

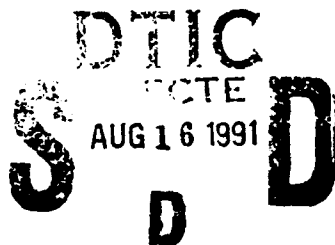
AD-A239 732



MOLECULAR BEAM EPITAXY 1990

①

Proceedings of the Sixth International
Conference on Molecular Beam Epitaxy
La Jolla, CA, USA, 27- 31 August 1990



Edited by:
C. W. Tu
J. S. Harris, Jr.

This document has been approved
for public release and sale; its
distribution is unlimited.

North Holland

91-07379

49



±

REPORT DOCUMENTATION PAGE

1a. REPORT SECURITY CLASSIFICATION UNCLASSIFIED			1b. RESTRICTIVE MARKINGS		
2a. SECURITY CLASSIFICATION AUTHORITY			3. DISTRIBUTION/AVAILABILITY OF REPORT Approved for public release, distribution is unlimited		
2b. DECLASSIFICATION/DOWNGRADING SCHEDULE					
4. PERFORMING ORGANIZATION REPORT NUMBER(S) Tu-MBE-90			5. MONITORING ORGANIZATION REPORT NUMBER(S)		
6a. NAME OF PERFORMING ORGANIZATION Univ. Calif. San Diego		6b. OFFICE SYMBOL (If applicable)		7a. NAME OF MONITORING ORGANIZATION Office of Naval Research Code 1114	
6c. ADDRESS (City, State, and ZIP Code) Dept. Electrical & Computer Engineering 0407 La Jolla, CA 92093-0407			7b. ADDRESS (City, State, and ZIP Code) Arlington, VA 22217-5000		
8a. NAME OF FUNDING/SPONSORING ORGANIZATION		8b. OFFICE SYMBOL (If applicable)		9. PROCUREMENT INSTRUMENT IDENTIFICATION NUMBER Grant No. N00014-90-J-1699	
8c. ADDRESS (City, State, and ZIP Code)			10. SOURCE OF FUNDING NUMBERS		
			PROGRAM ELEMENT NO.	PROJECT NO.	TASK NO.
11. TITLE (Include Security Classification) Proceedings of the Sixth International Conference on Molecular Beam Epitaxy					
12. PERSONAL AUTHOR(S) C.W. Tu (editor)					
13a. TYPE OF REPORT Final		13b. TIME COVERED FROM 8/27/90 TO 8/31/90		14. DATE OF REPORT (Year, Month, Day) 1991, August 5	
15. PAGE COUNT 1158					
16. SUPPLEMENTARY NOTATION This grant provided partial funding to the conference.					
17. COSATI CODES			18. SUBJECT TERMS (Continue on reverse if necessary and identify by block number) MBE, gas-source MBE, MOMBE, III-V, II-VI, IV		
FIELD	GROUP	SUB-GROUP			
19. ABSTRACT (Continue on reverse if necessary and identify by block number) The Proceedings contains the papers presented at the Sixth International Conference on Molecular Beam Epitaxy (MBE-VI), held at the San Diego campus of the University of California in La Jolla, California, from 27th to 31st August 1990.					
20. DISTRIBUTION/AVAILABILITY OF ABSTRACT <input checked="" type="checkbox"/> UNCLASSIFIED/UNLIMITED <input type="checkbox"/> SAME AS RPT. <input type="checkbox"/> DTIC USERS			21. ABSTRACT SECURITY CLASSIFICATION UNCLASSIFIED		
22a. NAME OF RESPONSIBLE INDIVIDUAL George Wright			22b. TELEPHONE (Include Area Code) (202) 696-4215		22c. OFFICE SYMBOL ONR

MOLECULAR BEAM EPITAXY 1990

MOLECULAR BEAM EPITAXY 1990

PROCEEDINGS OF THE SIXTH INTERNATIONAL
CONFERENCE ON MOLECULAR BEAM EPITAXY
LA JOLLA, CA, USA, 27-31 AUGUST 1990

EDITED BY

C.W. TU

University of California

J.S. HARRIS, Jr.

Stanford University



1991

NORTH-HOLLAND

© Elsevier Science Publishers B.V., 1991

All rights reserved. No part of this publication may be reproduced, stored in a retrieval system or transmitted in any form or by any means, electronic, mechanical, photocopying, recording or otherwise, without the written permission of the publisher, Elsevier Science Publishers B.V., P.O. Box 103, 1000 AC Amsterdam, The Netherlands.

Special regulations for readers in the USA - This publication has been registered with the Copyright Clearance Center Inc. (CCC), Salem, Massachusetts. Information can be obtained from the CCC about conditions under which photocopies of parts of this publication may be made in the USA. All other copyright questions, including photocopying outside of the USA, should be referred to the Publisher.

No responsibility is assumed by the Publisher for any injury and/or damage to persons or property as a matter of products liability, negligence or otherwise, or from any use or operation of any methods, products, instructions or ideas contained in the material herein.

This volume is printed on acid-free paper.

Reprinted from:
JOURNAL OF CRYSTAL GROWTH 111 (1991) Nos. 1-4

The Manuscripts of the Proceedings were
received by the Publisher: November/December 1990

Accession For	
NTIS CRA&I	<input checked="checked" type="checkbox"/>
DTIC TAB	<input type="checkbox"/>
Unannounced	<input type="checkbox"/>
Justification:	
By	
Distribution /	
Availability Codes	
Dist	Avail and/or Special
A-1	21



Printed in The Netherlands

SIXTH INTERNATIONAL CONFERENCE ON MOLECULAR BEAM EPITAXY
La Jolla, California, USA, 27-31 August 1990

Conference Chairman

L.L. Chang, IBM

Conference Co-Chairmen

A.C. Gossard, University of California
H. Okamoto, Furukawa Electric
G. Weimann, Walter Schottky Institute

Organizing Committee

C.W. Tu, Chairman, University of California
J.S. Harris, Jr., Co-Chairman, Stanford University
M.J. Delaney, Hughes
R.W. Grant, Rockwell
F.J. Grunthaner, Caltech
A. Madhukar, University of Southern California
J.N. Miller, Hewlett Packard
D.C. Streit, TRW
G. Sullivan, Rockwell
K.L. Wang, University of California

International Advisory Committee

J.R. Arthur (USA)	E. Kasper (Germany)
G. Bauer (Austria)	M. Kong (China)
A.Y. Cho (USA)	Y.V. Kovalchuk (USSR)
G.J. Davies (UK)	H. Kroemer (USA)
L.F. Eastman (USA)	H. Morkoç (USA)
L. Esaki (USA)	M.B. Panish (USA)
B. Etienne (France)	J.F. Schetzina (USA)
H. Hiyamizu (Japan)	Y. Shiraki (Japan)
M. Ilegems (Switzerland)	K. Takahashi (Japan)
B.A. Joyce (UK)	H.H. Wieder (USA)

Technical Program Committee

B.G. Streetman, Chairman, University of Texas
P.K. Bhattacharya, University of Michigan
L.R. Dawson, Sandia Laboratories
C.W. Farley, Rockwell
C.T. Foxon, Philips Research
A.Z. Li, Shanghai Metallurgical Institute
D.L. Miller, Pennsylvania State University
K. Ploog, Max Planck Institute
G.Y. Robinson, Colorado State University
H. Sakaki, University of Tokyo
G.E. Stillman, University of Illinois
W.T. Tsang, AT&T Bell Laboratories
J.M. Woodall, IBM

Acknowledgement

Financial support from the following organizations is gratefully acknowledged:

National Science Foundation
Air Force Office of Scientific Research
Army Research Office
Office of Naval Research
IBM, Yorktown Heights
Jet Propulsion Laboratories, Pasadena
University of California, San Diego
Hughes, Malibu
Hewlett-Packard, Palo Alto
Rockwell International, Thousand Oaks

Exhibitors

Aixtron, Wilsonville, Oregon, USA
Applied Science & Technology, Woburn, Massachusetts, USA
BIO-RAD, San Jose, California, USA
EPI Systems, St. Paul, Minnesota, USA
Epique AB, Lund, Sweden
FEI Co., Beaverton, Oregon, USA
GTE-Sylvania Emissive Products, Exeter, New Hampshire, USA
Instruments SA/Riber, Edison, New Jersey, USA
Métaux Spéciaux, Plombière, Moutiers, France
Precision Resources Technology, Melville, New York, USA
Oxford Applied Research, Oxfordshire, UK
Science and Engineering Research Council, Swindon, UK
Superior Vacuum Technology, Eden Prairie, Minnesota, USA
Union Carbide, Cleveland, Ohio, USA
United Mineral Chemical Co., Lyndhurst, New Jersey, USA
Varian, Santa Clara, California, USA
VG Instruments, Danvers, Massachusetts, USA
Wavemat, Plymouth, Michigan, USA

Preface

This issue of the Journal of Crystal Growth contains the papers presented at the Sixth International Conference on Molecular Beam Epitaxy (MBE-VI), held at the San Diego campus of the University of California (UCSD) in La Jolla, California, USA, from 27th to 31st August 1990. This conference is one in a biennial series, which rotates between the United States, Europe, and Japan. Previous international conferences were held in Sapporo, Japan (1988), York, United Kingdom (1986), San Francisco (1984), Tokyo (1982) and Paris (1978).

The organizing committee first thought that the attendance might be limited amidst reports of lower attendance in other conferences due to budget constraints in many laboratories. Furthermore, an increasing number of conferences are related to electronic materials and devices around the world. The day before the conference started, there were less than 400 pre-registrants. However, the number of walk-in registrants turned out to be over 100. The total number of participants was about 500, far exceeding the committee's expectation. Twenty countries were represented.

In MBE-VI, about 230 papers, including 21 invited talks, were selected from more than 300 submissions. The scope of the conference covered the entire spectrum of MBE technology, from material aspects of growth, characterization, to

physics and devices. Topics included growth kinetics, doping, migration-enhanced epitaxy, reflection high-energy-electron diffraction, quantum wells and wires, gas-source MBE, MOMBE, CBE, and structures based on GaAs, InP, II-VI compounds, antimonides, superconductors, magnetic materials, etc. In addition, 18 companies participated in an equipment and product exhibit.

The MBE-VI committee would like to thank first various federal agencies, UCSD, and companies for their financial support of the conference. The MBE-VI committee would also like to thank Lena Hartman and her able staff in the Conference Office at UCSD for arranging facilities, room and board and for running the conference very smoothly. The program committee is grateful to the session chairmen for handling their sessions very well.

About 95% of the 230 papers presented at the conference are included in this volume, resulting in a very thick proceedings. The editors would like to thank the many referees for their assistance in producing this volume and acknowledge the invaluable help of Vicki Postula and Karin Zirk at UCSD and Françoise Y. Verploegh Chassé and the staff at North-Holland/Elsevier.

C.W. Tu and J.S. Harris, Jr.

Contents

Preface	ix
SECTION I. MBE TECHNOLOGY	
Advances in molecular beam epitaxy (MBE)	
A.Y. Cho	1
$4 \times 10^{15} \text{ cm}^2 \text{ V}^{-1} \text{ s}^{-1}$ peak electron mobilities in GaAs grown by solid source MBE with As_2	
C.R. Stanley, M.C. Holland, A.H. Kean, J.M. Chamberlain, R.T. Grimes and M.B. Stanaway	14
Variation of background impurities in $\text{Al}_x\text{Ga}_{1-x}\text{As}$ ($0.3 \leq x \leq 0.4$) with growth temperature: implications for device leakage current and surface/heterointerface roughness	
N. Chand, T.D. Harris, S.N.G. Chu, E.E. Becker, A.M. Sergeant, M. Schnoes and D.V. Lang	20
Properties and applications of $\text{Al}_x\text{Ga}_{1-x}\text{As}$ ($0 \leq x \leq 1$) grown at low temperatures	
T.Y. Chu, A. Dodabalapur, A. Srinivasan, D.P. Neikirk and B.G. Streetman	26
Low-temperature growth of GaAs and AlGaAs by MBE and effects of post-growth thermal annealing	
J.N. Miller and T.S. Low	30
GaAs buffer layers grown at low substrate temperatures using As_2 and the formation of arsenic precipitates	
M.R. Melloch, K. Mahalingam, N. Otsuka, J.M. Woodall and A.C. Warren	39
Electrical and optical characterization of gas source and solid source MBE low temperature buffers	
R.A. Puechner, D.A. Johnson, H.T. Shiralagi, D.S. Gerber, R. Droopad and G.N. Maracas	43
Graded compositional heterostructures in the GaAs/ $\text{Al}_x\text{Ga}_{1-x}\text{As}$ system	
S. Giugni, T.L. Tansley and G.J. Griffiths	50
Precise computer control of the MBE process - application to graded InGaAlAs/InP alloys	
J.C. Vilek and C.G. Fonstad	56
Composition control of GaAsP grown by molecular beam epitaxy	
T. Nomura, H. Ogasawara, M. Miyao and M. Hagino	61
Dynamics and roughness spectrum of the GaAs(001) surface during the MBE process	
L. Däweritz, J. Griesche, R. Hey and J. Herzog	65
Growth uniformity studies in molecular beam epitaxy	
Z.R. Wasilewski, G.C. Aers, A.J. SpringThorpe and C.J. Miner	70
SECTION II. IN SITU CHARACTERIZATION	
MBE monolayer growth control by in-situ electron microscopy	
N. Inoue	75
Surface diffusion length observed by in situ scanning microprobe reflection high-energy electron diffraction	
M. Hata, A. Watanabe and T. Isu	83
A reflection high-energy electron diffraction study of growth processes at step edges during molecular beam epitaxy of GaAs and AlAs	
H. Tsuda and T. Mizutani	88
Modulated molecular beam study of group III desorption during growth by MBE	
J. Zhang, E.M. Gibson, C.T. Foxon and B.A. Joyce	93
Correlation between the dampening of RHEED oscillations and the photoluminescence of quantum wells in the presence of AsO	
T.R. Block and B.G. Streetman	98
Application of frequency-domain analysis to RHEED oscillation data: time dependence of AlGaAs growth rates	
G.W. Turner and S.J. Eglash	105

Initial growth stage of InAs/GaAs studied by RHEED-TRAXS method	
J. Shigetomi, K. Fuwa, S. Shimizu, H. Yamakawa and S. Ino	110
Reflectance-difference probing of surface kinetics of (001) GaAs during vacuum chemical epitaxy	
G. Paulsson, K. Deppert, S. Jeppesen, J. Jönsson, L. Samuelson and P. Schmidt	115
In-situ monitoring of antiphase domain evolution during atomic layer MBE (ALMBE) and MBE growth of GaAs/Si(001) by reflectance difference	
Y. González, L. González and F. Briones	120
Oscillatory As ₄ surface reaction rates during molecular beam epitaxy of AlAs, GaAs and InAs	
J.Y. Tsao, T.M. Brennan and B.E. Hammons	125
Accurate measurement of MBE substrate temperature	
W.S. Lee, G.W. Yoffe, D.G. Schlom and J.S. Harris, Jr.	131
A novel in-situ molecular beam epitaxy monitoring system using low energy ion scattering	
M. Kubo and T. Narusawa	136

SECTION III. GROWTH KINETICS

Surface segregation in III-V alloys	
J.M. Moisson, F. Houzay, F. Barthe, J.M. Gérard, B. Jusserand, J. Massies and F.S. Turco-Sandhoff	141
Thermodynamic analysis of segregation effects in MBE of A ^{III} -B ^V compounds	
S.V. Ivanov, P.S. Kop'ev and N.N. Ledentsov	151
Nonlinear diffusion equation for epitaxial growth and recovery on vicinal surfaces	
A.K. Myers-Beaghton and D.D. Vvedensky	162
Surface diffusion of Al and Ga atoms on GaAs (001) and (111)B vicinal surfaces in molecular beam epitaxy	
M. Tanaka, T. Suzuki and T. Nishinaga	168
Surface diffusion and atom incorporation kinetics in MBE of InGaAs and AlGaAs	
T. Suzuki and T. Nishinaga	173
Monte Carlo simulation of MBE growth of the 2 × 4 reconstructed GaAs(001) surface	
J.M. McCoy and P.A. Maksym	178
Control of initial surface configuration for GaAs-on-Si MBE using a Si buffer layer?	
G.E. Crook, L. Tapfer, L. Däweritz, R. Cingolani and K. Ploog	184
Gallium desorption from (Al,Ga)As grown by molecular beam epitaxy at high temperatures	
A.H. Kean, C.R. Stanley, M.C. Holland, J.L. Martin and J.N. Chapman	189

SECTION IV. MIGRATION ENHANCED EPITAXY

Atomic layer molecular beam epitaxy (ALMBE): growth kinetics and applications	
F. Briones and A. Ruiz	194
Optical investigation of GaAs growth process in molecular beam epitaxy and migration-enhanced epitaxy	
Y. Horikoshi, M. Kawashima and N. Kobayashi	200
Modulated molecular beam epitaxy: a successful route toward high quality highly strained heterostructures	
J.M. Gérard, J.Y. Marzin and B. Jusserand	205
Real-time μ -RHEED observations of GaAs surfaces during growth with alternating source supply	
T. Isu, M. Hata and A. Watanabe	210
Realization of mirror surface in (111)- and (110)-oriented GaAs by migration-enhanced epitaxy	
Y. Takano, M. Lopez, T. Torihata, T. Ikei, Y. Kanaya, K. Pak and H. Yonezu	216
Fabrication of AlAs/Al/AlAs heterostructures by molecular beam epitaxy and migration enhanced epitaxy	
T. Yao, H. Nakahara, H. Matuhata and Y. Okada	221
Strained layer epitaxy of InGaAs by MBE and migration enhanced epitaxy - comparison of growth modes and surface quality	
Y.C. Chen, P.K. Bhattacharya and J. Singh	228
Improved device performance by migration-enhanced epitaxy	
P. Ho, S.C. Wang, T. Yu, J.M. Ballingall, P.A. Martin, K.H.G. Duh, S.M.J. Liu, G.A. Hutchins and E.L. Hall	233

SECTION V. DOPING

Delta-doping of GaAs and Al _{0.33} Ga _{0.67} As with Sn, Si and Be: a comparative study	
J.J. Harris, J.B. Clegg, R.B. Beall, J. Castagné, K. Woodbridge and C. Roberts	239

Comparison of delta doped GaAs grown by MBE and GSMBE using different arsenic species M.T. Asom, G. Livescu, M. Geva, V. Swaminathan, L.C. Luther, R.E. Leibenguth, V.D. Mattera, E.F. Schaubert, J.M. Kuo and R. Kopf	246
Reduced silicon donor incorporation in MBE grown GaAs layers using cracker-generated dimer arsenic B.J. Wu, Y.J. Mii, M. Chen, K.L. Wang and J.J. Murray	252
Hydrogen passivation of delta doped GaAs M.T. Asom, V. Swaminathan, G. Livescu, M. Geva, L.C. Luther, R.E. Leibenguth, V.D. Mattera and T. Hayes	260
A comparison of atomic carbon versus beryllium acceptor doping in GaAs grown by molecular beam epitaxy J. Nagle, R.J. Malik and D. Gershoni	264
Carbon doping of MBE GaAs and $\text{Ga}_{0.7}\text{Al}_{0.3}\text{As}$ films using a graphite filament W.E. Hoke, P.J. Lemonias, P.S. Lyman, H.T. Hendriks, D. Weir and P. Colombo	269
Characterization of the GaAs:C and AlGaAs:C doping superlattice grown by chemical beam epitaxy T.H. Chiu, J.E. Cunningham, J.A. Ditzenberger, W.Y. Jan and S.N.G. Chu	274
Electrical properties and dopant incorporation mechanisms of Si doped GaAs and (AlGa)As grown on (111)A GaAs surfaces by MBE Y. Kadoya, A. Sato, H. Kano and H. Sakaki	280
Si doping and MBE growth of GaAs on tilted (111)A substrates M. Shigeta, Y. Okano, H. Seto, H. Katahama, S. Nishine, K. Kobayashi and I. Fujimoto	284

SECTION VI. MODULATION DOPED STRUCTURES

Effect of neutron irradiation on transport in heterostructures Junming Zhou, Weimin Jin, Jianmin Mao and Yi Huang	288
Modulation doped inverted and normal $\text{GaAs}/\text{Al}_x\text{Ga}_{1-x}\text{As}$ heterostructures: influence of Si-segregation on the two-dimensional electron gas K. Köhler, P. Ganser, M. Maier and K.H. Bachem	295
The growth and characterisation of back-gated high mobility two-dimensional electron gas structures D.A. Ritchie, J.E.F. Frost, D.C. Peacock, E.H. Linfield, A. Hamilton and G.A.C. Jones	300
The growth of shallow high mobility two-dimensional electron gas structures J.E.F. Frost, D.A. Ritchie and G.A.C. Jones	305
Anisotropy in electronic transport of modulation doped structures having strained InGaAs wells C. Webb, J.N. Eckstein and Y.M. Desai	309
High-quality $\text{In}_{0.1}\text{Ga}_{0.9}\text{As}/\text{InAlAs}$ modulation-doped heterostructures grown lattice-mismatched on GaAs substrates K. Inoue, J.C. Harmand and T. Matsuno	313
The growth and physics of high mobility two-dimensional hole gases A.G. Davies, J.E.F. Frost, P.A. Ritchie, D.C. Peacock, R. Newbury, E.H. Linfield, M. Pepper and G.A.C. Jones	318

SECTION VII. QUANTUM WELLS, WIRES AND SUPERLATTICES

Serpentine superlattice: concept and first results M.S. Miller, C.E. Pryor, H. Weman, L.A. Samoska, H. Kroemer and P.M. Petroff	323
Growth kinetics and electronic characteristics of quantum wires A.K. Myers-Beaghton, J.P.G. Taylor, D.D. Vvedensky, K.J. Hugill and A. MacKinnon	328
Quantum wire structures by MBE overgrowth on a cleaved edge L. Pfeiffer, H.L. Störmer, K. West and K.W. Baldwin	333
Indium incorporation in GaInAs/GaAs quantum wells grown on GaAs K. Woodbridge, K.J. Moore, N.L. Andrew and P.F. Fewster	339
Narrow luminescence linewidth in GaAs single quantum wells by insertion of thin AlAs smoothing layers K. Ploog, A. Fischer, L. Tapfer and B.F. Feuerbacher	344
Characterization of lateral correlation length of interface roughness in MBE grown GaAs/AlAs quantum wells by mobility measurement T. Noda, M. Tanaka and H. Sakaki	348
Re-examination of the formation mechanism of CuPt-type natural superlattices in alloy semiconductors T. Suzuki and A. Gomyo	353
MBE growth of tilted superlattices: advances and novel structures P.M. Petroff, M.S. Miller, Y.T. Lu, S.A. Chalmers, H. Metiu, H. Kroemer and A.C. Gossard	360

Fabrication of quasi-three-dimensional electron systems and superlattices in wide parabolic wells	
M. Santos, J. Jo, M. Shayegan and A.-M. Lanzillotto	366
Formation of quantum well wire-like structures by MBE growth of AlGaAs/GaAs superlattices on GaAs (110) surfaces	
S. Hasegawa, M. Sato, K. Maehashi, H. Asahi and H. Nakashima	371

SECTION VIII. STRAINED LAYER STRUCTURES

Stress accommodation in large-mismatch systems	
B.W. Dodson	376
Growth processes and relaxation mechanisms in the molecular beam epitaxy of InAs/GaAs heterostructures	
O. Brandt, L. Tapfer, K. Ploog, M. Hohenstein and F. Phillipp	383
Optical studies of InAs/GaAs on GaAs short-period strained-layer superlattices grown by MBE and MEE	
T.C. Hasenberg, D.S. McCallum, X.R. Huang, A.L. Smirl, M.D. Dawson and T.F. Boggess	388
Strain induced change in band offsets at pseudomorphically grown InAs/GaAs heterointerfaces characterized by X-ray photoelectron spectroscopy	
Y. Hashimoto, K. Hirakawa, K. Harada and T. Ikoma	393
Structural stability of ultrathin InAs/GaAs quantum wells grown by migration enhanced epitaxy	
M. Yano, K. Yoh, T. Iwawaki, Y. Iwai and M. Inoue	397
Fabrication and characterization of MBE grown InAs/GaAs strained-layer superlattices on variously oriented substrates	
K. Kudo, J.S. Lee, K. Tanaka, Y. Makita and A. Yamada	402
Indium desorption during MBE growth of strained InGaAs layers	
J.-P. Reithmaier, H. Riechert, H. Schlötterer and G. Weimann	407
A photoluminescence study of indium desorption from strained $Ga_{1-x}In_xAs/GaAs$	
M.T. Emeny, L.K. Howard, K.P. Homewood, J.D. Lambkin and C.R. Whitehouse	413
Molecular beam epitaxial growth and properties of highly strained $In_xGa_{1-x}As/GaAs$ multiple quantum wells	
S. Niki, W.S.C. Chang, H.H. Wieder and T.E. Van Eck	419
Realization of sharp excitonic features in highly strained $GaAs/In_xGa_{1-x}As$ multiple quantum wells grown on GaAs(100) substrates	
Li Chen, K.C. Rajkumar, A. Madhukar, Wei Chen, S. Guha and K. Kaviani	424
Observation of dark line defects in InGaAs/GaAs strained layer superlattices by photoluminescence topography	
K. Iizuka, T. Yoshida, T. Suzuki and H. Hirose	429
The nature and control of morphology and the formation of defects in InGaAs epilayers and InAs/GaAs superlattices grown via MBE on GaAs(100)	
S. Guha, K.C. Rajkumar and A. Madhukar	434
Electrooptic effects of piezo-electrically strained AlGaAs/GaAs(111) quantum wells	
S.M. Shank and G.W. Wicks	440

SECTION IX. InP-BASED STRUCTURES

Growth and characterization of low temperature AlInAs	
R.A. Metzger, A.S. Brown, W.E. Stanchina, M. Lui, R.G. Wilson, T.V. Kargodorian, L.G. McCray and J.A. Henige	445
Influence of nonuniform charge distribution in $In_{0.53}Ga_{0.47}As$ on the interpretation of dopant incorporation	
S.P. Svensson, W.A. Beck, D.C. Martel, P.N. Uppal and D.C. Cooke	450
Characterization of InGaAs and InAlAs layers on InP by four-crystal high resolution X-ray diffraction and wedge transmission electron microscopy	
R. Houdre, F. Gueissaz, M. Gailhanou, J.-D. Ganière, A. Rudra and H. Ilegems	456
MBE overgrowth of implanted regions in InP:Fe substrates	
H. Künzel, R. Gibis, W. Schlaak, L.M. Su and N. Grote	461
Effects of substrate orientation, pseudomorphic growth and superlattice on alloy scattering in modulation doped GaInAs	
A. Chin, T.Y. Chang, A. Ourmazd, E.M. Monberg, A.M. Chang and C. Kurdak	466
High electron density and mobility in single and double planar doped InGaAs/InAlAs heterojunctions on InP	
F. Gueissaz, R. Houdré and M. Ilegems	470
High quality GaInAs/AlGaInAs/AlInAs heterostructures on Si ion implanted semi-insulating InP substrates for novel high performance optical modulators	
T.Y. Chang, N.J. Sauer, J.E. Zucker, K.L. Jones, B. Tell, K. Brown-Goebeler, M. Wegener and D.S. Chemla	475
Orientation dependence of mismatched $In_xAl_{1-x}As/In_{0.53}Ga_{0.47}As$ HFETs	
S.K. Bahl, W.J. Azzam and J.A. del Alamo	479

MBE growth of graded index AlGaInAs MQW lasers on InP	
M. Allovon, M. Quillec, M. Blez and C. Kazmierski	484
Molecular beam epitaxial growth and structural design of $\text{In}_{0.52}\text{Al}_{0.48}\text{As}/\text{In}_{0.53}\text{Ga}_{0.47}\text{As}/\text{InP}$ HEMTs	
Y.C. Pao and J.S. Harris, Jr.	489

SECTION X. GAS-SOURCE MBE: HYDRIDES

High quality InP and $\text{In}_{1-x}\text{Ga}_x\text{As}_y\text{P}_{1-y}$ grown by gas source MBE	
M. Lambert, L. Goldstein, A. Perales, F. Gaborit, C. Starck and J.-L. Lievin	495
Gas source MEE (migration enhanced epitaxy) growth of InP	
N. Takeyasu, H. Asahi, S.J. Yu, K. Asami, T. Kaneko and S. Gonda	502
GSMBE growth of GaAs at low AsH_3 cracking temperatures	
M.J. Hafich, H.Y. Lee, P. Silvestre and G.Y. Robinson	507
Residual impurities originating from AsH_3 in GS-MBE grown GaAs	
S. Nagao, Y. Inoue, E. Kawanishi and H. Gotoh	511
Gas source molecular beam epitaxy growth of heterojunction bipolar transistors containing 1 monolayer δ -Be	
J.E. Cunningham, T.Y. Kuo, A. Ourmazd, K. Goossen, W. Jan, F. Storz, F. Ren and C.G. Fonstad	515
Abruptness of GaAs/AlInP hetero-interfaces grown by GS-MBE	
S. Nagao, M. Takashima, Y. Inoue, M. Katoh and H. Gotoh	521
Improved InGaP/GaAs heterointerfaces during gas-source MBE growth	
H.Y. Lee, M.J. Hafich, G.Y. Robinson, K. Mahalingam and N. Otsuka	525

SECTION XI. GAS-SOURCE MBE: MOMBE AND CBE

A review of CBE, MOMBE and GSMBE	
W.T. Tsang	529
A comparison of MBE and MOMBE/CBE growth mechanisms using modulated beam mass spectrometry and RHEED	
C.T. Foxon, E.M. Gibson, J. Zhang, B.A. Joyce and D.E. Lacklison	539
Background pressure dependence of GaAs and AlGaAs growth rates in gas-source molecular beam epitaxy	
J. Saito, T. Maeda, K. Ono and K. Kondo	544
The roles of group-V species in metalorganic molecular-beam epitaxy and chemical-beam epitaxy of III-V compounds	
B.W. Liang and C.W. Tu	550
Metalorganic molecular beam epitaxy of GaAs using hydrogen radical beam	
A. Watanabe, M. Hata and T. Ito	554
p ⁺ /n GaAs-AlGaAs heterostructures grown by gas source MBE using gaseous p- and n-type dopant sources	
A. Sandhu, T. Fujii, H. Ando, T. Takahashi, H. Ishikawa and N. Yokoyama	559
Use of CCl_4 and CHCl_3 in gas source molecular beam epitaxy for carbon doping of GaAs and $\text{Ga}_{1-x}\text{In}_x\text{P}$	
T.J. de Lyon, N.I. Buchan, P.D. Kirchner, J.M. Woodall, D.T. McInturff, G.J. Scilla and F. Cardone	564
In-situ selective-area epitaxy of GaAs using a GaAs oxide layer as a mask	
Y. Hiratani, Y. Ohki, Y. Sugimoto and K. Akita	570
The roles of aluminum and hydrogen in impurity contamination of AlGaAs grown by MOMBE	
C.R. Abernathy, S.J. Pearton, D.A. Bohling and G.T. Muhr	574
Chemical beam epitaxy growth of GaAs/ $\text{Ga}_{0.5}\text{In}_{0.5}\text{P}$ heterostructures: growth kinetics, electrical and optical properties	
J.C. Garcia, P. Maurel, P. Bove, J.P. Hirtz and A. Barski	578
MOMBE growth and characterization of heavily carbon-doped InGaAs	
T. Yamada, S. Nozaki, R. Miyake, T. Fukamachi, J. Shirakashi, M. Konagai and K. Takahashi	584
Luminescence and transport properties of high quality InP grown by CBE between 450 and 550°C	
A. Rudra, J.F. Carlin, M. Proctor and M. Illegems	589
The optimization of $\text{In}_{1-x}\text{Ga}_x\text{As}$ and InP growth conditions by CBE	
M.E. Sherwin, G.O. Munns, M.E. Elta, E.G. Woelk, S.B. Crary, F.L. Terry and G.I. Haddad	594
Growth of GaInAs and GaInAsP lattice matched to InP by metalorganic MBE	
H. Heinecke, B. Baur, R. Höger, A. Miklis and R. Treichler	599
The design of an ECR plasma system and its application to InP grown by CBE	
M.E. Sherwin, G.O. Munns, E.G. Woelk, T.J. Drummond, M.E. Elta, F.L. Terry and G.I. Haddad	605

SECTION XII. ANTIMONIDE STRUCTURES

Surface reaction of III-V compound semiconductors irradiated by As and Sb molecular beams M. Yano, H. Yokose, Y. Iwai and M. Inoue	609
Indium antimonide doped with lead telluride grown by molecular beam epitaxy D.L. Partin, J. Heremans and C.M. Thrush	614
Tellurium doping study of GaSb grown by molecular beam epitaxy using SnTe J.F. Chen and A.Y. Cho	619
Transport properties of heterostructures based on GaSb, InAs and InSb on GaAs substrates P.N. Uppal, D.M. Gill, S.P. Svensson and D.C. Cooke	623
Growth and properties of GaAsSb/InGaAs superlattices on InP J.F. Klem, S.R. Kurtz and A. Datye	628
Growth and properties of InAs _{1-x} Al _x Ga _{1-y} Sb _y and InAs _x Sb _{1-x} /Al _y Ga _{1-y} Sb heterostructures J.H. Kim, D. Yang, Y.-C. Chen and P. Bhattacharya	633
MOMBE growth of GaSb and InAsSb using triethylstibine and triethylarsine T. Kaneko, H. Asahi, Y. Itani, Y. Okuno and S. Gonda	638
Electrical characteristics dependence on aluminum mole fraction in (Al _{0.5} Ga _{0.5})Sb/InAs/(Al _x Ga _{1-x})Sb heterostructure K. Yoh, T. Moriuchi, M. Yano and M. Inoue	643
The growth of (Al, Ga)Sb tilted superlattices and their heteroepitaxy with InAs to form corrugated-barrier quantum wells S.A. Chalmers, H. Kroemer and A.C. Gossard	647
Resonant tunneling in polytype InAs/AlSb/GaSb heterostructures K.F. Longenbach, L.F. Luo, S. Xin and W.I. Wang	651
Studies of the tunneling currents in the InAs/AlSb/GaSb single-barrier interband tunneling diodes grown on GaAs substrates J.F. Chen, L. Yang, M.C. Wu, S.N.G. Chu and A.Y. Cho	659
Interband tunneling in InAs/GaSb/AlSb heterostructures D.A. Collins, D.Z.-Y. Ting, E.T. Yu, D.H. Chow, J.R. Söderström, Y. Rajakarunanyake and T.C. McGill	664
MBE growth of GaInAsSb/AlGaAsSb double heterostructures for infrared diode lasers S.J. Eglash, H.K. Choi and G.W. Turner	669
MBE growth and characterization of In _x Ga _{1-x} Sb/InAs strained layer superlattices R. Fashe, J.T. Zborowski, T.D. Golding, H.D. Shih, P.C. Chow, K. Matsuichi, B.C. Covington, A. Chi, J. Zheng and H.F. Schaake	677
Growth of InAs/Ga _{1-x} In _x Sb infrared superlattices D.H. Chow, R.H. Miles, C.W. Nieh and T.C. McGill	683
New MBE growth method for InSb quantum well boxes N. Koguchi, S. Takahashi and T. Chikyow	688
Strong nonlinear optical enhancement in MBE-grown Bi _{1-x} Sb _x E.R. Youngdale, J.R. Meyer, C.A. Hoffman, F.J. Bartoli, D.L. Partin, C.M. Thrush and J.P. Heremans	693

SECTION XIII. II-VI MBE: SMALL BANDGAPS

New development on the control of homoepitaxial and heteroepitaxial growth of CdTe and HgCdTe by MBE J.P. Faurie, R. Sporken, S. Sivananthan and M.D. Lange	698
Application of the RHEED oscillation technique to the growth of II-VI compounds: CdTe, HgTe and their related alloys L. Ulmer, N. Magnea, H. Mariette and P. Gentile	711
A novel technique for the MBE growth of twin-free HgCdTe R.W. Yanka, K.A. Harris, L.M. Mohnkern and T.H. Myers	715
Very low temperature growth and doping of Hg-based epilayers and superlattices Y. Lansari, Z. Yang, S. Hwang, F.E. Reed, A.T. Sowers, J.W. Cook, Jr. and J.F. Schetzina	720
Chemical beam epitaxy of CdTe, HgTe, and HgCdTe R.G. Benz II, B.K. Wagner, D. Rajavel and C.J. Summers	725
Heteroepitaxy of CdTe(100) on Si(100) using BaF ₂ -CaF ₂ (100) buffer layers A.N. Tiwari, W. Floeder, S. Blunier, H. Zogg and M.J. Proctor	730
Atomic layer epitaxy of (CdTe) _m (ZnTe) _n -ZnTe multiquantum wells on (001)GaAs substrate Jie Li, Li He, Wei Shan, Xingyu Cheng and Shixin Yuan	736

SECTION XIV. II-VI MBE: LARGE BANDGAPS

Surface stoichiometry effects on ZnSe/GaAs heteroepitaxy	
M.C. Tamargo, R.E. Nahory, B.J. Skromme, S.M. Shibli, A.L. Weaver, R.J. Martin and H.H. Farrell	741
ZnSe/GaAs heterovalent interfaces: interface microstructure versus electrical properties	
J. Qiu, D.R. Menke, M. Kobayashi, R.L. Gunshor, Q.-D. Qian, D. Li and N. Otsuka	747
High-quality ZnSe/GaAs superlattices: MBE growth, and structural and optical characterization	
S. Ramesh, N. Kobayashi and Y. Horikoshi	752
Growth and characterization of ZnSe on $(\text{NH}_4)_2\text{S}_x$ -treated GaAs substrates: effect of GaAs surface microstructure on the growth rate of ZnSe	
Y. Wu, Y. Kawakami, Sz. Fujita and Sg. Fujita	757
Molecular beam epitaxy of Zn(Se,Te) alloys and superlattices	
F.S. Turco-Sandroff, R.E. Nahory, M.J.S.P. Brasil, R.J. Martin, R. Beserman, L.A. Farrow, J.M. Worlock and A.L. Weaver	762
Quantum wells with zincblende MnTe barriers	
J. Han, S.M. Durbin, R.L. Gunshor, M. Kobayashi, D.R. Menke, N. Pelekanos, M. Hagerott, A.V. Nurmikko, Y. Nakamura and N. Otsuka	767
Substitutional doping of ZnSe films	
J. Ren, K.A. Bowers, S. Hwang, J.W. Cook, Jr. and J.F. Schetzina	772
n-Type and p-type conductivity control of ZnSe grown by metalorganic molecular beam epitaxy using methyl iodide and ammonia	
M. Migita, A. Taike and H. Yamamoto	776
Electric field assisted doping of semiconductors during epitaxial growth	
Y. Rajakarunanyake, J.O. McCaldin and T.C. McGill	782
Photo-assisted MBE growth of ZnSe on GaAs substrates	
N. Matsumura, T. Fukada, K. Senga, Y. Fukushima and J. Saraie	787
Ultraviolet irradiation effect on the MBE growth of ZnSe/GaAs observed by RHEED	
M. Ohishi, H. Saito, H. Torihara, Y. Fujisaki and K. Ohmori	792
Doping of nitrogen acceptors into ZnSe using radical beam during MBE growth	
H. Ohkawa, T. Karasawa and T. Mitsuyu	797
$(\text{ZnSe})_m-(\text{ZnTe})_n$ short-period strained layer superlattices prepared by atomic layer epitaxy	
Y. Takemura, H. Nakanishi, M. Konagai, H. Takahashi, Y. Nakamura and N. Otsuka	802
Determination of refractive index and study of absorption in wide gap II-VI semiconductor superlattices	
Aidong Shen, Jie Cui, Yunliang Chen, Hailong Wang and Aizhen Li	807
The study of phonons and lattice strains in ZnSe-ZnTe and ZnS-ZnSe strained-layer superlattices by Raman and far-infrared reflectivity spectra	
Jie Cui, Hailong Wang, Fuxi Gan and Aizhen Li	811
Growth and properties of new wide-gap quantum well structures: $\text{Zn}_{1-x}\text{Mn}_x\text{Se}/\text{Zn}_{1-x}\text{Cd}_x\text{Se}$	
N. Samarth, H. Luo, J. Buschert, J.K. Furdyna, W.J. Walecki, A.V. Nurmikko, R.G. Alonso, E.-S. Oh, A.K. Ramdas and N. Otsuka	816
Characterization of CdSe/ZnTe heterojunctions	
M.C. Phillips, E.T. Yu, Y. Rajakarunanyake, J.O. McCaldin, D.A. Collins and T.C. McGill	820
Fabrication of $\text{ZnS}/(\text{ZnSe})_n/\text{ZnS}$ single quantum well structures and photoluminescence properties	
T. Yao, M. Fujimoto, S.H. Chang and H. Tanino	823
Blue (ZnSe) and green $(\text{ZnSe}_{0.9}\text{Te}_{0.1})$ light emitting diodes	
J. Ren, K.A. Bowers, B. Sneed, F.E. Reed, J.W. Cook, Jr. and J.F. Schetzina	829

SECTION XV. GROUP IV MBE: Si AND Ge

Limited thickness epitaxy of semiconductors and Si MBE down to room temperature	
D.J. Eaglesham, H.-J. Gossmann, M. Cerullo, L.N. Pfeiffer and K.W. West	833
Buried, ordered structures: boron in Si(111) and Si(100)	
R.L. Headrick, B.E. Weir, A.F.J. Levi, D.J. Eaglesham and L.C. Feldman	838
Redistribution of delta-doped Sb in Si	
S.J. Fukatsu, S. Kubo, Y. Shiraki and R. Ito	843
Dopant incorporation in epitaxial germanium grown on Ge(100) substrates by MBE	
V.P. Kesan, S.S. Iyer and J.M. Cotte	847

B doping effect on gas source Si-MBE growth: a comparison of B_2H_6 gas doping and HBO_2 Knudsen cell doping	856
H. Hirayama, M. Hiroi, K. Koyama and T. Tatsumi	
Limitations of selective epitaxial growth conditions in gas-source MBE using Si_2H_6	860
H. Aketagawa, T. Tatsumi and J. Sakai	
Simulation with animation: microscopic growth kinetics of Si(001) homoepitaxy	864
M.R. Wilby, M.W. Ricketts, S. Clarke and D.D. Vvedensky	
Molecular dynamics and quasidynamics simulations of low-energy ion/surface interactions leading to decreased epitaxial temperatures and increased dopant incorporation probabilities during Si MBE	870
M. Kitabatake, P. Fons and J.E. Greene	
Scanning tunneling microscopy studies of the growth process of Ge on Si(001)	876
Y.-M. Mo and M.G. Lagally	

SECTION XVI. GROUP IV MBE: SiGe, SnGe AND SILICIDES

Group IV element (Si, Ge and α -Sn) superlattices - low temperature MBE	882
K. Eberl, W. Wegscheider and G. Abstreiter	
Silicon heteroepitaxy: interface structure and physical properties	889
H. von Känel, E. Müller, H.-U. Nissen, W. Bacsá, M. Ospelt, K.A. Mäder, R. Stalder and A. Baldereschi	
MBE Si_mGe_n strained monolayer superlattices	897
M.A. Kallel, V. Arbet-Engels, K.L. Wang and R.P.G. Karunasiri	
Structure dependence of photoluminescence in Ge_n/Si_m strained-layer superlattices	902
K. Miki, H. Okumura, K. Sakamoto, H. Matsuhata, T. Sakamoto and S. Yoshida	
Elemental boron and antimony doping of MBE Si and SiGe structures grown at temperatures below 600°C	907
A.R. Powell, R.A.A. Kubiak, S.M. Newstead, C. Parry, N.L. Matthey, D.W. Smith, J.C. Brighten, C.J. Emeleus, T. Naylor, E. Basaran, T.E. Whall, M.G. Dowsett, R.D. Barlow, E.H.C. Parker and D.K. Bowen	
High hole mobility in strained Ge channel of modulation-doped p- $Si_{0.5}Ge_{0.5}/Ge/Si_{1-x}Ge_x$ heterostructure	912
M. Miyao, E. Murakami, H. Etoh, K. Nakagawa and A. Nishida	
Transport properties of p-Si/SiGe single-modulation-doped heterostructures grown by MBE	916
D.J. Gravesteijn, T. Mishima, C.W. Fredriksz, G.F.A. van de Walle and R.A. van den Heuvel	
Dislocation-related photoluminescence in $Si_{1-x}Ge_x/Si(100)$ grown by molecular beam epitaxy	920
K. Terashima, M. Tajima, A. Sakai and T. Tatsumi	
The determination of strain in Si-Ge superlattices by electron diffraction in a scanning transmission electron microscope	925
W.T. Pike, L.M. Brown, R.A.A. Kubiak, S.M. Newstead, A.R. Powell, E.H.C. Parker and T.E. Whall	
Strain modification by ion-assisted molecular beam epitaxy in the Si_xGe_{1-x} alloy system: a kinetic analysis	931
C.J. Tsai, P. Rozenak, H.A. Atwater and T. Vreeland	
Si/SiGe heterostructures grown on SOI substrates by MBE for integrated optoelectronics	936
V.P. Kesan, P.G. May, F.K. LeGoues and S.S. Iyer	
The growth and electronic properties of α -Sn thin films grown on InSb(100) and $(\bar{1}\bar{1}\bar{1})$ substrates by molecular beam epitaxy (MBE)	943
W.T. Yuen, W.K. Liu, R.A. Stradling and B.A. Joyce	
Control of misoriented grains and pinholes in $CoSi_2$ grown on Si(001)	948
L.J. Schowalter, J.R. Jimenez, L.M. Hsiung, K. Rajan, S. Hashimoto, R.D. Thompson and S.S. Iyer	
Characterization and application of fine-patterned Si/ $CoSi_2$ /Si double heterostructures fabricated by self-aligned, two-step MBE	957
M. Miyao, K. Nakagawa, N. Nakamura and T. Ohshima	
$\sqrt{3} \times \sqrt{3}$ -B structure on a 5×5 $Ge_{1-x}Si_x/Si(111)$ surface and its electrical conduction	961
T. Tatsumi, I. Hirose, T. Niino, H. Hirayama and J. Mizuki	

SECTION XVII. SUPERCONDUCTORS, METALS, MAGNETIC SUPERCONDUCTORS AND OTHERS

Growth and properties of high T_c films in $Y_1Ba_2Cu_3O_{7-x}$ perovskite by molecular beam epitaxy	965
J. Kwo	
Growth of superconducting $Bi_2Sr_2Ca_{n-1}Cu_nO_x$ thin films by atomically layered epitaxy	973
J.N. Eckstein, I. Bozovic, D.G. Schlom and J.S. Harris, Jr.	
MBE growth of ferromagnetic metastable epitaxial MnAl thin films on AlAs/GaAs heterostructures	978
J.P. Harbison, T. Sands, R. Ramesh, L.T. Florez, B.J. Wilkens and V.G. Keramidas	
MBE growth and properties of $Fe_3(Al,Si)$ on GaAs(100)	984
M. Hong, H.S. Chen, J. Kwo, A.R. Kortan, J.P. Mannaerts, B.E. Weir and L.C. Feldman	

Overgrowth and strain in MBE-grown GaAs/ErAs/GaAs structures J.D. Ralston, J. Wagner, F. Fuchs, P. Hiesinger and J. Schmärlzin	989
RHEED studies of epitaxial growth of CoGa on GaAs by MBE – determination of epitaxial phases and orientations T.C. Kuo, T.W. Kang and K.L. Wang	996
Molecular beam epitaxial growth of Cr/Fe, Ag/Fe, Ag/Cr and Ag/Co superlattices on MgO (001) substrates P. Etienne, J. Massies, S. Lequien, R. Cabanel and F. Petroff	1003
p-Type diluted magnetic III–V semiconductors H. Munekata, H. Ohno, R.R. Ruf, R.J. Gambino and L.L. Chang	1011
Growth and novel properties of magnetic heterostructures by molecular beam epitaxy J.M. Hong, D.D. Awschalom, F. Agulló-Rueda and L.L. Chang	1016
Evaluation of a new plasma source for molecular beam epitaxial growth of InN and GaN films W.E. Hoke, P.J. Lemonias and D.G. Weir	1024
Heteroepitaxial growth by Van der Waals interaction in one-, two- and three-dimensional materials A. Koma, K. Ueno and K. Saiki	1029
Growth of MoSe ₂ thin films with Van der Waals epitaxy F.S. Ohuchi, T. Shimada, B.A. Parkinson, K. Ueno and A. Koma	1033
Reconstruction structure at Ge ₂ Se ₃ /GaAs epitaxial interface D. Li, Y. Nakamura, N. Otsuka, J. Qiu, M. Kobayashi and R.L. Gunshor	1038
 SECTION XVIII. DEVICES	
MBE as a production technology for AlGaAs lasers H. Tanaka and M. Mushiage	1043
Substrate temperature dependence of SQW alloy and superlattice lasers grown by MBE using As ₂ C.T. Foxon, P. Blood, E.D. Fletcher, D. Hilton, P.J. Hulyer and M. Vening	1047
Vertical cavity top-surface emitting lasers with thin Ag mirrors and hybrid reflectors M. Hong, L.W. Tu, J. Gamelin, Y.H. Wang, R.J. Fischer, E.F. Schubert, K. Tai, G. Hasnain, J.P. Mannaerts, B.E. Weir, J.D. Wynn, R.F. Kopf, G.J. Zydzik and A.Y. Cho	1052
Reduced current thresholds in GaAs/AlGaAs vertical cavity surface emitting lasers using 4° off-oriented (001) GaAs substrates Y.H. Wang, K. Tai, Y.F. Hsieh, S.N.G. Chu, J.O. Wynn, M. Hong, R.J. Fischer and A.Y. Cho	1057
GaInAs/InP MQW and DBR growth for surface emitting lasers by CBE T.K. Uchida, T. Uchida, K. Mise, N. Yokouchi, F. Koyama and K. Iga	1062
MBE grown, visible, surface emitting harmonic generation lasers R.L. Williams, F. Chatenoud and R. Normandin	1066
A simple way to reduce series resistance in p-doped semiconductor distributed Bragg reflectors M. Hong, J.P. Mannaerts, J.M. Hong, R.J. Fischer, K. Tai, J. Kwo, J.M. Vandenberg, Y.H. Wang and J. Gamelin	1071
MBE growth of InP/InGaAs MQW modulators E.G. Scott and M.A.Z. Rejman-Greene	1076
Quantum-confined Stark effect in InGaAs/InP multiple quantum wells grown by solid source molecular beam epitaxy P.A. Claxton, M. Hopkinson, J. Kovac, G. Hill, M.A. Pate and J.P.R. David	1080
Critical issues in the MBE growth of Ga _{0.47} In _{0.53} As for waveguide/PIN/JFET integration H. Künzel, R. Kaiser, W. Passenberg, D. Trommer and G. Unterbörsch	1084
Investigation of a double barrier resonant tunnelling structure which incorporates an optical window layer in the top contact N. Henini, C.R.H. White, P.E. Simmonds, L. Eaves, M.S. Skolnick, D.K. Maude, O.H. Hughes and J.C. Portal	1089
Transport in Al _x Ga _{1-x} As/In _x Ga _{1-x} As resonant tunneling diodes with asymmetric layers H. Yoo, S.M. Goodnick and J.R. Arthur	1095
MBE growth and post-growth annealing of GaAs-based resonant tunneling structures, viewed in relation to interface roughness H. Riechert, D. Bernklau, J.-P. Reithmaier and R.D. Schnell	1100
MBE growth of GaAs/AlAs double-barrier structures on GaAs channeled substrates S. Shimomura, N. Okamoto, M. Takeuchi, E. Tamaoka, Y. Yuba, S. Namba, S. Hiyamizu, M. Shigeta, T. Yamamoto and K. Kobayashi	1105
Highly strained pseudomorphic In _x Ga _{1-x} As/AlAs based resonant tunneling diodes grown on patterned and non-patterned GaAs(100) substrates R.M. Kapre, A. Madhukar and S. Guha	1110

Comprehensive analysis of epitaxial Al/Al _x Ga _{1-x} As Schottky barriers made by MBE: barrier heights and band edge discontinuities	
M. Missous, E.H. Rhoderick, K.E. Singer and W.S. Truscott	1116
Author index	1121
Subject index	1136

Advances in molecular beam epitaxy (MBE)

A.Y. Cho

AT&T Bell Laboratories, Murray Hill, New Jersey 07974, USA

Molecular beam epitaxy (MBE) continues to set the standard for the control of epitaxial layer thickness and uniformity over a large substrate area. Recent improvement in growth conditions allow us to prepare epitaxial materials free from oval defects with electrical and optical properties better than or as good as any other crystal growth technique. Artificially structured materials permit us to explore physical and chemical properties that do not exist in nature. In the area of crystal growth, there have been two main movements in recent years: one is to grow in selective areas by depositing on patterned substrates or with focussed ion beams; the other is to extend epitaxial growth beyond lattice-matched systems with strained layers. Alloy systems such as $\text{Al}_x\text{Ga}_{1-x}\text{In}_{1-x-y}\text{As}$, $\text{Al}_x\text{Ga}_{1-x}\text{As}_y\text{Sb}_{1-y}$, $\text{InAs}_x\text{Sb}_{1-x}$, $\text{Ga}_x\text{In}_{1-x}\text{P}$, SiGe , ZnSe , and CdZnTe/ZnTe are among the new materials explored. New devices grown by MBE with exciting results are surface emitting lasers, strained quantum well lasers, quantum well infrared photodetectors, and real-space transfer heterostructure transistors (NERFETs). This paper will review recent advances in the conventional solid source MBE.

1. Introduction

Molecular beam epitaxy (MBE) has not only brought experimental quantum physics to the classroom but has also become a manufacturing technology. For instance, more than 70% of the compact disc lasers in the world are now manufactured by MBE [1]. This technology has also led to scientific investigations ranging from understanding of material science for crystal growth to electron motion on an atomic scale [2–4]. Many recent advances in the understanding of crystal growth, such as elimination of oval defects [5], influence of surface induced Fermi-level-pinning on impurity drift [6], selective area growth [7–11], and strained layer epitaxy [12–14], were reported. By coupling the intensity oscillation in reflection high-energy electron diffraction (RHEED) with the computer controlled MBE shutters, the epitaxial layer thickness can be controlled to atomic layer precision. This was used to form phase-locked epitaxy (PLE) [15]. Stimulated emission from a CdTe/HgCdTe heterostructure [16], photodiodes fabricated with HgCdTe with semi-metal Schottky layers [17], and ZnSe light emitting diodes [18] were demonstrated for II–VI com-

pounds. The drive to have heterostructures in Si technology similar to those in the III–V system, prompted workers to study the SiGe alloy [19–21]. This paper will discuss the recent results of material processing, patterned growth, strained layer epitaxy, and some novel device performance with solid source MBE. One advantage of using solid source MBE over the gas source is the lower cost for safety installation. Since II–VI and group IV materials will be covered by other invited speakers, I will cover mostly III–V compounds.

2. Material processing

2.1. Elimination of gallium-source related oval defects

Oval defects have been seen in MBE GaAs or AlGaAs films grown on {100} substrates [22]. These are hillocks or {111} faceted growth around an impurity cluster or a Ga droplet with the major axis along $\langle 110 \rangle$. In a clean manufacturing environment, these defects have been reduced to below 300 cm^{-2} [23,24]. They were also not as noticeable when graphite lined Ga ovens were

used in early MBE studies. However, much higher density (10^3 – 10^4 cm $^{-2}$) is generally observed in an average MBE laboratory with pyrolytic BN crucibles depending on the growth thickness. It was recently reported that if the Ga charge was contained in a pyrolytic BN crucible which was previously used for the evaporation of aluminum, the grown GaAs layers were totally free from Ga-source related oval defects [5]. No defects were observed even with layers as thick as 20 μ m. Fig. 1 illustrates the reduction of oval defects with such an oven. This improvement was thought to be due to a change in the nature of the BN crucible (possibly coated with AlN) after prolonged high

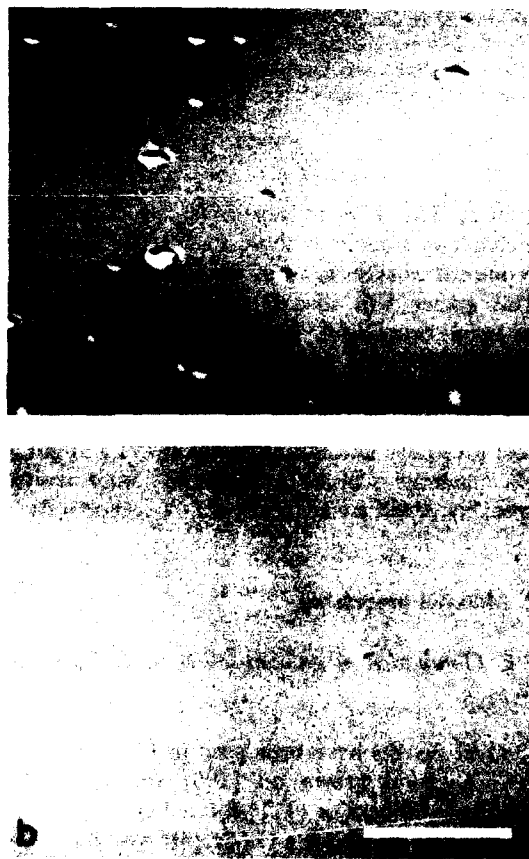


Fig. 1. Oval defects on 5 μ m thick MBE GaAs layers grown with (a) Ga charge in conventional BN crucible and (b) Ga charge in an Al-treated BN crucible [5]. Marker represents 50 μ m.

temperature heating with aluminum [5]. The presence of residual aluminum may also getter the gallium oxide in the Ga charge to further reduce Ga spitting from the oven [25]. An Al treated effusion cell produced a total of 600 μ m of GaAs layers before some oval defects began to appear.

2.2. Doping studies

The influence of Fermi-level pinning at a semiconductor surface can result in impurity drift during crystal growth by MBE [6]. The electrostatic dipole interaction between carriers localized in surface states and their parent donors causes the donors to segregate along with the growing surface. Appropriate background doping to reverse the field (screening) can reduce the segregation. This gives us good physical insight, but for practical devices, generally one does not have the freedom to provide such background doping. Growth under different reconstructed surface structures may give us different screening conditions and be more applicable to device preparations.

GaSb has an attractive characteristic which is unique to III-V compounds. It has comparable values for electron and hole mobilities and therefore can be useful for the fabrication of complementary circuits. $\text{Al}_x\text{Ga}_{1-x}\text{Sb}$ lattice matched to GaSb substrates covers the wavelengths from 0.78 to 1.71 μ m which is useful for applications in the optical fiber communications system. However, it is difficult to dope GaSb or $\text{Al}_x\text{Ga}_{1-x}\text{Sb}$ n-type with MBE. The conventional group IV elements such as Sn and Si are not incorporated as donors. Tellurium is a high vapor pressure element and does not evaporate in the form of monomers. Using a compound source of Sb_2Te_3 , GaSb was successfully doped from 10^{17} to 2×10^{18} cm $^{-3}$ [26]. For $n = 1.8 \times 10^{17}$ cm $^{-3}$, a room-temperature electron mobility of 3000 cm 2 /V \cdot s was obtained. Further increase in Te concentration to 2×10^{19} cm $^{-3}$ resulted in a reduction of both the carrier concentration and carrier mobility. When GaSb was doped with a SnTe compound source, electron concentration from 1.2×10^{16} cm $^{-3}$ to 4×10^{18} cm $^{-3}$ was obtained reproducibly [27]. Carrier mobility as high as 5100 cm 2 /V \cdot s was observed for $n = 3.2 \times 10^{16}$ cm $^{-3}$ at room temperature. Fig.

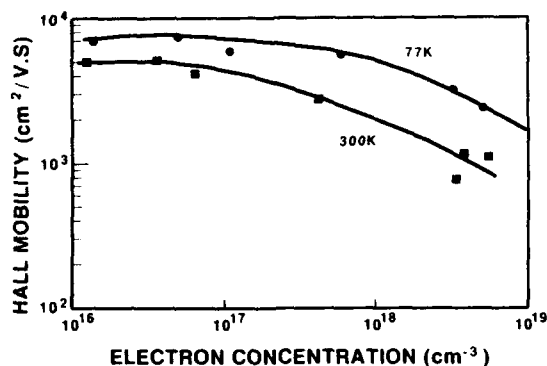


Fig. 2. Hall mobility as a function of electron concentration for SnTe doped GaSb [27].

2 shows the electron mobility of SnTe doped GaSb.

Many investigators studied carbon as a possible candidate in addition to the most commonly used beryllium for p-type dopant in III-V compounds. Carbon has a relatively low ionization energy, high solid solubility ($> 10^{20} \text{ cm}^{-3}$), and low diffusion coefficient in GaAs. Carbon doping with a resistively heated (1700–1900°C) graphite filament cut in a serpentine shape can achieve controlled acceptor concentration over a range from 10^{17} to 10^{20} cm^{-3} [28]. The room temperature hole mobility of the GaAs epitaxial layer as a function of the hole concentration is shown in fig. 3.

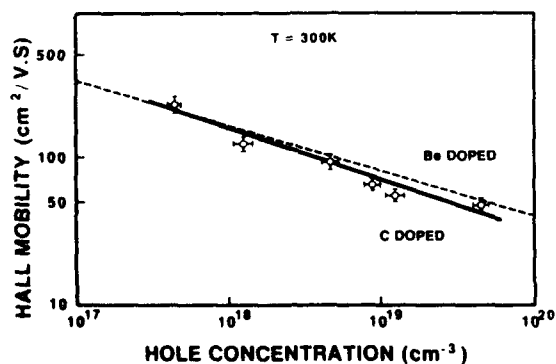


Fig. 3. Room temperature Hall mobility as a function of hole concentration for carbon doped GaAs [28].

2.3. New material systems

$\text{Ga}_x\text{Al}_y\text{In}_{1-x-y}\text{As}$ epitaxially grown on InP substrates covers the wavelengths from 0.855 to $1.65 \mu\text{m}$, similar to those of $\text{Ga}_x\text{In}_{1-x}\text{As}_y\text{P}_{1-y}$, which cover from 0.925 to $1.65 \mu\text{m}$. However, the former needs to control only one high vapor pressure group V element and it is more suited for the conventional solid source MBE. Device quality material without misfit dislocations was grown over the entire composition by keeping the In flux constant while changing the Ga and Al cell temperatures simultaneously to keep the total Ga plus Al flux constant such that $(x + y = 0.47)$ [29]. The renewed interest in this material [30,31] is due to the more available computer-automated MBE systems which allow one to accurately model the characteristics of the effusion cells, including not only the static flux versus temperature relationship, but also the time-dependent behavior of the cell [31]. This quaternary is viewed as a binary alloy of the two ternaries $\text{In}_{0.53}\text{Ga}_{0.47}\text{As}$ and $\text{In}_{0.52}\text{Al}_{0.48}\text{As}$ with two indium sources. Excellent lasers operating at an emission wavelength of $1.5 \mu\text{m}$ with a threshold current density as low as 830 A cm^{-2} were demonstrated [30].

$\text{Ga}_x\text{In}_{1-x}\text{P}$ lattice matched to GaAs is an important alloy system for photonic devices in the visible wavelength (6000–6800 Å). High quality epitaxial layers were recently demonstrated with MBE [32]. A solid red phosphorus source with a cracker cell has also been used to generate the dimetric phosphorus beam for the growth of $\text{Ga}_x\text{In}_{1-x}\text{P}$ at 510°C [33]. A $10 \mu\text{m}$ wide stripe-geometry GaInP/AlInP DH laser showed a low cw threshold current of 93 mA and an emission wavelength of 670 nm at room temperature [34].

Among the II-VI compounds, ZnSe has potential application as a blue light emitter. It can be doped n-type fairly easily, and much effort has gone into the more difficult problem of p-type doping. Most recently, ZnSe diodes were grown on n-type GaAs substrates at 225 to 325°C with special designed two-zone heated effusion cells [18]. ZnCl_2 was used to dope the n-type layer, and pure Li metal was used to dope the p-type layer. Large volumes of reproducible ZnSe blue light

emitting diodes ($\lambda = 471$ nm at 300 K) were produced [18].

We expect that it will be essential to develop silicon heterojunction technology. The two most promising candidate material systems are silicon-germanium and silicon carbide. The former can be grown with MBE and the latter has to be grown with plasma assisted epitaxy. Because of the large lattice mismatch between Si and Ge (4%), only a thin commensurate structure with relatively low Ge content can be grown without misfit dislocation [19,20]. Si-Ge_{0.4}Si_{0.6} quantum well structures were grown at 530 °C to demonstrate three-terminal resonant tunneling transistors [19]. Work on molecular doping species has successfully used boron oxide B₂O₃ and boric acid HBO₃ as boron doping sources. Carrier concentrations as high as 10^{20} cm⁻³ have been achieved [35].

3. Patterned growth

Single crystal growth in selective areas has been demonstrated earlier with patterned oxide as a mask over a substrate [36,37] or epitaxial growth on a pre-etched nonplanar (channel) substrate [38]. On a (001) GaAs surface, the side wall growth is smooth when the stripe is aligned in the $\bar{1}10$ direction and rough when aligned in the 110 direction [37]. There are many recent and excellent studies of MBE growth on nonplanar substrates [7-10]. The difference in the growth rate on planes of different orientations results both from the spatial variation in the flux of the source beams as well as from migration of the adsorbed atoms to a more favorable crystal plane. With various ratios of H₂SO₄:H₂O₂:H₂O, or different depths of etching, one may form different micro facets in the etched channels. Facet planes of {311}, {411}, {111}, {811}, {711}, and {544} were observed in the channel [8,10]. The migration length of Ga adatoms at the growth temperature is in the order of 1-2 μ m while the In adatom migration length on {100} plane is as long as 25 μ m [10]. It is this different migration rate on different facets and the formation of "kinks" in the channel that make MBE on nonplanar substrates potentially useful for optoelectronic devices. For instance, on a sub-

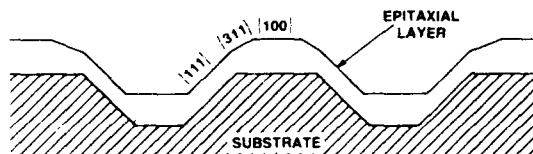


Fig. 4. Schematic of cross-sectional view of non planar substrate and epitaxial layer.

strate with {100} ridges and grooves formed with {111} side walls, the Ga atoms tend to migrate from the side walls to {100} plane resulting in a 20% to 50% thicker layer on the ridge and groove than on the side walls as shown in fig. 4. If we grow GaAs and AlGaAs superlattice over the whole channeled substrate, the resulting structure would have higher AlAs mole fraction on the side walls than on the {100} plane; a natural formation of an index guided injection laser structure with single-step growth is produced. Fig. 5 shows

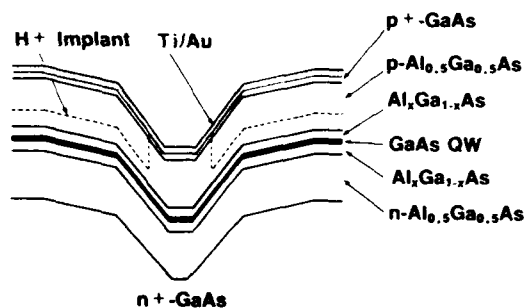


Fig. 5. Cross section of a one step MBE grown patterned graded-index separate confinement (GRINSCH) quantum well laser. This laser has a threshold current as low as 0.35 mA [9].

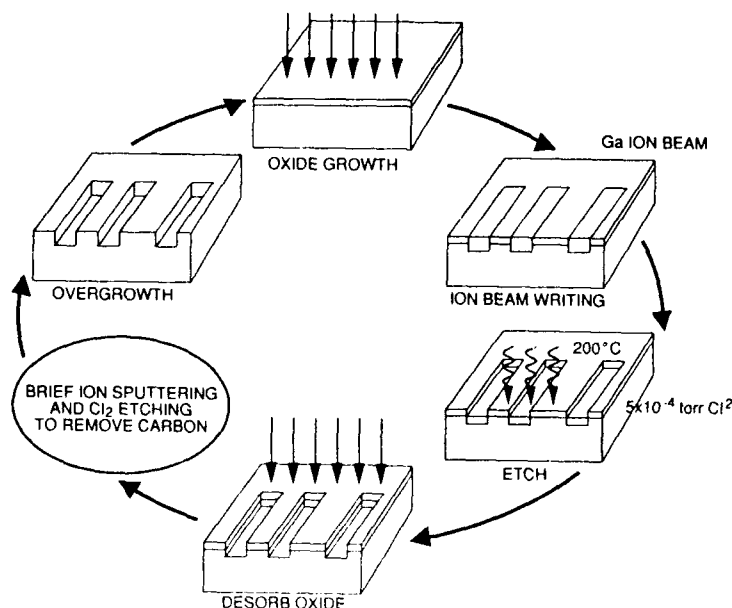


Fig. 6. A schematic diagram illustrating the processing sequence for the formation of in-situ patterning and regrowth [11].

such a structure which has a threshold current as low as 0.35 mA at room temperature [9].

One other way to achieve patterned growth is to combine focussed ion beams with MBE [13,39]. An in-situ patterning process is achieved by writing with a 20 keV Ga ion beam (10^{13} – 10^{15} cm $^{-2}$) on a very thin (20–30 Å) native oxide layer. The mask pattern is then transferred into the substrate by dry etching in a 10^{-4} Torr Cl $_2$ at 200°C with an etch rate of about 1000 Å/min. The oxide mask is then thermally removed. For regrowth on this patterned substrate, a brief low energy ion sputtering and Cl $_2$ etching to remove any carbon contamination is essential. Fig. 6 illustrates the vacuum lithography and regrowth process.

4. Strained layer epitaxy

The use of non-lattice-matched epitaxial materials to form strained quantum wells or periodic structures not only allows us to prepare materials operating at a wavelength which would otherwise not be accessible with lattice-matched materials

[40], but also provides desirable electronic properties for high-speed transistors [41] and optical properties for high-speed lasers [42] because of the biaxial strain.

In the crystal growth of strained layers, most studies were focussed on the thickness at which dislocations are first observed, referred to as the critical thickness [43–46]. InGaAs on GaAs and SiGe on Si substrates were studied extensively. The relaxation was found to be strain dependent as well as highly temperature dependent [46].

For epitaxial layers thicker than the critical thickness and without interface defects due to lattice mismatch, the growth may be conducted on a patterned substrate. It was found that by a reduction in growth area one can reduce dislocation multiplication and limit the glide of existing misfit dislocations [13,14,47]. Fig. 7 shows the drastic reduction of the linear density of misfit dislocations from > 5000 dislocations/cm in an unpatterned substrate to nearly zero for a 70 μ m mesa [13]. The photomicrograph is a cathodoluminescence image of an In $_{0.05}$ Ga $_{0.95}$ As epitaxial layer, 3500 Å thick, grown on a GaAs patterned

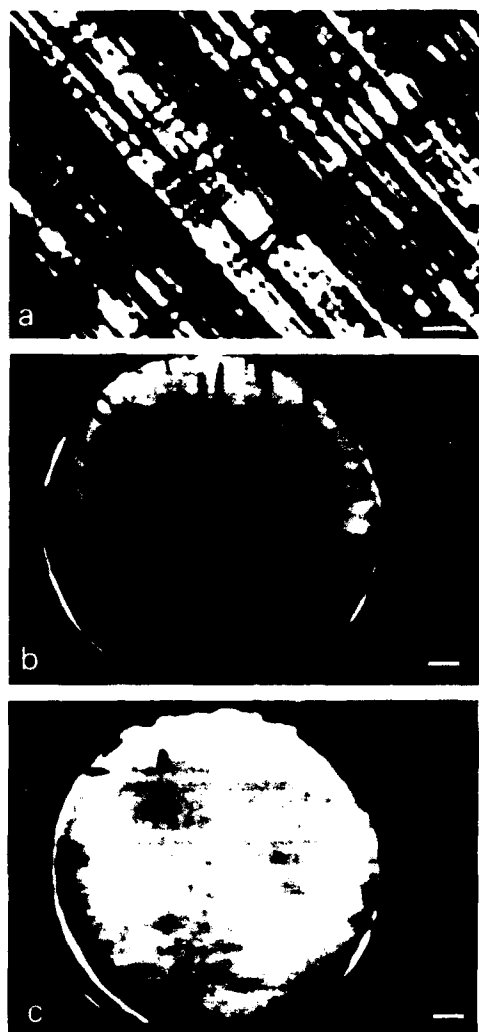


Fig. 7. Cathodoluminescence images of 3500 Å $\text{In}_{0.05}\text{Ga}_{0.95}\text{As}$ layer on GaAs (a) with no lateral restriction (b) on a 90 μm diameter patterned mesa substrate (c) on a 67 μm diameter mesa substrate [13]. Markers represent 10 μm .

substrate at 550°C. It is seen here that by reducing the lateral dimension of the growth surface, one can reduce misfit dislocation density for the growth which is greater than four times the previously accepted critical thickness.

5. Novel devices

5.1. Strained InGaAs/GaAs quantum well lasers

Strained InGaAs/GaAs quantum wells were grown on nonplanar substrates with (100) ridges and grooves formed with (311)A sidewalls. [48]. To study the In adatom migration effect on different widths of ridges, two 70 Å $\text{In}_x\text{Ga}_{1-x}\text{As}$ quantum wells were grown with $x = 0.10$ and 0.17 at 520°C on 4 and 40 μm wide structures. It was found that most of the In atoms on the (311)A sidewalls migrate to the (100) ridges and result in a larger InAs mole fraction on the ridges. Fig. 8 shows the 5 K cathodoluminescence spectra of these two quantum wells at two different widths of the ridges. The upper spectrum with peaks at 870.8 and 914.0 nm was taken at the middle of a 4 μm wide ridge while the lower spectrum with peaks at 863.0 and 902.5 nm was taken from the middle of a 40 μm wide ridge. The emission wavelength from an unpatterned substrate would be 859.6 and 897.6 nm, respectively. Graded index separate confinement heterostructure (GRINSCH) lasers were fabricated on patterned substrates with ridges varying from 3.5 to 40 μm wide [48]. Fig. 9 shows room temperature cw lasing energy of 70 Å $\text{In}_{0.15}\text{Ga}_{0.85}\text{As}$ quantum well GRINSCH lasers

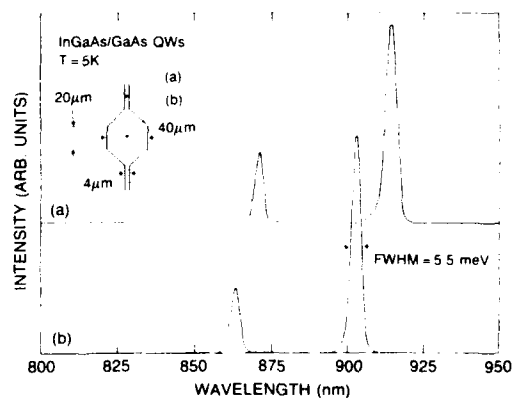


Fig. 8. Cathodoluminescence spectra at 5 K for $\text{In}_x\text{Ga}_{1-x}\text{As}/\text{GaAs}$ quantum wells (70 Å) with $x = 0.10$ and 0.17 taken at (a) 4 μm wide ridge and (b) 40 μm wide ridge. The peak emission wavelengths observed in a spectrum obtained from a (100) planar section are 859 nm and 897 [49].

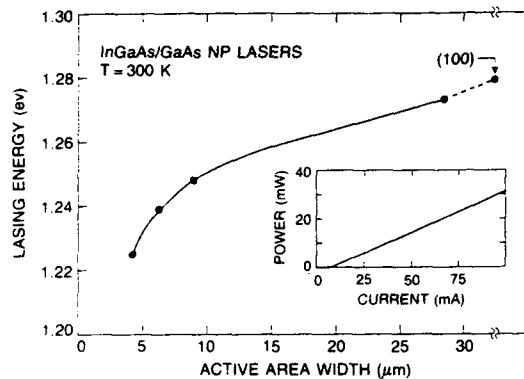


Fig. 9. Room temperature cw lasing energy of strained $\text{In}_{0.15}\text{Ga}_{0.85}\text{As}/\text{GaAs}$ GRINSLASERS grown on patterned substrates with various stripe width. Energy differences larger than 50 meV are achieved as the ridge width is decreased. The inset shows a typical cw power as a function of injection current curve for a $4\text{ }\mu\text{m} \times 750\text{ }\mu\text{m}$ device [48].

grown on different ridge widths. Threshold currents of $4\text{ }\mu\text{m} \times 750\text{ }\mu\text{m}$ uncoated devices lasing single mode at a wavelength of $1.01\text{ }\mu\text{m}$ were as low as 6 mA ($J_{\text{th}} = 320\text{ A}/\text{cm}^2$) [48].

5.2. Surface emitting lasers

The surface emitting laser which emits the light normal to the substrate surface, as shown in fig. 10 [49–51], is emerging as a promising solution for fabricating low-cost lasers because it can be

evaluated at the wafer level before separation into chips; it may be used for a high power source because it can readily be fabricated into a two-dimensional coherently coupled array (fig. 11); it can be used as a high performance single frequency laser because of its inherent dynamic single longitudinal mode operation which is due to the large mode spacing of the short cavity ($0.5\text{--}2\text{ }\mu\text{m}$).

Distributed Bragg reflectors (DBRs) consisting of periodic quarter wavelength stacks of low and high refractive index AlAs and GaAs are used for the reflecting mirrors of the laser. However, the energy bandgap difference at the hetero-interface results in potential barriers (spikes) which in turn creates a large series resistance for the device. This series resistance gives rise to thermal heating and thus deteriorates the laser performance. With “bandgap engineering”, either by compositional grading at the interface or by using a multi-stair case superlattice, we can eliminate the interface spike and reduce the series resistance. In the GaAs–AlGaAs DBR structure, about two orders of magnitude reduction in series resistance was achieved without deteriorating the optical reflectivity [52]. Fig. 12 shows a cross-sectional electron micrograph of the AlGaAs/GaAs surface emitting laser. It takes more than 20 pairs of this semiconductor superlattice to form a mirror with reflectivity higher than 98%. The structure consists of a total of 360 layers and is computer controlled for the entire growth. Fig. 13 shows the typical lasing

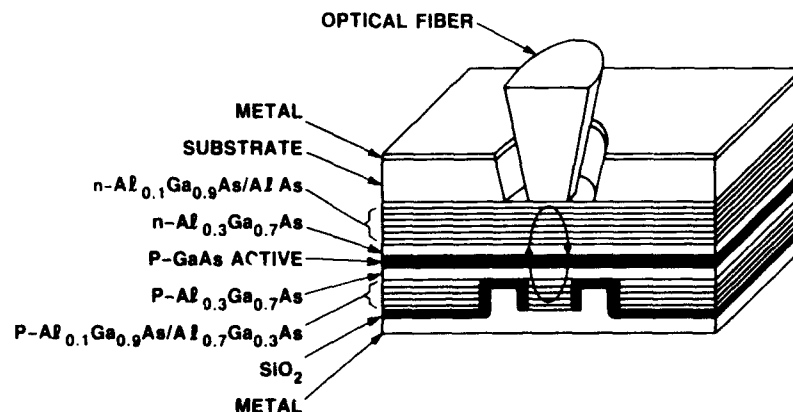


Fig. 10. Schematic of a surface emitting laser with all epitaxially grown superlattice reflecting mirrors [51].

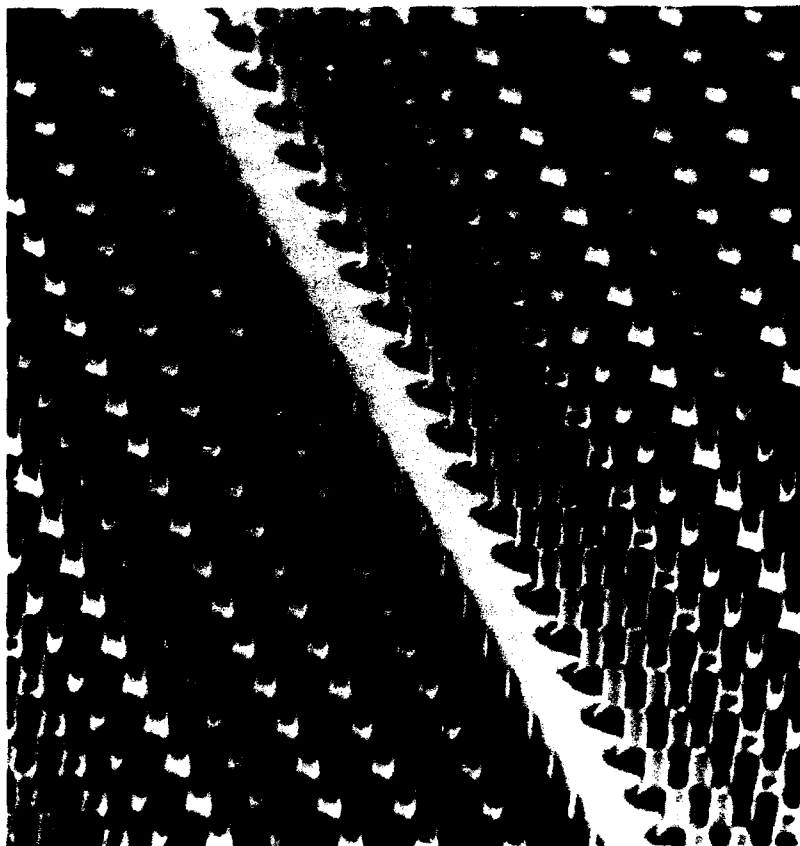


Fig. 11. Scanning electron micrograph of arrays of surface emitting lasers (R.A. Gottscho).

characteristics under cw at room temperature. Recent results showed that a $15\text{ }\mu\text{m}$ diameter device has a room temperature cw threshold current of 2.5 mA giving an output power of 0.2 mW with a temperature coefficient for lasing, $T_0 \approx 115\text{ K}$ [53].

Ion implantation may be used to isolate the surface emitting lasers and to preserve a planar geometry [54]. Most recently, deep H^+ -ion implantation (300 keV) was used to form an embedded insulating layer at the depth of the active region to isolate individual SEL devices [55] as shown in fig. 14. The active region consists of four $100\text{ }\text{\AA}$ thick GaAs quantum wells separated by

three $70\text{ }\text{\AA}$ thick $\text{Al}_{0.3}\text{Ga}_{0.7}\text{As}$ barriers. The threshold current is 2.2 mA for a $10\text{ }\mu\text{m}$ diameter laser operating cw at room temperature with differential quantum efficiency as high as 20%.

A two-dimensional phased coupled array of surface emitting lasers was also demonstrated [56,57]. The array was comprised of more than 160 lasers of $1.3\text{ }\mu\text{m}$ diameter with a separation of less than $0.1\text{ }\mu\text{m}$ between each lasing element. Due to strong optical coupling between lasers, the threshold current is only $280\text{ }\mu\text{A}$ for each elemental laser. The far-field beam angle of the array was as narrow as 7° indicating that phase locking had

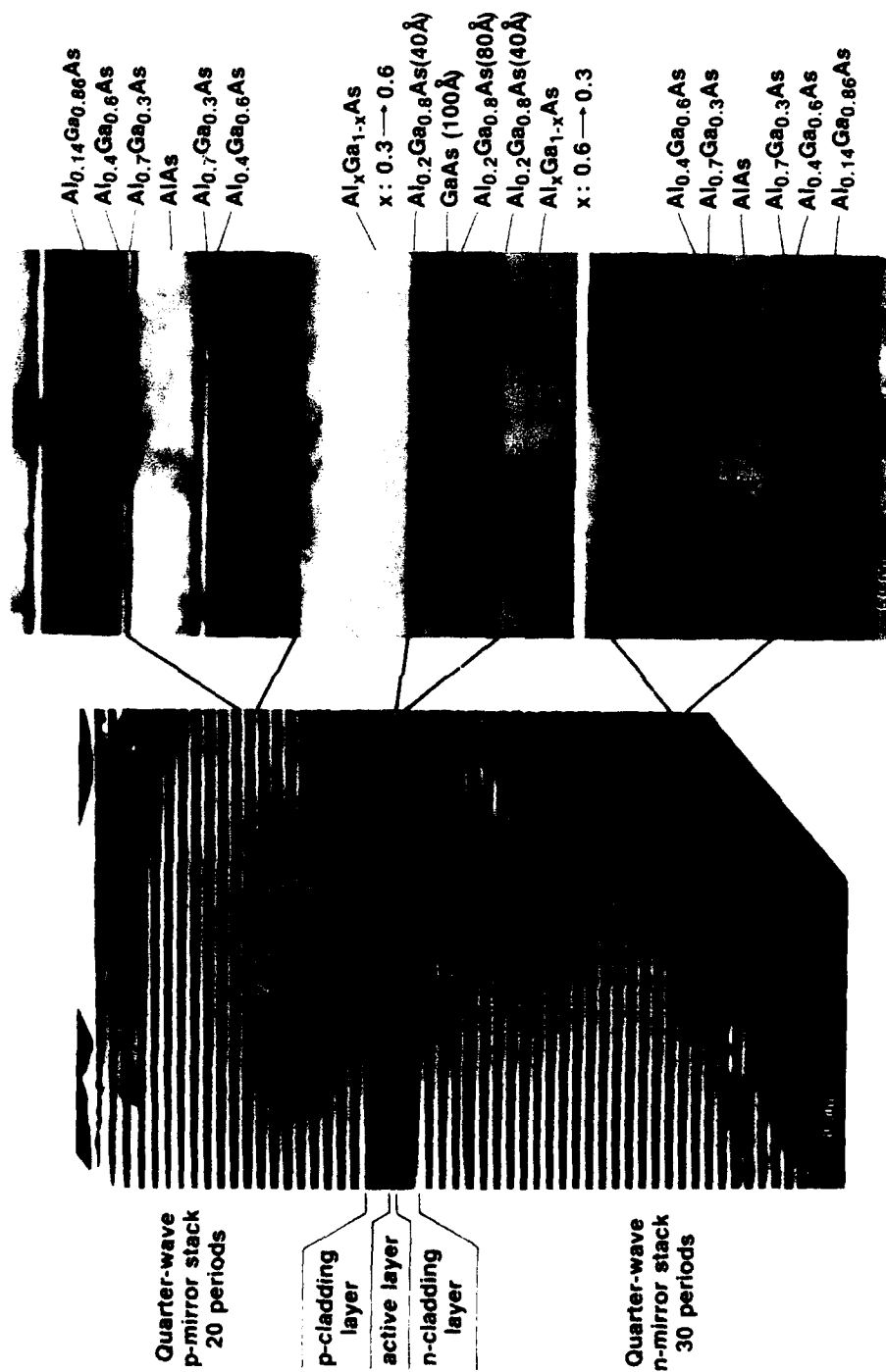


Fig. 12. A cross sectional electron micrograph of the AlGaAs/GaAs surface emitting laser (S.N.G. Chu).

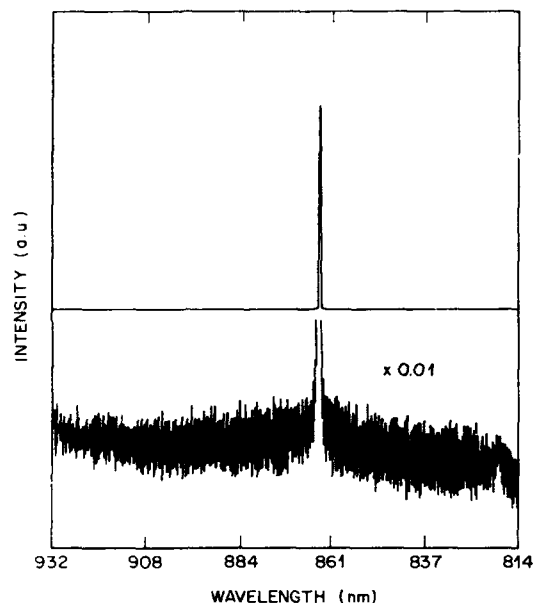


Fig. 13. Room temperature cw emission of the surface emitting laser. The side mode suppression ratio is better than 35 dB [53].

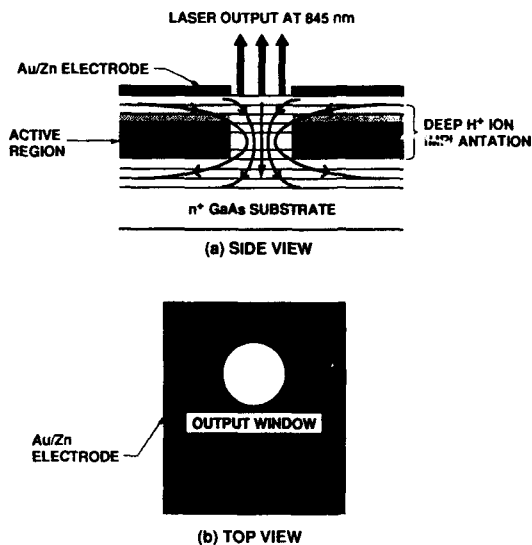


Fig. 14. Schematic of a deep ion-implantation to isolate individual lasers [55].

been achieved. A holographic reconstructed image was demonstrated with the two-dimensional phase-locked array [56].

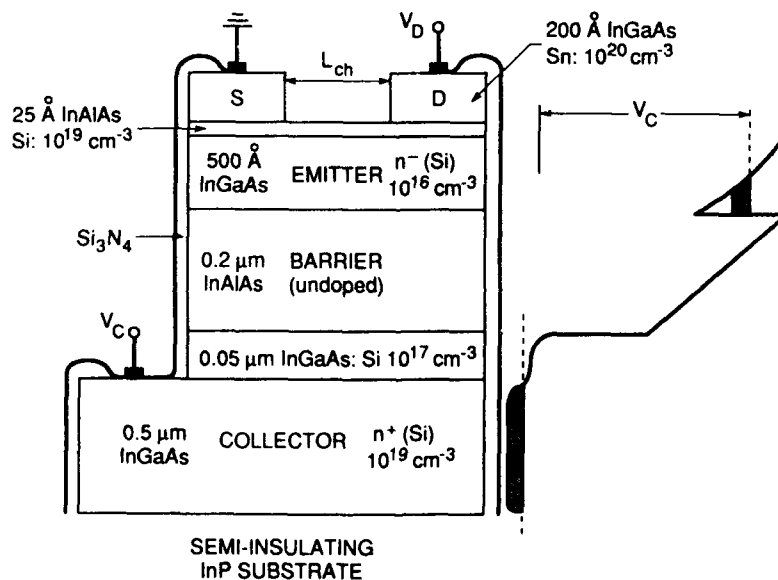


Fig. 15. Cross-section of a charge injection negative differential resistance field effect transistor. The energy-band diagram is under an applied collector bias condition [61].

5.3. Three-terminal real-space transfer devices

The charge-injection transistor is based on the real-space transfer of hot electrons between two low bandgap semiconducting layers separated by a large bandgap potential barrier layer [58,59]. The drain and source contacts are on one semiconducting layer and the collector contact is on the other, separated by the potential barrier layer (fig. 15). As one applies bias to the drain and source, the carriers get heated and are injected into the collector layer. A strong negative differential resistance develops in the drain current (I_D) as a function of drain voltage (heating voltage, V_D) characteristics.

A successful charge injection transistor was prepared with InGaAs/InAlAs lattice matched to InP substrate [59]. Advantages of this system for real space transfer (RST) transistors are the low effective electron mass which favors heating effects and large ΔE_C to reduce leakage current of "cold" electrons. Perhaps the most important factor in preparing such a structure is to be able to grow a non-alloyed (Sn-doped) ohmic contact [60] so that the multi-layers will not be shorted as would occur with the standard alloyed contacts.

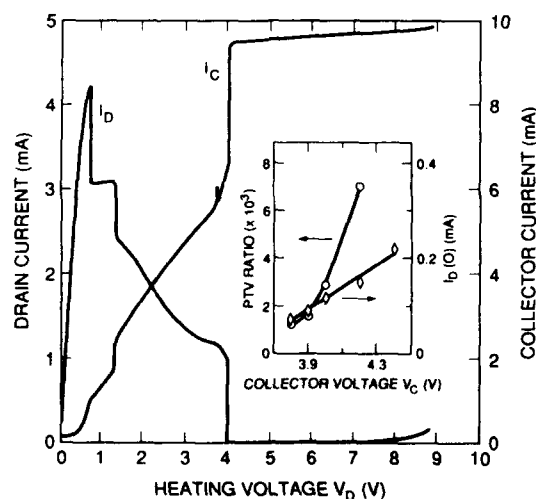


Fig. 16. The drain current (I_D) and collector current (I_C) as a function of the heating drain voltage (V_D) for a charge injection transistor. The collector bias, V_C , is 3.9 V. Inset: collector bias dependence of the drain current peak-to-valley ratio and the leakage current, defined as I_D at $V_D = 0$ [61].

Fig. 15 shows the cross-section of the device structure and the energy-band diagram under an applied collector bias. The trench in this heavily Sn-doped cap layer defines the emitter channel, whose length (L_{ch}) varied from 0.6 to 2 μm . Recent results showed that the peak-to-valley ratio of the negative differential resistance in the drain circuit routinely exceeds 1000 with a maximum observed value of 7000 (fig. 16). The measured peak transconductance typically exceeded 10 S/mm and the highest observed value was 23.1 S/mm. A single device structure that performs logic operations such as NOR and AND were demonstrated [61].

6. Future challenges

Molecular beam epitaxy (MBE) continues to advance and set standards for the control of epitaxial layer thickness and uniformity over a large substrate area while the electrical and optical properties of MBE epitaxial materials are either exceeding or comparable to any other crystal growth technique. New physics, new material characteristics, and new devices will continue to be discovered. There are several new challenges in material processing:

- Develop semiconductor materials for electronic and optical devices operating above 85°C.
- Develop new artificial structures for optical switching (large electro-optic effect).
- Develop regrowth technology for MBE so that one may fabricate high performance integrated circuits and the integration with photonics (in situ integrated processing)
- Develop MBE automated systems that can routinely produce highly uniform layers with variation less than 1% over 10 cm.

Acknowledgements

I would like to thank Russ Fischer, Naresh Chand, Jim Harbison, Y.L. Wang, Eugene Fitzgerald, Piotr Mensz, J.F. Chen, Y.H. Wang, and Debbie Sivco for many helpful discussions.

References

- [1] ROHM uses MBE to manufacture compact disc lasers and its market share is 70–75%:
see also H. Tanaka and M. Mushiage, *J. Crystal Growth* 111 (1991) 1043.
- [2] L.L. Chang, L. Esaki and R. Tsu, *Appl. Phys. Letters* 24 (1974) 593.
- [3] F. Capasso, Ed., *Physics of Quantum Electron Devices* (Springer, Berlin, 1990).
- [4] R. Beresford, L.F. Luo, K.F. Longenbach and W.I. Wang, *Appl. Phys. Letters* 56 (1990) 952.
- [5] N. Chand, *Appl. Phys. Letters* 56 (1990) 466;
also, N. Chand and S.N.G. Chu, *J. Crystal Growth* 104 (1990) 485.
- [6] E.F. Schubert, J.M. Kuo, R.F. Kopf, A.S. Jordan, H.S. Luftmann and L.C. Hopkins, *Phys. Rev. B* 42 (1990) 1364.
- [7] J.M. Hong, M.C. Wu, S. Wong, W.I. Wang and L.L. Chang, *Appl. Phys. Letters* 51 (1987) 886.
- [8] E. Kapon, M.C. Tamargo and D.M. Hwang, *Appl. Phys. Letters* 50 (1987) 347.
- [9] E. Kapon, S. Simhony, J.P. Harbison and L.T. Florez, *Appl. Phys. Letters* 56 (1990) 1825.
- [10] D.L. Arent, S. Nilsson, Y.D. Galenchet, H.P. Meier and W. Walter, *Appl. Phys. Letters* 55 (1989) 2611.
- [11] Y.L. Wang, L.R. Harriott, R.A. Hamm and H. Temkin, *Appl. Phys. Letters* 56 (1990) 749.
- [12] B.W. Dodson and J.Y. Tsao, *Appl. Phys. Letters* 55 (1989) 1345.
- [13] E.A. Fitzgerald, P.D. Kirchner, R. Proano, G.D. Pettit, J.M. Woodall and D.G. Ast, *Appl. Phys. Letters* 52 (1988) 1496.
- [14] S. Guha, A. Madhukar and L. Chen, *Appl. Phys. Letters* 56 (1990) 2304.
- [15] J.D. Walker, K. Malloy, S. Wang and J.S. Smith, *Appl. Phys. Letters* 56 (1990) 2493.
- [16] K.K. Mahavadi, J. Bleuse, S. Sivananthan and J.P. Faurie, *Appl. Phys. Letters* 56 (1990) 2077.
- [17] J.W. Sulhoff, J.L. Zyskind, C.A. Burrus, R.D. Feldman and R.F. Austin, *Appl. Phys. Letters* 56 (1990) 388.
- [18] J. Ren, B. Sneed, K.A. Bowers, J.W. Cook, Jr. and J.F. Schetzina, 48th Annual Device Research Conf., Santa Barbara, CA, June 1990;
also, J. Ren, K.A. Bowers, B. Sneed, F.E. Reed, J.W. Cook, Jr. and J.F. Schetzina, *J. Crystal Growth* 111 (1991) 829.
- [19] S.S. Rhee, G.K. Chang, T.K. Carns and K.L. Wang, *Appl. Phys. Letters* 56 (1990) 1061.
- [20] G.A. Northrop, D.J. Wolford, V.P. Kesan and S.S. Iyer, *Electronic Materials Conf.*, Santa Barbara, CA, June 1990;
also, S.S. Iyer, 6th Intern. Conf. on Molecular Beam Epitaxy, La Jolla, CA, August 1990.
- [21] G.L. Patton, J.H. Comfort, B.S. Meyerson, E.F. Craffe, G.J. Scilla, E. de Fresart, J.M.C. Stark, J.Y. Sun, D.L. Hareme and J.N. Burghartz, *IEEE Electron Device Letters* EDL-11 (1990) 171.
- [22] K. Fujiwara, K. Kanamoto, Y.N. Ohta, Y. Tokuda and T. Nakayama, *J. Crystal Growth* 80 (1987) 104.
- [23] P. Delescluse, A. Verotite, V. Parguel, J. Vatus, J.F. Rochette and Linh T. Nuyen, 5th Intern. Conf. on Molecular Beam Epitaxy, Sapporo, 1988. Recent results showed defects have been reduced to 3 cm^{-2} .
- [24] J. Saito, K. Nanbu, T. Ishikawa and K. Kondo, *J. Crystal Growth* 95 (1989) 322.
- [25] G.D. Pettit, J.M. Woodall, S.L. Wright, P.D. Kirchner and J.L. Freeouf, *J. Vacuum Sci. Technol. B* 2 (1984) 241.
- [26] T.H. Chiu, J.A. Ditzemberger, H.S. Luftman, W.T. Tsang and N.T. Ha, *Appl. Phys. Letters* 56 (1990) 1688.
- [27] J.F. Chen and A.Y. Cho, *J. Crystal Growth* 111 (1991) 619.
- [28] R.J. Malik, R.N. Nottenberg, E.F. Schubert, J.F. Walker and R.W. Ryan, *Appl. Phys. Letters* 53 (1988) 2661.
- [29] K. Alavi, A.Y. Cho, F. Capasso and J. Allan, *J. Vacuum Sci. Technol. B* 5 (1987) 802.
- [30] M. Quillec and M. Allovon, *Electronic Materials Conf.*, Santa Barbara, CA, June 1990;
also, M. Allovon, M. Quillec, M. Blez and C. Kazmierski, *J. Crystal Growth* 111 (1991) 484.
- [31] J.C. Vlcek and C.G. Fonstad, *Electronic Materials Conf.*, Santa Barbara, CA, June 1990;
also, J.C. Vlcek and C.G. Fonstad, *J. Crystal Growth* 111 (1991) 56.
- [32] K.Y. Cheng, J.N. Billargeon, K.C. Hsieh, D.W. Nam, E. Vesely, G.E. Fernandez, N. Holonyak, Jr. and R.J. Fu, *Electronic Materials Conf.*, Santa Barbara, CA, June 1990.
- [33] K. Takahashi, T. Hayakawa, M. Hosoda, S. Yamamoto and T. Hijikata, *J. Crystal Growth* 95 (1989) 333.
- [34] T. Hayakawa, K. Takahashi, M. Hosoda, S. Yamamoto and T. Hijikata, *Japan. J. Appl. Phys.* 27 (1988) L1553.
- [35] J.C. Bean, to be published.
- [36] A.Y. Cho and W.C. Ballamy, *J. Appl. Phys.* 46 (1975) 783.
- [37] A.Y. Cho, *J. Vacuum Sci. Technol.* 16 (1979) 275.
- [38] W.T. Tsang and A.Y. Cho, *Appl. Phys. Letters* 30 (1977) 293.
- [39] E. Miyauchi, T. Morita, A. Takamori, H. Arimoto, Y. Bamba and H. Hashimoto, *J. Vacuum Sci. Technol. B* 4 (1986) 189; *Appl. Phys. Letters* 56 (1990) 749.
- [40] M.C. Wu, N.A. Olsson, D. Sivco and A.Y. Cho, *Appl. Phys. Letters* 56 (1990) 221.
- [41] T.E. Zipperin, L.R. Dawson, T.J. Drummond, J.E. Schirber and I.J. Fritz, *Appl. Phys. Letters* 52 (1988) 975.
- [42] N.K. Dutta, J. Wynn, D.L. Sivco and A.Y. Cho, *Appl. Phys. Letters* 56 (1990) 2293.
- [43] J.W. Mathews, *J. Vacuum Sci. Technol.* 12 (1975) 126.
- [44] R. People and J.C. Bean, *Appl. Phys. Letters* 47 (1988) 322.
- [45] B. Dodson and J.Y. Tsao, *Appl. Phys. Letters* 51 (1987) 1325; 55 (1989) 1345.
- [46] G.J. Whalen and P.I. Cohen, *Appl. Phys. Letters* 57 (1990) 144.
- [47] E.A. Fitzgerald, *J. Vacuum Sci. Technol. B* 7 (1989) 782.
- [48] D.J. Arent, Y.D. Galeuchet, S. Nilsson and H.P. Meier, to be published.

- [49] K. Iga, F. Koyama, and S. Kinoshita, *IEEE J. Quantum Electron.* QE-24 (1988) 1845.
- [50] J.L. Jewell, A. Scherer, S.L. McCall, Y.H. Lee, S. Walker, J.P. Harbison and L.T. Florez, *Electron. Letters* 25 (1989) 1123.
- [51] K. Tai, R.J. Fischer, C.W. Seabury, N.A. Olsson, T.C.D. Huo, Y. Ota and A.Y. Cho, *Appl. Phys. Letters* 55 (1989) 2473.
- [52] K. Tai, L. Yang, Y.H. Wang, J.D. Wynn and A.Y. Cho, *Appl. Phys. Letters* 56 (1990) 2496; also, M. Hong, J.P. Mannaerts, J.M. Hong, R.J. Fischer, K. Tai, J. Kwo, J.M. Vandenberg, Y.H. Hwang and J. Gamelin, *J. Crystal Growth* 111 (1991) 1071.
- [53] Y.H. Wang, R.J. Fischer, J. Gamelin, K. Tai, T.F. Hsieh, S.N.G. Chu, J.D. Wynn, M. Hong and A.Y. Cho, to be published; also, Y.H. Wang, K. Tai, Y.F. Hsieh, S.N.G. Chu, J.D. Wynn, M. Hong, R.J. Fischer and A.Y. Cho, *J. Crystal Growth* 111 (1991) 1057.
- [54] K. Tai, R.J. Fischer, K.W. Wang, S.N.G. Chu and A.Y. Cho, *IEEE Electron Device Letters* EDL-24 (1989) 1644.
- [55] Y.H. Lee, B. Tell, K. Brown-Goebeler, J.L. Jewell and J.V. Hove, to be published.
- [56] H-J Yoo, A. Scherer, J.P. Harbison, L.T. Florez, E.G. Palk, B.P. van der Gaag, J.R. Hayes, A. von Lehmen, E. Kapon and Y.S. Kwon, *Appl. Phys. Letters* 56 (1990) 1198.
- [57] J.P. van der Ziel, D.G. Deppe, N. Chand, G.J. Zyzdik and S.N.G. Chu, to be published.
- [58] A. Kastalsky and S. Luryi, *IEEE Electron Device Letters* EDL-4 (1983) 334.
- [59] P.M. Mensz, S. Luryi, A.Y. Cho, D.L. Sivco and F. Ren, *Appl. Phys. Letters* 56 (1990) 2563.
- [60] P.A. Barnes and A.Y. Cho, *Appl. Phys. Letters* 33 (1978) 651.
- [61] S. Luryi, P.M. Mensz, M.R. Pinto, P.A. Garbinski, A.Y. Cho and D.L. Sivco, *Appl. Phys. Letters* 57 (1990) 1787; also, P.M. Mensz, S. Luryi, A.Y. Cho and D. Sivco, 5th Intern. Conf. on MBE, La Jolla, CA, August 1990.

$4 \times 10^5 \text{ cm}^2 \text{ V}^{-1} \text{ s}^{-1}$ peak electron mobilities in GaAs grown by solid source MBE with As_2

C.R. Stanley, M.C. Holland, A.H. Kean

Department of Electronics and Electrical Engineering, University of Glasgow, Glasgow G12 8QQ, UK

J.M. Chamberlain, R.T. Grimes and M.B. Stanaway

Department of Physics, University of Nottingham, Nottingham NG7 2RD, UK

A detailed study into the molecular beam epitaxy of high purity n-GaAs with arsenic dimers has been undertaken, culminating in the growth of a layer with a peak mobility of $\approx 4.0 \times 10^5 \text{ cm}^2 \text{ V}^{-1} \text{ s}^{-1}$ at 28–40 K, the highest ever recorded in bulk GaAs.

1. Introduction

Many advantages are gained from the use of arsenic dimers (As_2) rather than tetramers (As_4) in the growth of (Al,Ga)As by solid source molecular beam epitaxy (MBE). These include a reduction in the concentration of deep electron traps in GaAs [1], the elimination of the temperature window between ≈ 630 and 690°C within which the morphology of (Al,Ga)As is poor [2], and a reduction in the concentration of carbon incorporated into GaAs from the solid arsenic [3,4]. Generally, however, the total impurity densities in As_2 -grown GaAs have been higher than in layers grown under comparable MBE conditions with arsenic fluxes generated either conventionally from high purity arsenic lumps (As_4) [5] or from arsine (AsH_3) [6], where free electron concentrations, $n = N_d - N_a$ around $3 \times 10^{13} \text{ cm}^{-3}$ and peak electron mobilities, μ_{peak} up to $\approx 3 \times 10^5 \text{ cm}^2 \text{ V}^{-1} \text{ s}^{-1}$ have been recorded. This paper will address the use of a new As_2 -source, similar to that described by Chow et al. [7], in the growth by solid source MBE of thick unintentionally doped (hereafter referred to as “undoped”) n-GaAs layers with exceptional peak electron mobilities [8]. The investigations have culminated in the growth of the highest mobility bulk GaAs ever produced.

2. Experimental procedures

2.1. MBE system

The layers were grown in a Varian Modular Gen II MBE system equipped with standard sources for Ga, Al, As_4 , Si and Be, together with Varian “cracker” sources [7] for As_2 and P_2 . The procedures described by Larkins et al. [9] and recommended by Varian [10] were broadly followed to condition the sources and the growth environment of the MBE system. The gallium source was loaded with 8N’s gallium from Alcan Electronic Materials A.G. Both the conventional As_4 source and the sublimator section of the As_4 cracker were filled with 7N’s purity MBE-grade arsenic lumps from the same batch supplied by Preussag GmbH.

2.2. Wafer preparation

Undoped (semi-insulating) (100) GaAs wafers, 2 inch in diameter, were rinsed in H_2SO_4 and de-ionized water only, and heated in air at 250°C for 5 min to form a surface oxide [11]. The wafers were mounted without indium bonding into Mo holders, given an extensive degas at 500°C and a final degas at 620°C for 20 min in the inter-

mediate chamber of the MBE system, and then cooled to 400°C. This caused the desorption of the oxide layer (without an As overpressure) into the intermediate chamber and the observation by reflection high energy electron diffraction (RHEED) of well-defined reconstruction immediately the wafer surface was exposed to an arsenic flux in the growth chamber.

2.3. Growth parameters

The arsenic sublimator temperature was 290–300°C for As₂:Ga flux ratios, F_r of ≈ 2.5 –4.5:1 at a 1.0 $\mu\text{m/h}$ growth rate, while the cracker operated at $T_{cr} = 600$ –700°C. The As₄ → As₂ cracking efficiency was estimated to be $\approx 70\%$ at 600°C, rising to $\geq 95\%$ at 700°C [12]. Fluxes were determined from both RHEED intensity oscillations and beam equivalent pressures. Substrate temperatures T_s between 520 and 620°C were used, which were checked with an optical pyrometer. The minimum F_r for (2 × 4)-(100) As-stable growth at 1.0 $\mu\text{m/h}$ with $T_s \approx 520$ –610°C was 2.5:1. For $T_s \approx 520^\circ\text{C}$, the wafer was only 5°C above the temperature, which caused a tran-

sition from the c(4 × 4) to the (2 × 4) reconstruction. Details of the growth conditions are presented in table 1. All layers, with the exception of #B27, were grown at a rate of 1 $\mu\text{m/h}$ under (2 × 4)-(100) As-stable conditions. However, for #B50, a central region ≈ 25 mm diameter grew with a (2 × 4) pattern and had smooth morphology, while the outer ring of the wafer was (3 × 1) due to a slight temperature increase, and resulted in a rough surface.

2.4. Analytical techniques

A comprehensive evaluation of the electrical and optical properties of the layers has been undertaken using 4–300 K Hall measurements and 4.2 K far infrared photoconduction spectroscopy (FIRPC) [13], and by 5 K photoluminescence spectroscopy (PL). The discussion in section 3 is restricted to FIRPC results obtained with 302 μm radiation which excites the $1s \rightarrow 2p_{-1}$ transitions of the hydrogenic donor impurities; a full account of the FIRPC experiments has been presented elsewhere [14]. It is sufficient to note here that although FIRPC spectroscopy in isolation yields

Table 1

Summary of the growth parameters and Hall data for unintentionally doped n-GaAs grown with As₂; one sample of As₄-grown Si-GaAs, #B37, is also included for comparison; #B47 was grown undoped with As₄

Sample No.	Growth parameters				Hall and FIRPC data					
	Flux ratio	Substrate temperature (°C)	d (μm)	T_{cr} (°C)	n_{77} (10^{13} cm^{-3})	μ_{77} ($\text{cm}^2 \text{ V}^{-1} \text{ s}^{-1}$)	μ_{peak} ($\text{cm}^2 \text{ V}^{-1} \text{ s}^{-1}$)	N_a/N_d (ref. [18])	N_{Si} (10^{13} cm^{-3})	N_S (10^{13} cm^{-3})
B27	2.5:1	583	15	700	72	93000	106000 (70 K)	0.28	29.0	51.0
B38	4.5:1	583	10	700	16	161000	219000 (50 K)	0.31	4.0	15.0
B43	3.1:1	≈ 520	10	700	13	182000	278000 (40 K)	0.2	1.5	13.5
B45	3.2:1	580	15	700	9.7	184000	275000 (50 K)	0.3	4.0	5.0
B48	3.2:1	612	15	700	7.6	203000	327000 (42 K)	0.2	6.3	0.7
B49	3.2:1	618	15	700	9.5	191000	282000 (45 K)	0.24	—	—
B50 ^{a)}	2.5:1	580	15	700	9.8	211000	332000 (40 K)	< 0.1	3.2	3.8
B50 ^{b)}	2.5:1	≈ 580	15	700	4.6	174000	—	0.62	8.0	4.0
B52	3.2:1	610	15	700	10.3	191000	283000 (45 K)	0.2	6.7	3.3
B54	3.5:1	583	15	650	2.8	220000	402000 (28–40 K)	0.2	1.1	2.9
B55	4.1:1	583	20	600	SI	—	—	—	—	—
B56	4.1:1	580	30	635	SI	—	—	—	0.55	3.0
B64	2.9:1	585	15	700	6.9	195000	326000 (40 K)	0.28	5.0	3.0
B37	7.6:1	585	15	(As ₄)	2.4	160600	—	≈ 0.8	—	—
B47	5.5:1	581	15	(As ₄)	6.6	4055	(p-type)	—	—	—

^{a)} Centre.

^{b)} Edge.

only the relative donor densities in a particular sample, the concentration of individual shallow donors can be estimated from the FIRPC spectra used in conjunction with Hall measurements, provided the deep electron trap concentration is negligible. The 77 K Hall data, peak electron mobilities, and estimated donor impurity concentrations (N_{Si} and N_S) are summarised in table 1. An iterative procedure was used to produce consistency between the total depletion layer thicknesses and the free electron density, based on numerical values derived from ref. [15].

3. Results and discussion

All layers grown with As_2 were n-type, in contrast to As_4 growth from "conventional" Knudsen-type sources in two different Varian MBE systems, where un-GaAs produced from Preussag arsenic was always p-type. A test layer, #B47, was grown with $T_{cr} \approx 100^\circ C$ so that the flux from the cracker source was composed entirely of As_4 molecules; this layer was also p-type (table 1). The sequence of FIRPC spectra reproduced in fig. 1 shows that Si and S are the principal donors in

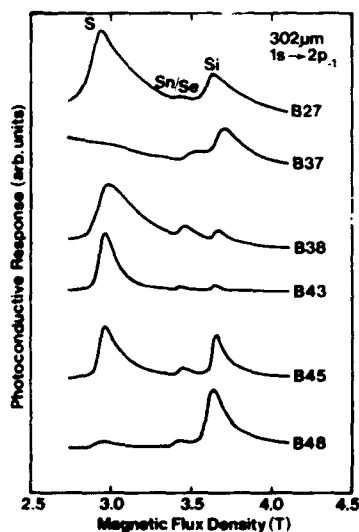


Fig. 1. Far infrared photoconductive response versus magnetic flux density due to $1s \rightarrow 2p_{1/2}$ donor transitions in As_2 -grown MBE n-GaAs under illumination with $302 \mu m$ radiation (samples #B27–#B48).

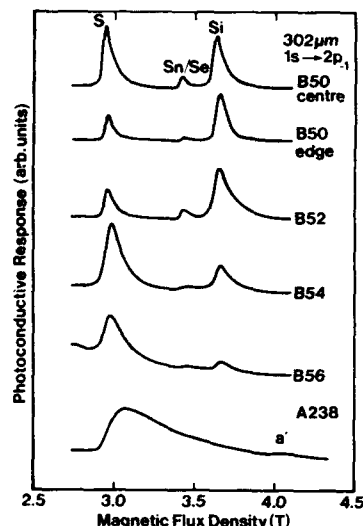


Fig. 2. Far infrared photoconductive response versus magnetic flux density due to $1s \rightarrow 2p_{1/2}$ donor transitions in As_2 -grown MBE n-GaAs under illumination with $302 \mu m$ radiation (samples #B50–#B56, and #A238).

As_2 -grown material, with traces of Se/Sn [13,14]. #B37 was grown with "conventional" As_4 and intentionally doped with Si for n-type behaviour. There is a noticeable absence of S, possibly because when As_2 is used, large S molecules (S_6 , S_8), released from the solid arsenic charge, are themselves cracked into lighter species (S_1 , S_2) in the cracker furnace, and then incorporated into the GaAs more effectively due to a higher sticking coefficient [16]. A second series of FIRPC spectra is shown in fig. 2. For #B50, N_S is found to be approximately constant between the centre and edge of the wafer, as expected for $T_c \approx 580^\circ C$ where desorption of S as Ga_2S is insignificant [16], but N_{Si} is unexpectedly higher near the edge where the increased As-vacancy concentration under (3×1) growth might influence a proportion of the incident Si flux to incorporate as acceptors rather than donors. The evaluation of N_{Si} and N_S for all As_2 -grown samples within #B27–#B52 suggests is a progressive clean-up of the As_2 source, after which N_{Si} and N_S equilibrate at approximately equal concentrations $\approx (3-6) \times 10^{13} cm^{-3}$ for growth at $T_s \approx 580^\circ C$ and $F_r \approx 3.2:1$. An exception is #B48 which has a lower

$N_S \approx 7 \times 10^{12} \text{ cm}^{-3}$ due to a higher value of T_s , driving the surface close to the (3×1) reconstruction where S loss becomes measurable. #A238 is included in fig. 2 to show that S can be the dominant impurity in undoped GaAs grown with As₄ (from Johnson-Matthey arsenic), resulting in n-type conductivity. Bearing in mind the previous comments regarding the enhanced sticking coefficients of smaller S molecules, the importance of selecting the "correct" arsenic for use in a cracker source becomes apparent. Arsenic with a high residual S content which produces n-type As₄-grown layers will yield even high background doping levels when used as As₂.

The approximately constant donor concentration is reflected in consistent values of n_{77} , μ_{77} and μ_{peak} (table 1), with most of the 77 K Hall data for samples prepared under similar conditions grouped around $n_{77} \approx 1 \times 10^{14} \text{ cm}^{-3}$ and $\mu_{77} \approx 2 \times 10^5 \text{ cm}^2 \text{ V}^{-1} \text{ s}^{-1}$. Plots of μ versus T from ≈ 4 to 300 K for samples #B27 (the first As₂-grown sample), #B38, #B45 and #B48, all grown with $T_{\text{cr}} = 700^\circ \text{C}$, are illustrated in fig. 3. The decreasing influence of ionized impurity scattering in #B27 through to #B48 is apparent

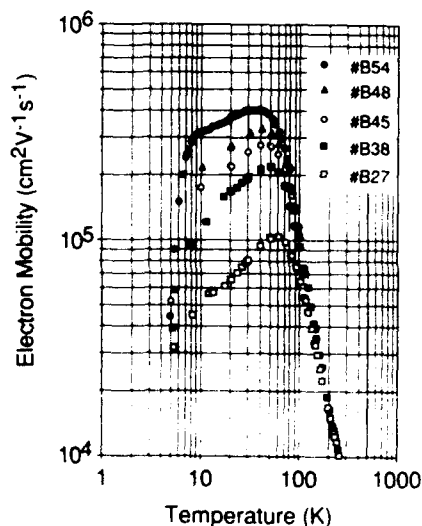


Fig. 3. Plots of mobility versus temperature for samples #B27, #B38, #B45, #B48 ($T_{\text{cr}} = 700^\circ \text{C}$) and #B54 ($T_{\text{cr}} = 650^\circ \text{C}$), showing progressive increase in μ_{peak} with decreasing total ionized impurity concentration (see table 1).

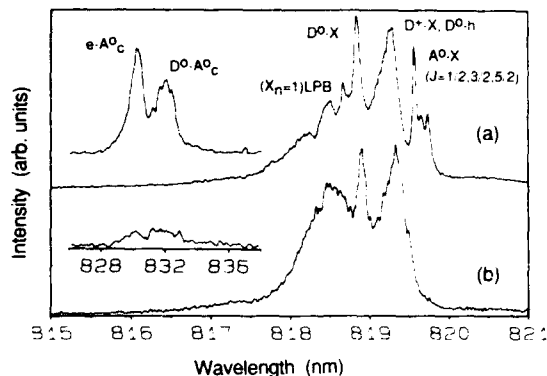


Fig. 4. 5 K photoluminescence spectra, reproduced on identical intensity scales, for 15 μm thick undoped GaAs layers grown by MBE with (a) As₄ (p-type) and (b) As₂ (n-type). The excitation conditions were the same for both spectra: wavelength 488 nm; intensity 50 mW cm^{-2} ; resolution $< 0.02 \text{ nm}$.

as μ_{peak} increases from 1.06×10^5 to $3.27 \times 10^5 \text{ cm}^2 \text{ V}^{-1} \text{ s}^{-1}$. The compensation ratios derived from theoretical data [17] are lower than in As₄-grown layers with comparable free electron densities. The main reason for this is revealed by the 5 K PL spectra (fig. 4), which show the virtual disappearance of the acceptor(carbon)-related transitions for growth with As₂ under (2×4) As-stable conditions.

The evidence from the FIRPC spectra (figs. 1 and 2) discussed below suggests that the Si originates from a component in, or close to the cracker furnace of the As₂ source, while the S is a residual contaminant in the solid As charge. Three layers were grown to assess the effect of varying T_{cr} between 600 and 700°C . #B54, #B55 and #B56. Compared with #B48, the ratio of the S and Si peaks in the FIRPC spectrum of #B54 ($T_{\text{cr}} = 650^\circ \text{C}$) (fig. 2) has changed such that $N_S > N_{\text{Si}}$ ($\gg N_{\text{Se}}$). The signatures of all three donors are better resolved and the linewidths for sample #B54 are almost half those for #B48, indicating an overall lowering in N_d . Further support comes from the Hall data where n_{77} for #B54 has been reduced to $2.8 \times 10^{13} \text{ cm}^{-3}$, while μ_{77} has increased to $2.2 \times 10^5 \text{ cm}^2 \text{ V}^{-1} \text{ s}^{-1}$, corresponding to compensation ratio of ≈ 0.2 [17]. N_d and N_a are, therefore, $\approx 4 \times 10^{13}$ and $\approx 1 \times 10^{13} \text{ cm}^{-3}$, respectively. The μ versus T plot for #B54 (re-

stricted to $\approx 4\text{--}100\text{ K}$ for clarity) is shown in fig. 3. The mobility peaks at the very high value of $\approx 4.0 \times 10^5\text{ cm}^2\text{ V}^{-1}\text{ s}^{-1}$ over a broad plateau of temperatures from ≈ 28 to 40 K , the highest mobility ever recorded in bulk GaAs irrespective of the growth technique employed. Values of μ_{peak} in the range $(3.8\text{--}4.1) \times 10^5\text{ cm}^2\text{ V}^{-1}\text{ s}^{-1}$ have been measured for several Van der Pauw and Hall-bar geometry samples prepared from wafer #B54, #B55 ($T_{\text{cr}} = 600^\circ\text{C}$) and #B56 ($T_{\text{cr}} = 635^\circ\text{C}$) have also been analysed. The $1s \rightarrow 2p_{-1}$ transitions for #B56 (fig. 2) show a further reduction by a factor of two in the Si peak relative to S, in sympathy with the decrease of T_{cr} to 635°C . #B55 could not be measured because of contacting problems, and no Hall data could be recorded for either #B55 or #B56 which were believed to be fully depleted. The estimated values of N_{Si} show a fall from $\approx 6 \times 10^{13}\text{ cm}^{-3}$ (typical for $T_{\text{cr}} = 700^\circ\text{C}$) to $\approx 1.1 \times 10^{13}\text{ cm}^{-3}$ in #B54 ($T_{\text{cr}} = 650^\circ\text{C}$), and $\approx 5.5 \times 10^{12}\text{ cm}^{-3}$ in #B56 ($T_{\text{cr}} = 635^\circ\text{C}$). If the cracker section of the As₂ source behaves as a Knudsen-type source, then the Si flux will vary as $\sim p_{\text{Si}}(T)/T^{1/2}$ where $p_{\text{Si}}(T)$ (in Torr) is the equilibrium vapour pressure of Si over Si at temperature T (in K), and from ref. [18], $\log_{10} p_{\text{Si}}(T) = -20,900/T - 0.565 \log_{10} T + 10.78$. N_{Si} is predicted to fall by 13.8 as T_{cr} is lowered from 700 to 650°C , and a further $\times 2.3$ as T_{cr} is decreased from 650 to 635°C . Both reductions are comparable to the estimates of $\approx \times 6$ and $\approx \times 2$ based on the FIRPC and Hall data, substantiating the view that the Si flux does originate from a component in, or close to, the hot cracker furnace.

4. Conclusions

n-GaAs layers with peak electron mobilities increasing progressively from 1.06×10^5 to $\approx 4 \times 10^5\text{ cm}^2\text{ V}^{-1}\text{ s}^{-1}$ at $28\text{--}40\text{ K}$, the highest value ever achieved in bulk n-GaAs, have been grown by solid source MBE using As₂. Total impurity concentrations of $\leq 5 \times 10^{13}\text{ cm}^{-3}$ have been realised, partly as a consequence of a marked reduction in the concentration of incorporated carbon for As₂ growth compared to growth under similar conditions with As₄ generated from the same batch

of arsenic. 4.2 K FIRPC spectroscopy and $4\text{--}300\text{ K}$ Hall measurements have provided evidence that Si from the As cracker contributes to the unintended n-type conductivity of the GaAs layers, although as T_{cr} is lowered below $\approx 650^\circ\text{C}$, S incorporated from the solid As charge becomes the major impurity. There may be scope for growing n-GaAs with even higher values of μ_{peak} using the 8N's Ga and 7N's As charges currently available. This would involve modifying the conditions used to grow #B48, again setting T_{cr} to $610\text{--}620^\circ\text{C}$ to initiate partial desorption of the incident S flux, but at the same time operating the cracker at $T_{\text{cr}} \leq 650^\circ\text{C}$ to minimize the Si contamination. A total impurity concentration of $\leq 1 \times 10^{13}\text{ cm}^{-3}$ is a realistic target with the present MBE equipment. However, Hall measurements on samples with low free carrier concentrations are hampered by the combined effects of the interface depletion layers [15], requiring physical thicknesses as large as $\approx 20\text{--}30\text{ }\mu\text{m}$ to avoid total depletion, depending on the precise value of n . One solution would be to cap the undoped GaAs layer with a thin layer intentionally doped with Si to $\approx 1 \times 10^{17}\text{ cm}^{-3}$, to partially absorb the depletion caused by surface states. The cap layer could then be fully depleted by applying reverse bias to a Schottky contact covering the sample between the ohmic contacts. A gated-Hall specimen of this nature would facilitate measurements on an underlying high mobility layer of more reasonable dimensions.

Acknowledgements

The authors wish to acknowledge the technical support of J. Cochrane, R. Hutchins, N. Johnson and W. Reid in the MBE laboratory. The research is funded by the UK Science and Engineering Research Council through grants GR/E/18186 and GR/E/50117 (University of Glasgow), and GR/E/17431 (University of Nottingham).

References

- [1] J.H. Neave, B. Blood and B.A. Joyce, Appl. Phys. Letters 36 (1980) 311.

- [2] L.P. Erickson, T.J. Mattord, P.W. Palmberg, R. Fischer and H. Morkoç, *Electron Letters* 19 (1983) 632.
- [3] J.C. Garcia, A.C. Beye, J.P. Contour, G. Neu, J. Massies and A. Barski, *Appl. Phys. Letters* 52 (1988) 1596.
- [4] T.M. Kerr, C.E.C. Wood, S.M. Newstead and J.D. Wilcox, *J. Appl. Phys.* 65 (1989) 2673.
- [5] N. Chand, R.C. Miller, A.M. Sergeant, S.K. Spitz and D.V. Lang, *Appl. Phys. Letters* 52 (1988) 1721.
- [6] J.E. Cunningham, T.H. Chiu, G. Timp, E. Agyekum and W.T. Tsang, *Appl. Phys. Letters* 53 (1988) 1285.
- [7] R. Chow, R. Fernandez, D. Atchley, K. Chan and D. Bliss, *J. Vacuum Sci. Technol.* B8 (1990) 163.
- [8] C.R. Stanley, M.C. Holland and A.H. Kean, *Appl. Phys. Letters* 57 (1990) 1992.
- [9] E.C. Larkins, E.S. Hellman, D.G. Schlom, J.S. Harris, Jr., M.H. Kim and G.E. Stillman, *Appl. Phys. Letters* 49 (1986) 391.
- [10] R. Chow and R. Fernandez, *Varian MBE Process Training Guide* (Varian MBE Operations, Santa Clara, CA, 1987).
- [11] H. Fronius, A. Fischer and K. Ploog, *Japan. J. Appl. Phys.* 25 (1986) L137.
- [12] J.C. Garcia, A. Barski, J.P. Contour and J. Massies, *Appl. Phys. Letters* 51 (1987) 593.
- [13] C.J. Armistead, P. Knowles, S.P. Najda and R.A. Stradling, *J. Phys. C (Solid State Phys.)* 17 (1984) 6415.
- [14] R.T. Grimes, M.B. Stanaway, J. Singleton, C.J.G.M. Langerak, J.M. Chamberlain, C.R. Stanley and T.S. Cheng, in: *Proc. 17th Intern. Symp. on GaAs and Related Compounds*, Jersey, 1990, *Inst. Phys. Conf. Ser.* 112, Ed. K.E. Singer (*Inst. Phys., London-Bristol*, 1991) ch. 4, pp. 213-218.
- [15] A. Chandra, C.E.C. Wood, D.W. Woodard and L.F. Eastman, *Solid State Electron.* 22 (1979) 645.
- [16] D.A. Andrews, R. Heckingbottom and G.J. Davies, *J. Appl. Phys.* 54 (1983) 4421.
- [17] M. Benzaquen, K. Mazuruk, D. Walsh, A.J. SpringThorpe and C. Miner, *J. Electron. Mater.* 16 (1987) 111.
- [18] O. Kubaschewski and C.B. Alcock, *Metallurgical Thermochemistry* (Pergamon, Oxford, 1979).

Variation of background impurities in $\text{Al}_x\text{Ga}_{1-x}\text{As}$ ($0.3 \leq x \leq 0.4$) with growth temperature: implications for device leakage current and surface/heterointerface roughness

Naresh Chand, T.D. Harris, S.N.G. Chu, E.E. Becker, A.M. Sergent, M. Schnoes and D.V. Lang
AT&T Bell Laboratories, Murray Hill, New Jersey 07974, USA

In a wide range of growth conditions, the residual impurity concentration is found to be higher in $\text{Al}_x\text{Ga}_{1-x}\text{As}$ ($0.3 \leq x \leq 0.4$) than in GaAs. Undoped AlGaAs is p-type for substrate growth temperature $T_s \leq 680^\circ\text{C}$ and n-type for $T_s \sim 700^\circ\text{C}$. In n-type $\text{Al}_{0.3}\text{Ga}_{0.7}\text{As}$, typical electron density and mobility were $5 \times 10^{14} \text{ cm}^{-3}$ and $2340 \text{ cm}^2 \text{ V}^{-1} \text{ s}^{-1}$ at 300 K and $5 \times 10^{12} \text{ cm}^{-3}$ and $8725 \text{ cm}^2 \text{ V}^{-1} \text{ s}^{-1}$ at 77 K, which we believe are the best values ever reported for this alloy. In p-type samples, hole density was $\leq 5 \times 10^{14} \text{ cm}^{-3}$ at 300 K for $T_s = 580^\circ\text{C}$, and $\geq 4 \times 10^{15} \text{ cm}^{-3}$ for $600^\circ\text{C} < T_s \leq 680^\circ\text{C}$. Photoluminescence (PL) intensity of near band to band emission at 1.5 K decreased with increasing T_s from 580°C but increased dramatically with sharper peaks for $T_s > 680^\circ\text{C}$. Leakage current in $0.5 \mu\text{m}$ n⁺-GaAs/ $0.2 \mu\text{m}$ undoped- $\text{Al}_{0.3}\text{Ga}_{0.7}\text{As}$ /n⁺-GaAs SIS heterostructure diodes increased with increasing T_s of AlGaAs from 580°C to 620°C but decreased several orders of magnitude for $T_s = 700^\circ\text{C}$. Thus, Hall, PL and leakage current measurements suggest degradation of AlGaAs properties with increasing T_s between 580 and 680°C but dramatic improvement for $T_s > 680^\circ\text{C}$. Misorienting the (100) GaAs substrates by 2° – 3° towards $\langle 111 \rangle$ A also caused marked improvements in material quality in non-optimum growth conditions. For up to $5 \mu\text{m}$ thick AlGaAs, there is no “forbidden” range of growth temperature for misoriented substrates, but $10 \mu\text{m}$ thick layers were equally hazy on both type of substrates for $630 < T_s < 680^\circ\text{C}$. For best performance, devices employing undoped AlGaAs should be grown at $\sim 580^\circ\text{C}$ or if structure permits at $\sim 700^\circ\text{C}$.

1. Introduction

Epitaxial growth of $\text{Al}_x\text{Ga}_{1-x}\text{As}$ with very low levels of background impurities is imperative for the success of AlGaAs/GaAs technology for switching, microwave and photonic device applications, especially in devices where undoped AlGaAs is used. Growth of smooth and high purity AlGaAs by molecular beam epitaxy (MBE) is fundamentally more difficult than that of GaAs due to complex growth kinetics and high reactivity of Al with oxygen and other impurities which are normally present in residual gases in an MBE system. While there have been numerous reports on the growth parameter dependent properties of MBE-AlGaAs [5–15], very few data are available [16] on the level of background impurities in undoped-AlGaAs and their variation with growth temperature. In addition, there exists a “forbidden range” [7–11] of substrate temperature, T_s , between 630 and 690°C where the surface mor-

phology of $\text{Al}_x\text{Ga}_{1-x}\text{As}$ degrades and becomes hazy. Furthermore, properties of AlGaAs also affect the AlGaAs/GaAs interface quality and the properties of overgrown GaAs [1–4,14]. The inverted interface (GaAs on AlGaAs) is usually rough in comparison with the normal interface (AlGaAs on GaAs) [14].

Despite extensive efforts, variation of properties of AlGaAs with growth temperature, the presence of “forbidden” growth temperature range, and the origin of heterointerface roughness are not well understood. It is not yet clear why growth of different devices require growth of AlGaAs at different temperatures [6]. We feel that answers to these questions lie with the background impurities in AlGaAs which vary with growth temperature and has not yet been well studied. Using our clean MBE system and the purer sources currently available, we have studied the background impurities and their effect on optical, electrical and surface morphological properties of undoped thick (> 10

μm) $\text{Al}_x\text{Ga}_{1-x}\text{As}$ ($x > 0.3$) layers as a function of growth temperature between 580 and 700°C. Effects of substrate misorientation were also studied. Details of the study are reported here.

2. Experimental

The $\text{Al}_x\text{Ga}_{1-x}\text{As}/\text{GaAs}$ structures were grown using As_4 flux in a Riber 32P MBE system discussed elsewhere [17]. For studying background impurities, 10 μm or thicker undoped layers of $\text{Al}_x\text{Ga}_{1-x}\text{As}$ ($0.3 \leq x < 0.4$) were grown at T_s varying between 580 and 700°C on exact (100) and 2° to 3° off (100) towards $\langle 111 \rangle$ A undoped semi-insulating GaAs substrates. We used 8N purity Ga, 7N5 purity As, and 6N purity Al rods. Due to the high purity As source used, we do not notice any marked effect of As_4/Ga flux ratio on the properties of AlGaAs and GaAs. Normally, As_4/Ga flux ratio was kept at the minimum necessary to achieve As-stabilized growth conditions. The growth rate of GaAs was kept fixed at 1.0 $\mu\text{m}/\text{h}$ in all the structures and AlAs growth rate ($\leq 0.5 \mu\text{m}/\text{h}$) was adjusted to obtain the desired value of x . For comparison, undoped and lightly Si-doped GaAs layers were also grown. The substrate temperature was measured by a 2000 series Ircon pyrometer within $\pm 5^\circ\text{C}$ accuracy. To study the surface roughness and the effect of substrate misorientation in obtaining smoother growth in the forbidden temperature zone, two monolayers thick GaAs marker layers were periodically incorporated in AlGaAs layers grown simultaneously on both types of substrates. The grown layers were characterized by Hall measurements at a magnetic field of 0.5 G and by 1.5 K photoluminescence (PL) using 514.5 nm line of an argon ion laser with 0.1 W/cm^2 excitation density.

To study the effect of growth temperature related background impurities on the leakage current in devices employing undoped AlGaAs layers, three semiconductor-insulator-semiconductor (SIS) (0.5 μm $n^+\text{-GaAs}/0.2 \mu\text{m}$ undoped- $\text{Al}_{0.3}\text{Ga}_{0.7}\text{As}/n^+\text{-GaAs}$) heterostructures were grown on $n^+\text{-GaAs}$ substrates with different growth temperatures for $\text{Al}_{0.3}\text{Ga}_{0.7}\text{As}$, which were 580, 620 and 700°C. T_s for GaAs was 580°C. On

each side of AlGaAs, 25 Å of GaAs was kept undoped to minimize diffusion of Si into undoped AlGaAs. Ga and Al cell temperatures were kept the same in all three structures. Consequently, the structure in which $\text{Al}_x\text{Ga}_{1-x}\text{As}$ was grown at 700°C should have $x \sim 0.33\text{--}0.35$ due to reduced sticking coefficient of Ga at this temperature. After growth, $n^+\text{-GaAs}/u\text{-AlGaAs}/n^+\text{-GaAs}$ mesa diodes of diameters 125, 250, and 500 μm were made by chemical etching of the top GaAs and AlGaAs layers in $3\text{NH}_4\text{OH}:1\text{H}_2\text{O}_2:15\text{H}_2\text{O}$ using Au-Sn-Au ohmic metal contacts as the mask. The resulting devices were characterized for leakage current at various temperatures between 77 and 300 K.

3. Results

3.1. Surface morphology

$\text{Al}_x\text{Ga}_{1-x}\text{As}$, irrespective of x , grown at $580 \leq T_s < 620^\circ\text{C}$ had featureless morphology. Between 630 and 680°C, all the $\text{Al}_x\text{Ga}_{1-x}\text{As}$ ($0.3 \leq x \leq 0.7$) layers ($> 0.5 \mu\text{m}$ thick) studied on (100) substrates had hazy surfaces. AlAs layers were smooth irrespective of the growth temperature. For 700°C growth, surfaces were smooth if $x \leq 0.5$ and hazy if x was between 0.6 and 0.7. If grown on 3° off (100) towards $\langle 111 \rangle$ A substrates, up to 5 μm thick $\text{Al}_x\text{Ga}_{1-x}\text{As}$ layers had smooth surfaces irrespective of the values of T_s ($\leq 700^\circ\text{C}$) and x , but after $\sim 5 \mu\text{m}$ of growth surfaces developed haziness during growth at 660°C, and 10 μm thick layers were as hazy as those on exact (100) substrates.

To illustrate the effect that substrate misorientation has in the forbidden temperature range on surface smoothness of AlGaAs, we show in figs. 1a and 1b the TEM cross-sectional images of 1.7 μm thick $\text{Al}_{0.35}\text{Ga}_{0.65}\text{As}$ grown simultaneously on both types of substrates at 660°C with GaAs marker layers at regular intervals. In the inset, Nomarski phase contrast images of the respective surfaces are also shown. The GaAs marker layers clearly illustrate that the AlGaAs surface is flat throughout on the misoriented substrate (fig. 1a), but becomes wavy after 0.5 μm of growth on the

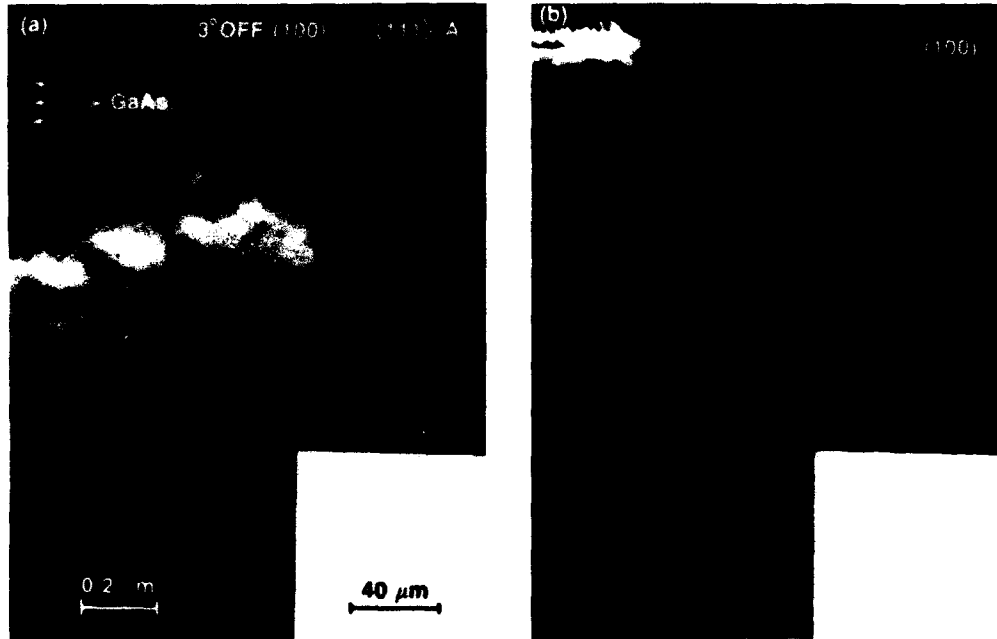


Fig. 1. [200] dark-field TEM images of $\text{Al}_{0.35}\text{Ga}_{0.65}\text{As}$ grown simultaneously at 660°C on (a) 3° off (100) towards $\langle 111 \rangle\text{A}$ substrate and (b) (100) substrate. GaAs marker lines show smooth growth on misoriented substrate and rough growth on exact (100) substrate. In inset, Nomarski phase contrast images of resulting surface morphology are also shown.

Table 1
Growth temperature dependent properties of undoped $\text{Al}_x\text{Ga}_{1-x}\text{As}$

Sample No.	Growth temperature ($^\circ\text{C}$)	AlAs content, x	Thickness (μm)	Background impurities (300 K)			Surface morphology
				Type	Density (cm^{-3})	Mobility ($\text{cm}^2 \text{V}^{-1} \text{s}^{-1}$)	
N444	700	0.33	11.4	n	5×10^{14} (5×10^{12} at 77 K)	2340 (8725 at 77 K)	Smooth
N462	680	0.34	11.0	p	4×10^{15}	88	Hazy
N464	660	0.35	15.0	p	4×10^{15} (1×10^{15}) ^{a1}	92 (150) ^{a1}	Hazy
N461	640	0.33	10.0	p	4×10^{15}	90	Hazy
N469	630	0.32	12.0	p	4×10^{15}	50	Hazy
N454	620	0.37	10.0	p	4×10^{16}	120	Smooth
N452	580	0.35	10.0	p	—	—	Smooth
N463	580	0.30	20.0	p	5×10^{14}	440	Smooth
N459 ^{b1}	580	0	12.0	p	$< 1 \times 10^{14}$	725	Smooth
N439 ^{b1}	580	0	13.0	n (Si-doped)	1×10^{15}	6715 (64000 at 77 K)	Smooth

^{a1} On 3° off (100) \rightarrow $\langle 111 \rangle\text{A}$ substrate.

^{b1} Undoped and Si-doped GaAs layers for comparison.

(100) substrate resulting in a hazy surface (fig. 1b). The waviness or surface roughness increases with thickness.

3.2. Hall measurements

Table 1 summarizes the growth temperature dependent properties of undoped $\text{Al}_x\text{Ga}_{1-x}\text{As}$ layers. Only the typical results are shown; the total number of wafers grown were more than those listed. The AlGaAs layers grown at 700°C were reproducibly n-type, and the layers grown between 500 and 680°C were always p-type. In n-type samples (N444), electron density and mobility measured in the dark were $5 \times 10^{14} \text{ cm}^{-3}$ and $2340 \text{ cm}^2 \text{ V}^{-1} \text{ s}^{-1}$ at 300 K and $5 \times 10^{12} \text{ cm}^{-3}$ and $8725 \text{ cm}^2 \text{ V}^{-1} \text{ s}^{-1}$ at 77 K . To the best of our knowledge, these are the best values ever reported. The sample was conductive up to 30 K and exhibited no persistent photoconductivity. Interestingly, in p-type samples, $N_A - N_D$ was $\leq 5 \times 10^{14} \text{ cm}^{-3}$ if grown at 580°C and $\geq 4 \times 10^{15} \text{ cm}^{-3}$ if grown between 600 and 680°C irrespective of the surface morphology. Reduced hole mobility for T_s between 630 and 680°C suggests a high level of impurity compensation; thus background impurity or stoichiometric defects density may even be higher than shown. These doping levels are significantly larger than the typical background doping ($N_A - N_D$) of $< 10^{14} \text{ cm}^{-3}$ measured in undoped GaAs grown using the same Ga and As sources. High hole mobility of $725 \text{ cm}^2 \text{ V}^{-1} \text{ s}^{-1}$ at 300 K (N459) in undoped and high electron mobility of $64000 \text{ cm}^2 \text{ V}^{-1} \text{ s}^{-1}$ at 77 K in Si-doped ($n = 1 \times 10^{15} \text{ cm}^{-3}$) GaAs (N439) (table 1) indicate very low level of impurity compensation in GaAs.

The level of background impurities, $N_A - N_D$, was either similar or lower within an order of magnitude, but never higher, in AlGaAs grown on misoriented substrates compared to those grown simultaneously on exact (100) surfaces. The difference was larger in samples grown in less than the optimum conditions.

3.3. Photoluminescence

The 1.5 K PL spectra of three samples, N444, N452 and N454, grown at 700 , 580 and 620°C ,

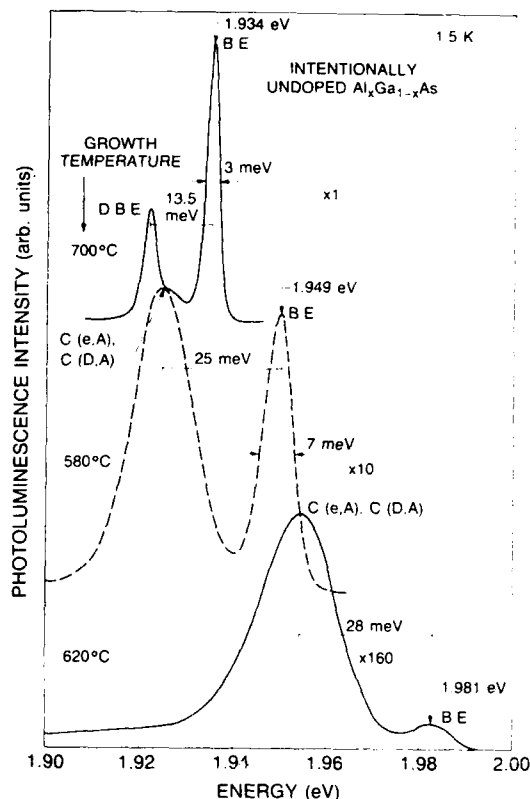


Fig. 2. 1.5 K PL spectra of samples N444, N452 and N454 grown at 700 , 580 and 620°C respectively.

respectively, are shown in fig. 2 from which several interesting observations can be made. Consistent with the earlier reported results [5], N444 ($x = 0.33$) grown at 700°C has the best PL spectra. It has a very sharp and intense shallow impurity bound exciton peak at 1.934 eV with full-width at half-maximum (FWHM) of 3 meV , and a donor or defect bound exciton peak at 1.9205 eV , and it shows little deep acceptor related emission. This agrees with the Hall measurement data which show the sample to be n-type. It is not clear whether the peak at 1.9205 eV is related to a defect or donor. If it is related to the donor, its depth of 13.5 meV agrees well with the earlier results of Chand and coworkers [15]. These authors observed a shallow donor, in addition to the deep donor, with an activation energy of 13 meV in Si-doped $\text{Al}_{0.32}\text{Ga}_{0.68}\text{As}$ by Hall measurements.

The bound exciton peak at 1.949 eV in sample N452 grown at 580°C is an order of magnitude less intense as compared to N444 and has an increased FWHM of 7.0 meV. In addition, in this sample, carbon acceptor related emission is more intense than the BE emission. This indicates the presence of a high level of carbon, consistent with the Hall measurement data which shows the sample to be p-type.

Surprisingly, sample N454 grown at 620°C, which had a smooth surface, has much weaker photoluminescence than samples N444 and N452. The spectrum is dominated by very weak C-related emission. This result is contrary to the earlier published results which indicate an improvement in optical properties of AlGaAs with increasing growth temperature. We expected N454 to be optically brighter than N452 but the reverse is observed. This behavior was reproducibly observed in several other samples grown at 580 and 620°C. The AlGaAs samples in table 1 grown between 630 and 690°C, which had hazy surfaces, had very broad and weak photoluminescence.

3.4. I - V characteristics of SIS structures

The I - V characteristics of three SIS structures discussed in section 2 in which undoped $\text{Al}_{0.3}\text{Ga}_{0.7}\text{As}$ layers were grown at 580, 620 and 700°C are shown in fig. 3 at 3300 and 100 K for voltages applied in both directions. The device

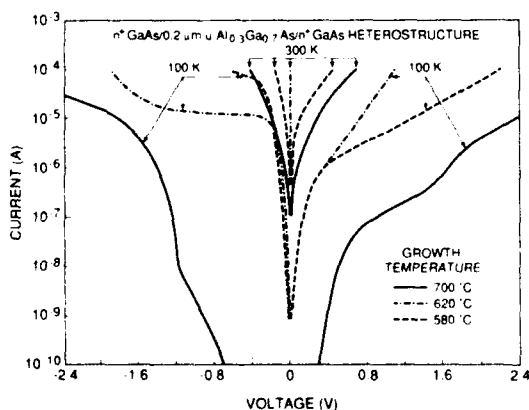


Fig. 3. I - V characteristics of 250 μm diameter three n^+ -GaAs/ u -AlGaAs/ n^+ -GaAs diodes measured at 300 and 100 K. The devices differed in the growth temperature of undoped AlGaAs which was 700, 620 and 580°C.

diameter in all three cases was 250 μm . Voltages are measured with respect to the substrate. The AlGaAs in these devices is expected to behave as an insulating barrier and the current should flow by thermionic emission over the AlGaAs barrier. Thus, the goal here is to examine the current blocking capability of the AlGaAs. These devices have both normal and inverted AlGaAs/GaAs heterointerfaces which dominate the current conduction process for positive and negative voltages, respectively. In most conditions, the leakage currents are smaller for positive voltages indicating the superior quality of the normal AlGaAs/GaAs heterointerfaces as compared to the inverted heterointerfaces.

Consistent with the Hall and PL measurements, the 700°C AlGaAs devices have the best and 620°C AlGaAs devices have the worst I - V characteristics both at 300 and at 100 K. At 300 K, the latter devices are short circuited indicating that the $\text{Al}_{0.3}\text{Ga}_{0.7}\text{As}$ grown at 620°C contains a large density of defects and/or impurities. Leakage current in 700°C AlGaAs devices is one to several orders of magnitude smaller than in the devices grown at the two lower temperatures. The somewhat higher AlAs content in this device, due to growth of AlGaAs at 700°C as discussed earlier, does not explain the observed smaller leakage current. An AlAs content of 0.35 instead of 0.3 can only decrease the leakage current by one order of magnitude at 100 K. Furthermore, the current in 700°C AlGaAs device exhibits strong temperature dependence, whereas in the other two devices the currents exhibit lack of temperature dependence, which is the characteristic of tunneling. This suggests that the current in 620°C AlGaAs devices is largely due to defects or impurity assisted tunneling, and the AlGaAs offers no barrier to the flow of electrons especially at 300 K. In 700°C AlGaAs devices, the current is largely due to thermionic emission over the AlGaAs barrier and thus the AlGaAs is presumed free from impurities and defects. The case of 580°C AlGaAs falls between these two categories at 300 K and for low voltages at 77 K. However, there is not much difference between 580°C and 620°C AlGaAs devices at 77 K for larger voltages when the AlGaAs barrier becomes ineffective. Notice

that if there was any thermal diffusion of Si impurities, it should have been more significant in 700°C AlGaAs devices. Thus, the effect of diffusion of Si on leakage current in all three devices can be discounted.

4. Summary

Hall and PL measurements, and the leakage current in SIS structures suggest degradation of undoped $\text{Al}_x\text{Ga}_{1-x}\text{As}$ ($0.3 \leq x \leq 0.4$) with increasing growth temperature (T_S) between 580 and 680°C, but a dramatic improvement at T_S 700°C. For some growth conditions, there is also a marked improvement in material quality if it is grown on 2°–3° off (100) towards $\langle 111 \rangle$ A substrate. We believe abnormal growth behavior of AlGaAs is largely due to the presence of background impurities incorporation of which vary with substrate growth temperatures.

Acknowledgments

We are grateful to J.P. van der Ziel, M.T. Asom, A.Y. Cho, D. Gershoni, A. Madhukar, H. Morkoc, R.J. Malik, L. Pfeiffer, R. Kopf, and D.L. Sivco for many fruitful discussions on the subject.

References

- [1] P.M. Petroff, R.C. Miller, A.C. Gossard and W. Wiegmann, *Appl. Phys. Letters* 44 (1984) 217.
- [2] R.C. Miller, W.T. Tsang and O. Munteanu, *Appl. Phys. Letters* 41 (1982) 374.
- [3] N. Chand and S.N.G. Chu, *Appl. Phys. Letters* 57 (1990) 1796.
- [4] M.T. Asom, S. N. G. Chu, M. Geva and R. E. Leibenguth, unpublished.
- [5] W.T. Tsang and V. Swaminathan, *Appl. Phys. Letters* 39 (1981) 486.
- [6] E.H.C. Parker, Ed., *The Technology and Physics of Molecular Beam Epitaxy* (Plenum, New York, 1985).
- [7] H. Morkoc, T.J. Drummond, W. Kopp and R. Fischer, *J. Electrochem. Soc.* 129 (1982) 824.
- [8] F. Alexandre, L. Goldstein, G. Leroux, M.C. Joncour, H. Thibierge and E.V.K. Rao, *J. Vacuum Sci. Technol.* B3 (1985) 950.
- [9] F. Alexandre, J.L. Lievin, M.H. Meynadier and C. Delalande, *Surface Sci.* 168 (1986) 454.
- [10] J. Massies, F. Turco, A. Saletes and J.P. Contour, *J. Crystal Growth* 80 (1987) 307.
- [11] D.C. Radulescu, G.W. Wicks, W.J. Schaff, A.R. Calawa and L.F. Eastman, *J. Appl. Phys.* 62 (1987) 954.
- [12] R.K. Tsui, J.A. Curless, G.D. Kramer, M.S. Peffley and G.W. Wicks, *J. Appl. Phys.* 59 (1986) 1508.
- [13] H.Z. Chen, A. Ghaffari, M. Morkoc and A. Yariv, *Appl. Phys. Letters* 51 2094.
- [14] N.M. Cho, D.J. Kim, A. Madhukar, P.G. Newman, D.D. Smith, T. Aucoin and G.J. Lafrate, *Appl. Phys. Letters* 52 (1988) 2037.
- [15] N. Chand, T. Henderson, J. Klem, W.T. Masselink, R. Fischer, Y.-C. Chang and M. Morkoc, *Phys. Rev.* B30 (1984) 4481.
- [16] A. Chandra and L.F. Eastman, *J. Electrochem. Soc.* 127 (1980) 211.
- [17] N. Chand, *J. Crystal Growth* 97 (1989) 415.

Properties and applications of $\text{Al}_x\text{Ga}_{1-x}\text{As}$ ($0 \leq x \leq 1$) grown at low temperatures

T.Y. Chu, A. Dodabalapur *, A. Srinivasan, D.P. Neikirk and B.G. Streetman

Microelectronics Research Center, Department of Electrical and Computer Engineering, The University of Texas at Austin, Austin, Texas 78712-1084, USA

We have used low temperature MBE growth to obtain highly resistive GaAs and AlGaAs layers with potential applications in a variety of devices. Using MIS structures, we have examined the resistivity of AlGaAs for various aluminum mole fractions and growth temperatures. A GaAs resistor structure was grown at 300°C and a resistivity of $5 \times 10^5 \Omega \text{ cm}$ is measured. This agrees well with the resistivity of $3 \times 10^5 \Omega \text{ cm}$ measured using an MIS structure. Furthermore, we have grown a HEMT structure with high mobility ($\mu = 156,000 \text{ cm}^2 \text{ V}^{-1} \text{ s}^{-1}$ at 77 K) and electron sheet density ($n_s = 6.0 \times 10^{11} \text{ cm}^{-2}$ at 77 K) on a highly resistive low-temperature grown (LTG) $\text{Al}_{0.3}\text{Ga}_{0.7}\text{As}/\text{GaAs}$ superlattice buffer. To test the LTG AlGaAs as a possible dielectric for microwave applications, a coplanar waveguide (CPW) was fabricated on a $0.75 \mu\text{m}$ epitaxial $\text{Al}_{0.3}\text{Ga}_{0.7}\text{As}$ layer grown at 270°C . There was virtually no difference in the measured S-parameters for the coplanar waveguide (CPW) fabricated on the $0.75 \mu\text{m}$ epitaxial $\text{Al}_{0.3}\text{Ga}_{0.7}\text{As}$ layer and the CPW made directly on a semi-insulating GaAs wafer.

1. Introduction

There has been considerable interest in the low-temperature growth of GaAs as a buffer layer. Using Ga and As_4 fluxes at 150 to 300°C to grow a resistive GaAs buffer, it has been shown that the output resistance and breakdown voltages improve for MESFETs fabricated on the low temperature GaAs buffer [1]. The GaAs buffer layer is effective since it is crystalline, highly resistive, and has a high breakdown electric field. This low-temperature grown (LTG) GaAs MESFET buffer technology has been used to fabricate GaAs SCFL frequency dividers with a maximum clock rate of 22 GHz [2]. Recently, there has been interest in explaining the material aspects of the LTG GaAs layers as well [3,4].

In addition to continuing the work on the growth of LTG GaAs, we have also begun growing and using LTG AlGaAs as a semi-insulating

layer. The low temperature growth (200 to 300°C) of AlGaAs using molecular beam epitaxy (MBE) results in layers which are more resistive than corresponding GaAs layers [5]. As with LTG GaAs, we find that an in situ arsenic anneal serves to increase the resistivity of the LTG AlGaAs layers.

In this study, we examined the resistivity of AlGaAs grown at low temperatures as a function of growth temperature and aluminum mole fraction. Resistivity serves as a useful monitor of the LTG material as well as determining the amount of vertical isolation such a layer can provide. We have also built a HEMT structure on LTG material and have tested LTG AlGaAs as a possible dielectric for microwave applications. We have used a Varian Gen II MBE system to grow GaAs and AlGaAs layers from 200 to 300°C . All samples were grown using dimeric arsenic under arsenic-rich conditions. The dimeric arsenic is generated by a refractory arsenic cracking source developed in our laboratory and discussed elsewhere [6].

* Current address: AT&T Bell Laboratories, Holmdel, New Jersey 07733, USA.

2. Results and discussion

A standard technique for measuring resistivity of a semiconductor sample involves making four-point probe measurements on Van der Pauw structures. Such measurements of an LTG AlGaAs layer grown on a semi-insulating (SI) substrate are complicated by parallel conduction in the SI substrate. Parallel conduction occurs because the LTG AlGaAs can have a resistivity comparable to or much higher than the underlying SI substrate.

To examine these highly resistive layers, MIS structures were grown. The V/III flux rate and growth rate calibrations were done on a calibration sample at 600°C prior to the actual growth of the LTG AlGaAs. The MIS structure consists of $1.0\text{ }\mu\text{m}$ of silicon-doped GaAs ($5 \times 10^{15}\text{ cm}^{-3}$) grown on an n^+ -GaAs substrate, followed by $2000\text{ }\text{\AA}$ of LTG AlGaAs. In addition, for MIS structures with an LTG AlGaAs layer having mole fractions above 0.3, a $120\text{ }\text{\AA}$ undoped GaAs cap layer is grown at 600°C on the LTG AlGaAs. The cap layer is important to prevent the formation of oxides at the surface after removal of the sample from the MBE system. A contact consisting of $2000\text{ }\text{\AA}$ aluminum is made to the LTG AlGaAs layer.

The I - V curves from an MIS structure consist of two regions: an exponential region and a linear region. The inverse of the slope measured in the linear region was taken to be the resistance of the LTG AlGaAs, from which we computed the resistivity of the material.

To verify the resistivity extracted from the MIS structure, we used a resistor structure as well. The resistor structure was grown on an n^+ (100) GaAs substrate and consisted of the following layer sequence: $2000\text{ }\text{\AA}$ of silicon-doped GaAs ($5 \times 10^{18}\text{ cm}^{-3}$) grown at 600°C followed by $1\text{ }\mu\text{m}$ of GaAs grown at 300°C , and capped by $2000\text{ }\text{\AA}$ of silicon-doped GaAs ($5 \times 10^{18}\text{ cm}^{-3}$) grown at 600°C . An ohmic contact consisting of $50\text{ }\text{\AA}$ of nickel, $1000\text{ }\text{\AA}$ of Au/Ge, and capped by $150\text{ }\text{\AA}$ of nickel, annealed at 450°C , was made to the resistor structure. A resistivity of $5 \times 10^5\text{ }\Omega\text{ cm}$ measured using this resistor structure agrees well with the resistivity of $3 \times 10^5\text{ }\Omega\text{ cm}$ extracted from an

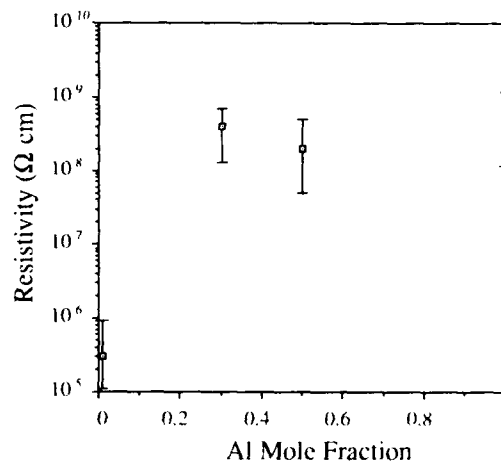


Fig. 1. Resistivity of AlGaAs grown at 270°C and $1\text{ }\mu\text{m/h}$, as a function of Al mole fraction.

MIS structure employing a LTG GaAs layer grown under the same growth conditions.

To investigate the resistivity of LTG $\text{Al}_x\text{Ga}_{1-x}\text{As}$ as a function of aluminum mole fraction, MIS structures were grown at 300°C and a growth rate of $1\text{ }\mu\text{m/h}$ with $x = 0, 0.3, 0.5$, and 1.0 . The resistivity for each of the layers was extracted from room temperature I - V curves under dark conditions using an HP 4145B Parameter Analyzer. From fig. 1 it is seen that the resistivity increases rapidly from that of GaAs to the higher value of AlGaAs and remains nearly constant for the larger mole fractions.

To investigate resistivity as a function of growth temperature, $\text{Al}_{0.3}\text{Ga}_{0.7}\text{As}$ and GaAs MIS structures were grown at $210, 240, 270$, and 300°C . As shown in fig. 2, the resistivity of both the GaAs and the $\text{Al}_{0.3}\text{Ga}_{0.7}\text{As}$ is nearly constant for the low temperature range of 210 to 300°C , and in each case, is much higher than the material grown at 600°C .

To explore the potential of LTG AlGaAs in device structures we have studied highly resistive LTG $\text{Al}_{0.3}\text{Ga}_{0.7}\text{As}/\text{GaAs}$ superlattice (SL) buffers and the incorporation of the LTG AlGaAs as a dielectric in coplanar waveguides.

The properties of $\text{Al}_{0.3}\text{Ga}_{0.7}\text{As}/\text{GaAs}$ superlattices grown at low temperatures (270°C) were studied to evaluate their performance as highly

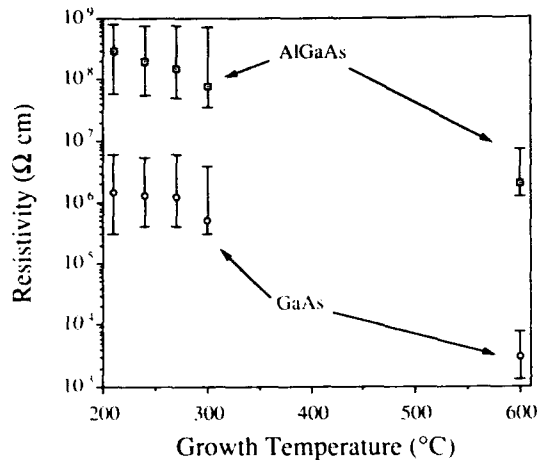


Fig. 2. Resistivity of $\text{Al}_{0.3}\text{Ga}_{0.7}\text{As}$ and GaAs grown with $1 \mu\text{m/h}$ and growth temperatures ranging from 210 to 600 °C.

resistive buffer layers. We studied the sheet resistance of a $10 \times (100 \text{ Å } \text{Al}_{0.3}\text{Ga}_{0.7}\text{As}, 100 \text{ Å } \text{GaAs})$ SL grown at 270 °C over a $1 \mu\text{m}$ undoped GaAs buffer grown on a semi-insulating GaAs substrate. After evaporating a 660 μm diameter aluminum contact, a sheet resistance of $1 \times 10^{12} \Omega/\square$ was measured. Such highly resistive layers can provide excellent vertical isolation to suppress backgating in field-effect transistors and also may find applications in providing isolation between levels in optoelectronic integrated circuits.

Next we grew a HEMT structure on an LTG AlGaAs/GaAs SL, as shown in fig. 3. A $5 \times (100 \text{ Å } \text{Al}_{0.3}\text{Ga}_{0.7}\text{As}, 100 \text{ Å } \text{GaAs})$ SL was grown at 270 °C over a $1 \mu\text{m}$ undoped GaAs buffer grown on a semi-insulating GaAs substrate. This was followed by a $5 \times (100 \text{ Å } \text{Al}_{0.3}\text{Ga}_{0.7}\text{As}, 100 \text{ Å } \text{GaAs})$ superlattice grown at 650 °C, followed by a high electron mobility transistor (HEMT) structure, also grown at 650 °C. The HEMT structure consists of a 1000 Å undoped GaAs buffer, a 200 Å undoped $\text{Al}_{0.3}\text{Ga}_{0.7}\text{As}$ spacer, a 300 Å $n^+\text{-Al}_{0.3}\text{Ga}_{0.7}\text{As}$ layer, and a 200 Å GaAs cap layer. This test structure is very useful in evaluating material quality, because of the sensitivity of the HEMT to defects and impurities in the 2DEG region. The low temperature photoluminescence (PL) linewidth of the SL grown at 650 °C on top of the

LTG buffer provides a good index of interface and crystalline quality.

In our test structure, the 4.2 K PL spectrum from the $\text{Al}_{0.3}\text{Ga}_{0.7}\text{As/GaAs}$ SL has a relatively small linewidth of 1.3 meV, which implies good quality interfaces [7]. Spectral evidence suggests that this luminescence is excitonic in origin. The 77 K Hall mobility of $156,000 \text{ cm}^2 \text{ V}^{-1} \text{ s}^{-1}$ and sheet concentration of $6.0 \times 10^{11} \text{ cm}^{-2}$ of the HEMT structure are also indicative of high quality material. HEMT structures grown under similar conditions in our MBE system, but without the low temperature grown SL buffer, have similar mobilities.

Examining another possible application of LTG AlGaAs , coplanar waveguides (CPWs) were fabricated consisting of a center metal strip with a metal ground plane on either side. The center strip and the ground planes are generally placed on a dielectric slab to make a CPW. Our coplanar

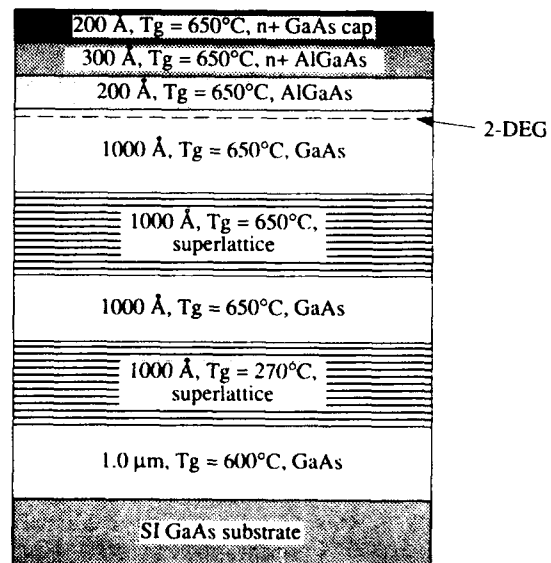


Fig. 3. Schematic diagram of a HEMT structure grown on an LTG superlattice $5 \times (100 \text{ Å } \text{Al}_{0.3}\text{Ga}_{0.7}\text{As}, 100 \text{ Å } \text{GaAs})$ and a superlattice $5 \times (100 \text{ Å } \text{Al}_{0.3}\text{Ga}_{0.7}\text{As}, 100 \text{ Å } \text{GaAs})$ grown at 650 °C. The HEMT structure has a measured 77 K mobility of $156,000 \text{ cm}^2 \text{ V}^{-1} \text{ s}^{-1}$ at a 2DEG concentration of $6.0 \times 10^{11} \text{ cm}^{-2}$. From 4 K PL, the measured FWHM linewidth was 1.3 meV from the $\text{Al}_{0.3}\text{Ga}_{0.7}\text{As}$ (100 Å) superlattice grown at 650 °C.

waveguide structure consists of $0.75\text{ }\mu\text{m}$ of LTG $\text{Al}_{0.3}\text{Ga}_{0.7}\text{As}$ grown (at 270°C) on a SI GaAs substrate. A contact consisting of $200\text{ }\text{\AA}$ Cr, $1.2\text{ }\mu\text{m}$ Ag, and $500\text{ }\text{\AA}$ Au is made to the $\text{Al}_{0.3}\text{Ga}_{0.7}\text{As}$ epitaxial layer. Using an HP 8510 Network Analyzer, microwave test frequencies up to 30 GHz revealed no difference in the measured S -parameters for the CPW employing the LTG $\text{Al}_{0.3}\text{Ga}_{0.7}\text{As}$ slab and a CPW employing a SI GaAs slab. This suggests that the low-temperature grown AlGaAs buffer material may be useful as a dielectric in devices which have microwave applications.

3. Summary and conclusions

We have reported several properties and potential applications of AlGaAs grown at low temperatures (200 to 300°C) using MBE. We have used Al, Ga, and As_2 fluxes to grow resistive buffers and have found the resistivity of AlGaAs for selected aluminum mole fractions and growth temperatures. The fact that the resistivity of LTG AlGaAs does not vary strongly with Al mole fraction of 0.3 or higher, or with growth temperature from 200 – 300°C , is encouraging for practical applications to devices. We have grown a HEMT structure with high mobility and electron sheet concentration on a highly resistive LTG $\text{Al}_{0.3}\text{Ga}_{0.7}\text{As}/\text{GaAs}$ superlattice buffer. In addition, the microwave properties of LTG AlGaAs in a coplanar waveguide were found to be comparable

to SI GaAs. The present evidence indicates that LTG GaAs and AlGaAs have useful properties, and we expect interesting device applications will be found for these materials.

Acknowledgements

We appreciate useful discussions with T.J. Mattord, S. Islam, and A. Tsao in this research. This work was supported by UT-Austin and by the Joint Services Electronics Program under contract AFOSR F 492620-89-C-0844.

References

- [1] F.W. Smith, A.R. Calawa and C. Chen, IEEE Electron Device Letters EDL-9 (1988) 77.
- [2] M.J. Delaney, C.S. Chou, L.E. Larson, J.F. Jensen, D.S. Deakin, A.S. Brown, W.W. Hopper, M.A. Thompson, L.G. McCray and S.E. Rosenbaum, IEEE Electron Device Letters EDL-10 (1989) 355.
- [3] M. Kaminska, Z. Liliental-Weber, E.R. Weber, T. George, J.B. Kortright, F.W. Smith, B.-Y. Tsaur and A.R. Calawa, J. Vacuum Sci. Technol. B7 (1989) 1881.
- [4] M. Kaminska, E.R. Weber, Z. Liliental-Weber and R. Leon, J. Vacuum Sci. Technol. B8 (1989) 710.
- [5] A.C. Campbell, G.E. Crook, T.J. Rogers and B.G. Streetman, J. Vacuum Sci. Technol. B8 (1990) 305.
- [6] T.J. Mattord, V.P. Kesan, G.E. Crook, T.R. Block, A.C. Campbell, D.P. Neikirk and B.G. Streetman, J. Vacuum Sci. Technol. B6 (1988) 1667.
- [7] B. Daveaud, A. Regreny, J.-Y. Emery and A. Chomette, J. Appl. Phys. 59 (1986) 1633.

Low-temperature growth of GaAs and AlGaAs by MBE and effects of post-growth thermal annealing

J.N. Miller and T.S. Low

Hewlett-Packard Laboratories, 3500 Deer Creek Road, Palo Alto, California 94304, USA

GaAs and $\text{Al}_{0.3}\text{Ga}_{0.7}\text{As}$ films were grown by molecular beam epitaxy (MBE) using substrate temperatures between 350 and 620°C. These samples were produced under otherwise identical conditions using either elemental As (tetrameric As) or GaAs (dimeric As) as the arsenic source, and using fixed fluxes of either Si or Sn, corresponding to an atomic dopant concentration of approximately $3 \times 10^{18} \text{ cm}^{-3}$. The samples were characterized by Hall effect measurements at 300 and 77 K, and by photoluminescence measurements at 300 K. In the as-grown samples, the free carrier concentration, n , the Hall mobility, μ , and the luminescence intensity all decrease as the substrate temperature decreases below 450°C. The lower values of n , μ , and luminescence intensity can, however, be improved by thermally annealing the films at 850°C for between 5 and 30 s. After the anneal, values of n , μ , and photoluminescence intensity are comparable to those observed in unannealed films grown at 620°C. For a given growth temperature, the measured electrical and optical properties and the annealing behavior of these samples are very similar, whether Si or Sn is used as the dopant, and whether a tetrameric or dimeric As source is used.

1. Introduction

The effect of growth temperature on the quality of epitaxial layers has been of fundamental interest since the early application of molecular beam epitaxy (MBE). In some early studies, Cho determined the temperature limits for epitaxial growth and in situ annealing [1]. Later, Metzger et al. contrasted the role of surface dynamic processes with that of atomic arrival rates on the electrical quality of GaAs films [2]. Recently, GaAs layers grown at low temperatures have generated a great deal of interest because field effect transistors (FETs) have shown reduced sidegating when placed atop these layers [3].

The original motivation for this work was to produce modulation-doped $\text{Al}_{0.3}\text{Ga}_{0.7}\text{As}/\text{GaAs}$ heterostructures doped with Sn by MBE. Sn is a shallower impurity level in AlGaAs [4] than the more commonly used Si, and Sn affords substantially higher maximum free electron concentrations in GaAs than Si ($\text{Si} \sim 7 \times 10^{18} \text{ cm}^{-3}$ versus $\text{Sn} \sim 2 \times 10^{19} \text{ cm}^{-3}$). Because of these properties, Sn modulation doped structures achieve higher two-dimensional sheet carrier concentrations, and

should lead to superior microwave performance of modulation doped FETs (MODFETs) compared to similar structures doped with Si. However, Sn as a dopant in MODFET layers, which require precision 20 Å spacer layers, is highly problematic. Sn segregates at the GaAs surface and incorporates in the growing layer in proportion to its surface concentration at conventional growth temperatures [5]. The characteristic incorporation distance required to reach steady state Sn doping is of the order of 1 μm at a substrate temperature of 620°C. It was clear that a new approach was necessary if Sn doping was to be successful in devices requiring abrupt doping profiles.

The motivation for this work evolved into finding a way to produce abrupt Sn doping profiles. It has been demonstrated that by decreasing the growth temperature, the incorporation rates for Sn and Te in GaAs can be increased such that the dopants are trapped in the subsequent atomic layers [6]. Our hypothesis is that, at sufficiently low growth temperatures, Sn would incorporate into the lattice with characteristic distances of a few monolayers, similar to distances for Si in GaAs. At these low temperatures, the as-grown

GaAs:Sn and $\text{Al}_{0.3}\text{Ga}_{0.7}\text{As}:\text{Sn}$ would be of electrically and optically poor quality, but after annealing, as in ion implanted material, the electrical properties would become comparable to material grown at conventional temperatures. The studies described below demonstrate the feasibility of this growth and annealing technique for Sn doping. Similar experiments with GaAs:Si and $\text{Al}_{0.3}\text{Ga}_{0.7}\text{As}:\text{Si}$ grown at low temperatures were used to compare and contrast the Sn doping results. Moreover, as a result of these experiments we were able to gain insight into the mechanisms which result in the reduced carrier concentrations at low growth temperatures.

2. Experiments

The MBE growth of GaAs and $\text{Al}_{0.3}\text{Ga}_{0.7}\text{As}$ was carried out in a Varian GEN II with a modified substrate holder [7]. All layers were grown on semi-insulating (100) GaAs wafers which were chemically prepared by a procedure described elsewhere [8]. The wafers were heated to 640°C in an As beam to desorb the surface oxide prior to growth. The substrate temperature was then decreased to one of four selected temperatures prior to growth: 620°C, 450°C, 400°C, 350°C. At 620°C the substrate temperature was set with a calibrated optical pyrometer, at the lower temperatures the temperatures were set using the substrate thermocouple. The substrate thermocouple temperature is notoriously inaccurate [7] but the substrate temperature is reproducible ($\pm 10^\circ\text{C}$, the temperature error was calculated from the variation of the heater power to achieve the same setpoint). The As flux was maintained at approximately 30% above the flux necessary to achieve an As stable surface reconstruction and we observed only a weak growth temperature dependence in the As flux necessary to maintain these growth conditions in the temperature range considered [2].

The GaAs specimens were 1.00 μm thick and were grown at a rate of 1.00 $\mu\text{m}/\text{h}$. The $\text{Al}_{0.3}\text{Ga}_{0.7}\text{As}$ specimens were a three layer stack consisting of a 0.1 μm buffer layer of GaAs, a 0.5 μm undoped $\text{Al}_{0.3}\text{Ga}_{0.7}\text{As}$ to preclude formation of a two-dimensional electron gas, and a 1.00 μm

doped $\text{Al}_{0.3}\text{Ga}_{0.7}\text{As}$ layer. The $\text{Al}_{0.3}\text{Ga}_{0.7}\text{As}$ growth rate was 1.43 $\mu\text{m}/\text{h}$. A 4.5 min Sn predeposition [9] was determined by secondary ion mass spectrometry to be necessary for a flat Sn profile for layers grown at 620°C, predepositions were not used for the other growths. The flux of Sn and Si was held constant by maintaining the same source temperatures for all experiments, resulting in GaAs free electrons of 2.5×10^{18} and $3.4 \times 10^{18} \text{ cm}^{-3}$, respectively.

The reflection high energy electron diffraction (RHEED) patterns showed the standard (2×4) pattern at 620°C and an apparent $c(2 \times 2)$ or (1×1) pattern during growth below 400°C. Two-fold and four-fold reconstructions persisted to low temperatures, but at the onset of growth these fractional order spots weakened. Newstead et al. [10] report mixed (2×4) and $c(4 \times 4)$ for GaAs grown in this temperature region. Neave et al. [11] also observed similar patterns with a low growth temperature. The crystal structure of the low temperature GaAs was also probed with X-ray diffractometer measurements. The Al K α (004) rocking curve halfwidth of a GaAs film grown at 350°C was 23 arc sec and indistinguishable from a similar film grown at 620°C.

Layers were produced with either tetrameric As_4 or dimeric As_2 sources. As_4 was produced by sublimating elemental As. The As_2 was produced by heating GaAs chunks in a 40 cm^3 effusion cell: the GaAs chunks were formed by crushing a 60 g piece of an undoped liquid-encapsulated Czochralski-grown boule. The Ga flux from this GaAs source was less than $6 \times 10^{12} \text{ cm}^{-2}/\text{s}$ at the substrate surface. This low value of Ga flux corresponds to less than 1% of the flux from the Ga cell, much less than expected theoretically [12], and is possibly due to a self "scavenging" [13] effect of the large quantity of GaAs in the cell.

After growth, the wafers were removed from the MBE system and quartered. The as-grown quarter was characterized by Hall measurements, for free electron concentration and mobility, and room temperature photoluminescence (PL). The remaining quarters were subsequently annealed in a rapid thermal annealing process. The films were uncapped and annealed at a temperature of 850°C for 5 to 30 s in Ar. The annealed quarters were

then characterized by Hall measurements and room temperature PL.

3. Results

3.1. As-grown material

The GaAs free-electron concentration data are plotted in fig. 1 as a function of growth temperature for films doped with Si or Sn, and grown with As_2 or As_4 . At the higher growth temperatures between 620 and 450°C, the free-electron concentration, n , decreased only about 20% when the temperature was decreased for the Si doped layers

and was independent of the species of As. Over the same growth temperature range the Sn doped films increased about 10%, the increase is presumably due to increased incorporation of the surface Sn. The mobility drops from an average value of 1900 to 1300 $\text{cm}^2/\text{V} \cdot \text{s}$ when the growth temperature drops from 620 to 450°C.

As the growth temperature is further decreased, the free-electron concentration drops dramatically over six orders of magnitude in the span of 100°C, and n is relatively insensitive to the dopant or the As species used. The mobility of these layers, both at room temperature and 77 K are tightly clustered. The room temperature mobility of the 400 and 350°C material averaged 500 and 700 cm^2/V

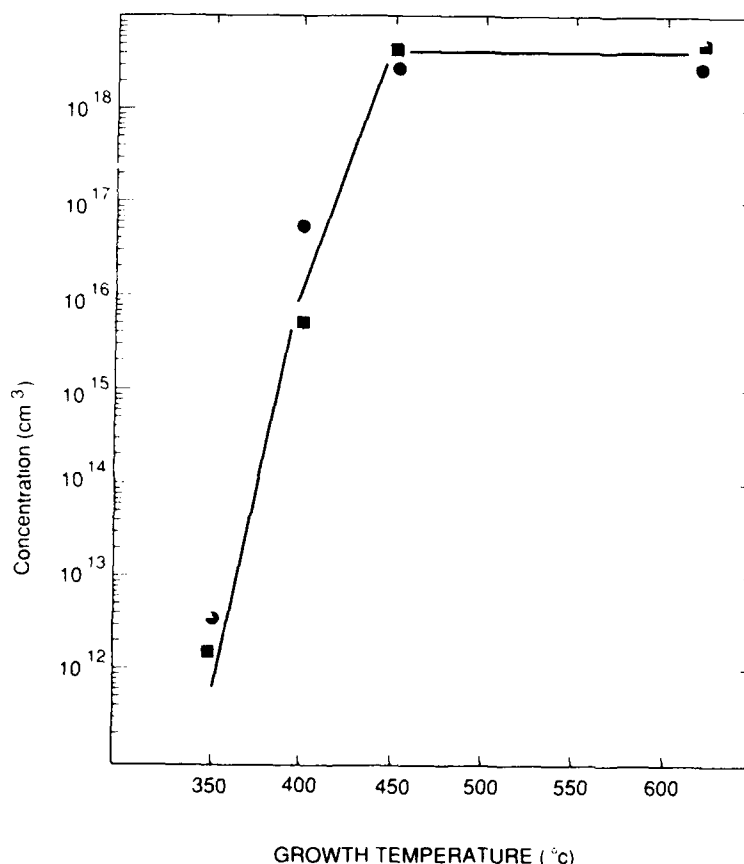


Fig. 1. The free-electron concentration of GaAs as a function of growth temperature. The symbols represent material produced using the following vapor species: (■) As_2 , Si; (△) As_4 , Si; (●) As_2 , Sn; (□) As_4 , Sn. The line serves only as a guide for the eye.

s, respectively, 77 K mobility of these same samples was less than $50 \text{ cm}^2/\text{V} \cdot \text{s}$ when reliable measurements were made.

In the case of $\text{Al}_{0.3}\text{Ga}_{0.7}\text{As}$, the same general trend is observed. Fig 2 shows the free-electron concentration data as a function of growth temperature for films grown with Si or Sn and As_2 or As_4 . The free-electron concentration is about one order of magnitude lower in the case of $\text{Al}_{0.3}\text{Ga}_{0.7}\text{As}$ due to the deeper donors [4] and, again, as in the case of GaAs, the carrier concentration changes very little when the growth temperature is reduced from 620°C to 450°C . However, as the growth temperature is reduced to 400°C and 350°C the electron concentration decreases about six orders of magnitude for the

AlGaAs grown with As_4 and about four orders of magnitude for the material grown with As_2 . There was no difference between Si and Sn within the experimental error. The average room temperature mobilities for the 620 , 450 , 400 , and 350°C samples were 650 , 500 , 300 , and $1000 \text{ cm}^2/\text{V} \cdot \text{s}$, respectively. The large mobility for the sample grown at 350°C is likely an artifact due to a small two-dimensional electron gas at the substrate interface. The other three indicate a monotonic decrease in μ as the growth temperature decreases.

3.2. Annealed material

The free-electron concentration, n , of the low temperature grown films tended to increase for

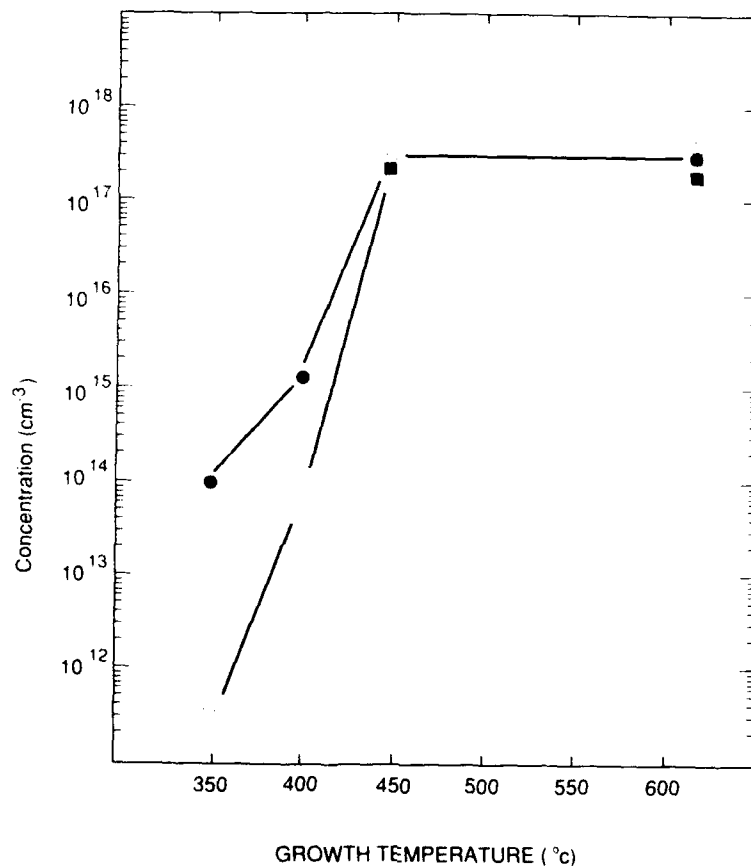


Fig.2. The free-electron concentration of $\text{Al}_{0.3}\text{Ga}_{0.7}\text{As}$ as a function of growth temperature. The symbols represent material produced using the following vapor species: (■) As_2 , Si; (Δ) As_4 , Si; (●) As_2 , Sn; (□) As_4 , Sn. The line serves only as a guide for the eye.

anneals at 850°C and for times between 5 and 20 s, longer annealing times resulted in reduced values of n . Since the anneals were performed without a cap, some loss of As from the near surface region was observed. The measured n after an 850°C, anneal is plotted versus growth temperature in figs. 3a and 3b for GaAs and $\text{Al}_{0.3}\text{Ga}_{0.7}\text{As}$, respectively. The overall trend for the n in GaAs and the $\text{Al}_{0.3}\text{Ga}_{0.7}\text{As}$ samples are qualitatively the same. The annealed samples tend to have free-carrier concentrations similar to those of samples grown at 620°C. The degree of recovery depends

on the growth temperature, with better recovery observed for samples grown at higher temperature within the temperature range from 350 to 450°C. The 450°C samples have recovered n completely within the measurement error. The 350°C specimens have, on the average, n values 1/3 of the 620°C values. A number of the samples recovered n completely with different duration anneals, so that with optimized annealing it would be possible to obtain complete recovery of n within the measurement error. The average mobility of the pulse annealed samples was nearly independent of

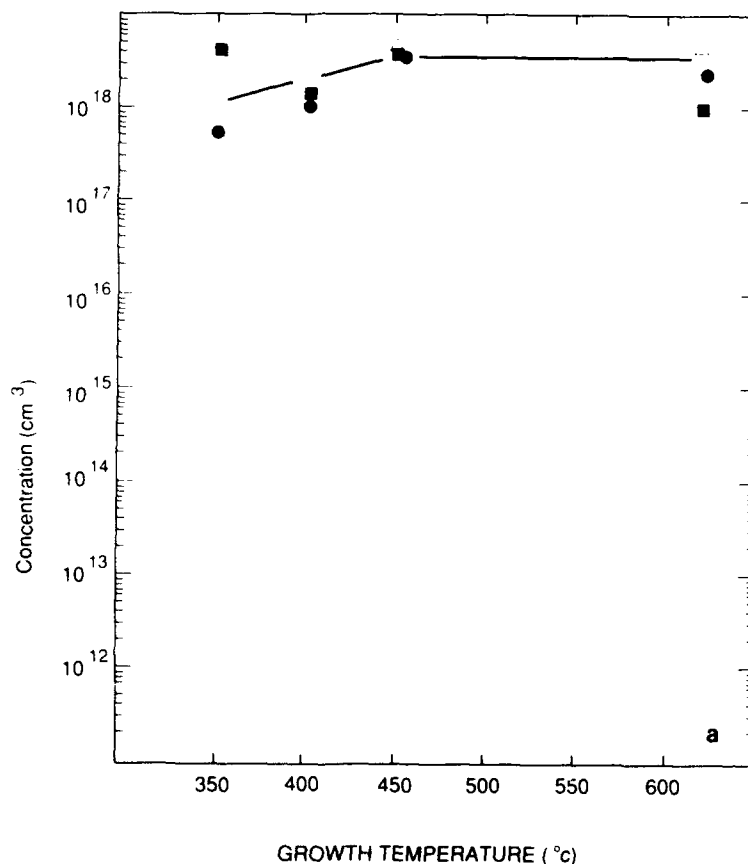


Fig. 3. (a) The free-electron concentration of GaAs as a function of growth temperature after annealing at 850°C for 5 s. (b) The free electron concentration of $\text{Al}_{0.3}\text{Ga}_{0.7}\text{As}$ as a function of growth temperature after annealing at 850°C for 5 s. The symbols represent material produced using the following vapor species: (■) As_2 , Si; (Δ) As_4 , Si; (●) As_2 , Sn; (□) As_4 , Sn. The line serves only as a guide for the eye.

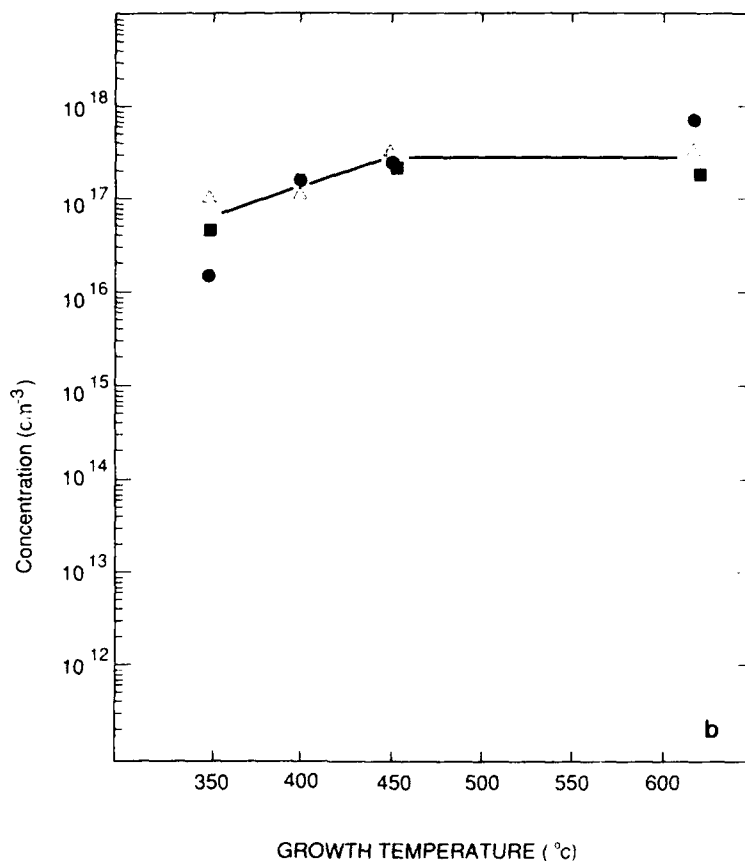


Fig. 3 (continued).

dopant species, As species, and growth temperature.

Hall effect transport measurements predominantly reflect majority carrier properties of these films. The annealed films could possess a significant number of deep donors and acceptors which would have only a minor effect on the electrical transport data. So we chose to measure the room temperature photoluminescence (PL) intensity in order to gain insight into the minority carrier properties of these films.

The PL intensity versus growth temperature was measured for $\text{Al}_{0.3}\text{Ga}_{0.7}\text{As}$ and GaAs. Photoluminescence was not detected in the films grown at 350 and 400°C (the detection limit is approximately two and a half orders of magnitude lower

than the values measured for the 620°C films). After pulse-annealing, the PL intensity of specimens grown at 620°C drops to 1/10 of their as-grown value. This is indicative of the damage our pulse-annealing process does to the near surface region due in part to a loss of As, as mentioned previously. The PL intensity of the pulse-annealed specimens grown at the other temperatures were comparable to the 620°C films. Because of the surface damage from the pulse annealing, a number of specimens were annealed in AsH_3 at 700°C for 15 min in order to minimize As loss during this processing. The PL intensities of these $\text{Al}_{0.3}\text{Ga}_{0.7}\text{As}$ samples, shown in fig. 4 were comparable to similar unannealed specimens grown at 620°C. This indicates that both the

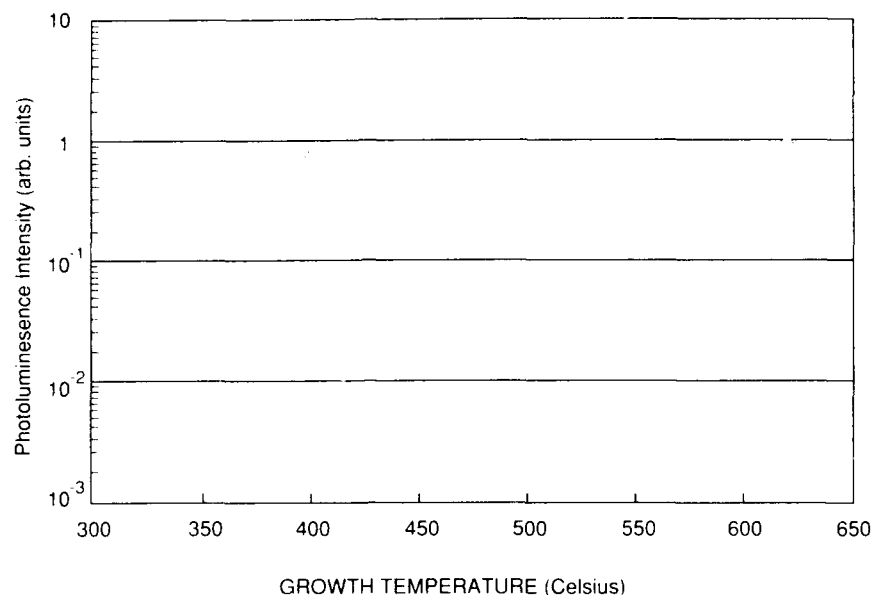


Fig. 4. The photoluminescence intensity of $\text{Al}_{0.3}\text{Ga}_{0.7}\text{As}$ as a function of the growth temperature after annealing at 700°C in arsine. The symbols represent material produced using the following vapor species: (\square) As_2 ; (\triangle) As_4 .

majority carrier properties and the minority carrier properties of these materials can be made comparable to material produced at 620°C .

4. Discussion

The current view of the crystal growth process requires that atoms land on the surface and migrate to an atomic step or kink where they are incorporated into the crystal. The atoms are unable to migrate to one of these propagating steps if the surface temperature is too low or the growth rate is too high. Because of insufficient thermal energy or time, fewer atoms reach equilibrium sites before growth of the next atomic layer and, as a result, many more point defects are incorporated into the crystal. These point defects may produce electronic states near the middle of the gap. Thus, as the growth temperature decreases the density of traps would be expected to increase and compensate the donors.

Autocompensation mechanisms may also play a role in producing the low n values. The dopant

atoms must migrate to the proper substitutional site. Columns IV donors such as Sn and Si normally reside on a Ga site. However, if they incorporate on an As site or other sites, they may form acceptors [14] which would result in highly compensated material.

Another potential defect generating mechanism particular to the MBE crystal growth involves the As species. It has been demonstrated that MBE GaAs grows via a reaction between As dimers and Ga surface atoms [15]. Elemental As sublimates as As tetramers which are thought to fission, via a reaction with Ga atoms, into incorporated As atoms and a tetramer ejected from the surface [15]. At lower temperatures the surface energies might be insufficient to break the tetramers and thus they might incorporate as electrically active point defects.

As we have noted, the reduced free carrier concentrations depend only weakly, if at all, on the As species used. And, the annealing behavior of these samples is independent of the As species used. From these data, it is clear that the primary electronic defect responsible for the drop in car-

rier concentration is not caused by the As tetramers [11]. The reduced values of n are also independent of the dopant species, Sn or Si. If the Sn and Si atoms were responsible for the compensating centers, the mobility of the autocompensating material would stay almost constant as n drops because $(N_D^+ + N_A^-)$ would be fixed; this is not the case. A significant reduction in mobility is even measured at growth temperatures above those where n drops. Also, a temperature dependent autocompensation mechanism, where dopant atoms site-switch, depends on a difference between the surface kinetics and thermodynamics for the dopant atoms. Künzel et al. [16], for example, found that autocompensation of Ge was highly dependent on the As species and the growth temperature in the range from 500 to 600°C. It is unlikely that this mechanism for n reduction would take place at the same temperature for Si and Sn given their vastly different surface incorporation rates at 620°C however we cannot completely rule out that part of the compensation is due to this mechanism.

Based on the foregoing, we suggest two trap generating mechanisms which are consistent with our data. First, the low Ga atom surface mobility at low temperature may play a significant role in the electrical traps responsible for the dramatically reduced n . Though there is minor difference between the material grown with As_4 and As_2 , it is possible that breaking the final As_2 bond becomes the rate limiting step at low temperatures with both As species and becomes the main trap generating mechanism.

5. Conclusions

GaAs and $Al_{0.1}Ga_{0.9}As$ films were grown by molecular beam epitaxy (MBE) using substrate temperatures between 350 and 620°C. These samples were produced under otherwise identical conditions using either As_2 or As_4 as the arsenic source, and using fixed fluxes of either Si or Sn corresponding to an atomic dopant concentration of approximately $3 \times 10^{18} \text{ cm}^{-3}$. In the as-grown samples, the free carrier concentration, n , the Hall mobility, μ , and the luminescence intensity all

decrease dramatically when the substrate temperatures are below 450°C. This decrease in n is primarily due to an increase in the concentration of compensating traps as the growth temperature decreases and not to an autocompensation mechanism for the dopants. A subsequent 5 to 30 s thermal anneal at 850°C of films grown between 350 and 450°C results in measured values of n , μ , and luminescence intensity that are comparable to those of similar unannealed samples grown at 620°C. For a given growth temperature, the measured electrical and optical properties and the annealing behavior of these samples are very similar, regardless of whether Si or Sn is used as the dopant, and regardless of whether a tetrameric or dimeric As source is used. The small free carrier concentrations in the samples are probably not caused by compensating centers that result from incomplete dissociation of As_4 at the growth surface, since samples grown with dimeric and tetrameric As behave in a similar manner.

Acknowledgments

We would like to acknowledge M. Pustorino, M. Kanemura, R. LaCoste, and A. Fischer-Colbrie for technical support, and Ron Moon and Rolf Jaeger for critical reading of the manuscript.

References

- [1] A.Y. Cho, *Surface Sci.* 17 (1969) 494.
- [2] G.M. Metzger, A.R. Calawa and J.G. Mavroides, *J. Vacuum Sci. Technol.* B1 (1983) 166.
- [3] F.W. Smith, A.R. Calawa, C.-L. Chen, M.J. Mantra and L.J. Mahones, *IEEE Electron Device Letters* EDL-9 (1988) 77.
- [4] D.V. Lang and R.A. Logan, in: *Proc. 14th Intern. Conf. on Physics of Semiconductors*, Edinburgh, 1978, *Inst. Phys. Conf. Ser.* 43, Ed. B.L.H. Wilson (Inst. Phys., London-Bristol, 1979) p. 433.
- [5] F. Alexandre, C. Raisin, M.I. Abdalla, A. Brenac and J.M. Masson, *J. Appl. Phys.* 51 (1980) 4296.
- [6] D.M. Collins, J.N. Miller, Y.G. Chan and R. Chow, *J. Appl. Phys.* 53 (1982) 3010.
- [7] D.E. Mars and J.N. Miller, *J. Vacuum Sci. Technol.* B4 (1986) 571.
- [8] D. Bimberg, D. Mars, J.N. Miller, R. Bauer and D. Oertel, *J. Vacuum Sci. Technol.* B4 (1986) 1014.

- [9] C.E.C. Wood and B.A. Joyce, *J. Appl. Phys.* 49 (1978) 4854.
- [10] S.M. Newstead, R.A.A. Kubiak and E.H.C. Parker, *J. Crystal Growth* 81 (1987) 49.
- [11] J.H. Neave, P. Blood and B.A. Joyce, *Appl. Phys. Letters* 36 (1980) 311.
- [12] J.R. Arthur, Jr., *J. Phys. Chem. Solids* 28 (1967) 2257.
- [13] M.J. Mondry, E.J. Caine and H. Kroemer, *J. Vacuum Sci. Technol.* A3 (1985) 316.
- [14] T.S. Low, B.J. Skromme and G.E. Stillman, in: *Proc. 10th Intern. Symp. on GaAs and Related Compounds*, Albuquerque, NM, 1982, *Inst. Phys. Conf. Ser.* 65, Ed. G.E. Stillman (Inst. Phys., London-Bristol, 1983) p. 515.
- [15] C.T. Foxon and B.A. Joyce, *Surface Sci.* 50 (1975) 434.
- [16] H. Kunzel, J. Knecht, H. Jung, K. Wünstel and K. Ploog, *Appl. Phys.* A28 (1982) 167.

GaAs buffer layers grown at low substrate temperatures using As_2 and the formation of arsenic precipitates

M.R. Melloch

School of Electrical Engineering, Purdue University, West Lafayette, Indiana 47907, USA

K. Mahalingam, N. Otsuka

Materials Engineering, Purdue University, West Lafayette, Indiana 47907, USA

J.M. Woodall and A.C. Warren

IBM Research Division, P.O. Box 218, Yorktown Heights, New York 10598, USA

We have grown GaAs layers by molecular beam epitaxy at low substrate temperatures (250°C) using the dimer arsenic source As_2 . Following a one hour anneal at 600°C , the GaAs layers were examined with transmission electron microscopy. The GaAs layers contained arsenic precipitates of average diameter 100 \AA and density of 10^{17} cm^{-3} .

GaAs buffer layers grown by molecular beam epitaxy (MBE) at low substrate temperatures (LTBLs) have been attracting attention because they can be used to eliminate sidegating in field effect transistors (FETs) [1–3]. In addition, the layers which are grown at normal substrate temperatures on top of LTBLs exhibit extremely high electrical quality [4]. By growing at low substrate temperatures, excess arsenic is incorporated into these buffer layers [5]. Raising the substrate temperature back to normal growth temperatures results in the excess arsenic forming precipitates [6]. These arsenic precipitates then act as buried “Schottky barriers” whose overlapping depletion regions render the material semi-insulating [7]. What is truly remarkable is that the GaAs material between the Schottky barriers exhibits mobility indicative of “normal” GaAs [8]. This combination of buried Schottky barriers in high quality GaAs makes LTBLs an excellent material for optoelectronic applications [8,9]. Previously, all LTBLs have been grown using the tetramer arsenic source As_4 . Using an LTBL grown with the dimer arsenic source As_2 as the photoconductive material in a broad-band

receiver, we have been able to generate and detect electrical pulses with full width at half maximum of 0.71 ps [8]. In this paper we describe the growth of LTBLs using the dimer arsenic source, present transmission electron microscopy (TEM) analysis of these LTBLs, and compare LTBLs grown with As_2 , and As_4 .

The films used in this work were grown in a Varian GEN II MBE system on 2-inch diameter undoped semi-insulating liquid-encapsulated Czochralski (100) GaAs substrates. The substrates were degreased, etched in a 60°C solution of $5:1:1$ of $\text{H}_2\text{SO}_4:\text{H}_2\text{O}_2:\text{H}_2\text{O}$ for 1 min and placed in non-bonded substrate mounts. The substrates were outgassed for 2 h at 200°C in the entry chamber of the MBE, moved to the buffer chamber where they were outgassed for 1 h at 300°C , and then loaded into the growth chamber. In the growth chamber, each sample was heated to 615°C for 2 min (the surface oxides desorbed at 580°C) and then lowered to the initial growth temperature of 600°C .

The growth rate for all layers was $1\text{ }\mu\text{m/h}$. For samples grown with As_2 the group V to group III

beam equivalent pressure was 22. For samples grown with As₄ the group V to group III, beam equivalent pressures were 16. Initially, 0.75 μm of undoped GaAs was grown. Then the substrate temperature was lowered from an actual temperature of 600°C to a thermal couple reading of 250°C during the growth of the next 0.25 μm of GaAs. (At the actual temperature of 600°C, the thermocouple reads in the neighborhood of 700°C.) After reaching a thermocouple reading of 250°C, 1 μm of undoped GaAs was grown. The substrate temperature was then ramped back to 600°C during the growth of the next 500 Å of GaAs. After attaining the normal growth temperature of 600°C, an additional 100 Å of undoped GaAs was grown. This was followed by an in-situ anneal in the As₂ or As₄ flux for 1 h at 600°C. The substrate was rotated at 5 rpm during the growth of all layers and during the one hour 600°C anneal.

The TEM examination of LTBLs grown with As₂ and As₄ was performed by using a JEM 2000 EX electron microscope. For the examination, [011] cross-sectional samples were prepared by the ion thinning technique. TEM images of both LTBLs have shown the existence of a large number of As precipitates, the appearance of which is similar to that observed in our earlier study [6]. Figs. 1a and 1b are bright field images taken from LTBLs grown with As₂ and As₄, respectively. The two images were taken under identical conditions; cross-sectional samples were tilted from the [011] axis by a few degrees to excite only one of the (111) type reflections. This condition gives rise to broad dark and bright bands of thickness contours in the images, which were used for the estimation of thicknesses of the observed areas. The small spacing of thickness contours in fig. 1b is caused by a large change of the thickness across the observed area of the sample. In the images, As precipitates appear with either dark or bright contrasts, depending on their locations with respect to those of the thickness contours. As seen in the two images, the sizes of the As precipitates are distinctly different between the two LTBLs; the average diameter of the precipitates in fig. 1a is 100 Å, while that in fig. 1b is 50 Å. Observations of other parts of the two LTBLs also showed this same

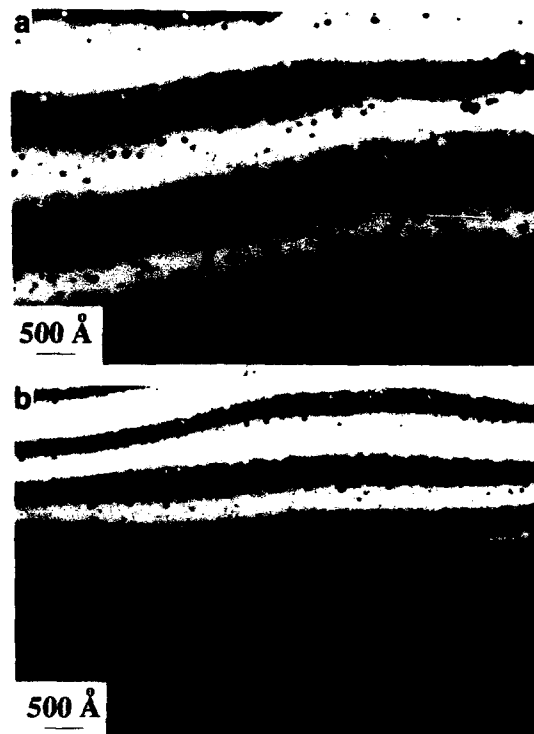


Fig. 1. Bright field images of cross-sectional samples of the LTBLs grown with (a) As₂ and (b) As₄.

difference in sizes of As precipitates. All observed precipitates in the LTBL grown with As₄ appear as nearly spherical particles. However the boundaries between the As precipitates and the GaAs for many of the large precipitates in the LTBL grown with As₂ exhibited flat sections, suggesting the formation of low energy boundaries along certain crystallographic planes. Fig. 2 is a high magnification bright field image showing such precipitates in the LTBL grown with As₂. In the image in fig. 2, many of the precipitates exhibit moire fringes.

Densities of the As precipitates were estimated from the bright field images. The thicknesses of the estimated areas were determined by using the extinction distance of 370 Å in GaAs for the (111) reflection of 200 kV electrons. Estimated densities are on the order of 10^{17} cm^{-3} for both LTBLs. No significant difference in the density of precipitates



Fig. 2. High magnification bright field image of As precipitates in the LTBL grown with As₂.

was observed between the two samples, although the estimated density for the LTBL grown with As₄ appears to be slightly greater than that for the other LTBL. Since arsenic precipitates play a key role in the electrical properties of LTBLs [7], LTBLs grown with As₂ and As₄ should exhibit similar electrical characteristics due to the similar densities of arsenic precipitates. Recently, similar electrical properties for GaAs LTBLs grown using dimer and tetramer arsenic sources have been observed [10,11].

In comparing the two film growths used in this work, the film grown with As₂ had a slightly higher arrival rate of As atoms than the film grown with As₄, as determined from the measured beam equivalent pressures for As₂ and As₄, and taking into account the variation in sensitivity of an ion gauge due to the difference in number of electrons in the two molecules [12]. However, we find that the volume fraction of the elemental As phase in the LTBL grown with As₂ is significantly greater than that in the LTBL grown with As₄, indicating a higher incorporation efficiency of As₂ than that of As₄. The larger sizes but the similar density of As precipitates in the LTBL grown with As₂, compared to those in the LTBL grown with As₄, may be explained by assuming that the evolution process of As precipitates in these two samples had already entered the coarsening stage due to the relatively long period of annealing; nearly all excess As was already incorporated in precipitates in these two LTBLs. This assumption may explain the high quality of the

GaAs matrix in these LTBLs [8]. In order to confirm these explanations, however, one needs to carry out further systematic study on the precipitation process of As in LTBLs.

In summary, we report the growth of GaAs LTBLs by MBE using the dimer arsenic source As₂. We have observed the formation of arsenic precipitates in these LTBLs. TEM analysis of the LTBLs indicates an average As precipitate diameter of 100 Å and a density in the range of 10¹⁷ cm⁻³ for the growth conditions used (beam equivalent pressure of As₂ to Ga of 22, a substrate temperature thermocouple reading of 250°C, and followed by a one hour anneal at a temperature of 600°C in the As₂ flux). We have also found that the incorporation of As in LTBLs is much more efficient when As₂ is used rather than As₄ during molecular beam epitaxy.

The work at Purdue University was partially funded by the Office of Naval Research under grant No. N00014-89-J-1864. M.R. Melloch would like to thank Dr. George N. Maracas of Arizona State University for preprints of LTBL work performed at ASU.

References

- [1] F.W. Smith, A.R. Calawa, Chang-Lee Chen, M.J. Mantra and L.J. Mahoney, IEEE Electron Devices Letters EDL-9 (1988) 77.
- [2] B.J.F. Lin, D.E. Mars, and T.S. Low, 46th Device Research Conf., University of Colorado at Boulder, June 1988.
- [3] B. Jia-Fu Lin, C.P. Kocot, D.E. Mars and R. Jaeger, IEEE Trans. Electron Devices ED-37 (1990) 46.
- [4] M.R. Melloch, D.C. Miller and B. Das, Appl. Phys. Letters 54 (1989) 943.
- [5] M. Kaminska, Z. Liliental-Weber, E.R. Weber, T. George, J.B. Kortright, F.W. Smith, B.-Y. Tsaur and A.R. Calawa, Appl. Phys. Letters 54 (1989) 1881.
- [6] M.R. Melloch, N. Otsuka, J.M. Woodall, A.C. Warren and J.L. Freeouf, Appl. Phys. Letters 57 (1990) 1531.
- [7] A.C. Warren, J.M. Woodall, J.L. Freeouf, D. Grischkowsky, D.T. McInturff, M.R. Melloch and N. Otsuka, Appl. Phys. Letters 57 (1990) 1331.
- [8] A.C. Warren, N. Katzenellenbogen, D. Grischkowsky, J.M. Woodall, M.R. Melloch and N. Otsuka, Appl. Phys. Letters 58 (1991).

- [9] F.W. Smith, H.W. Le, V. Diadiuk, M.A. Hollis, A.R. Calawa, S. Gupta, M. Frankel, D.R. Dykaar, G.A. Mourou and T.Y. Hsiang, *Appl. Phys. Letters* 54 (1989) 890.
- [10] R.A. Puechner, D.A. Johnson, K.T. Shiralagi, D.S. Gerber, R. Droopad and G.N. Maracas, *J. Crystal Growth* 111 (1991) 43.
- [11] D.A. Johnson, R.A. Puechner, A.M. Krizan, K. Shiralagi, D. Gerber, R. Droopad and G.N. Maracas, *Appl. Phys. Letters*, submitted.
- [12] S. Dushman and A.H. Young, *Phys. Rev.* 68 (1945) 278.

Electrical and optical characterization of gas source and solid source MBE low temperature buffers

R.A. Puechner, D.A. Johnson, K.T. Shiralagi, D.S. Gerber, R. Droopad and G.N. Maracas

Center for Solid State Electronics Research, ERC 120, Arizona State University, Tempe, Arizona 85287-6206, USA

MBE GaAs buffer layers grown at low substrate temperatures (200–300 °C) have been shown to significantly reduce backgating and sidegating in GaAs integrated circuits. The isolation provided by these buffers is attributed to a high level of compensating traps in the layers induced by excess arsenic and arsenic antisite defects. Structures were grown by both gas source and solid source MBE in a VG Semicon V80H dual chamber system. The structures allow us to study characteristics of the LTB itself as well as the quality of active layers grown upon these buffer layers. The insulating characteristics of the gas and solid source LTBs are comparable. However, in contrast to control layers grown on semi-insulating GaAs, we observe considerably higher trap concentrations in FET active layers grown on LTBs. Deep level transient spectroscopy (DLTS) measurements show several resolvable electron and hole traps, plus a band of shallow hole traps. Due to the differences in growth kinetics for gas and solid source growth such a close similarity was not expected. The resistivity of the LTBs and the traps incorporated into the active layers appear to be similar for solid source (As_4) and gas source (As_2) growth. Furthermore, the characteristics of proximity annealed layers continue to change for varied length low temperature anneals. This indicates that the excess arsenic continues to diffuse into the active device layers degrading device stability.

1. Introduction

Recently, Smith et al. [1] have demonstrated a dramatic backgating and sidegating reduction in GaAs MESFETs by employing a buffer grown at very low temperatures (200–300 °C) by MBE. The large reduction in backgating and sidegating is primarily due to a large increase in the trap filled limited voltage (V_{TFL}) for the low temperature buffers (LTB), which results from a high concentration of deep levels in this material. The nature of low temperature buffers grown by solid source MBE has been the subject of much research, however, LTBs grown by gas source MBE (GSMBE) have not been previously reported. Since the growth kinetics for GSMBE (As_2) are different from conventional solid source MBE (As_4), it is important to determine whether GSMBE LTBs have properties similar to those grown by solid source and if so, to determine an acceptable range of growth parameters (substrate temperature, As/Ga ratio). Furthermore, the stability and the quality of epitaxial layers grown upon LTBs must be studied in order to more completely evaluate

the effectiveness of LTBs for device applications. Lin et al. [2] have reported reductions in backgating and sidegating in HEMTs grown on LTBs. However, they also reported transient behavior which they attribute to gallium vacancies which diffuse from the LTB into the top epitaxial layer. In this paper we review the present understanding of LTBs, and then present our experimental results on bulk properties of LTBs as well as layers grown upon LTBs. We then comment on gas and solid source LTBs based upon the implications of our studies.

2. Background

Low temperature buffers may provide an effective way of increasing the isolation between devices for MESFET or HEMT based integrated circuits. As grown, these samples contain up to 1% excess arsenic which forms As_{Ga} antisites, As interstitials and various complexes [3]. These “as-grown” layers exhibit large conductivities due to hopping between a large numbers of defect sites,

with concentrations approaching $2 \times 10^{19} \text{ cm}^{-3}$. Annealing "as-grown" layers approximately 10 min at 600°C converts them to highly insulating material ($10^8 \Omega \text{ cm}$). During the annealing process, the excess As in the LTB material "self-getters" and forms hexagonal arsenic precipitates 20–100 Å in size and in concentrations of approximately $1 \times 10^{17} \text{ cm}^{-3}$ [4]. However, the precipitate density is a strong function of growth temperature, anneal time, and anneal temperature [5]. Concurrent with the formation of As precipitates is a reduction in the defect density in the material. At present, there are two proposed theories as to how conduction occurs in these layers. Look et al. [6] have proposed that the conduction in unannealed layers is due to variable range hopping (VRH) within a band of deep levels, at low temperatures, and nearest neighbor hopping (NNH) through the same impurity band at higher temperatures. In the VRH regime the conductivity follows the form [7]

$$\ln(\sigma) \propto T^{-\nu}, \quad (1)$$

with $\nu = 0.25$. On the other hand, Warren et al. [4] believe that the high resistivity of the material is due to local depletion around the As precipitates ($f_{\text{hAs}} = 0.8 \text{ eV}$). By this view, the high density of As precipitates results in a system of overlapping depletion regions. Conductivity then occurs by hopping between pockets of undepleted material. This view also predicts the $\nu = 0.25$ VRH behavior which has been reported.

3. Experimental

Table 1 summarizes the sample material parameters. The LTBs were grown on standard undoped semi-insulating (SI) GaAs 3 inch substrates in a VG Semicon V80H dual chamber MBE system. Samples A and E were grown utilizing elemental Ga and As sources while samples B, C and F were grown by GSMBE utilizing solid Ga and cracked arsine (AsH_3). Samples D and G were standard buffer layers, grown at normal growth temperatures and were used for purposes of comparison. Samples A, B, C and D were used for conductivity and photoluminescence (PL) mea-

surements. Samples E, F and G were grown with a $n = 1 \times 10^{17} \text{ cm}^{-3}$ Si doped FET channel on top of the LTB, for evaluation of epitaxial layer quality. Deep level transient spectroscopy (DLTS) and photoluminescence (PL) measurements were performed on these layers.

For the conductivity measurements, parallel, high aspect ratio ($1 \text{ mm} \times 20 \mu\text{m}$ with $40 \mu\text{m}$ separation) patterns with alloyed AuGe/Ni ohmic contacts were fabricated. DLTS measurements on the doped layers were made on Al Schottky diodes having AuGe/Ni guard rings.

The conductivity and PL measurements were performed in a Janis immersion cryostat with 1.4–300 K capabilities. Both measurements are completely automated utilizing LabView and a Mac II computer. The DLTS measurements are also computer automated with transient signals being digitally recorded for subsequent analysis. The light source used for the optical DLTS was a GaAs light emitting diode.

4. Results

The conductivity versus temperature measurements indicate that the LTBs grown by gas source (As_2) and solid source (As_4) MBE are very similar in nature. This is interesting in view of the differences in the growth kinetics for As_2 and As_4 , especially since good quality, high mobility, MBE GaAs has been grown at as low as 430°C using an As_2 source [8]. However, Foxon and Joyce [9] have shown that below 330°C As_2 undergoes an association reaction on the GaAs surface forming As_4 and thus, by this mechanism, the growth characteristics for As_2 and As_4 may be very similar for low substrate temperatures.

Fig. 1 shows dark conductivity versus temperature for three of the samples under study and a commercial undoped semi-insulating substrate. The conductivity of the $650 \mu\text{m}$ thick substrate was calculated assuming an LTB thickness of $2.0 \mu\text{m}$. In this way the intersection of the SI substrate conductivity curve and the LTB conductivity curves indicates that around 230 K substrate conduction dominates. As further evidence that the substrate is dominating the conduction at high

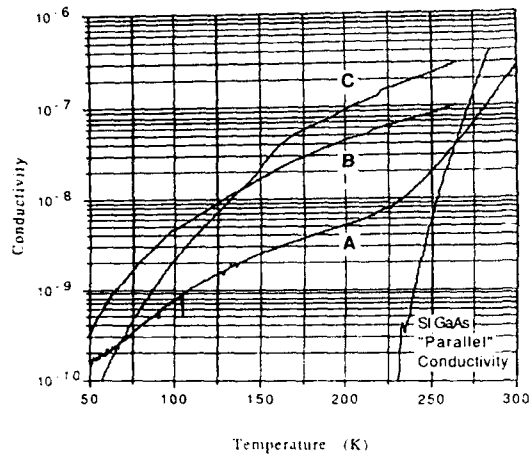


Fig. 1. Conductivity versus temperature for samples A, B and C compared with an undoped liquid encapsulated Czochralski (LEC) semi-insulating substrate. Substrate conduction dominates above 230 K as seen by the thermal activation of EL2.

temperatures, we observed room temperature mobilities in the range of $4000\text{--}6000\text{ cm}^2/\text{V}\cdot\text{s}$ and conductivity which is thermally activated with $\Delta E = 0.7\text{--}0.78\text{ eV}$ (above 250 K) which corresponds to the EL2 trap activation energy. In this region, the conductivity normal to the thin LTB dominates and substrate conduction occurs through the buffer. However, our measurements do not exclude the possibility of activated nearest neighbor hopping in the buffer as reported by Look et al. [6]. For these samples we simply would not observe this behavior due to the relatively high conductivity of the semi-insulating substrate. The mechanism of conduction below 50 K is not well understood and is highly sample dependent.

Clearly, in the range of about 50–200 K, conduction is occurring primarily in the epitaxial LTB layers. The conductivity of the layers grown by gas source is higher than that of the solid source layer (A). Sample A, however, was much thinner ($0.8\text{ }\mu\text{m}$) than the other layers and interface depletion may be contributing to the higher observed resistivity. It should be noted that determination of conductivity by this method (using parallel ohmic contacts with $L/W \gg 1$) is not exact. However, for thin layers ($\sim 2\text{ }\mu\text{m}$) it is not possible to use a Van der Pauw geometry with $L/W \approx 1$. For example, even for the most conductive layer (C), the resistivity at 200 K is approximately $1 \times 10^7\text{ }\Omega\text{ cm}$. For a square sample with a $2\text{ }\mu\text{m}$ thick layer this corresponds to a net resistance of $5 \times 10^{10}\text{ }\Omega$ with resistance increasing to $5 \times 10^{13}\text{ }\Omega$ at 50 K. Our Hall effect system cannot accurately measure samples if the resistance exceeds $1 \times 10^{10}\text{ }\Omega$.

We chose to study thin ($2\text{ }\mu\text{m}$) layers since it has been reported that at greater than $1\text{--}2\text{ }\mu\text{m}$ the material can become polycrystalline [10]. In addition, since typical LTBs used in FET devices are $0.5\text{--}2.0\text{ }\mu\text{m}$ thick, they are of practical interest. This is also important since it is likely that a thick annealed layer would be extremely nonuniform due to As out-diffusion.

Fig. 2 shows $\ln(\sigma)$ plotted versus $T^{-1/4}$ for the same data. The plots are all linear, however, they are also reasonably linear in $T^{-\nu}$ for $\nu < 0.25$ [11]. We acquired a large number of samples (≈ 500 points per curve) and were able to perform a chi-squared minimization to obtain the best fit for various values of ν . We found that the best fit is consistently obtained for $\nu < 0.25$. For sample A,

Table 1
Growth and anneal parameters for samples used in this study

Sample	As species	Growth temperature ($^{\circ}\text{C}$)	As/Ga ratio	Anneal temperature ($^{\circ}\text{C}$)	Anneal time (min)	Doped layer thickness (μm)
A	As ₄	245	20	600	10	–
B	As ₂	245	35	600	5	–
C	As ₂	310	52	600	10	–
D	As ₄	580	8	–	–	–
E	As ₄	245	20	600	10	0.2
F	As ₂	245	35	600	10	0.3
G	As ₄	580	12	–	–	1.0

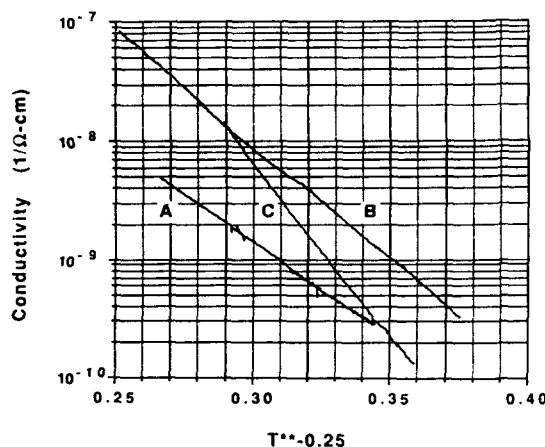


Fig. 2. Conductivity versus $T^{-0.25}$ for samples A, B and C. The linearity indicates hopping conduction. The best fits are obtained for an exponent of $\nu < 0.25$ which indicates that a modified form of variable range hopping conduction is occurring.

$\nu \approx 0.1$, and for sample B, $\nu \approx 0.18$. This indicates that a modified form of Mott's $T^{-1/4}$ variable range hopping could be dominating in these samples. Effects such as strong electron-phonon coupling or a rapidly varying density of states function could cause a lower exponent, such as we observe [12-14].

For the high As/Ga GSMBE sample (C), the data are not linear over a broad enough range to generate a good fit. This sample was grown at a higher substrate temperature and a higher As/Ga ratio than is normally employed. Therefore, both the concentration of As precipitates and native defects is expected to be higher. The higher conductivity for this samples supports this conclusion. Therefore, conduction may be occurring in this sample by a variety of mechanisms accounting for the deviation from simple behavior. This sample suggests that there is a limited range of growth conditions in which high resistivity LTBs can be grown by GSMBE. Our preliminary results indicate that the parameter range for growth by GSMBE is smaller than for solid source MBE.

Fig. 3 is a comparison of 4 K photoluminescence spectra of GaAs grown at low temperatures with As_4 and As_2 and an unintentionally doped buffer layer grown at 580°C . In both types of low

temperature buffer material, no excitons or acceptor-band carbon transitions are observed. The intensity of the carbon transitions is a factor of approximately 20 less in the low temperature buffers than in the standard buffer and the excitonic transitions are an additional factor of 10 stronger than the carbon transitions in the standard buffer. Clearly the LTBs are extremely optically inefficient and do not support the formation of excitons. However the most striking result is that the data indicates that As_4 and As_2 grown buffers are also nearly identical in their optical characteristics.

Figs. 4 and 5 show optical (top curves) and electrical (bottom curves) DLTS scans for solid source (sample E) and gas source (sample F) epitaxial layers grown on LTBs. Positive peaks indicate hole traps while negative peaks indicate electron traps. A reverse bias of -0.75 V was used to detect traps near the middle of the active region. In both layers there is an electron trap at 190 K with an activation energy of 0.28 eV and a capture cross section (CCS) of approximately $5 \times 10^{-15}\text{ cm}^2$. At 260 K there is an electron trap with an activation energy of 0.45 eV and a CCS of $1.5 \times 10^{-14}\text{ cm}^2$ and at 350 K there is another electron

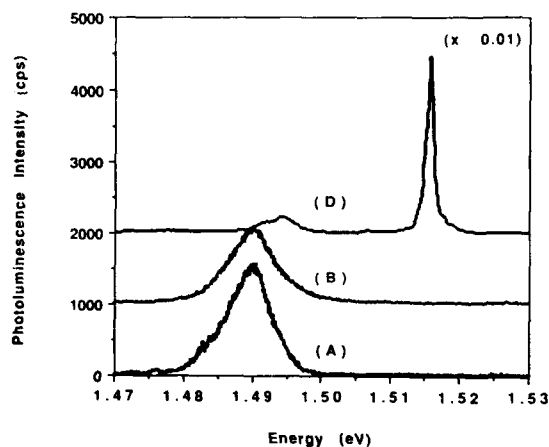


Fig. 3. 4.2 K photoluminescence spectra of low temperature GaAs buffers grown by solid (A) and gas source (B) MBE compared to an standard unintentionally doped buffer (D). No excitons or acceptor-band carbon transitions are observed in the low temperature buffers. (The intensity of sample D is divided by 100 and the curves are offset for clarity.)

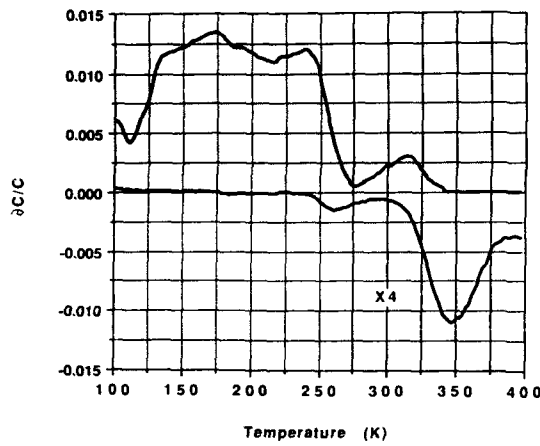


Fig. 4. Optical (top curve) and electrical (bottom curve) DLTS spectra of an FET channel grown by MBE on a LTB (sample E).

level with an activation energy of 0.53 eV and a CCS of $2 \times 10^{-16} \text{ cm}^2$. Both samples contain hole traps with activation energies of 0.38 and 0.52 eV which appear in the spectra at 236 and 320 K, respectively. The trap concentrations are below 10^{15} cm^{-3} . In addition, both layers have a band of unresolvable hole levels between 110 and 220 K. From these data we can easily see that the epitaxial layers grown on top of these LTBs are quite similar in their electrical characteristics. Perhaps

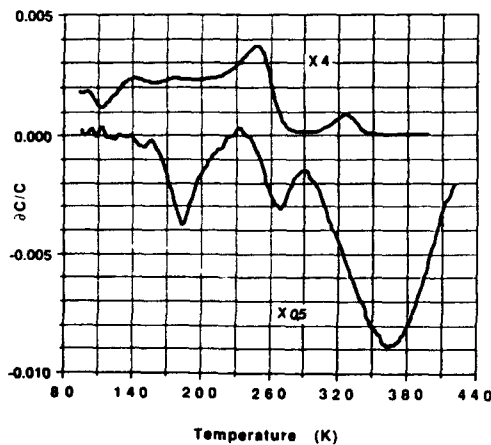


Fig. 5. Optical (top curve) and electrical (bottom curve) DLTS spectra of an FET channel grown by GSMBE on a LTB (sample F).

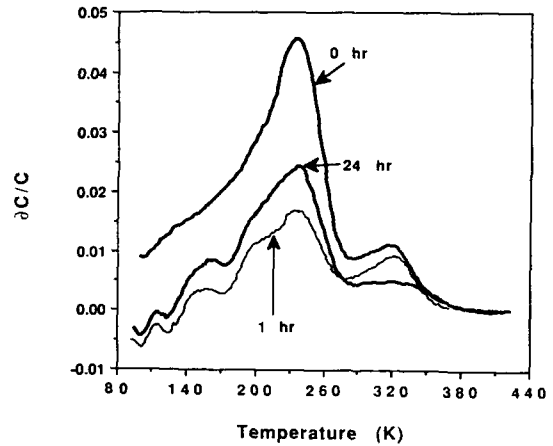


Fig. 6. Optical DLTS spectra of GSMBE FET active region (sample F) at various anneal times.

the most striking information though is that without the incorporation of the LTB, the control samples exhibited none of these electron or hole levels in detectable quantities. The limit of our detection level for this range of doping is approximately $2 \times 10^{14} \text{ cm}^{-3}$. Therefore, it is seen that the out-diffusion of As from the As-rich LTB seriously degrades the quality of the subsequently grown epitaxial layers.

The stability of the same epitaxial layers was studied for various proximity anneal times. Figs. 6

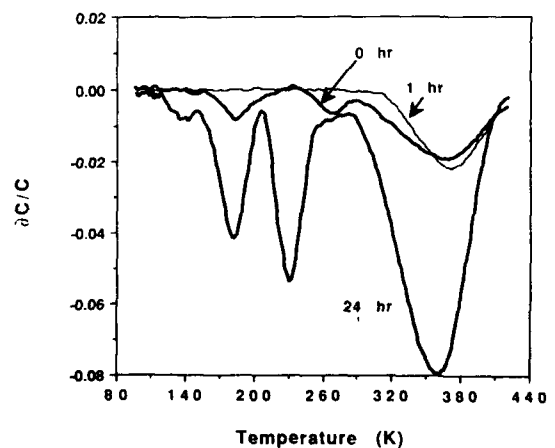


Fig. 7. Electrical DLTS spectra of GSMBE FET active region (sample F) at various anneal times.

and 7 show optical and electrical DLTS data on these layers respectively. A bias of -2 V was used to profile closer to the active/buffer interface. The reverse bias leakage currents remained constant in the low nA range for all samples. Hall effect and capacitance-voltage measurements show no appreciable change in the carrier concentration of the epitaxial layers. Samples were annealed for 1 and 24 h at 400°C in a nitrogen ambient and referenced to an unannealed sample. The distribution of trap levels is significantly altered by the annealing. The electrical DLTS shows an initial decrease in two of the levels and a slight increase in the highest temperature level after 1 h. After 24 h all of the electron traps increase in concentration and an entirely new level emerges at 240 K. The optical DLTS shows a steady decrease in the 320 K hole trap concentration and an initial decrease in the band of hole levels followed by an increase at 24 h. This shows that even during moderate temperature annealing the material properties of the epitaxial layers are changing. The trend is that the hole trap concentration decreases while the electron trap concentration increases with anneal time.

Fig. 8 shows 1.6 K PL spectra on the epitaxial layers used for the DLTS measurements above. The excitation and detection conditions were kept constant throughout the set of measurements. The

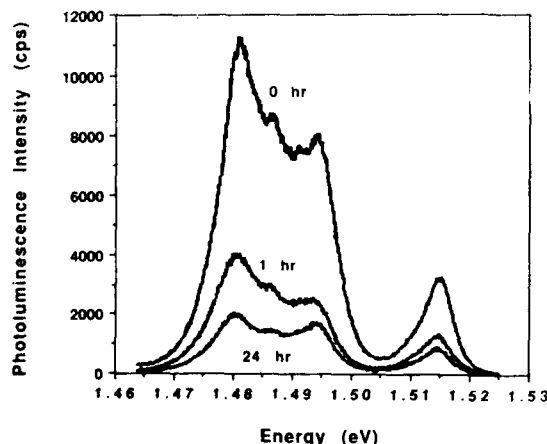


Fig. 8. 1.6 K photoluminescence for the same samples as studied with DLTS. Note the steady degradation in optical efficiency.

spectra show a degradation in optical efficiency versus anneal time. Differences in surface recombination velocity among the samples are not large enough to account for the changes observed. Thus we conclude that the degradation is due to the increase in nonradiative centers seen by DLTS.

5. Conclusions

GaAs LTBs have been grown by both gas and solid source MBE and it is found that the insulating characteristics of the buffers are very similar. The low temperature conduction properties indicate that the exponent in the temperature dependence of $\ln(\sigma)$ is less than 0.25 for both LTBs, which indicates that a modified form of the VRH mechanism proposed by Mott is dominating conduction in the buffer material. It is suggested that hopping is occurring between conduction band electrons separated by depletion regions formed by the arsenic precipitates in the material. We have also observed that the photoluminescence properties of both types of LTB are nearly identical.

The presence of deep levels in FET channels grown on LTBs has been detected. The type and concentrations of deep levels observed by DLTS are similar for both types of buffer. However, in layers grown on a standard high temperature undoped buffer none of these trap levels are observed. After variable time proximity anneals we found that the hole trap concentrations decreased while the electron trap concentrations increased with anneal time.

Acknowledgements

We would like to thank Frank Smith of MIT Lincoln Lab for useful discussions. This research was supported by the Army Research Office, Contract No. DAAL03-89-K-0038.

References

- [1] F.W. Smith, A.R. Calawa, C.L. Chen, M.J. Manfra and L.J. Mahoney, IEEE Trans. Electron Devices ED-9 (1988) 77.

- [2] B.J. Lin, C.P. Kocot, D.E. Mars and R. Jaeger, IEEE Trans. Electron Devices ED-37 (1990) 46.
- [3] M. Kaminska, Z. Liliental-Weber, E.R. Weber, T. George, J.B. Kortright, F.W. Smith, B.Y. Tsaur and A.R. Calawa, Appl. Phys. Letters 51 (1989) 1881.
- [4] A.C. Warren, J.M. Woodall, J.L. Freeouf, M.R. Melloch and N. Otsuka, Appl. Phys. Letters, submitted.
- [5] M.R. Melloch, N. Otsuka, J.M. Woodall, A.C. Warren and J.L. Freeouf, Appl. Phys. Letters, submitted.
- [6] D.C. Look, D.C. Walters, M.O. Manasreh, J.R. Sizelove, C.E. Stutz and K.R. Evans, Phys. Rev. B6 (1990) 3578.
- [7] N.F. Mott and E.A. Davis, Electronic Properties in Non-Crystalline Materials (Clarendon, Oxford, 1971).
- [8] M. Missous and K.F. Singer, Appl. Phys. Letters 50 (1987) 694.
- [9] C.T. Foxon and B.A. Joyce, Surface Sci. 64 (1977) 293.
- [10] Z. Liliental-Weber, F. Smith and A.R. Calawa, MRS Spring Conf., San Francisco, CA, April 1990.
- [11] K.L. Chopra and S.K. Bahl, Phys. Rev. B1 (1970) 2545.
- [12] V. Ambekar, B.I. Halperin and J.S. Langer, Phys. Rev. B4 (1971) 2612.
- [13] J.M. Luttinger and H.K. Sy, Phys. Rev. A7 (1973) 701.
- [14] A.M. Kriman et al., CSSER ESS6206, Arizona State University, manuscript in preparation.

Graded compositional heterostructures in the GaAs/Al_xGa_{1-x}As system

Stephen Giugni, T.L. Tansley

Semiconductor Science and Technology Laboratories (SSTL), Macquarie University, NSW 2109, Australia

and

Grant J. Griffiths

CSIRO Division of Radiophysics, P.O. Box 76, Epping, NSW 2121, Australia

A device exhibiting the characteristics of two anti-parallel Schottky diodes would allow the fabrication of a planar balanced mixer for millimetre wave communications. A suitable GaAs/Al_xGa_{1-x}As isotype heterostructure containing a highly symmetric triangular barrier of controlled height and width in the conduction band is described. Symmetric compositionally graded triangular barriers and quantum wells have been grown with barrier widths between 160 to 4000 Å using conventional solid source molecular beam epitaxy (MBE), by the continuous linear ramping of aluminium mole fraction from $x = 0$ to the order of $x = 0.3$. Current versus voltage ($I-V$) characteristics have been measured over a range of temperatures and correlated with theoretical predictions. Triangular quantum well structures were also grown in the range of widths from 50 to 500 Å and have been studied by photoreflectance (PR) and differential photoreflectance (DR) techniques. Both types of device exhibit excellent symmetry and short, steep compositional profiles have been confirmed by direct secondary ion mass spectrometry (SIMS) and transmission electron microscopy (TEM) analysis on representative samples.

1. Introduction

A pair of Schottky diodes, arranged in an anti-parallel configuration, can be used as a mixing element for mm-wave frequency conversion. Such an arrangement forms the basis of a conventional sub-harmonically pumped mixer in which the local oscillator frequency is set just below half the frequency of the incoming signal. This allows a low frequency oscillator to be used which has many advantages. The diode pair conducts for periods of both half cycles of the signal, producing a conductance waveform of twice the excitation frequency [2,3]. Two difficulties associated with this conventional arrangement are the need to match precisely the characteristics of the two diodes to ensure waveform symmetry, and to fabricate high quality Schottky contacts with low noise and minimal leakage. The physical construction of

such a balanced mixer is also difficult with discrete diodes. Schneider [4] and Allyn et al. [5] suggested that an analogous structure could be produced which incorporated a single, symmetrical barrier to majority carriers. This device would combine electrical characteristics suitable for pure sub-harmonic mixing with the benefits of a buried structure. Only ohmic contacts are required to produce a device, thereby eliminating all of the problems involved with Schottky contacts to GaAs.

The barrier is formed by symmetric triangular grading of the aluminium concentration in aluminium gallium arsenide to produce a triangular intrusion of forbidden states in the conduction band. The linear variation in band-gap offset with aluminium mole fraction, allows the required profile to be engineered by a relatively simple algorithm. A smooth compositional variation in mole

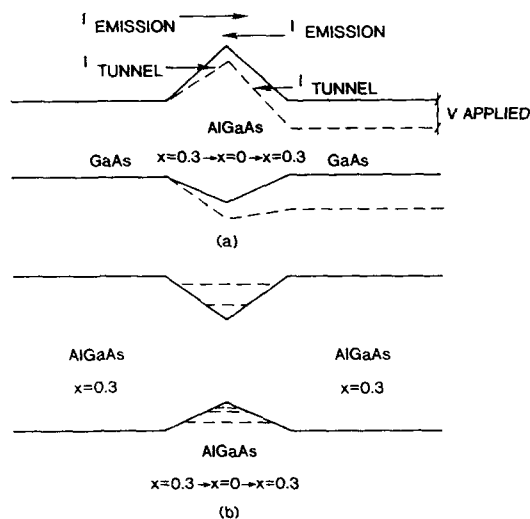


Fig. 1. Schematic band-gap structure for a graded barrier (a) and a graded quantum well (b).

fraction is preferable to a variable period superlattice structure due to the expected enhanced of electron scattering at to multiple interfaces [10].

To examine the efficacy of the grading control by optical techniques, symmetrical graded triangular wells were grown by inverting the above structure. Fig. 1 shows schematically the band-gap structure for a graded barrier and quantum well.

2. Growth of samples

The samples analysed in this work were grown in a VG Semicon V80H MBE system. The method of substrate preparation and growth are standard and will not be presented here. Alloy changes were effected by precise control of the aluminium source temperature, in contrast with previously reported attempts to grow well-defined graded structures by MBE [5–9].

The growth of very narrow, symmetric, linearly graded structures requires that the Knudsen cell temperature be ramped at a rate which maintains near-equilibrium conditions. This is particularly important in the region of temperature reversal, at the barrier peak or well bottom, where skewing of the contour will have the most significant effect.

By studying the relationship between beam flux arrival rates with temperature, growth rate, cell transient response and alloy composition, an algorithm was readily constructed to facilitate the growth of arbitrary profiles. A familiar feature of the GaAs/AlAs system is the very small lattice mismatch between the extremes of alloy composition allowing it to be varied without introducing strain. Equally attractive for the present purpose is the almost linear variation in the band-gap with increasing aluminium mole fraction up to the Γ -X crossover at approximately 40%. This makes the formulation of a suitable algorithm reasonably straightforward in this alloy system, although an understanding of the kinetics of the particular machine and a detailed characterisation of the source as a function of temperature changes and the amount of material present in the crucible are essential. The algorithm calculates the aluminium flux required for the evolution of the desired grading profile, setting the source temperature in real time by reference to measured flux/temperature calibration data.

3. Modelling

In order to form a basis for determining the performance of the grown structures, the electrical characteristics of the graded barrier diode and the optical response of graded triangular quantum wells have been modelled. The electrical response of the barriers includes contributions from both emission and tunnelling currents. The calculation of the tunnelling component was treated by the application of the WKB method to an arbitrary barrier shape, through a piece-wise approximation [11]. The tunnelling component is added to the emission current over the barrier and the total current calculated as a function of applied bias at a particular temperature. This numerical simulations shows excellent agreement with the exact calculation which solves the wave equations for the specific case of triangular barriers. The model includes the variation of effective mass with aluminium mole fraction, the effect of dopants in the graded region and the position of the Fermi level outside the barrier. A typical simulation is shown in fig. 2.

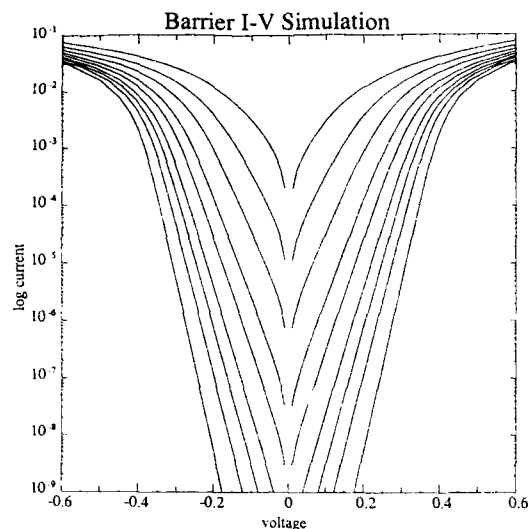


Fig. 2. Simulated current-voltage characteristics for a 750 Å barrier versus temperature. The simulation temperatures are from top to bottom 240, 195, 165, 140, 125, 110, 100, 90 and 77 K.

The quantum levels in graded symmetric triangular quantum wells have not been studied in great detail to date. Previously reported non-rectangular quantum wells [7-9] have either been half triangular or grown with an effective alloy composition change, achieved through a variable period superlattice, so-called digital grading. The exact quantum states have been calculated for the symmetric structures by an appropriate Airy function approach and, as expected, are found to be much further from the band edge than in a similar width square well. This means that the states should be more readily resolved optically.

4. Physical characterisation

In order to verify the structures and hence control of the growth parameters, selected samples were analysed by SIMS, Auger electron spectroscopy and sputtered neutral mass spectrometry. Fig. 3 shows the SIMS profile of a 400 Å triangular graded barrier which exhibits extremely good symmetry without any evidence of skewing. Further confirmation has been provided by TEM

analysis. By viewing a cleaved wedge sample, the compositional variation can readily be observed through the different atomic densities of the constituent alloys. The electron wave interference fringes thus produce an effective alloy composition profile, as shown in the micrograph of a 200 Å graded barrier (fig. 4). These profiles clearly demonstrate that the high degree of symmetry required for sub-harmonically pumped mixer devices can be achieved by conventional solid source MBE.

5. Optical characterisation of graded quantum wells

Graded triangular quantum wells were grown and the quantum energy levels determined by PR, DR and photoluminescence. Fig. 5 shows a typical PR/DR result from triangular well of nominal 125 Å width. The aluminium mole fraction is 0.36. The quantum states for the e_1-hh_1 and the e_2-hh_2

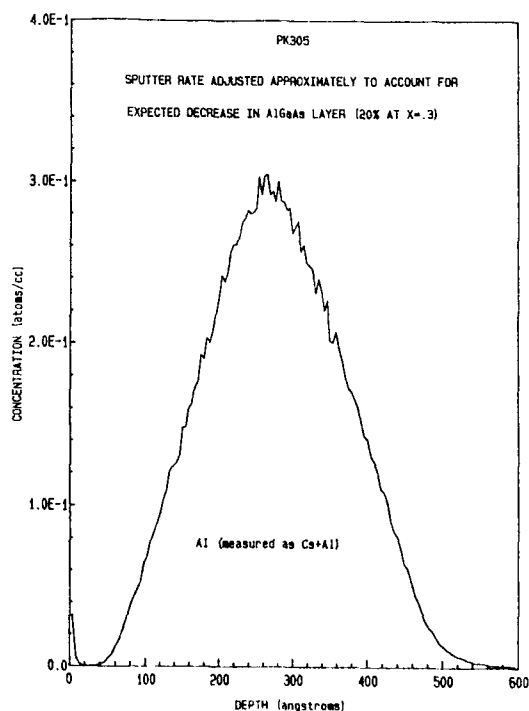
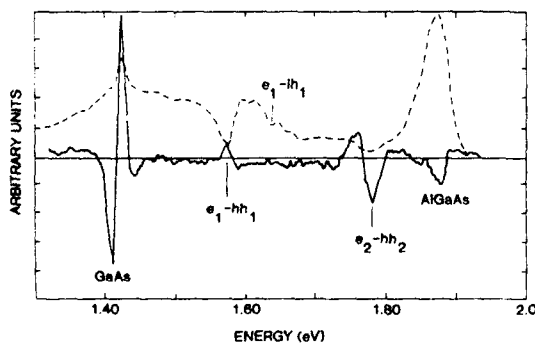


Fig. 3. SIMS analysis of a 400 Å graded barrier.



Fig. 4. TEM micrograph of a 200 Å graded barrier.

(electron to heavy hole) transitions are clearly visible and correspond to the predicted energy levels. The DR trace also provides an indication of

Fig. 5. PR and DR spectra for sample No. 220, a 125 Å graded quantum well. $T = 300$ K. (—) PR; (---) DR.

the e_1 - lh_1 (electron to light hole) transition. We believe this to be the first time a symmetrical continuously graded triangular quantum well has been grown and characterised. While the optical transitions are clearly resolved in this sample, many others showed degraded optical performance arising from the very low growth rates and the concomitant increase in impurity incorporation.

6. Electrical characterisation of graded barrier structures

A number of graded barrier structures have been fabricated and their electrical device characteristics measured at a range of temperatures.

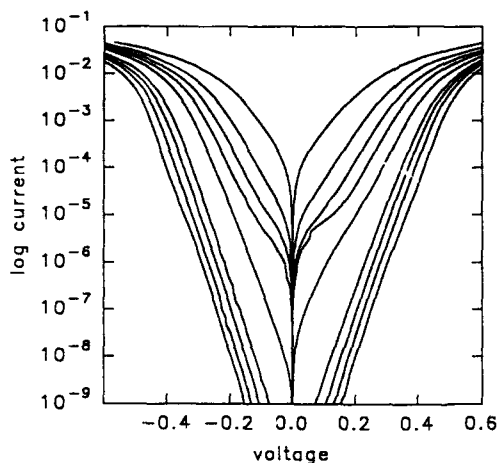


Fig. 6. Measured I - V characteristics for a 750 Å barrier with a contact diameter of 100 μm . The measurement temperatures are from top to bottom 240, 195, 165, 140, 125, 110, 100, 90 and 77 K.

Fig. 6 shows the results for a 750 Å barrier device measured between 77 K and room temperature. The barrier height of this device has been determined to be 230 meV. This is in accordance with the currently accepted theory of band offsets in the GaAs/AlAs system and in contrast to the previously published results for a similar structure [1].

Several interesting features appear in the measured characteristics. At low temperatures, the semi-logarithmic I - V curves are linear and closely parallel, indicating that tunnelling is the dominant means of current conduction. At higher temperatures emission current becomes dominant, the lines are no longer parallel and a uniform ideality factor is approached. The presence of optically filled traps in the barrier region and of various parasitic conductances are also evident in many samples. These and other departures from the idealised model and their respective contributions to device performance will form the basis for future study.

7. Conclusions

The theoretical and physical characteristics of highly symmetrical continuously linearly graded

triangular heterostructures have been developed and proven in the GaAs/AlAs system. Algorithmic control of the aluminium source temperature in a well-characterised MBE system allows the growth of compositionally graded Al_xGa_{1-x}As structures to required profiles with a high degree of precision. In particular, symmetrical triangular barriers and wells with heights/depths up to 300 meV and widths between 100 to 4000 Å can be grown with slope linearities and extrema geometries better than the resolution of SIMS, AES, and TEM. The current-voltage characteristics of barriers show the general features predicted by an appropriate simulation, of symmetry and nonlinearity, whilst they also demonstrate the involvement of an optically fillable/thermally emptyable trap in the conduction process.

Acknowledgments

Stephen Giugni acknowledges the support of CSIRO Division of Radiophysics, The Australian Telecommunications and Electronics Research Board (ATERB), and the Australian Postgraduate Research Awards (APRA) scheme. The authors are grateful for the participation in this work of CSIRO Division Of Radiophysics, and in particular Dr. John Archer, John Wiggins and Dr. Fred Green, of the Solid State Devices Group; Chit Shwe and Dr. Michael Gal of the University of New South Wales; and Dr. Rob Glaisher of the Electron Microscope Unit, University of Sydney. This work is supported in part by ATERB and the Australian Research Council.

References

- [1] A.C. Gossard, W. Brown, C.L. Allyn and W. Wiegmann, *J. Vacuum Sci. Technol.* 20 (1982) 694.
- [2] M.V. Schneider and W.W. Snell, *IEEE Trans. Microwave Theory Tech.* MTT-23 (1975) 271.
- [3] M. Cohn, J.E. Degenford and B.A. Newman, *IEEE Trans. Microwave Theory Techn.* MTT-23 (1975) 667.
- [4] M.V. Schneider, *IEEE Trans. Microwave Theory Tech.* MTT-28 (1980) 1169.
- [5] C.L. Allyn, A.C. Gossard and W. Wiegmann, *Appl. Phys. Letters* 36 (1980) 373.

- [6] C. Schwartz, IEEE J. Quantum Electron. QE-24 (1988) 1712.
- [7] A.C. Gossard, R.C. Miller and W. Wiegmann, Surface Sci. 174 (1986) 131.
- [8] W. Potz and D.K. Ferry, Phys. Rev. B32 (1985) 3863.
- [9] A.P. Long, M.J. Kelly, T.M. Kerr, K.M. Knowles, E.G. Britton and W.M. Stobbs, J. Appl. Phys. 63 (1988) 1603.
- [10] R.J. Malik and A.F.J. Levi, Appl. Phys. Letters 52 (1988) 651.
- [11] T.L. Tansley, S. Giugni, M.J. Batty and G.J. Griffiths, Thin Solid Films 163 (1988) 479.

Precise computer control of the MBE process – application to graded InGaAlAs/InP alloys

James C. Vleck and Clifton G. Fonstad

*Department of Electrical Engineering and Computer Science, Center for Materials Science and Engineering,
and Research Laboratory of Electronics, Massachusetts Institute of Technology, Cambridge, Massachusetts 02139, USA*

We report MBE growth techniques for the precise control of composition in both graded and uniform composition InGaAlAs alloys. Flux modulation through precise control of the effusion cell setpoint temperatures, including corrections for thermal transient effects, is used to achieve graded alloy compositions as well as to maintain a uniform composition in the presence of disturbances such as shutter operations.

1. Introduction

The $\text{In}_x(\text{Ga}_y\text{Al}_{1-y})_{1-x}\text{As}$ alloy system provides an excellent platform for the development of advanced computer controlled MBE growth techniques. It spans the same bandgap range (0.75–1.5 eV) and lattice-matches to the same substrate (InP) as $\text{In}_{1-x}\text{Ga}_x\text{As}_y\text{P}_{1-y}$, but does not suffer from the difficulties inherent in the growth of phosphorus-containing compounds. This advantage, coupled with the large conduction band offsets (up to 0.5 eV) available, makes InGaAlAs an ideal candidate for the ultra-precise techniques of bandgap engineering made possible by solid-source MBE.

We report here MBE growth techniques for the precise control of constituent mole fraction in both graded and uniform composition InGaAlAs alloys. Flux modulation through ramping of the effusion cell setpoint temperature was used to achieve graded composition alloys, and to maintain constant composition in the presence of disturbances in the cell flux due to shutter operation. We find from double-crystal X-ray diffraction studies that maintaining the lattice-matching condition through a graded region is no more difficult than achieving the initial lattice matching conditions for the two ternary constituents of the graded quaternary alloy. Time-dependent corrections to

the setpoint temperature profile are then used to remove transient effects resulting from finite thermal response times of the cells, and to remove flux overshoot transients resulting from shutter operation.

2. MBE growth procedure

The MBE growths were performed in a Riber 2300 three-chamber MBE system, from purely solid sources in Knudsen-type effusion cells. The constituent beams of In, Ga, Al, and As_4 were generated from sources of 7N In, 8N Ga, 7N Al, and 7N As slugs, respectively. Growths typically were performed at a rate of 0.6–0.8 $\mu\text{m}/\text{h}$ under a V/III beam equivalent pressure (BEP) ratio of 15:1 at a substrate temperature varying from 490 to 520 °C.

Flux vs. temperature relationships for each of the effusion cells were derived from measured data fit by least-squares approximation to an Arrhenius form:

$$\log F = A/T + C. \quad (1)$$

The activation energies A were measured periodically by simultaneously logging the beam flux and temperature of each cell while slowly ramping its

setpoint over the temperature range of interest. Since the mole fractions of In in $\text{In}_{0.53}\text{Ga}_{0.47}\text{As}$ and $\text{In}_{0.52}\text{Al}_{0.48}\text{As}$ are nearly equal, the In cell temperature is maintained constant during all growths; this has the effect of fixing the growth rate. Under these conditions, the constants C for Ga and Al are determined from those setpoint temperatures which yield lattice-matched $\text{In}_{0.53}\text{Ga}_{0.47}\text{As}$ or $\text{In}_{0.52}\text{Al}_{0.48}\text{As}$, respectively; these values are determined from X-ray diffraction measurements on a daily basis. Normalizing the Ga and Al fluxes to their values at the values at the lattice-matching value, their $F(T)$ relationships can be written as

$$\log F = T_0 \left(\frac{1}{T_\mu} - \frac{1}{T} \right), \quad (2)$$

where T_0 represents the activation energy, and the "unity flux temperature" T_μ is the setpoint temperature for lattice matching.

Compositional grading was achieved by varying the cell temperatures in accordance with a setpoint profile determined by inverting eq. (2) for the desired flux profile $F(r)$. A personal computer was used to generate a piecewise linear approximation to the desired setpoint profile, and to communicate with digital temperature controllers which governed the effusion cells.

The computer was also equipped for automatic shutter operation, and for logging of beam fluxes using the in-situ ion gauge on the growth manipulator. The latter capability facilitates the measurement of the temporal response of a cell's beam flux to disturbances in the cell's operating condition. Such disturbances would include changes in setpoint temperature or the opening or closing of the cell shutter.

3. Lattice matching

The maintainance of lattice-matching to the InP substrate is a key concern in the growth of $\text{In}_x(\text{Ga}, \text{Al}_{1-x})_{1-x}\text{As}$ alloys; should the synchrony of the flux gradients be lost, lattice mismatch may occur, resulting in undesired variations in material parameters and even misfit dislocations in the extreme case. We examine here the

effect of errors in the two cell flux parameters, T_0 and T_μ , on the maintainance of lattice-matching.

The lattice mismatch resulting from an error in cell flux can be shown to be proportional to the absolute error (as opposed to the relative error) in flux [1]. The errors in cell flux resulting from errors in the cell parameters are then determined by differentiating eq. (2). For T_0 , we find

$$\Delta F = \frac{\Delta T_0}{T_0} F \ln F,$$

whereas for T_μ we find

$$\Delta F = \frac{T_0 \Delta T_\mu}{T_\mu^2} F.$$

To maintain a lattice mismatch less than 0.1%, we then find from these expressions that the relative error in T_μ must be maintained less than 0.2%, whereas the relative error in T_0 need only be kept less than 10%.

To experimentally verify the effects of errors in T_μ on lattice matching, a sequence of five growths, each 0.74 μm thick and linearly graded over their entirety from $\text{In}_{0.52}\text{Al}_{0.48}\text{As}$ to $\text{In}_{0.53}\text{Ga}_{0.47}\text{As}$, were performed. The T_μ of the Ga cell used in this experiment was held constant over the five growths, while that of the Al cell was varied in 1°C increments between each growth, for a total spread of 4°C around the lattice matching point. Double-crystal X-ray diffraction scans of these five layers are shown in fig. 1. (Note that the T_μ of the Ga cell has been set so that all layers are slightly mismatched from the InP substrate: this is to clearly distinguish the epitaxial and substrate diffraction peaks.) The full width at half maximum (FWHM) of the epitaxial peak clearly goes through a minimum for $\Delta T_\mu = 0$ for the Al cell; the value of 24 arc sec for the FWHM is close to the theoretical minimum for this material system at this thickness [2]. The spread in the diffraction peak widths for $\Delta T_\mu(\text{Al}) \neq 0$, corresponding to the varying lattice constant through the graded layer, clearly demonstrates the importance of accuracy in determining T_μ . The very narrow peak for $\Delta T_\mu = 0$, on the other hand, demonstrates that extremely tight control of the lattice constant is easily maintained throughout a grading sequence

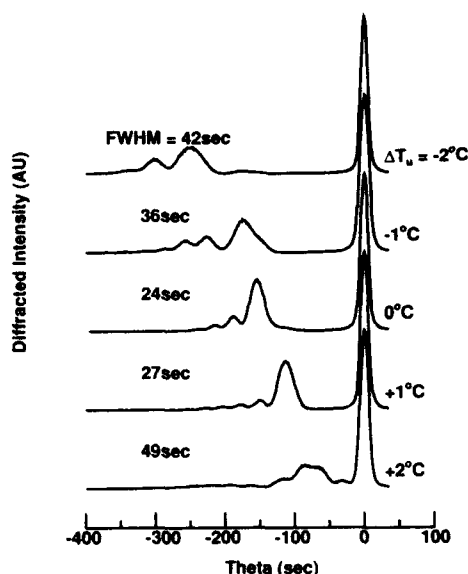


Fig. 1. Double crystal X-ray diffraction scans of uniformly graded $\text{In}_{1-x}(\text{Ga}_x\text{Al}_{1-x})_{1-y}\text{As}$ layers, where T_μ of Al cell is stepped 1°C between each growth. Note that InP substrate peaks (right) have been aligned for purpose of comparison.

provided that the constituent ternaries are closely lattice matched to each other. The observance of Pendellösung fringes in the diffraction signal for the $\Delta T_\mu = 0$ layer, with a period of 26 arc sec (in good agreement with the layer thickness of $0.74 \mu\text{m}$), is further testament to the high crystalline quality of these samples.

4. Time-dependent flux corrections

Since effusion cells have a finite thermal mass, their beam fluxes will not be able to respond instantaneously to changes in setpoint temperature. The resultant time lag in flux with respect to setpoint will lead to over- and undershoot errors in grading profiles if no corrective action is taken. We seek to overcome this difficulty by applying linear system techniques to the analysis of the response of an effusion cell to incremental changes in its setpoint.

Response functions for each of the effusion cells can be determined by measuring the time-de-

pendent flux emitted by the cell in response to a step change in its setpoint temperature. Differentiating this flux with respect to time yields the cell's impulse response; we choose to model this impulse response as a series (typically, one or two) of complex exponentials. Taking the Laplace transform then yields a system function of the form

$$H(s) = \sum_i \frac{c_i}{s + \alpha_i}. \quad (3)$$

To simplify the analysis, we take as the input not the setpoint temperature, but instead the desired flux profile, and as output the actual flux profile. This yields a system with unity gain in the steady state. The setpoint temperature profile is then determined by calculating the inverse system function $H^{-1}(s)$ from eq. (3), multiplying it by the Laplace transform of the desired flux profile, inverse transforming to find the deconvolved profile, and then calculating the setpoint temperature sequence corresponding to this deconvolved profile.

Taking $f_d(t)$ as the desired flux profile, and $f_e(t)$ as the "effective" flux profile obtained through the above procedure, we find that, for a system function characterized by a single time constant, the effective flux profile contains a proportional and a derivative term [3]:

$$f_e(t) = \left(A + B \frac{d}{dt} \right) f_d(t). \quad (4)$$

For a system function characterized by two independent transients with differing time constants, the effective flux profile contains proportional, integral, and derivative terms:

$$f_e(t) = \left(A + B \int_{-\infty}^t dt e^{-\sigma t} + C \frac{d}{dt} \right) f_d(t), \quad (5)$$

where σ is a weighted average of the two time constants. The time constants and coefficients in eq. (5) are determined from measurements of the response of a cell to a step change in setpoint temperature, an example of which is shown in fig. 2. Here, a model incorporating two time constants is fit to flux data measured for a gallium cell (both model and measured data are normalized to the change in steady-state flux). The two-time-con-

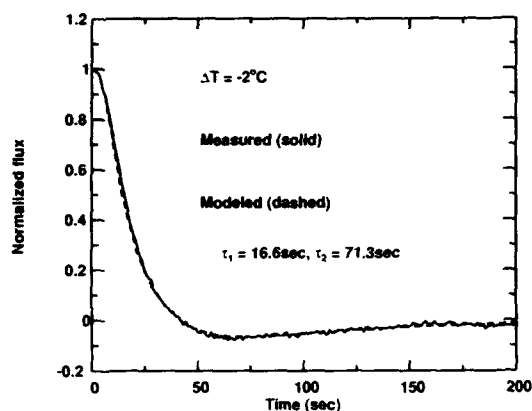


Fig. 2. Comparison of measured flux step response and model incorporating two exponential time constants.

stant model fits the measured data within 4% for times after the step greater than 5 s, and within 1% for times greater than 25 s. The cell's system response is now obtained simply by differentiating the step response.

Fig. 3 compares graded flux profiles with no correction for thermal lag times in the cell (profile "A"); with corrections only for the dominant, short time constant transient (profile "B"); and with corrections for both a short and a long time constant transient (profile "C"). It can be seen

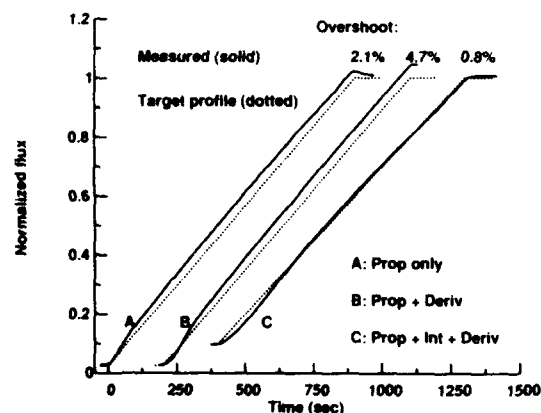


Fig. 3. Comparison of graded flux profiles with no correction for time response (A); correction for one exponential time constant (B), and correction for two exponential time constants (C).

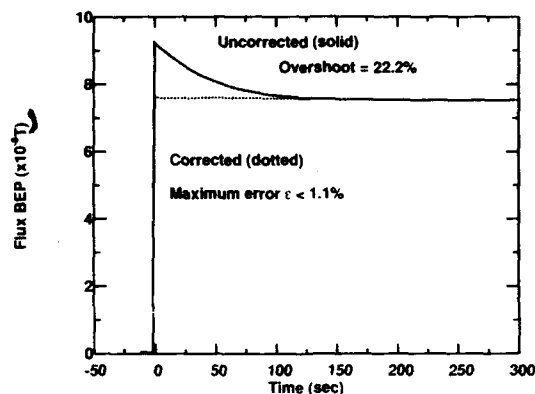


Fig. 4. Measured flux profiles from Al cell without (solid curve) and with (dotted curve) corrections for shutter transient.

that the inclusion of only the short time constant in fact worsens the overshoot at the end of the grading profile, whereas inclusion of both time constants reduces the overshoot to less than 1%.

A single time constant system function does, however, prove adequate in the removal of flux transients due to shutter operations. The opening of a cell shutter typically leads to a positive flux transient of the form:

$$F(t) = F_0 + \delta F e^{-t/\tau_s}$$

The "shutter time constant" τ_s is, in general, not equal to either of the time constants typically measured in the cell's step response, and usually lies between them. For a single time constant, we use Eq. (4) to find for the form of the "effective" flux profile:

$$f_e(t) = Au(t) + B(1 - e^{-t/\tau_s}),$$

where $u(t)$ is the unit step function. This approach is qualitatively similar to that taken by Chilton et al. [4].

Fig. 4 shows aluminium flux profiles, measured after shutter openings, with and without corrections for the transients. In the uncorrected case, the maximum overshoot is in excess of 20%, while the corrected profile is within 1.1% of the steady state value throughout the course of the measurement.

5. Conclusions

In summary, the growth of high-quality graded-composition $\text{In}_x(\text{Ga}_y\text{Al}_{1-y})_{1-x}\text{As}$ alloys on InP substrates has been demonstrated. Graded-composition alloys spanning the entire quaternary range between the two ternary end-points $\text{In}_{0.53}\text{Ga}_{0.47}\text{As}$ and $\text{In}_{0.52}\text{Al}_{0.48}\text{As}$ have been grown. The dominant factor in maintaining lattice matching while grading has been shown to be the initial establishment of lattice matching for the constituent ternaries: layers graded through their entirety over $0.74\text{ }\mu\text{m}$ have been measured with X-ray diffraction full widths at half maximum of 24 arc sec, close to the theoretical minimum. Time-dependent corrections to the setpoint temperature profile to take into account finite thermal response times of the cells have been shown to reduce overshoot effects in graded flux profiles and flux transients due to shutter operation to the 1% level.

Acknowledgements

The authors would like to thank Brian Bennett for performing the double-crystal X-ray scans. This work was supported by the National Science Foundation under Grant No. EET-87-03404, JSEP, through the MIT Research Laboratory of Electronics under Contract, No. DAAL 03-89-C-0001, and in part by the Charles Stark Draper Laboratory.

References

- [1] J. Vleck and C. Fonstad, *J. Vacuum Sci. Technol.*, submitted.
- [2] A.T. Macrander and K.E. Strege, *J. Appl. Phys.* 59 (1986) 442.
- [3] J. Vleck and C. Fonstad, unpublished.
- [4] P.A. Chilton, W.S. Truscott and Y.F. Wen, *J. Vacuum Sci. Technol. B6* (1988) 1099.

Composition control of GaAsP grown by molecular beam epitaxy

Takashi Nomura, Hiroshi Ogasawara, Masahiro Miyao * and Minoru Hagino

Research Institute of Electronics, Shizuoka University, 3-5-1 Johoku, Hamamatsu 432, Japan

This paper describes composition control of GaAsP alloy grown by molecular beam epitaxy. The relationship between the growth condition and the film composition is explained applying a precursor state growth model to GaAsP growth. The activation energies and the parameters appearing in the relationship are determined by fitting the calculated compositions to the experimental ones. The effect of flux intensities, substrate temperature and growth rate on the composition is discussed.

1. Introduction

Ternary or quarternary III–V alloys are important for optical device applications, and a precise control of the composition is required. Composition control of alloys with mixed group V elements is one of the important issues of molecular beam epitaxy (MBE), because there is no simple relationship between the group V fluxes and the film composition. Matsushima and Gonda [1] reported that the phosphorus composition of GaAsP is a function of substrate temperature. For GaAsSb growth, Chang et al. [2] found that the composition is controlled by Sb/Ga flux ratio when the flux ratio is less than unity. Foxon et al. [3] pointed out that the As/Ga flux ratio determines the film composition of GaAsP alloy for a constant P flux intensity. Woodbridge et al. [4] also reported that the composition is a function of the substrate temperature. However, the temperature dependence of the composition was the inverse of that reported by Matsushima and Gonda [1]. Calculation based on the thermodynamic model was reported by Seki and Koukitu [5]; however, the calculated results on GaAsP have not fully explained the experimental results.

In this paper, composition control of GaAsP alloy grown by MBE is described. The relation-

ship between the growth condition and the film composition is explained applying a precursor state growth model to GaAsP growth. The effect of substrate temperature and growth rate is discussed.

2. Growth model

The growth model describes the MBE growth of material i with four processes: the incidence of the atom to the precursor state (J_i), the desorption from the precursor state (D_i), the chemisorption to the film (G_i), and the sublimation to the precursor state by the dissociation of the film (E_i). The dissociation of molecules to atoms, association of atoms to molecules and migration of group V elements at the surface are treated as a precursor state. The concentration of the precursor state n_i is determined by these processes as:

$$dn_i/dt = J_i - G_i + E_i - D_i. \quad (1)$$

In the steady state condition, dn_i/dt is equal to zero. The net growth rate is expressed as $G_i - E_i$. This growth model was successfully extended to ZnSe growth by MBE [6,7].

We applied the growth model to GaAsP growth for the typical growth conditions: substrate temperature is low where the loss of Ga can be ignored, and the beam flux intensity of the group V element is larger than that of Ga beam. The

* Present address: Sendai National College of Technology, Kami-Ayashi, Sendai, Miyagi 989-31, Japan.

growth rate of GaAsP is determined by the arrival rate of Ga under these growth conditions.

For the GaAsP growth it is assumed that the chemisorption rates of group V elements are proportional to the product of the precursor state concentration and the probability of the reaction with Ga, and the interaction between the precursor state of As and that of P is ignored. G_{As} and G_P are expressed as:

$$G_{As}/G_P = q n_{As}/n_P, \quad (2)$$

where q is the ratio of incorporation probabilities of group V atoms with Ga atom at the surface. The sum of the growth rates of P and As is equal to the growth rate of Ga, since the growth rate of GaAsP is determined by the Ga flux intensity. The net growth rate of As and P is expressed as:

$$G_{As} - E_{As} = x J_{Ga}, \quad (3)$$

$$G_P - E_P = (1 - x) J_{Ga}, \quad (4)$$

where x denotes the As composition. The desorption and the sublimation are expressed to have an Arrhenius form:

$$D_i = n_i^m v_i \exp(-\epsilon_{i,d}/kT), \quad (5)$$

$$E_{As} = x L_{As}, \quad (6)$$

$$E_P = (1 - x) L_P, \quad (7)$$

where

$$L_i = a_i \exp(-\epsilon_{i,c}/kT), \quad (8)$$

and m is assumed to be 1. L_{As} and L_P represent the sublimation to the precursor state by the dissociation of GaAs and GaP, respectively. E_i is assumed to be proportional to the composition ratio. Reducing eqs. (1)–(8) gives:

$$\frac{r_{As} \exp\left(\frac{-\epsilon_{As,d}}{kT}\right) \left(1 + \frac{L_{As}}{J_{Ga}}\right)}{q r_P \exp\left(\frac{-\epsilon_{P,d}}{kT}\right) \left(1 + \frac{L_P}{J_{Ga}}\right)} = \frac{\frac{r_{As}}{x} - 1}{\frac{r_P}{1-x} - 1}, \quad (9)$$

where r_i represents the beam flux ratio:

$$r_{As} = J_{As}/J_{Ga}, \quad (10)$$

$$r_P = J_P/J_{Ga}. \quad (11)$$

Eq. (9) is an expression of the relationship between the composition ratio and the growth condition.

3. Results

The unknown parameters and activation energies in eq. (9) are determined by fitting the calculated compositions to the experimental results. The GaAsP layer is grown on GaAs (001) by MBE under various growth conditions. The growth rate is determined by RHEED intensity oscillation. The molecular beam of tetramers is used for As and P. The beam equivalent pressures of As flux and P flux are monitored with nude ion gauge. The As flux intensity is calibrated by a transition from As-stable reconstruction to Ga-stable one. The As composition ratio x is measured by the X-ray diffraction, assuming that the lattice constant of a ternary alloy follows Vegard's law. The layer thickness of GaAsP is 1.0 μm , to relieve the strain due to the lattice mismatch between the film and the substrate.

Fig. 1 shows the As composition of the GaAsP alloy as a function of the As/Ga beam flux ratio for different P flux intensities. Solid line and broken line show the composition calculated by eq. (9). The alloy composition depends on the growth condition in a complex way. No linear relationship was observed between the composi-

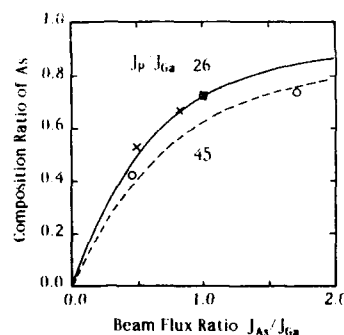


Fig. 1. As composition of the GaAsP alloy as a function of the As/Ga beam flux ratio for different P flux intensities. Solid line and broken line show the compositions calculated by eq. (9). The growth rate is 0.4 $\mu\text{m}/\text{h}$ and the substrate temperature is 470 $^{\circ}\text{C}$.

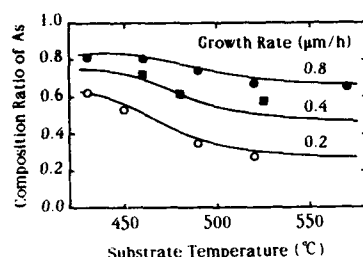


Fig. 2. As composition of GaAsP alloy as a function of the substrate temperature for different growth rates. Solid lines show the composition calculated by eq. (9). The As/Ga beam flux ratio is 1 and the P/Ga beam flux ratio is 45.

tion and the As/Ga flux ratio. The As composition decreases as the P flux intensity increases. The calculated and the experimental compositions agree well.

The effect of substrate temperature on the composition for various growth rates is shown in fig. 2. Solid lines show the composition calculated by eq. (9). The As composition decreases as the substrate temperature increases. However, the decrease of the composition is saturated at higher substrate temperatures. The influence of the substrate temperature on the composition ratio decreases with the growth rate. The saturation temperature is lowered for low growth rate.

Table 1 shows the parameters and activation energies in eq. (9) determined by fitting to the experimental results.

4. Discussions

A higher incorporation probability of As than P by a factor of 50 [3] is reported under the growth condition where excess group V elements

Table 1
Activation energies and parameters determined by fitting the calculated compositions to the experimental results

$\epsilon_{Asd} - \epsilon_{Pd}$	-8.53×10^{-2}	eV
$\nu_{As}/q\nu_P$	2.93×10^{-2}	
ϵ_{Ave}	2.55	eV
a_{As}	1.05×10^{23}	cm^{-2}
ϵ_{Pe}	3.67	eV
a_P	1.01×10^{26}	cm^{-2}

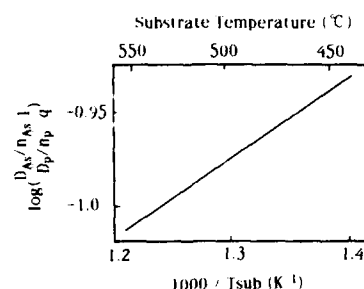


Fig. 3. Calculated value of the product of incorporation rate from the precursor state to the substrate and the desorption rate from the precursor state.

are supplied. The As composition of GaAsP alloy is controlled by adjusting the As/Ga beam flux ratio. However, the composition is varied by the beam flux intensity of P. This variation is explained by the concentration change of the precursor state. The beam flux intensity of P changes the concentration of the precursor state of P. Thus the concentration is varied through the change of the ratio of the reaction rates with Ga, $G_{As}/G_P = qn_{As}/n_P$.

The effect of the substrate temperature on the composition is clarified by calculating G_i , D_i and E_i as a function of substrate temperature. The product of the ratio of incorporation rates and the ratio of the desorption rates from the precursor state is calculated based on the determined activation energies. The product is plotted as a function of substrate temperature in fig. 3. The product decreases as the substrate temperature increases, which shows that the ratio of the incorporation rate G_{As}/G_P is increased and the ratio of the

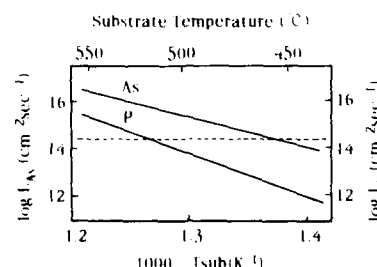


Fig. 4. Calculated value of the dissociation rate of As and P as a function of the substrate temperature. The broken line denotes the Ga flux intensity at the growth rate of 0.4 $\mu\text{m/h}$.

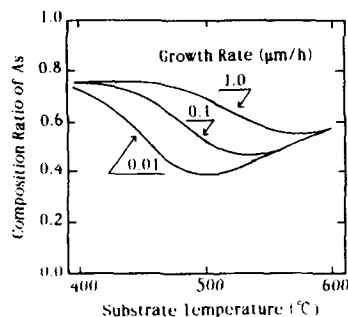


Fig. 5. Calculated film composition as a function of substrate temperature for various growth rates. The As/Ga beam flux ratio is 1 and the P/Ga beam flux ratio is 45.

desorption rate D_{As}/D_P is decreased. The effect of G_i and D_i increases the As composition as the substrate temperature increases.

Fig. 4 shows the calculated values of L_{As} and L_P . The broken line in the figure shows the number of incorporated Ga atoms for growth rate of $0.4 \mu\text{m/h}$. The sublimation of precursor state L_i increases with the substrate temperature. The sublimation of As is comparable to the growth rate at around 460°C . However, the sublimation of P is negligible because the sublimation of P is less than 1% of the growth rate. Thus the As is preferentially sublimated around 460°C . The effect of the sublimation decreases the As composition. On the other hand, sublimation of P becomes comparable to the growth rate around 520°C . The saturation of decrease of As composition around 500°C of substrate temperature is due to the sublimation of P.

The calculated As composition for a wider range of growth conditions is shown in fig. 5. The temperature dependence of the composition varies, depending on the substrate temperature and the growth rate.

5. Conclusion

The relationship between the composition of GaAsP and the MBE growth condition is determined. The expression of the relationship between the composition ratio and the growth condition is obtained with the precursor state growth model. The activation energies and parameters are determined by fitting the calculated compositions to the experimental results. The effects of the sublimation of group V material on the composition are discussed.

References

- [1] Y. Matsushima and S. Gonda, Japan. J. Appl. Phys. 15 (1976) 2093.
- [2] C.A. Chang, R. Ludeke, L.L. Chang and L. Esaki, Appl. Phys. Letters 31 (1977) 759.
- [3] C.T. Foxon, B.A. Joyce and M.T. Norris, J. Crystal Growth 49 (1980) 132.
- [4] K. Woodbridge, J.P. Gowers and B.A. Joyce, J. Crystal Growth 60 (1982) 21.
- [5] H. Seki and A. Koukitu, J. Crystal Growth 78 (1986) 342.
- [6] Z. Zhu, T. Nomura, M. Miyao and M. Hagino, J. Crystal Growth 95 (1989) 529.
- [7] Z. Zhu, T. Nomura, M. Miyao and M. Hagino, J. Crystal Growth 96 (1989) 513.

Dynamics and roughness spectrum of the GaAs(001) surface during the MBE process

L. Däweritz, J. Griesche *, R. Hey and J. Herzog

Zentralinstitut für Elektronenphysik, Hausvogteiplatz 5-7, O-1086 Berlin, Germany

The roughness spectrum of the GaAs(001) surface has been studied during growth and after growth interruption by combining the time-dependent recording of the RHEED specular beam intensity with intensity profile measurements of the specular streak. The profiles reflect drastic changes in the distances of Ga-terminated steps in $[1\bar{1}0]$ direction, the roughness of As-terminated steps in $[110]$ direction, and the number of levels included in the surface profile. The rates of the underlying kinetic and thermodynamic processes are estimated from the recovery of the specular beam intensity which shows a stepwise increase for growth interruptions after extended deposition.

1. Introduction

Previous conclusions on interface roughness of molecular beam epitaxy (MBE) grown interfaces differ considerably [1]. This provokes the question on the roughness spectrum of the growth front and of the annealed surface. The evolution of the surface can be studied in situ by reflection high-energy electron diffraction (RHEED). From intensity profile measurements of the specular streak the average terrace width on the GaAs(001) surface has been found to be in the order of about 500 Å during steady state growth and in the order of several 1000 Å after 10 min growth interruption [2]. The recovery of the specular beam intensity observed after depositions on a well annealed surface can be fitted by a two-exponential form [3,4]. This has been explained by considering the initial fast process as a rapid smoothing of the growth front profile and the following slow process as recovery of long range order. For integer or 0.12 less than integer monolayer depositions a dip in the recovery curve after the initial raise has

been reported [4,5]. In the present work, the growth is interrupted after extended growth leading to a higher surface roughness. Without provisions to interrupt the growth at a certain stage, the recovery curve shows an additional dip. By a combined analysis of this curve and of intensity profiles taken at defined stages deeper insight into the evolution of the roughness spectrum of the surface is obtained.

2. Experimental

Growth and annealing cycles were performed at a substrate temperature of 580°C, an As_4 :Ga beam equivalent pressure (BEP) ratio of 10 and a growth rate of 0.45 ML (monolayers) s^{-1} . At these conditions a clear (2×4) structure was observed and the specular beam intensity recorded in the $[110]$ azimuth at an out-of-phase condition reached the maximum for the static as well as the growing surface. The arrangement for intensity measurements consisted of a collimator, optical fibre, and photomultiplier. Intensity profiles along the 00 streak were measured by photodensitometry from RHEED patterns recorded photographically (exposure time 0.5 s).

* Sektion Physik, Humboldt-Universität zu Berlin, O-1040 Berlin, Germany.

3. Results

Three growth and annealing cycles were realized by Ga shutter opening and closing as indicated in fig. 1. In the first cycle the growth is interrupted after extended growth with a constant specular beam intensity indicating a steady state step distribution. Even after 5 min annealing a stable no-growth intensity is not reached. Nevertheless, step distances larger than the Ga migration length must exist since after growth initiation in the second cycle, the intensity decreases rapidly and oscillates. After several minutes growth, there is an additional decrease in intensity toward the steady state value. During the second growth break, a stepwise intensity increase in two stages is observed after the first rapid raise. In the third cycle, the growth is initiated on a smoother surface. Again a reordering of the growing surface toward the steady state is found. During a growth interruption of about 20 min, the intensity approaches a stable no-growth value. When depositing only a few monolayers on this surface, the usually studied recovery behaviour is found (fig. 2).

In a second series of experiments, RHEED patterns for intensity profile measurements have been recorded at the stages labelled a to i in fig. 1. The profiles compiled in fig. 3 consist of a peak with a fine structure (cf. also fig. 4 and ref. [6]) and diffuse wings. The full width at half maxi-

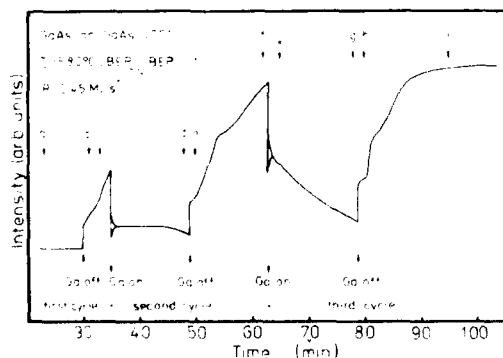


Fig. 1. Temporal behaviour of the specular beam intensity during three growth and annealing cycles. Oscillations are indicated by their envelopes. At stages labelled a to i and * RHEED patterns for intensity profile measurements were taken.

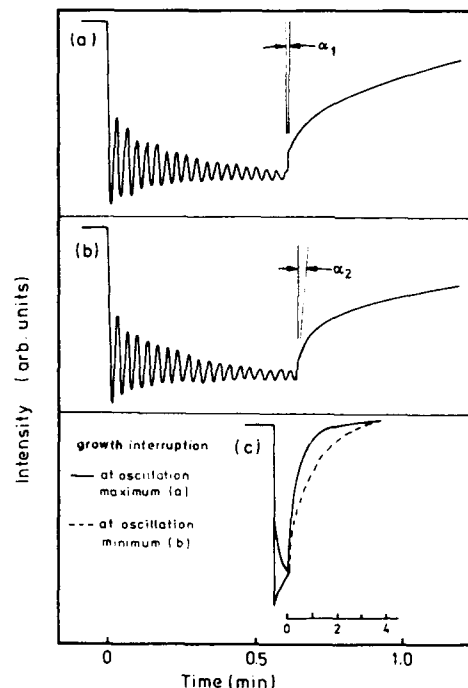


Fig. 2. Recovery of the specular beam intensity after deposition of 18 (a) and 18.5 ML GaAs (b). From $\alpha_1 < \alpha_2$ and the comparison in (c) follows that the growth front relaxes faster for growth interruption at monolayer completion.

um (FWHM) is inverse proportional to the average step distance. The fine structure with splittings $\Delta\theta_r$ and the diffuse wings, respectively, reflect larger and shorter distances, respectively. Taking into account the grazing incidence RHEED geometry, the corresponding correlation lengths in the [110] direction were calculated from the FWHM or $\Delta\theta_r$. The data are given in table 1. In addition, the step distribution is characterized by the ratio B of the profile width at 1/4 of maximum to that at 3/4 of maximum [7]. The width at 0.05 of maximum is a measure of the contribution of short distances to the roughness spectrum.

During the first growth interruption the average terrace width increases from 560 to 670 Å. The B value of 3.3 for steady state growth indicates a geometric step distribution [7], its decrease during growth interruption a transition to a narrower terrace width distribution. A reduction in

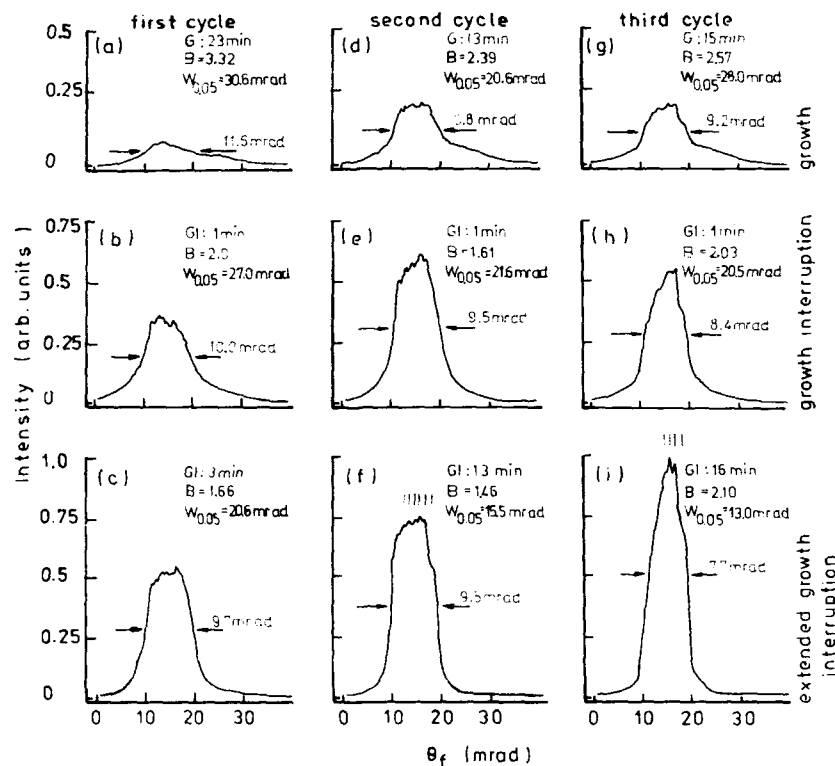


Fig. 3. Intensity profiles of the 00 streak measured for the growth (G) and growth interruption (GI) stages indicated in fig. 1.

the contribution of short distances to the roughness spectrum is evident also from the decreasing $W_{0.05}$ value. During the following deposition the reversal effects are found. Finally, during long-time annealing in the third cycle, the average and maximum terrace width increase to 830 and 6500 Å, respectively. The unexpected high B value for the well-annealed surface can be explained by considering not only a change in the lateral, but also in the vertical distribution of terraces over different levels. For a surface with only a few levels the profile consists of a broad shoulder and a central spike [8]. After separation of the central spike from the shoulder in the profile shown in fig. 3i, a B value of about 1.4 is obtained. This gives clear evidence that on the well-annealed surface, the number of terrace levels decreases.

The reflection of topography changes in the profiles becomes obvious in particular when the

profiles are normalized concerning their maxima. From the profiles presented in fig. 4, it can be clearly seen that the FWHM, $\Delta\theta_f$, and the contribution of diffuse wings increase during growth and decrease during growth interruption.

4. Discussion and conclusions

The model of the GaAs(001) surface shown in fig. 5 takes into account differences of As-terminated steps along the [110] direction and Ga-terminated steps along the $\bar{1}\bar{1}0$ direction regarding excess energy [9] and tendency to meandering [10]. With the given diffraction and recording conditions, the profiles measured are sensitive to a succession of strings of atoms sampled in a one-dimensional cut across the surface in [110] direction and averaged over cuts in $\bar{1}\bar{1}0$

Table 1

Average terrace width, shape ratio B as a measure of the width distribution, profile width $W_{0.05}$ as a measure of the contribution of short distances, and maximum terrace width for different growth and annealing stages

Growth/annealing stage	Average terrace width (Å) Distribution function, $B = W_{0.25}/W_{0.75}$ Contribution of small distances, $W_{0.05}$ (mrad)			Maximum terrace width (Å)
	Cycle 1	Cycle 2	Cycle 3	
	Cycle 1	Cycle 2	Cycle 3	
Growth				
2 min	—	—	710 2.1 25.1	4990
Extended	560 (23 min) 2.3 30.6	660 (13 min) 2.4 28.0	700 (15 min) 2.6 28.0	4700
Growth interruption				
1 min	640 2.0 27.0	680 1.6 21.6	770 2.0 20.5	4990
Extended	670 (3 min) 1.7 20.6	680 (13 min) 1.5 15.5	830 (16 min) 2.1 13.0	6430

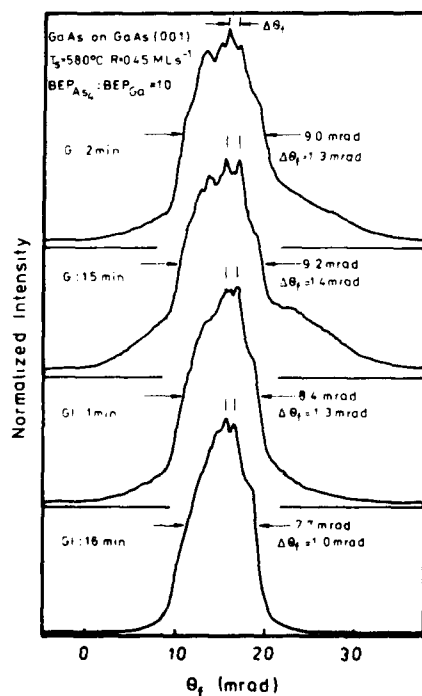


Fig. 4. Normalized intensity profiles for different growth (G) and growth interruption (GI) stages in the third cycle.

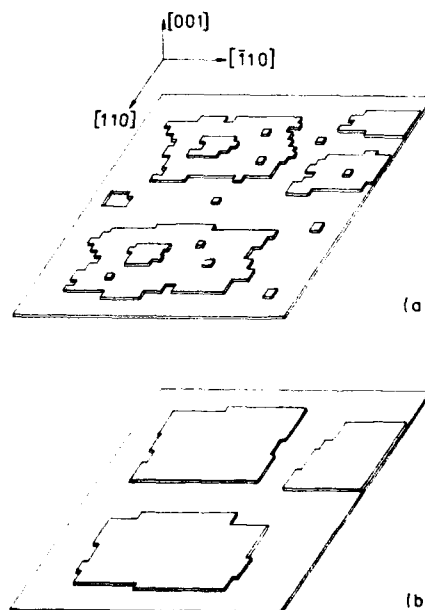


Fig. 5. Schematic illustration of the terrace-step-kink structure of the growing (a) and annealed GaAs (001) surface (b).

direction [11]. The string length distribution sampled is related to the distances of $\bar{1}10$ Ga steps and the roughness of 110 As steps. After growth interruption, the kink and step related free energy will reduce. The reduction of the broad components in the intensity profile can be explained by the dissolution of small clusters and diffusion of their constituents to neighbored islands as well as by the smoothing of 110 As steps. The decrease in the FWHM of the profile combined with an increase of its maximum evidences that finally the island size increases due to a reduction of the number of levels included in the surface profile. The rates of these processes can be estimated from the recovery of the specular beam intensity in the third cycle (cf. fig. 1). The first rapid raise within less than 1 s is tentatively ascribed to the migration of ad-atoms or small clusters to neighbored islands, the second increase within about 2 min to the establishing of a local thermodynamic equilibrium for each island by diffusion of atoms within the given island and smoothing of the step edges. To achieve a global thermodynamic equilibrium by diffusion of atoms between different islands and hopping to lower levels requires more time, as can be seen from the slow approach of the specular beam intensity to a stable no-growth value.

In conclusion, detailed information on the evolution of the surface topography after growth interruption regarding distances in the roughness spectrum and rates of the underlying kinetic and thermodynamic processes has been derived from combined intensity profile and intensity recovery measurements. Drastic changes in the topography

occur not only during the first intensity raise, but also during the slow stage of the intensity recovery.

Acknowledgements

The authors are grateful to Professor H. Berger and P. Krispin for encouraging interest and to K. Haupt for technical assistance.

References

- [1] A. Ourmazd, *J. Crystal Growth* 98 (1989) 72.
- [2] J.M. VanHove, C.S. Lent, P.R. Pukite and P.I. Cohen, *J. Vacuum Sci. Technol.* B1 (1983) 741.
- [3] J.H. Neave, B.A. Joyce, P.J. Dobson and N. Norton, *Appl. Phys.* A31 (1983) 1.
- [4] B.F. Lewis, F.J. Grunthaner, A. Madhukar, T.C. Lee and R. Fernandez, *J. Vacuum Sci. Technol.* B3 (1985) 1317.
- [5] A dip exists also in some of the recovery curves presented in P.R. Berger, P.K. Bhattacharya and J. Singh, *J. Appl. Phys.* 61 (1987) 2856.
- [6] Since the fine structure changes during growth and annealing in an opposite sense and no fine structure was found in profile measurements of fractional-order beams, an artefact of the fluorescent screen can be excluded.
- [7] M. Henzler, *Surface Sci.* 132 (1983) 82.
- [8] R. Altsinger, H. Busch, M. Horn and M. Henzler, *Surface Sci.* 200 (1988) 235.
- [9] D.K. Choi, S.M. Koch, T. Takai, T. Halicioglu and W.A. Tiller, *J. Vacuum Sci. Technol.* B6 (1988) 1140.
- [10] P.R. Pukite, G.S. Petrich, S. Batra and P.I. Cohen, *J. Crystal Growth* 95 (1989) 269.
- [11] D. Saloner, J.A. Martin, M.C. Tringides, D.E. Savage, C.E. Aumann and M.G. Lagally, *J. Appl. Phys.* 61 (1987) 2884.

Growth uniformity studies in molecular beam epitaxy

Z.R. Wasilewski, G.C. Aers

Institute for Microstructural Sciences, National Research Council of Canada, Ottawa, Ontario, Canada K1A 0R6

A.J. SpringThorpe and C.J. Miner

Bell Northern Research Laboratory, P.O. Box 3511, Station C, Ottawa, Ontario, Canada K1Y 4H7

We present the results of experimental measurements and numerical calculations of the layer uniformity of MBE grown GaAs layers on stationary and rotating wafers using different crucible geometries. We obtain excellent agreement between theory and experiment for the actual geometry used in the MBE deposition and describe the configuration required to obtain very good uniformity over a 3 inch rotating wafer. We also study the case of a trumpet crucible insert used as a simple way of improving layer uniformity.

1. Introduction

As the quality of MBE grown epilayers has improved an increasing number of laboratories, particularly those in the area of III–V materials, are shifting their main interest from material studies to device physics and development. Uniformity of layers is therefore a very important issue. Although some of the production oriented MBE systems now marketed offer very respectable growth uniformity, for many systems operating worldwide this is definitely not the case and several groups are experimenting with ways to improve the performance of their older machines. Development of an accurate numerical model for thickness profiles of MBE grown layers may help solve some of the existing problems with less time consuming trial-and-error experiment.

The flux distribution from effusion cells in MBE growth has been addressed by Curless [1] and Yamashita et al. [2]. The cosine law for emission of molecules from both the melt and the crucible walls was used and the re-emission from the crucible walls was calculated self-consistently. The growth rate at any given point on the substrate was calculated by integrating the flux contribution from all melt and wall elements in line of sight

from this point. Curless limited the model to the cylindrically symmetrical case, i.e. the melt surface perpendicular to the crucible axis. Calculations by Yamashita et al. aimed at generalizing Curless' model to the case of liquid loads where the melt surface is not perpendicular to the crucible axis.

Recently we have performed detailed studies [3] of thickness profiles of GaAs layers grown on stationary wafers with two different types of Gallium effusion cells. The first (labelled here CL1) contains an almost straight walled 40 cm³ crucible. The second (labelled CL2) contains a conical 30 cm³ crucible. We found that in order to explain the experimental results two additional effects typical to an MBE environment had to be included in the theoretical model, namely variation of the molecule re-emission coefficient along the crucible walls caused by the temperature gradient and shielding of the molecular flux by Ga droplets accumulated at the crucible orifice. Including such effects allowed us to reduce the maximum difference between calculated and experimentally measured layer thickness to less than 1% over the whole area of a stationary 3 inch wafer.

In the present paper we quote the main results of this model applied to the more practical situation where the wafer is rotating during growth. We

also present new experimental results obtained for a modified cell (labelled CL3) containing a straight walled 80 cm³ crucible with a conical insert and extend our model to cover this increasingly popular configuration.

2. Experimental

The GaAs layers studied were grown with V80H MBE systems. Fig. 1a shows a schematic of the crucible geometry used in the previous calculations [3]. The first cell investigated (CL1) was the standard VG single filament effusion cell with a 40 cm³ pyrolytic boron nitride (PBN) crucible. The second cell (CL2), using a 30 cm³ PBN conical crucible ($\beta \approx 8^\circ$), was supplied by EPI and had a dual filament design. Such an arrangement allows one to reverse the thermal gradient along the cell, thus strongly reducing accumulation of Ga droplets at the crucible orifice and associated spitting

of Ga. The tilt of the melt level with respect to the crucible axes, α , was calculated using the actual cell orientation within the system. Fig. 1b shows a schematic of the crucible geometry for the CL3 cell used for the present study. The cell was equipped with two filaments and no Ga accumulation was observed at the crucible orifice. The Ga charge is placed in a large volume straight wall PBN crucible which is capped with a "trumpet" made from a 30 cm³ conical crucible (the same as the crucible in the CL2 cell described above) with its bottom removed. In our case the distance $h = 81$ mm and the orifice diameter $d = 28$ mm. Such a design retains the uniformity improvement offered by the conical crucible without an associated drop in the useful volume. A similar design used for a Varian system was described by Maki et al. [4]. Fig. 1c shows a schematic of the crucible-substrate geometry and its spatial orientation for the case of a V80H MBE machine, together with the fundamental coordinate system. Note that the

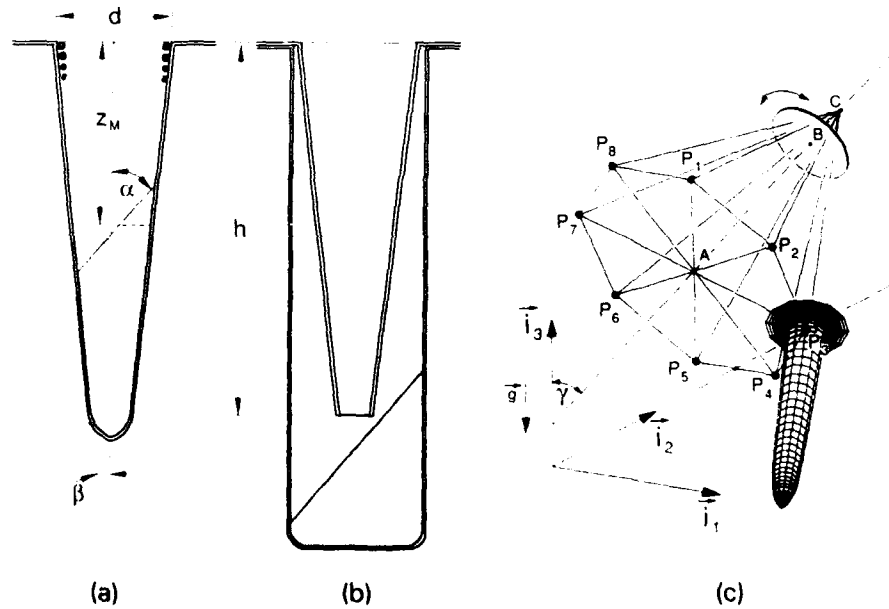


Fig. 1. Schematics of: (a) crucible, defining angles used in present numerical simulations; (b) crucible of cell CL3 containing trumpet insert constructed from a cut-off CL2 conical crucible; (c) crucible-substrate geometry and its spatial orientation for a V80H MBE machine. The plane $i_1 i_2$ is parallel to the floor, while i_3 indicates the vertical direction antiparallel to the direction of gravity g . Points P_1 to P_8 indicate the centres of the cell orifices. For this system $D_{AB} = 13.5$ cm, $D_{BC} = 5.6$ cm, $\gamma = 25^\circ$, $\angle ACP_1 = 24^\circ$, and $\angle P_1 A P_2 = 45^\circ$.

crucible axis does not point at the centre of the wafer.

Layers were grown in the following sequence. After desorption of native oxide thin GaAs (300 Å) and AlAs (300 Å) layers were deposited on a rotating wafer. At this point rotation was turned off, the wafer angular orientation established, and the growth of GaAs resumed. The arsenic pressure was adjusted to maintain arsenic stabilized reconstruction over the whole wafer. In all cases a 1 $\mu\text{m/h}$ GaAs growth rate, and 600°C substrate temperature (as read with calibrated infrared IRCON pyrometers) were used.

Measurements of layer thickness were carried out in two stages. First a map of relative thickness variation across the wafer was obtained using a scanning reflectance system and then an absolute thickness profile was constructed by establishing the exact thickness corresponding to one of the interference fringes using reflectance spectroscopy [3,5]. The absolute accuracy of layer thickness measured in such a way should be better than $\pm 1\%$.

3. Results

The main results of our theoretical studies on growth uniformity for rotating wafers are summarized in fig. 2. More details of these calculations are given in ref. [3]. The top panel indicates that the cell CL1 with the almost straight walled crucible, when used in the supplied machine configuration (fig. 1c), provides a very poor layer uniformity that is also heavily dependent on the level of the melt (z_M) in the gallium crucible. From the middle panel of fig. 2 it can be seen that the cell CL2 with the conical crucible provides better but still insufficient uniformity, again with considerable melt level dependence. These calculations are in good quantitative agreement with experimental results. In the bottom panel of fig. 2 we show results of calculations performed for the case where the CL2 cell crucible axis is tilted to point close to the centre of the wafer. This ensures that practically the whole wafer is in direct line of sight from all emitting surfaces of the crucible. Both uniformity and melt level dependence are

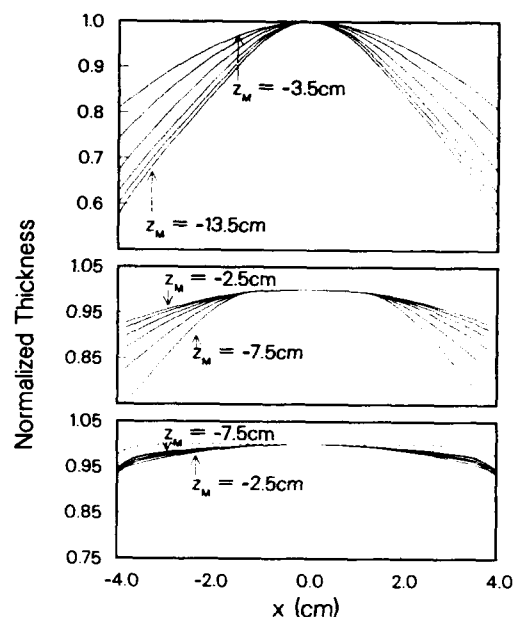


Fig. 2. Theoretical thickness cross-sections for GaAs layers grown on a rotating wafer in the configuration illustrated in fig. 1c. Curves are for a number of values of the distance z_M between the crucible orifice and the melt (measured prior to tilting with gravity). The top panel is obtained for cell CL1 and the middle panel is for CL2. The lower panel is for CL2 but with the crucible axes tilted to point very close to the centre of the wafer. The dashed curve on the lower panel is for the "optimum" case where the cell is directed at 45° to the wafer and the crucible axes is intersecting the wafer center [3].

dramatically improved. Also shown in this panel (dashed curve) is the result obtained for the same configuration but with the wafer rotated to be at 45° to the crucible axis. The resulting layer is calculated to be flat to better than 0.1% over most of a 3 inch wafer.

The geometry represented in this last calculation (dashed curve) is not easily or cheaply implemented in the MBE machines as supplied. However, modification of the effusion cell CL2 such that the conical crucible is rotated within the cell to "overlook" the whole wafer appears, at first sight, to be a workable solution. Unfortunately, since such a cell would have no cylindrical symmetry, it would be more expensive to make and would suffer from uneven heating by the cell heaters which may give rise to excessive melt

turbulence and material spitting. An alternative approach is to modify the crucible itself without changing its position in the cell. For example, the crucible in cell CL3 (see fig. 1b) could be modified to tilt the trumpet insert away from the crucible axis to point towards the centre of the wafer. Such a solution would avoid the disadvantages mentioned above, providing a cell which has higher capacity and better thermal stability than CL2.

The question which we need to answer is how well the beam profile of a cell like CL3 resembles that of a cell like CL2 with a simple conical crucible. Recall that the trumpet insert in CL3 is constructed from a conical crucible identical to that in CL2. More specifically, we wish to determine if the hole in the bottom of the trumpet produces a flux distribution similar to that of a melt surface. We have calculated self-consistently the spatial and angular distributions of the flux leaving a circular opening in a lid covering a straight walled crucible of the same dimension as the outer crucible in CL3. The size of the opening was taken to be the same as that at the bottom of the trumpet insert in CL3. The calculation was performed with the melt surface within the covered

crucible fixed at an angle to the crucible axis appropriate to the experimental arrangement. Within the error of the calculation the distribution from the hole in the covered crucible reproduced the one leaving a simple melt surface of the same dimensions. Furthermore, the results did not change when the covered crucible calculation was repeated with the melt surface normal to the crucible axis, indicating that even for such a large opening the momentum distribution of particles leaving the opening is randomized by multiple collisions with the inner walls. An important practical consequence of that result is the independence of the beam profile leaving the cell on the melt level below the trumpet insert. It is also clear that, to a very good approximation, we can neglect the large container in further calculations, at least for this system, replacing the actual hole in the trumpet with an equivalent melt surface. This simplifies the problem greatly, reducing it practically to the one already solved, that is to the case of CL2 cell. The fact that the melt level is perpendicular to the crucible axes in this case makes little difference to the final flux distribution, particularly for a melt surface deep in the crucible [3].

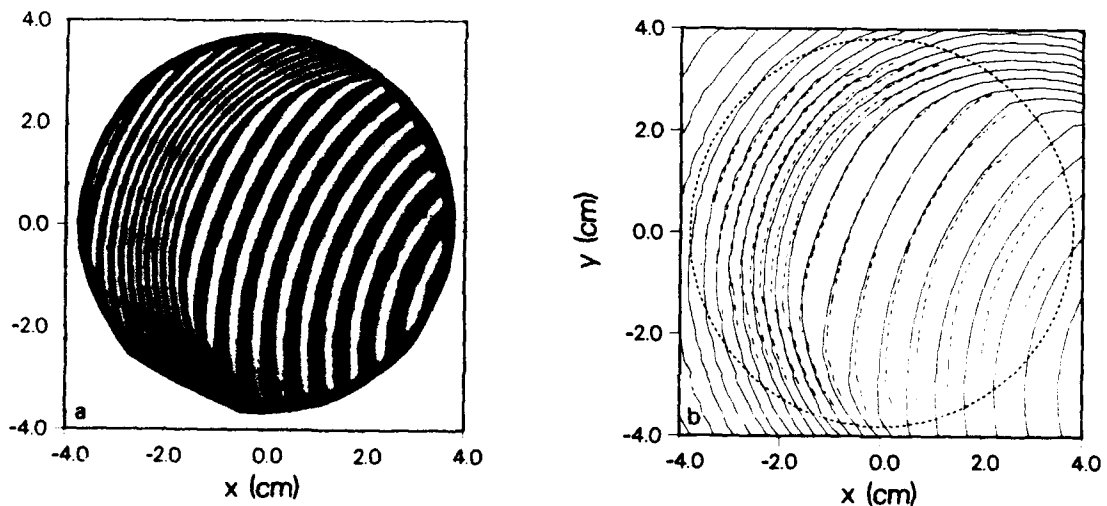


Fig. 3. (a) Reflectance scan of a GaAs layer grown on a stationary substrate with the CL3 cell. Each fringe indicates points on the wafer where the GaAs layer thickness is the same. (b) Comparison between theoretical (solid lines) and experimental (dashed lines) stationary growth thickness profiles for the CL3 cell. The spacings between contours are equal to 5% of the thickness at the wafer centre. The dimensions of the 3 inch wafer are indicated by the dashed circle.

We have carried out the calculations and compared them with the experimental thickness profile for the layer grown on a stationary wafer with the cell CL3. We found that a good fit was obtained only when the bottom 17 mm of the conical insert was assumed to be coated with emitting gallium. This is expected to happen if the Ga accumulated on the inner wall of the PBN trumpet, facing the melt, diffuses round the edge of the trumpet hole to the outer wall. Such diffusion was demonstrated in accurate equilibrium pressure measurements using Knudsen cells [6]. We found that an artificial shift in the position of the trumpet hole towards the crucible orifice has a similar effect on the beam profile. This supports our earlier conclusion [3] that the excellent fit obtained for the cells CL1 and CL2 may have been in part due to the equivalence of such diffusion to a shift of the melt level used in the calculations with respect to the actual one.

The experimentally obtained thickness map for a layer grown with CL3 is shown in fig. 3a. A comparison of the theoretical and experimental thickness contours are shown in fig. 3b. The maximum difference between theory and experiment is less than 2%. Note that the calculations were made with canonical values for all the geometrical parameters of the system except for a small 0.5° tilt in the trumpet insert. The trumpet was supposed to be seated so that its axis was colinear with the axis of the outer crucible but small deviations can be expected. The only additional degree of freedom introduced was the effect of gallium accumulation at the bottom of the trumpet (discussed above). We have also performed calculations for the case of a rotating wafer. As expected, the thickness profile is very similar to the one obtained with the cell CL2 for $z_M \approx -6.5$ (the second worst uniformity curve shown in the middle panel of fig. 2). This result, although rather

negative for the case of the present configuration, leads to an optimistic prediction. Simply rotating the trumpet within the outer crucible or better still using a trumpet already designed in this way, should improve the uniformity significantly, from slightly less than 20% to better than 3% over the area of a 3 inch wafer.

4. Summary and conclusions

We have performed numerical simulations of GaAs layer thickness uniformity for stationary and rotating wafers using a number of crucible geometries in the V80H MBE system configuration. Our calculations indicate that considerable improvements in layer uniformity could be achieved if the crucible were rotated to point at the centre of the wafer. Since this is expensive and technically difficult we investigated the use of crucible trumpet inserts as a simpler way of obtaining greater uniformity. Our results suggest that a trumpet insert may improve uniformity if it is rotated within the outer crucible towards the wafer centre.

References

- [1] J.A. Curless, *J. Vacuum Sci. Technol.* B3 (1985) 531.
- [2] T. Yamashita, T. Tomita and T. Sakuri, *Japan. J. Appl. Phys.* 26 (1987) 1192.
- [3] Z.R. Wasilewski, G.C. Aers, A.J. SpringThorpe and C.J. Miner, *J. Vacuum Sci. Technol.* B9 (1991) 120.
- [4] P.A. Maki, S.C. Palmateer, A.R. Calawa and B.R. Lee, *J. Vacuum Sci. Technol.* B4 (1986) 564.
- [5] L.E. Tarof, C.J. Miner and A.J. SpringThorpe, *J. Electron. Mater.* 18 (1989) 361; L.E. Tarof, C.J. Miner and C. Blaauw, *J. Appl. Phys.* 68 (1990) 2927.
- [6] W.L. Winterbottom and J.P. Hirth, *J. Chem. Phys.* 37 (1962) 784.

MBE monolayer growth control by in-situ electron microscopy

N. Inoue

NTT LSI Laboratories, Atsugi, Kanagawa 243-01, Japan

A molecular beam epitaxy/scanning reflection electron microscope/scanning electron microscope (MBE-SREM-SEM) hybrid system is developed as an in-situ observation technique for study and control of growth of GaAs and AlGaAs. The resolution is 50 nm for SREM and 30 nm for SEM at 10 s/frame observation rate. The highest observation rate is 1 s/frame for SREM and 1/60 s/frame for SEM. Three applications are established: The observation of quick, transient growth processes to clarify the growth mechanism, the measurement of material properties under actual growth conditions to understand and control growth, and growth control by in-process monitoring, in which a micron scale lateral growth of Ga/Al monolayer is developed.

1. Introduction

Precise growth control down to the monolayer is necessary for developing future devices using quantum effects. Additionally, a defect control is required to improve the performance of these advanced devices. In-situ observation of growth processes in molecular beam epitaxy (MBE) may provide new insights into the growth mechanism and defect formation mechanism necessary for such controls.

In-situ surface reflection electron microscopy (REM) during growth is possible in two ways. The original one is using a lens focusing-type electron microscope (called REM), where the sample is embedded between a pair of objective lenses of a transmission electron microscope (TEM) [1]. Here, resolution is good, but growth control is difficult within a narrow space. We have applied this to a terrace growth study on a (100) silicon surface during annealing [2]. The other possibility is a scanning reflection electron microscopy (SREM). This was first performed using TEM [3], but was developed using a scanning electron microscope (SEM) [4]. The resolution of SEM is poorer than that of TEM, but the wide sample space is favorable for realizing growth conditions compatible with those in a conventional MBE system. In-situ observation of Si MBE growth has been performed

[4]. We have developed an MBE-SREM-SEM system for GaAs growth [5]. The unique character of our system from the previous one for Si was the capability of real time observation. We established three applications. One of the main uses is revealing the quick, transient growth processes and clarifying the growth mechanism affecting the grown crystal's morphology and quality. The pictures of these processes have been only ambiguously provided, either from in-situ but averaged measurements over a wide surface by RHEED, or from the characterization of grown crystals. Another use is measuring material parameters under actual growth conditions that determine the growth mechanism and are necessary for developing new growth technologies. The last use is growth control by in-process monitoring.

In this paper, we shall outline this technique's feature and show these applications. For the above applications, high resolution and quick response are essential. The improvements in resolution and observation rate made recently [6] are also described.

2. Experimental

A cross-section of the instrument is illustrated in fig. 1. The main difference of our system from

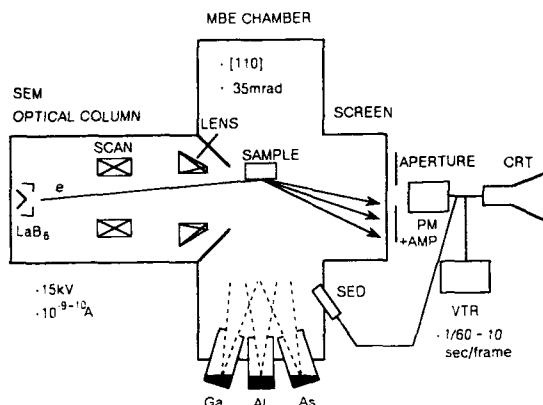


Fig. 1. The MBE-SREM-SEM system.

that previously developed for Si MBE observation is that the optic column of the electron microscope is mounted horizontally, not vertically, to the small MBE chamber, in place of a RHEED gun. This solved the most serious problem with GaAs, clouding of the lenses by the upward As flux. The other difference is that an LaB_6 filament is used which is more resistive to a low vacuum with As than the previous field emission gun [4]. The electron beam is scanned on the sample surface while maintaining the Bragg reflection condition. The RHEED pattern is obtained on the phosphor screen, and one of the diffracted beams is collected by the photomultiplier through the aperture. The SREM image is then viewed on the CRT. A conventional SEM mode is also available.

For in-situ observation, high resolution and quick response are essential and have been realized as follows [6]. The resolution is primarily determined by the electron probe size, but is degraded by contamination of lenses by growing species and sample vibration. The probe size is limited by the required current for forming high contrast images. When we started this study, the resolution was 200 nm for SEM and even worse for SREM at a beam current of 1 nA and an observation rate of 10 s/frame [5]. The probe size was then reduced to 20 nm at 1×10^{-10} A by using a bright, small top LaB_6 filament. To suppress the sample vibration, the whole system was set on the vibration isolation stage. The vibration-

resistant vertical sample holder was then developed to take advantage of our horizontal optics. Recently, the resolution is about 50 nm for SREM and 30 nm for SEM. The apparent resolution of SREM for crystalline feature is 200 nm, which is overestimated because there are no features smaller than 100 nm adequate for evaluation of the resolution.

The observation rate is limited by the S/N requirement. The time to obtain one frame is: (data acquisition time/pixel) \times (number of pixels in one frame). For convenience, pixel refers to the raster line length corresponding to a resolution. Previously it was 10 s/frame for both SREM and SEM [4]. However, the real time observation was possible: As shown later, a top end of a frame showed a surface feature at the start of scan, while a bottom showed that at the end of scan. Provided that the surface is homogeneous, the change during the scan was viewed as a variation within a frame. Recently, a fast, high-gain amplifier has been developed for SREM, and observation may be done at 1 s/frame. For SEM, due to the high yield of secondary electrons, TV rate observation is possible at the cost of resolution degradation. This quick observation contrasts to the Si MBE [4] and GaAs MBE observation [7] typically at a few minutes per frame.

The base pressure of the MBE chamber is about 2×10^{-10} Torr, and the growth control by RHEED, a flux monitor and a QMS is available using 6 Knudsen cells. In the experiment described here, the background As pressure was slightly below 10^{-6} Torr. Unique applications of observation in GaAs growth are to observe Ga droplets and localized Ga monolayers on As layer, which are not expected in Si MBE. Of course, the surface roughness change during growth are observed. The observed processes are recorded on a video tape.

3. Observation of transient growth processes

3.1. Ga-Al droplet formation and annihilation

It has been suggested that Ga droplets are formed in As deficient growth and responsible for

the interface roughness in a hetero-structure [8]. However, the formation mechanism is not clear, because they are not detected during growth. We have directly observed the Ga-Al alloy droplet formation under As-deficient MBE [5]. Next, the

droplet formation by supplying Ga atoms was examined [9]. It was found that Ga droplets are formed on a Ga-stabilized surface as soon as Ga atoms are supplied, as shown in fig. 2a. Therefore, it is clarified that Ga on a Ga layer cannot form a

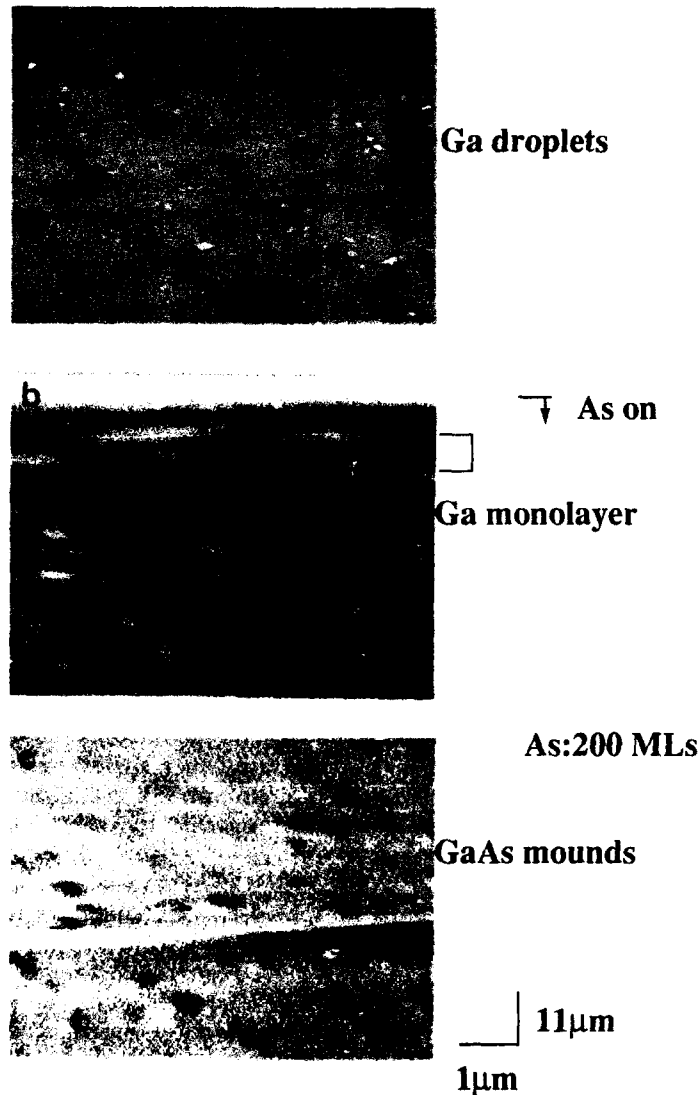


Fig. 2. Ga droplet and GaAs mound formation at 610°C observed by SEM. The images are foreshortened in the vertical direction by about 20 times. (a) Ga droplets (dark spots) are formed as soon as Ga atoms are supplied on a Ga stabilized surface. The gray ovals are GaAs mounds formed by previous experimental sequences. (b) Ga droplets shrink by absorption of As. The bright bands on the top are Ga overlayer around droplets (see section 5). (c) The droplets annihilate by absorbing As, leaving GaAs mounds behind.

continuous film. This opposes the previous suggestion from the RHEED study, but supports speculation by Neave et al. [10]. The RHEED study was wrong, because it observed the crystalline phase covering the most of the surface, while the excess Ga atoms are gathered within the small droplets. The droplet distance is as large as several microns and does not increase on further supply of Ga. So, all Ga atoms arrived between the droplets are captured by the droplets. No anisotropy was found (foreshortening limits the sensitivity to anisotropy). It was established that the droplets are formed through nucleation by supersaturation of Ga adatoms. The nucleation is diffusion limited, because the distance is inversely proportional to the root of the supply rate [11].

It was found that the mounds are formed on the droplets when droplets are annihilated by absorption of As, as shown in fig. 2c [9]. This is the first hard evidence supporting the previous suggestion that droplets cause roughening [8].

3.2. Surface roughening and smoothing

Preparation of an atomically smooth surface is essential for controlled growth of atomic layers. Surface roughening after growth, 20–1200 nm thick was observed step-by-step by Isu et al. [7]. Here, the surface roughening and smoothing processes by thin buffer layer growth were continuously observed in comparison to the RHEED pattern observation. Fig. 3 shows an example. First, after removing the oxide, a three-dimensional RHEED pattern is observed. In SREM, there are no features observed, suggesting that the small undulation below the resolution is on the surface. In some growth conditions, for example a slow growth rate at a high substrate temperature, a submicron scale cobbled structure appears in a very short growth period, as shown in fig. 3b. A particular RHEED pattern corresponds to the surface feature. However, under adequate growth condition, surface undulation disappears by growth of only 100 monolayers in 4 min, as shown in fig. 3d. During growth, the RHEED pattern changed to a 2×4 reconstruction, while the trace of rough features remained in the SREM image, as shown in fig. 3c.

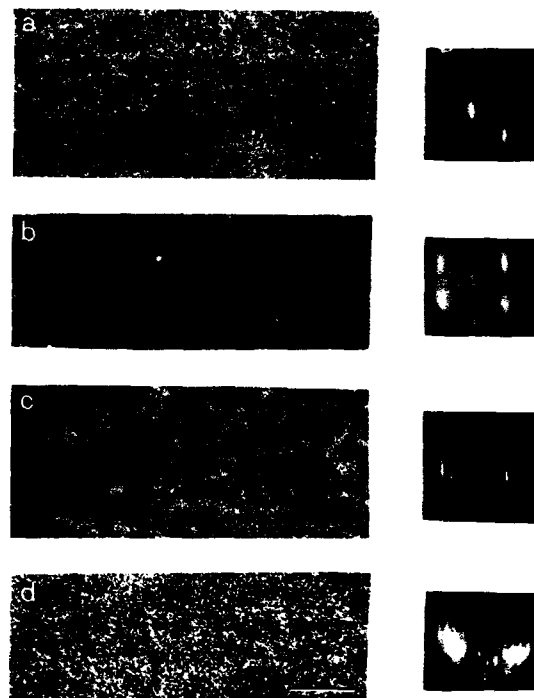


Fig. 3. Surface roughening and smoothing by buffer layer growth observed by SREM (left-hand column). The corresponding RHEED patterns are also shown (right-hand column). (a) before growth; (b) roughening; (c) smoothing; (d) after 100 layers (4 min). Marker represents 1 μm .

Thus, the high-rate SREM observations provide a great deal of information, such as surface feature size and how a smooth surface can be obtained, and are more sensitive to long range surface roughness than RHEED.

4. Material parameter determination during growth

4.1. Ga migration distance on a Ga top layer

The surface migration distance of growing species is a very important material parameter because it controls the growth mechanism and affects the terrace size. So far, this has been determined by RHEED oscillation under growth on the tilted substrate [12]. This method cannot measure migration distances larger than 30 nm because

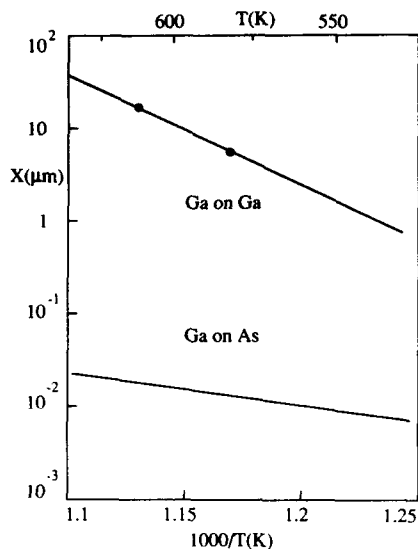


Fig. 4. Migration distance of Ga on Ga. Migration distance of Ga on As in conventional MBE [12] is shown for comparison.

a substrate has a terrace smaller than that due to misorientation. It is also difficult to be applied to an alternate supply growth. As shown above, half the distance between Ga droplets gives the lowest estimation of Ga migration distance on the surface covered with a Ga layer. This is a new, direct measurement method of migration [5]. Fig. 4 shows an example [9]. The migration distance exceeds $1\ \mu\text{m}$, 2 orders of magnitude larger than the Ga migration distance on the As surface from a RHEED oscillation study [12].

It is to be noted that the RHEED oscillation method observes the intralayer migration only. On the other hand, Ga atoms move over many steps in the present case. The interlayer migration is measured by the present method, which plays an important role in obtaining the smooth surface.

It was found that the Ga droplet size during normal MBE growth under Ga-rich conditions is as large as that in alternately supplying growth. This implies that coexisting As on the surface has little effect on Ga migration [5]. The other important result is that the droplet distance in Ga-Al alloy is nearly equal to that in Ga [5,9,13], because

the terrace size in AlGaAs is usually much smaller than that in GaAs [14].

4.2. Pseudo-self-limiting nature of Ga layer

Ga droplet formation was examined on both the Ga-stabilized and As-stabilized surfaces [9]. On a Ga-stabilized surface above 510°C , droplets appear as soon as the Ga supply begins. On the other hand, on an As-stabilized surface below 510°C , Ga droplets appear after more than 1 monolayer of Ga is supplied. In short, in both cases, only 1 Ga monolayer is stable with excess Ga atoms-forming droplets [9]. This behavior is similar to the self-limiting mechanism employed in atomic layer epitaxy (ALE) in MOCVD. Hence, the pseudo-self-limiting nature of Ga is established in MBE growth. This may be due to the weak Ga-Ga bond and large surface tension of Ga metal [8]. Ga-Al alloy also has a self-limiting nature [13]. This may be applicable to monolayer growth control in GaAs/AlGaAs hetero-structure fabrication.

4.3. Surface stoichiometry

Surface stoichiometry determines the reconstruction and affects the growth mechanism considerably. However, there has been little quantitative information [15] as there are no reliable measurement methods. In our study, Ga droplets always appeared on Ga supply as soon as the surface changed to a Ga-stabilized 4×2 structure. This agrees with the free Ga formation observed in the thermal treatment [15]. Thus, the 4×2 structure corresponds to 100% coverage by Ga. The amount of Ga atoms supplied until droplet formation equals the amount of As atoms on the initial surface. Therefore, the surface stoichiometry or As coverage can be precisely determined by droplet observation. Here, the Ga flux is calibrated by a RHEED oscillation period under normal MBE growth. The result is shown in fig. 5 [16]. In this case, measurements were performed at least several minutes after the As supply was stopped. Therefore, surface stoichiometry without As flux was obtained (background As pressure was slightly lower than 10^{-6} Torr and As evaporation might

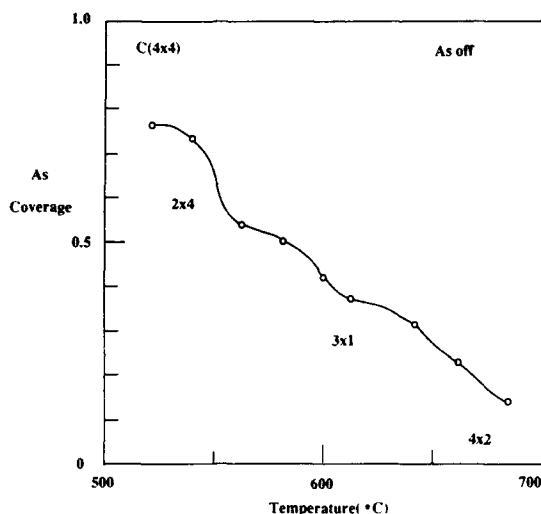


Fig. 5. Surface coverage of As without As flux. On supply of Ga, droplets appear as soon as a 4×2 reconstruction is developed, which is considered to be 100% Ga coverage.

be negligible before droplet formation). It is notable that the surface stoichiometry is not uniquely determined by the reconstruction, but As coverage decreases monotonically with the temperature increase. This is probably due to accelerated As evaporation at high temperature. Maximum As coverage on a 2×4 reconstructed surface is 75%, which confirms the missing dimer model [17] and suggests that this new measurement method is reliable. The measurements were also performed immediately after As was stopped. Here, the surface stoichiometry under As flux could be obtained so long as the As evaporation was negligible. In this case, the As coverage was always higher than that shown in fig. 5 [16].

5. Control of lateral growth of a Ga monolayer by in-process monitoring

As described earlier, it was found that the Ga top layer has two advantageous characteristics for atomic layer controlled epitaxy; (1) a pseudo-self-limiting nature and (2) a large Ga atom migration distance. Based on these, a new growth method is developed: a micron scale lateral growth of a Ga monolayer over an As top layer [18].

We found a novel growth process; when As was supplied on the Ga-stabilized surface with droplets, faint bright areas appeared in the SEM image (top of fig. 3b), which disappeared quickly. It was found that these were Ga layers developing laterally from the droplets over the As top layer and covered by As again. The locally separated coexisting Ga and As top layers were not expected, but observed by both SEM and SREM.

To establish complete monolayer growth, control by in-situ monitoring was used. An example of avoided condition is the continuous or more than 1 monolayer supply of As atoms, where the As covers the Ga overlayer and suppresses further lateral growth, and introduces mounds on the droplets (fig. 3). An insufficient Ga supply also results in incomplete coverage. Finally, the complete lateral growth of a Ga monolayer from a Ga droplet over a micron is realized by the following procedure.

The surface topography change is reproduced in fig. 6:

- (a) Ga droplets are formed by a supply of excess Ga.
- (b) As is supplied for 1 monolayer in a short pulse. Then, the surface darkens, showing the coverage by As. Bright areas, Ga monolayers, appear around the droplets and begin to extend.
- (c) Finally bright areas cover the entire surface, leaving shrunk droplets.

The growth model is shown in the right hand side of the figure.

- (b1) When the surface is covered by As, it is possible for Ga atoms in the droplets to find stable As sites. They come off the droplets and attach themselves to the nearest As atoms.
- (b2) The Ga atoms that follow migrate over the new Ga overlayer until they reach the As layer. Since migration occurs on a Ga layer, the migration distance is very large.
- (c) This process continues until the surface is completely covered by Ga. Growth is stopped by the self-limiting mechanism.

It takes about 10 s for complete growth. From material property point of view, the lateral growth provides information concerning the Ga migration in a time domain for the first time.

It is remarkable that the monolayer size ob-

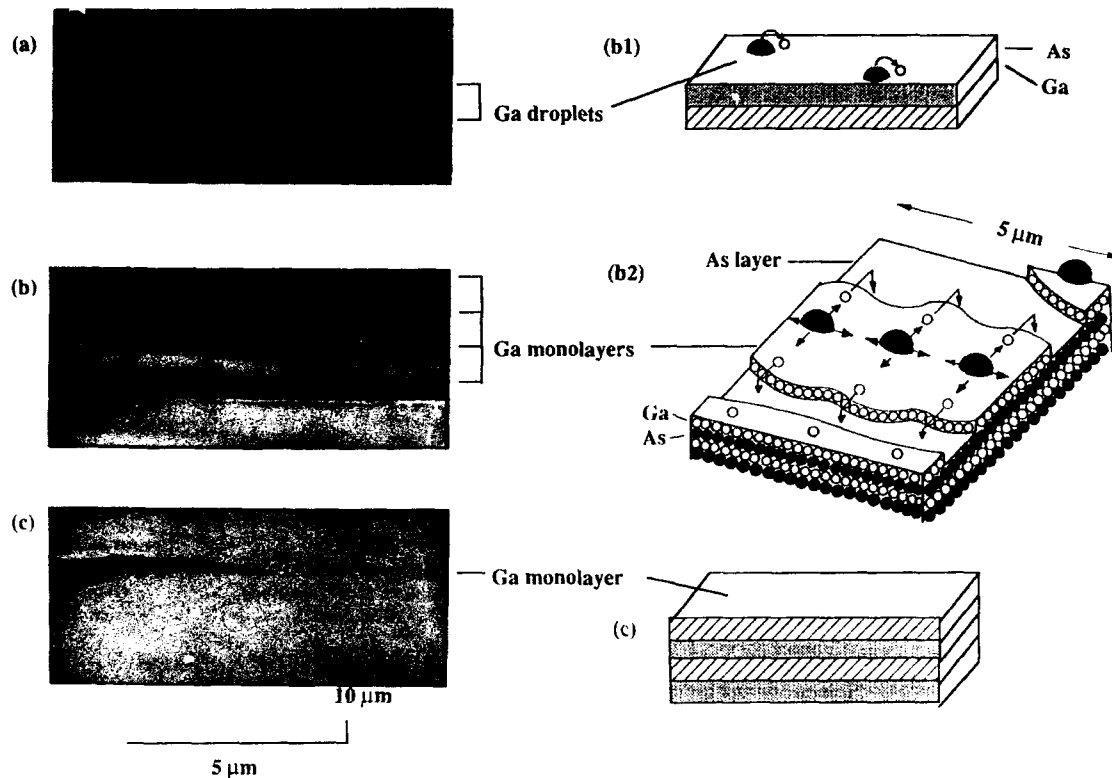


Fig. 6. Lateral growth of a Ga monolayer observed by SEM with schematic illustrations. (a) Ga droplets (dark dots) on Ga top layer. Dark horizontal band in the left side is a marker for focusing. (b) 0 s (top) to 5 s (bottom) after As supply. Dark areas are As top layer and the bright areas around the droplets are laterally growing Ga monolayers. The size increase toward bottom reproduces the growth history of monolayer islands. (c) 15 s (top) to 20 s (bottom) after. Complete coverage by Ga monolayer leaving tiny droplets.

tained here is two orders of magnitude larger than the terrace size realized so far [13]. We also observed micron-scale lateral growth of Ga-Al alloy monolayer [14]. This new growth technique is promising for atomic layer controlled growth for hetero-structures.

Now, lateral growth of monolayers and migration enhanced epitaxy (MEE) [19] are compared briefly. First, it is to be noted that when MEE is performed at high temperatures where the surface As coverage is less than 100% without As flux, 1 monolayer supply of Ga results in the formation of droplets like the present case. Therefore the growth model given previously must be modified taking into account the droplet formation, especially in the case of more than 1 monolayer supply of Ga atoms. Next, in MEE, Ga is generally

supplied only a few seconds after As is supplied. What takes place then? From the present result it is clear that Ga lateral monolayer growth is still going on then. The additional supply of Ga results in the simultaneous growth of lateral growth from droplets on the one hand and "normal" growth on the other hand. It is to be noted that in the latter growth, the Ga atoms migrate over the As layer, whose migration distance is much smaller than that on Ga. Therefore, the nucleation-and-growth takes place there.

6. Summary

An MBE-SREM hybrid system for in-situ observation of GaAs growth is outlined. A few ex-

amples are shown, demonstrating that this technology is a powerful tool for providing new insights into the growth mechanism and for developing new growth technologies. Although this technique has only been applied to GaAs related systems, it will be useful for other systems too: droplets may also be formed in InGaAs and play an important role in defect formation [20]. Further improvement in resolution will widen its application to nanostructure fabrication.

Acknowledgements

I am indebted to my colleagues Jiro Osaka, Koji Yamada, Kiyoshi Kanisawa and Shigeru Hirono for their contributions to the work reported here. Discussions with Professors J.W. Cowley, K. Yagi, P.M. Petroff and B.A. Joyce are gratefully acknowledged. I am also grateful to Akira Ishida and Kazuo Hirata for continuous encouragement.

References

- [1] J.S. Halliday and R.C. Newman, *Brit. J. Appl. Phys.* 11 (1960) 158.
- [2] N. Inoue, Y. Tanishiro and K. Yagi, *Japan. J. Appl. Phys.* 26 (1987) L293.
- [3] L.M. Cowley et al., *Rev. Sci. Instr.* 46 (1975) 826.
- [4] M. Ichikawa and T. Doi, *Appl. Phys. Letters* 50 (1987) 1141.
- [5] K. Yamada, N. Inoue, J. Osaka and K. Wada, 5th Intern. Conf. on Molecular Beam Epitaxy (MBE-V), Sapporo, 1988, LN-9; K. Yamada, N. Inoue, J. Osaka and K. Wada, *Appl. Phys. Letters* 55 (1989) 622.
- [6] N. Inoue, S. Hirono, J. Osaka and K. Kanisawa, *J. Appl. Phys.*, submitted.
- [7] T. Isu, A. Watanabe, M. Hata and Y. Katayama, *Japan. J. Appl. Phys.* 27 (1988) L2259.
- [8] R.A. Stall, J. Ziko, V. Swaminathan and N. Schumaker, *J. Vacuum Sci. Technol.* B3 (1985) 524.
- [9] J. Osaka, N. Inoue, Y. Mada, K. Yamada and K. Wada, *J. Crystal Growth* 99 (1990) 120.
- [10] J.H. Neave, B.A. Joyce and P.J. Dobson, *Appl. Phys.* A34 (1984) 179.
- [11] J. Osaka and K. Kanisawa, *J. Crystal Growth*, submitted.
- [12] J.H. Neave, P.J. Dobson and B.A. Joyce, *Appl. Phys. Letters* 47 (1985) 100.
- [13] M. Tanaka and H. Sakaki, *J. Appl. Phys.* 64 (1988) 4503.
- [14] K. Kanisawa, J. Osaka, S. Hirono and N. Inoue, *Appl. Phys. Letters*, to be published.
- [15] J.H. Neave and B.A. Joyce, *J. Crystal Growth* 44 (1978) 387.
- [16] J. Osaka, unpublished.
- [17] M.D. Pashley, K.W. Haberern and W. Fridav, *Phys. Rev. Letters* 60 (1988) 2176.
- [18] J. Osaka and N. Inoue, *Mater. Res. Soc. Symp. Proc.* 159 (1990) 33.
- [19] Y. Horikoshi, M. Kawashima and H. Yamaguchi, *Japan. J. Appl. Phys.* 25 (1986) L868.
- [20] A. Madhukar, private communication.

Surface diffusion length observed by in situ scanning microprobe reflection high-energy electron diffraction

Masayuki Hata, Akiyoshi Watanabe * and Toshiro Isu

Optoelectronics Technology Research Laboratory 5-5 Tohkodai, Tsukuba, Ibaraki 300-26, Japan

The dependence of surface diffusion phenomena of Ga adatoms on As flux during molecular beam epitaxy is investigated. Variations of growth rates of GaAs layers grown on the (001) surfaces adjacent to the (111) surfaces were measured by scanning microprobe reflection high-energy electron diffraction. The surface diffusion length is derived from the variations of the growth rates. It is found that the surface diffusion length of the Ga adatoms becomes larger under lower As flux.

1. Introduction

The surface diffusion phenomenon during molecular beam epitaxy (MBE) growth has recently received a great deal of attention. It is known that growth rates of layers grown by MBE on the (001) surface adjacent to the (111) surface vary with the distance from the edge of the (111) surface [1–6]. This is explained by analysis of the surface diffusion of Ga adatoms from or to the neighboring (111) surface. Consequently, the surface diffusion length on the (001) surface can be determined by measuring the variation of the growth rates on the (001) surface adjacent to the (111) surface.

It is well known that the intensity of reflection high-energy electron diffraction (RHEED) oscillates with a period corresponding to the periodic changes of the morphology of the growing surface on the atomic-scale during MBE growth [7]. Scanning microprobe RHEED makes it possible to measure the distribution of growth rates in a whole scan area simultaneously, because the growth rates can be measured from periods of this RHEED intensity oscillation according to growth at each point in the area. From the distributions of the growth rates measured by this method it was

estimated that the diffusion lengths of Ga adatoms along the [110] and along the $\bar{1}\bar{1}0$ directions were about 1 and 8 μm at 560 °C, respectively [5,6].

In this study, the dependence of surface diffusion length of Ga adatoms on As flux is investigated. Distributions of growth rates of GaAs layers grown by MBE on mesa-etched GaAs wafers are measured by scanning microprobe RHEED. The surface diffusion length is derived from the distribution of the growth rates.

2. Experimental

The growth apparatus used in the present work was described elsewhere [8]. GaAs MBE growth was carried out on the (001) substrate with mesa-grooves along the $\bar{1}\bar{1}0$ direction, whose depths were about 2 μm . The mesa-grooves were formed by chemical etching using $\text{H}_3\text{PO}_4:\text{H}_2\text{O}_2:\text{H}_2\text{O}$ (4:1:1) solution; they had (111)A sidewalls. The substrate was heated at 570 °C under arsenic pressure for surface cleaning. The growth temperature monitored by an infrared pyrometer was 550 °C. The growth rate of GaAs on the surface far from the edge of the (111) surface was about 0.1 nm/s. The amount of Ga flux on the (111)A surfaces was 60% of the amount on (001) surface because of the different incident angle of the flux. The flux of arsenic was in the range of 2.8×10^{-4} – 7.8×10^{-4}

* Present address: Central Research Laboratory, Hitachi, Ltd., Kokubunji, Tokyo 185, Japan.

Pa on a beam flux monitor. The RHEED patterns of the (001) surface showed the (2×4) reconstruction of As-stabilized surface before MBE growth. A buffer layer of a few tens of nm thickness was grown, before distributions of the growth rates were measured.

Scanning reflection electron microscope (SREM) images were obtained by using the intensity of the specular beam spot of the RHEED pattern for the (001) surface. Fig. 1a shows a typical SREM image during the growth of the GaAs surface near the edge of the (111)A surface illustrated in fig. 1b. The incident electron beam is in the $[\bar{1}10]$ azimuth at a glancing angle of 1° . The brighter area on the right-hand side of the photograph is the image of the upper (001) surface and the darker area on the left-hand side is that of the (111)A sidewall. The horizontal and vertical direc-

tions of the photograph represent the $[110]$ and $[\bar{1}\bar{1}0]$ directions, respectively. Because of the small glancing angle of the incident electron beam, the length along the vertical direction is reduced by a factor of about $1/20$ in comparison with that along the horizontal direction. The vertical direction also acts as time axis, because the scanning speed along this direction is much slower than that along the horizontal direction. It is seen in fig. 1a that horizontal stripes appear in the image of the upper (001) surface after the start of the MBE growth denoted by the arrow. Fig. 1c illustrates a schematic drawing of the SREM image shown in fig. 1a. The stripes appearing on the (001) surface correspond to RHEED intensity oscillations, as shown in fig. 1d. Intervals between the stripes represent periods of RHEED intensity oscillations. The growth rates at points of e, f, and

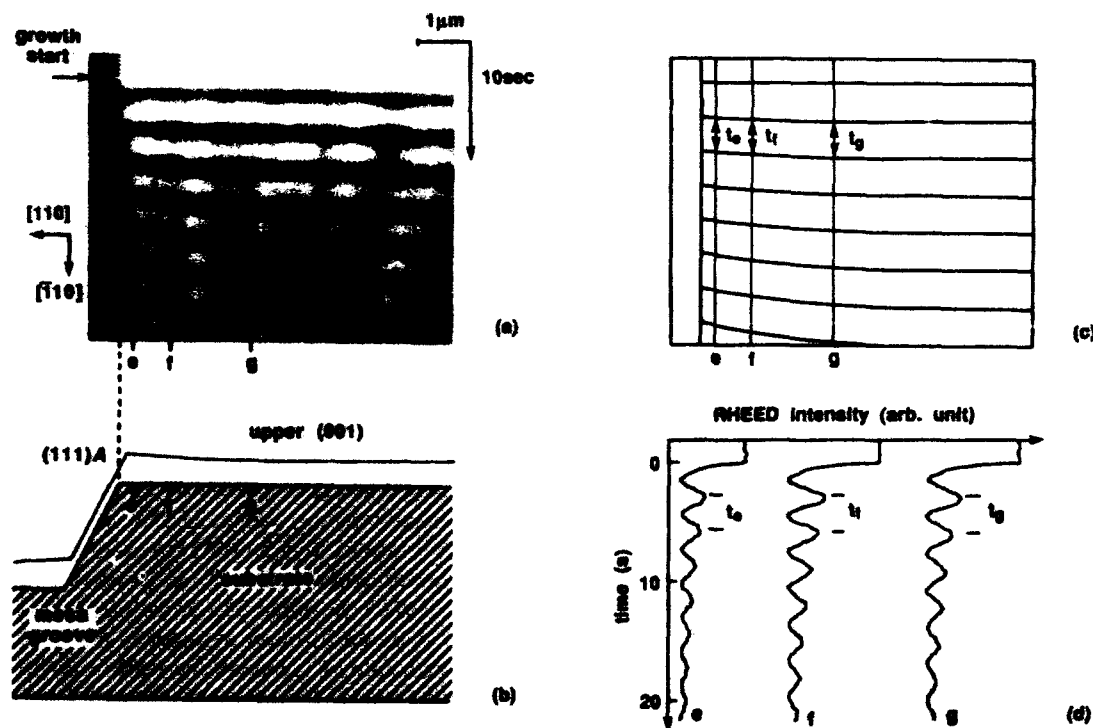


Fig. 1. (a) SREM image of the GaAs surface during growth on the (001) surface near the edge of the (111)A surface. (b) Schematic illustration of the substrate. (c) Schematic drawing of the SREM image shown in (a). (d) Variations of RHEED intensity at the points of e, f, and g in (b).

g in fig. 1b are derived from the RHEED intensity oscillations of e, f, and g in fig. 1d, respectively. When the RHEED intensity at a particular point in the scan area is observed, the growth rate at the point is measured in real time from its oscillation period. This measurement takes a growth of only about ten monolayers. Scanning microprobe RHEED makes it possible to measure growth rates in a whole scan area simultaneously.

3. Results

Fig. 2 shows relative increases in the growth rates on the (001) surface near the edge of the (111)A surface as a function of the distance from the edge under various conditions of As flux. The RHEED patterns of the (001) surface under the condition of As flux of 2.8×10^{-4} Pa showed the (3×1) reconstruction during MBE growth. Under the conditions of As flux higher than this, the surface keeps showing the (2×4) reconstruction during MBE growth. The relative increases in the growth rates decrease exponentially with the distance from the edge.

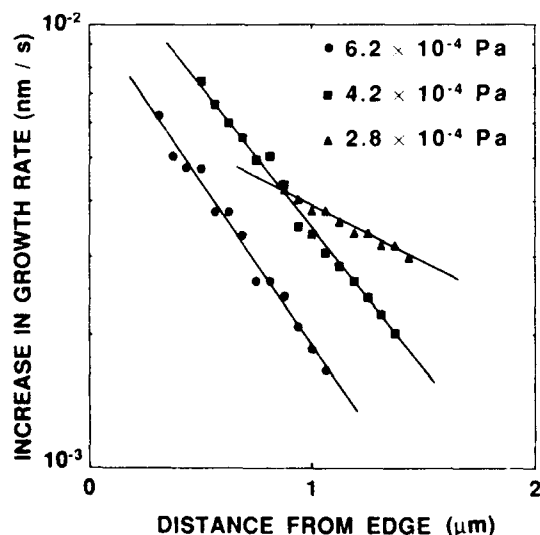


Fig. 2. Relative increases in growth rates on the upper (001) surface as a function of the distance from the edge of the (111)A surface.

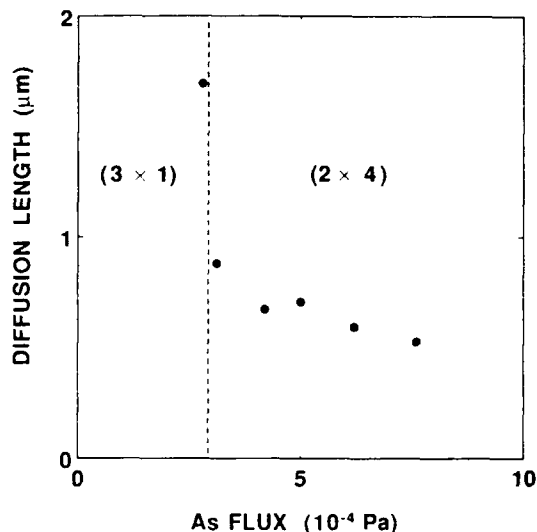


Fig. 3. Surface diffusion lengths as a function of As flux. The dashed line indicates the (2×4) to (3×1) phase transition of the surface reconstruction.

Ga adatoms incident on the (001) surface are not desorbed under the usual growth condition. If Ga adatoms are diffused from the neighboring (111) surface to the (001) surface, the distribution of the growth rate on the (001) surface varies with the distance from the edge of the (111) surface. When the Ga flux is supplied with density J and the Ga adatoms flow from the (111) surface with density I , the distribution of the growth rate R near the edge is given by

$$R = J + \frac{I}{\lambda} \exp\left(-\frac{x}{\lambda}\right). \quad (1)$$

where x and λ are the distance from the edge of the (111) surface and the surface diffusion length of Ga adatoms, respectively [6]. Eq. (1) shows that the relative increase in growth rate decreases exponentially with the distance from the edge. The surface diffusion length λ is, therefore, derived from the dependence of the growth rate on the distance from the edge of the (111) surface x .

The gradient of the relative increase in the growth rates as shown in fig. 2 corresponds to the inverse of the surface diffusion length of Ga along the [110] direction. Fig. 3 shows the diffusion lengths as a function of As flux. The dashed line

indicates the (2×4) to (3×1) phase transition of the surface reconstruction. The diffusion length becomes larger under lower As flux. In particular the surface diffusion length changes abruptly, when the phase transition of the surface reconstruction occurs. Because As is easily desorbed at the growth temperature, surface coverage of As decreased with decreasing As flux. The $3 \times$ streak has been reported in the (1×6) pattern in low-energy electron diffraction [9]. The (3×1) surface observed in this work seems to correspond to this surface, because it is difficult to confirm the $\times 6$ pattern with the scanning gun. The (3×1) surface is more As-deficient than the (2×4) surface, and more As-rich than the (4×2) surface. This suggests that the lower surface coverage of As makes the surface diffusion length of Ga adatoms larger.

4. Discussions

Horikoshi et al. performed AlGaAs growth in alternating source supply mode in which group III elements were provided under no As flux [10]. They reported that hetero-interfaces grown in this mode were flatter than those grown by conventional MBE method. They estimated that the large surface diffusion length caused the flat hetero-interfaces. The longer diffusion length on the (3×1) surface supports their result.

Several groups derived the surface diffusion length of Ga adatoms on GaAs surfaces by observing the transition of the growth modes [11–14]. The surface diffusion lengths of Ga adatoms on GaAs surfaces derived by this method are about 100 times smaller than those derived from the distribution of the growth rates, even if differences of growth conditions are taken into account. To explain this discrepancy, the authors proposed that the sticking coefficient of Ga adatoms to atomic steps is much smaller than unity [5,6]. If most of the Ga adatoms go through atomic steps when they arrive there, the surface diffusion lengths are probably much larger than the terrace widths on the vicinal surfaces. The transition of the growth mode occurs when the terrace width on the vicinal surface is equal to the diameter of the two-dimensional (2D) nucleus at its maximum.

The surface diffusion length derived by observing the transition of the growth modes would be underestimated.

Van Hove and Cohen reported that the surface diffusion length on the (2×4) surface did not vary with As flux [12]. They, however, derived the surface diffusion length from the transition of the growth mode. It should be thought that they did not measure the diffusion length, but the maximal diameters of the 2D nuclei. Therefore, the surface diffusion length observed in this work does not necessarily show the same dependence on As flux as the result derived by Van Hove and Cohen.

5. Conclusion

The dependence of surface diffusion length of Ga adatoms on As flux was investigated. It was found that the surface diffusion length becomes larger under lower As flux. In particular, the surface diffusion length changes abruptly with the (2×4) to (3×1) phase transition of the surface reconstruction.

Acknowledgements

The authors would like to thank Drs. I. Hayashi and Y. Katayama for enlightening discussions and continuous encouragement.

References

- [1] W.S. Tsang and A.Y. Cho, Appl. Phys. Letters 30 (1977) 293.
- [2] M. Ohtsuka and S. Miyazawa, J. Appl. Phys. 64 (1988) 3522.
- [3] S. Nilsson, E. Van Gieson, D.J. Arent, H.P. Meier, W. Walter and T. Forster, Appl. Phys. Letters 55 (1989) 972.
- [4] M. Kawabe and T. Sugaya, Japan. J. Appl. Phys. 28 (1989) L1077.
- [5] M. Hata, T. Isu, A. Watanabe and Y. Katayama, Appl. Phys. Letters 56 (1990) 2542.
- [6] M. Hata, T. Isu, A. Watanabe and Y. Katayama, J. Vacuum Sci. Technol. B8 (1990) 692.
- [7] J.H. Neave, B.A. Joyce, P.J. Dobson and N. Norton, Appl. Phys. A31 (1983) 1.

- [8] T. Isu, A. Watanabe, M. Hata and Y. Katayama, Japan. J. Appl. Phys. 27 (1988) L2259.
- [9] D.K. Biegelsen, R.D. Bringans, J.E. Northrup and L.-E. Swarts, Phys. Rev. B41 (1990) 5701.
- [10] Y. Horikoshi, M. Kawashima and H. Yamaguchi, Japan. J. Appl. Phys. 27 (1988) 169.
- [11] J.H. Neave, P.J. Dobson, B.A. Joyce and Jing Zhang, Appl. Phys. Letters 47 (1985) 100.
- [12] J.M. Van Hove and P.I. Cohen, J. Crystal Growth 81 (1987) 13.
- [13] K. Ohta, T. Kojima and T. Nakagawa, J. Crystal Growth 95 (1989) 71.
- [14] T. Nishinaga and Kyoung-Ik Cho, Japan. J. Appl. Phys. 27 (1988) L12.

A reflection high-energy electron diffraction study of growth processes at step edges during molecular beam epitaxy of GaAs and AlAs

Hiroshi Tsuda and Takashi Mizutani

Fundamental Research Laboratories, NEC Corporation, 34 Miyukigaoka, Tsukuba, Ibaraki 305, Japan

We have investigated molecular beam epitaxy of GaAs and AlAs on highly misoriented GaAs(001) substrates with reflection high-energy electron diffraction (RHEED). The substrate orientations studied are (117)A and (119)A. Facet-like structures are formed on GaAs surfaces under As stabilized conditions either during growth or during growth interruption. However, such structures disappear when AlAs is grown on these surfaces. Moreover, the surfaces without facet-like structures are maintained after AlAs growth is interrupted. This suggests not only the step flow growth of AlAs but also the stabilization of Al atoms on the surface, which is attributed to the stronger bonding of AlAs. On the other hand, the facet-like structures during GaAs growth shows the migration of Ga atoms across the step edges because of the weaker bonding of GaAs. The surface without facet-like structures during GaAs growth with a slightly insufficient As₄ flux are related to small As coverage on the surface.

1. Introduction

Molecular beam epitaxy (MBE) is one of the most fundamental techniques in fabricating semiconductor thin films. Understanding its growth mechanisms can help in intentionally fabricating such controlled structures as tilted superlattices [1]. Reflection high-energy electron diffraction (RHEED) is a useful in situ technique to monitor the surface during MBE growth. From RHEED studies, it has been revealed that Al is much less mobile than Ga on the GaAs(001) surface [2]. Similar results were reported concerning migration-enhanced epitaxy (MEE) [3]. Lateral growth studies also suggested the small diffusion length of Al [4].

As almost all growth seems to proceed at the step sites or kink sites, misoriented surfaces provide information concerning growth fronts and step properties. Step properties on vicinal surfaces concerning MBE have been studied by using RHEED [5–10].

In this paper, we observed RHEED patterns of two highly misoriented GaAs(001) substrates in order to study the growth behavior of GaAs and AlAs during MBE growth and growth interruption. Facet-like structures were observed on As

stabilized GaAs surfaces. However, no such structures were observed on AlAs surfaces. This is interpreted from the viewpoint of the growth behavior.

2. Experimental

RHEED observations were conducted in a continuous cycle of growth and growth interruption with the observed azimuth fixed. AlAs layers were grown on GaAs surfaces, while GaAs layers were grown on GaAs surfaces and AlAs surfaces. The electron primary energy was 12.1 keV. A high-sensitivity SIT (silicon intensified target) TV camera was used for observation with video signals recorded by VTR (video tape recorder). The RHEED patterns presented in this paper are observations made after changes, if any, had been completed. The time needed for change corresponded to about one layer growth for GaAs and about two layer growth for AlAs.

The samples used were n⁺-GaAs (117)A and (119)A substrates. These were misoriented (001) substrates inclined at 11.4°(117) and 8.9°(119) toward [110] azimuth, and were expected to have Ga atoms at the step edges. Before being loaded

into the MBE chamber, they were degreased with an organic solvent by ultrasonic cleaning, followed by chemical etching by $7\text{H}_2\text{SO}_4:2\text{H}_2\text{O}_2:2\text{H}_2\text{O}$ solution at around 60°C . After deoxidation under As_4 flux at 650°C , an undoped GaAs buffer layer of about 3000 \AA thickness was grown on each substrate at 600°C .

Growth rates were $0.8\text{ }\mu\text{m/h}$ for GaAs and $0.1\text{ }\mu\text{m/h}$ for AlAs. Substrate temperature (T_{sub}) was fixed at 600°C . An As_4 flux of $(1.5 \pm 0.2) \times 10^{-5}$ Torr monitored at the substrate growth position was applied for GaAs and AlAs growth. This is a usual amount for an As stabilized (2×4) RHEED pattern maintained on the GaAs(001) surface during GaAs growth with this growth rate and T_{sub} . An examination was also made of an As_4 flux of $(4.5 \pm 1.5) \times 10^{-6}$ Torr, which is a slightly insufficient amount for GaAs growth where the transient from a (2×4) to a diffused (3×1) begins to occur on the GaAs(001) surface during homoepitaxial growth with the same growth rate and T_{sub} .

3. Results and discussion

Fig. 1 shows RHEED patterns of GaAs surfaces on the (117) substrate observed at the $[\bar{1}10]$ azimuth under 4.5×10^{-6} Torr of As_4 flux. The incidence plane of the primary electrons was almost parallel to the step edges. The streaks before growth (fig. 1a) were slightly more diffused than those during GaAs growth (fig. 1b). After growth was interrupted, the pattern immediately became the same as that shown in fig. 1a. The existence of streaks in both figures demonstrates broadened two-dimensional reciprocal lattice rods, which result from many irregularities along the step edges. Nevertheless, there is no doubt that the GaAs surface during growth is somewhat more ordered than that during growth interruption. Furthermore, there were no three-dimensional islands of significant size on the surface, because patterns of electrons transmitted through the bulk were observed before buffer layer growth but disappeared after it.

The streaks in fig. 1b were almost perpendicular to the shadow edge of the substrate, while the averaged spacing of the streaks was the same as

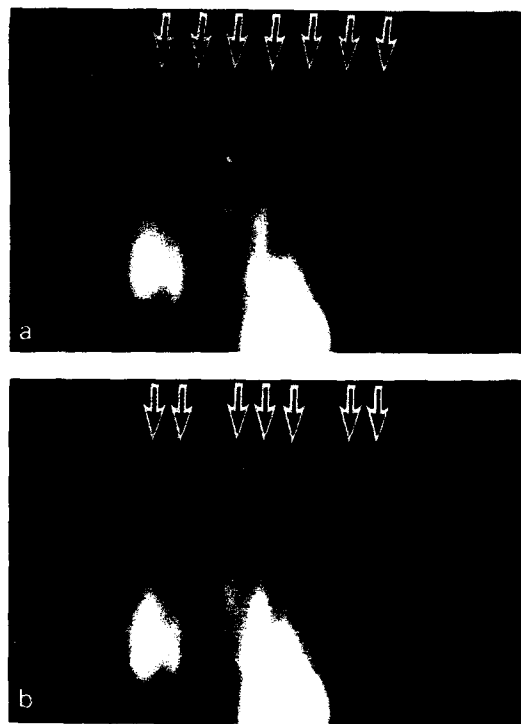


Fig. 1. RHEED patterns of (117) substrate observed at the $[\bar{1}10]$ azimuth under insufficient As conditions: (a) GaAs surface during growth interruption; (b) GaAs surface during growth. Averaged streak positions are indicated by arrows. (a) Suggests the existence of a rather disordered facet.

that expected for an ideal (117) surface. This shows the existence of a nearly ideal (117) surface, because the spacing of streaks corresponds to the step edge interval [11] and the direction of two-dimensional lattice rods represents the face azimuth. Yet, the averaged spacing in fig. 1a was about 1.3 times larger than that seen in fig. 1b. Moreover, in fig. 1a the streaks were not perpendicular to the shadow edge, but were at an angle of about 3° relative to those in fig. 1b at this azimuth. This shows that a facet-like structure appeared on the GaAs surface during growth interruption. It was (115)-like, but was not an exact (115) facet because the angle should be 4.4° if an exact (115) facet was formed on the (117) surface. (In this study, the error of angle measurement on RHEED patterns was at most half a degree for averaged

streaks.) On the other hand, it was neither a (114) facet nor a (116) facet based on the spacing of the streaks and their incline.

During GaAs growth with 1.5×10^{-5} Torr of As_4 flux, RHEED patterns of the (117) substrate showed the facet-like structure, and were the same as those during growth interruption (fig. 1a). Furthermore, when the growth rate of GaAs was reduced to $0.1 \mu\text{m/h}$, the patterns during growth were also the same as fig. 1a and showed the facet-like structures even though the As_4 flux was 4.5×10^{-6} Torr. Under the same conditions, an As stabilized (2×4) RHEED pattern was maintained on the GaAs(001) surface during growth. This implies that an As stabilized condition is essential to the formation of the facet-like structure on the GaAs surface. The minimization of surface energy would be the driving force of the formation, in the same way as when surface reconstruction takes place on singular surfaces.

In contrast, the facet-like structure disappeared only during growth of GaAs with a slightly insufficient As_4 flux, but was easily recovered under the same As_4 flux after growth was interrupted. Therefore, the surface without facet-like structures observed on the (117) substrate is caused by the structural changes related to a small As coverage on the surface. The surface without facet-like structure corresponds to the vicinal surface whose terrace length fluctuations are reduced under an As insufficient stoichiometry [6,8]. The minimization of surface energy would be also the driving force in this case.

The reason why the facet-like structure is maintained on GaAs surfaces during growth under As stabilized conditions is explained by the growth process at the step edges, that is, the migration of Ga atoms across the step edges. The Ga diffusion length on GaAs(001) terraces can be estimated at least to the order of 100 \AA in this situation [12]. Thus, all Ga atoms are apparently able to reach the step sites on this highly misoriented substrate, and two-dimensional nuclei do not form. If Ga atoms are easily incorporated into the crystal lattice at the step sites, then step flow growth must take place and the facet-like structure must disappear. However, the facet-like structure is maintained. Therefore, Ga atoms must migrate across

the step edges before they are incorporated into the crystal lattice. This result is consistent with the SEM [13] and scanning μ RHEED [14] studies on patterned substrates.

The maintenance of the surface without facet-like structures during growth with an insufficient As_4 flux can be explained by the small As coverage on the surface. MEE studies [15] revealed that Ga atoms migrate over a longer distance under insufficient As conditions than under As stabilized conditions. In other words, they are less willing to be incorporated into the crystal under insufficient As conditions. Therefore, the observed surface without facet-like structures is stable under these conditions due to the minimization of surface energy.

Fig. 2 shows RHEED patterns of (a) GaAs surface before growth and (b) AlAs surface during growth, observed near the $[\bar{1}10]$ azimuth for the (117) substrate under 1.5×10^{-5} Torr of As_4 flux. (Observation at a few angles off the $[\bar{1}10]$ azimuth made the difference clearer.) The patterns under 4.5×10^{-6} Torr of As_4 flux were the same as in fig. 2. The pattern of the GaAs surface (fig. 2a) shows the facet-like structure as described above, where the streaks were not perpendicular to the shadow edge and the averaged spacing of the streaks was larger than that expected for an ideal (117) surface. In contrast, the streaks in the pattern during AlAs growth (fig. 2b) were almost perpendicular to the shadow edge, and the averaged spacing of the streaks was the same as that expected for an ideal (117) surface. This shows that the facet-like structure disappears when AlAs growth is started on the GaAs surface in spite of the reduced growth rate. The stronger bond energy of AlAs would have Al atoms, reaching step sites, firmly incorporated into the crystal lattice even under As stabilized condition. Therefore, the initial growth of AlAs on this surface can be interpreted in terms of step flow growth.

After AlAs growth was interrupted, RHEED patterns observed for the (117) substrate were the same as those during AlAs growth. This confirms that Al atoms are not so mobile on the AlAs surface, while Ga atoms are so mobile that they easily leave the step sites and change the surface structure. This can be attributed to the bonding of

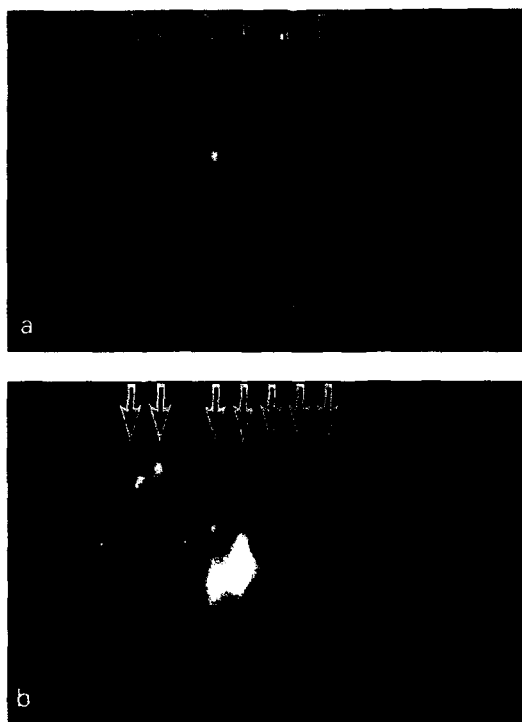


Fig. 2. RHEED patterns of (117) substrate observed near the $[110]$ azimuth under sufficient As conditions: (a) GaAs surface during growth interruption; (b) AlAs surface during growth. The shadow edge is parallel to the horizontal edge of the photograph. Averaged streak positions are indicated by arrows. (a) Suggests the existence of a rather disordered facet.

AlAs which is stronger than that of GaAs [16]. The interpretation in terms of differing bond energy is consistent with the mechanism of coherent tilted superlattices [17]. Although these superlattices were made by migration-enhanced epitaxy, the Al atoms were captured more easily at the step sites than the Ga atoms because of the stronger bonding of AlAs.

The trend of the (119) substrate was quite similar to that of the (117) substrate except for the patterns of GaAs surface under As stabilized conditions. Fig. 3 shows RHEED patterns of the (119) substrate observed near the $[1\bar{1}0]$ azimuth under 4.5×10^{-6} Torr of As_4 flux. Figs. 3a, 3b and 3c correspond to the GaAs surface during growth interruption, the GaAs surface during

growth and the AlAs surface during growth. The pattern of the AlAs surface during growth interruption was the same as that during AlAs growth

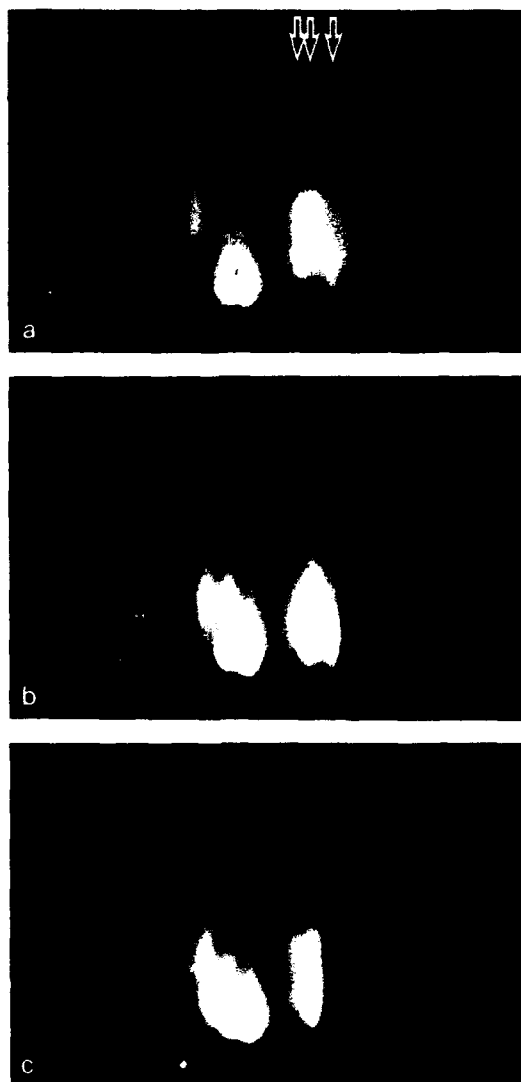


Fig. 3. RHEED patterns of (119) substrate observed near the $[110]$ azimuth under insufficient As conditions: (a) GaAs surface during growth interruption; (b) GaAs surface during growth; (c) AlAs surface during growth. The shadow edge is parallel to the horizontal edge of the photograph. Two different spacings in the right part of (a) show the existence of a rather complicated domain.

(fig. 3c). Furthermore, under 1.5×10^{-5} Torr of As_4 flux, the patterns of GaAs were the same as seen in fig. 3a and those of AlAs were the same as seen in fig. 3c.

There were at least two different spacings in the streaks as shown in fig. 3a, with the streaks being perpendicular to the shadow edge. This suggests that a complicated domain forms on the (119) substrate because one of the spacings does not seem to have the coincident relation to that expected for an ideal (119) surface. The streaks in figs. 3b and 3c were also almost perpendicular to the shadow edge, but the averaged spacings of the streaks for both figures were the same as those expected for an ideal (119) surface. This implies that there are no complicated domains on these surfaces. Note the difference in the intensity distribution between figs. 3b and 3c. This suggests that the atomic configuration of rather well ordered GaAs must be different from that of AlAs.

If the complicated domain is regarded as a facet-like structure, the phenomena observed for the (119) substrate can be explained in the same way as the (117) substrate.

From the observation at the [110] azimuth, where electrons go across the step edges, weak half order streaks were observed on both (117) and (119) GaAs surfaces under As stabilized conditions where facet-like structures were formed. Under conditions where facet-like structures were not observed, half order streaks were either terribly weak or not observed at all. This suggests the existence of As dimers on the GaAs surfaces with facet-like structures.

4. Conclusions

RHEED observations indicated the difference in growth properties of GaAs and AlAs on (117) and (119) substrates. Facet-like structures were formed on GaAs surfaces under As stabilized conditions either during growth or during growth interruption. However, no such structures were observed on AlAs surfaces under the same conditions. It was confirmed that Ga atoms migrate across the step edges because of the weaker bonding of GaAs, while it was interpreted that the

stronger bonding of AlAs would cause the step flow growth of AlAs. In addition, the surfaces without facet-like structures during GaAs growth with a slightly insufficient As_4 flux were determined to be related to small As coverage on the surface.

Acknowledgment

The authors would like to thank Y. Matsumoto for his constant support and encouragement.

References

- [1] J.M. Gaines, P.M. Petroff, H. Kroemer, R.J. Simens, R.S. Geels and J.H. English, *J. Vacuum Sci. Technol.* B6 (1988), 1378.
- [2] C.S. Lent and P.I. Cohen, *Phys. Rev.* B33 (1986) 8329.
- [3] Y. Horikoshi, H. Yamaguchi and M. Kawashima, *Japan. J. Appl. Phys.* 28 (1989) 1307.
- [4] T. Sugaya, S. Yokoyama and M. Kawabe, in: *Proc. 16th Intern. Symp. on GaAs and Related Compounds*, Karuizawa, 1989, *Inst. Phys. Conf. Ser.* 106, Eds. T. Ikoma and H. Watanabe (*Inst. Phys., London-Bristol*, 1990) p. 147.
- [5] J.M. Van Hove and P.I. Cohen, *J. Vacuum Sci. Technol.* 20 (1982) 726.
- [6] P.R. Pukite, C.S. Lent and P.I. Cohen, *Surface Sci.* 161(1985) 39.
- [7] P.I. Cohen, P.R. Pukite, J.M. Van Hove and C.S. Lent, *J. Vacuum Sci. Technol.* A4 (1986) 1251.
- [8] P.R. Pukite, G.S. Petrich, S. Batra and P.I. Cohen, *J. Crystal Growth* 95 (1989) 269.
- [9] S.A. Chalmers, A.C. Gossard, P.M. Petroff, J.M. Gaines and H. Kroemer, *J. Vacuum Sci. Technol.* B7 (1989) 1357.
- [10] S.A. Chalmers, A.C. Gossard, P.M. Petroff and H. Kroemer, *J. Vacuum Sci. Technol.* B8 (1990) 431.
- [11] M. Henzler, in: *Electron Spectroscopy for Surface Analysis*, Ed. H. Ibach (*Springer, Berlin*, 1977).
- [12] J.H. Neave, P.J. Dobson, B.A. Joyce and J. Zhang, *Appl. Phys. Letters* 47 (1985) 100.
- [13] H.P. Meier, E. Van Gieson, P.W. Epperlein, C. Harder, W. Walter, M. Krahle and D. Bimberg, *J. Crystal Growth* 95 (1989) 66.
- [14] M. Hata, T. Isu, A. Watanabe and Y. Katayama, *Appl. Phys. Letters* 56 (1990) 2542.
- [15] Y. Horikoshi, M. Kawashima and H. Yamaguchi, *Japan. J. Appl. Phys.* 27 (1988) 169.
- [16] R.C. Weast and M.J. Astle, Eds., *CRC Handbook of Chemistry and Physics*, 62nd ed. (*CRC Press, Boca Raton, FL*, 1981) p. E-99.
- [17] M. Tsuchiya, P.M. Petroff and L.A. Coldren, *Appl. Phys. Letters* 54 (1989) 1690.

Modulated molecular beam study of group III desorption during growth by MBE

J. Zhang, E.M. Gibson

ICR for Semiconductor Materials, Blackett Laboratory, Imperial College of Science, Technology and Medicine, Prince Consort Road, London SW7 2BZ, UK

C.T. Foxon

Philips Research Laboratories, Cross Oak Lane, Redhill, Surrey RH1 5HA, UK

and

B.A. Joyce

ICR for Semiconductor Materials, Blackett Laboratory, Imperial College of Science, Technology and Medicine, Prince Consort Road, London SW7 2BZ, UK

Direct measurements of Ga and In desorption rates from GaAs and InAs were made using modulated beam mass spectrometry (MBMS). Two distinct temperature dependences of In desorption from InAs were observed. One is shown to be independent of surface In adatom population. The other is shown to be dependent on In adatom population. They are the rate limiting processes at different temperature regions and are independent of one another. We suggest the latter is due to In clusters on the surface. Under As_2 , Ga desorption is largely dominated by a surface adatom independent process. However, there is a surface Ga adatom dependent contribution at low temperatures under As_4 .

1. Introduction

The desorption of group III elements during molecular beam epitaxy (MBE) of III–V semiconductors is of great importance in the control of the thickness and composition of the structures grown. There are two main techniques used in the study of this phenomenon. One is to observe the temperature dependence of the growth rate and infer the desorption rate [1,2]. The other is to measure the desorption flux directly using modulated beam mass spectrometry (MBMS) [3]. Measurement of the growth rate can be achieved in-situ by the reflection high energy electron diffraction (RHEED) intensity oscillation technique [4] or ex-situ by layer thickness measurements [5]. Although the desorption rate under Langmuir free evaporation can be measured directly using

RHEED intensity oscillations [2], the requirement of precisely orientated substrates restricts the application of this method to the investigation of desorption from growing surfaces. The MBMS technique can be applied to either Langmuir evaporation or growing surfaces. The absolute rate measurements can be achieved by calibration using the RHEED intensity oscillation method.

Ga desorption from GaAs and (Al,Ga)As has been studied extensively. Using RHEED, the activation energies for desorption under Langmuir evaporation and during growth were measured as 4.7 and 4.6 eV, respectively [1,2]. This is in agreement with the result of Heckingbottom's calculation based on a thermodynamic approach [6]. However, there have been conflicting reports on the influence of other growth parameters such as the arsenic flux and presence of Al on the Ga

desorption rate. Some RHEED observations have shown no dependence on the presence of Al and arsenic flux [7], whereas a recent non-modulating mass spectrometric measurement has shown a reduction in desorption rate as well as reduction in activation energy due to presence of Al at high temperatures [8,9]. Our recent results [10] have shown no dependence on arsenic flux and no significant difference between the Langmuir evaporation and evaporation during growth of GaAs and (Al,Ga)As at high temperatures (690°C). However, there is clear evidence of a difference in the desorption rate between the growing and static surface at the relatively low temperature of 630°C.

There have been few reports on the study of In desorption from InAs and (Ga,In)As [11,12]. Evans and co-workers [12] recently measured the desorption rate of In from InAs over the temperature range of 550–615°C and obtained an activation energy of 4.0 eV. Their experiments were performed at relatively high temperatures and an As₄ flux in excess of $10^{15} \text{ cm}^{-2} \text{ s}^{-1}$ was used.

Here we report on measurements of the desorption rate of group III elements from (001) surfaces of GaAs and InAs using the MBMS technique. Both Langmuir evaporation and evaporation during growth are investigated.

2. Experimental technique and results

The experimental facility consists of a purpose built MBE system and MBMS electronics. The MBE system is diffusion pumped with solid sources of Ga, Al, In and As. The solid arsenic source has a hot "cracker" so either As₂ or As₄ can be supplied by varying the temperature of the cracker. There are also gas sources available though they are not used in this study. The detector used is an EAI quadrupole mass spectrometer housed in a liquid nitrogen cooled tank. The ioniser has direct line of sight to the sample through a modulator and is otherwise exposed to liquid nitrogen cooled surfaces. The MBMS electronics include a custom-built multichannel scaler, described in a previous publication [13].

The molecular beam fluxes used in the experiments were set as follows:

$$J_{\text{Ga}} = 3.1 \times 10^{14} \text{ cm}^{-2} \text{ s}^{-1},$$

$$J_{\text{In}} = 3.1 \times 10^{14} \text{ cm}^{-2} \text{ s}^{-1},$$

$$J_{\text{As}_2} = 5 \times 10^{14} \text{ cm}^{-2} \text{ s}^{-1} \quad (\text{for GaAs}),$$

$$J_{\text{As}_4} = 5 \times 10^{14} \text{ cm}^{-2} \text{ s}^{-1} \quad (\text{for GaAs}),$$

$$J_{\text{As}_2} = 6.2 \times 10^{14} \text{ cm}^{-2} \text{ s}^{-1} \quad (\text{for InAs}).$$

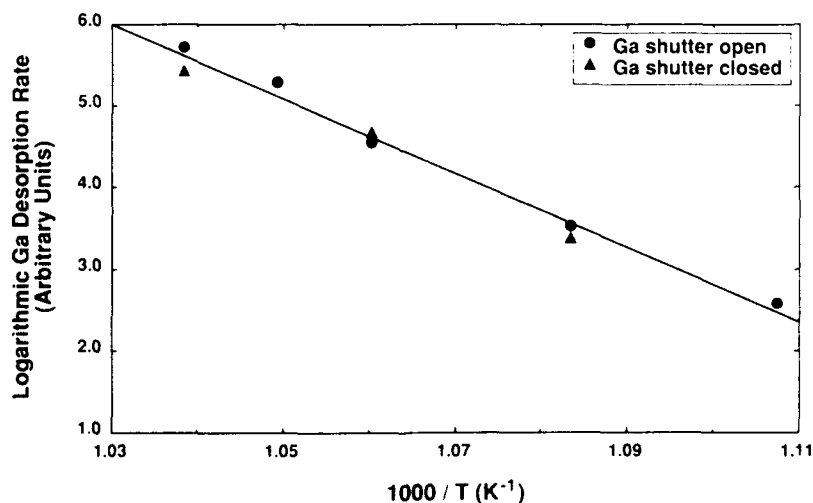


Fig. 1. Measurements of the desorption rate of Ga from GaAs under Langmuir evaporation and MBE growth conditions using As₂.

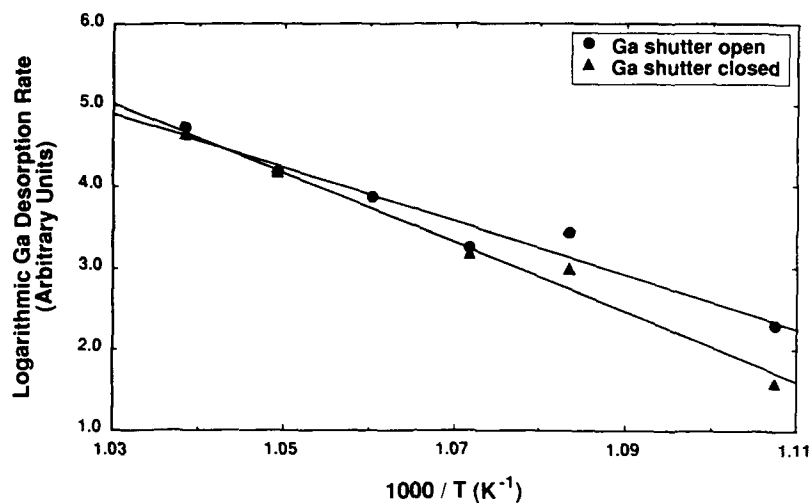


Fig. 2. Measurements of the desorption rate of Ga from GaAs under Langmuir evaporation and MBE growth conditions using As_4 .

These fluxes, including As_2 , and As_4 were measured using RHEED intensity oscillation [4,14]. The substrate temperature was measured by a thermocouple calibrated with a radiation pyrometer. The In desorption experiments were performed on fully relaxed InAs grown on GaAs(001)

surfaces. Before measurements of Langmuir evaporation were taken, GaAs or InAs was grown for 10 min at 580 and 430 °C, respectively. The substrate was then set to the desired temperature and allowed to settle. The measurements during Langmuir evaporation and during growth were taken

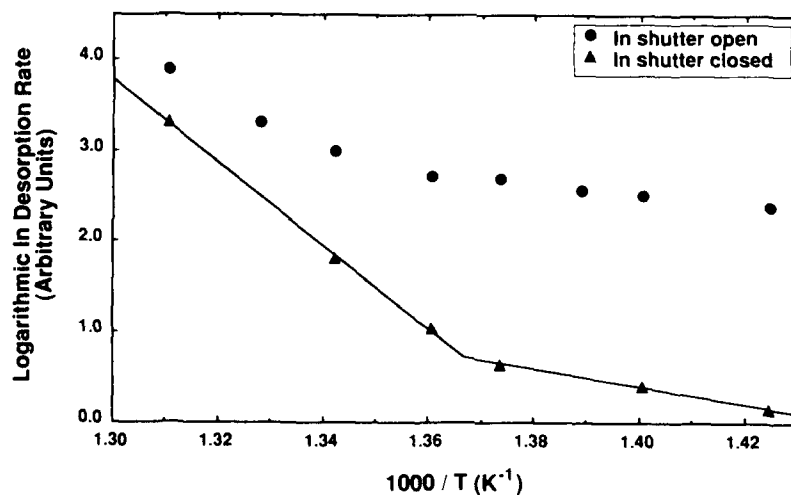


Fig. 3. Measurements of the desorption rate of In from InAs under Langmuir evaporation and MBE growth conditions using As_2 .

sequentially. The results are shown in the following three figures.

The logarithmic (natural) desorption rate of Ga from GaAs surfaces maintained by a constant flux of As_2 molecules is plotted against inverse temperature in fig. 1. Both Langmuir evaporation and growing conditions are shown. There is little difference in the desorption rate between the two cases and the activation energy for desorption is approximately 4.0 eV. Similar experiments were performed on a GaAs surface using As_4 and the results are shown in fig. 2. In this case the desorption rate during growth was generally higher than that under Langmuir evaporation. Activation energies of 2.9 and 3.6 eV were obtained for growth and Langmuir evaporation, respectively.

Fig. 3 shows the desorption data of In from an InAs surface maintained by a beam of As_2 molecules. In the case of Langmuir evaporation, two different temperature dependences are clearly shown. From temperatures of 460°C upwards, a rate limiting process with an activation energy of 4.0 eV exists, whereas a different process with activation energy of 0.8 eV exists below 460°C. Under growth conditions, the desorption rate is generally higher than the Langmuir evaporation case. Towards the high temperature region covered in this experiment, the relative difference between the growth and Langmuir evaporation conditions is reduced compared with the low temperature region.

3. Discussion

The results of In desorption during Langmuir evaporation exhibit two different temperature dependences at temperatures above and below 460°C. Let the two rate limiting processes with activation energies of 4.0 and 0.8 eV be called A and B. These two processes must be independent of one another. That is, they are not different processes in the same In desorption path. If the contrary is true, then process B should have been the rate limiting step at temperatures above 460°C since its projected rates at those temperatures are much smaller than those observed and process A would not have been present. The activation en-

ergy of process A agrees with that measured by Evans et. al. [12] at higher temperatures during growth. The agreement of this activation energy and the reduction of the difference in desorption rate between Langmuir evaporation and growth with increasing temperature suggest that process A is the same as the one observed by Evans [12]. The value of 4.0 eV for the activation energy indicates that the process involves the dissociation of InAs. Therefore, at temperatures above those covered by the present experiment, the difference in desorption rate during Langmuir evaporation and during growth would become insignificant. At lower temperatures, the desorption rate of In during growth is much larger than the corresponding rate under Langmuir evaporation conditions. The activation energy is, however, slightly lower than in process B. If the desorption mechanism is the same, then the large difference in desorption rate suggests that process B is dependent on the surface In adatom population. The likely source of In is therefore small In clusters.

The desorption rate of Ga from GaAs under an As_2 beam did not show a significant difference between Langmuir evaporation and growth. The activation energy obtained is similar to that obtained using the RHEED technique [1,2]. The corresponding rate limiting process is therefore independent of the surface Ga adatom population. With an As_4 beam however, a lower activation energy is observed and the desorption rate from a growing surface is higher than that from a static surface. The difference between the two surfaces, as in the case of InAs under As_2 , reduces when the temperature is increased. The activation energy is also influenced by the introduction of a Ga beam. Therefore the desorption process must be dependent on the surface Ga population. If Ga behaves in a similar way to In over InAs below 460°C, then the corresponding Ga desorption mechanism could also be due to clusters of Ga on the surface.

The desorption process which is dependent on the surface adatom population is dominated by other independent processes at high temperature. This could explain why the Ga desorption rate is dependent on arsenic overpressure and Al flux at high and low temperatures [13].

4. Summary

It is shown through desorption rate measurements that the desorption rate is dominated by an adatom independent process at high temperatures. At lower temperatures, other desorption processes dependent on the surface adatom population start to contribute towards desorption.

Acknowledgements

The authors wish to thank Mr. J.H. Neave and Mr. P.N. Fawcett for fruitful discussions and help in the preparation of the manuscript.

References

- [1] J.M. Van Hove and P.I. Cohen, *Appl. Phys. Letters* 47 (1985) 726.
- [2] T. Kojima, N.J. Kawai, T. Nakagawa, K. Ohta, T. Sakamoto and M. Kawashima, *Appl. Phys. Letters* 47 (1985) 286.
- [3] C.T. Foxon, M.R. Boudry and B.A. Joyce, *J. Crystal Growth* 44 (1978) 74.
- [4] J.H. Neave, B.A. Joyce, P.J. Dobson and N. Norton, *Appl. Phys.* A31 (1983) 1.
- [5] F. Alexandre, N. Duhamel, P. Ossart, J.M. Masson and C. Meillerat, *J. Physique* 43 (1982) C5-483.
- [6] R. Heckingbottom, *J. Vacuum Sci. Technol.* B3 (1985) 572.
- [7] C.T. Foxon, *J. Vacuum Sci. Technol.* B4 (1986) 867.
- [8] A.J. SpringThorpe and P. Mandeville, *J. Vacuum Sci. Technol.* B6 (1988) 754.
- [9] K.R. Evans, C.E. Stutz, T.K. Lorange and R.L. Jones, *J. Vacuum Sci. Technol.* B7 (1989) 259.
- [10] E.M. Gibson, C.T. Foxon, J. Zhang and B.A. Joyce, *Appl. Phys. Letters* 57 (1990) 1203.
- [11] C.T. Foxon and B.A. Joyce, *J. Crystal Growth* 44 (1978) 75.
- [12] K.R. Evans, C.E. Stutz, D.K. Lorange and R.L. Jones, *J. Crystal Growth* 95 (1989) 197.
- [13] E.M. Gibson, C.T. Foxon, J. Zhang, J.H. Batey and B.A. Joyce, *J. Vacuum Sci. Technol.* A8 (1990) 3141.
- [14] J.H. Neave, B.A. Joyce and P.J. Dobson, *Appl. Phys.* A34 (1984) 179.

Correlation between the dampening of RHEED oscillations and the photoluminescence of quantum wells in the presence of AsO

Thomas R. Block and B.G. Streetman

Department of Electrical and Computer Engineering, Microelectronics Research Center, The University of Texas at Austin, Austin, Texas 78712, USA

We have intentionally introduced AsO during the growth of GaAs and AlGaAs to study its effects on the dampening of RHEED oscillations and the photoluminescence (PL) of quantum well (QW) structures. The amount of AsO was found to increase as the temperature of the cracking section of our As source was increased. The dampening of the RHEED oscillations for GaAs and AlGaAs were studied as the amount of AsO was increased. We found that the dampening of the AlGaAs increased with increasing AsO concentrations. Little effect was found upon the dampening of the GaAs. PL of QW samples grown with increasing AsO displayed a dramatic decrease in the integrated intensity and an equally dramatic increase in the transition linewidths. After reducing the AsO contamination, the experiments were repeated. The RHEED dampening became essentially independent of the cracking section temperature. The PL of the QW layers was also dramatically improved. However, the PL still displayed a trend toward lower integrated intensity and larger linewidths as the cracking temperature was increased. PL is thus an extremely sensitive tool for determining the presence of AsO at low levels in an MBE system.

1. Introduction

Molecular beam epitaxy (MBE) is a well known crystal growing technique used in the production of compound semiconductor devices [1]. Extremely important to MBE is the in situ monitoring of growth processes by reflection high energy electron diffraction (RHEED) [2]. RHEED is routinely used to measure the growth rate and the column V to column III flux ratio [3,4], and has also been used to optimize the growth of quantum well (QW) structures by monitoring the average (damped) intensity [5,6]. Another aspect of the RHEED intensity oscillations which may be used as a diagnostic tool for crystal growth is the dampening of the oscillation [7,8]. As part of a study of the dampening of the RHEED oscillations, we examined the effects AsO would have on the growth of GaAs and AlGaAs. These data could then be compared to photoluminescence (PL) data which were expected to be sensitive to the presence of AsO.

2. Experiment

The samples in this study were grown in a Varian Gen II MBE system using a cryopump on the growth chamber instead of an ion pump. Sample substrates consisted of 5 mm squares of (100) undoped semi-insulating GaAs. A two-zone As cracking source developed in our laboratory was used to supply As₂ during growth [9]. The sublimator zone of the source was loaded with Furukawa 7N As granules. The Ga flux was supplied by a stock Varian 40 cc cell loaded with Alcan 8N Ga. The Al flux was supplied by a custom built hot-lipped 16 cc cell loaded with a single crystal Atomergic 6N Al ingot. The system was then baked for four days while the cracking section was kept at around 600°C. During the process of growing a series of quantum well (QW) structures, a degradation in the PL of these structures was noted as the cracking voltage was increased. A residual gas analysis (RGA) of the chamber using a UTI 100C mass analyzer revealed the presence

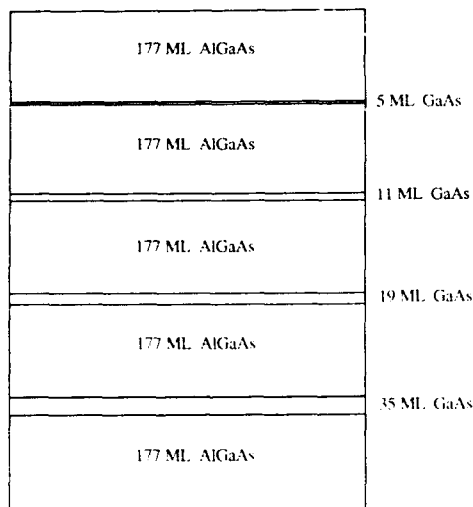


Fig. 1. Schematic cross-section of QW layers grown for PL study. Al mole fraction of 0.3.

of a small amount of mass 91 peak (AsO) during growth [10]. The mass 91 peak was found to increase with increasing cracking temperature, and varied from less than 1×10^{-12} to 4×10^{-12} A for cracking temperatures between 540 and 760 °C. This presented the opportunity of introducing a controlled amount of AsO into the films during growth to study its effects on both the PL of QW structures and the dampening of RHEED oscillations.

The samples grown for PL consisted of a 1 μ m buffer of GaAs followed by a set of four QWs of 35, 19, 11, and 5 monolayers (ML) of GaAs separated by 177 ML (500 Å) barriers of $\text{Al}_{0.3}\text{Ga}_{0.7}\text{As}$, as shown in fig. 1. All samples were grown at a nominal temperature of 620 °C with a GaAs growth rate of 0.7 ML/s and an AlAs growth rate of 0.3 ML/s. An attempt was made to keep all growth parameters the same except for the temperature of the As cracking section. The As cracking temperature was varied between 540 and 760 °C. The cracking section would normally be operated in this temperature range for a beam of predominantly As_2 . The cracking temperature was measured using a Vanzetti EITM2 dual wavelength pyrometer (no further corrections were made to the measured temperature). The As/Ga

ratio was kept within the range from 1.6 to 1.8. For this As overpressure the measured ratio of As to Ga + Al was found to be also in the range of 1.6 to 1.8. The first series of four samples were then grown at different cracking temperatures.

After the growth of the first series of samples, the cracking section was baked at maximum power, resulting in a temperature in excess of 1000 °C. Shutter and cracking temperature dependence during the bake indicated the AsO was either coming directly from the cracking section or from the radial vane cryo-shrouding around the cell. To assist in backing this cryo-shrouding, liquid nitrogen cooling to the radial vane was turned off and the cells adjacent to the As cell were run at elevated temperatures. During this bake, the mass 91 peak increased to about 1×10^{-11} A and then started to decrease. After three days the peak leveled out at 0.5×10^{-12} A and the bake was terminated. When the wheel was subsequently cooled with LN, there was no detectable AsO in the system, perhaps indicating that it had indeed come from the cryo-shrouding. Recently, Sacks et al. [11] have reported S contamination arising from the cryo-shrouding around their As cracking section. After baking, a second series of four samples were then grown under the same conditions as the previous series. There was no detectable mass 91 present during this second series.

Prior to the growth of each of the eight samples described above, RHEED data was taken on the growth oscillations of GaAs and AlGaAs to determine the amount of dampening of the RHEED oscillations. A 10 keV electron beam was used at an angle of incidence of about 1.0° along the twofold direction of the 2×4 reconstruction. For each run approximately 0.75 μ m would be grown, then seven GaAs spectra and seven AlGaAs spectra would be taken, followed by the growth of the rest of the buffer and then the QW layers.

After growth, the PL of each sample was measured. The samples were mounted in a cryostat and cooled to 4 K, immersed in liquid He. The samples were excited with the 514.5 nm line of an Argon ion laser at a power density of 1 W/cm². The luminescence was passed through a 1 m single grating spectrometer. The entrance and exit slits were set so that the broadening of each peak due

to the slits was always much less than the peak's intrinsic full width at half maximum (FWHM). The PL intensity was detected using photon counting from a cooled GaAs detector. From the PL measurements we determined the peak position of each QW transition, the FWHM linewidth of each transition, and the absolute and integrated intensity of each sample.

3. Photoluminescence results

The PL of the four samples grown before the bake are shown in fig. 2. The intensity of the spectrum in fig. 2a was used as the standard for the relative intensity scale. As the cracking temperature is increased the intensity of the PL drops, becoming dramatically lower, as seen in fig. 2d. The integrated intensities from 680 to 810 nm for these samples are shown in fig. 3 (lower curve). Here it is seen that the integrated intensity drops

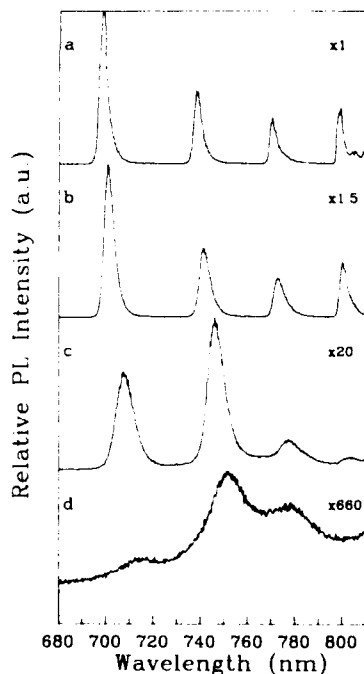


Fig. 2. PL spectra of the four samples grown before the bake of the As cracking section. Samples grown at cracking temperatures of (a) 540°C, (b) 610°C, (c) 690°C, and (d) 760°C are shown.

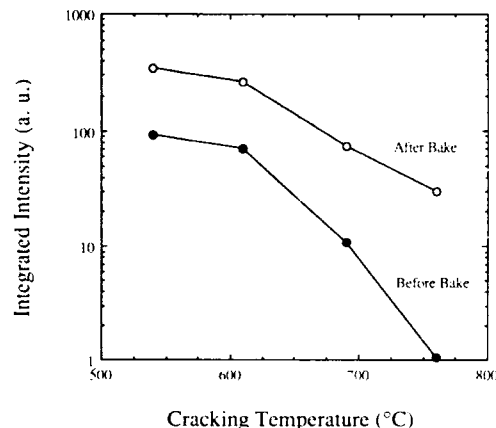


Fig. 3. Integrated PL intensity of samples grown before and after bake of the As cracking section.

by two orders of magnitude over the cracking temperature range. These integrated intensities are very similar to those of QW samples grown at different cracking temperatures at the time the AsO contamination was discovered. This indicates the generation of AsO with cracking temperature was very reproducible and stable. The presence of O₂ during the growth of AlGaAs is known to decrease the PL intensity [12]. This has been attributed to an aluminum-oxygen complex [13]. The measured FWHM linewidths are shown in fig. 4 for the various cracking temperatures. A pronounced trend in this data is the broadening of the linewidths over the cracking temperature range. The linewidths for the sample shown in fig. 2d were extremely broad and are not displayed in fig. 4.

The PL of the four samples grown after the As source was cleaned up are shown in fig. 5. These samples show a dramatic improvement in both intensity and linewidth. The integrated intensities for these samples are shown in fig. 3 (upper curve). Under the same growth conditions as the first series, the integrated intensities for the second series are between 30 and 300 times higher. Additionally, the integrated intensities drop only one order of magnitude over the cracking temperature range, compared with a drop of two orders of magnitude for the first series of samples. The measured FWHM linewidths for the samples of

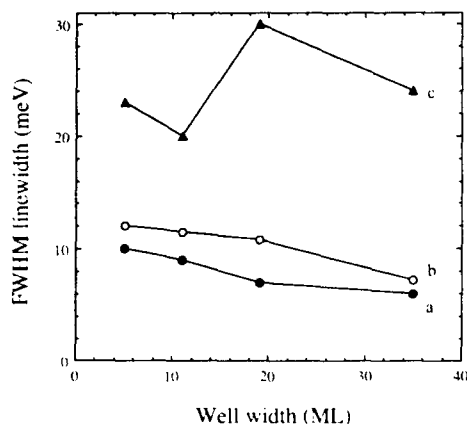


Fig. 4. Variation in the FWHM PL linewidth of the samples grown before the bake. Samples grown at cracking temperatures of (a) 540°C, (b) 610°C, and (c) 690°C are shown. (Linewidths of sample grown at 760°C too large to display.)

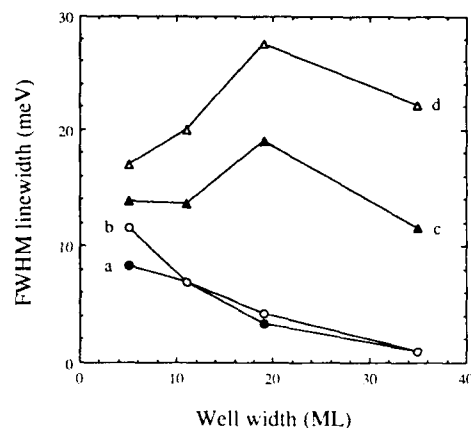


Fig. 6. Variation in the FWHM PL linewidth of the samples grown after the bake. Samples grown at cracking temperatures of (a) 540°C, (b) 610°C, (c) 690°C, and (d) 760°C are shown.

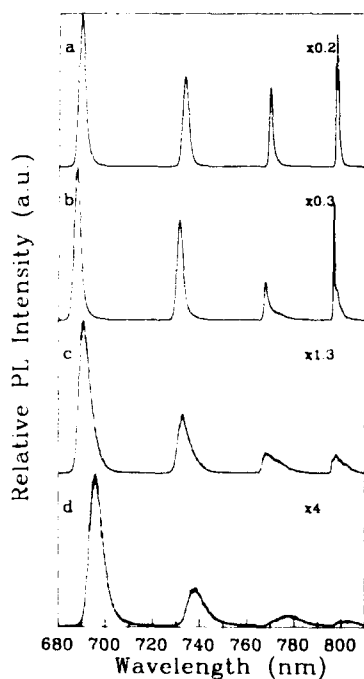


Fig. 5. PL spectra of the four samples grown after the bake of the As cracking section. Samples grown at cracking temperatures of (a) 540°C, (b) 610°C, (c) 690°C, and (d) 760°C are shown.

the second series are shown in fig. 6. The QW transitions are uniformly sharper after baking the cracking section. The linewidth for the samples shown in figs. 5a and 5b are comparable to those published in the literature [14]. The large improvement seen in the photoluminescence demonstrates the importance of removing AsO from the system. However, the fact remains that after the bake we will see a decrease in the integrated intensity and an increase in the linewidth as the cracking temperature is increased. We attribute this degradation to residual AsO present below our detection limits, which points out the difficulty of completely removing the AsO.

4. RHEED dampening results

The RHEED oscillation data was taken to determine what effect the AsO might have upon the dampening of the oscillations. This work is part of a larger study to understand the causes of the dampening and determine any diagnostic use they may have. For the first second of each spectrum only the As shutter was open to establish the initial intensity of the As stabilized surface; then the metal shutters were opened (60 s for GaAs and 45 for AlGaAs) and the intensity oscillated as the

layer grew. Then the metal shutters were closed again and the intensity recovered as the surface smoothed. After each AlGaAs spectrum GaAs was grown to smooth the surface.

The dampening of the oscillations was determined by extracting the normalized oscillation heights and fitting them with a single exponential. While most of the spectra seem to have both a fast and a slow component to the dampening, and are thus best fit by two exponentials, there is enough variance in the fit to make it difficult to compare spectra to one another. For the purposes of this paper, therefore, only a single exponential fit will be used. In fitting the data the first monolayer (starting intensity to 1st valley to 1st peak) was ignored. The remaining peak-to-valley (P-V, and valley-to-peak (V-P) heights were then determined and the oscillation height defined to be the geometric mean of each pair of P-V and V-P (this was done to reduce the effect of noise on the spectra). All the oscillation heights were then normalized by the first oscillation height. This series of heights was plotted versus oscillation number (i.e. monolayer) and fitted with a single exponential. From this a dampening constant in monolayers was determined, which represents how many layers can be grown before the oscillation height decays by e^{-1} . The extracted oscillation height data and fit for an AlGaAs RHEED spectrum are shown in fig. 7. Seven spectra of both GaAs and AlGaAs were taken at each growth condition to determine the mean and variance of the exponential fit. This treatment allows one to compare dampening independent of the growth rate or electron beam intensity. An additional benefit of treating the data in this way is its relative insensitivity to drift of the electron beam due to charging phenomena.

The presence of AsO primarily affects the dampening of the AlGaAs. Fig. 8 shows the RHEED oscillations for AlGaAs at different cracking temperatures before the bake. These correspond to the PL spectra shown in fig. 2. The oscillations are damped more as the cracking temperature is increased. The measured dampening constants for these curves are shown in fig. 9 (lower curve, fitted with a least squares line). The dampening constant decreases from 19 ± 1.7 ML

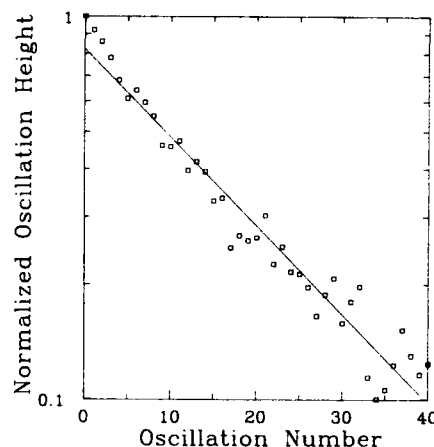


Fig. 7. Extracted oscillation heights and exponential fit for AlGaAs RHEED oscillations at As cracking temperature of 540°C before the bake.

to 12 ± 1 ML. One should also note the lack of recovery of the intensity in fig. 8d (corresponding to PL spectra fig. 2d). The RHEED oscillations

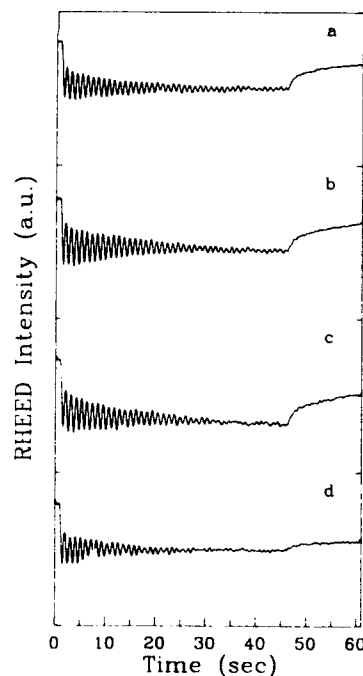


Fig. 8. RHEED oscillations for four samples grown before the bake. Samples grown at cracking temperatures of (a) 540°C , (b) 610°C , (c) 690°C , and (d) 760°C are shown.

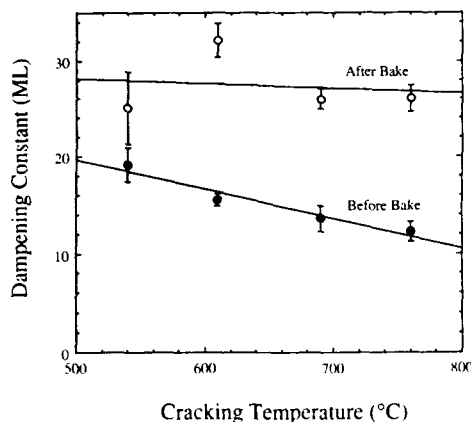


Fig. 9. Fitted dampening constants to AlGaAs RHEED oscillations. 1 ML/s growth rate, before and after baking the As cracking section. Error bars represent one standard deviation in the repeatability of the measurement.

taken after the bake are shown in fig. 10 and the dampening constants in fig. 9 (upper curve, fitted with a least squares line). There is no detectable

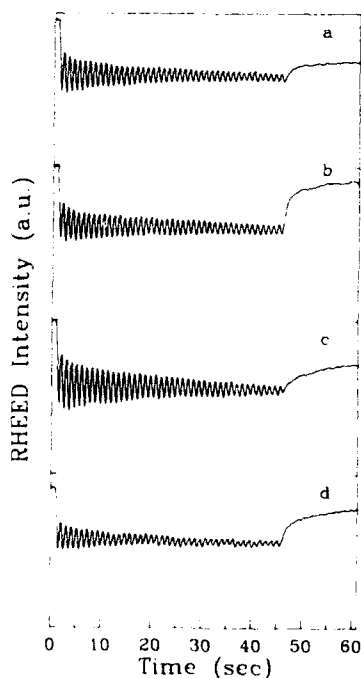


Fig. 10. RHEED oscillations for four samples grown after the bake. Samples grown at cracking temperatures of (a) 540 °C, (b) 610 °C, (c) 690 °C, and (d) 760 °C are shown.

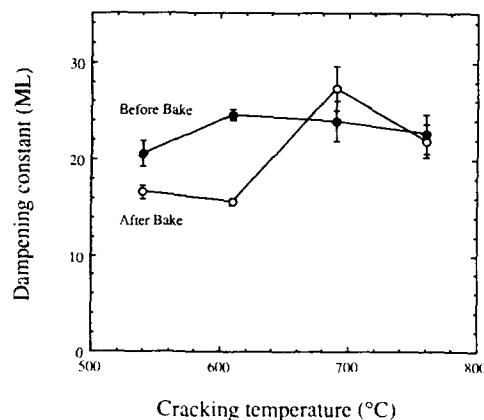


Fig. 11. Fitted dampening constants to GaAs RHEED oscillations. 0.7 ML/s growth rate, before and after baking the As cracking section. Error bars represent one standard deviation in the repeatability of the measurement.

increase in the dampening after the bake. This is in contrast to the PL result which degraded with increasing cracking temperature after the bake.

The GaAs dampening constants are shown in fig. 11. These results show a generally constant dampening of the GaAs before and after the bake. Somewhat puzzling are the smaller values obtained at the lower cracking settings after the bake, primarily the one point at 610 °C. This may have resulted from a lack of adequate control of all the variables. Nonetheless, the data as a whole indicate the dampening of the GaAs was relatively unaffected by the presence of AsO.

5. Discussion and conclusions

The dramatic effect of AsO on the PL of QW structures demonstrates the sensitivity of this measurement. AsO resulted in both a large decrease in the integrated intensity and a broadening of the QW linewidths. There has been much discussion recently over the relevance of PL linewidth to interface quality or smoothness in QW samples [15-17]. For these samples, the combination of both decreasing intensity and increasing linewidth argue that the samples become "worse" (optically) as AsO is introduced. The importance of this comes not when AsO is detectable by RGA, but

rather when it is not measurable. The integrated intensity and linewidth of QW transitions in PL offers an extremely sensitive diagnostic tool for determining the presence of AsO at low levels in an MBE system.

The degradation of the PL was correlated with increased dampening of AlGaAs RHEED oscillations when AsO was measurable. When no AsO was detectable, the dampening of the AlGaAs oscillations became constant. The presence of AsO seems to have had little effect on the RHEED oscillations of GaAs. The simplest explanation of these results would be that the AsO strongly binds the Al atoms incident on the surface, reducing their surface mobility. This would have the effect of making the surface rougher, broadening the PL linewidths. Consistent with this suggestion is the lack of the RHEED intensity recovery at maximum AsO exposure. The incorporation of oxygen into the films would decrease the PL intensity.

It is possible that the dampening of the RHEED oscillations could be used as a gross diagnostic tool for AsO contamination, but in its sensitivity range residual gas analysis is much simpler. Furthermore, interpreting the dampening of RHEED oscillations is very difficult. The dampening has been found to depend on the As overpressure [18], angle of incidence (potentially strong effect), azimuthal angle (relatively weak effect), sample position in the chamber (surprisingly strong effect), as well as other parameters [19,20]. Thus comparing dampening figures requires strict control of all these variables. At this point it is unclear whether the dampening of the RHEED oscillations can be used for reliable diagnostics during the growth process.

Acknowledgments

The authors would like to thank K. Sadra, D.P. Neikirk, and K. Eyink for discussion of the topics in this paper. This work was supported by the Joint Services Electronics Program under contract No. AFOSR F49260-89-C-0044 and the Army Re-

search Office under contract No. DAAL 03-88-K-0060.

References

- [1] A.Y. Cho and J.R. Arthur, *Progr. Solid State Chem.* 10 (1975) 157.
- [2] P.K. Larsen and P.J. Dobson, Eds., *Reflection High-Energy Electron Diffraction and Reflection Electron Imaging of Surfaces*, NATO Series B 188 (1988).
- [3] J.M. Van Hove, C.S. Lent, P.R. Pukite and P.I. Cohen, *J. Vacuum Sci. Technol.* B1 (1983) 741.
- [4] C.W. Farley, G.J. Sullivan, M.J. Mondry and D.L. Miller, *J. Crystal Growth* 96 (1989) 19.
- [5] A. Madhukar, in: *Thin Film Growth Techniques for Low-Dimensional Structures*, Eds. R.F.C. Farrow et al., NATO Series B 163 (1988) 37.
- [6] C. Deparis, J. Massies and G. Neu, *Appl. Phys. Letters* 56 (1990) 233.
- [7] J.H. Neave, B.A. Joyce, P.J. Dobson and N. Norton, *Appl. Phys.* A31 (1983) 1.
- [8] J.M. Van Hove, P.R. Pukite and P.I. Cohen, *J. Vacuum Sci. Technol.* B3 (1985) 563.
- [9] T.J. Mattord, V.P. Kesan, G.E. Crook, T.R. Block, A.C. Campbell, D.P. Neikirk and B.G. Streetman, *J. Vacuum Sci. Technol.* B6 (1988) 1667.
- [10] It is possible some other contaminant was being generated by the hot cracking source. However, considering the well known detrimental effects of oxygen on AlGaAs we consider AsO as the most likely agent for the effects seen in this paper.
- [11] R.N. Sacks, D.W. Eichler, R.A. Pastorello and P. Colombo, *J. Vacuum Sci. Technol.* B8 (1990) 168.
- [12] C.T. Foxon, J.B. Clegg, K. Woodbridge, D. Hilton, P. Dawson and P. Blood, *J. Vacuum Sci. Technol.* B3 (1985) 703.
- [13] K. Akimoto, M. Kamada, K. Taira, M. Arai and N. Watanabe, *J. Appl. Phys.* 59 (1986) 2833.
- [14] C.W. Tu, R.C. Miller, B.A. Wilson, P.M. Petroff, I.D. Harris, R.F. Kopf, S.K. Spitz and M.G. Lamont, *J. Crystal Growth* 81 (1987) 159.
- [15] R.C. Miller and R. Bhat, *J. Appl. Phys.* 64 (1988) 3647.
- [16] A. Ourmazd, J. Cunningham, D.W. Taylor, J.A. Reentschler and C.W. Tu, in: *Defects in Semiconductors 15*, *Material Science Forum*, Vols. 38-41 (1989) p. 689.
- [17] C.A. Warwick, W.Y. Jan, A. Ourmazd and T.D. Harris, *Appl. Phys. Letters* 56 (1990) 2666.
- [18] B.F. Lewis, F.J. Grunthaler, A. Madhukar, T.C. Lee and R. Fernandez, *J. Vacuum Sci. Technol.* B3 (1985) 131.
- [19] J.M. Van Hove, P.R. Pukite and P.I. Cohen, *J. Vacuum Sci. Technol.* B3 (1985) 563.
- [20] T.R. Block and B.G. Streetman, work in progress.

Application of frequency-domain analysis to RHEED oscillation data: time dependence of AlGaAs growth rates

G.W. Turner and S.J. Eglash

Lincoln Laboratory, Massachusetts Institute of Technology, Lexington, Massachusetts 02173-9108, USA

Frequency-domain techniques have been applied to the analysis of RHEED oscillation data taken during MBE growth of AlGaAs at substrate temperatures from 580 to 790°C and at various V/III ratios. In addition to permitting rapid and highly accurate measurements of RHEED oscillation frequencies under normal growth conditions, frequency-domain techniques allow these frequencies to be determined when the RHEED data are too noisy to be analyzed by conventional time-domain techniques. Frequency-domain techniques also have the capability of analyzing the time evolution of the RHEED frequencies obtained immediately after growth is restarted following interruption of the group III flux. For AlGaAs growth at substrate temperatures above 700°C, we have observed that the frequency decreases substantially during deposition of the first few monolayers. This variation leads to errors in growth rates evaluated by conventional RHEED analysis.

1. Introduction

For the analysis of reflection high-energy diffraction (RHEED) oscillation data obtained during MBE growth, frequency-domain techniques [1,2] such as the fast Fourier transform offer a number of advantages over the conventional time-domain method, which utilizes graphical analysis of intensity-versus-time plots. The frequency-domain techniques permit the oscillation frequency to be determined more rapidly and precisely, to be evaluated from even a single oscillation, and to be extracted from data that cannot be analyzed by the conventional technique because the oscillations are too weak to be detected by visual inspection. The latter capability permits the assessment of the validity of an assumption that is often made in performing MBE growth experiments, namely, that the growth rate determined from RHEED oscillations observed in the early stages of growth is the same as the rate during the later stages, when oscillations are no longer visible.

We have chosen to investigate the growth of AlGaAs at high substrate temperatures, since such growth is required in the fabrication of a variety of electronic and optoelectronic devices. For temperatures above 700°C, the RHEED oscillation

frequency decreases substantially during deposition of the first few monolayers.

2. Experimental procedure

A Varian GEN II modular 75 mm MBE system was used for the growth of AlGaAs and GaAs layers on semi-insulating GaAs substrates bonded with In to Mo mounting blocks. The substrates were prepared by chemical cleaning and etching followed by oxide desorption at ~600°C in the MBE growth chamber under an As flux. Substrate temperatures were measured with a narrow-band optical pyrometer positioned to view the substrate in the growth position. Emissivity values employed in the pyrometer measurements were determined by calibration experiments based on observations of the InSb melting point and the formation of the Al–Si eutectic. Relative substrate temperatures were monitored with a thermocouple located below the mounting block. The steady-state Ga and Al source fluxes were adjusted to give GaAs growth rates of 0.9 to 1.0 $\mu\text{m/h}$ and AlAs growth rates of 0.3 to 0.4 $\mu\text{m/h}$. Beam-equivalent pressures for the Ga, Al, and As fluxes

were determined from readings on an ion gauge located in the growth position. Initial Ga and Al flux transients were determined by computerized recording of the ion gauge readings for a few minutes after the opening of the source shutters. The Ga and Al fluxes decreased by less than 2% and 5%, respectively. The As_4 flux was varied to give uncorrected beam-equivalent V/III ratios between 7:1 and 20:1.

The computerized measurement system used for frequency-domain analysis has been described previously [1]. Briefly, the system is based on the observation of RHEED intensities by a TV camera focused on the phosphor screen. The intensity data for a selected pixel are digitized and read into a desktop computer for frequency analysis. In each frequency determination, data are collected for 30 or 60 s at rates of 70 and 30 samples/s respectively, then analyzed to obtain the power spectrum, after which a simple peak location algorithm is employed to extract the frequency. For these times and sampling rates it is predicted that the frequency can be measured with an uncertainty as low as ± 0.003 Hz. This value has been confirmed by the reproducibility of the frequency values measured on GaAs depositions performed under the same growth conditions. The uncertainty is higher for especially noisy spectra.

In performing a set of oscillation frequency measurements, a GaAs buffer layer at least $1\text{ }\mu\text{m}$ thick was first deposited on the substrate at $\sim 550^\circ\text{C}$, followed in most cases by deposition of $\sim 0.1\text{ }\mu\text{m}$ of AlGaAs at this temperature. The Al and Ga shutters were then closed for ~ 30 s, data collection was started, the Al and Ga shutters were reopened, and intensity data for the specular reflection in the (011) azimuth were collected for the desired time. The substrate temperature was then increased and allowed to stabilize, the Al and Ga shutters were closed, and the procedure was repeated. As-stabilized surface reconstructions were maintained. Generally the experiments were performed at a series of successively higher temperatures. If a measurement was then repeated at one of the lower temperatures, the frequency was found to be the same as the value measured earlier. In experiments at temperatures below 700°C , the frequency was found to be the same for AlGaAs

growth directly on GaAs as for growth on an AlGaAs layer; at higher temperatures, growth could not be performed directly on GaAs because of the difficulty of maintaining an As-stabilized GaAs surface.

3. Results

In fig. 1, the RHEED oscillation frequencies measured in two sets of AlGaAs growth experiments are plotted against substrate temperature over the range from 580 to 790°C . In one set of experiments the V/III beam-equivalent pressure ratio was 7.3 and the ratio of Al flux to the total group III flux was 0.31 (yielding $\text{Al}_x\text{Ga}_{1-x}\text{As}$ layers with $x = 0.31$ if the sticking coefficient is unity for both Ga and Al), while in the other set these ratios were 19 and 0.33, respectively. The frequency values were obtained by analysis of data collected for 60 s after opening the Ga and Al shutters. As previously reported [3], the persistence of the observed oscillations varied with substrate temperature, with the oscillations most clearly visible in the high-temperature and low-temperature regimes. With increasing temperature, the measured frequency is nearly constant up to $\sim 650^\circ\text{C}$, then decreases strongly as the growth rate decreases because of Ga desorption from the growing surface. The ratio of the growth rates at the highest and lowest temperatures approximates the ratio of the Al flux to the total group III flux, showing that the layers grown at the highest temperatures probably consist almost entirely of AlAs. This variation in growth rate with temperature is not shown as clearly by the earlier data of Ralston, Wicks and Eastman [3], which are plotted in fig. 1 for comparison.

The two curves for frequency-domain-analyzed data in fig. 1 show that the onset of significant Ga desorption was shifted to higher substrate temperature for the run with the higher V/III ratio. The results that we have obtained in similar experiments, as well as the limited data of ref. [3], are consistent with this trend. However, the magnitude of the temperature shift has not been determined accurately, because of the uncertainty in substrate temperature measurements.

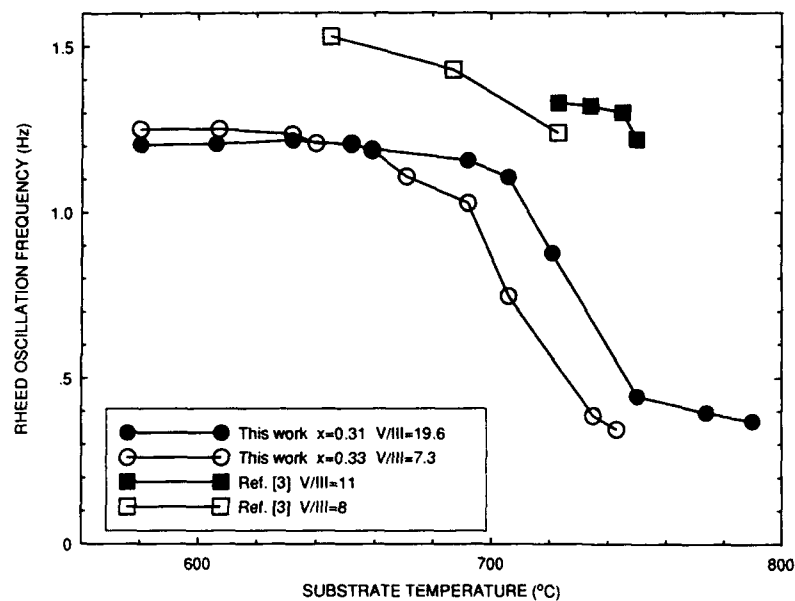


Fig. 1. RHEED oscillation frequency versus substrate temperature for growth of AlGaAs. For data represented by circles and squares, frequencies were obtained by frequency-domain and time-domain analysis, respectively.

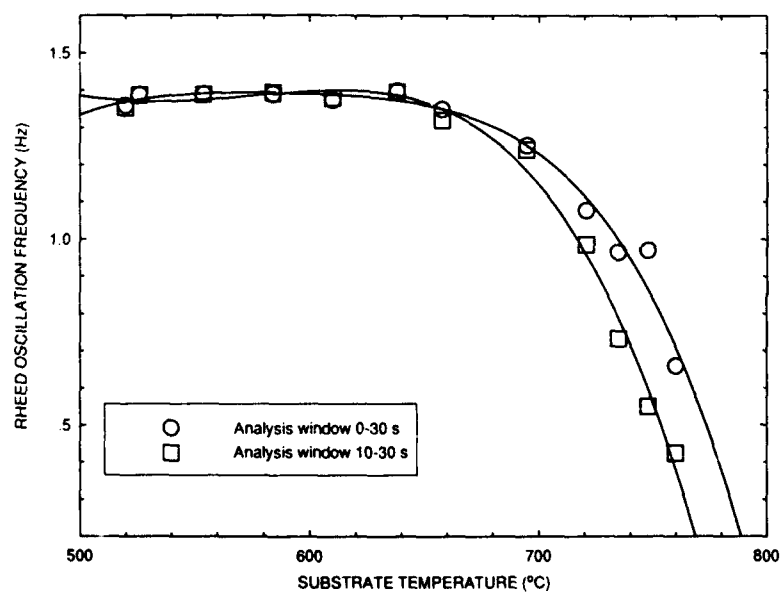


Fig. 2. RHEED oscillation frequency versus substrate temperature for growth of AlGaAs. For data represented by circles and squares, frequencies were obtained by frequency-domain analysis of data collected for 0-30 and 10-30 s, respectively, after opening the Al and Ga source shutters.

In another set of AlGaAs growth experiments, which were performed under conditions similar to those used in obtaining the results shown in fig. 1 for the lower V/III ratio, data were collected for 30 s after opening the Ga and Al shutters. For each substrate temperature, oscillation frequencies were determined by analyzing the data collected from 10 to 30 s as well as by analyzing the data for the entire 30 s. The results are shown in fig. 2. For temperatures below 700°C the frequencies obtained for the two analysis windows are the same. For higher temperatures, however, the values are lower for the 10–30 s window than for the 0–30 s window, showing that the growth rate during the first 10 s was greater than the steady-state rate.

To investigate the time evolution of the growth rate in greater detail, experiments were performed at temperatures from 520 to 760°C in which analysis windows of 5 s were used in analyzing data taken for 30 s after opening the Ga and Al shutters. The results are shown in fig. 3. At temperatures below 700°C the growth rate does not change with time, but at the higher temperatures

the initial rate is higher than the steady-state value by an amount that increases with increasing temperature. At 760°C, the initial rate is about twice the steady-state value. This change in growth rate (and therefore in composition) is much too large to be attributed to flux transients. It indicates the existence of complex interactions among the surface atoms that should be addressed in future investigations of the epitaxial growth of AlGaAs layers.

4. Conclusions

By using frequency-domain analysis of RHEED oscillation data taken during the growth of AlGaAs, the oscillation frequency has been measured over a wider range of substrate temperatures and V/III ratios than previously reported. By utilizing the capability of frequency-domain analysis to extract oscillation frequencies from data taken over short time intervals, it has been found that at high temperatures the growth rate immediately after opening the source shutters is sub-

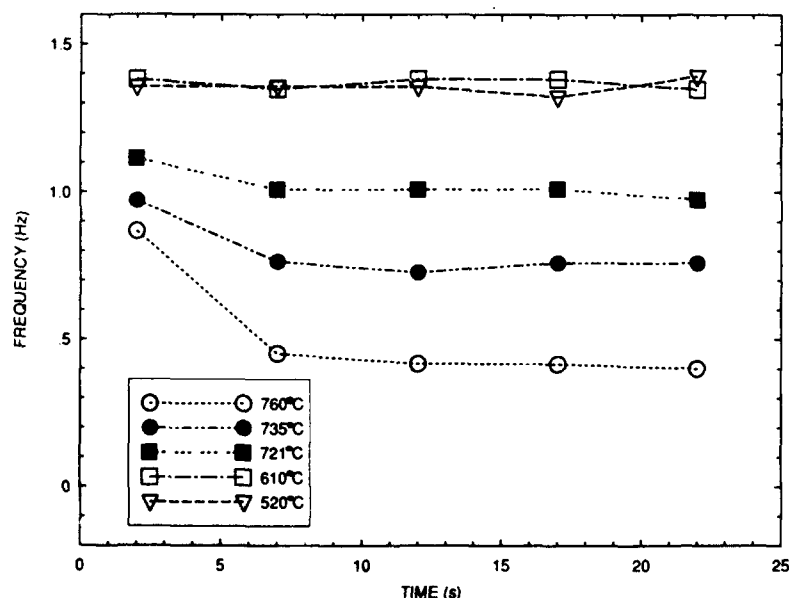


Fig. 3. RHEED oscillation frequency versus time following source shutter opening for AlGaAs growth at substrate temperatures from 520 to 760°C. Frequencies were obtained by frequency-domain analysis of data collected for 5 s periods.

stantially higher than the steady-state rate. Such measurements of the time evolution of epitaxial growth should assist in achieving a better understanding of the complex interactions at growing epitaxial surfaces.

Acknowledgments

The authors would like to acknowledge A.J. Strauss for helpful discussions, B.N. Nechay for continuing assistance with the analysis software, and M.K. Connors, L.J. Krohn, and J.V. Pantano

for technical assistance. This work was sponsored by the Defense Advanced Research Projects Agency and the Department of the Air Force.

References

- [1] G.W. Turner, B.N. Nechay and S.J. Eglash, *J. Vacuum Sci. Technol.* B8 (1990) 283.
- [2] J.S. Resh, K.D. Jamison, J. Strozier and A. Ignatiev, *Rev. Sci. Instr.* 61 (1990) 771.
- [3] J. Ralston, G.W. Wicks and L.F. Eastman, *J. Vacuum Sci. Technol.* B4 (1986) 594.

Initial growth stage of InAs/GaAs studied by RHEED–TRAXS method

J. Shigetomi, K. Fuwa, S. Shimizu, H. Yamakawa

ULVAC JAPAN, Ltd., Hagisono, Chigasaki-shi, Kanagawa 253, Japan

and

S. Ino

University of Tokyo, Hongo, Bunkyo-ku, Tokyo 113, Japan

RHEED–TRAXS (total reflection angle X-ray spectroscopy in RHEED experiments) technique has been focused on an observation of In desorption processes from GaAs(100) substrate surfaces. Results show that In desorption energy sensitively changes along with arsenic partial pressure, P_{As_4} . Furthermore, at 3.0×10^{-8} Torr of P_{As_4} , ITDS (isothermal desorption spectroscopy) curves have a refraction point below the In L α line intensity corresponding to one monolayer of InAs. RHEED intensity measurements indicate that the refraction point corresponds to the change of the growth manner, i.e. a single layer growth occurs followed by three-dimensional island growth, the Stranski–Krastanov growth mode, at this P_{As_4} . On the other hand, at 1.0×10^{-7} Torr of P_{As_4} , InAs grows with the Volmer–Weber growth mode.

1. Introduction

Reflection high energy electron diffraction (RHEED) has been extensively used for studying the atomic structure of crystal surfaces. Recently, the phenomenon of RHEED intensity oscillation has attracted a great deal of interest, since the intensity changes with time when epitaxy occurs in a layer-by-layer growth model. It is now widely accepted that RHEED is a powerful tool for tailoring “man-made” structures by molecular beam epitaxy (MBE). Although the layer thickness can be precisely controlled with atomic scale accuracy by measuring an intensity oscillation, only little detailed information on chemical composition during growth is available.

Ino et al. originally proposed X-ray spectroscopy for surface chemical analysis with high surface sensitivity in which an incident electron beam of RHEED was used as an excitation probe [1]. It was for the first time demonstrated by Hasegawa et al. [2,3]: when the X-ray take-off

angle is set closely corresponding to the critical angle for total reflection of the characteristic X-ray, the detection efficiency is remarkably improved. They called this technique RHEED–TRAXS (total reflection angle X-ray spectroscopy in RHEED experiments) and proved that the sensitivity of this technique is comparable to or higher than that of Auger electron spectroscopy (AES).

We have applied this RHEED–TRAXS technique to InAs thin film growth onto GaAs substrate for in-situ monitoring the chemical composition. The contact of InAs to GaAs is of considerable interest in its promising applications to infrared (IR) detectors and optoelectronic devices [4–11]. The large lattice mismatch between InAs and GaAs substrates, however, causes a significant obstacle in obtaining high electronic quality. It is very important to make the initial stages of InAs onto GaAs controllable in order to fabricate those devices.

In a previous paper [12] it was shown that the

composition x in the grown $\text{InAs}_{1-x}\text{Sb}_x$ film could be precisely controlled by measuring the characteristic X-ray peak ratio ($\text{Sb L}\alpha$)/($\text{Ga K}\alpha$) and by adjusting the composition of As_4 and Sb_4 beam flux.

InAs desorption processes from $\text{GaAs}(100)$ substrate are presently investigated by RHEED-TRAXS method as a function of P_{As_4} . In this paper the dependence of In desorption energy upon P_{As_4} is discussed. In addition, two types of growth mode, i.e. Stranski-Krastanov mode and Volmer-Weber mode, of InAs due to P_{As_4} , are also described.

2. Experiment

The MBE system (ULVAC model MBC-305) used in the present work was composed of a sample loading chamber and a growth chamber. A Li drifted Si solid state X-ray detector, Si(Li) detector, was combined so as to detect the arbitrary characteristic X-ray. The X-rays emitted from the sample surface pass successively through two Be windows and reach a Si(Li) detector. Details of the spatial arrangement of the electron gun, Si(Li) detector and specimen were described elsewhere [12]. X-ray take-off angle of In $\text{L}\alpha$ line was fixed at 0.74° , corresponding to a total reflection angle of the In $\text{L}\alpha$ line on the GaAs surface.

The substrates used here were (100)-oriented semi-insulating Cr-O doped GaAs, 20 mm square and 0.35 mm thick. After chemical etching by $\text{H}_2\text{SO}_4:\text{H}_2\text{O}_2:\text{H}_2\text{O}$ (5:1:1) solution, they were mounted on Mo blocks and inserted into the growth chamber. Prior to the growth, the substrate temperature, T_{sub} , was raised up to 600°C for 5 min in order to obtain a clean surface. After that, the InAs layers were grown at constant T_{sub} where P_{As_4} was fixed. Growth rates as well as film thickness were calibrated in advance by measuring thicknesses in direct proportion to the growth time. The InAs desorption processes were observed in-situ by RHEED-TRAXS in which RHEED intensity oscillations were simultaneously observed. The energy of the incident electron beam was 20 kV throughout the work.

3. Result and discussion

After the InAs films were grown up to 10 ML, the In K-cell shutter was closed. The In $\text{L}\alpha$ X-ray intensities were successively measured by RHEED-TRAXS, as a function of duration time of In desorption, which was the so-called ITDS (isothermal desorption spectroscopy) method [3]. P_{As_4} was kept constant from the growth to the desorption. At first, when ITDS was done at two values of P_{As_4} , i.e. 3.0×10^{-8} and 1.0×10^{-8} Torr, the difference of ITDS gradient depending upon P_{As_4} was observed. The results are shown in fig. 1, where T_{sub} was kept at 450°C . The abscissa of fig. 1 indicates the duration time of the desorption, and its ordinate, the intensity of the In $\text{L}\alpha$ line (3.29 keV), which is normalized by Ga $\text{K}\alpha$ intensity. Open and solid circles denote the case of P_{As_4} of 3.0×10^{-8} and 1.0×10^{-8} Torr, respectively. In the case of 3.0×10^{-8} Torr of P_{As_4} , the In $\text{L}\alpha$ line intensity decreases just a little even after 50 min of duration. However, it decreases rapidly after the As shutter was closed. The RHEED patterns at the positions (I), (II) and (III) in the

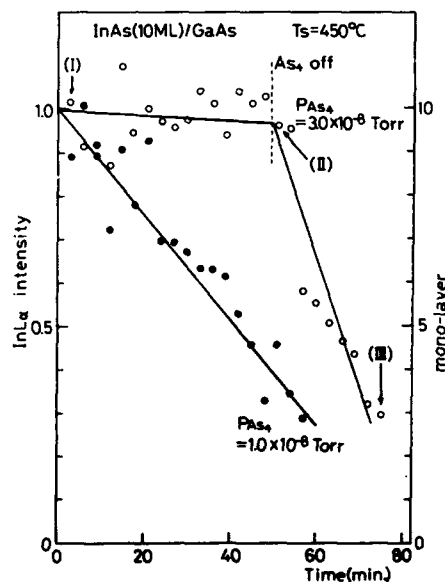


Fig. 1. Isothermal ($T_{\text{sub}} = 450^\circ\text{C}$) desorption curves of In $\text{L}\alpha$ line intensity versus duration time. Open and solid circles denote 3.0×10^{-8} and 1.0×10^{-8} Torr of P_{As_4} , respectively.

ITDS curve are represented in fig. 2. The RHEED pattern (I) indicates that InAs forms as the three-dimensional island formation onto GaAs(100) surfaces. The RHEED pattern (II), taken after the As shutter was closed, shows that the InAs spot intensities become rather weak as compared with (I), which corresponds to the In $L\alpha$ line intensity to be weakened. At the point (III), 25 min after the As shutter was closed, the InAs spots completely disappear. The In $L\alpha$ line intensity, however, is observed corresponding to three mono-layers of InAs. Because the As vapor pressure is much higher than that of In, In would remain on the substrate as a liquid-like metallic formation.

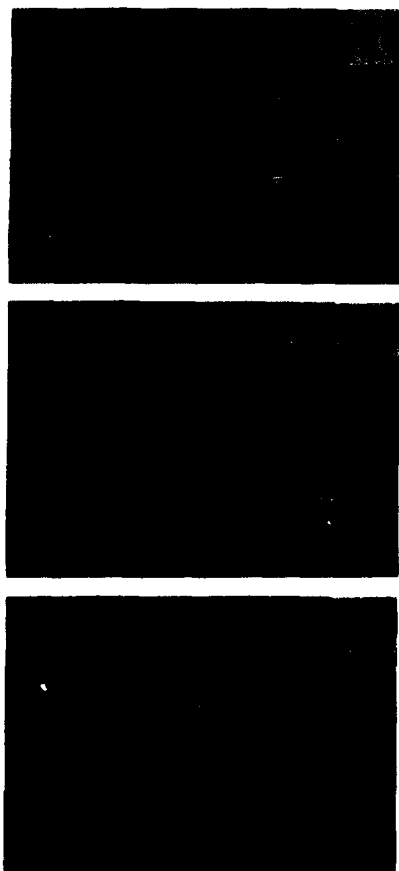


Fig. 2. The changes of RHEED pattern during In desorption at 3.0×10^{-8} Torr of P_{As_4} . (I), (II) and (III) correspond to the points indicated by the same number in fig. 1.

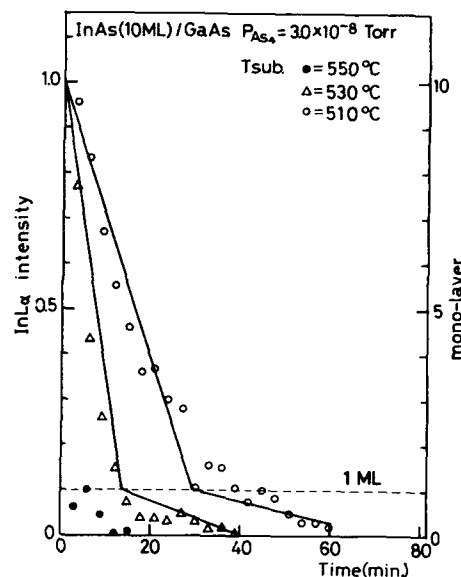


Fig. 3. Isothermal desorption curves ($P_{As_4} = 3.0 \times 10^{-8}$ Torr) at various substrate temperatures.

This suggests that a quantitative analysis for growing surface as well as a qualitative analysis is very important and indispensable to in-situ observation in MBE.

On the other hand, in the case of 1.0×10^{-8} Torr of P_{As_4} , the In $L\alpha$ intensity is abruptly decreased. It can be considered that the In desorption energy is very sensitive to P_{As_4} because of the difference of In desorption rate depending upon P_{As_4} .

Furthermore, In desorption energies are obtained from ITDS so as to clarify the dependence of In desorption energy upon P_{As_4} on GaAs(100) surfaces. Desorption energies are easily obtained from Arrhenius plots of ITDS curve, because the gradients of the ITDS curves directly correspond to the desorption rate of In atoms [3]. ITDS by RHEED-TRAXS measurements was done for 10 ML grown InAs at different P_{As_4} . Fig. 3 shows ITDS curves of In on GaAs(100) surface at 3.0×10^{-8} Torr of P_{As_4} . When T_{sub} is 550°C , In rapidly desorbs from the surface within 15 min. In desorption rates, however, become low with decreasing T_{sub} . Fig. 4 shows ITDS curves at 1.0×10^{-7} Torr of P_{As_4} . In desorption rates also decrease with

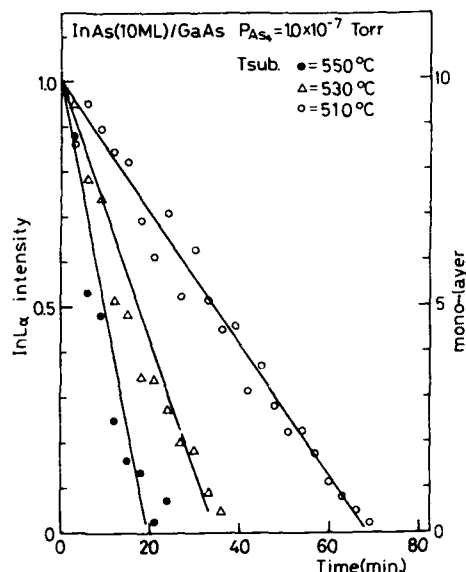


Fig. 4. Isothermal desorption curves ($P_{As_4} = 1.0 \times 10^{-7}$ Torr) at various substrate temperatures.

decreasing T_{sub} . As is evident from comparison with fig. 3, however, the desorption rate at the same T_{sub} seems different. Desorption energies are summarized in table 1 where the result of the AES experiment by Foxon and Joyce is also shown [13]. The present results agree approximately with those obtained by Foxon and Joyce. However, they did not take the important role of P_{As_4} into consideration. Our ITDS results by RHEED-TRAXS method indicate that In desorption energies are sensitively affected by P_{As_4} .

Further attention must be focused on the refraction point on the curve around one monolayer, as is shown in fig. 3. The refraction points appear at the same In coverage, i.e. around one monolayer, in both T_{sub} of 510°C and 530°C. In de-

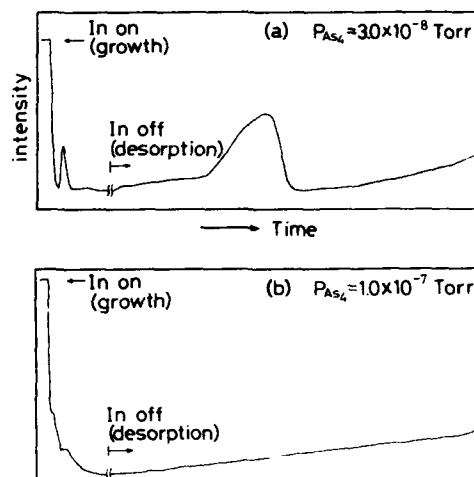


Fig. 5. RHEED intensity oscillation during growth and desorption processes, $T_{sub} = 530^\circ\text{C}$: (a) $P_{As_4} = 3.0 \times 10^{-8}$ Torr and (b) $P_{As_4} = 1.0 \times 10^{-7}$ Torr.

sorption energy below one monolayer is obtained as 2.1 eV, which is 0.7 eV higher than the energy above one monolayer. This indicates that In atoms hardly desorb below one monolayer. On the other hand, in the case of 1.0×10^{-7} Torr of P_{As_4} , the refraction point does not appear, as is shown in fig. 4. The observation of the RHEED patterns shows no differences around one monolayer. The intensity oscillation, however, reveals remarkable characteristics corresponding to desorption energy, as is shown in fig. 5. Fig. 5 shows the specular beam intensity as a function of time for InAs growth and desorption. In the figure, InAs grows between two arrows, denoted as In on and In off. The desorption process is represented after the point indicated by right hand arrow subscribed as In off. Figs. 5a and 5b correspond to 3.0×10^{-8} and 1.0×10^{-7} Torr of P_{As_4} , respectively. In the case of 3.0×10^{-8} Torr of P_{As_4} , when In atoms are supplied, the intensity oscillation is observed only once through growth. After the In shutter is closed, the intensity gradually increases with duration time and a wide oscillation peak appears as compared with the growth process. This can be considered as follows: since the period of RHEED intensity oscillation precisely coincides with one monolayer growth, a two-dimen-

Table 1
Indium desorption energies (in eV) from GaAs(100) surface

Present work	AES [13]
1.4 ($P_{As_4} = 3 \times 10^{-8}$ Torr)	1.5 ± 0.1
1.8 ($P_{As_4} = 1 \times 10^{-7}$ Torr)	1.5 ± 0.1
2.1 ($P_{As_4} = 3 \times 10^{-8}$ Torr ^{a)})	1.5 ± 0.1

^{a)} Below 1 monolayer.

sional InAs layer is formed onto GaAs(100) surface followed by three dimensional islands at this P_{As_4} . The increase of In desorption energy below one monolayer is also shown in fig. 5a. If the large peak of RHEED intensity on desorption process corresponds to the desorption of one monolayer just on the GaAs(100) surface with two-dimensional formation, the elongation of the oscillation period as compared with that of the growth process would indicate the increase of In desorption energy. This shows that the growth is made under Stranski-Krastanov mode at 3.0×10^{-8} Torr of P_{As_4} . On the contrary, in fig. 5b, oscillations cannot be clearly observed. This suggests that three-dimensional growth, i.e. Volmer-Weber type of growth, would occur at 1.0×10^{-7} Torr of P_{As_4} .

4. Conclusion

The RHEED-TRAXS technique has been applied to an observation of In desorption processes from GaAs(100) substrates. It is evidently observed that In desorption energies susceptibly change depending upon P_{As_4} . At 3.0×10^{-8} Torr of P_{As_4} , the ITDS curves have a refraction point below the In $L\alpha$ intensity corresponding to one monolayer of InAs. RHEED intensity measurement, which was simultaneously done with

TRAXS, shows that InAs grows with the Stranski-Krastanov mode. On the other hand, at 1.0×10^{-7} Torr of P_{As_4} , InAs grows with the Volmer-Weber mode.

References

- [1] S. Ino, T. Ichikawa and S. Okada, Japan. J. Appl. Phys. 19 (1980) 1451.
- [2] S. Hasegawa, S. Ino, Y. Yamamoto and H. Daimon, Japan. J. Appl. Phys. 24 (1985) L387.
- [3] S. Hasegawa, H. Daimon and S. Ino, Surface Sci. 186 (1987) 138.
- [4] D.T. Cheung, A.M. Andrews, E.R. Gertner, G.M. Williams, J.E. Clarke, J.G. Pasko and J.T. Longo, Appl. Phys. Letters 30 (1977) 587.
- [5] H. Sakaki, L.L. Chang, R. Ludeke, C. Chang, G.A. Halasz and L. Esaki, Appl. Phys. Letters 31 (1977) 211.
- [6] L.O. Bubulac, A.M. Andrews, E.R. Gertner and D.T. Cheung, Appl. Phys. Letters 36 (1980) 734.
- [7] W.J. Schaffer, M.D. Lind, S.P. Kowalczyk and R.W. Grant, J. Vacuum Sci. Technol. B1 (1983) 688.
- [8] D.I. Smith and C. Mailhot, J. Appl. Phys. 62 (1987) 2545.
- [9] C.G. Bethea, M.Y. Yen, B.F. Levine, K.K. Choi and A.Y. Cho, Appl. Phys. Letters 51 (1987) 1431.
- [10] R. Bean and K. Zanio, Appl. Phys. Letters 53 (1988) 1647.
- [11] M. Sato and Y. Horikoshi, Appl. Phys. Letters 55 (1989) 1689.
- [12] S. Shimizu, J. Shigetomi, H. Yamakawa and S. Ino, Vacuum, in press.
- [13] C.T. Foxon and B.A. Joyce, J. Crystal Growth 44 (1978) 75.

Reflectance-difference probing of surface kinetics of (001) GaAs during vacuum chemical epitaxy

G. Paulsson, K. Deppert *, S. Jeppesen, J. Jönsson, L. Samuelson and P. Schmidt *

Department of Solid State Physics, University of Lund, Box 118, S-221 00 Lund, Sweden

A reflectance-difference (RD) study of the kinetics of various surface processes involved in the growth of GaAs from triethylgallium and arsine is presented. During triethylgallium exposure of an As-stabilized (001) GaAs surface, an initial linear RD response is observed, similar to what has previously been reported for trimethylgallium. We show that in the case of triethylgallium an over-saturation of the surface occurs, which results in complex transients in the RD response and, for a critical dose, in a loss of the surface coherency as determined by the disappearance of RD growth oscillations. It is found that the arsine reactivity on the over-saturated surface is much higher than that on the Ga-stabilized surface. The arsine-induced RD transient is compared with the kinetics of the re-establishment of a perfect As-stabilized surface, using the amplitude of RD-detected growth oscillations as a probe of the status of the surface.

1. Introduction

Considerable effort has been devoted to increase the understanding of surface kinetics taking place during epitaxial growth. Some of these processes are: adsorption, desorption, diffusion of adsorbed species to steps, decomposition, and incorporation – not necessarily in this order. Results obtained from high-vacuum (HV) techniques may also be applicable to metalorganic vapor-phase epitaxy since the importance of gas-phase reactions and the hydrogen atmosphere has been questioned lately [1]. So far, reflection high-energy electron diffraction (RHEED) has been the dominating *in situ* method in high-vacuum techniques but recently a series of very powerful optical methods has been demonstrated, e.g. reflectance-difference (RD) [1], ellipsometry [2], and surface photo-absorption (SPA) [3]. Using optical methods it has been possible to follow various phenomena on the sub-monolayer scale during epitaxial growth, and since these very powerful *in*

situ techniques are indifferent to the pressure they can thus be used to link high-vacuum (HV) techniques to atmospheric pressure methods. In this paper we use RD to study the kinetics of the (001) GaAs surface when exposed to triethylgallium and/or arsine.

2. Experimental details

The experiments were carried out in a vacuum chemical epitaxy (VCE) reactor [4,5] using triethylgallium (TEG) and arsine as precursors. The vacuum system consists of an outer vacuum chamber which contains an inner growth chamber held at an elevated temperature of approximately 200 °C. This design allows multiple impingement which is necessary when using arsine as group V precursor. The arsine pressure inside the growth chamber was approximately 5×10^{-4} Torr and the V/III ratio was typically 20. Residual hydrocarbon and hydrogen molecules can leave the growth chamber through several small orifices. The 1 cm² sized (001) GaAs substrate is situated inside the growth chamber on a carbon susceptor heated by infra-red radiation. The RD system [5]

* Permanent address: Central Institute of Optics and Spectroscopy, Academy of Sciences, Rudower Chaussee 6, O-1199 Berlin, Germany.

is placed on top of the vacuum chamber where the light probe enters the vacuum chamber through a strain-free quartz window, and the growth chamber through a small hole. In our RD measurements the difference between normal-incidence reflectance of light polarized parallel and perpendicular to a principal crystallographic axis of the surface is measured as a function of time for a fixed wavelength equal to 632.8 nm. The GaAs surface is, from an optical absorption point of view, highly anisotropic mainly due to the dimer formation in the outermost atomic layer of the crystal [1]. Such intrinsic effects are caused by As-As and Ga-Ga dimer bonds directed in the $\bar{1}10$ and $[110]$ directions, respectively. It should be noted, however, that preferentially-oriented molecules adsorbed on the surface may also contribute to the RD signal.

3. Results and discussion

3.1. TEG and arsine monolayer saturation effects

Fig. 1 shows the time dependence of the RD signal during pure TEG exposure of a previously arsine-stabilized (001) GaAs surface. The time axis has been divided into four different periods, labelled A-D, corresponding to different events. During period A, which is equal to 10 s, a constant flow of TEG is injected into the growth chamber and under this phase the RD signal shows a linear time dependence until it reaches approximately 4/5ths of the first peak value. This is in good agreement with experiments reported for trimethylgallium (TMG) [1] in a hydrogen atmosphere. In the upper curve of fig. 1, this period is followed by an interval where the signal is more or less constant. During period B the arsine flow is resumed and the recovery towards the initial arsine-stabilized value has an exponential time dependence. In the lower curve of fig. 1 the TEG flow has been kept on for another 50 s, period C, in order to study the effects of over-saturation. Contrary to TMG, excess TEG adsorbs on top of the first Ga layer. After passing through the dip the RD signal increases further before saturation. When the over-saturated surface

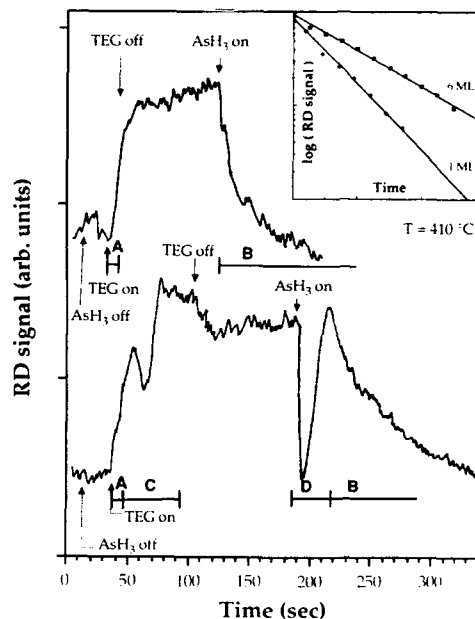


Fig. 1. The time dependence of the RD signal during pure TEG exposure of previously arsine-stabilized GaAs surfaces. The doses required to form one monolayer, period A in the upper curve, and six monolayers, period A+C in the lower curve, of GaAs during continuous growth. The RD signal experiences a rapid change when the over-saturated surface is exposed to arsine. The insert illustrates the exponential time dependencies of the arsine-stabilization recovery of the RD signal during period B following the two levels of saturation.

is exposed to arsine, during period D, a rapid change in the RD signal can be observed. The presence and magnitude of this feature are correlated to the amount of excess TEG, or derivatives thereof, at the surface. When the surface is over-saturated with TEG the arsine becomes highly reactive, indicated by the very fast change of the RD signal. The recovery of the RD response, during period B, towards the value corresponding to the arsine-stabilized surface is similar to that of the upper curve in fig 1 but the time constants differ as can be seen from the insert in the upper right corner. The fact that the kinetics is faster in the case of only one monolayer Ga coverage is reasonable since the transformation of an over-saturated surface involves more complex surface processes.

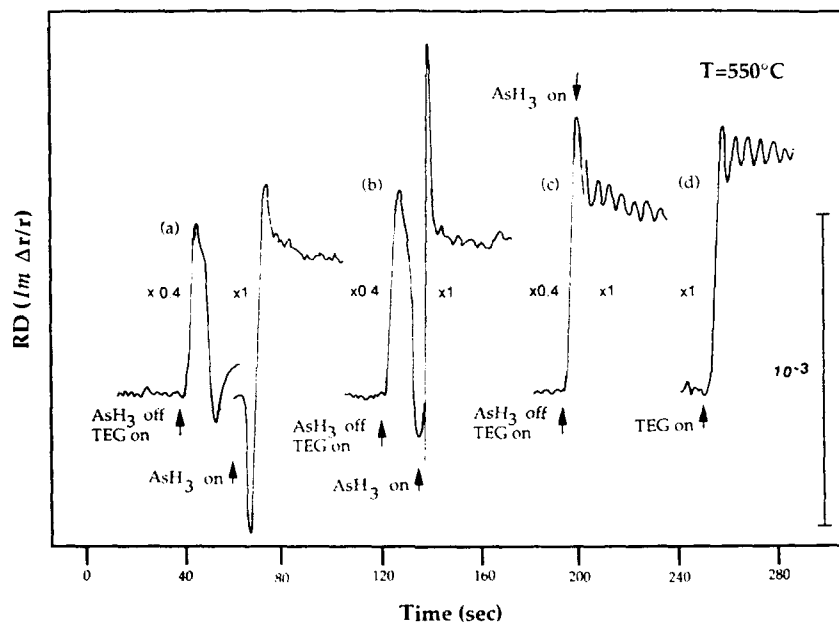


Fig. 2. RD-probing of TEG-exposed GaAs surfaces in order to evaluate the degree of surface coherence when continuous growth is started. The amount of TEG corresponds to the growth of: (a) 5–6 monolayers (ML); (b) 3 ML; (c) 1 ML. The presence and durability of the growth oscillations is a measure of how the TEG species adsorb to the surface. If the surface is exposed to more than one monolayer the surface coherence is lost. (d) RD response when the continuous growth is initiated from an arsine-stabilized surface.

3.2. Study of the surface roughening during TEG saturation

We have recently shown that it is possible, using the RD technique, to obtain growth oscillations in real time during continuous growth [7] as illustrated in fig. 2 (curve 2d). This phenomenon makes not only growth-rate measurements very convenient but can also be used to gain information about the surface from which the continuous growth is initiated. In the previous section, it was shown how excess TEG species on the surface affect the RD signal during arsine-only exposure. In this section, it will be discussed how the Ga species are adsorbed at the surface by using the presence and durability of the growth oscillations as a measure of the status of the surface [8]. During this experiment (curves 2a–2c), the valve-switching sequences are the same, starting with arsine stabilization which is followed by a period of TEG exposure the length of which is varied in

time. After a certain exposure of TEG the arsine flow is resumed which enables continuous growth. Curve 2a shows the RD response when the arsine-stabilized surface is exposed to an amount of TEG corresponding to six monolayers during continuous growth and the behavior of the RD signal when the continuous growth is initiated resembles somewhat the large feature seen in the lower curve in fig. 1. Contrary to the experiments described in fig. 1, the TEG is left on while resuming the arsine flow. Hence, the RD signal settles at a value characteristic of continuous growth using a certain V/III ratio. Curve 2d, where the TEG-only period is absent, has been included as a reference. Due to the large amount of TEG species, the growth front becomes statistically distributed over several monolayers and no growth oscillations can be observed. Reducing the TEG-only period to a time corresponding to three monolayers (curve 2b) gives rise to a larger feature when the arsine flow is resumed but still no sign

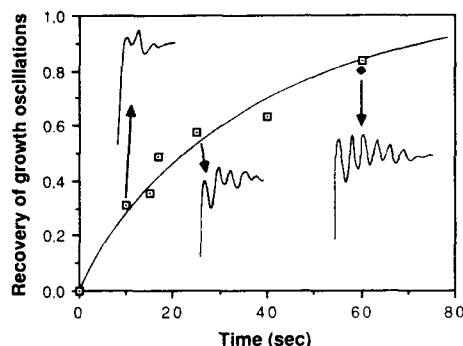


Fig. 3. The degree of recovery of the growth-oscillations (□) as a function of the arsine exposure of the surface. Starting from a continuous growth situation the TEG flow is terminated and after a certain time the TEG flow has been resumed. Three RD growth oscillation curves have been included corresponding to different recovery times. Note that the 60 s point is a double point also obtained by doubling the flow and reducing the exposure time to the half (♦).

of growth oscillations. The true shape of this feature is not resolved, due to the inherent time constant of the RD set-up. In curve 2c the TEG deposition is nominally one monolayer adsorbed Ga and when arsine is added together with TEG, after the shorter TEG-only period, the behavior of the RD signal is completely different. Clearly resolved growth oscillations can now be observed directly after the initiation of the continuous growth, demonstrating that the deposition of one Ga monolayer preserves the coherency of the

surface and no three-dimensional Ga deposits are formed.

3.3. The kinetics of the recovery of growth oscillations under arsine treatment

Even with optimal surface conditions when growth is initiated, clearly resolved RD growth oscillations decay within, typically, 20–30 periods. This is believed to be the time taken to establish a growth front which has reached the steady state equilibrium admixture of As–As and Ga–Ga dimers. An extensive exposure of the GaAs surface to arsine is necessary in order to regain the well-defined As-stabilized surface required for reinitiation of growth with the best conditions for the RD observation of growth oscillations. Using the same arsine flux as that used for the growth rate of 1 monolayer/10 s, it takes at least a few minutes for full (> 95%) recovery (at 550 °C). An attempt to evaluate the kinetics of this recovery process is presented in fig. 3, in which the average of the amplitude of the first oscillations is plotted as a function of the arsine exposure time. Three examples of such growth oscillations with different degrees of regeneration are shown as inserts for 10, 25 and 60 s arsine treatment.

During the arsine treatment an RD transient is also induced corresponding to the transformation of the partially Ga–Ga dimer-covered growing surface into the As-stabilized surface, assumed to be the frequently observed (2 × 4) reconstruction

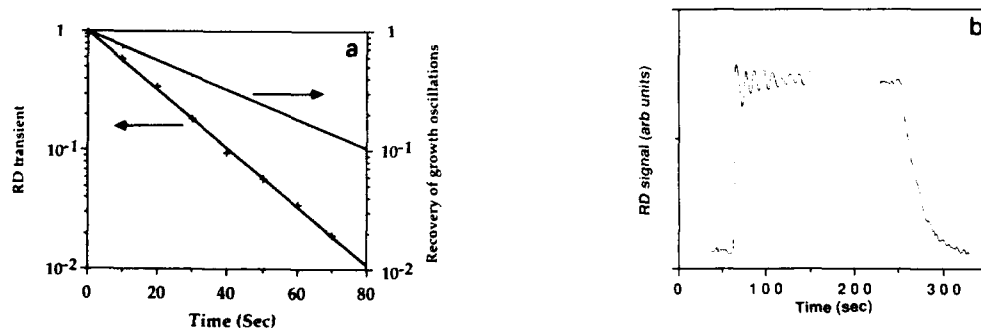


Fig. 4. (a) Measurement of the degree of recovery of the arsine-stabilized surface using two different definitions of surface recovery. The upper curve shows the logarithm of the recovery of growth oscillations as a function of time, as determined by the method illustrated in fig. 3. The lower curve is the logarithm of the transient of the RD signal in going from the level corresponding to continuous growth to the level corresponding to the arsine-stabilized surface. (b) Growth oscillations followed by such a transient.

(see fig. 4b). Obviously, the RD transient and the recovery transient measure different surface processes, a difference which can be illuminated by a comparison of the kinetics of the two processes. This comparison is made in fig. 4a, where the RD transient is plotted logarithmically versus the arsine exposure time (experimental points +), with the exponential line fitted to these points. The corresponding best exponential fit of the recovery process (from fig. 3) is also shown in fig. 4a. It is clear that the time constant for recovery of the ideal As-stabilized surface is longer, here by a factor of two, than the time constant for returning the RD signal from that of continuous growth to that of the As-stabilized surface. However, there is still too little experimental data available to judge if the factor of two is significant, but it is beyond doubt that the results in fig. 4 tell us that the recovery of the growth oscillations is a more complicated and slower process than the process monitored in the transient of the RD signal itself. An explanation of this difference in kinetics can be that the faster RD transient is primarily probing the arsine-induced breaking of Ga-Ga dimer bonds while the slower process of recovery of growth oscillations involves also surface reconstructions with the formation of the (2×4) periodic reconstruction of the As atoms.

5. Summary

We have shown that the RD method can be used to gain significant information about the surface kinetics during monolayer saturation as

well as under continuous growth. The time constants for the re-establishment of a perfect arsine-stabilized surface have been studied and we have shown that the arsine exposure of an over-saturated GaAs surface leads to very fast chemical reactions.

Acknowledgements

This work was supported by the Swedish Board for Technical Development and the Swedish Natural Science Research Council.

References

- [1] D.E. Aspnes, R. Bhat, E. Colas, V.G. Keramidas, M.A. Koza and A.A. Studna, *J. Vacuum Sci. Technol.* A7 (1989) 711.
- [2] L.V. Sokolov, M.A. Lamin, V.A. Markov, V.I. Mashanov, O.P. Pchelyakov and S.I. Stenin, *JETP Letters* 44 (1986) 357.
- [3] N. Kobayashi, T. Makimoto, Y. Yamauchi and Y. Hori-koshi, *J. Crystal Growth* 107 (1991) 62.
- [4] P. Schmidt, K. Deppert, S. Jeppesen, J. Jönsson, G. Paulsson and L. Samuelson, *J. Crystal Growth* 105 (1990) 306.
- [5] L.M. Fraas, P.S. McLeod, L.D. Partain and J.A. Cape, *J. Vacuum Sci. Technol.* B4 (1986) 22.
- [6] G. Paulsson, K. Deppert, S. Jeppesen, J. Jönsson, L. Samuelson and P. Schmidt, *J. Crystal Growth* 105 (1990) 312.
- [7] J. Jönsson, K. Deppert, S. Jeppesen, G. Paulsson, L. Samuelson and P. Schmidt, *Appl. Phys. Letters* 56 (1990) 2414.
- [8] L. Samuelson, K. Deppert, S. Jeppesen, J. Jönsson, G. Paulsson and P. Schmidt, *J. Crystal Growth* 107 (1991) 68.

In-situ monitoring of antiphase domain evolution during atomic layer MBE (ALMBE) and MBE growth of GaAs/Si(001) by reflectance difference

Y. González, L. González and F. Briones

Centro Nacional de Microelectrónica, CSIC Serrano, 144. 28006 Madrid, Spain

Reflectance difference technique is used to in-situ monitor the antiphase domain (APD) annihilation process during atomic layer MBE and MBE growth of GaAs on Si 2° and 4° off (001) towards (110). We show that this technique is able to provide quantitative information on the domain evolution. Experimental data obtained with reflectance difference show that thin GaAs layers (typically 50–100 nm) are enough for achieving a single domain growth front. APD evolution is characterized by a process which starts at the onset of growth and is thickness dependent. We observe a fast APD evolution during growth of the first 500 Å thick layer followed by a slow step in case a single domain growth front has not yet been achieved. We find that the rate of the APD annihilation process depends on growth conditions, although the GaAs thickness (~500 Å) at which kinetics changes is independent both on growth conditions and on density of steps in the starting surface (2° and 4° off (001) Si substrate). A possible relation between APD annihilation and lattice mismatch relaxation process is proposed based on these observations.

1. Introduction

The appearance of antiphase domains (APDs) in epitaxially grown GaAs on Si(001) is a direct consequence of growing a polar compound semiconductor on a non polar substrate [1].

GaAs antiphase domains could be avoided by growing on an atomically flat perfect (001) Si surface if the very first layer is formed by either Ga or As atoms. However, any real (001) Si surface will always exhibit steps. Again no APDs would be expected if the surface steps are two atomic layer high ($\frac{1}{2}a_0$), where the sublattice site allocation of Ga or As at both sides of the step are coincident. Achieving this kind of silicon surface requires very high annealing temperatures (above 1000°C) which are not compatible with current Si technology preprocessed wafers.

Experimental results have shown [2] that single domain GaAs is not achieved on exactly oriented (001) Si surfaces, but GaAs APDs can be effectively suppressed by growing on slightly misoriented (001) Si substrates, even though they present a high surface density of monoatomic steps ($\frac{1}{4}a_0$). In this case, the initially double domain GaAs

surface progressively evolves into a single domain growth front. How this simple recipe works is not known at present, but it is clear that other mechanisms besides the doubling of surface step height must be operative in APDs suppression.

The main characteristic of tilted (001) Si substrates is the alignment of a high density of steps with different structure in the direction of misorientation. So one would expect that the APD annihilation process is closely related to the preferent GaAs nucleation at inequivalent steps: one step will overgrow the other one, leading to APD suppression. However, there is no actual understanding of APD evolution, mainly due to the lack of an experimental technique to in-situ monitor the APD annihilation process.

In a previous work [3] we demonstrated the ability of the reflectance difference (RD) technique [4,5] to in-situ monitor the APD annihilation process. We showed that this technique can provide accurate quantitative data in comparison with the commonly used RHEED, which only gives qualitative information about the orientation and relative abundance of domains. In particular, we found that during the atomic layer molecular

beam epitaxy [6] (ALMBE) growth, the process of domain annihilation begins at the onset of growth, such that thin GaAs layers (typically ~ 50 – 100 nm) are sufficient for achieving a single domain growth front. In agreement with other authors [7], the orientation of the final domain only depends on the formation or not of an As stable layer on the Si surface created by heating the Si substrates at $T_s > 600^\circ\text{C}$ in the presence of arsenic [8].

However, the expectable relation between the high density of inequivalent steps present in the tilted Si substrates with the GaAs APD suppression mechanism remains unclear at the present moment.

In order to get a deeper insight, we have studied in the APD annihilation process during GaAs-on-Si growth under a broad range of experimental conditions, both by ALMBE and MBE. We have extended the growth conditions [9,10], trying to actuate the kinetics of the APD suppression process by selectively enhancing the GaAs growth in the surface steps against two-dimensional nucleation on the terraces. To monitor this process, we have used reflectance difference. This technique is sensitive primarily [4] to surface anisotropy induced by Ga–Ga dimers, and consequently to surface stoichiometry which is periodically changed every monolayer in case of ALMBE growth, or by intentionally interrupting the As beam flux (and/or supplying an extra amount of Ga) during conventional MBE growth under As stabilized conditions.

For epitaxial growth of GaAs on single crystal and single domain GaAs(001), the Ga–Ga dimers are all aligned along $\langle 110 \rangle$ direction. Then, the variations in surface stoichiometry produced during layer-by-layer ALMBE growth cause periodic changes in $R_{110} - R_{\bar{1}\bar{1}0}$ reflectance difference.

However, during atomic layer-by-layer growth of a two-domain GaAs layer on Si, different surfaces areas will show mutually perpendicular Ga–Ga dimer orientations and the resulting RD signal amplitude will be reduced by a factor proportional to the relative difference between the surface areas of the domains A and B:

$$\frac{\Delta R}{R} = \frac{A - B}{A + B} \frac{R_{110} - R_{\bar{1}\bar{1}0}}{R} \quad (1)$$

If we normalize the signal amplitude $\Delta R/R$ during growth of GaAs/Si to the amplitude during GaAs/GaAs single domain growth, we obtain a quite accurate measurement of the evolution of the relative extension of orthogonal domains, $(A - B)/(A + B)$.

For a well-defined detector polarization relative to the $\langle 110 \rangle$ and $\langle \bar{1}\bar{1}0 \rangle$ crystal directions, the absolute sign of the RD signal gives the azimuth of the initially predominant domain, as well as the final domain orientation, in agreement with qualitative RHEED observations.

In this way, using RD we are able to observe during growth (layer by layer in case of ALMBE growth) the APD concentration evolution and its eventual dependence on growth conditions.

2. Experimental

A description of the experimental reflectance difference technique set-up, as well as the Si surface preparation process has been published elsewhere [3,5]. (001) Si wafers misoriented by 2° and 4° towards $\langle 110 \rangle$ were used for this work.

ALMBE and MBE layers were grown under As_4 beam equivalent pressure (BEP) of $\sim 4 \times 10^{-6}$ Torr. The Ga flux was previously calibrated by RHEED oscillations in MBE grown GaAs on GaAs substrate, in order to establish the adequate As pulse frequency for ALMBE growth (one pulse per $1.0 N_s$ Ga dose, measuring Ga doses in units of $N_s = 6.25 \times 10^{14}$ sites/cm² on the ideal (001) plane).

Low temperature ($T_s = 350^\circ\text{C}$) ALMBE layers consisted of 2000 \AA GaAs grown at 0.8 monolayers per second (ML/s). Growth was initiated by opening first the Ga cell, followed by the As pulses. The duration of the As pulses was changed from some samples to others in order to achieve different growth conditions, from high arsenic excess to the just amount to combine with $1.0 N_s$ Ga dose.

Low temperature ($T_s = 300^\circ\text{C}$) MBE layers consisted of 500 \AA thick GaAs grown at 0.2 ML/s. High T_s MBE layers ($500 < T_s < 580^\circ\text{C}$) were grown at 0.8 ML/s after depositing a 100 \AA nucleation layer by ALMBE at $T_s = 350^\circ\text{C}$ in

order to avoid the formation of large three-dimensional islands at the onset of MBE growth at high T_s .

3. Results

A plot of the evolution of RD signal amplitude during GaAs growth is shown in fig. 1. Solid and open circles correspond to two GaAs samples grown on Si 2° and 4° off (001) respectively by ALMBE under As rich conditions at $T_s = 350^\circ\text{C}$ [3]. A rapid increase of the RD signal amplitude is followed by a saturation state reached when a thin layer of about 500 Å has been grown.

The non-zero intersection of the dashed straight line with the Y-axis shows that the starting Si surface presents an already larger area ($\sim 30\%$) of the 2×1 domain. By using RHEED observations alone, it would be impossible to detect this initial difference. Notice that under the same growth conditions, and the same relative distribution of domains in the Si starting surface, the APD evolution of both samples is identical, even when the initial average size of APDs in the 4° off substrate is expected to be half of that in the 2° off substrate.

The amplitude oscillations superposed on the RD signal are of purely optical origin and correspond to the periodic changes of surface reflectance due to interference between light reflected at

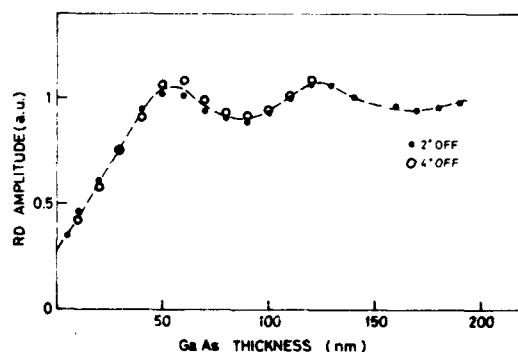


Fig. 1. Reflectance difference signal amplitude versus GaAs thickness during atomic layer MBE growth at $T_s = 350^\circ\text{C}$ of GaAs on Si 2° off (●) and 4° off (○) towards $\langle 110 \rangle$.

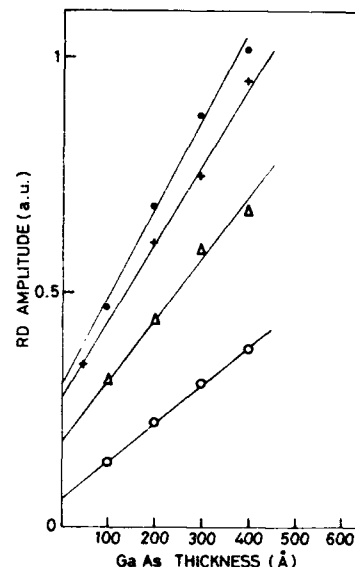


Fig. 2. Reflectance difference signal amplitude versus GaAs thickness during atomic layer MBE growth at $T_s = 350^\circ\text{C}$ of GaAs on Si 2° off (001) under "As-rich" growth conditions.

the growing surface and at the silicon surface substrate.

The RD signal behaviour shown in fig. 1 for samples grown on 2° and 4° off (001) Si substrates is completely general. Under different growth conditions, for ALMBE or MBE grown samples, we always observe an APD annihilation process characterized by a fast step, up to ~ 500 Å, followed by a slow step that can even exhibit a zero slope when APDs have been suppressed.

We have observed that under fixed growth conditions, the slope of the fast step depends on the relative abundance of A and B domains in the starting Si surface. Fig. 2 shows the evolution of RD signal, normalized to the amplitude during GaAs single domain growth, for four different samples grown by ALMBE at $T_s = 350^\circ\text{C}$ under "As-rich" growth conditions. Although the rate of APD evolution remains constant under fixed growth conditions, smaller GaAs thicknesses are needed to achieve a single domain growth front (RD amplitude = 1) when the starting surface shows larger areas of the domain that will be enlarged during the annihilation process.

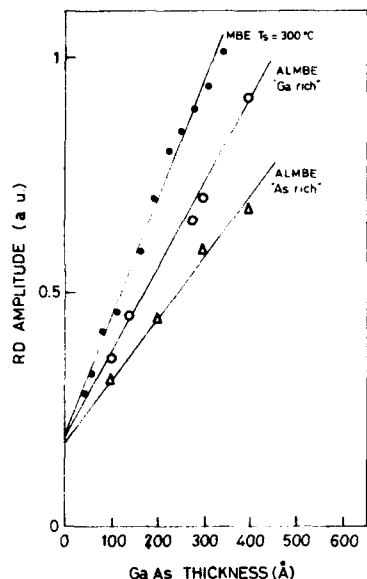


Fig. 3. Reflectance difference signal amplitude versus GaAs thickness during GaAs on Si 2° off (001) growth by ALMBE at $T_s = 350^\circ\text{C}$ under "As-rich" growth conditions (Δ), ALMBE $T_s = 350^\circ\text{C}$ "Ga-rich" growth conditions (\circ) and MBE $T_s = 300^\circ\text{C}$ (\bullet) for similar Si starting surfaces.

The small difference of relative size of domains (domain A surface occupation changes from 54% to 65% in different samples) will probably be due to differences in the prior to growth Si surface preparation process.

The same behaviour with the relative domain size in the Si starting surface is observed for MBE grown layers. In particular, we do not find any difference in APD annihilation rates for layers grown at $500 < T_s < 580^\circ\text{C}$. This range of T_s was chosen, according to other authors [9], to produce a change of growth mode (from 2D to step flow) in A surfaces, expecting so far a change in APD suppression kinetics.

We also have observed a dependence of APD suppression rate on the growth conditions. Fig. 3 shows the evolution of RD signal for three samples grown by MBE, $T_s = 300^\circ\text{C}$ (solid circles), ALMBE, $T_s = 350^\circ\text{C}$, under "Ga-rich" growth conditions (open circles), and ALMBE, $T_s = 350^\circ\text{C}$, under "As-rich" growth conditions (triangles). We can see that for comparable Si substrate

starting surfaces, MBE grown samples show an APD suppression process that is faster than ALMBE at "Ga-rich" conditions, which in turn is faster than "As-rich" growth conditions.

4. Discussion

Besides the observed dependence on growth conditions, as well as on the relative domain distribution in the Si starting surface, our experimental results show that the APD suppression process begins at the onset of growth and is thickness dependent. Although the rate of APD annihilation process depends on growth conditions, the GaAs thickness at which we observe a change of kinetics (about 500 \AA) is independent both on the density of steps (2° or 4° off Si substrates) and on the growth conditions.

These results seem to point out that the APD annihilation process must be related to some other property which is enhanced in stepped surface, like the preferential formation of misfit dislocations in steps [12]. At this stage we think that the GaAs on Si APD annihilation mechanisms are somehow related through the growth kinetics to the lattice relaxation mechanisms.

The different rates of APD suppression observed for different growth processes (ALMBE, MBE) could easily be explained in this context. GaAs deposited by MBE at low T_s forms 3D islands which grow and coalesce accommodating lattice mismatch by generating pure edge (misfit) and mixed dislocations. On the other hand, the initial GaAs nucleation by ALMBE is two-dimensional. This layer growth would perhaps cause a relaxation of lattice strain by generating a higher density of misfit dislocation as compared with MBE growth.

Preliminary TEM results seem to support this new approach: ALMBE grown GaAs on Si layers observed by this technique shows a precisely delimited 500 \AA thick highly defective region. Similar results were previously reported for GaAs on Si grown by MOCVD [11].

More experimental work is presently underway, including growth on Si substrates with lower misorientation angles, in order to confirm a possible

relation between APD suppression and lattice relaxation process.

5. Conclusions

In summary, reflectance difference technique has been used for in-situ monitoring antiphase domain (APD) evolution during ALMBE and MBE growth of GaAs on Si 2° and 4° off (001) towards $\langle 110 \rangle$ direction. We have observed that APD annihilation starts at the onset of growth, being characterized by a fast process, up to GaAs thickness of ~ 500 Å, followed by a slow process, if a single domain growth front has not been achieved during the deposition of the first 500 Å thick layer. Although the rate of the APD annihilation process depends on the growth conditions, the GaAs thickness at which we observe a change of kinetics is independent both on the density of steps (2° or 4° off Si substrates) and on the growth conditions.

In view of the above results, we feel that the APD annihilation process could be closely related to the lattice relaxation process.

Acknowledgements

The authors wish to acknowledge A. Cornet and J.R. Morante for preliminary TEM results.

The authors wish to thank the CEC for support under the ESPRIT II project 2289 (Optical Interconnections for VLSI and Electronic Systems).

References

- [1] H. Kroemer, *J. Vacuum Sci. Technol.* B5 (1987) 1150.
- [2] H. Kawanami, A. Hatoyama, K. Nagai and Y. Hagashi, *Japan. J. Appl. Phys.* 26 (1987) L173.
- [3] Y. González, L. González and F. Briones, *Japan. J. Appl. Phys.* 30 (1991), in press.
- [4] D.E. Aspnes, J.P. Harbison, A.A. Studna and L.T. Florez, *Phys. Rev. Letters* 59 (1987) 1687.
- [5] F. Briones and Y. Horikoshi, *Japan. J. Appl. Phys.* 29 (1990) 1014.
- [6] F. Briones, L. González and A. Ruiz, *Appl. Phys.* A49 (1989) 729.
- [7] P.R. Pukite and P.I. Cohen, *Appl. Phys. Letters* 50 (1987) 1739.
- [8] M. Kawabe and T. Ueda, *Japan. J. Appl. Phys.* 26 (1987) L114.
- [9] T. Shitara, J. Zhang, J.H. Neave, D.D. Vvedensky and B.A. Joyce, in: *Proc. 1st EPI Conf.*, Budapest, April 1990 (Trans Tech, Switzerland, in press).
- [10] M. Yamaguchi and Y. Horikoshi, *Japan. J. Appl. Phys.* 28 (1989) L1456.
- [11] D.J. Eaglesham, R. Devenish, R.T. Fan, C.J. Humphreys, H. Morkoç, R. Bradley and P.D. Augustus, in: *Microscopy of Semiconducting Materials 1987*, Inst. Phys. Conf. Ser. 87, Eds. A.G. Cullis and P.D. Augustus (Inst. Phys., London-Bristol, 1987) p. 105.
- [12] N. Otsuka, C. Choi, Y. Nakamura, S. Nagakura, R. Fischer, C.K. Peng and H. Morkoç, *Appl. Phys. Letters* 49 (1986) 277.

Oscillatory As_4 surface reaction rates during molecular beam epitaxy of AlAs, GaAs and InAs

J.Y. Tsao, T.M. Brennan and B.E. Hammons

Sandia National Laboratories, Albuquerque, New Mexico 87185-5800, USA

We report oscillations in the surface reaction rate of As_4 during molecular beam epitaxy of AlAs, GaAs and InAs. The oscillations are periodic with the bilayer-by-bilayer growth cycle, and correspond to a slightly lower reaction rate approximately 1/4 of the way, and a slightly higher reaction rate approximately 3/4 of the way, through that cycle.

Crystal growth has long been known to be mediated by surface microstructural defects such as adatoms, steps and kinks [1]. Measurements sensitive to that defect microstructure have therefore been central to advances in our understanding of crystal growth.

For molecular beam epitaxy (MBE) of III/V compounds, however, surface defect microstructure is only half the picture. In these systems, the growth species typically include stable molecules, such as As_4 , which must chemically react with the surface before growth can occur. Surface chemistry is therefore a crucial second half of the picture. Indeed, we expect the overall dynamics of crystal growth to be determined by a complex interplay between surface chemical reactivity and surface defect microstructure [2].

Thus far, however, very little is known about the dependence of surface chemical reactivity on surface defect microstructure during III/V MBE. Nearly all previous direct studies of surface chemistry during III/V MBE have been performed on surfaces having an “average” microstructure characteristic of steady-state growth [3,4].

In this paper, we report reflection mass spectrometry (REMS) studies of reactive sticking of As_4 and desorption of As_2 during MBE of AlAs, GaAs and InAs on carefully prepared, smooth (001) surfaces. We find, interestingly, that in all these systems the reaction rate of As_4 with the surface oscillates initially, before settling to an

average value characteristic of steady-state growth. These “REMS” oscillations are analogous to those seen in reflection-high-energy diffraction (RHEED) intensities [5,6], photoemission [7], secondary electron emission [8] and optical reflectance difference spectroscopy (RDS) [9], in that they are periodic with the bilayer-by-bilayer growth cycle. They are unique, though, in that they establish, for the first time, a periodic variation in the *chemical reactivity* of the surface during MBE.

Our experimental geometry is nearly the same as that described previously [10]. An unapertured UTI-100C mass spectrometer, recessed in a liquid-nitrogen-cooled housing, is attached directly to an effusion-cell port of a state-of-the-art (Riber 32P) III/V MBE chamber. Due to improved liquid-nitrogen transfer to the cryoshrouds of this chamber, background signals from volatile As_4 not originating from the wafer surface were somewhat lower (approximately one-sixth of the line-of-sight signals) than in our previous studies.

In this growth chamber, we routinely observe REMS oscillations during MBE of AlAs, GaAs and InAs on carefully smoothed vicinal surfaces of the same material. The oscillations are most intense, however, during MBE on “nearly singular” substrates. Therefore, in this paper we restrict ourselves to presenting measurements during MBE on a GaAs wafer miscut by less than one-twentieth of a degree from (001). We also restrict ourselves

to measurements during AlAs MBE, which is the system we have studied most systematically thus far, and in which REMS oscillations are quite reproducible. Even under such favorable conditions, of course, careful surface preparation is important: prior to these measurements, a 1 μm thick GaAs buffer layer was grown at 580°C, followed by a 1 μm thick buffer layer of AlAs at 620°C.

During buffer layer growth, and during all of the measurements described here, the surface was bathed in a flux of pure molecular As_4 . From previous studies [11], the As fluxes leaving such a surface are thought to consist exclusively of As_4 and As_2 . A superposition of the cracking patterns of these two parent molecules, weighted by their relative fluxes, determines the measured mass spectrum. Hence, to deduce the fluxes of these two

parent molecules, it is necessary to measure ion currents at two mass/charge (m/q) ratios.

In this study, by multiplexing the mass spectrometer at 0.025 s intervals, we measured ion currents "simultaneously" at $m/q = 150$ amu/e (nominally As_2^+), and $m/q = 300$ amu/e (nominally As_4^+). These ion currents can be linearly related to the fluxes leaving the surface according to:

$$i_{150}^{\text{REMS}} = m_{22}(2j_{\text{As}_2}^{\text{out}}) + m_{24}(4j_{\text{As}_4}^{\text{out}}), \quad (1)$$

$$i_{300}^{\text{REMS}} = m_{44}(4j_{\text{As}_4}^{\text{out}}). \quad (2)$$

The three matrix elements can be determined from the cracking pattern of known outgoing As_4 fluxes, and from the responses of outgoing As_4 and As_2 fluxes to variations in temperature and group III fluxes during MBE [14]. For the operating condi-

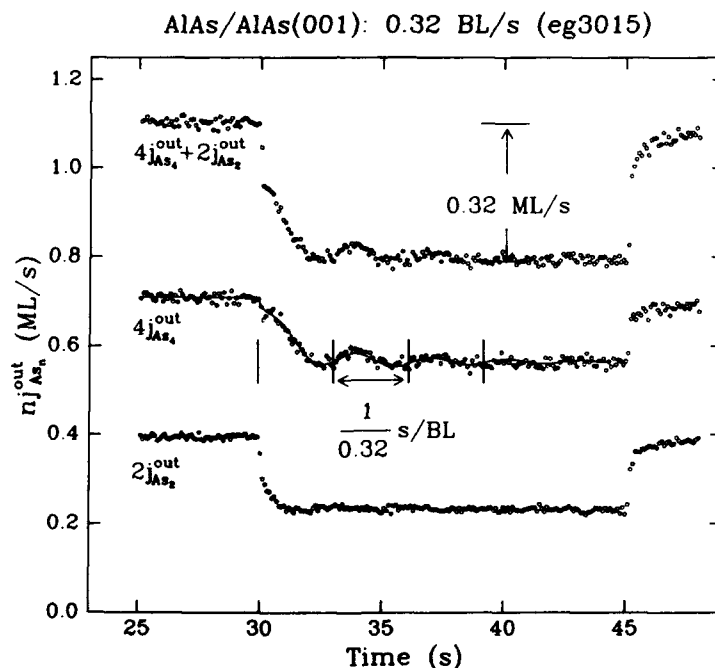


Fig. 1. Time-resolved As_4 and As_2 fluxes leaving the surface during AlAs MBE at 0.32 bilayers/s. Initially, the Al shutter is closed, so that all the As_4 that strikes the surface leaves, either as "reflected" As_4 , or as "desorbing" As_2 . At $t = 30$ s, the Al shutter is opened. As must now incorporate into the growing AlAs crystal, and both As fluxes leaving the surface decrease. Finally, at $t = 45$ s, the Al shutter is closed, and the As fluxes leaving the surface return to their initial steady-state values. The vertical lines indicate the 0, 2π , 4π and 6π points in the bilayer growth cycle, relative to the initiation of growth. The solid line drawn through the $4j_{\text{As}_4}^{\text{out}}$ data is a nonlinear-least-squares fit to eq. (3).

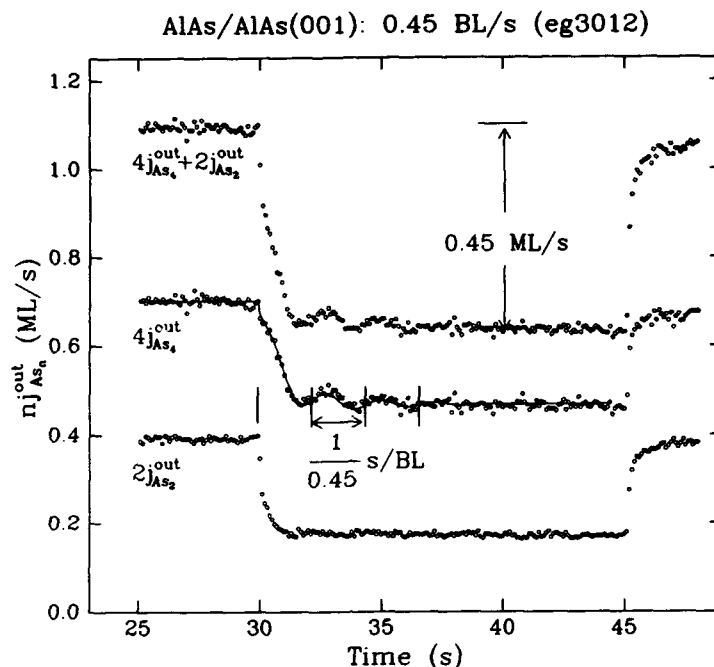


Fig. 2. Same as fig. 1, except at a growth rate of 0.45 bilayers/s.

tions of this study, they were found to be $m_{22} \approx 6.1$ nA s/ML, $m_{24} \approx 1.2$ nA s/ML, and $m_{44} \approx 1.7$ nA s/ML, where 1 ML represents the number density of As (or Al) atoms on a bulk-terminated As (or Al) surface of AlAs (001). Then, by inverting eqs. 1 and 2, outgoing fluxes can be deduced from measured ion currents. Note that the ion current at $m/q = 150$ amu/e is especially sensitive to the As_2 flux leaving the surface, while the ion current at $m/q = 300$ amu/e is sensitive exclusively to the As_4 flux leaving the surface [12].

In figs. 1 and 2, we show two examples of outgoing As fluxes during AlAs MBE on AlAs (001) at 620°C , deduced from REMS measurements and eqs. (1) and (2). For both figures the As_4 flux incident on the surface in units of equivalent As atoms was $4j_{\text{As}_4}^{\text{in}} \approx 1.1$ ML/s ($\approx 6.9 \times 10^{14} \text{ cm}^{-2} \text{ s}^{-1}$). For fig. 1 the Al flux incident on the surface was $j_{\text{Al}}^{\text{in}} \approx 0.32$ ML/s ($\approx 2.0 \times 10^{14} \text{ cm}^{-2} \text{ s}^{-1}$) for fig. 2 it was $j_{\text{Al}}^{\text{in}} \approx 0.45$ ML/s ($\approx 2.8 \times 10^{14} \text{ cm}^{-2} \text{ s}^{-1}$).

The sequence of events in both figures is as follows. Initially, for $t \leq 30$ s, the Al shutter is

closed. In the absence of growth, all the As_4 that strikes the surface ultimately leaves. Not all the As leaving the surface, though, leaves as As_4 . At this relatively high temperature, approximately 36% of the incident As_4 cracks and ultimately leaves the surface as As_2 .

At $t = 30$ s, the Al shutter is opened, AlAs MBE is initiated, and both the reflecting As_4 and desorbing As_2 fluxes decrease. The total As flux leaving the surface decreases by 0.32 ML/s in fig. 1 and by 0.45 ML/s in fig. 2, so as to consume exactly the Al fluxes incident on the surface.

Finally, at $t = 45$ s, the Al shutter is closed, and all the outgoing As fluxes recover to their initial steady-state values. Note that in neither figure is a "tail" observed in those recoveries. The absence of such a tail indicates that the incident Al had already been entirely consumed by As. For lower V/III flux ratios, not all the incident Al need be so consumed, and pronounced tails are observed in the recovery of the outgoing As fluxes [14]. In this study, we deliberately avoided V/III flux ratios (defined as $j_{\text{As}_4}^{\text{in}}/j_{\text{Al}}^{\text{in}}$) lower than 0.53, both

to avoid such tails, as well as to avoid deviations from the usual As-stabilized 2×4 surface reconstruction during growth.

The overall features seen in figs. 1 and 2 can be qualitatively understood on the basis of a balance between (a) cracking of incident As_4 followed by chemisorption of As, which increases the As coverage, and (b) desorption of As_2 and chemisorption of Al, which decrease the As coverage [13]. Turning on the Al flux decreases the As coverage, and thereby increases the (presumably Al-coverage-dependent) cracking of As_4 and decreases the (also presumably As-coverage-dependent) desorption of As_2 .

These overall features are always present, even on vicinal surfaces, or on nearly-singular surfaces imperfectly prepared. They therefore probably represent some sort of average behavior of a quasi-steady-state distribution of surface defects. However, on well-prepared, nearly-singular surfaces, we see, superimposed on this average behavior, oscillations in the As_4 flux leaving the surface. Qualitatively, these "REMS oscillations" are most intense under approximately the same conditions that RHEED oscillations are most intense (for AlAs, in the temperature range 590–640 °C). They are, however, somewhat more sensitive than are RHEED oscillations to the smoothness of the starting surface. We have found, e.g., that oscillations during AlAs MBE can only be reproduced consistently at 620 °C if the surface is first smoothened by a growth interruption greater than ≈ 30 s. At lower growth temperatures, either longer interruptions or higher temperature annealing is required.

To quantify the oscillations in figs. 1 and 2, we have performed nonlinear least-squares fits (shown as solid curves through the decaying portions of the outgoing As_4 fluxes) to the empirical form,

$$f(t) = A + B e^{-k_1(t-t_0)} + C e^{-k_2(t-t_0)} \times \cos[2\pi\nu(t-t_0) - \phi], \quad (3)$$

where $t_0 \approx 29.92$ s is the time at which the Al shutter was opened. The first two terms correspond to the non-oscillatory part of the overall decay of the outgoing As_4 flux. The third term corresponds to an exponentially damped sinusoidal

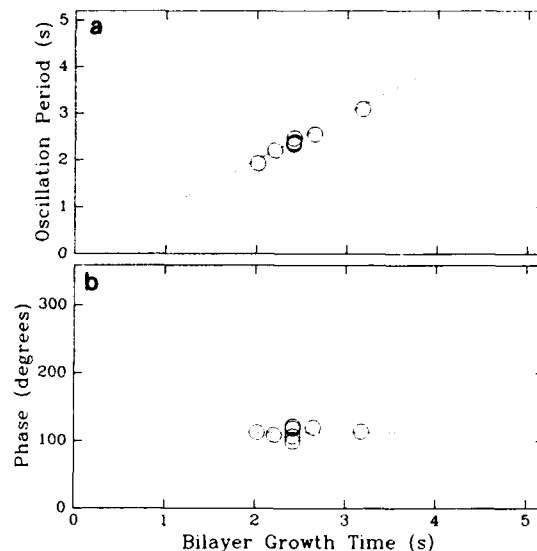


Fig. 3. REMS oscillation periods $1/\nu$ (a) and phase offsets ϕ (b) deduced from fits to time-resolved reflected As_4 fluxes such as those shown in figs. 1 and 2, as a function of bilayer growth periods known from thickness and RHEED oscillation calibrations. The dashed lines represent equivalence between the two periods (a) and 113° (b).

oscillation with frequency ν and phase offset ϕ .

The best-fit oscillation periods, $1/\nu$, for measurements at various growth rates are shown in fig. 3a. As can be seen, they agree quite well with growth rates deduced from the periodicity of RHEED oscillations. They also agree, from inspection of figs. 1 and 2, with the decrease in the total As flux leaving the surface upon opening the Al shutter. Therefore, from a technological point of view, REMS oscillations and As REMS "deficits" are both potentially useful alternatives to RHEED oscillations for real-time measurement of growth rate.

It is evident from figs. 1 and 2, however, that the REMS oscillations are relatively weak. They damp quickly (on a time scale comparable to the oscillation periods themselves), and their initial amplitudes are small (roughly 5% of the total As_4 flux incident on the surface). It is therefore not implausible that they be caused directly by step density oscillations during growth, since the am-

plitude of such oscillations might be expected to be of that same order of magnitude [15].

Interestingly, over the range of growth conditions studied here, the phase offset of the oscillations relative to the initiation of growth is $\phi \approx 113^\circ$, as shown in fig. 3b. In other words, As₄ reacts with the surface least rapidly approximately 1/4 of the way through the bilayer growth cycle, and most rapidly approximately 3/4 of the way through the bilayer cycle. Although there is currently some uncertainty as to the interpretation of phase offsets observed in RHEED oscillations, one anticipates that at the 1/4 bilayer point the creation rate of steps might be highest, and that at the 3/4 bilayer point the annihilation rate of steps might be highest [16]. If so, then the creation of new steps would seem, counterintuitively, to be associated with a decrease in surface As, while the annihilation of steps would seem to be associated with an increase in surface As.

Finally, it is interesting to note that, although the reflected As₄ flux oscillates measurably, the desorbing As₂ flux does not. Partly, this may be because at these growth temperatures the As₂ desorption fluxes are much lower than As₄ reflected fluxes; superimposed oscillations might be too weak to observe with our present signal-to-noise ratio. However, it also may be that As₂ desorbs only slightly differently from steps as from terraces.

In summary, we have observed oscillations in As₄ incorporation rates during molecular beam epitaxy of AlAs, GaAs and InAs. The oscillations are periodic with the bilayer-by-bilayer growth cycle, and suggest that AlAs, GaAs and InAs surface chemistry depend on surface microstructure. It will be exciting to explore and understand the origin of that dependence.

In particular, it will be interesting to understand the atomic structure of steps on AlAs, GaAs and InAs (001) at a level of detail comparable to our current understanding of the terrace reconstructions [17,18]. It might then be possible to apply electron counting arguments [19] to deduce likely sequences of intermediate structures during incorporation at steps [20]. Such electron counting arguments have already been used to deduce likely intermediate structures for "homogeneous" incor-

poration of Ga and As species on terraces [21]. Indeed, the measurements reported here appear to be consistent with such a mechanism. However, experimental evidence appears to favor the dominance, at least for some growth conditions, of mechanisms for "heterogeneous" incorporation at defects such as steps [22,23]. Perhaps both mechanisms are important, but under different growth conditions.

Ultimately, it will of course be interesting to finally combine a microscopic understanding of microstructure-dependent elementary attachment mechanisms with rate-equation models [24] or Monte Carlo simulations [25] of the large-scale evolution of III/V surface microstructure, and to eventually predict macroscopic measurements such as those reported here.

We would like to acknowledge helpful conversations with Jack Houston and Paul Peercy. This work, performed at Sandia National Laboratories, was supported by the United States Department of Energy under Contract No. DE-AC04-76DP00789.

References

- [1] W.K. Burton, N. Cabrera and F.C. Frank, *Phil. Trans. Roy. Soc. London* A243 (1951) 299.
- [2] A. Madhukar and S.V. Ghaisas, *CRC Critical Rev. Solid State Mater. Sci.* 14 (1988) 1.
- [3] See, e.g., C.T. Foxon and B.A. Joyce, in: *Current Topics in Materials Science*, Vol. 7, Ed. E. Kaldis (North-Holland, Amsterdam, 1981) ch. 1.
- [4] J.Y. Tsao, T.M. Brennan and B.E. Hammons, *Appl. Phys. Letters* 53 (1988) 288.
- [5] J.J. Harris, B.A. Joyce and P.J. Dobson, *Surface Sci.* 103 (1981) L90.
- [6] C.E.C. Wood, *Surface Sci.* 108 (1981) L441.
- [7] J.N. Eckstein, C. Webb, S.-L. Weng and K.A. Bertness, *Appl. Phys. Letters* 51 (1987) 1833.
- [8] L.P. Erickson, M.D. Longbone, R.C. Youngman and B.E. Dies, *J. Crystal Growth* 81 (1987) 55.
- [9] J.P. Harbison, D.E. Aspnes, A.A. Studna, L.T. Florez and M.K. Kelly, *Appl. Phys. Letters* 52 (1988) 2046.
- [10] J.Y. Tsao, T.M. Brennan, J.F. Klem and B.E. Hammons, *Appl. Phys. Letters* 55 (1989) 777.
- [11] C.T. Foxon, J.A. Harvey and B.A. Joyce, *J. Phys. Chem. Solids* 34 (1973) 1693.
- [12] We neglect possible dimer recombination in the mass spectrometer itself.

- [13] J.Y. Tsao, T.M. Brennan, J.F. Klem and B.E. Hammons, *J. Vacuum Sci. Technol.* A7 (1989) 2138.
- [14] T.M. Brennan, J.Y. Tsao and B.E. Hammons, in preparation.
- [15] C.S. Lent and P.I. Cohen, *Phys. Rev.* B33 (1986) 8329.
- [16] S. Clarke and D.D. Vvedensky, *J. Appl. Phys.* 63 (1988) 2272.
- [17] D.J. Chadi, *J. Vacuum Sci. Technol.* A5 (1987) 834.
- [18] D.K. Biegelsen, R.D. Bringans, J.E. Northrup and L.-E. Swartz, *Phys. Rev.* B41 (1990) 5701.
- [19] J.A. Appelbaum, G.A. Baraff and D.R. Hamann, *Phys. Rev.* 14 (1976) 1623.
- [20] E. Kaxiras, O.L. Alerhand, J.D. Joannopoulos and G.W. Turner, *Phys. Rev. Letters* 62 (1989) 2484.
- [21] H. H. Farrell, J.P. Harbison and L.D. Peterson, *J. Vacuum Sci. Technol.* B5 (1987) 1482.
- [22] P.M. Petroff, A.C. Gossard and W. Wiegmann, *Appl. Phys. Letters* 45 (1984) 620.
- [23] J.H. Neave, P.J. Dobson, B.A. Joyce and J. Zhang, *Appl. Phys. Letters* 47 (1985) 100.
- [24] T. Shitara and T. Nishinaga, Japan. *J. Appl. Phys.* 28 (1989) 1212.
- [25] M. Thomsen and A. Madhukar, *J. Crystal Growth* 80 (1987) 275.

Accurate measurement of MBE substrate temperature

W.S. Lee, G.W. Yoffe, D.G. Schlom and J.S. Harris, Jr.

Department of Electrical Engineering, Stanford University, Stanford, California 94305, USA

The behavior of real substrate temperature for radiatively heated MBE holders is measured using changes in the bandgap and refractive index with temperature. The infra-red spectroscopy techniques utilized are not sensitive to window coating and have no adjustable parameters. Using bandgap changes with temperature, we observed that the change in real substrate temperature is approximately 60% that of the indicated thermocouple change and that variations as large as 15°C occurred between "nominally identical" substrate holders. The real substrate temperature also changes by up to 10°C during growth and with opening and closing of high temperature doping furnaces.

1. Introduction

Accurate substrate temperature measurement has been a problem for molecular beam epitaxy (MBE) since the introduction of rotating substrate holders. This problem was further exacerbated by non-In-bonded, radiatively heated substrate holders. While these innovations have significantly improved MBE growth, they have created problems for both accurate substrate temperature measurement and control because the monitoring thermocouple is not in direct contact with the substrate. This separation causes a discrepancy between the real substrate temperature and the monitoring thermocouple measured temperature, since the thermocouple senses the combined effects of the substrate heater, the holder, the source furnaces and the substrate. It is also sensitive to the thermocouple location in the cavity. Because of the question of how strongly the thermocouple is coupled to the substrate versus the cavity, we have examined the sensitivity of the thermocouple to measure changes in the radiation environment resulting from a variety of effects.

In this work, we have extended our previous work utilizing optical spectroscopy to measure substrate temperature using the temperature dependence of the bandgap energy [1]. We also report a new method utilizing the temperature dependence of the refractive index in either trans-

mission or reflection mode, which is useful with opaque substrates or at low temperatures. Both methods use material-dependent parameters with no adjustable factors, such as emissivity. Both utilize spectral shape rather than absolute radiated power as the measurable quantity and are thus unaffected by window absorption or coating with time. We utilize these techniques to clearly demonstrate some of the long suspected problems of current MBE thermocouple measurements; temperature changes during growth, run to run variations with different, but "nominally identical" substrate holders and the effects of opening hot furnace shutters during growth.

2. Experimental procedure

Our MBE system is a 3 inch Varian GEN-II machine. The optical spectroscopy measurement system is identical to that which we utilized before [1], with the exception of the detector, which is now a 1 mm² germanium avalanche photodiode operated at room temperature. The system resolution is ~ 2 Å depending on spectrometer slit width. This corresponds to about 1°C temperature resolution, which can be achieved at higher temperatures (> 700°C). At lower temperatures, because of lower radiated power from the heater,

the resolution is $\sim 2^\circ\text{C}$ and the limiting factor is noise from the uncooled Ge detector.

The wafers used in these experiments were 500 μm thick, double side polished, 2 inch diameter GaAs wafers. They were mounted on standard Varian 2 inch Mo inserts, fitted to the 3 inch substrate holder [2]. Substrates are viewed through a 1 inch diameter sapphire window in the center of the source shroud. For transmission mode measurements, the substrate heater is used as the light source; for reflection mode measurements, a tungsten lamp is incident through the viewport and the reflected beam is collected by the fiber bundle without an imaging lens.

3. Results and discussion

3.1. Temperature measurement by absorption edge shift

Since GaAs is a direct bandgap material, it has a well defined, sharp absorption edge. Proper extraction of the absorption characteristic can provide an accurate measure of the substrate temperature. A series of transmission spectra through a semi-insulating (SI) GaAs substrate at various thermocouple settings are shown in fig. 1. There are three regions in the spectra and all three are utilized to extract a reproducible bandedge for analysis. (We pick the 800°C curve to define the three regions.) The first region, between 11,000

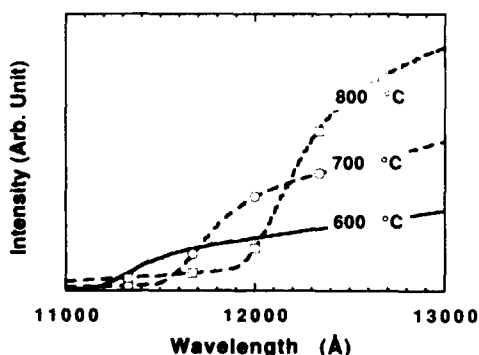


Fig. 1. Transmission spectra through a semi-insulating GaAs substrate at various thermocouple temperatures.

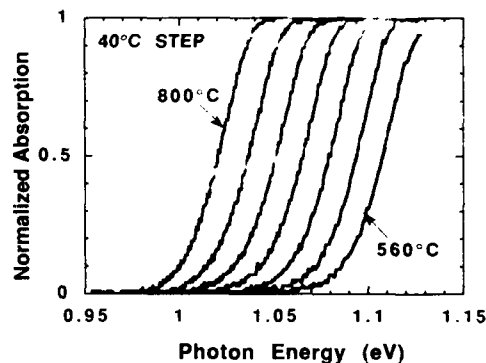


Fig. 2. Normalized transmission vs wavelength curves extracted from the data of fig. 1.

and 12,000 \AA , corresponds to blackbody radiation from the substrate. In this region, light from the heater is completely absorbed. The second region, between 12,000 and 12,400 \AA , is due to the absorption characteristic of the wafer. The third region, between 12,600 and 13,000 \AA , is due to blackbody radiation from the heating element because the wafer is transparent in this region.

In order to extract reliable absorption characteristics from these curves, we first measure the combined characteristics of the heater blackbody emission and measurement system transfer characteristic (window, lens, fiber, spectrometer and detector) without a wafer in the holder. We then divide the spectrum in fig. 1 by this emission spectrum-system transfer function. The blackbody emission from the substrate is then subtracted and the spectrum is normalized. A series of normalized spectrum spectra corresponding to different thermocouple temperatures are shown in fig. 2. These spectra clearly show sharp absorption characteristics for different temperatures; however, the expected exponential variation of the absorption coefficient at the bandgap is hidden by residual blackbody radiation from the wafer. With this uncertainty, we have opted to use an extrapolation between the 30% and 70% points to find the 50% point of the normalized spectra as the measure of bandgap energy.

The extracted bandgap variation versus MBE thermocouple temperature (dE_g/dT) exhibits a substantial difference compared to the values

measured by Thurmond [3] with a thermocouple connected directly to the substrate. The variation in real temperature is approximately 60% that indicated by the MBE thermocouple between 600 and 800°C. This same discrepancy in temperature has been observed by pyrometer [2]. We believe this discrepancy is largely from coupling between the radiative heating element and the temperature controlling thermocouple, which is located about 2 mm behind the center of the substrate. Since the heating element is much hotter than the substrate, even weak coupling from the radiator will seriously effect the thermocouple reading. In our system, a 1°C increase in thermocouple reading is composed of a 0.6°C increase in real substrate temperature and a 0.4°C increase due to thermal coupling.

It has long been suspected that the actual substrate temperature changes during growth. We have measured the thermal effect of GaAs coating a shiny substrate holder during growth. The holder starts out freshly etched and metallic. We first measure the transmission spectrum of a semi-insulating GaAs substrate at 600, 620 and 640°C on a clean holder. Spectra were measured with and without substrate rotation and there was no difference. The measurement was repeated after growing 20 µm of undoped GaAs with a constant set point of 620°C, as shown in fig. 3. After 20 µm of GaAs deposition, the holder becomes dark. While the substrate set-point and thermocouple reading are identical, the actual substrate temperature on the darker holder is lower by 10°C. We

believe that the emissivity of the substrate insert increases both because the emissivity of GaAs is larger than Mo and because the deposited GaAs is polycrystal with a roughened and darkened surface. The measured radiation from the heater indicates a temperature increase to maintain the same cavity and thermocouple temperature. Since the thermocouple reading is a weighted average of the heating element and real substrate temperature, the higher heating element temperature means a lower real substrate temperature for the same thermocouple reading.

Using this same technique, we measured the temperature variation between 3 different, but "nominally identical" holders. These holders were all freshly etched, baked and had ~5 µm of GaAs deposited on them. However, for the same set point and thermocouple reading of 600°C, we observed a holder to holder variation of 15°C in real substrate temperature as measured by the bandedge shift. We also compared the real temperature of an n⁺ substrate with a SI substrates. Not surprisingly, the added free carrier absorption of the doped substrate results in a 25°C higher temperature for the doped substrate.

3.2. Temperature measurement from refractive index change

Yoffe et al. [4] demonstrated that an AlGaAs/GaAs quarter-wave interference filter has a significant spectral shift with changes of temperature. A quarter-wave filter consists of alternating layers of two materials with different refractive indices, but identical quarter-wave optical length (thickness × refractive index). Yoffe [5] demonstrated that the peak shift in these filters is linear with refractive index changes up to more than 10%. Since the refractive indices of GaAs and AlAs are sensitive to temperature changes, these structures can be used to measure the actual substrate surface temperature by measuring shifts of either the transmission or reflection spectra. The experimental structures consisted of alternating layers of GaAs and AlAs with the same optical length. Since the detectivity of Ge detectors drops rapidly beyond 1.5 µm and the bandgap of GaAs at 550°C is ~1.1 eV (1.1 µm), the available

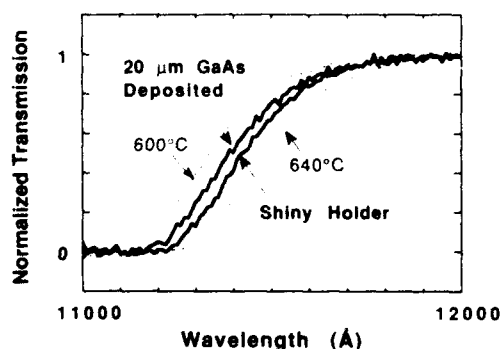


Fig. 3. Normalized transmission spectra of a SI GaAs substrate for shiny and dark (coated by 20 µm of GaAs) holder surface.

window for the present set-up for transmission measurements is between 1.1 and 1.5 μm . We thus selected GaAs and AlAs thicknesses of 900 and 1050 \AA , respectively. The growth rate was calibrated by reflection high-energy electron diffraction (RHEED) oscillations just prior to growth. After the growth, the transmission spectra shift with temperature was measured. Due to constraints of our experimental set-up, the calibration spectral shift measurements were made between 30 and 150 $^{\circ}\text{C}$. The shift was linear with a slope of 0.98 $\text{\AA}/^{\circ}\text{C}$. Since the refractive index versus temperature of GaAs and AlAs [6] are not known for the higher temperature range of MBE interest, accurate measurements need to be done to obtain accurate absolute temperatures. Transmission spectra are normalized by the substrate heater radiation intensity. The spectra shown in fig. 4 clearly demonstrate the temperature shift, with little spectral shape change. However, we observe a change in the rate of the shift from a low temperature value of 0.98 to 0.84 $\text{\AA}/^{\circ}\text{C}$ at 600 $^{\circ}\text{C}$. This same type of discrepancy between thermocouple and actual substrate temperature was observed in the band edge measurement described previously.

Using the transmission spectra shift of the above quarter-wave filters, we measured the effect of source furnace shutter opening on substrate temperature. The system is set to maintain a constant value of the substrate thermocouple and the substrate is not rotated to eliminate layer nonuniformity effects. The transmission spectrum is first

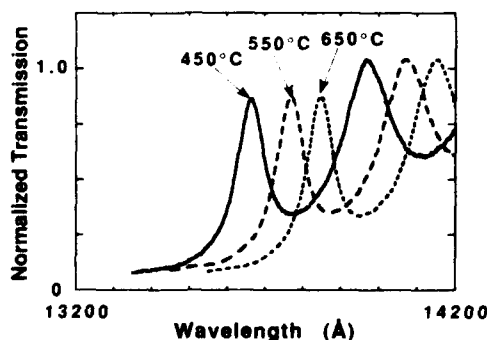


Fig. 4. Normalized transmission spectra through a quarter-wave filter as a function of measured thermocouple temperature.

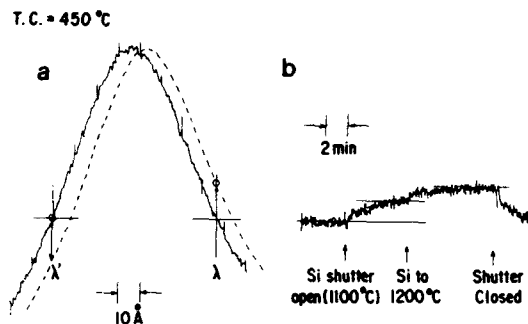


Fig. 5. Substrate temperature variation with source furnace shutter opening and furnace temperature change. (a) Optical intensity as a function of wavelength at 450 (solid curve) and 458 $^{\circ}\text{C}$ (dashed curve), respectively. The substrate thermocouple reading was constant at 450 $^{\circ}\text{C}$ during this measurement. (b) Intensity increase as a function of time for first, the shutter opening with an 1100 $^{\circ}\text{C}$ furnace temperature, and second, an increase in furnace temperature to 1200 $^{\circ}\text{C}$.

scanned, and the spectrometer is then set to a wavelength (λ or λ' in fig. 5a). Since the transmission spectrum moves by $\sim 1 \text{ \AA}/^{\circ}\text{C}$, the intensity change at a given wavelength is a direct measure of the substrate temperature fluctuation. The intensity change when a source shutter is opened is shown in fig. 5b. In fig. 5a, the solid line corresponds to a transmission spectrum at 450 $^{\circ}\text{C}$. The dashed line is shifted 8 \AA from the solid line, thus corresponding to an increase of 8 $^{\circ}\text{C}$ in the substrate temperature due to substrate heating from the open source. In order to verify that this intensity change is not due to heater emission intensity change or stray light from the source furnace, the same measurement was done at λ' . The measurement shows a dip, corresponding to the same spectral shift as before. In this measurement, the thermocouple reading has been kept at the same temperature. Since high temperature sources, like Ga, Al, and Si, are open during the growth, the actual temperature during this time might be much higher than that measured with all the sources closed. This effect might explain some of the temperature discrepancies which occur between different MBE systems. Some growers use the substrate thermocouple for maintaining temperature during the entire growth, while others set the growth temperature by infrared pyrometer with all

of the sources closed. During growth, the thermocouple maintains the same cavity and thermocouple temperature, however, the real substrate temperature might easily vary by 25°C or more due to deposition on the substrate holder and different furnace operating temperatures and configurations.

Another variation of temperature measurement with the quarter-wave filter is in a system where no light source is available (i.e. either the substrate heater is at too low a temperature to provide useful radiation or the substrate is opaque). Since very little absorption is involved in the quarter-wave filter, reflection can be used as well as transmission. Using a pencil like beam from a well collimated light source, the reflection mode can be used to measure temperature. It is also useful to measure temperature variations across a wafer [7].

4. Conclusions

Using bandgap changes with temperature, we observed that the real substrate temperature does not accurately follow the thermocouple reading. The real substrate temperature for identical substrate holders showed approximately 15°C variation in the actual substrate temperature at the same thermocouple reading. Also, the real substrate temperature exhibited differences depending upon holder finish or coating with GaAs. Using a quarter-wave filter, we found that the real substrate temperature varies by as much as 10°C when a single Si doping furnace at 1200°C is

opened while the thermocouple was maintaining the same set point temperature. All of these results show that in growths requiring accurate temperature measurement and control, we cannot rely on the current MBE thermocouple configuration for adequate input for system temperature control.

Acknowledgements

We would like to thank E.S. Hellman, E.C. Larkins and Y.C. Pao for discussions, collaborating measurements and help on the optical measurement system. This work was supported by DARPA and ONR under Contract N0. N00014-84-K-0077.

References

- [1] E.S. Hellman and J.S. Harris, Jr., *J. Crystal Growth* 81 (1987) 38.
- [2] E.S. Hellman, P.M. Pitner, A. Harwit, D. Liu, G.W. Yoffe, J.S. Harris, Jr., B. Caffee and T. Hierl, *J. Vacuum Sci. Technol.* B4 (1986) 574.
- [3] C.D. Thurmond, *J. Electrochem. Soc.* 122 (1975) 1133.
- [4] G.W. Yoffe, D.G. Schlom and J.S. Harris, Jr., *Appl. Phys. Letters* 51 (1987) 1876.
- [5] G.W. Yoffe, *Modulation of Light by Electronically Tunable Multi-Layer Optical Interference*, PhD Thesis, Stanford University (1989).
- [6] O. Madelung, M. Schulz and H. Weiss, *Numerical Data and Functional Relationship in Science and Technology*, Landolt-Börnstein III.17a (Springer, Berlin, 1982).
- [7] W.S. Lee, *Thin Barrier Type AlGaAs/GaAs Heterojunction Bipolar Transistor Structure with Reduced Surface Effects*, PhD Thesis, Stanford University (1990).

A novel in-situ molecular beam epitaxy monitoring system using low energy ion scattering

Minoru Kubo and Tadashi Narusawa

Semiconductor Research Center, Matsushita Electric Industrial Co., Ltd., Moriguchi, Osaka 570, Japan

Low energy ion scattering (LEIS) is introduced as a novel in-situ molecular beam epitaxy (MBE) monitor, which is highly sensitive to local atomic structures of the substrate surface and provides information complementary to the conventional electron diffraction techniques. LEIS is applied to a study of surface steps of GaAs substrates during MBE growth. By demonstrating the sensitivity of the new monitor to atomic steps on the substrate surface, we demonstrate its usefulness for analyses of dynamical surface defect processes, which often play a crucial role in the growth of sophisticated device structures.

1. Introduction

In-situ monitoring of molecular beam epitaxy (MBE) has been carried out mainly by methods of electron diffraction, namely, reflection high-energy electron diffraction (RHEED) and variations such as micro-beam RHEED and scanning RHEED. These techniques have provided useful information towards improving epitaxial film growth [1–3]. These diffraction techniques require long range order in the substrate/film atomic structure, and therefore detailed local structural information such as surface step densities and other structural parameters has not been obtained. We introduce here a novel in-situ MBE monitoring system [4], low energy ion scattering (LEIS), as a structure-sensitive analytical method [5,6]. It utilizes keV He^+ ion scattering at the surface which is particularly sensitive to the local surface atomic structure during MBE growth. Therefore, the information provided by our method is complementary to conventional RHEED techniques, and useful for precise control of MBE growth conditions.

In this paper we describe the apparatus and apply LEIS to a study of surface steps during the MBE growth of GaAs. We first observe a characteristic variation of the He^+ ion scattering intensity with respect to the incident angles of He^+

ions to substrate surface, then find a linear correlation between the surface step density and the He^+ ion scattering intensity under a certain scattering geometry. These results demonstrate a unique application of LEIS.

2. Experimental

The MBE–LEIS system is shown schematically in fig. 1. The LEIS beam line and spectrometer is combined with a MBE chamber via a 70 mm port. The He^+ ion beam is produced in an ion source of electron-impact type, and accelerated in the range of 0.5–5 keV. After being shaped into a pulsed beam by two pairs of electrostatic deflection plates, the ion beam impinges on the substrate surface. The beam current and diameter are 10 nA and ~ 10 mm, respectively, at the substrate surface. Scattered particles, both ions and neutrals, are energy-analyzed by a time-of-flight (TOF) spectrometer and detected by a microchannel plate (MCP) with 1 ns resolution. Two MCPs are located at the scattering angles of 160° and 180° , but the 180° detector is mainly used in the present study for the ease of analysis. Details of the system are described elsewhere [4].

Experiments were carried out by iteration of MBE growths and LEIS measurements. The MBE

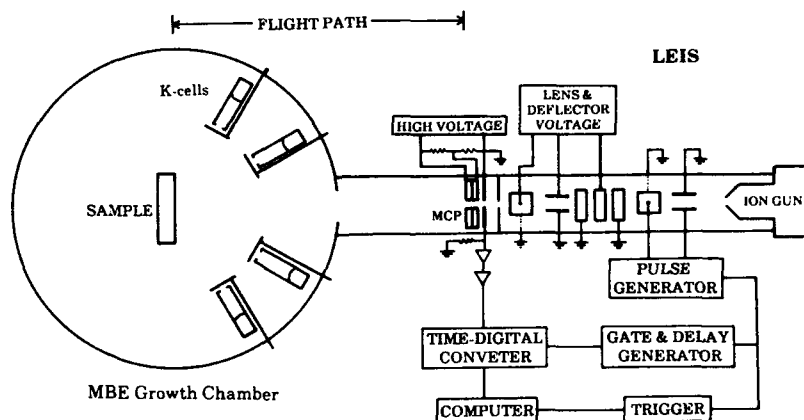


Fig. 1. Schematics of MBE-LEIS apparatus.

growth used conventional K-cell and shutter systems. The substrates were n-type GaAs miss-oriented off the [100] axis by 2° – 6° . These wafers were used for calibration measurements of surface step densities. The substrates were mounted on a 2-axis UHV goniometer. Angular distribution of scattering intensities was measured by rotating the substrate with a stepping motor. The ion dosage per spectral measurement was approximately $0.02 \mu\text{C}/\text{cm}^2$, which is 2–3 orders below the value that may cause a damage to surface atomic structure.

3. Results and discussion

3.1. Angular distribution of LEIS intensity

Fig. 2 shows typical TOF spectra of He particles scattered by thermally cleaned GaAs(100) surface. The incident angles of He ion beam to the substrate surface (α) are at 43.2° and 57.6° in the (001) plane. Although we cannot clearly distinguish between Ga and As in the spectrum there exists a drastic change in the scattering intensity. When $\alpha = 45^\circ$, the incidence is along the $\langle 110 \rangle$ channeling direction, and scattering is limited only from a few topmost layers because of shadowing effects. In contrast, the scattering intensity at $\alpha = 60^\circ$ is greatly enhanced. The shadow cone radius

$R(\text{\AA})$ at distance $L(\text{\AA})$ in the present regime is represented by [7,8]:

$$R = (0.924 - 0.182 \ln(\alpha) + 0.0008\alpha) \times 2(bL)^{1/2},$$

$$\alpha = 2(bL)^{1/2}/a, \quad b = Z_1 Z_2 e^2/E,$$

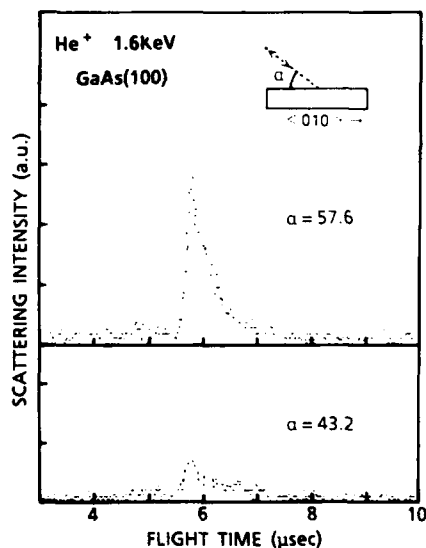


Fig. 2. Time of flight spectra of He particles scattered by GaAs(100) surface. The incident angle of the He⁺ ion beam at the substrate surface is 57.6° (upper panel), and 43.2° (lower panel).

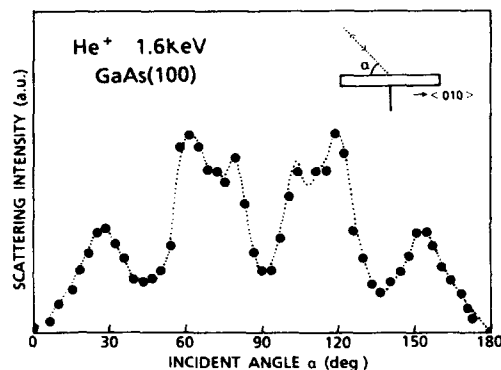


Fig. 3. Scattering intensity as a function of incident angles for GaAs(100) surface.

where E is the ion beam energy (eV), a is the screening length, $0.4685/(Z_1^{1/2} + Z_2^{1/2})^{2/3}$, for the atomic numbers Z_1 and Z_2 , and $e^2 = 14.4$ eV Å. Putting appropriate values for these parameters in the equation, we find that the envelope of the shadow cone by the 1st layer atom coincides with the location of the 2nd layer atom within an error of 0.1 Å. This is the so-called focussing effect of ion beams.

The overall angular distribution of scattering intensity is shown in fig. 3. The profile is symmetric reflecting the high crystalline quality of the substrate. The channeling dips can be seen at $\alpha = 45^\circ$, 90° , and 135° together with the focussing peaks at several angles. In the next section, we pay attention to the profile in the vicinity of 0° , which provides surface step-related information.

3.2. Scattering by surface steps

As schematically shown in fig. 4, if the substrate surface is ideally flat and when the incident

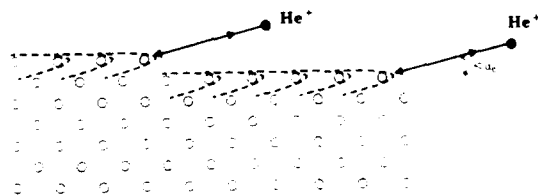


Fig. 4. Schematics of surface step structure and the principle of surface step detection by LEIS.

angle of ion beam is smaller than a certain critical value (α_c), the backward ion scattering cannot be observed [9–11]. We call this the surface shadowing effect. In practical measurements by LEIS in the (110) and (010) planes, the critical angles are calculated to be about 15° and 12° , respectively from $\alpha_c = \tan^{-1}(R/L)$, where L is the nearest-neighbor distance along each azimuthal direction. These rather large values of the critical angle originate from the large scattering cross sections for low energy ions, and enable measurements of the profile near α_c . As we see in fig. 4, surface imperfections such as vacancies and steps bring about the backward scattering even when the incident angle is below α_c . The scattering intensity in such a geometry, therefore, offers a sensitive measure of the density of surface imperfections.

In order to calibrate the scattering intensity near the critical angle against the surface step density, we have made measurements using just (100) oriented and slightly off-angled GaAs wafers. The wafers were thoroughly cleaned thermally at 500°C in an As environment. Off-angled wafers were assumed to contain equally spaced di-atomic steps. The density of such surface steps was calculated for each off-angled wafer, and expressed in units of cm^{-1} , i.e. the total length of step per unit area.

Results of measurements and calculation are shown in figs. 5 and 6. Since the wafers are off-angled toward the $\langle 111 \rangle$ direction, angular scans were made in the (110) plane, so that the ion beam hits the step line perpendicularly. The profile for the just oriented wafer in fig. 5 shows a steep decrease in the scattering intensity near the critical angle, whereas those for off-angled wafers have significant bumps around $\alpha = 10^\circ$ indicating the scattering by surface steps. The scattering intensity evaluated for each profile is plotted against the calculated surface step density in fig. 6. The three plots show a fair linearity and suggest that the scattering intensity at just below the critical angle is, in fact, proportional to the surface step density. However, the extrapolated line does not pass through the origin of the coordinate. The content of this offset is not clear, but may result from a misassumption that the just oriented wafer is completely step-free, or a misvaluation of the

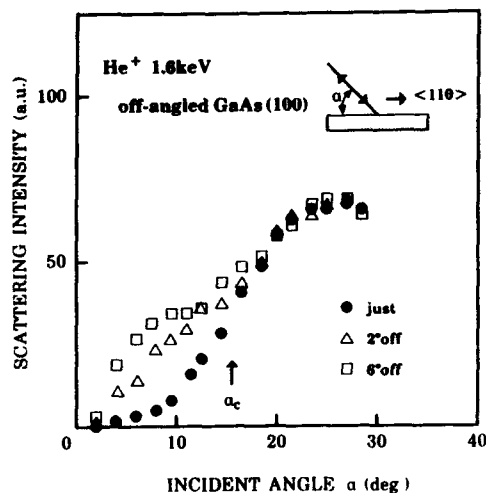


Fig. 5. Angular profiles of scattering intensity from several off-angled substrate surface.

extra scattering intensity. In any case, further study is necessary to clarify the point.

3.3. As incorporation into Ga clusters

We have applied LEIS to monitor the surface steps during MBE growth of GaAs. By opening only the shutter for the Ga K cell, Ga clusters were formed on a clean GaAs(100) substrate at

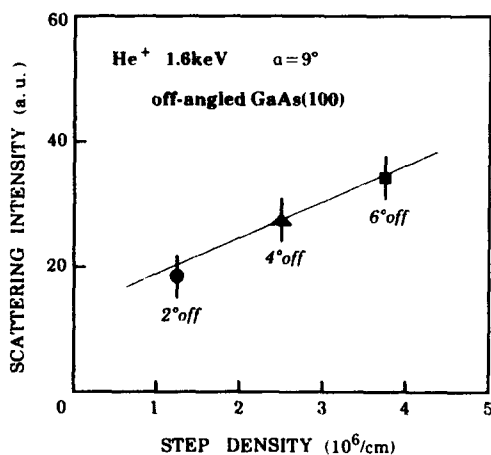


Fig. 6. Dependence of scattering intensity (at $\alpha = 9^\circ$) on step density.

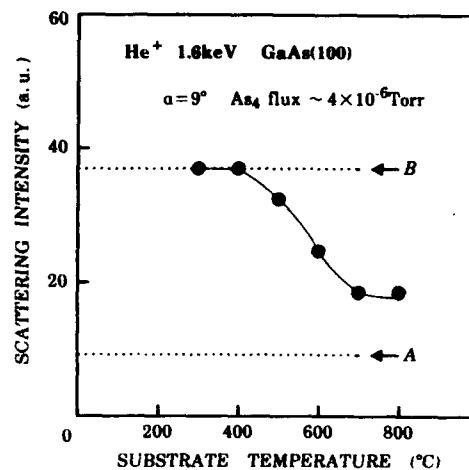


Fig. 7. Dependence of scattering intensity on substrate temperature during MBE growth.

$\sim 400^\circ\text{C}$. The average film thickness was ~ 20 monolayers. At this stage, the scattering intensity at $<\alpha_c$ was very high, reflecting a roughness of the substrate surface. Then the As_4 flux of $\sim 4 \times 10^{-6}$ Torr was supplied with the substrate temperature raised step by step. Variation of the scattering intensity at $\alpha = 9^\circ$ ($<\alpha_c$) in the course of this temperature increase is shown in fig. 7. The scattering intensity from the clean surface and from as-Ga-deposited surface are labeled A and B, respectively. With the increase in the substrate temperature, the scattering intensity decreases. The tendency is notable in the temperature range of $500\text{--}600^\circ\text{C}$. In fig. 7 the scattering intensity does not recover completely from the level B to A even after heating at $\sim 800^\circ\text{C}$ for several minutes. This indicates that ~ 20 monolayers of Ga atoms are too thick to be flattened out thermally. Another possibility is a spontaneous formation at such a high temperatures as $\sim 800^\circ\text{C}$.

The results described above suggest that the initial Ga clusters are flattened out due to a competitive phenomenon of the migration of Ga atoms and adsorption of As atoms. Once a migrating Ga atom reacts with an As atom, a stable GaAs "molecule" is formed and is bound to a certain site in the substrate surface. The As atoms do not adsorb onto such sites but only to free Ga atoms. If this is the case, the incorporation of As atoms

into Ga clusters would strongly depend on the As₄ flux, the substrate temperature, and the size of the Ga clusters. When the size is too big, migration of Ga atoms out of the cluster may be restrained because the average migration distance is limited under a given As₄ flux and a substrate temperature. This speculation has been confirmed by observing the complete recovery of the scattering intensity in the case of the initial Ga coverage of ~ 3 monolayers.

4. Summary

We have developed a novel in-situ MBE monitoring, LEIS, which is highly sensitive to local atomic structures of the substrate surface, and provides us with information which is complementary to conventional electron diffraction techniques. The monitor is useful in dynamical analyses of local surface structures like surface vacancies and steps, and applied to a study of surface steps on GaAs substrates during MBE growth. We have demonstrated the use of the surface shadowing effect, the linearity between the surface step density and He⁺ ion scattering intensity under the surface shadowing geometry, and the usefulness of our monitor in analyses of dynamical surface phenomena such as the incorporation of As atoms into Ga clusters.

Acknowledgments

The authors would like to thank T. Onuma for his encouragement throughout the present study. They also acknowledge Professor K. Oura of Osaka University and Dr. M. Aono of the Institute of Physical and Chemical Research for their useful comments, advice, and discussions.

References

- [1] J.H. Neave and B.A. Joyce, *J. Crystal Growth* 44 (1978) 387.
- [2] M. Ichikawa and T. Doi, *Appl. Phys. Letters* 50 (1987) 1141.
- [3] S. Clarke and D.D. Vedensky, *Phys. Rev. Letters* 58 (1987) 2235.
- [4] M. Kubo and T. Narusawa, *J. Vacuum Sci. Technol.* B8 (1990) 697.
- [5] M. Aono, M. Katayama, E. Nomura, T. Chassé, D. Choi and M. Kato, *Nucl. Instr. Methods B37/38* (1989) 264.
- [6] K. Sumitomo, K. Tanaka, Y. Izawa, I. Katayama, F. Shoji, K. Oura and T. Hanawa, *Appl. Surface Sci.* 41/42 (1989) 112.
- [7] H. Nakamatsu, A. Sudo and S. Kawai, *Surface Sci.* 194 (1988) 265.
- [8] M. Aono, Y. Hou, R. Souda, C. Oshima, S. Otani, Y. Ishizawa, K. Matsuda and R. Shimizu, *Japan. J. Appl. Phys.* 21 (1982) L670.
- [9] C.S. Chang, T.L. Porter and I.S.T. Tsong, *Vacuum* 39 (1989) 1195.
- [10] C.H. Patterson and T.M. Buck, *Surface Sci.* 218 (1989) 431.
- [11] M. Kato, M. Katayama, T. Chassé and M. Aono, *Nucl. Instr. Methods B39* (1989) 30.

Surface segregation in III–V alloys

J.M. Moison, F. Houzay, F. Barthe, J.M. Gérard, B. Jusserand

Laboratoire de Bagneux, Centre National d'Etudes des Télécommunications, 196 Avenue Henri Ravéra, F-92220 Bagneux, France

J. Massies and F.S. Turco-Sandroff *

Laboratoire de Physique du Solide et Energie Solaire, Parc de Sophia Antipolis, Rue Bernard Grégory, F-06560 Valbonne, France

Recent measurements which demonstrate the occurrence of surface segregation during the MBE growth of $\text{III}_a\text{III}_b\text{-V}$ ternary semiconductor alloys and $\text{III}_a\text{-V}/\text{III}_b\text{-V}$ heterostructures are reviewed. This preferential segregation drives to the surface one of the third-column elements involved, to the expense of the other, within their common sublattice. In ternary alloys, the surface is found to be nearly binary, and a short-scale interface roughness is detected in heterostructures. For arsenides, the direction and extent of the segregation process follow the $\text{In} > \text{Ga} \geq \text{Al}$ order. We discuss possible origins for the segregation process and the ability of standard segregation models to describe the results on ternary alloys and to predict composition profiles for any given heterostructure. These predictions are compared to recent measurements by high-resolution microscopy, ion scattering, photo-luminescence, or Raman scattering. Possible applications of the segregation process, and also remedies for avoiding it are finally discussed.

1. Introduction

High-quality materials can now be built by molecular-beam epitaxy (MBE) into complex tailored structures with pattern sizes down to atomic distances such as superlattice alloys, ultra-thin quantum wells with lattice-mismatched compounds, tilted superlattices obtained by fractional monolayer growth, etc. At such pattern sizes, and with such steep composition and lattice parameter gradients, the heterointerface roughness is all the more important. Obviously, maximum care must be exercised in MBE procedures, for instance by optimizing the accuracy of fractional deposits and smoothing the layers by growth interruptions. However, even with optimal precautions, leading to a perfectly flat growth surface at the completion of each monolayer, can intrinsic atomic displacements still limit the abruptness of the final interface? In other words, is there some kind of quantum limit to the quality of interfaces on the

atomic level? At usual growth temperatures ($\leq 600^\circ\text{C}$), bulk diffusion is not operative due to the lack of vacancies; atomic arrangements are determined during growth by surface or near-surface processes and frozen after burial. Surface-located displacements which provide the surface mobility are necessary to obtain high-quality material, but they can simultaneously lead to exchanges between substrate atoms and impinging atoms, for instance at growth steps, which would degrade the planned composition gradients. We show here that preferential segregation of some third-column atoms at the surface is one possible driving force for such exchanges.

Preferential segregation at surfaces, interfaces, grain boundaries, etc. have been known for a long time in metallurgical science, both in the domain of impurities (e.g. carbon segregation to iron grain boundaries) and alloys (e.g. surface enrichment in Cr of Fe–Cr alloys) [1]. Similar alloy effects have been reported in III–V ternary alloys, where they involve bulk–surface redistribution within one sublattice, the third-column metal one for the case of arsenides. Preferential segregation effects may

* Present address: Bellcore, 331 Newman Springs Road, Red Bank, New Jersey 07701, USA.

also lead to dopant redistribution. At heterointerfaces, phenomena which drive substrate atoms to the top of the growing overlayer have also been observed [2]. We review here the data obtained in ternary arsenides and discuss their description by standard segregation theory, considering their deviations from true thermodynamic equilibrium. Predictions of this approach for heterointerfaces and atom-sized structures are then compared with recent experimental data. We finally evaluate possible ways to use or rather fight this phenomenon.

2. Ternary alloys

2.1. Experimental data

Surface segregation in ternary alloys is most easily measured by surface analytical techniques. Thick layers of the desired material $\text{Ga}_x\text{Al}_{1-x}\text{As}$, $\text{In}_x\text{Ga}_{1-x}\text{As}$, or $\text{In}_x\text{Al}_{1-x}\text{As}$ have been grown by MBE. The bulk composition x_b was measured using RHEED oscillations, X-ray diffraction and photoluminescence. After cooling down the sample, the surface composition gradient was measured by in situ ultra-high-vacuum techniques such as Auger electron spectroscopy (AES), X-ray photoemission spectroscopy (XPS), UV Photoemission spectroscopy (UPS) or electron energy loss spectroscopy (EELS). As a result, AES, XPS, UPS, and EELS spectra show clearly surface enrichments [2-8], in Ga for $\text{Ga}_x\text{Al}_{1-x}\text{As}$, and in In for $\text{In}_x\text{Ga}_{1-x}\text{As}$ and $\text{In}_x\text{Al}_{1-x}\text{As}$ (see an example in fig. 1). The rules for predicting the segregating element will be discussed in section 4.

More quantitative information may be obtained from XPS and AES intensities through some simple assumptions such as uniform primary excitation and exponential attenuation of emitted electrons, same arsenic content in binaries and ternaries, and unidimensional distribution of third-column atoms (planar interfaces). Under these assumptions, the XPS signals depend only on parameters such as the ionization cross-sections or the electron escape depth [9], i.e. the probed depth (10-50 Å), and on the composition gradient at the surface. For thick ternary layers which have reached a stationary composition

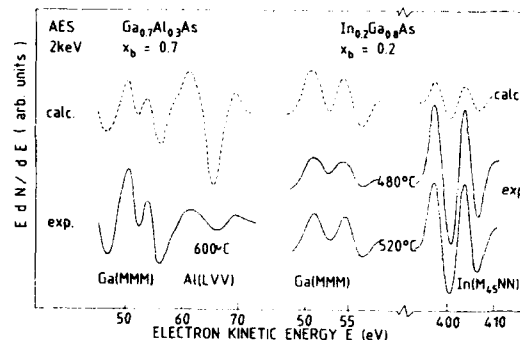


Fig. 1. AES spectra of $\text{Ga}_{0.7}\text{Al}_{0.3}\text{As}$ (a) and $\text{In}_{0.2}\text{Ga}_{0.8}\text{As}$ (b) (full lines) [7]. For the second alloy, data corresponding to as-grown samples and post-annealed samples are shown; the temperature indicated is either the growth temperature or the anneal temperature. The top spectra (dashed lines), expected for no segregation, are constructed by scaling each peak from the corresponding binary alloy by its fraction in the ternary alloy, after reduction to the same As peak.

gradient with a representative bulk composition, the gradient can exist only very close to the surface, and can be summarized by a "surface" composition x_s . The "surface" may be considered to encompass either the topmost surface monolayer (ML) defined as one metal and one As (001) planes, or a thicker (several ML) subsurface layer. In the first case [7,8], systematic $x_s(x_b)$ XPS/AES measurements (see fig. 2) with various probed depths indicate that most of the segregation is concentrated in the topmost layer. In the second case [4,6], the maximum of segregation reported from XPS data for $\text{Ga}_x\text{Al}_{1-x}\text{As}$ can be accounted for by either 2 ML of GaAs on top of a ternary or 3 ML of $\text{Ga}_x\text{Al}_{1-x}\text{As}$ of variable composition, and for $\text{In}_x\text{Ga}_{1-x}\text{As}$ by either 2 ML of InAs or 4 ML of $\text{In}_x\text{Ga}_{1-x}\text{As}$ of variable composition.

We consider now to what extent those results can be considered as equilibrium data, taken into account by classical segregation theory, and used to predict phenomena occurring at heterointerfaces or more complex structures.

2.2. Equilibrium and growth-induced stationary state

From a thermodynamical point of view, the ideal surface segregation experiment involves a bulk phase (semi-infinite solid alloy M_{1-x}N_x of x_b

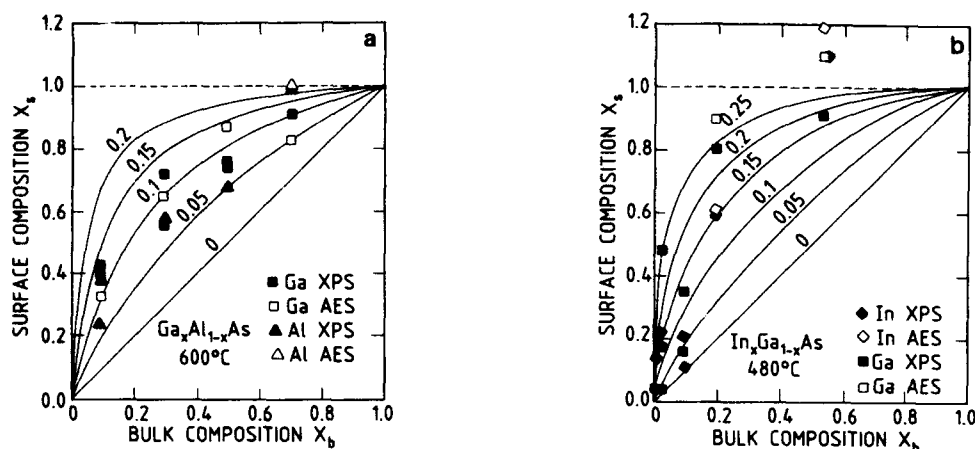


Fig. 2. Experimental segregation isotherms $x_s(x_b)$ deduced from XPS measurements for the (a) $\text{Ga}_x\text{Al}_{1-x}\text{As}$ alloys at 600°C and $\text{In}_x\text{Ga}_{1-x}\text{As}$ alloys at 480°C (b), and theoretical expectations for various values of E_s (indicated in eV) [7].

composition), a surface phase (surface of the latter with an x_s composition) and a gas phase (atmosphere of M and N under their gaseous form). Thermodynamic equilibrium requires the adjustment of chemical potentials in all phases, i.e. of x_b , x_s , and of the partial pressures of M and N in the gas phase. This ideal situation is almost never found. Most experiments on metals only consider a bulk-surface equilibrium reached after annealing samples cleaned or fractured under vacuum. Performing similar experiments in (M,N)As arsenides is not possible since long enough diffusion paths cannot be obtained in reasonable times except at temperatures ($> 1000^\circ\text{C}$) where the material rapidly evaporates. This evaporation cannot be counteracted by an adequate (M,N,As) atmosphere as in the "ideal" experiment for practical reasons.

The actual experiment for ternary arsenides then differs from the ideal one in two ways: (i) the (M,N) partial pressures in the gas phase have the correct $(x_b, 1 - x_b)$ proportion but are in excess in terms of chemical potential (this excess causes the growth) and (ii) the temperature is not high enough to allow any significant bulk diffusion and induce the bulk/surface equilibrium. However, the concentration excess $x_s - x_b$ as the surface necessary to attain equilibrium of chemical potentials, which cannot be produced by diffusion from the

bulk to a fixed surface, can be obtained by accumulation of segregated atoms at a surface moving due to the growth flux. In this case, the excess is provided by a depleted zone corresponding to the growth start, where the incorporation of the segregating species into the bulk is smaller, and is then constantly renewed and transported along the growth. Growth – and the fast surface exchanges – acts here as a substitute to failing bulk diffusion. In these conditions which are discussed at length elsewhere [7], though the equilibrium is not reached by the usual means, the x_s values obtained are nevertheless similar to the ones which would be obtained in the hypothetical ideal experiment. We may then discuss them with standard segregation models.

2.3. Surface segregation models

In the case of a simple bulk/surface equilibrium, we consider only the balance of chemical potentials of the segregating species in these two phases. The most simple quantitative model known as McLean's involves only the entropy term and the "chemical" energy E_s as contributions to the free energy [1]. We must also introduce here a term corresponding to the elastic deformation caused to the surface by its pseudomorphism with the bulk. For instance, such a segregation iso-

therm correctly fits the experimental $x_s(x_b)$ data of fig. 2, with $E_s \approx 0.15 \pm 0.1$ eV for $\text{In}_x\text{Ga}_{1-x}\text{As}$ alloys and 0.1 ± 0.05 eV for $\text{Ga}_x\text{Al}_{1-x}\text{As}$ alloys. This in turn allows us to predict the equilibrium surface concentration of any ternary alloy at any temperature. For the rather high x_b concentrations and the rather low temperatures involved in most common cases, the chemical potential in the bulk phase and the segregation energy are too high to be counteracted by disorder or elastic strains and x_s is always much higher than x_b , although variations with temperature are observed (see fig. 3). Except by using kinetic limitations, the only way to change strongly x_s is then desorption whose activation energy is higher than E_s , but which involves a chemical potential in the neighbouring phase (a pure As atmosphere) considerably lower. For instance, in $\text{Ga}_x\text{Al}_{1-x}\text{As}$ at temperatures higher than 650°C , the desorption of Ga becomes significant. The difference between x_s and x_b is seen to decrease above this value (see fig. 3), meaning that the desorption of Ga then overrides the preferential segregation of Ga.

Concentration profiles at heterojunctions can also be predicted by assuming simply that at the deposition of every monolayer, the concentrations of segregating element in this monolayer and in the underlying one reach an equilibrium according to the $x_s(x_b)$ relation and to the matter conserva-

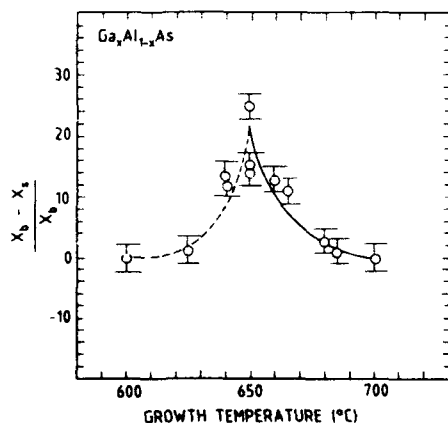


Fig. 3. Variation of $(x_s - x_b)/x_b$ deduced from XPS measurements with the growth temperature, for various $\text{Ga}_x\text{Al}_{1-x}\text{As}$ alloys [4]. Lines are tentative fits by exponential laws.

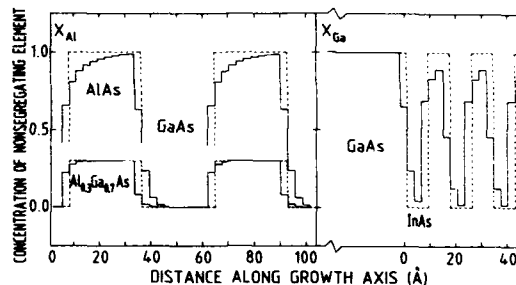


Fig. 4. Profile of composition in non-segregating element for selected heterostructures [7]. Each step corresponds to a single monolayer. Planned profiles are the dotted lines and model profiles calculated at usual growth temperatures are full lines.

tion relation. The underlying monolayer is then "frozen" for the rest of the growth. This model generates an interface roughness expressed as a concentration gradient different from the as-planned step function. It tells nothing a priori about the distribution of atoms within atomic planes parallel to the growth axis. It is also assumed that the growth is otherwise geometrically perfect: the growth surface is ideally flat at the completion of each monolayer and each deposition stops after the strict completion of its last monolayer. Concentration profiles obtained by this method will be called model profiles. Some examples are shown in fig. 4. One interesting feature is that, although for instance Ga tends to segregate to replace Al, the first pure GaAs monolayer deposited on top of AlAs is not in equilibrium: the stable point is obtained for a topmost layer of $\text{Ga}_{0.7}\text{Al}_{0.3}\text{As}$ and an underlying layer of $\text{Ga}_{0.3}\text{Al}_{0.7}\text{As}$. Hence the GaAs-on-AlAs interface with the segregating element atop ("inverse" in the MBE terminology) is not abrupt; it is narrower but rougher than the other ("normal") interface AlAs-on-GaAs (see fig. 4).

3. Heterointerfaces

Various experiments demonstrate the existence of surface segregation during the formation of heterointerfaces, leading to interface roughening. We consider first the evidence coming from surface analysis techniques.

3.1. Surface and analytical techniques

Three types of test structures have been used to decide whether B atoms segregate to the surface when A-As is grown on B-As: (i) a single atomic layer of an A-As deposited onto B-As, (ii) for lattice-matched materials, a thin (≤ 100 Å) overlayer of the A-As material, and (iii) for lattice-mismatched materials, sandwich structures (B-As, 1 ML of A-As, and thin, ≤ 100 Å, overlayer of B-As) in order to avoid the switch from 2D laminar growth to 3D island growth, and hence to keep the system as homogeneous as possible in the growth plane. The reduced signal of A is compared to the expectations yielded by various models, such as abrupt interface or equilibrium profile. From all data obtained on various test structures built by steps or in a continuous manner, it is clear that segregation does occur at interfaces. Atoms which should be long buried if no segregation occurred are observed by surface-sensitive techniques [7,9] (see fig. 5). The tendency for segregation found is $\text{In} > \text{Ga} \geq \text{Al}$ as for ternary alloys. The interface width can reach tens of ML in the worst case (AlAs-on-InAs), while it is nearly invisible (≤ 1 ML) in the best cases (AlAs-on-GaAs) [7,10]. For the InAs/GaAs case, several experiments showed no significant influence of temperature from 420 to 560°C, growth rate from 0.1 to 1 $\mu\text{m/h}$, or compressive strain from 0 to 7% [7]. Similar results have been obtained for sandwich structures built at very low temperatures (300°C) by alternating arsenic and metal fluxes (migration-enhanced epitaxy or MEE) [11].

3.2. High-resolution microscopy

High-resolution transmission electron microscopy (HRTEM), which could in principle give a straightforward answer to the question of the interface geometry, has actually encountered problems due to interpretation of contrasts, in-plane roughness and homogeneity of samples. In the GaAs/AlGaAs system, HRTEM has imaged near-flat interfaces with 1 ML high steps separating wide terraces [12]. However, a recent subtle analysis of HRTEM results concludes that even the best interfaces exhibit roughness on the atomic

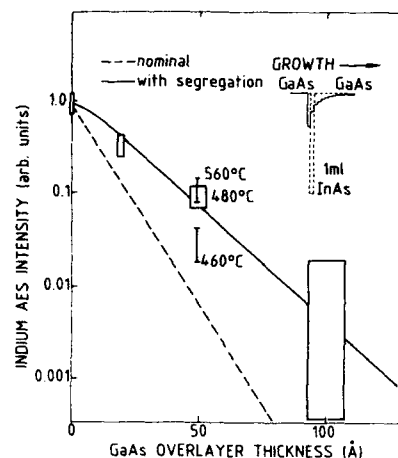


Fig. 5. Evolution of AES signals in sandwich heterostructures GaAs/1 ML InAs/GaAs with thickness of the final layer. Signals are normalized to the signal corresponding to the absence of final layer. Full and dashed lines correspond to predictions for the planned and model profiles.

scale [13]. HRTEM pictures by d'Anterroches et al. [14] of GaAs/1 ML InAs/GaAs structures indicate indium redistribution in the top GaAs layer with a complex concentration gradient. The InAs-on-GaAs interface appears planar, while the reverse one is rough and extends from 2 ML in some places to 4 ML in others. This in-plane roughness occurs on a rather short distance (≈ 40 Å). This shows the limitations of the unidimensional model used here.

3.3. Rutherford backscattering

GaAs/1 ML InAs/GaAs sandwich structures have also been analyzed ex situ by Rutherford backscattering with 1 MeV He^+ ions by Cohen and co-workers [15]. If the structure had indeed the planned geometry, the InAs monolayer should be distorted quadratically – in-plane compression and normal extension – in order to take the in-plane GaAs parameter which is 7% smaller than the InAs unstrained one. This structure should then be seen by ions channeled in off-normal directions as a stacking fault, which should increase the minimum yield χ_{\min} to $\approx 15\%$. Fur-

thermore, indium atoms lying outside the off-normal channels should have a substantial backscattering yield. Actually, the low χ_{\min} ($\approx 4\%$) observed in both (100) and (110) directions (see fig. 6a) shows that atoms in the whole heterostructure are approximately located at the substrate lattice positions. The indium yield is also very low with respect to the expected value. The indium atoms are therefore redistributed in the GaAs overlayer. Fits of angular scans of indium yield (fig. 6b) show that it is redistributed over ≈ 5 ML, in fair agreement with the model profile.

3.4. Photoluminescence

Photoluminescence (PL) line splittings in GaAs-AlGaAs quantum wells have been interpreted for long as originating from a long-range fluctuation of plus or minus one monolayer of the otherwise perfectly constant well width [16]. This conclusion must be weighted by the relatively low sensitivity of the probing particle, the exciton, to small-scale in-plane roughness. The small deviations to perfection shown in the model profile of fig. 4 for GaAs/AlGaAs interfaces are probably

invisible to PL, all the more since the well width is preserved by the segregation process; actually, the direct interface should be seen by PL as abrupt. However, for very thin wells with important band discontinuities, such as a few ML of InAs in GaAs, PL becomes a good probe of interface roughness. For a well thickness corresponding to a non-integer number of atomic layers, e.g. 1.2 ML, a single PL peak – and not separated peaks corresponding to 1, 2 or 3 ML – is observed [17]. The energy of this peak varies continuously with the well width. This is found to be in agreement with a redistribution of indium atoms over 4 to 5 ML.

Further evidence of this redistribution is obtained in more sophisticated structures, where the previous sequence GaAs/1 ML InAs/GaAs is inserted inside AlGaAs barriers [17]. The PL signal considered here originates from the GaAs quantum well on which the 1 ML InAs acts as a perturbation [18]. InAs layers placed in symmetrical positions with respect to the middle of the GaAs well should induce the same perturbation, because they are identical except for the growth direction. Actually a quite significant difference between the corresponding PL energies is ob-

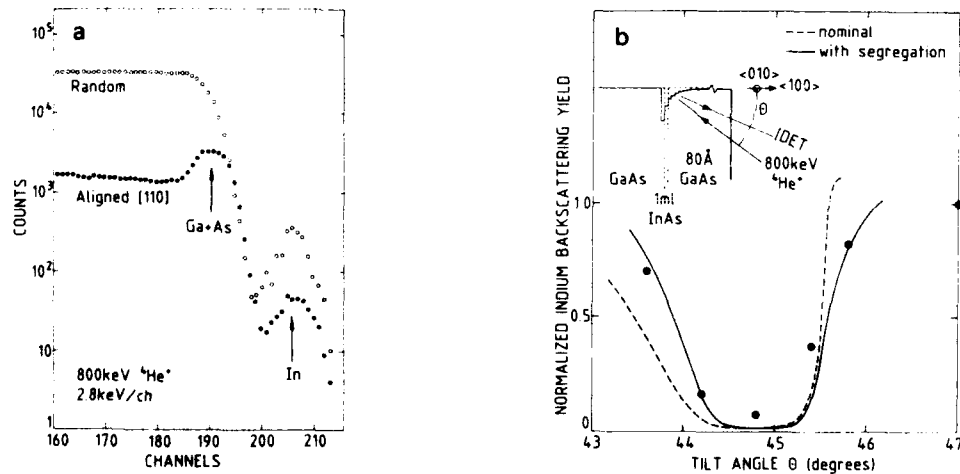


Fig. 6. (a) Rutherford backscattering yield spectrum for sandwich heterostructures GaAs/1 ML InAs/80 Å GaAs; (b) angular scan of the In peak area [15]. Full and dashed lines correspond to predictions for the planned and model profiles.

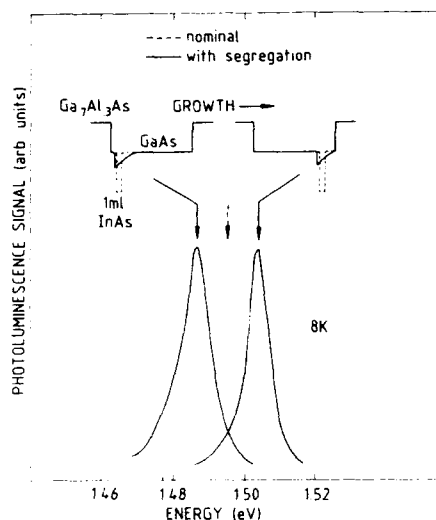


Fig. 7. Photoluminescence spectra for two structures similar except for the growth direction, involving an InAs ML inserted within a GaAs/Ga_{0.9}Al_{0.1}As quantum well [18]. Full and dashed lines and arrows correspond to predictions for the planned and model profiles.

served (see fig. 7), revealing an overall displacement of the indium layer in the growth direction. This overall displacement is estimated to be about 2 ML, again in fair agreement with the model profile.

3.5. Raman scattering

Recently, Raman scattering has proven to be a powerful probe of interface roughness in GaAs/AlAs structures, due to the frequency separation of the optical phonon branches in GaAs and AlAs, and hence to the strict confinement of GaAs- and AlAs-type phonons in their respective layers. Phonon frequencies are therefore very simply connected to individual layer thicknesses for ideally flat interfaces, and also very sensitive to interface roughness. Short-period superlattices, such as (AlAs)₄(GaAs)₃(AlAs)₁(GaAs)₃ or (AlAs)₄(GaAs)₃(AlAs)₁(GaAs)₃, which are identical except for the growth direction, have been considered by Jusserand et al. [19]. While the superlattice period is checked by X-ray diffraction to be the one expected, the optical phonon spectrum reveals in-

dividual layer thicknesses significantly lower than planned ones, e.g. ≈ 1.5 ML instead of 3 nominal for a GaAs layer grown at 600°C (fig. 8). This apparent thickness depends on growth temperature, but also on the thickness of the underlying AlAs layer. Considering the strict confinement of optical vibrations of, say GaAs in the GaAs layer, even by a fraction of Al atoms inserted in the boundary atomic layers, such deviations directly detect the roughening and widening of interfaces (mainly the "inverse" one GaAs-on-AlAs) on the atomic scale. It may be noted that this is not inconsistent with the observation by PL of flat interfaces on a larger scale due to the exciton size.

At the standard growth temperature of 600°C where segregation data have been obtained by surface analytical techniques, the phonon frequencies calculated with the model profile and their dependence on the underlying layer thickness (saturation above 4 ML) are in excellent agreement with experimental values (see fig. 8). However, the extrapolation of model profiles to lower temperatures (400°C) yields only a small variation, while Raman scattering sees a strong de-

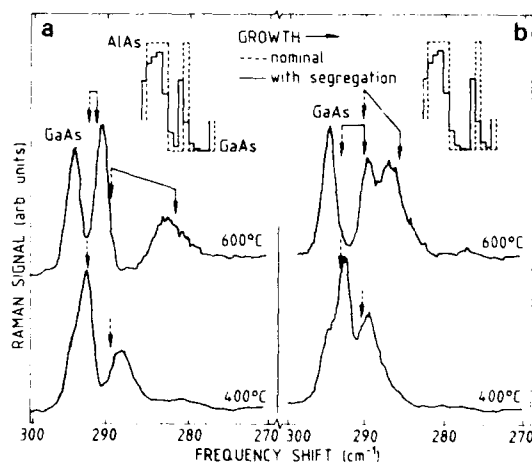


Fig. 8. Raman spectra in two GaAs/AlAs short-period superlattices equivalent except for the growth direction [20]. Inserts show the planned (dashed lines) and model (full lines) composition profiles. The peak indexed by "GaAs" corresponds to the signal from the GaAs substrate. The frequencies calculated for vibrations confined in GaAs layers according to the planned (respectively model) profile are indicated by dashed (respectively full) arrows.

crease of the atomic-scale roughness. A possible reason for this discrepancy is the influence of kinetics (see section 4).

4. Discussion

4.1. Driving force

We consider here briefly the question of the microscopic origin or driving force for surface segregation. If we define the tendency to surface segregation of an atom M as the energy gain E provided when it moves from the bulk to the surface, M will segregate to the surface of the (M,N)As alloy if $E_M > E_N$. Experimental observations yield $E_{In} > E_{Ga} \geq E_{Al}$, both for ternary alloys and heterointerfaces. A similar order is observed in neighbouring reactions known as exchange reactions which take place during the deposition of a third-column metal on arsenides without arsenic pressure [20]. In the absence of other information, it has been suggested that correlations of these segregation energies with other data could indicate the origin of the driving force [4,5,21]. The correlation with the heats of formation or the bonding energies of bulk arsenides (the less strongly bonded atom comes to the surface) seems to indicate the preeminence of the chemical energy, but the reverse correlation is observed in antimonides. The correlation with covalent radii (the biggest atom comes to the surface) seems to indicate the preeminence of the elastic energy, but this disagrees with the weak influence of elastic strain mentioned above. Other correlations of the segregation energy, for instance with the incorporation energy or the surface diffusion coefficient, have also been put forward. Finally, a pessimistic way to consider such correlations is to say that all quantities involved are expected to follow somehow the Periodic Table order (Al,Ga,In) for arsenides. Furthermore, some puzzling experiments and theories on segregation in metal alloys [22] show that the prediction of the segregating component is by no means straightforward. It may be reversed for instance by changing the crystal orientation of the surface, when conflicting effects like atom size (surface strain), pair-interaction

(surface energy), and surface reconstruction energy oppose.

4.2. Microscopic mechanisms

Data show that the microscopic mechanisms involved in segregation are fast i.e. not strongly limited by kinetics or growth rates, which is expected since they are probably similar to those of surface diffusion. Like any atom movement at the surface, they are likely to take place preferentially at defects such as growth steps or steps associated with reconstructions which are the only sites where the reaction can proceed by successive movements without any direct atom exchange: indeed, exchanges in metal/semiconductor systems depend very strongly on defect density [23]. Furthermore, it has been shown [5,24] that on $Ga_{1-x}Al_xAs$ the surface segregation correlates with the development of the growth interface roughness: all published results [25] indicate that the $Ga_{1-x}Al_xAs$ surface roughening is maximum at growth temperatures around 650°C, which is also the case for Ga segregation (see fig. 3).

In all these problems, it is clear that significant data are missing. We can also mention that the assumption that processes in successive layers are not correlated, which leads to an unidimensional description, neglects actual observations of in-plane unhomogeneities, i.e. 2D clustering even in unstrained systems [26]. This is a strong and basic limitation to the discussion.

4.3. Consequences, and possible cures ...

We consider first the consequences of surface segregation on the concentration profile in III-V ternary alloys and heterostructures. During the growth of a ternary alloy, the bulk composition is in principle set by the ratio of metal fluxes and is therefore as homogeneous as these fluxes are stable. However, the fluxes must pass through the surface whose composition is very different from this ratio, and only the regularity of the speed of segregation mechanisms insures that fluxes entering the bulk are identical to the impinging ones. If this regularity is impaired for some reason, variations of the bulk will appear. The problem of

heterointerfaces is different in the sense that they are expected to be abrupt, which segregation processes oppose, since a fraction of the substrate topmost monolayer "floats" on the growing layer and is gradually incorporated. As a consequence, the geometrical accuracy of short-scale structures is degraded, since all interfaces are enlarged in a manner which depends on the materials considered and on the growth direction. It has been suggested, among other explanations, that this was the origin of the differences between GaAs/Al_{0.3}Ga_{0.7}As "normal" and "inverse" interfaces. It may be stressed that this interface roughness also depends in a sense on the probe used to measure it.

Beside the roughening of interfaces, segregation has further consequences. In the case of a ternary alloy, or shortly after an heterointerface, the composition of the sample surface is not as expected. This composition error may be important if the properties of this surface are used in devices (low surface recombination, chemical reactivity or passivation, further growth, etc.). It may also be noted that the reconstruction of the surface and its (temperature, As pressure) "phase diagram", which helps tuning growth conditions, are dictated by the surface composition: two monolayers of InAs on InP have the same "phase diagram" as bulk InAs [27]. Therefore, the growth conditions should be set in principle with respect to the actual surface and not to the presumed overlayer material surface. Conversely, segregation may explain some puzzling successions of RHEED patterns observed during the growth of short-period structures. Finally, segregation has a number of consequences, most of them negative with respect to the quality of the interface. A positive one is the possibility of obtaining layers without having to build them with atom fluxes, with possible applications to atomic-layer epitaxy. However, much work must still be performed before putting segregation into actual use and rather the present problem is to get rid of it.

Our present data show that reducing significantly the segregation would need too high temperatures ($> 1000^\circ\text{C}$) if thermodynamic equilibrium is to be maintained. We may then try slow down the kinetics, with the counterpart of getting

off-equilibrium interfaces. First, it seems that the growth rate cannot be increased enough to beat the process by burying the atoms before they could reach equilibrium. Temperature has a mixed effect. Low temperatures increase the equilibrium segregation but decrease the surface mobility of atoms towards the reaction sites, and the rate of exchange at these sites. Observations on Ga_xAl_{1-x}As ternary alloys by XPS [4,6] and on GaAs/AlAs superlattices by Raman scattering [19] indicate a positive effect of reduced growth temperatures. The foreseeable corresponding loss in material quality may be obviated by MEE (alternating arsenic and metal fluxes) which restores a high surface mobility of metal atoms now unimpeded by excess arsenic. No significant reduction of segregation in GaAs/InAs/GaAs structures is indeed obtained by this method. A possible solution could be the modulation of the surface mobility: (i) high mobility during the growth of the substrate up to the topmost monolayer, coupled with a growth interruption at its exact completion in order to decrease the number of reaction sites if they are defects, and (ii) low mobility during the growth of the first monolayers of the overlayer in order to build a barrier to segregation, with the risk of obtaining sharp but faulted interfaces.

Acknowledgements

We gratefully acknowledge fruitful collaboration and discussions with J.Y. Marzin, C.A. Sébenne, C. d'Anterrockes, F. Alexandre, M. Quillec, L. Goldstein, F. Mollot, R. Planel, C. Cohen, A. l'Hoir, F. Abel, D. Schmaus, J.P. Contour, and C. Deparis.

References

- [1] See, for instance: G.A. Chadwick and D.A. Smith, Eds., *Grain Boundary Structure and Properties* (Academic Press, London, 1975); J. Bénard, Ed., *Adsorption on Metal Surfaces* (Elsevier, Amsterdam, 1983).
- [2] An extended list of papers dating before 1989 is given in ref. [7]; some later papers are listed below.

- [3] T.C. Chiang, R. Ludeke and D.E. Eastman, *Phys. Rev. B* 25 (1982) 6518.
- [4] J. Massies, F. Turco, A. Salètes and J.P. Contour, *J. Crystal Growth* 80 (1987) 307.
- [5] R.A. Stall, J. Zilko, V. Swaminathan and N. Schumaker, *J. Vacuum Sci. Technol. B* 3 (1985) 524.
- [6] F.S. Turco and J. Massies, *Appl. Surface Sci.* 37 (1989) 160;
F.S. Turco, Thesis, Institut National Polytechnique de Grenoble, Grenoble (1988).
- [7] J.M. Moison, C. Guille, F. Houzay, F. Barthe and M. Van Rompay, *Phys. Rev. B* 40 (1989) 6149.
- [8] F. Houzay, J.M. Moison, C. Guille, F. Barthe and M. Van Rompay, *J. Crystal Growth* 95 (1989) 35.
- [9] M.P. Seah and D.A. Dench, *Surface Interface Anal.* 1 (1979) 2;
Ping Chen, D. Bolmont and C.A. Sébenne, *J. Phys. C* 15 (1982) 6101;
C.R. Brundle, *Surface Sci.* 48 (1975) 99.
- [10] C. Guille, F. Houzay, J.M. Moison and F. Barthe, *Surface Sci.* 48 (1975) 99.
- [11] J.Y. Marzin, J.M. Gérard, J.A. Brum and P. Voisin, *Semiconductors and Semimetals* 32 (1990) 55.
- [12] J.Y. Laval, C. Delamarre, A. Dubon, G. Schiffmacher, G. DeSagey and B. Guesnais, in: *Electron Microscopy and Analysis 1985*, Inst. Phys. Conf. Ser. 78, Ed. G.J. Tatlock (Inst. Phys., London-Bristol, 1986) p. 359;
T. Nakamura, M. Ikeda, S. Muto and I. Imebu, *Appl. Phys. Letters* 53 (1988) 379.
- [13] A. Ourmazd, D.W. Taylor, J. Cunningham and C.W. Tu, *Phys. Rev. Letters* 62 (1989) 933.
- [14] C. d'Anterrosches, in: *Proc. NATO Workshop on The Evaluation of Advanced Semiconductor Materials by Electron Microscopy*, Bristol, 1988.
- [15] F. Abel, C. Cohen, C. Guille, F. Houzay, A. l'Hoir, J.M. Moison and D. Schmaus, to be published.
- [16] B. Deveaud, A. Regreny, J.Y. Emery and A. Chomette, *J. Appl. Phys.* 59 (1986) 1633;
M. Tanaka, H. Sakaki, J. Yoshino and T. Furuta, *Surface Sci.* 174 (1986) 65.
- [17] J.Y. Marzin and J.M. Gérard, in: *Proc. NATO Workshop on Spectroscopy of Semiconductor Microstructures*, Venice, 1989, NATO ASI Series B206 (Plenum, New York, 1989).
- [18] J.Y. Marzin and J.M. Gérard, *Phys. Rev. Letters* 62 (1989) 2172.
- [19] B. Jusserand, F. Mollot, J.M. Moison, and G. Le Roux, *Appl. Phys. Letters* 57 (1990) 560.
- [20] M. DelGuidice, M. Grioni, J.J. Joyce, M.W. Ruckman, S.A. Chambers and J.H. Weaver, *Surface Sci.* 168 (1986) 309;
F. Houzay, M. Bensoussan and F. Barthe, *Surface Sci.* 168 (1986) 347;
Zhangda Lin, F. Xu and J.H. Weaver, *Phys. Rev. B* 36 (1987) 5777.
- [21] A. Rosato, K.J. Strandburg, F. Prinz and R.H. Swendsen, *Phys. Rev. Letters* 58 (1987) 1038.
- [22] Y. Gauthier, Y. Joly, R. Baudoin and J. Rundgren, *Phys. Rev. B* 31 (1985) 6216;
G. Trégia and B. Legrand, *Phys. Rev. B* 35 (1987) 4338.
- [23] R. Ludeke, *Surface Sci.* 132 (1983) 143;
C.A. Sébenne, in: *Proc. NATO Workshop on Metallization and Metal-Semiconductor Interfaces*, Ed. I.D. Batra (Plenum, New York, 1989).
- [24] J. Massies, J.F. Rochette and P. Delescluse, *J. Vacuum Sci. Technol. B* 3 (1985) 613;
J. Massies, F. Turco, A. Salettes and J.P. Contour, *Semicond. Sci. Technol.* 2 (1987) 179.
- [25] W.I. Wang, S. Judaprawira, C.E.C. Wood and L.F. Eastman, *Appl. Phys. Letters* 38 (1981) 708;
H. Morkoç, T.J. Drummond, W. Kopp and R. Fisher, *J. Electrochem. Soc.* 129 (1982) 824;
F. Alexandre, L. Goldstein, G. Le Roux, M.C. Joncour, H. Thibierge and E.V.K. Rao, *J. Vacuum Sci. Technol. B* 3 (1985) 950;
A. Regreny, P. Auvray, A. Chomette, B. Deveaud, G. Dupas, J.Y. Emery and A. Poudoulec, *Rev. Physique Appl.* 22 (1987) 273.
- [26] M. Tsuchiya, P.M. Petroff, and L.A. Coldren, *Appl. Phys. Letters* 54 (1989) 1690;
Y.T. Lu, P.M. Petroff and H. Metu, *Appl. Phys. Letters* 57 (1990) 2683.
- [27] J.M. Moison, C. Guille, M. Van Rompay, F. Barthe and F. Houzay, *Phys. Rev. B* 39 (1989) 1772.

Thermodynamic analysis of segregation effects in MBE of A^{III}–B^V compounds

S.V. Ivanov, P.S. Kop'ev and N.N. Ledentsov

A.F. Ioffe Physico-Technical Institute, Academy of Sciences of the USSR, Politekhnikeskaya 26, Leningrad 194021, USSR

The main features of MBE growth (growth rate, composition and doping control) can be predicted in the framework of a thermodynamic description, *ab initio*. In this paper, special attention is given to the thermodynamic analysis of segregation effects (base elements and impurities) as well as to the interplay between impurity surface segregation and diffusion.

1. Introduction

During the first stage of MBE investigations it was generally assumed that this technology is a fundamentally nonequilibrium process and that a thermodynamic consideration is completely inappropriate, so that information on the growth processes can be obtained only by investigation of the surface reaction kinetics. Experiments on modulated beams led to a theory according to which the main role in MBE of III–V compounds is played by elementary processes of atoms and molecules adsorption, migration and desorption on the surface [1]. However, in the case of binary compounds the real growth picture is very complex and cannot be analyzed by simple representations [2].

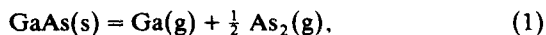
The fact that the MBE process occurs under strongly nonequilibrium conditions does not provide formal justification for the conclusion that it is impossible to use the thermodynamic approach to describe an MBE system on the basis of mass action equations in combination with equations describing conservation of the mass of the interacting elements. This approach is in fact used widely and successfully in the description of many chemical reactions that occur under strongly nonequilibrium conditions. In the case of sublimation of binary compounds (which is also a strongly nonequilibrium process), the conclusions of the thermodynamic description have been confirmed

by numerous experimental data well before the appearance of MBE (see, for example, ref. [3]).

So one may consider the MBE growth as a quasi-equilibrium process where the equilibrium between a vapor phase and a solid phase (or between vapor, liquid and solid phases, in the case of a segregation layer formation) is established at the surface of a growing layer. The system temperature is governed by the substrate temperature, and equilibrium partial pressures are those corresponding to the fluxes of atoms and molecules from the substrate surface, as in ref. [3].

2. MBE of binary compounds

The reactions between the main components in the case of MBE (e.g. GaAs) [4] are:



The equation of mass action for reaction (1) is

$$P_{\text{Ga}} P_{\text{As}_2}^{1/2} / \alpha_{\text{GaAs}} = K_{\text{GaAs}} = 2.73 \times 10^{11} \times \exp(-4.72/kT), \quad (3)$$

where P_{Ga} and P_{As_2} are the partial equilibrium pressures of gallium and arsenic over the substrate surface (in atmospheres), α_{GaAs} is the activity of GaAs in the solid phase equal to 1 for a binary

compound, and K_{GaAs} is the value of the equilibrium constant according to ref. [5]; kT is in eV. In the case of reaction (2), we have [5]:

$$K_{\text{As}} = P_{\text{As}_4} P_{\text{As}_2}^{-2},$$

$$\log K_{\text{As}} = 27.3 \times 10^3/T - 19.8. \quad (4)$$

It follows from the law of mass conservation that

$$P_{\text{Ga}}^0 - P_{\text{Ga}} = P_{\text{As}}^0 - (4P_{\text{As}_4} + 2P_{\text{As}_2}), \quad (5)$$

where P_{As}^0 and P_{Ga}^0 correspond to the fluxes of arsenic and gallium atoms onto the surface. If $T_s \geq 500^\circ\text{C}$ and $P_{\text{As}}^0 = 10^{-5}$ Torr, it follows from eq. (4) that $P_{\text{As}_2} \gg P_{\text{As}_4}$, so that if $P_{\text{As}}^0 \gg P_{\text{Ga}}^0$, $P_{\text{As}}^0 = 2P_{\text{As}_2}$ and

$$v_g = t(P_{\text{III}}^0 - P_{\text{III}})$$

$$= t \left[P_{\text{Ga}}^0 - K_{\text{GaAs}} (P_{\text{As}}^0/2)^{-1/2} \right]. \quad (6)$$

This dependence describes the GaAs growth rate variation with substrate temperature during MBE well [6]. The enthalpy of GaAs evaporation, determined experimentally for MBE conditions in ref. [7], is +4.6 eV (compare with the value 4.72 eV in (3)) and the evaporation rate at a given temperature is inversely proportional to the square root of the arsenic flux, which agrees well with eqs. (3) and (6). When $P_{\text{As}}^0/P_{\text{Ga}}^0 \sim 1$ (under Ga-rich conditions), the value of P_{As_2} is governed by the arsenic partial pressure along the Ga-GaAs liquidus of GaAs [33]:

$$(P_{\text{As}_2}^{\text{GaAs}})^{1/2} = 9.49 \times 10^5 \exp(-1.98/kT). \quad (7)$$

Arsenic precipitates do not form on the GaAs surface in MBE, because at typical substrate temperatures, the equilibrium arsenic pressure over metallic arsenic ranges from a few Torr to tens of atmospheres.

3. MBE of III-V alloys

When a solid solution (for example, $\text{Ga}_x\text{In}_{1-x}\text{As}$) is grown by MBE, the equilibrium partial pressure of more volatile metal component is [8]

$$P_{\text{In}} = \gamma_{\text{InAs}}(1-x)K_{\text{InAs}}P_{\text{As}_2}^{-1/2}$$

$$= (1-x) \exp(\Omega x^2/kT)K_{\text{InAs}}P_{\text{As}_2}^{-1/2}. \quad (8)$$

Synthesis of solid alloys containing two group V elements (for example, $\text{GaAs}_x\text{P}_{1-x}$) is characterized at $T_s \geq 500^\circ\text{C}$ and $P_{\text{As}}^0, P_{\text{P}}^0 \gg P_{\text{Ga}}^0$ [8] by

$$x = \left[(\gamma_{\text{GaAs}}K_{\text{GaAs}}/\gamma_{\text{GaP}}K_{\text{GaP}})(P_{\text{P}}^0/P_{\text{As}}^0)^{1/2} + 1 \right]^{-1}. \quad (9)$$

4. Point defect equilibria

No reliable experimental data for point defect equilibria under the typical MBE growth conditions are available. Nevertheless, the data obtained in LPE and VPE [5] may be used to evaluate the effect of growth parameters and conditions on the point defect concentration in MBE grown layers.

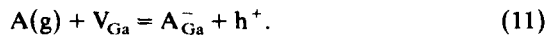
In addition to the reaction in ref. [5], one should use the electroneutrality equation

$$N_{\text{D}} + [\text{As}_i^+] + [\text{V}_{\text{As}}^+] + p = [\text{V}_{\text{Ga}}^-] + N_{\text{A}} + n, \quad (10)$$

where N_{D} and N_{A} are the ionized donor and acceptor concentrations during MBE growth. The calculation in accordance with ref. [5] shows that at typical MBE growth conditions ($T_s > 550^\circ\text{C}$) the ionized arsenic vacancy concentration may be sufficiently high and govern the electroneutrality condition, especially in the case of heavily p-type doping [5,8].

5. Doping in MBE

We shall consider the doping in MBE (for example, the case of an acceptor impurity incorporation from the gaseous phase A(g) into the gallium sublattice of GaAs [9]):



Applying the law of mass action to (11) gives

$$[\text{A}_{\text{Ga}}^-] p / P_{\text{A}} [\text{V}_{\text{Ga}}] = K_{\text{A}}, \quad (12)$$

where p is the hole concentration during growth (h^+), P_{A} is the equilibrium partial pressure of the impurity vapor over the surface corresponding to

the flux from the surface, V_{Ga} is the gallium vacancy, and the square brackets denote the concentration. One should also allow for the electro-neutrality equation

$$p + [V_{\text{As}}^+] + N_{\text{D}^+} = n + N_{\text{A}^-} + [A_{\text{Ga}}^-], \quad (13)$$

and the law of mass conservation

$$P_{\text{Ga}}^0 [A_{\text{Ga}}^-] = P_{\text{A}}^0 - P_{\text{A}}, \quad (14)$$

where P_{A}^0 corresponds to a flux of impurity atoms arriving at the surface [8].

6. More volatile group III element surface segregation in MBE of III-V alloy (Ga in Al_xGa_{1-x}As)

The minimum arsenic equilibrium partial pressure is determined by the arsenic pressure over the Ga-GaAs liquidus given by (7). According to (3), the corresponding gallium partial pressure is

$$P_{\text{Ga}}^{\text{GaAs}} = 2.88 \times 10^5 \exp(-2.74/kT) \quad (15)$$

Thus, in the thermodynamic approach the minimum excess arsenic pressure $P_{\text{As}_2, \text{exc}} = \frac{1}{2} [P_{\text{As}}^0 - (P_{\text{Ga}}^0 - P_{\text{Ga}})]$, which provides the epitaxial growth of GaAs without liquid phase (Ga droplets) formation on the surface, coincides with $P_{\text{As}_2}^{\text{GaAs}}$. The value of $P_{\text{As}_2}^{\text{GaAs}}$ calculated from (7) agrees well with the experimental arsenic pressure corresponding to the transition from As- to Ga-stabilized conditions [11].

In the case of a ternary compound, unlike the binary one, the arsenic equilibrium pressure over the Al-Ga-Al_xGa_{1-x}As liquidus depends on the solid phase composition x and, respectively, on the composition of the liquid phase, which is in equilibrium with it.

The general expression for the Ga equilibrium pressure over the complex liquid phase is [10]:

$$P_{\text{Ga}} = P_{\text{Ga}}' \gamma_{\text{Ga}} [Ga_L], \quad (16)$$

where $[Ga_L]$ and γ_{Ga} are the concentration (in mole percent) and activity coefficient of Ga in the liquid phase respectively; P_{Ga}' is Ga equilibrium pressure over the Ga melt which coincides with $P_{\text{Ga}}^{\text{GaAs}}$ (see (15)) with a very high accuracy.

For the Ga-Al-As liquid phase, which is in equilibrium with the solid solution Al_xGa_{1-x}As, the aluminium and arsenic concentrations are negligible in comparison with gallium at substrate temperatures $T_s < 800^\circ\text{C}$ and solid phase compositions $x < 0.8$ [10], i.e.

$$[As_L] \ll 1, [Al_L] \ll 1, [Ga_L] \sim 1. \quad (17)$$

The calculation of γ_{Ga} according to ref. [10] for $T_s = 700^\circ\text{C}$, and $x = 0.5$ gives the value of $\gamma_{\text{Ga}} = 1.0002$. Thus, in the above temperature and composition regions

$$P_{\text{Ga}}^{\text{L}} = P_{\text{Ga}}^{\text{GaAs}} = 2.88 \times 10^5 \exp(-2.74/kT). \quad (18)$$

The equilibrium equation for the formation of GaAs in the case of Al_xGa_{1-x}As can be written as follows:

$$P_{\text{Ga}} P_{\text{As}_2}^{1/2} = \gamma_{\text{GaAs}} (1-x) \times 2.73 \times 10^{11} \times \exp(-4.72/kT), \quad (19)$$

where γ_{GaAs} is the GaAs activity coefficient in the solid solution ($\gamma_{\text{GaAs}} = 1$ for Al_xGa_{1-x}As [8]). It follows from (18) and (19) for Al_xGa_{1-x}As alloys that the expression for the arsenic equilibrium partial pressure over the Al-Ga-Al_xGa_{1-x}As liquidus is:

$$\begin{aligned} (P_{\text{As}_2}^{\text{L}})^{1/2} &= [(1-x) \times 2.73 \times 10^{11} \exp(-4.72/kT)] \\ &/ P_{\text{Ga}}^{\text{GaAs}} = (1-x) (P_{\text{As}_2}^{\text{GaAs}})^{1/2}. \end{aligned} \quad (20)$$

That is,

$$P_{\text{As}_2}^{\text{L}} = (1-x)^2 P_{\text{As}_2}^{\text{GaAs}}. \quad (21)$$

Fig. 1a shows the dependences of arsenic equilibrium partial pressures $P_{\text{As}_2}^{\text{L}}$ over the Al-Ga-As liquid phase (which is in equilibrium with the solid solution Al_xGa_{1-x}As) on x at different T_s values (see (21)). The excess arsenic partial pressure during a given growth run determined from the mass conservation law is:

$$P_{\text{As}_2, \text{exc}} = \frac{1}{2} [P_{\text{As}}^0 - (P_{\text{Ga}}^0 - P_{\text{Ga}}) - P_{\text{Al}}^0]. \quad (22)$$

P_{Ga} can be calculated from (19) for given $P_{\text{As}_2} = P_{\text{As}_2, \text{exc}}$. P_{Al} is negligible in comparison with com-

monly used P_{Al}^0 at $T_s < 800^\circ\text{C}$. The temperature dependences of P_{Ga} at some fixed values of solid phase compositions x and $P_{As_2,exc}$ are presented in fig. 1b by the dashed and broken lines. The solid line in this figure corresponds to the gallium partial pressure over the Ga-Al- Al_xGa_{1-x} As liquidus (P_{Ga}^L) (see (18)), being the maximum possible Ga pressure. The solid horizontal lines show the beam equivalent pressures of incident Ga flux (P_{Ga}^0) at different growth rates.

Let the excess arsenic pressure $P_{As_2,exc}$ be less than the equilibrium arsenic pressure over the Ga-GaAs liquidus ($P_{As_2}^{GaL}$) ($x = 0$) at given T_s (see fig. 1a, curve 2). Then, there always exists the equilibrium solid phase composition x_{eq} corresponding to this $P_{As_2,exc}$. On the other hand, the composition of the bulk solid phase is determined

by the input gallium and aluminium partial pressures as follows:

$$x_b = P_{Al}^0 / [P_{Al}^0 + (P_{Ga}^0 - P_{Ga})] \quad (23)$$

If, for instance, $x_b = x_1 < x_{eq}$, then a quasi-liquid phase ("floating" Ga layer) should appear on the growth surface, because $P_{As_2,exc}$ during growth is less than $(P_{As_2}^L)_1$, corresponding to the Ga-Al-As liquidus for the composition x_1 .

When the excess arsenic pressure is higher than that determined by the expression (21) for a given bulk solid solution composition (see fig. 1a, the case of $x_b = x_2$), the situation with $x_{surf} = x_2$ (the absence of a Ga segregation layer) may also become equilibrium, since $P_{As_2,exc}$ is higher than the pressure corresponding to the Al-Ga-As liquidus boundary for a given composition. The system

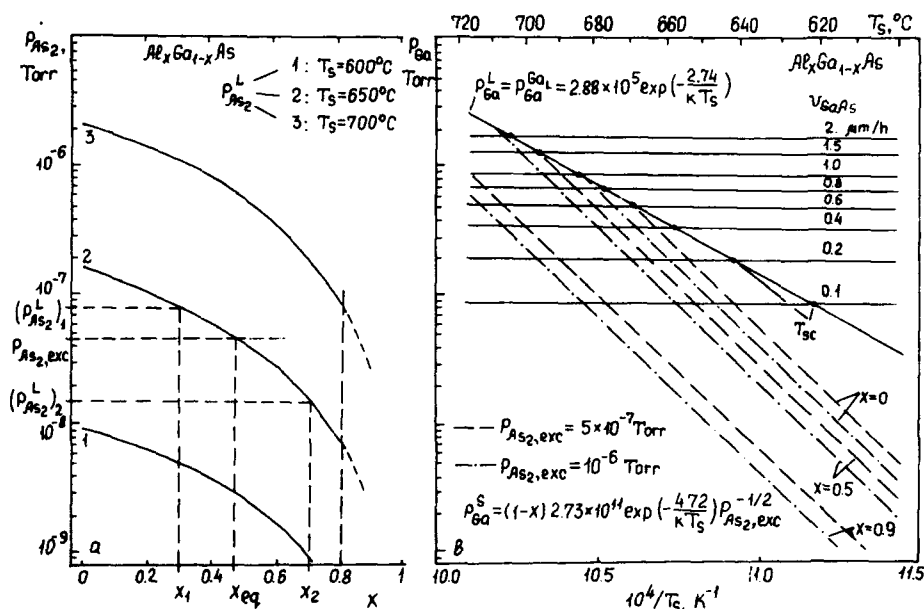


Fig. 1. (a) The arsenic equilibrium partial pressure over the Al-Ga-As liquid phase, which is in equilibrium with the solid solution $Al_xGa_{1-x}As$, versus x at different T_s (solid lines) (see (21)). Scheme of a quasi-liquid phase formation mechanism: x_1 and x_2 are the different bulk compositions (see (23)), and x_{eq} is the equilibrium surface solid phase monolayer composition corresponding to $P_{As_2,exc}$. (b) The temperature dependences of Ga equilibrium partial pressure: over the Al-Ga-As- Al_xGa_{1-x} As liquidus (solid line); over the free surface $Al_xGa_{1-x}As$ solid phase at different x and P_{As_2} (dashed and broken lines). Solid horizontal lines correspond to beam equivalent pressure of incident Ga flux at different growth rates. T_w are the "forbidden" range upper boundaries at different GaAs growth rate component.

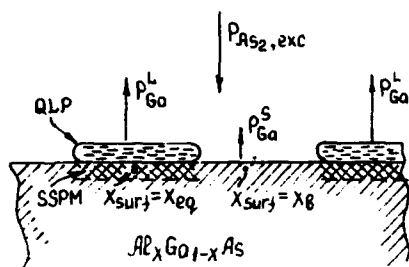


Fig. 2. Schematic diagram of a Ga quasi-liquid phase on the surface of $\text{Al}_x\text{Ga}_{1-x}\text{As}$.

that has a tendency to increase its area with time will be stable during growth. At the same arsenic excess pressure, the gallium equilibrium pressure over the liquid phase is higher than that over the solid $\text{Al}_x\text{Ga}_{1-x}\text{As}$ (see fig. 1b). This means that the Ga vapour over the liquid phase regions is supersaturated with respect to the free $\text{Al}_x\text{Ga}_{1-x}\text{As}$ surface regions and will evidently give rise to the condensation of Ga atoms on the free alloy surface. Since the gallium atom flux from the surface corresponding to the equilibrium partial pressure is maximum over the liquid phase regions, the GaAs component of the $\text{Al}_x\text{Ga}_{1-x}\text{As}$ growth rate for these regions is lower and the solid solution composition x_b is higher, as follows from the mass conservation law (see (6) and (23)). Furthermore, the higher growth rate in the free surface regions should prevent quasi-liquid phase propagation over the substrate surface, giving rise to the formation of localized liquid phase islands. A schematic diagram of Ga quasi-liquid phase on the surface of $\text{Al}_x\text{Ga}_{1-x}\text{As}$ is presented in fig. 2.

It is obvious that this quasi-liquid phase formation may cause composition and thickness nonuniformity over the substrate surface and, hence, be the origin of the $\text{Al}_x\text{Ga}_{1-x}\text{As}$ surface morphology degradation. The increase of x_b , i.e. the decrease of P_{Ga}^S compared to P_{Ga}^L , should result in a rougher morphology for the same growth time.

Thus, to prevent Ga segregation layer formation during the growth of $\text{Al}_x\text{Ga}_{1-x}\text{As}$, it is necessary either for the arsenic excess pressure to be higher than its equilibrium partial pressure over the Ga-GaAs liquidus at a given T_s (As-stabilized growth conditions), or for the beam equivalent

pressure of the Ga incident flux P_{Ga}^0 to be lower than the gallium equilibrium partial pressure along the Ga-GaAs liquidus (but higher than P_{Ga}^S) (see fig. 1b, the T_{sc} values determine the upper substrate temperature "forbidden" range boundaries). In this case the Ga "floating" layer cannot appear because of evaporation. The latter can be reached by both an increase of the substrate temperature and a decrease of the GaAs growth rate component.

Another way is a predeposition of several Ga monolayers immediately before the growth of $\text{Al}_x\text{Ga}_{1-x}\text{As}$, i.e. when the quasi-liquid phase just begins to form. The growth through this liquid thermodynamically-stable and uniform Ga floating layer ("floating layer epitaxy") allowed us to obtain high quality $\text{Al}_{0.35}\text{Ga}_{0.65}\text{As}$ layers with nearly smooth morphology ($\sim 1 \mu\text{m}$ thick; $n_{300\text{K}} = 1.5 \times 10^{16} \text{ cm}^{-3}$, $\mu_{300\text{K}} = 1140 \text{ cm}^2/\text{V} \cdot \text{s}$, $n_{77\text{K}} = 2.2 \times 10^{16} \text{ cm}^{-3}$, $\mu_{77\text{K}} = 1600 \text{ cm}^2/\text{V} \cdot \text{s}$; FWHN of the PL peak corresponds to that of GaAs) at an intermediate substrate temperature ($T_s \sim 650^\circ\text{C}$, i.e. inside the "forbidden" range) even in poor vacuum conditions. The better results may seem to be obtained with this method when growth interruptions are used after each 200–500 Å of Al-GaAs growth to evaporate this Ga floating layer and, then, to form it again.

Fig. 3 shows the calculated temperature dependence of arsenic equilibrium partial pressure over the Ga-GaAs liquidus and over the Al-Ga-As liquid phase, which is in equilibrium with $\text{Al}_x\text{Ga}_{1-x}\text{As}$ solid solution (dashed lines, see (21)). The dotted line is the minimum possible arsenic beam equivalent pressure experimentally obtained in ref. [11], corresponding to the transition from As- to Ga-stabilized conditions on the GaAs surface at zero growth rate. The temperature dependence of minimum possible arsenic beam equivalent pressure at which the Al-Ga-As quasi-liquid phase does not appear according to the model proposed is presented in fig. 3 by the solid lines which correspond to different alloy growth rates. These last dependences were calculated using the expression:

$$P_{\text{As}_2}^0 = \frac{1}{2} [(P_{\text{Ga}}^0 - P_{\text{Ga}}) + P_{\text{Al}}^0] + (P_{\text{As}_2}^{\text{Ga}_1})', \quad (24)$$

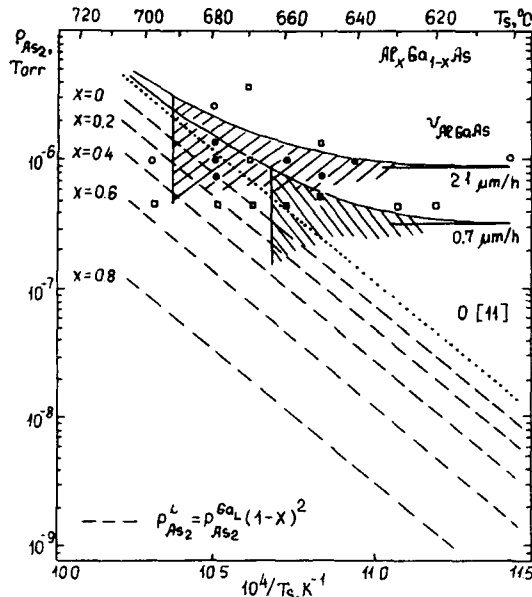


Fig. 3. The experimentally obtained (in ref. [11]) minimum possible arsenic beam equivalent pressure corresponding to the transition from As- to Ga-stabilized conditions on the GaAs surface at zero growth rate (dotted line). The calculated temperature dependences of arsenic equilibrium partial pressure over the Al-Ga-As-Al_xGa_{1-x}As liquidus at different x (dashed lines) and minimum possible arsenic beam equivalent pressure, which are necessary to provide As-stabilized growth conditions at different alloy growth rates of 2.1 and 0.7 $\mu\text{m/h}$ (solid lines). The shaded regions show the theoretically predicted growth condition ranges, within which a Ga segregation layer should appear at the growth rates of 2.1 and 0.7 $\mu\text{m/h}$. The full and open circles are the experimental data of ref. [13], corresponding to rough and smooth morphology of Al_{0.3}Ga_{0.7}As layers, respectively, provided that the arsenic beam equivalent pressure for the layer grown at 600 °C is believed to be equal to 10^{-6} Torr. Our experimental results for the Al_{0.3}Ga_{0.7}As growth rate of 0.7 $\mu\text{m/h}$ are also shown by closed (rough morphology) and open (smooth morphology) squares.

where $P_{\text{As}_2}^{\text{GaAs}}$ is taken from the experimental curve (dotted line). As is seen from fig. 3, the effect of a $(P_{\text{As}_2}^{\text{GaAs}})'$ increase becomes noticeable within the substrate temperature range of 630–640 °C, which is in a good agreement with the lower boundary of the T_s “forbidden” range [12–14]. It is obvious that the larger the solid solution growth rate at the same V/III ratio, the larger $P_{\text{As}_2, \text{exc}}$ and, hence, the higher the lower “forbidden” range boundary.

According to our consideration, the very low solid solution growth rates and high V/III ratio should result in the disappearance of a T_s “forbidden” range because of the merging of its upper and lower boundaries (see fig. 1b and fig. 3).

The shaded regions in fig. 3 show the growth condition ranges within which, according to the thermodynamic analysis, a Ga segregation layer should appear at the growth rates of 2.1 and 0.7 $\mu\text{m/h}$. The full and open circles are the experimental data of ref. [13] corresponding to rough and smooth morphology of Al_{0.3}Ga_{0.7}As layers respectively. Our experimental results for the Al_{0.3}Ga_{0.7}As growth rate of 0.7 $\mu\text{m/h}$ are also shown by closed and open squares (rough and smooth morphology respectively). The experimental conditions and the method of arsenic excess pressure measurement and calculation are practically the same as in ref. [25].

The case of indium segregation on the surface of Ga_{1-x}In_xAs and Al_{1-x}In_xAs can be considered in the same way.

7. Dopant segregation in MBE of III–V compounds (Sn segregation in GaAs)

At present the kinetic models of the impurity segregation process in MBE are widely used [15]. Among them, the segregation models for tin in GaAs are the most developed [16,17]. The first thermodynamic consideration of tin doping of GaAs was performed in refs. [4,18].

Here, using the thermodynamic approach developed in the previous section, we consider the arsenic equilibrium partial pressure over the Ga–As–Sn liquid phase, which is in equilibrium with GaAs doped with Sn.

Within the substrate temperature range of interest ($T_s < 800$ °C), the arsenic concentration in the liquid phase can be neglected [19]:

$$[\text{As}_L] \ll 1, \quad [\text{Ga}_L] + [\text{Sn}_L] \approx 1. \quad (25)$$

The gallium equilibrium partial pressure over the Ga–Sn–GaAs : Sn liquidus is as follows (see (16)):

$$P_{\text{Ga}}^{(\text{Ga-Sn})_L} = \gamma_{\text{Ga}} [\text{Ga}_L] P_{\text{Ga}}^{\text{GaAs}}, \quad (26)$$

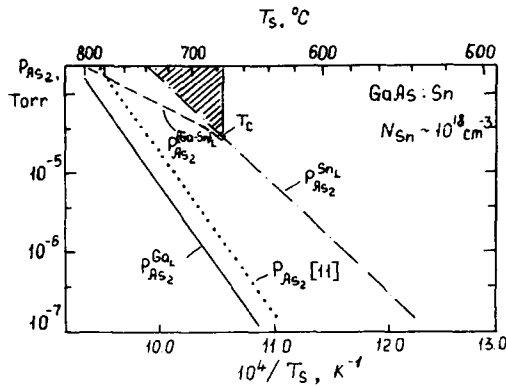


Fig. 4. The temperature dependences of arsenic equilibrium partial pressure: over the Ga-GaAs liquidus (see (7)) (solid line), over the Ga-As-Sn liquid phase, which is in equilibrium with GaAs doped with Sn up to the concentration $\sim 10^{18} \text{ cm}^{-3}$ ($P_{\text{As}_2}^{\text{Ga-As-Sn}}$) (dashed line), and over the GaAs saturated solution in Sn ($P_{\text{As}_2}^{\text{Sn}}$) [20] (broken line). The dotted line is the same as in fig. 3. The shaded region corresponds to growth conditions at which the Sn segregation layer cannot occur at a doping level of $\sim 10^{18} \text{ cm}^{-3}$.

where γ_{Ga} is the Ga activity coefficient in the liquid phase. The calculation of γ_{Ga} using ref. [10] for $T_s = 700^\circ \text{C}$ and Sn concentration in GaAs $\sim 10^{18} \text{ cm}^{-3}$ ($[\text{Sn}_L] \sim 0.8$, $[\text{As}_L] \sim 0.015$, $[\text{Ga}_L] \sim 0.2$) [19,32] gives the value $\gamma_{\text{Ga}} = 1.04$. Further, taking into account the fact that $\gamma_{\text{Ga}} = 1$, we obtain from (3), (7), (15), (25) and (26) the following expression for the arsenic equilibrium pressure:

$$P_{\text{As}_2}^{\text{Ga-As-Sn}} = P_{\text{As}_2}^{\text{GaAs}} / (1 - [\text{Sn}_L])^2. \quad (27)$$

Fig. 4 presents the temperature dependences of arsenic equilibrium partial pressure: (1) over the Ga-GaAs liquidus boundary ($P_{\text{As}_2}^{\text{GaAs}}$), (2) over the Ga-As-Sn liquid phase (Ga-rich), which is in equilibrium with GaAs doped with Sn up to the concentration $\sim 10^{18} \text{ cm}^{-3}$ ($P_{\text{As}_2}^{\text{Ga-As-Sn}}$) (calculated according to (27) using the data of Hurle [32]), and (3) over the GaAs saturated solution in Sn ($P_{\text{As}_2}^{\text{Sn}}$) [20], which is the maximum arsenic equilibrium pressure for tin-rich solution. The interception point of the $P_{\text{As}_2}^{\text{Ga-As-Sn}}$ and $P_{\text{As}_2}^{\text{Sn}}$ dependences determines the minimum critical substrate temperature (T_c) at which a given Sn doping concentration corresponds to the maximal Sn con-

centration in the melt (maximal tin vapor pressure).

By analogy with the gallium segregation case, one can show that $P_{\text{As}_2, \text{exc}}$ should exceed $P_{\text{As}_2}^{\text{Sn}}$ at given $T_s > T_c$ to prevent Sn surface segregation, i.e. it should be essentially increased compared to the pressure commonly used to grow undoped GaAs (compare solid and broken lines in fig. 4). When $P_{\text{As}_2, \text{exc}}$ is increased to a value higher than $P_{\text{As}_2}^{\text{Sn}}$, the liquid phase becomes tin depleted, so $P_{\text{As}_2}^{\text{Sn}}$ decreases and $P_{\text{As}_2}^{\text{Sn}}$ over the tin-rich solid phase becomes higher than $P_{\text{As}_2}^{\text{Sn}}$. In this case the quasi-liquid phase seems to be unstable. The shaded region in fig. 4 corresponds to growth conditions at which the Sn segregation layer cannot occur at a doping level of $\sim 10^{18} \text{ cm}^{-3}$.

8. Interplay of impurity segregation and diffusion in MBE (Be in GaAs)

In general, impurity segregation depends on the rate of atom arrival from the bulk to the surface. Thus it is necessary to take into consideration the balance of the atomic fluxes (the mass conservation law). This is true for the case of Be in GaAs. In this case by analogy with that of Sn in GaAs, we may consider the arsenic equilibrium pressure over the Ga-As-Be quasi-liquid phase, which is in equilibrium with GaAs heavily doped with Be. Although the Be melting point is 1283°C , the Be-rich surface segregation layer may be regarded as the quasi-liquid phase, which we assume to be thin enough for Be microprecipitates not to form. It will also be a reasonable assumption to neglect the arsenic concentration in the quasi-liquid phase at the substrate temperatures of interest, i.e.

$$[\text{As}_L] \ll 1, \quad [\text{Be}_L] + [\text{Ga}_L] \approx 1. \quad (28)$$

Omitting intermediate calculation procedures, one can obtain

$$P_{\text{As}_2}^{\text{Be-GaAs}} = P_{\text{As}_2}^{\text{GaAs}} / (1 - [\text{Be}_L])^2, \quad (29)$$

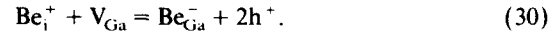
where $P_{\text{As}_2}^{\text{GaAs}}$ is the arsenic equilibrium pressure over the Ga-GaAs liquidus of undoped GaAs, and the Ga activity coefficient in the quasi-liquid phase is taken equal to 1 for a simplicity.

Thus, as it follows from (29) at $T_s \approx 600$ – 630°C , when $P_{\text{As}_2}^{\text{Ga}_L}$ becomes noticeable, and at high Be concentration in the quasi-liquid phase, $[\text{Be}_L] \sim 1$, $([\text{Be}_{\text{Ga}}^-] \sim [\text{Be}_{\text{Ga}}^-]_{\text{max}}$ for a Be-rich melt), the As equilibrium pressure over the Ga-Be-GaAs:Be liquidus $P_{\text{As}_2}^{\text{Be}_L} = (P_{\text{As}_2}^{\text{Ga-Be}_L})_{\text{max}}$ becomes much higher than $P_{\text{As}_2}^{\text{Ga}_L}$. At low temperatures of about 500°C , $P_{\text{As}_2}^{\text{Ga-Be}_L}$ should be small enough due to the commonly observed decrease in the As solubility in a metal solution with temperature.

As is also seen from (29), the dependence of $P_{\text{As}_2}^{\text{Ga-Be}_L}$ on $[\text{Be}_{\text{Ga}}^-]$ is very steep only in the vicinity of $[\text{Be}_{\text{Ga}}^-]_{\text{max}}$. So any $P_{\text{As}_2, \text{exc}}$ high enough compared to $P_{\text{As}_2}^{\text{Ga}_L}$ will be in equilibrium with a surface

solid phase layer with very high beryllium concentration close to $[\text{Be}_{\text{Ga}}^-]_{\text{max}}$. This means that, in practice, for MBE Be doping of GaAs under the As-rich condition, when the Be bulk concentration is low enough compared to the Be concentration corresponding to Be-rich melt ($[\text{Be}_{\text{Ga}}^-]_b \leq 10^{20} \text{ cm}^{-3}$), the Be concentration in the surface solid phase layer must be close to $[\text{Be}_{\text{Ga}}^-]_{\text{max}}$.

As has been proposed by Miller et al. [21] and confirmed experimentally by Miller and Asbeck [22], the diffusion of Be in GaAs (and AlGaAs) may proceed by a movement of the highly mobile positively charged Be interstitials (Be_i^+), while the resulting profile of electrically active substitutional Be acceptors is determined by an interaction of these interstitials with gallium vacancies [21]:



The concentration of interstitials is assumed to be small compared to substitutional, i.e. $[\text{Be}_i^+] \ll [\text{Be}_{\text{Ga}}^-]$. Applying the law of mass action to (30) gives:

$$K_{\text{Be}}^{\text{dif}} = [\text{Be}_{\text{Ga}}^-] p^2 / [\text{Be}_i^+] [V_{\text{Ga}}]. \quad (31)$$

According to ref. [23], the expression for the Be diffusion coefficient can be written as:

$$D_{\text{Be}} \sim [\text{Be}_i^+] / [\text{Be}_{\text{Ga}}^-] = (K_{\text{Be}}^{\text{dif}})^{-1} p^2 / [V_{\text{Ga}}]. \quad (32)$$

For $[\text{Be}_{\text{Ga}}^-] > 10^{18} \text{ cm}^{-3}$ and T_s in the range of 500 – 700°C , the Be diffusion coefficient for MBE growth may be written as (all symbols as in ref. [5]):

$$\begin{aligned} D_{\text{Be}} &\sim K_{\text{cv}}^2 K_{\text{As}_2}^1 (K_{\text{fa}} K_{\text{av}}^2 K_{\text{s}} K_{\text{Be}}^{\text{dif}})^{-1} P_{\text{As}_2}^{1/2} [\text{Be}_{\text{Ga}}^-]^2 \\ &= K_1 [\text{Be}_{\text{Ga}}^-]^2, \end{aligned} \quad (33)$$

where K_1 is a proportionality coefficient depending on the temperature and having a comparatively weak dependence on the arsenic equilibrium pressure. Using the Be diffusion coefficients experimentally measured at different doping levels and substrate temperatures and taking into account (33), it is possible to estimate the distance (L), which is reached by the diffusion front in one second after a contact of doped and undoped regions

$$L = \sqrt{D_{\text{Be}}} \sim [\text{Be}_{\text{Ga}}^-]. \quad (34)$$

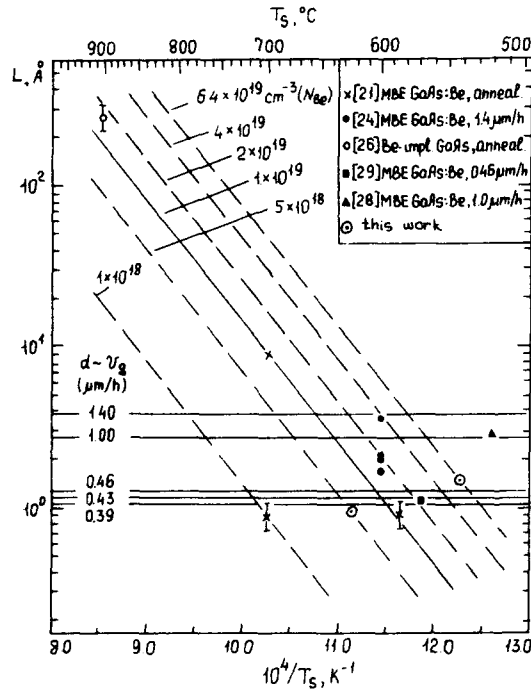


Fig. 5. The temperature dependences of diffusion length in 1 s (L) at different Be doping levels (the solid line at $1 \times 10^{19} \text{ cm}^{-3}$ corresponds to the experimental data of ref. [21] (\times), the dashed lines are calculated with respect to that according to (34)). The solid horizontal lines show layer thicknesses in 1 s (d) at different growth rates. Comparison of experimental and theoretical results on the annealing of GaAs:Be layers and on the effect of growth parameters and doping levels on the onset of fast Be in-diffusion and surface morphology degradation in MBE GaAs:Be (see text).

Let d signify the thickness of the GaAs layer grown in 1 s. If $L > d$, the Be concentration in a surface monolayer reaches $[\text{Be}_{\text{Ga}}^-]_b$ for its growth time even without the input Be flux. Thus, the input Be flux turns excessive and may lead to surface enrichment with beryllium and, as a consequence, segregation layer formation, if this is thermodynamically favourable.

Fig. 5 presents the L (see (34)) temperature dependences at different Be doping levels. They were plotted using the experimental data of high resolution secondary ion mass spectroscopy (SIMS) profile measurements of Miller et al. [21] at 1×10^{19} and $1 \times 10^{18} \text{ cm}^{-3}$ (crosses and solid line) and the data of ref. [24] at 600°C from the normal Be diffusion region (four closed circles in the range of $(1.4-3.8) \times 10^{19} \text{ cm}^{-3}$), which agree well with the square-law dependence of the diffusion coefficient on $[\text{Be}_{\text{Ga}}^-]$ (32). The other dependences (dashed lines) were calculated according to (34), assuming the same diffusion coefficient behaviour with temperature. One should note the good agreement between the Be diffusion coefficients in the Be-implanted up to $2.2 \times 10^{19} \text{ cm}^{-3}$ GaAs layer annealed at 900°C , which was referred to in ref. [26], (open circle), and the later reported data on as-grown MBE GaAs:Be. An estimation of the D_{Be} temperature dependence from fig. 5 gives

$$D_{\text{Be}} \sim \exp[(-3.0 \pm 0.2)/kT]. \quad (35)$$

Further, the horizontal solid lines show the d values corresponding to different growth rates.

Usually the arsenic excess pressure during growth is higher than $P_{\text{As}_2}^{\text{eq}}$, corresponding to any given beryllium bulk doping level according to (29), but less than $P_{\text{As}_2}^{\text{Be}_1}$. The Be concentration $[\text{Be}_{\text{Ga}}^-]_b$ is determined by the Be to Ga flux ratio [8]

$$[\text{Be}_{\text{Ga}}^-]_b \approx P_{\text{Be}}^0/P_{\text{Ga}}^0. \quad (36)$$

At low $[\text{Be}_{\text{Ga}}^-]_b$, the diffusion coefficients are very small and all the Be atoms arriving onto the growth surface incorporate as substitutional acceptors on the Ga sites. As $[\text{Be}_{\text{Ga}}^-]_b$ rises, L increases. At last, when $L \geq d$, the input Be flux becomes excessive and a quasi-liquid phase of segregated Be atoms arises. It is in equilibrium

with the surface solid phase monolayer (SSPM) with $[\text{Be}_{\text{Ga}}^-] = [\text{Be}_{\text{Ga}}^-]_{\text{surf}} > [\text{Be}_{\text{Ga}}^-]_b$. Since the beryllium concentration at the SSPM is much higher than the bulk one, the Be interstitial concentration $[\text{Be}_i^+]$ in the SSPM drastically increases (it may be shown that $[\text{Be}_i^+] \sim [\text{Be}_{\text{Ga}}^-]^3$). Thus, in this case the growth surface serves as Be interstitial generation region stimulating the strong Be diffusion into the bulk. This makes it impossible to obtain a high Be concentration in a thin layer. This claim is confirmed by the data of Pao et al. [24], who observed the drastic increase in Be diffusion coefficient from $\sim 1.4 \times 10^{-15}$ to $\sim 2 \times 10^{-12} \text{ cm}^2/\text{s}$ with a Be doping increase from $\sim 3.8 \times 10^{19}$ to $\sim 5.3 \times 10^{19} \text{ cm}^{-3}$ at 600°C and growth rate of $1.4 \mu\text{m}/\text{h}$ (see fig. 5, closed circles and the solid horizontal line corresponding to $v_g = 1.4 \mu\text{m}/\text{h}$). In the case of thin heavily doped layers, this effect prevents the Be segregation layer from appearing, because the strong increase in Be in-diffusion results in the increase of the doped layer thickness, with P_{Be}^0 , instead of in the increase of $[\text{Be}_{\text{Ga}}^-]$. On the other hand, the increase of Be_i^+ concentration in the growing layer, which was found in ref. [30] to participate in the formation of nonradiative centers, may result in a pronounced reduction of luminescence intensity [31] at doping levels determined by the condition of $L \approx d$.

Further, as the substrate temperatures commonly used in MBE are small compared to the beryllium melting point (1223°C), it is possible for segregated Be atoms to form solid phase precipitates on the growth surface, leading to the layer morphology deterioration. The morphology degradation has been also reported in ref. [28] to be normally associated with the onset of the fast Be diffusion.

To prevent the Be segregation layer formation in the case when $d \leq L$ at constant growth rate and Be doping level, it is necessary either to reduce the substrate temperature for $P_{\text{As}_2}^{\text{Be}_1}$ to be less than the $P_{\text{As}_2, \text{exc}}$ used (see (29)) or to increase $P_{\text{As}_2, \text{exc}}$. The former has been demonstrated by L'evin and Alexandre [27], when reducing the substrate temperature from 550 to 500°C at a Be concentration of $1 \times 10^{20} \text{ cm}^{-3}$. Recently Pao et al. [28] have succeeded in suppressing the fast Be diffusion completely and obtaining good surface

morphology by a strong increase of the As_4/Ga ratio. This has been found to be possible only at $T_s = 520^\circ C$ for a Be concentration of $1 \times 10^{20} \text{ cm}^{-3}$, but not at $T_s = 580^\circ C$. This result also agrees well with the conclusions from eq. (29). Moreover, the D_{Be} measured in ref. [28] at an As_4/Ga ratio corresponding to the transition from fast to normal Be diffusion had a value at which L is equal to d at the growth rate of $1 \mu\text{m/h}$ (see fig. 5, closed triangle at $520^\circ C$).

It is also obvious from the model proposed that the effects connected with the Be surface segregation could be observed at the lower doping levels, if the growth rates are small enough. Iimura and Kawabe [29] reported the transition from smooth to rough morphology at $2.2 \times 10^{19} \text{ cm}^{-3}$ at a growth rate of $0.46 \mu\text{m/h}$ (closed square in fig. 5 at $T_s = 570^\circ C$). The same transition was observed in this work at $v_g = 0.39 \mu\text{m/h}$ and the lower doping level of $\sim 5 \times 10^{18} \text{ cm}^{-3}$ (encircled dot in fig. 5 at $T_s = 620^\circ C$) (for the experimental conditions, see elsewhere [25]). The encircled dot at $T_s = 540^\circ C$ corresponds to a smooth surface morphology layer with $p = 6.4 \times 10^{19} \text{ cm}^{-3}$ grown at $v_g = 0.43 \mu\text{m/h}$ and at an arsenic excess pressure much higher compared to the undoped GaAs growth.

9. Conclusion

One may conclude that the thermodynamic description of segregation effects in MBE of $III-V$ compounds proposed here is in good qualitative and in some cases quantitative agreement with the experimental results, and provides a very useful guide for controllable change of growth parameters to obtain high quality epitaxial structures with abrupt composition and doping profiles and perfect surface morphology. This approach may be used for the description of MBE growth and doping of other semiconductor compounds, such as $II-VI$, $Si-Ge$, etc.

References

- [1] C.T. Foxon, *Acta Electron.* 21 (1978) 139.
- [2] A. Madhukar, *Surface Sci.* 132 (1983) 344.
- [3] F.A. Kröger, *The Chemistry of Imperfect Crystals* (North-Holland, Amsterdam, 1964).
- [4] R. Heckingbottom, G.J. Davies and K.A. Prior, *Surface Sci.* 132 (1983) 375.
- [5] D.T.J. Hurle, *J. Phys. Chem. Solids* 40 (1979) 613.
- [6] R. Heckingbottom, *J. Vacuum Sci. Technol.* B3 (1985) 572.
- [7] J.M. Van Hove and P.I. Cohen, *Appl. Phys. Letters* 47 (1985) 727.
- [8] P.S. Kop'ev and N.N. Ledentsov, *Soviet Phys.-Semicond.* 22 (1988) 1093.
- [9] N.N. Ledentsov, B.Ya. Ber, P.S. Kop'ev, S.V. Ivanov, B.Ya. Meltser and G.M. Minchev, *Zh. Tekh. Fiz.* 35 (1985) 142.
- [10] M.B. Panish and M. Ilegems, in: *Progress in Solid State Chemistry*, Vol. 7, Ed. H. Reiss and J. McCaldin (Pergamon, Oxford, 1972) p. 39.
- [11] J.C. Harmand, F. Alexandre and J. Beerens, *Rev. Physique Appl.* 22 (1987) 821.
- [12] R.A. Stall, J. Zilko, V. Swaminathan and N. Schumaker, *J. Vacuum Sci. Technol.* B3 (1985) 524.
- [13] F. Alexandre, L. Goldstein, G. Leroux, M.C. Joncour, H. Thiberge and E.V.K. Rao, *J. Vacuum Sci. Technol.* B3 (1985) 950.
- [14] H. Morkoç, T.J. Drummond, W. Kopp and R. Fisher, *J. Electrochem. Soc.* 129 (1982) 824.
- [15] J.E. Greene, S.A. Barnett, A. Rockett and G. Bajor, *Appl. Surface Sci.* 22/23 (1985) 520.
- [16] C.E.C. Wood and B.A. Joyce, *J. Appl. Phys.* 49 (1978) 4854.
- [17] J. Harris, D.E. Ashenford, C.T. Foxon, P.J. Dobson and B.A. Joyce, *Appl. Phys.* A 33 (1984) 87.
- [18] R. Heckingbottom, in: *Molecular Beam Epitaxy and Heterostructures*, Eds. L.L. Chang and K. Ploog (Nijhoff, Dordrecht, 1985).
- [19] D. Dutartre and M. Gavand, *J. Crystal Growth* 66 (1984) 647.
- [20] S.S. Strelchenko and V.V. Lebedev, $A^{III}-B^V$ Compounds (Metallurgiya, Moscow, 1984) (in Russian).
- [21] J.N. Miller, D.M. Collins and N.J. Moll, *Appl. Phys. Letters* 46 (1985) 960.
- [22] D.L. Miller and P.M. Asbeck, *J. Appl. Phys.* 57 (1985) 1816.
- [23] F.C. Frank and D. Turnbull, *Phys. Rev.* 104 (1956) 617.
- [24] Yi. Ching Pao, T. Hierl and T. Cooper, *J. Appl. Phys.* 60 (1986) 201.
- [25] P.S. Kop'ev, S.V. Ivanov, A.Yu. Yegorov and D. Yu. Uglov, *J. Crystal Growth* 96 (1989) 533.
- [26] W.V. McLevige, K.V. Vaidyanathan, B.G. Streetman, M. Ilegems, J. Comas and L. Plew, *Appl. Phys. Letters* 33 (1978) 127.
- [27] J.L. Lievin and F. Alexandre, *Electron. Letters* 21 (1985) 413.
- [28] Y.C. Pao, J. Franklin and J.S. Harris, Jr., *J. Crystal Growth* 95 (1989) 301.
- [29] Y. Iimura and M. Kawabe, *Japan. J. Appl. Phys.* 25 (1986) L81.

- [30] N. Duhamel, P. Henoc, F. Alexandre and E.V.K. Rao, Appl. Phys. Letters 39 (1981) 49.
- [31] J.F. Bresse and A.C. Papadopoulos, Appl. Phys. Letters 51 (1987) 183.
- [32] D.T.J. Hurle, J. Phys. Chem. Solids 40 (1979) 639.
- [33] M. Tmar, A. Gabriel, C. Chatillion and I. Ansara, J. Crystal Growth 69 (1984) 421.

Nonlinear diffusion equation for epitaxial growth and recovery on vicinal surfaces

Andrea K. Myers-Beaghton and Dimitri D. Vvedensky

The Bluckett Laboratory and Interdisciplinary Research Centre for Semiconductor Materials, Imperial College, London SW7 2BZ, UK

Recently, we derived a theoretical model for molecular-beam epitaxy (MBE) on vicinal surfaces that includes both adatom diffusion and a nonlinear term for diatomic island formation. The model was shown to reproduce and explain both the transient behavior of reflection high-energy electron-diffraction measurements of MBE on stepped surfaces and their dependence on the growth conditions. Here, we refine the model to include the formation of higher-atomic islands (with up to ten atoms) as well as their decay and incorporate a simple model for atom attachment and detachment kinetics at the step edges. We show that incorporation of island break-up is necessary for a realistic model of recovery.

1. Introduction

A realistic model of molecular-beam epitaxy (MBE) on vicinal (stepped) surfaces must include both the migration of adatoms on the substrate and the interaction among these adatoms in the form of cluster formation and break-up. Previous analytical models of MBE growth have generally treated each process separately. Kinetic rate equations can be used to model island formation alone [1]; however, this approach is not suitable for stepped surfaces for which a diffusion-controlled concentration gradient is present along the terraces. A different approach is based on the near-equilibrium crystal growth theory of Burton, Cabrera and Frank (BCF) [2], in which linear diffusion equations are solved for the step velocity and adatom concentration along the terrace. Extensions of this theory to MBE have been reported which include corrections due to the non-equilibrium growth conditions [3–6]. However, although it was recognized that nucleation phenomena would be important under typical MBE conditions [7,8], none of these treatments have explicitly combined both adatom diffusion and a mechanism for island formation.

Recently we have introduced a theoretical model for MBE on vicinal surfaces based on the BCF diffusion equations which includes a nonlinear term for the formation of diatomic islands in

addition to adatom diffusion [9,10]. The inclusion of a mechanism for nucleation was shown to be essential to reproduce and explain the transient behavior of reflection high-energy electron diffraction (RHEED) measurements of MBE growth on stepped surfaces [10]. In this paper, we show how this model can be further extended to model recovery processes as well as growth by including formation of higher order islands and island break-up. We also discuss the difficulties of including the intrinsically two-dimensional kinetics of atom attachment and detachment at the step edges into the one-dimensional model.

2. Theoretical model

First, we briefly review the original theory, before incorporation of atom detachment kinetics and higher-order island formation is discussed. The vicinal surface consists of an infinite train of flat terraces of width h in the x -direction (fig. 1). The effective diffusion equation for the adatom concentration $n(x, t)$ in the continuum limit is

$$\begin{aligned} \frac{\partial n(x, t)}{\partial t} &= D \frac{\partial^2 n(x, t)}{\partial x^2} + J + v(t) \frac{\partial n(x, t)}{\partial x} \\ &\quad - R[n(x, t)], \\ n(0, t) &= n(h, t) = 0. \end{aligned} \quad (1)$$

The above equation is written with respect to a coordinate system moving with the velocity $v(t)$ of the steps. In (1), D is the diffusion constant of the adatoms on the terraces, J is the adatom flux to the surface, and $R[n]$ is the rate of adatom nucleation, specified below. The diffusion constant is taken to be

$$D = \nu a^2 \exp(-E_D/k_B T),$$

where ν is an adatom vibrational frequency on the order of 10^{13} s^{-1} , a is the nearest-neighbor hopping distance, E_D is the effective activation energy for diffusion of a lone adatom, k_B is Boltzmann's constant, and T is the substrate temperature.

In the original model, we included adatom nucleation on the terraces to a first-order approximation by allowing the formation only of diatomic islands. We now consider inclusion of higher-order island-formation as well as a mechanism for break-up of the islands. The concentration of a species with j atoms is denoted by $n_j(x, t)$. We assume that an adatom attached to an island detaches itself from the island with a probability per unit time of k_d . Thus the net rate at

which an island with j atoms is formed is given by:

$$\begin{aligned} R_j(n_1, n_{j-1}, n_j, n_{j+1}) \\ = \sigma D n_1 (n_{j-1} - n_j) + J \left(m_{j-1} \frac{n_{j-1}}{n_0} - m_j \frac{n_j}{n_0} \right) \\ - k_d (n_j - n_{j+1}), \quad j \geq 2. \end{aligned} \quad (2)$$

The first term on the right-hand side of (2) represents the rate at which single mobile adatoms collide with existing atoms or islands and is proportional to D and to σ , a capture efficiency of order one [1]. The second term accounts for the direct collision of incoming atoms with adsorbed adatoms or islands and is proportional to the total fraction of incoming adatoms that arrive at island-forming sites, n_j/n_0 , where n_0 is the concentration of lattice sites. The factor m_j is the number of sites around an adsorbed entity with j atoms that will form a $(j+1)$ -atom island when filled. The third term accounts for island decay.

If we now assume that islands have a finite probability of breaking up, then we must also include the detachment of single adatoms from the step edge. We employ boundary conditions [6,11] which identify the flux into the step from

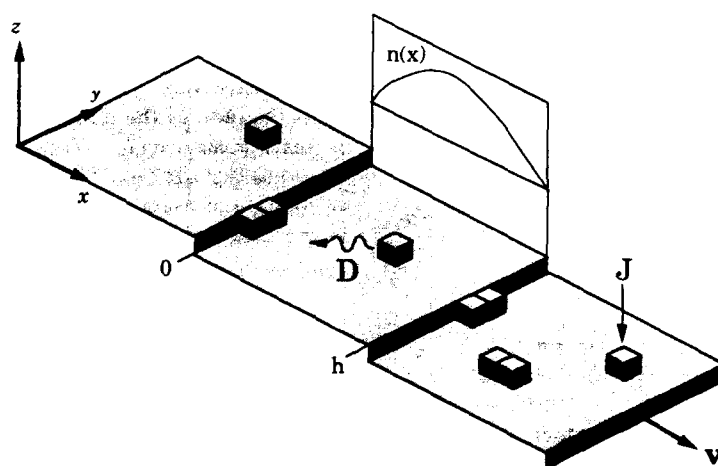


Fig. 1. Schematic representation of a section through the stepped crystal.

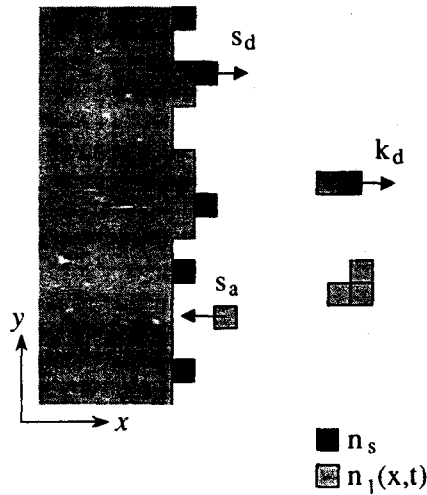


Fig. 2. Depiction of adatom attachment and detachment kinetics below the step edge and island break-up on the terraces.

either above or below to be given by the next rate at which atoms hop into the step edge (fig. 2):

$$\begin{aligned} D \frac{dn}{dx} \Big|_{x=0} &= s_a n(0, t) - s_d n_s, \\ D \frac{dn}{dx} \Big|_{x=h} &= -s_a n(h, t) + s_d n_s. \end{aligned} \quad (3)$$

Above, the rate constant for adatom incorporation into a step is s_a , and s_d is the rate of detachment of atoms from the step edge, where n_s is the concentration of singly-bonded or kink-site atoms on the step edge which may detach.

Inclusion of island and step breakup leads to the introduction of several new parameters: k_d , s_a , s_d and n_s . Assuming that the energy of attachment between two nearest-neighbor atoms is E_N yields

$$k_d = \nu \exp[-(E_D + E_N)/k_B T].$$

Estimation of the step kinetic parameters s_a , s_b , and n_s is more difficult since the values of these parameters will depend on the two-dimensional morphology of the step edge, which is not included in our one-dimensional averaged theory. As a first approximation, we will assume that n_s is

the concentration of singly bonded atoms on the step edge and is a constant; thus

$$s_d = \nu a \exp[-(E_D + E_N)/k_B T]/4,$$

where the factor of four occurs because only one hop in four directions (assuming a (001) surface) will result in detachment of the atom below (or above) the step. Furthermore, we assume that the rate of attachment of an atom to the step is proportional to its mobility; hence

$$s_a = \nu a \exp(-E_D/k_B T)/4.$$

It is convenient to introduce dimensionless variables by $y_j \equiv Dn_j/Jh^2$, $x \rightarrow x/h$, $t \rightarrow t/(n_0/J)$, and $n \rightarrow \nu n_0/Jh$. This results in the following set of nonlinear equations including islands with up to N atoms:

$$\begin{aligned} \alpha \frac{\partial y_1}{\partial t} &= \frac{\partial^2 y_1}{\partial x^2} + 1 + \nu \alpha \frac{\partial y_1}{\partial x} - 2\alpha y_1(\beta y_1 + m_1) \\ &\quad - \alpha \sum_{j=2}^{N-1} y_j(\beta y_1 + m_j) + K_d \left(2y_2 + \sum_{j=3}^N y_j \right), \\ \alpha \frac{\partial y_j}{\partial t} &= \nu \alpha \frac{\partial y_j}{\partial x} + \alpha [\beta y_1(y_{j-1} - y_j) \\ &\quad + (m_{j-1}y_{j-1} - m_j y_j)] \\ &\quad + K_d [y_{j+1} - y_j], \quad j \geq 2. \end{aligned} \quad (4)$$

The dimensionless parameter $\alpha = Jh^2/Dn_c$ represents the ratio of the diffusion time for an adatom to reach a terrace (h^2/D) to the interarrival time of atoms per site (n_0/J). $\beta = \sigma n_0 h^2$ is a measure of the rate of island formation, and $K_d = k_d h^2/D$ is the ratio of the diffusion time to the average lifetime of a diatomic island.

3. Results and discussion

To compare the transient behavior of our nonlinear theory with RHEED measurements of MBE on stepped surfaces [12-14], we calculate the

kinematic intensity down the staircase at the off-Bragg angle [5]:

$$I(S_x = \pi/h, S_z = \pi/a; t) = \left| \int_0^1 \left[1 - 2 \sum_{j=1}^N j y_j(x, t) \right] e^{i\pi x} dx \right|^2. \quad (5)$$

Fig. 3 shows the intensity as a function of α for $\beta = 324$, calculated numerically from (4) using a finite difference method [15]. At the left is shown the intensity for the original theory with diatomic islands only and infinitely "sticky" adatoms ($E_N \rightarrow \infty$, $k_d, s_d = 0$, and $s_a \rightarrow \infty$). The transient behavior of the calculated intensity *during growth* exhibits a remarkable resemblance to temporal RHEED measurements of MBE on stepped surfaces [12–14]. At high α (low temperature), the nucleation rate is substantial and the pair concentration builds up until at a time equivalent to deposition of one monolayer, a large proportion of the surface is covered. Then, the velocity suddenly increases sharply as these islands are incorporated

into the step edge and the step effectively shoots across the surface, forming a less densely-populated fresh terrace and an oscillation in the intensity. The build-up of islands is then repeated but to a lesser extent until the intensity oscillations are damped out. At low α (high temperature), growth proceeds predominantly by incorporation of mobile adatoms into the step edges. The velocity and kinematic intensity do not oscillate but instead evolve monotonically to their steady-state value.

In the RHEED measurements, a temperature T_c was defined as the temperature where temporal oscillations are no longer detectable during growth; this was interpreted to correspond to the onset of step flow, i.e. growth dominated by incorporation of atoms at the step edge [12]. We have shown that T_c can be predicted from our original model [9] as the point at which pair-formation may be neglected and epitaxial growth proceeds predominantly by step propagation:

$$T_c = (E_D/k_B) [\ln(\nu a^2/2Jh^4)]^{-1}.$$

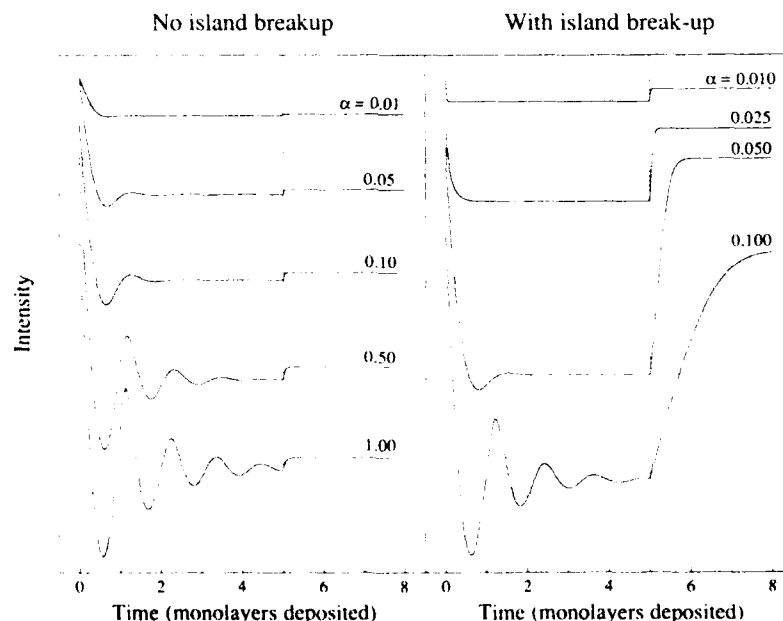


Fig. 3. Kinematic intensity at $S_x = \pi/h$ and $S_z = \pi/a$ for growth and recovery. The left-hand panel shows the nonlinear theory including nucleation with diatomic islands only for $\beta = 324$, and the right-hand panel includes islands with up to ten atoms as well as atom detachment from the islands and step edges.

We obtained excellent agreement between the values of T_c determined by the nonlinear model and those obtained from both Monte Carlo simulations and measurements on vicinal GaAs (001) surfaces for different Ga and As_2 fluxes [9]. Nucleation reduces the effective diffusivity of the adatoms by several orders of magnitude, and therefore a realistic model of MBE on vicinal surfaces must include the nonlinear interactions responsible for island formation.

Although inclusion of diatomic island formation is sufficient to quantitatively predict the transition to step flow, several refinements are necessary for a detailed model of MBE on stepped surfaces. On the right-hand side of fig. 3, we show the intensity for inclusion of islands with up to ten atoms in (4), with a finite probability of detachment $E_N/E_D = 0.2$ and with $n_s/n_0 = 0.25$, which was chosen to yield a total concentration of material under the step edge at T_c to be close to that for the previous model, about one percent. Several differences are apparent between the original and modified theory.

Firstly, the intensity does not recover after the cessation of growth for the original model since the diatomic islands are not allowed to decay. The recovery profile for the modified theory, on the other hand, compares qualitatively well to measurements [12]. Recovery is swifter at lower α (high temperature) and proceeds from an initial decrease of single adatom concentration due to incorporation at steps and nucleation, and a slower decay of the islands themselves.

Secondly, we note that oscillations appear more quickly with increasing α when a greater degree of nucleation is included. Fig. 4 shows the total number of atoms in each type of surface species at steady state for two different α corresponding to a step flow regime and to an island-formation dominated regime. At $\alpha = 0.1$ it is clear that at least 10-atom islands must be included; for lower temperature it will be necessary to include terms for coalescence of islands, and other models for deposition on flat surfaces are probably more appropriate. However, at step flow $\alpha = 0.0014$, the total concentration of material on the terrace is very small, and formation of triatomic islands or higher only counts for a small percentage of the

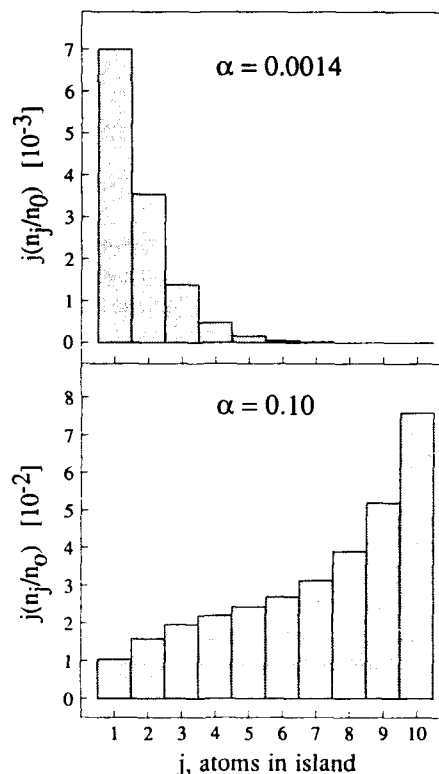


Fig. 4. Number of atoms in each species on the terraces, $j(n_j/n_0)$, as a function of α for $\beta = 324$, $E_N/E_D = 0.2$ eV, $J = 1$ ML/s, and $n_s/n_0 = 0.25$ in the modified theory (4). Note the difference in scale.

total material on the terrace. This confirms the assumption of our original theory, that *near step flow* inclusion of only diatomic islands is sufficient.

Although qualitatively superior to our original model, the increase in the number of parameters in the modified theory means an inevitable loss of predictive power. From the success of the original model in predicting T_c for simulations and measurements of MBE growth [9], it was apparent that at least for determining the dependence of T_c on the growth conditions, detachment of atoms from islands balanced with detachment from the step and could be ignored to a first approximation. In this paper we attempt to *explicitly* include kinetics at the step edge. Since the model is one-

dimensional, we are however decoupling growth along the step train from fluctuations along the step edge, which STM images have shown can be quite large [16]. The step kinetic parameters s_a , s_b , and n_s vary in a complicated way with growth conditions through the roughness of the step, which is not treated explicitly in our model. For example, we have assumed that n_s/n_0 is a constant for all growth conditions when in reality it will depend on the morphology of the step edge. We plan to incorporate the y -dimension into our growth equations in the future so that the effects of step-edge fluctuations may be treated more exactly.

4. Conclusions

The inclusion of adatom interactions in BCF theory is shown to provide a realistic model of MBE on stepped surfaces over a wide range of growth conditions. The nonlinear theory reproduces the full time-dependent behavior of RHEED measurements of MBE during growth on stepped surfaces, including intensity oscillations, decay, and dependence on the growth conditions. Here, we have shown that recovery of the stepped surface as well as growth can be modeled by including break-up of atoms from the islands and the step edge. Additionally we have extended the applicability of the original model (with diatomic nucleation only) further away from step flow by including the formation of islands with an increasing number of atoms in the equation. It is also possible to extend the theory to model growth of semiconductor alloys or quantum wires by explicitly including two or more diffusing species [17]. In conclusion, the nonlinear diffusion model provides a fairly complete picture of MBE on vicinal

surfaces, within the intrinsic limitations of the assumption of one-dimensionality of the step train.

Acknowledgement

A.K.M.-B. acknowledges the support of a NATO Postdoctoral Fellowship.

References

- [1] J.A. Venables, G.D.T. Spiller and M. Hanbücken, *Rept. Progr. Phys.* 47 (1984) 399.
- [2] W.K. Burton, N. Cabrera and F.C. Frank, *Phil. Trans. Roy. Soc. London A*243 (1951) 299.
- [3] K. Voigtlaender and H. Risken, *Appl. Phys.* A39 (1986) 31.
- [4] V. Fuenzalida and I. Eisele, *J. Crystal Growth* 74 (1986) 597.
- [5] G.S. Petrich, P.R. Pukite, A.M. Wowchak, G.J. Whaley, P.I. Cohen and A.S. Arrott, *J. Crystal Growth* 95 (1989) 23.
- [6] R. Ghez and S.S. Iyer, *IBM J. Res. Develop.* 32 (1988) 804.
- [7] T. Shitara and T. Nishinaga, *Japan. J. Appl. Phys.* 26 (1989) 1212.
- [8] S. Stoyanov, *Appl. Phys.* A50 (1990) 439.
- [9] A.K. Myers-Beaghton and D.D. Vvedensky, *Phys. Rev. B*42 (1990) 5544.
- [10] A.K. Myers-Beaghton and D.D. Vvedensky, *J. Phys. A (Math. Gen.)* 23 (1990) L995.
- [11] R. Ghez, *Surface Sci.* 20 (1970) 326.
- [12] J.H. Neave, P.J. Dobson, B.A. Joyce and J. Zhang, *Appl. Phys. Letters* 47 (1985) 100.
- [13] J.H. Neave, B.A. Joyce, P.J. Dobson and N. Norton, *Appl. Phys.* A31 (1983) 1.
- [14] J.M. Van Hove, C.S. Lent, P.R. Pukite and P.I. Cohen, *J. Vacuum Sci. Technol.* B1 (1983) 741.
- [15] B. Carnahan, H.A. Luther and J. Wilkes, *Applied Numerical Methods* (Wiley, New York, 1969).
- [16] A.J. Hoeven, D. Dijkamp, E.J. van Loenen, J.M. Lenssen and J. Dieleman, *J. Vacuum Sci. Technol.* A8 (1990) 207.
- [17] A.K. Myers-Beaghton and D.D. Vvedensky, *Surface Sci.* 240 (1990) L591.

Surface diffusion of Al and Ga atoms on GaAs (001) and (111)B vicinal surfaces in molecular beam epitaxy

M. Tanaka, T. Suzuki and T. Nishinaga

Department of Electronic Engineering, Faculty of Engineering, The University of Tokyo, 7-3-1 Hongo, Bunkyo-ku, Tokyo 113, Japan

We have measured the critical temperature where the growth mode transition between step-flow and 2D nucleation takes place by RHEED measurements during the molecular beam epitaxial growth of GaAs and AlAs on (001) and (111)B GaAs vicinal surfaces. Combining the experimental results with our theory and taking into account the surface diffusion and supersaturation ratio of adatoms on the terraces, the intrinsic surface diffusion length λ_s of Al and Ga atoms is estimated on both (001) and (111)B GaAs vicinal surfaces with various misorientation directions.

1. Introduction

There has been much interest in the growth on vicinal surfaces which are slightly misoriented from a particular low index plane, not only because it is useful to study the elemental growth process of molecular beam epitaxy (MBE) [1–4] and metal-organic chemical vapor deposition (MOCVD), but also because planar superlattices (PSLs) and quantum wires can be formed by depositing fractional monolayers (MLs) of GaAs and AlAs alternately on the vicinal substrate [5–11]. For implementing these novel structures as intended, one must understand the elemental growth processes on vicinal surfaces.

Although it was pointed out that surface diffusion is one of the most important growth processes in MBE [2], very little is known about the atomic details of surface diffusion and various physical parameters characterizing the process such as diffusion length, residence time, activation energy and so on. In this paper, we study theoretically and experimentally the surface diffusion process in MBE growth of GaAs and AlAs on both (001) and (111)B GaAs vicinal surfaces.

2. Theoretical model

Previously, Neave et al. [1] tried to determine the diffusion coefficient D_s of Ga atoms by mea-

suring the critical temperature T_c of the appearance or disappearance of RHEED oscillations. They assumed that at T_c the diffusion length $\lambda (= \sqrt{D_s \tau})$ took the same value as the interstep distance λ_0 on vicinal surfaces, where they took τ as the time for monolayer growth. However, in the sense of their measurements, τ should be the average time τ_{nuc} for two-dimensional (2D) nucleation to occur, which is much smaller than the time for monolayer growth. Thus the diffusion length $\lambda (= \sqrt{D_s \tau_{nuc}})$ is a function of the surface step density.

Unlike the oversimplified analysis of Neave et al. [1], the principal idea of our theory [2,3] is that the growth mode transition between step-flow and 2D nucleation occurs when the surface supersaturation on the terrace becomes equal to the critical supersaturation for 2D nucleation. Here we apply this theory to the estimation of intrinsic diffusion length λ_s of Al and Ga atoms on various vicinal surfaces.

We assume that when the growth mode is by step-flow, the step acts as a uniform sink for the diffusion of adatoms and that there is no other sink of adatoms. It is also assumed that the density of adatoms on the surface n_s takes the value of equilibrium density of adatoms n_e at the step edges and that GaAs or AlAs grows macroscopically with stoichiometric composition. Since chemical equilibrium is assumed at the step edges, the

following equation is realized between column III atoms (Ga or Al) and column V molecules (As_4) during the step-flow growth:

$$\frac{n_e^{\text{III}}(n_e^{\text{V}})^{1/4}}{\tau_s^{\text{III}}(\tau_s^{\text{V}})^{1/4}} = \frac{K_{p4}}{(2\pi m^{\text{III}}kT_s)^{1/2}(2\pi m^{\text{V}}kT_s)^{1/8}}, \quad (1)$$

where τ_s is the mean resident time, m is the mass of adatoms, k and T_s are Boltzmann's constant and substrate temperature, and K_{p4} is the equilibrium constant for the reaction given by $\text{Ga(Al)} + \frac{1}{4}\text{As}_4 \rightleftharpoons \text{GaAs(AlAs)}$. Here, the mass action law was employed for the GaAs (AlAs) crystal and gaseous Ga(Al) and As_4 . The value of K_{p4} is derived from the recent results of Seki and Koukitu [12]. While eq. (1) is true for step-flow growth, the following equation is satisfied when 2D nucleation begins to appear:

$$\alpha_{\text{max}}^{\text{III}} \alpha_{\text{max}}^{\text{V}} = \alpha_{\text{crit}} = \exp\left(\frac{\Omega\pi h\sigma^2}{(65 - \ln 10^{12})k^2T_s^2}\right). \quad (2)$$

Here we assume that disk-shaped 2D nucleation occurs once a second per 10 nm^2 . Ω is the atomic volume, h is the height of the disk, σ is the surface free energy whose value we tentatively choose as $n_0 \times 0.70 \text{ eV}$ for GaAs and $n_0 \times 0.86 \text{ eV}$ for AlAs, where n_0 is the density of lattice sites and 0.70 eV (0.86 eV) is half the bond energy of GaAs (AlAs). α is the supersaturation ratio, and α_{max} its maximum value given by

$$\alpha_{\text{max}}^{\text{III}} = 1 + \frac{\tau_s^{\text{III}} n_0 \lambda_0}{n_e^{\text{III}} \tau \cdot 2\lambda_s^{\text{III}}} \tanh \frac{\lambda_0}{4\lambda_s^{\text{III}}}, \quad (3)$$

$$\alpha_{\text{max}}^{\text{V}} = 1 + \frac{\tau_s^{\text{V}} n_0 \lambda_0}{n_e^{\text{V}} 4\tau \cdot 2\lambda_s^{\text{V}}} \tanh \frac{\lambda_0}{4\lambda_s^{\text{V}}}, \quad (4)$$

where τ is the time of monolayer growth, λ_0 is the average terrace width, and λ_s is the surface diffusion length.

At the critical temperature T_c where the growth mode transition between step-flow to 2D nucleation takes place, both eq. (1) and eq. (2) are satisfied simultaneously. When the flux of As_4 is much higher than that of Ga (or Al), the supersaturation ratio of As is nearly equal to unity [2],

and thus the following equation is derived from eqs. (2) and (3):

$$\begin{aligned} \frac{\lambda_0}{4\lambda_s^{\text{III}}} \tanh \frac{\lambda_0}{4\lambda_s^{\text{III}}} \\ = \frac{\tau}{2n_0} (\alpha_{\text{crit}} - 1) \frac{K_{p4}}{(P_e^{\text{V}})^{1/4} (2\pi m^{\text{III}}kT_s)^{1/2}}, \quad (5) \end{aligned}$$

where P_e^{V} is the vapor pressure of As_4 at equilibrium and is assumed to be equal to the incident flux of As_4 .

3. Experimental results and estimation of intrinsic surface diffusion length on (001) and (111)B surfaces

To determine the critical growth parameters in eq. (5), we measured them where the RHEED oscillation begins to appear or disappear on various vicinal surfaces. GaAs misoriented substrates which are slightly (1° – 2°) tilted from the (001) plane towards $[110]$ (we denote here (001) "A" surface), and towards $[\bar{1}10]$ ((001) "B" surface), and 1° tilted from the (111)B plane towards $[\bar{1}00]$, $[110]$ and $[0\bar{1}1]$ are used. MBE growth was carried out mainly by ULVAC MBC-508. After removing the native oxide by heating the substrates up to 600°C under the incident As_4 flux, a GaAs buffer layer of 3000 \AA was grown at 600°C and then the growth was interrupted for 2 min to make the surface atomically smooth. The V/III flux ratio (As_4/Ga and As_4/Al) was maintained at 2.0–2.5 for the growth of both GaAs and AlAs. The growth rate was varied from 0.1 to $1.0 \mu\text{m/h}$. An electron beam with an acceleration voltage of 20 kV was used in the RHEED and the specular beam intensity was measured at the orthogonal azimuth to the misorientation direction. In each experimental run, after a GaAs layer of more than 100 \AA was grown under the step-flow conditions and the growth was interrupted for 2 min, GaAs or AlAs was grown on GaAs.

While the details of the RHEED patterns which show splittings of integral order beams and their dependence on the growth conditions were reported elsewhere [13], here we focus on the

RHEED intensity oscillations with the incident electron beam parallel to the step edges, and measure the critical temperature for mode transition T_c under various growth conditions. The results showed that: (1) T_c increases as the off-angle decreases (average terrace width increases); (2) T_c increases as the incident column III atoms (growth rate) increase; (3) T_c on the (001) "A" surface is higher than that on the (001) "B" surface; (4) T_c on the (001) surface is higher than that on the (111)B surface; (5) T_c of AlAs is higher than that of GaAs; (6) little difference was found between different directions of misorientation on (111)B.

First, the surface diffusion lengths of Ga and Al atoms on (001) GaAs vicinal "A" surface and "B" surface are calculated by eq. (5) and plotted in figs. 1a and 1b. Theoretically, the diffusion length of III atoms is given by

$$\lambda_s = a \exp(Q/2kT_s), \quad (6)$$

where a ($= 4.0 \text{ \AA}$) is the jump distance, $Q = E_{\text{des}} - E_{\text{diff}}$, and E_{des} and E_{diff} are the activation energies for desorption and surface diffusion, respectively. Fitting this equation with the experimental data, we can estimate the value of $Q/2$ as 0.69 eV for Al and 0.37 eV for Ga on the "A" surface, and 0.74 eV for Al and 0.43 eV for Ga on the "B" surface. In all cases, λ_s increases with the

decrease of temperature, indicating that the desorption energy is larger than the diffusion energy, and therefore, with the decrease of temperature, the residence time becomes large so that the atoms can migrate a long way on the surface if there are no steps and kinks. These results also indicate that the surface diffusion length λ_s of Al is much larger than that of Ga. This is because AlAs has a larger bond energy than GaAs and is more difficult to reevaporate. Note here that λ_s is the average diffusion length during the resident time τ_s on the surface without steps and kinks, and hence, is intrinsic to the material, depending on temperature.

In the present model, it is assumed that chemical equilibrium is established at the steps on each "A" and "B" surface. We have to consider, however, the possibility that the step-edge structure is different between the "A" surface and the "B" surface, as we discussed in previous papers [3,14]. Studies on the step structures and their dependence on the growth conditions are in progress.

Next, we have performed the same experiments on (111)B vicinal surfaces. Figs. 2a and 2b show typical data of RHEED specular beam intensity when we grow (a) GaAs and (b) AlAs on GaAs (111)B vicinal surfaces with an off-angle of 1° tilted towards $[1\bar{1}0]$. The behaviour of RHEED

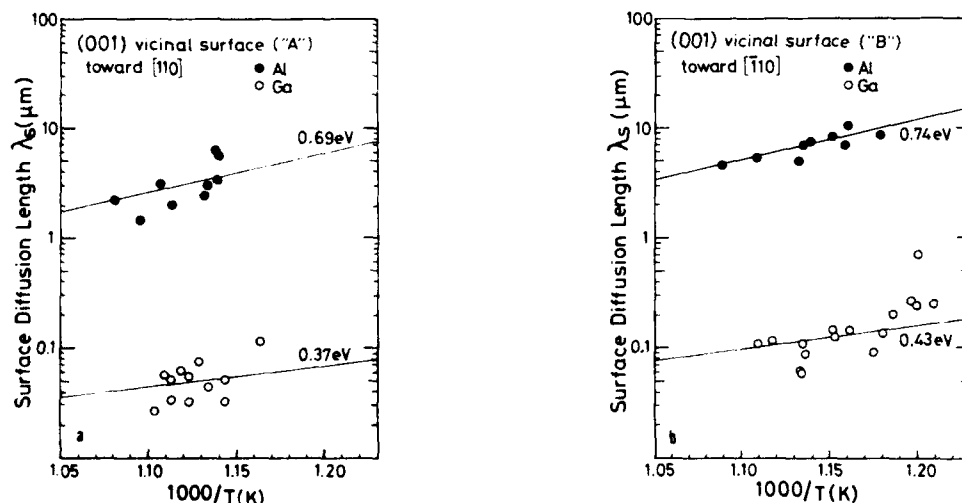


Fig. 1. Surface diffusion length of Al (●) and Ga (○) on GaAs vicinal surface misoriented from (001) towards (a) $[110]$ ("A" surface) and (b) $[1\bar{1}0]$ ("B" surface).

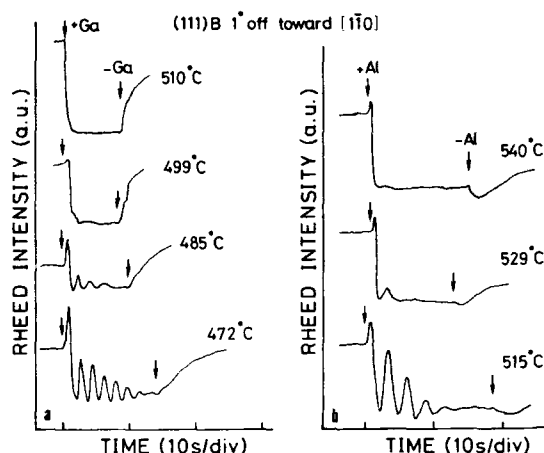


Fig. 2. Typical data sets of time evolution of RHEED specular beam intensity during the growth of (a) GaAs and (b) AlAs on GaAs vicinal surfaces misoriented from (111)B towards [110].

specular beam intensities on (111)B is qualitatively similar to that on (001). The critical temperature of AlAs is higher than that of GaAs. For GaAs, RHEED oscillations can be seen under the As stabilized (2×2) region near the transition region between ($\sqrt{19} \times \sqrt{19}$) and (2×2). Initially, the

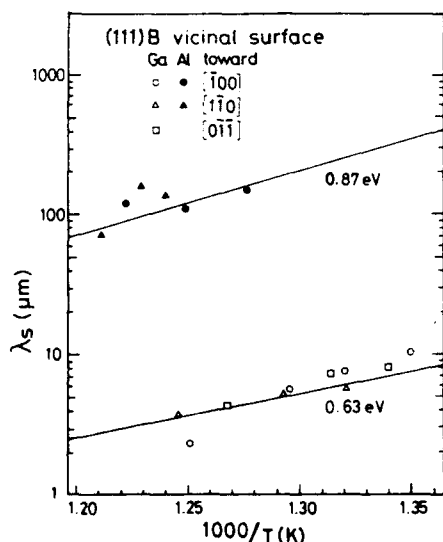


Fig. 3. Surface diffusion length of Al (●, ▲) and Ga (○, △) on GaAs vicinal surfaces misoriented from (111)B towards [100], [110] and [011].

RHEED intensity increases rapidly, and then decreases and oscillates with the rapid decay of amplitude. The most striking difference from the (001) surface is the much lower critical temperature in both GaAs and AlAs. This means that 2D nucleation is more difficult on the (111)B surface than on the (001) surface.

By using the measured critical growth conditions and eq. (5), we plotted in fig. 3 the surface diffusion length λ_s of Ga and Al atoms on various (111)B vicinal surfaces tilted towards $[100]$, $[110]$ and $[011]$. λ_s is estimated to be much larger than that on (001), and in contrast to the (001) surface, there is little dependence on misorientation direction both for GaAs and for AlAs. By fitting eq. (6) with the experimental data, we estimate the value of $Q/2$ as 0.87 eV for Al and 0.63 eV for Ga on the GaAs (111)B surface.

4. Conclusions

We have measured the critical temperature where the growth mode transition takes place by RHEED during the growth of GaAs and AlAs on GaAs (001) and (111)B vicinal surfaces. Combining the experimental results with our theory and taking into account the surface diffusion and supersaturation ratio of adatoms on the terraces, the intrinsic surface diffusion length λ_s of Al and Ga atoms is estimated on both (001) and (111)B GaAs vicinal atoms surfaces with various misorientation directions. The main conclusions are:

- (1) λ_s increases as the temperature decreases due to the increase of τ_s .
- (2) λ_s of Al is larger than λ_s of Ga because Al atoms are more difficult to reevaporate than Ga atoms.
- (3) λ_s on (111)B is a little larger than that on (001).
- (4) From the temperature dependence of λ_s derived from our experiments and theory, the value of $E_{\text{des}} - E_{\text{diff}}$ was estimated.

References

- [1] J.H. Neave, P.J. Dobson, B.A. Joyce and J. Zhang, Appl. Phys. Letters 47 (1985) 100.

- [2] T. Nishinaga and K.I. Cho, Japan. J. Appl. Phys. 27 (1988) L12.
- [3] T. Shitara and T. Nishinaga, Japan. J. Appl. Phys. 28 (1989) 1212.
- [4] M. Tanaka, T. Suzuki and T. Nishinaga, Japan. J. Appl. Phys. 29 (1990) L706.
- [5] T. Fukui and H. Saito, Appl. Phys. Letters 50 (1987) L824.
- [6] T. Fukui and H. Saito and Y. Tokura, Japan. J. Appl. Phys. 27 (1988) L1320.
- [7] J.M. Gaines, P.M. Petroff, H. Kroemer, R.J. Simes, R.J. Geels and J.H. English, J. Vacuum Sci. Technol. B6 (1988) 1738.
- [8] M. Tanaka and H. Sakaki, Japan. J. Appl. Phys. 27 (1988) L2025.
- [9] M. Tsuchiya, J.M. Gaines, R.H. Yan, R.J. Simes, P.O. Holtz, L.A. Coldren and P.M. Petroff, Phys. Rev. Letters 62 (1989) 466.
- [10] M. Tanaka and H. Sakaki, Appl. Phys. Letters 54 (1989) 1326.
- [11] J. Motohisa, M. Tanaka and H. Sakaki, Appl. Phys. Letters 55 (1989) 1214.
- [12] H. Seki and A. Koukitu, J. Crystal Growth 78 (1986) 342.
- [13] M. Tanaka, G. Tanaka and T. Nishinaga, in: Record 9th Symp. of Alloy Semiconductor Physics and Electronics, Izu-Nagaoka, July 1990, pp. 195-202.
- [14] P.R. Pukite, G.S. Petrich, S. Batra and P.I. Cohen, J. Crystal Growth 95 (1988) 269.

Surface diffusion and atom incorporation kinetics in MBE of InGaAs and AlGaAs

T. Suzuki and T. Nishinaga

Department of Electronic Engineering, Faculty of Engineering, The University of Tokyo, 7-3-1 Hongo, Bunkyo-ku, Tokyo 113, Japan

We have developed a theory to obtain the surface flux of growing species in MBE, taking account of step kinematics as well as surface diffusion. This treatment makes it possible to understand the elemental growth process in MBE of III–V alloys. The MBE experiments are carried out and the solid composition of InGaAs and AlGaAs is measured for the different faces with a different off angle. Theory shows qualitatively a good agreement with the present experiments suggesting that the role of step kinetics is important in controlling the alloy composition.

1. Introduction

Many efforts to obtain surface diffusion length or surface diffusion coefficient have been made to account for the growth mechanism of MBE in which surface smoothness is accomplished with the insensitivity of the growth rate to the temperature and the substrate orientation [1,2]. In the usual growth of III–V MBE where reevaporation can be neglected, the surface incorporation length of the group III element, which is defined as the distance from the adsorption on the surface to the incorporation into the crystal is the most important to understand the growth mechanism, but it is a complicated function of many kinds of growth parameters, for example, step density, step orientation, growth temperature, arsenic pressure and so on. In this situation, in some cases the incorporation of the diffusing atoms into the steps becomes the main rate determining process, and the surface diffusion might play a minor role.

In this paper, we propose a growth model in which step kinetics plays an important role in addition to the surface diffusion. Then experimental results for the growth of InGaAs and AlGaAs on the substrates with a different off-angle are shown and explained by the present model in which step kinetics is taken into account.

2. Theoretical consideration

Fig. 1 illustrates schematically the model of the present theory. An equi-distance step train on a vicinal surface is assumed. Therefore, the problem can be treated as one-dimensional. According to BCF theory [3], one obtains the surface flux incident to the step edges $J^s(\lambda_0/2)$ as [4,5]

$$J^s\left(\frac{\lambda_0}{2}\right) = \left(J^{in} - \frac{n_{step}}{\tau_s}\right) \lambda_s \tanh\left(\frac{\lambda_0}{2\lambda_s}\right). \quad (1)$$

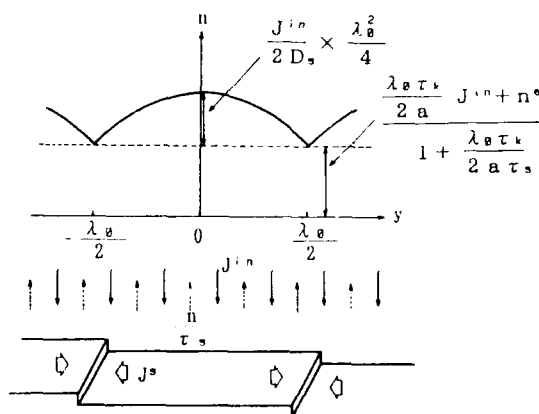


Fig. 1. Schematic illustration of the present model with distribution of surface diffusion adatoms. An equi-distance step train is postulated.

where n_{step} , λ_s , J^{in} and τ_s are the concentration of adatoms at the steps, the surface diffusion length, the flux incident to the growing surface and the resident time of adatoms, respectively. Here it is important to mention that this expression contains the surface diffusion length which is defined as $(D_s \tau_s)^{1/2}$, where D_s is the diffusion coefficient and plays a major role in the BCF theory. However, under the usual MBE conditions, and even if the reevaporation cannot be neglected at rather high growth temperature, the residence time of the adatoms is longer than the time for diffusing atoms to reach the step edge. Then we can postulate $\lambda_s \gg \lambda_0$ and obtain the more simple form

$$J^{\text{in}} \left(\frac{\lambda_0}{2} \right) = \left(J^{\text{in}} - \frac{n_{\text{step}}}{\tau_s} \right) \frac{\lambda_0}{2}. \quad (2)$$

Next, we define the concentration at the step edges, n_{step} . There are experiments where we must assume that adatoms can diffuse as far as $1 \mu\text{m}$ [6]. This means that all the surface atoms entering the step are not always incorporated into the crystal, but many are reflected back or pass over the steps. To include this process, we introduce a relaxation time τ_k [7], the inverse of which is the probability per unit time for adatoms within a jump distance to be incorporated into the step and so far neglected in our previous treatments [5].

The flux into the step from one side on the surface is determined by the average number of adatoms within an elemental surface jump distance a . Since n_{step} is the number of adatoms per unit surface adjacent to the step, $n_{\text{step}}a$ is the number per unit step length and $n_{\text{step}}a/\tau_k$ is the number per unit step length per time going to the step from that side. On the other hand, the flux leaving the step is $n^e a/\tau_k$ where n^e is the equilibrium concentration of adatoms. Then the net flux incorporated to the steps is given by

$$J^{\text{in}} \left(\frac{\lambda_0}{2} \right) = \frac{a}{\tau_k} n_{\text{step}} - \frac{a}{\tau_k} n^e. \quad (3)$$

From eqs. (2) and (3), n_{step} can be calculated and eq. (2) leads to

$$J^{\text{in}} \left(\frac{\lambda_0}{2} \right) = \left(J^{\text{in}} - \frac{n^e}{\tau_s} \right) \frac{1}{1 + \lambda_0 \tau_k / 2 a \tau_s} \frac{\lambda_0}{2}. \quad (4)$$

It is important to mention that in the limit of $\tau_k = 0$, where the microscopic process is neglected, eq. (4) expresses the macro-equilibrium between vapor-solid phase calculated by thermodynamic technique [8,9]. In this treatment, τ_k is defined for a step, which allows us to employ a one-dimensional model. In the actual case, τ_k depends on the kink density, the step shape, the surface reconstruction, etc. Hence, if we know τ_k in detail as a function of various growth parameters, we can get the information about the growth mechanism of MBE.

3. Experimental results

GaAs(100) substrates with different misorientation, nominal (100) ($< 0.5^\circ$), 2° , 5° off to $\langle 111 \rangle \text{B}$ and 2° off to $\langle 111 \rangle \text{A}$ and nominal (111)B ($< 0.1^\circ$) were degreased and after chemical etching, they were mounted with indium on the same Mo block. After removal of the native oxide by heating up to 620°C under incident As_4 flux, GaAs buffer layer more than 3000\AA was grown at 580°C . Then the substrate temperature was set at the temperature higher than the normal growth temperature for III-V alloys.

In the case of InGaAs, the growth conditions are chosen such that the flux ratio $F_{\text{In}}/F_{\text{Ga}}$ is $0.49/0.51$, and the growth rate and the thickness of the layer are nominally about $0.7 \mu\text{m/h}$ and $1.4 \mu\text{m}$, respectively. The growth thickness is much larger than the so-called critical thickness for the strain relaxation, hence one can neglect the effect of lattice strain in the following analysis. After the growth, the concentration of the In was determined by X-ray diffraction. For the growth of AlGaAs, the incident flux ratio $F_{\text{Al}}/F_{\text{Ga}}$ is chosen as $0.133/0.867$; the growth rate of $1.0 \mu\text{m/h}$ and the thickness of layer of $1.0 \mu\text{m}$ are nominally employed. After the growth, the concentration of Al was estimated by photoluminescence (PL) at 77 K .

It is difficult to reproduce the substrate temperature accurately in many growth sequences. Therefore, the following method has been used to calibrate the growth temperature. Curve (1) in fig. 2a shows the dependence of the concentration of

In on the growth temperature obtained from the periods of RHEED specular intensity oscillations in the growth of $\text{In}_x\text{Ga}_{1-x}\text{As}$ ($x = 0.18$) on a GaAs(100) substrate. With this curve, it is possible to get curve (2) for $x = 0.49$ with the thermodynamic theory [8], and experimental results of InGaAs on GaAs(100) substrate were fitted to this curve (2). In this way, the true temperature for the set of substrates on one Mo block was determined. In the case of AlGaAs, the data of GaAs(100) are calculated by the thermodynamic theory with the parameter fitted to experimental conditions and the true temperature for the set of substrates was determined with the same technique employed for InGaAs. Figs. 2a and 2b show the experimental results for InGaAs and AlGaAs, respectively, after the calibration. The concentration of In and Ga respectively in InGaAs and AlGaAs decreases rapidly with increasing growth temperature because of the reevaporation of In and Ga, respectively. In the growth of InGaAs, however, the In concentration has a large orientational dependence which cannot be explained by thermodynamic theory and the following relationship is found in this experiment. Increasing the off-angle at the same off-axis, the concentration of In becomes higher, and at the same off-angle (2° off)

the concentration of In is higher for the substrate misoriented off to $\langle 111 \rangle_B$ than off to $\langle 111 \rangle_A$. On the other hand, the Ga concentration in AlGaAs shows no orientation dependence at all.

4. Discussion

To understand these two results of great contrast, we use eq. (4) to determine the alloy composition dependence on the growth temperature. In the case of InGaAs, In atom reevaporates preferentially and the reevaporation of Ga atom can be neglected. Then from eq. (4) one gets the concentration x in $\text{In}_x\text{Ga}_{1-x}\text{As}$ as

$$x = \frac{J_{\text{In}}^s}{J_{\text{In}}^s + J_{\text{Ga}}^s} = \frac{\left(J_{\text{In}}^{\text{in}} - \frac{n_{\text{In}}^e}{\tau_{\text{sIn}}} \right) \frac{1}{1 + \omega_{\text{In}}}}{\left(J_{\text{In}}^{\text{in}} - \frac{n_{\text{In}}^e}{\tau_{\text{sIn}}} \right) \frac{1}{1 + \omega_{\text{In}}} + J_{\text{Ga}}^{\text{in}}} \quad (5)$$

with

$$\omega_{\text{In}} = \frac{\lambda_0 \tau_{\text{kIn}}}{2a\tau_{\text{sIn}}} \quad (6)$$

where the subscripts mean the values for each atom. From eq. (5) it is shown that as the step

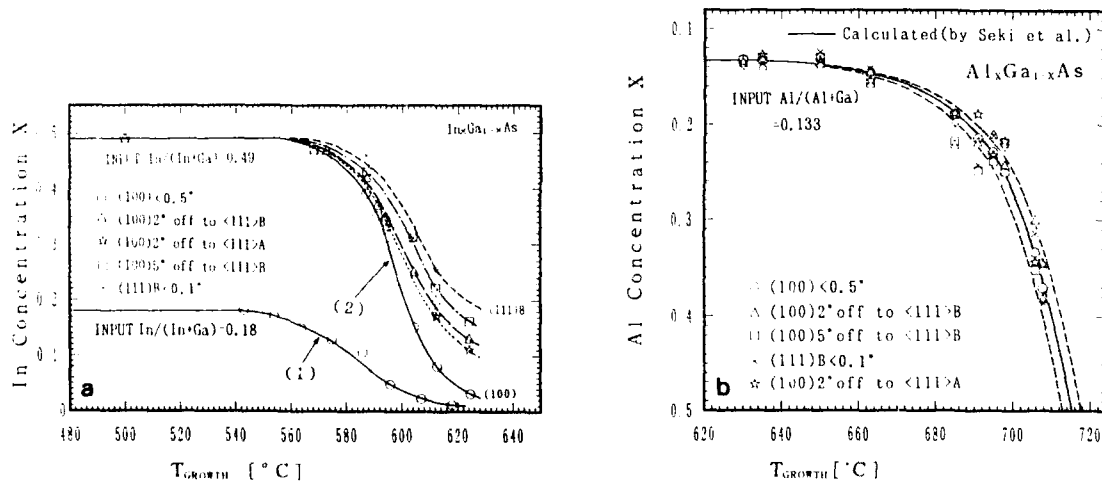


Fig. 2. Substrate temperature and orientation dependence of (a) InGaAs and (b) AlGaAs. Curve (1) in (a) shows the experimental results on In concentration versus substrate temperature obtained by RHEED intensity oscillations and curve (2) shows the composition for $x = 0.49$ after calibration. The shaded portion in (b) shows the range of the experimental error which comes mainly from the nonuniformity among the substrate temperatures on the same Mo block ($\pm 2.5^\circ\text{C}$).

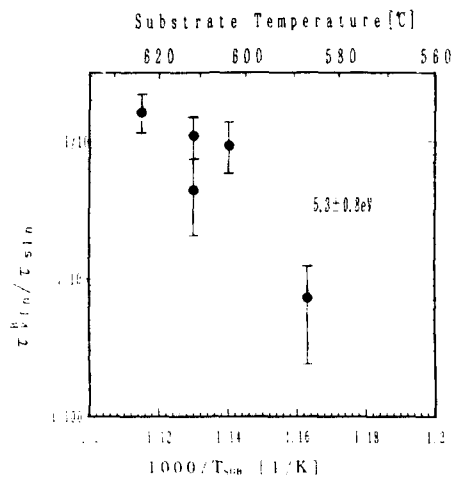


Fig. 3. τ_{kIn}^B/τ_{sIn} versus growth temperature in the InGaAs obtained from the experimental results with the substrates of GaAs (100) 2°, 5° off to $\langle 111 \rangle B$. The experimental error bar corresponds to the nonuniformity among the substrate temperature and the activation energy was found to be 5.3 ± 0.8 eV.

distance is increased at the same substrate temperature, the concentration of In is decreased and that as the growth temperature increases, which corresponds to decreasing the residence time τ_s , the step kinetics which is expressed by τ_k plays a more important role in determining the alloy composition. Hence, from the alloy composition which contains the combined process of the reevaporation and the incorporation, the ratio τ_{kIn}^B/τ_{sIn} can be calculated from the experimental data and is shown in fig. 3 where τ_{kIn}^B means the value for $\langle 111 \rangle B$ off surface. The activation energy of τ_{kIn}^B/τ_{sIn} was found as 5.3 ± 0.8 eV which contains the desorption energy of In and the step incorporation energy. Since τ_{kIn} depends on the structure of the step, τ_{kIn}^A for the surface off to $\langle 111 \rangle A$ is not necessarily equal to τ_{kIn}^B . Actually, τ_{kIn}^A is found to be larger than τ_{kIn}^B qualitatively.

Since the reevaporation of Al can be neglected for AlGaAs, we can get the composition of AlGaAs like eq. (5) on analogy of InGaAs. However, in the case of AlGaAs, the experimental results show no dependence of Ga concentration on the off-angle or on the crystal orientation. There are two ways to explain these phenomena as follows:

(1) The number of steps on the surface may

become infinitely large since the presence of Al might produce a large number of 2D or 3D nucleations. Once this happens, λ_0 becomes nearly zero and we get

$$x = \frac{J_{Al}^s}{J_{Ga}^s + J_{Al}^s} = \frac{J_{Al}^{in}}{\left(J_{Ga}^{in} - \frac{n_{Ga}^c}{\tau_{sGa}} \right) + J_{Al}^{in}} \quad (7)$$

for $Al_xGa_{1-x}As$. Eq. (7) takes the same expression as the one which the thermodynamic theory gives and it shows no dependence on the orientation, in agreement with the experimental results.

(2) It can be assumed that although the growth occurs in the step flow mode, the growth reaction at the front becomes much more closer to equilibrium than the case of InGaAs. Then we can assume $\tau_{kGa} \ll \tau_{sGa}$ and we get the same form as eq. (7). In this situation the main point of great contrast between InGaAs and AlGaAs exists in the difference in incorporation kinetics of In and Ga at the steps, respectively. It means that the In atom is difficult to be incorporated into the crystal (steps) and it passes over or is reflected back at the step edges more frequently than Ga in the growth of AlGaAs. In other words, the difference exists in the degree of equilibrium established at the step edge, namely, Ga in AlGaAs is expected to be much closer to equilibrium than In in InGaAs. Up to now, it is difficult to conclude which explanation is correct.

5. Conclusions

A theory is developed to understand the growth of III-V alloys taking account of the step kinetics in addition to the surface diffusion. MBE experiments have revealed that the solid composition of InGaAs and AlGaAs grown at higher temperature shows a great contrast, in such a way that the former depends very much on the degrees of the off-angle and the off-axis; however, the latter does not depend on these conditions within an experimental error. This clearly indicates that the step kinetics plays an important role in the growth of MBE. The different behavior in the solid composition between InGaAs and AlGaAs has been explained by using the present model.

Acknowledgements

The present authors thank Dr. M. Tanaka, Ms. M. Washiyama and Mr. R. Sasagawa of the University of Tokyo for their valuable help to carry out this work. This work was supported by the Grant-in-Aid No. 02352027 for Co-operative Research (B) on "Studies on crystal growth mechanism in atomic scale", from the Ministry of Education, Science and Culture.

References

- [1] J.H. Neave, P.J. Dobson, B.A. Joyce and J. Zhang, *Appl. Phys. Letters* 47 (1985) 100.
- [2] K. Ohta, T. Kojima and T. Nakagawa, *J. Crystal Growth* 95 (1989) 71.
- [3] W.K. Burton, N. Cabrera and F.C. Frank, *Phil. Trans. Roy. Soc. London A*243 (1951) 299.
- [4] T. Nishinaga and K.I. Cho, *Japan. J. Appl. Phys.* 27 (1988) L12.
- [5] T. Shitara and T. Nishinaga, *Japan. J. Appl. Phys.* 28 (1989) 1212.
- [6] H. Hata, T. Isu, A. Watanabe and Y. Katayama, *Appl. Phys. Letters* 56 (1990) 2542.
- [7] P. Bennema and G.H. Gilmer, in: *Crystal Growth: An Introduction*, Ed. P. Hartman (North-Holland, Amsterdam, 1973) ch. 10.
- [8] R. Heckingbottom, *J. Vacuum Sci. Technol.* B3 (1985) 572.
- [9] H. Seki and A. Koukitu, *J. Crystal Growth* 78 (1986) 342.

Monte Carlo simulation of MBE growth of the 2×4 reconstructed GaAs(001) surface

J.M. McCoy and P.A. Maksym

Department of Physics and Astronomy, University of Leicester, University Road, Leicester LE1 7RH, UK

A Monte Carlo model is used to simulate the MBE growth of the As-stabilized GaAs(001) 2×4 surface. Atomistic detail of the bilayer growth cycle, derived from a proposed model of the growth, is incorporated in a phenomenological manner. Despite the large size of the reconstructed unit cell, this approach is not significantly more computationally-demanding in the updating of rates than simulations which neglect the reconstruction and the atomistic growth model details. Preliminary results indicate that the inclusion of these additional ingredients in the simulation produces significant differences in the grown surface. Simulated growth of the 2×4 system produces surfaces which reproduce features reported in STM studies of the real surface.

1. Introduction

Valuable information about the behavior of atoms at semiconductor crystal surfaces during MBE growth has been provided by a number of Monte Carlo (MC) computer simulations (e.g., refs. [1,2]). Reconstruction of the surface has a significant influence upon the kinetics of surface atoms and, consequently, upon the manner in which the growth proceeds. However, reported MC growth simulations which incorporate the effects of reconstruction in an explicitly atomistic fashion have been limited to systems having small and relatively simple reconstructed surface unit cells (e.g., Si(001) 2×1 [2,3], GaAs(001) 2×2 [4]). In case of GaAs(001) 2×2 , a significant increase was found in the roughness of the growth front in a simulation in which the effect of the surface reconstruction was included, compared with a simulation which neglected the reconstruction [4]. MBE growth of the important As-stabilized GaAs(001) 2×4 system has so far not been simulated using a MC model and this is the purpose of the present work. Our model is a MC implementation of the model proposed by Farrell et al. [5] which is based upon a consideration of steric and electron-counting constraints imposed on the surface atoms during growth. The MC model em-

ploys a method of calculating the rates of surface kinetic processes which avoids the computationally-intensive task of searching further out than second nearest neighbor sites, despite the large size of the reconstructed unit cell. We will first present briefly the pertinent features of the proposed growth model. An account of the computer model and details of the way in which the growth model is formulated within a MC framework will then be given. Finally, results will be presented of simulations of the initial stages of growth. Comparison will be made with simulations for which the effects of reconstruction are absent and the simulated surface will be compared with reported STM observations of the real surface.

2. Proposed growth model

The model of Farrell et al. describes the growth sequence of a 2×4 unit cell in the As-stabilized system from a flux of monatomic Ga and an excess flux of As_2 , both of which provide physisorbed diffusing species on the surface prior to chemisorption. The initial structure of the 2×4 cell in the presence of an As flux but in the absence of a Ga flux prior to the start of growth comprises a three-quarter coverage of As in the

form of As dimers in the "missing row" configuration. This structure, predicted by a tight-binding total-energy calculation [6], and observed using STM [7,8], consists of three aligned surface As dimers and one dimer vacancy per unit cell. Growth begins when Ga atoms are introduced onto the surface and become a monatomic diffusing species. Space forbids a complete description of the growth model here, but the model postulates the sequence of stable intermediate surface atom configurations occurring during the bilayer growth cycle, starting from the "missing row" structure, with the same structure being recovered after the deposition of the bilayer. In between these stable intermediate structures, the surface is expected to experience various short-lived, excited configurations. The growth model also explains how the $c(2 \times 8)$ reconstruction arises from the juxtaposition of two neighboring 2×4 units aligned along the $[110]$ direction (the direction of their $4 \times$ periodicity) but having an antiphase boundary in the $[\bar{1}10]$ direction [7].

3. The MC model

The MC algorithm governing the growth simulation of the semiconductor surface is the fast MBE growth algorithm of Maksym [9], extended to incorporate surface dimerization, with dimer reorientation events ("dimer flips") [2] also included. The surface is represented by a square of $n \times n$ sites with periodic boundary conditions. The GaAs tetrahedral crystal structure is explicitly accounted for, the current structure (including the reconstruction) being mapped into an integer array. Other ingredients of the model are closely based upon reported work also. The As is assumed to arrive as diatomic As_2 from a physisorbed reservoir and to dissociate on any pair of second neighbor sites which each have a Ga first neighbor [9,10]. Diffusion and evaporation events of single atoms have rates calculated from interaction energies derived from the number and atom kind of all first and second nearest neighbor atoms surrounding the atom. There is an additional energy term present, representing the additional binding, if the given atom is one of a dimer pair. Finally,

the total interaction energy, E_h or E_e , for diffusion or evaporation respectively, is multiplied by a phenomenological factor α ($0 < \alpha \leq 1$) which depends upon both the local environment of the atom and the current stage of growth in the unit cell occupied by the atom. The factor α promotes the correct manner of growth. The inclusion of this factor is one of the novel parts of the simulation and will be treated in greater depth below. Explicitly, the rates for diffusion, h , and evaporation, e , respectively, are given by the Arrhenius expressions

$$h = R_h \exp\left(-\frac{\alpha E_h}{kT}\right), \quad e = R_e \exp\left(-\frac{\alpha E_e}{kT}\right). \quad (1)$$

The interaction energies and the prefactor for diffusion rates are derived from the RHEED oscillation measurements of Neave et al. [11], whilst the parameters for evaporation are those used by Singh and Madhukar [10] (see also ref. [12]). The additional contribution to the energies in the rate expressions if the atom is dimerized are in the range 0.5–0.6 eV for both diffusion and evaporation rates and for both As and Ga dimers. Detailed information on the accuracy of these values is lacking, but they are satisfactory in reflecting the increase in stability caused by dimerization.

Rates for dimer reorientation events are calculated in a way similar to that in ref. [2]. These events are important as they allow reordering in intermediate structures during the growth and maintain coherence between neighboring surface unit cells. The flip rate is given by the Arrhenius expression,

$$f = R_f \exp(-E_f/kT). \quad (2)$$

E_f is given by $E_f = E_d - mE_m$, where E_d is a constant activation energy and mE_m is a term describing the influence on the flip rate of the configuration of first nearest neighbor dimers in the same layer and of the same atom type. E_m is a constant and m is an integer having a value in the range 0–4, depending on the presence and orientation of adjacent dimers. The main result of this formulation is that dimers tend to arrange themselves in rows rather than in any other configuration [2]. We use the values $R_f = 10^{12} \text{ s}^{-1}$, $E_d = 1.9$

eV and $E_m = 0.2$ eV for both As and Ga dimers. Again, accurate values for these parameters are difficult to estimate [3], but these values are close to those used in Si(001) 2×1 simulations [2,3] and they are sufficiently accurate to produce satisfactory dimer reorientation behavior during the simulated growth.

The value of α used for a given diffusion or evaporation rate at a given stage of the growth is the key to ensuring that growth follows, at least in an approximate manner, the proposed growth model. Indeed, the use of the phenomenological factor, α , avoids the necessity of having to update diffusion and evaporation rates by searching sites further out than second nearest neighbors, despite the large size of the reconstructed unit cell. Hence, the procedure is of comparable computational speed to reported simulations employing site searches out to second nearest neighbor displacements (e.g., refs. [1,2,9]).

In detail, the procedure to update diffusion and evaporation rates involves, at a given stage of the growth, determining the position of the atom within the 2×4 unit cell, calculating the interaction energy by searching out to second nearest neighbor sites and then multiplying by the factor α to promote (low α) or suppress (high α) a given type of event. The relevant value of α varies in accordance with the location of the atom and the current stage of growth within the growth cycle. The growth stage attained in a given unit cell is maintained by the value of a flag in each unit cell. Typical values of α are $\alpha = 1$ if an atom is located at a stable site at the current stage of the growth cycle and $\alpha = 0.2$ – 0.3 if an atom is resident at an unstable site, with intermediate values also used. The effect of this is that atoms at unstable sites, as given by the proposed growth model, rapidly diffuse to another site or (more rarely) evaporate, whilst atoms occupying stable sites remain in place and may be considered as being chemisorbed. This provides a close correspondence to the behavior of the real system, the physical relevance of α being to reflect the degree of stability in an atom's occupation of a given site at a given stage of the growth cycle. For example, the value of α for an undimerized Ga atom located on one of the three As dimers at the very beginning of the growth

cycle is $\alpha = 0.7$, whilst, for a Ga atom between the As dimer rows, $\alpha = 0.5$. This ensures that, in the former case, Ga atoms are fairly mobile before they eventually stabilize as dimers with other Ga atoms upon the As dimers, whilst in the latter case, the Ga atoms are more mobile, rarely stabilizing as Ga dimers at all. This produces the kind of structure predicted in ref. [5], the growth at this stage of the cycle being limited to sites above the initial As dimers. At later stages the value of α changes to allow the growth to proceed on the remaining sites, in accordance with the growth model. This procedure is only capable of providing an approximate description, since the relevant values of α are subject to some uncertainty.

Finally, a further feature of the model is the inclusion of a simultaneous As/Ga dimer chemisorption event to describe the two instances during the growth cycle which involve the coupled chemisorption of both a Ga and an As dimer (see ref. [5]). The model approximates such chemisorptions as being exactly simultaneous. These events occur whenever two Ga atoms dimerize on the correct two sites at the two correct stages of the growth cycle, the As dimer being inserted as part of the same event. A simplifying assumption is that the As dimer is always added at the same location within a unit cell. In the real system the situation is more complex as, most generally, there is a number of sites available for the addition of the As dimer.

4. Results

We present results of the initial stages of growth. Fig. 1 shows a representation of a typical sequence describing the growth of the first bilayer. The intermediate stable surface configurations in this simulated sequence correspond well to those proposed in ref. [5]. For clarity a 8×8 site subregion of a simulation run on a system size of 60×60 sites at a temperature of 875 K is shown. Fig. 1a ($t = 0.100$ s) shows the surface at approaching the completion of the first stage of the cycle which involves, on average, the chemisorption of one Ga dimer upon each triplet of As dimers [5]. Also displayed is one example of the first type of

simultaneous As/Ga dimer chemisorption event arising from the formation of a Ga dimer between two others located upon the initial As dimer triplets and which produces the simultaneous chemisorption of an As dimer in the "missing row". In fig. 1b ($t = 0.295$ s) the Ga coverage has increased, and sufficient simultaneous As/Ga chemisorptions have occurred to fill the "missing rows" with As. The initial stages of growth of the uppermost layer are also evident. The undimerized As atoms are highly mobile but attain more stability by dimerizing. In fig. 1c ($t = 0.360$ s) the Ga layer is approaching completion and for those cells in which the Ga layer is already complete, the uppermost As layer is rapidly increasing in coverage. The structure at approaching the completion of the bilayer is shown in fig. 1d ($t = 0.565$ s). Details

of this structure will be discussed later, but it is clear that a high degree of layer-by-layer growth is occurring.

The high quality of the grown surface in fig. 1 is a consequence of the incorporated details of the growth model. According to the growth model, the uppermost As layer cannot form beyond one-quarter coverage until the complete Ga layer has been chemisorbed and this mechanism is responsible for the extremely high degree of layer-by-layer growth. This contrasts with simulations not incorporating the reconstruction and which omit such atomistic detail of the growth model (the model reported in [9]), these simulations producing a rougher surface and a lower degree of layer-by-layer growth. Fig. 2 shows a comparison of a simulation not incorporating the reconstruction

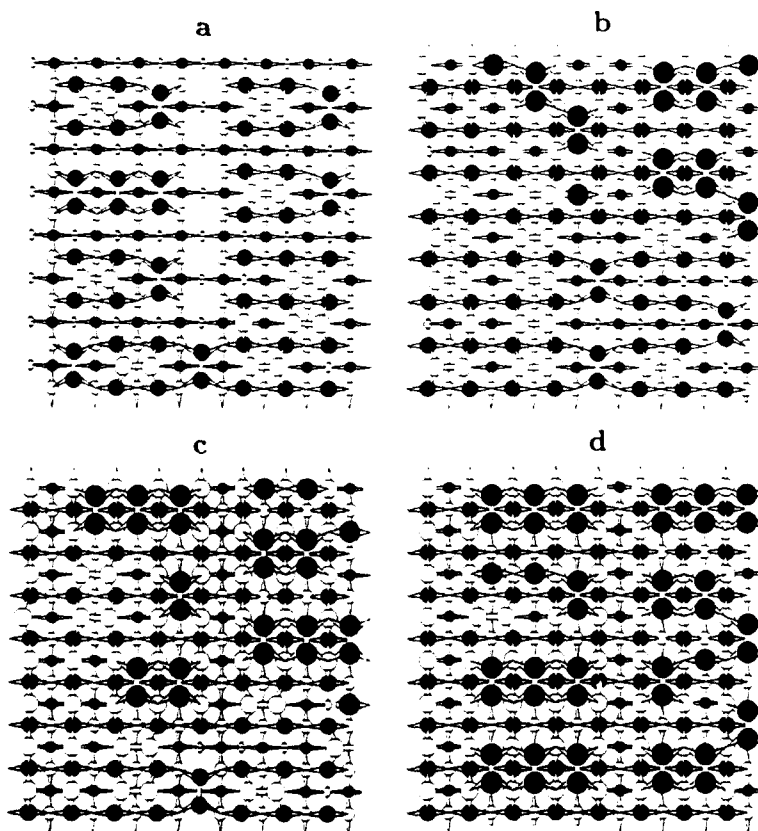


Fig. 1. Simulated growth sequence based on the Farrell et al. growth model. Displayed is a subregion of the surface at the times (a) 0.100 s, (b) 0.295 s, (c) 0.360 s and (d) 0.565 s. Key: Ga atoms are shown in white and As atoms in black.

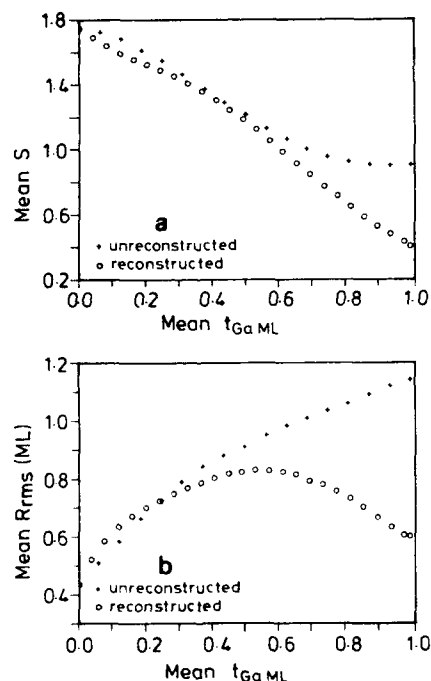


Fig. 2. Comparison of simulations incorporating both the 2×4 reconstruction and the atomistic details of the Farrell et al. growth model with simulations omitting both of these features. In (a) is plotted S , an index of layer-by-layer growth, and in (b) the rms surface roughness, R_{rms} . Times are normalized to $t_{\text{Ga ML}}$ (see text).

and the atomistic growth model details [9] and a simulation incorporating both of these features. Apart from those rate parameters relevant to reconstruction phenomena, all other rate parameters are identical between the two models. Fig. 2a is a plot of the quantity S which is a measure of layer-by-layer growth defined in [9]. Ideal layer-by-layer growth is characterized by S oscillating between the values 2 and 0. The $t=0$ value is, however, 1.75, corresponding to the initial three-quarter coverage of As upon one complete layer of Ga. For comparison the times are normalized to $t_{\text{Ga ML}}$ which is the earliest time at which sufficient deposited Ga atoms are present on the surface to form 1 ML. ($t_{\text{Ga ML}} = 0.32$ s for the unreconstructed model and $t_{\text{Ga ML}} = 0.49$ s for the reconstructed case.) The plotted data are average of five simulations on system sizes of 60×60 sites, using

different random number sets at the temperature 875 K. During this simulated stage of growth the degree of layer-by-layer growth is clearly significantly greater for the reconstructed model relative to that for the unreconstructed model. The reason is that, in the reconstructed model, growth is almost exclusively limited to the first bilayer, whilst in the unreconstructed model, no growth constraints prevent growth from progressing on layers above the first bilayer. This means that at the time $t_{\text{Ga ML}}$ nearly every chemisorbed Ga atom in the reconstructed model resides in one nearly-complete monolayer, whilst in the unreconstructed model the same Ga atoms are, most generally, distributed over more than one monolayer. Similarly, significant differences are evident in the rms surface roughness, R_{rms} , between the two models. R_{rms} is as defined in [2] and is expressed in units of ML. R_{rms} data are plotted in fig. 2b and are taken from the same five simulations as in fig. 2a. Indeed for $t > t_{\text{Ga ML}}$ and with the Ga flux maintained, for the reconstructed model the rms roughness oscillates, whilst for the unreconstructed model this quantity monotonically increases. Furthermore, for this latter case, our simulations have shown that R_{rms} continues monotonically increasing beyond $t_{\text{Ga ML}}$. These results are further explained by our observation that, in the case of the reconstructed surface, Ga atoms arriving on top of the As atoms in the uppermost layer when the underlying Ga layer is not yet complete very rarely stabilize as dimers with neighboring Ga atoms whilst the lower Ga layer remains incomplete. Such Ga adatoms tend to diffuse to fill holes, whilst they exist, rather than initiate a new layer, and the uppermost As layer rapidly reaches its full three-quarter coverage before the second Ga layer is initiated. This is the reason why for $t > t_{\text{Ga ML}}$ such a high degree of layer-by-layer growth is evident in the simulation in fig. 1. In summary, the additional features of the growth model which have been incorporated, which are in essence the inclusion of details of the order in which stable chemisorption sites become available during the growth cycle, have a significant effect upon the manner of growth and the quality of the surface. Since such details are important we suggest that simulations not considering such features are ne-

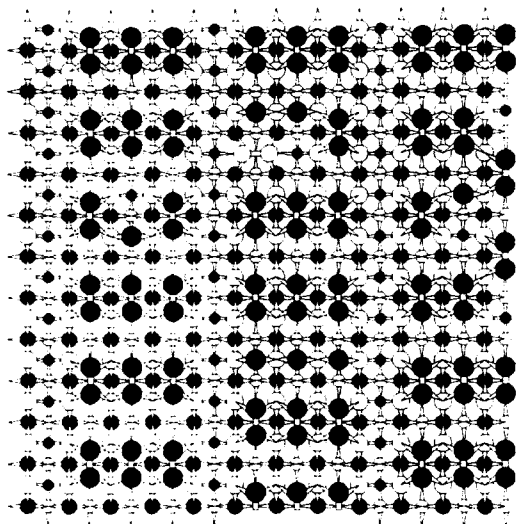


Fig. 3. 12×12 site subregion of a simulation on a 60×60 site system at 875 K after the growth of the first bilayer, showing the coexistence of small 2×4 and $c(2 \times 8)$ domains. Present also are examples of local disorder and defects (see text). (Key as in fig. 1.)

glecting a significant ingredient. It is possible that this is the cause of the qualitative discrepancy between our data and that reported for GaAs(001) 2×2 [4], mentioned in section 1.

Finally, in fig. 3 we show a typical simulated region of 12×12 sites, again a subregion of a 60×60 site system with growth conditions as in fig. 1. Certain features of the simulated surface reproduce those found in STM images (e.g., ref. [7]). Particularly well reproduced is the coexistence of small domains, having sizes of a few unit cells across, of both the 2×4 and the $c(2 \times 8)$ reconstruction. Examples of the disorder and the defects evident on the simulated surface bear a close correspondence to some of those reported in ref. [7]. As in ref. [7], we find local disorder involving rows of three undimerized As atoms along [110] which has the effect of turning an in-phase boundary into an antiphase boundary, and also

we find examples of unit cells having less than three dimers. However, the perfect "missing row" structure is a consequence of the model formulation and such a degree of ordering is rarely found in the real system.

5. Concluding remarks

The gross features of MBE growth of the As-stabilized GaAs(001) 2×4 surface have been simulated using a MC model. Significant differences in growth occur when the 2×4 reconstruction is included. The simulated surface reproduces certain features on the real surface as revealed by STM studies.

Acknowledgements

We acknowledge financial support from the Science and Engineering Research Council, UK. P.A.M. is grateful for the support of the Nuffield Foundation.

References

- [1] S.V. Ghaisas and A. Madhukar, Phys. Rev. Letters 56 (1986) 1066.
- [2] S.A. Barnett and A. Rockett, Surface Sci. 198 (1988) 133.
- [3] A. Rockett, Surface Sci. 227 (1990) 208.
- [4] S.B. Ogale, M. Thomsen and A. Madhukar, Mater. Res. Soc. Symp. Proc. 94 (1987) 83.
- [5] H.H. Farrell, J.P. Harbison and L.D. Peterson, J. Vacuum Sci. Technol. B5 (1987) 1482.
- [6] D.J. Chadi, J. Vacuum Sci. Technol. A5 (1987) 834.
- [7] M.D. Pashley, K.W. Haberern, W. Friday, J.M. Woodall and P.D. Kirchner, Phys. Rev. Letters 60 (1988) 2176.
- [8] D.K. Biegelsen, R.D. Bringans, J.E. Northrup and L.-E. Swartz, Phys. Rev. B41 (1990) 5701; 42 (1990) 3195 (E).
- [9] P.A. Maksym, Semiconductor Sci. Technol. 3 (1988) 5^c.
- [10] J. Singh and A. Madhukar, Phys. Rev. Letters 51 (1983) 794.
- [11] J.H. Neave, P.J. Dobson, B.A. Joyce and J. Zhang, Appl. Phys. Letters 47 (1985) 100.
- [12] A. Madhukar and S.V. Ghaisas, CRC Critical Rev. Solid State Mater. Sci. 14 (1988) 1.

Control of initial surface configuration for GaAs-on-Si MBE using a Si buffer layer?

G.E. Crook, L. Tapfer, L. Däweritz *, R. Cingolani and K. Ploog

Max-Planck-Institut für Festkörperforschung, Heisenbergstrasse 1, W-7000 Stuttgart 80, Germany

Gallium arsenide layers were grown by molecular beam epitaxy on (100) Si substrates misoriented by 1.7° and 4° toward [011], with a thin Si buffer layer deposited before GaAs growth for some samples. Reflection high energy electron diffraction observations showed that the substrates misoriented by 1.7° had mostly single-layer steps, while those misoriented by 4° had mostly double-layer steps, regardless of the conditions for the Si buffer layer growth. For 3 μm thick GaAs layers, the measured full widths at half-maximum of the GaAs (400) X-ray reflection ranged from 680 to 870 μrad (about 140 to 180 arc sec), with linewidths about 15% lower for the layers grown on the 4° misoriented substrates. Photoluminescence spectra for the GaAs layers were dominated by carbon-related luminescence, possibly caused by contamination during in situ annealing cycles. However, a GaAs/AlAs superlattice grown on a GaAs-on-Si buffer layer exhibited a single luminescence peak with a linewidth of 8 meV.

1. Introduction

Vicinal Si(100) surfaces have been very important in molecular beam epitaxy (MBE) of GaAs on silicon substrates. For example, growth on Si substrates misoriented toward a $\langle 011 \rangle$ direction results in GaAs without antiphase domains [1,2]. For some time it was thought that substrates with single-domain surfaces (having steps an even number of atomic layers high) were required for this antiphase domain suppression. However, GaAs grown on double-domain (having domains with both (2×1) and (1×2) reconstruction) vicinal Si substrates also shows no evidence of antiphase domains when examined using reflection high-energy electron diffraction (RHEED) [3,4]. In this work we examine the effect of Si substrates with single-layer and double-layer steps on the structural and optical properties of GaAs-on-Si layers.

There has been a great deal of interest in the nature of steps on vicinal Si(100) surfaces [5]. Double-layer steps are observed for surfaces with

larger misorientations toward $\langle 011 \rangle$ (4° or more), while surfaces with smaller misorientations (2° or less) generally have single-layer steps. Recently it has been reported that Si growth on vicinal Si surfaces can produce double-layer steps on surfaces which normally have single-layer steps [6–8], and single-layer steps on surfaces normally having double-layer steps [6]. We will investigate the use of a resistively heated Si source in the MBE growth chamber to alter the step configuration on vicinal substrates, and then examine GaAs layers grown on these substrates by double-crystal X-ray diffraction and photoluminescence.

2. Experimental procedure

The MBE system used has a RIBER 2300 MBE growth chamber, with a standard 3-inch RIBER substrate manipulator, and custom-built preparation and load-lock chambers. The substrate heaters in the preparation chamber can reach about 1100°C, with uniform heating across a 2-inch wafer mounted in an indium-free holder (radiative heating). A Si effusion cell which sublimates high-purity Si by passing current through it [9] is used

* On leave from Zentralinstitut für Elektronenphysik, O-1086 Berlin, Germany.

in the growth chamber to grow Si at a rate of about 0.1 nm/min.

The substrates used were Si(100) with misorientations of 1.7° and 4° toward [011]. Quarters of 2-inch wafers were put into concentrated H₂SO₄ with ultrasonic agitation for 10 min (to help reduce particulate contamination [10]), rinsed in DI water, and blown dry with N₂ before mounting in In-free holders and loading into the MBE machine. After outgassing in the loadlock chamber, the substrates were thermally cleaned in the preparation chamber by heating to 850°C and then raising the temperature by about 10°C/s until the chamber pressure reached 10⁻⁸ Torr, at which time the temperature was brought to 850°C again. The substrates were typically flashed 4 to 8 times to temperatures of 1000–1050°C (as read by a thermocouple behind the substrate).

Silicon was grown at a rate of about 0.1 nm/min at substrate temperatures between 400 and 800°C (measured with a thermocouple calibrated using GaAs and Si oxide desorption temperatures). For examination of the Si growth using RHEED, successive Si layers about 1 nm thick were grown on a given substrate. After growth at one substrate temperature, the substrate was moved to the preparation chamber for high-temperature flash annealing (as described above) in order to provide a smooth surface for growth at the next substrate temperature. The RHEED results are described in the next section. For the samples which had GaAs grown on a Si buffer layer, one Si layer about 1.5 nm thick was grown at 450°C. This layer was then flash-annealed in the preparation chamber before GaAs growth.

For GaAs growth, substrates were brought to 300°C in the growth chamber before heating the As₄ source. The first 0.1 μm was then grown using the "migration-enhanced epitaxy" (MEE) method [11], with one monolayer of GaAs deposited per cycle (cycle: 1 s Ga, 1 s interrupt, 1 s As, 1 s interrupt). After annealing this layer at 600°C for 15 min under As₄ flux, the next 0.4 μm was grown by MBE with a substrate temperature of 500°C and a growth rate of 0.5 μm/h. This layer was annealed at 650°C for 15 min, and the next 0.5 μm was grown at 600°C with a growth rate of 1 μm/h. At this point in the growth (1 μm total

thickness) three cyclic thermal anneals were performed under As₄ flux. In each cycle, the substrate temperature was raised to 650°C for 5 min, lowered to 300°C for 5 min, and raised again to 600°C. A cycle took about 35 min, and 20 nm of GaAs was grown at the end of each cycle to provide a fresh GaAs surface. We have found that this thermal cycling treatment significantly improves the X-ray diffraction linewidths of our GaAs-on-Si layers [12]. Another 1 μm GaAs was then grown at 600°C with a growth rate of 1 μm/h, and the layer was again thermally cycled three times. Finally, 1 μm more of GaAs was grown (600°C, 1 μm/h) with no further thermal treatment, so that the final layer thickness was 3 μm. In one of the samples, a 1 μm thick GaAs/AlAs superlattice was grown instead of the final 1 μm of GaAs.

3. Results

3.1. Si buffer layer growth

Although control of the step configuration on vicinal Si substrates by growing Si under appropriate conditions has been reported by other authors as described above, we were unable to reproduce these results in our experiments. Typical RHEED patterns taken with the electron beam directed along the step edges of substrates misoriented by 4° and 1.7° toward [011] are shown in fig. 1. The weakened 1/2 order streaks and the spacing of the splitting in the major streaks (denoted by arrows) of the pattern from the 4° substrate indicate a mostly single-domain surface with regularly spaced double-layer steps [5]. The pattern from the 1.7° substrate has strong 1/2 order spots, indicating a double-domain surface. The apparent splitting in the 00 streak of fig. 1b, though not well resolved, has a spacing consistent with that expected for an array of double-layer steps at this misorientation. The double-domain surface may therefore arise from single-layer islands with double-layer steps rather than regular single-layer steps. Silicon growth on the substrates appeared to roughen the surfaces, and did not result in RHEED patterns indicating predomi-

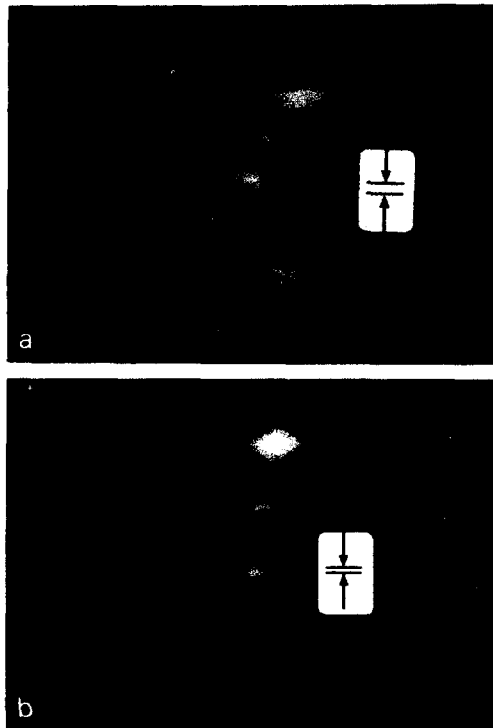


Fig. 1. RHEED patterns from Si(100) after flash annealing, observed with the 20 keV electron beam directed parallel to the step edges of substrates misoriented by (a) 4° and (b) 1.7° toward [011]. Step-induced splitting of RHEED streaks is shown by arrows. (Magnification is not the same in (a) and (b).)

nantly single-layer steps on the 4° surfaces or double-layer steps on the 1.7° surfaces. We believe that the most likely explanation for this inconsistency with the results of other authors is contamination from As around the Si source in the growth chamber. Before growing GaAs on

samples with Si buffer layers, the substrates were moved to the preparation chamber for an additional flash annealing treatment to remove any contamination associated with the Si growth.

3.2. GaAs layers

The GaAs layers grown on both substrate misorientations, with or without 1.5nm-thick Si buffer layers, all had (2 × 4) reconstructions which appeared during the anneal of the initial 0.1 μm thick layer. The "4 × " pattern was seen with the electron beam parallel to the step edges, and there was no indication in the RHEED patterns of antiphase domains. Double-crystal X-ray diffraction measurements of the (400) and (511) reflections for four GaAs-on-Si layers are summarized in table 1. Measurements were made with the X-ray beam directed along each of the four <011> directions; the average of the two measurements made with the beam parallel to the step edges and the two with the beam perpendicular to the step edges is recorded for each sample. The misorientation between the GaAs layer and the Si substrate was calculated from the variation in the angle between the GaAs and Si peaks [13]. For both substrate misorientations, the tilt of the GaAs lattice planes with respect to those of the Si substrate was such that the GaAs [100] direction lay between the surface normal and the Si [100] direction, as has been seen before for misorientations larger than 1° [13,14].

The broadening of the (511) linewidths with respect to the (400) linewidths is primarily caused by dispersion arising from the use of different reflections in the monochromator crystal and the sample (the (400) reflection from a Ge crystal is

Table 1
X-ray diffraction results on 3 μm thick GaAs layers

Substrate misorientation → [011] (deg)	Si buffer? (1.5 nm thick)	Misorientation between GaAs and Si (deg)	GaAs FWHM (μrad)			
			(400) reflection		(511) reflection	
			to steps	⊥ to steps	to steps	⊥ to steps
1.7	No	0.060	870	810	940	850
1.7	Yes	0.074	860	840	900	890
4	No	0.158	720	690	770	770
4	Yes	0.156	730	680	790	730

used for the monochromator). It can be seen from the table that for both reflections, the FWHM for the layers grown on substrates misoriented by 4° are about 15% smaller than for the layers grown on the 1.7° misoriented substrates. The presence or absence of the Si buffer layer did not appear to affect the X-ray results. The linewidths measured with the X-ray beam perpendicular to the step edges were always less than or equal to those measured with the beam parallel to the step edges. This could be indicative of an anisotropy for defects in the layers, and will be studied further.

A typical 5 K photoluminescence (PL) spectrum for the GaAs-on-Si layers is shown in the inset of fig. 2. The spectra are dominated by impurity-related transitions at the characteristic energy for carbon acceptors. The carbon was presumably incorporated during the long interrupts for thermal cycling, and possibly during the initial MBE growth. The spectra were similar for the GaAs layers grown on both substrate misorientations, with and without a Si buffer layer. The main part of fig. 2 shows the PL spectrum for a sample with a $1\text{ }\mu\text{m}$ thick GaAs/AlAs superlattice (100 periods, nominally 5.0 nm GaAs/5.0 nm AlAs)

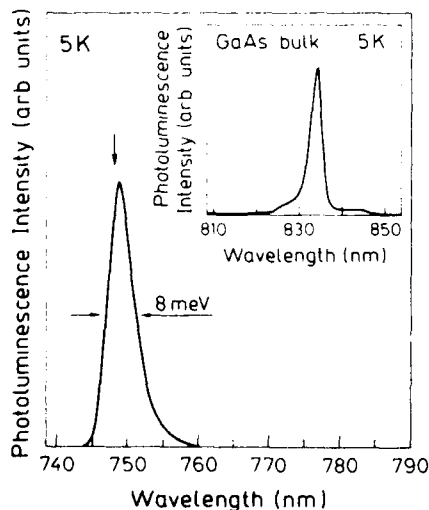


Fig. 2. Photoluminescence spectrum at 5 K for GaAs/AlAs superlattice grown on a $2\text{ }\mu\text{m}$ thick GaAs buffer on a Si substrate misoriented by 1.7° toward [011]. The inset shows a typical spectrum for the $3\text{ }\mu\text{m}$ thick GaAs layers on Si.

grown instead of the top $1\text{ }\mu\text{m}$ of GaAs. This structure exhibited intense luminescence from the superlattice layer. The arrow indicates the wavelength of the fundamental interband electron-to-heavy-hole transition calculated for 5 nm wells and 5 nm barriers with the usual Kronig-Penney model. The calculation neglected strain effects and used a 65:35 band offset ratio. The 8 meV linewidth is similar to those previously reported for GaAs/AlGaAs quantum wells on silicon [15,16]. In contrast to the spectra from the GaAs layers, the spectrum from the superlattice sample does not contain strong impurity-related luminescence. This suggests that any impurities which were incorporated into the GaAs buffer layer did not diffuse very far into the superlattice layer.

4. Conclusions

X-ray diffraction linewidths for GaAs layers grown by MBE on vicinal Si(100) were found to be about 15% lower for layers grown on substrates misoriented by 4° toward [110] than for layers on substrates with a 1.7° misorientation, suggesting that single-domain Si surfaces indeed result in better GaAs-on-Si layers. The PL spectra for the GaAs layers were qualitatively the same for the different substrates, but the large extrinsic luminescence could be masking any differences. Finally, the in situ thermal cycling which leads to improvement of the X-ray linewidths (reflecting reduced dislocation densities) is probably the reason for the strong impurity-related PL transitions in the GaAs-on-Si layers. Faster thermal cycling and/or growing during the cycling may be a way to mitigate this impurity incorporation while retaining good structural properties.

Acknowledgements

We would like to thank A. Fischer for his expert technical assistance, W. Stolz for several helpful discussions, and E. Böckenhoff (Thomson-CSF) for providing some of the silicon wafers. This work was sponsored by the Bundesmini-

sterium für Forschung und Technologie of the Federal Republic of Germany.

References

- [1] R. Fischer, N. Chand, W. Kopp, H. Morkoç, L.P. Erickson and R. Youngman, *Appl. Phys. Letters* 47 (1985) 397.
- [2] M. Kawabe and T. Ueda, *Japan. J. Appl. Phys.* 25 (1986) L285.
- [3] P.R. Pukite and P.I. Cohen, *Appl. Phys. Letters* 50 (1987) 1739.
- [4] M. Kawabe and T. Ueda, *Japan. J. Appl. Phys.* 26 (1987) L944.
- [5] G.E. Crook, L. Däweritz and K. Ploog, *Phys. Rev.* B42 (1990) 5126, and references therein.
- [6] K. Sakamoto, T. Sakamoto, K. Miki and S. Nagao, *J. Electrochem. Soc.* 136 (1989) 2705.
- [7] A.J. Hoeven, E.J. van Loenen, D. Dijkamp, J.M. Lenssinck and J. Dieleman, *Thin Solid Films* 183 (1989) 263.
- [8] N. Aizaki and T. Tatsumi, *Surface Sci.* 174 (1986) 658.
- [9] Si source made by KEKO, Wildmoosstrasse 2, W-8047 Karlsfeld/München, Germany.
- [10] H. Fronius, A. Fischer and K. Ploog, *Japan. J. Appl. Phys.* 25 (1986) L137.
- [11] Y. Horikoshi, M. Kawashima, and H. Yamaguchi, *Japan. J. Appl. Phys.* 25 (1986) L868.
- [12] W. Stolz, G.E. Crook, L. Tapfer and K. Ploog, in: *Proc. 1st Intern. Conf. on Epitaxial Crystal Growth*, Budapest, April 1990 (*Trans Tech.*, to be published).
- [13] H. Nagai, *J. Appl. Phys.* 45 (1974) 3789.
- [14] R.J. Matyi, J.W. Lee and H.F. Schaake, *J. Electron. Mater.* 17 (1988) 87.
- [15] M. Naganuma, W. Stolz and Y. Horikoshi, in: *Extended Abstracts 19th Conf. on Solid State Devices and Materials*, Tokyo, 1987, p. 513.
- [16] C. Jagannath, S. Zemon, P. Norris and B.S. Elman, *Appl. Phys. Letters* 51 (1987) 1268.

Gallium desorption from (Al,Ga)As grown by molecular beam epitaxy at high temperatures

A.H. Kean, C.R. Stanley, M.C. Holland

Department of Electronics and Electrical Engineering, University of Glasgow, Glasgow G12 8QQ, UK

J.L. Martin and J.N. Chapman

Department of Physics and Astronomy, University of Glasgow, Glasgow G12 8QQ, UK

We report on a detailed study by cross-sectional transmission electron microscopy (XTEM) of gallium desorption from (Al,Ga)As structures grown by molecular beam epitaxy (MBE) at substrate temperatures in the range 680–730 °C. The Ga desorption rate (D_i) depends only on substrate temperature, with an activation energy, E_a for re-evaporation of 2.56 eV, comparable to E_a for Ga evaporation from liquid gallium. The presence of aluminium has no measurable influence on D_i except where the desorbing gallium flux exceeds the incident flux ($D_i \gg G_i$), when a few monolayers of residual GaAs can be detected on an AlAs surface. No As_4 overpressure dependence has been observed. In practice, therefore, multilayer structures of (Al,Ga)As with controlled thicknesses and compositions can be grown with As_4 in the temperature regime investigated by making a constant allowance for D_i , irrespective of the compositional fraction of the (Al,Ga)As.

1. Introduction

It has been shown [1] that higher substrate temperatures, T_s than normally used during the molecular beam epitaxial (MBE) growth of GaAs are required to produce optical and laser devices in the (Al,Ga)As materials system. The low temperature photoluminescence recombination efficiency and associated linewidth of thick $\text{Al}_{1-x}\text{Ga}_x\text{As}$ layers ($x < 0.37$) improve and laser threshold current densities decrease as T_s is increased, particularly for growth with a $(3 \times 1)-(100)$ surface reconstruction. The improvement in optical quality results from the decreased probability of the formation of non-radiative recombination centres. In practice, a temperature in excess of 680 °C is required to avoid the window of temperature between ≈ 630 and 680 °C where the morphology of the (Al,Ga)As grown with As_4 is extremely poor [2]. Above ≈ 660 °C, desorption of gallium from the epilayer becomes significant, and the control of layer thicknesses and compositions to the desired accuracies becomes difficult.

However, there is still considerable controversy over the desorption behaviour of the more volatile group III element in the MBE growth of ternary alloys such as (Al,Ga)As and (Ga,In)As, and the influence exerted by the less volatile species. Conflicting evidence has been published on whether the process of gallium desorption from an (Al,Ga)As surface at high temperatures (≈ 700 °C) is dependent on the Al molar fraction [3–5] and/or the proximity of the GaAs to an underlying (Al,Ga)As interface [6].

This paper examines by two different methods the process of gallium desorption from (Al,Ga)As structures containing quantum wells (QWs) grown under different conditions. In the first series of experiments, (Al,Ga)As nett growth rates were measured by reflection high energy electron diffraction (RHEED) oscillations for $T_s \approx 580$ –720 °C. Secondly, RHEED oscillations were used to set up low temperature growth rates where gallium desorption does not occur. These growth rates were then used to grow structures at high T_s where gallium desorption is significant, but with

growth times set on the assumption of no desorption. The resulting layer thicknesses in the structures were then examined by cross-sectional transmission electron microscopy (XTEM).

2. Experimental procedures

The layers were grown in a standard 3-chamber Varian Modular Gen II MBE machine equipped with solid-source effusion furnaces. Note that growth was carried out using arsenic tetramers, As_4 , with a flux of $\approx 1 \times 10^{15}$ As atoms/ $\text{cm}^2 \cdot \text{s}$ and a growth rate of $\approx 1 \mu\text{m/h}$. This arsenic flux is ≈ 2 – 3 times higher than the flux used for GaAs growth. Two-inch diameter (100) GaAs wafers were cleaned by a standard method employing sulphuric acid and a de-ionised water rinse, and a protective surface oxide was formed by heating in air at $\approx 250^\circ\text{C}$ for 5 min [7]. The wafers were mounted on indium-free wafer holders and deoxidised in the intermediate chamber at a real temperature of 580°C for 10 min without an As overpressure. When transferred to the growth chamber, the GaAs surface exhibited well defined reconstruction when examined by 15 keV RHEED. A small 5 mm^2 calibration sample was mounted with indium at the centre of a molybdenum platen. An initial wafer temperature was determined by measuring T_i , the temperature at which the RHEED pattern changed from a $c(4 \times 4)$ As-rich to a (2×4) As-stable surface, which could be established to $\leq 5^\circ\text{C}$. Note, however, that T_i is a function of the As_4 overpressure. T_i was also measured with an infrared optical pyrometer (T_p). The growth rates of (Al,Ga)As, GaAs and AlAs were measured using RHEED intensity oscillations of the specularly reflected spot, which was difficult at high substrate temperatures when the diffraction pattern became diffuse.

3. Results and discussion

RHEED measurements. Fig. 1 shows the growth rates of $\text{Al}_{1-x}\text{Ga}_x\text{As}$ ($x = 0.3$ at low T_i), GaAs and AlAs as a function of substrate temperature between 580 and 720°C . Both the GaAs and

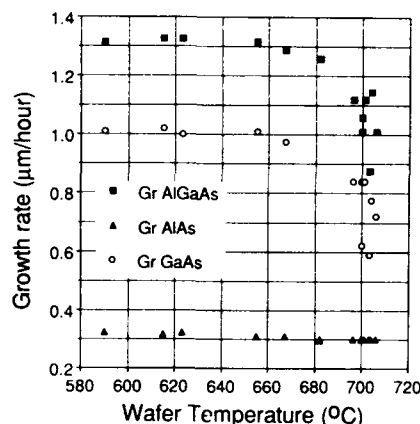


Fig. 1. Growth rates for GaAs, AlAs, and $\text{Al}_{1-x}\text{Ga}_x\text{As}$ ($x = 0.3$ for $T_i \leq 650^\circ\text{C}$) as a function of wafer temperature, determined from RHEED intensity oscillation.

(Al,Ga)As growth rates decrease as T_i is raised above $\approx 660^\circ\text{C}$, while the AlAs growth rate remains constant. Above 700°C , the gradient of the curves increases rapidly indicating that control of the growth rate at these temperatures becomes extremely difficult. It is more revealing, however, to display the data as a reduction in nett G_r versus T_i as shown in fig. 2, which in the absence of Al loss is just Ga desorption or re-evaporation.

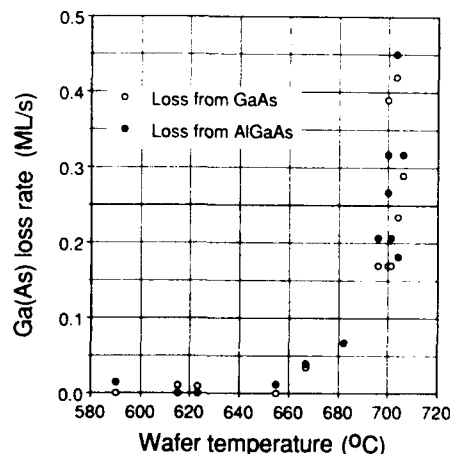


Fig. 2. Reduction in nett growth rate of GaAs and (Al,Ga)As (defined as $G_r(T_i \leq 650^\circ\text{C}) - G_r(T_i)$) as a function of wafer temperature.

$D_r(T)$ (monolayers per second (ML/s) $\approx \mu\text{m/h}$). The curves for $D_r(T)$ from GaAs and from $\text{Al}_x\text{Ga}_{1-x}\text{As}$ are indistinguishable indicating that within the errors of this experiment the presence of aluminium has no influence on Ga desorption.

XTEM. Several structures were grown for XTEM studies to measure GaAs layer thicknesses over a range of substrate temperatures after the fluxes had initially been set up using RHEED intensity oscillations at low T_s from the calibration wafer. The first experiment was designed to determine the variation of D_r with T_s , layer thickness and aluminium content. Sample No. A164 consisted of seven sets of 100 and 200 Å GaAs wells grown at T_s from $T_i + 180^\circ\text{C}$ ($T_p = 640^\circ\text{C}$) to $T_i + 260^\circ\text{C}$ ($T_p = 710^\circ\text{C}$), followed by six GaAs wells with intended thicknesses of 50–250 Å grown on 400 Å thick $\text{Al}_{0.4}\text{Ga}_{0.6}\text{As}$ barrier layers at $T_i + 240^\circ\text{C}$ ($T_p = 700^\circ\text{C}$), where gallium desorption is significant. Finally, 100 and 200 Å GaAs wells were grown on $\text{Al}_x\text{Ga}_{1-x}\text{As}$ layers with $x = 0.2, 0.4$ and 0.6 . The resultant GaAs well thicknesses were found to decrease as T_s increased, indicating a desorption rate up to 0.53 monolayers per second (ML/s) at a growth temperature of $T_i + 260^\circ\text{C}$ ($T_p = 710^\circ\text{C}$). The reduced thicknesses of the (Al,Ga)As barrier layers could be accounted for solely on the basis of Ga desorbing at the same rate as from GaAs. No dependence of D_r on the molar fraction $x = 0.2, 0.4$ and 0.6 has been observed. The measured thickness versus intended thickness for the 50–250 Å wells is plotted in fig. 3. The linear dependence indicates that D_r is constant at 0.32 ML/s, and is not influenced to any significant extent by the thickness of the GaAs overlaying the (Al,Ga)As surface, in contrast to the result of Ralston et al. [6]. Fig. 4 is a plot of the logarithm of gallium loss rate versus $1/T_s$ measured from the group of 100 and 200 Å thick QW grown at $T_i + 180 \rightarrow 260^\circ\text{C}$ ($T_p \approx 640 \rightarrow 710^\circ\text{C}$). The gradient of the plot yields the enthalpy for re-evaporation, ≈ 2.56 eV, close to the enthalpy of gallium evaporation from liquid gallium [8]. In a separate experiment, No. A195 was grown which included five sets of QWs varying from 25 to 300 Å in thickness grown at temperatures again ranging from $T_i + 180 \rightarrow 260^\circ\text{C}$. D_r was calculated to be 0.26 ML/s for

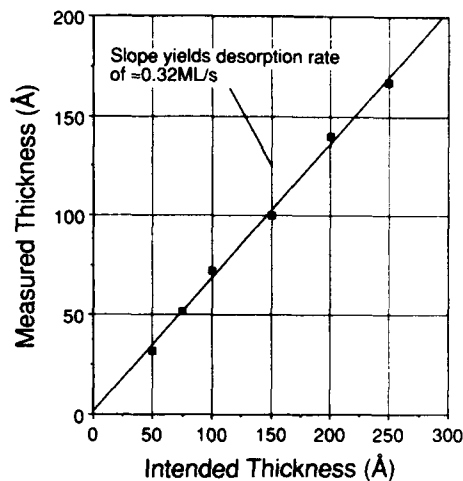


Fig. 3. Plot of thickness of quantum well measured by XTEM versus intended thickness for a wafer temperature of $\approx 700^\circ\text{C}$. The loss, or desorption rate, of Ga from GaAs is ≈ 0.32 ML/s.

$T_s = T_i + 260^\circ\text{C}$. The important observation here is that between individual experiments, there was a variation in the measured values of D_r for the same notional wafer temperature. This serves to emphasise that the sensitivity of D_r to T_s makes direct comparison between experiments difficult so that as much information as possible should be contained in a single, but complex structure.

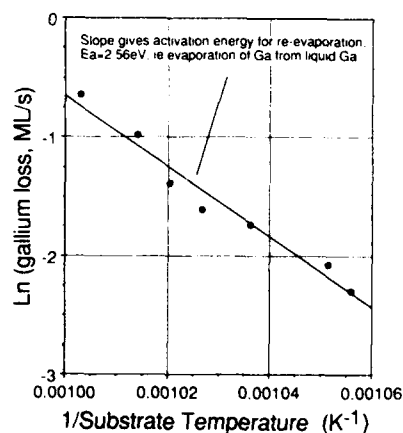


Fig. 4. Plot of $\ln(\text{Ga loss})$ versus $1/T_s$. The activation energy for the Ga re-evaporation is ≈ 2.56 eV.



Fig. 5. XTEM micrograph of a section of No. A257 showing residual GaAs layers (darker bands), highlighted by the arrows, embedded on AlAs (lighter bands) when grown under conditions where $D_r \gg G_r$.

The effect of As_4 overpressure on D_r was examined by growing a set of GaAs wells at $T_i + 240^\circ\text{C}$ and then repeating the experiments with a 50% increase in the As_4 flux. There was no apparent difference in the measured D_r between the two sets of data, although if the As_4 overpressure is increased by at least an order of magnitude then the desorption of gallium might be suppressed [5].

Finally, the growth of extremely thin wells at high temperatures has been examined where $D_r > G_r$ (the growth rate). Sample No. A257 contained twelve sets of four GaAs wells with 200 Å AlAs barriers. The thicknesses of the single wells were 2, 4, 8 and 16 ML. Each set was grown at three different growth rates (1.0, 0.5 and 0.1 ML/s) and repeated at four different substrate temperatures: $T_i + 130^\circ\text{C}$ ($T_p = 610^\circ\text{C}$), where $D_r \ll G_r$, providing a calibration of layer thicknesses, $T_i + 225^\circ\text{C}$ and $T_i + 250^\circ\text{C}$ where D_r is significant and $T_i + 275^\circ\text{C}$ ($T_p \approx 725^\circ\text{C}$) where $D_r \gg G_r$. As T_i is increased, the measured thicknesses of the QWs should decrease to zero according to the relationship $d = (G_r - D_r)t$ as D_r approaches G_r , where d is the thickness of the measured layer and t is the time taken to grow that particular layer. Thereafter, there will be no nett growth and no QWs

should be detected by XTEM. As T_i is increased, the measured thicknesses of the layers do decrease as expected, but significantly, at the highest temperature $T_i + 275^\circ\text{C}$ ($T_p \approx 725^\circ\text{C}$) and at the lowest growth rate of 0.1 ML/s where $D_r \gg G_r$, there is evidence for one or two residual monolayers of GaAs on the AlAs barriers. This is illustrated in the XTEM micrograph, fig. 5, where three sets of four thin GaAs wells can be seen (darker lines). The set identified by the white arrows was grown with $D_r \gg G_r$. The four wells appear to be the same thickness although absolute dimensions are difficult to measure because the resolution of the XTEM technique used here is around 7 Å. The presence of residual GaAs implies that D_r is severely retarded for the first monolayers of deposition, an effect observed by Ohta and co-workers [9,10] using RHEED sublimation oscillations.

4. Conclusions

The gallium desorption rate from GaAs or $\text{Al}_x\text{Ga}_{1-x}\text{As}$ ($0 \leq x \leq 1.0$) is dependent only on the substrate temperature except for an initial few

monolayers of deposited GaAs, which remain even when the gallium desorption flux is greater than the incident gallium flux. For most practical purposes, therefore, at the high values of T_s and minimum As_4 :Ga flux ratios required for the growth of optical quality (Al,Ga)As, a constant allowance for Ga re-evaporation can be assumed. The measured activation energy for gallium re-evaporation is ≈ 2.56 eV, close to the value for re-evaporation of gallium from liquid gallium, and substantiates recent modulated beam mass spectrometry studies of Ga desorption from (Al,Ga)As under similar experimental conditions by Gibson and co-workers [11]. The results presented here also provide support for the models which postulate surface segregation of gallium on (Al,Ga)As at higher temperatures [12,13].

Acknowledgements

The authors wish to acknowledge the technical support of J. Cochrane, R. Hutchins, N. Johnson and W. Reid in the MBE laboratory. The research is funded by the UK Science and Engineering Research Council through grants GR/E/18186 and GR/E/50117.

References

- [1] W.T. Tsang, Molecular beam epitaxy of III-V compound semiconductors, in: Semiconductors and Semimetals, Vol. 22, part A, Eds. R.K. Willardson and A.C. Beer (Academic Press, New York, 1985) pp. 95-207, and references therein.
- [2] H. Morkoç, T.J. Drummond, W. Kopp and R. Fischer, J. Electrochem. Soc. 129 (1982) 824.
- [3] R. Fischer, J. Klem, T.J. Drummond, R.E. Thorne, W. Kopp, H. Morkoç and A.Y. Cho, J. Appl. Phys. 54 (1983) 2508.
- [4] J.M. Van Hove and P.I. Cohen, Appl. Phys. Letters 47 (1985) 726.
- [5] R. Heckingbottom, J. Vacuum Sci. Technol. B3 (1985) 572.
- [6] J. Ralston, G.W. Wicks and L.F. Eastman, J. Vacuum Sci. Technol. B4 (1986) 594.
- [7] H. Fronius, A. Fischer and K. Ploog, Japan. J. Appl. Phys. 25 (1986) L137.
- [8] R.E. Honig and D.A. Kramer, RCA Rev. 30 (1969) 285.
- [9] K. Ohta, private communication.
- [10] T. Kojima, N.J. Kawai, T. Nakagawa, K. Ohta, T. Sakamoto and M. Kawashima, Appl. Phys. Letters 47 (1985) 286.
- [11] E.M. Gibson, C.T. Foxon, J. Zhang and B.A. Joyce, Appl. Phys. Letters 57 (1990) 1203.
- [12] J. Massies, J.F. Rochette and P. Delescluse, J. Vacuum Sci. Technol. B3 (1985) 613.
- [13] J. Massies, F. Turco and J.P. Contour, Semicond. Sci. Technol. 2 (1987) 179.

Atomic layer molecular beam epitaxy (ALMBE): growth kinetics and applications

F. Briones and A. Ruiz

Centro Nacional de Microelectrónica, CSIC, Calle Serrano 144, 28006 Madrid, Spain

MBE basic growth mechanisms for III–V compounds on (100) surfaces, step flow and 2D nucleation, are shown to be modified by a periodic modulation of the molecular beams in synchronism with the layer-by-layer growth sequence characteristic of optimized MBE. Beam modulation is shown to enhance nucleation on completed monolayers, leading to a better 2D or layer-by-layer growth (NEMBE). The possibility of growing in a kind of atomic layer-by-layer mode (ALMBE) is studied by optical (RDS) and RHEED in-situ analysis. Applications to the growth of III–V_A–V_B pseudoalloys and III_AV_B–III_CV_D superlattices and heterostructures are presented. Finally, exploratory growth experiments on low index surfaces (311), (211)A, (211)B, (111) and (110) by using modulated beams are discussed.

1. Remarks on MBE kinetics

The extraordinary ability of MBE to fabricate nearly perfect surfaces and interfaces of III–V semiconductors arises from the peculiar growth kinetics of the commonly used (100) surface. In particular, the layer-by-layer growth mechanism originates from the existence of a kinetic barrier for the nucleation of a new monolayer on a flat, defect-free surface such as the As stabilized, 2×4 reconstructed GaAs surface. The first kinetic obstacle is that sufficient Ga oversaturation must be achieved on the growing surface in order to allow some probability for the coincidence of two migrating Ga atoms and to incorporate simultaneously as a Ga–Ga dimer by bridging two As–As dimers [1]. A second requirement is the catalytic dissociation of an As₄ molecule on two of such Ga–Ga dimers to form the first stable GaAs nucleus [2]. This complicated process establishes an effective kinetic barrier for 2D nucleation as compared with the much more straightforward incorporation of migrating species at monolayer height steps [3].

The step flow growth mechanism will, therefore, predominate as long as terrace or islands sizes will not exceed the migration range of the impinging species. When the size of a growing

island surpasses this range or when steps are annihilated by 2D island coalescence, Ga oversaturation will increase up to a point in which 2D nucleation will be statistically possible and growth of a new monolayer will proceed by flow of islands steps [4].

Studies of RHEED intensity oscillations have been very helpful to modelize this process and to determine migration parameters [4,5]. The time and local random character of the 2D nucleation events are responsible for the observed RHEED oscillation damping and the evolution of the growth front into a multilevel one [6]. The scarcity of nucleation events is responsible for the large islands size and growth front flatness under optimized MBE conditions (high T_s , minimum group V flux to stabilize, 2×4 surface, large migration range).

2. Nucleation enhanced MBE (NEMBE)

Some years ago [6] we found that, by interrupting the As₄ beam for a short time during stationary MBE growth, damped out RHEED oscillations would recover. Moreover, by repeating the brief interruption periodically, in synchronism

with the monolayer-by-monolayer growth sequence, the oscillation amplitude will persist, not damp out, with growing time. We proposed that the mechanism behind it was an enhancement and synchronization of the nucleation events over the whole surface caused by the periodic group III surface enrichment, during interruptions as a consequence of the continuing group III deposition and As desorption at sufficiently high substrate temperature.

The optimum timing for the periodic interruptions of the As_4 flux in order to enhance RHEED oscillation amplitude and improve growth front flatness, is just after a RHEED I_{00} maximum has been achieved. It is known that, for the usual 2×4 reconstructed surface, I_{00} maxima correspond to the completion of a monolayer. If we provoke an As_4 interruption precisely at this moment, while continuing to supply Ga, the surface will be momentarily group III enriched and eventually will turn to the 3×1 or 4×2 reconstructions. When now As_4 flux is restored, it will find a Ga stabilized highly reactive surface and impinging As_4 molecules will catalytically dissociate and incorporate as homogeneously distributed nuclei of a new monolayer. The effect is that of synchronized suppression of the kinetic barrier for 2D nucleation. Further growth of the monolayer will proceed by lateral expansion of a high density of 2D islands. Notice that, even when at this stage group III and group V species are supplied simultaneously as in MBE, due to the availability of a large density of steps at the islands edges, the step propagation mechanism will predominate and nucleation of a second monolayer will be kinetically hindered until the growing one is completed. Notice also that the need for a large surface migration range for the impinging species is greatly reduced due to the small lateral dimensions of the islands at coalescence, and growth temperature can be lowered. Consequently, materials with reduced migration, such as AlGaAs or AlAs, can be grown layer by layer at temperatures well below 600°C [7]. At the same time, by minimizing the effect of inhomogeneous nucleation at defects (impurities or dislocations), epitaxial layer morphology (flatness) is greatly improved even for thick AlGaAs or highly doped materials ($n = 2 \times$

10^{19} cm^{-3} GaAs) and oval defects are totally suppressed [8]. Recognizing the importance of the nucleation enhancement, we denominated this process *nucleation enhanced MBE* (NEMBE) [8]. In particular, the ability of this mechanism to force 2D growth mode has led to successful applications of NEMBE to the growth of highly mismatched systems [9].

At low substrate temperatures, a periodic group III enrichment of the surface will not take place by arsenic desorption, but simply by letting group III arrive alone at the surface during a longer arsenic beam interruption. Meanwhile, an enhanced migration of group III species over the already group III stabilized areas in the absence of As_4 flux helps promoting a homogeneous group III atomic layer coverage. Homogeneous nucleation and growth of a monolayer will take place during the As_4 supply time. Now, this can be reduced to a small fraction of the modulation period and therefore we can consider operating with a pulsed As_4 cell (pulsed mode).

Notice that the group III flux does not need to be modulated during NEMBE. However, as a limit case, we can separate completely the group III and group V supply periods by alternating both beams. This particular mode, developed independently by Horikoshi et al. [10], has been called MEE by emphasizing the enhanced migration of species, when supplied separately, as the determining mechanism to improve growth.

We have shown that alternated (MEE) or pulsed (NEMBE) beam operation modes are totally equivalent and produce epilayers of similar quality [7]. The advantages for the group V pulsed mode are that it does not pose any large mechanical load on the group III cell, uses its content more efficiently and reduces by a half the total growth time.

Both MEE and NEMBE modes need As_4 cells with an on/off flux ratio ≥ 10 to avoid As incorporation during Ga supply time. We use specially designed, fast operating valved cells (0.1 s opening and closing time) with measured on/off flux ratio ≈ 200 and equipped with a high temperature cracking section. Cells of the same kind are used also for P_4 or P_2 pulses from solid red phosphorus with great advantage over conventional designs.

Because most of the time P_4 and As_4 cells are valved off, their operation does not have negative consequence on ion pumps or vacuum background and their high on/off ratio allows one to alternate phosphorus and arsenic in epitaxial structures with little cross contamination.

3. Atomic layer MBE (ALMBE)

In a previous work based on RHEED oscillation analysis we have shown that, in a certain range of substrate temperatures and by carefully adjusting the beam modulation frequency to the actual growth rate in monolayers/s, surface stoichiometry oscillates during NEMBE (or MEE) growth with an amplitude of $1 N_s$, where N_s is the density of Ga or As sites in an atomic layer ($N_s = 6.26 \times 10^{14} \text{ cm}^{-2}$ for (001) GaAs). This means that using the above modulation schemes, MBE growth kinetics can be modified into an atomic layer by atomic layer kind of growth. Our denomination atomic layer MBE (ALMBE) wants to emphasize precisely this character. It should be clearly stated, however, that ALMBE is conceptually and practically different from atomic layer epitaxy (ALE) [11]. During ALMBE, no natural mechanism will stop accumulation of group III atoms on the surface once a complete atomic layer had been deposited. Therefore an accurate computer control of shutters is mandatory. Group V adsorption on the growing surface is, however, self-limited and its saturation coverage can be controlled by substrate temperature, pulsed beam intensity and previous group III coverage (pulse width and phase). This self-limited adsorption adds to the forced 2D growth capabilities inherent of NEMBE, a new application range: the controlled growth of pseudoalloys or alternate monolayer compounds (AMC), short period superlattices and sharp interfaces including two different group V elements. This has been normally beyond the possibilities of MBE due to the known problem of group V competition for incorporation. During ALMBE, P_4 or P_2 and As_4 or As_2 are supplied in successive pulses to group III terminated intermediate surfaces, therefore avoiding competition.

Applications of ALMBE to the growth of Ga

As/GaP SSLs and QWs with excellent structural and optical properties have been previously published [12,13]. Recent results on the growth of complex periodic decoupling structures like $(GaP)_l/(GaAs)_m/(InP)_n$ for GaAs/Si shows the possibilities of combining several strained systems containing both P and As. Also, $(GaP)_m/(InP)_n$ strained layer QWs confined by $Al_{0.7}Ga_{0.3}As$ have been grown successfully, opening a new field for MBE growth of band engineered structures.

However, general problems of interface formation like exchange reactions, segregation and different incorporation efficiencies during growth of heterostructures based on compounds with highly different chemical reactivities cannot be ruled out and need to be investigated in detail.

4. Optical and RHEED investigations during ALMBE

Reflectance difference spectroscopy (RDS), a new optical in-situ analysis technique, useful to monitor surface chemical composition changes [14,15], has been added to RHEED analysis in order to study ALMBE kinetics and to control interface formation. A simplified reflectance difference set-up at the fixed wavelength of a He-Ne laser has been developed and currently used to follow in real time surface stoichiometry changes during alternate or pulsed beam growth [16]. At $\lambda = 6328 \text{ \AA}$, reflectance difference for light polarized parallel to $[1\bar{1}0]$ and $[110]$ directions supplies a signal of comparable amplitude for all investigated compounds (AlAs, GaAs, GaP, InAs, InP and their alloys) and is specially suited to follow surface stoichiometry changes during alternated or pulsed growth of heterostructures.

According to Aspnes et al. [14], the main component of the RD signal originates from the differential absorption of polarized light with the electric vector parallel to the group III surface dimers (along $[110]$ direction) and is therefore proportional to the density of such dimers on the surface.

Referring to fig. 1 in which RHEED, I_{00} , for $[110]$ azimuth is plotted together with RD signal, $R_{110} - R_{1\bar{1}0}$, for two cyclic alternations of Ga and

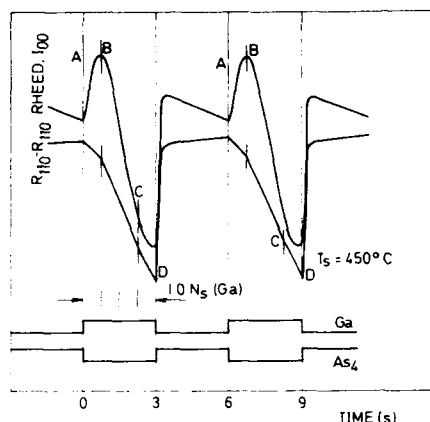


Fig. 1. Simultaneous recordings of RHEED, I_{00} , for $[110]$ azimuth and reflectance difference signal, $R_{110} - R_{\bar{1}\bar{1}0}$, for cyclic growth of GaAs under alternative supply of Ga and As_4 . Substrate temperature $T_s = 450^\circ\text{C}$, BEP $\text{As}_4 = 5 \times 10^{-6}$ mbar. Letters mark different stages of the growth sequence described in the text.

As_4 at $T_s = 450^\circ\text{C}$, we would like to point out some specific details as an example of the kind of information that can be obtained. A complete analysis under a range of substrate temperatures and modulation sequences will be published elsewhere. At the bottom of the figure the beam sequence is schematized and the dose of Ga supplied per cycle, $1 N_s$, indicated. RHEED intensity can be assumed to be sensitive mainly to the density of steps (along $[110]$ direction) as long as the surface is 2×4 reconstructed.

At point A, the beginning of the Ga supply, a low I_{00} intensity indicates that the cycle starts at a rough, incomplete monolayer of GaAs. By supplying $0.25 N_s$ of Ga, I_{00} achieves at point B a maximum intensity comparable with that of a good (flat) As stabilized and 2×4 reconstructed GaAs surface which, according to the well-established Chadi model, is built of three As-As dimers and one dimer vacancy units. Nucleation of further supplied Ga on this surface (few steps available) occurs by Ga-Ga dimer formation, as shown by the linear decrease of the $R_{110}/R_{\bar{1}\bar{1}0}$ signal until at point C, corresponding to the deposition of $0.5 N_s$ Ga atoms in dimer form on the 2×4 surface, a change of slope in RD is seen in coincidence with a change of reconstruction of the RHEED di-

agram into the 3×1 reconstruction. This part of the cycle corresponds exactly to the nucleation model of Farrell et al. [1]. Without As supply, it is not possible to accommodate more than $0.5 N_s$ of Ga-Ga dimers on a 2×4 surface without changing reconstruction into the (3×1) . Further Ga supply, up to $0.75 N_s$, induces a reconstruction change into the 4×2 . Now, at point D, the As_4 beam is supplied again and a fast recovery of the 2×4 reconstruction is observed together with that of the RD signal level as Ga-Ga dimers are buried. However, RHEED, I_{00} , intensity does not recover completely under the As_4 beam but evolves into that of a 0.75 completed monolayer. This was expected, as we had only $0.75 N_s$ of Ga-Ga dimers on the surface. From this point on, the cycle starts again with the supply of Ga to finish growing the incomplete monolayers. The necessary arsenic had to be stored on the surface in an adsorbed state (probably in As_2 form originating from the previous catalytic decomposition of As_4). During this initial part of the cycle, the RD signal has a different slope and originates on a surface absorption for light polarized in the $[110]$ direction, not related to Ga-Ga dimers but to the reduction of surface anisotropy during island coalescence of the incomplete monolayer [16].

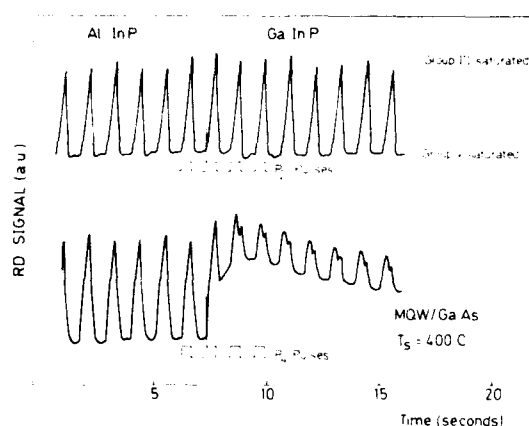


Fig. 2. RD signal during growth of an $\text{Al}_{0.5}\text{In}_{0.5}\text{P}/\text{Ga}_{0.5}\text{In}_{0.5}\text{P}$ heterojunction on GaAs substrate by pulsed mode ALMBE. Bottom level corresponds to surface saturation with phosphorus. Upper level (peaks) corresponds to group III stabilized surface. Lower level (flat) corresponds to group V saturation. Incomplete saturation with P_4 is observed for GaInP.

Besides the good correlation of the observed features and the current models of the GaAs surface, an important consequence of this type of detailed analysis is that, in principle, it is possible to use it to adjust the pulsed beams timing precisely to operate in an ALMBE mode and therefore to obtain atomically sharp buried interfaces also for group V elements.

The effects associated with different chemical activity across the interfaces, as pointed out before, can be investigated by means of this technique and taken into account during the design of the adequate beam sequence to fabricate an optimized interface. For example, during the formation of GaInP/AlInP heterostructures, the use of P_2 instead of P_4 is necessary to achieve full coverage of phosphorus on GaInP, while good incorporation is obtained in more reactive AlInP using P_4 , as shown with the help of RD recordings in fig. 2.

5. Low index surfaces

What kind of kinetics is expected for NEMBE on low index surfaces different from the (100)? Can we still obtain synchronized enhanced nucleation by Ga-Ga dimer promotion and perhaps define an atomic layer-by-layer (ALMBE) growth mode? Exploratory studies have been started using RD signal as an analysis tool during GaAs growth on (311), (211), (111) and (110) surfaces.

In fig. 3 we show experimental recordings of RD signal $R_{110}-R_{\bar{1}\bar{1}0}$ during Ga supply while

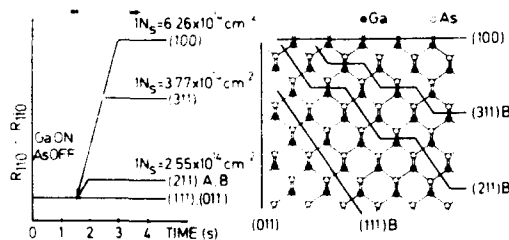


Fig. 3. Experimental recordings of $R_{110}-R_{\bar{1}\bar{1}0}$ during $As_4(off)/Ga(on)$ transient on various low index cut substrates. $T_s = 580^\circ C$, BEP $As_4 = 5 \times 10^{-6}$ mbar. Nominal Ga site densities are included, together with a schematic view of the lattice along [110] direction.

growing under alternated beams on substrates cut an carefully polished in those orientations. High quality, mirror like, GaAs epitaxy was always obtained by using alternated or pulsed beams at $400^\circ C$ and supplying $1 N_s(Ga) = 6.26 \times 10^{14} \text{ cm}^{-2}$ per cycle. For comparison we include in the figure the nominal density of "dimerizable" Ga sites and a scheme of their geometrical location.

Surprisingly good agreement is obtained between the RD signal relative amplitude, or also the saturation Ga dose and the expected surface densities of dimerizable (two dangling bonds) Ga sites.

According to the previous ideas, no atomic layer growth would be possible on totally polar (111)A, (111)B or non-polar (110) surfaces where no alternation of As and Ga planes takes place, and of course, no RD signal can be expected. Nominally, on (311)B the number of "dimerizable" Ga sites is approximately half of that on (100) ($N_{s(100)} = 6.26 \times 10^{14} \text{ cm}^{-2}$). The (100) surface saturates with $0.75 N_{s(100)}(Ga)$ and the experimental value for the (311)B is $0.75 N_{s(311)}(Ga)$ ($N_{s(311)} = 3.77 \times 10^{14} \text{ cm}^{-2}$) in such a good coincidence with the geometrical value that it seems to indicate that on the (311)B surface most of the Ga dimerize and that the As stabilized surface has the same coverage and probably reconstructs in a similar way as the (100). On the (211) surface (A and B), the RD signal is clearly observable, but it saturates for A Ga dose smaller than the nominal density of Ga sites ($N_{s(211)} = 2.55 \times 10^{14} \text{ cm}^{-2}$). Also, the signal amplitude is smaller. Of course, we cannot expect to have all Ga (or As) dimerized on a surface that will contain an enormous density of steps or rearrange to lower its total energy in an unknown way. In favour of such rearrangement, we should point out that very similar RD signals are obtained for the, in principle, quite different (211)A and (211)B surfaces.

Although no signal at all is observed, as expected, on (111)A or (111)B and (110) surfaces, the fact that a good growth morphology is obtained anyway by pulsing the beams shows that some beneficial effect of the surface stoichiometry modulation is still operating. More growth experiments, including superlattice growth, are underway trying to clarify these points.

6. Conclusions

A modulation of the molecular beams in synchronism with the layer-by-layer growth sequence causes a substantial modification of the MBE growth kinetics in two ways: enhancing and synchronizing 2D nucleation (NEMBE) and enhancing migration of surface species (MEE).

As a consequence, 2D growth mode is promoted even for low substrate temperatures or during growth of highly doped materials and strained systems.

Adequately designed pulse sequence leads to approximate atomic layer-by-layer growth (AL-MBE). It allows for the first time, using new valved pulsed cells, the growth of heterostructures, pseudoalloys $\text{III-V}_A\text{-V}_B$, superlattices and sharp heterostructures of the form $\text{III}_A\text{V}_B\text{-III}_C\text{V}_D$ from solid sources in an otherwise conventional MBE system.

Analysis of simultaneous RHEED and RD recordings allows us to control and optimize the modulated beam sequence and to investigate interface formation and growth on low index and off-oriented surfaces.

In summary, the range of applications of MBE can be greatly extended through the engineering of growth kinetics by pulsed beam techniques.

Acknowledgements

The authors wish to acknowledge the collaboration of G. Armelles, M. Recio, J.M. Rodríguez, J. Meléndez, P.S. Domínguez and A. Mazuelas with

the optical and structural characterization of the grown heterostructures. They thank especially Dr. K. Ploog, Max-Planck Institut für Festkörperforschung, for valuable discussions and for his collaboration with the low index surface experiments.

References

- [1] H.H. Farrell, J.P. Harbison and L.D. Peterson, *J. Vacuum Sci. Technol.* B5 (1987) 1482.
- [2] C.T. Foxon and B.A. Joyce, *Surface Sci.* 50 (1975) 435.
- [3] Y. Horikoshi, H. Yamaguchi, F. Briones and M. Kawashima, *J. Crystal Growth* 105 (1990) 326.
- [4] T. Nishinaga, T. Shitara, K. Mochizuki and K.I. Cho, *J. Crystal Growth* 99 (1990) 482.
- [5] J.H. Neave, B.A. Joyce, P.J. Dobson and N. Norton, *Appl. Phys.* A31 (1983) 1.
- [6] F. Briones, D. Golmayo, L. González and A. Ruiz, *J. Crystal Growth* 81 (1987) 19.
- [7] F. Briones, L. González, M. Recio and M. Vázquez, *Japan. J. Appl. Phys.* 26 (1987) L1125.
- [8] F. Briones, L. González and A. Ruiz, *Appl. Phys.* A49 (1989) 729.
- [9] A. Ruiz, L. González, A. Mazuelas and F. Briones, *Appl. Phys.* A49 (1989) 543.
- [10] H. Horikoshi, M. Kawashima and H. Yamaguchi, *Japan. J. Appl. Phys.* 25 (1986) L868.
- [11] C.H. Goodman and M.V. Pessa, *J. Appl. Phys.* 60 (1986) 1265.
- [12] M. Recio, G. Armelles, A. Ruiz, A. Mazuelas and F. Briones, *Surface Sci.* 228 (1990) 139.
- [13] M. Recio, G. Armelles, J. Meléndez and F. Briones, *J. Appl. Phys.* 67 (1990) 2044.
- [14] D.E. Aspnes, J.P. Harbison, A.A. Studna, L.T. Florez and M.K. Kelly, *J. Vacuum Sci. Technol.* B6 (1988) 1127.
- [15] F. Briones and Y. Horikoshi, *Japan. J. Appl. Phys.* 29 (1990) 1014.
- [16] F. Briones et al., to be published.

Optical investigation of GaAs growth process in molecular beam epitaxy and migration-enhanced epitaxy

Yoshiji Horikoshi, Minoru Kawashima and Naoki Kobayashi

NTT Basic Research Laboratories, Musashino-shi, Tokyo 180, Japan

Epitaxial growth process of GaAs by molecular beam epitaxy and migration-enhanced epitaxy is investigated using a newly developed optical monitoring method called *surface photo-absorption*. This method is based on the reflectivity measurement of p-polarized light incident at the Brewster angle on the growing surface. This configuration minimizes the bulk GaAs contribution to the light reflection. The small signal from the growing surface is thus detected with a high signal-to-noise ratio. It was found that this optical method is useful for monitoring the surface chemical composition during molecular beam epitaxy, and the fractional layer growth during migration-enhanced epitaxy. An optimization of As₄ deposition rate during growth is also demonstrated using the recorded surface photo-absorption signal.

1. Introduction

Reflection high energy electron diffraction (RHEED) [1] is a useful in-situ monitoring method for molecular beam epitaxy (MBE) and migration-enhanced epitaxy (MEE) [2]. RHEED is sensitive to structural characteristics such as surface atomic arrangement and surface roughness in an atomic scale [3]. Reflectance difference spectroscopy (RDS) [4], an optical in-situ monitoring method developed recently by Aspnes et al., has been used to provide chemical information on the growing surface, which complements the structural information provided by RHEED. With this method, the difference between normal incidence reflectances is measured for light polarized along the [110] and $\bar{1}\bar{1}0$ principal axes about the (001) surface. Therefore, RDS is primarily applicable to anisotropic surfaces.

Recently, the authors developed a new optical in-situ monitoring method called *surface photo-absorption* (SPA) where p-polarized light is irradiated at the Brewster angle on the growing surface [5]. In this method, the *E* vector of incident light includes components both parallel and perpendicular to the growing surface. Therefore, unlike RDS, SPA is applicable both to isotropic and anisotropic surfaces.

In this paper, we demonstrate the usefulness of SPA in monitoring the chemical composition of the growing surface and the fractional layer growth, and in optimizing the As₄ deposition rate during growth.

2. Surface photo-absorption method

When p-polarized light is irradiated on the growing surface, the reflected light intensity can be minimized by setting the incident angle close to the Brewster angle. The residual reflected light intensity observed around the Brewster angle is caused by the optical absorption near the surface. Thus, the deposition of an absorbing thin film can be easily detected by measuring the amount of reflected light.

McIntyre and Aspnes [6] have discussed theoretically the reflectivity change which occurs when a very thin film is deposited on the substrate. This reflectivity change, $\Delta R/R$, can be expressed by

$$\frac{\Delta R}{R} = \frac{R(d) - R(0)}{R(0)}, \quad (1)$$

where $R(0)$ and $R(d)$ represent, respectively, the reflectivity of the substrate before and after the deposition of a thin film with thickness d .

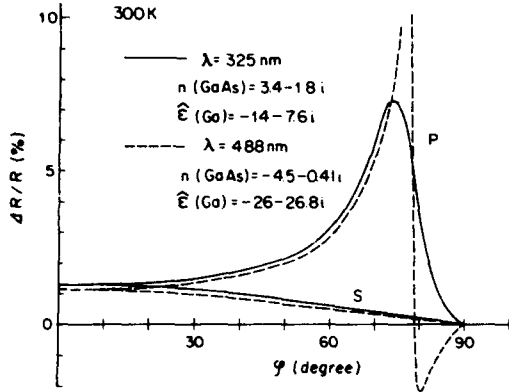


Fig. 1. Reflectivity change on the GaAs (001) substrate covered with 1 atomic Ga layer as a function of the incident angle. The optical constants of GaAs and Ga used in the calculation are shown in the text.

Let $\hat{\epsilon}_{\text{sub}}$ and $\hat{\epsilon}$ be the dielectric constant of the substrate and the deposited thin film, respectively. Then the reflectivity change for s- and p-polarized light can be expressed by [6]

$$\left(\frac{\Delta R}{R}\right)_s = \frac{8\pi d \cos \varphi}{\lambda} \text{Im} \left(\frac{\hat{\epsilon} - \hat{\epsilon}_{\text{sub}}}{1 - \hat{\epsilon}_{\text{sub}}} \right). \quad (2)$$

$$\left(\frac{\Delta R}{R}\right)_p = \frac{8\pi d \cos \varphi}{\lambda} \times \text{Im} \left(\frac{\hat{\epsilon} - \hat{\epsilon}_{\text{sub}}}{1 - \hat{\epsilon}_{\text{sub}}} \times \frac{1 - (1/\hat{\epsilon}\hat{\epsilon}_{\text{sub}})(\hat{\epsilon} + \hat{\epsilon}_{\text{sub}}) \sin^2 \varphi}{1 - (1/\hat{\epsilon}_{\text{sub}})(1 + \hat{\epsilon}_{\text{sub}}) \sin^2 \varphi} \right). \quad (3)$$

Fig. 1 shows the reflectivity change calculated using eqs. (2) and (3) for a (001) GaAs substrate with 1 atomic Ga layer (N_s Ga atoms) on top. The wavelength of incident light is set at 325 and 488 nm, and the corresponding refractive index of GaAs is assumed to be $3.4 - 1.8i$ and $4.5 - 0.41i$, respectively [7]. Although the dielectric constant of a Ga mono-atomic layer is not known, the value obtained for thicker layers is assumed to be valid for 1 atomic layer. Thus, the dielectric constant used in the calculation is $-14 - 7.6i$ for 325 nm, and $-26 - 26.8i$ for 488 nm [8].

The results graphed in fig. 1 clearly indicate that the detection of ultra thin film deposition is

maximized at the Brewster angle. If the term $\text{Im}(\dots)$ of eq. (3) varies slowly when the thickness d is increased, eq. (3) predicts a linear increase in the SPA signal as a function of d .

3. Experimental

The experimental setup used in the present work is shown in fig. 2. A conventional MBE system with two quartz windows at the Brewster angle ($\varphi = 75^\circ$), together with a RHEED gun with an acceleration voltage of 15 kV. Two-inch GaAs (001) substrates were chemically polished in a $\text{H}_2\text{SO}_4\text{-H}_2\text{O}_2\text{-H}_2\text{O}$ solution and then rinsed in deionized water. The resulting oxide was removed by thermal desorption at 630°C in an As_4 flux prior to the SPA experiment. The beam intensities of Ga and Al from effusion cells were determined from the periods of the RHEED specular beam intensity oscillation, while the As_4 beam intensity was measured by the flux monitor gauge placed at the substrate position. p-Polarized 325 nm light (He-Cd laser) was used for the SPA experiments. The reflected light was detected by the Si-PIN photodiode. The results were compared with those obtained by the RHEED observation.

4. Experimental results and discussion

4.1. Application to MBE growth of GaAs

As discussed in a previous paper [5], the SPA signal increases linearly with the number of Ga atoms (N_{Ga}) deposited on the surface until the full

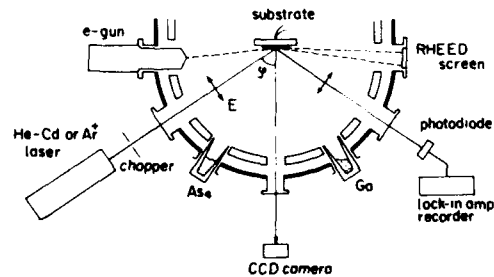


Fig. 2. Experimental MBE setup used for the SPA experiment.

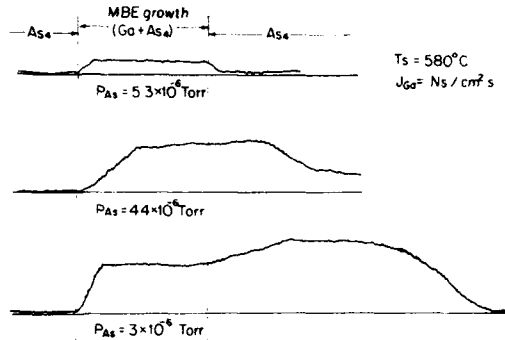


Fig. 3. SPA signal intensity variation during the MBE growth of GaAs. The incident light wavelength was 325 nm.

coverage is accomplished ($N_{\text{Ga}} = N_s$, the number of surface sites). This phenomenon makes it possible to monitor the surface chemical composition during MBE growth.

Fig. 3 demonstrates the SPA signal variation during MBE growth of GaAs under different As_4 pressure (P_{As}) conditions. The growth was continued for 10 s using the Ga flux intensity of N_s (cm^2/s). Before opening the Ga effusion cell shutter, the As-stable surface with (2×4) reconstruction was confirmed by RHEED observation. During MBE growth using $P_{\text{As}} = 5.3 \times 10^{-6}$ Torr (uppermost trace in fig. 3), the SPA signal showed higher intensity than that before and after growth, indicating increased Ga concentration in the growing surface. However, the corresponding RHEED observation showed a distinct specular beam intensity oscillation throughout the entire growth

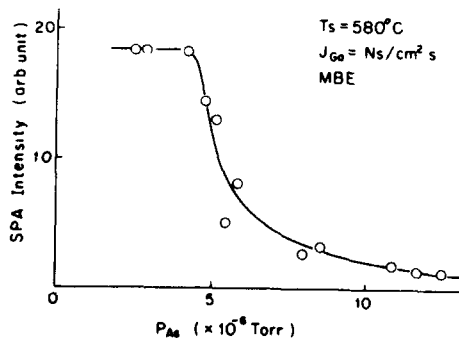


Fig. 4. Steady state SPA signal intensity during MBE growth of GaAs as a function of the As_4 pressure.

duration (10 s). This result indicates that SPA is not sensitive to structural changes in the growing surface. For the reduced As_4 pressure conditions (lower two traces of fig. 3), the SPA signal intensity increases during growth and finally saturates. This saturation value corresponds to the intensity of the (001) GaAs surface fully covered with Ga atoms. After saturation, excess Ga atoms are stored in the form of droplets on the growing surface. Thus, it takes a long time to recover the original As-stable surface after growing. These low P_{As} conditions produce no specular surfaces for the continued growth.

Fig. 4 shows the stationary SPA signal intensity during growth as a function of P_{As} . The saturated intensity in the $P_{\text{As}} < 5 \times 10^{-6}$ Torr region corresponds to the complete coverage by Ga atoms, indicating insufficient As_4 deposition. For the region of $P_{\text{As}} > 5 \times 10^{-6}$ Torr, specular surfaces were obtained even for the thick epitaxial layer growth. Thus, the surface chemical composition can be monitored during growth, which may affect the defect incorporation into the grown layer.

4.2. Application to MEE growth of GaAs

In a previous section, it was demonstrated that the SPA method is useful for monitoring of surface chemical composition during MBE growth, and therefore for optimizing the As_4 deposition rate. Optimization of the As_4 deposition rate is also

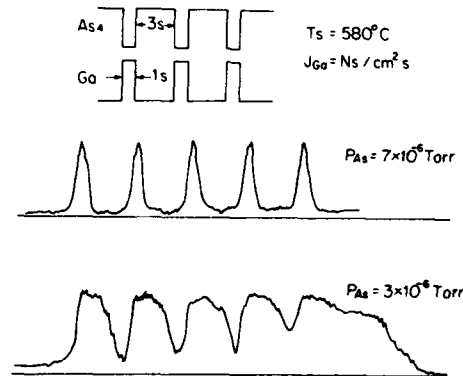


Fig. 5. SPA signal intensity traces observed using $\lambda = 325$ nm light for 5-cycle MEE growth of GaAs at 580°C . Optimization of As_4 deposition rate can be done.

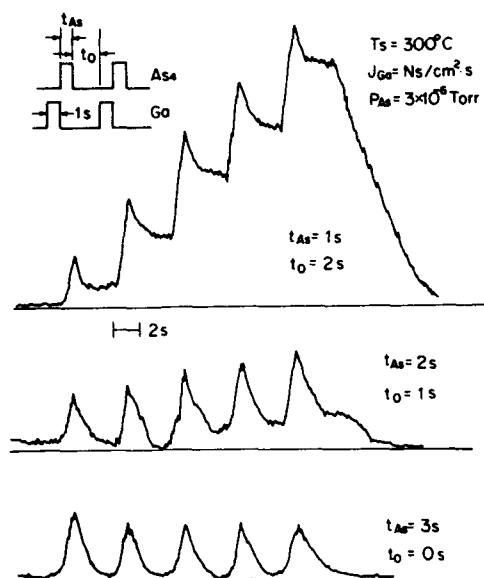


Fig. 6. SPA signal intensity traces of 5-cycle MEE growth of GaAs at 300°C.

possible in the MEE growth using SPA. Fig. 5 indicates the SPA intensity traces for 5-cycle MEE growth of GaAs. The growth rate was fixed at 1 monolayer per cycle. A steady oscillation in SPA signal intensity (upper trace) was obtained using $P_{As} = 7 \times 10^{-6}$ Torr. In this case, As_4 deposition was continued for 3 s in each cycle. However, the As-stable surface was recovered within 1 s deposition (see the time needed for the complete intensity drop to the original level in each cycle). When P_{As} was reduced to 3×10^{-6} Torr, the SPA signal intensity drop in the As_4 deposition duration occurred very slowly and incompletely, indicating that excess Ga atoms agglomerate on the growing surface.

The results obtained for a reduced substrate temperature (300°C) are shown in fig. 6. The deposition sequence is depicted in the inset. In this case, P_{As} was fixed at 3×10^{-6} Torr and the deposition duration was changed for different traces. When the deposition duration is 1s (uppermost trace), no steady oscillation was observed because of insufficient As_4 deposition. Even for the first cycle, no complete recovery to the As-sta-

ble surface was obtained. In contrast to the high temperature result (see the lower trace in fig. 5), the SPA signal intensity grows continuously. This phenomenon implies that no large Ga droplet is formed on the growing surface even when excess Ga atoms are accumulated on the surface Ga layer. Instead, the growing surface is probably covered by higher density but very small Ga droplets at this substrate temperature. By increasing the As_4 deposition duration, stationary SPA oscillation can be achieved as shown in the lower most trace in fig. 6. From these results, it is easy to optimize the As_4 deposition rate.

5. Conclusion

The newly developed optical in-situ monitoring method, SPA was applied to the growth of GaAs by MBE and MEE. This method is based on the measurement of reflected light intensity of p-polarized light incident at the Brewster angle on the growing surface. In this method, the *E*-vector of incident light includes components both parallel and perpendicular to the growing surface. Thus, unlike the RDS method, SPA can be applied both to isotropic and anisotropic surfaces. The SPA method proved useful for monitoring surface chemical composition during MBE and fractional layer growth by MEE.

Acknowledgements

The authors would like to thank Drs. Tatsuya Kimura and Tatsuo Izawa for their encouragement throughout the work.

References

- [1] A.Y. Cho, J. Appl. Phys. 42 (1971) 2074.
- [2] Y. Horikoshi, M. Kawashima and H. Yamaguchi, Japan. J. Appl. Phys. 27 (1988) 169.
- [3] J.J. Harris, B.A. Joyce and P.J. Dobson, Surface Sci. 103 (1981) L90.

- [4] D.E. Aspnes, J.P. Harbison, A.A. Studna and L.T. Florez, Phys. Rev. Letters 59 (1987) 1687.
- [5] N. Kobayashi and Y. Horikoshi, Japan. J. Appl. Phys. 28 (1989) L188C.
- [6] J.D.E. McIntyre and D.E. Aspnes, Surface Sci. 24 (1971) 417.
- [7] B.O. Seraphin and H.E. Bennett, in: *Semiconductors and Semimetals*, Vol. 3, Eds. R.K. Willardson and A.C. Beer (Academic Press, New York, 1966) p. 519.
- [8] O. Hunderi and R. Ryberg, J. Phys. F (Metal Phys.) 4 (1974) 2084.

Modulated molecular beam epitaxy: a successful route toward high quality highly strained heterostructures

J.M. Gérard *, J.Y. Marzin and B. Jusserand

Centre National d'Etudes des Télécommunications, 196 Avenue Henri Ravera, F-92220 Bagneux, France

InAs/GaAs highly strained short period superlattices exhibit clearly improved structural and optical properties when grown by modulated MBE at low temperature (350 °C) instead of conventional MBE. This technique forces a layer by layer growth of the strained layers. Current descriptions of the growth mechanism are discussed, and an alternative model is proposed for it.

1. Introduction

One of the major recent trends in strained layer epitaxy is the growth of highly strained heterostructures. Besides their potential interest in the field of devices as a high mobility substitute for InGaAs random alloy, InAs/GaAs short period superlattices (SPSs) also constitute simple test structures to study the impact of large strains (7% lattice mismatch between InAs and GaAs) on the growth mode and stability of heterostructures. The growth by MBE of $(\text{InAs})_n(\text{GaAs})_m$ approximately lattice matched to InP has been reported for a long time [1–3]. Such layers display, however, rather poor structural and optical properties, as a result of a degraded growth mode. We first recall that a clear improvement results from an alternate delivery of arsenic and metal atoms by monolayer increments at low temperature (350 °C) [4]. The adequation of this modulated MBE (MMBE) technique to the growth of highly strained II–V layers allows one to discuss the validity of the “migration enhanced epitaxy (MEE)” [5] and “atomic layer MBE (ALMBE)” [6] models which have been used to describe the microscopic growth process in MMBE. We pro-

pose a novel model to explain how MMBE induces a layer-by-layer growth.

2. Experimental results

An extended characterization of MMBE grown $(\text{InAs})_n(\text{GaAs})_m$ SPSs has been performed for $m, n \leq 8$. In the following, we compare briefly the data obtained for a 1000 Å thick $(\text{InAs})_4(\text{GaAs})_3$ SPS (sample S43) to those available in the literature for MBE grown layers. X-ray diffraction

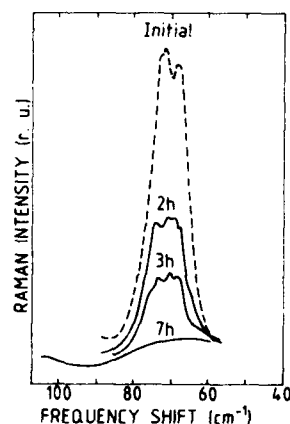


Fig. 1. Evolution of the first folded Raman acoustic doublet of an $(\text{InAs})_4(\text{GaAs})_3$ SPS for successive thermal annealings at 740 °C.

* Member of the Direction des Recherches Etudes et Techniques (French Ministry of Defense).

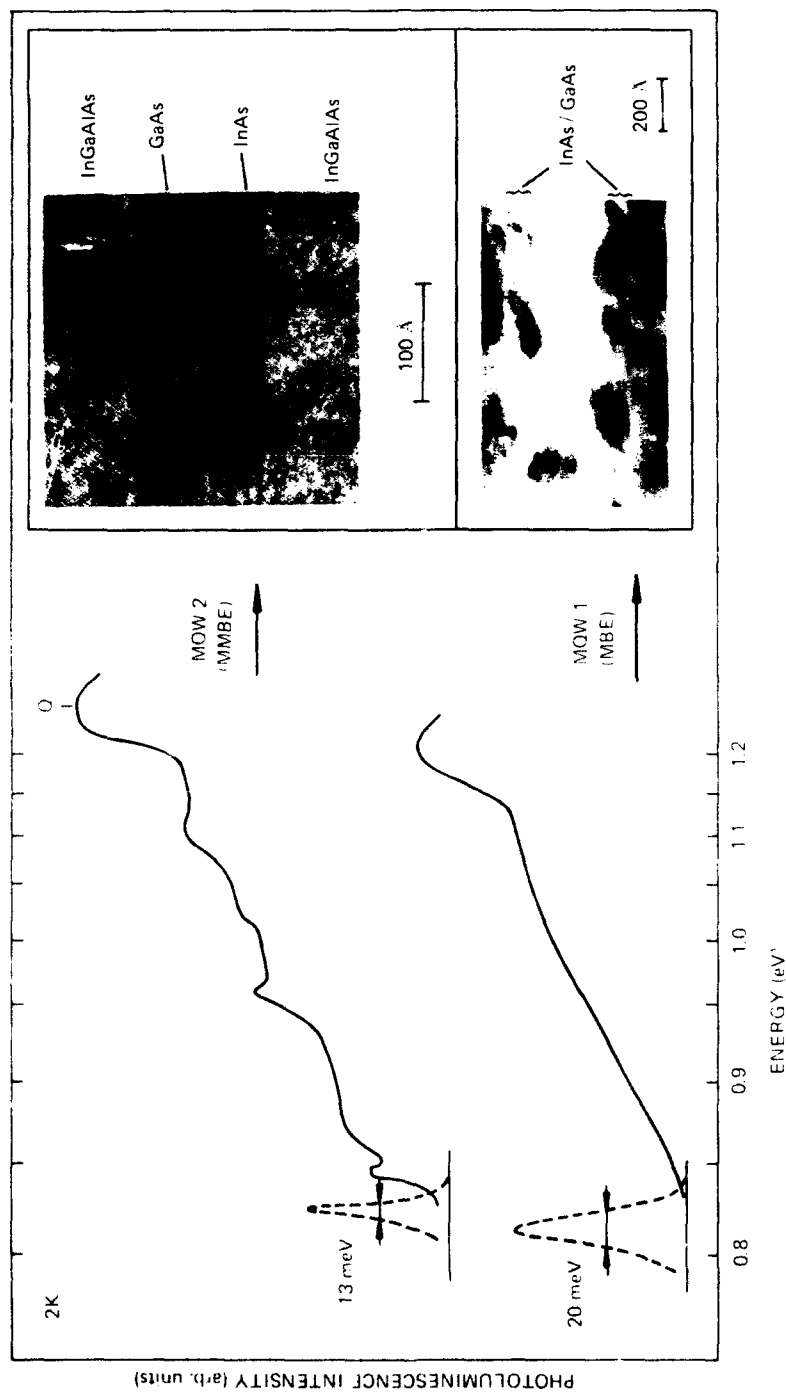


Fig. 2. PL and PL excitation spectra obtained at 2 K and high resolution transmission electron micrographs (insets) for two $(\text{InAs})_2(\text{GaAs})_2/\text{InGaAlAs}$ MQW samples. The well material has been grown by MMBE at 350 °C (MQW1) or conventional MBE at 520 °C (MQW2). Q marks the absorption edge of the InGaAlAs barrier layers.

satellites with full width at half maximum as low as $100''$ appear on θ - 2θ diffraction profiles [4] (typically 1° for MBE grown layers [1-3]). Raman scattering experiments performed on MMBE samples allowed us to observe confined optical modes and folded acoustic modes for the first time in this system [4]. MMBE grown SPSs thus have a well-defined periodicity and a good in-plane homogeneity.

The stability of sample S34 has been tested by performing thermal annealing; the decreasing intensity of the first folded acoustic mode is studied by Raman scattering at different stages of a thermal treatment (fig. 1). A nearly complete intermixing requires 7 h annealing at 750°C . Interesting comparisons can be undertaken with InAs/GaAs and GaAs/AlAs SPSs grown by MBE. Complete intermixing is achieved for 10 Å–10 Å SPSs after 2 h at 500 or 700°C respectively [7]. For a given period, InAs/GaAs MMBE grown SPSs are thus much more stable than MBE grown InAs/GaAs SPSs, and at least as stable as GaAs/AlAs unstrained structures. The very large strains experienced by the sublayers are in fact not likely to jeopardize the SPS stability, since the amount of elastic energy (about 50 meV per metal atom for InAs/GaAs on InP) is much smaller than the bulk diffusion activation energy.

Improved optical properties also result from the growth by MMBE. The low temperature photoluminescence (PL) of S43 is intense, with a 10 meV spectral width [4] (50–100 meV for MBE grown SPS [8]). Its Stokes shift with respect to the bandgap absorption edge (studied by PL excitation spectroscopy) is only 10 meV, instead of typically 50 meV for MBE grown layers.

InGaAlAs/(InAs)₂(GaAs)₂ multiquantum wells (MQWs) have also been studied so as to compare further the quality of thin SPS layers grown using different techniques. The buffer and barrier layers are grown by MBE at 520°C ; the 105 Å thick SPSs are either built by standard MBE (MQW1) or by MMBE at 350°C (MQW2). PL and PL excitation spectra obtained at 2 K for both samples are shown in fig. 2. The excitation spectrum is smooth for MQW1, which indicates that the MQW structure has no two-dimensional character. Contrasted areas on the high resolution

transmission micrograph obtained for MQW1 reveal fluctuations of the composition within the well material. The 2D features of the MQW excitation spectrum are smeared out if the bandgap variations they entail are of the order of the spacing between the optical transitions. For a 105 Å thick quantum well, this effect reveals compositional fluctuations exceeding 5%. On the other hand, the observation of two-dimensional step-like features and the recovery of excitonic peaks in the excitation spectrum for MQW2 confirm a remarkable improvement for the MMBE grown (InAs)₂(GaAs)₂SPS. Its homogeneity is also revealed by the high resolution micrograph displayed in fig. 2, on which alternate bilayers are clearly identified.

These results stem of course from the very different SPS growth modes in MBE and MMBE, which can be studied by reflection high-energy electron diffraction (RHEED). A shift from 2D to 3D growth mode is revealed by a bulk type spotty pattern when about 5 monolayers (ML) InAs or GaAs have been deposited by MBE on a buffer layer lattice-matched to InP under standard growth conditions (500°C , As-stabilized surface). During the growth of a (InAs)_n(GaAs)_n SPS, for n smaller than that apparent critical thickness for 3D growth of the individual layers ($2 \leq n < 5$), a continuous shift to 3D growth is observed by RHEED. Some intensity modulation of the integral order streaks gradually appears and a bulk-type spotty pattern is finally obtained, when typically 500 Å ($n = 4$) or 900 Å ($n = 3$) thick layers have been deposited. This degraded growth mode is responsible for the poor structural and optical quality of MBE grown SPS.

On the other hand, MMBE at 350°C allows one to deposit two-dimensional InAs and GaAs layers on InP up to the critical thickness for plastic relaxation (and obviously after). No degradation of the growth mode is observed for (InAs)_n(GaAs)_n ($n \leq 8$) for 1000 Å thick films. The alternate deposition of As₄ and metal atoms forces a layer-by-layer growth mode of the highly strained layers, thus allowing one to grow high quality material. However, this forced 2D growth mode is only observed for temperatures lower than about 400°C .

3. Discussion

The shift to 3D growth of highly strained layers grown by MBE has a thermodynamical origin (sufficiently large islands of relaxed material are more stable than the pseudomorphic 2D epilayer), but proceeds from a progressive roughening of the surface [9], and is essentially controlled by kinetics. It is therefore possible to delay or suppress the shift to 3D growth by changing the growth conditions.

MMBE overcomes the intrinsic tendency of highly strained layers to grow three-dimensionally. This result allows one to discuss more precisely the growth mechanism in MMBE. The quite different MEE and ALMBE models have been introduced to account for the growth of good quality (unstrained) GaAs at very low temperature ($\approx 200^\circ\text{C}$). Neither is, however, fully satisfying for the MMBE of strained material.

In the ALMBE model [6], an enhancement of the two-dimensional nucleation process results from the cyclic perturbation of the surface stoichiometry. However, preliminary experiments performed at 500 and 370°C indicate that short periodic interruptions of the As_4 flux during the growth by MBE do not improve the quality of the InAs/GaAs SPS, although they entail surface reconstruction (and stoichiometry) changes.

In the MEE model detailed for GaAs [5], a layer-by-layer growth mode is favoured by the enhancement of the cation migration under very low arsenic pressure. A large migration has been surmised for Ga adatoms on a surface covered with As (encountered at the beginning of each Ga deposition) as well as with Ga (end of the deposition of 1 ML Ga), even at low temperature ($\approx 200^\circ\text{C}$) [5]. However, the Ga diffusion length l_{Ga} for a very low As_4 flux has only been measured at 550°C (1900 Å) and for a metal-stable surface [10]. l_{Ga} is drastically smaller at 200°C on a surface covered with As, due to the temperature lowering, and to the larger cohesion of Ga adatoms to an As plane than to a Ga plane:

- When more than 1 ML Ga is deposited on a surface covered with arsenic, atoms of the first ML establish covalent Ga-As bonds, whereas excess Ga atoms tend to gather into droplets [11]

and establish metallic bonds. Ga adatoms on the first Ga ML are thus weakly bound to it, and should migrate much more easily than Ga adatoms on an As plane.

- To calculate the decrease of l_{Ga} between 550 and 200°C , one has to estimate the (unknown) activation energy E_m of the migration of Ga atoms on an As stable surface. E_m can be (very roughly) estimated from the Ga desorption activation energy. Ga migration or desorption involve indeed the breaking or distortion of a number of Ga-As bonds which depends on the growth conditions; we assume that their activation energies E_m and E_d vary proportionally to each other. E_d is 4.7 eV under large As_4 flux (4 bonds to break) [12], 2.5 eV for a free evaporation of GaAs [13] (2 bonds to break since Ga and As desorb alternately) and intermediate (3.6 eV) during the standard MBE growth of GaAs [14]. Since the migration activation energy E_m is 1.3 eV in the latter case [15], we find a rather large but not unreasonable E_m ($\approx 1\text{eV}$) for Ga adatoms on a surface covered with As in the vacuum. As a result, the related Ga diffusion length would be 250 times smaller at 200°C than at 550°C . Surface migration of metal atoms might thus be *much smaller* during low temperature MMBE (on a surface covered with As) than during standard MBE ($\approx 70\text{ Å}$ [15]).

Finally, a large surface transport (also involved in the Volmer-Weber 3D growth mode) could not explain *alone* that a 2D growth of highly strained material is obtained by MMBE.

We propose a modified model for the growth mechanism in low temperature ($\approx 350^\circ\text{C}$) MMBE, which only involves a large migration of metal atoms on metal stable surfaces and is illustrated in fig. 3 in the case of GaAs. 1 ML Ga is first deposited under As-poor atmosphere on a surface covered with As. The migration of Ga might be small on such a surface at the beginning of the deposition, but a rapid diffusion of Ga on Ga terraces is expected. Ga atoms deposited on top of a Ga terrace migrate until they reach its edge and establish stable covalent bonds with As atoms (fig. 3a). A complete atomic layer of Ga is thus obtained at the end of the Ga deposition (fig. 3b). As_4 molecules are then sent to this highly reactive surface which is quickly and homoge-

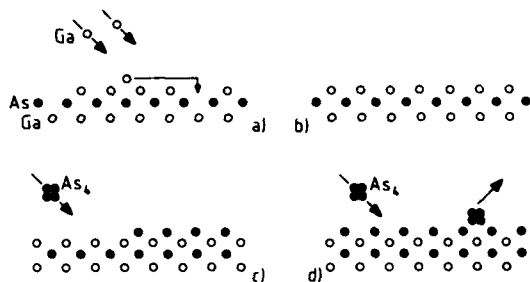


Fig. 3. Schematic model for the MMBE growth of a GaAs monolayer at low temperature ($\approx 350^\circ\text{C}$).

neously covered with arsenic (fig. 3c). Excess As_4 molecules fully desorb if the substrate temperature T_s is sufficiently high (e.g. $T_s > 50^\circ\text{C}$). At the end of this sequence, 1 ML GaAs has been deposited without any terrace formation (fig. 3d).

The key feature of this model is of course the intrinsic tendency of metal atoms to form a smooth atomic layer rather than to gather into droplets (for a submonolayer or monolayer deposition). As for unstrained material [5], this effect is confirmed experimentally during the growth by MMBE of InAs or GaAs strained on InP [4,6]: at 370°C , well-established (4×4) , 4×2 and 3×1 reconstructions are observed at the end of As_4 , Ga and In deposition sequences, respectively, thus showing that the surface stoichiometry is homogeneously changed at each step of the deposition cycle.

Finally, the need for a low growth temperature ($T_s < 400^\circ\text{C}$) can also be explained within this simple frame. At higher temperature, an As-stable surface is not stable in the vacuum, and desorption of arsenic from the surface monolayer after As_4 deposition becomes efficient. More than 1 atomic layer of metal atoms is then at the surface when metal atoms have been deposited. This can lead during the subsequent delivery of As_4 to the formation of terraces, which constitute a germ for the roughness increase, and the shift to 3D growth of the highly strained layer.

4. Conclusions

A clear breakthrough for the quality of InAs/GaAs highly strained short period superlattices is obtained when metal atoms and arsenic are deposited alternately by monolayer increments at low temperature ($\approx 350^\circ\text{C}$). This modulated MBE technique forces a layer-by-layer growth of the strained material.

Acknowledgments

The authors gratefully acknowledge J. Primot (CNET Bagneux), C. D'Anterrosches (CNET Meylan) and P. Voisin (Ecole Normale Supérieure) for their respective contributions to this work, and M. Quillec for constant advice and encouragement.

References

- [1] M.C. Tamargo, R. Hull, L.H. Greene, J.R. Hayes and A.Y. Cho, *Appl. Phys. Letters* 46 (1985) 569.
- [2] Y. Matsui, H. Hayashi, M. Takahashi, K. Kikuchi and K. Yoshida, *J. Crystal Growth* 71 (1985) 280.
- [3] H. Ohno, R. Katsumi, T. Takama and H. Hasegawa, *Japan. J. Appl. Phys.* 24 (1985) L682.
- [4] J.M. Gérard, J.Y. Marzin, B. Jusserand, F. Glas and J. Primot, *Appl. Phys. Letters* 54 (1989) 30.
- [5] Y. Horikoshi, M. Kawashima and H. Yamaguchi, *Japan. J. Appl. Phys.* 27 (1988) 169.
- [6] F. Briones, L. Gonzalez and A. Ruiz, *Appl. Phys.* A49 (1989) 729.
- [7] K. Kakimoto, H. Ohno, R. Katsumi, Y. Abe, H. Hasegawa and T. Katoda, in: *Proc. 11th Intern. Symp. on GaAs and Related Compounds*, Biarritz, 1984, *Inst. Phys. Conf. Ser.* 74, Ed. B. de Cremoux (Inst. Phys., London-Bristol, 1975) p. 253.
- [8] P. Voisin, M. Voos, J.Y. Marzin, M.C. Tamargo, R.E. Nahory and A.Y. Cho, *Appl. Phys. Letters* 48 (1986) 1476.
- [9] J.M. Gérard, in: *Proc. NATO ARW on Condensed Systems of Low Dimensionality*, Marmaris, Turkey, 1990 (Plenum, New York, to be published).
- [10] S. Nagata and T. Tanaka, *J. Appl. Phys.* 48 (1977) 940.
- [11] Y. Horikoshi, H. Yamaguchi and M. Kawashima, *Japan. J. Appl. Phys.* 26 (1989) 1307.
- [12] J.M. Van Hove and P.I. Cohen, *Appl. Phys. Letters* 47 (1985) 726.
- [13] B. Goldstein, D.J. Szostak and V.S. Ban, *Surface Sci.* 57 (1986) 733.
- [14] J.C. Harmand, PhD Thesis, Paris (1988).
- [15] J.H. Neave, P.J. Dobson, B.A. Joyce and J. Zhang, *Appl. Phys. Letters* 47 (1985) 100.

Real-time μ -RHEED observations of GaAs surfaces during growth with alternating source supply

Toshiro Isu, Masayuki Hata and Akiyoshi Watanabe *

Optoelectronics Technology Research Laboratory, 5-5 Tohkodai, Tsukuba, Ibaraki 300-26, Japan

The microscopic surface features of GaAs and AlAs during growth with an alternating source supply were observed by scanning microprobe reflection high-energy electron diffraction in real time. Scanning reflection electron microscope images were obtained in the TV scan mode (50 frames per second). The creation of Ga droplets was observed when Ga atoms over the critical amount depending on the substrate temperature were supplied. They disappeared after a sufficient amount of As was supplied. When 5 monolayers of Ga atoms were supplied per cycle, small islands with bright contrast appeared due to three-dimensional nucleation after As was supplied.

1. Introduction

Reflection high-energy electron diffraction (RHEED) is a very useful technique for observing surface structures during molecular beam epitaxy (MBE) growth. The growth mechanism of GaAs in MBE has been investigated through intensity variations of RHEED spots [1–3]. Scanning microprobe reflection high-energy electron diffraction (μ -RHEED) is a powerful tool for investigating the growth mechanism through microscopic surface observations during growth. Using this technique, images of monolayer steps at Si surfaces were obtained and their behavior during MBE was observed [4]. The surface morphology of MBE-grown layers of GaAs were observed, revealing that anisotropic surface undulations developed during growth [5]. It was also found that Ga droplets were formed under deficient arsenic pressure and shrank due to a sufficient supply of arsenic [6].

In this study, the microscopic surface features of GaAs and AlAs during growth with an alternating source supply, so-called migration enhanced

epitaxy (MEE), were observed in real-time by the μ -RHEED technique.

2. Experimental

The μ -RHEED system comprises a scanning electron gun, a signal-detection system of the μ -RHEED spot intensity and an MBE growth system. Details concerning the system have been reported elsewhere [7]. Utilizing the intensity signal of the RHEED pattern to modulate the display brightness, a scanning reflection electron microscope (SREM) image was obtained. The secondary electron microscope (SEM) image was also obtained using a secondary electron detector facing the substrate in the growth chamber. We have developed an image storage system for real-time observations. The images can be taken in real time during growth in a TV scan mode at 50 frames per second; they are monitored and recorded with a video system. Integrated images of any number of frames from 2 to 2000 can also be monitored as an averaged picture. The electron beam was designed to be focused to 10 nm diameter, and the spatial resolution of the image was about 50 nm for the direction perpendicular to the incident azimuth.

* Present address: Central Research Laboratory, Hitachi, Ltd., Kokubunji, Tokyo 185, Japan.

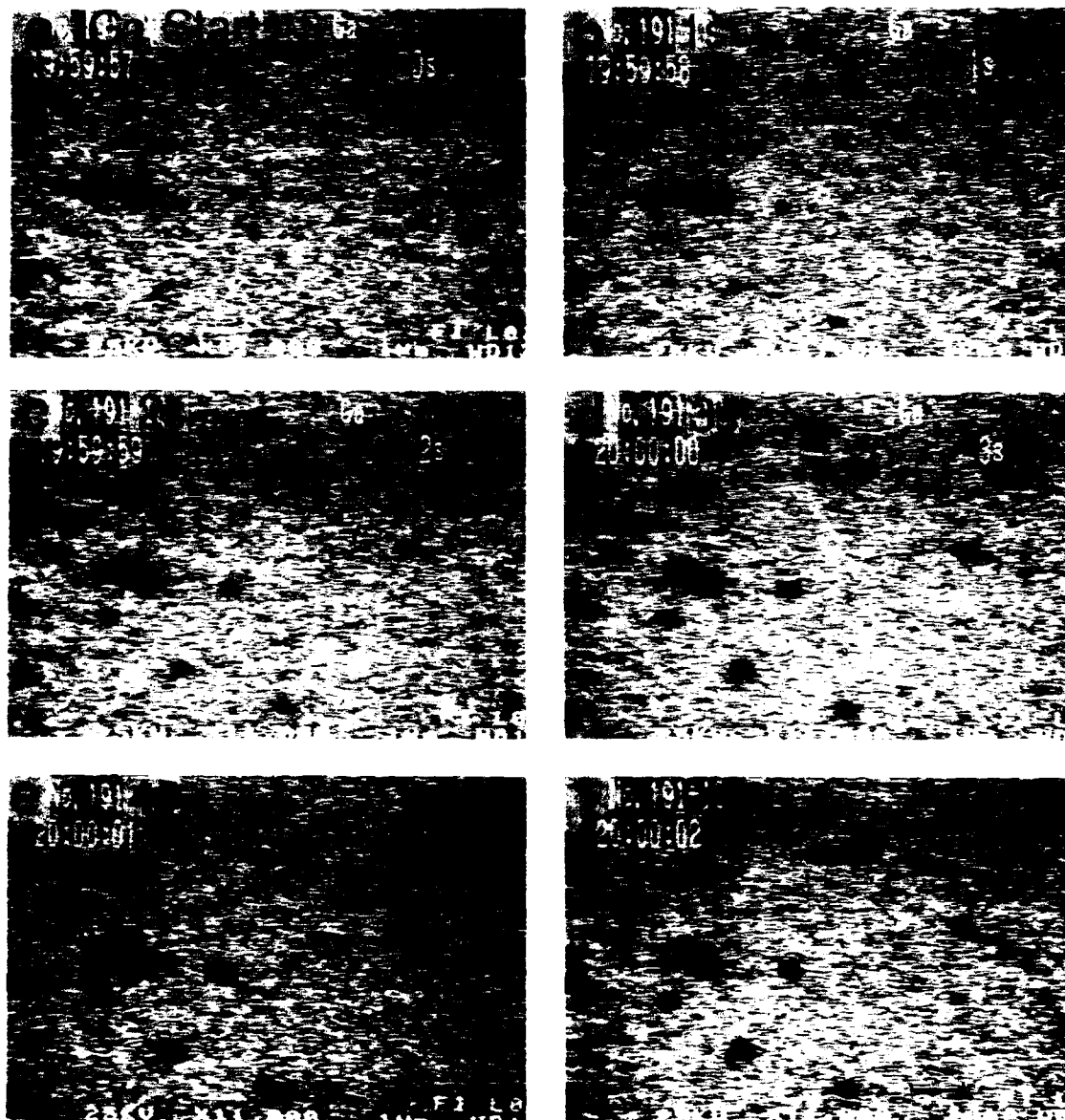


Fig. 1. SREM images during Ga supply on the GaAs substrate at 610°C. The time from the start of Ga supply is shown in each photograph: (a) just after starting; (b)–(d) at 1, 2 and 3 s after starting, respectively; (e) stopping; (f) 1 s after stopping the supply. Marker represents 1 μm .

The spatial resolution was mainly restricted by the mechanical vibration of the specimen, which was caused by the MBE system under the growth conditions.

In the present experiment, n-type GaAs (001) $\pm 0.1^\circ$ wafers were mainly used as substrates; the substrate temperature was set at 550–630°C. The azimuth of the incident beam was along $[110]$,

with a glancing angle of about 1° . The SREM image was taken using the specular beam spot. The Ga and Al flux corresponded to 0.25–1.5 and 0.2 ML/s growth, respectively. The beam equivalent pressure of As was $(5\text{--}10) \times 10^{-4}$ Pa. Ga or Al was supplied alternatively with As on GaAs layers and/or AlAs with a 3 s interval between each source supply.

3. Results and discussion

Fig. 1 shows SREM images at every one second when Ga was supplied in an amount of 1 ML per cycle at a substrate temperature of 610°C . Each image was taken from a still of the video. The video signal comprised an image integrated over 10 frames of TV scanning of the electron beam (an averaged picture for 0.2 s). The dark areas in the left-center in fig. 1a represent a marker showing the focusing condition. After 1 s from the start of Ga supply, several dark spots appeared, as shown in fig. 1b. Though they increased in size during Ga supply, their number remained constants as shown in figs. 1c–1e. The surface features were unchanged after the Ga supply stopped, as shown in fig. 1f. It was reported that Ga droplets were formed when excess Ga atoms over As atoms were supplied during MBE growth [6,8,9]. These dark spots are considered to be Ga droplets. At substrate temperatures lower than 580°C , Ga droplets were observed after more than 1 ML Ga atoms were supplied. At higher temperatures than 610°C , the droplets appeared after only 0.25 ML Ga supply. A Ga droplet is formed by the excess surface Ga atoms which have no bonds to arsenic. Because arsenic is easily desorbed at higher substrate temperatures, the surface coverage of arsenic is decreased during the interval before Ga supply. The position where the droplet appeared was random and different for each cycle. The density of Ga droplets decreased, being strongly dependent on increase in the substrate temperature. Since the droplet is an agglomeration of excess Ga atoms on a Ga-covered surface, the density is considered to be determined by the surface diffusion of excess Ga atoms, the flux density of Ga and such thermodynamic prop-

erties as the critical supersaturation ratio and the equilibrium concentration of Ga atoms. Although the average distance between the droplets reflects the diffusion coefficient of excess Ga atoms on a Ga-covered surface, further investigation concerning the characteristics of Ga atoms is necessary in order to estimate the diffusion length.

Fig. 2 shows SREM images when As was supplied to the surface shown in fig. 1. The Ga droplets shrank and then disappeared after sufficient amounts of As were supplied. Bright regions around the droplets were observed before they disappeared, as shown in fig. 2c. Since the Ga-rich surface was brighter than the As-stabilized surface under the present conditions of RHEED, the bright region seemed to be Ga-rich regions. It is considered that Ga atoms diffuse from the droplets and form a monolayer of GaAs within the first 3 s of As supply.

Growth on a vicinal surface (2° off toward [110]) showed similar features regarding both the creation and annihilation of droplets. The density of the droplets was nearly the same as that on an exactly oriented surface. A 2° vicinal surface would have an extra monolayer step at every 80 nm on the average, although it was obviously not observed. This implies that the surface monolayer steps accompanying the misorientation of the surface have little effect on the surface migration of excess Ga atoms. In other words, it is thought that more steps than those due to the misorientation of the surface would exist even on a smooth surface. On a rough surface which was prepared by growth under As-deficient conditions, however, the droplet density was increased. This is considered to be due to a reduction of the diffusion of excess Ga atoms. These facts mean that the monolayer steps do not make nuclei of agglomerated excess Ga atoms but, rather, reduce the diffusion.

When more than 5 ML Ga atoms were supplied in a cycle, a different surface feature was observed. Fig. 3 shows sequential SREM images when a 5 ML amount of Ga were supplied and followed by an As supply. Just at the start of Ga supply (fig. 3a), only contrast coming from surface morphology was observed. Ga droplets were observed on the surface after the Ga supply (fig. 3b). When As was supplied, the Ga droplets started to

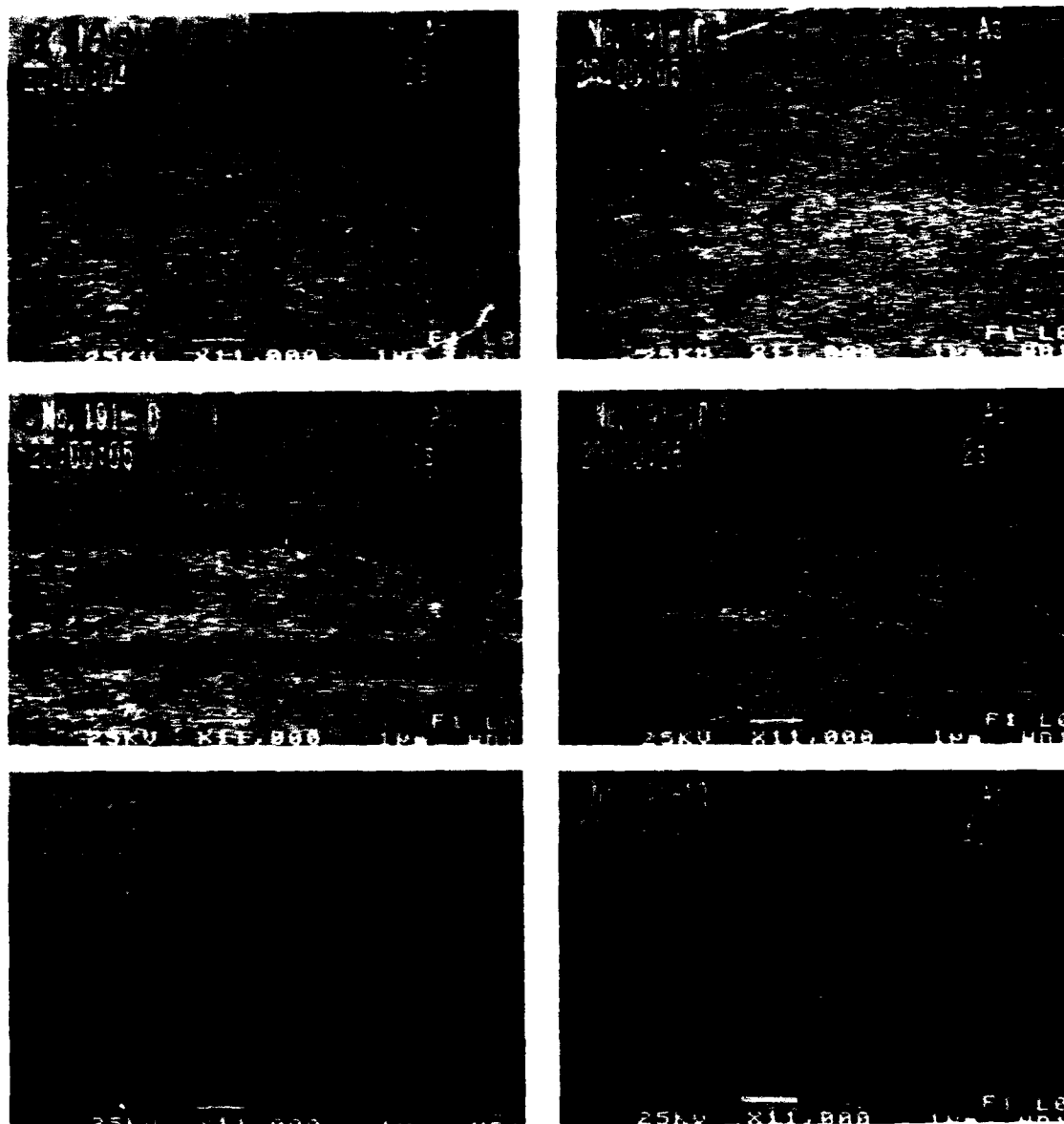


Fig. 2. SREM image during the succeeding As supply on the surface shown in fig. 1. The time from the start of the As supply is shown in each photograph. Marker represents 1 μ m.

shrink and then disappeared (figs. 3c–3e). Bright spots appeared at the same positions where the droplets had existed (figs. 3e and 3f), and became clear after sufficient As was supplied (fig. 3g). The RHEED pattern at the bright spot showed the

typical three-dimensional (3D) diffraction. Images were taken using the specular beam spot. It was at nearly the same position on the screen where a 3D diffraction spot appeared under the present diffraction conditions. The bright areas are therefore

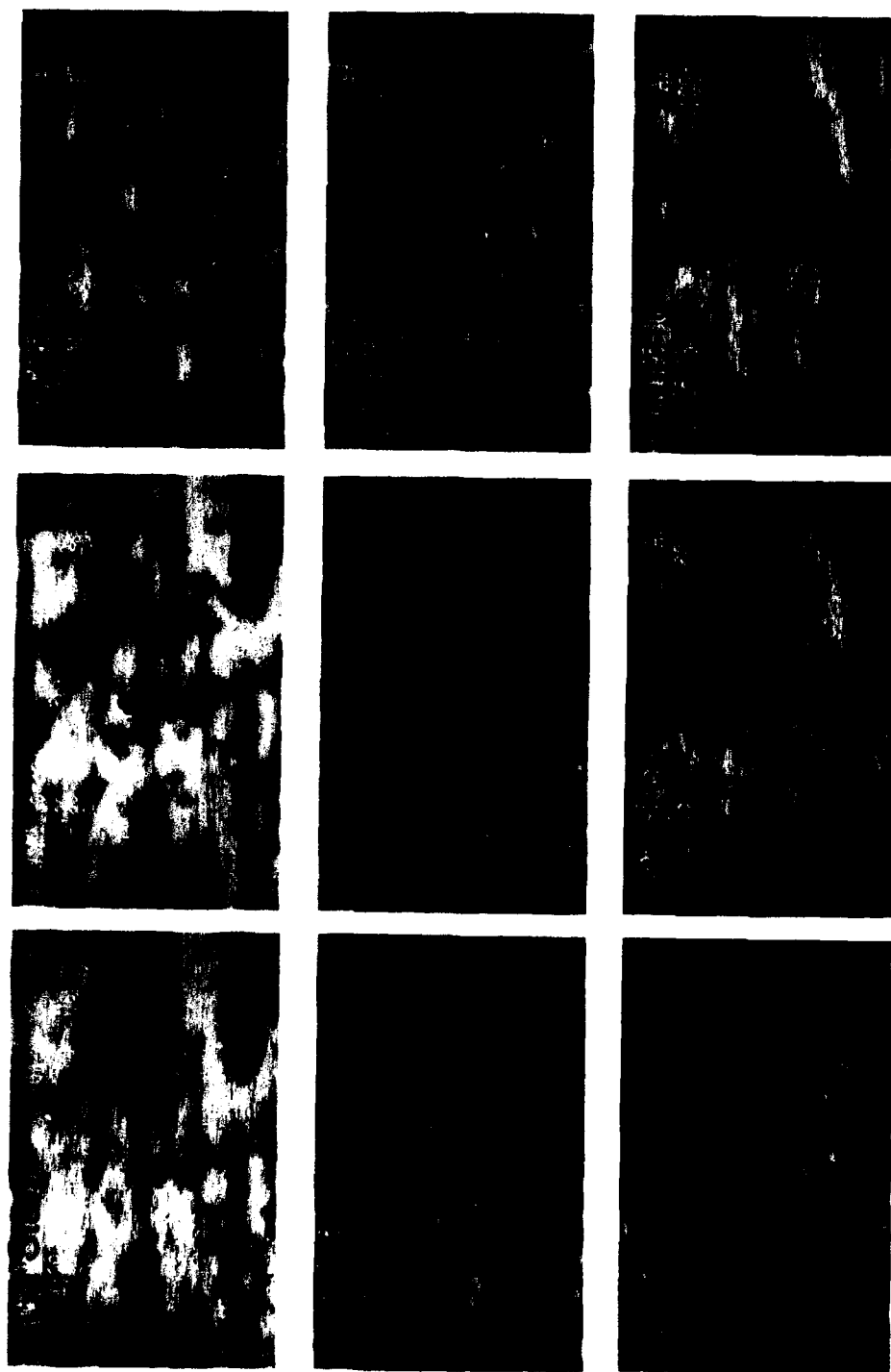


Fig. 3 SREM images during MBE growth for 5 ML of Ga supply per cycle: (a) just after starting Ga supply, (b) during Ga supply, (c) just after starting As supply (d)–(i) at 1, 2, 3, 4, 60 and 100 s after starting the As supply, respectively. Marker represents 1 μ m.

considered to be 3D nuclei. It is well known that a surface becomes rough when an amount of Ga over several monolayers is supplied in a cycle of MEE growth. This is a direct observation of the 3D nucleation which causes surface roughness. After a long interruption of growth under As pressure, it was observed that the bright spots became diffuse and disappeared (figs. 3g and 3h). The disappearance of the 3D nuclei was confirmed by the RHEED pattern at every point of the image. This phenomenon is thought to correspond to the RHEED intensity recovery after growth interruption.

In AlAs growth on GaAs substrates, similar features were observed. The droplets appeared within several cycles of growth. In AlAs growth on AlAs layers, however, no droplets were observed below 690°C of substrate temperature. When Ga was supplied on the AlAs layer, nearly the same number of droplets were observed as those on GaAs layers. The proposed reason for the absence of Al droplets on AlAs layers is supposed to be as follows. The surface of AlAs has so many trap sites that the diffusion length of adatoms is shortened. Hence, the droplets are too small to be observed with the resolution of the present system. This interpretation, however, is not compatible with the observed features of GaAs growth on the AlAs layer. These facts imply that a very complicated behavior of Al atoms might exist on both the GaAs and the AlAs surfaces. Further investigation is necessary to explain the features of surface adatoms.

4. Summary

GaAs (001) surfaces during an alternating supply of Ga and As were microscopically ob-

served in real time by scanning microprobe RHEED. The features of creation and annihilation of Ga droplets were observed. In the case of a large amount of Ga supply per cycle, 3D nucleation of GaAs was observed. The 3D nuclei were found to diffuse after a long interruption of growth. In AlAs growth on a GaAs layer similar features were observed, but no droplets were observed on AlAs layers. The real-time observations by the μ -RHEED will provide important information concerning the epitaxial growth mechanism.

Acknowledgements

The authors would like to thank Dr. Y. Katayama for valuable discussions and comments. They are also grateful to Dr. I. Hayashi for helpful discussions and continuous encouragement.

References

- [1] J.H. Neave and B.A. Joyce, *J. Crystal Growth* **44** (1978) 387.
- [2] J.J. Harris and B.A. Joyce, *Surface Sci.* **108** (1981) L90.
- [3] C.E.C. Wood, *Surface Sci.* **108** (1981) L441.
- [4] M. Ichikawa, T. Doi, M. Ichihashi and K. Hayakawa, *Japan. J. Appl. Phys.* **23** (1984) 913.
- [5] T. Isu, A. Watanabe, M. Hata, Y. Katayama, *Japan. J. Appl. Phys.* **27** (1988) L2259.
- [6] K. Yamada, N. Inoue, J. Osaka and K. Wada, *Appl. Phys. Letters* **55** (1989) 622.
- [7] T. Isu, M. Hata, A. Watanabe and Y. Katayama, *J. Vacuum Sci. Technol.* **B7** (1989) 714.
- [8] J.H. Neave, B.A. Joyce and P.J. Dobson, *Appl. Phys.* **A34** (1984) 179.
- [9] J. Osaka, N. Inoue, Y. Mada and K. Wada, *J. Crystal Growth* **99** (1990) 120.

Realization of mirror surface in (111)- and (110)-oriented GaAs by migration-enhanced epitaxy

Y. Takano, M. Lopez, T. Torihata *, T. Ikei, Y. Kanaya **, K. Pak and H. Yonezu

Department of Electrical and Electronic Engineering, Toyohashi University of Technology, Tempaku-cho, Toyohashi 441, Japan

The layer-by-layer growth mode was readily realized on exactly oriented GaAs(111)B and GaAs(110) substrates by migration-enhanced epitaxy. This growth mode results in a mirror surface with low hillock density of $\sim 10^3 \text{ cm}^{-2}$ which is 3 orders of magnitude lower than the density obtained by conventional MBE growth.

1. Introduction

In III–V epitaxial layers, (111) oriented structure has features attractive for optical devices [1,2]. The (110) plane has the advantage of being the non-polar plane, which could solve the problem of charge imbalance in the interface for the zinc-blende on diamond systems [3] such as GaAs on Si(110) [4]. Layers of GaAs(110) are also attractive because of the applications in avalanche devices due to high impact ionization efficiency [5]. For both orientations, the homoepitaxial growth on the exactly oriented substrates produced a poor surface morphology covered with many hillocks. The growth conditions for specular surface morphology were investigated by using misoriented substrates [6–8] or migration-enhanced epitaxy (MEE) [9]. Few have reported on this growth mode in exactly oriented substrates [10,11].

In this paper, the growth mode was revealed by reflection high energy electron diffraction (RHEED) intensity oscillation for GaAs(111)B and GaAs(110). The layer by layer growth was realized in (111) and (110) orientations by MEE [12], which resulted in mirror surfaces. These results were compared with those on GaAs(100) growth.

* Present address: Fuji Photo Film Co., Ltd., 798, Miyanodai, Kaisei-machi, Ashigarakami-gun, Kanagawa, 258, Japan

** Present address: Anritsu Co., Onna 1800, Atsugi, Kanagawa 243, Japan.

2. Experimental

MEE and MBE growth were conducted on exactly oriented GaAs(111)B and GaAs(110) substrates with an accuracy for orientation of less than 0.1° and 0.5° , respectively. They were degreased and etched in 3:1:1 $\text{H}_2\text{SO}_4:\text{H}_2\text{O}_2:\text{H}_2\text{O}$ solution at 50°C . Then, they were heated in the MBE growth chamber at 650°C for 10 min with an As_4 flux in order to desorb a thin oxide film on the substrates. The growth was conducted at temperatures between 500 and 600°C . The substrate temperatures were measured by a pyrometer.

The Ga beam flux intensity was estimated from the period of the RHEED specular beam intensity oscillation during MBE growth of GaAs. The typical Ga and As_4 beam flux intensities were 2.2×10^{-7} and 1.0×10^{-5} Torr, respectively. In MEE, the number of Ga atoms supplied in one cycle was adjusted to half of the number of surface Ga sites (0.5 monolayer) in order to investigate the growth mode [14]. In one cycle of the MEE growth, the Ga shutter was opened for 1.1 s and then the As_4 shutter was opened (Ga closed) for 2 s. Then, both Ga and As_4 shutters were closed for 1 and 2 s in GaAs(111)B and GaAs(110) growth, respectively. Epilayers of exactly oriented GaAs(100) were also grown by MBE and MEE as references.

The specular beam intensity was monitored along the [110] azimuth using 25 keV primary beam energy during the growth [14]. The epilayers

were grown by MBE and MEE to a thickness of 1200 Å and the surface morphology was observed by Normarski-interference contrast optical microscope.

3. Results and discussion

Fig. 1a shows the typical specular beam intensity observed in MBE growth of GaAs(100) at 500°C. Specular beam intensity oscillations were easily observed, which indicated the two-dimensional nucleation mode [15]. The specular beam intensity during MBE growth of GaAs(111)B at 580°C is shown in fig. 1b. The intensity oscillation was found during 3 monolayer (ML) of deposition, but the specular beam intensity decreased rapidly and no oscillation was observed after 3 ML of deposition. The RHEED oscillation has not been observed except under the above conditions. Fig. 1c shows the specular beam intensity during MBE growth of GaAs(110) at 540°C. After the initiation of MBE growth, the specular beam intensity decreased without showing oscillation. No intensity oscillation has been found in MBE growth of GaAs(110).

The two-dimensional nucleation mode is readily obtained in MBE growth of GaAs(100) with a large range of growth parameters. In GaAs(111)B

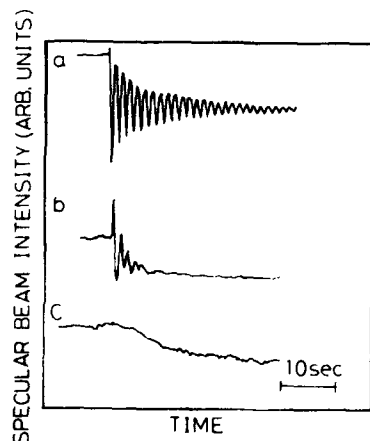


Fig. 1. Specular beam intensity during MBE growth for (a) GaAs(100), (b) GaAs(111)B and (c) GaAs(110).

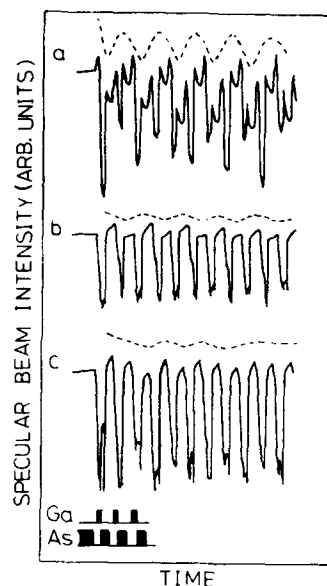


Fig. 2. Specular beam intensity observed in MEE growth of GaAs(100): (a) at 500°C; (b) at 540°C; (c) at 600°C.

and (110), however, the rapid decrease in specular beam intensity indicates the roughening of the growth surface, which coincides with the faceted growth (three-dimensional island growth) observed. Layer-by-layer growth is difficult to be realized by codeposition of Ga and As₄.

The specular beam intensity in MEE growth of GaAs(100) at 500°C is shown in fig. 2a. The peak intensity of the As-stable surface was modulated with a period of two cycles. Fig. 2b and fig. 2c are the specular beam intensities during the growth of GaAs(100) at 540 and 600°C, respectively. The amplitude of peak intensity modulation decreased with increasing temperature.

Fig. 3 shows the results on the typical specular beam intensity during MEE growth of GaAs(111)B at 500, 530 and 560°C. At 500°C (fig. 3a), the peak intensity modulation was observed with a period of two cycles. At 530°C (fig. 3b), the amplitude of the peak intensity modulation became small. At 560°C (fig. 3c) no peak intensity modulation was observed.

Fig. 4 shows the specular beam intensity observed in MEE growth of GaAs(110) at 500, 530 and 560°C. The peak intensity was modulated

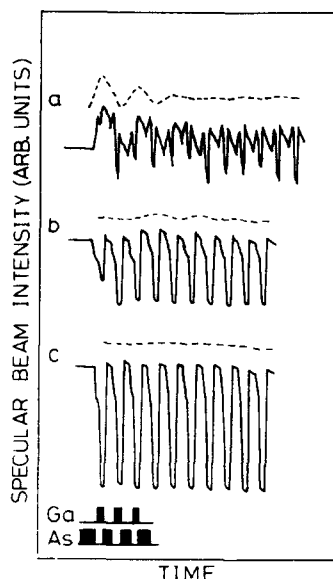


Fig. 3. Specular beam intensity observed in MEE growth of GaAs(111)B: (a) at 500°C; (b) at 530°C; (c) at 560°C.

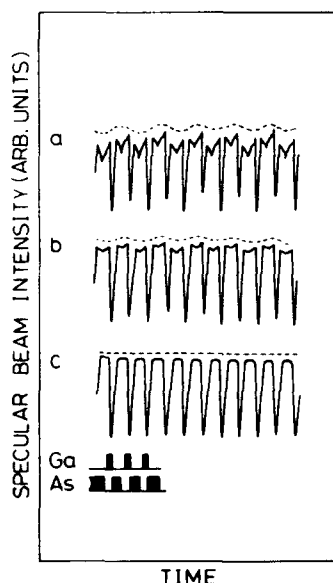


Fig. 4. Specular beam intensity observed in MEE growth of GaAs(110): (a) at 500°C; (b) at 530°C; (c) at 560°C.

with a period of 2 cycles at 500 and 530°C. The amplitude of modulation became small with increasing temperature and the modulation disappeared at 560°C.

When the two-dimensional nucleation mode occurs in MEE, the peak intensity of the As-stable surface should oscillate with a period of two cycles due to 0.5 ML of GaAs growth per cycle [13]. When the step flow mode occurs, the roughness of the surface should not change, which leads to a constant peak intensity in spite of the 0.5 ML of GaAs growth per cycle [13]. The two-dimensional nucleation mode was readily realized by using MEE for (111)B and (110) orientations at 500°C. No peak intensity modulation was observed above a temperature of 530°C, indicating that the step flow mode was predominant in (111)B and (110) orientations. This result suggests that a certain amount of steps exist even in the exactly oriented substrates. The difference in growth mode between MEE and MBE is remarkable for these orientations.

The (100) and (111)B GaAs epilayers consist of alternating planes of Ga and As atoms, while the (110) GaAs has a non-polar surface which is composed of equal numbers of Ga and As atoms. The excess As_4 adsorption results in the facet formation in MBE growth of (110) orientation [7]. In MEE growth of (110) orientation, the incoming Ga atoms during no As_4 deposition adhere preferentially to the As atoms of the (110) surface because of low excess As_4 adsorption. The next incoming As_4 molecules react with the predeposited Ga atoms and form a GaAs(110) surface. Therefore, there is no cause for three-dimensional island growth (faceted growth) in one cycle of MEE growth unless Ga droplets are formed. This is consistent with the layer-by-layer growth mode obtained in the (110) orientation. The desorption of As_4 in excess [16] was realized by introducing a period in which both shutters were closed. This was confirmed by the result that the specular beam intensity increased during this period, as seen in figs. 3a and 4a. Alternate supply of Ga and As_4 , and the reduction of excess As_4 adsorption, is believed to suppress the faceted growth of the (110) orientation.

In MEE growth of GaAs(100), the two-dimen-

sional nucleation mode occurred at temperatures between 460 and 600°C. The decrease in peak intensity modulation with increasing temperature indicates that the step flow mode partially occurred at high temperatures. However, the two-dimensional nucleation mode exists even at 600°C where the step flow mode is dominant in (111)B and (110) orientations. This difference could be due to the migration length of Ga atoms on the As-stable surface during no As₄ flux. For the (111)B and (110) orientations, each As atom of the surface, without excess As₄ adsorption, has only one back bond to the incoming Ga atoms. Therefore, Ga atoms on the surfaces are unstable and can migrate freely to reach the steps under As₄ free conditions. On the other hand, each As atom of the (100) surface possesses two back bonds to the incoming Ga atoms, which suppresses the migration of Ga atoms and the step flow mode.

Fig. 5 shows the hillock densities of GaAs(111)B and GaAs(110) epilayers with 1200 Å growth thickness. For MBE grown epilayers, the density was of the order of 10⁶ cm⁻² for both orientations. The hillocks covered the whole surfaces, as shown in the microphotographs. The MEE growth reduced the hillock density by two to three orders of magnitude and yielded a mirror surface for both orientations, as shown in the microphotographs. During the MEE growth, no damping was observed in the amplitude of the specular beam intensity oscillation (the difference between the intensity during Ga deposition and that during As₄ deposition). The specular beam intensity of the As-stable surface remained constant or slightly increased during growth, which has not been observed in MBE growth. The hillock density decreased with increasing growth temperature.

Good surface morphology of AlGaAs and GaAs was obtained by Hayakawa et al. [1] using 0.5° misoriented substrates and by Tsutsui et al. [6] using 1.5° misoriented GaAs(111)B substrates. For GaAs(110), 6° misoriented substrates were required for a specular surface [7]. The steps are considered to serve as growing fronts on the surfaces which have one back bond to the incoming Ga atoms. The use of MEE increases the average migration length of the Ga atoms. Therefore, less step density could be required for the

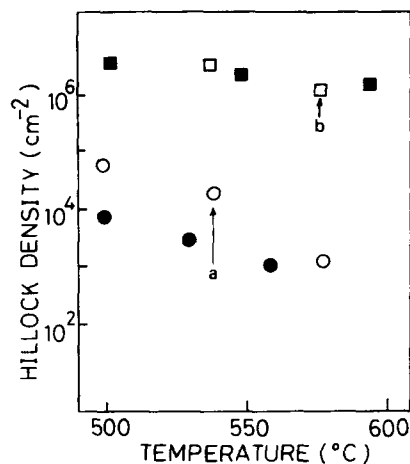


Fig. 5. Hillock densities for GaAs(111)B and GaAs(110) epilayers: (□) GaAs(111)B by MBE; (■) GaAs(110) by MBE; (○) GaAs(111)B by MEE; (●) GaAs(110) by MEE. Surface morphologies of the epilayers are also shown. Markers represent 10 μm.

layer-by-layer growth in MEE growth than in MBE growth. This leads to mirror surfaces of MEE grown epilayers on exactly oriented substrates. The decrease of hillock density with temperature is due to the increase of the migration length of Ga atoms.

4. Conclusions

The layer-by-layer growth mode, which is hardly obtained by MBE, was readily observed by MEE for (111)B and (110) orientations. This growth mode and low excess As₄ adsorption can suppress facet growth and realize mirror surfaces with low hillock density.

References

- [1] T. Hayakawa, M. Kondo, T. Suyama, K. Takahashi, T. Yamamoto and T. Hijikata, *Japan. J. Appl. Phys.* 26 (1987) L302.
- [2] Mau-Phon Houng, Yia-Chung Chang and W.I. Wang, *J. Appl. Phys.* 64 (1988) 4609.
- [3] H. Kroemer, K.J. Polasco and S.C. Wright, *Appl. Phys. Letters* 36 (1980) 763.
- [4] M. Lopez, T. Ikei, Y. Takano, K. Pak and H. Yonezu, *Japan. J. Appl. Phys.* 29 (1990) 551.
- [5] T.P. Pearsall, F. Capasso, R.E. Nahory, M.A. Pollack and J.R. Chelikowsky, *Solid State Electron.* 21 (1978) 297.
- [6] K. Tsutsui, H. Mizukami, O. Ishiyama, S. Nakamura and S. Furukawa, *Japan. J. Appl. Phys.* 29 (1990) 468.
- [7] L.T.P. Allen, E.R. Weber, J. Washburn, Y.C. Pao and A.G. Elliot, *J. Crystal Growth* 87 (1988) 193.
- [8] T. Shitara, E. Kondo and T. Nishinaga, *J. Crystal Growth* 99 (1990) 530.
- [9] H. Imamoto, F. Sato, K. Imanaka and M. Shimura, *Appl. Phys. Letters* 55 (1989) 115.
- [10] M.Y. Yen, T.W. Haas, *Appl. Phys. Letters* 56 (1990) 2533.
- [11] Y. Takano, T. Torihata, T. Kawai, K. Pak and H. Yonezu, *Japan. J. Appl. Phys.*, to be published.
- [12] Y. Horikoshi, M. Kawashima and H. Yamaguchi, *Japan. J. Appl. Phys.* 27 (1988) 169.
- [13] H. Yamaguchi and Y. Horikoshi, *Japan. J. Appl. Phys.* 28 (1989) L1456.
- [14] Y. Takano, Y. Kanaya, T. Torihata, K. Pak and H. Yonezu, *J. Crystal Growth* 102 (1990) 341.
- [15] J.H. Neave, P.J. Dobson, B.A. Joyce and J. Zhang, *Appl. Phys. Letters* 47 (1985) 100.
- [16] Y. Horikoshi and M. Kawashima, *Japan. J. Appl. Phys.* 28 (1989) 200.

Fabrication of AlAs/Al/AlAs heterostructures by molecular beam epitaxy and migration enhanced epitaxy

Takafumi Yao

Department of Electrical Engineering, Hiroshima University, Higashi-Hiroshima 724, Japan

and

Electrotechnical Laboratory, Tsukuba, Ibaraki 305, Japan

Hiroaki Nakahara *, Hirofumi Matuhata and Yasumasa Okada

Electrotechnical Laboratory, Tsukuba, Ibaraki 305, Japan

AlAs/Al/AlAs heterostructures are fabricated on (001)GaAs by molecular beam epitaxy (MBE) and migration enhanced epitaxy (MEE). The Al and successive AlAs layers are grown at room temperature by MBE and MEE, respectively, while the underlying AlAs layer is grown at 600 °C by MBE. Single crystal Al layers are grown successfully. The epitaxy relationship of Al with the underlying AlAs layer is $(011)\bar{1}100\text{Al}|| (001)\bar{1}110\text{AlAs}$. Detailed RHEED analysis elucidates the lattice relaxation processes of Al on AlAs as well as the growth process. It is suggested that the initially deposited 2(1) ML thick Al layers occupy sublattice sites in the AlAs lattice with the same lattice spacing as AlAs on As- (Al-) stabilized AlAs and that the lattice relaxation and the formation of the fcc Al lattice is initiated during deposition of the 3rd (2nd) layer on As- (Al-) stabilized AlAs. The top AlAs layer is single crystalline and grows in an island growth mode. The observed epitaxy relationship of AlAs on Al is $(001)\bar{1}110\text{AlAs}|| (011)\bar{1}100\text{Al}$.

1. Introduction

Recently, the epitaxy of semiconductor/metal/semiconductor structures have attracted considerable attention because of their potential application to metal-base transistors, permeable base transistors, superconductor FETs, and various novel devices [1]. In particular, the growth of such structures on GaAs substrate is technologically important, because of high electron mobility in GaAs, which may enable one to couple high-speed GaAs devices with metal-base transistors. Moreover, semi-insulating GaAs is available, which is indispensable to fabricate monolithic devices. However, there have been only few reports

on successful fabrication of device-quality semiconductor/metal heterostructures on GaAs substrates [1,2].

In order to fabricate device-quality semiconductor/metal heterostructures, interdiffusion between layers should be suppressed. We have examined Al epitaxy, since Al is most frequently used as a Schottky barrier metal. However, the diffusion of Al and As is a serious problem in the Al/GaAs system [3,4]. Hence we have used AlAs instead of GaAs to avoid the interdiffusion problem.

In this paper, we report the growth of AlAs/Al/AlAs heterostructures by MBE and MEE, where Al and the underlying AlAs layers are grown by MBE and the successive AlAs layer by MEE. The growth processes have been investigated by RHEED. The following points are elucidated: (1) the growth processes at the initial

* On leave from Tokai University, 117 Kitakaname, Hiratsuka, Kanagawa 259-23, Japan. Present address: Chichibu Works, Showa Denko K.K., Chichibu 369-18, Japan.

stage of heteroepitaxy; (2) the growth processes of metal layer on semiconductor surfaces; (3) growth processes of semiconductor layers on metal surfaces.

2. Experimental

We prepared a GaAs buffer layer of 1–2 μm at 500–550°C on Cr-doped (001) GaAs with a conventional MBE system (ANELVA 830S). Subsequently, a 50 ML thick AlAs layer was grown at 600°C, which showed a (2×4) reconstruction pattern. In order to obtain an As-stabilized surface at room temperature, the substrate temperature was cooled down to room temperature after the temperature of the As effusion cell was cooled down. Then (2×4) As-stabilized or occasionally $c(4 \times 4)$ As-rich AlAs surfaces were obtained. A (4×1) Al-stabilized surface was formed by a brief dose of Al at 500°C under reduced As background pressure. After the reduction of the background pressure of As, the substrate was cooled down to room temperature. The deposition of Al was carried out at room temperature with a deposition rate of 2.7×10^{14} atoms cm^{-2} s^{-1} as determined by RHEED oscillation, after the background pressure was reduced below 1×10^{-9} Torr. After the growth of an Al layer, the temperature of As was raised again. The successive AlAs layer was grown at room temperature by MEE, in which the shutter sequence was set as follows: As of 1 ML (2.4 s) \leftrightarrow interval (5 s) \leftrightarrow Al of 1 ML (2.4 s). This period was repeated 100 times to grow a 100 ML thick AlAs layer. The AlAs layer was covered by a GaAs capping layer.

The evolution of RHEED patterns was recorded by a RHEED observation system to investigate the growth process of Al and the change in lattice spacing at the surface. The RHEED observation system used in the present experiment is described elsewhere [5], but with a better resolution of 512×512 pixels with 8 bit intensity data.

Selected films were subsequently studied by cross-sectional transmission electron microscopy (TEM) in a JEOL 400FX 400 keV instrument. The structural quality was evaluated with double crystal X-ray diffraction technique.

3. MBE growth of Al on AlAs

The evolution of the RHEED pattern during epitaxial growth of Al on (001)AlAs with the [110] azimuth is shown in fig. 1. Al was grown either on an As-stabilized surface (fig. 1a) or on an Al-stabilized surface (fig. 1b). The RHEED patterns after growth of 50 ML thick AlAs prior to Al deposition showed twofold reconstruction indicative of (2×4) reconstruction on an As-stabilized surface and fourfold reconstruction indicative of (4×2) reconstruction on an Al-stabilized surface. On commencing the Al deposition, the streaky pattern of AlAs gradually disappeared and diffusive diffraction spots corresponding to Al growth began to appear. A clear spotty pattern was observed at the deposition of ca. 80×10^{14} Al atoms/ cm^2 or approximately 10 ML thick Al layers.

Fig. 2 shows RHEED patterns of an Al layers of 50 ML grown on an As-stabilized surface with azimuthal directions of [110] (fig. 2a) and $[1\bar{1}0]$ (fig. 2b). Similar RHEED patterns were observed on an Al layer grown on an Al-stabilized surface. Figs. 2c and 2d show corresponding schematic RHEED patterns with indices. From this analysis, the orientation relationship of Al epitaxy on AlAs was found to be: $(011)[100]\text{Al} \parallel (001)[110]\text{AlAs}$, that is, the so-called (011)Al-R orientation [6]. This epitaxy relationship was first suggested and demonstrated by Ludeke et al. for the Al/GaAs heterostructure [9]. It is interesting to note that only single orientation was observed from the very beginning of Al epitaxy in the present experiments, although it was reported that thin Al layers contain domains of different orientation in the Al/GaAs epitaxy [7,8]. As the deposition proceeded, the spotty pattern became elongated. Eventually, a streaky RHEED pattern was observed after the deposition of a more than 1000 Å thick Al layer, which is indicative of smoothing of the surface. Moreover, the (001)Al surface showed a (4×1) reconstruction pattern after the deposition of a 3000 Å thick layer, which confirms the observation by Massies and Linh [8]. The observed orientation relationship in the Al/AlAs epitaxy is the same as the orientation relationship observed for Al/GaAs at high temperature. It is

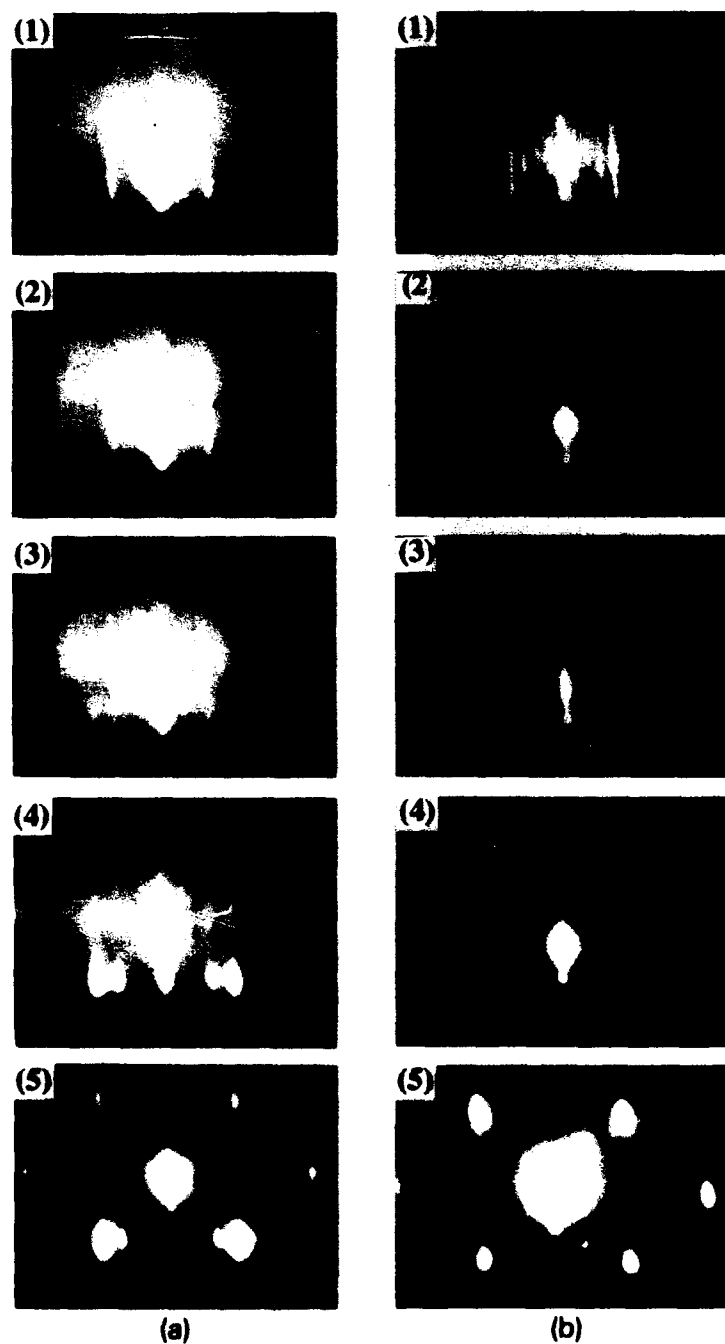


Fig. 1. Evolution of RHEED pattern during Al growth on AlAs buffer layers with (a) As-stabilized or (b) Al-stabilized surfaces with [110] azimuth. In (a), pattern (1) is a RHEED pattern from an As-stabilized surface, while patterns (2)–(5) are those after the deposition of Al: (2) 7.6×10^{14} Al atoms/cm²; (3) 17.9×10^{14} Al atoms/cm²; (4) 25.5×10^{14} Al atoms/cm²; (5) 75.5×10^{14} Al atoms/cm². In (b), pattern (1) is a RHEED pattern from an Al-stabilized surface, while patterns (2)–(5) are those after the deposition of Al: (2) 8.4×10^{14} Al atoms/cm²; (3) 19.7×10^{14} Al atoms/cm²; (4) 28.2×10^{14} Al atoms/cm²; (5) 84.0×10^{14} Al atoms/cm².

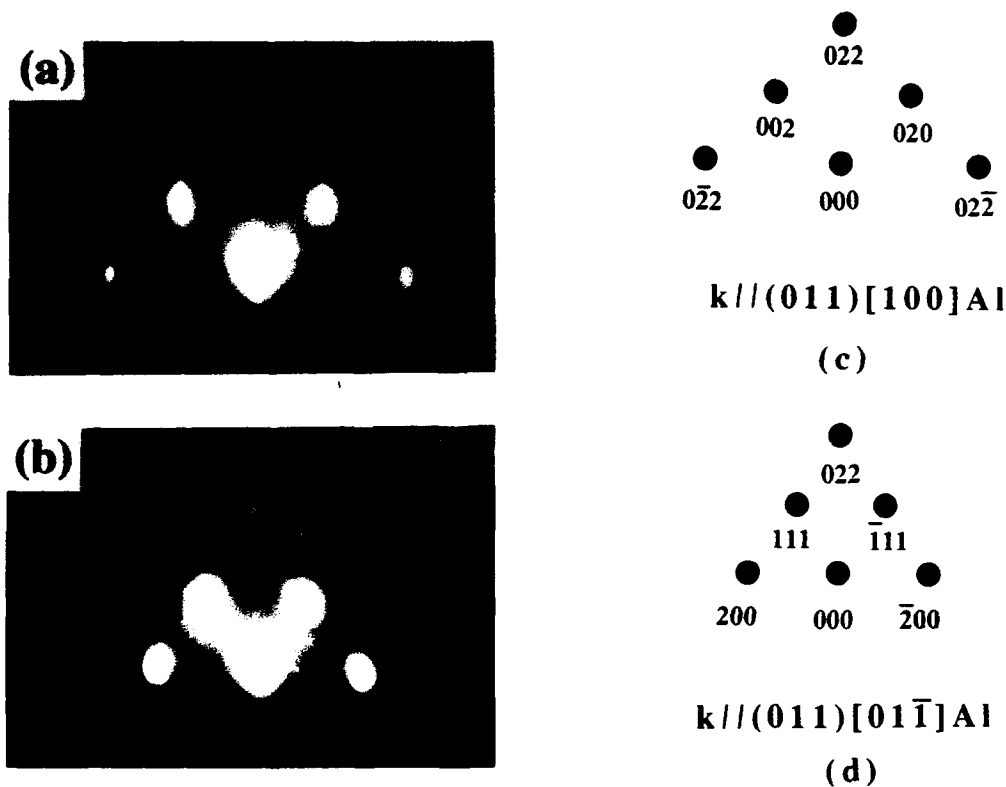


Fig. 2. RHEED patterns of a 200 Å thick Al layer grown on an As-stabilized surface with (a) [110] and (b) $\bar{1}\bar{1}0$ azimuths; (c), (d) corresponding schematic RHEED patterns with crystallographic indices.

suggested [6] that the latter is a consequence of strong chemical reaction between Al and As leading to Ga-As bond-breaking and formation of

tetrahedral Al-As bond. Hence, it is natural that the (001)Al-R orientation becomes dominant in the Al/AlAs epitaxy.

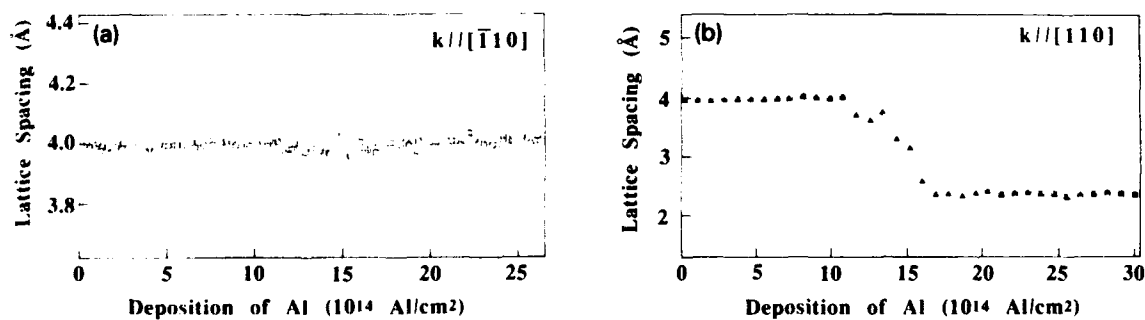


Fig. 3. Al surface lattice spacings along (a) [110]AlAs and (b) $\bar{1}\bar{1}0$ AlAs directions as a function of Al flux: (\square) on As-stabilized surface; (Δ) on Al-stabilized surface.

With the orientation relationship of Al epitaxy on AlAs described above, the lattice misfit along the $[1\bar{1}0]$ AlAs direction of AlAs is estimated to be 28.3% while that along the $[110]$ AlAs direction is 1.3%. Therefore, it is expected that the surface lattice spacing of Al along the $[01\bar{1}]$ Al \parallel $[\bar{1}10]$ AlAs direction shows a drastic change due to the surface lattice strain relaxation at the initial stage of epitaxy, while that along $[100]$ Al \parallel $[110]$ AlAs shows only slight change. In fig. 3a is plotted the surface lattice spacing of an Al layer along the $[100]$ Al \parallel $[110]$ AlAs direction against Al deposition. The surface lattice spacing remains almost unchanged and the onset of strain relaxation is hardly observed. In fig. 3b, the variation of lattice spacing at the surface along the $[01\bar{1}]$ Al \parallel $[\bar{1}10]$ AlAs during growth of Al is plotted against the amount of Al deposition (N_{Al}). The surface lattice spacing of Al along the $[01\bar{1}]$ Al \parallel $[\bar{1}10]$ AlAs direction at the initial stage of Al growth on an As-stabilized surface coincides with that of AlAs when N_{Al} is less than $N_{c1}(As) = 18.6 \times 10^{14}$ atoms cm^{-2} , while it decreases abruptly with further deposition and eventually reaches that of bulk Al when N_{Al} is larger than $N_{c2}(As) = 21.5 \times 10^{14}$ atoms cm^{-2} . On an Al-stabilized AlAs surface, the surface lattice spacing of Al in the same direction coincides with that of AlAs when N_{Al} is less than $N_{c1}(Al) = 11 \times 10^{14}$ atoms cm^{-2} , while it agrees with that of bulk Al when N_{Al} is larger than $N_{c2}(Al) = 16.8 \times 10^{14}$ atoms cm^{-2} . The surface atom density of Al on (001) AlAs and (011) Al surfaces is $C_{AlAs} = 6.25 \times 10^{14}$ atoms cm^{-2} and $C_{Al} = 8.66 \times 10^{14}$ atoms cm^{-2} , respectively. We note that $N_{c1}(As) = 3C_{AlAs}$ and $N_{c2}(As) = 2C_{AlAs} + C_{Al}$, while $N_{c1}(Al) = 2C_{AlAs}$ and $N_{c2}(Al) = C_{AlAs} + C_{Al}$.

From these experimental data, we propose a model for the initial stage of growth process of Al on AlAs. On depositing Al atoms on As-stabilized AlAs surface, Al atoms occupy Al sites on the AlAs surface due to tetrahedral covalent bonding between Al adatoms and As on the surface. It is suggested that the second and part of the third Al layers occupy the As and Al sites of (001) AlAs, respectively, because no lattice strain relaxation occurs until $N_{Al} = N_{c1}(As) = 3C_{AlAs}$. Additional Al deposition of more than $3C_{AlAs}$ causes lattice strain relaxation due to the formation of Al lattice.

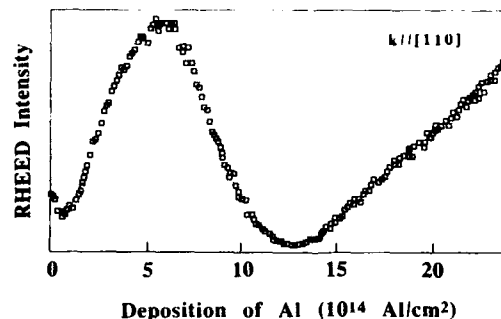


Fig. 4. The intensity variation of the (01) diffraction spot at the initial stage of Al epitaxy with $k \parallel [\bar{1}10]$ AlAs.

The surface lattice spacing of Al along the $[01\bar{1}]$ Al \parallel $[\bar{1}10]$ AlAs direction completely relaxes at around $N_{Al} = N_{c2}(As) = 2C_{AlAs} + C_{Al}$, while that along the $[100]$ Al \parallel $[110]$ AlAs shows almost no change. Then, the third layer would form a (011) Al surface with a relationship of $[01\bar{1}]$ Al \parallel $[\bar{1}10]$ AlAs and $[100]$ Al \parallel $[110]$ AlAs.

The first and part of the second Al atomic layers deposited on an Al-stabilized surface would occupy the As and Al sites of (001) AlAs, respectively, because no lattice relaxation occurs until $N_{Al} = N_{c1}(Al) = 2C_{AlAs}$. On depositing more Al atoms, the lattice strain begins to relax due to the formation of Al lattice and the lattice spacing of Al at the surface along the $[10\bar{1}]$ Al \parallel $[\bar{1}10]$ AlAs completely relaxes at around $N_{Al} = N_{c2}(Al) = C_{AlAs} + C_{Al}$, while the lattice spacing of Al along the $[100]$ Al \parallel $[110]$ AlAs shows almost no change. Therefore, the second Al layer would eventually form a (011) Al surface with the same orientation relationship as on an As-stabilized surface.

Fig. 4 shows the intensity variation of the (01) diffraction spot at the initial stage of Al epitaxy on the As-stabilized surface with the electron azimuthal parallel to $[\bar{1}10]$ AlAs. Note that with this azimuthal direction, the change in lattice spacing at the initial stage of growth was hardly observed (see fig. 3a). On commencing Al deposition, the intensity of the diffraction spot initially increases and reaches a maximum at the deposition of ca. 6×10^{14} Al atoms/ cm^2 ($= C_{AlAs}$), after which the intensity decreases and becomes minimum at the deposition of 13×10^{14} atoms/ cm^2 .

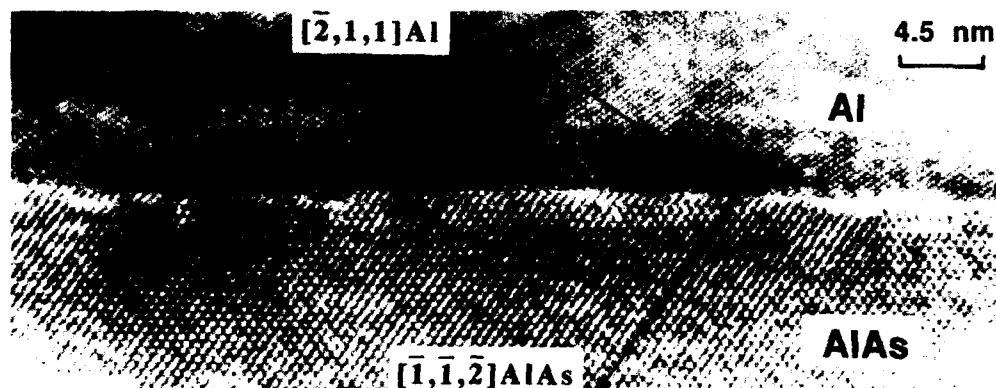


Fig. 5. Cross-sectional TEM image of the interface between Al and AlAs.

($= C_{\text{AlAs}}$). More deposition monotonically increases the diffraction intensity. Such behavior suggests that the first and the second Al layers grow two-dimensionally, while the three-dimensional growth starts during growth of the third Al layer.

The Al/AlAs structure characterized during growth by RHEED in fig. 1 was imaged in the cross-sectional TEM micrograph of fig. 5. The direction of the atom rows in Al and AlAs epilayers is consistent with the observed epitaxy relationship. For instance, the $[1\bar{1}\bar{2}]$ AlAs direction is perpendicular to the $[211]$ Al direction. The interface is relatively smooth on an atomic scale, and the intrusion of As into Al layers is not observed. The initial accommodation of Al without an exchange reaction and its position corresponding to that of AlAs does not contradict with the model. On the other hand, in an Al layer at around the interface, almost periodic array of dislocations, which relax the lattice strain in Al, were observed by the electron microscope.

We have characterized Al epilayers by double crystal X-ray diffraction technique. The diffraction showed only (220) reflection which is consistent with the observed epitaxy relationship. The full width at half maximum of the X-ray rocking curve of (220) diffraction from a 3000 Å thick Al layer was 0.06° . Although this value is larger than that of the GaAs substrate (0.013°), which implies

that the Al epilayer contains more crystalline imperfection than GaAs, it would be possible to apply the epitaxial Al film to device applications.

4. MEE growth of AlAs on Al

In order to avoid interdiffusion of As into the Al layer, AlAs was successively grown at room temperature on an Al epilayer. Fig. 6 shows the evolution of the RHEED pattern during AlAs deposition with the azimuthal of $[110]$ AlAs direction. On commencing AlAs growth, the streaky RHEED pattern changes into a diffusive spotty one with weakened intensity, which suggests the growth of single crystalline AlAs film in an island growth mode. The observed epitaxy relationship in the AlAs/As system was $(001)[110]\text{AlAs} \parallel (011)[100]\text{Al}$, which implies that the AlAs overgrowth has the same crystallographic orientation as the GaAs substrate.

5. Conclusions

The structure and growth processes of single crystal Al layers on AlAs by MBE and of AlAs

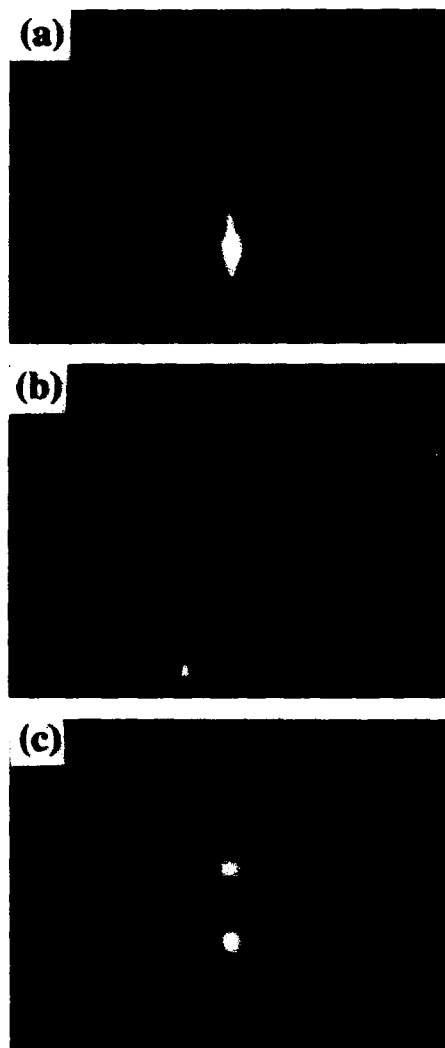


Fig. 6. Evolution of RHEED pattern during AlAs deposition with $k \parallel [\bar{1}10]$ AlAs: (a) Al single crystal layer; (b) 20 ML thick AlAs layer; (c) 100 ML thick AlAs layer.

layers successively grown by MEE on the Al layers were studied using RHEED. The epitaxy relationships of Al on AlAs and AlAs overgrowth on Al

are $(011)[100]\text{Al} \parallel (001)[110]\text{AlAs}$ and $(001)[110]\text{AlAs} \parallel (011)[100]\text{Al}$, respectively. The surface lattice spacing of Al along the $[01\bar{1}]\text{Al} \parallel [\bar{1}10]\text{AlAs}$ direction suffers from abrupt lattice relaxation at the deposition of 18.6×10^{14} Al/cm^2 and 11×10^{14} Al/cm^2 , respectively on an As- and Al-stabilized AlAs and completely relaxed at the deposition of 21.5×10^{14} and 16.8×10^{14} Al/cm^2 , respectively on the As- and Al-stabilized surfaces. However, that along the $[100]\text{Al} \parallel [110]\text{AlAs}$ remains almost unchanged. It is suggested that initially deposited 2(1) ML thick Al layers form a sphalerite lattice with the same lattice spacing as AlAs on As- (Al-) stabilized AlAs, and that the deposition of additional Al layers induced the relaxation of lattice misfit strain and formed an fcc lattice with bulk Al lattice constant. No interdiffusion of As into Al was observed in terms of TEM observation. Single crystal AlAs grows on the Al epilayer in an island growth mode.

References

- [1] T. Sands, J.P. Harbison, W.K. Chan, S.A. Schwartz, C.C. Chang, C.J. Palmstrom and V.G. Keramidas, *Appl. Phys. Letters* 52 (1988) 1216.
- [2] J.P. Harbison, T. Sands, N. Tabatabaie, W.K. Chan, L.T. Florez and V.G. Keramidas, *Appl. Phys. Letters* 53 (1988) 1717.
- [3] K. Okamoto, C.E.C. Wood, L. Rathbun and L.F. Eastman, *J. Appl. Phys.* 53 (1982) 1532.
- [4] B. Tadayon, S. Tadayon, M.G. Spencer, G.L. Harris, L. Rathbun, J.T. Bradshaw, W.J. Schaff, P.J. Tasker and L.F. Eastman, *Appl. Phys. Letters* 53 (1988) 2664.
- [5] T. Yao, H. Nakao, H. Kawanami and R. Toba, *J. Crystal Growth* 95 (1989) 107.
- [6] R. Ludeke and G. Landgren, *J. Vacuum Sci. Technol.* 19 (1981) 667.
- [7] P.M. Petroff, L.C. Feldman, A.Y. Cho and R.S. Williams, *J. Appl. Phys.* 52 (1981) 7317.
- [8] J. Massies and N.T. Linh, *Surface Sci.* 114 (1982) 147.
- [9] R. Ludeke, L.L. Chang and L. Esaki, *Appl. Phys. Letters* 23 (1973) 201.

Strained layer epitaxy of InGaAs by MBE and migration enhanced epitaxy – comparison of growth modes and surface quality

Y.C. Chen, P.K. Bhattacharya and J. Singh

Solid State Electronics Laboratory, Department of Electrical Engineering and Computer Science, The University of Michigan, Ann Arbor, Michigan 48109-2122, USA

Our measurements on a series of pseudomorphic n-type modulation doped field effect transistors have shown that the mobility of the two-dimensional carriers appears to suffer from increased interface roughness as the strain increases. Reflection high energy electron diffraction oscillation studies in $\text{In}_x\text{Ga}_{1-x}\text{As}$ grown by molecular beam epitaxy show that as the strain in the overlayer increases, the growth modes change from layer-by-layer to three-dimensional island growth. However, in migration enhanced epitaxy, we find that the growth remains in the layer-by-layer mode even for high strain. Reflection high energy electron diffraction oscillations also show that surface roughness in strained layers grown by molecular beam epitaxy can be smoothed by just a few monolayers grown by migration enhanced epitaxy. This suggests that for pseudomorphic devices most of the strained active layer might be grown by molecular beam epitaxy but just a few monolayers before interface formation by migration enhanced epitaxy to produce an abrupt interface. Our device results validate this observation.

1. Introduction

Increased efforts have concentrated on the growth of pseudomorphic heterostructure systems, including $\text{In}_x\text{Ga}_{1-x}\text{As}/\text{AlGaAs}$ (on GaAs substrates) and $\text{In}_{0.53+x}\text{Ga}_{0.47}\text{As}/\text{In}_{0.52}\text{Al}_{0.48}\text{As}$ (on InP substrates). Modulation doped field effect transistors (MODFETs) based on these pseudomorphic heterostructures have several advantages over their lattice-matched counterparts [1,2]. Pseudomorphic MODFETs contain a highly strained pseudomorphic quantum well channel. It is extremely important to understand the epitaxial growth modes of such highly strained layers, since the growth modes control the growth front and interface roughness. The latter, in turn, controls the transport properties of the pseudomorphic channel and ultimately the device performance [3,4]. In this study we have investigated the suitability of molecular beam epitaxy (MBE), and its variation, commonly known as migration enhanced epitaxy (MEE), for the realization of high quality pseudomorphic heterostructures.

2. Growth modes in molecular beam epitaxy

In the growth of $\text{In}_x\text{Ga}_{1-x}\text{As}$ by MBE, since atoms and molecules (Ga , In , As_4) impinge randomly on the substrate, kinetics and thermodynamics both play important roles in establishing the growth modes. Thermodynamic parameters such as surface bond-strengths and substrate temperature (free energy = internal energy – $T_{\text{sub}} \times$ entropy) decide whether in equilibrium the surface is atomically abrupt or three-dimensional in nature. Kinetic parameters (surface migration and evaporation) decide whether the thermodynamical equilibrium is reached. If the surface migration rate of the impinging atoms is high and thermodynamics favor an atomically abrupt surface, a layer-by-layer growth mode results. On the other hand if the surface kinetics are very small or the thermodynamics equilibrium state is not atomically flat, a three-dimensional growth mode will result [5]. These growth modes can be studied in-situ by reflection high energy electron diffraction (RHEED) oscillation studies [6,7]. In (100)-

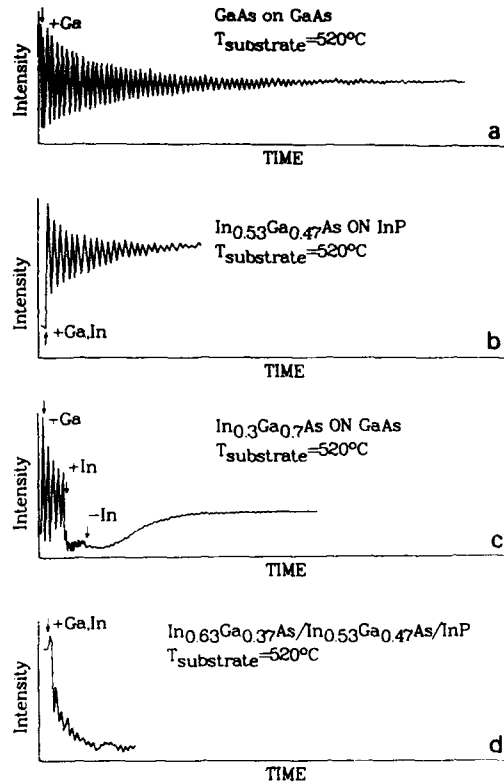


Fig. 1. RHEED oscillations observed during MBE growth of (a) GaAs on GaAs, (b) $\text{In}_{0.53}\text{Ga}_{0.47}\text{As}$ on InP, (c) $\text{In}_{0.3}\text{Ga}_{0.7}\text{As}$ on GaAs and (d) $\text{In}_{0.63}\text{Ga}_{0.37}\text{As}/\text{In}_{0.53}\text{Ga}_{0.47}\text{As}$ on InP.

oriented growth, the energy difference between an atomically abrupt and a rough surface results from second neighbor bond strengths under the appropriate surface reconstruction. In absence of biaxial strain, if the second neighbor bond energy ω_2 is larger than kT_{sub} , the equilibrium state is atomically abrupt and a layer-by-layer growth mode can result if the surface kinetics are sufficiently high [8]. In figs. 1a and 1b we show RHEED oscillations for the lattice matched growth of GaAs and $\text{In}_{0.53}\text{Ga}_{0.47}\text{As}$ on InP. As can be seen from the sustained oscillations, layer-by-layer growth occurs.

In strained system, besides the second neighbor bond energy, ω_2 , one has to consider the strain energy in determining the thermodynamic equilibrium state. Using a simple model and energy

minimization techniques we have shown that the surface prefers to be formed from islands rather than have an atomically flat profile and that the height (in monolayers) of the islands is given by

$$n^3 \approx 2 \frac{\omega_1}{\omega_2} \frac{R_0}{d_c}, \quad (1)$$

where ω_1/ω_2 is the ratio of the nearest to second neighbor bond energies, R_0 is the substrate lattice constant and d_c is the critical thickness. At critical thickness the strain energy equals the dislocation formation energy. For lattice matched system ($d_c \rightarrow \infty$), n goes to zero, i.e., to an atomically flat surface. However, as the value of d_c decreases (i.e., the lattice mismatch increases) we expect a three-dimensional surface. In figs. 1c and 1d we have shown RHEED oscillation data for growth of strained $\text{In}_{0.3}\text{Ga}_{0.7}\text{As}$ on GaAs and InGaAs on InP, respectively. As can be seen from this figure, in presence of strain the layer grows in a 3D mode which is reflected by the abrupt decay of the RHEED oscillations.

3. Migration enhanced epitaxy

Since the minimum free energy for a strained system favors a 3D surface, the growth of strained systems cannot be improved by simply enhancing the surface migration rate of the adatoms. One expects the free energy to depend upon the surface reconstruction during growth. In MBE the surface

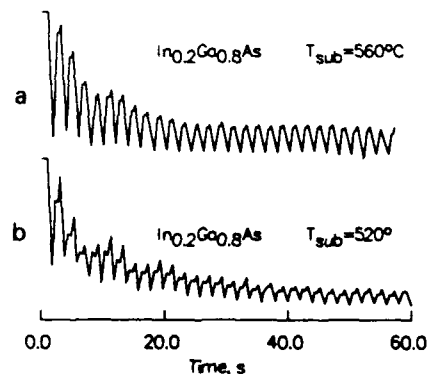


Fig. 2. RHEED oscillations observed during growth of $\text{In}_{0.2}\text{Ga}_{0.8}\text{As}$ by MBE.

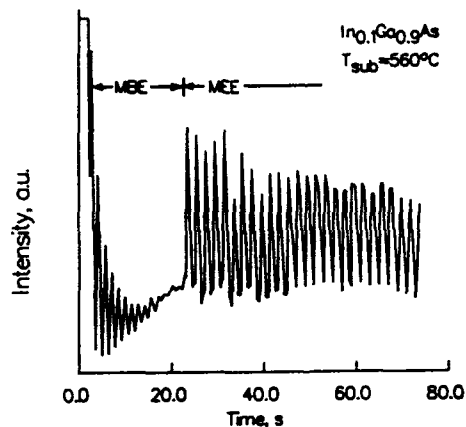


Fig. 3. RHEED oscillations observed during growth of $\text{In}_{0.1}\text{Ga}_{0.9}\text{As}$ with first fifteen monolayers grown by MBE then followed immediately by MEE.

is anion stabilized with a (2×4) or $c(2 \times 8)$ reconstruction. It is therefore important to examine other possible surface reconstructions which might change the surface chemical energy. Since MBE of III-V semiconductors cannot be carried out under cation-rich conditions because the excess cation causes non-stoichiometric growth, a practical approach is migration enhanced epitaxy (MEE) [9,10].

During MEE growth, group III and group V fluxes are delivered alternately by shutter control. The surface reconstruction thus alternates between cation and anion stabilized. If the shutter opening time is adjusted such that one monolayer of atoms are deposited in each shutter opening, layer-by-

layer growth is possible, with long-lasting oscillations. Shown in fig. 2 are the observed RHEED oscillations for growth of $\text{In}_{0.2}\text{Ga}_{0.8}\text{As}$ by MEE. Differences in RHEED patterns between MBE and MEE are also observed for $\text{In}_x\text{Ga}_{1-x}\text{As}$ with $x = 0.3$. In MBE growth, the RHEED pattern becomes spotty after a few monolayers are deposited. During MEE, the pattern remains streaked even after 20 monolayers, suggesting the growth is two-dimensional. RHEED studies also show that surface roughness in strained layers grown by MBE can be smoothed by just a few monolayers overgrown by MEE, as evidenced by the restoration of strong oscillations (fig. 3). This suggests that for pseudomorphic devices most of the strained active layer might be grown by MBE and just a few monolayers before interface formation by MEE to produce an abrupt interface.

4. Transport properties and device performance

We have carried out experiments on both GaAs-based and InP-based pseudomorphic MODFET heterostructures. We will first discuss the results obtained from InP-based structures grown by MBE. The schematic of a typical InP-based structure is shown in fig. 4a. The sheet electron density in all the samples varied in the range $(2.0 \times 3.2) \times 10^{12} \text{ cm}^{-2}$. In fig. 4b we show a plot of the 300 and 77 K mobilities versus excess In content in the channel. MODFETs, with $0.8 \mu\text{m}$ gate stripes, were fabricated on the hetero-

a		
150 Å	$\text{In}_{0.53}\text{Ga}_{0.47}\text{As}$	$n^+ (5 \times 10^{18} \text{ cm}^{-3})$
200 Å	$\text{In}_{0.52}\text{Al}_{0.48}\text{As}$	i
150 Å	$\text{In}_{0.52}\text{Al}_{0.48}\text{As}$	$n^+ (5 \times 10^{18} \text{ cm}^{-3})$
50 Å	$\text{In}_{0.52}\text{Al}_{0.48}\text{As}$	i
100 Å	$\text{In}_x\text{Ga}_{1-x}\text{As}$	i
400 Å	$\text{In}_{0.53}\text{Ga}_{0.47}\text{As}$	i
4000 Å	$\text{In}_{0.52}\text{Al}_{0.48}\text{As}$	i
InAlAs/InGaAs Superlattices		
S. I. InP (100) Substrate		

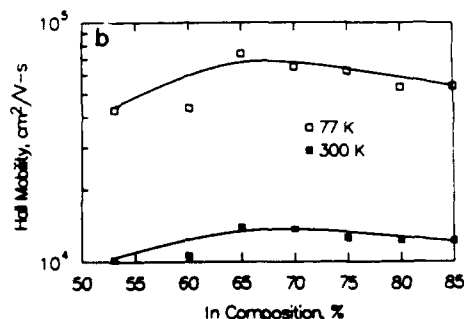


Fig. 4. (a) Schematic of MBE-grown n-type pseudomorphic MODFET on InP. (b) Hall mobilities of pseudomorphic MODFETs with increasing indium content in the channel at 77 and 300 K.

Table 1
DC and microwave characteristics of $0.8 \times 150 \mu\text{m}$ gate MODFETs with pseudomorphic $\text{In}_x\text{Ga}_{1-x}\text{As}/\text{In}_{0.52}\text{Al}_{0.48}\text{As}$ quantum wells

x	$g_{m,\text{max}}$ (mS/mm)	$I_{ds,\text{max}}$ (mA/mm)	f_T (GHz)	f_{max} (GHz)
53	440	530	30	44
60	390	270	30	40
65	510	500	40	52
70	550	510	45	62
75	370	310	36	47
80	430	270	41	50
85	400	420	33	51

structures by standard photolithography and liftoff techniques. All the samples exhibited good pinch-off characteristics and output conductances in the range of 10 to 25 mS/mm. The devices were biased near their peak g_m value for microwave measurements. From the measured S -parameter, the extrinsic values of f_T and f_{max} were extrapolated. Table 1 shows the summary of DC and microwave characteristics measured for each of the samples. The good DC and microwave results indicate the high quality of these layers.

The trend in the mobility data as a function of In content observed by us – an initial increase followed by a decrease at higher values of strain (In content) – has been observed by other authors [11]. Since the carrier mass is not expected to show a turnaround, to explain the mobility data it is important to examine other scattering mechanisms. The dominant mechanisms which could explain the decreased mobility at higher In composition are interface scattering and alloy scattering. For the GaAs based structures, the alloy scattering continuously increases as In composition x is increased (since $\mu \propto 1/x^2(1-x)^2$). However, for the InP based systems the alloy scattering should decrease since the alloy scattering peaks for a 50:50 alloy, assuming the mass does not vary. Thus unless some unusual clustering effects occur in strained epitaxy, one has to consider interface roughness as the source of the turnaround in mobility as the excess In composition increases beyond $\sim 15\%$. The interface

roughness scattering can be described by the scattering rate [4]:

$$\frac{1}{\tau} = \frac{\pi e^4 m^*}{\hbar^3 \epsilon_s^2} N_s \Delta^2 \int_0^\pi J_1(k_F L \sin \phi)^2 d\phi, \quad (2)$$

where N_s is the sheet charge density, Δ is the height of the 3D island describing the interface roughness, L is the lateral extent of the island, and k_F is the Fermi vector. From the discussion section 2 we expect Δ to increase abruptly when the strain increases $\sim 2\%$. We expect that if Δ increase to ~ 4 monolayers around this value of strain, the mobility decreases at high In content can be accounted for. The RHEED data of figs. 1c and 1d suggest that this is quite likely the case. The existence of point defects is possible, but is difficult to identify. However, in-situ scanning tunneling microscopy (STM) data for $\text{In}_{0.35}\text{Ga}_{0.65}\text{As}$ on GaAs did clearly show that 3D growth occurs in the case of strained-layer epitaxy with large misfits. This supports our RHEED measurement results.

A MODFET grown by the MEE technique should suffer less from interface roughness scattering and, thus, have improved transport properties. To verify this argument, we have compared the properties of GaAs-based $\text{Al}_{0.3}\text{Ga}_{0.7}\text{As}/\text{In}_{0.2}\text{Ga}_{0.8}\text{As}$ MODFETs with 100 \AA $\text{In}_{0.2}\text{Ga}_{0.8}\text{As}$ channels. In one set the entire structure is grown by MBE at 560°C while in the other the last five monolayers of the $\text{In}_{0.2}\text{Ga}_{0.8}\text{As}$ channel is grown by MEE at 560°C . The latter exhibits improved

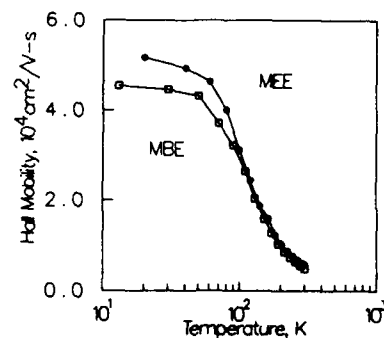


Fig. 5. Hall mobility as a function of temperature in $\text{Al}_{0.3}\text{Ga}_{0.7}\text{As}/\text{In}_{0.2}\text{Ga}_{0.8}\text{As}$ MODFET structures grown by MBE and MEE.

mobilities at temperatures ranging from 13 to 300 K (fig. 5). The channel electron density in the two structures is $\sim 1.5 \times 10^{12} \text{ cm}^{-2}$. $1 \mu\text{m}$ gate MODFETs made of the MEE samples also show improved DC transconductance and microwave performance. For example, at room temperature $g_m = 108$ and 59 mS/mm in the devices grown by MEE and MBE, respectively. Note that the low g_m values are partly due to the low electron densities and part of the difference is due to process variation. In this MODFET structure, the modulation-doped layer has thickness of 150 \AA and nominal doping concentration of $2 \times 10^{18} \text{ cm}^{-3}$. The spacer layer has thickness of 120 \AA . This structure was intended for high electron mobility in the channel. For higher current capability and g_m , we would increase the doping level and reduce the spacer thickness. We have also made $0.2 \mu\text{m}$ gate $\text{In}_{0.7}\text{Ga}_{0.3}\text{As}/\text{In}_{0.52}\text{Al}_{0.48}\text{As}$ MODFETs with the channel grown by MEE. The measured g_m and f_{max} are 570 mS/mm and 140 GHz , respectively, showing the suitability of the MEE technique for realizing high-performance devices.

5. Conclusions

In conclusion, we have addressed the issue of growth modes in MBE grown strained layers in the context of the performance characteristics and transport properties of pseudomorphic MODFETs. The advantages of MEE over MBE are also discussed. From RHEED oscillation measurements and energy minimization considerations it is apparent that once the misfit strain in the InGaAs channel increases above $\sim 1.5\text{--}2.0\%$, the growth occurs in a 3D island mode, leading to a

rough interface. From RHEED oscillation studies we note that it is possible to achieve layer-by-layer growth even at high strain by MEE. MODFETs with the last several monolayers of the channel grown by MEE also exhibit better performance than those with entire structure grown by MBE.

Acknowledgements

The authors acknowledge help and comment provided by R. Lai and J. Pamulapati. This work was supported by the Office of Naval Research under Grant N00019-89-J1519.

References

- [1] G.I. Ng, W.-P. Hong, D. Pavlidis, M. Tutt and P.K. Bhattacharya, IEEE Electron Device Letters EDL-9 (1988) 439.
- [2] T.J. Drummond, T.E. Zipperian, I.J. Fritz, J.E. Schirber and T.A. Plut, Appl. Phys. Letters 49 (1986) 461.
- [3] T. Ando, J. Phys. Soc. Japan 51 (1982) 3900.
- [4] W.-P. Hong, J. Singh and P.K. Bhattacharya, IEEE Electron Device Letters EDL-7 (1986) 480.
- [5] J. Singh and K.K. Bajaj, Superlattices and Microstructures 2 (1986) 185.
- [6] J.H. Neave, P.J. Dobson, B.A. Joyce and J. Zheng, Appl. Phys. Letters 47 (1985) 100.
- [7] J.M. Van Hove, P.R. Pukite, G.J. Whaley, A.M. Wouchak and P.I. Cohen, J. Vacuum Sci. Technol. B3 (1985) 1116.
- [8] P.R. Berger, K. Chang, P.K. Bhattacharya, J. Singh and K.K. Bajaj, Appl. Phys. Letters 53 (1988) 684.
- [9] Y. Horikoshi, M. Kawashima and H. Yamaguchi, Japan. J. Appl. Phys. 27 (1988) 169.
- [10] F. Briones, L. Gonzalez and A. Ruiz, Appl. Phys. A49 (1989) 729.
- [11] C.K. Peng, S. Sinha and H. Morkoç, J. Appl. Phys. 62 (1987) 2880.

Improved device performance by migration-enhanced epitaxy

Pin Ho, S.C. Wang, T. Yu, J.M. Ballingall, P.A. Martin, K.H.G. Duh, S.M.J. Liu

General Electric Electronics Laboratory, Syracuse, New York 13221, USA

G.A. Hutchins and E.L. Hall

General Electric Corporate Research & Development Center, Schenectady, New York 12301, USA

Migration-enhanced epitaxy (MEE) has been employed successfully to grow high quality GaAs buffer and InGaAs channel layers at 300°C. Planar-doped GaAs MESFETs with a thin MEE GaAs buffer layer have been fabricated for comparison with devices using conventional MBE buffers. Our preliminary data indicate that the MEE buffer alternative offers reduced side-gating effect, lower output conductance, better pinch-off characteristics and higher channel current. RF measurements indicate an improvement in output power density, gain and efficiency for the MEE-buffered MESFETs. High electron mobility transistor (HEMT) devices fabricated on modulation-doped pseudomorphic AlGaAs/InGaAs/GaAs heterostructures with a thin MEE buffer layer yield higher transconductance (g_m), transistor gain, and unity current gain cutoff frequency (f_T) compared to the conventional MBE-buffered devices. Moreover, HEMT devices with an MEE InGaAs channel grown at 300°C achieve comparable g_m and f_T to those with a conventional MBE channel grown at ~500°C. Critical layer thickness of InGaAs on GaAs using the MEE method, under the growth conditions reported here, is found to exceed that of MBE.

1. Introduction

Migration-enhanced epitaxy (MEE), first introduced by Horikoshi et al. [1] in 1986 as an alternative to conventional molecular beam epitaxy (MBE), has stimulated a great deal of interest due to its two-dimensional layer-by-layer growth mechanism and low substrate growth temperatures. This method has been employed successfully to grow high quality materials such as GaAs [1,2], GaAs/AlGaAs [3], AlAs/GaAs [1], or InAs/GaAs [4] quantum-well layers and to reduce surface morphological defects [5]. Recently, Tadayon et al. [6] reported improved electron transport properties of Si-doped GaAs by the MEE method. Nevertheless, no beneficial effects on device performance using this technique, to our knowledge, have been reported.

In this paper, we demonstrate improved DC and RF performance of the devices incorporating MEE buffer layers, and also report for the first time the results using MEE InGaAs channel layers based on our preliminary data. Results of Hall

effect, photoluminescence (PL), and transmission electron microscopy (TEM) are discussed. The critical layer thickness of InGaAs on GaAs using MEE and MBE methods are compared.

2. Material growth and measurements

All of the samples were grown in a Varian Gen-II reactor on (100) LEC GaAs substrates and yielded good surface morphology. The beam flux intensities were set to $(4.3\text{--}6.3) \times 10^{14}$ and $(1.1\text{--}1.8) \times 10^{14} \text{ cm}^{-2} \text{ s}^{-1}$ for Ga and In respectively. The As_4 beam equivalent pressure was about 6×10^{-6} Torr. A substrate temperature of 300°C was utilized for all of the MEE layers except as mentioned. Group III and Group V beam fluxes were alternately supplied to the growing substrate with no interruption between switching. For instance, for the growth of InGaAs layers, Ga and In shutters were opened simultaneously. The In content was based on the calibration of the conventional MBE InGaAs layer.

300Å	Undoped	GaAs	
	Si-PlanarDoping	$5 \times 10^{12} \text{ cm}^{-2}$	
700Å	Undoped	GaAs	
	Si-Planar Doping	$5 \times 10^{12} \text{ cm}^{-2}$	
0.85µm	Undoped	GaAs	
0.15µm	Undoped	MEE	GaAs
GaAs Substrate			

Fig. 1. Layer structure of planar-doped GaAs MESFET with a 0.15 µm MEE buffer layer.

A simple, non-optimized layer structure of the planar-doped GaAs MESFET, with a thin MEE GaAs buffer layer, is shown schematically in fig. 1. All the MBE layers in the MESFET structure were grown at 600°C. Fig. 2 shows the AlGaAs/InGaAs/GaAs pseudomorphic HEMT heterostructures with an MEE-grown InGaAs channel layer. Modulation doping was provided by silicon atomic planar doping at a concentration of $5 \times 10^{12} \text{ cm}^{-2}$ on top of a 40 Å thick undoped Al GaAs spacer layer. The MBE buffer layer was grown at 600°C; the rest of the layers, except for

300Å	n	GaAs	
400Å	n	AlGaAs	
Si-Planar Doping			
40Å	Undoped	AlGaAs	
	Undoped	MEE	InGaAs
1 μm	Undoped	GaAs	
GaAs Substrate			

Fig. 2. Layer structure of AlGaAs/InGaAs/GaAs pseudomorphic HEMT with an MEE channel layer.

the MEE InGaAs layer, were grown at 480–520°C.

The samples were characterized by Hall effect, PL, and TEM. The Hall effect samples were step-etched to the point of maximizing the measured 77 K electron mobility in order to minimize the effect of parallel conduction in the GaAs and AlGaAs overlayers. TEM measurements were performed on cross-sectional samples utilizing both bright field and dark field imaging modes. Plan-view imaging utilized two-beam diffracting conditions in the bright field mode for assessing dislocation densities down to a detection limit of 10^4 cm^{-2} .

3. Device fabrication

Devices were fabricated on planar-doped GaAs MESFETs shown in fig. 1 with a thin MEE buffer layer in comparison with the conventional MBE buffer, with a 0.7 µm gate-length. The gate-width and source-drain separation were 150 and 4 µm, respectively. For side-gating experiments, the gate-width was reduced to 50 µm with a 25 µm separation between pads. The mesa isolation breakdown voltages were measured at 10 µm spacing between mesas, after etching the mesas 0.15 µm past the planar doped active layer. 150 µm wide HEMTs, with layer structure as illustrated in fig. 2, with 0.15 µm T-shaped gates were also fabricated by E-beam lithography. The ohmic contacts were formed by alloyed AuGeNi and the gates by non-alloyed Ti/Pt/Au.

4. Material characteristics and device results

For the 0.7 µm gate-length MESFETs, though the extrinsic transconductances, g_m , are comparable, 200 and 210 mS/mm for MBE- and MEE-buffered devices respectively, the general trend is that the MEE-buffered devices offer lower output conductance, better pinchoff characteristics, and higher saturation channel current (I_{ds}), as summarized in table 1. The mesa isolation breakdown voltage of 45 V was obtained for the MEE-buffered devices in comparison with a typical 30 V for conventional MBE buffer.

Table 1
DC results of 0.7 μm planar-doped MESFETs

Buffer	g_m (mS/mm)	I_{dss} (mA)	$V_{pinchoff}$ (V)	Mesa breakdown (V)
MEE	210	50	2.0–2.5	45
MBE	200	45	2.5–3.5	30

Fig. 3 shows the side-gating characteristics for the devices. With the gate grounded, the channel current I_{ds} was measured at $V_{ds} = 2.5$ V as a

function of side-gate voltage. The I_{ds} was then normalized to the I_{dss} . As can be seen in the figure, the MEE buffer layer eliminates the side-gating effect up to a side gate voltage of about 6 V, then the I_{ds}/I_{dss} ratio decreases monotonically with increasing voltage. Note that the thickness of the MEE buffer layer used in this study is only 0.15 μm . Further reduction of side-gating effect can be expected by using a thicker MEE buffer layer.

Table 2 summarizes the RF results of power and gain performance at 10 GHz for 0.7 μm

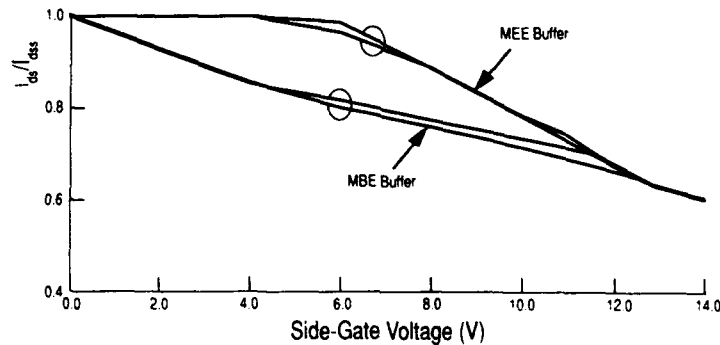


Fig. 3. Side-gating characteristics for 0.7 μm planar-doped MESFETs with an MEE buffer or an MBE buffer.

Table 2
RF results for 0.7 μm planar-doped MESFETs measured at 10 GHz

Buffer	V_{ds} (V)	Maximum PAE (%)	Gain (dB)	Output power density (W/mm)	MSG or MAG (dB)
MEE	5.5	35.8	7.1	0.34	13.6
MBE	5.5	26.0	5.6	0.27	12.5

Table 3
77 K Hall effect and growth data for modulation-doped $\text{In}_{0.5}\text{Ga}_{0.5}\text{As}$ HEMTs

Sample No.	x	Thickness (Å)	Growth method	Growth temperature (°C)	Mobility ($\text{cm}^2/\text{V}\cdot\text{s}$)	Sheet charge density (cm^{-2})
791	0.30	80	MEE	480	1000	2.6×10^{12}
797	0.30	80	MEE	300	10000	
1041	0.22	100	MEE	520	1200	2.3×10^{12}
1043	0.22	100	MEE	300	16700	
1044	0.22	100	MBE	300	2800	1.9×10^{12}
1046	0.22	100	MBE	520	14700	
1049 ^{a)}	0.22	100	MBE	520	15100	3.0×10^{12}

^{a)} With an MEE buffer layer grown at 300 °C.

planar-doped MESFETs. All the measurements were done at the bias conditions where the maximum power-added efficiencies (PAEs) were obtained. Significant improvements in output power density, gain and efficiency can be seen and demonstrate the superior performance utilizing MEE buffer layers. The maximum stable gain (MSG) and maximum available gain (MAG) values determined from the *S*-parameter measurements also illustrate an improved gain for the MEE-buffered devices.

Table 3 lists Hall effect data for the AlGaAs/InGaAs/GaAs pseudomorphic HEMTs with an MEE or an MBE InGaAs channel layer grown at various temperatures. As shown in the table, the low growth temperatures are optimal for the MEE InGaAs layers, while for the MBE channel growth, the temperature has to be high ($\geq 470^\circ\text{C}$). The degradation in electron mobility correlates with the dislocations as detected by TEM, or the InGaAs quantum well emissions by PL. Cross-sectional TEM image of sample 791 shows a high defect density. The wavy contrast observed at the InGaAs/AlGaAs interface is due to interface roughness [7,8]. Planar faults and threading dislocations extend from the InGaAs/AlGaAs interface toward the top surface of the sample. 4 K PL scans show no emissions attributed to the quantum well. Sample 1044 with an InGaAs channel grown by MBE at 300°C yields a 77 K Hall mobility of only $2800\text{ cm}^2/\text{V}\cdot\text{s}$ (see table 3). Though cross-sectional TEM micrographs of this sample are defect-free, point defects may still exist. Plan-view TEM shows some interfacial dislocations. Again, there is no PL quantum well emission from this sample. Samples 1043, 1046 and 1049, on the other hand, with good 77 K Hall mobility and PL emissions, show no dislocations in the cross-sectional TEM images, or in the plan-view mode down to a detection limit of 10^4 cm^{-2} . The InGaAs channel in samples 1043, 1044, 1046 and the MEE buffer layer in sample 1049 have been carefully examined using high resolution TEM imaging. Sample 1049 is similar to the other layers except for a $0.15\text{ }\mu\text{m}$ thick MEE buffer grown directly on the substrate and subsequently overgrown with a $0.85\text{ }\mu\text{m}$ thick MBE GaAs layer. No evidence of arsenic precipitates, or defects,

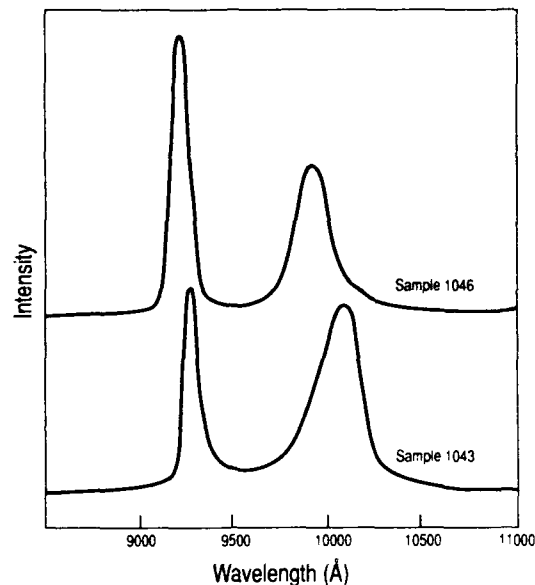


Fig. 4. 4 K photoluminescence scans of AlGaAs/InGaAs/GaAs pseudomorphic HEMTs with an MEE (sample 1043) or an MBE (sample 1046) channel layer. Laser power density = 31 W/cm^2 .

other than dislocations as mentioned above, was observed in those layers. This is an interesting result, because GaAs grown by MBE at 300°C and then heat-treated at a higher temperature (600°C) for a short time exhibits small ($\sim 100\text{ Å}$) arsenic precipitates [9–11]. Their absence here may be due to MEE growth, the small thickness of the layers, or the low growth temperature ($\sim 500^\circ\text{C}$) of the overlayers.

Low temperature PL was performed on these samples in an attempt to determine the quality of the MEE InGaAs and GaAs layers. Fig. 4 shows the PL spectra for samples 1043 and 1046, with an MEE and a conventional MBE InGaAs channel layer respectively. Two peaks observed in each spectrum are attributed to the $n=1$ and $n=2$ conduction-band quantized states in the InGaAs quantum wells. The peak widths, or full widths at half maximum (FWHM), are very similar for both samples. Also, the FWHMs are typical of modulation-doped pseudomorphic layers with a sheet density of $(2\text{--}3) \times 10^{12}\text{ cm}^{-2}$, indicating high material quality for both MEE- and MBE-grown

Table 4
77 K Hall effect data for $\text{Al}_{0.25}\text{Ga}_{0.75}\text{As}/\text{In}_{0.21}\text{Ga}_{0.79}\text{As}/\text{GaAs}$ pseudomorphic HEMTs with a 300 °C MEE channel

Sample No.	Channel thickness (Å)	Mobility ($\text{cm}^2/\text{V}\cdot\text{s}$)	Sheet charge density (cm^{-2})
1228	100	12600	2.4×10^{12}
1230	150	11400	2.3×10^{12}
1231	175	10900	2.4×10^{12}
1235	200	6100	2.2×10^{12}

InGaAs layers [12]. The shift of peak position is partly due to a slight change of composition. All of the GaAs, AlGaAs and InGaAs PL peaks observed in sample 1049 (not shown) are similar to those of sample 1046. Since, sample 1049 has an MEE buffer layer, these PL data indicate that with an MEE buffer, the quality of the MBE overlayers remains unaffected. The data also suggest that the MEE buffer is of reasonably high quality as has been reported previously [1,3]. An MEE GaAs layer grown separately exhibited emission spectra due to free exciton and impurity-bound excitons, confirming that this is indeed the case.

We have previously established the critical layer thickness (CLT) for single quantum well pseudomorphic structures grown at low substrate temperatures ($\sim 480^\circ\text{C}$). At 480°C , the CLT can substantially exceed the Matthews–Blakeslee limit for the single-kink failure mechanism because of the slowed misfit dislocation kinetics [7]. For instance, the CLT for $x = 0.21$ is found to be about 140 Å. The typical 77 K mobility is $14000 \text{ cm}^2/\text{V}\cdot\text{s}$ for a pseudomorphic structure with a 120 Å channel and $x = 0.21$. Table 4 lists Hall effect data for several pseudomorphic structures with varying the

InGaAs channel thickness ($x = 0.21$). With increasing the MEE channel layer thickness from 100 to 175 Å, the 77 K Hall mobility slightly decreases. For 200 Å the mobility drops drastically to only $6100 \text{ cm}^2/\text{V}\cdot\text{s}$. Therefore, we can say that the CLT of MEE InGaAs grown on GaAs, under the growth conditions in this report, exceeds that of MBE for $x = 0.21$. The MEE technique, in principle, could be exploited to achieve higher CLT, because of the low substrate temperature and the reduced growth rate, but in practice the sample temperature needs to be elevated back to above 470°C in order to grow conducting GaAs and AlGaAs overlayers for modulation doping. Further development of low temperature MEE growth for the overlayers might lead to successful growth of the entire structure at 300°C .

HEMT devices were also fabricated on samples 1043, 1046 and 1049 for comparison. Table 3 lists the growth parameters and Hall data for these samples. Preliminary DC and RF data are presented in table 5. The room temperature extrinsic g_m was measured at $V_{ds} = 2.5 \text{ V}$. Maximum g_m of 1000 mS/mm was obtained from sample 1049 with a thin MEE buffer layer, while 930 and 880 mS/mm were obtained for samples 1043 and 1046 with MEE and MBE channels, respectively. RF measurements at 18 GHz yielded a minimum noise figure (F_{min}) of 0.8 dB at room temperature with an associated gain (G_a) of 13.2 dB for sample 1049, which is the best in terms of noise performance among those samples. Moreover, the f_T value of 113 GHz was extrapolated from the h_{21} value for sample 1049, while samples 1043 and 1046 yielded comparable f_T values of 84 and 86 GHz respectively. Notice that the RF measurements were performed on passivated devices. This study demonstrates the superior performance of

Table 5
DC and RF results for $0.15 \times 150 \mu\text{m}$ AlGaAs/InGaAs/GaAs pseudomorphic HEMTs

Sample No.	Maximum extrinsic g_m (mS/mm)	Channel current at maximum g_m (mA/mm)	Minimum noise figure at 18 GHz (dB)	Associated gain at 18 GHz (dB)	f_T (GHz)
1043	930	260	0.9	12.0	84
1046	880	250	1.2	12.6	86
1049	1000	285	0.8	13.2	113

the devices incorporating an MEE buffer layer. Also comparable device performance can be achieved by using a low temperature MEE or a conventional MBE InGaAs channel layer in the pseudomorphic HEMT structures, indicating MEE as an alternative growth technique for device applications.

5. Conclusions

The MEE technique has been employed successfully to grow high quality GaAs buffer and InGaAs channel layers incorporated in MESFET and AlGaAs/InGaAs/GaAs HEMT structures. We have demonstrated improved DC and RF performance of the devices incorporating 300°C MEE buffer layers based on our preliminary data. We also demonstrate that MEE is an alternative technique for the growth of InGaAs layers for device applications.

Acknowledgements

We wish to thank Dr. Gerry Witt for helpful discussions. The support of Alan Swanson and Walter Butler at General Electric is also gratefully appreciated. This research is partially sponsored

by the Air Force Office of Scientific Research (AFSC) under Contract F49620-88-C-0054.

References

- [1] Y. Horikoshi, M. Kawashima and H. Yamaguchi, Japan. J. Appl. Phys. 25 (1986) L868.
- [2] Y. Horikoshi and M. Kawashima, Japan. J. Appl. Phys. 28 (1989) 200.
- [3] Y. Horikoshi, M. Kawashima and H. Yamaguchi, Japan. J. Appl. Phys. 27 (1988) 169.
- [4] J.M. Gerard and J.Y. Marzin, Appl. Phys. Letters 53 (1988) 568.
- [5] A. Salokatve, J. Varrio, J. Lammasniemi, H. Asonen and M. Pessa, Appl. Phys. Letters 51 (1987) 1340.
- [6] B. Tadayon, S. Tadayon, M.G. Spencer, G.L. Harris, J. Griffin and L.F. Eastman, Appl. Phys. Letters 67 (1990) 589.
- [7] J.M. Ballingall, P. Ho, P.A. Martin, G.J. Tessmer, T. Yu, N. Lewis and E.L. Hall, J. Electron. Mater. 19 (1990) 509.
- [8] J. Pamulapati, R. Lai, G.I. Ng, Y.C. Chen, P.R. Berger, P.K. Bhattacharya, J. Singh and D. Pavlidis, J. Appl. Phys. 68 (1990) 347.
- [9] Z. Liliental-Weber, F. Smith and A.R. Calawa, Materials Research Society Spring Meeting, San Francisco, CA, April 1990.
- [10] M.R. Melloch, Workshop on Low Temperature GaAs Buffer Layers, San Francisco, CA, April 1990.
- [11] J.M. Ballingall, Workshop on Low Temperature GaAs Buffer Layers, San Francisco, CA, April 1990.
- [12] J.M. Ballingall, P. Ho, G.J. Tessmer, P.A. Martin, T.H. Yu, P.C. Chao, P.M. Smith and K.H.G. Duh, Mater. Res. Soc. Symp. Proc. 160 (1990) 759.

Delta-doping of GaAs and $\text{Al}_{0.33}\text{Ga}_{0.67}\text{As}$ with Sn, Si and Be: a comparative study

J.J. Harris, J.B. Clegg, R.B. Beall, J. Castagné, K. Woodbridge and C. Roberts

Philips Research Laboratories, Redhill, Surrey RH1 5HA, UK

We have performed a study of the contributions of segregation, diffusion and aggregation to the broadening of delta-doped planes of Sn, Si and Be in GaAs and $\text{Al}_{0.33}\text{Ga}_{0.67}\text{As}$. Sn planes are severely broadened by all three processes, but sharp spikes of Si and Be can be obtained in both host materials for sheet densities below 10^{13} cm^{-2} and growth temperatures of 500°C or less. At higher temperatures or densities, segregation or concentration-dependent rapid diffusion may occur, causing significant spreading even during growth. Co-deposition of Si and Be dramatically reduces this broadening, and various mechanisms are considered to explain these effects.

1. Introduction

There are a number of mechanisms which can influence the incorporation and distribution of impurities in GaAs during growth by molecular beam epitaxy (MBE); these are principally surface segregation and diffusion, although dopant aggregation and autocompensation may also play a role. The presence of any of these processes at the growth temperatures and dopant concentrations used for the preparation of MBE samples may have undesirable consequences for the production of controlled dopant profiles, a particularly stringent situation being the growth of delta-doped (δ -doped) structures [1–3], in which the aim is to confine the impurities to a single atomic plane in the crystal.

We have studied the incorporation and diffusion processes of δ -doped planes of Sn, Si and Be in GaAs [4–9] and $\text{Al}_{0.33}\text{Ga}_{0.67}\text{As}$, using secondary ion mass spectrometry (SIMS) to determine the total impurity distribution and electrochemical capacitance–voltage (C – V) profiling to measure the electrical activity of the dopant. From these results, we have deduced the temperature and impurity concentration ranges in which the various mechanisms are important in causing departures from the ideal δ -doping structures; these ranges differ widely for the three dopants

studied. We have also investigated samples in which Be and Si have been deposited simultaneously on the same plane, and have found that the incorporation and migration of each species is strongly affected by the presence of the other.

2. Experimental

The samples were prepared by MBE in a modified Varian MBE-360 system, using growth temperatures in the range 300 – 640°C and, in most cases, a growth rate of $1 \mu\text{m/h}$, although values between 0.1 and $2 \mu\text{m/h}$ were sometimes used for comparison. The δ -doping planes were formed by depositing the impurity atoms (up to $4 \times 10^{13} \text{ cm}^{-2}$) whilst growth was interrupted by closing the Ga shutter; the As flux to the surface was maintained during this time. Usually, three planes were included in each layer grown. Three basic types of sample were prepared, with:

- (a) planes of constant impurity density, but successively lower deposition temperatures, for surface segregation studies;
- (b) planes of constant density at constant deposition temperature, where growth was also interrupted between planes without adding impurities in order to enhance diffusion at the growth temperature of the previously-deposited dopant;

(c) planes of different density at constant, low growth temperature, in which concentration dependent diffusion effects were studied using post-growth annealing; the samples were placed face-to-face with undoped GaAs in an evacuated quartz ampoule, and heated in a three-zone furnace whose temperature could be controlled to $\pm 0.5^\circ\text{C}$.

SIMS profiling was carried out in an Atomika system using 2 keV O_2^+ primary ions. The instrument resolution function has been determined using Si [10] and Be dopant planes deposited at very low temperatures ($\leq 400^\circ\text{C}$), where the profiles have been shown to be temperature independent, and hence not limited by diffusion or segregation effects. These measurements have shown that the minimum SIMS resolution is a full-width-at-half-maximum (FWHM) of $42 \pm 2 \text{ \AA}$ for Si and $56 \pm 2 \text{ \AA}$ for Be. The profiles are characterised by an exponential decay of impurity content towards the surface, at a rate λ_L (expressed here in $\text{\AA}/\text{decade}$), and towards the substrate at a rate λ_T . The minimum values of λ_L were 14 and 16 $\text{\AA}/\text{decade}$ for Si and Be, respectively, and of λ_T , 35 and 75 $\text{\AA}/\text{decade}$; the greater values for λ_T are due to a SIMS "knock-on" mixing effect.

3. Results and discussion

In the following sections, we will consider the role of each broadening mechanism, i.e. segregation, diffusion (both during and post growth) and surface aggregation, in determining the distribution of the three impurities Sn, Si and Be, and the combination of Si + Be, when deposited as a dopant plane.

3.1. Surface segregation

This is manifest as a preferential spreading of the dopant in the growth direction, usually with an exponential decay of the concentration towards the surface. It has been known for many years that Sn exhibits this effect very strongly, and we have previously [5] interpreted the temperature and flux dependence on a model which takes account of kinetic limitations due to the competition between the GaAs deposition rate and the

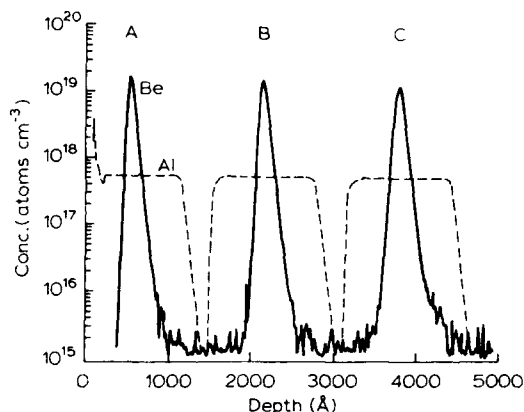


Fig. 1. SIMS profile of 10^{13} cm^{-2} Be δ -doped planes in $\text{Al}_{0.33}\text{Ga}_{0.67}\text{As}$ grown at (A) 500, (B) 550 and (C) 600 $^\circ\text{C}$. (The Al signal is scaled for convenience of display.)

dopant segregation. Si and Be also show asymmetric spreading which increases with temperature [6,9,11], as illustrated in fig. 1 for three planes of

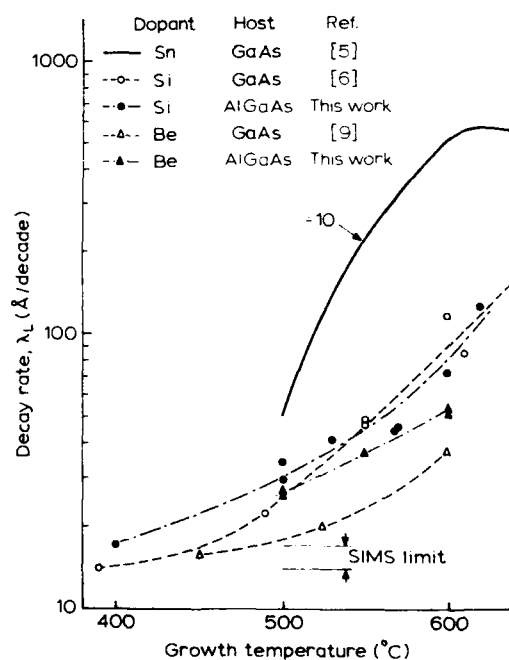


Fig. 2. Surface segregation behaviour of Sn, Si and Be in GaAs and $\text{Al}_{0.33}\text{Ga}_{0.67}\text{As}$. The exponential decay rate of the impurity concentration in the growth direction is plotted as a function of growth temperature.

Be in $\text{Al}_{0.33}\text{Ga}_{0.67}\text{As}$, deposited at 500, 550 and 600°C. The slope of the profile on the surface side of each peak, λ_L , increases from 28 Å/decade at 500°C to 53 Å/decade at 600°C, whereas λ_T is constant at 88 Å/decade, and results from SIMS mixing. These results, together with other data for Sn in GaAs and Si and Be in both GaAs and $\text{Al}_{0.33}\text{Ga}_{0.67}\text{As}$ are compared in fig. 2. This shows that, while the segregation rates of Si in GaAs and $\text{Al}_{0.33}\text{Ga}_{0.67}\text{As}$ are similar, and comparable to that of Be in $\text{Al}_{0.33}\text{Ga}_{0.67}\text{As}$, Be in GaAs shows a significantly smaller effect; Sn in GaAs, on the other hand, segregates over dis-

tances 10 to 100 times greater than those observed for Si and Be. In all these samples, the values of λ_T were independent of temperature, and the increase in FWHM was consistent with the increase in λ_L , indicating that diffusion effects were not contributing significantly to the shape of the profiles.

It has been suggested [11,12] that band-bending at the surface during growth would provide a field in which the ionized dopants would drift, giving rise to the observed spreading. In order to test the role of this and other charge-related effects in dopant migration, two samples were prepared at 600°C with 3 and 4 planes of 10^{13} cm^{-2} Si atoms, different amounts of Be being deposited simultaneously on each plane; the nominal Be densities used were 0, 1, 2.5, 5, 7.5, 10 and $15 \times 10^{12} \text{ cm}^{-2}$. Fig. 3a shows a composite profile of the two layers as-grown, and fig. 3b, the result of annealing for 3.5 h at 650°C. In the as-grown state, all the Si spikes show asymmetric broadening, with λ_L values of 90 ± 6 Å/decade, independent of the amount of Be deposited, even though in one plane (G) it exceeds the Si density. Since the net charge on the δ -plane will have a strong effect on the surface field during the subsequent growth of GaAs, this seems convincing evidence that the surface field is not responsible for Si surface segregation. However, λ_L for the Be peaks increased systematically from 24 to 37 Å/decade as the Be density increased, supporting the proposal [11] that surface field effects are influencing the surface segregation of Be.

3.2. Diffusion

A planar impurity profile may broaden by diffusion either during the growth time required to deposit the rest of the sample, or subsequently during post-growth heating such as may be required for device processing.

3.2.1. Growth-time diffusion

Fig. 4 shows the gradual broadening of Si δ -doped planes with time (up to 75 min) at a growth temperature for $\text{Al}_{0.33}\text{Ga}_{0.67}\text{As}$ of 550°C, with the FWHM increasing from 74 Å at the surface to 180 Å for the deepest spike; this corresponds to a

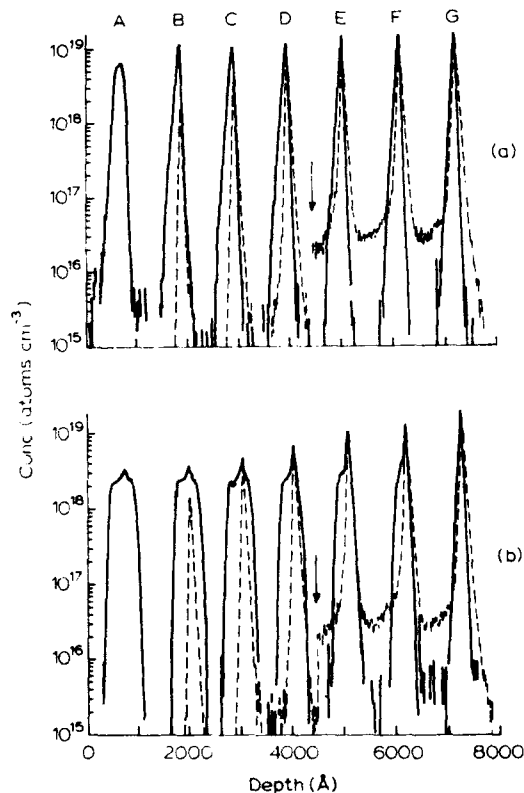


Fig. 3. SIMS profile of δ -doped planes, co-doped with Si (solid lines) and Be (broken lines). (The arrow marks the surface of the layer containing peaks E, F and G). The measured Si density on each plane is $1.3 \times 10^{13} \text{ cm}^{-2}$, and the Be densities are (A) 0, (B) 0.098×10^{13} , (C) 0.25×10^{13} , (D) 0.47×10^{13} , (E) 0.70×10^{13} , (F) 0.95×10^{13} and (G) $1.40 \times 10^{13} \text{ cm}^{-2}$. (a) As-grown; (b) after 3.5 h at 650°C.

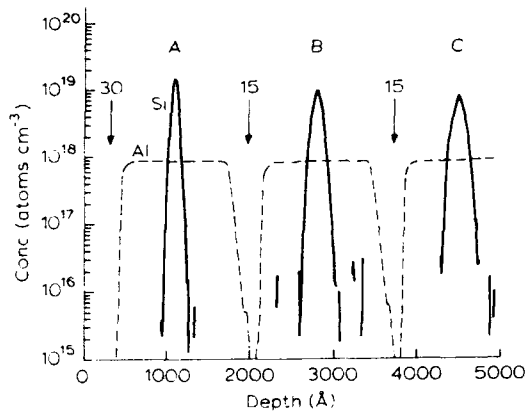


Fig. 4. SIMS profile of 10^{13} cm^{-2} Si δ -doped planes in $\text{Al}_{0.33}\text{Ga}_{0.67}\text{As}$ grown at 550°C , with arrows corresponding to growth interrupts for the number of minutes indicated.

diffusion coefficient of $1 \times 10^{-16} \text{ cm}^2 \text{ s}^{-1}$. The equivalent results for the other dopants are summarised in table 1, from which it can be seen that, at a sheet density of 10^{13} cm^{-2} , Si and Be have the same diffusion coefficients in GaAs and $\text{Al}_{0.33}\text{Ga}_{0.67}\text{As}$, with the values for Be being slightly lower than those for Si. (All diffusion constants quoted here have an estimated error of a factor of 2.) The result for Sn in GaAs was achieved by using a sample in which the growth temperature was lowered from 550 to 295°C immediately after deposition of the Sn, at which temperature 100 Å of GaAs was grown to incorporate all the Sn before returning the sample temperature to 550°C . This was repeated three times, with 1100 Å of undoped GaAs, plus a 30 min growth interruption, between each plane. The observed spreading

corresponded to a diffusion coefficient, D , at 550°C of $\sim 5 \times 10^{-16} \text{ cm}^2 \text{ s}^{-1}$. This is about three orders of magnitude greater than expected [13], although more recent work [14] has suggested that D is concentration dependent, which may explain the discrepancy. Indeed, there is a wide range of literature values of D for all these dopants, a situation which we believe can only be reconciled by taking into account the concentration dependence and non-Fickian behaviour of the diffusion process. There is an indication of non-ideal diffusive behaviour in fig. 3a, where we observed a clear difference in FWHM between the "Si only" spike, A, which is 200 Å wide, and all the others (FWHM = $90 \pm 10 \text{ Å}$), suggesting that the co-deposited Be has reduced growth-time diffusion of the Si. However, more convincing evidence has been obtained from post-growth diffusion studies of samples with planes of different dopant density, and these are discussed below.

3.1.2. Post-growth diffusion

The concentration dependence of the diffusion process for Be in $\text{Al}_{0.33}\text{Ga}_{0.67}\text{As}$ is clearly demonstrated in fig. 5a, which is the SIMS profile through three planes of nominal densities (A) 0.4×10^{13} , (b) 1×10^{13} and (C) $4 \times 10^{13} \text{ cm}^{-2}$ at 500°C . At this relatively low growth temperature, peak B is narrower than the corresponding 600°C spike (B in fig. 4), but the highest density peak C is broadened to a FWHM of 380 Å , indicating a much higher diffusion coefficient. Similar behaviour has been observed for Si in $\text{Al}_{0.33}\text{Ga}_{0.67}\text{As}$, and for Si and Be in GaAs [8,9,11]. Post-growth annealing of these layers reveals that, even after correcting for the instrument response function of the SIMS [10], the spreading of the profiles with time, t , does not obey Fick's Law, which for a Gaussian profile gives

$$(\text{FWHM})^2 = 16 \ln 2 (Dt). \quad (1)$$

Instead, the effective diffusion constant, D' , obtained from fitting eq. (1) to the data, gradually decreases as the anneals progress. This is, of course, consistent with a diffusion rate which depends on concentration, since the impurity density falls as the profile broadens. In order to make a meaning-

Table 1
Growth-time diffusion of 10^{13} cm^{-2} delta-doped planes of Sn, Si and Be in GaAs and $\text{Al}_{0.33}\text{Ga}_{0.67}\text{As}$

Dopant	Host	Temperature ($^\circ\text{C}$)	Diffusion constant ($\text{cm}^2 \text{ s}^{-1}$)
Sn	GaAs	550	5×10^{-16}
Si	GaAs	550	1×10^{-16}
	AlGaAs	550	1×10^{-16}
Be	GaAs	600	1.5×10^{-16}
		600	4×10^{-17}
		600	4×10^{-17}

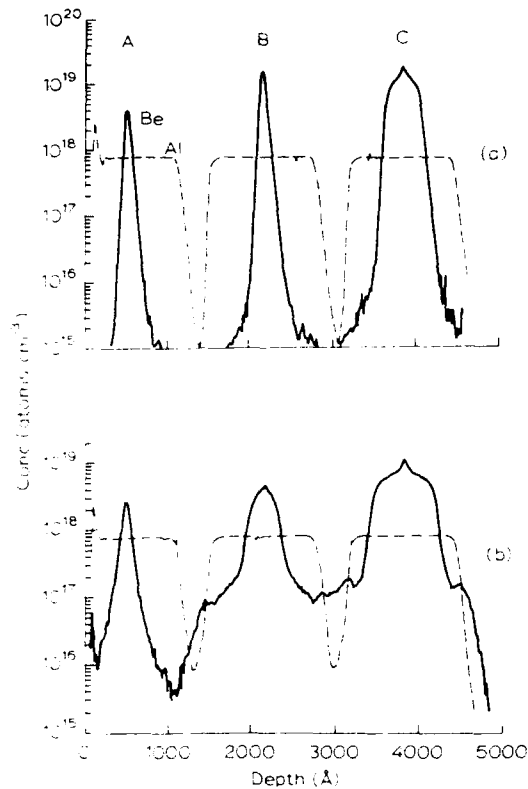


Fig. 5. SIMS profiles of Be δ -doped planes in $\text{Al}_{0.33}\text{Ga}_{0.67}\text{As}$, of densities (A) 0.4×10^{13} , (B) 1×10^{13} and (C) $4 \times 10^{13} \text{ cm}^{-2}$, (a) As-grown at 500°C ; (b) after 1.5 h at 650°C .

ful comparison, we have listed in table 2 the values of D' for Si and Be in GaAs and $\text{Al}_{0.33}\text{Ga}_{0.67}\text{As}$ with three different densities on the original planes, after annealing for 3.5 h at 650°C . These results indicate a strong dependence on carrier density, with slightly higher diffusion rates in $\text{Al}_{0.33}\text{Ga}_{0.67}\text{As}$ than in GaAs [15]. The data for Si planes of $4 \times 10^{12} \text{ cm}^{-2}$ indicate that diffusion is Fickian at this density, and, for the GaAs layer, good agreement is obtained with the value obtained by Schubert et al. [16] for this density of dopant after a 5 s rapid thermal anneal at 650°C . However, their results for Si in $\text{Al}_{0.33}\text{Ga}_{0.67}\text{As}$ [17] and Be in GaAs [11] are considerably higher than ours; since we observe non-Fickian diffusion for Be even at $4 \times 10^{12} \text{ cm}^{-2}$,

the latter result is consistent with our data, but the origin of the difference in the Si results is unclear.

Several models have been proposed to account for these rapid, concentration-dependent diffusion effects: for Si, the observation of auto-compensation in the diffused profiles (a factor which we have confirmed by $C-V$ and local vibrational mode (LVM) measurements [8]), has led to the suggestion that $\text{Si}_{\text{Ga}}-\text{Si}_{\text{As}}$ pairs are the diffusing species [18], while Be is expected to behave like Zn, for which an interstitial-substitutional mechanism has been proposed [19]. Recently Schubert et al. [3,11] have pointed out that mutual repulsion between the charged dopant atoms might be expected to add a drift component to the dopant migration; however, this is only expected to be significant at densities above 10^{20} cm^{-3} . Nevertheless, the results for the co-doped layers shown in fig. 3, particularly the data after annealing at 650°C (fig. 3b) indicate that ionic charge effects can apparently be significant: for Be, diffusive broadening of the type shown in fig. 5b is completely removed by the presence of co-deposited Si, and the Be concentration is clearly having a systematic effect on the rapid diffusion of Si. Since the dopant densities are below 10^{20} cm^{-3} , it seems likely that drift effects are not responsible, and that a different model is required to explain

Table 2

Effective diffusion coefficient for Si and Be delta-doped planes in GaAs and $\text{Al}_{0.33}\text{Ga}_{0.67}\text{As}$ after post-growth annealing for 3.5 h at 650°C

Dopant	Host	Sheet density (10^{13} cm^{-2})	Effective diffusion coefficient ($\text{cm}^2 \text{ s}^{-1}$)
Si	GaAs	0.4	2×10^{-17}
		1	2×10^{-16}
		4	7×10^{-16}
	AlGaAs	0.4	4×10^{-17}
		1	5×10^{-16}
		4	1×10^{-15}
Be	GaAs	0.4	$2 \times 10^{-17.41}$
		1	2×10^{-17}
		4	8×10^{-17}
	AlGaAs	0.4	6×10^{-18}
		1	1×10^{-16}
		4	4×10^{-16}

⁴¹ After 1.5 h.

the stability of the Be peaks in fig. 3b. One possibility is suggested by the LVM measurements of Mohades-Kassai et al. [20] on thick layers co-doped with Si and Be, where evidence of $\text{Si}_{\text{Ga}}^+ - \text{Be}_{\text{Ga}}^-$ next-nearest-neighbour pairing was found; such a complex may have a low diffusion coefficient. Alternatively, the presence of Si may simply inhibit the transfer of Be from a substitutional site to the rapidly-diffusing interstitial state [21]. The effect of post-growth annealing on the Si impurity distribution is more complex, with varying amounts of rapid diffusion being apparent; as the amount of Be increases, the diffusion profiles narrow asymmetrically, with a more pronounced effect on the substrate side of the δ -plane than on the surface side. Again, the "drift plus diffusion" model does not seem applicable in this case, and the results may once more be due to the formation of low-mobility Si-Be complexes. However, an alternative explanation is also offered by the work of Mohades-Kassai et al. [20] on thick co-doped layers, where it was found that in the presence of excess Be, Si will not occupy As sites. This Fermi-level related effect will thus inhibit the formation of $\text{Si}_{\text{Ga}} - \text{Si}_{\text{As}}$ pairs, and prevent the rapid diffusion process. The asymmetry seen in the profiles is simply the consequence of the original surface segregation of the Si; this means that the surface side of the co-doped peaks will be more n-type than the substrate side, and hence more likely to exhibit rapid diffusion.

3.3. Surface aggregation

If, during deposition of the δ -plane, the surface diffusion distance of an impurity exceeds the inter-impurity spacing, it is possible for islands of dopant to form; these will influence the subsequent incorporation and diffusion behaviour. In the case of Sn, the presence of islands results in a flat-topped segregation profile [4], whereas for Si the characteristic feature is a sharp central spike superimposed on the diffusion profile (e.g. peak A in fig. 3b). This is due to the presence of electrically neutral Si [8], which we believe is Si aggregated into islands during deposition. This feature is seen in both GaAs and $\text{Al}_{0.33}\text{Ga}_{0.67}\text{As}$ when the sheet density is 10^{13} cm^{-2} or greater, and may be

the reason why the free electron concentration of δ -doped planes appears to saturate at about this level [1], the excess Si being incorporated into the islands. A central spike is also visible in peak C of fig. 5b, for Be in $\text{Al}_{0.33}\text{Ga}_{0.67}\text{As}$, although none were observed for Be in GaAs [9,11]. It is possible that this also corresponds to aggregated material [22], but further work is required to confirm this.

4. Conclusions

We have compared the segregation, diffusion and aggregation behaviour of Sn, Si and Be in GaAs and $\text{Al}_{0.33}\text{Ga}_{0.67}\text{As}$. Delta-doped planes of Sn exhibit severe broadening due to all three mechanisms, whereas for sheet densities of less than 10^{13} cm^{-2} relatively sharp spikes of Si and Be can be obtained in both host materials at growth temperatures of 500°C or below. For higher temperatures and/or densities, diffusion becomes important, with concentration-dependent rapid diffusion processes coming into play. Significant changes in behaviour have been observed by co-depositing Si and Be on the same plane, suggesting that drift effects due to ionic charges may play a part in the broadening process; however, other interpretations are also possible, so that the situation remains unclear.

References

- [1] A. Zrenner, F. Koch and K. Ploog, in: Proc. 14th Intern. Symp. on GaAs and Related Compounds, Heraklion, Crete, 1987, Inst. Phys. Conf. Ser. 91, Eds. A. Christou and H.S. Rupprecht (Inst. Phys., London-Bristol, 1988) p. 171.
- [2] M. Santos, T. Sajoto, A. Zrenner and M. Shayegan, Appl. Phys. Letters 53 (1988) 2504.
- [3] E.F. Schubert, J. Vacuum Sci. Technol. A8 (1990) 2980.
- [4] J.J. Harris, B.A. Joyce, J.P. Gowers and J.H. Neave, Appl. Phys. A28 (1982) 63.
- [5] J.J. Harris, D.E. Ashenford, C.T. Foxon, P.J. Dobson and B.A. Joyce, Appl. Phys. A33 (1983) 87.
- [6] R.B. Beall, J.B. Clegg and J.J. Harris, Semicond. Sci. Technol. 3 (1988) 612.
- [7] R.B. Beall, J.J. Harris, J.B. Clegg, J.P. Gowers, B.A. Joyce, J. Castagné and V. Welch, in: Proc. 15th Intern. Symp. on GaAs and Related Compounds, Atlanta, GA, 1988, Inst. Phys. Conf. Ser. 96, Ed. J.S. Harris (Inst. Phys., London-Bristol, 1989) p. 17.

- [8] R.B. Beall, J.B. Clegg, J. Castagné, J.J. Harris, R. Murray and R.C. Newman, *Semicond. Sci. Technol.* 4 (1989) 1171.
- [9] J.J. Harris, J.B. Clegg, R.B. Beall and J. Castagné, *Semicond. Sci. Technol.* 5 (1990) 785.
- [10] J.B. Clegg and R.B. Beall, *Surface Interface Anal.* 14 (1989) 308.
- [11] E.F. Schubert, J.M. Kuo, R.F. Kopf, H.S. Luftmann, L.C. Hopkins and N.J. Sayer, *J. Appl. Phys.* 67 (1990) 1969.
- [12] K.H. Nichols, R.E. Goldwasser and C.M. Wolfe, *Appl. Phys. Letters* 36 (1980) 601.
- [13] B. Tuck and M.H. Badawi, *J. Phys. D (Appl. Phys.)* 11 (1978) 2541.
- [14] N. Arnold, R. Schmitt and K. Heime, *J. Phys. D (Appl. Phys.)* 17 (1984) 443.
- [15] A-M. Lanzillotto, M. Santos and M. Shayegan, *Appl. Phys. Letters* 55 (1989) 1445.
- [16] E.F. Schubert, J.B. Stark, T.H. Chiu and B. Tell, *Appl. Phys. Letters* 53 (1988) 293.
- [17] E.F. Schubert, C.W. Tu, R.F. Kopf, J.M. Kuo and L.M. Lunardi, *Appl. Phys. Letters* 54 (1989) 2592.
- [18] M.E. Greiner and J.F. Gibbons, *Appl. Phys. Letters* 44 (1984) 750.
- [19] B. Tuck and M.A.H. Khadim, *J. Mater. Sci.* 7 (1972) 585.
- [20] A. Mohades-Kassai, M.R. Brozel, R. Murray and R.C. Newman, in: *Proc. 16th Intern. Symp. on GaAs and Related Compounds, Karuizawa, 1989*, Inst. Phys. Conf. Ser. 106, Eds. T. Ikoma and H. Watanabe (Inst. Phys., London-Bristol, 1990) p. 471.
- [21] M.D. Deal and H.G. Robinson, *Appl. Phys. Letters* 55 (1989) 1990.
- [22] A. Ourmazd, J. Cunningham, W. Jan, J.A. Rentschler and W. Schroter, *Appl. Phys. Letters* 56 (1990) 85.

Comparison of delta doped GaAs grown by MBE and GSMBE using different arsenic species

M.T. Asom, G. Livescu, M. Geva, V. Swaminathan, L.C. Luther, R.E. Leibenguth, V.D. Mattera

AT & T Bell Laboratories, Breinigsville, Pennsylvania 18031, USA

E.F. Schubert, J.M. Kuo and R. Kopf

AT & T Bell Laboratories, Murray Hill, New Jersey 07974, USA

We have compared the extent of spatial confinement and the optical properties of Be and Si delta doped GaAs grown by gas source and solid source MBE. The delta doped samples were grown at a substrate temperature of 500°C. The two-dimensional doping density we employed in our comparisons was less than $5 \times 10^{12} \text{ cm}^{-2}$. Secondary ion mass spectrometry and capacitance-voltage measurements indicate insignificant differences in the spatial distribution of Si and Be for structures grown using As_4 , As_2 and AsH_3 . Optical measurements indicate that the quality of the doped layers grown with AsH_3 are superior to those grown with solid As source. Our results are explained in terms of defect passivation by H and by the presence of As monomers as the dominant arsenic specie during gas source MBE. We shall also discuss a novel method of obtaining planar doping.

1. Introduction

Delta doping of semiconductors is becoming increasingly important because of scientific benefits of engineering two-dimensional structures [1–3] and the potential technological applications in electronic and photonic devices. Delta doped structures can be used as non-alloyed ohmic contacts to GaAs [4], as Schottky gates in field effect transistors [5] and as doping superlattice in spatial light modulators and edge emitting diodes [2]. In the conventional delta doping of GaAs, growth of GaAs is interrupted while a dopant atom is deposited on the crystal surface and subsequently the growth is resumed. Ideally, the profile width of the dopant should be comparable to a lattice constant. Experimentally, however, deviations from the ideal delta function occur, the profiles may become as broad as 200 Å at high growth temperatures. Two factors that affect the spatial confinement of the dopants are the diffusion and segregation of the impurities. Recently, Zrenner [6] has argued that the discrepancies between theoretical calculations based on self-consistent and

semiclassical methods, and experimental data on the dopant localization can be resolved if background doping and extrinsic defects such as DX centers are taken into consideration. There has also been a report on improved localization of Be and Si for growth by GSMBE [7] as compared to conventional MBE growth using As_4 . In this paper, we report on a study in which we have examined the role of unintentional background doping and the influence of the crystal growth method on delta doped GaAs. We have compared for the first time spatial confinement and photoluminescence properties of Be and Si delta doped GaAs grown using As_1 (from AsH_3), As_2 , and As_4 .

2. Experimental

The delta doped GaAs samples were grown in a Varian Gen II gas source MBE chamber at a growth temperature of 500°C. The V/III ratio was obtained by measuring the beam equivalent flux ratio with an ion gauge in the substrate position. An AsH_3 flow rate of 4 SCCM was em-

ployed in order to maintain a V/III ratio equivalent to that obtained by using solid As sources. A GaAs growth rate of 2.5 \AA/s was employed. The chamber was fitted with an elemental As cracking furnace [8] and a low pressure hydride injector. The solid As cracker provided As_4 and As_2 species. In the GSMBE approach, the group III fluxes are provided by elemental Ga and the group V sources are hydrides; in this case, arsine. The conventional delta doping was accomplished by interrupting growth of Ga (closing the Ga shutter) and opening the dopant shutter (Si or Be) for a given duration of time and subsequently resuming growth of GaAs. (We have also accomplished planar confinement by a novel method whereby the Ga and dopant atoms are introduced at the same time. The advantage of this method is that it eliminates growth interruptions which may result in accumulation of impurities during the delta doping phase.) Two-dimensional doping densities between 8×10^{11} and $4 \times 10^{12} \text{ cm}^{-2}$ were employed for the comparisons. The growth temperature was maintained at 500°C in order to minimize impurity diffusion and redistribution that would occur at higher substrate temperatures. A typical growth sequence consists of a Si or Be doped or undoped buffer layer on top of a $\langle 100 \rangle$ oriented n-type or

semi-insulating GaAs substrate. An undoped spacer layer of GaAs was grown on top of the buffer, followed by deposition of the dopants. Finally an undoped GaAs cap layer, $200\text{--}2000 \text{ \AA}$ thick was grown. The delta doped samples were characterized by capacitance-voltage measurements on reverse biased Ti/Au Schottky diodes, mercury Schottky barriers and also by an electrochemical profiling method (Polaron). Secondary ion mass spectrometer (SIMS) profiles of the dopants were obtained with a Cameca IMF-4F SIMS instrument using O_2^+ primary ion source. Photoluminescence (PL) measurements were performed at room temperature and also at low temperature using the 5145 \AA excitation line from an argon laser.

3. Results and discussion

Figs. 1a and 1b show typical C-V profiles of Si and Be delta doped GaAs grown by conventional MBE with As_4 sources. The Si peak in fig. 1a occurs at a depth of 986 \AA from the surface, as expected from reflection high energy electron diffraction calibrations. The maximum electron concentration is $7.7 \times 10^{18} \text{ cm}^{-3}$ and the full width at

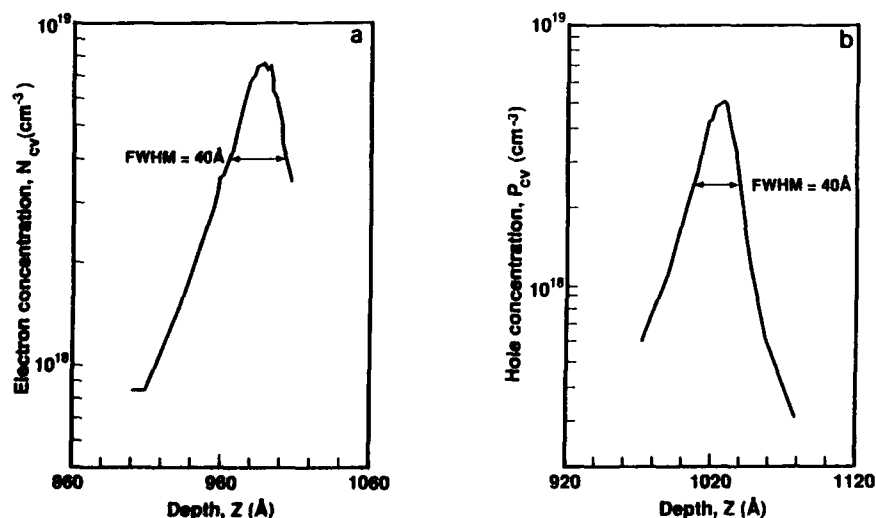


Fig. 1. C-V doping profiles of Si and Be delta doped GaAs. The samples were grown at 500°C using As_4 . We did not observe significant differences between the FWHM of the C-V profiles of samples grown with As_4 , As_2 , and As_1 (AsH_3).

half maximum (FWHM) is 40 Å corresponding to a two-dimensional density of $3.2 \times 10^{12} \text{ cm}^{-2}$. Fig. 1b shows the $C-V$ profile of Be delta doped GaAs grown using As_4 . The Be peak is located at a depth of 1002 Å and the maximum hole concentration is $5.1 \times 10^{18} \text{ cm}^{-3}$. The FWHM is measured to be 40 Å resulting in a two-dimensional doping density of $2 \times 10^{12} \text{ cm}^{-2}$. We obtained identical results on samples grown under the same growth conditions except with As_1 and As_2 replacing As_4 . $C-V$ measurements were also done on Si delta doped GaAs with a $C-V$ doping density of $1 \times 10^{12} \text{ cm}^{-2}$. The FWHM of these profiles were generally of the order of 75–80 Å for growth using As_1 , As_2 , and As_4 .

Fig. 2a shows the SIMS profile of Si delta doped GaAs grown using As_4 , the maximum Si concentration is $4 \times 10^{19} \text{ cm}^{-3}$ and a FWHM of 47 Å is measured. The sample grown under identical conditions by GSMBE yield a FWHM of 45 Å. A SIMS profile of Be delta doped GaAs is shown in fig. 2b. The Be concentration is measured to be $8.9 \times 10^{18} \text{ cm}^{-3}$ with a FWHM of 47 Å. A similar profile was obtained for growth using As_2 with maximum Be concentration of $8.9 \times 10^{18} \text{ cm}^{-3}$, occurring at a depth of 1000 Å and a FWHM of 49 Å. The SIMS profile of Be grown using AsH_3 indicates Be concentration of $6 \times 10^{18} \text{ cm}^{-3}$ and a FWHM of 45 Å.

It is clear from the $C-V$ and SIMS measurements that the distribution of Be and Si in GaAs

grown at a low temperature of 500°C is unaffected by the nature of the As species employed during growth. The main difference between our results and those in refs. [7,9] is that we employed low two-dimensional $C-V$ doping densities ($< 5 \times 10^{12} \text{ cm}^{-2}$). The dependence of $C-V$ width on two-dimensional doping density has been given by Schubert et al. [10]. The $C-V$ FWHM is found to decrease as the doping increases. Our measured value of 40 Å for Si is lower than the theoretical prediction from self-consistent calculations. An interesting observation from these measurements can be made regarding the activation efficiency of the dopant atoms for growth at 500°C. The electrical activation efficiency of Si and Be is calculated by taking the ratio of the $C-V$ concentration and the SIMS concentration. The donor and acceptor activation efficiencies of 26% and 57% were obtained for Si and Be, respectively.

Fig. 3 depicts a SIMS profile taken from a structure consisting of two Be delta doped spikes. The sample was grown at 515°C with AsH_3 source. The first spike at 200 Å was obtained with the novel approach and the peak at 650 Å was obtained following conventional delta doping. The FWHM of both spikes is approximately 55 Å. This result reveals an alternative method of obtaining delta doping without growth interruption. A similar method has recently been reported by Kim et al. [11].

PL measurements were employed in order to

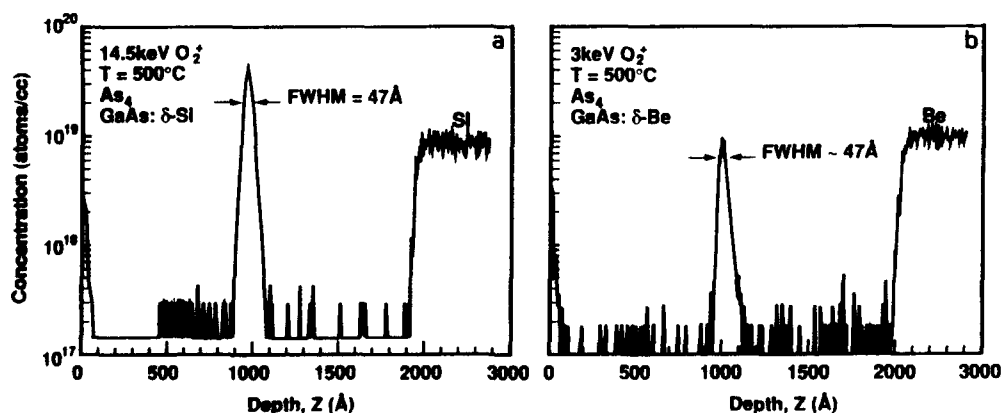


Fig. 2. SIMS depth profiles of Si and Be delta doped GaAs showing a FWHM of 47 Å. Identical FWHMs of the delta spikes were measured for samples grown with As_4 , As_2 , and As_1 (AsH_3).

assess the optical properties of the delta doped structures. The low temperature luminescence from Si delta doped GaAs grown with As_4 and AsH_3 is depicted in fig. 4a. Two peaks are apparent at 1.513 and 1.493 eV. The peak at 1.513 eV is related to a donor bound exciton. The peak at 1.493 eV is assigned to a donor-to-acceptor transition involving C. There is a slight decrease in the PL intensity of the AsH_3 grown sample. We have previously observed the same effect in our hydrogenated delta doped samples [12] and we attribute the decrease to the passivation of the Si donor atoms in the presence of H in GSMBE. The appearance of this exciton line with a FWHM of 4.4 meV indicates that high quality GaAs can be grown at 500°C. At room temperature, we find that the integrated PL intensity in the GSMBE grown sample is stronger than in the MBE grown sample, as shown in fig. 4b.

The low temperature luminescence from Be delta doped GaAs grown using AsH_3 , As_2 and As_4 is shown in fig. 4c. The main luminescence peak occurs at 1.483 eV and has a FWHM of 23 meV. We have assigned this peak to a donor-to-acceptor-like transition involving Be acceptors. The FWHM and the position of the peak are con-

sistent with heavily doped p-type GaAs, and are a result of formation of tail states and band gap narrowing [13,14]. It should be noted that similar luminescence features were observed from a single Be delta doped sample grown on an undoped buffer layer and a Si substrate. The integrated PL intensity of Si and Be delta doped GaAs at room temperature, is strongest in the AsH_3 grown samples and clearly demonstrates that hydrogen plays a very active role in modifying the growth kinetics in GSMBE. The increased PL intensity can be attributed to two factors: (1) The presence of H as the primary by-product of AsH_3 decomposition may serve to passivate nonradiative centers, thus enhancing the PL intensity. This is consistent with our results on hydrogenated As_4 grown samples [12]. (2) We have evidence that the predominant As species in our system is As monomers [15]. The differences in the growth kinetics between As_2 , As_4 and As_1 (AsH_3) has strong influence on the formation of native defects such as V_{Ga} , especially at the low growth temperature of 500°C. Such differences have been previously observed by Kunzel and Ploog [16] for As_4 and As_2 , and Calawa [17] and Cunningham et al. [18] for As monomers. At room temperature, the lumines-

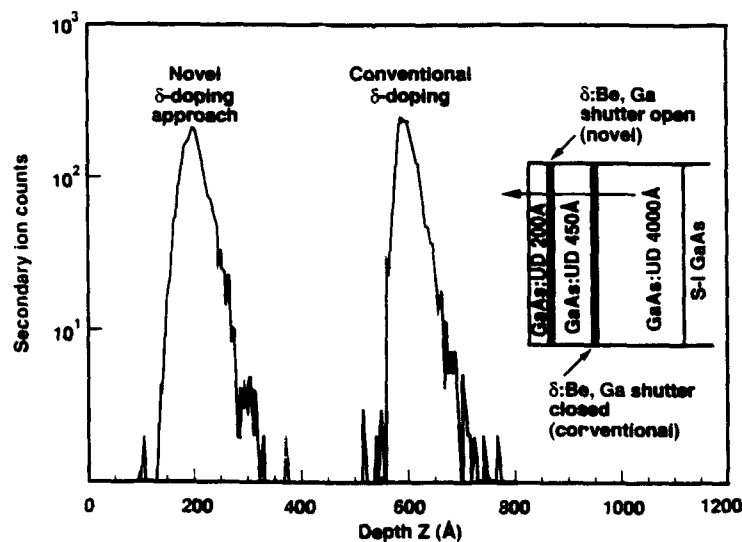


Fig. 3. SIMS profiles of Be delta doped GaAs grown with As_1 at a substrate temperature of 515°C. The peak at 200 Å was obtained with both Ga and Be shutters open. The peak at 650 Å was obtained with the Ga shutter closed. A schematic illustration of the growth sequence is also shown.

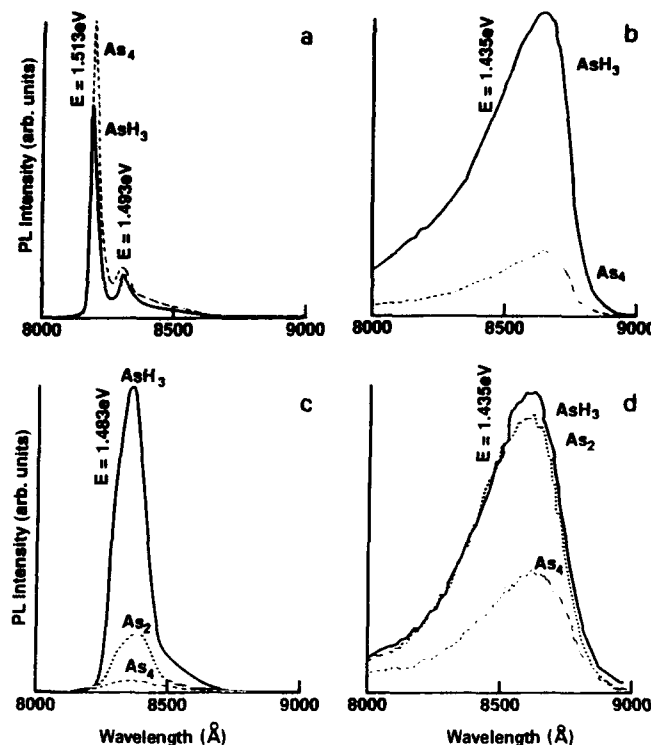


Fig. 4. PL spectra from Si and Be delta doped GaAs grown with As_4 , As_2 , and As_1 (AsH_3): (a) and (b) show low temperature (a) and room temperature (b) PL from Si delta doped GaAs; (c) and (d) show low temperature (c) and room temperature (d) PL from Be delta doped GaAs. Note that enhanced PL efficiency in samples grown with As_1 at room temperature.

cence from Be delta doped GaAs occurs at 1.435 eV and it is again strongest for AsH_3 grown sample as shown in fig. 4d.

4. Conclusion

We have compared the spatial confinement and the optical quality of delta doped GaAs shown grown using As_2 , As_4 , and AsH_3 sources. The spatial distribution of Be and Si is unaffected by the type of As species used during growth of delta doped GaAs with doping densities $< 5 \times 10^{12} \text{ cm}^{-2}$ and growth temperature of 500°C . The optical quality of the delta doped structures is enhanced with growth using As monomers (AsH_3). We attribute the enhanced PL efficiency in GSMBE grown samples to reduction of point defects such as V_{Ga} and related complexes and to

passivation of nonradiative centers by atomic hydrogen in the chamber.

Acknowledgements

The authors wish to acknowledge the discussions with M.B. Panish, J. Zilko, L.C. Kimmerling and the support of P.J. Anthony.

References

- [1] K. Ploog, J. Crystal Growth 81 (1987) 304.
- [2] E.F. Schubert, J. Vacuum Sci. Technol. A8 (1990) 2980.
- [3] E.F. Schubert, A. Fischer, Y. Horikoshi and K. Ploog, Appl. Phys. Letters 47 (1985) 219.
- [4] E.F. Schubert, J.E. Cunningham, W.T. Tsang and T.H. Chiu, Appl. Phys. Letters 49 (1986) 292.
- [5] T.Y. Kuo, J.E. Cunningham, E.F. Schubert, W.T. Tsang.

- T.H. Chiu, F. Ren and C.G. Fonstad, *J. Appl. Phys.* 64 (1988) 3324.
- [6] A. Zrenner, *Appl. Phys. Letters* 55 (1989) 156.
- [7] J.E. Cunningham, T.H. Chiu, B. Tell and W. Jan, *J. Vacuum Sci. Technol. B8* (1990) 157.
- [8] R.N. Sacks, D.W. Eichler, R.A. Pastorello and P. Colombo, *J. Vacuum Sci. Technol. B8* (1990) 163.
- [9] T.H. Chiu, J.E. Cunningham, B. Tell and E.F. Schubert, *Appl. Phys. Letters* 64 (1988) 1578.
- [10] E.F. Schubert, T.H. Chiu, J.E. Cunningham, B. Tell and J.B. Stark, *J. Electron. Mater.* 17 (1988) 527.
- [11] H.K. Kim, T.E. Schlesinger and A.G. Milnes, *J. Electron. Mater.* 19 (1990) 139.
- [12] M.T. Asom, V. Swaminathan, G. Livescu, M. Geva, L.C. Luther, R.E. Leibenguth, V.D. Matterna and T. Hayes, *J. Crystal Growth* 111 (1991) 260.
- [13] K. Saito, T. Yamada, T. Akatsuka, T. Fukamachi, E. Tokumitsu, M. Konagai and K. Takahashi, *Japan. J. Appl. Phys.* 28 (1989) 12081.
- [14] T. Takamori, T. Fukunaga, J. Kobayashi, K. Ishidu and H. Nakashima, *Japan. J. Appl. Phys.* 26 (1987) 1097.
- [15] We find that the dominant As species emanating from cracking AsH₃ is As₁ (As monomer). The ratio of As₁/As₄ is an order of magnitude higher than the As₂/As₄ ratio.
- [16] H. Kunzel and K. Ploog, *Appl. Phys. Letters* 37 (1980) 416.
- [17] A.R. Calawa, *Appl. Phys. Letters* 38 (1981) 701.
- [18] J.E. Cunningham, G. Timp, T.H. Chiu, J.A. Ditzenberger, W. Tsang, M. Sergent and D.V. Lang, *J. Crystal Growth* 95 (1989) 185.

Reduced silicon donor incorporation in MBE grown GaAs layers using cracker-generated dimer arsenic

B.J. Wu, Y.J. Mii, M. Chen, K.L. Wang

Device Research Laboratory, Department of Electrical Engineering, 7619 Boelter Hall, University of California at Los Angeles, Los Angeles, California 90024-1600, USA

and

J.J. Murray

Intel Corporation, 3065 Bowers Avenue, SC2-24, Santa Clara, California 95052-8126, USA

Si dopant incorporation in GaAs layers is shown to be reduced when dimer arsenic is used. Si doped GaAs layers grown by molecular beam epitaxy under different arsenic cracker conditions are studied by a Polaron doping profiles and secondary ion mass spectrometry. Throughout the doping range of investigation, 5×10^{16} to $2 \times 10^{18} \text{ cm}^{-3}$, strong reduction in Si incorporation is observed as the fraction of dimer arsenic is increased. The reduction of Si incorporation is enhanced as the growth temperature is increased. Evidence is given to show that, instead of Si self-compensation, Si dopants are actually desorbed in the presence of dimer arsenic. The formation of volatile Si_xAs_y compound(s) due to the reaction between the impinging dimer arsenic species and the Si dopants at the substrate surface may be responsible for this phenomenon. The activation energy of this reaction is estimated.

1. Introduction

Elemental arsenic is the major group V source used in the molecular beam epitaxy (MBE) growth of GaAs and related films because of its convenient and easy use. Depending upon the availability of an As cracker, As_4 (tetramer) as well as As_2 (dimer) can be generated and both are routinely used for growth. The dimer arsenic is obtained by dissociation of the arsenic tetramer via a catalytic effect by passing As_4 through a high temperature cracker [1]. The growth mechanisms of GaAs using As_4 and As_2 are known to be very different [2,3]. For the former, the growth involves a complicated bi-molecular interaction of As_4 with adjacent Ga atoms, and as a result, four arsenic atoms are desorbed in form of As_4 and it is known to be a second order reaction. For the latter, growth simply involves a dissociative chemisorption of As_2 to Ga atoms and is known to be a first order reaction. The difference in growth mechanism using

different arsenic species leads to the conclusion that the maximum sticking coefficient of As_2 is close to unity and that of As_4 is 0.5 on a Ga-rich surface. Therefore the use of dimer arsenic minimizes the consumption of the arsenic source and should be able to prolong substantially the MBE machine operation time without replenishing the source charge. In addition to the conservation of arsenic source material, there are several reports indicating improvements of the MBE grown GaAs and related layers using As_2 such as elimination of defect-induced bound exciton peaks in PL spectra [4], minimizing the size and the number of oval defects [5], and reduction of deep level concentration [6] and carbon incorporation [7].

Si is one of the most commonly used n-type dopants in MBE GaAs, owing to its relatively non-amphoteric behavior and low diffusivity. The behavior of Si incorporation into GaAs grown by As_4 has been extensively studied [8,9]. It has been reported that, as long as the solubility limit for Si

in GaAs is not exceeded, the Si doping concentration is simply proportional to the Si arrival rate, or in other words, the sticking coefficient of Si to GaAs is unity [9,10]. The decrease in free carrier concentration for Si doped GaAs at elevated substrate temperatures and for a large Ga/As₄ ratio is attributed to the Si amphoteric property. On the other hand, although the As₂ grown MBE GaAs and related films have been demonstrated to possess superior properties as mentioned before, studies concerning the Si dopant incorporation, unlike the As₄ case, remain lacking. Therefore, comprehensive studies of dopant incorporation behavior for MBE grown GaAs and related compounds using As₂ are needed, especially for those applications where doping control is crucial.

In this work, a strong reduction of Si donor incorporation in MBE grown GaAs layers at high cracker temperatures is reported. The reduction of Si incorporation is seen to enhance at increasing substrate temperature. The objective of this study is to investigate the influence of different cracker and substrate temperatures on the Si incorporation and to explore the reaction mechanism(s) leading to this dopant reduction phenomenon.

2. Experimental

Si doped GaAs layers are grown in a Perkin-Elmer 430 MBE system equipped with an As cracking cell. The cracking cell consists of an As bulk evaporator (low temperature furnace) and a molybdenum cracker (high temperature furnace). The bulk evaporator is used to control the arsenic flux and the cracker is used to dissociate As₄ into As₂. Since there is no thermocouple installed in the cracker, the control of cracker temperature can only be made by adjusting the cracker current. In growth, (100) oriented n⁺-GaAs wafers are indium mounted onto molybdenum sample holders. After being introduced into vacuum, the samples are outgassed at 300°C for 20 min and then transferred into the growth chamber. Before growth, the samples are heated to 620°C for oxide removal and thermal cleaning. Throughout each growth, the temperatures of the arsenic bulk evaporator and Si doping cell are kept constant,

while the cracker current (corresponding to cracker temperature) is varied, ranging from 5.0 to 6.5 A, unless otherwise stated, for each layer of 0.4 μm thick at a specific growth temperature. In order to stabilize the change of the cracker current in step, the growth is interrupted for 30 min between the layers. For different samples, the substrate temperature is changed from 570 to 660°C and the Si doping level is varied from 5×10^{16} to 2×10^{18} cm⁻³.

A UTI 100 residual gas analyzer (RGA) is used to investigate the arsenic dissociation efficiency of the cracker by monitoring the peak intensities of major arsenic species. A Polaron doping profiler is used to determine active Si dopant concentrations of the grown samples. Secondary ion mass spectrometry (SIMS) profiles are also made for some of the samples to determine the total Si concentrations. An ion-implanted sample is used as the standard reference for the quantitation of all SIMS profiles.

3. Results and discussion

The carrier concentration profiles, obtained from the Polaron profiles, as functions of the substrate temperature and the cracker current are shown in figs. 1 and 2, respectively. It is clear that the carrier concentration as measured by Polaron decreases as the cracker current increases and the effect is enhanced as the substrate temperature is increased. In this study, for samples grown at 660°C, the Si doping concentration drops from 1.6×10^{18} cm⁻³ at a cracker current 5.0 A, to 5.9×10^{17} cm⁻³ at 6.5 A, a decrease of nearly a factor of 3. However, for those grown at 570°C with the same cracker condition, the Si doping concentration drops only from 1.9×10^{18} to 1.7×10^{18} cm⁻³, showing a rather weak cracker temperature (current) dependence.

Carbon contamination [11] and Si self-compensation [8] are among possible mechanisms, at least for the As₄ case, that could lead to this dopant reduction effect. Although we did observe carbon distribution near the epilayer and substrate interface in the SIMS profile measurement, the carbon contamination caused by increasing cracker

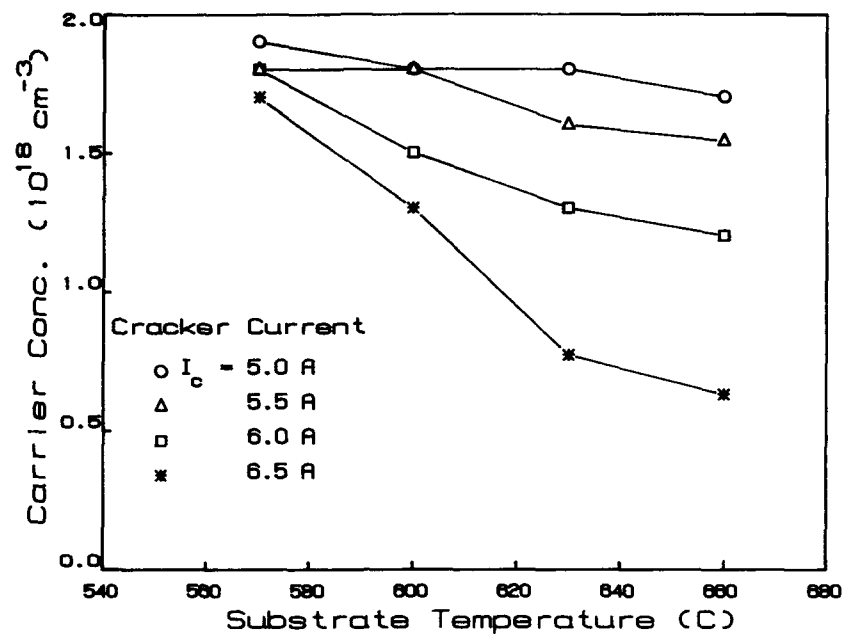


Fig. 1. Polaron-measured Si doping concentration as a function of substrate temperature with different cracker currents. The Si doping concentration decreases with increasing growth temperature.

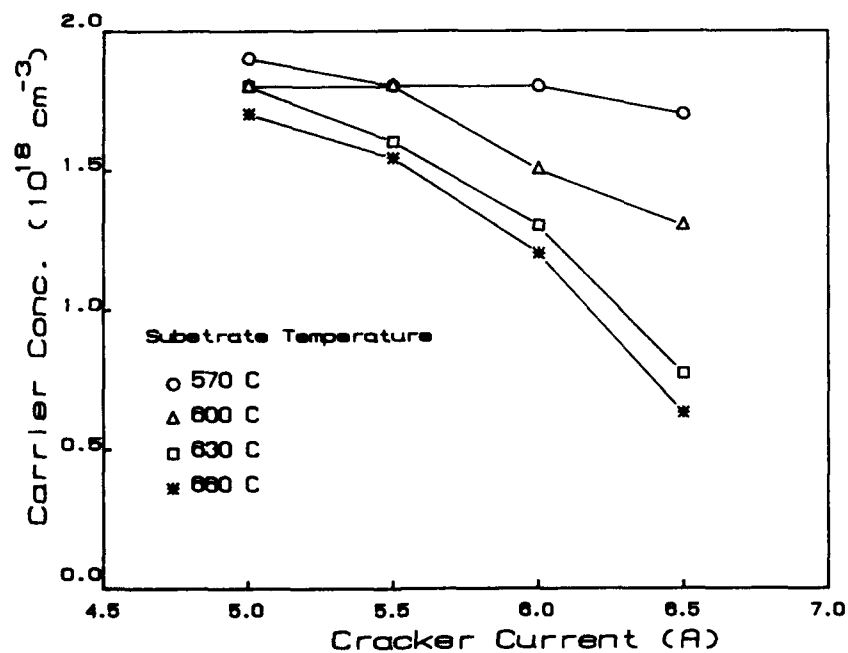


Fig. 2. Polaron-measured Si doping concentration as a function of cracker current with different substrate temperatures. The decrease of the Si doping becomes substantial when the cracker current is larger than 5.0 A.

current is very unlikely to be the main reason for this effect based on the following arguments. We have examined the dopant reduction effect as a function of dopant level ranging from 5×10^{16} to $2 \times 10^{18} \text{ cm}^{-3}$. If the carbon contamination from the cracker were the cause of the effect, because of the same cracker conditions used for these samples with different doping levels, we would have seen a stronger reduction at lower doping level. However, this is not the case. For the doping levels investigated, similar dependences are observed for the Si incorporation on the cracker temperature (current) and substrate temperature. Typical Polaron profiles for the samples grown at 630°C with a Si doping level at $\sim 2 \times 10^{18} \text{ cm}^{-3}$ is shown in fig. 3a. The $\sim 2 \times 10^{17} \text{ cm}^{-3}$ doping case is shown in the inset. In addition, by comparing with a standard sample, we have estimated only $\sim 10^{14} \text{ cm}^{-3}$ unintentional carbon incorporation in GaAs layers from our preliminary photoluminescence results, which is in agreement with those reported by Cho and Arthur [11]. The carbon

concentration, far below the doping range that we investigated, is too low to result in such a severe change in the measured doping density. Furthermore, we have also experimented different heating cycles at growth [12] and observed that the doping reduction appeared to be independent of the different heating cycles. If the carbon contamination were the reason, we would expect some dependence correlated with outgassing due to different heating cycles, which we did not. This further support that the carbon contamination can be ruled out from the possible causes of the observed effect.

Before discussing Si self-compensation, understanding of the influence of the cracker current (temperature) on the composition of different arsenic species is needed. To do so, the RGA arsenic peaks at 75 (As_1^+), 150 (As_2^+), 225 (As_3^+) and 300 (As_4^+) amu are monitored with the cracker current varying from 0 to 7 A while the substrate temperature held at 630°C . In order to investigate the cracking effect and minimize the background con-

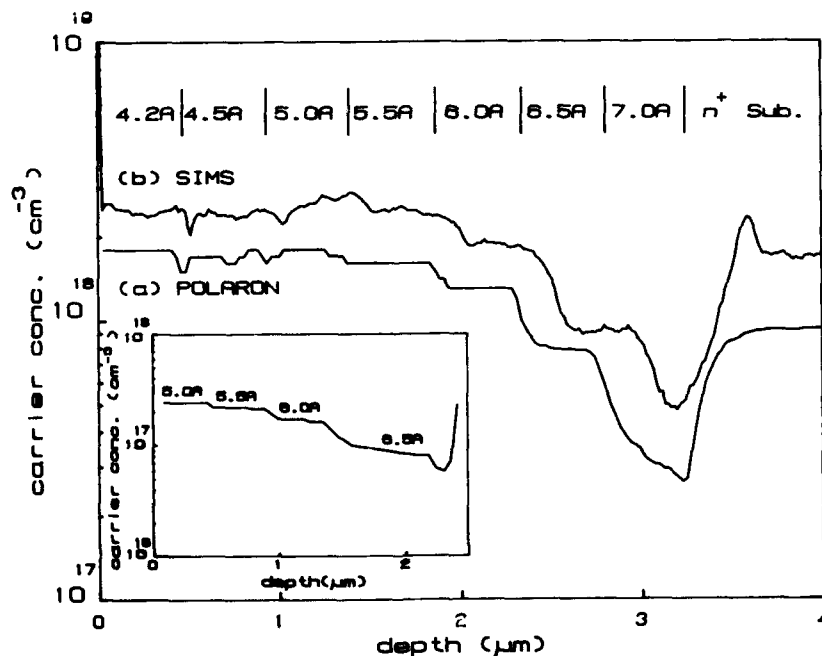


Fig. 3. (a) Carrier concentration measured by Polaron profiler and (b) Si concentration measured by SIMS profiler for the GaAs films grown at 630°C with different cracker currents shown in the figure. The inset shows a typical Polaron profile at lower doping level, in this case, $\sim 2 \times 10^{17} \text{ cm}^{-3}$.

tribution, the peaks are normalized to As_4 . The As_3/As_4 ratio stays constant for the entire cracker current range examined. Meanwhile, there is a slow increase of the As_1/As_4 ratio up to a factor of 1.5, believed to be the result of increase in As_2 as the cracker current is increased; consequently when passing through RGA, the probability of cracking As_2 into As_1 is increased. The most important feature in this investigation is the drastic increase of the As_2/As_4 ratio occurring approximately in the current range of 5.0 to 7.0 A, as shown in fig. 4a. The ratio remains low when the cracker current is less than 4 A, and reaches its maximum as the cracker current approaches 7 A. The triangles represent the data taken during the increasing of cracker current, while the circles are for the decreasing of cracker current. Between measurements, 30 min is waited for stabilizing the arsenic flux after changing the cracker current. Even so, there is a seeming hysteresis effect observed, which is believed to be the result of insufficient time for stabilization. Nevertheless, the data

taken from both the increasing and decreasing cracker current shows almost the same influence of the cracker current on the As_2/As_4 ratio.

For the As_4 case, the growth temperature dependence on the reduced net carrier concentration was reported to be mainly due to the Si amphoteric behavior [8], i.e. some Si dopants incorporating into As sites instead of the expected Ga sites. The similar growth temperature dependence of Si incorporation observed in the present work, as shown in fig. 1, would appear to suggest a similar mechanism. However, from the previously described cracker behavior, we know that the amount of dimer arsenic increases rapidly as the cracker increases from 5.0 to 7.0 A. This fact along with the reported higher sticking coefficient of As_2 [2,3] indicates that the increase of the cracker current should reduce the arsenic vacancies on the substrate surface and as a result Si incorporating into As sites should also reduce. In this case, the net carrier concentration observed should increase rather than decrease with the cracker current. This

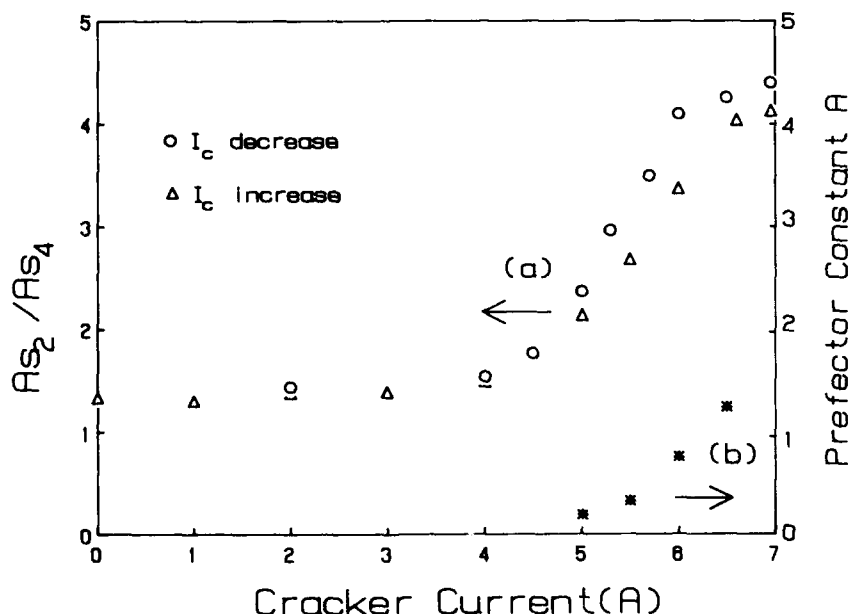


Fig. 4. (a) As_2/As_4 ratio as a function of cracker current measured from RGA peaks. The triangle data were measured with increasing cracker current, and the circle data were measured with decreasing cracker current. (b) Prefactor A in the kinetic equation as a function of cracker current.

is opposite to what we observed in fig. 2; therefore the Si amphoteric behavior can not be used to account for the phenomenon. Moreover, if the Si self-compensation were the case we would expect to see no reduction of atomic Si concentration from the SIMS profile, no matter what sites the Si dopants are incorporated in.

To illustrate the contrary, we show in fig. 3 the carrier concentrations measured by a Polaron profile (fig. 3a), along with the Si concentrations measured by SIMS (fig. 3b), for the layers grown at 630°C with the cracker current varying from 4.2 to 7.0 A. Note that the layers are marked with respect to the Polaron thickness data. It is obvious that the Si SIMS profile follows almost exactly the same profile as the Polaron carrier concentration, except that the SIMS result shows a depth scale of about 10% difference and the Si concentration is measured to be roughly twice larger than the Polaron result. The observed distinctions are believed to be the result of the differences in etching and calibration procedures used in these two characterization techniques. The general agreement of the two profiles, a reduction in both Polaron and SIMS data, indicates that it is actually the escape of Si atoms from the substrate surface that is responsible for the carrier reduction. Since the Si vapor pressure is so low at the growth temperature ($\sim 600^\circ\text{C}$), the direct escape of the Si atoms from the substrate surface is too little to introduce such a substantial change. There should be some other kinetics involved to cause the Si desorption.

It is evident from figs. 2 and 4 that the doping concentration is strongly dependent on the As_2 to As_4 ratio, suggesting that the As_2 species produced by the cracker plays an important role in the reduction of the Si concentration. It is very likely that the Si dopants arrived at the GaAs surface react with the impinging As_2 , form volatile Si_xAs_y compounds and desorb from the sample surface. If this is the case, the desorption is enhanced and the carrier concentration decreases as the cracker current increases, or as the fraction of As_2 increases. Furthermore, as the substrate temperature increases, the Si_xAs_y formation and desorption is enhanced through a thermally activated kinetics, and therefore, the atomic Si concentration and carrier concentration drops. This pro-

posed model can be used to explain the observations in this study. Although there is no direct evidence in observing the compound for this model, there are several reported phenomena that can be used to support this mechanism. Cho and Arthur [11] reported a net background donor level of $(5-8) \times 10^{15} \text{ cm}^{-3}$ in unintentionally doped MBE GaAs layers using polycrystalline GaAs as an arsenic source containing a $\sim 10^{16} \text{ cm}^{-3}$ Si impurity level. However, from the vapor pressure of pure Si at the temperature that the polycrystalline GaAs cell is operated, it is straightforward to verify that, even with intentionally doped GaAs layers using a Si doping cell, at this temperature the doping level cannot be as high as $(5-8) \times 10^{15} \text{ cm}^{-3}$. The direct evaporation of Si from such a low Si impurity polycrystalline GaAs source (being less than 2×10^{-7} in terms of the fractional concentration of volumetric atomic sites) is very unlikely to introduce an approximately 10^{15} cm^{-3} background dopant concentration. The preferential escape of volatile Si-As compound(s) (such as Si_xAs_y) from the source is more likely to occur. In addition, there is another supportive evidence in a gas phase pickup mechanism of Si, which has been reported for Si incorporation in GaAs-on-Si heteroepitaxy by MOCVD [13]. In their work, the authors have observed high unintentional doping levels caused by the gas phase pickup of Si, either from the substrate edge or from a Si piece placed next to the substrate, and incorporated into the GaAs layer. It is entirely possible that in their work, the formation of a similar, but not necessarily the same as our MBE case, volatile Si-As compound(s) occurs on the Si surface in the gas flow and the compound(s) is then carried to deposit into the epitaxial layer. Moreover, from the p - T - x phase diagram of the Si-As system, Ugai et al. [14] reported the existence of two compounds in this system: SiAs , which melts congruently at 1083°C with an equilibrium vapor pressure of 0.5 atm, and SiAs_2 , which decompose through a peritectic reaction at 944°C with an equilibrium pressure of 1.25 atm. It is reasonable to expect, based on the high vapor pressure natures of these compounds just mentioned, that at the growth temperature ($\sim 600^\circ\text{C}$) the vapor pressure of the compound(s) is high enough to

escape from the sample surface. This further supports our model: formation of the volatile Si-As compounds.

Invoking this model, the net carrier concentration measured can be estimated from the competition between incorporation and desorption of the Si dopants. The measured net carrier concentration, n , can be modelled by

$$n = N_0 [1 - A \exp(-E_a/kT)],$$

where N_0 is the atomic concentration of dopants reaching the GaAs surface, A is a constant proportional to As_2 fraction, E_a is the desorption activation energy, k is the Boltzmann constant and T is the substrate temperature in kelvin. The $A \exp(-E_a/kT)$ term accounts for the desorption of Si dopants due to arsenic dimers. In order to estimate the activation energy, a determination of N_0 is needed. As seen from fig. 3, the carrier concentration remains almost constant as the cracker current becomes lower than 5 A. This observation along with the reported unity sticking

coefficient of Si at low (or no) arsenic dimer case suggest that it is reasonable to choose the carrier concentration corresponding to a growth temperature of 570°C and a cracker current of 5 A for N_0 . The plot of $\log(1 - n/N_0)$ versus $1000/T$ is depicted in fig. 5. It is not surprising that the slopes of all the curves correspond to different cracker currents are very close to each other, indicating a unique activation energy. The activation energies obtained for cracker currents ranging from 5.0 to 6.5 A are calculated to range from 1.29–1.51 eV (average 1.4 eV). It is worth noting that the large relative errors introduced by the choice of N_0 and the measured concentrations for layers grown at low temperature (570°C) will result in a large error in the calculated activation energies. The substantial variation of the activation energies obtained above is the result of this error. However, the close calculated values are indeed a good indication that only one reaction (or compound) leads to the Si dopant reduction, unless different volatile compounds are formed and they have

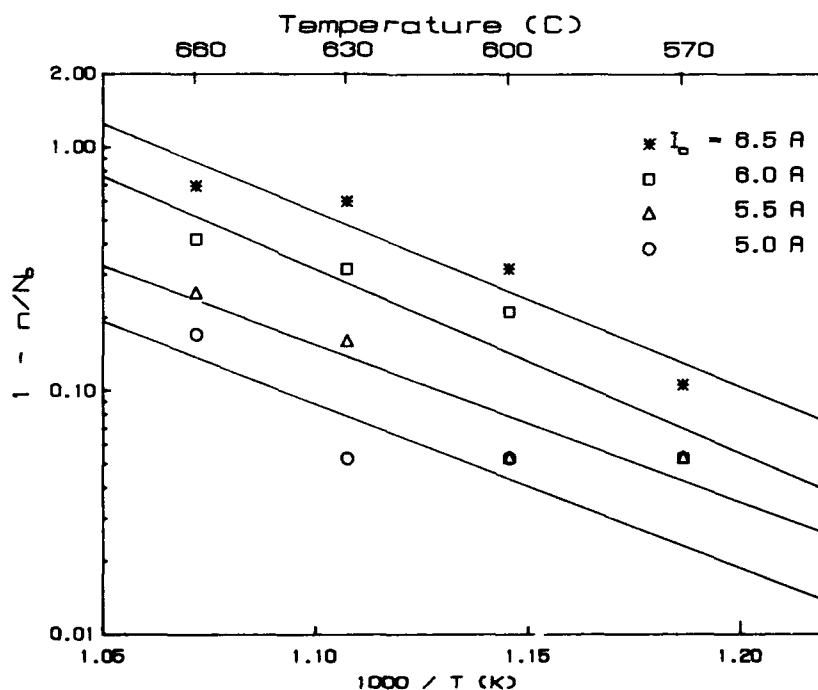


Fig. 5. Plot of $\log(1 - n/N_0)$ versus $1000/T$ for the cracker current ranging from 5.0 to 6.5 A. The slopes corresponding to activation energies are estimated to be ~ 1.4 eV.

close desorption activation energies. Besides, the $\log(1 - n/N_0)$ values become smaller as the cracker current decreases, also shown in fig. 5, and this is in agreement with the decrease of As_2 species. For the temperature range of interest, prefactors A in the kinetic equation for different cracker currents are determined and plotted in fig. 4b with the right-hand side abscissa. It is clear that the A value as a function of cracker current follows the same trend of the As_2/As_4 ratio. This and the close activation energy calculated support the proposed mechanism of the formation Si-As volatile compound(s). Further experiments and mechanism studies are actively under way to explore the exact reaction and kinetics of this observed doping reduction.

4. Conclusion

A reduction of Si incorporation in MBE GaAs layers with increased cracker current and substrate temperature is reported. We have observed that, unlike As_4 , As_2 tends to reduce Si donor concentration. Si self-compensation and carbon contamination cannot be used to account for the observed effect. Instead, Si appears to desorb in the presence of As_2 . Formation of volatile Si-As compound(s) with As_2 is proposed to account for the escape of Si dopants. The activation energy of the desorption is estimated to be ~ 1.4 eV for the cracker current ranging from 5.0 to 6.5 A. The exact Si-As compound is yet to be determined.

Acknowledgement

This work done at UCLA is supported in part by ONR and ARO.

References

- [1] J.C. Garcia, A. Barski, J.P. Contour and J. Massies, *Appl. Phys. Letters* 51 (1987) 593.
- [2] C.T. Foxon and B.A. Joyce, *Surface Sci.* 50 (1975) 434.
- [3] C.T. Foxon and B.A. Joyce, *Surface Sci.* 64 (1977) 293.
- [4] H. Kunzel and K. Ploog, *Appl. Phys. Letters* 37 (1980) 416.
- [5] S. Matteson and H.D. Shih, *Appl. Phys. Letters* 48 (1986) 47.
- [6] J.H. Neave, P. Blood and B.A. Joyce, *Appl. Phys. Letters* 36 (1980) 311.
- [7] J.C. Garcia, A.C. Beye, J.P. Contour, G. Neu, J. Massies and A. Barski, *Appl. Phys. Letters* 52 (1988) 1596.
- [8] Y.G. Chai, R. Chow and C.E.C. Wood, *Appl. Phys. Letters* 39 (1981) 800.
- [9] T. Shimanoe, T. Murotani, M. Nakatani, M. Otsubo and S. Mitsui, *Surface Sci.* 86 (1979) 126.
- [10] A.Y. Cho and I. Hayashi, *Met. Trans.* 2 (1971) 777.
- [11] A.Y. Cho and J.R. Arthur, *Progr. Solid State Chem.* 10 (1975) 157.
- [12] B.J. Wu, Y.J. Mii, M. Chen and K.L. Wang, *Appl. Phys. Letters* 58 (1991) 391.
- [13] S. Nozaki, J.J. Murray, A.T. Wu, T. George, E.R. Weber and M. Umeno, *Appl. Phys. Letters* 55 (1989) 1674.
- [14] Y.A. Ugai, S.N. Miroshnichenko and E.G. Goncharov, *Russ. Inorg. Mater.* 10 (1974) 1523.

Hydrogen passivation of delta doped GaAs

M.T. Asom, V. Swaminathan, G. Livescu, M. Geva, L.C. Luther, R.E. Leibenguth, V.D. Mattera

AT & T Bell Laboratories, Breinigsville, Pennsylvania 18031, USA

and

T. Hayes

AT & T Bell Laboratories, Murray Hill, New Jersey 07974, USA

We report on hydrogen passivation of Si and Be delta doped GaAs grown by molecular beam epitaxy. The delta doped structures were exposed to low energy and low frequency hydrogen and deuterium plasmas. Secondary ion mass analysis shows hydrogen and deuterium incorporation at the dopant sites. Electrical analysis of the samples reveals total deactivation of the Si atoms and only a partial (35%–50%) deactivation of the Be atoms. Photoluminescence measurements of the hydrogenated Si doped structures indicate a disappearance of above band gap transitions associated with free carriers and enhancement of transitions related to background acceptors.

1. Introduction

Hydrogenation in III–V semiconductors is known to render donors, acceptors and deep levels inactive. This phenomenon, commonly known as passivation, has been utilized for improved material properties such as enhancement of mobility in epitaxial and bulk grown GaAs. Recently hydrogenation has been used in the fabrication of a new device called a hydrogenated channel FET [1]. In addition AlGaAs/GaAs quantum well lasers have been fabricated where hydrogenation is used to provide current-guiding through the heterostructure [2]. It has become clear that unintentional introduction of H_2 in III–V processing steps, such as plasma etching, bulk and epitaxial crystal growth by LEC, and MOCVD, results in hydrogen incorporation, which may contribute to the modification of the properties of the material [3].

While numerous studies exist in the literature on passivation of acceptors and donors in III–V compounds [3], there has been no report on the effect of hydrogen on lamella doped structures

where dopant atoms are confined to a two-dimensional plane in the III–V matrix. We have examined the effect of hydrogenation on the electrical, chemical and optical properties of Si and Be delta doped GaAs. Our results are presented in this paper.

2. Experimental

The delta doped samples were grown in a Varian Gen II chamber with As_4 at a growth temperature of 540°C. Delta doping was accomplished by interrupting GaAs growth (closing Ga shutter only), simultaneously opening the dopant shutter and subsequently resuming GaAs growth [4]. The substrates used were semi-insulating and N^+ , (100) oriented GaAs. Two sample structures were employed, the first sample consists of an undoped GaAs buffer layer, 5000 Å thick, two delta doped layers separated by 500 Å of undoped GaAs and a 500 Å undoped GaAs cap. The second structure consists of a 5000 Å Be doped buffer layer, a 2500 Å undoped GaAs layer, two Be delta doped re-

gions that are separated by another 2500 Å thick GaAs and a 2500 Å GaAs cap layer. Hydrogenation was done by exposing the as-grown structures to a low frequency (30 kHz) and low power density (0.08 W cm^{-2}) hydrogen or deuterium (D) plasma at 250°C for 30 min under a pressure of 0.75 Torr. These conditions were chosen in order to minimize surface degradation of the samples and reduce deep level defect introduction [5]. Deuterated samples were used for secondary ion mass spectrometry (SIMS) analysis because of the increased detection sensitivity for D in contrast to the detection limit for H. Following hydrogenation, the samples were characterized by capacitance-voltage ($C-V$), Hall effect, SIMS and photoluminescence (PL) measurements.

3. Results and discussion

Fig. 1a depicts the SIMS profile of the as-grown and deuterated Si delta doped samples. Two peaks are evident and are located at a depth 500 and 1000 Å from the surface. The Si peaks illustrate the delta doping, and the ^2D peak indicates the

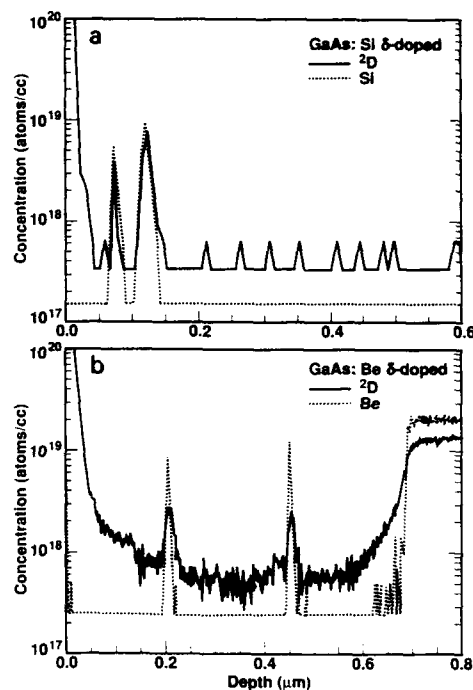


Fig. 1. SIMS depth profiles of Si and Be delta doped GaAs showing as-grown (Si and Be) and deuterium peaks at the dopant sites.

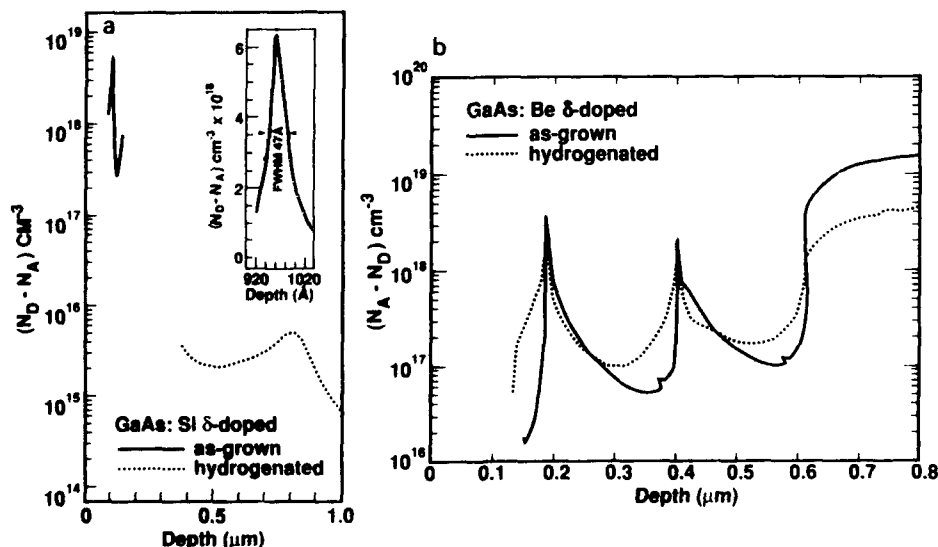


Fig. 2. $C-V$ profiles of Si and Be before and after hydrogenation. The Si concentration is decreased by three orders of magnitude. The Be concentration is decreased by 35%–50%.

bonding of D to the Si atoms after exposure to the plasma. Fig. 1b illustrates the Be doping and the bonding of ^2D to the Be atoms after subjecting the sample to the plasma. A ^2D concentration of $2.5 \times 10^{18} \text{ cm}^{-3}$ is measured in the Be delta doped spikes and $1 \times 10^{19} \text{ cm}^{-3}$ in the uniformly doped buffer.

Fig. 2a shows the electrical profile of the Si delta doped sample before and after hydrogenation. The as-grown sample indicates only a single peak instead of the actual two spikes because of the high electric field breakdown during $C-V$ profiling. The Si doping is measured to be $6 \times 10^{18} \text{ cm}^{-3}$ in the as-grown sample. The insert shows a detailed $C-V$ profile and it indicates a full width at half maximum of 47 \AA in spite of the relatively high growth temperature (540°C) for delta doping [6]. Following hydrogenation, $C-V$ profiles indicate broad peaks with a concentration of less than 10^{16} cm^{-3} . The peak located at about $0.8 \text{ }\mu\text{m}$ is due to unintentional Si accumulation at the epitaxy-substrate interface [7]. It is clear from these measurements that in the delta doped regions, most of the Si donor atoms are passivated after hydrogenation.

Fig. 2b depicts the doping profiles of as-grown and the hydrogenated Be delta doped GaAs. We see that the hole concentration has decreased from 3.5×10^{18} to $1.8 \times 10^{18} \text{ cm}^{-3}$ in the first Be spike and from 1.3×10^{19} to $8.4 \times 10^{18} \text{ cm}^{-3}$ in the uniformly doped region. Only 35%–50% of the dopants are passivated. This is in sharp contrast to the donor case (Si) where most of the donor atoms are passivated. Such differences in the magnitude of passivation between donors (Si) and acceptors (Be) has been observed in hydrogenated uniformly doped GaAs [8,9].

Low temperature PL measurements on the delta doped and hydrogenated samples show enhancements in the PL intensity in the hydrogenated samples. Fig. 3a shows PL spectra from the as-grown and hydrogenated Si delta doped sample. The as-grown sample luminescence consists of three main peaks at 1.521, 1.516, and 1.489 eV. We associate the above band gap peak at 1.521 eV with the free carrier luminescence, and the 1.516 eV peak to a bound exciton. The 1.489 eV peak is ascribed to the donor-acceptor transi-

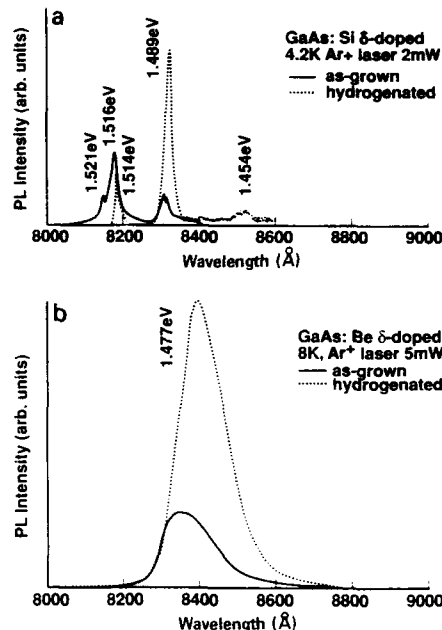


Fig. 3. Photoluminescence from the delta doped samples before and after hydrogenation. Note the absence of the above band gap luminescence in (a) and the increase of the impurity related peaks at 1.489 and 1.477 eV following hydrogenation in (a) and (b), respectively.

tion involving a contaminant such as carbon. The location in energy of the 1.489 eV peak from the band edge would support our C assignment since C has an ionization energy of 27 meV. The above band gap luminescence at 1.521 eV is due to the free carriers; we have observed it only in highly Si doped ($N > 10^{18} \text{ cm}^{-3}$) GaAs samples. The luminescence is related to recombination between the photoexcited holes and the free electrons distributed between the Fermi level and the bottom of the conduction band (Moss-Burstein shift) [10,11]. After hydrogenation, we find that the above band gap luminescence disappears, supporting our interpretation that the peak is related to the free carriers, since we have observed total passivation of the free carriers. We see an increase by a factor of 10 in the C related peak at 1.489 eV. We associate the increased PL intensity with passivation of nonradiative centers such as M1, M3 and M4 [12] in MBE grown GaAs and to en-

hanced recombination of photoexcited carriers via the C acceptor.

Fig. 3b represents the low temperature PL of Be delta doped GaAs before and after hydrogenation. The only peak present in this spectrum is related to a donor-to-acceptor or free-to-acceptor transition involving Be acceptors and it has a FWHM of 25 meV. This large width may be due to the high Be concentration in the delta doped region. Similar spectra have been observed in highly Si doped GaAs [13]. It is clear from this figure that an enhancement of the acceptor related luminescence peak at 1.477 eV has occurred after hydrogenation analogous to the Si delta doped case. The lower PL intensity in the as-grown sample may be caused by nonradiative centers such as native defects [12] and Be precipitates (Be_2) [14,15]. Be_2 are introduced in homogeneously doped GaAs if the doping level exceeds $4 \times 10^{18} \text{ cm}^{-3}$ [15] and Be_2 have been shown to participate in the formation of non-radiative centers [15].

4. Conclusion

We have shown that Be and Si delta doped GaAs can be passivated when exposed to a hydrogen plasma. We find that all donors are passivated, whereas only 35%–50% of the acceptors are passivated. The implications of this work is that it offers device designers a method of introducing lamella regions of hydrogen and may also have

applications in two dimensional planar component isolation in processing steps for devices.

References

- [1] E. Constant, J. Chevallier, J.C. Pesant and N. Caglio, *Electron. Letters* 23 (1987) 841.
- [2] G.S. Jackson, N. Pan, M.S. Feng, G.E. Stillman, H. Holonyak and R.D. Burnham, *Appl. Phys. Letters* 51 (1987) 1629.
- [3] W.C. Dautremont-Smith, in: *Mater. Res. Soc. Symp. Proc.*, Vol. 104, Eds. M. Stavola, S.J. Pearton and G. Davies (Mater. Res. Soc., Pittsburgh, PA, 1987) p. 313.
- [4] C.E.C. Wood, G. Metze, J. Berry and L. Eastman, *J. Appl. Phys.* 51 (1980) 383.
- [5] A. Jalil, A. Heurtel, Y. Marfaing and J. Chevallier, *J. Appl. Phys.* 66 (1980) 5854.
- [6] M. Santos, T. Sajota, A. Zrenner and M. Shayegan, *Appl. Phys. Letters* 53 (1988) 2504.
- [7] E.F. Schubert, J. Stark, T.H. Chiu and B. Tell, *Appl. Phys. Letters* 53 (1988) 293.
- [8] N.M. Johnson, R.D. Burnham, R.A. Street and R.L. Thornton, *Phys. Rev. B* 33 (1986) 1102.
- [9] S.J. Pearton, W.C. Dautremont-Smith, J. Lopata, C.W. Tu and C.R. Alberathy, *Phys. Rev. B* 36 (1987) 4260.
- [10] Jiang De-Sheng, Y. Makita, K. Ploog and H.J. Queisser, *J. Appl. Phys.* 53 (1982), 999.
- [11] T. Lideikus and G. Treideris, *Semicond. Sci. Technol.* 4 (1989) 938.
- [12] W.C. Dautremont-Smith, J.C. Nabity, V. Swaminathan, M. Stavola, J. Chevallier, C.W. Tu and S.J. Pearton, *Appl. Phys. Letters* 49 (1986) 1098.
- [13] T. Takomori, T. Fukunaga, J. Koboyashi, K. Ishida and H. Nakashima, *Japan. J. Appl. Phys.* 26 (1987) 1097.
- [14] N. Duhamel, P. Henoc, E. Alexander and F.V.K. Rao, *Appl. Phys. Letters* 39 (1981) 49.
- [15] J.F. Bresse and A.C. Papadopoulos, *Appl. Phys. Letters* 51 (1987) 183.

A comparison of atomic carbon versus beryllium acceptor doping in GaAs grown by molecular beam epitaxy

J. Nagle, R.J. Malik and D. Gershoni

AT&T Bell Laboratories, Murray Hill, New Jersey 07974, USA

Atomic carbon doping by solid-source molecular beam epitaxy (MBE) using a resistively heated graphite filament is investigated. Reproducible doping levels up to 10^{20} cm^{-3} are obtained with good hole mobilities. Results concerning the high limit of bulk doping and δ -doping with carbon are presented. A systematic variation of the V/III ratio showed no evidence of an amphoteric behavior of carbon. Comparison with beryllium doped layers grown in the same MBE system shows similar optical quality for the low doping range and degradation for carbon doping only above 10^{19} cm^{-3} . Carbon memory effects are found to be negligible after the growth of thin doped layers. These results show that carbon could replace advantageously beryllium in most electronic and optical devices.

1. Introduction

There has been considerable interest in recent years on p-type doping of GaAs with carbon. The high solubility of carbon in GaAs, its straightforward behavior as a shallow acceptor and its extremely low diffusion coefficient render it an excellent candidate for high doping of GaAs. Controlled incorporation of carbon as an acceptor up to high levels has been demonstrated from trimethylgallium or trimethylaluminum using metal-organic molecular beam epitaxy [1–4] and metal-organic chemical vapor deposition [5]. The incomplete dissociation of the metal–C bond is in all cases responsible for the high efficiency of the carbon incorporation in the As sublattice as an acceptor.

In conventional solid-source molecular beam epitaxy (MBE), Be is commonly used as p type dopant [6]. The maximum doping level is limited to about $1 \times 10^{20} \text{ cm}^{-3}$ due to thermal diffusion and interstitial incorporation of Be when growing around 580°C . A higher maximum doping level of $2 \times 10^{20} \text{ cm}^{-3}$ can be achieved when growing at lower temperatures [7].

Carbon doping in solid-source MBE using a resistively heated graphite filament has recently been successfully demonstrated [8]. In the present work we concentrate on growth issues and on

basic characterizations aiming at increased knowledge of the quality of carbon-doped materials grown by this novel technique. In order to clearly discriminate the specific effects related to the presence of carbon as dopant from the high doping effects, we compare directly with Be-doped layers grown in exactly identical conditions since a conventional beryllium effusion cell is also available in the same MBE system. Hall, SIMS, and photoluminescence (PL) measurements were performed on the samples.

2. Experimental

Samples were grown in a VG V80H MBE system on (100) oriented GaAs substrates. The graphite filaments were cut in a serpentine shape from rectangular sheets of high purity graphite to have a resistance of approximately 1Ω . Two filaments were mounted side by side with tantalum nuts on tantalum rods and surrounded by a cylindrical tantalum radiation shield. The rods were connected to a triple vacuum current feedthrough attached to one of the cell ports.

The structure of the samples we used for this study was one of the following three: (i) 5000 \AA doped GaAs; (ii) samples comprising $1 \mu\text{m}$ of

doped GaAs sandwiched between two 1000 Å $\text{Al}_{0.3}\text{Ga}_{0.7}\text{As}$ layers and capped with a thin GaAs layer, specifically designed for optical measurements to avoid the recombination of photoexcited carriers at the free surface and to ensure that there are no photoexcited carriers in the buffer layers; (iii) sequence of doped or undoped GaAs quantum wells separated by 300 Å $\text{Al}_{0.3}\text{Ga}_{0.7}\text{As}$ and capped by 1500 Å $\text{Al}_{0.3}\text{Ga}_{0.7}\text{As}$. All samples were grown on an unintentionally doped buffer including a short period superlattice sequence for type (ii) and (iii) samples. All samples were grown using As_2 beams with a GaAs growth rate of 1 $\mu\text{m}/\text{h}$. The growth temperature was measured by a calibrated near-infrared pyrometer. It was varied between 550 and 600°C for Be-doped samples and between 580 and 630°C for C-doped samples.

The photoluminescence spectra were taken at 6 K with a He-Ne laser ($\lambda = 632.8$ nm, $P_{\text{exc}} = 1$ W/cm²), at 300 K with an Ar⁺ laser ($\lambda = 514$ nm, $P_{\text{exc}} = 1$ kW/cm²) and detected with a Ge detector or an optical multichannel analyzer.

3. Results

3.1. Carbon incorporation

C-doped GaAs samples with mobilities comparable to those of Be-doped samples were obtained for doping densities up to 1×10^{20} cm⁻³, with smooth surfaces below 3×10^{19} cm⁻³. Fig. 1 shows that the doping follows the total carbon vapor pressure [9]. The temperature of the graphite filament was measured using a hot-wire pyrometer. Single readings have large error bars (± 25 K) but the fact that the measured temperatures follow exactly a $P^{1/4}$ law between 1600 and 2400 K indicates that (i) temperature values measured by the hot-wire pyrometer are reliable and (ii) heat losses are dominated by radiant losses. Using the electrical power and the corresponding filament temperature as inputs in Stefan's law with an emissivity factor of 0.8 [9], we find a radiant area of 3.6 cm² very close to the geometrical area (3.2 cm²) of the thin part of the filament. Using the Hertz-Knudsen formula with the esti-

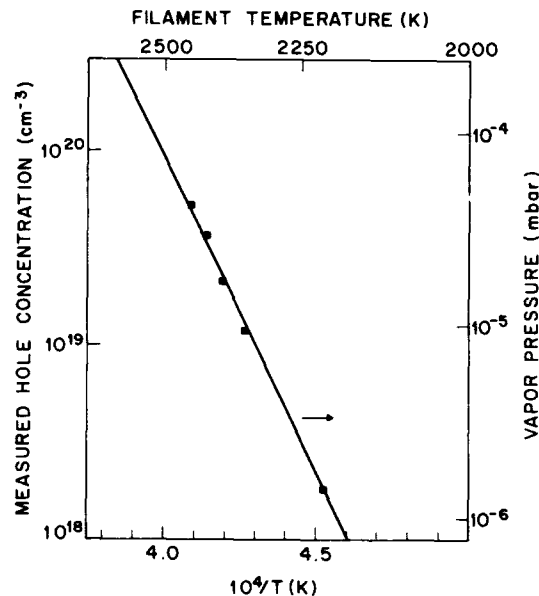


Fig. 1. Measured concentration of holes at 300 K in GaAs:C as a function of the temperature of the graphite filament measured with a hot-wire pyrometer. The data points follow the total carbon vapor pressure over graphite from ref. [9] shown as a solid line.

mated filament-substrate distance ($d = 15$ cm) and with carbon evaporation coefficient $a_v = 0.18$ [10], we calculate from fig. 1 a total number of carbon atoms impinging on the substrate two times larger than the actual doping. This discrepancy can be attributed to the large uncertainty of the vapor pressure data and of the geometrical factors or to the fact that C_2 and C_3 molecular species are present in the vapor pressure and can even dominate C_1 atoms for the highest temperatures of the filament [10].

Attempts to grow layers doped above 1×10^{20} cm⁻³ gave consistently hole concentrations much smaller than expected from fig. 1 together with reduced mobilities. Nomarski microscope pictures of the surface of these samples showed a characteristic isotropic short-scale roughness. For all doping ranges a correlation is observed between reduction of the carrier density and appearance of roughness. The carbon concentration was measured by SIMS on some of the samples. It is found to agree within 30% with the measured Hall car-

rier concentration below $1 \times 10^{20} \text{ cm}^{-3}$ and with the intended concentration extrapolated using the vapor pressure curve above $1 \times 10^{20} \text{ cm}^{-3}$. This electrical inactivity of carbon for the highest concentrations could be related to the incorporation of the already mentioned C_2 and C_3 molecular species or to the incorporation of C_1 as interstitial.

3.2. V/III ratio dependence

The incorporation of carbon atoms as acceptors in substitutional sites for As atoms should be favored by a low As pressure during growth if the carbon has an amphoteric behavior. We varied systematically the V/III ratio for a series of samples grown at 580°C and nominally doped at a density of $9 \times 10^{18} \text{ cm}^{-3}$. The electrical activity of carbon is found to be quite independent of the V/III ratio as long as the growth takes place under As-stabilized conditions (fig. 2). The PL intensity at room temperature and at low temperature is also independent of the V/III ratio for As-stabilized conditions. In contrast, the sample grown under Ga-rich conditions has a slightly reduced hole density and PL intensities reduced

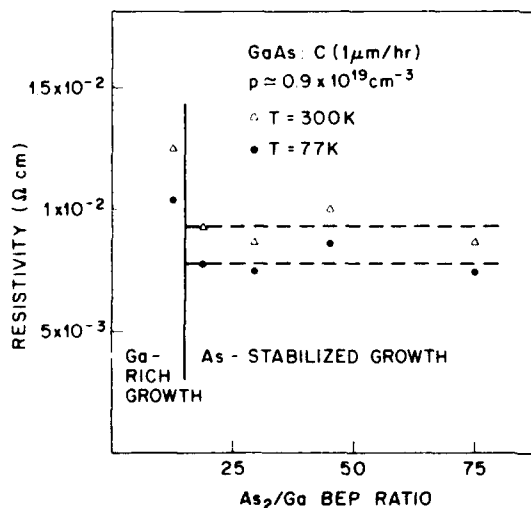


Fig. 2. Resistivity at 300 and 77 K of C-doped samples with the same nominal doping as function of the V/III beam equivalent pressure ratio. Above the threshold for As stabilization the resistivity is approximately constant.

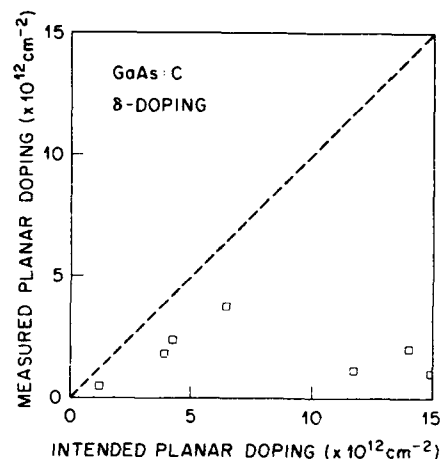


Fig. 3. Carrier density measured at 300 K in GaAs δ -doped with carbon as a function of the expected density. The highest value obtained is $3.8 \times 10^{12} \text{ cm}^{-2}$. Attempts to further increase the planar doping result in compensation.

by a factor of 10 as compared to the other samples, correlated with its degraded morphology. These results imply that carbon is not exhibiting any amphoteric behavior at this doping level and that successful doping with carbon is possible in a very wide range of growth conditions.

3.3. δ -doping

Results on the electrical activity of carbon in δ -doped planes are summarized in fig. 3. The various samples have been grown under very different conditions and at different times, but they clearly show a general tendency. The maximum doping obtained in a single plane is $3.8 \times 10^{12} \text{ cm}^{-2}$. δ -Doped planes with intended densities higher than $1 \times 10^{13} \text{ cm}^{-2}$ are systematically strongly compensated.

3.4. PL results

The PL spectra of Be-doped samples (fig. 4) show the expected behavior of highly doped p-type GaAs [11] with a low energy peak associated to k -conserving transitions and a high energy shoulder at the Fermi level of holes due to k -nonconserving transitions. This Fermi edge is clearly visi-

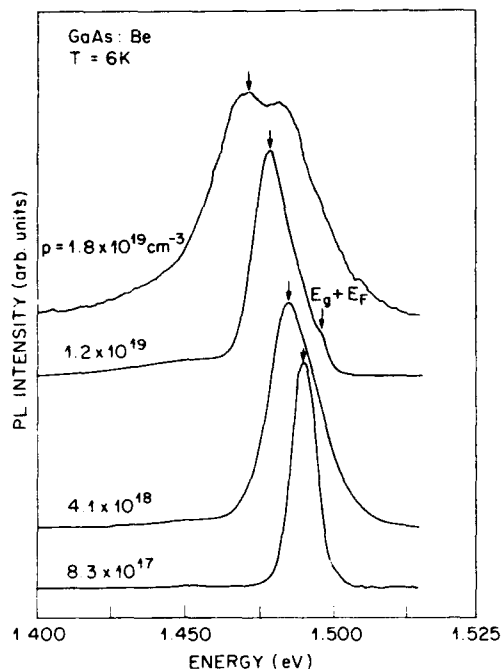


Fig. 4. Normalized low temperature PL spectra of thick (0.5–1 μm) Be-doped GaAs samples for various doping levels. Note the red shift of the peak associated to k -conserving transitions with increasing band-gap renormalization.

ble in the spectrum for $p = 1.2 \times 10^{19} \text{ cm}^{-3}$ (the doping concentrations were measured by the Hall–Van der Pauw method at room temperature). The band gap renormalization effect is responsible for the red shift of the principal peak for increased carrier concentrations. The integrated PL intensity goes through a maximum for doping in the low- 10^{19} cm^{-3} range.

The PL spectra for carbon doping up to $\approx 5 \times 10^{18} \text{ cm}^{-3}$ are similar in lineshape and intensity to those of beryllium. On the other hand the intensity ratio starts degrading for higher doping indicating the presence of non-radiative recombination centers. In none of the samples did we detect luminescence between 0.7 eV (limit of the Ge detector) and the band-edge luminescence. The PL intensity ratio results at room temperature replicated those at 6 K. The presence of defects in the C-doped layers is confirmed by the fact that the integrated PL intensity can be improved by a

factor of 1.5 to 8 after 10 s rapid thermal annealing at 900°C .

3.5. Memory effects of carbon doping

The band–acceptor PL transition at 6 K of two undoped quantum wells sandwiching a highly carbon doped quantum well was used as an optical probe for the presence of carbon atoms 300 Å away from their intended incorporation region. The PL of this sample after 10 s annealing at 860°C is presented in fig. 5. The spectrum of the non-annealed sample is identical except that annealing has enhanced by a factor of 8 the PL intensity of the doped well (QW2). The undoped wells show PL intensity and lineshape identical to what is obtained in samples having no doped well. This implies that the doping of QW2 introduces no degradation of the interfaces. The $e\text{--}A^0$ transitions of QW3 (hardly visible at the scale of fig. 5) are not more intense than those of QW1 which was grown before any doping in the sample. This indicates no significant memory effect or segregation during growth. Furthermore, the unchanged

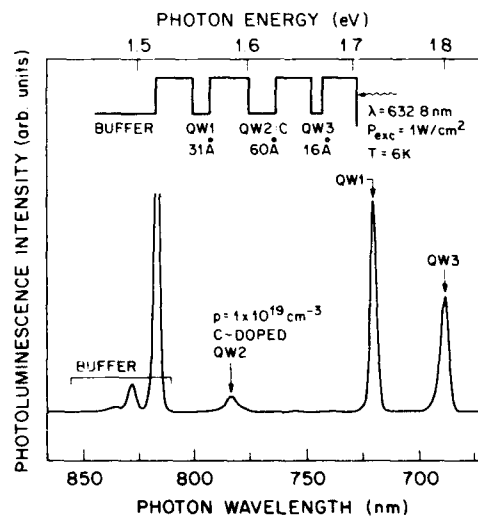


Fig. 5. PL spectrum of one heavily C-doped quantum well sandwiched between two unintentionally doped quantum wells. The spectrum demonstrates the absence of sizeable segregation, diffusion or memory effects of carbon dopant atoms over the 300 Å AlGaAs barriers (see text).

PL of QW1 and QW3 after annealing shows that there is no outdiffusion of defects or carbon atoms to the neighbouring wells.

4. Discussion

The reason for the observed saturation of carbon doping in bulk and δ -spikes is not understood yet. This saturation is associated with degraded morphology and minority carrier lifetime. Possible causes include (i) incorporation of non-dissociated C-C bonds in form of C_2 or C_3 molecules present in the vapor pressure and (ii) incorporation of excess carbon atoms in interstitial sites similarly to the case of beryllium. Carbon pairing is less likely given the absence of amphoteric behavior of carbon. Since we observed the same high-doping limit using filaments cut from high grade purity and less pure graphite, the incorporation of impurities from the filament is probably not the reason. We can also rule out the side effects of the presence of the elevated filament temperature in the system (i.e. impurity ionization, outgassing from the shrouds, high H_2 pressure) since the same maximum doping ($\sim 1 \times 10^{20} \text{ cm}^{-3}$) was obtained with a filament placed 25 cm away from the substrate instead of 15 cm, necessitating therefore a much higher operating temperature for the same doping level.

5. Conclusions

Reproducible carbon doping levels up to 10^{20} cm^{-3} with good electrical properties have been obtained in GaAs using a resistively heated graphite filament in conventional solid-source MBE. The V/III ratio during growth has been varied and no evidence of an amphoteric behavior of carbon has been observed.

Comparison with Be-doped layers grown in the same system shows similar optical quality for the low doping range and degradation for carbon

doping only above 10^{19} cm^{-3} . Excellent optical properties are conserved in the immediate vicinity of highly C-doped layers.

These results combined with the extremely low diffusion coefficient of carbon in GaAs [2,8] and the high toxicity of beryllium show that carbon doping can be used advantageously instead of beryllium doping in any electronic or optical devices for doping levels below 10^{19} cm^{-3} . For higher levels carbon doping may still be preferable in cases where absence of diffusion is more important than optical quality.

Acknowledgements

The authors would like to thank L.C. Hopkins for SIMS measurements and R.W. Ryan for expert technical assistance.

References

- [1] M. Weyers, N. Pütz, H. Heinecke, M. Heyen, H. Lüth and P. Balk, *J. Electron. Mater.* 15 (1986) 57.
- [2] N. Kobayashi, T. Makimoto and Y. Horikoshi, *Appl. Phys. Letters* 50 (1987) 1435.
- [3] M. Konagai, T. Yamada, T. Akatsuka, K. Saito, E. Tokumitsu and K. Takahashi, *J. Crystal Growth* 98 (1989) 167.
- [4] C.R. Abernathy, S.J. Pearton, R. Caruso, F. Ren and J. Kovalchik, *Appl. Phys. Letters* 55 (1989) 1750.
- [5] T.F. Kuech, M.A. Tischler, P.-J. Wang, G. Scilla, R. Potemski and F. Cardone, *Appl. Phys. Letters* 53 (1988) 1317.
- [6] K. Ploog, A. Fischer and H. Künzel, *J. Electrochem. Soc.* 128 (1981) 400.
- [7] J.L. Lievin and F. Alexandre, *Electron. Letters* 21 (1985) 413.
- [8] R.J. Malik, R.N. Nottenburg, E.F. Schubert, J.F. Walker and R.W. Ryan, *Appl. Phys. Letters* 53 (1988) 2261.
- [9] W.N. Reynolds, *Physical Properties of Graphite* (Elsevier, Amsterdam, 1968).
- [10] I.A. Dimitriev, V.I. Kostikov, I.A. Berezin and L.N. Yurchenko, *Izv. Akad. Nauk SSSR, Neorg. Mater.* 16 (1980) 1945.
- [11] D. Olego and M. Cardona, *Phys. Rev. B* 22 (1980) 886.

Carbon doping of MBE GaAs and $\text{Ga}_{0.7}\text{Al}_{0.3}\text{As}$ films using a graphite filament

W.E. Hoke, P.J. Lemonias, P.S. Lyman, H.T. Hendriks, D. Weir

Raytheon Research Division, Lexington, Massachusetts 02173, USA

and

P. Colombo

EPI Division, Chorus Corp., St. Paul, Minnesota 55101, USA

Carbon doped GaAs and $\text{Ga}_{0.7}\text{Al}_{0.3}\text{As}$ films have been grown by molecular beam epitaxy using a resistively heated graphite filament. At moderate doping levels, the effect on carbon doping of the V/III flux ratio and the nature of the arsenic species was found to be minor. The GaAs films were doped from 1×10^{15} to $5 \times 10^{19} \text{ cm}^{-3}$ and the resulting hole mobilities were equivalent to beryllium doped films. Excellent doping uniformity was obtained for 3-inch diameter films. $\text{Ga}_{0.7}\text{Al}_{0.3}\text{As}$ films were also doped from 9×10^{17} to $3.4 \times 10^{19} \text{ cm}^{-3}$. For the highest carbon doped films, lattice contractions were observed which were greater than for beryllium doping. The lattice contractions were analyzed with a model using tetrahedral covalent radii.

1. Introduction

Presently, beryllium is the acceptor dopant of choice for GaAs in conventional molecular beam epitaxy (MBE) due to its high doping efficiency, good hole transport properties, and acceptable diffusion rate at moderate doping levels. However, for doping levels in excess of $1 \times 10^{19} \text{ cm}^{-3}$, concentration dependent diffusion becomes important [1] and is enhanced by the presence of nearby n-type layers [2]. In our laboratory we have observed degraded heterojunction bipolar transistor (HBT) performance due to beryllium in the heavily doped base layer diffusing into the n-type emitter. The development of carbon as an acceptor dopant in GaAs is motivated by its much smaller diffusion coefficient than beryllium [3,4]. Also hole concentrations in GaAs in excess of $1 \times 10^{20} \text{ cm}^{-3}$ have been demonstrated [3–6].

Initial reports on carbon doping using a graphite filament have been published [7,8]. In this work, we report carbon doping of GaAs over a wide range of concentrations with transport prop-

erties equivalent to beryllium doped films. The doping uniformity for 3-inch diameter films is excellent. The effect on doping from the As_4/Ga flux ratio is investigated and a comparison is made for carbon doping using As_2 and As_4 . The carbon doping of $\text{Ga}_{0.7}\text{Al}_{0.3}\text{As}$ films is reported. Finally heavily doped films exhibit lattice contractions which are analyzed with calculations utilizing tetrahedral covalent radii.

2. Experimental

The carbon doped films were grown in a VG-80H MBE machine which was loaded with conventional solid sources. Arsenic was supplied to the growth surface as either As_2 or As_4 , which was determined by the cracking zone temperature of an EPI arsenic cracker. The films were deposited at a substrate temperature of 530–600°C for GaAs and 600–650°C for $\text{Ga}_{0.7}\text{Al}_{0.3}\text{As}$. The growth rates for GaAs and $\text{Ga}_{0.7}\text{Al}_{0.3}\text{As}$ were 0.5 and 0.7

$\mu\text{m/h}$, respectively. The carbon doping source was fabricated by EPI and contained a graphite strip which was resistively heated by a regulated power supply without thermocouple feedback control. Filaments with resistances at operating temperature of 0.25 and 0.4 Ω were used. The filament temperature was measured with an optical pyrometer and was varied from approximately 1550 to 2100°C to vary the doping from 1×10^{15} to $5 \times 10^{19} \text{ cm}^{-3}$. The highest doping level required 600 W of power. For comparison, beryllium doped samples were also grown by conventional MBE.

The electrical properties of the films were determined by Hall measurements at 4000 G as well as by capacitance-voltage ($C-V$) profiling. At high doping levels, lattice contractions perpendicular to the film surface were observed by X-ray double crystal measurements. Copper $K\alpha_1$ radiation was used with the (400) reflection of GaAs.

3. Results and discussion

Since carbon acceptors must occupy arsenic sites, the effect of the arsenic environment on

carbon doping was initially examined for moderate doping levels. In one experiment, the As_4 flux was varied with the other growth conditions held constant. Fig. 1 is a doping versus depth profile of a film containing six 0.8 μm thick layers delineated by small doping spikes and grown with different ratios of V/III beam equivalent pressures. The first and last layers were grown with similar flux ratios to ensure that the results were consistent and not a result of a long term drift effect. Fig. 1 shows that a three fold increase in flux ratio leads to a small depression in doping of approximately 20%. Around the commonly used flux ratio of 10, the effect of flux ratio is quite small and probably within experimental uncertainty. The limited dependence of carbon doping on arsenic flux is an attractive doping property due to the difficulty of achieving a constant and reproducible arsenic flux in solid source MBE.

The effect on carbon doping of using As_2 or As_4 was investigated. As_2 is more reactive and has a higher sticking coefficient than As_4 [9] which could effect carbon doping. Comparison films were grown at doping levels of 2×10^{17} , 5×10^{17} , and $1.5 \times 10^{19} \text{ cm}^{-3}$ with cracked (As_2) and un-

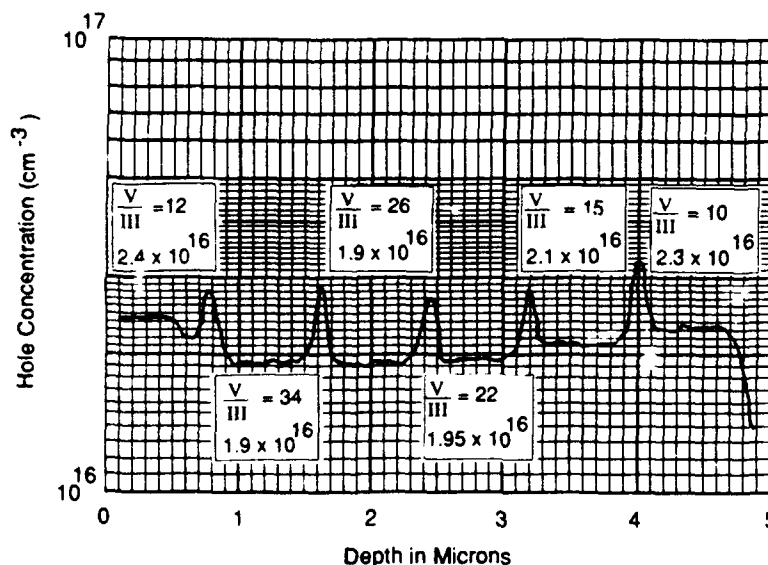


Fig. 1 Hole concentration versus depth for a film containing six 0.8 μm -thick layers grown with different As_4/Ga flux ratios. The layers are delineated by small doping spikes.

cracked (As₄) arsenic. The resulting carrier concentrations with the two arsenic species agreed within 10% and the mobilities agreed within 4%.

These two experiments indicate that the arsenic environment plays a limited role in carbon doping of GaAs at moderate doping levels despite carbon occupying sites on the arsenic sublattice. A possible explanation is that site occupation is primarily determined by the stronger gallium-carbon bond (61 kcal/mol) than the arsenic-carbon bond (57 kcal/mol) [10]. A relative bond strength model has been proposed to explain the carbon doping behavior as p-type in GaAs, n-type in InAs, and compensated in Ga_{0.5}In_{0.5}As [8].

The lateral uniformity with carbon doping was examined. Fig. 2 is a compilation of 16 C-V measurements taken along the wafer radius for a 2.8-inch diameter film. The film was grown with gallium evaporated from a large diameter VG 70 cm³ cell which produces a thickness uniformity of $\pm 1\%$. Fig. 2 contains two types of uniformity measurements. The depth profile is obtained by differentiating the capacitance as a function of applied voltage in the conventional manner [11]. The maximum variation in the doping level is $\pm 2.5\%$ with a considerably smaller standard deviation. Also given in fig. 2 is the zero bias depletion capacitance, C_0 , which has a maximum variation

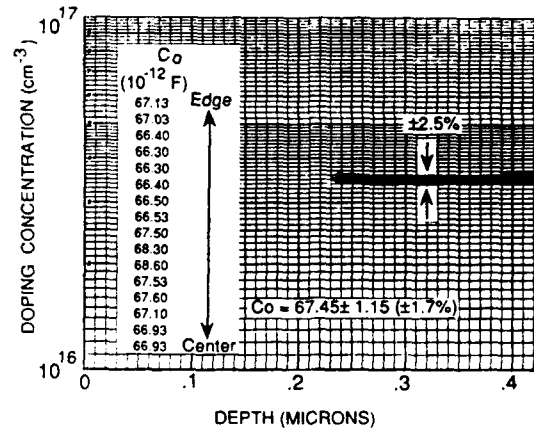


Fig. 2. Capacitance-voltage depth profiles obtained from 16 Schottky diodes placed along the radius of a 3-inch wafer. C_0 is the zero bias capacitance of the diode.

of $\pm 1.7\%$. Since C_0 is proportional to the square root of the doping concentration in the depletion layer, this measure of doping variation gives $\pm 1.3\%$.

Two other characteristics of the carbon doping source are worth noting. As shown in figs. 1 and 2, the doping levels are quite flat using a regulated power supply without temperature feedback control. Also the filament has a very small thermal

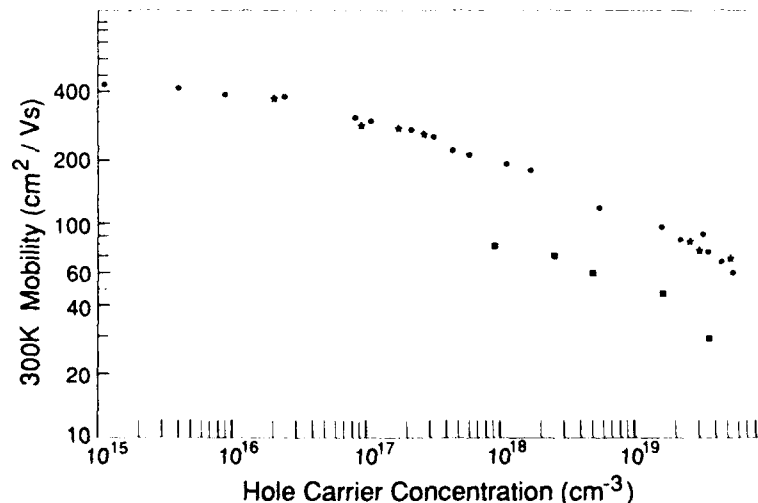


Fig. 3. Room temperature mobility versus hole concentration for carbon (●) and beryllium (○) doped GaAs films and carbon (■) doped Ga_{0.7}Al_{0.3}As films.

mass which rapidly equilibrates radiatively with its thermal environment. Consequently the filament temperature can be changed several hundred degrees in approximately 10 s for growth of multiple doping levels.

GaAs films were doped with carbon with resulting hole concentrations from 1.2×10^{15} to $5.3 \times 10^{19} \text{ cm}^{-3}$. For hole concentrations up to $3 \times 10^{19} \text{ cm}^{-3}$, the surfaces were quite specular with no microscopic texture observable under Nomarski contrast. At $5 \times 10^{19} \text{ cm}^{-3}$ a background texture was present. The maximum doping level was limited by filament failure due to hot spots in the filament. Higher doping levels should be possible by optimizing filament design.

Room temperature Hall mobilities are given in fig. 3 for carbon and beryllium doped GaAs films and the results compare well with literature values

[12]. For a given hole concentration, the mobilities of the beryllium and carbon doped films are the same within experimental uncertainty. A variable temperature Hall measurement was performed on the $1.2 \times 10^{15} \text{ cm}^{-3}$ sample which gave mobilities of $440 \text{ cm}^2/\text{V} \cdot \text{s}$ at 300 K, $7200 \text{ cm}^2/\text{V} \cdot \text{s}$ at 77 K, and $13,700 \text{ cm}^2/\text{V} \cdot \text{s}$ at 40 K. Data for carbon doped Ga_{0.7}Al_{0.3}As films are also given in fig. 3 for doping levels from 9×10^{17} to $3.4 \times 10^{19} \text{ cm}^{-3}$.

Lattice contractions in heavily carbon and beryllium doped films were observed using double crystal X-ray measurements. As illustrated in the fig. 4 insert, the (400) diffraction peaks of the doped film and substrate are separated. The separations or splittings are caused by a contraction in the lattice constant perpendicular to the growth plane due to the smaller atomic size of carbon or beryllium compared to gallium or arsenic. The measured splittings in fig. 4 are larger for carbon than beryllium doping which is qualitatively consistent with the smaller tetrahedral covalent radius of carbon compared to beryllium [13]. Also the splittings in fig. 4 exhibit a linear dependence on doping concentration.

The relationship between doping and lattice contraction is now considered. The splitting, $\Delta\theta$, between the X-ray diffraction peaks of the GaAs substrate with lattice constant a_0 and the tetragonally distorted GaAs film with perpendicular lattice constant, a_\perp , is given by:

$$(a_\perp - a_0)/a_0 = \Delta a/a_0 = -\Delta\theta \cot(\theta), \quad (1)$$

where θ is the substrate diffraction angle. For Cu K α_1 radiation and the (400) reflection of GaAs, θ is 33.024° . Assuming interstitial dopant atoms do not perturb the lattice constant, the expected lattice contraction for a doped GaAs layer can be straightforwardly calculated using the molecular density and tetrahedral covalent radii to determine bond lengths. The relationship is then:

$$\frac{\Delta a}{a_0} = \frac{4[N_{\text{CGa}}(r_{\text{C}} - r_{\text{Ga}}) + N_{\text{CAs}}(r_{\text{C}} - r_{\text{As}})](1 + \nu)}{\sqrt{3}(2.21 \times 10^{22})a_0(1 - \nu)}, \quad (2)$$

where N_{CGa} and N_{CAs} are the densities (cm^{-3}) of carbon atoms on gallium and arsenic sites, respectively, r_x is the tetrahedral covalent radius of atom

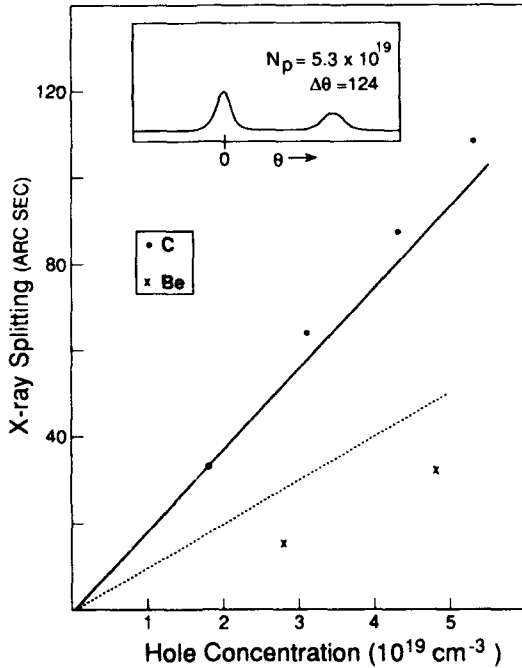


Fig. 4. Measured (400) X-ray splittings for carbon (●) and beryllium (×) doped GaAs films compared to calculated values for carbon (—) and beryllium (---) doping. Insert is an X-ray spectrum for a carbon doped film with hole concentration, N_p , of $5.3 \times 10^{19} \text{ cm}^{-3}$. The (400) substrate peak is at 0° .

x , and ν is the Poisson ratio for GaAs. Eq. (2) is pertinent for pseudomorphically strained films such as in this study. For thick, completely strain relaxed films, the factors containing the Poisson ratio are eliminated, as previously discussed [6]. Eq. (2) can be simplified since the calculated values for the tetrahedral covalent radii of gallium and arsenic are reported to be the same (1.225 Å) [13] which yields:

$$\frac{\Delta a}{a_0} = \frac{1.04 \times 10^{-22} N_{\text{CAs}} (r_{\text{C}} - r_{\text{As}}) (1 + \rho) (1 + \nu)}{a_0 (1 - \nu)}, \quad (3)$$

where ρ is the compensation ratio, $N_{\text{CAs}}/N_{\text{CAs}}$, and the constants have been combined. The calculated splittings in fig. 4 were obtained with $r_{\text{C}} = 0.774$ Å [13], $\nu = 0.31$ [12] and assuming no compensation. For beryllium doping, an analogous eq. (3) is obtained and $r_{\text{Be}} = 0.975$ Å [13].

Qualitatively eq. (3) describes the linear dependence of lattice contraction on carbon doping concentration as well as the smaller effect of beryllium doping on lattice contraction. Quantitatively the measured and calculated lattice contractions given in fig. 4 for carbon doped GaAs agree well with the measured values being typically 10% larger than the calculated value. The good agreement indicates that the material is not heavily compensated. The measured lattice contractions with beryllium doping are smaller than calculated. Additional data are needed to further examine this effect.

Lattice contraction was also observed for a Ga_{0.72}Al_{0.28}As sample doped at $1.6 \times 10^{19} \text{ cm}^{-3}$. The measured splitting between the GaAlAs film and GaAs substrate peaks was 47 arc sec compared to an expected splitting of 109 arc sec for an undoped film. Using the analysis above for an uncompensated Ga_{0.72}Al_{0.28}As sample doped at $1.6 \times 10^{19} \text{ cm}^{-3}$, the expected splitting is 75 arc sec. The observed smaller splitting indicates that the carbon concentration in the film is greater

than the doping concentration. Possible explanations are compensation and/or electrically inactive carbon. These initial results indicate that double crystal measurements may become a useful technique to assess material quality of heavily doped samples.

In summary, a carbon filament furnace has been used to dope GaAs films over a wide range with hole mobilities equivalent to beryllium. At moderate doping levels the arsenic environment plays a minor role in doping efficiency. The doping uniformity is excellent for 3-inch diameter material. Ga_{0.7}Al_{0.3}As films have also been doped with carbon. At high doping levels lattice contractions are observed with carbon and beryllium doping. The contractions have been analyzed with a model using tetrahedral covalent radii.

References

- [1] Y.-C. Pao, T. Hiern and T. Cooper, *J. Appl. Phys.* 60 (1986) 201.
- [2] D. Deppe, *Appl. Phys. Letters* 56 (1990) 370.
- [3] K. Saito, E. Tokumitsu, T. Akatsuka, M. Miyauchi, T. Yamada, M. Konagai and K. Takahashi, *J. Appl. Phys.* 64 (1988) 3975.
- [4] C. Abernathy, S. Pearton, R. Caruso, F. Ren and J. Kovalchik, *Appl. Phys. Letters* 55 (1989) 1750.
- [5] N. Pütz, H. Heinecke, M. Heyen, P. Balk, M. Weyers and H. Lüth, *J. Crystal Growth* 74 (1986) 292.
- [6] T. de Lyon, J. Woodall, M. Goorsky and P. Kirchner, *Appl. Phys. Letters* 56 (1990) 1040.
- [7] R. Malik, R. Nottenberg, E. Schubert, J. Walker and R. Ryan, *Appl. Phys. Letters* 53 (1988) 2661.
- [8] H. Ito and T. Ishibashi, *Mater. Res. Soc. Symp.*, Boston, MA, Nov. 1989, Paper G9.38.
- [9] L.P. Erickson, T. Mattord, G. Carpenter, P. Palmberg, P. Pearah, M. Klein and H. Morkoç, *J. Appl. Phys.* 56 (1984) 2231.
- [10] F. Hartley and S. Patai, *The Chemistry of the Metal-Carbon Bond* (Wiley, New York, 1982) pp. 53–71.
- [11] W.C. Johnson, *IEEE Trans. Electron Devices* ED-18 (1971) 965.
- [12] J. Blakemore, *J. Appl. Phys.* 53 (1982) R123.
- [13] J. Van Vechten and J. Phillips, *Phys. Rev. B* 2 (1970) 2160.

Characterization of the GaAs:C and AlGaAs:C doping superlattice grown by chemical beam epitaxy

T.H. Chiu, J.E. Cunningham, J.A. Ditzenberger, W.Y. Jan

AT&T Bell Laboratories, Holmdel, New Jersey 07733, USA

and

S.N.G. Chu

AT&T Bell Laboratories, Murray Hill, New Jersey 07974, USA

We report the growth of high quality GaAs and AlGaAs carbon doping superlattice homostructures using trimethyl-Ga, triethyl-Ga and trimethylamine alan by chemical beam epitaxy. The periodic change in lattice parameter resulting from the change in carbon doping level is useful for the structural characterization of these samples by double crystal X-ray diffraction. With minimal contribution to the X-ray scattering intensity due to atomic form factors of the chemical modulation, the satellite intensities of the GaAs/GaAs:C superlattice are found to scale with order index as n^{-4} , which conforms to a square waveform of strain modulation. Analysis of the intensity reduction of the annealed GaAs sample yields unambiguous information about the carbon diffusion in GaAs.

1. Introduction

Recently, carbon doped GaAs has received increasing attention because of its high doping efficiency [1–3] and low impurity diffusivity [4,5]. Compared to Be, C doping profile in GaAs is also stable against Zn diffusion which is a process often employed for contact purpose [6]. These properties are technologically important for device application such as heterojunction bipolar transistor (HBT) [1,7]. In chemical beam epitaxy (CBE) of GaAs, C doping is conveniently obtained by using trimethyl-Ga (TMGa) as a precursor for the growth. The concentration of C can be controlled by growth conditions [8] or mixing triethyl-Ga (TEGa) with TMGa. Successful C doping using separate doping sources has been demonstrated by using graphite filament in molecular beam epitaxy (MBE) [1] and CCl_4 in organometallic vapor phase epitaxy (OMVPE) [9]. One less desirable property of heavily C doped GaAs is a significant change in lattice parameter [2,10] with C concentration above

10^{19} cm^{-3} . This is not necessarily a problem for device application if the strained C doped region is thinner than the critical thickness. Here we show that this inherent strain due to C doping is useful in preparing strain modulated GaAs and AlGaAs superlattice homostructures for X-ray diffraction study. By comparing the satellite intensities of the as-grown and the annealed samples, Arrhenius dependence of the carbon diffusion coefficient in GaAs can be determined. This method can also be applied to the study of C diffusion in AlGaAs.

2. Crystal growth

In the CBE growth of GaAs:C, pure TMGa without carrier gas was used. Carbon incorporation results from the incomplete Ga–C bond cleavage. Thus, C will preferentially sit on the As site as an acceptor. The concentration of C de-

depends on how efficiently the CH_3 radical is cleaved away and removed from the surface. With increasing As flux, the C level is generally found to decrease. The presence of hydrogen, in particular ionized species [11], also reduces the C impurity level. Therefore, a small V/III ratio is desirable for CBE growth of GaAs: C. From a chemical kinetics point of view, lower growth temperature favors C incorporation because of slower Ga-C cleavage rate. However, at low growth temperature, hydrogen passivation [12] may reduce the electrical activity of C. Furthermore, the growth rate becomes more sensitive to any change in substrate temperature which may lead to fluctuations in the layer thickness of superlattice. In order to obtain high C doping level with good periodicity, here the GaAs/GaAs: C superlattice is grown at 550°C using a V/III ratio of 2. The nominally undoped region ($\text{C} \sim 1 \times 10^{16} \text{ cm}^{-3}$) is grown by using TEGa.

For the growth of AlGaAs, trimethylamine alane (TMAAl) from Cyanamid was used as the Al source gas. Very recently, the use of alane along with TEG has been shown to result in much improved AlGaAs layers with lower oxygen and carbon contamination [13]. This makes possible the preparation of entirely CBE grown HBTs with both uniform and graded bases [14]. Whereas, heavily carbon doped AlGaAs is obtained by using TMAAl and TMGa. The AlGaAs/AlGaAs: C su-

perlattice is grown by alternating injection of TEGa and TMGa with a constant TMAAl flow.

3. Characterization of the C doped GaAs and superlattice

Earlier we have shown that a mismatch of about $(\Delta a/a)_\perp = 1.3 \times 10^{-3}$ is measured for a $2 \mu\text{m}$ thick GaAs: C epilayer [8]. The C concentration, $7.2 \times 10^{19} \text{ cm}^{-3}$, will result in a mismatch of about 6×10^{-4} for unstrained epilayer if a Ga-C bond length is assumed by replacing the covalent radius of As with that of C. This approach has been employed to account for the partially relaxed heavily C doped GaAs [10]. Thus, the measured mismatch suggests an unrelaxed tetragonally distorted lattice, consistent with the narrow X-ray diffraction peak width.

In fig. 1, intense satellite peaks of the GaAs/GaAs: C superlattice with reflection up to order $n = 7$ are clearly observable. Satellites up to order $n = 10$ are resolved at improved signal/noise level. The narrow width of satellites suggests that inhomogeneity in strain and thickness along the growth direction is very small. The abrupt interface can also be observed using transmission electron microscopy (TEM). Fig. 2a shows sharp contrast of the GaAs: C/GaAs interface. The thickness mea-

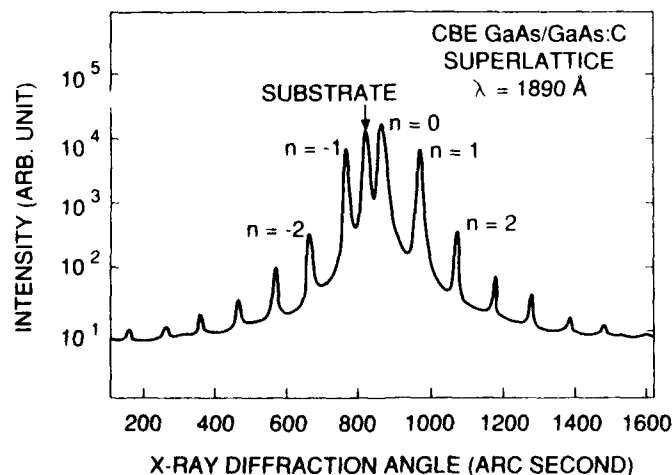


Fig. 1. X-ray rocking curve of a 30 period GaAs(950 Å)/(GaAs: C(940 Å) doping superlattice.

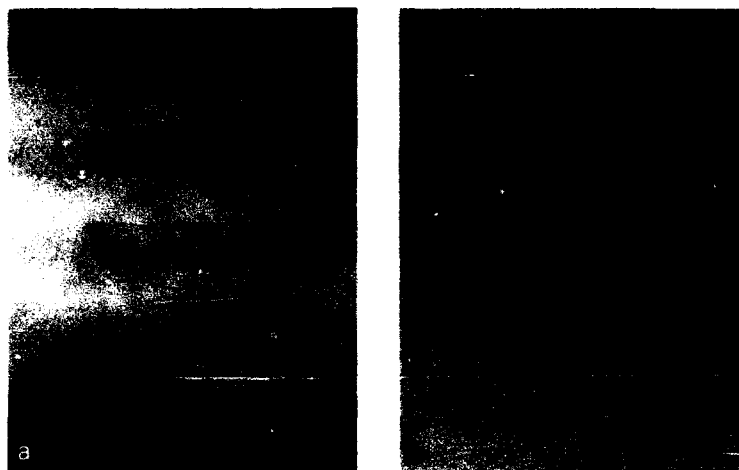


Fig. 2. Cross sectional TEM micrographs of the GaAs/GaAs:C superlattice (a) before (b) after a 900 °C anneal for 1 h.

sured from TEM agrees with the X-ray measurement to within 3%. It should be noted that even if the chemical interface is abrupt at monolayer scale, a gradient in the strain field still exists and is

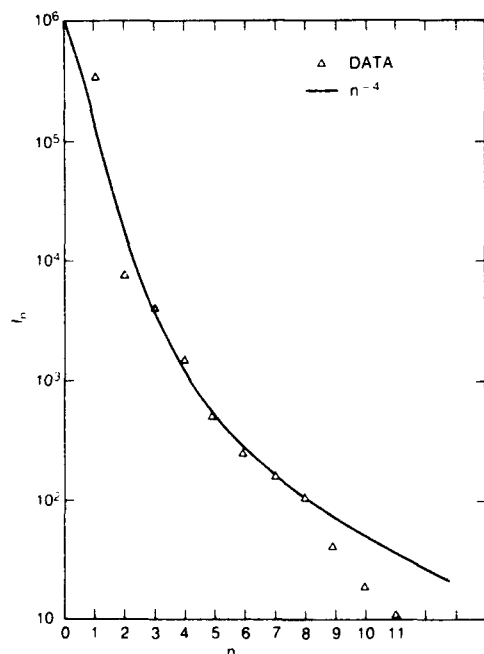


Fig. 3. Satellite intensity of the GaAs/GaAs:C superlattice versus order index n .

expected to extend across tens of angstroms at the interface.

The reduction in satellite intensity scales with increasing order as n^{-4} , which is illustrated in fig. 3. This dependence can be approximated by assuming a square waveform in the strain modulation. Whereas, chemical modulation in composition will scale as n^{-2} . Attempts to fit the satellite intensity using sinusoidal or trapezoidal waveforms are not successful. This is an indication of abrupt doping interface. Small deviation from n^{-4} dependence for high order index suggests a small statistical imperfection of the interfaces which can either be caused by small thickness variation or change in strain field across the interface.

4. Strain and composition modulated AlGaAs superlattice

The chemical configuration of trimethylamine alane, $[(CH_3)_3N]_2AlH_3$, indicates this compound contains no Al-C bond [15]. The $N(CH_3)_3$ group cleaves away easily at low temperature leaving an unstable adsorbed AlH_3 molecules, which results in efficient Al deposition above 200 °C. Thus, the carbon incorporation in the growth of AlGaAs using TMAAl and TEGa is not expected to be any higher than in the case of using Al-alkyl contain-

ing Al-C bond, of which a carbon level below 10^{17} cm^{-3} has been reported [16]. The X-ray diffraction scan of a CBE grown $\text{Al}_{0.1}\text{Ga}_{0.9}\text{As}/\text{GaAs}$ superlattice is comparable to that of the MBE grown superlattice samples. From a Si doping study, the oxygen contamination in the AlGaAs layer is estimated to be on the order of $1 \times 10^{18} \text{ cm}^{-3}$, which has also been observed in the high quality AlGaAs layers using TMAAl from a different source supplier [13]. There is no indication that oxygen contamination at this level will lead to any noticeable change in lattice parameter.

When TMAAl and TMGa are used for the growth, heavily C doped AlGaAs is obtained. The hole concentration of the nominal $\text{Al}_{0.1}\text{Ga}_{0.9}\text{As}$ epilayer grown at 570°C is about $1 \times 10^{20} \text{ cm}^{-3}$, about 30% higher when compared to GaAs: C using similar low V/III ratio. In the growth study of arsenide compounds using trimethyl-In (TMIn) [17] and TMGa [8], the non-linear region in growth rate characteristics, where the recombination of adsorbed methyl radicals and fragmented alkyl molecules is significant, occurs at much higher temperatures for TMGa. This indicates a stronger methyl-Ga bond, and a much higher C level is obtained in GaAs than InAs. Considering the bond strength of Al-C, the presence of Al is expected to enhance the carbon incorporation of AlGaAs.

Fig. 4 shows the X-ray diffraction of an AlGaAs/AlGaAs: C superlattice grown by using a

constant TMAAl flux. Although the TMGa and TEGa flow rates are chosen to give equal Al compositions based on the GaAs/GaAs: C growth, fig. 4 indicates clear asymmetry due to Al composition modulation in the satellite intensities, which no longer scale with order index n^{-4} . This suggests the presence of TMAAl affects the GaAs growth rates differently for TMGa and TEGa. Nevertheless, the $n=0$ superlattice peak shifts to larger diffraction angle indicating a compressive strain in the superlattice as a result of heavily carbon doped AlGaAs layers. With optimized composition control, it is possible to grow AlGaAs superlattice with strain modulation alone for X-ray characterization.

5. Effect of thermal annealing

Anneal experiments of the GaAs/GaAs: C superlattice are carried out in quartz ampoule sealed with controlled amount of As. Fig. 2b shows the smearing of interfaces as a result of noticeable diffusion of C into the undoped region of the sample annealed at 900°C for 1 h. Hall measurements of the unannealed sample give an average hole concentration of $3.43 \times 10^{19} \text{ cm}^{-3}$ and a mobility of $58 \text{ cm}^2/\text{V} \cdot \text{s}$. After annealing at 900°C , this sample shows an average hole concentration of $1.55 \times 10^{19} \text{ cm}^{-3}$ with an increased mobility of

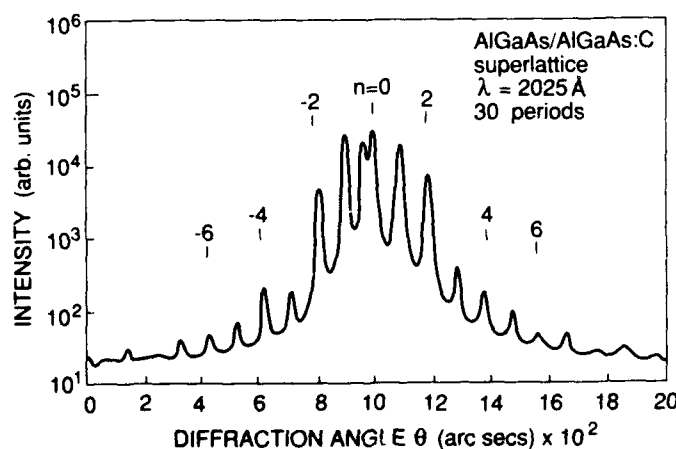


Fig. 4. X-ray diffraction rocking curve of the AlGaAs/AlGaAs: C superlattice.

$77 \text{ cm}^2/\text{V} \cdot \text{s}$. Similar results are measured for the sample annealed at 700°C for 16 h. Contrary to the case of bulk GaAs: C where annealing usually results in reduced mobility, the higher mobility indicate the contribution of hole conduction in the undoped region resulting from diffusive transport of C from the heavily doped layer. The reduction in hole density suggests the occurrence of self-compensation due to site changing of C, or positively charged C interstitial. This implies that the carbon diffusion may also involve Ga sublattice as opposed to the mechanism via As vacancy [4] or interstitial As which is easily formed under our annealing conditions with excessive As overpressure.

The long anneal time under equilibrium condition results in homogeneous diffusion of C throughout the entire superlattice. A systematic shift of the zeroth order peak toward the substrate peak is observed, indicating the reduction in the overall strain. The satellite peak height reduces as a consequence of the reduced asymmetry in the carbon concentration between the doped and un-

doped region. However, the width of the satellite peaks remains insensitive to the annealing. Quantitative information of the C diffusion coefficient, D , can be estimated from the reduction of satellite intensity of high order superlattice harmonics [18]. Fig. 5 shows the Arrhenius dependence of D for samples annealed at 700, 755, 800 and 900°C for 16, 16, 8 and 1 h, respectively. The activation energy for C diffusion is 2.8 eV. Also shown is the Be diffusion coefficient with an activation of 2.0 eV obtained from capacitance-voltage measurement of the annealed Be δ -doped GaAs samples.

6. Summary

We have shown that high quality strain modulated GaAs and AlGaAs carbon doping superlattice can be prepared by CBE using TMGa, TEGa and TMAAl. Localization of the carbon impurity has been examined by TEM and X-ray diffraction analysis, which confirms the abruptness of the interfaces on an atomic scale. By comparing the satellite intensities of the as-grown and annealed GaAs/GaAs: C samples, the C diffusion coefficient is found to be almost 2 orders of magnitude lower than that of Be in the temperature range from 700 to 900°C .

References

- [1] R.J. Malik, R.N. Nottenberg, E.F. Schubert, J.F. Walker and R.W. Ryan, *Appl. Phys. Letters* 53 (1989) 2661.
- [2] M. Konagai, T. Yamada, T. Akatsuka, K. Saito, T. Tokumitsu and K. Takahashi, *J. Crystal Growth* 98 (1989) 167.
- [3] C.R. Abernathy, S.J. Pearton, R. Caruso, F. Ren and J. Kovalchik, *Appl. Phys. Letters* 55 (1989) 1750.
- [4] B.T. Cunningham, L.J. Guido, J.E. Baker, J.S. Major, Jr., N. Holonyak, Jr. and G.E. Stillman, *Appl. Phys. Letters* 55 (1989) 687.
- [5] T.F. Kuech, M.A. Tischler, P.J. Wang, G. Scilla, R. Potemski and F. Cardone, *Appl. Phys. Letters* 53 (1988) 1317.
- [6] E. Tokumitsu, T.H. Chiu, H.S. Luftman and N.T. Ha, to be published.
- [7] T.Y. Kuo, T.H. Chiu, J.E. Cunningham, K.W. Goossen, C.G. Fonstad and F. Ren, *Electron. Letters* 26 (1990) 1260.

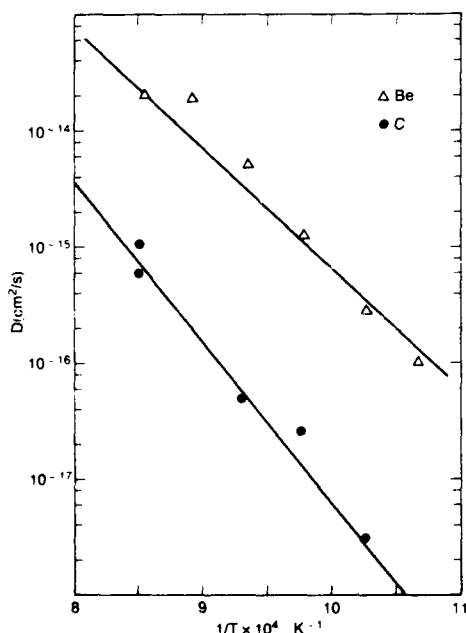


Fig. 5. Arrhenius dependence of the C and Be diffusion coefficients in GaAs.

- [8] T.H. Chiu, J.E. Cunningham, J.A. Ditzenberger and W.Y. Jan, Appl. Phys. Letters 57 (1990) 171, and references therein.
- [9] B.T. Cunningham, M.A. Haase, M.J. McCollum, J.E. Baker and G.E. Stillman, Appl. Phys. Letters 54 (1989) 1905.
- [10] T.J. de Lyon, J.M. Woodall, M.S. Goorsky and P.D. Kirchner, Appl. Phys. Letters 56 (1990) 1040.
- [11] E. Tokumitsu, Y. Kudou, M. Konagai and K. Takahashi, Japan. J. Appl. Phys. 24 (1985) 1189.
- [12] R. Iga, H. Sugiura, T. Yamada and K. Wada, Appl. Phys. Letters 55 (1989) 451.
- [13] C.R. Abernathy, A.S. Jordan, S.J. Pearton, W.S. Hobson, D.A. Bohling and G.T. Muhr, Appl. Phys. Letters, to be published.
- [14] T.H. Chiu, T.Y. Kuo and C.G. Fonstad, IEEE Electron Device Letters, submitted.
- [15] W.L. Gladfelter, D.C. Boyd and K.F. Jensen, Chem. Mater. 1 (1989) 339.
- [16] Y.M. Houng, B.J. Lee, T.S. Low and N.N. Miller, J. Vacuum Sci. Technol. B8 (1990) 355.
- [17] T.H. Chiu and J.A. Ditzenberger, Appl. Phys. Letters 56 (1990) 2219.
- [18] J.E. Cunningham, T.H. Chiu and J.A. Ditzenberger, to be published.

Electrical properties and dopant incorporation mechanisms of Si doped GaAs and (AlGa)As grown on (111)A GaAs surfaces by MBE

Y. Kadoya, A. Sato, H. Kano

Quantum Wave Project, JRDC, Keyaki House 302, 4-3-24, Komaba, Meguro-ku, Tokyo 153, Japan

and

H. Sakaki

University of Tokyo, Roppongi 7-22-1, Minato-ku, Tokyo 106, Japan

and

Quantum Wave Project, JRDC, Keyaki House 302, 4-3-24, Komaba, Meguro-ku, Tokyo 153, Japan

The relation of Si incorporation site and the growth parameters in MBE growth of GaAs and (AlGa)As on (111)A surface is systematically investigated. Both n- and p-type GaAs and (AlGa)As layers with reasonably low compensation are achieved, and the dependencies of Si incorporation on the parameters can be qualitatively understood by the change of the population of As atoms at the surface. Two-dimensional electron and hole gas (2DEG, 2DHG) structures are successfully grown on (111)A substrates.

1. Introduction

The epitaxial growth on patterned substrates is receiving much attention for its importance in the formation of advanced quantum structures such as quantum wires (QWI) and quantum boxes. This will be a key process, especially, for the V-groove-edge QWIs, where QWIs are to be formed by the overgrowth of n- or p-type wide-gap material on V-grooves cut into undoped quantum well structures [1]. The growth of high quality GaAs and (AlGa)As and the control of dopant incorporation on (111)A Ga stabilized surfaces are extremely important since anisotropic and chemical etching suitable for the formation of such V-grooves tends to expose (111)A surfaces. Several works have shown, however, that the MBE growth on (111)A surfaces is quite different from that on (100) surfaces, and that p-type conduction [2,3] and both p- and n-type conduction [4] are obtained on Si doped GaAs and (AlGa)As.

In order to elucidate the mechanisms of growth and impurity incorporation and to control the electrical properties of the layer grown on V-groove surfaces, we report here a systematic study on the MBE growth and characterization of Si doped GaAs and (AlGa)As layers on flat (111)A surfaces. We study, in particular, how the Si incorporation site can be controlled by the growth conditions. We report also the successful formation of both two-dimensional electron and hole gases on (111)A GaAs surfaces by the use of silicon dopants.

2. Experimental procedure

Semi-insulating (CrO-doped) HB grown (100) and (111)A GaAs substrates were used. The substrates were prepared by standard procedure: degreasing, 1 min etch in $8\text{H}_2\text{SO}_4:1\text{H}_2\text{O}_2:1\text{H}_2\text{O}$, rinse in DI water, and drying with N_2 gas. The

(100) and (111)A substrates were then mounted side by side on a Mo holder with In solder. All samples were grown in a conventional MBE system. Arsenic pressures (fluxes) were measured with B-A ion gauge, and substrate temperatures were measured with a thermocouple which was calibrated at the dissociation temperature of native oxide on GaAs. Growth rates were measured using RHEED intensity oscillation.

3. Si doping of GaAs grown on (111)A surfaces

Since the original (111)A GaAs plane consists of rows of Ga atoms with single dangling bond on each site, arsenic atoms are bonded only weakly to the surface and may easily desorb from the growing surface as compared with (100) surface [2]. Hence, it is expected that the surface population of As atoms can be easily controlled by the change of growth conditions. If the amphotericity of Si is influenced by the relative occupancy of As on the surface, the incorporation site of Si may be controlled by growth parameters such as substrate temperature and arsenic fluxes. Indeed, we show here how the Si incorporation site is related to and controlled by the growth conditions.

The structures grown to assess the carrier density and mobility consists of 5000 Å GaAs buffer, 5000 Å Si doped GaAs, and 1000 Å undoped cap GaAs layers. Si flux was adjusted to obtain the

electron densities of $7 \times 10^{17} - 2 \times 10^{18} \text{ cm}^{-3}$ in (100) samples.

Suppose that the total density of Si in GaAs is represented by N_{Si} and that the density of Si incorporated in As (acceptor) site and in Ga (donor) site are respectively denoted as N_{A} and N_{D} ($N_{\text{Si}} = N_{\text{A}} + N_{\text{D}}$). Since the compensation is negligible in the n-GaAs growth on (100) surfaces, N_{Si} can be determined from the electron density measured at 300 K on (100) samples, which are grown simultaneously with the (111)A sample. Since the electron or hole concentration measured on the (111)A sample is equal to $(N_{\text{D}} - N_{\text{A}})$ or $(N_{\text{A}} - N_{\text{D}})$, N_{A} and N_{D} can be separately determined from measured carrier densities and N_{Si} . In order to cancel out the fluctuation of Si flux between each growth, we discuss here the normalized values: the fraction of acceptor-site silicon f_{A} ($f_{\text{A}} = N_{\text{A}}/N_{\text{Si}}$), and the fraction of donor-site silicon f_{D} ($f_{\text{D}} = N_{\text{D}}/N_{\text{Si}}$).

Fig. 1a shows the measured fraction f_{A} of As-site Si as a function of arsenic pressure (P_{As_4}) with the substrate temperature (T_{S}) during growth as a parameter. The growth rate was about $0.6 \mu\text{m/h}$ ($0.54 - 0.63$). One can see that f_{A} varies in a wide range when P_{As_4} and T_{S} are varied. There is a tendency that Si atoms are predominantly incorporated in the acceptor site ($f_{\text{A}} \sim 1$) when P_{As_4} is lowered or T_{S} is raised, whereas they get in the donor site under the opposite condition. At $T_{\text{S}} = 530^\circ\text{C}$, f_{A} depends almost linearly on P_{As_4} , while

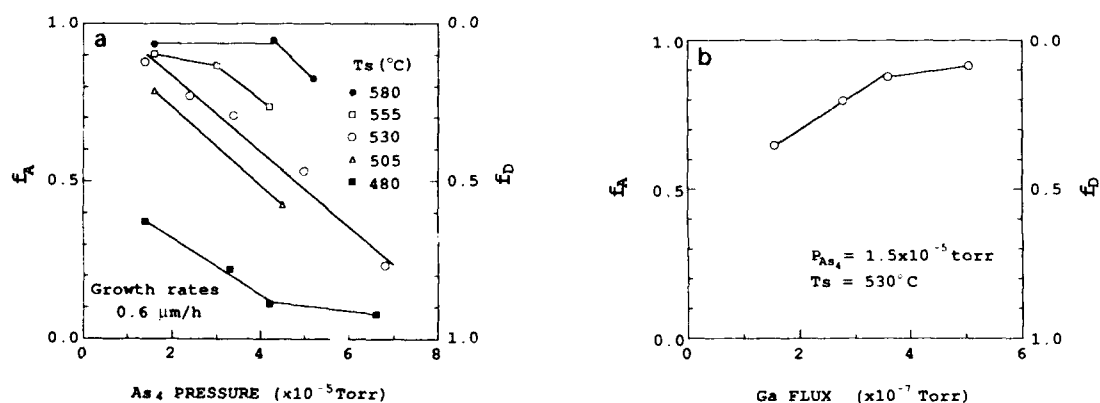


Fig. 1. Fraction of Si atoms in As site (f_{A}) and in Ga site (f_{D}) as a function of growth parameters. (a) Dependencies of f_{A} and f_{D} on arsenic pressure (flux) are shown with substrate temperature as a parameter. Growth rate is $0.6 \mu\text{m/h}$. (b) Dependency of f_{A} and f_{D} on Ga flux. Arsenic pressure is $1.5 \times 10^{-5} \text{ Torr}$ and growth temperature is 530°C .

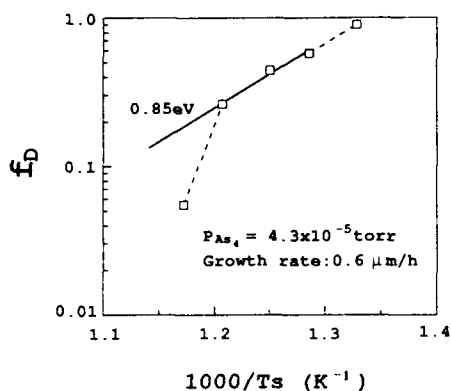


Fig. 2. Replot of the fraction of Si atoms in Ga site (f_D) as a function of inverse substrate temperature $1000/T_s$. Growth rate is $0.6 \mu\text{m/h}$ and arsenic pressure is 4.3×10^{-5} Torr. From the middle three points, an activation energy of 0.85 eV is obtained.

the increment of f_A saturates when P_{As_4} is lowered at higher T_s . At $T_s = 480^\circ\text{C}$, on the other hand, f_A decreases and approaches a saturatory value when P_{As_4} is raised. Fig. 1b shows the relation between f_A and Ga flux at $T_s = 530^\circ\text{C}$ and $P_{\text{As}_4} = 1.5 \times 10^{-5}$ Torr. It is apparent that f_A increases almost linearly with Ga flux except for the point where f_A is very close to unity, indicating that the supply of Ga enhances the Si incorporation in an As site. The replot of f_D for $P_{\text{As}_4} = 4.3 \times 10^{-5}$ Torr as a function of inverse temperature $1000/T_s$ is shown in fig. 2. Since f_D represents the state of the GaAs surface where Si is incorporated in a Ga site, f_D is related to the density of As atoms bonded to surface. Since the two end data points that are close to $f_D = 0.0$ and $f_D = 1.0$ may include larger experimental errors and also may deviate from the simple linear model, we pay greater attention here to the middle three points in fig. 2. They fall on the exponential relationship $\exp(-E_a/kT_s)$ with the activation energy E_a of 0.85 eV . This activation energy term may be related to the desorption process of As atoms during the growth on (111)A surface.

The results shown above clearly point out that the fraction f_A of As-site Si, or the fraction f_D of Ga-site Si, varies in a wide range when arsenic pressure, substrate temperature and Ga flux are changed, and one can control quantitatively the

incorporation site of Si by the choice of these parameters. It should be emphasized that both n- and p-type conduction can be achieved with reasonably low compensation. The observed dependencies of f_A and f_D on these parameters suggest that the change of Si incorporation with these growth parameters can be qualitatively understood by the change of As population at growing (111)A surfaces. To establish the microscopic understanding of Si incorporation beyond this simple picture, detailed analysis of the above results is needed in future.

4. Formation of two-dimensional electron and hole gases

Since the precise determination of f_A or f_D on Si doped (AlGa)As layers from the measured carrier concentration gets quite complex because of the formation of DX centers, we studied how the room temperature carrier densities of Si doped (AlGa)As grown on (111)A surfaces are related to growth temperature. The result is qualitatively similar to that on Si doped GaAs, except that Si seems to be incorporated more to Ga site in (AlGa)As growth than in GaAs growth. It is probably due to the stronger bonding of As to Al atoms.

Choosing the appropriate growth conditions, we successfully formed the two-dimensional electron and hole gas (2DEG, 2DHG) structures on (111)A substrates. The grown structure for 2DHG is $1 \mu\text{m}$ GaAs buffer layer followed by 100 \AA undoped $\text{Al}_{0.3}\text{Ga}_{0.7}\text{As}$ spacer, 1000 \AA Si doped $\text{Al}_{0.3}\text{Ga}_{0.7}\text{As}$, and 100 \AA undoped GaAs cap layers. The 2DEG structure is $1 \mu\text{m}$ buffer GaAs layer followed by 3500 \AA Si-doped $\text{Al}_{0.3}\text{Ga}_{0.7}\text{As}$ and 100 \AA cap GaAs layers, and Si was doped heavily

Table 1
Growth conditions for 2DHG and 2DEG structures

	Growth rate ($\mu\text{m/h}$)	Substrate temperature ($^\circ\text{C}$)	As_4 pressure ($\times 10^{-5}$ Torr)
2DHG	0.6	580	1.0
2DEG	0.2	480	3.0

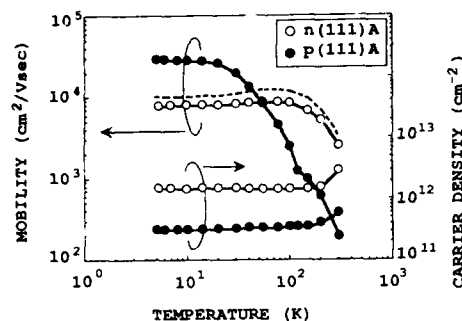


Fig. 3. Temperature dependence of carrier densities and mobilities of 2DEG and 2DHG grown on (111)A substrate. Open circle corresponds to 2DEG and solid circle to 2DHG. Broken line shows the mobility of a (100) sample that is grown simultaneously with (111)A sample of 2DEG structure.

$((2-3) \times 10^{18} \text{ cm}^{-3})$ in the (AlGa)As layer in order to obtain high two-dimensional electron densities. The growth parameters are summarized in table 1. It is worth noting here that we could obtain the 2DEG only at low growth rate ($0.2 \mu\text{m/h}$).

Fig. 3 shows the temperature dependence of carrier densities and mobilities of 2DEG and 2DHG. The 2DHG sample showed a maximum hole mobility of $32000 \text{ cm}^2/\text{V} \cdot \text{s}$ and a hole density of $3.2 \times 10^{11} \text{ cm}^{-2}$ at 4.2 K. On the other hand, a sheet electron density of $1.5 \times 10^{12} \text{ cm}^{-2}$ is obtained on the 2DEG sample grown on the (111)A substrate. This value is almost the same as on the (100) sample which was grown simultaneously with the (111)A sample. In the figure, the mobility of a 2DEG on (100) substrate is also shown (broken line). Although the mobilities of these samples are relatively low, this figure indicates that, in this mobility range, the mobility of two-dimensional electrons on a (111)A sample is comparable with that on a (100) sample, as long as the same structure and the same growth conditions are used. These relatively low mobilities may be caused by (1) heavy doping in AlGaAs layer, (2) the absence of spacer layer, and (3) low growth temperature which enhances the incorporation of residual impurity. To improve these mobilities, optimization of these points is necessary.

5. Conclusion

We have shown in this paper how the incorporation site of Si in the growth of GaAs on (111)A surfaces is related to the growth parameters such as substrate temperature, arsenic pressure, and gallium flux. The fraction of As-site Si or Ga-site Si is found to be controlled in a wide range by the appropriate choice of these growth parameters, and both n- and p-type GaAs and (AlGa)As layer with reasonably low compensation are achieved. Dependencies of Si incorporation on these parameters can be qualitatively understood by the change of the population of As atoms at the surface. Two-dimensional electron and hole gases were successfully formed on (111)A surfaces. The 2DEG on (111)A surface showed comparable mobility with (100) samples and the mobility of 2DHG was as high as $32000 \text{ cm}^2/\text{V} \cdot \text{s}$ at 4.2 K. Hence one can conclude that one of the important problems for the formation of V-groove-edge quantum wire structures and other advanced quantum devices which use the modification of epitaxial surface has been solved. Detailed study on the chemistry of Si incorporation is a subject of future research and its clarification is necessary to improve qualities of the layer grown on (111)A surface.

Acknowledgements

The authors wish to thank Dr. M. Tsuchiya, Mr. T. Noda, and Mr. Y. Nakamura for helpful discussions.

References

- [1] H. Sakaki, Japan. J. Appl. Phys. 19 (1980) 94.
- [2] W.I. Wang, E.E. Mendez, T.S. Kuan and L. Esaki, Appl. Phys. Letters 47 (1985) 826.
- [3] D.L. Miller, Appl. Phys. Letters 47 (1985) 1309.
- [4] D.L. Miller and P.M. Asbeck, J. Crystal Growth 81 (1987) 368.
- [5] M. Shigeta, Y. Okano, H. Seto, K. Katahama, S. Nishine, K. Kobayashi and I. Fujimoto, in: Record of Alloy Semiconductor Physics and Electronics Symp., Japan, 1990, p. 447.

Si doping and MBE growth of GaAs on tilted (111)A substrates

M. Shigeta, Y. Okano, H. Seto, H. Katahama, S. Nishine, K. Kobayashi

ATR Optical and Radio Communications Research Laboratories, Sanpeidani, Inuidani, Seika-cho, Soraku-gun, Kyoto 619-02, Japan

and

I. Fujimoto

Science and Technical Research Laboratories of NHK, Kinuta, Setagaya-ku, Tokyo 157, Japan

Molecular beam epitaxy of GaAs doped with Si on a vicinal surface of (111)A, (211)A and (311)A have been examined. The variations of the impurity concentrations are dependent on the growth conditions and are affected by the angle of the substrates. The impurity concentrations are compared with a model calculation which is based on microscopic surface structures and kinematical surface reactions. Growth modes are monitored by reflection high-energy electron diffraction intensity oscillations. A doping mechanism of Si atoms into GaAs films is proposed.

1. Introduction

Substrate surface microscopic processes during molecular beam epitaxy (MBE) growth are involved in realizing mesoscopic structures. Microscopic surface structures on tilted substrates [1,2] and lateral variations of doping properties on patterned substrates [3] have been reported. The microscopic growth mechanism has received considerable attention for device fabrication as well as for basic physics studies. The nature of the growth modes in MBE, i.e. two-dimensional nucleation and step propagation, has been investigated by reflection high-energy electron diffraction (RHEED) intensity oscillations [4]. On the other hand, as Si is the amphoteric dopant, the incorporation mechanism during MBE growth would be greatly affected by the growth modes. It is well known that the conductivities of GaAs films doped with Si on nonplanar substrates, which have (111)A steps and (100) terraces, are p-type on the step and n-type on the terrace [3]. This result is similar to that of planar substrates [5,6].

Recently, we have studied the conductivities of MBE grown GaAs on tilted (111)A substrates due

to growth conditions [7,8]. In this paper, we investigate the growth and Si doping mechanism of MBE grown GaAs on tilted (111)A substrates including (211)A and (311)A. The ionized impurity concentrations on tilted substrates are compared with the model calculation. The roles of microscopic bond structure on growth modes and doping mechanism are studied by RHEED, and electronic properties are studied by photoluminescence.

2. Experimental

The MBE growth of Si doping into GaAs was conducted as follows. The substrates employed are 1°, 3° and 5° off (111)A toward (100) in addition to (111)A, (211)A and (311)A. The substrate temperatures were varied from 500 to 600°C. The flux intensities of Ga (7.3×10^{-7} Torr) and Si were fixed. The Si source temperature was 1330°C. The flux ratio $\gamma = J_{\text{As}_4}/J_{\text{Ga}}$ was varied from 1 to 7. The growth rate was about 1 $\mu\text{m/h}$ and the film thickness was 1 μm . The conductivity types and ionized impurity concentrations were measured by

the $C-V$ method. Photoluminescence spectra were measured at 11 K using the 514.5 nm line of an argon ion laser.

3. Results and discussion

3.1. Doping and growth modes

The tilted substrates of (111)A have two different types of bonds ((100) and (111)A) which might appear on the step and terrace of the surface. The amphoteric dopant Si dominantly acts as donor on (100) and acceptor on (111)A. The amounts and occupation sites of incorporated Si during MBE growth were treated independently for both surface bonds. We assume that the Si incorporation rates on the terraces having N_T sites are determined by the following rate equations. These are

$$dN_D/dt = JN_T K_3 \theta_2$$

for Si into Ga sites and

$$dN_A/dt = JN_T K_4 \theta_1$$

for Si into As sites, where N_D and N_A are respectively the impurity concentrations of donor and acceptor, J is the Si flux, K_3 and K_4 are respectively the sticking coefficients of Si onto the As and Ga surfaces, and θ_1 and θ_2 are respectively the surface coverages of Ga and As atoms. Similar equations are written for incorporation rates of Si on the steps with N_S sites. The sticking coefficients and coverages are denoted by a prime. Finally, the ionized impurity concentration $N_A - N_D$ is written as

$$N_A - N_D = JN_T (K_4 \theta_1 - K_3 \theta_2) + JN_S (K_4' \theta_1' - K_3' \theta_2').$$

The surface coverages (θ_1 , θ_2) were written using the flux (J_1 , J_2) and sticking coefficients (K_1 , K_2) of Ga and As as

$$\theta_1 = \theta_1' = K_1 J_1 / (K_1 J_1 + K_2 J_2),$$

$$\theta_2 = \theta_2' = K_2 J_2 / (K_1 J_1 + K_2 J_2).$$

For simplicity, desorptions of the atoms are neglected. The ratio of site numbers N_T/N_S is approximated by $N_T/N_S \sim 0.94/\tan \psi$ for a small tilt angle (ψ) of the substrates, and is 2 and 1 for (211) and (311) substrates, respectively.

Fig. 1 shows the conductivity map in the plane of tilt angle ψ and flux ratio γ . We note that the incorporated Si concentration was little influenced by substrate misorientation with secondary ion mass spectroscopy (SIMS) measurements. The dotted line in fig. 1 shows the neutral condition $N_D = N_A$ of the above equation. The values of the fitting parameters are chosen as follows: $K_2/K_1 = 0.5$, $K_3/K_4 = 0.3$, $K_3'/K_4' = 1$ and $K_4' = 0$. The normalized impurity concentration variations with respect to flux ratio are shown in fig. 2. The experimental values are well fitted to the calculated values, except for the 5° of substrate in both figures. In this case, the conductivity tends to be n-type, which resembles the feature of the step bonds (100) on the surface. From the above discrepancy we believe that the growth mode is step propagation rather than two-dimensional nucleation as is the case of 5° off substrate.

The films on the tilted (111)A substrates, observed by a scanning electron microscope (SEM), commonly have a somewhat rough surface morphology with pyramidal facets. But the pyramidal structures fade out with the increase in substrate misorientation. This result suggests the difference

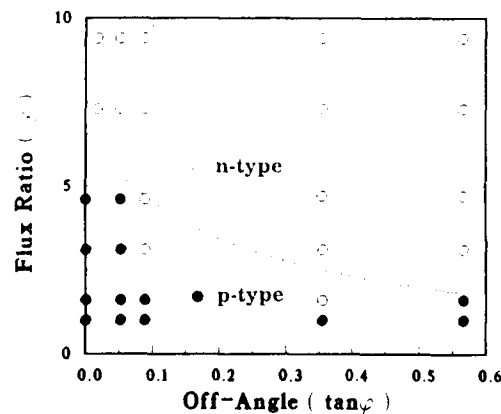


Fig. 1. Conductivity map in plane of tilting angle (ψ) and flux ratio (γ).

in growth behaviour of tilted and exact (111)A substrates.

The growth modes of GaAs on tilted (111)A substrates were investigated by RHEED intensity oscillation. Figs. 3a and 3b show the RHEED patterns of 3° off substrate with incident direction $[0\bar{1}1]$ parallel to the step and $[2\bar{1}\bar{1}]$. As the angular profile of the RHEED pattern in fig. 3a is broader than that of fig. 3b, there is a large fluctuation in the terrace length [9]. The RHEED intensity of tilted (111)A was measured using integral order spots. Calculated from the growth rate measurements of 3° off substrate in fig. 3c, one period of oscillation corresponds to an atomic-layer ($\frac{1}{2}a_0/\sqrt{3} = 1.6 \text{ \AA}$) growth. But no oscillation has been observed 5° off substrate. The growth mode results are coincident with the impurity concentration results.

3.2. Photoluminescence

Fig. 4 shows the results of PL measurements of the samples with $\gamma = 4.8$. The shapes of PL spectra for the compensated (3° off) and non-compensated (5° off and (311)) are shown in fig. 4a. The low-energy edge of the compensated sample falls gradually and resembles the edge of the Gaussian [10] and the high energy edge reflects the fluctuation of local potential. The peak energy in the compensated sample is varied logarithmically

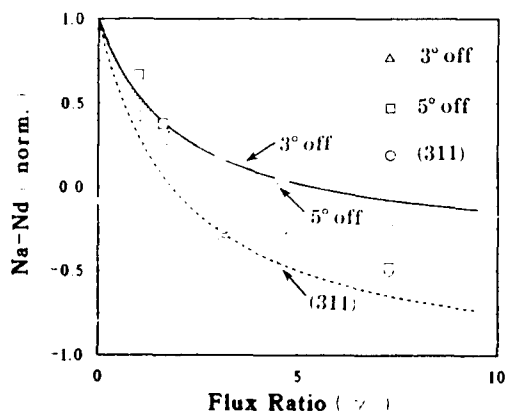


Fig. 2. Impurity concentration as a function of flux ratio (γ) for different substrates; 3° off, 5° off and (311)A.

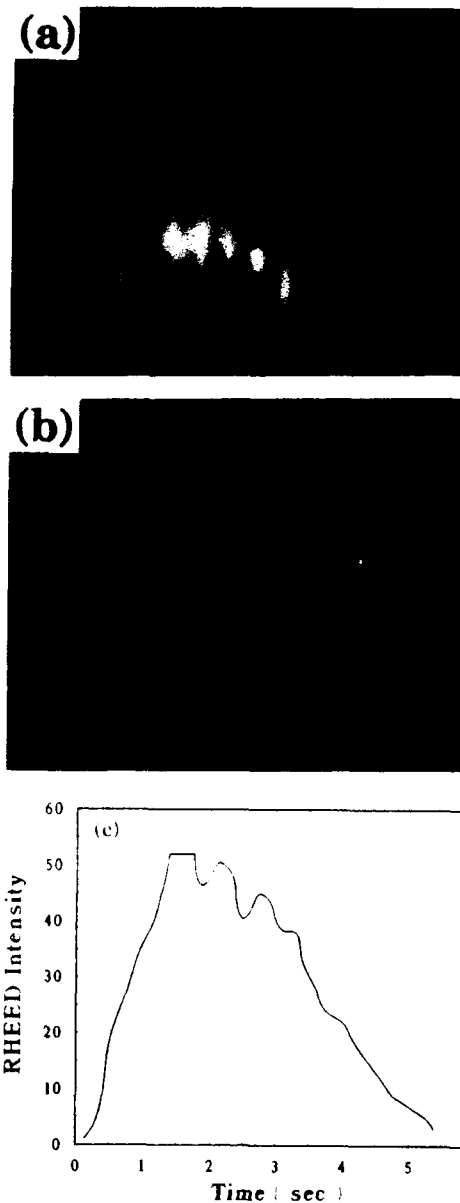


Fig. 3. RHEED patterns along $[0\bar{1}1]$ (a) and $[2\bar{1}\bar{1}]$ (b) azimuthal directions. RHEED intensity oscillation 3° off substrate is shown in (c).

with respect to excitation intensity, as shown in fig. 4b. The shifts are associated with band tails in compensated samples [10]. On the other hand,

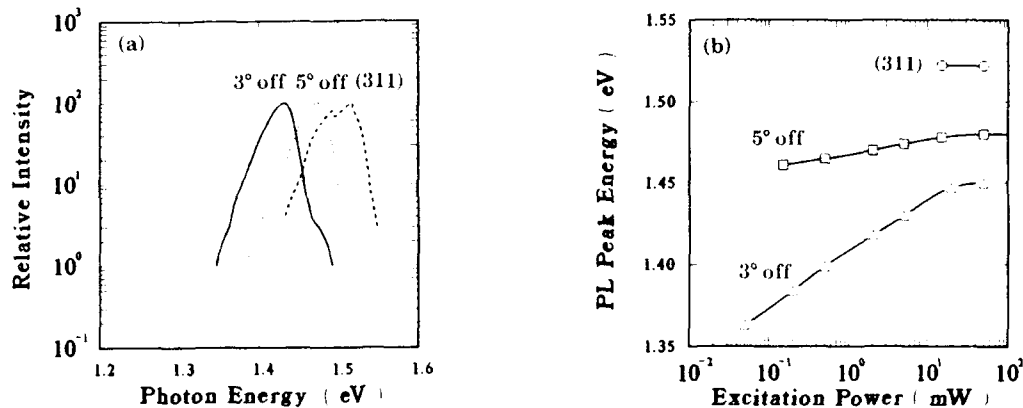


Fig. 4. PL spectra for $\gamma = 4.8$ are shown in (a). Excitation intensity is 5 mW. Excitation intensity dependences of peak energy with different substrates are shown in (b). Substrate orientations are 3° off, 5° off and (311)A.

non-compensated samples have sharp peaks and show no peak shift. PL spectra of the films show a behaviour corresponding to the impurity concentration.

3.3. Discussion

The surface microscopic processes of MBE growth change the doping characteristics of the amphoteric dopant Si. The results indicate that the small misorientation of the substrate alters not only the carrier concentration, but also the conductivity type. The conductivities of the films in MBE growth would be determined by the bond structures of the surface, namely, films with p-type conductivity would be grown on a Ga surface and the n-type on a As surface. As the roles of macroscopic surface orientations and microscopic surface bonds are essentially the same, the carrier concentration will be related to the growth modes on nonplanar substrates.

4. Summary

A model calculation of impurity concentration of Si doped into GaAs films was proposed. The growth modes alter the Si incorporation mechanism into GaAs films. The RHEED oscillation of a 3° tilted (111)A substrate shows the atomic-layer growth. The relationship between growth modes

and doping mechanism are confirmed by RHEED and PL spectra.

Acknowledgement

The authors would like to thank Dr. Y. Furuhama for his encouragement throughout this work.

References

- [1] T. Fukui and H. Saito, *Appl. Phys. Letters* 50 (1987) 824.
- [2] P.M. Petroff, A.C. Gossard and W. Wiegmann, *Appl. Phys. Letters* 45 (1984) 620.
- [3] D.L. Miller, *Appl. Phys. Letters* 47 (1985) 1309.
- [4] T. Sakamoto, N.J. Kawai, T. Nakagawa, K. Ohta and T. Kojima, *Appl. Phys. Letters* 47 (1985) 617.
- [5] W.I. Wang, E.E. Mendez, T.S. Kuan and L. Esaki, *Appl. Phys. Letters* 47 (1985) 826.
- [6] W.I. Wang, R.F. Marks and L. Vina, *J. Appl. Phys.* 59 (1986) 937.
- [7] Y. Okano, H. Seto, M. Shigeta, H. Katahama, S. Nishine, I. Fujimoto and T. Suzuki, in: *Proc. 1989 Fall Meeting of Materials Research Society, Boston, 1989* (Mater. Res. Soc., Pittsburgh PA, 1990).
- [8] Y. Okano, M. Shigeta, H. Seto, H. Katahama, S. Nishine and I. Fujimoto, *Japan. J. Appl. Phys. Letters* 29 (1990) L1357.
- [9] P.R. Pukita, G.S. Petrich, S. Batra and P.I. Cohen, *J. Crystal Growth* 95 (1989) 269.
- [10] M.I. Nathan and T.N. Morgan, in: *Physics of Quantum Electronics*, Eds. P.L. Kelley, B. Lax and P.E. Tannenwald (McGraw-Hill, New York, 1966) p. 478.

Effect of neutron irradiation on transport in heterostructures

Junming Zhou, Weimin Jin, Jianmin Mao and Yi Huang

Institute of Physics, Chinese Academy of Sciences, P.O. Box 603, Beijing 100080, People's Rep. of China

The effects of fast ($E_n = 14$ MeV) and thermal ($E_n = 0.025$ eV) neutron irradiation on quantum transport in modulation-doped heterostructures and double barrier resonant tunneling diodes have been investigated. In the case of modulation doped heterostructures, both concentration and mobility of the 2DEG at 4.2 K decreased in the dark after fast neutron irradiation. The Hall plateau broadened and the SdH oscillation was clearly enhanced under high magnetic fields. The increase of the concentration and mobility of 2DEG, Hall plateau broadening and SdH oscillation enhancing as well as parallel conductance were observed at 4.2 K in samples irradiated by thermal neutrons. All the changes disappeared gradually with time. In double barrier resonant tunneling structures irradiated by fast neutrons, the peak current position V_p , valley current I_p and peak-to-valley ratio (PTVR) decreased.

1. Introduction

Many experiments on the effect of neutron irradiation in GaAs bulk materials have been performed [1–4]. Classification of the defects produced and their energy spectrum of the irradiated materials were the main subject of interest. Experiments have revealed that the anion antisite $\text{As}_{\text{Ga}}^{1-}$ configuration and complexes of $\text{As}_{\text{Ga}}-\text{V}_{\text{Ga}}$ exist in semi-insulating GaAs irradiated by fast neutrons. Fast neutron irradiation of n-GaAs mainly induces two deep electron traps in the band gap. The first is referred to as EL6 with an energy level at $E_c + 0.6$ eV. The second has a wide energy distribution around $E_c - 0.5$ eV and is referred to as the U band.

As is well known, in quantum Hall effects localized states play an important role in interpreting the existence of Hall plateaus. Fast neutron irradiation can introduce artificial defects to the heterostructure. Hence the effect of localized state on Hall plateaus can be investigated in 2DEG samples irradiated by fast neutron. In addition, in the GaAs channel of 2DEG, the background impurity concentration may be in a range of low 10^{14} to high 10^{14} cm^{-3} , and electrons with high concentration (the high 10^{17} cm^{-3}) in the 2D channel screen the background ionized impurities. Therefore, the screening effect results in much higher

mobilities than lightly doped bulk GaAs at low temperatures. We reasoned that the electrons in the channel would screen the defects induced by the neutron irradiation as well, so that devices made from modulation doped heterostructure would stand against irradiation more strongly.

In the first experiments of fast neutron irradiation [5,6], we observed several phenomena which could not be explained solely by the defects introduced by fast neutron irradiation. We attributed this to the effect of mixed beam irradiation where the fast neutrons dominated, but the thermal neutron effect could not be ignored. In this paper, the effects of fast and thermal neutron irradiation on transport in heterostructures will be reported.

2. Sample preparation and neutron irradiation

The modulation doped heterojunctions and resonant tunneling diodes used for neutron irradiation experiments were prepared in a home made MBE system in our group.

The samples for QHE studies were grown at a substrate temperature of 600°C and a growth rate of $1 \mu\text{m/h}$ for GaAs layers, and $0.6 \mu\text{m/h}$ for AlGaAs layers. A $1 \mu\text{m}$ thick undoped GaAs buffer layer, followed by a 200 \AA undoped $\text{Al}_{0.3}\text{Ga}_{0.7}\text{As}$ space layer, and a 400 \AA thick Si-

doped $\text{Al}_x\text{Ga}_{1-x}\text{As}$ layer and 150 Å GaAs cap layer were grown on a (100) oriented Si GaAs substrate. Standard Hall bridges were fabricated by lithography and indium balls were used for ohmic contact.

The double-barrier structures used here consist of a buffer layer, an AlAs–GaAs–AlAs double barrier and a cap layer. The thickness of symmetric barriers is 25 Å and the GaAs well width is 70 Å. The spacer layers are undoped GaAs layers of 15 Å. Circular mesas were prepared by wet etching with diameters ranging from 30 to 80 μm. AuGe/Ni was deposited and alloyed as Ohmic contact.

Two sources of fast neutrons were used. One source used for low dose irradiations was from the reaction $\text{T} + \text{d} \rightarrow \alpha + \text{n} + \text{Q}$, with the outgoing neutrons of about 14 MeV energy and unit flux of $1.2 \times 10^9 \text{ n/cm}^2 \cdot \text{s}$. Another source for higher dose irradiation experiments was from the ^{235}U nuclear fusion reaction with neutrons of energies ranging from 1 to 20 MeV and a flux of $1.2 \times 10^{11} \text{ n/cm}^2 \cdot \text{s}$. The high thermal neutron flux was reduced by lining the watertight container with a layer of cadmium.

The nuclear splitting reaction of heavy-nucleus actinium in a light-water moderated nuclear reactor was used as a source of thermal neutrons. Apart from a small number of high-energy neutrons, the majority of neutrons from the thermal neutron pile had an energy of about 0.025 eV with unit flux of $1.0 \times 10^{11} \text{ n/cm}^2 \cdot \text{s}$.

3. Modulation doped heterostructures under neutron irradiation

3.1. Effect of fast neutron irradiation [7]

Six Hall bridges were used in these experiments and neutron irradiation was performed with the fast neutron source of lower flux intensity. After 5 h of irradiation, the total neutron flux was $\phi = 2.1 \times 10^{13} \text{ n/cm}^2$. By monitoring the irradiation process, it was found that the longitudinal resistance of the samples at room temperature increased gradually, which gives evidence that defects have been induced in the samples. In Si– $\text{Al}_x\text{Ga}_{1-x}\text{As}$ /

Table 1

The concentration n_{2D} and mobility μ_{2D} of 2DEG before and after fast-neutron irradiation of $2.1 \times 10^{13} \text{ n/cm}^2$, which were measured in the dark and with light, respectively, and at 4.2 K

	$n_{2D} (10^{11} \text{ cm}^{-2})$	$\mu_{2D} (10^4 \text{ cm}^2/\text{V} \cdot \text{s})$
Before irradiation		
Dark	2.74	15.8
Light	5.18	25.7
After irradiation		
Dark	2.65	10.5
Light	5.32	19.0

GaAs modulation-doped heterostructures, the constituent elements have nuclei with intermediate masses in the range from 25 to 80. When the samples are bombarded with fast neutrons of about 14 MeV, elastic scattering (n, n) processes are dominant. As a result, a large number of defects, such as $\text{As}_{\text{Ga}}^{4+}$, $\text{V}_{\text{Ga}}^{2-}$ and $\text{As}_{\text{Ga}}\text{--V}_{\text{Ga}}$ occur. Since it is difficult for a fast, high energy neutron to be captured by a nucleus, the probability of nucleus capture (n, γ) is so small that the irradiated samples are free from β decay and γ radiation. Therefore, the characteristics of the transport in such an irradiated sample will be time independent, contrary to the situation in the thermal neutron irradiated samples.

3.1.1. Mobility reduction of 2DEG

Table 1 shows the changes of carrier concentration and mobility from a typical sample before and after fast neutron irradiation. Although the carrier concentration decreased in the dark after irradiation, the change was very small. This implies that the resulting electron traps were few in number compared with the electron concentration in the 2DEG channel after a dose of 10^{13} cm^{-2} neutron irradiation. In the fast neutron irradiation experiments on GaAs bulk materials, the defect introduction rate has been determined to be $20\text{--}30 \text{ cm}^{-1}$. Therefore, in our Si doped $\text{Al}_x\text{Ga}_{1-x}\text{As}$ layer and 2DEG channel region with a total thickness of 700 Å, the defect concentration was estimated to be around $3 \times 10^9 \text{ cm}^{-2}$, which could not cause a large change in the channel electron concentration through trapping in the samples used for the experiments.

As is well known, at low temperatures the most important scattering mechanism is Coulomb scattering. As a rough estimate, it may be assumed that there is strong Coulombic scattering between ionized defects and 2D electrons only in regions of 200 Å on both sides of 100 Å wide 2DEG channel. For neutron irradiation of $2 \times 10^{13} \text{ cm}^{-2}$, the induced defects in the 500 Å thick layer are about $3 \times 10^9 \text{ cm}^{-2}$, which is comparable with the amount of residual impurities in the channel. Therefore, the effect of neutron irradiation on carrier scattering by induced defects is much stronger than that on carrier trapping by those defects.

3.1.2. Hall plateau broadening and SdH oscillation enhancement

Quantization of the Hall resistance of the 2DEG was observed by von Klitzing et al. in 1980 [8]. The Hall plateaus appear when the Fermi level resides in the Landau localized states. In the case of fast-neutron irradiation, the elastic and inelastic scattering give rise to geometric distortion of the lattice in our samples. As the scatterer concentration increases, the localized states of the 2DEG also increase. As a result, the energy band of the Landau extended state is compressed, while the impurity band of the Landau localized state is expanded under strong magnetic fields. Naturally, we can see the Hall plateaus are broadened just as shown in fig. 1.

The peak value of the SdH oscillation is observed when the Fermi level lies in the Landau

extended states which are associated with short-range scattering. In the case of high concentration of scatterer, the conductivity has a maximum $(N + 1/2)e^2/\pi^2 h$. In the case of low concentration of scatterer, the conductivity has a maximum $2\pi e^2 N_i (N + 1/2)e^2 h$ (N_i stands for scatterer concentration, N for Landau level index). In our samples the undoped spacer is about 200 Å thick and electrons at the heterojunction are influenced by the weak scatterer potential, so the maximum conductivity would increase with scatterer concentration. After calculation and approximation, the peak value of the SdH oscillation of the N th Landau level is given by

$$(R_{xx})_{\max} = N_i \frac{2\alpha(N + 1/2)B}{\pi en^2}, \quad (1)$$

which is enhanced with increasing scatterer concentration N_i , as shown in fig. 1.

3.2. The effect of thermal neutron irradiation [9]

Six Al_xGa_{1-x}As/GaAs modulation doped heterojunction samples, divided into three groups, have been irradiated by thermal neutrons for 2 min, 20 min and 1 h, with a total flux of 1.2×10^{13} , 1.2×10^{14} and $3.6 \times 10^{14} \text{ n/cm}^2$, respectively. When such samples are bombarded by thermal neutrons of about 0.025 eV, nuclear capture (n, γ) should be the dominant process. After capturing a neutron, the neutron-proton ratio of a nucleus rises, followed by β^- decay and γ radiation which decrease gradually. Therefore, the behaviour of the 2DEG depends strongly on the time elapsed after thermal neutron irradiation.

3.2.1. Time dependent effect

The time dependence of the concentration and mobility of 2DEG for a sample irradiated by a $1.2 \times 10^{14} \text{ cm}^{-2}$ of thermal neutron is shown in table 2. The measurements were performed under low magnetic field at 4.2 K. Fig. 2 shows that the Hall plateau broadening and the SdH oscillation enhancement under strong magnetic field at 4.2 K are time dependent also.

The time dependent effect may be explained as follows. The irradiated samples are dominated by continuous, extremely strong β^- decay and γ

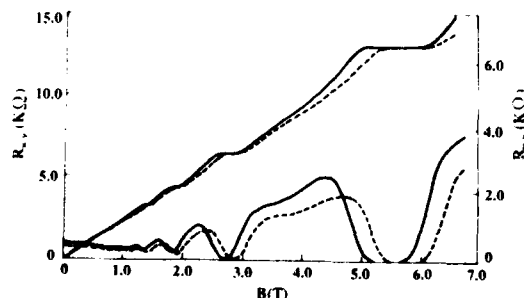


Fig. 1. Hall resistance R_H and diagonal resistance R_{xx} as a function of magnetic field B before (dashed lines) and after (solid lines) fast-neutron irradiation.

Table 2
Changes in n_{2D} and μ_{2D} at 4.2 K with time after thermal-neutron irradiation of 1.2×10^{14} n/cm²

	n_{2D} (10^{11} cm ⁻²)	μ_{2D} (10^4 cm ² /V·s)
Before irradiation	2.80	10.5
30 h later	3.54	11.8
65 h later	3.41	11.4
2 months later	2.67	9.3

radiation, which are followed by a series of secondary processes. The nucleus after β^- decay may capture a shell electron to give off X-rays or Auger electrons. Meanwhile, the internal conversion process may occur accompanied by γ radiation, i.e., the interaction between the electromagnetic field of the nucleus and shell electrons gives rise to a transition whereby excited energy is transferred to shell electrons to release internal shell electrons. Moreover, other processes relating to the energy band structure of semiconductors may occur with these radioactive rays. The first is the excitation of electrons of the DX center in the doped $Al_{1-x}Ga_xAs$ layer and the second is the transition of electrons from the valence band to the conduction band generating electron-hole pairs. The electrons produced by these processes make direct contributions to the 2DEG in the case of irradiation doses lower than 1.2×10^{14} cm⁻².

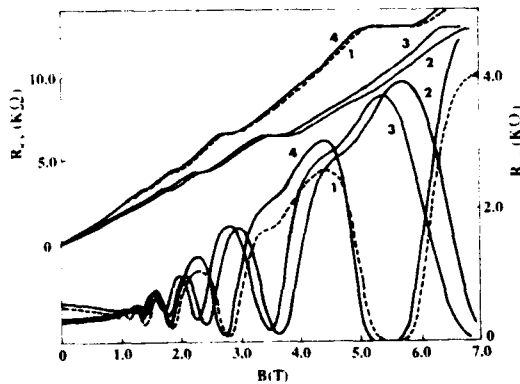


Fig. 2. Hall resistance R_H , and the diagonal resistance R_{xx} , drawn as a function of magnetic field B . Dashed line 1 is the original one before thermal-neutron irradiation. Solid lines 2, 3 and 4 were measured 30 h, 65 h and 2 months later, after the irradiation, respectively.

As a result, the concentration of the 2DEG in the heterointerface increases, as also the mobility enhances owing to the increase in Fermi wavevector with electron concentration. This is similar to the illumination effect of the optical flux.

The decrease of 2DEG concentration can be described as an exponential decay with time:

$$\Delta n(t) = n_0 \exp(-t/\tau). \quad (2)$$

One should notice that part of the carriers described by $n_0 - n(\infty)$ is captured by defects caused by higher-energy pile neutrons. Letting $\Delta n(t) = n(t) - n(\infty)$ and $\Delta n_0 = n(0) - n(\infty)$, and using the data in table 2, we obtain $\Delta n_0 \approx 1.0 \times 10^{11}$ cm⁻² and $\tau \approx 216$ h.

The radiation field immediately after thermal neutron irradiation is extremely strong and thermal neutron irradiation does have a contribution to the Landau localized states, leading to some slightly broadening of Hall plateaus according to our observation. But it is difficult to verify this, unless we make more accurate measurements. Because of the small probability of elastic and inelastic scattering between thermal neutrons and atoms in the sample, after irradiation, the Hall plateaus turn out to be broadened, but less than one created by fast neutron irradiation. This was also confirmed by a small reduction in mobility measured two months later, as shown in table 2.

For both fast- and thermal-neutron irradiation we have observed that the peak values of the SdH oscillations are intensified in the limit of short-range scattering, but the reasons in the two cases are quite different. In the former case, the increase of scatterer concentration is responsible. In the latter case, however, the strong radiation field produced by nuclear reaction is the cause. Under such a radiation field, the interaction between the strong β^- (or γ) rays and the 2DEG has basically the nature of short range scattering, leading to a large increase of the peak value of the longitudinal conductivity corresponding to the extended state of the N th Landau level.

With the elapse of time, β^- decay and γ radiation decrease, the changes related to the radiation field also decrease gradually, as shown in table 2 and fig. 2.

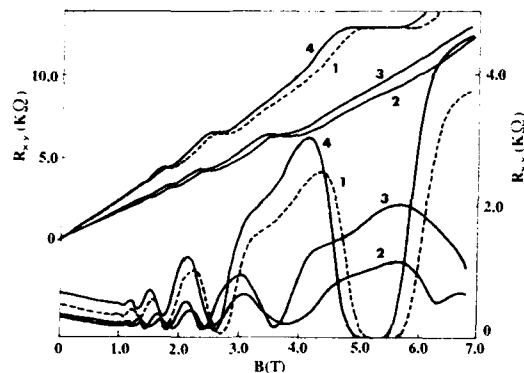


Fig. 3. Hall resistance R_H and diagonal resistance R_{xx} drawn as a function of magnetic field B with time as a parameter: line 1, before thermal neutron irradiation; line 2, 24 h later; line 3, 70 h later; line 4, 2 weeks later, after thermal neutron irradiation with a dose of $3.6 \times 10^{14} \text{ cm}^{-2}$. The parallel conduction appears in lines 2 and 3, and disappears in line 4.

3.2.2. Parallel Conductance

To investigate the persistent photoconductivity (PPC) in modulation doped heterojunctions the usual experiments are always performed by illuminating samples with monochromatic light or white light. By contrast, in the samples irradiated by thermal neutrons, parallel conductance can sometimes be observed without illumination from outside. When the samples were irradiated by thermal neutrons with a total flux of $1.2 \times 10^{14} \text{ cm}^{-2}$, the 2DEG concentration increased and no parallel conductance occurred, as shown in fig. 2 and table 2.

When the total flux of thermal neutrons was increased up to $3.6 \times 10^{14} \text{ cm}^{-2}$, the parallel conduction effect was observed 24 h and 70 h later, after the irradiation, and then disappeared two weeks later, as shown in fig. 3. The relative concentrations and mobilities are listed in table 3. As described above, a number of electrons are pro-

duced by the radiation field through various excitation processes. Usually the electrons produced may make direct contributions to the 2DEG in the case of low radiation field. However, in the case of higher radiation field, the full width of the depletion layers becomes less than that of the doped and undoped AlGaAs layers, and a parallel conduction channel appears in the AlGaAs layer. With the elapse of time, the nuclear radiation decreases and the excited electrons decrease too. The parallel conduction effect tends to decrease and after two weeks disappears completely. After the radiation disappears, the characteristics of the quantum transport of the 2DEG are completely determined by the degree of damage and the defects in the samples. Then it becomes impossible to find the parallel conductance without illumination.

4. Effect of neutron irradiation on resonant tunneling [10]

The samples were divided into 5 groups, each one consisting of two double barrier diodes. Two of the groups were irradiated by 14 MeV neutrons with doses of 1×10^{12} and $1 \times 10^{13} \text{ cm}^{-2}$, respectively. The other three groups were irradiated by the ^{235}U nuclear reactor for 14 min, 2.3 h and 23.12 h with doses of 1×10^{14} , 1×10^{15} and $1 \times 10^{16} \text{ cm}^{-2}$, respectively. The fast neutron reaction with the atoms in the samples is dominated by the primary knock-on (PKO) process resulting in a large amount of atom displacement. The defects could form clusters due to possible nuclear cascades. Measuring the I - V curve after fast neutron irradiation, we found there was no change for low dose irradiation such as 1×10^{12} and $1 \times 10^{13} \text{ cm}^{-2}$. However, there were changes for high doses – the higher the dose, the larger the changes. Fig. 4 shows the current-voltage characteristics for a DBD sample irradiated by fast neutron dosage of $1 \times 10^{16} \text{ cm}^{-2}$. Samples irradiated by ^{235}U nuclear reactor neutrons were measured one month later to avoid the radiation effect. For all samples after irradiation with doses above $1 \times 10^{14} \text{ cm}^{-2}$, the peak positions of current V_p and valley current V_v shifted to a higher voltage while the peak current

Table 3
Changes in n_{2D} and μ_{2D} at 4.2 K with time after thermal-neutron irradiation of $3.6 \times 10^{14} \text{ n/cm}^2$

	$n_{2D} (10^{11} \text{ cm}^{-2})$	$\mu_{2D} (10^4 \text{ cm}^2/\text{V}\cdot\text{s})$
Before irradiation	2.65	10.5
30 h later	3.65	13.9
65 h later	3.50	13.4
2 months later	2.47	8.80

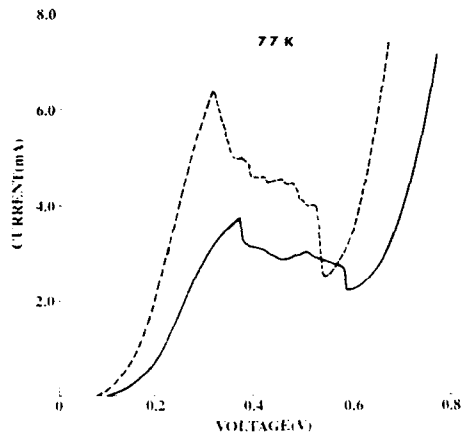


Fig. 4. Static current-voltage characteristics of resonant tunneling diode before irradiation (solid line) and after fast neutron irradiation with a dose of $1 \times 10^{16} \text{ n/cm}^2$ (dashed line).

I_p and PTVR decreased. The valley current I_v had a small increase for doses of 1×10^{14} and $1 \times 10^{15} \text{ cm}^{-2}$, but decreased for a dose of $1 \times 10^{16} \text{ cm}^{-2}$. The change of I_p was larger than that of I_v for all doses. There was a decrease of current for all samples beyond the negative differential resistance region and an increase of resistance of the samples.

Fast neutron irradiation produces ionized impurities also in the emitter and the collector regions, resulting in an increase of resistance. This is similar to connecting a series resistance in the I - V measuring system. However, an increase of the resistance in the collector cannot cause such a change. This was demonstrated from the results of the experiment on an unirradiated double barrier diode connected with a series resistance of 11Ω , in which the same shift of V_p as that in fig. 4 occurred, but little change was observed in I_p and I_v .

As_{Ga} defects in a quantum well create an attractive Coulomb potential for electrons such that the bound energy level is lowered, whereas V_{Ga} and $\text{As}_{\text{Ga}}\text{-V}_{\text{Ga}}$ type defects in the well have a repulsive Coulomb potential for electrons, resulting in the raising of the energy level. Since fast neutron irradiation produces a nearly equal number of As_{Ga} and V_{Ga} types, the repulsive potential

is stronger than the attractive potential, causing a net increase in the energy level in the well. The ionized impurities produced by neutron irradiation in ALAs barriers raise the effective tunneling barrier, so that the energy level is raised further, albeit by a small amount. These two facts lead to a shift of V_p and V_v to higher voltages in the experimental I - V curve. Calculation [11] shows that impurities in the well would reduce PTVR in a resonant tunneling diode. Thus, the experimentally observed reduction of PTVR may be attributed to elastic scattering from impurities, lattice defects, etc., produced by fast neutron irradiation. Fig. 4 shows that the full width at half maximum of the current (FWHM) on the low bias side broadened from 85 to 110 mV, which implies the 12.5 meV broadening of the bound energy level. This broadening of the I - V curve can be attributed to impurity scattering itself and not to fluctuations of impurities, because fast neutron irradiation causes a homogeneous doping in the well. The tunneling current is determined by the tunneling probability and the net distribution of incoming particles. The decrease of the Fermi energy in the emitter reduces this distribution, and the decrease of the total relaxation time reduces the tunneling probability. Hence, I_p , PTVR and the tunneling current beyond the negative differential resistance region are reduced by fast neutron irradiation. I_v depends on many factors: the increase of impurities will increase impurity assisted tunneling so that I_v will increase; the decrease of electron density in the accumulation region and V_{Ga} and As_{Ga} acting as traps for electrons will reduce I_v . The change of I_v is determined by all these factors.

5. Conclusion

We have studied the characteristics of quantum transport in heterostructures irradiated by fast and thermal neutrons. The defects caused by the fast neutron irradiation are the origin of all phenomena observed both in modulation doped heterostructures and resonant tunneling diodes. Because there is no Coulomb scattering between a neutron and a charged particle, a neutron can

penetrate a sample more easily than charged particles. Fast neutron irradiation is therefore a useful method to study the role of defects in quantum transport phenomena.

In the thermal neutron irradiation experiments, nuclear radiation is the origin of all these time-dependent effects. The persistent conductivity due to the radiation field produced results in time dependent increases of electron mobility and electron density only at low temperature. No measurable changes in the resonant tunneling diodes irradiated by thermal neutrons have been observed.

Acknowledgements

We would like to thank Professor H.Z. Zheng and Professor W.Y. Lai for helpful discussions. This work is mostly supported by the national science fund.

References

- [1] A. Goltzene, C. Schwab, J.P. David and A. Roizes, *Appl. Phys. Letters* 49 (1986) 862.
- [2] G.M. Martin, E. Esteve, P. Langlade and S. Makram-Ebeid, *J. Appl. Phys.* 56 (1984) 2655.
- [3] R. Worner, U. Kaufman and J. Schneider, *Appl. Phys. Letters* 40 (1981) 141.
- [4] M. Satoh, K. Kuriyama, M. Yahagi, K. Lwamura, C. Kim, T. Kawakubo, K. Yoneda and L. Kimura, *Appl. Phys. Letters* 50 (1987) 580.
- [5] Wu Yongsheng, Huang Yi, Zhou Junming and Meng Xiangli, *Chinese Phys. Letters* 4 (1987) 373.
- [6] Y.S. Wu, Y. Huang, Y.K. Li, Z.X. Yang and J.M. Zhou, *J. Appl. Phys.* 63 (1988) 2154.
- [7] W.M. Jin, Z.M. Zhou, Y. Huang and L.H. Cai, *Phys. Rev. B* 38 (1988) 13086.
- [8] K. von Klitzing, G. Dorda and M. Pepper, *Phys. Rev. Letters* 45 (1980) 494.
- [9] W.M. Jin, J.M. Zhou, Y. Huang and L.H. Cai, *Phys. Rev. B* 38 (1988) 13090.
- [10] J.M. Mao, J.M. Zhou, R.L. Zhang, W.M. Jin, C.L. Bao and Y. Huang, *Appl. Phys. Letters* 56 (1990) 548.
- [11] B.Y. Gu, C. Coluzza, M. Mangiantini and A. Frova, *Superstructures and Microstructures* 7 (1990) 29.

Modulation doped inverted and normal GaAs/ $\text{Al}_x\text{Ga}_{1-x}\text{As}$ heterostructures: influence of Si-segregation on the two-dimensional electron gas

K. Köhler, P. Ganzer, M. Maier and K.H. Bachem

Fraunhofer-Institut für Angewandte Festkörperphysik, Tullastrasse 72, W-7800 Freiburg, Germany

Modulation doped GaAs/ $\text{Al}_x\text{Ga}_{1-x}\text{As}$ heterostructures have been grown by molecular beam epitaxy in the temperature range of 350–850°C. Special emphasis is laid on the two different types of heterostructures: doped $\text{Al}_x\text{Ga}_{1-x}\text{As}$ on top of undoped GaAs (normal heterostructure) and undoped GaAs on top of doped $\text{Al}_x\text{Ga}_{1-x}\text{As}$ (inverted heterostructure). The electrical properties, determined by Hall effect measurements at 77 and 300 K, were investigated as a function of growth temperature. At 77 K the normal heterostructures exhibit a maximum mobility of 120,000 $\text{cm}^2/\text{V}\cdot\text{s}$ at a substrate temperature of 750°C. In contrast, the maximum mobility of 45,000 $\text{cm}^2/\text{V}\cdot\text{s}$ for inverted heterostructures is found at a substrate temperature of 500°C, whereas at a temperature of 750°C a drastic reduction of mobility of 3500 $\text{cm}^2/\text{V}\cdot\text{s}$ is observed which is attributed to the segregation of Si atoms into the channel. SIMS depth profiles indeed show Si segregation in the spacer layer at a growth temperature of 700°C. Based upon these results we have grown inverted heterostructures at 750°C with suppressed Si segregation by growing the doped $\text{Al}_x\text{Ga}_{1-x}\text{As}$ layer at 500°C.

1. Introduction

Modulation doped GaAs/ $\text{Al}_x\text{Ga}_{1-x}\text{As}$ heterostructures exhibit two-dimensional electron gases (2DEG) with enhanced electron mobilities. The normal heterostructure, used for high electron mobility transistors (HEMTs), is achieved by the growth of the doped higher band gap $\text{Al}_x\text{Ga}_{1-x}\text{As}$ on top of the undoped lower band gap GaAs. By adding an undoped $\text{Al}_x\text{Ga}_{1-x}\text{As}$ spacer layer with a thickness greater than 20 nm, low temperature mobilities ($T = 4$ K) larger than $1 \times 10^6 \text{ cm}^2/\text{V}\cdot\text{s}$ measured in the dark have been reported, where the electron concentration is reduced to below $3 \times 10^{11} \text{ cm}^{-2}$ [1–4]. HEMT structures suitable for microelectronic application, which need maximum conductivity at room temperature, have smaller spacer layers and therefore higher electron concentration and low temperature mobilities of $(1-3) \times 10^5 \text{ cm}^2/\text{V}\cdot\text{s}$ [1].

In comparison with the normal heterostructure, remarkably little is known about the inverted heterostructure where the undoped GaAs is grown on top of the doped $\text{Al}_x\text{Ga}_{1-x}\text{As}$. This structure is

the basis of the inverted HEMT (I-HEMT). There are some technological advantages of the I-HEMT structure, such as easy formation of ohmic contacts to the 2DEG channel and simplified gate recessing schemes [5]. Attempts to realize I-HEMT structures have been reported [6–9]. The problems which have to be solved are attributed to the higher degree of interface disorder and accumulation of impurities at the inverted interface [6,7] as well as to the segregation or outdiffusion of the Si-dopant across the inverted interface into the 2DEG channel [8,9]. I-HEMT structures with highest mobilities (130,000 $\text{cm}^2/\text{V}\cdot\text{s}$ at $T = 77$ K and 460,000 $\text{cm}^2/\text{V}\cdot\text{s}$ at $T = 4.2$ K) were grown by Shtrikman et al. [10] by using growth interruption and low growth temperature together with reduced growth rates during growth of the doped $\text{Al}_x\text{Ga}_{1-x}\text{As}$ layer.

One of the reasons for the inferior properties of the I-HEMT structures, segregation of the Si-dopant, has been reported by several authors. Segregation is found in doped GaAs and $\text{Al}_x\text{Ga}_{1-x}\text{As}$ -films [11,12], selectively doped heterostructures [12,13], and quantum wells [14], as

well as in Si planar doped GaAs with doping concentrations $> 10^{19} \text{ cm}^{-3}$ [15]. In contrast, Gonzales et al. [16] found concentration dependant diffusion but no preferential migration towards or away from growth direction.

In this paper, we report on the growth and comparison of HEMT and I-HEMT structures for electrical devices with respect to electrical properties for different growth temperatures. The influence of segregation on the quality of I-HEMT structures will be discussed. Special emphasis is laid on identical growth conditions for both structures. Finally, we will show that we can achieve high quality I-HEMT structures mainly by suppressing Si-segregation.

2. Preparation and growth

The GaAs/Al_{0.3}Ga_{0.7}As layers were grown by molecular beam epitaxy (MBE) in a Varian Gen II with substrate holders for indium free mounting. The (100) GaAs substrates used for epitaxy were semiinsulating LEC grown 2-inch wafers. Substrates are prepared before growth on an especially designed spinner. The sequence of cleaning and etching steps as well as the supply of etchant and de-ionized water are automatically controlled. Etching is carried out in a solution of NH₄OH, H₂O₂ and H₂O (5:1:5). The growth temperatures for the samples are chosen between $T_c = 350^\circ\text{C}$ and 850°C measured by thermocouples [17]. The growth rate for GaAs, determined by reflection high energy electron diffraction (RHEED) intensity oscillations, is $1.25 \mu\text{m/h}$ over the whole temperature range.

A schematic description of the layer configuration is shown on the right side of fig. 1 (HEMT structure) and fig. 2 (I-HEMT structure). The respective conduction band diagram is on the left side of the figures. First an undoped 300 nm GaAs buffer layer is grown for both structures, followed by a GaAs/Al_{0.3}Ga_{0.7}As superlattice to improve the layer quality in the region of the 2DEG [18]. The layer sequence of the HEMT structure (fig. 1) grown on top of the buffer continues with a 600 nm thick undoped GaAs layer. Then an Al_{0.3}Ga_{0.7}As layer follows, consisting of a 5 nm un-

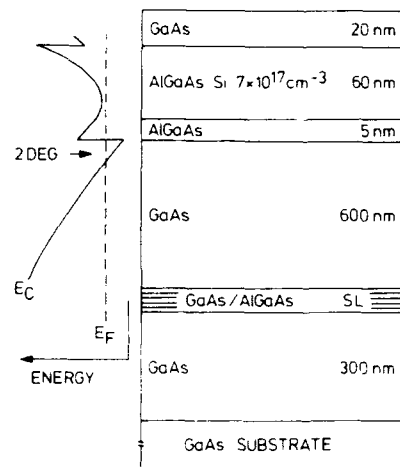


Fig. 1. Cross sectional view of the GaAs/Al_{0.3}Ga_{0.7}As HEMT structure with a normal interface. A schematic of the conduction band diagram is shown on the left side of the figure.

doped spacer and a 60 nm electron supply layer doped with $7 \times 10^{17} \text{ cm}^{-3}$ Si atoms. The structure is capped by an undoped 20 nm GaAs layer. The layer sequence of the I-HEMT structure (fig. 2) continues from its superlattice with an Al_{0.3}Ga_{0.7}As layer consisting of a 200 nm first spacer followed by a 40 nm electron supply layer doped

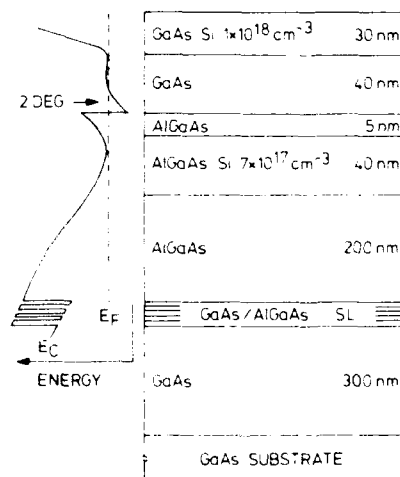


Fig. 2. Cross sectional view of the GaAs/Al_{0.3}Ga_{0.7}As I-HEMT structure with an inverted interface. A schematic of the conduction band diagram is shown on the left side of the figure.

with $7 \times 10^{17} \text{ cm}^{-3}$ Si atoms and a second spacer of 5 nm. The first spacer prevents a 2DEG from forming at the normal interface. The 2DEG channel at the inverted interface is in the succeeding undoped 40 nm GaAs layer. The structure is capped by a Si-doped 30 nm GaAs layer with a doping concentration of $1 \times 10^{18} \text{ cm}^{-3}$. This cap is designed so as to be just depleted by the surface potential, and to ensure that the GaAs conduction band edge at the heterojunction is below the Fermi level.

The spacer thickness of 5 nm in the above structures is chosen to obtain sufficiently high carrier concentration in the channel for two reasons: first to reduce the influence of residual impurities in the GaAs channel [1] and second to achieve optimum conductivity for electrical devices. A possible effect of different Si diffusion times during the growth of HEMT and I-HEMT structures, as mentioned by Gonzales et al. [16] as the main influence of the different performance of HEMT and I-HEMT, is also considered. The doped cap layer for the I-HEMT structure allows a growth time of about 200 s after the incorporation of the dopant for the 2DEG which is nearly the same for the HEMT structure.

3. Results and discussion

The electrical properties of the 2DEG in the HEMT and I-HEMT structures are determined by Hall effect measurements using then Van der Pauw method. Measurements were carried out in the dark at temperatures of 300 and 77 K. The results at 77 K are summarized in fig. 3. The mobility of the HEMT structures (dashed line) and the I-HEMT structures (full line) is plotted versus T_g . The respective carrier concentration is plotted below. Results at room temperature show similar behavior.

The mobilities of the HEMT structures cover a broad range around $10^5 \text{ cm}^2/\text{V} \cdot \text{s}$. The maximum mobility of $120,000 \text{ cm}^2/\text{V} \cdot \text{s}$ is achieved at $T_g = 750^\circ\text{C}$. At $T_g > 750^\circ\text{C}$, we obtained a slight decrease in mobility which we attribute to interface roughness due to Ga desorption [19]. A strong decrease in mobility is observed at $T_g < 500^\circ\text{C}$

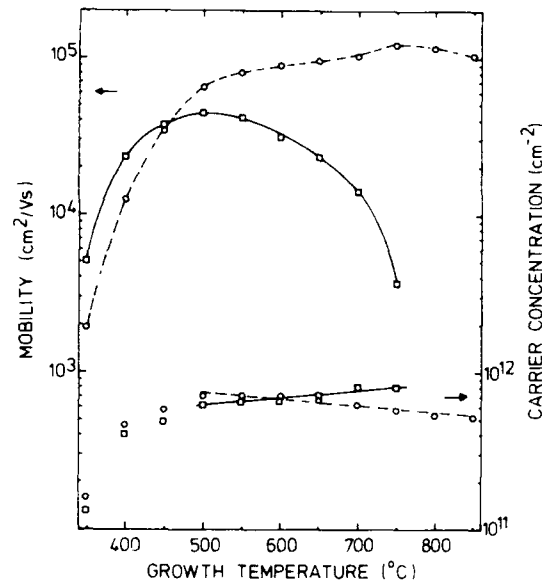


Fig. 3. Hall mobility and carrier concentration measured at 77 K of the HEMT (dashed lines) and I-HEMT (full lines) structure versus growth temperature. The lines are intended only as a guide.

presumably due to an increase of intrinsic crystal defects [20].

The I-HEMT structures show maximum mobility of $45,000 \text{ cm}^2/\text{V} \cdot \text{s}$ at a decisively lower T_g of 500°C . The difference in mobilities of HEMT and I-HEMT structures is less than a factor of 1.5 at this temperature which indicates that in principal both interfaces (inverted and normal) are of the same quality. Below $T_g = 500^\circ\text{C}$, we also observed a drop in mobility for the I-HEMT structure due to the reduced crystal quality. In comparison to the HEMT structure, the behavior above $T_g = 500^\circ$ is totally different. A clear drop of the mobility down to a value of $3500 \text{ cm}^2/\text{V} \cdot \text{s}$ at $T_g = 750^\circ\text{C}$ is observed. This value is comparable to that of homogeneously doped GaAs with an electron concentration of 10^{17} – 10^{18} cm^{-3} . We attribute the drop in mobility to the segregation of the Si dopant through the spacer towards the GaAs channel. The actual spacer thickness is reduced and the influence of Coulomb scattering increases. This trend ends when the Si atoms reach the nominally undoped GaAs channel and the mobil-

ity is similar to that of doped GaAs. In comparison with the mobility of the HEMT structure for $T_s = 750^\circ\text{C}$ we can exclude the effect of diffusion which would act on both structures by reduction of the mobility.

The respective carrier concentration in fig. 3 shows two regions. Below $T_s = 500^\circ\text{C}$ the carrier concentration drops due to the increasing amount of trapping centers [20]. The behavior above $T_s = 500^\circ\text{C}$ is dominated by the influence of Si segregation. Although expected constant from the growth parameters, the actual spacer increases with increasing T_s for the HEMT structure. Here the spacer is grown before the Si doped layer is grown and the Si segregates away from the 2DEG. Thus we observe a decrease of the carrier concentration (dashed line). For the I-HEMT structure, where the dopant is incorporated before the spacer is grown, the actual spacer decreases with increasing T_s . Here we observe a slight increase in carrier concentration (full line).

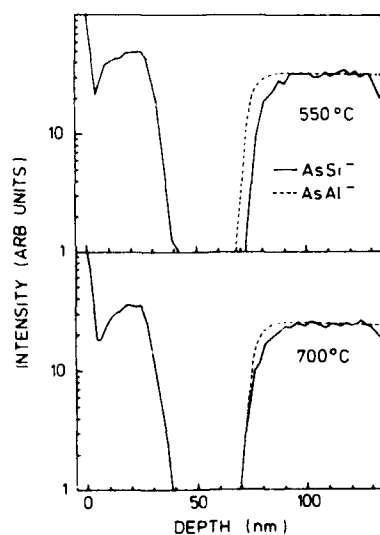


Fig. 4. SIMS profile of I-HEMT structures grown at 550 and 700°C versus sputter depth. Negative secondary ions of AsSi, AsAl were recorded. The normalized profiles represent the Si and Al distribution.

Based on the electrical data we can interpret the results to be caused by Si segregation. Further proof is given by SIMS depth profiles of I-HEMT structures. Measurements of profiles representing Si and Al distribution are shown in fig. 4. The normalized profiles for two I-HEMT structures grown at $T_s = 550^\circ\text{C}$ and 700°C are plotted versus sputter depth. For a description of the experimental conditions, see Maier et al. [12]. In the sample grown at $T_s = 550^\circ\text{C}$ the rise of the Si (full line) and the Al profiles (dashed line) are very similar and the profiles are well separated, as shown in the upper part of fig. 4. Therefore, the Si concentration in the spacer layer is lower than the detection limit of 1×10^{17} Si atoms/cm³. Thus we conclude that Si is confined to the intentionally doped layer. The situation changes significantly upon increasing the growth temperature to $T_s = 700^\circ\text{C}$ (lower part of fig. 4). Whereas the Al profile is unchanged, a distinct modification of the Si profile is observed in comparison with the Al profile. The Si profile first drops below the Al profile in the spacer region. However, the slope is smaller so that the profiles approach each other demonstrating that Si indeed has segregated into the spacer.

Using the fact that segregation dominates the electrical quality of I-HEMT structures we have grown I-HEMT structures (fig. 2) at the optimized T_s for HEMT structures, $T_s = 750^\circ\text{C}$. The only difference was the growth of the doped Al_xGa_{1-x}As layer, which was grown at $T_s = 500^\circ\text{C}$ to reduce segregation. Mobility values of up to 60,000 cm²/V·s at $T = 77$ K indicate suppressed segregation and an improved quality of the inverted interface.

4. Conclusion

We have demonstrated the influence of Si segregation by comparison of normal and inverted heterostructures grown by MBE at different T_s . Segregation was confirmed by SIMS analysis of I-HEMT structures. In temperature ranges where segregation is suppressed, HEMT and I-HEMT structures are of comparable quality concerning the electrical properties.

Acknowledgement

We gratefully acknowledge the technical assistance of S. Emminger in sample preparation.

References

- [1] K. Hirakawa and H. Sakaki, *Phys. Rev.* B33 (1986) 8291.
- [2] G. Weimann, in: *Festkörperprobleme (Advances in Physics)*, Vol. 26, Ed. P. Grosse (Vieweg, Braunschweig, 1986) p. 231.
- [3] L. Pfeiffer, K.W. West, H.L. Störmer and K.W. Baldwin, *Appl. Phys. Letters* 55 (1989) 1888.
- [4] C.T. Foxon, J.J. Harris, D. Hilton, J. Hewett and C. Roberts, *Semicond. Sci. Technol.* 4 (1989) 582.
- [5] S. Nishi, T. Saito, S. Seki, Y. Sano, H. Inomata, T. Itoh, M. Akiyama and K. Kaminishi, in: *Proc. 13th Intern. Symp. on GaAs and Related Compounds*, Las Vegas, NV, 1986, *Inst. Phys. Conf. Ser.* 83, Ed. W.T. Lindley (Inst. Phys., London-Bristol, 1987) p. 515.
- [6] H. Morkoç, T.J. Drummond and R. Fischer, *J. Appl. Phys.* 53 (1982) 1030.
- [7] T.J. Drummond, J. Klem, D. Arnold, R. Fischer, R.E. Thorne, W.G. Lyons and H. Morkoç, *Appl. Phys. Letters* 42 (1983) 615.
- [8] S. Sasa, J. Saito, K. Nanbu, T. Ishikawa and S. Hiyamizu, *Japan. J. Appl. Phys.* 23 (1984) 573.
- [9] N.M. Cho, D.J. Kim, A. Madhukar, P.G. Newman, D.D. Smith, T. Aucoin and G.J. Iafrate, *Appl. Phys. Letters* 52 (1988) 2037.
- [10] H. Shtrikman, M. Heiblum, K. Seo, D.E. Galbi and L. Osterling, *J. Vacuum Sci. Technol.* B6 (1988) 670.
- [11] A. Rockett, J. Klem, S.A. Barnett, J.E. Greene and H. Morkoç, *J. Appl. Phys.* 59 (1986) 2777.
- [12] M. Heiblum, *J. Vacuum Sci. Technol.* B3 (1985) 820.
- [13] M. Maier, P. Hiesinger, K. Köhler and W. Jantz, *Vacuum*, in press.
- [14] K. Inoue, H. Sakaki, J. Yoshino and Y. Yoshioka, *Appl. Phys. Letters* 46 (1985) 973.
- [15] R.B. Beall, J.B. Clegg and J.J. Harris, *Semicond. Sci. Technol.* 3 (1988) 612.
- [16] L. Gonzalez, J.B. Clegg, D. Hilton, J.P. Gowers, C.T. Foxon and B.A. Joyce, *Appl. Phys.* A41 (1986) 237.
- [17] Substrate temperatures up to $T_s = 500^\circ\text{C}$ are also measured by transmission measurements using the temperature dependence of the GaAs band edge. The substrate heater is used as a light source. The temperatures are comparable to the thermocouple readout. However, at $T_s = 750^\circ\text{C}$ measured by thermocouple the value of a pyrometer measurement is 660°C .
- [18] A.C. Gossard, *IEEE J. Quantum Electron.* QE-22 (1986) 1649.
- [19] T. Kojima, N.J. Kawai, T. Nakagawa, K. Ohta, T. Sakamoto and M. Kawashima, *Appl. Phys. Letters* 47 (1985) 286.
- [20] T. Muratoni, T. Shimano and S. Mitsui, *J. Crystal Growth* 45 (1978) 302.

The growth and characterisation of back-gated high mobility two-dimensional electron gas structures

D.A. Ritchie, J.E.F. Frost, D.C. Peacock *, E.H. Linfield, A. Hamilton and G.A.C. Jones

Cavendish Laboratory, University of Cambridge, Madingley Road, Cambridge CB3 0HE, UK

This paper presents a description and analysis of two back-gated high mobility GaAs/AlGaAs two-dimensional electron gas (2DEG) structures. The results show the carrier density in the 2DEG varying over a wide range with a low leakage current from the 2DEG to the n^+ substrate, which acts as the back-gate. With the carrier density enhanced, a second 2DEG formed in a different part of the structure from the first one. These samples will be used for the study of low-dimensional structures by using a patterned front gate on the surface of the epilayer to define the shape of the structure and the back-gate to vary the carrier density.

1. Introduction

The control of the electron carrier density in two-dimensional electron gas (2DEG) structures is important for investigation of the quantum Hall effect as well as studies of electrons confined in low-dimensional structures.

One technique to control the carrier density is to deposit a gate onto the surface of the epilayer either in-situ [1] or outside the MBE environment [2]. Combining this with the fabrication of low dimensional structures involves complex sample processing [3,4]. The provision of a back-gate on the sample to control the electron density however allows the use of patterned gates [5] on the epilayer surface to independently confine the electrons. Back-gates have been evaporated onto the rear of samples thinned to $\sim 120 \mu\text{m}$ [2] but this approach has problems of uniformity and low sensitivity to back-gate bias. A conducting substrate has been used to back-gate an “inverted” GaAs on AlGaAs heterostructure [6] and this work has been extended to the manufacture of a one-dimensional structure [7]. The “inverted” structures suffer however from having a lower mobility than conventional AlGaAs on GaAs heterostructure [8].

For all ex-situ evaporated gates the uniformity over the sample is worse than for those deposited in-situ because of surface contamination. For all fabricated gates it is necessary to have a leakage current of order 1 nA over the range of bias required to avoid electron heating at milli-kelvin temperatures.

In this paper a discussion is presented of the growth and properties of conventional high mobility heterostructures grown on a barrier structure on top of conducting n-type substrates.

2. Epilayers

Sample growth took place in a VG V80H GaAs/AlGaAs MBE machine using conventional thermal sources. Silicon and beryllium were used as dopants and the typical background impurity level for the system was $1 \times 10^{14} \text{ cm}^{-3}$ n-type. Growth occurred on 2 inch diameter silicon doped n^+ wafers mounted in indium free holders, the substrate temperature being determined by an Ircon infra-red pyrometer.

Two structures grown are depicted in fig. 1. They each consist of a conventional high mobility heterostructure [8] separated from the conducting substrate or back-gate, by a barrier structure designed to give a low gate leakage current whilst

* Also at GEC Hirst Research Centre, East Lane, Wembley HA9 7PP, UK.

allowing variation of the 2DEG concentration by changing the gate bias. The first barrier, in sample C190, consisted of $0.79\ \mu\text{m}$ thick AlGaAs layer between two $0.25\ \mu\text{m}$ GaAs layers. The GaAs was grown at 530°C to make it insulating, the rest of the structure was grown at 640°C . The structure also has two superlattice buffers to prevent the diffusion of impurities and dislocations. These superlattices have been shown by measurements on other samples not to provide a sufficient electrical isolation barrier in themselves.

The second sample C319 contained in p-n junction with a variable period multiple quantum well structure at its centre. This structure is based on that used by Couch et al. [9] for a low leakage diode. The p-type doping level was $10^{16}\ \text{cm}^{-3}$, in another sample with this layer doped in the $10^{18}\ \text{cm}^{-3}$ range, varying the back-gate bias only made a tiny change to the 2DEG density. A superlattice buffer was grown after the p-n structure for the reasons given above. The growth temperature throughout this structure was 655°C .

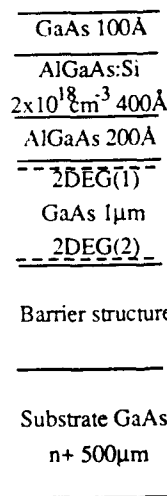
3. Measurements

The samples were processed by photolithography and wet etching into Hall bars of length $400\ \mu\text{m}$ and width $60\ \mu\text{m}$ with eight contacts made by evaporating a Au/Ge/Pd structure followed by optical annealing. Contact to the substrate (the back-gate) was by another evaporated contact. The samples were characterised in a ^4He cryostat at temperatures $\geq 1.5\ \text{K}$ and magnetic fields $\leq 8\ \text{T}$. All measurements reported here were made without illumination.

The gate to 2DEG leakage current was measured with a picoammeter as a function of the applied voltage. For sample C190, the range of bias over which the leakage current was below $1\ \text{nA}$ was -7 to $+13\ \text{V}$ and for C319 it was -1.8 to $+2.0\ \text{V}$, some data presented are outside these ranges.

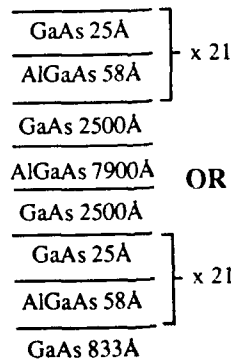
The samples were further characterised by passing an AC current of 1 or $0.1\ \mu\text{A}$ along the Hall bar and by using phase sensitive detection tech-

Main structure

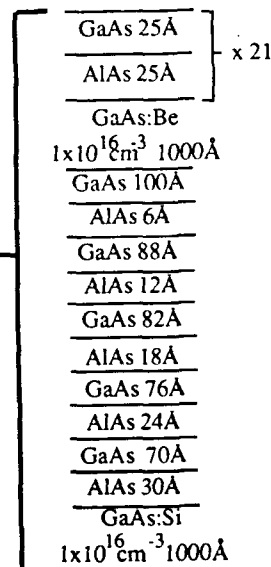


Barrier structures

C190



C319



Note: The Al Ga As mole fraction, x was 0.37 for C190 and 0.33 for C319.

Fig. 1. The structure of the two MBE samples C190 and C319. The position of the two 2DEGs is shown.

niques to measure the four terminal resistivity and the Hall voltage at 0.4 T. These measurements were carried out at 5 K and as a function of gate voltage. The results were the same for different sets of contacts. From these data the values of electron mobility and density were obtained.

Measurements were made at fixed gate voltage of the resistivity and Hall voltage as a function of magnetic field, giving rise to Shubnikov-De Haas (SdH) oscillations and observation of the quantum Hall effect. By plotting the SdH oscillations as a function of B^{-1} and Fourier analysing the result, the 2DEG density was obtained. Under certain conditions two oscillation frequencies were obtained, which are discussed later.

4. Results and discussion

Figs. 2 and 3 show the carrier density and electron mobility plotted as a function of gate voltage V_g for C190 and C319, respectively. For C190 the Hall carrier density, n_{Hall} , varied over a

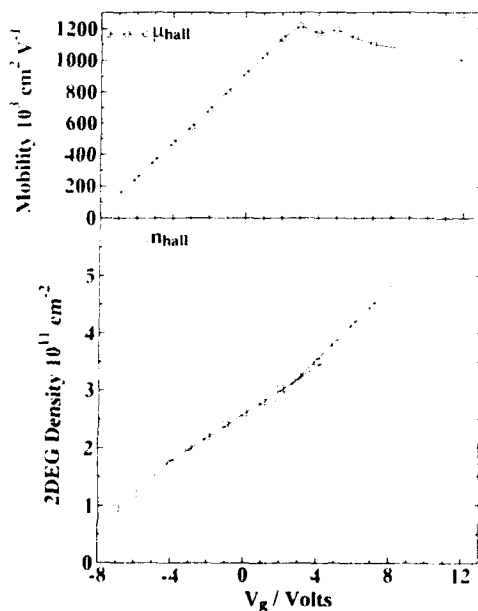


Fig. 2. Carrier density, n_{Hall} , and mobility, μ_{Hall} , from Hall data as a function of back gate bias, V_g , for sample C190. The linear regions of different gradients are shown.

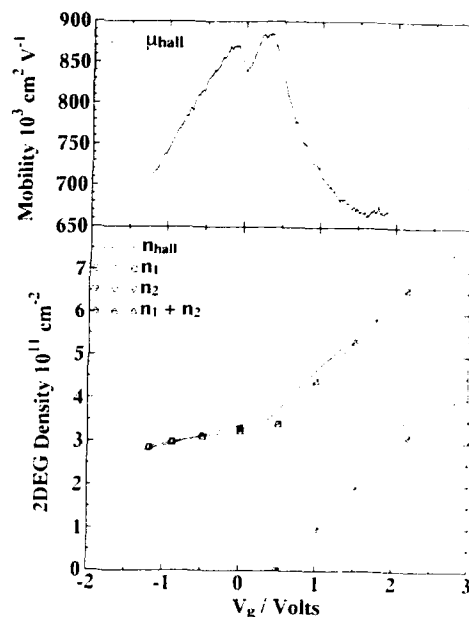


Fig. 3. Carrier density, n_{Hall} , with n_1 and n_2 from SdH data plotted with mobility, μ_{Hall} , as a function of back gate bias, V_g , for sample C319.

wide range, between 9×10^{10} and $5.2 \times 10^{11} \text{ cm}^{-2}$, whilst the mobility increased steadily over this range from 1.3×10^5 to over $1.2 \times 10^6 \text{ cm}^2 \text{ V}^{-1} \text{ s}^{-1}$ before falling away slightly. The results for C319 follow a similar pattern at larger carrier densities.

For both structures the value of n_{Hall} increased linearly with V_g at low carrier concentration. At certain positive values of V_g , 2.7 V for C190 and 0.5 V for C319, the gradient changed. This change corresponded to the peak in the mobility characteristic. In addition a second frequency was observed in the SdH oscillations as the carrier density increased into this second region. This suggests that in this regime a second 2DEG became populated. In fig. 3 carrier density values from the SdH data are plotted together with the Hall carrier density and mobility data for sample C319. The SdH results for $V_g < 0.5$ V were in good agreement with the Hall results. For $V_g > 0.5$ V two SdH oscillation frequencies were observed showing that the SdH carrier density, n_1 , from the first 2DEG remained constant while the carrier

density in the second 2DEG, n_2 , increased steadily. As expected, the sum of the two SdH densities equalled the Hall density. Eventually the second SdH density became greater than the first. C190 showed similar properties. In both structures in the first region of gate bias, the SdH oscillations reached zero resistivity at certain magnetic fields. This confirms the absence of parallel conduction in the doped AlGaAs near the surface of the heterostructures.

At first it was believed that the two oscillation periods corresponded to two electrical subbands in one location, it is now believed that there are two 2DEGs at separate locations in the structure, the first at the usual heterointerface and the second at the top of the barrier structure, as shown in fig. 1. It is thought that the first 2DEG stops filling as the second one begins since the second 2DEG screens the first from the attractive charge on the gate. This explanation is also consistent with the change in gradient of n_{Hall} with V_g since this is a measure of the capacitance per unit area between the gate and the 2DEG and is given by

$$c = C/A = \epsilon_0 \epsilon_r / d = e \, dn_{\text{Hall}} / dV_g.$$

Here, d is the distance between capacitor plates and $\epsilon_r = 12.5$ for GaAs at low temperatures. For two 2DEGs at different distances from the gate the capacitance was different, which gave dissimilar gradients in the two regions of the graph. The distance from the first 2DEG to the gate was calculated, this gave results larger than expected by 23% for C190 and 18% for C319. The ratio of the two gradients for each sample was used to find the position of the second 2DEG, 580 Å above the superlattice buffer for C190 and 14 Å above it for C319. These values are within experimental error of the position shown in fig. 1.

The electron mobilities of the two 2DEGs in sample C319 were calculated by two methods, that of Kane et al. [10] and by a fit to the low field magnetoresistance from the SdH data. These gave the same result, the second 2DEG has a mobility of $4.25 \times 10^5 \text{ cm}^2 \text{ V}^{-1} \text{ s}^{-1}$ at low carrier densities rising to $4.5 \times 10^5 \text{ cm}^2 \text{ V}^{-2} \text{ s}^{-2}$ at a density of $2.5 \times 10^{11} \text{ cm}^{-2}$. This is a large but not an unprecedented value for a 2DEG located on an "inverted" heterojunction [6].

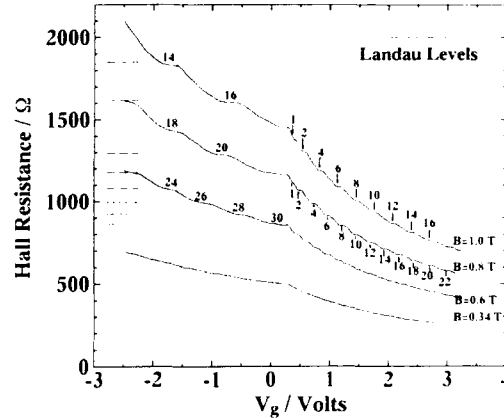


Fig. 4. Hall resistance as a function of back gate bias, V_g , for C319, the expected quantum Hall plateaux are marked.

As further evidence of this double 2DEG structure, fig. 4 shows the Hall resistance, $R_{\text{Hall}} = V_{\text{Hall}}/I$ at 1.5 K as a function of gate voltage for several different magnetic fields, I is the current passing along the Hall bar. The data shown are from C319. In the range $V_g < 0.5$ V a series of quantum Hall plateaux were observed given by $R_{\text{Hall}} = h/ie^2$ for even integer i . For $V_g > 0.5$ V further plateaux were observed which were attributed to the increasing occupation of the second 2DEG. These plateaux are not quantised because the measurement is a parallel combination of the Hall resistance from the first 2DEG with that from the second. The Hall resistance of the first 2DEG is constant in this region and therefore may be subtracted from the measurements. In that case these plateaux became quantised, their indices being marked on the graph. This structure therefore provides a way of observing the properties of low order Landau levels at low magnetic fields. The results shown in fig. 4 also confirmed the high quality and uniformity of the gate in this structure as well as confirming the high mobility of the second 2DEG. These results also imply that the contacts must have penetrated to the second 2DEG when the gate was used to enhance the carrier density.

At present experiments are being carried out to determine the optimum design of low leakage barrier as well as applying this technique to the

fabrication of back-gated low-dimensional devices.

5. Conclusions

High mobility heterojunction samples have been manufactured which show a large variation of two-dimensional carrier density with back-gate bias. The leakage current is less than 1 nA making these devices suitable for experiments at the lowest temperatures.

The occupation of a second 2DEG has also been observed. This has been shown to be located above the superlattice buffer in the structure. The quantum Hall effect has been clearly observed in both 2DEGs in this structure as a function of gate voltage, illustrating the high quality of the back-gated structure.

Acknowledgements

The authors would like to acknowledge discussions with M.J. Kelly and the technical assistance

of D. Heftel, D.R. Charge and A.E.R. Stone. This work was funded in part by the SERC. E.H.L. was supported by a studentship from Trinity College Cambridge and A.H. by an SERC CASE studentship with GEC-Marconi.

References

- [1] C.E. Timmering, J.M. Lagemaat, C.T. Foxon and J.J. Harris, *Semicond. Sci. Technol.* 3 (1988) 1139.
- [2] K. Hirakawa and H. Sakaki, *Phys. Rev. B* 33 (1986) 8291.
- [3] K. Owusu-Sekyere, A.M. Chang and T.Y. Chang, *Appl. Phys. Letters* 52 (1988) 1246.
- [4] E.H. Linfield, D.A. Ritchie, G.A.C. Jones, J.E.F. Frost, D.C. Peacock and M. Pepper, *Microelectron. Eng.* 11 (1990) 19.
- [5] T.J. Thornton, M. Pepper, H. Ahmed, D. Andrews and G.J. Davies, *Phys. Rev. Letters* 56 (1986) 1198.
- [6] U. Meirav, M. Heiblum and F. Stern, *Appl. Phys. Letters* 52 (1988) 1268.
- [7] U. Meirav, M.A. Kastner, M. Heiblum and S.J. Wind, *Phys. Rev. B* 40 (1989) 5871.
- [8] J.J. Harris, C.T. Foxon, K.W.J. Barnham, D.E. Lacklison, J. Hewitt and C. White, *J. Appl. Phys.* 61 (1987) 1219.
- [9] N.R. Couch, D.G. Parker, M.J. Kelly and T.M. Kerr, *Electron. Letters* 22 (1986) 636.
- [10] M.J. Kane, N. Apsley, D.A. Anderson, L.L. Taylor and T. Kerr, *J. Phys. C* 18 (1985) 5629.

The growth of shallow high mobility two-dimensional electron gas structures

J.E.F. Frost, D.A. Ritchie and G.A.C. Jones

Cavendish Laboratory, University of Cambridge, Madingley Road, Cambridge CB3 0HE, UK

GaAs/AlAs heterostructures are described in which the two-dimensional electron gases (2DEGs) are in close proximity to the crystalline surface. Measurements are presented from samples in which the 2DEGs were 15 and 25 nm below the GaAs/vacuum interface. The sheet carrier concentrations were 6.7×10^{11} and $3.4 \times 10^{11} \text{ cm}^{-2}$ and Hall mobilities were 5×10^7 and $1.2 \times 10^6 \text{ cm}^2 \text{ V}^{-1} \text{ s}^{-1}$, respectively, at 4 K. The two samples were examined by transmission electron microscopy. Hall measurements are given both as a function of temperature and as a function of surface Schottky gate voltage at 4 K. A simple capacitor model was used to relate the sheet carrier concentration versus gate voltage dependence to the depth of the 2DEG below the gate. Variable temperature Hall measurements suggest that ionized impurity scattering is less significant than phonon scattering at 4 K.

1. Introduction

Electron beam lithography combined with molecular beam epitaxy (MBE) has advanced the development of device fabrication technology in which electrons exhibit a physical behaviour characteristic of reduced dimensionality at low temperatures. Electrons may be confined close to a modulation doped AlGaAs/GaAs heterojunction grown by MBE to form a two-dimensional electron gas (2DEG). Further confinement may be achieved by fabricating split Schottky gates on the sample surface by electron beam lithography (EBL) so that the electrons are confined to exist in either 1D or even 0D by the imposed electric field. The current line-width resolution limit set by EBL metallisation lift-off is ca. 50 nm and to realize its full potential, the 2DEG should be formed at a distance, d , less than this limit below the surface of the epitaxial layer. Novel physical effects may be observed, for example electron interference at sharp Schottky gate corners.

High mobilities are required in low-dimensional structures in order to increase the inelastic scattering time and preferably at a low sheet carrier concentration, where the Fermi wavelength is larger. A mobility of $10^6 \text{ cm}^2 \text{ V}^{-1} \text{ s}^{-1}$ at a carrier

concentration of $2.2 \times 10^{11} \text{ cm}^{-2}$ has been achieved previously elsewhere with $d = 33 \text{ nm}$ [1]. Layers of a comparable mobility and sheet carrier concentration but with the value of d reduced to 15 nm have been grown. We describe two layers from this series and compare their properties with more conventional structures with $d = 70 \text{ nm}$ and $d = 260 \text{ nm}$ grown in the same system.

2. Sample growth and characterisation

A series of structures was grown in a solid source VG Semicon V80H MBE machine at substrate temperatures between 600 and 640°C as measured with an Ircon infra-red pyrometer during the GaAs buffer growth (fig. 1). Two inch diameter GaAs substrates were mounted in an indium-free holder of proprietary design. The growth rate in each case was 2 $\mu\text{m/h}$ and doping was changed by variation of the planar doping duration with the silicon cell temperature constant. Each layer contained a GaAs buffer followed by two AlAs barriers separated by a 2.2 nm GaAs or 2.8 nm $\text{Al}_{0.3}\text{Ga}_{0.7}\text{As}$ quantum well planar doped with silicon. The intended AlAs barrier thickness were 10 and 5 nm for A381 and A384.

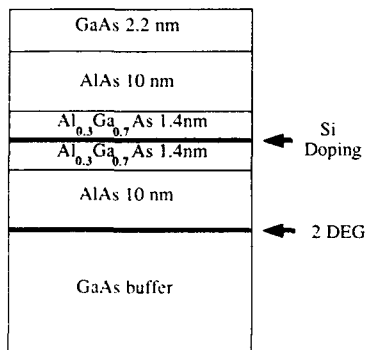


Fig. 1. Schematic diagram of the shallow 2DEG structures.

respectively, and all layers were capped with 2.2 nm of GaAs. The sheet doping concentrations in A381 and A384 were estimated to be 1.0×10^{13} and $1.5 \times 10^{13} \text{ cm}^{-2}$, respectively. A 2DEG forms between the GaAs buffer and the first AlAs barrier and the sheet doping concentrations were chosen to eliminate parallel conduction.

The epitaxial layers were processed into eight contact Hall bars using conventional photolithography. AuGeNi ohmic contacts were annealed at 360°C for 15 s which is lower than the 430°C used for our standard 2DEG heterostructure with $d = 70 \text{ nm}$. Some Hall bars had Schottky gates with either gold or palladium followed by gold metallisation. The more conventional layer A304 had a GaAs buffer, a 40 nm $\text{Al}_{0.3}\text{Ga}_{0.7}\text{As}$ undoped spacer, a 200 nm doped $\text{Al}_{0.3}\text{Ga}_{0.7}\text{As}$ layer and finally a 20 nm GaAs cap and A281 had a GaAs buffer, a 20 nm $\text{Al}_{0.3}\text{Ga}_{0.7}\text{As}$ undoped spacer, a 40 nm doped $\text{Al}_{0.3}\text{Ga}_{0.7}\text{As}$ layer and finally a 10 nm GaAs cap.

The processed devices were characterised in a continuous flow ^4He cryostat from room temperature to 4 K and in a 1.5 K cryostat in the dark and after illumination by a red LED. Measurement currents of 0.1 and 1 μA were used and gated samples were biased with a Keithley 236 which allowed simultaneous monitoring of the gate voltage and leakage current. Fixed and swept magnetic field measurements up to 6 T were made.

3. Results and discussion

Two of the samples, A381 and A384, were examined using TEM. The total distances to the 2DEG heterointerfaces below the surface were less than 31 and 20 nm, respectively.

Fig. 2 shows the dependence of sheet carrier concentration and mobility for A381 with $d = 25 \text{ nm}$ and A384 with $d = 15 \text{ nm}$. The mobilities of these samples with dopant to 2DEG separations of 11 and 6 nm respectively compare favourably with published data from samples with similar spacer thicknesses, and at lower sheet carrier concentrations [2]. At the lowest temperatures the mobility is still increasing, and this suggests for these two samples that the temperature dependence of the mobility is dominated by phonon

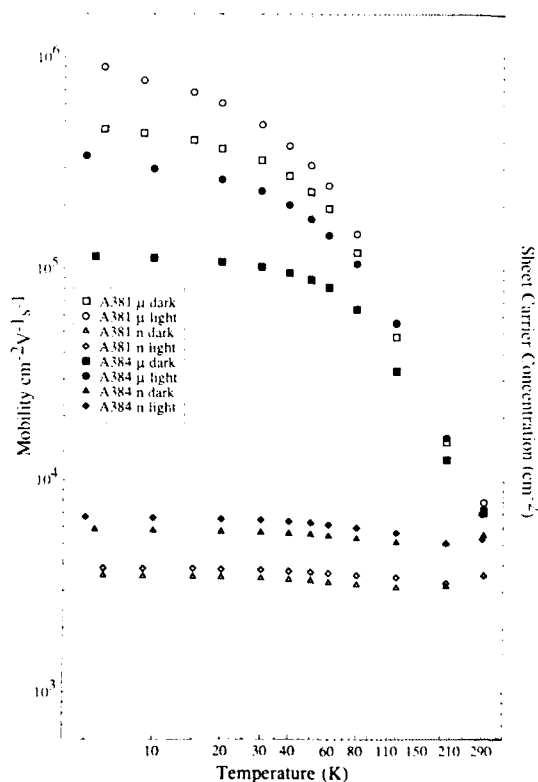


Fig. 2. Temperature dependence of the sheet carrier concentration and mobility in the dark and after illumination for A381 and A384.

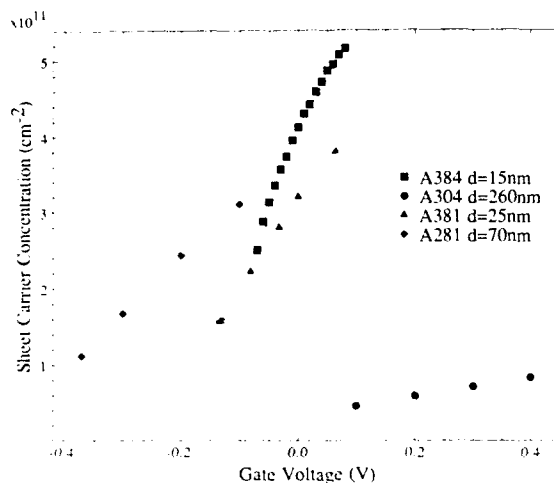


Fig. 3. Sheet carrier density as a function of surface Schottky gate bias for A381, A384, A304 and A291.

scattering. If this were not the case, and ionized-impurity scattering dominated, then a decrease in mobility below about 50 K would be expected [3]. A gated sample of A381 did indeed have this decrease in mobility with temperature when negatively biased, and hence at a lower sheet carrier density. This in turn suggests that for these carrier concentrations, the distance d may be reduced further without degrading the mobility.

Fig. 3 shows the variation of sheet carrier concentration with applied gate voltage for two shallow 2DEG structures and two more conventional structures. The four samples shown, A384, A381, A281 and A304, have expected d values of 15, 25, 70 and 260 nm, respectively, but the simple capacitor model used gives d values of 40, 56, 91 and 533 nm. The absolute values may be given incorrectly due to the presence of trapped charges between the 2DEG and the gate or because the thickness has been increased by oxidation prior to metallisation, but the trend in the two depths is apparent.

Parallel conduction is deleterious to performance in low dimensional structures and may degrade the quality of low temperature results by, for example, eliminating zeroes in Shubnikov-De Haas plots. The double barrier structure described by Horikoshi et al. [4] containing a doped quan-

tum well had barriers of different Al content and hence barrier height in order to preclude a bound electron energy level and therefore remove parallel conduction. In this work we have both barriers of AlAs because it was found that parallel conduction occurred in the $\text{Al}_{0.3}\text{Ga}_{0.7}\text{As}$ upper barrier if the thickness of the AlAs barrier nearer the 2DEG was increased from 20 to 40 nm. By using this combination of $\text{Al}_{0.2}\text{Ga}_{0.7}\text{As}$ well and AlAs barrier the lowest electron energy levels in the well are above the X-band in the barrier [5]. The silicon donor binding energy in AlAs is about 57 meV and any conduction in these layers will freeze out at low temperature [6]. We believe that parallel conduction is absent in these samples, confirmed by the appearance of zeroes in the Shubnikov-De Haas data, because the electronic energy levels in the doped quantum well lie above the Fermi level for the 2DEG. Carriers reach the 2DEG from the quantum well by thermionic excitation at room temperature and additionally by photoexcitation at low temperatures. Parallel conduction is eliminated at higher sheet carrier concentrations by using an $\text{Al}_{0.3}\text{Ga}_{0.7}\text{As}$ instead of a GaAs well, as the electron energy levels in the well are raised. This is demonstrated by comparing A381, which had an $\text{Al}_{0.3}\text{Ga}_{0.7}\text{As}$ well, with A382, which was identical except that it had a GaAs well. The sample had mobility and sheet carrier concentrations of $1.35 \times 10^6 \text{ cm}^2 \text{ V}^{-1} \text{ s}^{-1}$ at $3.4 \times 10^{11} \text{ cm}^{-2}$ in the dark and $1.52 \times 10^6 \text{ cm}^2 \text{ V}^{-1} \text{ s}^{-1}$ at $3.6 \times 10^{11} \text{ cm}^{-2}$ after illumination but then showed signs of parallel conduction.

Planar doping was used for two reasons: Firstly, planar doping is by definition the method of introducing dopant atoms in the minimum epilayer thickness and secondly, the number of free carriers generated per dopant atom is maximised, allowing the lowest doping levels to be used. Although the layers are described as planar doped, work by Harris et al. [7] and Shayegan and co-workers [8] has shown that at the substrate temperatures used here of between 870 and 910 K, the Si may be spread over a depth comparable with the thickness of the AlAs barriers and this may make the sheet carrier concentration and mobility a function of the time elapsed between the deposition of the Si and the cessation of growth. This

suggests that the highest mobilities possible for such structures have not yet been achieved. Further work, including reduction of the growth temperature, is underway to optimise this part of the structure.

4. Conclusions

A series of GaAs/AlAs heterostructures with silicon planar doping have been grown by MBE in which a 2DEG is formed at a distance as small as 15 nm from the crystalline surface. Electrical measurements made on two of these structures are described and it is shown that their quality is sufficient to allow the fabrication of ultrasmall Schottky gated structures for low-dimensional physics experiments, for example electron interference from edges sharp compared to the electron Fermi wavelength.

Acknowledgements

We are grateful to N. Rimmer for the TEM sample analysis. We would like to thank D.R. Charge and D. Heftel for their technical assistance.

References

- [1] K. Ploog, *J. Crystal Growth* 81 (1987) 304.
- [2] J.J. Harris, C.T. Foxon, D.E. Lacklinson and K.W.J. Barnham, *Superlattices and Microstructures* 2 (1986) 563.
- [3] K. Hirakawa and H. Sakaki, *Phys. Rev. B* 33 (1986) 8291.
- [4] Y. Horikoshi, A. Fischer, E.F. Schubert and K. Ploog, *Japan. J. Appl. Phys.* 26 (1987) 263.
- [5] P.M. Solomon, S.L. Wright and C. Lanza, *Superlattices and Microstructures* 2 (1986) 521.
- [6] N. Chand, T. Henderson, J. Klem, W.T. Masselink, R. Fischer, Y.-C. Chang and H. Morkoç, *Phys. Rev. B* 30 (1984) 4481.
- [7] J.J. Harris, R.B. Beall, J.B. Clegg, C.T. Foxon, S.J. Battersby, D.E. Lacklinson, G. Duggan and C.M. Hellon, *J. Crystal Growth* 95 (1989) 257.
- [8] A.M. Lanzillotto, M. Santos and M. Shayegan, *Appl. Phys. Letters* 55 (1989) 1445.

Anisotropy in electronic transport of modulation doped structures having strained InGaAs wells

C. Webb, J.N. Eckstein and Y.M. Desai

Varian Research Center, Palo Alto, California 94303, USA

We have investigated electron mobilities of modulation doped structures grown by molecular beam epitaxy having strained InGaAs wells, and have found that there exists a strong anisotropy in $\langle 011 \rangle$ directions. The anisotropy may be conveniently characterized by the ratio of the mobilities in the two orthogonal directions; this ratio varies with well thickness, becoming significantly greater but less predictable as the well thickness exceeds the critical thickness for dislocation formation. Although most of our data are applicable to growths on the (100) crystal face, we also demonstrated that there is no dependence on slight wafer misorientation. We interpret our results as implying that some small number of dislocations is generated at the onset of InGaAs growth with larger numbers as the critical thickness is passed. Our results have obvious implications for device optimization.

InGaAs is an important III–V semiconductor, having a narrower band-gap and higher electron mobility and saturated velocity than GaAs. These properties are desirable for modulation-doped field effect transistors (MODFETs) where the lower band-gap leads to a larger conduction band discontinuity resulting in more charge transfer to the conducting channel, while the higher saturated velocity and mobility permit higher speed devices. Unfortunately the requirements of lattice matching present difficulties in the incorporation of InGaAs into device structures. Unlike AlGaAs, which is essentially lattice matched to GaAs over the entire compositional range, there exists an approximately 7% lattice constant difference between InAs and GaAs. One way in which InGaAs can be exploited for GaAs based MODFETs is the “pseudomorphic” MODFET [1–3], where only a very thin (typically ~ 150 Å of $\text{In}_{0.15}\text{Ga}_{0.85}\text{As}$) layer is utilized. Provided the layer thickness is sufficiently small, i.e. below the Matthews–Blakeslee limit [4] or critical thickness, it is energetically favorable for the entire InGaAs layer to deform as a strained layer rather than form dislocations.

In this study we have investigated electron transport properties of pseudomorphic MODFET

structures as the InGaAs layer thickness is systematically varied through a range of values above and below the critical thickness. Layers were deposited by molecular beam epitaxy (MBE) in a Varian GEN II system on (100) oriented GaAs. Both double and single heterojunction (DH and SH, respectively) structures were grown at a variety of growth temperatures. Although outside the useful range of our pyrometer (Minolta 52C), such data obtained at higher temperatures were used to calibrate the thermocouple; the best linear fit was extrapolated to lower temperatures so that thermocouple readings could be converted to pyrometer-based values which are quoted here. Hall bar samples were prepared in which conduction occurred along definite crystallographic directions. To be specific, we note that for the wafers used in this work the primary flat is located on the (011) plane below the (111)As face (SEMI flats). The wafer referred to its crystallographic orientation is shown in fig. 1. We shall refer to electron transport perpendicular to the primary flat as the “V” direction since it is parallel to the V-groove etch direction produced, e.g. by ammonia/peroxide etches, and transport parallel to the primary flat the “P” direction. We also grew on deliberately misoriented substrates: (a) tilted $2^\circ > (111)\text{A}$, i.e.

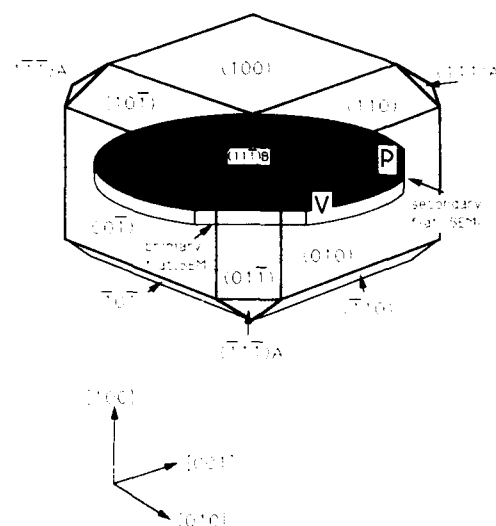


Fig. 1. The wafer is referred to its crystallographic orientation and the "V" and "P" directions are defined.

towards the secondary flat. (b) $2^\circ > (111)B$, and (c) $2^\circ > (110)$. In crystallographic terms, the first two cases are tilted in orthogonal directions while the case (c) tilt direction is midway between. In practical terms case (b) was generated by polishing the reverse face of the same wafers as in (a), resulting, in this case only, in EJ standard flats with the "V" direction perpendicular to the secondary flat.

Hall measurements were obtained in the V and P directions at 300 and 77 K for approximately 75

Table 1

Measured values of electron mobility for a small representative sampling of runs; these runs were made on a single day with fixed growth conditions and the well thickness as a parameter; carrier sheet densities showed little variation being generally $\sim 1.4 \times 10^{12}$

Run No.	Well (\AA)	μ at 300 K ($\text{cm}^2/\text{V}\cdot\text{s}$)		μ at 77 K ($\text{cm}^2/\text{V}\cdot\text{s}$)		μ Ratio at 77K, V/P
		V	P	V	P	
TH369	120	7360	7070	35200	29800	1.18
TH366	150	7270	7060	34700	30200	1.15
TH368	200	7100	5930	24800	14300	1.74
TH367	250	6600	6750	16800	23900	0.70
TH370	300	6500	5130	24300	14900	1.63

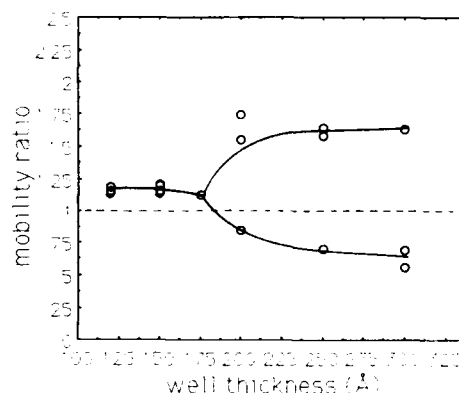


Fig. 2. The ratio of electron mobility in the V/P directions is plotted as a function of InGaAs well thickness for single heterojunction layers grown under the same growth conditions at 523°C.

runs in all. Table 1 shows a representative sampling of data for fixed growth conditions with the well thickness as a parameter; these data refer to runs made on a single day. The electron mobilities exhibit marked anisotropy particularly at 77 K and the discussion that follows considers only this measurement temperature. The anisotropy is most conveniently seen by plotting the ratio of mobilities in the V and P directions. Fig. 2 shows this ratio, as a function of well thickness, for all those samples which were grown on (100) oriented wafers at a nominal substrate temperature of 523°C and having the SH structure. These data, which include those of table 1, are chosen as the largest group with fixed growth conditions, and are representative of the trends seen in all the data. The ratio, which has the V direction mobility in the numerator, is mostly greater than unity indicating the V direction to be the preferred one for electron transport. For well thicknesses above the critical thickness, which for the 15% InGaAs used here is approximately 200 Å, the ratio deviates from unity more than for the thinner wells, and further there are several cases where the P direction is preferred, giving fig. 2 its double-branched appearance. However, the P direction is only preferred at values of well width greater than or equal to the critical thickness. The sheet carrier densities are generally very close for a given sam-

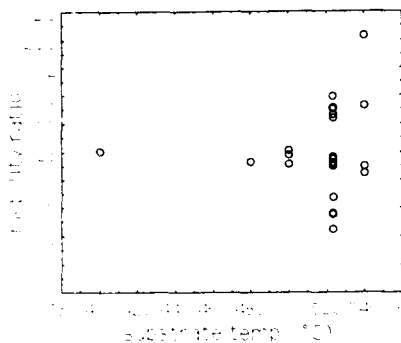


Fig. 3. The ratio of electron mobility of the V/P directions is plotted as a function of substrate temperature. In this case all growths which have single heterojunctions on (100) orientations are included.

ple as would be expected and fig. 2 is not substantially modified if sheet resistance ratios are used instead of mobility ratios.

The existence of several cases where the mobility is enhanced in the P direction was initially surprising. We considered the possibility that small differences in substrate orientation could influence the mobility outcome, and in order to test this hypothesis we grew on differently oriented substrates as described above. Without exception, all of the mobility ratios were found to be greater than unity indicating no orientation dependence. In fig. 3 we show all SH data for (100) orientations, plotting the mobility ratio against the substrate temperature during growth. Although there are more layers grown at 523°C than at the other temperatures employed, there is a suggestion that growth temperature may be involved in the reversal of the preferred direction.

The anisotropy can only be understood in terms of crystal defects, and in view of the relationship which we observe with the critical thickness, we believe that the defects in question are dislocations. If there are more dislocations running parallel to one of the two $\langle 011 \rangle$ directions then it would be expected that electron transport would be better when parallel to the majority of dislocations. In discussing these results, we need to consider the basic processes involved in lattice mismatched growth. In view, however, of symmetry we might expect both that dislocations would form

equally in both orthogonal $\langle 011 \rangle$ directions and that this would be required to completely relieve the strain. In accordance with the Matthews-Blakeslee model, initial deposition of InGaAs on GaAs should occur with perfect registry over the 2D plane of the substrate surface. In the absence of dislocations the deposited layer would take the substrate lattice constant in the plane parallel to the surface but there is no restriction perpendicular to the plane and in that direction the lattice constant should expand relative to the InGaAs bulk in order to reduce the strain energy. When a dislocation – which is by definition a line defect – forms to reduce the strain energy further, it may do so most effectively if it is parallel to the surface. The effect of a single edge dislocation is to relax the strain in a second direction and at least locally near the dislocation there may again be some expansion of the lattice constant in this case perpendicular to the line defect or parallel to the Burgers vector, further reducing the strain energy. The point is to demonstrate that despite symmetry considerations, dislocations along a single direction may effectively reduce the strain energy of the whole layer. We should expect this argument to be less applicable for layers many times the critical thickness, but that is not the case here. In fact during the growth, the symmetry is in general broken by surface reconstruction as observed by RHEED, so that a mechanism by which dislocations may form preferentially in a particular direction is quite possible.

At the growth temperatures involved here the surface reconstruction in the absence of a group III flux is the As-rich $c(4 \times 4)$, but changes to a somewhat "fuzzy" (2×4) (i.e. still As stable) with a group III flux. We interpret our results as implying that this reconstruction determines the most frequently observed directional preference for the electron mobility. We suggest that below the critical thickness some small number of dislocations is generated all parallel to one another, and since the (2×4) reconstruction is lost immediately with the initiation of an In flux, we further suggest that they are essentially all generated near the onset of InGaAs growth. This is consistent with the fact that the ratio of electron mobilities for the two orthogonal directions is not

particularly dependent on the well thickness when below the critical value. It is also consistent with calculations of Ghaisas and Madhukar [5] based upon a kinetic approach called the "configuration-dependent reactive incorporation" model. They suggest that strain will result in the formation of dislocations at the earliest stages of growth – the first monolayer in the case of 2D growth – in numbers controlled by the growth kinetics. Our results further suggest that, near the critical thickness, dislocations are generated spontaneously in greater numbers, and it is apparent from these results that they tend to be aligned to one another but not necessarily to those formed below the critical thickness. We do not at present understand what determines the direction chosen by the dislocations above the critical thickness, though as indicated by fig. 3 the growth temperature may play a role.

In summary, we have observed anisotropy in the electron mobilities of pseudomorphic MOD-FET structures in orthogonal $\langle 011 \rangle$ directions for

layers grown on GaAs(100). In general the anisotropy is such as to give higher mobilities in the "V" direction, but for well thicknesses which exceed the critical thickness, the anisotropy becomes larger and the preferred direction is less predictable. We have shown that the effect is not related to crystal misorientation.

References

- [1] J.J. Rosenberg, M. Benlarmi, P.D. Kirchner, J.M. Woodall and G.D. Pettit, IEEE Electron Device Letters EDL-6 (1985) 491.
- [2] T. Henderson, M.I. Aksun, C.K. Peng, H. Morkoç, P.C. Chao, P.M. Smith, K.-H.G. Duh and L.F. Lester, IEEE Electron Device Letters EDL-7 (1986) 649.
- [3] G.M. Metze, A. Cornfeld, E. Carlson, G. Dahrooge, E. Chang, J. Singer, J. Bass, H.-L. Hung and T. Lee, IEEE Electron Device Letters EDL-10 (1989) 165.
- [4] J.W. Matthews and A.E. Blakeslee, J. Crystal Growth 27 (1974) 118.
- [5] S.V. Ghaisas and A. Madhukar, J. Vacuum Sci. Technol. B7 (1989) 264.

High-quality $\text{In}_x\text{Ga}_{1-x}\text{As}/\text{InAlAs}$ modulation-doped heterostructures grown lattice-mismatched on GaAs substrates

K. Inoue, J.C. Harmand and T. Matsuno

Semiconductor Research Center, Matsushita Electric Industrial Co. Ltd., 3-15, Yagumo-Nakamachi, Moriguchi, Osaka 570, Japan

We report on the lattice-mismatched growth and properties of $\text{InGaAs}/\text{InAlAs}$ modulation-doped heterostructures on GaAs substrates for a full In composition range, by molecular beam epitaxy using a linearly graded InGaAs or InGaAlAs buffer layer grown at a relatively low temperature. High electron mobilities of 25,000 to 118,000 $\text{cm}^2/\text{V}\cdot\text{s}$ were obtained at 77 K for In composition from 0.3 to 0.8. The observed monotonical increase of mobility in this In composition range agreed well with the theoretical calculation. It has been shown that the use of wider bandgap material, such as InGaAlAs , in the graded buffer layer is very effective in reducing the residual carrier concentration from 1×10^{12} to less than $1 \times 10^{11} \text{ cm}^{-2}$.

1. Introduction

The lattice-mismatched growth of $\text{InGaAs}/\text{InAlAs}$ heterostructures on GaAs substrates has attracted much attention, not only because it will improve the performance of GaAs-based devices, but also because it will expand the freedom in the choice of In composition. Although the feasibility of $\text{InGaAs}/\text{InAlAs}$ HBTs and MODFETs on GaAs substrates has been demonstrated [1,2], the problem of the lattice mismatch between epilayers and the substrate was still left unsolved. We have previously shown that the use of a compositionally graded InGaAs buffer layer grown at a relatively low temperature of about 400°C greatly improves the electron mobility in such a lattice mismatched system [3,4].

In this paper, we first describe the successful growth of $\text{InGaAs}/\text{InAlAs}$ modulation-doped heterostructures for a full In composition range by using this growth technology. Then, the experimental dependence of electron mobility in these heterostructures on In composition has been analyzed and compared with that obtained by the theoretical calculation. Finally, we describe the effect of the buffer layer structure on the residual carrier distribution, which is important for the

device fabrication, and report some preliminary results on the MODFETs fabricated on these lattice-mismatched structures.

2. Layer structure

A schematic cross section of the modulation-doped $\text{InGaAs}/\text{InAlAs}$ heterostructure on GaAs is shown in fig. 1. The growth was performed by solid source MBE on (001) semi-insulating GaAs

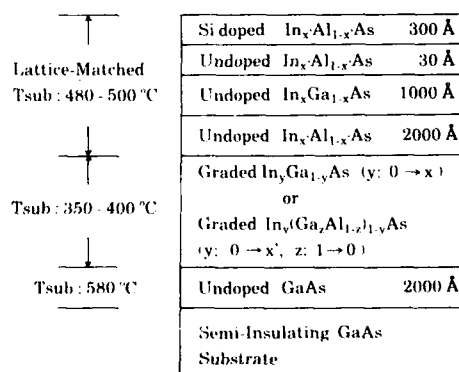


Fig. 1. Schematic cross section of $\text{InGaAs}/\text{InAlAs}$ modulation-doped heterostructure grown on a GaAs substrate.

substrates. The growth of the structure was initiated with a 2000 Å thick GaAs layer at about 580°C. Then, an $\text{In}_x\text{Ga}_{1-x}\text{As}$ or $\text{In}_x(\text{Ga}_{1-x}\text{Al}_{1-x})_{1-x}\text{As}$ with a linearly graded In composition (y) from 0.02 to the desired value (x or x') was grown at a temperature of 350–400°C. The In composition gradient was fixed to about 50%/μm. The growth was then interrupted for several minutes and the substrate temperature was raised to 480–500°C. After that, a 2000 Å thick $\text{In}_{1-x}\text{Al}_x\text{As}$ layer was grown to separate the active layers from the former buffer layer. These active layers consist of a 1000 Å thick undoped $\text{In}_x\text{Ga}_{1-x}\text{As}$ channel layer, a 30 Å thick undoped $\text{In}_{1-x}\text{Al}_x\text{As}$ spacer layer and a 300 Å thick $\text{In}_{1-x}\text{Al}_x\text{As}$ donor layer doped with Si to $2 \times 10^{18} \text{ cm}^{-3}$. The layers on top of the graded buffer layer were lattice-matched to each other except for the case of high In composition of more than 80%, where the conduction-band discontinuity between InGaAs and InAlAs becomes quite small. In such a case, a pseudomorphic InAlAs spacer and donor layers were used ($\text{In}_{0.7}\text{Al}_{0.3}\text{As}$ for $x = 0.8$ and $\text{In}_{0.8}\text{Al}_{0.2}\text{As}$ for $x = 1.0$).

3. Electron mobility

Fig. 2 shows electron mobilities measured at 300 and 77 K and sheet electron concentration (N_s) at 77 K as a function of In composition in the InGaAs channel layer. In the figure, the data obtained from similar heterostructures grown lattice-mismatched on InP substrates are also plotted, for which a graded $\text{In}_{1-x}\text{Al}_x\text{As}$ buffer layer was used. As a general tendency, the electron mobility at 300 K is seen to monotonically increase with the increase of In composition, from 7000 $\text{cm}^2/\text{V}\cdot\text{s}$ at $x = 0.2$, 10,500 $\text{cm}^2/\text{V}\cdot\text{s}$ at $x = 0.53$ to 20,000 $\text{cm}^2/\text{V}\cdot\text{s}$ at $x = 1.0$. On the other hand, at 77 K, the mobility showed its minimum value at x about 0.3 and increased almost monotonically with the increase of In composition: from 25,000 $\text{cm}^2/\text{V}\cdot\text{s}$ at $x = 0.3$, 51,000 $\text{cm}^2/\text{V}\cdot\text{s}$ at $x = 0.53$ to 118,000 $\text{cm}^2/\text{V}\cdot\text{s}$ at $x = 0.8$. These high mobility values indicate that the dislocations created to relieve the strain accumulated in the graded buffer layer are efficiently

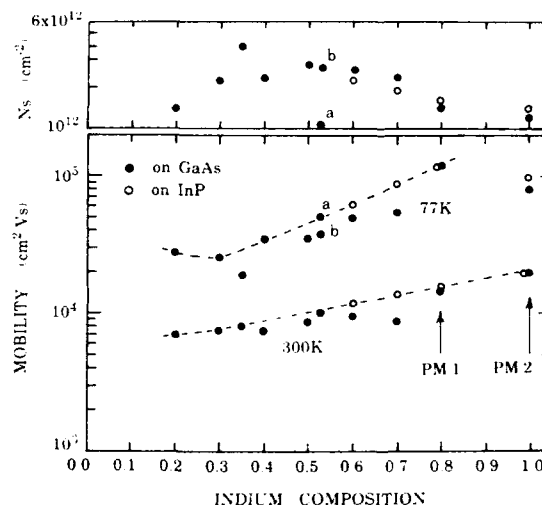


Fig. 2. Electron mobility and concentration (N_s) as a function of In composition. PM1 and PM2 indicate the samples with pseudomorphic InAlAs spacer and donor layers.

confined in this layer and the propagation of threading dislocations to the active layer is well suppressed in these heterostructures, as revealed by TEM observation reported previously [4].

In order to confirm the validity of these dependences of electron mobility on the In composition, a theoretical calculation has been performed assuming a single-subband transport and using the Stern–Howard variational wave function [5]. For the total mobility and that limited by polar optical phonon scattering (PO), we have used the iteration method developed by Nag [6]. The calculated results at 77 K with $N_s = 1 \times 10^{12} \text{ cm}^{-2}$ is shown in fig. 3. From this figure, the In composition dependence of electron mobility is mostly determined by alloy-scattering-limited mobility (AL) and at about $x = 0.3$, the mobility takes the minimum value. The solid circles in the figure indicate the highest mobility obtained in the experiment for each In composition. The agreement between the experimental results and the calculated ones is excellent in spite of the difference in N_s value between experiment and calculation. Anyway, this result also supports the good crystallinity of the active layer in our heterostructures.

It should be noted that if we look at fig. 2 carefully, the mobility value for $x > 0.5$ tends to

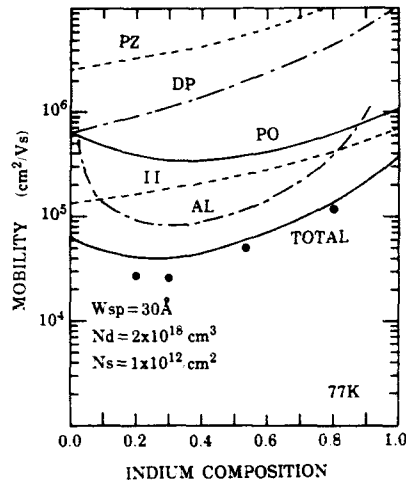


Fig. 3. Calculated 77 K mobility as a function of In composition in the channel layer. Each symbol represents electron mobility limited by polar-optical phonon scattering (PO), alloy scattering (AL), ionized impurity scattering (II) acoustic-phonon deformation potential scattering (DP) and acoustic-phonon piezoelectric scattering (PZ).

saturate and the structures on InP or those with pseudomorphic InAlAs spacer and donor layers show higher values than the standard samples on GaAs substrates. The cause for such differences is not clear at present, but the contribution of parallel conduction in the donor layer or in the thick buffer layer is considered to be one of the factors.

4. Residual carrier and its distribution

When the MODFETs were fabricated on the epilayers grown on graded $\text{In}_{0.53}\text{Ga}_{0.47}\text{As}$ buffer

layers, the device isolation by mesa-etching and Schottky diode characteristics were found to be very poor. In order to clarify the cause for such high leakage currents, we have grown some undoped $\text{In}_{0.53}\text{Ga}_{0.47}\text{As}/\text{InAlAs}$ heterostructures either on a graded InGaAs buffer layer (sample B) or on a graded InGaAlAs buffer layer (sample D) and measured the residual carrier concentration in these structures. The results are summarized in table 1, together with those for modulation-doped heterostructures (samples A and C). The residual carrier concentration in the undoped structure on a graded InGaAs buffer layer was found to be surprisingly high, about $1 \times 10^{12} \text{ cm}^{-2}$, while that on a graded InGaAlAs was one order of magnitude lower, about $1 \times 10^{11} \text{ cm}^{-2}$ or less. The high residual carrier concentration in sample B is probably due to the narrower bandgap and/or higher background carrier concentration of the undoped InGaAs graded buffer layer than those of the InGaAlAs graded buffer layer.

The locations of the residual electron concentration were then studied using a capacitance-voltage carrier profiling method. Two samples were prepared for this experiment using n-type GaAs substrates: one is an undoped $\text{In}_{0.53}\text{Ga}_{0.47}\text{As}/\text{InAlAs}$ heterostructure on a graded InGaAs buffer layer via a 1000 Å thick InAlAs (fig. 4a) and the other is a modulation-doped heterostructure on a graded InGaAlAs buffer layer (fig. 4b). As seen in fig. 4a, for the undoped heterostructure on a graded InGaAs buffer layer, a sharp peak of electron concentration is located at the heterointerface between the 1000 Å thick InAlAs and the graded InGaAs buffer layer, just like a two-dimensional electron gas accumulated in modulation-doped

Table 1
Electron mobility (μ) and concentration (N_s) for modulation-doped (MD) and undoped (U) $\text{In}_{0.53}\text{Ga}_{0.47}\text{As}/\text{InAlAs}$ heterostructures grown on graded InGaAs buffer layer or graded InGaAlAs buffer layer

Sample	Buffer layer	Structure	300 K		77 K	
			μ ($\text{cm}^2/\text{V}\cdot\text{s}$)	N_s (cm^{-2})	μ ($\text{cm}^2/\text{V}\cdot\text{s}$)	N_s (cm^{-2})
A	Graded InGaAs	MD	10400	1.7×10^{12}	45000	1.8×10^{12}
B		U	9000	1.1×10^{12}	32000	9.4×10^{11}
C	Graded InGaAlAs	MD	9500	2.1×10^{12}	41000	2.1×10^{12}
D		U	5400	8.6×10^{10}	18000	1.1×10^{11}

heterostructures. This fact suggests that the electrons are flowing through two InGaAs channels in the samples in fig. 2 grown on InGaAs buffer layers. This also explains the good agreement of the theoretical calculation with the experiment in fig. 3. On the other hand, for the modulation-doped heterostructure grown on InGaAlAs buffer layer in fig. 4b, the peak of residual electron concentration is seen inside the InGaAlAs buffer layer, the amount of which is about one order of magnitude lower than that observed in fig. 4a.

The $0.5\text{ }\mu\text{m}$ gate $\text{In}_{0.5}\text{Ga}_{0.5}\text{As}$ / InAlAs MODFETs were fabricated using a heterostructure with a graded InGaAlAs buffer layer on a semi-insulating GaAs substrate, the layer structure of which is

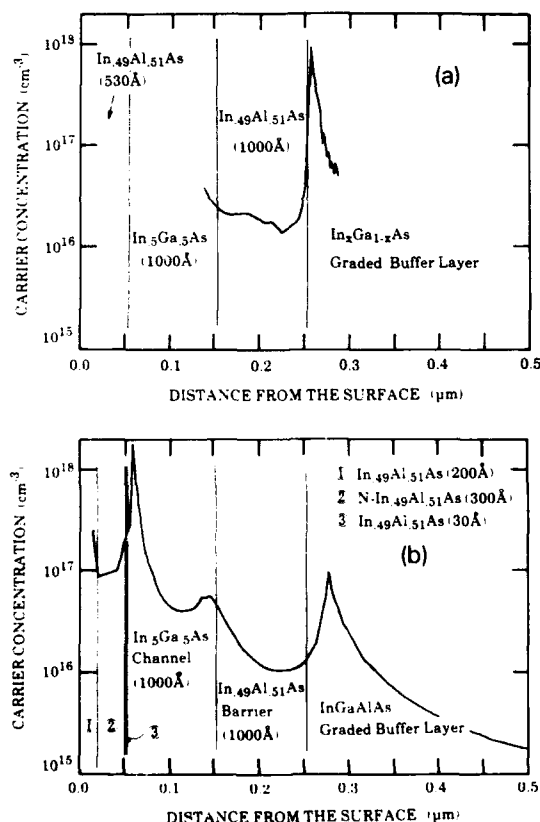


Fig. 4. Carrier profiles in (a) an undoped $\text{In}_{0.5}\text{Ga}_{0.5}\text{As}$ / InAlAs heterostructure grown on a graded $\text{In}_{0.5}\text{Ga}_{0.5}\text{As}$ buffer layer and in (b) a modulation-doped $\text{In}_{0.5}\text{Ga}_{0.5}\text{As}$ / InAlAs heterostructure grown on a graded $\text{In}_{0.5}(\text{Ga}_{0.5}\text{Al}_{0.5})_{1-x}\text{As}$ buffer layer.

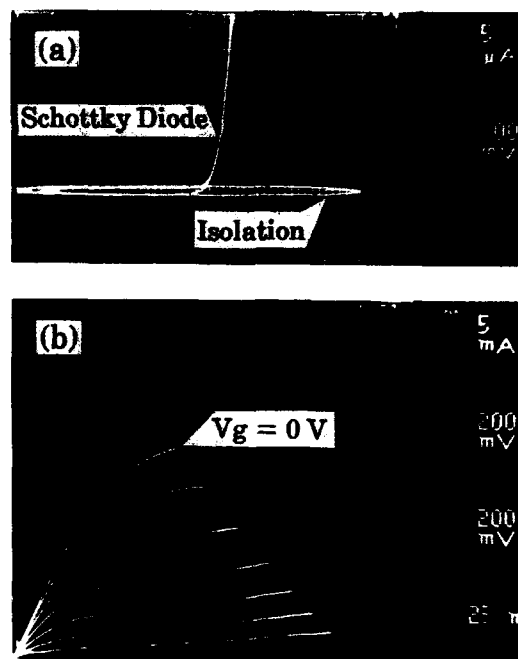


Fig. 5. (a) Schottky diode and device isolation characteristics and (b) drain I - V characteristics for the fabricated $0.5\text{ }\mu\text{m}$ gate MODFET. The gate width is $80\text{ }\mu\text{m}$.

the same as the one shown in fig. 4b. The device isolation and the Schottky diode characteristics were found to be good, as shown in fig. 5a. These improvements are probably due to the use of InGaAlAs for the graded buffer layer. The leakage current between two MODFETs about $100\text{ }\mu\text{m}$ apart was less than $1\text{ }\mu\text{A}$ at an applied voltage of 10 V . Although a high transconductance of 370 mS/mm was obtained, the pinch-off characteristics are still needed to be improved, as seen in fig. 5b. We believe that these MODFET characteristics will be further improved by optimizing the layer structure and reducing the residual carrier concentration, for which a use of wider bandgap material such as InAlAs as a graded buffer layer will be effective.

5. Summary

In summary, we have successfully grown InGaAs / InAlAs modulation-doped heterostructures

lattice mismatched to GaAs substrates for a full In composition range. The dependence of mobility on In composition was theoretically analyzed, and agreed very well with the experimental results. The importance of using wide gap material for the buffer layer has been pointed out, to reduce the residual carrier concentration and to improve the MODFET characteristics.

Acknowledgments

The authors would like to thank Dr. S. Horiuchi and T. Onuma for their continuous encouragement throughout this work.

References

- [1] T. Won S. Agarwala and H. Morkoç, Appl. Phys. Letters 53 (1988) 2311.
- [2] G.W. Wang, Y.K. Chen, W.J. Schaff and L.F. Eastman, IEEE Trans. Electron Devices ED-35 (1988) 818.
- [3] J.C. Harmand, T. Matsuno and K. Inoue, Japan. J. Appl. Phys. 28 (1989) 1101.
- [4] J.C. Harmand, T. Matsuno and K. Inoue, in: Proc. 16th Intern. Symp. on GaAs and Related Compounds, Karuizawa, 1989, Inst. Phys. Conf. Ser. 106, Eds. T. Ikoma and H. Watanabe (Inst. Phys., London-Bristol, 1990) p. 177.
- [5] F. Stern and W.E. Howard, Phys. Rev. 163 (1967) 816.
- [6] B.R. Nag, J. Phys. C (Solid State Phys.) 7 (1974) 3541.

The growth and physics of high mobility two-dimensional hole gases

A.G. Davies, J.E.F. Frost, D.A. Ritchie, D.C. Peacock *, R. Newbury, E.H. Linfield, M. Pepper and G.A.C. Jones

Cavendish Laboratory, University of Cambridge, Madingley Road, Cambridge CB3 0HE, UK

Modulation-doped p-type GaAs–Al_xGa_{1-x}As heterojunctions have been grown by molecular beam epitaxy (MBE) on the (311)A GaAs surface using silicon as the acceptor. Two-dimensional hole gases with mobilities as high as 570,000 cm² V⁻¹ s⁻¹ at 50 mK have been obtained. It is shown that the sample mobility is dependent upon the direction of orientation of the fabricated Hall bar on the MBE wafer which could be due to the anisotropic nature of the Fermi surface in p-type systems. Experimental results on the fractional quantum Hall effect (FQHE) in these high mobility hole gases are also presented.

1. Introduction

The majority of experimental work on GaAs–Al_xGa_{1-x}As heterojunctions grown by MBE has been performed upon n-type material. The properties of p-type heterojunctions have been neglected mainly because their quality has generally been much poorer than that of n-type systems. Most MBE growth takes place on the (100) GaAs surface and beryllium is traditionally used as an acceptor. It has been reported, however, that high quality epitaxial growth can take place on the (311)A GaAs surface as confirmed by low temperature photoluminescence studies for bulk GaAs [1] and for single quantum wells [2]. Furthermore, it has been shown that silicon is an acceptor for growth on this surface and very high mobility material can be achieved [1,3]. This paper reports the growth of such p-type heterojunctions having mobilities as high as 570,000 cm² V⁻¹ s⁻¹ at 50 mK. The highest quality samples have been used to investigate the FQHE [4].

The larger heterojunction mobility resulting from this method of growth has been attributed to the reduced carbon and sulphur impurity incorporation onto the (311)A surface during MBE growth

[3]. Silicon MBE sources are intrinsically more pure than beryllium sources and furthermore, silicon does not have the tendency to diffuse during growth as much as beryllium. The use of silicon as a p-type dopant also eliminates the possibility of beryllium contamination of subsequent n-type wafers grown in the same MBE chamber.

2. Sample growth and characterisation

A series of p-type structures was grown on (311)A GaAs substrates in a solid-source VG Semicon V80H MBE machine with substrate temperatures between 630 and 680 °C as measured by an Ircon infra-red pyrometer during the GaAs buffer growth. A silicon cell temperature of 1083 °C gave an n-type carrier concentration of 1.7×10^{18} cm⁻³ in bulk GaAs grown on (100) wafers at 1 μm/h which doubled when the temperature was increased by 20 °C. A Keithley electrometer connected to the collector of a nude ion gauge mounted on the back of the substrate manipulator was used to monitor the beam flux. Both “D” shaped chromium-doped horizontal Bridgman substrates with a two inch major axis and circular undoped two inch LEC substrates were used and were mounted in indium-free holders of proprietary design. Each wafer con-

* Also at GEC Hirst Research Centre, East Lane, Wembley HA9 7PP, UK.

tained a GaAs buffer, an $\text{Al}_x\text{Ga}_{1-x}\text{As}$ undoped spacer layer, a 40 nm silicon-doped $\text{Al}_x\text{Ga}_{1-x}\text{As}$ layer and finally a 10 nm GaAs capping layer. Wafers were grown at growth rates of both 1 and 2 $\mu\text{m/h}$. The aluminium fraction, x , was usually 0.3 but four wafers were grown with $x = 0.5$. Some wafers also contained a superlattice buffer consisting of $20 \times (2.5 \text{ nm AlAs} + 2.5 \text{ nm GaAs})$ layers situated 1 μm below the heterointerface. This structure leads to the formation of a two-dimensional hole gas in the GaAs buffer just below the undoped $\text{Al}_x\text{Ga}_{1-x}\text{As}$ spacer layer.

The epitaxial layers were processed into Hall bar geometries by means of conventional photolithography and wet-etching techniques. It was noted, however, that our standard mesa etch of $\text{H}_2\text{SO}_4:\text{H}_2\text{O}_2:\text{H}_2\text{O}$ (1:8:80 by volume) had a reduced etch-rate for the (311)A samples compared with those on the more usual (100) substrate. Both InZn alloy contacts annealed at 350°C and evaporated AuZnAu ohmic contacts annealed at 435°C were employed depending upon the size of the Hall bar contact pads, the smaller Hall bars having the evaporated contacts. Electrical transport measurements were performed using conventional low-frequency AC lock-in techniques.

3. Results and discussion

Fig. 1 shows the variation of sheet carrier density with spacer thickness for the p-type wafers. A

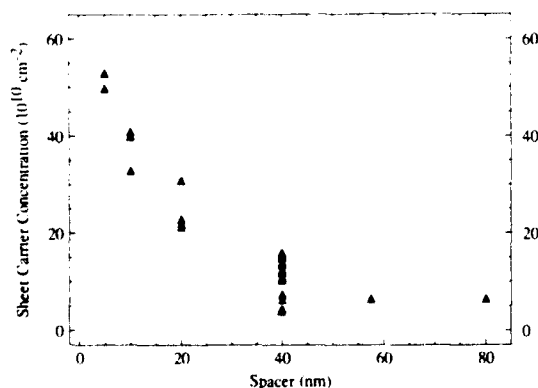


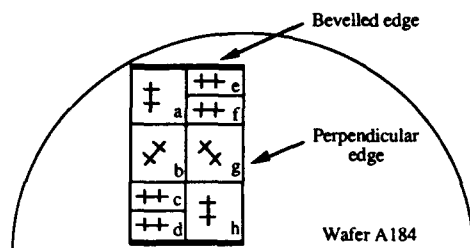
Fig. 1. The variation of sheet carrier density with spacer layer thickness for twenty four p-type $\text{GaAs-Al}_x\text{Ga}_{1-x}\text{As}$ heterojunctions.

systematic and reproducible variation can be seen, with the sheet carrier density reducing rapidly with increased spacer thickness in a similar way to that reported for n-type samples [5]. The mobility was not a simple function of spacer thickness and a peak value of about $250,000 \text{ cm}^2 \text{ V}^{-1} \text{ s}^{-1}$ at 4.2 K was attainable for all spacer thicknesses between 10 nm and 40 nm. It has been reported for n-type heterostructures that the mobility of successive nominally identical wafers tends to increase slowly following a reload of the cells [5,6]. This may explain the scatter in the mobility data and suggests that accurate conclusions concerning the dependence of mobility on growth parameters may only be drawn from the properties of samples grown in close succession.

Wafers A326, A327 and A328 each contained 40 nm spacer layers and were grown at a rate of 2 $\mu\text{m/h}$ with an As/Ga ratio of 7.5, an aluminium fraction $x = 0.3$ and a substrate temperature of 640°C but with silicon-cell temperatures of 1083, 1103 and 1063°C, respectively. Wafers A326 and A327 had very similar carrier densities ($n = 1 \times 10^{11} \text{ cm}^{-2}$) and mobilities ($\mu = 180,000 \text{ cm}^2 \text{ V}^{-1} \text{ s}^{-1}$) at 4.2 K but wafer A328, grown with the lowest silicon-cell temperature, had a factor of two decrease in the carrier density and an order of magnitude reduction in the mobility. These results indicate that although the carrier density increases with increasing silicon flux there is a saturation of carrier densities for high silicon flux.

Wafers A165 and A188 were grown during the same growth-run and each contained a 40 nm spacer layer and had an aluminium fraction $x = 0.5$. These wafers were grown at a rate of 1 $\mu\text{m/h}$ with a silicon-cell temperature of 1083°C and a substrate temperature of 650°C. Sample A165 was grown with an As/Ga ratio of 5.7 and had a resulting carrier density of $1.5 \times 10^{11} \text{ cm}^{-2}$ and a mobility of $180,000 \text{ cm}^2 \text{ V}^{-1} \text{ s}^{-1}$ at 4.2 K. Sample A188, however, was grown with an As/Ga ratio of only 4.9 and this wafer was found to be highly resistive at 4.2 K.

The mobility of the best samples was found to continue to increase as the temperature was reduced below 4.2 K. For example, samples processed from wafer A198 had an average mobility of around $540,000 \text{ cm}^2 \text{ V}^{-1} \text{ s}^{-1}$ at 50 mK



Hall Bar	μ ($10^5 \text{ cm}^2 \text{ V}^{-1} \text{ s}^{-1}$)	n (10^{11} cm^{-2})
a (+)	2.18	2.41
b (/)	1.97	2.21
c (-)	1.71	2.19
d (-)	1.77	2.27
e (-)	1.73	2.40
f (-)	1.69	2.27
g (\)	2.04	2.16
h (+)	2.44	2.11

Fig. 2. A schematic diagram of MBE wafer A184 showing the positions and orientations of the eight Hall bars. The table gives the mobilities and carrier densities of the eight Hall bars at 4.2 K.

which was twice the 4.2 K mobility. The carrier concentration of this wafer was $1.2 \times 10^{11} \text{ cm}^{-2}$ which did not change appreciably over this temperature range.

Due to the anisotropic nature of the Fermi surface in p-type material, the magnitude of the Fermi wave vector is directionally dependent [7]. It is possible, therefore, that the mobility of p-type devices will depend upon the direction of current flow since carriers with a large wave vector are less susceptible to ionised impurity scattering. In order to investigate this, eight Hall bars were processed in different orientations on MBE wafer A184 and the mobility and carrier density of these devices was obtained at 4.2 K. A schematic diagram showing the positions of the eight Hall bars on the "D" shaped wafer is given in fig. 2 together with the resulting mobilities and carrier densities. It can be seen that there was a large variation in the mobility with Hall bar orientation, ranging from an average of $230,000 \text{ cm}^2 \text{ V}^{-1} \text{ s}^{-1}$ with the Hall bars in the "vertical" direction to an average of $170,000 \text{ cm}^2 \text{ V}^{-1} \text{ s}^{-1}$ for the "horizontal" orientation. The

mobilities of the "diagonal" Hall bars lay between these limits. The variation of the carrier density between samples was about 13% which is typical across an MBE wafer and was not obviously linked to the Hall bar direction or to the resulting sample mobility. Thus, although the transport is diffusive and any carrier will be scattered and change its wave vector many times a second, there was still a systematic variation of sample mobility with current direction. This shows that it is important to orientate the Hall bars correctly if the highest mobility devices are to be obtained. When (311)A wafers were cleaved into rectangular samples, it was found that the edges are either bevelled or perpendicular to the sample surface as shown in fig. 2. Assuming that the (311)A samples cleave preferentially along the {110} set of planes as is expected for zincblende crystals, the perpendicular edges must correspond to the (011) plane. For rectangular samples, the bevelled edges must represent the (011) plane. The presence of these bevelled and perpendicular edges allows the consistent orientation of Hall bars on different wafers. The highest mobilities were found for current flow in the "vertical" orientation in fig. 2 which is the $[\bar{2}33]$ direction.

The FQHE has attracted considerable experimental and theoretical attention recently [8]. The FQHE is driven by the Coulomb interactions between the carriers in a two-dimensional system and is destroyed by excessive disorder in the material. It is for this reason that most experimental investigations of this effect have been performed on high mobility n-type $\text{GaAs-Al}_{1-x}\text{Ga}_x$ As heterojunctions although p-type systems have also been studied [9]. Fig. 3 shows the Hall (ρ_{xy}) and diagonal (ρ_{xx}) magnetoresistivity of a silicon-doped (311)A p-type sample of mobility $\mu = 540,000 \text{ cm}^2 \text{ V}^{-1} \text{ s}^{-1}$ and carrier density $n = 1.2 \times 10^{11} \text{ cm}^{-2}$ at dilution refrigerator base temperature ($< 40 \text{ mK}$). Structure associated with both the integer and fractional quantum Hall effects can be observed. Fractional states are seen at filling factors $\nu = 5/3, 7/5, 2/3, 3/5, 4/7, 3/7$ and $2/5$, in conjunction with quantised plateaux in the Hall resistance for the stronger fractions. The magnetic field was not large enough for the $1/3$ fraction to be observed in this sample, al-

though this fraction has been seen in material with a lower carrier density.

An unusual aspect of this data is the absence of the $4/3$ fraction even though the $5/3$ and $7/5$ states are present. It was found that if the sample was tilted in situ in the magnetic field, the $4/3$ state emerges [4]. In n-type samples of comparable carrier densities, the $4/3$ is present at low fields and is seen to be destroyed gradually as the sample is tilted before finally re-emerging [10]. This behaviour is explained by finite-size calculations which show that at low magnetic fields the interacting carriers forming certain fractional states can possess spins aligned both parallel and anti-parallel to the applied field [11]. As the sample is tilted, a given fraction is pushed to higher magnetic fields. This increases the Zeeman energy of the reversed spins causing these fractional states to change. The fact that much lower magnetic fields seem to be required to destroy and recover the $4/3$ state in p-type material in comparison with n-type material suggests that the Zeeman energy of a fractional state at a given magnetic field is larger in the p-type samples [4].

4. Conclusions

The growth of silicon-doped p-type GaAs-Al_xGa_{1-x}As heterostructures on the (311)A GaAs surface has been investigated. It is found that very high mobility structures can be achieved. The mobility of a processed Hall bar has been shown to be dependent upon its orientation on the MBE wafer which is possibly caused by the anisotropic nature of the Fermi surface in these systems. The FQHE has been studied in the best quality samples. The behaviour of the fractional structure as the sample is tilted in the applied magnetic field suggests that the Zeeman energy of the fractional states at a given magnetic field is larger in this material than in comparable n-type devices.

Acknowledgements

We are grateful for the technical assistance of Mr. D.R. Charge, Mr. D.W. Heftel and Mr. D.I. Swainston. The financial support of the SERC is acknowledged.

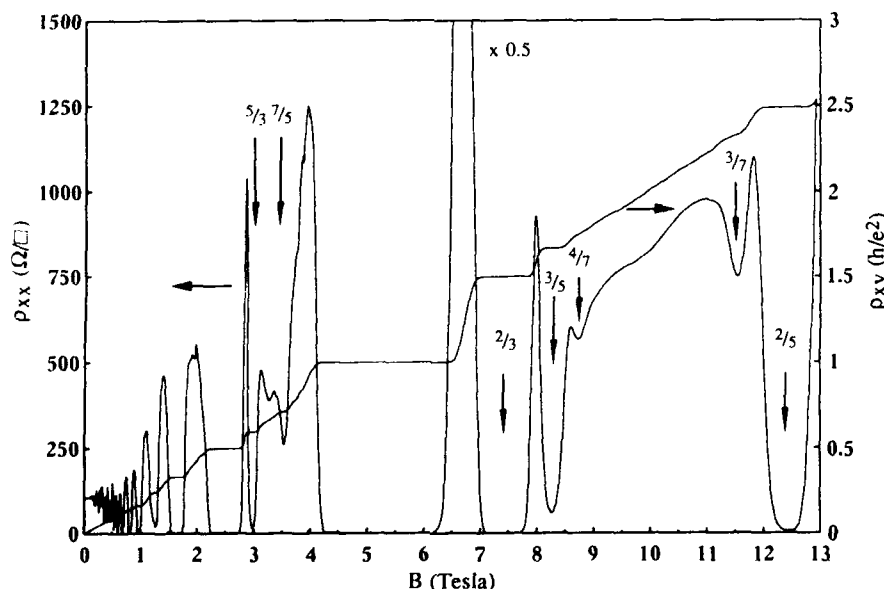


Fig. 3. The ρ_{xx} and ρ_{xy} magnetoresistivity of p-type GaAs-Al_xGa_{1-x}As sample A198F3 ($n = 1.2 \times 10^{11} \text{ cm}^{-2}$, $\mu = 540,000 \text{ cm}^2 \text{ V}^{-1} \text{ s}^{-1}$).

References

- [1] W.I. Wang, R.F. Marks and L. Vina, *J. Appl. Phys.* 59 (1986) 937.
- [2] T. Fukunaga, T. Takamori and H. Nakashima, *J. Crystal Growth* 81 (1987) 85.
- [3] W.I. Wang, E.E. Mendez, Y. Iye, B. Lee, M.H. Kim and G.E. Stillman, *J. Appl. Phys.* 60 (1986) 1834.
- [4] A.G. Davies, to be published;
A.G. Davies, in: *Proc. 20th Intern. Conf. on Physics of Semiconductors*, Thessaloniki, Greece, 1990 (World Scientific, Singapore).
- [5] J.J. Harris, C.T. Foxon, D.E. Lacklinson and K.W.J. Barnham, *Superlattices and Microstructures* 2 (1986) 563.
- [6] C.T. Foxon and J.J. Harris, *Philips J. Res.* 41 (1986) 313.
- [7] U. Ekenberg and M. Altarelli, *Phys. Rev.* B32 (1985) 3712.
- [8] See, for example, T. Chakraborty and P. Pietiläinen, *The Fractional Quantum Hall Effect* (Springer, Berlin, 1988).
- [9] H.L. Störmer, A. Chang, D.C. Tsui, J.C.M. Hwang, A.C. Gossard and W. Wiegmann, *Phys. Rev. Letters* 51 (1983) 1953;
E.E. Mendez, *Surface Sci.* 170 (1986) 561.
- [10] R.G. Clark, S.R. Haynes, A.M. Suckling, J.R. Mallett, P.A. Wright, J.J. Harris and C.T. Foxon, *Phys. Rev. Letters* 62 (1989) 1536.
- [11] P.A. Maksym, *J. Phys. Condens. Matter* 1 (1989) 6299.

Serpentine superlattice: concept and first results

M.S. Miller ^a, C.E. Pryor ^b, H. Weman ^{c,e}, L.A. Samoska ^d, H. Kroemer ^{a,d} and P.M. Petroff ^{d,a}

University of California, Santa Barbara, California 93106, USA

We present an epitaxial growth technique for vicinal substrates which avoids the geometric tilt sensitivity inherent to the cyclic growth of such structures as tilted superlattices. This cyclical deposition and growth technique produces a serpentine superlattice (SSL) (M.S. Miller et al., in: Proc. 20th Intern. Conf. on Physics of Semiconductors, Thessaloniki, August 1990). Purposefully varying the per-cycle growth rate produces a lateral superlattice with a variable, meandering tilt, with 1 D, microscopically confined electronic states formed where the superlattice bends over. The quantum wire electronic confinement is principally determined by the SSL shape near these widest regions, near places with a vertical tangent. This shape is accurately established through the smooth adjustment of the fractional monolayer growth rates. If a large enough range of growth rates is spanned, then a particular confinement structure is guaranteed: With a SSL, quantum wire arrays with particular energy levels may be precisely realized. Not only is this true at a particular place on the substrate, but the growth rate variations across a substrate are automatically accommodated and uniform wires are realized over the entire wafer. Calculations of the two-dimensional subband structure were performed for (Ga,Al)As SSLs to confirm the 1D electronic states, determine optimal structure parameters and explain experimental results. Such (Ga,Al)As SSLs have been prepared by MBE and characterized with photoluminescence. We find emitted light in several samples that is polarized parallel to the direction of the vicinal substrate's steps, which we interpret to be consistent with quasi-1D confinement.

1. Introduction

Epitaxially grown heterostructures give one dimension of microscopic compositional control, typified by 1D quantum wells and modulation doped heterostructures, and can also, in principle, provide good confinement in two dimensions. Approaches to epitaxial 2D confining heterostructures in III–V semiconductor systems include techniques of cyclic deposition and growth on vicinal substrates, giving tilted superlattices (TSLs) [2,3] or fractional layer superlattices [4], and regrowth techniques on either finely patterned substrates, which exploit the differing growth of barrier and well materials at the bottom of a trench [5], or on cleaved epitaxial layers [6]. In particular,

TSLs have not successfully been used to form two-dimensional confinement structures with good electrical and optical properties. One reason for poorly defined confinement is because of the thermodynamic difficulty of having fractional layers segregate fully on the vicinal terraces in the (Ga,Al)As system. Perhaps this may be avoided through a better understanding of the growth processes in this system or by turning to other systems such as the (Ga,Al)Sb system [7]. Another problem, intrinsic to the growth geometry, is that the tilt is not a well controlled parameter. This stems from the facts that the deposition and growth rates cannot be characterized to within less than about one percent and that growth rate variations across a substrate are typically greater than one percent. One percent errors in the growth rate variously give tilts of 14° and 30° on vicinal GaAs substrates misoriented 2° and 1°, respectively, from the (100) surface [2]. Electronic confinement energies, and resulting electrical and optical properties, will change with the tilt and are thus not well controlled in a TSL. We present here

^a Department of Computer and Electrical Engineering.

^b Department of Physics.

^c QUEST Center for Science and Technology.

^d Department of Engineering Materials.

^e Permanent address: Linköping University, Linköping, Sweden.

another cyclic deposition and epitaxial growth technique for vicinal surfaces. The resulting structures, named serpentine superlattices (SSLs) for their purposefully meandering shapes, may be employed to obtain quantum wires (QWs) [1]. These structures inherently accommodate the geometric sensitivity to absolute growth rates. The calculations of the electronic subband structure and envelope wavefunctions we present confirm the quality of this 2D confining geometry. To date we have prepared a number of (Ga,Al)As SSL QW samples using molecular beam epitaxy (MBE) to characterize their optical and structural properties. The polarization dependence of the emitted photoluminescence data that we present suggests that we have achieved electronic states confined to 1D, but is not conclusive.

Serpentine superlattices are produced with a cyclic deposition and growth technique on vicinal substrates, taking the relative coverage between successive deposition cycles as a variable, controlled parameter. During such a growth with MBE, for example, the shuttering of the molecular

beams is under computer control and may be changed each cycle by a certain amount relative to the other cycles. Smoothly sweeping the per-cycle coverage back and forth through a range including monolayer coverage gives a structure with a continuously varying tilt, as is schematically represented in fig. 1a. Two-dimensional electronic confinement may be obtained at the wide places in the winding wells, where the structure turns a corner. The shape near these regions determines the energy spectrum of the confinement. Perhaps the most interesting case occurs for a linear ramping of the per-cycle coverage through a range including vertical growth. This instance gives a SSL with a cross section of periodically displaced parabolas having curvatures determined by the mis-orientation angle and the per-cycle coverage ramping rate $1/z_0$. The confinement energies are determined by z_0 , the lateral well and barrier widths, and the barrier height. The confinement in this case is insensitive to errors in the absolute growth rates. An error shifts the vertices of the parabolas up or down in the growth direction but

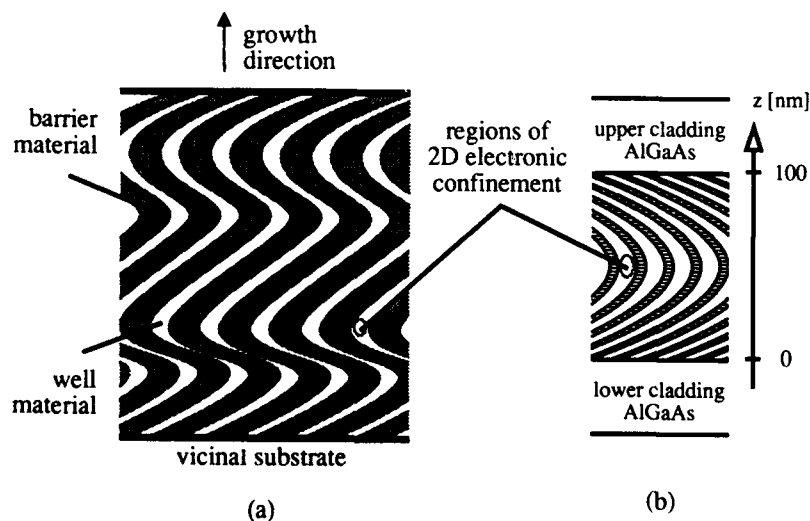


Fig. 1. A SSL cross section is shown (a) that would result from sweeping the per-cycle coverage back and forth through a range that includes exact monolayer coverage. At such places, where the tangent to the structure is vertical, electronic states are confined to two dimensions. The 2D potential energy minima near these regions may be characterized by the lateral barrier and well widths, lateral barrier height and the local curvature of the SSL. (b) Most of the simulated and grown structures have been single-crescent, parabolic geometries with barriers cladding the SSL region above and below.

does not change their shape. Thus a confinement may be obtained that is quite insensitive to growth rate variations across an entire substrate.

2. Calculations and experimental results

We have calculated energy levels, superlattice subbands, density of states (DOS) and envelope wavefunctions for the two-dimensional SSL confinement geometry in order to quantify the quality of the quantum confinement, understand the variation of confinement energies with the available design parameters and model problems with actual structures. A typical configuration for which we have computed energy levels is depicted in fig. 1b, a parabolic single-crescent serpentine structure placed between upper and lower cladding layers. For the calculation the SSL potential energy is defined on a grid with hard-wall boundaries above and below and lateral periodic boundary conditions. The effective mass varies with the alloy composition. This is solved as a series of eigenvalue problems at increasingly finer grid spacings with the final result being an extrapolation to zero grid spacing. Fig. 2 gives contour plots of conduction band electron envelope wavefunctions and DOS for a single-crescent, parabolic SSL configured similar to the structure of fig. 1b. The simulated structure had a per-cycle growth-rate ramping constant of $z_0 = 125$ nm, vertical barriers of $x = 1$, and both the lateral barrier and well thicknesses of 5.4 nm. The wavefunction results of fig. 2a show the good confinement of this structure in the growth direction, where the lowest state is localized to about 10 nm in the growth direction. Fig. 2b clearly demonstrates the expected 1D-like DOS for such a confining potential. The first and second conduction band electron subbands are seen to be separated by 34 meV. Other calculations we have performed include examining gated SSL structures and modeling the effects of unintentional Al in the GaAs well.

A number of (Ga,Al)As samples have been grown by MBE for characterization of their optical and structural properties. Most of these specimens have been single-crescent parabolic structures prepared with a 20% change in the per-cycle

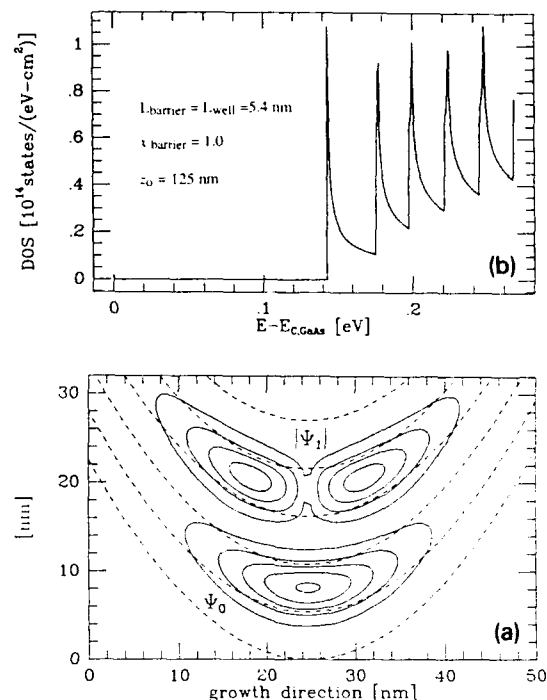


Fig. 2. Calculated results for a single-crescent serpentine superlattice are presented. (a) Contour plots of the conduction band envelope wavefunction of the ground state, Ψ_0 , and of the absolute value of the first excited state, $|\Psi_1|$, are superimposed on dashed lines that define the well and barrier regions. The lowest contour is more than an order of magnitude below the highest. (b) The electron density of states (DOS) is also given for this structure. Note the very good 1D-like shape of the lower bands.

coverage over approximately 100 nm of growth, thus having $z_0 = 500$ nm. These have been produced on vicinal (100) GaAs substrates misoriented towards [111]A. The SSL layers are deposited in an alternating beam, migration enhanced epitaxy mode at substrate temperatures between 600 and 610°C on two or more substrates simultaneously. The principal characterization technique has been the measurement of polarization dependent photoluminescence (PL) spectra at 1.4 K. Fig. 3 gives PL data for a single-crescent SSL grown on a 2° misoriented substrate. The spectra were obtained by exciting the sample obliquely with 488 nm light and observing the light emitted normal to the surface through a polarizing

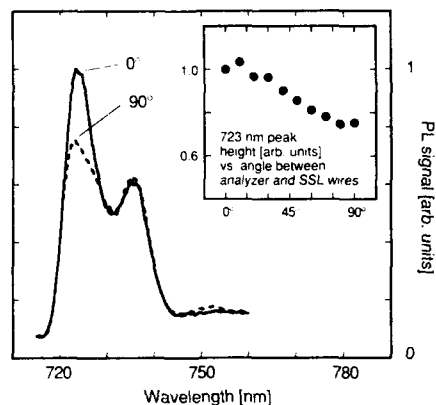


Fig. 3. The polarization dependence of the photoluminescence from a single-crescent SSL on a 2° substrate (81 nm step width) with the layer dimensions of fig. 2b is given. The SSL (Ga,Al)As barriers nominally cover $3/7$ of a step and have $x = 1/3$. A polarizer has been placed between the sample and the monochromator in order to analyze the emitted light. The light from the shoulder peak around 735 nm is seen to be unpolarized. The weak signal at longer wavelengths is also seen to be polarized. The main peak is assigned to recombination from quantum wire states in the SSL, and the shoulder peak to defect-related recombination.

analyzer. The angles in the figure are taken between the anticipated wire direction and the analyzer's orientation. The larger peak at 723 nm exhibits a polarization dependence, where most of the luminescence is polarized parallel to the wire direction. The polarization dependence of this main peak is what is expected from a simple theory for recombination from a heavy hole-like quantum wire state [8]. The intensity of this peak, as well as corresponding peaks in most of the other SSL samples prepared to date, is comparable to the intensity of witness quantum wells which are placed in the cladding layers. The position of this peak is approximately determined by the nominal total average alloy composition of the SSL structure, which is well above, by perhaps 80 meV, what would be expected for this SSL in which all of the AlAs resides in well defined barriers, and none in the wells. We have modeled this poor segregation with a calculation which assumes that much of the AlAs from the barriers is uniformly distributed into the wells and then estimates the actual segregation in the structure

with a fit to the measured peak position. However, because the peak position is set by alloy composition, which is not known better than to several percent, and because the energy difference between the poorly segregated barriers and wells is relatively small, we are unable to make a reliable estimate. The polarization effects have been seen on 1° and 2° mis-oriented substrates, but are much weaker or absent on 0.5° and 4° substrates. The states which give the lower energy shoulder peak at 735 nm emit unpolarized light normal to the sample surface. Photoluminescence excitation measurements confirm that this shoulder peak originates from states within the structure that gives the main SSL peak. This peak is only present in some of the SSL samples grown to date and has lifetime that is typically two orders of magnitude longer than that of the main peak. We have concluded that this is a defect-related peak in the SSL. A weak polarization dependence in the background at energies below the main peaks is also seen.

3. Conclusions and future work

We have presented here a technique for growing epitaxial 2D confining heterostructures. Our calculations predict the serpentine superlattice geometry may give good confinement in (Ga,Al)As structures. The initial PL results we have presented are qualitatively consistent with confinement to 1D. SSL structures might well have applications in studying 1D systems and in devices. Towards these ends we have prepared samples for transport measurements and begun to calculate the responses of gated structures. A particular device application currently being pursued is that of using a SSL in a quantum wire laser.

Acknowledgements

This work has been supported by the National Science Foundation. We would like to thank A.C. Gossard, J.H. English, M. Tsuchiya, J.M. Gaines, D.B. Young and S.A. Chalmers for their help in MBE growth on vicinal surfaces.

References

- [1] M.S. Miller, C.E. Pryor, H. Weman, L.A. Samoska, H. Kroemer and P.M. Petroff, in: *Proc. 20th Intern. Conf. on Physics of Semiconductors*, Thessaloniki, August 1990, Eds. E.M. Anastassakis and J.D. Joannopoulos (World Scientific, Singapore).
- [2] J.M. Gaines, P.M. Petroff, H. Kroemer, R.J. Simes, R.S. Geels and J.H. English, *J. Vacuum Sci. Technol. B6* (1988) 1378.
- [3] M. Tsuchiya, P.M. Petroff and L.A. Coldren, *Appl. Phys. Letters* 43 (1989) 1690.
- [4] T. Fukui and H. Saito, *J. Vacuum Sci. Technol. B6* (1988) 1373.
- [5] Yia-Chung Chang, L.L. Chang and L. Esaki, *Appl. Phys. Letters* 47 (1985) 1324.
- [6] E. Kapon, D.M. Hwang and R. Bhat, *Phys. Rev. Letters* 63 (1989) 430.
- [7] S.A. Chalmers, A.C. Gossard and H.K. Kroemer, *Appl. Phys. Letters*, in press.
- [8] S.W. Corzine, R.H. Yan and L.A. Coldren, unpublished UCSB preprint.

Growth kinetics and electronic characteristics of quantum wires

A.K. Myers-Beaghton *, J.P.G. Taylor, D.D. Vvedensky *, K.J. Hugill * and A. MacKinnon

The Blackett Laboratory, Imperial College, London SW7 2BZ, UK

The fabrication and characterization of narrow quantum wires is studied with a combination of theoretical techniques. Using the compositional integrity as a measure of quality, our earlier work has shown that quantum wires generated by a Monte Carlo simulations of crystal growth attain the highest quality within a narrow range of substrate temperatures that depends upon the beam flux and terrace width. We examine the factors that influence the electronic density of states of such quantum wires within a tight-binding framework and discuss the compositional integrity of the structures in relation to the quantum mechanical integrity. The effects of migrating species with different mobility parameters are then considered by appealing to recent work describing growth on vicinal surfaces with an effective nonlinear diffusion equation.

1. Introduction

The control of interface compositional disorder is implicit in many of the predicted characteristics of narrow quantum wells and quantum wires [1]. However, in the growth of quantum wells, there is a lower limit to the superlattice period below which the benefits of the reduced dimensionality are lost and some of the material characteristics are more similar to those of an alloy with the corresponding average composition [2]. In part, this is due to imperfect layer-by-layer growth, since even under optimum conditions of molecular-beam epitaxy (MBE), the growth front is spread over several layers. In the case of quantum-wires, interface disorder is compounded by the reduced dimensionality of the growth front, i.e., the step edges, because fluctuations in the step-edge profile are far more facile than the fluctuations in the planar growth front of a quantum well. This leads to a more irregular lateral interface for quantum wires and thus to more stringent kinetic restrictions on the lower limit of the lateral dimension of quantum wires.

The basic principle behind quantum-wire growth by conventional MBE stems from the work

of Neave et al. [3], who showed that the growth mode on a vicinal surface is temperature-dependent. At low temperatures, growth proceeds by the formation and coalescence of two-dimensional clusters on terraces, while at higher temperatures, enhanced surface mobility promotes the direct incorporation of migrating atoms at the step edges, with growth occurring by step advancement. In principle, the high-temperature growth mode may be exploited for growing (Al,Ga)As quantum wires by arranging the substrate temperature(s), Ga and Al fluxes, and misorientation angle to favor growth by step advancement for both group III species. Quantum wire arrays or tilted superlattices are then achieved by alternately depositing appropriate fractional monolayers of the constituent materials.

In practice, quantum wires are grown either by MBE [4,5] or as coherent tilted superlattices [6] under conditions known as migration-enhanced epitaxy (MEE) [7,8]. However, since simulations of MEE growth kinetics are only beginning to emerge [9], we will concentrate on the kinetic limitations to the growth of narrow quantum wires by conventional MBE. By using a combination of Monte Carlo simulations, nonlinear diffusion equations, and tight-binding calculations of electronic structure we will examine the factors that degrade the compositional integrity of the wire

* Also at Interdisciplinary Research Centre for Semiconductor Materials.

due to the interaction between Ga and a less-mobile species such as Al, and determine the effects of various types of disorder upon the electronic density of states of the lowest subbands of the quantum wires.

2. Theoretical methods

The Monte Carlo simulations are based upon a solid-on-solid model of MBE, wherein the substrate is modeled as a simple cubic lattice on which overhangs are not permitted. Growth is initiated by the random deposition of atoms onto the lattice at a rate JA , where J is the flux and A is the substrate area. The migration of adatoms is treated as a nearest-neighbor hopping process, with the hopping rate given by

$$k(E, T) = k_0 \exp(-E/k_B T),$$

where k_0 is an adatom vibrational frequency ($\approx 10^{13} \text{ s}^{-1}$), k_B is Boltzmann's constant, T is the substrate temperature, and E is the barrier to migration. The barrier consists of a substrate term E_S and a contribution E_N from each nearest neighbor along the substrate. Thus, $E = E_S + nE_N$, where $n = 0, 1, \dots, 4$. By direct comparison with the experiments of Neave et al. [3], the optimum values of these diffusion barriers for GaAs(001) have been determined to be $E_S = 1.45 \text{ eV}$ and $E_N = 0.3 \text{ eV}$ [10]. By choosing isotropic mobility parameters, we have neglected the effects of the surface reconstruction. The generalization of the model to explicitly include the reconstruction is analogous to the case of simulations of (001) homoepitaxy [11], and is discussed elsewhere [12].

Our analytic work is based upon a nonlinear continuum model for MBE that includes diffusion and an approximation to adatom interactions in the form of diatomic island formation [13]. A natural outcome of the model is the identification of the transition temperature, T_c , at which growth by step propagation dominates island-formation:

$$T_c = (E_{\text{eff}}/k_B) [\ln(k_0 a^2 / 2Jh^4)]^{-1},$$

where E_{eff} is an effective diffusion barrier, h is the terrace length, and a is the nearest-neighbor

distance of the square lattice. Excellent agreement is obtained between the values of T_c determined by the nonlinear model, with $E_{\text{eff}} = 1.4 \text{ eV}$, and those obtained from both Monte Carlo simulations and measurements on vicinal GaAs (001) surfaces for different Ga and As₂ fluxes [10]. This result, together with the considerable reduction in effective diffusivity predicted by the model [13] and observed experimentally [3], highlight the role of the adatom interactions as an essential ingredient in a realistic model of MBE.

The electronic structure of quantum wires is calculated using a single-band nearest-neighbor tight-binding Hamiltonian, which allows the disorder at the interfaces to be treated exactly [14]. The effective Schrödinger equation can be written in terms of site components as

$$\epsilon_i c_i + \sum_j V_{ij} c_j = E c_i,$$

where c_i is the amplitude of the wavefunction at site i , and ϵ_i is the potential, which takes either the value ϵ_{Ga} or ϵ_{Al} . The hopping elements V_{ij} are the kinetic energy terms, which will be taken to have the constant value, V , between nearest neighbors and zero otherwise. For GaAs/AlAs wires, we must choose $\epsilon_{\text{Al}} \gg \epsilon_{\text{Ga}}$. In the limit $\epsilon_{\text{Al}} \rightarrow \infty$, the Ga subband can be studied by considering only the Ga sites. This provides a considerable saving in the computer time and has little effect on the results when compared with more realistic values for ϵ_{Al} . It must be stressed, however, that this treatment is not intended to represent in detail any realistic GaAs/AlAs system, but only to treat on a quantum mechanical level a system for which the scattering structure is similar to that of a realistic system.

3. Results and discussion

Following previous work [15], we model quantum-wire growth by first considering a system in which the two constituent components have identical kinetic properties, and are distinguished solely by a label. In this way we can focus upon the key features that determine the morphology of these

structures before addressing the effect of a second species. The growth of quantum wires was simulated by alternately depositing half monolayers of "B" and "A" material for a total of ten layers upon a substrate of "A".

To quantify the compositional integrity of these structures, the "quality" has been defined as the average percentage of "B" atoms present within the region that would be completely occupied with "B" atoms if the wire growth was perfect. Our earlier work showed that the quality so defined exhibited a flux-dependent maximum as a function of substrate temperature. At low temperatures, the poor quality is due to the residual formation of clusters on the terraces, while at higher temperatures, the decreasing wire quality results from large-amplitude fluctuations in the step-edge profile, which lead to the meandering of the step edge outside of the target area.

The important growth-induced features that can degrade the electronic structure of quantum wires are (i) the disorder at the interface, (ii) residual island-formation within the wire, and (iii) the long-wavelength meandering of the wire. Since achieving the required resolution in energy for a density of states profile necessitates generating wires of length up to 50,000 lattice spacings, we first present the result of a preliminary study that successively incorporates the effects of (i)–(iii) in wires constructed from the statistics of simulated wires. The integrated density of states was calculated for two-dimensional planar wires since the computational requirements for treating wires with a full two-dimensional cross-section are at the moment prohibitive. However, planar structures similar to those whose electronic structure we are calculating have been grown by MBE [16], so this idealization is not as drastic as it may first appear.

Sections of the three types of wires studied are shown in fig. 1, with a fixed-width meandering structure in fig. 1a to which interface fluctuations are added in fig. 1b and islands in fig. 1c. The mean width in all three cases is 10 atomic units and the statistics used to generate these structures were taken from the appropriate correlation functions of simulated wires (fig. 1d). The corresponding densities of states near the band edge are shown in fig. 2. The physically interesting region

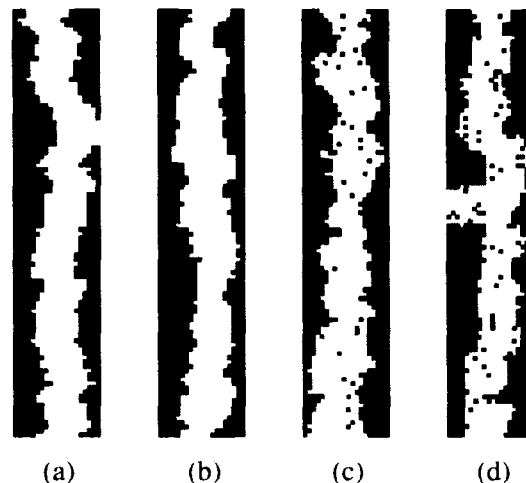


Fig. 1. Sections of 20-atom-wide quantum wires generated from the statistics of simulated wires, with (a) with fixed-width meandering only and (b) with fluctuations in the width included, and (c) with islands, compared with (d) simulated wires at the optimum temperature as measured by compositional integrity. The dark and light shading indicate regions of Al(As) and Ga(As), respectively.

of the spectrum is that close to the band edge, where the wavefunctions with long wavelengths along the wire direction should be least sensitive to perturbations of the wire width. The effect of meandering on the density of states in fig. 2a is seen to be quite small, with the first three subbands being clearly discernible. However, the inclusion of width fluctuations has an evident detrimental effect, with only the first subband showing sharp definition (fig. 1b). The addition of islands has an even stronger degrading effect, presumably by forcing nodes in the wavefunction, which wipes away the remaining characteristic features of the density of states. These results are expected to be a strong function of the width of the quantum wire, with the effects of the interface disorder diminishing with increasing lateral extent. The morphologies in figs. 1a–1c also indicate that the characterization of wire quality based upon structural integrity can be a misleading measure of *quantum mechanical integrity*, since increasing the substrate temperature decreases both the island density and the interface disorder.

The presence of a second, less mobile species,

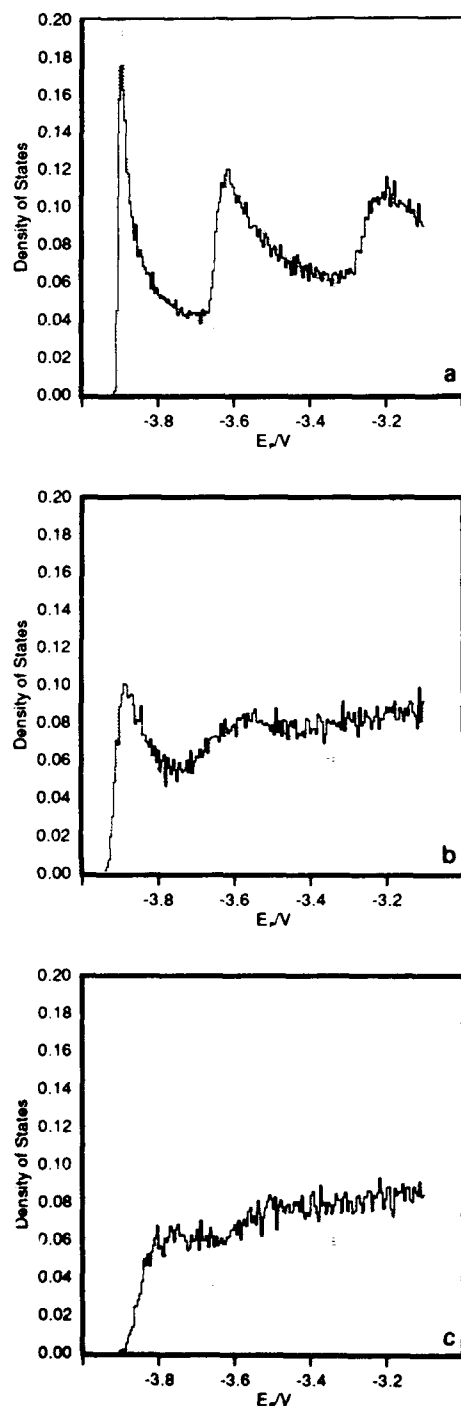


Fig. 2. The densities of states near the band edge of monolayer slices of quantum wires generated from the statistics of simulated wires shown in figs. 1a–1c.

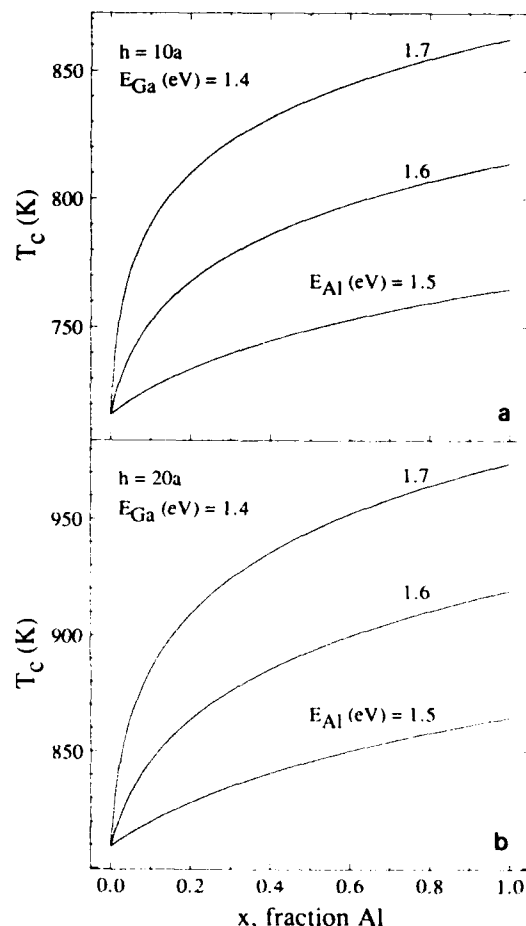


Fig. 3. The variation in T_c as function of Al concentration for growth of $\text{Al}_x\text{Ga}_{1-x}\text{As}$, $0 \leq x \leq 1$ on a vicinal surface with terraces of length $h = 10a$ and $h = 20a$. The total flux has been set to 1 ML/s.

e.g. Al, can affect the morphology of the quantum wires in several ways. First, the growth temperature must be chosen so that the growth of the alloy proceeds by step advancement. Since adatom interactions decreases the effective mobility of Ga by providing capture sites for diffusing Ga atoms, the appropriate growth temperature depends upon the Al concentration. Furthermore, Al is expected to increase the density of step-edge kink sites, which leads to a rough step profile and increases the width fluctuations of the wire.

Although the mobility parameters of Al have not been determined because of complications in-

volved in growing at the required elevated temperatures, the values of T_c can be estimated for a given value of the effective diffusion barrier of Al by appealing to the nonlinear diffusion equation adapted to account for two diffusing species. The calculated transition temperatures are shown in fig. 3a for $\text{Al}_x\text{Ga}_{1-x}\text{As}$, $0 \leq x \leq 1$ on a vicinal surface with terraces of length $h = 10a$, with the corresponding calculation for $h = 20a$ shown in fig. 1b. The diffusion barrier for Ga was set to 1.4 eV as determined above, while for Al, calculations with the values 1.5, 1.6, and 1.7 eV are shown. Figs. 4a and 3b suggest that even if the RHEED measurements were performed for an $\text{Al}_x\text{Ga}_{1-x}\text{As}$ alloy at a single concentration (for $x \geq 0.1$), there is sufficient discrimination between the curves corresponding to different values of E_{Al} to permit an estimate of the effective diffusion barrier for Al.

4. Conclusions

We have identified several important factors that determine the growth and electronic characteristics of (Al,Ga)As quantum wires. Tight-binding calculations for monolayer slices of wires generated from the statistics of the simulated wires reveal the importance of the interface profile fluctuations and islands in determining the appearance of quasi-one-dimensional electronic characteristics. These calculations imply that the interaction between Ga and Al both on the terraces and at the step edges under growth conditions of conventional MBE are expected to lead to a degradation of wire quality in terms of the electronic structure. Future calculations will explore more detailed analytical models for growth

on vicinal surfaces as well as extending the calculations on the simulated quantum wires to transport phenomena.

Acknowledgements

This work was supported by NATO, through a Postdoctoral Fellowship to A.K.M.-B., and by the UK Science and Engineering Research Council.

References

- [1] G. Bastard, *Wave Mechanics Applied to Semiconductor Heterostructures* (Editions de Physique, Les Ulis, 1988).
- [2] K.J. Moore, G. Duggan, P. Dawson and C.T. Foxon, *Phys. Rev. B* 38 (1988) 5535.
- [3] J.H. Neave, P.J. Dobson, B.A. Joyce and J. Zhang, *Appl. Phys. Letters* 47 (1985) 100.
- [4] M. Tanaka and H. Sakaki, *J. Appl. Phys.* 64 (1988) 4503.
- [5] H. Sakaki, M. Tanaka and J. Yoshino, *Japan. J. Appl. Phys.* 24 (1988) L417.
- [6] M. Tsuchiya, P.M. Petroff and L.A. Coldren, *Appl. Phys. Letters* 54 (1989) 1690.
- [7] Y. Horikoshi, M. Kawashima and H. Yamagushi, *Japan. J. Appl. Phys.* 25 (1986) L868.
- [8] Y. Horikoshi, M. Kawashima and H. Yamagushi, *Japan. J. Appl. Phys.* 27 (1988) 169.
- [9] Y.-T. Liu, P. Petroff and H. Metiu, *Appl. Phys. Letters* 57 (1990) 2683.
- [10] D.D. Vvedensky and S. Clarke, *Surface Sci.* 225 (1990) 373.
- [11] M.R. Wilby, S. Clarke, T. Kawamura and D.D. Vvedensky, *Phys. Rev. B* 40 (1989) 10617.
- [12] B.A. Joyce, J.H. Neave, J. Zhang, D.D. Vvedensky, S. Clarke, K.J. Hugill, T. Shitara and A.K. Myers-Beaghton, *Semiconductor Sci. Technol.* 5 (1990) 1147.
- [13] A.K. Myers-Beaghton and D.D. Vvedensky, *Phys. Rev. B* 42 (1990) 5544.
- [14] A. MacKinnon and B. Kramer, *Z. Physik* B53 (1983) 1.
- [15] K.J. Hugill, S. Clarke, D.D. Vvedensky and B.A. Joyce, *J. Appl. Phys.* 66 (1989) 3415.
- [16] M. Tanaka and H. Sakaki, *Appl. Phys. Letters* 54 (1989) 1326.

Quantum wire structures by MBE overgrowth on a cleaved edge

Loren Pfeiffer, H.L. Störmer, K. West and K.W. Baldwin

AT&T Bell Laboratories, Murray Hill, New Jersey 07974, USA

We have recently demonstrated the existence of a high mobility ($6.1 \times 10^5 \text{ cm}^2/\text{V}\cdot\text{s}$) two-dimensional electron gas (2DEG) at the (110) vicinal surface formed by cleaving [L. Pfeiffer et al., Appl. Phys. Letters 56 (1990) 1697] a (100) GaAs wafer. We have now expanded this work to modulation-doped overgrowth on the cleaved edge of a multiperiod superlattice. We report here the first observation of the quantum Hall characteristics in such a two-dimensional system containing an atomically precise 71 Å GaAs by 31 Å $\text{Al}_{0.24}\text{Ga}_{0.76}\text{As}$ compositional superlattice. The onset of Shubnikov–De Haas oscillations occurs at only 3000 G, implying the Landau cyclotron orbits are phase coherent over diameters as large as 5000 Å, corresponding to more than 200 GaAs/AlGaAs interface crossings.

Our recent demonstration of the MBE growth of high quality AlGaAs on the cleaved edge [1] of a GaAs wafer opens up exciting new possibilities for all sorts of laterally confined quantum structures having unprecedented atomic precision in two or even three dimensions. We will describe the cleaved growth method, review our initial results establishing the quality of the MBE overgrowth, and then describe new work on modulation-doping over cleaved multiperiod superlattices, including a demonstration of phase coherence over Landau cyclotron orbits that cross 200 or more GaAs/AlGaAs interfaces.

The concept of quantum wire fabrication by MBE growth on a cleaved edge of a GaAs wafer is

illustrated in fig. 1. As can be imagined from the figure the idea is sufficiently straightforward to have occurred to many people over the past 15 years [2]. Until now, however, technical difficulties with the quality of the second MBE growth have prevented successful experiments along these lines. The technical difficulties are of two types: (i) One must find a new set of MBE conditions for high quality growth on the (110) atomic surfaces of GaAs. We must grow on the (110) surface because GaAs crystals show a strong natural preference for cleavage on (110) lattice planes. (ii) Any cleavage must be performed in UHV and preferably in situ in the MBE growth chamber, because exposure to atmospheric contamination will irre-

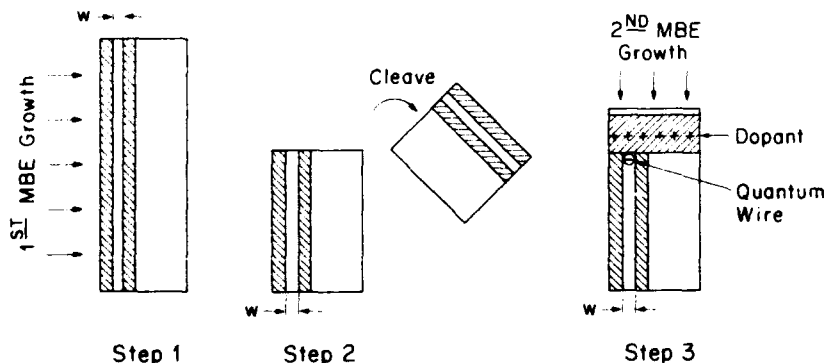


Fig. 1. The concept of laterally confined quantum wire fabrication by MBE growth on a cleaved edge.

versibly damage the fresh (110) atomic surface, particularly so of those layers containing aluminum.

The literature of III-V epitaxy contains very few accounts of growth on surfaces other than (100), and only a handful [3-6] that discuss GaAs growth on or near (110). However, these references make it clear that good epitaxy on an exact (110) surface is very difficult, because As_4 does not readily stick to the non-polar (110) surface even in a Ga flux. The proposed solutions include increasing the As_4 overpressure, lowering the substrate temperature, using As_2 in lieu of As_4 , or choosing a surface misaligned by a degree or so from exact (110) GaAs. But misaligned (110) surfaces are not useful here, because the cleave will expose an *exact* (110) GaAs surface. We found use of an As_2 beam did improve the morphology of the overgrowth, but so far we have been unable to find suitable conditions for good (110) epitaxy using As_2 . In growth tests using 5 cm diameter GaAs wafers polished on (110) surfaces to within 0.1° we generally confirm the conditions found by Zhou, Huang, Li and Jia [6]. We use a beam-equivalent As_4 ion gauge pressure of 1.6×10^{-5} Torr measured at the substrate position, and a substrate temperature of $480\text{--}500^\circ\text{C}$ measured using an Ircon Type V infrared pyrometer [7] calibrated assuming a congruent sublimation temperature for GaAs of 640°C . Modulation-doped 250 Å wide quantum wells grown on (110) wafers under these conditions at a growth rate of 0.5 monolayers/s show smooth featureless morphology free of excess Ga and clean 4-point Shubnikov-De Haas (SdH) spectra (see fig. 2), and 2DEG mobilities in the range 3 to 5×10^5 $\text{cm}^2/\text{V}\cdot\text{s}$ in the dark, after exposure to light at 1K. This mobility is an order of magnitude better than the best previous reported [6] for epitaxial material.

We decided to use a cleave as opposed to *ex situ* lapping or etching in order to provide the cleanest possible surface on which to proceed with further epitaxial growth. A clean surface can only degrade with time and handling. So it is obvious that ideally the sample should be in the MBE growth chamber, at the proper growth temperature, with the proper orientation, and in the proper

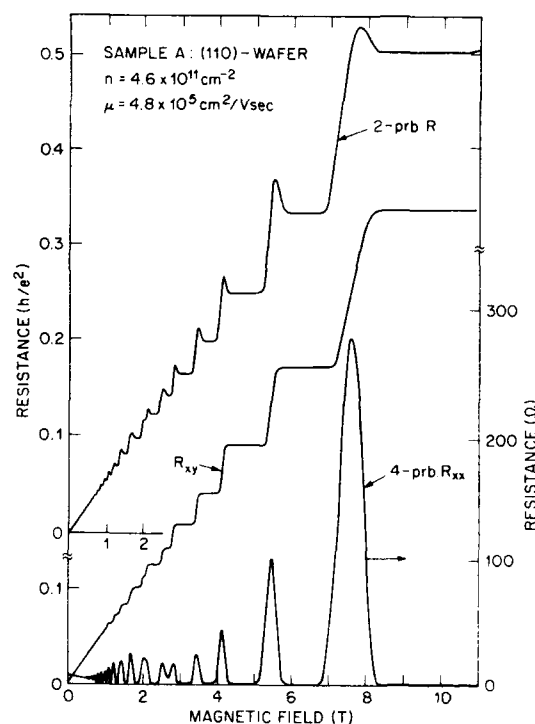


Fig. 2. Four-probe and 2-probe magneto-resistance (4-probe R_{xx}) and Hall resistance R_{xy} of a two-dimensional electron gas in a $4\text{ mm} \times 4\text{ mm}$ planar (110) modulation-doped sample grown at the same time as the edge cleaved sample of fig. 3.

molecular fluxes before the cleave. The cleave then becomes the last step before overgrowth on the newly exposed (110) edge. We modified our Varian Gen II MBE equipment [8] to accomplish the *in situ* cleave.

In order to establish the quality of the MBE growth on a cleaved interface, we decided to postpone our quest for novel quantum wire physics, and instead to look for the quantum Hall effect in a two-dimensional electron gas (2DEG) at the cleave of previously MBE grown GaAs material. The sample was prepared for the cleave by growing 1000 Å of undoped GaAs, then 7 μm of superlattice consisting of alternating layers of 100 Å $\text{Al}_{0.33}\text{Ga}_{0.67}\text{As}$ and 30 Å GaAs, then 10 μm of GaAs, followed by 7 μm of superlattice cap. In this case the GaAs wells of the superlattice are kept very narrow so that only the 10 μm thick

GaAs layer later supports a 10 μm wide 2DEG. After growth the wafer is removed from the machine, lapped from the backside to a thickness of 150 μm , and cleaved into rectangular pieces 5 mm \times 10 mm. A scratch 0.5 mm long is made where the future in situ cleave is to occur. After cleaning these pieces are mounted using Ga metal solder on a special Ta metal substrate holder. The pieces are soldered against a 3 mm high Ta bracket so that their 10 mm length extends in free space normal to the plane of the sample holder's front surface. To monitor the quality of the growth, and to provide a surface of proper emissivity for the pyrometer, a (110) oriented wafer is mounted conventionally with Ga solder on the front surface of the Ta holder not occupied by the edge growth samples. The holder is in all other respects compatible with the Varian Gen II sample transfer equipment. Thus the sample is put into the load-lock of the MBE machine, vacuum outgassed, and loaded into the growth chamber in the usual way.

The non-rotated sample holder is oriented in the growth chamber so the multilayer side of the yet-to-be-cleaved sample pieces do not see any flux from the Si furnace. The oxide from the (110) planar sample is desorbed at $\sim 630^\circ\text{C}$ in the As_4 flux. Subsequently, the substrate temperature is lowered to 485°C , and the precleave growth on the (110) planar substrate begins. The precleave layer sequence is as follows: 3000 \AA GaAs, a 1300 \AA superlattice consisting of alternating layering of 100 \AA $\text{Al}_{0.3}\text{Ga}_{0.7}\text{As}$ and 30 \AA GaAs, and finally a 1000 \AA GaAs wide layer which will become the 2DEG channel in the (110) planar sample.

All growth is then stopped for a few seconds during the cleave. The cleave is accomplished by moving a Ta metal bar against the upright un-cleaved pieces along a path parallel to and ~ 7 mm above the front surface of the substrate holder. Within about 1–2 s after the cleave, the MBE growth resumes. But now the growth proceeds on both the newly exposed cleave as well as the adjacent (110) planar wafer. The post-cleave layer sequence is as follows: 300 \AA $\text{Al}_{0.3}\text{Ga}_{0.7}\text{As}$ undoped setback, Si δ -doping at 10^{12} cm^{-2} , 3000 \AA $\text{Al}_{0.3}\text{Ga}_{0.7}\text{As}$, completed by a 50 \AA GaAs cap.

Fig. 2 shows standard magneto-transport measurements on the (110) planar sample using both

4-probe and 2-probe transport geometries. We show this comparison for reference because the growth on the cleaved surface (see fig. 3) produces a narrow stripe of 2D electrons, which makes the common 4-probe measurement very difficult. In the less common 2-probe geometry R_{xx} and R_{xy} are admixed as seen in the magneto-transport spectrum in fig. 3 marked 0° . In this case the magnetic field is perpendicular to the 2D electron system. We observe the characteristic magnetic field dependence of a 2D electron system which resembles the Hall resistance in a 4-probe configuration. As compared to fig. 2 the mixing of R_{xx} into R_{xy} is much stronger due to the much larger aspect ratio of 10 μm /600 μm of the edge sample as compared to 4 mm/4 mm in planar sample. Nevertheless, in the high-field regime a clear plateau of $R_{xy} = h/2e^2$ is well resolved from which we can deduce the electron density $n = 3.6 \times 10^{11}\text{ cm}^{-2}$. This is only slightly less than in the simultaneously grown planar sample shown in fig. 2. From the resistance of the 600 μm long, 10 μm

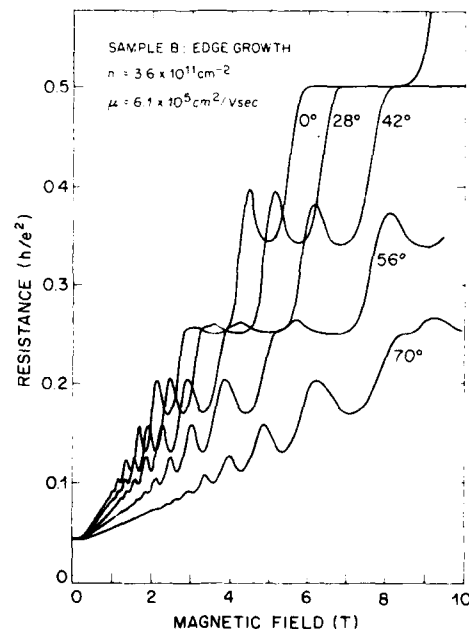


Fig. 3. Two-probe magneto-resistance data of a two-dimensional electron gas in a modulation-doped sample regrown with MBE on a (110) surface after an in situ edge cleave.

wide stripe we infer a mobility of $\mu = 6.1 \times 10^5$ $\text{cm}^2/\text{V} \cdot \text{s}$; slightly in excess of the planar sample. The other traces show the magneto-resistance of the cleaved sample as the cleaved surface normal is rotated at various angles away from the direction of the magnetic field. The magneto-resistance pattern shows the orderly $\cos \theta$ shift which is expected from a 2D electron gas located in the plane of the (110) cleave. The lack of any additional oscillations proves that the 2DEG exists only on the cleaved surface and that no other 2DEG has been grown accidentally on any other of the exposed surfaces.

Having established that our MBE growth following an in situ cleave can produce high quality material, we turned our attention to the compositional 2D-superlattice structure shown in fig. 4. The sample preparation is similar to the previous case except that now the MBE growth before the cleave is a superlattice consisting of the repeating pair 71 \AA GaAs/ 31 \AA $\text{Al}_{0.24}\text{Ga}_{0.76}\text{As}$. This superlattice is grown with $1 \times 10^{18} \text{ cm}^{-3}$ Si doping for the first $1 \mu\text{m}$, then undoped for $3 \mu\text{m}$, and finally with $1 \times 10^{18} \text{ cm}^{-3}$ Si doping for the last $3 \mu\text{m}$. After growth the sample is prepared for cleaving

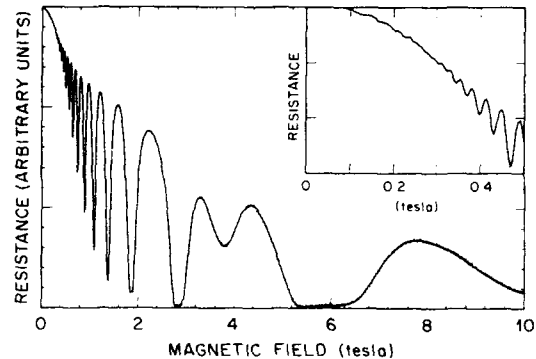


Fig. 5. Magneto-resistance of the modulation-doped compositional 2D superlattice.

as described before with the cleaned, backside lapped, $5 \text{ mm} \times 10 \text{ mm}$ pieces mounted so their 10 mm lengths point toward the MBE source ovens. The proper conditions for (110) epitaxy are then established in the MBE growth chamber. The cleave and post-cleave growth sequence are also the same as before except that now the undoped $\text{Al}_{0.33}\text{Ga}_{0.67}\text{As}$ setback is reduced to 250 \AA to increase the 2DEG carrier concentration.

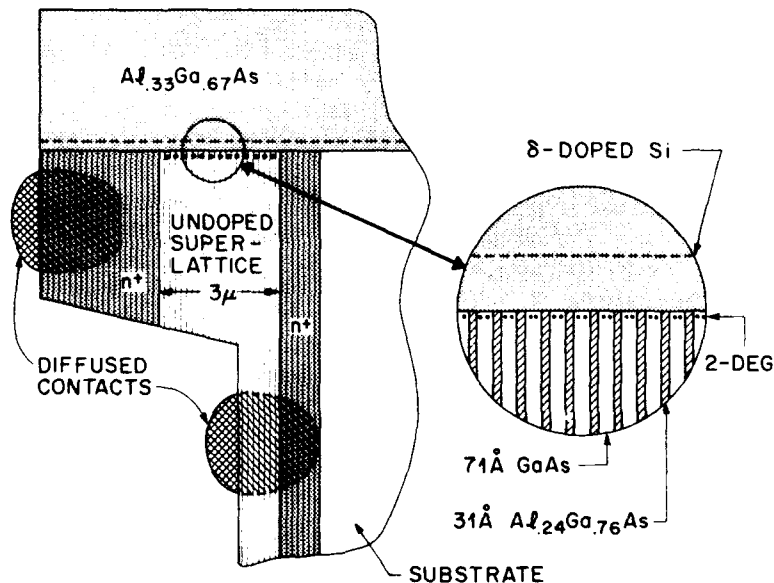


Fig. 4. Structure of the modulation-doped compositional 2D superlattice.

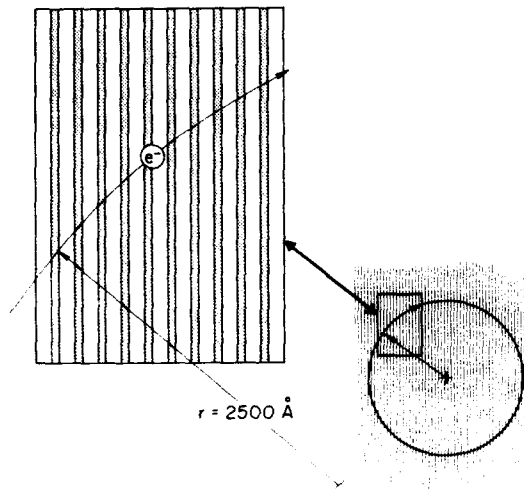


Fig. 6. Schematic diagram of the electron orbit corresponding to the Shubnikov-De Haas onset.

The magneto-transport measurements are made using diffused contacts to the n^+ layers shown in fig. 4. Fig. 5 shows the well established broad zero-resistance minima associated with the existence of a quantum Hall effect (QHE) in this compositional 2D-superlattice sample. The spin

splitting corresponding to a filling factor $\nu = 3$ is clearly resolved at 4.06 T. From the period of the oscillations we deduce a 2D electron density of $3.0 \times 10^{11} \text{ cm}^{-2}$. The onset of the SdH oscillations occurs at only 0.3 T (see inset of fig. 5). Using the classical cyclotron orbit formula

$$m^*v^2/r = eBv,$$

and regarding the system as isotropic with an effective mass $m^* = 0.07 m_0$, we deduce a cyclotron orbital radius of $r = m^*v/eB$. Here e is the electron charge, v the electron velocity which in this case is the Fermi velocity $\approx 2 \times 10^7 \text{ cm/s}$, and B is the magnetic field. At the onset field $B = 0.3 \text{ T}$ the orbital radius r corresponds to $\approx 2500 \text{ Å}$. Thus, at onset, the nearly circular orbit (see fig. 6) must cross more than 200 GaAs/AlGaAs interfaces while maintaining sufficient phase coherence to show a distinct oscillation in magneto-transport.

Due to the contact resistance no direct measure of the sample mobility is available for the 2D superlattice. However, we can obtain a lower bound estimate by assuming $\omega\tau \approx 1$, at the onset of the SdH oscillations. Recalling $eB/m^* = \omega$ from the cyclotron formula and using the resulting

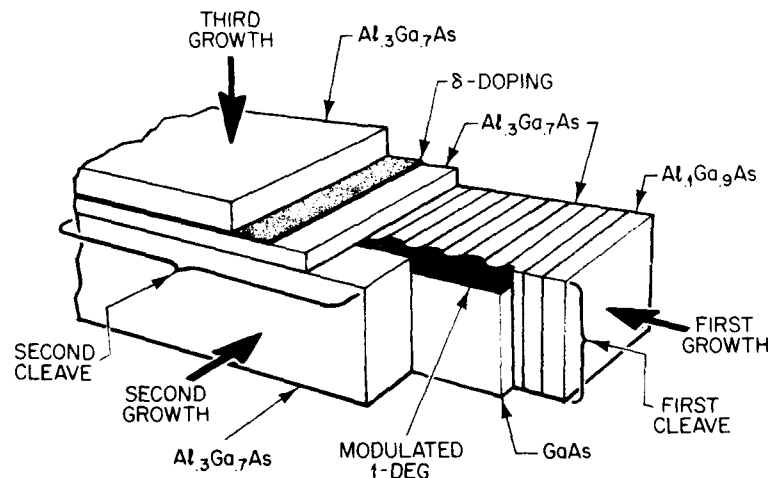


Fig. 7. Proposed structure of a modulation-doped quantum wire (1DEG) that is longitudinally modulated with an adjacent superlattice.

relaxation time τ_s as a lower limit for the mobility scattering time τ_l we arrive at $\mu = e\tau_l/m^* \geq e\tau_s/m^* = 33,000 \text{ cm}^2/\text{V} \cdot \text{s}$. As is known from the literature [9], this procedure characteristically vastly underestimates the true mobility. From the spectrum in fig. 5 it is clear in any case that the compositional 2D superlattice of fig. 4 is of excellent quality which justifies a serious look for the long predicted Bloch oscillation radiation [10,11] that such structures are expected to emit under proper bias.

We conclude with a proposal for a still more complex compositional superlattice structure. This structure shown in fig. 7 employs an adjacent superlattice to longitudinally modulate a modulation-doped quantum wire or 1DEG. The proposal is complex because its physical realization involves three separate MBE growths separated by 2 in situ cleaves. It is definitely worth the effort, however, as a superlattice modulated 1DEG is the most ideal realization of the Bloch oscillator concept.

References

- [1] L. Pfeiffer, K.W. West, H.L. Störmer, J.P. Eisenstein, K.W. Baldwin, D. Gershoni and J. Spector, *Appl. Phys. Letters* 56 (1990) 1697.
- [2] H.L. Störmer, A.C. Gossard and W. Wiegmann, unpublished results, 1978;
J.P. Kotthaus, private communication, 1980;
L. Esaki, in: *Recent Topics in Semiconductor Physics*, Eds. H. Kamimura and Y. Toyazawa (World Scientific, Singapore, 1983) p. 1.
- [3] W.I. Wang, *J. Vacuum Sci. Technol.* B1 (1983) 630.
- [4] L.T. Parachanian, E.R. Weber and T.L. Hierl, *Mater. Res. Soc. Symp. Proc.* 46 (1985) 391.
- [5] L.T. Allen, E.R. Weber, J. Washburn and Y.C. Pao, *Appl. Phys. Letters* 51 (1987) 670.
- [6] J. Zhou, Y. Huang, Y. Li and W.Y. Jia, *J. Crystal Growth* 81 (1987) 221.
- [7] Ircon, Inc., Niles, IL 60648, USA.
- [8] Varian Associates, Inc., Santa Clara, CA 95054, USA.
- [9] S. Das Sarma and F. Stern, *Phys. Rev.* 32 (1985) 8442, and references therein.
- [10] L.V. Keldysh, *Soviet Phys.-JETP* 16 (1963) 471.
- [11] L. Esaki and R. Tsu, *IBM J. Res. Develop.* 15 (1970) 61.

Indium incorporation in GaInAs/GaAs quantum wells grown on GaAs

K. Woodbridge *, K.J. Moore, N.L. Andrew and P.F. Fewster

Philips Research Laboratories, Redhill, Surrey RH1 5HA, UK

We report RHEED studies on the growth of GaInAs on GaAs over a range of growth conditions. Above about 550 °C there is a steady fall in In incorporation and a temperature-dependent reconstruction change from an As stable 2×4 to an In stable 4×2 . Recovery time data indicate that the In surface concentration is highest at 560 °C and decreases at higher temperatures due to increasing re-evaporation rate. An upturn in recovery time at longer deposition times and lower temperatures may be due to strain limited incorporation. Compositional homogeneity of GaInAs/GaAs quantum wells grown with full and partial In incorporation show marked differences which are discussed in relation to the above results.

1. Introduction

The growth and characterisation of strained layer structures has been the subject of a great deal of study in recent years. One of the most widely studied systems has been GaInAs/GaAs which has a number of potential device applications such as pseudomorphic HEMTs and strained layer lasers. The incorporation of In into GaInAs is complex and has been the subject of many studies using RHEED surface reconstruction and oscillation data. The gradual decrease of InAs growth rate as a function of temperature has been observed by a number of authors [1–3] and appears to be a significant effect above about 550 °C. Below this temperature, many groups have observed a transition from a two-dimensional to three-dimensional growth mode [4–7] at a “critical thickness” thought to be related to the onset of misfit dislocation generation. Above this temperature a transition from an As stable 2×4 to a metal stable 4×2 has been reported [2,6]. This has been linked to the presence of In on the growing surface and indeed In surface segregation has been reported to occur at higher growth tem-

peratures [3,6,8,9]. In addition, in this materials system, the further effect of strain must be considered to possibly influence the growth mode [3,10]. It is clearly important to determine the In content of these strained layers as accurately as possible in order to allow meaningful interpretation of optical and electrical data. In this work we have used RHEED studies on GaInAs in order to investigate the incorporation behaviour of In under a variety of growth conditions. These results have then been related to the actual In content of GaInAs/GaAs multiple quantum well (MQW) structures grown under conditions of both full and partial incorporation of In. In contents of these structures were directly determined by low temperature photoluminescence (LTPL) and X-Ray diffraction (XRD) techniques.

2. Experimental

Layers for this work were grown in a commercial 3 inch MBE system equipped with a 15 kV electron gun for RHEED analysis. Diffraction patterns were viewed on a coated phosphor screen and RHEED intensity oscillations were monitored via an optic fibre coupling and a photomultiplier. Undoped GaAs(001) substrates were In mounted on to a bonded platten for RHEED studies but

* Present address: Department of Electronic and Electrical Engineering, University College London, Torrington Place, London WC1E 7JE, UK

were fitted in non-bonded 2 inch holders for growth of complete MQW structures. The substrate was rotated during growth of the MQWs. Growth rates were measured using the RHEED oscillation technique and were 1 monolayer per second (ML/s) for the GaAs. InAs growth rates that are quoted in the text were deduced from GaAs and GaInAs RHEED oscillations at a substrate temperature below that at which In re-evaporation occurs. All growth occurred under an overpressure of As_4 and a V/III beam flux of about 15–20/1 was maintained during layer deposition. The LTPL measurements were made at 4 K using a He–Ne laser, as the excitation source. XRD measurements were made by double-crystal diffractometer using $\text{Cu K}\alpha$ radiation and simulation of the rocking curves with dynamical theory [11].

3. Results

3.1. Surface studies

Several papers have previously reported the decrease of InAs growth rate as a function of substrate temperature and those experiments were repeated here initially to give some reference point for substrate temperatures in the following experiments. The InAs growth rate was deduced from the RHEED oscillation period of GaInAs over a range of substrate temperatures and was found to start to drop significantly above about 550 °C decreasing by a factor of 2 by 590 °C. We also found that in the partial In incorporation regime the RHEED oscillations terminate abruptly after a certain time and the reconstruction changes from 2×4 to 4×2 . The time for this to occur decreases with both increasing In flux and increasing substrate temperature consistent with non-incorporated In segregating to the surface. These data in themselves do not prove that In segregation is occurring since increased As loss from the InAs component of the material could also result in a group III stable surface. We therefore carried out a series of experiments to examine the time it takes for the GaInAs surface to recover the 2×4 reconstruction from the In stable 4×2 after either the In or both the In and Ga fluxes are terminated.

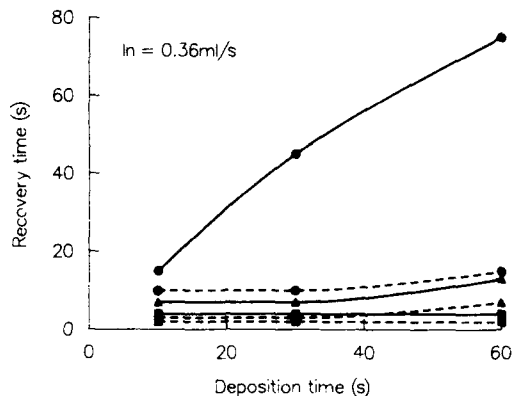


Fig. 1. Time for surface reconstruction to return to 2×4 following termination of the In flux (dashed line) or Ga and In fluxes (solid line). Substrate temperatures are 560 °C (●), 580 °C (▲) and 600 °C (■).

Recovery times were measured as a function of deposition times up to 60 s using an In flux equivalent to 0.36 ML/s. The data are presented in fig. 1 for three different substrate temperatures. The long recovery times in these cases would appear to confirm that In surface segregation is occurring. The recovery time becomes longer as the substrate temperature is lowered for both In off and total growth stop situations. This result clearly implies that the surface In population is larger at 560 °C than at 600 °C so that although the amount of In segregating must be lower at the lower temperature, this is more than compensated for by the lower re-evaporation rate. This result is in general agreement with the data of Ebner and Arthur [3]. When the Ga flux remains incident on the surface, as would be the case in the growth of GaInAs/GaAs quantum wells, the recovery time is longer for all temperatures. The recovery time appears constant with deposition time for higher temperatures or shorter deposition times implying a constant In surface population is maintained under these conditions. This situation does not seem to hold for either longer deposition times or lower temperatures especially in the case of the GaAs growth continuing. The marked increases in recovery time in these cases suggests a gradual build up of surface In. This could be related to a strain induced reduction in In incorporation which

might be expected to be more pronounced at lower temperatures where the initial incorporation of In is higher. Chang et al. [5] have reported that surface recovery times increase with increasing strain and have proposed an island growth mode for strained GaInAs at higher temperatures. In the case where the Ga flux is left on and the GaAs continues to grow, then the re-evaporation of In is suppressed resulting in longer recovery times compared to the total growth stop situation for the same In surface coverage.

3.2. MQW studies

It is apparent from the above data that, for growth of GaInAs at higher temperatures, the In incorporation behaviour is complex and involves segregation, re-evaporation and possibly strain and thickness dependent effects. This section of work describes the growth and compositional analysis of two typical GaInAs/GaAs strained layer structures grown at temperatures above and below the point at which In re-evaporation and segregation becomes significant. The layers were both twenty period GaInAs/GaAs MQW structures with 100 Å barriers and 20–25 Å wells. Growth was started with a 1 µm GaAs buffer and terminated with a 200 Å GaAs cap. The structures were not intentionally doped and were grown at 530°C (M247) or 580°C (M149). The InAs growth rates were set at 0.13 ML/s for the low temperature sample and at 0.21 ML/s for the high temperature sample in order to try and compensate for some of the In loss. The layers were cleaved in half and sectioned into 1 cm square pieces for examination by XRD in order to determine the mean (well + barrier) In content of each piece. The results were then extrapolated to a whole 2 inch wafer as a 3D graphical plot generated of In composition as a function of position on the slice. The mean In composition was also confirmed by atomic absorption spectroscopy while direct measurement of well composition was obtained from LTPL for comparison with the XRD data [12]. The plot for M247 can be seen in fig. 2 and shows that good lateral uniformity is obtained with the mean In content being 2.3% with variations of about 1% in absolute In content. LTPL on this wafer shows sharp ex-

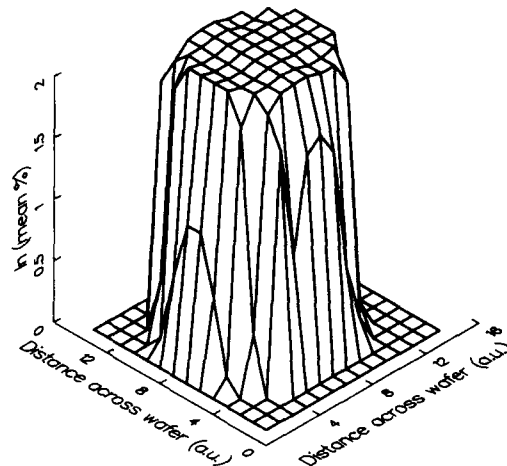


Fig. 2. Mean In content across 2 inch wafer for GaInAs/GaAs MQW sample grown at 530°C (M247).

citonic features with less than 1 meV shift in transition energy across the wafer indicating little lateral In content fluctuation. The results for the wafer grown at 580°C are quite different (fig. 3) showing a mean In content of about 1% with up to 50% variation in absolute In content across the slice. LTPL on this wafer also shows quite different behaviour with significant exciton peak position shifts up to 3 or 4 meV across the wafer indicating variations in well In content of up to 50%. These data correlate well with the large lateral mean In content variations which have been mea-

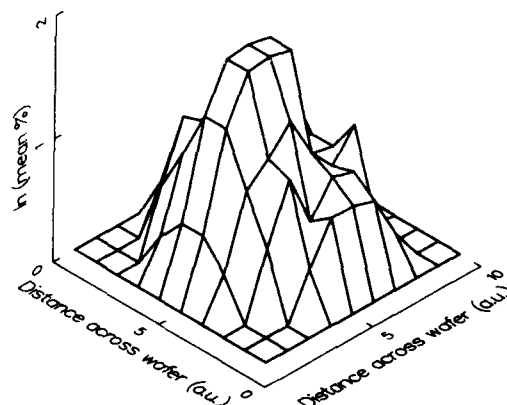


Fig. 3. Mean In content across 2 inch wafer for GaInAs/GaAs MQW sample grown at 580°C (M149).

sured by XRD. Despite these large fluctuations in In content the optical efficiency of this sample remains high. We also see some fine structure in the spectra of both samples which suggests some smaller inter- or intra-well fluctuations in In content of about 0.5%, similar to that which we have previously reported [13].

These results clearly show that growth of GaInAs/GaAs MQW structures at high substrate temperatures produces both a reduction in In incorporation, as expected, but also large lateral compositional inhomogeneities. The origin of these composition variations is difficult to determine from the current data but could be related to temperature variations across the wafer during growth. This possibility is currently being investigated.

4. Conclusions

We have studied the incorporation behaviour of In in InGaAs using RHEED oscillation and recovery data. Above a temperature of about 550 °C In begins to segregate to the surface of the growing layer and forms an in surface population. This In surface population is dependent on the competing processes of segregation and re-evaporation but appears to increase with both In flux and deposition time. When growth is terminated there is a finite time in which the In surface population decreases which becomes larger as the substrate temperature is lowered. The surface population therefore appears to be largest at 560 °C due to segregation and then decreases up to 600 °C as a result of increasing rate of re-evaporation. In addition, a gradual increase in recovery time as deposition time increases is observed for lower temperatures or higher In fluxes. This may be due to strain limited incorporation effects becoming dominant especially since this is most marked in the case of continuing GaAs growth, with the associated large increases in strain between the overlayer and the growing GaAs surface. GaInAs/GaAs multiple quantum well structures grown below and above the In evaporation temperature show very marked differences in In content and uniformity. Layers grown at 530 °C show

a mean In content which agrees well with the measured InAs growth rate and good uniformity while those grown at 580 °C show a significant drop in In content in addition to large variations in mean In content of up to 50% across the wafer as measured by XRD. LTPL data agree well with the XRD results but also show that high optical quality material is still obtained at high temperatures. Sharp PL lines suggest that the lateral In variation is on a much coarser scale than the 50 µm PL probe size. There is also some indication of small well-to-well fluctuations being present in all samples. The In incorporation into quantum wells at high temperature is clearly complex and is strongly affected by the segregation and re-evaporation which is observed by RHEED for GaInAs growth. Further experiments, possibly using modulated beam mass spectrometry techniques are required to determine In surface lifetimes and re-evaporation rates directly.

Acknowledgements

The authors would like to thank Tom Foxon for useful discussions on the manuscript and results, Geoff Duggan for support in the interpretation of the LTPL data, Christine Roberts for assistance with MBE growth and Ian Gale for the atomic absorption spectroscopy measurements.

References

- [1] S. Chika, H. Kato, M. Nakayama and N. Sano, *Japan. J. Appl. Phys.* 25 (1986) 1441.
- [2] S.-L. Weng, C. Webb and J.N. Eckstein, *J. Vacuum Sci. Technol.* B7 (1989) 361.
- [3] J.T. Ebner and J.R. Arthur, *J. Vacuum Sci. Technol.* A5 (1987) 2007.
- [4] B.F. Lewis, T.C. Lee, F.J. Grunthaner, A. Madhukar, R. Fernandez and J. Maserjian, *J. Vacuum Sci. Technol.* B2 (1984) 419.
- [5] K.H. Chang, P.R. Berger, R. Gibala, P.K. Bhattacharya, J. Singh, J.F. Mansfield and R. Clarke, *Dislocations and Interfaces in Semiconductors* (Metallurgical Society, 1988) p. 157.
- [6] D.C. Radulescu, W.J. Schaff, L.F. Eastman, J.M. Ballingall, G.O. Ramseyer and S.D. Hersee, *J. Vacuum Sci. Technol.* B7 (1989) 111.

- [7] B. Elman, E.S. Koteles, P. Melman, C. Jagannath, J. Lee and D. Dugger, *Appl. Phys. Letters* 55 (1989) 1659.
- [8] J. Massies, F. Turco, A. Saletes and J.P. Contour, *J. Crystal Growth* 80 (1987) 307.
- [9] C.T. Foxon and B.A. Joyce, *J. Crystal Growth* 44 (1978) 75.
- [10] K.R. Evans, C.E. Stutz, D.K. Lorange and R.L. Jones, *J. Crystal Growth* 95 (1989) 197.
- [11] P.F. Fewster and C. Curling, *J. Appl. Phys.* 62 (1987) 4154.
- [12] K. J. Moore, G. Duggan, A. Raukema and K. Woodbridge, *Phys. Rev. B* 42 (1990) 1326.
- [13] K.J. Moore, G. Duggan, K. Woodbridge and C. Roberts, *Phys. Rev. B* 41 (1990) 1090.

Narrow luminescence linewidth in GaAs single quantum wells by insertion of thin AlAs smoothing layers

K. Ploog, A. Fischer, L. Tapfer and B.F. Feuerbacher

Max-Planck-Institut für Festkörperforschung, W-7000 Stuttgart 80, Germany

We propose a new approach to produce high-quality GaAs single quantum wells with smooth interfaces by molecular beam epitaxy, avoiding long growth interruption times. The insertion of ultrathin AlAs smoothing layers at the constituent GaAs/ $\text{Al}_x\text{Ga}_{1-x}\text{As}$ heterointerfaces and growth interruptions of not more than 15 s yields an improvement of the luminescence linewidth (FWHM) to 0.56 meV for a 13 nm wide GaAs well and to a value as low as 0.195 meV for a 27 nm wide GaAs well. In addition, no Stokes shift between absorption and emission and no line splitting due to monolayer fluctuations in the well width are observed.

1. Introduction

The potential for exciton confinement in quantum wells (QWs) made of III–V semiconductors is often not ideal. The potential perturbation originates from microscopic well width fluctuations due to the existence of growth islands of different lateral extent at the interfaces and from statistical composition fluctuations of ternary alloy (e.g. $\text{Al}_x\text{Ga}_{1-x}\text{As}$) barriers. This interface roughness has a strong impact on the electronic properties of GaAs/ $\text{Al}_x\text{Ga}_{1-x}\text{As}$ heterostructures and superlattices (SLs), including broadening or splitting of excitonic luminescence lines [1], irregularities in luminescence quenching under resonance conditions [2], perpendicular-localization of excitons in SLs [3], variations of tunneling times induced by barrier width fluctuations [4], and modification of exciton dynamics through inhomogeneous broadening of exciton states [5].

The currently accepted status of optimized conditions during conventional molecular beam epitaxy (MBE) is the application of growth interruption for generation of growth islands with atomically flat terraces of area comparable to or larger than the exciton diameter [6] and sometimes the additional use of all-binary AlAs/GaAs short-period SL barriers [3]. However, although interruption of the group III flux for a few minutes can

result in a smoothing of the interfaces, there is also a concomitant increase of the impurity concentration at the interfaces, incorporated from gaseous background species of the vacuum system. Moreover, the interface and bulk composition of the ternary alloy can differ considerably because of surface segregation [7], i.e. the most weakly bound group III element segregates at the surface during growth interruption. Recent structural investigations by high-resolution transmission electron microscopy (HRTEM) [8] of the samples originally grown by Tu et al. [9] did not confirm the existence of atomically abrupt material transitions and flat terraces of large area. In addition, the splitting of the luminescence lines due to monolayer fluctuations in the same sample was found to vary considerably and not in integer steps as a function of position of the laser spot on the wafer [10].

The latter two findings led to the conclusion that apparently even the island regions are rough on atomic scale (note the difference in length scale: for excitonic properties the roughness over the exciton diameter is crucial, whereas for electrical transport properties the roughness over the Fermi wavelength becomes important). We have, therefore, developed a new approach for obtaining smooth GaAs/ $\text{Al}_x\text{Ga}_{1-x}\text{As}$ heterointerfaces on the length scale of the exciton diameter, avoiding

long growth interruptions. The insertion of ultra-thin AlAs smoothing layers at the constituent interfaces yields an improvement of the luminescence linewidth to 0.56 MeV for a 13 nm wide GaAs single quantum well (SQW) and to a value as low as 0.195 MeV for a 27 nm wide well. In addition, no Stokes shift between absorption and emission and no line splitting due to monolayer fluctuations in the well width are observed.

2. Experiment

The GaAs SQWs of the present study are grown in a three-chamber MBE system similar to that described previously [11] using tetrameric arsenic and elemental Al and Ga sources. The exactly (001) oriented [$<0.1^\circ$ off] semiinsulating GaAs substrate is heated to 600°C without In soldering. The growth rates of 1 ML/s for GaAs, 0.5 ML/s for AlAs and 1.5 ML/s for $\text{Al}_x\text{Ga}_{1-x}\text{As}$ with $x = 0.3$ have been calibrated by measurements of the RHEED intensity oscillations and by layer thickness measurements in previous growth runs. The layer sequence of the sample comprising three GaAs SQWs of 44, 27, and 13 nm width is as follows: the buffer layer next to the substrate consists of 60 periods of 10 ML GaAs/10 ML AlAs short-period superlattice (SPS), 0.7 μm $\text{Al}_x\text{Ga}_{1-x}\text{As}$, and another 60 periods of 10 ML GaAs/10 ML AlAs SPS. Then 0.2 μm GaAs, 0.1 μm $\text{Al}_x\text{Ga}_{1-x}\text{As}$, and the 44 nm GaAs QW sandwiched between 3 ML AlAs follow. This first wide QW is separated by 30 nm $\text{Al}_x\text{Ga}_{1-x}\text{As}$ from the second GaAs QW of 27 nm width also sandwiched between 3 ML AlAs. Another 30 nm $\text{Al}_x\text{Ga}_{1-x}\text{As}$ barrier separates the final 13 nm GaAs QW surrounded again by 3 ML AlAs smoothing layers. The top layer is 0.1 μm $\text{Al}_x\text{Ga}_{1-x}\text{As}$ and 2 nm GaAs. At each constituent interface the group III flux is interrupted for 12 to 15 s, mainly in order to adjust and synchronize the position of the rotating (6 rpm) substrate to the appropriate layer thickness. The structural parameters of the whole epilayer, including the thicknesses of the constituent GaAs, $\text{Al}_x\text{Ga}_{1-x}\text{As}$, and AlAs layers are determined by high-resolution double-crystal X-ray diffraction using $\text{Cu K}\alpha_1$

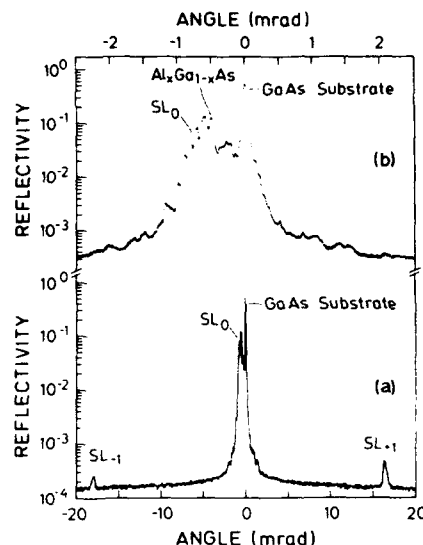


Fig. 1. X-ray diffraction patterns of the studied epilayer taken with $\text{Cu K}\alpha_1$ radiation in the vicinity of the (400) GaAs reflection; (a) overall diffraction pattern including satellite peaks; (b) very close to (400) GaAs reflection on expanded scale.

radiation [12]. The photoluminescence (PL) and photoluminescence excitation (PLE) experiments are carried out in a He bath cryostat at 2.1 K. The sample is excited with a CW Styryl 9 dye laser pumped by an Ar^+ ion laser using excitation densities below 5 W/cm^2 for direct excitation of the respective SQW. The luminescence is dispersed by a 0.85 m double monochromator and detected with a cooled GaAs photomultiplier tube. The spectral resolution of the PL experiments is approximately 0.05 MeV and the width of the PLE spectra is limited by the 1 meV bandwidth of the exciting dye laser.

3. Results

In fig. 1 we show the X-ray diffraction patterns of the epilayer recorded around the (400) reflection. Besides the substrate peak and the main epitaxial layer peaks, the spectrum of fig. 1a exhibits the +1 and -1 satellite peaks of the two GaAs/AlAs short-period superlattices composing

the buffer layer next to the substrate. The angular distance between the first-order satellite peaks gives the superlattice period of $\Lambda_{SL} = 5.4$ nm. The detailed features of the diffraction pattern very close to the (400) GaAs reflection are displayed in fig. 1b. The observed peaks can be attributed to individual layers only by using a computer simulation based on the dynamical diffraction theory [12]. We indicate the zeroth-order superlattice peak SL_0 and the peak of the ternary $Al_xGa_{1-x}As$ layers ($x = 0.3$). The other peaks are Pendellösung fringes caused by the interference of the X-rays between epitaxial layers with different lattice parameters, i.e. different mole fractions x [12]. The observation of these interference features clearly indicates the high structural perfection and the chemical homogeneity of the entire heterostructure. Due to the complicated buffer layer sequence, the three GaAs SQWs cannot be resolved in the present case. However, extrapolation of the data obtained for the buffer SPS and the ternary $Al_xGa_{1-x}As$ layers gives us the widths of the three GaAs SQWs to 43.8, 27.3, and 13.8 nm, respectively, and of the $Al_xGa_{1-x}As$ barriers to 30.7 nm as well as the thickness of the thin AlAs smoothing layers at the GaAs/ $Al_xGa_{1-x}As$ interfaces to be 3 ML. All these values are in good agreement with the nominal values.

In fig. 2 we show the PL and PLE spectra obtained from the 27 nm GaAs SQW at 2.1 K. The energy of the exciting laser line is always below the bandgap of the $Al_xGa_{1-x}As$ barriers so that each GaAs QW is excited directly and selectively. The energies of the lowest electron to heavy-hole (E_{1hh}) and electron to light-hole (E_{1lh}) transitions and the full widths at half maximum (FWHM) of the respective E_{1hh} luminescence transitions are summarized in table 1 for the three GaAs SQWs of the present study. Inspection of the spectral features depicted in fig. 2 reveals the important results of the present study. First, there is no Stokes shift between the E_{1hh} transitions observed in luminescence and in luminescence excitation. Second, to our knowledge the spectral widths (FWHM) for these single quantum wells measured directly are narrower than those reported previously [13] and thus constitute the narrowest linewidths to date. Third, even under widely

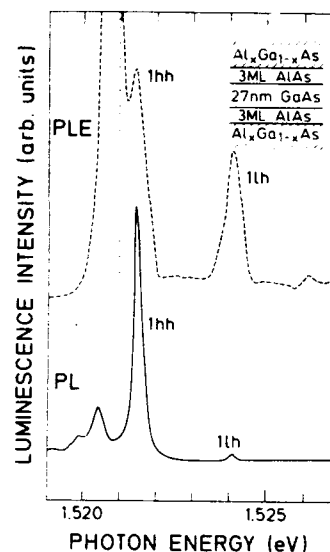


Fig. 2. Low-temperature PL and PLE spectra taken from 27 nm GaAs SQW. PL excitation is at 1.53500 eV with 2 W/cm^2 . Detection for PLE (dotted vertical line) is set at 1.52091 eV.

varying excitation conditions there is no line splitting of the PL and of the PLE spectra arising from any changes of the well width by one monolayer. The application of the PLE leads to the unambiguous identification of free excitons from large areas which are uniform in well width. The insertion of 3 ML AlAs at both GaAs/ $Al_xGa_{1-x}As$ heterointerfaces obviously results in a smoothing of the interfaces to better than one monolayer over very large lateral regions. On the other hand, this ultrathin smoothing layer has only a minor effect on the barrier height of the ternary $Al_xGa_{1-x}As$ (direct gap for $x = 0.3$) and on the lattice strain which might be imposed on GaAs SQWs confined by thicker AlAs barriers.

Table 1

Observed well widths L_w (by X-ray diffraction) and lowest-energy electron to heavy-hole (E_{1hh}) and electron to light-hole (E_{1lh}) free-exciton transitions in the three GaAs single quantum wells at 2.1 K; also given is the line-width (FWHM) of the E_{1hh} PL transition

L_w (nm)	E_{1hh} (eV)	FWHM (meV)	E_{1lh} (eV)
13.8	1.54361	0.56	1.55335
27.3	1.52173	0.195	1.52446
43.8	1.51702	0.28	1.51801

In the low-temperature PL spectra obtained from these high-quality GaAs SQWs we always observe a low-energy line which is red-shifted by 0.87 MeV for the 44 nm well, by 1.24 MeV for the 27 nm well, and by 1.42 meV for the 13 nm well. These low-energy features do not contribute to the PLE spectra and they readily saturate in luminescence with increasing excitation intensity. We, therefore, assign them to excitons bound to shallow donors (impurities or donor-like defects). If we assume the observed red-shift to be comparable to the shallow-donor-level binding energies in GaAs QWs, these values are in good agreement with recent calculations [14] (see impurity position at $z_0 = \frac{1}{8}$ in table 1b of this reference).

4. Conclusions

We have developed a method to considerably reduce the overall value of interrupted growth for high-quality GaAs SQWs during molecular beam epitaxy. The insertion of ultrathin AlAs smoothing layers (3 ML) at the constituent GaAs/Al_{0.3}Ga_{0.7}As heterointerfaces and growth interruptions of not more than 15 s yields an improvement of the PL linewidth (FWHM) to 0.56 meV for a 13 nm wide GaAs well and to a value as low as 0.195 meV for a 27 nm wide GaAs well. In addition, no Stokes shift between absorption and emission and no line splitting due to monolayer fluctuations in the well width is observed. The detailed mechanism for the observed interface smoothing is at present not fully understood. The ultrathin AlAs layers certainly eliminate statistical composition fluctuations of ternary alloy interfaces as well as problems arising from surface segregation. On the microscopic scale, the different incorporation behaviour of Al during MBE may induce a preferential filling of areas not covered by monolayer islands. This mechanism would involve three monolayers in growth direction and would result in a smooth averaged Al mole fraction along the interfaces.

Acknowledgements

This work was sponsored by the Bundesministerium für Forschung und Technologie of the Federal Republic of Germany. One of the authors (K.P.) expresses his gratitude to Dr. Tatsuya Kimura and Dr. Seigo Tarucha for their kind hospitality at the NTT Basic Research Laboratories, Tokyo 180, Japan, where part of this work was finished.

References

- [1] C. Weisbuch, R. Dingle, A.C. Gossard and W. Wiegmann, *Solid State Commun.* 38 (1981) 709; L. Goldstein, L. Y. Horikoshi, S. Tarucha and H. Okamoto, *Japan. J. Appl. Phys.* 22 (1983) 1491; M. Kohl, D. Heitmann, S. Tarucha, K. Leo and K. Ploog, *Phys. Rev. B* 39 (1989) 7736.
- [2] S. Tarucha and K. Ploog, *Phys. Rev. B* 38 (1988) 4198.
- [3] K. Fujiwara, R. Cingolani and K. Ploog, *Phys. Rev. B* 43 (1991) 3117.
- [4] S. Tarucha and K. Ploog, *Phys. Rev. B* 39 (1989) 5353.
- [5] J. Kuhl, A. Honold, L. Schultheis and C.W. Tu, in: *Festkörperprobleme*, Vol. 29, Ed. U. Rössler (Vieweg, Braunschweig, 1989) p. 157.
- [6] M. Tanaka, H. Sakaki and J. Yoshino, *Japan. J. Appl. Phys.* 25 (1986) L155; F. Voillot, A. Madhukar, J.Y. Kim, P. Chen, N.M. Cho, W.C. Tang and P.G. Newman, *Appl. Phys. Letters* 48 (1986) 1009; R.C. Miller, C.W. Tu, S.K. Sputz and R.F. Kopf, *Appl. Phys. Letters* 49 (1986) 1245.
- [7] J. Massies, F. Turco and J.P. Contour, *Semicond. Sci. Technol.* 2 (1987) 179; F. Turco and J. Massies, *Appl. Surface Sci.* 37 (1989) 160.
- [8] A. Ourmazd, in: *Low-Dimensional Semiconductors*, Eds. H.G. Grimmeis and A.R. Peaker (Plenum, New York, 1991).
- [9] C.W. Tu, R.C. Miller, B.A. Wilson, P.M. Petroff, T.D. Harris, R.F. Kopf, S.K. Sputz and M.G. Lamont, *J. Crystal Growth* 81 (1987) 159.
- [10] C.A. Warwick, W.Y. Jan, A. Ourmazd, T.D. Harris and J. Christen, *Appl. Phys. Letters* 56 (1990) 2666.
- [11] K. Ploog, *Angew. Chem. Intern. Ed. Engl.* 27 (1988) 593.
- [12] L. Tapfer and K. Ploog, *Phys. Rev. B* 33 (1986) 5565; *B40* (1989) 9802.
- [13] A. Honold, L. Schultheis, J. Kuhl and C.W. Tu, *Phys. Rev. B* 40 (1989) 6442.
- [14] M. Stopa and S. Das Sarma, *Phys. Rev. B* 40 (1989) 8466.

Characterization of lateral correlation length of interface roughness in MBE grown GaAs/AlAs quantum wells by mobility measurement

T. Noda, M. Tanaka * and H. Sakaki **

Institute of Industrial Science, University of Tokyo, 7-22-1 Roppongi, Minato-ku, Tokyo 106, Japan

The correlation length (Λ) of interface roughness in GaAs/AlAs quantum wells (QWs) prepared by molecular beam epitaxy (MBE) was studied by measuring and analyzing the electron concentration dependences of mobilities. When the bottom AlAs barrier of QWs is prepared by alternate beam MBE and/or by the use of superlattice buffer beneath the QW, the mobility of two-dimensional electrons is substantially enhanced. The lateral correlation length Λ of such samples is found to become as large as 200–300 Å. We have found that Λ of the bottom (GaAs-on-AlAs) interface of the QW is about 70 Å when prepared by conventional MBE.

In a variety of quantum heterostructures, most of the electronic and optical properties are determined by the interaction of electrons with heterointerfaces [1]. Hence, the understanding of the atomic structures of interfaces and their controls is extremely important. Key parameters to characterize interface roughness are the amplitude and the lateral correlation length. Interfaces of GaAs/AlAs quantum wells (QWs) grown by conventional molecular beam epitaxy (MBE) have a roughness of monoatomic fluctuation. This results in the broadening of photoluminescence (PL) spectra [2,3] and a substantial decrease in mobility, particularly in the case of thin QWs [4]. From PL studies in GaAs/AlAs QWs, it is established that the GaAs surface or AlAs-on-GaAs (top) interface can be made atomically flat by growth interruption (GI), whereas the roughness on the AlAs surface or GaAs-on-AlAs (bottom) interface has a short correlation length Λ (< 100 Å) and is difficult to smooth out at the growth temperature

of 600 °C [5]. Our earlier mobility study has clarified that Λ of roughness at the bottom interface is typically 50–70 Å [4].

We present in the first part of this paper our continuing effort to determine the correlation length by measuring and analyzing the mobility as a function of electron concentration. In the second part, we study the possibility of the enhancement of surface migration of adatoms by modification of MBEs. In particular, we evaluate the influence of the periodic reduction of arsenic pressure [6,7], referred to as alternate beam MBE or migration enhanced epitaxy [8] and the use of superlattice (SL) buffer. We show that these modifications are effective in enhancing Λ of the bottom interface to 200–300 Å or more. In addition, we also discuss the dependence of the mobility on in-plane crystallographic orientation.

Samples used are selectively doped GaAs/AlAs QWs with the well width L_w ranging from 17 monolayers (ML) to 30 ML. We prepared three sample groups (I, II, and III) on (001) Cr-doped semi-insulating GaAs at 590–600 °C. Groups I and II were prepared by growing successively 8000 Å-thick undoped GaAs, an SL buffer consisting of 21 periods of undoped AlAs(14 ML)/GaAs(14 ML) with GI of 60 s prior to form the top interfaces, a 21-ML-thick undoped AlAs spacer, an

* Present address: Department of Electronic Engineering, University of Tokyo, 7-3-1 Hongo, Bunkyo-ku, Tokyo 113, Japan.

** Also at Research Center for Advanced Science and Technology, University of Tokyo, 4-6-1 Komaba, Meguro-ku, Tokyo 153, Japan.

undoped GaAs QW with various L_w , a 21-ML-thick undoped AlAs spacer, a 800-Å-thick Si-doped $\text{Al}_{0.3}\text{Ga}_{0.7}\text{As}$ with a donor density N_D of $7 \times 10^{17} \text{ cm}^{-3}$, and finally a 100-Å-thick undoped GaAs capping layer. For group III, the structure is the same as for groups I and II except that the buffer layers are 5000 Å GaAs and 2000 Å $\text{Al}_{0.3}\text{Ga}_{0.7}\text{As}$, and N_D is $1 \times 10^{18} \text{ cm}^{-3}$.

The AlAs layer just below the GaAs well was prepared by alternate beam MBE for group I, and by conventional MBE for groups II and III. In alternate beam MBE, the Al flux corresponding to 1 ML coverage and the As_4 flux for 5 s are alternately supplied with no interval. The beam flux is $1.4 \times 10^{14} \text{ cm}^{-2} \text{ s}^{-1}$ for Al and $8 \times 10^{14} \text{ cm}^{-2} \text{ s}^{-1}$ for As_4 . When the As_4 cell shutter is closed, the beam equivalent pressure of As_4 is reduced from 1×10^{-5} to 6×10^{-7} Torr, or the As_4 beam flux of about $5 \times 10^{13} \text{ cm}^{-2} \text{ s}^{-1}$. In these thin QWs, the roughness at the bottom interface plays a dominant role in the scattering process because the top interface prepared with GI of 60 s is expected to have a Λ of more than 1000 Å and contributes little to the scattering [5]. The reduction of mobility due to possible contamination of growth surfaces during GI is negligibly small since the mobility of selectively doped single heterostructures with GI of 60 s exceeds $10^5 \text{ cm}^2/\text{V} \cdot \text{s}$ at 4.2 K. Typical growth rates in usual MBE growth are 0.55, 0.23 and $0.79 \mu\text{m/h}$ for GaAs, AlAs and $\text{Al}_{0.3}\text{Ga}_{0.7}\text{As}$, respectively.

It has been clarified [4,9] that interface roughness (IFR) scattering can be theoretically evaluated as long as the roughness is characterized by the height Δ and the lateral correlation length Λ of the Gaussian fluctuation. Since the fluctuation of the well width L_w leads to the spatial fluctuation of the ground level E_0 , the potential fluctuation ΔV responsible for the scattering is given by

$$\Delta V = (\partial E_0(L_w, V_0)/\partial L_w) \Delta.$$

Then, the roughness limited mobility (μ_r) is theoretically expressed as [4,9]:

$$\mu_r = \left(\frac{\partial E_0}{\partial L_w} \Delta \right)^{-2} g(\Lambda, N_s, T), \quad (1a)$$

$$\mu_r = \text{const} \frac{L_w^6}{\Delta^2} g(\Lambda, N_s, T) \quad (\text{when } V_0 = \infty), \quad (1b)$$

where V_0 is the barrier height, and g is a function of Λ , the electron concentration N_s , and the temperature T . Eq. (1b) indicates that the dependence of μ_r on L_w , Δ and N_s is separable and not interlinked. In particular, the N_s dependence of μ_r is determined primarily by Λ , and independent of Δ as long as T is constant. This is because the change of μ_r with N_s results mainly from the Fermi wavelength dependence of the scattering probability.

We plot 4.2 K mobilities (μ) of three sample groups, measured as a function of L_w , in fig. 1. Closed circles are the data for group I, the closed triangle for group II, and closed squares for group III. These sets of mobility data are strongly dependent on L_w , approximately proportional to L_w^6 , indicating that the mobilities are dominated

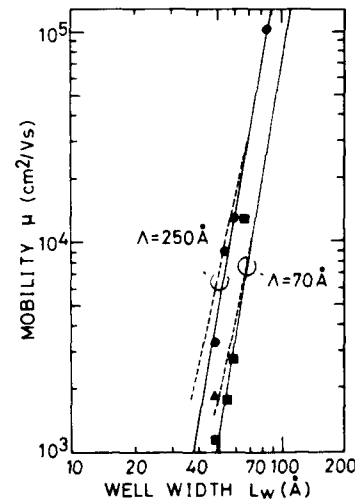


Fig. 1. Calculated and measured mobilities at 4.2 K as a function of the well width L_w . Closed circles are the data for group I, the closed triangle for group II and closed squares for group III. N_s of each sample in the unit of 10^{11} cm^{-2} is shown in the following form $N_s(L_w)$. For group I: 4.0(30 ML), 2.0(21 ML), 2.7(19 ML), 1.6(17 ML). For group II: 4.2(17 ML). For group III: 4.3(23 ML), 1.9(21 ML), 3.2(19 ML), 3.1(17 ML). Solid and broken lines are the roughness dominated mobilities calculated for $V_0 = \infty$ and $V_0 = 1.2 \text{ eV}$, respectively, at $N_s = 2 \times 10^{11} \text{ cm}^{-2}$.

by IFR scattering at the bottom interface and all other scattering mechanisms are far less important. Mobilities of group I are higher than those of group III, indicating that alternate beam MBE and/or the use of an SL buffer suppresses IFR scattering to some extent. When $L_w = 17$ ML, μ of group II has an intermediate value, between those of groups I and III. This suggests that the use of an SL buffer alone enhances the mobility in thin QWs. For comparison, theoretical mobilities (μ_r) for $T = 0$ K and $N_s = 2 \times 10^{11} \text{ cm}^{-2}$ are plotted in fig. 1 for the correlation lengths Λ of 250 and 70 Å; solid lines are for $V_0 = \infty$ and $\Delta = 2.83$ Å, and broken lines for $V_0 = 1.2$ eV and $\Delta = 3.7$ Å. Note that the slope of μ versus L_w at other values of N_s is almost the same as that for $N_s = 2 \times 10^{11} \text{ cm}^{-2}$ because μ_r has a stronger dependence on L_w than on N_s (see fig. 2). Although the data have some spread, primarily due to the difference of N_s in different samples, the L_w dependence of μ is close to the theoretical prediction.

Although a good agreement can be found in

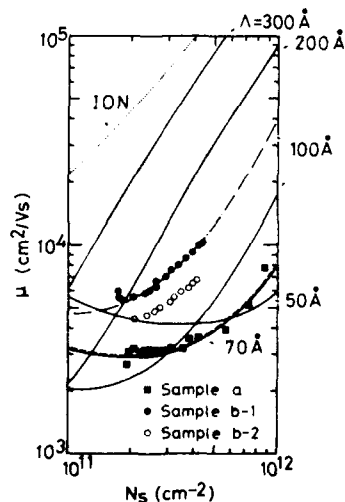


Fig. 2. The N_s dependences of mobilities of group III. Measured data are plotted by closed squares for a QW (sample a) with $L_w = 21$ ML, closed and open circles for QWs (samples b-1 and b-2) with $L_w = 23$ ML. Solid, broken and chained lines are the roughness dominated mobilities calculated at 0 K. Dotted line is the impurity dominated mobility calculated at 0 K.

fig. 1, one cannot determine Λ and Δ separately only from the L_w dependence of μ . The best way to determine Λ is to study the N_s dependence of μ because it is determined by Λ , as indicated in eq. (1). As examples, we show by solid lines in fig. 2 the N_s dependence of μ_r for a QW with $L_w = 21$ ML for various correlation lengths Λ . Note that the N_s dependence of μ_r is primarily determined by Λ , and does not depend on V_0 or Δ . We also show, by a broken line in fig. 2, μ_r for a QW with $L_w = 23$ ML, $V_0 = 1.2$ eV and $\Delta = 3.4$ Å. To show the role of impurity scattering, we plot by a dotted line the mobility for a QW with $L_w = 21$ ML dominated by ionized donors in AlGaAs.

Now we plot in fig. 2 the measured μ at 4.2 K as a function of N_s for three samples (a, b-1 and b-2) of group III. Closed squares are for a QW (sample a) with $L_w = 21$ ML and N_s was changed by using the persistent photoconductivity (PPC) effect. The current is along the $(1\bar{1}0)$ direction. Closed and open circles are the mobilities measured for QWs (samples b-1 and b-2) with $L_w = 23$ ML and N_s was changed by a gate electric field in a FET configuration. The current directions are along the $(1\bar{1}0)$ direction for sample b-1 and along (110) for sample b-2.

We first discuss μ of sample a (shown by closed squares), which is almost constant when $N_s < 4 \times 10^{11} \text{ cm}^{-2}$ and gradually increases with increase of N_s . This N_s dependence of μ agrees very well with a theoretical prediction of IFR scattering only when we assume $\Lambda = 70$ Å. To achieve the complete fit in the absolute magnitude, we find $\Delta = 4.2$ Å since $V_0 = 1.2$ eV. These values of Δ and Λ are consistent with our previous results obtained from the μ - T characteristic [4]. To avoid ambiguities due to the PPC effect, we also examine μ of sample b (closed and open circles). The measured μ of this sample is a little more strongly dependent on N_s . By adopting the same process, we find that Λ is 100 Å for both samples. We find also that Δ is 3.4 Å for $(1\bar{1}0)$ channel orientation and $\Delta = 3.8$ Å for (110) channel orientation. These values are close to those of sample a. The reason for finding a larger value of Λ and a smaller value of Δ is probably due to small changes in the growth condition, such as the As_4 flux or the substrate temperature. We find from these results

that the roughness at the bottom interface of group III has a typical correlation length Λ of 70–100 Å and a effective height Δ of 1–1.5 ML.

Next, we study whether or not Λ is enhanced by alternate beam MBE and/or the use of SL buffer. Mobilities of three samples (c, d-1 and d-2) of group I are plotted in fig. 3. Closed circles are measured μ for a QW (sample c) with $L_w = 21$ ML with current flowing along $(1\bar{1}0)$ direction. Closed and open squares are measured μ for QWs (samples d-1 and d-2) with $L_w = 21$ ML with current flowing along $(1\bar{1}0)$ for sample d-1 and (110) for sample d-2. In samples d-1 and d-2, not only the bottom AlAs but also the central GaAs well layer is prepared by alternate beam MBE. However, the main feature of bottom interfaces is the same as sample c because the top interface contributes little to the scattering process. Note in these samples (c, d-1 and d-2) that μ is strongly dependent on N_s , suggesting that the nature of bottom interfaces has changed as compared with those of group III. Although the ionized impurity

(ION) scattering plays some role, particularly at high N_s , the mobility is still mostly affected by IFR scattering. This indicates that a steep μ - N_s characteristic of samples c, d-1 and d-2 originates from the interface with Λ larger than that of group III. By analyzing the data, Λ is estimated to be 200 Å or longer. Note that the N_s dependence of μ is no longer sensitive to Λ when Λ exceeds 200 Å and the exact determination of Λ gets difficult. Hence, one may conclude that Λ is 250–300 Å if we assume $\Delta = 4.2$ Å (broken lines), and Λ is about 200 Å if $\Delta = 2.83$ Å (chained lines). A similar conclusion is obtained for group I with $L_w = 19$ ML. This implies that Λ of bottom interfaces prepared by modified MBE with alternate supply of beams and SL buffer becomes about three times larger than those prepared by the usual MBE. Further study is necessary to clarify which of the two modifications has a major contribution.

In conclusion, we have determined the correlation length Λ of roughness at the bottom interface by measuring and analyzing the μ - N_s characteristics. It is shown that Λ of the bottom interface is short (70–100 Å when prepared with conventional MBE but Λ can be enhanced to 200–300 Å by the use of alternate beam MBE and/or SL buffer layer. In addition, we have clarified the dependence of the mobility on intraplane orientation.

This work is supported by a Grant in Aid from the Ministry of Education and by the Research Development Corporation of Japan through the ERATO program for Quantum Wave Project.

References

- [1] H. Sakaki, in: Proc. Intern. Symp. on the Foundations of Quantum Mechanics, Tokyo, 1983 (Phys. Soc. Japan, Tokyo, 1984) p. 94.
- [2] L. Goldstein, Y. Horikoshi, S. Tarucha and H. Okamoto, Japan. J. Appl. Phys. 22 (1983) 1489.
- [3] H. Sakaki, M. Tanaka and J. Yoshino, Japan. J. Appl. Phys. 24 (1985) L417; T. Fukunaga, K.L.I. Kobayashi and H. Nakashima, Japan. J. Appl. Phys. 24 (1985) L510.

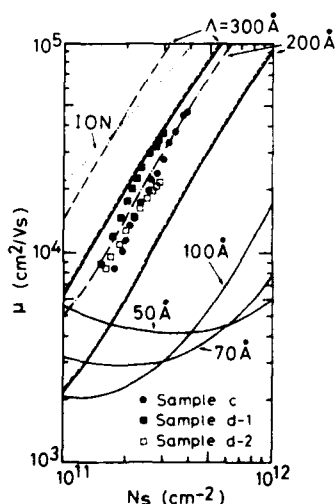


Fig. 3. The N_s dependences of mobilities of group I with $L_w = 21$ ML. Measured data are plotted by closed circles (sample c), and closed and open squares (samples d-1 and d-2). Solid, dotted and chained lines are the roughness dominated mobilities calculated at 0 K. Dotted line is the impurity dominated mobility calculated at 0 K.

- [4] H. Sakaki, T. Noda, K. Hirakawa, M. Tanaka and T. Matsusue, *Appl. Phys. Letters* 51 (1987) 1934.
- [5] M. Tanaka, H. Sakaki and J. Yoshino, *Japan. J. Appl. Phys.* 25 (1986) L155.
- [6] M. Tanaka and H. Sakaki, *J. Crystal Growth* 81 (1987) 153.
- [7] J.M. Van Hove and P.I. Cohen, *J. Crystal Growth* 81 (1987) 13.
- [8] F. Briones, D. Golmayo, L. Gonzales and A. Ruiz, *J. Crystal Growth* 81 (1987) 19.
- [9] Y. Horikoshi, K. Kawashima and H. Yamaguchi, *Japan. J. Appl. Phys.* 25 (1986) L868.
- [10] A. Gold, *Z. Physik* B74 (1989) 53.

Re-examination of the formation mechanism of CuPt-type natural superlattices in alloy semiconductors

Tohru Suzuki and Akiko Gomyo

Opto-Electronics Research Laboratories, NEC Corporation, 4-1-1, Miyazaki, Miyamae-ku, Kawasaki-shi, Kanagawa 213, Japan

The previously proposed natural superlattice (NSL) formation mechanism is experimentally re-examined by using $\text{Ga}_{0.5}\text{In}_{0.5}\text{P}$ grown on (001) vicinal (6° off towards the $[\bar{1}10]$ direction) GaAs substrate by metalorganic vapor phase epitaxy (MOVPE). Based mainly on the experimental results: non-existence of the (111)B micro-facets at the growing interface and extremely large (several hundred Å) single NSL domain sizes compared with the average terrace width (~ 27 Å), a new NSL formation (step-terrace-reconstruction (STR)) mechanism is presented. The mechanism assumes a reconstruction of the steps and terraces at the column V atom stabilized vicinal (001) surface, on which parity of the number of the column III atoms for each terrace is even.

1. Introduction

Natural superlattices (NSLs), spontaneous structural ordering on a sublattice, are now widely observed in III–V alloy semiconductors grown by various growth methods: molecular beam epitaxy (MBE), metalorganic vapor phase epitaxy (MOVPE) and chloride transport vapor phase epitaxy [1–19]. Among them, MOVPE grown AlGaInP, especially its end ternary GaInP shows CuPt type NSL and has been a most intensively studied material [4–10,12–16,20]. The AlGaInP is used as a key material system for 600 nm band visible laser diodes and has been found to show a correlation between the band-gap energy (thus, lasing wavelength) and the degree of ordering [5]. These facts have enhanced studies on understanding and control of the ordering [8] and on its effects on the electronic properties [21].

Previously we proposed a formation mechanism for the CuPt-type NSL [8]. The proposition included several postulates. This paper experimentally examines their validity. Based on the experimental results, a new formation mechanism is presented, which will also be applicable for MBE grown crystals. The issues to be studied in the present work include: (1) do (111)B microfacets on a growing surface really exist and (2) does terrace-parity mismatch introduce a disorder, e.g.

anti-phase-boundary (APB); here, “terrace-parity” [8] means the parity of the number of the column-III-atom lines on the (001) terrace between the nearest two steps.

2. Experimental

Crystal growths of GaInP and GaAs for this study were carried out by low-pressure (70 Torr) MOVPE. The growth details were described previously [12].

Sample #N1 has a structure of GaAs/ $\text{Ga}_{0.5}\text{In}_{0.5}\text{P}$ /GaAs (buffer layer). The thickness of the GaInP layer was $0.14\ \mu\text{m}$. These three layers were grown on a (001)GaAs substrate with a misorientation of 6° off towards $[\bar{1}10]$. The growth temperature was 660°C . The growth for GaInP was under a V/III ratio of 140 with a PH_3 flow rate of 150 SCCM. The $\text{Ga}_{0.5}\text{In}_{0.5}\text{P}$ layer is lattice-matched to the GaAs substrate. A V/III ratio of 54.7 was used for the GaAs growth with an AsH_3 flow rate of 500 SCCM. Triethylgallium and trimethylgallium were used for GaInP and GaAs growth, respectively.

Samples for cross-section transmission electron microscopy (TEM) studies were prepared by the same method described previously [9].

3. Results and discussion

3.1. Examination of step heights

A previous paper [5] described that $[110]$ steps, whose edge lines are in the $[110]$ direction, are playing an essential role in the NSL formation, and furthermore that $[110]$ step arrays descending towards $[\bar{1}10]$ are responsible for the $(\frac{1}{2}\frac{1}{2}\frac{1}{2})$ NSL formation. Based on this fact, we asserted that the steps are acting as "phase-lockers" [8]. In order to explain the phase-locking action at the steps, we postulated that the step edges may form $(111)B$ micro-facets and preferential Ga-sticking may occur on the micro-facets.

In order to examine whether or not the postulated $(111)B$ micro-facets exist, the interfaces of the sample #N1 consisting of the GaAs/GaInP/

GaAs structure grown on (001) GaAs substrate with a misorientation of 6° off towards $[\bar{1}10]$ were observed by TEM. In the GaInP layer there can be seen significant NSL formation with only one variant: $(\frac{1}{2}\frac{1}{2}\frac{1}{2})$, as reported already in ref. [9]. Fig. 1 shows the TEM images for the two interfaces; (a) GaAs/GaInP (upper interface) and (b) GaInP/GaAs (lower interface). The interfaces show misorientations from (001) towards $[\bar{1}10]$ with angles of, on average, 5° to 6° , which are close to the nominal angle of 6° . Grazing angle examination of these photographs enables us to more easily observe the structures at the interfaces.

It is seen that both interfaces do not appear to include $(111)B$ micro-facets, i.e. steps equal to or higher than two molecular-layer (ML) height with $(111)B$ surface, but show one-ML-height

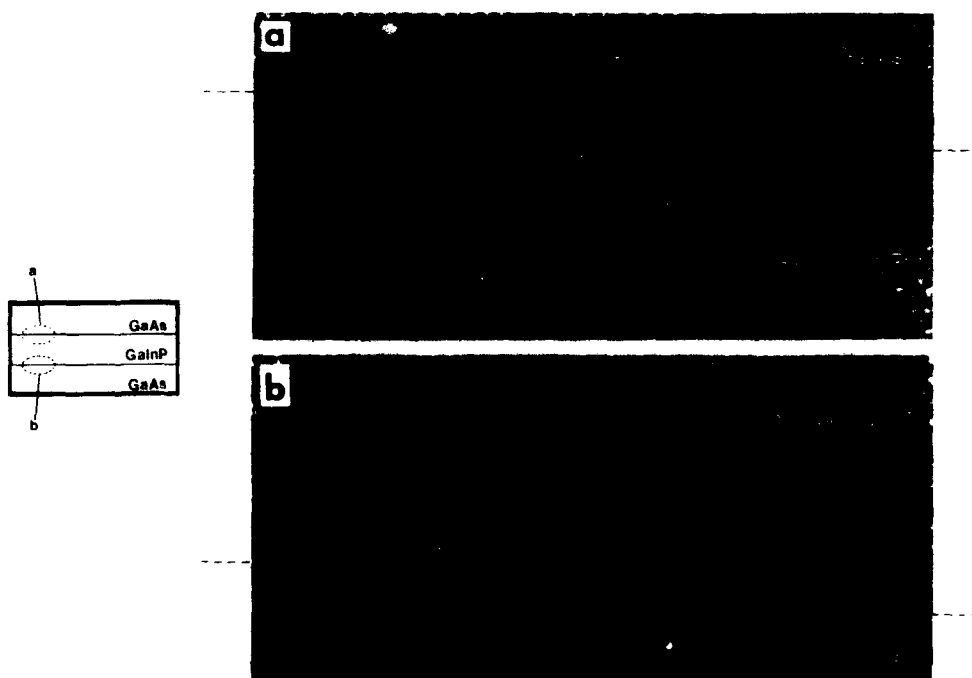


Fig. 1. $[110]$ pole lattice images for the two interface regions of a GaAs-on-GaInP-on-GaAs grown on a (001) GaAs substrate with a misorientation of 6° off towards $[\bar{1}10]$ direction: (a) GaAs-on-GaInP interface and (b) GaInP-on-GaAs. Shown on the left is the $[\bar{1}10]$ direction. Average inclination angles of 5° to 6° of the interfaces from the $[001]$ axis are visible. Dashed lines at both sides of these photographs show the interface edges. $(111)B$ micro-facets, whose heights are equal to or larger than two-ML-height, are scarcely seen at the steps. Instead, one-ML-high steps are observed for both interfaces. Grazing angle observation of the photographs makes inspection of the interface structures easier.

(~ 2.8 Å) steps. This was consistently observed in other similar samples. The fact that the upper interface also does not appear to include (111)B micro-facets and show one-ML-height steps, excludes the following possibility: GaInP growth starts on the GaAs (001) surface with one-ML-height steps and when growth proceeds, (111)B micro-facets with step heights higher than or equal to two-ML might develop; if this were the case, the upper interface would show (111)B micro-facets. This means that during the GaInP growth the successive (001) GaInP surface exhibits only one-ML-height steps, because the upper interface structure may represent a general feature of the growth-surface structure during the GaInP growth. Our present observations reveal that the GaAs and GaInP (001) vicinal surfaces also exhibit one-ML-height steps. Figs. 2a and 2b diagrammatically illustrate the structures with one-ML-height steps at the upper and lower interfaces, respec-

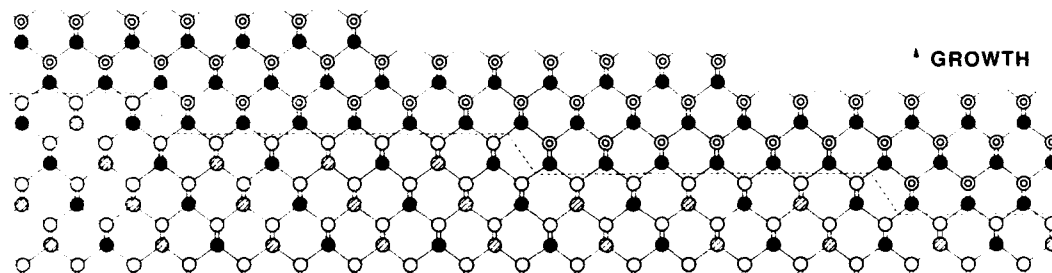
tively. The average interface angle is approximately 6° . The calculated average terrace width which corresponds to 6° is 27 Å. The particular terrace width shown in figs. 2a and 2b is 26 Å.

In relation to (111)B micro-facets, it will be appropriate to mention here the following. The previous paper [8] assumed that GaInP growth at the steps proceeds in the direction perpendicular to $[\bar{1}11]$. It will be, however, natural to assume that steps move towards the $[\bar{1}10]$ direction during the growth, considering the recent observations [23].

3.2. Size of a single NSL domain

Fig. 3 shows a dark field TEM image for an interface region between GaInP and GaAs. NSL formation appears to occur *almost from the interface*. We notice that coherent single domains as large as 400 Å are formed with almost no defects.

(a) GaAs on GaInP interface



(b) GaInP on GaAs interface

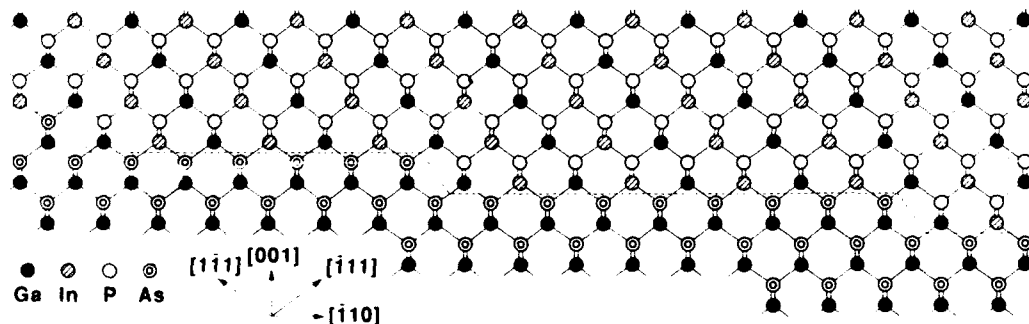


Fig. 2. Diagrammatic drawings of atomic structures for the two interfaces shown in figs. 1a and 1b. One-ML step height is about 2.8 Å.

These large single domains have also been observed consistently for other crystals grown under the similar conditions, using a substrate with the same orientation. The 400 Å domain size is quite large compared with the 27 Å average terrace width for a 6° off-angle substrate. This means that a single domain contains over 15 steps on average. In the (110) cross-section view, the central two terraces shown in fig. 2(b) accommodate column III atoms with 6 and 8 atom sites; thus only 3 and 4 period NSLs can stem from each of the terraces, as shown in the figure.

At first it seemed [8] that step terraces may have randomly both even and odd "terrace-parity", which has been defined in section 1. If every step acts as a "phase-locker" for the alternate arrangement of Ga-line and In-line, the terraces with odd terrace-parity, which will occur at 50% probability, may give rise to lattice defects such as anti-phase boundaries (APBs). Thus the defects would be observed, on average, for every 6 periods of NSL in GaInP grown on a 6° off angle substrate, because each step includes a 3 period NSL, on average, as mentioned in the last section. However, we have failed to see such a large number of lattice defects. We rather observe quite

large (several hundred Å) single NSL domains compared with the average terrace length (~ 27 Å), as is visible in fig. 3. This raises the question how the NSL is formed in such a coherent manner without generating lattice defects, e.g. APBs. This question includes how each one-ML-height step acts as a phase-locker.

3.3. Step-terrace-reconstruction (STR) model

The question raised in the last part of the previous section may be answered if each terrace-parity is *all even* and if some additional assumptions are made. Each of the two terraces in the center position of fig. 2b has been drawn to have 6 and 8 atom sites for column III atoms; both terraces have even terrace parity. With Ga atoms at the step corner, no atom arrangement mismatch has been generated. The even nature of terrace-parity, if it is the case, may result from reconstruction of the terraced (001) surface. Scanning tunneling microscopy (STM) has directly demonstrated that As stabilized (001) surface of MBE grown GaAs is reconstructed to form As dimers [24]. A similar surface reconstruction is expected also for P-stabilized GaInP (001) surface.



Fig. 3. [110] pole dark-field TEM image for GaInP-on-GaAs interface shown in fig. 1b. Dense line array in GaInP layer corresponds to NSL. Spacing is 6.5 Å. Interface is inclined about 6° from (001) towards $\bar{1}\bar{1}0$. The average terrace width corresponds to about three periods of natural superlattice (NSLs) in the horizontal direction. Note the very large coherence length (several hundred Å) for NSL instead of the short terrace width (~ 27 Å). Also note that the NSL appears to stem almost from the interface. A photograph obtained from the same negative film with a lower light exposure time has more clearly showed the structure at the interface.

Figs. 4a–4c show some of the possible reconstructed As (or P for GaInP case) stabilized (001) surfaces with terraces, where terraces are assumed to be reconstructed to have column V atom dimers. Fig. 4a illustrates terraces with *even parity* ($\dots, s_1-s_6, t_1-t_8, \dots$). Here we define “terrace width” as the number of the group III atoms on a terrace in the projected (110) plane. For example, terraces s and t in fig. 4a are drawn to have terrace widths of $n=6$ and 8. Terrace widths for (001) GaAs with a 6° off-angle may distribute like 2, 4, 6, 8, 10, \dots with even parity around an average of 6. We assume that each step edge, e.g. s_6-t_1 and t_8-u_1 , shows a specific reconstruction as in fig. 4a or fig. 4b. Depending on whether t_1 forms a

dimer or not, the reconstructed terraced surfaces are referred to as Even-II and Even-I, respectively. We tentatively assume that the Even-I type is the most stable reconstructed surface. We refer to this model as step-terrace-reconstruction (STR) model.

Let $\text{Ga}_{0.5}\text{In}_{0.5}\text{P}$ growth begin with an As-stabilized terraced (001) surface. Here, however, we start to examine the growth process after the completion of the growth of the first ML (molecular-layer) GaInP. Thus, this time, in fig. 4a, we regard double circles at the outermost “monolayer” surfaces as phosphorus (P) atoms, and imagine that beneath them there is one column-III-atom-monolayer $\text{Ga}_{0.5}\text{In}_{0.5}$, where both Ga and In are expressed as closed circles. Underneath this one-

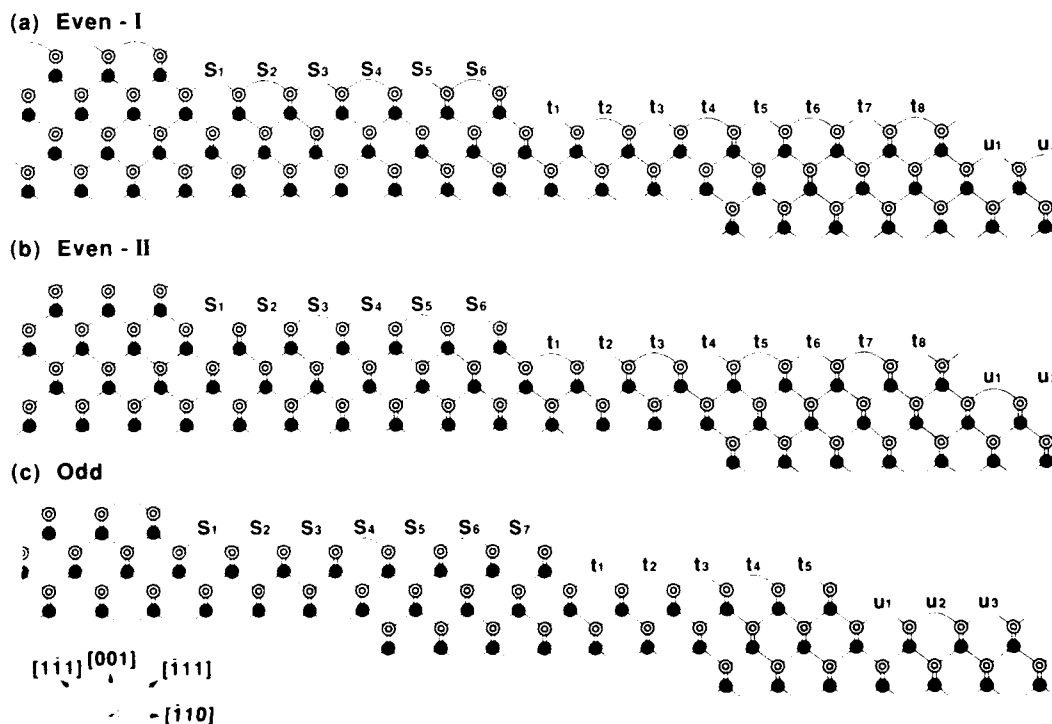


Fig. 4. Bond-stick models for reconstructed surfaces for terraced (001) III-V semiconductors. Closed circles stand for column III atoms and double circles stand for column V atoms in this figure. The curved line and unconnected line on one end mean a dimer and a dangling bond, respectively. Two types of reconstructions are shown in (a) and (b). The difference lies at the step edges. Both cases are for even “terrace parity”. An odd terrace parity case is shown in (c). Another odd terrace parity case is obtained by replacing dangling bonds and dimers by each other for (c).

ML GaInP, a GaAs substrate exists, which is also represented as closed circles (Ga) and double circles (As). As for the first one-ML GaInP growth, we will mention it later.

On the P-stabilized terraced surface (see fig. 4a), growth may begin from each step edge, s_1, t_1, u_1, \dots . If the following requirements are satisfied, a growth of a large scale single domain NSL, will be automatically assured;

(R1): Preferential sticking of either of column III atoms (Ga or In) to the step edges occurs.

(R2): Alternate arrangement of Ga and In lines is preferred.

(R3): Every terrace width has even terrace parity.

The first requirement (R1) may be satisfied, considering that Ga has a larger Ga-P bonding energy compared with that for In-P (see ref. [8]). The requirement (R2) will be satisfied if we remember the "stress minimum principle", proposed previously [8]. Each Ga which has stucked at the sites s_1, t_1, u_1, \dots form two Ga-P bonds between one Ga atom and two P atoms at the surface. Because the order of the bond lengths (b) is $b(\text{In-P}) > b(\text{Ga-As}) > b(\text{Ga-P})$, after the Ga sticking, the distance between the two P atoms may become less than d_0 (4 Å), which is the distance between two corresponding As atoms in bulk GaAs crystal. After the Ga sticking at the step edge sites s_1, t_1, u_1, \dots , the sites s_2, t_2, u_2, \dots will be preferred by In atoms, in order to minimize the strain energy. The In sticking at these sites tends to compensate the strain which was introduced by the previous Ga sticking. The requirement (R3) is supported by the present step-terrace-reconstruction (STR) model. An example of the grown NSL is shown in fig. 2b, in which the first one ML beneath the dotted line should be understood as one disordered GaInP layer, as mentioned above.

Here we will discuss the growth of the first one-ML layer GaInP just on the GaAs substrate. For this discussion, we use fig. 4a to represent GaAs substrate; all closed circles and double circles are Ga and As atoms, respectively. Sites s_1, t_1, u_1, \dots will be occupied by Ga atoms for the same reason as for the P-stabilized surface. This time, however, the next sites s_2, t_2, u_2, \dots have no apparent reason to preferentially accept In

atoms, because the previous Ga sticking and resultant Ga-As bond does not seem to introduce extra strain energy. This is simply because the substrate is GaAs itself. Thus the first ML GaInP may be a disordered layer; from the second GaInP layer the NSL formation will begin.

The stress-minimum principle assumed in (R2) seems also necessary if we remember that AlGaAs has not been reported to show CuPt type NSL [1], in spite of the large bonding energy difference between Al-As and Ga-As. [8]. Though the large bonding energy difference may cause preferential sticking of Al atoms at the step edges, the requirement (R2) is not satisfied due to the fact that bond lengths are virtually equal; $b(\text{AlAs}) \sim b(\text{GaAs})$.

The growth condition (growth temperature, V/III ratio [20]) dependence of NSL formation [5,6] and in turn band-gap energy [4,20] may be interpreted in terms of growth condition dependence of both surface reconstruction and atom mobility at growing surfaces.

4. Conclusion

Based mainly on the experimental results for GaInP on a (001) vicinal (6° towards $[\bar{1}10]$) surface: (1) non-existence of (111)B micro-facets at the interface between GaAs substrate and GaInP epi-layer and at the growing surface and (2) extremely large (~ 400 Å) sizes of single natural superlattice domains compared with the average terrace width (six column III atom: ~ 27 Å), a new NSL formation mechanism (step-terrace-reconstruction (STR) model) was presented, in which reconstruction of a column V atom stabilized (001) surface with one-ML-high terraces is assumed to give even parity for the numbers of column III atoms on (001) terraces. This STR model automatically assures a large single domain NSL formation. The stress minimum principle and the preferential Ga sticking at step edges are also assumed.

Acknowledgements

The authors would like to thank K. Kobayashi, Y. Ueno, S. Kawata and H. Hotta for growing many crystals and for discussions, N. Hamada and T. Kurimoto for helpful discussions, and I. Hino for discussions and supporting this work. The authors also would like to thank M. Sakaguchi for his continuous encouragement.

Note added in proof

Although the present paper assumed preferential Ga sticking at the step edges, by considering a steric effect due to the contraction of P-P dimer distances preferential In sticking becomes plausible. This model allows the ordering even for the first GaInP mono-molecular layer on GaAs substrate. The model is discussed in an article by Suzuki, Gomyo and Iijima [25]. The NSL formation in III-V-V type alloys is also discussed briefly in this article.

References

- [1] T.S. Kuan, T.F. Kuech, W.I. Wang and E.L. Wilkie, *Phys. Rev. Letters* 54 (1985) 201.
- [2] I.J. Murgatroyd, A.G. Norman, G.R. Booker and T.M. Kerr, in: *Proc. 11th Intern. Congr. on Electron Microscopy*, Kyoto, 1986, Eds. T. Imura, S. Maruse and T. Suzuki (Japan. Soc. Electron Microscopy, Tokyo, 1986).
- [3] M.A. Shahid, S. Mahajan and D.E. Laughlin, *Phys. Rev. Letters* 58 (1987) 2567.
- [4] A. Gomyo, T. Suzuki, K. Kobayashi, S. Kawata, I. Hino and T. Yuasa, *Appl. Phys. Letters* 50 (1987) 673.
- [5] A. Gomyo, T. Suzuki and S. Iijima, *Phys. Rev. Letters* 60 (1988) 2645.
- [6] T. Suzuki, A. Gomyo, S. Iijima, K. Kobayashi, S. Kawata, I. Hino and T. Yuasa, *Japan. J. Appl. Phys.* 27 (1988) 2098.
- [7] A. Gomyo, T. Suzuki, S. Iijima, H. Hotta, H. Fujii, S. Kawata, K. Kobayashi, Y. Ueno and I. Hino, *Japan. J. Appl. Phys.* 27 (1988) L2370.
- [8] T. Suzuki, A. Gomyo and S. Iijima, *J. Crystal Growth* 93 (1988) 396.
- [9] A. Gomyo, S. Kawata, T. Suzuki, S. Iijima and I. Hino, *Japan. J. Appl. Phys.* 28 (1989) L1728.
- [10] A. Gomyo, H. Hotta, I. Hino, S. Kawata, K. Kobayashi and T. Suzuki, *Japan. J. Appl. Phys.* 28 (1989) L1330.
- [11] Y.E. Ihm, N. Ohtsuka, J. Klem and H. Morkoç, *Appl. Phys. Letters* 51 (1987) 3013.
- [12] O. Ueda, M. Takikawa, J. Komeno and I. Umebu, *Japan. J. Appl. Phys.* 26 (1987) L1824.
- [13] P. Bellon, J.P. Chevallier, G.P. Martin, E. Dupont-Nivet, C. Thievaux and J.P. Andre, *Appl. Phys. Letters* 52 (1988) 567.
- [14] F.P. Dabkowski, P. Gavrilovic, K. Meehan, W. Stutius, J.E. Williams, M.A. Shahid and S. Mahajan, *Appl. Phys. Letters* 52 (1988) 2142.
- [15] E. Morita, M. Ikeda, O. Kumagai and K. Kaneko, *Appl. Phys. Letters* 53 (1988) 2164.
- [16] S. Yasuami, C. Nozaki and Y. Ohba, *Appl. Phys. Letters* 52 (1988) 2031.
- [17] H.R. Jen, D.S. Cao and G.B. Stringfellow, *Appl. Phys. Letters* 54 (1989) 1890.
- [18] W.E. Plano, D.W. Nam, J.S. Major, K.C. Hsieh and N. Holonyak, Jr., *Appl. Phys. Letters* 53 (1989) 2537.
- [19] I.J. Murgatroyd, A.G. Norman and G.R. Bokker, *J. Appl. Phys.* 67 (1990) 2310.
- [20] A. Gomyo, K. Kobayashi, S. Kawata, I. Hino, T. Suzuki and T. Yuasa, *J. Crystal Growth* 77 (1986) 367.
- [21] T. Kurimoto and N. Hamada, *Phys. Rev.* B40 (1989) 3889.
- [22] K. Kobayashi, I. Hino, A. Gomyo, S. Kawata and T. Suzuki, *IEEE J. Quantum Electron.* QE-23 (1987) 704.
- [23] H.M. Cox, P.S. Lin, A. Yi-Kan, K. Kash, M. Seto and P. Bastos, *Appl. Phys. Letters* 55 (1989) 472.
- [24] M.D. Pashley, K.W. Haberen, W. Friday, Woodall and P.D. Kirchner, *Phys. Rev. Letters* 21 (1988) 2176.
- [25] T. Suzuki, A. Gomyo and S. Iijima, Natural superlattice as a result of surface reconstruction, in: *Ordering at Surfaces and Interfaces*, Eds. A. Yoshimori, T. Shinjo and H. Watanabe (Springer, Berlin, to be published).

MBE growth of tilted superlattices: advances and novel structures

P.M. Petroff^a, M.S. Miller^a, Y.T. Lu^b, S.A. Chalmers^a, H. Metiu^b, H. Kroemer^a
and A.C. Gossard^a

University of California, Santa Barbara, California 93106, USA

The vicinal surface ordering required for the TSL deposition has been studied as a function of temperature and composition for Ga_{1-x}Al_xAs, GaSb and AlSb surfaces. The interface sharpness observed during the Al–Ga co-deposition and self-organization on a vicinal surface has been modeled using a stochastic kinetics method. The modeling reproduces well the observations. To avoid critical effects of the tilt parameter variations, a novel structure, the serpentine superlattice, has been proposed. This structure has a “build in” two-dimensional confinement and yields uniform luminescence properties over large wafer areas. Finally, the TSL concept has been demonstrated for a novel system, the GaSb–AlSb system.

1. Introduction

Conceptually, the tilted superlattices (TSLs) are extremely attractive as a structure for introducing new degrees of freedom in tailoring the band gap in compounds semiconductors. For example, the direct growth of quantum wire superlattices or corrugated interfaces with a band gap modulation parallel to an heterostructure interface have been demonstrated [1,2]. An added attraction is that the structures have been demonstrated for both MBE [3] and MOCVD [4] deposition.

The TSL is fabricated by alternate deposition of fractional monolayers of two III–V compounds on a vicinally oriented substrate. First demonstrated for the GaAs–AlGaAs system, TSL structures have recently been demonstrated for the GaSb–AlGaAs system [5]. The method allows for TSLs whose periodicity is function of the substrate misorientation angle and of the TSL tilt angle β , with respect to the terraces normal. The TSL periodicity for a given substrate misorientation angle α can be continuously tuned by chang-

ing the tilt parameter p . The TSL period is given by:

$$T = \frac{pd}{[\tan^2\alpha + (1-p)^2]^{1/2}}.$$

The fraction of monolayers for the two semiconductors are m and n and the tilt parameter is $p = m + n$. The step height d for GaAs is 2.83 Å. A small change in p or α will induce large variations in the period and hence in the confined states energies. Hence the need for an accurate control of these parameters.

The 3 difficulties associated in the TSL deposition are:

- (a) the requirement of a periodic step array over the entire substrate, during the TSL deposition as well as the deposition of the buffer layer and the cladding layers required for the fabrication of a quantum wire superlattice;
- (b) the requirements of a uniform tilt angle of the TSL over the entire wafer;
- (c) the necessity of maintaining sharp interfaces between the quantum wells and the cladding layers.

We examine subsequently the recent progress made in solving these 3 problems.

^a Department of Engineering Materials and Department of Computer and Electrical Engineering.

^b Chemistry Department.

2. Step ordering on a vicinal semiconductor surface

The vicinal surface as delivered by the manufacturer has a mean misorientation α , which does not correspond to the presence of a periodic step array on the surface. A Gaussian distribution of terraces with a mean dimension $L = d/(\tan \alpha)$ is present on the surface. Fortunately, for the GaAs [6] and the AlAs [7], and GaSb [5] {100} substrates, nature provides us with a self-correcting process which allows us to obtain a periodic step lattice out of a gaussian distribution of steps around a mean misorientation α . If a potential barrier to atomic motion prevents atoms from going down from one terrace to the other before they are incorporated at the step as part of the growing layer, an equalization of the terrace length takes place providing that a layer growth regime is established. This effect was demonstrated analytically and by Monte Carlo simulations [8]. The existence of a potential barrier to atom motion from one terrace to the other is found to be necessary to the self-correcting process. The origin of this potential barrier is not clear, however one might speculate that the bond breaking mechanism is more difficult if hybridized bonds are formed at step edges and more bond have to be broken when an atoms jump from one terrace to another. Intuitively, the short terrace will grow laterally faster than the larger adjacent one since the number of atoms impinging on the long terrace is larger.

The preparation of the vicinal surface is done by observing during growth of the buffer layer, the double peak structure of the specular beam in the RHEED pattern when the incident electron beam is orthogonal to the step edges [6,7]. The full width at half maximum is directly correlated to the step periodicity and the distance between these peaks is related to the vicinal surface misorientation. The proper conditions [7] for producing a periodic array of steps will depend on the surface composition, the growth temperature T and whether growth is taken place in the molecular beam epitaxy (MBE) or the migration enhanced epitaxy (MEE) mode.

For the $\text{Al}_x\text{Ga}_{1-x}\text{As}$ system grown in the MEE mode, a phase diagram has been established ex-

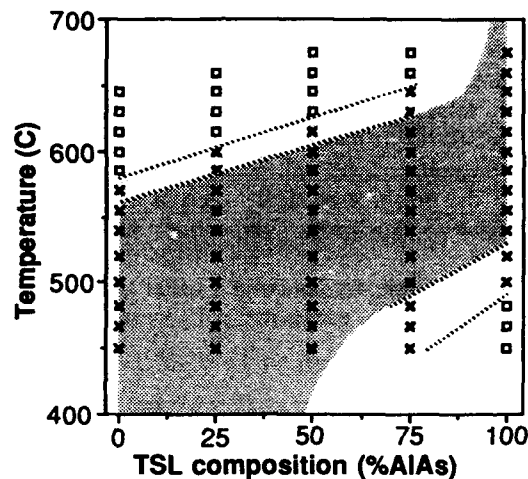


Fig. 1. Phase diagram of TSL growth surface morphology as a function of substrate temperature and AlAs composition obtained from the RHEED data analysis. MEE deposition. (\square) Data points represent smooth growth. Lightly shaded area represent regions where growth is mostly smooth but appreciable island nucleation is taking place on the terraces. Heavily shaded area represents rough growth [7].

perimentally as a function of x and T . As shown in fig. 1 for a As/Ga flux ratio of 6, there is not a unique deposition temperature that will preserve steps for both GaAs and AlAs surfaces during MEE deposition of a TSL. However, a GaAs- $\text{Al}_x\text{Ga}_{1-x}\text{As}$ TSL can be grown while preserving a good step structure at a temperature $T > 600^\circ\text{C}$ for $x < 0.5$.

The preservation of a step lattice at lower temperatures $T < 500^\circ\text{C}$ for $x > 0.75$ is not presently understood. The optimal growth temperature for the $(\text{Al}_{0.5}\text{Ga}_{0.5}\text{As})_m-(\text{GaAs})_n$ TSL is around 600°C for MEE deposition.

3. Tilt angle uniformity issue

The rapid variation of the tilt angle with the tilt parameter has serious consequences on the uniformity of the TSL characteristics grown on a wafer scale. As seen in fig. 2, small (1% or 2%) variations of the flux incident on the wafer will induce large changes (20° – 30°) in the TSL orientation. This type of variations is expected even

with wafer rotation during growth. Fig. 2a shows for a 2° vicinal surface the computed variations of the tilt angle with the tilt parameter.

A solution to this problem has recently been proposed [9]. It involves insuring that everywhere on the wafer, there will be a region of material with the proper periodicity. This is obtained by growing a so-called "serpentine superlattice" (SSL).

For example, by imposing a linear time dependence of the tilt parameter p between A and B

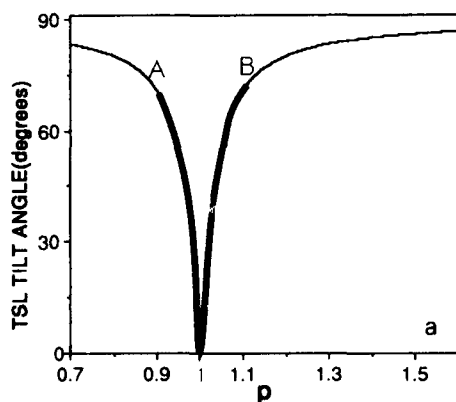


Fig. 2. (a) TSL tilt angle versus tilt parameter for a 2° vicinal surface. (b) A "C" shaped serpentine tilted superlattice schematic. The GaAs regions are shown as clear regions while the shaded regions represent the AlGaAs. The curvature of the GaAs quantum wells is determined by continuously varying p with time from a value smaller than 1 to a value larger than 1.

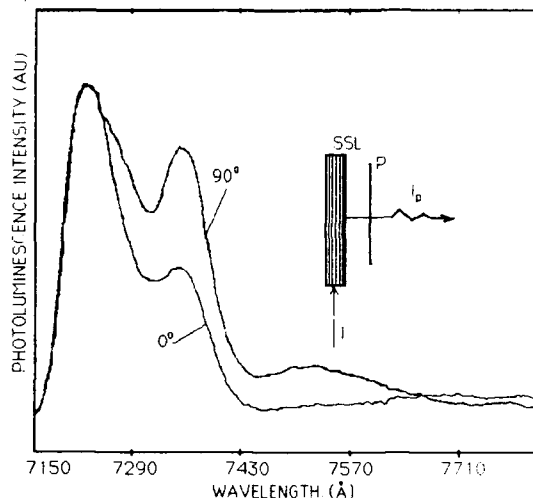


Fig. 3. PL spectrum of a "C" shaped serpentine superlattice deposited on a 2° vicinal surface. With the polarizer P set at 90° the electric vector is perpendicular to the wires. The wires are running vertically in the sample and are excited end on [9].

(heavy line, fig. 2a) during the growth of the SSL, one can insure that there will always be on the wafer a region for which $p = 1$. A schematic of the resulting SSL is shown in fig. 2b. This type of superlattice structure warrants that a uniform quantum wire superlattice is formed everywhere on the wafer. Two-dimensional carrier confinement is "built in" the regions of the SSL with the smallest radius of curvature [9]. A three-dimensional QWW superlattice is formed by continuously varying the p value alternatively between 2 values which span the $p = 1$ value. The resulting SSL has an S shape. By changing the p dependence with time during growth, the curvature of the SSL quantum well can be varied at will.

Because of the variable width in the SSL's quantum wells, the SSL yields a quantum-wire-like confinement in the region of largest curvature. The photoluminescence spectrum of a "C" shaped serpentine superlattice deposited on a 2° vicinal substrate is shown in fig. 3. The main peak is attributed to recombination in parts of the SSL which are essentially a random alloy and shows no polarization dependence when a polarized filter is placed in between the sample and the monochromator. The shoulder, which shows a pronounced

polarization dependence, is tentatively assigned to recombination from a quantum wire state. The PL intensity is at a maximum, in the curve labeled 90° , when the polarizer passes light perpendicular to the quantum wire. A weak polarization dependence can also be seen in the background at lower energies. These polarization effects have been seen on 1° and 2° substrates, but are much weaker or absent on 0.5° and 4° substrates. A fuller interpretation of these spectra is still being developed.

4. The interface sharpness in the TSL structures

One of the more serious issues remaining in the TSL or SSL structures is that of interface sharpness. Transmission electron microscopy experiments [10] have indicated that the interface roughness of 4 to 5 monolayers is usually present in the TSL. The interface sharpness is controlled by the diffusion kinetics of atoms at the surface and by the equilibrium shape of steps during growth. The presence of kinks at the step edges, which is required to ensure a layer growth regime, is one of the essential components affecting interface sharpness. Since there are no experimental data on this problem, a modeling approach has been adopted.

An attempt at understanding the partitioning of Al and Ga at the surface is achieved by using a stochastic kinetics simulation method [11] aimed at reproducing the Al-Ga segregation which has been recently observed [12] during MEE growth of the coherent tilted superlattice (CTSL).

The CTSL is realized through the self-organization and phase segregation which take place when Al and Ga atoms are co-deposited on a vicinal surface with a 2° misorientation. The self-organization and phase segregation are detected by depositing sequentially Al-Ga and As. If the amount of co-deposited Al and Ga is equal to a monolayer and if an appreciable phase separation takes place, a CTSL will be formed. The CTSL has been detected by transmission electron microscopy (TEM) and the Al has been shown to preferentially segregate at the step edges when these are parallel to $[110]$.

In the numerical simulation of the CTSL

growth, the Al and Ga are randomly deposited onto a 30×40 square lattice plane according to the rate of deposition. The migration of atoms on the surface takes place through a succession of uncorrelated jumps, each jump taking the atom from its lattice site to one of the nearest neighbor sites. The jump rate depends on the temperature, the jump direction, and the neighboring configuration. The jump frequency is determined by the largest jumping rate (e.g. Ga in a most favorable neighbor configuration) which is normalized to have probability of success 1 in each attempting jump, and the probability of jump for Al or Ga in other configurations will have jumping probability less than 1 in each attempt. The jump frequency is typically a thousand times the atom deposition frequency.

The modeling is based on the following physical considerations:

- (1) The migration energy of a diffusing atom, E_m is taken as: $E_m = E_s + E_i$. E_s and E_i are respectively the atom interaction energy with the substrate and with the neighboring surface adatoms. Indeed both these energies are direction dependent. However, the modeling results appear to be weakly dependent on the directional dependence of E_s .
- (2) The Ga migrates about 3 times faster than the Al at 600°C .
- (3) The group III atoms have a pair of dangling bonds pointing along the fast diffusion direction, $[110]$, therefore two atoms lined in the fast diffusion direction will have stronger interaction than with those in the orthogonal direction. We use a Morse potential for taking into account the interactions between atoms. We have reduced the strength of the atom-atom interactions along the slow-diffusion direction, $[1\bar{1}0]$, by a factor (anisotropy) varying from 0 to 1 to study the effect of anisotropic interactions. The strength of the anisotropy factor is atom position dependent and takes into account the distance of the first and second nearest neighbors.
- (4) The Al-Al interaction is stronger than the Ga-Ga, or Al-Ga interactions. The dissociation energies in the Morse potential are 0.18, 0.09, 0.04 eV for Al-Al, Ga-Ga, Al-Ga, respectively. The contributions from both the nearest neighbors and

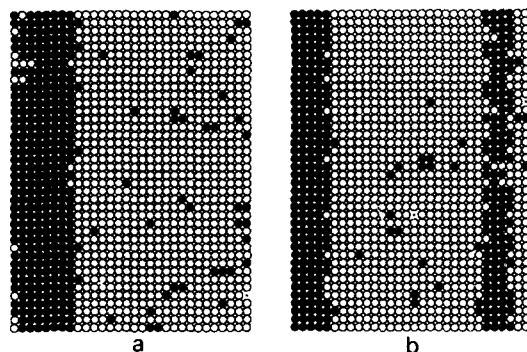


Fig. 4. Surface image of the Al-Ga (ratio of Al to Ga atoms is 0.33) deposition on a 1.5° vicinal surface. Full circles denote Al atoms and open ones the Ga atoms. (a) After complete deposition of a monolayer (1200 atoms are deposited) at the optimal temperature ($T = 600^\circ\text{C}$). (b) After complete deposition of a monolayer at lower temperature (475°C). The $[1\bar{1}0]$ step edge is located on the left side of each figure [11].

next nearest neighbors are taken into account in the calculation of the hopping energy barrier.

(5) The step provides an extra attractive potential to both the Ga and Al when they arrive at step sites. This results in a larger barrier for them when leaving the step. We use 0.135 eV as the extra step attraction energy for both Ga and Al.

The simulations using this model with anisotropy factors for E_i of 0 and 0.5 (with atoms perpendicular to the moving atom) reproduce well the observed self-organization and phase segregation. Fig. 4a shows the result of $\text{Ga}_{0.7}\text{Al}_{0.3}$ deposition at 600°C . Most of the Al are able to penetrate through the Ga layer and reach the step. The successful segregation is due to factors like: the lower deposition rate, the high temperature and the weak Ga-Ga interaction. The first two factors allow the Al enough time and mobility for reaching the step, and the third factor allows the Al to penetrate the Ga islands in the later stage of deposition. The simulation is also able to reproduce qualitatively the narrow temperature window which was observed in the experiment. Fig. 4b shows a simulation at 475°C . Some of the Al fails to segregate to the step and form a second band on the terrace (the position of this band with respect to the step edge is located randomly). There are two reasons for this failure: (1) Lower

temperature reduces the mobility of Al. (2) At lower temperature the islands of Ga become more rigid; this prevents Al penetration through the Ga in the later stage of deposition.

The failure of growing TSL on a B face vicinal surface is also understood from the simulation. Different geometrical structure at the B face may result the weaker step attraction. However, we found that this is not the essential factor. Since both Ga and Al have a propensity to grow as strips along the slow diffusion direction, $[1\bar{1}0]$, the simulation with the B face results in Al and Ga forming bands in the direction perpendicular to the step (this is still true even if the B face step attracts atoms as strongly as the A face step).

5. Extension of the TSL concept to other systems

In principle the TSL growth concept should be applicable to other systems providing a vicinal surface with monolayer height steps can be formed and preserved during growth. The step-flow growth mode should also be established to grow these systems. Recently, the TSL concept has been tested successfully on the GaSb-AlSb system [5]. The GaSb-AlSb TSL was grown either on GaAs or GaSb $\{100\}$ vicinal surfaces. The growth was carried out by MBE and MEE in the temperature range $490\text{--}510^\circ\text{C}$.

The effects of the strain on the interface sharpness appear to be minimal. Thus we expect that TSL can be produced in a large number of heterostructure systems irrespective of the strain.

6. Conclusions

The vicinal surface ordering needed during the TSL deposition has been studied as a function of temperature and composition for $\text{Ga}_x\text{Al}_{1-x}\text{As}$, GaSb and AlSb surfaces. The interface sharpness observed during the Al-Ga co-deposition and self-organization on a vicinal surface has been modeled using a stochastic kinetics method. This type of modeling should lead to establishing conditions for the deposition of better TSLs. To avoid critical effects of the tilt parameter variations a

novel structure, the serpentine superlattice has been proposed. This structure has a "built in" two-dimensional confinement and yields uniform luminescence properties over large wafer areas. Finally, the TSL concept has been demonstrated for a novel system, the GaSb-AlSb system.

Acknowledgements

It is a pleasure to thank J. English for his valuable help with the MBE growth. We acknowledge financial support by the AFOSR and QUEST, a National Science Foundation Science and Technology center.

References

- [1] J.M. Gaines, P.M. Petroff, H. Kroemer, R.J. Simes, R.S. Geels and J.H. English, *J. Vacuum Sci. Tech* B6 (1988) 1378.
- [2] M. Tsuchiya, J.M. Gaines, R.H. Yan, R.J. Simes, P.O. Holtz, L.A. Coldren and P.M. Petroff, *Phys. Rev. Letters* 62 (1989) 466.
- [3] P.M. Petroff, J.M. Gaines, M. Tsuchiya, R. Simes, L.A. Coldren, H. Kroemer, J.H. English and A.C. Gossard, *J. Crystal Growth* 95 (1989) 260.
- [4] T. Fukui and T. Saito, *J. Vacuum Sci. Technol.* B6 (1988) 1373.
- [5] S.A. Chalmers, A.C. Gossard and H. Kroemer, *Appl. Phys. Letters* 57 (1990) 1751; S.A. Chalmers, H. Kroemer and A.C. Gossard, *J. Crystal Growth* 111 (1991) 647.
- [6] S.A. Chalmers, A.C. Gossard, P.M. Petroff, J. Gaines and H. Kroemer, *J. Vacuum Sci. Technol.* B7 (1990) 1357.
- [7] S.A. Chalmers, A.C. Gossard, P.M. Petroff and H. Kroemer, *J. Vacuum Sci. Technol.* B8 (1990) 431.
- [8] H-G. Gossmann, S.W. Siden and L.C. Feldman, *J. Appl. Phys.* 67 (1990) 745.
- [9] M.S. Miller, H. Weman, L.A. Samoska, C.E. Pryor, H. Kroemer and P.M. Petroff, in: *The Physics of Semiconductors*, Vol. 2, Eds. E.M. Anastassakis and J.D. Joannopoulos (World Scientific, Singapore, 1990) p. 1717; M.S. Miller, C.E. Pryor, H. Weman, L.A. Samoska, H. Kroemer and P.M. Petroff, *J. Crystal Growth* 111 (1991) 323.
- [10] P.M. Petroff, *Ultramicroscopy* 31 (1989) 67.
- [11] Y.T. Lu, P.M. Petroff and H. Metiu, *Appl. Phys. Letters* 57 (1990) 2683.
- [12] M. Tsuchiya, P.M. Petroff and L.A. Coldren, *Appl. Phys. Letters* 54 (1989) 1690.

Fabrication of quasi-three-dimensional electron systems and superlattices in wide parabolic wells

M. Santos, J. Jo, M. Shayegan

Department of Electrical Engineering, Princeton University, Princeton, New Jersey 08544, USA

and

A.-M. Lanzillotto

David Sarnoff Research Center, Princeton, New Jersey 08543, USA

We report the realization of quasi-three-dimensional electron systems in selectively-doped wide parabolic quantum wells, focusing on a novel superlattice which contains a high-mobility ($\approx 1.1 \times 10^5 \text{ cm}^2/\text{V}\cdot\text{s}$ at 4 K) *degenerate* electron system. This molecular beam epitaxy grown structure is a wide undoped $\text{Al}_x\text{Ga}_{1-x}\text{As}$ well bounded by undoped (spacer) and doped layers of $\text{Al}_x\text{Ga}_{1-x}\text{As}$ ($x > x_c$) on both sides. The alloy composition in the well is graded in a way that results in a parabolic potential with a sinusoidal modulation superimposed on it. Once transferred into this well, the electrons screen the parabolic potential and an electron system with a modulated charge density profile is obtained. We present self-consistent quantum mechanical calculations of the electronic system and our characterization of the structure by secondary ion mass spectrometry and magnetotransport measurements.

Selectively-doped semiconductor structures that exhibit three dimensional behavior [1–3] attract current attention in part because they provide nearly ideal systems for the possible observation of a variety of predicted collective phenomenon [4]. In these systems electrons are confined in wide $\text{Al}_x\text{Ga}_{1-x}\text{As}$ quantum wells with quadratically graded Al composition which, when empty, leads to a quadratic dependence of the conduction band edge on the distance from the well center. As a consequence of the self-consistent electrostatic potential, the electrons in the parabolic well screen the quadratic potential and a system of nearly uniformly distributed electrons in a flat potential is obtained.

To demonstrate the electronic structure of such systems, fig. 1 shows calculations of the charge distribution and the potential in a typical parabolic well. These calculations were done by self-consistently solving the Poisson and Schrödinger equations while taking the exchange correlation into account via the local-density approximation.

As expected, the charge distribution in the central part of the well is nearly uniform. Small oscillations in the charge density exist because only a

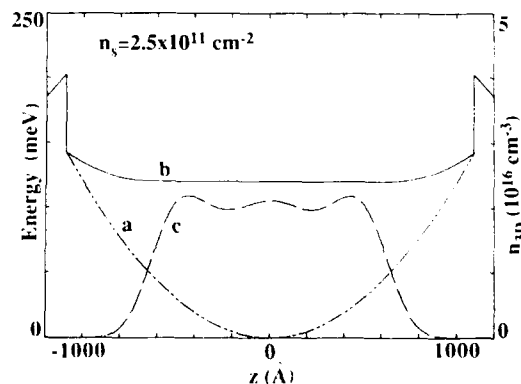


Fig. 1. Self-consistent calculations of the conduction band edge (curve b) and the charge density profile (curve c) are shown for a typical parabolic well. The conduction band edge for the empty well is indicated by curve a. These calculations were done for a total electron areal density $n_s = 2.5 \times 10^{11} \text{ cm}^{-2}$.

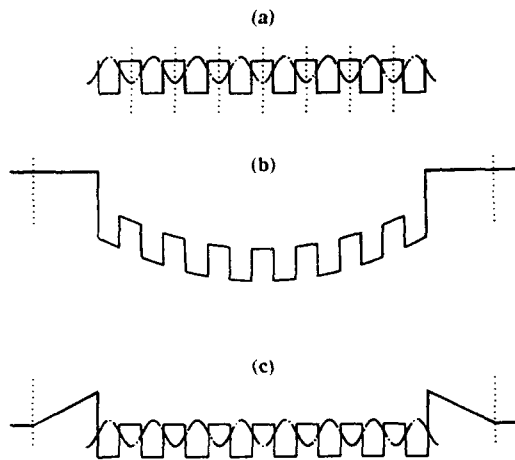


Fig. 2. The idea behind using a parabolic well with a periodic modulation to fabricate a high-quality superlattice is schematically presented. Solid, dash-dotted, and dotted curves represent the conduction band edge, the charge distribution, and the dopant atoms respectively. The structure of a conventional superlattice (a) and our proposed structure without (b) and with (c) electrons are shown.

finite number of electric subbands are occupied. In the case shown in fig. 1 there are four occupied subbands. Quantitative evidence for the realization of electron systems like this one is provided by comparing the calculated densities of these subbands with densities experimentally determined from a Fourier analysis of Shubnikov-De Haas oscillations seen at low applied magnetic fields [1]. We analyzed data obtained in a number of parabolic wells and found the experimental results in excellent agreement with the calculations, verifying the realization of electron systems similar to that shown in fig. 1 [1].

By adding a small periodic modulation to the Al composition of the parabolic well, a novel superlattice containing a low-disorder (high-mobility) degenerate electron system can be obtained [5]. In this structure *all* intentional dopants are placed *outside* the superlattice, a major advantage over conventional superlattice structures. This paper focuses on the fabrication and characterization of such a system.

Fig. 2a shows the conduction band edge, E_c , of a conventional GaAs/ $\text{Al}_x\text{Ga}_{1-x}\text{As}$ superlattice. To obtain a degenerate electron system, the bar-

riers in such a structure are doped. The ionized dopant atoms are therefore in close proximity to the electrons, encouraging substantial disorder and scattering of electrons by ionized impurities. This results in a system with low electron mobility, typically less than $10^4 \text{ cm}^2/\text{V} \cdot \text{s}$ at 4 K [6]. Fig. 2b schematically shows E_c of our proposed structure in the absence of any space charge. Note that the dopant atoms on both sides are placed outside the well, separated from the well by undoped (spacer) $\text{Al}_y\text{Ga}_{1-y}\text{As}$ ($y > x$) layers. Once transferred into the well, the electrons screen the parabolic potential and an electron system with a modulated charge density profile is expected (fig. 2c).

The structure was grown by molecular beam epitaxy on an undoped (100) GaAs substrate. The Al concentration, x , of a 3000 Å wide $\text{Al}_x\text{Ga}_{1-x}\text{As}$ well was quadratically varied between $x = 0.04$ at the well center and $x = 0.14$ at the well edges and contained an additional *sinusoidal* variation with a period of 200 Å and a peak-to-peak amplitude of 0.05. This variation in x along the growth direction was achieved by slowly changing the Al oven temperature during the growth. A sinusoidal modulation was chosen over a square-wave potential because the latter effectively requires two Al furnaces which we currently do not have [7]. The spacer between each parabolic well edge and the nearest Si dopant is 370 Å of $\text{Al}_{0.3}\text{Ga}_{0.7}\text{As}$ and the doping consists of five Si δ -doped layers, each with a density of $2.5 \times 10^{11} \text{ cm}^{-2}$ and spaced 37 Å apart.

Compositional characterization of the grown structure was made using secondary ion mass spectrometry (SIMS), the experimental details of which were reported elsewhere [8]. Fig. 3 is the SIMS depth profile for Al. The horizontal axis was calibrated (converted from sputtering time to depth) based on a profilometer measurement of the crater depth to an estimated accuracy of $\pm 10\%$. The profile shows a fifteen-period sinusoidal superlattice superimposed on a parabolic background. The measured width of the well and period of oscillation are both in agreement with the growth parameters to within the experimental accuracy. Measurements of the curvature of the parabolic Al profile and the amplitude of the sinusoidal oscillations can be made to within

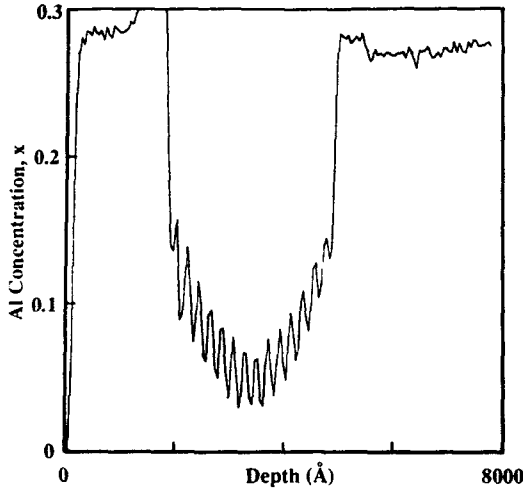


Fig. 3. SIMS profile measuring Al concentration as a function of depth.

$\pm 30\%$ using SIMS and, within this accuracy, they agree with the intended parameters [9].

Self-consistent calculations for this structure are shown in fig. 4 for several total areal densities, n_s , in the well. For each n_s , as long as the well is not overfilled, the charge density profile is nearly periodic with the same period as the superlattice potential. Because of the finite size of the well, the wavevector along the growth direction, k_z , and the energy are quantized. The additional slow variation in the charge density arises from a finite number of energy levels being occupied. Note that as n_s increases, the electrons spread over a larger distance in the well so that the peak value of the charge density profile remains nearly constant. This is the expected behavior of electrons in a partially-filled parabolic well [1–3]. Once the parabolic well is overfilled, electrons start to accumulate near the two edges of the well as shown in fig. 4d. These calculations therefore indicate that effective screening of the parabolic potential takes place even in the presence of the additional periodic potential.

Low-temperature magnetotransport measurements were performed to characterize the electronic properties of the grown structure. The transverse (ρ_{xx}) and Hall (ρ_{xy}) resistivities shown in fig. 5a were measured in the conventional

manner with the applied magnetic field, B , perpendicular to the sample plane. The high field data exhibit the integral quantum Hall effect, QHE. From the position in B of the ρ_{xx} minimum and ρ_{xy} plateau for the Landau-level filling factor $\nu = 2$, 3.0 T, we deduce an electron density $n_s \approx 1.5 \times 10^{11} \text{ cm}^{-2}$. The low-temperature mobility measured for the structure is $\approx 1.1 \times 10^5 \text{ cm}^2/\text{V} \cdot \text{s}$. This exceeds the value reported for a degenerate electron system in a conventional superlattice [6] by more than a factor of ten.

In fig. 5b the energy versus B fan-diagram for our structure is shown. At $B = 0$, self-consistent calculations for $n_s = 1.5 \times 10^{11} \text{ cm}^{-2}$ (fig. 4) indicate that five electric subbands are occupied. According to this figure, when $B \geq 0.7$ T only the lowest ($N = 0$) Landau levels of the electric subbands are occupied. Since the separation between

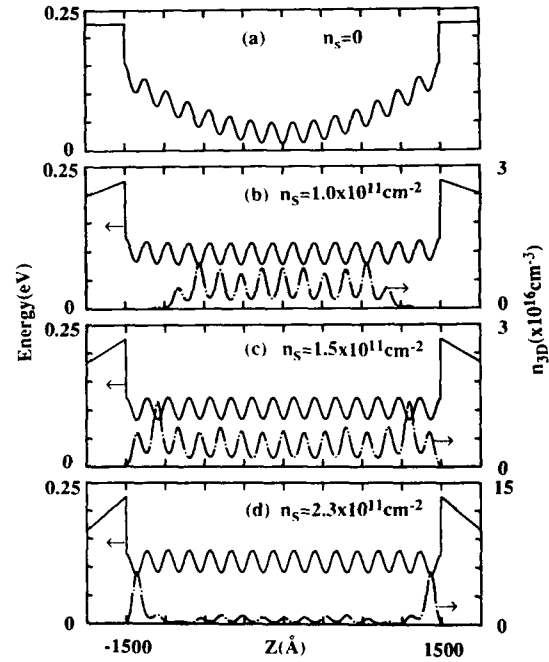


Fig. 4. Self-consistent calculations of the conduction band edge (solid curves) and the charge density profile (dash-dotted curves) are shown for several areal densities, n_s , in the well. The well is empty in (a), underfilled in (b), approximately full in (c), and overfilled in (d). We used $\Delta E_c = 750 \text{ x (meV)}$ for the conduction band offset of $\text{GaAs}/\text{Al}_x\text{Ga}_{1-x}\text{As}$ and $m^*/m_0 = 0.067$ for the effective mass.

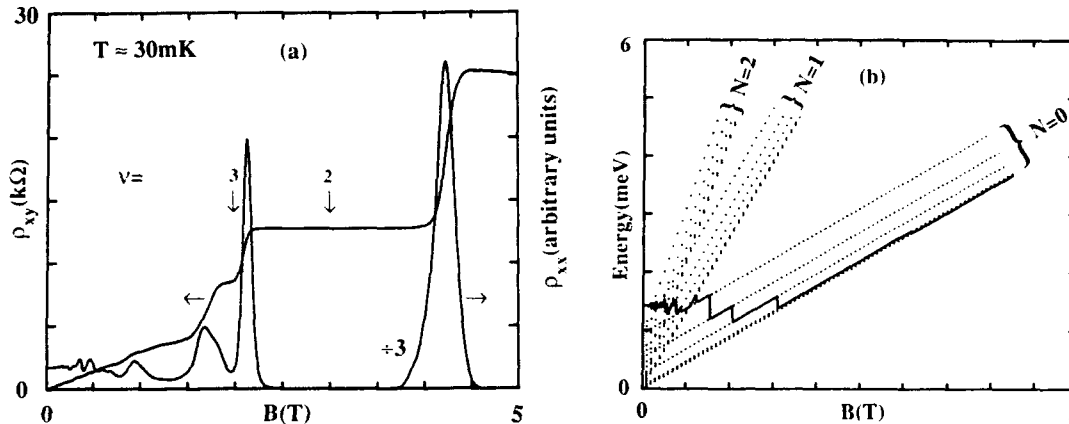


Fig. 5. Magnetotransport coefficients ρ_{xy} and ρ_{xx} measured at $T \approx 30$ mK are shown in (a). The energy versus B fan-diagram (dotted lines) and the position of the Fermi level (solid curve) are shown in (b). The zero-field energies are obtained from the self-consistent calculations shown in fig. 4c. Only the first three Landau levels ($N=0, 1$, and 2) for each of the electric subbands are shown. Spin splitting is not included.

the lowest electric subbands is small (≈ 0.1 meV), well developed QHE features (i.e., $\rho_{xy} \rightarrow 0$ and $\rho_{xx} \rightarrow$ plateau) are expected only at very low temperatures. This is consistent with our observation (not shown here) that the high-field QHE for this structure already becomes weak at a temperature of ≈ 300 mK. The addition of spin-splitting complicates the picture; it results in possible overlap of (spin-split) energy levels near certain integer filling factors and can lead to the absence of QHE at these filling factors. The filling factors at which such missing QHE states should occur critically depend on the electronic subband structure and consequently on the electron density and the parameters of the superlattice. Uncertainties in the exact shape of the potential well (curvature of the parabolic potential and amplitude and periodicity of the modulation) preclude us from a more quantitative comparison of the data with the calculations. Preliminary experiments, however, reveal that small changes in the electron density in the well (via application of a back-gate voltage) result in a dramatic disappearance and reappearance of the QHE states.

In summary, we report the fabrication and characterization of a superlattice in a wide parabolic well which includes a periodic potential modulation. Calculations of the electronic struc-

ture were also presented to demonstrate the self-consistent charge density profile in the system. Such high-quality superlattices can provide rich systems for the study of phenomena arising from interlayer Coulomb interactions in low-disorder multilayer electron systems.

We thank H.D. Drew, K. Karrai, and D.C. Tsui for fruitful discussions and Y.W. Suen and L.W. Engel for assistance with the low-temperature measurements. This work is supported by the National Science Foundation (Grant No. ECS-85-53110 and DMR-89-21073), the US Army Research Office (Contract No. DAAL03-89-K-0036), the New Jersey Commission on Science and Technology, GTE Laboratories Inc., Xerox Corporation, and the Alfred P. Sloan Foundation.

References

- [1] M. Shayegan, T. Sajoto, M. Santos and C. Silvestre, Appl. Phys. Letters 53 (1988) 791;
T. Sajoto, J. Jo, H.P. Wei, M. Santos and M. Shayegan, J. Vacuum Sci. Technol. B7 (1989) 311;
T. Sajoto, J. Jo, L.W. Engel, M. Santos and M. Shayegan, Phys. Rev. B39 (1989) 10464;
T. Sajoto, J. Jo, M. Santos and M. Shayegan, Appl. Phys. Letters 55 (1989) 1430.

- [2] M. Sundaram, A.C. Gossard, J.H. English and R.M. Westervelt, *Superlattices Microstruct.* 4 (1988) 683.
- [3] K. Karrai, H.D. Drew, M.W. Lee and M. Shayegan, *Phys. Rev. B* 39 (1989) 1426;
K. Karrai, X. Ying, H.D. Drew and M. Shayegan, *Phys. Rev. B* 40 (1989) 12020.
- [4] B.I. Halperin, *Japan. J. Appl. Phys.* 26, Suppl. 26-3 (1987) 1913.
- [5] A preliminary report on the fabrication, characterization, self-consistent calculations of the subband structure, and magnetotransport data of this superlattice was recently given by J. Jo, T. Sajoto, M. Santos and M. Shayegan, *Bull. Am. Phys. Soc.* 35 (1990) 682. Also, as this manuscript was being prepared, we received a preprint by L. Brey, N.F. Johnson and J. Dempsey reporting calculations of the electronic and optical properties of a superlattice similar to that shown in fig. 2c.
- [6] H.L. Störmer, J.P. Eisenstein, A.C. Gossard, W. Wiegmann and K. Baldwin, *Phys. Rev. Letters* 56 (1986) 85.
- [7] The structure in fig. 2b can also be grown using a short-period superlattice of GaAs/ $\text{Al}_x\text{Ga}_{1-x}\text{As}$ with varying $\text{Al}_x\text{Ga}_{1-x}\text{As}$ thickness, similar to the method used in ref. [2] to grow parabolic wells.
- [8] A.-M. Lanzillotto, M. Santos and M. Shayegan, *Appl. Phys. Letters* 55 (1989) 1445.
- [9] The amplitudes of the oscillations in Al concentration in fig. 2 are larger on the left (surface) side of the parabolic well. It is likely that this is related to the worsening of our SIMS resolution with increasing crater depth (because of the non-uniformity of the crater depth). See ref. [8] for details.

Formation of quantum well wire-like structures by MBE growth of AlGaAs/GaAs superlattices on GaAs (110) surfaces

Shigehiko Hasegawa, Masamichi Sato, Kenzo Maehashi, Hajime Asahi and Hisao Nakashima

The Institute of Scientific and Industrial Research, Osaka University, Mihogaoka, Ibaraki, Osaka 567, Japan

We report on molecular beam epitaxial (MBE) growth of AlGaAs/GaAs superlattices on several GaAs (110) substrates, i.e. nominal (110) substrates and vicinal (110) substrates misoriented toward (111)A and (111)B. MBE growth of the superlattices on vicinal (110) substrates misoriented toward (111)B has been found to produce quantum well wire-like structures being coherently aligned toward the $\langle 110 \rangle$ direction with almost equal spacing. We discuss the formation mechanism of the quantum well wire-like structures which is closely related with the MBE growth mechanism on (110) surfaces.

In order to fabricate quantum well wire structures, several techniques, such as the ion implantation induced disordering [1] and the molecular beam epitaxial (MBE) growth of GaAs-AlAs “tilted superlattices” [2], have been reported and examined intensively. Recently, we have reported that quantum well wire-like structures are formed spontaneously during the MBE growth of AlGaAs/GaAs superlattices on cleaved GaAs (110) substrates [3]. In order to study this phenomenon, AlGaAs/GaAs superlattices were grown by MBE on various GaAs (110) substrates, i.e. nominal (110) substrates oriented within $\pm 0.5^\circ$ and vicinal (110) substrates misoriented 6° toward (111)A and (111)B. Scanning electron microscopic (SEM) observations revealed that quantum well wire-like structures were formed on vicinal (110) substrates misoriented 6° toward (111)B as well as on cleaved (110) substrates. In this paper we discuss the formation mechanism of these quantum well wire-like structures in terms of the MBE growth mechanism on (110) surfaces reported by Allen et al. [4,5].

Superlattices composed of 300 Å thick $\text{Al}_{0.5}\text{Ga}_{0.5}\text{As}$ layers and 300 Å thick GaAs layers with 8 periods were grown on vicinal (110) substrates misoriented 6° toward (111)A and (111)B, and on nominal (110) substrates oriented within $\pm 0.5^\circ$ for comparison. Growth temperature, growth rate of GaAs layers and flow rate of AsH_3 were 580°C ,

0.1 $\mu\text{m}/\text{h}$ and 1.5 SCCM, respectively. Substrate surfaces were thermally cleaned at 720°C for 20 min in As_2 atmosphere. Total thickness of grown superlattice layers was about 0.5 μm .

SEM micrograph of the surface of the sample grown on the vicinal (110) substrate misoriented 6° toward (111)B is shown in fig. 1. Giant steps are observed being coherently aligned along the $\langle 110 \rangle$ direction. The distance between the steps is

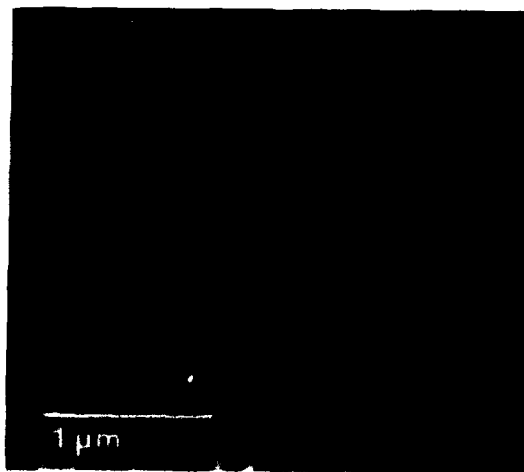


Fig. 1. SEM micrograph on the surface of the $\text{Al}_{0.5}\text{Ga}_{0.5}\text{As}(300 \text{ Å})/\text{GaAs}(300 \text{ Å})$ superlattice grown on a vicinal GaAs (110) substrate misoriented 6° toward (111)B.

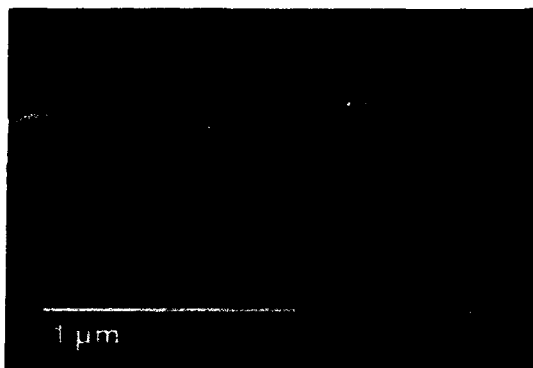


Fig. 2. Cross-sectional SEM micrograph of the sample shown in fig. 1. $\text{Al}_{0.5}\text{Ga}_{0.5}\text{As}$ layers of the sample were selectively etched by 1:21:20 solution of $\text{HF}:\text{H}_2\text{O}:\text{C}_2\text{H}_5\text{OH}$. The dark regions in the SEM micrograph correspond to AlGaAs layers.

about 3000 Å. From the off-angle of the substrate and this terrace width, the step height is estimated at about 300 Å. In contrast, SEM observation of the sample grown on a vicinal (110) substrate misoriented 6° toward (111)A revealed smooth surface morphology. This result is consistent with the report by Allen et al. [4].

Fig. 2 shows the cross-sectional SEM micrograph of the sample shown in fig. 1, i.e. the superlattice grown on vicinal (110) substrates misoriented 6° toward (111)B. $\text{Al}_{0.5}\text{Ga}_{0.5}\text{As}$ layers of the sample were selectively etched by 1:21:20 solution of $\text{HF}:\text{H}_2\text{O}:\text{C}_2\text{H}_5\text{OH}$. The dark regions in the SEM micrograph correspond to AlGaAs layers. The SEM micrograph reveals that quantum

well wire-like structures are formed being aligned toward the $\langle 111 \rangle$ direction. These quantum well wire-like structures are observed only for the sample grown on vicinal (110) substrates misoriented toward (111)B. A precise investigation of the cross-sectional SEM micrograph shows that during earlier stages of the MBE growth, steps become higher and coherent as the growth proceeds, and then two kinds of facets are formed at the giant step edges. As schematically shown in fig. 3, these facets are determined to be mainly composed of (111)A and (111)B surfaces from the relative angles between facets and (110) terraces. Polarities of (111) facets were determined from the orientation relative to the surfaces of the mesa structure shown later. The terraces between giant steps incline about 5° to the interface between the epitaxial layer and substrate, which means that the terraces are oriented exact $\langle 110 \rangle$ direction.

The quantum well wire-like structures in fig. 2 originate in the (111) facets formed at giant step edges. So, the AlAs mole fraction of AlGaAs layers on (111)A and/or (111)B facets is thought to be different from that on the (110) terraces, as schematically shown in fig. 3. Then, a $1\text{ }\mu\text{m}$ thick $\text{Al}_{0.5}\text{Ga}_{0.5}\text{As}$ layer was grown on a GaAs (110) substrate with mesa structures composed of (110), (111)A, (111)B and (100) surfaces. The mesa structures were made with anisotropic etchant ($\text{H}_2\text{SO}_4:\text{H}_2\text{O}_2:\text{H}_2\text{O} = 1:8:1$). The surface of the $\text{Al}_{0.5}\text{Ga}_{0.5}\text{As}$ layer was covered with a 2500 Å thick GaAs cap layer. Growth temperature and

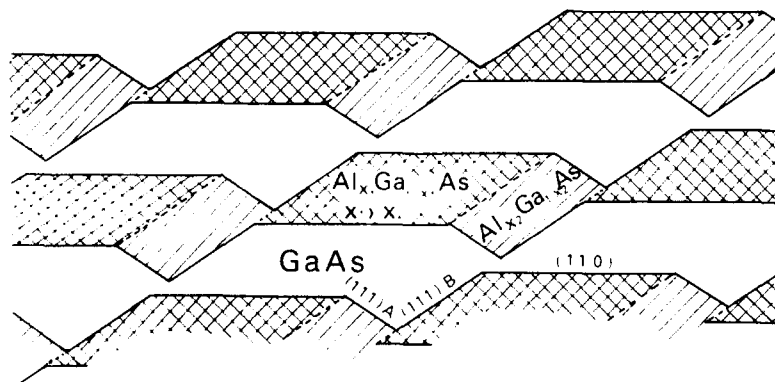


Fig. 3. Schematic illustration of the superlattice structure shown in fig. 2.

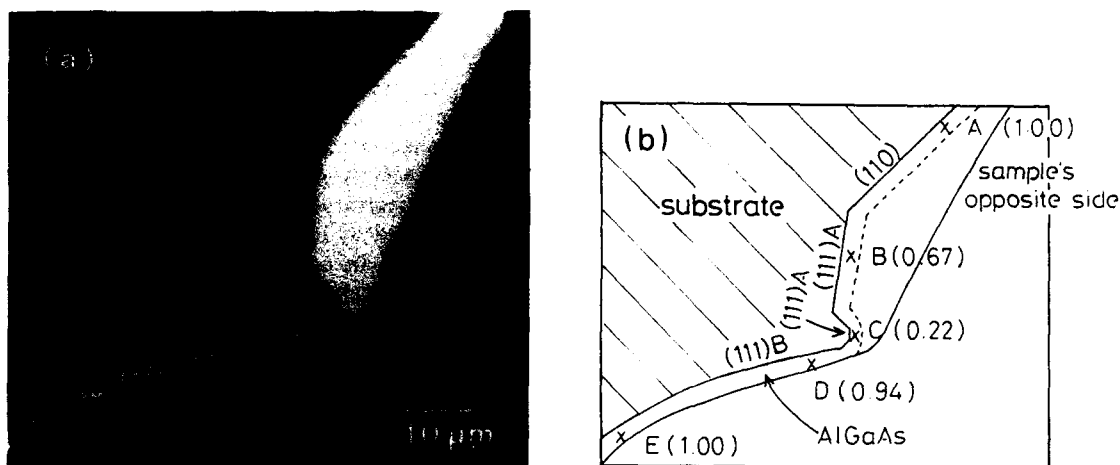


Fig. 4. Cross-sectional structure of the sample used for EPMA measurements: (a) SEM micrograph; (b) schematic illustration. EPMA measurements were carried out at each point (A, B, C, D and E). Figure in parentheses at each point shows Al $K\alpha$ intensity normalized by that at A.

growth rate were 580°C and $0.5\ \mu\text{m/h}$, respectively. Fig. 4 shows a cross-sectional SEM micrograph (fig. 4a) and schematic cross section (fig. 4b) of the sample. Electron probe microanalysis (EPMA) measurements were carried out at each point (A, B, C, D and E) shown in fig. 4b. The Al $K\alpha$ intensity at each point is normalized by that at A and is also shown in fig. 4b. The AlAs mole

fraction of the AlGaAs layer on (111)A surfaces is smaller than that on (110) surfaces. This result is very consistent with that of cathodoluminescence measurements which showed an orientation dependent AlAs mole fraction in AlGaAs epitaxial layers [6]. This orientation dependent AlAs mole fraction can be explained by the orientation dependence of the Al sticking coefficient and/or

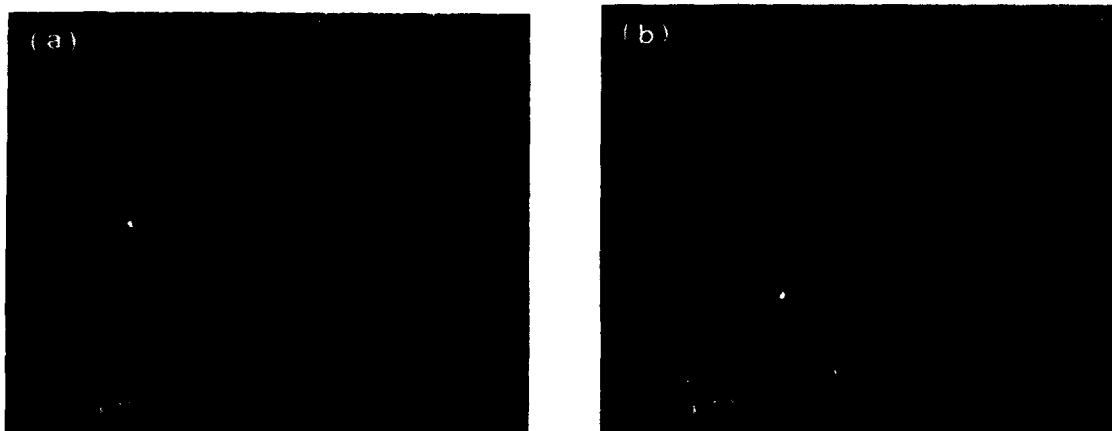


Fig. 5. SEM micrographs of the vicinal (110) substrates misoriented 6° toward (111)A (a) and (111)B (b) after thermal cleaning at 700°C in As_2 atmosphere.

surface diffusion length. The quantum well wire-like structures shown in fig. 2 are considered to be due to the (111)A facet formation and orientation dependent AlAs mole fraction.

Fig. 2 also shows that the quantum well wire-like structures originate in the vicinity of the interface between the superlattice layer and substrate. This result suggests that the giant growth steps with (111) facets are formed during earlier stages of MBE growth or thermal cleaning of (110) surfaces. Figs. 5a and 5b show SEM micrographs of the vicinal surfaces misoriented 6° toward (111)A and (111)B after thermal cleaning at 700°C in As_2 atmosphere, respectively. For the surface misoriented 6° toward (111)A, zig-zag steps are observed. In contrast, the morphology of the surface misoriented 6° toward (111)B is free from any structure. Therefore, the giant steps observed in figs. 1 and 2 are considered to be formed during earlier stages of the MBE growth. Allen et al. have reported that two-dimensional growth initiates at Ga-rich ledges and the epitaxial growth proceeds in a layer-by-layer growth mechanisms on vicinal (110) surfaces misoriented 6° toward (111)A [4,5]. Their result is very consistent with ours that the growth on vicinal (110) surfaces misoriented 6° toward (111)A provides the smooth surface morphology although the thermally cleaned surface is rough. The zig-zag steps observed at the thermally cleaned vicinal surface misoriented toward (111)A provide a number of the stable chemisorption sites of Ga atoms. Resultant Ga-rich ledges serve as a basis for layer-by-layer growth, and facet free films are grown. Therefore, on the vicinal (110) substrates misoriented toward (111)A, the AlGaAs/GaAs superlattices are grown without quantum well wire-like structures. On the vicinal (110) surfaces misoriented 6° toward (111)B, we considered that the (111)B facets at step edges interrupt lateral growth initiated at Ga-rich ledges. As a result, (111)A facets shown in fig. 3 are formed at the step edges as the MBE growth proceeds. This (111)A facet formation and orientation dependent AlAs mole fraction induce the quantum well wire-like structures in this sample. The nominal (110) surfaces are not exactly as flat as cleaved (110) surfaces and are locally misoriented toward different directions. The local mis-

orientation produces the grown surfaces with differently oriented facets and incoherent superlattices without quantum well wire-like structures.

In conclusion, we have found that the quantum well wire-like structures are formed by the MBE growth of AlGaAs/GaAs superlattices on vicinal GaAs(110) substrates misoriented 6° toward (111)B as well as cleaved GaAs(110) substrates. The structures are coherently aligned along $\langle 110 \rangle$ direction with almost equal spacing. SEM observations and EPMA measurements confirm that the (111)A facet formation during growth and orientation dependent AlAs mole fraction of AlGaAs layers induce the quantum well wire-like structures. The size of quantum well wire-like structures may be controlled by varying the off angle of vicinal (110) substrates and/or growth condition such as growth temperature, thickness of AlGaAs/GaAs layers and so on. Using this phenomenon, therefore, we think that we can easily fabricate quantum well wire structures without any sophisticated process.

The authors would like to thank Dr. T. Narusawa of Matsushita Electric Industrial Co., Ltd., for his help in fabrication of mesa structures, T. Tanaka of Osaka University for EPMA measurements and Y. Okuda of Osaka University for his help in computer control of MBE. They would also like to thank K. Kamon of Sumitomo Electric Industry Ltd. and T. Inada of Hitachi Cable Ltd. for supplying GaAs substrates, and Professor S. Gonda for his support. This work was supported by a grant from the Research Program on "Creation of New Materials through Intelligent Design" of ISIR, Osaka University.

References

- [1] Y. Hirayama, Y. Suzuki and H. Okamoto, Japan. J. Appl. Phys. 24 (1985) L516.
- [2] P.M. Petroff, A.C. Gossard and W. Wiegmann, Appl. Phys. Letters 45 (1984) 620.
- [3] M. Sato, K. Maehashi, H. Asahi, S. Hasegawa and H. Nakashima, in: Proc. 5th Intern. Conf. on the Physics of

- Electro-Optic Microstructures and Microdevices. Crete, 1990, in press.
- [4] L.T.P. Allen, E.R. Weber, J. Washburn and Y.C. Pao, Appl. Phys. Letters 51 (1987) 670.
- [5] L.T.P. Allen, E.R. Weber, J. Washburn, Y.C. Pao and A.G. Elliot, J. Crystal Growth 87 (1988) 193.
- [6] M.E. Hoenk, H.Z. Chen, A. Yariv, H. Morkoc and K.J. Vahala, Appl. Phys. Letters 54 (1989) 1347.

Stress accommodation in large-mismatch systems

Brian W. Dodson

Sandia National Laboratories, Albuquerque, New Mexico 87185, USA

Accommodation of lattice mismatch is investigated for the case of large ($\epsilon > 0.02$) mismatch. In particular, the regime where the separation D between misfit dislocations is much less than the strained layer thickness h is considered here. The conventional Matthews–Blakeslee mechanism for creation of misfit dislocations is found to be inadequate for the case of large lattice relaxation owing to interactions amongst the misfit dislocations at the interface. According to St. Venant's principle, the stress fields of the dislocation network are screened beyond a distance D from the dislocation cores. This observation has several consequences, including large densities of threading dislocations and the "melting" of moderately relaxed heterointerfaces at conventional semiconductor growth temperatures. A number of experimental observations may be explained via these models.

1. Introduction

The problem of accommodation of lattice mismatch at a heterointerface is one of great practical and scientific concern. On the practical side, strained-layer epitaxial structures offer the ability to tailor the electronic properties of semiconductors such that a broad continuum of material systems is made available for application. Beyond this, however, the formation and properties of interfacial structures which accommodate differing bulk structures is a wideranging and little understood problem. We are used to considering a tiny subset of this field, namely those structures in which the two materials making up the system have essentially the same crystal structure and nearly the same lattice constant. In this case, a reasonable approximation is that the mismatch is taken up by a lattice of misfit dislocations, whose introduction can be described using the Matthews–Blakeslee model. There are many situations, however, in which this description is inadequate. The problem is complicated considerably when the materials involved do not have the same crystal structure. In addition, when high densities of misfit dislocations appear, the interaction of those dislocations amongst themselves, rather than solely with the misfit stress, can dominate the energetics of relaxation. Finally, a dense network

of misfit dislocations at or near an interface can be considered another, nearly two-dimensional, material in its own right. The special properties of that interfacial material can strongly affect structural relaxation and/or stability.

In this paper, I will seek to examine the consequences of certain of these phenomena. The systems considered will be limited to materials having the same crystal structure, but having lattice parameters which differ by significantly more than one percent. This number will come out of the upcoming analyses, but is also motivated by a large number of experimental studies in which "something bad" happens to structures grown from materials having lattice mismatch of about 2% or greater. Initially, the Matthews–Blakeslee mechanism for strained-layer relaxation will be reviewed. The unusual nature of misfit dislocations will then be briefly examined, to establish a basis for treating highly relaxed structures. The stress field of a regular network of misfit dislocations will be described, primarily to justify our later use of a valuable qualitative rule for stress analysis of such structures, St. Venant's principle. This rule will then be applied to two specific problems, the observation of very large threading dislocation densities, and the loss of rectilinear form in the misfit dislocation network, in large mismatch structures. The treatment will be tu-

torial in places, to make the material accessible to the widest possible audience.

2. Matthews-Blakeslee relaxation mechanism

For over four decades, the possibility that lattice mismatch ϵ between two materials can be accommodated via a network of misfit dislocations at their interface has been appreciated. At that time, a simple atomistic model for the energetics controlling this process, in the limit where the spacing D between misfit dislocations is much greater than the layer thickness h , was developed [1]. This model, however, did not address the process of formation of the misfit dislocation network. That question was first seriously addressed by Matthews and Blakeslee [2], who observed that threading dislocations become unstable against formation of misfit dislocations when the misfit strain is large enough. As shown in fig. 1, the portion of a threading dislocation which lies in a strained layer is subjected to a force along its glide plane. As the remainder of the threading dislocation experiences

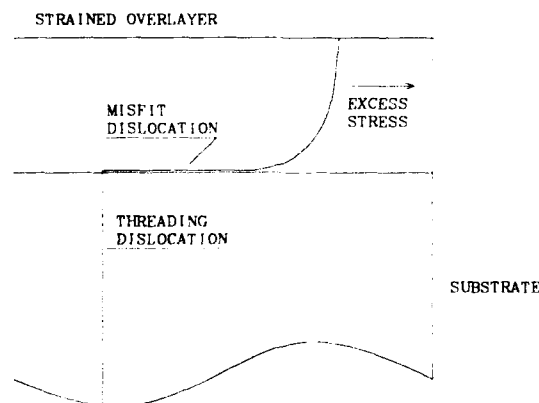


Fig. 1 Schematic of the Matthews-Blakeslee mechanism for formation of misfit dislocations. The segment of the threading dislocation in the strained overlayer is forced to the right by the misfit stress. If that stress is greater than the line tension of a misfit dislocation, the excess stress is greater than zero, and the threading dislocation becomes unstable against formation of a misfit dislocation at the interface, as illustrated.

only self-forces transmitted via a line tension, it tends to stay near its original position. If the line tension of a misfit dislocation at the strained layer interface is less than the force on the threading dislocation, the portion of the threading dislocation in the strained layer is free to move along its glide plane, leaving behind a misfit dislocation. It is important to note that, despite the restricted nature of this model, in reality strong assumptions are not being made concerning the original source of the misfit dislocations. Even if a local event, such as nucleation at inclusions or operation of a Frank-Read-type source, is originally responsible for the dislocations, once the misfit dislocations extend beyond the locality of the source further extension is the result of a Matthews-Blakeslee mechanism.

It is convenient to describe the stability of threading dislocations in a strained layer structure by defining an excess stress σ_{ex} [3]. If we take the case of (001) diamond-cubic strained interfaces and 60° dislocations (typical for small-mismatch group IV and III-V semiconductors), the excess stress is

$$\sigma_{ex} = 2 \frac{1+\nu}{1-\nu} \mu \epsilon - \frac{\mu b}{2\pi} \frac{1-\nu \cos^2 \beta}{1-\nu} \frac{\ln(4h/b)}{h}, \quad (1)$$

where μ is shear modulus, ν is Poisson's ratio, b is the magnitude of the Burgers vector of the dislocation, and β is the angle between the Burgers vector and the line of the dislocation. The first term reflects the force on the threading dislocation from interaction with the strained layer, and the second term describes the line tension of the misfit dislocation. Given the excess stress, the net glide force on the threading dislocation is simply

$$F = 0.5hb\sigma_{ex}. \quad (2)$$

Clearly, misfit dislocations will be produced when σ_{ex} is greater than zero. Although the rate of dislocation formation, and hence of stress relaxation, depends on a number of additional kinetic factors [4], the Matthews-Blakeslee model has had a remarkable degree of success in describing the equilibrium behavior of small-mismatch strained-layer structures.

3. Misfit dislocations in highly relaxed structures

In a formal sense, a misfit dislocation is defined by a line and a Burgers vector, as are conventional dislocations. It is natural, however, to wonder if these structures are truly analogous. In a normal edge dislocation, for example, an additional plane of atoms is inserted into the material (fig. 2a). This produces a hoop stress which varies inversely with the distance from the dislocation core. ($2\pi r + d$ matter is compressed into $2\pi r$ circumference. The resulting strain is $\sim d/2\pi r$.) The dislocation energy, which is obtained by integration from the core region, is logarithmically dependent on distance from the core.

An edge misfit dislocation appears to be a rather different entity (fig. 2b). In this case, the extra plane of atoms is not inserted by force, but rather is the natural result of the lattice mismatch of the materials on either side of the dislocation. In the vicinity of the core ($r < b/\epsilon$), therefore, there is little residual strain. Since the energy is obtained by integration over space, it would appear that a misfit dislocation has smaller energy than a formally equivalent conventional dislocation.

Of course, the dilemma set up above is specious: formally equivalent dislocations have identical material displacements, stress fields, and energies. The confusion results from inconsistent choices of reference systems in the two cases. As

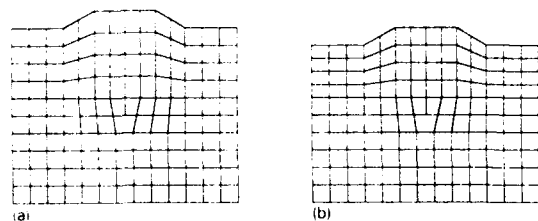


Fig. 2. Dislocations as displacements from a dislocation-free reference state. In (a) appears an edge dislocation below the surface of a monolithic structure. In (b) is shown an edge misfit dislocation at the interface between an unstrained substrate and a strained overlayer. Although the region above the edge dislocation is strained in compression, and the same region above the misfit dislocation is roughly free of strain, the displacements from the respective dislocation-free reference states are the same.

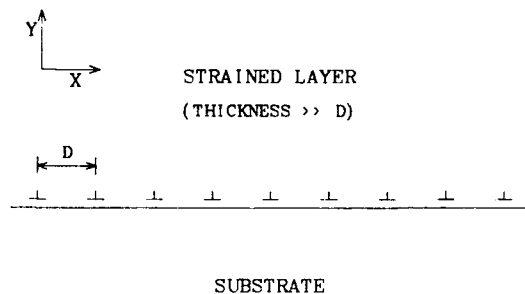


Fig. 3. An interfacial wall of misfit dislocations.

illustrated in fig. 2, in both cases a surface bulge results from the dislocation, which is a result of the excess material added. In fact, the displacements are actually identical (assuming equal elastic constants) if the displacements are measured *relative to their respective dislocation-free structures*!. If the reference structure happens to be strained, then that strain must be added to the dislocation strain to obtain the total structural strain (and hence stress and energy).

A particularly clear (and useful) illustration of this point is to consider an interfacial wall of edge misfit dislocations, as shown in fig. 3. The stress field of such a distribution of dislocations is [5]:

$$\sigma_{xx} = -\frac{\mu b}{2\pi(1-\nu)} \sum_{n=-\infty}^{\infty} \frac{y[3x^2 + (y-nD)^2]}{[x^2 + (y-nD)^2]^2} \quad (3)$$

or

$$\sigma_{xx} = -\frac{\mu b}{2D(1-\nu)(\cosh 2\pi Y - \cos 2\pi X)^2} \times [2 \sinh 2\pi Y (\cosh 2\pi Y - \cos 2\pi X) - 2\pi Y (\cosh 2\pi Y \cos 2\pi X - 1)] \quad (4)$$

where D is the dislocation separation, $X = x/D$, and $Y = y/D$. Only σ_{xx} has a long-range stress component. In the limit of large Y , σ_{xx} converges to $\mu b/D(1-\nu)$. This is the total stress if a wall of edge dislocations is placed in a single unstrained material.

In the present case, however, the wall is positioned at the interface between two materials hav-

ing lattice mismatch ϵ . The dislocation-free reference structure is that in which one of the materials (chosen to be $Y > 0$) is subjected to a uniform biaxial strain, resulting in a coherent interface. The resulting stress is $(1 + \nu)\mu\epsilon/(1 - \nu)$, which must be subtracted from the stress field of the dislocation wall to obtain the total stress of the structure.

If the mismatch is entirely accommodated by the dislocation wall, the limiting stress of the dislocation wall and the mismatch stress of the dislocation-free structure must be equal and opposite, so that the total structure has no long-range stress fields. This condition allows us to solve for D_0 , the equilibrium separation between misfit dislocations.

$$D_0 = b/(1 + \nu)\epsilon. \quad (5)$$

This is not precisely correct when systems of finite extent are considered, but is a very good approximation when the layer thickness h is substantially greater than D_0 .

4. Relaxation energetics and St. Venant's principle

The later stages of Matthews-Blakeslee relaxation in a strained-layer structure thick enough that

$D \ll h$ will be dominated by the interaction of the dislocation wall stress field (rather than the biaxial misfit stress alone) with threading dislocations. This total stress $\sigma = \sigma_{\text{ex}} - (1 + \nu)\mu\epsilon/(1 - \nu)$ is shown in a contour plot in fig. 4 for the case where the dislocation separation is D_0 ; the misfit stress is exactly compensated by the dislocation wall far away from the interface. (The contours are labeled in GPa.) Whereas an isolated dislocation would have stress levels of about 0.3 GPa at a distance of $D = 2$ in silicon, the structure considered here has stress levels less than 0.001 GPa at that distance from the interface. As a result, when relaxation is nearly complete, the primary elastic interactions take place very near the interface, where the stresses are large.

A useful tool for considering the interaction of dislocations with such complex dislocation structures is St. Venant's principle [6]. This states that statically equivalent forces applied to a local region of a body cause no long-range changes in the total stress field, and that the characteristic distance of the changes in the internal stress distribution is roughly that of the linear dimensions of the local region. For example, the stress distribution of two bodies whose surfaces are pressed, with equal forces, by a sharp needle and a rod of diameter d are essentially equivalent at distances

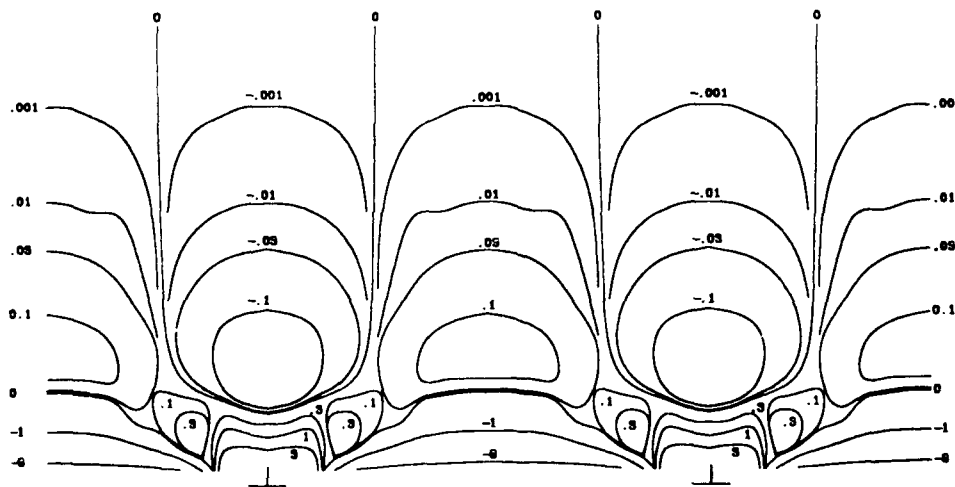


Fig. 4. Stress contours for the dislocation configuration in fig. 3. Stress here is in GPa. The dislocation separation was chosen to cancel the misfit strain far from the interface. Note that very little of the stress appears beyond one dislocation separation from the interface.

substantially greater than d from the pressure point.

St. Venant's principle also allows the stress distribution of a periodic array of dislocations to be estimated. If we refer again to fig. 4, it will be seen that there is little stress beyond a distance of $Y = 1$ from the dislocation wall. As a result, it is a reasonable approximation to eschew exact calculations, which become intractable for more complex configurations, and take the total stress as the superposition of the individual fields of the dislocations cut off at a distance equal to the dislocation separation D . (Comparison with exact calculations will sometimes suggest that the length scale should vary somewhat from D . This will generally affect only quantitative estimates, but not qualitative conclusions.) Although this procedure will not reproduce the exact stress field of a given dislocation distribution, it does allow relatively easy evaluation of the merit of possible mechanisms for structural change.

5. Appearance and unfilterability of large threading dislocation densities

A common (indeed, nearly ubiquitous) feature of growth of highly strained layers is the appearance of very high ($\sim 10^{12} \text{ cm}^{-2}$) densities of threading dislocations near the interface. (This phenomenon also appears occasionally in structures having little strain.) Although the threading dislocation density becomes smaller with continued growth, annealing, and the inclusion of dislocation filtering structures, there appears to be a minimum density of residual dislocations which varies as a function of layer thickness. In the case of GaAs layers on Si with a thickness of several microns, that density appears to be in the neighborhood of 10^7 cm^{-2} .

This is a problem of considerable practical importance, as this density of dislocations is enough to render the epilayer useless for a number of desirable applications. There have been many experimental studies of such structures, primarily aimed at testing various schemes for reducing the residual threading dislocation density. There has been, however, very little examination of why these

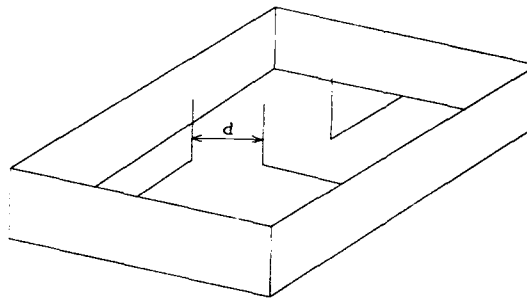


Fig. 5. Threading dislocation arms interacting to prevent further generation of misfit dislocations by the Matthews-Blakeslee mechanism.

enormous densities appear, and why they are so resistant to being removed from the system. I believe that one of the major factors involved is that, as strain relaxation proceeds, the interactions of the threading dislocation segments in the strained layer amongst themselves can become larger than the interactions with the remaining layer strain which is driving the relaxation process. At this point, the dislocations become "frozen" in place. In this section, a simple model for this phenomenon will be discussed.

Consider a strained layer relaxing by the Matthews-Blakeslee mechanism. This involves a number of threading dislocation arms moving through the strained epilayer (fig. 5). We want to determine at what threading dislocation density the inter-arm interaction is equal to the arm-strained layer interaction, as at this point the motion of the arms will be frozen. The force between two segments of threading dislocation is roughly

$$F_{\text{td}} = (\mu b^2 / 2\pi) h \rho^{-1}, \quad (6)$$

where ρ is the threading dislocation density and h is the strained layer thickness.

The force on the threading dislocation arms driving Matthews-Blakeslee relaxation is obtained from eqs. (1) and (2) by substituting the distance D between misfit dislocations at the strained layer interface for the layer thickness h . This substitution is allowed by St. Venant's principle when the layer is nearly relaxed. At this point, $D \sim b/(\epsilon_0 - \epsilon)$, where ϵ_0 is the total mismatch of the materials

and ϵ is the residual misfit. As $\epsilon \ll \epsilon_0$ is assumed, we can substitute $\epsilon_0 = \epsilon_0 - \epsilon$. This yields

$$F_{mb} = \frac{1+\nu}{1-\nu} \mu b^2 \frac{\epsilon}{\epsilon_0} - \frac{\mu b}{4\pi} \ln\left(\frac{4}{\epsilon_0}\right). \quad (7)$$

The condition for interference with dislocation arm motion is $F_{td} = F_{mb}$. This yields

$$\rho = \left[\frac{2\pi(1+\nu)\epsilon}{(1-\nu)\epsilon_0} - \frac{1}{2} \ln\left(\frac{4}{\epsilon_0}\right) \right]^2 h^{-2}. \quad (8)$$

The dislocation density for interference with mismatch relaxation can now be estimated. In practical use, the second term of eq. (8) dominates because $\epsilon/\epsilon_0 \ll 1$. For the GaAs/Si system, then, $\rho \sim 5h^{-2}$. For a thickness of 100 Å, this would predict a density of $5 \times 10^{12} \text{ cm}^{-2}$. For a thickness of 5 μm , the density would be roughly $2 \times 10^7 \text{ cm}^{-2}$. Both of these values are consistent with experimental values. Even though the above discussion is a sketch of a complete model, rather than an accurate description of the interference phenomenon, agreement with numerous experiments lends credence to the ideas developed here.

6. Dislocation "melting" at the strained-layer interface

Another phenomenon which is commonly observed in structures exhibiting lattice mismatch larger than about 2–3% is a transition from a rectilinear network of long 60° dislocations to a tangled mess of edge and mixed dislocations in the interfacial region. The resulting structures are reminiscent of those expected in the dislocation theory of melting. In that theory, a liquid is supposed to be a solid densely packed with dislocations, so that the shear strength of the resulting material would be minimal. This may or may not be an appropriate model of a liquid, but it is a reasonably good description of the material near the interface of a highly strained structure. I will investigate below the possibility that dislocation "melting" is active in producing such structures.

Mizushima [7] has produced an equilibrium model of dislocation "melting", which provides a

basis for our discussion. The energy of an atomic length of dislocation is roughly

$$U = \frac{b^2 \mu}{4\pi} \ln\left(\frac{D}{\delta b}\right) = -\frac{b^3 \mu}{4\pi} \ln(\delta \epsilon). \quad (9)$$

We use here $D \sim h/\epsilon$ in a (nearly) relaxed structure. This reflects the two-dimensional distribution of the misfit dislocations. The other notation is consistent with our earlier usage, and δ is a core energy parameter which will be fit to experiment. Nabarro [5] has estimated the entropy of a dislocation array, including terms from positional entropy, vibrational entropy of the dislocation line, and vibrational entropy of the surrounding lattice. He obtains an estimate of $-5k$ for the total entropy per atomic length of the dislocation line. Using this, the free energy per atom in an interfacial region of a relaxed structure with an initial mismatch of ϵ is

$$F(\epsilon, T) = -\frac{b^3 \mu}{4\pi} \epsilon \ln(\delta \epsilon) - 5k\epsilon T. \quad (10)$$

In the conventional melting theory, the "melting" point T_m is taken as that temperature satisfying $F(0, T_m) = F(1, T_m)$. In the current situation, however, the initial density of dislocations is not

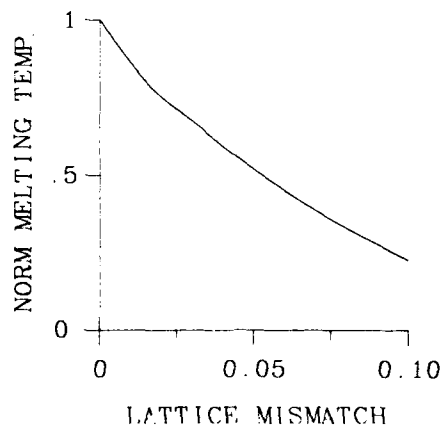


Fig. 6. Reduction in "melting" temperature of an interfacial region due to the presence of a high density of misfit dislocations. This calculation assumes that nearly all of the mismatch is accommodated by such dislocations prior to melting, which allows the initial dislocation density to be expressed in terms of the lattice mismatch. This is not necessary for the reduction to appear.

zero, but instead can be very large. The condition for "melting" is thus

$$T_m: F(\epsilon, T_m) = F(1, T_m). \quad (11)$$

A small value of ϵ can produce a large change in T_m . The adjustable parameter δ is set by requiring that the "melting" temperature for a dislocation-free material be equal to that observed experimentally. The relative "melting" point as a function of initial mismatch is then

$$\frac{T_m(\epsilon)}{T_m(0)} = 1 - \frac{\epsilon}{1-\epsilon} \frac{\ln \epsilon}{\ln \delta}. \quad (12)$$

Using this relation, T_m as a function of ϵ is shown in fig. 6 for a strained silicon-like material. Observe that the melting temperature is reduced to the range of typical growth temperatures for a mismatch of about 4%, in reasonable agreement with experiment.

7. Conclusion

In this paper, I have attempted to establish that it is reasonable that the relaxed structure of structures composed of materials having large lattice

mismatch differs qualitatively from that characteristic of systems with small mismatch. The stress distributions and interactions associated with a member of a dense network of misfit dislocations are quite different from the equivalent quantities for an isolated dislocation. In particular, models have been presented suggesting that the common observations both of large densities of threading dislocations and of dense non-rectilinear networks of dislocations near the interface in large misfit relaxed structures are collective effects reflecting the effect of dislocation-dislocation interactions.

References

- [1] F.C. Frank and J.H. van der Merwe, *Proc. Roy. Soc. (London)* A198 (1949) 216.
- [2] J.W. Matthews and A.E. Blakeslee, *J. Crystal Growth* 27 (1974) 118.
- [3] J.Y. Tsao, B.W. Dodson, S.T. Picraux and D.M. Cornelson, *Phys. Rev. Letters* 59 (1987) 2455.
- [4] B.W. Dodson and J.Y. Tsao, *Appl. Phys. Letters* 51 (1987) 1325.
- [5] F.R.N. Nabarro, *Theory of Crystal Dislocations* (Clarendon, Oxford, 1967).
- [6] S. Timoshenko and J.N. Goodier, *Theory of Elasticity* (McGraw-Hill, New York, 1951).
- [7] S. Mizushima, *J. Phys. Soc. Japan* 15 (1960) 70.

Growth processes and relaxation mechanisms in the molecular beam epitaxy of InAs/GaAs heterostructures

O. Brandt, L. Tapfer, K. Ploog

Max-Planck-Institut für Festkörperforschung, Heisenbergstrasse 1, W-7000 Stuttgart 80, Germany

M. Hohenstein and F. Phillipp

Max-Planck-Institut für Metallforschung, Heisenbergstrasse 1, W-7000 Stuttgart 80, Germany

The very first stages of growth during the molecular beam epitaxy of InAs on GaAs are studied. The growth mode is found to be closely related to the mechanisms of strain relaxation. The onset of 3D nucleation initiates strain relief by the formation of relaxed islands with subsequent segregation and intermixing of the group III elements. In multilayer structures, a competition between different relaxation paths is observed, regulated by the individual layer thickness rather than by the net strain in the structure.

In this work, we study the nucleation and strain relief processes in the molecular beam epitaxy of InAs on GaAs. Single as well as multiple InAs/GaAs structures are investigated by a combination of different methods. *In situ* reflection high energy electron diffraction (RHEED) provides a sensitive probe of the growth mode of the epilayer. High-resolution electron microscopy (HRTEM) and high-resolution double-crystal X-ray diffractometry (HRDXD) are combined for an accurate determination of the structural properties.

The InAs/GaAs structures are grown on undoped (100) GaAs substrates by conventional solid-source molecular beam epitaxy (MBE). Prior to the growth of the InAs/GaAs heterostructures, a 1 μm thick GaAs buffer layer is deposited. In the single layer samples, the InAs layer is capped with 200 nm GaAs. The structural parameters of the presented samples as determined by HRDXD and Raman spectroscopy are given in table 1. The growth process itself is identical for all of the samples. Each of the InAs layers is grown at 420°C, whereas the GaAs buffer and barrier layers are grown at 540°C. To avoid In desorption, a few monolayers of GaAs are deposited at 420°C

on top on the InAs layer, before heating up again to 540°C. In order to obtain smooth and homogeneous layers and to minimize the density of atomic steps at the growth surface, the InAs layers are deposited in half-monolayer increments, annealing the surface after each deposition under As_4 for 120 s at the growth temperature of 420°C. The reference for the calibration of the substrate temperature is given by the desorption of the native oxide at 580°C observed in the RHEED pattern. The RHEED monitoring of the growth process will be discussed below. The X-ray measurements are performed with a computer-controlled high-resolution double-crystal diffractometer [1] using $\text{Cu K}\alpha_1$ radiation in the vicinity of the symmetrical (400) and the asymmetrical (422) and (511) GaAs reflections, respectively. The entire X-ray spectrum between $\theta_B = 2^\circ$ and $\theta_B = 55^\circ$ is recorded by using the powder diffractometer with a post-sample curved graphite monochromator. The cross-sectional samples for the HRTEM investigation are prepared by the conventional sandwich technique. They are cut into $\langle 110 \rangle$ slices and thinned to approximately 20 nm by ion milling. The investigation is performed with a JEOL

Table 1

Parameters of the InAs/GaAs heterostructures under consideration; listed are the number of periods n , the thickness of the InAs layer d , the period as determined by X-ray diffraction (λ_X) and Raman scattering (λ_{Ra}), the lattice mismatch parallel (δ_{\parallel}) and perpendicular (δ_{\perp}) to the layer plane, the degree of relaxation R and the critical thickness of the whole structure (H_c)

Sample No.	n	$d^{a)}$ (Å)	λ_X (Å)	λ_{Ra} (Å)	$\delta_{\parallel}^{b)}$	$\delta_{\perp}^{b)}$	R	$H_c^{c)}$ (Å)
6660	1	2.15	—	—	1.49×10^{-1}	0	0	—
6664	1	9.55	—	—	— ^{d)}	— ^{d)}	— ^{d)}	—
6665	1	10.33	—	—	— ^{d)}	— ^{d)}	— ^{d)}	—
6720	20	4.39	25.8	26.2	2.23×10^{-2}	3.15×10^{-3}	0.256	105
6722	10	4.00	53.4	52.2	1.03×10^{-2}	3.86×10^{-4}	0.07	224

^{a)} The InAs layer thickness corresponds to the unstrained value and represents thus the amount of In atoms incorporated.

^{b)} In the case of multilayers, the measured mismatch is weighted with the respective thicknesses of the constituent layers.

^{c)} According to the model of Matthews and Blakeslee [6].

^{d)} The lattice images of this structures reveal a fractional strain relief. However, no quantitative determination by means of HRDXD is possible due to the angular shift of the interference fringes.

4000EX microscope, including diffracted beams up to the {400} reflection in the diffraction aperture.

Information about processes occurring during the deposition of the InAs layers is obtained by in situ RHEED. The InAs layers are grown near the boundary to the In-stabilized region, as manifested by a sharp transition from a well defined (2×4) reconstruction to a (4×1) reconstruction for a slightly increased growth temperature of 430°C . The occurrence of sharp reconstruction streaks reflects a 2D layer-by-layer growth and is observed during the deposition of the first two monolayers. The annealing cycle after the deposition of half-monolayer increments results in a sharpening of the reconstruction streaks in the RHEED pattern, indicating a smoothing of the growth surface due to the dissociation of spontaneously formed InAs islands and the subsequent incorporation of migrating In atoms in surface step sites [2]. When monitoring the growth of thicker InAs layers (up to 10 monolayer (ML)), a sharp transition from the (2×4) reconstruction to a spotty RHEED pattern at a thickness of 2.5 ML is observed, revealing the onset of three-dimensional nucleation. This transition is interpreted as a change in growth mode caused by the large lattice misfit between the two materials (Stranski-Krastanov growth) [3].

In fig. 1 we show the symmetrical (400) and the asymmetrical (422) diffraction patterns of a single

layer InAs on GaAs, capped with 200 nm GaAs. The InAs thickness is determined to be 0.8 ML, referring to the tetragonally distorted unit cell of

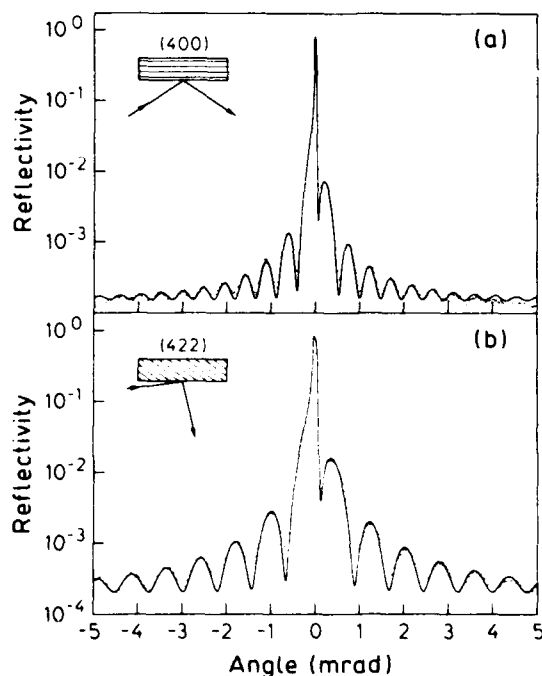


Fig. 1. Experimental (dotted line) and simulated (solid line) X-ray diffraction patterns recorded in the vicinity of the symmetrical (400) (a) reflection and the asymmetrical (422) reflection (b), respectively, with Cu $K\alpha_1$ radiation, for sample #6660.

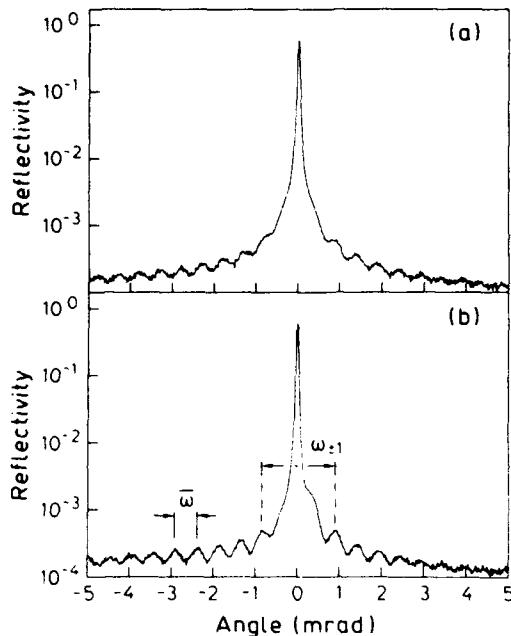


Fig. 2. Experimental X-ray diffraction patterns in the vicinity of the symmetrical (400) reflection, recorded with Cu $K\alpha_1$ radiation for samples #6664 (a) and #6665 (b), respectively.

strained InAs. The RHEED pattern during growth exhibits a (2×4) reconstruction as discussed above. The excellent agreement between the experimental and simulated diffraction patterns reveals the perfect crystal quality of the sample. In addition, diffraction around asymmetric reflections demonstrates a coherent growth of the InAs layer, i.e., the lattice mismatch is accommodated entirely by an elastic tetragonal distortion of the InAs unit cell.

Fig. 2 shows the experimental diffraction pattern of samples with InAs layer thicknesses of 3.4 ML (fig. 2a) and 3.7 ML (fig. 2b), respectively. For both of the samples, a spotty RHEED pattern develops during the growth. The onset of 3D nucleation as indicated by the RHEED observation manifests itself in an decreasing amplitude and an angular shift of the interference fringes adjacent to the main epitaxial reflection ($\omega_{\pm 1}$), resulting from the loss of phase coherence of the X-ray wave fields in the crystal [4].

The systematic comparison of the actual growth rates of the ultrathin strained layers with those derived from the measured thickness of bulk samples grown under identical conditions reveals a strong impact of the strain on the In incorporation [5]. Additionally, the In incorporation drops abruptly when the layer thickness exceeds the onset for 3D growth. This important phenomenon will be discussed in connection with the HRTEM measurements presented below.

In fig. 3, the high resolution lattice images from the structures of fig. 1a and fig. 2b are shown. The projected InAs layer appears as a dark line in the brighter GaAs matrix. The structure shown in fig. 3a is found to be free from dislocations, having in fact the excellent structural quality as suggested by the X-ray investigation. In contrast, in fig. 3b a strong fluctuation of the InAs layer is observed, which directly reflects the first stage of island nucleation. Symmetrically introduced 60° -type dislocations with their Burgers vector inclined on opposing $\{111\}$ planes are detected at the edges of the islands [4]. Furthermore, the upper interface is not well defined but is strongly intermixed with the adjacent GaAs layer. This experimental finding suggests that the initial relaxation of InAs islands results in an enhanced segregation of In during the overgrowth with the GaAs cap layer (strain enhanced diffusion). This segregation process is thought to be responsible for the sharply decreasing growth rate mentioned above, since In atoms floating at the growing surface can readily be desorbed during the heating cycle.

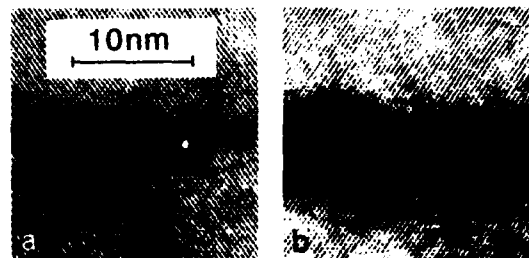


Fig. 3. High resolution lattice images of sample #6660 (a) and #6665 (b), respectively. The (100) InAs layer appears as a dark line in the GaAs matrix.

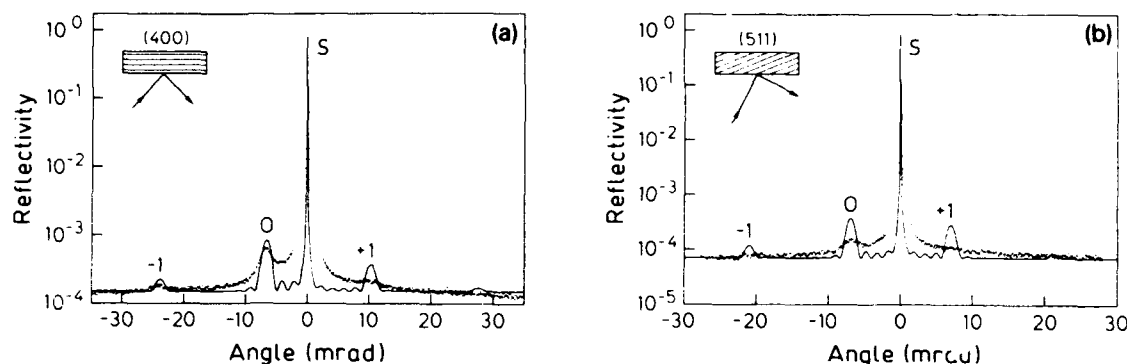


Fig. 4. Experimental (dotted line) and simulated (solid line) diffraction patterns in the vicinity of the symmetrical (400) and asymmetrical (511) reflection, respectively, for sample #6722.

Fig. 4 shows the diffraction patterns of sample #6722 around the symmetric (400) (fig. 4a) and the asymmetric (511) (fig. 4b) reflections, respectively. The data obtained from these measurements yield the mean lattice misfit perpendicular, δ_{\perp} , and parallel, δ_{\parallel} , to the (100) layer plane. The structural parameters derived from these measurements are summarized in table 1. It is worth noting that the degree of relaxation is always much smaller than expected from the equilibrium

elasticity theory [6], which predicts almost complete relaxation (95%) for the structures presented here.

The individual layer thicknesses of all multi-layer structures are well within the limit for coherent 2D growth. It is thus expected that the relaxation takes place only at the substrate-superlattice interface, i.e. the superlattice as a whole is characterized by an in-plane mismatch δ_{\parallel} . This allows us to determine the elastic strain components of

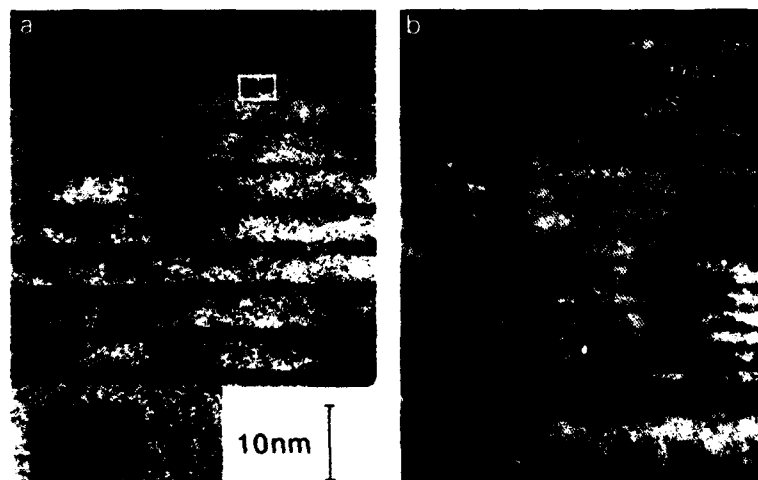


Fig. 5. High resolution lattice images for samples #6722 (a) and #6720 (b), respectively. In the upper part of (a), the whole superlattice structure is shown. In the inset below, the InAs/GaAs interface depicted by the white frame is shown in magnification.

the individual layers which enter the simulation shown in fig. 4. The position of the superlattice peaks in the experimental diffraction patterns are well reproduced by the simulation. However, the experimental superlattice satellites are apparently broadened with respect to the theoretical ones. The broadening and the reduced intensity of the first order satellites (± 1) can be attributed to the incoherent X-ray scattering at heterointerface inhomogeneities (thickness fluctuations). The broadening of the main satellite (0) indicates the presence of defects such as clusters or threading dislocations within the superlattice structure. Thus, the relaxation process severely affects the quality of the whole structure, although the misfit dislocations are most likely generated at the superlattice base.

In fig. 5, we show lattice images of two samples with the same InAs layer thickness (1.5 ML) but different GaAs thickness and number of periods (see table 1). In fig. 5a misfit dislocation formation at the base of the superlattice is observed. The individual interfaces are homogenous and essentially free from defects (see the inset of fig. 5a where one interface is shown in magnification). In contrast, in fig. 5b a strong intermixing of the individual layers is apparent. These results indicate that the strain relaxes initially by the formation of misfit dislocations at the superlattice base. The residual strain within the whole superlattice is then preferentially relieved by layer intermixing.

Finally, we should mention that the vibrational as well as the optical properties of the investigated samples can readily be understood by considering both the structural and chemical disorder induced by strain relaxation [4,7].

To conclude, the nucleation of InAs on GaAs was found to take place by the Stranski-Krastanov

growth mode. The analysis of both the HRDXD patterns and the HRTEM lattice images has revealed the strong correlation of the growth mode of the InAs layer to the mechanism of strain relaxation. The onset of 3D growth initiates strain relaxation by the formation of relaxed islands with subsequent intermixing of the group III elements. This segregation process is considerably enhanced by the strain between relaxed InAs islands and the GaAs cap layer, resulting in an abrupt drop of the In incorporation. In multilayer structures with individual InAs layer thicknesses below those required for the onset of 3D growth, but with a total thickness exceeding the critical one, the structural stability is governed by the total thickness of the superlattice as predicted by the equilibrium elasticity theory. However, in addition to the initial relaxation at the superlattice base strain relief proceeds at the internal interfaces, regulated by the individual layer thickness.

This work has been partly supported by the Bundesministerium für Forschung und Technologie of the Federal Republic of Germany.

References

- [1] L. Tapfer and K. Ploog, *Phys. Rev. B* **33** (1986) 5565.
- [2] Y. Horikoshi and M. Kawashima, *J. Crystal Growth* **95** (1989) 17.
- [3] S.M. Pintus, S.I. Stenin, A.I. Toporov, E.M. Trukhanov and V.Y. Karasyov, *Thin Solid Films* **151** (1987) 275.
- [4] O. Brandt, L. Tapfer, K. Ploog, M. Hohenstein and F. Philipp, unpublished.
- [5] O. Brandt, L. Tapfer, R. Cingolani, K. Ploog, M. Hohenstein and F. Philipp, *Phys. Rev. B* **41** (1990) 12599.
- [6] J.W. Matthews and A.E. Blakeslee, *J. Crystal Growth* **27** (1974) 990.
- [7] G. Scamarcio, O. Brandt, L. Tapfer, D.J. Mowbray, M. Cardona, and K. Ploog, *J. Appl. Phys.*, to be published.

Optical studies of InAs/GaAs on GaAs short-period strained-layer superlattices grown by MBE and MEE

T.C. Hasenberg

Hughes Research Laboratories, 3011 Malibu Canyon Road, Malibu, California 90265, USA

D.S. McCallum, X.R. Huang, A.L. Smirl, M.D. Dawson and T.F. Boggess

Center for Laser Science and Engineering, University of Iowa, 124 AMRF, Oakdale Campus, Iowa City IA, Iowa 52242, USA

We have grown InAs/GaAs short-period strained-layer superlattices (SPSLs) by both conventional molecular beam epitaxy (MBE) and migration enhanced epitaxy (MEE). Our efforts have been directed towards the optimization of growth parameters including shutter times, growth interrupt times, and substrate temperatures for both growth techniques. We have investigated several structures with different numbers and thicknesses of InAs and GaAs layers. Optical measurements, including absorbance, CW photoluminescence (PL), and time resolved PL, have been employed to determine the quality of the samples. We have grown samples with 50 repetitions of the SPSLS separated by 20 nm GaAs barrier layers which have exhibited excellent 5 K CW PL peaks with full width at half maximum (FWHM) of less than 9 meV. In addition, several samples have shown room temperature exciton features in absorbance spectra. A synchronously mode-locked Styryl 9 dye laser has been used in conjunction with a streak camera to perform time resolved PL measurements, thereby determining carrier lifetimes in the samples. We will discuss our results, comparing the growth conditions as well as the different SPSLS structures, in terms of the optical data that we have obtained.

There has been great interest in indium-containing III–V strained-layer superlattice (SLS) semiconductor structures because they can exhibit relatively small in-plane effective hole masses and hence large hole mobilities. This low effective mass can significantly reduce the threshold current in semiconductor lasers [1,2] as well as increase the speed of complementary electronic circuits [3]. In addition, strained indium-containing compounds have been investigated because they have absorption edges at wavelengths associated with low loss and minimum dispersion in silica fibers, and hence are compatible with optical communications applications.

The majority of the previous work involving indium-containing SLSs on GaAs substrates has employed ternary $\text{In}_{1-x}\text{Ga}_x\text{As}$ compounds [4–6]. We have grown and characterized an SLS system which employs only the binary constituents InAs and GaAs [7,8]. The use of binary compounds has some distinct advantages over the random InGaAs

alloy: firstly, during the growth of InAs/GaAs, accurate control of the InAs and GaAs layer thicknesses yields the desired effective composition and bandgap. When growing binary compounds, layer thicknesses can be precisely monitored by in-situ reflection high-energy electron diffraction (RHEED) oscillations [9,10]. Fig. 1 shows RHEED intensity oscillations observed during the growth of one of our samples. Each period

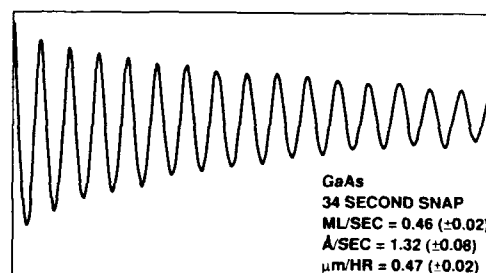


Fig. 1. RHEED oscillations from a GaAs spacer layer during the growth of an InAs/GaAs SPSLS.

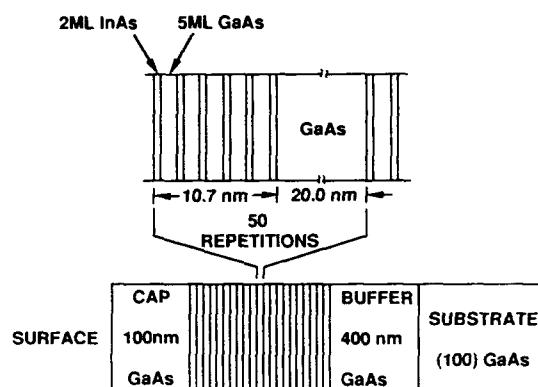


Fig. 2. Schematic diagram of a $2 \times 5 \times 6$ SPSLS on a GaAs substrate.

of the oscillation corresponds to the deposition of one full monolayer of material (i.e. half of a unit cell). In contrast, during InGaAs growth, reliable measurement and control of the group III flux ratio is difficult and therefore it is less easy to control the composition, and hence the bandgap, of the ternary material. Secondly, replacing the ternary compound with an all-binary one has the effect of reducing or eliminating alloy disorder scattering, which may improve the transport properties of the material and remove the alloy-disorder broadening contribution to the absorption linewidth.

We have grown various InAs/GaAs short-period, strained-layer superlattice (SPSLS) structures, and have employed the notation $i \times j \times k$ to specify the SPSLS. Here, i and j give the thicknesses, in monolayers (ML), of each layer of InAs and GaAs, respectively. Then k designates the number of layers of the InAs that alternate with the $(k-1)$ layers of GaAs to form each superlattice. The samples investigated in this work are all $2 \times 5 \times k$; the upper part of fig. 2 depicts a $2 \times 5 \times 6$ SPSLS. The 5 ML GaAs layers are too thin to prevent strong overlap of electron and hole wave functions between adjacent InAs layers, and therefore each SPSLS can be treated as being, in effect, a single quantum well.

Clearly, samples containing many such quantum wells are required for practical materials or devices involving optical absorption. Therefore,

we have grown samples containing up to 50 repetitions of the SPSLS structure, with adjacent SPSLSs separated by 14 to 25 nm thick GaAs barrier layers. These structures are described as multiple SPSLSs or M-SPSLSs. Fig. 2 depicts a 50-repetition $2 \times 5 \times 6$ M-SPSLS used in our work. Such samples are coherently strained; when observing the photoluminescence (PL) spectrum of the samples at 5 K, we have measured only a slight increase (~ 2 meV) of the linewidth of a 50-repetition $2 \times 5 \times 6$ M-SPSLS compared to a single repetition $2 \times 5 \times 6$ SPSLS.

We have investigated several structures in an attempt to obtain high optical quality material with various bandgaps (wavelengths). We have confirmed (for the growth conditions discussed below) that the critical thickness [11] of InAs on GaAs is 2 ML. Depending on the values of i and j , different numbers of InAs layers (k in our notation) can be grown in each SPSLS without relaxation of the strain. The upper limit for k in the $2 \times 5 \times k$ structure is not known explicitly, although it lies between 10 and 50, which may be determined by comparing the 5 K PL spectra for a $2 \times 5 \times 10$ and a $2 \times 5 \times 50$ SPSLS. The PL peak for the $2 \times 5 \times 10$ sample was centered on 919 nm and had a linewidth (full width at half maximum height) of 9 meV, whereas the PL peak for the $2 \times 5 \times 50$ sample had a much lower peak intensity, a line center at 1420 nm and a linewidth of 185 meV. Such a large wavelength shift in the PL cannot be ascribed simply to the loss of quantum confinement in the $2 \times 5 \times 50$ structure, but must be associated with the relaxation of the strain.

The M-SPSLSs have been grown by molecular beam epitaxy (MBE) as well as by migration enhanced epitaxy (MEE) [12]. Excellent results have been obtained with both growth techniques if the substrate temperature is held below 530°C during the growth of the M-SPSLS. Furthermore, the arsenic (As_2) overpressure is just adequate to maintain an arsenic stabilized surface. This is verified by the observation of a (2×4) reconstruction pattern via RHEED. In all of the samples, a 400–500 nm buffer layer is grown with a substrate temperature of 600°C after successfully desorbing the native oxide layer. Next, the substrate is ramped down to 530°C in 5 min as we continue

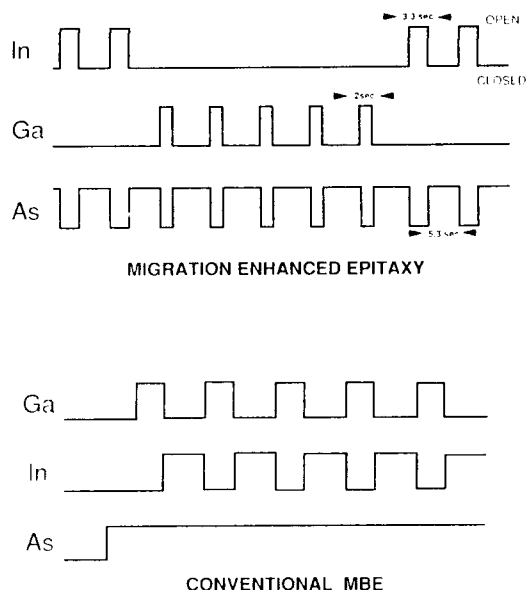


Fig. 3. Shutter sequences for conventional MBE versus MEE.

to grow GaAs. The GaAs growth rate is reduced from 0.28 nm/s to about 0.14 nm/s at the beginning of the substrate temperature ramp. Finally, the M-SPSLS is grown on the buffer layer by either conventional MBE or by MEE.

The shutter sequence for the MEE growth is depicted in fig. 3. Note that the group III flux is deposited in the absence of an arsenic flux in MEE in contrast to MBE where the arsenic flux is not interrupted during the entire growth. It has been found that the quality of the MEE grown films are strongly dependent on the group III shutter times [13]. Unlike arsenic, the growth of elemental group III constituents (In and Ga) is not self-limiting. Hence, we must carefully control the shutter times for the In and Ga in order to deposit an exact ML of material and maintain a stoichiometric layer. Low temperature (5 K) PL linewidths as narrow as those from the highest quality MBE grown M-SPSLS samples are obtained by careful shutter control while utilizing the MEE method.

Fig. 4 shows the wavelength of the 5 K CW PL emission peaks plotted against number of InAs layers (k) for five different 50-repetition samples

— two $2 \times 5 \times 6$, one $2 \times 5 \times 8$, and two $2 \times 5 \times 10$ M-SPSLS samples. Four of the samples were grown by MEE whereas one of the $2 \times 5 \times 10$ samples was grown by conventional MBE. Furthermore, the two $2 \times 5 \times 10$ samples were grown months apart with the effusion cells recharged between the growths. All five of the samples contain 20 nm barrier layers between each of the 50 SPSLSs. The run-to-run reproducibility of the growth is clearly evident; the PL peaks for the two $2 \times 5 \times 6$ structures are essentially indistinguishable, as are those for the two $2 \times 5 \times 10$ structures. In addition, the uniformity of the 50 individual SPSLSs within each sample is excellent since the PL linewidths range between 6 and 10 meV FWHM for the five samples.

We have examined the optical quality of the 50-repetition samples using time resolved PL. Fig. 5 depicts typical 15 K time-resolved PL scans of a 50 period $2 \times 5 \times 8$ M-SPSLS at various laser excitation intensities. The samples were excited with a frequency-doubled Nd:YAG-pumped, mode-locked, Styryl 9 dye laser which generates pulses of 5 ps duration at 810 nm. Photoluminescence at 915 nm, corresponding to recombination of the $n = 1$ heavy-hole exciton, was detected with a streak camera operated in the synchroscan mode. For the lowest excitation intensity of 1.4×10^5 W/cm², which generated an average carrier den-

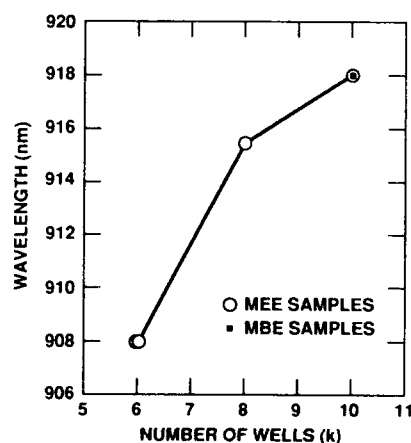


Fig. 4. Low temperature (5 K) PL peak versus number of InAs wells (k) for five different $2 \times 5 \times k$ M-SPSLS samples.

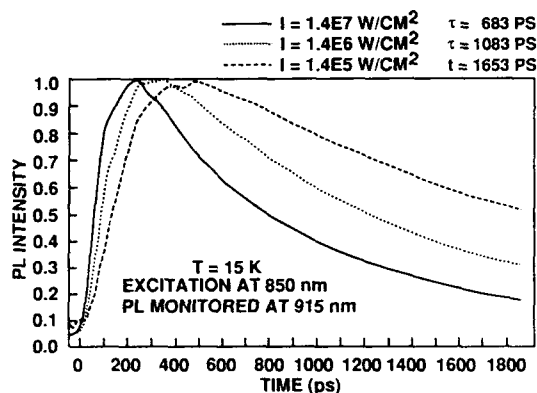


Fig. 5. Time resolved photoluminescence of an InAs/GaAs $2 \times 5 \times 8$ M-SPSLS at various excitation intensities.

sity of $2.1 \times 10^{16} \text{ cm}^{-3}$ in the SPSLS, the photoluminescence was observed to decay exponentially with a decay constant 1.65 ns. This long exciton lifetime attests to the high quality of the M-SPSLS samples. At higher excited carrier densities, somewhat shorter photoluminescence lifetimes were observed, along with a clear decrease in the PL risetime. A detailed discussion of the time-resolved PL will be the subject of a future publication.

Room temperature absorption spectra were obtained for each of the $2 \times 5 \times k$ M-SPSLS sam-

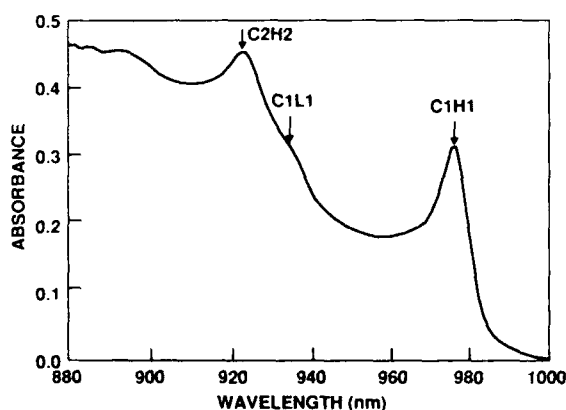


Fig. 6. Room temperature absorbance from an InAs/GaAs $2 \times 5 \times 8$ M-SPSLS.

ples. Fig. 6 depicts the absorbance spectrum of a 50-repetition $2 \times 5 \times 8$ sample, with tentative identifications for the more prominent features on the curve. The peaks corresponding to the $n = 1$ conduction band to heavy hole (C1H1) and $n = 2$ conduction band to heavy hole (C2H2) transitions indicate the presence of enhanced excitonic absorption strengths due to two-dimensional confinement in the sample. In contrast, the feature we identify as the $n = 1$ conduction band to light hole (C1L1) transition is poorly resolved at this temperature. Similar curves have been obtained for the $2 \times 5 \times 6$ and $2 \times 5 \times 10$ M-SPSLSs, with corresponding features shifted to longer wavelengths as k increases. This is consistent with the $2 \times 5 \times k$ SPSLS forming a single effective quantum well, the width of which increases as k is increased.

We have attempted to do standard tight binding calculations and envelope wave function calculations for these structures in order to determine theoretically the wavelengths of the transitions. However, the theoretical wavelength predictions are always shifted to the red with respect to the experimental results. We are developing a model which completely accounts for the large strain in these structures by employing deformation potentials, in order to successfully calculate the wavelength of the transitions.

In conclusion, we have demonstrated that very high optical quality (InAs/GaAs)-on-GaAs samples with strong excitonic transitions in the 900–1000 nm wavelength range can be obtained by employing the M-SPSLS structure. Clearly, the optical properties depend on the M-SPSLS structure and not on the growth technique, since strong room temperature excitonic features have been observed in samples grown by both MBE and MEE. We are presently working on a model to calculate the energy levels in single or multiple SPSLSs. In addition, we plan to investigate additional $i \times j \times k$ M-SPSLSs by varying j and k in an attempt to further vary the emission wavelengths of the samples. We intend to incorporate the SPSLS as an active region in a GaAs/Al-GaAs-based GRINSCH laser. We expect very low threshold currents and should easily obtain a 980 nm wavelength which is optimum for pumping lasers based on Er-doped fibers.

Acknowledgement

The portion of the work performed at the University of Iowa was supported by the US Office of Naval Research.

References

- [1] A.R. Adams, *Electron. Letters* 22 (1986) 249.
- [2] E. Yablonovitch and E.O. Kane, *IEEE J. Lightwave Technol.* LT-4 (1986) 504.
- [3] G.C. Osbourn, *J. Vacuum Sci. Technol.* A3 (1986) 826.
- [4] I.J. Fritz, L.R. Dawson and T.E. Zipperian, *J. Vacuum Sci. Technol.* B1 (1983) 387.
- [5] N.G. Anderson, W.D. Laidig and Y.F. Lin, *J. Electron. Mater.* 43 (1983) 846.
- [6] J.Y. Marzin, M.H. Charasse and B. Sermage, *Phys. Rev.* B31 (1985) 8298.
- [7] F.J. Grunthaner, M.Y. Yen, R. Fernandez, T.C. Lee, A. Madhukar and B.F. Lewis, *Appl. Phys. Letters* 46 (1985) 983.
- [8] L. Goldstein, F. Glas, J.Y. Marzin, M.N. Charasse and G. Le Roux, *Appl. Phys. Letters* 47 (1985) 1099.
- [9] K. Ploog, in: *Spectroscopy of Semiconductor Microstructures*, NATO ASI Series B, Vol. 206, Eds. G. Fasol, A. Fasolino and P. Lugli (Plenum, New York 1989) p. 1.
- [10] Y.C. Chen, P.K. Battacharya and J. Singh, *Appl. Phys. Letters* 57 (1990) 692.
- [11] F.C. Frank and J.H. van der Merwe, *Proc. Roy. Soc.* A198 (1949) 216.
- [12] Y. Horikoshi, M. Kawashima and M. Yamaguchi, *Japan. J. Appl. Phys.* 25 (1986) L868.
- [13] T.C. Hasenberg, D.S. McCallum, X.R. Huang, A.L. Smirl, M.D. Dawson and T.F. Boggess, presented at March Meeting of American Physical Society, Anaheim, CA, 1990.

Strain induced change in band offsets at pseudomorphically grown InAs/GaAs heterointerfaces characterized by X-ray photoelectron spectroscopy

Y. Hashimoto, K. Hirakawa, K. Harada and T. Ikoma

Institute of Industrial Science, University of Tokyo, 7-22-1 Roppongi, Minato-ku, Tokyo 106, Japan

We studied the heterojunction band offsets (HBOs) at highly-strained InAs/GaAs(100) heterointerfaces with an emphasis on the effects of strain. The core level energy differences between In 4d and Ga 3d levels in InAs/GaAs heterostructures are measured by in-situ X-ray photoelectron spectroscopy and found to be only slightly dependent on the substrate lattice constant. The effect of strain on the core level energies relative to the valence band maxima (VBM) was theoretically taken into account. The determined valence band offset $\Delta E_V [= E_V(\text{InAs}) - E_V(\text{GaAs})]$ is 0.53 eV on GaAs substrates and -0.16 eV on InAs substrates, clearly indicating a large effect of strain on the valence band offset (~ 0.7 eV) in this system.

Recently, the InAs/GaAs short period superlattice has attracted much attention for its possibility to replace disordered $\text{In}_{1-x}\text{Ga}_x\text{As}$ alloy [1]. In spite of its importance, only a few works have been done to determine InAs/GaAs heterojunction band offset (HBO) experimentally [2]. The main difficulty arises from the fact that this system has about 7% lattice mismatch and that the critical thickness for generating misfit dislocations is as thin as 2 monolayers (MLs) [3]. This makes it very difficult to determine HBOs accurately by the conventional methods which have been successfully applied to the lattice-matched systems.

In this work, we studied HBOs at pseudomorphic InAs/GaAs(100) interfaces by X-ray photoelectron spectroscopy (XPS). It was found that the core level energy difference ΔE_{CL} between In 4d level and Ga 3d level in InAs/GaAs heterostructures only slightly depends on the in-plane lattice constant. Furthermore, we took into account theoretically the strain-induced shifts of the energy distance between the core levels and the valence band maxima (VBM), which were neglected in the previous work [2]. The determined valence band offset ΔE_V is found to be strongly dependent on the in-plane lattice constant and is compared with recent experimental and theoretical results [2,4].

All the samples used in this study were grown by molecular beam epitaxy (MBE). We prepared unstrained bulk GaAs and InAs and two types of heterojunctions; i.e. GaAs/InAs/GaAs double heterostructures (DHs) on GaAs substrates (type I) and the reversed InAs/GaAs/InAs DHs grown on InAs substrates (type II). Type-I samples were prepared by growing successively 1 μm thick Si-doped n^+ -GaAs buffer layer, 2 ML thick undoped InAs strained interlayer, and 5 ML thick GaAs capping layer on Si-doped n -type GaAs(100) substrates. The type-II structures were grown on undoped n -type InAs(100) substrates in the reversed growth sequence. The strained interlayer is sufficiently thin to avoid the generation of misfit dislocations. The capping layers minimize the experimental uncertainty originated from the surface chemical shift. Samples with clean mirror surfaces were obtained at substrate temperatures around 450°C. The reflection high energy electron diffraction (RHEED) patterns were recorded by photographs to ensure that the lattice relaxation does not occur in these samples. MBE-grown samples were immediately transferred to the XPS chamber via the ultra high vacuum transfer tube. XPS measurements were performed with a monochromatic AlK α X-ray source ($h\nu = 1486.6$ eV).

Table 1
Measured and calculated energy differences (in eV)

Sample	E_{CL}^{V0}	ΔE_{CL}	E_{CL}^{CVS}	E_{hh}^u	E_{lh}^u	E_{CV}^{CS}
GaAs	18.75 ± 0.05		18.53	-0.17	0.59	0.86
InAs	17.36 ± 0.05		17.25	0.39	0.18	0.90
InAs/GaAs (type I)		1.64 ± 0.02				
GaAs/InAs (type II)		1.60 ± 0.02				

First, we measured the core level binding energies relative to VBM, E_{Ga3d}^{V0} and E_{In4d}^{V0} , on MBE-grown unstrained bulk GaAs and InAs samples, respectively. (Superscript 0 denotes the unstrained bulk values.) The energy positions of core levels and VBM were determined in the same manner as described in ref. [2]. Obtained values of E_{Ga3d}^{V0} and E_{In4d}^{V0} are tabulated in table 1.

The core level energy distance ΔE_{CL} between In 4d and Ga 3d levels was obtained from XPS measurements on DH samples. A typical core level XPS spectrum of a type-I InAs/GaAs DH is shown in fig. 1. We carried out three independent experiments for each type of structure. Least squares fitting by the reference spectra of Ga 3d and In 4d core levels was used to separate the two closely-spaced core levels. The determined ΔE_{CL} was 1.64 ± 0.02 eV and 1.60 ± 0.02 eV for type-I

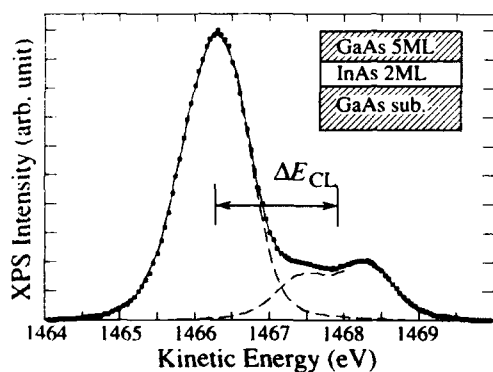


Fig. 1. A typical XPS spectrum measured on an InAs/GaAs heterostructure grown on a (100) GaAs substrate (type-I sample). The background function is subtracted as described in ref. [2]. The dots are the XPS data and the solid line denotes the curve obtained by fitting with the reference spectra of Ga 3d and In 4d core levels measured on bulk samples (broken lines). The inset shows the sample structure.

and type-II samples, respectively, only slightly depending on the in-plane lattice constant.

Fig. 2 shows schematic energy band diagrams at InAs/GaAs heterointerfaces grown on GaAs substrates (fig. 2a) and on InAs substrates (fig. 2b). The valence band offsets $\Delta E_v \equiv E_v(\text{InAs}) - E_v(\text{GaAs})$ can be obtained as follows:

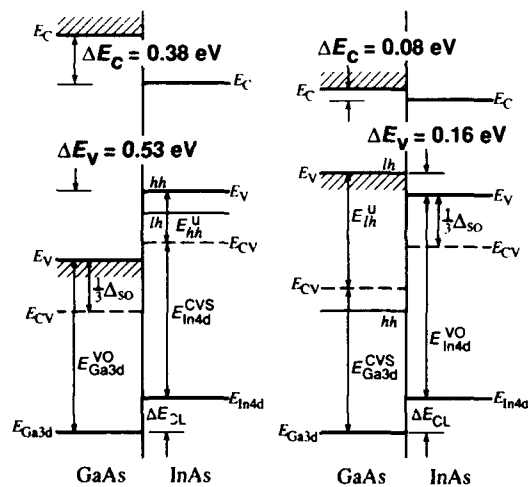
$$\Delta E_v = -E_{Ga3d}^{V0} + E_{In4d}^{VS} + \Delta E_{CL} \quad (1)$$

for GaAs substrates,

$$\Delta E_v = -E_{Ga3d}^{VS} + E_{In4d}^{V0} + \Delta E_{CL} \quad (2)$$

for InAs substrates.

Here, E_{Ga3d}^{VS} and E_{In4d}^{VS} are the core level energies referenced to the top of the strain-split VBM. (Superscript S denotes the values for strained



(a) InAs strained (type-I) (b) GaAs strained (type-II)

Fig. 2. Schematic energy band alignments at InAs/GaAs heterointerfaces grown (a) on GaAs substrates and (b) on InAs substrates.

layers.) Although $E_{\text{Ga3d}}^{\text{V0}}$, $E_{\text{In4d}}^{\text{V0}}$, and ΔE_{CL} are measurable quantities by XPS, it is very difficult to determine $E_{\text{Ga3d}}^{\text{VS}}$ and $E_{\text{In4d}}^{\text{VS}}$ experimentally. In the previous work [2], $E_{\text{Ga3d}}^{\text{VS}}$ and $E_{\text{In4d}}^{\text{VS}}$ were replaced with their unstrained values. However, this approximation is not always correct. Therefore, the key point in predicting HBOs in the strained InAs/GaAs systems is to estimate $E_{\text{Ga3d}}^{\text{VS}}$ and $E_{\text{In4d}}^{\text{VS}}$ accurately by theoretical considerations [5].

The biaxial strain associated with pseudomorphic epitaxy can be decomposed into the hydrostatic part and the uniaxial part. Van de Walle and Martin have theoretically shown that the energy difference between the centroid of the valence band maximum (CVBM) and the core level is influenced by the hydrostatic part, and that the uniaxial part splits VBM around CVBM without shifting the centroid [6].

First, we consider the effect of the hydrostatic part of the strain. Within the framework of the tight binding (TB) theory and the $Z+1$ approximation [7], we calculated the strain-induced shift $\Delta E_{\text{CL}}^{\text{CV}}$ in the core level binding energy relative to CVBM, $E_{\text{CL}}^{\text{CV}}$ [8]. The calculated value of $\Delta E_{\text{CL}}^{\text{CV}}$ is +0.02 eV for compressed InAs (type I) and -0.11 eV for tensile GaAs (type II). $E_{\text{CL}}^{\text{CVS}}$ is then obtained by $E_{\text{CL}}^{\text{CV0}} + \Delta E_{\text{CL}}^{\text{CV}}$. Here, $E_{\text{CL}}^{\text{CV0}}$ is given by $(E_{\text{CL}}^{\text{V0}} - \Delta_{\text{so}}/3)$, with Δ_{so} the spin-orbit splitting energy (0.34 eV for GaAs and 0.38 eV for InAs). Obtained $E_{\text{CL}}^{\text{CVS}}$ is also tabulated in table 1. By combining $E_{\text{CL}}^{\text{CVS}}$ with experimentally obtained ΔE_{CL} , the offsets of CVBM, ΔE_{CV} , are determined to be 0.25 eV on GaAs substrates and 0.30 eV on InAs substrates, which show about 0.05 eV dependence on the in-plane lattice constant.

Furthermore, the uniaxial part of the strain splits the three-fold degenerate VBM into heavy hole (hh), light hole (lh), and spin-orbit split off (so) band around the CVBM. With the shear deformation potential constant b , we calculated the shifts of energy positions of heavy and light hole bands relative to CVBM, E_{hh}^{u} and E_{lh}^{u} [6]. To obtain the conduction band offset ΔE_{C} , the energy position of the conduction band minimum relative to CVBM, E_{C}^{CS} , was calculated by using the hydrostatic deformation potential constant a . These values are also tabulated in table 1.

Table 2

Determined band offsets (in eV); ΔE_{CV} , ΔE_{hh} and ΔE_{lh} denote the offset in CVBM, the heavy hole band and the light hole band, respectively; ΔE_{V} represents the offset of VBM and ΔE_{C} denotes the conduction band offset defined by $\Delta E_{\text{C}} \equiv E_{\text{C}}(\text{InAs}) - E_{\text{C}}(\text{GaAs})$

	InAs strained case (type I)	GaAs strained case (type II)
ΔE_{CV}	0.25	0.30
ΔE_{hh}	0.53	0.60
ΔE_{lh}	0.32	-0.16
ΔE_{V}	0.53	-0.16
ΔE_{C}	-0.38	-0.08

Consequently, large ΔE_{V} of 0.53 eV and ΔE_{C} of 0.38 eV are obtained for type-I structure, as shown in fig. 2a. In this case, the top of the valence band in InAs is the heavy hole band. In contrast, a characteristic band alignment is expected for type-II structure (fig. 2b), where the light hole (heavy hole) band in GaAs layer is higher (lower) than VBM in InAs by 0.16 eV (0.60 eV), and ΔE_{C} is 0.08 eV. These results are summarized in table 2. It should be noted that ΔE_{V} shows a very large dependence (~ 0.7 eV) on the in-plane lattice constant.

It would be very interesting to verify such a big change of ΔE_{V} in the valence band density-of-states (VBDOS) spectra measured by XPS. However, this is very difficult due to the fact that the XPS signals from the VBDOS in type-I and type-II samples are dominated by the bulk GaAs and InAs VBDOS signals, respectively, since the inter-layer thickness is limited to be less than 2 MLs.

Kowalczyk et al. obtained ΔE_{V} of 0.17 eV by XPS measurements on an InAs/GaAs single heterojunction [2]. The discrepancy between our result and the result by Kowalczyk et al. is considered to arise from the lattice relaxation in their 20 Å thick InAs layer. Cardona and Christensen, on the other hand, predicted ΔE_{V} to be 0.52 eV (on GaAs substrates) from their dielectric midgap energy theory [4], which is in excellent agreement with our ΔE_{V} of 0.53 eV.

In summary, the valence band offsets at strained InAs/GaAs heterojunctions were determined for InAs/GaAs heterostructures grown on GaAs and InAs substrates. The core level energy difference

ΔE_{CL} between In 4d and Ga 3d levels in InAs/GaAs heterostructures were measured by in-situ XPS and found to depend only slightly on the in-plane lattice constant. By taking into account theoretically the strain-induced shifts of the energy distance between the core levels and VBM, the offsets of the centroid of VBM, ΔE_{CV} , are determined to be 0.25 eV on GaAs substrates and 0.30 eV on InAs substrates. Furthermore, by adding the splitting of VBM due to the uniaxial part of the strain, the valence band offsets ΔE_V are determined to be 0.53 eV on GaAs substrates and -0.16 eV on InAs substrates, demonstrating a large effect of strain on ΔE_V .

We are grateful to Dr. T. Saito for valuable discussions. This work is partly supported by the Grant-in-Aid from the Ministry of Education, Science, and Culture, Japan and also by the Industry-University Joint Research Program "Mesoscopic Electronics".

References

- [1] G. Osbourn, Phys. Rev. B27 (1983) 5126;
T. Yao, Japan. J. Appl. Phys. 22 (1983) L680.
- [2] S.P. Kowalczyk, W.J. Schaffer, E.A. Kraut and R.W. Grant, J. Vacuum Sci. Technol. 20 (1982) 705.
- [3] H. Nakao and T. Yao, Japan. J. Appl. Phys. 28 (1989) L352.
- [4] M. Cardona and N.E. Christensen, Phys. Rev. B35 (1987) 6182.
- [5] G.P. Schwartz, M.S. Hybertsen, J. Bevk, R.G. Nuzzo, J.P. Mannaerts and G.J. Gualtieri, Phys. Rev. B39 (1989) 1235. In this paper, they calculated strain-induced shifts in the core to valence energies in pseudomorphic Si/Ge heterostructures. However, their calculation does not take into account the XPS core-hole relaxation effect.
- [6] C.G. Van de Walle and R.M. Martin, Phys. Rev. B34 (1986) 5621.
- [7] R. Enderlein and W.A. Harrison, Phys. Rev. B30 (1984) 1867. In our calculation, we used the nonorthogonality shift of $(1.28/3.22)^2 V_0/2$, following the results by W.A. Harrison and E.A. Kraut [Phys. Rev. B37 (1988) 8244].
- [8] K. Hirakawa, Y. Hashimoto and T. Ikoma, Unpublished.

Structural stability of ultrathin InAs/GaAs quantum wells grown by migration enhanced epitaxy

Mitsuaki Yano, Kanji Yoh, Takanori Iwawaki, Yoshio Iwai and Masataka Inoue

New Material Research Center, Osaka Institute of Technology, Asahi-ku Ohmiya, Osaka 535, Japan

In order to study the strained-structure of InAs films on GaAs substrates, photoluminescence (PL) properties have been examined for ultrathin InAs/GaAs single quantum well (SQW) structures grown by migration enhanced epitaxy. Observed PL spectra from SQWs are discussed in conjunction with in-situ monitored growth conditions of the heterostructure by using reflection high energy electron diffraction. Rapid thermal annealing on the grown samples has been performed to understand the stability of strained heterostructure. By the PL analysis on the annealing effect, the critical thickness for the stably strained heterostructure is determined to be 2–3 MLs and nearly 1 ML for samples grown at 520 and 420 °C, respectively.

1. Introduction

An ultrathin InAs layer clad with GaAs is one of the typical examples of highly strained heterostructure because InAs has a 7% lattice mismatch to GaAs. The initial growth stage of heteroepitaxial InAs on GaAs by molecular beam epitaxy (MBE) has been studied by many workers trying to understand the pseudomorphic two-dimensional (2D) growth. For instance, Nakao et al. experimentally determined the critical thickness to be 1.5 monolayers (MLs) for the pseudomorphic growth of InAs on GaAs by using reflection high-energy electron diffraction (RHEED) [1]. Recently, photoluminescence (PL) analysis has been performed for ultrathin InAs/GaAs single quantum well (SQW) structures prepared by various growth techniques such as metalorganic chemical vapor deposition (MOCVD) [2–4] and MBE [5]. However, different PL energies were reported for SQWs with the same thickness of InAs. For instance, the PL energy from SQWs with 2 MLs of InAs in ref. [3] is about 1.46 eV which is more than 100 meV higher in comparison with the result in ref. [4]. This considerably large discrepancy has not been explained reasonably yet [6,7]. There are some possibilities that this discrepancy is due to the structural difference of InAs layer in an atomic scale because the well width of these SQWs

is close to the critical thickness expected for the pseudomorphic growth of InAs. In previous works, however, the relationship between the PL spectra and the microscopic structure has not been understood sufficiently.

In this paper, we report PL properties of ultrathin InAs/GaAs SQW structures prepared by migration enhanced epitaxy (MEE). The growth condition was monitored by RHEED to study the interface structure in relation to the PL properties. Observed PL spectra were compared with calculations to understand the electron recombination in the quantum well structure. In order to study the stability of strained-structure, we examined the effect of annealing on the PL spectra for these SQWs.

2. Growth condition

The heterostructure, with ultrathin InAs layer capped by a 50 nm thick GaAs layer, was grown on a (100) surface of Si-doped GaAs by using ANELVA-620 type MBE apparatus. Two series of SQWs, grown at $T_s = 420^\circ\text{C}$ and 520°C , were examined to understand the effect of growth temperature. We have grown these heterostructures by MEE because it is known as a powerful technique

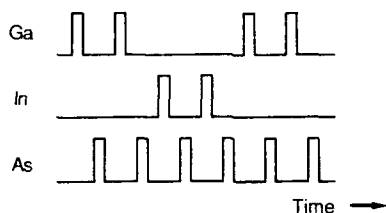


Fig. 1. Timing of molecular beams during the growth of SQW structures. Illustrated is the case of 2 MLs growth of InAs between GaAs.

to realize high quality epitaxial layers even at low growth temperatures [8]. We can also control the thickness precisely by MEE in the growth of ultrathin SQW structures. Fig. 1 shows the typical timing of molecular beams used for the 2 ML growth of InAs between GaAs. The short period of pulses, such as 2.4 s, was taken to form just one atomic plane of the respective materials. Under these conditions, a precisely controlled 1 ML of

InAs was grown by introducing a pulse of In between those of Ga.

Typical RHEED patterns of the growing surface are shown in fig. 2, in which the growth temperature was controlled to be 520 °C. The reconstructed (2×4) As pattern of fig. 2a was observed from the GaAs surface before the deposition of InAs. The same pattern shown in fig. 2b was continued during the deposition period of InAs as far as the thickness was less than 2 MLs. This reconstructed pattern disappeared after 3 MLs of InAs growth although the elemental diffraction continued to be streaky, as shown in fig. 2c. After depositing 4 MLs of InAs, the elemental diffraction changed to a spot pattern, as shown in fig. 2d. These results indicate that the critical thickness is between two and three monolayers for the present 2D growth of heteroepitaxial InAs. The interface strain due to the lattice-mismatch will be relaxed to form a 3D island structure as the thickness of

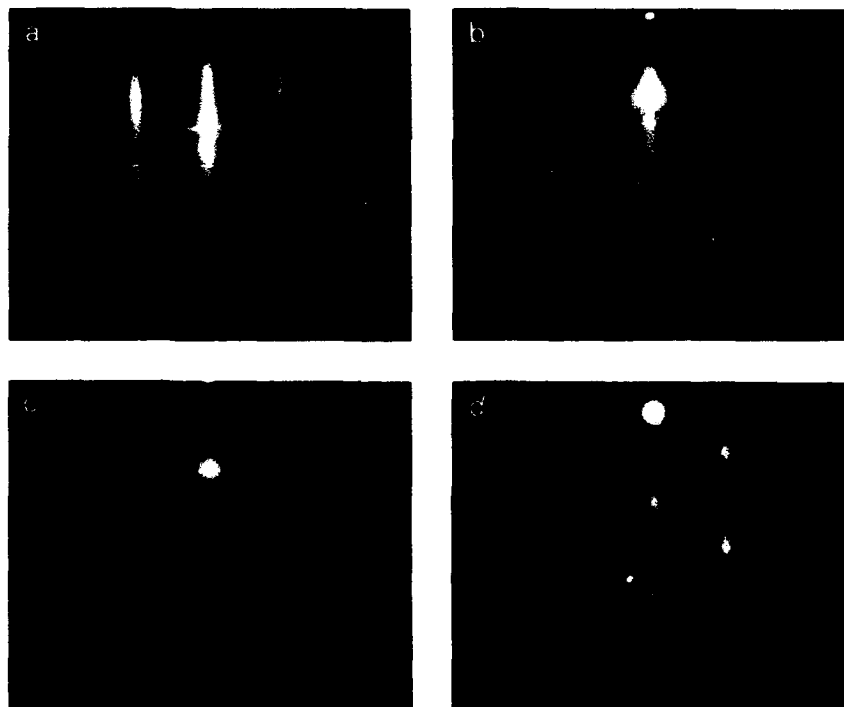


Fig. 2. RHEED patterns from the growing surface of InAs on GaAs: (a) is the pattern from GaAs before the deposition of InAs; (b), (c) and (d) are patterns from InAs surface with the controlled thickness of 2 MLs, 3 MLs and 4 MLs, respectively.

InAs exceeds the critical value. When the SQWs were grown at $T_s = 420^\circ\text{C}$, the change from streak to spot occurred at the same thickness, 3 MLs. The streak pattern from 1 or 2 MLs of InAs, however, was not so sharp in comparison with the case of $T_s = 520^\circ\text{C}$. This result of $T_s = 420^\circ\text{C}$ should imply that deterioration of the 2D strained-structure has been introduced into these films below the apparent critical thickness.

3. Analysis of PL spectra

We measured PL signals from these SQWs at 12 K under the excitation of the 632.8 nm line of a He-Ne laser. Fig. 3 and fig. 4 show typical PL spectra from SQWs with 1–4 MLs of InAs, of which growth temperatures were controlled to be 520 and 420°C , respectively. At $T_s = 520^\circ\text{C}$, single sharp emissions were observed from the respective SQW structures with thin (1–2 MLs) InAs quantum wells. With increasing the quantum well width (3–4 MLs), the spectrum became broader, as shown in fig. 3. For samples grown at $T_s = 420^\circ\text{C}$, however, spectra from SQWs with 1–2 MLs of InAs became much broader than the case of $T_s = 520^\circ\text{C}$, as shown in fig. 4. Broadening of the PL spectrum is a reflection of the interface roughness in the SQW. Hence, SQWs with broad PL emissions should have a 3D heterointerface caused by the imperfect 2D growth of InAs. As shown in fig. 3, the high quality of the

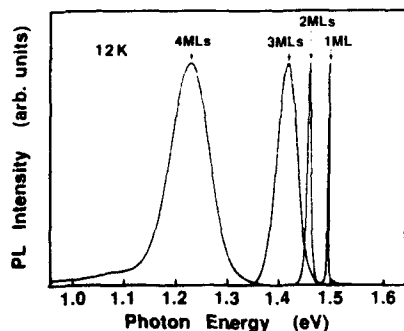


Fig. 3. PL spectra from SQWs with different thickness of InAs. These SQW structures were grown at $T_s = 520^\circ\text{C}$.

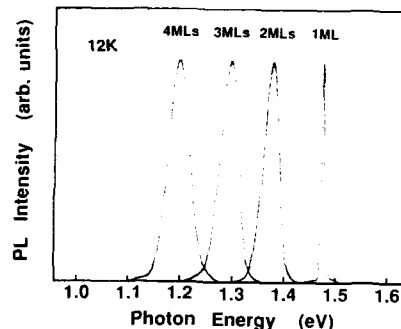


Fig. 4. PL spectra from SQWs with different thickness of InAs. These SQW structures were grown at $T_s = 420^\circ\text{C}$.

heterointerface is deteriorated abruptly at 3 MLs when the SQW structure is grown at $T_s = 520^\circ\text{C}$. On the other hand, fig. 4 indicates that rather gradual deterioration has been introduced at 1 ML of InAs when we use a growth temperature of $T_s = 420^\circ\text{C}$. This thickness dependence of PL spectra is consistent with the above-mentioned RHEED observation.

In fig. 5, we summarize the peak energy of PL spectra as a function of the well width. Solid circles denote the peak energy observed from samples grown at $T_s = 520^\circ\text{C}$. Solid squares indicate the case of $T_s = 420^\circ\text{C}$. The dashed lines are drawn to guide the eye. The solid line is the theoretical result estimated for the electron transition energy in quantum wells by using the effective mass approximation. In the calculation, we assumed the band line-up to be a completely strain-relaxed structure, as shown in the inset of fig. 5 [9]. The conduction band discontinuity is determined from the difference of electron affinities between the two semiconductors, GaAs and InAs. For the case of $T_s = 520^\circ\text{C}$, we can see a considerable decrease of PL peak energy at 3–4 MLs. On the other hand, continuous decrease is observed for samples grown at $T_s = 420^\circ\text{C}$. Between 1 and 3 MLs, the PL energy for samples grown at $T_s = 520^\circ\text{C}$ clearly lies above the case of $T_s = 420^\circ\text{C}$. This result seems to be caused by the structural difference of InAs epitaxial layers. At $T_s = 420^\circ\text{C}$, considerable part of the interface strain might be relaxed, independent of the well width because the peak energy is close to the

nearly 1 ML for samples grown at 520 and 420 °C, respectively.

4. Summary

Optical properties of SQW structure composed of ultrathin InAs and GaAs barriers have been studied. From the in-situ analysis of RHEED signals, we have determined the critical thickness to be 2–3 MLs for pseudomorphic growth of InAs. Below the critical thickness, however, the PL properties of the strained-structure is dependent on the growth temperature. By PL analysis on the annealing effect, the critical thickness for the stably-strained heterostructure is determined to be 2–3 MLs and nearly 1 ML for samples grown at 520 and 420 °C, respectively.

Acknowledgements

The authors wish to thank H. Yokose and A. Kawaguchi for the experimental assistance on MEE growth. This work was supported in part by Japan Private School Promotion Foundation on The Scientific Research Promotion Foundation

and by Grant-in-Aid for Scientific Research from The Ministry of Education, Science and Culture.

References

- [1] H. Nakao and T. Yao, *Japan. J. Appl. Phys.* 28 (1989) L352.
- [2] M.A. Tischeler, N.G. Anderson and S.M. Bedair, *Appl. Phys. Letters* 49 (1986) 1199.
- [3] K. Taira, H. Kawai, I. Hase, K. Kaneko and N. Watanabe, *Appl. Phys. Letters* 53 (1988) 495.
- [4] M. Sato and Y. Horikoshi, *J. Appl. Phys.* 66 (1989) 851.
- [5] J.M. Gerard and J.Y. Marzin, *Appl. Phys. Letters* 53 (1989) 568.
- [6] M. Sato and Y. Horikoshi, *Appl. Phys. Letters* 55 (1989) 1689.
- [7] K. Taira, H. Kawai, I. Hase, K. Kaneko and N. Watanabe, *Appl. Phys. Letters* 55 (1989) 1690.
- [8] Y. Horikoshi and M. Kawashima, *J. Crystal Growth* 95 (1989) 17.
- [9] M. Yano, T. Iwawaki, H. Yokose, A. Kawaguchi, Y. Iwai and M. Inoue, in: *Quantum-Well and Superlattice Physics III*, Eds. G.H. Döhler, E.S. Koteles and J.N. Schulman [Proc. SPIE 1283 (1990) 221].
- [10] P.R. Berger, K. Chang, P. Bhattacharya, J. Singh and K.K. Bajaj, *Appl. Phys. Letters* 53 (1989) 684.
- [11] W. Gillin, Y.S. Tang, N.J. Whitehead, K.P. Homewood, B.J. Sealy, M.T. Emeny and C.R. Whitehouse, *Appl. Phys. Letters* 56 (1990) 1116.

Fabrication and characterization of MBE grown InAs/GaAs strained-layer superlattices on variously oriented substrates

Kazuhiro Kudo, Jong Sik Lee, Kuniaki Tanaka

Faculty of Engineering, Chiba University, 1-33 Yayoi-cho, Chiba 260, Japan

Yunosuke Makita and Akimasa Yamada

Electrotechnical Laboratory, 1-1-4 Umezono, Tsukuba-shi, Ibaraki 305, Japan

InAs/GaAs strained-layer superlattices (SLSs), grown by molecular-beam epitaxy on variously oriented GaAs substrates, have been investigated. X-ray diffraction and photoluminescence (PL) studies reveal the formation of coherent SLS and microstructures due to the three-dimensional nucleation is strongly dependent on the substrate orientation and the growth parameters. The relationship between PL spectra and growth modes and potential applications of self-aligned microstructures, including quantum pyramids, are described.

1. Introduction

Epitaxial growth of strained-layer superlattices (SLSs) on variously oriented substrates is of interest for the fundamental understanding of growth phenomena and also in relation to the development of optoelectronic devices. The fabrication of microstructures, such as quantum wires [1,2] and quantum boxes [3,4], is expected to lead to the realization of a variety of devices using lateral quantum confinement. Two approaches reported in this field are the methods using lithography [5,6] and epitaxial growth on vicinal substrates [7,8]. In particular, the fabrication of self-aligned microstructures using critical thickness due to mismatch [9] and the migration of atoms on misoriented substrates [7,8] is a promising technique for future devices. Among highly strained systems, InAs/GaAs is particularly interesting, since two or three-dimensional nucleation due to 7% lattice mismatch takes place over a critical thickness of 2–3 monolayers [9–11].

In this report, we describe the growth and characterization of InAs/GaAs SLSs on variously oriented GaAs substrates. Photoluminescence (PL) and X-ray measurements were made to investigate

the formation of the microstructures and the dependence on the substrate orientation and the growth conditions.

2. Experimental procedures

All the samples used in this study were grown by a usual molecular beam epitaxy (MBE) system. Cr-doped (100)A, (711)A, (311)A, and (111)A oriented GaAs wafers were used as substrates. After the chemical etching of the substrates, a set of four differently oriented substrates were mounted on a molybdenum block and SLS were grown at the same time. The growth process is as follows. First, a 0.5 μm GaAs buffer layer was grown. Next, InAs and GaAs layer were alternately grown for 4 and 40 s, respectively. Before and after the growth of the InAs layer, the growth was interrupted for 8 s to enhance the migration of atoms. In order to examine the influence of the SLS's growth periods on the surface features and the optical properties, one, five, and twenty period InAs/GaAs SLSs were fabricated. The growth temperature, T_s , was varied between 400 and

550 °C. The flux ratios of As₄/Ga and As₄/In were 3 and 20, respectively, and the growth rate of the GaAs layer was about 1 μm/h. From the experimental evaluation, the thicknesses of the InAs well and the GaAs barrier layer were 3–15 Å (1–5 monolayers) and 200–300 Å (70–80 monolayers), respectively, and these values strongly depend on T_g .

Double-crystal X-ray diffraction patterns were obtained using Cu Kα₁ radiation. PL measurements were carried out at 77 K, using the 514.5 nm line of an Ar⁺ ion laser for excitation. In this report we are interested in the emission from ultra-thin InAs quantum-wells and microstructures, including defects; hence the PL spectra in the wavelength range between 800 and 1500 nm

were measured using a liquid-nitrogen-cooled Ge detector.

3. Results and discussion

3.1. Surface morphology of epitaxial layer

Surface morphologies of InAs/GaAs SLs were varied depending on both the growth temperature and the substrate orientation. Fig. 1 shows typical scanning electron microscopy (SEM) images of the normal view of the sample surface. The SEM images in figs. 1a–1d correspond to the twenty period SLs, grown at 475 °C on (100)A, (711)A, (311)A, and (111)A GaAs substrates. A smooth

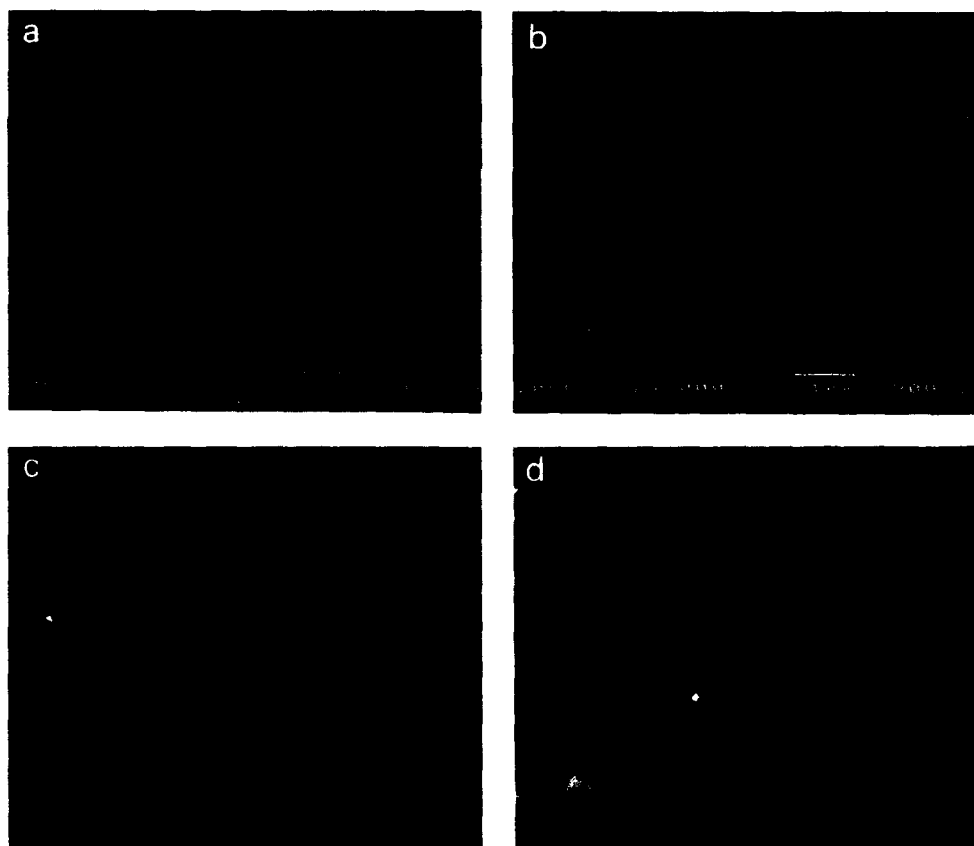


Fig. 1. Surface SEM images for the samples grown on (a) (100)A, (b) (711)A, (c) (311)A and (d) (111)A GaAs substrates at 475 °C.

and featureless surface was achieved on (100) and (711) substrates and in the T_s range of 400 to 550 °C. However, submicron size pyramid structures, as shown in figs. 1c and 1d, were observed on the surface of the SLS grown on (311) and (111) substrates. The size and the shape of these microstructures are closely related to the growth conditions and the substrate orientation.

3.2. X-ray diffraction patterns

X-ray diffraction patterns of the twenty period SLS grown on a (100) substrate are shown in fig. 2. In this case, X-ray diffractions made around a (422) reflection are shown as a function of T_s . The sample grown at 500 °C exhibits the most well-defined and sharp X-ray satellite pattern, which indicates that coherent SLS structure is realized in the epitaxial layer. The zero-order satellite peak shifts towards the GaAs substrate peak at higher growth temperatures. However, the satellite peaks vanish in the sample grown at 550 °C. This phenomenon can be easily explained by the fact that the desorption of In atoms and the revaporization of the InAs layer are enhanced at higher T_s . On

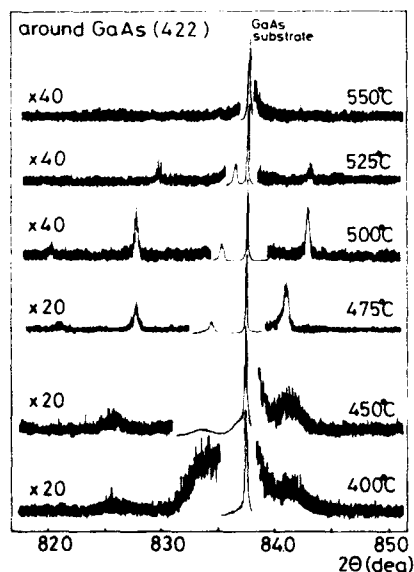


Fig. 2. X-ray diffraction patterns of the twenty period SLS grown on (100) GaAs substrate.

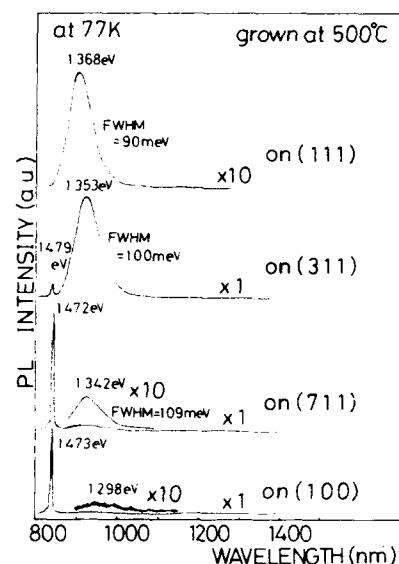


Fig. 3. Photoluminescence spectra of the twenty period SLSs grown on (100), (711), (311), and (111) GaAs substrates at 500 °C.

the other hand, the satellite peaks of the samples grown at T_s lower than 475 °C suddenly change to a broad and smeared shape. These results indicate that three-dimensional nucleation takes place and the effect of disorder is thought to be strong. The variation of the InAs layer thickness and the three-dimensional nucleation with T_s are in good agreement with the results of PL measurements. Similar results are obtained for the samples grown on (711) and (311) substrates. However, none of the samples grown on (111) substrates showed clear satellite patterns. This might be attributed to the surface roughness of the epitaxial layer, as shown in fig. 1d.

3.3. Photoluminescence spectra

Figs. 3 and 4 show the PL spectra at 77 K for the samples grown at 500 and 475 °C, respectively. As shown in fig. 3, a sharp peak at around 1.47 eV is dominant for the samples grown on (100) and (711) substrates. However, this peak is weak for the sample on the (311) substrate and completely disappears for that on the (111) substrate. On the

contrary, the broad peak in the lower energy region between 1.29 and 1.37 eV becomes larger for the samples grown on the substrate tilted towards the (111) orientation. In fig. 4, it may be noticed that more than two broad peaks are observed for all the samples grown at 475°C. These critically depend both on T_s and on the substrate orientation for T_s in the range of 475–500°C. The samples grown at higher and lower T_s show no clear dependence on the substrate orientation. The peak at the high energy side shifts towards higher energies with increasing T_s . The emission energy of 1.50–1.44 eV corresponds to the SLSs with an InAs well between zero and two monolayers [10,11] and the energy shift is in good agreement with the thinning of InAs layers at high T_s . The experimental results demonstrate that the InAs layer is fully strained for up to 2 monolayers and that three-dimensional nucleation takes place beyond 2 monolayers as reported by other authors [9–11]. Moreover, the nucleation occurs at the initial stage of the growth with the substrate tilted towards (111) orientation.

In order to determine whether the number of the SLS's period has any effect on the PL spectra,

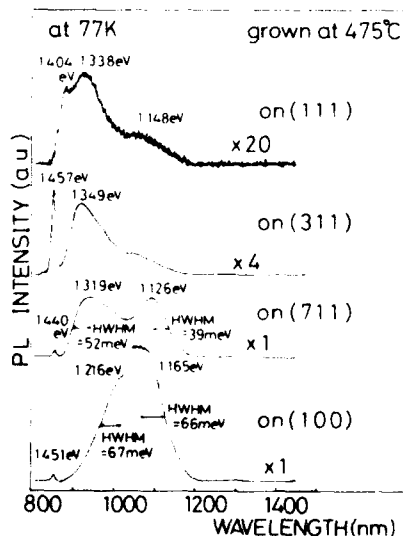


Fig. 4. Photoluminescence spectra of the twenty period SLSs grown on (100), (711), (311), and (111) GaAs substrates at 475°C.

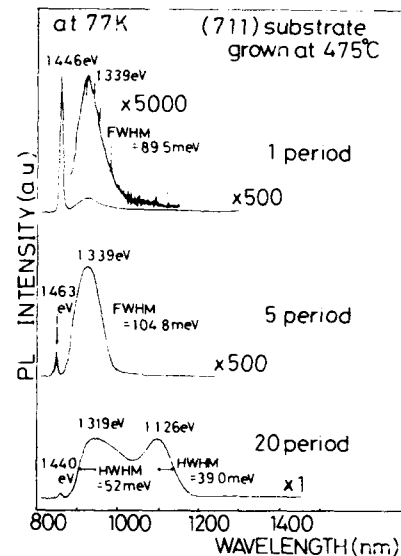


Fig. 5. Photoluminescence spectra of the SLSs with 1, 5, and 20 periods. The samples grown on (711) substrate at 475°C.

we have measured the samples with 1, 5, 20 period SLSs. Fig. 5 shows typical PL spectra for samples grown on a (711) substrate at T_s of 475°C. As is clear from the figure, though a strong and sharp peak at higher energies is dominant for the single quantum well (one period) structure, the intensity of the broad peak at lower energies increases as the period increases and an additional new peak at 1.126 eV appears for the sample with 20 period. The origin of the broad peaks at the low energies is directly related to the generation of three-dimensional nucleation. However, the microstructures due to the three-dimensional nucleation might be too small to be observed in the SEM image, as shown in fig. 1b. Whether the emission comes from microstructure or misfit dislocations cannot be determined fully; however, distinguishing characteristics were observed in polarization resolved PL spectra. A strong anisotropy in relation to the direction of the micro-pyramids was observed in the emission at around 1.3 eV for the samples grown on (311) substrates. From this result, we conclude that the emission at around 1.3 eV is closely related to the formation of a self-aligned micro-pyramidal structure. However, the

emissions have a large full width at half maximum (FWHM) or half width at half maximum (HWHM) in figs. 3–5, which indicates that the size of the microstructures have not been fully controlled under the conditions reported here.

4. Conclusion

We have investigated the formation and the properties of microstructures in InAs/GaAs strained-layer superlattices grown on variously oriented GaAs substrates. The observed PL spectra and X-ray diffraction patterns show a clear dependence on the substrate orientation and the growth conditions. The experimental results obtained here demonstrate the formation of self-aligned microstructures without lithographic processes. However, the present difficulty in achieving controlled microstructures is thought to be related to the occurrence of the three-dimensional nucleation and the migration and/or desorption of atoms during growth and interruption. We believe that detailed investigation of the growth modes and the substrate orientation would overcome the difficulty.

Acknowledgements

The authors would like to express their thanks to Dr. Y. Toyoda and Mr. K. Mutoh for help in the X-ray diffraction measurements and also for fruitful discussions. We also thank Dr. H. Shibata and Mr. M. Watanabe for their help in fabricating the samples.

References

- [1] Y. Arakawa, K. Vahala, A. Yariv and K. Lau, *Appl. Phys. Letters* 48 (1986) 384.
- [2] H. Sakaki, K. Wagatsuma, J. Hamasaki and S. Saito, *Thin Solid Films* 36 (1976) 497.
- [3] Y. Arakawa and H. Sakaki, *Appl. Phys. Letters* 40 (1982) 939.
- [4] Y. Miyamoto, M. Cao, Y. Shingai, K. Furuya, Y. Suematsu, K.G. Ravikumar and S. Arai, *Japan. J. Appl. Phys.* 26 (1987) L225.
- [5] S.R. Andrews, H. Arnot, P.K. Rees, T.M. Kerr and S.P. Beaumont, *J. Appl. Phys.* 67 (1990) 3472.
- [6] K. Kash, A. Scherer, J.M. Worlock, H.G. Craighead and M.C. Tamargo, *Appl. Phys. Letters* 49 (1986) 1043.
- [7] P.M. Petroff, A.C. Gossard and W. Wiegmann, *Appl. Phys. Letters* 45 (1984) 620.
- [8] T. Fukui and H. Saito, *Appl. Phys. Letters* 50 (1987) 824.
- [9] J.W. Matthews and A.E. Blakeslee, *J. Crystal Growth* 27 (1974) 118.
- [10] J.M. Gerard and J.Y. Marzin, *Appl. Phys. Letters* 53 (1988) 568.
- [11] F.J. Grunthaner, M.Y. Yen, R. Fernandez, T.C. Lee, A. Madhukar and B.F. Lewis, *Appl. Phys. Letters* 46 (1985) 983.

Indium desorption during MBE growth of strained InGaAs layers

J.-P. Reithmaier *, H. Riechert, H. Schlötterer

Siemens Research Laboratories, Otto-Hahn-Ring 6, W-8000 München 83, Germany

and

G. Weimann

Walter Schottky Institut, Technische Universität, W-8046 Garching, Germany

We have investigated the In desorption during growth of pseudomorphic InGaAs/GaAs SQWs at various substrate temperatures (500–700°C) and In contents (5–45%) by photoluminescence and transmission electron microscopy. We present data about temperature dependent growth rates at different In contents. The evaluation of these data shows a strain dependent activation energy for In desorption, which at the low strain limit approaches that of unstrained relaxed InGaAs layers. Our results are in agreement with published data of growth investigations of InAs on GaAs. TEM images of highly strained InGaAs layers show a temperature range, where three-dimensional growth dominates, even for thicknesses far below the critical thickness.

1. Introduction

In applications of MBE growth, where high optical material quality is required, especially in heterostructures with Al-containing layers, elevated growth temperatures are used, at which a significant reevaporation may occur. Of the group III atoms used, In is most critical with respect to desorption because it has the lowest binding energy to As [1]. For a more accurate growth control in the high temperature region a better understanding of the In desorption and growth behaviour is necessary.

We present a systematic investigation about strain dependent In desorption behaviour during MBE growth parameters generally used for device applications (growth rate $\approx 1 \mu\text{m/h}$, V/III beam flux ratio > 10). At the low strain limit, we find overall activation energies for In desorption during InGaAs growth which are comparable with values from unstrained InGaAs. Published data

about In desorption during submonolayer growth of InAs on GaAs [2] are in agreement with our values of relaxed (unstrained) samples, and corresponding data during growth of a few monolayers of InAs [3,4] agree very well with values which we obtain from highly strained samples.

With transmission electron microscopy (TEM) we have investigated the morphology of the interface region. In samples with high In content we could observe a temperature range, where three-dimensional growth dominates even for well thicknesses below the critical layer thickness of Matthews and Blakeslee [5], while for lower In content no growth defects or significant interface roughness are detectable over the whole investigated temperature range.

2. Experiment

We have grown pseudomorphic InGaAs/GaAs single quantum well structures on semi-insulating (100) GaAs substrates in a VG V80H molecular beam epitaxy system with elemental sources. Each

* Present address: IBM Research Laboratories, Säumerstrasse 4, CH-8803 Rüschlikon, Switzerland.

sample consists of about 10 wells with 1 or 3 reference wells grown at low temperature ($\approx 500^\circ\text{C}$) and the other wells grown at different higher temperatures (increased by a certain value from well to well). The growth temperature of the 60 nm thick barriers was always constant at 600°C . The temperature change was made at the beginning and at the end of each barrier with fast ramps. The surface temperature of the In-free mounted substrate was measured by a short wavelength pyrometer during growth and calibrated before each run at the desorption point of the native Ga oxide (582°C [6]). The growth rate was around $1\ \mu\text{m/h}$ and the beam flux ratio > 10 , which are generally used growth parameters for device applications. No growth interruptions were applied.

Photoluminescence (PL) measurements were performed at low temperature ($< 2\ \text{K}$) and with an excitation power of a few W/cm^2 . The TEM images were made on cleaved wedge samples [7].

3. Results and discussion

Fig. 1 shows a PL spectrum of a sample with an In concentration of 5% at low growth temperatures. The sample consists of three reference wells grown at 510°C and 7 wells grown at increasing temperatures. The well thickness is 20 nm. Each PL peak corresponds to a well grown at one temperature. We reach line widths which are significantly lower than 1 meV and which show the high optical quality of the sample. Also for samples with higher In content, the peaks are well resolved, which can be seen in fig. 2. This PL spectrum was measured from a sample with an In concentration of 24% and a well width of 5 nm for the reference well.

From the PL transition energies we can deduce the In concentration according to calculations previously published [8]. For samples with higher In concentrations and small well widths ($< 10\ \text{nm}$), a self-consistent procedure was applied for the

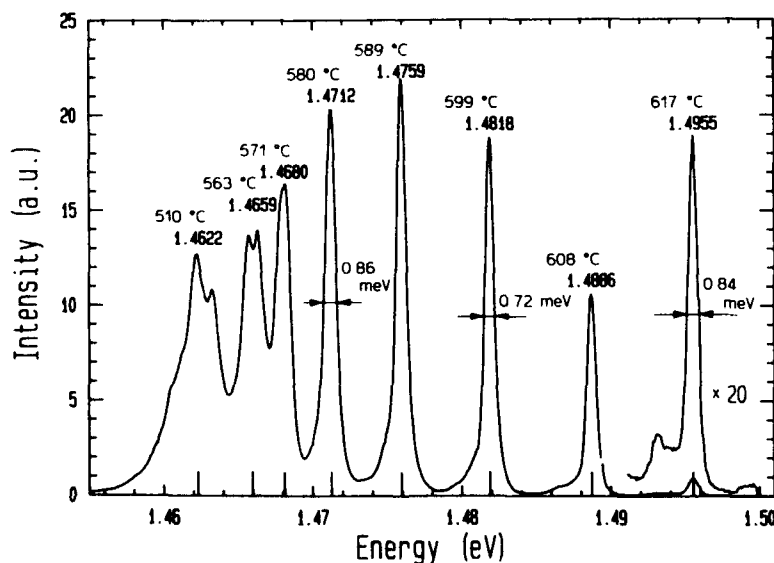


Fig. 1. PL spectrum of an InGaAs/GaAs sample with a sequence of SQWs grown at different temperatures (values above each peak position). The starting In concentration was about 5% and corresponds to the PL peak grown at 510°C . PL was performed at 2 K with an excitation power of $1.5\ \text{W}/\text{cm}^2$.

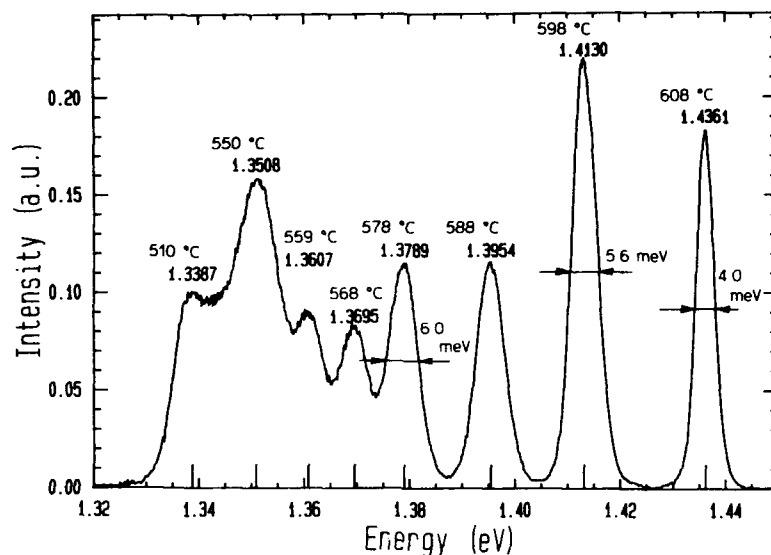


Fig. 2. PL spectrum of an InGaAs/GaAs desorption sample with a starting In concentration of 24% and a well width of 5 nm.

evaluation, which takes into account the decreasing well width because of In loss. For temperatures below 640 °C the assumption of no Ga loss

was made, while for higher temperatures the GaAs growth rate was corrected according to results of Van Hove and Cohen [9] neglecting strain effects.

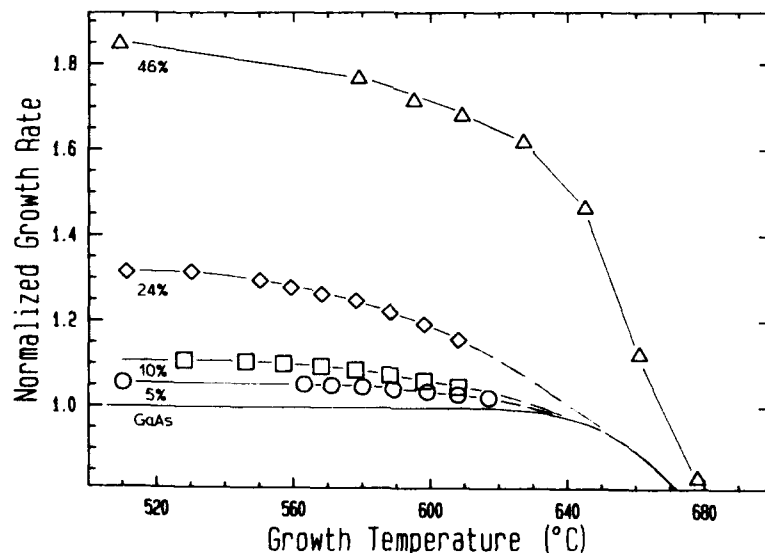


Fig. 3. Dependence of the InGaAs growth rate on the growth temperature for different starting In concentrations (percentage values). The growth rate is normalized to the GaAs growth rate for low temperatures (no Ga loss). For comparison, the GaAs growth rate (solid line) is added which was measured from Van Hove and Cohen [9].

The deduced growth rate, normalized to the GaAs growth rate at low temperatures, is plotted versus the substrate temperature in fig. 3 for four samples with different starting In concentrations (controlled by the incident In/Ga flux ratio). For comparison, the experimental curve from Van Hove and Cohen for GaAs growth is added. For high In concentrations and growth temperatures above 640°C, the InGaAs growth rate shows, as expected, a strong dependence on the temperature, which makes it difficult to control the growth.

From the calculated In concentration of each well we can deduce the desorption part from the following rate equation:

$$r_{\text{incident}} = r_{\text{desorption}} + r_{\text{growth}} \quad (1)$$

where r_{growth} is the InAs growth rate, r_{incident} the rate equivalent to the offered In beam flux and $r_{\text{desorption}}$ the desorption rate which can be expressed as

$$r_{\text{desorption}} = \frac{x_0 - x}{(1 - x_0)(1 - x)} r_0 \quad (2)$$

with the GaAs growth rate r_0 as reference, x_0 as the starting In concentration according to the

Table 1

Activation energies E_a for In desorption during MBE growth of InGaAs on (100) GaAs deduced from PL measurements; the first line corresponds to the desorption experiment with relaxed unstrained InGaAs samples with an In starting concentration of 12%; the lattice mismatch ϵ was calculated according to Vegard's law (linear dependence on the In content); the activation energies were evaluated using the Arrhenius plot of fig. 4

In content (%)	$\epsilon = \Delta a/a_{\text{GaAs}}$ (%)	E_a (eV)
0.6–12	(Relaxed)	2.60 ± 0.3
2.8–4.9	0.20–0.35	2.74 ± 0.3
4.4–9.1	0.32–0.65	2.65 ± 0.3
13.5–21.7	0.97–1.55	1.87 ± 0.3
33.1–43.4	2.37–3.11	1.44 ± 0.5

In/Ga flux ratio and x as the measured In content of each well.

These values are shown in an Arrhenius plot in fig. 4, where we can calculate the activation energy E_a by a linear fit. For the evaluation a comparable temperature range was used for all samples.

The activation energies are listed in table 1. The strain was calculated according to Vegard's law from the In concentration. The error for the

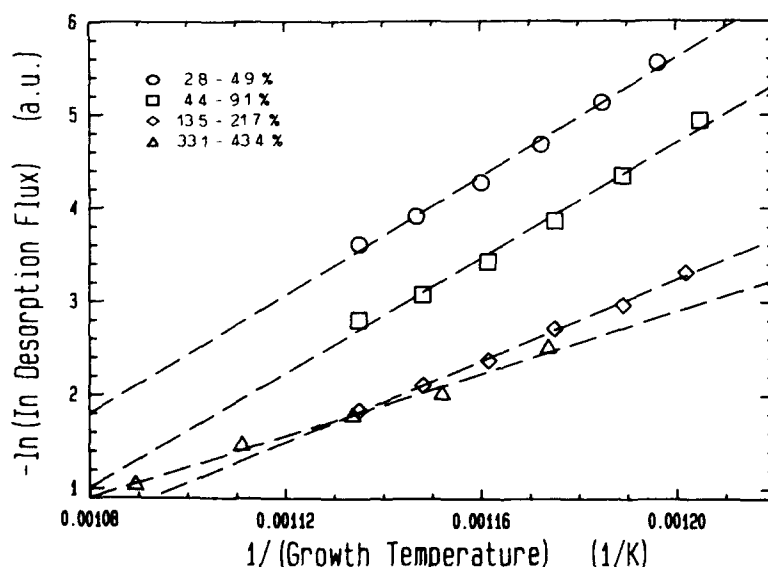


Fig. 4. Arrhenius plot of the reevaporated In flux which was evaluated from PL measurements. For all linear fits, comparable temperature ranges were used, which correspond to the labeled ranges for the In concentration for each sample.

activation energy results from the inaccuracy of the growth rate determination. An increase of the accuracy because of averaging over several measurement points was not taken into account. In table 1, a fifth value for zero stress is added (first line). This value was deduced from a sample sequence with unstrained, i.e. relaxed, thick InGaAs layers (12% In content at a growth temperature of 500 °C, layer thickness $\geq 2 \mu\text{m}$). Each of these samples was grown at a different temperature (500, 580 and 620 °C). The In concentration was determined by PL and verified by X-ray fluorescence analysis. This value agrees very well with the results of the low strain samples and is in excellent agreement with the activation energy of 2.6 eV determined by Evans et al. [2] for sub-monolayer growth of InAs on GaAs in the comparable temperature range ($< 650^\circ\text{C} = 2 \times 2$ surface reconstruction). In that case no strain should significantly affect the growth mechanism; therefore it is equivalent to the low strain limit. Foxon and Joyce [3] and Kanter et al. [4] have investigated the growth of few monolayers of InAs on GaAs with a modulated beam technique and reflection high energy electron diffraction, respectively, combined with quadrupole mass spectrometry. These investigations corresponds to the high strain growth regime. The authors have published activation energies between 1.3 and 1.5 eV, which agree also very well with the value we find for the most highly strained sample.

In fig. 5, TEM images of two samples with an In content of 5% (fig. 5a) and 45% (fig. 5b) are shown. The low strain sample has sharp interfaces and no well fluctuations are observable over the whole temperature range, while the high strain sample (fig. 5b) shows significant interface roughness which must be due to three-dimensional growth. With a well thickness of the reference well of 3.5 nm, this sample is still 30% below the critical thickness according to the theory of Matthews and Blakeslee. During growth of the GaAs barriers the roughness is smoothened until the InGaAs growth starts again. Therefore only the second interface in growth direction is disturbed. This feature already occurs at a temperature range below 560 °C (3rd to 5th well from the bottom in fig. 5b), at which the In desorption is low and the

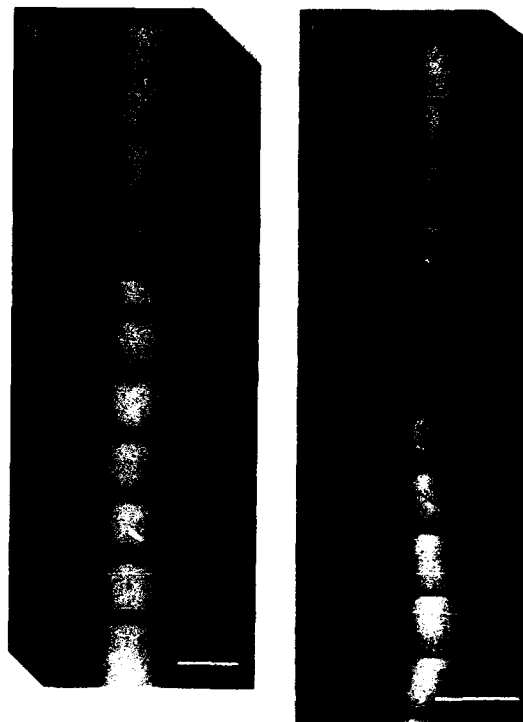


Fig. 5. TEM images (dark field, (200) reflex) of two InGaAs/GaAs samples with 5% (a) and 45% (b) In content, respectively. The first three wells (at the bottom) of the 5% sample were grown at 510 °C. The temperature for the following wells, starting at 560 °C, was increased by 10 K from well to well. For the 45% sample, the growth temperature was increased from 500 to 650 °C in 15 K steps. The white lines in the middle of each well are due to a contrast inversion [10]. Markers represent 100 nm.

strain nearly constant. Only above 640 °C, where significant In loss occurs and therefore the strain and the well width are strongly decreased, the interface fluctuations disappear. This behaviour is more pronounced in samples with thicker well widths, but it is still possible to get sharper interfaces at lower temperatures ($\leq 500^\circ\text{C}$), at least for well thicknesses below the critical thickness.

4. Conclusions

By PL and TEM, we have investigated pseudomorphic InGaAs/GaAs samples with a sequence

of SQWs grown at different substrate temperatures. The In concentration was varied from 5% to 45%, the growth temperature from 500 to 700 °C. From the deduced In loss during growth we have evaluated strain dependent activation energies for In desorption. We find that for the activation energy the low strain limit agrees very well with our value deduced from an investigation with relaxed, i.e. unstrained, samples and also with published data for submonolayer growth of InAs on GaAs [2]. Published data from investigations about In desorption from a few monolayers of InAs on GaAs [3,4] are in good agreement with our results from highly strained samples.

In TEM images of samples with high In content, we observe three-dimensional growth at temperatures above 530 °C, even for well thicknesses below the critical thickness. But only the second interface in growth direction, i.e. InGaAs to GaAs, is disturbed. At higher temperatures, at which the well thickness and the strain is reduced because of significant In reevaporation, both interfaces are sharp again.

Acknowledgements

We wish to thank D. Bernklau for substrate preparation, A. Miklis for assistance in optical

measurements, C. Fruth for TEM images, M. Schuster and Mr. Worthington for X-ray fluorescence analysis and R. Höger for helpful discussions.

References

- [1] H. Seki and A. Koukitu, *J. Crystal Growth* 74 (1986) 172.
- [2] K.R. Evans, C.E. Stutz, D.K. Lorange and R.L. Jones, *J. Vacuum Sci. Technol.* B7 (1989) 259.
- [3] C.T. Foxon and B.A. Joyce, *J. Crystal Growth* 44 (1978) 75.
- [4] Y.O. Kanter, A.K. Gutakovsky, A.A. Fedrow, M.A. Revenko, S.V. Rubanov and S.I. Stenin, *Thin Solid Films* 163 (1988) 497.
- [5] J.W. Matthews and A.E. Blakeslee, *J. Crystal Growth* 27 (1974) 118.
- [6] A.J. SpringThorpe, S.J. Ingre, B. Emmerstorfer, P. Mandeville and W.T. Moore, *Appl. Phys. Letters* 50 (1987) 77.
- [7] H. Kakibayashi and F. Nagata, *Japan. J. Appl. Phys.* 25 (1986) 1644.
- [8] J.-P. Reithmaier, R. Höger, H. Riechert, A. Heberle, G. Abstreiter and G. Weimann, *Appl. Phys. Letters* 56 (1990) 536.
- [9] J.M. Van Hove and I. Cohen, *Appl. Phys. Letters* 47 (1986) 726.
- [10] C.S. Baxter, W.M. Stobbs, K.J. Monserrat and J.N. Tothill, in: *Analytical Electron Microscopy*, Ed. G.W. Lorimer (Institute of Metals, London, 1988) p. 209.

A photoluminescence study of indium desorption from strained $\text{Ga}_{1-x}\text{In}_x\text{As}/\text{GaAs}$

M.T. Emeny

Royal Signals and Radar Establishment, St. Andrews Road, Great Malvern, Worcs. WR14 3PS, UK

L.K. Howard *, K.P. Homewood **, J.D. Lambkin *

University of Surrey, Guildford, Surrey GU2 5XH, UK

and

C.R. Whitehouse

Royal Signals and Radar Establishment, St. Andrews Road, Great Malvern, Worcs. WR14 3PS, UK

In this paper we present detailed measurements of the thermal desorption rates of indium from strained GaInAs grown off a GaAs substrate. We have made these measurements by monitoring the photoluminescence (PL) of the groundstate emission from strained quantum wells. We show that this method can be an accurate and highly sensitive technique for measuring desorption rates. The measurements have been made as a function of composition and arsenic overpressure. A simple model for the indium incorporation is developed and an activation energy for the desorption process has been obtained.

1. Introduction

Preferential desorption of the more volatile of the group III elements during the MBE growth of ternary III–III–V materials can lead to errors in composition and thickness of grown layers. While this problem can be avoided by growth at sufficiently low temperatures where desorption can be made negligible this may lead to unacceptable compromises in material quality and subsequent device performance, particularly in multilayered structures. One may then be obliged to work in regimes where substantial desorption of at least one of the group III elements is occurring. Under these conditions it is clearly essential to have the group III loss rate accurately characterised. Group

III desorption in ternary materials is not trivial. In addition to the temperature the desorption will in general depend on the group V flux, the flux of the other group III element, the overall growth rate, the composition of the ternary and when present any strain in the system.

Previously [1] the main method used to study desorption rates has been thickness measurements using cross-sectional scanning electron microscopy (SEM) or transmission electron microscopy (TEM) of layers or multilayers grow at different temperatures. However, as well as being extremely time consuming, these techniques lack the sensitivity to measure low loss rates, particularly for compositions where the desorbing element is the smaller mole fraction, as in GaInAs. Because of this sensitivity problem SEM and TEM may also require layers that are thicker than the critical thickness for strain relaxation making it difficult to assess

* Strained Layer Structures Group.

** Department of Electronic and Electrical Engineering.

the influence of strain, which will be expected to increase the desorption, on the desorption rates. We have therefore used low-temperature photoluminescence from strained multilayer stacks to monitor the indium incorporation in InGaAs grown pseudomorphically on GaAs. When the well is formed from a ternary alloy, as in this case, and the cladding is the larger band-gap binary constituent we show that the PL from quantum wells provides a fast, accurate and sensitive technique for measuring desorption rates.

2. Experimental details

All of the samples were grown by molecular beam epitaxy (MBE) in a Vacuum Generators V80H reactor on (100) orientated GaAs substrates. The growth rates for all samples were determined by RHEED oscillation measurements, and the growth rates for the alloy were kept constant at 1 monolayer/s. The samples consisted of a series of multiquantum well stacks grown under a variety of conditions of interest. Each sample contained a stack of seven nominally identical quantum wells each of which had been grown at a different temperature. The first well was always grown at a temperature well below the regime for any appreciable desorption and therefore provides a reference point. The wells within a stack were separated by 500 Å of GaAs to provide optical and structural isolation between wells. The growth temperature was adjusted during growth of the GaAs barriers. After some initial test structures all the samples were grown with wells at real temperatures of 470, 565, 590, 610, 620, 628 and 636°C grown sequentially. These temperatures were found to give approximately equally spaced well separated PL peaks and to cover a reasonable range of desorption rate. Initial substrate temperatures were determined by reference to the sharp $c(4 \times 4)$ to (4×2) transition in the surface reconstruction monitored by RHEED, 530°C at a 5:1 arsenic to gallium flux ratio and subsequently monitored by optical pyrometry [2]. RHEED reconstruction temperatures were found to vary by less than 3°C from beginning to end of growth. To ensure consistency the substrate temperature

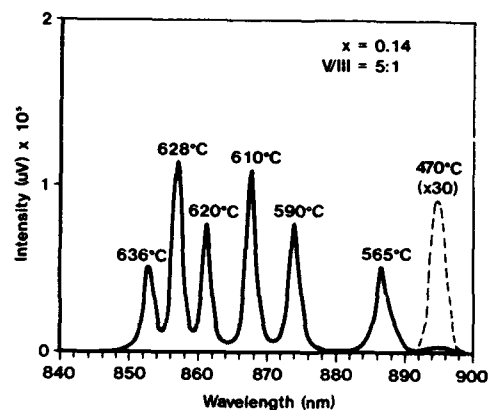


Fig. 1. A typical photoluminescence spectrum from a multi-quantum well stack (sample ME655, seven nominally 100 Å $Ga_{0.86}In_{0.14}As$ wells in GaAs grown at various temperatures).

was set under identical arsenic fluxes (3×10^{15} atoms $cm^{-2} s^{-1}$) for all samples and the arsenic flux actually used during growth adjusted subsequently. The arsenic flux was set by measurement of arsenic induced RHEED oscillations [3].

The photoluminescence measurements were made at a temperature of 77 K using a 514 nm argon laser excitation, a 1 m grating spectrometer, and a nitrogen cooled Ge pin detector. A plot of a typical spectrum from a sample is shown in fig. 1. As can be seen there is a shift in the PL peak position to higher energies for wells grown at successively higher temperatures as a result of indium desorption and a consequent reduction in the indium incorporated. By far the biggest contribution to this up-shift is the change in the band gap of the well material, ~ 11 meV for a 0.01 change in the indium mole fraction. There are small second order contributions to the PL shift due to changes in the confinement energies in the conduction and valence band wells as a result of the reduction in the well depths and thicknesses. We have taken all of these effects into account in our calculation of the composition of the well material. The composition of the quantum wells was calculated from the energies of the peak positions to high precision by solving the Schrödinger equation in the structure to obtain the ground state energies for the conduction and valence band wells. We use hole effective masses of 0.35 for

both GaAs and InAs and the electron effective masses are taken to be 0.0665 and 0.023, respectively, in the binaries and are linearly interpolated for the alloys. The strained energy gap and band-offset ratios were calculated from the solid-model method of Van de Walle [4]. While the absolute values of the composition can be slightly in error using this approach the shift in the composition, from that of the control well, can nevertheless be obtained to a high accuracy and it is this shift that contains the information on the indium desorption rate. Applying this method iteratively accounts fully for the second order effect on the PL peak positions of the changes in the well thickness due to desorption of the indium fraction in the well.

We have performed two main experiments. Firstly we have investigated the effect of the indium mole fraction on the indium desorption rate from strained InGaAs, and secondly we have studied the effect of varying the arsenic flux. The results from these experiments are described in the following section.

3. Results and discussion

In fig. 2a we have plotted the indium incorporation factor (the actual over the expected indium content) for five samples varying in indium content from $\sim 6\%$ to 40% as a function of temperature. The expected, zero desorption, indium concentration is obtained by measuring the peak energy of the PL from the reference well grown at the lowest temperature and calculating the composition using the method described in the previous section. All these samples were grown under an identical arsenic overpressure with an arsenic to total group III flux ratio of nominally 5:1. As can be seen, appreciable indium desorption occurs only above $\sim 550^\circ\text{C}$ after which the indium incorporation decreases monotonically with increasing temperature with only approximately half of the incident indium being incorporated by $\sim 640^\circ\text{C}$. In fig. 2b the indium incorporation factor has been plotted over the same temperature range but for five samples in which we have varied the arsenic to total group III flux ratio from 2.5:1

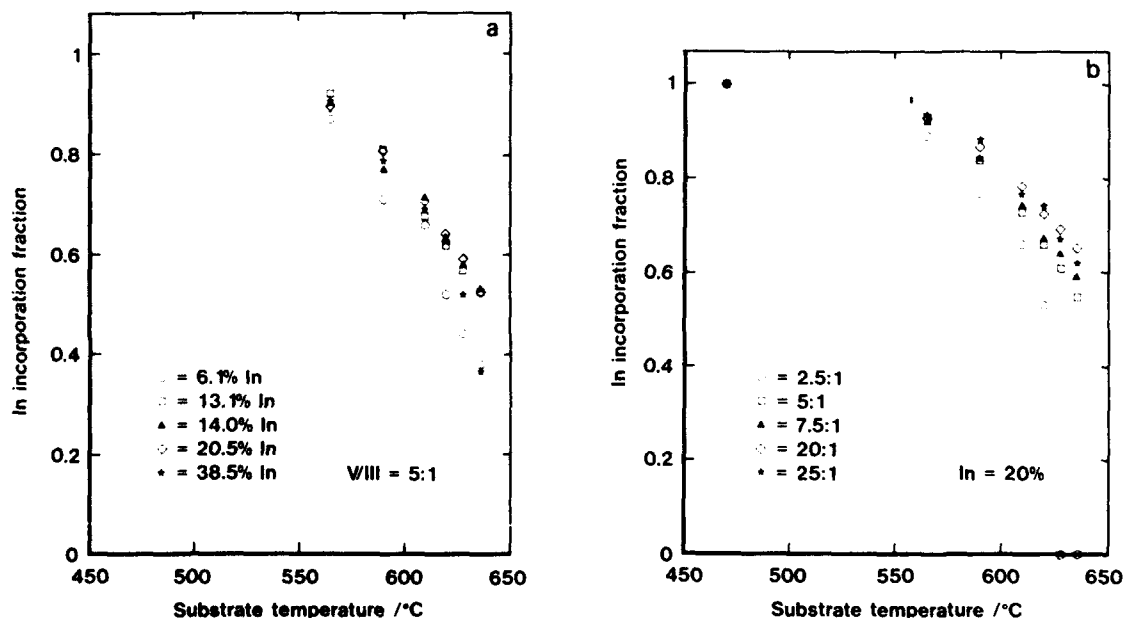


Fig. 2. Indium incorporation fraction as a function of temperature for (a) various low temperature indium mole fractions η_0 and (b) various arsenic to group III flux ratios.

to 25:1. All these samples were grown with an intended indium mole fraction of 0.2. The curves are seen to be of the same form as in the previous experiment. However, it should be noted that for the lowest arsenic:group III ratio, 2.5:1, the indium desorption has apparently increased dramatically above $\sim 620^\circ\text{C}$. Indeed, only five of the wells could be observed implying that no indium was incorporated at growth temperatures above 628°C for this low arsenic flux, or that growth quality is vitiated by the combination of high temperatures and low arsenic flux.

The results of these two experiments are summarised for clarity in figs. 3a and 3b where we have plotted, respectively, the indium incorporation factor as a function of strained indium content and arsenic to group III flux for various growth temperatures. The indium incorporation is seen to be essentially constant with nominal composition, the composition for no indium desorption, over most of the range studied with a slight reduction in indium incorporation for low indium concentrations, while small this reduction is greater than that expected from the dependence of the incorporation fraction on the nominal composition implicit in eqs. (4) and (6). A similar reduction has been previously observed [5] in Ga incor-

poration in the growth of GaAlAs, at high temperature, as the gallium mole fraction is reduced. This was speculatively attributed, to an exchange reaction between surface Al and subsurface Ga atoms. A slight drop off in the indium incorporation for the highest indium content sample $\sim 40\%$ is also observed, but only at a high growth temperature, this is attributed primarily to the effects of surface segregation of indium although there may also be some contribution as a result of increased strain which will tend to reduce incorporation. Fig. 3b shows a similar behaviour of the indium incorporation as a function of arsenic to group III flux ratio. Again the indium incorporation is constant over most of the range studied. The incorporation is reduced at lower flux ratios, indeed, apparently dramatically reduced at high growth temperatures for the lowest flux ratios and high temperatures when the arsenic sticking factors will also be reduced we believe that the surface may have turned metal rich and this quite probably kills the PL intensity. We are currently undertaking TEM to check the number of wells in this sample. A fall off in group III incorporation at low group V to group III flux ratios has been previously observed in the GaAlAs/GaAs system [6] and was attributed to a change in the growth regime from

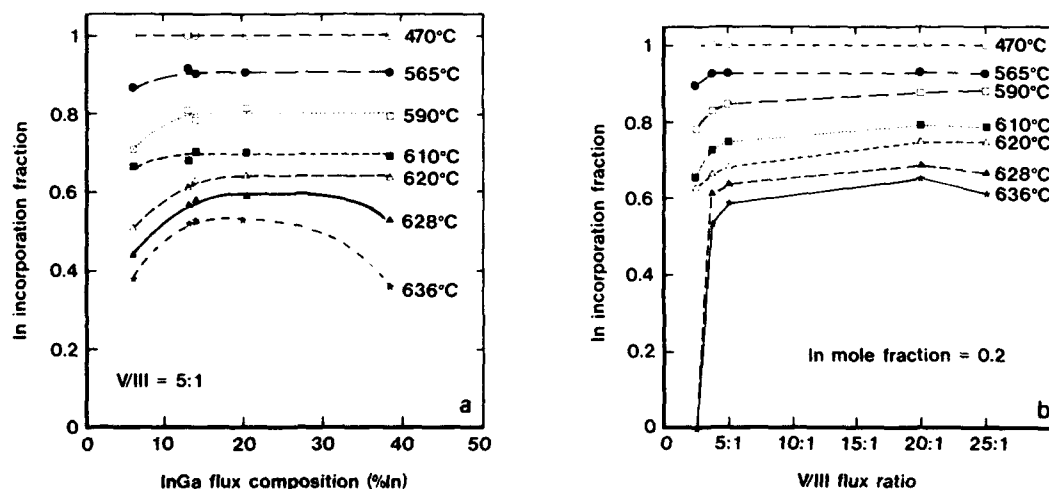


Fig. 3. Indium incorporation fraction, at various temperatures, as a function of (a) the low temperature indium mole fraction η_0 , and (b) arsenic to group III flux ratio. The solid lines are best fits to the data and are provided as a guide to the eye.

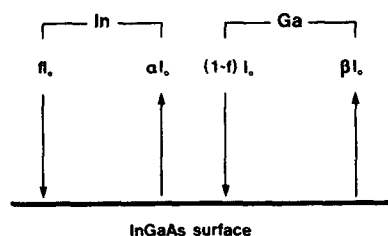


Fig. 4. A schematic of the growth model. I_0 is the total incident group III flux, f the incident indium flux, $1-f$ the incident gallium flux, α the indium fraction desorbed and β the gallium fraction desorbed.

configuration limited reactive (CLR) incorporation, where the arsenic flux is sufficient to provide essentially complete arsenic coverage of the growing surface and the group III incorporation will be independent of arsenic flux, to reaction limited (RL) incorporation, a group III stabilised regime, where group III incorporation will depend on the surface coverage of arsenic which is incomplete and therefore on the arsenic flux.

We have analysed these results using a simple rate-equation model shown schematically in fig. 4. The incident and emitted fluxes are defined as shown in the figure and figure legend.

We assume that we are operating in a temperature regime where the Ga desorption is negligible, we can therefore set $\beta = 0$. The mole fraction η_1 of indium incorporated is then given by

$$\eta_1 = \frac{f - \alpha}{(f - \alpha) + (1 - f)} = \frac{f - \alpha}{1 - \alpha}. \quad (1)$$

The intended indium mole fraction, η_0 , for no desorption, is then given by setting α equal to 0. So

$$\eta_0 = f. \quad (2)$$

We assume the desorbing flux αI_0 is proportional to the surface concentration of indium, which is just equal to the incorporated indium fraction of monolayers, if no surface segregation is occurring, and is exponentially activated. We can then write the indium flux desorbed as

$$\alpha I_0 = \eta_1 \omega_0 \exp(-E_A/kT), \quad (3)$$

where ω_0 is a factor incorporating an attempt frequency. The incorporated indium concentration η_1 monolayers is then

$$\eta_1 = \alpha I_0 / \omega_0 \exp(E_A/kT). \quad (4)$$

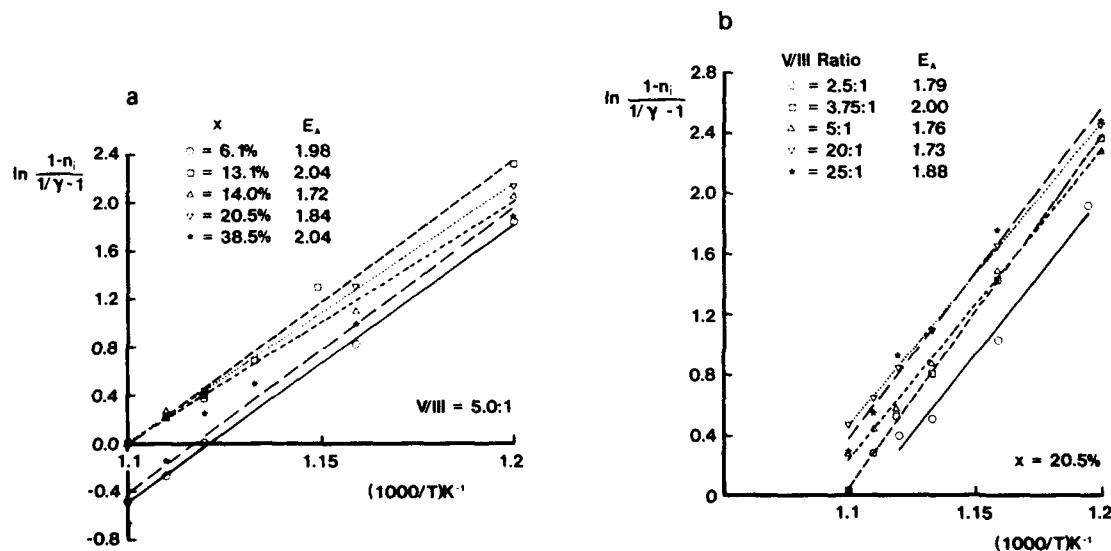


Fig. 5. Arrhenius plots of eq. (6) for (a) various nominal, low temperature, indium concentrations and (b) various arsenic to group III flux ratios. The lines are least squares fits to the data.

where α can be expressed as

$$\alpha = (\eta_0 - \eta_1)/(1 - \eta_1). \quad (5)$$

Substituting and rearranging we obtain

$$\frac{1 - \eta_1}{\eta_0/\eta_1 - 1} = \frac{I_0}{\omega_0} \exp\left(\frac{E_A}{kT}\right), \quad (6)$$

where η_1/η_0 is the incorporation coefficient γ .

We can therefore obtain the activation energy E_A and the prefactor I_0/ω_0 from an Arrhenius plot of $\log[(1 - \eta_1)/(\eta_0/\eta_1 - 1)]$ against $1/T$.

In figs. 5a and 5b we show Arrhenius plots of the data shown in figs. 2a and 2b, respectively. Within experimental error the activation energy for indium desorption is found to be constant both as a function of indium concentration and group V to group III flux ratios. We obtain an average value of 1.88 ± 0.15 eV for this activation energy. We make no correction for any temperature dependence of the prefactor.

4. Conclusion

To summarise, we have shown that PL can be used as a valuable tool for studying desorption in alloy systems. We have measured indium desorption from strained GaInAs as a function of both indium mole fraction and V:III flux ratio. The indium incorporation at any fixed temperature is found to be essentially constant as a function of both composition and V:III flux ratio over most of the range studied although a reduction in indium incorporation occurs both at low compositions and low V:III flux ratios. The activation energy for desorption is found to be independent,

within experimental error, of both arsenic to total group III flux ratio and of composition. A value of 1.88 ± 0.15 eV is obtained for this energy.

We are currently investigating the influence of growth rate on desorption and will be extending the study to higher indium concentrations by studying wells grown off relaxed InGaAs buffer layers. This will enable us to deconvolve the effects of composition and strain on the indium desorption rate. We will also be studying indium desorption rate from a metal rich surface as a function of metal alloy composition. These results will be presented in future papers.

Acknowledgements

We are grateful to the SERC and MOD for financial support under the UK joint SERC/MOD scheme.

References

- [1] R. Fischer, J. Klem, T.J. Drummond, R.E. Thorne, W. Kopp, H. Morkoç and A.Y. Cho, *J. Appl. Phys.* 54 (1983) 2508.
- [2] C.R. Whitehouse, M.T. Emeny, L. Davis, G. Williams and T. Martin, 4th Intern. Conf. on Molecular Beam Epitaxy, York, September 1986.
- [3] B. Lewis and R. Fernandez, *J. Vacuum Sci. Technol.* B4 (1986) 560.
- [4] C.G. Van de Walle, *Phys. Rev.* B39 (1989) 1871.
- [5] K.R. Evans, C.E. Stutz, D.K. Lorange and R.L. Jones, *J. Vacuum Sci. Technol.* B7 (1989) 259.
- [6] R. Köhbrück, S. Munnix, D. Bimberg, E.C. Larkins and J.S. Harris, Jr., *J. Appl. Phys. Letters* 54 (1989) 623.

Molecular beam epitaxial growth and properties of highly strained $\text{In}_x\text{Ga}_{1-x}\text{As}/\text{GaAs}$ multiple quantum wells

S. Niki, W.S.C. Chang, H.H. Wieder

Department of Electrical and Computer Engineering, Mail code R-007, University of California at San Diego, La Jolla, California 92093, USA

and

T.E. Van Eck

Lockheed Missiles and Space Co., Inc., 3251 Hanover Street, Palo Alto, California 94304-1191, USA

Strained-layer $\text{In}_x\text{Ga}_{1-x}\text{As}/\text{GaAs}$ multiple quantum well (MQW) structures with indium compositions of $0.15 \leq x \leq 0.28$ grown on GaAs by molecular beam epitaxy were investigated with the emphasis on their material characteristics intended for surface-normal electroabsorption modulators. The interposition of an appropriate buffer layer between the GaAs substrate and QW structure has made possible the growth of 30–80 period $\text{In}_x\text{Ga}_{1-x}\text{As}/\text{GaAs}$ MQWs with thicknesses of the strained layers well beyond the pseudomorphic limit. Optical investigations of such QW structures showed distinct exciton peaks and clear quantum confined Stark effect. An exciton absorption peak can be selected by changing the indium composition of the ternary alloy up to the wavelength of $\lambda = 1.08 \mu\text{m}$.

1. Introduction

Since Van Eck et al. [1] first observed the quantum confined Stark effect in 10-period pseudomorphically strained $\text{In}_{0.13}\text{Ga}_{0.87}\text{As}(100 \text{ \AA})/\text{GaAs}(150 \text{ \AA})$ quantum wells (QWs), a great deal of attention has been focused on the growth and fabrication of strained-layer $\text{In}_x\text{Ga}_{1-x}\text{As}/\text{GaAs}$ multiple quantum well (MQW) modulators [2–6] for the following reasons: (1) The GaAs substrate is transparent at the wavelength of the excitonic absorption in the $\text{In}_x\text{Ga}_{1-x}\text{As}/\text{GaAs}$ material system. (2) The wavelength of exciton lines can be tuned widely in the infrared spectrum range which can not be obtained in a common $\text{AlGaAs}/\text{GaAs}$ material system. (3) New coherent light sources have been developed in this wavelength range.

We have investigated during the past few years [4,7] $\text{In}_x\text{Ga}_{1-x}\text{As}/\text{GaAs}$ multiple quantum wells (MQWs) for surface-normal electroabsorption

(EA) modulator applications. The modulation depth and the operating wavelength are the most critical parameters for the device design in such applications. The modulation depth can be enhanced by increasing the number of QW period, and the exciton lines can be tuned to longer wavelengths by increasing the indium composition of the ternary alloy. However, both of these requirements impose growth of $\text{In}_x\text{Ga}_{1-x}\text{As}/\text{GaAs}$ MQWs well beyond the pseudomorphic limit.

This paper reports on the growth of 30–80 period $\text{In}_x\text{Ga}_{1-x}\text{As}/\text{GaAs}$ QWs ($0.15 < x < 0.28$) on a lattice-mismatched buffer layer by molecular beam epitaxy (MBE) and the characterization of their material properties determined primarily by means of absorption (AB) and EA spectroscopy, and transmission electron microscopy (TEM). The results obtained from AB and EA experiments made at room temperature will be discussed in terms of the linewidths of the exciton lines.

Cross-sectional images of the samples taken by TEM will be examined and compared with the results obtained from optical measurements.

2. Molecular beam epitaxial growth and device fabrication

Three different types of samples have been grown by conventional MBE on (100) oriented GaAs substrates at substrate temperatures between 500 and 530°C. Their detailed configurations are illustrated in figs. 1a–1c, and their growth parameters are listed in table 1. The substrates were precleaned prior to the MBE growths by a common cleaning process using an etching solution made of a $\text{NH}_4\text{OH}:\text{H}_2\text{O}_2:\text{H}_2\text{O} = 5:2:10$ mixture for sample 6 and a $\text{H}_2\text{SO}_4:\text{H}_2\text{O}_2:\text{H}_2\text{O} = 5:1:1$ mixture for the other specimens. The samples were rotated with an azimuth rotation speed of 18 rpm during the outgas and growth in the growth chamber. A 0.1–0.3 μm undoped GaAs buffer was grown before starting the growth of lattice-mismatched layers. A 20 s growth interruption was used between the growth of each QW layer for improving the surface smoothness [8]. A superlattice buffer which consists of 125 period $\text{In}_{0.13}\text{Ga}_{0.87}\text{As}(25 \text{ \AA})/\text{GaAs}(25 \text{ \AA})$ with the same indium concentration as the QW layers was used for samples 3 and 4. A 500 nm thick $\text{In}_{0.13}\text{Ga}_{0.87}\text{As}$

ternary alloy buffer and a 50-period $\text{In}_{0.25}\text{Ga}_{0.75}\text{As}(50 \text{ \AA})/\text{GaAs}(50 \text{ \AA})$ superlattice buffer were interposed between the GaAs substrate and QWs, followed by a 200 nm thick $\text{In}_{0.13}\text{Ga}_{0.87}\text{As}$ cap layer for sample 6. The cap layer of sample 6 was beryllium doped and those of the other samples were silicon doped with doping concentrations of $n(p) \sim (1-5) \times 10^{17} \text{ cm}^{-3}$. The ternary compositions and thicknesses of the epitaxial layers were determined nominally by reflection high energy electron diffraction (RHEED), and their thicknesses were calibrated by cross-sectional TEM.

p-i-n diodes with a ring-shaped electrode 300 μm inner diameter and 500 μm outer diameter were fabricated on such samples using standard photolithographic processes. Zn–Au metal contact was used for p-type substrates and Ge–Au contact for n-type substrates. Cr–Au contact was used for the cap layers. Each device was mesa etched to the substrate with a solution, $\text{H}_3\text{PO}_4:\text{H}_2\text{O}_2:\text{H}_2\text{O} = 8:1:1$ for electrical isolation. I – V traces of such diodes showed small leakage currents of less than 1 μA , under the electrical field of up to $F \sim 70$ –90 kV/cm.

3. Material properties

Optical properties of such QW structures were investigated by means of both AB and EA spec-

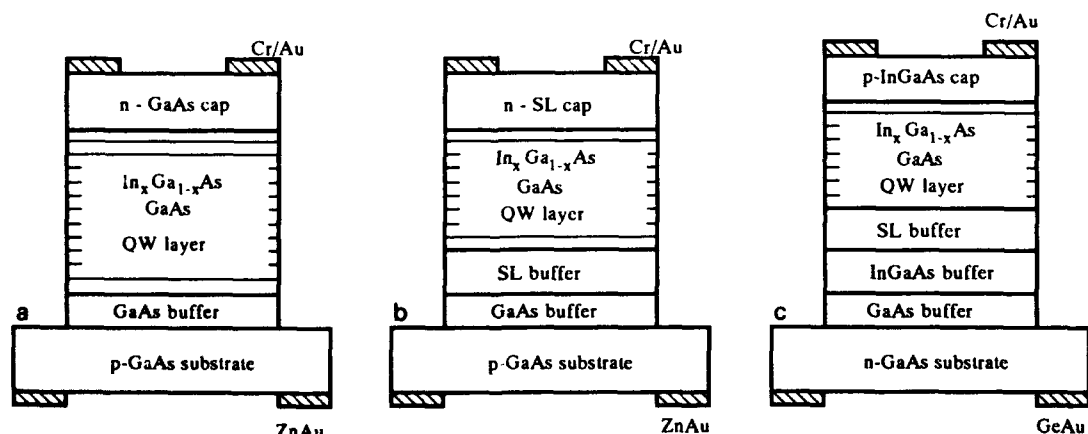


Fig. 1. Schematic diagram of $\text{In}_{1-x}\text{Ga}_x\text{As}/\text{GaAs}$ multiple quantum wells: (a) type 1 (samples 1, 2, and 5); (b) type 2 (samples 3 and 4); (c) type 3 (sample 6).

Table 1
Comparison of growth parameters and optical characteristics of strained-layer $\text{In}_{1-x}\text{Ga}_x\text{As}/\text{GaAs}$ multiple quantum wells

Sample No.	In composition	Periods	Well width (Å)	Barrier width (Å)	Buffer layer	Wavelength of exciton peak (μm)	Linewidth FWHM (meV)
1	0.15	80	120	120	None	0.993	14.0
2	0.19	80	120	120	None	1.021	23.6
3	0.15	50	120	120	SL	0.985	11.4
4	0.22	50	120	120	SL	1.035	16.4
5	0.15	50	100	100	None	0.962	13.4
6	0.25	30	100	100	Alloy + SL	1.058	18.0

troscopy made at room temperature. Monochromatic light was applied normal to the layers and the transmitted light was detected by a Si or Ge photodiode. The reflection from the surfaces and residual absorption in the substrate were subtracted from the raw signal by using a reference substrate.

A distinct exciton peak with a linewidth of 14 meV, which is comparable to those obtained from pseudomorphically grown QWs [9], was observed from sample 1. A smaller linewidth of 11.4 meV was obtained from sample 3. The linewidth of sample 2 is distinctly larger than those of the other specimens. A small linewidth is observed for sample 4 despite the larger lattice-mismatch. This suggests that a superlattice buffer may play an important role in the growth of strained $\text{In}_{1-x}\text{Ga}_x\text{As}/\text{GaAs}$ QWs. The linewidths of these exciton peaks are also listed in table 1.

The cross sectional images of the samples were obtained by means of TEM. It was found that misfit dislocations are created within the first few QW periods and no propagating dislocations are found in the remaining active layers of sample 1. TEM pictures of sample 2 show dislocations propagating throughout the QW layers, showing a poor crystalline quality. This result is consistent with that obtained from the optical characterization.

EA characteristics of the samples were measured by applying a DC reverse bias to a p-i-n diode fabricated from such structures. The linewidths of the exciton peaks as a function of electric field are shown in fig. 2. A severe linewidth broadening was observed with increasing of electric field for sample 2, but not for the other specimens. It is possible that the interface rough-

ness could cause the broadening of the exciton lines: However, no clear evidence of such surface roughness was obtained from the TEM pictures of sample 2. Therefore, we believe the broadening of the exciton lines is due to the enhanced scattering and/or greater tunneling probability with or via deep traps generated by dislocation loops.

The strained-layer superlattice buffers have successfully confined misfit dislocations at the superlattice/GaAs interface for sample 3 and 4. A cross-sectional image of sample 4 is shown in fig. 3. Therefore, most of the QW layers are elastically deformed. Since we have observed misfit dislocations, in-plane lattice constant of the epitaxial layers can be relaxed from that of GaAs. It implies that each $\text{In}_{1-x}\text{Ga}_x\text{As}/\text{GaAs}$ QW layer shares a strain in opposite directions, making possible the growth of the strained QW layer well above the pseudomorphic limit. However, the detailed information on such relaxation is lacking.

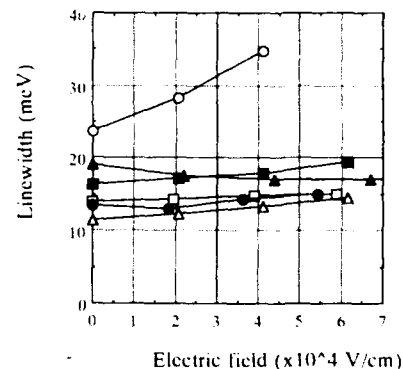


Fig. 2. Linewidths of the exciton peaks as a function of electric field. (□) sample 1; (○) sample 2; (△) sample 3; (■) sample 4; (●) sample 5; (▲) sample 6.

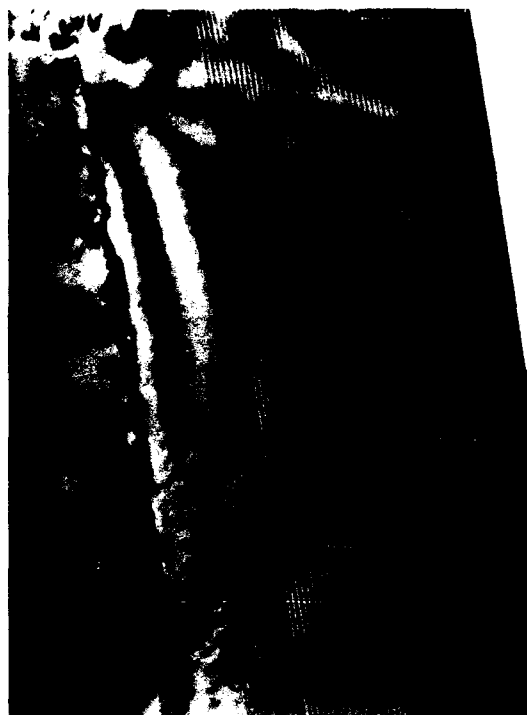


Fig. 3. A cross-sectional image of sample 4, by means of transmission electron microscopy.

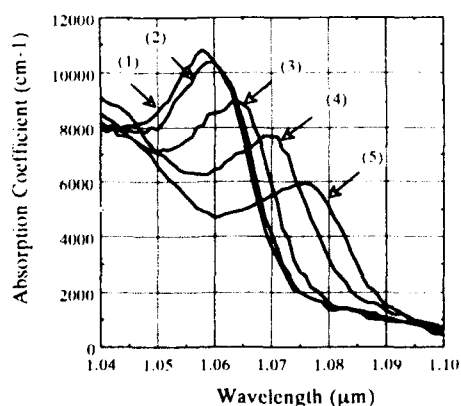


Fig. 4. Electroabsorption spectra obtained from sample 6: (1)–(5) correspond to electric fields of 0, 2.2×10^4 , 4.4×10^4 , 6.7×10^4 and 8.9×10^4 V/cm.

Similar QW structures as in type 2 with $x \geq 0.25$ were grown intended to shift the exciton line to longer wavelengths. However, no distinct exciton peak was observed. A bulk ternary alloy buffer, instead of the alternating strained layer, was introduced for relaxing the in-plane lattice constant of the epitaxial layer presumably up to the average of $\text{In}_x\text{Ga}_{1-x}\text{As}$ and GaAs for sample 6. It is theoretically predicted [10] that an alternating strained layer structure whose weighted strains are equal but opposite will remain commensurate if each layer is below the critical layer thickness limit. EA spectra obtained from sample 6 exhibit a large AB coefficient change of up to $\Delta\alpha = 5900 \text{ cm}^{-1}$ at $\lambda = 1.05\text{--}1.09 \mu\text{m}$ as shown in fig. 4. Similar QW structures as sample 6 with $x = 0.28$ also exhibit sharp exciton peaks at $\lambda \sim 1.08 \mu\text{m}$. TEM investigations on such a specimen with $x = 0.28$ show that misfit dislocations are confined in the ternary alloy layer [6]. The use of such a bulk ternary alloy buffer may provide a better balanced strain in each QW layer and/or provide more uniform spatial distribution of strain than using an alternating strained layer buffer.

4. Summary

$\text{In}_x\text{Ga}_{1-x}\text{As}/\text{GaAs}$ ($0.15 \leq x \leq 0.28$) multiple quantum wells were grown with the total thickness of the strained layer well above the critical layer thickness limit. The optical and electrooptic properties as well as the crystalline quality of such QW structures suggest potential applications for surface-normal EA modulators in the $0.9\text{--}1.1 \mu\text{m}$ wavelength range.

Acknowledgments

This work is supported in part by the Air Force Office of Scientific Research. We wish to thank J.C.P. Chang and Dr. A.J. Mardinly for taking TEM pictures, and A. Cheng for her cooperation in material growth and device fabrication.

References

- [1] T.E. Van Eck, P. Chu, W.S.C. Chang and H.H. Wieder, *Appl. Phys. Letters* 49 (1986) 135.
- [2] U. Das, P.R. Burger and P. Bhattacharya, *Cpt. Letters* 12 (1987) 820.
- [3] U. Das, Y. Chen, P.K. Bhattacharya and P.R. Berger, *Appl. Phys. Letters* 53 (1988) 2129.
- [4] S. Niki, H.H. Wieder and W.S.C. Chang, in: *Digital Optical Computing II*, Proc. SPIE, Los Angeles, CA, 1990, to be published.
- [5] T.K. Woodward, T. Sizer II, D.L. Sivco and A.Y. Cho, *Appl. Phys. Letters* 57 (1990) 548.
- [6] S. Niki, A. Cheng, J.C.P. Chang, W.S.C. Chang and H.H. Wieder, *Japan. J. Appl. Phys.*, to be published.
- [7] T.E. Van Eck, S. Niki, P. Chu, W.S.C. Chang, H.H. Wieder, A.J. Mardinly, K. Aron and G.A. Hansen, presented at the Quantum Wells for Optical and Optoelectronics, Topical Meeting, Salt Lake City, UT, 1989, paper WA 3-1.
- [8] K.H. Chung, P.R. Berger, J. Singh and P.K. Bhattacharya, *Appl. Phys. Letters* 51 (1987) 261.
- [9] D.A. Dahl, L.J. Dries, F.A. Junga, W.G. Opyd and P. Chu, *J. Appl. Phys* 61 (1987) 2079.
- [10] R. Hull, J.C. Bean, F. Cerdeira, A.T. Fiory and J.M. Gibson, *Appl. Phys. Letters* 48 (1986) 56.

Realization of sharp excitonic features in highly strained GaAs/In_xGa_{1-x}As multiple quantum wells grown on GaAs(100) substrates

Li Chen, K.C. Rajkumar, A. Madhukar, Wei Chen, S. Guha and K. Kaviani

Photonic Materials and Devices Laboratory, University of Southern California, Los Angeles, California 90089-0241, USA

The relation between the exciton linewidth and the quantum well width is studied for various In compositions in InGaAs/GaAs quantum wells. A region of minimum exciton linewidth is observed. Thick multiple quantum wells, grown in this minimum linewidth region, show sharp excitonic features when grown under RHEED determined optimized growth conditions. Ultrathin strained multiple quantum wells with good optical quality are realized by exploiting strain relief via growth on pre-patterned substrates.

1. Introduction

In_xGa_{1-x}As/GaAs multiple quantum wells (MQWs) grown on GaAs are of interest since their exciton transition energies lie in the transparent region of the substrate. Used as the active region in spatial light modulators (SLMs), this system gives more flexibility in geometry and processing than the AlGaAs/GaAs based SLMs. However, due to the presence of lattice mismatch, taking such advantage is hindered by the small critical thickness for defect generation. Efforts are devoted to realizing sharp excitonic features in these highly strained QWs. In this paper we show that sharp excitonic features can be achieved by a combination of quantum well design and MBE growth procedure. We first present results for single quantum well (SQW) exciton linewidth dependence on the well width and In composition and identify a region of linewidth minimum. Results for MQWs grown in this regime are then presented. Finally, the role of growth on pre-patterned substrates to further improve the optical properties is examined. Although due to space limitations only photoluminescence and optical transmission measurement results are reported here, this study included extensive structural examination via transmission electron microscopy and electrical examination via *C-V* measure-

ments. Readers are referred to ref. [1] for these results as well as good electro-modulation behavior observed on these samples.

2. Experimental

The samples were grown in the USC RIBER 32P MBE system on GaAs(100) substrates (either Cr-doped semi-insulating or Si-doped *n*⁺). Reflection high energy electron diffraction (RHEED) pattern and intensity behavior was monitored to determine the growth condition [2] (i.e., substrate temperature, growth rate, arsenic pressure and alloy composition) as well as to ensure their reproducibility, independent of the machine gauges, etc. This is absolutely critical to having confidence in comparisons made between different samples and interpretations of the underlying physics. The substrate temperatures used varied from 580 to 520 °C with increasing In content from 0.10 to 0.25 so as to maintain control on In composition since In desorption rate is a strong function of the temperature above 520 °C. The In composition typically varies ±1% across a 2 cm square wafer. The photoluminescence (PL) and PL excitation (PLE) measurements were performed with an Ar⁺ laser pumped Ti-sapphire laser, a Spex 1704 monochromator, and a LN₂ cooled Ge detector. For absorp-

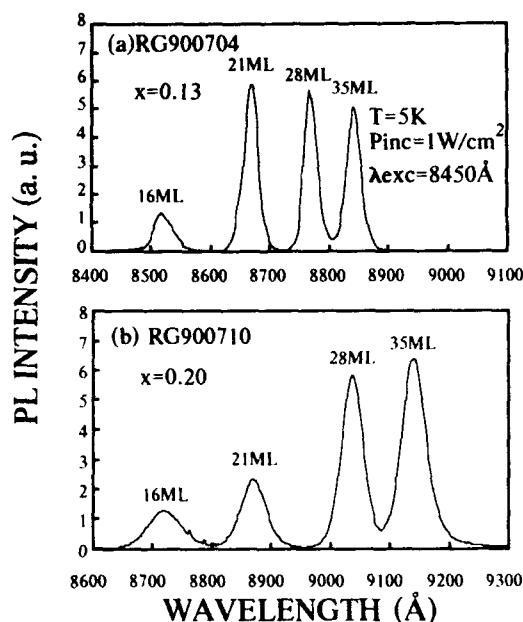


Fig. 1. 5 K photoluminescence from (a) sample RG900704 and (b) sample RG900710.

tion measurements, a halogen-tungsten lamp was used as the source and either a Si or Ge detector was used for detection

3. Results and discussion

In order to investigate the dependence of the exciton linewidth on the QW well width and In composition, samples containing multiple single quantum wells of different well widths were examined for different In compositions. Figs. 1a and 1b show the 5 K PL results on two typical samples (RG900704 and RG900710), each containing four SQW of well widths 16 monolayer (ML), 21 ML, 28 ML and 35 ML and In content 0.13 and 0.20, respectively. They were chosen to cover the range of practical value to quantum confined Stark effect (QCSE) devices and to be distributed evenly in both well width and exciton transition energy scale. The growth sequence is thin well to thick well in order to minimize the possibility of dislocations generated in one well propagating into the

subsequent wells. Very thick GaAs barriers of 180 ML are grown between SQW to prohibit electronic communication between wells. Such thickness is also found through RHEED studies to be adequate for recovering the surface to the same condition as the starting point of the previous wells.

In the PL measurements, the excitation energy of Ti-sapphire laser was tuned at 8450 Å, slightly below the GaAs bandgap and above all the QW exciton transition energies of interest. The excitation power was varied from 0.01 to 10 W/cm². The peaks are quite symmetric and remain unshifted under all excitation powers, indicating the excitonic nature of these transitions. The PL is found to be very efficient and is estimated to be 1 to 2 orders of magnitude more efficient than that from GaAs/Al_{0.3}Ga_{0.7}As SQW samples. Unlike the GaAs/AlGaAs QWs in which the exciton PL intensity is found to increase linearly or superlinearly with increasing power [3], it is found to increase sublinearly with increasing power in these InGaAs/GaAs samples. The linewidths remain almost constant for excitation power ≤ 1 W/cm² and start to increase beyond 1 W/cm², the behavior near the exciton tail changing faster than that at half maximum. The PL peak positions and full widths at half maximum (FWHMs) at an excitation power of 1 W/cm² are listed in table 1. These linewidths are generally amongst the narrowest found in the literature [4–6]. Note that there exists a minimum linewidth in the well width range studied. For the $x = 0.13$ sample (RG900704), this minimum linewidth is found to lie in a rather wide region, between 28 ML and 35 ML. This mini-

Table 1

The peak positions and linewidths (FWHMs) of sample RG900704 ($x = 0.13$) and sample RG900710 ($x = 0.20$) for 5 K photoluminescence of fig. 1

Well width (ML)	$x = 0.13$		$x = 0.20$	
	E (eV)	FWHM (meV)	E (eV)	FWHM (meV)
16	1.4553	6.3	1.3896	10.4
21	1.4296	4.6	1.3663	7.8
28	1.4137	4.2	1.3416	6.2
35	1.4018	4.3	1.3268	6.8

imum behavior becomes more evident at higher In composition as seen in sample RG900710 ($x = 0.20$) where the minimum is located at 28 ML. This behavior is different from the linewidth-well width relation previously reported for the GaAs/AlGaAs [6,7] and the InGaAs/GaAs [6] systems. The minimum linewidth of 4.2 meV for the $x = 0.13$ sample and 6.2 meV for the $x = 0.20$ sample is found to satisfy the $x(1-x)$ rule [8] closely, indicating that the alloy scattering contributes an important factor to the linewidth in this class of samples. This phenomenon can be understood by taking into account the interfacial and alloy scattering, as well as the possible degradation in growth front for thicker InGaAs layers. Since the primary focus of this paper is on the realization of the sharpest exciton features, the mechanism responsible for this line width behavior will be analyzed elsewhere [9].

Next we present results on the role of growth procedure in realizing good exciton features. Samples in the p-i(MQW)-n configuration were grown on substrates containing a region of square mesas of 10 to 20 μm linear size. The choice of the mesa size was motivated by a balance between effectiveness in intrinsic defect reduction in this In composition range as revealed by previous studies [10,11] and a usable size for a single pixel in a two-dimensional array of a SLM. Fig. 2 shows the room temperature absorption behavior of sample RG900420 (50 period In_{0.12}Ga_{0.88}As(35 ML)/GaAs(70 ML) MQW). Note that the QW well width is in the linewidth minimum region. The absorption coefficient is obtained by considering the thickness of the total active InGaAs layers. In the mesa region, the behavior is the average over the mesa and trench regions with the mesas occupying $\sim 13.5\%$ of the area since the beam size is approximately 0.5 mm² and the mesa size is 18 $\mu\text{m} \times 12 \mu\text{m}$. The slightly shorter wavelength of the exciton peak in the patterned area can be mostly attributed to the slightly lower In composition expected from the overall mapping of In composition in this sample. Based on our earlier studies [12], it is expected that the higher degree of homogeneous strain in the mesa region also contributes to this effect. The half width at half maximum (HWHM) of the exciton in the pat-

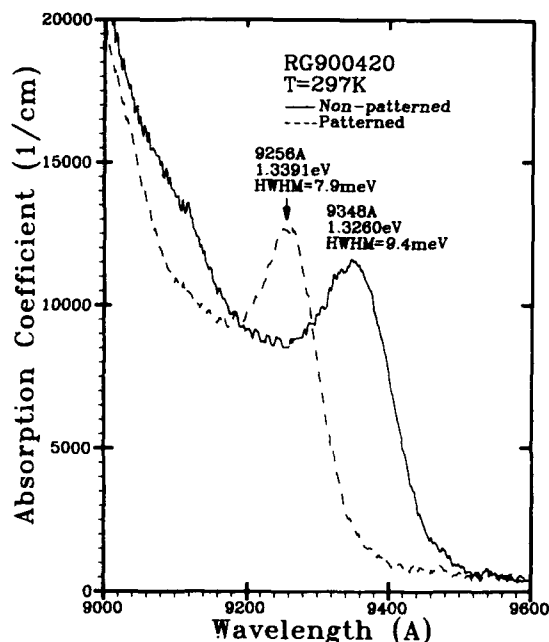


Fig. 2. The room temperature absorption behavior of a 50 period In_{0.12}Ga_{0.88}As(35 ML)/GaAs(70 ML) MQW (sample RG900420) from the non-patterned (solid curve) and patterned (broken curve) regions.

terned region is 7.9 meV, slightly narrower than the 9.4 meV HWHM in the non-patterned region. Though not discussed here, electro-absorption experiments reveal that these line widths are distorted by an inhomogeneous distribution of electric field across the MQW at zero bias [1]. The intrinsic HWHM obtained from these experiments is approximately 5.5 meV at room temperature and 2.5 meV at LN₂ temperature for the non-patterned region. These linewidths are generally comparable to or even narrower than those obtained earlier [13,14] for the much thinner 10 period similar structures, indicating the high quality of the MQWs in both patterned and non-patterned regions even for a total MQW thickness as high as 1.5 μm .

The advantage of growth on a pre-patterned substrate when the In composition is higher can be seen clearly in the following example. Fig. 3 shows the 5 K transmission behavior of sample RG891110 (100 period In_{0.20}Ga_{0.80}As(28 ML)/

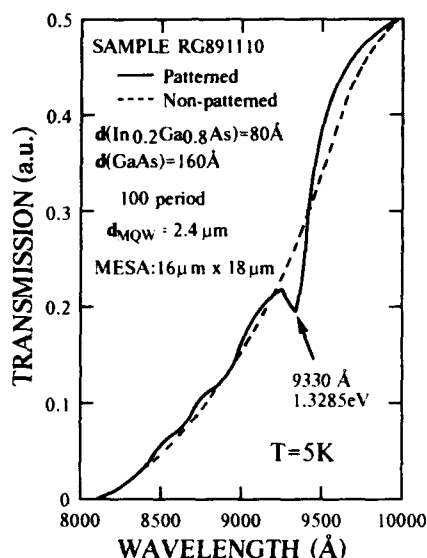


Fig. 3. Optical transmission behavior of sample RG891110 for the MQW in the non-patterned region (broken curve) and patterned region (solid). The first heavy hole-to-first confined electron (1hh-1e), light hole to first confined electron (lh-1e), and second heavy hole-to-second confined electron (2hh-2e) excitons are observed indicating high quality quantum wells on the mesas.

GaAs(56 ML)) from the non-patterned region (broken curve) and patterned region containing $18 \mu\text{m} \times 16 \mu\text{m}$ size mesas (solid curve). Note again that since the In composition is higher, the well width was decreased accordingly to meet the minimum linewidth requirement. While in the non-patterned region no excitonic features are observed, a sharp 1hh-1e excitonic transition can be clearly seen in the patterned region. Even the lh-1e and 2hh-2e transitions can be resolved. This finding clearly indicates the good quality of the MQWs grown on top of the mesas and is consistent with our XTEM studies [1,15] which showed that while a high density of defects, including threading dislocations, is present in the non-patterned region, the MQWs grown on the mesas contain much lower defect density.

4. Conclusions

In summary, the relationship between exciton linewidth and QW well width in GaAs/InGaAs quantum wells is studied for various In composition. A line width minimum is observed in the well width range of practical importance to QCSE based devices. Thick MQW samples, grown using RHEED determined growth conditions, with well width in this linewidth minimum region exhibit sharp excitonic features. The usefulness of growth on pre-patterned substrates in improving the optical quality of ultrathick strained MQW is demonstrated.

Acknowledgments

This work was supported by the AFOSR, ARO, and the URI on Integration of Optical Computing administered by AFOSR.

References

- [1] Li Chen, A. Madhukar, K.C. Rajkumar, Kezhong Hu and J.J. Jung, in: Proc. 20th Intern. Conf. on Physics of Semiconductors, Thessaloniki, 1990, Ed. J. Joannopoulos (World Scientific, Singapore, 1991).
- [2] P. Chen, J.Y. Kim, A. Madhukar and N.M. Cho, J. Vacuum Sci. Technol. B4 (1986) 890.
- [3] R.C. Miller, D.A. Kleinman, W.A. Nordland, Jr. and A.C. Gossard, Phys. Rev. B22 (1980) 863.
- [4] K.F. Huang, K. Tai, S.N.G. Chu and A.Y. Cho, Appl. Phys. Letters 54 (1989) 2026.
- [5] D.J. Arent, K. Deneffe, C. Van Hoof, J. De Boeck and G. Borghs, J. Appl. Phys. 66 (1989) 1739.
- [6] D.C. Bertolet, Jung-Kuei Hsu, K.M. Lau, E.S. Koteles and D. Owens, J. Appl. Phys. 64 (1988) 6562.
- [7] S.B. Ogale, A. Madhukar, F. Voillot, M. Thomsen, W.C. Tang, T.C. Lee, J.Y. Kim and P. Chen, Phys. Rev. B36 (1987) 1662.
- [8] E.F. Schubert, Z.O. Gobel, Y. Horikoshi, K. Ploog and H.J. Queisser, Phys. Rev. B30 (1984) 813.
- [9] Li Chen and A. Madhukar, unpublished.
- [10] S.V. Ghaisas and A. Madhukar, J. Vacuum Sci. Technol. B7 (1989) 264, and references therein.
- [11] S. Guha, A. Madhukar, K. Kaviani and R. Kapre, J. Vacuum Sci. Technol. B8 (1990) 149; see also Appl. Phys. Letters 56 (1990) 2304.

- [12] Li Chen, K.C. Rajkumar and A. Madhukar, Appl. Phys. Letters 57 (1990) 2478.
- [13] T.E. Van Eck, P. Chu, W.S.C. Chang and H.H. Wieder, Appl. Phys. Letters 49 (1986) 135.
- [14] J.Y. Marzin, M.N. Charasse and B. Sermage, Phys. Rev. B31 (1985) 8298.
- [15] A. Madhukar, K.C. Rajkumar, Li Chen, S. Guha, K. Kaviani and R. Kapre, Appl. Phys. Letters 57 (1990) 2007.

Observation of dark line defects in InGaAs/GaAs strained layer superlattices by photoluminescence topography

Kanji Iizuka, Takashi Yoshida, Toshimasa Suzuki and Haruo Hirose

Nippon Institute of Technology, 4-1 Gakuendai, Miyashiro, Minami-Saitama, Saitama 345, Japan

The behavior of dark line defects (DLDs) in molecular beam epitaxy grown InGaAs/GaAs strained layer superlattices (SLSs) has been studied by photoluminescence (PL) topography. The density of DLDs parallel to the [011] was larger than that of those perpendicular to the [011] and increased with increasing number of SLS periods. These DLDs were considered to be originated from the locally deformed lattices by the misfit stress. The relaxation model of stress in MBE-grown InGaAs/GaAs SLSs was proposed from the obtained results.

1. Introduction

The strained InGaAs/GaAs system has been actively studied in recent years because of its potential applications to electronic and optoelectronic devices [1]. This system was revealed to have a large number of dislocations caused by large lattice mismatches ($\sim 7\%$) [2]. Fitzgerald et al. [3] have observed scanning cathodoluminescence (CL) and transmission electron microscopy (TEM) images of AlGaAs/InGaAs/GaAs heterostructures and discussed the relation between the direction of the dislocations and the residual elastic strains.

Photoluminescence (PL) topography, which gives us information on spatial variations of PL emission using an image detector instead of measuring PL spectra, also enables us to characterize the nonradiative centers such as dark spots (DSs) or dark line defects (DLDs) [4]. We have been evaluating the crystallinity of various GaAs wafers and molecular beam epitaxy grown (MBE-grown) InGaAs/AlGaAs/GaAs multilayer or superlattice structures by PL topography [5,6].

In this study, the misfit strains in MBE-grown InGaAs/GaAs strained-layer superlattices (SLSs) with various superlattice periods and growth temperatures were characterized by PL topography.

Finally the relaxation mechanism of stress in this system was discussed.

2. Experimental

InGaAs/GaAs SLSs were grown by MBE using a Riber model MBE 2300 R&D system. Substrates were prepared from the indium-doped semi-insulating (100) GaAs wafers (EPD: 10^3 cm^{-2}). The growth temperature was varied from 500°C to 575°C . The SLS samples were composed of alternation of 70 \AA thick $\text{In}_{0.1}\text{Ga}_{0.9}\text{As}$

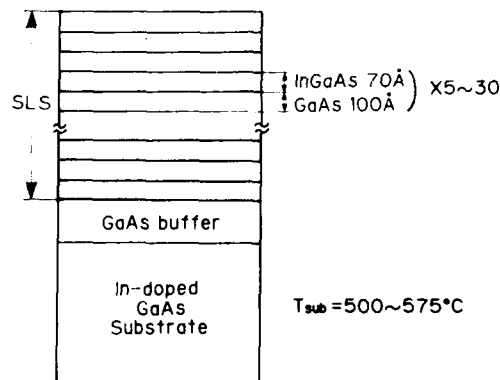


Fig. 1. A Schematic illustration of sample structure.

and 100 Å thick GaAs layers, and the related period was varied from 5 to 30 as shown in fig. 1. The thickness of each layer was controlled by observing reflection high energy electron diffraction (RHEED) intensity oscillation.

PL topography was carried out at the temperature about 50 K using an infrared Vidicon TV camera (Hamamatsu C-1965) where a cw krypton ion laser light (6471 Å, 600 mW) was used as an excitation source and an IR-80 high-pass filter was adopted to suppress the laser light and to observe the PL emission only.

3. Results and discussion

Fig. 2 shows the PL topograph patterns of the samples with various SLS periods at the substrate temperature: 550°C. The cross-stripe pattern of dark lines as seen in the figure was observed in all SLS samples. Similar patterns have also been observed by CL observations [1,2]. Such dark lines were not observed so far in a thicker layer (1 µm thick $\text{In}_{0.1}\text{Ga}_{0.9}\text{As}$); however, a cross-hatch pattern was revealed by Nomarski microscope observation on the surface. It was concluded that this pattern was caused by the misfit stress between GaAs and $\text{In}_{0.1}\text{Ga}_{0.9}\text{As}$ [6]. On the other hand, the cross-hatch pattern has never been observed on the surface of SLSs, although a similar pattern in the DLDs with a different density was observed by PL topography. This result suggests that the misfit stress in thick $\text{In}_{0.1}\text{Ga}_{0.9}\text{As}$ on GaAs will be relaxed by forming wrinkles on its surface, but that in SLSs by introducing some defects it is observed as dark lines.

The density of the DLDs was increased with increasing the number of the SLS period. The internal stress in the SLS structures is relaxed by the lattice relaxation of each layer whose thickness is thinner than the critical value [7]. The layer thickness of all $\text{In}_{0.1}\text{Ga}_{0.9}\text{As}$ layers was smaller than the critical value. Therefore we consider that we could take the standpoint that these DLDs were not caused by the misfit dislocation, but were caused by the misfit stress between the $\text{In}_{0.1}\text{Ga}_{0.9}\text{As}$ layers and the GaAs layers. However, PL topography observations indicate the difference in PL

aspects between misfit stress and dislocation qualitatively. In order to confirm this point, the cross section of the SLSs should be observed by transmission electron microscopy (TEM).

It is not known why we could observe the relaxation of the misfit stress by PL topography. We consider the direction of the DLDs. The DLDs were lines parallel or perpendicular to the [011] direction. The density of DLDs parallel to the [011] was about 400 lines/cm and it was larger than that of those perpendicular to the [011]. We think that this difference is caused by the growth mechanism of the layer on the surface. Asai [8] reported on anisotropic lateral growth in GaAs layers on (001) substrates and found that the fastest growth direction is the [110] and the slowest is the $\bar{[110]}$ direction. Therefore the progress of the [011] steps on the GaAs (100) surface in our case should be more preferential than that of the $\bar{[011]}$ steps. As a result, the surface stress in the [011] direction is relaxed in a shorter distance than in the $\bar{[011]}$ direction as the $\text{In}_{0.1}\text{Ga}_{0.9}\text{As}$ layers grow. This difference in the direction of the progress of steps corresponded well to the difference in the density of DLDs. We think that the $\text{In}_{0.1}\text{Ga}_{0.9}\text{As}$ lattice will be deformed locally by the compressive stress, as Grundmann et al. [9] reported from the results of double-crystal X-ray diffraction, and therefore the PL emission efficiency in the deformed region will be degraded to be observed as a DLD by PL topography.

If the generation of DLDs is dependent on the progress of steps, the behavior of DLDs should be changed by the growth temperature. Fig. 3 shows the change of the PL topograph pattern of the samples with 10 SLS periods when the growth temperature was varied from 500 to 575°C. When the growth temperature was 575°C, no stripe pattern was observed. This situation might be understood in such a way that the growth temperature was so high that the stuck indium atoms were eliminated from the surface, and, as a result, the superlattice structure was not completed. When the growth temperatures were lower than 550°C, the densities of the DLDs in the [011] and $\bar{[011]}$ directions were increased with decreasing growth temperature. For example, the density in the [011] direction was about 400 lines/cm at 550°C and it

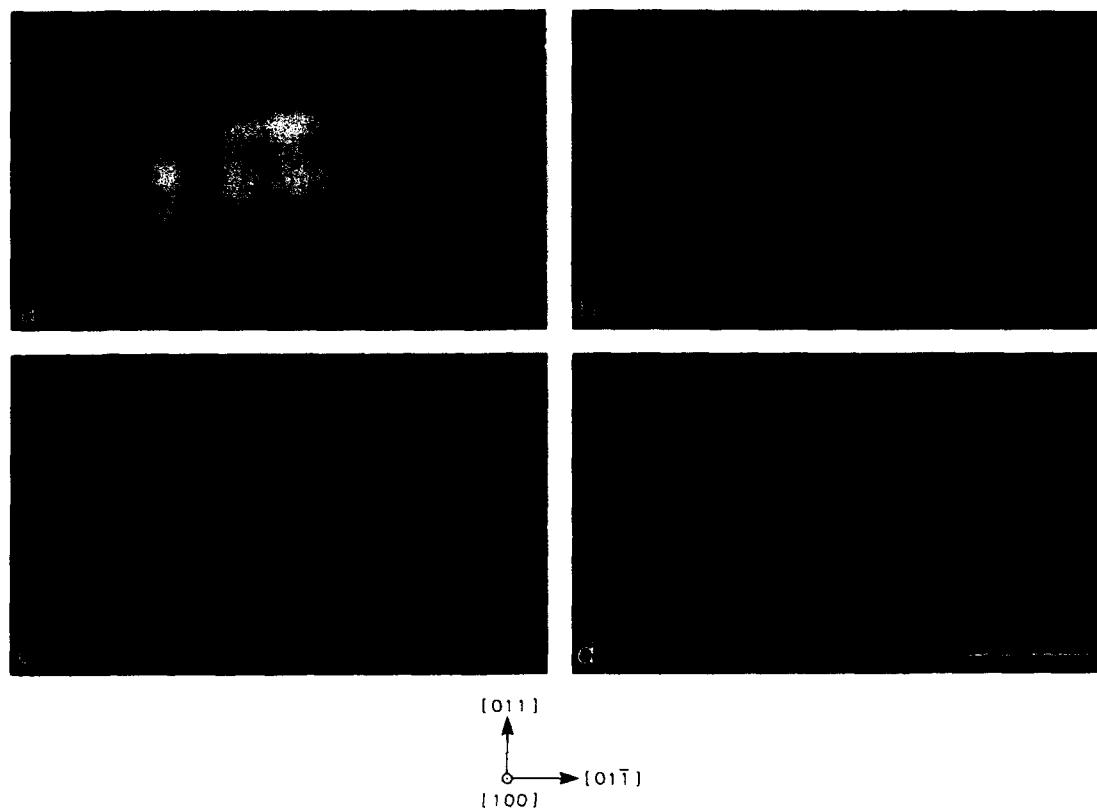


Fig. 2. PL topograph patterns from four MBE-grown $\text{In}_{0.1}\text{Ga}_{0.9}\text{As}/\text{GaAs}$ SLSs which have various superlattice periods: (a) 5 periods; (b) 10 periods; (c) 20 periods; (d) 30 periods. The substrate temperature was 550°C . Marker represents $100\ \mu\text{m}$.

was about 700 lines/cm at 500°C . We consider that this was caused by the change in the surface migration of the atoms. That is to say, the diffusion length is decreased with decreasing growth temperature, and the density of the DLDs, caused by the local relaxation of the misfit stress, was increased.

Here we propose a model for relaxation anisotropy of the stress in InGaAs/GaAs SLSs, as shown in fig. 4. The compressive stress is acting to the growing surface of the $\text{In}_{0.1}\text{Ga}_{0.9}\text{As}$ layer. This stress is accumulated with increasing layer thickness, and relaxed by deforming local lattices. But misfit dislocation will not be introduced because the thickness of the $\text{In}_{0.1}\text{Ga}_{0.9}\text{As}$ layers is thought to be thinner than the critical layer thickness. The lattice deformation in the $[011]$ direction is more

preferential than that in the $[01\bar{1}]$ direction, since the lateral growth rate has an anisotropy. In other words, the compressive stress is relaxed within a shorter distance in the $[011]$ direction than that in the $[01\bar{1}]$ direction, since the growth of steps in the $[01\bar{1}]$ direction is slower than in the $[011]$ direction. These locally deformed $\text{In}_{0.1}\text{Ga}_{0.9}\text{As}$ lattices are observed as anisotropic DLD patterns by PL topography.

4. Conclusion

InGaAs/GaAs SLSs with various periods and growth temperatures were grown by MBE and characterized by PL topography. Cross-stripe patterns were observed in all samples except in the

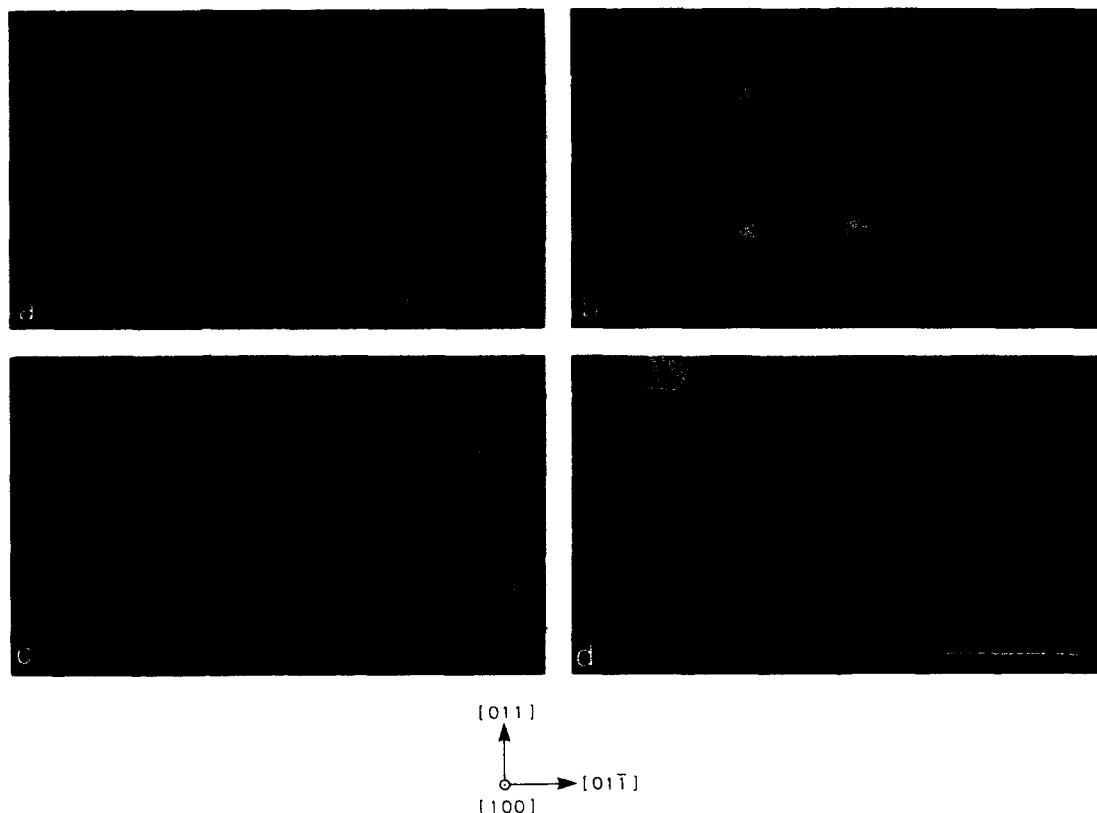


Fig. 3. Temperature dependence of the PL topograph patterns from MBE-grown $\text{In}_{0.1}\text{Ga}_{0.9}\text{As}/\text{GaAs}$ SLSs whose SLS period was ten. The growth temperature was: (a) 500°C ; (b) 525°C ; (c) 550°C ; (d) 575°C . Marker represents $100\ \mu\text{m}$.

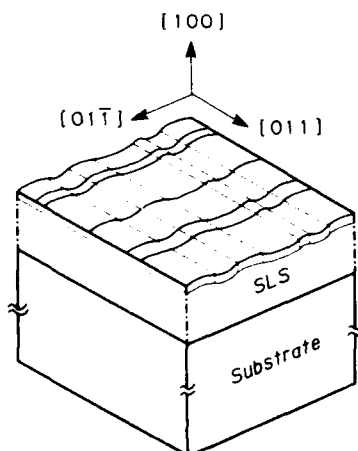


Fig. 4. A proposed model for the relaxation anisotropy of the stress in InGaAs/GaAs SLS.

one grown at 575°C . The density of the DLDs was increased with increasing SLS period and with decreasing growth temperature. The density of the DLDs parallel to the $[011]$ was about 400 lines/cm and it was larger than that of those perpendicular to the $[011]$. This difference was thought to be caused by the anisotropy in the growth rates of steps in $\text{In}_{0.1}\text{Ga}_{0.9}\text{As}$ layers. That is to say, relaxation of the misfit stress in the $[011]$ direction is more preferential than that in the $[01\bar{1}]$. This relaxation is accompanied with the deformation of the local lattices in the $\text{In}_{0.1}\text{Ga}_{0.9}\text{As}$ layers without introducing the misfit dislocations, because the thickness of the $\text{In}_{0.1}\text{Ga}_{0.9}\text{As}$ layer is thinner than the critical value. This lattice deformation results in the degradation of the efficiency of PL emission. As a result, this lattice deformation is ob-

served as DLD by PL topography. Finally, we proposed a relaxation model of the stress which explains sufficiently the relaxation of the stress in InGaAs/GaAs SLs.

References

- [1] I.J. Fritz, P.L. Dawson and J.E. Schirber, *Appl. Phys. Letters* 53 (1988) 1098.
- [2] A. Aydinli, M. Berti, A.V. Drigo, C. Ferrari, G. Salviati, F. Genova and L. Moro, in: *Proc. 14th Intern. Symp. on GaAs and Related Compounds*, Heraklion, 1987, *Inst. Phys. Conf. Ser.* 91, Eds. A. Christou and H.S. Rupprecht (*Inst. Phys.*, London-Bristol, 1988) p. 331.
- [3] E.A. Fitzgerald, Y. Ashizawa, L.F. Eastman and D.G. Ast, *J. Appl. Phys.* 63 (1988) 4925.
- [4] R. Ito, H. Nakashima and O. Nakada, *Japan. J. Appl. Phys.* 12 (1973) 1272.
- [5] K. Iizuka and T. Suzuki, in: *Proc. 2nd Intern. Symp. on Defect Recognition and Image Processing in III-V Compounds (DRIP II)*, Monterey, 1987, *Materials Science Monographs* 44, Ed. E. Weber (*Elsevier*, Amsterdam, 1987) p. 233.
- [6] K. Iizuka, A. Nomura, M. Hasobe and T. Suzuki, *Superlattices and Microstructures* 6 (1989) 13.
- [7] J.W. Matthews and A.E. Blakeslee, *J. Crystal Growth* 27 (1974) 118.
- [8] H. Asai, *J. Crystal Growth* 80 (1987) 425.
- [9] M. Grundmann, U. Lienert, D. Bimberg, A. Fischer-Colbrie and J.N. Miller, *Appl. Phys. Letters* 55 (1989) 1765.

The nature and control of morphology and the formation of defects in InGaAs epilayers and InAs/GaAs superlattices grown via MBE on GaAs(100)

S. Guha, K.C. Rajkumar and A. Madhukar

University of Southern California, Los Angeles, California 90089-0241, USA

Initial stages of molecular beam epitaxial (MBE) growth of highly mismatched $\text{In}_{1-x}\text{Ga}_x\text{As}/\text{GaAs}(100)$ have been studied by planar and cross-sectional transmission electron microscopy. For $\text{In}_{0.5}\text{Ga}_{0.5}\text{As}$ growth, we find drastic differences in morphology obtained by reducing the growth temperature from 475 to 420 °C. We also observe differences in morphology between alloy growth and short period superlattice $((\text{InAs})_n/(\text{GaAs})_m)$ ($m = 1$ monolayer, $n = 2$ monolayers) growth of equivalent effective composition. In the case of growth by formation of large islands, we present direct evidence of strain relief at the island edges and discuss defect formation in these islands.

1. Introduction

Technical exploitation of the lattice mismatched $\text{In}_{1-x}\text{Ga}_x\text{As}/\text{GaAs}$ ($x \geq 0.30$) is limited due to roughening of the growth front due to a change in the growth mode from 2D layer-by-layer to 3D islanding beyond a certain composition dependent thickness. Computer simulations show that a 3D growth mode is brought about by a strain induced anisotropy in interplanar cation migration [1]. A change in the growth mode also brings about a change in the observed defect structure with the introduction of a large number of threading dislocations [2,3]. Various schemes have been proposed in the literature that link the formation of threading dislocations with island growth and coalescence [1,2,4]. Recently, experimental work on $\text{In}_{1-x}\text{Ga}_x\text{As}/\text{GaAs}$ at low levels of mismatch strain ($\Delta a/a \leq 1.4\%$) point to benefits obtained in terms of defect reduction by growth on pre-patterned substrates [3,5,6]. However, this development appears to be beneficial only in the layer-by-layer growth regime, with no significant differences being observed between patterned and non-patterned regions once the mis-

match strain is high enough for 3D island growth to commence [3]. Provided one can maintain a layer-by-layer mode of growth even at high values of mismatch strain, one might expect defect reduction from patterning. Additionally, a layer-by-layer growth mode produces smoother interfaces – a necessity for interface sensitive devices such as resonant tunnelling diode (RTD) structures. For these reasons, our recent efforts have focussed on preserving a 2D layer-by-layer growth mode even for highly mismatched $\text{In}_{1-x}\text{Ga}_x\text{As}$ on GaAs(100) by controlling the attendant growth kinetics. Initial stages of InAs/GaAs growth have been studied earlier by a variety of techniques [7–9]. In particular, transmission electron microscopy (TEM) is a very powerful tool in studying the initial stages of growth and defect formation. Cross-section transmission electron microscopy (XTEM) has been used earlier in studying highly strained thin InAs/GaAs layers [10,11]. A study of the early stages of InAs/GaAs growth has been carried out by Glas et al. [12], where they have analysed different stages of growth under fixed growth conditions. In our case, the aim has been more in terms of varying the growth parameters and ob-

serving its effects on a fixed amount of growth. We present below the results of some TEM studies in this regard.

2. Experimental

Samples were grown by molecular beam epitaxy (MBE) in a Riber 32P system. Following growth of a suitable GaAs buffer layer on GaAs (100), $\text{In}_x\text{Ga}_{1-x}\text{As}$ ($x = 0.33$ and 0.5) layers with thicknesses between 7 monolayers (ML) and 15 ML were grown on different substrates at substrate temperatures of 420 to 520 °C and at group V to group III incorporation rate ratios of 1.5 to 5.0. The growth rate of $\text{In}_x\text{Ga}_{1-x}\text{As}$ was kept at 0.25 ML/s unless otherwise mentioned. In some samples the $\text{In}_x\text{Ga}_{1-x}\text{As}$ growth was covered by a 2 ML GaAs cap deposited at 0.125 ML/s. Planar and cross-section samples for transmission electron microscope (TEM) studies were prepared by mechanical polishing followed by Ar ion thinning. TEM studies were carried out in a Philips 420T microscope at 120 kV. High resolution electron microscope observations were carried out in an Akashi EM-002B microscope at 200 kV.

3. Results and discussion

Let us begin with the results on two samples each with 11 ML $\text{In}_{0.5}\text{Ga}_{0.5}\text{As}$ followed by 2 ML of GaAs cap grown at 475 °C (sample 1) and 420 °C (sample 2), respectively. The group V to group III incorporation rate ratio in both cases was 1.5. The RHEED patterns at the end of GaAs cap growth are shown as insets in figs. 1 and 3. Additionally, for (1) the pattern had turned metal stabilized after about 7.5 ML of $\text{In}_{0.5}\text{Ga}_{0.5}\text{As}$ growth with the appearance of quarter order streaks which subsequently vanished during the GaAs cap growth.

Fig. 1A shows a TEM (200) dark field cross-section image of sample (1). As expected from the spotty RHEED pattern, one observes the formation of large islands (typically 240 to 400 Å wide and 55 to 100 Å high). The compositional contrast obtained from the (200) image clearly shows the

islands joined laterally by a thin (about 6 ML) InGaAs layer, suggesting a Stranski–Krastanov growth mode. Fig. 1B is a (400) dark field cross-sectional image in which the white patches in the substrate below each island are strain contrast contours indicating deformation of the (100) planes below each island and implying a normal force exerted by the island on the substrate region below it. These strain fields are observed to extend to about 200 to 250 Å into the substrate below the interface. Similar deformations have been observed recently by Eaglesham and Cerullo for the Ge/Si(100) system [13]. Figs. 2A–2C are dark field micrographs of a set of islands taken with different $\mathbf{g} = \{022\}$ vectors in plan view (i.e. the electron beam is normal to the growth plane). One observes a large number of islands exhibiting a pair of bright and dark contrast lobes adjacent to one another. The bright-dark contrast switches on reversing \mathbf{g} (compare figs. 2A and 2B) and the line of demarcation between the bright-dark lobes is perpendicular to \mathbf{g} (compare fig. 2B with fig. 2C). The diffraction contrast behaviour observed is found to be consistent with a symmetric deformation of the $\{220\}$ lattice planes of the island and the substrate region adjacent to the island on either side of the central axis of the island. Glas et al. observed similar contrast behaviour in their TEM studies of InAs/GaAs [12] and inferred presence of deformations in the (100) substrate planes. However, apart from deformation of the substrate planes, one would expect a deformation of the planes in the island itself due to free expansion at its unconstrained lateral edges resulting in strain relief. This is demonstrated later in the paper. Note the fringing in larger islands (lateral dimensions ≥ 400 Å) suggesting a departure from coherence in these islands.

Fig. 3A shows a (200) dark field cross-sectional image of sample (2). A dramatic difference in growth morphology brought about by reducing the growth temperature to 420 °C is observed. Unlike sample (1), large scale islands are not observed. The growth front roughness at the end of the GaAs cap is within about 3 ML. The 2 ML GaAs cap appears to be discontinuously distributed laterally. Fig. 3B shows $\mathbf{g} = \{022\}$ plan view dark field images. One again observes black/white

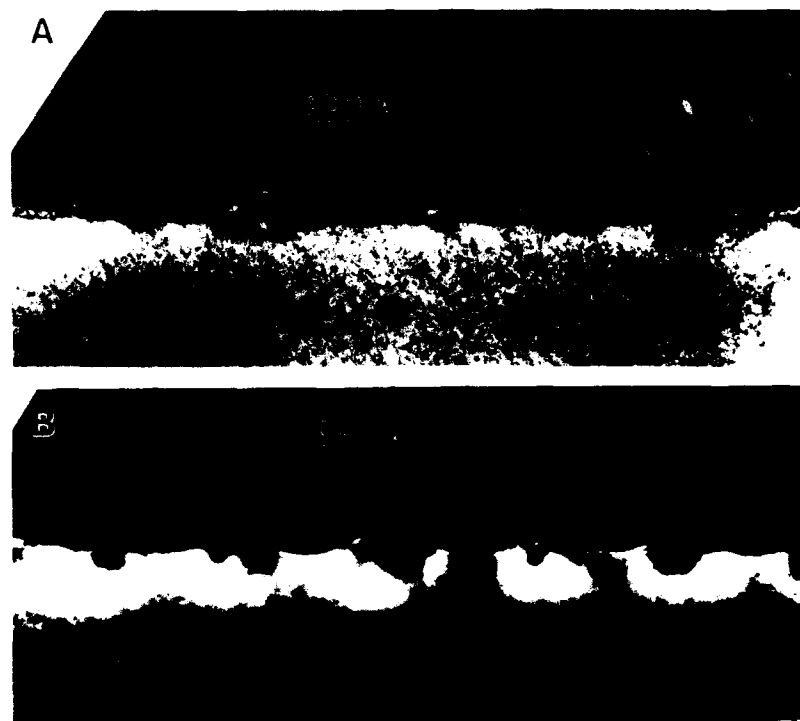


Fig. 1. Cross-sectional dark field images showing growth at 475°C of 11 ML $\text{In}_{0.5}\text{Ga}_{0.5}\text{As}$ followed by a 2 ML GaAs cap: (A) image with $g = (002)$ and (B) image with $g = (004)$. Inset shows RHEED pattern at the end of the cap growth.

strain contrast whose lateral extent indicates the lateral length scale of these islands to be $\leq 240 \text{ \AA}$, much smaller than for sample (1). The island

distribution appears to be about 3 times denser than sample (1). From the cross-section image one concludes that any InGaAs islands that are formed



Fig. 2. Plan view dark field micrographs with different $g = \{022\}$ reflections showing strain contrast exhibited due to islands for 11 ML $\text{In}_{0.5}\text{Ga}_{0.5}\text{As}$ followed by 2 ML GaAs cap grown at 475°C.

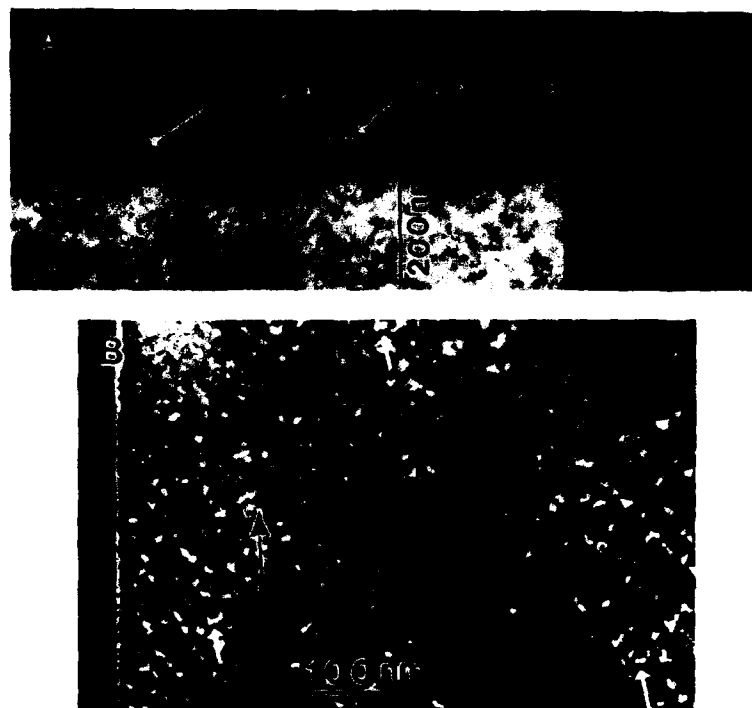


Fig. 3. Dark field micrographs showing the growth at 420 °C of 11 ML $\text{In}_{0.5}\text{Ga}_{0.5}\text{As}$ followed by a 2 ML GaAs cap: (A) $g = \{200\}$ cross-sectional image and (B) $g = \{022\}$ plan view image. Inset shows RHEED pattern at the end of the GaAs cap growth.

on top of the uniform InGaAs layer are not as well developed as those in sample (1) and are ≤ 3 ML in height. However, from the plan view micrographs we find clearly the presence of small islands indicating a Stranski–Krastanov growth

mode. Note also the presence of some very small features (a few are marked by white arrows in fig. 3B) which appear near island edges. We speculate that these may be very small dislocation loops appearing at island edges.



Fig. 4. (A) HREM image showing a coherent and defected island for the growth of 7 ML of $\text{In}_{0.5}\text{Ga}_{0.5}\text{As}$ on GaAs at 520 °C. (B) Plot showing variation of the $\{011\}$ lattice spacing (d_{011}) with distance from the interface d_{011} is normalized to d_{ref} , the spacing measured 85 Å below interface.

Fig. 4A shows a high resolution cross-sectional image of a sample in which 7 ML of $\text{In}_{0.5}\text{Ga}_{0.5}\text{As}$ was deposited at 520°C . In this case the RHEED pattern had turned spotty after 3 ML of growth indicating commencement of 3D island growth. The presence of islands which grew to heights of $\sim 80 \text{ \AA}$ and widths of $\sim 250 \text{ \AA}$ without defects (i.e. coherent) and larger incoherent islands is seen in fig. 4A. From HREM of coherent islands we have measured the spacing (d_{011}) of the {011} planes normal to the interface as a function of distance from the interface. The results are plotted in fig. 4B. d_{011} has been normalized to the spacing (d_{ref}) measured 85 \AA below the interface in the substrate. In order to ensure measurement accuracy, 29 lattice spacings in the lateral direction were averaged to obtain each d_{011} value. Thus we have averaged out any lateral variation of d_{011} . One clearly observes a relaxation of the d_{011} spacing in the islands. This is a clear and direct demonstration of lateral strain relief occurring at the island edge. For large islands we frequently observe that defects appear to be symmetrically introduced near either end of the growing island. In the defected island in fig. 4A, two stacking faults can be seen symmetrically near either end of the island. These are likely the consequence of partial dislocation half loop nucleation near the island edge. For a growing island there will be stress

concentrations for both the interfacial shear stress and the normal stress (along a direction that lies in the interfacial plane) components at the island edges. This would make the island edge the most likely site for defect incorporation.

Finally, we examine differences between alloy growth and growth of short period superlattice of equivalent effective composition. Two samples, one containing $(\text{InAs})_m/(\text{GaAs})_n$ ($m = 1 \text{ ML}$, $n = 2 \text{ ML}$) and another containing a straight $\text{In}_{0.33}\text{Ga}_{0.67}\text{As}$ alloy, both grown to a thickness of 15 ML, are discussed below. Note that the SLS corresponds to an averaged composition of $\text{In}_{0.33}\text{Ga}_{0.67}\text{As}$. Both samples were grown at 475°C . For the SLS, the InAs and GaAs growth rates were 0.23 and 0.26 ML/s, respectively, as the As:(In/Ga) incorporation rate ratios were 3.4 and 3.0. Following deposition of each cycle (i.e. 1 ML InAs and 2 ML GaAs), there was an interruption of 60 s under As_4 flux. For the straight alloy, the In flux was kept the same as the SLS and the Ga flux was increased to obtain an $\text{In}_{0.33}\text{Ga}_{0.67}\text{As}$ composition with a resulting growth rate of 0.69 ML/s. The group V to group III ratio in this case was 2.3. At the end of growth, the RHEED pattern from the SLS structure had turned to a "stubby" pattern (similar to inset in fig. 3) while for the straight alloy the pattern had remained streaky throughout. Fig. 5A shows a plan view

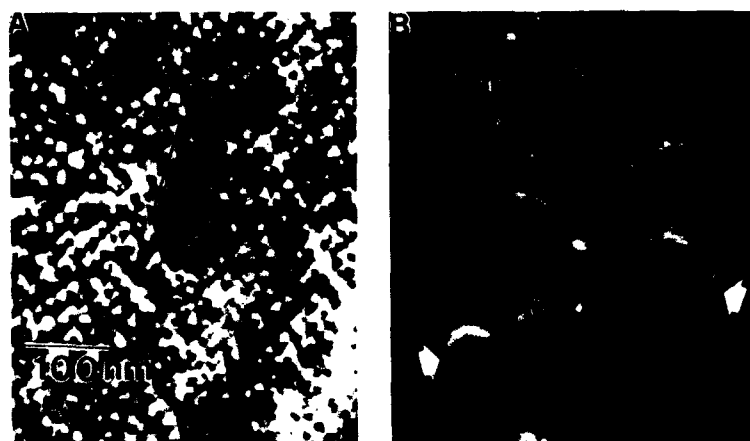


Fig. 5. Plan view {022} dark field micrographs showing: (A) the 5 period $(\text{InAs})_{1\text{ML}}/(\text{GaAs})_{2\text{ML}}$ SLS growth; (B) 15 ML $\text{In}_{0.33}\text{Ga}_{0.67}\text{As}$ growth.

dark field micrograph of the SLS sample. Typical island contrast of the type exhibited in fig. 2 is observed. The lateral dimensions of the islands vary from 150 to 180 Å. No defects are observed. Fig. 5B is a dark field plan view micrograph showing the $\text{In}_{0.33}\text{Ga}_{0.67}\text{As}$ alloy growth. The growth morphology appears to be quite different from the SLS case. The strain contrast effects appear on a much larger length scale (400 to 1400 Å). The TEM observations are consistent with the presence of islands/clusters that are relatively flat and have the above-mentioned lateral dimensions. Such flat and large islands are also consistent with the observation of a streaky RHEED pattern. From the dark field micrographs, the lateral strain fields appear to extend to about 150 Å. Again, no defects are observed. It should be mentioned here that we have recently been able to grow the SLS structure to thicknesses of 18 ML in a smooth layer-by-layer fashion by lowering the substrate temperature to 425°C [14].

4. Conclusions

In conclusion, we have carried out TEM studies of the initial stages of MBE growth of highly strained $\text{In}_x\text{Ga}_{1-x}\text{As}$ ($x = 0.33$ and 0.5). Under the operative growth rate and As_4 overpressure, we observe a drastic reduction in the extent of islanding for the growth of $\text{In}_{0.5}\text{Ga}_{0.5}\text{As}$ by reducing the growth temperature from 475 to 420°C. We present evidence for strain relief at island edges and, in a large number of cases, find defects generated near island edges. Finally, we compare the growth of a 5 period $(\text{InAs})_{1\text{ML}}/(\text{GaAs})_{2\text{ML}}$ SLS (resulting in an average composition of

$\text{In}_{0.33}\text{Ga}_{0.67}\text{As}$) with that of a straight $\text{In}_{0.33}\text{Ga}_{0.67}\text{As}$ alloy grown to the same thickness and find clear morphological differences between the two.

References

- [1] S.V. Ghaisas and A. Madhukar, J. Vacuum. Sci. Technol. B7 (1989) 264.
- [2] K.H. Chang, P.K. Bhattacharya and R. Gibala, J. Appl. Phys. 66 (1989) 2993.
- [3] S. Guha, A. Madhukar, Li Chen, K.C. Rajkumar and R. Kapre, in: SPIE Proc., Vol. 1285, Society of Photo-Optical Instrumentation Engineers, Bellingham, WA, 1990.
- [4] T. George, E.R. Weber, S. Nozaki, A.T. Wu, N. Noto and M. Umeno, J. Appl. Phys. 67 (1990) 2441.
- [5] E.A. Fitzgerald, G.P. Watson, R.E. Proano, D.G. Ast, P.D. Kirchner, G.D. Pettit and J.M. Woodall, J. Appl. Phys. 65 (1989) 2220.
- [6] S. Guha, A. Madhukar and Li Chen, Appl. Phys. Letters 56 (1990) 2304.
- [7] H. Munekata, L.L. Chang, S.C. Woronick and Y.H. Kao, J. Crystal Growth 81 (1987) 237.
- [8] W.J. Schaffer, M.D. Lind, S.P. Kowalczyk and R.W. Grant, J. Vacuum Sci. Technol. B1 (1983) 688.
- [9] F. Houzay, C. Guille, J.M. Moison, P. Henoc and F. Barthe, J. Crystal Growth 81 (1987) 67.
- [10] F.J. Grunthaner, M.Y. Yen, R. Fernandez, T.C. Lee, A. Madhukar and B.F. Lewis, Appl. Phys. Letters 46 (1985) 983.
- [11] M.Y. Yen, A. Madhukar, B.F. Lewis, R. Fernandez, L. Eng and F.J. Grunthaner, Surface Sci. 174 (1986) 606.
- [12] F. Glas, C. Guille, P. Henoc and F. Houzay, in: Microscopy of Semiconducting Materials 1987, Inst. Phys. Conf. Ser. 87, Eds. A.G. Cullis and P.D. Augustus (Inst. Phys., London-Bristol, 1987) section 2, p. 71.
- [13] D.J. Eaglesham and M. Cerullo, Phys. Rev. Letters 64 (1990) 1943.
- [14] R. Kapre, A. Madhukar and S. Guha, J. Crystal Growth 111 (1991) 1110.

Electrooptic effects of piezo-electrically strained AlGaAs/GaAs(111) quantum wells

S.M. Shank and G.W. Wicks

The Institute of Optics, University of Rochester, Rochester, New York 14627, USA

The electrooptic effects, electroabsorption and the electric field induced change in birefringence (electrobirefringence), have been measured in 100 Å (111) and (100) GaAs/AlGaAs quantum wells. It is determined that electrobirefringence at $\lambda = 1.06 \mu\text{m}$ is 43% larger in (111) quantum wells than in (100) oriented wells. The primary cause of this increased electrobirefringence of (111) oriented wells is the anisotropy of the effective mass of the heavy holes. The increased effective mass of the heavy hole in the (111) direction causes a larger quantum confined Stark effect, which causes larger electrobirefringence. A mass anisotropy for light holes is also observed. A second effect, the converse piezo-electric effect (electric field induced strain), exists in the (111) wells, and is an additional contribution to the difference between the electrooptic effects of the two orientations. The electric field dependent strain of the (111) wells shifts the exciton absorption features, as does the quantum confined Stark effect. Unlike the quantum confined Stark effect, however, the electrooptic effects induced by the converse piezo-electric effect should be dependent on the sign of the electric field. This dependence of the electrooptic behavior on the sign of the electric field has been observed in (111) quantum wells.

1. Introduction

Electrooptic effects in GaAs/AlGaAs quantum wells are of importance due to their potential for efficient electrooptic devices. There is interest as well in the investigation of fundamental effects that occur in this material system. The quantum confined Stark effect (QCSE) is the basic driving mechanism for many useful electrooptic effects of quantum wells, and has been thoroughly studied for epitaxial growth along the [100] crystal direction [1]. Intensity and phase modulators have been proposed and demonstrated using the electroabsorptive and electrorefractive properties of the QCSE [2,3]. Another important electrooptic effect is the electric field induced change in birefringence, which is termed electrobirefringence in this report. Electrobirefringence, which can be used to electrically control the rotation of the optical polarization, is caused by a difference in the electrorefraction of perpendicular polarizations. Electrobirefringence in GaAs/AlGaAs quantum wells has been previously investigated in (100) quantum wells [4]. It was found that the magnitude of the

electrobirefringence at a wavelength of $1.1523 \mu\text{m}$ is approximately equal to that of bulk GaAs.

Two studies have examined electrooptic effects of GaAs/AlGaAs lattice matched epitaxial growth along the [111] crystal direction. It has been experimentally shown that the electric field induced shift of the $n = 1$ heavy hole to electron transition (hh1-e1) is greater for (111) quantum wells than for (100) wells [5]. It has also been shown that the energy separation between the $n = 1$ light hole transition (lh1-e1) and that of the heavy hole (hh1-e1) transition is larger, and the heavy hole transition oscillator strength is greater, in (111) quantum wells [6]. Both experiments imply a heavy hole mass anisotropy, $m_{hh}^*[111]/m_{hh}^*[100] = 2.65$.

Electrobirefringence is primarily dependent on the rate of energy shift of the hh1-e1 transition and is less influenced by the shift of the lh1-e1 transition. This is due to the fact that the difference between the electrorefraction of two perpendicular polarizations is related to these polarizations' absorption coefficients through the Kramers-Kronig equation. The absorption coefficients for light polarized parallel to the plane of

the quantum well, α_{TE} , and perpendicular to the plane, α_{TM} , are used to define the birefringence through the relation

$$\Delta n_{TE}(\omega, V) - \Delta n_{TM}(\omega, V) = \frac{c}{\pi} P \int_{\omega_1}^{\omega_2} \frac{[\Delta \alpha_{TE}(\omega', V) - \Delta \alpha_{TM}(\omega', V)] d\omega'}{\omega'^2 - \omega^2} \quad (1)$$

The selection rules in quantum wells are such that the $hh1-e1$ transition affects both $\Delta \alpha_{TE}$ and $\Delta \alpha_{TM}$, however $hh1-e1$ affects only $\Delta \alpha_{TE}$. Thus the integrand in (1) and the electrobirefringence are dominated by the heavy hole exciton feature. The heavy hole mass anisotropy should therefore be a dominant influence on the crystal orientation dependence of the electrobirefringence.

There have also been several studies on electro-optic effects in strained quantum wells. It has been theoretically shown that, compared with that of a lattice matched (111) $Ga_{0.47}In_{0.53}As/Al_{0.48}In_{0.52}As$ quantum well, the $hh1-e1$ transition of a lattice mismatched (111) $Ga_{0.47}In_{0.53}As/Al_{0.70}In_{0.30}As$ quantum well shifts more rapidly with an applied electric field [7]. This is caused by an internal piezo-electric field, which occurs only in the mismatched [111] direction, due to the direct piezo-electric effect [8]. The strain induced piezo-electric field has been experimentally observed in (111) strained layer GaInAs quantum wells on GaAs substrates [9,10]. In either lattice matched or mismatched quantum wells grown on a (111) substrate, a related effect, the converse piezo-electric effect, must occur [8], but has not previously been reported. The converse effect produces an internal strain in response to an externally applied electric field along a piezo-electric direction, e.g. [111]. This electric field induced strain will influence the electronic and optical properties of the crystal as would any other type of strain, such as strain caused by external forces or by mismatched epitaxy. The converse piezo-electric effect will occur in both lattice mismatched as well as lattice matched materials, however it does not occur for electric fields applied along a [100] direction. Although the direct piezo-electric effect in GaAs quantum wells has been

reported, this is the first report of the converse piezo-electric effect in III-V quantum wells.

This report demonstrates that the heavy hole mass anisotropy and the converse piezo-electric effect cause the electrobirefringence in (111) AlGaAs/GaAs quantum wells to be enhanced over that of (100) wells. This is the first experimental study to compare the electrobirefringence of (100) and (111) quantum wells.

2. Experimental procedure

The samples examined in this study consisted of two 100 Å GaAs wells centered in the cores of leaky waveguides with AlGaAs cladding layers [11]. The structures were grown simultaneously by MBE on pairs of (100) and (111)B substrates. The growths occurred at temperatures of 620–650 °C with As_4/Ga beam equivalent pressure ratios of 34–44. The devices are contacted by etched mesas with 50 μm stripe widths. Light at $\lambda = 1.06 \mu m$ from a Nd-YAG laser is endfired into the leaky waveguide. Interaction of the quantum wells with only the lowest order mode of the waveguide is assured by the leaky waveguide structure. The incident polarization is at an angle 45° to both the growth axis and the plane of the quantum wells so that propagation is allowed for the lowest order TE and TM waveguide modes. The transmitted light is elliptically polarized due to the birefringence of the sample. The transmitted light passes through an analyzer and is incident on a silicon photodiode operated with synchronous detection. The magnitudes of the major (a) and minor (b) axes and the vertical (a_1) and horizontal (a_2) components of the ellipse are measured as a function of applied dc voltage across the quantum wells. The orientation (α) of the major axis of the ellipse relative to the horizontal axis is determined by

$$\tan(2\alpha) = \frac{2a_1a_2 \cos \phi}{a_1^2 - a_2^2} \quad (2)$$

and its phase (ϕ) by

$$\sin \phi = ab/a_1a_2 \quad (3)$$

where phase is defined by the electric field vector of the transmitted light.

$$E(x, y) = a_1 \cos(\omega t) \hat{x} + a_2 \cos(\omega t + \phi) \hat{y}. \quad (4)$$

Fig. 1 shows a typical ellipse measurement. The x and y components of eq. (4) are plotted at 0 and -15 V. The electrorefractive index is given by

$$\Delta n_{TE}(V) - \Delta n_{TM}(V) = \frac{\lambda}{2\pi} \frac{\Delta\phi(V)}{L}. \quad (5)$$

Three waveguide lengths of each orientation, (100) and (111)B, were examined, and electrorefractive index determined.

The measured electrorefractive index as a function of applied voltage is shown in fig. 2. The figure shows that the electrorefractive index at a reverse bias of 10 V is 43% larger in the (111) quantum wells than in the (100) wells. This increase is comparable to the 29% increase in the energy shift of the $n=1$ heavy hole transition in (111) wells measured by Kajikawa et al. [5].

The electrorefractive index data shown in fig. 2 were taken from samples grown at 620°C with an As_4/Ga beam equivalent pressure ratio of 34. The (111) samples exhibited very broad exciton absorption features which became unresolvable at a reverse bias of 5 V. Samples grown at 650°C with a beam equivalent pressure ratio of 44 had sharp exciton features for both (100) and (111) structures beyond -15 V. Despite these differences in the exciton absorption features, the electrorefractive

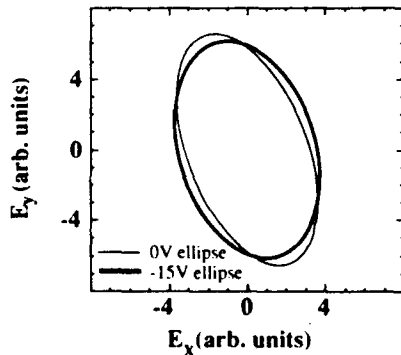


Fig. 1. Measured polarization ellipses of transmitted light through waveguide for a (111) quantum well. x and y components of the ellipse are plotted at 0 and -15 V.

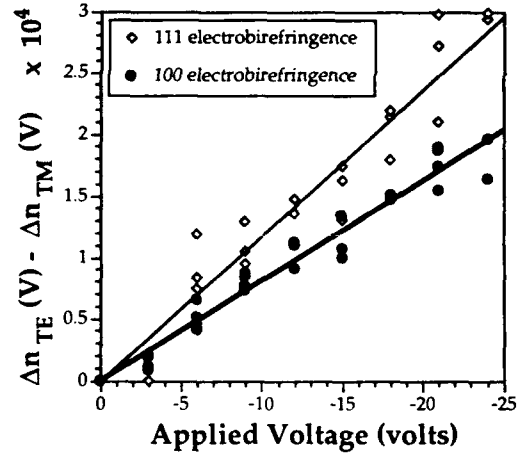


Fig. 2. Electrorefractive index data for (100) and (111) quantum wells. Data are fit linearly.

fringe was the same as the samples with broad excitons.

The converse piezo-electric effect was examined in three sample geometries, two (111)'s and one (100). The (111) samples were designed to be identical except for the sign of the applied electric field. The first (111) sample is identical to the

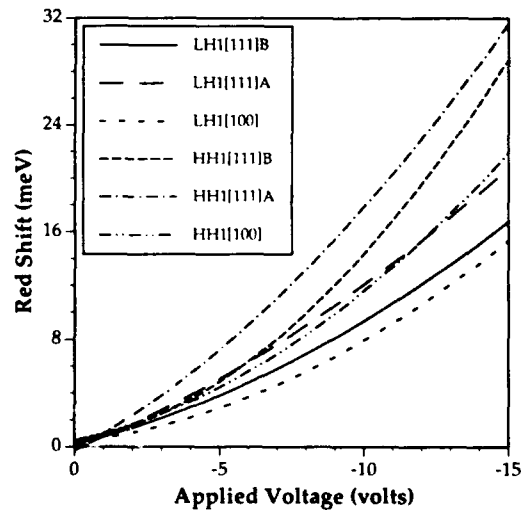


Fig. 3. Energy level shifts for (100), (111)A, and (111)B quantum wells. Quadratic fits of electroabsorption and photocurrent data of three samples for each sample geometry.

(111) sample used to measure electrobirefringence. An applied reverse bias on this diode is in the [111]A direction. A reverse bias on the second (111) diode produces an electric field in the [111]B direction. The third sample is grown on a (100) substrate and thus has an electric field produced by a reverse bias in a $\langle 100 \rangle$ direction. Fig. 3 shows the energy level shift versus applied voltage for the hh1-e1 and lh1-e1 transitions for samples 1, 2, and 3. For each sample geometry, three samples were measured. Photocurrent and electroabsorption spectroscopies were used to measure the energy levels of the two transitions as a function of applied voltage.

3. Discussion

Several predominant features stand out. The heavy hole transition of both (111) samples red shifts faster than the (100) sample. Since the rate of electrical field induced shift of the energy of a quantum well transition is roughly proportional to effective mass [12], this observation can be explained by the effective mass anisotropy of the heavy hole, as previously mentioned.

Additionally, the lh1-e1 transition of sample 1 red shifts as fast as the hh1-e1 transition of the (100) sample. Since the effective masses are quite different, $m_{hh(100)}^* = 0.34$ and $m_{lh(111)}^* = 0.094$ [13], this behaviour is not expected. One possible explanation could be that the thickness of the (111) quantum well is thicker than that of the (100) well. Since the rate of energy level shift is proportional to the well thickness to the fourth power [12], this would account for both the heavy hole and light hole transitions shifting faster for sample 1 than for sample 3. Using measured zero volt energy levels and a finite square well model, the well width difference between samples 1 and 3 is 1 Å. This difference will not cause such an effect. Also, the samples were grown at the same time, and although one might imagine slightly different gallium desorption rates for (111) and (100) substrates, a large difference in quantum well width seems unlikely. We therefore conclude that any difference in the well thicknesses of the two samples is not large enough to explain the above

observations. It is therefore proposed that the converse piezo-electric effect, which operates in the (111) samples, enables the lh1-e1 (111) transition to shift as fast as the hh1-e1 (100) transition. The strain which results from converse piezo-electricity can affect the electrooptic properties of quantum wells in two different ways. Strain can directly shift the valence band edges [14]. Additionally, strain alters the effective masses of the light and heavy holes [14], which will substantially influence the QCSE and its resultant electrooptic properties.

Also seen in fig. 3 is an anisotropy between the energy level shifts for (111) samples 1 and 2. Since the quantum confined Stark effect is not sensitive to the sign of the electric field, this observation must also be attributed to the converse piezo-electric effect.

4. Conclusion

The magnitude of electrobirefringence has been determined for (111) quantum wells, and it has been shown that at an applied reverse bias of 10 V, there is a 43% increase from that of (100) quantum wells. This makes the [111] crystal direction attractive for electrooptic device applications. An introductory study of the converse piezo-electric effect and its effects on the optical and electronic properties of quantum wells has also been presented.

Acknowledgements

This work is supported in part by a US Army Research Office graduate student fellowship, and in part by the New York State Center for Advanced Optical Technology.

References

- [1] D.A.B. Miller, D.S. Chemla, T.C. Damen, A.C. Gossard, W. Wiegmann, T.H. Wood and C.A. Burrus, *Phys. Rev. B* 32 (1985) 1043.
- [2] T.H. Wood, *J. Lightwave Tech.* 6 (1988) 743.

- [3] J.E. Zucker, T.L. Hendrickson and C.A. Burrus, *Appl. Phys. Letters* 52 (1988) 945.
- [4] M. Glick, F.K. Reinhart and G. Weimann, *Helv. Phys. Acta* 58 (1985) 403.
- [5] Y. Kajikawa, N. Sugiyama, T. Kamijoh and Y. Katayama, *Japan. J. Appl. Phys. Letters* 28 (1989) L1022.
- [6] T. Hayakawa, K. Takahashi, M. Kondo, T. Suyama, S. Yamamoto and T. Hijikata, *Phys. Rev. Letters* 60 (1988) 349.
- [7] D.L. Smith and C. Mailhot, *Rev. Mod. Phys.* 62 (1990) 173.
- [8] J.F. Nye, *Physical Properties of Crystals* (Clarendon, Oxford, 1957).
- [9] B.K. Laurich, K. Elcess, J.G. Beery, C. Mailhot and D.L. Smith, *Phys. Rev. Letters* 62 (1989) 649.
- [10] E.A. Caridi, T.Y. Chang, K.W. Goossen and L.F. Eastman, *Appl. Phys. Letters* 56 (1990) 659.
- [11] J.S. Weiner, D.A.B. Miller, D.S. Chemla, T.C. Damen, C.A. Burrus, T.H. Wood, A.C. Gossard and W. Wiegmann, *Appl. Phys. Letters* 47 (1985) 1148.
- [12] G. Bastard, E.E. Mendez, L.L. Chang and L. Esaki, *Phys. Rev. B* 28 (1983) 3241.
- [13] R.C. Miller, D.A. Kleinman and A.C. Gossard, *Phys. Rev. B* 29 (1984) 7085.
- [14] B.K. Ridley, *Quantum Processes in Semiconductors* (Clarendon, Oxford, 1982).

Growth and characterization of low temperature AlInAs

R.A. Metzger, A.S. Brown, W.E. Stanchina, M. Lui, R.G. Wilson, T.V. Kargodorian,
L.G. McCray and J.A. Henige

Hughes Research Laboratories, 3011 Malibu Canyon Road, M/S RL 61, Malibu, California 90265, USA

$\text{Al}_{0.48}\text{In}_{0.52}\text{As}$ lattice matched to InP and grown by MBE over a temperature range of 250 to 100 °C and under an As_4 pressure of 1×10^{-6} to 2×10^{-5} Torr has been investigated. Over this temperature range of 250 to 100 °C, resistivity decreases from 2×10^7 to 3×10^6 Ω cm while photoluminescence intensity decreases by two orders of magnitude. Resistivity showed little sensitivity to change in As_4 overpressure over the range investigated. Single crystal samples grown in the range of 100 to 150 °C showed nonstoichiometric excess As of up to 1.4% as determined by secondary ion mass spectrometry, and lattice expansion of 0.1% as determined by X-ray diffraction. Samples grown at temperatures greater than 200 °C showed no excess As or lattice expansion.

1. Introduction

$\text{Ga}_{0.47}\text{In}_{0.53}\text{As}$ and $\text{Al}_{0.48}\text{In}_{0.52}\text{As}$ lattice matched to InP are extremely useful for high-speed electronic and optical devices [1,2]. Device applications often require high resistivity, low lifetime material to act as buffers for electrical isolation and reduction of backgating and sidegating [3–5]. It has been demonstrated that these characteristics can be obtained using lattice matched materials grown at temperatures substantially below those of normal growth conditions [3–5]. We have investigated the properties of low temperature (LT) $\text{Al}_{0.48}\text{In}_{0.52}$ (AlInAs) material lattice matched to InP, grown by molecular beam epitaxy (MBE) and investigated as a function of growth temperature (100 to 250 °C) and arsenic overpressure, As_4 (1×10^{-6} to 2×10^{-5} Torr). This LT AlInAs has been evaluated using resistivity and breakdown voltage measurements, photoluminescence (PL) intensity, X-ray diffraction, and secondary ion mass spectrometry (SIMS).

2. Experiment

The epitaxial layers were grown in a Riber-2300 and Perkin-Elmer PHI-430 equipped with a 3 inch rotating substrate heater. Substrate temperatures

and beam equivalent pressures were set with a thermocouple and ion gauge. The growth rate was 600 nm/h. The native oxide of the InP surface was desorbed at approximately 500 °C under an As_4 overpressure where the desorption point was determined by reflection high-energy electron diffraction (RHEED) patterns. Specific details of the growth of AlInAs at normal temperatures (500 °C) are described elsewhere [6]. During the low temperature growth of AlInAs for these experiments, an As_4 overpressure was maintained during all substrate temperature ramps between low temperature and normal temperature growths – there was no interruption of As_4 overpressure. All samples grown are single crystal as determined by RHEED patterns and X-ray diffraction unless otherwise stated. Figs. 1a–c show the sample profiles grown to evaluate LT AlInAs resistivity and breakdown voltages (fig. 1a), PL and X-ray diffraction (fig. 1b), and SIMS (fig. 1c).

3. Results

3.1. Resistivity / breakdown voltage

It has been reported that low temperature growth of GaAs enhances both its resistivity and breakdown characteristics [4,5]. We wanted to de-

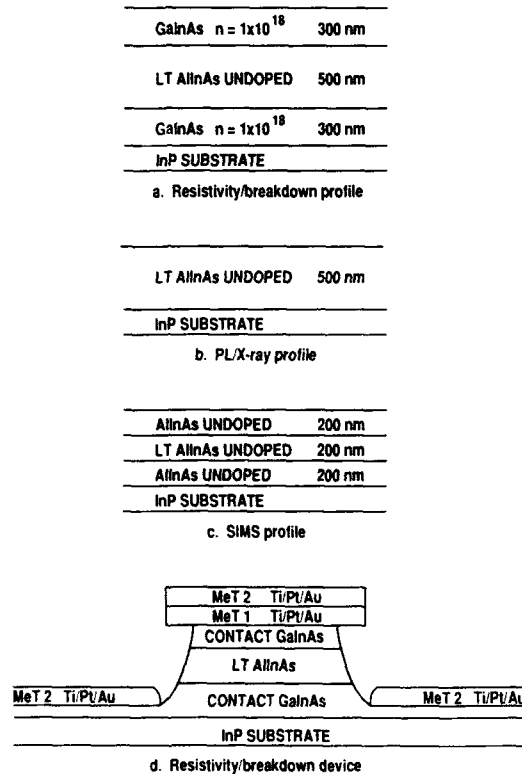


Fig. 1. Film profiles for measurement of (a) resistivity/breakdown voltage, (b) PL and X-ray, (c) SIMS, and (d) device structure for measurement of resistivity/breakdown voltage.

termine whether this was also true for LT AlInAs. We initially attempted to measure the resistivity of LT AlInAs films using the structure in (fig. 1b) by utilizing a conventional Hall measurement technique, but found that the resistivity measurements were limited to values of less than $10^3 \Omega \text{ cm}$ because of the parallel conduction path of interface states at the AlInAs-InP interface [7]. We therefore grew the structure shown in fig. 1a in which the resistivity can be determined by measuring the I - V characteristics in a serial (top to bottom) fashion, thereby eliminating the effect of interface parallel conduction. This structure also offers the advantage of determining the breakdown voltage of the LT AlInAs. The structure used to make this measurement is shown in fig. 1d. The LT AlInAs was 500 nm thick and differ-

ent samples were grown over a temperature range of 100 to 250 °C and under an As₄ pressure range of 1×10^{-6} to 2×10^{-5} Torr. The LT AlInAs was sandwiched between GaInAs contact layers which were heavily Si doped ($1 \times 10^{18} \text{ cm}^{-3}$) and grown at 500 °C to produce ohmic contact to the metallization while adding negligible resistance to the I - V measurement. Positive resist lithography was performed to open a dot pattern for the top contact (area = $8 \times 10^{-6} \text{ cm}^2$), Ti/Pt/Au (50 nm/50 nm/50 nm) was evaporated, and the resist lifted off in a solvent soak to produce a dot pattern. A mesa etch was performed (citric acid-hydrogen peroxide-water-phosphoric acid) using the metal dot as a mask, resulting in the undercut profile shown in fig. 1d. A blanket evaporation of Ti/Pt/Au (50 nm/50 nm/150 nm) was performed to form the bottom contact, self aligned to the top contact and electrically isolated from it due to the undercut of the mesa etch. The sample was annealed in forming gas at 300 °C for 1 min. Table 1 shows the results of both resistivity and breakdown as a function of growth conditions. The resistivity increases from 2.7×10^6 to $2.0 \times 10^7 \Omega \text{ cm}$ over the temperature range of 100 to 250 °C with a breakdown voltage in the range of 13–15 V which results in a breakdown field of $(2.6\text{--}3.0) \times 10^5 \text{ V/cm}$. A control sample was grown in which the AlInAs was grown under normal growth conditions (500 °C) and it demonstrated a resistivity of $1 \times 10^7 \Omega \text{ cm}$ which is equivalent to that of LT AlInAs grown at 250 °C.

Table 1
Resistivity/breakdown voltage as a function of growth temperature and As₄ overpressure

Temperature (°C)	As (Torr)	ρ ($\Omega \text{ cm}$)	V_{BD} (V)
100	5.0×10^{-6}	2.7×10^6	15
175	5.0×10^{-6}	3.5×10^6	13
250	5.0×10^{-6}	2.0×10^7	13
200	1.0×10^{-6}	2.2×10^6	13
200	5.0×10^{-6}	3.7×10^6	13
200	2.0×10^{-5}	1.1×10^6	11
500	5.0×10^{-6}	1.6×10^7	15
100 ^{a)}	5.0×10^{-6}	1.0×10^8	15

^{a)} Annealed at 550 °C for 1 h before top GaInAs contact.

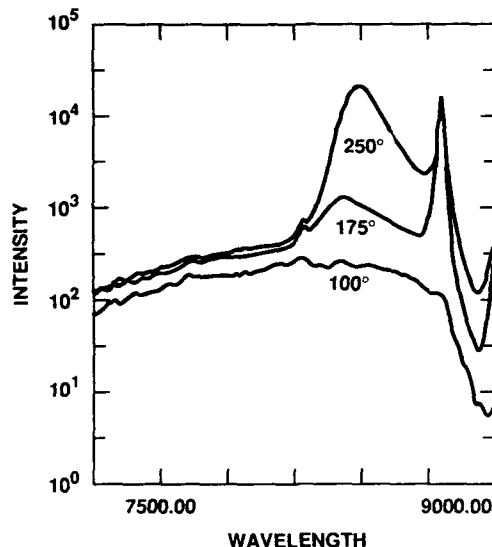


Fig. 2. Photoluminescence of 500 nm AlInAs grown at 100, 175 and 250 °C.

Unlike LT GaAs in which the resistivity increases rapidly as growth temperatures are decreased from 600 to 200 °C [5], this is not observed for LT AlInAs. Change in As_4 overpressure from 1×10^{-6} to 2×10^{-5} Torr does not produce any significant change in resistivity, but may show some slight degradation at the higher As_4 levels. No anneals were given to these LT AlInAs films other than the heating to 500 °C during the growth of the top GaInAs contact. A sample grown at 100 °C was given an additional anneal of 550 °C for 1 h while under an As_4 overpressure of 5×10^{-6} Torr, after the LT AlInAs growth, but before the final GaInAs contact layer, resulting in the highest observed resistivity of $1.0 \times 10^8 \Omega \text{ cm}$ and showing no degradation in breakdown voltage.

3.2. Photoluminescence

Photoluminescence (PL) done on 500 nm of LT AlInAs grown over a temperature range of 100 to 250 °C and under an As_4 overpressure of 5×10^{-6} Torr, and measured at 10 K, is shown in fig. 2. The sample grown at 100 °C is optically "dead", showing no detectable signal above background, in addition to not showing any PL response from

the InP substrate (890 nm). RHEED pattern and X-ray diffraction showed that this film was single crystal. Growth at 175 and 250 °C show intensity that is respectively one and two orders of magnitude greater than that of the 100 °C sample. Additionally, these samples do show signal from the InP substrate (890 nm). AlInAs grown at a temperature of 500 °C and under an As_4 overpressure of 5.0×10^{-6} Torr shows a peak intensity that is 10^4 times greater than that of the LT AlInAs grown at 250 °C. Therefore, over the growth range of 100 to 500 °C, the PL intensity response increases by approximately six orders of magnitude, illustrating that electron-hole recombination in AlInAs is extremely sensitive to growth temperature.

3.3. SIMS and X-ray

It has been reported that LT GaAs exhibits nonstoichiometric excess quantities of As, with samples that are grown at 200 °C showing excess As on the order of 1.0% as determined by Auger [5] and X-ray diffraction [8]. We have investigated this effect by using SIMS, from the structure shown in fig. 1C. Because this is a relative measurement (small changes in As concentration), the LT AlInAs is sandwiched between AlInAs grown at normal temperatures (500 °C), so that the change in As can be observed at the two interfaces. The SIMS was performed in a Cameca 4f SIMS instrument, detecting As negative secondaries, and using a 14.5 keV Cs primary beam with a current of 3.5×10^{-6} A and a raster of 250 μm . A large signal level was obtained (greater than 5×10^5 per channel) allowing statistically measurable variations in the As signal of 0.2%. Fig. 3 shows the resultant profile for growth at 140 °C, which exhibits excess As of 1.2%. Table 2 shows the excess As as a function of growth temperature. The spread in temperature range is due to spread in temperature calibration between the two MBE systems used (Riber-2300 and PHI-430) for these sample growths, with the resultant excess As values averaged over several samples in a given temperature range. For substrate temperatures below 100 °C, the samples were not single crystal as determined by RHEED patterns and

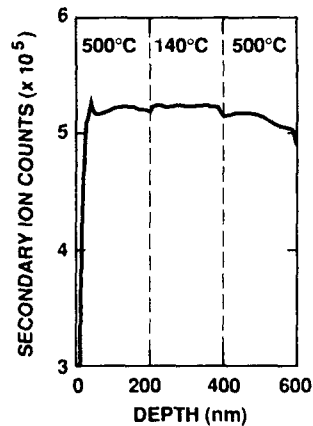


Fig. 3. Secondary ion mass spectrometry profile of As in AlInAs grown at 500 and 140 °C.

X-ray double crystal diffraction, and showed excess As greater than 3.0%. X-ray diffraction of unannealed samples showed no observable peak shift due to the excess As, but samples that had been annealed at 500 °C after growth, and under an As₄ overpressure of 1×10^{-6} Torr showed increasing compressive stress for increasing amounts of excess As, with lattice mismatch, f , approaching 1×10^{-3} for samples that maintained single crystallinity. Similar lattice mismatches have been seen in LT GaAs [8]. A possible explanation for this difference between annealed and unannealed samples may be because of the different location of As within the LT AlInAs as a result of those annealing conditions. It has been observed in LT GaAs that samples as grown at 200 °C show As uniformly distributed throughout the lattice, while after annealing, large As precipitates of 10 nm in diameter are observed by TEM [9]. It

is possible that this change in As structure as a result of annealing conditions may produce the different X-ray results that were observed here.

4. Conclusion

LT AlInAs has been grown over a temperature range of 100 to 250 °C and As₄ overpressures of 1×10^{-6} to 2×10^{-5} Torr. Resistivity and breakdown voltage were relatively constant over this temperature range, actually increasing by one order of magnitude from 2.7×10^6 to 2.0×10^7 Ω cm and then remaining constant up to normal growth temperatures (500 °C). As₄ overpressure showed no strong effect on resistivity. While the resistivity was not a strong function of growth temperature, the PL response was extremely sensitive to growth temperature, showing six orders of magnitude increases over a range of 100 to 500 °C. Both SIMS and X-ray diffraction measurements showed excess As present over the temperature range of 100 to 250 °C, with maximum excess As of 1.4% for single crystal samples grown just above 100 °C. Because this excess As distorts the lattice, inducing strain, it may be possible to grow single crystal AlInAs films with As in excess of 1.4% and at temperatures less than 100 °C, if the overall film thickness/strain product is kept beneath the critical level at which dislocations and subsequent polycrystalline growth occur [10].

References

- [1] A.S. Brown, U.K. Mishra, J.A. Henige and M.J. Delaney, J. Vacuum Sci. Technol. B6 (1988) 678.
- [2] Y. Kawamura, K. Wakha and H. Asahi, in: Proc. 12th Intern. Symp. on GaAs and Related Compounds, Karuizawa, 1985, Inst. Phys. Conf. Ser. 79, Ed. M. Fujimoto (Inst. Phys., London-Bristol, 1986) p. 451.
- [3] A.S. Brown, U.K. Mishra, C.S. Chou, W.E. Hooper, M.A. Melendes, M. Thompson, L.E. Larson, S.E. Rosenbaum and M.J. Delaney, IEEE Electron Device Letters EDL-10 (1989) 565.
- [4] F.W. Smith, C.L. Chen, G.W. Turner, M.C. Finn, L.J. Mahoney, M.J. Manfra and A.R. Calawa, in: IEDM Tech. Digest, 1988, p. 838.
- [5] F.W. Smith, A.R. Calawa, C.L. Chen, M.J. Manfra and L.J. Mahoney, IEEE Electron Device Letters EDL-9 (1988) 77.

Table 2

Excess As and lattice mismatch of LT AlInAs as a function of growth temperature for an As₄ overpressure of 5×10^{-6} Torr

Temperature (°C)	Excess As (SIMS) (%)	$f = \Delta a/a_0$ (X-ray)
< 100	> 3.0	Poly
100–150	1.4	8.1×10^{-4}
150–200	0.4	1.2×10^{-4}
200–250	0.0	0.0×10^{-4}

- [6] A.S. Brown, U.K. Mishra, J.A. Henige and M.J. Delaney, *J. Appl. Phys.* 64 (1988) 3476.
- [7] D. Look, University Research Center, Wright State University, Dayton, OH 45435, USA, private communication.
- [8] M. Kaminska, Z. Liliental-Weber, E.R. Weber, T. George, J.B. Kortright, F.W. Smith, B-Y. Tsaur and A.R. Calawa, *Appl. Phys. Letters* 54 (1989) 1881.
- [9] M.R. Melloch, K. Mahalingam, N. Otsuka, J.M. Woodall and A.C. Warren, *J. Crystal Growth* 111 (1991) 39.
- [10] J.W. Matthews and A.E. Blakeslee, *J. Crystal Growth* 27 (1974) 118.

Influence of nonuniform charge distribution in $\text{In}_{0.53}\text{Ga}_{0.47}\text{As}$ on the interpretation of dopant incorporation

Stefan P. Svensson, W.A. Beck, D.C. Martel, P.N. Uppal and D.C. Cooke

Martin Marietta Laboratories, 1450 S. Rolling Road, Baltimore, Maryland 21227, USA

The electrical properties of $\text{In}_{0.53}\text{Ga}_{0.47}\text{As}$ grown on full two-inch InP wafers have been studied. Special emphasis was placed on investigations of the vertical and lateral uniformity of the material quality. Using the Mobility Spectrum Technique, a way of unambiguously analyzing Hall effect data from samples with multiple conduction paths, a conducting substrate-epi interface layer was found in some $\text{In}_{0.53}\text{Ga}_{0.47}\text{As}$ films. Despite the presence of the interface layer, good, vertically uniform mobilities in n-doped samples were still measured in the film. A large-scale lateral nonuniformity in the sheet resistance was associated with variations in the interface layer. A 1.5 μm thick undoped $\text{In}_{0.53}\text{Ga}_{0.47}\text{As}$ layer with an $\text{In}_{0.52}\text{Al}_{0.48}\text{As}$ buffer layer exhibited a 77 K mobility of $65,100 \text{ cm}^2/\text{V}\cdot\text{s}$ with no sign of interface conduction. Some lateral nonuniformity in the sheet resistance similar to the doped sample was still observed, indicating that the substrate surface quality still affects the film quality to some degree. However, the lateral variations in films with AlInAs buffers are much smaller and are not expected to affect, e.g., modulation-doped structures.

1. Introduction

The material combination of $\text{In}_{0.53}\text{Ga}_{0.47}\text{As}$ and $\text{In}_{0.52}\text{Al}_{0.48}\text{As}$, which is lattice matched to InP, is attracting increased interest for use in modulation-doped field effect transistors (MODFETs). So far, the best low-noise transistor results have been obtained using this material combination [1]. In order to reach the same acceptance as GaAs-based MODFETs, the growth parameter tolerances of the structures on InP must be established. It should be possible to produce uniform, high quality structures without introducing significantly more calibration time or other preparation work before growth.

Historically, the problem with growth of $\text{In}_{0.53}\text{Ga}_{0.47}\text{As}$ has been the fact that it always turns out n-type, many times with a disappointingly low mobility. However, when looking at published growth conditions used to obtain good mobilities and low background concentrations, one observes a great spread in the data (see, e.g., refs. [2,3]). A certain degree of mismatch, particularly on the indium-rich side, can also be accommodated without serious degradation of the film [4–6]. This is encouraging in the sense that the

material must indeed be tolerant to wide variations in substrate temperature, flux ratios and growth rate. However, the fact that films with good mobilities are not always obtained points to the existence of other more dominant factors. In this paper we have studied the lateral uniformity of the sheet resistance across undoped layers, as well as the vertical uniformity through the film, and related these properties to the starting substrate surface.

2. Experimental

All material in this study was grown on full two-inch substrates mounted in In-free holders. Since we are reporting on the purity and uniformity of the $\text{In}_{0.53}\text{Ga}_{0.47}\text{As}$ we mention for reference that thick spacer MODFETs with GaAs channels grown in this system routinely exhibit 77 K mobilities above $200,000 \text{ cm}^2/\text{V}\cdot\text{s}$. The uniformity of the sheet resistance of any layers grown on GaAs substrates normally is excellent and near the 1% repeatability of the contactless probe (Tencor M-Gage).

The growth rate used was 1.5 $\mu\text{m}/\text{h}$. Oxide

desorption was done by heating the substrate in an As flux such that the temperature quickly reached 540°C and then dropped down to the growth temperature of 520°C. These numbers were obtained with an optical pyrometer, calibrated on GaAs according to the procedure developed by SpringThorpe et al. [7]. The group V/III beam equivalent pressure ratio was ~ 13 .

The wafers were analyzed using X-ray diffraction, electro-chemical capacitance-voltage ($C-V$) profiling (Polaron), and Hall effect with multi-carrier analysis capability.

The multi-carrier Hall effect analysis technique plays an important role in this investigation and will therefore be reviewed in some more detail. Its most generalized form, the Mobility Spectrum Technique [8], has been used to study many types of materials [8–11] and is useful for all systems in which the transverse elements of the conductivity tensor can be described by a (possibly continuous) sum of contributions, each with semi-classical magnetic field dependence, yielding the expressions [8]:

$$\sigma_{xx}(B) = \int_{-\infty}^{\infty} \frac{s(\mu) d\mu}{1 + (\mu B)^2}, \quad (1)$$

$$\sigma_{xy}(B) = \int_{-\infty}^{\infty} \frac{\mu B s(\mu) d\mu}{1 + (\mu B)^2}. \quad (2)$$

Here B is the magnetic induction (which, for simplicity, will be referred to as the magnetic field) and μ is mobility. $s(\mu)$ is a positive definite conductivity density function that is assumed to be independent of magnetic field and that includes the contributions of all of the parallel conduction paths.

The function of μ that is equal to the maximum conductivity contribution, and is consistent with σ_{xx} and σ_{xy} measured at a finite number of magnetic fields, is called the mobility spectrum. This can be calculated by a direct mathematical transform. It can be shown that if the sample contains N types of carriers, each with a single mobility, then the mobility spectrum generated from Hall data at at least $N + 1$ magnetic fields will consist of N sharp peaks whose position and amplitude correspond to the correct properties of the carriers.

If it is known that the sample contains N types of carriers, each with a single mobility, then we can restrict $s(\mu)$ to have the form:

$$s(\mu) = \sum_{i=1}^N S_i \delta(\mu - \mu_i), \quad (3)$$

so that the integrals in eqs. (1) and (2) collapse to sums. We can then use a conventional nonlinear least-squares fitting technique to extract more precise values for the carrier properties.

3. Results

Data from two particular $\text{In}_{0.53}\text{Ga}_{0.47}\text{As}$ films are reported on. The first sample was 1 μm thick grown directly on the InP substrate. The first half micron (closest to the substrate) of this film was undoped, and the second half micron was doped to $1 \times 10^{16} \text{ cm}^{-3}$ using Si. The other sample was 1.5 μm thick grown on top of a 0.25 μm thick $\text{Al}_{0.52}\text{In}_{0.48}\text{As}$ buffer layer.

In fig. 1, we show three-dimensional maps of the sheet resistance from the two samples. For $\text{In}_{0.53}\text{Ga}_{0.47}\text{As}$ grown directly on the InP substrate the lateral variations in the sheet resistance are generally significantly larger than when an AlInAs buffer layer is used (in this case 40% versus 10%). In addition the pattern of the variations is roughly reproduced on all wafers, indicating a substrate dependence.

When the mobility spectrum analysis was used, the sample grown without AlInAs buffer was found to have two conducting layers. Without this analysis method the Hall mobility from the film would have been measured to be around $6500 \text{ cm}^2/\text{V} \cdot \text{s}$ at 77 K. Stepwise etching was then performed on the sample to further demonstrate the usefulness of the Mobility Spectrum Technique. As can be seen in fig. 2 a single-carrier Hall effect model leads one to the incorrect conclusion that film quality improves monotonically with thickness since the mobility seems to increase, and the doping concentration decrease, away from the substrate. This behavior has been observed earlier [5,6] (and may indeed be representative of the true sample quality in some cases).

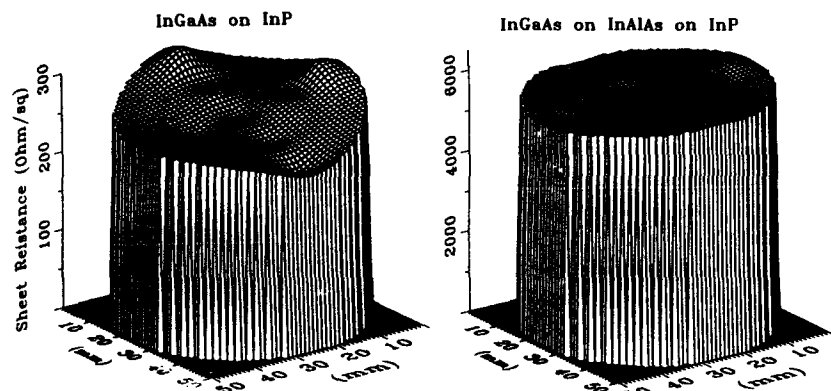


Fig. 1. Sheet resistance variations in two $\text{In}_{0.53}\text{Ga}_{0.47}\text{As}$ layers grown on InP. The sample at left hand is doped. The sample at right is undoped and also has an undoped AlInAs buffer layer.

The multi-carrier analysis gives a completely different view of the film quality. Fig. 3 shows the development of the mobility spectrum as the film surface is gradually etched away. We observe (i) a high-mobility component that maintains its mobility position but whose conductivity decreases and

(ii) a low-mobility peak that remains essentially unchanged throughout the etch sequence. Details of the mobility and carrier concentration from the two layers are shown in fig. 4. We can see that the charge concentration of the high-mobility component decreases linearly, with a slope corresponding

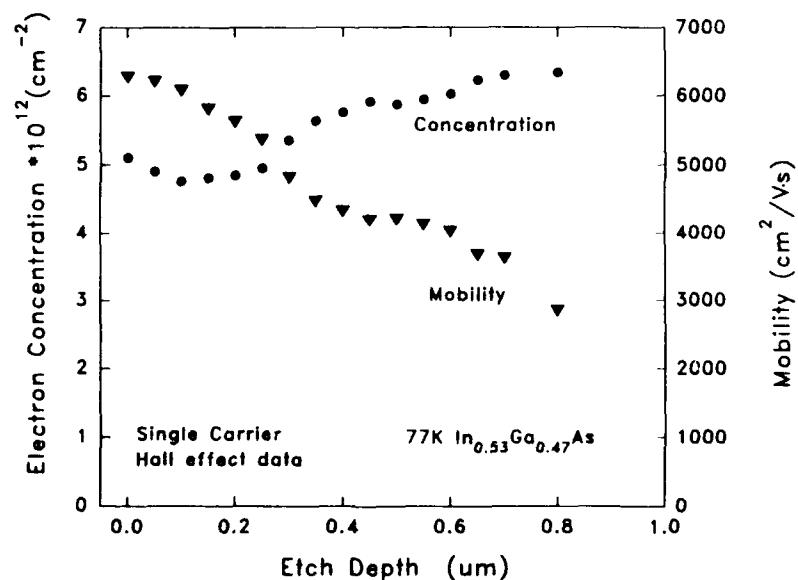


Fig. 2. 77 K Hall effect mobility and charge concentration as a function of etch depth. The results are interpreted with a single-carrier model which gives a false impression of continuously improving material quality towards the surface (see text).

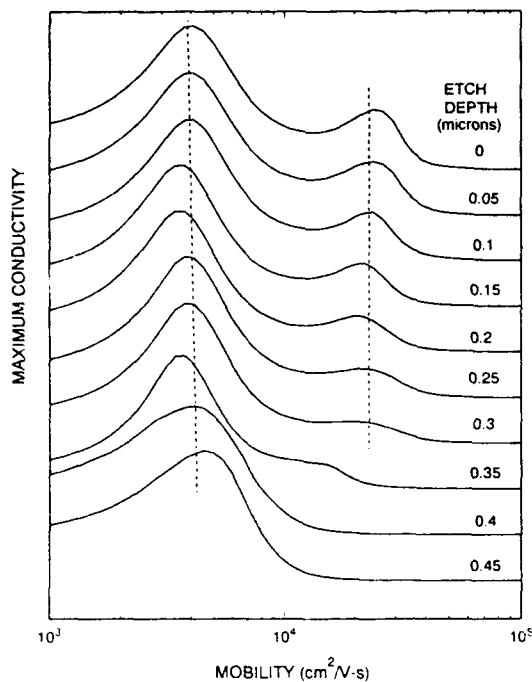


Fig. 3. 77 K mobility spectra recorded at each etch-step interval. Two carriers with distinctly different mobilities are observed initially. Note how the high-mobility component vanishes as the etch progresses.

to a bulk concentration of $1 \times 10^{16} \text{ cm}^{-3}$. These factors identify this component as the top $1/2 \mu\text{m}$ doped layer. The concentration and mobility of the low-mobility component, on the other hand, remain constant until the entire layer is removed. Thus the low-mobility peak could only have its origin at the solid-vacuum, or epi-substrate, interface. $C-V$ profiling confirmed the location to be at the substrate.

This analysis shows that vertically, the quality of the film is very uniform, apart from a layer at the substrate interface where a large concentration of charge resides. The mobility of $26,000 \text{ cm}^2/\text{V} \cdot \text{s}$ is quite respectable for a doping level of $1 \times 10^{16} \text{ cm}^{-3}$ as can be seen in fig. 5. The purity of the material grown in the system is further demonstrated by the mobility of the film with the AlInAs buffer. This layer exhibited only one mobility spectrum peak at $65,100 \text{ cm}^2/\text{V} \cdot \text{s}$ and a corresponding background concentration around 10^{15} cm^{-3}

(the exact number depends on the interface depletion width, which is unknown). To our knowledge this is the highest 77 K mobility reported for MBE-grown $\text{In}_{0.53}\text{Ga}_{0.47}\text{As}$.

Full Hall effect mapping of the wafers could not be done. However, samples taken at typical areas indicated that the main part of the difference in conductivity appeared to be in the interface layer. It is worth pointing out again that our high-mobility film with the AlInAs buffer also shows sheet resistance variations across the wafer, although with smaller variations.

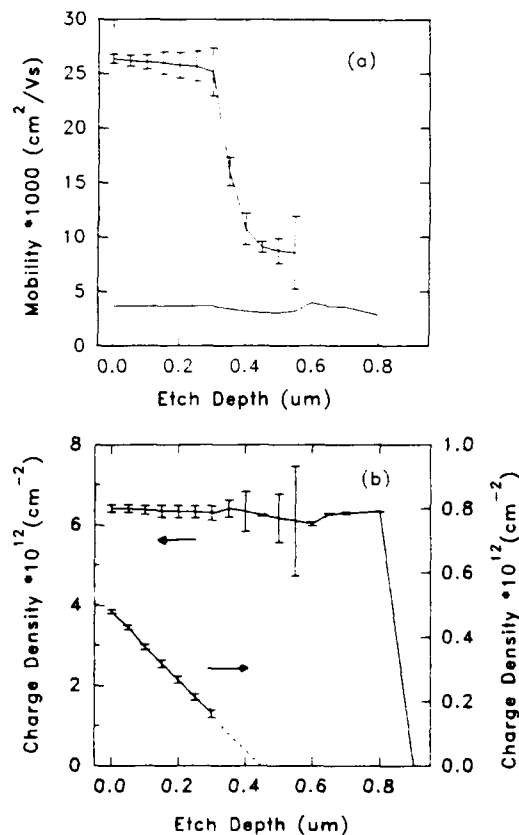


Fig. 4. (a) Two-carrier Hall mobility and (b) concentration data plotted as a function of etch depth. In the region between 0.35 and 0.55 μm , the mobilities are similar enough that correct separation into two components is not possible.

4. Discussion

The interface quality between the substrate and the epi-film obviously plays an important role in determining the quality of the rest of the layer. Our observations indicate that lateral variations in substrate surface quality affect the interface conduction. The magnitude of the variations can be quite large as was seen in fig. 1. However, even when a conducting interface layer is formed, films of good quality can be grown. The interface conduction can be largely eliminated by use of an AlInAs buffer layer, which is normally the case in devices, such as MODFETs. The origin of the interface charge could be either the background donors in the InGaAs or InAlAs layers or interface donor states (see, e.g., ref. [13]). It is less clear where exactly the electrons are moving. It is well known that an interface layer of InAs is formed on InP when it is heated in an As flux [14,15]. However, since the thickness of this layer is only one [15] or two [14] monolayers, one would not expect the quantum well that the layer forms to have a bound state near its bottom. This would be required if charge should be able to accumulate in the well. (We assume that the band lineup is close to $dE_c/E_g = 65\%$ and that the Fermi level is pinned close to mid-gap in the InP [16]. Based on Raman studies of InP surfaces prepared in different ways, Boudart et al. [17] have suggested that a conducting surface layer can be formed under

certain conditions on an otherwise semi-insulating wafer. The origin of such a layer and its relationship to the structure or composition of the InP surface is not understood at present. Further studies to resolve these issues are needed.

5. Summary

We have shown that conducting interface layers sometimes form between InGaAs films and InP substrates. The presence of such a layer was detected using the Mobility Spectrum Technique. The presence of a conducting layer did not seem to affect the quality of the epitaxial film. The development of interface layers can be minimized by use of an AlInAs buffer layer. The exact origin of the conducting layer is presently unknown.

References

- [1] K.H.G. Duh, P.C. Chao, P. Ho, A. Tessler, S.M.J. Liu, M.Y. Kao, P.M. Smith and J.M. Ballingal, in: IEEE Microwave Theory and Techniques Society Intern. Microwave Symp. Digest, 1990, p. 595.
- [2] T. Fujii, T. Inata, K. Ishii and S. Hiyaizumi, Electron. Letters 22 (1986) 191.
- [3] W. Lee and C.G. Fonstad, J. Vacuum Sci. Technol. B4 (1986) 536.
- [4] R.A. Kubiak, J.J. Harris and P. Dawson, J. Appl. Phys. 55 (1984) 598.
- [5] J.S. Whiteley and S.K. Ghandhi, Thin Solid Films 104 (1983) 145.
- [6] E.G. Scott, D. Wake, A.W. Livingstone, D.A. Andrews and G.J. Davies, J. Vacuum Sci. Technol. B3 (1985) 816.
- [7] A.J. SpringThorpe, S.J. Ingre, B. Emmerstorfer, P. Mandeville and W.T. Moore, Appl. Phys. Letters 50 (1987) 77.
- [8] W.A. Beck and J.R. Anderson, J. Appl. Phys. 62 (1987) 541.
- [9] C. Colvard, N. Nouri, D. Ackley and H. Lee, J. Electrochem. Soc. 136 (1989) 3463.
- [10] R.T. Huang, Y.Y. Tu, D. Kasemset, N. Nouri, C. Colvard and D. Ackley, J. Appl. Phys. 67 (1989) 550.
- [11] W.A. Beck, F. Crowne, J.R. Anderson, M. Gorzka and Z. Dziuba, J. Vacuum Sci. Technol. A6 (1988) 2772.
- [12] Y. Takeda, in: GaInAsP Alloy Semiconductors, Ed. T.P. Pearsall (Wiley, New York, 1982) p. 213.
- [13] M. Ogura, M. Mizuta, K. Onaka and H. Kukimoto, Japan. J. Appl. Phys. 22 (1983) 1502.

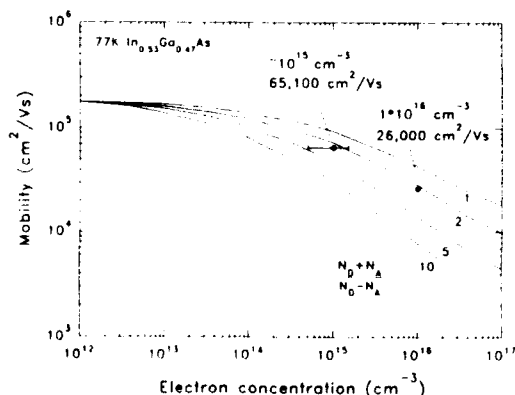


Fig. 5. Calculated [12] and measured mobility as a function of electron concentration.

- [14] J.M. Moison, M. Bensoussan and F. Houzay, *Phys. Rev.* 34 (1986) 2018.
- [15] J. Kanski, P.O. Nilsson, U.O. Karlsson and S.P. Svensson, in: *Proc. 20th Intern. Conf. on Semiconductors*, Thessaloniki, 1990, to be published.
- [16] J.M. Moison and M. Bensoussan, *Surface Sci.* 168 (1986) 68.
- [17] B. Boudart, B. Prevot, C. Schwab, E.V.K. Rao and R. Coquillé, in: *Proc. 6th Conf. on Semi-Insulating Materials*, Toronto, May 1990, in press.

Characterization of InGaAs and InAlAs layers on InP by four-crystal high resolution X-ray diffraction and wedge transmission electron microscopy

R. Houdré, F. Gueissaz, M. Gailhanou, J.-D. Ganière, A. Rudra and M. Illegems

Institut de Micro- et Optoélectronique, Ecole Polytechnique Fédérale de Lausanne, CH-1015 Lausanne, Switzerland

The indium desorption rates from InGaAs and InAlAs grown on InP substrates have been measured by wedge transmission electron microscopy as a function of the growth temperature. Desorption becomes significant at 545°C for both materials. No automatching effects could be observed under the growth conditions of the experiment. The bandgap of In_xAl_{1-x}As has been measured at 77 K as a function of the indium content. The composition and the strain have been measured by four-crystal high resolution X-ray diffraction with symmetrical (004) and asymmetrical (115 ±) Bragg reflections. The intrinsic bandgap follows the relation $E_g(x) = 2.774 - 2.411x$ and the strained material the relation $E_g(x) = 0.671 + 5.236x - 6.929x^2$.

1. Introduction

Despite the increasing interest in InAlAs and InGaAs alloys, some important parameters such as the bandgap energy versus indium content or indium desorption rate versus growth temperature (T_g) are still not fully established, especially for InAlAs. The purpose of this paper is to show that by using newly developed characterization techniques such as four-crystal high resolution X-ray diffraction (HRXD) or wedge transmission electron microscopy (WTEM), some of these parameters can be investigated.

All the samples used in the present study have been grown in a VG V80H solid source MBE system. Sumitomo InP {001} ± 0.5° oriented substrates were loaded with indium mounting and without any substrate preparation, as better results on modulation doped heterostructures have been obtained in our group with this procedure [1]. InAlAs was grown at a low V/III ratio (i.e. significantly lower than the ratio used for GaAs at a similar growth rate) and a high V/III ratio was used for InGaAs.

2. Wedge transmission electron microscopy (WTEM)

Perfect 90° wedges can easily be produced by cleavage along any {±110} planes. An image of the wedge along the [001] growth axis can thus be obtained at any chosen point of the wafer. The wedge is transparent to electrons over a distance of a few hundred ångströms. Observation is often done along, or close to, the [100] zone axis, i.e. with the epilayers running parallel to the incident beam. The WTEM technique is interesting in several aspects:

- the specimen preparation is fast, and only a few square millimetres of material are needed;
- the contrast interpretation is made easier due to the precise knowledge of the thickness of the observed area;
- artefacts due to conventional thinning process are avoided;
- buckling and strain relaxation effects are reduced because the substrate is not removed;
- the steep variation of thickness across the sample allows new possibilities to have information concerning the chemical composition of the layers.

For more details about WTEM, see, for example, ref. [2].

It is now well established that indium desorption from InGaAs or InAlAs becomes significant for T_g close to the usual growth temperature, but the published values range from 500°C up to 650°C [3,4]. We have measured the desorption rate as a function of T_g . The sample structure consists of 10 layers 1000 Å thick InGaAs (respectively InAlAs) separated by 100 Å InAlAs (respectively InGaAs) markers. T_g was increased by ~10 K at each step. WTEM has been used to obtain an accurate estimation of the epilayer thicknesses. With this procedure the entire desorption curve can be measured using only one sample, which eliminates discrepancy problems from one growth to another. The growth temperature was carefully monitored with a 0.95 μm IRCON Modline V pyrometer, which was calibrated against the melting point of InSb at 525°C and the oxygen desorption temperature of Ga₂O oxide from GaAs at 630°C. The temperature measurements were done with the group III shutters in the closed position in order to prevent parasitic reflection from the K-cells. The temperature was stable within ±2 K from the beginning to the end of each step. A typical WTEM picture is shown in fig. 1 and indium desorption curves versus T_g are shown in fig. 2 and fig. 3. From a practical point of view, significant desorption occurs at 545–550°C for both materials. This confirms the lowest values published for InAlAs. An Arrhenius plot



Fig. 1. Wedge transmission microscopy of a structure consisting of ten 1000 Å thick InGaAs (respectively InAlAs) layers separated by 100 Å InAlAs (respectively InGaAs) markers. [310] zone axis, bright field, 300 kV. Marker represents 500 nm.

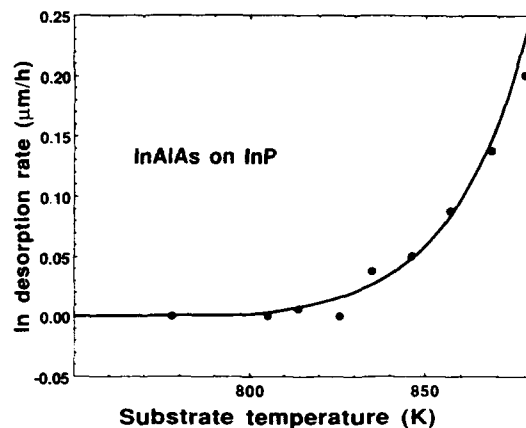


Fig. 2. Indium desorption rate of InP lattice matched InAlAs versus growth temperature.

gives an activation energy of 3.15 eV (respectively 5.2 eV) for InAlAs (respectively InGaAs). These values must not be interpreted as representing the binding energies of indium on the surface. Corrections have to be made because the indium coverage at the surface is not kept constant from one step to another. Moreover, as T_g is increased, the arsenic coverage decreases, which may affect the indium desorption [5].

Automatching effects have been reported [4] on InAlAs for growth conditions where indium desorption occurs. We have studied this effect using

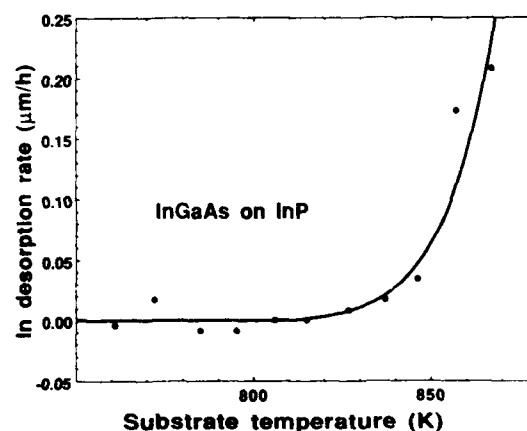


Fig. 3. Indium desorption rate of InP lattice matched InGaAs versus growth temperature.

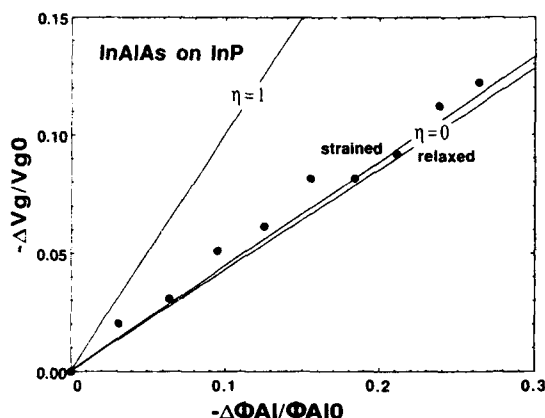


Fig. 4. Growth rate relative variation versus aluminium incident flux relative variation for InAlAs on InP. The straight line comes from theoretical calculations, $\eta=1$ is for automatching conditions, $\eta=0$ is for constant Indium sticking coefficient. The $\eta=0$ condition is calculated assuming the InAlAs is relaxed or strained on the InP substrate.

the technique described above with similar structures grown at ~ 550 – 560°C , but now decreasing the aluminium incident flux in several steps. The incident indium flux is maintained constant; we assume that the aluminium sticking coefficient is unity. We define two cases: (i) $\eta=0$ if no automatching occurs, i.e. the indium sticking coefficient is constant; (ii) $\eta=1$ if automatching occurs, i.e. the indium sticking (S_{In}) coefficient adjusts itself in order to keep the composition equal to the lattice matched one. The growth rate is given by the relation

$$V_g = 4k(y) (S_{\text{In}}\Phi_{\text{In}} + \Phi_{\text{Al}}).$$

where Φ_{In} (respectively Φ_{Al}) is the indium (respectively aluminium) incident flux and $k(y)$ represents the volume of the strain or relaxed unit cell. Φ_i^0 are the corresponding values under lattice matching conditions. The relative variation of the growth rate with varying aluminium flux is then given by:

if $\eta=1$, then

$$\frac{\Delta V_g}{V_g^0} = \frac{\Delta \Phi_{\text{Al}}}{\Phi_{\text{Al}}^0};$$

if $\eta=0$, then

$$\frac{\Delta V_g}{V_g^0} = \frac{\Delta k(y)}{k(y_0)} + (1 - y_0) \frac{k(y)}{k(y_0)} \frac{\Delta \Phi_{\text{Al}}}{\Phi_{\text{Al}}^0}.$$

The relative variation of the growth rate is plotted as a function of the relative variation of the aluminium flux in fig. 4. The slope of the data points closely follows the behaviour calculated for the $\eta=0$ case, with or without strain relaxation of the layers. We conclude that no automatching effects are observed for both InAlAs and InGaAs material under the conditions of our experiment and for y values in the range from 53% to 60%.

3. Four-crystal high resolution X-ray diffraction (HRXD)

X-ray measurements were carried out using a high resolution diffractometer (Philips HR1). The four-crystal monochromator was configured in its 220 setting providing an intense parallel monochromatic beam. An interesting feature of this set-up is that any Bragg reflection on any material can be observed with no change in the monochromator setting, in contrast to X-ray double diffraction. 004 X-ray rocking curves demonstrate the high crystalline quality and excellent vertical composition uniformity of the GaInAs layers, as evidenced by the low full width at half maximum (FWHM) of the layer diffraction peaks and the

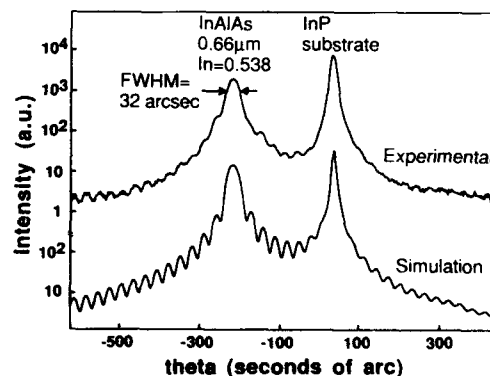


Fig. 5. Four-crystal high resolution X-ray diffraction (HRXD) rocking curve of a $0.66 \mu\text{m}$ thick InAlAs layer on InP.

presence of at least 15 Pendellösung fringes obtained for both materials. Fig. 5 shows the good agreement between experimental and calculated curves for a $0.66 \mu\text{m}$ thick AlInAs layer. To our knowledge, no observation of this kind has yet been made on InAlAs, the growth of which is more critical than that of InGaAs. The simulation is based on the dynamical X-ray diffraction theory [6]. The 32 arc sec FWHM is very close to the theoretical value. A similar fit is obtained on a $1 \mu\text{m}$ thick GaInAs layer (FWHM = 24 arc sec). Previous reports can be found for InGaAs grown on InP [7] and for the AlGaAs/GaAs system [8].

A $0.5 \mu\text{m}$ thick AlInAs layer was grown with no substrate rotation in order to induce a large lateral change of the indium content (y). Mapping using the 004, 115 and $\bar{1}\bar{1}5$ Bragg reflections shows that y varies from 46% up to 57% over a quarter of a 2-inch wafer. Asymmetrical reflection measurements show that no significant strain relaxation occurs for y between 46% and 55%. However, a relaxation as high as 30% was measured for an indium content of 57%. A long and very narrow stripe was then cleaved from this layer, so that a convenient relation of y as a function of the position along the stripe could be used, and photoluminescence (PL) studies as a function of y have been performed. A typical 77 K PL spectrum is shown in fig. 6. The spectrum exhibits a sharp band-to-band emission line with maximum inten-

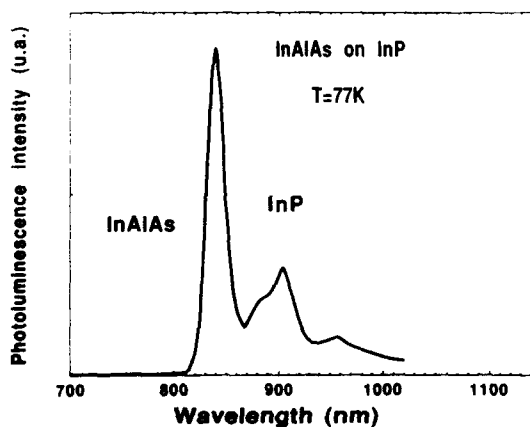


Fig. 6. 77 K photoluminescence of lattice matched InAlAs on InP.

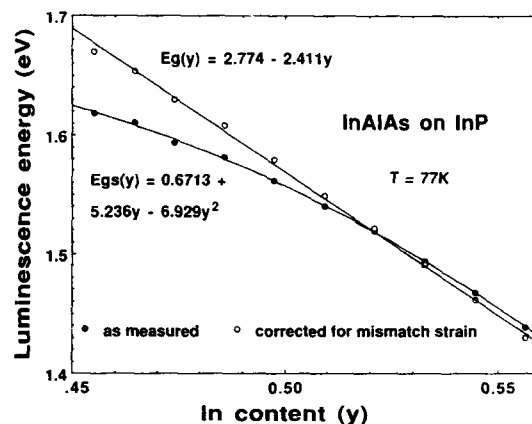


Fig. 7. 77 K luminescence energy of InAlAs versus indium content and intrinsic bandgap corrected for mismatch strain.

sity for the lattice matched material. The aluminium-rich material presents a low energy impurity line with a constant binding energy of 100 meV, while for the indium-rich material, two low energy lines were found. PL intensity versus excitation power density measurements shows a quadratic dependence for the high energy line and a linear dependence for the low energy one, thereby confirming the nature of these lines. Fig. 7 shows the measured 77 K bandgap of $\text{In}_y\text{Al}_{1-y}\text{As}$ versus y and the values corrected for mismatch strain according to a simple and classical model [9]. The bandgap values measured on the as-grown (strained) layers follow the relationship $E_g(y) = 0.671 + 5.236y - 6.929y^2$. Applying the strain corrections, we deduce the relation $E_g(y) = 2.774 - 2.411y$ for the intrinsic material. It is important to notice that the intrinsic bandgap has a linear dependence and does not show any particularity at the lattice matched value, in contrast to the measured values for which the bandgap is determined by electron-to-heavy-hole transition when $y > 0.52$ and electron-to-light-hole transition when $y < 0.52$.

The lattice matched bandgap of AlInAs at 77 K was found to be $E_g = 1.511 \text{ eV}$. This result is in close agreement with values from refs. [3,10]. Preliminary measurements at 4 K show a 17 meV wide PL line at 1.507 eV for the lattice matched

material, which gives a bandgap $E_g = 1.516$ eV after binding exciton energy correction.

4. Conclusion

We have measured by WTEM the indium desorption rate from InGaAs and InAlAs grown on InP substrates as a function of the growth temperature. We deduce that desorption becomes significant at 545°C for both materials. With the same procedure, automatching effects have been investigated, and we conclude that no effects could be observed under the growth conditions of the experiment. The bandgap of $\text{In}_y\text{Al}_{1-y}\text{As}$ has been measured at 77 K as a function of y . The indium content and the strain were carefully measured by HRXD. The intrinsic bandgap follows the relation $E_g(y) = 2.774 - 2.411y$ and the strained material the relation $E_g(y) = 0.671 + 5.236y - 6.929y^2$.

Acknowledgement

This work was supported by Thomson-CSF (France).

References

- [1] F. Gueissaz, R. Houdré and M. Illegems, *J. Crystal Growth* 111 (1991) 470.
- [2] P.A. Buffat, J.D. Ganière and P. Stadelmann, in: *Evaluation of Advanced Semiconductor Materials by Electron Microscopy*, NATO Workshop, Bristol, 1988, NATO ASI Series B: Physics, Vol. 203 (1989) pp. 319–334.
- [3] G.J. Davies, T. Kerr, C.G. Tuppen, B. Wakefield and D.A. Andrews, *J. Vacuum Sci. Technol. B2* (1984) 219.
- [4] M. Allovon, J. Primot, Y. Gao and M. Quillec, *J. Electron. Mater.* 18 (1988) 505.
- [5] E.G. Scott, D.A. Andrews and G.J. Davies, *J. Vacuum Sci. Technol. B4* (1986) 534; C.T. Foxon and B.A. Joyce, *J. Crystal Growth* 44 (1978) 75.
- [6] D. Taupin, *Bull. Soc. Franç. Crist.* 87 (1969) 469.
- [7] A.T. Macrander and K.E. Strege, *J. Appl. Phys.* 59 (1986) 442.
- [8] L. Tapfer and K. Ploog, *Phys. Rev. B33* (1986) 5565.
- [9] J.Y. Marzin, in: *Heterojunctions and Semiconductor Superlattices*, Eds. G. Allan, G. Bastard, M. Lannoo and M. Voos (Springer, Berlin, 1986) p. 161.
- [10] D. Oertel, D. Bimberg, R.K. Bauer and K.W. Carey, *Appl. Phys. Letters* 55 (1989) 140.

MBE overgrowth of implanted regions in InP:Fe substrates

H. Künzel, R. Gibis, W. Schlaak, L.M. Su and N. Grote

Heinrich-Hertz-Institut für Nachrichtentechnik Berlin GmbH, Einsteinufer 37, W-1000 Berlin 10, Germany

The MBE growth of InGaAs layers on Si-implanted InP:Fe substrates was investigated. Ion doses and energies used were in the range of 5×10^{12} – 5×10^{14} cm $^{-2}$ and 100–700 keV, respectively. Among the different annealing conditions tested, i.e. in-situ annealing in the MBE growth chamber at 500°C, rapid thermal annealing at 650°C, and high temperature annealing at 750°C under PH $_3$ /H $_2$ partial pressure, only the latter method was found to ensure restoration of the substrate crystal and high-quality overgrowth as assessed by RHEED and X-ray diffractometry. Heterojunction bipolar transistors employing an implanted overgrown collector were successfully fabricated.

1. Introduction

For advanced long-wavelength integrated optoelectronics the use of semi-insulating InP:Fe substrate material is a prerequisite to allow for electrical isolation of the devices involved. Unfortunately, most of the components to be used in integrated optoelectronic circuits (OEIC) exhibit a vertical (e.g. laser, photodiode, heterojunction bipolar transistor (HBT)) rather than a lateral design which generally leads to mesa-type devices the height of which can amount up to a few microns. In particular, a contacting layer with a sheet resistance as low as possible needs to be incorporated at the bottom of the epitaxial device structure to provide low ohmic current access. As such layers require a substantial thickness they may considerably contribute to the total device height, thereby impeding the fabrication technology. The use of buried contact layers embedded into the semi-insulating substrate provides a means to minimize this problem. Moreover, applying this scheme to other layers of the device structure can help reduce parasitic elements as is true for the HBT structure shown below. Embedded layers can be created either by selective infill growth into grooves or by selective dopant incorporation to locally convert semi-insulating into conductive material. Both diffusion (p-type) and ion implan-

tation (n- and p-type) represent suitable techniques for selective doping.

In this study multiple ion implantation was applied to selectively define the n $^+$ /n-doped sub-collector (contact) collector region of an InP-based HBT which is taken as an example for a device making use of embedded layers.

Different annealing conditions were investigated to provide a substrate surface suitable for the MBE overgrowth of an In $_{0.52}$ Al $_{0.48}$ As/In $_{0.53}$ Ga $_{0.47}$ As layer sequence (referred to as InAlAs/InGaAs), completing the HBT layer structure. Results on single medium-size transistors and integrated laser driver circuits will be presented demonstrating that the developed implantation based buried layer technology is well suited for the fabrication of devices.

2. Embedded collector HBT (EC-HBT)

In fig. 1, a schematic cross-section of the embedded collector HBT (EC-HBT) is shown. The n $^+$ /n collector region is formed by selective ion implantation of Si into a Fe-doped InP substrate. To improve the quality of the InP:Fe material an episubstrate approach [1] can be applied as an alternative. In this case, a > 10 μ m thick MOVPE InP:Fe layer is first grown onto an n $^+$ -InP:S

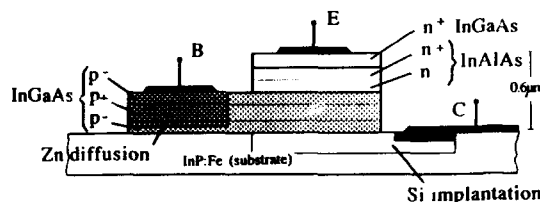


Fig. 1. Schematic cross-section of EC-HBT employing a Si-implanted collector and a MBE grown InGaAs/InAlAs base/emitter layer structure.

substrate. This approach not only ensures a well-defined Fe concentration, adjusted at $(1-2) \times 10^{16} \text{ cm}^{-3}$, but also a reduced density of defects due to the use of a low EPD n^+ -substrate. For the MBE growth studies homogeneously n^+/n -implanted InP:Fe substrates were employed whereas for the growth of HBT layer structures selectively implanted episubstrates were used.

To synthesize the n^+/n dopant profile in the substrate, multiple implantation is employed with the ion energies and the doses ranging from 100 to 700 keV and 5×10^{12} to $5 \times 10^{14} \text{ cm}^{-2}$, respectively. Double-ionized Si is used for energies > 400 keV. The resulting carrier depth profile of the implanted region as measured by $C-V$ profiling after annealing is shown in fig. 2. The resulting sheet resistance is measured to be approximately $40 \Omega/\square$. In some instances the use of InP:Fe substrate material gave distorted implantation profiles in the highly doped subcollector region, which is attributed to a non-homogeneous Fe distribution.

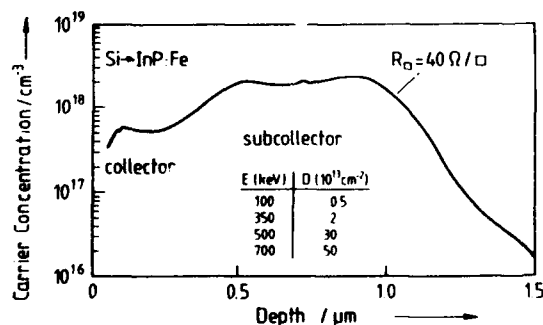


Fig. 2. Doping concentration depth profile in Si-implanted InP:Fe (implantation parameters given in the inset).

The base and emitter layers are grown by MBE directly onto the implanted substrate after annealing such that the collector/base heterojunction corresponds to the substrate/layer interface. The base consists of a 150 nm thick Be doped InGaAs layer ($p = 1 \times 10^{18} \text{ cm}^{-3}$) with p^- -doped 30 nm thick spacer regions ($p = 5 \times 10^{16} \text{ cm}^{-3}$). For the emitter a 150 nm thick Si-doped InAlAs layer ($n = 2 \times 10^{17} \text{ cm}^{-3}$) is employed. The layer sequence is completed by a 150 nm InAlAs:Si layer and a 100 nm thick n^+ -InGaAs:Si contact layer on top ($n^+ = 2 \times 10^{19} \text{ cm}^{-3}$). Within the upper InAlAs layer the donor doping concentration is gradually increased from the emitter to the contact layer value. Further details on the device structure are given in ref. [2]. Due to the use of an embedded collector the device height amounts to only $0.6 \mu\text{m}$ which may be further reduced.

3. MBE growth on implanted surfaces

In principle, ion implantation leaves a distorted crystalline region near the surface. Although microscopic inspection of the samples used in this work revealed no difference between the implanted and unimplanted regions with respect to surface morphology, MBE growth on non-annealed implanted regions yielded polycrystalline deposits exhibiting high electrical resistivity [3]. In order to obtain surfaces suitable for subsequent MBE growth, three different annealing techniques were compared. Firstly, to achieve an in-situ annealing/MBE growth process thermal treatment of the substrate in the growth chamber was tried using an annealing time of 1 h in a stabilizing As_4 beam [4] after oxide desorption. Secondly, rapid thermal annealing (RTA) which has proven suitable for fully activating the incorporated Si ions was utilized. This thermal treatment was carried out in an inert atmosphere at a temperature of 650°C for 30 s. As the third method, high-temperature annealing performed at 750°C for 20 min, with the surface of the implanted substrates being stabilized in a PH_3/H_2 ambient, was studied. After implantation and annealing the samples were cleaned in a diluted HF solution and are introduced into the MBE growth chamber without any

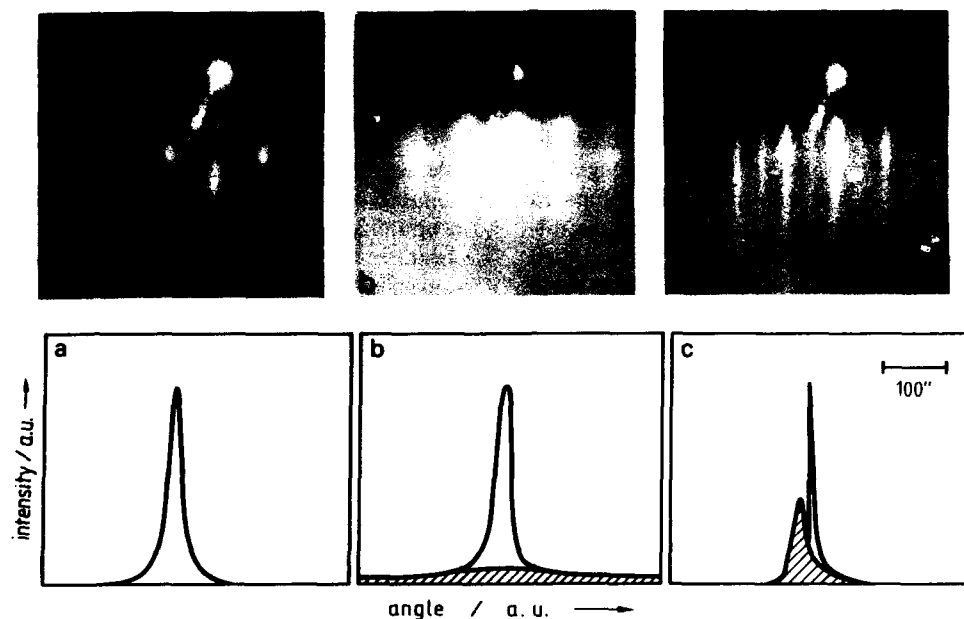


Fig. 3. Dependence of substrate status and epitaxial layer quality on annealing conditions measured by RHEED ((2×4) RHEED patterns of Si-implanted InP:Fe) and X-ray diffraction (X-ray diffraction patterns of 0.6 μm MBE GaInAs), respectively: (a) in-situ annealing, 1 h, 500 °C; (b) rapid thermal annealing, 30 s, 650 °C; (c) high-temperature annealing in PH_3 ambient, 20 min, 750 °C.

additional etching procedure. The results of this study in terms of the quality of the substrate surface and of overgrown MBE InGaAs layers are presented in fig. 3 which also summarizes the different annealing conditions.

The crystalline condition of the uppermost atomic layers of the substrate was examined by means of the RHEED pattern. Mainly the (2×4) reconstruction of the surface was observed to judge the surface state. In the case of in-situ annealing in the MBE system at temperatures below 400 °C, the RHEED pattern shows a circular intensity distribution being characteristic of an amorphous surface layer. With increasing the substrate temperature to 500 °C broken bulk-type reflection lines tend to appear. After an annealing time of 1 h at this temperature the amorphous contribution of the RHEED pattern disappears and the intensity of the reflection lines increases which, however, are still interrupted, as shown in fig. 3a. In fig. 3b, a RHEED pattern is displayed which was taken on a RTA annealed wafer after oxide desorption. It can be seen to be composed of non-in-

terrupted bulk-type reflection lines being strongly intensity modulated indicating a still imperfect restoration of the crystal lattice. In addition, the onset of surface reconstruction lines is visible. However, using the long-term high temperature annealing process under PH_3/H_2 yields a RHEED pattern which is comparable to that of unimplanted substrate material. The achievement of homogeneous and complete reconstruction of the bulk and surface region is clearly demonstrated in fig. 3c.

InGaAs layers with a thickness of 0.6 μm were subsequently deposited by MBE onto fully implanted substrates, annealed as discussed above. The surface morphology and the crystalline quality of these layers were assessed using interference contrast microscopy and X-ray diffractometry, respectively. Diffraction patterns were recorded in the vicinity of the symmetric (400) reflection using $\text{Cu K}\alpha_1$ radiation.

As a result, growth on substrates exhibiting a non-ideal surface state gives rough InGaAs surfaces. In the case of the in-situ annealing pro-

cess the surface is extremely deteriorated characterized by a roughness of the order of 100 nm. The respective diffraction spectrum shows only one peak which is related to the substrate (fig. 2a). The use of the RTA process results in some improvement of the morphology with the roughness being reduced by a factor of about five compared to the former procedure. Additionally, in the diffraction pattern a very broad structure, illustrated by the shaded area in fig. 2b, is indicative of some ordering. The center of this band which almost coincides with the substrate peak demonstrates the properly matched alloy composition of the MBE InGaAs layer. As expected from the RHEED studies on substrates annealed at 750°C under PH_3 partial pressure, overgrown layers exhibit a smooth surface comparable to layers grown on unimplanted substrates. The X-ray diffraction spectrum of such samples is composed of two closely neighbouring sharp peaks with the FWHM value amounting to 30–40 arc sec for the 0.6 μm InGaAs layer compared to 15 arc sec for the substrate. These figures are in agreement with data given in the literature for high quality MBE growth [5]. As a conclusion, high quality MBE growth is achievable on heavily implanted InP substrates provided proper annealing conditions are chosen. It remains to be investigated, however, whether this also holds for even higher ion doses and ion energies different from those used in this study.

4. MBE growth and device characteristics of EC-HBT

Based on the process described above complete layer structures for EC-HBT devices (section 2) were grown by MBE using a substrate temperature of 500°C. Slightly As-stabilized flux ratios were applied. Under these growth conditions InAlAs layers were found to exhibit an optimum surface morphology [6]. For InGaAs no variation of the crystalline and electrical properties was observed when grown between 450 and 580°C. Despite the incorporation of the InAlAs layer an ideal morphology was obtained for the entire layer stack due to InGaAs grown as the starting layer

[7]. A reduction of the growth temperature for the Be-doped based layer to minimize acceptor diffusion was considered to be not necessary because the doping level of $1 \times 10^{18} \text{ cm}^{-3}$ used here is below those concentration levels which give rise to enhanced diffusion [8]. At the p/p⁺ and the heterointerface MBE growth was interrupted for 90 s to optimize the acceptor profile and to minimize variation in the alloy composition due to flux transients. This interruption however, has no negative influence on the heterojunction built-up as confirmed by an interface state density of $1 \times 10^{10} \text{ cm}^{-2}$. Following the MBE growth, EC-HBT devices were fabricated according to the design illustrated in fig. 1 and as described in ref. [2]. Here the performance of the devices will be briefly summarized only to demonstrate that the growth on implanted areas yields epitaxial material which meets the demands of high-quality devices. The electrical quality of the growth interface between the implanted region and the epitaxial base layer forming the collector p/n junction is crucial for the I/V properties of the HBTs. A representative forward I/V characteristic of the collector diode is given in fig. 4. The ideality factor obtained is mostly less than 2, with typical values being around 1.8, which gives another indication of the high quality overgrowth achieved on the implanted substrates. This result also suggests that the relatively high density of interface states measured by the $C-V$ profiling techniques does not cause a

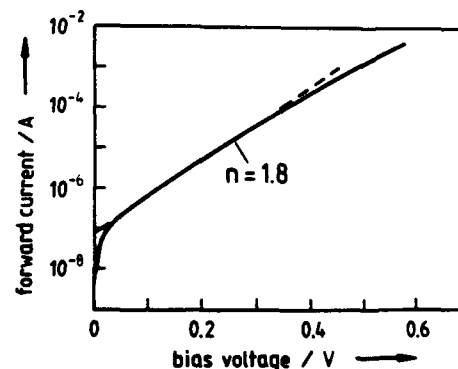


Fig. 4. I/V forward characteristic of EC-HBT base/collector diode.

noticeable degradation of the electrical behaviour of the collector heterodiode.

Well behaved common emitter characteristics with a breakdown voltage of more than 3 V and current gains of the order of 100 at collector current densities of 10^2 – 10^4 A cm⁻² (emitter area: 8×32 μm^2) were attained. The transit frequency (f_T) was measured to be approximately 9 GHz for these medium-size devices. Moreover, an integrated laser driver circuit consisting of three EC-HBTs and a resistor was fabricated which is capable of current modulation at bitrates of up to 4 Gbit/s [9].

5. Conclusions

A study on the MBE growth of InGaAs layers on selectively Si-implanted InP: Fe substrates was performed. Three different methods for annealing, i.e. in-situ annealing prior to MBE growth, rapid thermal annealing (650 °C), and high-temperature annealing at 750 °C in PH₃/H₂, have been investigated. Only the latter procedure was found to ensure high-quality overgrowth which allows the fabrication of devices employing implanted layers buried in the substrate. The successful realization of HBTs with an embedded collector demon-

strates the usefulness of this technological approach.

References

- [1] N. Grote, H.G. Bach, D. Franke, P. Harde, B. Sartorius and P. Wolfram, in: Proc. 19th ESSDERC, Eds. A. Heuberger, H. Ryssel and P. Lange (Springer, Berlin, 1989) p. 275.
- [2] L.M. Su, H. Künzel, R. Gibis, G. Mekonnen, W. Schlaak and N. Grote, in: Proc. 20th ESSDERC, Nottingham, Sept. 1990, to be published.
- [3] P. Favennec, L. Henry, A. Regreny and M. Salvi, Electron. Letters 18 (1982) 933.
- [4] G.J. Davies, R. Heckingbottom, H. Ohno, C.E.C. Wood and A.R. Calawa, Appl. Phys. Letters 37 (1980) 290.
- [5] C. Ferrari, P. Franzosi, L. Gastaldi and F. Tataroli, J. Appl. Phys. 63 (1988) 2628.
- [6] A. Hase, J. Böttcher, R. Gibis and H. Künzel, unpublished results.
- [7] C. Schramm, H. Künzel, C. Bornholdt, L.M. Su and H.H. Wehmann, in: Proc. 19th ESSDERC, Eds. A. Heuberger, H. Ryssel and P. Lange (Springer, Berlin, 1989) p. 59.
- [8] W. Passenberg, P. Harde, H. Künzel and D. Trommer, in: Proc. 2nd Intern. Conf. on Indium Phosphide and Related Materials, Denver, CO, 1990, IEEE Catalog No. 90 CH 2859-7 (1990) p. 195.
- [9] L.M. Su, H. Künzel, H.G. Bach, W. Schlaak and N. Grote, in: Proc. 17th Intern. Symp. on GaAs and Related Compounds, Jersey, 1990, Inst. Phys. Conf. Ser. (Inst. Phys., London-Bristol, 1991).

Effects of substrate orientation, pseudomorphic growth and superlattice on alloy scattering in modulation doped GaInAs

Albert Chin *, T.Y. Chang, A. Ourmazd, E.M. Monberg **, A.M. Chang

AT & T Bell Laboratories, Crawford's Corner Road, Holmdel, New Jersey 07733-1988, USA

and

C. Kurdak

Department of Electrical Engineering, Princeton University, Princeton, New Jersey 08540, USA

The possibility of reducing alloy scattering in MBE $\text{Ga}_{1-x}\text{In}_x\text{As}$ has been studied experimentally by growing modulation doped heterostructures (A) with an InAs/GaInAs superlattice 2DEG channel, (B) on a vicinal (110) InP substrate, and (C) with a strain compensated pseudomorphic channel. The maximum 77 K mobility obtained in each case is (A) 60,600, (B) 69,300, and (C) 123,100 $\text{cm}^2/\text{V}\cdot\text{s}$, using $x = 0.50$, 0.53, and 0.80, respectively. Partial alloy ordering is observed in case (B). Cyclotron resonance measurements indicate that the reduction of m^* contributes much less to the enhancement of mobility in case (C) than the alloy composition factor $x(1-x)$. Alloy ordering may also be important.

1. Introduction

Heterostructures of $\text{Ga}_{1-x}\text{In}_x\text{As}/\text{Al}_{0.48}\text{In}_{0.52}\text{As}$ grown on InP substrates, in addition to being important for photonic devices in the 1.3 to 1.7 μm spectral range, have been proven advantageous over those of the GaAs/AlGaAs system for high speed electronic devices, due to several superior electronic transport properties. At cryogenic temperatures, the electron mobility in GaInAs is, however, generally lower than that in GaAs, due to alloy scattering. At room temperature, alloy scattering is less important but still significant. In this paper, we present the results of experimental investigations in which three different avenues towards reduced alloy scattering in modulation doped heterostructures are explored. These approaches involve the use of (A) a short period

InAs/ $\text{Ga}_{0.5}\text{In}_{0.5}\text{As}$ superlattice channel on (100) InP, (B) lattice matched layers on vicinal (110) InP, and (C) highly In rich pseudomorphic layers grown on (100) InP.

Our results show record high mobilities in all three categories. For vicinal (110) growth, enhancement of mobility over (100) growth is achieved for the first time. The highest 77 K mobility of 123,100 $\text{cm}^2/\text{V}\cdot\text{s}$ is obtained on (100) substrate in a pseudomorphic channel of $x = 0.80$ by using a novel strain compensation structure [1]. This high mobility enabled us to observe sizeable h/e Aharonov–Bohm effect in GaInAs for the first time. The improvement of mobility with the x value is interpreted with the help of cyclotron resonance data.

2. Experimental

The heterostructures used in the present study were grown at $\sim 500^\circ\text{C}$ in a solid-source MBE

* Current address: General Electric Co., Electronics Park, Syracuse, New York 13221, USA.

** AT & T Bell Laboratories, Murray Hill, New Jersey 07974-2070, USA.

system. Two sets of In and Ga cells were used to facilitate calibration and growth of various layers. In general, the modulation doped heterostructures consist of a 300 nm undoped $\text{Al}_{0.48}\text{In}_{0.52}\text{As}$ buffer layer, an undoped $\text{Ga}_{0.47}\text{In}_{0.53}\text{As}$ smoothing layer, a two-dimensional electron-gas (2DEG) channel, a 10 nm undoped $\text{Al}_{0.48}\text{In}_{0.52}\text{As}$ spacer layer, a 20 nm Si doped $((2-3) \times 10^{18} \text{ cm}^{-3})$ $\text{Al}_{0.48}\text{In}_{0.52}\text{As}$ layer, a 30 nm undoped $\text{Al}_{0.48}\text{In}_{0.52}\text{As}$ Schottky barrier layer, and finally a 20 nm Si doped $(3 \times 10^{18} \text{ cm}^{-3})$ $\text{Ga}_{0.47}\text{In}_{0.53}\text{As}$ cap layer for ohmic contact. The combined thickness of the $\text{Ga}_{0.47}\text{In}_{0.53}\text{As}$ smoothing layer and the channel layer are held to stay within a narrow range between 50 and 55 nm for consistency.

The three groups of samples differed mainly in the design of the 2DEG channel. Structure A consisted of l periods of $(\text{InAs})_m/(\text{Ga}_{0.50}\text{In}_{0.50}\text{As})_n$ superlattice channel, where m and n indicate the number of monolayers. Three samples of structure A were grown with (l, m, n) values of (5, 1, 3), (5, 2, 3) and (4, 3, 3). Structure B is grown on vicinal (110) InP and contains a lattice matched $\text{Ga}_{0.47}\text{In}_{0.53}\text{As}$ channel. These vicinal (110) substrates are tilted 6° toward the (111) pole to promote quasi 2D growth. The structure C contains a pseudomorphic $\text{Ga}_{1-x}\text{In}_x\text{As}$ channel with various x values from 0.53 to 0.85. For $x \leq 0.70$, a channel thickness of 15 nm is used. For $x > 0.70$, a strain compensation layer of 3.5 nm $\text{Ga}_{0.75}\text{In}_{0.25}\text{As}$ is incorporated just beneath the channel layer to partially balance the strain in the structure.

The low field transport properties were investigated by Hall measurement. The n^+ cap layer was removed after ohmic contact formation to avoid parallel conduction. The dependence of electron effective mass on InAs mole fraction in the pseudomorphic channel was characterized by cyclotron resonance (CR) measurements at wavelengths of 70.6 and 118.8 μm .

3. Results and discussion

The growth conditions used in the present study are similar to those used previously to obtain high quality ternary and quaternary layers [2]. Hall

measurement of a 2 μm thick $\text{Ga}_{0.47}\text{In}_{0.53}\text{As}$ layer grown on top of a 0.4 μm AlInAs buffer layer yields an unintentional doping level of $N_D - N_A = 1.6 \times 10^{14} \text{ cm}^{-3}$ and a 300 K mobility of 12,000 $\text{cm}^2/\text{V} \cdot \text{s}$. In 2DEG channels of this purity, ionized impurity scattering at 77 K is relatively low and alloy scattering is expected to play a significant role in limiting the electron mobility.

Summarized in table 1 are the measured Hall data for the superlattice-channel samples (Structure A) along with those for a lattice matched modulation doped heterostructure sample grown in the same series. The best mobilities were obtained for the (5, 2, 3) sample, being 11,600 and 60,600 $\text{cm}^2/\text{V} \cdot \text{s}$ at 300 and 77 K respectively. These values are superior to those for the lattice matched sample grown during the same period of time in the same MBE system. More significantly, they are much superior to the best values reported previously for $(\text{InAs})_m(\text{GaAs})_n$ superlattices which are considered to be the ideal structure for suppressing alloy scattering [3].

The samples on vicinal (110) substrates were grown at 470 and 510 $^\circ\text{C}$. The Hall data for these samples along with the data for (100) samples grown side by side with them are summarized in table 2. For 470 $^\circ\text{C}$ growth, the mobility is lower for the vicinal (110) sample. When the growth temperature is raised to 510 $^\circ\text{C}$, the mobility values for the (100) orientation improves slightly while those for vicinal (110) orientation improve significantly and surpass the (100) values. Considering the typical dependence of mobility on the 2DEG density [4], the 77 K mobility for vicinal (110) case is seen to be enhanced over that for the (100) case by at least 10% for the same 2DEG

Table 1
Measured Hall data for $(\text{InAs})_m/(\text{GaInAs})_n$ SL channel modulation-doped heterostructures

(l, m, n)	$\mu \text{ (cm}^2/\text{V} \cdot \text{s)}$		$n_{2\text{DEG}} \text{ (cm}^{-2}\text{)}$	
	300 K	77 K	300 K	77 K
(5, 1, 3)	7200	—	2.02×10^{12}	—
(5, 2, 3)	11600	60600	1.78×10^{12}	1.68×10^{12}
(4, 3, 3)	5800	—	2.00×10^{12}	—
Lattice-matched	10700	48000	1.45×10^{12}	1.43×10^{12}

Table 2
Measured Hall data for GaInAs/AlInAs modulation-doped heterostructures grown on (100) and vicinal (110) orientations

T_{growth} (°C)	Orientation	Mobility (cm ² /V·s)		2DEG density (cm ⁻²)	
		300 K	77 K	300 K	77 K
470	(100)	11100	63000	1.81×10^{12}	1.56×10^{12}
	(110)v	9600	56400	2.32×10^{12}	1.68×10^{12}
510	(100)	11100	64200	1.23×10^{12}	1.13×10^{12}
	(110)v	11320	69300	1.75×10^{12}	1.65×10^{12}

density. Cross-sectional electron diffraction patterns from thicker GaInAs layers reveal moderately strong Ga-In ordering in the vicinal (110) case [5] and essentially random Ga-In distribution in the (100) case. The observed small enhancement of mobility for this orientation may be due to the partial ordering and/or the reduced incorporation of background acceptors. Further details including the electron diffraction patterns will be published elsewhere.

Improvement of 2DEG mobility and MOD-FET performance by the use of In rich pseudomorphic channel layer has been limited previously to $x \leq 0.65$ due to rapidly diminishing critical layer thickness with increasing x [6,7]. We have demonstrated that the unacceptably small critical layer thickness for $x > 0.7$ can be significantly increased by the use of a novel strain compensated structure [1]. By this technique we have achieved new record high mobilities of 15,300 and 123,100 cm²/V·s at 300 and 77 K respectively at a high 2DEG density of $\sim 1.8 \times 10^{12}$ cm⁻² in GaInAs.

Table 3
Measured Hall data for strain compensated modulation-doped heterostructures

In (%)	Mobility (cm ² /V·s)		2DEG density (cm ⁻²)		m_{CR}^*/m_e at 4 K
	300 K	77 K	300 K	77 K	
53	11100	64200	1.23×10^{12}	1.13×10^{12}	0.0521
60	12500	73100	1.39×10^{12}	1.21×10^{12}	0.0507
65	12800	83000	1.48×10^{12}	1.41×10^{12}	-
75	14100	113000	1.71×10^{12}	1.65×10^{12}	-
80	15200	123100	1.84×10^{12}	1.81×10^{12}	0.0500
85	15300	70700	1.84×10^{12}	1.81×10^{12}	0.04845

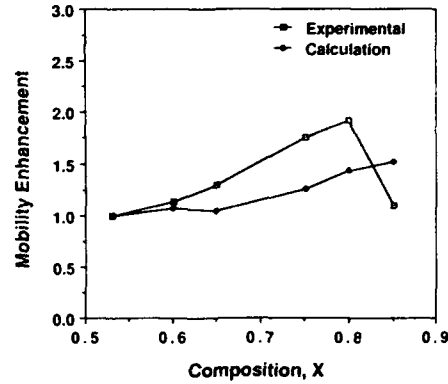


Fig. 1. Enhancement of measured 77 K mobility in pseudomorphic Ga_{1-x}In_xAs 2DEG channels over the $x = 0.53$ value as a function of x (open squares). The solid symbols show calculated enhancement of alloy limited mobility.

The Hall data are summarized in table 3. Included in the last column of the table are the experimental values of the electron effective mass in these samples measured by far infrared cyclotron resonance. The decrease of m_{CR}^* with increasing InAs mole fraction is seen to be relatively minor. This is due to the high Fermi level in these samples and the increasing nonparabolicity with increasing x value. The band-edge effective mass values deduced from these data, however, are in reasonably good agreement with the values interpolated between those of GaAs and InAs after correcting for the effect of strain. Further details will be published elsewhere [8].

The enhancement of these measured mobilities over the lattice matched value are plotted in fig. 1 as open squares. The sudden drop of enhancement beyond $x = 0.8$ is believed to be due to the development of misfit dislocations.

The alloy scattering limited mobility in a 2DEG channel is given theoretically by [9]:

$$\mu_{\text{AL}} = \frac{e\hbar^3}{m^{*2}\Omega x(1-x)S(\Delta U)^2} \frac{16}{3(b_0 + b_{\text{eff}})}, \quad (1)$$

where Ω is the volume of the primitive cell, S is the degree of randomness, ΔU is the alloy scattering potential, and b_0 and b_{eff} are depth parameters related to the extent of the wave function in the 2DEG channel obtained here by using the

triangular potential approximation. The calculated enhancement of μ_{AL} over its lattice matched value is plotted as solid symbols in fig. 1 assuming $S = 1$. Since m^* is nearly constant in our samples, most of the enhancement arises from the alloy composition factor $x(1-x)$. The observed enhancement is seen to be considerably larger than the calculated enhancement for μ_{AL} . The discrepancy is too large to be reconciled by possible dependences of ΔU and ionized impurity scattering on x [10]. A possible explanation is increasing degree of alloy ordering ($S < 1$) in these samples.

Record high mobilities achieved in these samples enabled us to observe quantum interference in GaInAs for the first time. Large h/e Aharonov-Bohm oscillations with periods of 13.5 and 25 G were observed at 0.4 to 1.9 K in two different square ring structures of 0.45 μm wide ridges 1.8 and 1.3 μm long on each side. These rings were fabricated by electron-beam lithography on a pseudomorphic sample with $x = 0.80$ and a 4 K mobility of 154,000 $\text{cm}^2/\text{V} \cdot \text{s}$. Comparative studies using this and the AlGaAs/GaAs heterostructure system should allow us to answer some fundamental questions related to the quantum interference effects.

4. Conclusion

Three different means of reducing alloy scattering in GaInAs have been studied by MBE growth. In each case, a record high mobility has been achieved. The best results are obtained by using very In rich GaInAs strain compensated heterostructures. For samples with highly degenerate 2DEG, the improvement of mobility is seen to

arise mostly from the alloy composition factor $x(1-x)$ and possibly from the increased degree of alloy ordering rather than from the reduction of m^* . This type of heterostructure is very promising for very high speed transistors. Small enhancement of mobility has also been demonstrated for vicinal (110) growth. This unconventional substrate orientation is interesting for novel devices and for its demonstrated ability to provide greater threshold voltage uniformity [11]. High mobility has also been demonstrated for the first time in an InAs/GaInAs superlattice channel. This structure is, however, not yet competitive with pseudomorphic heterostructures.

References

- [1] A. Chin and T.Y. Chang, *J. Vacuum Sci. Technol.* B8 (1990) 364.
- [2] D. Biswas, A. Chin, J. Pamulapati and P. Bhattacharya, *J. Appl. Phys.* 67 (1990) 2450.
- [3] T. Fukui and H. Saito, *Japan. J. Appl. Phys.* 23 (1984) L521.
- [4] L. Aina, M. Mattingly and B. Potter, *Appl. Phys. Letters* 51 (1987) 1735.
- [5] T.S. Kuan, W.I. Wang and E.L. Wilkie, *Appl. Phys. Letters* 51 (1987) 51.
- [6] J.M. Kuo, B. Lalevic and T.Y. Chang, *J. Vacuum Sci. Technol.* B5 (1987) 782.
- [7] G.I. Ng, D. Pavlidis, M. Quillec, Y.J. Chan, M.D. Jaffe and J. Singh, *Appl. Phys. Letters* 52 (1988) 728.
- [8] A. Chin, T.Y. Chang, M.J. Yang and R.J. Wagner, to be published.
- [9] J.A. Brum and G. Bastard, *Solid State Commun.* 53 (1985) 727.
- [10] M.A. Littlejohn, J.R. Hauser, T.H. Glisson, D.K. Ferry and J.W. Harrison, *Solid State Electron.* 21 (1978) 107.
- [11] T. Onodera, H. Kawata, H. Nishi, T. Futatsugi and N. Yokoyama, *IEEE Trans. Electron Devices* ED-36 (1989) 1586.

High electron density and mobility in single and double planar doped InGaAs/InAlAs heterojunctions on InP

F. Gueissaz, R. Houdré and M. Illegems

Institut de Micro-et Optoélectronique, Ecole Polytechnique Fédérale de Lausanne, CH-1015 Lausanne, Switzerland

We present results of a growth study concerning the electrical properties of lattice matched InAlGa/InGaAs single planar doped (SPD) and double planar doped (DPD) heterostructures grown on InP by molecular beam epitaxy (MBE). It is shown that room temperature electron mobilities (μ_H) as high as $11000 \text{ cm}^2/\text{V}\cdot\text{s}$ at high sheet densities of $2.8 \times 10^{12} \text{ cm}^{-2}$ can be obtained by optimizing the growth temperatures of each material in the SPD structure. High performance two-dimensional electron gas field effect transistors (TEGFET's) are demonstrated, with transconductances as high as 420 mS/mm at $1 \mu\text{m}$ gatelength and f_T 's of 46 GHz at $0.7 \mu\text{m}$ gatelength. The DPD heterostructures further boost the n_s values up to $6.2 \times 10^{12} \text{ cm}^{-2}$ at $\mu_H (300 \text{ K}) = 6000 \text{ cm}^2/\text{V}\cdot\text{s}$.

1. Material growth

All samples used in the present study have been grown in a VG V80H solid sources MBE system. Sumitomo InP:Fe {001} $\pm 0.5^\circ$ substrates were loaded without any substrate preparation, as better results in terms of defect density and surface morphology have been obtained in this manner, without significant difference in the electrical properties of modulation doped heterostructures.

The growth temperature was measured with a $0.95 \mu\text{m}$ IRCON Modline V pyrometer, which was calibrated against the melting point of InSb at 525°C and the oxygen desorption temperature from GaAs at 630°C . Prior to growth, the substrates were heated up to $500\text{--}505^\circ\text{C}$ under arsenic flux for a few minutes and growth was initiated when surface reconstruction lines could be observed by RHEED. The temperature was subsequently adjusted to the desired values for the different ternary alloys. Fast temperature transients of up to 50°C in less than 40 s were obtained by following a carefully calibrated substrate heater power schedule.

Undesired flux transients at the opening of K-cells have been reduced from 5% down to 0.5% by increasing the cell temperature set point at the

opening of the shutter. Prior to growth, the group III element fluxes were measured with an ion gauge. Although we do not believe in absolute flux measurements by this method, we found the indium over gallium, or indium over aluminium beam equivalent pressure (BEP) ratios to give a reliable indication of the alloy compositions. The group III fluxes were then finely tuned by using a previously calibrated $y/(1-y)$ versus In/Ga or In/Al BEP curve, where y is the InAs content

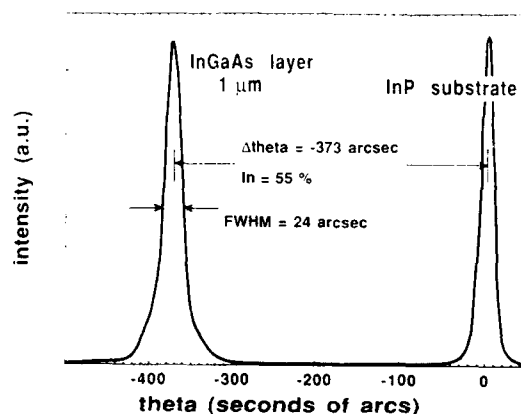


Fig. 1. 004 X-ray rocking curve of a $1 \mu\text{m}$ thick InGaAs layer grown on InP.

measured by four crystal high resolution X-ray diffraction (HRXD). A single K-cell generated the arsenic flux and the growth rate was kept constant at 0.65–0.7 $\mu\text{m/h}$. With this procedure, lattice parameter control and reproducibility to better than 500 ppm could be achieved.

The good material quality has been evidenced by 004 X-ray rocking curves with a full width at half maximum of 25 arc sec for 1 μm thick InGaAs (fig. 1). This value is very close to the theoretical one [1].

2. Sample design and device fabrication

We consider here three different single planar doped (SPD) samples labeled A, B and C as well as one double planar doped (DPD) sample labeled D. The labels follow the increasing order of electron sheet densities measured on the samples.

Fig. 2 (left) shows the structure of samples A through C, which consisted of, starting from the InP:Fe substrate interface, a 4000 Å InAlAs buffer layer, a 500 Å InGaAs channel layer, a 70 Å (sample A) or 50 Å (samples B and C) InAlAs channel spacer layer, a Si doping plane containing $6.0 \times 10^{12} \text{ cm}^{-2}$ (samples A and C) or $5.2 \times 10^{12} \text{ cm}^{-2}$ (sample B) donors, a 200 Å InAlAs undoped top layer and a 50 Å n^+ -InGaAs cap layer (fully depleted). Samples A and C were grown at a constant temperature of 530°C while the temperature of sample B was lowered to 500°C prior to growing the InGaAs channel layer and kept constant for the remaining layers.

Fig. 2 (right) shows the structure of sample D, which consisted of, starting from the InP:Fe substrate interface, a 4000 Å InAlAs buffer layer, a

first Si doping plane containing $2.8 \times 10^{12} \text{ cm}^{-2}$ donors, a first 70 Å InAlAs channel spacer layer, a 200 Å InGaAs channel layer, a second 70 Å InAlAs channel spacer layer, a second Si doping plane containing $6.0 \times 10^{12} \text{ cm}^{-2}$ donors, a 200 Å InAlAs top undoped layer and a 50 Å n^+ -InGaAs cap layer (fully depleted). The growth temperatures for the InAlAs and InGaAs layers were 535 and 485°C, respectively.

Schottky diodes for the capacitance versus bias measurement were made on sample A and D by Ti/Au (500 Å/4500 Å) evaporation after recessing approximately 90 Å from the surface. The necessary side-ohmic contacts were made by Ni/Ge/Au/Ti/Au evaporation and followed by an alloy cycle at 360°C under protective atmosphere.

Chips containing 0.7 to 5 μm gatelength TEGFET's were fabricated on all samples by a standard process using optical UV lithography and consisting of mesa etching, Ni/Ge/Au/Ti/Au ohmic contact deposition and alloying at 360°C, electrically controlled gate recess etching, TiAu gate overlay metal deposition.

All access pads were designed for on-wafer probing with 50 Ω tapered waveguides. This technique allows accurate $C(V)$ measurements and microwave measurements up to 18 GHz on TEGFETs.

3. Electrical characterization at low field

The electron sheet densities (n_s) measured by Hall effect are nearly constant for temperatures between 13 and 77 K with a small increase of less than 5% toward 300 K. The n_s values at 300 K for samples A, B and C are 2.6×10^{12} , 2.8×10^{12} and $2.9 \times 10^{12} \text{ cm}^{-2}$, respectively. It follows that increasing the InAlAs channel spacer layer from 50 to 70 Å reduces n_s by about 10%. The slight difference of n_s between samples B and C is due to a small doping variation. Sample D, having an additional Si doping plane underneath the channel, exhibits the highest n_s of $6.2 \times 10^{12} \text{ cm}^{-2}$ at 300 K.

A relatively weak (<5% change in n_s) persistent photoconductivity (PPC) effect was ob-

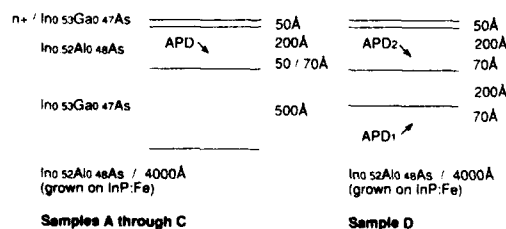


Fig. 2. Layer design of single planar doped samples A through C (left) and double planar doped sample D (right).

served on all four samples at 13 K. After illumination at 13 K, the typical decay time constants are of the order of an hour. The n_s value itself and the Δn_s observed in PPC do not seem to be affected by the growth temperature between 485 and 535 °C.

Fig. 3 shows the electron mobilities in the InGaAs channel as a function of the temperature for samples A through D. The highest mobilities are obtained from sample A which has the widest InAlAs channel spacer layer of 70 Å, the room temperature mobility is 11300 cm²/V·s and rapidly saturates below 77 K to attain 51000 cm²/V·s at 13 K. The mobilities above 77 K are primarily limited by optical phonon scattering whereas the saturation characteristics toward lower temperatures is clearly due to alloy disorder scattering which is about maximum for lattice matched InGaAs. These mobilities are among the highest reported; higher values can be obtained either at lower electron sheet densities or by growing strained InGaAs channels [2,3]. Reducing the channel spacer from 70 to 50 Å in sample C strongly affects the mobility characteristics, the room temperature value dropping to 8400 cm²/V·s and reaching 21000 cm²/V·s at 13 K. Sample B has the same structure as sample C but exhibits mobilities almost as high as sample A, indicating that the crystalline quality of the InGaAs channel is improved at the lower growth temperature. The

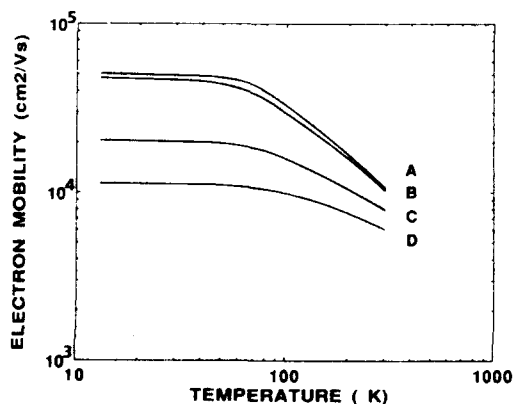


Fig. 3. Electron mobilities of samples A through D as a function of the temperature from 13 to 300 K.

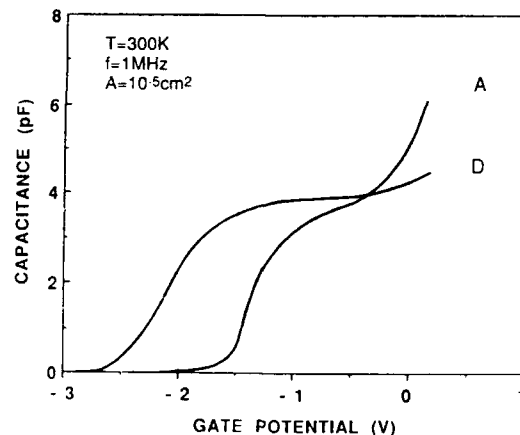


Fig. 4. Capacitance versus bias of a single planar doped sample (A) and a double planar doped sample (D).

room temperature mobility of sample D is decreased to 6000 cm²/V·s and reaches 11200 cm²/V·s at 13 K. These figures are fairly good if one considers the extremely high n_s , involving electron filling of more than two energy subbands, and the thin InGaAs channel confining the bidimensional electron gas near the inverted heterointerface.

The comparison of PPC effects on the mobility shows that the $\Delta\mu_H$ is positive and smaller than 4% for all samples excepting sample B (-1.8%) having the planar doped InAlAs layer grown at 500 °C. Higher growth temperatures for the InAlAs are thus necessary to insure good interfaces and efficient Si atom incorporation.

Fig. 4 shows capacitance measurements at 300 K and 1 MHz as a function of the potential applied on a Schottky diode processed on sample A (SPD) and sample D (DPD). Samples A and D are compared since they have the same structure from the top heterointerface to the cap layer. Both curves integrated from the threshold voltage to 0 V yield n_s values close to the results obtained by Hall effect. The average 2DEG capacitance is about 3.8×10^{-7} F/cm² which yields an average distance of about 290 Å between the 2DEG and the Schottky barrier, in good agreement with the expected values. The broad plateau on the char-

acteristics of sample D accounts for the very high n_s which can be modulated while maintaining an excellent confinement in the InGaAs channel.

Computer simulations of the n_s versus bias dependence for samples A and D using a self-consistent resolution of the Schrödinger effective mass equation coupled with the Poisson equation [4] at different potentials at the Schottky interface agreed very well (within 10%) with the experimental values of n_s . Further, these show that two energy subbands are normally filled in the SPD structure, whereas three are filled in the DPD structure. The electron mobilities in sample D could be reduced by the increased intersubband scattering effects, and alloy disorder scattering effects, which are also dependent on the n_s [5].

4. Electrical characterization of TEGFETs

DC measurements on 1 μm gatelength TEGFETs yielded saturation mode ($V_{DS} = 1\text{--}2\text{ V}$) transconductances as high as 420, 410 and 360 mS/mm for samples A, B and C respectively.

Fig. 5 shows the typical transfer characteristics of 1 μm gatelength TEGFETs processed out of sample A. TEGFETs with $0.7 \times 100\text{ }\mu\text{m}^2$ gatelength times width have been measured at microwave frequencies from 1 to 18 GHz. A 13-element equivalent electrical model was used to fit the measured scattering parameters with excellent

agreement. The extrapolated current gain and maximum power gain cutoff frequencies were as high as 46 and 82 GHz.

The DC TEGFETs characteristics are influenced both by the intrinsic material parameters and by the processing technology (gate recess and Schottky barrier). An effort was made to keep the technological parameters constant so as to obtain identical threshold voltages for all TEGFETs. The peak transconductances occur at typically 140 mA/mm drain current for both samples B and C, as expected since both structures are identical. However, the peak transconductance of sample A, with a 70 Å channel spacer, occurs at 220 mA/mm drain current, indicating that more carriers can be modulated with an equally high transconductance compared to sample B, with a 50 Å channel spacer. This indicates that parallel conduction (resulting in a decrease of modulation efficiency degrading the transconductance [6,7]) in the top InAlAs layers of sample A is not significant up to higher bidimensional electron densities. Samples B and C should intrinsically attain their maximum transconductance values at drain currents of at least 220 mA/mm because of the reduced spacer thickness used. The lower values encountered here are attributed to an improper adjustment of the gate recess and hence of the threshold voltage. Finally, we observe that the reduced electron mobility of sample C will mainly increase the access resistances to the channel and degrade the transconductance characteristics.

Sample D showed a very broad peak of transconductance as expected from the capacitance versus potential measurements. However, we were confronted with the low breakdown voltage of the Schottky gates on AlInAs (typically 2.5–3.5 V). The threshold voltage of TEGFETs processed on sample D is about -2.7 V and unacceptable gate to drain potentials are required to achieve pinch-off of the channel in the saturation mode. Moreover, the drain current characteristics of the TEGFETs did not saturate properly, while the transfer characteristics showed a steady increase of the peak transconductance as the drain potential was raised (up to breakdown). It is clear, therefore, that a further optimization of the double planar doped heterostructure is necessary to

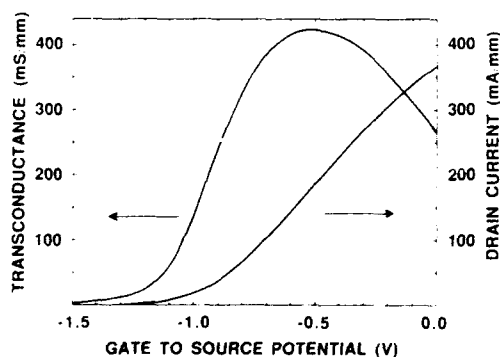


Fig. 5. Transfer characteristics of a 1 μm gatelength TEGFET, at $V_{DS} = 1\text{ V}$, processed on a single planar doped sample (A).

fully exploit the high n_s values achievable with this design.

5. Conclusions

Growth parameters such as substrate temperature and design parameters such as spacer thickness have a determining influence on the electrical properties of TEGFETs. These have to be simultaneously optimized in order to yield high performance two-dimensional electron gas heterostructures.

The single planar doped TEGFETs realized exhibit current gain cutoff frequencies and power gain characteristics which are among the best reported for 0.7 μm gatelength devices.

Acknowledgements

Dr. J. Favre of Thomson-CSF (France) is gratefully acknowledged for his work on simulating

our heterojunctions. We thank Mrs. S.P. Liu for her constant help in preparing the samples. This work was supported by Thomson-CSF (France).

References

- [1] M.A.G. Halliwell and M.H. Lyons, *J. Crystal Growth* 68 (1984) 523.
- [2] W. Walukiewicz, H.E. Ruda, J. Lagowski and H.C. Gatos, *Phys. Rev. B* 30 (1984) 4571.
- [3] C.K. Peng, S. Shinha and H. Morkoç, *J. Appl. Phys.* 62 (1987) 2880.
- [4] B. Vinter, *Appl. Phys. Letters* 44 (1984) 307.
- [5] G. Bastard, *Wave Mechanics Applied to Semiconductor Heterostructures* (Editions de Physique, Les Ulis, 1988).
- [6] K. Lee, M.S. Shur, T.J. Drummond and H. Morkoç, *IEEE Trans. Electron Devices* ED-31 (1984) 29.
- [7] M.C. Foisy, P.J. Tasker, B. Hughes and L.F. Eastman, *IEEE Trans. Electron Devices* ED-35 (1988) 871.

High quality GaInAs/AlGaInAs/AlInAs heterostructures on Si ion implanted semi-insulating InP substrates for novel high performance optical modulators

T.Y. Chang, N.J. Sauer, J.E. Zucker, K.L. Jones, B. Tell, K. Brown-Goebeler, M. Wegener *
and D.S. Chemla

AT&T Bell Laboratories, Crawfords Corner Road, Holmdel, New Jersey 07733-1988, USA

The wide range of conduction-band discontinuity available in the GaInAs/AlGaInAs/AlInAs material system has enabled us to demonstrate high sensitivity, high speed optical modulators and switches based on the band filling effect in the novel blockaded reservoir and quantum well electron transfer structure (BRAQWETS). As phase modulators, these devices also offer linear response and very low attendant absorption modulation. High quality samples have been obtained on Si⁺ implanted InP:Fe substrates which will permit predefinition of conduction patterns for optoelectronic integration. Experimental results and design principles are presented.

1. Introduction

The ability of MBE to grow complex, high quality GaInAs/AlGaInAs/AlInAs heterostructures on InP offers opportunities to create novel bandgap engineered optoelectronic devices for the important spectral range of 1.3 to 1.6 μm . This material combination has several attributes that are of fundamental importance to optoelectronic devices; namely, large conduction-band discontinuities (typically 0.5 eV), high room-temperature mobilities (greater than $10,000 \text{ cm}^2/\text{V} \cdot \text{s}$), and an optically transparent substrate. A novel blockaded reservoir and quantum well electron transfer structure (BRAQWETS) made possible by this versatile materials technology is described in this paper. BRAQWETS makes it possible for the first time to synchronously control the charge density in multiple quantum wells. The related band filling effect gives rise to strong electroabsorption at

wavelengths above the absorption edge and to strong electrorefraction below the absorption edge. Experimental results indicate that for a given absorption loss the maximum achievable phase shift in a waveguide is one order of magnitude greater than what is possible in a quantum confined Stark effect (QCSE) modulator containing similar quantum wells. Consequently, we are able to achieve 180° phase shift in a compact waveguide structure with low absorption loss and very low attendant absorption modulation. Furthermore, the electric field dependence of Δn in BRAQWETS devices is linear rather than quadratic. In contrast to carrier injection type devices, the absence of holes in BRAQWETS makes it low in power consumption and high in response speed. These properties can be used to advantage in intersecting waveguide optical switches. These device structures have been grown with high quality on Si ion implanted semi-insulating InP. This technique would allow the fabrication of optoelectronic integrated circuits on substrates with predefined conduction patterns. Finally, we consider the speed and sensitivity of BRAQWETS devices and their optimization.

* Current address: Fachbereich Physik, Universität Dortmund, W-4600 Dortmund, Germany

2. Device structure and experimental results

The energy-band diagrams under (a) equilibrium, and (b) strong forward bias for two periods of prototype BRAQWETS are shown in fig. 1. Each period comprises an electron reservoir ($R_s + R_b$) of lattice matched AlGaInAs (1.00 to 1.06 eV band gap) doped with Si to 1 to $3 \times 10^{18} \text{ cm}^{-3}$ with a total thickness of 28 to 50 nm, a 10 to 26 nm undoped spacer layer (S) of the same quaternary material, an undoped 7 to 9 nm quantum well (W) of $\text{Ga}_{0.47}\text{In}_{0.53}\text{As}$, and a 32 to 72 nm blocking barrier (B) of $\text{Al}_{0.48}\text{In}_{0.52}\text{As}$. The blocking barrier is undoped except for a 15 nm region near the center where it is doped with Be to 1.24 to $2.5 \times 10^{18} \text{ cm}^{-3}$. The two ends of this building block are securely anchored in the Fermi level owing to the n^+ doping. The identical and well defined boundary conditions on each end permit repeated stacking of the basic period. The depleted p doping in the blocking barrier induces partial depletion of the reservoir and appropriate band bending in the spacer and the quantum well. Each waveguide sample contains five to eight periods of BRAQWETS, terminating at both ends in a 60 nm reservoir followed by an n^+ -doped superlattice grading layer, and an n^+ AlInAs:Si clad-

ding layer. The top surface of each device is further capped with 30 nm of n^{++} quaternary layer to facilitate ohmic contact. The absence of free holes in the device helps minimize the optical waveguide loss.

Under forward bias (fig. 1b), the external voltage is divided exactly equally among all periods and the transfer of electrons from reservoirs to quantum wells takes place synchronously. The leakage current is identical from period to period and remains small (less than $2.5 \mu\text{A}$ for a $100 \times 200 \mu\text{m}^2$ mesa for bias voltages between -2 and $+4 \text{ V}$) owing to the high blocking barrier.

The MBE growth was carried out at a substrate temperature of $\sim 500^\circ\text{C}$. The lattice mismatches for AlInAs, AlGaInAs, and GaInAs were kept well within 2×10^{-3} by using five precalibrated group III effusion cells including one for In, two for Ga, and two for Al. Mesa diodes (some with an $80 \mu\text{m}$ diameter optical window) and rib waveguides were subsequently fabricated by standard photolithography and lift off techniques. Since the refractive index of InP is lower than those of all the epitaxial layers used, we find it necessary to limit the thickness of the bottom cladding layer to $\sim 0.25 \mu\text{m}$ to avoid multimoding in the waveguide. To facilitate processing of the bottom ohmic contact when a semi-insulating substrate is used in the interest of minimizing parasitic capacitance and/or future optoelectronics integration, we introduce an $\sim 0.8 \mu\text{m}$ conducting surface layer to the pre-etched substrate by Si ion implantation. The implant is activated at 775°C for 15 s and then a $\sim 0.2 \mu\text{m}$ layer is removed by chemical etching before the substrate is loaded into the MBE system. We have been able to obtain devices on this type of substrates with quality equivalent to those grown on InP:S. This technique will allow us to predefine conduction patterns on semi-insulating substrates for optoelectronic integration.

A differential absorption spectrum (DAS) for a five-period samples measured at normal incidence is shown in fig. 2 as a dashed curve. It gives the change of absorption coefficient $\Delta\alpha$ (all assigned to the quantum wells) for a bias-voltage swing of 2–6 V. The steepness of the low energy edge attests to the synchronousness of band filling in

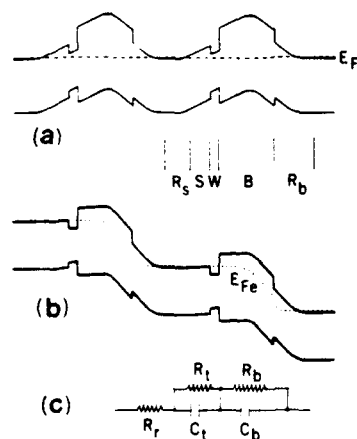


Fig. 1. Energy-band diagrams for two periods of BRAQWETS: (a) at equilibrium and (b) under large forward bias ($R_s + R_b$: electron reservoir, S: spacer, W: quantum well, B: blocking barrier); (c) Small signal equivalent circuit.

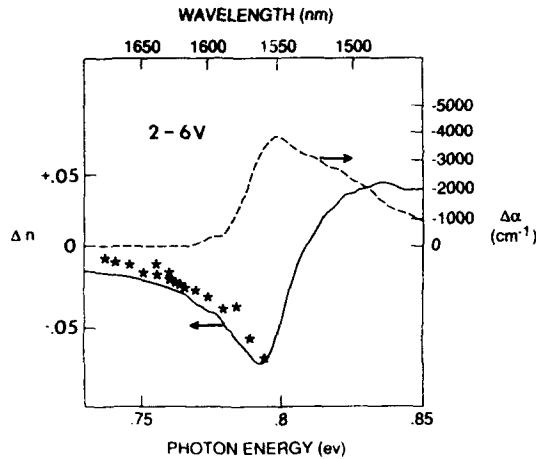


Fig. 2. Measured Δn for 2–6 V modulation of the bias (dashed curve) and the corresponding Δn calculated from Kramers-Kronig transformation (solid curve). The asterisks are interferometrically measured data points.

all five quantum wells. Further details on DAS have been given elsewhere [1,2].

In the waveguide configuration, we obtain a 22 dB change of transmitted intensity at $1.539 \mu\text{m}$ for a bias voltage swing from -2 to 7 V for a 1.04 mm long device fabricated from a five-period prototype BRAQWETS. The experimental data are shown in fig. 3. The propagation loss in the "on" state is 3 dB.

The induced change of refractive index Δn for 2–6 V voltage excursion (corresponding to $\Delta E =$

9.3×10^4 V/cm) calculated from $\Delta \alpha$ by Kramers-Kronig transform is shown as the solid curve in fig. 2. The calculated value of $|\Delta n|$ at 0.775 eV (0.031 eV below the heavy hole exciton at 2 V bias) is 0.04 (in quantum wells only). This is 4.3 times larger than Δn available from QCSE for similar quantum wells and the same electric field [3]. Direct measurements of Δn were also carried out by inserting the sample in a high contrast tunable Mach-Zehnder interferometer. The measured values are plotted in fig. 2.

The dependence of Δn on the bias voltage was found to be linear over a wide voltage range once the quantum wells started to fill. Below this threshold, Δn was negligibly small. The values of the threshold voltage was adjustable by varying the spacer layer thickness and/or the p-type doping in the blocking barrier [1,2].

Monolithic Mach-Zehnder interferometers with $5 \mu\text{m}$ wide rib waveguides have been fabricated. The active regions are electrically isolated by ion bombardment. Shown in fig. 4 are the dependences of the transmitted intensity at $1.58 \mu\text{m}$ as a function of bias voltage applied to one arm of the interferometer for active lengths of 350 and 650 μm . For the latter, the voltage swing required to produce 180° phase shift is 5.4 V. Recent studies show that, by using a more optimized layer structure and by increasing the number of BRAQWETS period from five to eight, the voltage-length

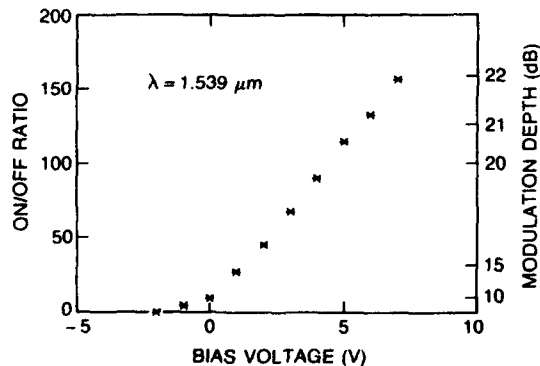


Fig. 3. Transmitted intensity as a function of bias voltage for a 1.04 mm long waveguide with 3dB propagation loss in the "on" state.

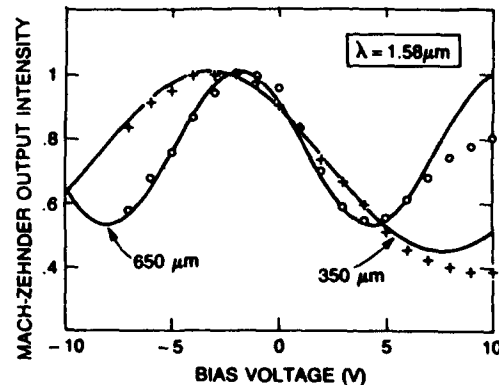


Fig. 4. Output intensity of Mach-Zehnder rib waveguide interferometer as a function of applied voltage at $1.58 \mu\text{m}$ wavelength for two different active lengths, 650 and 350 μm .

product for 180° phase shift can be an order of magnitude smaller than what has been achieved previously by using bulk semiconductor layers. Preliminary results also show BRAQWETS to be effective for fabricating intersecting waveguide optical switches. Owing to the absence of holes, BRAQWETS based switches are expected to be vastly faster and require much less power than current-injection switches.

3. Discussion

At moderate detuning (25 to 35 meV) below the heavy hole exciton, phase modulation by QCSE is seriously encumbered by the induced absorption due to the red shifting absorption edge. In contrast, the absence of induced absorption below the band gap (since the absorption edge blue shifts) makes BRAQWETS much superior for phase modulators. The values of two important figures of merit, namely, $\Delta n / \Delta k$ (where $\Delta k = \lambda_0 \Delta \alpha / 4\pi$) and $\Delta \phi_L = 2\pi \Delta n / \lambda_0 \alpha_{\max}$ (the phase shift induced in one adsorption length), are both higher by an order of magnitude in BRAQWETS than in QCSE for the same amount of detuning below the band edge [2-4]. The difference is particularly striking at high fields ($\sim 10^5$ V/cm).

A small signal equivalent circuit, when the quantum wells are at least partly filled, is shown in fig. 1c. The resistance of the reservoir, R_r , is very small, typically $< 10^{-7} \Omega \text{ cm}^2$. The transfer capacitance, C_t , is determined by the thickness of the transfer barrier (thickness of the space layer plus that of the right depletion layer of the reservoir), while the transfer resistance, R_t , by its height. The blocking capacitance, C_b , and the blocking resistance, R_b , are similarly determined by the combination of the blocking barrier and the left depletion layer of the reservoir. The intrinsic speed of the device is limited by $R_t C_t$ which is $\sim 10^{-11}$ s for present designs. This can be reduced by reducing the quaternary band gap. It can be even more effectively reduced by stepwise or continuous grading of the spacer-layer band gap. The

intrinsic speed would be significantly slower if the electrons were required to transfer laterally over a much larger distance to and from a source contact located outside the waveguide.

The actual speed of a BRAQWETS device is given approximately by $[(R_d/N) + R_t]C_b$, where R_d is the source resistance of the drive circuit and N is the number of BRAQWETS period [2]. If $R_d/N = 10 \Omega$, then the response time is $\sim 10^{-10}$ s for a 1 mm long waveguide.

Increasing doping concentrations allows one to reduce the doping layer thicknesses and hence increases the optical confinement factor. Reducing the blocking barrier thickness also improves the confinement factor and furthermore enhances the voltage sensitivity. However, since C_b is increased as a result of this, the improvement may come about at the expense of the response speed unless N is increased at the same time. To achieve the highest possible speed, it would be necessary to have integrated source or emitter followers on the same chip to reduce R_d .

4. Conclusions

High performance optical modulators and switches based on the band filling effect in BRAQWETS have been demonstrated. As phase modulators, this novel device concept offers not only high sensitivity and high speed but also linear response and very low attendant absorption loss and absorption modulation.

References

- [1] M. Wegener, J.E. Zucker, T.Y. Chang, N.J. Sauer, K.L. Jones and D.S. Chemla, Phys. Rev. B41 (1990) 3097.
- [2] T.Y. Chang, M. Wegener, J.E. Zucker, N.J. Sauer, K.L. Jones and D.S. Chemla, in: IEEE Intern. Electron Devices Meeting, Washington, DC, 1989, Tech. Digest, p. 737.
- [3] J.E. Zucker, I. Bar-Joseph, G. Sucha, U. Koren, B.I. Miller and D.S. Chemla, Electron. Letters 24 (1988) 458.
- [4] J.E. Zucker, T.Y. Chang, M. Wegener, N.J. Sauer, K.L. Jones and D.S. Chemla, IEEE Photonics Technol. Letters 2 (1990) 29.

Orientation dependence of mismatched $\text{In}_x\text{Al}_{1-x}\text{As}/\text{In}_{0.53}\text{Ga}_{0.47}\text{As}$ HFETs

Sandeep R. Bahl, Walid J. Azzam and Jesús A. del Alamo

Massachusetts Institute of Technology, Cambridge, Massachusetts 02139, USA

A device perspective is applied to the issue of critical layer thickness and the impact of strain relaxation on electrical characteristics. We have fabricated $\text{In}_x\text{Al}_{1-x}\text{As}/\text{n}^+\text{-In}_{0.53}\text{Ga}_{0.47}\text{As}$ HFETs with InAs mole fractions in the 300 Å thick $\text{In}_x\text{Al}_{1-x}\text{As}$ insulator of $x = 0.52$ (lattice-matching), 0.48, 0.40, and 0.30. The $x = 0.40$ and 0.30 samples, with thicknesses greater than the critical limit, show unidirectional surface ridges that reveal misfit dislocations at the $\text{In}_x\text{Al}_{1-x}\text{As}/\text{In}_{0.53}\text{Ga}_{0.47}\text{As}$ hetero-interface. Dislocations are found to severely degrade the performance of devices when the current in the device flows perpendicular to them. Excellent HFETs were obtained with current flow parallel to the surface ridges for $x = 0.40$, in spite of the unequivocal evidence of dislocations in the devices.

1. Introduction

The critical layer thickness of a strained semiconductor layer is ultimately determined by its application. For devices, performance is the ultimate goal. In many III–V semiconductor devices, the use of intentionally mismatched layers has the potential of significantly improving device characteristics. The appearance of misfit dislocations, however, is expected to degrade device performance, but to determine how much and in what manner, there is no substitute to studying the devices fabricated using these mismatched layers.

In an effort to increase the conduction band discontinuity in the $\text{In}_{0.52}\text{Al}_{0.48}\text{As}/\text{In}_{0.53}\text{Ga}_{0.47}\text{As}$ system (lattice-matched to InP), we have strained the $\text{In}_x\text{Al}_{1-x}\text{As}$ layer to negative mismatch by reducing its InAs fraction. This results in many benefits to the device characteristics of $\text{In}_x\text{Al}_{1-x}\text{As}/\text{n}^+\text{-In}_{0.53}\text{Ga}_{0.47}\text{As}$ HFETs [1,2]. In our structure the $\text{In}_x\text{Al}_{1-x}\text{As}$ is undoped, as contrasted with the more familiar modulation-doped FET (MODFET). The absence of dopants in the insulator prevents some common problems that plague the MODFET [1,2]: transconductance and cutoff-frequency collapse at high gate-source bias from parasitic channel formation, and a reduced gate-breakdown voltage. Here we focus on the

effect of mismatch on device performance. Our main result is the finding of strong orientation dependence in device characteristics beyond the Matthews–Blakeslee critical layer thickness [3].

2. Experimental

A cross section of the device structure is shown in fig. 1. Four wafers were grown by MBE in MIT's Riber 2300 system with InAs mole fractions in the $\text{In}_x\text{Al}_{1-x}\text{As}$ gate insulator layer of

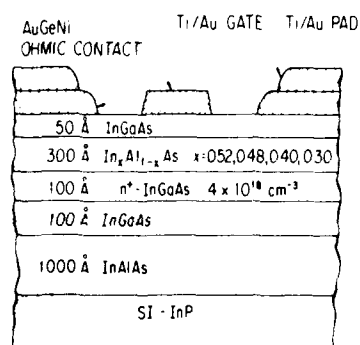


Fig. 1. Schematic cross section of the fabricated $\text{In}_x\text{Al}_{1-x}\text{As}/\text{n}^+\text{-In}_{0.53}\text{Ga}_{0.47}\text{As}$ HFETs.

0.52 (lattice-matching), 0.48, 0.40 and 0.30. The starting material was SI (100) InP. The device structure consists (from bottom to top) of a 1000 Å undoped $\text{In}_{0.52}\text{Al}_{0.48}\text{As}$ buffer layer, a 100 Å undoped $\text{In}_{0.52}\text{Ga}_{0.48}\text{As}$ subchannel, a 100 Å heavily Si doped ($N_D = 4 \times 10^{18} \text{ cm}^{-3}$) $\text{In}_{0.52}\text{Ga}_{0.48}\text{As}$ channel, a 300 Å undoped $\text{In}_x\text{Al}_{1-x}\text{As}$ gate insulator layer, and an undoped 50 Å $\text{In}_{0.52}\text{Ga}_{0.48}\text{As}$ cap. The subchannel serves as a smoothing layer to prevent the growth of the active channel directly on the poor $\text{In}_{0.52}\text{Al}_{0.48}\text{As}/\text{In}_{0.52}\text{Ga}_{0.48}\text{As}$ reverse interface [4]. The four wafers were grown subsequently and device processing was carried out simultaneously. Device processing is described in ref. [2].

HFETs were fabricated with gate-widths of 30 μm and gate-lengths, L_g , of 1, 1.5, 2, 3, 5, and 10 μm with current flow along the $[0\bar{1}1]$ (defined here as 0° with respect to the flat), $[001]$ (45°), and $[011]$ (90°) directions.

3. Results

Fig. 2 shows the channel sheet resistance, R_{sh} , on each of the four wafers as a function of orientation. R_{sh} was measured using the actual HFETs by the all-electrical floating gate transmission-line

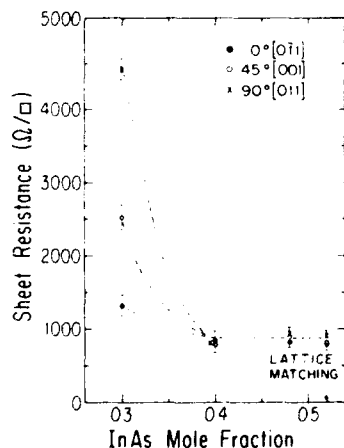


Fig. 2. Channel resistance versus InAs mole fraction, x , in the $\text{In}_x\text{Al}_{1-x}\text{As}$ insulator layer, for current flow along the 0° , 45° , and 90° direction with respect to the flat.

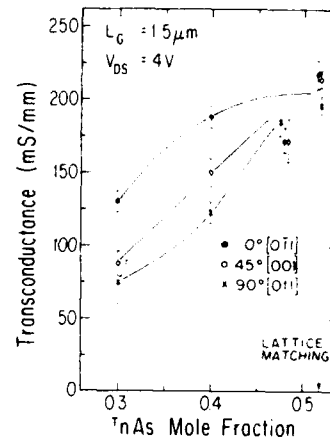


Fig. 3. A plot of the peak transconductance versus x for the 0° , 45° , and 90° devices with $L_g = 1.5 \mu\text{m}$ at $V_{ds} = 4 \text{ V}$.

model (FGTLM) technique [5]. Each point represents an average over five FGTLMs. For wafers with InAs mole fractions, x , of 0.52, 0.48, and 0.40, R_{sh} remains constant at approximately $850 \Omega/\square$ independent of orientation. However, upon decreasing x from 0.40 to 0.30, the channel sheet resistance increases for all three orientations, showing a very pronounced orientation dependence with $R_{sh} [011] > R_{sh} [001] > R_{sh} [0\bar{1}1]$.

Fig. 3 shows the average peak transconductance, g_m , over ten devices versus x for the three orientations. These values are for devices with nominal gate-lengths of $1.5 \mu\text{m}$, measured at $V_{ds} = 4 \text{ V}$. The $x = 0.52$ and 0.48 devices do not show any orientation dependence. The $x = 0.40$ devices have a high source resistance and are anomalously low in g_m . A pronounced orientation dependence is seen for devices with both $x = 0.40$ and 0.30 , with the 0° device being the best and the 90° device the most degraded. This result applies regardless of L_g from 1 to $10 \mu\text{m}$. An additional significant result is that $g_m(0^\circ, x = 0.40)$ is 189 mS/mm , which is very close to the average $g_m = 209 \text{ mS/mm}$ of the $x = 0.52$ sample.

4. Discussion

The $x = 0.40$ and 0.30 devices were grown with thicknesses greater than the Matthews–Blakeslee

critical layer limit [3]. This suggests that, in these devices, misfit dislocations may be responsible for the decrease in g_m and the appearance of orientation dependence. Since the presence of misfit dislocations has been correlated to the appearance of a cross-hatched surface [8], we have taken dark field microscope images of the surface of the four wafers (fig. 4). Figs. 4a and 4b are the surfaces of the $x = 0.52$ and $x = 0.48$ wafers, respectively. There are no ridges or cross-hatches on the surface. Figs. 4c and 4d are the surfaces of the $x = 0.40$ and $x = 0.30$ wafers, respectively. We see the ap-

pearance of a unidirectional array of surface ridges, faint and short, in fig. 4c, and brighter and longer in fig. 4d, running along the $[0\bar{1}1]$ direction. This is the direction of current flow in the better (0°) devices. We could not distinguish any ridges along the $[011]$ direction, neither in the Nomarski, nor in the dark-field mode of the microscope. The ridges could not be imaged at higher magnification, so a density count was impossible. Brighter and longer streaks would result from greater surface relief, indicating a greater dislocation density, with a greater bunch of dislocations associated with each

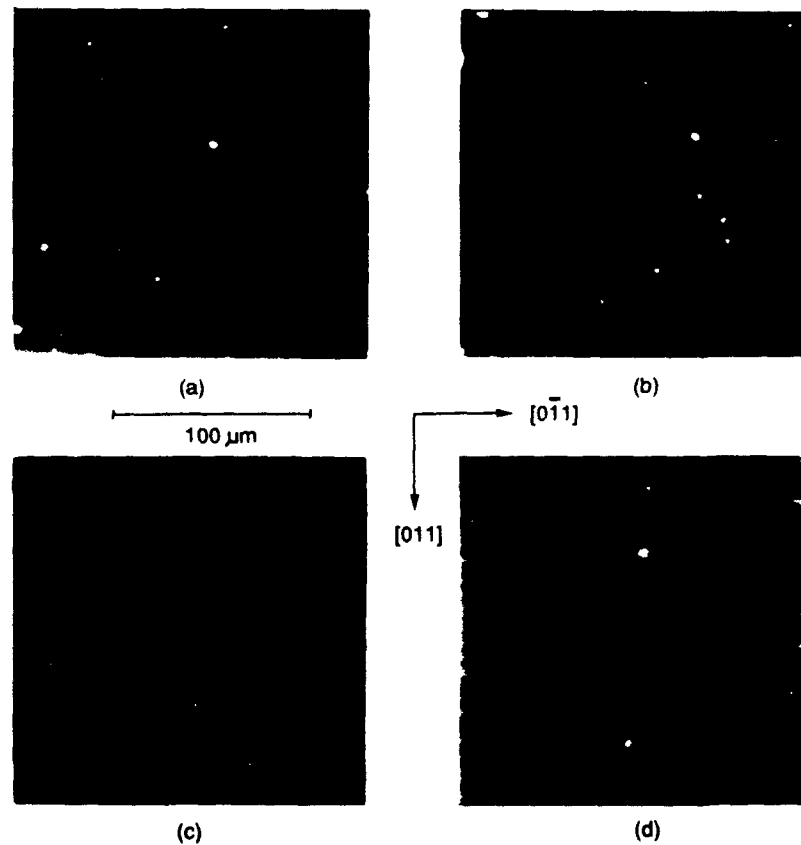


Fig. 4. Dark-field optical microscope photographs of the surface of the HFET layer structure for (a) $x = 0.52$, showing a plain surface, (b) $x = 0.48$ showing a plain surface, (c) $x = 0.40$, showing the appearance of short faint surface ridges along the $[0\bar{1}1]$ direction, and (d) $x = 0.30$, showing a dense unidirectional array of ridges in the $[0\bar{1}1]$ direction.

surface streak [9]. The unidirectional hatch observed is consistent with that reported [6] for thin strained samples.

In III-V semiconductors, orthogonal 60° dislocations in the zinc-blende lattice occur on different sublattices and show an asymmetry relative to each other [9]. The so-called α dislocations have an extra half plane ending on a row of group III atoms, and the β dislocations have an extra half plane ending on a row of group V atoms [10]. For strained (100) InGaAs/GaAs, it has been shown that the first dislocations to form are $60^\circ \alpha$ dislocations along the [011] direction [6,7]. For our samples, in contrast, the dislocations run unidirectionally along the $[0\bar{1}1]$ direction, perpendicular to the preferred dislocation direction we have seen reported in the literature. However, these reports [6,7,11] have been done for epilayers under compression, i.e. the relaxed lattice constant for the epilayer is larger than that of the substrate. It has also been suggested that the $60^\circ \alpha$ and β dislocations should interchange directions when the epilayer is grown in tension [12], which is consistent with our results, assuming that the α dislocations still nucleate preferentially. We believe we are the first to report observations of this behavior.

Our 0° devices, which have current flowing along the dislocations, are better than our 90° devices, which have current flowing perpendicular to them. The 45° devices fall in between. Our results are in agreement with the findings of Sun et al. [11], who report that for mismatched $\text{In}_x\text{Ga}_{1-x}\text{As}/\text{GaAs}$, with surface ridges preferentially along the [011] direction, the low-field mobility is degraded along the $[0\bar{1}1]$ direction, i.e. normal to the lines of preferred (α) dislocations. Esquivel et al. [10] also show a decrease in mobility for current flow perpendicular to the α dislocations.

Woodall et al. [13] have proposed that misfit dislocations pin the Fermi-level, depleting a cylindrical region around them. Fig. 5 shows a schematic cross-section of the dislocation depletion regions in a semiconductor slab with misfit dislocations running along the $[0\bar{1}1]$ direction. Based on this figure, we can hypothesize an explanation for our observations: For our 0° devices, current flows along the dislocation direction $[0\bar{1}1]$, while

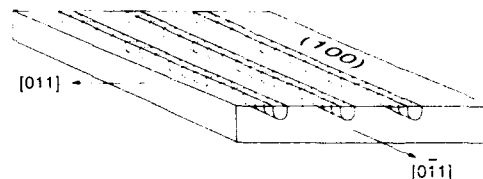


Fig. 5. A schematic cross-section of the channel region of the HFET under tension, showing the effect of the depletion regions of misfit dislocations on current flowing parallel and perpendicular to them.

for our 90° device, current flow along $[0\bar{1}1]$ is normal to it. If the dislocation density is low, as in the $x = 0.40$ sample, a dislocation would be associated with a small depletion region in the channel. If this depletion depth is smaller than the equilibrium depletion associated with Fermi-level pinning at the wafer surface or underneath the gate, then R_{sh} should not be affected by the presence of the dislocations. However, the pinning at the dislocation would prevent the gate voltage from modulating the portion of the channel underneath it. This should result in the degradation of g_m more severe for current flow perpendicular to the dislocations, because of their constricting effect, than for flow parallel to them. For a higher misfit (such as in the $x = 0.30$ sample), the surface relief becomes more pronounced, indicating a greater bunching of the dislocations [9], and producing depletion regions that exceed the depth of the one associated with the wafer surface. This should result in an asymmetry in both R_{sh} and g_m .

$\text{In}_{0.40}\text{Al}_{0.60}\text{As}/n^+-\text{In}_{0.53}\text{Ga}_{0.47}\text{As}$ devices with $L_g = 1.5 \mu\text{m}$ and current flow along the $[0\bar{1}1]$ direction show excellent characteristics in spite of the presence of misfit dislocations: a reverse breakdown voltage of 23 V, a maximum drain current of 308 mA/mm, a peak transconductance of 189 mS/mm and reduced real-space transfer of hot electrons from the channel to the gate [2]. Our result shows that although dislocations degrade device performance, excellent devices may be obtained by orienting the current parallel to them, if they are sufficiently sparse.

5. Conclusion

We have studied the electrical properties of strained-insulator $\text{In}_x\text{Al}_{1-x}\text{As}/\text{n}^+-\text{In}_{0.53}\text{Ga}_{0.47}\text{As}$ HFETs with the insulator composition below and above the Matthews–Blakeslee criteria for dislocation formation. For devices with the $\text{In}_x\text{Al}_{1-x}\text{As}$ layer above its critical thickness, we see a unidirectional array of surface ridges and measure a strong orientation dependence of peak transconductance. By aligning the current in the direction of the ridges, the impact of dislocations is greatly minimized, resulting in excellent devices, if their density is not too high.

Acknowledgements

This work has been partially funded by the Joint Services Electronics Program through the Research Laboratory of Electronics (DAAL-03-86-K-0002), the C.S. Draper Laboratory (DL-H-404180), and a TRW Scholarship from the Undergraduate Research Opportunities Program at MIT (W.J.A.). The authors acknowledge Professor Clifton G. Fonstad for the use of his MBE, and Hewlett Packard for an equipment donation.

References

- [1] J.A. del Alamo and T. Mizutani, IEEE Electron Device Letters EDL-8 (1987) 534.
- [2] S.R. Bahl, W.J. Azzam and J.A. del Alamo, IEEE Trans. Electron Devices, submitted.
- [3] J.W. Matthews and A.E. Blakeslee, J. Crystal Growth 27 (1974) 118.
- [4] A.S. Brown, J.A. Henige and M.J. Delaney, Appl. Phys. Letters 52 (1988) 1142.
- [5] W.J. Azzam and J.A. del Alamo, IEEE Trans. Electron Devices ED-37 (1990) 2105.
- [6] K.L. Kavanagh, M.A. Capano, L.W. Hobbs, J.C. Barbour, P.M.J. Marée, W. Schaff, J.W. Mayer, D. Pettit, J.M. Woodall, J.A. Strosio and R.M. Feenstra, J. Appl. Phys. 64 (1988) 4843.
- [7] E.A. Fitzgerald, G.P. Watson, R.E. Proano, D.G. Ast, P.D. Kirchner, G.D. Pettit and J.M. Woodall, J. Appl. Phys. 65 (1989) 2220.
- [8] K.H. Chang, R. Gibala, D.J. Srolovitz, P.K. Bhattacharya and J.F. Mansfield, J. Appl. Phys. 67 (1990) 4093.
- [9] M.S. Abrahams, J. Blanc and C.J. Buiochi, Appl. Phys. Letters 21 (1972) 185.
- [10] A.L. Esquivel, S. Sen and W.N. Lin, J. Appl. Phys. 47 (1976) 2588.
- [11] Q. Sun, D. Morris, C. Lacelle and A.P. Roth, Mater. Res. Soc. Symp. Proc. 160 (1990) 783.
- [12] W.J. Bartels and W. Nijman, J. Crystal Growth 37 (1977) 204.
- [13] J.M. Woodall, G.D. Pettit, T.N. Jackson and C. Lanza, Phys. Rev. Letters 51 (1983) 1783.

MBE growth of graded index AlGaInAs MQW lasers on InP

M. Allovon, M. Quilic, M. Blez and C. Kazmierski

Centre National d'Etudes des Télécommunications, Laboratoire de Bagneux, 196 Avenue Henri Ravéra, F-92220 Bagneux, France

AlGaInAs SCH MQW lasers with continuously graded bandgap active region have been grown by MBE lattice matched to InP. The design of the structure and the MBE growth technique used to grow graded quaternary layers are reported in details. Improved laser results are reported both for broad area devices and for buried ridge stripe processed lasers. A threshold current density as low as 820 A/cm^2 is obtained for a $1180 \mu\text{m}$ long device. A record cw threshold current of 17 mA is reported for a AlGaInAs laser, with a resonance frequency of 6.7 GHz.

1. Introduction

During the last years, the GaInAs/AlInAs material system has attracted considerable interest, especially in MBE because of the ease of growth of these "arsenide only" ternaries and quaternary. Many impressive results have been obtained in the microelectronic or electro-optic fields, but good results have been reported only recently in the laser field [1-3], probably because of the relatively poor optical quality of AlInAs compared to InP.

We show here how the modification of the standard SCH structure by avoiding the use of AlInAs near the active region of the lasers has allowed us to obtain state-of-the-art threshold current densities with "phosphorus-free" MBE multi quantum well structures, using graded quaternary layers in the optical guide. Then we explain how we have successfully grown well lattice matched linearly graded AlGaInAs layers, in spite of the indirect flux control inherent to solid source MBE. Finally we present recent results on buried ridge stripe (BRS) lasers made from these structures in a two-steps process, including low cw threshold currents and preliminary dynamic measurements of these promising MQW lasers.

In the following, AlGaInAs quaternary layers lattice matched to InP will be written as follows: $(\text{Ga}_{0.47}\text{In}_{0.53}\text{As})_{1-z}(\text{Al}_{0.48}\text{In}_{0.52}\text{As})_z$, where z is the

quaternary composition often expressed in percent.

2. Design of AlGaInAs MQW laser structure

The MQW graded index separate confinement heterostructure (GRINSCH) used in this work is detailed in fig. 1. Compared to previous work on MQW lasers in this material system [4-6], we have avoided to use a thick AlInAs bottom layer be-

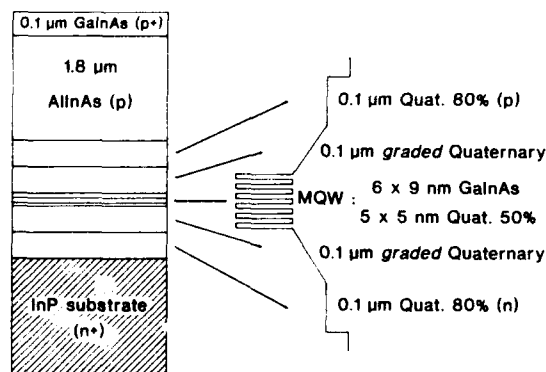


Fig. 1. Detailed MQW GRINSCH laser structure. The n- and p-layers are doped about $5 \times 10^{17} \text{ cm}^{-3}$. The n⁺-InP substrate and p⁺-GaInAs contact layer are doped about $2 \times 10^{19} \text{ cm}^{-3}$. Other layers (active region) are undoped (n-type residual doping level about $2 \times 10^{15} \text{ cm}^{-3}$).

cause it is likely to introduce a rough interface between the n-type cladding layer and the first quaternary guiding layer. And the presence of a "bad" interface at this position in the structure should decrease the luminescence efficiency of the laser because the dwelling time of the carriers in the guiding layers is long enough to give rise to significant losses if the non-radiative lifetimes in these layers are too short, or if the recombination rates at the interfaces are too high.

For these reasons we have decided to use the InP substrate as n-type optical cladding layer, and we have grown only a thin 80% quaternary buffer layer of 0.1 μm below the first guiding layer, in order to confine further the carriers in the active region and to prevent them to be lost at the substrate interface which is always highly recombinant. On the p-side of the structure we have grown symmetrically a 0.1 μm 80% quaternary layer to separate the guiding layer from the AlInAs optical confinement layer. Another advantage of using quaternary instead of AlInAs for the buffer layer is to minimize the injection problems which might result from the conduction band discontinuity at the InP/AlInAs interface.

A plain SCH structure was then difficult to realize, since it needs to shift from a 80% quaternary layer to another composition like 50% for the guiding region. We have tried two different solutions, as already reported [3], either by using a short period superlattice pseudo-alloy for the guiding layers, or by gradually modifying the quaternary composition between 80% and 50%. We report here on the MBE growth of the second type of structure ie the GRINSCH one, which gave the best results, but which is the most difficult to realize, since it needs to control the growth of *lattice matched* quaternary layers with continuously graded composition.

3. MBE growth of continuously graded layers

We use RIBER 2300 equipment, with a home made growth automation software. The quaternary AlGaInAs material is grown by using two indium sources In_1 and In_2 , which makes composition tuning very easy, as described in previous work

[7]. The two ternaries GaIn_1As and AlIn_2As can be separately tuned for lattice matching with the substrate. The quaternary alloy $\text{GaAl}(\text{In}_1 + \text{In}_2)\text{As}$ is then also lattice matched, its composition being a function of the growth rates of the two ternaries:

$$r_Q = r_G + r_A, \quad z = r_A/r_Q,$$

where r_G , r_A and r_Q are the growth rates of GaIn_1As , AlIn_2As and GaAlInAs respectively, and z is the composition of the quaternary written as $(\text{GaIn}_1\text{As})_{1-z}(\text{AlIn}_2\text{As})_z$.

It is obvious from the preceding equations that one simple way to grow linearly graded quaternary layers versus layer thickness is to ramp *linearly* r_A and r_G versus time in opposite sense, keeping r_Q constant.

At this point it is important to note that this kind of simple solution does not work for the GaInAsP quaternary alloy, because the competition between As and P incorporation turns out in interdependence between GaAs and InP growth rates [8].

On the other hand, in solid source MBE, linear ramping of growth rates is not trivial, because growth rates are proportional to cell *fluxes* (assuming unity sticking coefficients), but the only controllable parameters during growth are the cell *temperatures*. And the relationships between them

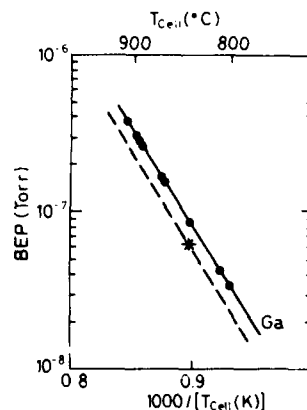


Fig. 2. Calibrated correspondence between emitted flux (BEP) and reciprocal absolute temperature for a gallium cell. The solid line is fitted on initial flux measurements. The broken line is deduced from one daily measurement and is used to compute actual correspondences.

are not linear but rather exponential. In order to overcome the difficulty we proceed as follows:

- *Initial flux calibration:* After opening the growth chamber the values of beam equivalent pressure (BEP) at different temperatures are measured for each group III cell. These pressure measurements taken with an ion gauge located in the substrate position, give a good idea of the atomic flux impinging at the substrate during growth, and can be considered to be proportional to the growth rate of the corresponding arsenide if the sticking coefficient of this element is unity. These points align on a straight line in adequate coordinates (fig. 2) and give an initial calibration of the cell fluxes.

- *Daily corrections:* During a run which lasts several weeks, the absolute value of the flux for a given temperature changes significantly, so that it was found necessary to adjust daily this initial calibration by measuring each morning only one point for each cell, assuming a constant slope for the straight line. This gives the broken line of fig. 2, which is then used to compute the actual correspondence between fluxes and temperatures. In a similar way the linear relationship between the cell's BEP and the growth rate of the corresponding binary, is calibrated using thickness and mismatch measurements of ternary layers. In practice this procedure allows us to grow lattice matched (or purposely mismatched) ternary layers of any growth rate (and thus quaternaries of any desired composition) in a reliable way.

- *Ramps with linear flux grading:* Besides, this method is also usable to achieve linear ramping of cell fluxes. Indeed, at any point of a ramp, instead of interpolating the current setpoint between the final and initial temperatures, it is easy to do the linear interpolation between the corresponding fluxes, computed in real time using the already calibrated correspondences. This is illustrated in fig. 3: The recording of the actual cell's temperature (solid upper curve) departs from the broken line during the ramp because the setpoints are computed to achieve linear ramping of the flux and not of the temperature. The result is shown on the bottom curve which is the simultaneous recording of the actual flux (BEP) emitted by this cell. It is important to note that in order to obtain

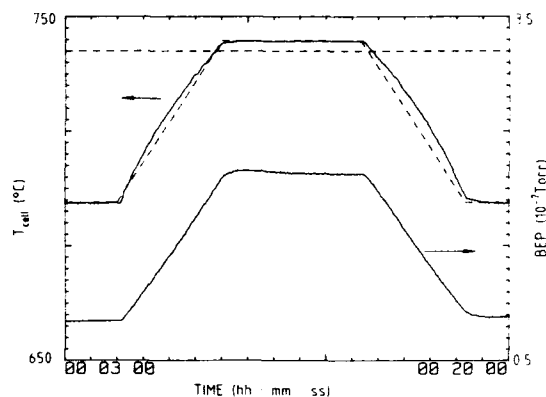


Fig. 3. Temperature ramps for linear grading of cell flux. Upper solid curve is the recording of actual temperature variations compared to linear ramping of temperature setpoint (broken line). Bottom curve is the simultaneous recording of the emitted flux, showing linear flux variations during the ramps, with a flat plateau in between.

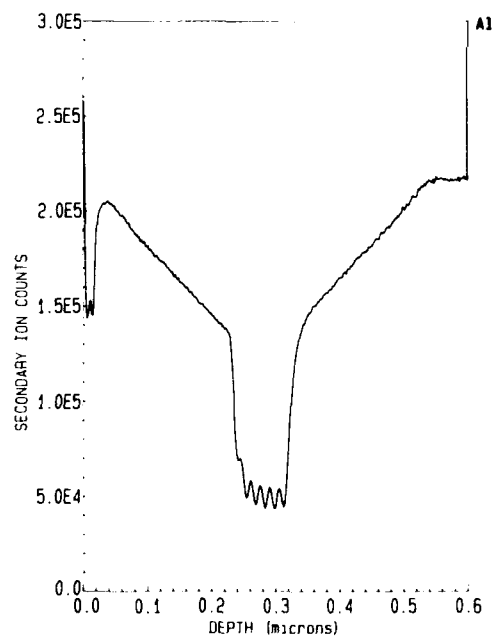


Fig. 4. SIMS profile of the aluminum content in the active region of a GRINSCH laser, demonstrating linear grading in composition versus layer thickness (note the unusual linear scale on the left). The six quantum wells of the active region are clearly visible.

such a good flux profile (in particular good symmetry between increasing and decreasing ramps and a flat plateau in between), it is also necessary to set adequate values for the PID constants of the cell temperature regulator during the ramp. This is also done automatically, according to the ramp's slope, by our automation software.

Thus the problem is solved, because two ramps of this kind are enough to grow a ternary layer whose growth rate varies linearly versus time, and which is lattice matched all along because the two cell fluxes remain in the same ratio. As explained before, four simultaneous such ramps are needed to grow a quaternary graded layer with linear composition grading versus thickness, by superimposing the growths of two independent ternaries whose growth rates are linearly varying in opposite sense, in order to keep a constant growth rate for the graded layer.

This technique has been successfully applied to the growth of MQW lasers. Fig. 4 shows the aluminum SIMS profile in such a structure (without p-type cladding layer). Due to SIMS memory effects (visible also on the first QW record), the ramps do not appear very symmetric, but are conclusively linear (note the unusual linear scale for the aluminum content). X-ray measurements also don't show increased FWHM for the peaks corresponding to such graded layers.

4. Broad area lasers

Laser structures were grown at 560°C (calibrated using InSb melting point), under an As_4 beam of about 2×10^{-5} . The typical growth rate of quaternary layers was 1.5 $\mu\text{m}/\text{h}$. Broad area laser diodes were processed from these structures. Series of chips with cavity length L ranging from 0.2 to 1.2 mm were tested. The threshold current densities of the four best wafers are reported as a function of L in fig. 5. Since our first report of low threshold MBE grown lasers [3], we have further improved the threshold values: best figures are now: 1090, 890 and 820 A/cm^2 for 420, 870 and 1180 μm long devices, respectively. The mean values for about 10 devices of the same cavity length are not very different: 1140, 910 and 830

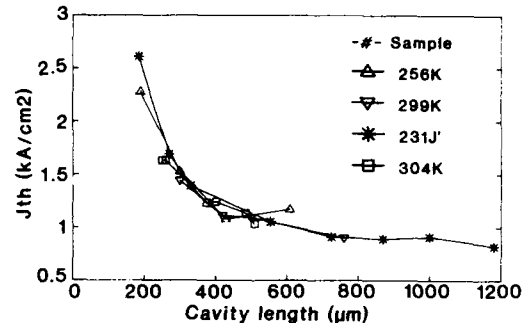


Fig. 5. Variations of threshold current densities versus cavity length, for four different wafers grown in two different MBE runs. Laser structure is detailed in fig. 1.

A/cm^2 , respectively, showing the good homogeneity of these wafers. Moreover, fig. 5 shows the good reproducibility of these results, with very similar values obtained on four wafers, even when grown in different runs and for different wavelengths (ranging from 1.5 to 1.6 μm by using different well widths).

5. BRS lasers

These MBE GRINSCH structures have also been processed in buried ridge stripe (BRS) lasers in order to perform cw and frequency measurements. We started from the structure presented in fig. 1, but without the upper AlInAs and GaInAs p-type cladding and contact layers. A 1.8 μm wide ridge stripe was etched down to the InP substrate, then a second epitaxial growth of 1.5 μm p-doped InP confinement layer and a 0.2 μm p⁺-GaInAs contact layer was performed using a horizontal MOVPE reactor. Details of the process can be found in our recent report of the preliminary results obtained with these lasers [9].

We have improved the homogeneity of our laser results, and also some of the figures already published: at a wavelength of 1.485 μm , threshold currents as low as 15 mA have been measured under pulsed operation, and 17 mA under cw operation, for 250 μm long devices. The maximum optical power was about 8 mW. These already good figures can probably be improved because they seem to be limited by leakage currents through

the side p-n homojunction, which is located inside the heavily doped substrate ($n^+ > 10^{19} \text{ cm}^{-3}$).

The dynamic behaviour of these lasers has also been studied. A resonance frequency of 6.7 GHz has been measured on a 300 μm long device at about 5 mW. Although this figure is also limited by the maximum optical power available, its steep dependence versus optical power (bandwidth move-out rate of about $4 \text{ GHz mW}^{-1/2}$) is very promising for the ultimate high frequency performances of these MQW AlGaInAs lasers.

6. Conclusions

We have reported on the design and the MBE growth of continuously graded index SCH laser structures in the AlGaInAs material system lattice matched to InP. We have also reported further improvements in our laser results, both for broad area devices and for buried ridge stripe processed lasers: very low threshold current densities are obtained reproducibly, with a best value as low as 820 A/cm^2 for a 1180 μm long device. For BRS lasers, a record threshold current of 17 mA has been measured on a AlGaInAs device, and, although limited by the maximum optical power available, an encouraging value of 6.7 GHz has been obtained for the resonance frequency of these promising MBE AlGaInAs MQW lasers.

Acknowledgements

We wish to thank particularly Jacques Primot for many X-ray measurements, Yumin Gao for SIMS analysis, Annick Godin for technical assistance, Didier Robein for MOVPE regrowth experiments and Bernard Sermage for helpful discussions. We are also very grateful to Giovanni De Stefanis and his collaborators from CSELT in Turin (Italy) for broad area laser characterization of one of our wafers. This work was supported by the "AQUA" European project RACE 1057.

References

- [1] P.J. Williams, D.J. Robbins, T.J. Reid, J.I. Davies, A.C. Marshall and A.C. Carter, *Electron. Letters* 25 (1989) 5.
- [2] R.W. Glew, B. Garrett and P.D. Greene, *Electron. Letters* 25 (1989) 1103.
- [3] M. Quillec, M. Allovon, F. Brillouet, A. Gloukhian, J.P. Praseuth and B. Sermage, *Electron. Letters* 25 (1989) 1731.
- [4] H. Temkin, K. Alavi, W.R. Wagner, T.P. Pearsall and A.Y. Cho, *Appl. Phys. Letters* 42 (1983) 845.
- [5] Y. Matsushima, K. Utsuka, K. Sakai and O. Takeuchi, *Electron. Letters* 23 (1987) 1271.
- [6] R. Gessner, M. Druminski and M. Beschoner, *Electron. Letters* 25 (1989) 516.
- [7] J.P. Praseuth, M.C. Joncour, J.M. Gérard, P. Hénoc and M. Quillec, *J. Appl. Phys.* 63 (1988) 400.
- [8] H. Temkin, T. Tanbun-Ek, R.A. Logan, J.A. Lewis and N.K. Dutta, *Appl. Phys. Letters* 56 (1990) 1222.
- [9] C. Kazmierski, M. Blez, M. Quillec, M. Allovon and B. Sermage, *Electron. Letters* 26 (1990) 889.

Molecular beam epitaxial growth and structural design of $\text{In}_{0.52}\text{Al}_{0.48}\text{As}/\text{In}_{0.53}\text{Ga}_{0.47}\text{As}/\text{InP}$ HEMTs

Yi-Ching Pao * and J.S. Harris, Jr.

Department of Electrical Engineering, Stanford University, Stanford, California 94305, USA

Lattice-matched $\text{In}_{0.52}\text{Al}_{0.48}\text{As}$ and $\text{In}_{0.53}\text{Ga}_{0.47}\text{As}$ layers and two-dimensional electron gas (2DEG) structures have been grown on (100) InP substrates by molecular beam epitaxy (MBE) with dimeric or tetrameric arsenic species. Surface morphology of $0.5\text{ }\mu\text{m}$ $\text{In}_{0.53}\text{Ga}_{0.47}\text{As}$ layers is strongly influenced by the As_4 to group III flux ratio, and also by the arsenic species used in the growth. The RHEED oscillation study shows that the uses of As_2 or higher As_4 flux reduce the group III adatoms surface diffusion, hence improving the interface or surface roughness caused by the alloy clustering. This behavior is more obvious in the growth of $\text{In}_{0.53}\text{Ga}_{0.47}\text{As}$ layers than $\text{In}_{0.52}\text{Al}_{0.48}\text{As}$. Two-dimensional electron mobilities of over $11,080\text{ cm}^2/\text{V}\cdot\text{s}$ at 300 K and $33,500\text{ cm}^2/\text{V}\cdot\text{s}$ at 77 K with sheet charge of $3.9 \times 10^{12}\text{ cm}^{-2}$ have been achieved from this study.

1. Introduction

The ternary compound, $\text{In}_{0.53}\text{Ga}_{0.47}\text{As}$, lattice matched to InP has attracted growing attention in recent years because its superior electron transport properties for ultra high speed operations [1] and its band gap compatibility to the $1.3\text{--}1.6\text{ }\mu\text{m}$ wavelength window of low transmission loss optical fiber [2]. Though considerable progress has been made to achieved better device performance, the fundamental growth process of these ternary compounds is still not well understood.

During the MBE growth of GaAs, in order to obtain smooth and atomically abrupt interface, it is sometimes desirable to enhance the cation surface migration so that the two-dimensional MBE growth process can be enhanced. This process is evident by observing the oscillation in the refraction high electron energy diffraction (RHEED) pattern [3]. However, in the case of ternary compounds such as $\text{Al}_x\text{Ga}_{1-x}\text{As}$ and $\text{In}_{0.53}\text{Ga}_{0.47}\text{As}$, this enhancement of cation surface

migration does not yield the same improvement, possibly due to preferential cation clustering [4]. The growth conditions which give good RHEED oscillations do not produce smooth and featureless surface morphology, thus disconnecting the correlation between growth front smoothness and the growth conditions set by the initiation of RHEED oscillation.

Earlier efforts using As_2 and optimizing the growth conditions have made considerable progress in producing higher quality $\text{In}_{0.52}\text{Al}_{0.48}\text{As}$ and $\text{In}_{0.53}\text{Ga}_{0.47}\text{As}$ layers [5–7]. However, a comprehensive study of the various growth conditions on both uniform and planar doped $\text{In}_{0.52}\text{Al}_{0.48}\text{As}/\text{In}_{0.53}\text{Ga}_{0.47}\text{As}/\text{InP}$ HEMT structures has yet to be reported. In this paper, we present a comparative study of As_2 and As_4 growth of $0.5\text{ }\mu\text{m}$ $\text{In}_{0.52}\text{Al}_{0.48}\text{As}$ and $\text{In}_{0.53}\text{Ga}_{0.47}\text{As}$ epitaxial layers, and report the resulting 2DEG properties of the $\text{In}_{0.52}\text{Al}_{0.48}\text{As}/\text{In}_{0.53}\text{Ga}_{0.47}\text{As}/\text{InP}$ HEMT structures with uniform and planar doping schemes under optimized growth conditions. Based upon this study, we have achieved state-of-the-art 2DEG material properties and planar doped HEMT performance.

* Y.C. Pao is also with Varian Associates, Solid State Operation, Santa Clara, California 95054, USA.

2. Experimental

MBE growth of lattice-matched $\text{In}_{0.52}\text{Al}_{0.48}\text{As}$ / $\text{In}_{0.53}\text{Ga}_{0.47}\text{As}$ epitaxial layers and 2DEG heterostructures was performed in a modified Varian MBE GEN-II system with two-inch non-indium bonded semi-insulating InP substrates. The typical growth rate of $\text{In}_{0.52}\text{Al}_{0.48}\text{As}$ and $\text{In}_{0.53}\text{Ga}_{0.47}\text{As}$ is $0.3 \mu\text{m/h}$, with a normal substrate temperature of 490°C . The composition of the ternary layers was determined using the RHEED oscillation technique performed on both GaAs and InP substrates. The epitaxial surface morphology was studied by Nomarski phase contrast microscopy, and Hall measurements were used to provide electrical characterization of the 2DEG sheet charge density and electron mobility. The basic HEMT structure used in this study is as follows: a 2500 \AA $\text{In}_{0.52}\text{Al}_{0.48}\text{As}$ undoped buffer, a 320 \AA undoped $\text{In}_{0.53}\text{Ga}_{0.47}\text{As}$ layer to form the 2DEG channel, a 30 \AA $\text{In}_{0.52}\text{Al}_{0.48}\text{As}$ undoped spacer, either a uniform or pulse planar Si-doped $\text{In}_{0.52}\text{Al}_{0.48}\text{As}$ layer, where the doped sheet charge or/and pulse layer thickness were varied to study the resulting electrical properties, a 250 \AA undoped $\text{In}_{0.52}\text{Al}_{0.48}\text{As}$ layer, and a 30 \AA undoped $\text{In}_{0.53}\text{Ga}_{0.47}\text{As}$ surface layer was grown to reduce the effects of oxidation and surface contamination on the 2DEG electron properties.

3. Results and discussion

Fig. 1 shows some typical RHEED oscillation data taken during the growth of $\text{In}_{0.52}\text{Al}_{0.48}\text{As}$ and $\text{In}_{0.53}\text{Ga}_{0.47}\text{As}$ on InP. It is shown that the specular beam intensity damps faster in the case of As_2 compared to As_4 for both $\text{In}_{0.52}\text{Al}_{0.48}\text{As}$ and $\text{In}_{0.53}\text{Ga}_{0.47}\text{As}$ growth, indicating reduced cation diffusion on the growth front with As_2 coverage [8]. Fig. 2 shows the surface morphology of $0.5 \mu\text{m}$ thick, moderately Si-doped $\text{In}_{0.52}\text{Al}_{0.48}\text{As}$ epitaxial layers grown with As_4 (figs. 2a and 2b) and As_2 (figs. 2c and 2d) sources, with the same group V to group III flux ratio of 14. There was almost no difference in either surface morphology or electron mobility ($\sim 410 \text{ cm}^2/\text{V} \cdot \text{s}$ at 300 K) between the dimeric and tetrameric arsenic growth. Further

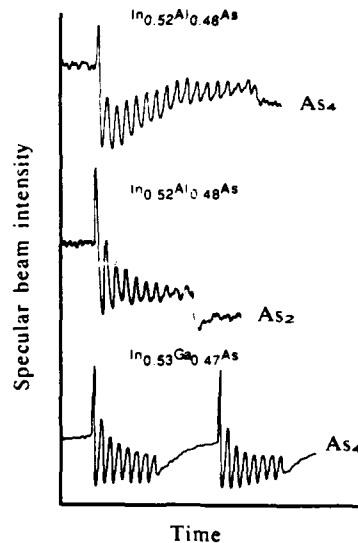


Fig. 1. RHEED intensity oscillations of $\text{In}_{0.52}\text{Al}_{0.48}\text{As}$ and $\text{In}_{0.53}\text{Ga}_{0.47}\text{As}$ with As_2 and As_4 sources.

increase of the As_4 or As_2 V/III flux ratios showed little change in either surface morphology or electrical properties of the $\text{In}_{0.52}\text{Al}_{0.48}\text{As}$ epitaxial layers. However, in the case of $\text{In}_{0.53}\text{Ga}_{0.47}\text{As}$, the situation is quite different. Fig. 3 shows how the growth morphology of $\text{In}_{0.53}\text{Ga}_{0.47}\text{As}$ is influenced by the arsenic species and its strong dependence on the V/III flux ratio with As_4 growth. The poor surface morphology of fig. 3a occurred at a relative low $V(\text{As}_4)/\text{III}$ flux ratio of 16; however, this is the same flux ratio used in fig. 1 where RHEED oscillations were observed during the growth of $\text{In}_{0.53}\text{Ga}_{0.47}\text{As}$. If the As_4 flux is increased further, the $\text{In}_{0.53}\text{Ga}_{0.47}\text{As}$ surface morphology improves, as shown in figs. 3b and 3c. This is a clear indication that the growth of the $\text{In}_{0.53}\text{Ga}_{0.47}\text{As}$ is vulnerable to cation (i.e., Ga and In) surface segregation, which is strongly affected by the cation surface mobility which is mainly controlled by the surface arsenic coverage. Since the surface texture in figs. 3a and 3b is not microscopically uniform throughout the surface, it is not likely that the poor surface morphology is due to As-vacancies or their related defect complexes as intuitively speculated. Fig. 3d shows a smooth epitaxial surface of $\text{In}_{0.53}\text{Ga}_{0.47}\text{As}$ achieved with As_2

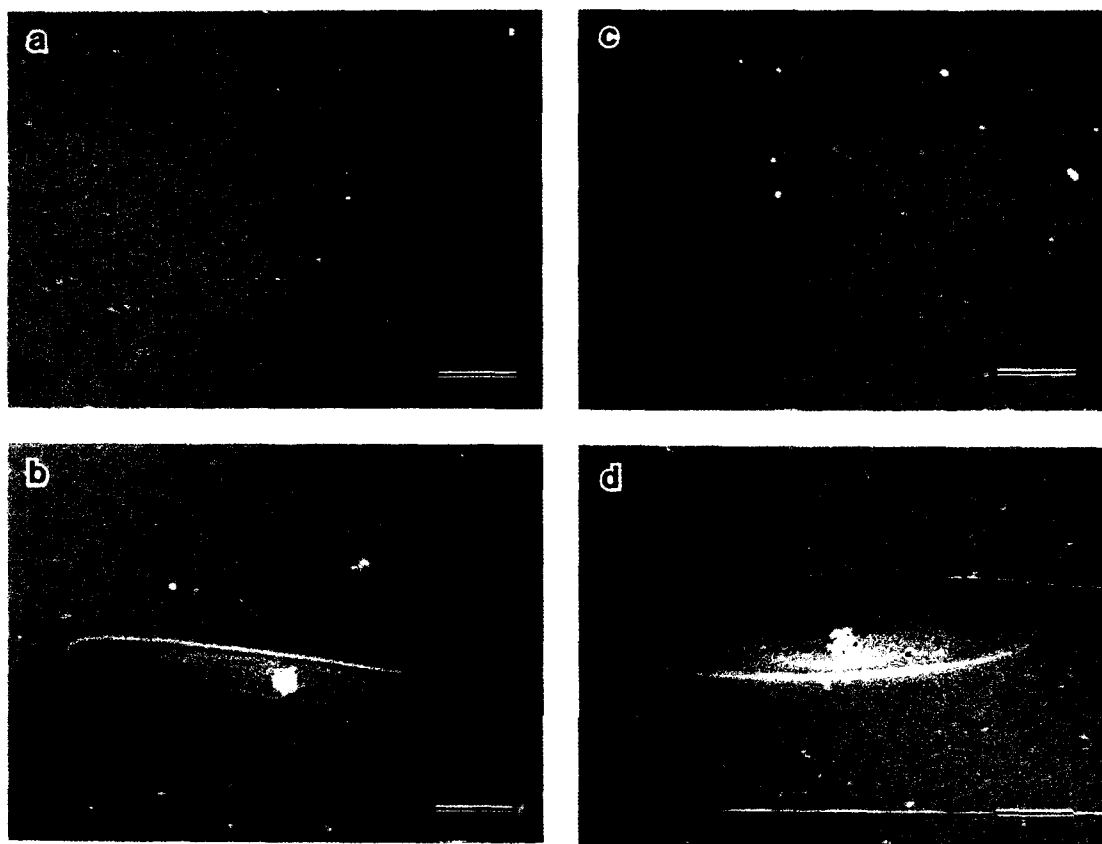


Fig. 2. Epitaxial surface morphology and particle related growth defect on $\text{In}_{0.52}\text{Al}_{0.48}\text{As}$ grown under As_4 (a, b) and As_2 (c, d). The markers represent 50 μm (a, c) and 20 μm (b, d).

growth, even at a relatively low V/III flux ratio of 14.

After recognizing the influence of arsenic species on thick ternary compounds of $\text{In}_{0.52}\text{Al}_{0.48}\text{As}$ and $\text{In}_{0.53}\text{Ga}_{0.47}\text{As}$, the next step was to examine the influence of arsenic species on 2DEG structures. Fig. 4 shows the planar doped 2DEG electron sheet charge density and mobilities as a function of spacer layer thickness, with the doped sheet charge held constant at $5 \times 10^{12} \text{ cm}^{-2}$. The major difference in 2DEG properties between As_2 or As_4 growth appears to be in the 77 K electron mobility, where a substantial increase (30–50%) of mobility is obvious with As_2 growth. Since the 2DEG sheet charge densities remain relatively constant, the most reasonable explanation is that

the heterointerface of the 2DEG quantum well is microscopically smoother with As_2 growth. This is consistent with our earlier discussion on surface morphology.

To show the influence of different doping schemes (i.e., uniform versus planar doped structures) on 2DEG electrical properties, table 1 gives the results of varying the doping structure from a three-dimensional uniformly doped layer to a two-dimensional, planar pulse doped layer. The sheet doping densities were constant at $5 \times 10^{12} \text{ cm}^{-2}$ and As_4 was used as arsenic species. It is evident that the 2DEG sheet charge increases as the doping pulse width decreases (thus increasing the heterointerface 2DEG confining electric field). The electron mobility, on the other hand, in-

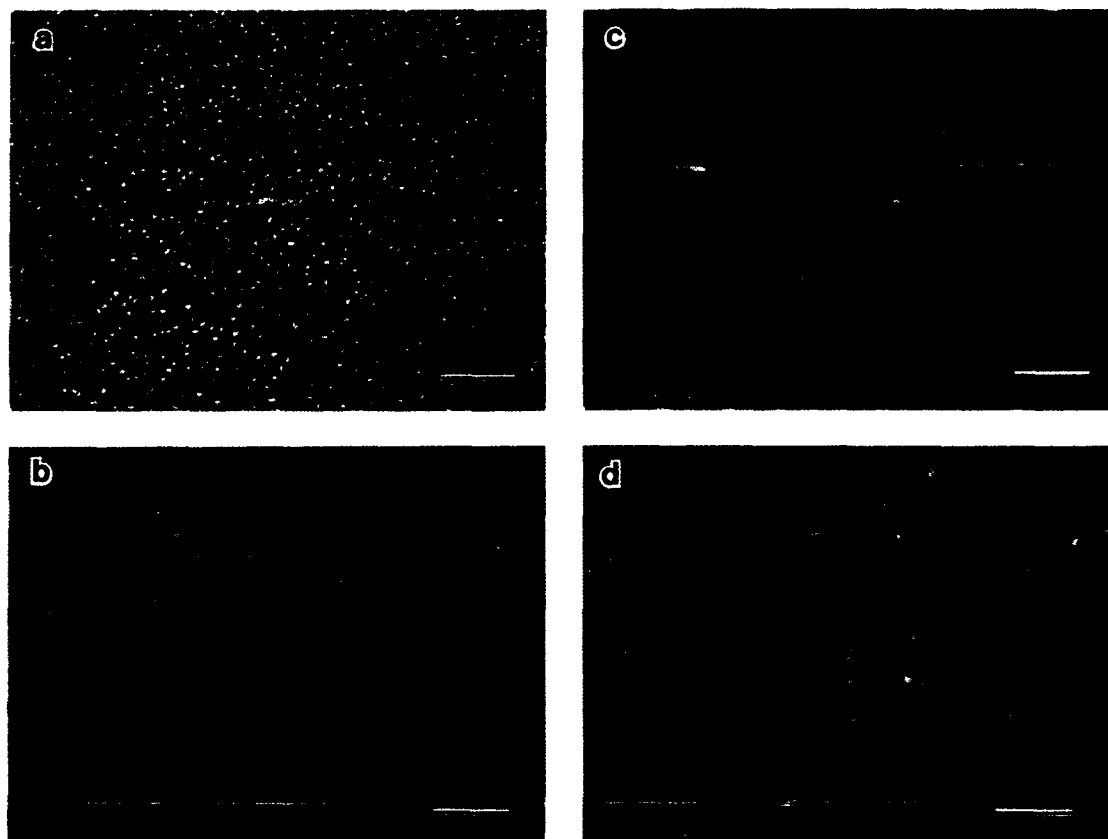


Fig. 3. Epitaxial surface morphology of $\text{In}_{0.53}\text{Ga}_{0.47}\text{As}$ layers grown under different arsenic conditions: (a) As_4 with V/III ratio of 16; (b) As_4 with V/III ratio of 26; (c) As_4 with V/III ratio of 36; (d) As_2 with V/III ratio of 14. The marker represents $50\ \mu\text{m}$.

creases gradually with increasing 2DEG sheet charge density, consistent with increased electron screening [9] of the Coulombic interaction (i.e., scattering) with the host impurities. This experi-

ment showed definite advantages of the planar doped structure over uniformly doped ones. In order to acquire even higher 2DEG sheet charge with planar doped structure, we undertook the

Table 1
Comparison of 2DEG properties between uniform and planar doped HEMT structures

Structure type	Doping level/thickness	Spacer (Å)	2DEG (300 K)	
			Sheet charge (cm^{-2})	Mobility ($\text{cm}^2/\text{V}\cdot\text{s}$)
Uniform	$2 \times 10^{18}\ \text{cm}^{-3}/250\ \text{Å}$	30	2.35×10^{12}	10,100
Uniform	$4 \times 10^{18}\ \text{cm}^{-3}/125\ \text{Å}$	30	2.72×10^{12}	10,500
Planar	$5 \times 10^{12}\ \text{cm}^{-2}$	30	2.95×10^{12}	11,020

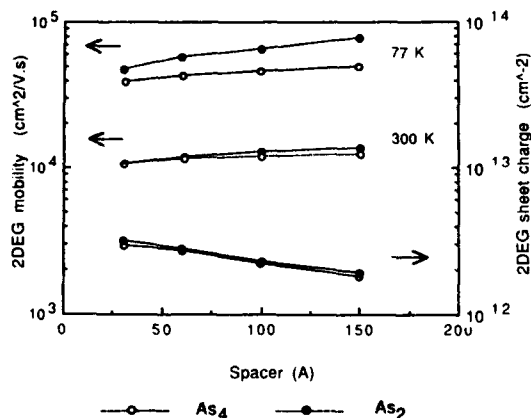


Fig. 4. Comparison of the planar doped 2DEG electron sheet charge density and electron mobility as functions of the spacer layer thickness and arsenic species. The Si sheet doping density was constant at $5 \times 10^{12} \text{ cm}^{-2}$.

following experiment with As_2 growth, since As_2 offers superior 2DEG electrical properties. Fig. 5 shows that with further increase in the planar Si-doped sheet charge, the 2DEG sheet charge density increases continuously, without degrading the room temperature electron mobility. 2DEG electron mobilities of $11,080 \text{ cm}^2/\text{V} \cdot \text{s}$ at 300 K and $33,500 \text{ cm}^2/\text{V} \cdot \text{s}$ at 77 K with sheet charge of $3.9 \times 10^{12} \text{ cm}^{-2}$ have been achieved; this is so far the best reported room temperature mobility with such high sheet charge density.

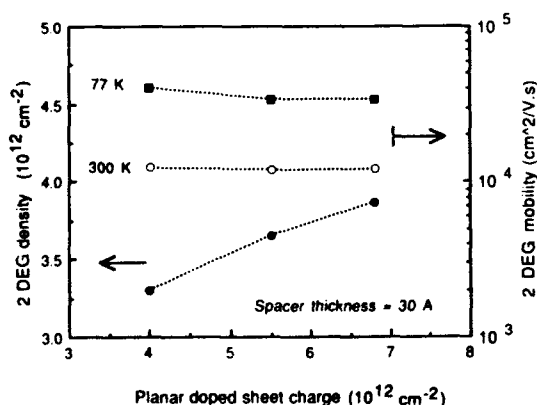


Fig. 5. Planar doped 2DEG electron sheet charge density and mobility as a function of the sheet charge density in Si pulse doped layer, with a 30 Å thick spacer layer.

Based on these epitaxial material results, we have fabricated a state-of-the-art, $\text{In}_{0.52}\text{Al}_{0.48}\text{As}/\text{In}_{0.53}\text{Ga}_{0.47}\text{As}/\text{InP}$ HEMT with sub- $0.1 \mu\text{m}$ gate length. This device has achieved an intrinsic current gain cut-off frequency of over 288 GHz [10], which is among the highest cut-off frequencies reported to date for any three-terminal devices.

4. Conclusion

The MBE growth of $\text{In}_{0.52}\text{Al}_{0.48}\text{As}/\text{InP}$ is relatively insensitive to both the arsenic species used and the V/III flux ratio. However, $\text{In}_{0.53}\text{Ga}_{0.47}\text{As}$ is strongly influenced by these parameters. The use of dimeric arsenic produces superior epitaxial $\text{In}_{0.53}\text{Ga}_{0.47}\text{As}$ surface morphology and higher low temperature 2DEG electron mobility. This improvement of low temperature 2DEG mobility is attributed to the microscopically smoother hetero-interface obtained with As_2 growth. Due to the large $\Gamma-L$ valley separation of the $\text{In}_{0.53}\text{Ga}_{0.47}\text{As}$ channel layer, the room temperature 2DEG electron mobility remains relatively constant over a wide range of 2DEG sheet charge density, between 2.3 to $3.9 \times 10^{12} \text{ cm}^{-2}$. A room temperature 2DEG mobility of $11,080 \text{ cm}^2/\text{V} \cdot \text{s}$ with a corresponding sheet charge density of $3.9 \times 10^{12} \text{ cm}^{-2}$ has been demonstrated, and state-of-the-art device performance has been achieved with MBE grown, planar doped HEMT structures.

Acknowledgments

The authors would like to thank J. Franklin, T. Han and Dr. N.G. Bechtel for their technical support and helpful discussions.

References

- [1] A. Cappy, B. Carnez, R. Fauquembergues, G. Salmer and E. Constant, IEEE Trans. Electron Devices ED-27 (1980) 2158.
- [2] H. Osanai, T. Shioda, T. Moriyama, S. Araki, M. Horiguchi, T. Izawa and H. Takata, Electron. Letters 12 (1976) 549.

- [3] B.A. Joyce, J. Zhang, J.H. Neave and P.J. Dobson, Appl. Phys. A45 (1988) 255.
- [4] P.M. Petroff, A.Y. Cho, F.K. Reihart, A.C. Gossard and W. Wiegmann, Phys. Rev. Letters 48 (1982) 170.
- [5] G. Wicks, C.E.C. Wood, H. Ohno and L.F. Eastman, J. Electron. Mater. 11 (1982) 435.
- [6] W.T. Tsang, J.A. Ditzenberger and N.A. Olsson, IEEE Electron Device Letters EDL-4 (1983) 275.
- [7] W. Lee and C.G. Fonstad, J. Vacuum Sci. Technol. B4 (1986) 536.
- [8] B.A. Joyce, P.J. Dobson, J.H. Neave and K. Woodbridge, Surface Sci. 168 (1986) 423.
- [9] S. Mori and T. Ando, J. Phys. Soc. Japan 48 (1980) 865.
- [10] M. Riazat, C. Nishimoto, S. Silverman, Y.C. Pao, S.L. Weng, M. Glenn, S. Bandy, R. Majidi-Ahy and G. Zdasiuk, in: Proc. 2nd Intern. Conf. on InP and Related Materials, 1990.

High quality InP and $\text{In}_{1-x}\text{Ga}_x\text{As}_y\text{P}_{1-y}$ grown by gas source MBE

Marc Lambert *, Léon Goldstein, Antonina Perales, Fabienne Gaborit, Christophe Starck and Jean-Louis Lievin

Laboratoires de Marcoussis, Route de Nozay, F-91460 Marcoussis, France

The growth of high quality InP and $\text{In}_{1-x}\text{Ga}_x\text{As}_y\text{P}_{1-y}$ by gas source molecular beam epitaxy is reported. 77 K mobilities up to $112,000 \text{ cm}^2/\text{V}\cdot\text{s}$ for high purity InP have been measured. Fe-doped semi-insulating InP has been grown using an iron effusion cell, and resistivities as high as $10^9 \Omega \text{ cm}$ have been obtained. Selective epitaxy of InP on Si_3N_4 -patterned substrates is also presented.

1. Introduction

Gas source molecular beam epitaxy (GSMBE) has, over the last few years, demonstrated high potential for the production of high quality layers as well as a wide range of optoelectronic devices including double heterostructure lasers [1], quantum well structures [2], DFB lasers [3] and optical amplifiers [4].

GSMBE offers number of advantages over other growth techniques. The epitaxial process requires a much lower flow of hydrides than metalorganic vapor phase epitaxy (MOVPE). As opposed to chemical beam epitaxy (CBE), the growth kinetics and alloy composition of ternary and quaternary materials are almost independent of substrate temperature. The absence of MO compounds in the growth chamber avoids any carbon contamination of dopant effusion cells, cracking cells as well as hot parts of the growth chamber.

In this paper, we review our results on the growth of high purity InP and $\text{In}_{1-x}\text{Ga}_x\text{As}_y\text{P}_{1-y}$ using GSMBE. We also report, for the first time, the ability of GSMBE to grow high quality semi-insulating InP using an iron effusion cell. Selective epitaxy of InP on Si_3N_4 -patterned substrates is also described.

2. GSMBE system

The GSMBE experiments were carried out in a commercial MBE chamber fitted with a 2200 l/s turbomolecular pump to provide adequate pumping of hydrogen produced by the decomposition of the hydrides. A gas handling system with mass flow controllers and switching valves was used to introduce pure AsH_3 and PH_3 into the reactor through a low pressure cracking cell. Three effusion cells (2 In and 1 Ga) and 4 hydride lines permit the growth of InP and $3\cdot\text{In}_{1-x}\text{Ga}_x\text{As}_y\text{P}_{1-y}$ alloys with minimum growth interruptions at the heterointerfaces. Before growth, the Ga and In beam flux calibrations were computer controlled using an ion gauge.

The MBE system was installed in a class 10,000 clean room with entry chamber connected to a class 100 laminar flow station for loading and unloading wafers. The growth chamber was carefully prepared: after venting, the system was baked out (200°C) and each cell was individually outgassed. 7N purity indium sources (Johnson Matthey), 8N purity gallium source (Rhône-Poulenc) and Si, Be and Fe dopant sources were loaded before a final bake out (150°C). The cryoshrouds were continuously filled with liquid nitrogen, reducing the partial pressures of background impurities (H_2O , CO, etc.). Before growth, the base pressure of the chamber was in the 10^{-9} Torr range, due to residual hydrogen outgassing from

* Present address: ALCATEL-CIT, Département Transmission sur Câbles, Nozay, F-91620 La Ville-du-Bois, France.

hot sources. Other partial pressures were below 10^{-11} Torr.

3. $\text{In}_{1-x}\text{Ga}_x\text{As}_y\text{P}_{1-y}$ growth

We have studied the growth conditions of $\text{In}_{1-x}\text{Ga}_x\text{As}_y\text{P}_{1-y}$ alloys lattice matched to InP over the entire range of composition ($y \approx 2.2x$, $0 \leq y \leq 1$).

The growth mechanisms in GSMBE and in conventional MBE are very similar: the sticking coefficients of Ga and In are equal to unity for substrate temperatures lower than the re-evaporation limit of the group III elements, and independent of group V element fluxes. Growth rates ranging from 0.5 to 2 $\mu\text{m/h}$ were typically used.

The thermal decomposition of AsH_3 and PH_3 generates As_2 and P_2 beams which allow low V/III ratio during growth (between 2 and 10). The hydride flows needed are much lower than in MOVPE. The variation of the arsenic concentration in the solid (y) versus the flux ratio $Y = \text{As}_2/(\text{As}_2 + \text{P}_2)$ is plotted in fig. 1. Two regions are shown: for the As-rich alloys, the ratio of group V elements incorporated in the solid is almost the same as in the gas phase, whatever the substrate temperature: As_2 and P_2 have ap-

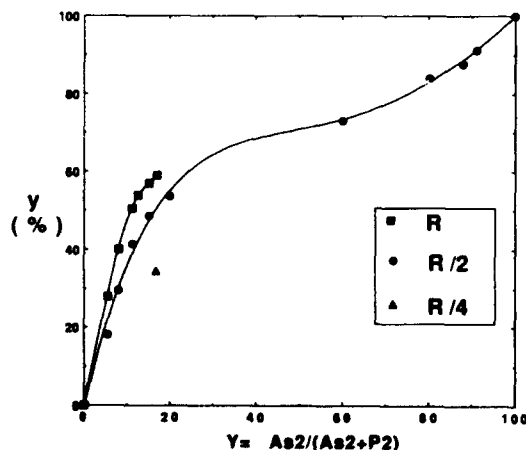


Fig. 1. Arsenic concentration in the solid as a function of the flux ratio $\text{As}_2/(\text{As}_2 + \text{P}_2)$, with different V/III ratios R ($T_s = 500^\circ\text{C}$).

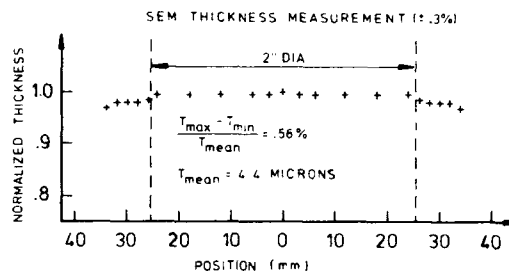


Fig. 2. $\text{In}_{0.53}\text{Ga}_{0.47}\text{As}$ thickness uniformity over a 2 inch diameter wafer.

proximately the same sticking coefficient. For the high phosphorus-content alloys ($y < 0.6$), the relative sticking coefficient of As increases. In this region, we have observed a stronger incorporation of arsenic for reduced growth temperature [5]. As plotted in fig. 1, we have also observed a relative decrease of arsenic incorporation when V/III ratio decreased. This is in good agreement with theoretical predictions given by Seki and Koukitu [6].

Composition and thickness uniformities of $\text{In}_{0.53}\text{Ga}_{0.47}\text{As}$ have been checked using respectively double-crystal X-ray diffraction and scanning electron microscope (SEM) measurements. High homogeneities over a 2 inch diameter wafer have been obtained, with thickness variation lower than 1% and composition variation lower than 0.1% (see figs. 2 and 3). Photoluminescence wavelength mapping obtained at room temperature on a $\text{In}_{0.53}\text{Ga}_{0.47}\text{As}/\text{In}_{0.82}\text{Ga}_{0.18}\text{As}_{0.40}\text{P}_{0.60}$ quantum well structure grown on a 2 inch substrate gave a wavelength variation lower than 1 nm, confirming the homogeneity in thickness and composition of the alloys [7].

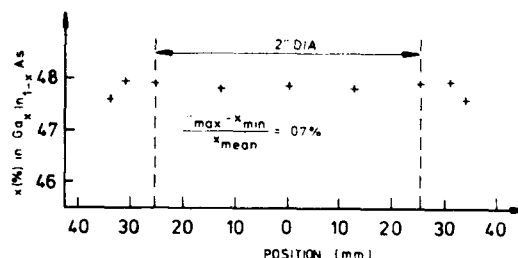


Fig. 3. $\text{In}_{0.53}\text{Ga}_{0.47}\text{As}$ composition uniformity over a 2 inch diameter wafer.

4. High purity InP growth

GSMBE is well adapted to the growth of high purity materials, as previously reported by Cunningham et al. on GaAs [8]. We have also demonstrated that high purity InP can be obtained by this technique [9]. The growth has been performed at 500°C under a cracked- PH_3 flow giving a H_2 pressure in the growth chamber of 5×10^{-5} Torr, as described in ref. [9].

Fig. 4 shows a photoluminescence spectrum of a high purity InP epilayer, obtained at 4.2 K. The free exciton (X) and neutral donor bound exciton ($\text{D}^0\text{-X}$) transitions are clearly resolved at 1.4187

and 1.4175 eV, respectively. A shoulder at 1.4166 eV can be attributed to neutral donor–hole transitions ($\text{D}^0\text{-h}$). The low intensity of acceptor related transitions observed in this spectrum confirms the high purity of the sample. Hall effect measurements performed at 77 K without illumination have routinely shown residual carrier concentrations in the 10^{14} cm^{-3} range with mobilities in the range of 70,000–100,000 $\text{cm}^2/\text{V} \cdot \text{s}$, with a best value of 112,000 $\text{cm}^2/\text{V} \cdot \text{s}$ for $N_D - N_A = 2 \times 10^{14} \text{ cm}^{-3}$. These values, which are not corrected for surface depletion effects, are comparable to the results obtained on very pure InP grown by CBE [10,11].

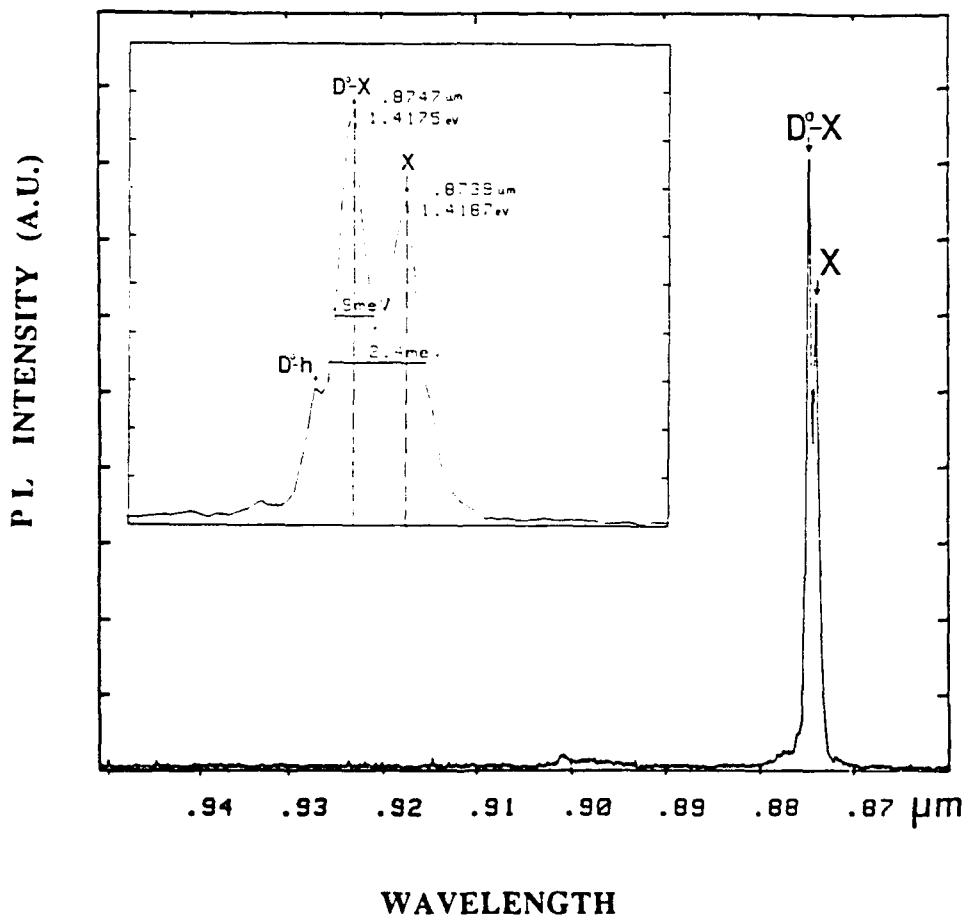


Fig. 4. 4.2 K photoluminescence spectrum of a pure InP epilayer.

These pure undoped InP epilayers were grown over a several months period, alternatively with InGaAsP/InP optoelectronic structures with beryllium, silicon or iron doped layers. No special procedures were adopted to avoid contamination from dopants, demonstrating the versatility of the GSMBE technique.

5. Semi-insulating InP

Many optoelectronic devices such as integrated waveguides, high speed lasers as well as integrated circuits require high resistivity (semi-insulating) InP layers.

Fe-doped semi-insulating InP has been grown by MOVPE [12,13] using ferrocene ($\text{Fe}(\text{C}_5\text{H}_5)_2$) and $\text{Fe}(\text{CO})_5$ sources. More recently, Tsang et al. [14] have successfully grown Fe-doped semi-insulating InP by CBE using a conventional iron effusion source. We have used a 6N purity iron source as dopant for GSMBE semi-insulating InP. As shown in fig. 5, the iron concentration is well controlled by the effusion cell temperature as calibrated by SIMS measurements. For iron concentrations below 10^{17} cm^{-3} , InP epilayers exhibit

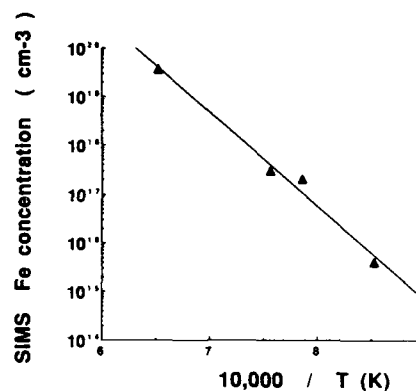


Fig. 5. Variation of iron doping level (SIMS measurements) as a function of the reciprocal of the iron cell temperature.

smooth surface, comparable to undoped layers (fig. 6a). For higher doping levels, a degradation of the morphology is observed. Fig. 6b shows the surface morphology of an InP layer with an estimated iron concentration of 10^{18} cm^{-3} . The poor morphology is presumably induced by FeP precipitates as observed by Chu et al. in InP:Fe grown by MOVPE [15,16].

For electrical characterization, an epitaxial structure consisting in a $3 \mu\text{m}$ Fe-doped InP layer

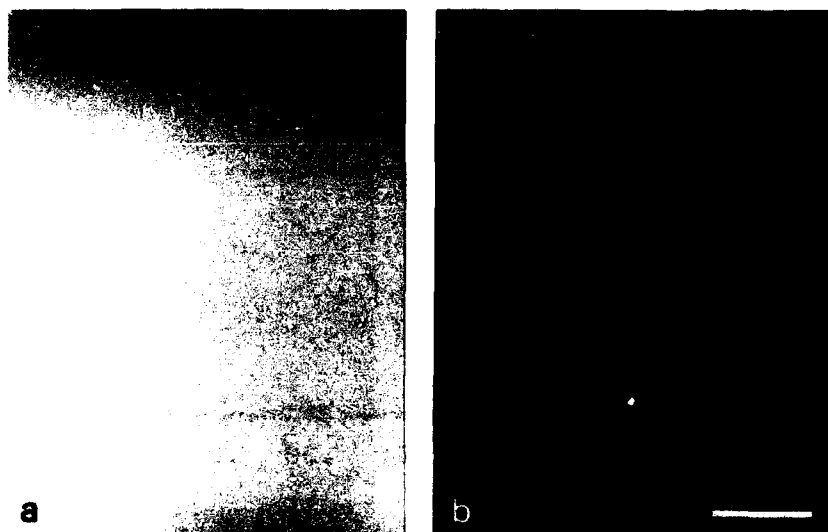


Fig. 6. Surface morphology of InP:Fe samples with estimated iron concentration of: (a) 10^{17} cm^{-3} ; (b) 10^{18} cm^{-3} . Marker represents $20 \mu\text{m}$.

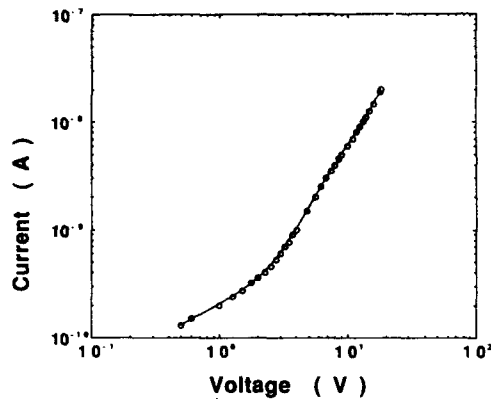


Fig. 7. Current-voltage characteristic of a 90 μm diameter mesa $n^+-\text{SI}-n^+$ structure with a 3 μm thick InP:Fe layer.

sandwiched between two n^+ doped InP layers has been grown on an n^+ doped substrate. The iron concentration was estimated to 10^{17} cm^{-3} . Ti/Au contacts have been evaporated on both sides of the structure and 90 μm chemical etched mesas have been processed. A typical current-voltage characteristic of the structure is given in fig. 7. As previously described by Macrander et al. [17], two regimes are shown: an ohmic regime occurs at low voltage, and for voltages higher than 3 V, a quadratic regime, characteristic of space-charge limited current, is observed. The resistivity in the ohmic region is as high as $10^9\ \Omega\text{ cm}$. This result,

which is one of the best published, is of particular interest for device applications.

6. Selective epitaxy

Whereas VPE [18], MOVPE [19] and CBE [11,20] have demonstrated excellent selectivity, GSMBE and conventional MBE have been considered to have poor selectivity because of the high sticking coefficients of group III elements. We have studied selective epitaxy of InP on partially masked and grooved (100) InP substrates. Grooves along the $\langle 110 \rangle$ directions were formed using Si_3N_4 masks and wet etching or reactive ion etching (RIE) processes.

For standard growth conditions, polycrystalline deposition occurs on the dielectric mask. However, for high growth temperatures ($> 560^\circ\text{C}$), selective epitaxy has been achieved with no deposition on Si_3N_4 , as shown by the SEM pictures in fig. 8. Such effect, which has already been reported for MBE-grown InAs [21], is due to the enhanced re-evaporation rate of indium on dielectric surface as compared to InP substrate at these temperatures.

The beam nature of GSMBE has been observed with regrowth on a non-rotating substrate. A cross-patterned mask has been used to etch the substrate. Fig. 9 gives a schematic representation

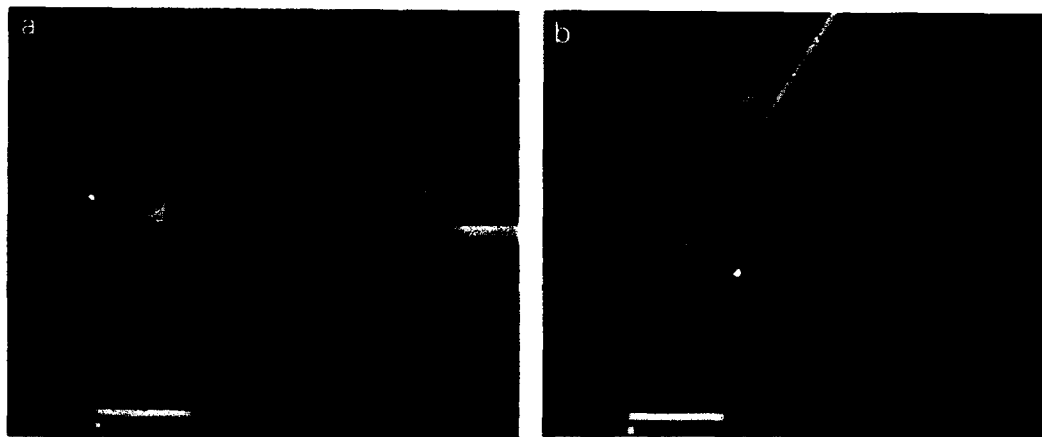


Fig. 8. SEM photographs of InP growth on Si_3N_4 -masked substrate with RIE grooves. Markers represent 1 μm .

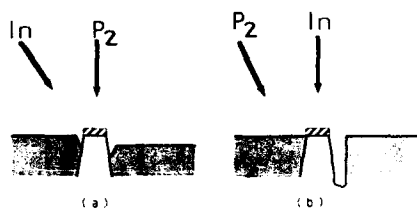


Fig. 9. Schematic representation of InP regrowth on a non-rotating engraved substrate. The spatial separation between the indium cell and the gas injector gives the difference in the molecular beam angles.

of the cross-section in both $\langle 110 \rangle$ directions. The spatial separation between the indium cell and the gas injector gives the difference in the molecular beam angles. SEM pictures exhibit assymetric growth on the different sides of the grooves. The group III element shadow effect is shown in fig. 10a.

Fig. 10b clearly shows a shadow effect due to the phosphorus beam tilt: at one edge of the mesa, unexposed to P_2 flux, there is even evidence for a depletion zone due to local reevaporation of InP at this temperature (550°C).

7. Conclusion

In summary, we have reported on the epitaxy of high quality InP and $\text{In}_{1-x}\text{Ga}_x\text{As}_y\text{P}_{1-y}$ grown by GSMBE. Residual carrier concentration of $2 \times 10^{14} \text{ cm}^{-3}$ has been obtained on InP with 77 K mobility of $112,000 \text{ cm}^2/\text{V} \cdot \text{s}$. Semi-insulating InP grown by GSMBE using an Fe effusion cell has

been reported for the first time. Resistivities as high as $10^9 \Omega \text{ cm}$ have been obtained. We have also demonstrated the selective epitaxy of InP at substrate temperature in the range of $550\text{--}560^\circ\text{C}$.

These results demonstrate that GSMBE is now strongly established as a powerful growth technique to provide high quality InP based materials and is particularly attractive for the realization of future optoelectronic integrated circuits.

Acknowledgments

The authors wish to thank L. Le Gouezigou for wafer processing, D. Bonnevie, J.P. Chardon and R. Vergnaud for technical assistance, C. Audry for X-Ray measurements and C. Hervo for SIMS profiles.

References

- [1] M.B. Panish, H. Temkin and S. Sumski, *J. Vacuum Sci. Technol.* B3 (1985) 657.
- [2] M.B. Panish, H. Temkin, R.A. Hamm and S.N.G. Chu, *Appl. Phys. Letters* 49 (1986) 164.
- [3] L. Goldstein, C. Artigue, D. Bonnevie, B. Fernier, A. Peralès and J. Benoit, *J. Crystal Growth* 95 (1989) 375.
- [4] B. Mersali, G. Gelly, A. Accard, J.L. Lafragette, P. Dousiere, M. Lambert and B. Fernier, *Electron. Letters* 26 (1990) 124.
- [5] L. Goldstein, M. Lambert, B. Fernier, D. Bonnevie, C. Starck and M. Boulou, in: *Proc. 14th Intern. Symp. on GaAs and Related Compounds*, Heraklion, 1987. *Inst. Phys. Conf. Ser.* 91, Eds. A. Christou and H.S. Rupprecht (Inst. Phys., London-Bristol, 1988) p. 211.
- [6] H. Seki and A. Koukitu, *J. Crystal Growth* 78 (1986) 342.



Fig. 10. SEM pictures of InP regrowth on a non-rotating engraved substrate, showing Indium (a) and phosphorus (b) shadows. Markers represent $1 \mu\text{m}$.

- [7] L. Goldstein, *J. Crystal Growth* 105 (1990) 93.
- [8] J.E. Cunningham, G. Timp, T.H. Chiu, J.A. Ditzenberger, W.T. Tsang, A.M. Sergent and D.V. Lang, *J. Crystal Growth* 95 (1989) 185.
- [9] M. Lambert, A. Peralès, R. Vergnaud and C. Starck, *J. Crystal Growth* 105 (1990) 97.
- [10] Y. Kawaguchi, H. Asahi and H. Nagai, in: *Proc. 12th Intern. Symp. on GaAs and Related Compounds*, Karuizawa, 1985, Inst. Phys. Conf. Ser. 79, Ed. M. Fujimoto (Inst. Phys., London-Bristol, 1986) p. 79.
- [11] H. Heinecke, R. Höger, B. Baur and A. Miklis, *Electron. Letters* 26 (1990) 213.
- [12] J.A. Long, V.G. Riggs and W.D. Johnston, Jr., *J. Crystal Growth* 69 (1984) 10.
- [13] P. Speier, G. Schemmel and W. Kuebart, *Electron. Letters* 22 (1986) 1216.
- [14] W.T. Tsang, A.S. Subdo, L. Yang, R. Camarda and R.E. Leibenguth, *Appl. Phys. Letters* 54 (1989) 2336.
- [15] S.N.G. Chu, S. Nakahara, J.A. Long, V.G. Riggs and W.D. Johnston, Jr., *J. Electrochem. Soc.* 132 (1985) 2795.
- [16] S. Nakahara, S.N.G. Chu, J.A. Long, V.G. Riggs and W.D. Johnston, Jr., *J. Crystal Growth* 72 (1985) 693.
- [17] A.T. Macrander, J.A. Long, V.G. Riggs, A.F. Bloemeke and W.D. Johnston, Jr., *Appl. Phys. Letters* 45 (1984) 1297.
- [18] M. Hoshino, K. Tanaka, J. Komeno, K. Kitahara, K. Kodama and M. Ozeki, *Appl. Phys. Letters* 48 (1986) 186.
- [19] M. Oishi and K. Kuroiwa, *J. Electrochem. Soc.* 132 (1985) 1209.
- [20] M. Gailhanou, L. Goldstein, M. Lambert, M. Boulou, C. Starck and L. Le Guezigou, presented at ESSDERC '89, Berlin, 1989, to be published.
- [21] A. Okamoto and K. Ohata, *Japan. J. Appl. Phys.* 26 (1987) L1174.

Gas source MEE (migration enhanced epitaxy) growth of InP

Nobuyuki Takeyasu, Hajime Asahi, Soon Jae Yu, Kumiko Asami, Tadaaki Kaneko
and Shun-ichi Gonda

The Institute of Scientific and Industrial Research, Osaka University, 8-1, Mihogaoka, Ibaraki, Osaka 567, Japan

High-quality InP layers are grown by gas source MEE (migration enhanced epitaxy) method at 350°C. It is found that even at a substrate temperature as low as 350°C, the desorption of some amount of phosphorus from the InP surface occurs when the PH₃ flow is interrupted, although the RHEED pattern is still showing the (2×4) reconstructions. As a result, the perfectly alternating supply of indium and phosphorus can be achieved only when PH₃ is supplied with a proper interruption time before the supply of In. It is also found that InP layers grown by gas source MEE at 350°C have optical properties equal to or better than those grown by conventional gas source MBE (molecular beam epitaxy) at 470°C.

1. Introduction

InGaAs/InP superlattice (SL) and quantum well (QW) structures consist of two group III and two group V atoms and have two different types of hetero-interfaces (InGaP and InAs) depending on the growth sequence even when ideally formed. Recently, the existence of two different types of hetero-interfaces was confirmed with high-resolution X-ray diffraction [1]. Under the usual growth conditions, the hetero-interfaces have uncontrolled interfaces because group V atoms are usually supplied during growth owing to high growth temperature. Furthermore, in the growth of InGaAs/InP heterostructures, the changeover of As and P flows is necessary and the incorporation of As (P) into the InP (InGaAs) layer and the desorption of As (P) from the InGaAs (InP) layer near the interfaces are easy to occur.

The atomic arrangement at the interfaces will influence the physical properties of the SL/QW structures. For example, this will be one of the reasons of the scattered reported values for ΔE_c at InGaAs/InP hetero-interfaces [2–4]. In fact, PL peak energy shift is observed for QWs prepared by different growth schedules [5], namely QW PL peak energy changes depending on the composi-

tion of the hetero-interface. The optical and electrical qualities of the SL/QW structures will be also influenced by the precise atomic arrangement at the interfaces. These situations are common in all the SL/QW structures having two group III and two group V atoms, such as InGaP/GaAs and InAs/AlSb.

To control the physical properties of the SL/QW structures, the atomically controlled growth of the hetero-interfaces is necessary. Migration enhanced epitaxy (MEE) is an attractive method to form tailored hetero-interfaces because of low growth temperature and alternating supply of group III and group V atoms. However, the MEE growth of InGaAs/InP heterostructures is difficult in the conventional solid source MBE system, because these heterostructures have two group V atoms.

In this paper, we will report, for the first time, the results on the MEE growth of InP using PH₃ as group V atom source (gas source MEE). The effects of the interruption times of the PH₃ flow before and after the In supply and the In supply time on the RHEED (reflection high energy electron diffraction) patterns and the intensity recovery are described. The results of photoluminescence (PL) measurements on gas source MEE-

grown InP layers and conventional gas source MBE-grown InP layers are also presented.

2. Experimental

The gas source MBE system (ANELVA GBE830) used here is evacuated by an oil diffusion pump with a liquid nitrogen trap. Solid indium and gas phosphine (PH_3) were used as group III and group V sources, respectively. PH_3 was introduced into the growth chamber through a mass flow controller (MFC) and a gas cracker cell ($\sim 900^\circ\text{C}$). The substrates used were Fe-doped (001) InP. The substrate surface was thermally cleaned prior to growth with a PH_3 flux of 1.0 SCCM at 500°C for 10 min. The InP layers were grown at substrate temperatures (T_s) of 350 and 400°C with a PH_3 flux of 0.2 SCCM by MEE method. The T_s was monitored with an infrared optical pyrometer. The PH_3 gas flow is rapidly supplied or interrupted by using electronically operated block valves located close to the gas cracker cell.

The RHEED measurements were carried out with an incident electron beam energy of 25 keV. The RHEED intensity oscillation was measured on the specular spot in the $[100]$ azimuth.

PL measurements were also carried out at 77 K with a He-Ne gas laser (6328 Å, 15 mW) as an excitation light source.

3. Results and discussion

InP layers exhibit (2×4) reconstructions in the phosphorus-stable region at a value of T_s , such as 470°C , for the usual MBE growth. At a lower value of T_s , clear (2×4) RHEED patterns were observed on the InP surface when the PH_3 flow was interrupted (fig. 1a). However, with a PH_3 flux of 1.0 SCCM at 350°C , the (2×4) patterns became diffused, as shown in fig. 1b. And this was more noticeable with increasing PH_3 flow rate. It can be said that the supply of excess P atoms at 350°C induces the additional adsorption of P on the surface and changes surface reconstructions.

Figs. 2b and 2c demonstrate RHEED intensity

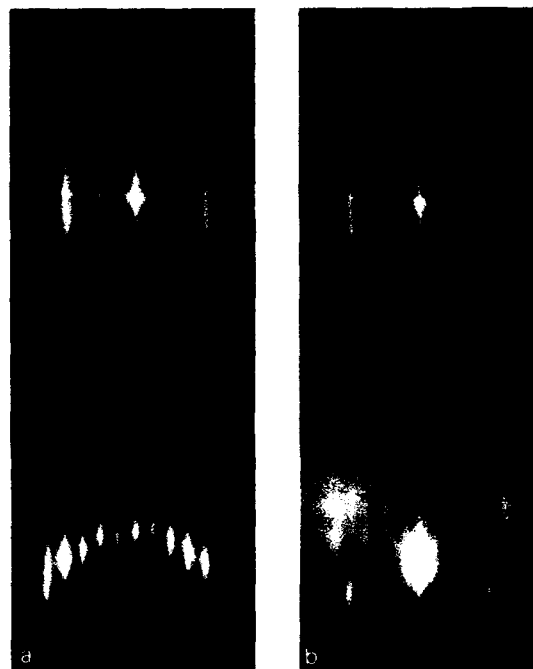


Fig. 1. RHEED patterns from (001) InP surface at 350°C for $[110]$ and $[\bar{1}10]$ azimuths: (a) without PH_3 flow and (b) with a PH_3 flux of 1.0 SCCM.

traces recorded during the alternating supply of In and P when the supply of P is interrupted for over 30 s before the supply of In, as shown in fig. 2a, at 350°C (fig. 2b) and 400°C (fig. 2c) for various In supply times (t_{In}). The RHEED patterns were still exhibiting the (2×4) reconstructions throughout the interruption time. The In supply time when RHEED intensity recovers the most quickly for the 350°C growth is 1.8 s, which is shorter than the growth time (2.5 s) of one monolayer which is measured from RHEED oscillation traces in the usual MBE growth at 350°C . It is also found that the In supply time when RHEED intensity recovers the most quickly at 400°C is still shorter (1.0 s). This indicates that at 350°C some amount of P atoms desorb from the surface and excess In atoms exist there, although the RHEED pattern is still showing the (2×4) reconstructions, and that only In atoms less than one monolayer are necessary to be deposited there to complete one monolayer growth, i.e., the number of In atoms neces-

sary to be deposited on the surface decreases from the number of In atoms equivalent to one monolayer. This is quite different from the MEE growth of GaAs [6], where the number of Ga atoms necessary to be deposited on the surface to achieve the quickest recovery of the RHEED intensity is equal to the number of surface sites. This observation in the InP growth will be closely related to the fact that the (4×2) reconstructions cannot be observed in the (gas source) MBE growth and that the InP surface changes from the (2×4) reconstructed surface to a matted surface without (4×2) region [7]. It is important to take the above experimental facts into account to form the controlled interface of InGaAs/InP.

It is also important that succeeding In atoms are deposited on the surface covered with one monolayer of P atoms. This is achieved by means of giving the interruption of the PH_3 flow before the In supply. Fig. 3b shows RHEED intensity traces by the sequence as shown in fig. 3a as a function of the interruption time (t_0) of the PH_3 flow before the In supply, where the In supply time (t_{In}) is chosen to be 2.5 s, which is the one

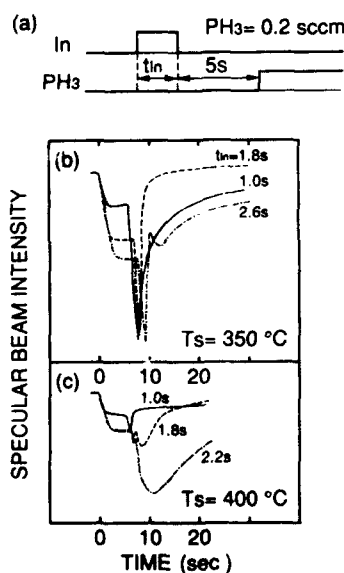


Fig. 2. (a) Deposition diagram of In and P, (b) RHEED intensity recovery at 350°C as a function of In supply time (t_{In}) using the deposition diagram shown in (a) and (c) RHEED intensity recovery at 400°C .

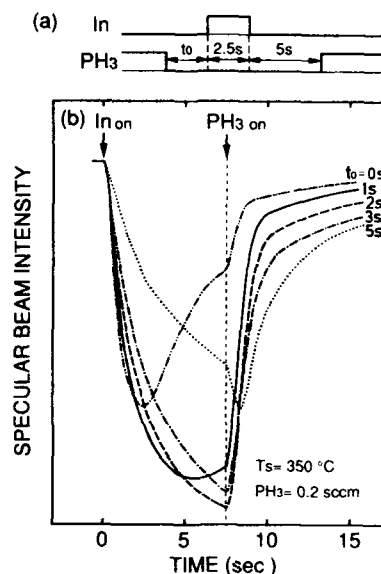


Fig. 3. (a) Deposition diagram of In and P and (b) RHEED intensity recovery at 350°C as a function of the interruption time (t_0) of the PH_3 flow using the deposition diagram shown in (a).

monolayer growth time in the usual MBE growth at 350°C . The recovery of RHEED intensity is observed before the P supply when t_0 equals 0 and 1 s. This indicates that the RHEED intensity recovers by the incorporation of supplied In atoms and excess P atoms which remain on the surface or in the atmosphere before the P supply. On the other hand, when t_0 increases to 5 s, the RHEED intensity just falls and then recovers by the P supply; this suggests that some amount of P atoms desorb from the surface during the P supply interruption time of t_0 . When t_0 is chosen to be 2–3 s, the regular RHEED intensity recovery is observed.

Fig. 4b shows RHEED intensity traces with $t_0 = 3.0\text{ s}$ by the sequence as shown in fig. 4a as a function of t_{In} . It is found that the RHEED intensity recovers the most quickly when t_{In} equals 2.5 s. This time just corresponds to the growth time of one monolayer in the usual MBE growth. This indicates that neither excess phosphorus exists nor deficiency of phosphorus occurs on the surface during growth.

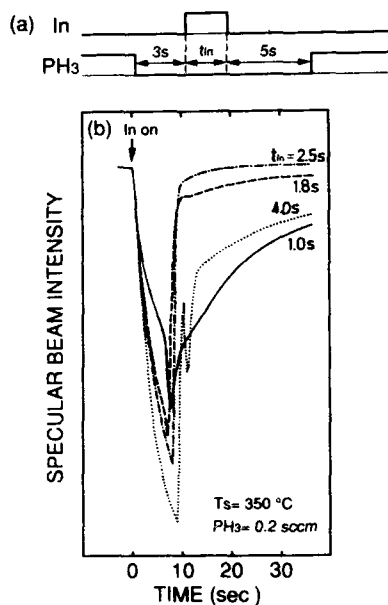


Fig. 4. (a) Deposition diagram of In and P and (b) RHEED intensity recovery at 350°C as a function of In supply time (t_{in}) using the deposition diagram shown in (a).

The gas source MEE growth was done by alternately supplying an optimum amount of In and P atoms. Fig. 5b shows the RHEED intensity traces during the growth of InP by gas source MEE at 350°C by the sequence as shown in fig. 5a. In this case, the In supply time equivalent to one mono-

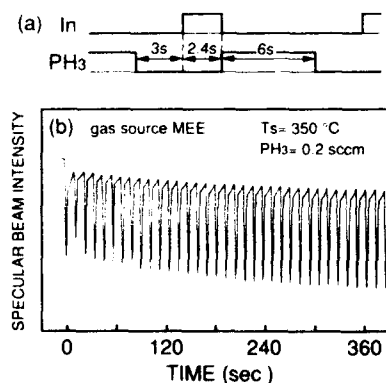


Fig. 5. (a) Deposition diagram of In and P and (b) RHEED intensity trace during gas source MEE growth of InP at 350°C using the deposition diagram shown in (a).

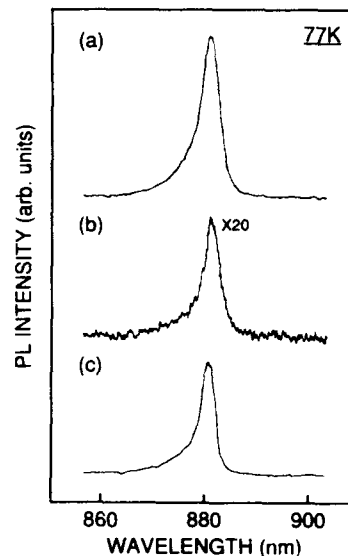


Fig. 6. 77 K PL spectra for three types of 3000 Å thick InP layers grown by (a) gas source MEE at 350°C, (b) gas source MBE at 350°C and (c) gas source MBE at 470°C, respectively, in the same growth chamber. Top: (110); bottom: (110).

layer in the usual MBE mode is 2.4 s, which is slightly different from the 2.5 s in figs. 3 and 4, due to the slight difference in the In cell temperature. Persistent RHEED oscillations were observed with the same amplitude during the growth of over 1000 cycles, as shown in fig. 5b. During the growth of InP by gas source MEE, the (2 × 4) RHEED patterns were observed either during In supply or during P supply.

The 77 K PL spectra are shown in fig. 6 for three types of 3000 Å thick samples grown by gas source MEE at 350°C (fig. 6a), gas source MBE at 350°C (fig. 6b) and gas source MBE at 470°C (fig. 6c), respectively, in the same growth chamber. The FWHM (full width at half maximum) values are almost the same, but the PL intensity of gas source MEE-grown InP is about twenty times as large as that of gas source MBE-grown InP at the same temperature and about one and a half times as large as that of gas source MBE-grown InP at 470°C. This indicates that the gas source MEE-grown InP at 350°C has optical properties equal to or better than the gas source MBE-grown InP at 470°C.

4. Conclusion

Even at a substrate temperature as low as 350°C, the desorption of some amount of phosphorus from the InP surface is observed when PH₃ flow is interrupted, although the RHEED pattern is still showing (2 × 4) reconstructions. The perfectly alternating supply of In and P can be achieved only when PH₃ is supplied with a proper interruption time before the supply of In, where neither excess phosphorus exists nor deficiency of phosphorus occurs on the surface before the supply of In. Under this condition, the recovery of the RHEED intensity induced by the incorporation of phosphorus after the supply of one atomic layer of In is observed at the shortest time period and the RHEED intensity oscillation continues over 1000 cycles with the same amplitude. The optical properties of gas source MEE-grown InP at 350°C are favorably compared with those of InP grown at 470°C by the usual MBE mode.

It is concluded that the gas source MEE method is useful to grow high quality InP layers at low temperatures and will be promising for the growth

of InGaAs/InP SL/QWs with tailored hetero-interfaces.

Acknowledgement

This work was supported in part by the Scientific Research Grant-in-Aid No. 2650014 from the Ministry of Education, Science and Culture of Japan.

References

- [1] J.M. Vandenberg, M.B. Panish, H. Temkin and R.A. Hamm, *Appl. Phys. Letters* 53 (1988) 1920.
- [2] S.R. Forrest, P.H. Schmidt, R.B. Wilson and M.L. Kaplan, *Appl. Phys. Letters* 45 (1984) 1199.
- [3] R. Saner, T.D. Harris and W.T. Tsang, *Phys. Rev.* B34 (1986) 9023.
- [4] K. Uomi, S. Sasaki, T. Tsuchiya and N. Chinone, *J. Appl. Phys.* 67 (1990) 904.
- [5] T.Y. Wang, E.H. Reihlen, H.R. Jen and G.B. Stringfellow, *J. Appl. Phys.* 66 (1989) 5376.
- [6] Y. Horikoshi, M. Kawashima and H. Yamaguchi, *Japan. J. Appl. Phys.* 27 (1988) 169.
- [7] M.B. Panish, *J. Electrochem. Soc.* 127 (1980) 2729.

GSMBE growth of GaAs at low AsH₃ cracking temperatures

M.J. Hafich, H.Y. Lee, P. Silvestre and G.Y. Robinson

Department of Electrical Engineering and Center for Optoelectronic Computing Systems, Colorado State University, Fort Collins, Colorado 80253, USA

A series of nominally undoped GaAs layers were grown by gas source MBE (GSMBE) with an elemental Ga source and AsH₃ cracked by a low pressure Ta gas cracker at cracking temperatures, T_{gas} , between 500 and 1100 °C. For T_{gas} below 800 °C the AsH₃ flow rate was increased to maintain an As-stabilized surface. All samples were found to be p-type. The net carrier concentrations decreased linearly as T_{gas} was decreased from 800 to 500 °C; for $T_{\text{gas}} = 800$ °C, $\mu_{77\text{K}} = 4300 \text{ cm}^2/\text{V}\cdot\text{s}$, whereas when $T_{\text{gas}} = 500$ °C, $\mu_{77\text{K}} = 6400 \text{ cm}^2/\text{V}\cdot\text{s}$. Low temperature photoluminescence (PL) on samples grown at $T_{\text{gas}} = 900$ °C and $T_{\text{gas}} = 500$ °C showed carbon to be the dominant acceptor and a much lower level of carbon incorporation at the lower gas cracking temperature. Quadrupole mass spectrometer measurements of the AsH₃ pyrolysis by the gas cell indicate only partial cracking occurring for $T_{\text{gas}} = 500$ to 800 °C; thus, AsH₃ fragments may be affecting carbon incorporation at the growth surface.

1. Introduction

The use of thermally decomposed arsine as a source of arsenic during MBE growth was begun by Panish [1] more than a decade ago; since then the use of arsine and elemental Ga or an organometallic Ga compound for the growth of GaAs by MBE has been employed by numerous groups. The utilitarian advantages to the use of arsine are well established: gas flow control is precise, reproducible, and very quick; flux is constant throughout the life of the supply; and the arsine supply may be easily replenished without venting the MBE vacuum chamber. The use of arsine and elemental Ga for the growth of GaAs has repeatedly produced high quality epilayers [2,3]; this may be due in part to the hydrogen ambient resulting from the thermal cracking of arsine. Calawa [4] demonstrated that a hydrogen ambient during GaAs growth significantly reduces the incorporation of carbon and oxygen in the epilayer. It has also been speculated in the literature that "the presence of the AsH radical on the growth surface can play a key role in inhibiting hydrocarbon pyrolysis since a surface can play a key role in inhibiting hydrocarbon pyrolysis since a surface population of atomic hydrogen is neces-

sarily made available" [3]. It is the role of the partially cracked arsine species that we have examined in the present work.

We report here the growth of a series of unintentionally doped GaAs epilayers by gas source molecular beam epitaxy (GSMBE) where the temperature (T_{gas}) of the low-pressure gas cracking cell was varied between 500 and 1100 °C. Hall measurements of these layers show a distinct decrease in carrier concentration as T_{gas} decreased from 900 to 500 °C along with a corresponding increase in Hall mobility. Low temperature photoluminescence measurements indicated a decrease in carbon incorporation when $T_{\text{gas}} = 500$ °C. Upon examining a quadrupole mass spectrometer measurement of the thermal decomposition of arsine as a function of T_{gas} , we believe that the partially cracked species of arsine were responsible for improved GaAs characteristics at low AsH₃ cracking temperatures.

2. Experimental

The vacuum system used for this work was a Perkin-Elmer Model 433 MBE system with an Ulvac gas cell and a cryopump to remove excess

hydrogen. The Ulvac gas cell is a hydride gas cracking oven that operates in the low-pressure region (below 10 Torr) and consists of a gas flow region baffled with 11 Ta discs inside a 12 cm long, 1.5 cm diameter, heated Ta tube. AsH₃ (and/or PH₃ for the growth of other materials) was supplied to the gas cell by a delivery system using closed loop pressure control to regulate the flow of gas. The gas cell was used to crack both AsH₃ and PH₃; although no PH₃ was used during the growth of these epilayers, phosphide materials were grown during this time period and we did observe a small amount of phosphorus in these samples. During the six month period when this series of layers were grown the vacuum system was not vented and only a single cylinder of AsH₃ [5] was used.

The growth conditions for each of the GaAs layers were kept as identical as possible. The substrate material used was undoped, semi-insulating (100) GaAs and a single wafer was cleaved and used for the growth of all of the layers. The temperature of the gas cell was constant in the range from 500 to 1100°C, each of the GaAs layers was grown with a substrate temperature of 620°C, the GaAs growth rate was 1.05 ± 0.10 $\mu\text{m/h}$, and the epilayer thickness was nominally 5 μm . The AsH₃ flow varied from 2.5 to 7.0 SCCM over the series of layers grown; during the growth of each layer the V/III ratio was held constant at a value between 1 and 2.

3. Characterization

All of the layers in this study were p-type and fig. 1 shows the net carrier concentration ($N_a - N_d$) and Hall mobility of each layer versus the temperature of the gas cell during epitaxial growth. The open circles are data from Hall measurements at 300 K and the filled circles are data from Hall measurements at 77 K. The change in net carrier concentration with measurement temperature is consistent with the expected change in occupation of acceptor impurities in GaAs. Fig. 1 shows the data can be divided into two regions: at or below 800°C the net carrier concentration decreases with T_{gas} and at or above 900°C the net carrier concentration has little dependence upon T_{gas} . From fig. 1b, the 77 K hole mobility increases with decreasing T_{gas} for T_{gas} below 800°C. The combined changes in carrier concentration and mobility indicate that the number of acceptor impurities incorporated in the epitaxial film decreased as T_{gas} was decreased. Assuming the 77 K mobility was due to only impurity scattering and lattice scattering, the temperature dependence of the hole mobility in GaAs (summarized by Blakemore [6]) yields a decrease in acceptor concentration of N_a of about a factor of 2 while the donor concentration N_d remained approximately constant. For T_{gas} above 800°C, the decreasing mobilities indicate additional impurities which may have been produced by the gas cell at the high operating

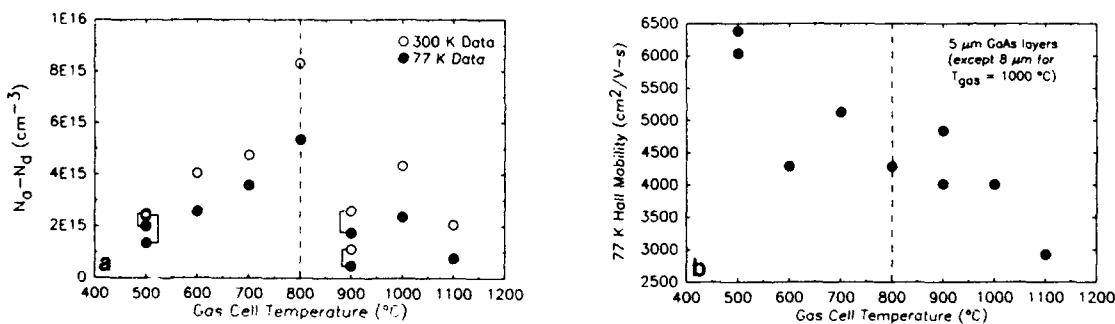


Fig. 1. (a) The net carrier concentration $N_a - N_d$ for the unintentionally doped GaAs layers plotted against the gas cell temperature used during epitaxial growth. The open circles were obtained from Hall measurements at 300 K and the filled circles were obtained from Hall measurements at 77 K in the dark. (b) The measured Hall mobility at 77 K as a function of T_{gas} . The vertical dashed line in both plots denotes the division in the data between effects at low T_{gas} and at high T_{gas} .

temperatures. Finally, two of the growths were repeated, one with $T_{\text{gas}} = 900^\circ\text{C}$ and the other with $T_{\text{gas}} = 500^\circ\text{C}$, and the trends in the net carrier concentration and 77 K Hall mobility were reproducible. Low temperature photoluminescence (PL) measurements were performed on two of the samples in this study: one grown with $T_{\text{gas}} = 900^\circ\text{C}$ and the other grown with $T_{\text{gas}} = 500^\circ\text{C}$. The PL spectra are shown in fig. 2. Both spectra were observed to be shifted to higher energies due to the differing amounts of residual phosphorus incorporated in films during growth (measured by double crystal X-ray diffraction). If the energy shift due to the residual phosphorus is removed [7] then the peak assignments shown in fig. 2 agree within 0.5 meV of published values [8,9] and it is clear that the dominant residual impurity in these films was carbon as is typical of MBE material. Lu et al. [9] demonstrated that estimates of both the compensation ratio, N_a/N_d , and the magnitude of N_a can be obtained from integrated peak intensities in the low temperature PL spectrum of GaAs. Based on that analysis, the implications for the spectra of fig. 2 are: (1) for the sample grown with $T_{\text{gas}} = 900^\circ\text{C}$ the similar intensities of the excitonic peaks indicates a large compensation ratio whereas for the sample grown with $T_{\text{gas}} = 500^\circ\text{C}$ the dominance of the (A^0 , X) peak indicates only slight compensation, and (2) the ratio of the (e, C)/(A^0 , X) peaks in each sample shows that the sample grown with $T_{\text{gas}} =$

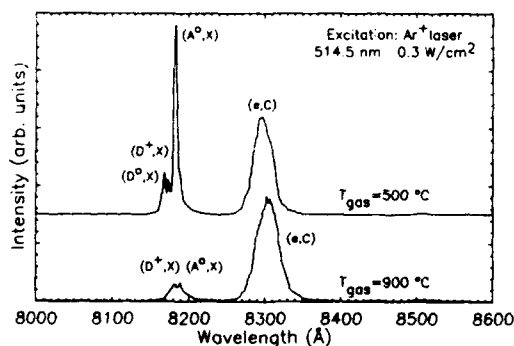


Fig. 2. 2 K photoluminescence spectra of a GaAs epilayer grown with a gas cell temperature of 500°C (upper spectrum) and a GaAs epilayer grown with a gas cell temperature of 900°C (lower spectrum).

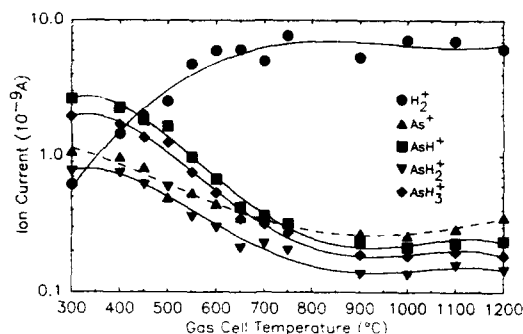


Fig. 3. The uncorrected ion currents from a quadrupole mass spectrometer for H_2^+ (2 amu) and the singly ionized fragments of AsH_3 : As^+ (75 amu), AsH^+ (76 amu), AsH_2^+ (77 amu) and AsH_3^+ (78 amu). The ion currents were measured as a function of the gas cell temperature and with an AsH_3 flow of 0.5 SCCM.

500°C had a significantly lower acceptor (carbon) concentration. These results agree qualitatively with the electrical data presented in fig. 1, indicating that the residual acceptor is carbon and the carbon incorporated in the GaAs epilayers decreases as T_{gas} is lowered.

Fig. 3 shows the hydrogen and the fragments of arsine observed in the quadrupole mass spectrometer (QMS) of the GSMBE system as a function of T_{gas} . The QMS ionizer was located 2–3 cm above the growth position of the sample and not on the axis of the gas cell. A large noise level and very small electron multiplier gain in the QMS during the measurement prevented us from observing the arsenic peaks above 75 amu. The measurement was performed with 0.5 SCCM of AsH_3 flowing to minimize nonlinear effects when the QMS operates at pressures exceeding 10^{-5} Torr [10]. With 0.5 SCCM of AsH_3 , the flow in the gas cell was molecular and gas-wall collisions dominated the cracking process; not much change from this condition was expected for the higher gas flows used during epitaxy since flow in the gas cell does not enter the viscous flow region. At $T_{\text{gas}} = 300^\circ\text{C}$ the relative magnitudes of the arsine fragments agreed with published fragmentation patterns. As T_{gas} was raised, the increase of the H_2^+ peak and the relative increase in the As^+ peak (shown as the triangular data points and the

dashed line) above the AsH⁺, the AsH₂⁺, and the AsH₃⁺ peaks resulted from the cracking operation of the gas cell. The most important effect to be observed from fig. 3 is that the change in the cracking of the arsine by the gas cell occurs in the temperature region from 400 to 800°C, the same temperature region in fig. 1a where the net carrier concentration in the GaAs epilayer was changing.

4. Conclusion

We have observed an increase in 77 K hole mobility and decrease in carbon incorporation for GaAs grown by GSMBE as the temperature of the gas cell was decreased. The temperature region where these effects occurred corresponds to that where arsine is partially pyrolyzed in the low pressure gas cell, thus it is the partially cracked fragments of arsine that reduce the incorporation of carbon into the GaAs layer.

Acknowledgements

The authors wish to thank S.D. Hersee and P.A. Martin of the Electronics Laboratory at General Electric for the low temperature photo-

luminescence measurements. The authors gratefully acknowledge the support of the Air Force Office of Scientific Research (Grant 89-0513) and the Center for Optoelectronic Computing Systems, sponsored by the National Science Foundation/Engineering Research Center Grant CDR-86-22236 and by the Colorado Advanced Technology Institute, an agency of the State of Colorado, and the support of the General Electric Company.

References

- [1] M.B. Panish, J. Electrochem. Soc. 127 (1980) 2729.
- [2] A.R. Calawa, Appl. Phys. Letters 38 (1981) 701.
- [3] J.E. Cunningham, G. Timp, T.H. Chiu, J.A. Ditzenberger, W.T. Tsang, A.M. Sergent and D.V. Lang, J. Crystal Growth 95 (1989) 185.
- [4] A.R. Calawa, Appl. Phys. Letters 33 (1978) 1020.
- [5] Phoenix Research Corp., 8075 Alvarado Road, La Mesa, CA 92401, USA.
- [6] J.S. Blakemore, J. Appl. Phys. 53 (1982) R123.
- [7] H.C. Casey, Jr. and M.B. Panish, Heterostructure Lasers, Part B: Materials and Operating Characteristics (Academic Press, New York, 1978).
- [8] S. Ambros, M. Kamp, K. Wolter, M. Weyers, H. Heinke, H. Kurz and P. Balk, J. Appl. Phys. 64 (1988) 5098.
- [9] Z.H. Lu, M.C. Hanna, D.M. Szmyd, E.G. Oh and A. Majerfeld, Appl. Phys. Letters 56 (1990) 177.
- [10] J. Steinhaus, UTI Instruments Co., 497 S. Hillview Drive, P.O. Box 40008, Milpitas, CA 95035-2008, USA.

Residual impurities originating from AsH₃ in GS-MBE grown GaAs

S. Nagao, Y. Inoue, E. Kawanishi and H. Gotoh

Thin Films Laboratory, Research Center, Mitsubishi Kasei Corp., 1000 Higashimamiana, Ushiku, Ibaraki 300-12, Japan

The dependence of residual impurities in GS-MBE grown GaAs on cracking temperature and differences between batches of AsH₃ has been studied. Samples were characterized using Hall measurement, photoluminescence and SIMS analysis. Silicon and sulfur were identified as dominant residual donors, and these impurities were concluded to come from gaseous impurities in AsH₃. The residual donor concentration and the dominant donor species were found to depend mainly on differences between batches of AsH₃, reflecting differences in methods used to produce and purify AsH₃.

1. Introduction

It is well known that the presence of residual impurities in gas source molecular beam epitaxy (GS-MBE) grown GaAs depends on the cracking temperature of AsH₃ [1]. This is thought to be due to impurities from the gas cell used in the GS-MBE system. A few reports describe the relationship between residual impurities in GaAs grown not only by GS-MBE, but also by metalorganic vapor phase epitaxy (MOVPE) and those in the source AsH₃ [2,3]. It is considered that information about impurities in AsH₃ will contribute toward obtaining higher quality epitaxial films by GS-MBE, chemical beam epitaxy (CBE) and MOVPE.

This paper reports on residual impurities in GS-MBE grown GaAs originating from the source AsH₃, and examines the stability of source AsH₃ quality. The characteristics of high electron mobility transistor (HEMT) structures grown by GS-MBE are also evaluated.

2. Experiments

The GS-MBE system (VG V80H) employed in this study was equipped with a high-pressure gas cell (HP-GC), and was evacuated by an oil diffusion pump. Two batches of AsH₃ (AsH₃-1 and AsH₃-2) from different suppliers were used. Each

supplier has its own purification method that mainly reduces the amount of water in AsH₃. Both batches of AsH₃ had purities of 5N according to the suppliers' specifications. The methods used by the suppliers to reduce water have not been revealed yet. The group V gas cell was made of PBN and alumina. Group III sources of Ga and Al have purities of 8N and 5N, respectively, and were held within PBN crucibles.

Undoped GaAs films were grown on (100) oriented Cr-doped GaAs substrates at a temperature of 600°C and a growth rate of 1.0 μm/h. The cracking temperature of AsH₃ was varied from 700 to 900°C. The total beam intensity of the cracked AsH₃ was 5×10^{-3} Pa. The stability of the source AsH₃ quality was also examined. The source AsH₃ was connected for three months to the gas handling system of the GS-MBE apparatus, then undoped GaAs films were grown under identical conditions. Finally, HEMT structures were grown on the condition that high purity GaAs had been obtained.

The characteristics of grown films were evaluated by Hall measurement, photoluminescence (PL) spectroscopy and secondary ion mass spectroscopy (SIMS) analysis. Photoluminescence was measured at 4.2 K, and the excitation source was the chopped 5145 Å line of an Ar laser. 0.25 μm gate length, low noise HEMTs were also fabricated.

3. Results and discussion

The dependence of residual carrier concentration in GS-MBE grown undoped GaAs on cracking temperature and differences between batches of AsH_3 is shown in fig. 1. All films grown from AsH_3 -1 exhibited n-type conduction, and carrier concentration increased as cracking temperature increased. Films grown from AsH_3 -2 under the higher cracking temperatures also exhibited n-type conduction, and they had almost the same temperature dependence except that the level was lower than that of films grown from AsH_3 -1. Undoped GaAs grown from AsH_3 -2 at the lower cracking temperature exhibited p-type conduction and a carrier concentration of below 10^{14} cm^{-3} . The fact that the difference in residual carrier concentration level depended on AsH_3 batch indicates that the residual impurities originated from the source AsH_3 . The dependence of residual carrier concentration on cracking temperature suggests the possibility that impurities in AsH_3 exist as gaseous compounds; they are thermally decomposed in the gas cell and they are incorporated into GaAs

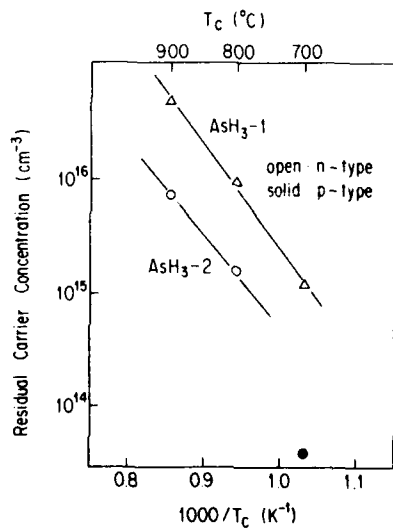


Fig. 1. Residual carrier concentration versus cracking temperature (T_c) in GaAs films grown by GS-MBE from AsH_3 -1 and AsH_3 -2. Activation energies of carrier concentration are 1.76 and 1.69 eV, respectively.

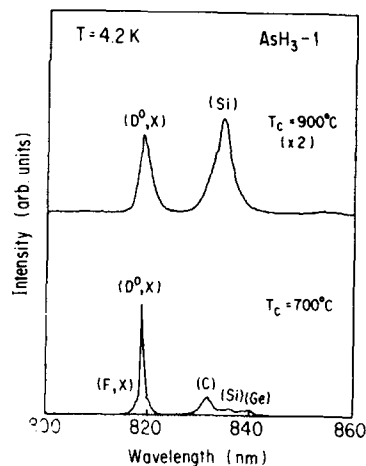


Fig. 2. PL spectra of GaAs grown by GS-MBE at $T_c = 900$ and 700°C using AsH_3 -1, measured at 4.2 K.

films. The activation energies of carrier concentration in GaAs grown from AsH_3 -1 and AsH_3 -2 are estimated to be 1.76 and 1.69 eV, respectively.

Fig. 2 shows the PL spectra at 4.2 K of undoped GaAs grown from AsH_3 -1. There is a strong luminescence related to Si acceptors in the PL spectrum of GaAs grown at the higher cracking temperatures. In addition, there are three prominent peaks which are related to C, Si and Ge from the GaAs at the lower cracking temperature. Therefore silicon must be a dominant n-type impurity in the GaAs grown from AsH_3 -1. In contrast, there are not prominent peaks except for a C-related one in the PL spectrum of GaAs grown from AsH_3 -2, as shown in fig. 3. Dominant n-type impurities in GaAs grown from AsH_3 -2 cannot be identified at this point. The prominent peaks in the exciton luminescence region in all films grown using AsH_3 -1 and the film grown at the cracking temperature of 900°C using AsH_3 -2 are due to the recombination of excitons bound to neutral donors (D^0, X). On the other hand, in the film grown at the cracking temperature of 700°C using AsH_3 -2, the free-exciton recombination line (F, X) and the neutral acceptor bound exciton transition (A^0, X) are clearly observed, as well as excitons bound to donors. Carbon acts as an acceptor in the GaAs from both batches of AsH_3 .

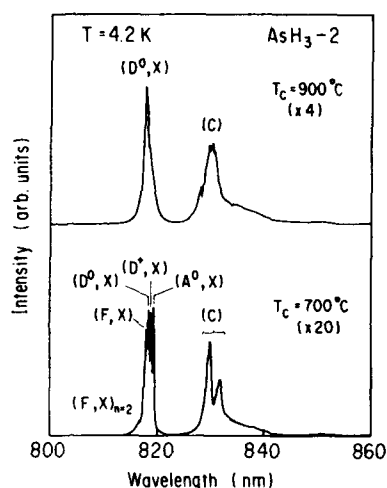
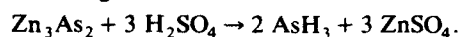


Fig. 3. PL spectra of GaAs grown by GS-MBE at $T_c = 900$ and 700°C using AsH₃-2, measured at 4.2 K.

AsH₃-1 may have been contaminated by Si-related compounds during the production and purification of the AsH₃. The observed activation energy of 1.76 eV is close to values obtained during the thermal decomposition process of SiH₄ [4,5]. Thus, SiH₄ is one possible gaseous impurity in AsH₃-1. However, the exact mechanism of Si incorporation in GS-MBE grown GaAs is not obvious. Complicated processes such as the thermal decomposition of SiH₄, the generation of various kinds of radicals or Si sticking to the gas cell and re-evaporating from it may be involved.

The results of SIMS analysis are shown in table 1. Silicon dominates the residual impurity concentration in GaAs grown from AsH₃-1. This result is consistent with that obtained from observa-

tion of the PL spectra. On the other hand, there was no Si detectable by SIMS in the GaAs grown from AsH₃-2, and the S concentration corresponds to the residual carrier concentration. The S level is almost the same as that of the GaAs grown from AsH₃-1. Incorporation of S into AsH₃ is probably related to the production of AsH₃ by the following reaction:



It is well known that H₂S is also generated during the above reaction. The observed activation energy of residual carrier concentration in the GaAs grown from AsH₃-2 is 1.69 eV, which corresponds to the decomposition enthalpy of H₂S [6]. Sulfur may exist in the AsH₃ as a gaseous compound of H₂S, and be thermally decomposed and stick to GaAs films [7,8].

All undoped GaAs films grown from AsH₃-2, after it was left attached to the system for three months after the first series of growths was done, exhibited p-type conduction, even at the high cracking temperature of 1100°C . The carrier concentration of all films were on the order of 10^{13} cm^{-3} . Sulfur was not detected by SIMS analysis in any of the films. This may be attributed to the adsorption of H₂S onto the walls of the AsH₃ cylinder. The hole mobilities were all about $450 \text{ cm}^2/\text{V} \cdot \text{s}$ at room temperature.

Typical two-dimensional electron gas (2DEG) mobilities of AlGaAs/GaAs HEMT structures grown in the same MBE system by conventional solid source and by gas source MBE were examined. Each structure had layers consisting of 1 μm undoped GaAs, 6 nm undoped Al_{0.3}Ga_{0.7}As spacer, 70 nm Si-doped Al_{0.3}Ga_{0.7}As (1×10^{18}

Table 1
Impurities in GS-MBE grown GaAs using different AsH₃ batches, measured by SIMS analysis

Sample No.	Carrier concentration (cm^{-3})	Carrier type	Impurity concentration (cm^{-3})					T_c ^{a)} ($^\circ\text{C}$)	AsH ₃ batch No.
			Si	Ge	S	Se	Te		
064C	4.9×10^{16}	n	3.5×10^{16}	ND	2.8×10^{15}	ND	ND	900	1
068C	1.4×10^{15}	n	1.2×10^{15}	ND	ND	ND	ND	700	1
451C	7.6×10^{15}	n	ND	ND	7.8×10^{15}	ND	ND	900	2
458C	1.8×10^{15}	n	ND	ND	1.6×10^{15}	ND	ND	800	2
473C	6.5×10^{13}	p	ND	ND	1×10^{13}	ND	ND	700	2
Background level			1×10^{15}	1×10^{16}	5×10^{14}	7×10^{13}	9×10^{12}		

^{a)} T_c is the cracking temperature of AsH₃.

cm⁻³) and 5 nm undoped GaAs cap layers. In this case, AsH₃-2 was used for the GS-MBE growth. A typical 2DEG mobility at 77 K in a structure obtained by conventional MBE was about 9×10^4 cm²/V·s with a sheet carrier concentration of 7×10^{11} cm⁻². The value for structures obtained by GS-MBE was 1.1×10^5 cm²/V·s with the same carrier concentration.

Next, 0.25 µm gate length, low-noise HEMTs were fabricated using AsH₃. The transconductance g_m of these HEMTs was found to be about 360 mS/mm, and the minimum noise figure at 12 GHz was 0.86 dB. These values are almost the same as those of low-noise HEMTs obtained by conventional solid source MBE.

4. Conclusions

Residual impurities in GS-MBE grown GaAs are related not only to cracking temperature, but also to the batches of the source AsH₃. Two kinds of n-type impurities, Si and S, were found to be present. Both Si and S are believed to originate from impurities in the source AsH₃, in the form of gaseous compounds such as SiH₄ and H₂S. Silicon was found in only the films grown from one of two different batches of AsH₃. This reflects differences in purification of AsH₃. On the other hand, S was detected at a similar level in films

grown from two different batches of AsH₃. The incorporation of S into AsH₃ is related to reactions in the production of AsH₃. Low noise HEMTs obtained by GS-MBE using high-purity AsH₃ were of high quality.

Acknowledgements

The authors would like to thank I. Sakamoto, K. Shimoyama, M. Katoh, J. Saitoh and T. Okano for their useful discussion and continuous encouragement.

References

- [1] A.R. Calawa, Appl. Phys. Letters 38 (1981) 702.
- [2] S.P. Watkins, G. Haacke and H. Burkhard, Appl. Phys. Letters 52 (1988) 401.
- [3] S.P. Watkins, G. Haacke, H. Burkhard, M.L.W. Trewalt and S. Charbonneau, J. Appl. Phys. 64 (1988) 3205.
- [4] D.C. Gupta and R. Yee, J. Electrochem. Soc. 116 (1969) 1561.
- [5] H. Ohno, E. Ikeda and H. Hasegawa, J. Crystal Growth 68 (1984) 15.
- [6] M.E.D. Rayment, Alberta Sulphur Quart. Bull. 8 (1971) 24.
- [7] J. Massies, F. Dezaly and N.T. Linh, J. Vacuum Sci. Technol. 17 (1980) 1134.
- [8] H. Gotoh, K. Sasamoto, S. Kuroda, T. Yamamoto, K. Tamamura, M. Fukushima and M. Kimata, Japan. J. Appl. Phys. 20 (1981) L893.

Gas source molecular beam epitaxy growth of heterojunction bipolar transistors containing 1 monolayer δ -Be

J.E. Cunningham

AT&T Bell Laboratories, Holmdel, New Jersey 07733, USA

T.Y. Kuo

Massachusetts Institute of Technology, Cambridge, Massachusetts 02139, USA

A. Ourmazd, K. Goossen, W. Jan, F. Storz, F. Ren

AT&T Bell Laboratories, Holmdel, New Jersey 07733, USA

and

C.G. Fonstad

Massachusetts Institute of Technology, Cambridge, Massachusetts 02139, USA

We present results on AlGaAs/GaAs Heterostructure Bipolar Transistors containing a 1 monolayer δ -Be doped sheet in a GaAs base 100 Å wide that is grown by gas source molecular beam epitaxy. Also, diffraction measurements performed on 1 monolayer δ -Be layers show the planar doping widths are 40 and 200 Å for gas source and molecular beam epitaxial growth, respectively. Be diffusion measurements versus varying anneal conditions are presented and shown to be consistent with a kick-out mechanism involving interstitial Be.

1. Introduction

The use of a widegap emitter in a heterostructure bipolar transistor [1], HBT, allows for extremely high base doping to improve high speed device performance. Also, the carrier transit time through the base of a HBT may be reduced in structures containing narrow δ -doped bases as was successfully demonstrated at the 0.04 monolayer (ML) δ -Be level by Malik et al. [2]. However, the Be planar densities employed in HBTs to date produce effective doping concentrations close to the homogeneous doping solubility limit [3]. Furthermore, it becomes questionable whether Be, at the 1 ML ($6 \times 10^{14} \text{ cm}^{-2}$) level, can be confined

in ultra thin bases of HBT as a δ -dopant owing to significant dopant redistribution [4] and diffusion [5] accompanying crystal growth. Although the origin of the latter phenomenon remains incompletely understood, it is clear that planar out-diffusion becomes increasingly severe as the Be concentration extends further beyond the doping solubility limit.

In this work we present results on AlGaAs/GaAs HBT structures containing a sheet of δ -Be dopant up to 1 ML in a GaAs base 100 Å wide that are grown by GSMBE, gas source molecular beam epitaxy. We report diffraction measurements from structures containing up to a 1 ML δ -Be concentration in GaAs that show the spread

of planar dopants is below 40 and 200 Å for GSMBE and MBE growth methods, respectively. The dependence of Be diffusion on anneal time, temperature and δ -Be concentration are measured and found compatible with a kick-out mechanism involving a singly ionized interstitial donor.

2. Localization of δ -Be below the 0.02 ML level

Our investigation of the planar confinement of Be begins at $\delta = 0.016$ ML, where the doping concentration just lies near the 3D homogeneous doping solubility limit. We profile by capacitance-voltage (CV) techniques structures containing the above δ -Be sheet grown 1000 Å below the GaAs surface by GSMBE and examine the dependence of the CV profile FWHM on growth temperature. A III-V flux ratio less than 1:2 was used. For comparison, measurements were performed on the identical structures grown by MBE using As₄ under similar growth conditions. The CV FWHM are 11 and 20 Å for GSMBE growth at 510 and 580°C, respectively. The CV FWHM of 11 Å is the narrowest CV profile width ever measured in a semiconductor. On the other hand, the respective FWHM were 28 and 56 Å for growth of the same δ -Be concentration by MBE at 530 and 600°C. Clearly, our results reveal the planar confinement of Be is a growth dependent phenomenon. We have examined in detail the thermal broadening of the CV profile of δ -Be during growth and found it to be diffusion limited in the GSMBE case where as surface segregation is the principal broadening mechanism in the MBE case [6]. For growth at 500°C the difference in planar confinement of Be between growth methods is as small as 20 Å, however, this difference can become magnified as the δ -Be/GaAs system moves to higher instability brought on by δ -Be concentrations that greatly exceed the solubility limit. At present, the mechanism that drive surface segregation of Be during MBE growth and its reduction by GSMBE are unknown. The latter difficulty is in part caused by the behavior of Be diffusion which both remains incompletely understood to date and is an essential step in the surface segregation process.

3. δ -Be diffusion

The present study aims at identifying the defect structure and attendant exchange mechanism that underlies Be diffusion when δ -doped into GaAs 1000 Å below the surface. Key aspects of the problem are interwoven in the way the doping profile of δ -doped Be specimens broaden as the thermal, temporal conditions of the anneals vary for a particular Be concentration. The width of the doping distribution was estimated from the FWHM of the CV profile. At a δ -Be concentration of 0.015 ML our measured CV FWHM and corresponding annealing information is tabulated in table 1. We determine the Be diffusion coefficient, D , from our data by use of procedures described previously [7]. Thermal dependences of D at the 0.015 ML level (solid circles) are plotted in fig. 1 and show an Arrhenius behavior with an activation energy, E_a , of 2.0 eV and an ordinate intercept, D_0 , of 1×10^{-5} cm²/s. For comparison a slower Be diffusivity is observed at the 0.008 ML level (solid square) and is fit with an Arrhenius expression in which $E_a = 1.7$ eV and $D_0 = 2 \times 10^{-8}$ cm²/s. The factor two increase in Be concentration results in a factor two/three increase in Be diffusivity. The Be diffusivity found here is similar to other measurements on δ -Be layers [7].

The inset shows the dependence of the Be diffusion length, x_d , on the anneal time, t , when the anneal temperature is held fixed at 700°C. The data is fit by an expression $x_d^2 \propto t^{1.1}$. The data follow classical impurity diffusion where x_d^2 scales like $2Dt$ and D is time independent. Non-classical

Table 1
Capacitance-voltage FWHM versus anneal temperature for anneal time of 10 s

Temperature (°C)	FWHM (Å)
As-grown	16
650	19
680	22
700	24
750	40
800	67
850	130
900	143
950	150

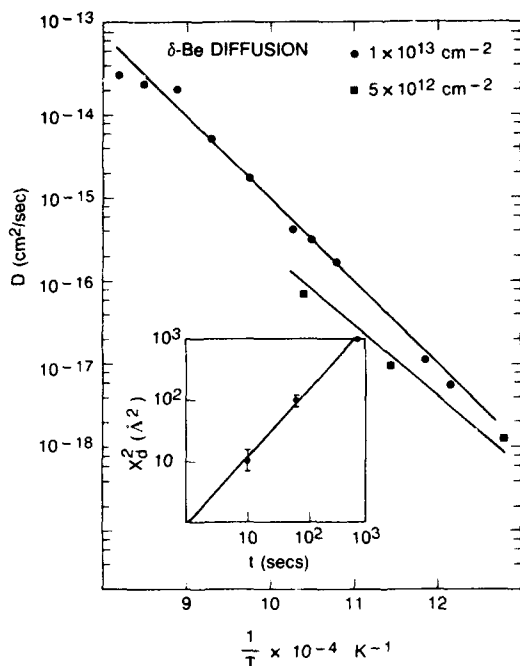


Fig. 1. Be diffusion coefficient versus inverse temperature. Inset. Be diffusion length versus time.

diffusion, i.e. D is time dependent, can also occur when thermodynamic equilibrium conditions have not been achieved in defect concentration at the dopant position during short anneal times. This is because defects may be kinetically hindered from reaching a dopant layer buried well below the crystal surface owing to an inherently large migration energy for the defect. The latter conditions would indeed be expected for the case of a Ga vacancy point defect and δ -Be layers considered here. This is because Ga vacancies diffuse slowly from the crystal surface as reported previously by Chiang and Pearson [8], and thus their concentration would not achieve a thermodynamic equilibrium value at the δ -position over the anneal time-temperature range explored here. The resulting Be diffusion coefficient would be nonlinear both temporally and kinetically and hence not follow the simple dependences depicted by the data shown in fig. 1. On the other hand, Ga interstitials may rapidly diffuse from the crystal surface well into the bulk and cause Be diffusion

to follow equilibrium classical behavior much like what is observed in fig. 1. This is because the Ga interstitials are expected to possess lower migration energies in comparison to Ga vacancy motion processes. Be diffusion, when controlled by interstitials, can proceed by a kick-out mechanism. One choice of the site exchange mechanism is, Be_{Ga}^- , Be acceptor on the Ga sublattice, combining with I_{Ga}^+ , Ga interstitial donor, to produce a Be_i^+ , interstitial Be ion, and an electron. Alternative reaction paths have been suggested for Column II diffusion on the Ga sublattice and differ with the above choice in either ionization charge state of a constituent or the defect type [4,5,9]. The chemical configuration considered here was chosen for qualitative reasons i.e. (i) defects that have low migration energy and (ii) low charge states of constituents to minimize the concentration dependence of D .

4. Diffraction from δ -Be near 1 ML

In this section we examine localization of δ -Be at high concentrations, when measured by high resolution transmission electron microscopy, HR-TEM, and high resolution X-ray diffraction, HR-XRD, respectively. Diffraction techniques have distinct advantages over alternative methods (i.e. CV and SIMS) in that the ultimate width of the dopant distribution measured is not limited by the intrinsic resolution of the technique but instead, can be measured to distances smaller than a few Å. In earlier work [10], Ourmazd et al. reported a HRTEM view of our 0.3 ML δ -Be layer grown at 500°C by GSMBE that showed spatially localized contrast at the δ -Be position. The profile width of this chemically sensitive contrast was 15 Å which indicates the degree of δ -Be confinement. A HRTEM plan view of the δ plane further reveals the contrast is not uniform but, instead, consists of clusters of diameter 12 Å. We have also examined δ -Be localization using HRXRD methods. In this approach a multiple array of δ -Be sheets at the 0.8 ML level are periodically grown in GaAs. They produce superlattice diffraction characteristics around the (400) Bragg reflection as shown in fig. 2. The measurements were obtained using

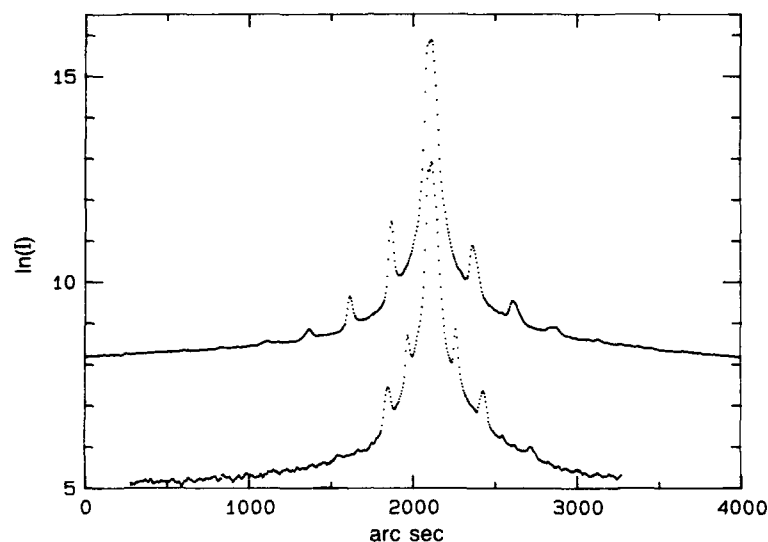


Fig. 2. X-ray diffraction from 0.9 ML δ -Be superlattice grown by GSMBE (top) and MBE (bottom).

Cu K α incident radiation and the diffractometer operated in double crystal diffraction geometry. The diffraction traces in fig. 2 correspond to the above structure grown by GSMBE and conventional MBE in which the growth temperatures were 470 and 450°C, the III/V ratios were 1:5 and 1:10 and the period lengths were 750 and 1200 Å, respectively. It is clear that the higher order satellites are much more distinct in the GSMBE grown structure and thus indicate improved characteristics for δ -Be planar confinement. We will show elsewhere that the spatial confinement of the Be is localized to 34 and 200 Å for GSMBE and MBE layers, respectively.

5. δ -Be HBT

Growth of HBT structures by GSMBE methods consists of a 5000 Å collector layer Si doped to $5 \times 10^{16} \text{ cm}^{-3}$ on a n-type substrate then followed by a δ -Be concentration near 1 ML in GaAs base of 50–200 Å thickness. The emitter component consists of a 1000 Å layer of graded AlGaAs ($x = 0.3$ to 0.0) Si doped to $5 \times 10^{17} \text{ cm}^{-3}$, then followed by Si δ -doped GaAs and epitaxial Al metal for non-alloyed ohmic contact

[11]. The base and emitter components of the structure were grown at 500°C. A description of selective contacting, processing and device planarization has been reported elsewhere by Goossen et al. [12] and Kuo et al. [13].

We have explored device characteristics of this structure on the concentration of δ -Be doping in the base as it varies from 0.09 to 0.9 ML. The effect of changing the base width from 50 to 200 Å at the 0.33 ML level is also examined. Evaluation of device transport on the above dependences provides information on growth abnormalities such as Be redistribution into the emitter and trap formation. In fig. 3a we present a Gummel plot of the emitter–base junction, EB, and corresponding collector response for the 0.3 ML device at a 200 Å base layer width. From an I – V of the base–collector (BC) junction, not shown, the diode ideality factor, n , is 1.08 and is a general feature of the BC diode quality found in all the structures listed above. The EB junction also appeared perfectly ideal (i.e., $n = 1.0$ to 1.2) for driving currents above 100 μA . Hence, nearly perfect diffusive transport from injector to the base occurred in our devices under typical HBT operation.

At lower currents, the Gummel plots of the EB junction reveals components in the diode I – V

having ideality in the range 1.7–1.9. The contribution of the higher order ideality components to the I – V relation varies considerably with the δ -Be concentration. At the 0.08 and 0.9 δ -Be levels, the $n \neq 1$ components become visible below the 100 nA and μ A level, respectively. This strong δ -Be dependence of the $n \neq 1$ components in the EB diode I – V characteristic, and also their low temperature characteristics, are indicative of tunneling assisted transport processes in the AlGaAs emitter much like those found in homogeneously doped heterojunction diodes reported previously by Chand et al. [14]. Tunneling assisted processes at the low current level in the EB junction could arise from traps formed in the AlGaAs owing to the low growth temperature employed to localize Be. Nevertheless, our devices work as excellent HBTs at temperatures as low as 2 K and hence the number of traps is insufficient to affect the device performance under typical operation.

An example of the output performance of an HBT containing δ -Be at the 0.3 level is shown in fig. 3b. The current gain is 10. It is uniform versus collector current and the device has low output

conductance. The gain falls to 5 for a 50 Å base width because of hole back injection into the emitter. The dependence of the gain on δ -Be concentration is strong but remarkable systematic. Our preliminary measurements give gain versus δ -Be concentration as 250:0.08, 30:0.16, 10:0.3 and 0.1:0.9 ML. The strong gain reduction in the device at higher δ -Be concentration is indicative of limitations comprising higher order p-type dependences such as Auger processes [15] or hole back injection [16]. At present there is no consensus view of the dominance of either process to the gain limitation in HBTs nor is there sufficient space to further discuss our results on this important matter.

At 77 K the 0.3 ML device has a current gain of 100 and sheet base resistance of $150 \Omega/\square$. Thus, the δ -Be HBT device appears well suited for high frequency applications.

6. Conclusion

In summary, HBTs have been grown by GSMBE methods in which δ -Be concentrations up

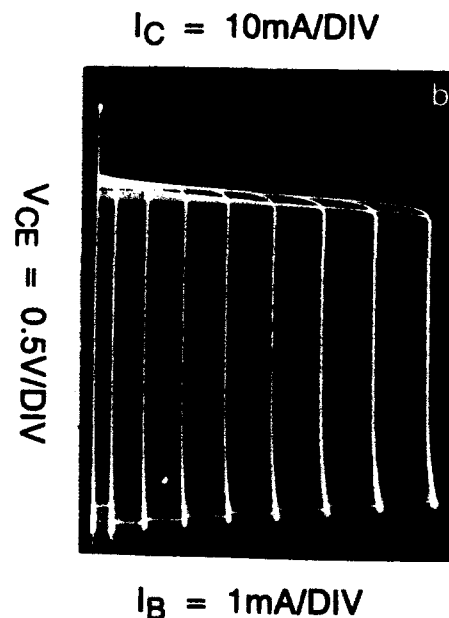
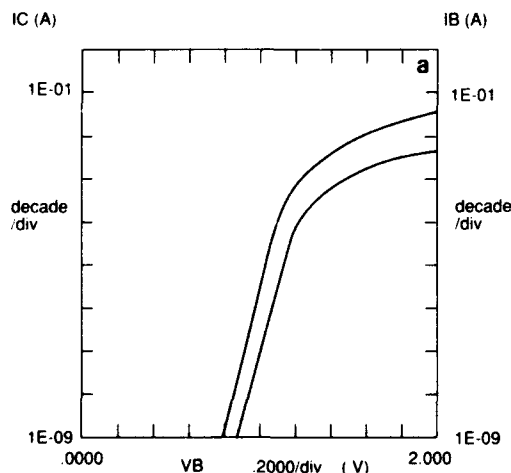


Fig. 3. (a) The Gummel plot of 0.3 ML δ -Be HBT (50 μ m diameter emitter). (b) Output characteristics of δ -doped base HBT (50 μ m diameter emitter).

to 1 ML are spatially confined in a GaAs base of width less than 100 Å. These devices work as excellent transistors with a current gain of 15 and a sheet resistance of 280 Ω/\square for δ -Be at the 0.3 ML level. For δ -Be at the 0.8 ML level diffraction measurements show that the width of spread of Be during growth is less than 40 Å for GSMBE but is 200 Å for conventional MBE. Although the mechanism responsible for dopant surface segregation during MBE growth and its absence during GSMBE remain incompletely understood, we have shown that Be diffusion increases linearly with increasing Be concentration. Further, the linear concentration dependence to Be diffusion is compatible with a kick-out mechanism involving singly ionized interstitial donors of Be and Ga. Since impurity diffusion increases with Be concentration and hence surface segregation then becomes more rapid, it follows that Be is more difficult to localize in the δ plane at the 1 ML level during growth.

References

- [1] H. Kroemer, Proc. IEEE 70 (1982) 13.
- [2] R.J. Malik, L.M. Lunardi, J.F. Walker and R.W. Ryan, IEEE Electron Device Letters EDL-9 (1988) 7.
- [3] J.L. Lievin, C. Dubon-Chevallier, F. Alexandre, G. Le Roux, J. Dangla and D. Ankri, IEEE Electron Device Letters EDL-7 (1986) 129.
- [4] J.N. Miller, D.M. Collins and N.J. Moll, Appl. Phys. Letters 45 (1985) 960.
- [5] P. Enquist, G.W. Wicks, L.F. Eastman and C. Hitzman, J. Appl. Phys. 58 (1985) 4130.
- [6] J.E. Cunningham, T.H. Chiu, A. Ourmazd, W. Jan and T.Y. Kuo, J. Crystal Growth 105 (1990) 111.
- [7] E.F. Schubert, in: Semiconductors and Semimetals: Artificially Structured Semiconductors, Ed. A.C. Gossard (Academic Press, New York, 1990).
- [8] S.Y. Chiang and G.L. Pearson, J. Appl. Phys. 46 (1975) 2986.
- [9] See review by D.G. Deppe and N. Holonyak, J. Appl. Phys. 64 (1988) R93.
- [10] A. Ourmazd, J. Cunningham, W. Jan and J. Rentschler, Appl. Phys. Letters 56 (1990) 854.
- [11] K.W. Goossen, J.E. Cunningham, T.H. Chiu, D.A.B. Miller and D.S. Chemla, in: Proc. IEDM 89 (1989) p. 409.
- [12] K.W. Goossen, T.Y. Kuo, J.E. Cunningham, A. Ourmazd, C.G. Fonstad, F. Ren and W. Jan, IEEE Electron Device Letters, submitted.
- [13] T.Y. Kuo, K.W. Goossen, J.E. Cunningham, A. Ourmazd, C.G. Fonstad, F. Ren and W. Jan, IEEE Electron Device Letters, in press.
- [14] N. Chand, R. Fischer, J. Klem and H. Morkoç, J. Vacuum Sci. Technol. B4 (1986) 2.
- [15] S. Tiwari and S. Wright, Appl. Phys. Letters 56 (1990) 563.
- [16] B. Jalali, R.N. Nottenburg, A.F. Levi, R.A. Hamm, M.B. Panish, D. Sivco and A.Y. Cho, Appl. Phys. Letters 56 (1990) 1460.

Abruptness of GaAs/AlInP hetero-interfaces grown by GS-MBE

S. Nagao, M. Takashima, Y. Inoue, M. Katoh and H. Gotoh

Thin Films Laboratory, Research Center, Mitsubishi Kasei Corp., 1000 Higashimamiana, Ushiku, Ibaraki 300-12, Japan

The effect of the exposure of GaAs and AlInP surfaces to phosphorus and arsenic beams were studied using HR-TEM, RHEED, XPS, AES, and Raman scattering. The GaAs surface was found to be fairly reactive with respect to the phosphorus beam. The exposure of GaAs to a phosphorus beam for 60 s caused a surface roughness of at least 20 Å, caused by the formation of a GaP-rich island. However, a flat surface of AlInP was found to be structurally stable with respect to the arsenic beam. The arsenic beam was found to induce a replacement of a few percent of P atoms by As atoms in an AlInP surface layer. An atomically flat AlInP-on-GaAs interface was obtained by a sequence in which the GaAs surface was not exposed to a P beam.

Recently, AlGaInP lattice matched to GaAs has been widely studied as a material for visible lasers grown by metalorganic vapor phase epitaxy (MOVPE) or by molecular beam epitaxy (MBE). However, the properties of interfaces between AlGaInP and As-based materials, such as GaAs, are not well known. The valence band offset for an AlGaInP/GaAs interface is known to be larger than that for an AlGaAs/GaAs interface [1,2]. Therefore, a hetero-interface between AlGaInP and GaAs is considered to be attractive for appli-

cations to heterostructure devices such as heterostructure bipolar transistor (HBT) [1] and complementary high-electron-mobility transistor (HEMT) devices. It is important to understand and control the properties of hetero-interfaces.

We have already reported that AlInP/GaAs single quantum wells (SQWs) grown by gas source MBE (GS-MBE) have a high quality [3]. However, the abruptness of AlInP/GaAs interfaces strongly depends on the sequence in which molecular beams are switched. Growth interruptions are indis-



Fig. 1. $\langle 110 \rangle$ HR-TEM image of the GaAs/AlInP quantum well grown on GaAs (001) by sequence A. Marker represents 100 Å.

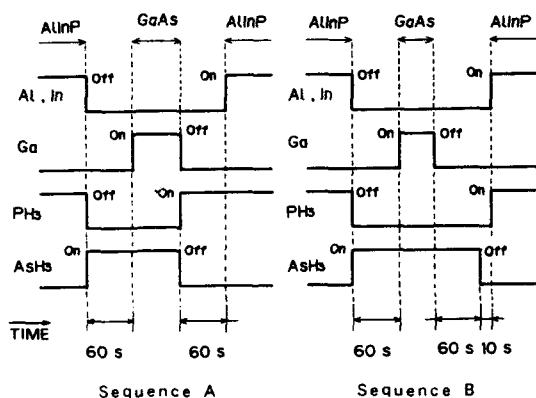


Fig. 2. Switching sequences of shutters and valves for source materials in the growth of AlInP/GaAs hetero-interfaces. In sequence A, GaAs and AlInP surfaces were exposed to a P beam and an As beam, respectively, during the growth interruptions of 60 s prior to the interface formation. In sequence B, GaAs surfaces were not exposed to the P beam during the growth interruptions.

pensable for the switching of group-V beams to form hetero-interfaces. Reactions between crystal surfaces and group-V beams must occur during these growth interruptions [4]. In this paper, we report on the effect of the exposure of GaAs and AlInP surfaces to phosphorus and arsenic beams.

AlInP/GaAs SQWs were grown on GaAs (001) at 540°C by GS-MBE, with various sequences of beam switches during the interface growth. Details of the growth procedure have been published elsewhere [3]. The structural properties of the resultant interfaces were observed by high resolution transmission electron microscopy (HR-TEM), using a Hitachi H-9000 UHR which was operated at an accelerating voltage of 300 kV. Fig. 1 shows a $\langle 110 \rangle$ HR-TEM lattice image of an AlInP/GaAs quantum well grown with the sequence of beam switches shown in fig. 2 (sequence A). In this

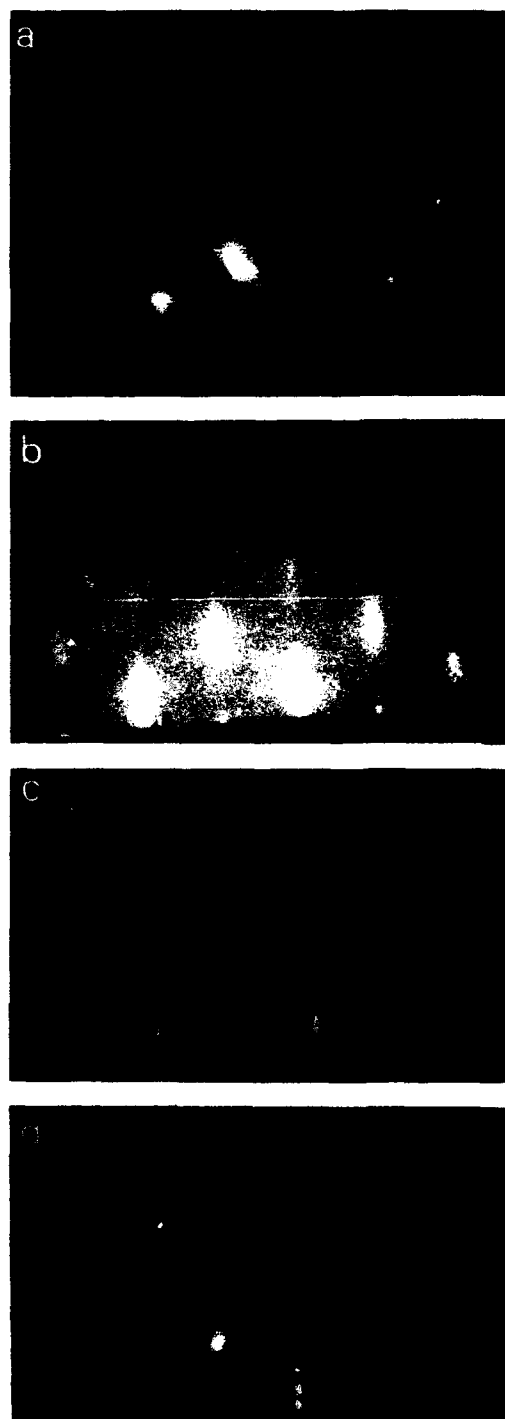


Fig. 3. RHEED patterns from GaAs (001) along [110] azimuth (a) before and (b)–(d) after exposition to a P beam for 60 s at different surface temperatures: (b) $T_s = 590^\circ\text{C}$; (c) $T_s = 540^\circ\text{C}$; (d) $T_s = 490^\circ\text{C}$. The P beam was produced from decomposed PH_3 at 900°C . The dominant species of the P beam were monomer P and dimer P_2 . The total flux was about 1×10^{-2} Pa.

sequence, group-V beams were switched at the same time that group-III beams were shut off. Then, after a pause of 60 s, additional growth was resumed by opening the appropriate group-III shutters. The resultant GaAs-on-AlInP interface was seen to be atomically flat, while the resultant AlInP-on-GaAs interface had a roughness of at least 20 Å, with slight lattice deformation.

Next, the effect of group-V beams on the surfaces of GaAs and AlInP was studied using reflection high energy electron diffraction (RHEED), X-ray photoelectron spectroscopy (XPS), Auger electron spectroscopy (AES), and Raman spectroscopy. GaAs samples were exposed for 60 s to the beam from decomposed PH_3 at 900 °C (with a total flux was about 1×10^{-2} Pa) in the MBE system. The surface temperature was varied from 490 to 590 °C. The dominant species of the phosphorus beams were P and P_2 .

Fig. 3 shows RHEED patterns obtained from GaAs before and after exposure to the phosphorus beam. The initial GaAs surface exhibited a 2×4 pattern with strong spots on the Laue ring during the exposition to an As beam, indicating that the surface was atomically flat. The RHEED patterns became spotty after exposure to the phosphorus beam. With the higher substrate temperatures, the RHEED patterns became more spotty and diffused.

XPS, AES, and Raman scattering measurements were also carried out on these GaAs samples. XPS and AES analyses showed that the exposure of GaAs to the P beam resulted in a remarkably P-rich, As-poor layer at the surface. The ratios of the numbers of P atoms to As atoms (P/As), averaged over a 20 Å depth from the surface, were estimated to be 0.54 ($T_s = 490^\circ\text{C}$), 1.1 ($T_s = 550^\circ\text{C}$) and 1.4 ($T_s = 590^\circ\text{C}$), respectively, from the results of XPS. Using AES, the thickness of the P-rich, and As-poor layer was evaluated to be about 20 to 30 Å, and it became thicker with increasing substrate temperature.

Fig. 4 shows the XPS signals of P_{2p} of GaAs surfaces exposed to P beams. The signals contain two components attributed to different bonding configurations. The lower energy peaks correspond to chemical shifts caused by Ga-P bonding, while the higher peaks are possibly due to P

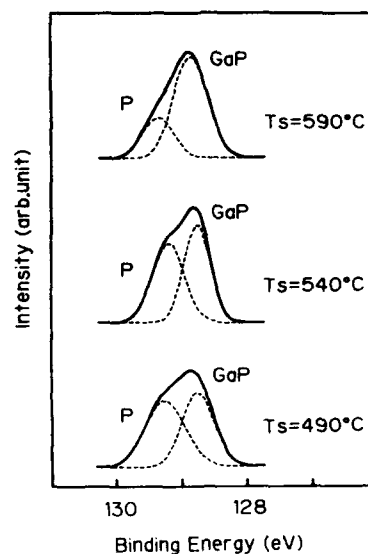


Fig. 4. XPS signals of P_{2p} of the GaAs surfaces exposed to a P beam for 60 s, at different surface temperatures T_s . The observed signals (—) consist of two components (---), corresponding to chemical shifts caused by amorphous P and Ga-P bonding, respectively.

atoms in amorphous form. Amorphous P was found to have condensed into surface defects on the basis of AES and micro-Raman scattering data. These defects were presumably related to dislocations. The intensity of the signal which was attributed to P atoms forming GaP bonds increased as the substrate temperature rose. The GaAs surface and P beam reacted more vigorously at the higher substrate temperatures. This result is consistent with Raman scattering data.

We cannot explain this phenomenon as a simple process consisting of As atoms evaporating from the GaAs surface and subsequently P atoms being adsorbed by the surface. Unidentified strong, fast chemical reactions seem to proceed between the GaAs surface and the P beam. This surface reaction is considered to be due to a large binding energy of GaP in comparison with that of GaAs. The surface roughness of GaAs exposed to P beam can presumably be explained by the formation of islands to reduce misfit strain of the GaP rich layer.

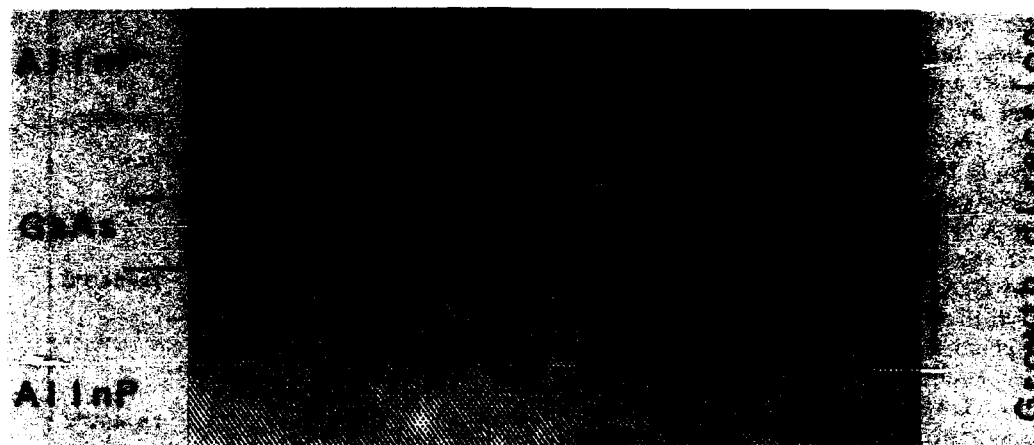


Fig. 5. $\langle 110 \rangle$ HR-TEM image of the GaAs/AlInP quantum well grown on GaAs (001) by sequence B. Marker represents 100 Å.

The exposure of AlInP to an As beam resulted in no appreciable change in the streak RHEED pattern, with strong spots on the Laue ring being observed during the exposition to the P beam. A few percent of excess As atoms were found from AES analysis to be in a few monolayers of the AlInP surface exposed to the As beam.

Fig. 5 shows a $\langle 110 \rangle$ HR-TEM lattice image of an AlInP/GaAs quantum well grown in sequence B shown in fig. 2. In this sequence, the GaAs surfaces were not exposed to the P beam during the growth interruptions. This sequence cured the roughness caused by the reaction between the GaAs surface and the P beam, resulting in an atomically flat AlInP-on-GaAs interface with a fluctuation of 1 or 2 monolayers, as well as a GaAs-on-AlInP interface. We also checked the fact that a heterostructure with insufficient growth interruptions at the interface from AlInP to GaAs had a roughened interface. An ordered AlInP structure was not observed in the samples we prepared.

In conclusion, we have studied the abruptness of AlInP/GaAs interfaces for different sequences during GS-MBE growth. We found that a vigorous reaction takes place between a GaAs surface and a P beam, resulting in an interface roughness attributed to the formation of GaP-rich islands on the GaAs surface. A flat AlInP surface was found to be structurally stable with respect to an As

beam. However, the substitution of a few percent of P atoms into As atoms occurs in a few monolayers of an AlInP surface exposed to an As beam. The roughness of the AlInP-on-GaAs interface was suppressed by a growth sequence that avoided the exposure of the GaAs surface to the P beam.

The authors would like to thank Dr. T. Nakamura, N. Ishikawa and Y. Abe for XPS and AES measurements, Dr. M. Yano for Raman measurements and Y. Higuchi for assistance in MBE sample growth. They also thank I. Sakamoto, K. Shimoyama, J. Saitoh and T. Okano for helpful discussions and continuous encouragement.

References

- [1] H. Kroemer, *J. Vacuum Sci. Technol.* B1 (1983) 126.
- [2] M.O. Watanabe and Y. Ohba, *Appl. Phys. Letters* 50 (1987) 906.
- [3] S. Nagao, Y. Inoue, M. Katoh, K. Shimoyama and H. Gotoh, *J. Crystal Growth* 95 (1989) 163.
- [4] M. Yano, H. Yokose, A. Kawaguchi, R. Hagiwara, Y. Iwai and M. Inoue, *J. Crystal Growth*, to be published.

Improved InGaP/GaAs heterointerfaces during gas-source MBE growth

H.Y. Lee, M.J. Hafich, G.Y. Robinson

Center for Optoelectronic Computing Systems and Department of Electrical Engineering, Colorado State University, Fort Collins, Colorado 80523, USA

K. Mahalingam and N. Otsuka

School of Materials Engineering, Purdue University, West Lafayette, Indiana 47907, USA

The conditions for obtaining InGaP/GaAs heterointerfaces which are laterally uniform and atomically abrupt when grown by gas-source MBE are reported. Using in-situ reflection high-energy electron diffraction, double crystal X-ray diffraction, and transmission electron microscopy, the effects of a growth pause on the interfacial structure and composition of lattice-matched InGaP/GaAs multiple quantum well structures were studied. It was found that by providing sufficient time for annealing of the growth surface, interfacial regions which correspond to an intrinsic strain model of ideal InGaP/GaAs heteroepitaxial interfaces could be obtained.

1. Introduction

MBE growth of $\text{In}_{0.48}\text{Ga}_{0.52}\text{P}/\text{GaAs}$ quantum-well structures requires switching of the arsenic and phosphorous molecular beams at each heterointerface. We have recently reported that the switching of the group-V molecular beams can produce compositional intermixing and localized strain at the InGaP/GaAs heterointerfaces [1]. We report here the conditions for obtaining InGaP/GaAs interfaces which are atomically abrupt, in structure and composition, when grown by gas-source MBE. Reflection high energy electron diffraction (RHEED), double crystal X-ray diffraction (DCXR), and transmission electron microscopy (TEM) were used to study the effects of a growth pause on the interfacial abruptness and composition during MBE growth of lattice-matched InGaP/GaAs multiple quantum well (MQW) structures. It was found that by allowing the interface to anneal before switching and by keeping the time after switching the As and P

beams to a minimum, laterally uniform, atomically abrupt interfaces can be obtained.

2. Experimental

MQW samples were grown on (100) GaAs substrates at approximately 530 °C (which was found to be 90 °C below GaAs oxide desorption temperature) using conventional Ga and In MBE effusion cells and As_2 and P_2 molecular beams produced by thermal decomposition of AsH_3 and PH_3 , respectively, in a single low-pressure cracking oven held at 900 °C [2]. All InGaP layers were grown at a rate of 1.0 $\mu\text{m}/\text{h}$ and PH_3 flow rate of 8 SCCM. All GaAs layers were grown at 0.5 $\mu\text{m}/\text{h}$ and AsH_3 flow rate of 4 SCCM. For purposes of this study the growth pause at each interface was divided into two time periods: the interval (denoted by t_1) after stopping growth by closing the group-III shutters but before switching the group-V beams, and the interval (t_2) after

switching the group-V beams but before recommencing growth. In a previous report [1], we showed that during the interval t_2 , significant compositional intermixing occurs at the interfaces if $t_2 \geq 6$ s. For this report we have kept $t_2 = 1$ s to minimize intermixing and examined the effects of changing only t_1 .

Each sample consisted of a $1 \mu\text{m}$ InGaP buffer layer, followed by a 20-period MQW region of InGaP ($\sim 240 \text{ \AA}$)/GaAs ($\sim 95 \text{ \AA}$), capped off with $0.25 \mu\text{m}$ of InGaP. The InGaP/GaAs MQWs were examined by computer controlled DCXR diffractometer using $\text{Cu K}\alpha_1$ radiation and the (400) reflection. Computer simulations using the analytical Takagi-Taupin equations of dynamical X-ray scattering theory were performed for structural analysis of the MQWs [3]. TEM was performed with a JEM 2000EX microscope operated at 200 kV.

3. Results and discussion

For the substrate temperature used, a (2×1) RHEED reconstruction pattern was observed during growth of both the GaAs and InGaP layers. During the growth pause, the two-fold patterns on the GaAs surface became sharper with increasing t_1 , with the first-order Laue ring appearing at $t_1 \sim 10$ s. No noticeable change in RHEED pattern on the InGaP surface was observed for t_1 lasting up to 90 s, unlike our earlier observations during interval t_2 where the RHEED pattern became diffuse and eventually spotty [1].

The interface quality and layer thickness of the InGaP/GaAs MQW samples of [011] and [001] cross-sections were determined by TEM. Layer thicknesses agreed with DCXR data and high resolution TEM lattice images showed coherent MQWs with uniform layer thicknesses and heterointerfacial regions of 1–3 biatomic layers in thickness.

The measured X-ray spectra for a sample with $t_1 = 90$ s, shown in fig. 1a, exhibits a large number of intense, well-defined satellite peaks. The full width at half maximum (FWHM) of the peaks for the InGaP cap layer, the GaAs substrate, and the MQW for $n = 0$ were 28, 19, and 35 arc sec,

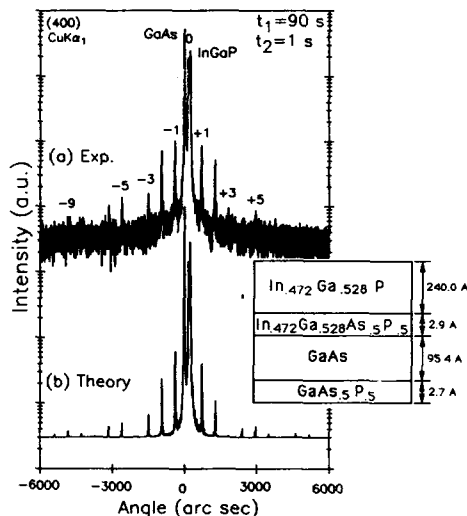


Fig. 1. DCXR diffraction spectra for InGaP/GaAs MQW heterostructures. (a) Experimental data for $t_1 = 90$ s and $t_2 = 1$ s. The MQW period is $341 \pm 7 \text{ \AA}$. (b) Simulated spectrum using the model shown in the insert for one period of the MQW region.

respectively. The FWHM averaged over the four strongest satellite peaks was 51 arc sec for $t_1 = 1$ s, 30 arc sec for $t_1 = 7$ s, and 26 arc sec for $t_1 = 90$ s. For DCXR diffraction of MQW structures, narrow satellite peaks are an indication of strong periodicity, a high degree of lateral uniformity, and well-defined interfaces. Thus, the observed change in the satellite peaks implies the interface quality improved as t_1 was increased.

For comparison, the simulated DCXR spectrum in fig. 1b was obtained using the four-layer model shown for each period of the MQW stack in the insert. In the model, each interfacial region consists of a layer differing in composition from that of the InGaP barrier layer or the GaAs well layer. Here the thicknesses and composition of the interfacial regions were based on the intrinsic strain model of Vandenberg et al. [4], where the switching of the As and P beams at alternating interfaces during growth produces asymmetrical ordering of the atomic layers. The strained interfacial regions arise because of the differences in

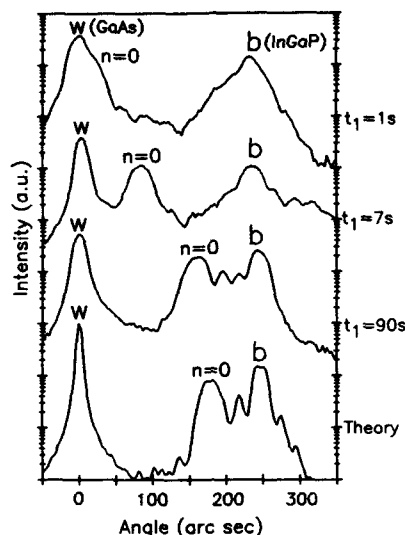


Fig. 2. Experimental DCXR diffraction spectra for $t_1 = 1$, 7, and 90 s, and calculated spectrum using an intrinsic strain model, in the expanded region near the $n = 0$ MQW peak.

atomic bond length between As and P [4]. We assume here that the intrinsic strain model represents ideal InGaP/GaAs interfaces. The alloy composition $\text{In}_{0.472}\text{Ga}_{0.528}\text{P}$ was determined from the separation of the InGaP and GaAs peaks. The overall experimental spectrum for $t_1 = 90$ s is seen to match reasonably well the simulated spectrum based on the intrinsic strain model.

By examining the effect of varying t_1 on the position of the $n = 0$ DCXR peak, additional information about the interfaces can be obtained. Fig. 2 shows the measured DCXR spectra for three different samples with $t_1 = 1$, 7, and 90 s along with the simulated spectrum from the intrinsic strain model. The experimental DCXR spectra were carefully measured at a location in each sample with the same alloy composition, as shown by identical separations of the GaAs (w) and $\text{In}_{0.472}\text{Ga}_{0.528}\text{P}$ (b) peaks. With increasing t_1 the measured $n = 0$ peak is observed to shift toward the position of the $n = 0$ peak of the theoretical spectra. The $n = 0$ angular position represents the average strain present in the MQWs and is a function of the strain and thicknesses of the well,

barrier, and interfacial layers [1,2]. Small variations in the well and barrier thicknesses from sample to sample can not explain such a large shift in the $n = 0$ peak. Since the angular separation between the w and b peaks in fig. 2 does not change with t_1 , the strain produced by the mismatch of the well and barrier layers is not changing with t_1 . Thus, the interfacial layers must be responsible for the observed shift. Furthermore, since the $n = 0$ peak is shifting towards the $n = 0$ position calculated from the model, it can be concluded that the heterointerfaces become more ideal as t_1 increases.

4. Conclusions

In summary, the effect of varying the time t_1 , the interval during the growth pause before switching the group-V molecular beams, on the quality of InGaP/GaAs interfaces grown by gas-source MBE has been investigated. To minimize intermixing of the As and P at the interfaces, the time t_2 after switching the group-V molecular beams was kept small. It was found that longer values of t_1 produced laterally uniform, atomically abrupt interfaces, as evidenced by narrow DCXR satellite peak widths and high resolution TEM images. Furthermore, it was shown that by increasing t_1 interfacial regions which correspond to an intrinsic strain model of ideal InGaP/GaAs heteroepitaxial interfaces could be obtained.

Acknowledgements

The authors gratefully acknowledge the support of the GE Electronics Laboratory and the Center for Optoelectronic Computing Systems, sponsored by the National Science Foundation ERC grant CDR 86-22236 and by the Colorado Advanced Technology Institute, an agency of the State of Colorado, and the support at Purdue University of National Science Foundation grant DMR-85-20866.

References

- [1] H.Y. Lee, M.J. Hafich and G.Y. Robinson, *J. Crystal Growth* 105 (1990) 244.
- [2] H.Y. Lee, M.D. Crook, M.J. Hafich, J.H. Quigley, G.Y. Robinson, D. Li and N. Otsuka, *Appl. Phys. Letters* 55 (1989) 2322.
- [3] M.J. Hill, B.K. Tanner, M.A.G. Halliwell and M.H. Lyons, *J. Appl. Cryst.* 13 (1985) 446.
- [4] J.M. Vandenberg, M.B. Panish, H. Temkin and R.A. Hamm, *Appl. Phys. Letters* 55 (1989) 1920.

A review of CBE, MOMBE and GSMBE

W.T. Tsang

AT&T Bell Laboratories, Murray Hill, New Jersey 07974, USA

This paper reviews briefly the recent progress in III–V compound semiconductor epilayer and heterostructure preparations by the three different approaches: chemical beam epitaxy (CBE, employing both vapor group III and group V sources), metalorganic molecular beam epitaxy (MOMBE, employing vapor group III and solid group V sources), and gas source molecular beam epitaxy (GSMBE, employing solid group III and vapor group V sources). The results obtained so far clearly demonstrated that high quality InGaAsP/InP materials and heterostructures suitable for state-of-the-art device applications can be routinely prepared by CBE. With new metalorganic aluminum compounds becoming available, high quality GaAs/AlGaAs with low residual carbon background also has successfully been prepared recently. GaAs/AlGaAs modulation doped field-effect transistors prepared by CBE have similar device performance as those prepared by molecular beam epitaxy. Recently, there is also a great interest in using CBE for the preparation of Si, SiGe, and II–VI compound semiconductor layers.

1. Introduction

Within the past few years the progress in chemical beam epitaxy (CBE) has been tremendous [1]. At present, almost every major electronics laboratory has a research and development effort in CBE or related growth process. The results obtained so far clearly demonstrated that high quality InGaAsP/InP materials and heterostructures suitable for state-of-the-art device applications can be routinely prepared by CBE. With new metalorganic aluminum compounds becoming available, high quality GaAs/AlGaAs with low residual carbon background also has successfully been prepared recently. GaAs/AlGaAs modulation doped field-effect transistors prepared by CBE have similar device performance as those prepared by molecular beam epitaxy (MBE).

Here, some of the important recent research results will be reviewed briefly. Due to the short interval between this conference review and the one at the Workshop on MOMBE, CBE, GSMBE, and Related Techniques, Aachen, Germany, in June 1990, the content of this review is similar to that presented at the Workshop. A special issue of

the Journal of Crystal Growth containing papers in this area can be found in Vol. 105, Nos. 1–4, October 1990.

To date, the commonly recognized definitions of the various techniques are:

Chemical beam epitaxy (CBE) is taken to employ both vapor group III and group V starting sources. *Metalorganic MBE (MOMBE)* employs vapor group III and elemental group V sources.

Gas source MBE (GSMBE) employs elemental group III and vapor group V sources.

These techniques are bridging the gap between the now established techniques of molecular beam epitaxy and metalorganic vapor phase epitaxy (MOVPE). The increasing use of new metalorganic starting sources and the reduction in reactor pressure are major factors in the novel effects and advantages that are beginning to become apparent from these crystal growth methods. In particular, the combination of the versatility of MOVPE together with the molecular beam properties of MBE was seen to be a powerful tool for both the crystal growers and the device designers.

Important and rapid progress has been made in several areas: (1) system designs, (2) understand-

ing of growth kinetics, (3) preparation of high-quality compound semiconductor materials and heterostructures, (4) electronic and photonic device applications, (5) silicon epitaxial growth, (6) new vapor sources, (7) photon and electron assisted growths, and (8) atomic layer epitaxy. In particular, the use of metalorganic compounds has stimulated a very active and fruitful research into growth mechanisms. This will also undoubtedly lead to a greater understanding of the two parent technologies, MBE and MOVPE. The commercial success of these new technologies, in terms of simpler and more efficient equipment, was always in evidence.

2. GSMBE

For GSMBE, Lambert et al. [2] reported the growth of high purity InP having 77 K mobilities as high as $112,000 \text{ cm}^2/\text{V} \cdot \text{s}$ with residual carrier concentrations of $2 \times 10^{14} \text{ cm}^{-3}$. 4.2 K photoluminescence spectra are dominated by free-exciton and neutral donor-exciton transitions. Goldstein [3] also reported the preparation of high performance InGaAsP/InP optical devices, i.e., semiconductor amplifier and multiquantum well distributed feedback (MQW-DFB) lasers. MQW-DFB base wafers have performance similar to those prepared by MOVPE. Davies et al. [4] reported results that state-of-the-art quantum confined stark effect 4×4 arrays of modulators can be prepared by GSMBE. In order to further improve the characteristics of the modulators, they developed the double sided epitaxy, where matched pairs of MQWs were grown on both sides of the same InP wafer. This enables devices on either side of the wafer to be optically coupled through the transparent substrate, but individually addressed. Nakajima et al. [5] reported the electrical, optical and structural properties of GSMBE grown $\text{Al}_{0.5}\text{In}_{0.5}\text{P}$ and $\text{Ga}_{0.5}\text{In}_{0.5}\text{P}$ epilayers for visible laser applications. Kishino et al. [6] recently succeeded the preparation of GaInP/AlInP lasers using a multiple quantum barrier. They obtained threshold current density as low as 840 A/cm^2 operating at 660 nm.

3. MOMBE

For MOMBE, the advantage lies in safety. This is very suitable for investigating the growth mechanisms using metalorganic sources. Two major surface diagnostic techniques commonly used in these experiments are the reflection high energy electron diffraction (RHEED) intensity oscillations and modulated beam mass spectrometry (MBMS). The RHEED intensity oscillation measurements were first employed by Tsang et al. [7] to study the dependence of growth rates on substrate temperatures and flow rates during CBE. Robertson et al. [8] of the same laboratories subsequently devised a model to explain the observed results. Martin and Whitehouse [9] using MBMS confirmed several areas of the model particularly relating to the dominant role of diethylgallium (DEGa) in the GaAs growth process and its subsequent desorption in the higher substrate temperature regime. Further, their results also support the assumption that the desorption reactions of monoethylgallium (MEGa) do not play a major role in the growth process. Fig. 1 shows the desorption of DEGa, MEGa and Ga ions flux as a function of substrate temperature. Data are corrected for TEGa cracking-pattern due to the mass spectrometer. Another important experiment carried out by them is to study the competing surface reactions between TEGa and triethylindium, TEIn in an effort to try to shed some light on the anomalous changes in alloy growth and composition observed in InGaAs CBE growth. They observed that with the presence of incident TEIn flux, DEGa desorption is substantially enhanced and hence reduced the Ga uptake in growing InGaAs during CBE or MOMBE. This effect becomes serious at high temperatures. Iimura et al. [10] also reported the observation of surface segregation of indium during CBE growth of InGaAs.

4. CBE

An extensive review on the progress in CBE is given by Tsang in ref. [1]. Very high quality epilayers of InGaAs, InP, InGaAsP were reported. InGaAs lattice-matched to InP was reproducibly

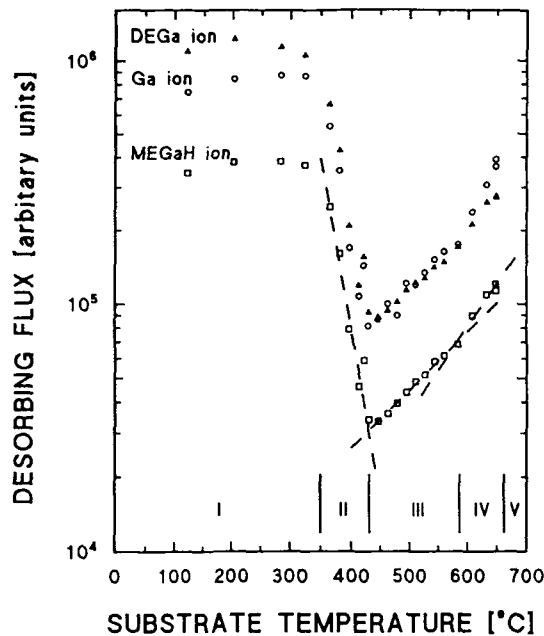


Fig. 1. Desorbing DEGa, MEGa, and Ga ion signed flux as a function of substrate temperature as measured by modulated beam mass spectrometry. Data corrected for TEGa cracking-pattern contribution. After ref. [8].

grown by several laboratories having the (004) X-ray Bragg reflection linewidth as narrow as 17 arc sec for $\sim 2 \mu\text{m}$ thick layers. Such extreme composition uniformity was also supported by results from Auger depth profiles and 2 K photoluminescence (PL) measurements. Very intense efficient luminescence peaks due to excitonic transitions with linewidths (FWHM) as narrow as 1.2 meV were obtained. This represents the narrowest linewidth ever reported for GaInAs grown. Hall measurements of 2–5 μm thick epilayers grown on InP substrates have mobilities of 10,000–12,000 and 40,000–67,000 $\text{cm}^2/\text{V} \cdot \text{s}$ at 300 and 77 K with n in the range of 5×10^{14} – $5 \times 10^{15} \text{ cm}^{-3}$, as summarized in fig. 2. Though these results were obtained in 1986 by Tsang, they still represent the best results thus far. Much work has also been done on the growth of InP by CBE. Benchimol et al. [11], Heinecke et al. [12] and Rudra et al. [13] have prepared InP epilayers with background impurities as low as $2 \times 10^{14} \text{ cm}^{-3}$ and 77 K mobilities as high as $1.54 \times 10^5 \text{ cm}^2/\text{V} \cdot \text{s}$. Low-temperature PL reveals excitonic peaks (D^0, X) n with n up to 6. Excitonic linewidths as narrow as 0.08

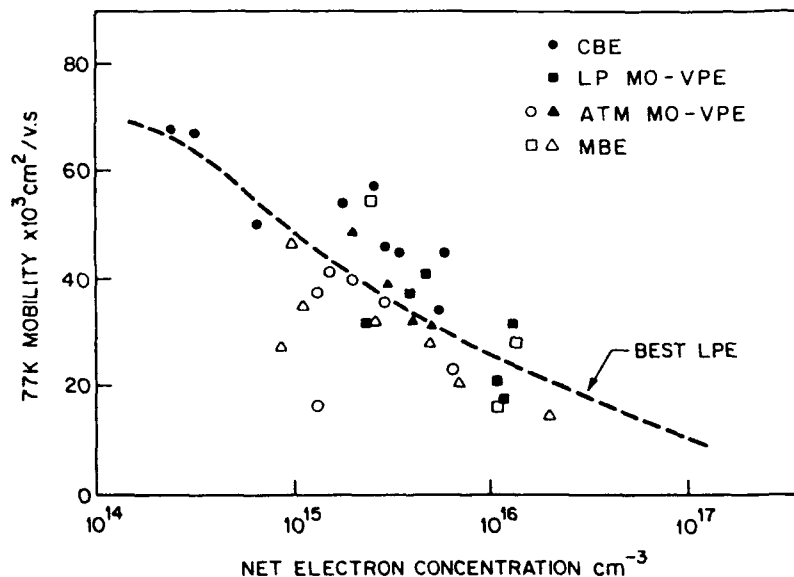


Fig. 2. 77 K Hall mobility versus background net electron concentration for closely lattice-matched InGaAs epilayers without two-dimensional electron gas effect. After ref. [1].

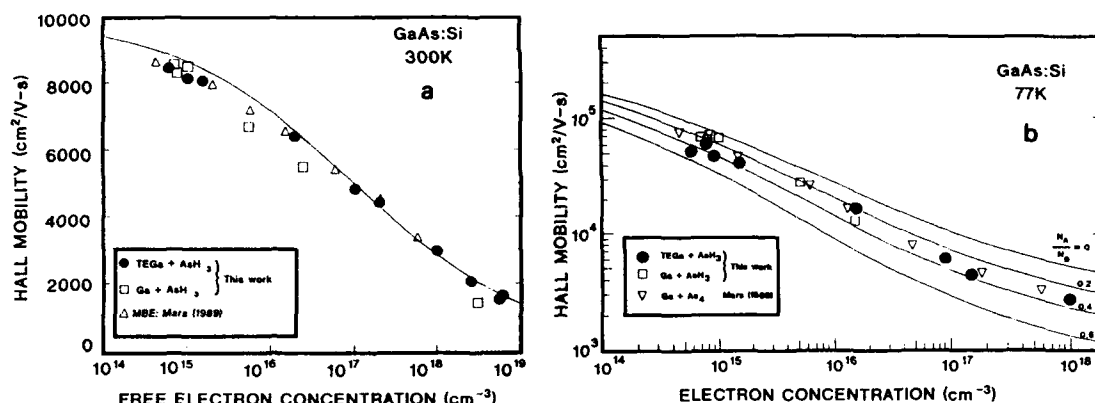


Fig. 3. Hall mobility as a function of free carrier concentration in Si-doped GaAs at 300 K (a) and 77 K (b). Experimental data for GSMBE grown using AsH₃ + TEGa (●), AsH₃ + Ga (□), and MBE grown using As₄ + Ga (△). The solid lines in (b) are Hall mobilities calculated for different compensation ratios N_A^-/N_D^+ . The solid line in (a) is calculated using Hilsum's empirical formula. After ref. [14].

meV were obtained. Such results are similar to those obtained by low-pressure MOVPE InP.

Ga_xIn_{1-x}As_yP_{1-y} epilayers closely lattice-matched, $\Delta a/a \sim < 5 \times 10^{-4}$, have been reproducibly grown over the whole range of compositions ($y \approx 2.2x$, $1 > y > 0$). Very intense efficient luminescence peaks due to excitonic transitions with linewidths (FWHM) as narrow as 3 meV were obtained [2]. Such a linewidth corresponded closely to the intrinsic linewidth due to alloy scattering in GaInAsP alloys.

Houng [14] and Chiu et al. [15] reported GaAs epilayers with $2 \times 10^{14} \text{ cm}^{-3}$ and 300 K mobility of 490–518 $\text{cm}^2/\text{V}\cdot\text{s}$. Intentional Si doping of GaAs epilayers using an elemental Si source, yielded controlled carrier concentrations from 7×10^{14} to $8 \times 10^{18} \text{ cm}^{-3}$ with 77 K mobilities from 62.700 to 2500 $\text{cm}^2/\text{V}\cdot\text{s}$, as shown in figs. 3a and 3b for 300 and 77 K results, respectively [14]. Residual carbon incorporation was reduced in AlGaAs by growing at 560°C and using triisobutylaluminum such that 77 K two-dimensional electron gas mobilities as high as 88,600 $\text{cm}^2/\text{V}\cdot\text{s}$ were obtained [16]. The Al_{0.23}Ga_{0.77}As spacer layer is 150 Å. The resulting 77 K sheet concentration is $5.6 \times 10^{11} \text{ cm}^{-2}$. Such value is similar to those obtained by MBE. In this case, for sheet concentration of $4.6 \times 10^{11} \text{ cm}^{-2}$, the 77 K mobility is 93,400 $\text{cm}^2/\text{V}\cdot\text{s}$. Recently, high quality AlGaAs

epilayers were also prepared by CBE using trimethylamine alane (TMAAl) [17]. Fig. 4 shows the carbon concentration versus AlAs mole fraction of AlGaAs grown from TEGa and either TEAl or TMAAl. In fig. 5 the carbon concentration versus

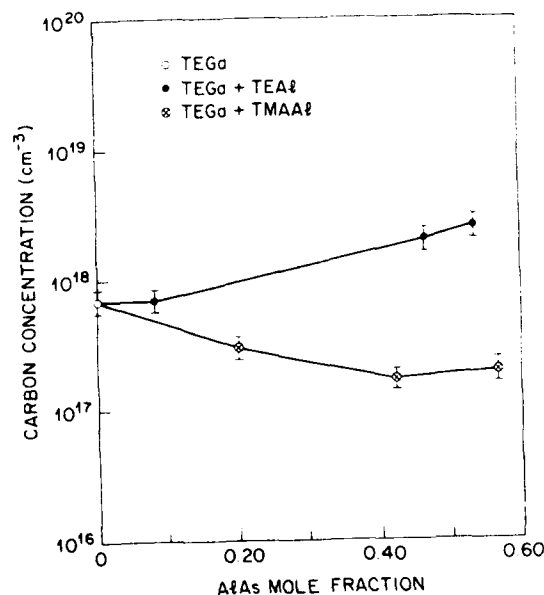


Fig. 4. The carbon concentration versus AlAs mole fraction of AlGaAs grown from TEGa and either TEAl or TMAAl. After ref. [17].

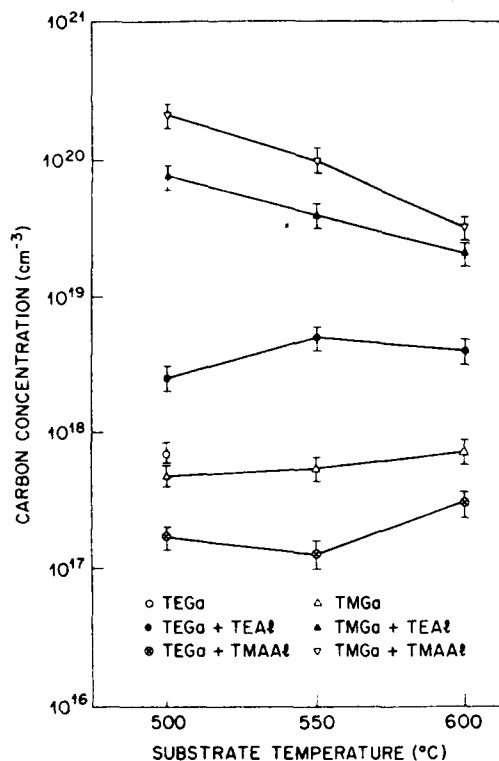


Fig. 5. The carbon concentration versus growth temperature for GaAs and AlGaAs using different combinations of metal-organic sources. After ref. [17].

growth temperature for GaAs and AlGaAs is shown for different source combinations.

Excellent results continue to be reported on InGaAs/InP quantum wells and superlattices. Significant improvement was also obtained from GaAs/AlGaAs quantum wells.

5. Doping studies

Impurity doping from vapor sources is more advantageous over solid sources in CBE. Weyers and co-workers [18] have carried out a rather extensive study surveying the suitability of various vapor sources as n- and p-type dopants in GaAs and InP. The following dopant sources were studied by them: silane (SiH_4), disilane (Si_2H_6), triethylsilane (TESiH , $(\text{C}_2\text{H}_5)_3\text{SiH}$), diethyltel-

luride (DETe , $\text{Te}(\text{C}_2\text{H}_5)_2$) and tetraethyltin (TESn , $\text{Sn}(\text{C}_2\text{H}_5)_4$) as n-type dopants, biscyclopenta-dienylmagnesium (Cp_2Mg , $\text{Mg}(\text{C}_5\text{H}_5)_2$), diethylzinc (DEZn , $\text{Zn}(\text{C}_2\text{H}_5)_2$) and diethylberyllium (DEBe , $\text{Be}(\text{C}_2\text{H}_5)_2$) as p-type dopants. Trimethylgallium (TMGa , $\text{Ga}(\text{CH}_3)_3$), trimethylarsenic (TMAAs , $\text{As}(\text{CH}_3)_3$) and acetylene (C_2H_2) as carbon dopant in GaAs.

Carbon is becoming a very important p-type dopant in GaAs. Its incorporation is particularly convenient in CBE and MOMBE growth. It can be incorporated by simply using some TMGa flow and adjusting the growth conditions properly during growth of GaAs using TEGa. Konagai and co-workers [19] reported that carbon concentration up to 10^{21} cm^{-3} have been obtained and they are electrically active. It is also confirmed that C does not segregate or diffuse [20]. This is demonstrated by the δ -doped structure shown in fig. 6. The doping spike of $7 \times 10^{19} \text{ cm}^{-3}$, as measured by Polaron profiling, has a full-width at half-maximum of $\sim 50 \text{ \AA}$. This is very important for device applications, especially for bipolar transistors where high doping and sharp profiles are required.

InP epilayers having high resistivities ($\geq 10^7 \Omega \text{ cm}$) were reported by Tsang et al. [21] over a wide

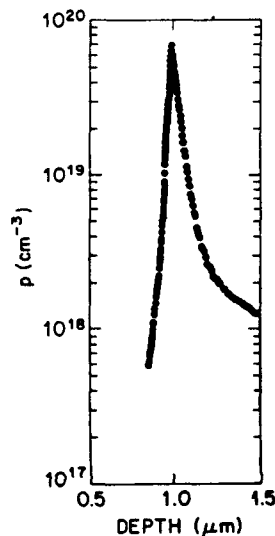


Fig. 6. Polaron profile of carbon δ -doped sample. After ref. [18].

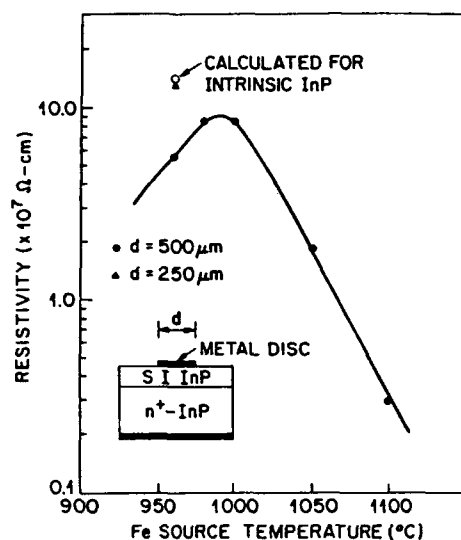


Fig. 7. Plot of measured resistivities as a function of Fe source temperatures. The inset shows the device structure for resistivity measurement.

range of Fe concentrations. Resistivities as high as $1.3 \times 10^8 \Omega \text{ cm}$ have been obtained, as shown in fig. 7. Such resistivity is almost equal to the theoretical value of $1.37 \times 10^8 \Omega \text{ cm}$ that is estimated for intrinsic InP.

6. Alternative sources

The hazard posed by the group V hydrides, AsH_3 and PH_3 , together with the desire for precursor molecules producing higher quality layers has motivated the development of new, metalorganic group V and even group III precursor molecules. Stringfellow [22] gives a very thorough survey. For group III alternate sources, triisobutyl-gallium and -aluminum (TIBGa and TIBAl), and alane ($\text{AlH}_3(\text{CH}_3)_3\text{N}$) are very promising sources for further reducing the carbon residual incorporation problem in the CBE and MOMBE growth of GaAs and AlGaAs. As for group V alternate sources, triisobutyl-arsine and -phosphine, and phenyl-arsine appear to be quite promising as replacements for the hydrides. When phenyl-arsine is used, no pre-cracking is needed.

Excellent InGaAs/InP quantum well results were obtained by Ritter et al. [23] using triisobutyl-arsine and -phosphine.

7. Laser-assisted CBE and ALE

Laser-assisted CBE and atomic layer epitaxy (ALE) has been studied employing a multi-line Ar^+ laser and RHEED technique by Doi, Aoyagi and Namba [24]. Two major findings are: (1) the decomposition rate of TEGa is enhanced to a greater extent on an As surface in comparison with that on a Ga surface under Ar^+ laser irradiation, (2) the laser irradiation also enhances the surface migration of the absorbed surface molecules. Chiu et al. [25] also conducted atomic layer epitaxy of GaAs employing CBE using TMGa . The one-monolayer self-limiting process is clearly observed using RHEED intensity oscillations.

8. Si CBE

In order to maximize the technological impact of Si MBE and completely eliminate the particulate problems associated with conventional Si MBE, silicon CBE using gas sources is very attractive and potentially important. Silicon CBE also adds the capability of deposition on selected areas of the substrate wafer, which conventional Si MBE cannot do. Hirayama and Koyama [26] investigated the growth using disilane and obtained a low-temperature growth rate of 1 Å/s . They found that B, Sb and P doping are possible using HBO_2 cell, ionization cell and PH_3 gas doping method, respectively. Transistors show normal common-emitter I - V characteristics ($h_{\text{FE}} \sim 30$). Selective epitaxial growth was employed to fabricate $\text{Si}_{1-x}\text{Ge}_x$ base heterojunction bipolar transistors (HBTs) using disilane and germane.

9. CBE of II-VI compound semiconductors

Research has also been started by several groups to use CBE for the growth of II-VI compounds, e.g. ZnSe , ZnS , CdTe , HgTe , and HgCdTe , etc.

The major advantage offered by CBE is the superior flux control and stability throughout the run and from run to run. Recently, Benz II et al. [27] reported the growth of high quality CdTe, HgTe, and their alloys by CBE using diethylcadmium, diisopropyltelluride and Hg vapor.

10. Device applications

With such high quality materials and heterostructures, a large variety of optical and electronic devices with very high performance have been grown by CBE, mostly due to Tsang and his co-workers [1]. These include GaInAs p-i-n photodiodes, APDs, photoconductive detectors, photo-transistors, GaAs double-heterostructure (DH) lasers, 1.3 and 1.5 μm wavelength GaInAsP DH lasers, GaInAs/InP QW lasers, very-low-loss GaInAs/InP optical waveguides, superlattice optical logic etalons, GaInAs/InP high-mobility two-dimensional electron gas FETs, GaInAs/InP MIS-FETs, very-thin-base (150 Å) bipolar, tunnel-

ing diodes, distributed Bragg reflector (DBR) laser, Fe-doped InP/InGaAs metal-semiconductor-metal (MSM) photodetector, and integrated MSM-FET photoreceivers, QW optical modulation, quantum switched heterojunction bipolar transistors, etc. For a review, see ref. [1]. Though some of these devices were prepared several years ago, their performance results still are among the best today.

Recently, Tsang et al. [28] have demonstrated the first successful preparation of InGaAs/InGaAsP multiquantum well (MQW) lasers grown by CBE. The broad-area threshold current densities of standard (not graded index) separate confinement heterostructure (SCH) MQW lasers were as low as 860 and $\sim 590 \text{ A/cm}^2$ for cavity lengths of 500 and 1500–3500 μm . Such values are similar to those obtained from MQW wafers employing the more advanced graded index SCH (GRIN-SCH) grown by MOVPE [29–31]. Buried heterostructure lasers [32,33] also have similar threshold currents, i.e., 25–40 mA for 300–1500 long cavities as shown in fig. 8. Pulses and CW output

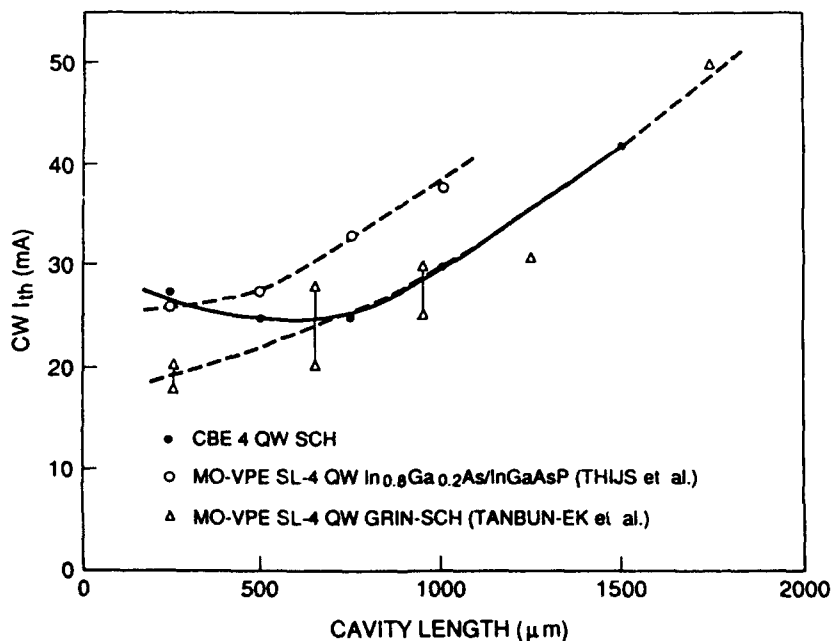


Fig. 8. The threshold currents as a function of cavity lengths of CBE-grown standard SCH MQW BH lasers, MOVPE-grown strained SCH. After ref. [32].

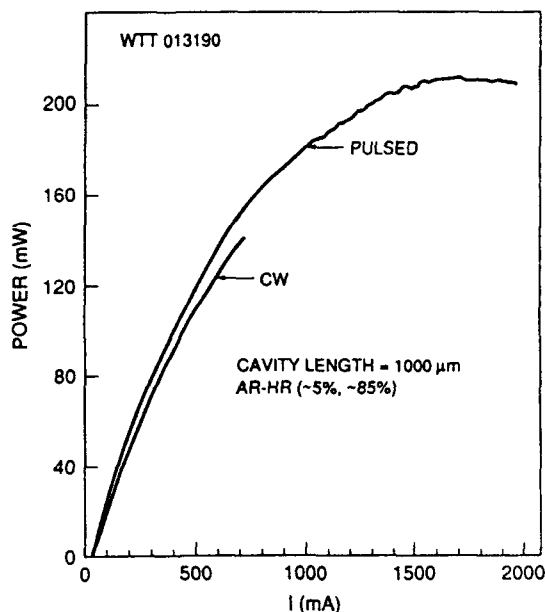


Fig. 9. The pulsed and CW output power versus current for a SCH MQW BH laser with AR-HR coating of $\sim 5\%$ and $\sim 85\%$.

power at $1.57 \mu\text{m}$ as high as 216 and 140 mW were obtained from 1 mm long lasers having anti-reflection and high reflection coatings of $\sim 5\%$ and

$\sim 85\%$, as shown in fig. 9. The layer thickness uniformity is better than $\pm 1\%$ across a 2-inch diameter wafer. By introducing strain into the $\text{In}_x\text{Ga}_{1-x}\text{As}$ quantum wells, threshold current density as low as 370 A/cm^2 was obtained for a four quantum well laser having $x = 0.65$ and well thickness of 50 \AA . Such value is among the lowest threshold current densities obtained for $1.5 \mu\text{m}$ multiple quantum well lasers. Fig. 10 shows a comparison of lattice-matched and strained quantum well lasers.

In short, it has been thoroughly investigated and demonstrated that the InGaAsP/InP optoelectronic devices prepared by CBE are no doubt among the best performance as those similar devices prepared by MOVPE and LPE. (Note that MBE is not suited for preparing InGaAsP materials.) With the improved qualities of AlGaAs grown by CBE using new Al compounds, there is also a significant improvement in the AlGaAs/GaAs device performance reported.

Houng and co-workers [14,16] have optimized the CBE growth conditions for GaAs and AlGaAs using TEGa and TEAl. Table 1 shows the 2DEG properties of the CBE AlGaAs/GaAs modulation-doped heterostructure with a thin spacer layer (30 \AA). The values are comparable to that of films of a similar structure grown by OMVPE or ele-

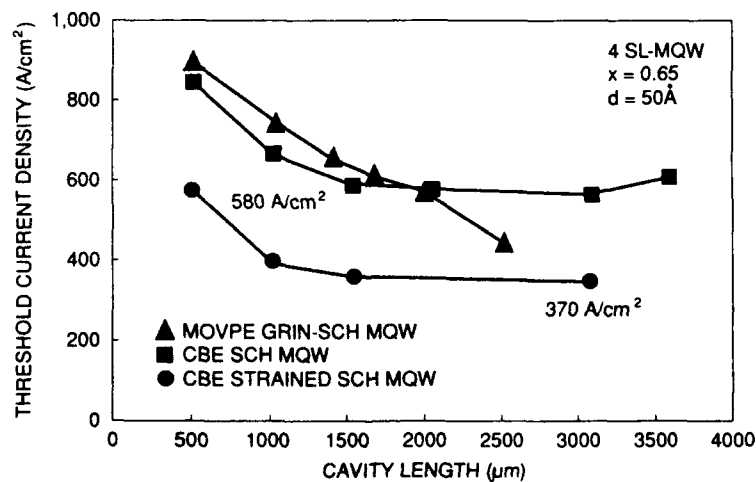


Fig. 10. A comparison of the threshold current densities for lattice-matched CBE-grown, MOVPE-grown and CBE-grown strained-layer multiple quantum well lasers.

Table 1
Electrical properties of modulation-doped structure with a 30 Å AlGaAs spacer layer

Technique	N_s (cm^{-2})		μ ($\text{cm}^2/\text{V}\cdot\text{s}$)	
	300 K	77 K	300 K	77 K
CBE	1.1×10^{12}	1.0×10^{12}	7100	47400
MOCVD	1.4×10^{12}	1.4×10^{12}	6300	42000
MBE	1.2×10^{12}	1.0×10^{12}	7060	54600

mental-source MBE technique. It is seen that for practical device structure applications, the two-dimensional electron gas (2DEG) mobilities are very similar. In a more recent experiment using triisobutylaluminum (TIBAl) instead of TEAl, further improvement is obtained. In a 2DEG structure having 150 Å AlGaAs spacer layer, a 2DEG mobility at 77 K of $88,600 \text{ cm}^2/\text{V}\cdot\text{s}$ is obtained using TIBAl versus $64,900 \text{ cm}^2/\text{V}\cdot\text{s}$ using TEAl. The sheet carrier concentration is $6 \times 10^{11} \text{ cm}^{-2}$. This is the highest 2DEG mobility in AlGaAs/GaAs grown by CBE.

Quarter-micron gate length MODFETs have been fabricated on this CBE film grown using TEGa and TEAl sources. These devices have a maximum transconductance g_m of 380 mS/mm at $V_G = -0.17 \text{ V}$. Typical noise figures of 1.7 dB with an associated gain of 10.5 dB at 18 GHz and an f_T of 38 GHz were obtained from these devices when operated at room temperature. These devices exhibited characteristics equivalent to devices fabricated from material grown by elemental-source MBE and processed using the same mask set. Table 2 shows a comparison with MBE grown transistors. Further improvement of CBE MODFET device performance can be obtained by using TIBAl instead of TEAl as an Al source for the growth of MODFET structure.

Table 2
MODFET device performance: $L_g = 0.25 \text{ }\mu\text{m}$ and $b_g = 150 \text{ }\mu\text{m}$

Technique	g_m (mS/mm)	NF ^{a1} (dB)	f_T (GHz)
CBE	380	1.7	38
MBE	300–340	1.4–1.5	35–40

^{a1} Measured at 18 GHz.

Carbon doping in Gas using TMGa proves to be important for HBT applications for two important reasons: (1) Very high C concentration, which is electrically active, up to 10^{20} cm^{-3} can be obtained, (2) carbon does not diffuse during growth or high temperature (700°C) annealing. Abernathy and co-workers [20] have fabricated similar devices in which the entire structure is grown by CBE. For a base doping of 10^{19} cm^{-3} a gain of 140 was measured for 90 μm diameter devices. $2 \text{ }\mu\text{m} \times 6 \text{ }\mu\text{m}$ devices showed a gain of 28 and an f_T to 40 GHz. Though further work is needed to optimize the performance of these structures, these preliminary results are quite encouraging and suggest that carbon may indeed fulfill its promise as a p-type dopant in high-speed III–V devices. Excellent results were also reported by Hewlett-Packard group on AlGaAs/GaAs travelling-wave electro-optic waveguide modulations, which require low-defect 10 μm thick epilayers, and light-emitting diode arrays at 710 μm .

11. Conclusion

In short, the recent rapid progress and widespread interest has confirmed the importance and ensured the future of CBE. In fact, the development of CBE is in some way a necessity without choice if epitaxial growth technology is to go beyond MOVPE and MBE. MOVPE and MBE have been under development for the last two decades and matured. Their respective advantages and disadvantages, their unique capabilities and limits are well understood. It is only natural and timely for researchers to develop new techniques for the future that preserve and even create new advantages and capabilities, and at the same time eliminate or circumvent the shortcomings.

References

- [1] For a review, see:
W.T. Tsang, J. Crystal Growth 95 (1989) 121;
W.T. Tsang, Chemical beam epitaxy, in: VLSI Electronics Microstructure Science, Vol. 21, Ed. N.G. Einspruch (Academic Press, New York, 1989) ch. 6, pp. 255–357;
W.T. Tsang, J. Crystal Growth 105 (1990) 1.

- [2] M. Lambert, A. Peralès, R. Vergnaud and C. Starck, *J. Crystal Growth* 105 (1990) 97.
- [3] L. Goldstein, *J. Crystal Growth* 105 (1990) 93.
- [4] G.J. Davies, E.G. Scott, M.H. Lyons, M.A.Z. Rejman-Greene and D.A. Andrews, NATO Conf. on Spectroscopy of Semiconductor Microstructures, Venice, May 1989.
- [5] M. Nakajima, A. Takamori, T. Yokotsuka, K. Uchiyama and T. Abe, *J. Crystal Growth* 105 (1990) 116.
- [6] K. Kishino, A. Kikuchi, Y. Kaneko and I. Nomura, 12th Intern. Conf. on Semiconducting Lasers, paper PD-10, Davos, Sept. 1990.
- [7] W.T. Tsang, T.H. Chiu, J.E. Cunningham and A. Robertson, Jr., *Appl. Phys. Letters* 50 (1987) 1376.
- [8] A. Robertson, Jr., T.H. Chiu, W.T. Tsang and J.E. Cunningham, *J. Appl. Phys.* 64 (1988) 877.
- [9] T. Martin and C.R. Whitehouse, *J. Crystal Growth* 105 (1990) 57.
- [10] Y. Iimura, K. Nagata, Y. Aoyagi and S. Namba, *J. Crystal Growth* 105 (1990) 230.
- [11] J.L. Benchimol, F. Alaoui, Y. Gao, G. Le Roux, E.V.K. Rao and F. Alexandre, *J. Crystal Growth* 105 (1990) 135.
- [12] H. Heinecke, B. Baur, H. Höger and A. Miklis, *J. Crystal Growth* 105 (1990) 143; *Electron. Letters* 26 (1990) 213.
- [13] A. Rudra, J.F. Carlin, M. Proctor and M. Ilegems, *J. Crystal Growth* 111 (1991) 589.
- [14] Y.M. Houn, *J. Crystal Growth* 105 (1990) 124.
- [15] T.H. Chiu, W.T. Tsang, J.A. Ditzenberger, C.W. Tu, F. Fen and C.S. Wu, *J. Electron. Mater.* 17 (1988) 217.
- [16] B.J. Lee, Y.M. Houn, J.N. Miller and J.E. Turner, *J. Crystal Growth* 105 (1990) 168.
- [17] D.A. Bohling, G.T. Muhr, C.R. Abernathy, A.S. Jordan, S.J. Pearton and W.S. Hobson, *J. Crystal Growth* 107 (1991) 1068.
- [18] M. Weyers, J. Musolf, D. Marx, A. Kohl and P. Balk, *J. Crystal Growth* 105 (1990) 383.
- [19] M. Konagai, T. Yamada, T. Akasuka, S. Nogaki, R. Miyake, K. Saito, T. Fukamachi, E. Tokumitsu and K. Takahashi, *J. Crystal Growth* 105 (1990) 359.
- [20] C.R. Abernathy, *J. Crystal Growth* 107 (1990) 982.
- [21] W.T. Tsang, A.S. Sudbo, L. Yang, R.M. Camarda and R.E. Leibenguth, *Appl. Phys. Letters* 54 (1989) 2336.
- [22] G.B. Strongfellow, *J. Crystal Growth* 105 (1990) 260.
- [23] D. Ritter, M.B. Panish, R.A. Hamm and D. Gershoni, 2nd Intern. Conf. on Chemical Beam Epitaxy and Related Growth Techniques, Houston, Dec. 1989.
- [24] A. Doi, Y. Aoyagi and S. Namba, *Appl. Phys. Letters* 48 (1986) 1787.
- [25] T.H. Chiu, J.E. Cunningham, A. Robertson, Jr. and D.L. Malm, *J. Crystal Growth* 105 (1990) 155.
- [26] H. Hirayama and K. Koyama, *J. Crystal Growth* 105 (1990) 46.
- [27] R.G. Benz II, B.K. Wagner, D. Rajavel and C.J. Summers, *J. Crystal Growth* 111 (1991) 725.
- [28] W.T. Tsang, M.C. Wu, T. Tanbun-Ek, R.A. Logan, S.N.G. Chu and A.M. Sergent, *Appl. Phys. Letters*, in press.
- [29] A. Kasukawa, I.J. Murgatroyd, Y. Imajo, N. Matsumoto, T. Fukushima, H. Okamoto and S. Kashiwa, *Japan. J. Appl. Phys.* 28 (1989) L661.
- [30] T. Tanbun-Ek, R.A. Logan, H. Temkin, K. Berthold, A.F.J. Levi and S.N.G. Chu, *Appl. Phys. Letters* 55 (1983) 2283.
- [31] K. Berthold, A.F.J. Levi, T. Tanbun-Ek and R.A. Logan, *Appl. Phys. Letters* 56 (1990) 122.
- [32] H. Temkin, T. Tanbun-Ek, R.A. Logan, J.A. Lewis and N.K. Dutta, *Appl. Phys. Letters* 56 (1990) 1210.
- [33] P.J.A. Thijs, T. van Dongen and B.H. Verbeek, OFC, San Francisco, 1990.

A comparison of MBE and MOMBE/CBE growth mechanisms using modulated beam mass spectrometry and RHEED

C.T. Foxon

Philips Research Laboratories, Redhill, Surrey RH1 5HA, UK

E.M. Gibson, J. Zhang, B.A. Joyce

Semiconductor Materials IRC, The Blackett Laboratory, Imperial College, London SW7 2BZ, UK

and

D.E. Lacklison

Philips Research Laboratories, Redhill, Surrey RH1 5HA, UK

MOMBE and CBE growth has until recently been based on largely empirical studies of the epitaxial process. We have used modulated beam mass spectrometry (MBMS) and reflection high energy electron diffraction (RHEED), previously applied to the study of MBE, to investigate the interaction of metalorganics with As_2 and As_4 with a view to understanding more completely the MOMBE/CBE process. The decomposition of metalorganic (MO) sources under quasi-equilibrium conditions has been studied using time-of-flight (TOF) techniques. The cracking pattern of trimethylgallium (TMGa) has been established using this method. The interaction of TMGa with As_2 and As_4 has been studied in detail on both singular and vicinal plane samples. The growth rate is a complex function of both substrate temperature and group III incident flux and is also influenced by the nature of the group V species and the group V/III ratio. Studies of the species desorbing from the surface during growth by MOMBE using TMGa have shown that in addition to the metalorganics, only methyl radicals are observed, the methane and ethane seen in mass spectrometer studies which have not used modulation techniques are formed in the system. Modulating the adsorbed beam (TMGa) has shown that, in the temperature range where significant growth is achieved, no TMGa is desorbed from the surface. The presence of CH_3 (no CH_4 or C_2H_6 is detected) desorbing from the surface suggests the pyrolysis of TMGa via sequential release of methyl radicals. The reaction mechanism for the decomposition of TMGa under MOMBE conditions is complicated with at least one slow step limiting the growth rate of GaAs.

1. Introduction

Considerable interest has been generated in metalorganic molecular beam epitaxy (MOMBE) in recent years [1,2] as a method that potentially combines the advantages of MBE and MOCVD [3] in III–V compound semiconductor growth. Because growth takes place in ultra-high vacuum equipment, modulated beam mass spectrometry (MBMS) and reflection high energy electron diffraction (RHEED) monitoring techniques can be used to clarify the growth mechanisms.

We have studied in detail the pyrolysis of trimethylgallium (TMGa) under MOMBE growth conditions. There are various mechanisms proposed for the decomposition of TMGa that involve the loss of methane or the methyl radicals. We have recently reported our preliminary data using MBMS and RHEED studies under true MOMBE conditions [4], which show that only the methyl radical (CH_3) is desorbed from the surface in addition to the metalorganics. The metalorganic (MO) species desorbing change with temperature as radicals are lost via a sequential pyrolysis.

Memmert and Yu [5] used a combination of pulsed molecular beam and time resolved mass spectrometry to study the kinetics of pyrolysis of TMGa and also concluded that only CH_3 is observed, in agreement with our data.

In this paper, we present more detailed data obtained from MBMS [6,7] and RHEED studies [7]. These two techniques combined give information on the complex surface kinetics under dynamic growth conditions for both MOMBE and MBE. We have extended our earlier RHEED study by working on vicinal plane samples and for singular surfaces used smaller substrates to avoid geometrical beating effects in the RHEED intensity oscillations [4]. In addition we have modulated the adsorbed TMGa beam in order to study the time dependence of desorbing species.

2. Experimental

The MBMS and RHEED studies were performed in an MBE system equipped with additional MO sources: TMGa, TEGa, TEAl and TMIn. Elemental sources containing In, Ga, Al, As and P were also present. The group V sources had additional hot (cracker) zones to provide either the dimer or tetramer. In this present study only TMGa and As_2 were used. Absolute measurement of the TMGa flux was not possible because the sticking coefficient never reached unity. The approximate values quoted in this paper were obtained from the maximum growth rate, determined using the RHEED oscillation technique, assuming a unity incorporation rate for TMGa, which is not quite the case. The (001) oriented GaAs substrate was etched in $\text{H}_2\text{SO}_4 : \text{H}_2\text{O}_2 : \text{H}_2\text{O}$, mounted with In onto a Mo block and the oxide was removed by heating in a beam of As_2 at 620°C . The temperature of the substrate was monitored using both a thermocouple shielded to prevent direct radiation from the heaters and a radiation pyrometer ($2\text{ }\mu\text{m}$ with an emissivity setting of 0.62 for a Si doped substrate). The two estimates agreed to $< 10^\circ\text{C}$.

The ioniser of the quadrupole mass spectrometer used for the MBMS studies was surrounded by a liquid nitrogen cooled assembly with collimation

to ensure that it can only detect molecules directly desorbed from the sample surface. The adsorbed or desorbed beam can be modulated to distinguish real signals from those resulting from background gases arising in the ioniser region. This is especially crucial in the case of metalorganics which have relatively high background pressures within the MOMBE chamber, typically in the mid 10^{-7} Torr range. Since the ioniser in the mass spectrometer collects typically 10^{-3} of the flux desorbed from the surface, the true signal is small compared to the background. So-called "reflection mass spectrometry" in which line of sight combined with a simple mechanical shutter arrangement is used cannot give satisfactory data under these conditions. Fourier transform techniques are used to extract both phase and amplitude information on the surface processes from the overall signal [6]. An additional DC flux is available to study non-linear higher order reactions.

There is a separate time-of-flight (TOF) facility, which is used to study the cracking patterns from the various MO sources. The mass spectrometer has an additional RF only pre-filter and behaves as a ideal density detector under suitable conditions [8].

3. Results and discussion

The preliminary results of our earlier study in which the desorbed beam was modulated are shown schematically in fig. 1. This shows a peak in the growth rate followed by a small decreased and finally a second increase as the substrate temperature is increased.

We have now studied the same process by modulating the adsorbed beam which allows us to determine the surface lifetime of the various species desorbing from the surface. In order to obtain surface lifetime from the overall delay, we need to know the adsorbed and desorbed species to determine and remove the flight times from the modulator to the surface and from the surface to the detector [6]. The adsorbed beam in this case is TMGa, but the nature of the desorbed species is not clear, since the cracking patterns of the vari-

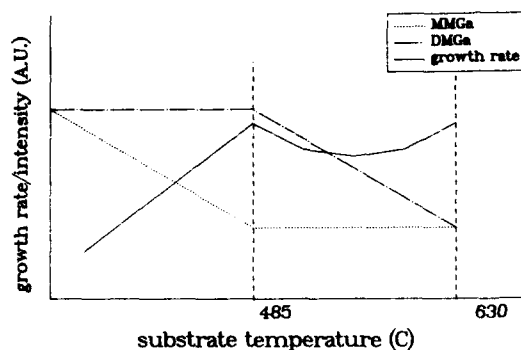


Fig. 1. Schematic diagram depicting the variation of growth rate of GaAs and the desorption of TMGa fragments with temperature, applied to either As_2 or As_4 .

ous possibilities are not known. As a first approximation we have therefore used the detected ion mass for the mass of the desorbed beam. The maximum error resulting from this possibly incorrect procedure will be < 0.5 ms. The results of this study are shown in fig. 2, the delays in the signals for Ga^+ , MMGa^+ and DMGa^+ are all negligible over the whole temperature range studied (420 to 620°C) but for the TMGa^+ a constant, temperature independent delay of about 4 ms is observed. This can only be explained by the signal arising as an association reaction on the

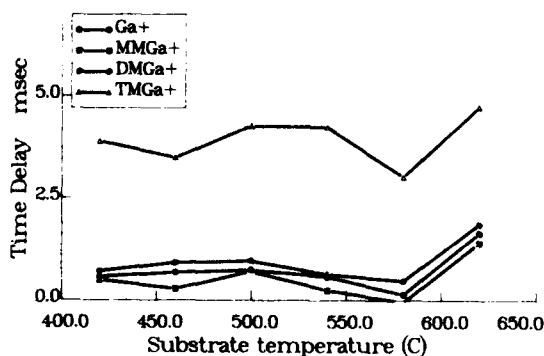


Fig. 2. Delay in the signals in the mass spectrometer with respect to modulation of the adsorbed beam of TMGa during growth using As_2 as a function of substrate temperature. Contributions due to the flight times of the adsorbed and desorbed beam have been removed but uncertainties ~ 0.5 ms exist due to the unknown mass of the desorbing species and the behaviour of the mass spectrometer which does not act as an ideal density detector.

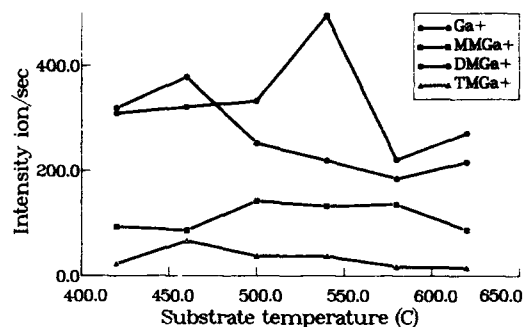


Fig. 3. Amplitude of the signals in the mass spectrometer for modulation of the adsorbed beam of TMGa during growth using As_2 as a function of substrate temperature.

walls of the ioniser of the mass spectrometer or in the collimating apertures. It is important to point out that in studies using reflection mass spectrometry this signal would be incorrectly identified as coming from the surface. Only phase information obtained by modulating the incident beam can reveal this as spurious information.

Fig. 3 shows the intensity of the various signals observed in the mass spectrometer as a function of temperature over the same temperature range. The functional dependence observed follows closely that seen in our previous study, in which the desorbing flux was modulated [4]. From an analysis of the amplitude of the various Fourier components present in the signals we can also see that for the Ga^+ and DMGa^+ no second harmonic is present, but for the TMGa^+ and in some instances for the MMGa^+ this is not always the case.

Plotting the ratios of the intensities of Ga^+ to MMGa^+ , as shown in fig. 4 shows that this correlates closely with the observed growth rate dependence shown in fig. 1.

From this additional data we can see that the original model proposed for the decomposition of TMGa during growth by MOMBE is essentially correct [4]. Radicals are lost sequentially and in the temperature range where significant growth is observed ($> 400^\circ\text{C}$) no TMGa is desorbed from the surface. This implies that the energy required to break the first bond is small, but that DMGa and MMGa are relatively stable surface species. The changing relative intensities of Ga^+ , MMGa^+

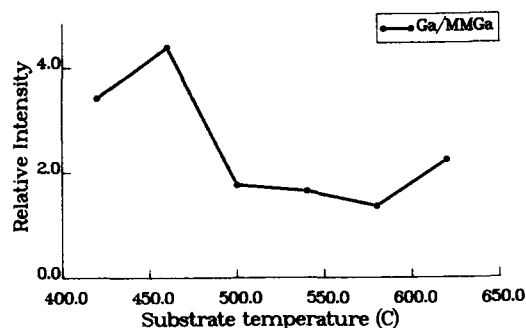


Fig. 4. Ratio of the amplitudes of the Ga^+ to MMGa^+ signals in the mass spectrometer for modulation of the adsorbed beam of TMGa during growth using As_2 as a function of substrate temperature.

and DMGa^+ observed in the MBMS studies show that both DMGa and MMGa are lost by desorption, unlike the situation with TEGa , where the growth rate is determined by the desorption of DEGa [9–11]. This difference may explain why a more complex dependence of growth rate on substrate temperature is observed for TMGa than for TEGa .

We have extended our previous study of the relative damping of RHEED oscillations in MBE and MOMBE growth. To avoid the inherent problem of different growth rate variations across the substrate in MBE and MOMBE due to geometrical factors [4], we have used much smaller substrates than previously ($1 \times 1 \text{ mm}^2$ cf. $5 \times 5 \text{ mm}^2$). The difference in damping rate is still observed to persist, with the oscillations damping much more slowly in MOMBE than in MBE grown under the same conditions. This we do not ascribe to higher mobility for the metalorganics on the surface. It implies that a longer time is needed to reach the steady state step distribution in MOMBE compared to MBE under otherwise identical conditions. This is perhaps consistent with the notion that the metalorganics are less mobile than Ga atoms.

Finally we have studied by RHEED the dependence of growth on substrate temperature on vicinal plane samples. In the low temperature region ($< 480^\circ\text{C}$) we find an enhanced growth rate for samples cut off orientation with steps running parallel to the $[\bar{1}10]$ direction; for samples cut off

in the orthogonal direction no difference compared to a singular surface is observed. This finding implies that specific surface sites are responsible for the pyrolysis of the TMGa or DMGa molecules and will be the subject of a more detailed study.

4. Summary

Growth of GaAs by MOMBE using TMGa takes place by the sequential release of methyl radicals which are lost by desorption. Over the temperature range where significant growth takes place (above 400°C) DMGa and MMGa are lost by desorption from the surface; TMGa signals seen in reflection mass spectrometry studies are false and are formed in the ioniser region of the mass spectrometer. The reduced rate of damping of RHEED oscillations observed in MOMBE growth compared with MBE is probably due to lower surface mobility for metalorganics compared to elemental Ga. Specific sites are involved in the pyrolysis of DMGa or TMGa.

Acknowledgements

The authors would like to thank J.H. Neave for helpful discussions and P. Cheale, B. Heaton, R.B. Maddox and G. Terry for invaluable assistance with constructing and maintaining the MBMS/RHEED equipment.

References

- [1] R. Heckingbottom and K.A. Prior, *Surface Sci.* 175 (1986) 38.
- [2] W.T. Tsang, *J. Crystal Growth* 95 (1989) 121.
- [3] M. Uneta, Y. Watanabe and Y. Ohmachi, *Japan. J. Appl. Phys.* 27 (1988) L2411.
- [4] E. Gibson, C.T. Foxon, J. Zhang and B.A. Joyce, *J. Crystal Growth* 105 (1990) 81.
- [5] U. Memmert and M.L. Yu, *Appl. Phys. Letters* 56 (1990) 1883.
- [6] C.T. Foxon, M.R. Boudry and B.A. Joyce, *Surface Sci.* 44 (1974) 69.

- [7] B.A. Joyce, Rept. Progr. Phys. 48 (1985) 1637.
- [8] E.M. Gibson, C.T. Foxon, J. Zhang, J.H. Batey and B.A. Joyce, J. Vacuum Sci. Technol. A8 (1990) 3141.
- [9] A.J. Murrell, A.T.S. Wee, H. Fairbrother, N.K. Singh, J.S. Foord, G.J. Davies and D.A. Andrews, J. Crystal Growth 105 (1990) 199.
- [10] T. Martin and C.R. Whitehouse, J. Crystal Growth 105 (1990) 57.
- [11] A. Robertson, T.H. Chiu, W.T. Tsang and J.E. Cunningham, J. Appl. Phys. 64 (1988) 877.

Background pressure dependence of GaAs and AlGaAs growth rates in gas-source molecular beam epitaxy

Junji Saito, Takeshi Maeda, Katsuji Ono and Kazuo Kondo

Fujitsu Laboratories Ltd., 10-1 Morinosato-Wakamiya, Atsugi 243-01, Japan

The rate of GaAs and AlGaAs epitaxial growth by molecular-beam epitaxy using two gas systems – arsine (AsH_3), triethylgallium (TEG) and Al, and AsH_3 , Ga and Al – decreased exponentially as the AsH_3 flow rate increased. We find that growth rate R can be represented using AsH_3 flow rate F as $R = B \exp(-AF)$, where A and B are constants. A was the same for GaAs and AlGaAs. In these systems, the background pressure during growth increased from 10^{-5} to 10^{-4} Torr. In the As_4 and TEG system, the GaAs growth rate was independent of the As_4 beam intensity from 10^{-5} to 10^{-4} Torr, unlike in the AsH_3 systems. The background pressure in this As_4 pressure range was also constant. We explain these results in terms of an increase of the collision frequency between the group III and background molecules. The value A calculated from our growth conditions using the kinetic theory of gases agreed well with the results of experiments.

1. Introduction

Background pressure during growth in molecular-beam epitaxy (MBE) growth using metalorganic compounds and/or hydrides is typically 10^{-4} to 10^{-5} Torr, mid-range between conventional MBE using a metal source and metalorganic chemical vapor deposition (MOCVD). The growth of gas-source MBE differs from standard MBE and MOCVD [1,2]. In GaAs growth using triethylgallium (TEG), an excessive arsenic (As_4) beam intensity [3,4] or arsine (AsH_3) flow rate [5–7] suppresses carbon incorporation into the epitaxial layer during growth. However, the growth rate of GaAs grown using TEG and AsH_3 also decreases with the AsH_3 flow rate or as additional H_2 pressure increases [8–10].

Nagata et al. [8] reported that the reduction of growth rate in GaAs grown using As_4 or AsH_3 and TEG was caused by additional hydrogen and excessive AsH_3 flow rate. They explained these results saying that chemical adsorption of hydrogen atoms on the growth surface prevents the adsorption of TEG molecules. Chiu et al. [9] also

reported that the growth rate of GaAs grown using AsH_3 and TEG decreases with increasing AsH_3 flow rate over a wide range of substrate temperature. They explained this by the preferential site catalytic effect, which may exist because the excessive As reduces the probability for diethylgallium produced by decomposition of TEG to move to the proper site for epitaxial growth. Maruno et al. [10] reported that the growth rate in GaAs grown using TEG and AsH_3 decreased when additional hydrogen or nitrogen was introduced, or that there was an excessive AsH_3 flow rate. They refuted the chemical adsorption model reported by Nagata, claiming the growth rate reduction was caused by nitrogen as well as hydrogen. They explained their results by assuming that transient residence of hydrogen or nitrogen molecules on the growing surface impedes adsorption of TEG molecules.

This paper discusses the AsH_3 flow rate and As_4 beam intensity dependence of the growth rate and the AlAs mole fraction in GaAs and AlGaAs layers grown using three systems: AsH_3 , TEG and Al; AsH_3 , Ga and Al; and As_4 and TEG. It also

discusses the growth mechanism of GaAs and AlGaAs layers in a high-pressure region caused by an excessive AsH_3 flow rate.

2. Experiments

The experiments were performed in a modified ISA-Riber 2300P, equipped with gas lines for AsH_3 and TEG, conventional effusion cells for As_4 , Ga and Al, and evacuated with a turbo-molecular pump (2200 l/s) during growth [4]. The distance between effusion cells and substrate was 25 cm. AsH_3 was introduced through a high-temperature cracking cell maintained at 920°C . The flow rate was controlled with a mass flow controller (MFC), and varied from 5 to 50 standard cm^3/min (SCCM). Since the AsH_3 flow rate was less than 3 SCCM, the surface morphology of epitaxial layers degraded because few As_2 molecules were incident on the growth surface. Therefore, we used an AsH_3 flow rate of more than 5 SCCM. TEG was introduced into the growth chamber through a low-temperature effusion cell using hydrogen as a carrier gas. The total flow rate of 10 SCCM was also controlled with a MFC. The TEG flow rate as calculated from the partial pressure was 2.5 SCCM. A conventional arsenic effusion cell was used to produce an As_4 molecular beam which was varied from 1.5×10^{-5} to 3.0×10^{-4} Torr. The As_4 molecular beam intensity was measured with a Bayard-Alpert ionization gauge in place of the substrate.

A semi-insulating (100)-oriented GaAs substrate was mounted on a molybdenum block by indium solder, and introduced into the growth chamber. The substrate temperature, measured by an infrared pyrometer calibrated to the melting point of aluminum, was 550°C . This temperature is in a mass-transport limited region [11,12]. Background pressure during growth was measured using a Bayard-Alpert ionization gauge. The growth rate was determined by measuring the layer thickness using a stylus profilometer on GaAs substrates which were partly masked by $0.8 \mu\text{m}$ thick SiO_2 films. The thickness of GaAs and AlGaAs layers in the heterostructure were determined using

a depth profile of Al by secondary-ion mass spectroscopy (SIMS).

3. Results

GaAs and AlGaAs layers were grown on the GaAs substrates using AsH_3 , TEG and Al sources. Background pressure during growth increased linearly from 7×10^{-5} to 7×10^{-4} Torr as the AsH_3 flow rate increased from 5 to 50 SCCM. The growth rates of GaAs and AlGaAs decreased exponentially from 0.79 and 1.04 to 0.42 and 0.55 $\mu\text{m}/\text{h}$ as the AsH_3 flow rate increased (fig. 1). We found that the growth rate R is expressed in terms of AsH_3 flow rate F (SCCM) as $R = B \exp(-AF)$, where A and B are constants. A is the same for GaAs and AlGaAs. The lines in fig. 1 represent the equation of growth rate $R = 0.872 \exp(-0.0146F)$ for GaAs and $R = 1.12 \exp(-0.0146F)$ for AlGaAs.

The AlAs mole fraction of AlGaAs as determined from the growth rates of GaAs and AlGaAs was 0.24 for an AsH_3 flow rate of 5 to 50 SCCM. We identified that the intensity ratio of Al to Ga signals measured using SIMS was also independent of the AsH_3 flow rate (fig. 2). These results indicate that GaAs and AlAs growth rates

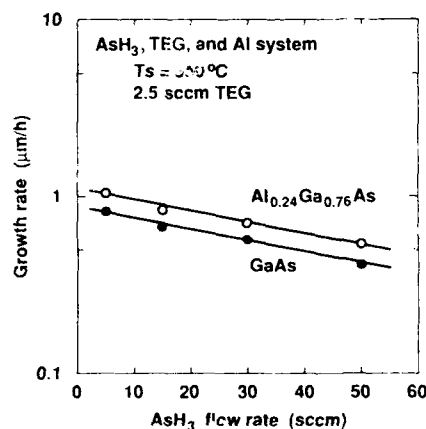


Fig. 1. Growth rates of GaAs (●) and AlGaAs (○) as a function of AsH_3 flow rates. GaAs and AlGaAs were grown using AsH_3 , TEG and Al sources. Lines represent growth rate $R = B \exp(-AF)$, where F is AsH_3 flow rate and A is 0.0146.

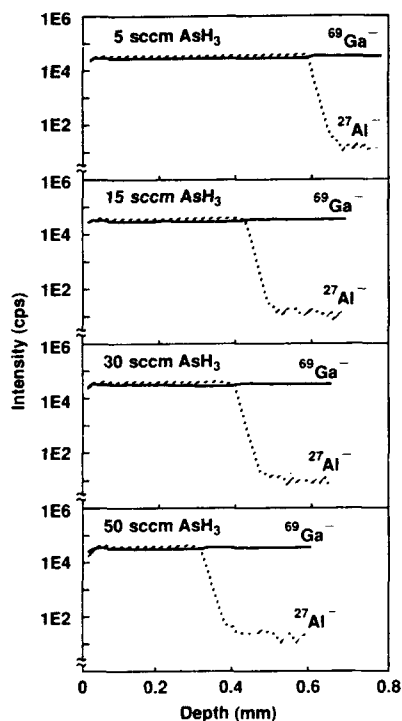


Fig. 2. Ga and Al depth profiles measured using SIMS in AlGaAs for various AsH_3 flow rates. The AlGaAs layers were grown using AsH_3 , TEG and Al sources.

decreased at the same rate as the AsH_3 flow increased.

GaAs/AlGaAs heterostructures were grown on semi-insulating GaAs substrates using AsH_3 , Ga and Al sources. The designed heterostructure consisted of a $0.44 \mu\text{m}$ GaAs, then a $0.11 \mu\text{m}$ $\text{Al}_{0.28}\text{Ga}_{0.72}\text{As}$, then a $0.05 \mu\text{m}$ GaAs, then a $0.1 \mu\text{m}$ $\text{Al}_{0.28}\text{Ga}_{0.72}\text{As}$, followed by a $0.01 \mu\text{m}$ GaAs cap layer. We measured the depth profile of Al using SIMS for GaAs/AlGaAs heterostructures grown at various AsH_3 flow rates. The thickness of the first layer of GaAs decreased from 0.44 to $0.27 \mu\text{m}$ as the AsH_3 flow rate increased from 5 to 50 SCCM. The thickness of the second layer of AlGaAs also decreased from 0.11 to $0.058 \mu\text{m}$. We plotted the thickness of first, second and third layers as functions of the AsH_3 flow rate (fig. 3). The lines in fig. 3 show the exponential curves with gradient of 0.0146 as a function of AsH_3

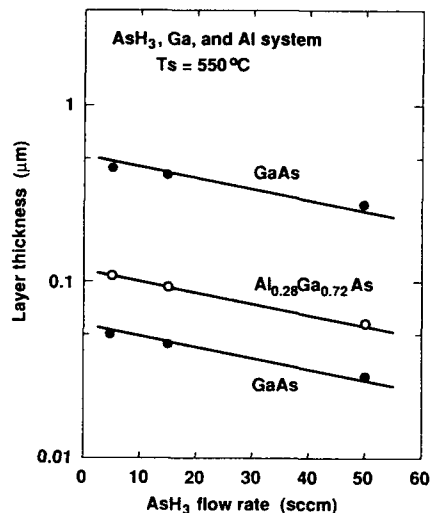


Fig. 3. Thickness of GaAs (●) and AlGaAs (○) in the GaAs/AlGaAs heterostructure (fig. 1) as a function of AsH_3 flow rate. Lines represent the equation for thickness $T \propto \exp(-AF)$, where F is AsH_3 flow rate and A is 0.0146, the same as the equation in fig. 1.

flow rate F . This gradient value is the same for the growth rate R in the AsH_3 , TEG and Al system shown in fig. 1.

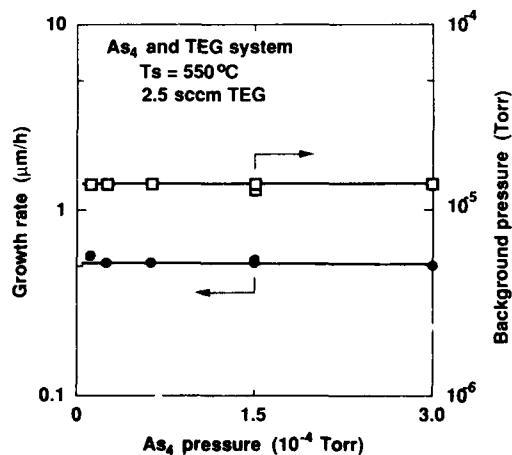


Fig. 4. Dependence of As_4 beam flux intensity on growth rate of GaAs and background pressure during growth. GaAs was grown using As_4 and TEG at substrate temperature of 550°C . The As_4 beam flux was varied from 1.5×10^{-5} to 3.0×10^{-4} Torr. The TEG flow rate was kept at 2.5 SCCM.

GaAs was grown on partially masked substrates using As_4 and TEG sources. While the As_4 molecular flux increased from 1.5×10^{-5} to 3.0×10^{-4} Torr, the background pressure during growth was constant at 1.4×10^{-5} Torr (fig. 4). This background pressure was largely dominated by the hydrogen carrier gas for TEG. The GaAs growth rate was independent of the As_4 pressure, unlike that in the AsH_3 systems.

4. Discussion

We explain these results using the kinetic theory of gases. While a molecular beam passes through a gas, the intensity of the molecular beam is decreased by the elastic collision with gas molecules. The number of group III (TEG, Ga and Al) molecules in a beam L cm away from the gas or effusion cell is given by

$$N(L) = N_0 \exp(-L/\lambda), \quad (1)$$

where N_0 is the original number of molecules and λ is the mean free path for the gases in the growth chamber. The mean free path λ (cm) can be calculated using background pressure P (Torr) as

$$\lambda = 2.33 \times 10^{-20} T / P d^2, \quad (2)$$

where d is the molecular diameter in cm and T the gas temperature in K. Eq. (1) can now be written as

$$N(L) = N_0 \exp(-4.29 \times 10^{19} L d^2 P / T). \quad (3)$$

We used a substrate temperature of 550°C in a mass-transport limited region. Therefore growth rate R is proportional to $N(L)$. The growth rate can be written by

$$R = B \exp(-A'P), \quad (4)$$

where B is constant and

$$A' = 4.29 \times 10^{19} L d^2 / T. \quad (5)$$

In the AsH_3 system, the background pressure P (Torr) is dominated by the AsH_3 flow rate F (SCCM) and effective pumping speed S (l/s) of the growth chamber as

$$P = 0.0127 F / S. \quad (6)$$

Therefore, the growth rate is represented by

$$R = B \exp(-AF), \quad (7)$$

the same as the empirical equation described for the AsH_3 systems, where

$$A = 5.45 \times 10^{17} L d^2 / TS. \quad (8)$$

The effective pumping speed S in this AsH_3 system was examined experimentally. As AsH_3 was introduced through a high-temperature cracking cell at 920°C , the pressure P (Torr) of the growth chamber was measured as a function of the AsH_3 flow rate F (SCCM). The pressure increased linearly according to empirical equation as $P = 7.5 \times 10^{-6} F$. We found that the effective pumping speed S was 1700 l/s.

To calculate A in eq. (8), we chose the molecular diameter $d = 2.75 \times 10^{-8}$ cm of hydrogen as the diameter of the main molecules in this AsH_3 system. We introduced arsine through a cracking cell maintained at 920°C , a temperature sufficient to induce thermal decomposition of arsine. The molecular beams effused from the arsine cracking cell would consist mainly of As dimers and hydrogen, with arsine molecules negligibly few. Most of the As dimers contribute to growth. The remainders, including those re-evaporated from the substrate, are deposited on the shroud wall at liquid nitrogen temperature. Hydrogen, however, does not adsorb on the wall, so the background pressure is dominated by hydrogen molecules. The gas temperature is dominated by the temperature of the wall the gas impinges on. We therefore simply chose a gas temperature $T = 450$ K as an average of the substrate temperature of 550°C and liquid nitrogen of 77 K. The distance L between effusion cells and substrate was 25 cm. With these growth conditions, A , as calculated from eq. (8), is 0.0135. This agrees well with the measured results using two AsH_3 systems. This shows that the reduction of GaAs and AlGaAs growth rates in the AsH_3 systems is caused by an increase of the collision frequency between group III and background molecules. We believe that background molecules consist mainly of hydrogen from the cracked AsH_3 flux. The growth rate reduction caused by the increase in AsH_3 flow

rate appeared when various group III molecules as such as TEG, Ga and Al were used. This indicates that this phenomenon does not depend on the kind of molecule. This also supports the explanation using kinetic theory.

Collision with the background pressure gas also applies to As dimers derived from the thermal decomposition of arsine. Although there is collision, As dimers flux-impinging on the substrate surface increase by a factor of 5 where the arsine flow rate increases from 5 to 50 SCCM.

In the As₄ and TEG system, the background pressure during growth did not increase as the As₄ flux increased. It remained at 1.4×10^{-5} Torr. According to eqs. (4) and (5), the growth rate does not decrease. This also agrees with our measurements.

In the calculation of eqs. (4) and (5), the background pressure deviation of 10^{-6} Torr corresponds to a growth rate deviation of 0.2%, 10^{-5} Torr to 2% and 10^{-4} Torr to 20%. This shows that the growth rate in MBE using gas source is dominated by the background pressure above 10^{-5} Torr.

Chiu et al. [9] show that the GaAs growth rate decreases as the arsine flow rate increases in a substrate temperature range of 380 to 600 °C. The substrate temperature from 380 to 420 °C is within the range of the decomposition-limited region. They show that, in this range, the growth rate was sensitive to an arsine flow rate of 1 to 4 SCCM. They explain this by the preferential site catalytic effect, which may exist because excessive As flux will reduce the number of sites available for TEG pyrolysis. We agree with their argument on this temperature range (380–420 °C) and arsine flow rate range (1–4 SCCM). However, in Chiu et al.'s data, the growth rate gradient in an arsine flow rate of 4 to 20 SCCM is nearly the same for various substrate temperatures. Their experiments were performed in a system where pressure was maintained at less than 5×10^{-5} Torr during growth. This pressure corresponds to our experiments at an arsine flow rate of 5 SCCM. If there are background pressure deviations of 10^{-5} Torr in Chiu et al.'s experiments, we can estimate, using our equations (4) and (5), that the growth rate deviation is several percent. This estimate

agrees with their growth rate reduction in the arsine flow rate over 4 SCCM at various substrate temperatures.

Maruno et al. [10] maintained that the growth rate reduction was not caused by a decrease in the arrival rate of TEG because the collision probability with hydrogen is small enough at background pressures of 0.3 to 3×10^{-4} Torr. At 3×10^{-4} Torr, however, the actual hydrogen pressure is 6.8×10^{-4} Torr, because the gauge sensitivity of hydrogen with a Bayard–Alpert gauge is 0.44 [13]. At this pressure, the mean free path of hydrogen (calculated using eq. (2)) is 20 cm, comparable to the distance between effusion cell and substrate. Therefore, when group III molecules pass through hydrogen from effusion cell to substrate, collision with hydrogen is not negligible. They show that the reciprocal of growth rate ($1/R$) is proportional to the arsine flow rate within an error of 8%. We have plotted their growth rate data in semi-logarithm and find that their data agree with the simple exponential curve of $R = B \exp(-AF)$ within an error of 8%. We believe that the collision with hydrogen reduces the growth rate.

5. Conclusion

The growth rate of GaAs and AlGaAs layers grown by two MBE systems (AsH₃, TEG and Al; and AsH₃, Ga and Al) decreased exponentially as the AsH₃ flow rate increased from 5 to 50 SCCM. We found that the growth rate R is represented in terms of the AsH₃ flow rate F as $R = B \exp(-AF)$, where A and B are constants. In the As₄ and TEG system, the GaAs growth rate was independent of the As₄ beam flux, unlike the AsH₃ system. We explained these results using the kinetic theory of gases. The growth rate gradient as a function of AsH₃ flow rate, which was derived from our growth conditions, agreed well with our measurements. This proves that the reduction of GaAs and AlGaAs growth rates in MBE using the AsH₃ system is caused by an increase in the number of collisions between group III and background molecules. This shows that MBE using gas sources in the background pres-

sure of 10^{-5} to 10^{-4} Torr occurs in the boundary region between molecular and gas flows.

Acknowledgements

We thank T. Misugi, M. Kobayashi, H. Ishikawa, M. Abe, and T. Mimura for their encouragement and support.

References

- [1] W.T. Tsang, Appl. Phys. Letters 45 (1984) 1234.
- [2] W.T. Tsang, in: Extended Abstracts 18th (1986 Intern.) Conf. on Solid State Devices and Materials Tokyo, 1986, pp. 611-617.
- [3] K. Kimura, S. Horiguchi, K. Kamon, M. Mashita, M. Mihara and M. Ishii, Japan. J. Appl. Phys. 26 (1987) 419.
- [4] J. Saito, K. Ono, K. Nanbu, T. Ishikawa and K. Kondo, Japan. J. Appl. Phys. 27 (1988) L1144.
- [5] N. Pütz, H. Heinecke, M. Heyen, P. Balk, M. Weyers and H. Lüth, J. Crystal Growth 74 (1986) 292.
- [6] S. Horiguchi, K. Kimura, K. Kamon, M. Mashita, M. Shimazu, M. Mihara and M. Ishii, Japan. J. Appl. Phys. 25 (1986) L979.
- [7] T.H. Chiu, W.T. Tsang, E.F. Schubert and E. Agyekum, Appl. Phys. Letters 51 (1987) 1109.
- [8] K. Nagata, Y. Iimura, Y. Aoyagi, S. Namba, S. Den and A. Moritani, J. Crystal Growth 93 (1988) 265.
- [9] T.H. Chiu, J.E. Cunningham and A. Robertson, Jr., J. Crystal Growth 95 (1989) 136.
- [10] S. Maruno, Y. Nomura, H. Ogata, M. Gotoda and Y. Morishita, J. Crystal Growth 97 (1989) 578.
- [11] J. Saito, K. Ono and K. Kondo, Japan. J. Appl. Phys. 28 (1989) L738.
- [12] T. Maeda, J. Saito and K. Kondo, J. Crystal Growth 105 (1990) 191.
- [13] T.A. Flaim and P.D. Ownly, J. Vacuum Sci. Technol. 8 (1971) 661.

The roles of group-V species in metalorganic molecular-beam epitaxy and chemical-beam epitaxy of III–V compounds

B.W. Liang and C.W. Tu

Department of Electrical and Computer Engineering, University of California at San Diego, La Jolla, California 92093-0407, USA

Our kinetic model for metalorganic molecular-beam epitaxy (MOMBE) and chemical-beam epitaxy (CBE) of GaAs has been extended to GaSb. This model can fit experimental data for growth with triethylgallium (TEGa) and antimony. The roles of group-V species in MOMBE of III–V compounds are summarized. Group-V species are as important as group-III species in determining the growth rates in MOMBE and CBE.

1. Introduction

More and more people are interested in metalorganic molecular-beam epitaxy (MOMBE) or chemical-beam epitaxy (CBE) [1,2] because of its special properties, such as different growth kinetics from conventional MBE [3–5], atomic layer epitaxy (ALE) [7,10,11], high carbon doping [6,7], and selective-area epitaxy [8,9]. In previous papers [4,5], we have studied the growth kinetics of MOMBE of GaAs and InAs. We found that arsenic plays an important role in MOMBE or CBE. The growth rate is very sensitive to arsenic beam flux. Our kinetic model can fit experimental results very well and provide more insights into the growth process.

In this paper, we extend our model to MOMBE of GaSb with triethylgallium (TEGa) and antimony and summarize the roles of group-V species in MOMBE of III–V compounds.

2. Growth kinetics

2.1. MOMBE of GaSb

Because the mean free paths of molecules are very long compared to the source-to-substrate distance, one can expect that gas-phase reactions are unimportant in MOMBE, unlike in metalorganic

chemical vapor deposition (MOCVD). Surface reactions dominate the growth process. The first kinetic model proposed by Robertson et al. considered only triethylgallium (TEGa) decomposition paths [3]. The role of arsenic species was presumed secondary. Subsequently, group-V species, unlike in conventional MBE, were found to have a strong effect on the growth rate. This model therefore cannot explain the arsenic dependence of growth rates. Another model proposed by Kaneko et al. [12] for MOMBE of GaSb assumes the growth rate is controlled by the antimony vacancy and provides a relation between growth and antimony surface concentration with $R_g \sim f(T)[\text{Sb}]^{-n}$, where n is the number of antimony vacancy. According to their model, if $[\text{Sb}] = 0$, growth rate of GaSb is infinite. Obviously, it is not right because the growth rate of GaSb must be zero without antimony. We have proposed a new kinetic model [4], taking into account the effect of arsenic species for the first time, for CBE of GaAs using TEGa and arise (AsH_3). The model can fit the experimental data of Chiu [11] very well.

The model assumes that diethylgallium (DEGa) decomposition, in the presence of arsenic, is the rate-limiting step for growing GaAs. We expect that monoethylgallium (MEGa), with two ethyl radicals cleaved off, would be very reactive and chemisorb strongly to the surface. Cleavage of the last ethyl radical and subsequent incorporation of

GaAs would occur very fast due to small activation barrier. This situation is similar to Robertson's model. What differentiates our model is that this DEGa decomposition step includes an arsenic species. Experimentally, the growth rate decreases with increasing arsine flow rate, and this has been attributed to the site-blocking effect [11]. In our preliminary study, the site-blocking mechanism does not agree with experimental data. We therefore propose enhanced desorption of TEGa by excess arsenic on the surface in the continuous CBE or MOMBE process. Similar to GaSb, for GaSb, the proposed surface chemical reactions are as follows:

- (1) $\text{TEGa(g)} \xrightarrow{FS_0} \text{TEGa(ad)},$
- (2) $\text{TEGa(ad)} \xrightarrow{k_1} \text{DEGa(ad)},$
- (3) $\text{TEGa(ad)} + \text{Sb}_2(\text{ad}) \xrightarrow{k_2} \text{TEGa(g)} + \text{other products},$
- (4) $\text{DEGa(ad)} \xrightarrow{k_3} \text{DEGa(g)},$
- (5) $\text{DEGa(ad)} + \text{Sb}_2(\text{ad}) \xrightarrow{k_4} \text{GaSb} + \text{other products}.$

In reaction (1), F is the TEGa beam flux, and S_0 is the adsorption probability. The k 's are various reaction rate coefficients. Similar to Robertson's model, we postulate the cleavage of the second ethyl radical to be the rate-limiting step. In our model, the growth rate (R_g) depends not only on the DEGa surface concentration X_2 , but also on the antimony surface concentration C_{Sb} :

$$R_g = kX_2C_{\text{Sb}}. \quad (1)$$

In the steady-state condition, the concentration of adsorbed TEGa (X_1) and DEGa (X_2) are independent of time. Solving for X_2 and X_3 , and assuming Arrhenius behavior for the reactions $k_i = A_i \exp(-E_i/kT)$, we obtain

$$R_g = \{FS_0\} \left\{ \left[1 + (A_1/C_{\text{Sb}}) \times e^{-\Delta E_1/RT} \right] \left(1 + A_2C_{\text{Sb}} e^{-\Delta E_2/RT} \right) \right\}^{-1}. \quad (2)$$

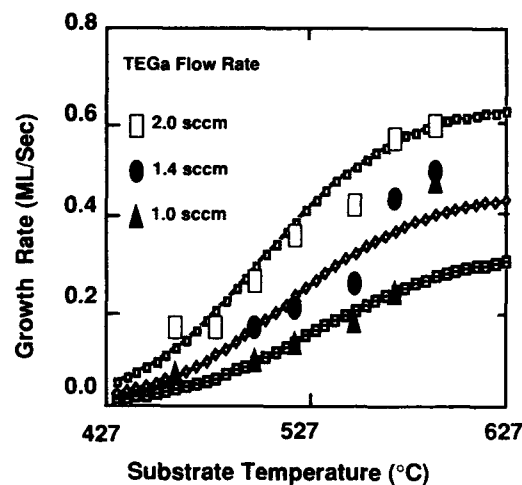


Fig. 1. The relation between growth rate of GaSb by MOMBE and substrate temperature.

where $A_1 = A_{-2}/A$, $A_2 = A'/A_3$, $\Delta E_1 = E_{-2} - E$ and $\Delta E_2 = E' - E_3$. There are six unknown parameters (A_1 , A_2 , ΔE_1 , ΔE_2 , FS_0 and C_{Sb}). Note that in this model, we have further assumed that (1) there is no Ga desorption because the growth temperature is below that of Ga desorption and (2) the temperature dependence of S_0 and C_{Sb} is small in the range studied.

We use eq. (2) to fit experimental data from ref. [12]. First, we fit the growth rate versus substrate temperature at 2.0 SCCM of TEGa flow rate and 1.2×10^{-6} Torr of antimony beam equivalent pressure since their data points under this condition look relatively complete and have relatively small scatter compared with the other two sets of data. We obtain the fitting parameters as follows: $A_1 = 3000$ ML, $\Delta E_1 = 21$ kcal/mol, $A_2 = 5 \times 10^{-10}$ ML⁻¹, $\Delta E_2 = -34.8$ kcal/mol, $FS_0 = 0.7$ ML/cm²·s, and $C_{\text{Sb}} = 0.48$ ML. ML stands for monolayers. Then we fix the values of A_1 , A_2 , ΔE_1 , and ΔE_2 , and adjust FS_0 and C_{Sb} to fit other growth-rate curves, as shown in fig. 1. It should be mentioned that because the data points scatter, we ignored the highest point in the set of points for which TEGa flow rate is 1.0 SCCM.

Using these parameters, we calculate the growth rate as a function of C_{Sb} , as shown in fig. 2 for various substrate temperatures used in ref. [12].

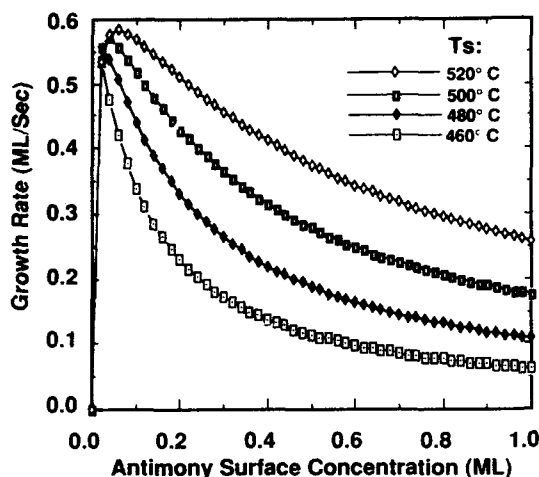


Fig. 2. The dependence of growth rate of GaSb on antimony surface concentration resulting from our model.

Qualitatively these curves agree well with the data in ref. [12].

We now discuss the parameter obtained from the model. Consider first $\Delta E_1 = E_{-2} - E$, where E_{-2} is the activation energy of DEGa desorption and E is the activation energy for reaction (5). Since DEGa and Sb_2 are reactive, E is probably small. Therefore, $\Delta E_1 \approx E_{-2}$, which means $E_2 \approx 21$ kcal/mol. This value is almost the same as our previous result for GaAs [4], and it indicates that the DEGa desorption activation energy is the same on GaSb as on GaAs surface. Now, consider $\Delta E_2 = E' - E_3$, where E' is the activation energy of antimony-enhanced desorption, and E_3 is the

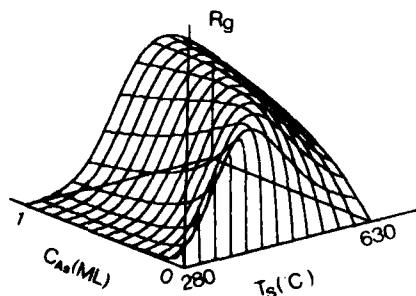


Fig. 3. Growth rate of InAs using TMIn and As_4 as a function of substrate temperature (from 280 to 630°C) and arsenic surface concentration.

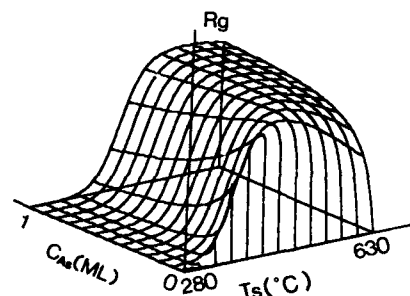


Fig. 4. Growth rate of GaAs using TEGa and arsine as a function of substrate temperature (from 280 to 630°C) and arsenic surface concentration.

activation energy for TEGa decomposing into DEGa. Since the binding energy for physisorbed molecules should be in the range of 1–10 kcal/mol, E_3 is in the range of 35.8–45 kcal/mol. This value is reasonable compared with the gas-phase value of 46 kcal/mol.

2.2. The roles of group-V species in MOMBE and CBE

Surveying the growth behavior of MOMBE of GaAs, InAs and GaSb, as shown in figs. 3, 4 and 5, we can come to a conclusion that group-V species play very important roles in MOMBE and CBE. For TEGa, in the low group-V surface concentration range, the group-V affects growth rates very seriously, especially in low substrate temperature range. For TMIn, even though arsenic affects the growth rate too, but not as much as that in

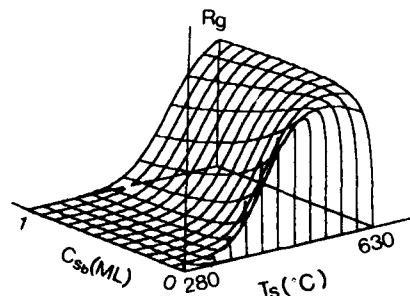


Fig. 5. Growth rate of GaSb using TEGa and Sb_4 as a function of substrate temperature (from 280 to 630°C) and antimony surface concentration.

TEGa. This may be because of the difference between TEGa and TMIn in chemistry. According to our kinetic model, there are two competing reactions, reactions (2) and (3), during MOMBE or CBE of III-V compounds. For example, in GaSb, one is TEGa decomposing into DEGa and the other is antimony-enhanced TEGa desorption. At low substrate temperature, reaction (2) is slow, and thus reaction (3) plays the major role. The growth rate increases with increasing the surface concentration of group-V species first and then decreases very quickly. But at high substrate temperature, both reaction (2) and reaction (5) are very fast. So, reaction (3) does not play an important role anymore. The growth rate behaves like conventional MBE.

In summary, group-V species play an important role in MOMBE and CBE, especially in low substrate temperature. On the one hand, group-V species on the surface react with alkyl-group-III radical, such as DEGa, and this kind of reaction limits the growth rate. The higher the surface concentration of group-V species, the higher the growth rate. On the other hand, too much group-V species on the surface may enhance desorption of alkyl-group-V molecules, and then growth rate decreases with increasing group-V beam flux. Therefore, accurate control of both group-V beam flux and substrate temperature is a critical issue in MOMBE and CBE. We have succeeded in extending our kinetic model for MOMBE of GaAs and InAs to GaSb. The model can fit the experimental data very well and explain how TEGa flow rate

and antimony surface concentration influence the growth rate.

Acknowledgments

This work was partially supported by the Air Force Wright Research and Development Center and the Office of Naval Research. We wish to thank H.Q. Hou for help in fitting the data.

References

- [1] E. Veuhoff, W. Pletschen, P. Balk and H. Lüth, *J. Crystal Growth* 55 (1981) 30.
- [2] W.T. Tsang, *Appl. Phys. Letters* 45 (1984) 1234.
- [3] R. Robertson, Jr., T.H. Chiu, W.T. Tsang and J.E. Cunningham, *J. Appl. Phys.* 64 (1988) 877.
- [4] B.W. Liang and C.W. Tu, *Appl. Phys. Letters* 57 (1990) 689.
- [5] B.W. Liang, L.Y. Wang and C.W. Tu, in: *Proc. 12th Conf. on State-of-the-Art Progress on Compound Semiconductors*, in press.
- [6] M. Weyers, N. Pütz, H. Heinecke, M. Heyen, H. Lüth and P. Balk, *J. Electron. Mater.* 15 (1986) 57.
- [7] C.W. Tu, B.W. Liang, T.P. Chin and J. Zhang, *J. Vacuum Sci. Technol.* B8 (1990) 293.
- [8] V.M. Donnelly, C.W. Tu, J.C. Beggy, V.R. McGrary, M.G. Lamont, T.D. Harris, F.A. Baiocchi and R.C. Farrow, *Appl. Phys. Letters* 52 (1988) 1065.
- [9] H. Sugiura, R. Iga, T. Yamada and M. Yamaguchi, *Appl. Phys. Letters* 54 (1989) 335.
- [10] B.W. Liang, T.P. Chin and C.W. Tu, *J. Appl. Phys.* 67 (1990) 4393.
- [11] T.H. Chiu, *Mater. Res. Soc. Symp. Proc.* 145 (1989) 47.
- [12] T. Kaneko, H. Asahi, Y. Okuno, T.W. Kang and S. Gonda, *J. Crystal Growth* 105 (1990) 69.

Metalorganic molecular beam epitaxy of GaAs using hydrogen radical beam

Akiyoshi Watanabe *, Masayuki Hata and Toshiro Isu

Optoelectronics Technology Research Laboratory, 5-5 Tohkodai, Tsukuba, Ibaraki 300-26, Japan

The effects of a hydrogen radical beam on metalorganic molecular beam epitaxy are examined. An oxide layer of GaAs is removed by hydrogen radical irradiation. Self-limiting growth is suppressed when trimethylgallium (TMGa) and arsine (AsH_3) are supplied alternately under hydrogen radical pressure. When triethylgallium (TEGa), TMGa and AsH_3 are supplied sequentially, the growth rate of GaAs increases with total amount of TEGa supply plus TMGa supply, while the growth rate increases with only amount of TEGa without hydrogen radicals. It is considered that hydrogen radicals cut the bonds of both a methyl radical and an ethyl radical with Ga atom in TMGa and TEGa molecules.

1. Introduction

Atomic layer epitaxy (ALE) is an interesting growth technique that has good controllability of growth layer thickness [1–5]. In metalorganic chemical vapor deposition (MOCVD) [1,4], good optical and electrical characteristics of grown layers have been reported using the ALE technique. Good electrical characteristics have not been obtained in layers by metalorganic molecular beam epitaxy (MOMBE) using trimethylgallium (TMGa) as a source. Under MOMBE, a grown layer contains carbon impurities with 10^{19} – 10^{21} cm^{-3} carrier concentration. We have reported that under the ALE conditions the adsorbed molecules on the surface are not decomposed into Ga atoms for both cases of TMGa and triethylgallium (TEGa) [5,7]. In other words, the adsorbed molecules have a bond to carbon during the ALE growth process. In order to decrease the carbon concentration, it is desired to cut the bond of carbon and Ga of metalorganic molecules by some method.

It was reported that the native oxide on a surface of a GaAs substrate was removed by hy-

drogen radicals produced by ECR plasma [6]. This suggests that hydrogen radicals are so active that they can cut the bond of oxygen and a gallium or arsenic atom. Therefore, it is thought that hydrogen radicals can cut the bond of carbon and a Ga atom.

In this paper, the effects of hydrogen radicals on MOMBE growth are examined from an ALE viewpoint. Removal of a GaAs oxide layer is examined by Auger electron spectroscopy. In addition, it is examined as to whether hydrogen radicals do cut the bond of a Ga atom and carbon in TMGa and TEGa molecules through measurement of the thickness of the layer grown by the ALE procedure.

2. Experimental apparatus

The MOMBE system used in the present experiment consists of a conventional MBE system with three chambers for introduction, preheating and Auger analysis, and growth, respectively, and a specially designed gas-handling system [7]. A hydrogen radical beam gun, Oxford Applied Research MPD20, is installed in a port of the growth chamber. Hydrogen radicals are produced by an electrodeless discharge at 13.56 MHz and 150 W

* Present address: Central Research Laboratory, Hitachi, Ltd., Kokubunji, Tokyo 185, Japan.

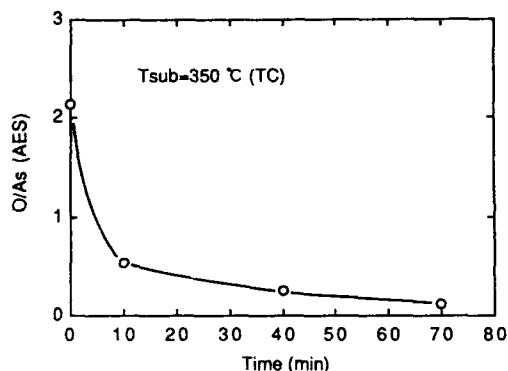


Fig. 1. The ratio of oxygen and arsenic Auger peak intensity as a function of time. The substrate temperature is 350 °C at a thermocouple behind the Mo block. The pressure of hydrogen radicals is 2.5×10^{-2} Pa.

of RF power with 20 SCCM of H_2 flow. It is considered that hydrogen ions are hardly produced by the radical beam gun. Arsine (AsH_3) is cracked by the tantalum baffles, which are maintained at 850 °C.

3. Removal of native oxide of GaAs substrate

An n-type GaAs(100) $\pm 0.1^\circ$ wafer was used as the substrate. After a chemical treatment with sulfuric acid, the wafer was mounted on a molybdenum block using indium metal, and it was then introduced into the growth chamber. It was heated at 350 °C at a thermocouple behind the Mo block. Then hydrogen radicals were supplied for a sufficient time, and the wafer was transferred to the analysis chamber in order to obtain an Auger electron spectrum from the surface of the wafer. These procedures were repeated several times.

Fig. 1 shows the dependence of intensity ratio of oxygen and arsenic Auger peak as a function of irradiation time of hydrogen radicals. In the figure, the intensity ratio of oxygen and arsenic Auger peak decreases with time; therefore, the native oxide on the surface of the GaAs wafer was removed. When hydrogen was supplied without electrodeless discharge, the intensity of the oxygen Auger peak did not decrease at 350 °C. It was

considered that hydrogen radicals produced by electrodeless discharge remove the native oxide on the surface of GaAs. In other words, hydrogen radicals are thought to cut the bond of oxygen and a gallium or arsenic atom.

4. Effects on ALE

4.1. Source supply (ALE)

After the wafer was introduced into the growth chamber as mentioned above, the substrate was heated at 570 °C under arsenic pressure for surface cleaning. The wafer temperature was measured by an infrared pyrometer.

The flow rates of TMGa, TEGa, AsH_3 and H_2 were 0.6, 0.6, 1.5 and 20 SCCM, respectively. The pressure in the growth chamber was 2.5×10^{-2} Pa with H_2 flow and 1.5×10^{-3} Pa without H_2 flow. The pressures of TMGa, TEGa and AsH_3 were 4×10^{-4} , 2×10^{-4} and 1.9×10^{-3} Pa, respectively, on the beam flux monitor in the MBE chamber.

Prior to the ALE growth, an about 200 nm thick undoped GaAs layer was grown using Ga metal and AsH_3 . The reflection high energy electron diffraction (RHEED) pattern of the surface showed the 2×4 surface reconstruction of an arsenic stabilized surface. When the substrate temperature was decreased to 500 °C, the RHEED pattern of the surface was changed into the $c(4 \times 4)$ pattern. The growth rates of the GaAs layer using TMGa and TEGa were both 4 nm/min without H_2 flow and both 3 nm/min with H_2 flow, respectively.

In the ALE experiments, TMGa, TEGa and AsH_3 were supplied sequentially, as shown in fig. 2. These sequences were repeated for 150 cycles. Grown layer thicknesses were measured from cross-sectional views using the Hitachi S-900 scanning electron microscope with a resolution of 0.8 nm.

4.2. The effect of hydrogen radicals on ALE

Fig. 3 shows the thickness of GaAs per cycle as a function of TMGa supply duration for the se-

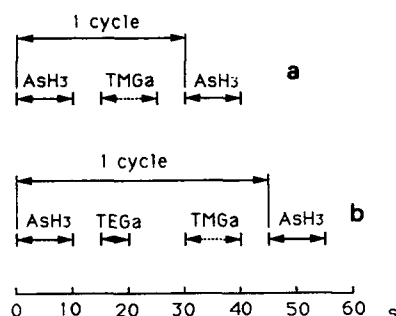


Fig. 2. Time sequences of source supplies: (a) TMGa and AsH₃ supplied alternately for a GaAs substrate and (b) TEGa, TMGa and AsH₃ supplied sequentially. The TMGa supply duration is varied from 5 to 20 s and the TEGa supply duration is 5 s, which corresponds to 1 ML of GaAs growth. AsH₃ supply duration is 10 s.

quence of fig. 2a at a growth temperature of 500°C. In the figure, the thickness of GaAs per cycle increases with TMGa supply duration and no saturation phenomena are observed, whereas the thickness of GaAs per cycle was saturated at 1 monolayer (ML) when hydrogen radicals were not supplied [5]. We already reported that TMGa molecules do not adsorb on TMGa molecules or their derivatives but adsorb on Ga atoms, and that TMGa molecules do not decompose into Ga atoms [5]. The fact that the thickness of GaAs per cycle did not saturate at 1 ML shows that the hydrogen

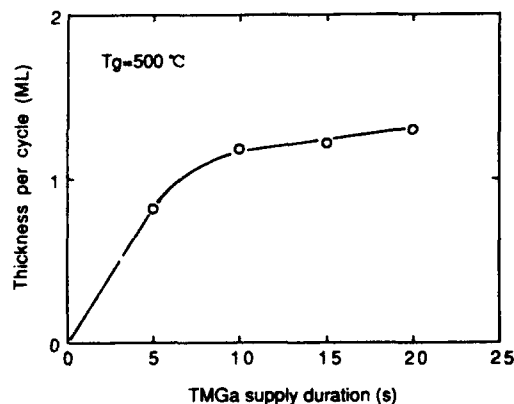


Fig. 3. Thickness of GaAs per cycle as a function of TMGa supply duration for the sequence of fig. 2a at a growth temperature of 500°C. The pressure of hydrogen radicals is 2.5×10^{-2} Pa.

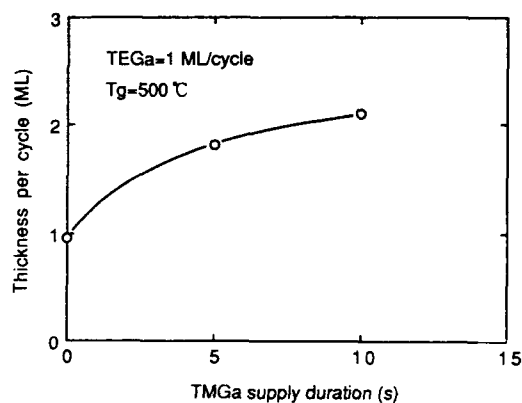


Fig. 4. Thickness of GaAs per cycle as a function of TMGa supply duration for the sequence of fig. 2b at a growth temperature of 500°C. The TEGa supply duration is 5 s, which corresponds to 1 ML of GaAs growth. The pressure of hydrogen radicals is 2.5×10^{-2} Pa.

radicals removed the layer that limited adsorption of excess TMGa molecules.

4.3. The effect of hydrogen radicals on TEGa molecule

It is well known that in the case of using TEGa as a source, self-limiting growth does not occur when TEGa and AsH₃ are supplied alternately at a growth temperature of 500°C. We already examined the growth rate of GaAs for the sequence shown in fig. 2b without hydrogen radical pressure [7]. As a result, it is considered that TEGa molecules do not decompose into Ga atoms and TMGa molecules do not adsorb on TEGa molecules or their derivatives. In order to examine the effect of hydrogen radicals on a layer that was produced by TEGa molecules and limited adsorption of TMGa molecules, the thickness of GaAs per cycle was examined for the sequence of fig. 2b with irradiation of hydrogen radicals. Fig. 4 shows the thickness of GaAs per cycle as a function of TMGa supply duration for the sequence of fig. 2b at a growth temperature of 500°C. In the figure, the thickness of GaAs increases with TMGa supply duration. Therefore it is considered that hydrogen radicals can remove a layer that limits adsorption of TMGa molecules.

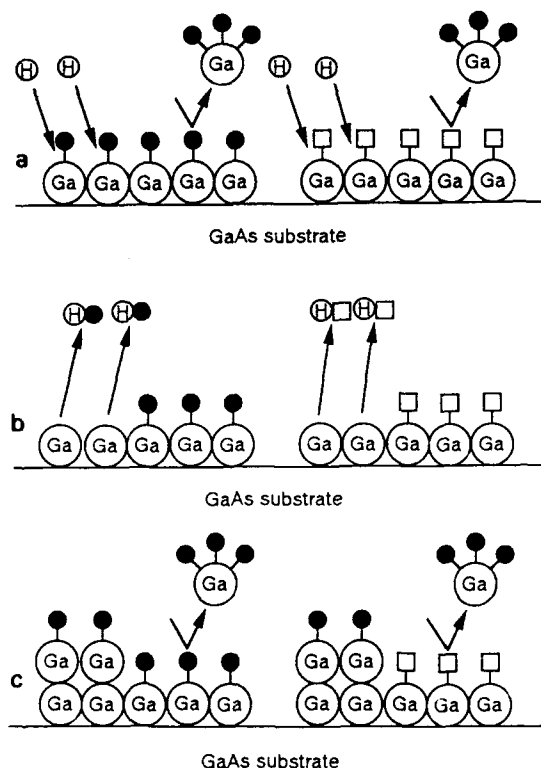


Fig. 5. Growth kinetic model for surface chemical reactions of hydrogen radicals and metalorganic molecules: (●) CH₃; (□) C₂H₅.

5. Discussion

Fig. 5 shows schematically a model for surface chemical reactions of hydrogen radicals and metalorganic molecules. When TMGa or TEGa molecules are irradiated onto the GaAs surface, TMGa or TEGa molecules decompose into molecules such as monomethylgallium (MMGa) or monoethylgallium (MEGa), and these molecules adsorb on the GaAs surface, as shown in fig. 5a. When TMGa molecules are irradiated onto adsorbed MMEGa or MEGa, they cannot adsorb on MMEGa or MEGa. When hydrogen radicals are irradiated onto adsorbed MMEGa or MEGa, they react with MMEGa or MEGa. As a result of the hydrogen radical reaction with MMEGa or MEGa, either methane or ethane may be produced and

desorbed from the surface, as shown in fig. 5b. Therefore, the Ga atom remains on the GaAs surface. As TMGa molecules adsorb on a Ga atom [5] an excess GaAs layer of 1 ML is grown for 1 cycle, as shown in fig. 5c.

In these experiments, the thickness of GaAs layer per cycle was not proportional to TMGa supply duration. The reasons are considered as follows. Hydrogen radicals produced by the radical beam gun are insufficient, and the reaction time of hydrogen radicals with the adsorbed TMGa molecules is longer compared with that of the source supply.

It was considered that hydrogen radicals do have the ability to cut the bond of a Ga atom and carbon in both TMGa and TEGa molecules. It is important that the amount of carbon impurities is decreased maintaining the characteristics of self-limiting growth. In this experiment, self-limiting growth was not achieved, since hydrogen radicals were constantly supplied during growth. We believe that ALE growth with low carbon concentration can be achieved by the following procedure. First, 1 ML of TMGa molecules is adsorbed on a GaAs surface by the excess 1 ML supply of TMGa. Next, hydrogen radicals are supplied for a sufficient time, and 1 ML of Ga atom without carbon may remain. 1 ML of GaAs is grown when AsH₃ is supplied.

6. Summary

The effects of hydrogen radicals on MOMBE were examined. It was found that native oxide of GaAs can be removed under hydrogen radical exposure. The growth rates of GaAs were measured in sequence where TMGa, TEGa and AsH₃ were supplied under hydrogen radical pressure. The self-limiting growth to 1 ML of GaAs growth was not observed when TMGa and AsH₃ were supplied alternately to a GaAs substrate under hydrogen radical pressure. It was also observed that TEGa did not limit TMGa adsorption on it. It was considered that TMGa molecules adsorb on TMGa and TEGa molecules or their derivatives on the surface of a GaAs substrate under hydrogen radical pressure. It was also considered that

hydrogen radicals were effective to cut the bond of a Ga atom and methyl or ethyl radical.

Acknowledgments

The authors would like to thank Drs. Y. Katayama and I. Hayashi for helpful discussions and continuous encouragement.

References

- [1] S.M. Bedair, M.A. Tischer, T. Katsuyama and N.A. El-Masry, *Appl. Phys. Letters* 47 (1985) 51.
- [2] J. Nishizawa, H. Abe and T. Kurabayashi, *J. Electrochem. Soc.* 132 (1985) 1197.
- [3] A. Usui and H. Sunakawa, *Japan. J. Appl. Phys.* 25 (1986) L212.
- [4] M. Ozeki, N. Ohtsuka and K. Kodama, *Appl. Phys. Letters* 53 (1988) 1509.
- [5] A. Watanabe, T. Isu, M. Hata, T. Kamijoh and Y. Katayama, *Japan. J. Appl. Phys.* 28 (1989) L1080.
- [6] Y. Tanaka, Y. Kunitsugu, I. Suemune, Y. Honda, Y. Kan and M. Yamanishi, *J. Appl. Phys.* 64 (1988) 2778.
- [7] A. Watanabe, T. Kamijoh, M. Hata, T. Isu and Y. Katayama, *Vacuum* 41 (1990) 965.

p^+/N GaAs–AlGaAs heterostructures grown by gas source MBE using gaseous p- and n-type dopant sources

A. Sandhu, T. Fujii, H. Ando, T. Takahashi, H. Ishikawa and N. Yokoyama

Fujitsu Laboratories Ltd., 10-1 Morinosato-Wakamiya, Atsugi 243-01, Japan

We report on the first growth of p^+/N GaAs–Al_xGa_{1-x}As heterostructures using all gaseous sources by gas source MBE (GSMBE). GaAs was doped p-type ($1.3 \times 10^{20} \text{ cm}^{-3}$) using trimethylgallium as both a dopant and group III source and Al_xGa_{1-x}As ($x = 0.0.28$) was doped n-type ($5 \times 10^{17} \text{ cm}^{-3}$) using uncracked disilane as an n-type dopant and triethylgallium and triethylaluminium as group III sources. In both cases 100% arsine was used as the group V source. The current–voltage ideality factor of the heterojunctions was found to depend on the aluminium mole fraction of Al_xGa_{1-x}As ($x = 0.12, 0.23, 0.28$) and the width ($\Delta s = 5, 10, 20 \text{ nm}$) of an undoped GaAs spacer layer at the heterojunction. A value of 1.17 was obtained for a heterostructure with $x = 0.23$ and $\Delta s = 20 \text{ nm}$.

1. Introduction

The growth of III–V semiconductors in ultra-high vacuum using metalorganic group III sources and hydride group V sources has become an extremely active field of research [1–4]. Henceforth, this growth method will be referred to as gas source MBE (GSMBE). From this research, it has become apparent that the reproducible doping of III–V compound semiconductors using conventional “hot” solid sources contained in Knudsen cells is not reproducible over long periods of time, due to the formation of nonvolatile metalorganic related species in the effusion cell [5]. Thus for practical applications of GSMBE, it is important to be able to reproducibly dope III–V semiconductors both n-type and p-type. Without such a doping ability it will be very difficult to reproducibly realize high performance electron devices, such as heterojunction bipolar transistors (HBTs), where it is necessary to grow appropriately designed p^+/N heterojunctions. Possible alternatives to “hot” solid sources would be “cold” gaseous sources which do not require any form of cracking and which incorporate readily under normal growth conditions. We have previously reported on the growth of n-type Al_xGa_{1-x}As ($x = 0–0.28$)

and p-type GaAs by gas source MBE using disilane (Si_2H_6) and trimethylgallium ($\text{Ga}(\text{CH}_3)_3$, TMG) as gaseous dopant sources [6]. We have taken this investigation a stage further, and in this paper report the first growth of p^+/N GaAs–AlGaAs heterostructures by GSMBE using the aforementioned gaseous dopant sources. We present the electrical and secondary ion mass spectroscopy data on the (Al, Ga)As epilayers and heterostructures doped using Si_2H_6 and TMG, and show that “cold” dopant sources are a practical alternative to “hot” solid sources for the growth of p^+/N GaAs–AlGaAs heterostructures by GSMBE.

2. Experimental

All the epilayers were grown on semi-insulating (100) GaAs substrates in a VG80H MBE growth chamber using a totally independently designed gas handling system. Cracked AsH_3 (100%, 1100°C) was used as a group V source and its flow rate was regulated using a mass flow controller. In the n-type growth of the Al_xGa_{1-x}As ($x = 0–0.28$), triethylgallium ($\text{Ga}(\text{C}_2\text{H}_5)_3$, TEG) and triethylaluminium ($\text{Al}(\text{C}_2\text{H}_5)_3$, TEA) were

used as group III sources, and uncracked 10% disilane in hydrogen (Si_2H_6) as the *n*-type dopant source. Growth of *p*-type GaAs was carried out using trimethylgallium ($\text{Ga}(\text{CH}_3)_3$, TMG) as both the *p*-type dopant and group III source. All metal-organics were introduced into the growth chamber without the use of a carrier gas and the flow rate was controlled by measuring the pressure difference at a flow element and then feeding the signal to a control valve. A detailed account of the group III gas handling system has been published elsewhere [7]. The GaAs-AlGaAs heterostructures were grown at a substrate temperature of 580°C, which was monitored using a calibrated infrared pyrometer.

The electron concentration of *n*-type $\text{Al}_x\text{Ga}_{1-x}\text{As}$ ($x = 0-0.28$) was determined by *C-V* measurements on aluminium Schottky diodes, and the hole concentration and mobility of *p*-type GaAs were measured at room temperature by the standard Van der Pauw-Hall method using indium ohmic contacts. The atomic concentrations of Si in the *n*-type $\text{Al}_x\text{Ga}_{1-x}\text{As}$ epilayers and Si and C in the *p*⁺/*N* GaAs-Ga_xAl_{1-x}As heterostructures were obtained from secondary ion mass spectroscopy (SIMS) measurements using Cs^+ ions for sputtering. The atomic concentrations of C and Si were determined by comparison with ion-implanted reference samples. In the case of *n*-type AlGaAs, the reference samples were Si-implanted GaAs and $\text{Al}_{0.3}\text{Ga}_{0.7}\text{As}$. Current-voltage measurements were made on mesa diodes having a diameter of 200 μm, which were fabricated by

photo-lithographic processes, and conventional wet chemical etching.

3. Results and discussion

Figs. 1a and 1b show the variation of the GaAs hole concentration and mobility with substrate temperature and V/III ratio, respectively. All the *p*-type GaAs epilayers studied had excellent mirror morphologies. The GaAs epilayer mobilities varied between 100 $\text{cm}^2/\text{V} \cdot \text{s}$ at a hole concentration of $6.3 \times 10^{18} \text{ cm}^{-3}$ and 60 $\text{cm}^2/\text{V} \cdot \text{s}$ at hole concentration of $1.3 \times 10^{20} \text{ cm}^{-3}$. These results are considered to be comparable or better than those of *p*-type GaAs epilayers grown by other methods [8]. It can be seen that the GaAs epilayer hole concentration is relatively insensitive to substrate temperature, but is strongly dependent on the V/III ratio. Our results show opposite trends from results on the growth of *p*-type GaAs using a combination of TMG-As₄, where the hole concentration was reported to decrease drastically with increasing substrate temperature and to be very weakly dependent on the V/III ratio [9]. It can be speculated that carbon incorporation using the TMG-AsH₃ combination is governed by the reaction of TMG by-products with active hydrogen (which is abundantly present as a by-product of cracked arsine), and not by thermal pyrolysis of TMG as has been proposed in the case of TMG-As₄. From the practical point of view, our results show that the hole concentration of GaAs can be

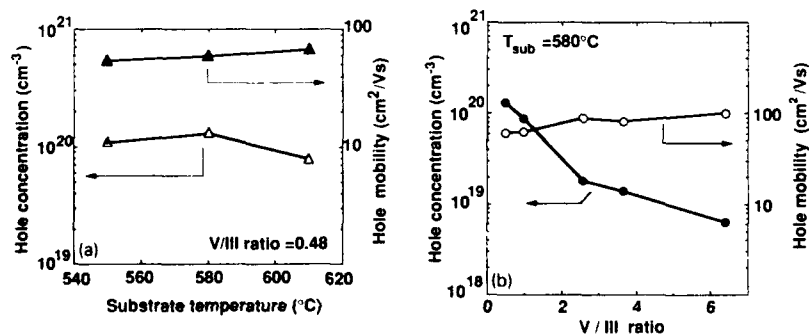


Fig. 1. Variation of GaAs epilayer hole concentration and mobility with (a) substrate temperature and (b) V/III ratio.

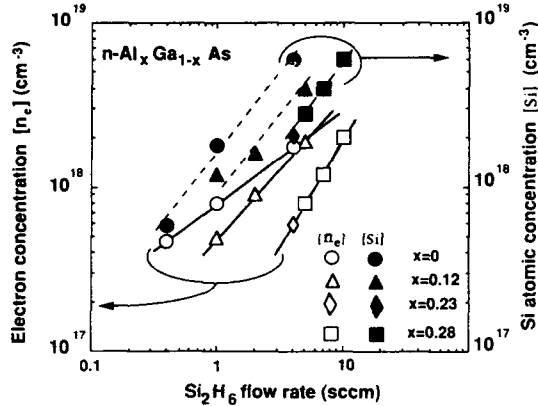


Fig. 2. Variation of the electron and silicon atomic concentration of $\text{Al}_x\text{Ga}_{1-x}\text{As}$ ($x=0-0.28$) epilayers with Si_2H_6 flow rate. The data are normalized to an epilayer growth rate of $1 \mu\text{m/h}$. For $x=0$ (GaAs) $T_{\text{sub}}=610^\circ\text{C}$ and $\text{AsH}_3=2 \text{ SCCM}$. For $x=0.12, 0.23$ and 0.28 , $T_{\text{sub}}=580^\circ\text{C}$ and $\text{AsH}_3=4 \text{ SCCM}$. The dashed lines indicate a unity slope and the solid lines are inserted to make reading of data easier.

changed between 6.3×10^{18} and $1.3 \times 10^{20} \text{ cm}^{-3}$ by varying the TMG and AsH_3 flow rates (i.e. V/III ratio), which is much more accurate and simpler than if it were necessary to adjust the substrate temperature.

Fig. 2 shows the variation of the electron and silicon atomic concentration of n-type $\text{Al}_x\text{Ga}_{1-x}\text{As}$ ($x=0, 0.12, 0.23, 0.28$) with Si_2H_6 flow rate. All the silicon doped epilayers had excellent mirror morphologies. It can be seen that the atomic concentration of silicon varies linearly with Si_2H_6 flow rate for all aluminium compositions (dashed lines indicate a slope of unity). However, the electron concentration of $\text{Al}_x\text{Ga}_{1-x}\text{As}$ for $x=0$ and 0.12 varies sublinearly (approximately square root) with the Si_2H_6 flow rate and for $x=0.23$ and 0.28 , the dependence becomes superlinear. The electron concentration dependencies are different from those of n-type (Al, Ga)As grown by low pressure MOCVD using disilane as a dopant, where the electron concentration was reported to exhibit a linear dependence on the Si_2H_6 flow rate and to be independent of the Al mole fraction [10]. Further investigations are necessary in order to be able to explain the different trends because the dissociation paths of Si_2H_6 and the consequent incorporation mechanisms of silicon in GSMBE are not understood, but the role of the stagnant layer (which does not exist under normal GSMBE growth conditions where the pressure during growth is typically 5×10^{-5} Torr) appears to be the key factor in explaining the differences in the results. However, our results clearly show

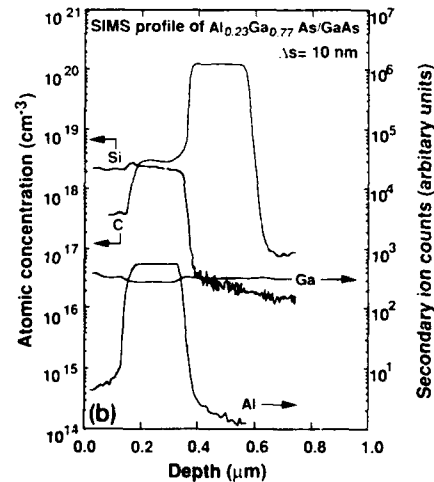
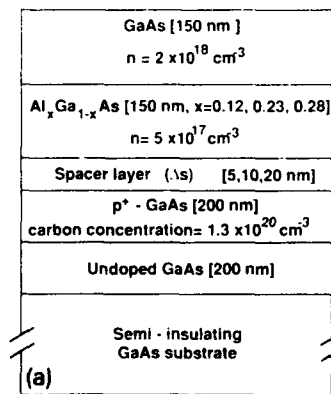


Fig. 3. (a) The specifications of all the p^+ /N $\text{Al}_x\text{Ga}_{1-x}\text{As}$ heterostructures investigated. (b) The SIMS profile of a p^+ /N $\text{Al}_{0.23}\text{Ga}_{0.77}\text{As}$ heterostructure ($\Delta s = 10 \text{ nm}$).

that Si_2H_6 dissociates readily at normal growth temperatures and that it is a suitable n -type "cold" dopant source for $\text{Al}_x\text{Ga}_{1-x}\text{As}$ ($x = 0-0.28$) grown by GSMBE.

Based on the doping results described above, a series of p^+/N GaAs- $\text{Al}_x\text{Ga}_{1-x}\text{As}$ heterostructures were grown and the electrical properties of the heterojunctions evaluated from the ideality factor of the heterojunction I - V characteristics. The variable growth parameters were the aluminium composition (x) of the $\text{Al}_x\text{Ga}_{1-x}\text{As}$ layer and the width of an undoped GaAs spacer layer (Δs) inserted between p^+ -GaAs and n - $\text{Al}_x\text{Ga}_{1-x}\text{As}$ layers. The specifications and SIMS profile (for $x = 0.23$ and $\Delta s = 10$ nm) of the p^+/N GaAs- $\text{Al}_x\text{Ga}_{1-x}\text{As}$ heterostructures are shown in figs. 3a and 3b, respectively. The SIMS data shows that the carbon profile of the p^+ -GaAs layer ($1.3 \times 10^{20} \text{ cm}^{-3}$) is very abrupt, falling to the background carbon level of the adjacent $\text{Al}_{0.23}\text{Ga}_{0.77}\text{As}$ layer within about 25 nm. This result confirms the previous reports on the extremely small diffusion constant of carbon in GaAs at high doping level [11]. It can be seen that the carbon concentration is higher than that of Si in the $\text{Al}_{0.23}\text{Ga}_{0.77}\text{As}$ layer. This would suggest that the AlGaAs should be p -type. However, as we have previously reported [12], the background carbon in AlGaAs epilayers grown by GSMBE is not 100% electrically active and, for example, when SIMS data from an undoped AlGaAs layer show a back-

ground carbon concentration of $1 \times 10^{18} \text{ cm}^{-3}$, the C - V data from the same epilayer reveal a hole concentration of only $1 \times 10^{17} \text{ cm}^{-3}$. In the case of these p^+/N heterostructures, C - V measurements were used to confirm that the AlGaAs layers were n -type having electron densities of $5 \times 10^{17} \text{ cm}^{-3}$.

Fig. 4a shows the typical I - V characteristics of the p^+/N GaAs- $\text{Al}_x\text{Ga}_{1-x}\text{As}$ heterostructures grown in this study. The characteristics are of a p^+/N GaAs- $\text{Al}_{0.23}\text{Ga}_{0.77}\text{As}$ heterostructure having a spacer layer width of 10 nm. The ideality factors (η) of the heterojunctions were determined from such I - V data and fig. 4b shows the variation of η with Al mole fraction (x) and spacer layer width (Δs) of all the heterostructures grown. A value of 1.17 was obtained for $x = 0.23$ and $\Delta s = 20$ nm. It can be seen that η is relatively insensitive to the spacer layer width, but that it has a more pronounced dependence on x . Further investigations are now underway in order to explain the observed increase in the magnitude of η with increasing aluminium mole fraction, with particular emphasis on the role of recombination centres in the vicinity of the heterojunction depletion region.

The very encouraging ideality factor results of the p^+/N GaAs-AlGaAs heterostructures indicate that TMG and uncracked Si_2H_6 are practical alternatives to conventional solid dopant sources for the growth of such structures by GSMBE. These results are very promising for the potential

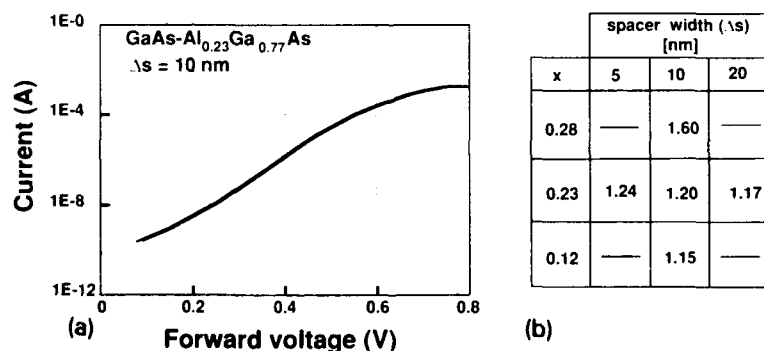


Fig. 4. (a) The I - V characteristics of a p^+/N GaAs- $\text{Al}_{0.23}\text{Ga}_{0.77}\text{As}$ heterostructure ($\Delta s = 10$ nm). (b) The variation of the ideality factor (η) with Al mole fraction (x) and spacer layer width (Δs) of all the heterostructures investigated.

realization of high performance HBT structures by this growth method.

4. Conclusion

We reported on the first growth of p^+/N GaAs-Al_xGa_{1-x}As heterostructures using all gaseous sources by GSMBE. The current-voltage ideality factor of the heterojunctions was found to depend on the aluminium mole fraction of the Al_xGa_{1-x}As layer and spacer layer width. A value of 1.17 was obtained for a heterostructure with $x = 0.23$ and $\Delta x = 20$ nm.

These results will have significant implications for the successful realization of devices such as GaAs/AlGaAs heterojunction bipolar transistors by GSMBE.

Acknowledgements

The authors would like to thank Miss K. Okada, Mr. Y. Yamaguchi and Mr. T. Kurihara for technical assistance and Dr. O. Otsuki for encouragement during this work.

References

- [1] M.B. Panish, J. Electrochem. Soc. 127 (1980) 2729.
- [2] E. Veuhoff, W. Pletschen, P. Balk and H. Lüth, J. Crystal Growth 55 (1981) 30.
- [3] N. Vojdani, A. Lemarch and H. Paradan, J. Physique Colloq. 43 (1982) C5-339.
- [4] W.T. Tsang, J. Crystal Growth 105 (1990) 1.
- [5] P.J. Skevington, D.A. Andrews and G.J. Davies, Appl. Phys. Letters 56 (1990) 1546.
- [6] A. Sandhu, T. Fujii, H. Ando and H. Ishikawa, Japan. J. Appl. Phys. 29 (1990) L1033.
- [7] H. Ishikawa, H. Ando, K. Kondo, A. Sandhu, E. Miyauchi, T. Fujii and S. Hiyamizu, J. Vacuum Sci. Technol. A8 (1990) 805.
- [8] J.D. Wiley, in: Semiconductors and Semimetals, Vol. 10, Eds. R.K. Willardson and A.R. Beer (Academic Press, New York, 1975) p. 154.
- [9] K. Saito, E. Tokumitsu, T. Akatsuka, M. Miyauchi, T. Yamada, M. Konagai and K. Takahashi, in: Proc. 15th Intern. Symp. on GaAs and Related Compounds, Atlanta, GA, 1988, Inst. Phys. Conf. Ser. 96, Ed. J.S. Harris (Inst. Phys., London-Bristol, 1989) p. 69.
- [10] T.F. Kuech, E. Veuhoff and B.S. Meyerson, J. Crystal Growth 68 (1984) 48.
- [11] C.R. Abernathy, S.J. Pearton and A.S. Jordan, Appl. Phys. Letters 56 (1990) 1251.
- [12] H. Ando, A. Sandhu, H. Ishikawa, Y. Sugiyama and T. Fujii, in: Proc. 16th Intern. Symp. on GaAs and Related Compounds, Karuizawa, 1989, Inst. Phys. Conf. Ser. 106, Eds. T. Ikoma and H. Watanabe (Inst. Phys., London-Bristol, 1990) p. 217.

Use of CCl_4 and CHCl_3 in gas source molecular beam epitaxy for carbon doping of GaAs and $\text{Ga}_x\text{In}_{1-x}\text{P}$

T.J. de Lyon, N.I. Buchan, P.D. Kirchner, J.M. Woodall, D.T. McInturff, G.J. Scilla and F. Cardone

IBM Research Division, Thomas J. Watson Research Center, P.O. Box 218, Yorktown Heights, New York 10598, USA

Carbon tetrachloride (CCl_4) and chloroform (CHCl_3) have been studied as carbon doping sources for the compound semiconductors GaAs, GaP, InP, and $\text{Ga}_{0.51}\text{In}_{0.49}\text{P}$ grown by gas source MBE from elemental Group III sources and thermally cracked Group V hydride sources. Hole concentrations up to $1.3 \times 10^{20} \text{ cm}^{-3}$ have been measured by Hall effect in CCl_4 -doped GaAs, which agrees closely with the atomic C concentration from secondary ion mass spectrometry, indicating complete electrical activity of the incorporated carbon. For comparable dopant flow rates, use of CHCl_3 results in carbon and hole concentrations approximately a factor of 15 lower than that from CCl_4 . The sensitivity of carbon incorporation to varying substrate temperature and V/III ratio has been observed to be significantly reduced with CCl_4 and CHCl_3 from that obtained under similar growth conditions with trimethylgallium (TMG) in metalorganic MBE (MOMBE). The GaAs growth rate is unaffected by the CCl_4 flux over the range of CCl_4 flow investigated. CCl_4 has also been successfully employed as a carbon doping source for GaP, with a hole concentration of $1 \times 10^{20} \text{ cm}^{-3}$ achieved for growth at 600°C . Films of $\text{Ga}_{0.51}\text{In}_{0.49}\text{P}$ grown at 515°C exhibit only marginal p-type conductivity with $\rho = 5 \times 10^{16} \text{ cm}^{-3}$ when doped with CCl_4 , despite an incorporated atomic concentration of $[\text{C}] = 5 \times 10^{19} \text{ cm}^{-3}$. Films of InP grown at 515°C are n-type with $n = 9 \times 10^{17} \text{ cm}^{-3}$ despite substantial incorporated carbon equal to $1 \times 10^{20} \text{ cm}^{-3}$.

1. Introduction

The use of carbon as an intentional p-type dopant species for films of GaAs and $\text{Al}_x\text{Ga}_{1-x}\text{As}$ has recently become a topic of great interest because of the extremely high substitutional concentration that can be achieved, with doping in excess of $1 \times 10^{19} \text{ cm}^{-3}$ having been demonstrated by organometallic vapor phase epitaxy (OMVPE) [1,2] and beyond $1 \times 10^{21} \text{ cm}^{-3}$ in the case of metalorganic molecular beam epitaxy (MOMBE) [3]. Such high levels of carbon doping facilitate the formation of ohmic contacts to p-type GaAs and $\text{Al}_x\text{Ga}_{1-x}\text{As}$ layers and minimize the parasitic sheet and bulk resistances associated with p-type layers in device structures such as the Npn heterojunction bipolar transistor. Just as important as the high doping level achievable with carbon doping sources is the extremely low diffusion coefficient [1] of carbon relative to other p-type doping species such as beryllium, magnesium, and zinc.

CCl_4 has recently been studied as a carbon doping source for GaAs grown by OMVPE [2,4]. Similar investigations in the case of MBE have not yet been undertaken. Carbon doping in MBE has thus far been limited to studies utilizing either a graphite filament source [5] in conventional solid source MBE or trimethylgallium (TMG) in metalorganic MBE (MOMBE) [6]. Likewise, very little work has been reported to date on the incorporation and electrical activity of high concentrations of carbon in III–V compound semiconductors other than GaAs [7,8]. Because of their visible emission spectrum, GaP and $\text{Ga}_{0.51}\text{In}_{0.49}\text{P}$ are important semiconductor materials for optical devices such as light-emitting diodes and laser diodes. It is of interest, therefore, to investigate the possibility of extending the usefulness of carbon as a dopant species beyond $\text{Al}_x\text{Ga}_{1-x}\text{As}$ to other related III–V optoelectronic materials. In this paper, we report on the first use of CCl_4 and the related halomethane, CHCl_3 , as carbon doping

sources for the MBE growth of GaAs, GaP, InP, and $\text{Ga}_{0.51}\text{In}_{0.49}\text{P}$ (GaInP).

2. Experimental details

All epitaxial films reported in this study were grown in a Varian Gen II Modular Gas Source MBE system. Pure PH_3 (99.9992% purity) and AsH_3 (99.9995% purity) were thermally cracked in a low pressure cracking furnace operated in the range 850–950°C. Elemental Ga and In sources in conventional MBE Knudsen cells were utilized for the growth of all films doped with CCl_4 or CHCl_3 . For comparison, GaAs films were also grown with TMG, in which case the TMG was transported by palladium-purified hydrogen carrier gas metered with mass flow controllers. Electronic grade CCl_4 and CHCl_3 were transported from temperature-controlled stainless steel bubblers with a hydrogen carrier gas during the doping experiments. The growth rates of all epilayers were in the range of 0.65–1.0 μ/h . Substrate heating of the GaAs and InP substrates was accomplished radiatively, while GaP substrates were bonded with In/Ga eutectic solder to molybdenum blocks. After ex situ chemical cleaning, the substrates were thermally cleaned in the growth chamber at 620°C (GaAs), 550°C (InP), or 650°C (GaP) under the appropriate Group V flux. During epilayer growth, the chamber pressure was in the range $(1-7) \times 10^{-5}$ T.

For characterization of the carbon incorporation, Hall effect and secondary ion mass spectrometry (SIMS) measurements were performed. For calibration of the SIMS measurements, ^{12}C -implanted standards of GaAs, GaP, InP, and GaInP were utilized. The SIMS characterizations of the samples were performed in a Cameca IMS 3f instrument, using Cs^+ ion bombardment at 10 kV with negative secondary ion detection of the $^{12}\text{C}^-$ ion. The $^{12}\text{C}^-$ background signal corresponded to a carbon concentration of about $(1-2) \times 10^{17} \text{ cm}^{-3}$. Double crystal X-ray diffraction measurements were made to confirm lattice-matching of the GaInP films to the GaAs substrates with mismatch less than 2×10^{-3} .

For computation of the actual halomethane

flow delivered to the growth chamber, the Antoine equations for the temperature dependence of the vapor pressures of CCl_4 and CHCl_3 were used [9].

3. Results and discussion

3.1. GaAs growth

Films of GaAs doped with either CCl_4 or CHCl_3 exhibit 100% electrical activation of the carbon dopant over the concentration range of 10^{18} – 10^{20} cm^{-3} . The dependence of SIMS carbon concentration on dopant flow rate is summarized in fig. 1. With both doping sources, the atomic carbon concentration varies in a well-controlled, linear fashion with dopant flow. The CCl_4 curve shows slight saturation as the atomic carbon concentration reaches $2 \times 10^{20} \text{ cm}^{-3}$. In addition, the surface morphology and hole mobilities are significantly degraded for CCl_4 flow beyond about 4 SCCM corresponding to a hole concentration of $1.5 \times 10^{20} \text{ cm}^{-3}$. For comparable dopant flow rates, CCl_4 appears to be a more efficient doping source than CHCl_3 by about a factor of 15, which is similar to the result obtained in OMVPE [9].

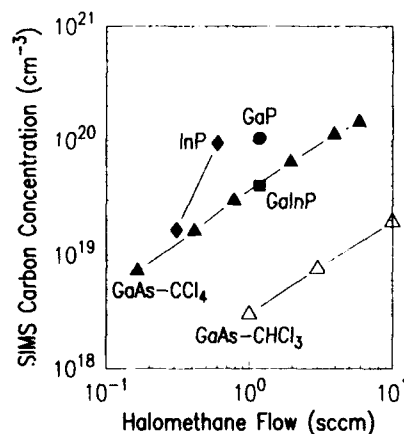


Fig. 1. SIMS carbon incorporation for CCl_4 in GaAs (\blacktriangle), GaP (\bullet), InP (\blacklozenge), and $\text{Ga}_{0.51}\text{In}_{0.49}\text{P}$ (\blacksquare), and for CHCl_3 in GaAs (\triangle) as a function of the dopant flow rate. The dopant flow rates have been determined from carrier gas flow rates using vapor pressure data [9] and the carbon concentrations have been scaled for a common growth rate of 1.0 $\mu\text{m/h}$.

It should be noted that neither CCl_4 nor CHCl_3 affected the GaAs growth rate over the doping range displayed in fig. 1. Direct control of doping levels with dopant flow rate and the decoupling of doping level from growth rate are advantages of these doping sources with respect to either TMG or triethylgallium (TEG). With TMG and TEG, variations in growth parameters such as precursor flow rate, substrate temperature, or V/III ratio that might be utilized to control carbon incorporation also have the undesirable effect of significantly perturbing the growth rate [10,11], thus complicating control of the epitaxial process. With CCl_4 and CHCl_3 , the doping level can be changed simply by changing the hydrogen carrier gas flow without affecting the GaAs growth rate, which is determined solely by the Ga arrival rate.

The carbon doping from CCl_4 and CHCl_3 is much less sensitive to variation in substrate temperature during growth than that associated with either TMG/ AsH_3 or TMG/ As_4 . Fig. 2 is a direct comparison of the growth temperature dependences of atomic carbon concentration for these sources with a fixed AsH_3 flow of 3 SCCM. The carbon incorporation from $\text{CCl}_4/\text{AsH}_3$ is a factor of 2–3.5 above that achieved with TMG/ AsH_3 and increases at higher growth temperature, in contrast to the decrease in carbon concentration observed for TMG with increasing growth temperature. The level of carbon incorporation is determined by the competition between decomposition and desorption processes involving adsorbed CH_x (TMG doping) and CCl_x (CCl_4 or CHCl_3 doping) species. Higher growth temperatures would tend to enhance both the decomposition and desorption rates of surface-adsorbed CH_x and CCl_x , so that the temperature dependence of the incorporated carbon would be determined by the relative magnitudes of the activation energies (E_A) for these two processes. If the value of E_A for surface decomposition is higher than that for desorption, then the carbon level would increase with increasing growth temperature, as in the case of CCl_4 doping. The temperature dependence of carbon incorporation from TMG/ AsH_3 suggests that the activation energy for desorption of surface-adsorbed CH_x is higher than that for decomposition over the temperature range of 520–

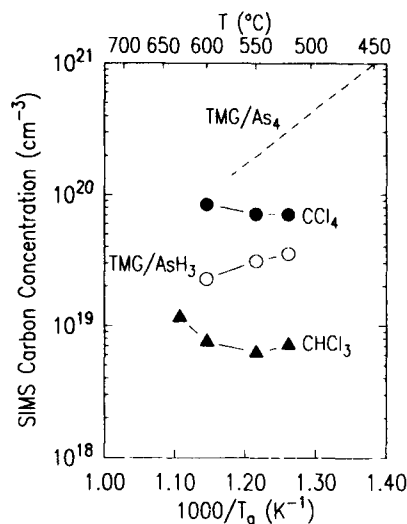


Fig. 2. Growth temperature dependence of the SIMS carbon concentration in GaAs doped with various precursors. The data for TMG/ As_4 are taken from ref. [3]. The AsH_3 , CCl_4 , and CHCl_3 flow rates are each fixed at 3 SCCM and the growth rate is $1 \mu\text{m/h}$.

600°C. It can be concluded that replacing CH_x surface species with more weakly bound CCl_x species allows surface decomposition to more effectively compete with desorption as the temperature increases. This property of Cl ligands suggests that CCl_4 is to be preferred over TMG as a dopant source in situations requiring heavy carbon doping at growth temperatures greater than 600°C.

Sequential replacement of strongly bound H ligands ($\sim 104 \text{ kcal/mol}$) with weakly bound Cl ligands ($\sim 78 \text{ kcal/mol}$ [12]) in the halomethane precursor affects not only the temperature dependence of carbon incorporation, but also the efficiency of the doping source, which is evident in the data for CCl_4 and CHCl_3 in fig. 1. Decomposition is expected to occur more rapidly in the more highly substituted halomethane, leading to increased carbon incorporation efficiency. A similar trend has been reported in OMPVE [9]. Controlled p-type doping at levels below $1 \times 10^{19} \text{ cm}^{-3}$ might then be obtained by utilizing halomethanes with fewer replacement halogen atoms, such as CH_3Cl or CH_2Cl_2 .

In order to achieve the very highest levels of carbon incorporation with TMG, i.e., approaching $1 \times 10^{21} \text{ cm}^{-3}$, As_4 rather than cracked AsH_3 is usually employed [3], although a high doping level of $5 \times 10^{20} \text{ cm}^{-3}$ has also been reported for GaAs grown at $1.8 \mu\text{m/h}$ with TMG/ AsH_3 [13]. In addition, He is generally used as a carrier gas for the TMG rather than H_2 , and the growth temperature must be reduced below 550°C . As we have been unable to achieve this level of carbon doping with CCl_4 due to degradation in layer morphology, TMG continues to be the only available doping system for applications requiring extremely high carbon doping beyond $2 \times 10^{20} \text{ cm}^{-3}$.

In addition to its favorable temperature dependence, CCl_4 is also less sensitive as a dopant source to V/III ratio than is TMG. Fig. 3 compares the dependence of carbon incorporation on AsH_3 flow rate for films grown with CCl_4 , CHCl_3 , and TMG at 600°C . While the carbon incorporation varies inverse linearly with AsH_3 flow rate for the TMG case, the carbon incorporation from CCl_4 and CHCl_3 is approximately inversely proportional to the square root of the AsH_3 flow rate. This behavior of CCl_4 and CHCl_3 in GSMBE differs from that observed in OMVPE [9], in which the carbon incorporation varies with an inverse superlinear dependence on AsH_3 flow. The reason

for the reduced variation of carbon content with AsH_3 flow in GSMBE using halomethanes is not understood at present, although it may be related to differences in the form of the predominant As species employed in the two growth techniques, e.g., As or As_2 in GSMBE versus AsH_3 in OMVPE.

The electrical, optical, and structural properties of heavily carbon-doped films of GaAs grown with CCl_4 appear to be quite similar to those of films grown with TMG. For films with $p = 1 \times 10^{20} \text{ cm}^{-3}$, 300 K Hall mobilities of $60 \text{ cm}^2/\text{V} \cdot \text{s}$ are measured for both CCl_4 and TMG doping. Likewise, the FWHM of epilayer X-ray diffraction peaks are also almost identical for both CCl_4 and TMG at 40–50 arc sec for $1.35\text{-}\mu\text{m}$ -thick films doped at $1.2 \times 10^{20} \text{ cm}^{-3}$. The 300 K photoluminescence peak intensity of layers grown with CCl_4 is within a factor of 2 of that from films comparably doped with TMG. The abruptness of doping turn-on and turn-off is estimated to be less than $150\text{--}200 \text{ \AA/decade}$ for both CCl_4 and TMG, corresponding to the depth resolution limit of SIMS analyses.

The potential for Cl contamination of epilayers must be considered with chloromethane doping sources. SIMS measurements indicate that the Cl content of films grown with either CCl_4 or CHCl_3 is below the SIMS detection limit of $1 \times 10^{16} \text{ cm}^{-3}$.

3.2. GaP growth

We have previously demonstrated that TMG can be used to carbon-dope GaP in a manner similar to GaAs [8]. In this present study, CCl_4 has also been successfully applied to carbon-dope GaP films grown with elemental Ga and thermally cracked PH_3 . At a growth temperature of 600°C , a growth rate of $0.65 \mu\text{m/h}$, and with 4 SCCM of PH_3 , a hole concentration of $1 \times 10^{20} \text{ cm}^{-3}$ and a 300 K hole mobility of $25 \text{ cm}^2/\text{V} \cdot \text{s}$ have been measured for a CCl_4 flow of 1.2 SCCM. The doping efficiency of CCl_4 in GaP is only slightly higher than that observed in GaAs under similar growth conditions (see the GaP data point in fig. 1), suggesting that the carbon incorporation from CCl_4 is relatively insensitive to differences in

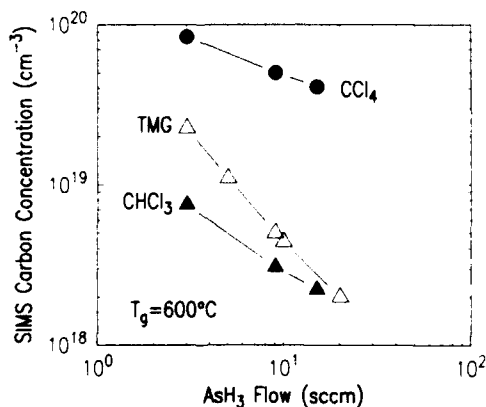


Fig. 3. Variation of SIMS carbon concentration with AsH_3 flow rate in GaAs doped with various precursors at a growth temperature of 600°C . The CCl_4 and CHCl_3 flow rates are each 3 SCCM, and the growth rate is $1 \mu\text{m/h}$.

surface chemistry associated with the different Group V species, PH_3 and AsH_3 .

3.3. GaInP growth

Previous attempts to carbon-dope $\text{Ga}_{0.51}\text{In}_{0.49}\text{P}$ by using TMG and elemental In in MOMBE have been unsuccessful [8]. At a high growth temperature of 560°C , carbon incorporation in $\text{Ga}_{0.51}\text{In}_{0.49}\text{P}$ is reduced by the presence of In in the films, with the carbon concentration dropping by 1 decade for each 1.5% increase of InP mole fraction above 5%. At a lower growth temperature of 500°C , TMG results in $5 \times 10^{18} \text{ cm}^{-3}$ carbon incorporation, but the $\text{Ga}_{0.51}\text{In}_{0.49}\text{P}$ films are generally n-type with $n = 2 \times 10^{17} \text{ cm}^{-3}$. An even higher concentration of carbon can be incorporated in GaInP from CCl_4 than has been possible thus far with either TMG or TEG, as indicated by the datum for $\text{Ga}_{0.51}\text{In}_{0.49}\text{P}$ in fig. 1 at a growth temperature of 515°C . Despite this atomic carbon concentration of $5 \times 10^{19} \text{ cm}^{-3}$, however, Hall effect measurements indicated a hole concentration of only $5 \times 10^{16} \text{ cm}^{-3}$. We have not been able to determine whether the low carrier concentrations in GaInP doped with either TMG or CCl_4 are due to nonsubstitutionality of carbon, self-compensation by occupation of both Group III and Group V sublattice sites, and/or compensation by electrically active native defects. In summary, even though CCl_4 can carbon-dope $\text{Ga}_{0.51}\text{In}_{0.49}\text{P}$ an order of magnitude more heavily than TMG, the resulting p-type conductivity is too marginal at present to be of practical utility.

3.4. InP growth

CCl_4 has not heretofore been studied as a doping source for InP grown by GSMBE. When used in OMVPE in the temperature range of 580 – 630°C , CCl_4 has been shown to fail to incorporate any measurable amount of carbon [14]. In contrast, the data for InP in fig. 1 suggest that in GSMBE, CCl_4 incorporates at least as efficiently in InP grown at 515°C as in GaAs grown at 600°C . Even with $[\text{C}] = 1 \times 10^{20} \text{ cm}^{-3}$, however, the InP epilayer is n-type with $n = 9 \times 10^{17} \text{ cm}^{-3}$

and a low 77 K Hall mobility of $740 \text{ cm}^2/\text{V} \cdot \text{s}$. By comparison, a nominally undoped InP epilayer grown in our system typically has a measured 77 K mobility of $2650 \text{ cm}^2/\text{V} \cdot \text{s}$ at an electron concentration of $3.2 \times 10^{17} \text{ cm}^{-3}$. If these 77 K mobilities are primarily determined by ionized impurity scattering, then this result suggests that the carbon is self-compensating in InP grown by GSMBE. The closeness of the compensation might be an indication of a C–C pairing mechanism, although further work is clearly necessary to clarify the behavior of carbon in epitaxial InP. This work has demonstrated, though, that the use of CCl_4 in GSMBE is the only available epitaxial technique for incorporating a substantial carbon concentration in InP, which should facilitate future studies of carbon electrical activity in InP.

4. Conclusions

CCl_4 and CHCl_3 have been demonstrated to be useful p-type dopant sources for carbon doping of GaAs and GaP grown by GSMBE. At comparable dopant flow rates, CCl_4 is about 15 times more efficient as a carbon doping source for GaAs than CHCl_3 . In comparison with TMG, CCl_4 and CHCl_3 result in carbon doping that is less sensitive to variation in substrate temperature and V/III ratio, and in addition allow for control of the carbon doping level independent of growth rate. For doping in excess of $2 \times 10^{20} \text{ cm}^{-3}$, TMG must still be used, but for doping around $1 \times 10^{20} \text{ cm}^{-3}$ at high growth temperatures ($> 550^\circ\text{C}$) and high V/III ratios with AsH_3 , CCl_4 can be used to obtain substantially higher carbon doping than is possible with TMG/ AsH_3 under similar growth conditions.

The CCl_4 doping results in GaAs extend readily to GaP, with $1 \times 10^{20} \text{ cm}^{-3}$ doping achievable using elemental Ga and cracked PH_3 . In $\text{Ga}_{0.51}\text{In}_{0.49}\text{P}$ and InP, however, CCl_4 does not result in high levels of p-type conductivity, in spite of extremely high levels of incorporated atomic carbon. The exact cause of the poor electrical activity of carbon in these In-containing compounds is currently not understood.

Acknowledgements

The authors wish to thank H. Hovel and D.K. Sadana for providing the carbon and chlorine-implemented SIMS standards and M.S. Goorsky for assistance with X-ray diffraction measurements and analysis.

References

- [1] T.F. Kuech, M.A. Tischler, P.-J. Wang, G. Scilla, R. Potemski and F. Cardone, *Appl. Phys. Letters* 53 (1988) 1317.
- [2] B.T. Cunningham, M.A. Haase, M.J. McCollum, J.F. Baker and G.E. Stillman, *Appl. Phys. Letters* 54 (1989) 1905.
- [3] M. Konagai, T. Yamada, T. Akatsuka, K. Saito, E. Tokumitsu and K. Takahashi, *J. Crystal Growth* 98 (1989) 167.
- [4] N.I. Buchan, T.F. Kuech, G. Scilla, F. Cardone and R. Potemski, *J. Electron. Mater.* 19 (1990) 277.
- [5] R.J. Malik, R.N. Nottenburg, E.F. Schuber, J.F. Walker and R.W. Ryan, *Appl. Phys. Letters* 53 (1988) 2661.
- [6] E. Tokumitsu, Y. Kudou, M. Konagai and K. Takahashi, *J. Appl. Phys.* 55 (1984) 3163.
- [7] M. Kamp, R. Contini, K. Werner, H. Heinecke, M. Wevers, H. Lüth and P. Balk, *J. Crystal Growth* 95 (1989) 154.
- [8] T.J. de Lyon, J.M. Woodall, P.D. Kirchner, D.T. McInturff, G.J. Scilla and F. Cardone, *J. Vacuum Sci. Technol. B*, in press.
- [9] N.I. Buchan, T.F. Kuech, G. Scilla, and F. Cardone, *J. Crystal Growth* 110 (1991) 405; see also T. Boublik, V. Fried and E. Hala, *The Vapour Pressures of Pure Substances* (Elsevier, Amsterdam, 1984).
- [10] M. Uneta, Y. Watanabe and Y. Ohmachi, *Appl. Phys. Letters* 54 (1989) 2327.
- [11] T.H. Chiu, J.E. Cunningham, J.A. Ditzenberger and W.Y. Jan, *Appl. Phys. Letters* 57 (1990) 171.
- [12] S.W. Benson, *Thermochemical Kinetics* (Wiley-Interscience, New York, 1976) pp. 288–297.
- [13] C.R. Abernathy, S.J. Pearton, F. Ren, W.S. Hobson, T.R. Fullowan, A. Katz, A.S. Jordan and J. Kovalchick, *J. Crystal Growth* 105 (1990) 375.
- [14] B.T. Cunningham, J.F. Baker, S.A. Stockman and G.E. Stillman, *Appl. Phys. Letters* 56 (1990) 1760.

In-situ selective-area epitaxy of GaAs using a GaAs oxide layer as a mask

Y. Hiratani, Y. Ohki, Y. Sugimoto and K. Akita

Optoelectronics Technology Research Laboratory, 5-5 Tohkodai, Tsukuba, Ibaraki 300-26, Japan

Selective-area epitaxy of GaAs was performed by metalorganic molecular beam epitaxy using a GaAs oxide mask. No deposition of polycrystalline GaAs was observed on a GaAs oxide mask after the selective-area epitaxy using a trimethylgallium (TMG) and As_4 as source materials. An observation of the decomposition of TMG indicated that it occurred above 350°C on an oxide-free surface of GaAs, while decomposition did not occur below 550°C on a GaAs oxide surface. This surface-catalyzed decomposition of TMG explains the selectivity of GaAs growth.

1. Introduction

The selective-area epitaxy of a III–V compound semiconductor is one of the promising techniques for the fabrication of devices with new structures, such as quantum wires or quantum boxes. In conventional selective-area epitaxy, the surface of the wafer was often contaminated by air exposure. It is well known that contamination of the surface and interface degrades the characteristics of the devices. Then, there has been increasing interest concerning in-situ selective-area epitaxy aimed at eliminating contamination of a wafer surface. Here, “in-situ” means that all of the required processes are performed continuously in an ultra-high vacuum (UHV) or in a high-purity gas without exposing the wafer to air.

To realize in-situ selective-area epitaxy, the following processes have to be carried out without exposing the wafer to air. They are (i) the formation of a mask layer, (ii) patterning of the mask and (iii) removal of any residual mask for overgrowth. In conventional selective-area epitaxy of GaAs, a thin film of SiO_2 [1] or SiN_x [2] is widely used as the mask. However, those mask materials do not meet the conditions of (ii) patterning and (iii) removal of those material without exposing the wafer to air.

Regarding the patterning and the removal of a mask, GaAs oxide is one of the promising mask materials. Since the GaAs oxide layer can be patterned using an electron-beam-assisted chlorine etching (EB etching) technique [3], the GaAs oxide layer can be removed by heating a wafer under an arsenic flux [4].

There have been several reports [5,6] on selective-area epitaxy combining a GaAs oxide mask with molecular beam epitaxy (MBE) [5] or an atmospheric metalorganic chemical vapor deposition (MOCVD) [6] method. In those studies, polycrystalline GaAs was deposited on the GaAs oxide layer. Since the deposited polycrystalline GaAs prevents the removal of the GaAs oxide layer, the deposition must be suppressed. On the other hand, no deposition of polycrystalline GaAs on the SiO_2 mask was reported [1] using metal organic molecular beam epitaxy (MOMBE). Therefore, a combination of GaAs oxide mask and the MOMBE method is expected to be helpful for the in-situ selective-area epitaxy of GaAs.

In this paper, we report on selective-area epitaxy of GaAs combining MOMBE and a GaAs oxide mask. In terms of the results of mass spectrometric measurements on the decomposition of the source material, the mechanism of the selective area epitaxy is discussed.

2. Experimental apparatus

A MOMBE system [7] and an EB etching system [3] were used for this experiment. The formation of a GaAs oxide layer and the growth of GaAs were carried out using the MOMBE system modified by adding an oxygen-supply line and a halogen-lamp unit. The patterning of the GaAs oxide layer was performed in the EB etching system.

To study the mechanism of selective-area epitaxy, an apertured, cryoshrouded quadrupole mass spectrometer [7] (QMS) and reflection high-energy electron diffraction (RHEED), attached the MOMBE system, were used.

3. Results and discussion

3.1. In-situ selective-area epitaxy of GaAs

An n-type (100) GaAs wafer was used as the substrates. The wafer was cleaned at 600–630°C under an arsenic (As_4) flux in the MOMBE system. Then, a GaAs oxide layer was formed on the wafer by light irradiation from a halogen lamp under oxygen atmosphere. The oxidation conditions were fixed as follows: the oxygen pressure was 1×10^{-1} Pa, the oxidation time was 15 min and the power density of the light was 2.0 W/cm^2 at the surface of the substrate. The thickness of

the formed oxide layer was about 3 nm (measured using ellipsometry).

The wafer was then removed from the MOMBE system, and was loaded into the EB etching system. A rectangular window ($20 \times 300 \mu\text{m}^2$) was opened on the GaAs oxide layer by scanning a 10 keV electron beam under Cl_2 flux. The etching conditions were as follows: the substrate temperature was 70°C, the electron dose was 3.8×10^{16} electrons/ cm^2 and the Cl_2 flux density was 7×10^{16} molecules/ $\text{cm}^2 \cdot \text{s}$.

The patterned wafer was transferred from the EB etching system to the MOMBE system (within 2 min). Selective-area growth of GaAs was carried out at 450°C by simultaneous (or alternating) source supply mode. Trimethylgallium (TMG) and As_4 were used as source materials. The beam equivalent pressures of TMG and As_4 were 4×10^{-6} and 1×10^{-4} Pa, respectively.

Fig. 1a shows a Nomarski microphotograph of the wafer surface after selective-area epitaxy performed by alternating the source supply mode. The supply duration of TMG and As_4 were 50 and 30 s, respectively. The sequence for the source supply was repeated 270 times. The rectangular area corresponds to the window of the GaAs oxide layer. No deposition of polycrystalline GaAs was observed on the oxide layer. Fig. 1b shows a cross sectional profile of the wafer shown in fig. 1a. It was measured using a stylus profilometer.

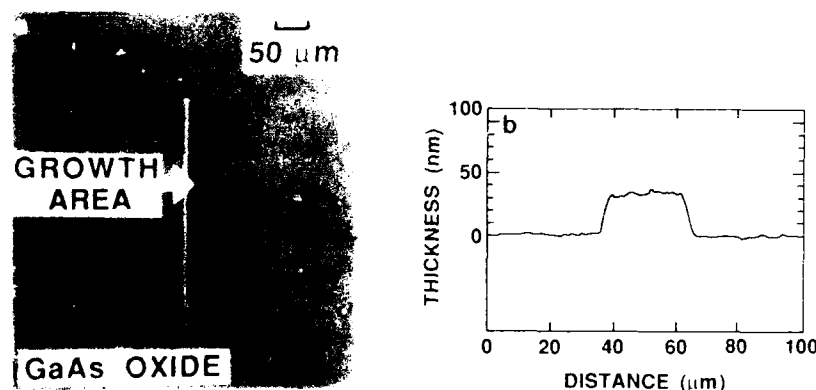


Fig. 1. Surface morphology and cross-sectional profile of the wafer after selective-area epitaxy of GaAs. (a) Nomarski microphotograph of the selectively grown GaAs layer. The rectangular area corresponds to the window of the GaAs oxide layer. (b) Cross-sectional profile of the wafer shown in (a).

The measured thickness of the selectively grown GaAs layer was about 30 nm.

The same selectivity of GaAs growth was observed in selective-area epitaxy performed by a simultaneous source supply mode.

The results of this experiment concerning selective-area epitaxy demonstrate the possibility of an in-situ process from the formation of a mask film to overgrowth, followed by selective-area epitaxy.

3.2. Mechanism of selective-area epitaxy of GaAs

The mechanism of the selective-area epitaxy of GaAs was studied by measuring the desorbed species under a TMG (or TMG + As₄) flux using mass spectrometry. The study was carried out on two types of surfaces: one was the surface of a GaAs oxide layer and the other was a (2 × 4) reconstructed surface which simulated the window of the mask. A GaAs oxide layer was formed on a (100) GaAs wafer (5 cm in diameter) under the same conditions as the mask formation for the selective-area epitaxy. The (2 × 4) reconstructed surface was prepared by heating the substrate at 600–630°C under an As₄ flux.

Under a TMG (or TMG + As₄) flux, the substrate was heated from 150 to 550°C at a rate of 10°C/min. The intensity of Ga⁺ and dimethylgallium (DMG⁺) was measured as a function of substrate temperature using an apertured,

cryoshrouded QMS. The flux densities of TMG and As₄ were fixed at 4×10^{-6} and 1×10^{-4} Pa, respectively.

The temperature dependence of the signal intensity of Ga⁺ and intensity ratio of DMG⁺/Ga⁺ are shown in fig. 2. When TMG was supplied to the (2 × 4) reconstructed surface (fig. 2a), the ratio of DMG⁺/Ga⁺ was independent of the substrate temperature up to 350°C, and the RHEED pattern showed the structure of (2 × 4). Above 350°C, the intensity of Ga⁺ decreased as the temperature increased. The ratio of DMG⁺/Ga⁺ changed above 350°C. The variation of Ga⁺ and DMG⁺/Ga⁺ indicates that the partially decomposed species desorbed from the substrate. When the changes of Ga⁺ and DMG⁺/Ga⁺ were observed, the RHEED pattern also changed from (2 × 4) to (1 × 2). Under an UHV atmosphere, the (2 × 4) reconstructed surface was maintained up to 500°C in the separate experiment. Thus, the change in the RHEED pattern suggests that the adsorption of a gallium-containing species occurred on the (2 × 4) reconstructed surface above 350°C.

When TMG was supplied to the surface of the GaAs oxide layer (fig. 2b), the ratio DMG⁺/Ga⁺ was independent of the substrate temperature below 550°C. The intensity ratio showed good agreement with that observed in the (2 × 4) reconstructed surface below 350°C. A steep decrease of

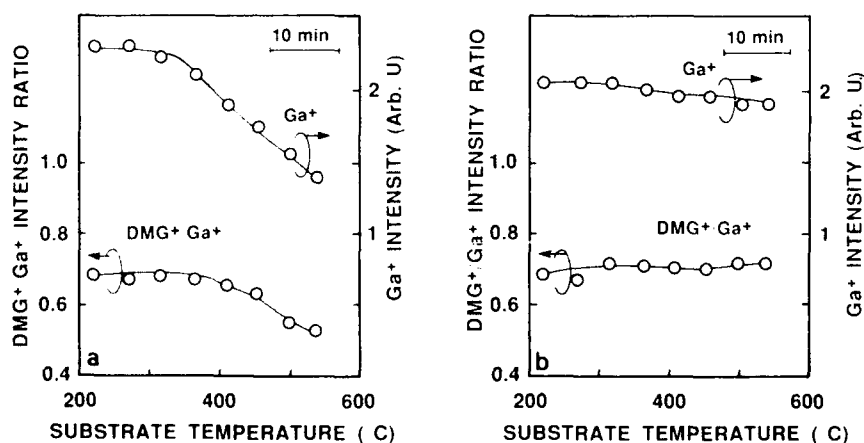


Fig. 2. Variation of QMS signal (the Ga⁺ intensity and DMG⁺/Ga⁺ intensity ratio) versus temperature during heating the substrate at a rate of 10°C/min under TMG flux: (a) on a GaAs substrate with a (2 × 4) reconstructed surface; (b) on the GaAs oxide layer.

intensity in the Ga^+ was not observed within the measured temperature range. The RHEED pattern showed a halo pattern in the temperature range from 150 to 550°C. This means that most of the TMG molecules were reflected from the GaAs oxide layer without any adsorption or decomposition below 550°C.

When TMG and As_4 were supplied simultaneously to the GaAs oxide layer, the Ga^+ intensity, the ratio DMG^+/Ga^+ , and the RHEED pattern were similar to the case of an experiment under TMG flux only. This means that the decomposition of TMG did not occur on the GaAs oxide layer under an As_4 flux.

These experimental results show that the decomposition of TMG did not occur on the GaAs oxide layer below 550°C, even under an As_4 flux. On the other hand, the decomposition occurred on the oxide-free surface of GaAs above 350°C. Thus, the oxide-free surface (such as the (2×4) reconstructed surface) of GaAs acted as a catalyst for the decomposition of TMG. The surface-catalyzed decomposition of TMG explains the mechanism for the selective-area epitaxy of GaAs at 450°C.

4. Summary

The possibility of *in-situ* selective-area epitaxy was demonstrated by combining a GaAs oxide mask and the MOMBE method. GaAs was grown selectively on the window of a GaAs oxide mask without any deposition of polycrystalline GaAs on the GaAs oxide layer. Mass spectrometric measurements of the decomposition of TMG on the

substrate surface revealed that TMG molecules were reflected from the GaAs oxide surface without any decomposition below 550°C. On the other hand, the decomposition of TMG was observed above 350°C on a GaAs surface. The surface-catalyzed decomposition of TMG can explain the mechanism of the selective area epitaxy of GaAs. The combination of a GaAs oxide mask, MOMBE and EB etching [3] will provide a continuous process of crystal growth and selective etching under UHV conditions.

Acknowledgements

The authors would like to thank Mr. M. Taneva and Mr. H. Hidaka for helpful discussions, and Dr. Y. Katayama and Dr. I. Hayashi for valuable discussions and continuous encouragement during this study.

References

- [1] E. Tokumitsu, Y. Kudou, M. Konagai and K. Takahashi, *J. Appl. Phys.* 55 (1984) 3163.
- [2] K. Kamon, S. Takagishi and H. Mori, *J. Crystal Growth* 73 (1985) 73.
- [3] M. Taneva, Y. Sugimoto, H. Hidaka and K. Akita, *Japan. J. Appl. Phys.* 28 (1989) L515.
- [4] J. Saito, K. Nanbu, T. Ishikawa and K. Kondo, *J. Appl. Phys.* 63, (1989) 754.
- [5] G.M. Metze, H.M. Levy, D.W. Woodard, C.E.C. Wood and L.F. Eastman, *Appl. Phys. Letters* 37 (1980) 628.
- [6] S.H. Jones and K.M. Lau, *J. Electrochem. Soc.* 134 (1987) 3149.
- [7] Y. Ohki, Y. Hiratani and M. Yamada, *Japan. J. Appl. Phys.* 28 (1989) L1486.

The roles of aluminum and hydrogen in impurity contamination of AlGaAs grown by MOMBE

C.R. Abernathy, S.J. Pearton

AT&T Bell Laboratories, Murray Hill, New Jersey 07974, USA

D.A. Bohling and G.T. Muhr

Air Products and Chemicals, Inc., Allentown, Pennsylvania 18195, USA

We have investigated the effect of Al in the form of triethylaluminum (TEAl), trimethylamine alane (TMAAl), or elemental Al and hydrogen, bonded to Group III or Group V precursors, on the oxygen and carbon concentrations of AlGaAs grown by metalorganic molecular beam epitaxy (MOMBE). Al was found to increase both the oxygen and carbon incorporation rates relative to GaAs. The primary source of the oxygen has been determined to be alkoxide contamination of the alkyl Group III sources. Similarly, the carbon contamination is due to carbon released from the decomposition of the alkyl Ga sources. For films grown with TEGa, this enhancement of the carbon uptake can be suppressed through the use of TMAAl which releases atomic hydrogen at the growth surface. Hydrogen does not appear to remove carbon generated from methyl radicals, as AlGaAs grown from TMGa exhibits hole concentrations $>10^{19} \text{ cm}^{-3}$, regardless of Al source, which increase with increasing AsH_3/As_2 ratio. We have also determined that increasing the AsH_3/As_2 ratio does not improve the crystallinity of the AlGaAs layers as determined by ion channelling analysis.

1. Introduction

While previous reports have demonstrated the sensitivity of TEGa decomposition to elemental Al [1] and the dramatic increase in carbon concentration which occurs during growth of AlGaAs by MOMBE [2,3], little information has been available regarding the roles of Al and hydrogen in the growth process. We have examined the effect of these elements on the oxygen and carbon incorporation in AlGaAs by comparing various Ga, Al, and As precursors, and by varying the temperature of the AsH_3 cracker. Three different Al sources, elemental Al, triethylaluminum (TEAl), and trimethylamine alane (TMAAl) have been used, as have two different Ga sources, triethylgallium (TEGa) and trimethylgallium (TMGa), so that the effect of the Al can be separated from that of the hydrocarbon side groups.

Hydrogen has been introduced via the Group V species, i.e. by using partially cracked AsH_3 , and via the Group III species by using TMAAl which

contains three Al–H bonds. While the uncracked AsH_3 would be expected to produce only small quantities of hydrogen at the growth surface, due to poor cracking efficiencies at the growth temperature, TMAAl should produce significant surface concentrations of hydrogen. Thus, it is possible to determine what effect, if any, these components have on the growth of AlGaAs.

2. Experimental procedure

The samples were grown in a Varian Gas Source Gen II on 2 inch diameter GaAs substrates which received no treatment prior to growth. The TEGa flux was adjusted to give a GaAs growth rate of 0.22 ML/s at 500°C under an AsH_3 flow of 5 SCCM. The TMGa flux was set to give the same growth rate under the same conditions. The TEAl flux was fixed at a rate which yielded an AlAs growth rate of 0.26 ML/s, while the TMAAl flux

was fixed at a rate of 0.24 ML/s. AlGaAs layers were grown using the same Al and Ga fluxes as the binaries. Samples were grown from TEAl first. Then the TEAl bubbler was replaced with a bubbler of TMAAl. No other changes were introduced into the gas handling system. The TMGa was transported by a He carrier gas while the other Ga and Al sources were transported with hydrogen. For both gaseous Al sources, the H_2 flow rate was 20 SCCM. Some layers were grown by replacing the gaseous Al source with elemental Al, generated from a conventional effusion oven, while some samples were grown by a similar replacement of the gaseous Ga source with elemental Ga. The Al and Ga fluxes were set to give approximately the same Al content as the films grown with only gaseous Group III sources. The AsH_3 was cracked in a Varian low pressure cracker whose temperature was varied from 950 to 1100 °C. For layers grown with As_4 , the pressure of the As_4 beam was 2×10^{-5} Torr as measured by the beam flux gauge. Prior to deposition of the AlGaAs, 1000 Å GaAs buffer layers were grown at 500 °C under 5 SCCM of AsH_3 at a rate of 1.2 $\mu\text{m}/\text{h}$.

For samples grown with TMGa, carbon levels were determined from Hall measurements. For those grown with TEGa, the carbon and oxygen concentrations were determined by SIMS using a Cameca IMS 3f system with a Cs^+ beam. The carbon and oxygen concentrations were determined by comparison with ion implanted standards. The thickness and AlAs mole fraction of the AlGaAs films were determined from Rutherford backscattering analysis using 2.120 MeV He^+ ions. The Al mole fraction is determined within ± 0.02 . Ion channeling analysis was used to evaluate the crystalline quality of these films. In particular, the data were used to determine the minimum backscattering yield (χ_{min}), defined as the ratio of the near-surface backscattering count rate measured in a channelled configuration to that measured in a random or non-channelled direction. High-quality, single crystal films have χ_{min} values of 3%–4%, as this is the minimum ratio which can be accurately detected. χ_{min} values above this baseline are measured within an accuracy of $\pm 0.5\%$.

3. Results and discussion

Previous work has shown that replacing TEAl with TMAAl leads to a significant reduction in oxygen in AlGaAs grown by MOMBE due to the elimination of volatile Al–O–C species present in commercially available TEAl [4]. This reduction is reflected in the data of table 1, which shows a decrease of $\sim 80 \times$ in oxygen when TMAAl is used instead of TEAl. However, the residual oxygen concentration is still $\sim 10\text{--}100 \times$ higher than the background normally seen in material grown by conventional MBE. Replacement of the TMAAl with element Al also shows severe oxygen contamination at $7 \times 10^{18} \text{ cm}^{-3}$. This suggests that the oxygen concentration is due to contamination of the TEGa source with Ga alkoxides, which are similar in nature to the Al alkoxides discussed previously. Confirmation of this can be seen in the material grown with elemental Ga which shows an oxygen background, $2 \times 10^{17} \text{ cm}^{-3}$, similar to levels observed in material grown by conventional MBE. Clearly, the Al at the growth surface getters oxygen from the impurities present in the TEGa, as GaAs grown under the same conditions does

Table 1

Oxygen and carbon concentrations as determined by SIMS analysis in AlGaAs grown from various Group III and Group V sources; all samples are grown at 600 °C unless otherwise indicated

Sources	O (cm^{-3})	C (cm^{-3})
TEAl, TEGa, AsH_3 ($X_{Al} = 0.57$)	8×10^{20}	5×10^{18}
TEAl, TEGa, As_4 ($X_{Al} = 0.42$)	$\sim 10^{21}$	5×10^{19}
TMAAl, TEGa, AsH_3 ($X_{Al} = 0.44$)	1×10^{19}	5×10^{17}
TMAAl, TEGa, AsH_3 (500 °C, $X_{Al} = 0.35$)	1.5×10^{18}	$2.5 \times 10^{16, a)}$
TMAAl, TEGa, As_4 ($X_{Al} = 0.42$)	$^{b)}$	$3 \times 10^{16, a)}$
TMAAl, Ga, AsH_3 ($X_{Al} = 0.4$)	2×10^{17}	$3 \times 10^{16, a)}$
TMAAl, Ga, As_4 ($X_{Al} = 0.4$)	2×10^{17}	$1 \times 10^{16, a)}$
Al, TEGa, As_4 ($X_{Al} = 0.33$)	7×10^{18}	1×10^{17}

^{a)} SIMS detection limit.

^{b)} Oxygen concentration not measured.

not show oxygen beyond the detection limit of SIMS. This interaction may also explain the reduction in oxygen with growth temperature in material grown with TMAAl and TEGa. In conventional MBE, decreasing growth temperature tends to increase the oxygen uptake due to reduced desorption of oxygen containing species from the growth surface. In contrast, lower growth temperatures in MOMBE appear to reduce the oxygen level, possibly due to a reduced interaction between the adsorbed Al and Ga-O-C species at the lower temperature.

Al also produces a dramatic increase in carbon concentration. GaAs grown with TEGa typically does not show carbon beyond the detection limit of SIMS. As shown in table 1, AlGaAs grown from TEAl and TEGa shows carbon at least two orders of magnitude higher. Much of the carbon

in these samples is due to incomplete cleavage of the Al-C bond in the parent molecule. However, even when elemental Al is used, the carbon contamination is significantly higher than in GaAs [3]. It appears that Al getters carbon from the TEGa, possibly through the transfer of ethyl or methyl groups from the adsorbed Ga species to the adsorbed Al [3,5,6]. TMAAl suppresses the uptake of carbon even further, yielding carbon levels at the background of SIMS. This reduction is probably due in part to removal of ethyl species from the surface by the atomic hydrogen generated from decomposition of the TMAAl. However, the carbon background does depend somewhat on impurities in the TEGa, as purging of the TEGa bubbler prior to growth is often necessary to produce the lowest carbon levels.

The impurity in the TEGa responsible for the carbon uptake may involve $(\text{CH}_3)_x\text{Ga}$ species. Fig. 1 shows the dramatic increase in carbon in AlGaAs grown with TMGa relative to GaAs grown with the same flux. Clearly, the hydrogen attached to the TMAAl is not effective in removing methyl groups from the surface. Thus, any contamination of the TEGa bubbler with $(\text{CH}_3)_x\text{Ga}$ would lead to an increase in the carbon concentration. Since the pressure of TMGa is greater than that of TEGa, purging would remove the TMGa or other $(\text{CH}_3)_x\text{Ga}$ species at a much faster rate than the TEGa, leaving a cleaner source and hence cleaner AlGaAs.

As with hydrogen generated from the TMAAl, hydrogen introduced via the Group V source does not appear to remove methyl groups from the surface since films grown with TMGa show a decrease in carbon with increasing cracker temperature (fig. 1). Previous work has shown that the ratio of AsH_x to As_2 can be decreased significantly by increasing the temperature of the hydride cracker from 950 to 1100°C [7]. Since more of the AsH_x species are converted to As_2 , the V/III ratio is increased at higher cracker temperatures while the AsH_x/As_2 ratio is decreased. Thus a reduction in carbon with increasing cracker temperature is in agreement with previous reports which have shown the carbon level to be strongly dependent on V/III ratio in films grown with TMGa [8-10].

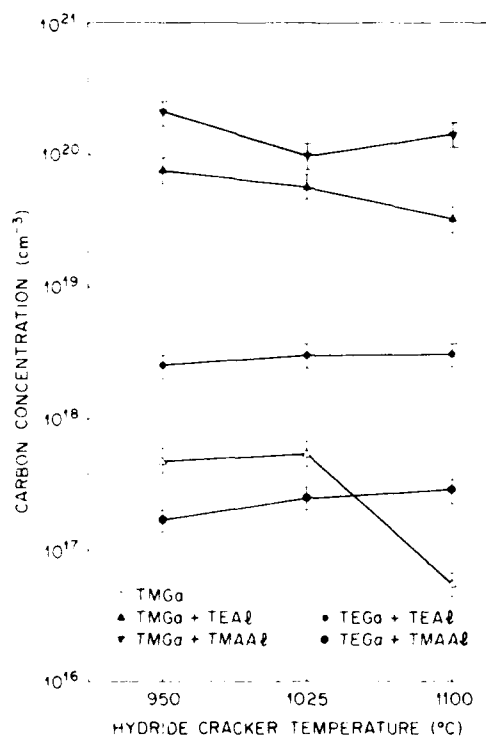


Fig. 1. Carbon concentration versus hydride cracker temperature for GaAs and AlGaAs grown at 500°C from various Ga and Al precursors.

The effect of hydrogen on removal of ethyl groups can also be inferred from the lack of variation of carbon with cracker temperature for AlGaAs grown with TEGa. Houg and co-workers [2,3] have shown that carbon levels decrease with increasing V/III ratio in AlGaAs grown with TEAl and TEGa. Since this decrease does not occur with increasing cracker temperature, even though the V/III ratio is increasing, one might suggest that the effect of increasing the As_2 flux is being offset by the reduction in the AsH_x concentration at the growth surface. This is consistent with the previous discussion regarding the hydrogen generated by the dissociation of the TMAAl, and with the data of table 1, where replacement of AsH_3 with As_4 produces a significant increase in the carbon concentration in films grown with TEAl but has no effect in films grown with TMAAl. In contrast, the AsH_x does not appear to remove oxygen from the growth front, as As_4 and cracked AsH_3 yield similar oxygen levels for any given combination of sources.

Finally, it is necessary to examine what role the composition of the Group V beam plays in the issue of crystallinity. From fig. 2, it is apparent that increasing the cracker temperature generally improves the crystallinity. Again, these results are consistent with previous work which has shown

that higher V/III ratios tend to improve the crystallinity [4]. Further, we have found that $\text{Al}_{0.4}\text{Ga}_{0.6}\text{As}$ with $\chi_{\min} = 4\%$ can be grown using TMAAl, TEGa and As_4 instead of AsH_3 . Thus it does not appear that AsH_x species are needed to produce high quality AlGaAs.

In conclusion, we have found that Al plays a major role in determining both the oxygen and carbon concentrations in AlGaAs, particularly when gaseous Ga sources are used. In contrast, hydrogen attached to either Al or As only seems to significantly affect the growth chemistry when TEGa is used as the Ga source.

Acknowledgements

The authors would like to acknowledge C. Magee of Evans East for the SIMS analysis and S.S. Pei and A.S. Jordan for their encouragement and support. This work was partially funded by the Materials Laboratory, WRDC, under US Air Force contract No. F33615-87-C-5244.

References

- [1] N. Kobayashi, J.L. Benchimol, F. Alexandre and Y. Gao, Appl. Phys. Letters 51 (1987) 1907.
- [2] Y.M. Houg, Y.C. Pao and P. McLeod, Mater. Res. Soc. Symp. Proc. 145 (1989) 63.
- [3] B.J. Lee, Y.M. Houg, J.N. Miller and J.E. Turner, J. Crystal Growth 105 (1990) 168.
- [4] C.R. Abernathy, S.J. Pearton, F.A. Baiocchi, T. Ambrose, A.S. Jordan, D.A. Bohling and G.T. Muhr, J. Crystal Growth 110 (1991) 457.
- [5] B.E. Bent, R.G. Nuzzo and L.H. Dubois, J. Am. Chem. Soc. 111 (1989) 1634.
- [6] C.R. Abernathy, A.S. Jordan, S.J. Pearton, W.S. Hobson, D.A. Bohling and G.T. Muhr, Appl. Phys. Letters 56 (1990) 2654.
- [7] C.R. Abernathy, J. Crystal Growth 107 (1991) 982.
- [8] N. Pütz, H. Heinecke, M. Heyen, P. Baltz, M. Weyers and H. Lüth, J. Crystal Growth 74 (1986) 292.
- [9] K. Saito, E. Tokamitsu, T. Akatsuka, M. Miyauchi, T. Yamada, M. Konagai and K. Takahashi, J. Appl. Phys. 64 (1988) 3975.
- [10] C.R. Abernathy, S.J. Pearton, F. Ren, W.S. Hobson, T.R. Fullowan, A. Katz, A. S. Jordan and J. Kovalchick, J. Crystal Growth 105 (1990) 375.

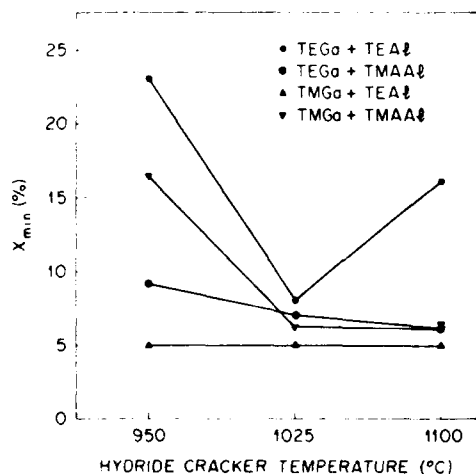


Fig. 2. χ_{\min} versus hydride cracker temperature for AlGaAs grown at 500°C from various Ga and Al precursors.

Chemical beam epitaxy growth of GaAs/Ga_{0.5}In_{0.5}P heterostructures: growth kinetics, electrical and optical properties

J.C. Garcia, P. Maurel, P. Bove, J.P. Hirtz

Laboratoire Central de Recherches, Thomson-CSF, F-91404 Orsay Cedex, France

and

A. Barski

Instrument S.A. Riber, BP 231, F-92503 Rueil Cedex, France

We report the growth kinetics, together with electrical and optical properties of undoped chemical beam epitaxy GaAs/GaInP structures grown using triethylgallium (TEGa), trimethylindium (TMIn), arsine and phosphine as starting materials for group III and group V elements. Undoped GaAs layers were found to be p-type, independent of the gallium-to-arsenic ratio, with free hole concentration ranging from 1×10^{15} to $9 \times 10^{15} \text{ cm}^{-3}$, depending on the growth temperature. Undoped GaAs/GaInP heterojunctions exhibit a two-dimensional electron gas with $T = 4 \text{ K}$ mobilities ranging from 20,000 to 25,000 $\text{cm}^2/\text{V}\cdot\text{s}$. The optical characteristics of GaAs/GaInP multiquantum wells as a function of growth interruptions at the interfaces were investigated by photoluminescence measurements. The growth kinetics of GaAs and GaInP were studied by reflection high energy electron diffraction (RHEED) oscillations. The composition of GaInP was found to be controlled mainly by the growth rate dependence of the binaries (GaP, InP) on growth parameters. The indium composition was found to be proportional to the flux of TMIn at a fixed TEGa flow. A lattice matching better than 5×10^{-4} can be routinely obtained. However, the composition exhibits a strong dependence on temperature. At temperatures above 510°C indium desorption occurs and the composition tends toward a Ga-rich phase, while below 510°C, the indium composition is enhanced by the decrease of the binary GaP growth rate. The PH_3 flow also affects significantly the ternary growth rate, mainly through indium incorporation modification. At low PH_3 flow (1–5 SCCM), the indium concentration decreases. This fact is attributed to the preferential Ga–P compared to In–P bond formation.

1. Introduction

In the past few years, chemical beam epitaxy (CBE) has emerged as a promising epitaxial technique which combines the respective advantages of both MBE and MOCVD. Indeed, high quality CBE growth of a wide range of III–V materials has already been demonstrated [1,2], in particular for phosphorus-based alloys. GaInP lattice-matched to GaAs, for example, is a very promising alternative to GaAlAs as a wide band gap barrier to GaAs in heterojunction devices, since GaAlAs suffers from various disadvantages. As an example, aluminium acts as a very efficient getter of both oxygen and carbon impurities. Therefore, the growth of high quality GaAs/GaAlAs struc-

tures requires extremely rigorous experimental growth procedures and very low reactor impurities levels. In contrast, this does not occur for GaInP growth. Furthermore, GaInP lattice matched to GaAs has been reported to exhibit low deep level concentrations [4].

Little work has been done on the molecular beam epitaxy (MBE) growth of these structures, due to the operational difficulties associated with the handling and control of MBE phosphorus sources and also to the limited material quality achievable, which is mainly limited by the purity of phosphorus charges available [3]. On the other hand, high quality GaAs/GaInP heterostructures have already been grown successfully by metalorganic chemical vapour deposition (MOCVD) [4].

but specific difficulties have been encountered, such as good homogeneity over large area substrates or problems of immiscibility [5].

The high level of flux control, stability and uniformity available with CBE coupled with its ability to produce very high quality phosphorus containing materials and extremely sharp hetero-interfaces, make it extremely attractive for the Ga_{0.5}In_{0.5}P material system. However, the basic aspects of the kinetics involved in CBE growth of these alloys are still poorly understood, and parallel studies of growth mechanisms and material properties are necessary.

In this paper, we report the CBE growth and characterization of GaAs/GaInP structures. Kinetics aspects as well as optical and electrical properties are presented, giving an overall view of the CBE growth of this system.

2. Experimental

Starting gaseous sources were triethylgallium (TEGa), trimethylindium (TMIn), pure phosphine and arsine. The details of the CBE growth system have been described elsewhere [6]. The growth rate of both GaP and InP was obtained using reflection high energy electron diffraction (RHEED) oscillations. The Ga_{0.5}In_{0.5}P composition was determined by X-ray diffraction analysis. The temperature was controlled using an infrared pyrometer calibrated with the melting point of InSb (525°C).

2.1. GaAs bulk layers

GaAs bulk materials grown by CBE have been extensively studied by various authors [7,8]. GaAs layers grown in the 500–650°C temperature range showed p-type conductivity. As expected, carbon was the main acceptor. The hole concentration increases from 1×10^{15} to $9 \times 10^{15} \text{ cm}^{-3}$ when the temperature is increased from 500 to 650°C. The apparent activation energy for carbon incorporation is found to be 25 kcal/mol, which is close to the value reported by Benchimol et al. [9]. Surprisingly, no significant dependence on the III/V ratio has been observed, as has been previously

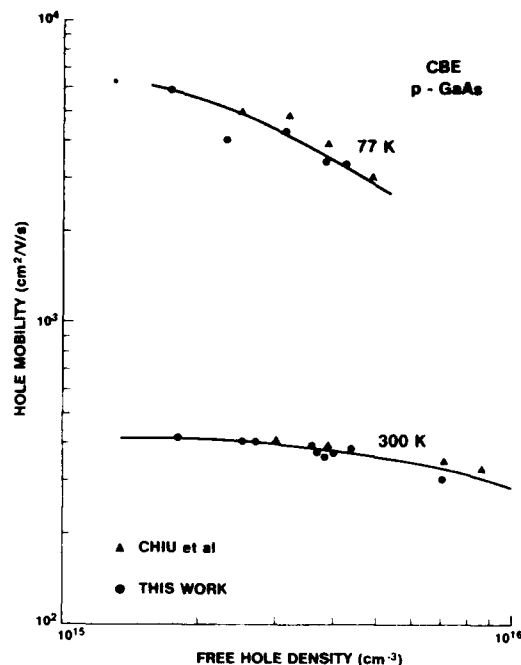


Fig. 1. 300 and 77 K mobilities of GaAs bulk layers as a function of free hole concentration.

reported by different authors [8,10]. Fig. 1 summarizes the results of the mobility at 300 and 77 K as a function of hole concentration. Good agreement is obtained with the data of Chiu et al. [7], which have been reported in the same figure.

RHEED intensity oscillation investigations of the GaAs growth by CBE have already led to valuable information on the understanding of the growth mechanisms involved in the use of organometallic starting sources [11]. Fig. 2 shows the dependence of the growth rate as a function of both arsine and hydrogen flow. As previously reported by various authors [11,12], the growth rate decreases with increasing arsine [11] or hydrogen [12] flow. Since molecular hydrogen does not adsorb efficiently on the GaAs (001) surface [13], as has been previously shown, it seems unlikely that H₂ molecules cause such effects. Considering the fact that GaAs growth using uncracked AsH₃ is extremely slow or even impossible [14], one possibility is that hydrogen interacts with arsenic on the surface, forming thermodynamically stable

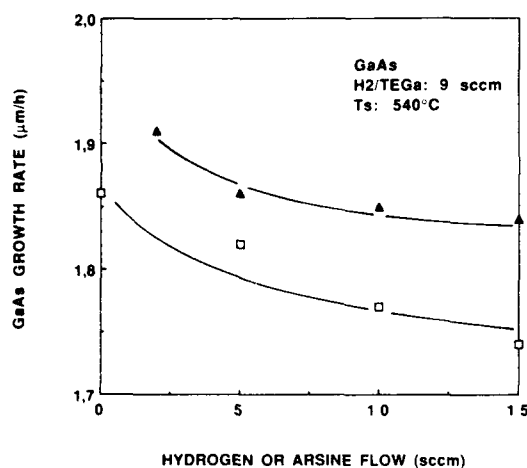


Fig. 2. GaAs growth rate as a function of arsine (▲) and hydrogen (□) flow rates. The arsine flow rate was kept at 5 SCCM when hydrogen was introduced.

chemisorbed AsH_n molecules [15], which block the gallium deposition sites and consequently induce a greater TEGa desorption.

2.2. Ga_{0.5}In_{0.5}P bulk material

Fig. 3a shows the X-ray double diffraction pattern of a 1 μm thick GaInP layer grown at 520°C.

The lattice mismatch is about 4×10^{-4} and the crystalline perfection of the layer is comparable to that of the GaAs substrate, with a full width at half maximum (FWHM) value of 15". At temperatures below 520°C, the crystal quality is drastically degraded, leading to a broad diffraction peak for the ternary alloy. Fig. 3b shows the variation, at a constant H₂/TEGa flow rate kept at 5 SCCM, of the indium composition as a function of the H₂/TMIn flow rate. The indium composition is found to vary linearly, regardless of the temperature used. However, the composition depends strongly on the temperature. This contrasts with the GaInP composition behaviour previously reported by Ozasa et al. [16], who observed both constant growth rate and indium composition over a large temperature range (400–520°C). In fact, these authors used triethylindium as a starting source and it seems likely that the temperature behaviour of the GaInP growth rate differs from that using TMIn. The temperature behaviour we observed can be explained by considering the growth rate of the two binaries GaP and InP [17]. The growth rate of GaP increases with increasing temperature and reaches a maximum near 550°C. Beyond this temperature, the growth rate slightly decreases. In the case of InP, a constant growth rate is observed over a large temperature range

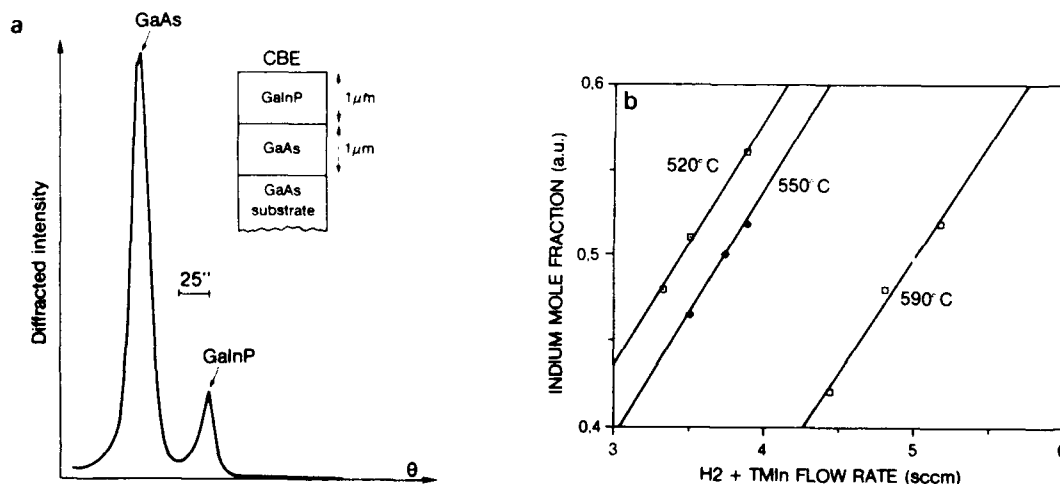


Fig. 3. (a) Double X-ray diffraction pattern of a bulk GaInP layer grown on GaAs substrate. Growth temperature was 520°C. (b) Indium composition as a function of (TMIn + H₂) flow. Temperature is taken as a parameter.

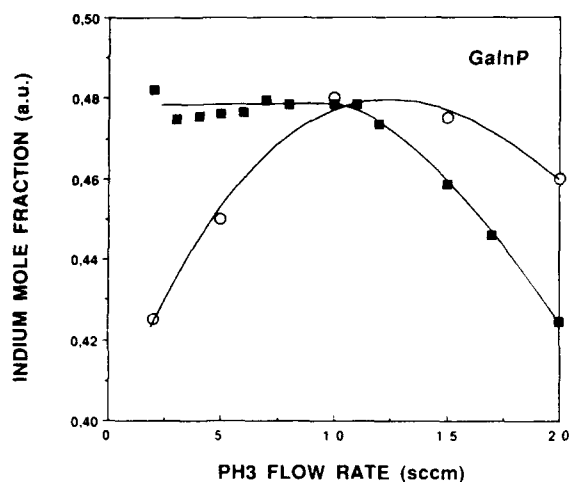


Fig. 4. Indium mole fraction (○) in GaInP and expected indium composition (■) deduced from the phosphine flow rate dependence of the two binaries as a function of phosphine flow rate. Note the strong decrease of indium composition obtained at low phosphine flow rates.

(420–510°C). At higher temperatures, the InP growth rate decreases significantly. Therefore, at temperatures higher than 510°C, the indium incorporation in GaInP is mainly limited by the desorption of the indium species, while at lower temperatures the increase in the indium composition is analogous to the decrease of the GaP binary growth rate. More detailed results of RHEED intensity oscillation measurements of the growth rate of the two binaries will be reported elsewhere [17].

The dependence of the indium composition as a function of the phosphine flow is shown in fig. 4. At low and high phosphine flow rate, the indium composition decreases. At high phosphine flow rates, the measured indium concentration agrees well with that deduced from the phosphine flow dependence of the growth rate of both binaries GaP and InP [17], the InP growth rate being reduced more significantly than the GaP growth rate while increasing the phosphine flow. At low phosphine flow rates, the expected indium mole fraction, deduced from the binaries growth rates is found to be constant. As seen in fig. 4, experimental results indicate that indium mole

fraction decreases with decreasing phosphine flow rates. The strong enhancement in Ga composition can be related to the energy difference between the Ga–P and In–P bonds. Since it has been reported that the GaP bond is stronger than the InP one [5], it seems reasonable to conclude that at low phosphorus coverage, the GaP bonds are preferentially formed, thus leading to a desorption of In species.

2.3. GaAs/GaInP heterostructures

Hall measurements on undoped GaAs/GaInP heterostructures revealed the existence of a two-dimensional electron gas (2DEG) with the following mobilities: $\mu(300\text{ K}) = 3000\text{--}4000\text{ cm}^2/\text{V}\cdot\text{s}$ and $\mu(4\text{ K}) = 20,000\text{--}26,000\text{ cm}^2/\text{V}\cdot\text{s}$ with $N_s = (2\text{--}4) \times 10^{11}\text{ cm}^{-2}$. The two-dimensionality of the electron gas has been established by the mobility plateau obtained at low temperature measurements, demonstrating the good quality of the interface. Growth interruption at the interface was necessary in order to obtain such 2DEG.

Multiquantum well (MQW) structures were grown to further assess the quality of the interfaces. The GaAs growth rate was $1\text{ }\mu\text{m/h}$, while GaInP growth rate was fixed to $1.5\text{ }\mu\text{m/h}$. Growth interruption was necessary at the normal GaAs/GaInP interface in order to obtain reasonably good confinement energies. The experimental procedure is the following: At the normal interface, the growth of GaAs is stopped and the surface is stabilized under phosphine flow for 15 s, the RHEED pattern showing a well defined 2×4 reconstruction. Finally, GaInP growth is initiated simply by switching both the TEGa and TMIn flows from the vent to the growth chamber. It should be noted that for higher durations of exposure of the GaAs surface to a phosphine flow, the surface becomes rough. Similarly, the GaInP surface also becomes rough with arsenic exposure up to 10 s. It seems reasonable to suggest that for long time stabilization under phosphine or arsine, intermediates GaInAsP alloys are formed at the interfaces. These observations can be correlated with the work of Lee et al. [18], who have to include intermediate GaP and GaInAsP layers at the GaAs/GaInP and GaInP/GaAs interfaces,

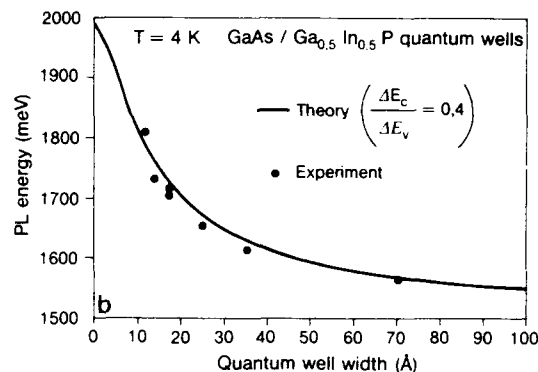
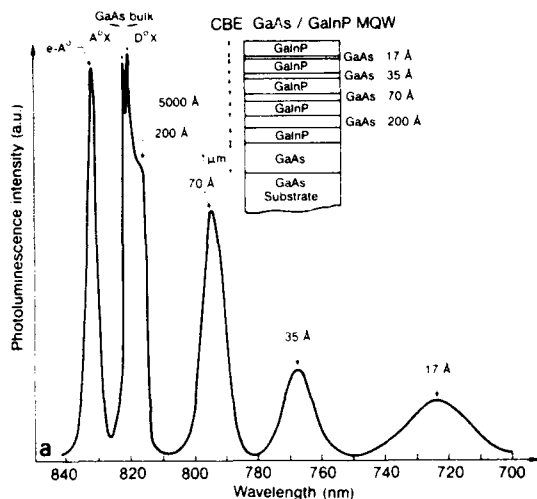


Fig. 5. (a) Low temperature photoluminescence of a typical GaAs/GaInP MQW structure. (b) both theoretical and experimental optical confinements of GaAs/GaInP quantum wells.

respectively, in order to fit the double crystal X-ray diffraction spectrum of a superlattice structure. On the other hand, if no growth interruption occurs, the preferential incorporation of arsenic, if compared with phosphorus, leads to the formation of an intermediate GaInP(As) layer at the normal interface, which does not happen at the inverted interface.

The GaInP/GaAs MQW structures were characterized by low temperature photoluminescence (PL) using an excitation wavelength of 0.63 μm . Fig. 5a shows a typical spectrum of such a structure. The energy shift due to quantum confinement relative to GaAs band gap is shown in fig. 5b as a function of the well width. Good agreement is obtained between the theoretical calculation, performed using a simple square well model assuming a conduction band valence band discontinuity ratio ($\Delta E_c/\Delta E_v$) of 0.4, and the experimental values. Wells as thin as 10 Å have been obtained with associated energy shifts up to 310 meV. This demonstrates the high quality of the interfaces achievable by CBE.

In summary, high quality GaAs/GaInP structures were grown by CBE with a good reproducibility, although a strong composition dependence of the ternary alloy with growth parameters such

as temperature and phosphine flow was observed. Monolayer growth control can be achieved, as demonstrated by the growth of thin quantum wells.

Acknowledgement

This work has been supported by EEC under ESPRIT contract No. 5031.

References

- [1] W.T. Tsang, Appl. Phys. Letters 48 (1986) 511.
- [2] H. Heinecke, R. Höger, B. Baur and A. Miklis, Electron. Letters 26 (1990) 213.
- [3] T. Martin, C.R. Stanley, A. Iliadis, C. Whitehouse and D.E. Sykes, Appl. Phys. Letters 46 (1985) 994.
- [4] M. Razeghi, P. Maurel, F. Omnes, M. Defour, C. Boothroyd, W.M. Stobbs and M. Kelly, J. Appl. Phys. 63 (1988) 451.
- [5] K. Ozasa, M. Yuri, S. Nishino and H. Matsunami, J. Crystal Growth 89 (1988) 485.
- [6] P. Maurel, P. Bove, J.C. Garcia and M. Razeghi, Semicond. Sci. Technol. 5 (1990) 638.
- [7] T.H. Chiu, W.T. Tsang, E.F. Schubert and E. Agvekm, Appl. Phys. Letters 51 (1987) 1109.
- [8] N. Pütz, H. Heinecke, M. Heyen, P. Balk, M. Weyers and H. Lüth, J. Crystal Growth 74 (1986) 292.

- [9] J.L. Benchimol, F. Alexandre, Y. Gao and F. Alaoui, *J. Crystal Growth* 95 (1989) 150.
- [10] J. Saito, K. Ono, K. Nambu, T. Ishikawa and K. Kono, *Japan. J. Appl. Phys.* 127 (1988) L114.
- [11] T.H. C'kui, J.E. Cunningham and A. Robertson, *J. Crystal Growth* 95 (1989) 136.
- [12] S. Maruno, Y. Nomura, H. Ogata, M. Gotoda and Y. Morishita, *J. Crystal Growth* 97 (1989) 578.
- [13] R.Z. Bachrach and R.D. Bringans, *J. Vacuum Sci. Technol.* B1 (1983) 142.
- [14] N. Vojdani, A. Lemarchand and H. Paradan, *J. Physique Colloq.* 43 (1982) C5-339.
- [15] D.M. Joseph, R.F. Hicks, L.P. Sadwick and K.L. Wang, *Surface Sci.* 204 (1988) L721.
- [16] K. Osaza, M. Yuri, S. Tanaka and H. Matsunami, *J. Appl. Phys.* 65 (1989) 2711.
- [17] J.C. Garcia, P. Maurel, P. Bove and J.P. Hirtz, *J. Appl. Phys.*, submitted.
- [18] H.Y. Lee, M.D. Crook, M.J. Hafich, J.H. Quigley, G.Y. Robinson, D. Li and N. Otsuka, *Appl. Phys. Letters* 55 (1989) 2322.

MOMBE growth and characterization of heavily carbon-doped InGaAs

Takumi Yamada, Shinji Nozaki *, Ryuji Miyake, Taichi Fukamachi, Jun-ichi Shirakashi,
Makoto Konagai and Kiyoshi Takahashi

Department of Electrical and Electronic Engineering, Tokyo Institute of Technology, 2-12-1, O-okayama, Meguro-ku, Tokyo 152, Japan

A series of recent experimental results show that carbon is a more suitable acceptor for GaAs than beryllium. One reason for this is the capability of ultra-high doping up to $1 \times 10^{21} \text{ cm}^{-3}$ with carbon. However, the lattice constant significantly decreases with increasing hole concentration at such high doping levels. To solve the lattice-mismatch problem at the interface between heavily carbon-doped GaAs and moderately-doped or Si GaAs, we have grown heavily carbon-doped InGaAs lattice-matched to Si GaAs by metalorganic molecular beam epitaxy (MOMBE). Hall and X-ray diffraction measurements were performed to study the carrier concentrations and the lattice constants, respectively, of the heavily carbon-doped InGaAs with various In contents both before and after annealing.

1. Introduction

Although recent improvements in the speed and the integration level of semiconductor devices are remarkable, a further increase in the speed and the maximum operational frequency requires a technique to produce heavily doped semiconductors. Especially, the demand for stable, well-controlled p-type doping in the 10^{20} cm^{-3} range has been growing for fabrication of heterostructure bipolar transistors (HBTs). We have already reported MOMBE growth of carbon-doped GaAs with a hole concentration of $1.5 \times 10^{21} \text{ cm}^{-3}$ [1,2]. While it is difficult to achieve a doping level higher than $(1-2) \times 10^{19} \text{ cm}^{-3}$ in n-type GaAs due to self-compensation mechanism [3], carbon, in contrast, was found to incorporate as an acceptor up to $1 \times 10^{21} \text{ cm}^{-3}$ without self-compensation. Since then, carbon has been intensively studied as a potential acceptor to replace beryllium at many institutions, and many benefits from the use of carbon as an acceptor have been confirmed [4–6]. The lattice constant of the heavily carbon-doped GaAs, however, decreases with increasing carbon

content at high doping levels due to a difference in the radii of Ga, As, and C atoms [2,5,7,8]. The lattice mismatch at the emitter-base and the collector-base junctions may degrade the HBT performance if the heavily carbon-doped GaAs is used as a base layer. To avoid the lattice mismatch, we grew heavily carbon-doped InGaAs lattice-matched with Si GaAs using elemental In and As and trimethylgallium (TMG) as sources [9]. Although the diffusion coefficient of carbon in GaAs is known to be extremely small, it is important to study the thermal stability of electrical properties of heavily carbon-doped GaAs and InGaAs, because the material can be exposed to high temperatures in the process of device fabrication. In this paper, we report the carrier concentration and the lattice constant of heavily carbon-doped InGaAs with various indium contents before and after annealing, and propose a model to explain the experimental results.

2. Experiments

The system used in this experiment is a V-80H made by VG Semicon. In the MOMBE growth of GaAs and InGaAs, TMG and elemental As and In were used as Ga, As₄ and In sources, respec-

* On leave from Intel Corporation, Santa Clara, California 95052, USA.

tively. The details of the growth were described elsewhere [7]. Substrate temperature is a key parameter of the MOMB growth of carbon-doped GaAs [1]. The substrate temperature must be low enough to obtain the heavily carbon-doped GaAs. In this experiment, the substrate temperature was kept at 450°C. The pressure-equivalent beam flux of TMG and As₄ was kept at 1.1×10^{-5} and 0.8×10^{-5} Torr, respectively. The indium pressure-equivalent beam flux was varied from 0 to 1.5×10^{-7} Torr to obtain InGaAs with various indium contents. It should be noted that the absolute indium content in the heavily carbon-doped InGaAs cannot be determined directly from the lattice constant since a large amount of the incorporated carbon reduces the lattice constant. Determination of the indium content in the heavily carbon-doped InGaAs was described elsewhere [9].

The as-grown InGaAs was annealed at 900°C for 4 h under N₂ flow. A dummy GaAs substrate was placed on the surface of the InGaAs to minimize arsenic loss during annealing. Double-crystal X-ray diffraction and Hall measurements were performed to study the lattice constant and the carrier concentration before and after annealing.

3. Results and discussion

Fig. 1 shows the dependence of the carrier concentration on the indium pressure-equivalent beam flux. All samples show p-type conductivity, and the hole concentration decreases with increasing the indium beam flux. Since the monomethylgallium resulted from decomposition of TMG plays a significant role in carbon doping, the carbon concentration incorporated in the epilayer is determined by dissociation of TMG [1]. The effect of presence of the In atoms on the dissociation of TMG must be considered to explain the observed dependence. The catalytic effect of the In atoms may promote the complete dissociation of TMG, which leads to less incorporation of carbon into the epilayer. This hypothesis will be confirmed by the SIMS analysis. However, there is another possibility that the electrical activation rate of carbon as an acceptor decreases with the In

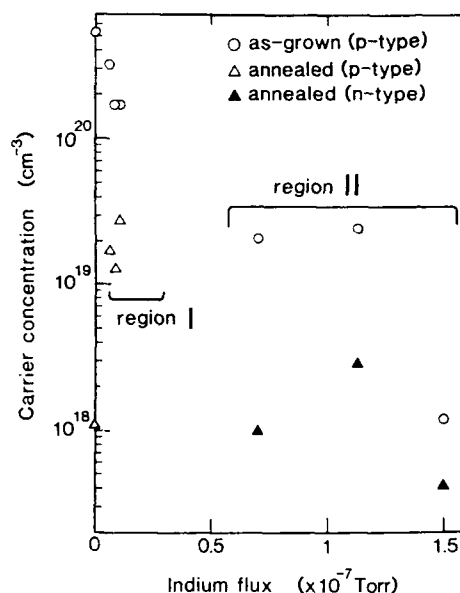


Fig. 1. Carrier-concentration dependence on the indium pressure-equivalent beam flux for the heavily carbon-doped InGaAs before (\circ) and after (Δ , \blacktriangle) annealing.

mole fraction, which may result in self-compensation for higher In mole fraction [10].

The carrier concentrations after annealing at 900°C for 4 h are also shown in fig. 1. The hole concentration decreases more than one order of magnitude after annealing for smaller indium contents (region I). A similar decrease of the hole concentration was observed for heavily C-doped GaAs with hole concentrations higher than 10^{20} cm^{-3} [5]. For larger indium content (region II), the conductivity changes to n-type after annealing. A simple model to explain these experimental results will be proposed later.

Fig. 2 shows the lattice constant as a function of the indium pressure-equivalent beam flux before and after annealing. The strain in the heavily C-doped GaAs and InGaAs is relaxed after annealing. Aberrathy et al. attributed the relaxation of the strain in the heavily carbon-doped GaAs to the site switching, which also accounts for a decrease of the hole concentration after annealing. However, even if the carbon atom moves to the Ga site from the As site, it does not significantly reduce the local strain. Therefore, the lattice re-

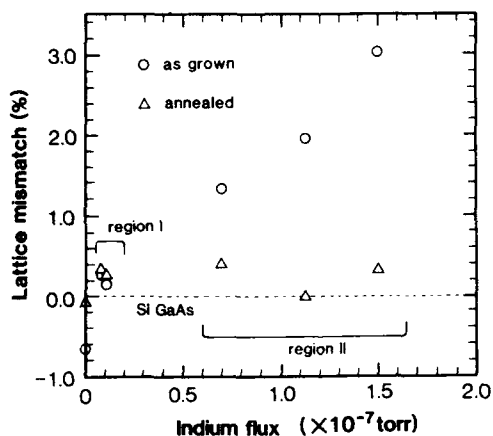


Fig. 2. Lattice-constant dependence on the indium pressure-equivalent beam flux for the heavily carbon-doped InGaAs before (\circ) and after (Δ) annealing.

laxation in GaAs cannot be explained simply by the site switching model. For the heavily carbon-doped InGaAs, the lattice relaxation is also observed in region II, but the strain slightly increases in region I.

The SEM micrograph in fig. 3 shows surface morphology of the heavily carbon-doped InGaAs with a larger indium content after annealing. Figs. 4a and 4b show the elemental analyses by the energy dispersive X-ray spectroscopy (EDX) on the points A and B in fig. 3. They indicate the indium precipitation at the surface. The GaAs-like Raman spectrum also confirms this result. It may be concluded that the majority of the In atoms in the InGaAs segregate toward the surface and then precipitate, leaving a large amount of indium vacancies in the epilayer. This indium segregation is significant for the heavily carbon-doped InGaAs with larger In content.

Next, we propose a simple model to explain the observed variations in the lattice constant and the carrier concentration due to annealing. Let us start with the heavily carbon-doped GaAs. As reported [2], the activation rate of the carbon atom as an acceptor is close to 100%, and almost all of the incorporated carbon atoms are substitutional [8] and occupy the As sites. The X-ray quasi-forbidden reflection (XFR) technique [11] supports this hypothesis, as seen in fig. 5. The

details of the analysis by the XFR technique applied to the heavily carbon-doped GaAs will be reported elsewhere, but the result well agrees with a calculation based on the strain between the C and the nearest Ga atoms. However, the Ga-C bond is broken by thermal energy during annealing, and as a result the local strain is relaxed after annealing. The C atoms with the broken bonds may form interstitials and become electrically inactive. The number of the carbon atoms with the broken bonds is determined from the thermal equilibrium during annealing. Therefore, the hole concentration decreases after annealing.

The argument for the heavily carbon doped GaAs can be applied to the heavily carbon-doped InGaAs with smaller indium contents. The breakage of the Ga-C bond results in an increase of the lattice constant and a decrease of the hole concentration.

In the InGaAs with larger indium contents, the indium segregation during annealing causes a large number of indium vacancies. Some unbonded carbon atoms may move to the indium vacancies



Fig. 3. SEM micrograph of surface morphology of the heavily carbon-doped InGaAs with a larger In content after annealing. Marker represents 6 μ m.

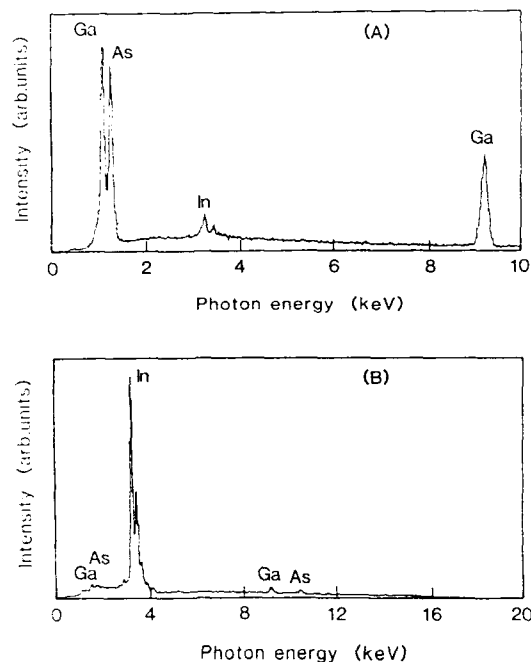


Fig. 4. Elemental analyses by EDX for points A and B in fig. 3. Point B shows the indium precipitation.

and become a donor, resulting in the conversion of the conductivity from p-type to n-type. As observed in fig. 4, there still remain some In atoms

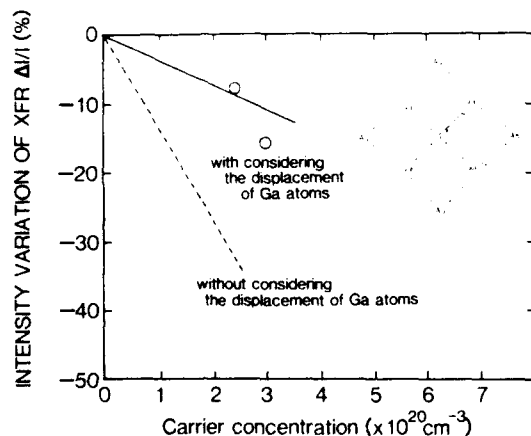


Fig. 5. Intensity variation of the X-ray (200) quasi-forbidden peak as a function of the hole concentration. The insert shows the local strain around C atoms used in this calculation.

in the epilayer. The remaining small number of In atoms increase the lattice constant, but the carbon atoms decrease the lattice constant. The balance between the effects of the indium and carbon atoms on the lattice constant results in the nearly complete lattice relaxation seen in fig. 2.

4. Conclusions

We have grown heavily carbon-doped InGaAs with various indium contents by MOMBÉ. The hole concentration decreases with increasing indium content, but p-type conductivity is observed even for larger indium contents. However, large variations in the carrier concentration and the lattice constant due to annealing were found. The hole concentration of the InGaAs with smaller indium contents decreases, but the conductivity of the InGaAs with larger indium content changes from p-type to n-type after annealing. The lattice constant increases for smaller In content, while the lattice constant decreases and approaches that of SI GaAs for larger In content. A simple model was proposed to explain the observed effects of annealing.

The study raises a serious question regarding the thermal stability of the heavily carbon-doped GaAs and InGaAs. A further investigation of the thermal stability is needed before using these materials in various devices.

Acknowledgements

The authors wish to thank Dr. I. Fujimoto at the Science and Technical Research Laboratories of NHK for the X-ray quasi-forbidden reflection measurements and technical discussions, and Drs. A. Yamada, S. Yamanaka, and F. Sugimoto at the Tokyo Institute of Technology for technical assistance.

References

- [1] T. Yamada, E. Tokumitsu, K. Saito, T. Akatsuka, M. Miyauchi, M. Konagai and K. Takahashi, *J. Crystal Growth* 95 (1989) 145.

- [2] M. Konagai, T. Yamada, T. Akatsuka, K. Saito, E. Tokumitsu and K. Takahashi, *J. Crystal Growth* 98 (1989) 167.
- [3] E. Tokumitsu, *Japan. J. Appl. Phys.* 29 (1990) L698.
- [4] M. Weyers, N. Pütz, H. Heinecke, M. Heyen, H. Lüth and P. Balk, *J. Electron. Mater.* 15 (1986) 57.
- [5] C. R. Abernathy, S.J. Pearton, R. Caruso, F. Ren and J. Kovalchik, *Appl. Phys. Letters* 55 (1989) 1750.
- [6] T.H. Chiu, J.E. Cunningham, J.A. Ditzenberger and W.Y. Jan, *Appl. Phys. Letters* 57 (1990) 171.
- [7] M. Konagai, T. Yamada, T. Akatsuka, S. Nozaki, R. Miyake, K. Saito, T. Fukamachi, E. Tokumitsu and K. Takahashi, *J. Crystal Growth* 105 (1990) 359.
- [8] T.J. de Lyon, J.M. Woodall, M.S. Goorsky and P.D. Kirchner, *Appl. Phys. Letters* 56 (1990) 1040.
- [9] T. Akatsuka, R. Miyake, S. Nozaki, T. Yamada, M. Konagai and K. Takahashi, *Japan. J. Appl. Phys.* 29 (1990) L537.
- [10] H. Ito and T. Ishibashi, *Mater. Res. Soc. Symp. Proc.* 163 (1989) 887.
- [11] I. Fujimoto, N. Kamata, K. Kobayashi and T. Suzuki, in: *Proc. 12th Intern. Symp. on GaAs and Related Compounds*, Karuizawa, 1985, *Inst. Phys. Conf. Ser.* 79, Ed. M. Fujimoto (Inst. Phys., London-Bristol, 1986) p. 199.

Luminescence and transport properties of high quality InP grown by CBE between 450 and 550°C

A. Rudra, J.F. Carlin, M. Proctor and M. Illegems

Institute for Micro- and Optoelectronics, Ecole Polytechnique Fédérale de Lausanne, CH-1015 Lausanne, Switzerland

A Hall mobility as high as $153,800 \text{ cm}^2 \text{ V}^{-1} \text{ s}^{-1}$ at 77 K with $N_D - N_A = 1.5 \times 10^{14} \text{ cm}^{-3}$ has been obtained by adjusting the growth temperature and the phosphine cracking temperature. The 4 K photoluminescence spectra show finely resolved excitonic transitions for layers grown above 535°C with linewidths as narrow as 0.07 meV. The use of substrates misoriented 2° and 3.5° towards (111)A significantly improves the morphology at the cost of a slight increase in the impurity incorporation.

1. Introduction

Early attempts to grow InP/GaInAsP by conventional molecular beam epitaxy (MBE) were hindered by the large quantities of solid phosphorus that were needed and by the difficulty in precisely stabilizing and switching the P_4 flux [1]. The use of cracked phosphine has overcome this problem and is now the accepted answer. High purity InP was obtained by chemical beam epitaxy (CBE), first by using triethylindium (TEIn) [2,3], and more recently by using trimethylindium (TMIn) [4], as well as with gas source MBE (GSMBE) [5] using a solid In source. In this paper, we present a detailed description of the optical and electrical properties of InP as a function of growth conditions, particularly of substrate temperature, phosphine cracking temperature and substrate misorientation. At the present time, mobility values obtained on CBE-grown InP closely approach the record values published from metalorganic vapour phase epitaxy (MOVPE) [6], so that the different techniques appear capable of equivalent performance as far as the intrinsic material quality is concerned.

2. Experimental

The growth experiments were carried out inside a VG V80H growth chamber evacuated through a

cryogenic trap by a diffusion pump. Pure TMIn from Epichem was introduced via a leak aperture in a low temperature cell (50–100°C) and the flow rate was established by controlling the upstream pressure at 0.77 and 1.3 Torr, resulting in a growth rate of 0.5 and 1 $\mu\text{m/h}$, respectively. Pure, undried PH_3 (Phoenix grade, Union Carbide) was decomposed at high pressure (300 to 1000 Torr) inside a pyrolytic boron nitride and molybdenum cracking cell usually kept at 880°C and run down to 760°C in a specific set of experiments. The phosphine flux was varied between 1.5 and 3 SCCM. Iron-doped (001) oriented InP wafers from Sumitomo, standard grade and pre-etched, were In-mounted without any additional preparation. The substrate temperature was continuously monitored with an accuracy and repeatability of $\pm 3^\circ\text{C}$ by using an infrared pyrometer responding at 950 nm and regularly calibrated against the melting point of InSb (525°C). RHEED diffraction was used to monitor the heat treatment prior to growth.

Low temperature (4.5 K) photoluminescence (LTPL) measurements were carried out using an Oxford Instruments CF1204LT continuous flow cryostat and a SPEX 14018 0.85 m double grating spectrometer. The detector is a Peltier-cooled GaAs photomultiplier with a photon counting multichannel analyser to record the spectra. The number of measured points was 80 per meV. The excitation energy could be tuned between 1.75 and 1.55 eV, from a CR 590 Pyridine 2 dye laser

pumped with all emission lines of an Ar⁺ Spectra Physics 2016 laser. The spot size was nominally 130 μm and the sample was at an angle of 45° with respect to the incident and collected beam axis.

3. Effect of substrate temperature

Layers grown between 445 and 480 °C show high n-type residual doping levels (mid- 10^{15} to mid- 10^{16} cm^{-3}). Hall mobilities are usually below $3000 \text{ cm}^2 \text{ V}^{-1} \text{ s}^{-1}$ at 300 K and do not exceed $20,000 \text{ cm}^2 \text{ V}^{-1} \text{ s}^{-1}$ at 77 K. The compensation ratio is in the 0.6 to 0.8 range. The substrate–layer interface sometimes shows an enhanced carrier concentration, the origin of which is not clear.

The LTPL spectra usually show two broad emission lines. The first one, at 1.418 eV, is about 10 meV wide and is attributed to band-to-band recombination. About 33 meV below, the second emission is due to a donor-to-acceptor ($\text{D}^0\text{--A}^0$) recombination.

Between 480 and 520 °C, the residual doping level slowly decreases to the low- 10^{15} cm^{-3} range and mobilities between $30,000$ and $50,000 \text{ cm}^2 \text{ V}^{-1} \text{ s}^{-1}$ are obtained. The major LTPL line is now due to the exciton bound to a neutral donor ($\text{D}^0\text{--X}$). The free exciton X is clearly visible (fig. 1A). The ($\text{D}^0\text{--A}^0$) impurity emission is much weaker, usually undetectable.

Above 520 °C, the residual doping level falls below $5 \times 10^{14} \text{ cm}^{-3}$ at 77 K and mobilities are routinely over $80,000 \text{ cm}^2 \text{ V}^{-1} \text{ s}^{-1}$ (fig. 2). Relia-

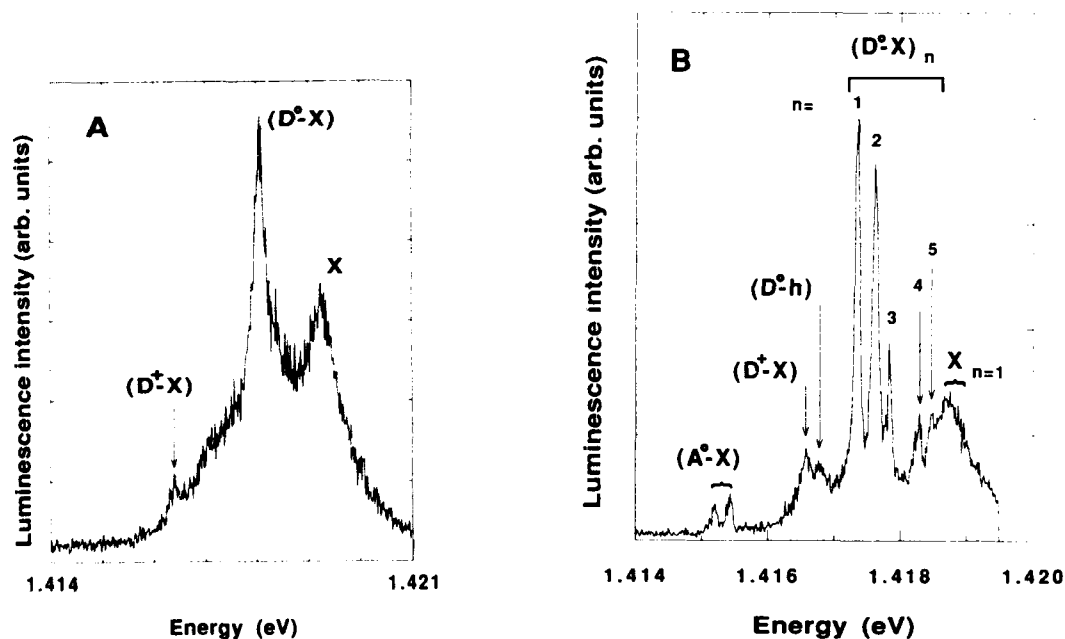


Fig. 1. Photoluminescence spectra at 6 K of two InP layers grown at 520 °C (A) and 540 °C (B).

Sample	Excitation density (mW cm^{-2})	Excitation energy (eV)	$N_d - N_a$ at 77 K (cm^{-3})	μ at 77 K ($\text{cm}^2 \text{ V}^{-1} \text{ cm}^{-1}$)	Layer thickness (μm)
A	480	1.75	1.5×10^{15}	51,000	2
B	75	1.75	4.3×10^{14}	105,000	7

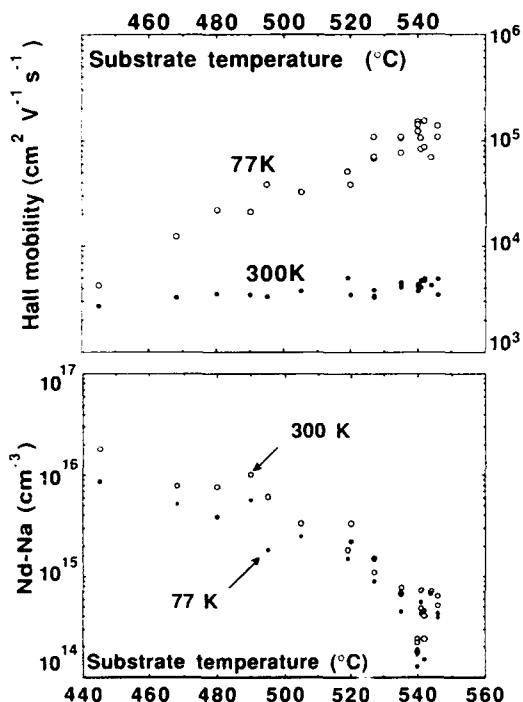


Fig. 2. Growth temperature dependence of the Hall mobility and the residual electron concentration of InP layers grown under similar other conditions.

ble measurements can only be made on thick layers (at least 4 μm) because the depleted layers at the surface and substrate interfaces are expected to account for more than 1 μm .

The Hall data are confirmed by profiling into layers grown with different substrate temperature stages. The carrier concentration measured by $C-V$ increases step by step as the temperature decreases and the measured electron concentrations show a good fit with the Hall data.

On LTPL spectra, transitions due to excited states of the exciton bound to the neutral donor, $(D^0-X)_n$ up to $n = 5$, are now clearly resolved, as well as (D^+-X) and (D^0-h) lines (fig. 1B). These features, only found on high purity material, have been described in detail in several publications [7–9].

4. Effect of cracking temperature

The highest purity layers were finally obtained by lowering the phosphine cracking temperature from 880 to 810 °C. Hall mobilities as high as 4700 $\text{cm}^2 \text{V}^{-1} \text{s}^{-1}$ at 300 K and 153,800 $\text{cm}^2 \text{V}^{-1} \text{s}^{-1}$ at 77 K with $N_d - N_a = 1.5 \times 10^{14} \text{cm}^{-3}$ have been measured for a 5.5 μm thick layer grown at 541 °C. Lowering the cracking cell temperature further down to 760 °C did not bring any more improvement to the purity of the layers.

This result complements the observation of Kawaguchi et al. [10] for layers with $N_d - N_a$ in the 10^{15} to 10^{17}cm^{-3} range. It is not clear whether the nature and distribution of chemical species inside the beam resulting from the cracking of PH_3 is more favourable at lower cracking temperature or if reduced outgassing from the cracker is the essential reason for the growth of higher purity layers.

The usual reference for computation of the compensation ratio is Walukiewicz et al. [11].

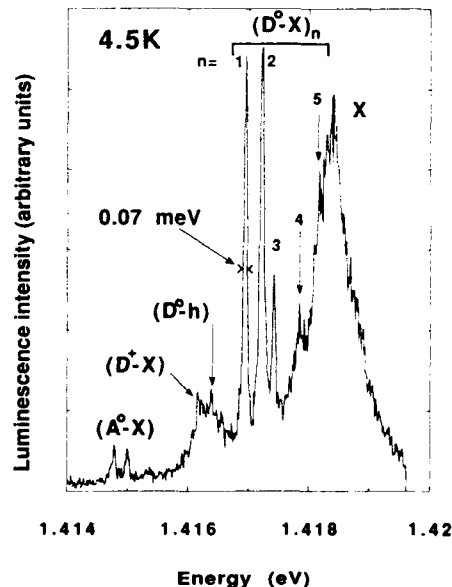


Fig. 3. 4 K photoluminescence spectrum of a 4.5 μm thick InP layer grown at a low phosphine cracking temperature (760 °C). Excitation density is 240 mW cm^{-2} , excitation energy is 1.55 eV, $N_d - N_a$ (at 77 K) is $1.3 \times 10^{14} \text{cm}^{-3}$ and μ (at 77 K) is 150,000 $\text{cm}^2 \text{V}^{-1} \text{s}^{-1}$.

However, for high purity layers the compensation ratio and the maximum mobility seems to be underestimated. As a result, the compensation ratios calculated from this model are close to zero or even negative. Using a more recent model by Tagushi and Yamada [12], we find that most of our layers stand below 0.4 with lowest values below 0.2.

An example of a LTPL spectrum of a very high purity sample is given in fig. 3. The linewidth of the $(D^0-X)_1$ emission is 0.07 ± 0.01 meV. With increasing excitation density, the free exciton rapidly dominates the spectra but the $(D^0-X)_{1,2}$ lines remain visible on the lower energy shoulder. These photoluminescence spectra stand among the best which have ever been reported for InP, whichever growth technique was employed [4,7,13].

5. Effect of substrate misorientation

On standard grade, exactly (001) oriented substrates, the layer morphology is excellent up to about 500°C. A residual defect density varying from 200 to 600 cm⁻² is attributed to particulates contaminating the surface during cleavage. In bonding, handling in the class 100 hood and transfers inside the vacuum system. An increasing density of elongated defects appears when the temperature is risen from 500°C. Their density is 10⁴ cm⁻² at 520°C. Above 545°C the morphology is seriously degraded. Etching the wafers in a bromine-methanol solution prior to In-mounting is not found to be beneficial. In contrast, the use of pre-etched grade wafers brings a dramatic improvement in the defect density; however, under our growth conditions of low V/III ratio, it cannot be reduced below 10⁴ cm⁻² for 5 µm thick layers grown at 540°C. Because the highest purity layers are precisely obtained at these higher temperatures, we have run comparative experiments on wafers disoriented by 2° and 3.5° towards (111)A. To exclude any problem linked to variations from growth to growth, we mounted one exactly oriented and 2 misoriented wafers side by side. Four growth experiments were carried out at 527, 535, 540 and 546°C. In each case, the wafer-to-wafer temperature variation was measured to

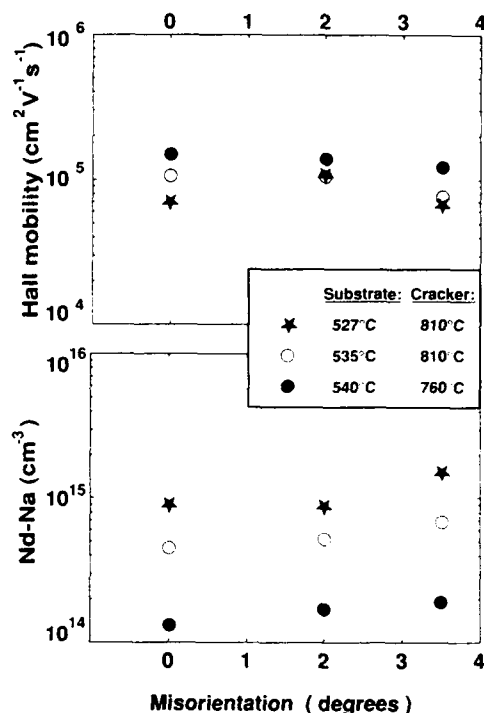


Fig. 4. Influence of substrate misorientation on the transport properties of layers grown side by side in 3 different runs.

be less than 2°C. In all four layers, the misorientation significantly improved the layer morphology. On 4.2 to 5 µm thick layers grown on 3.5° off oriented substrates, the defect density falls below 600 cm⁻² at 540°C, below 500 cm⁻² at 535°C and below 360 cm⁻² at 527°C. The surface roughness is otherwise not visible under phase contrast optical microscope examination.

The misorientation has a slight detrimental effect on the impurity uptake during growth (fig. 4). A small increase in the intensity of the (A^0-X) peaks is also perceptible on one, otherwise unchanged, LTPL spectrum. Clearly, the tradeoff seems to be quite acceptable. This result complements the study by Benchimol et al. [3] on layers of higher residual doping levels obtained with TEIn where no deterioration was found.

6. Conclusion

InP layers with 77 K Hall mobilities over $100,000 \text{ cm}^2 \text{ V}^{-1} \text{ s}^{-1}$, residual donor concentrations below $5 \times 10^{14} \text{ cm}^{-3}$ and defect densities below 600 cm^{-2} are routinely grown on our CBE equipment. Growth temperatures between 525 and 545°C , phosphine fluxes between 2 and 3 SCCM and low cracking temperatures ($800\text{--}850^\circ\text{C}$) are the required growth conditions.

A residual donor concentration as low as $1.5 \times 10^{14} \text{ cm}^{-3}$, room temperature and 77 K mobilities as high as $4700 \text{ cm}^2 \text{ V}^{-1} \text{ s}^{-1}$ and $153,800 \text{ cm}^2 \text{ V}^{-1} \text{ s}^{-1}$ and very finely resolved PL spectra add up to characterize to the best of our knowledge, the highest purity InP layer reported so far for CBE, MOMBE or GSMBE grown InP. These results demonstrate that the best results obtained by CBE concerning the quality of high purity InP are approaching the record values obtained by MOVPE, indicating that both techniques should ultimately be capable of achieving the same intrinsic material quality.

Acknowledgements

We are grateful to A. Mahé for very valuable technical support and to I. Kocijancic for sus-

tained help during the layer growth program. This work was supported by Thomson-CSF.

References

- [1] D. Huet, M. Lambert, D. Bonnevie and D. Dufresne, *J. Vacuum Sci. Technol.* B3 (1985) 823.
- [2] Y. Kawaguchi, H. Asahi and H. Nagai, in: *Proc. 12th Intern. Symp. on GaAs and Related Compounds*, Karuizawa, 1985, *Inst. Phys. Conf. Ser.* 79, Ed. M. Fujimoto (Inst. Phys., London-Bristol, 1986) p. 79.
- [3] J.L. Benchimol, F. Alaoui, Y. Gao, G. Le Roux, E.V.K. Rao and F. Alexandre, *J. Crystal Growth* 105 (1990) 135.
- [4] H. Heinecke, R. Höger, B. Baur and A. Miklis, *Electron. Letters* 26 (1990) 213.
- [5] M. Lambert, A. Peralès, R. Vergnaud and C. Starck, *J. Crystal Growth* 105 (1990) 97.
- [6] S.S. Bose, *Appl. Phys. Letters* 56 (1990) 752.
- [7] P.J. Dean and M.S. Skolnick, *J. Appl. Phys.* 54 (1983) 346.
- [8] W. Rühle and W. Klingenstein, *Phys. Rev.* B18 (1978) 7011.
- [9] D.C. Herbert, *J. Phys.* C10 (1977) 3327.
- [10] Y. Kawaguchi, H. Asahi and H. Nagai, *Japan. J. Appl. Phys.* 24 (1985) L221.
- [11] V. Walukiewicz, J. Lagowski, L. Jastrzebski, P. Rava, M. Lichtensteiger, C.H. Gatos and H.C. Gatos, *J. Appl. Phys.* 51 (1980) 2659.
- [12] A. Taguchi and S. Yamada, *J. Appl. Phys.* 61 (1987) 2412.
- [13] M. Razeghi, Ph. Maurel, M. Defour, F. Omnes, G. Neu and A. Kozacki, *Appl. Phys. Letters* 52 (1988) 117.

The optimization of $\text{In}_x\text{Ga}_{1-x}\text{As}$ and InP growth conditions by CBE

M.E. Sherwin, G.O. Munns, M.E. Elta, E.G. Woelk, S.B. Crary, F.L. Terry and G.I. Haddad

Center for High Frequency Micro-Electronics, Solid State Electronics Laboratory, 2435 EECS Building, The University of Michigan, Ann Arbor, Michigan 48109-2122, USA

Minimization of the number of experiments needed to fully characterize and optimize the growth of epitaxial material is the first important step in realizing state of the art device structures. While widely used in some fields such as chemical engineering, response surface modeling (RSM) has been little used in crystal growth applications. Using RSM, input parameters such as substrate temperature, hydride injector temperature and V/III ratio, were simultaneously adjusted to characterize the crystal growth process. This technique identified interactions among parameters, minimized the number of experiments necessary to understand and optimize the process, and minimized the variability of the growth process. RSM has been applied to the CBE growth of InGaAs and InP with the purpose of generating an operating point at which both good surface morphology and high mobility material can be produced. Although the best 77 K InP mobility was $70,000 \text{ cm}^2/\text{V}\cdot\text{s}$, in order to improve the surface quality the input parameters were changed so that the final mobility was $37,000 \text{ cm}^2/\text{V}\cdot\text{s}$. Although the quality of the InGaAs layers showed a dependence on the reactor history, there did not appear to be any sensitivity to variations made in the operating conditions. The best 77 K InGaAs mobility was $62,500 \text{ cm}^2/\text{V}\cdot\text{s}$.

1. Introduction

Response surface modeling (RSM) is a powerful technique for process optimization [1,2] but has been little used in crystal growth applications. One of the primary advantages of RSM is its ability to reduce the number of experiments required to fully characterize and optimize a process. This can be very important for CBE growth, where the large number of possible material systems precludes a factorial design of experiments. An integral part of RSM is the design of experiments. The choice of experimental points has a profound effect upon the uncertainty in the results. All of the experiments carried out in this study were performed using a first generation Varian Gen II MOMBE reactor. Source materials used were TMI, TEG, AsH_3 and PH_3 . During this study the flow rates of the group III elements were held constant. During InP growth, the TMI flow rate was 1.25 SCCM. During InGaAs growth, the TMI flow rate was 0.87 SCCM and the TEG flow rate was 1.13 SCCM. The control variables that were adjusted were: substrate temperature (T_{sub}), hydride injector temperature (T_{inj}), and V/III

ratio. The goal was to find an operating point that produces high mobility InGaAs and InP with good surface morphology.

Grown layers were evaluated for mobility and background carrier concentration, surface morphology, composition and growth rate. All mobility measurements were carried out at room temperature and 77 K using patterned Hall samples. Surface morphology was evaluated by visual inspection of Nomarski photographs. By comparing sample photographs against a present standard a rough measure of hillock density was determined. Surfaces were rated from zero to ten, with ten indicating a perfect surface.

2. Design of experiments

A common approach to experimentation involves holding all parameters fixed, except the one being explored. The response would then be maximized with respect to the first variable, which would then be fixed at its "optimal" point while the second variable is varied. This process proceeds, cycling through all the variables, multiple

times if necessary, until no further improvement in the response is observed. Unfortunately, this method can be very inefficient and there is no guarantee of finding the true maximal response [1]. One way of avoiding this problem is to set up a rectangular grid of operating points evenly distributed over the input parameter space. This has the disadvantage of requiring a large number of experiments.

For the optimization of InGaAs a central composite design of experiments was used. It is recommended that all input variables be normalized [3], so that they range from roughly -1 to 1 . This is especially true with this problem since T_{inj} can vary by $\pm 75^\circ\text{C}$ while the V/III ratio varies by only ± 5 . By normalizing all variables, all changes will be of the same order of magnitude. Assuming that the responses, morphology and mobility, could be modeled by second order equations and with three input variables, T_{sub} , T_{inj} and V/III ratio, a central composite design requires a minimum of 15 experiments [1]. The experimental points are divided into three categories: cube, star and center points. The cube portion consists of eight points arranged in a first order 2^3 factorial design, $(\pm 1, \pm 1, \pm 1)$. The star portion consists of six points, $(0, 0, \pm \alpha)$, $(0, \pm \alpha, 0)$ and $(\pm \alpha, 0, 0)$. Although the choice of α is up to the experimenter, a value of 1.682 was used following the advice in ref. [2]. This choice of α results in spherical contours of the expected error in the response surface around the center point. This feature names the design rotatable. The minimum number of center points $(0, 0, 0)$ is one, but for this experiment three center points were used to help obtain a better idea of the variance of the individual measurements. The 17 experiments were arranged in random order and conducted sequentially.

For the optimization of InP a minimum point near I-optimal design was used. Whereas a rotatable central composite design is arranged so that the response error is symmetrically distributed around the central point, an I-optimal design is arranged so as to minimize the average expected error in the response surface over the entire domain of the parameter space. As before, all input variables were normalized from -1 to 1 . Being a

minimum point design, only ten points were needed to model the second order response with three independent variables. One of the disadvantages of a minimum point design is its inability to provide a measure of the error of the fitted response surface. The ten experimental points were: $(0.96, 0.1, -0.1)$, $(-1, -1, -1)$, $(1, -1, 1)$, $(-0.1, 0.1, 0.96)$, $(-0.1, -0.96, -0.1)$, $(1, -1, -1)$, $(-1, 1, 0.25)$, $(1, 1, 1)$, $(-1, -0.25, -1)$ and $(0.26, 1, -1)$.

3. Results

The primary goal of this study is to determine a single operating point where both good InGaAs and InP can be grown. T_{sub} and T_{inj} are common variables for both InGaAs and InP, while the arsine and phosphine flow rates are independent for each material. The actual substrate temperature is estimated to be 55°C below the setpoint [4]. The morphology scale is from zero to ten. In order to scale the mobility, the natural log of the mobility was linearly scaled so that $10,000\text{ cm}^2/\text{V}\cdot\text{s}$ was equal to zero and $100,000\text{ cm}^2/\text{V}\cdot\text{s}$ was equal to ten. All of the statistical analyses performed for this study were carried out using RS/1, a statistical package donated to the University of Michigan by BBN Software Products Corporation of Cambridge, MA.

3.1. InGaAs

The center point of the central composite design was: $T_{sub} = 580^\circ\text{C}$, $T_{inj} = 900^\circ\text{C}$ and the V/III ratio was 10.0. The distances from the cube center to the cube faces were 20°C for T_{sub} , 50°C for T_{inj} and 2.5 for the V/III ratio. The distance to the star points was the distance to the cube face multiplied by 1.682.

The highest mobility InGaAs grown had a 77 K mobility of $62,500\text{ cm}^2/\text{V}\cdot\text{s}$, with a background carrier density of $5.3 \times 10^{14}\text{ cm}^{-3}$. The 77 K mobility showed a linear increase with sample number, with no discernible dependence on any of the three input parameters. It is believed that this is due to the outgassing of the hydride injector. The last four experiments with drastically different

operating conditions all showed 77 K mobilities over $50,000 \text{ cm}^2/\text{V} \cdot \text{s}$ while the surfaces of all 17 samples were featureless, showing no dependence on operating conditions. This indicates that the InGaAs is not very sensitive to the operating conditions.

Over the explored range of operating points, both the misfit and growth rate showed variation with the input parameters. The growth rate, as measured with a selective etch, showed a linear dependence on the V/III ratio and the injector temperature. This dependence is shown in fig. 1. The misfit, as measured by double crystal X-ray diffraction, is shown in fig. 2. The quadratic dependence of the misfit on the substrate temperature agrees with the findings of Andrews and Davies [5]. In determining the relationship for the misfit a small long term system drift observed earlier was ignored [4].

3.2. InP

The center point of the minimal point I-optimal design was: $T_{\text{sub}} = 580^\circ\text{C}$, $T_{\text{inj}} = 900^\circ\text{C}$ and the V/III ratio was 12.5. The excursions from the cube center to the cube faces were 25°C for T_{sub} , 60°C for T_{inj} and 5.0 for the V/III ratio. Initial

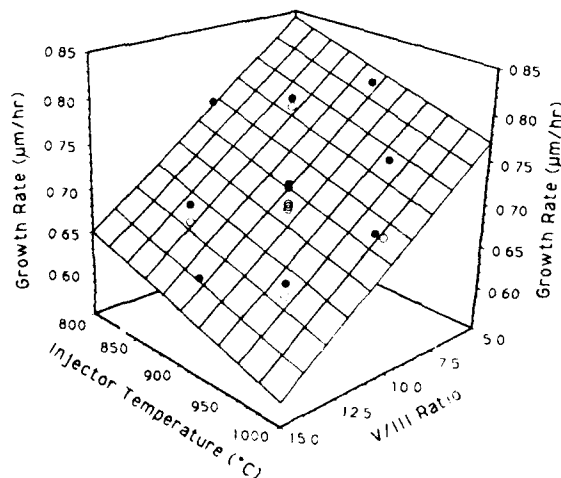


Fig. 1. InGaAs growth rate as a function of V/III ratio and hydride injector temperature. The filled symbols are above the fitted surface, while the empty symbols are below the fitted surface.

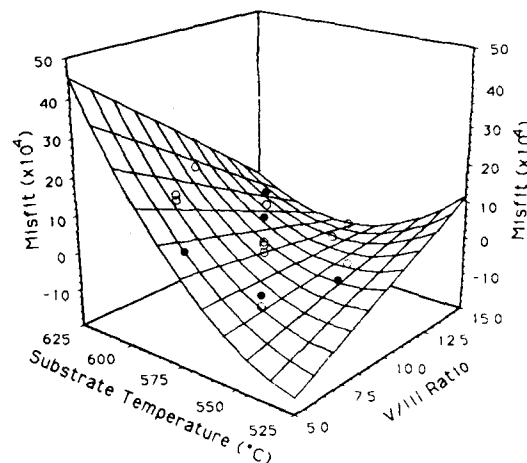


Fig. 2. InGaAs lattice misfit as a function of substrate temperature and V/III ratio. The filled symbols are above the fitted surface, while the empty symbols are below the fitted surface.

data analysis after the 10 experiments were completed indicated that the quadratic models for mobility and morphology were unacceptable. Since there were only 10 data points and 10 terms in the quadratic equation, the equation would pass through each data point. This would be adequate if the system had very low noise. In order to improve the validity of the fitted equations, data from previously grown InP layers were added to the data set. Although the group III flow rate was somewhat different, it was felt that this variation was secondary to the three variables being explored. A total of 16 data points was used to obtain the final fits to the mobility and morphology. The growth rate, as measured by an interface stain, did not show any statistically significant variation over the operating conditions.

Both the mobility and morphology showed significant dependence on the input parameters, with no discernible dependence on reactor history. Table 1 shows the correlation matrix between the input parameters and the response variables, scaled mobility and morphology. The most striking feature is the difference in signs between the scaled mobility and the morphology correlations with all three input parameters. This is further borne out in the fitted equations given below.

Table 1
Correlation matrix for InP 77 K scaled mobility (μ) and surface morphology (M) versus T_{sub} , T_{inj} and the V/III ratio

	T_{sub}	T_{inj}	V/III	μ	M
T_{sub}	1.0	0.065	0.196	0.347	-0.217
T_{inj}	0.065	1.0	0.107	-0.519	0.244
V/III	0.196	0.107	1.0	-0.211	0.353
μ	0.347	-0.519	-0.211	1.0	-0.358
M	-0.217	0.244	0.353	-0.358	1.0

Morphology

$$\begin{aligned}
 &= 8.8892 - 0.03862(T_{\text{sub}} - 580) \\
 &\quad + 0.01004(T_{\text{inj}} - 900) \\
 &\quad + 0.3399(V/\text{III} - 12.5) \\
 &\quad + 0.00531(T_{\text{inj}} - 900)(V/\text{III} - 12.5) \\
 &\quad - 0.00438(T_{\text{sub}} - 580)^2 \\
 &\quad - 0.04824(V/\text{III} - 12.5)^2, \\
 \mu &= 5.1347 + 0.036178(T_{\text{sub}} - 580) \\
 &\quad - 0.01905(T_{\text{inj}} - 900) \\
 &\quad - 0.1343(V/\text{III} - 12.5) \\
 &\quad + 0.01104(T_{\text{sub}} - 580)(V/\text{III} - 12.5) \\
 &\quad - 0.00298(T_{\text{inj}} - 900)(V/\text{III} - 12.5) \\
 &\quad - 0.02203(V/\text{III} - 12.5)^2.
 \end{aligned}$$

A graphical representation of this equation is difficult to obtain since this would require a four-dimensional graph. It is very important to take great care in trying to visualize this information [6]. A series of three-dimensional graphs with one of the input parameters chosen as a grouping variable is the best option.

These equations indicate that good morphology and high mobility do not occur at the same operating point. The highest 77 K mobility measured was 70,000 cm²/V·s, with a background carrier concentration of 1.0×10^{15} cm⁻³, but the sample had a very rough surface. The strong relationship between the surface morphology and the hydride injector temperature would involve a reaction with only partially decomposed phosphine as proposed

by Karlicek et al. [7]. Using the above equations and the optimization routine available in RS/1, we were able to determine an operating point that had both acceptable morphology and good mobility. This operating point was: $T_{\text{sub}} = 580^\circ\text{C}$, $T_{\text{inj}} = 894^\circ\text{C}$ and the V/III ratio = 14.2. Confirmation runs at this operating point gave a 77 K mobility of 37,000 cm²/V·s with good morphology. Both the surface quality and the 77 K mobility agreed well with the predicted values.

Some further work will be done to determine the effects of substrate misorientation and growth rate. It is anticipated that with these additional parameters it should be possible to obtain a good surface at the highest mobility available.

4. Conclusions

The results presented here show the applicability of response modeling techniques to the CBE growth process. As shown by the problems encountered with the minimum point near I-optimal design, it appears necessary to perform additional experiments to be able to test the model and to determine the error of the fit. Using RSM, a compromise operating point has been found which produces both good InP and InGaAs for future heterostructure work. A future effort will also involve modeling those elements of the growth process that drift in time.

Acknowledgments

The authors would like to thank 3-D Visions for their assistance in developing methods of visualizing some of the data. This work was supported by the US Army Research Office, URI Program, Contract DAAL03-86-K-0007.

References

- [1] G.E.P. Box, W.G. Hunter and J.S. Hunter, *Statistics for Experimenters* (Wiley, New York, 1978).

- [2] G.E.P. Box and N.R. Draper, *Empirical Model-Building and Response Surfaces* (Wiley, New York, 1978).
- [3] A.I. Khuri and J.A. Cornell, *Response Surface* (Dekker, New York, 1987).
- [4] E.G. Woelk, M.E. Sherwin and G.O. Munns, *J. Crystal Growth* 107 (1991) 1074.
- [5] D.A. Andrews and G.J. Davies, *J. Appl. Phys.* 67 (1990) 3187.
- [6] P. Hirsch, *Sci. Computing & Automation* 6 (1990) 19.
- [7] R.F. Karlick, Jr., D. Mitcham, J.C. Ginocchio and B. Hammarlund, *J. Electrochem. Soc.* 134 (1987) 470.

Growth of GaInAs and GaInAsP lattice matched to InP by metalorganic MBE

H. Heinecke, B. Baur, R. Höger, A. Miklis and R. Treichler

Siemens Research Laboratories, Otto-Hahn-Ring 6, W-8000 München 83, Germany

This study reports on the growth of GaInAs and GaInAsP single layers and heterostructures by metalorganic MBE (MOMBE) using trimethylindium (TMI), triethylgallium (TEG), arsine (AsH_3) and phosphine (PH_3) as starting materials. The growth parameters were optimized for a temperature range where also high quality InP is available. Ternary and quaternary layers exhibiting excellent uniformity across a wafer diameter of 3 inches were obtained with regard to layer thickness ($\leq 1.5\%$) and material composition. SIMS measurements on GaInAs/InP and GaInAsP/InP double heterostructures revealed even for the problematic element As an abrupt modulation of about three orders of magnitude or more depending on the structure.

1. Introduction

Metalorganic MBE (MOMBE, CBE) has been developed intensively during the last years. Although this technique offers specific advantages for the epitaxial growth of InP based materials, there are only a few reports on GaInAs [1,2] and GaInAsP growth [3,4]. The principal advantage of MOMBE for the deposition of As and P containing materials is given by the precracking of the hydrides AsH_3 and PH_3 in the gas injectors. In contrast to this, the situation seems to be more complex in metalorganic vapour phase epitaxy (MOVPE), where the hydrides have to be dissociated in the high temperature zones at the substrate area. Consequently, the different thermal stabilities of AsH_3 and PH_3 lead to a complicated As/P incorporation behaviour and require relatively high deposition temperatures [5,6]. However, also for the MOMBE growth there are anomalies reported concerning the incorporation of lattice constituent elements. Here the Ga uptake can be affected due to a growth temperature stimulated desorption of Ga containing molecules if TEG is used as an Ga source [1,7,8].

The intention of this investigation was to optimize the growth conditions for GaInAs and GaInAsP in a temperature range (515–530 °C)

where we obtain high quality InP layers. Special attention was paid to the modulation of the elements in InP/GaInAs/GaInAsP heterostructures and the achievable uniformity concerning layer thickness and material composition.

2. Experimental

As starting materials for the growth of InP/GaInAs/GaInAsP, pure AsH_3 , PH_3 (both thermally decomposed in a cracker), TMI and TEG were injected into the growth chamber. The mass flux of the gases was adjusted by high precision pressure control loops. Technical details of the growth equipment and the procedure of substrate preparation are given in ref. [9].

Half 2 inch InP wafers (iron doped 2° off (100) towards next (110) plane) were In – mounted on the 3 inch substrate holder excentrically, so that more than the radius of the holder is covered by the wafer. The wafers were analysed with regard to thickness, material composition and electrical properties (Hall measurements), 5/25/45 mm (positions A/M/B) counted radially inwards from the limit of the holder. Layer thicknesses were evaluated by SIMS analysis with an accuracy of better than 1.5%. The As/Ga profiles of the dou-

ble heterostructures were recorded by SIMS using O_2^+ or Cs^+ ion beams at an energy of 5.5 keV in a Cameca IMS 3F.

The material composition was determined by double-crystal X-ray diffraction and 300 K/2 K photoluminescence measurements.

3. Results and discussion

3.1. GaInAs growth

The dependence of the lattice matching of the GaInAs layers with respect to InP (evaluated from the X-ray data) on the growth temperature is shown in fig. 1a focusing on the most interesting temperature range between 510 and 545°C. The results marked using squares were obtained by injection of TMI and TEG through a multiple gas cell. This ensures even without substrate rotation an excellent compositional uniformity [10]. The data show that for a lattice matching of $\Delta a/a < 2 \times 10^{-4}$ (at fixed beam pressures), the substrate temperature has to be controlled in the range

between 525 and 531°C. The evaluation of the corresponding binary growth rates is in line with the earlier findings in ref. [1] that the GaAs growth rate is reduced by increasing the growth temperature (see fig. 1b). This phenomenon was recently explained by the desorption of diethylgallium molecules, which is promoted in the presence of indium [8,11].

Since TMI and TEG were injected via a multiple gas cell, alkyl exchange reactions which were indeed observed at room temperature [12] could also affect the growth mechanism. In order to achieve more insight, the TEG was injected via a separate second gas cell. Substrate rotation was used for these experiments. The data in fig. 1a (symbols: circles and triangles) indicate a more efficient incorporation of Ga in the case of separate injection since the TMI flux was exactly the same in all experiments. It can also be estimated that for strong Ga-rich conditions, the effect of the growth temperature on lattice matching is reduced.

The observed effect cannot be explained by errors in gas flux calibration, since a common injection through the second gas cell yields at 524°C a mismatch of -400 ppm. This finding is then in agreement with the upper curve in fig. 1a. However, the difference between separate and common injection needs further investigation.

Fig. 2 presents the dependence of the GaInAs growth rate and of the In concentration on the beam pressures of TMI and TEG. There is only a small tendency to In-rich conditions for lower growth rates which can be caused by crosstalk effects in the multiple gas cell or by the increased V/III ratio used for these experiments. These results show that growth rate ramping is possible without affecting material composition and that the above discussed Ga-molecule desorption must depend in a nearly linear way on the TEG adsorption flux for closely lattice matched GaInAs growth.

Fig. 3 gives an overview of the (004) X-ray Bragg reflection linewidths versus the lattice mismatch $\delta a/a$ for samples grown under different experimental conditions. The layer thicknesses vary between 1.6 and 2.1 μm . There are a number of samples with linewidths between 15 and 20 arc

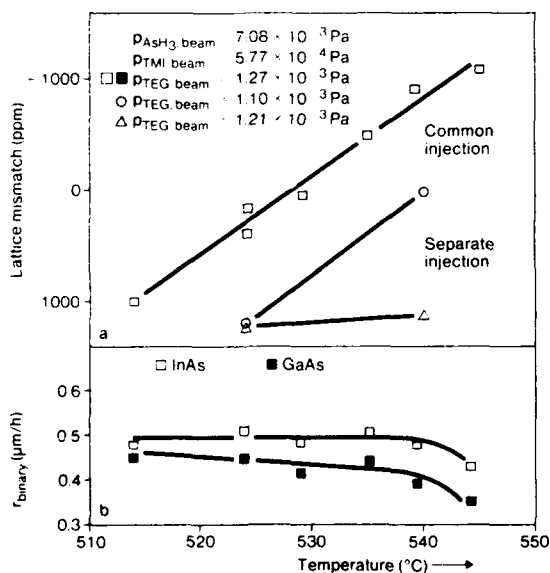


Fig. 1. Effect of growth temperature on: (a) GaInAs lattice matching using various TEG injection conditions; (b) InAs and GaAs growth rates.

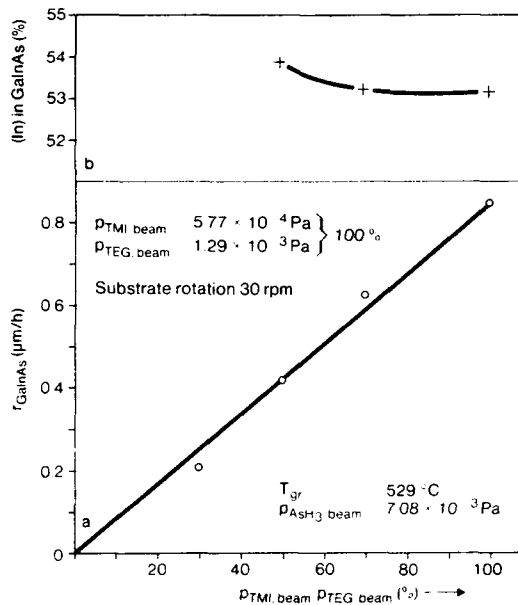


Fig. 2. Dependence of TMI and TEG beam pressure on: (a) GaInAs growth rate; (b) indium concentration in GaInAs.

sec. Even at a strong mismatch of minus 2500 ppm the FWHM value is only about 33 arc sec (this layer is only 1 μm thick). The data of figs. 2

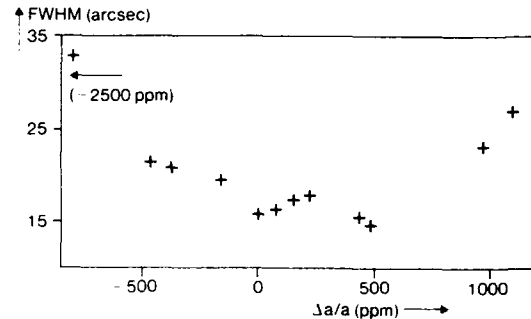


Fig. 3. Dependence of X-ray linewidths on lattice matching between GaInAs layer and InP substrate.

and 3 reflect the high degree of control over the material composition.

The free carrier concentration (always n-type) in the nominally undoped layers grown directly on semi-insulating substrates lies between 6×10^{14} and $2 \times 10^{15} \text{ cm}^{-3}$, depending on the process parameters. Hall mobilities between 10000 and $11000 \text{ cm}^2/\text{V} \cdot \text{s}$ were measured at 300 K and between 40000 and $47000 \text{ cm}^2/\text{V} \cdot \text{s}$ at 77 K.

The layers show intensive photoluminescence and the spectra are clearly dominated by bound exciton recombination. The FWHM of the bound exciton recombination is only 2.3 meV [10].

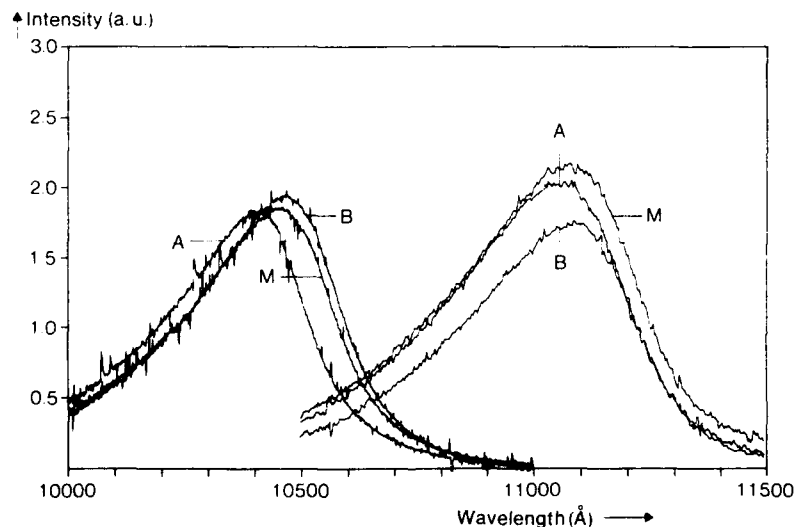


Fig. 4. Room temperature photoluminescence recorded on GaInAsP layers showing 1.05 and 1.11 μm energy gap wavelength material composition, measured at the positions A/M/B (beam pressures: $P_{\text{PH}_3} = 5.8 \times 10^{-3} \text{ Pa}$; $\lambda_{\text{R}} = 1.11 \mu\text{m}$: $P_{\text{AsH}_3} = 4.7 \times 10^{-4} \text{ Pa}$, $P_{\text{TMI}} = 3.2 \times 10^{-4} \text{ Pa}$, $P_{\text{TEG}} = 5.9 \times 10^{-4} \text{ Pa}$; $\lambda_{\text{R}} = 1.05 \mu\text{m}$: $P_{\text{AsH}_3} = 3.3 \times 10^{-4} \text{ Pa}$, $P_{\text{TMI}} = 5.5 \times 10^{-4} \text{ Pa}$, $P_{\text{TEG}} = 7.3 \times 10^{-4} \text{ Pa}$).

3.2. GaInAsP growth

According to the results of the preceding section, the quaternary materials were deposited at a temperature of 529°C. Fig. 4 presents the 300 K photoluminescence spectra of GaInAsP having an energy gap wavelength of 1.05 and 1.11 μm , respectively. The growth rate was 0.22 $\mu\text{m}/\text{h}$ for the 1.11 μm material and 0.4 $\mu\text{m}/\text{h}$ for the 1.05 μm material. Lattice matching to InP is better than 4×10^{-4} for the 1.11 μm wavelength materials. The spectra are recorded at the positions A/M/B of the layer (see also table 1). The FWHM of the 300 K photoluminescence lines varies between 42 and 46 meV. The flux ratios of $P_{\text{PH}_3, \text{beam}} / (P_{\text{PH}_3, \text{beam}} + P_{\text{AsH}_3, \text{beam}})$ for both material compositions fit quite reasonably into the curve presented in ref. [3]. Hall measurements revealed mobilities between 3000 and 4800 $\text{cm}^2/\text{V} \cdot \text{s}$ at 300 K and between 20000 and 31000 $\text{cm}^2/\text{V} \cdot \text{s}$ at 77 K with free carrier concentrations in the high 10^{14} cm^{-3} range.

3.3. Uniformity of grown materials

As already pointed out in section 3.1, extreme composition uniformity in GaInAs layers can be obtained even without substrate rotation. However, for the best thickness uniformity, substrate rotation is required in our MOMBE system based on a conventional MBE chamber. In table 1 the results are summarized with regard to thickness measurements, X-ray data and gap wavelength for InP, GaInAs and GaInAsP layers. The data are measured in the positions A/M/B on a half 2 inch wafer. Since substrate rotation was used for

these experiments, the same uniformity data from table 1 should be achieved over a real 3 inch substrate area.

The absolute thickness variation for all three materials is less than 1.5%, which is roughly the accuracy of the used measurement technique.

4. Growth of heterostructures

For the growth of InP/GaInAs/GaInAsP heterostructures, group V element switching at the interface is an important factor. In order to study the modulation of As, double stacks of double heterostructures were grown under different growth parameters. Since all single layer growth parameters are optimized in the same temperature range, the structure could be grown without growth interruption at 529°C. The material fluxes were switched by gas valves and not by cell shutters.

Fig. 5 presents the SIMS depth profiles of the As signal in sputtering through the structures. The $\text{Ga}_{0.47}\text{In}_{0.53}\text{As}$ layers in fig. 5a were grown under a high AsH_3 supply. The DH layer sequence closer to the substrate was grown at a constant In flux, whereas the upper structure (left side, fig. 5a) was grown at a nearly constant growth rate ($\approx 1 \mu\text{m}/\text{h}$). There is a sharp drop in the As signal by more than two orders of magnitude. The shape of the profiles prove that As interdiffusion at the growth temperature of 529°C plays only a minor role. The slopes of the As decay are affected by the growth speed, as can be seen in fig. 5a by comparing the As signal in the two InP cover layers.

At the higher growth rate, the As uptake is levelling out slower (surface layer). These ob-

Table 1
Data on lateral uniformity for thickness and material composition measured at three points (see section 2)

Position	InP layer thickness (μm)	GaInAs		GaInAsP		
		Layer thickness (μm)	$\Delta a/a$	Layer thickness	$\Delta a/a$	λ_{gap} (μm)
A	1.99	0.821	1.5×10^{-4}	0.807	-6.5×10^{-4}	1.048/1.107
M	2.02	0.830	0	0.800	-2×10^{-4}	1.050/1.108
B	1.99	0.818	0	0.795	0	1.052/1.109
Variation	1.5%	1.5%		1.5%		4 nm 2 nm

servations indicate that there must be a small but constant source of As, possibly coming from hot filaments [13], and a more intensive but depleting source which is built up by a positive adsorption-desorption balance at intermediate temperature spots in the system. The latter can be only detected directly after the growth of an As containing material and the amount depends on the As supply during that growth period. This is confirmed by the SIMS profile of an InP/GaInAsP/InP structure grown under a much lower AsH₃ supply (see fig. 5b). Similar but more pronounced effects of As uptake in InP are observed in MOVPE grown InP/GaInAs heterostructures [14]. In MOVPE these effects can be explained by autodoping originating from material grown on the susceptor.

Furthermore, fig. 5a reveals that also some Ga is carried into the InP cover layers, however, at a significantly lower level than As. Due to the fact that Ga molecules are desorbing during the growth of GaInAs or GaInAsP, a certain amount of these species can enter the hot cell areas. During the InP

growth these hot cells and filaments are then a rapidly depleting source of Ga.

It is worth mentioning that the observed Ga and As memory effects are at a very low absolute level (log scale in fig. 5!) so that the characteristics of the heterostructure and single layers are not disturbed. This is proved by the fact that the 2 K photoluminescence spectra of the InP cover layers from fig. 5a do not exhibit any peculiarities. In addition, GaInAs/InP single quantum well structures have been grown on 2° off oriented substrates without growth interruption at the interface.

The 2 K photoluminescence of 100 Å thick wells reveals symmetric and sharp PL lines with linewidths of only 4.3 to 4.5 meV.

5. Conclusions

The results of this study have shown that the epitaxial growth of high quality GaInAs and GaInAsP layers can be obtained. An optimized

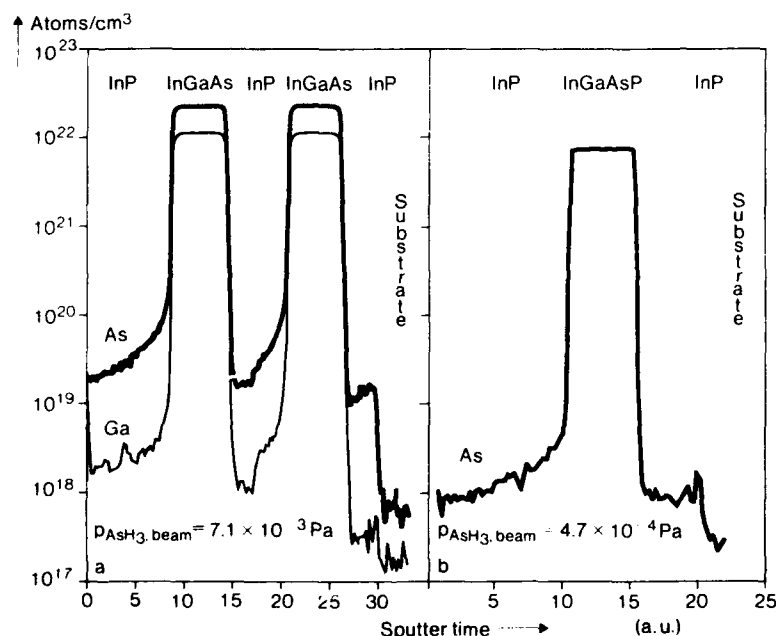


Fig. 5. SIMS depth profiles of arsenic and gallium measured on: (a) double InP/GaInAs/InP structure grown under different parameters (see text); layer thickness (in μm) from left to right: 0.5/0.22/0.4/0.22/0.22/ substrate; (b) GaInAsP ($\lambda_g = 1.1 \mu\text{m}$) DH structure; layer thickness (in μm) from left to right: 1.0/0.45/0.45/ substrate.

growth temperature equal for the growth of the binary, ternary and quaternary materials has been proved to enable the preparation of high quality layered heterostructures with extreme uniformity concerning layer thickness and material composition in lateral and vertical direction.

For the growth of InP/GaInAs/GaInAsP heterostructures it was demonstrated that a sharp modulation also of the critical element As can be achieved. For low InP growth rates the As uptake in InP is more localized at the heterointerface, whereas for higher InP growth rates the incorporation of As is more distributed over an increased thickness of the InP layer, however, at an even lower level.

This result can be of significant importance for the growth of quantum well and critical device heterostructures.

Acknowledgements

The authors are indebted to B. Jobst for performing X-ray measurements on a number of samples and to K. Beer and T. Hillmer for technical assistance.

References

- [1] Y. Kawaguchi, H. Asahi and H. Nagai, in: Extended Abstracts 18th (1986 Intern.) Conf. on Solid State Devices and Materials, Tokyo, 1986, p. 619.
- [2] W.T. Tsang, J. Electron. Mater. 15 (1985) 235.
- [3] W.T. Tsang, E.F. Schubert, T.H. Chiu, J.E. Cunningham, E.G. Burkhardt, J.A. Ditzenberger and E. Agyekum, Appl. Phys. Letters 51 (1987) 761.
- [4] J.L. Benchimol, G. Le Roux, H. Thibierge, C. Daguet, F. Alexandre and F. Brillouet, J. Crystal Growth 107 (1991) 978.
- [5] G.B. Stringfellow, J. Crystal Growth 68 (1984) 111.
- [6] S. Sugou, A. Kameyama, Y. Miyamoto, K. Furuya and Y. Suematsu, Japan. J. Appl. Phys. 23 (1984) 1182.
- [7] T.H. Chiu, W.T. Tsang, J.E. Cunningham and A. Robertson, Jr., J. Appl. Phys. 62 (1987) 2302.
- [8] T. Martin, C.R. Whitehouse and P.A. Lane, J. Crystal Growth 107 (1991) 969.
- [9] H. Heinecke, B. Baur, R. Höger and A. Miklis, J. Crystal Growth 105 (1990) 143.
- [10] H. Heinecke, B. Baur, R. Höger, A. Miklis and B. Jobst, J. Crystal Growth 107 (1991) 1062.
- [11] A. Robertson Jr., T.H. Chiu, W.T. Tsang and J.E. Cunningham, J. Appl. Phys. 64 (1988) 877.
- [12] P.D. Agnello and S.K. Ghandhi, J. Crystal Growth 94 (1982) 311.
- [13] J.L. Benchimol, F. Alaoui, Y. Gao, G. Le Roux, E.V.K. Rao and F. Alexandre, J. Crystal Growth 105 (1990) 135.
- [14] P.A. Houston, C. Blaauw, A. Margittai, M.N. Svilans, N. Pütz, D.J. Day, F.R. Shepherd and A.J. SpringThorpe, Electron. Letters 23 (1987) 931.

The design of an ECR plasma system and its application to InP grown by CBE

M.E. Sherwin, G.O. Munns, E.G. Woelk, T.J. Drummond *, M.E. Elta, F.L. Terry
and G.I. Haddad

Center for High Frequency Micro-Electronics, 2435 EECS Building, The University of Michigan, Ann Arbor, Michigan 48109-2122, USA

An electron cyclotron resonance (ECR) plasma system has been designed for the purpose of using an excited beam of gases during CBE growth. The system was designed to use hydrogen, nitrogen and argon. An ECR plasma system has the ability to ignite a low pressure and low temperature plasma with very low ion energies, which should minimize any damage to the growing layer. The motivation behind using a plasma during growth is the ability of atomic hydrogen to remove contaminants from the growing layer and to enhance the decomposition of organometallic precursors at low substrate temperatures. InP grown with a hydrogen plasma showed an n-type background carrier concentration of $6.0 \times 10^{16} \text{ cm}^{-3}$, with a rough surface and a strong photoluminescence peak at 1.378 eV. A control sample grown with excess hydrogen but without the plasma had a background carrier concentration of $1.0 \times 10^{15} \text{ cm}^{-3}$, a 77 K mobility of $65,000 \text{ cm}^2/\text{V}\cdot\text{s}$ and a very weak photoluminescence peak at 1.378 eV. The most likely cause for the layer degradation during plasma growth is an intrinsic defect such as an antisite defect or a vacancy. The n-type nature of the layer and the relatively high carrier concentration would seem to exclude the possibility of carbon or any other unintentional impurities.

1. Introduction

Hydrogen and nitrogen plasmas have been used to aid in the growth of GaAs, GaN and other materials [1–3]. When the epitaxial process occurs at very low pressures, below 1×10^{-4} Torr, an ECR plasma source is one of the most convenient techniques to generate a plasma. An ECR plasma system is a powerful method for generating an excited beam of gases during CBE growth.

ECR plasmas have been proven effective for the growth of nitrides, specifically GaN and AlN. For nitride growth without plasma assistance, it was found that hydrazine is a better source of nitrogen than ammonia [4]. However, work done with ECR plasmas and nitride growth have shown that nitrogen can be an effective source material [5]. The reactivity of ionized nitrogen eases some of the constraints on the growth conditions. The substrate temperature is no longer limited by the

decomposition temperature of the group V precursor. Meikle et al. [5] have suggested that the addition of hydrogen to a nitrogen plasma should help prevent the formation of Al–C during the growth of AlN from trimethylaluminum. In designing an ECR system for CBE growth of nitrides, it is important to have the ability to arbitrarily vary the composition of the plasma.

The ECR plasma injector was installed in a first generation Varian Gen II MOMBE reactor. The source materials used were trimethylindium (TMI) and 100% phosphine. The CBE system has been described elsewhere [6]. The experiments were carried out with a TMI flow rate of 1.25 SCCM, a V/III ratio of 14.2, a substrate setpoint of 580°C , an alkyl injector temperature of 50°C , and a hydride injector temperature of 894°C . The actual substrate temperature is estimated to be 525°C [6]. The samples were analyzed with patterned Hall measurements, etching C–V measurement and photoluminescence (PL). The excitation wavelength for the PL measurements was 488 nm, and the intensity was approximately $1.2 \text{ W}/\text{cm}^2$. The PL measurements were done at 14 K.

* Present address: Sandia National Laboratories, Albuquerque, New Mexico 87185, USA.

2. The ECR plasma system

The plasma injector was purchased from Wavemat, Inc. [7]. The injector was designed to fit in a standard Knudsen cell port in the source flange of the Varian Gen II MOMBE. A schematic of the injector is shown in fig. 1. The injector was designed to take advantage of the resonance that occurs when microwave energy couples with the resonance frequency of electrons in a static magnetic field [8]. Making use of this resonance allows the plasma to be ignited at low pressures and low temperatures, minimizing damage to the growing layer. The injector was designed to minimize plasma recombination within the discharge region. The materials located near the discharge region are quartz and stainless steel.

The gas delivery system was designed to allow independent control of gas composition and flow rate into the reactor. The present system was developed for use with nitrogen, hydrogen and argon. A layout of the gas delivery system is shown in fig. 2. There are two distinct portions of the gas delivery system, composition control and flow control into the reactor. The composition of

the gas stream is controlled by 3 parallel MKS 1259 mass flow controllers, allowing any mixture of hydrogen, nitrogen and argon. The flow rate into the growth chamber is controlled by a molecular flow element (MFE). By varying the pressure across the MFE, the flow rate can be varied up to 50 SCCM, with a resolution better than 0.1 SCCM. However, due to the low conductance of the plasma injector itself (3.7×10^{-3} l/s) [7], at flow rates over 5 SCCM the pressure drop of the injector itself is used to control the gas flow. It is postulated that replacing the MFE with a laminar flow element, which can sustain a larger pressure drop across the element, will result in a more controllable flow rate in the 10 to 20 SCCM range.

3. Results

In order to test the applicability of a hydrogen plasma during the growth of InP three layers were grown: bulk undoped InP, InP with a hydrogen plasma, and InP with excess hydrogen but no plasma. The electrical properties are summarized

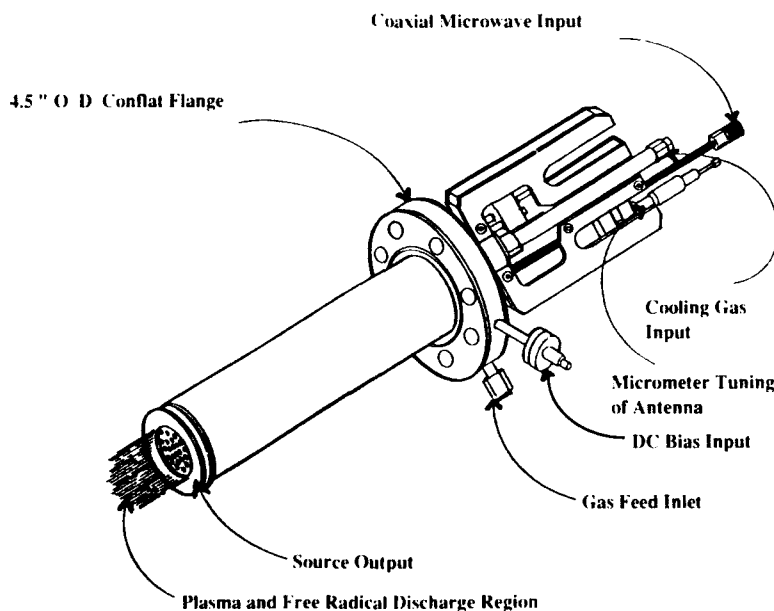


Fig. 1. The ECR plasma injector purchased from Wavemat, Inc.

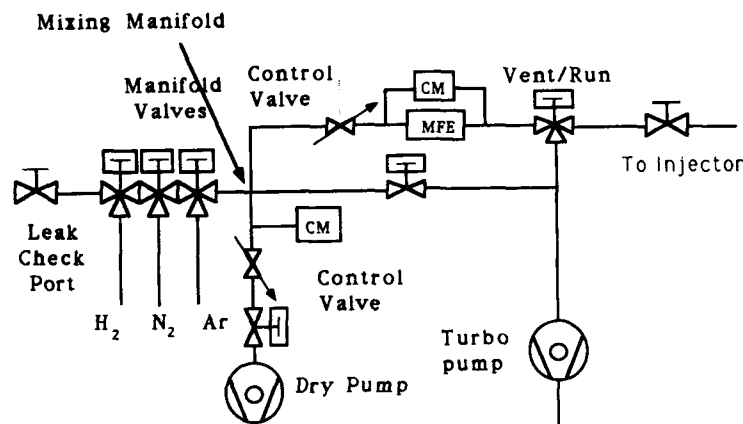


Fig. 2. Layout of the gas delivery system.

in table 1. Samples 135 and 136 had an excess hydrogen flow of 9.5 SCCM, while the plasma for sample 135 was ignited with 50 W. Sample 135 showed significant deterioration in surface quality, while samples 134 and 136 had excellent surfaces.

Photoluminescence spectra were taken of the three samples in the 1.2 to 1.5 eV range. Sample 134 shows a band-to-band peak at 1.413 eV with a FWHM of 4.8 meV. Sample 135 shows a band-to-band peak at 1.410 eV with a FWHM of 16.8 meV and a strong second peak at 1.378 eV with a FWHM of 20.7 meV. Sample 136 shows a band-to-band peak at 1.413 eV with a FWHM of 4.8 meV and a weak second peak at 1.378 eV. Fig. 3 shows the photoluminescence spectra of samples 134, 135 and 136.

The presence of the high background carrier concentration in sample 135 seems to indicate an unintentional elemental impurity. However, it appears that a more likely cause is an intrinsic

crystal defect such as an anti-site defect or a vacancy. After installing the ECR plasma system, hydrogen and nitrogen were flowed into the growth chamber and analyzed with a UTI-100 quadrupole mass spectrometer both with and without igniting a plasma. No contaminants were observed over the range from 1 to 100 amu. The energy of the second PL peak corresponds to a carbon acceptor level [9], but the n-type nature of the layer and the relatively high carrier concentration precludes carbon as the unintentional impurity.

The original purpose behind introducing the hydrogen plasma during growth was to prevent the incorporation of unwanted contaminants.

Table 1
Electrical data for bulk InP, bulk InP with a hydrogen plasma and bulk InP with excess hydrogen

Sample No.	Hydrogen	Plasma	Growth rate ($\mu\text{m/h}$)	n (77 K) (cm^{-3})	μ (77 K) ($\text{cm}^2/\text{V}\cdot\text{s}$)
134	No	No	0.717	1.5×10^{15}	57000
135	Yes	Yes	0.724	6.0×10^{16}	2700
136	Yes	No	0.590	1.9×10^{15}	65000

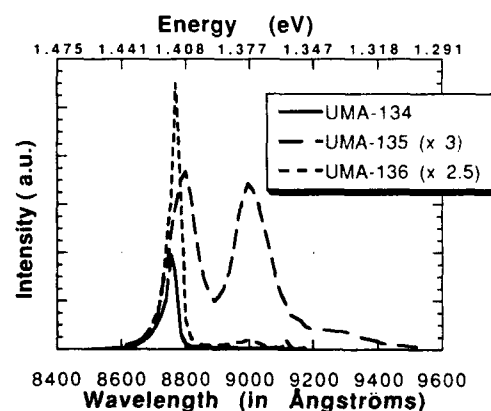


Fig. 3. Photoluminescence spectra of samples 134, 135 and 136. The measurements were done at 14 K.

However, it appears that the hydrogen plasma interfered with the growth process. The atomic hydrogen can tie up surface sites, and can also form volatile compounds on the surface, preventing their incorporation into the growing layer. Reactions between partially decomposed phosphine and the atomic hydrogen would form phosphine, which would not decompose at the substrate. Similar behavior has been seen during hydride vapor phase epitaxy of InP with partially decomposed phosphine [10]. The partially decomposed phosphine would form volatile compounds on the surface, leaving a phosphorus deficient surface. Karlicek et al. [10] have also observed a deterioration in surface quality during growth with a phosphorus deficient surface. Dry etching of InP with hydrogen plasmas results in the formation of indium droplets on the surface [11,12]. The formation of indium droplets during etching can even occur at 50°C, demonstrating the highly reactive nature of the hydrogen plasma. During the growth of InP, the preferential etching of phosphorus by the hydrogen plasma will result in the growth of a phosphorus deficient layer.

Sample 136, grown with excess hydrogen but no plasma, showed only a weak PL signal at 1.378 eV. Since the reactivity of molecular hydrogen is much less than that of atomic hydrogen, the corresponding decrease in the defect level signal was expected. Also the good electrical properties and the excellent surface of sample 136, indicates that it is the high reactivity of the atomic hydrogen that damaged sample 135. The reduction of the growth rate of sample 136 may be a result of molecular hydrogen tying up surface sites on the growing surface.

Although it is impossible to say with certainty what type of intrinsic crystal defect is responsible for the quality of sample 135, it does seem that crystal defects and not contamination appears to be the cause of the high carrier concentration, the PL peak at 1.378 eV and the surface degradation.

4. Conclusions

An electron cyclotron resonance plasma system has been constructed for the injection of a hydrogen, nitrogen or argon plasma during CBE growth.

Initial experiments carried out with a hydrogen plasma during the growth of InP resulted in layers with a high n-type carrier concentration and a strong photoluminescence peak at 1.378 eV. The most likely cause for this is an intrinsic defect such as an antisite or a vacancy. Although hydrogen plasmas have been effective during the low temperature growth of GaAs, it does not appear that the use of a hydrogen plasma at normal growth temperatures ($\approx 500^\circ\text{C}$) is useful for InP growth. Future work will focus on determining the type of crystal defect and developing a better model of the interaction between hydrogen and the growing surface.

Acknowledgments

The authors would like to thank Mr. Larry Davis for performing the photoluminescence measurements. The authors would also like to acknowledge the assistance provided by both MKS Instruments Inc. and Wavemat, Inc. This work was supported by the US Army Research Office, URI Program, Contract DAAL03-86-K-0007.

References

- [1] S. Sugata, A. Takamori, N. Takado, K. Asakawa, E. Miyauchi and H. Hashimoto, *J. Vacuum Sci. Technol.* B6 (1988) 1087.
- [2] S. Zembutsu and T. Sasaki, *J. Crystal Growth* 77 (1986) 250.
- [3] G.V. Jagannathan, M.L. Andrews and A.T. Habig, *Appl. Phys. Letters* 56 (1990) 2019.
- [4] S. Fujieda, M. Mizuta and Y. Matsumoto, *Japan. J. Appl. Phys.* 26 (1987) 2067.
- [5] S. Meikle, H. Nomura, Y. Nakanishi and Y. Hatanaka, *J. Appl. Phys.* 67 (1990) 483.
- [6] E.G. Woelk, M.E. Sherwin and G.O. Munns, *J. Crystal Growth* 110 (1991) 452.
- [7] Wavemat, Inc., 44780 Helm St. Plymouth, MI 48170, USA.
- [8] J. Asmussen, *J. Vacuum Sci. Technol.* A7 (1989) 883.
- [9] L.D. Zhu, K.T. Chan, D.K. Wagner and J.M. Ballantyne, *J. Appl. Phys.* 57 (1985) 5486.
- [10] R.F. Karlicek, Jr., Mitcham, J.C. Ginocchio and B. Hammarlund, *J. Electrochem. Soc.* 134 (1987) 470.
- [11] R.P.H. Chang, C.C. Chang and S. Darack, *J. Vacuum Sci. Technol.* 20 (1982) 45.
- [12] J.H. Thomas III, G. Kaganowicz and J.W. Robinson, *J. Electrochem. Soc.* 135 (1988) 1201.

Surface reaction of III–V compound semiconductors irradiated by As and Sb molecular beams

Mitsuaki Yano, Hisakazu Yokose, Yoshio Iwai and Masataka Inoue

New Material Research Center, Osaka Institute of Technology, Asahi-ku Ohmiya, Osaka 535, Japan

For the growth of III–V_A/III–V_B heterostructures with a sharp interface, it is important to suppress the interchanging reaction of column V elements between the impinging molecules (V_A) and atoms of the substrates (V_B). In order to obtain a systematic understanding, the chemical reaction has been examined for eight different substrate materials with beams of As and Sb. We have determined the critical temperature at which this reaction becomes predominant by using reflection high energy electron diffraction. Raman scattering measurement was also used to analyze the composition of beam-irradiated surface. Experimental results are interpreted reasonably well by the thermochemical property of these III–V compound semiconductors.

1. Introduction

Different types of heterostructure using III–V compound semiconductors have been widely examined as a fundamental material for opto-electronic and high-speed device applications in the last decade. In order to realize these devices with high quality performance, fine control of heterointerface must be achieved at an atomic scale. Excepting GaAs/AlGaAs, however, there are still problems on the interface control by molecular beam epitaxy (MBE). On the MBE growth of III–V_A/III–V_B type heterostructures, the dominant problem to control interface properties is an interchanging reaction between V_A molecules in the beam and V_B atoms in the epitaxial layer. Tuttle et al. reported a strong dependence of electronic properties on the growth condition of InAs channel clad with AlSb [1]. They found that controlled growth of the interface bondings, InSb-like or GaAs-like, is important to obtain high mobility electrons in the channel. We have also found that the heterointerface between GaAs and GaSb becomes graded in composition [2]. These interface properties should be governed by the chemical reaction of highly volatile column V elements between the molecular beam and the crystal surface.

In this paper, we report systematic analysis on the surface reaction of impinging molecular beams with various III–V compound semiconductors. We focus on the reaction of As and Sb beams with the following various semiconductors: AlAs, AlSb, GaP, GaAs, GaSb, InP, InAs and InSb. The observed results will be discussed from a viewpoint of thermochemical property of III–V compound semiconductors.

2. Experimental procedure

The apparatus used here is ANELVA-620 type conventional MBE system. Pure metals of Al, Ga, In, As and Sb were used as sources of molecular beams. In-situ grown epitaxial layers, AlAs, AlSb, GaAs, GaSb, InAs and InSb on (100) oriented GaAs substrates, were used for studying surface reaction with As and Sb molecular beams. All the epitaxial layers used for experiments were grown for 1 μm and were confirmed to have a smooth surface by using reflection high energy electron diffraction (RHEED). In the case of GaP and InP, surfaces of (100) oriented single crystals were used for the experiment. Crystals of GaP and InP were heated in As beam irradiation for a few minutes to

of 514.5 nm line from Ar ion laser to analyze the characteristic phonon mode.

3. Results of RHEED experiment

In fig. 1, we summarize the results of RHEED experiment for the series of III-V compound semiconductors. This figure shows the reconstructed RHEED pattern observed at each temperature under various conditions. As we can see, the surface structure has changed with increasing substrate temperature. For instance, the surface of InAs changed the structure from (2×4) As to (4×2) In at 440°C when it was heated without beam irradiation. Such a structural change would be due to the selective sublimation of column V atoms [4]. With increasing the temperature in addition, the streaky RHEED signal has been changed into the spotty or the diffused ring patterns. Open and solid circles in fig. 1 show the critical temperatures at which the spot and the ring patterns have appeared, respectively. The spot pattern indicates the formation of three-dimensional (3D) surface structure. The ring pattern denotes the buildup of amorphous or polycrystalline films on the irradiated surface. Here, we name the critical temperatures of this change in RHEED pattern as T_c .

When the samples are heated without beam irradiation, T_c should correspond to the critical temperature for dominant compositional sublimation of column V atoms. As shown in fig. 1, we observed considerable shift of T_c from the sublimation temperature when the sample was heated under the beam irradiation. When the column V atoms in the beam are the same as the component of the crystal, the beam irradiation increases T_c and stabilizes the surface to prevent compositional sublimation. This increase of T_c should be due to the shift of equilibrium vapor pressure between the sublimed column V atoms and the molecular beam. When the column V beam is different from the component element in crystal, on the other hand, the critical temperature does not necessarily increase by the irradiation. T_c of the series of antimonides decreases by the irradiation of As beam, while T_c of phosphides

and arsenides increases by the irradiation of As and Sb beams. For the case of AlAs, we could not see any signs of deterioration in surface morphology up to 800°C , independent of the beam irradiation.

4. Analysis of thermochemical properties

Fig. 2 summarizes sublimation temperatures (T_c without beam irradiation) for the various compound semiconductors appearing in fig. 1. These temperatures are also compared with the binding energies, i.e., cohesive energies per bond [5]. As can be seen in fig. 2, the sequence of T_c is in qualitative agreement with that of the binding energy. Thus we have confirmed experimentally that the sublimation temperature is governed by the binding energy. Note that T_c for AlAs is probably well over 800°C .

Next, we discuss the shift of T_c caused by the irradiation of two different beams, As or Sb. In order to understand the shift of T_c by the beam irradiation, we measured Raman spectra from these beam-irradiated samples. It is revealed by the measurement that compositional change has been introduced to the irradiated surface. For instance, fig. 3 shows the Raman signals from GaSb surface irradiated by As beam. The irradiation period was 30 min and the substrate temperatures for the irradiation were 520 and 420°C for samples (a) and (b), respectively. The spectrum (a) contains two major peaks characteristics of TO and LO phonon modes from GaAsSb alloy crystals

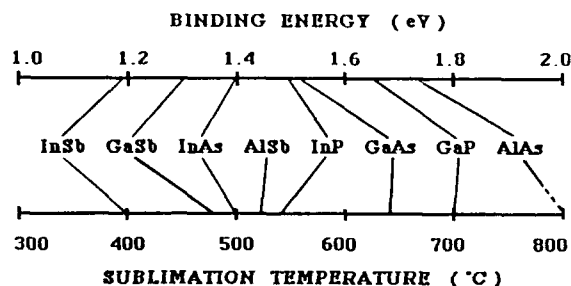


Fig. 2. Relationship between the sublimation temperature (observed T_c for without beam irradiation) and the binding energy.

and a weak peak from LO of GaSb, i.e., phonons from GaSb were replaced by those from GaAsSb by the irradiation of the As beam. This result indicates that the irradiation of the As beam at 520°C has turned the GaSb surface to GaAsSb. Because the skin depth of the probing light is expected to be about 120 nm for GaAs, this result indicates that about 60 nm thick GaSb surface has been turned to GaAsSb by the As irradiation. On the contrary, the surface of GaSb irradiated by As at 420°C did not show any trace of GaAs or GaAsSb phonon modes as shown by spectrum (b). As well as the Raman signal, the RHEED pattern from the sample did not show any appreciable change by the irradiation, which indicates that GaSb at 420°C does not react with the As beam to produce a GaAs bond.

On the left and right axes of fig. 4, we show the material's name (framed) of which the Raman signal has been detected on each surface after the beam irradiation. The beam-irradiated surface is always a transition layer which consists of binary or ternary compounds. In the transition layer, the

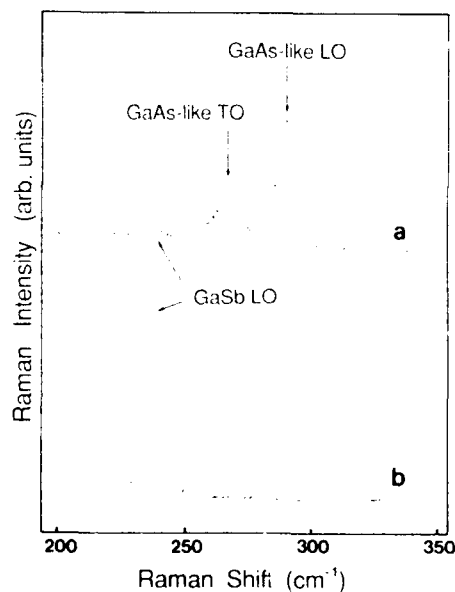


Fig. 3. Recorder traces of Raman spectra from GaSb surface irradiated by As beam. The irradiation period was 30 min and the substrate temperatures were 520 and 420°C for samples (a) and (b), respectively.

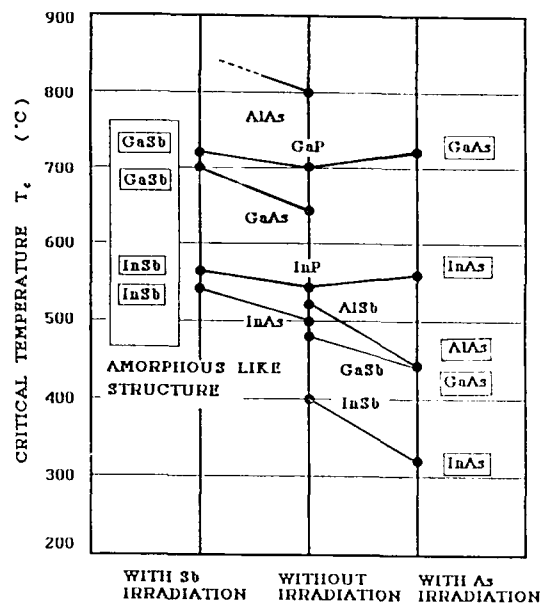


Fig. 4. Shift of critical temperatures due to the beam irradiation. On the central axis, T_c without beam irradiation (sublimation temperature) is shown for various compound semiconductors. Under the beam irradiation, different T_c shown on the left and right axes were observed. In frames, we show the material's name of which the Raman signal has been detected on each surface after the beam irradiation.

column V element of the original crystal has been replaced by other atoms from the molecular beam. We also note in fig. 4 that Sb atoms of any antimonides are easily replaced by As even if they have been kept at lower temperatures below the sublimation temperature. On the contrary, As atoms of any arsenides are stable for Sb irradiation until they are heated to higher than the sublimation temperature. Phosphides do not react with beams of As and Sb, unless they are heated above the sublimation temperature. This behavior is probably the direct reflection of the binding energy, i.e., atoms in crystals react at high temperatures with molecular beams to stabilize the surface by forming the cap layer with higher binding energy. As seen in fig. 2, the sequence for the binding energy is as follows: phosphides > arsenides > antimonides if the column III component is the same.

This type of chemical reaction is not desirable to obtain a sharp interface by MBE. If V_A atoms in a III- V_A crystal are easily replaced by V_B atoms in the molecular beam, the same chemical reaction should form a graded heterointerface in the III- V_A /III- V_B structures [6]. Moreover, the heterointerface under such a conditions should be rough at an atomic scale. This is because the beam-irradiated surface easily becomes a 3D structure even at lower temperatures below the sublimation temperature, which has been mentioned above in the RHEED analysis. The similar interchanging reaction will be observed for surface atoms of arsenides and antimonides when they are irradiated by P beam [7]. In order to prevent the chemical reaction and to obtain a sharp heterointerface, it is important to maintain the growth temperature as low as possible.

5. Summary

We have studied the surface stability of III-V compound semiconductors under the irradiation of column V molecular beams. When the crystals are heated without beam irradiation, decomposition sublimation of the column V atoms is observed. The critical temperature for sublimation is governed by the binding energy of the binary compound. When the samples are irradiated by beams, we have observed different critical temperatures. The shift of critical temperatures is attri-

buted to the chemical reaction between the molecular beam and the crystal surface. For the controlled growth of heterostructures, it is important to minimize this type of chemical reaction.

Acknowledgements

The authors wish to thank A. Kawaguchi and R. Hagiwara for their experimental assistance. This work was supported in part by the Japan Private School Promotion Foundation on The Scientific Research Promotion Foundation and a Grant-in-Aid for Scientific Research from The Ministry of Education, Science and Culture.

References

- [1] G. Tuttle, H. Kroemer and J.H. English, *J. Appl. Phys.* 67 (1990) 3032.
- [2] M. Yano, M. Ashida, A. Kawaguchi, Y. Iwai and M. Inoue, *J. Vacuum Sci. Technol.* B7 (1989) 199.
- [3] G.J. Davies, R. Heckigbottom, H. Ohno, C.E.C. Wood, and A.R. Calawa, *Appl. Phys. Letters* 37 (1980) 290.
- [4] C.E.C. Wood, K. Singer, T. Ohashi, L.R. Dawson and A.J. Noreika, *J. Appl. Phys.* 54 (1983) 2732.
- [5] J.C. Phillips, *Bonds and Bands in Semiconductors* (Academic Press, New York, 1973) pp. 40-50.
- [6] M. Yano, M. Ashida, Y. Iwai and M. Inoue, *Appl. Surface Sci.* 41-42 (1989) 457.
- [7] S. Nagao, M. Takashima, Y. Inoue, M. Katoh and H. Gotoh, *J. Crystal Growth* 111 (1991) 521.

Indium antimonide doped with lead telluride grown by molecular beam epitaxy

D.L. Partin, J. Heremans and C.M. Trush

Physics Department, General Motors Research Laboratories, Warren, Michigan 48090-9055, USA

A PbTe dopant source has been used to grow n-type InSb using the molecular beam epitaxy growth technique. From Auger electron spectroscopy studies, no surface segregation of tellurium or lead is observed up to $\sim 10^{19} \text{ cm}^{-3}$ doping levels. The correlation between the PbTe flux used during growth and the electron density in the grown films is very good, suggesting that the incorporation of tellurium is near unity. Six-probe Hall measurements of carrier transport gave room temperature mobilities as high as $51,300 \text{ cm}^2 \text{ V}^{-1} \text{ s}^{-1}$ at an electron density of $2.9 \times 10^{16} \text{ cm}^{-3}$ (54,300 at an electron density of $1.9 \times 10^{16} \text{ cm}^{-3}$ at 110 K) for a film of $4.0 \mu\text{m}$ thickness on an InP substrate.

1. Introduction

Indium antimonide is a narrow energy band gap semiconductor with a very small electron effective mass and thus may be useful for long wavelength optoelectronic devices and for transport devices such as magnetoresistors. Epitaxial InSb films grown by molecular beam epitaxy (MBE) may potentially be doped n-type with Si or Sn, or with the group VI elements S, Se, or Te. Of the group VI elements, Te may be advantageous because of its relatively lower vapor pressure, increasing its incorporation efficiency at relatively high film growth temperatures. Use of a captive Te source, such as PbTe, is suggested by studies of Te and PbTe as Te dopant sources for MBE-grown GaAs, GaSb, and AlSb. Near stoichiometric PbTe sublimates predominantly as a molecule, liberating a Te dopant atom on the growing surface and a Pb atom, which may re-evaporate. In GaAs, use of an elemental Te source results in surface accumulation of Te, possibly in the form of Ga_2Te or Ga_3Te_2 , which tends to complicate growth [1]. Use of a PbTe dopant source still resulted in Te surface accumulation and desorption at growth temperatures above 570°C [2]. Lead appears to have

negligible incorporation efficiency in GaAs at typical MBE growth temperatures $> 480^\circ\text{C}$ [2,3]. The use of PbTe source material alloyed with about 10% elemental Pb appears to alleviate the problem of Te surface accumulation, since it reduces the residual amount of Te_2 , which sublimates from PbTe [3,4]. This results in an atomic Pb flux which is only a factor of 2 less than the PbTe flux. However, this is not a problem, with apparently complete thermal desorption of Pb from a GaAs surface [3].

These encouraging results led naturally to the evaluation of PbTe as an n-type dopant for the antimonides GaSb and AlSb [2,5]. In GaSb, it appears that Te (from a PbTe source) does not surface accumulate. This behavior differs from that of Te in GaAs, apparently because of atomic size effects [2]. In GaSb, Te desorption has been measured above $500\text{--}540^\circ\text{C}$ [2,5]. By contrast, Te incorporation in AlSb decreases at low temperatures, possibly because of solid solubility limitations. The free electron concentration in PbTe-doped GaSb is generally lower than would be obtained if all incident Te at the growth surface resulted in a free electron. Pb was not clearly detected in GaSb doped from an apparently

stoichiometric PbTe source oven [2], but was clearly observed in GaSb which was heavily doped with a Pb-rich PbTe source oven [5].

2. Experiment

The encouraging results obtained in PbTe-doped GaSb and AlSb led us to evaluate PbTe as a dopant source for MBE-grown InSb. These studies were done in a Physical Electronics Model 400 MBE system which was previously used to grow $\text{Pb}_{1-x}\text{Eu}_x\text{Se}_{1-y}\text{Te}_y$ for long wavelength diode lasers [6]. The main source ovens previously used contained PbTe, PbSe, Eu, and Te. A new stainless steel cryoshroud surrounding the source ovens was installed, and new source ovens for In and Sb were used. The Sb source oven was not equipped with a cracker, and hence its flux was mainly composed of Sb_4 . The PbTe was compounded from 6-9's pure Pb and Te in a quartz ampoule at 975°C . The compounded ingot was then heated in a thermal gradient to drive off relatively volatile impurity species. This left the material slightly Pb-rich, but still single phase PbTe. From thermoelectric voltage measurements, it was estimated that the PbTe contained a Te vacancy concentration of $< 10^{18} \text{ cm}^{-3}$. However, during sublimation in the MBE source oven, the surface composition of the PbTe shifts to give congruently evaporating material [7]. Our starting material was probably sufficiently near to the stoichiometric composition that a congruently subliming vapor was achieved. Others who use $\sim 10\%$ Pb-rich material have a two phase mixture. With relatively little material sublimed for dopant studies, they would presumably obtain a Pb-rich and Te_2 -deficient flux, just as they desired.

Semi-insulating, iron-doped, (100) oriented InP substrates [8] were used for InSb film growth. Earlier studies indicated that it was somewhat more straightforward to obtain high electron mobilities in MBE-grown InSb films grown on these substrates than on GaAs substrates [9]. After etching the InP substrates in a dilute bromine-methanol solution, the substrates were heated to 400°C in an Sb_4 flux. We note that in the previous study of InSb/InP, thermal oxide desorption

was done in the more conventional arsenic flux. Our procedure gave a streaked RHEED pattern, and an Auger electron spectroscopy (AES) study of the resultant surface (using an AES instrument attached to the MBE system) showed that some surface oxide was still present. The same sample was then briefly heated to 460°C in an Sb_4 flux. The resultant AES spectrum showed little or no oxygen. However, the RHEED streaks were less clear, and InSb films grown on this surface had somewhat lower electron mobilities than films which were grown on InP surfaces which were preheated at 400°C .

The In, Sb, and PbTe fluxes were measured before and after growth using a water-cooled quartz crystal deposition monitor which could be moved into the sample growth position, thus giving an absolute flux measurement in the absence of re-evaporation phenomena. The (atomic) Sb/In flux ratio was adjusted to 1.15 before growth. Growth was abruptly initiated at 360°C and a growth rate of $0.9 \mu\text{m/h}$. These conditions were held constant during growth.

3. Transport studies

Our initial attempts to grow undoped InSb films resulted in heavily n-type material ($n = 1 \times 10^{18} \text{ cm}^{-3}$), as determined by Van der Pauw measurements. After growing many films (encompassing 4 reloads of the In and Sb ovens), the background free electron density at 300 K dropped to $(4-5) \times 10^{16} \text{ cm}^{-3}$. We then analyzed these films with a secondary ion mass spectrometer (SIMS) [10], and found that the main impurity was selenium. This implies that a residual background existed inside the MBE machine due to the previously evaporated PbSe, and that it was gradually becoming coated with In and Sb. Apparently, the higher vapor pressure of Se compared to Te is the reason for the appearance of Se as the residual background donor. However, additional growths failed to further reduce the electron density. SIMS analysis of the Sb source material (SbA) revealed (in units of counts per second) ^{80}Se (37) and ^{126}Te (2). This led us to evaluate another Sb source (SbB). SIMS analysis of SbB showed that it had

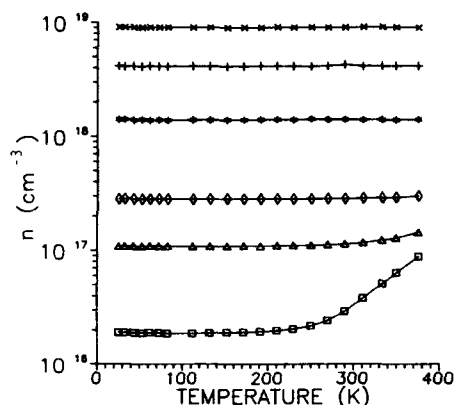


Fig. 1. Electron densities (n) of PbTe-doped InSb versus temperature.

^{34}S (5) and no ^{80}Se . Other impurities, especially donors (Si, Sn, Te, and Pb) were sought but not found. These data cannot be readily quantified, since the relative sensitivity factors in an Sb matrix are not known. Our most recent growths using SbB give a room temperature carrier density of $1.9 \times 10^{16} \text{ cm}^{-3}$ and a mobility of $63,000 \text{ cm}^2 \text{ V}^{-1} \text{ s}^{-1}$ for a film $5.0 \mu\text{m}$ thick. Since the intrinsic carrier density in InSb at room temperature is $\sim 2 \times 10^{16} \text{ cm}^{-3}$, the films are intrinsic at this temperature. At 77 K, $n = 1.24 \times 10^{15} \text{ cm}^{-3}$ and the mobility is $99,000 \text{ cm}^2 \text{ V}^{-1} \text{ s}^{-1}$. All other growths of PbTe-doped InSb reported in this paper were done using SbA with a background electron density of $(4-5) \times 10^{16} \text{ cm}^{-3}$.

Six-probe DC Hall effect measurements were made on PbTe-doped samples at temperatures from 25 to 370 K in magnetic fields from 0.25 to 2 T. The samples with donor concentrations above $1 \times 10^{17} \text{ cm}^{-3}$ showed little intrinsic magnetoresistance, and had a constant Hall coefficient. Carrier densities and mobilities are shown in figs. 1 and 2, respectively, as measured in fields up to 0.25 T. For all samples, even the highest doped one, the mobility decreases as the temperature is increased.

The free electron concentration versus tellurium concentration is shown in fig. 3. The tellurium concentration was calculated under the following conditions. (1) Our PbTe source material sublimates mainly as a molecule (which has been verified by observations with a quadrupole mass

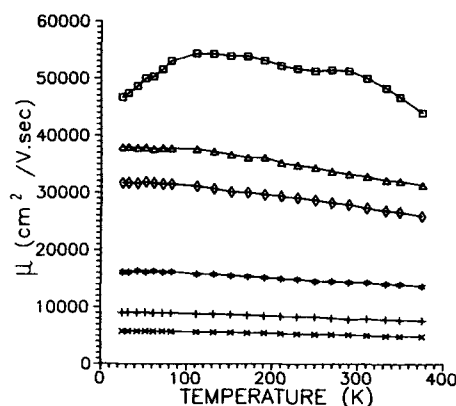


Fig. 2. Electron mobilities (μ) of PbTe-doped InSb versus temperature. Samples are identified by the same symbols as in fig. 1.

spectrometer). (2) The PbTe flux incident upon the quartz crystal deposition monitor has unity deposition coefficient. This has been verified by PbTe film thickness measurements during previous PbTe film growths. (3) All PbTe molecules incident upon the InSb surface dissociate into Te atoms which are incorporated into the InSb lattice

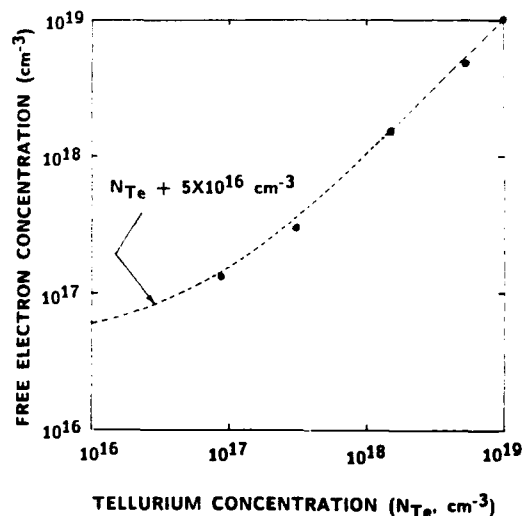


Fig. 3. Free electron concentration versus tellurium concentration in InSb films at 300 K. The "background" electron concentration at 300 K in these experiments was $5 \times 10^{16} \text{ cm}^{-3}$.

(presumably as single donors on Sb lattice sites), and into Pb atoms which re-evaporate. These assumptions are also consistent with our data, since the free electron density is equal to the calculated tellurium concentration plus the background density (see fig. 3). This differs from the case of PbTe-doped GaSb, where only about half of the incident flux incorporates into the film [2]. Even more interesting is the fact that free electron concentrations up to 10^{19} cm^{-3} were obtained with unity dopant utilization in our InSb films. Comparable PbTe fluxes gave a saturated free electron concentration of $\sim 2.5 \times 10^{18} \text{ cm}^{-3}$ in GaSb, and lower PbTe fluxes were not proportional to the free electron concentrations.

The fact that tellurium donors are fully ionized at concentrations of 10^{19} cm^{-3} implies that the tellurium donor level is located high in the conduction band and not just below the conduction band edge as in GaAs and GaP [11]. This is consistent with the fact that Te has zero ionization energy in InSb [12].

The 300 K electron mobilities of these PbTe-doped films are shown in fig. 4. The horizontal axis is given as "net donor concentration". This is done so that mobility values for bulk crystals doped below the intrinsic carrier concentration of $2 \times 10^{16} \text{ cm}^{-3}$ can be shown. The concentrations shown for films doped with Te and Se are actually free electron concentrations measured with the Van der Pauw technique at 300 K. The difference between the net donor and free electron con-

centrations is only significant near the intrinsic concentration. An experimental curve for bulk InSb are also shown for comparison. Some of our earlier, unintentionally Se-doped films are also shown. All of the PbTe-doped films are only $1 \mu\text{m}$ thick. The electron mobilities of the PbTe-doped and Se-doped films are comparable, and approach the mobilities of bulk InSb crystals. Since the group VI dopants Se and Te generally reside only on the group V sublattice in these compounds, it is not unexpected that near bulk-like mobilities may be attained with them.

4. Auger studies

As discussed in the introduction, Te surface accumulation has been observed in MBE-grown, PbTe-doped GaAs (and possibly in AlSb [5]) but not in GaSb. In our case, InSb films were studied with Auger electron spectroscopy (AES) immediately after growth without breaking UHV vacuum. The main Te AES peaks have energies near those of Sb, but we estimate our sensitivity to Te on an InSb surface to be ~ 0.02 monolayer. The AES spectrum of a film doped at $N_{\text{Te}} = 1 \times 10^{19} \text{ cm}^{-2}$ was identical to the spectrum of an undoped film. Hence, within the sensitivity limitation of AES, no Te surface accumulation is observed. No lead was observed on the surface either, with an estimated sensitivity of ~ 0.05 monolayer.

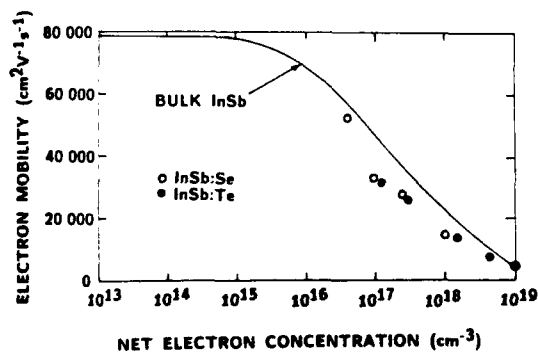


Fig. 4. Electron mobility versus net donor concentration in InSb films doped with (Pb)Te or from Se in the background vacuum at 300 K.

References

- [1] A.Y. Cho and J.R. Arthur, *Progr. Solid State Chem.* 10 (1975) 157.
- [2] S.M. Newstead, T.M. Kerr and C.E.C. Wood, *J. Appl. Phys.* 66 (1989) 4184.
- [3] J. De-Sheng, Y. Makita, K. Ploog and H.J. Queisser, *J. Appl. Phys.* 53 (1982) 999.
- [4] R.F. Brebrick and A.J. Strauss, *J. Chem. Phys.* 40 (1964) 3230.
- [5] S. Subbanna, G. Tuttle and H. Kroemer, *J. Electron. Mater.* 17 (1988) 297.
- [6] D.L. Partin, *IEEE J. Quantum Electron.* QE-24 (1988) 1716.
- [7] T.A. Smorodina and A.P. Tsuranov, *Inorg. Mater.* 15 (1980) 1068.
- [8] The iron-doped semi-insulating InP substrates used in this

- study were obtained from Crystacomm, Inc., Mountain View, CA, USA.
- [9] J.E. Oh, P.K. Bhattacharya, Y.C. Chen and S. Tsukamoto, *J. Appl. Phys.* 66 (1989) 3618.
- [10] The Cameca IMS-3f SIMS was located at Surface Science Western, University of Western Ontario, London, Ontario, Canada.
- [11] A.G. Milnes, *Deep Impurities in Semiconductors* (Wiley, New York, 1973).
- [12] K.F. Hulme and J.B. Mullin, *Solid State Electron.* 5 (1962) 211.

Tellurium doping study of GaSb grown by molecular beam epitaxy using SnTe

J.F. Chen and A.Y. Cho

AT & T Bell Laboratories, Murray Hill, New Jersey 07974, USA

The application of SnTe as a tellurium source of donor impurities in the growth of n-type GaSb by molecular beam epitaxy (MBE) is investigated. We obtained Hall carrier concentrations ranging from 1.23×10^{16} to $3.7 \times 10^{18} \text{ cm}^{-3}$. At a growth temperature of 500°C , the estimated donor concentrations are proportional to the arrival rate of the molecular dopants up to $3 \times 10^{18} \text{ cm}^{-3}$. Room-temperature Hall mobilities as high as $5114 \text{ cm}^2/\text{V}\cdot\text{s}$ were measured for a GaSb layer with $n_{\text{H}} = 3.8 \times 10^{16} \text{ cm}^{-3}$. These results, coupled with the insensitivity of the electron concentration to the Sb_4/Ga flux ratio, at a growth temperature of 500°C , may lead to SnTe being one of the donor dopants of choice in the MBE growth of n-type GaSb.

1. Introduction

Semiconductor III–V compounds containing antimony are promising materials for optical devices in the spectral region $1.3\text{--}1.7 \mu\text{m}$ grown by molecular beam epitaxy (MBE) [1]. In these devices, a controllable n-type doping of MBE-grown GaSb is required. Unintentionally doped GaSb is p-type and the common n-dopants used for III–V MBE (silicon and tin) are amphoteric and lead to heavily compensated p-type epilayers in GaSb [2]. A group VI element such as Te is required for n-doping in GaSb. Yano et al. [3] have used the elemental Te and achieved satisfactory n-typed doping up to $1.7 \times 10^{18} \text{ cm}^{-3}$. However, the elemental Te has high vapor pressure to cause considerable concern about possible memory effects and complicated reactions with Ga [4]. A number of workers have investigated the use of compound sources Ga_2Te_3 [5], PbSe [6], PbTe [7], Sb_2Te_3 [8] and an electrochemical cell of Ag_2S [9] to alleviate the above negative effects. However, problems such as limited carrier concentrations, significant lead incorporation and doping incorporation inefficiency for growth temperature above 500°C still remain. It is the purpose of this work to investigate the incorporation of Te in GaSb by using the alternative compound source SnTe. For the SnTe

source, measurements using the quadrupole mass analyzer indicate that it evaporates predominantly as the molecular species (i.e. SnTe) [10]. This helps prevent a surface reaction between the elemental Te and Ga at the surface forming gallium telluride (Ga_2Te or Ga_2Te_3) [4,12], which may complicate the growth. This paper describes the incorporation of Te in GaSb using a SnTe source. In addition, the effects of the MBE growth conditions such as the antimony-to-gallium flux ratio on Te incorporation in GaSb are investigated.

2. Experiment

The GaSb layer was grown on a Cr-doped semi-insulating GaAs (100) substrate in Riber-2300 MBE system, which has been reported previously [11]. The sources used were Ga, Sb_4 , and SnTe. The GaSb epitaxial layers were grown at 500°C and a growth rate of $0.5 \mu\text{m/h}$ with a beam equivalent pressure (BEP) ratio of Sb_4 to Ga of about 2, an optimal growth condition found for the GaSb layer in our system. This flux ratio, corresponding to the lowest ratio to maintain a Sb-stabilized 3×1 surface reconstruction, has been found to give rise to the highest crystal quality at each deposition temperature [13]. As

soon as the growth of GaSb was initiated, the reflection high energy electron diffraction (RHEED) pattern turned spotty, indicating three-dimensional nucleation due to the large lattice mismatch (7%) between GaAs and GaSb. However, the RHEED patterns recovered within about 10 nm thick growth of GaSb to show a streaky 3×1 reconstruction. The unintentionally doped GaSb layers were p-type with a typical carrier concentration of $(0.9\text{--}2) \times 10^{16} \text{ cm}^{-3}$ and a room temperature mobility of $(0.6\text{--}1.1) \times 10^3 \text{ cm}^2/\text{V} \cdot \text{s}$. All grown layers had smooth mirror-like surfaces with morphologies almost as good as GaAs homo-epitaxial layers seen under the phase contrast microscope. For the growth of Te-doped GaSb layers, the operation temperature range of SnTe source was between 200 and 350 °C. Ohmic contacts were made by alloying Sn dots to low-doped n-type GaSb layers. Ohmic contacts to undoped p-type and highly doped n-type layers were obtained by alloying In dots.

3. Results and discussion

The electrical properties for 2 μm thick GaSb layers doped with Te were obtained from Hall measurements at room temperature and 77 K. A wide range of Hall concentrations from 1.0×10^{16} to $3.7 \times 10^{18} \text{ cm}^{-3}$ is obtained by varying the SnTe source temperature, indicating the effectiveness of the controlled n-type doping by SnTe source. It should be noted here that the measured Hall concentration, particularly at room temperature, is not considered to be the total free carrier concentration. To analyze our Hall measurement results, a two-conduction band model is required. According to Sagar [14], the L-valleys of GaSb, which have a high density of states and a low mobility, lie very close in energy to the central Γ -minimum. The measured Hall concentration is weighted average of the Γ -valley and L-valley mobility. Therefore, the Hall measurement will underestimate the total carrier concentration, particularly so at high temperature due to more carriers transferring to the upper band [6]. The total electron concentration is closer to the measured Hall concentration at lower temperatures. There-

fore, the total donor concentration was estimated by adding the measured Hall concentration at 77 K to the estimated acceptor background concentration (10^{16} cm^{-3}). An Arrhenius plot of the estimated donor concentration as a function of SnTe source temperature is shown in fig. 1. Also included in fig. 1 is the dash line representing the vapor pressure of SnTe from a previously reported value ($1.99 \pm 0.11 \text{ eV}$) of the enthalpy of sublimation [10]. The values of the donor concentrations estimated in a way described above lie reasonably close to this line for $n < 3 \times 10^{18} \text{ cm}^{-3}$. Therefore, at a growth temperature of 500 °C used in the present work, the observed donor level is simply proportional to the arrival rate of the molecular dopant species up to about $n < 3 \times 10^{18} \text{ cm}^{-3}$. Beyond this doping level, the dopant incorporation efficiency saturates, as shown in fig. 1. This dopant saturation level is much higher than $4 \times 10^{16} \text{ cm}^{-3}$, the highest level achievable for n-type GaSb by using H_2S [15] under practical MBE-growth conditions. A similar doping saturation level ($3 \times 10^{18} \text{ cm}^{-3}$) in n-type GaSb was observed previously by using PbTe [7], Ga_2Te_3 [5] and Sb_2Te_3 [8].

The measured Hall mobilities both at room temperature and 77 K for n-type GaSb layers are

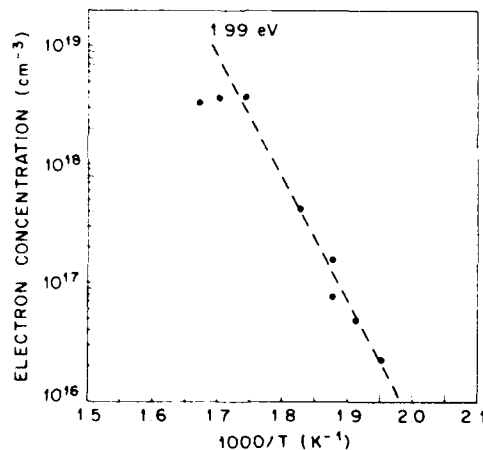


Fig. 1. Arrhenius plot of the donor concentration as a function of SnTe source temperature. The donor concentration is estimated by adding the Hall concentration at 77 K to the estimated acceptor background concentration (10^{16} cm^{-3}). The dashed line represents the vapor pressure of SnTe with the literature value ($1.99 \pm 0.11 \text{ eV}$) of the enthalpy of sublimation.

shown in fig. 2 against room-temperature Hall concentrations. Mobilities shown in fig. 2 have not been corrected from the two-band model. The thickness of the GaSb layer is 2 μm . Room-temperature mobility as high as 5114 $\text{cm}^2/\text{V}\cdot\text{s}$ was measured for a GaSb layer with $n_{\text{H}} = 3.8 \times 10^{16} \text{ cm}^{-3}$. The mobilities were reduced to 4200 and 2770 $\text{cm}^2/\text{V}\cdot\text{s}$ for $n_{\text{H}} = 6.5 \times 10^{16}$ and $n_{\text{H}} = 4 \times 10^{17} \text{ cm}^{-3}$, respectively. Also included in fig. 2 are some previously reported results of MBE-grown GaSb films using other dopant sources. Our measured mobilities are compared favorably to those from previous reports, indicating good quality of the grown layers. Similar to the previous reports for n-type GaSb, the mobilities at 77 K are only slightly higher than those at room temperature, suggesting that ionized impurity scattering dominates throughout the temperature range measured. A considerably low mobility was observed for a GaSb layer when doped with Te higher than the saturation level.

The effects of the Sb_4/Ga flux ratio on the incorporation of Te in GaSb are investigated. Fig. 3 shows the measured Hall concentrations for several GaSb layers grown with different Sb_4/Ga flux ratio. The growth temperature was kept constant at 500 $^\circ\text{C}$. The SnTe source temperature was fixed at 260 $^\circ\text{C}$ to given an electron concentration around mid- 10^{16} cm^{-3} as determined in fig. 1. It can be seen that for the range of Sb_4/Ga flux ratio studied (beam equivalent pressure ratio from

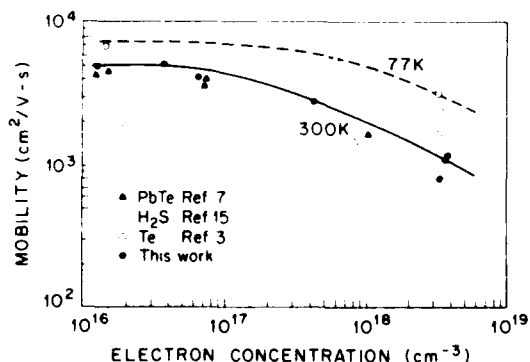


Fig. 2. Hall mobilities against carrier concentrations for n-type GaSb layers both at 300 and 77 K. The thickness of the GaSb layer is 2 μm .

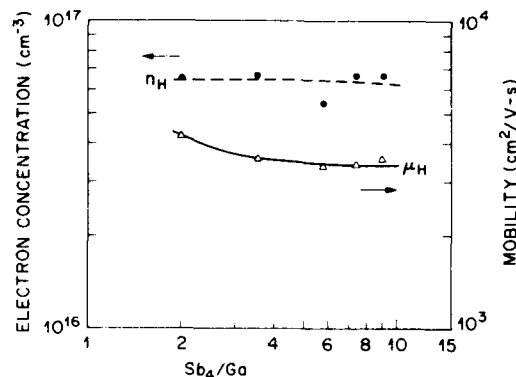


Fig. 3. Room-temperature Hall concentration and mobility for n-type GaSb layers versus the Sb_4/Ga beam equivalent pressure used for the GaSb growth at a substrate temperature of 500 $^\circ\text{C}$.

2 to 9), the measured Hall concentration is insensitive to the Sb_4/Ga flux ratio, indicating a controllability for Te doping using SnTe. Except for one sample, the variation of n_{H} from the average value is only about 1.5%, a value within the measurement uncertainty. The largest deviation of n_{H} (about 16%) for the sample grown with $\text{Sb}_4/\text{Ga} = 5.8$ is probably due to a variation of the substrate growth temperature. A decrease in Te incorporation in GaSb using Sb_2Te_3 source has been observed (up to a factor 4) at a growth temperature of 560 $^\circ\text{C}$ [8]. This insensitivity of Te incorporation in GaSb to Sb_4/Ga flux ratio is in contrast to the result reported by Poole et al. [9] for sulphur doping in GaSb. They reported that the incorporation of Sulphur increases by a factor of 3 on changing the Sb_4/Ga flux ratio from 1:1 to 4:1. As shown in fig. 3, the highest mobility was obtained for the GaSb layer grown with the lowest Sb_4/Ga flux ratio (BEP = 2) at a growth temperature of 500 $^\circ\text{C}$. This flux ratio, corresponding to the lowest ratio to maintain a Sb-stabilized surface reconstruction, is found to give rise to the highest crystal quality.

4. Summary

The Te incorporation in MBE-grown GaSb layers using SnTe source is investigated. A wide doping range from 1.23×10^{16} to $3.7 \times 10^{18} \text{ cm}^{-3}$

has been obtained by varying SnTe source temperature. High room-temperature Hall mobilities above $5000 \text{ cm}^2/\text{V} \cdot \text{s}$ are obtained for the low-doped GaSb layers. These results, coupled with the insensitivity of the electron concentration to the Sb_4/Ga flux ratio, at a growth temperature of 500°C , may lead to SnTe being one of the donor dopants of choice in the MBE growth of n-type GaSb.

Acknowledgments

The authors wish to thank R. Nottenburg, S.N.G. Chu, L. Yang, Y.H. Wang, and E.F. Schubert for useful discussions.

References

- [1] A.Y. Cho, *Thin Solid Films* 100 (1983) 291.
- [2] C.A. Chang, R. Ludeke, L.L. Chang and L. Esaki, *Appl. Phys. Letters* 31 (1977) 759.
- [3] M. Yano, Y. Suzuki, T. Ishii, Y. Matsushima and M. Kimata, *Japan. J. Appl. Phys.* 17 (1978) 2091.
- [4] D.M. Collins, J.N. Miller, Y.G. Chai and R. Chow, *J. Appl. Phys.* 53 (1982) 3010.
- [5] Y. Ohmori, S. Tarucha, Y. Horikoshi and H. Okamoto, *Japan. J. Appl. Phys.* 23 (1984) L94.
- [6] T.D. Mclean, T.M. Kerr, D.I. Westwood, C.E.C. Wood and D.F. Howell, *J. Vacuum. Sci. Technol.* B4 (1986) 601.
- [7] S. Subbanna, G. Tuttle and H. Kroemer, *J. Electron. Mater.* 17 (1988) 297.
- [8] T.H. Chiu, J.A. Ditzenberger, H.S. Luftman, W.T. Tsang and N.T. Ha, *Appl. Phys. Letters* 56 (1990) 1688.
- [9] I. Poole, M.E. Lee, K.E. Singer, J.E.F. Frost, T.M. Kerr, C.E.C. Wood, D.A. Andrews, W.J.M. Rothwell and G.J. Davies, *J. Appl. Phys.* 63 (1988) 395.
- [10] R. Colin and J. Drowart, *Trans. Faraday Soc.* 60 (1964) 673.
- [11] K.Y. Cheng, A.Y. Cho and W.A. Bonner, *J. Appl. Phys.* 52 (1981) 4672.
- [12] D.M. Collins, *Appl. Phys. Letters* 35 (1979) 67.
- [13] M.E. Lee, D.J. Nicholas, K.E. Singer and B. Hamilton, *J. Appl. Phys.* 59 (1986) 2895.
- [14] A. Sagar, *Phys. Rev.* 117 (1960) 93.
- [15] H. Gotoh, K. Sasamoto, S. Kuroda, T. Yakanoto, K. Tamamura, M. Fukushima and M. Minata, *Japan. J. Appl. Phys.* 20 (1981) L893.

Transport properties of heterostructures based on GaSb, InAs and InSb on GaAs substrates

P.N. Uppal, D.M. Gill, S.P. Svensson and D.C. Cooke

Martin Marietta Laboratories, 1450 S. Rolling Road, Baltimore, Maryland 21227-3898, USA

We have grown heterostructures based on low band-gap channels of $\text{Ga}_x\text{In}_{1-x}\text{Sb}$ ($x = 0.5$) and $\text{InAs}_x\text{Sb}_{1-x}$ ($x = 0.4-1$) alloys, and characterized them using Hall measurements. For barrier layers, we used $\text{Al}_x\text{In}_{1-x}\text{Sb}$ ($x = 1-0.5$), with a composition chosen to be closely lattice matched to the channel layers, $\text{Ga}_x\text{In}_{1-x}\text{Sb}$ and $\text{InAs}_x\text{Sb}_{1-x}$. We also grew a $\text{Al}_x\text{Ga}_{1-x}\text{As}/\text{GaAs}_y\text{Sb}_{1-y}/\text{GaAs}$ pseudomorphic heterostructure, which is an analog of the $\text{In}_x\text{Ga}_{1-x}\text{As}$ pseudomorphic MODFET. In the case of $\text{Al}_x\text{In}_{1-x}\text{Sb}/\text{Ga}_x\text{In}_{1-x}\text{Sb}$ and $\text{Al}_x\text{In}_{1-x}\text{Sb}/\text{InAs}_x\text{Sb}_{1-x}$ heterostructures, the barrier layers were undoped but we observed two-dimensional electron densities of about 7×10^{11} to $2 \times 10^{12} \text{ cm}^{-2}$ at 300 K. For the AlSb/InAs and $\text{Al}_{0.7}\text{In}_{0.3}\text{Sb}/\text{Ga}_{0.7}\text{In}_{0.3}\text{Sb}$ heterostructures, the 300 K mobilities were 24,000 and 3000 $\text{cm}^2/\text{V}\cdot\text{s}$, respectively. Mobilities for the $\text{Al}_x\text{In}_{1-x}\text{Sb}/\text{InAs}_x\text{Sb}_{1-x}$ heterostructures were around 12,000 $\text{cm}^2/\text{V}\cdot\text{s}$. Hall measurements on the $\text{Al}_x\text{Ga}_{1-x}\text{As}/\text{GaAs}_y\text{Sb}_{1-y}/\text{GaAs}$ heterostructures indicated 2D electron densities of $3 \times 10^{12} \text{ cm}^{-2}$ and mobilities of 3,000 $\text{cm}^2/\text{V}\cdot\text{s}$. These results indicate the potential of the $\text{Al}_x\text{In}_{1-x}\text{Sb}/\text{InAs}_x\text{Sb}_{1-x}$ ($x = 0.4$) heterostructures to be used as high-speed MODFETs and of the $\text{Al}_x\text{Ga}_{1-x}\text{As}/\text{GaAs}_y\text{Sb}_{1-y}/\text{GaAs}$ heterostructures to be used as power MODFETs.

1. Introduction

$\text{In}_x\text{Ga}_{1-x}\text{As}$ pseudomorphic MODFETs on GaAs yield higher performance than conventional $\text{GaAl}/\text{Al}_x\text{Ga}_{1-x}\text{As}$ MODFETs due to a higher 2D electron density and a higher electron velocity [1]. $\text{In}_x\text{Ga}_{1-x}\text{As}$ lattice-matched to InP produces the best performance to date of any MODFET [2],

but from the point of view of device processing, having such a MODFET on a GaAs substrate would be the most desirable. GaAs is preferred because its processing technology is much further advanced than that for InP, and GaAs substrates are much higher in quality and have higher mechanical strength than InP substrates.

Because it is clearly better to use a larger (pure

Table 1
Transport data for III-V compounds

Material	Lattice constant (Å)	Energy gap at 300 K (eV)	Electron mobility at 300 K ($\text{cm}^2/\text{V}\cdot\text{s}$)	Γ -L Spacing (eV)	Specific electron mass	Coefficient of thermal expansion (K^{-1})
GaAs SI substrate	5.65	1.42 (direct)	8000	0.3	0.068	5.93×10^{-6}
InP SI substrate	5.87	1.35 (direct)	5000	0.6	0.067	4.5×10^{-6}
AlSb	6.11	1.7 (indirect), 2.22 (direct)	200		0.33	5×10^{-6}
GaSb	6.09	0.7 (direct)	5000	0.15	0.045	5.93×10^{-6}
InAs	6.60	0.36 (direct)	33000	0.9	0.023	5.19×10^{-6}
InSb	6.48	0.17 (direct)	78000	1.5	0.013	4.90×10^{-6}

InAs would be preferred) InAs mole fraction for the $\text{In}_x\text{Ga}_{1-x}\text{As}$ channel, it would be a major technological step to be able to grow MODFETs on GaAs with a high InAs content. Recently, Tuttle et al. [3] and Luo et al. [4] proposed AlSb/InAs MODFETs and reported very good transport properties for this type of heterojunction. InAs and InSb offer substantially higher low-field mobility, no intervalley scattering, and much higher velocity overshoot [4]. In table 1, which shows some of the material parameters, the intervalley (Γ -L) InAs and InSb are seen to possess very favorable transport properties for MODFETs. Using channel materials with very narrow bandgaps may lead to pinch-off problems in the FET. That is, electrons may be excited across the band gap, either thermally or through impact ionization during transport from source to drain. Although we believe that such effects will be a comparatively small problem for low-noise applications or digital circuits, where smaller accelerating voltages are used, they must be studied, resulting in trade-offs between narrow gap (mobility) and pinch-off properties. One promising way of increasing the effective bandgap of these small-gap materials is through the use of the quantum confinement effect, which increases the energy of the lowest bound state. This effect occurs because the energy of the bound states in a quantum well is inversely proportional to the quantum well width and the carrier effective mass. The effective mass dependence makes the effect stronger in InAs and InSb than in, e.g. GaAs.

In this paper, we report on the growth of new MODFET structures based on GaSb, InAs, and InSb.

1.1. $\text{Al}_x\text{Ga}_{1-x}/\text{GaAs}_y\text{Sb}_{1-y}/\text{GaAs}$ structure

This structure is the analog of $\text{In}_x\text{Ga}_{1-x}\text{As}$ pseudomorphic MODFET in which the $\text{In}_x\text{Ga}_{1-x}\text{As}$ pseudomorphic channel has been replaced by a $\text{GaAs}_y\text{Sb}_{1-y}$ pseudomorphic channel. $\text{GaAs}_y\text{Sb}_{1-y}$ does not offer any benefits over $\text{In}_x\text{Ga}_{1-x}\text{As}$ in terms of higher mobility and saturation velocity, but it does have several other advantages: (1) the energy gap change with alloy composition (for small Sb concentration) is much

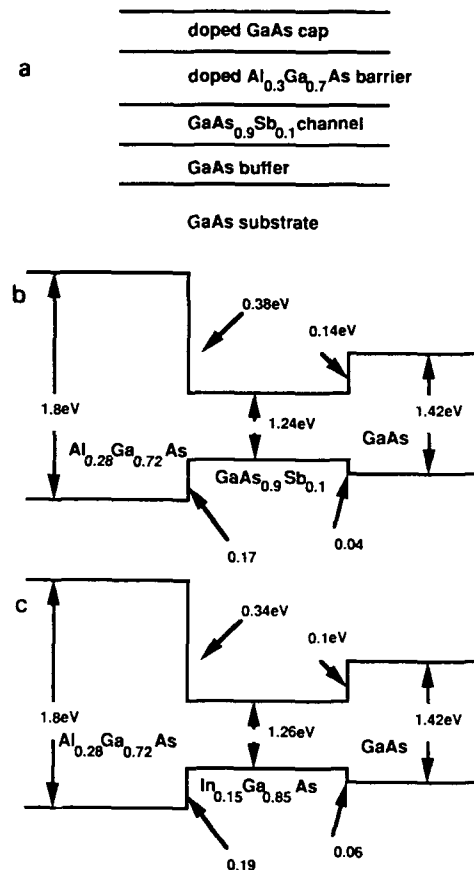


Fig. 1. (a) Schematic diagram of the GaAsSb HFET and energy band diagrams of (b) the GaAsSb and (c) the InGaAs pseudomorphic HFETs.

larger than that for $\text{In}_x\text{Ga}_{1-x}\text{As}$ [5], so that a deeper quantum well forms for a smaller change in alloy composition, and (2) the conduction band discontinuity (ΔE_c) of 0.14 eV between GaAs and $\text{GaAs}_{0.9}\text{Sb}_{0.1}$ [6] is larger than that between GaAs and $\text{In}_{0.15}\text{Ga}_{0.85}\text{As}$, resulting in better charge confinement, higher charge transfer, and potential applications for power FETs. Fig. 1 shows the energy band diagrams for the two pseudomorphic structures. Since the $\text{Al}_x\text{Ga}_{1-x}\text{As}/\text{GaAs}_y\text{Sb}_{1-y}/\text{GaAs}$ device does not offer better high-frequency or switching operation than the $\text{In}_x\text{Ga}_{1-x}\text{As}$ MODFET, its only use would be for power appli-

cations (because of its higher 2D charge density). Hall measurement results for this heterojunction are presented later.

1.2. $Al_xIn_{1-x}Sb/GaIn_{1-x}Sb$ and $Al_xIn_{1-x}Sb/InAs_xSb_{1-x}$ structures

$Al_xIn_{1-x}Sb$ alloys show the highest rate of change of the direct energy gap with increasing lattice constant of all III-V alloys. Further, the binaries GaSb and AlSb maintain a layer-by-layer two-dimensional growth on GaAs right from the start of growth, despite a large lattice mismatch. We observed the same growth pattern for the ternaries $Al_xIn_{1-x}Sb$ and $Ga_xIn_{1-x}Sb$. Because very high mobilities have been reported for InAs and InSb, we expected an alloy $InAs_xSb_{1-x}$ of these two also possess these favorable properties.

We also preferred the $Al_xIn_{1-x}Sb/InAs_xSb_{1-x}$ system (to the already studied AlSb/InAs system) because we could controllably dope $Al_xIn_{1-x}Sb$ (for $x > 0.5$) with Si, which is not possible with AlSb. We were able to n-type dope $Al_xIn_{1-x}Sb$ for $x = 0.5$ or above with Si, below which the layers were p-type and compensated. Since there is no high-bandgap material that is perfectly lattice matched to InSb, we can use an alloy of $Al_xIn_{1-x}Sb$ lattice-matched to a suitable composition of $InAs_xSb_{1-x}$. The same argument can be made for the use of $Ga_xIn_{1-x}Sb$: its bandgap will be much higher than that of $InAs_xSb_{1-x}$, leading to lower leakage currents. As another benefit, $Ga_xIn_{1-x}Sb$ will have the highest hole mobility of the III-V compounds, although we did not explore any p-type MODFETs. Fig. 2 shows the expected energy-band diagrams for the $Al_xIn_{1-x}Sb/Ga_xIn_{1-x}Sb$ and $Al_xIn_{1-x}Sb/InAs_xSb_{1-x}$ structures.

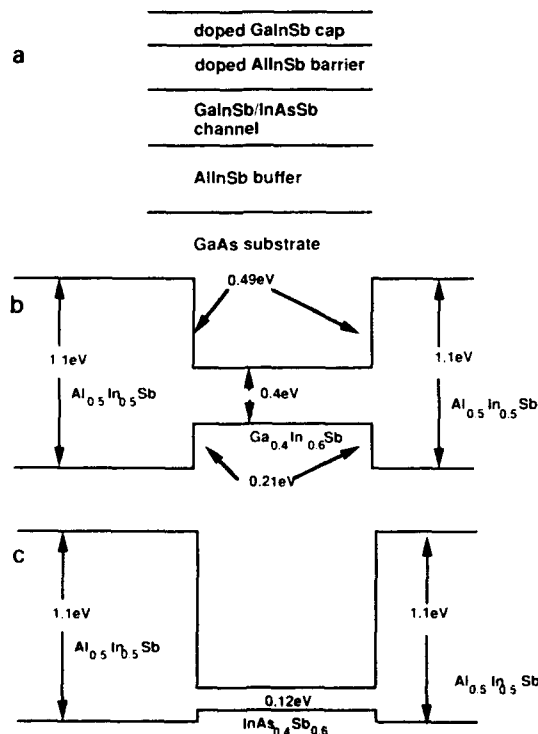


Fig. 2. (a) Schematic diagram of the GaInSb and InAsSb HFETs and expected energy band diagrams of (b) AlInSb/GaInSb and (c) AlInSb/InAsSb structures.

2. Experimental

All the layers were grown in a Perkin-Elmer PHI 425B molecular beam epitaxy (MBE) machine equipped with an arsenic cracker. Sb_4 was used for the antimonide layers and As_2 was used for layers containing arsenides. GaAs, Sb_{1-x} layers were grown at 500 °C. The substrate temperature was 450 °C for the growth of $Ga_xIn_{1-x}Sb$ and $Al_xIn_{1-x}Sb$, 480 °C for InAs growth, and 400 °C for both InSb and $InAs_xSb_{1-x}$ growth. Most of the layers reported here were grown on GaAs(100), although some of the AlSb/InAs heterojunction structures were grown on GaAs(211)B. Alloy composition was determined by X-ray diffraction. Unintentionally doped layers of AlSb had very high resistivity with a p-type background of $5 \times 10^{14} \text{ cm}^{-3}$. GaSb layers were p-type with a background doping of $1 \times 10^{15} \text{ cm}^{-3}$. Unintentionally doped layers of InAs, InSb and $InAs_xSb_{1-x}$ had an n-type background doping of $2 \times 10^{16} \text{ cm}^{-3}$. Except for the $Al_xGa_{1-x}As/GaAs_xSb_{1-x}/GaAs$ structures all the other layers were grown with 0.5 μm AlSb buffer layers followed by a 0.5 μm $Al_xIn_{1-x}Sb$ buffer layer.

3. Results and discussion

3.1. $Al_xGa_{1-x}As/GaAs_ySb_{1-y}/GaAs$ structure

Hall measurements were made on the pseudomorphic MODFET structure $Al_xGa_{1-x}As/GaAs_ySb_{1-y}/GaAs$, where the Al mole fraction was 0.26 and the Sb mole fraction was 0.15. The $Al_xGa_{1-x}As$ layer was doped to $2 \times 10^{18} \text{ cm}^{-3}$ and the $GaAs_ySb_{1-y}$ thickness was chosen to be 150 Å; the spacer thickness was 25 Å. The Hall measurement results indicate that the room-temperature mobility was $3000 \text{ cm}^2/\text{V} \cdot \text{s}$, which is about a factor of two lower than that for a comparable pseudomorphic $In_xGa_{1-x}As$ MODFET and the carrier density was $3 \times 10^{12} \text{ cm}^{-2}$. The 2D electron density was about a factor of two higher. These results clearly show that the ΔE_c of the $Al_{0.26}Ga_{0.74}As/GaAs_{0.85}Sb_{0.15}$ heterojunction is higher than that of the $Al_{0.26}Ga_{0.74}As/In_{0.15}Ga_{0.85}As$ heterojunction. The results also indicate that these devices can be used for power applications, which require higher carrier densities.

3.2. $Al_xIn_{1-x}Sb/Ga_xIn_{1-x}Sb$ and $Al_xIn_{1-x}Sb/InAs_xSb_{1-x}$ structures

We were able to reproduce the results of Tuttle et al. [3] on the AlSb/InAs heterojunctions for the case of undoped InAs, as shown in table 2. The undoped InAs with the so-called InSb-like [3] interface had the highest mobility at 77 K, although the 2D electron density is $7 \times 10^{11} \text{ cm}^{-2}$, which may not be very useful for actual devices. To increase the carrier density, we also doped the InAs channel with Si. The 2-D electron density doubled thereby, but the mobility at 300 K dropped to $14,000 \text{ cm}^2/\text{V} \cdot \text{s}$. The carrier density for an $InAs_{0.7}Sb_{0.3}$ channel was about four times higher than that for undoped InAs, but the mobility was lower, probably due to alloy scattering.

Table 2 shows the results for an InAs/AlSb structure grown on GaAs(211)B. In the case of the (211) surface, there are two Sb bonds for one Al bond, so that the interface character will be 2/3 InSb-like and 1/3 AlAs-like. Hall results confirm this description by indicating mobilities and carrier density numbers in between those for an

Table 2
Hall measurement results on AlSb/InAs/GaAs(100) and AlSb/InAs/GaAs(211)B

	Temperature (K)	Carrier density (cm^{-2})	Mobility ($\text{cm}^2/\text{V} \cdot \text{s}$)
Results on AlSb/InAs/GaAs(100): channel InSb-like ^{a)}			
InAs undoped	300	7×10^{11}	23000
	77	4×10^{11}	76000
InAs doped	300	1.4×10^{12}	14000
	77	9.5×10^{11}	24000
$InAs_{0.7}Sb_{0.3}$ undoped	300	2.1×10^{12}	9400
	77	1.5×10^{12}	12100
Results on AlSb/InAs/GaAs(100): channel AlAs-like ^{a)}			
InAs undoped	300	9.9×10^{12}	510
	77	3.8×10^{12}	825
Results on AlSb/InAs/GaAs(211)B: channel InSb-like ^{a)}			
InAs undoped	300	5.4×10^{12}	3400
	77	2.5×10^{12}	5750

^{a)} AlSb/InAs/GaAs(100) can have two types of interfaces at the AlSb/InAs interface (see ref. [3]), one in which the interface has InSb bonds and the other having AlAs bonds. In the case of AlSb/InAs/GaAs(211)B, there is a mixed interface because there are two Sb bonds for each Al bond. Thus, the interface character will be 2/3 InSb-like and 1/3 AlAs-like.

Table 3
Al_{0.7}In_{0.3}Sb/InAs_{0.7}Sb_{0.3} Hall measurement results

Channel	Temperature (K)	Carrier density (cm ⁻²)	Mobility (cm ² /V·s)
InAs _{0.7} Sb _{0.3}	300	3.2×10^{12}	8100
	77	2.8×10^{12}	12000
Ga _{0.7} In _{0.3} Sb	300	2.8×10^{11}	3100
	77	3.0×10^{11}	4000

InSb-like and an AlAs-like interface on (100). In the case of the Al_xIn_{1-x}Sb/Ga_xIn_{1-x}Sb structure, we observed lower-than-expected mobilities (table 3), whereas for the Al_xIn_{1-x}Sb/InAs_xSb_{1-x} structure, both the charge density and the mobility were higher. The origin of electrons in these structures is unclear because Si in Al_xIn_{1-x}Sb and Ga_xIn_{1-x}Sb acts an acceptor for x -values less than 0.5. We believe that arsenic produces interface states or antisite defects in AlSb and Al_xIn_{1-x}Sb which pin the Fermi level at mid-gap in Al_xIn_{1-x}Sb, where it is higher than the bottom of the conduction band of the lower gap material. It seems that the residual arsenic in the MBE chamber is enough to cause these defects, as evidenced by the presence of electrons in the Al_xIn_{1-x}Sb/Ga_xIn_{1-x}Sb structure.

It should be noted that none of these structures was optimized in any sense and careful lattice matching was not done. Nevertheless, these structures show high enough room-temperature mobilities and carrier densities to make them promising for future work. However, a considerable effort on ohmic contacts and Schottky barriers will be required before actual MODFETs can be fabricated from these structures.

4. Conclusions

(1) We have demonstrated the high-quality growth of pseudomorphic heterostructures based upon GaAs_ySb_{1-y}. The pseudomorphic Al_x

Ga_{1-x}As/GaAs_ySb_{1-y}/GaAs heterostructures is a viable alternative to the widely studied In_xGa_{1-x}As-based heterostructures. The GaAs_ySb_{1-y}-based heterostructures offer almost twice the carrier densities obtained in the In_xGa_{1-x}As-based heterostructures, making it very suitable for power FET applications.

(2) The InSb-like channels in the AlSb/InAs and the Al_xIn_{1-x}Sb/InAs_xSb_{1-x} heterostructures offer very high room-temperature as well as 77 K electron mobilities and thus have potential as very-high-speed MODFETs. The Al_xIn_{1-x}Sb/InAs_xSb_{1-x} heterostructures can be modulation doped with Si (for $x > 0.5$), the regular n-type dopant in MBE, which offers a controllable method of doping. The AlAs-like channel offers very high carrier densities but very low mobilities. As expected, the Al_xIn_{1-x}Sb/Ga_xIn_{1-x}Sb heterostructures did not display very high mobilities. The origin of electrons in all these heterostructures is not clear but it has been speculated (3) that they are due to the presence of deep or mid-gap traps in AlSb. The same seems to be true for the case of Al_xIn_{1-x}Sb.

(3) Doping the InAs channel offers a viable method of increasing the carrier density in the AlSb/InAs heterojunctions.

References

- [1] L.F. Lester, P.M. Smith, P. Ho, P.C. Chao, R.C. Tiberio, K.H.G. Duh and E.D. Wolf, in: IEEE/IEDM Tech. Digest IEDM-88 (1988) p. 172.
- [2] U.K. Mishra, A.S. Brown, S.E. Rosenbaum, C.E. Hooper, M.W. Pierce, M.J. Delaney, S. Vaughn and K. White, IEEE Electron Device Letters EDL-9 (1988) 647.
- [3] G. Tuttle, H. Kroemer and J.H. English, J. Appl. Phys. 67 (1990) 3032.
- [4] L.F. Luo, R. Beresford, W.I. Wang and H. Mune-kata, Appl. Phys. Letters 55 (1989) 789.
- [5] H.C. Casey and M.B. Panish, Heterostructure Lasers, Part B (Academic Press, New York, 1978).
- [6] J.H. Zhao, A.Z. Li, T.E. Schlesinger and A.G. Milnes, J. Electron. Mater. 17 (1988) 255.

Growth and properties of GaAsSb/InGaAs superlattices on InP

J.F. Klem, S.R. Kurtz

Sandia National Laboratories, P.O. Box 5800, Albuquerque, New Mexico 87185, USA

and

A. Datye

Department of Chemical and Nuclear Engineering, University of New Mexico, Albuquerque, New Mexico 87131, USA

GaAsSb/InGaAs superlattices of varying thicknesses have been grown nominally lattice matched to InP and characterised by X-ray diffraction, transmission electron microscopy, Hall measurement, and photoluminescence. These structures exhibit net Hall electron densities of $\sim 5 \times 10^{17} \text{ cm}^{-3}$ at room temperature. X-ray diffraction results demonstrate the existence of an intrinsic interfacial strain between these two materials. Low-temperature photoluminescence in the range 2.3–2.8 μm is consistent with the expected type II band alignment in this system, and allows determination of the band offsets between these materials.

1. Introduction

GaAsSb remains one of the more poorly characterised of the III–V ternary alloys, primarily due to the difficulty of preparing high quality material. This difficulty stems mainly from the fact that a large miscibility gap exists in this system, precluding the preparation of homogeneous alloys by equilibrium techniques [1]. Recent studies, however, have demonstrated improvements in the quality of this alloy as grown by molecular beam epitaxy (MBE) and organometallic vapor phase epitaxy, and have elucidated the nature of thermodynamic contributions to material inhomogeneities [2–7]. Relatively little work has been done, however, to characterise heterojunction systems containing this alloy. We have therefore undertaken a study of the GaAsSb/InGaAs system by examining nominally lattice-matched superlattices on InP substrates.

2. Experimental

The GaAsSb/InGaAs superlattices were grown by MBE at 500°C on n^+ or semi-insulating InP

substrates with a thin ($< 0.5 \mu\text{m}$) InGaAs buffer. Growth rates were approximately 3.2 and 1.5 Å/s for the InGaAs and GaAsSb, respectively, and total thickness of the superlattices was 1.5 μm . Sb_2 flux was supplied by a cracking cell consisting of a pyrolytic boron nitride (PBN) sublimator and a tantalum-baffled PBN cracking zone. As_4 flux was supplied by two sources to allow for optimal III/V ratios for the two different materials. Measured As_4/Ga beam equivalent pressure ratios were approximately 13 and 40 for the GaAsSb and InGaAs, respectively. During growth, RHEED patterns displayed a 2×4 reconstruction for both materials, with no noticeable change at the interfaces.

The superlattices were characterised by 300 and 77 K Hall measurement, cross-sectional transmission electron microscopy, and 10 K photoluminescence.

3. Results

The superlattices had smooth surfaces, with no roughness detectable by phase-contrast optical microscopy, but had densities of oval-shaped defects

on the order of $3 \times 10^4 \text{ cm}^{-2}$. Because similar defects have sometimes been seen in InGaAs layers grown on InP, these defects appear to originate at the InP/InGaAs interface, and thus seem not to be intrinsic to the GaAsSb/InGaAs system. These defects most likely originate during the oxide desorption step of the pre-growth sequence for the InP substrate.

Fig. 1 shows a cross-sectional TEM photograph of a portion of a 55 Å/55 Å superlattice. No dislocations or other defects were visible either in the superlattice layers or at the superlattice/buffer interface, demonstrating a good lattice match of the materials. The interfaces appear abrupt, but with a small amount of roughness. No evidence of ordering or compositional inhomogeneity was evident in the GaAsSb either in the TEM images or TEM diffraction patterns.

Hall results for the unintentionally doped structures showed net n-type conductivity, with electron concentrations approximately 5×10^{15}



Fig. 1. Cross-sectional transmission electron micrograph of a 55 Å/55 Å GaAsSb/InGaAs superlattice.

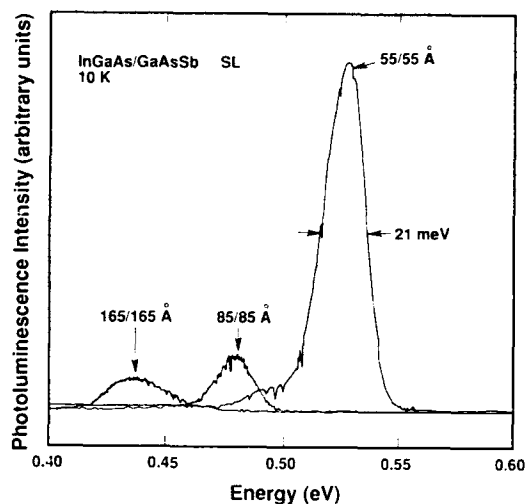


Fig. 2. Low-temperature photoluminescence spectra for GaAsSb/InGaAs superlattices of various periods.

cm^{-3} at 300 K, and mobilities of 2500–4500 $\text{cm}^2/\text{V} \cdot \text{s}$ for superlattices with periods from 110 to 330 Å. At 80 K, electron densities decreased to $(2\text{--}4) \times 10^{15} \text{ cm}^{-3}$, and mobilities were 1600–10,000 $\text{cm}^2/\text{V} \cdot \text{s}$, with shorter-period superlattices exhibiting the lower mobilities. The contribution of the thin unintentionally doped InGaAs buffer, known to be n-type, was neglected in our analysis of the Hall data.

Low-temperature photoluminescence measurements, as shown in fig. 2, reveal spectra consisting of a major peak in the 0.4 to 0.55 eV range for structures of different periods, with a weak low-energy shoulder (evident only for the 55 Å/55 Å structure in fig. 2). This corresponds to an energy considerably below the known bandgaps of either material, in accordance with the expectation of a type II band alignment between these materials. In addition, the intensity of the luminescence increases as the superlattice period decreases, due to the increased spatial overlap of the electron and hole wavefunctions in shorter-period superlattices of the type II alignment. The full width at half maximum of the luminescence peaks is $\sim 20 \text{ meV}$.

X-ray diffraction rocking curve measurements revealed strong zero-order peaks for the superlattices slightly offset from the substrate and buffer

layer peaks. In some cases, the InGaAs buffer layer peak was sufficiently displaced from the substrate peak to be resolved. The InGaAs composition in the superlattice was assumed to be the same as that of the buffer. Also resolved were from 7 to 16 superlattice satellite peaks over the 3–4 decade dynamic range of the measurement. Intensities calculated in a kinematical diffraction model [8] were fit to the (004) experimental intensities to obtain the layer thicknesses and GaAsSb composition and strain. Results of this process indicated that the GaAsSb layers were under a slight compressive strain ($\Delta a/a$) of less than -4×10^{-3} .

4. Discussion

Conduction and valence band offsets for this heterojunction system have been investigated previously by Sai-Halasz et al. [9] with absorption measurements on GaAsSb/InGaAs superlattices and by Sugiyama et al. [10] with single-barrier thermionic emission structures. In the work by Sai-Halasz et al., 10 K measurements were performed on structures lattice-mismatched to the substrate, from which we derive an estimated InGaAs conduction band to GaAsSb valence band gap of 0.23 eV for compositions lattice-matched to InP. Sugiyama et al. obtained for lattice-matched structures a value of 0.25 eV from measurements between 300 and 410 K.

To determine band offsets in these structures, we have calculated $n = 1$ transition energies for GaAsSb/InGaAs superlattices of varying periods, with equal layer thicknesses, with the conduction band offset between the materials as an adjustable parameter. The model is a three-band envelope function approximation [8], and layer thicknesses, compositions, and strains were obtained from the X-ray diffraction modeling described below. In contrast to systems where a type I band lineup is found, in this type II system the lowest subband transition energy is a sensitive function of the band offsets. Comparison of this model to the 10 K photoluminescence peak energies determines the conduction band discontinuity.

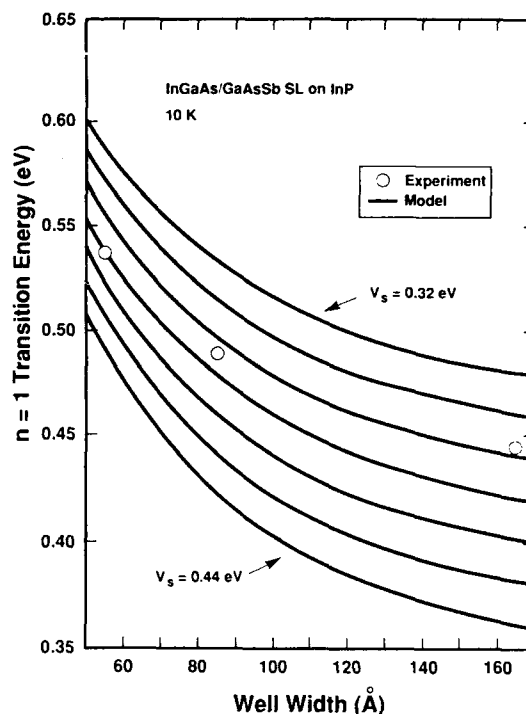


Fig. 3. Modeled $n = 1$ transition energies for GaAsSb/InGaAs superlattices as a function of period, with conduction band discontinuity energy V_s as an adjustable parameter. Experimental data are also shown.

Shown in fig. 3 are calculated and experimental results, assuming the PL peak falls 10 meV below the band-to-band transition energy, for three superlattices. We have assumed bandgaps of 0.80 and 0.81 eV for the GaAsSb and InGaAs, respectively. The results indicate a conduction band offset of 0.37 eV, with the GaAsSb conduction band higher in energy, which implies an InGaAs conduction band to GaAsSb valence band gap of 0.43 eV. This effective bandgap value is somewhat larger than those obtained by either Sai-Halasz et al. or Sugiyama et al. Comparison with the more recent measurements of Sugiyama et al. is difficult without some knowledge of the temperature shifts of the relevant bands.

We have also attempted to model the superlattice atomic structure through a comparison of X-ray diffraction spectra and spectra generated by a kinematical diffraction model. As demonstrated

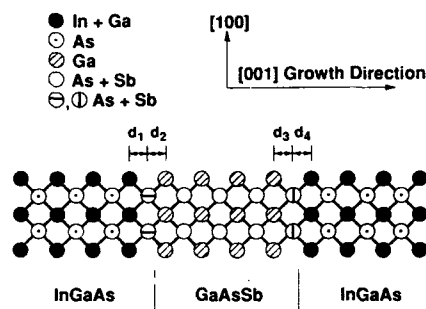


Fig. 4. Schematic cross-section of heterojunction interfaces, showing interface atomic spacings which depend on composition of group V interface planes.

for systems such as InP/InGaAs [11], where superlattice layers differ both in the group III and group V sublattice species, interfacial strain is expected to be present even when the component layers are lattice matched. This strain arises as a result of bonding of the group III species of one layer with the group V species of the other, e.g. In-As and InGa-P in the case of InP/InGaAs, or Ga-As and InGa-AsSb in the present case. This is illustrated in fig. 4. The atomic spacings d_1 through d_4 are a function of the group V species which occupy the interfacial lattice positions. If we assume that each monolayer of material is terminated by the correct group V species, then these interface planes are As and 50% As + 50% Sb, for transitions from InGaAs to GaAsSb, and GaAsSb to InGaAs, respectively.

We have examined various possible chemical compositions of these group V interface planes and their resulting lattice parameters in the diffraction model. The ideal interfaces described above provide a relatively poor fit between calculated and experimental diffraction peak intensities as shown in fig. 5 for "interface configuration No. 1". The best fit, as shown for "interface configuration No. 2", results from assuming that the interface group V planes are As and approximately 83% As + 17% Sb, for transitions from InGaAs to GaAsSb, and GaAsSb to InGaAs, respectively. This implies that atomic spacings d_2 and d_3 are smaller than the spacings within either the In-

GaAs or GaAsSb layers, while d_4 is larger and d_1 is the same. The departure of the composition of the GaAsSb-to-InGaAs group V interface plane from ideal can be characterised as grading, although it is important to realise the interface strain, while modified by grading, is present even in the ideal case. The depletion of Sb from this interface may be related to the increase in As beam flux, which competes for group V lattice sites, at the beginning of the InGaAs layer growth.

The fit of the diffraction model spectra to the experimental data is consistently better, for structures with various periods, assuming a graded GaAsSb-to-InGaAs interface (83% As + 17% Sb), rather than an ideal interface. We estimate the uncertainty in interface composition as $\pm 10\%$ mole fraction. Some discrepancies still exist between experimental and theoretical data, however. In most cases, the model underestimates the intensities of higher-order satellites while overestimating the intensities of the +1 and -1 satellites. The cause of this disagreement has not been determined.

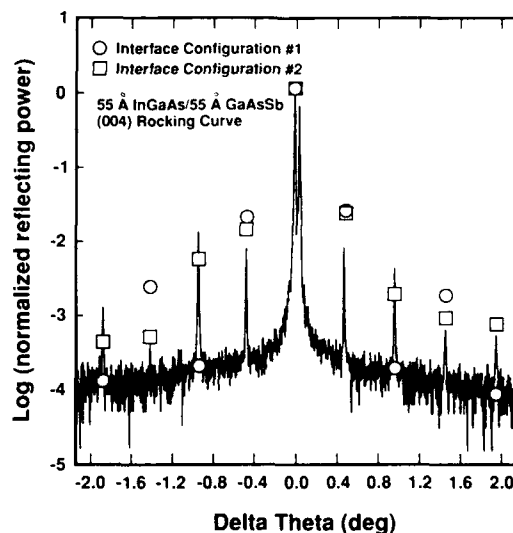


Fig. 5. Experimental and calculated (004) X-ray diffraction spectrum for a 55 Å/55 Å superlattice, with calculated satellite intensities corresponding to ideal and graded interface configurations detailed in text.

5. Conclusions

We have investigated GaAsSb/InGaAs superlattices grown on InP substrates by molecular beam epitaxy. These structures displayed low temperature photoluminescence in the 2.3 to 2.8 μm range which allowed determination of the conduction band discontinuity to be made. We obtained a value of 0.37 eV at 10 K, which is somewhat smaller than previous values obtained by electrical and optical characterisation of similar heterostructures. Interfacial strain was demonstrated to be present in these structures, and a simple model including one monolayer of interface grading was shown to provide a good fit to X-ray diffraction data.

Acknowledgements

The authors would like to thank R. Biefeld and J. Nelson for helpful discussions on modeling strain effects in these structures, B. Doyle for providing facilities for X-ray analysis, and J. Avery for technical assistance. This work was supported by the United States Department of Energy under Contract Number DE-AC04-76D00789.

References

- [1] R.E. Nahory, M.A. Pollack, J.C. DeWinter and K.M. Williams, *J. Appl. Phys.* 48 (1977) 1607.
- [2] T.H. Chiu, W.T. Tsang, S.N.G. Chu, J. Shah and J.A. Ditzenberger, *Appl. Phys. Letters* 46 (1985) 408.
- [3] M.J. Cherng, Y.T. Cherng, H.R. Jen, P. Harper, R.M. Cohen and G.B. Stringfellow, *J. Electron. Mater.* 15 (1986) 79.
- [4] I.J. Murgatroyd, A.G. Norman, G.R. Booker and T.M. Kerr, in: *Proc. 11th Intern. Conf. on Electron Microscopy*, Kyoto, 1986, Eds. T. Imura, S. Maruse and T. Suzuki (Japan. Soc. of Electron Microscopy, Tokyo, 1986).
- [5] J. Klem, D. Huang, H. Morkoç, Y.E. Ihm and N. Otsuka, *Appl. Phys. Letters* 50 (1987) 1364.
- [6] Y.E. Ihm, N. Otsuka, J. Klem and H. Morkoç, *Appl. Phys. Letters* 51 (1987) 2013.
- [7] Y. Nakata, T. Fujii, A. Sandhu, Y. Sugiyama and E. Miyauchi, *J. Crystal Growth* 91 (1988) 655.
- [8] J.Y. Marzin, in: *Heterojunctions and Semiconductor Superlattices*, Eds. G. Allan, G. Bastard, N. Boccara, M. Lannoo and M. Voos (Springer, Berlin, 1986).
- [9] G.A. Sai-Halasz, L.L. Chang, J.-M. Welter, C.-A. Chang and L. Esaki, *Solid State Commun.* 27 (1978) 935.
- [10] Y. Sugiyama, T. Fujii, Y. Nakata, S. Muto and E. Miyauchi, *J. Crystal Growth* 95 (1989) 363.
- [11] J.M. Vandenberg, M.B. Panish, H. Temkin and R.A. Hamm, *Appl. Phys. Letters* 53 (1988) 1920.

Growth and properties of $\text{InAs}_x\text{Sb}_{1-x}$, $\text{Al}_y\text{Ga}_{1-y}\text{Sb}$, and $\text{InAs}_x\text{Sb}_{1-x}/\text{Al}_y\text{Ga}_{1-y}\text{Sb}$ heterostructures

J.H. Kim, D. Yang, Y.-C. Chen and P. Bhattacharya

Solid State Electronics Laboratory, Department of Electrical Engineering and Computer Science, The University of Michigan, Ann Arbor, Michigan 48109-2122, USA

A series of undoped InSb and $\text{InAs}_x\text{Sb}_{1-x}$ layers were grown using tetramer Sb_4 and As_4 sources on (100)-oriented semi-insulating GaAs and InP substrates with different growth parameters. Very high electron mobilities (70,000 and 110,000 $\text{cm}^2/\text{V}\cdot\text{s}$ in InSb at 300 and 77 K, respectively) and n-type conductivity are obtained for all alloy compositions. The flux ratio $P_{\text{Sb}}/P_{\text{In}}$ played a crucial role in determining the surface morphology and the mobility of InSb films. Barrier heights of $\text{Al}_y\text{p-Al}_y\text{Ga}_{1-y}\text{Sb}$ Schottky diodes are measured and are 0.4 eV. A 300 Å Si-doped $\text{InAs}_{0.8}\text{Sb}_{0.2}$ channel region sandwiched between undoped $\text{Al}_{0.4}\text{Ga}_{0.6}\text{Sb}$ buffer and gate barrier regions has $\mu = 1000 \text{ cm}^2/\text{V}\cdot\text{s}$ and $n_i = 5.4 \times 10^{12} \text{ cm}^{-2}$ at 300 K. 1 μm gate FETs made with this heterostructure have shown a maximum extrinsic $g_m = 160 \text{ mS/mm}$ and $f_T = 5 \text{ GHz}$ at 300 K.

1. Introduction

The Sb-containing alloys, and their heterostructures are becoming increasingly important for long-wavelength optoelectronic and cryogenic electronic device applications. In particular, the $\text{InAs}_x\text{Sb}_{1-x}$ alloys produce the lowest bandgap in the family of III-V compounds. They are therefore suitable for detectors and sources operating at wavelengths in the 3–5 μm and 8–12 μm windows where the atmospheric absorption goes to a minimum [1–3]. However, in the development of materials and heterostructures for application to high speed and high frequency microelectronics, the antimony-bearing compounds have lagged behind. There are several reasons for this. Lack of suitable substrates and their large lattice mismatch to GaAs and InP is one. The existence of large miscibility gaps precludes the growth of high quality materials at lower temperatures by equilibrium and non-equilibrium techniques. On the other hand, because of their low bandgaps, the transport properties are expected to improve considerably at low temperatures and therefore these materials and devices would be important for cryogenic applications. However, recent epitaxial materials

grown by molecular beam epitaxy (MBE) exhibit type conversion and degradation of the transport properties as the measurement temperature is lowered from 300 K [4–6].

InAs , InSb , and their binary alloys have favorable transport properties compared to GaAs or InP. As mentioned above, they have higher low-field mobility. In addition, the Γ -L and Γ -X intervalley separations are about 1 eV or larger, leading to negligible intervalley scattering and higher peak velocities. This will potentially improve the performance of submicron devices also. Therefore, if some of the problems mentioned earlier can be alleviated, one stands to gain from the superior materials characteristics.

In this paper, we report the growth and transport properties of $\text{InAs}_x\text{Sb}_{1-x}$ heteroepitaxial layers, and the characteristics of $\text{Al}_y\text{Ga}_{1-y}\text{Sb}/\text{Al}$ Schottky diodes. We have also investigated $\text{InAs}_x\text{Sb}_{1-x}/\text{Al}_y\text{Ga}_{1-y}\text{Sb}$ heterostructures grown by MBE on GaAs and InP substrates for the realization of field effect transistors (FETs). Finally, we report the structure of $\text{InAs}_x\text{Sb}_{1-x}/\text{Al}_y\text{Ga}_{1-y}\text{Sb}$ heterostructure field effect transistor (HFET) and its performances. The DC and high frequency performance of 1 μm gate FETs made

with $\text{InAsSb}/\text{AlGaSb}$ heterostructures are described.

2. The growth and transport properties of $\text{InAs}_x\text{Sb}_{1-x}$

Heteroepitaxial $\text{InAs}_x\text{Sb}_{1-x}$ layers ($0 \leq x \leq 1$) were grown on Fe-doped (100) InP substrates and semi-insulating GaAs (100) substrates in a Riber 2300P MBE system. Elemental arsenic and antimony were used as the group V sources, producing predominantly As_4 and Sb_4 species. After oxygen desorption under As_4 overpressure (1.5×10^{-5} Torr), the growth of InAsSb was initiated as substrate temperature ranging from 350–500 °C, as measured by an infrared pyrometer. The growth rate varied in the range 0.8–1.0 $\mu\text{m}/\text{h}$ and the flux ratio $J_{\text{Sb}_4}/J_{\text{In}}$ was varied in the range of 0.3 to 4.0. The thickness of these directly grown layers varied in the range of 1.0–14.0 μm . In-situ examination of the crystalline nature of growth was done by reflection high energy electron diffraction (RHEED) measurements with 10 keV electron beams along the (110) azimuth. The observed spotty nature of the RHEED pattern at the initiation of growth indicates a three dimensional growth mode resulting from the large lattice mismatch. After growth of a few hundred ångströms, the spots change to streaks with a (1×3) reconstruction, indicating continuous coverage and smoothening of the growth front. Our observations were essentially same as those in previous reports [7].

We have grown InSb films (1 μm thick) on (100) InP substrates with different partial pressure ratios $P_{\text{Sb}_4}/P_{\text{In}}$. The measured room-temperature Hall mobilities of 1 μm InSb films grown on InP with different partial pressure ratios are shown in fig. 1 as a function of the partial pressure ratio. All the samples are n-type and the highest electron mobility can be observed in the sample with $P_{\text{Sb}_4}/P_{\text{In}}$ ratio of 6 and a corresponding beam flux ratio $J_{\text{Sb}_4}/J_{\text{In}}$ of 2. The above observations suggest that the flux ratio, $J_{\text{Sb}_4}/J_{\text{In}}$, plays a crucial role in determining the surface morphology and the electron mobility in the heteroepitaxial InSb films due to the high sticking coefficient of Sb_4 molecules at

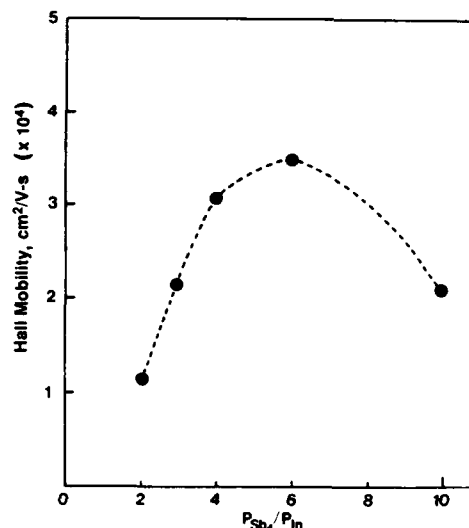


Fig. 1. Variation of measured Hall mobilities with $P_{\text{Sb}_4}/P_{\text{In}}$ in 1 μm InSb films grown on InP at 380 °C and 1 $\mu\text{m}/\text{h}$. The dashed line joins the data points.

the growth temperature used. Similar results were obtained in the InSb films grown on (100) GaAs substrates. The measured mobilities of $\text{InAs}_x\text{Sb}_{1-x}$ with different composition ratios are shown in fig. 2. All samples are n-type. The mobility of InSb is 70,000 $\text{cm}^2/\text{V}\cdot\text{s}$ at room temperature and 110,000

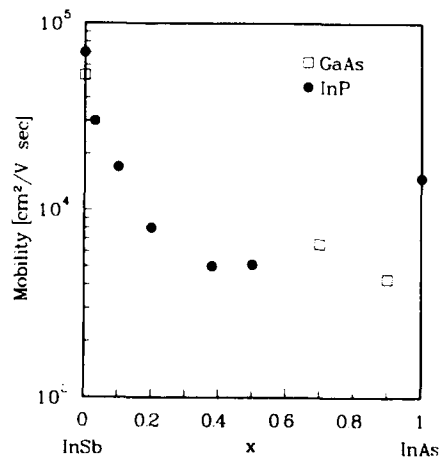


Fig. 2. Variation of measured room-temperature electron mobility with alloy compositions in $\text{InAs}_x\text{Sb}_{1-x}$ films grown on GaAs and InP.

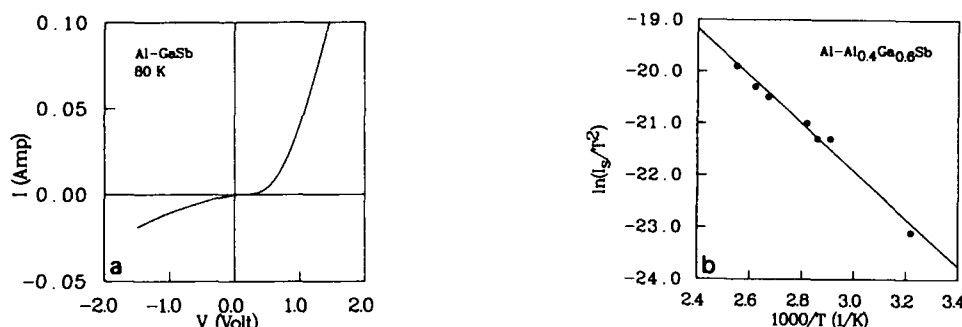


Fig. 3. (a) I - V characteristics at 80 K of Al/GaSb diodes and (b) $\ln(I_s/T^2)$ versus $10^3/T$ plot of Al/ $\text{Al}_{0.4}\text{Ga}_{0.6}\text{Sb}$ diode.

$\text{cm}^2/\text{V} \cdot \text{s}$ at 77 K, and the mobility of InAs on InP is $15,000 \text{ cm}^2/\text{V} \cdot \text{s}$ at room temperature. The mobility rapidly drops with alloying, probably due to a combination of increased lattice mismatch and clustering effects. However, the mobility values compare very favorably with $\text{InAs}_x\text{Sb}_{1-x}$ films grown by liquid phase epitaxy on InSb substrates. This also indicates that clustering effects rather than dislocation effects are responsible for the degradation in mobility.

3. The growth and schottky diode characteristics of $\text{Al}_y\text{Ga}_{1-y}\text{Sb}$ epitaxial layers

An important parameter in the design and fabrication of FETs are the barrier height and leakage current of the Schottky gate contact. Since in our heterostructures, the Schottky diode is fabricated on an AlGaSb layer, we have examined the properties of Al/AlGaSb Schottky diodes. A $1 \mu\text{m}$ layer of AlGaSb Be-doped p-type $5 \times 10^{16} \text{ cm}^{-3}$ was grown on P⁺-GaSb substrates. 500 μm diameter Al Schottky diodes were made on the layers by electron beam evaporation through a shadow mask. Forward and reverse-bias current-voltage measurements were made on the diodes as a function of temperature in the range 80–400 K. The I - V characteristics of a GaSb diode at 80 K are shown in fig. 3a. The reverse saturation current is $8.83 \mu\text{A}$ and the breakdown voltage is 3 V. Fig. 3b shows the $\ln(I_s/T^2)$ versus $10^3/T$ plot for an $\text{Al}_{0.4}\text{Ga}_{0.6}\text{Sb}$ diode in accordance with the Richardson equation. The barrier heights obtained

from the analysis of these data are 0.37 and 0.4 eV for GaSb and $\text{Al}_{0.4}\text{Ga}_{0.6}\text{Sb}$, respectively. Mead and Spitzer [8,9] and Sadiq and Joullie [10] have reported barrier heights of 0.55 and 0.7 eV for Au/p-type AlSb Schottky diodes. Mead and Spitzer cleaved the samples in vacuum before depositing the Au layer. Assuming an increase of barrier height with bandgap, our results are in fair agreement with the data of Mead and Spitzer. These are first reported data on barrier height of MBE grown AlGaSb.

4. The structures and the performance of $\text{InAs}_{0.8}\text{Sb}_{0.2}/\text{Al}_{0.4}\text{Ga}_{0.6}\text{Sb}$ HFET

For an FET it is important to realize a thin channel with good transport properties. We used InAsSb as a channel and AlGaSb as a barrier material. The schematics of the doped-channel heterostructure FET grown on semi-insulating GaAs is shown in fig. 4. The sheet electron concentration and mobility in the 300 Å Si-doped $\text{InAs}_{0.8}\text{Sb}_{0.2}$ channel at 300 K are $5.4 \times 10^{12} \text{ cm}^{-2}$

100 Å	$n = 2 \times 10^{18} \text{ cm}^{-3}$ InAs
400 Å	Undoped AlGaSb Barrier
300 Å	$n = 2 \times 10^{18} \text{ cm}^{-3}$ InAsSb Channel
7 μm	Undoped AlGaSb Buffer
S. I. GaAs Substrate	

Fig. 4. Schematic of $\text{InAsSb}/\text{AlGaSb}$ heterostructure FET grown by MBE on GaAs.

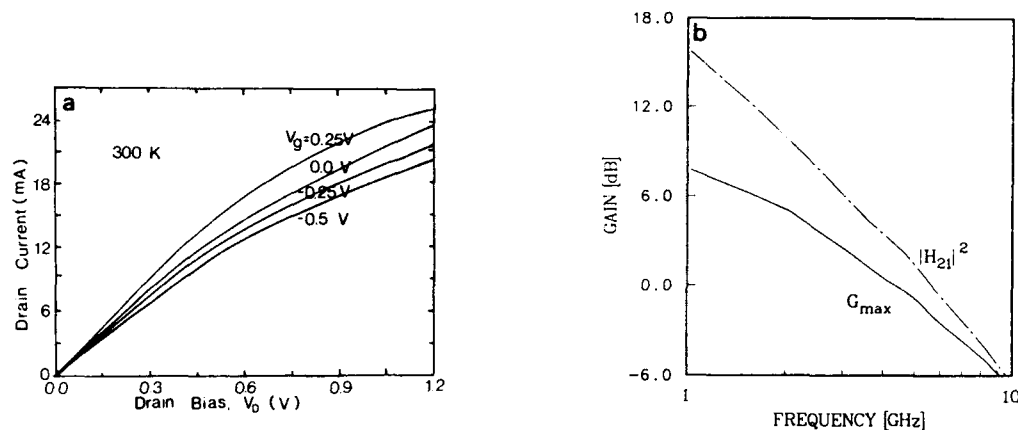


Fig. 5. Measured (a) DC and (b) microwave performance at room temperature for $\text{InAsSb}/\text{AlGaSb}$ heterostructure FET.

and $1000 \text{ cm}^2/\text{V} \cdot \text{s}$, respectively. Recently, FETs with an undoped channel using the $\text{InAs}/\text{AlGaSb}$ (or AlSb) heterostructure were reported by Tuttle and Kroemer [11] and Luo et al. [12].

$1 \mu \times 50 \mu \text{m}$ gate FETs with a source-drain spacing of $3.5 \mu \text{m}$ were made by standard photolithography techniques. The source and drain contacts were made with electron beam evaporated $\text{Au}/\text{Ge}/\text{Ni}$ and subsequent alloying. Al gate contacts were formed by electron beam evaporation. Measured room-temperature current-voltage characteristics of the devices are shown in fig. 5a. The devices cannot be pinched off due to a large parallel conduction. The maximum measured transconductance at 300 K is 160 mS/mm . The S-parameter measurements were made on the devices with a CASCADE probe station and a 8510 automatic network analyzer. The measured current gain is shown in fig. 5b. The unity gain cut-off frequency f_T is found to be 5 GHz.

5. Conclusion

We have grown high quality $\text{InAs}_x\text{Sb}_{1-x}$ ($0 \leq x \leq 1$) directly on InP and GaAs substrates by molecular beam epitaxy. The undoped crystals are all n-type at 300 K and at low temperature. The surface morphology and electrical transport properties are strongly dependent on the $J_{\text{Sb}_4}/J_{\text{In}}$ flux ratio and substrate temperature. The highest mo-

bilities in InSb ($10 \mu \text{m}$ thick) are $70,000 \text{ cm}^2/\text{V} \cdot \text{s}$ and 300 K and $110,000 \text{ cm}^2/\text{V} \cdot \text{s}$ at 77 K, and lower values are measured in the alloys.

We have also investigated the suitability of $\text{Al}_y\text{Ga}_{1-y}\text{Sb}$ as a buffer and gate barrier layer in heterostructure FETs. Al Schottky contacts were evaporated on these p-type films and temperature-dependent current-voltage measurements were made. Barrier heights of 0.37 and 0.39 eV are measured in GaSb and $\text{Al}_{0.4}\text{Ga}_{0.6}\text{Sb}$, respectively.

We have made a 300 Å Si-doped $\text{InAs}_{0.8}\text{Sb}_{0.2}$ channel structure, sandwiched between undoped $\text{Al}_{0.4}\text{Ga}_{0.6}\text{Sb}$ buffer and gate barrier region. It shows $\mu = 1000 \text{ cm}^2/\text{V} \cdot \text{s}$ and $n_s = 5.4 \times 10^{12} \text{ cm}^{-2}$ at 300 K. $1 \mu \text{m}$ gate FETs made with this heterostructure, showed a maximum extrinsic $g_m = 160 \text{ mS/mm}$ and $f_T = 5 \text{ GHz}$ at 300 K.

Acknowledgements

The work is supported by NASA-Lewis under grant NAG-3-988 and the ARO (URI Program) under Contract DAALO03-87-K0007.

References

- [1] G.C. Osbourn, J. Vacuum Sci. Technol. B2 (1984) 176.
- [2] S.R. Kurtz, L.R. Dawson, T.E. Zipperian and S.R. Lee, Appl. Phys. Letters 52 (1988) 1581.

- [3] J.H. Kim, P.K. Bhattacharya and J. Singh, Appl. Phys. Letters 56 (1990) 1901.
- [4] J.K. Abrokwhah and M. Gershenson, J. Electron. Mater. 10 (1981) 379.
- [5] M.Y. Yen, R. People, K.W. Weckl and A.Y. Cho, Appl. Phys. Letters 52 (1988) 489.
- [6] J.-I. Chyi, S. Kalem, N.S. Kumar, C.W. Litton and H. Morkoç, Appl. Phys. Letters 53 (1988) 1092.
- [7] G.M. Williams, C.R. Whitehouse, C.F. McConville, A.G. Cullies, T. Ashiley, S.J. Courtney and C.T. Elliott, Appl. Phys. Letters 53 (1988) 1189.
- [8] A. Mead and W.G. Spitzer, Phys. Rev. Letters 10 (1963) 471.
- [9] A. Mead and W.G. Spitzer, Phys. Rev. A134 (1963) 713.
- [10] S. Sadiq and A. Joullie, J. Appl. Phys. 65 12 (1989) 15.
- [11] G. Tuttle and H. Kroemer, IEEE Trans. Electron Devices ED-34 (1987) 2358.
- [12] L.F. Luo, R. Beresford, W.I. Wang and H. Munekata, Appl. Phys. Letters 55 (1989) 789.

MOMBE growth of GaSb and InAsSb using triethylstibine and triethylarsine

Tadaaki Kaneko, Hajime Asahi, Yasushi Itani, Yasutoshi Okuno and Shun-ichi Gonda

Institute of Scientific and Industrial Research (ISIR), Osaka University, 8-1, Mihogaoka, Ibaraki, Osaka 567, Japan

We report metalorganic molecular beam epitaxial (MOMBE) growth of GaSb and InAsSb using triethylgallium (TEGa), trimethylindium (TMIn), triethylstibine (TESb), and triethylarsine (TEAs). For GaSb growth, the maximum growth rate is observed at a substrate temperature of 500°C. This is associated with the use of TESb instead of solid Sb, where the alkyl species coming from thermally cracked TESb also play important roles in the pyrolysis of TEGa. For InAsSb growth, it is found that pyrolysis of TMIn at substrate temperatures below 400°C is decomposition limited. Precise control of solid composition for $\text{InAs}_{1-x}\text{Sb}_x$ in the range of $0 \leq x \leq 0.6$ is confirmed in the temperature range from 400 to 500°C.

1. Introduction

Alloys of InGaAsSb lattice matched to GaSb have attracted considerable interest for 2–4 μm wavelength optical devices [1] and high speed electronic devices [2]. Several authors have reported the epitaxial growth of Sb-containing materials by MBE [3] and MOVPE [4]. However, this system has a wide miscibility gap and contains two group V atoms where the reproducibility of the composition of the alloys is strictly dependent on flux stability. In solid source MBE, it is difficult to control the composition of materials containing two group V atoms. MOMBE (metalorganic molecular beam epitaxy), which is a non-thermal-equilibrium growth technique and has an advantage in good controllability of gas sources, is a promising method for growing this material system. Furthermore, the study of MOMBE growth using group V metalorganic gas sources gives important information to the MOMBE growth mechanism.

We have previously reported [5,6] the first trial on MOMBE growth of GaSb, InAs and InSb on GaSb substrates using metalorganics only for group III atoms, where the Sb-related growth kinetics of group III metalorganics have been discussed [6]. This paper describes the first MOMBE growth of GaSb and InAsSb using group V metal-

organics instead of solid sources. The employment of these materials without the use of a toxic group V hydride compressed gas is of much interest from a safety point of view. In the growth of GaSb using triethylgallium (TEGa) and triethylstibine (TESb), the effect of the thermal cracking process of TESb on the pyrolysis of TEGa on the surface is investigated from the growth rate variation with the growth conditions. In the growth of $\text{InAs}_{1-x}\text{Sb}_x$ using trimethylindium (TMIn), triethylarsine (TEAs) and TESb, the control of alloy composition in the range of $0 < x < 0.6$ is reported. At the same time, the effect of the surface pyrolytic process of TMIn is described in terms of the growth temperature dependence of the constituent binary growth rates.

2. Experiment

The MOMBE growth experiments were performed using the conventional MBE growth chamber equipped with an oil diffusion pump having a liquid nitrogen trap and with gas supplying systems. The sources used were TEGa, TMIn, TESb, and TEAs. No carrier gas was employed. The substrates used were Te-doped (001) GaSb ($n = 1 \times 10^{18} \text{ cm}^{-3}$) and (001) semi-insulating

GaAs. The group III gases were directly introduced into the growth chamber, and the group V gases were introduced through a cracker cell ($\approx 800^\circ\text{C}$) after mixing. At this cracking temperature, both TESb and TEAs were expected to efficiently decompose judging from the mass spectrometric measurement in the MOMBE system. The gas flow rates were controlled by mass flow controllers. Further experimental details have been described elsewhere [5,6].

GaSb layers were grown on GaSb substrates over temperature range of 400 to 580°C . The flow rates of TEGa and TESb were varied from 0.2 to 2.0 and 0.1 to 0.4 SCCM, respectively. The growth rate of GaSb was determined from the period of RHEED (reflection high energy electron diffraction) intensity oscillations. For the growth of InAsSb on GaSb substrates, the temperatures were varied from 350 to 500°C . The TMIn flow rate was 0.1 SCCM, where the outlet of the group III gas cell was rearranged to get four times closer to the substrate than during growth of GaSb. The flow rates of TEAs and TESb were varied from 0.06 to 0.2 and 0.05 to 0.4 SCCM, respectively. The solid composition was determined using X-ray diffraction measurements by assuming Vegard's law. Growth rate was confirmed by the cross-sectional observation of cleaved epilayers with a scanning electron microscope, and by the measurement of the step height between the epilayer surface and the substrate surface masked with a small Ta piece during the growth. Typical background pressure during growth is less than 3×10^{-6} Torr.

3. GaSb growth

Mirror surfaces were obtained for GaSb growth over the entire range of growth conditions employed here except at a V/III ratio less than unity. The surface reconstruction during growth exhibited (1×3) pattern, similar to the result observed in the conventional MBE growth [7]. RHEED oscillations were observed at substrate temperatures in the range of 400 to 580°C . The amplitudes of RHEED intensity oscillations ob-

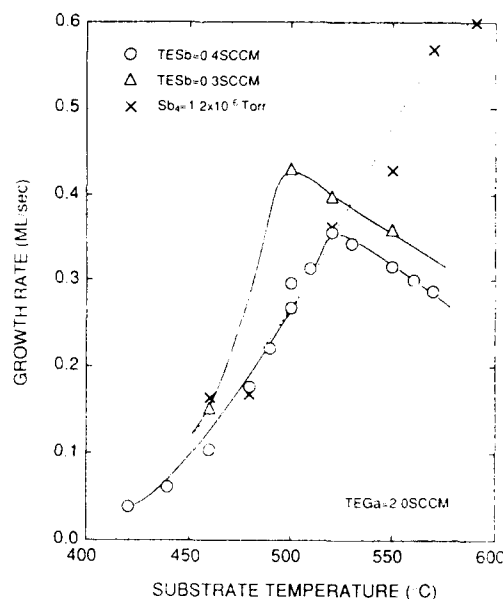


Fig. 1. MOMBE GaSb growth rate versus substrate temperature for a given TESb flow rate with a constant TEGa flow rate of 2.0 SCCM. The broken line shows the temperature dependence of growth rate for MOMBE GaSb using solid Sb₄ with the same TEGa flow rate.

served here were larger than those using Sb₄ under the same growth conditions.

A significant variation of the MOMBE GaSb growth rate with substrate temperature is shown in fig. 1 for two different given TESb flow rates at a constant TEGa flow rate of 2.0 SCCM (solid lines). The variation of growth rate for the GaSb layers grown using Sb₄ under the same TEGa flow rate is also shown with a broken line for comparison. The use of TESb instead of Sb₄ induces changes in the growth rate variation curve with substrate temperature. The growth rate of GaSb grown from TESb shows a maximum at around 500°C . However, the growth rate at 500°C is lower than that in the GaAs growth using the same TEGa flux by a factor of 3. Since a decrease in the growth rate can be observed with increasing TESb flow rate even at higher temperatures, the growth rate reduction above 500°C is not related to an Sb deficiency on the surface, but to the surface pyrolytic process of TEGa. This indicates that the alkyl species coming from thermally

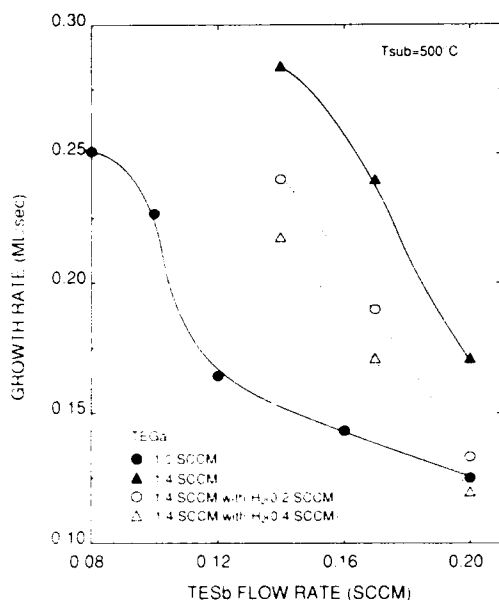


Fig. 2. MOMBE GaSb growth rate versus TESb flow rate for given TEGa flow rates at a substrate temperature of 500 °C.

cracked TESb also play an important role in the MOMBE growth process by suppressing the ethyl-gallium bond cleavage reaction.

Fig. 2 shows the TESb flow rate dependence of the growth rate for different TEGa fluxes. The growth temperature was kept at 500 °C. At the leftside points of each curve the V/III ratio corresponds to unity. The remarkable reduction of the growth rate with an increase in the TESb flow rate can be seen near the region at V/III ratio close to unity. A similar reduction in growth rate with increased group V flux has been observed in the MOMBE growth of GaSb using Sb₄ [6] and GaAs using AsH₃ [8]. This indicates that oversaturated alkyl molecules coming from thermally cracked TESb reduces the number of sites available for TEGa pyrolysis. Since the mass spectrometric measurement showed that one of the main species of TESb by cracking was hydrogen, we also investigated the overpressure effect of hydrogen on the MOMBE GaSb growth, shown as broken lines in fig. 2, by introducing hydrogen into the cracker cell for group V sources. We can see the decrease of the growth rate with increasing hydrogen flow

rate. However, since the rate of the growth rate reduction with increasing TESb has little dependence on the magnitude of additional hydrogen, it is considered that alkyl species cracked from TESb play a relatively important role in the site blocking effect on the pyrolysis of TEGa, compared to hydrogen.

The electrical properties of GaSb layers grown on a (001) GaAs substrate were evaluated by Hall measurement. The 1.2 μm thick undoped GaSb layer grown at 520 °C using TEGa of 2.0 SCCM and TESb of 0.4 SCCM showed a relatively low hole concentration of $2 \times 10^{17} \text{ cm}^{-3}$ and mobility of 660 cm²/V · s at 77 K.

4. InAsSb growth

In the MOMBE growth of InAsSb, mirror-like surfaces were obtained only in the narrow region of TEAs/TMIn flux ratio close to unity. Under this condition, the InAs layers grown on GaSb substrate using TMIn and TEAs exhibit cross-

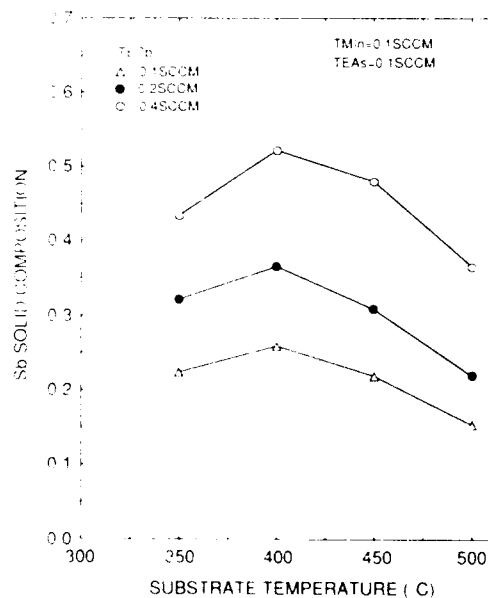


Fig. 3. Substrate temperature dependence of Sb solid composition for MOMBE InAsSb as a function of TESb flow rate with constant TMIn and TEAs flow rates of 0.1 SCCM.

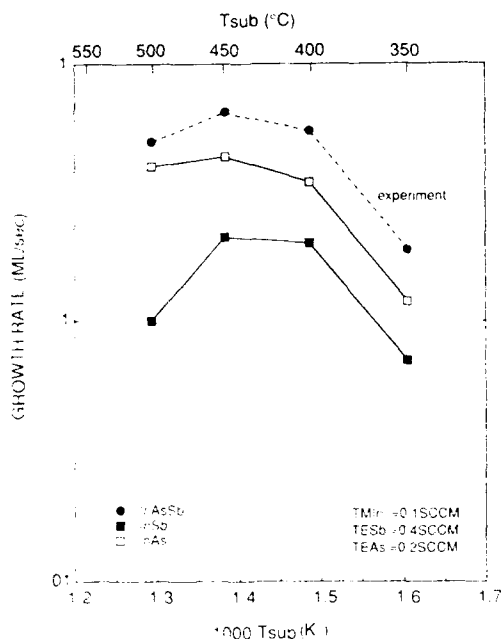


Fig. 4. Growth rates of InAsSb and calculated constituent binary compounds InSb and InAs as a function of reciprocal temperature for MOMBE grown InAsSb with TMIn, TESb and TEAs flow rates of 0.1, 0.4 and 0.2 SCCM, respectively.

hatched appearance in the temperature range of 350 to 500°C. The InAsSb layers during growth show (2×6) RHEED patterns.

Fig. 3 shows the temperature dependence of Sb solid composition x of $\text{InAs}_{1-x}\text{Sb}_x$ as a function of TESb flow rate with constant TMIn and TEAs flow rates of 0.1 SCCM. As shown in this figure, two distinct temperature dependent regions can be seen. The first is the low temperature region below 400°C, where the Sb solid composition increases with increasing temperature. This region seems to be characteristic of MOMBE growth, because pyrolytic process of TMIn in this temperature range is expected to be decomposition limited from the result reported on the MOMBE growth of InAs using TMIn and solid As [6]. The second is the region above 400°C where the Sb solid composition decreases with increasing temperature. Similar observations were reported on both MOVPE and MBE growths of InAsSb [3,4]. The tendency of the lower Sb content at the higher substrate

temperature is considered to reflect an increased Sb desorption rate from the growth front [9].

Fig. 4 shows temperature dependence of InAsSb and constituent binary growth rates at TMIn, TEAs and TESb flow rates of 0.1, 0.2 and 0.4 SCCM, respectively. The growth rates of binaries obtained here were calculated from the total growth rate and solid composition. From the temperature dependence of the constituent InSb and InAs growth rates, the pyrolytic process of TMIn is found to be decomposition limited below 400°C and the activation energy is almost the same. It is considered that the catalytic efficiency of TMIn has no difference between the constituent InAs growth and the InSb growth in this growth condition. In the temperature region of 400 to 450°C, nearly flat regions can be seen, corresponding to the transport limited region. Thus, adopting the temperature within this range during MOMBE InAsSb growth may offer a reproducible control of the solid composition. At higher temperatures of more than 450°C, the growth rates decrease with increasing temperature, which is caused by

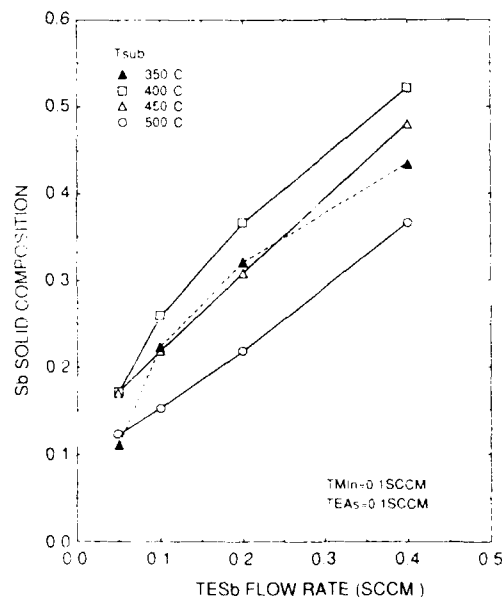


Fig. 5. Sb solid composition versus TESb flow rate for MOMBE InAsSb as a function of substrate temperature with constant TMIn and TEAs flow rates of 0.1 SCCM.

the desorption of In atoms, as in conventional MBE.

Since the temperature dependence of the constituent InAs growth rate is quite similar to the result observed in the growth of binary InAs using TMIn and As₄ [6], the existence of Sb molecules does not play an important role energetically in the decomposition of TMIn on InAs. Therefore, it is expected that the decomposition of TMIn on binary InSb may obey the temperature dependence of the constituent InSb growth rate obtained here as shown in fig. 4.

A variation of the Sb solid composition with TESb flow rate is shown in fig. 5 as a function of substrate temperature. The composition can be controlled precisely, as can be seen in this figure, except for the curve at 350°C, as long as using an infrared optical pyrometer during growth to control the substrate temperature with a deviation of less than 5°C.

The 1 µm thick undoped InAsSb layer ($x = 0.27$) on a GaAs substrate was n-type with a carrier concentration of $1.7 \times 10^{17} \text{ cm}^{-3}$ and mobility of $3030 \text{ cm}^2/\text{V} \cdot \text{s}$ at 77 K.

5. Conclusion

We have grown for the first time GaSb and InAsSb layers by MOMBE method using TEGa and TMIn as group III sources, and TESb and TEAs as group V sources. In the growth of GaSb, the growth rate showed a maximum at around 500°C without the monotonic increase of the growth rate observed in MOMBE GaSb growth using Sb₄. It is considered that the alkyl species coming from thermally cracked TESb also play an important role in the MOMBE growth process suppressing the ethyl-gallium bond cleavage reaction. In the growth of InAsSb, we have confirmed that the solid composition can be controlled precisely. In the temperature region lower than

400°C, the reduction of the Sb solid composition with decreasing temperature was observed. From the temperature dependence of constituent InSb and InAs growth rates, the pyrolytic process of TMIn was found to be decomposition limited below 400°C having almost the same activation energy.

Acknowledgements

The authors would like to thank Fumio Kimijima of Ulvac Co. Ltd. for the MBE apparatus, Masashi Isemura of Sumitomo Chemical Co. Ltd. for the metalorganic gas sources, and Hiroshi Okamoto and Haruo Nagai for the GaSb substrates. This work was supported in part by a grant from the Research Program on "Creation of New Materials through Intelligent Design" of ISIR, Osaka University.

References

- [1] C. Caneau, A.K. Srivastava, A.G. Dentai, J.L. Zyskind, C.A. Burrus and M.A. Pollak, *Electron. Letters* 22 (1986) 992.
- [2] T.H. Chiu, W.T. Tsang, J.A. Ditzenberger and J.P. van der Ziel, *Appl. Phys. Letters* 49 (1986) 1051.
- [3] G.S. Lee, Y. Lo, Y.F. Lin, S.M. Bedair and W.D. Laidig, *Appl. Phys. Letters* 47 (1985) 1219.
- [4] P.K. Chiang and S.M. Bedair, *J. Electrochem. Soc.* 131 (1984) 2422.
- [5] T. Kaneko, H. Asahi, Y. Okuno and S. Gonda, *J. Crystal Growth* 95 (1989) 158.
- [6] T. Kaneko, H. Asahi, Y. Okuno, T.W. Kang and S. Gonda, *J. Crystal Growth* 105 (1990) 69.
- [7] M. Lee, D.J. Nicholas, K.E. Singer and B. Hamilton, *J. Appl. Phys.* 59 (1986) 2895.
- [8] T.H. Chiu, J.E. Cunningham and A. Robertson, Jr., *J. Crystal Growth* 95 (1989) 158.
- [9] K.R. Evans, C.E. Stutz, P.W. Yu and C.R. Wie, *J. Vacuum Sci. Technol.* B7 (1989) 271.

Electrical characteristics dependence on aluminum mole fraction in $(\text{Al}_{0.5}\text{Ga}_{0.5})\text{Sb}/\text{InAs}/(\text{Al}_x\text{Ga}_{1-x})\text{Sb}$ heterostructure

Kanji Yoh, Toshiaki Moriuchi, Mitsuaki Yano and Masataka Inoue

Department of Electrical Engineering, Osaka Institute of Technology, 5-16-1 Omiya, Asahi-ku, Osaka 535, Japan

We have studied the electrical characteristics of the $(\text{Al}_{0.5}\text{Ga}_{0.5})\text{Sb}/\text{InAs}/(\text{Al}_x\text{Ga}_{1-x})\text{Sb}$ heterosystems in a variety of samples with different aluminum mole fraction, x . Negative photoconductivity has been observed when the aluminum mole fraction is between 0.2 and 1.0. Reduction of both electron mobility and sheet carrier concentration by the light illumination was most pronounced at $x = 0.75$. The negative photoconductivity of an $(\text{Al}_{0.5}\text{Ga}_{0.5})\text{Sb}/\text{InAs}/(\text{Al}_{0.5}\text{Ga}_{0.5})\text{Sb}$ structure was found to disappear at high electric fields by pulsed Hall-effect measurements suggesting increased Coulombic scattering being the origin of the negative photoconductivity.

1. Introduction

$\text{InAs}/(\text{Al}_x\text{Ga}_{1-x})\text{Sb}$ heterostructures provide not only interesting band alignment [1,2] in physical point of view, but also practical applications such as high performance field-effect transistors [3] and quantum interference devices. High speed electron transport is expected because of its extremely high low-field mobility [4] and high overshoot velocity of the electrons in the channel under high electric field. However, the characterization done so far on this system is not sufficient enough to optimize the heterostructure for any realistic device application. For example, the lack of knowledge includes spacial distribution and the concentration of the not-intentionally-doped donors [4] in the $(\text{AlGa})\text{Sb}$ barriers, their dependence on the aluminum composition, and negative photoconductivity [4] dependence on the heterostructure. We have studied the electrical characteristics of the $(\text{Al}_{0.5}\text{Ga}_{0.5})\text{Sb}/\text{InAs}/(\text{Al}_x\text{Ga}_{1-x})\text{Sb}$ heterosystems in a variety of samples with different aluminum mole fraction (x) and then, other similar but slightly different structures such as $(\text{Al}_{0.5}\text{Ga}_{0.5})\text{Sb}/\text{InAs}/\text{GaSb}$ heterostructures with thin $(\text{Al}_x\text{Ga}_{1-x})\text{Sb}$ layers inserted at the InAs/GaSb interface. Finally, pulsed Hall-effect

measurement on an $(\text{Al}_{0.5}\text{Ga}_{0.5})\text{Sb}/\text{InAs}/(\text{Al}_{0.5}\text{Ga}_{0.5})\text{Sb}$ heterostructure will be discussed in conjunction with the negative photoconductivity effect on high field electron transport.

2. Experimental

The heterostructures have been grown on GaAs substrates by molecular beam epitaxy (MBE) using the ANELVA-620 system. As shown in fig. 1a, the standard structure consists of 1.0 μm of GaSb buffer layer, 0.75 μm of AlSb, 2000 Å of $(\text{Al}_{0.5}\text{Ga}_{0.5})\text{Sb}$, 150 Å of InAs, 150 Å of $(\text{Al}_{0.5}\text{Ga}_{0.5})\text{Sb}$, and 100 Å of GaSb cap layer. Growth conditions were carefully chosen in order to avoid the arsenic mixing into the $(\text{AlGa})\text{Sb}$ layers [5]. The insertion of the initial GaSb buffer plays an important role to obtain good surface morphology and high low-field mobility of electrons in the InAs channel. In order to avoid the parallel conduction of holes in the GaSb buffer layer, all the devices have been fabricated using non-alloyed ohmic contacts to the InAs channel. The substrate temperature, T_{sub} , during the growth of InAs channel and the rest of the layers above it was set to 480°C, while the T_{sub} during the growth of the layers under the

channel was set to 550 °C. Beam pressure ratio of As to In was chosen in such a way that the InAs surface reconstruction falls into the transition region from 2×4 to 4×2 [6]. The aluminum composition of the top barrier has almost no effect on the electrical characteristics (similar results obtained in ref. [7]). Accordingly, the aluminum mole fraction of the top barrier has been set to be 0.5, because it provides both moderate inertness to the water vapor and moderate barrier height at the same time. The first set of experiments were done by Hall-effect measurements (Van der Pauw method) of a series of standard structures which are otherwise identical but with different x , in order to investigate the effects of aluminum mole fraction in the bottom barrier on the electrical characteristics of the InAs channel. A second set of experiments were done by inserting thin $(\text{Al}_x\text{Ga}_{1-x})\text{Sb}$ layers at the bottom interface of the InAs channel in $(\text{Al}_{0.5}\text{Ga}_{0.5})\text{Sb}/\text{InAs}/\text{GaSb}$ heterostructures in order to extract the effects of interface materials on the electrical characteristics. A third set of experiments were done by high-field pulsed Hall-effect measurements on Hall-bar devices with a spacing of 50 μm , in order to investigate the aluminum mole fraction effects on the electron transport under high fields.

3. Results and discussions

The Hall-effect measurements by Van der Pauw method on the standard structure (with $x = 0.5$) showed mobility of 20100 and 60600 $\text{cm}^2/\text{V} \cdot \text{s}$ at 300 and 77 K, respectively. The corresponding sheet carrier densities were 1.38×10^{12} and $9.96 \times 10^{11} \text{ cm}^{-2}$, respectively. Fig. 2 shows Hall mobility and sheet carrier concentration dependence on temperature, respectively. As can be seen, both mobility and the sheet carrier concentration decreases at low temperatures upon light (green LED) illumination. This negative photoconductivity, which was found in a $\text{AlSb}/\text{InAs}/\text{AlSb}$ system by Tuttle et al. [4], was observed as well in the $(\text{Al}_{0.5}\text{Ga}_{0.5})\text{Sb}/\text{InAs}/(\text{Al}_x\text{Ga}_{1-x})\text{Sb}$ heterosystem in a wide range of aluminum mole fractions. The compositional parameter, x , in the lower barrier significantly affects the electrical characteristics of the InAs channel layer. The room temperature mobility is always near 20000 $\text{cm}^2/\text{V} \cdot \text{s}$, independent of the aluminum mole fraction. Low temperature mobilities at 77 K are rather scattered and range between 40000 and 80000 $\text{cm}^2/\text{V} \cdot \text{s}$. The mobility reduction upon light illumination occurs if the bottom barrier, $(\text{Al}_x\text{Ga}_{1-x})\text{Sb}$, of the samples contains more than 25% of aluminum.

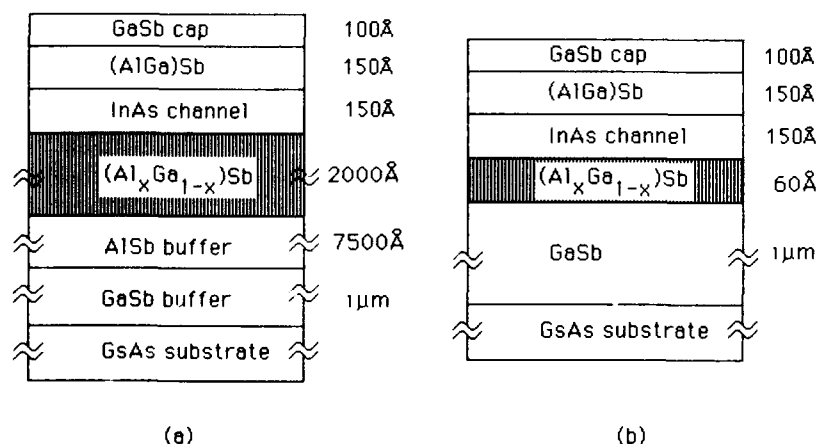


Fig. 1. Schematic diagrams of (a) standard $(\text{Al}_{0.5}\text{Ga}_{0.5})\text{Sb}/\text{InAs}/(\text{Al}_x\text{Ga}_{1-x})\text{Sb}$ heterostructure and (b) $(\text{Al}_{0.5}\text{Ga}_{0.5})\text{Sb}/\text{InAs}/(\text{Al}_x\text{Ga}_{1-x})\text{Sb}/\text{GaSb}$ heterostructure with thin barrier.

The carrier concentrations at 300 K are rather scattered and range from 1.5×10^{12} to $2.5 \times 10^{12} \text{ cm}^{-2}$. The sheet carrier concentrations at 77 K roughly stay near the $1 \times 10^{12} \text{ cm}^{-2}$ range except in the vicinity of $x = 1$ where the concentration slightly goes up. At 77 K, reduction of the sheet carrier concentration upon LED flash has been observed in the aluminum mole fraction range of 0.25 to 1.0, which matches the mobility reduction range as discussed above. The electron mobility and the sheet carrier concentration after LED flash at 77 K are plotted in fig. 3 (solid curves), where all data are normalized by the results without LED flash. From this figure, it is obvious that almost the same amount of reduction occurs in both sheet carrier concentration and electron mobility in the same range of aluminum mole fraction upon the light illumination. From fig. 3, the threshold aluminum mole fraction above which negative photoconductivity occurs reads around 0.2.

The suppression of the negative photoconductivity has been observed in the heterostructures with a thin ($\approx 60 \text{ \AA}$) $(\text{Al}_{0.5}\text{Ga}_{0.5})\text{Sb}$ layer inserted between the InAs channel and the bottom GaSb layer, which is depicted in fig. 1b. The aluminum mole fraction of the bottom thin barrier has very

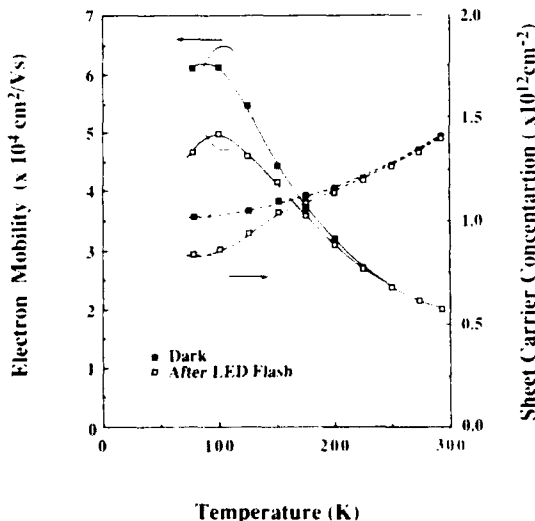


Fig. 2. Hall mobility and sheet carrier concentration dependence on temperature. Open squares denote the results after LED flash.

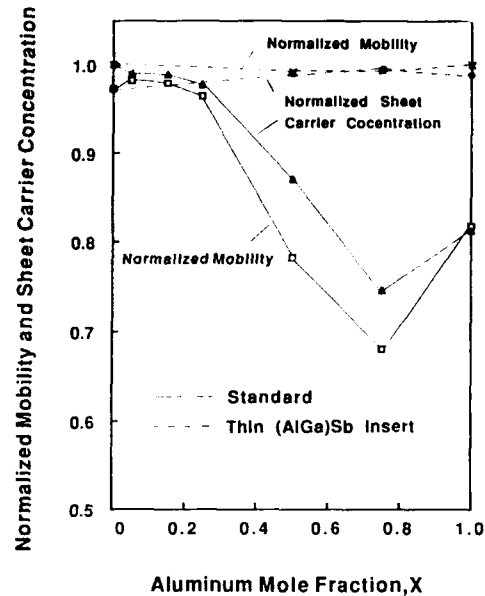


Fig. 3. The electron mobility and the sheet carrier concentration measured at 77 K after LED flash. Data are normalized by the results without LED flash.

little effect on the electrical characteristics, as shown in fig. 3 (dashed curves). Furthermore, both electron mobility and the sheet carrier concentration were always higher than the standard structures with the same barrier compounds. On the other hand, in the otherwise identical structure but with the bottom GaSb layer replaced by $(\text{Al}_{0.5}\text{Ga}_{0.5})\text{Sb}$, the negative photoconductivity did not disappear. These results show that the bulk $(\text{Al}_{0.5}\text{Ga}_{0.5})\text{Sb}$ layer ($0.25 < x < 1.0$) is responsible for the negative photoconductivity effect, not something that has the origin at the InAs/ $(\text{Al}_{0.5}\text{Ga}_{0.5})\text{Sb}$ interface. These results suggest that the donors are not localized at the bottom interface of the channel where possible AlAs bonds are formed as suggested by ref. [7]. Rather, the donors seem to be distributed uniformly in $(\text{AlGa})\text{Sb}$ layers.

Electron transport properties under high electric fields have been studied by pulsed Hall-effect measurements. As shown in fig. 4, both the sheet carrier concentration and the electron mobility measured after LED flash catch up the corresponding results measured without LED flash at

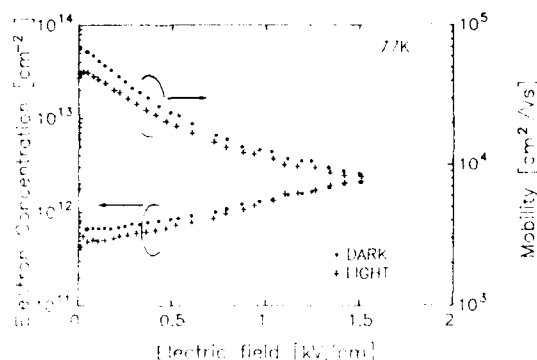


Fig. 4. The electron mobility and the sheet carrier concentration of an $(\text{Al}_{0.5}\text{Ga}_{0.5})\text{Sb}/\text{InAs}/(\text{Al}_{0.5}\text{Ga}_{0.5})\text{Sb}$ structure measured by pulsed electric-field Hall-effect measurements.

high electric fields. This asymptotic approach in high fields indicates that the mobility reduction is caused by scattering from some kinds of "ions" because electrons suffer less Coulombic scattering under high fields. Taking account of the fact that the decrease of the electron density in the InAs channel accompanies the mobility decrease, the "ions" should be negatively charged. Further experiment is needed to determine the origin of the negative photoconductivity.

4. Conclusions

In conclusion, the electrical characteristics dependence of the $(\text{Al}_{0.5}\text{Ga}_{0.5})\text{Sb}/\text{InAs}/(\text{Al}_{0.5}\text{Ga}_{0.5})\text{Sb}$ heterostructures on the aluminum mole fraction of the bottom barriers has been investigated. The negative photoconductivity effect has been shown to occur at the aluminum mole frac-

tion range of 20% to 100%. The aluminum mole fraction of the bottom thin barrier had very little effect on the electrical characteristics, but rather the bulk $(\text{Al}_x\text{Ga}_{1-x})\text{Sb}$ under the thin barrier affected the negative photoconductivity effect. Pulsed Hall measurement on an $(\text{Al}_{0.5}\text{Ga}_{0.5})\text{Sb}/\text{InAs}/(\text{Al}_{0.5}\text{Ga}_{0.5})\text{Sb}$ heterostructure showed suppression of the negative photoconductivity effect at high electric fields, suggesting the increased Coulombic scattering being the origin of the negative photoconductivity.

Acknowledgements

The authors would like to thank H. Taniguchi, K. Kiyomi and T. Kamiyoshi for their technical assistance. This work was supported in part by the Japan Private School Promotion Foundation on the Scientific Research Promotion Foundation and Grant-in-Aid for Science Research from the Ministry of Education, Science and Culture.

References

- [1] G.A. Sai-Halasz, L. Esaki and W.A. Harrison, *Phys. Rev.* B18 (1978) 2812.
- [2] G. Bastard, E.E. Mendez, L.L. Chang and L. Esaki, *J. Vacuum Sci. Technol.* 21 (1982) 531.
- [3] K. Yoh, T. Moriuchi and M. Inoue, in: *Proc. Device Research Conf.*, Santa Barbara, CA, 1990, paper IIA-3.
- [4] G. Tuttle, H. Kroemer and J.H. English, *J. Appl. Phys.* 15 (1989) 5239.
- [5] M. Yano, M. Ashida, Y. Iwai and M. Inoue, *Appl. Surface Sci.* 41/42 (1989) 457.
- [6] J.R. Soderstrom, D.H. Chow and T.C. MacGill, *Mater. Res. Soc. Symp. Proc.* 145 (1989) 409.
- [7] G. Tuttle, H. Kroemer and J.H. English, *J. Appl. Phys.* 67 (1990) 3032.

The growth of (Al,Ga)Sb tilted superlattices and their heteroepitaxy with InAs to form corrugated-barrier quantum wells

S.A. Chalmers, H. Kroemer and A.C. Gossard

Electrical and Computer Engineering Department and Materials Department, University of California, Santa Barbara, California 93106, USA

We have demonstrated the molecular beam epitaxial growth of (Al,Ga)Sb tilted superlattices (TSLs) on 2° vicinal (100) GaSb and GaAs substrates. The existence of (Al,Ga)Sb TSLs proves that step-flow growth can occur in this material system, and in the presence of strain. Lateral fluctuations in the tilt angle of the superlattice are observed and are found to be caused by a non-uniform distribution of incorporated adatoms which is correlated with the surface step density. The (Al,Ga)Sb TSL growth was also combined with InAs growth to form an InAs quantum well with "corrugated" barriers consisting of (Al,Ga)Sb TSLs. The electron mobilities in this structure exceeded $6 \times 10^5 \text{ cm}^2/\text{V} \cdot \text{s}$.

1. Introduction

Aluminum antimonide, gallium antimonide, and indium arsenide form an interesting family of compounds for molecular beam epitaxial (MBE) growth because they are nearly lattice-matched and they can be combined to form heterojunctions with straddling, staggered, and broken gap lineups. To learn more about the MBE growth of these compounds we have investigated their step-flow growth on vicinal surfaces, which gives information on the surface diffusion of the deposited adatoms and on the morphology of the growing surface. Successful step-flow growth of these compounds also raises the possibility of fabricating new structures in this material system, such as tilted superlattices (TSLs) [1,2]. The growth of more conventional structures may also be improved by step-flow growth on vicinal surfaces, which may be more ordered and better controlled than layer-by-layer growth on singular surfaces, because we can choose the orientation and therefore the bonding nature of the surface steps. This may be particularly important when forming interfaces across which the relatively volatile anion atoms are changed.

To investigate the step-flow growth of AlSb and GaSb we attempted to grow (Al,Ga)Sb TSLs, and found that in spite of the 0.65% lattice mismatch between these two materials, they can be grown together by step-flow to form uniform TSLs. We also demonstrated that AlSb and GaSb step-flow growth can be successfully combined with InAs growth by growing an InAs quantum well with "corrugated" (Al,Ga)Sb TSL barriers, which exhibits electron mobilities inside the well in excess of $6 \times 10^5 \text{ cm}^2/\text{V} \cdot \text{s}$.

2. Experimental

All growths were performed in a Varian Gen II MBE system with solid sources and an arsenic cracker. Both not-intentionally-doped GaSb and semi-insulating GaAs substrates were used, with the surfaces misoriented from (100) by 2° toward [011], which produces terraces with an average width of 20 atoms. The GaSb substrates were cleaned with a standard de-grease sequence and etched in 1 HF:1 H_2O_2 :100 H_2O for 2 min, while the GaAs substrates were used as received. All growth rates were approximately 0.3 mono-

layers/s. The Sb_4 beam equivalent pressure (BEP) was approximately 1×10^{-6} Torr, and the As_2 BEP was approximately 2×10^{-6} Torr.

3. Results and discussion

We grew the (Al,Ga)Sb TSLs by sequentially depositing approximately 0.4 monolayers (ML) of AlSb and 0.6 ML of GaSb. To lower the temperature for AlSb step-flow during TSL growth, we deposited the AlSb by migration-enhanced epitaxy (MEE) [3,4] (i.e., by alternating the Al and Sb beams), while we grew the GaSb by concurrent Ga and Sb deposition. We found that in this growth mode we were able to grow well-defined (Al,Ga)Sb TSLs at substrate temperatures from 450 to 510°C, on both GaSb and GaAs substrates. Fig. 1 shows a transmission electron microscopic (TEM) cross-section of four 12 nm thick TSLs grown on a GaAs substrate at 490°C after buffer layers of 100 nm of GaAs (600°C), 50 nm of AlSb (560°C), and 300 nm of GaSb (510°C) were deposited, in that order. We can see from the figure that even these relatively thin buffer layers resulted in a fairly uniform surface, as manifested in the uniform periodicity of the TSLs. This is surprising considering the 7% lattice mismatch between the GaAs substrate and the (Al,Ga)Sb layers which results in a high density of threading dislocations, and can be attributed to the smoothing properties of

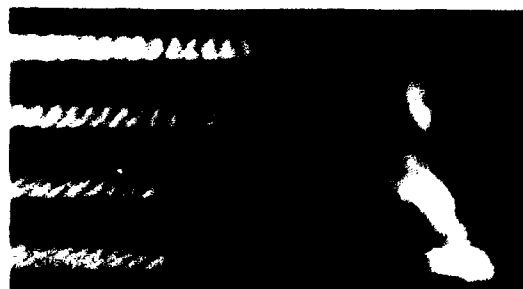


Fig. 1. Dark-field TEM micrograph of 12 nm thick (Al,Ga)Sb TSLs grown on 2° A-type GaAs substrate, with $p = 1.00$, 1.01, 1.03, and 1.05 (top to bottom). The steps descend left to right. The diagonal feature of the right side is a threading dislocation, resulting from the lattice mismatch due to growing on a GaAs substrate.



Fig. 2. Dark-field TEM micrograph of a 12 nm thick (Al,Ga)Sb TSL grown on a 2° A-type GaSb substrate, which shows variations in the TSL tilt angle.

the AlSb and GaSb buffer layers. TSLs grown on the GaSb substrates, with a 300 nm GaSb buffer layer grown at 510°C, were similar but exhibited better uniformity than those grown on GaAs substrates. The exact number of monolayers of AlSb and GaSb deposited per cycle, p , for the different TSLs in fig. 1 was 1.00, 1.01, 1.03, and 1.05 from top to bottom, as determined from the resulting tilt angles. The TSLs exhibit a high contrast between the AlSb-rich and GaSb-rich regions, indicating that these components are well separated, but there is also contrast between the GaSb-rich regions and the GaSb spacer layers, indicating that the separation is not complete. Although strain in the region of the dislocation seen in fig. 1 makes TEM imaging in that area difficult, we can see that TSLs formed, and therefore step-flow growth occurred, even very close to the dislocation.

An interesting feature of the (Al,Ga)Sb TSLs is that their tilt angle can vary with position, as seen in fig. 2. This TEM cross-section shows a 12 nm thick TSL grown on a GaSb substrate after a 300 nm GaSb buffer was grown at 510°C. Careful analysis of the local TSL thickness shows that the changing tilt angles are due to a variation in the local growth rate across the TSL, resulting in varying p -values. The resulting variations in p are much too great to be explained by inhomogeneous strain or non-uniform adatom deposition, but must rather be caused by a non-uniform redistribution of the group III adatoms that occurs *after* deposition. Because step edges play a dominant role in determining adatom distribution during step-flow growth, we might expect there to be a relation between an area's growth rate and its step density. Fig. 3 plots the p -value versus average step density for various locations of the TSL in fig. 2. The strong correlation between the two indicates that p is greater in regions that contain more steps. This sort of correlation, to differing degrees, was

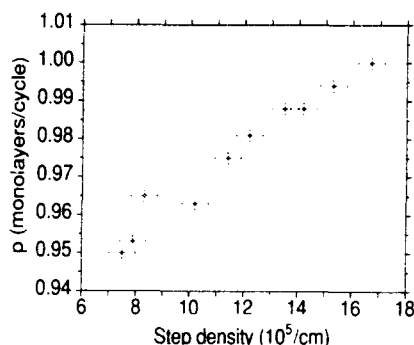


Fig. 3. Plot showing the correlation between the average local step density at various locations of the TSL in fig. 2 and the local p -value calculated from the TSL tilt.

seen in all the (Al,Ga)Sb TSLs examined. This behavior and therefore the tilt variations can be explained if we consider two different models of step-flow growth.

In one extreme limit where diffusing adatoms stick to the nearest step edge, p would be independent of terrace width, and the terrace widths would eventually equalize, in contradiction both to fig. 3 and to the actual appearance of the TSL pattern.

In the opposite limit, a model that assumes that the adatoms are *completely* free to diffuse over distances large compared to the terrace widths and that the sticking probability of an adatom at a step is the same at all step edges, would lead to a local growth rate that is simply proportional to the local step density, a correlation far stronger than what is observed.

Our data can be explained by a model between these two extremes, where some of the adatoms diffuse over distances equal to several terrace widths. Considering the bonding energies of AlSb and GaSb, and the analogous situation in the (Al,Ga)As system, the adatoms diffusing over these long distances are probably Ga. This result suggests that to grow TSLs with less tilt angle variation, we need to grow them on a surface with a more uniform step distribution, which may be accomplished by simply growing a thicker buffer layer.

To demonstrate that step-flow growth in the (Al,Ga)Sb system can be successfully combined

with InAs growth, we grew a corrugated-barrier quantum well (CBQW) that consisted of a 20 nm wide InAs quantum well with 12 nm (Al,Ga)Sb TSL barriers, as diagrammed in fig. 4a. The average barrier composition was chosen to be 30% Al (i.e. 0.3 ML of AlSb and 0.7 ML of GaSb deposited sequentially per cycle), so that any TSL formation in the barriers would result in the well/barrier interface being alternately broken gap (GaSb-rich barrier regions) and staggered gap (AlSb-rich barrier regions), which we felt might result in interesting transport effects. The structure was grown on a 2° A-type GaAs substrate, preceded by 50 nm of AlSb grown at 560°C and a 2.5 μ m thick GaSb buffer layer grown at 500°C. The InAs well was grown at 500°C and the TSL barriers at 490°C.

It has been shown that to achieve high electron mobilities in an InAs quantum well with AlSb barriers, it is critical that the bottom barrier/well interface be InSb-like [5]. To achieve this, we grew the bottom interface in the sequence 0.3 ML of Al, 6s of Sb, 0.5 ML of In, 3 s of As, and then the

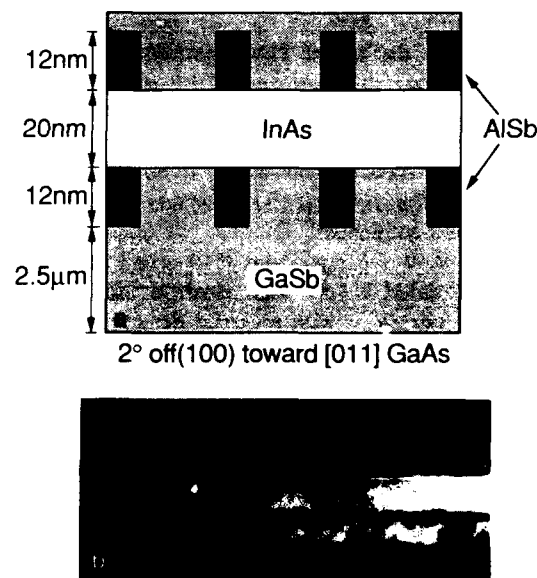


Fig. 4. (a) Schematic diagram of the corrugated-barrier quantum well (CBQW) that we attempted. (b) Dark-field TEM micrograph of the corrugated-barrier quantum well diagrammed in (a).

remainder of the InAs well by concurrent In and As deposition. After the InAs well was complete, we had a growth interruption of 50 s with As on to smooth the InAs surface, and then we started the top barrier with a 0.7 ML GaSb deposition. A TEM cross-section of the resulting structure is shown in fig. 4b. We can see that TSLs formed in both barriers, but they appear to be of lower quality than TSLs shown in fig. 1. Aside from a thicker buffer layer and a slightly lower Al content, the only difference in the growth of the bottom TSL of the CBQW and the TSLs shown in fig. 1 was the presence of a background As₂ pressure of approximately 3×10^{-7} Torr BEP during the CBQW growth, which was unavoidable since As₂ was needed for the InAs well growth. We suspect that the presence of As₂ on the growing surface may have interfered with the step-flow growth and therefore caused the poor TSL quality. In any case, a survey over the entire TEM sample revealed no apparent degradation of the top TSL with respect to the bottom one, indicating that the InAs layer itself had little adverse effect on the TSL formation. A puzzling feature of the micrograph in fig. 4b is the appearance of dark regions at both InAs/(Al,Ga)Sb TSL interfaces, which are visible over the entire TEM sample. We do not know whether they are caused by strain, or are due to a different compound, such as InSb, having formed at the interfaces, but it should be noted that the two dark regions appear to be very similar in spite of the fact that the interfaces were grown in different sequences.

Shubnikov-De Haas and Hall effect measurements revealed a very high electron mobility of 6.1×10^5 cm²/V·s with a carrier density of 9.8×10^{11} cm⁻² at 2 K, which we believe is the highest reported mobility for an InAs quantum well to date. Another sample, which was grown simultaneously with this sample but on a semi-insulating (100) GaAs substrate, had an electron mobility of only 3.6×10^5 cm²/V·s with a carrier density of 1.1×10^{12} cm⁻² at 2 K. Neither sample exhibited negative persistent photoconductivity, in contrast to high mobility AlSb/InAs wells [5]. Surprisingly, the measurements showed no significant anisotropy of the transport properties, relative to the direction of the TSL stripes. We speculate that

the absence of any anisotropy might be related to the presence of the intervening dark layers in fig. 4b, which may somehow shield the electrons in the well from the corrugations in the barrier. This point clearly needs more research, as does the understanding of the mechanism responsible for the high electron mobility. Of particular interest will be the effects of different substrate orientations and different interface growth sequences.

4. Conclusions

We have shown that AlSb and GaSb can be grown by step-flow and can be combined to grow tilted superlattices on 2° A-type GaAs and GaSb substrates, in spite of a 0.65% lattice mismatch. Lateral fluctuations in the tilt angle of the superlattice are observed and are found to be caused by a non-uniform adatom redistribution which is correlated with the surface step density. (Al,Ga)Sb TSL growth was also combined with InAs to form a corrugated-barrier quantum well (CBQW) with electron mobilities greater than 6×10^5 cm²/V·s, and which showed no anisotropy relative to the stripe direction of the corrugated barriers.

Acknowledgements

This work was supported by the National Science Foundation Science and Technology Center for Quantized Electronic Structures (S.A.C. and A.C.G.) and by the Office of Naval Research (H.K.).

References

- [1] P.M. Petroff, A.C. Gossard and W. Wiegmann, *Appl. Phys. Letters* 45 (1984) 620.
- [2] J.M. Gaines, P.M. Petroff, H. Kroemer, R.J. Simes, R.S. Geels and J.H. English, *J. Vacuum Sci. Technol.* B6 (1988) 1378.
- [3] F. Briones, D. Golmayo, L. Gonzalez and A. Ruiz, *J. Crystal Growth* 81 (1987) 19.
- [4] Y. Horikoshi, M. Kawashima and H. Yamaguchi, *Japan. Appl. Phys.* 27 (1988) 169.
- [5] G. Tuttle, H. Kroemer and J.H. English, *J. Appl. Phys.* 67 (1990) 3032.

Resonant tunneling in polytype InAs/AlSb/GaSb heterostructures

K.F. Longenbach, L.F. Luo, S. Xin and W.I. Wang

Department of Electrical Engineering, Columbia University, New York, New York 10027, USA

Polytype heterostructures of GaSb/AlSb/InAs show interband tunneling due to the ~ 0.14 eV overlap of the InAs conduction band and the GaSb valence band. This broken-gap configuration results in several novel mechanisms for negative differential resistance (NDR) that have potential applications in high-speed devices. Double-barrier structures exhibit resonant interband tunneling with high peak-to-valley current ratios due to the resonance enhancement of the tunneling current and the bandgap blocking of the nonresonant current components. Using InAs as the base in a double-barrier polytype heterostructure, resonant tunneling at room temperature through a quantum well as wide as 110 nm has been demonstrated. Also, GaSb/InAs/AlSb/GaSb structures have exhibited interband resonant tunneling with peak-to-valley ratios as high as 20:1 at 300 K and peak current densities up to 28 kA/cm². In addition to tunneling experiments, Ge and Sn have been shown to be well behaved p-type dopants for GaSb grown by molecular beam epitaxy (MBE), exhibiting free acceptor concentrations as high as 2×10^{19} and 5×10^{18} cm⁻³, respectively.

1. Introduction

Negative differential resistance arising from electron tunneling processes has been studied intensively for use in devices. The tunnel diode, which operates via interband tunneling, has circuit applications in the gigahertz frequency range. Resonant tunneling devices fabricated from quantum wells have shown the potential for operation at terahertz frequencies [1–3], but have not yet achieved adequate peak-to-valley current ratios at room temperature. Recently, resonant interband tunnel diodes were proposed [4–7] as a way to combine features of both interband and resonant tunneling in one device. In this article we review some of the recent results of interband tunneling in polytype heterostructures of GaSb/AlSb/InAs including both double-barrier and zero-barrier experiments. High peak-to-valley ratios are observed in these devices since bandgap blocking is effective in suppressing inelastic as well as elastic tunneling processes. Furthermore, resonant tunneling via a confined state in a quantum well gives rise to a large negative differential conductance.

In addition to tunneling devices grown by molecular beam epitaxy (MBE), we have demonstrated p-type doping of GaSb by Ge and Sn. The

observed p-type nature of Ge and Sn dopants in GaSb as well as the absence of Sn segregation is attributed to the large covalent bond radius of Sb. These dopants are important since they provide an excellent alternative to Be for p-type doping of MBE grown Sb based materials.

2. Double barrier polytype tunneling

High peak-to-valley ratios are realized in interband tunneling because bandgap blocking is effective in suppressing inelastic as well as elastic tunneling processes. Compared to a conventional double-barrier heterostructure, a polytype heterostructure operates with a more nearly ideal peak-to-valley ratio. For example, we have observed peak-to-valley ratios for polytype heterostructures (GaSb electrodes/InAs well) more than three times larger than those for the corresponding conventional heterostructure (InAs electrode/InAs well [8]). Interband tunneling in the InAs/AlSb/GaSb system can be observed because of the unique band alignment of these materials. As shown in fig. 1, the GaSb/AlSb valence band offset is 0.4 eV while the GaSb/InAs valence band offset is about 0.5 eV [10,11]. InAs and

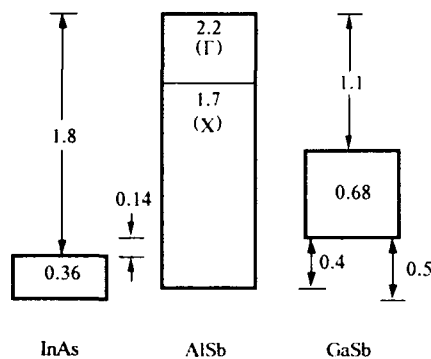


Fig. 1. Energy band alignment for the InAs/AlSb/GaSb. Approximate values of the bandgaps and offsets are shown in eV.

GaSb thus form a broken-gap heterojunction, with the InAs conduction band overlapping the GaSb valence band by about 0.14 eV.

Therefore, in this material system, two polytype configurations are possible: InAs well with GaSb electrodes, and GaSb well with InAs electrodes. Both show improved characteristics compared to the corresponding monotype structure. However, for fabricating wide wells, the smaller effective mass material (InAs) is more desirable. To understand the operation of these devices, a double-barrier structure as shown in fig. 2a is considered. The first confined state in the InAs well occurs at about 40 meV for a well width of 15 nm. For applied biases less than about 0.14 eV, interband tunneling can occur across both barriers, and a

large resonant current will flow in the structure. Here the holes in the GaSb anode tunnel first through the AlSb barrier to the quantum-confined electron states in the InAs well and then through the second AlSb barrier to the hole states in the GaSb cathode. In the two-band model, it is the light holes that will couple to the electron states in the well.

At higher bias, the valence band edge in the anode drops below the confined state energy in InAs, and the tunneling channel is cut off (fig. 2b). The interband tunneling does not depend on quantization effects. However, with thinner InAs wells, the quantization of states in the InAs well leads to large peak current densities.

In order to demonstrate this tunneling process, we prepared samples by MBE on GaSb substrates [11]. A 1 μm thick buffer layer of GaSb is grown first, followed by a GaSb electrode (10^{17} cm^{-3} p type). Then the quantum well structure is grown, consisting of 2.5 nm AlSb barriers and a 15 nm InAs well. The top electrode mirrors the bottom one, so that the structure is symmetric. A heavily doped GaSb cap layer completes the sequence. The top contact metal is Au/Ge, which served as the etch mask in forming mesas.

The I - V characteristics of this structure at room and liquid nitrogen temperatures are shown in fig. 3a. The valley is broad and deep, with a peak-to-valley ratio of 62:1 at 77 K (13:1 at 300 K) and a peak current density of 2.0 kA/cm^2 [7]. The hysteresis in the characteristic can be ac-

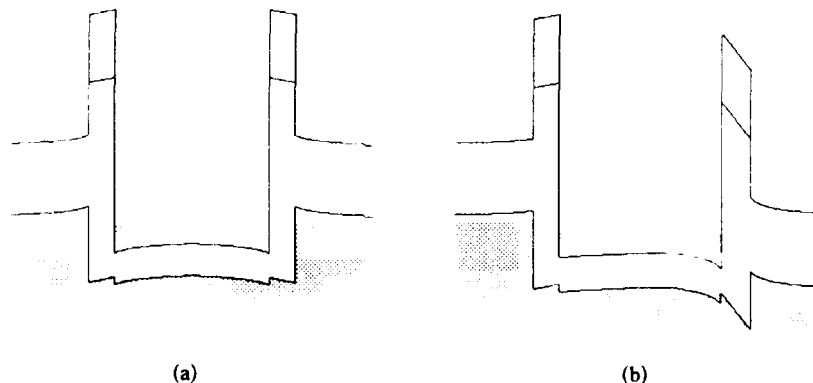


Fig. 2. Schematic energy band diagrams showing the operation of resonant interband tunneling (a) and the bandgap blocking at the anode barrier (b).

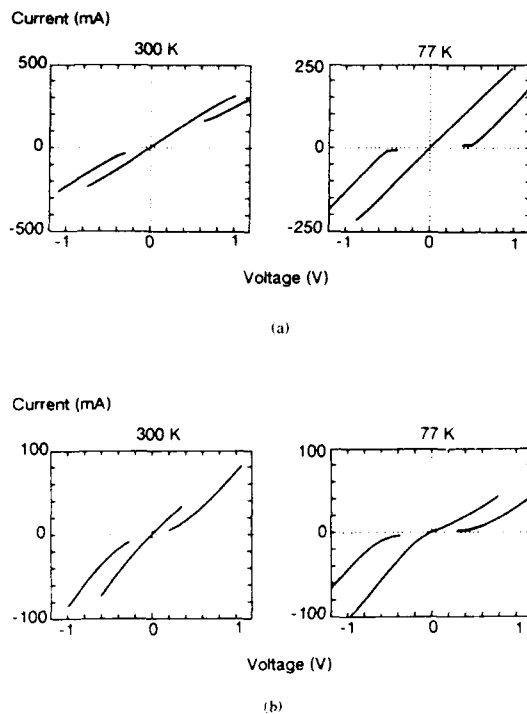


Fig. 3. I - V characteristics for double-barrier polytype heterostructures with a 2.5 nm barrier and (a) a 15 nm InAs well and (b) a 110 nm InAs well. Both devices are approximately 125 μm diameter dots.

counted for by the series resistance which is on the order of a few ohms and is not present in devices of much smaller area. The large peak-to-valley ratio is attributed to the reduced valley current compared to conventional resonant tunneling diodes, in which a high density of transverse momentum states is available off resonance. In contrast, excess valley current in interband tunneling arises from relatively rare defect levels in the bandgap, or from higher order scattering processes.

As noted previously, the small electron effective mass of InAs allows for the fabrication of devices with wide quantum wells. Thus, polytype structures with InAs well widths from 15 to 110 nm were grown and resonant tunneling I - V characteristics observed at room and liquid nitrogen temperatures [12]. For well widths up to 60 nm, the peak current density is typically 2 kA/cm^2 ;

above 60 nm the peak values are reduced. Nonetheless, resonant interband tunneling was observed for 110 nm InAs wells with low-temperature peak-to-valley ratios of 44:1 (fig. 3b). The achievement of resonant tunneling in a very wide quantum well has striking implications for potential three-terminal devices based on this phenomenon. Compared to the GaAs/AlGaAs system, InAs/AlSb/GaSb offers up to 20 times wider quantum wells, about 5 times higher base conductivity, and the critical advantage of the availability of good ohmic contacts.

3. Zero-barrier polytype interband coupling

In addition to the polytype double barrier structures, large negative differential resistance at room temperature has also been observed in GaSb/InAs/GaSb and InAs/GaSb/InAs structures and attributed to resonant interband coupling [13-15]. These structures represent the zero barrier thickness limit of double-barrier resonant tunneling experiments and exhibit large peak current densities due to the resonant coupling of electron states in InAs with light hole states in GaSb without a true "barrier" region. However, peak-to-valley ratios lower than double-barrier polytype structures are observed because in the absence of AlSb barriers complete bandgap blocking does not occur.

Resonant interband tunneling has also been observed in GaSb/InAs/AlSb/GaSb structures [16]. These structures combine the high peak-to-valley ratios of double-barrier polytype structures and high current densities of zero-barrier resonant interband coupling devices. These devices demonstrate that even in the absence of one AlSb barrier, confinement of a quasibound state in the well region still occurs and large resonant currents are observed. Peak-to-valley ratios comparable to double-barrier structures are also exhibited since bandgap blocking occurs in one bias direction due to the presence of an AlSb barrier.

An equilibrium schematic band diagram of a GaSb/InAs/AlSb/GaSb structure is shown in fig. 4a. Under low reverse biases (right GaSb electrode positive with respect to the left), a large resonant

current will flow in the structure. Light holes in the right hand GaSb electrode couple with the quasibound electron state in the InAs well and tunnel through the AlSb barrier into available hole states on the left (fig. 4b). At higher bias (fig. 4c), the valence band of the GaSb anode moves below the confined state energy in InAs and eventually below the InAs conduction band, thus cutting off the tunneling current by bandgap blocking.

For low forward biases a large resonant current will also flow as light holes in GaSb electrode align with the quasibound state in the InAs well. At higher biases the occupied hole states in GaSb move below the confined state, cutting off the resonant current (fig. 4d). However, complete bandgap blocking does not occur and nonresonant

current is still able to flow through a barrier width consisting of the AlSb barrier and a triangular portion of the InAs well.

Calculations based on the two-band model for asymmetric double-barrier structures with finite barrier thickness indicate that the forward resonant current will be greater than in the reverse bias direction. However, valley currents in the forward direction will also be greater due to the absence of complete bandgap blocking. Therefore, an asymmetric current-voltage (I - V) characteristic is anticipated for these devices. Under forward bias an NDR feature similar to that exhibited by GaSb/InAs/GaSb structures is expected. However, the NDR feature in the reverse direction will resemble GaSb/AlSb/InAs double-barrier results

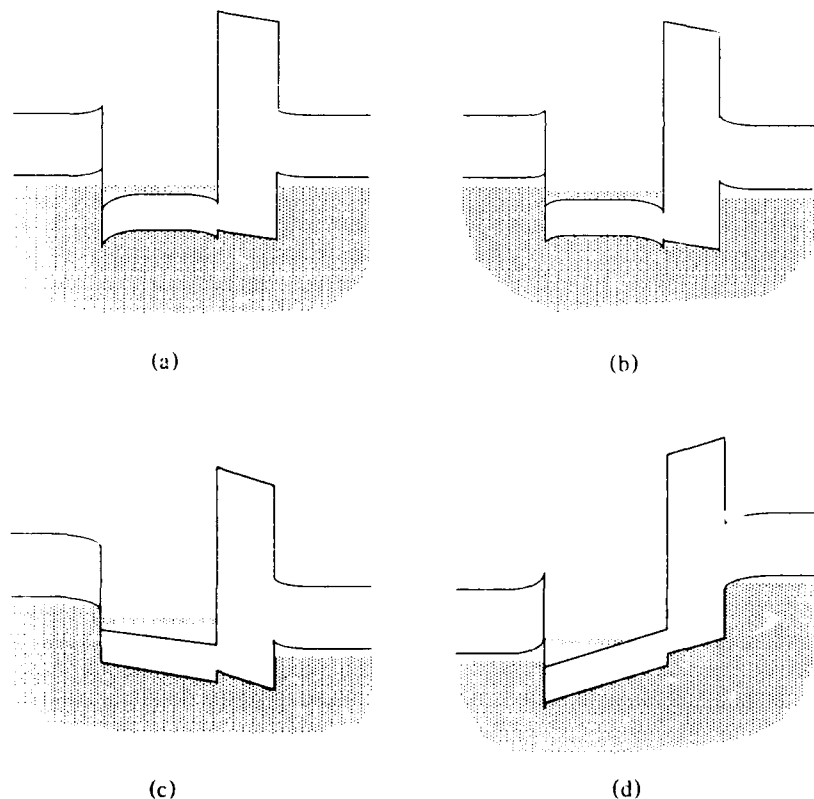


Fig. 4. (a) Schematic band diagram of GaSb/InAs/AlSb/InAs structure at equilibrium. (b) Conduction at low reverse bias. (c) Cut-off due to bandgap blocking at higher reverse bias. (d) Cut-off in the forward bias direction.

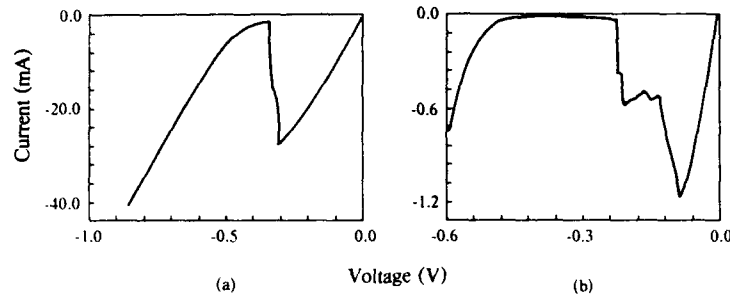


Fig. 5. The reverse bias region of the current-voltage characteristic for GaSb/InAs/AlSb/GaSb structures with a 20 nm InAs well and 1.5 nm AlSb barrier at room temperature (a) and a 40 nm InAs well and 2.5 nm barrier at 80 K (b). The device area is 10^{-6} cm^2 .

exhibiting a lower peak current density and a larger peak-to-valley ratio compared to the forward bias direction.

To demonstrate these ideas, samples of various well and barrier widths were prepared by MBE [11]. The reverse region of the current-voltage (I - V) characteristics of a device with a 20 nm InAs well width and 1.5 nm AlSb barrier (fig. 5a) exhibit peak-to-valley ratios of 20:1 (40:1 at 80 K) with peak current densities as high as 28 kA/cm^2 (35 kA/cm^2 at 80 K) at room temperature. At these high current densities, these values represent the highest peak-to-valley ratio measured in polytype tunneling structures. Higher peak-to-valley ratios were demonstrated in similar structures consisting of a 40 nm well and 2.5 nm barrier (fig. 5b). A peak-to-valley ratio of 80:1 (17:1 at 300 K) was measured at 80 K but with a peak current density of 1.2 kA/cm^2 . The large valley region of fig. 5b is indicative of the band-gap blocking mechanism. Although not shown, a small NDR feature in the forward bias direction is also commonly observed in low-current density samples. This feature as predicted exhibits higher peak current density and lower peak-to-valley ratios compared to the NDR feature in the reverse bias region.

4. Ge and Sn p-type doping of GaSb

In fabricating these tunneling devices the GaSb electrodes were doped with Be, which to date has

been the only available p-type dopant for GaSb and other Sb based materials grown by molecular beam epitaxy. Alternative p-type dopants for GaSb are desirable since Be is highly toxic and has the problem of surface segregation at high doping levels. We report here the first results of p-type doping of GaSb by the group IV atoms Ge and Sn. Typically, group IV atoms such as Si, Ge and Sn are well known amphoteric dopants of III-V compounds; they can incorporate on group III lattice sites as donors or on group V lattice sites as acceptors. The site on which the impurity is incorporated depends upon the covalent radius of the impurity relative to the host atoms and upon the relative availability of the two lattice sites. Usually, the impurity will occupy a lattice site which most closely matches its covalent radius, since this will minimize the lattice strain and therefore the free energy of the crystal. Roughly speaking, the free energy does not increase much for incorporation of an impurity on a larger lattice site, but increases rapidly with incorporation of a large impurity on a smaller lattice site. Thus impurities will tend to incorporate themselves on a host site larger than itself rather than one smaller than itself. Since the covalent radius of Sb is much larger than Ga and As it is reasonable to expect a different behavior for group IV impurities in GaAs and GaSb.

Typically, Ge and Sn will act as donors in GaAs [17]. The covalent radius of Ge (1.22 Å) is larger than that of As (1.18 Å) and smaller than Ga (1.26 Å). Therefore Ge will tend to occupy Ga

lattice sites. In the case of Sn (1.40 Å), its covalent radius is larger than both Ga and As and therefore tends to occupy the larger Ga site in order to minimize the strain in the lattice. The tendency of Ge and Sn to occupy Ga sites is further supported by the fact that more Ga sites are available since MBE is an arsenic-rich growth process. However, one difficulty associated with Sn doping in GaAs is a segregation of the impurity on the surface [17,18]. This effect is partially attributed to the large covalent radius of Sn compared to both Ga and As, which makes it difficult to squeeze itself into either host site. The result is a slow rate of incorporation and an excess accumulation of Sn on the surface. Therefore Ge and Si are favored as n-type dopants in GaAs.

Group IV impurities are expected to behave differently in GaSb. Since the covalent radius of Sb (1.36 Å) is larger than Ga, group IV atoms should tend to occupy Sb sites. A prior study by Subbanna et al. [19] demonstrated that Si was a partially compensated acceptor in GaSb. This behavior has been confirmed by us and we have further found that Si is actually highly compensated in AlSb. The high degree of compensation is observed because Si has a small covalent radius compared to Al, Ga and Sb, and thus has little difficulty occupying either lattice site. Nonetheless, in GaSb the results indicate that Si prefers occupation of the larger Sb site over the more closely matched Ga site. Ge and Sn should also be acceptors in GaSb since their covalent radii are larger than Si and thus are even less likely to occupy Ga sites.

To study these dopants, samples were grown by MBE on (100) InP substrates [11]. GaSb layers of 1 μm thickness were grown and doped with either Ge or Sn at a variety of dopant cell temperatures. The layers were grown under an Sb rich environment at a substrate temperature of 500–550°C. Unintentionally doped samples are typically p-type of concentration 10^{16} cm^{-3} . Hall effect measurements were used to characterize the carrier density of the samples.

The results of our Ge doping experiments are given in fig. 6 which shows the free acceptor concentration versus inverse cell temperature. The characteristic is linear with carrier densities up to

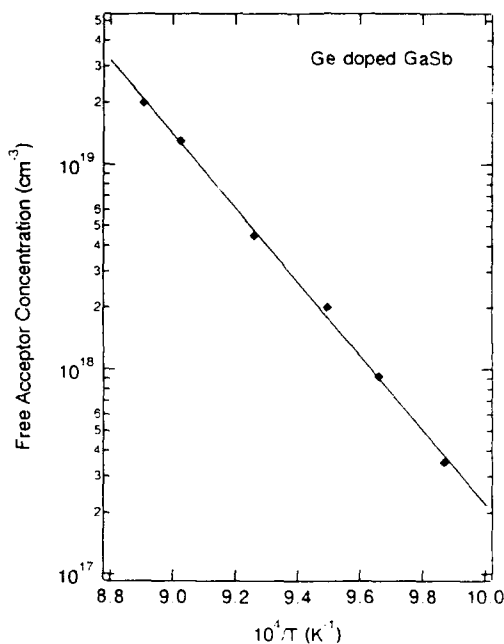


Fig. 6. Free acceptor concentration in GaSb as a function of reciprocal temperature for the Ge source.

$2 \times 10^{19} \text{ cm}^{-3}$. The samples also exhibit Hall mobilities slightly lower than our typical Be doped samples, indicating a low level of compensation. These results also indicate that although the covalent radius of Ge is slightly smaller than Ga and the growth is Sb rich, incorporation into the much larger Sb site is preferred. Thus, Ge acts similarly to Si but exhibits a lower level of compensation due its larger covalent radius.

Compared to Si and Ge, the p-type nature of Sn is less surprising since its covalent radius is much larger than Ga and comparable to Sb. Thus, the occupation of the Sb site by Sn is clearly favored. For Sn the free acceptor concentration versus inverse cell temperature (fig. 7) is quite linear with carrier densities up to $5 \times 10^{18} \text{ cm}^{-3}$. In addition to this well behaved acceptor nature of Sn, Sn does not appear to exhibit surface segregation in GaSb as it does in GaAs. This conclusion is based upon RHEED observations during the GaSb layer growth. During the growth of undoped GaAs, the surface reconstruction pattern is

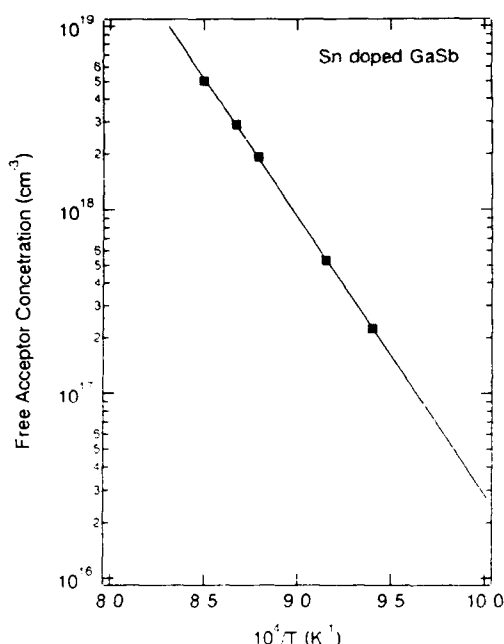


Fig. 7. Free acceptor concentration in GaSb as a function of reciprocal temperature for the Sn source.

observed to be (2×4) . With the addition of Sn as a dopant the surface reconstruction of the GaAs surface changes to (1×2) . This change in surface reconstruction is attributed to the surface segregation of Sn during growth. In contrast, growth of GaSb under Sb stabilized conditions exhibits a (1×3) pattern both in the absence of any dopant and in the presence of Sn introduced at dopant levels. These RHEED results provide evidence that Sn surface segregation does not occur in GaSb as in GaAs. The absence of segregation can be explained by the fact that since Sn is comparable in size to Sb it can easily occupy Sb sites in the lattice. Therefore, in addition to the uniform behavior with cell temperature, there is evidence to suggest that dopant segregation is not a problem in GaSb.

5. Summary

We have demonstrated resonant interband tunneling in double-barrier and zero-barrier InAs/

AlSb/GaSb structures. Room temperature peak-to-valley ratios as high as 20:1 at peak-current densities of 28 kA/cm^2 have been observed. These results, in addition to the observed resonant tunneling in 110 nm InAs well devices, demonstrate the potential for three-terminal resonant tunneling device applications. Finally, results on Ge and Sn doping in GaSb clearly indicate that they offer an excellent alternative to Be for p-type doping of MBE grown GaSb and AlSb. These materials are also important for infrared detectors and lasers with wavelengths up to $1.7 \mu\text{m}$.

Acknowledgements

This work is supported by the Office of Naval Research and the Air Force Office of Scientific Research, with additional support from an industrial grant of the Columbia University Center for Telecommunications Research. Kort F. Longenbach is supported by IBM East Fishkill.

References

- [1] R. Tsu and L. Esaki, *Appl. Phys. Letters* 22 (1973) 562.
- [2] L.L. Chang, L. Esaki and R. Tsu, *Appl. Phys. Letters* 24 (1974) 593.
- [3] T.C.L.G. Sollner, W.D. Goodhue, P.E. Tannenwald, C.D. Parker and D.D. Peck, *Appl. Phys. Letters* 43 (1983) 588.
- [4] L. Esaki, L.L. Chang and E.E. Mendez, *Japan. J. Appl. Phys.* 20 (1981) L529.
- [5] M. Sweeney and J. Xu, *Appl. Phys. Letters* 54 (1989) 546.
- [6] J.R. Söderström, D.H. Chow and T.C. McGill, *Appl. Phys. Letters* 55 (1989) 1094.
- [7] L.F. Luo, R. Beresford and W.I. Wang, *Appl. Phys. Letters* 55 (1989) 2023.
- [8] L.F. Luo, R. Beresford and W.I. Wang, *Appl. Phys. Letters* 53 (1988) 2320.
- [9] H. Kroemer, *Surface Sci.* 174 (1986) 299.
- [10] J. Tersoff, *Phys. Rev. Letters* 56 (1986) 2755.
- [11] A.Y. Cho, *Thin Solid Films* 100 (1983) 291.
- [12] R. Beresford, L.F. Luo, K.F. Longenbach and W.I. Wang, *Appl. Phys. Letters* 56 (1990) 551.
- [13] L.F. Luo, R. Beresford, K.F. Longenbach and W.I. Wang, *J. Appl. Phys.* 68 (1990) 2854.
- [14] K. Taira, I. Hase and Kawai, *Electron. Letters* 25 (1989) 1708.
- [15] D.A. Collins, D.H. Chow, F.T. Yu, D.Z.-Y. Ting, J.R. Söderström, Y. Rajakarunanyake and T.C. McGill, presented at NATO Workshop on Resonant Tunneling, El Escorial, 1990.

- [16] K. Longenbach, L.F. Luo and W.I. Wang, Appl. Phys. Letters 57 (1990) 1554.
- [17] A.Y. Cho, J. Appl. Phys. 46 (1975) 1733.
- [18] C.E.C. Wood and B.A. Joyce, J. Appl. Phys. 49 (1978) 4854.
- [19] S. Subbanna, G. Tuttle and H. Kroemer, J. Electron. Mater. 17 (1988) 297.

Studies of the tunneling currents in the InAs/AlSb/GaSb single-barrier interband tunneling diodes grown on GaAs substrates

J.F. Chen, L. Yang, M.C. Wu, S.N.G. Chu and A.Y. Cho

AT&T Bell Laboratories, Murray Hill, New Jersey 07974, USA

This paper studies the tunneling currents in the single-barrier InAs/AlSb/GaSb interband tunneling structures, with an emphasis on correlating with the bandedge alignment. The WKB approximation combined with the $k \cdot p$ two-band model are used to analyze the interband tunneling currents versus the barrier widths to obtain the energy level in the AlSb barrier through which the peak tunneling currents occur. The obtained energy level (0.48 ± 0.1 eV above the valence band maximum of the AlSb) agrees with the valence-band offset between AlSb and GaSb. A good agreement of the measured peak voltages and the $C-V$ data with the predicted values by the theory using a self-consistent Schrödinger-Poisson solver is obtained, with a value of 0.15–0.2 eV for the InAs/GaSb band overlap.

1. Introduction

The large conduction-band offset (between InAs and AlSb) and the band overlap (between InAs and GaSb) have drawn the use of the InAs/AlSb/GaSb material system in the application of tunneling devices [1–8] recently. Among these devices, the InAs/AlSb/GaSb single-barrier interband tunneling structure utilizing this unique band lineups offers flexible designs of the barrier thickness and the doping concentrations. The interband tunneling based on the InAs/AlSb/GaSb material system was first studied by Takaoka et al. [1]. Recently, Luo et al. [6] reported their observations of negative differential resistance (NDR) at room temperature in the InAs/AlSb/GaSb interband tunneling structure. An improved peak-to-valley current ratio (PVR) of 4.5:1 with a peak current density of 3.5 kA/cm^2 at room temperature was recently obtained in this structure [8]. In spite of these achievements, the band alignments in this material system are still not completely understood [9]. This paper reports our studies of the tunneling currents in the single-barrier InAs/AlSb/GaSb interband tunneling structures by experimentally varying the barrier thickness to ob-

tain the information about the bandedge alignment.

2. Experimental

The structure of the InAs/AlSb/GaSb tunneling device was grown on a n^+ -GaAs (100) substrate in Riber-2300 molecular beam epitaxy (MBE) [10] system. A buffer layer of a $1 \mu\text{m}$ thick InAs (heavily Si-doped) was grown at 400°C (growth rate of $0.5 \mu\text{m/h}$) with a comparable As to In flux ratio. After the growth of InAs buffer layer, the substrate temperature was raised to 500°C and the whole diode structure was subsequently grown. The n^+ -InAs layer was doped by Si with a doping concentration about $1 \times 10^{18} \text{ cm}^{-3}$. AlSb and GaSb were grown at 500°C and a growth rate of $0.5 \mu\text{m/h}$ with beam equivalent pressure (BEP) ratio of Sb to Al or Ga about 3:1. The undoped AlSb layer had a relatively high resistivity on the order of $10^3 \Omega \text{ cm}$ found in a separate calibration. All the epitaxial layer thicknesses were precisely confirmed by the cross-sectional transmission electron micrographs (TEM). All the grown samples show mirror-like surfaces

and smooth interfaces, even the growth started with a lattice mismatch of 7.2%.

3. InAs / AlSb / GaSb single-barrier interband tunneling diodes

The band diagram of the single-barrier InAs / AlSb / GaSb tunneling diode with a small forward bias is shown in fig. 1a. Fig. 1b shows typical room temperature I - V characteristics of the devices ($60\text{ }\mu\text{m}$ dots) with a 1.5 and a 5.0 nm thick AlSb barrier, respectively. A distinct negative differential resistance, presumably due to the interband tunneling process as shown in fig. 1a, with a PVR as high as 4.5 can be seen at the forward bias (GaSb positive with respect to InAs). A peak current density of 3.5 kA/cm^2 was observed for this device. The device with a 5 nm thick AlSb barrier showed a rectified characteristic. Conductance plot showed a shoulder with a current density of 1.68 A/cm^2 (PVR = 2 at 77 K). This relatively low peak current density was due to the reduction of the interband tunneling probability by the thick AlSb barrier layer.

3.1. The effects of AlSb barrier width

Fig. 2 shows both the peak current densities and the valley current densities at room tempera-

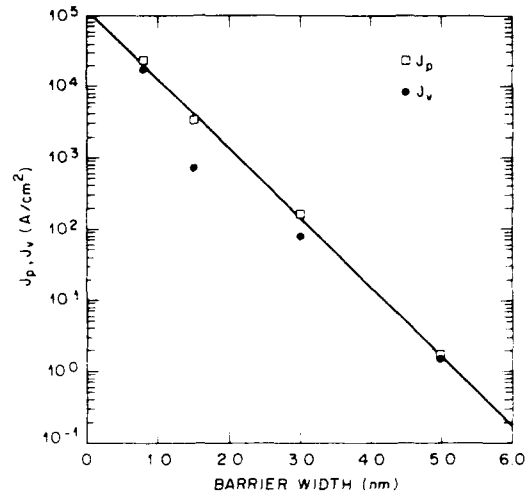


Fig. 2. Dependence of the peak current density and the valley current density at room temperature on the barrier width. The solid line represents a best fit to the experimental peak currents.

ture as a function of the AlSb barrier widths. The values of the peak current density shown in fig. 2 display an excellent exponential dependence on the AlSb barrier widths. This behavior suggests the usage of the Wentzel Kramers-Brillouin (WKB) approximation [11] for the tunneling probability. According to our calculation, at the peak-current bias condition, the potential drop across

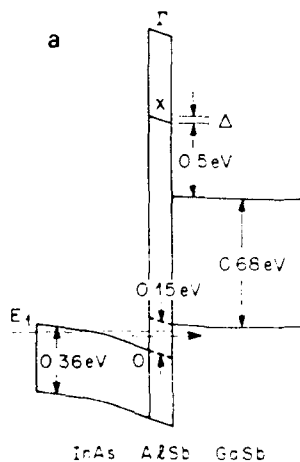
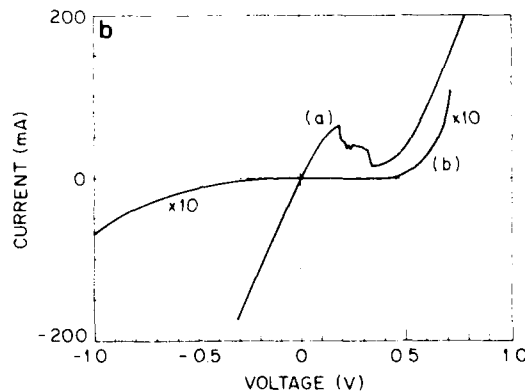


Fig. 1. (a) The band diagrams of a InAs / AlSb / GaSb single barrier tunneling diode at a bias of 0.02 V. (b) The current-voltage characteristics of a tunneling diode ($60\text{ }\mu\text{m}$ diameter dots) with a 1.5 and a 5.0 nm AlSb barrier, respectively.



the AlSb is very small (for example, 0.012 eV across a 0.8 nm thick barrier). This small potential drop across the AlSb allows us to use a constant effective wave vector in the WKB approximation. To obtain the energy level in the AlSb barrier through which the peak tunneling currents occur, we use the dispersion relation using Kane's $k \cdot p$ two-band model [12]. The direct bandgap of the AlSb (2.22 eV for the Γ valley) was used in this calculation. Because the tunneling energy level is close to the valence band edge of AlSb, the value of the light hole mass of AlSb ($m^* = 0.11m_e$) was used for the effective mass [13]. By using the slope of J_p versus L_B as the effective wave vector, the value of E_t thus obtained was -1.74 ± 0.10 eV (or 0.48 ± 0.10 eV above the valence band maximum of the AlSb). This value agrees with the valence-band offset (0.40 ± 0.15 eV) between AlSb and GaSb obtained by X-ray photoemission measurement [9]. While this method may not be the best way to determine the valence-band offset between AlSb and GaSb, our result indicates: (a) that the experimental dependence of the peak current on the barrier width suggests the usage of the WKB approximation for the tunneling probability; (b) the application of Kane's $k \cdot p$ two-band model in calculating the wave vector of the tunneling carriers.

3.2. The effects of barrier widths on peak voltages

The peak voltage (voltage value at which peak current is observed) was measured for each device and compared with the predicted values. As a function of applied voltage, the band bending and the associated quantum states are obtained by solving the Schrödinger and Poisson equations self-consistently. The detailed numerical calculation can be found in ref. [7]. When the first subband of the electron in the InAs accumulation region begins to exceed the valence band of the GaSb layer, a cut-off of the interband tunneling process occurs. The predicted cut-off voltages as a function of the AlSb barrier widths are shown in fig. 3 for different values of the band overlap between InAs and GaSb. The experimentally measured peak voltages for each sample, after subtracting the parasitic resistance drop, are

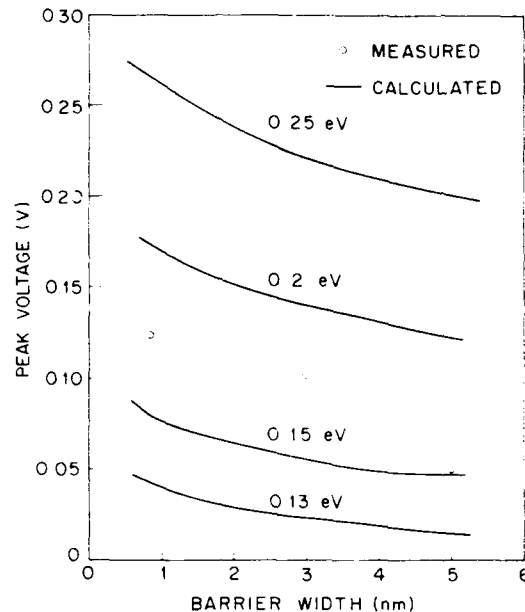


Fig. 3. Dependence of the peak voltage on the barrier width for several different values of band overlap between InAs and GaSb. The experimentally measured peak voltages (open circles) lie between the curves of 0.15 and 0.2 eV for the band overlap between InAs and GaSb.

plotted as open circles in fig. 3. It can be seen that the measured peak voltages lie between the curves of 0.15 and 0.2 eV for the band overlap between InAs and GaSb. This value of the band overlap agrees with the value (0.15 eV) reported in ref. [14]. Considering the difficulties in obtaining the intrinsic peak voltage, agreement between the intrinsic peak voltages and the cut-off voltages calculated by using a value of 0.15 eV as the band overlap was obtained.

3.3. C-V measurements

The low conduction of the tunneling diode with a 5 nm thick AlSb barrier layer permits an accurate capacitance-voltage measurement. The measurements were performed with frequencies of 130 MHz, 400 MHz, and 1 GHz, and almost identical capacitance-voltage curves were obtained. Fig. 4 shows that in the forward bias condition, the

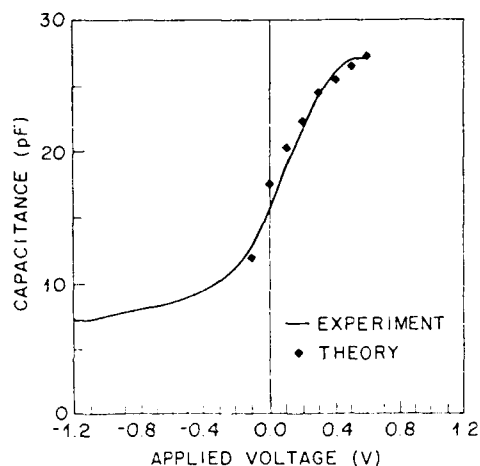


Fig. 4. The measured (—) and calculated (◆) capacitance-voltage characteristics. The calculation was done using a Schrödinger-Poisson solver. The carriers with a sheet concentration of $3.7 \times 10^{12} \text{ cm}^{-2}$ accumulate at the interfaces at 0.6 V.

capacitance first increases from 16 pF at zero bias linearly with the bias and then begins to saturate to 27 pF after 0.5 V. Under the forward bias condition, both electrons in the InAs side and the holes in the GaSb side accumulate at the AlSb heterointerfaces. However, unlike what is usually seen in the $C-V$ curve of a Si/SiO₂ capacitor, the capacitance does not saturate to a constant as soon as the accumulation occurs. This is because the width of the wave-packet of the bound electrons in the triangular well at the InAs/AlSb interface is comparable to or even wider than the AlSb barrier thickness. The linear increase of capacitance with the applied voltage is mainly due to the narrowing of width of the electron envelop wave-packet in the InAs/AlSb interface. A very good quantitative agreement (within 10%) between the measured $C-V$ data and the calculated results, from a self-consistent Schrödinger-Poisson solver using a value of 0.15 eV for the band overlap between InAs and GaSb, was obtained. From the $C-V$ measurement, we estimated a sheet concentration of $3.7 \times 10^{12} \text{ cm}^{-2}$ accumulated at the interfaces at forward bias 0.6 V.

4. Summary

The tunneling currents in the InAs/AlSb/GaSb single-barrier interband tunneling structures was studied experimentally. We summarize our results as follows: (a) The experimental dependence of the peak current on the barrier width suggests the usage of the WKB approximation for the interband tunneling probability. (b) By using Kane's $k \cdot p$ two-band model in calculating the wave vector of the tunneling carriers, the energy level in the AlSb barrier through which the peak tunneling currents occur was obtained. The energy level (0.48 ± 0.10 eV above the valence band maximum of the AlSb) corresponds to the valence-band offset between AlSb and GaSb. (c) The experimentally measured peak voltages agree with the predicted cut-off voltages calculated by using a value of 0.15 to 0.2 eV for the band overlap between InAs and GaSb. (d) Good quantitative agreement between the measured $C-V$ data and the calculated results was obtained, using a value of 0.15 eV for the band overlap between InAs and GaSb.

Acknowledgments

The authors would like to thank Y.K. Chen, Y.F. Hsieh, and Y.H. Wang for providing helpful suggestions.

References

- [1] H. Takaoka, Chin-An Chang, E.E. Mendez, L.L. Chang and L. Esaki, *Physica B* 117 (1983) 741.
- [2] L.F. Luo, R. Beresford and W.I. Wang, *Appl. Phys. Letters* 53 (1988) 2320.
- [3] R. Beresford, L.F. Luo and W.I. Wang, *Appl. Phys. Letters* 54 (1989) 1899.
- [4] H. Munekata, T.P. Smith III and L.L. Chang, *J. Vacuum Sci. Technol.* B7 (1989) 324.
- [5] J.R. Soderstrom, D.H. Chow and T.C. McGill, *Appl. Phys. Letters* 55 (1989) 1094.
- [6] L.F. Luo, R. Beresford and W.I. Wang, *Appl. Phys. Letters* 55 (1989) 2023.
- [7] L. Yang, M.C. Wu, J.F. Chen, Y.K. Chen, G.L. Snider and A.Y. Cho, *J. Appl. Phys.* 68 (1990) 4286.
- [8] J.F. Chen, L. Yang, M.C. Wu, S.N.G. Chu, and A.Y. Cho, *J. Appl. Phys.* 68 (1990) 3451.

- [9] G.J. Gualtieri, G.P. Schwartz, R.G. Nuzzo and W.A. Sunder, *Appl. Phys. Letters* 49 (1986) 1037.
- [10] A.Y. Cho, *Thin Solid Films* 100 (1983) 291.
- [11] L.D. Landau and E.M. Lifshitz, *Quantum Mechanics* (Addison-Wesley, Reading, MA, 1958) p. 174.
- [12] E.O. Kane, *J. Appl. Phys.* 32 (1961) 83.
- [13] M. Cardona, F.H. Pollak and K.L. Shaklee, *Phys. Rev. Letters* 16 (1966) 644.
- [14] L.L. Chang and L. Esaki, *Surface Sci.* 98 (1980) 70.

Interband tunneling in InAs/GaSb/AlSb heterostructures

D.A. Collins, D.Z.-Y. Ting, E.T. Yu, D.H. Chow, J.R. Söderström *, Y. Rajakarunanayake and T.C. McGill

Thomas J. Watson, Sr., Laboratory of Applied Physics, California Institute of Technology, Pasadena, California 91125, USA

We report the experimental observation of negative differential resistance (NDR) at room temperature from a structure consisting of a single InAs(n)-GaSb(p) interface. The peak current densities ranged from 4.2×10^4 to 8.0×10^4 A/cm² depending on how the structure is doped. The mechanism that causes the NDR is similar to that of an Esaki tunnel diode. We have also observed NDR at room temperature in a second class of novel devices. These structures consist of a thin layer of AlSb displaced from a single InAs(n)-GaSb(p) interface. NDR with peak current densities greater than 1.6×10^5 A/cm² is seen in these structures. We attribute the increase in peak current densities with the addition of the AlSb barrier to the formation of a quasi-bound state between the AlSb layer and the InAs-GaSb interface. This quasi-bound state forms either in the conduction band of InAs or the valence band of GaSb, depending on where the AlSb barrier is placed and leads to a resonance enhancement of the current in the structures.

1. Introduction

Quantum mechanical tunneling in semiconductors as well as negative differential resistance (NDR) were first demonstrated in forward biased Esaki diodes which consist of a degenerately doped p-n junction [1]. The discovery of NDR generated a tremendous amount of interest and research into Esaki diodes since they can be used to fabricate amplifiers, oscillators and high speed switches [2]. Although Esaki diode amplifiers have been built that operate at frequencies as high as 85 GHz, they have two important weaknesses: their small current densities limit them to much lower output powers than Gunn-effect or IMPATT diodes, and their large junction capacitance limits them to much lower frequencies than InAs/AlSb double barrier diodes which can be made to oscillate at fundamental frequencies greater than 700 GHz [3].

In this work we report on a group of novel devices which show room temperature NDR due to a mechanism similar to that of an Esaki diode

but with peak current densities of between 10^4 and 10^5 A/cm² (compared to $< 10^3$ A/cm² for Esaki diodes [2]). These devices can be realized because of the unique staggered band alignment of InAs and GaSb in which the conduction band of InAs is 150 meV below the valence band of GaSb [4]. A schematic representation of the InAs/GaSb band alignments, which is strongly reminiscent of the band structure of an Esaki diode, is shown in fig. 1a. Because of this staggered band alignment a layer of GaSb(p⁺) grown on InAs(n⁺) will show NDR due to a mechanism similar to that of an Esaki diode. Such devices, which we call heterojunction Esaki diodes (HED), have been grown and show NDR at room temperature with peak current densities ranging from 4.2×10^4 to 8.0×10^4 A/cm² depending on how the structure is doped.

We have also grown a second class of novel structures, which we call resonance enhanced heterojunction Esaki diodes (REHED), which combine favorable aspects of the HED with those of double barrier diodes. The structures consist of a thin layer of AlSb displaced from a single InAs(n)/GaSb(p) interface. Schematic band-edge diagrams of these heterostructures are shown in figs. 1b and 1c. These devices also showed NDR

* Present address: Department of Physics, Chalmers University of Technology, S-41296 Göteborg, Sweden.

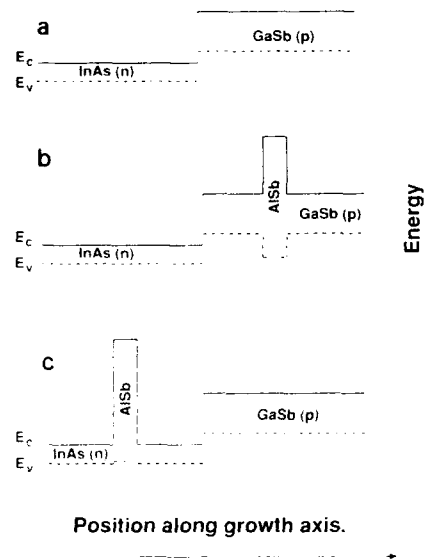


Fig. 1. Schematic band edge diagrams (neglecting band bending) of the structures grown for this study.

at room temperature with peak current densities greater than 10^5 A/cm². We attribute the increase in peak current densities with the addition of a thin AlSb barrier to the formation of a quasi-bound state between the InAs/GaSb interface and the AlSb layer, which leads to a resonant enhancement of the device's current.

2. Experimental

In table 1 we give the layer sequences and thicknesses for the samples grown for this study. The samples studied were grown on GaAs sub-

strates in a Perkin-Elmer 430 molecular beam epitaxy system equipped with cracked Sb and As sources. The details of the crystal growth have been reported elsewhere [5]. Elemental Si was used to dope the InAs electrodes n-type ($n \approx 2 \times 10^{17}$ cm⁻³) and the GaSb p-type ($p \approx 5 \times 10^{18}$ cm⁻³) [6]. 100 Å undoped spacer layers were grown on each side of the InAs(n)/GaSb(p) interface in sample 1; there were no undoped spacer layers in sample 2. In samples 3, 4 and 5, the AlSb layers, quantum wells, and an additional 100 Å spacer layers on the InAs sides of the active regions were undoped.

After growth, device mesas 6 µm in diameter were fabricated using photolithography and a wet etch. The etch was stopped in the InAs epilayer so that no current flowed through the GaAs substrate. Au/Ge was used to make ohmic contact to the individual devices. Current-voltage (*I-V*) curves were measured at room temperature and 77 K by probing the mesas with a thin gold wire.

3. Results

The dashed line in fig. 2 shows a representative *I-V* curves for the HED structure (see fig. 1a) without undoped spacer layers at the heterointerface. Both HED structures show NDR at room temperature with peak current densities greater than 8.2×10^4 (4.0×10^4) A/cm² for the structure with (without) undoped spacer layers at the heterointerface. The HED's *I-V* curves are virtually unchanged when measured at 77 K, which indicates that thermionic emission plays only a minor role in the large valley current. The oh-

Table 1
Layer sequences for the samples

Sample number	Band diagram	Peak current density (A/cm ²)	Layer sequence
1	Fig. 1a	8.0×10^4	InAs(n)/undoped InAs(100 Å)/undoped GaSb(100 Å)/GaSb(p)
2	Fig. 1a	4.2×10^4	InAs(n)/GaSb(p)
3	Fig. 1b	1.6×10^5	InAs(n)/GaSb(51 Å)/AlSb(12 Å)/GaSb(p)
4	Fig. 1c	6.7×10^4	InAs(n)/AlSb(21 Å)/InAs(120 Å)/GaSb(p)
5	Fig. 1c	No NDR	InAs(n)/AlSb(21 Å)/InAs(75 Å)/GaSb(p)

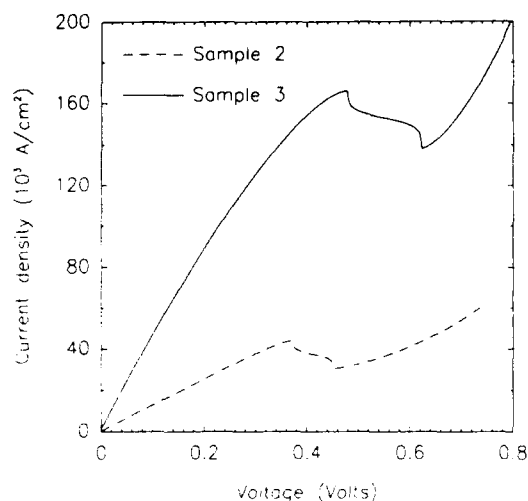


Fig. 2. I - V curves for samples 2, a HED structure (dashed line), and 3, a REHED structure (solid line.) The enhanced current density in sample 3 is consistent with resonant tunneling via a quasi-bound state in the GaSb quantum well.

served temperature stability of these devices between 77 and 300 K is similar to that of conventional Esaki diodes [2].

The results for the REHED structures, whose schematic band edge diagrams are shown in figs. 1b and 1c are more complicated. Both types of REHED structures showed NDR at room temperature with peak current densities ranging from 6.7×10^3 to 1.6×10^5 A/cm² depending on the thickness of the AlSb layer used. These structures also show a strong dependence of the peak current density on the distance between the AlSb barrier and the InAs/GaSb interface. In fact, if the separation is too small, no NDR is observed. The qualitative behavior of both variants of the REHED can be explained by the existence of a quasi-bound state as will be shown in the discussion section.

4. Discussion

Because the NDR observed in HED structures (see fig. 1a) is not associated with a quasi-bound state, which may have a long lifetime, they hold

promise for the fabrication of high speed devices. The intrinsic upper limit of this structure's oscillation frequency will be determined by the transit time across the heterointerface and the inherent frequency response of the materials, as well as the device's RC time constant. Furthermore, because this device can be grown without undoped spacer layers, limiting processes such as transit time delays across depleted regions which can be important in conventional double barrier heterostructures will be eliminated in this device [7].

In fig. 2 we compare typical I - V curves for samples 2 and 3 (see table 1). The solid curve is for the REHED structure (see fig. 1b) and the dashed curve is from the previously discussed HED structure (see fig. 1a). As the data show, the structure with the AlSb barrier is more conductive with a peak current density of more than 1.6×10^5 A/cm². This unintuitive behavior can be understood by examining the transmission coefficients of these structures. Fig. 3 displays transmission coefficients for samples 2 (dashed line) and 3 (solid line), calculated at flat band conditions using a two-band model which incorporates electrons and light holes [8]. The InAs conduction band

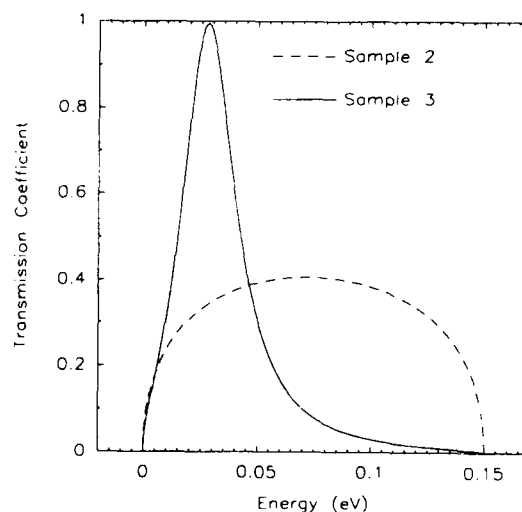


Fig. 3. Transmission coefficients for samples 2, a HED structure (dashed line), and 3, a REHED structure (solid line), calculated at flat band conditions, using a two-band model which incorporates electrons and light holes. The InAs conduction band edge is taken to be the zero of energy.

edge is taken to be the zero of energy. The calculation shows that sample 3 possesses a broad resonance, in the region between the InAs conduction band and the GaSb valence band, which peaks well above the maximum transmission probability for the HED structure. The calculation indicates that a quasi-bound state forms in the region of the crystal between the InAs/GaSb interface and the AlSb barrier in sample 3, leading to resonant tunneling of carriers across the structure. The formation of a quasi-bound state in the REHED structure, as indicated by the calculation, is consistent with the experimentally observed enhancement in the peak current density.

As a further demonstration of the tunneling mechanism described above, we grew structures corresponding to the band edge diagram of fig. 1c. In these samples, a quasi-bound state will be formed in the InAs quantum well due to the confinement of the AlSb barrier and the partially reflecting InAs/GaSb interface. The current densities in these samples are smaller than those in sample 3 due to the thicker AlSb barrier (see table 1). In fig. 4 we show $I-V$ curves for samples 4

(solid line) and 5 (dashed line). The only difference between them is the width of the InAs well. As the figure shows for a narrow well there is no NDR present in the structure. This can be readily explained since our calculations show that for a 75 Å InAs well the confinement energy of the quasi-bound state pushes it above the valence band edge of the GaSb. As a result, this resonant level is unavailable to electrons tunneling across the structure leading to a quenching of the NDR. This demonstrates the diode's sensitivity to the exact placement of the AlSb barrier, as well as that resonant interband tunneling can be observed with the AlSb barrier placed on either side of the InAs/GaSb interface. A more detailed study of the REHED structure is being published elsewhere [9].

5. Conclusions

In conclusion, we have demonstrated three novel variants of the Esaki diode: HEDs which consist of a single InAs(n)/GaSb(p) interface and two types of REHED structures consisting of a thin AlSb barrier displaced from a single InAs(n)/GaSb(p) interface. The operation of these structures is dependent on the unique staggered band alignment of InAs and GaSb as shown in fig. 1a. The mechanism that gives rise to NDR in these structures is similar to that of an Esaki diode. For devices consisting of an InAs(n)/GaSb(p) interface we observed peak current densities ranging from 4.2×10^{-4} to 8.0×10^{-4} A/cm² depending on how the structure is doped. We have also observed NDR at room temperature in a novel class of devices consisting of a thin AlSb barrier displaced from an InAs/GaSb interface. In structures with the thinnest AlSb barriers we observed peak current densities of 1.6×10^{-5} A/cm² which is larger than in devices without the AlSb barrier. We also found that the device's $I-V$ characteristics were extremely sensitive to the placement of the AlSb barrier. This sensitivity as well as the enhancement in the peak current density is consistent with the formation of a quasi-bound state in the region of the crystal bounded by the InAs/GaSb interface and the AlSb barrier layer.

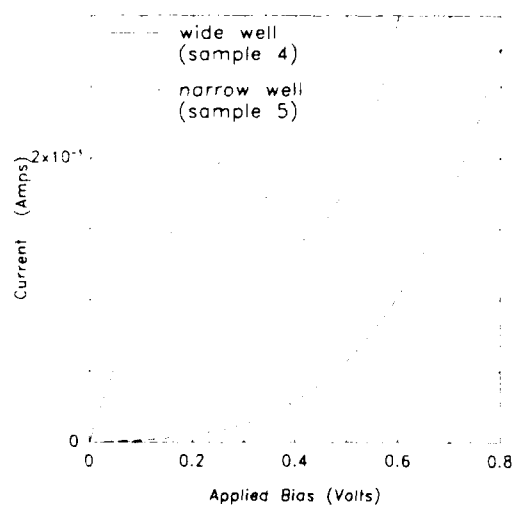


Fig. 4 $I-V$ curves for samples 4 and 5 showing the dramatic effect that the separation between the AlSb barrier and the InAs/GaSb interface has on device performance. The solid (dashed) line corresponds to a structure with a 120 Å (75 Å) InAs quantum well.

Acknowledgments

The authors would like to thank P.C. Sercel for helpful discussions. This work was supported by the Office of Naval Research under contract No. N00014-89-J-1141 and the Air Force Office of Scientific Research under contract No. AFOSR-86-0306. E.T. Yu was supported in part by the AT&T Foundation.

References

- [1] L. Esaki, Phys. Rev. 109 (1958) 603.
- [2] S.N. Levine and R.M. Kurzrok, Eds., Selected Papers on Semiconductor Microwave Electronics (Dover, New York, 1964).
- [3] E.R. Brown, C.D. Parker, L.J. Mahoney, J.R. Söderström and T.C. McGill, IEEE Trans. Electron Devices, in press.
- [4] G.J. Gaultieri, G.P. Schwartz, R.G. Nuzzo, R.J. Malik and J.F. Walker J. Appl. Phys. 61 (1987) 5337.
- [5] D.A. Collins, E.T. Yu, Y. Rajakarunayake, J.R. Söderström, D.Z.-Y. Ting, D.H. Chow and T.C. McGill, Appl. Phys. Letters 57 (1990) 683.
- [6] T.M. Rossi, D.A. Collins, D.H. Chow and T.C. McGill, Appl. Phys. Letters 57 (1990) 2256.
- [7] E.R. Brown, W.D. Goodhue and T.C. L.G. Sollner, J. Appl. Phys. 64 (1988) 1519.
- [8] D.Z.-Y. Ting, E.T. Yu, D.A. Collins, D.H. Chow and T.C. McGill, J. Vacuum Sci. Technol. B8 (1990) 810.
- [9] D.Z.-Y. Ting, D.A. Collins, E.T. Yu, O.H. Chow and T.C. McGill, Appl. Phys. Letters 57 (1990) 1257.

MBE growth of GaInAsSb/AlGaAsSb double heterostructures for infrared diode lasers

S.J. Eglash, H.K. Choi and G.W. Turner

Lincoln Laboratory, Massachusetts Institute of Technology, Lexington, Massachusetts 02173-9108, USA

For the fabrication of diode lasers emitting near $2.3\ \mu\text{m}$, molecular beam epitaxy has been used to grow double heterostructures consisting of a $\text{Ga}_{0.84}\text{In}_{0.16}\text{As}_{0.14}\text{Sb}_{0.86}$ active layer and $\text{Al}_{0.50}\text{Ga}_{0.50}\text{As}_{0.04}\text{Sb}_{0.96}$ confining layers lattice matched to a GaSb substrate. Because the sticking coefficient is much greater for Sb than for As, high concentrations of Sb can be incorporated into the alloy layers even though the As flux during growth is much greater than both the Sb flux and the total group III flux. The n- and p-type dopant sources were GaTe and Be, respectively. The lasers have threshold current densities as low as $1.5\ \text{kA cm}^{-2}$, differential quantum efficiencies as high as 50%, and pulsed output power as high as 900 mW per facet.

1. Introduction

Development of efficient semiconductor diode lasers with a specified emission wavelength requires the availability of an active layer material having the appropriate bandgap together with high radiative recombination efficiency and low optical absorption, and also confining layer material having a larger bandgap and smaller refractive index than the active layer. In addition, it must be possible to dope the confining layer material both n and p type. For alloy materials, accurate composition control is necessary to obtain uniform layers having the desired bandgap and lattice constant. Control of the lattice constant is important because excessive lattice mismatch produces a high density of dislocations, which are detrimental to laser performance.

The only efficient, long-lived diode lasers fabricated to date utilize GaAs, GaInAs, or AlGaAs active layers grown on GaAs substrates for emission from 0.8 to $1.1\ \mu\text{m}$, and GaInAsP active layers on InP for emission from 1.1 to $1.6\ \mu\text{m}$. High-performance diode lasers with emission wavelengths in the range from 2 to $5\ \mu\text{m}$ would be of both practical and fundamental interest. Such lasers would be useful for a variety of applications, including optical communications employ-

ing low-loss fluoride-based fibers, laser radar exploiting atmospheric transmission windows, remote sensing of atmospheric gases, and molecular spectroscopy. Furthermore, measurements of laser performance could help to elucidate the band-structure dependence of loss and absorption mechanisms such as Auger recombination and free-carrier absorption.

Heterostructures composed of GaInAsSb active layers and AlGaAsSb confining layers lattice matched to GaSb substrates meet the basic requirements for efficient diode lasers. As shown in fig. 1, where the bandgap is plotted against lattice constant for a number of III–V alloys, lasers incorporating these materials can potentially provide room-temperature emission from 1.7 to $4.4\ \mu\text{m}$ [1,2]. Room-temperature cw operation at wavelengths from 2.0 to $2.3\ \mu\text{m}$ has been reported [3,4] for GaInAsSb/AlGaAsSb double-heterostructure lasers grown by liquid phase epitaxy on GaSb substrates, and pulsed room-temperature operation has been demonstrated for such lasers grown by molecular beam epitaxy (MBE) [5,6]. We have used MBE to grow lasers of this type emitting at $2.3\ \mu\text{m}$ with threshold current density J_{th} as low as $1.5\ \text{kA cm}^{-2}$, differential quantum efficiency η_d as high as 50%, and pulsed output power as high as 900 mW per facet. This J_{th} value

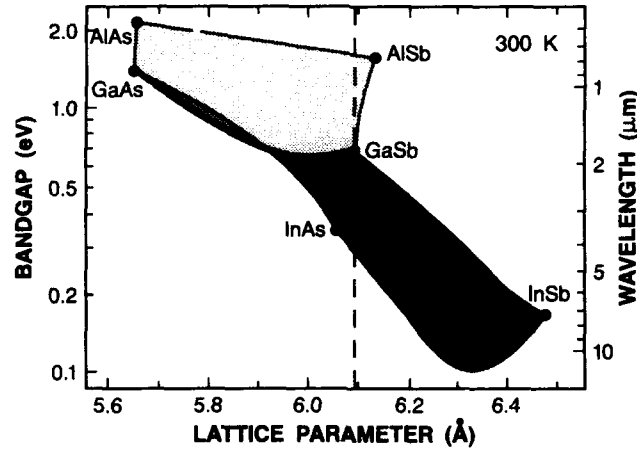


Fig. 1. Bandgap versus lattice parameter at 300 K for selected III-V alloys.

is equal to the lowest reported previously for GaInAsSb/AlGaAsSb diode lasers [3]. The η_d and output power values are the highest reported for the room-temperature operation of diode lasers emitting beyond 2 μm . In this paper we discuss the MBE growth procedures that have been used to achieve these results.

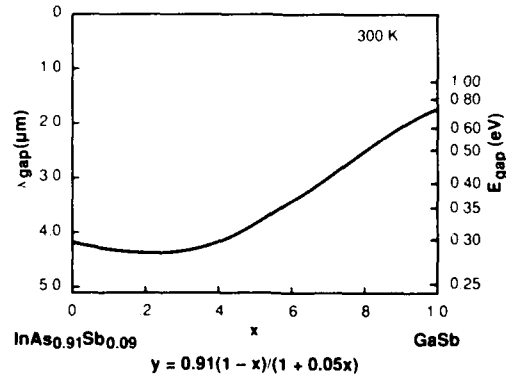
2. Quaternary alloy compositions

In the present work we chose to develop GaInAsSb/AlGaAsSb lasers with an emission wavelength of 2.3 μm at 300 K. For a quaternary alloy, the composition dependence of the bandgap, $E_g(x, y)$, is given by an expression that represents a weighted average of binary bandgaps and ternary bowing parameters. For $\text{Ga}_x\text{In}_{1-x}\text{As}_y\text{Sb}_{1-y}$, this expression is

$$\begin{aligned}
 E_g(x, y) &= xyE_{g,\text{GaAs}} + (1-x)yE_{g,\text{InAs}} \\
 &+ x(1-y)E_{g,\text{GaSb}} \\
 &+ (1-x)(1-y)E_{g,\text{InSb}} \\
 &+ x(1-x)[y\Gamma_{\text{GaInAs}} + (1-y)\Gamma_{\text{GaInSb}}] \\
 &+ y(1-y)[xE_{g,\text{GaAsSb}} + (1-x)\Gamma_{\text{InAsSb}}], \quad (1)
 \end{aligned}$$

where the Γ 's are the bowing parameters of the indicated ternary alloys [2]. To avoid the formation of misfit dislocations, it is necessary for the active and confining layers to be matched to GaSb to within $\Delta a/a_{\text{sub}} \approx 10^{-3}$ or less [7], where $\Delta a = a_{\text{epi}} - a_{\text{sub}}$, and a_{epi} and a_{sub} are the lattice constants of the epitaxial layer and substrate, respectively. For $\text{Ga}_x\text{In}_{1-x}\text{As}_y\text{Sb}_{1-y}$ alloys that are lattice matched to GaSb, application of Vegard's Law gives

$$y = 0.91(1-x)/(1+0.05x). \quad (2)$$

Fig. 2. Bandgap versus x in $\text{Ga}_x\text{In}_{1-x}\text{As}_y\text{Sb}_{1-y}$ alloys lattice matched to GaSb.

The solution of eq. (1) subject to this condition gives a function relating E_g and x for the GaInAsSb alloys that are lattice matched to GaSb. This function is plotted in fig. 2. The calculated lattice-matched composition with E_g corresponding to 2.3 μm is $\text{Ga}_{0.84}\text{In}_{0.16}\text{As}_{0.14}\text{Sb}_{0.86}$. The composition must be maintained to within 1% of these values to achieve $\Delta a/a_{\text{sub}} < 10^{-3}$ and $\Delta E_g < 0.01$ eV.

Although GaSb has a larger bandgap than $\text{Ga}_{0.84}\text{In}_{0.16}\text{As}_{0.14}\text{Sb}_{0.86}$, GaSb is not a satisfactory material for the confining layers of diode lasers with this active layer composition, because the valence band offset is too small to provide sufficient confinement of holes and because the refractive index of GaSb in the vicinity of 2.3 μm is not small enough to provide good optical confinement. The addition of Al increases the band offset and decreases the refractive index. Even for moderate Al concentrations, however, the lattice mismatch between $\text{Al}_x\text{Ga}_{1-x}\text{Sb}$ and GaSb at 300 K, $\Delta a/a_{\text{sub}} = 6.5 \times 10^{-3}x$, is too large to be accommodated elastically in the thick confining layers required for diode lasers. (This mismatch is five times larger than in the AlGaAs/GaAs system.) The incorporation of small concentrations of As yields AlGaAsSb alloys lattice matched to GaSb. For the present work we have chosen confining layers of $\text{Al}_{0.50}\text{Ga}_{0.50}\text{As}_{0.04}\text{Sb}_{0.96}$. The Sb content must be maintained to within 1.4% of this value to achieve $\Delta a/a_{\text{sub}} < 10^{-3}$.

3. Experimental procedure

3.1. Growth and flux calibration

Layers were grown on commercial Te-doped n-GaSb and semi-insulating GaAs (100) substrates. The GaAs substrates were used for growing test layers for electrical measurements, while the GaSb substrates were used for the other test layers, as well as for the laser structure. The substrates were cleaned in solvents and etched, mounted with In on 75 mm Mo holders, loaded into a Varian Gen II modular MBE system, and heated in the presence of the appropriate group V flux to desorb surface oxides and other contami-

nants. At this point a sharp, group-V-stabilized diffraction pattern could generally be observed by reflection high-energy electron diffraction (RHEED).

The sources used for MBE growth were the group III and group V elements, which yielded beams of Al, Ga, and In atoms and of As_4 and Sb_4 molecules. In all cases the As flux was much larger than the total group III flux. At the substrate temperatures employed in the present work, the group III elements have sticking coefficients of approximately unity, and the growth rate is determined by the total group III flux. The individual group III fluxes were calibrated by measuring the frequency of the RHEED intensity oscillations [8,9] observed during the growth of test layers of GaSb, AlSb, and InAs.

The calibration of the group V fluxes is more difficult because these elements do not have unity sticking coefficients under typical growth conditions. The effective Sb flux incorporated on a Ga-rich surface, J_{Sb}^* , was determined from the frequency of the RHEED oscillations observed during growth of GaSb under Sb-limited conditions [10,11]. The result of this measurement was consistent with a determination of the minimum Sb flux necessary for growing GaSb layers with good surface morphology. Calibration of the As flux was unnecessary because the absolute magnitude is not critical under the excess As conditions used in the present work.

3.2. Measurement and adjustment of alloy compositions

The initial conditions used for $\text{Ga}_{1-x}\text{In}_x\text{As}_y\text{Sb}_{1-y}$ and $\text{Al}_x\text{Ga}_{1-x}\text{As}_y\text{Sb}_{1-y}$ growth were established in the following manner. The group III fluxes were chosen to yield the desired Ga/In or Al/Ga ratio and a growth rate of approximately 1 $\mu\text{m h}^{-1}$. An As beam-equivalent pressure of approximately 4×10^{-6} Torr was used, to give a large excess As flux. The effective Sb flux, J_{Sb}^* , was set at $(1-y)\Sigma J_{\text{III}}$, where ΣJ_{III} is the total group III flux. Because Sb is incorporated more readily than As [12], the efficiency of Sb incorporation is expected to be high even in the presence of a large As flux. Layers grown under these initial conditions were characterized as described below.

the fluxes were changed to adjust the composition, and additional layers were grown and characterized until the desired bandgap and lattice constant were obtained.

The approximate bandgap of the GaInAsSb test layers was obtained from the peak wavelength of the photoluminescence spectrum measured at 4.2 K, using the 647 nm line of a Kr ion laser with a power density on the sample of approximately 600 W cm^{-2} , a SPEX 0.5 m spectrometer, and a PbS detector cooled to 77 K. To determine the lattice constants of both the GaInAsSb and AlGaAsSb layers, the lattice mismatch between these layers and the GaSb substrate was found by double-crystal X-ray diffraction measurements, using a GaSb first crystal, of the (400) reflection. The alloy composition was measured by Auger electron spectroscopy, as calibrated by Auger analysis of AlSb, GaSb, and GaAs layers and also of a thick GaInAsSb test layer whose composition had been determined by electron microprobe analysis.

For the GaInAsSb test layers, the composition was calculated from the measured photoluminescence wavelength and lattice mismatch by using eq. (1) for the bandgap and Vegard's law for the lattice constant. The ratio of the Ga and In fractions calculated in this way, as well as the ratios obtained by Auger analysis, are in good agreement with the ratio of the Ga and In fluxes. The growth rates determined by cross-sectional thickness measurements are in agreement with the rates calculated from the Ga and In fluxes by assuming that these elements are incorporated with unity efficiency. Fig. 3 shows the measured Sb content ($1-y$) of a number of $\text{Ga}_{1-x}\text{In}_x\text{As}_y\text{Sb}_{1-y}$ layers as a function of J_{Sb}^* normalized to the total group III flux. The scatter in the data can be attributed to the dependence of Sb incorporation efficiency on As flux and substrate temperature which were not the same in all the runs. The four points falling on the solid straight line in fig. 3 were obtained for layers grown in four runs with nominally the same As flux and substrate temperature. These runs were the ones that led to successful growth of the active layer in the laser structure.

For the $\text{Al}_x\text{Ga}_{1-x}\text{As}_y\text{Sb}_{1-y}$ layers, the value of ($1-y$) was determined from the measured lattice mismatch, on the assumption that the ratio of x to

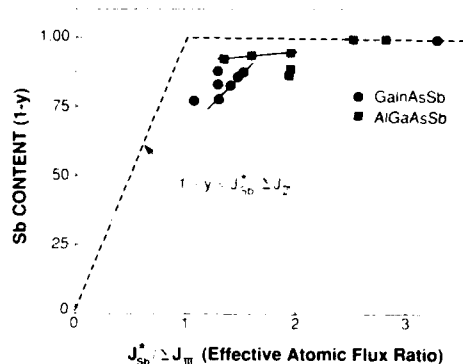


Fig. 3. Antimony content ($1-y$) of $\text{Ga}_{1-x}\text{In}_x\text{As}_y\text{Sb}_{1-y}$ and $\text{Al}_x\text{Ga}_{1-x}\text{As}_y\text{Sb}_{1-y}$ alloys versus effective Sb flux J_{Sb}^* normalized to total group III flux. The dashed line shows the values that would be obtained if the Sb incorporation efficiency were the same as the value for Ga-rich GaSb.

($1-x$) is equal to the ratio of the Al and Ga fluxes. This assumption is supported by the observation that the growth rate calculated from the total group III flux was equal to the value determined by cross-sectional thickness measurements. The three AlGaAsSb points in fig. 3 that fall on a solid straight line were obtained for layers grown in runs with nominally the same As flux and substrate temperature. These runs were the ones used to establish the conditions for growing the confining layers of the laser structure.

The results plotted in fig. 3 demonstrate that substantial Sb concentrations can be obtained even in the presence of an As flux that is much greater than the Sb flux. The dashed line in fig. 3 shows the values of ($1-y$) that would be obtained if the Sb incorporation efficiency were the same as the value for Ga-rich GaSb. The experimental values for ($1-y$) fall below this line, indicating that some additional Sb desorption occurs in the presence of a concurrent As flux. Furthermore, the very weak dependence of ($1-y$) on J_{Sb}^* exhibited by AlGaAsSb indicates that the Sb incorporation efficiency is reduced even further when the As flux is large and ($1-y$) is close to unity. These results are consistent with those obtained for GaAsSb by other workers [12-14].

4. Impurity doping and transport properties

Nominally undoped layers of GaSb and AlGaAsSb are p type. Silicon is commonly used for n-type doping of III-V semiconductors grown by MBE, but neither Si [13] nor Sn [12] is a donor in GaSb and AlGaAsSb, so the group VI elements S, Se, and Te are used instead. In this work, the impurity used for n-type doping was Te provided by the sublimation of GaTe [15]. The p-type dopant was Be, which is conventionally used in the MBE growth of III-V materials. The Van der Pauw technique was used to measure the carrier type, concentration, and mobility in doped test layers, typically 1 to 2 μm thick, grown on semi-insulating GaAs substrates. For n-type AlGaAsSb, undoped AlGaAsSb buffer layers were used to prevent the formation of a two-dimensional electron gas. Although GaSb and AlGaAsSb layers grown on GaAs substrates will contain a high density of misfit dislocations, only a slight degradation of the majority carrier transport properties is expected.

In fig. 4, the electron concentration n at 300 K in GaSb and $\text{Al}_{0.50}\text{Ga}_{0.50}\text{As}_{0.04}\text{Sb}_{0.96}$ layers doped with GaTe is plotted versus inverse GaTe source temperature. The values of n for GaSb layers range from 8×10^{15} to $1 \times 10^{18} \text{ cm}^{-3}$. At moderate GaTe source temperatures, n exhibits an

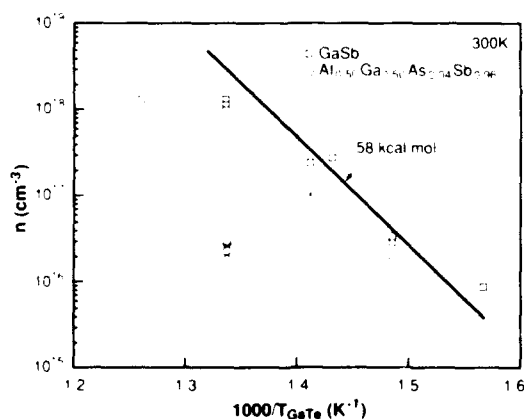


Fig. 4. Electron concentration n at 300 K versus inverse GaTe source temperature for n-GaSb and n-AlGaAsSb layers grown on semi-insulating GaAs substrates at $1 \mu\text{m h}^{-1}$.

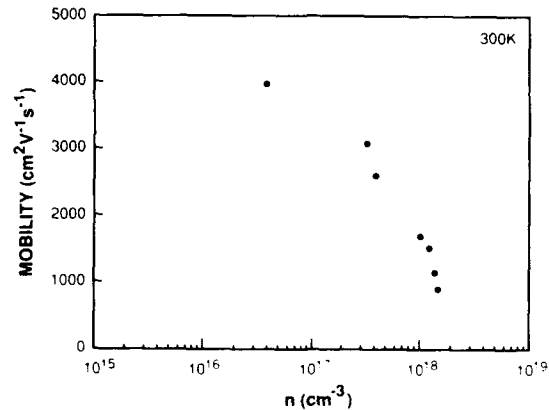


Fig. 5. Hall mobility at 300 K versus n for GaTe-doped n-GaSb layers grown on semi-insulating GaAs substrates.

Arrhenius dependence on temperature. The line drawn in fig. 4 corresponds to a sublimation heat of 58 kcal/mol. At the highest GaTe source temperatures, the values of n fall below this line. The electron mobility of n-GaSb layers at 300 K is shown in fig. 5. A mobility of $4000 \text{ cm}^2 \text{ V}^{-1} \text{ s}^{-1}$ was obtained for $n = 4 \times 10^{16} \text{ cm}^{-3}$. As expected, lower mobilities are observed at higher values of n . Somewhat higher mobilities were obtained at 77 K, with a value of $5850 \text{ cm}^2 \text{ V}^{-1} \text{ s}^{-1}$ for $n = 6 \times 10^{17} \text{ cm}^{-3}$. The n-type doping of GaSb grown by MBE has been investigated by other workers using S [16,17], PbSe [18], Te [19], Sb_2Te_3 [20], and PbTe [21]. The electron concentrations and mobilities obtained in this study by using GaTe are comparable to the best values that have been obtained with the other dopant sources.

For comparison, a GaTe-doped GaAs sample was grown with a GaTe source temperature of 435°C . The electron mobility is consistent with minimal compensation. The value of n is $5 \times 10^{17} \text{ cm}^{-3}$, nearly the same as that obtained in layers of GaSb grown with the same GaTe source temperature. This result, together with the Arrhenius behavior described above, suggests that unity incorporation and doping efficiency of Te occur in GaSb layers grown at moderate GaTe source temperatures.

For GaTe-doped $\text{Al}_{0.50}\text{Ga}_{0.50}\text{As}_{0.04}\text{Sb}_{0.96}$, values of n as high as $1 \times 10^{17} \text{ cm}^{-3}$ were obtained.

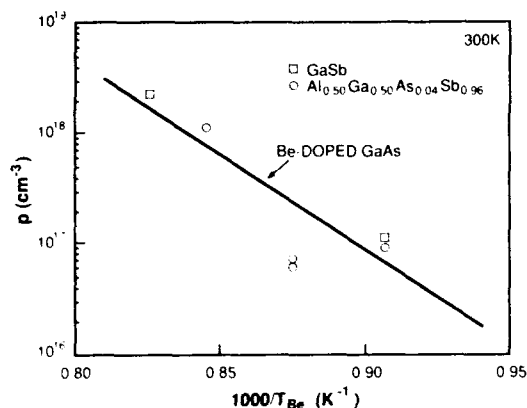


Fig. 6. Hole concentration at 300 K versus inverse Be source temperature for p-GaSb and p-AlGaAsSb layers grown on semi-insulating GaAs substrates at $1 \mu\text{m h}^{-1}$.

as shown in fig. 4. (The plotted values of n have not been corrected for simultaneous electron conduction in the Γ , L, and X conduction bands.) For GaTe source temperatures of 435°C ($1000/T = 1.412$) or lower, the results are relatively well behaved. For higher source temperatures, however, n decreases with increasing GaTe temperature, and the measured mobilities are anomalously high. Anomalously high Hall mobilities observed in other semiconductors were shown by Wolfe, Stillman, and Rossi [22] to result from conducting inhomogeneities such as metallic inclusions. It therefore seems probable that conducting inclusions of Te or some Te-containing species are incorporated in our AlGaAsSb layers grown with high GaTe source temperatures.

The results for Be doing of p-type GaSb and AlGaAsSb are straightforward. Fig. 6 is a plot of hole concentration p versus inverse Be source temperature. Values of p up to $2 \times 10^{18} \text{ cm}^{-3}$ have been obtained. Also shown is the line representing our data for Be-doped GaAs. Many workers have found that unity incorporation and doping efficiency occur for Be doping of GaAs under normal growth conditions. Since most of our measured points for Be-doped GaSb and AlGaAsSb fall near the line for Be-doped GaAs, we conclude that unity incorporation and doping efficiency also occur for the Be doping of these materials. The deviations shown in fig. 6 for two

samples of AlGaAsSb may have resulted from unintentional variations in growth rate or from non-optimum growth conditions.

5. Laser characteristics

The laser structure consists of the following layers: $0.75 \mu\text{m}$ thick n^+ -GaSb buffer, $2 \mu\text{m}$ thick $n\text{-Al}_{0.50}\text{Ga}_{0.50}\text{As}_{0.04}\text{Sb}_{0.96}$ confining, $0.4 \mu\text{m}$ thick $\text{Ga}_{0.84}\text{In}_{0.16}\text{As}_{0.14}\text{Sb}_{0.86}$ active, $3 \mu\text{m}$ thick $p\text{-Al}_{0.50}\text{Ga}_{0.50}\text{As}_{0.04}\text{Sb}_{0.96}$ confining, and $0.05 \mu\text{m}$ thick p^+ -GaSb contacting. Following growth, Ti/Au and Au/Sn layers were deposited and alloyed at 300°C to form ohmic contacts to the p^+ - and n -GaSb surfaces, respectively, and broad-stripe diode lasers $300 \mu\text{m}$ wide were fabricated.

The lasers exhibited uniform near-field emission patterns. The emission spectrum is composed of multiple longitudinal modes centered at $2.27 \mu\text{m}$, as shown in fig. 7. Two other wafers having a layer structure similar to the present one had been grown on consecutive days about a year earlier. Lasers fabricated from these two wafers had emission spectra centered at $2.29 \mu\text{m}$ [6]. A shift in bandgap from 2.29 to $2.27 \mu\text{m}$ corresponds to a change in the $\text{Ga}_{1-x}\text{In}_x\text{As}_y\text{Sb}_{1-y}$ composition of $\Delta x = 0.006$ or $\Delta y = 0.02$.

The light output L versus current I has been measured at room temperature for lasers with cavity lengths from 300 to $700 \mu\text{m}$. Fig. 8 shows the L - I curve for a $300 \mu\text{m}$ long device measured

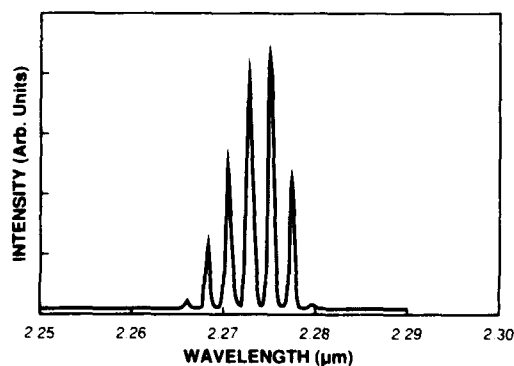


Fig. 7. Emission spectrum at 295 K of a GaInAsSb/AlGaAsSb diode laser.

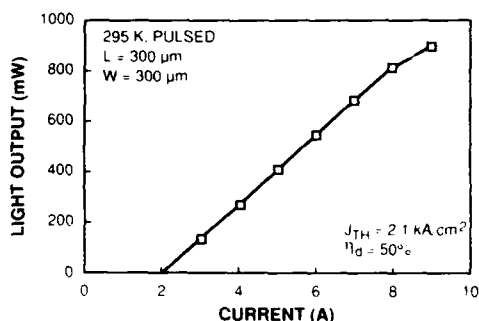


Fig. 8. Light output versus current characteristic of a GaInAsSb/AlGaAsSb laser under pulsed conditions.

with 200 ns pulses. From this curve, $J_{th} = 2.1 \text{ kA cm}^{-2}$ and $\eta_d = 50\%$. The maximum power output is 900 mW per facet, limited by failure of the probe point contact to the Ti/Au metallization. Values of J_{th} as low as 1.5 kA cm^{-2} were obtained for devices with a cavity length of $700 \mu\text{m}$. Such low values indicate that Auger recombination is not a serious problem in these lasers, contrary to earlier predictions [23]. The value of $1/\eta_d$ was found to depend linearly on cavity length; the length dependence yields an internal loss coefficient of less than 45 cm^{-1} . This low value indicates that free-carrier absorption is not a serious problem in these lasers. The values for η_d and power output are much higher than the best values reported previously for any diode laser emitting beyond $2 \mu\text{m}$ at room temperature.

6. Conclusions

MBE has been used to grow lattice-matched GaInAsSb/AlGaAsSb double heterostructures on GaSb substrates. The required alloy compositions were obtained by adjusting the group III and Sb fluxes on the basis of bandgap and lattice constant measurements on test layers. Carrier concentrations as high as 1×10^{18} and $1 \times 10^{17} \text{ cm}^{-3}$ were obtained for n-GaSb and n-AlGaAsSb, respectively, and as high as 2×10^{18} and $1 \times 10^{18} \text{ cm}^{-3}$ for p-GaSb and p-AlGaAsSb, respectively. Mobilities as high as 4000 and $5850 \text{ cm}^2 \text{ V}^{-1} \text{ s}^{-1}$ were

obtained for n-GaSb at 300 and 77 K, respectively.

Diode lasers emitting near $2.3 \mu\text{m}$ fabricated from these double heterostructures exhibited a threshold current density as low as 1.5 kA cm^{-2} , differential quantum efficiency as high as 50%, and pulsed power as high as 900 mW per facet. Auger recombination and free-carrier absorption do not appear to be serious problems for these lasers.

Acknowledgments

We are grateful to D.R. Calawa, J.W. Chludzinski, M.C. Finn, K.A. McIntosh, P.M. Nitishin, and J.V. Pantano for materials characterization and expert technical assistance, and to L.R. Dawson, S.H. Groves, L. Lassabaterre, and J.N. Walpole for helpful discussions. We would like to acknowledge the substantial contributions of A.J. Strauss to our development of these materials. This work was sponsored by the Department of the Air Force.

References

- [1] H.C. Casey, Jr. and M.B. Panish, *Heterostructure Lasers*, Part B (Academic Press, New York, 1978).
- [2] J.C. DeWinter, M.A. Pollack, A.K. Srivastava and J.L. Zyskind, *J. Electron. Mater.* 14 (1985) 729.
- [3] A.E. Bochkarev, L.M. Dolginov, A.E. Drakin, P.G. Eliseev and B.N. Sverdlov, *Soviet J. Quantum Electron.* 18 (1988) 1362.
- [4] A.N. Baranov, A.N. Imenkov, M.P. Mikhailova, A.A. Rogachev and Yu.P. Yakovlev, *Proc. SPIE* 1048 (1989) 188; A.N. Baranov, T.N. Danilova, B.E. Dzhurtanov, A.N. Imenkov, S.G. Konnikov, A.M. Litvak, V.E. Usmanski and Yu.P. Yakovlev, *Soviet Tech. Phys. Letters* 14 (1988) 727.
- [5] T.H. Chiu, W.T. Tsang, J.A. Ditzenberger and J.P. van der Ziel, *Appl. Phys. Letters* 49 (1986) 1051.
- [6] S.J. Eglash and H.K. Choi, *Appl. Phys. Letters* 57 (1990) 1292.
- [7] See, for example, B.W. Dodson and J.Y. Tsao, *Ann. Rev. Mater. Sci.* 19 (1989) 419.
- [8] J.H. Neave, B.A. Joyce, P.J. Dobson and N. Norton, *Appl. Phys.* A31 (1983) 1.
- [9] G.W. Turner, B.A. Nechay and S.J. Eglash, *J. Vacuum Sci. Technol.* B8 (1990) 283.

- [10] R. Fernandez, *J. Vacuum Sci. Technol.* B6 (1988) 745.
- [11] D.L. Miller, personal communication.
- [12] C.-A. Chang, R. Ludeke, L.L. Chang and L. Esaki, *Appl. Phys. Letters* 31 (1977) 759.
- [13] T.D. McLean, T.M. Kerr, D.I. Westwood, J.D. Grange and I.J. Murgatroyd, in: *Proc. 11th Intern. Symp. on GaAs and Related Compounds*, Biarritz, 1984, Inst. Phys. Conf. Ser. 74, Ed. B. de Cremoux (Inst. Phys., London-Bristol, 1985) p. 145.
- [14] M. Yano, M. Ashida, A. Kawaguchi, Y. Iwai and M. Inoue, *J. Vacuum Sci. Technol.* B7 (1989) 199.
- [15] A. Furukawa and M. Mizuta, *Electron. Letters* 24 (1988) 1378.
- [16] H. Gotoh, K. Sasamoto, S. Kuroda, T. Yamamoto, K. Tamamura, M. Fukushima and M. Kimata, Japan. *J. Appl. Phys.* 20 (1981) L893.
- [17] M.E. Lee, I. Poole, W.S. Truscott, I.R. Cleverly, K.E. Singer and D.M. Rohlfing, *J. Appl. Phys.* 68 (1990) 131.
- [18] T.D. McLean, T.M. Kerr, D.I. Westwood, C.E.C. Wood and D.F. Howell, *J. Vacuum Sci. Technol.* B4 (1986) 601.
- [19] M. Yano, Y. Suzuki, Y. Ishii, Y. Matsushima and M. Kimata, Japan. *J. Appl. Phys.* 17 (1978) 2091.
- [20] T.H. Chiu, J.A. Ditzenberger, H.S. Luftman, W.T. Tsang and N.T. Ha, *Appl. Phys. Letters* 56 (1990) 1688.
- [21] S. Subbanna, G. Tuttle and H. Kroemer, *J. Electron. Mater.* 17 (1988) 297.
- [22] C.M. Wolfe, G.E. Stillman and J.A. Rossi, *J. Electrochem. Soc.* 119 (1972) 250.
- [23] A. Sugimura, *IEEE J. Quantum Electron.* QE-18 (1982) 352.

MBE growth and characterization of $\text{In}_x\text{Ga}_{1-x}\text{Sb}/\text{InAs}$ strained layer superlattices

R. Fashe, J.T. Zborowski, T.D. Golding, H.D. Shih, P.C. Chow, K. Matsuichi *

Space Vacuum Epitaxy Center and Department of Physics, University of Houston, Houston, Texas 77204, USA

B.C. Covington, A. Chi, J. Zheng

Department of Physics, Sam Houston State University, Huntsville, Texas 77341, USA

and

H.F. Schaake

Central Research Laboratories, Texas Instruments Incorporated, Dallas, Texas 75265, USA

An experimental investigation of the artificially structured $\text{In}_x\text{Ga}_{1-x}\text{Sb}/\text{InAs}$ strained layer superlattice (SLS) system proposed by Mulhot and Smith in 1987 for long-wavelength infrared detection was carried out. The SLS structures were grown on $\text{GaSb}(100)$ substrates using MBE and were characterized by reflection high-energy electron diffraction, Auger electron spectroscopy, double-crystal X-ray diffraction, Raman spectroscopy, transmission electron microscopy and Fourier transform infrared spectroscopy. Far infrared absorption was observed at a wavelength of $12.6\text{ }\mu\text{m}$ in a 25-period, $150\text{ }\text{\AA}$ \times $150\text{ }\text{\AA}$ $[\text{In}_x\text{Ga}_{1-x}\text{Sb}/\text{InAs}]/\text{GaSb}(100)$ sample, thereby demonstrating the feasibility of this material system for long-wavelength infrared detection.

1. Introduction

A significant amount of effort has recently been devoted to the development of intrinsic semiconductor detectors for infrared (IR) imaging in the $10\text{--}12\text{ }\mu\text{m}$ wavelength range [1]. These devices are usually made from the II-VI $\text{Hg}_{1-x}\text{Cd}_x\text{Te}$ ternary alloy [2], because no bulk III-V materials have sufficiently small bandgaps at 77 K for operation in this wavelength range. Because of the noise considerations, photovoltaic infrared detectors are usually preferred over photoconductive devices [3]. The photovoltaic infrared detectors, mainly metal insulator semiconductor (MIS) and diode devices, are limited in their performance by dark currents caused mostly by electron tunneling

from the valence band to the conduction band. The problem intensifies at long wavelengths beyond $10\text{ }\mu\text{m}$ where bandgaps are less than 0.1 eV because, in a conventional bulk semiconductor, the bandgap and the effective mass are not independent: a narrow bandgap leads to a small effective mass, which in turn causes large tunnel currents. In view of this problem with bulk semiconductors, a number of alternative material systems were proposed and studied for IR applications over the past ten years. All proposed material systems [4-7] are artificially structured superlattices that require synthesizing using advanced epitaxial growth techniques such as molecular beam epitaxy (MBE). These synthesized materials have unique properties not found in the conventional semiconductors. For IR sensing applications, the artificially structured superlattices offer a significant advantage over the conventional

* Also at the Texas Center for Superconductivity at the University of Houston.

semiconductors: the decoupling of the bandgap and the effective mass to first order approximation in a superlattice structure. In other words, the bandgap and the effective mass can be independently tuned in a superlattice, and it is possible to design an IR detector with both a *small* bandgap and a *large* effective mass [4]. In addition to the requirements of having a small bandgap and a large effective mass, a potential superlattice candidate for IR applications should also have a large absorption coefficient, which depends on the density of states. The novel, type II strained-layer superlattice (SLS) system of $\text{InAs-In}_{1-x}\text{Ga}_x\text{Sb}$ proposed by Mailhot and Smith in 1987 meets all three requirements [7].

In the $\text{InAs-In}_{1-x}\text{Ga}_x\text{Sb}$ superlattice system proposed by Mailhot and Smith, the two constituent layers are not lattice matched. The internal strain effects caused by the mismatch are used to reduce the bandgap of the InAs quantum wells. Calculations showed that the $\text{In}_{1-x}\text{Ga}_x\text{Sb-InAs}$ has an effective mass greater than that of $\text{Hg}_{1-x}\text{Cd}_x\text{Te}$ and an absorption coefficient comparable to that of $\text{Hg}_{1-x}\text{Cd}_x\text{Te}$ [8], thereby making the InAs-InGaSb SLS a promising material for long-wavelength IR detection.

Experimental study of the $\text{In}_{1-x}\text{Ga}_x\text{Sb-InAs SLS}$ system was recently reported by Chow et al. [9], with all epitaxial structures grown on GaSb(100) substrates by MBE. We have undertaken a similar study of this potentially useful material system with MBE. However, all our epitaxial structures were grown on GaSb(100) substrates in order to reduce lattice mismatch between the free-standing superlattice structure and the substrate. Some of the preliminary experimental results are reported here. A more detailed report will appear elsewhere.

2. Experimental

All epitaxial structures reported here were prepared in a commercial Riber MBE system equipped with a growth chamber and an analysis chamber. The reflection high-energy electron diffraction (RHEED) facility was installed in the growth chamber, while the Auger electron spec-

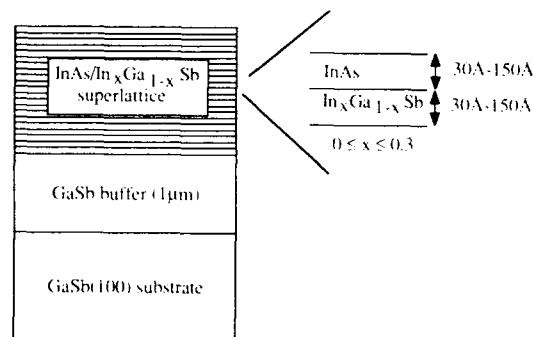


Fig. 1. Schematic diagram of a typical InGaSb-InAs SLS structure.

troscopy (AES) facility, comprising a double-pass cylindrical mirror analyser, was installed in the analysis chamber. The growth chamber had one antimony cell producing Sb_4 and two arsenic cells, a standard cell producing As_4 and a cracker cell producing As_2 . The GaSb substrates (typically $1 \text{ cm} \times 1 \text{ cm}$) were mounted by indium soldering onto the 3-inch molybdenum blocks. $\text{In}_{1-x}\text{Ga}_x\text{Sb}$ epilayers, InAs epilayers and $\text{In}_{1-x}\text{Ga}_x\text{Sb-InAs SLSs}$ were grown on GaSb(100) substrates buffered by $1.0 \mu\text{m}$ homoepitaxial GaSb layers. A schematic diagram of the SLS structure is shown in fig. 1. The substrate temperatures above 430°C were measured using an optical pyrometer and those below 430°C were estimated by extrapolating the substrate heater currents. The GaSb and InAs growth rates were calibrated from in situ RHEED oscillations and were 0.9 and $0.1 \mu\text{m/h}$, respectively.

Superlattice period thicknesses between 60 and 300 Å were investigated with growth temperatures ranging from 370 to 500°C . The films and resulting structures were characterized by in situ RHEED, AES, double-crystal X-ray spectroscopy and Fourier transform infrared (FTIR) spectroscopy. To characterize the samples with X-rays, a sealed copper source, in point geometry and running typically at 40 kV and 30 mA , was employed. The monochromator was a (220) germanium single crystal. To eliminate the $\text{K}\alpha_2$ component, an adjustable slit was placed from the monochromator. The main beam dimensions were $0.5 \times 3 \text{ mm}^2$. This arrangement gave a radial resolution

of about 0.03° FWHM in 2θ at the 400 reflection of InAs.

For FTIR analysis, all data were collected with a Bomem DA 3.01 Fourier transform spectrophotometer using a KBr beamsplitter, a glowbar source and a HgCdTe detector. The spectra were collected at a resolution of 2 cm^{-1} and a temperature of about 6 K. A total of 100 scans were co-added to improve the signal to noise ratio. The samples were mounted to the cold finger of a Janus continuous flow cryostat which had been calibrated to allow positioning the sample at angles at 0° , 20° , 40° and 65° with respect to the incident infrared beam. Angle dependence was obtained to confirm the two-dimensional nature of the observed transitions. This consisted of obtaining spectra at each of the chosen angles starting with 0° and increasing to larger angles and then repeating the process but starting at 65° and decreasing to smaller angles. The data were then compared for repeatability.

3. Results

A great deal of effort was devoted to growth of InAs/GaSb heterostructures using $(\text{As}_4, \text{Sb}_4)$ and $(\text{As}_2, \text{Sb}_4)$. We found, with the aid of Auger electron spectroscopy, that in using $(\text{As}_4, \text{Sb}_4)$ InAs could not be grown following growth of GaSb. Fig. 2 shows two Auger spectra from two different InAs/GaSb samples, one prepared using $(\text{As}_4, \text{Sb}_4)$ and the other $(\text{As}_2, \text{Sb}_4)$. Each of these two samples consisted of a nominal 150 Å InAs epilayer. The upper spectrum was obtained from the InAs/GaSb sample prepared using $(\text{As}_4, \text{Sb}_4)$ and shows a large Sb peak at 454 eV, while the lower spectrum was recorded from the sample prepared using $(\text{As}_2, \text{Sb}_4)$ and shows a substantially smaller Sb peak at 454 eV. In samples prepared using $(\text{As}_4, \text{Sb}_4)$, the absence of InAs on GaSb was also confirmed by Raman spectroscopy. In all heterostructure growth, the RHEED patterns remained streaky, indicating the presence of

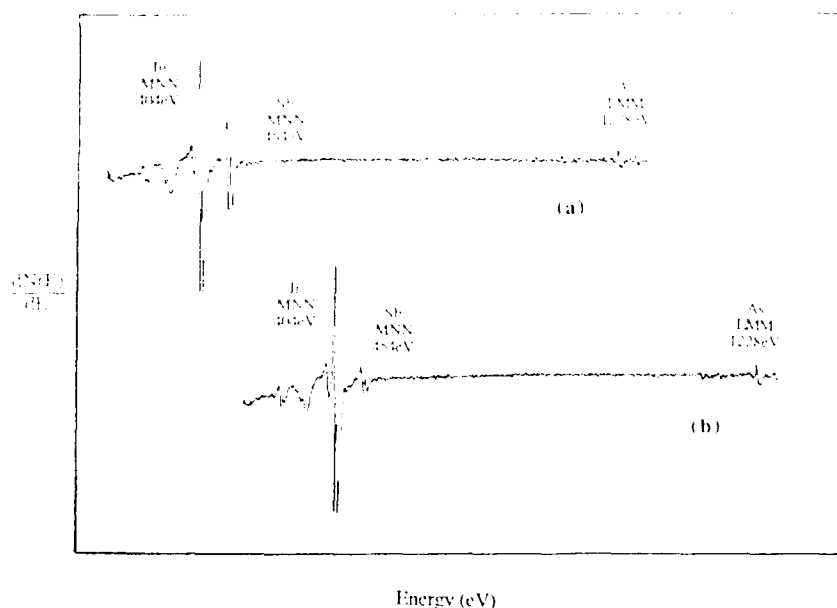


Fig. 2 Auger spectra for a nominal 150 Å InAs epilayer on a GaSb layer grown at 380°C utilizing (a) As_4 and (b) As_2 . The inability to grow InAs on GaSb using As_4 is evidenced by the presence of a large Sb peak in the upper spectrum (a).

a two-dimensional growth mode. The inability to grow InAs on GaSb using As_4 necessitated the use of As_2 in growth of all superlattice structures.

X-ray diffraction was used to analyze a series of 25-period $150 \text{ \AA}/150 \text{ \AA}$ $\text{In}_{0.2}\text{Ga}_{0.8}\text{Sb}/\text{InAs}$ SLS structures grown on GaSb(100) substrates at different substrate temperatures. Fig. 3 shows two X-ray diffraction spectra obtained from two samples grown at different substrate temperatures. The upper spectrum was obtained from Sample 381, which had a growth temperature of 420°C . The lower spectrum was obtained from Sample 281, which had a growth temperature of 380°C . The spectra were taken with $\text{Cu K}\alpha_1$ radiation near the 400 fundamental of the GaSb(100) substrate. The sample grown at 420°C was optically

inactive in the infrared region, whereas the sample grown at 380°C showed infrared absorption at a 12.6 \mu m wavelength. The diffraction profile for Sample 281 indicates a series of equally spaced superlattice peaks centered about the 400 superlattice fundamental. From the peak positions the average perpendicular lattice parameter of the superlattice is 6.093 \AA with a periodicity of 300 \AA . The theoretical value for an ideal $150 \text{ \AA}/150 \text{ \AA}$ $\text{In}_{0.2}\text{Ga}_{0.8}\text{Sb}/\text{InAs}$ coherently strained free standing SL based on elastic energy density minimization is 6.13 \AA for the average perpendicular lattice parameter. In contrast, the diffraction profile for Sample 381 is complex, showing superlattice peaks which yield a periodicity of 220 \AA . The high-angle peak, closest to the GaSb 400 peak, does not fall

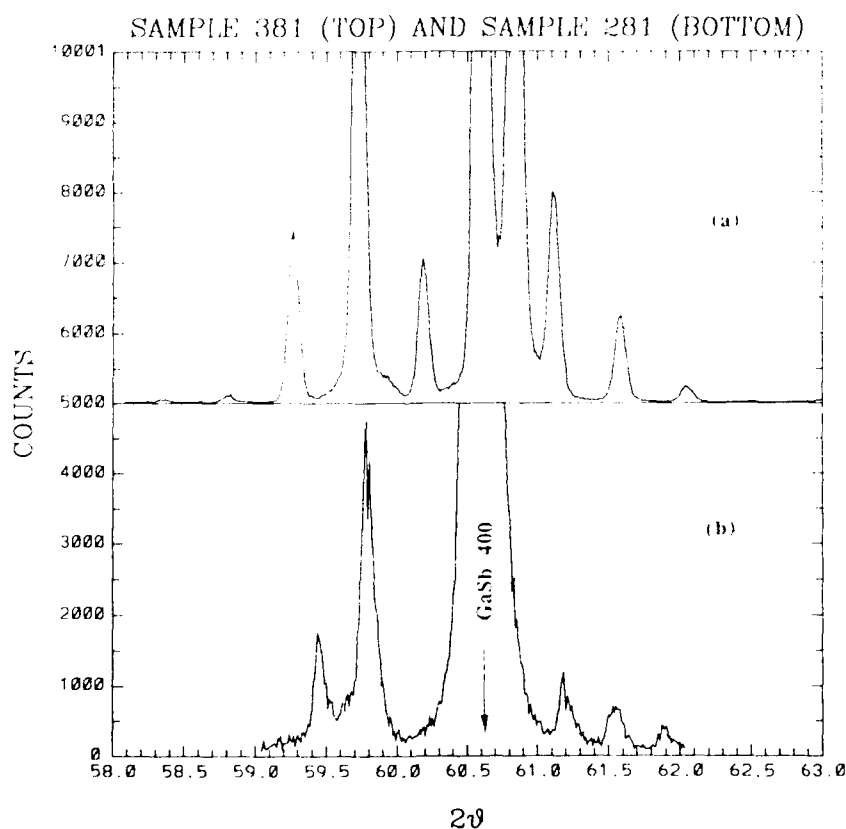


Fig. 3 Double-crystal X-ray diffraction spectra obtained from a 25-period, nominally grown $150 \text{ \AA}/150 \text{ \AA}$ $\text{In}_{0.2}\text{Ga}_{0.8}\text{Sb}/\text{InAs}$ SLS prepared under identical flux conditions at growth temperatures of (a) 420°C (Sample 381) and (b) 380°C (Sample 281). The ordinate is arbitrary and the intense peaks truncated.

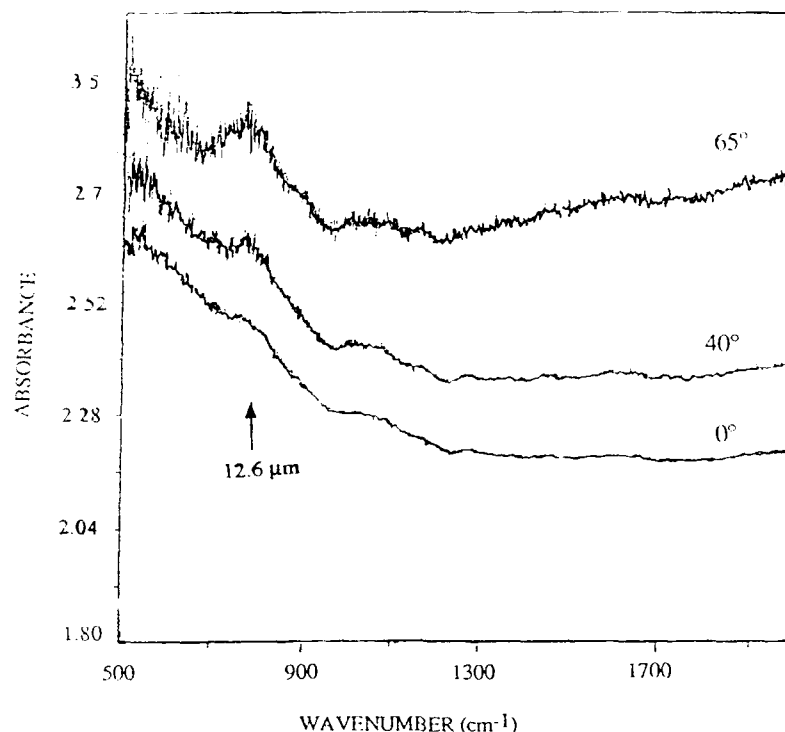


Fig. 4. Fourier transform infrared (FTIR) spectra for a 25-period, nominally grown 150 Å/150 Å $\text{In}_{0.2}\text{Ga}_{0.8}\text{Sb}$ -InAs SLS grown at 380°C. The spectra are displayed as a function of incident angle. The absorbance scale reflects the values obtained for each spectrum and is not drawn to scale.

into the superlattice spacing sequence and is probably due to interdiffusion between the InAs and $\text{In}_{0.2}\text{Ga}_{0.8}\text{Sb}$ constituent layers.

In addition to X-ray diffraction, the SLS samples were also characterized by FTIR for infrared absorption. Fig. 4 shows three FTIR spectra obtained from Sample 281 at three incident angles of 0°, 40° and 65°. These spectra were measured at 6 K. The strong absorption at a wavelength of 12.6 μm indicates that the InGaSb-InAs SLS system is a viable material for long-wavelength infrared detection. Further optimization of the epitaxial structure and the growth conditions is in progress.

4. Summary

We have experimentally investigated the InGaSb-InAs SLS system proposed by Mailhot

and Smith for long-wavelength infrared detection. The epitaxial structures were all grown on GaSb(100) substrates to minimize lattice mismatch. FTIR measurements indicate that this material is suitable for long-wavelength infrared detection. However, the quality of this material is highly dependent on growth conditions. Further optimization of the growth conditions is essential and is underway in our laboratory.

Acknowledgments

We thank Dr. Christian Mailhot, now at Lawrence Livermore National laboratory, for his interest in our work and for many stimulating discussions and valuable inputs. This work was supported in part by NASA Grant No. NAGW-977 and by the Advanced Research Program of the Texas Higher Education Coordinating Board.

References

- [1] R.A. Reynolds, J. Vacuum Sci. Technol. A7 (1989) 269.
- [2] M.B. Reine, A.K. Sood and T.J. Tredwell, in: Semiconductors and Semimetals, Vol. 18, Eds. R.K. Willardson and A.C. Beer (Academic Press, New York, 1981) p. 201.
- [3] M.A. Kinch and S.R. Borrello, Infrared Phys. 15 (1975) 111.
- [4] J.N. Schulman and T.C. McGill, Appl. Phys. Letters 34 (1979) 663.
- [5] G.C. Osbourn, L.R. Dawson, R.M. Biefeld, T.E. Zipperian, I.J. Fritz and B.L. Doyle, J. Vacuum Sci. Technol. A5 (1987) 3150.
- [6] K.K. Choi, B.F. Levine, C.G. Bethea, J. Walker and R.J. Walker, Appl. Phys. Letters 50 (1987) 1814.
- [7] C. Mailhot and D.L. Smith, J. Vacuum Sci. Technol. B5 (1987) 1268.
- [8] C. Mailhot and D.L. Smith, J. Vacuum Sci. Technol. A7 (1989) 445.
- [9] D.H. Chow, R.H. Miles, J.R. Söderström and T.C. McGill, Appl. Phys. Letters 56 (1990) 1418.

Growth of $\text{InAs}/\text{Ga}_{1-x}\text{In}_x\text{Sb}$ infrared superlattices

D.H. Chow *, R.H. Miles, C.W. Nieh

Hughes Research Laboratories, Malibu, California 90265, USA

and

T.C. McGill

T.J. Watson, Sr., Laboratory of Applied Physics, California Institute of Technology, Pasadena, California 91125, USA

A set of $\text{InAs}/\text{Ga}_{1-x}\text{In}_x\text{Sb}$ superlattices has been grown by molecular beam epitaxy. The superlattices are deposited on thick, stress-relaxed buffer layers of GaSb on (100)-oriented GaAs substrates. A short-period, heavily strained superlattice has been inserted at the GaAs/GaSb interface. Transmission electron microscope (TEM) images reveal that a dense network of dislocations forms at this interface, with the vast majority of threading dislocations propagating no further than the first 1000 Å of the GaSb buffer layer. Planar superlattice layers are observed, with no evidence of stress relaxation between the layers or between the $\text{InAs}/\text{Ga}_{1-x}\text{In}_x\text{Sb}$ superlattice and GaSb buffer. Analysis of X-ray diffraction satellites reveals that cross-incorporation of As in GaSb and $\text{Ga}_{1-x}\text{In}_x\text{Sb}$ layers is virtually eliminated at low growth temperatures. Photoconductivity spectra from the superlattices display sharp photocurrent threshold energies, in agreement with previously published energy gaps derived from calculations and photoluminescence data. Thresholds in the 8–14 μm range are obtained from superlattices with very thin layers (≈ 40 Å), which are necessary for strong optical absorption in a type II superlattice. Finally, an absorption coefficient of $\approx 2000\text{ cm}^{-1}$ is measured at 10 μm from a superlattice with an energy gap of 11.4 μm . This value is comparable to that of bulk $\text{Hg}_{1-x}\text{Cd}_x\text{Te}$, the current industry standard for infrared detectors in the 8–14 μm range.

1. Introduction

$\text{InAs}/\text{Ga}_{1-x}\text{In}_x\text{Sb}$ superlattices show promise as materials for infrared detection in the 8–14 μm range [1–4]. In comparison to $\text{Hg}_{1-x}\text{Cd}_x\text{Te}$, the current industry standard, $\text{InAs}/\text{Ga}_{1-x}\text{In}_x\text{Sb}$ superlattices are expected to hold several advantages: (i) a higher degree of uniformity, which is crucial for the fabrication of large infrared detector arrays, (ii) smaller leakage currents, due to the tunable increase in effective mass available in a superlattice, (iii) reduced Auger recombination rates, due to the substantial splitting of the light and heavy hole bands and the increase in electron effective mass [5], (iv) better understood device processing techniques, and (v) compatibil-

ity with GaAs-based readout electronics. Furthermore, the performance of infrared detectors based on $\text{InAs}/\text{Ga}_{1-x}\text{In}_x\text{Sb}$ superlattices should not be limited by the high thermal generation rates which preclude large D^* 's in multiquantum well infrared detectors (such as GaAs/AlGaAs multiquantum wells, for example) [6].

The conceptual basis for achieving far-infrared energy gaps in $\text{InAs}/\text{Ga}_{1-x}\text{In}_x\text{Sb}$ superlattices has been discussed previously [1–4]. Briefly, the broken-gap band alignment between the two constituent materials yields a small energy gap for the superlattice once quantum confinement effects are considered (assuming reasonably thin layers). The presence of coherent strain between the InAs and $\text{Ga}_{1-x}\text{In}_x\text{Sb}$ layers shifts the band edges such that the superlattice energy gap is reduced. This shift is advantageous because narrower energy gaps (longer cutoff wavelengths) can be obtained with

* Formerly at California Institute of Technology, Pasadena, California, USA.

reduced layer thicknesses, leading to enhanced optical absorption and carrier transport properties.

In this paper, we present structural and optical characterization of a set of InAs/Ga_{1-x}In_xSb superlattices grown by molecular beam epitaxy (MBE). Layer thicknesses and compositions have been varied, resulting in samples with energy gaps ranging from 80 to 340 meV (3.5 to 15 μ m). Structural characterization of the superlattices consisted of reflection high energy electron diffraction (RHEED), X-ray diffraction, and (in some cases) transmission electron microscopy (TEM). Spectrally resolved photoconductivity and optical transmission experiments have also been performed. Absorption coefficients comparable to those of bulk Hg_{1-x}Cd_xTe have been observed.

2. Growth and structural characterization

All of the samples discussed here have been grown by MBE on (100)-oriented GaAs substrates in a Perkin-Elmer 430 system equipped with both arsenic and antimony crackers. Measurements of the substrate temperature were obtained through a thermocouple, which was either in contact with a molybdenum block (in the case of indium-soldered substrates), or a heat diffuser (in the case of indium-free substrate mounts). In both cases, the thermocouple readings were calibrated to optical pyrometer readings above 500°C. At lower substrate temperatures, a transition in the GaSb surface reconstruction under an Sb₂ flux from 1 \times 3 to 1 \times 5 was used as a point of calibration for thermocouple readings. Nominal growth rates were calibrated via bulk film thickness measurements and RHEED oscillations measured during homoepitaxial growth of GaAs and InAs. A "nude" ion gauge was used to monitor the Sb₂ and As₂ fluxes.

Growth of each of the superlattices studied here commenced with 3000 Å of GaAs, grown at a substrate temperature of 600°C. Following the GaAs layer, a ten period, 1 monolayer/1 monolayer, GaSb/GaAs superlattice was deposited at 520°C. Spotty RHEED patterns, indicative of a three-dimensional growth mode, were observed al-

most immediately upon commencement of the short period superlattice. However, streaky RHEED patterns were recovered within the first 100 Å of a 5000 Å GaSb buffer layer, grown at 420–450°C on top of the short period superlattice. A 1 \times 3 RHEED pattern was observed throughout the deposition of the GaSb buffer layer, which is stress relaxed (free standing) as determined by X-ray diffraction. Growth was completed by deposition of an InAs/Ga_{1-x}In_xSb superlattice on top of the buffer layer. The choice of GaSb as a buffer layer material for the strained-layer InAs/Ga_{1-x}In_xSb superlattices was made because of the intermediate value of the lattice constant of GaSb with respect to the two constituent materials of the superlattice. Substrate temperatures ranging from 350 to 400°C were selected for the InAs/Ga_{1-x}In_xSb superlattices studied here. Ga_{1-x}In_xSb and InAs displayed 1 \times 3 and 1 \times 2 surface reconstructions, respectively, as observed via RHEED patterns during growth of the superlattices. For substrate temperatures below 370°C (approximately), a transition to a 1 \times 5 RHEED pattern was observed during growth interrupts (in an Sb flux) on Ga_{1-x}In_xSb surfaces.

A cross-sectional TEM photograph of an InAs/Ga_{1-x}In_xSb superlattice grown by the method described above is shown in fig. 1. The figure reveals a dense network of dislocations at the GaSb/GaAs interface, the vast majority of which do not propagate past the first 1000 Å of buffer layer growth. The remaining threading dislocations persist through the entire structure, with a density of approximately 10⁹ cm⁻². There is no evidence of plastic stress relaxation in any of the superlattice layers, nor between the superlattice and buffer layer. In spite of the high threading dislocation densities, TEM images reveal smooth, planar, InAs/Ga_{1-x}In_xSb superlattice layers over most of the sample area. It is likely that substantial improvements in structural quality can be achieved by growing InAs/Ga_{1-x}In_xSb superlattices on GaSb substrates. However, GaAs substrates are substantially less expensive and provide the possibility of monolithic integration with read-out circuitry.

Fig. 2 displays (400)-like, $\theta/2\theta$ X-ray diffraction data from an 80 period, 41 Å/25 Å, InAs/



Fig. 1. Cross-sectional TEM image of an InAs/Ga_{1-x}In_xSb superlattice grown on a GaAs substrate by the method described in the text. A dense network of dislocations is observed at the GaAs/GaSb interface; most of these dislocations do not propagate past the first 1000 Å of the GaSb buffer layer.

Ga_{0.75}In_{0.25}Sb superlattice, grown by the method described previously. The period and average interatomic spacing of the superlattice has been determined from the X-ray data by measuring the satellite spacings and zeroth order satellite posi-

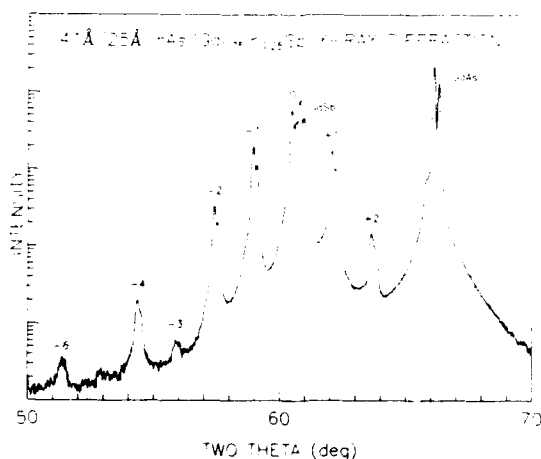


Fig. 2. $\theta/2\theta$ X-ray diffraction data for an 80 period, 41 Å/25 Å, InAs/Ga_{0.75}In_{0.25}Sb superlattice, showing (400)-like diffraction peaks. The sample was irradiated with Cu K α X-rays. Each peak in the figure is bimodal due to the K α doublet. The GaSb buffer and GaAs substrate peaks are labeled.

tion, respectively. This information is sufficient to compute the In and Ga fluxes used during growth (two measured quantities, two determined variables), assuming the structure is in a known strain state. Hence, the layer thicknesses and Ga_{1-x}In_xSb composition, x , of the superlattice can be determined from the X-ray data without relying on nominal growth rates. The intensities of the superlattice satellite peaks shown in fig. 2 are in excellent agreement with those predicted by kinematical theory. The widths of the peaks are limited by the resolution of the X-ray diffractometer used here. The intensity and narrowness of the satellite peaks is indicative of highly regular superlattice growth with limited interdiffusion between layers [7].

The position of the GaSb buffer layer peak in fig. 2 indicates that there is virtually no cross-incorporation of As into the layer (<0.1%). We have previously reported that growth of GaSb (with a cracked Sb source), in an As background produced by a hot, shuttered, As cracker, yields substantial cross-incorporation (7–30%) of As over the substrate temperature range 450–530 °C; in that study, lower substrate temperatures were found to yield lesser degrees of As-incorporation [8]. A substrate temperature of approximately

425°C was chosen for growth of the GaSb buffer layer in the sample used to produce fig. 2, resulting in the virtual elimination of As from the layer. These results suggest that: (i) increased coverage of Sb on the GaSb surface occurs as the substrate temperature is lowered, and (ii) the As-sticking coefficient is more strongly dependent on surface composition (Sb-coverage) than substrate temperature over the temperature range studied here. The effects of increased Sb-surface coverage would be enhanced if As₄ molecules dominate the As-background pressure when the As shutter is closed, since adjacent lattice sites are required for incorporation of As₄ into GaAs [9,10]. We have, furthermore, estimated the cross-incorporation of arsenic in the Ga_{1-x}In_xSb layers of the superlattice used to produce fig. 2 to be no greater than 1%. This estimate was made by assuming that the nominal GaSb growth rate was accurate to $\pm 20\%$, and applying the X-ray analysis described in the previous paragraph to determine the In flux and the degree of As-incorporation.

3. Optical characterization

Photoconductive devices have been fabricated for this study by chemically etching mesa structures into the InAs/Ga_{1-x}In_xSb superlattices. Evaporated aluminum contacts were then placed on the tops of the mesas and etched surfaces, forming sets of diodes. Fig. 3 displays spectrally resolved photocurrent data from five InAs/Ga_{1-x}In_xSb superlattices. The spectra were obtained under backside illumination at different applied biases. All of the data presented in fig. 3 were obtained at 5 K; to date, temperature dependence has been studied in only the 25 Å/25 Å InAs/Ga_{0.75}In_{0.25}Sb superlattice, revealing no appreciable changes in photoconductive response up to 100 K. As can be seen from the figure, photoconductive thresholds shift to lower energies as the InSb fraction and/or InAs layer thickness are increased. The photoconductive thresholds displayed in fig. 3 are in excellent agreement with previously published energy gaps derived from calculations and photoluminescence spectra [4]. It should be noted that operation in the 8–14 μm

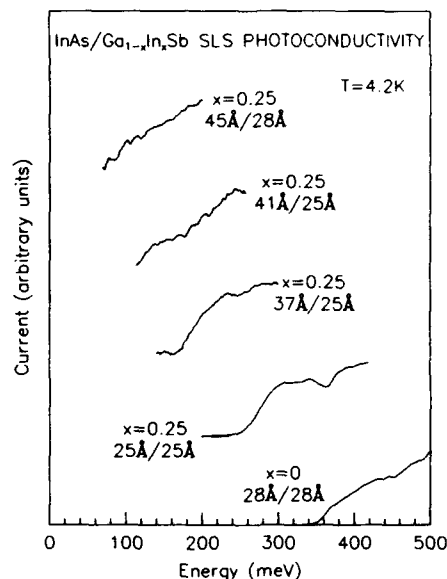


Fig. 3. Photoconductivity spectra from five in InAs/Ga_{1-x}In_xSb superlattices.

range is obtained for reasonably thin layers (≈ 40 Å), which are necessary for strong optical absorption.

Fig. 4 contains an experimental absorption spectrum, taken from the 41 Å/25 Å InAs/

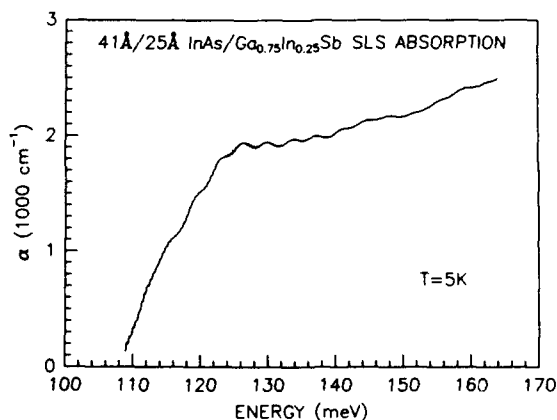


Fig. 4. Measured absorption coefficient for a 41 Å/25 Å InAs/Ga_{0.75}In_{0.25}Sb superlattice. Absorption at 10 μm is comparable to that of bulk Hg_{1-x}Cd_xTe with the same energy gap. The small amplitude oscillations observed in the figure are interference fringes resulting from a difference in thickness between the sample and a reference piece of a GaAs substrate.

Ga_{0.75}In_{0.25}Sb superlattice for which X-ray and photocurrent data are displayed in figs. 2 and 3, respectively. The superlattice absorption edge is abrupt (the absorption increases by one order of magnitude within 10 meV of the threshold energy), attaining a value of approximately 2000 cm⁻¹ at 10 μm. This value is comparable to that of bulk Hg_{1-x}Cd_xTe with the same energy gap. The observation of large absorption coefficients from a type II superlattice is consistent with the prediction of large electron effective masses in these structures, which may reduce leakage currents and Auger recombination rates. Comparison of figs. 3 and 4 reveals that the absorption edge of the superlattice is coincident with its photoconductive threshold, as expected.

4. Conclusions

In summary, we have grown a set of InAs/Ga_{1-x}In_xSb strained-layer superlattices by molecular beam epitaxy. The superlattices were deposited on thick, stress relaxed GaSb buffers layers on GaAs substrates. A two-dimensional growth mode is recovered within the first 100 Å of the buffer layer when a short period, heavily strained superlattice is inserted at the GaAs/GaSb interface. TEM images reveal planar superlattice layers, with residual threading dislocation densities of approximately 10⁹ cm⁻². However, no evidence of stress relaxation in the superlattice layers has been observed. X-ray diffraction data from the superlattices show intense, sharp satellite peaks, which have been used to determine the layer thicknesses and compositions of our samples. Further analysis of the X-ray data is consistent with the virtual elimination of cross-incorporated As in the GaSb buffer and Ga_{1-x}In_xSb superlattice layers at low growth temperatures. The InAs/Ga_{1-x}In_xSb superlattices studied here display sharp photocon-

ductive thresholds at energies which agree well with calculated energy gaps. Finally, an absorption coefficient of 2000 cm⁻¹ at 10 μm has been measured from a superlattice with an 11 μm energy gap. As this value is comparable to that of bulk Hg_{1-x}Cd_xTe, we feel it is a promising result for detectors based on InAs/Ga_{1-x}In_xSb superlattices.

Acknowledgments

The authors are grateful for fruitful discussions with D.L. Smith of Los Alamos National Laboratories and C. Mailhot of Lawrence Livermore Laboratories. We also wish to acknowledge discussions with R. Baron, J.P. Baukus, D.A. Collins, T.C. Hasenberg, A.T. Hunter, O.J. Marsh, J.R. Söderström, and M.H. Young, and the timely technical assistance of C. Haeussler. Parts of this work were performed under Contract Nos. N00014-89-C-0203 and N00014-89-J-3196 from the Defense Advanced Research Projects Agency and the Office of Naval Research.

References

- [1] D.L. Smith and C. Mailhot, *J. Appl. Phys.* 62 (1987) 2545.
- [2] Mailhot and D.L. Smith, *J. Vacuum Sci. Technol.* A7 (1989) 445.
- [3] D.H. Chow, R.H. Miles, J.R. Söderström and T.C. McGill, *Appl. Phys. Letters* 56 (1990) 1418.
- [4] R.H. Miles, D.H. Chow, J.N. Schulman and T.C. McGill, *Appl. Phys. Letters* 57 (1990) 801.
- [5] D.L. Smith, private communication.
- [6] M.A. Kinch and A. Yariv, *Appl. Phys. Letters* 55 (1989) 2093.
- [7] B.M. Clemens and J.G. Gay, *Phys. Rev.* B35 (1987) 9337.
- [8] D.H. Chow, R.H. Miles, J.R. Söderström and T.C. McGill, *J. Vacuum Sci. Technol.* B8 (1990) 710.
- [9] C.T. Foxon and B.A. Joyce, *Surface Sci.* 50 (1975) 434.
- [10] C.T. Foxon and B.A. Joyce, *Surface Sci.* 64 (1977) 293.

New MBE growth method for InSb quantum well boxes

Nobuyuki Koguchi, Satoshi Takahashi and Toyohiro Chikyow

National Research Institute for Metals, Tsukuba Laboratories, 1-2-1 Sengen, Tsukuba, Ibaraki 305, Japan

We propose a new MBE growth method for InSb microcrystals on CdTe which has a nearly equal lattice constant to InSb. The average size of the InSb microcrystals was about $150\text{ nm} \times 200\text{ nm} \times 70\text{ nm}$. This method is based on the Sb incorporation into In droplets and thought to be useful for fabricating quantum well boxes.

1. Introduction

Predictions of enhanced electron mobility [1] and drastic improvements of laser diode characteristics [2] have been made for quantum well box systems. In spite of the fundamental interest in making quantum well boxes, progress in their fabrication has been very slow. Although the electron beam lithography and subsequent argon ion milling have been demonstrated for the fabrication of the quantum well boxes [3] these dimensions are quite difficult to handle and radiation damage is inevitable. It appears highly desirable to look for alternative methods to fabricate quantum well boxes without resort to lithography.

In this paper, we propose a new MBE growth method for InSb microcrystals on a CdTe epitaxial layer. Since the CdTe has a nearly equal lattice constant to InSb and a larger energy gap than that of InSb, it may be possible to fabricate a quantum well box system by covering the InSb microcrystals by a CdTe epitaxial overlayer.

2. Experimental

The MBE system used in this work was a conventional commercial system (ANELVA-620) with a cluster of 40 cm^3 boron nitride effusion cells in a common liquid nitrogen shroud and an electron gun for reflection high energy electron diffraction (RHEED) with a primary beam energy

of 30 keV. This system was capable of an ultimate pressure in the low 10^{-10} Torr range.

Elemental In and Sb and compound CdTe in the Knudsen cells were used as molecular beam sources. The incident fluxes of In, Sb and CdTe were separately determined by measuring the weights of these films deposited on glass substrates held at 20°C and beam equivalent pressure (BEP).

Prior to loading, an InSb (001) substrate of $5 \times 5\text{ cm}^2$ area was solvent cleaned and mounted onto molybdenum support blocks using gallium solder. Immediately before growth, the native oxide was removed from the substrate surface by heating at 460°C in an Sb flux.

At first, an InSb buffer layer was grown onto the substrate at 430°C for 30 min. The thickness of the InSb buffer layer was about 500 nm. The In and Sb fluxes during growth were 4×10^{14} and $9 \times 10^{14}\text{ atoms/cm}^2 \cdot \text{s}$, respectively. Then 200 nm thick CdTe epitaxial layer was grown onto the InSb buffer layer at 200°C for 30 min. Next, In which had the same flux during growth of the InSb buffer layer was deposited on the CdTe epitaxial layer for 30 s at 200°C . After deposition of the In droplets, an Sb flux which was $1 \times 10^{14}\text{ atoms/cm}^2 \cdot \text{s}$ was supplied for 100 s.

The structures of the samples were analyzed by a field emission type high resolution scanning electron microscope (HRSEM) and transmission electron microscope (TEM).

3. Results and discussions

The RHEED patterns observed on each stage of the growth process are shown in fig. 1 along complementary $\langle 110 \rangle$ and $\langle \bar{1}\bar{1}0 \rangle$ azimuths. The surface reconstruction of the InSb buffer layer is

pseudo (1×3) during growth, which corresponds to that observed by Noreika et al. [4] for the flux ratio of the antimony and indium being larger than unity. The surface reconstruction changed to In-stabilized $c(8 \times 2)$ at 200°C . Tellurium stabilized (2×1) surface reconstruction [5] appeared

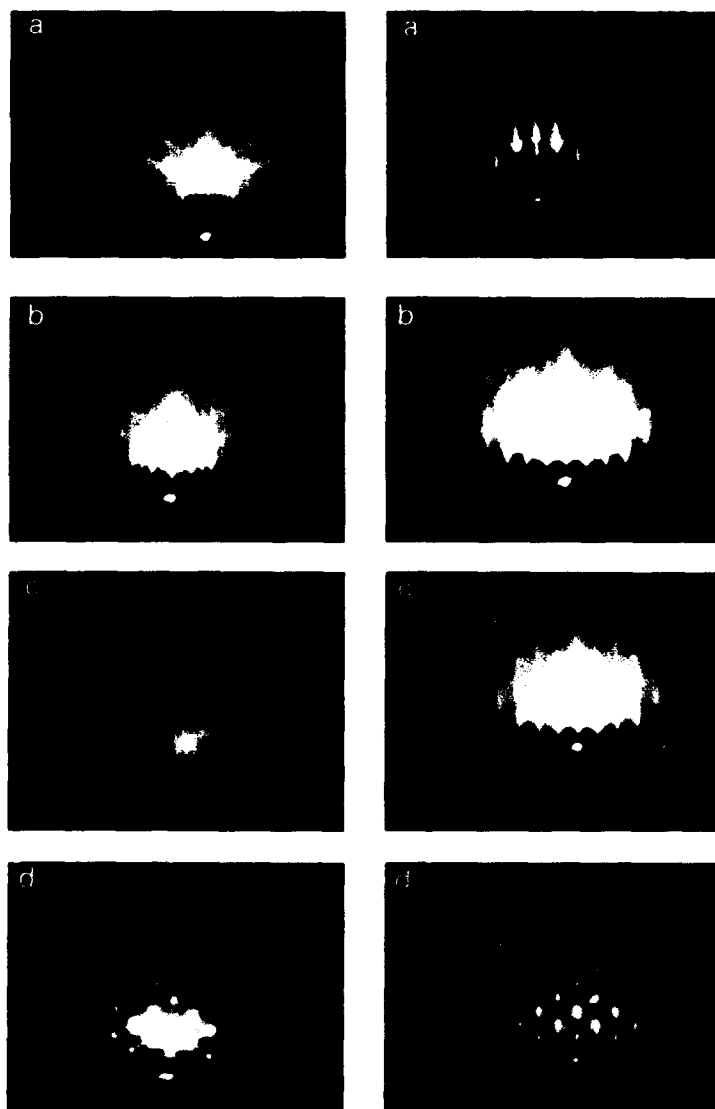


Fig. 1. RHEED patterns observed on the growth process along the complementary $\langle 110 \rangle$ azimuths: (a) surface of the InSb buffer layer at 200°C ; (b) surface of the CdTe epitaxial layer; (c) In deposited surface on the CdTe epitaxial layer; (d) surface after the Sb supply. Left column: $[110]$; right column: $[1\bar{1}0]$.

on the CdTe epitaxial layer. Simultaneous diffraction patterns of halo and (2×1) reconstruction were observed on the In deposited surface. Immediately after the Sb molecular beam radiation, the RHEED pattern changed to the spotty feature with streaks along $\langle 111 \rangle$ and $\langle 100 \rangle$ azimuths. The $\langle 111 \rangle$ streaks were clearly observed along the $\langle 110 \rangle$ azimuth rather than those along the $\langle \bar{1}\bar{1}0 \rangle$ azimuth. Some twin spots were observed along both azimuths. The Debye rings caused by antimony were observed simultaneously after about 60 s supply of antimony molecular beam.

These RHEED observations revealed that the In droplets deposited on the CdTe epitaxial layer changed to InSb epitaxial microcrystals truncated by (111) and (100) facets after the antimony molecular beam supply. The $(\bar{1}\bar{1}1)$ facets of micro-

crystals are well defined, but the (111) facets are not so clear.

The HRSEM photographs of In droplets on the CdTe epitaxial layer and the microcrystals grown by the Sb molecular beam supply to the In droplets are shown in fig. 2. The surface and slightly oblique side views are shown simultaneously in the figures. The shape of the In droplets is a hemisphere and the average diameter of the droplets is 120 nm. The standard deviation of the size distribution of the In droplets is about 10% in any sample prepared. These In droplets changed to truncated pyramidal shape microcrystals having (111) and (100) facets after the antimony flux supply. The base size of the pyramidal microcrystals is $150 \text{ nm} \times 200 \text{ nm}$ and the height is about 70 nm. The $(\bar{1}\bar{1}1)$ facets of the microcrystals

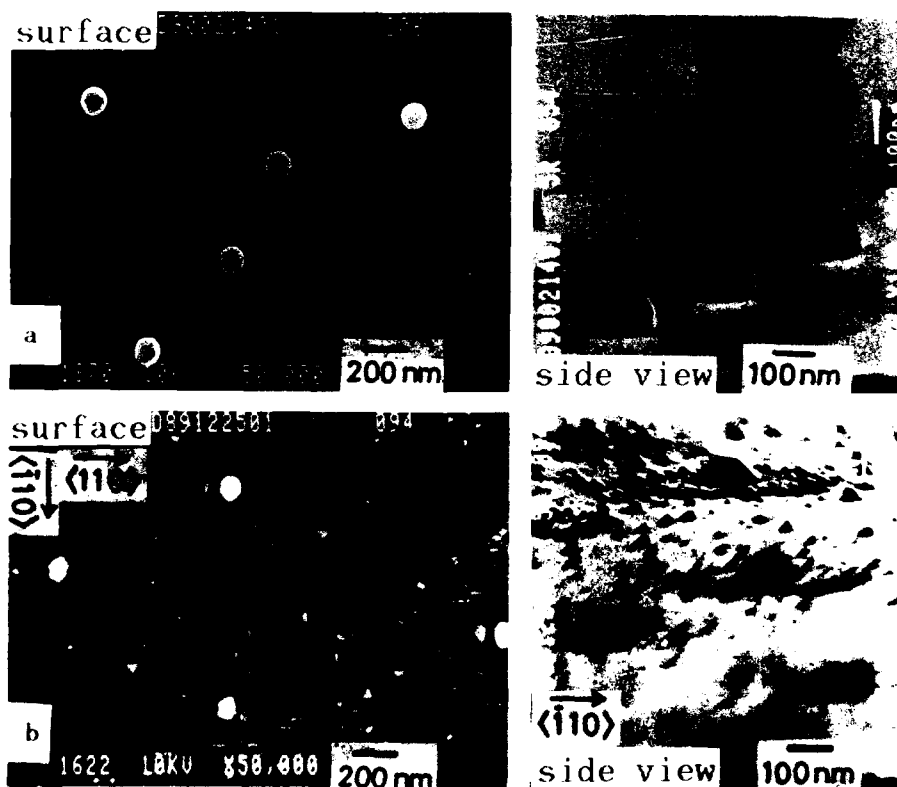


Fig. 2. HRSEM photographs: (a) In droplets deposited on the CdTe epitaxial layer; (b) microcrystals grown by the Sb molecular beam supply to In droplets.

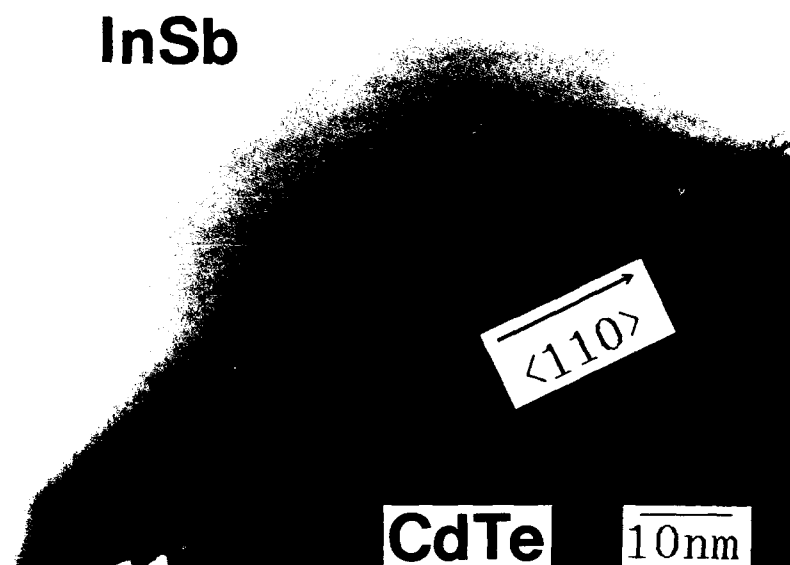


Fig. 3. TEM photograph of the InSb microcrystal.

are well defined, but the (111) facets are not so clear. These results correspond to those of the RHEED observation.

A TEM photograph of the microcrystal taken with the incident electron beam along the $\langle 110 \rangle$ direction for the cleaved sample is shown in fig. 3. The (111) lattice fringes appearing in the microcrystal are identified as those of InSb. Some InSb

microcrystals covered by the non-reacting In were observed simultaneously for the same specimen.

Irregularly shaped microcrystals, whose size was smaller than that of the InSb microcrystals, were deposited on the substrate simultaneously, as shown in fig. 2. These crystals were crowded around the InSb microcrystals. These irregularly shaped microcrystals and the Debye rings from

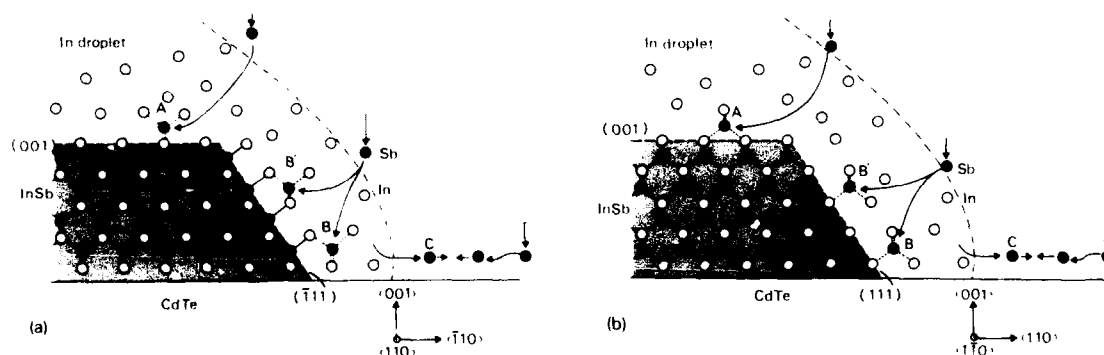


Fig. 4. Schematic explanation of growth mechanism of the InSb microcrystals: (a) cross sectional view along $\langle 110 \rangle$ azimuth; (b) cross sectional view along $\langle 110 \rangle$ azimuth.

antimony disappeared after 10 min of subsequent annealing at 300°C. So we can conclude that the irregularly shaped microcrystals around the InSb microcrystals were antimony.

These results show that three-dimensional growth of InSb microcrystals occurs by the antimony molecular beam supply to the In droplets deposited on the CdTe epitaxial layer. Two-dimensional lateral growth of GaAs was observed by the As molecular beam supply to the Ga droplets deposited on the GaAs substrate [6]. In this case, As monoatomic layer adsorption, which was suitable for the lateral growth of GaAs, occurred on the GaAs surface. On the other hand, Sb monoatomic layer adsorption with zinc-blende type surface structure may not occur on the CdTe surface.

Fig. 4 shows a speculated growth mechanism of the InSb microcrystal. Dissolved Sb atoms in the In droplet diffuse to the interface of In and CdTe. Then InSb crystallized at interface epitaxially. The microcrystals of InSb grow up by the adsorption of Sb atoms like A and B in the figure. On the $(\bar{1}\bar{1}1)$ surface, B and B' are nearly equivalent site; however, site B is more stable than site B' on the (111) surface for the growth. Then well defined $(\bar{1}\bar{1}1)$ facet appears but (111) facet is not so clear. Also the base size expansion of the microcrystals is easier in the $\langle 110 \rangle$ direction than in the $\langle \bar{1}\bar{1}0 \rangle$ direction. Since the excess Sb atoms, which were not soluble in the In droplets migrate on the CdTe surface (C), the supersaturation of the Sb atoms around the In droplets increases and then the density of Sb microcrystals is high around the In droplets.

The size of InSb microcrystals depend on that of In droplets. The average diameter of the In droplets on the CdTe epitaxial layer may decrease with a decrease of the substrate temperature and/or an increase of the In flux. Provided the In droplets changed to InSb completely by the supply of Sb molecular beam, a quantum well box system composed of InSb wells and CdTe barriers may be fabricated by the epitaxial growth of an CdTe overlayer on the InSb microcrystals. Zahn et al. [7] reported that the thin interfacial layer of the In_2Te_3 is formed in the InSb-CdTe interface. They

pointed out that the thickness of this layer was dependent on the substrate temperature, but that it was below some tens of angstroms thick at temperatures between about 180 and 330°C. Although we have not investigated the interfacial layer in this work, it may be necessary for decreasing substrate temperature during the growth process to fabricate an abrupt interface.

4. Conclusion

We have observed three-dimensional growth of InSb microcrystals by supplying a antimony molecular beam to the In droplets deposited on the CdTe epitaxial layer. Provided the In droplets changed to InSb completely by supply of an antimony molecular beam, the quantum well box system composed of InSb wells and the CdTe barrier may be fabricated by growing a CdTe epitaxial layer over the InSb microcrystals.

Acknowledgments

The authors wish to thank S. Yamamoto of the Tokai University for the MBE growth experiments, and Dr. K. Nii and Dr. K. Ogawa of the National Research Institute for Metals for their continuous encouragement. Thanks are also due to K. Ishige of the same institute for valuable discussions.

References

- [1] H. Sakaki, Japan. J. Appl. Phys. 28 (1989) L314.
- [2] Y. Arakawa and H. Sakaki, Appl. Phys. Letters 40 (1982) 939.
- [3] H. Temkin, G.J. Dolan, M.B. Panish and S.N.G. Chu, Appl. Phys. Letters 50 (1987) 413.
- [4] A.J. Noreika, M.H. Francombe and C.E. Wood, J. Appl. Phys. 52 (1981) 7416.
- [5] G.M. Williams, C.R. Whitehouse, N.G. Chew, G.W. Blackmore and A.G. Cullis, J. Vacuum Sci. Technol. B3 (1985) 704.
- [6] J. Osaka, N. Inoue, Y. Mada, K. Yamada and K. Wada, J. Crystal Growth 99 (1990) 120.
- [7] D.R.T. Zahn, K.J. Mackey, R.H. Williams, H. Munder, J. Geurts and W. Richter, Appl. Phys. Letters 50 (1987) 742.

Strong nonlinear optical enhancement in MBE-grown $\text{Bi}_{1-x}\text{Sb}_x$

E.R. Youngdale, J.R. Meyer, C.A. Hoffman, F.J. Bartoli

Naval Research Laboratory, Washington, DC 20375, USA

D.L. Partin, C.M. Thrush and J.P. Heremans

Physics Department, General Motors Research Laboratories, Warren, Michigan 48090, USA

We report an experimental study of the linear and nonlinear optical properties of $\text{Bi}_{1-x}\text{Sb}_x$ alloy layers grown by MBE. Non-degenerate four-wave mixing experiments at CO_2 laser wavelengths yield a large third-order nonlinear susceptibility ($\chi^{(3)} \approx 3.5 \times 10^{-4}$ esu). Furthermore, due to the high reflectivity of the $\text{Bi}_{1-x}\text{Sb}_x$ films at both the air and substrate interfaces, the etalon formed can enhance the nonlinear optical signal by over an order of magnitude.

It has been demonstrated that due to a strong optical modulation of the electron–hole plasma temperature, zero-gap and narrow-gap semiconductors such as HgTe [1], $\text{Hg}_{1-x}\text{Cd}_x\text{Te}$ [2], HgTe – CdTe superlattices [3,4], and $\alpha\text{-Sn}_{1-x}\text{Ge}_x$ [4,5] tend to have quite large third-order nonlinear susceptibilities ($\chi^{(3)}$) at CO_2 laser wavelengths. Response times are generally found to be in the picosecond range, and in some cases there is little saturation of the nonlinear signal at high optical intensities. In a recent publication [6], we reported the first nonlinear optical study of another narrow-gap system: $\text{Bi}_{1-x}\text{Sb}_x$ films grown by MBE. It was noted that the band structure and optical constants of $\text{Bi}_{1-x}\text{Sb}_x$ are quite favorable for large optical nonlinearities, and measurements confirmed that even at ambient temperatures, the $\chi^{(3)}$'s at high CO_2 laser intensities are among the largest ever measured. It was further noted that due to high reflectivities at both the ambient and substrate interfaces, the as-grown films form a relatively efficient Fabry–Pérot etalon. However, the films studied in the preliminary work were of arbitrary thickness, t , and hence were not optimized to take advantage of the etalon properties.

It was pointed out in an earlier study [6] that by adjusting t to match $\lambda/2$ in the medium, a significant etalon enhancement of the nonlinear

optical signal should be achievable. In this paper, ambient temperature four-wave mixing measurements on an MBE-grown $\text{Bi}_{1-x}\text{Sb}_x$ film of optimized thickness are presented and compared with data for the non-optimized samples. It will be seen that the correlation of etalon oscillations in the linear reflectivity spectrum with the frequency dependence of the four-wave signal (P_4) confirms a strong etalon enhancement of the nonlinear optical response.

$\text{Bi}_{1-x}\text{Sb}_x$ films were grown by MBE onto [111] BaF_2 substrates in a system which has been described elsewhere [7]. The growth temperature was 250°C , and the growth rate was $0.5 \mu\text{m/h}$. Electrical studies indicate that the films are single crystals, with electron and hole mobilities comparable to those in high-quality bulk $\text{Bi}_{1-x}\text{Sb}_x$. Compositions and thicknesses for four films are listed in table 1, along with linear and nonlinear optical properties to be discussed below. The composition was determined from the flux rate during growth, and was verified in one sample to be correct to within 5% by a neutron activation analysis.

The strong etalon effects in $\text{Bi}_{1-x}\text{Sb}_x$ films result because there is a large mismatch of the index of refraction at both the air and the BaF_2 substrate interfaces. The refractive index for BaF_2

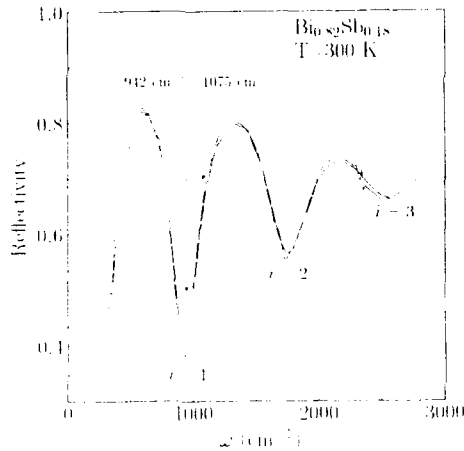


Fig. 1. Linear reflectivity as a function of frequency. The solid curve is experimental, while the dashed curve gives the results of the fit to the reflectivity data.

is only 1.4 [8], while that for $\text{Bi}_{1-x}\text{Sb}_x$ is > 10 . The linear reflectivity spectra [6] for samples 1–3, which all have thicknesses on the order of $1.1 \mu\text{m}$, indicate that for those films one does not expect pronounced etalon effects on P_4 because the available laser frequencies fall midway between etalon minima and maxima. However, the thickness of sample 4 was specifically chosen so as to maximize the etalon enhancement of the nonlinear response. The effect of the etalon is clearly shown in the linear reflectivity spectrum in fig. 1. The solid curve in this figure represents data taken using a Perkin-Elmer Model 180 spectrometer, while the dashed curve is a calculation based on a generalization of the Drude model to include multiple internal reflections. We modeled the dielectric properties of the BaF_2 substrate based on parameters in the literature [8]. Fitting the calcu-

lated curve to the experimental data yielded the values listed in table 1 for the high-frequency dielectric constant, plasma energy, and momentum relaxation time. These results are in good agreement with those obtained previously from bulk reflectivities in $\text{Bi}_{1-x}\text{Sb}_x$ [9,10]. Also listed in the table are the absorption coefficients at 942 cm^{-1} , which are obtained from the decay of the etalon oscillations and are therefore unavailable from bulk measurements. The arrows in fig. 1 indicate the positions in the spectrum corresponding to the range of CO_2 laser wavelengths. Note that $\omega = 942 \text{ cm}^{-1}$ is at a reflectivity minimum (where constructive interference of the internal optical fields is greatest), while $\omega = 1075 \text{ cm}^{-1}$ is midway between a minimum and a maximum.

The non-degenerate four-wave mixing experiments, described in detail elsewhere [3,4], utilize two grating-tuned, synchronously Q -switched CO_2 lasers, which generate $\approx 150 \text{ ns}$ pulses at frequencies ω_1 and ω_2 . The $\text{TEM}_{(0,0)}$ beams are aligned co-linearly and weakly focussed to a $1/e$ diameter of $560 \mu\text{m}$ on the sample, where mixing signals at frequencies $\omega_3 = 2\omega_1 - \omega_2$ and $\omega_4 = 2\omega_2 - \omega_1$ are generated. A 0.85 m Spex double monochromator is used to separate the four-wave signal P_4 at frequency ω_3 from the more intense pump beams. Beam intensities are varied by means of calibrated CaF_2 attenuators. The four-wave signal is measured using a HgCdTe photodiode operating at 77 K, and normalized to that obtained for a sample of optical grade germanium. P_4 is measured as a function of the difference frequency, $\Delta\omega = \omega_1 - \omega_2$, and intensity.

In fig. 2, we show measured $\chi^{(3)}$ as a function of laser difference frequency $\Delta\omega$. The values of $\chi^{(3)}$ are for a laser intensity of 10^6 W/cm^2 , and have been corrected for the presence of the etalon.

Table 1

$\text{Bi}_{1-x}\text{Sb}_x$ sample characteristics; the listed $\chi^{(3)}$'s are for $T = 300 \text{ K}$, $\Delta\omega = 1.8 \text{ cm}^{-1}$ and $P_0 = 2 \times 10^5 \text{ W/cm}^2$

Sample No.	x	t (μm)	ϵ_∞	$\hbar\omega_p$ (meV)	τ_m (ps)	$\alpha(\omega = 942 \text{ cm}^{-1})$ (cm^{-1})	$\chi^{(3)}$ (esu)
1	0.020	1.10	114.8	401	0.109	8240	2.1×10^{-4}
2	0.087	1.09	117.4	387	0.057	9510	2.6×10^{-4}
3	0.146	1.09	122.0	400	0.072	1.11×10^4	3.1×10^{-4}
4	0.186	0.508	127.9	468	0.063	1.30×10^4	3.5×10^{-4}

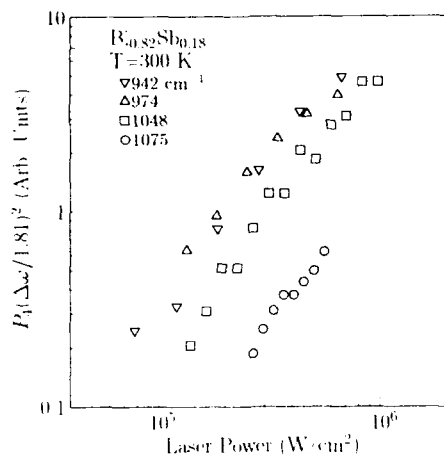


Fig. 2. $\chi^{(3)}$ as a function of laser difference frequency, $\Delta\omega$, at a laser power of 10^5 W/cm^2 . The straight line represents a $(\Delta\omega)^{-1}$ dependence.

The data clearly show a $1/(\Delta\omega)$ dependence down to the smallest $\Delta\omega$ used, from which we conclude that the relaxation time is greater than 3 ps [1,2].

It was pointed out above that the reflectivity spectrum for sample 4 implies a strong variation of the etalon enhancement with CO_2 laser frequency. To test this prediction, fig. 3 plots P_4 as a function of incident laser intensity at four

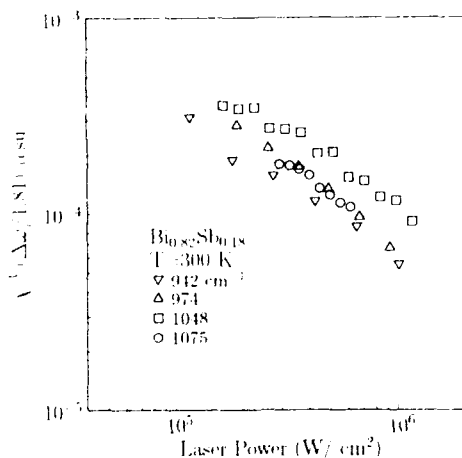


Fig. 3. Four-wave signal as a function of intensity for four different laser frequencies (scaling by $\Delta\omega$ make the data directly comparable). The strong dependence of the four-wave power on laser frequency confirms etalon enhancement.

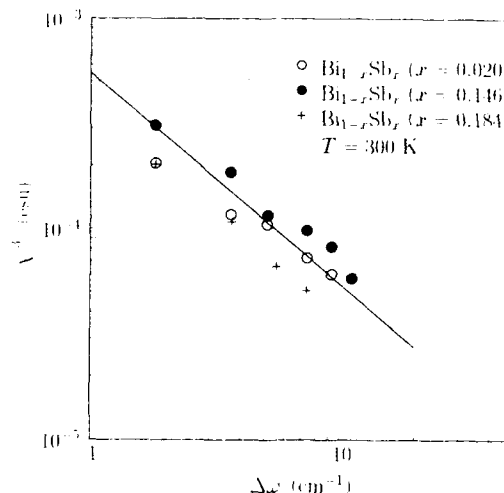


Fig. 4. $\chi^{(3)}$ as a function of laser intensity for the same four laser frequencies shown in fig. 3. The effects of the etalon have been accounted for in the analysis, and as a result there is no systematic dependence of $\chi^{(3)}$ on laser frequency.

different frequencies [11]. The data clearly confirm strong etalon enhancement, since P_4 at the optimum frequency (944 cm^{-1}) is nearly an order of magnitude larger than the value at 1075 cm^{-1} . In the appendix, we present a theoretical analysis of the effect of the etalon on nonlinear optical measurements. This analysis predicts an enhancement of P_4 by 29.5 at $\omega = 942 \text{ cm}^{-1}$, 19.6 at $\omega = 974 \text{ cm}^{-1}$, 4.0 at $\omega = 1048 \text{ cm}^{-1}$, and 1.7 at $\omega = 1075 \text{ cm}^{-1}$. For wavelengths closer to the reflectivity maximum, this factor would be less than unity.

Incorporating etalon effects into the analysis, $\chi^{(3)}$ at each laser frequency has been obtained from the data in fig. 3. Fig. 4 shows that whereas P_4 depends strongly on ω , the corrected $\chi^{(3)}$'s have no systematic dependence on frequency. The magnitude of the nonlinearity is quite high: $\chi^{(3)} = 3.5 \times 10^{-4} \text{ esu}$ at $\approx 10^5 \text{ W/cm}^2$. Partial saturation is observed with increasing laser intensity. A preliminary calculation of the nonlinear optical coefficients [1,3,4] in $\text{Bi}_{1-x}\text{Sb}_x$ was performed, which assumed that the mechanism responsible for the nonlinearity was a modulation of the dielectric constant due to thermally-generated electrons and holes induced by optical heating of the

free carrier plasma. The calculation yielded $\chi^{(3)}$'s in agreement with the experimental values to within a factor of ≈ 3 .

In summary, we have carried out a nonlinear optical investigation of the $\text{Bi}_{1-x}\text{Sb}_x$ alloy system, using nondegenerate four-wave mixing at CO_2 laser wavelengths. Due to favorable band structure and material parameters, the third-order nonlinear susceptibility at 300 K is quite high ($\chi^{(3)} \approx 3.5 \times 10^{-4}$ at 10^5 W/cm^2), although it shows a partial saturation. The data are interpreted in terms of modulation of the dielectric constant due to thermally-generated electrons and holes induced by optical heating of the free carrier plasma. Due to constructive interference of the optical fields within the as-grown films, we observe enhancement of the nonlinear optical response by an order of magnitude.

Work at NRL was supported by SDIO/IST and the Office of Naval Research.

Appendix

It is convenient to reduce the etalon enhancement problem to a two step process: we calculate a base $\chi^{(3)}$ by assuming that the reflected light plays no role in nonlinear optical generation, and then calculate a correction factor to account for etalon effects on P_4 . The correction factor itself consists of several parts: corrections for the electric field strength of each of the pump beams, and a correction for the non-linear signal that is generated.

The correction factor for each pump beam can be found by summing the infinite series of electric field contributions by each pass of the beam. For the etalon correction to the internal optical intensity one obtains [12]:

$$F(k) = \left[\frac{1}{1 - r_1(k)r_2(k) e^{2ikL}} \right]^2, \quad (1)$$

where $k = (2\pi n/\lambda)$ is the complex wavevector, and L is the film thickness, the reflection coefficients for the electric field are given by

$$r_i(k) = \frac{n_i(k) - n_{i+1}(k)}{n_i(k) + n_{i+1}(k)}.$$

Here n_i is the complex, frequency-dependent index of refraction in medium i , and the r_i are also complex, since at an interface with an absorbing medium there is a phase shift in the reflected light.

The correction factor for the four-wave beam at frequency $\omega_3 = 2\omega_1 - \omega_2$ can be found by decomposing the nonlinear field into two components, a beam traveling from left to right (E_{3r}), and a beam traveling from right to left ($E_{3r'}$). We take the incident pump beams to be traveling from left to right. The equations that these field intensities must obey are as follows:

$$E_{3r}(\mathbf{r}, L) = E_{3r}(\mathbf{r}, 0) e^{ik_3 L} + K E_{1r}^2(\mathbf{r}, 0) E_{2r}^*(\mathbf{r}, 0), \quad (2)$$

$$E_{3r'}(\mathbf{r}, 0) = E_{3r'}(\mathbf{r}, L) e^{ik_3 L} + K E_{1r'}^2(\mathbf{r}, L) E_{2r'}^*(\mathbf{r}, L), \quad (3)$$

$$E_{3r}(\mathbf{r}, L) = r_2(k_3) E_{3r}(\mathbf{r}, L), \quad (4)$$

$$E_{3r'}(\mathbf{r}, 0) = r_1(k_3) E_{3r'}(\mathbf{r}, 0), \quad (5)$$

where K is the nonlinear optical gain (including absorption losses) in a single pass. The pump beams must satisfy the relation:

$$E_{1r}^2(\mathbf{r}, L) E_{2r}^*(\mathbf{r}, L) = E_{1r}^2(\mathbf{r}, 0) E_{2r}^*(\mathbf{r}, 0) r_2^2(k_1) r_2^*(k_2) e^{i(2k_1 - k_2^*)L}, \quad (6)$$

since they must pass through the sample once and be reflected before there is a leftward beam. We can solve eqs. (2)–(6) for the electric field of the nonlinear beam just before it exits the sample:

$$E_3(\mathbf{r}, L) = K E_1^2(\mathbf{r}, 0) E_2^*(\mathbf{r}, 0) \times \left\{ \left[1 + r_1(k_3) r_2^2(k_1) r_2^*(k_2) \times e^{iL(2k_1 - k_2^* + k_3)} \right] \times \left[1 - r_1(k_3) r_2(k_3) e^{2ik_3 L} \right]^{-1} \right\}. \quad (7)$$

The term in brackets is the etalon correction for the nonlinear beam, which reduces to unity in the absence of multiple internal reflections ($r_1 r_2 \rightarrow 0$).

The net etalon correction for the nonlinear intensity P_4 is thus given by:

$$C_4 = F^2(k_1) F(k_2) \times \left\{ \left[1 + r_1(k_3) r_2^*(k_1) r_2^*(k_2) \right] \times e^{iL(2k_1 - k_2^* + k_3)} \right\} \times \left[1 - r_1(k_3) r_2(k_3) e^{2ik_3L} \right]^{-1} \}^2. \quad (8)$$

References

- [1] P.A. Wolff, S.Y. Yuen, K.A. Harris, J.W. Cook, Jr. and J.F. Schetzina, *Appl. Phys. Letters* 50 (1987) 1858.
- [2] S.Y. Auyang, P.A. Wolff, K.A. Harris, J.W. Cook, Jr. and J.F. Schetzina, *J. Vacuum Sci. Technol.* A6 (1988) 2693.
- [3] E.R. Youngdale, C.A. Hoffman, J.R. Meyer, F.J. Bartoli, X. Chu, J.P. Faurie, J.W. Han, J.W. Cook, Jr. and J.F. Schetzina, *J. Vacuum Sci. Technol.* A7 (1989) 365.
- [4] E.R. Youngdale, C.A. Hoffman, J.R. Meyer, F.J. Bartoli, J.W. Han, J.W. Cook, Jr., J.F. Schetzina, N.A. Engelhardt, E.W. Niles and H. Hochst, *J. Vacuum Sci. Technol.* A8 (1990) 1215.
- [5] E.R. Youngdale, C.A. Hoffman, J.R. Meyer, F.J. Bartoli, N.A. Engelhardt and H. Hochst, *Semicond. Sci. Technol.* 5 (1990) S253.
- [6] E.R. Youngdale, J.R. Meyer, C.A. Hoffman, F.J. Bartoli, D.L. Partin, C.M. Thrush and J.P. Heremans, *Appl. Phys. Letters* 57 (1990) 336.
- [7] D.T. Morelli, D.L. Partin and J.P. Heremans, *Semicond. Sci. Technol.* 5 (1990) S257.
- [8] S. Takaoka and K. Murase, *J. Phys. Soc. Japan* 54 (1985) 2250.
- [9] V.D. Kulakovskii and V.D. Egorov, *Fiz. Tverd. Tela* 15 (1973) 2053 [*Soviet Phys.-Solid State* 15 (1974) 1368].
- [10] E. Gerlach, P. Grosse, M. Rautenberg and W. Senske, *Phys. Status Solidi (b)* 75 (1976) 553.
- [11] The laser difference frequencies were $\Delta\omega \approx 1.81 \text{ cm}^{-1}$ for 942 and 1048 cm^{-1} , and $\Delta\omega \approx 2.59 \text{ cm}^{-1}$ for 974 and 1075 cm^{-1} . Since $\chi^{(3)}$ has a $1/\Delta\omega$ dependence (see fig. 2), the four-wave powers in fig. 3 are scaled by $(\Delta\omega/1.81)^2$ in order to make the data at different wavelengths directly comparable.
- [12] M. Born and E. Wolf, *Principles of Optics*, 2nd ed. (MacMillan, New York, 1964) section 7.6.

New development on the control of homoepitaxial and heteroepitaxial growth of CdTe and HgCdTe by MBE

J.P. Faurie, R. Sporken, S. Sivananthan and M.D. Lange

Microphysics Laboratory, Physics Department, University of Illinois at Chicago, Chicago, Illinois 60680, USA

It is reported that rotation twins as well as reflection twins are easily formed in CdTe and HgCdTe grown by MBE in the (111) orientation. Twinning can be avoided by carefully controlling the substrate preparation and by applying very stringent growth conditions, mostly for the stability of Hg pressure and the real surface temperature of the substrate, which is extremely difficult to control when the substrate rotates. A comparison between HgCdTe twinned layers and twin-free layers has shown that electrically active acceptors and high hole mobility are associated with the presence of reflection twins and/or mercury-rich alloy zones due to Hg overpressure during the growth. Twin-free HgCdTe layers can exhibit etch pit density count two orders of magnitude lower than twinned layers. Twin-free CdTe layers have been grown on GaAs and Si substrates. Excellent thickness uniformities have been reported: 0.24% for the standard deviation of a 2-inch diameter CdTe layer grown on GaAs(100) and 2.3% for a 5-inch diameter CdTe grown on Si(100).

1. Introduction

HgCdTe has been the object of extensive research effort during the last twenty years. HgCdTe was originally investigated because of its tunable direct energy bandgap, a strong absorption coefficient at the bandgap energy, and a reasonable dielectric constant even in the narrow bandgap range. Therefore, HgCdTe has been considered to be the best material for infrared (IR) detection until recently when the concept of IR photodetection by intersubband absorption in superlattices, first proposed by Smith et al. [1], has become the subject of intensive work using the GaAs/AlGaAs system [2].

A recent paper [3] has compared the ultimate performances of HgCdTe and GaAs/AlGaAs superlattice (SL) systems in terms of their potential application in infrared systems. In this paper it is reported that the limiting performance of the GaAs/AlGaAs SLs is found to be orders of magnitude below that of HgCdTe for any specific cutoff wavelength and operating temperature. This paper has triggered a comment [4] and a response to the comment [5] from which it appears that although the fundamental limits for the two

materials are not really questionable, the shortcomings of HgCdTe might represent a severe limitation for the fabrication of large focal plane arrays (FPAs). Nevertheless, although the picture is not as dark as it looks in the comment [4], and while impressive progress has been made these last ten years, there are still material shortcomings to be solved before high yield (low cost) large FPAs or large scale consumer opto-electronic device applications can be envisioned industrially for HgCdTe. It is fair to say that the GaAs/AlGaAs SL has a number of drawbacks of its own.

One of the problems with the HgCdTe alloy is its sensitivity to elevated temperature. Molecular beam epitaxy (MBE), which has been used to grow HgCdTe for almost ten years now, is the lowest temperature growth technique for this alloy. The low temperature of the growth, in addition, limits the interdiffusion process which allows better control of doping and compositional profile, making MBE the best technique to achieve bandgap engineering.

Another major problem encountered in the growth of CdTe and HgCdTe when a vapor phase technique such as MBE is utilized is the formation of twins. It is well known that twinning is com-

monly observed in crystals exhibiting the zincblende (ZnS) structure. The (111) orientation is particularly vulnerable to twin formation but other orientations such as (211) or (311) are also sensitive to twinning; and hillock formation, observed during the growth in the (100) orientation, is also twin-related [6-9].

It has been reported by different laboratories involved in the fabrication of IR photodiodes and metal-insulator-semiconductor (MIS) diodes that the presence of twins or hillocks is highly deleterious for photodiode performance, although no electrical activity associated with these defects has been previously found.

In recent years, the growth of HgCdTe by MBE has made impressive progress towards a solution to the problems arising from structural, electrical and optical properties. Infrared photodiodes with excellent performance are currently fabricated on MBE grown layers [10,11]. In addition, MBE offers a unique potential in terms of heterostructures such as homojunctions [12], heterojunctions, laser heterostructures [13,14], tunneling structures [15-17], and MIS heterostructures [18] which are extremely important for future technology.

MBE has now reached a stage where it is planned to be used for the production of electronic devices in competition with other techniques such as liquid phase epitaxy (LPE) or metalorganic chemical vapor deposition (MOCVD). Three fields of interest are currently actively pursued in order to bring the technique to the level of electronic-device manufacturing:

- (1) understanding and control of intrinsic and extrinsic doping;
- (2) growth of high quality epilayer on large foreign substrates such as GaAs and Si;
- (3) improvement of existing photodetector performances through new device concepts such as heterojunctions or quantum devices.

It is clear from our recent investigations that intrinsic doping in HgCdTe is mostly controlled by extended defects such as dislocations, twin boundaries, antiphase boundaries and clusters, for example, and point defects such as Hg vacancies, Te in antisites, and atoms in interstitial site. It appears also that the formation of these defects is crystallographic orientation dependent. The con-

trol of the extrinsic doping strongly depends on the control of the intrinsic doping since the doping levels for both dopings are not extremely different.

The purpose of this paper is to give an updated overview of the current understanding about the formation of twins in the (111)B orientation and their role, if any, in the electrical properties of HgCdTe epilayers grown on CdTe substrates. A brief overview on the important aspects of the heteroepitaxy of CdTe on GaAs and Si substrates will also be presented. Needless to say, the quality of the HgCdTe epilayer strongly depends on the crystalline quality of the alternate substrate, i.e. CdTe/GaAs or CdTe/Si.

2. Twin formation

While the presence of microstructural defects in MBE layers has been established for several years, information regarding their elimination has been scarce because such elimination is not a trivial problem. Only a few groups have reported some success in the elimination of twins in the (111) orientation [19-21]. Harris et al. [21] using photo-assisted MBE on a non-rotating substrate under very demanding parameter control have obtained a twin-free material yield of less than 20%. A clear improvement in structural properties is shown when twins are avoided but no information is given about change in electrical properties.

Therefore, since growing in the (111)B direction is so difficult, why not use another orientation? The (111)B orientation, despite its propensity to form twins is a very important orientation because the mercury consumption is lower than for the (100) orientation surfaces. Interfaces are usually very smooth in the (111)B plane, CdTe and CdZnTe substrates are obtained in high yield in this orientation and it is so far the most favorable orientation for growth on GaAs(100) and Si(100) substrates.

Although this problem seems less dramatic or at least can be more easily solved, in other directions such as (211)B, (311)B and (100), the progress achieved towards the control of twinning in the (111) should be beneficial for the other orientations. In the (100) orientation the formation of

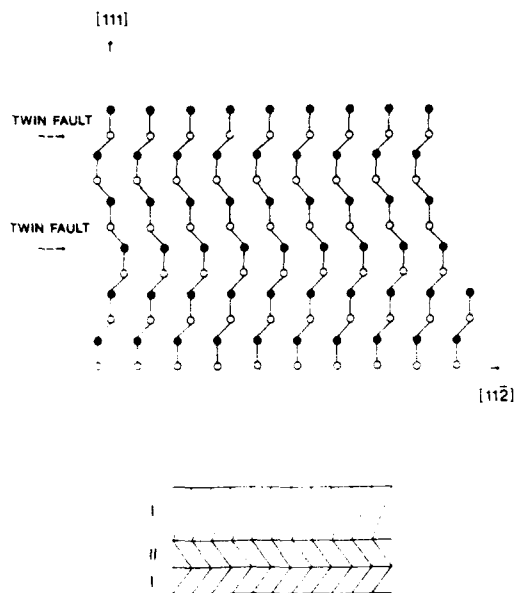


Fig. 1. Lamellar or stacking fault twin formed by a 180° rotation about the $[111]$ direction.

facets and hillocks is a major problem for focal plane arrays and MIS structures; also hillocks are twin-related defects [21].

Therefore the identification and control of twin formation is probably the most difficult and most important problem in the MBE growth of HgCdTe. The presence of twins in CdTe and HgCdTe epilayers can be revealed by detailed investigations involving electron microscopy, cathodoluminescence, chemical etching, and X-ray diffraction as well as electron channeling pattern (ECP).

In the zinc-blende structure, the twinning illustrated in fig. 1 is very often observed. It is a "rotation" type of twin corresponding to a 180° rotation about the $[111]$ normal direction. The stacking of (111) plane in the fcc structure changes from the abc type I configuration to acb type II configuration. The two stackings are equivalent, the changes require very low formation energy since the Cd(Hg)-Te bonds are preserved. This change can therefore occur several times during the growth. This kind of twinning is sometimes called lamellar twinning.

During the first step of epitaxial growth, islands can be formed which will grow and coalesce to form the epitaxial film. These islands may be of type I or type II configuration since they are energetically almost equivalent (fig. 2). Therefore, twin boundaries will exist after island coalescence and twin domains will grow in a columnar form. This kind of twinning which is also of a rotation type, is sometimes called double positioning twinning.

These two kinds of rotation twins can coexist in the crystal, but one or both can disappear during the growth. It is difficult to observe rotation twins during MBE growth by electron diffraction because the streaked (2D) patterns of the type I and type II configuration are identical to twin-free streaked patterns; and sometimes roughening of the surface, which allows 3D diffraction, is not large enough. The twinned domains present in the crystal are visible on the surface of the crystal under scanning electron microscopy or cathodoluminescence investigations in the form of close loops as illustrated in fig. 3 for a CdTe layer.

Electron channeling patterns can also help in the discovery of twins. Fig. 4a and 4b show two simulated ECPs of a twin-free and a twinned crystal. The (113) plane family has a 3-fold symmetry revealed in the form of a regular triangle in the twin-free configuration whereas in a twinned configuration a second inverted triangle is revealed. Fig. 4c shows the ECP pattern of a twinned CdTe layer similar to the one illustrated in fig. 4b.

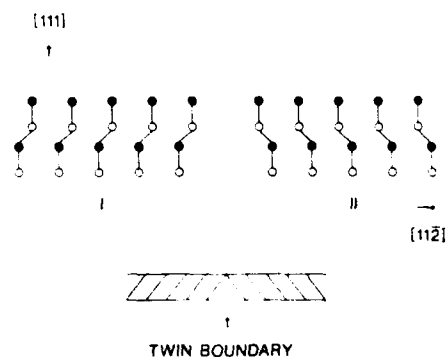


Fig. 2. Double positioning twin formed by a 180° rotation about the $[111]$ direction.

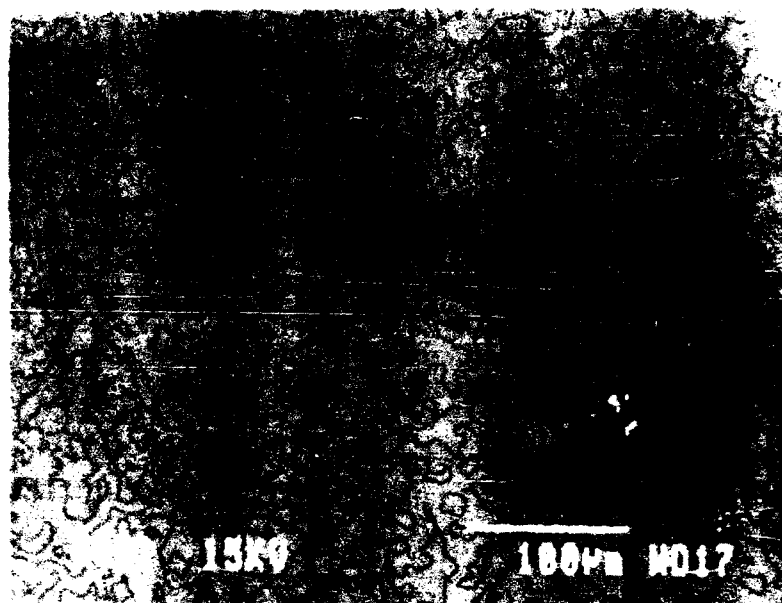


Fig. 3. Cathodoluminescence image of a twinned CdTe(111)B epilayer.

These two kinds of twinning can occur in both CdTe and HgCdTe. In HgCdTe, however, due to the high mercury flux used during the growth, we think that a third kind of twinning illustrated in fig. 5 can occur. This reflection type twin is formed by a mirror reflection with respect to the (111) twin plane. This produces a change in the polarity of the face by creating an anti-phase boundary. As shown in fig. 5, Hg-Hg bonds which usually require high formation energy occur at the plane of the reflection twin when the Hg flux is too high. This twinning does not occur across the entire area of the wafer; therefore, the growing surface exhibits (111)B and (111)A orientation simultaneously. The growth rate of (111)B and (111)A faces being different [22], a surface roughening allowing the observation of extra dots in the RHEED pattern is associated with this kind of twinning.

During the growth of HgCdTe in the (111)B orientation, extra dots due to twinning are observed when the Hg flux is too high for a selected substrate temperature. A decrease in the Hg flux or an increase in the substrate temperature pro-

duces a rapid change in the RHEED pattern, extra dots are disappearing and the spotty pattern is transformed into a streaky one. This is as expected, since a (111)A face is a Hg terminated unstable face requiring a high Hg flux. A new antiphase boundary with Te-Te bond is created reverting the (111)A to a (111)B face.

Fig. 6 is a TEM picture of a HgCdTe (111)B layer grown on a CdTe(111)B/GaAs(100) substrate. It can be seen that the CdTe layer grown on GaAs is full of lamellar twins. At the initiation of HgCdTe growth twins were visible on the RHEED pattern. The growth conditions were kept the same for a while and then the substrate temperature was increased by 5°C. Almost instantaneously the RHEED changed to a twin-free related electron diffraction pattern. The TEM micrograph confirms our in situ observation since a twin is visible in the HgCdTe layer and the position where the twin has disappeared corresponds very precisely to the change in the substrate temperature and the RHEED pattern. High resolution transmission electron microscopy (HRTEM) has not been able to confirm yet the "reflection"

nature of the twin since it is extremely difficult to reveal fine details of atomic structure. However, it is highly probable that this kind of twinning occurs when the Hg flux is too high.

2.1. CdTe (111)B twin-free epilayers

Surface cleaning and growth parameters have been thoroughly investigated in order to prevent twinning. Concerning CdTe, "reflection" type

twinning is very unlikely to occur when using a single effusion source which delivers a highly constant Cd/Te flux ratio. Therefore, in the case of CdTe, only the formation of the two kinds of "rotation" type twins has to be prevented. Double positioning twinning which starts at the substrate epilayer interface seems to be substrate surface preparation related. Regarding lamellar twins, which form during the growth, we have not yet precisely identified which parameter is triggering

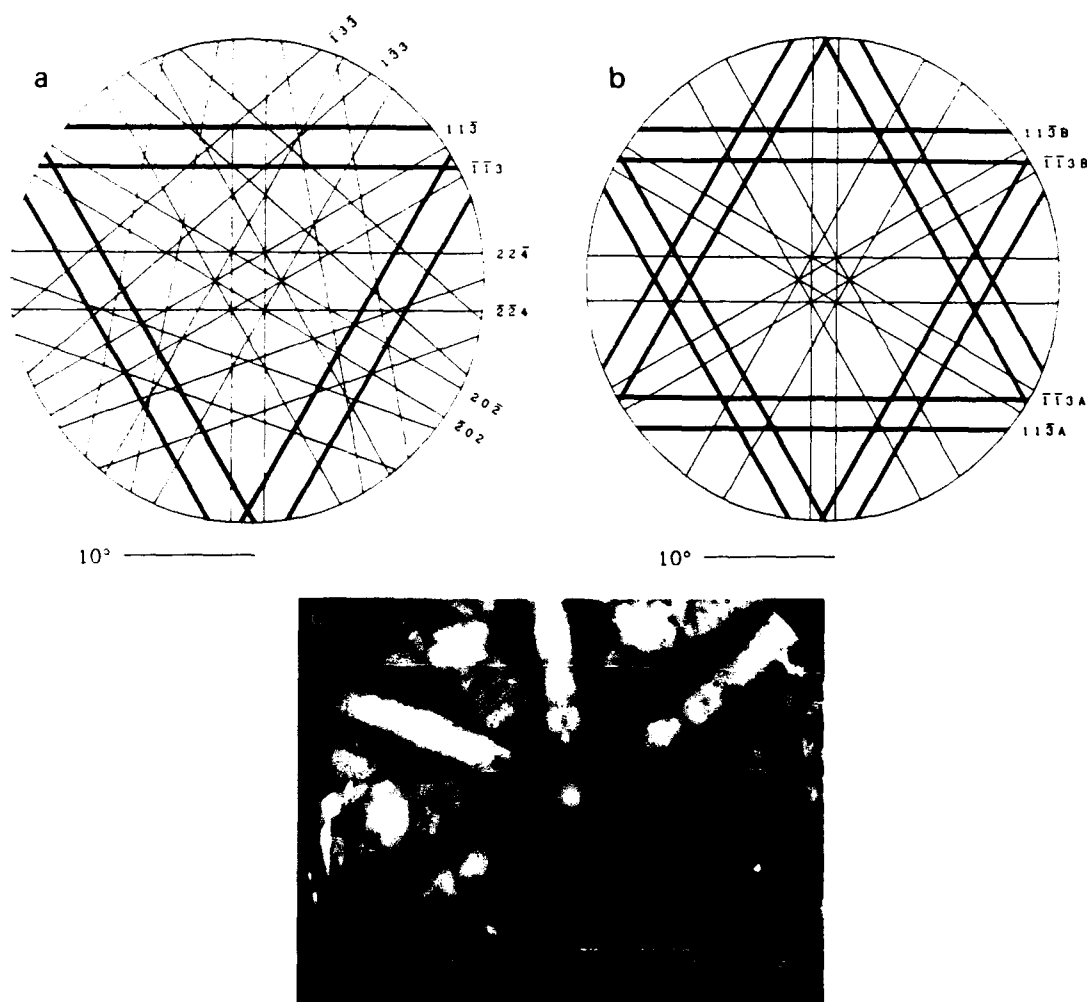


Fig. 4. Electron channeling pattern simulation of a CdTe crystal along the (111) axis: (a) twin-free crystal, 15.0 kV, fcc lattice, $a = 6.481 \text{ \AA}$; (b) twinned crystal, 25.0 kV, fcc lattice, $a = 6.481 \text{ \AA}$. (c) ECP pattern of a twinned CdTe crystal.

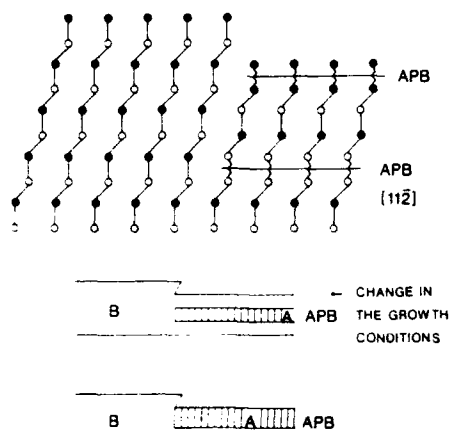


Fig. 5. Reflection twin formed by a mirror reflection with respect to the (111) plane.

their formation. Concerning CdTe (111)B homoepitaxial growth, it has been found that twinning does not occur when the growth temperature is around 335°C, nor does it occur if the CdTe substrate is cleaned at 335°C before growth at 250°C. The heteroepitaxial growth of CdTe (111)B on GaAs and Si substrates is also subject to twinning. The twinning in CdTe(111)B/GaAs(100) heteroepitaxy has been the object of investigations during the last few years. It has been found that twinning can be avoided by using GaAs substrates tilted 2° off (100) towards [110] [23–26]. CdTe(111)B grown on Si(100) is also subject to twinning. More details about CdTe growth on GaAs and Si substrates will be given later.

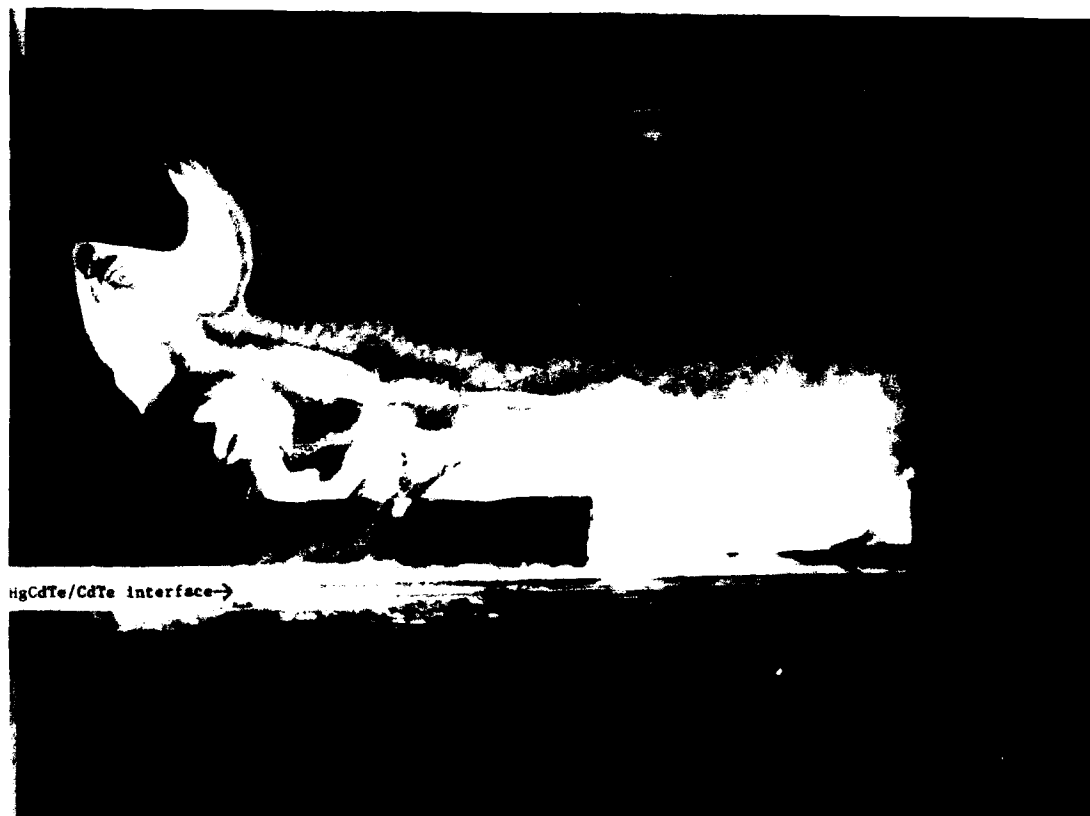


Fig. 6. Transmission electron microscopy of a HgCdTe(111)B/GaAs(100) substrate. Only CdTe epilayer exhibiting numerous lamellar twins and HgCdTe epilayer are visible.

2.2. HgCdTe (111)B twin-free layers

The growth of twin-free (111)B HgCdTe represents a real challenge. In addition to rotation type twins, reflection type twins have been observed. First of all the substrate or the buffer layer should be twin-free. Therefore great care must be taken during substrate preparation and buffer layer growth as discussed before. The same precautions must be observed during the first steps of the HgCdTe growth in order to prevent double positioning twin formation. During the growth we have seen that an increase in the Hg flux or a decrease in the substrate temperature can trigger the formation of an antiphase boundary.

The control of the Hg flux is achieved through the use of a constant level Hg cell. During the growth and from run-to-run the Hg flux monitored by an ion gauge is kept within less than 5% fluctuation. The control of the substrate temperature T_s is the most difficult task because what has to be controlled is, in fact, the temperature of the substrate surface T_{ss} . We have verified that the temperature indicated by the thermocouple located in the back of the substrate which rotates (1) does not give an accurate reading of the substrate temperature and (2) does not account quickly for surface temperature changes.

The use of an IR pyrometer does not represent an ideal solution either. When T_{ss} is kept constant at 190°C, by using a front thermocouple, at the

initiation of HgCdTe growth a jump of approximately 25°C (in our MBE configuration) occurs in the pyrometer reading T_p due to scattered IR radiation primarily from the hot CdTe cell as illustrated in fig. 7. Immediately T_p falls steeply due to both the rapid decrease in reflectance of the block and the fall toward the first minimum in the interference pattern related to the presence of a thin HgCdTe layer. Once the first minimum is reached, T_p rises toward the next maximum. Several more oscillations of decreasing amplitude follow. After about 1.5 μm of growth, the oscillations are almost completely gone. At this point T_p is approximately 15°C higher than the reading before growth. This increase is primarily due to increased emittance since the cutoff wavelength of the HgCdTe is longer than the 2.0 to 2.6 μm sensitivity region of the pyrometer.

During this time the back thermocouple T_B reading has increased by 15–20°C. In other words, if T_B is kept constant, T_{ss} will decrease. In this case, a constant Hg flux will become too high, since the Hg sticking coefficient changes drastically with temperature, and reflection twins visible in the RHEED pattern will be formed. From these experiments it appears that the control of the substrate surface temperature T_{ss} which is a key parameter and should be kept constant within 1°C is an extremely difficult task. The Microphysics Laboratory has devoted much time in order to achieve the best control of T_{ss} .

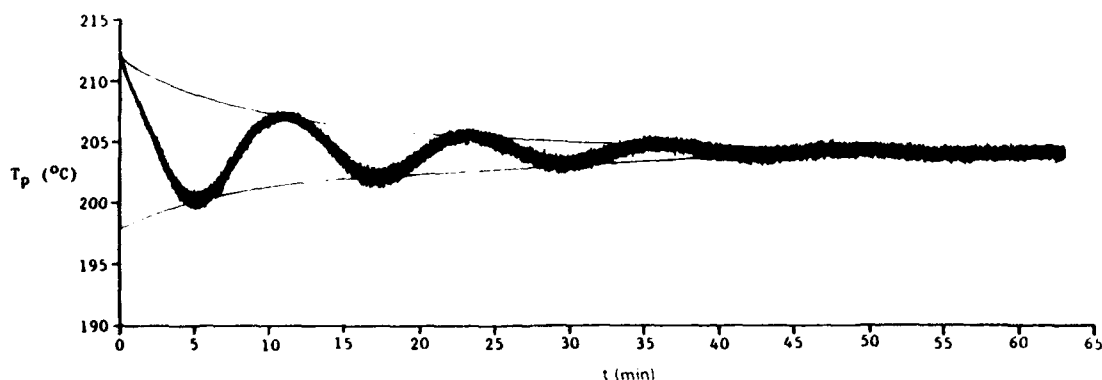


Fig. 7. Plot of the temperature pyrometer reading T_p versus t for $\text{Hg}_{1-x}\text{Cd}_x\text{Te}$ ($x \approx 0.26$) grown on CdTe (111)B. During the experiment the surface temperature of the substrate T_{ss} is kept constant at 190°C.



Fig. 8. Electron channeling pattern along the (111) axis of a twin-free HgCdTe (111)B layer grown on CdZnTe (111)B substrate.

Since a front thermocouple cannot be left in place during conventional growth using rotation, a double control involving a back thermocouple and an IR pyrometer along with the knowledge based on tedious experiments identical to the one described before, is currently utilized in the Microphysics Laboratory. It is very important to point out that since these observations are certainly valid for MBE growth of HgCdTe carried out in any MBE machine and using a substrate mounted with gallium on a molybdenum block, the magnitude of relative changes between T_B , T_P and T_{SS} will depend strongly on the substrate heater technology and effusion cell geometry. These investigations have resulted in better control of the surface preparation, of the stability and reproducibility of all the fluxes, and of the substrate surface temperature. This improvement has been confirmed by the growth of twin-free HgCdTe (111)B illustrated in the ECP of fig. 8 and excellent results for epilayers grown in (211)B orientation presented in section 4.

3. HgCdTe (111)B – comparison between twinned and twin-free layers

Hg_{1-x}Cd_xTe twinned layers grown by the Microphysics Laboratory in the (111)B orientation usually exhibit a p-type character with hole mobil-

ity approaching or even exceeding $10^3 \text{ cm}^2 \text{ V}^{-1} \text{ s}^{-1}$ [27] and excess carrier lifetime in the range of $(20-100) \times 10^{-9} \text{ s}$ [28]. An excellent electrical mobility is often considered to be associated with excellent crystal quality. It turns out that this is not precisely the case here.

All the layers exhibiting $10^3 \text{ cm}^2 \text{ V}^{-1} \text{ s}^{-1}$ have been investigated using X-ray diffraction. X-ray rocking curves recorded for (422) reflections have shown for every layer 6 peaks when rotating the sample about the $\langle 111 \rangle$ axis, whereas only three peaks should be observed in a twin-free epilayer. These findings were confirmed by ECP experiments. The first thought was that the presence of twins does not degrade the hole mobility. In order to confirm this, two HgCdTe epilayers ($x = 0.25$) have been grown under the same growth conditions, except that the Hg flux was increased several times for several minutes during the growth of layer A, whereas for layer B the twin-free growth conditions have been applied. X-ray diffraction confirmed that layer B is twin-free and layer A is twinned. Both layers have a p-type character; however, layer A exhibits a hole mobility of $900 \text{ cm}^2 \text{ V}^{-1} \text{ s}^{-1}$, whereas layer B has only a hole mobility of $300 \text{ cm}^2 \text{ V}^{-1} \text{ s}^{-1}$ at 23 K. All the twin-free p-type layers grown so far have a hole mobility not exceeding $500 \text{ cm}^2 \text{ V}^{-1} \text{ s}^{-1}$.

In addition, the carrier concentration $N_A - N_D$ for p-type twinned layers has been consistently found to be in the $(1-5) \times 10^{16} \text{ cm}^{-3}$ range and from Hall data curve fitting N_A has been calculated to be in the $(5-8) \times 10^{16} \text{ cm}^{-3}$ range, as reported before [29]. For p-type twin-free layers, the carrier concentration is much lower: $N_A - N_D$ is in the low 10^{15} cm^{-3} range. The decrease in $N_A - N_D$ is so drastic for twin-free layers that many of them are n-type. Anyway the lower hole mobility in twin-free layers cannot be explained by an increase in scattering due to a larger acceptor concentration since it is the opposite. Therefore, it is concluded that electrically active acceptors and high hole mobility are related to a high Hg flux during growth, which has triggered the formation of reflection twins along with Hg-rich alloy zones in the crystal.

Hg_{1-x}Cd_xTe grown at 200°C under Te-rich conditions (such as MBE) but under thermal equi-

Table 1

Main differences between (111)B twinned and twin-free layers grown by MBE

	Conduction type	$N_A - N_D$ (p-type layers) (cm^{-3})	Hole mobility ($\text{cm}^2 \text{V}^{-1} \text{s}^{-1}$)	EPD (cm^{-2})	Residual doping level after isothermal annealing (cm^{-3})
Twinned layer	p-Type	$(2-5) \times 10^{16}$	800-1600	10^6-10^7	$5 \times 10^{15}-2 \times 10^{16}$ (n-type)
Twin-free layer	p-Type or n-type	$(1-2) \times 10^{15}$	300-500	10^4-10^5	$5 \times 10^{15}-2 \times 10^{16}$ (n-type)

librium conditions (unlike MBE) should produce an intrinsic hole concentration due to Hg vacancies close to $1 \times 10^{16} \text{ cm}^{-3}$ [30,31]. It appears that in the (111)B orientation MBE grown twinned layers have p-type doping levels exceeding that expected from growth under thermodynamic equilibrium at the same temperature. In addition, the fact that fast low temperature isothermal (mercury-rich) anneals make the (111)B materials even more p-type leads us to believe that extended defects are mostly responsible for the electronic activity in the as-grown material. The increase in the acceptor level could be explained by the presence of numerous (111)A planes in the twin boundaries and antiphase boundaries. As reported before [22] a (111)A plane which is Hg terminated is very unstable and thus should have a Hg-vacancy density higher than the one thermodynamically calculated for a bulk crystal. The existence of Hg-rich alloy zones might also explain a higher Hg vacancy concentration.

Concerning the high hole mobility no clear explanation has yet been found. However, the excess of mercury induces the formation of Hg antiphase boundaries, as well as Hg-rich alloy zones. Therefore, numerous type III (semimetal-semiconductor) interfaces exist within the crystal. It has been discovered and explained [32,33] that a high hole mobility due to light heavy hole effective mass is associated with Type III interface. However, it is possible that with the presence of Hg-rich antiphase boundaries and therefore the existence of type III (semimetal-semiconductor) interfaces, similarities with the high hole mobility observed in type III HgTe-CdTe superlattices exist [32,33]. Indium diffusion experiments which have been carried out in doped quantum well (111)B structures [34] have shown that several In diffusion coefficients are required to explain the observed

secondary ion mass spectrometry data. A fraction of the indium has been found to be fast diffusing through a defect related matrix.

Another important difference related to etch-pit density (EPD) has been found between twinned and twin-free layers in good agreement with ref. [21]. EPD count which is related to dislocation density, is determined using a defect chemical etching solution suitable for the investigated crystallographic orientation. One can see in table 1 that by eliminating twins, EPD can drop tremendously, indicating a drastic improvement in the crystal quality unexpectedly associated with a decrease in the hole mobility measured by Hall in p-type layers.

Very long isothermal annealings have been performed on twinned and twin-free (111)B HgCdTe layers and very similar residual doping levels have been found. The materials are n-type with a background levels in the 5×10^{15} to $2 \times 10^{16} \text{ cm}^{-3}$ range. This background does not seem to be controlled by residual impurities. SIMS analysis indicates that MBE layers are very clean. Although all the complex relationships between growth parameters and intrinsic doping are not fully understood it is currently postulated that the residual donor doping level in MBE grown HgCdTe layers is due to tellurium atoms in antisite positions, i.e. replacing Hg atoms [35].

Table 1 provides a brief summary of the main differences between (111)B twinned and twin-free layers grown by MBE.

4. Growth in (211)B orientation

The progress accomplished in the growth in the (111)B orientation has been used to control in a better way the growth in different orientations.

We have devoted our recent efforts to grow along the $\langle 211 \rangle$ azimuth where the twinning problem does not appear as severe as in the (111)B. The layers grown in the (211)B orientation under the stringent growth control previously discussed exhibit excellent properties. As an example the layer No. 1008 has the following characteristics:

$x = 0.18$;

thickness: $16.2 \mu\text{m}$;

$N_d - N_a$: $1.9 \times 10^{14} \text{ cm}^{-3}$ at 15 K;

electron mobility: $1.1 \times 10^6 \text{ cm}^2 \text{ V}^{-1} \text{ s}^{-1}$ at 15 K;

lifetime: $9 \times 10^{-6} \text{ s}$ at 250 K; $2.2 \times 10^{-6} \text{ s}$ at 77 K.

This result reflects the state-of-the-art of the growth of HgCdTe alloys in the Microphysics Laboratory. These results are at least as good as the best results ever reported for HgCdTe grown by any technique for this composition. Diodes fabricated on twin-free (211)B layers showed improved operational yields [36].

5. Heteroepitaxial growth on GaAs and Si

An increasingly important aspect of molecular beam epitaxy is the heteroepitaxy between dissimilar materials. For the growth of HgCdTe and related compounds, the use of GaAs and Si substrates is particularly attractive. While the growth of CdTe and HgCdTe on GaAs by MBE has been studied for many years [24,37,38], the direct growth of single-crystalline CdTe and HgCdTe on silicon was reported only recently [39].

The advantage of GaAs compared to CdTe or CdZnTe substrates is its low cost, better mechanical strength and surface area. Regarding these characteristics, silicon substrates are even superior to GaAs, and in addition, if good HgCdTe can be grown on silicon, it could eventually become possible to produce large-area monolithic infrared focal-plane arrays, combining HgCdTe infrared detectors with silicon integrated circuits for signal processing.

On any kind of substrate, HgCdTe is usually grown on a CdTe buffer layer. Therefore, it is very important to optimize the growth of CdTe on GaAs and Si. We have characterized MBE-grown

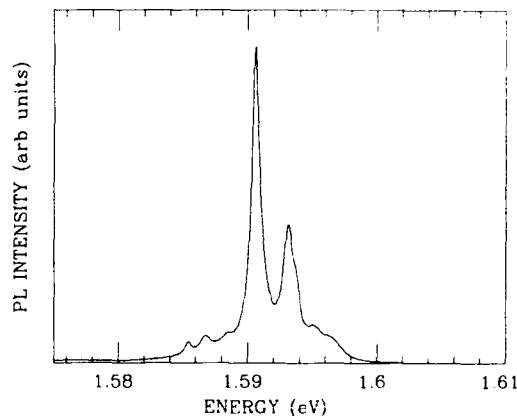


Fig. 9. 10 K photoluminescence spectrum of CdTe on GaAs(100) tilted 2° towards [110], excited with a 50 mW Ar laser at $514.5 \mu\text{m}$ wavelength.

layers of CdTe on GaAs and Si by reflection high-energy electron diffraction, double-crystal X-ray diffraction, photoluminescence (PL) spectroscopy and scanning electron microscopy (SEM).

In MBE, CdTe normally grows in the (111)B orientation on GaAs(100). A full-width at half-maximum (FWHM) of the X-ray double-crystal rocking curves (DCRCs) on the order of 120–140 arc sec is now obtained on a routine basis. Slightly lower values are obtained on misoriented substrates, which have the additional advantage of suppressing twinning in the CdTe layers. These layers yield strong PL spectra at 10 K (fig. 9), with a FWHM of only 0.7 meV of the acceptor bound exciton peak at 1.590 eV attributed to the presence of acceptors such as Cu or Li, Na [40]. This confirms the high structural quality of these layers. Their morphology is excellent, with no features detected by SEM. Finally, for CdTe(111)B on 2-inch diameter GaAs(100) wafers, the standard deviation of the layer thickness is only 0.24%, with a total thickness variation of $\pm 0.5\%$ when the growth is carried out in the new multiwafer RIBER OPUS 45 MBE machine.

CdTe(100) can also be grown on GaAs(100) by MBE, but these layers are usually of inferior quality as compared to CdTe(111)B on GaAs(100). Whether CdTe(100) or (111)B is obtained depends

on the details of the substrate cleaning procedure [38].

Because the problem of twinning is less severe for the (211) orientation as compared to the (111), we recently grew CdTe on GaAs(211)B. Similar to what was found on GaAs(100), we observed two growth orientations, which depended on the cleaning temperature. For cleaning temperatures above 550°C, (211) growth occurred, whereas for cleaning temperatures of about 540°C, (133) growth was obtained. The coincidence axes for CdTe(133)/GaAs(211)B are CdTe<011> || GaAs<011> and CdTe<611> || GaAs<111>. We also found that, whereas the CdTe(133) planes have no tilt with respect to the GaAs(211)B planes, the CdTe(211) planes tilt 3° toward the GaAs[011]

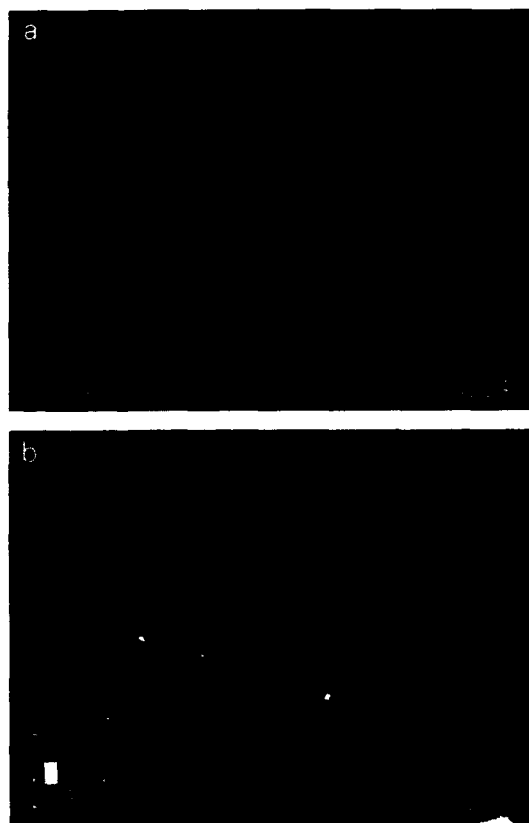


Fig. 10. Scanning electron microscope image of the surface of two CdTe layers grown on Si: (a) 9 μm thick CdTe on Si(100); (b) 4 μm thick CdTe on Si(100) tilted 8° towards [110].

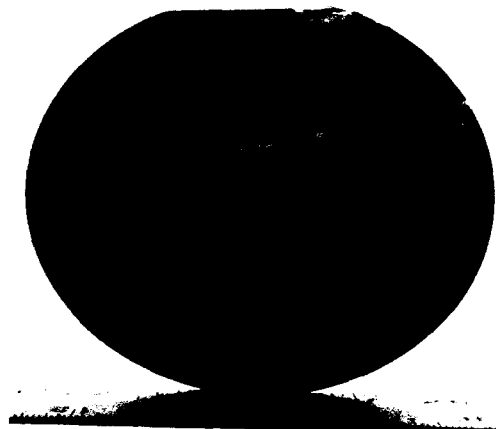


Fig. 11. 6 μm thick CdTe layer on a 5-inch Si(100) substrate.

axis. The X-ray DCRC full-width at half-maximum (Γ) of the CdTe(333) reflections furthermore revealed that the crystalline quality of the CdTe(133) growth is better than that of the CdTe(211) growth, as might be expected since the mismatch in the surface nets is only 2.0% along the CdTe<611> || GaAs<111> coincidence axis, as opposed to 14.6% mismatch in the bulk lattices. For the CdTe(133), $\bar{\Gamma} = 134$ arc sec, while for the (211), $\bar{\Gamma} = 160$ arc sec. These results are not far from our best results on GaAs tilted 2° off (100) toward [110].

CdTe grows in the (111)B orientation on Si(100) [39]. Two epitaxial relationships are possible between the two materials, corresponding to the $\bar{2}11$ CdTe axis parallel to either the $0\bar{1}1$ or the 011 Si axis. This introduces two domains oriented 90° apart in the epilayers. If the substrates are tilted towards <011>, the 011 and $0\bar{1}1$ directions are no longer equivalent, and single-domain films are grown. These situations result in very different surface morphologies. This is illustrated in fig. 10, showing the SEM images of CdTe grown on Si(100) and on Si(100) tilted 8° towards 011 . As expected, the single-domain films have better surface morphology. Furthermore, twin-free layers of CdTe(111)B can be grown on Si(100) tilted 8° towards 011 , whereas the layers on Si(100) are highly twinned. This is deduced from

electron channeling patterns as well as from transmission electron microscopy [41].

PL spectra measured at 12 K confirm the superior quality of the layers grown on tilted substrates. The FWHM of the 1.593 eV bound-exciton peak is 3 meV for CdTe on Si(100) 8° off towards [011] and 4 meV for CdTe on nominal Si(100). Also, under low excitation, the intensity ratio between the bound exciton peak and the defect bands is much higher for CdTe on tilted silicon substrates. Because CdTe can be grown on Si(100), it is now possible to produce very large monocrystalline layers of CdTe by MBE.

Recently, a 6 μm thick 5-inch diameter layer of CdTe was grown on Si(100) by MBE [42]. This is the largest single crystal of a II-VI semiconductor ever produced by any technique. This film is very shiny and mirror-like over its entire surface, as illustrated by fig. 11. The thickness of this layer is very uniform with a standard deviation of only 2.3% and a total thickness variation of $\pm 3.3\%$. Furthermore, it is interesting to note that this layer has the narrowest DCRC measured so far for CdTe on silicon, with an average FWHM of 514 arc sec versus 570 arc sec for the best of our 2-inch samples. The structural uniformity is also excellent; the standard deviation of the FWHM of the DCRCs is only 17 arc sec for the 5-inch diameter layer.

6. Conclusion

Rotation twins are easily formed in CdTe(111) and HgCdTe(111) epilayers. In addition, reflection twins which are related to a change in the Hg pressure and/or the substrate surface temperature can be formed during the growth of HgCdTe.

A careful substrate preparation with a proper thermal cleaning can prevent the formation of double positioning twins. To avoid the formation of reflection twins, stringent control in the stability of Hg ($\pm 2.5\%$), Te and CdTe fluxes, growth rate and surface substrate temperature ($\pm 0.5\%$) is required, which is very difficult when the substrate is rotating. Such control has been achieved in the Microphysics Laboratory and twin-free CdTe and HgCdTe(111)B layers have been grown.

A comparison between HgCdTe twinned layers and twin-free layers shows that electrically active acceptors along with high hole mobility arise from a mercury overpressure during HgCdTe growth. Etch pit densities as low as $8 \times 10^4 \text{ cm}^{-2}$ have been counted on twin-free HgCdTe layers which are two orders of magnitude lower than EPDs of twinned layers. From annealing experiments it has been found that a residual donor doping level in the range between 5×10^{15} and $2 \times 10^{16} \text{ cm}^{-3}$ has been measured in both twinned and twin-free HgCdTe epilayers. It is currently thought that this residual doping is due to antisite Te atoms.

CdTe and HgCdTe have been grown for several years now on GaAs(100) substrates but much more recently on Si(100) substrates. The quality of CdTe grown on GaAs has been improved as confirmed by a FWHM of the acceptor bound exciton peak at 1.59 eV of only 0.7 meV at 10 K. Single domain CdTe twin-free films have been grown on Si(100) tilted 8° towards [011]. Excellent thickness uniformities have been obtained for CdTe. On 2-inch diameter GaAs(100) the standard deviation of the layer thickness is only 0.24% and is 2.3% on 5-inch diameter Si(100).

Acknowledgements

This work has been supported by DARPA/AFOSR contract #F-49620-87-C0021 and also by DARPA/US Army Research Office contract #DAAL03-87K-0092. One of us (R.S.) is a senior research assistant of the Belgian National Fund for Scientific Research. We want also to acknowledge the contributions of G. Monfroy for electron microscopy and X-ray diffraction experiments, of J. Bleuse for electron channeling pattern simulation and interpretation, of P.S. Wijewarnasuriya for annealing experiments and of K. Mahavadi for photoluminescence experiments.

References

- [1] J.S. Smith, L.C. Chiu, S. Margulit, A. Yariv and A.Y. Cho, *J. Vacuum Sci. Technol.* B1 (1983) 376.
- [2] B.F. Levine, C.G. Bethea, G. Hasnain, J. Walker and R.J. Malik, *Appl. Phys. Letters* 53 (1988) 2196.
- [3] M.A. Kinch and Y. Yariv, *Appl. Phys. Letters* 55 (1989) 2093.

- [4] B.F. Levine, Appl. Phys. Letters 56 (1990) 2354.
- [5] M.A. Kinch and Y. Yariv, Appl. Phys. Letters 56 (1990) 2355.
- [6] R.D. Horning and J.L. Staudenman, Appl. Phys. Letters 49 (1986) 1590.
- [7] A. Million, L. Di Giocciio, J.P. Gaillard and K. Piaguet, J. Vacuum Sci. Technol. A6 (1988) 2813.
- [8] R.J. Koestner and H.F. Schaake, J. Vacuum Sci. Technol. A6 (1988) 2834.
- [9] J.M. Arias, S.H. Shin, J.G. Pasko and E.R. Gertner, Appl. Phys. Letters 53 (1988) 39.
- [10] J.M. Arias, S.H. Shin, J.G. Pasko, R.E. DeWames and E. Gertner, J. Appl. Phys. 65 (1989) 1747.
- [11] S.S. Yoo, M. Boukerche, M. De Souza and J.P. Faurie, SPIE Proc. 1106 (1989) 173.
- [12] M. Boukerche, S.S. Yoo, I.K. Sou, M. De Souza and J.P. Faurie, J. Vacuum Sci. Technol. A6 (1988) 2623.
- [13] K.K. Mahavadi, J. Bleuse, S. Sivananthan and J.P. Faurie, Appl. Phys. Letters 56 (1990) 2077.
- [14] N.C. Giles, Z. Yang, J.W. Han, J.W. Cook, Jr. and J.F. Schetzina, J. Vacuum Sci. Technol. A8 (1990) 1206.
- [15] J.N. Schulman and C.L. Anderson, Appl. Phys. Letters 48 (1986) 1684.
- [16] M.A. Reed, R.J. Koestner and M.W. Goodwin, Appl. Phys. Letters 49 (1986) 1293.
- [17] D.H. Chow, T.C. McGill, I.K. Sou, J.P. Faurie, C.W. Nieh, Appl. Phys. Letters 52 (1988) 54.
- [18] M.W. Goodwin, M.A. Kinch and R.J. Koestner, J. Vacuum Sci. Technol. A8 (1990) 1226.
- [19] A. Million, to be published.
- [20] J.P. Faurie, DARPA IR Focal Plane Array Materials and Processing, April 1989, unpublished.
- [21] K.A. Harris, T.H. Myers, R.W. Yanka, L.M. Mohnkern, R.W. Green and N. Otsuka, J. Vacuum Sci. Technol. A8 (1990) 1013.
- [22] S. Sivananthan, X. Chu, J. Reno and J.P. Faurie, J. Appl. Phys. 60 (1986) 1359.
- [23] G. Monfroy, S. Sivananthan, J.P. Faurie and J. Reno, J. Vacuum Sci. Technol. A7 (1989) 326.
- [24] J.L. Reno, P.L. Gourley, G. Monfroy and J.P. Faurie, Appl. Phys. Letters 53 (1988) 1747.
- [25] J. Cibert, Y. Gobil, K. Saminadaya, S. Tatarenko, A. Chami, G. Feuillet, Le Si Dang and E. Ligeon, Appl. Phys. Letters 54 (1989) 828.
- [26] J.L. Reno, M.J. Carr and P.L. Gourley, J. Vacuum Sci. Technol. A8 (1990) 1006.
- [27] S. Sivananthan, M.D. Lange, G. Monfroy and J.P. Faurie, J. Vacuum Sci. Technol. B6 (1988) 788.
- [28] M.E. de Souza, M. Boukerche and J.P. Faurie, J. Appl. Phys. 68 (1990) 5195.
- [29] M. Boukerche, S. Sivananthan, P.S. Wijewarnasuriya, I.K. Sou and J.P. Faurie, J. Vacuum Sci. Technol. A7 (1989) 31.
- [30] G.L. Destéfanis, J. Crystal Growth 86 (1988) 700.
- [31] H.R. Vydyanath and C.H. Hiner, J. Appl. Phys. 65 (1989) 3080.
- [32] J.P. Faurie, M. Boukerche, S. Sivananthan, J. Reno and C. Hsu, Superlattices and Microstructures 1 (1985) 237.
- [33] J.R. Meyer, C.A. Hoffman, F.J. Bartoli, J.W. Han, J.W. Cook, Jr., J.F. Schetzina, X. Chu, J.P. Faurie and J.N. Schulman, Phys. Rev. B38 (1988) 2204.
- [34] I.K. Sou, PhD Thesis, University of Illinois at Chicago (June 1990).
- [35] J.P. Faurie, HgCdTe MBE Workshop DARPA-CNVEO, Washington, 1987, unpublished results.
- [36] S.S. Yoo, M. Boukerche and J.P. Faurie, unpublished results.
- [37] J.P. Faurie, S. Sivananthan, M. Boukerche and J. Reno, J. Appl. Phys. Letters 45 (1984) 1307.
- [38] J.P. Faurie, C. Hsu, S. Sivananthan and X. Chu, Surface Sci. 168 (1986) 473.
- [39] R. Sporken, S. Sivananthan, K.K. Mahavadi, G. Monfroy, M. Boukerche and J.P. Faurie, Appl. Phys. Letters 55 (1989) 1879.
- [40] J.M. Francou, K. Saminadaya, J.L. Pautrat, J.P. Gaillard, A. Million and C. Fontaine, J. Crystal Growth 72 (1985) 220, and references therein.
- [41] J. Petruzello, R. Sporken and J.P. Faurie, unpublished.
- [42] R. Sporken, M.D. Lange, C. Masset and J.P. Faurie, Appl. Phys. Letters 57 (1990) 1449.

Application of the RHEED oscillation technique to the growth of II–VI compounds: CdTe, HgTe and their related alloys

L. Ulmer, N. Magnea, H. Mariette * and P. Gentile

*Service de Physique, Département de Recherche Fondamentale, Centre d'Etudes Nucléaires de Grenoble,
85 X, F-38041 Grenoble Cedex, France*

The RHEED oscillation technique has been used to study the growth mechanism of (001) oriented CdTe, HgTe and $\text{Cd}_{1-x}\text{Hg}_x\text{Te}$ II–VI compounds. For Cd or Hg stabilized surfaces, the two-dimensional layer-by-layer growth provides intense oscillations. They are used to measure the influence of growth parameters (substrate temperature, flux ratio, growth interruption) on growth rate and alloy composition. It appears that the molecular beam epitaxy of these II–VI compounds is strongly affected by the non-unity sticking coefficient of Cd in a very wide temperature range (140–400 °C) and that kinetic effects are important.

1. Introduction

The development of high quality CdTe – $\text{Cd}_{1-x}\text{Hg}_x\text{Te}$ heterostructures for infrared detection or emission systems requires a tight control of layer thicknesses and interface smoothness. The reflection high energy electron diffraction (RHEED) oscillations can provide such information [1].

In this paper we report on the use of this technique for an extensive study of the growth of (001) oriented CdTe, HgTe and $\text{Cd}_{1-x}\text{Hg}_x\text{Te}$ alloys by molecular beam epitaxy.

After a short description of the experimental procedure in section 2, section 3 deals with the sublimation and growth mode measurements of CdTe. We demonstrate the non unity value of the Cd sticking coefficient S_{Cd} and the need to work under Cd-rich conditions. The growth of $\text{Cd}_{1-x}\text{Hg}_x\text{Te}$ is developed in section 4. Intense RHEED oscillations are observed for the whole composition range and show that the growth of Hg compounds also takes place by a 2D layer-by-layer mode. The main result, obtained from a comparison between the RHEED data and chem-

ical measurements of alloy compositions, is that S_{Cd} is strongly affected by the interactions with Hg atoms and that kinetic phenomena are important for the incorporation rate of Cd and Hg.

2. Experimental

The samples are grown in a Riber 32 P system on (001) $\text{Cd}_{0.96}\text{Zn}_{0.04}\text{Te}$ and CdTe wafers. The substrate temperature T_s is measured with a thermocouple in contact with the rear face of the Molyholder. Prior to growth, the substrates are annealed at 340 °C and a thin layer of CdTe is grown to produce a smooth surface. For CdTe growth, a CdTe cell is used in conjunction with a Cd cell to vary the flux ratio $R = \text{Cd}/\text{Te}$. A constant level Hg cell, a CdTe and a Te cell are used to grow $\text{Cd}_{1-x}\text{Hg}_x\text{Te}$ (CMT) layers. The RHEED oscillations are recorded with a 40 kV e[−] gun and standard collection optics (lens, fiber) [2].

3. (001) CdTe growth

The growth and sublimation of CdTe layers are performed between 140 and 420 °C. For a Cd/Te flux ratio $R = 1$, the surface exhibits the (2×1)

* Laboratoire de Spectrométrie Physique, Université J. Fourier, F-38042 Grenoble Cédex, France.

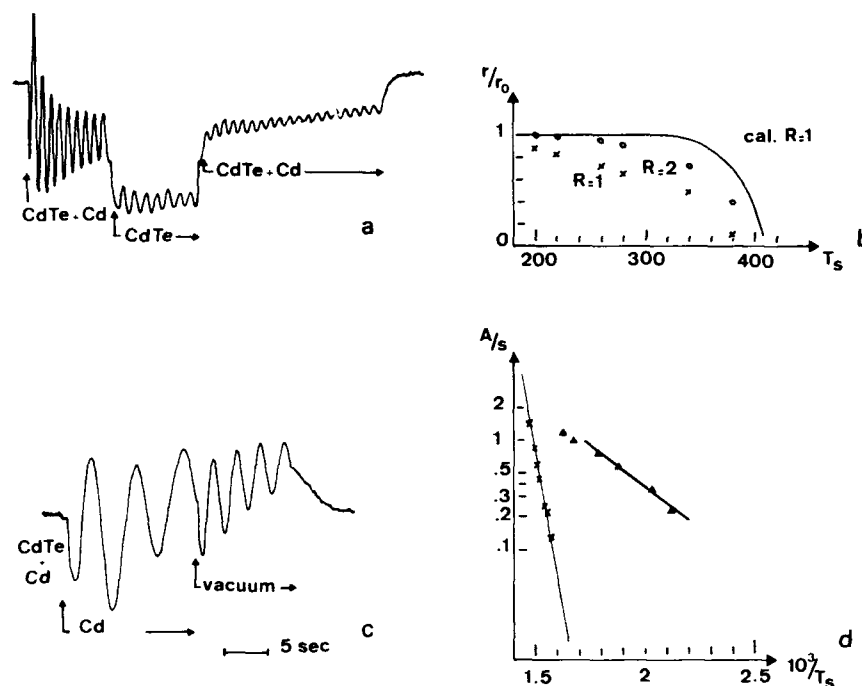


Fig. 1. (a) RHEED oscillations recorded during the growth of CdTe at $T_s = 240^\circ\text{C}$ with and without Cd additional flux. (b) Growth rate versus T_s for $R=1$ (x) and $R=2$ (o). The solid line corresponds to the growth rate variation deduced from an equilibrium thermodynamic calculation for $R=1$. (c) RHEED oscillations recorded during CdTe sublimation under vacuum or with a 3×10^{-7} Cd overpressure at $T_s = 385^\circ\text{C}$. (d) Plot of the desorbing rate during sublimation (x) and growth (Δ). The activation energies are 1.9 eV for sublimation and ~ 0.3 eV during growth for $T_s \leq 260^\circ\text{C}$.

Te-rich reconstruction. With an additional Cd flux ($R \approx 2$), this structure is strongly damped and a faint $c(2 \times 2)$ is observed, which becomes predominant at growth interruption under Cd flux [3]. Fig. 1a shows the RHEED oscillations recorded for a growth temperature of 240°C with and without an additional Cd flux. The growth rate and its dependence on R are then measured directly by opening or closing the Cd cell shutter. This is observed as a function of T_s in fig. 1b. We observe a net enhancement of growth rate when R increases with a saturation below 180°C , where desorption rate becomes negligible. On the same curve we have plotted the growth rate for $R=1$ calculated by assuming that desorption of CdTe is given by the equilibrium vapor pressure of Cd and Te_2 over CdTe. For this calculation the $K_p(T)$ reaction constant has been obtained from the sublimation rate obtained between 350 and 420°C

from RHEED oscillations (figs. 1c and 1d). The strong difference between the calculated and experimental curves for $R=1$ indicates that variation of growth rate with T_s is not due to CdTe sublimation, but to the sticking coefficient of Cd which is less than 1 above 200°C . In addition, if we plot as a function of T_s (fig. 1d (Δ)), the evaporation rate during growth (i.e. the difference between the growth rate r measured at T_s and the growth rate r_0 measured below 180°C where the Cd incorporation is equal to 1), we obtain an activation barrier of 0.3 eV to be compared to 1.9 eV for the sublimation rate (fig. 1d (x)). As a consequence of this low value of S_{Cd} , Te adatoms should also desorb to maintain surface stoichiometry and to provide high quality growth. Above 250°C , excess Te reevaporates easily and it is then possible to grow CdTe with $R=1$, but the high evaporation rate of CdTe induces surface

roughening and macroscopic defects [4]. Additional Cd flux is then needed to have a smooth growth front with high surface mobility in order to get sharp interfaces [2]. Below 220°C, Te desorption rate is lower, so that additional Cd is still necessary to "consume" the Te excess and to provide high quality layers [5].

4. (001) $\text{Cd}_x\text{Hg}_{1-x}\text{Te}$ growth

An example of the RHEED oscillations obtained for CMT growth at $T_s = 180^\circ\text{C}$ is shown in fig. 2. As we use a Te and a CdTe cell, it is possible to observe oscillations for the growth of HgTe (fig. 2a). "CdTe" (meaning CdTe grown under Hg flux) (fig. 2b) and $\text{Cd}_x\text{Hg}_{1-x}\text{Te}$ (fig. 2c). Each oscillation corresponds to the growth of one monolayer for each component and we verify that $r_{\text{CMT}} = r_{\text{HgTe}} + r_{\text{CdTe}}$, where r is the growth rate. During growth and interruptions, the Hg cell is kept open and the surface exhibits the $c(2 \times 2)$ structure. After damping out, the oscillations are recovered by a 30 s growth interruption under Hg

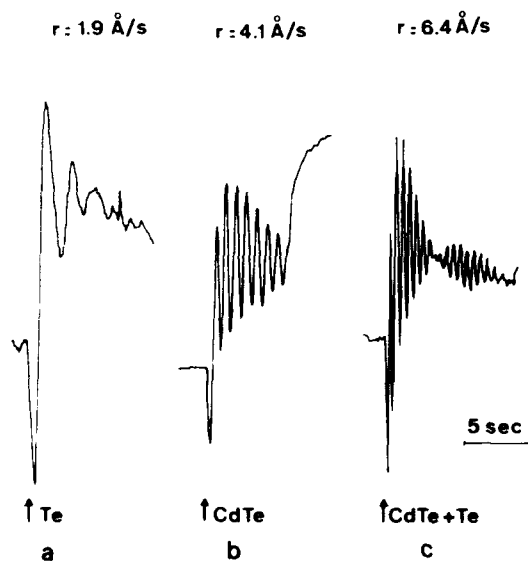


Fig. 2. RHEED oscillations at $T_s = 180^\circ\text{C}$ for (a) HgTe, (b) "CdTe" under Hg flux and (c) $\text{Cd}_{0.45}\text{Hg}_{0.55}\text{Te}$ growth. The Hg cell shutter is kept open during the growth and the interruptions.

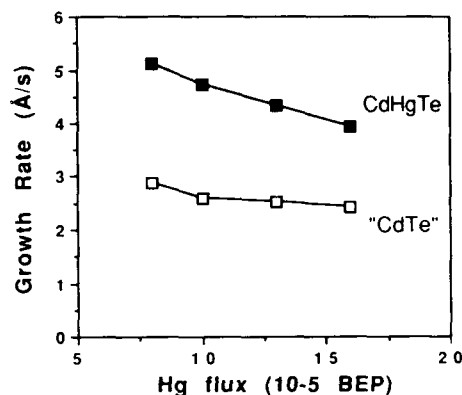


Fig. 3. Variation of $\text{Cd}_{0.45}\text{Hg}_{0.55}\text{Te}$ and "CdTe" growth rate measured by RHEED oscillations versus the Hg beam equivalent pressure (BEP).

flux, indicating appreciable surface mobilities of Te and Cd at such low temperature. The in-situ measurements of growth rate allow us to measure its dependence on the Hg flux. From fig. 3 it is evident that r_{CMT} decreases when the Hg flux increases. This effect results from the reduction of the mean free path of Cd and Te_2 species by collision with Hg atoms whose pressure is typically 10^{-4} Torr [6]. This reduction is totally independent of the substrate temperature (it is also observed at 340°C for CdTe growth with and without the Hg flux), confirming that it does not involve a surface reaction effect.

As shown in fig. 2, the growth rates of HgTe, "CdTe" and CMT can be obtained simultaneously and the alloy composition can be calculated, depending on the Cd incorporation rate. If the sticking coefficient S_{Cd} of Cd is unity (case 1) then the alloy composition x_{Cd} is given by

$$x_{\text{Cd}}^{\text{RHEED}} = \frac{r_{\text{"CdTe"}}}{r_{\text{"CdTe"}} + r_{\text{HgTe}}} = \frac{r_{\text{"CdTe"}}}{r_{\text{CMT}}} \quad (1)$$

If S_{Cd} is below unity (case 2), then by opening the CdTe cell with a Hg flux impinging on the substrate we grow $\text{Cd}_x\text{Hg}_{1-x}\text{Te}$ instead of CdTe as case 1 and x cannot be given directly by relation (1). In order to know the amount $(1 - S)$ of Hg incorporation, we have grown several $4 \mu\text{m}$ thick "CdTe" layers under Hg and in the same run CMT layers under the same conditions. The

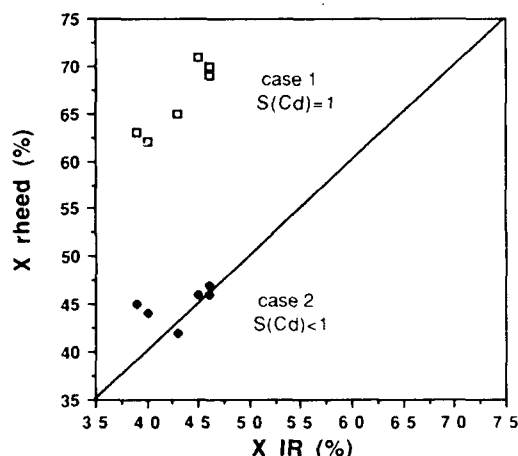


Fig. 4. Composition of MCT alloys (X^{RHEED}) deduced from RHEED oscillations and compared to IR transmission measurements (X^{IR}). Case 1: X_{Cd} calculated from RHEED by assuming a Cd sticking coefficient of 1 at 180°C. Case 2: X_{Cd} calculated from RHEED after correction by the actual value of S_{Cd} deduced for each sample from the composition measurement of "CdTe" grown under Hg flux.

RHEED oscillations are recorded for each sample and the compositions are deduced from the band gap energy position given by IR transmission (the band gap is determined at 50% transmission). It is shown firstly that an important amount of Hg ($1 - S \approx 30\%$) is incorporated in "CdTe" grown under Hg [7], indicating that case 2 should be considered, and secondly that the incorporation rate depends on substrate temperature and growth rate. The knowledge of S_{Cd} allows us to calculate X_{Cd} with the RHEED oscillations:

$$X_{\text{Cd}}^{\text{RHEED}} = S_{\text{Cd}} r_{\text{CdTe}} / r_{\text{CMT}} \quad (2)$$

Fig. 4 shows effectively that when the $X_{\text{Cd}}^{\text{RHEED}}$ value deduced from RHEED data (case 1) is corrected for the non-unity incorporation rate of Cd (case 2), good agreement is obtained with the IR transmission measurements X^{IR} . At 180°C with a Hg flux of 2×10^{-4} Torr, S_{Cd} is then close to 0.7. It is worth noting that by combining RHEED oscillations measurements and IR transmission data, the Cd sticking coefficient and its dependence on growth parameters can be evaluated by growing CMT layers without growing thick "CdTe" layers.

5. Discussion and conclusion

The real time growth measurements carried out by the RHEED oscillation technique show that cation stabilized growth of CdTe and $\text{Cd}_x\text{Hg}_{1-x}\text{Te}$ proceeds by 2D nucleation. In this regime the growth rate for CdTe and the CMT alloy compositions are mainly determined by the sticking coefficient of Cd which can be far below unity and depends strongly on substrate temperature and Hg overpressure for the CMT case. The most striking effect is that S_{Cd} , which is measured as ~ 1 at 180°C for CdTe, falls to 0.7 when a Hg flux is added. This shows that kinetic interactions take place between cation species on the growing surface leading to a competition between Cd and Hg adatoms to occupy available sites for incorporation. This is confirmed by the growth of $\text{Cd}_x\text{Hg}_{1-x}\text{Te}$ on (001) misoriented substrate where an enhancement of S_{Cd} is observed due to a more efficient incorporation of Cd at step edges. All these observations enlighten the importance of surface kinetics in MBE of II-VI compounds.

Acknowledgements

The authors wish to thank C. Denaeyer and K. Saminadayar for IR measurements and M. Rommeluere for microprobe analysis.

References

- [1] J.H. Neave, B.A. Joyce, P.J. Dobson and N. Norton, Appl. Phys. A31 (1983) 1.
- [2] G. Lentz, A. Ponchet, N. Magnea and H. Mariette, Appl. Phys. Letters 55 (1989) 2733.
- [3] J.D. Benson, B.K. Wagner, A. Torabi and C.J. Summers, Appl. Phys. Letters 49 (1986) 1034.
- [4] R.D. Feldman, R.F. Austin, P.M. Bridenbaugh, A.M. Johnson, W.M. Simpson, B.A. Wilson and C.E. Bonner, J. Appl. Phys. 64 (1988) 1191.
- [5] J.M. Arias, S.H. Shin, D.E. Cooper, M. Zandian, J.G. Pasko, E.R. Gertner and R.E. Dewames, J. Vacuum Sci. Technol. A8 (1990) 1025.
- [6] A. Million, L. Di Cioccio, J.P. Gailliard and J. Piagnet, J. Vacuum Sci. Technol. A6 (1988) 2813.
- [7] J. Reno, R. Sporken, Y.J. Kim, C. Hsu and J.P. Faurie, Appl. Phys. Letters 51 (1987) 1545.

A novel technique for the MBE growth of twin-free HgCdTe

R.W. Yanka, K.A. Harris, L.M. Mohnkern and T.H. Myers

Electronics Laboratory, General Electric Company, Syracuse, New York 13221, USA

A novel photon-assisted MBE technique, compositionally modulated structures (CMSs), has been developed to suppress twinning in MBE HgCdTe growth. Strain effects, introduced by thin CdTe layers, suppress planar twinning as well as lowering dislocation densities. A CMS epilayer consists of multiple repeats of a basic unit comprised of a thick (500-1500 Å) layer of HgCdTe and a thin (20-50 Å) layer of CdTe. The CMS epilayer is then interdiffused in a sealed quartz ampoule at temperatures consistent with n-type (or p-type) annealing producing isotropic HgCdTe suitable for infrared detector array fabrication. CMS has also been successfully applied to the low defect density growth of HgCdTe on the slightly lattice-mismatched CdTe substrates. This is an important result because CdTe substrates are less expensive, more chemically pure, and more readily available than the lattice-matched substrate CdZnTe.

1. Introduction

Molecular beam epitaxy (MBE) has become an important technology for the growth of the important infrared (IR) ternary $\text{Hg}_{1-x}\text{Cd}_x\text{Te}$ (MCT). MBE is particularly suited for MCT growth because the slow, controlled growth rates and low growth temperatures make possible the growth of multilayer structures and superlattices for advanced device applications.

However, the growth of MCT by MBE has been plagued by the formation of microstructural twinning defects and a high level of line dislocations. These defects are sources of dark currents and noise generation in IR MCT detectors. The reduction of these defects has been a major hurdle for the routine use of MBE MCT for fabricating high performance IR detectors. Twin defects occur on the (111)B orientation in the form of laminar twin domains arising from hexagonal stacking faults. Line dislocation defects are produced by non-optimal growth parameters and from lattice mismatched heterointerfaces. The reduction of these defects has been a non-trivial problem due to the relative instability of MCT.

The first application of the photo-assisted MBE (PAMBE) technique to the growth of MCT produced significant improvement in the crystalline

quality of MCT epilayers [1]. In this paper, we first report on the significant improvements achieved at General Electric (GE) for the growth of MCT on (111)B oriented CdTe and CdZnTe substrates using PAMBE in conjunction with tight control of critical growth parameters using GE's custom MBE equipment. We then report the results of our novel growth technique, compositionally modulated structures (CMSs), used in conjunction with the PAMBE technique to grow high yields of twin-free, low dislocation MCT quite suitable for the fabrication of high performance IR detector arrays.

2. Experimental

The growth of MCT epilayers was carried out in two custom-made MBE machines modified for PAMBE growth [1]. An argon ion laser equipped with broadband optics was used as the illumination source for all growths. Epilayers were grown without buffer layers directly onto CdZnTe and CdTe substrates obtained from II-VI, Inc. GE's proprietary substrate preparation, which includes a combination of standard wet etching techniques and thermal processing prior to growth, has been shown to produce high quality growth interfaces

without the complexity of a buffer layer [2]. Epilayers were grown at temperatures ranging from 170 to 180°C during this study. A Varian beam flux monitor was used to provide a precise determination of the flux from the thermal sources, thus enabling reproducible growth conditions.

The composition of MCT epilayers grown for this study was determined by IR transmission and IR photoluminescence. Defect etching was accomplished through the use of standard etches [3]. Double crystal X-ray diffraction rocking curves (DCRCs) were measured at GE Corporate Research and Development Center. Transmission electron microscopy (TEM) characterizations were performed at Purdue University under the direction of Professor Nobuo Otsuka using iodine thinning techniques.

3. Twin-free growth by parameter control

MCT grown by MBE on the (111)B orientation typically contains a high density of laminar twinning arising from hexagonal stacking faults during growth. Fig. 1a shows a defect etch micrograph which reveals laminar twinning typically observed in (111)B MCT grown by conventional MBE. Twin domains also affect the DCRC full width at half maximum (FWHM) as evidenced by the large value of 150 arc sec observed for this layer. By changing the growth kinetics through the use of in situ laser illumination of the substrate, a dramatic improvement in the laminar twinning density was observed, as illustrated in fig. 1b by the defect etch micrograph obtained from a (111)B MCT layer grown by PAMBE. A reduction of twinning



Fig. 1. Defect etch micrographs of (a) a (111)B MCT epilayer grown by conventional MBE, and (b) one grown by PAMBE, along with (c) a TEM cross-section obtained from the layer grown by PAMBE. The smooth defect-free interface indicates proper initial growth conditions. The onset of twinning after the deposition of about 1 μm of material indicates that twinning occurs due to inadequate parameter control.

is clearly observed as evidenced by the larger twin domains. The DCRC FWHM of 40 arc sec observed for this sample also attests to the reduction

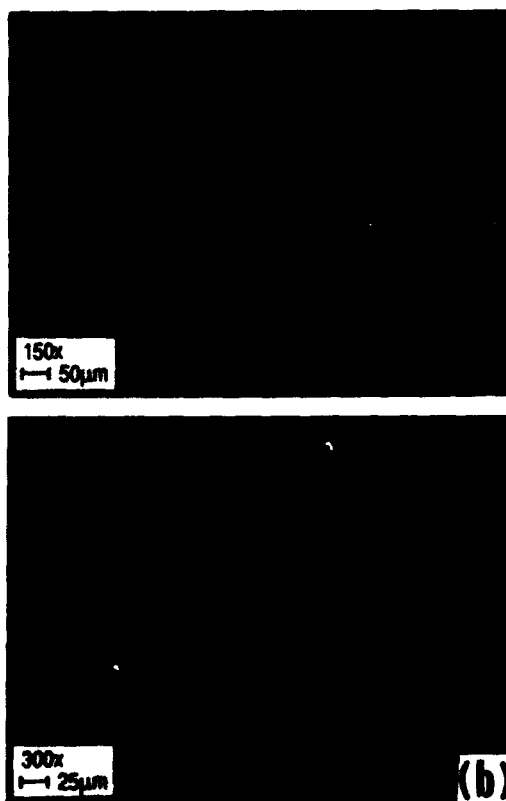
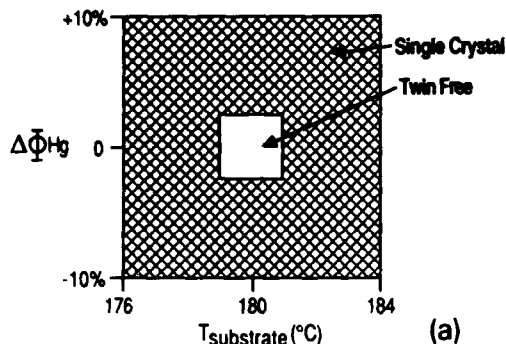


Fig. 2. (a) Graphic representation of the twin-free existence domain as a function of Hg flux and substrate temperature and (b) defect etch micrographs of a 10 μm thick (111)B MCT epilayer grown by PAMBE within this existence domain illustrating twin-free growth.

of laminar twinning. The etch pit density (EPD) count of line dislocations inside a twin domain was $5 \times 10^6 \text{ cm}^{-2}$. Although this EPD count is comparable to that of many LPE MCT films, the density is still an order of magnitude larger than that required for advanced detector fabrication.

The TEM cross-section micrograph of fig. 1c obtained from the (111)B MCT layer shown in fig. 1b illustrates that laminar twinning arose as a result of deviation from optimal growth parameters during deposition as evidenced by the onset of twinning after the growth of 1 μm of material beyond a smooth, dislocation-free substrate-epilayer interface. A systematic study of the effects of altering Hg overpressure and substrate temperature during growth determined that these parameters had to be tightly controlled in order to produce twin-free (111)B MCT epilayers. Fig. 2a graphically illustrates that the substrate temperature must be maintained to within $\pm 1^\circ\text{C}$ of the optimum while simultaneously controlling the Hg flux to within a few percent in order to achieve twin-free growth. The absence of twin domains in the defect etch micrograph (fig. 2b) from a 10 μm thick (111)B HgCdTe epilayer grown by PAMBE within this twin-free existence domain illustrates laminar-twin-free growth. Laminar-twin-free films also exhibited reduced DCRC FWHMs of 13–25 arc sec and EPD counts of $1 \times 10^5 \text{ cm}^{-2}$, well within the range required for fabrication of high performance IR detectors.

4. The CMS technique

The critical control of the Hg flux and the substrate temperature required for twin-free (111)B MCT growth is difficult to achieve and has limited the yield to less than 20%. To circumvent this problem, we have developed a new MBE MCT growth approach, compositionally modulated structures (CMSs). The first step of this two-step process is to grow an epilayer consisting of alternating layers of MCT (500–1500 Å thick) and CdTe (20–50 Å thick). The second step is to anneal the epilayer in a closed quartz ampoule under standard conditions in order to interdiffuse the layers to produce isotropic MCT. The ra-

tionale behind such an approach is that the thin CdTe layers will serve to suppress planar twinning due to interface strain caused by the slight lattice mismatch between the constituent layers. The multiple layers in the CMS structure also serve to block threading dislocations, analogous to that observed in III-V systems.

Indeed, the CMS approach was found to result in the growth of twin-free (111)B MCT with a substantially improved yield of 87%. This result indicates that the CMS technique allows for a greater latitude in parameter control. Also, CMS epilayers typically exhibit EPD counts lower than that observed for the substrates on which they are grown, indicating that line dislocations are suppressed by the CMS technique. Stronger evidence for this claim is given by the TEM cross-section of an unannealed CMS structure grown on a CdTe

substrate shown in fig. 3. Dislocations due to the slight lattice mismatch are observed at the interface, as well as threading dislocations arising from the substrate. The dislocations die out at about $0.2 \mu\text{m}$ from the interface, consistent with the CMS growth technique suppressing the propagation of threading dislocations through dislocation bending.

CMS is also effective in blocking dislocations which arise from the use of lattice mismatched substrates. Fig. 3b shows two MCT epilayers grown on (211)B CdTe substrates. The layer grown without CMS has the high EPD consistently found with the use of slightly lattice mismatched CdTe. The layer grown by CMS, however, exhibits a significantly reduced EPD indicative of the suppression of line dislocations. This is an important result because the CMS technique allows for the

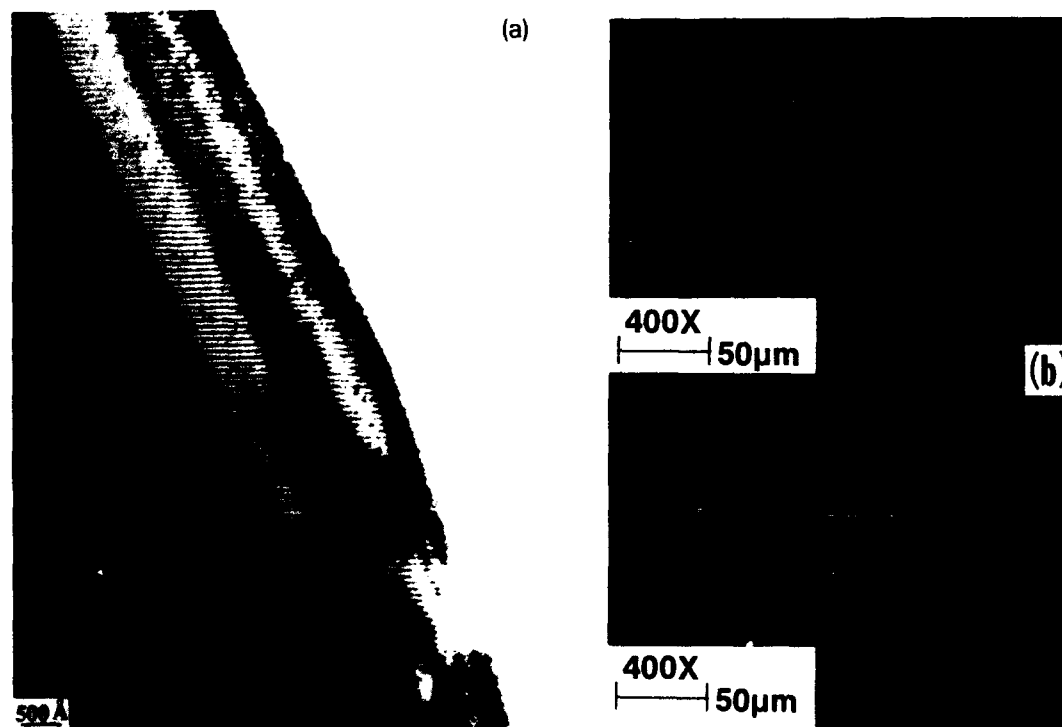


Fig. 3. Illustration of the line dislocation bending property of the CMS technique. The TEM cross-section (a) obtained from a CMS epilayer grown on a CdTe substrate shows elimination of the dislocation structure at about $0.2 \mu\text{m}$. The defect etch micrographs (b) show a reduction in EPD counts upon going from the PAMBE technique (upper micrograph) to the PAMBE/CMS technique (lower micrograph) for MCT growth on slightly lattice mismatched CdTe substrates.

growth of low dislocation density MCT on CdTe substrates suitable for advanced IR detector fabrication. CdTe substrates are cheaper, purer, and more readily available than lattice matched CdZnTe substrates. In addition, the ability of the CMS technique to block threading dislocations is attractive for the potential use of substrates with even greater lattice mismatch, such as GaAs.

5. Summary

A small existence region, constrained by the Hg flux and the substrate temperature, was shown to exist for achieving twin-free growth of (111)B MCT by PAMBE on a limited-yield basis. A novel concept in MBE growth, CMS, in conjunction with PAMBE was shown to be a viable, high yield technique for producing isotropic, twin-defect-free

(111)B MCT. The CMS technique was also shown to bend line dislocations allowing for the potential growth of low dislocation density MCT on lattice-mismatched substrates, such as CdTe or GaAs.

Acknowledgement

This work was supported by GE Internal Research and Development funding.

References

- [1] T.H. Myers, R.W. Yanka et al., *J. Vacuum Sci. Technol.* A7 (1989) 300.
- [2] K.A. Harris, T.H. Myers et al., *J. Vacuum Sci. Technol.* A8 (1990) 1013.
- [3] H.F. Schaafe, J.H. Tregilgas, A.J. Lewis and P.M. Everett, *J. Vacuum Sci. Technol.* A1 (1983) 1625.

Very low temperature growth and doping of Hg-based epilayers and superlattices

Y. Lansari, Z. Yang, S. Hwang, F.E. Reed, A.T. Sowers, J.W. Cook, Jr. and J.F. Schetzina

Department of Physics, North Carolina State University, Raleigh, North Carolina 27695-8202, USA

Photoassisted MBE growth of Hg-based thin films at very low temperatures (125–150 °C) is reported. Substitutionally doped superlattices were also prepared at low temperatures, using modulation doping techniques in which In and As were used as n-type and p-type dopants, respectively. The doped superlattices exhibit excellent electrical properties and optical properties characteristic of 2D quantum structures. Analysis of the measured absorption data yields a valence band offset of ~ 350 meV for the HgTe–CdTe interface.

1. Introduction

In recent years, molecular beam epitaxy (MBE) growth of HgCdTe for infrared (IR) detectors and of related superlattice structures has seen steady improvements. Advances in device fabrication [1,2] as well as in understanding of the fundamental physics of this material [3,4] have been made. However, a few difficulties still remain to be overcome. In particular, p-type substitutional doping of the $\text{Hg}_{0.8}\text{Cd}_{0.2}\text{Te}$ alloy, suitable for IR detectors in the 8–12 μm range, has not been achieved to date, although viable alternatives have been demonstrated [5]. Additionally, growth on (100) is still plagued by structural defects, namely pyramidal hillocks of densities 10^5 – 10^6 cm^{-2} , which seriously limit device applications [6]. Other issues of concern are the interdiffusion effects observed in SLs grown at conventional MBE temperatures [7]. A possible solution to several of these problems is offered by very low temperature MBE growth, which is feasible by use of the photoassisted MBE technique [8].

In this paper, we present results of an investigation of the growth parameters for very low temperature growth (125–150 °C) of Hg-based films and multilayers by photoassisted MBE. This appreciable reduction in growth temperature has allowed us to substantially reduce the Hg source

flux use in the growth experiments: beam equivalent pressures as low as 5×10^{-5} Torr were employed, nearly an order of magnitude less than fluxes used for ordinary MBE growth at conventional temperatures. The layers were grown on (100) CdZnTe substrates with the CdTe and Te source fluxes adjusted to obtain 0.6–3 Å/s growth rates. HgTe layers and HgTe–HgCdTe superlattices grown under these conditions exhibited good structural quality, with double-crystal X-ray diffraction peak FWHMs in the range 28–300 arc sec. Pyramidal hillock densities in the range 10^4 – 10^5 cm^{-2} were measured for all samples.

Substitutionally doped superlattices were also prepared at low temperatures, using modulation doping techniques in which In and As were used as n-type and p-type dopants, respectively. The doped superlattices exhibit excellent electrical properties ($\mu_n > 10^5$ $\text{cm}^2/\text{V} \cdot \text{s}$, $\mu_p \sim 10^4$ $\text{cm}^2/\text{V} \cdot \text{s}$) and optical properties characteristic of 2D quantum structures. Analysis of the measured absorption data yields a valence band offset of ~ 350 meV for the HgTe–CdTe interface.

2. Experimental details

The HgTe epilayers and the HgTe–HgCdTe SLs included in this study were grown on 5 mm \times 7

mm high-quality (100) CdZnTe (4% Zn) substrates furnished by SBRC and II-VI, Inc. The substrates were chemimechanically polished and etched in a 2% bromine-in-methanol solution, then degreased and briefly etched into a 1:1 HCl and DI water solution. Immediately prior to growth, the substrates were preheated in vacuum at about 300°C to desorb the Te surface layer. The growth temperatures used were in the range 125–150°C. These values represent actual substrate temperatures, as determined from temperature calibrations based on the melting points of several metals. In the photoassisted MBE process, the beam-expanded, broad-band output (458–514 nm) of a Spectra-Physics 2016-05 argon-ion laser was used to uniformly illuminate the substrate during film growth. Laser power densities at the substrate ranging from 35 to 80 mW/cm² were utilized. As the temperature was lowered, the laser power density was increased to compensate for the decrease in the thermal energy supplied to the substrate surface. These power densities do not produce any significant heating of the substrate surface.

In the modulation doped superlattices, In and As were used as the n-type and p-type dopants, respectively. The dopants were incorporated uniformly in the barrier layers (no setback), and the temperatures of the In and As ovens were varied from run to run, resulting in a range of doping levels obtained for the series of SLs. Each of the superlattices consisted of 200 double layers of HgTe–Hg_{0.15}Cd_{0.85}Te. The individual layer thicknesses for each SL were determined by using DEKTAK total thickness measurements, the angular separation of X-ray satellite peaks relative to the main diffraction peak, and the growth rates of HgTe and HgCdTe determined using calibration layers grown under the same conditions.

Double-crystal X-ray rocking curve measurements were performed on all the SLs included in this study. The full-width at half-maximum (FWHM) of the main (400) diffraction peak was used as a measure of structural quality. Electrical characterization of the SLs consisted of standard Van der Pauw–Hall measurements over the temperature range between 30 and 300 K. Optical absorption coefficients for selected SLs were determined by measuring their transmittance and

reflectance at room temperature. Photographs of selected sample surfaces were obtained using a JEOL-6400 scanning electron microscope (SEM).

3. Results and discussion

3.1. HgTe epilayers

A series of growth experiments was undertaken, where the substrate temperature was systematically lowered to cover the range 125–150°C. As the temperature was lowered, the laser power density was increased to compensate for the decrease in thermal energy supplied to the substrate surface. HgTe growth rates between 1 and 3 Å/s were used, and Hg fluxes with BEPs of 5×10^{-5} to 1×10^{-4} Torr were employed. The layers obtained exhibit good structural quality, with DCRC X-ray peak FWHMs within the range 40–200 arc sec. The best results (40 arc sec) were obtained for HgTe grown at 125°C using a laser power density at the substrate of 48 mW/cm², a Hg flux BEP of $\sim 6.5 \times 10^{-5}$ Torr, and a growth rate of ~ 1 Å/s. Layers grown under similar conditions but with higher growth rates (2–3 Å/s) yielded comparable results for the structural quality (60–100 arc sec).

The surface morphology of these HgTe epilayers is similar for the different growth conditions employed: the films appear specular to the eye, but examination using a SEM reveals the presence of rectangular pyramidal hillocks. Hillocks of this type always occur for (100) growth of Hg-based materials and have been observed by many others [9–11]. This growth defect is illustrated by the SEM photos shown in fig. 1. In fig. 1a is shown the surface of film A107, a HgTe epilayer grown at 125°C (hillock density $\sim 9 \times 10^4$ cm⁻²). In fig. 1b is shown the surface of A63, a HgTe epilayer grown at 150°C (hillock density $\sim 1 \times 10^4$ cm⁻²). To our knowledge, this hillock density is comparable to the lowest ever obtained for a Hg-based layer grown by conventional MBE at higher temperatures.

3.2. HgTe–Hg_{0.15}Cd_{0.85}Te superlattices

n-Type and p-type modulation-doped SLs were successfully grown for a range of layer thicknesses

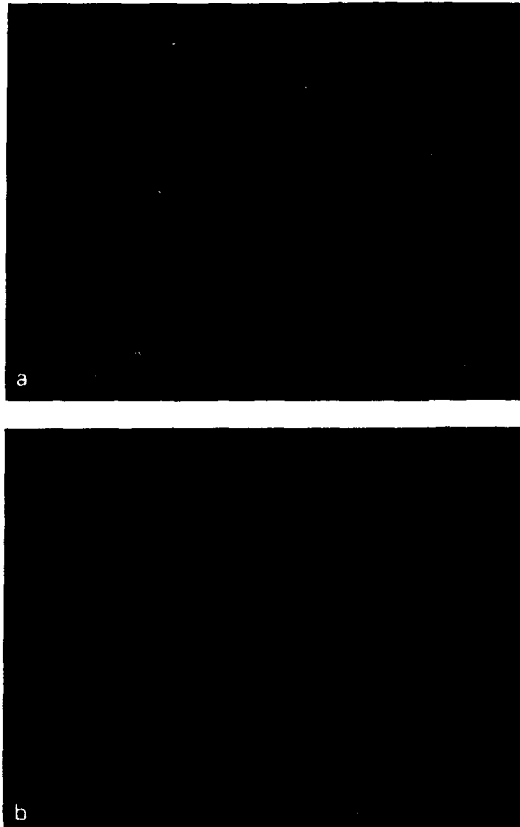


Fig. 1. Surface morphology of (a) HgTe epilayer A107 grown at 125 °C (hillock density $\sim 9 \times 10^4 \text{ cm}^{-2}$) and (b) HgTe epilayer A63 grown at 150 °C (hillock density $\sim 1 \times 10^4 \text{ cm}^{-2}$).

and doping levels (4×10^{14} – $1 \times 10^{17} \text{ cm}^{-3}$) at low temperatures). Fig. 2 shows Hall data for two representative modulation-doped samples, both grown at 140 °C by photoassisted MBE, which clearly manifest the effects of doping. Sample A69A is an n-type SL ($T_{\text{in}} = 475^\circ \text{C}$) having a well thickness of 58.3 Å and a barrier thickness of 48.6 Å, corresponding to a band gap $E_g = 19.5 \text{ meV}$ at 77 K. The electron concentration is constant, due to modulation doping, and equal to $1.1 \times 10^{17} \text{ cm}^{-3}$ at temperatures below $\sim 100 \text{ K}$, as shown in fig. 2a. The electron mobility increases with decreasing temperature and reaches a maximum of $32,000 \text{ cm}^2/\text{V} \cdot \text{s}$ at 30 K.

A74 (fig. 2b) is a p-type modulation-doped SL for which $L_z = 25.9 \text{ Å}$ and $L_b = 35.6 \text{ Å}$. These layer thicknesses correspond to a band gap $E_g = 171 \text{ meV}$ at 77 K. In this case, the Hall coefficient becomes positive at $\sim 285 \text{ K}$. At temperatures below $\sim 180 \text{ K}$, the hole concentration is constant and equal to $\sim 7 \times 10^{16} \text{ cm}^{-3}$. The hole mobility is approximately $250 \text{ cm}^2/\text{V} \cdot \text{s}$ over this temperature range, which is quite reasonable for a $\sim 7 \mu\text{m}$ band gap structure.

Optical absorption coefficients versus photon energy for two SLs A69A and A112 are shown in

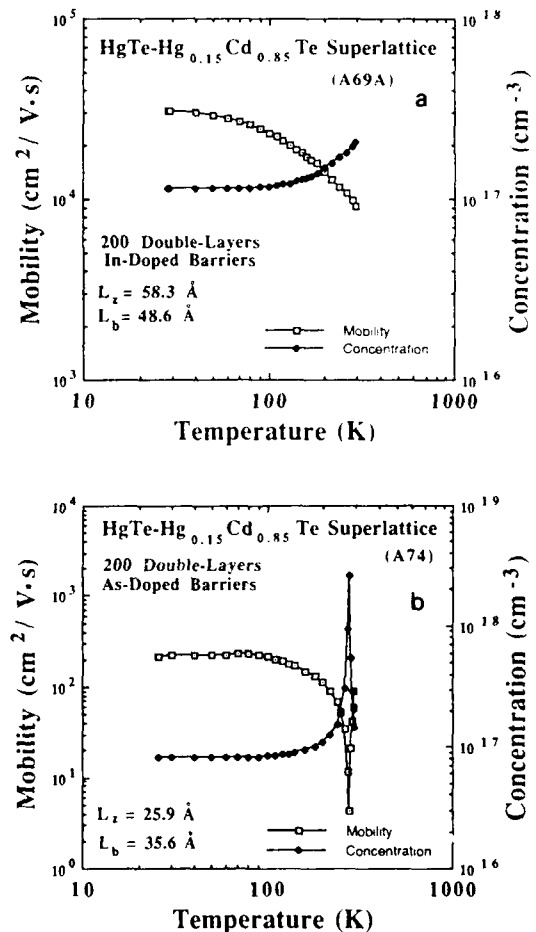


Fig. 2. Hall effect data for (a) an n-type modulation-doped SL ($T_{\text{in}} = 475^\circ \text{C}$) and (b) a p-type substitutionally doped superlattice ($T_{\text{As}} = 220^\circ \text{C}$).

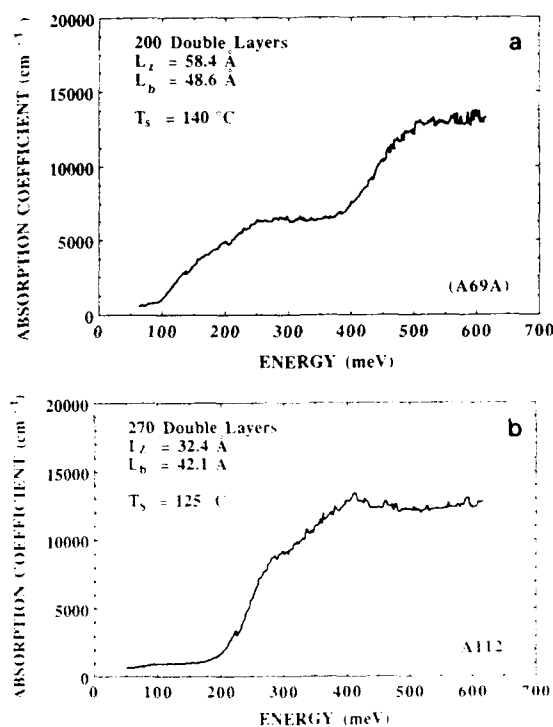


Fig. 3. Optical absorption coefficient versus photon energy for (a) SL A69A grown at $T_s = 140^\circ\text{C}$ and (b) SL 112 grown at $T_s = 125^\circ\text{C}$.

fig. 3. Each spectrum contains several distinct steps and plateaus, which are clear manifestations of the 2D quantum nature of these structures. Note that for SL A69A, which was prepared using a substrate temperature $T_s = 140^\circ\text{C}$, the onset of absorption (heavy hole H1 to conduction band E1 transition) occurs at about 100 meV and a second transition is barely discernable at about 210 meV. This second transition corresponds to the light hole L1 to conduction band E1 transition. The energy separation between these two transitions (~ 110 meV) is thus a measure of the light and heavy hole energy splitting in the valence band due to quantum confinement. The observed splitting is consistent with a large valence band offset (about 350 meV for the HgTe/CdTe binary interface). Note that the absorption spectrum of SL

A112, prepared using $T_s = 125^\circ\text{C}$, appears sharper due to the reduced growth temperature, which gives rise to sharper interfaces between the SL layers.

Measured hillock densities for the (100) superlattices tend to be somewhat higher ($\geq 10^5 \text{ cm}^{-2}$) than for the best HgTe epilayers grown at low temperatures. We believe the hillock density on our best HgTe layers is determined by substrate dislocations, in accord with earlier studies [9–11]. In the case of SL growth at low temperatures, the observed increase in hillock density may be related to less-than-ideal parameters for growth of the $\text{Hg}_{0.15}\text{Cd}_{0.85}\text{Te}$ barrier layers. These layers are grown using a single CdTe MBE source in the presence of a mercury ambient. We have found that thick layers of $\text{Hg}_{0.15}\text{Cd}_{0.85}\text{Te}$ grown in this way have even higher hillock densities (often $> 10^6 \text{ cm}^{-2}$). Modification of the technique used for growth of these barrier layers (by using a second supplemental Te source, for example) may be necessary to reduce the SL hillock density to below 10^4 cm^{-2} , a requirement for certain infrared detector applications.

4. Summary

Photoassisted MBE growth of Hg-based thin films at very low temperatures ($125\text{--}150^\circ\text{C}$) is reported. Substitutionally doped superlattices were also prepared at low temperatures, using modulation doping techniques in which In and As were used as n-type and p-type dopants, respectively. The doped superlattices exhibit excellent electrical properties and optical properties characteristic of 2D quantum structures. Analysis of the measured absorption data yields a valence band offset of ~ 350 meV for the HgTe/CdTe interface. Growth at low temperatures ($\sim 125^\circ\text{C}$) produces SLs of superior interfaces, as exemplified by improved optical absorption spectra. Hillock densities for the SLs were found to be an order of magnitude higher than for the best HgTe epilayers grown at low temperatures.

Acknowledgements

The authors wish to acknowledge J. Matthews, M. Bennett, and A. Mohan for their assistance with substrate preparation. This work was supported by NRL contract N00014-89-J-2024.

References

- [1] D.L. Dreifus, R.M. Kolbas, R.L. Harper, J.R. Tassitino, S. Hwang and J.F. Schetzina, *Appl. Phys. Letters* 53 (1988) 1279.
- [2] D.L. Dreifus, R.M. Kolbas, J.W. Han, J.W. Cook, Jr. and J.F. Schetzina, *J. Vacuum Sci. Technol.* A8 (1990) 1221.
- [3] J.R. Meyer, C.A. Hoffman, F.J. Bartoli, J.W. Han, J.W. Cook, Jr., J.F. Schetzina, X. Chu, J.P. Faurie and J.N. Schulman, *Phys. Rev.* B38 (1988) 2204.
- [4] Z. Yang, J.F. Schetzina and J.K. Furdyna, *J. Vacuum Sci. Technol.* A7 (1989) 360.
- [5] J.W. Han, S. Hwang, Y. Lansari, Z. Yang, J.W. Cook, Jr. and J.F. Schetzina, *J. Vacuum Sci. Technol.* B8 (1990) 205.
- [6] K.A. Harris, T.H. Myers, R.W. Yanka, L.M. Mohnkern, R.W. Green and N. Otsuka, *J. Vacuum Sci. Technol.* B8 (1990) 1013.
- [7] D.K. Arch, J.L. Staudenmann and J.P. Faurie, *Appl. Phys. Letters* 48 (1986) 1588.
- [8] R.N. Bicknell, N.C. Giles and J.F. Schetzina, *Appl. Phys. Letters* 49 (1986) 1095.
- [9] R.J. Koestner and H.F. Schaake, *J. Vacuum Sci. Technol.* A6 (1988) 2834.
- [10] A. Million, L. Di Cioccio, J.P. Gailliard and J. Piagnet, *J. Vacuum Sci. Technol.* A6 (1988) 2813.
- [11] K.A. Harris, T.H. Myers, R.W. Yanka, L.M. Mohnkern, R.W. Green and N. Otsuka, *J. Vacuum Sci. Technol.* A8 (1990) 1013.

Chemical beam epitaxy of CdTe, HgTe, and HgCdTe

R.G. Benz II, B.K. Wagner, D. Rajavel and C.J. Summers

Physical Sciences Laboratory, Georgia Tech Research Institute, Atlanta, Georgia 30332, USA

A chemical beam epitaxy (CBE) system has been implemented for the growth of CdTe, HgTe, and their alloys. The system is briefly described. Results on the cracking of the organometallic source gases are presented. Epitaxial layers have been grown from gas sources of diethylcadmium, diisopropyltelluride and Hg vapor, as well as conventional solid sources. Optical and electrical properties are reported, demonstrating the potential of CBE for growing high quality solar cell and infrared detector material.

1. Introduction

The development of chemical beam epitaxy (CBE) has principally involved III–V semiconductors and more recently wide bandgap electroluminescent II–VI materials such as ZnSe and ZnS. We have recently extended this growth technique to Te-based large bandgap (ZnTe/CdTe) and small bandgap (HgTe/HgCdTe) materials. This paper describes further developments and results of this work.

For HgCdTe we believe that CBE offers significant advantages in addressing both the material science and implementation issues of the growth of these materials [1]. The high volatility of the alloy components, the low Hg sticking coefficient ($< 10^{-3}$) and fast diffusion on the cation sublattice all require growth temperatures for alloy and superlattice growth of less than 230 and 150°C, respectively. Thus, material and interface quality are critically dependent on optimization of the nucleation kinetics and on maintaining very stable flux control throughout layer growth. CBE addresses both of these aspects by enabling chemical manipulation and precise regulation of the flux species. Thus, growth can be achieved using monomer Te, which has been shown to enhance the Hg sticking coefficient, and also monomer or dimer arsenic for p-type doping. Additionally, the use of gas dopant sources also enables an investigation of group VII, n-type dopants, which are difficult to control in conventional MBE systems.

These dopants also are expected to substitute on the Te sublattice and thus will be less susceptible to diffusion.

2. Experimental

2.1. CBE system

Growth was performed in a Varian GEN II MBE system with extensive modifications to convert it to a CBE system. The system is shown in fig. 1. These modifications have been described in detail elsewhere [2], and will be briefly reviewed here.

The CBE system currently has operational gas sources for the host elements tellurium, cadmium and zinc, and also arsenic and iodine for p- and n-type doping. For HgCdTe growth, diisopropyltelluride (DipTe) and diethylcadmium (DeCd) flow rates were controlled by MKS Instruments 1150B flow controllers, which operate through pressure control and thus do not require the use of carrier gases. Both the DeCd and DipTe were directly injected into group II or group VI gas injectors, respectively, where they are cracked and directed onto the substrate. For p-type doping arsine is used as the As source, although any of the organometallic As gases could be used. The dopant source works on the same principle as the MKS 1150B flow controllers except for the use of

a manual leak valve as a variable orifice. The arsine is cracked in the group VI gas injector before entering the CBE chamber. Mercury flux is provided by the Hg-pressure controlled vapor source (Hg-PCVS) reported previously [3]. Solid sources of Cd, Te, Zn and CdTe are used for MBE growth in the CBE system. The system is equipped with a UTI-100C quadrupole mass analyzer (QMA) and a reflection high energy electron diffraction (RHEED) system with computer-based image analysis. Other features of the CBE system are shown in the figure, but will not be described here.

Four vacuum pumps are currently used on the CBE system. During CBE growth, a Balzers MBE series turbomolecular pump and a Varian Cryosack 8 cryopump evacuate the growth chamber. The gases exhausted from the turbomolecular pump are pumped by an Alcatel 50 cfm Corrosive Series mechanical pump and then pass through an Emcore toxic gas scrubber filled with activated charcoal capable of scrubbing both Hg and the organometallic vapors. Both of these pumps are

used only for CBE growth and otherwise are turned off to prolong their working life. In addition, the substrate cryoshroud is continually cooled with liquid nitrogen to pump Hg vapor and uncracked organometallics. During MBE growth a 400 l/s ion pump and a titanium sublimation pump are used.

3.2. Growth conditions

Epitaxial layers of CdTe, HgTe, and HgCdTe were grown on chemically polished (001)-oriented CdTe, ZnCdTe and GaAs substrates. All layers were grown on CdTe buffer layers deposited by CBE or from a binary CdTe source. The Hg-based layers were grown at a substrate temperature of 165–185°C and the CdTe layers were grown at substrate temperatures ranging from 185–320°C. All substrate surface temperatures below 230°C were calibrated by a Te-condensation technique [4]. Growth rates for all layers were ~0.5–0.6 $\mu\text{m/h}$ and layer thickness varied from 2–6 μm . Hg-based materials were capped by a thin CdTe layer to prevent surface degradation.

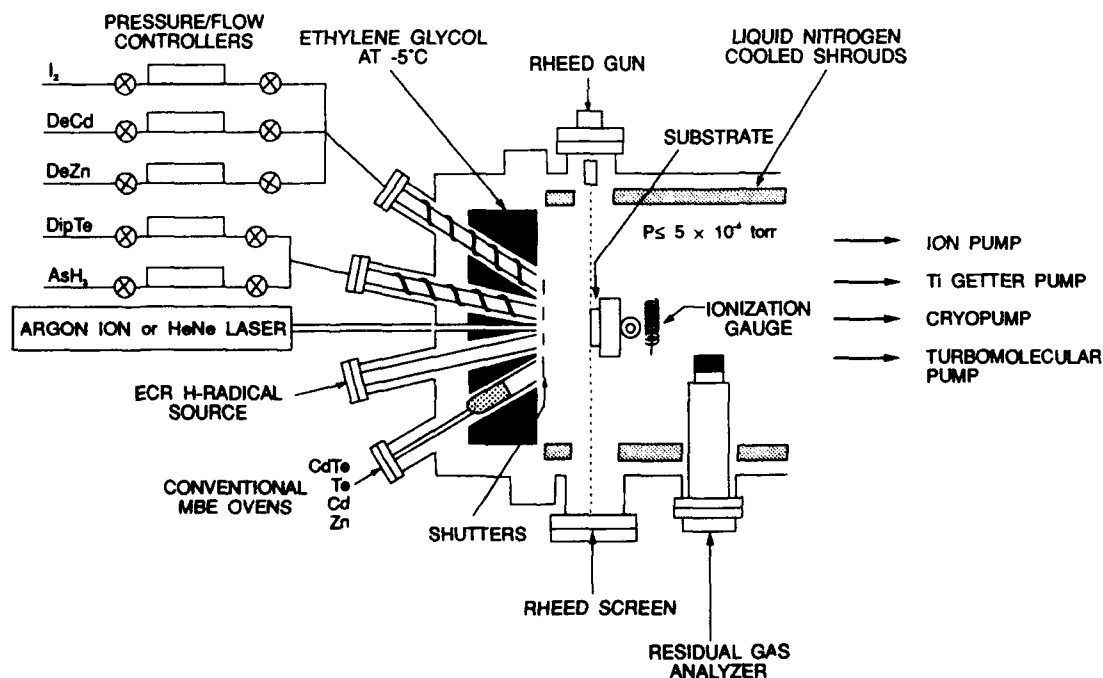


Fig. 1. Schematic of CBE system.

3. Results

3.1. Gas injector characterization

In order to remove the cracking dependence of the source gases from the substrate temperature, the source gases are precracked in a high temperature injector. To prevent gas phase reactions separate injectors are utilized for the group II elements and group VI elements. Both can accept three separate gas lines. Each injector uses a specially designed boron nitride diffuser element to enhance cracking efficiency. The group II injector uses a Ta delivery tube while the group VI utilizes a pyrolytic boron nitride (pBN) delivery tube to avoid any reaction between Te and Ta [5]. Both injectors are capable of operating at diffuser temperatures of 1300°C and have dual thermocouples for monitoring temperature gradients along the delivery tubes.

Studies have been implemented to determine cracking efficiency for both DeCd and DipTe. In the analysis, corrections to the data have been made for quadrupole transmission, ionization probability, multiplier gain, and fragmentation of the polyatomic molecules. Fig. 2 shows the ratio of monomer Te to the total Te species in the beam, defined as the monomer Te production

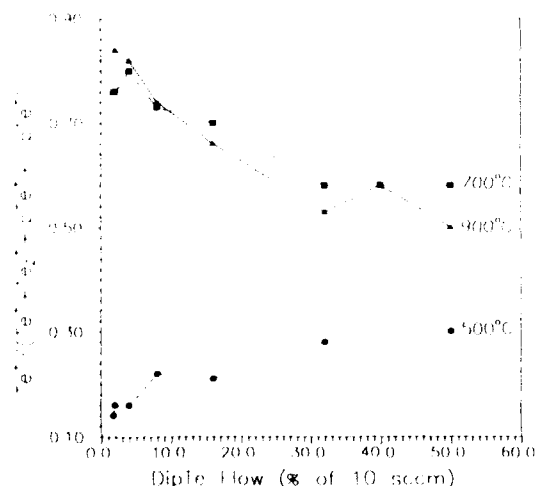


Fig. 2. Monomer Te production (MTeP) ratio versus DipTe flow for three diffuser temperatures.

ratio (MTeP), versus DipTe flow rate at different diffuser temperatures. A MTeP ratio of 25% was observed for a diffuser temperature of 500°C and was found to be almost independent of flow rate. For diffuser temperatures greater than 700°C, all of the DipTe has been cracked. The majority of the Te species from the injector is monomer and dimer Te, with a large increase in the MTeP ratio to approximately 80% and a corresponding Te/Te₂ ratio of 10 for low flow rates. At higher flows, the MTeP ratio gradually decreases to ~55% at flow rates greater than 30% of 10 SCCM FS. Further increases in diffuser temperature up to 1300°C had little effect on the MTeP ratio. The decrease in the MTeP ratio at high flow rates is attributed to two effects. For high gas pressures in the injector, monomer Te combines in the gas phase to form dimer Te. The other effect which influences the MTeP ratio at all flow rates is deposition and reevaporation of Te in the delivery tube. Since there is an appreciable thermal gradient along the delivery tube, at higher diffuser temperatures more DipTe cracks farther from the injector exit. The monomer Te then can deposit in the tube and subsequently reevaporate as dimer Te. Te deposition has been verified by examination of the inside of the delivery tube during operation and by plotting the total Te species versus flow rate for increasing diffuser temperatures. A significant decrease in the total flux of Te species is seen at high diffuser temperature due to Te deposition in the tube. This effect is seen during AsH₃ cracking [6]. Although the MTeP ratio decreases at the large flows, most growth occurs in the 1–2 SCCM range, where the MTeP ratio is maximum. The cracking of DeCd in the group II injector is similar in behavior to DipTe. DeCd is completely cracked to Cd at 500°C for flows up to 60% of 5 SCCM FS.

3.2. CdTe characterization

Photoluminescence (PL) results were obtained for CdTe layers grown by CBE on CdTe substrates. Fig. 3 shows photoluminescence spectra taken at 10 K of four CdTe layers grown with various DipTe/DeCd flux ratios. These measurements were obtained using the 6328 Å line of a HeNe laser as the excitation source. Each of the

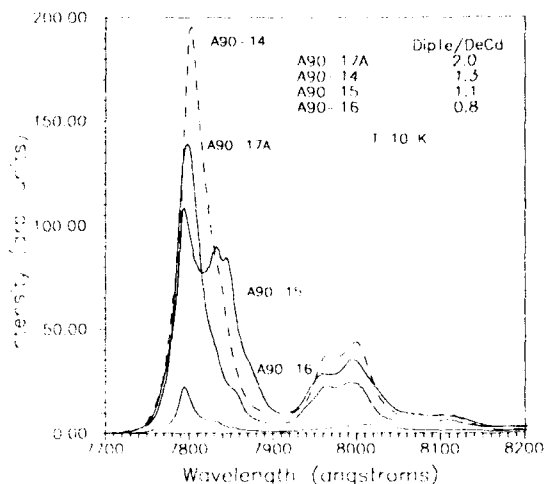


Fig. 3. Photoluminescence spectra at 10 K for four CBE CdTe layers grown at different DipTe/DeCd flux ratios.

spectra exhibit donor bound excitonic emission near 7800 Å and acceptor bound transitions at ~ 7832 Å. The features at 7960 and 8000 Å are attributed to free to acceptor and donor-acceptor transitions, respectively. LO-phonon replicas of the donor-acceptor pair transitions are also visible at lower energies. All samples exhibited n-type conductivity except for sample A90-16 which was insulating. The PL spectra agree qualitatively with electrical measurements performed on the samples. For example, sample A90-16, which appears to be the most compensated also has the lowest mobility of the four samples. Nonradiative defects may be the cause of the low luminescence intensity for sample A90-16 as well as its insulating character.

3.3. Hg-based layer characterization

HgTe layers have been grown and characterized in-situ by RHEED and ex-situ by optical microscopy and the Hall effect. Under the proper growth conditions, all HgTe layers showed no twinning as determined by RHEED. The layers were specular to the eye, although slight surface texturing was observed by optical microscopy.

Fig. 4 shows a plot of Hall mobility versus temperature for two HgTe layers. The CBE grown layer has a peak mobility of 109,000 $\text{cm}^2/\text{V} \cdot \text{s}$ at 24 K. This layer had the highest mobility of the HgTe layers grown and compares well with the highest values quoted by Feldman et al. [7]. The MBE grown layer had a peak mobility of 54,000 $\text{cm}^2/\text{V} \cdot \text{s}$, and was the highest mobility obtained for a MBE HgTe layer grown in the system, although no efforts were made to optimize the layers. These results illustrate the benefits of precise flux control and monomer Te for growing high mobility HgTe layers.

HgCdTe layers have also been grown by CBE. RHEED analysis confirmed the absence of twinning for layers grown under the proper flux and substrate temperature conditions. Evaluations of the optical and electrical properties of the HgCdTe layers indicate that x -values between 0.16 and 0.22 have been grown. For the best samples low-temperature electron concentrations between 5×10^{14} and $1 \times 10^{15} \text{ cm}^{-3}$ have been obtained with peak mobility values as high as $3.2 \times 10^5 \text{ cm}^2/\text{V} \cdot \text{s}$. These values were obtained on unannealed samples and are very competitive with published MBE results [8].

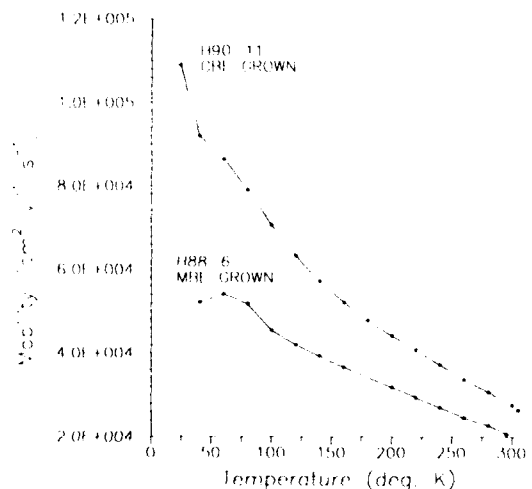


Fig. 4. Hall mobility versus temperature for two HgTe layers, one grown by MBE and one grown by CBE.

4. Conclusions

A chemical beam epitaxy system has been constructed and evaluated for the growth of HgCdTe alloys. The system comprises direct injection flow control, high-temperature gas injectors for group II and group VI elements, and a toxic gas pumping system. Efficient thermal cracking of diisopropyltelluride to form monomer Te was demonstrated. Using this system, CdTe, HgTe and HgCdTe layers were grown and characterized. The results presented demonstrate that low temperature growth of these materials can be achieved by CBE with results comparable to MBE.

Acknowledgements

This work was supported by the Solar Energy Research Institute (contract XH-9-19056-1), Wright Development and Research Center (contract F33615-89-C-1066) and the Georgia Tech Research Institute Internal Research Program.

Special thanks are given to Mr. Don Swank for construction of components of the CBE system, and to Ms. Marsha Moore for preparing the manuscript.

References

- [1] C.J. Summers, R.G. Benz II, B.K. Wagner, J.D. Benson and D. Rajavel, SPIE Proc. 1106 (1989) 1.
- [2] R.G. Benz II, B.K. Wagner and C.J. Summers, J. Vacuum Sci. Technol. A8 (1990) 1020.
- [3] B.K. Wagner, R.G. Benz II and C.J. Summers, J. Vacuum Sci. Technol. A7 (1989) 295.
- [4] D. Rajavel, F. Mueller, J.D. Benson, B.K. Wagner, R.G. Benz II and C.J. Summers, J. Vacuum Sci. Technol. B8 (1990) 192.
- [5] J.W. Cook, Jr., D.B. Eason and K.A. Harris, J. Vacuum Sci. Technol. B8 (1990) 192.
- [6] C. Lohe and C.D. Kohl, J. Vacuum Sci. Technol. B7 (1989) 217.
- [7] R.D. Feldman, M. Oron, R.E. Austin and R.L. Opila, J. Appl. Phys. 63 (1988) 2872.
- [8] J.M. Arias, S.H. Shin, J.T. Cheung, J.S. Chen, A. Sivananthan, J. Reno and J.P. Faurie, J. Vacuum Sci. Technol. A5 (1987) 3133.

Heteroepitaxy of CdTe(100) on Si(100) using BaF₂–CaF₂(100) buffer layers

A.N. Tiwari, W. Floeder, S. Blunier, H. Zogg

AFIF (Arbeitsgemeinschaft für industrielle Forschung) at Swiss Federal Institute of Technology, ETH – Hönggerberg, CH-8093 Zürich, Switzerland

and

M.J. Proctor

Institute of Micro- and Optoelectronics, EPFL, CH-1015 Lausanne, Switzerland

Epitaxial CdTe(100) layers have been grown on Si(100) by conventional molecular beam epitaxy (MBE) and photo-assisted MBE (PAMBE) using stacked BaF₂–CaF₂ as a buffer layer. Two-dimensional (2D) growth of BaF₂(100) is obtained using a two-temperature growth method. In conventional MBE, CdTe grows 2D for substrate temperatures above 270°C with a 2×1 surface reconstruction indicating a Te-stabilized surface. In PAMBE, 2D growth of CdTe is obtained at lower substrate temperatures ($\approx 200^\circ\text{C}$) with 1×1 RHEED patterns indicating that Ar laser illumination induces Te desorption. PAMBE grown layers have superior structural quality than layers grown by conventional MBE. Sb doped CdTe layers grown by PAMBE exhibit a 2×2 surface reconstruction, their 10 K photoluminescence spectra show a single dominant (A⁰, X) peak at 1.588 eV, and resistivities of 10⁻¹ Ω cm are measured.

1. Introduction

Heteroepitaxial growth of CdTe has received considerable attention for many optoelectronic devices, in particular for applications as a buffer layer for further growth of CdHgTe infrared sensors. High quality CdTe layers have been grown by MBE on sapphire, InSb and GaAs. However, much less work has been done on the growth of CdTe on Si, which is technologically a more important substrate. CdTe on Si would allow fabrication of monolithic active devices with the signal processing performed in the substrate.

There are only few published works on the epitaxial growth of CdTe on Si [1–5]. We have reported [6] MBE growth of good quality (111) oriented CdTe on Si(111) and recently [7] that of CdTe(100) on Si(100) by using BaF₂–CaF₂ as

buffer layers. The stacked fluoride buffer helps to overcome the large ($\approx 19\%$) lattice mismatch between CdTe and Si and relieves mechanical strain caused by thermal expansion mismatch [8]. We have also used these II-a fluorides as buffers to grow high quality epitaxial IV–VI based narrow gap semiconductors on Si and have fabricated infrared sensor arrays with cut-off wavelengths up to 12 μm [9]. Further, using a lift-off technique for the removal of CdTe layers from Si, we have shown the possibility of making thin film single crystal CdTe solar cells on reusable substrates [10].

The problem of substitutional doping in CdTe caused by self-compensation has been overcome by using a photo-assisted MBE (PAMBE) technique [11,12]. Here, illumination of the substrate by an Ar laser beam during MBE growth en-

hances the doping efficiency. However, all these works were confined to CdTe layers grown on lattice matched substrates. To our knowledge, there is no report on the doping in heteroepitaxial CdTe grown on lattice mismatched substrates (like Si) using PAMBE. This paper presents a comparative study of heteroepitaxial CdTe(100) grown by conventional MBE and PAMBE on Si(100) with intermediate fluoride buffer layers. Results on Sb doping of CdTe will also be discussed.

2. Experimental details

The MBE growth procedure of epitaxial CaF₂-BaF₂(100) on Si(100) has been described elsewhere [8]. Briefly, Si(100) wafers are cleaned using a Shiraki procedure and the protective oxide is removed by in-situ annealing at $\approx 900^\circ\text{C}$ for a few minutes just before starting fluoride growth. The substrate temperature is then lowered to 550°C and about 10 nm CaF₂ (0.6% lattice mismatch with Si at room temperature) is deposited. The RHEED patterns are spotty at this stage. The BaF₂ growth is then started without interruption at 550°C . After ~ 100 nm growth, the substrate temperature is raised to 700°C and the initial spotty RHEED patterns develop in to streaks, indicating 2D growth. The lattice has now widened by 14% to the higher lattice constant value of BaF₂, but is still 4.5% below that of CdTe [8].

For the growth of CdTe the fluoride covered Si wafers were transferred to another MBE chamber without breaking the vacuum. The substrate temperature was varied in the range of 200 to 350°C and a typical growth rate was 0.2 nm/s. The pressure in the chamber during CdTe growth was below 10^{-8} mbar. For PAMBE growth of CdTe, the substrate was illuminated with an Ar ion laser with ≈ 150 mW/cm² power density at the substrate. Photoluminescence (PL) measurements at 10 K were made using an Oxford Instruments continuous flow cryostat and a double grating spectrometer. Ar ion laser (514.5 nm) was used as an excitation source. Resistivity was measured using Van der Pauw technique and evaporated Au on CdTe was used for making ohmic contacts.

3. Results and discussion

3.1. Undoped CdTe layers

For CdTe films grown without Ar laser illumination above 270°C , streaky RHEED patterns are observed from the beginning of growth. The streaks become more intense with growing thickness. Fig. 1a shows the RHEED patterns of a ≈ 1.3 μm thick CdTe layer deposited at 300°C . The streaky patterns indicate 2D growth and the sharp Kikuchi bands illustrate a good crystal quality. Also a 2×1 surface reconstruction is observed which has been attributed to a Te-stabilized surface [13]. For the films deposited at lower temperature ($\approx 220^\circ\text{C}$), spotty RHEED patterns indicate 3D growth. These patterns transform to streaks showing a 2×1 reconstruction when annealed at $\approx 350^\circ\text{C}$ for ≈ 5 min.

Remarkable changes in the RHEED patterns occur when the substrate is illuminated with the Ar laser beam. The 2×1 surface reconstruction transforms to 1×1 when the sample is illuminated. This indicates that laser illumination induces Te desorption [14]. For PAMBE grown CdTe, streaky RHEED 1×1 patterns indicating 2D growth are obtained down to substrate temperatures of 200°C (fig. 1b). The RHEED patterns of PAMBE grown CdTe are sharper and the Kikuchi bands more intense compared to layers grown without illumination.

Layers grown by both MBE and PAMBE are crack-free and have specular surfaces. However, scanning electron microscopy reveals a smoother surface morphology and sharper electron channelling patterns for PAMBE layers. X-ray rocking curve widths of PAMBE grown CdTe are always smaller as compared to conventional MBE grown layers, but still as high as 580 arc sec (for 5 μm thick layers) due to some mosaicity. In contrast, much lower rocking curve values ~ 200 arc sec were obtained for (111) oriented CdTe on BaF₂-CaF₂/Si(111) [6,7]. We expect that CdTe(100) with smaller X-ray rocking curve widths can be obtained using misoriented Si substrates, by increasing the thickness of CdTe, and optimizing deposition parameters. A detailed comparative study of structure and morphology of conventional MBE

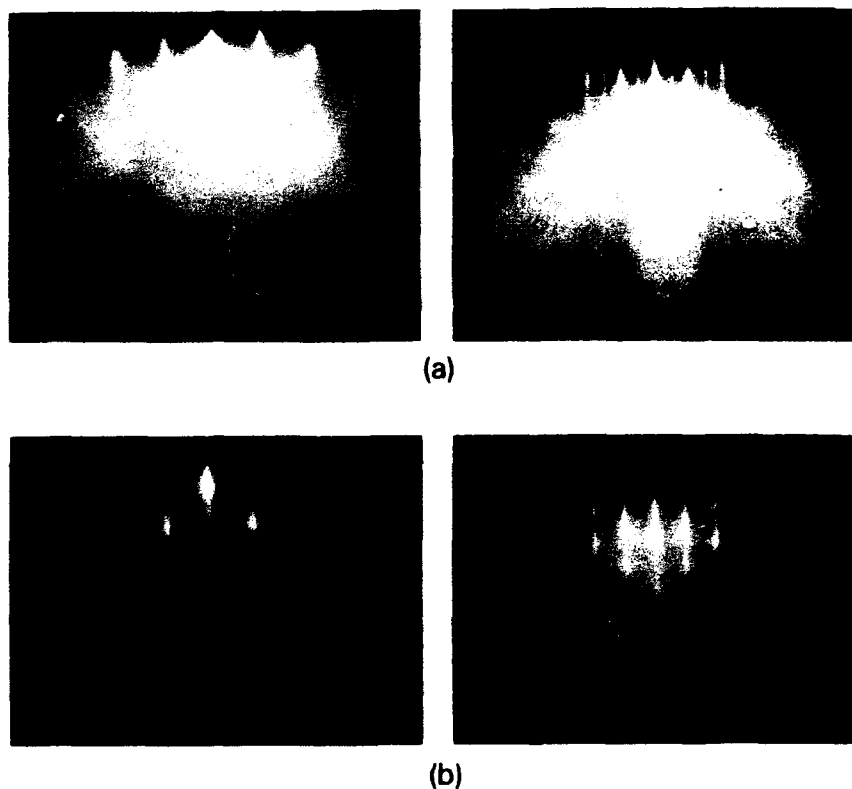


Fig. 1. 15 keV RHEED pattern of CdTe(100) on $\text{BaF}_2\text{-CaF}_2/\text{Si}(100)$: (a) MBE growth without Ar laser illumination, 2×1 Te-stabilized surface reconstruction; (b) photoassisted growth (PAMBE), 1×1 reconstruction. The electron beam is along the [001] (left) and [011] (right) direction.

and PAMBE grown CdTe epilayers will be published elsewhere.

The photoluminescence spectra of PAMBE and conventional MBE grown CdTe are significantly different. Fig. 2 shows the 10 K PL spectra of 5 μm thick layers deposited at 300°C . The spectrum for conventional MBE grown CdTe shows a peak due to combination of bound excitonic (BE) transitions which are not well resolved. On the low energy side, an intense broad band centered around 1.47 eV and originating from crystalline defects [15,16] is observed. The full width at half maximum (FWHM) value of the BE peak is 7 meV. The spectrum of PAMBE grown CdTe shows well resolved peaks at 1.590 and 1.583 eV in the excitonic region and a doublet band with peaks at

1.546 and 1.541 eV. The native defect related band at 1.463 eV has a low intensity. The (D^0, X) peak at 1.590 eV with 5.3 meV FWHM has been assigned to excitons bound to shallow donors and the (A^0, X) peak at 1.583 eV is due to recombination of acceptor bound excitons [11,16,17]. The doublet band at about 1.54 eV is due to recombination of an electron bound on a donor with a hole bound on an acceptor (DAP) with pairing effects [17].

The PL measurements clearly show that PAMBE grown layers are of superior quality, consistent with our other structural measurements. Similar changes in the PL spectra have been observed for homoepitaxial CdTe layers grown by conventional and photo-assisted MBE [11,12].

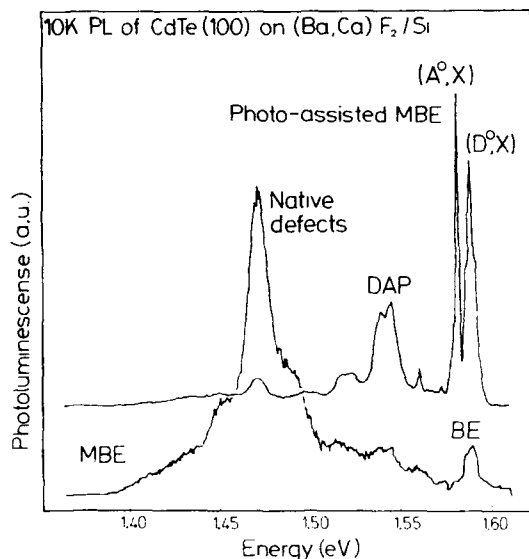


Fig. 2. 10 K photoluminescence spectra of MBE and PAMBE grown undoped CdTe(100) on BaF₂-CaF₂/Si(100). The 5 μ m thick layers were deposited at 300 °C.

3.2. Sb doped CdTe

The PAMBE technique has been successfully used for p- and n-type doping of homoepitaxial CdTe layers [11,12]. However, we were not able to reproduce the high doping activations reported in these works in our lattice mismatched heteroepitaxial CdTe layers. For the doping experiments, first about 1.5 μ m thick undoped CdTe was de-

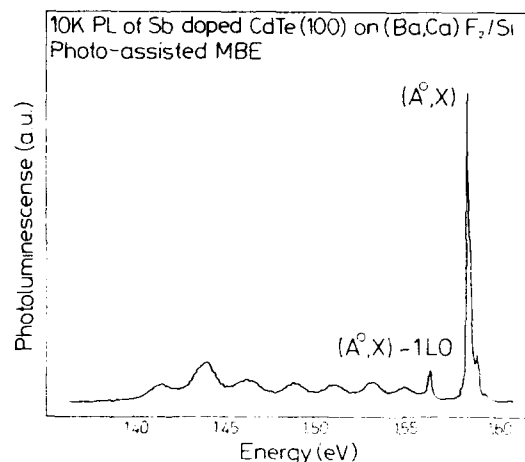


Fig. 4. 10 K photoluminescence spectrum of a 3.5 μ m thick PAMBE grown Sb doped CdTe(100) on BaF₂-CaF₂/Si(100). The (A⁰,X) peak is dominant. The resistivity of the p-type layer is $\approx 10^3 \Omega$ cm.

posited on BaF₂-CaF₂/Si(100) at 300 °C with laser illumination. As described above, streaky 1 \times 1 RHEED patterns are observed. Sb-doped CdTe layers were subsequently grown at an optimum substrate temperature of 260 °C and an Sb cell temperature of 400 °C. With the Sb shutter open, half order streaks in the RHEED patterns appear as shown in fig. 3; the surface reconstruction changes to 2 \times 2. Such a 2 \times 2 reconstruction has already been observed in homoepitaxial CdTe, and it was suggested that the laser illumination



Fig. 3. 15 kV RHEED pattern of PAMBE grown Sb doped CdTe layer showing a 2 \times 2 surface reconstruction. Electron beam parallel [001] (left) and [011] (right) direction. Sb effusion cell and substrate temperatures were 400 and 260 °C, respectively.

causes Te desorption and Sb gets incorporated into the Te vacancy sites [14].

The PL spectrum of a 3.5 μm thick Sb doped CdTe layer is shown in fig. 4. A strong luminescence peak with 2.3 meV FWHM value is observed at 1.588 eV and is assigned to an exciton bound to a neutral acceptor (A^0 , X). Its phonon replica, (A^0 , X)-1 LO is observed at 1.566 eV. On the high energy side of the dominant peak a well resolved shoulder at 1.593 eV and a small peak at 1.597 eV are also present. Bicknell et al. [11,18] have obtained (A^0 , X) and its replica at 1.5896 and 1.5687 eV, respectively, in 1.6 K PL spectra of heavily doped CdTe:Sb on CdTe substrates. On the high energy side they observed peaks at 1.5950 and 1.597 eV. Our values are about 2 meV higher. The (A^0 , X) transition is due to the acceptor level introduced by Sb and the peaks at 1.593 and 1.597 eV are due to the excited states of the excitons bound to the (A^0 , X) level [18]. We do not observe any DAP or native defect related deep level luminescence.

The resistivity of our layers decreases from $\approx 10^6 \Omega \text{ cm}$ for undoped CdTe to $\approx 10^3 \Omega \text{ cm}$ for p-type CdTe:Sb layers. Lower resistivities, previously reported for CdTe grown on lattice matched substrates [11,18], were not obtained. Larger Sb flux or lower substrate temperature yielded poor RHEED patterns indicating segregation or polycrystalline growth in these experiments.

4. Conclusions

According to the structural and photoluminescence data presented, illumination of the substrate with an Ar laser beam improves the quality of CdTe layers on fluoride covered Si-substrates and allows 2D growth at even lower substrate temperatures than conventional MBE. The different surface reconstructions observed with and without laser beam or Sb flux agree with the results reported for homoepitaxial growth. Ar laser illumination, which provides low energy photons, influences surface reconstructions which have low activation energies. However, we found that X-ray line widths remain still much larger compared to homoepitaxial growth, and dopant activation is

much less pronounced in our case. The lowest resistivities we achieved are three orders of magnitude higher than in Sb doped CdTe homoepitaxial layers. Thus, a convincing explanation why self-compensation can be suppressed drastically by PAMBE for lattice matched epitaxy only and not for mismatched heteroepitaxy must take into account the difference in structural qualities of CdTe layers achieved with homoepitaxy and lattice mismatched heteroepitaxy.

Acknowledgements

We would like to thank Professor F.K. Reinhart, EPFL-Lausanne, Switzerland, for the permission to use the photoluminescence system. The work is sponsored by the National Energy Research Foundation and the Swiss National Science Foundation.

References

- [1] R.N. Bicknell, T.H. Myers and J.F. Schetzina, *J. Vacuum Sci. Technol.* A2 (1984) 423.
- [2] R.L. Chou, M.S. Lin and K.S. Chou, *Appl. Phys. Letters* 48 (1986) 523; *J. Crystal Growth* 94 (1989) 551.
- [3] A. Nouhi, G. Radhakrishnan, J. Katz and K. Koliwad, *Appl. Phys. Letters* 52 (1988) 2028.
- [4] R. Bean, K. Zanio and J. Ziegler, *J. Vacuum Sci. Technol.* A7 (1989) 343.
- [5] R. Sporken, S. Sivananthan, K.K. Mahavadi, G. Monfroy, M. Boukerche and J.P. Faurie, *Appl. Phys. Letters* 55 (1989) 1879.
- [6] H. Zogg and S. Blunier, *Appl. Phys. Letters* 49 (1986) 1531.
- [7] A.N. Tiwari, W. Floeder, S. Blunier, H. Zogg and H. Weibel, *Appl. Phys. Letters* 57 (1990) 1108.
- [8] S. Blunier, H. Zogg and H. Weibel, *Appl. Phys. Letters* 53 (1988) 1512.
- [9] H. Zogg, C. Maissen, J. Masek, S. Blunier, A. Lambrecht and M. Tacke, *Appl. Phys. Letters* 55 (1989) 969.
- [10] W. Floeder, A.N. Tiwari, S. Blunier, H. Zogg and H. Weibel, in: *Proc. 9th European Photovoltaic Solar Energy Conf.*, Freiburg, 1989, p. 157.
- [11] R.N. Bicknell, N.C. Giles and J.F. Schetzina, *J. Vacuum Sci. Technol.* B5 (1987) 701.
- [12] J.M. Arias, S.H. Shin, D.E. Cooper, M. Zandian, J.G. Pasko, E.R. Gertner, R.E. DeWames and J. Singh, *J. Vacuum Sci. Technol.* A8 (1990) 1025.

- [13] J.D. Benson, B.K. Wagner, A. Torabi and C.J. Summers, Appl. Phys. Letters 49 (1986) 1034.
- [14] J.D. Benson and C.J. Summers, J. Crystal Growth 86 (1988) 354.
- [15] D.J. Leopold, J.M. Ballingall and M.L. Wroge, Appl. Phys. Letters 49 (1986) 1473.
- [16] T. Taguchi and M. Suita, Japan. J. Appl. Phys. 28 (1989) L1889.
- [17] J.M. Francou, K. Saminadayar, J.L. Pautrat, J.P. Gaillard, A. Million and C. Fontaine, J. Crystal Growth 72 (1985) 220.
- [18] R.N. Bicknell, N.C. Giles and J.F. Schetzina, Appl. Phys. Letters 49 (1986) 1735.

Atomic layer epitaxy of $(\text{CdTe})_m(\text{ZnTe})_n$ -ZnTe multiquantum wells on (001)GaAs substrate

Jie Li, Li He, Wei Shan, Xingyu Cheng and Shixin Yuan

Shanghai Institute of Technical Physics, Academia Sinica, 420 Zhong Shan Bei Yi Road, Shanghai 20083, People's Rep. of China

$(\text{CdTe})_m(\text{ZnTe})_n$ -ZnTe multiquantum well structure has been proposed and grown on (001)GaAs substrate by atomic layer epitaxy. Growth has been investigated using reflection high energy electron diffraction. Material characterizations have been performed by X-ray diffraction and photoluminescence. With this structure, great improvements have been made in crystalline quality compared with CdTe-ZnTe multiquantum wells, due to the reduction of misfit dislocations.

1. Introduction

The multilayers of II-VI wide-gap compound semiconductors are of current interest for their potential applications in short wavelength optoelectronic devices. CdTe-ZnTe system belongs to this category. CdTe-ZnTe multilayers possess direct band gap and the band gap can be tailored from 1.6 to 2.2 eV by varying the thicknesses of the CdTe and ZnTe layers. Selective acceptor doping of ZnTe and donor doping of CdTe have been achieved successfully [1,2], indicating the possibility of fabricating p-n junction in the CdTe-ZnTe system. These characteristics make it promising for the applications of light emitter and detector devices. But the large lattice constant mismatch (6.4%) between CdTe and ZnTe makes it very difficult to grow a CdTe-ZnTe system of high quality because of the easy relaxation of mismatch-strain through misfit dislocation generation. It was reported [3] that the critical thickness of CdTe/ZnTe epitaxy was only several monolayers at the MBE growth temperature. Although it is thought that strained multilayers can be grown perfectly with the thickness of individual layers being restricted to below their critical value, the realization of ultrathin-layer-control and meanwhile achieving periodical coherence within the device-needed thickness are not easy using the conventional growth techniques. Molecular beam epitaxy (MBE) [4] and organometallic vapor phase

epitaxy [5] have been applied to prepare CdTe-ZnTe multilayer structures, but the crystalline quality has not met, at the present stage, the needs of device applications. CdZnTe-CdTe and CdZnTe-ZnTe systems have been proposed for obtaining relatively well-matched lattice constants between contacted layers, but the growth of CdZnTe alloy is now far from optimized in the whole composition range [6].

Here, we report a novel structure grown by atomic layer epitaxy (ALE) technique for reduction of mismatch-induced dislocations in the CdTe-ZnTe system without introducing CdZnTe alloy. Ultrashort period $(\text{CdTe})_m(\text{ZnTe})_n$ superlattices were confined to ZnTe barriers to form $(\text{CdTe})_m(\text{ZnTe})_n$ -ZnTe multiquantum wells (MQWs). ALE technique is superior in growing ultrathin epilayers under precise control. Taking the advantages of the ALE technique, we controlled the thickness of individual layers of superlattices in quantum wells thinner than the critical value and adjusted the thickness ratio of CdTe to ZnTe to obtain "lattice constants" in potential wells closer to that of ZnTe barriers.

2. Material growth

The sample growth were carried out in a Shenyang Scientific Instrument FW-III MBE machine equipped with a computer-controlled

shutter system. $(\text{CdTe})_m(\text{ZnTe})_n$ -ZnTe MQWs were deposited on (001)ZnTe/(001)GaAs hybrid substrates, where (001)ZnTe is a buffer layer grown by MBE. Details of (001)GaAs substrate surface preparation were previously described elsewhere [7]. Three effusion cells containing elemental Cd, Zn and Te separately were employed for MBE growth of ZnTe buffer layers and subsequent ALE growth of MQW structures. The substrate temperature for ALE growth was 230–270°C, and 310–340°C for the ZnTe buffer layer growth. During ALE growth of CdTe or ZnTe, the shutters of the two constituent elemental sources were opened alternatively with an interval of 2 s. In CdTe growth, considering that the sticking coefficient of Cd on the Te surface is smaller than that of Te on the Cd surface, the Cd and Te source shutters were opened for 10 and 6 s separately in a growth cycle. The beam flux intensities were adjusted to deposit about 30 monolayers of Cd and 4 monolayers of Te within each opening time assuming no re-evaporation. By the same consideration, in ZnTe growth the opening times of the Zn and Te source shutters were 7 and 6 s separately producing about 15 monolayers of Zn and 4 monolayers of Te.

There exists a large lattice mismatch (7.6%) between GaAs and ZnTe, which introduces misfit dislocations at the film-substrate interface. In order to reduce the effects of these dislocations on the quality of the MQWs, a (001)ZnTe buffer layer of 0.5 to 1 μm was first deposited by MBE. To achieve an atomically flat surface for subsequent ALE growth, reflection high energy electron diffraction (RHEED) was used to investigate the growth conditions. It was found that the Zn-to-Te₂ flux ratio $R = P_{\text{Zn}}/P_{\text{Te}}$ influenced the smoothness of growth surface, where P_{Zn} and P_{Te} are the vapor pressures of Zn and Te₂ flux, respectively, measured at the sample position. Immediately as the growth (under $R \approx 1$) of ZnTe started, the initially streaked RHEED pattern became spotty, indicating a rough surface. Large lattice constant mismatch between ZnTe and GaAs caused three-dimensional growth. Unless Te-rich growth conditions were employed, the three-dimensional growth would persist. Once a smooth surface was achieved, two-dimensional growth could occur under Zn-rich conditions. The maximum R under which two-di-

mensional growth could be maintained is closely dependent on the extent of surface smoothness. For the smoothest surface in our experiments, two-dimensional growth could occur even for $R = 6$. For $R \approx 1.2$, both (2×1) and $c(2 \times 2)$ surface reconstructions were observed implying coexistence of Zn-terminated and Te-terminated surfaces. In our experiments, a ratio of $R = 0.8$ was used in the initial stage of ZnTe growth. After the front surface became smooth, R was increased and growth proceeded under Zn-rich conditions in order to reduce the density of the Zn-vacancy in the ZnTe buffer layer [8].

While ALE growing, the RHEED patterns exhibited well-defined streaks. It was clearly observed that Cd- and Zn-covered surfaces showed $c(2 \times 2)$ reconstruction and Te-covered surfaces showed (2×1) reconstruction, with no sign of mixture of $c(2 \times 2)$ and (2×1) reconstructed surface. ALE stepwise growth led to a variation of surface reconstructions from $c(2 \times 2)$ to (2×1) , and vice versa.

In the growth of $(\text{CdTe})_m(\text{ZnTe})_n$ short period superlattices on ZnTe barriers, it was observed that the RHEED streaks became broad and weak when the epitaxial thickness exceeded a certain value. The onset of RHEED pattern degradation corresponded to the critical thickness. This means that the critical thickness of epitaxy of the superlattice on ZnTe could also be determined by Yao's method [9]. To avoid misfit strain relaxation, it is absolutely necessary to investigate critical thicknesses of epitaxy of $(\text{CdTe})_m(\text{ZnTe})_n$ superlattices on ZnTe.

3. Characterization

A series of $(\text{CdTe})_m(\text{ZnTe})_n$ -ZnTe MQW samples, which have different average superlattice constants in the potential wells and different well-widths, were prepared by ALE. Characterization by X-ray diffraction using Cu-K α (400) Bragg reflection and photoluminescence using a cw argon laser as a pump source were performed. Sample No. SL-27 with a designed structure of $\{[(\text{CdTe})_2(\text{ZnTe})_4] \times 7 (\text{ZnTe})_{80}\} \times 6$ is shown here as an example. A schematic demonstration of this struc-

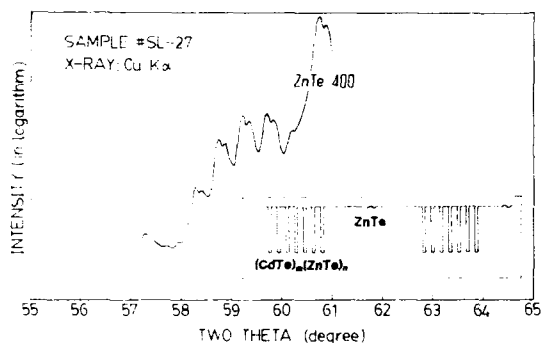


Fig. 1. θ - 2θ X-ray diffraction scan from No. SL-27, showing (400)-like satellite peaks. The inset is a schematic demonstration of present structure in energy gap.

ture is given in the inset of fig. 1. An X-ray diffraction scan of No. SL-27 around the (400) Bragg diffraction of bulk ZnTe is also shown in fig. 1. The measurements were carried out in a $\theta/2\theta$ arrangement. The spectrum shows the (400)-like superlattice peaks originated from coherent scattering of MQW periods. The thickness of each period was derived from the interspacing of satellite peaks. The measured period thickness is about half of the value calculated according to the growth design, assuming that two monolayers, i.e., $1/2$ lattice constant thickness was produced in each growth cycle. In fig. 1, the position of the envelope, which slowly modulates the superlattice peaks in amplitude on the lower angle side of the ZnTe (400) Bragg peak, corresponds to the average lattice constant of superlattice in the quantum wells according to Bragg's law. The position of this envelope is much closer to the ZnTe (400) Bragg peak than that of CdTe-ZnTe MQWs [7]. This means that the lattice constant of the quantum wells matches better with ZnTe barriers than that of CdTe potential wells does. In addition, $K\alpha_1$ and $K\alpha_2$ peaks were clearly separated in the spectrum indicating very sharp superlattice peaks. This attests to a high structural quality in terms of high degree of periodical coherence and crystalline perfection in the individual layers.

The curve denoted by (1) in fig. 2 shows the photoluminescence spectrum at 90 K from the same sample. The linewidth of the luminescence

peak is 14 meV which is much smaller than the reported values, measured at 5 K, of MBE grown CdTe-ZnTe superlattices [10,11]. The luminescence spectrum has a single intense exciton peak. Defect-related transitions which should appear on the lower energy side of the exciton peak [12] can not be detected within the detector limit under the used pump condition (< 5 mW). Despite the effective luminescence thickness of our sample is very thin, intense light emission was observed under the weak pump condition. The high luminescence efficiency is mainly attributed to carrier confinement in quantum wells [13] and also due to high structural perfection because high-density defects provide strong nonradiative decay channels [14]. Up to here, it is obvious that great improvement has been made in crystalline quality by using the proposed structure and ALE technique.

As a contrast, we show a CdTe-ZnTe MQW grown by ALE under the previously used growth conditions with a designed structure: $[(\text{CdTe})_{18}(\text{ZnTe})_{66}] \times 10$. Its characterization results of X-ray diffraction and photoluminescence are shown by fig. 3 and curve (2) of fig. 2, respectively. Comparing fig. 3 with fig. 1, more satellite peaks are obvious but the $K\alpha_1$ and $K\alpha_2$ peaks are not resolved. The appearance of more satellite peaks is mainly due to narrower quantum wells and larger lattice mismatch between the quantum wells and barriers. Because the width and lattice constant of the wells determine the linewidth and the position of the 400-like envelope of satellite peaks beside

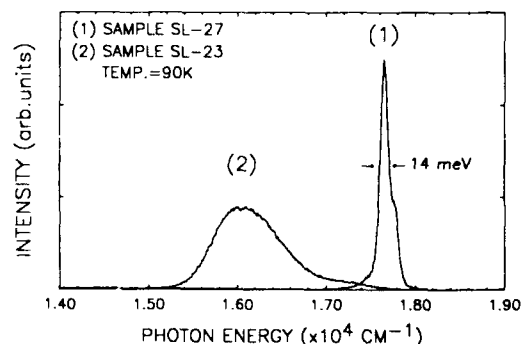


Fig. 2. Photoluminescence spectrum from No. SL-27 (1) and No. SL-23 (2) at 90 K.

ZnTe 400 Bragg peak. For narrower wells and larger barrier-well lattice mismatch, more satellite peaks would appear at the angle position farther apart from the ZnTe 400 Bragg peak. Fig. 3 does not resolve $K\alpha_1$ and $K\alpha_2$ peaks, attesting to poor crystalline quality. To this, fig. 3 also gives further evidence. The curve in dashed line is a calculation in the kinematical approximation for the unstrained case. The theoretical curve is in good agreement with the experimental one, indicating that the mismatch strain is completely relaxed. Therefore, a large number of misfit dislocations exist in the individual layers. In addition, the linewidth of photoluminescence peak (2), which is 106 meV, is much larger than that of peak (1) in fig. 2. This is in agreement with the result of X-ray diffraction measurement.

For the investigation of strain relaxations in the CdTe-ZnTe system and for further confirmation of the advantages of the $(\text{CdTe})_m(\text{ZnTe})_n$ -ZnTe MQW structure, a sample which has a designed structure of $[(\text{CdTe})_4-(\text{ZnTe})_{60}] \times 4 + [(\text{CdTe})_8-(\text{ZnTe})_{60}] \times 3 + [(\text{CdTe})_{12}-(\text{ZnTe})_{60}] \times 2$ was prepared by ALE. Its photoluminescence result is shown in fig. 4. The three peaks, denoted by (1), (2) and (3), have linewidths 14, ~41 and ~50 meV, respectively, and correspond to the three quantum well groups possessing different CdTe well widths. Corresponding to the narrowest peak,

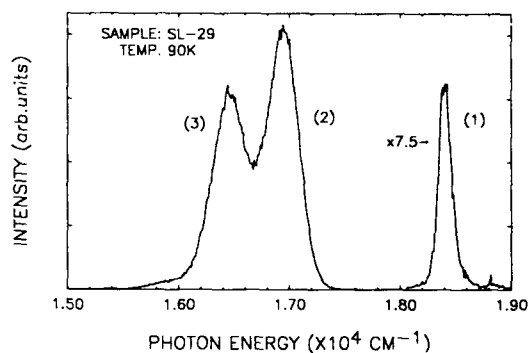


Fig. 4. Photoluminescence spectrum from No. SL-29 at 90 K.

the CdTe wells have a width below the critical thickness and the lattice constant mismatch is completely accommodated by elastic strain. The abrupt broadening of the other two peaks is due to strain relaxation through dislocation generation. Although sample No. SL-27 has much wider quantum wells, its linewidth of the photoluminescence peak is comparable with that of peak (1). This fact suggests that with $(\text{CdTe})_m(\text{ZnTe})_n$ -ZnTe structure, misfit dislocations induced by lattice constant mismatch between quantum wells and barriers were largely reduced in No. SL-27. In addition, it should be pointed out that the 14 meV linewidth of peak (1) indicates a very high degree of interface abruptness and periodical coherence, because even for wider CdTe wells, only one monolayer thickness fluctuation in quantum wells could cause 30 meV energy variation in the band gap [15] due to the heavy strain and strong carrier confinement. Here, the advantages of ALE are shown in the growth of heavily strained and ultrathin multilayer structures.

We have shown our success in improving the crystalline quality with the $(\text{CdTe})_m(\text{ZnTe})_n$ -ZnTe MQW structure. We believe that better quality could be achieved by optimizing the ALE growth conditions. For the purpose of providing reference for the structure design, the onset of mismatch-strain relaxation in the epitaxy of $(\text{CdTe})_m(\text{ZnTe})_n$ superlattices on bulk ZnTe should be investigated in detail.

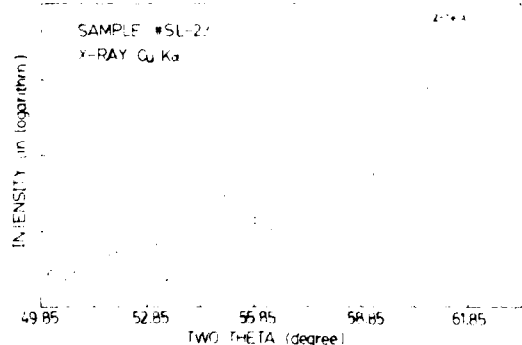


Fig. 3. $\theta/2\theta$ X-ray diffraction scan from No. SL-23. Also shown in dashed line is a spectrum calculated in the kinematical approximation for the unstrained case.

4. Conclusion

A CdTe-ZnTe multilayer system was, for the first time, grown by ALE technique. The $(\text{CdTe})_m(\text{ZnTe})_n\text{-ZnTe}$ MQW structure has been proposed and successfully produced on (001)GaAs substrate. Growth has been investigated using RHEED. Material characterizations have been performed by X-ray diffraction and photoluminescence. Taking the advantages of the ALE technique, the lattice constant mismatch between the quantum wells and barriers was designed by controlling the average lattice constant of the ultra-short period superlattice in the quantum wells through adjusting the layer thickness ratio of CdTe to ZnTe. Proper design of the mismatch and the width of quantum wells could prevent the occurrence of mismatch-strain relaxation. In contrast with CdTe-ZnTe MQWs and superlattices, the $(\text{CdTe})_m(\text{ZnTe})_n\text{-ZnTe}$ structure has great advantage in achieving high crystalline quality, due to large reduction of misfit dislocations. In addition, it was found that the ALE technique is superior in the growth of heavily strained and ultra-thin period multilayers.

Acknowledgments

The present work is supported by the National Committee of Science and Technology. The authors would like to express sincere thanks to professor Aizhen Li for her encouragement, and also to Meifang Yu and Yiming Qiao for their technical assistance.

References

- [1] M. Kobayashi, R. Kimura, M. Konagai and K. Takahashi, *J. Crystal Growth* 81 (1987) 495.
- [2] T. Yao, in: *The Technology and Physics of Molecular Beam Epitaxy*, Ed. E.H.C. Parker (Plenum, New York, 1985) p. 313.
- [3] J. Cibert, Y. Gobil, Le Si Dang and S. Tatarenko, G. Feuillet, P.H. Jouneau and K. Saminadayar, *Appl. Phys. Letters* 56 (1990) 292.
- [4] G. Monfroy, S. Sivananthan, X. Chu, J.P. Faurie, R.D. Knox and J.L. Staudenmann, *Appl. Phys. Letters* 49 (1986) 152.
- [5] D.W. Kisker, P.H. Fuoss, J.J. Krajewski, P.M. Amirtharaj, S. Nakahara and J. Menendez, *J. Crystal Growth* 86 (1988) 210.
- [6] R.D. Feldman, R.F. Austin, A.H. Dayem and E.H. Westervick, *Appl. Phys. Letters* 49 (1986) 797.
- [7] Jie Li, Li He, Wenguo Tang, Zhongling Peng and Shixin Yuan, CdTe-ZnTe multiquantum wells grown by atomic layer epitaxy on (001)GaAs substrate, in: *Proc. Sino-Soviet Seminar on Spectroscopy and Optoelectronics in Semiconductors and Related Materials*, Eds. S.C. Shen and Z.P. Wang (World Scientific, Singapore, 1990).
- [8] R.D. Feldman, R.F. Austin, P.M. Bridenbaugh, A.M. Johnson, W.M. Simpson, B.A. Wilson and C.E. Bonner, *J. Appl. Phys.* 64 (1988) 1191.
- [9] T. Yao, H. Nakao, H. Kawanami and R. Toba, *J. Crystal Growth* 95 (1989) 107.
- [10] H. Shtrikman and E. Finkman, *Superlattices and Microstructures* 6 (1989) 55.
- [11] R.H. Miles, G.Y. Wu, M.B. Johnson, T.C. McGill, J.P. Faurie and S. Sivananthan, *Appl. Phys. Letters* 48 (1986) 1383.
- [12] He-Xiang Han, B.J. Feldman, M.L. Wroge, D.J. Leopold and J.M. Ballingall, *J. Appl. Phys.* 61 (1987) 2670.
- [13] H. Jung, A. Fischer and K. Ploog, *Appl. Phys.* A33 (1984) 97.
- [14] M.D. Camras, J.M. Brown, N. Holonyak, Jr., M.D. Nixon, R.W. Kaliski, M.J. Ludowise, W.T. Dietze and C.R. Lewis, *J. Appl. Phys.* 54 (1983) 6183.
- [15] R.H. Miles, T.C. McGill, S. Sivananthan, X. Chu and J.P. Faurie, *J. Vacuum Sci. Technol.* B5 (1987) 1263.

Surface stoichiometry effects on ZnSe/GaAs heteroepitaxy

M.C. Tamargo, R.E. Nahory, B.J. Skromme *, S.M. Shibli **, A.L. Weaver, R.J. Martin
and H.H. Farrell

Belcore, 331 Newman Springs Road, Red Bank, New Jersey 07701, USA

We describe a simple model, based on counting of valence electrons at the interface, which can predict the surface reconstructions which provide optimal heteroepitaxial growth. Vertical photocurrent measurements on a series of ZnSe/GaAs heterostructures grown by molecular beam epitaxy, using various GaAs surface reconstructions, support the model predictions that surfaces which provide nearly equal number of the constituent atoms for interface bonds produce the highest quality interfaces.

1. Introduction

In the past several years the possibility of fabricating heterostructures combining II–VI and III–V semiconductors has been actively pursued in several laboratories [1–4]. In particular, recent reports demonstrate novel devices for which the II–VI/III–V heterointerface is a critical part of the device [5–7]. This differs from the more usual situation in which a III–V substrate is used for the growth of a II–VI buffer layer in that, for these new structures, the quality of the heterointerface is of utmost importance, not only from a structural and crystalline point of view, but also from an optical and electronic transport perspective. In these recent results, the key has been in the preparation of the III–V surface prior to II–VI growth [6,7], confirming earlier predictions [2].

In this study, we describe a method for predicting the surface structures which provide the most favorable conditions for the ideal interface formation. The method is based on a principle of electronic balance at the II–VI/III–V interface [8]. It

depends on the same formulation of electrostatics for polar interfaces proposed by Harrison et al. [9], and provides a simple, intuitive approach based on valence electron counting at the interface. To support our model we have grown a set of ZnSe/GaAs heterostructures, using a dual chamber molecular beam epitaxy (MBE) system, with various GaAs surface reconstructions on which the ZnSe layer was grown. We performed measurements of vertical photocurrent which reflect the ZnSe/GaAs interface quality in these heterostructures. These results support the model prediction that GaAs surfaces which expose equal number of the two constituent atoms, Ga and As, provide the most favorable surfaces for ZnSe epitaxy [8]. These surfaces produce electronically balanced interfaces with no excess charge, and therefore minimal densities of interface states. These observations, although derived from measurements on the specific case of ZnSe/GaAs are applicable in general to other II–VI/III–V systems. Our results indicate that, although under some experimental conditions the formation of a non-optimal separate phase (e.g., Ga_2Se_3) between the GaAs and the ZnSe may be forced to occur, as has been proposed [10,11], ideal interfaces which are abrupt and stable can be formed without a need to invoke these interfacial layers and without any evidence for their formation.

* Present address: Department of Electrical Engineering, Arizona State University, Tempe, Arizona 85287-5706, USA

** Present address: Instituto de Física “Gleb Wataghin”, Unicamp, 13081 Campinas, SP, Brazil

2. The electron counting method

In the bulk, the stability of both diamond and zinc-blende structure semiconductors rests on the fact that the individual atoms are tetrahedrally bonded with two electrons per bond. For diamond structure semiconductors, e.g., Si or Ge, this situation is achieved in an almost trivial fashion as each atom has four valence electrons distributed among the four bonding orbitals. Therefore each bond has the optimal configuration of a total of two electrons: one from each of the two atoms that it connects.

In the zinc-blende compound semiconductors (e.g., GaAs or ZnSe), this requirement is also satisfied as the cation contributes more than one electron and the anion less than one electron for a net occupancy of two. For example, in III-V compounds, each bonding orbital contains, on the average, $3/4$ of an electron from the group III atom and $5/4$ of an electron from the group V atom.

In the case of II-VI/III-V heteroepitaxy, we first consider the hypothetical situation of an unreconstructed interface. This involves abutting, for example, a completely As terminated GaAs surface to a Zn terminated ZnSe surface. As Zn contributes $2/4$ of an electron and As $5/4$ of an electron to each bonding orbital, there will be a charge deficit of $1/4$ of an electron per bond ($7/4 = 2 - 1/4$), resulting in a deficit of $1/2$ of an electron per atomic site. The opposite situation obtains for the abutment of Ga terminated and Se terminated surfaces, where there will be an excess of $1/2$ of an electron per site. This excess or deficit cannot remain localized at the interface, thus charge will flow either in or out of the interface region. This will result in a loss of local charge neutrality and formation of interface states, which, in turn, will produce band bending and very high electric fields at the interface. In order to reduce these high electrostatic fields, compensatory processes such as electron field enhanced diffusion or desorption are expected to occur, which may destroy the ideal, planar nature of the interface [12].

The solution to the electronic imbalance at the interface is, in principle, rather simple. A mixed interface, containing 50% Ga and 50% As atoms

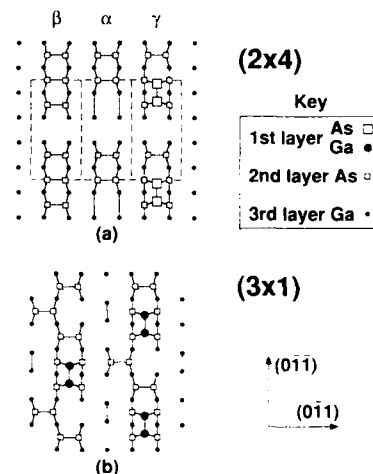


Fig. 1. Several surface reconstructions of the GaAs (100) surface: (a) The $(2 \times 4)\beta$ GaAs surface with a 75% As coverage, an As-lean $(2 \times 4)\alpha$ variant with a 50% As coverage and an As-rich $(2 \times 4)\gamma$ variant with excess chemisorbed As. (b) A possible (3×1) surface structure with a 50% As coverage.

should provide no excess charge at the interface. In practice, stable surface reconstructions are produced on the GaAs (100) surface which determine the surface stoichiometries available for growth. Thus, very accurate control of the experimental conditions which produce a particular surface reconstruction is needed to form the ideal II-VI/III-V heterointerface.

The most frequently observed GaAs surface reconstruction during MBE growth is the (2×4) As rich reconstruction [13–15]. It has been shown [16] that this reconstruction actually consists of a family of structures, the simplest of which contains three As dimers and as As dimer vacancy per unit cell. This gives an As coverage of 75%. However, both more As-rich and less As-rich members of the (2×4) family have been identified [16]. Fig. 1a shows three representative surface reconstructions for the three regimes, denoted as α , β and γ for the As-lean, 75%, and As-rich range of compositions, respectively. Of these, only the As-lean $(2 \times 4)\alpha$ approaches the desired 50% surface stoichiometry. The Ga-rich (4×2) surface reconstruction is also often observed in MBE growth. While it is not as well established, this diffraction pattern is believed to correspond to a 75% Ga

coverage under ideal conditions, and higher effective coverage can occur due to the formation of Ga droplets.

Several transitional reconstructions have been observed in going from the (2×4) to the (4×2) regimes [17]. It is therefore reasonable to expect that these may take us close to the ideal 50% surface stoichiometry. Two of these intermediate structures which have been observed show a (4×6) or a (3×1) reflection high energy electron diffraction (RHEED) pattern. They are believed to represent two different paths in the evolution from a (2×4) to a (4×2) surface reconstruction. Both represent a family of surfaces which possess a range of surface compositions and can provide, in some of their members, nearly stoichiometric interfaces [8]. Fig. 1b shows an example of a surface with a (3×1) surface reconstructions, a disordered form of the $c(6 \times 4)$, which provides nearly equal number of As and Ga atoms at the surface and which will be discussed below. Recently, Qiu et al. [6] and Kobayashi [7] have reported extremely good optical and electrical properties from ZnSe/GaAs interfaces. They both observe the formation of a (4×2) surface reconstruction on the GaAs substrate prior to ZnSe deposition. This surface is believed to be a Se-modified version of the (4×6) GaAs surface which may provide nearly 50:50 Ga-to-As ratio [8].

3. Evaluation of interface quality: RHEED and photoluminescence studies

Several means are available to evaluate interface quality, each of which provides information on different aspects of the interface. Thus, an ideal interface must aim to optimize as many of the criteria as possible. The most immediate indication of a good or bad interface is the evolution of the RHEED pattern as one initiates heteroepitaxial growth. As we had previously reported [1], instantaneous two-dimensional nucleation of ZnSe is typically observed on the (2×4) surface reconstructions, while a long lasting three-dimensional initial growth, which we refer to as transition time, occurs on the (4×2) GaAs surfaces. In the latter case, this disordered initial growth mode lasts for

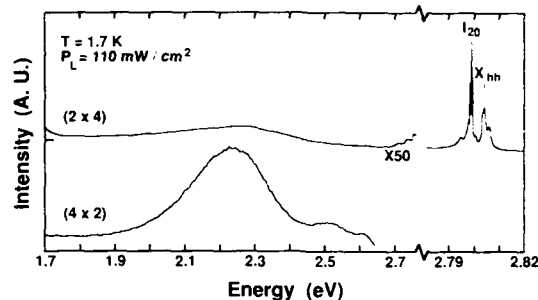


Fig. 2. Low temperature photoluminescence spectra for two samples consisting of a thin (1000 Å) ZnSe layer grown on $\text{In}_{0.04}\text{GaAs}$ substrates; one having a (2×4) and another a (4×2) surface reconstruction.

more than 30 s (up to several minutes), depending on the details of the growth conditions used, representing growth of a relatively thick (50–100 Å) layer before smoothing of the growth surface takes place. Transition times on the (3×1) surface, although always short, vary from negligible (less than 5 s) to approximately 15 s, apparently depending upon sample thermal history. Low temperature photoluminescence (PL) from 1000 Å ZnSe layers grown on $\text{In}_{0.04}\text{GaAs}$ bulk substrates are shown in fig. 2. In one case the ZnSe layer was grown on the (4×2) , Ga stabilized substrate surface, produced upon de-oxidation of the substrate in the absence of an As flux. In the other, the substrate was heated in the presence of As, thus obtaining a (2×4) surface reconstruction prior to ZnSe growth. The sample grown on a (4×2) surface exhibits an initial three-dimensional growth mode. Its PL is dominated by deep level emission indicating poor quality of the ZnSe near the interface region. By contrast, a similar sample grown on a (2×4) surface, which gave a negligible RHEED transition time, exhibits a PL spectrum with almost exclusively band edge luminescence and very sharp excitonic features.

The apparent insensitivity of the initial RHEED transition times to the degree of As coverage within the (2×4) family of structures may be explained by electric field enhanced desorption of excess As from the GaAs surface. This compensatory process, which would reduce the effect of the electronic imbalance at the interface, would actually take us closer to ideally stoichiometric composi-

tions. On the other hand, surfaces which contain an excess of Ga atoms cannot undergo such a compensatory desorption due to the relatively low vapor pressure of Ga. In these cases, roughening of the surface and intermixing may become the preferred mechanisms to relieve the interface imbalance. This roughening may in some cases lead to the formation of gallium selenide phases at the interface.

4. Vertical photocurrent studies

In addition to the structural properties of the heterointerface, one must establish the quality of the interface with respect to electronic transport across it. Here we propose a method based on vertical photocurrent (PC) through the interface. By this we mean that current flows perpendicular to the interface, between the epilayers and the substrate. Although transport across the interface is a complex process which is not well understood, photocurrents are well known to be very sensitive to the presence of traps, so that driving carriers directly across an interface is a good measure of interface quality. Thus, all else being equal, the magnitude of the photocurrent will vary with the density of interface states.

For these purposes a structure was considered consisting of an n^+ -GaAs substrate, an n -GaAs(Si) epilayer ($n = 10^{16} \text{ cm}^{-3}$, $d = 500 \text{ nm}$) and an n -ZnSe(Ga) layer ($n = 10^{17} \text{ cm}^{-3}$, $d = 500 \text{ nm}$). A series of such structures were grown, varying only the reconstruction of the surface of the GaAs epilayer, as observed by RHEED, prior to the growth of the ZnSe layer. We note here that as a side experiment some samples also included an additional GaAs layer as a thin cap ($\sim 20 \text{ nm}$) on top of the ZnSe to passivate the free surface.

The samples were grown in a dual chamber MBE system. In detail, a $0.5 \mu\text{m}$ layer of GaAs (n^+) was grown on GaAs(100) n^+ substrates in a chamber dedicated to GaAs grown, under typical MBE growth conditions. The samples were then cooled below 400°C in the presence of an As background. This typically gave a very As-rich (2×4) surface reconstruction, which served as a starting condition for all cases. The samples were

Table 1
Summary of the parameters of interest in the ZnSe/GaAs heterostructures studied

Sample No.	GaAs surface structure	RHEED transition time (s)	Cap layer
270	$(2 \times 4)\gamma$	5	No
306	(3×1)	15	No
335	$(2 \times 4)\gamma$	10	No
347	(3×1)	5	Yes
348	(4×1)	5	Yes

then transferred via UHV to the II-VI chamber where the ZnSe was grown. Prior to ZnSe growth the samples were heated in order to obtain the desired GaAs surface reconstructions, as determined by RHEED. For one case, sample temperatures were raised until the (2×4) RHEED pattern first appeared (designated as the more As-rich $(2 \times 4)\gamma$) and immediately cooled to 270°C for growth of ZnSe. In others, the temperature was raised further until, upon the disappearance of the (2×4) pattern, a (3×1) reconstruction could be identified. They were then immediately cooled, also, for ZnSe growth. One sample was heated to slightly higher temperatures, in which case a (4×1) surface evolved upon cooling. This reconstruction may be related to the previously reported [6,7] (4×3) surface. As stated earlier, in all the samples used in this study the RHEED transition times were less than 15 s. The relevant parameters compared in this study are summarized in table 1.

A Schottky diode was prepared from each structure by fabricating a thin, 10 nm , Cr disk ($450 \mu\text{m}$ diameter) and Au ring contact on the ZnSe surface. A Au-Ge ohmic contact was applied on the n^+ -GaAs substrate, and after dicing, individual diodes were bonded to TO-18 headers for measurement. Light from a tungsten lamp/monochromator source was used, incident directly through the thin Cr Schottky dot. Spectra were measured with wavelengths covering the range from 0.4 to $1.0 \mu\text{m}$, spanning the bandgaps of both GaAs and ZnSe. Light was thus absorbed on either the ZnSe or the GaAs side of the interface and the resulting photocurrent observed and

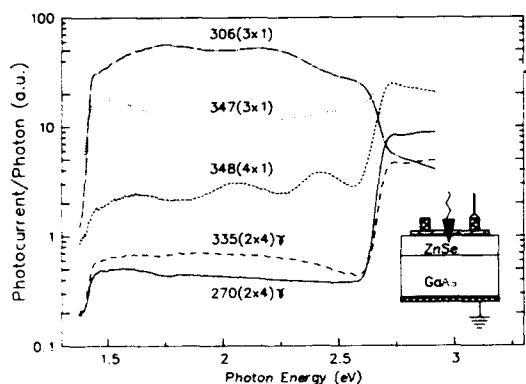


Fig. 3. Vertical photocurrent spectra for a series of GaAs/ZnSe heterostructures differing from each other in the GaAs surface reconstruction obtained before ZnSe deposition. The inset shows a schematic of the device configuration.

evaluated with transport through the heterointerface. The resulting photocurrent spectra are presented in fig. 3. Both the GaAs and the ZnSe absorption edges are clearly seen near 1.4 and 2.7 eV, respectively. We plot the log of the photocurrent versus photon energy, where the vertical scale, although in arbitrary units, preserves the relative magnitudes from sample to sample. (The quantum efficiency in GaAs for the best case is about 4%, a good value considering that the layer thicknesses were not optimized for this and that there is a large valence band offset.) The data clearly reflect the changes in surface reconstruction. For absorption in GaAs, observed for photon energies < 2.5 eV, the pC signals were largest for samples with a (3×1) reconstruction, while the lowest were for the As-rich $(2 \times 4)\gamma$ surface reconstructions. An intermediate value was observed for the (4×1) surface. These differences are large, ranging from 1 to 2 orders of magnitude. Large photocurrents corresponding to absorption in the GaAs were never observed for the $(2 \times 4)\gamma$ reconstruction, while the large photocurrents seen for the (3×1) interface could be reproduced. We attribute the differences in photocurrent to interface states which dominate in the $(2 \times 4)\gamma$ case, giving carrier trapping and recombination. We conclude that the (3×1) case gives reduced trapping because of better interface stoichiometry, and therefore large photocurrents.

For photon energies greater than 2.9 eV we obtain PC due to absorption in the ZnSe. The magnitude of this photocurrent is apparently dominated by the free surface due to surface recombination. This is evidenced by variations from diode, as well as by variations due to ambient conditions (e.g. room air versus vacuum). Improvement of these effects occurs when a thin 20 nm GaAs cap layer is included on the ZnSe. For example, samples 347 and 348, which show the largest ZnSe PC signals both contain a GaAs cap layer, while the others do not. More precise studies need to be made of these ZnSe surface effects.

5. Conclusions

We propose a simple model, based on electronic balance at the interface, to predict the surface reconstructions which form the most favorable II-VI/III-V heterointerfaces. The electron counting method in this model predicts that surfaces with equal number of the constituent atoms available for formation of interface bonds will produce ideal, abrupt interfaces with overall electronic balance, and a reduction of interface states. This was demonstrated by vertical photocurrent measurements made on a series of samples prepared with various GaAs interface stoichiometries, with minimum interface states for the (3×1) reconstruction. These samples also show short transition times upon initiation of ZnSe growth. These two results indicate that very high quality, abrupt ZnSe/GaAs interfaces have been obtained for growth on the nearly stoichiometric GaAs (3×1) surface. Our results provide no evidence for the existence of a distinct interfacial layer, as has sometimes been proposed [10,11]. In this initial study, only three reconstructions were examined to establish the correlation between interface quality and interface stoichiometry. A more gradual variation of the reconstructions may identify intermediate cases that approach even more closely electronic balance at the interface, producing an optimal heterointerface.

References

- [1] M.C. Tamargo, J.L. de Miguel, D.M. Hwang and H.H. Farrell, *J. Vacuum Sci. Technol.* B6 (1988) 784.
- [2] M.C. Tamargo, J.L. de Miguel, F.S. Turco, B.J. Skromme, D.M. Hwang, R.E. Nahory and H.H. Farrell, in: *Growth and Optical Properties of Wide-Gap II-VI Low Dimensional Semiconductors*, Eds. T.C. McGill, C.M. Sotomayor-Torres and W. Gebhardt (Plenum, New York, 1988).
- [3] R.L. Gunshor, L.A. Kolodziejski, M.R. Melloch, N. Otsuka and A.V. Nurmikko, in: *Growth and Optical Properties of Wide-Gap II-VI Low Dimensional Semiconductors*, Ed. T.C. McGill, C.M. Sotomayor-Torres and W. Gebhardt (Plenum, New York, 1988).
- [4] N. Kobayashi, *Japan. J. Appl. Phys.* 27 (1988) L1597.
- [5] Q.D. Qian, J. Qiu, M.R. Melloch, J.A. Cooper, Jr., L.A. Kolodziejski, M. Kobayashi and R.L. Gunshor, *Appl. Phys. Letters* 54 (1989) 1359.
- [6] J. Qiu, Q.-D. Qian, R.L. Gunshor, M. Kobayashi, D.R. Menke, D. Li and N. Otsuka, *Appl. Phys. Letters* 56 (1990) 1272.
- [7] N. Kobayashi, *Appl. Phys. Letters* 55 (1989) 1235.
- [8] H.H. Farrell, M.C. Tamargo and J.L. de Miguel, *Appl. Phys. Letters* 58 (1991) 355.
- [9] W.A. Harrison, E.A. Kraut, J.R. Waldrop and R.W. Grant, *Phys. Rev. B* 6 (1978) 4402.
- [10] D.-W. Tu and A. Kahn, *J. Vacuum Sci. Technol.* A3 (1985) 922.
- [11] D. Li, J.M. Gonsalves, N. Otsuka, J. Qiu, M. Kobayashi and R.L. Gunshor, *Appl. Phys. Letters* 57 (1990) 449.
- [12] E.A. Kraut, *J. Vacuum Sci. Technol.* B1 (1983) 643.
- [13] J.P. Harbison and H.H. Farrell, *J. Vacuum Sci. Technol.* B6 (1988) 733.
- [14] D.J. Chadi, *J. Vacuum Sci. Technol.* A5 (1987) 834.
- [15] M.D. Pashley, K.W. Haberern and J.M. Woodall, *J. Vacuum Sci. Technol.* B6 (1988) 1468.
- [16] H.H. Farrell and C.J. Palmstrom, *J. Vacuum Sci. Technol.* B8 (1990) 903.
- [17] W. Mönch, in: *Molecular Beam Epitaxy and Heterostructures*, Eds. L.L. Chang and K. Ploog (Nijhoff, Dordrecht, 1985), and references therein.

ZnSe/GaAs heterovalent interfaces: interface microstructure versus electrical properties

J. Qiu *, D.R. Menke, M. Kobayashi, R.L. Gunshor, Q.-D. Qian **

School of Electrical Engineering, Purdue University, West Lafayette, Indiana 47907, USA

D. Li and N. Otsuka

School of Materials Engineering, Purdue University, West Lafayette, Indiana 47907, USA

Epitaxial ZnSe/epitaxial GaAs interfaces are formed by molecular beam epitaxy and evaluated by several techniques including capacitance–voltage ($C-V$) measurements. The GaAs surface stoichiometry is systematically varied prior to the nucleation of ZnSe. A dramatic reduction of interface state density occurred when the GaAs epilayer is made As deficient. The ZnSe/GaAs interfaces exhibiting low interface state densities are associated with the presence of an interfacial layer of zincblende Ga_2Se_3 . In situ X-ray photoelectron spectroscopy (XPS) is used to study the nature of the bonding at the interfacial layer. The character of Se 3d core level features from the interfacial region and from separately grown Ga_2Se_3 epilayers support the identification of the interfacial layer as Ga_2Se_3 .

1. Introduction

In recent years there has been considerable activity involving the growth and study of various heterostructures and heterojunctions. The majority of this effort is focused on heterojunctions formed between III–V compounds. Unlike the homovalent III–V heterostructures, ZnSe/GaAs is characterized by a chemical valence mismatch at the interface. Previously it has been shown that, despite this valence mismatch across the interface, it was possible to obtain (at least in the case of epilayer/epilayer structures) heterovalent interface state densities comparable to those achieved from (Al,Ga)As/GaAs structures, by employing a post-growth annealing procedure [1–8]. In this paper we present a growth technique, involving the selection of an appropriate GaAs surface stoichiometry prior to nucleation of ZnSe [9], that

results in as-grown samples exhibiting nearly ideal $C-V$ characteristics without the necessity for post-growth annealing. The interface between the ZnSe epilayer and the GaAs epilayer is evaluated by in situ X-ray photoelectron spectroscopy (XPS).

2. Sample preparation and electrical properties

Both the ZnSe and GaAs epilayers were grown in separate growth chambers of a modular MBE system in order to avoid cross-contamination; transfer between growth chambers occurred in an ultrahigh vacuum (UHV) transfer module. The Be doped p-type ($1.0 \times 10^{17} \text{ cm}^{-3}$) GaAs epilayers were grown on (100) oriented Zn doped GaAs substrates at a substrate temperature of 582°C. Reflection high energy electron diffraction (RHEED) was used to monitor the film growth; a (2×4) reconstruction pattern was observed throughout the GaAs epilayer growth. When the temperature of the GaAs epilayer was lowered after the growth, an As-rich $c(4 \times 4)$ reconstruction pattern was observed. Following the growth

* Present address: 3M Company, St. Paul, Minnesota 55144, USA.

** Present address: Intel Corporation, Santa Clara, California 95052-8125, USA.

of the GaAs epilayer, samples were transferred in UHV to a second growth chamber for the nucleation of ZnSe. The ZnSe epilayers were grown using elemental sources at a substrate temperature of 320°C. The flux ratio was set at unity using a quartz crystal monitor placed at the substrate position.

A series of experiments were performed in the ZnSe growth chamber wherein the GaAs epilayer surface stoichiometry was altered prior to the nucleation of ZnSe [9]. Starting from the as-transferred sample which had the arsenic-rich $c(4 \times 4)$ reconstructed surface, the GaAs epilayers were heated to different temperatures to reduce the surface As content, resulting in four different GaAs interface reconstructions. When the GaAs was heated to approximately 460°C, a (2×4) surface reconstruction was observed. At about 510°C, a (4×6) surface reconstruction pattern appeared. As the GaAs epilayer temperature continued to be raised above the temperature where the (4×6) pattern was observed, in the vicinity of 535°C the reconstruction again changed. Although one might expect that a (4×2) Ga-stabilized pattern would follow the (4×6) as the temperature was increased [10], the reconstruction pattern recorded was a (4×3) [5]. The latter reconstruction, differing from the conventionally reported Ga-rich GaAs surface reconstruction patterns, may have resulted from the "decoration" [11] of the heated GaAs surface by high vapor pressure species such as Se or Zn, or by the formation of a submonolayer coverage of Ga_2Se_3 . Such a modification of the GaAs reconstruction pattern seemed not unlikely since the background chamber pressure rose from about 5×10^{-11} Torr to as high as 5×10^{-9} Torr as the GaAs epilayers (and contiguous substrate mounting hardware) were heated to increase the degree of As deficiency.

Following the growth of the epitaxial ZnSe/GaAs heterojunctions, circular capacitors with Al metalization were fabricated by an evaporation lift-off procedure, and series of C - V measurements were performed. All of the data shown here were taken in the dark. Fig. 1 shows the room temperature, 1 MHz C - V characteristics of Al/ZnSe/p-GaAs capacitors fabricated on as-

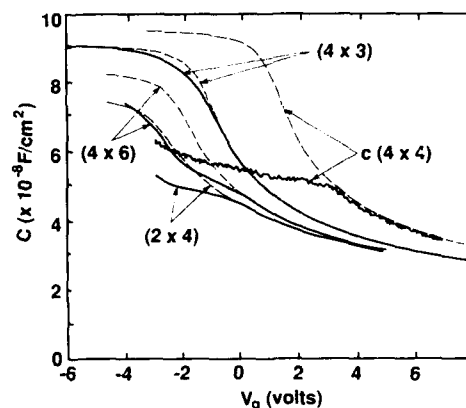


Fig. 1. Experimental (solid line) and theoretical (dashed line) C - V characteristics of the ZnSe/p-GaAs heterojunctions at room temperature. All of the data were taken at 1 MHz in the dark with a sweep rate of 0.1 V/s. The theoretical curves are calculated corresponding to the doping densities obtained from C - V profiling and the ZnSe epilayer thickness measured from TEM images.

grown heterostructures. For comparison, ideal (neglecting the effect of interface states) theoretical C - V curves were calculated corresponding to the doping densities obtained from C - V profiling and the ZnSe thicknesses measured from TEM images. In all cases the flat-band voltages of the theoretical curves were shifted to facilitate comparison with the experimental data. (The variation in the flat band voltage, caused by the presence of fixed charge at the interfacial region, did not affect the total range of band bending.) As shown in fig. 1, a typical sample, nucleated on a Ga-rich surface, as-grown, exhibited a clear accumulation ledge; the thickness of the ZnSe epilayer calculated from the accumulation capacitance was 840 Å, a value which agreed closely with the TEM measurement. The samples associated with both (2×4) and (4×6) GaAs surfaces showed a tendency to form a hole accumulation layer before current started to flow across the ZnSe layers. For these samples, an interface state-related stretching could be clearly seen from the depletion portion of the C - V curves. (The C - V characteristics of such samples improved to nearly ideal following the same thermal annealing procedure as described above [6,7].) Among the four types of as-grown samples, the

capacitors associated with the $c(4 \times 4)$ GaAs surface exhibited the most pronounced interface state-induced stretching near the mid-gap, while those capacitors formed on a Ga-rich GaAs surface had no indication of such stretching, indicating a virtual elimination of interface states in this region of the band gap. The only remaining interface states in those samples were distributed near the valence band edge. The $C-V$ characteristics were virtually independent of frequency from 1 kHz to 4 MHz.

The interface state density distributions were measured using Terman's method. By comparing the interface state densities near the mid-gap for the series of samples, a clear trend showing a reduction in the interface state density as the GaAs epilayer surface became increasingly As deficient was observed. For the samples grown on Ga-rich GaAs the interface state density, integrated over the lower portion of the GaAs band gap, was approximately $3 \times 10^{11} \text{ cm}^{-2}$.

It had been previously speculated that the ZnSe/GaAs interfaces exhibiting the low interface state densities were associated with the presence of an interfacial layer of Ga_2Se_3 [4,5,9]. Recent TEM cross-sectional dark field and high resolution images of heterojunctions formed on (4×3) reconstructed GaAs surface indicated the presence of an uniform band interpreted as an interfacial compound having an average thickness of 2 monolayers [12]. Image simulations strongly supported the identification of zincblende Ga_2Se_3 as the interfacial layer formed on As-deficient GaAs epilayers. As described in the next section, the TEM results have been further supported by an investigation of the interfacial bonding using XPS.

3. XPS analysis of the interfacial region

The XPS measurements were performed using a PHI series 5000 XPS system integrated into the modular MBE system. The pressure inside the XPS chamber during the measurements was less than 2.5×10^{-10} Torr.

In a typical experiment designed to analyze the interfacial region using XPS, the growth of ZnSe was interrupted 5 s after the nucleation ($\sim 2 \text{ \AA/s}$

growth rate), whereupon the sample (as-grown interfacial layer) was transferred under UHV to the XPS chamber. Subsequent to the binding energy measurement of interface species, the sample was transferred back to the ZnSe growth chamber for completion of the ZnSe layer growth. In additional alternative experiments, Se was intentionally reacted with the Ga-rich (4×3) surface. This was accomplished by first heating the GaAs epilayer until the (4×3) reconstruction was observed and then exposing it to a $2.0 \times 10^{14} \text{ atoms/cm}^2 \cdot \text{s}$ Se flux for 25 s while at high temperature. The temperature was then reduced to 320°C and ZnSe was grown as in the other experiments. $C-V$ profiles of samples having the "Se-reacted interface" are essentially the same as those of samples having as grown interfacial layers; both have nearly ideal interface properties (as discussed in ref. [9]).

To aid in the identification of the interfacial layer, a 450 Å thick epitaxial layer of Ga_2Se_3 was grown on a GaAs epilayer. The Ga_2Se_3 was nucleated on an As-deficient, (4×3) reconstructed GaAs surface at a substrate temperature of 400°C using a Se-to-Ga flux ratio of 3:1. A (2×1) reconstruction pattern was observed during the growth. Upon completion of the growth, the Ga_2Se_3 epilayer was transferred under UHV to the XPS chamber for analysis.

Fig. 2 shows Se 3d core level photoemission energy distribution curves for (a) the ZnSe epilayer, (b) the Ga_2Se_3 epilayer, (c) the interfacial layer, and (d) the Se reacted layer. The Se 3d features from ZnSe (fig. 2a) consist of a dominant doublet (two spin-orbit components: $3d_{5/2}$ and $3d_{3/2}$) originating from the bulk of the ZnSe epilayer, plus a very small peak at higher binding energy attributed to surface Se. As seen in figs. 2c and 2d, a very broad Gaussian component is needed to fit the Se 3d of the interfacial region. This peak is identified as the plasmon loss feature of As 3d electrons [13]. In fig. 2c the Se 3d feature can be resolved into three peaks including a component corresponding to Se bound to Zn (ZnSe). The other two components can be assigned to the interfacial layer. The binding energy of the feature attributed to Se bound to Zn is located at 0.2 eV lower than the higher energy feature from the interfacial region. It is apparent that the line shape

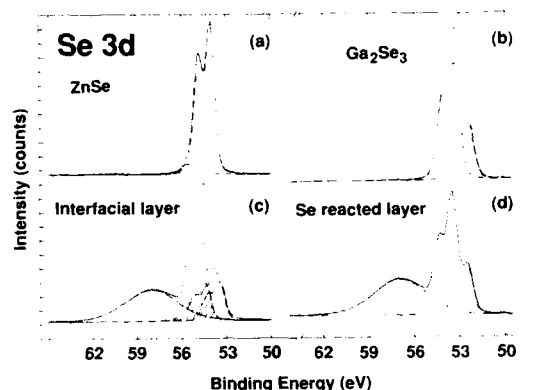


Fig. 2. The Se 3d core level photoemission energy distribution curves for (a) the ZnSe epilayer, (b) the Ga_2Se_3 epilayer, (c) the as-grown interfacial layer, and (d) the Se reacted layer. The features are resolved into several doublets which are attributed to spin-orbit splitting. Both the interfacial layer and the Se reacted layer include the As 3d plasmon loss feature in addition to the Se 3d peaks. In fig. 2c the Se 3d feature can be resolved into three components including a component (shaded in the figure) corresponding to Se bound to Zn (ZnSe).

of the Se 3d peaks originating from the interfacial layer, the Se reacted layer, and those from the Ga_2Se_3 epilayer are quite similar. The Se 3d peaks from the interfacial layer, the Se reacted layer, and those from the Ga_2Se_3 epilayer show two doublets of comparable magnitude separated by 0.95 eV, each having the same branching ratio (the same as the Se in the ZnSe epilayer), and with the area ratio of the high binding energy feature to the low binding energy feature of 2:1. This ratio is expected as it corresponds to the ratio of the number of Se atoms having vacancies in one nearest neighbor site to the number of Se atoms having two nearest neighbor site vacancies. A more detailed discussion concerning the origin of the area ratio is given elsewhere [14].

The binding energy difference between Se 3d and Ga 3d was compared for the Ga_2Se_3 epilayer, the as-grown interfacial layer, and the Se-reacted layer. The binding energy difference for the Ga_2Se_3 epilayer was 34.7 meV. Ga 3d spectra from the interfacial regions have a large feature originating from the GaAs and a smaller component [15] at a higher binding energy. The energy difference between the smaller Ga 3d component

and the Se features associated with Ga_2Se_3 is 34.6 meV, a value seen to be close to that determined from spectra from the Ga_2Se_3 epilayer.

4. TEM analysis of Ga_2Se_3 epilayer

The 450 Å Ga_2Se_3 epilayer has been examined by TEM. Observations of diffraction patterns have shown that the epilayer has a zincblende type structure and formed a good epitaxial relation with the GaAs epilayer. In [011] diffraction patterns of cross-sectional samples and [100] diffraction patterns of plan-view samples, each Bragg spot of GaAs is accompanied by a spot from the epilayer. The lattice parameter of the zincblende structure of the epilayer is determined from the diffraction patterns. The estimated value is 5.43 ± 0.02 Å which is smaller than the lattice parameter of GaAs by about 4%. The reported lattice parameter of Ga_2Se_3 is 5.418 Å [16], a value close to our estimate, indicating that the epilayer is nearly stoichiometric Ga_2Se_3 .

5. Conclusion

In conclusion, the as-grown heterointerfaces between ZnSe and p-GaAs are evaluated under device-like conditions by means of $C-V$ measurements. It is shown that the interface state density can be reduced by orders of magnitude when an appropriate GaAs epilayer surface stoichiometry is chosen for the subsequent nucleation of a ZnSe epilayer. In situ XPS is used to analyze the nature of the bonding at the interfacial layer. The character of Se 3d core level features from the ZnSe epilayer surface, from the interfacial region, and from separately grown Ga_2Se_3 epilayers supports the identification of the interfacial layer as Ga_2Se_3 .

Acknowledgements

The authors are grateful to L.A. Kolodziejski for her extensive involvement in the Purdue work involving ZnSe/GaAs interfaces. The authors would like to express their thanks to J.H. Weaver

for providing the curve fitting software for the XPS data analysis. The authors are indebted to W.N. Delgass and his co-workers for fruitful discussions about the XPS technique. The authors would also like to acknowledge the contributions to this work by D.A. Lubelski and S.M. Durbin. This work was supported by the Air Force Office of Scientific Research (AFOSR-89-0438) and the Defense Advanced Research Projects Agency/Office of Naval Research University Research Initiative Program (218-25015).

References

- [1] R.L. Gunshor, L.A. Kolodziejski, M.R. Melloch, M. Vaziri, C. Choi and N. Otsuka, *Appl. Phys. Letters* 50 (1987) 200.
- [2] G.D. Studtmann, R.L. Gunshor, L.A. Kolodziejski, M.R. Melloch, J.A. Cooper, Jr., R.F. Pierret, D.P. Munich, C. Choi and N. Otsuka, *Appl. Phys. Letters* 52 (1988) 1249.
- [3] M.C. Tamargo, J.L. de Miguel, D.M. Hwang and H.H. Farrell, *J. Vacuum Sci. Technol.* B6 (1988) 784.
- [4] I. Suemune, K. Ohmi, T. Kanda, K. Yukutake, Y. Kan and M. Yamanishi, *Japan. J. Appl. Phys.* 25 (1986) L827.
- [5] N. Kobayashi, *Japan. J. Appl. Phys.* 27 (1988) L1597.
- [6] Q.-D. Qian, J. Qiu, M.R. Melloch, J.A. Cooper, Jr., L.A. Kolodziejski, M. Kobayashi and R.L. Gunshor, *Appl. Phys. Letters* 54 (1989) 1359.
- [7] Q.-D. Qian, J. Qiu, M. Kobayashi, R.L. Gunshor, M.R. Melloch and J.A. Cooper, Jr., *J. Vacuum Technol.* B7 (1989) 793.
- [8] Y.R. Lee, A.K. Ramdas, L.A. Kolodziejski and R.L. Gunshor, *Phys. Rev.* B38 (1988) 13143.
- [9] J. Qiu, Q.-D. Qian, R.L. Gunshor, M. Kobayashi, D.R. Menke, D. Li and N. Otsuka, *Appl. Phys. Letters* 56 (1990) 1272.
- [10] A.Y. Cho, *J. Appl. Phys.* 47 (1976) 2841.
- [11] L.A. Kolodziejski, R.L. Gunshor, N. Otsuka and C. Choi, *J. Vacuum Sci. Technol.* A4 (1986) 2150.
- [12] D. Li, J.M. Gonsalves, N. Otsuka, J. Qiu, M. Kobayashi and R.L. Gunshor, *Appl. Phys. Letters* 57 (1990) 449.
- [13] H. Raether, *Excitation of plasmons and Interband Transitions by Electrons*, Springer Tracts in Modern Physics, Vol. 88 (Springer, Berlin, 1980) p. 53.
- [14] J. Qiu, D.R. Menke, R.L. Gunshor, M. Kobayashi, Q.-D. Qian, D. Li and N. Otsuka, to be published.
- [15] The association of the smaller Ga 3d feature in our interfacial region spectra with Ga bound to Se is consistent with the observation of similar peak separations for the Ga₂Se₃ epilayer. However, one or more surface features at binding energies located a similar increment above the GaAs bulk feature are commonly observed from GaAs samples having various surface reconstructions, and measured by synchrotron radiation photoemission spectroscopy.
- [16] H. Hahn and W. Klinger, *Z. Anorg. Chem.* 259 (1949) 135.

High-quality ZnSe/GaAs superlattices: MEE growth, and structural and optical characterization

S. Ramesh, N. Kobayashi and Y. Horikoshi

NTT Basic Research Laboratories, Musashino-shi, Tokyo-180 Japan

High-quality ZnSe/GaAs superlattices were grown by migration-enhanced epitaxy (MEE) and characterized using X-ray diffraction, electron microscopy and photoluminescence. The streaky reflection high-energy electron diffraction (RHEED) pattern and strong, persistent RHEED oscillations observed during the MEE growth of the superlattices indicate a smooth growing surface. The sharp satellite peaks observed clearly in the double-crystal X-ray diffraction rocking curve of a 21-period ZnSe/GaAs superlattice confirm the excellent crystalline and interfacial quality of the superlattice. Cross-section transmission electron microscopy (TEM) shows flat, abrupt heterointerfaces. Superlattice photoluminescence spectra show that both photo-excited electrons and holes are confined in GaAs wells; also seen are the sharp excitonic features from the coherently strained ZnSe cap and barrier layers of the superlattice.

1. Introduction

ZnSe/GaAs superlattice and quantum-well structures are attractive because of the small lattice mismatch (0.27%) between ZnSe and GaAs, and the wide band gap and small dielectric constant of ZnSe. A large optical non-linear effect is expected in these structures [1]. A number of studies have been reported on the ZnSe-on-GaAs heterostructures [2–4]; however, it is difficult to form the GaAs-on-ZnSe heterostructure by conventional molecular beam epitaxy (MBE) and metal organic chemical vapor deposition techniques. This difficulty is primarily due to the large difference in optimal growth temperatures of ZnSe ($\sim 300^\circ\text{C}$) and GaAs ($\geq 550^\circ\text{C}$). Recently, migration-enhanced epitaxy (MEE) [5] has been developed as a low-temperature growth technique to form compound semiconductor heterostructures with sharp interfaces. The optimal growth temperature mismatch between ZnSe and GaAs was solved by applying MEE for lowering the growth temperature of GaAs to 250°C . The problem of low sticking coefficient of As on ZnSe surface was circumvented by As_4 deposition at very low temperatures. Thus, a ZnSe/GaAs superlattice has recently been fabricated [6]. Here, we describe the

growth of high-quality ZnSe/GaAs superlattices with careful preparation and monitoring of the superlattice growth surface, reduction of impurity contamination, and optimization of (low-temperature) As_4 and Ga deposition conditions to facilitate GaAs-on-ZnSe growth; this allows growth of large number of periods of the superlattice of high quality and enables characterization using X-ray diffraction and photoluminescence.

2. Experimental

A conventional MBE apparatus equipped with a 10 kV RHEED (reflection high-energy electron diffraction) system was used for MEE growth. Both GaAs and ZnSe were grown in the same growth chamber. During growth the RHEED pattern was observed and the specular beam intensity variations were monitored along the [100] azimuth at an incident angle of 1.5° .

The substrates used were all (001)-oriented semi-insulating GaAs wafers. The surface oxide layer was removed by annealing the wafer in the growth chamber at about 580°C in an As_4 flux. At this stage the (2×4) RHEED pattern due to

As-stabilized surface of GaAs is observed. A GaAs buffer layer (180 nm thick) was grown by conventional MBE at 590°C at a growth rate of 1.5 \AA/s and a streaky RHEED pattern was confirmed. To further improve the flatness of the buffer layer a 20 nm layer of GaAs was grown at a temperature of 250°C by MEE. The beam equivalent pressure (BEP) values for GaAs growth by MEE at 250°C are 1.5×10^{-7} Torr for Ga and 1.6×10^{-6} Torr for As_4 ; flux durations were 1.8 and 8.2 s for Ga and As_4 , respectively.

ZnSe/GaAs superlattice (nominal layer thickness: ZnSe 20 nm, GaAs 20 nm) was then grown by MEE at a growth temperature of 250°C ; the topmost ZnSe layer (28 nm thick) acts as the cap. Growth and characterization of these structures is briefly reported in our recent paper [7]. MEE growth of the ZnSe layer after growth of the GaAs layer was done with the Ga and As_4 cells at room temperature and the chamber pressure down to $\sim 10^{-10}$ Torr. (this takes about 90 min). These precautions were sufficient to ensure that the ZnSe growth proceeded without deterioration of the growing surface as monitored by RHEED. For the growth of the ZnSe layer, the BEP values were 1.5×10^{-7} Torr each for Zn and Se and the beam flux durations were 10 s each. The RHEED pattern observed along the [100] azimuth changed clearly from $c(2 \times 2)$ on completion of the Zn supply to (2×1) on completion of the Se supply, as the Zn and Se beams were alternated (fig. 1). The RHEED specular beam intensity oscillation amplitude saturated at the maximum at the end of each Zn supply duration and at the minimum at the end of each Se supply duration. For the growth of GaAs on ZnSe, the low sticking coefficient of As_4 on ZnSe surface necessitates initiation of GaAs growth by deposition of amorphous gallium arsenide at a low temperature, followed by solid phase epitaxial regrowth. This is achieved by As_4 deposition onto Zn-stabilized ZnSe surface at an optimum temperature of 25°C followed by deposition of two atomic layers of Ga also at 25°C and in situ annealing for a few minutes at 250°C . (Whereas 1 ML of Ga may be sufficient, 2 ML are deposited to ensure that after the annealing step, subsequent growth will occur on crystalline GaAs at all locations.) At the end of this procedure a

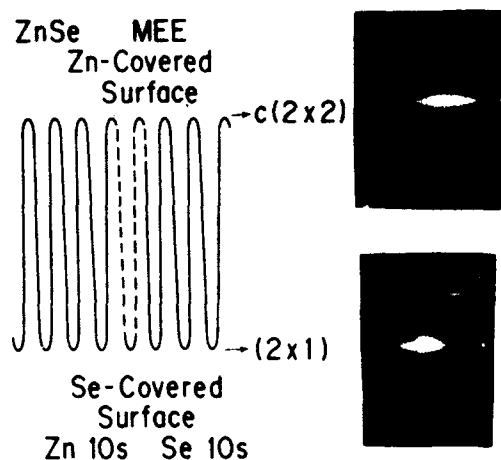


Fig. 1. RHEED specular beam intensity oscillation and alternating RHEED patterns during MEE growth of a ZnSe layer of the ZnSe/GaAs superlattice ([100] azimuth).

streaky (2×4) RHEED pattern is seen indicating the formation of a thin crystalline GaAs layer. The RHEED specular beam intensity, which decreases after the As_4 and Ga deposition at room temperature, recovers and saturates after the few minutes of annealing at 250°C (fig. 2). MEE growth of the 20 nm thick GaAs layer is then carried out at 250°C with no deterioration of the growing surface; this is evidenced by the strong,

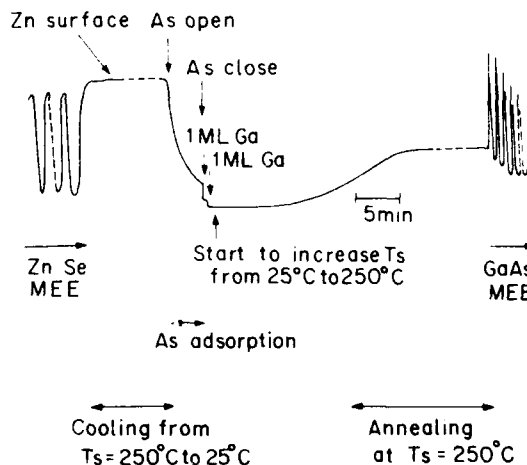


Fig. 2. Evolution of RHEED specular beam intensity during surface preparation for GaAs growth on ZnSe ([100] azimuth).

persistent RHEED oscillations. The RHEED oscillation amplitude was equally large even at the highest period numbers of superlattice grown.

3. Results and discussion

Fig. 3 shows a double-crystal X-ray rocking-curve obtained from a 21-period ZnSe/GaAs superlattice in the vicinity of the (004) GaAs Bragg angle. The sharpness of the diffraction satellite peaks, with full-width at half-maximum of 100 arc sec, indicates the high crystalline and interfacial quality of the superlattice. The period thickness of this superlattice, calculated in the usual manner from the angular spacing of the superlattice satellite peaks, is 40.8 nm, which is in agreement with the average period thickness obtained from transmission electron microscopy measurements. TEM was used to examine the superlattice structure in greater detail. Cross-section bright-field TEM image (fig. 4) shows flat, abrupt heterointerfaces and no dislocations or stacking faults, confirming that strained pseudomorphic growth of the superlattice layers occurs. The interface microstructure of the superlattice observed over wide areas using

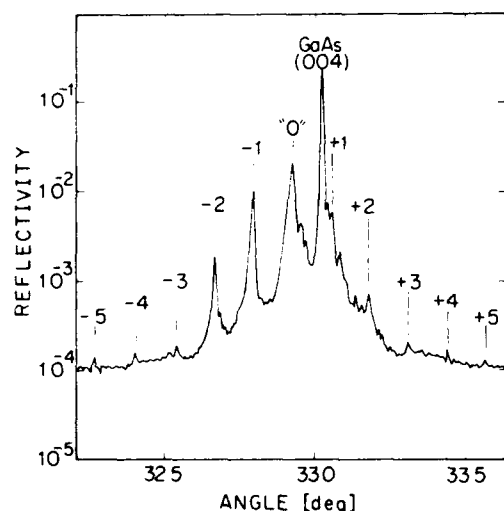


Fig. 3. Double-crystal X-ray rocking-curve of a 21-period ZnSe/GaAs superlattice obtained in the vicinity of the (004) GaAs Bragg reflection.



Fig. 4. Cross-section TEM bright-field image of a ZnSe/GaAs superlattice grown by MEE.

cross-section high-resolution electron microscopy imaging shows featureless, perfectly coherent heterointerfaces at both the ZnSe-on-GaAs and GaAs-on-ZnSe interfaces.

The thickness of the GaAs layers of the superlattice obtained from the TEM micrographs is as expected from a MEE growth rate of about one monolayer/cycle. However, the thickness of the ZnSe layers of the superlattice obtained from TEM micrographs yields an MEE growth rate of less than 0.67 monolayer/cycle for ZnSe growth at 250°C. Reported values of growth rate of ZnSe during atomic-layer controlled epitaxy range from 1/3 ML/cycle [9] and 1/2 ML cycle [6] to 1 ML/cycle [8]. In our study of MEE growth of ZnSe at 250°C, the alternate observation of the $c(2 \times 2)$ and (2×1) RHEED patterns does not appear to guarantee complete monolayer coverage per cycle. Strain may play some role in the resistance to complete monolayer coverage. However, additional experiments on MEE growth of ZnSe layers using various values of Se/Zn flux ratio, cycle durations and substrate temperatures shows that a growth rate of 1 ML/cycle can in fact be achieved over a wide temperature range [10]. Using this growth conditions we have fabricated high-quality single quantum well structures.

Photoluminescence characterization of the superlattice structures was done at a temperature of 4.2 K using the 325 nm wavelength excitation from a He-Cd laser. The luminescence observed from a superlattice (20 nm GaAs wells, total superlattice thickness of 880 nm) is shown in fig. 5.

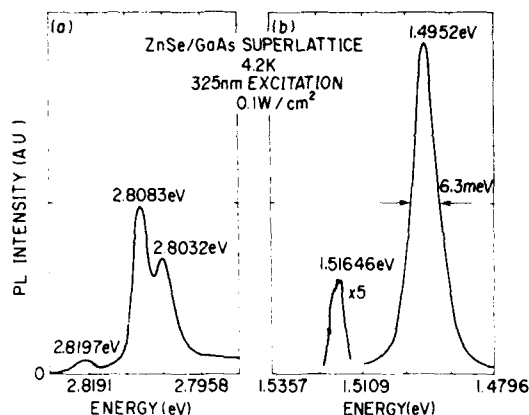


Fig. 5. 4.2 K photoluminescence spectrum of a ZnSe/GaAs superlattice (20 nm thick GaAs wells). Luminescence from (a) ZnSe cap and barrier layers of the superlattice and (b) from GaAs wells.

The reasonably sharp peaks seen in the luminescence from the GaAs wells (fig. 5b) indicate that photoexcited electrons and holes are confined in the wells. The small blue shift (to 1.5165 eV) of the excitonic luminescence from the 20 nm thick quantum wells is as expected from the small conduction band discontinuity for the GaAs/ZnSe heterojunction. The full width at half maximum of this excitonic peak is 2.5 meV. The luminescence peak at 1.4952 eV is probably due to band to Zn-acceptor emission. (This indicates residual doping of Zn in GaAs, even though the concentration is below the detection limits of Auger and SIMS.) Fig. 5a shows the luminescence from the ZnSe layer of the superlattice (primarily from the 28 nm thick cap). The ZnSe luminescence is qualitatively similar to that observed by other groups [3,4,11] for high-quality, coherently-strained layers of ZnSe grown directly on GaAs epilayers. The efficiency and sharpness of the luminescence from the ZnSe cap grown on top of the superlattice is a confirmation of the high quality of the ZnSe layer as well as (indirectly) of the quality of the superlattice. The excitonic features in our case are blue-shifted relative to the luminescence from a 1000 Å ZnSe layer [3]. This is

consistent with the layer thickness effect noted in ref. [11,3,4]. The 2.8083 eV (heavy hole) and 2.8197 eV (light hole) transitions are free exciton features, while the 2.8032 eV feature is probably associated with a neutral donor bound exciton. The 11.4 meV hh-lh splitting corresponds to a strain of $\sim 0.31\%$, which is approximately that expected for fully coherent growth on GaAs.

4. Conclusion

In this study we have demonstrated the MEE-growth of high-quality ZnSe/GaAs superlattices at the low growth temperature of 250°C. In situ monitoring of the growth using RHEED indicated smooth growing surface. Double-crystal X-ray rocking curve measurements and transmission electron microscopy confirm the excellent interfacial and crystalline quality of the superlattices. Sharp excitonic features have been observed in the photoluminescence spectra for the first time from any multilayer structure involving GaAs-on-ZnSe growth.

Acknowledgements

It is a pleasure to thank Dr. S. Tarucha and Dr. K. Ploog for discussions and Dr. T. Kimura for his encouragement and interest in this work.

References

- [1] M. Kumagai and T. Takagahara, *Phys. Rev.* B40 (1989) 12359.
- [2] T. Yao, in: *The Technology and Physics of MBE*, Ed. E.H.C. Parker (Plenum, New York, 1985) ch. 10, and references therein.
- [3] R.L. Gunshor and L.A. Kolodziejski, *IEEE J. Quantum Electron.* QE-24 (1988) 1744, and references therein.
- [4] R.N. Bhargava, *J. Crystal Growth* 86 (1988) 873, and references therein.
- [5] Y. Horikoshi, M. Kawashima and H. Yamaguchi, *Japan. J. Appl. Phys.* 25 (1986) L868.

- [6] N. Kobayashi and Y. Horikoshi, Japan. J. Appl. Phys. 29 (1990) L236.
- [7] S. Ramesh, N. Kobayashi and Y. Horikoshi, Appl. Phys. Letters 57 (1990) 1102.
- [8] T. Yao and T. Takeda, Appl. Phys. Letters 55 (1989) 1225.
- [9] J. Lilja, J. Keskinen, H. Asonen and M. Pessa, J. Crystal Growth 95 (1989) 522.
- [10] S. Ramesh and Y. Horikoshi, to be published.
- [11] B.J. Skromme, M.C. Tamargo, J.L. de Miguel and R.E. Nahory, Appl. Phys. Letters 53 (1988) 2217.

Growth and characterization of ZnSe on $(\text{NH}_4)_2\text{S}_x$ -treated GaAs substrates: effect of GaAs surface microstructure on the growth rate of ZnSe

Yi-hong Wu, Yoichi Kawakami, Shizuo Fujita and Shigeo Fujita

Department of Electrical Engineering, Kyoto University, Kyoto 606, Japan

We report the growth study of ZnSe onto $(\text{NH}_4)_2\text{S}_x$ -pretreated GaAs substrates. In situ reflection high-energy electron diffraction (RHEED) showed that the $(\text{NH}_4)_2\text{S}_x$ -treated GaAs (001) surface took a streaky (1×1) RHEED pattern at room temperature and a new surface reconstruction after heating up to 200°C . The new reconstruction pattern is characterized by curved lines between the integral reflection diffraction rods. We attributed this pattern to the composite of a (2×1) reconstruction pattern of the (001) surface and the reflection diffraction at $\{11n\}$ (n is estimated to be 5) surfaces of terraces formed at the (001) surface in the $(\text{NH}_4)_2\text{S}_x$ solution. We speculate that these terraces are enlarged at the surface of the overgrown ZnSe and contribute to enhance the growth rate of ZnSe throughout the entire stage of the heteroepitaxy.

1. Introduction

GaAs wafers have exclusively been employed as the substrates for epitaxial growth of ZnSe because of their high quality and small lattice-mismatch to ZnSe. In the case of epitaxial growth of ZnSe by a molecular beam epitaxy (MBE) system with one growth chamber, the removal of the GaAs surface oxide layer has usually been performed at high temperature, e.g., > 500 – 600°C without As beam irradiation. This process causes a rough GaAs surface because of the re-evaporization of As, which is not desirable for the ZnSe growth.

In order to overcome the above-mentioned difficulties, we have recently employed a new pretreatment technique for GaAs substrate by $(\text{NH}_4)_2\text{S}_x$ solution for metalorganic molecular beam epitaxy (MOMBE) of ZnSe [1–4]. Compared to the conventional thermal etching process, the $(\text{NH}_4)_2\text{S}_x$ -pretreatment resulted in (i) two-dimensional growth from an earlier stage of the growth, (ii) better optical properties of pseudomorphic ZnSe epilayers, and (iii) lower state densities at ZnSe/GaAs heterointerfaces. In the present study, we focus on the growth rate and discuss

the growth process in terms of surface structures of the $(\text{NH}_4)_2\text{S}_x$ -pretreated GaAs substrates.

2. Experimental

The growth was carried out in an ANELVA KMV-101 MOMBE system. A diffusion pump maintains the background pressure of the growth chamber below 2×10^{-9} Torr. Dimethylzinc (DMZn) and dimethylselenide (DMSe) were used as the sources for Zn and Se, and were cracked at 950 and 850°C through tantalum crackers, respectively. The results of quadrupole mass analysis suggest that the cracking efficiencies of DMZn and DMSe at these temperatures are 70–80% [5]. An indium-free holder was used to mount the GaAs substrate. The growth processes were in situ monitored by a RHEED observation system which consists of a CCD camera, a video recorder and an image processing unit. For sulfur passivation, we used the $(\text{NH}_4)_2\text{S}_x$ solution. In order to discuss the effect of sulfur passivation on the growth of ZnSe, we also applied the conventional pretreatment technique, i.e., thermal etching. Detailed procedures have been described in previous papers [1–4].

3. Results and discussion

3.1. Growth rate

As a first step, we investigated the growth rate of ZnSe epilayers grown on the GaAs substrates pretreated by the two different methods. We measured the epilayer thickness by ellipsometer and calculated the average growth rate. The results suggest that the growth rate tends to increase by the $(\text{NH}_4)_2\text{S}_x$ pretreatment. Fig. 1 demonstrates the increment of the growth rate on $(\text{NH}_4)_2\text{S}_x$ -pretreated GaAs substrates compared to that on conventionally pretreated GaAs substrates. As can be seen from the figure, the growth rate on the $(\text{NH}_4)_2\text{S}_x$ -pretreated substrate is about 20% higher than that on the substrate pretreated by thermal etching, less depending on the thickness of the overgrown epilayer. Prior to the growth, $(\text{NH}_4)_2\text{S}_x$ -pretreated GaAs substrates were preheated at 420°C.

The fact that $(\text{NH}_4)_2\text{S}_x$ pretreatment results in higher growth rate not only for thin (e.g. 0.03 μm) but also for thick (0.8 μm) epilayers suggests that the growth rate enhancement is hardly attributed to the influence of sulfur atoms adsorbed on the GaAs surfaces. It was reported that the coverage rate of sulfur on GaAs surfaces after heating around the growth temperatures used in this study

was less than unity [6–8]. Therefore, the adsorbed sulfur atoms may influence the growth rate at the initial stages, but it is hardly expected that they have any influence on the growth processes when the underlying ZnSe layer is as thick as 0.8 μm .

3.2. Surface structure

Excluding the possibility of influence by adsorbed sulfur atoms, the other factor which can be responsible for changing the growth rate is the surface structure of the GaAs (001) surface treated by the $(\text{NH}_4)_2\text{S}_x$ solution. Hirayama et al. [6] reported that the $(\text{NH}_4)_2\text{S}_x$ -treated surface showed a streaky 1×1 RHEED pattern before annealing, and a 2×1 surface reconstruction after annealing at 260 and 420°C. We also observed a streaky 1×1 RHEED pattern at room temperature; however, after annealing, there appeared a new RHEED pattern which was characterized by curved lines between the integral reflection diffraction rods. This pattern is clearly different from the 2×1 pattern reported by Hirayama et al., because the half order reflection diffraction rods of a 2×1 RHEED pattern should be straight lines.

From the geometrical relations between the curved lines and the integral reflection diffraction rods, we consider that the new RHEED pattern is composed of a 2×1 pattern from the (001) surfaces and those resulting from the $\{11n\}$ facets of the terraces formed by the pretreatment using the $(\text{NH}_4)_2\text{S}_x$ solution. Based on these considerations, a surface model of the $(\text{NH}_4)_2\text{S}_x$ -pretreated GaAs (001) substrate and the corresponding RHEED pattern with $[110]$ azimuth are shown schematically in figs. 2a and 2b, respectively. Since the reflection diffraction rods from the surfaces of the terraces look like curved lines due to the overlapping of the half-order reflection diffraction rods of the (001) surfaces upon them, it is difficult to determine the exact value of n . However, from an enlarged photograph we calculated the angle θ shown in fig. 2b to be 8.13°, suggesting that n is likely to be 5. However, the curved lines appeared very broad, and thus errors may be included in the calculations of θ and estimation of n .

However, we should point out that the new

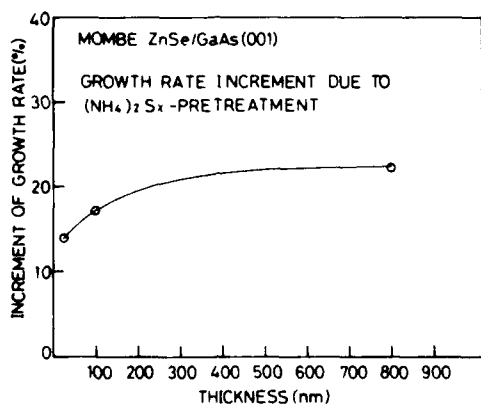


Fig. 1. Increment of the growth rate as a function of the thickness of the overgrown ZnSe layer. Prior to the growth, $(\text{NH}_4)_2\text{S}_x$ -pretreated GaAs substrates were preheated at temperatures of 420°C for 10 min.

RHEED pattern was not observed during the growth of ZnSe. Although the reason is not clear now, we are considering that the terraces become large during the growth, the major reflection diffraction occurs from the (001) surfaces rather than the $\{11n\}$ facets, and thus the curved lines appear very faint with the proceeding of the epitaxial growth.

3.3. Influences of terraces on growth rate

In order to know how the terraces affect the growth rate of ZnSe epilayers, we investigated the relationship between the RHEED patterns prior to the growth and the frequencies of RHEED oscillations. After the growth of a 0.12 μm thick pseudomorphic ZnSe epilayer and an interruption of 2 min, we observed the specular beam intensity oscillations. The results are given in fig. 3, and the corresponding RHEED patterns prior to the growth are shown in fig. 4. Here, (a), (b), (c) and (d) denote the experiments with $(\text{NH}_4)_2\text{S}_x$ -treated GaAs substrates after annealing at 420, 520, 600 and 650 $^\circ\text{C}$, respectively, and (e) is that with conventionally pretreated GaAs substrate.

In the RHEED patterns (fig. 4), curved lines are clearly seen in (a) and (b), become faint in (c), and completely disappear in (d). As can be seen from fig. 3, the growth rate is highest and nearly equal in (a) and (b) and decreases with the increase of the pretreatment temperature of GaAs substrate. The growth rate in (d) is almost the

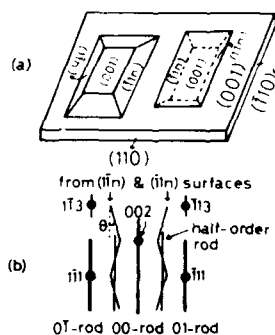


Fig. 2. (a) Model of the surface structure of the GaAs substrate pretreated by the $(\text{NH}_4)_2\text{S}_x$ solution and (b) schematic RHEED pattern from the surface structure shown in (a).

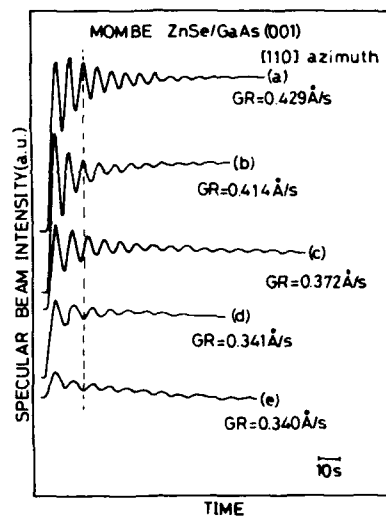


Fig. 3. RHEED intensity oscillations of ZnSe observed after an interruption of 2 min on a 0.12 μm thick pseudomorphic buffer layer: (a), (b), (c) and (d) are the results when we used the $(\text{NH}_4)_2\text{S}_x$ -pretreated GaAs substrates which were annealed at 420, 520, 600 and 650 $^\circ\text{C}$, respectively, prior to the growth; (e) is the result when we used the conventionally pretreated GaAs substrate.

same as that in (e) which is grown on the GaAs substrate pretreated by the conventional manner. Therefore, there is a clear correlation between the surface microstructures of GaAs substrate and the growth rate.

According to refs. [6] and [7], the sulfur coverage at the surface after annealing at 420 $^\circ\text{C}$ is equal or less than unity, and the sulfur atoms are desorbed at temperatures above 520 $^\circ\text{C}$. Therefore, if the adsorbed sulfur atoms cause the growth rate enhancement, variation in growth rate should have occurred in (b) as compared to (a). However, as we have seen in fig. 3, there is almost no difference in growth rate between (a) and (b).

Fig. 5 shows the dependence of the growth rate on the time interval of dipping of GaAs substrate into the $(\text{NH}_4)_2\text{S}_x$ solution. The time intervals for (a), (b), (c) and (d) are 10 s, 1 min, 2 min and 10 min, respectively. It was clearly observed that the growth rate increases with the time interval as far as it is less than 2 min. This fact means that a certain time interval (about 2 min) is necessary for completing the formation of terraces, although the

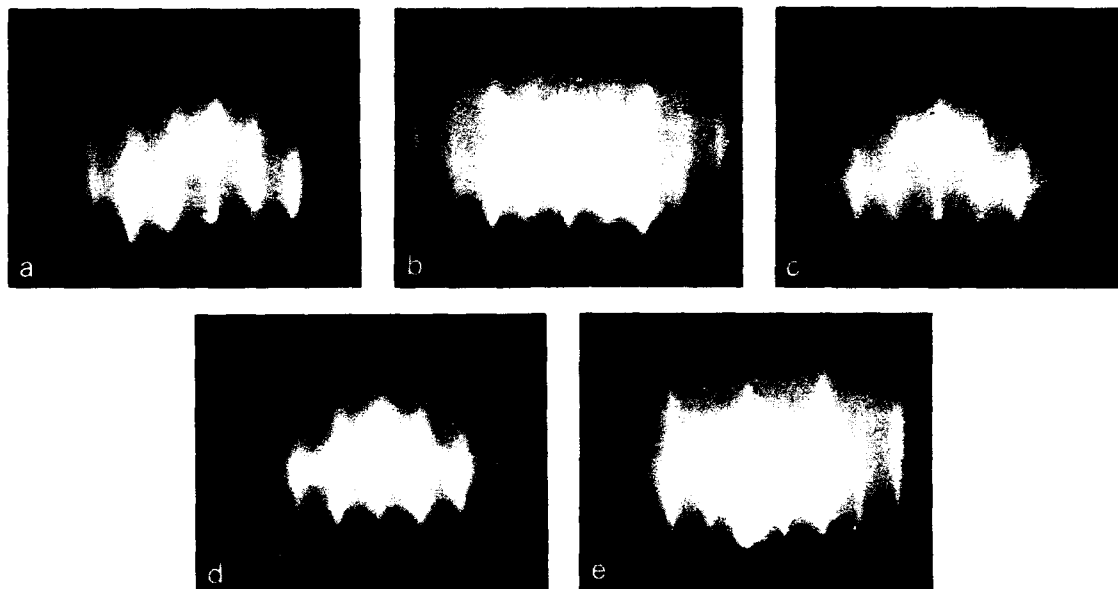


Fig. 4. RHEED patterns of GaAs substrates prior to the growth: (a)–(e) in this figure correspond to those in fig. 3.

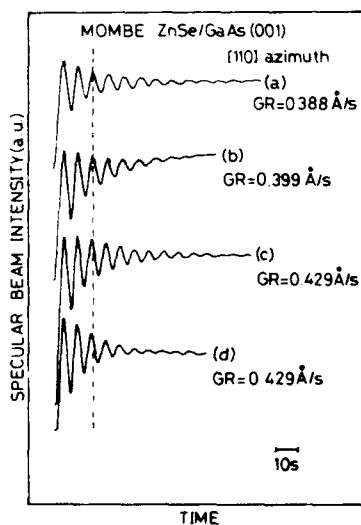


Fig. 5. RHEED intensity oscillations of ZnSe observed after an interruption of two min on a $0.12\text{ }\mu\text{m}$ thick pseudomorphic buffer layer. The intervals for dipping the GaAs substrates in the $(\text{NH}_4)_2\text{S}_x$ solution are: (a) 10 s (b) 1 min, (c) 2 min and (d) 10 min.

coverage of sulfur on GaAs (001) surface in the $(\text{NH}_4)_2\text{S}_x$ solution saturates within 2 s [8].

4. Conclusion

We have shown that the RHEED pattern of a $(\text{NH}_4)_2\text{S}_x$ -treated GaAs (001) surface is composed from the (2×1) pattern of the (001) surface and that of the $\{11n\}$ (n is estimated to be 5) surfaces of the terraces formed at the GaAs surface, rather than the simple (2×1) pattern. Our results provide direct evidence that the growth rate of ZnSe is greatly influenced by the surface structures of GaAs surface and point out the importance of surface pretreatment in heteroepitaxy.

Acknowledgments

The authors would like to express their gratitude to Sumitomo Chemical Industry Co., Ltd.,

for supplying the source materials. This work was supported in part by a Grant-in-Aid for Scientific Research on Priority Areas, New Functionality Materials – Design, Preparation and Control, from the Ministry of Education, Science and Culture, Nos. 01604011 and 02204011.

References

- [1] Y. Wu, T. Toyoda, Y. Kawakami, Sz. Fujita and Sg. Fujita, Japan. J. Appl. Phys. 29 (1990) L144.
- [2] Y. Kawakami, T. Toyoda, Y. Wu, Sz. Fujita and Sg. Fujita, Japan. J. Appl. Phys. 29 (1990) 2440.
- [3] Y. Wu, Y. Kawakami, Sz. Fujita and Sg. Fujita, Japan. J. Appl. Phys. 29 (1990) L1062.
- [4] Sg. Fujita, Y. Wu, Y. Miyazaki, T. Toyoda, Y. Kawakami and Sz. Fujita, presented at 1990 Intern. Conf. on Solid State Devices and Materials, Sendai, August 1990.
- [5] Sz. Fujita, N. Yoshimura, Y. Wu and Sg. Fujita, J. Crystal Growth 101 (1990) 78.
- [6] H. Hirayama, Y. Matsumoto, H. Oigawa and Y. Nannichi, Appl. Phys. Letters 64 (1989) 2565.
- [7] M.S. Carpenter, M.R. Melloch, B.A. Cowans, Z. Dardas and W.N. Delgass, J. Vacuum Sci. Technol. B7 (1989) 845.
- [8] H. Oigawa, J. Fan, Y. Nannichi, K. Ando, K. Saiki and A. Koma, Japan. J. Appl. Phys. 28 (1989) L340.

Molecular beam epitaxy of Zn(Se,Te) alloys and superlattices

F.S. Turco-Sandroff, R.E. Nahory, M.J.S.P. Brasil ^{*}, R.J. Martin, R. Beserman ^{**}, L.A. Farrow, J.M. Worlock and A.L. Weaver

Belcore, 331 Newman Springs Road, Red Bank, New Jersey 07701, USA

ZnSe_{1-x}Te_x ternary alloys have been grown over the entire range of composition by molecular beam epitaxy on GaAs or InP substrates. A good control of the composition is obtained by growing the ternary in Zn-rich conditions. The band gap energy versus the composition shows a very large bowing with a minimum at room temperature of 2.05 eV and a Te concentration of 0.65. ZnSe/ZnTe superlattices have been grown and show a strong absorption at 1.8 eV supporting the hypothesis of a type II superlattice.

1. Introduction

Wide band gap II-VI semiconductors are attractive materials for visible light emitters in the blue/green spectrum. Binaries, such as ZnSe, have been extensively studied for both p- and n-type doping. ZnSe can be efficiently n-type doped, [1] but efficient p doping remains an unsolved issue. In fact all the wide band gap II-VI semiconductors are n-type or semi-insulating residual and can be doped n-type, except ZnTe which presents a p-type residual. It is therefore interesting to study ZnTe and ZnSe mixed in the ternary alloy ZnSe_{1-x}Te_x and ZnSe/ZnTe superlattices. Moreover, the bandgap of ZnSeTe materials has been found to pass through a minimum at 0.1 eV below that of ZnTe [2,3]. All these results were measured on materials grown long ago by growth techniques using extremely high temperatures and resulting in polycrystalline material [4]. Nevertheless, these materials have been reported both n- and p-type for Te content of 0.4 to 0.6 [5].

In order to try to achieve better quality materials, molecular beam epitaxy has been recently used for growing ZnSeTe [6]. However, mono-crystalline ZnSeTe layers of good quality are dif-

ficult to achieve, and rather broad X-ray diffraction peaks having been found [6]. Reproducible composition has been underlined as an important issue, the range 0-0.2 being especially hard to control [7]. In fact, the solid solution presents some immiscibility with a critical temperature of about 430°C [8]. Strained ZnSe/ZnTe [9] and ZnSe/ZnSeTe [10] superlattices have already been demonstrated by MBE.

We report the growth by molecular beam epitaxy of ZnSe_{1-x}Te_x alloys and ZnSe/ZnTe superlattices on both GaAs and InP substrates. The ternary alloy has been grown for compositions x varying from 0 to 1. Single crystal ZnSe_{1-x}Te_x has been achieved as seen by RHEED and X-ray data. The influence of the initial substrate and the growth conditions as a function of substrate temperature and flux ratio are investigated. Choosing the right (Se,Te)-to-Zn flux gives us high reproducibility over the entire range of composition. Using spectral photoconductivity (PC) measurements, we determine the room temperature band gap energy versus Te concentration in the ZnSe_{1-x}Te_x ternary. A very strong bowing of E_g versus x is observed presenting a minimum of 2.05 eV at room temperature for a composition of about $x = 0.65$. We also present results on ZnSe/ZnTe superlattices constituted of equal thicknesses d of ZnSe and ZnTe layers ranging from 15 to 90 Å. PC spectra at room temperature

^{*} Unicamp, 13081 Campinas, SP, Brazil.

^{**} On leave from the Technion Institute of Technology, Haifa, Israel.

show strong absorption around 1.8 eV supporting a type II ZnSe/ZnTe superlattice. Raman scattering data and low temperature photoluminescence (PL) spectra show that strained ZnSe/ZnTe superlattices have been grown on InP and on GaAs substrates for $d \leq 45$ Å. For $d > 45$ Å, the critical thicknesses of both materials are exceeded and no PL emission is observed, suggesting the formation of a large number of structural defects.

2. MBE growth and characterization of ZnSeTe ternary alloys

The binaries ZnSe and ZnTe present lattice constants respectively equal to 5.6684 and 6.104 Å. The $\text{ZnSe}_x\text{Te}_{1-x}$ ternary obeys the Vegard law [2], and has lattice constants which present a lattice mismatch with GaAs substrates ranging 0.27% to 7.97% for x varying from 0 to 1 with critical thicknesses ranging from 1500 to ≈ 20 Å. Over InP substrates, $\text{ZnSe}_x\text{Te}_{1-x}$ presents a lattice mismatch of -3.4% to 4.01% for x varying from 0 to 1.

2.1. MBE growth of ZnSeTe on GaAs and InP substrates

The ZnSeTe layers are grown in a conventional 2300 Riber MBE system equipped with elemental sources of Zn, Se and Te. (001) GaAs and InP substrates are chemically etched in the standard $\text{H}_2\text{SO}_4:\text{H}_2\text{O}_2:\text{H}_2\text{O}$ solution of 4:1:1 and 2:1:1 respective concentrations. After being thermally outgassed at 300 and 200°C respectively, GaAs and InP substrates are transferred into the II-VI MBE chamber for thermal deoxidation, with no impinging fluxes, monitored by reflection high energy electron diffraction (RHEED). After thermal desorption of the oxide at $\approx 580^\circ\text{C}$, GaAs presents a superposition of the (3×1) and (4×6) surface reconstructions. For InP substrates, the thermal deoxidation occurs at ≈ 400 – 420°C providing a (2×4) surface reconstruction.

Growth temperatures from 270 to 400°C have been used for growing ZnSeTe on both GaAs and InP substrates. VI-rich conditions ensured by Se and Te excess have first been used giving a (2×1)

surface reconstruction during the growth of the ternary. For growth temperatures of 270 to 350°C, a VI/II flux ratio of 5 is enough to ensure a (2×1) surface reconstruction, while for higher temperatures of 350 to 400°C the ratio VI/II is increased to 10. Various Se/Te ratios have been used depending on the desired composition of the ternary. When the growth is started on a GaAs substrate presenting the superposition of (3×1) and (4×6) surface reconstructions, the RHEED pattern shows a three-dimensional transition of 0–30 Å possibly due to the lattice relaxation. Then, abruptly, the RHEED pattern presents a nice and streaky (2×1) surface reconstruction. When the growth is started on an InP substrate, presenting a (2×4) surface reconstruction, the RHEED becomes three-dimensional over the $[110]$ direction while the perpendicular axis only shows the bulk diffraction lines, giving a $(\infty \times 1)$ RHEED pattern. This disorder observed on the first axis finally disappears giving way to the usual (2×1) reconstruction. The higher the substrate temperature is when the growth is started, the longer the transition time from $(\infty \times 1)$ to (2×1) . This may be due to the outdiffusion of In from the InP substrate maintained at high temperature under UHV. This interpretation is supported by observation of a broadened InP absorption edge in PC spectra. Independently of the final growth temperature, we always start the growth at 270°C in order to limit the transition region and after the RHEED pattern recovers the temperature can be increased to the final growth temperature.

A second set of samples has been grown on GaAs and InP substrates in Zn-rich conditions where the flux ratio $\text{VI/II} = (\text{Se} + \text{Te})/\text{Zn}$ is equal to 0.3–1. A $c(2 \times 2)$ surface reconstruction appears very soon after the growth is started. However, if the temperature is lower than or equal to 300°C, ZnSeTe becomes amorphous as shown by the circles observed on the RHEED pattern. This is probably due to a lower migration of the different species at the surface of the growing crystal under Zn-rich conditions compared to the growth achieved under an overpressure of (Se,Te). The temperature has therefore to be higher than 300°C to grow monocrystalline material. After about 1.5 μm , the $c(2 \times 2)$ RHEED pattern slowly degrades

from streaky to spotty but always keeping the surface reconstruction. This may be due to a rougher growth front of the layer which does not however prevent the growth of a final good (100) crystal.

2.2. X-ray measurements

The bulk composition X_b is measured by X-ray diffraction. Fig. 1a shows the predicted concentration calculated from the Se/Te flux ratio $X_f = \varphi_{Te}/(\varphi_{Te} + \varphi_{Se})$ versus X_b . It can be seen that the X_b of the ternary grown on either GaAs or InP is not proportional to X_f . In fact, these samples have been grown in element VI overpressure, which means that Se and Te are in competition for their incorporation. This competition leads to ternaries leaner than expected in Te. The growth conditions have therefore to be modified to control the ternary composition in a reproducible way. A second set of samples has been grown under Zn-rich overpressure, the conditions being described in the previous section. The values of the composition are reported in fig. 1b and X_b is in very close agreement with X_f . In fact when the growth is

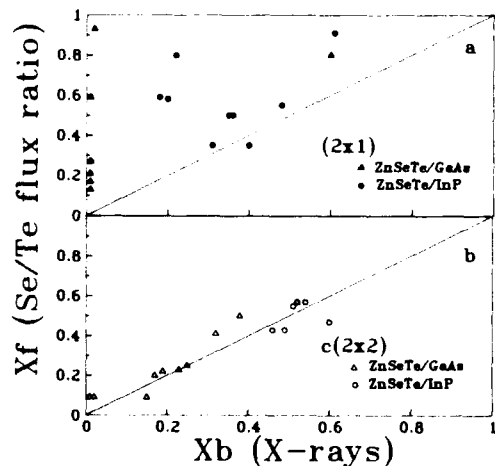


Fig. 1. Predicted Te concentration calculated from the Se/Te flux ratio X_f versus bulk composition X_b determined by X-ray diffraction for $ZnSe_{1-x}Te_x$ samples grown on GaAs and InP substrates under element-VI-rich conditions (a) and under element-II-rich conditions (b).

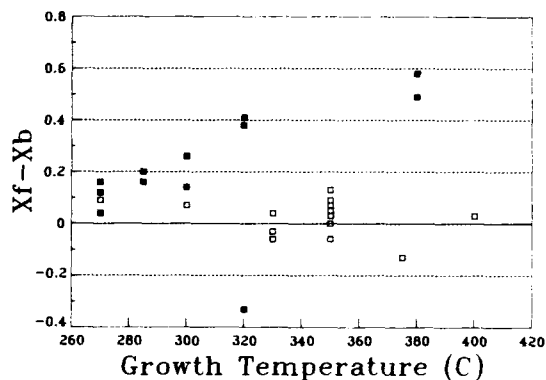


Fig. 2. Difference of the predicted Te concentration calculated from the Se/Te flux ratio X_f and the bulk concentration X_b versus the growth temperature.

carried out in Zn-rich conditions, both Se and Te are incorporated with no competition, as long as the sticking coefficient of Se and Te is near 1.

We report in fig. 2 the difference between X_f and X_b as a function of the growth temperature. As we can observe $X_f - X_b$ increases with the growth temperature when the sample is grown under (Se,Te)-rich composition. An increase of the overpressure from 4-6 to 10-12 is not sufficient to limit this difference. The samples grown are leaner in Te for higher temperature which is consistent with the thermodynamic values of heat of vaporization of ZnTe (152 kcal/mol) compared to ZnSe (175 kcal/mol) [11]. On the other hand, when the samples are grown under Zn-rich conditions, the difference ($X_f - X_b$) averages zero, especially when the (Se + Te)/Zn ratio is equal to 0.3-0.4. Under Zn-rich conditions the (Se,Te) desorption is therefore negligible. This observation is consistent with the lower mobility observed at the surface of ZnSeTe under Zn-rich conditions than under (Se,Te)-rich conditions.

The X-ray full width at half maximum (FWHM) does not seem to vary directly with the growth temperature or the fluxes. The measurements have been done with a single crystal X-ray apparatus where the GaAs or InP substrates present a FWHM of 200-250 arc sec. The FWHMs of the ZnSeTe layers are typically of 500-600 arc sec, the best being about 300 arc sec for low Te content

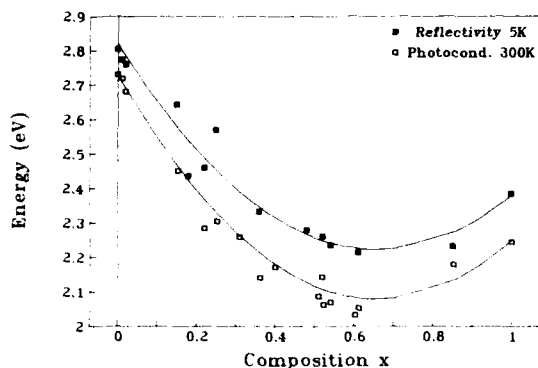


Fig. 3. Bandgap energy variation versus the Te concentration at room and low (5 K) temperature.

(0–2%) or perfectly lattice matched ternary on InP substrates.

2.3. Electrical and optical measurements

The variation of the bandgap with the concentration of these ZnSeTe layers has been measured at room temperature by PC measurements and at low temperature (5 K) by reflectivity measurements. Fig. 3 presents the variation of the bandgap versus the Te concentration at room and low temperature. A very strong bowing is observed, presenting a minimum at about 2.05 eV at room temperature at $x(\text{Te}) = 0.65$. The ternary ZnSeTe presents therefore a wide bandgap variation from 2.73 eV for ZnSe (blue) to 2.05 eV for $\text{ZnSe}_{0.35}\text{Te}_{0.65}$ (yellow). Low temperature (5 K) photoluminescence measurements have been performed using an Ar laser operating at 488 nm on $\text{ZnSe}_{1-x}\text{Te}_x$ for $x > 0.15$. Spectra are dominated by a transition involving an impurity, the depth of which varies with composition. The linewidth of this transition decreases regularly from 150 to 12 meV for a Te concentration increasing from ≈ 0.2 to 0.8. Details of this effect will be reported elsewhere.

Raman scattering has been performed on these ZnSeTe layers. The line width of the Raman line, providing an indication of the crystalline quality of the alloy, presents a maximum of 15 cm^{-1} for Te concentration of 40%. For lower or higher concentrations, it decreases monotonically to 6

cm^{-1} obtained for pure ZnSe and ZnTe. This shows that for concentrations close to 50%, the crystalline quality of the alloy may be perturbed, probably related to the very big difference between the bond length of the two binaries and the strains involved in the ternary. Further investigation of these results will be detailed elsewhere.

3. MBE growth and characterization of ZnSe/ZnTe superlattices

3.1. MBE growth of ZnSe/ZnTe on GaAs and InP substrate

ZnSe/ZnTe superlattices have been grown under VI-rich conditions, at growth temperatures of 270 to 300 °C on InP and GaAs substrates. The flux ratios used are 4–5 for ZnTe and 5–6 for ZnSe. The growth rate was monitored with the Zn flux remaining constant throughout the superlattice growth. The superlattices grown are constituted of equal thicknesses d of ZnSe and ZnTe, ranging nominally from 15 to 90 Å. The growth has been started at 270 °C. On GaAs substrates a very short transition 0–15 Å is observed between the initial $(3 \times 1) + (4 \times 6)$ GaAs surface reconstruction and the (2×1) surface reconstruction observed during the growth of the superlattice. When 15/15 or 30/30 Å layers are grown the RHEED shows a good (2×1) surface reconstruction. For 45/45 Å and up to 90/90 Å the RHEED is still streaky but the bulk lines are somewhat broadened indicating the beginning of some disorder. This can be due to the partial relaxation of the layers over the substrate.

3.2. Electrical and optical measurements

For $d \leq 45$ Å PC and Raman scattering have been performed. A strong absorption around 1.8 eV is observed by PC, well below the binaries bandgap energies supporting the hypothesis that ZnSe/ZnTe is a type II superlattice. The same 45/45 nominal ZnSe/ZnTe superlattice grown on GaAs and InP substrates has been studied by Raman scattering. The similarity between the phonon frequencies suggests that the superlattice is in

a free standard configuration. [12] Both Raman scattering and photoluminescence show that for $d > 45$ Å the quality of the material decreases. This is due to the partial relaxation of the strains of the two binaries as shown by Raman scattering, leading to the generation of dislocations at the interface.

4. Conclusion

We have presented here the growth of $\text{ZnSe}_{1-x}\text{Te}_x$ layers of good crystallinity on both GaAs and InP substrates. The layers grown on either substrate are very rapidly relaxed. Reproducible composition can be obtained over the entire range $0 \leq x \leq 1$ when the layers are grown under Zn-rich conditions at temperatures between 320 and 400 °C. These layers have been measured by room temperature PC, showing a very strong bowing in the variation of the bandgap with the composition. Now that good quality material can be achieved, doping studies are in process. ZnSe/ZnTe superlattices constituted of equal thicknesses d of both binaries have also been studied. For $d \leq 45$ Å, a strong absorption is observed at around 1.8 eV supporting a type II superlattice. Raman scattering indicates that these superlattices are in free-standing configuration whereas for $d > 45$ Å, the superlattices begin to relax.

References

- [1] J.L. de Miguel, S.M. Shibli, M.C. Tamargo and B.J. Skromme, *Appl. Phys. Letters* 53 (1988) 2065.
- [2] S. Larach, R.E. Shrader and D.F. Stocker, *Phys. Rev.* 108 (1957) 587.
- [3] A. Ebina, M. Yamamoto and T. Takahashi, *Phys. Rev.* 6 (1972) 3786.
- [4] W.W. Piper and S. Polish, *J. Appl. Phys.* 32 (1961) 1278.
- [5] M. Aven and W. Garwacki, *Appl. Phys. Letters* 5 (1964) 160.
- [6] T. Yao, Y. Makita and S. Maekawa, *J. Crystal Growth* 45 (1978) 309.
- [7] L.A. Kolodziejski, R.L. Gunshor, A.V. Nurmikko and N. Otsuka, in: *Growth and Optical Properties of Wide-Gap II-VI Low Dimensional Semiconductors*, NATO ASI Series B 200, Eds. T.C. McGill, C.M. Sotomayor Torres and W. Gebhardt (1989) p. 269.
- [8] V.A. Sanitarov, A.V. Altunin, E.M. Ivashura and I.P. Kalinkin, *Izv. Akad. Nauk SSSR, Neorg. Mater.* 25 (1989) 1211.
- [9] M. Kobayashi, N. Mino, H. Katagiri, R. Kimura, M. Konagai and K. Takahashi, *Appl. Phys. Letters* 48 (1986) 296.
- [10] Y. Rajakarunanyake, M.C. Philips, J.O. McCaldin, D.M. Chow, D.A. Collins and T.C. McGill, unpublished; M.C. Philips, Y. Rajakarunanyake, J.O. McCaldin, D.M. Chow, D.A. Collins and T.C. McGill, unpublished.
- [11] P. Goldfinger and M. Jeunehomme, *Trans. Faraday Soc.* 59 (1963) 2851; W.P. Gluscho et al., *Thermodynamic Constants*, Parts 1, 2 and 6 (Academy of Sciences of the USSR, Moscow, 1965-1973).
- [12] K. Shahzad, D.J. Olego, C.G. Van de Walle and D.A. Cammack, *J. Luminescence* 46 (1990) 109.

Quantum wells with zincblende MnTe barriers

J. Han, S.M. Durbin, R.L. Gunshor, M. Kobayashi, D.R. Menke

School of Electrical Engineering, Purdue University, West Lafayette, Indiana 47907, USA

N. Pelekanos, M. Hagerott, A.V. Nurmikko

Division of Engineering, Brown University, Providence, Rhode Island 02912, USA

Y. Nakamura * and N. Otsuka

School of Materials Engineering, Purdue University, West Lafayette, Indiana 47907, USA

In this paper we describe a series of MnTe/CdTe/MnTe and MnTe/InSb/MnTe single quantum well structures. For the CdTe quantum wells we report the observation of luminescence covering the entire visible range from red to blue; a quantized state in the InSb well is used to implement resonant tunneling. X-ray diffraction and transmission electron microscopy (TEM) were used to evaluate the microstructural quality of the structures. Dark-field TEM showed that, in spite of the 2.3% lattice mismatch, the MnTe layers remained pseudomorphic and dislocation-free. High resolution images (also used to determine dimensional details) indicated that the interfaces were atomically abrupt, and that the CdTe and InSb wells were essentially unstrained in each of the structures; most of the strain was contained in the MnTe barrier layers. Optical properties of the single quantum well structures have been studied using photoluminescence and photoluminescence excitation spectroscopy. Blue luminescence at 2.59 eV ($n = 1$ transition) has been observed from a structure with a 10 Å CdTe well. The negative differential resistance observed from MnTe/InSb resonant tunneling structures represents, to our knowledge, the first report of a dimensionally quantized state in InSb.

1. Introduction

This paper describes the growth and evaluation of quantum structures incorporating the metastable zincblende phase of MnTe. The MBE growth technique enables single crystal growth of the zincblende phase [1,2], whereas bulk-grown crystals of MnTe exhibit the hexagonal NiAs crystal structure [3]. The difference in bandgap energy between the two crystal structures is dramatic; the NiAs phase has an optical bandgap of 1.3 eV while the bandgap of the zincblende phase is 3.18 eV at 10 K [1,4] which is in the near ultraviolet portion of the spectrum. The motivation for the research reported here is the development of a suitable widegap semiconductor to serve

as the barrier layer to quantum well structures in the lattice constant range of InSb and CdTe. Epilayers of zincblende MnTe are grown up to a thickness of 0.5 μm , while a series of strained single quantum wells are fabricated with MnTe forming widegap barrier layers for quantum wells of CdTe, ZnTe, and InSb. The microstructure of the MnTe epilayers and quantum well structures is characterized using transmission electron microscopy (TEM) and X-ray diffraction; optical properties are determined using a combination of reflectance, photoluminescence (PL), Raman, and resonant Raman spectroscopies.

2. CdTe/MnTe single quantum well structures

The structures having CdTe quantum wells were grown on InSb substrates with a buffer layer of

* Permanent address: Tokyo Institute of Technology, Tokyo 152, Japan.

InSb. Preparation of the CdTe and InSb substrates used in this work has been described previously [5,6]. The InSb buffer layer was grown in a III-V growth chamber of the modular MBE system, and transferred under ultrahigh vacuum to a second chamber for the growth of the MnTe and CdTe epilayers. The InSb buffer layer was grown on the InSb substrate to provide an optimal surface prior to nucleation of the CdTe buffer layer at 200°C. During the growth of the CdTe buffer layer, the substrate temperature was raised to 300°C for the subsequent growth of the MnTe/CdTe quantum well structure. The CdTe layers were grown at a rate of 1.2 Å/s using a compound source, while the MnTe was grown at a rate of 1.1 Å/s from elemental sources at a unity cation/anion flux ratio. Flux measurements were performed using a quartz crystal monitor positioned near the substrate position.

During the sequential growth of barrier and well layers for the MnTe/CdTe structures, the RHEED patterns appeared to be virtually unchanged as the layers were alternated, with each exhibiting a (2×1) reconstruction suggesting an anion stabilized surface [7]. TEM measurements were used to determine the MnTe barrier layer thickness.

TEM observations of the single quantum well structures were made using [010] and [011] cross-sectional samples. For the preparation of cross-sectional samples, iodine ions were used at the final stage of ion thinning in order to reduce damage in the CdTe crystals. Although the samples were kept at low temperature with liquid nitrogen, the MnTe layers in these structures were found to rapidly intermix with the CdTe layers during ion thinning. Single quantum well structures were observed only from the samples for which a close contact with the cold stage of the ion milling machine was carefully maintained.

Lattice fringe patterns in HREM images directly show that the MnTe layers in the single quantum well structures have a cubic zincblende structure (also confirmed in electron diffraction of cross-sectional samples), and have been grown epitaxially on the CdTe layers. In the HREM image, more distinct 200 and 002 lattice fringes are seen in areas of MnTe than those of CdTe due

to the larger value of the crystal structure factor of 200 type reflections of MnTe. No misfit dislocations are observed in bright field or dark field images of these single quantum well structures, indicating the pseudomorphic nature of MnTe/CdTe interfaces.

In the several MnTe/CdTe/MnTe single quantum well structures, spanning CdTe well thicknesses from approximately 10 to 56 Å, strong photoluminescence originating from the well is detected in all samples, even for excitation at energies below the MnTe barrier layer absorption edge. (The MnTe barrier layer thicknesses are kept constant at approximately 35 Å.) Separate optical reflectance measurements on relatively thick MnTe films yield an approximate value of 3.2 eV for the s-p bandgap at $T = 10$ K. Thus the (unstrained) bandgap difference in the heterostructure is about 1.6 eV which suggests the possibility of strong confinement-induced effects. Direct evidence of carrier confinement is indeed apparent in the systematic shift to higher photon energies of the PL emission with decreasing CdTe quantum well thickness. Fig. 1 compares the experimentally determined energy shift of excitonic features with the predictions based on the calculated transmission coefficients [8] through the double barrier structure forming the quantum well. The calculation employs a heavy hole valence band offset of

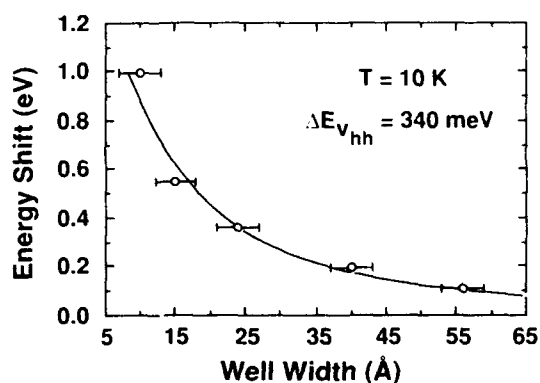


Fig. 1. The photoluminescence energy shift relative to the excitonic band edge of CdTe based on the average energy of the excitonic emission originating from the quantum well. (The error bars represent the expected uncertainty in TEM thickness measurement.)

340 meV which is determined from photoluminescence and photoluminescence excitation spectroscopy (PLE) measurements [9]. The PLE provides a measure of the valence band splitting due to the combination of strain (in the barriers) and quantum confinement in the well. (The configuration of the structure ensures that the well is essentially strain free.) For the narrowest well sample (10 Å), an energy shift (due to confinement) of approximately 1 eV is realized, corresponding to photon emission in the blue. The PL emission is usually composed of two or more emission lines which are 40–60 meV apart. These lines, each approximately 20 meV in width, are associated with transitions between $n = 1$ confined valence band states and the $n = 1$ conduction band state. Since the spectral peaks show the same sign of circular polarization in an external magnetic field, it is likely that they are associated with the same hole state. We presently attribute the peaks to monolayer scale fluctuations in the quantum well width. Important ingredients acting to shape the photoluminescence features are the operative band offsets, including the role of the large lattice constant mismatch (2.3%), the degree and nature of exciton binding, the exchange of electron–hole states with the Mn ion d-electron moments, and possible deviations from an ideal square well due to interfacial steps. We mention in passing that the temperature dependence of the PL linewidth has given us a quantitative measure of the exci-

ton–LO phonon interaction in this quantum well system [9].

3. InSb/MnTe resonant tunneling structures

In addition to incorporation in the CdTe quantum well structures, zincblende MnTe has also been applied to InSb-based quantum well structures which, due to the lack of appropriate barrier materials, have eluded realization. Study of the InSb/MnTe heterovalent tunneling structures was motivated by the potential application of resonant tunneling at high frequencies (InSb has the highest electron mobility of the conventional semiconductors), with improved device performance at room temperature. Computer simulations of InSb/MnTe double barrier resonant tunneling has been performed using a two-band model of electron dispersion in the band gap with the inclusion of the nonparabolicity of the InSb band structure [10–12]. A sample calculation predicted peak-to-valley ratio of the order of several thousand, and peak current densities of 5×10^3 A/cm² from a particular InSb/MnTe resonant tunneling structure with barrier and well dimensions of 20 and 50 Å, respectively. The current–voltage (I – V) characteristics were expected to remain approximately the same between 77 K and room temperature; the conduction band barriers formed by zincb-

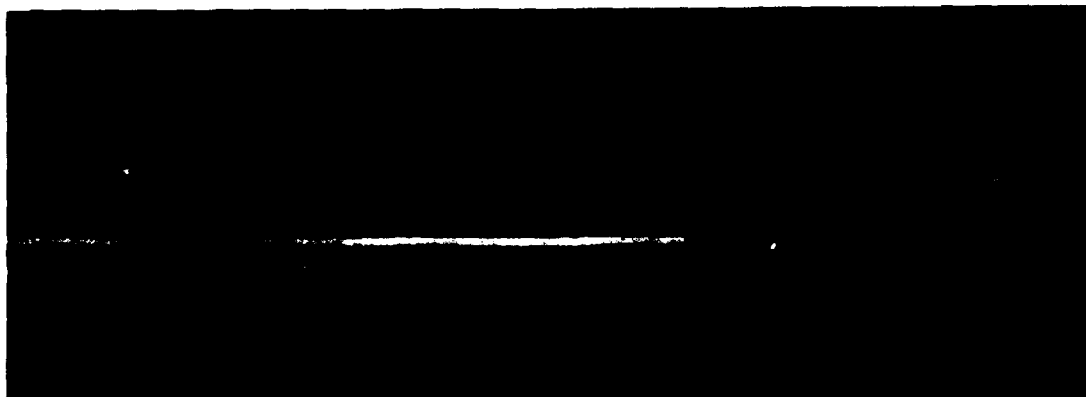


Fig. 2. 200 dark field electron microscope image of the InSb/MnTe resonant tunneling structure. Marker represents 200 Å.

lende MnTe (with an estimated band offset of 1.86 eV [9,13]) block most of the thermionic current.

The film growth was started in a III-V growth chamber where an InSb buffer layer was grown on a (100) InSb substrate at a temperature of 420°C. The sample was subsequently transferred under ultrahigh vacuum to another growth chamber (used for the CdTe quantum well structures described above) in which the InSb/MnTe resonant tunneling structures were grown using elemental sources at a substrate temperature of 300°C. An antimony cracker was employed to aid in the low temperature growth of the InSb quantum well and cap layers. Resonant tunneling structures consisting of MnTe/InSb/MnTe layers were grown by alternatively opening and closing the shutters without interruption of the growth. Fig. 2 shows a 200 dark field image of a InSb/MnTe resonant tunneling structure. The barrier and well thicknesses were measured to be 35 and 70 Å, respectively, which agreed with the dimension estimated from the growth rate. The image reveals the high microstructural quality of the resonant tunneling structure with abrupt and smooth interfaces. Dislocations were not observed in any imaged area of the sample.

Diodes are fabricated by evaporating Ti/Au on the InSb cap layer, followed by the etching of mesa structures. The I - V characteristics are measured at various temperatures. Preliminary I - V results employing pulse measurement (to avoid sample heating) are shown in fig. 3. A peak-to-valley ratio of 1.7:1 is observed at 77 K with a peak current density of 980 A/cm². Asymmetry about the origin in the I - V characteristics is observed with the resonant peak appearing at a higher voltage for the reverse bias condition compared to the forward bias condition. For these initial samples tested, the negative differential resistance becomes less pronounced with increasing temperature, and disappears at about 140 K. The origin of the deviation of the I - V characteristics from theoretical predictions is not yet known, and is still under investigation. One could speculate about such factors as interface scattering (MnTe/InSb interfaces have not been previously reported), leakage current paths along the side wall of the etched mesas, etc. In any case, to our knowledge,

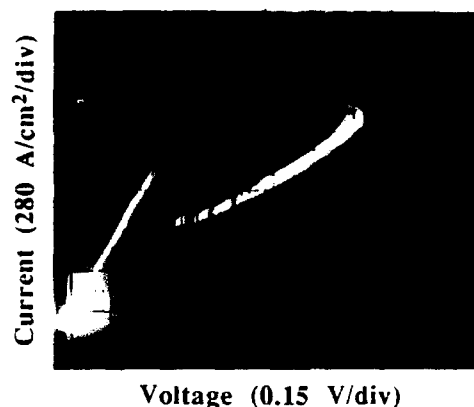


Fig. 3. I - V characteristic of the InSb/MnTe resonant tunneling structure. The measurement is carried out at 77 K.

the resonant tunneling represents the first report of a quantized state in InSb.

4. Summary

In summary, the MBE growth technique has presented an opportunity for the growth and study of novel structures incorporating the previously hypothetical magnetic semiconductor, zincblende MnTe. The MnTe layers were used in the formation of single quantum well structures which exhibited strong electron and hole confinement. Blue luminescence at 2.59 eV ($n=1$ transition) has been observed from a 10 Å CdTe well which is the largest confinement induced shift in quantum well structures reported so far. A dimensionally quantized state in InSb was observed from the InSb/MnTe resonant tunneling structure.

Acknowledgments

The authors gratefully acknowledge numerous insightful discussions with L.A. Kolodziejski, and the assistance of D.L. Mathine, Y.R. Lee, A.K. Ramdas, and D.A. Lubelski. Research support was provided by National Science Foundation grants MRG-8913706 (Purdue) and ECS-8916026 (Brown), Defense Advanced Research Projects

Agency/Office of Naval Research University Research Initiative Program 218-25015, and Office of Naval Research (ONR) grants N00014-89-J1604 (Purdue), and N00014-90-J1168 (Brown).

References

- [1] S.M. Durbin, J. Han, Sungki O. M. Kobayashi, D.R. Menke, R.L. Gunshor, Q. Fu, N. Pelekanos, A.V. Nurmikko, D. Li, J. Gonsalves and N. Otsuka, *Appl. Phys. Letters* 55 (1989) 2087.
- [2] S. Durbin, M. Kobayashi, Q. Fu, N. Pelekanos, R.L. Gunshor and A.V. Nurmikko, *Surface Sci.* 228 (1990) 33.
- [3] J.W. Allen, G. Lucovsky and J.C. Mikkelsen, Jr., *Solid State Commun.* 24 (1977) 367.
- [4] Y. Lee and A.K. Ramdas, *Phys. Rev. B* 38 (1988) 10600.
- [5] Q.-D. Qian, J. Qiu, J.L. Glenn, Jr., Sungki O. R.L. Gunshor, L.A. Kolodziejski, M. Kobayashi, N. Otsuka, M.R. Melloch, J.A. Cooper, Jr., M. Hagerott, T. Heyen and A.V. Nurmikko, *J. Crystal Growth* 95 (1989) 567.
- [6] J.L. Glenn, Jr., Sungki O. L.A. Kolodziejski, R.L. Gunshor, M. Kobayashi, D. Li, N. Otsuka, M. Hagerott, N. Pelekanos and A.V. Nurmikko, *J. Vacuum Sci. Technol. B* 7 (1989) 249.
- [7] J.D. Benson, B.K. Wagner, A. Torabi and C.J. Summers, *Appl. Phys. Letters* 49 (1986) 1034.
- [8] R.L. Gunshor, M. Kobayashi, L.A. Kolodziejski, N. Otsuka and A.V. Nurmikko, *J. Crystal Growth* 99 (1990) 390.
- [9] N. Pelekanos, Q. Fu, J. Ding, W. Walecki, A.V. Nurmikko, S.M. Durbin, J. Han, M. Kobayashi and R.L. Gunshor, *Phys. Rev. B* 41 (1990) 9966.
- [10] M.J. McLennan and S. Datta, *SEQUAL 2.1 User's Manual*, Purdue University (TR-EE 89-17, 1989).
- [11] E.T. Yu and T.C. McGill, *Appl. Phys. Letters* 53 (1988) 60.
- [12] R.G. van Welzenis and B.K. Ridley, *Solid State Electron* 27 (1984) 113.
- [13] J. Tersoff, *Phys. Rev. Letters* 56 (1986) 2755.

Substitutional doping of ZnSe films

J. Ren, K.A. Bowers, S. Hwang, J.W. Cook, Jr. and J.F. Schetzina

Department of Physics, North Carolina State University, Raleigh, North Carolina 27695-8202, USA

Molecular beam epitaxy has been successfully employed to grow n-type ZnSe:Cl epilayers on (100) GaAs substrates at 275 °C. The ZnSe:Cl epilayers are highly conducting and exhibit bright blue-violet edge luminescence at room temperature. A Hall mobility of 2480 cm²/V·s at 40 K was measured for an n-type ZnSe:Cl film doped to a level of $\sim 3 \times 10^{17}$ cm⁻³ and for which a compensation ratio $N_A/N_D \sim 4\%$ was calculated. Carrier concentrations as large as 7×10^{18} cm⁻³ were obtained by increasing the temperature of the MBE oven containing the Cl dopant. p-Type ZnSe films were prepared using Li as a substitutional dopant. The ZnSe:Li films exhibit photoluminescence spectra at 4 K dominated by an acceptor-bound exciton peak at 2.791 eV, providing clear evidence of p-type doping.

1. Introduction

ZnSe is a wide band gap II–VI semiconductor that is currently under investigation in a number of laboratories throughout the world. Its room temperature band gap of ~ 2.7 eV makes it an attractive candidate for the fabrication blue light emitting devices [1,2]. Although p-type doping is currently the major obstacle in making such devices, efficient activation of n-type dopants is of equal importance, particularly if blue light emitting semiconductor lasers are to be developed. n-Type doping is also required for other related devices such as optical modulators, transistor amplifiers, and diode detectors which together might form the basis of a new blue-green optoelectronics technology. Recent investigations by MBE [3] and MOVPE [4] have shown that very high n-type doping levels can be achieved in ZnSe films using group VII elements as dopants. However, the samples reported to date generally exhibit low Hall mobilities compared to n-type ZnSe:Ga doped films [2]. In this paper we report the successful MBE growth of high quality n-type ZnSe:Cl films at low temperatures. The films exhibit excellent electrical and optical properties. p-Type ZnSe layers were also obtained by using Li as a substitutional dopant [5].

2. Experimental details

The ZnSe:Cl samples were grown in an MBE system designed and built at North Carolina State University (NCSU) [6]. The growth chamber has a base pressure of 6×10^{-11} Torr and is equipped with seven MBE sources. The MBE sources feature special two-temperature-zone furnaces, designed and constructed at NCSU specifically for the growth of II–VI materials, which are capable of producing highly stable beam fluxes [7]. To calibrate the molecular beam flux density from each of the primary MBE ovens, films were deposited at room temperature and their thicknesses were measured. The beam flux was calculated assuming unity sticking coefficient and correlated with the beam equivalent pressure (BEP) measured with a nude ion gauge at the exact location of the substrate [6]. Both the Zn and Se source beams were calibrated in this way so that an accurate beam flux ratio (BFR) could be obtained. High purity (6N grade) Zn and Se were used as primary source materials, and ultra dry ZnCl₂ (5N grade) and Li metal (3N grade) were used as n-type and p-type dopant sources, respectively.

As (using a Zn₃As₂ source) and O (using a ZnO source) were also investigated as potential p-type dopants. However, our results for these

added impurities are discouraging to date - we have obtained no evidence for p-type doping of ZnSe using either As or O for the film growth conditions that we have employed.

Semi-insulating (100) GaAs wafers were used as substrates. Prior to MBE film growth, the GaAs substrate was first degreased in standard solvents and then etched in an $\text{H}_2\text{SO}_4 : \text{H}_2\text{O}_2 : \text{H}_2\text{O}$ (8:1:1) solution at 0°C for 3 min. The substrate was preheated to 580°C for 10 min in the MBE system to desorb the surface oxide.

The ZnSe:Cl epilayers were characterized by means of Hall effect and photoluminescence (PL) studies. It was not possible for us to complete Hall effect studies on the ZnSe:Li samples because of problems associated with non-ohmic contacts. The ZnSe:Li films were, however, investigated by means of low temperature photoluminescence (PL) studies. The PL was excited using the 360 nm UV output from an Ar^+ ion laser and was measured using a SPEX 1403 double monochromator equipped with a GaAs photomultiplier tube and computer-controlled photon counting electronics. Double-crystal X-ray diffraction rocking curve measurements were completed to assess the structural perfection of the doped epilayers.

3. Results and discussion

In order to achieve high quality electrical and optical properties, we found it necessary to use relatively low growth temperatures and to maintain the proper stoichiometry of the surface during film growth. Growth mechanisms of II-VI materials have been studied by several groups [8,9]. In a recent study, Zhu et al. [9] showed that the film growth rate is influenced by the Se desorption from the growing surface into the precursor states when the Zn-to-Se beam flux ratio (BFR) is greater than 1. When the $\text{BFR} \leq 1$, the growth rate is influenced by both Zn and Se desorption. Thus, it appears that it may be easier to control the surface stoichiometry by using $\text{BFR} > 1$. This generally requires lower growth temperatures ($\leq 275^\circ\text{C}$).

We have grown ZnSe films at $225-275^\circ\text{C}$ with Zn-to-Se BFR ranging from 0.5 to 2. Under Se-rich conditions ($\text{BFR} < 1$), the films exhibit relatively

poor surface morphologies and broad X-ray rocking curves. In contrast, films grown at $225-275^\circ\text{C}$ under Zn-rich conditions exhibit mirror-like surfaces. Double-crystal X-ray rocking curves for films $2-3\ \mu\text{m}$ thick typically exhibit full-widths-at-half-maxima (FWHMs) of ~ 150 arc sec.

3.1. n-Type ZnSe:Cl films

ZnSe:Cl films grown under Zn-rich conditions exhibit low resistivity. Room temperature carrier concentrations ranging from $1.5 \times 10^{17}\ \text{cm}^{-3}$ to $6.7 \times 10^{18}\ \text{cm}^{-3}$ have been reproducibly obtained by varying the ZnCl_2 oven temperature. Hall data for a degenerately-doped sample C21 exhibits a constant carrier concentration of $\sim 6.7 \times 10^{18}\ \text{cm}^{-3}$, independent of temperature. The electron mobility $\mu_p = 170\ \text{cm}^2/\text{V}\cdot\text{s}$ is also independent of temperature.

The carrier concentration of moderately-doped samples (such as C35 in fig. 1) is, however, clearly activated over the temperature range from 20 to 300 K. In order to determine the compensation ratio and donor ionization energy, we have calculated the carrier concentration by solving the charge-neutrality equation assuming non-degenerate statistics [10]. The conduction band effective mass was taken to be 0.17. The solid curve in fig. 1 shows the best fit which was obtained using a donor ionization energy $E_D = 16.5\ \text{meV}$, a donor density $N_D = 2.3 \times 10^{17}\ \text{cm}^{-3}$, and an acceptor density $N_A = 6.0 \times 10^{15}\ \text{cm}^{-3}$. The low compensa-

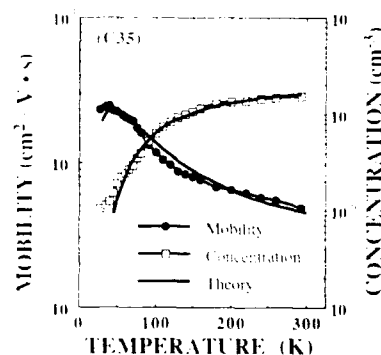


Fig. 1. Hall data and theoretical curves for moderately doped ZnSe:Cl film.

tion ratio ($< 4\%$) provides clear evidence of the exceptional electrical quality of this ZnSe:Cl sample.

Sample C35 exhibits a room temperature mobility of $485 \text{ cm}^2/\text{V} \cdot \text{s}$ and a maximum mobility of $2480 \text{ cm}^2/\text{V} \cdot \text{s}$ at 40°C , as shown in fig. 1. To our knowledge, this is the highest mobility ever obtained for n-type ZnSe doped to this concentration by any technique. To further analyze the data, we calculated the electron mobility by numerically solving the Boltzmann equation using the iteration method [11,12]. Four scattering mechanisms were taken into account, including polar mode phonon scattering, acoustic mode (deformation-potential coupling), acoustic mode (piezoelectric coupling), and ionized impurity scattering. The result of this mobility calculation is shown as the solid curve in fig. 1. The impurity concentration N_{imp} for the mobility calculation was taken to be $2N_A + n_0$ [13], where N_A is the acceptor concentration and n_0 is the equilibrium electron concentration. Both n_0 and N_A were obtained from the carrier concentration analysis described above. Note the good agreement between the theoretical calculation and experimental data, supporting the low compensation ratio obtained from the carrier concentration analysis.

The 4.2 K PL spectra of the ZnSe:Cl films is dominated by a donor-bound exciton D^0, X peak at 2.796–2.797 eV, depending on the doping level. The fact that both the free exciton and deep level emissions are absent, but the D^0, X line remains narrow (FWHM = 6.2 meV), implies that the Cl atoms have been successfully incorporated into the ZnSe lattice at tetrahedral sites, in accord with the electrical results described above. At 300 K, the PL spectrum of the ZnSe:Cl films is dominated by a strong near-band-edge emission peak centered at 2.693 eV. This peak energy is consistent with that reported by Ohkawa et al. for Cl-doped ZnSe, who attributed the peak to donor-to-valence-band recombination [3].

3.2. p-Type ZnSe:Li films

The use of Li as a p-type dopant produced immediate positive results, in marked contrast to the use of As and O as p-type dopants. This is

illustrated by the PL spectra shown in fig. 2. The spectrum at the top of the figure is for an undoped ZnSe film (C43) and features a donor-bound exciton peak D^0, X at 2.796 eV, along with a free exciton peak at a higher energy (2.801 eV). Next is shown a representative PL spectrum for an arsenic doped ZnSe film (C39). Note that the PL spectrum again features a donor-bound exciton peak D^0, X at 2.796 eV, but no evidence of p-type impurity incorporation. In the case of ZnSe:O (C48), the PL spectrum consists of two broad peaks at 2.787 and 2.734 eV, respectively. Using the film growth parameters reported in this paper, we have not been able to reproduce the results of Akimoto et al. [15] who obtained PL spectra for p-type ZnSe:O consisting of an acceptor-bound exciton peak A^0, X at 2.791–2.792 eV and a main donor-acceptor pair (DAP) peak at 2.715–2.722 eV, depending on the doping level. In contrast, the PL spectrum for a representative ZnSe:Li film C63, shown at the bottom of fig. 2, displays an intense acceptor-bound exciton peak A^0, X at 2.791 eV, providing clear evidence of p-type doping. In preparation for using the ZnSe:Li layers to fabricate light emitting diodes, several ZnSe:Cl–ZnSe:Li double-layered structures were fabricated.

Fig. 3 shows near-band-edge 4.2 K PL spectra for both ZnSe:Cl (C55A) and ZnSe:Li (C63B)

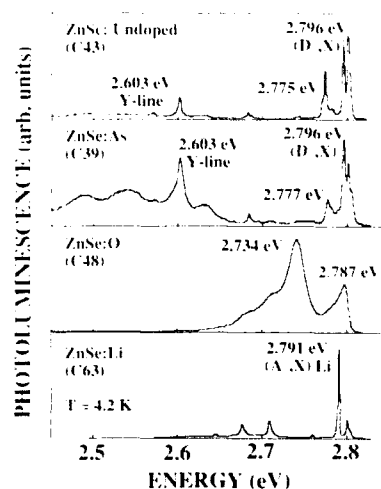


Fig. 2. PL spectra for selected ZnSe films.

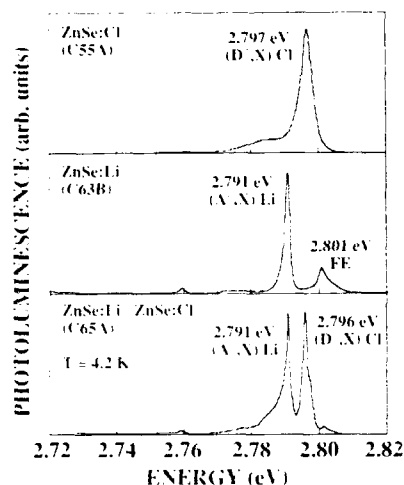


Fig. 3. PL spectra for doped ZnSe films.

films, which show D⁰, X and A⁰, X peaks, respectively. At the bottom of fig. 3 is shown the PL spectrum of a p-on-n double layer consisting of a 1.7 μm thick ZnSe:Cl film onto which a 0.8 μm thick ZnSe:Li layer was deposited. Note that in this case, both donor-bound and acceptor-bound peaks are present in the PL spectrum, indicating the presence of both n-type and p-type impurities in the region probed by the PL experiment. We have used double-layers of this type to successfully fabricate blue light emitting diodes [16].

4. Summary and conclusions

High quality Cl-doped ZnSe films have been grown by MBE under Zn-rich conditions at low temperatures (225°C). The epilayers exhibit mirror-like surface morphologies, good X-ray rocking curves, low compensation ratios, high electron mobilities, and sharp, bright near-band-edge photoluminescence with minimal deep level emissions. Our results provide clear evidence that Cl is a very acceptable and efficient n-type donor in ZnSe films.

We have not been able to demonstrate p-type doping of ZnSe using either As or O as the dopant

species. In contrast, Li was found to be a viable and reproducible p-type dopant for ZnSe. However, ohmic contacts to p-type ZnSe remain a key issue that needs to be addressed before detailed electrical characterization experiments can be completed.

Acknowledgements

This work was supported by the Defense Advanced Research Projects Agency (DARPA) through a University Research Initiative (URI) grant administered by the Office of Naval Research. Joe Matthews and M. Bennett provided assistance with some of the experiments.

References

- [1] R.N. Bhargava, *J. Crystal Growth* 86 (1988) 873.
- [2] T. Yao, *J. Crystal Growth* 72 (1985) 31.
- [3] K. Ohkawa, T. Mitsuyu and O. Yamazaki, *J. Appl. Phys.* 62 (1987) 3216.
- [4] A. Yoshikawa, H. Nomura, S. Yamaga and H. Kasai, *J. Appl. Phys.* 65 (1989) 1223.
- [5] H. Cheng, J.M. DePuydt, J.E. Potts and T.L. Smith, *Appl. Phys. Letters* 52 (1988) 147.
- [6] K.A. Harris, S. Hwang, D.K. Blanks, J.W. Cook, Jr., N. Otsuka and J.F. Schetzina, *J. Vacuum Sci. Technol.* A4 (1986) 2061.
- [7] J.W. Cook, Jr., D.B. Eason and K.A. Harris, *J. Vacuum Sci. Technol.* B8 (1990) 196.
- [8] A. Koukitu, H. Nakai, T. Suzuki and H. Seki, *J. Crystal Growth* 84 (1987) 425.
- [9] Z. Zhu, T. Nomura, M. Miyao and M. Hagino, *J. Crystal Growth* 95 (1989) 529.
- [10] J.S. Blakemore, *Solid State Physics*, 2nd ed. (Cambridge University Press, Cambridge, 1985) p. 320.
- [11] D.L. Rode, *Phys. Rev.* B2 (1970) 4036.
- [12] S. Hwang, PhD Thesis, North Carolina State University (1988), unpublished.
- [13] H.H. Woodbury, *Phys. Rev.* B9 (1974) 5188.
- [14] T. Yao, M. Ogura, S. Matsuoka and T. Morishita, *Appl. Phys. Letters* 43 (1983) 499.
- [15] K. Akimoto, T. Miyajima and Y. Mori, *Phys. Rev.* B39 (1989) 3138.
- [16] J. Ren, K.A. Bowers, B. Sneed, F.E. Reed, J.W. Cook, Jr. and J.F. Schetzina, *J. Crystal Growth* 111 (1991) 829.

n-Type and p-type conductivity control of ZnSe grown by metalorganic molecular beam epitaxy using methyl iodide and ammonia

Masahito Migita, Akira Taike and Hajime Yamamoto

Central Research Laboratory, Hitachi, Ltd., P.O. Box 2, Kokubunji, Tokyo 185, Japan

Electrical properties of ZnSe heavily doped with iodine or nitrogen have been investigated. The film crystals of ZnSe were grown by metalorganic beam epitaxy with methyl iodide or ammonia as a dopant source. Iodine doping provides highly conductive n-type ZnSe with resistivity as low as $0.02 \Omega \text{ cm}$ and a carrier concentration of $2.2 \times 10^{18} \text{ cm}^{-3}$ at room temperature. For ZnSe:N, ohmic electrodes have been formed with gold by annealing at 360°C for 5 min in N_2 atmosphere. The activation energy of p-type conductivity, E_A , is 90–110 meV when the growth temperature (T_g) is 350°C , while E_A is 80–100 meV when $T_g = 400^\circ\text{C}$. The acceptor concentration N_A decreases from 9×10^{16} – $3 \times 10^{17} \text{ cm}^{-3}$ to 3×10^{16} – $7 \times 10^{16} \text{ cm}^{-3}$ as T_g is elevated from 350 to 400°C . However, the difference between the acceptor and residual donor concentration ($N_A - N_D$) is about 5 times larger for 400°C than for 350°C . $N_A - N_D$ is 4×10^{17} – $7 \times 10^{17} \text{ cm}^{-3}$ for 350°C and 2×10^{16} – $4 \times 10^{16} \text{ cm}^{-3}$ for 400°C . This result indicates that electrical properties of the p-type ZnSe:N are improved as T_g increases. Photoluminescence properties of n-ZnSe:I and p-ZnSe:N are also reported.

1. Introduction

Zinc selenide (ZnSe) with a direct band-gap of 2.7 eV at RT is a promising material for fabrication of efficient blue LEDs and laser diodes. Recently, there has been considerable progress in conductivity control for n- and p-type ZnSe through the use of low temperature growth techniques such as metalorganic vapor phase epitaxy (MOVPE) [1–7] and molecular beam epitaxy (MBE) [8–10]. However, it is still controversial how to control conductivity well enough for device application for both n- and p-type ZnSe.

We have already reported that metalorganic molecular beam epitaxy (MOMBE) is a good technique for preparing highly conductive and electrically stable p-type ZnSe by doping of nitrogen [11–13]. In this paper, we report electrical transport properties as well as photoluminescence for both ZnSe:I and ZnSe:N grown on GaAs (100) substrates by MOMBE.

2. Experimental

The details of our MOMBE apparatus have been published elsewhere [12]. Iodine-doped and

nitrogen-doped ZnSe were grown on semi-insulating GaAs substrates ($> 10^7 \Omega \text{ cm}$). The growth chamber was evacuated to a pressure below 1×10^{-8} Torr before growth. Dimethylzinc (DMZ) and hydrogen selenide (H_2Se) were used as starting gases, and methyl iodide and ammonia (NH_3) were used as dopant sources. The flow rates of DMZ, H_2Se , NH_3 and methyl iodide were 20, 40, 20 and $10 \mu\text{mol/min}$, respectively. Although the $[\text{H}_2\text{Se}]/[\text{DMZ}]$ molar ratio is 2, the growth rate is limited by the H_2Se supply. In this sense, the growth occurs under a Zn-rich condition. The gas-cell temperature was maintained at 350°C for nitrogen-doping and at 100°C for iodine-doping. The pressure during the growth was about 2×10^{-4} Torr. The typical thickness of these layers is about $1 \mu\text{m}$.

Prior to growth, halogens contained in DMZ and H_2Se were analyzed. Inductively-coupled plasma spectroscopy (ICPS) shows that the DMZ used in this study contains about 1 ppm of Cl. In contrast, in H_2Se , Cl, Br and I of more than 0.01 ppm were not detected by diphenylcarbazone method.

The GaAs substrates were cleaned in the following way before growth: (1) rinsed in trichloro-

ethane, (2) rinsed in methanol, (3) etched in 4:1:1 $\text{H}_2\text{SO}_4:\text{H}_2\text{O}_2:\text{H}_2\text{O}$ at 40°C for 30 s and (4) etched in 1:1 $\text{HF}:\text{H}_2\text{O}$ at room temperature for 60 s. After this wet cleaning, the substrates were heated in a reactor at $550\text{--}630^\circ\text{C}$ for 10 min.

Photoluminescence (PL) spectra were measured at temperatures between 4.7 K and RT under He-Cd laser excitation at wavelength of 325 nm with a power density of less than $50\text{ mW}/\text{cm}^2$.

3. Results and discussion

3.1. Iodine-doped *n*-type ZnSe

Fig. 1 shows the PL spectra of ZnSe:I grown at 350°C measured at 4.7 K and RT. The inset shows details of the exciton emission region. The broad emission with a peak energy of 2.132 eV (581.1 nm) at RT comes from the self-activated (SA) center of a (Zn vacancy)-iodine complex. The peak of an emission line at the band edge region is located at an energy of 2.802 eV at 4.7 K, which is close to the peak energy of a free exciton emission in ZnSe [19]. The line has a tail developing on the lower energy side, which is characteris-

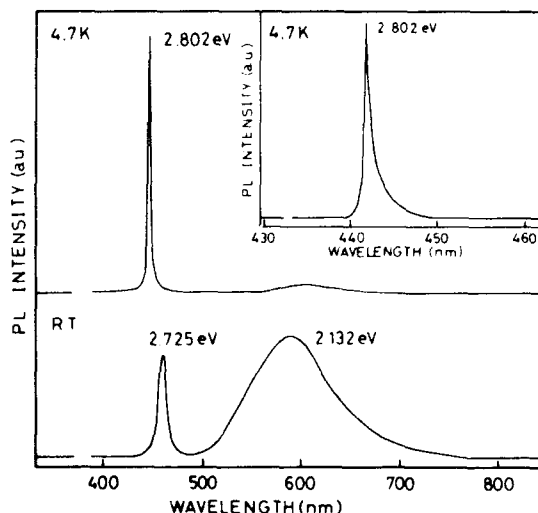


Fig. 1. Photoluminescence spectra of *n*-ZnSe:I ($T_g = 350^\circ\text{C}$) measured at 4.7 K and 23°C . The inset is the detailed spectrum in the exciton emission region at 4.7 K.

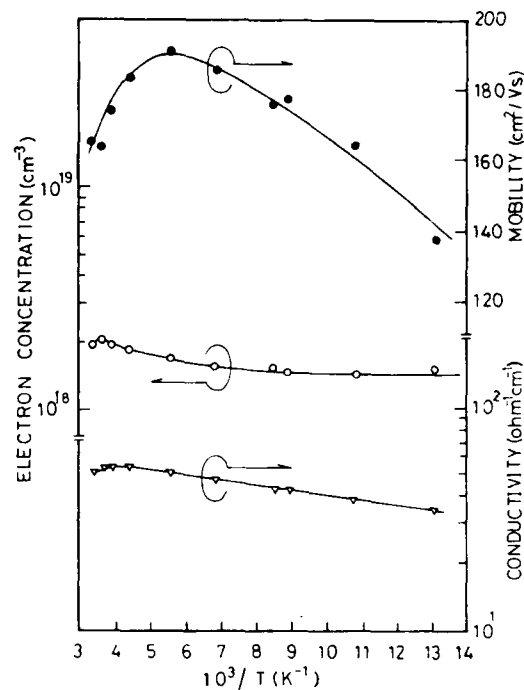


Fig. 2. Electric transport properties of *n*-ZnSe:I measured by the Van der Pauw configuration at various temperatures below RT.

tic of band-tailing caused by highly-doped iodine [4,15].

The electron concentration (n), conductivity (σ) and mobility are shown in fig. 2 as a function of temperature (T) for a ZnSe:I film grown at 350°C . The measurements were made in the Van der Pauw configuration. Ohmic electrodes were obtained by deposition of indium followed by annealing at 270°C for 5 min. At room temperature, the electron concentration is $2.2 \times 10^{18}\text{ cm}^{-3}$, Hall mobility $160\text{ cm}^2/\text{V}\cdot\text{s}$ and resistivity ($\rho = \sigma^{-1}$) $1.9 \times 10^{-2}\text{ }\Omega\text{ cm}$. The maximum mobility of $190\text{ cm}^2/\text{V}\cdot\text{s}$ occurs at 180 K with $n = 1.7 \times 10^{18}\text{ cm}^{-3}$. The log n versus $1/T$ curve indicates an electron transport mechanism with two kinds of activation energy. The first slope is 8 meV at a temperature region higher than 180 K. The second slope has zero activation energy at a temperature lower than 120 K for electron transport. The corresponding activation energy for the conductivity

is 5 meV, which was estimated from the slope below 200 K. The Bohr radius can be calculated to be 2.9 nm for ZnSe with a dielectric constant κ of 9.1 and an effective mass ratio of 0.17 [14,15]. From this Bohr radius, the minimum impurity concentration (N_i^{min}) causing the wave-function overlap can be estimated to be $1 \times 10^{18} \text{ cm}^{-3}$, which is well below the observed carrier concentration ($2.2 \times 10^{18} \text{ cm}^{-3}$). It is, therefore, concluded that the small activation energy results from the conduction through the interaction between iodines, as usually observed in highly doped semiconductors.

3.2. Nitrogen-doped p-type ZnSe

Nitrogen concentrations N_A^0 in the N-doped ZnSe were measured by secondary ion mass spectrometry (SIMS) with 13 keV Cs^+ ions as the primary beam. Instead of monitoring a $^{14}\text{N}^+$ ion, a $^{94}\text{SeN}^-$ ion was used to determine the amount of nitrogen in ZnSe because of its higher ionization efficiency than that of $^{14}\text{N}^+$. Integration of the $^{94}\text{SeN}^-$ signal gives the nitrogen concentration in comparison with reference samples implanted with N^+ ions at concentrations of 10^{17} , 10^{18} or 10^{19} cm^{-3} . The detectable N_A^0 in ZnSe is more than $1 \times 10^{17} \text{ cm}^{-3}$ when $^{94}\text{SeN}^-$ is used. Typical depth profiles for N-doped ZnSe are shown in the inset in fig. 3. In this figure, the N_A^0 tends to increase from $2 \times 10^{17} \text{ cm}^{-3}$ up to about 10^{19} cm^{-3} as the growth temperature (T_g) increases from 250 to 350°C. However, over 350°C, the concentration is slightly reduced.

Fig. 4 shows a PL spectrum of ZnSe:N grown at 350°C, in the band edge region at 5.6 K. The lines appearing at 2.792 eV (444.1 nm) and 2.797 eV (443.3 nm) can be attributed to an exciton bound to a neutral nitrogen acceptor (I_1^N) and to an exciton bound to a neutral donor (I_2), respectively. The nitrogen activation energy of 98–108 meV is obtained from the donor-acceptor (DA) formula [17] by using a zero-phonon peak of DA pair emission, i.e. 2.704 eV. These results show that nitrogen in ZnSe acts as a shallow acceptor.

In advance of the Hall measurements, the ohmic contact conditions were determined by varying annealing temperature. Formation of ohmic elec-

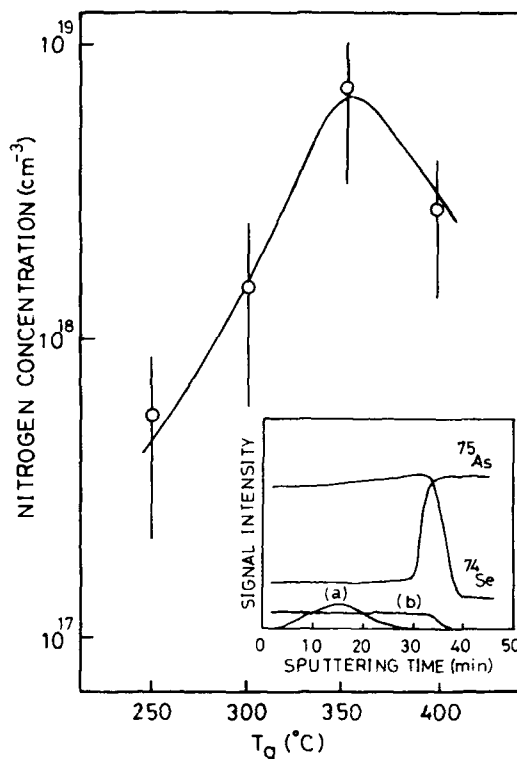


Fig. 3. Nitrogen concentration in ZnSe as a function of growth temperature (T_g) analyzed by secondary ion mass spectrometry. The inset shows typical depth profiles of $^{94}\text{SeN}^-$ in nitrogen-doped ZnSe: (a) implanted with N^+ ion concentration of 10^{19} cm^{-3} and (b) doped by MOMBE at $T_g = 350^\circ\text{C}$.

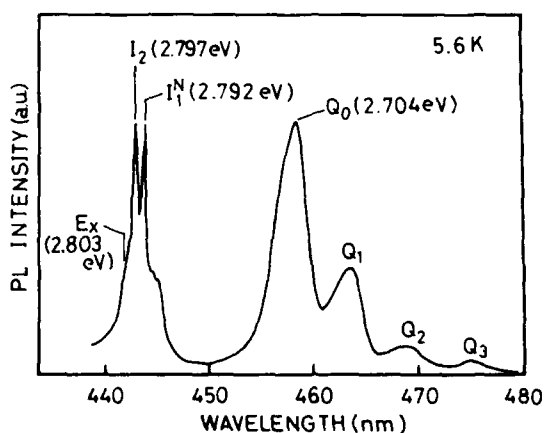


Fig. 4. PL spectrum of ZnSe:N grown at 350°C in the band edge region at 5.6 K.

trodes for ZnSe:N was attained as follows: gold was deposited and annealed at various temperatures between 260 and 460°C in an N₂ atmosphere for 5 min. With electrodes formed in this way on ZnSe:N films, current-voltage (I - V)

characteristics were measured at RT as a function of annealing temperature. As shown in fig. 5, the ohmic electrodes are obtained between 310 and 410°C. Electrical properties of ZnSe:N were measured with electrodes formed at 360°C where

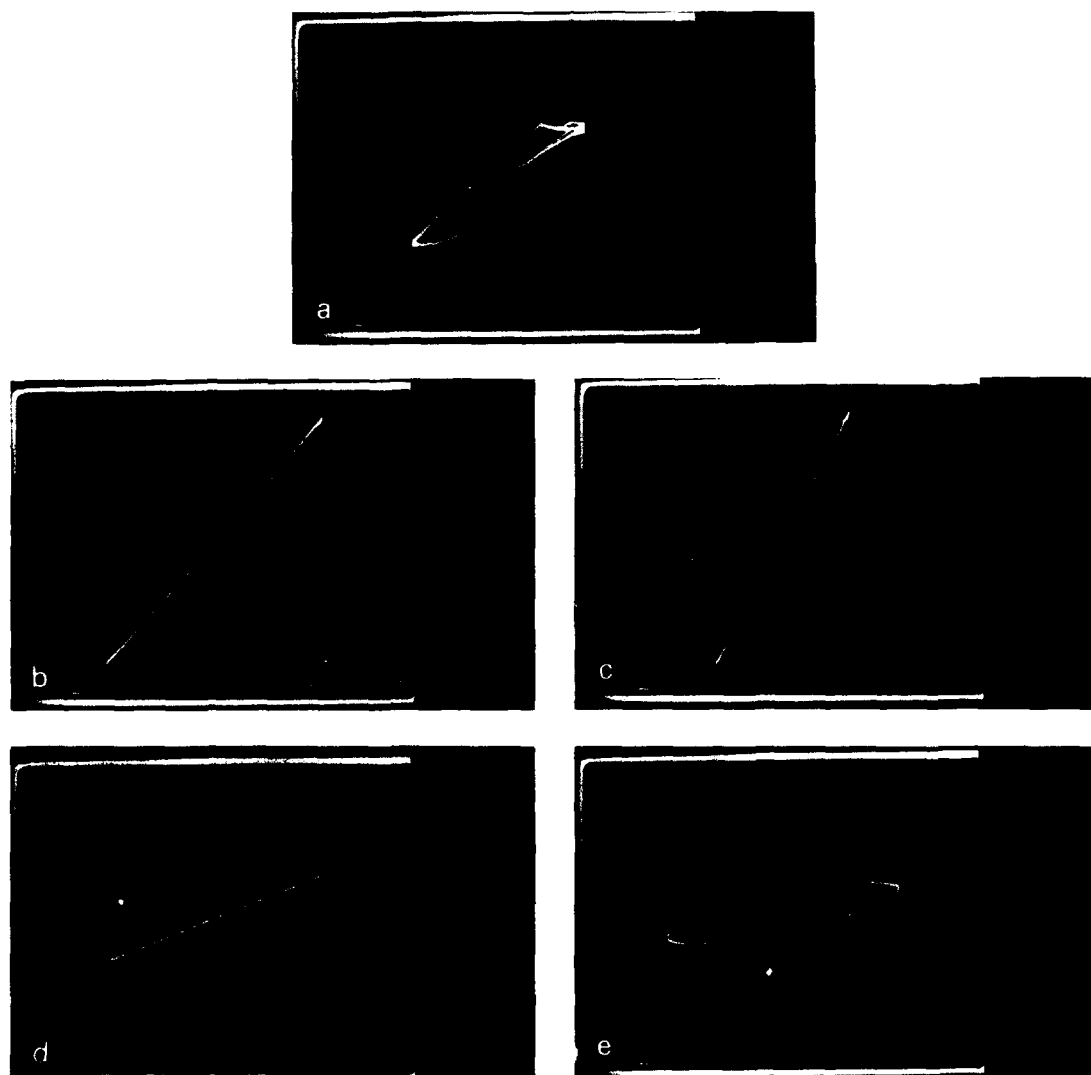


Fig. 5. Current-voltage (I - V) characteristics of Au contacts on ZnSe:N at RT as a function of annealing temperature: (a) 260°C, (b) 310°C, (c) 360°C, (d) 410°C and (e) 460°C. The vertical and horizontal scales are 10 μ A and 10 V for (a), 10 μ A and 2 V for (b)-(d) and 1 μ A and 10 V for (e).

the resistance has the minimum value. Those contacts remain ohmic from RT to the liquid nitrogen temperature.

Fig. 6a shows the hole concentration of ZnSe:N grown at 350 and 400°C as a function of $1/T$. The hole concentration at RT is $2.0 \times 10^{15} \text{ cm}^{-3}$ for $T_g = 350^\circ\text{C}$ and $4.0 \times 10^{15} \text{ cm}^{-3}$ for $T_g = 400^\circ\text{C}$. For p-ZnSe grown at 350°C, the hole concentration decreases as T decreases. Assuming that the acceptor concentration N_A is larger than the donor concentration N_D , the activation energy of the p-type conductivity E_A , the acceptor concentration N_A and the donor concentration N_D can be calculated from the following equation:

$$\frac{p(p + N_D)}{N_A - N_D - p} = \frac{N_V}{g} \exp\left(-\frac{E_A}{kT}\right), \quad (1)$$

where p is the hole concentration, N_V the density of states of the valence band, $N_V = 2(2\pi m_h kT/h^2)^{3/2}$. The hole effective mass is taken here as $m_h = 0.75m_0$ [21] and the degeneracy factor as $g = 4$. Then eq. (1) gives $N_A = 9 \times 10^{16} - 3 \times$

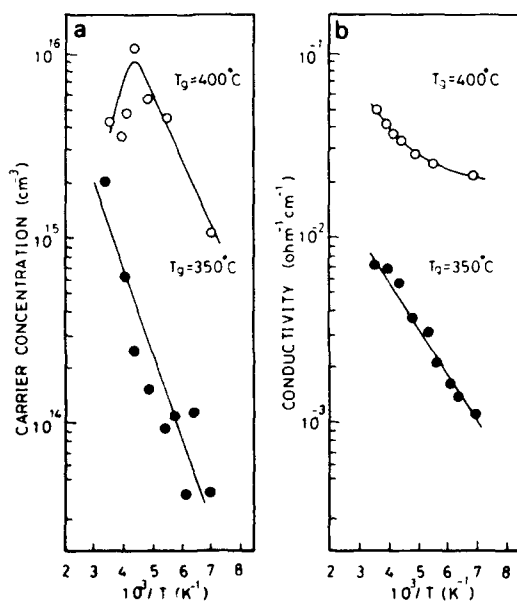


Fig. 6. Electric properties of p-type ZnSe:N grown at $T_g = 350^\circ\text{C}$ and 400°C measured at various temperatures below room temperature: (a) carrier concentration and (b) conductivity.

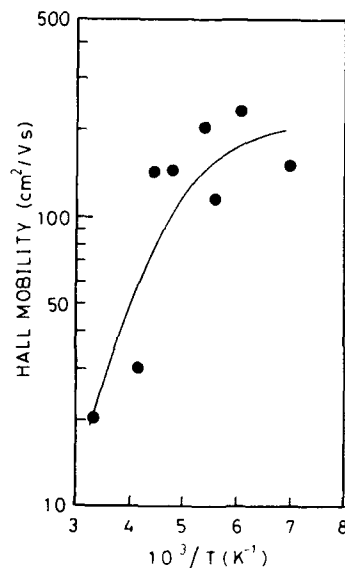


Fig. 7. Dependence of Hall mobility on measurement temperature. The sample is ZnSe:N grown at 350°C .

10^{17} cm^{-3} , $N_A - N_D = 4 \times 10^{15} - 7 \times 10^{15} \text{ cm}^{-3}$ and $E_A = 90 - 110 \text{ meV}$. The obtained value of E_A agrees well with that estimated from the PL spectrum described above. The conductivity has the same dependence as that of the hole concentration and is $6.7 \times 10^{-3} \Omega^{-1} \text{ cm}^{-1}$ at RT for the film grown at 350°C (fig. 6b). The Hall mobility for the sample of $T_g = 350^\circ\text{C}$ increases with a decrease in temperature and is about $20 \text{ cm}^2/\text{V} \cdot \text{s}$ at room temperature, as shown in fig. 7.

The conductivity of the film grown at 400°C was obtained to be $4.1 \times 10^{-2} \Omega^{-1} \text{ cm}^{-1}$ at RT, as shown in fig. 6b. The temperature dependence of conductivity cannot be fitted by a single exponential curve, which is different from the case of $T_g = 350^\circ\text{C}$. The hole concentration of the ZnSe:N grown at 400°C increases with a slope of about 150–200 meV from RT to 220 K. This is followed by a decrease in the hole concentration as the temperature decrease below 220 K. This result suggests that the donors with the activation energy of 150–200 meV compensate for nitrogen acceptors at around RT. Assuming that N_A is larger than N_D at a temperature below 220 K, one can calculate E_A , N_A and N_D from eq. (1); N_A is

$3 \times 10^{16} - 7 \times 10^{16} \text{ cm}^{-3}$, $N_A - N_D$ is $2 \times 10^{16} - 4 \times 10^{16} \text{ cm}^{-3}$ and E_A is about 80–100 meV. Although N_A is larger for the film of $T_g = 350^\circ\text{C}$ than for the film of $T_g = 400^\circ\text{C}$, a comparison of $N_A - N_D$ between the two T_g 's shows that the donor concentration N_D decreases as T_g increases. Since the ratio N_A/N_A^0 is 1–4% and is almost same for both films, this result indicates that the T_g -dependence of N_D is mainly responsible for the increase in hole concentration with T_g . The donors presumably come from residual impurities contaminating the source material such as DMZ. These results give an account of the T_g -dependence of the electrical properties of p-type ZnSe:N. We have already reported that the electrical properties such as hole concentration and resistivity were improved as T_g increases from 250 to 450°C [11,12].

4. Conclusions

This paper shows that the technique of MOMBE has a capability to provide both n-type and p-type ZnSe with high conductivity. It has been described that n-type ZnSe heavily doped with iodine shows a resistivity (ρ) low enough for device application ($\rho = 1.9 \times 10^{-2} \Omega \text{ cm}$ at RT). The electrical properties such as E_A , N_A , N_D , p , σ and μ of p-type ZnSe:N grown using ammonia as a dopant source have been elucidated. The activation efficiency (p/N_A^0 , where N_A^0 is the nitrogen concentration in ZnSe:N detected by SIMS) of nitrogen acceptors is improved with an increase in growth temperature presumably due to a decrease in residual donor concentration. Since impurities in DMZ such as Cl give rise to donors, further purification of source materials is one of the essential ways to control conductivity of ZnSe:N. Besides, the ratio N_A/N_A^0 for the ZnSe:N is at

most 4%, which suggests that the crystallinity of the p-type films has also to be improved, so as to enhance the p-type conductivity. A combination of these n-type ZnSe:I and p-type ZnSe:N films must be very promising to bring forth efficient blue-light emitting diodes.

References

- [1] W. Stutius, *J. Crystal Growth* 59 (1982) 1.
- [2] W. Stutius, *Appl. Phys. Letters* 38 (1981) 352.
- [3] A. Kamata, T. Ueno, M. Okajima, K. Hirahara, M. Kawachi and T. Beppu, *J. Crystal Growth* 86 (1989) 285.
- [4] N. Shibata, A. Ohki and S. Zembutsu, *Japan. J. Appl. Phys.* 27 (1988) L251.
- [5] T. Yasuda, I. Mitsuishi and H. Kukimoto, *Appl. Phys. Letters* 52 (1988) 57.
- [6] A. Yoshikawa, S. Muto, S. Yamaga and H. Kasai, *J. Appl. Phys.* 27 (1988) L260.
- [7] A. Ohki, N. Shibata and S. Zembutsu, *Japan. J. Appl. Phys.* 27 (1988) L909.
- [8] H. Cheng, J.M. DePuydt, J.E. Potts and T.L. Smith, *Appl. Phys. Letters* 52 (2) (1988) 147.
- [9] T. Yao and Y. Okada, *Japan. J. Appl. Phys.* 25 (1986) 821.
- [10] K. Akimoto, T. Miyajima and Y. Mori, *Japan. J. Appl. Phys.* 28 (1989) L523.
- [11] M. Migita, A. Taike, M. Shiiki and H. Yamamoto, *J. Crystal Growth* 101 (1990) 835.
- [12] A. Taike, M. Migita and H. Yamamoto, *Appl. Phys. Letters* 56 (1990) 1989.
- [13] M. Migita, A. Taike and H. Yamamoto, *J. Appl. Phys.* 68 (1990) 880.
- [14] N.F. Mott and W.D. Twose, *Advan. Phys.* 10 (1961) 107.
- [15] W. Stutius, *J. Appl. Phys.* 53 (1982) 284.
- [16] R.N. Bhargava, *J. Crystal Growth* 59 (1982) 15.
- [17] J.S. Prener and F.E. Williams, *J. Electrochem. Soc.* 103 (1956) 342.
- [18] T. Taguchi, T. Kusao and A. Hiraki, *J. Crystal Growth* 72 (1985) 46.
- [19] S. Satoh and K. Igaki, *Japan. J. Appl. Phys.* 19 (1980) 1953.
- [20] G.E. Hite, D.T.F. Marple and B. Segall, *Phys. Rev.* 156 (1967) B850.

Electric field assisted doping of semiconductors during epitaxial growth

Y. Rajakarunanayake, J.O. McCaldin and T.C. McGill

Thomas J. Watson, Sr. Laboratory of Applied Physics, California Institute of Technology, Pasadena, California 91125, USA

We describe a novel technique to improve doping in semiconductors, by the application of external electric fields during crystal growth. The dopants are modeled as charged, mobile species that are free to diffuse and drift under electric fields. In the case of molecular beam epitaxial (MBE) growth, we solve for the steady state of these species in a moving coordinate frame that travels with the growth front. We have specifically applied our analysis to Li donors in n-type ZnTe. Our results indicate that excellent improvements in the doping concentrations could be obtained under normal MBE growth conditions, with the applications, with the application of substantial electric fields.

1. Introduction

Wide band gap II–VI semiconductors have not realized their potential as visible light emitters because of inability to achieve p–n junctions with selective doping in both conduction types [1–4]. For example, ZnSe can only be easily doped n-type, while ZnTe can only be easily doped p-type. Although there have been many attempts to reverse the preferred conduction types of these materials within the past few decades, the results have at best produced very limited success [5,6]. Molecular beam epitaxy (MBE) and metalorganic chemical vapor deposition (MOCVD) have received the interest in wide bandgap II–VI semiconductors by permitting abrupt heterojunctions and novel doping techniques and producing heterojunctions [7–9]. Recent successes in producing Li doped p-ZnSe have attracted much attention [10–13]. We propose that the application of an electric field during epitaxial growth can produce enhanced doping and reduce self-compensation overcoming some of the difficulties associated with II–VI doping. We will use a simple example of Li donors grown into ZnTe by MBE for illustration, but the general idea is readily applicable to other semiconductors and growth techniques.

2. Physics of phenomena

Under external fields applied during growth, band bending is introduced near the growth surface, fig. 1a. The x -axis of fig. 1a corresponds to the distance from the growth surface measured in the moving coordinate frame that travels with the growth front. For simplicity we assume the bands are flat in the absence of the external electric fields. If additional band bending occurs because of Fermi level pinning at the surface [16], it is straightforward to include such effects in our calculations.

As a result of upward band bending at the surface, it is possible to enhance the incorporation of an ionized donor species while suppressing the incorporation of ionized acceptor species. The ionization of donors inside the semiconductor produces a donor concentration N_D^S and an electron concentration n^S near the surface. Using the fact that these donors are in equilibrium with the external phase, we can adopt the arguments given by Lander [17] to show that [17,18]:

$$n^S N_D^S = K, \quad (1)$$

where K is a constant determined by the temperature and the concentration of neutral donors in the external phase. If we assume that the electron

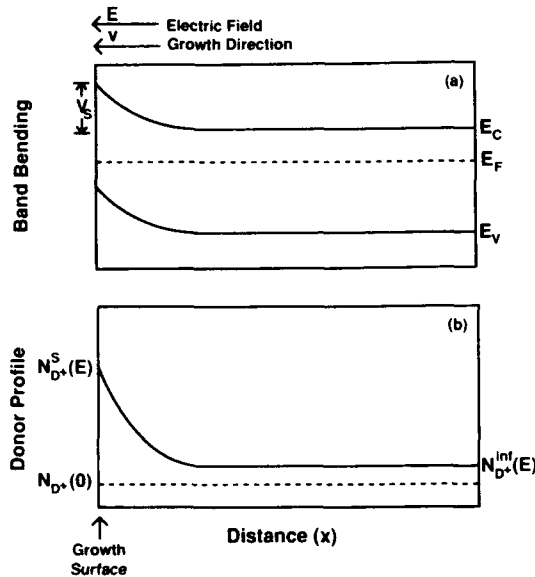


Fig. 1. Schematic diagram of the band bending in the presence of external electric fields is shown in (a). The figure is drawn in the moving coordinate frame that travels with the growth front. In (b) the expected enhancement of the doping concentration is shown. The dashed line of (b) corresponds to the doping concentration under zero electric field, while the solid line corresponds to the expected donor concentration under a substantial electric field.

concentration is given by a classical Maxwell-Boltzmann distribution, then

$$n^S \sim \exp\left(-\frac{E_{D^+}^S - E_F}{kT}\right), \quad (2)$$

where $E_{D^+}^S$ is the position of the donor level at the surface and the Fermi level for electrons is given by E_F . Using eqs. (1) and (2) we can express the ionized donor concentration at the surface as

$$N_{D^+}^S \sim \exp\left(\frac{E_{D^+}^S - E_F}{kT}\right). \quad (3)$$

Since it is possible to easily change the donor level $E_{D^+}^S$ at the surface by applying external electric fields, from eq. (3) we see that it is also possible to directly alter the concentration of the ionized donors at the surface. If we compare the concentration of ionized donors at the surface $N_{D^+}^S(E)$ corresponding to the case of doping under an

electric field E , to the concentration of ionized donors $N_{D^+}(0)$ with no electric fields, from eq. (3) we obtain

$$\frac{N_{D^+}^S(E)}{N_{D^+}(0)} = \exp\left(\frac{qV_s}{kT}\right), \quad (4)$$

where V_s is the surface band bending as shown in fig. 1a.

Next, it is necessary to bury the enhanced surface concentration of donors given by eq. (4) deep inside the epilayer to obtain thick layers with improved doping concentrations. Since new material is created constantly at the growth rate, the surface concentrations gets buried at the growth rate. However, at the same time it is possible for ionized donors to drift back towards the growth surface because the high electric fields present in the depletion region of fig 1a tend to exert a force that pushes them towards the surface. If the growth occurs faster than this drift process, then it is possible to obtain thick epitaxial layers with enhanced doping concentrations. This situation is shown in fig. 1b where $N_{D^+}^{int}(E) > N_{D^+}(0)$.

We choose a particularly simple example to illustrate field assisted doping, in which the only mobile specie is interstitial Li. Interstitial Li has been widely studied [19] in Ge and Si and its behavior found to follow simple laws of drift and diffusion under most circumstances; here we assume similar behavior of Li in a ZnTe host. It should be pointed out, however, that this simple example comes at a price in that interstitial Li is highly mobile, which causes the expected doping enhancement to be modest.

3. Theory

In this section we analyze the diffusion and drift of dopants under the conditions present in electric field assisted doping. If we assume that the growth rate is v , and denote the mobility, diffusion coefficient, and concentration of donors by μ , D , and N_{D^+} , respectively, then the particle current j in the moving coordinate frame can be written as

$$j = -D \frac{dN_{D^+}}{dx} + \mu E N_{D^+} + v N_{D^+}. \quad (5)$$

Eq. 5 has the familiar drift and diffusion currents plus an extra convection current that describes the fact that in moving coordinate frame material is buried at rate v . Using the continuity equation and requiring steady state, we obtain a second order differential equation for $N_{D^+}(E, x)$. The solution to finite values at infinity, is given by

$$\begin{aligned} \frac{N_{D^+}(E, x)}{N_{D^+}^{inf}(E)} &= \frac{v}{D} \exp\left(\frac{qV(x)}{kT} + \frac{vx}{D}\right) \\ &\times \int_0^\infty \exp\left(-\frac{qV(x')}{kT} - \frac{vx'}{D}\right) dx'. \end{aligned} \quad (6)$$

where $V(x)$ is the band bending, and $N_{D^+}^{inf}(E)$ is the concentration of ionized donors deep inside the bulk as shown in fig. 1a. The form of the band bending $V(x)$ is given by the solution to the Poisson equation which depends on N_{D^+} . However, valuable information about the electric field assisted doping could still be obtained by assuming a simple exponential form for the band bending given by

$$V(x) \equiv V_s \exp\left(-\frac{x}{\lambda}\right) = \lambda E \exp\left(-\frac{x}{\lambda}\right), \quad (7)$$

where λ corresponds to the Debye screening length of an electron concentration of $N_{D^+}^{inf}(E)$. With this form for the potential, it is straightforward to obtain the form of $N_{D^+}(E, x)$ from eq. (6) in terms of three dimensionless parameters $q\lambda E/kT$, $D/v\lambda$, and x/λ .

4. Results

Quantitative results obtained for Li donors in ZnTe are given in fig. 2. In this example, we assume the growth temperature to be 300°C, the diffusion coefficient of Li donors to be $10^{-11} \text{ cm}^2 \text{ s}^{-1}$ [22,9] and the growth rate $v \approx 10^{-7} \text{ cm s}^{-1}$ corresponding to attainable values in II-VI MBE [23]. Also, we assume a net donor concentration $N_{D^+}(0)$ obtainable in bulk n-ZnTe without electric fields of 10^{12} cm^{-3} , based on the results of Fischer et al. [6].

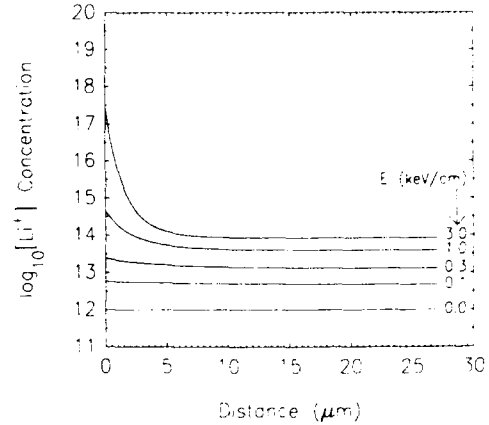


Fig. 2. The figure shows the Li donor concentration profiles obtained under electric field assisted doping. The enhancement of the Li concentration for several electric field strengths is shown. We have assumed that it is possible to obtain n-type ZnTe with Li at 10^{12} cm^{-3} under zero electric field [6]. The application of a 3 keV cm^{-1} electric field at the surface can produce roughly two orders of magnitude improvement in bulk doping.

Notice that under these conditions, the region near the surface is more heavily n-type doped while the region deep inside the semiconductor is less heavily n-type doped. However, the donor concentrations deep inside the bulk are still larger than for the case with zero electric fields. Fig. 2 shows that it is possible to attain bulk doping concentrations of $n \approx 10^{14} \text{ cm}^{-3}$ in ZnTe for electric field strengths of 3 keV cm^{-1} . The surface doping concentration produced in this case is $\approx 3.0 \times 10^{14} \text{ cm}^{-3}$. At lower electric field strengths ($E \approx 0.3 \text{ keV cm}^{-1}$), bulk doping can still be enhanced by about an order of magnitude over the zero field case, without the formation of a heavily doped surface region.

In fig. 3 we show a contour plot of the $\log[N_{D^+}^{inf}(E)/N_{D^+}(0)]$ as a function of the dimensionless parameters $q\lambda_0 E/kT$ and $\log[D/v\lambda_0]$. The length λ_0 is the Debye length corresponding to an electron concentration equal to $N_{D^+}(0)$. This value of λ_0 is different from the quantity λ used in eq. (7) which corresponds to the Debye screening length of an electron concentration of $N_{D^+}^{inf}(E)$. Positive values of the electric field (pointing out of the semiconductor) produce an increase in the

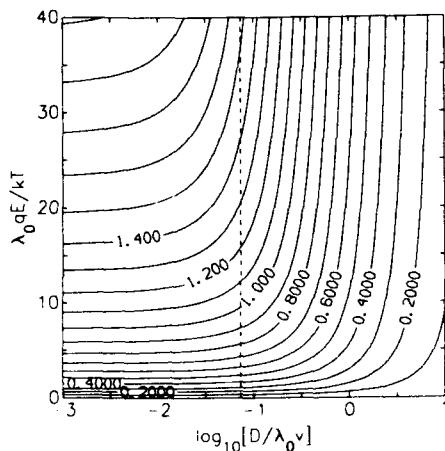


Fig. 3. Contour plot of the $\log [N_D^{\text{int}}(E)/N_D^{\text{int}}(0)]$ is shown as a function of the dimensionless parameters $D/\lambda_0 v$ and $\lambda_0 qE/kT$. The quantities $N_D^{\text{int}}(E)$ and $N_D^{\text{int}}(0)$ are illustrated in Fig. 1b. The Debye screening length for an electron concentration of $N_D^{\text{int}}(0)$ is given by λ_0 . An enhancement in the doping concentration can be produced by increasing the strength of the electric field E . The figure also shows that it is harder to obtain large enhancements in doping concentration if the diffusion coefficients are large. The specific situation corresponding to the Li donor in ZnTe is indicated by the dashed line.

doping concentrations while negative values of the electric field (pointing into the semiconductor) produce a decrease in the doping concentrations compared to the case with zero electric fields. If the value of $D/v\lambda_0 \ll 1$, then the surface concentrations are efficiently buried by the electric field assisted doping process. However, if the value of $D/v\lambda_0 \gg 1$, then it is quite difficult to obtain enhanced doping deep inside the bulk even for large applied electric field strengths. Using values of $D \approx 10^{-11} \text{ cm}^2 \text{ s}^{-1}$ [22], $v \approx 10^{-7} \text{ cm s}^{-1}$, and $\lambda_0 \approx 18.8 \text{ } \mu\text{m}$ corresponding to the Debye screening length for an electron concentration of 10^{12} cm^{-3} , we obtain $D/v\lambda_0 \approx 0.053$. This position is indicated by the dashed line of fig. 3. If we had chosen a dopant other than the very mobile interstitial Li, the dashed line in fig. 3 would lie considerably further left, yielding a larger doping enhancement.

5. Conclusion

We have shown that the application of electric fields during the epitaxial growth of semiconductors produces band bending at the growth surface that could enhance the incorporation of donors near the surface. In addition to producing improved doping concentrations near the surface, it is also possible to bury the enhanced surface concentration deep inside the bulk to obtain thick epilayers with improved doping. Although, for the sake of simplicity, we have applied this technique to the analysis of Li donors in ZnTe, the general idea is widely applicable to other dopants and growth techniques. This method could also be easily applied to reduce self-compensation in semiconductors, since the formation of compensating acceptor complexes near the surface could be suppressed.

Acknowledgement

This work was supported by the Office of Naval Research under contract N00014-90-J-1742.

References

- [1] F.A. Kröger, *The Chemistry of Imperfect Crystals* (North-Holland, Amsterdam, 1973).
- [2] R.E. Halstead, *J. Phys. Chem. Solids* 22 (1965) 109.
- [3] M.R. Lorenz and B. Segall, *Phys. Letters* 7 (1963) 18.
- [4] M. Aven and R.E. Halstead, *Phys. Rev.* 137 (1965) 228A.
- [5] F.T.J. Smith, *Solid State Commun.* 9 (1971) 957.
- [6] A.G. Fischer, J.N. Carides and J. Dresner, *Solid State Commun.* 2 (1964) 157.
- [7] T.C. McGill, R.H. Miles, Y. Rajakarunanyake and J.O. McCaldin, in: *Growth and Optical Properties of Wide-Gap II-VI Low-Dimensional Semiconductors*, Eds. T.C. McGill, C.M. Sotomayor-Torres and W.B. Gebhardt (Plenum, New York, 1989).
- [8] M. Kobayashi, N. Mino, H. Katagiri, R. Kimura, M. Konagai and K. Takahashi, *Appl. Phys. Letters* 48 (1986) 296.
- [9] J.O. McCaldin, *J. Vacuum Sci. Technol.* A8 (1990) 1188.
- [10] T. Yasuda, I. Mitsuishi and H. Kukimoto, *Appl. Phys. Letters* 52 (1987) 57.
- [11] H. Cheng, J.M. Depuydt, J.E. Potts and T.L. Smith, *Appl. Phys. Letters* 52 (1988) 147.
- [12] Y. Akihiko, S. Muto, S. Yamaga and H. Kasai, *Japan. J. Appl. Phys.* 27 (1988) L260.

- [13] T. Yodo and K. Yamashita, *Appl. Phys. Letters* 53 (1988) 2403.
- [14] S. Hwang, R.L. Harper, K.A. Harris, N.C. Giles, R.N. Bicknell, J.W. Cook, J.F. Schetzina and M. Chu, *J. Vacuum Sci. Technol. A6* (1988) 2821.
- [15] N.C. Giles, R.N. Bicknell, R.L. Harper, S. Hwang, K.A. Harris and J.F. Schetzina, *J. Crystal Growth* 86 (1988) 348.
- [16] A.K. Wahi, G.P. Carey, T.T. Chiang, I. Lindau and W.E. Spicer, *J. Vacuum Sci. Technol. A7* (1989) 494.
- [17] J.J. Lander, in: *Semiconductors*, Ed. N.B. Hannay (Reinhold, New York, 1959).
- [18] C.S. Fuller, in: *Semiconductors*, Ed. N.B. Hannay (Reinhold, New York, 1959).
- [19] E.M. Pell, *J. Appl. Phys.* 31 (1960) 291.
- [20] W.D. Baker and A.G. Milnes, *J. Appl. Phys.* 43 (1972) 5152.
- [21] A.K. Wahi, G.P. Carey, K. Miyano, T.T. Chiang, I. Lindau and W.E. Spicer, *J. Vacuum Sci. Technol. A8* (1990) 1152.
- [22] D. Shaw, *J. Crystal Growth* 86 (1988) 778.
- [23] T. Yao, in: *The Technology and Physics of Molecular Beam Epitaxy*, Ed. E.H.C. Parker (Plenum, New York, 1985).

Photo-assisted MBE growth of ZnSe on GaAs substrates

N. Matsumura, T. Fukada, K. Senga, Y. Fukushima and J. Saraie

Department of Electronics and Information Science, Faculty of Engineering and Design, Kyoto Institute of Technology, Matsugasaki, Kyoto 606, Japan

ZnSe epilayers have been grown by photo-assisted MBE on GaAs substrates at various substrate temperatures and under various molecular beam intensity ratios of group VI to group III element. A He–Cd laser with 441.6 nm wavelength was used as a light source. From the temperature dependence of the photo-desorption rate constants, the activation energies of photo-desorption of Zn and Se adatoms from the physical adsorption state (E_{Zn}^p , E_{Se}^p) and from the chemical adsorption state (E^c) are obtained, that is, $E_{Zn}^p = 7.8$ kcal/mol, $E_{Se}^p = 6.7$ kcal/mol and $E^c = 16.1$ kcal/mol. Thus, the photo-desorption observed is photo-enhanced “thermal” desorption. ZnSe epilayers have been successfully grown at a temperature as low as 150 °C. A sharp and strong free-excitation emission is observed in photoluminescence spectra at 11 K in the low-temperature grown samples, which shows that the crystallinity is almost comparable with that of the unirradiated epilayer grown at 340 °C (the optimum growth temperature without irradiation).

1. Introduction

ZnSe has been recognized as one of the most promising materials for blue light emitting devices. To prepare highly efficient devices, it is necessary to establish a growth method for obtaining high-quality epilayers.

Recently, we have reported the effects of light irradiation on MBE growth of ZnSe and ZnSSe on GaAs substrates [1,2]. The photo-desorption of adatoms from the growing surface is observed at a substrate temperature of 340 °C, and the desorption rate constants of Zn, Se and S atoms are obtained under He–Cd laser (441.6 nm) irradiation. The intensity of the free-excitation emission in the photoluminescence spectra increases with light irradiation during growth, which indicates an improvement of the crystallinity of the epilayers. These effects are attributed to the photons whose energies are larger than the bandgap of the epilayers [2]. As for CdTe, improved doping control at low growth temperatures was previously reported by photo-assisted MBE growth [3,4].

In this report, we have studied the temperature dependence of the photo-desorption of adatoms

and the low-temperature epitaxial growth under He–Cd laser irradiation.

2. Experimental

The substrates used were Cr–O doped GaAs-(100) wafers. Source materials were elemental 6N-Zn and 6N-Se (Osaka Asahi Metal Mfg. Co., Ltd.). The molecular beam intensity ratio of group VI to group II element (J_{VI}/J_{II} ratio) was changed from 0.4 to 2.1. The substrate temperature was varied from 150 to 340 °C.

A He–Cd laser (Kimmon Electric Co. Ltd., CD4601R) with a wavelength of 441.6 nm was used as an irradiation light source. The laser beam was expanded to a diameter of 5 mm. The irradiation intensity and photon density on the substrate were about 300 mW/cm² and about 7×10^{17} photons/cm²·s, respectively. The beam was introduced on part of the substrate surface at an angle of about 20°. Another part of the epilayer was irradiated by the light after the growth for 4–10 h in the growth chamber with maintaining the temperature equal to that used during growth, in

order to investigate irradiation effects on the completed chemical bond. Thus, in a single growth run, we obtained three kinds of epilayers; an epilayer irradiated during growth, an epilayer irradiated after growth and an unirradiated epilayer. Details of the growth procedure have been reported elsewhere [1].

The growth rates without irradiation were 0.25–0.5 $\mu\text{m/h}$ and the growth times was 3–4 h. The thicknesses of the unirradiated epilayers were measured by SEM observation of the (110) cleavage plane of the epilayers. The thickness reduction of the irradiated epilayers was measured by multiple beam interference microscope. The crystallinity of the grown layers was evaluated by medium energy electron diffraction (MEED) with an acceleration voltage of 4 kV. Photoluminescence spectra were measured at 11 K using an ultrahigh-pressure Hg lamp as an exciting source (365 nm, 400 mW/cm²).

3. Results and discussion

3.1. Photo-desorption of Zn and Se adatoms

The growth rates of the epilayers are reduced by laser irradiation during growth. The reduction rates depend both on the $J_{\text{VI}}/J_{\text{II}}$ ratio and on the substrate temperature. We already proposed the growth-rate equations including photo-desorption rate constants of the Zn and Se adatoms on the growing surface [1]. The growth rate under laser irradiation (G_p) is obtained as

$$G_p = \left[k_{\text{Zn}} k_{\text{Se}} (1 - D_{\text{Zn}}^p) (1 - D_{\text{Se}}^p) J_{\text{Zn}} J_{\text{Se}} - (D^c N_s)^2 \right] \left[k_{\text{Zn}} (1 - D_{\text{Zn}}^p) J_{\text{Zn}} + k_{\text{Se}} (1 - D_{\text{Se}}^p) J_{\text{Se}} + 2D^c N_s \right]^{-1},$$

where D_{Zn}^p (D_{Se}^p) is the photo-desorption rate constant of the Zn (Se) adatoms from the physical adsorption state on Se (Zn) exposed surface. k_{Zn} and k_{Se} are the sticking probabilities of the Zn atoms on the Se exposed surface and the Se atoms on the Zn exposed surface, respectively. J_{Zn} and J_{Se} are the molecular beam intensities of the Zn

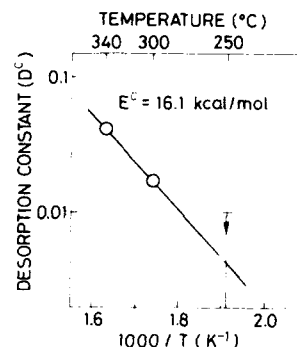


Fig. 1. Temperature dependence of photo-desorption rate constant of Zn or Se atoms from the chemical adsorption state.

atoms and Se atoms, respectively. D^c is the photo-desorption rate constant of the Zn or Se atoms from the chemical adsorption state. N_s is the surface concentration of the Zn or Se atoms (6.2×10^{14} atoms/cm² in ZnSe(100) surface).

The film thicknesses are reduced by laser irradiation after growth with maintaining the substrate at the growth temperature. This means that the chemically bonded atoms photo-desorb from the surface. Fig. 1 shows the temperature dependence of the photo-desorption rate constant D^c from the chemical adsorption state. The constant D^c decreases with the decreasing substrate temperature. The value of D^c at 250°C is calculated to be smaller than 0.01, which is the detection limit of our measurement. The activation energy of the photo-desorption was obtained from the slope of the line as 16.1 kcal/mol. Thus, the photo-desorption from the chemical-adsorption state is photo-enhanced thermal desorption.

Yao and Takeda [5] and Farrell et al. [6] observed the Se desorption from the ZnSe surface from the change in the RHEED reconstruction pattern from the Se stabilized surface to the Zn stabilized surface. They measured the temperature dependence of the Se desorption time and reported the activation energy of Se desorption as 15.1 kcal/mol [5] or 13.8 ± 2.3 kcal/mol [6]. The change in reconstruction pattern means surface-atom desorption from the chemical adsorption state. Farrell et al. reported that this desorption is electron-stimulated thermal desorption of Se adatoms. The activation energy of the photo-de-

sorption from the chemical adsorption state (16.1 kcal/mol) in our case is similar to the above activation energies of Se desorption obtained by RHEED observation. However, they only observed the Se atom desorption and not the Zn atom desorption in the electron-stimulated thermal desorption process. In our case, both Se and Zn atoms desorb with the light irradiation judging from the fact that the film thicknesses are reduced by the irradiation. The mechanism of the photo-enhanced thermal desorption from the chemical adsorption state is not the same as that of electron-stimulated desorption.

The activation energy of the simple thermal evaporation is 30 kcal/mol [5]. The activation energy of the photo-desorption is smaller than that of the thermal evaporation. It can be said that the light irradiation reduces the bonding energy of chemically adsorbed atoms to the underlying layer.

Samples with various J_{VI}/J_{II} ratio and substrate temperature were grown under laser irradiation during growth. The thicknesses are reduced much more than those of the samples irradiated after growth. Using the J_{Zn} , J_{Se} and D^C values, and taking k_{Zn} and k_{Se} to be unity [7], the temperature dependence of D_{Zn}^P and D_{Se}^P was obtained as shown in fig. 2. The constants D_{Zn}^P and D_{Se}^P decrease with the decreasing substrate temperature. The activation energies of the photo-desorption of Zn and Se from the physical adsorption

state (E_{Zn}^P and E_{Se}^P) are obtained from the slope of the lines:

$$E_{Zn}^P = 7.8 \text{ kcal/mol}, \quad E_{Se}^P = 6.7 \text{ kcal/mol}.$$

Thus, it is clarified that the desorption from the physical-adsorption state is also photo-enhanced thermal desorption. The Zn or Se molecules do not have absorption bands at 441.6 nm. The photo-enhancement of the desorption of the physically adsorbed atoms by 441.6 nm light indicates that the photons, whose energies are larger than the bandgap of the epilayers, are absorbed in the epilayer and the photo-generated carriers reduces the attractive adsorption forces between the adatoms and the surface. It is considered that the reduction of adsorption forces comes from the reduction of Van der Waals forces between the adatoms and the surface including excess photo-generated free carriers. The possibility of excitation of adatoms by energy transfer from the photo-generated carriers cannot be excluded, however. It should be noted that the activation energies obtained (E^C , E_{Zn}^P , E_{Se}^P) may depend on the light intensity.

3.2. Low-temperature growth by photo-assisted MBE

As mentioned in section 3.1, the attractive adsorption forces of physically adsorbed atoms are decreased by laser irradiation. Therefore, the light irradiation possibly enhances the migration of adatoms, which will help epitaxial growth at low temperatures. Thus, the low-temperature epitaxial growth has been tried.

Fig. 3 shows MEED patterns of the grown layers with or without irradiation. Above the substrate temperature of 250°C the MEED patterns show that the grown layers are single-crystalline and the patterns are almost the same whether the sample was irradiated or not. The unirradiated layer grown at 225°C shows the MEED pattern with spots and oriented rings. Therefore, a substrate temperature above 250°C is needed for growing single-crystalline ZnSe epilayers on GaAs(100) substrates by MBE without laser irradiation. The MEED pattern of the layer grown at 150°C with irradiation shows a single-crystal-

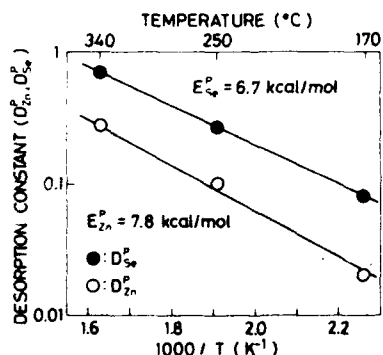


Fig. 2. Temperature dependence of photo-desorption rate constants of Zn (D_{Zn}^P) and Se (D_{Se}^P) adatoms from the physical adsorption state.

line spotty pattern (fig. 3c), that is, with He-Cd laser irradiation during MBE growth, the epitaxial temperature was successfully lowered down to 150°C. Fig. 3e shows a MEED pattern at 150°C under laser irradiation of 90 mW/cm² (30% of that in fig. 3c). This pattern shows an oriented polycrystalline pattern. It revealed that the lower limit of 150°C in this study relates with the laser power, and the epitaxial temperature could be lowered more with higher photon-density irradiation.

Fig. 4 shows photoluminescence spectra of the grown layers with (at 150°C) or without irradiation (at 340°C). The free exciton emission (F_{Ex}) of the irradiated epilayer grown at 150°C is sharp and strong, comparable to that of the unirradiated epilayer grown at 340°C, which is the optimum growth temperature without irradiation. Almost

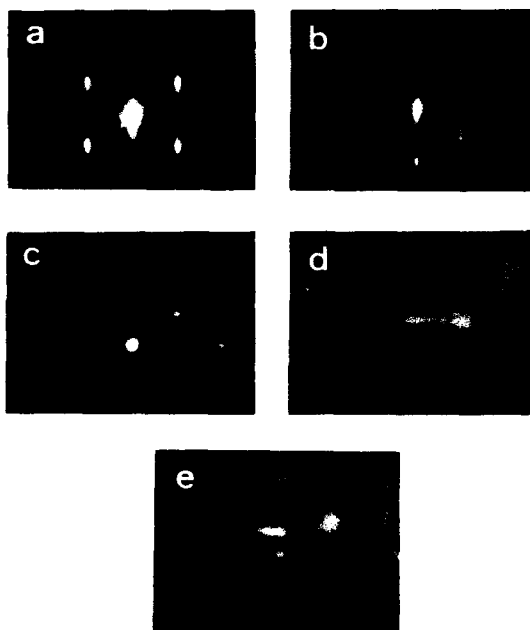


Fig. 3. MEED patterns of the grown layers with and without laser irradiation at substrate temperatures of (a), (b) 250°C and (c)–(d) 150°C. (a), (c) Patterns with 100% irradiation; (e) patterns with 30% irradiation; (b), (d) patterns without irradiation.

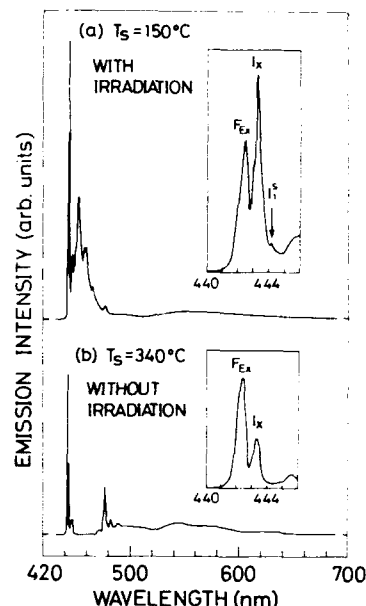


Fig. 4. Photoluminescence spectra of the grown layers: (a) spectrum of the layer grown at 150°C with irradiation and (b) spectrum at 340°C without irradiation.

no emissions were observed in the unirradiated polycrystalline layer grown at 150°C.

The donor-bound-exciton emission is observed at 443.2 nm. The binding energy of this emission is almost the same as that of the usually observed I_x (D^0, X) emission in MBE-ZnSe epilayers [8]. The intensity ratio of I_x emission to F_{Ex} emission decreases with the increasing substrate temperature. The intensities of F_{Ex} are almost the same in the epilayers for the substrate temperature from 150 to 340°C. The large I_x/F_{Ex} ratio of the low-temperature-grown layers suggests that the sticking probability of donor impurities increases at low temperature. The bound-exciton emission of neutral shallow acceptor (I_1^0) is observed in the epilayer grown at 150°C, whereas it is not observed in the epilayers grown at 340°C whether or not they were laser-irradiated. Therefore, impurities are easily incorporated into the epilayers grown at low temperature, that is, the low-temperature growth will be advantageous for intentional donor and acceptor doping.

4. Conclusion

ZnSe epilayers have been grown by photo-assisted MBE using a He-Cd laser (441.6 nm). The substrate-temperature dependence of the photo-desorption of adatoms on the surface clarified that the photo-desorption from the physical- or the chemical-adsorption state is photo-enhanced "thermal" desorption. The activation energies are determined.

The epitaxial layers of ZnSe have been obtained at a temperature as low as 150°C under light irradiation. The free-exciton emission of the irradiated epilayer grown at 150°C is sharp and strong, comparable to that of the unirradiated epilayer grown at 340°C, which is the optimum growth temperature without irradiation. Photo-assisted MBE growth of ZnSe is a useful method to prepare high-quality epilayers at low temperatures.

Acknowledgements

This study was partly supported by a Grant-in-Aid for Scientific Research on Priority Areas.

New Functionality Materials - Design, Preparation and Control, the Ministry of Education, Science and Culture of Japan, No. 02204001, and also by a Grant-in-Aid from the Akai Foundation and the Murata Science Foundation.

References

- [1] N. Matsumura, T. Fukada and J. Saraie, *J. Crystal Growth* 101 (1990) 61.
- [2] N. Matsumura, M. Tsubokura, K. Miyagawa, N. Nakamura, Y. Miyanagi, T. Fukada and J. Saraie, *Japan. J. Appl. Phys.* 29 (1990) L723.
- [3] R.N. Bicknell, N.C. Giles and J.F. Schetzina, *Appl. Phys. Letters* 49 (1986) 1095.
- [4] R.L. Harper, Jr., S. Hwang, N.C. Giles, J.F. Schetzina, D.L. Dreifus and T.H. Myers, *Appl. Phys. Letters* 54 (1989) 170.
- [5] T. Yao and T. Takeda, *J. Crystal Growth* 81 (1987) 43.
- [6] H.H. Farrell, J.L. de Miguel and M.C. Tamargo, *J. Appl. Phys.* 65 (1989) 4084.
- [7] N. Matsumura, M. Tsubokura, J. Saraie and Y. Yodogawa, *J. Crystal Growth* 86 (1988) 311.
- [8] T. Yao, Y. Makita and S. Maekawa, *Japan. J. Appl. Phys.* 20 (1981) L741.

Ultraviolet irradiation effect on the MBE growth of ZnSe/GaAs observed by RHEED

Masakazu Ohishi, Hiroshi Saito, Hiroshi Torihara, Yasunori Fujisaki and Kenzo Ohmori

Department of Applied Physics, Faculty of Science, Okayama University of Science, Ridai-cho 1-1, Okayama 700, Japan

Ultraviolet light irradiation effects on the MBE growth of ZnSe/GaAs(001) were investigated by means of RHEED observation. One of the prominent effects induced by the UV irradiation is to enhance the desorption of Se molecules. The other is that the decay of the RHEED oscillations becomes faster. These results imply the enhanced possibility of three-dimensional growth, which leads to the inferior surface morphology of the ZnSe/GaAs epilayers grown under photo-irradiation. Possible speculation on photo-MBE growth mechanisms is also given.

1. Introduction

Photo-assisted MBE is a new technique that has been developed to control epitaxial growth, and several photo-irradiation effects on the growth have been noted [1–5]. So far, the photo-irradiation effects on growth rate, surface morphology and photoluminescence properties have been investigated mostly on the grown epilayers. Photoluminescence properties are greatly improved, i.e., stronger excitonic and weak deep luminescence lines. The surface morphology, however, becomes considerably worse compared with that of un-irradiated layers. The growth rate is still a controversial point. The MBE growth mechanisms under photo-irradiation are not clearly understood yet. The in-situ observation of intensity variation of specular spot in RHEED is desirable to confirm them.

In this paper, we report the experimental results on the variation of RHEED specular intensity during the MBE growth of ZnSe/GaAs under UV light irradiation. Furthermore, the specular intensity variation during the adsorption and desorption processes of Zn atoms or Se atoms (molecules) are also discussed. These in-situ RHEED observations are the direct confirmation of the UV irradiation effect during the growth of ZnSe/GaAs.

2. Experimental procedure

Epitaxial ZnSe layers were grown by a conventional MBE system equipped with a 20 kV RHEED gun. Semi-insulating Cr-, O-doped GaAs wafers with surface orientation of (001) were used as substrate crystals. They were etched chemically in a solution of $5\text{H}_2\text{SO}_4:1\text{H}_2\text{O}_2:1\text{H}_2\text{O}$, rinsed in deionized water, and dried with N_2 gas. Prior to the growth, they were thermally cleaned at 620°C for 5 min in the growth chamber (base pressure of 1×10^{-7} Pa, without As flux), confirming the appearance of distinct 2×4 reconstruction streaks. The beam pressure was measured at the substrate position by a nude ion gauge. Prior to the observation of RHEED characteristics, ZnSe buffer layer was grown by the conventional MBE mode. He–Cd laser light (325 nm lasing wavelength, 10 mW output power) was introduced from the direction of one of the effusion cells, which was replaced by a quartz window.

The specular spot intensity in the RHEED pattern was detected by a photomultiplier via a glass fiber located on the focal plane of a camera lens, and the output signal was processed by a microcomputer. The shutters of effusion cells were driven by microcomputer-controlled stepping motors. The time required to open or to close the shutter completely was about 0.1 s or less. The

high energy electron beam (15 kV) exerts an unfavorable influence of the epilayer surface, which prevents us from studying in detail the growth mechanisms [6,7]. We used, therefore, the lowered acceleration voltage V_p of typically 4–6 kV with the current of 18–30 μ A.

3. Experimental results and discussion

3.1. The UV light irradiation effect on the desorption process of Se

The specular intensity (I_{sp}) variations observed from the direction of $k_{0||}$ [110] during the adsorption and desorption of Se were depicted in fig. 1 for several UV light levels from 0 to 220 mW/cm^2 . Experiments were performed using the shutter sequences for Zn and Se beams shown in the figure under $P_{Zn} = 1.5 \times 10^{-4}$ Pa, $P_{Se} = 3.2 \times 10^{-4}$ Pa and $T_{sub} = 300^\circ\text{C}$. Following the buffer layer

growth, the interruption of Se beam flux (Se off and Zn on, formation of the Zn stabilized surface) results in the increase of I_{sp} . After a short interval (both Se and Zn off), the reversed shutter openings (Se on and Zn off, formation of the Se stabilized surface) result in a decrease of I_{sp} . Then the interruption of both the Zn and the Se beams (both Se and Zn off brings about a gradual recovery of I_{sp} to the intensity level of the Zn stabilized surface.

These results indicate that Se on the surface desorbs gradually, and finally the surface changes to the Zn stabilized one. This fact is also confirmed by the change of the initial Se 2×1 reconstruction pattern to the final Zn $c(2 \times 2)$ reconstruction pattern. The recovery rate (and therefore the desorption rate of Se), however, depends upon the UV light intensity, i.e., the rate becomes larger with increasing UV intensity. At lower T_{sub} the recovery becomes slower, but at higher T_{sub} it becomes faster at a fixed UV light intensity. The two-stage recovery as in the unirradiated and 25 W/cm^2 cases in fig. 1 is generally observed when the desorption rate is low enough, i.e., at low V_p , low T_{sub} and low UV light intensity, and can be ascribed to the desorption of excess Se molecules in the first stage and that of Se adatoms in the next one. A detailed discussion will be shown in ref. [7]. The results in fig. 1 lead us to the conclusion that the UV irradiation enhances the desorption of the excess Se molecules and Se adatoms. In other words, the UV irradiation reduces the effective VI/II ratio on the surface. We also tried experiments similar to those fig. 1, in which the initial surface was the Zn stabilized one to measure Zn desorption. It is noted that almost no contribution of the UV light to the enhancement of Zn desorption is observed.

The chemical bonds between Se atoms on the outermost surface and Zn atoms behind are composed of sp^3 orbits. UV light irradiation larger than the band gap energy creates free electron-hole pairs. The free holes may be captured by the electrons in the sp^3 bond, resulting in bonded Se atoms to escape easily from the surface. Experimentally, this can be observed as the reduction of the VI/II ratio, in other words, the reduction of the sticking coefficient of Se. In the experiments,

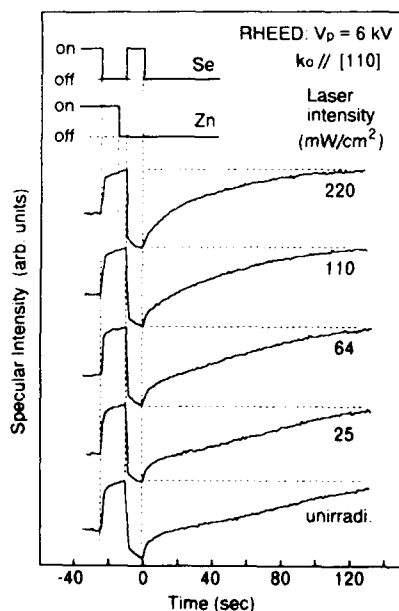


Fig. 1. RHEED specular intensity variations during growth interruption under several UV light levels from 0 to 220 mW/cm^2 . Experimental conditions were $P_{Zn} = 1.5 \times 10^{-4}$ Pa, $P_{Se} = 3.2 \times 10^{-4}$ Pa, $T_{sub} = 300^\circ\text{C}$, $V_p = 6$ kV and incident azimuth of $k_{0||}$ [110].

the photo-irradiation effect is hardly observed for the Zn surface. This difference in contribution to Se and to Zn cannot be understood yet.

3.2. The UV light irradiation effect on the RHEED oscillation

The UV irradiation effect during the MBE growth was studied also by monitoring the RHEED intensity oscillation of the specular spot. The results are shown in fig. 2 for several irradiation levels. The experiments were performed under the same flux conditions as those in fig. 1 at elevated T_{sub} of 400°C. After growing the ZnSe buffer layer, the surface was exposed only to the Zn flux by interrupting the Se flux for 30 s. This relatively long interruption of the Se flux is necessary to obtain a distinct RHEED oscillation. During the Se interruption, the Zn terraces on the surface coalesce and/or the ZnSe molecules and micro-terraces evaporate, giving rise to a smoother surface. Interruption of Zn flux, on the other hand, gives only poor RHEED oscillation. Without Zn flux, not only Se but also Zn atoms evaporate

from the vicinal surface, resulting in the degradation of the surface morphology. It should be noted that at this high T_{sub} no sudden increase of I_{sp} by exposing to Zn flux as in fig. 1 was observed, but I_{sp} gradually decreases. Fig. 2 clearly shows that the RHEED oscillation decays faster with increasing UV intensity. The RHEED oscillation is the measure of layer-by-layer growth. The results in fig. 2, therefore, point out that the UV irradiation has an unfavorable effect on the layer-by-layer growth, and rather enhances the possibility of three-dimensional growth.

In the present experiment, no change in the oscillation period is observed within the experimental accuracy, and also, the initial amplitude of the oscillation is almost the same irrespective of the UV light intensity. In the MBE growth of GaAs, it is well known that no RHEED oscillation becomes to be observed at higher T_{sub} because the growth mechanism changes from the nucleation and growth to the step flow growth [8]. The experimental results rule out the occurrence of the step flow growth in ZnSe/GaAs. It is also noted that the growth rate is kept almost unchanged in spite of the fact that the UV irradiation enhances the Se desorption.

Se atoms or molecules near the surface will combine with Zn atoms forming ZnSe molecules. The epilayer growth may take place with these ZnSe molecules. It seems that the probability of the molecule formation increases by photo-irradiation, because an increased number of Se atoms or molecules should exist near the surface, compared with the unirradiated case. This growth mechanism prevents each surface atom or molecule from migrating, which results in the enhancement of the three-dimensional growth and in the inferior morphology of the grown epilayers [3-5].

3.3. The UV light irradiation effect during the growth

The two effects caused by the UV irradiation mentioned above are clearly seen in the experiments shown in fig. 3, where the specular intensities during the conventional MBE and photo-MBE growths are observed. Experiments were performed under nearly the same flux conditions as in fig. 1, i.e., $P_{\text{Zn}} = 1.6 \times 10^{-4}$ Pa, $P_{\text{Se}} = 3.3 \times$

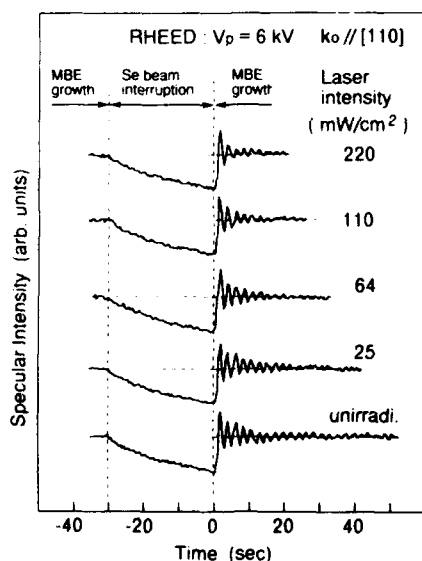


Fig. 2. RHEED oscillations under UV light irradiation with several intensity levels. Experimental conditions were $P_{\text{Zn}} = 1.5 \times 10^{-4}$ Pa, $P_{\text{Se}} = 3.2 \times 10^{-4}$ Pa, $T_{\text{sub}} = 400^\circ\text{C}$, $V_p = 6$ kV and incident azimuth of $k_{\text{in}} \parallel [110]$.

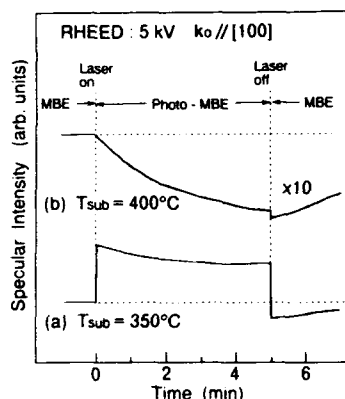


Fig. 3. RHEED specular intensities during conventional and photo-MBE growths for (a) $T_{\text{sub}} = 350^\circ\text{C}$ and (b) $T_{\text{sub}} = 400^\circ\text{C}$. Experimental conditions are $P_{\text{Zn}} = 1.6 \times 10^{-4}$ Pa, $P_{\text{Se}} = 3.3 \times 10^{-4}$ Pa, $V_p = 5$ kV and incident azimuth of $k_0 \parallel [100]$.

10^{-4} Pa and $T_{\text{sub}} = 350^\circ\text{C}$ in fig. 3a and $T_{\text{sub}} = 400^\circ\text{C}$ in fig. 3b. In these experiments the incident azimuth of $k_0 \parallel [100]$ is utilized, because the separation between each diffraction spot due to the bulk crystal is larger than that of $k_0 \parallel [110]$, which results in better spatial resolution between the specular spot and the diffraction spots. The I_{sp} variation in $k_0 \parallel [100]$ becomes qualitatively the same as that in $k_0 \parallel [110]$, because the I_{sp} variation in $k_0 \parallel [110]$ is very weak.

At $T_{\text{sub}} = 350^\circ\text{C}$ (fig. 3a), I_{sp} increases immediately after the UV irradiation is initiated and then decreases gradually and tends to saturate during the irradiation period. When the UV irradiation is stopped, I_{sp} drops with the same amount of the increase observed at the onset of the UV irradiation. Thus I_{sp} once drops below the unirradiated intensity level (the dashed line), and then it returns gradually to the unirradiated intensity level. At $T_{\text{sub}} = 400^\circ\text{C}$ (fig. 3b), I_{sp} shows similar behavior to that in fig. 3a, except that no steep rise and only a small drop are observed. The decay rate of I_{sp} during the photo-irradiation is also smaller compared with that in fig. 3a.

The steep rise and drop are ascribed to the increase and decrease in the effective VI/II ratio caused by the photo-irradiation, respectively. The

atomic composition on the surface or the surface stoichiometry depends on the VI/II ratio. If the surface becomes in Zn-rich condition, I_{sp} moves toward that of the Zn stabilized surface, i.e., I_{sp} increases, and vice versa. The fact that almost no increase or only a small amount of decrease of I_{sp} is observed at $T_{\text{sub}} = 400^\circ\text{C}$ indicates that the UV irradiation plays a minor role in changing the VI/II ratio. That is, the thermally activated desorption of Se dominates at high T_{sub} .

The gradual decreases in I_{sp} during the photo-MBE growth reflect the surface roughening due to the enhanced possibility of the three-dimensional growth. At high T_{sub} of 400°C , increased probability of thermally stimulated migration of the surface atoms will reduce the effect of the photo-induced three-dimensional growth, which results in a slower decay of I_{sp} . The recovery of I_{sp} toward the conventional MBE level after the UV light is stopped indicates that the surface becomes smoother again.

4. Summary

To study the UV irradiation effect on the MBE growth of ZnSe/GaAs, the RHEED specular beam intensity variations during the growth and during the adsorption and desorption processes of Se atoms and molecules on the (001) ZnSe surface were investigated. The obtained results are as follows:

- (1) UV light affects the bonding between the outermost Se atoms and the Zn atoms behind to unbind the Se atoms, resulting in an increase of the desorption rate of Se; in other words, an decrease of the effective VI/II ratio on the surface. Almost no effect on the outermost Zn atoms is observed.
- (2) The damping of RHEED oscillations is enhanced. This result implies that the UV irradiation rather prevents the surface atoms from migrating, i.e., causes three-dimensional growth, which leads to inferior surface morphologies of the grown epilayers. It still remains an open question why the epilayers with the worse morphologies show improved photoluminescence properties.

Acknowledgments

The authors would like to thank Messrs. J. Fujiwara, M. Kuyama, K. Takizawa, K. Takushima and T. Saeki for their continuous assistance throughout the experiments. This work was financially supported in part by a Grand-in-Aid for Scientific Research from the Ministry of Education, Science and Culture of Japan.

References

- [1] R.N. Bicknell-Tassius, N.C. Giles and J.F. Schetzina, Appl. Phys. Letters 49 (1986) 1735.
- [2] M. Kitagawa, Y. Tomomura, K. Nakanishi, A. Suzuki and S. Nakajima, J. Crystal Growth 101 (1990) 52.
- [3] M. Ohishi, H. Saito, H. Okano and K. Ohmori, J. Crystal Growth 95 (1989) 539.
- [4] N. Matsumura, T. Fukuda and J. Saraie, J. Crystal Growth 101 (1990) 61.
- [5] N. Matsumura, M. Tsubokura, K. Miyanagi, N. Nakamura, Y. Miyanagi, T. Fukuda and J. Saraie, Japan. J. Appl. Phys. 29 (1990) L723.
- [6] H.H. Farrell, J.L. de Miguel and M.C. Tamargo, J. Appl. Phys. 65 (1989) 4084.
- [7] M. Ohishi, H. Saito, H. Torihara, Y. Fujisaki and K. Ohmori, to be published.
- [8] J.H. Neave, P.J. Dobson and B.A. Joyce, Appl. Phys. Letters 47 (1985) 620.

Doping of nitrogen acceptors into ZnSe using a radical beam during MBE growth

K. Ohkawa, T. Karasawa and T. Mitsuyu

Central Research Laboratories, Matsushita Electric Ind. Co., Ltd., Moriguchi, Osaka 570, Japan

A new method of doping for ZnSe was attempted by using a neutral radical beam during the MBE growth. The radical beam dominantly consisted of N_2 molecular radicals at $A^3\Sigma_u^+$ state. The sticking coefficient of nitrogen was remarkably enhanced; thus this doping method was able to incorporate N into ZnSe by 10^{19} cm^{-3} . The existence of shallow N acceptors was confirmed by photoluminescence measurements; recombination of free electrons and acceptor holes (FA) at room temperature and recombination of donor–acceptor pairs at low-temperature were observed. The FA emission was observed only for ZnSe layers with moderate doping level, which shows p-type conduction. The carrier concentration was the order of 10^{15} cm^{-3} . The activation of N in ZnSe was less than 1%.

1. Introduction

It is difficult to control the electrical conduction in wide band-gap II–VI semiconductors such as ZnSe and ZnS. High-quality n-type ZnSe with carrier concentration up to 10^{19} cm^{-3} has been successfully controlled by Cl-doping in molecular beam epitaxial (MBE) growth [1]. On the contrary, many attempts in the MBE process were made to incorporate shallow acceptors in ZnSe to realize low-resistivity p-type conduction [2–5]. It is extremely difficult to grow p-type ZnSe with high carrier concentration like the n-type ZnSe. Nitrogen is the most promising element as a p-type dopant [6]. Doping of N in MBE process is very difficult, because of the low sticking coefficient of N_2 and NH_3 neutral molecules. In previous work, we attempted ion doping with high-purity N^+ or N_2^+ ion beam during the MBE growth of ZnSe to enhance the sticking coefficient of nitrogen [7]. The N-doped ZnSe layers grown by this method exhibited good low-temperature photoluminescence (PL) spectra: a dominant acceptor-bound exciton line (I_1) and well-suppressed other emissions. However, the electrical properties of the sample exhibited high resistivity. The crystallinity was degraded by ion damage under heavy doping condition attempting to realize p-type conduction.

Considering this result, we have attempted a new doping method using a neutral radical beam during the MBE growth. The kinetic energy of the radical beam is the order of the thermal energy. Then we can expect that by this method one can dope with low damage.

In this paper, we describe the energy states of the radicals and the characterization of the N-doped ZnSe layers with various N concentrations. The results of Hall measurements are also described.

2. Experimental procedure

The substrates used were undoped semi-insulating GaAs wafers with (100) orientation. The substrate was treated in an ordinary cleaning process [1]. Source materials are elemental Zn, Se and N_2 or NH_3 gas for the nitrogen radical beam. The substrate was irradiated with Zn, Se and the nitrogen-radical beams simultaneously. The substrate temperature during the growth was 325°C . The beam flux ratio ($J_{\text{Se}}/J_{\text{N}}$) was usually kept at about 1. The layer thickness was 1.5–4 μm . The background pressure was about 1×10^{-9} Torr, but the pressure at the radical beam operation was of the order of 10^{-6} Torr.

The PL properties were measured at 12 K or room temperature. The excitation was the 325 nm line from a He-Cd laser. The excitation power density was as low as 0.1 W/cm².

3. Characteristics of nitrogen radical beam

The radical beam source (Oxford Applied Research) was mounted in the MBE chamber. The beam source operated by means of an electrical discharge created from inductively-coupled RF excitation at 13.56 MHz.

We measured optical emission spectra of the N₂ and NH₃ plasma from 220–700 nm. The second ($C^3\Pi_u \rightarrow B^3\Pi_g$) and the first ($B^3\Pi_g \rightarrow A^3\Sigma_u^+$) positive emission bands of the N₂ molecules were observed, but the N atomic lines and the N⁺ ionic lines were not observed in the spectra. Strong H atomic lines were observed in the spectrum of the NH₃ plasma. The spectra indicate that the nitrogen radicals consist of metastable N₂ molecules in the case of both the N₂ and the NH₃ gas sources.

It was confirmed by mass spectroscopy analysis that NH_n ($n = 0, 1, 2, 3$) molecules were not observed in the MBE chamber at the radical beam operation using NH₃ gas. Considering the lifetime of each state [8,9], the N₂ radicals from the beam source would be the $A^3\Sigma_u^+$ state.

We evaluated the vibrational temperature of the N₂ radicals to be about 4500 K from the second positive emission bands of the spectra. It is natural to estimate its rotational temperature from classical equipartition of energy to be of same value of kinetic energy. The kinetic energy equals the temperature around 1100 K of the RF discharge cell, as the pressure in the cell would be about 50 mTorr. These thermal energies are fairly weak compared with the ion energy of about 100 eV in our previous work [7].

4. Results and discussion

Fig. 1a shows a typical PL spectrum of an undoped ZnSe layer at 12 K. It is found that the

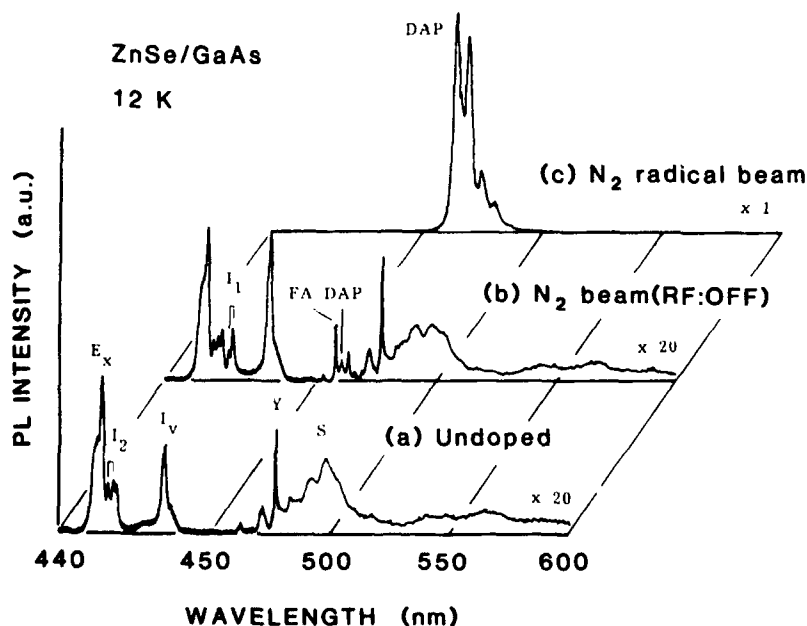


Fig. 1. 12 K PL spectra obtained from (a) undoped ZnSe, (b) lightly N-doped ZnSe grown by irradiation of N₂ beam and (c) N-doped ZnSe ($[N] = 2.2 \times 10^{18} \text{ cm}^{-3}$) grown by using a radical beam source.

undoped ZnSe layer exhibits a dominant free exciton peak (E_x) at 2.801 eV, well suppressed donor-bound exciton lines (I_2) at 2.798 and 2.796 eV, and a Y line at 2.602 eV, indicating that a high-quality crystal with low donor and acceptor impurities is obtained.

Lightly N-doped ZnSe layers were grown by irradiation of the N_2 gas beam from the radical beam source without RF power. The background pressure of the MBE chamber was about 2×10^{-5} Torr. The PL spectrum of the sample is shown in fig. 1b. This PL spectrum was almost the same as that of the undoped ZnSe shown in fig. 1a except for the weak I_1 lines at 2.792 and 2.790 eV, radiative recombination of free electrons and acceptor holes (FA) at 2.711 eV and radiative recombination of donor-acceptor pair (DAP) at 2.696 eV. This result indicates the low sticking coefficient of the unexcited nitrogen.

Strong DAP emission at 2.681 eV was observed in N-doped ZnSe layers grown by using the N_2 radical beam as shown in fig. 1c, in spite of the same N_2 flow level with the above N_2 beam without RF power. The I_1 line was very weak, of the order of 10^{-2} , compared with intensity of the DAP emission, and deep-level emission was not observed except for the case of the NH_3 gas for the radical beam source. The deep-level emission was observed at around 2.15 eV. We suppose that hydrogen is responsible for the deep level. This strong DAP emission indicates that the N_2 radicals at the $A^3\Sigma_u^+$ state have a higher sticking coefficient than N_2 at the ground state and the radicals are doped into ZnSe as a shallow acceptor. One of the reasons for the enhancement of the N doping would be due to a decrease of the dissociation energy, namely, the dissociation energy of the N_2 molecules at the ground state is 9.9 eV, but that of the N_2 radical at the $A^3\Sigma_u^+$ state is 3.9 eV. Furthermore, the radical has thermal energy (kinetic, rotational and vibrational energy) of about 0.6 eV.

We have carried out secondary ion mass spectroscopy (SIMS) analysis of N-doped ZnSe layers, and evaluated the N concentration using SeN secondary ions. The best detection limit was $3 \times 10^{17} \text{ cm}^{-3}$. Other acceptor impurities, K and Na, were detected in the N-doped ZnSe layers. The

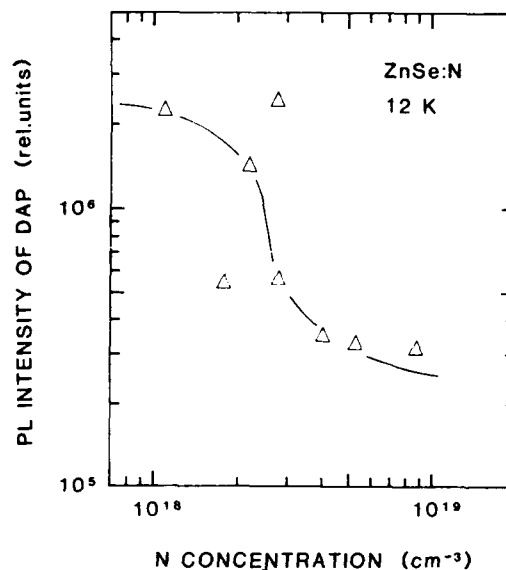


Fig. 2. Peak intensity of DAP emission from N-doped ZnSe layers at various N concentrations.

signal levels of K and Na were as low as the undoped ZnSe layer which showed a high-purity PL spectrum in fig. 1a, and these concentrations were less than 10^{15} cm^{-3} . In addition, the N concentration decreased in higher beam flux ratio J_{sc}/J_{zn} . From these results, it is believable that the acceptors in the doped layers have actually originated from N. A step-like profile of the N concentration was observed clearly, which well coincided with the structure of the sample, i.e., N-doped/undoped/GaAs. It was found that the diffusion of N in ZnSe at the growth conditions (325°C, 4 h) was less than 0.1 μm . The diffusion of N is very slight compared with that of Li [10], which is the typical dopant for p-type conduction.

Peak intensity of DAP emission depends on the N concentration, as shown in fig. 2. The maximum N concentration attained about $1 \times 10^{19} \text{ cm}^{-3}$. It is found that the DAP peak intensity decreases with an increase of the N concentration, indicating that non-radiative centers are induced by the doping. Although the N concentration depended on various parameters, there is a tendency that a lower pressure of the discharge cell causes higher

N concentration. It means that the N_2 radicals were quenched by collisions with other molecules.

ZnSe with high N concentration around $1 \times 10^{19} \text{ cm}^{-3}$ was still single crystal in this radical doping technique. This is a remarkable improvement on our previous work [7]; ZnSe layers grown by ion doping technique were polycrystal even for N concentration of $2 \times 10^{18} \text{ cm}^{-3}$.

Electrical properties of the N-doped ZnSe layers were measured with the Van der Pauw method. Most samples exhibited high resistivity. The sample with the N concentration of $2.2 \times 10^{18} \text{ cm}^{-3}$ showed p-type conduction at room temperature. The hole concentration is $4.4 \times 10^{15} \text{ cm}^{-3}$, thus activation of N in ZnSe is as low as 0.2%. The Hall mobility is $86 \text{ cm}^2/\text{V} \cdot \text{s}$. More heavily-doped layers ($[N] \geq 4 \times 10^{18} \text{ cm}^{-3}$) did not exhibit p-type conduction. Considering the abrupt decrease of the DAP peak intensity around $[N] = 3 \times 10^{18} \text{ cm}^{-3}$ in fig. 2, the nonradiative centers which relate with carrier traps would be created by over-doping.

The PL spectra of p-type ($[N] = 2.2 \times 10^{18} \text{ cm}^{-3}$, $p(300\text{K}) = 4.4 \times 10^{15} \text{ cm}^{-3}$), n-type (Cl-doped, $n(300\text{K}) = 6.7 \times 10^{16} \text{ cm}^{-3}$) and high-resistivity (undoped) ZnSe layers at room temperature are shown in fig. 3. The dominant peak at 2.687 eV in each sample is an emission due to recombination of donor electrons and free holes in the valence band (DF). A peak at 2.616 eV was observed only for the p-type ZnSe. A similar peak was observed in the p-type Li-doped ZnSe [11]. This is 2.616 eV peak would be recombination of free electrons in the conduction band an acceptor holes (FA). These DF and FA peak energies can be calculated from the equations $\hbar\omega_{\text{DF}} = E_g - E_D + 3.5 \text{ meV}$, $\hbar\omega_{\text{FA}} = E_g - E_A + \frac{1}{2}kT$, where E_D and E_A are the donor and acceptor ionization energies, respectively [12]. Inserting $E_g = 2.715 \text{ eV}$ [13], E_D and E_A are estimated to be 31 and 112 MeV, respectively. These E_D and E_A are in good agreement with the values for Cl donors and N acceptors determined by optical measurements [14,15].

5. Conclusion

We have grown N-doped ZnSe layers by MBE using the radical beam source. Dominant radicals created by RF discharge were N_2 molecular radicals at the $A^3\Sigma_u^+$ state. This new method was able to incorporate N around $1 \times 10^{19} \text{ cm}^{-3}$ with low damage. The FA peak was observed in room temperature PL measurement only for N-doped ZnSe with p-type conduction. The carrier concentration was $4.4 \times 10^{15} \text{ cm}^{-3}$. Activation of N doped in ZnSe was as low as 0.2%. More work will be needed to enhance the activation of N. The over-doped layers showed high resistivity; thus the non-radiative centers would be created by the over-doping. N atoms in ZnSe scarcely diffuse ($< 0.1 \mu\text{m}$) under our growth conditions.

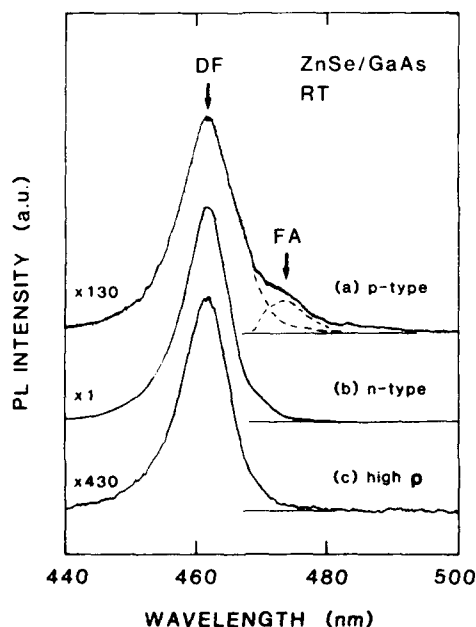


Fig. 3. Room-temperature PL spectra from (a) p-type, (b) n-type and (c) high-resistivity ZnSe layers.

References

- [1] K. Ohkawa, T. Mitsuyu and O. Yamazaki, J. Appl. Phys. 62 (1987) 3216.
- [2] R.M. Park, H.A. Mar and N.S. Salansky, J. Appl. Phys. 58 (1985) 1047.

- [3] T. Mitsuyu, K. Ohkawa and O. Yamazaki, *Appl. Phys. Letters* 49 (1986) 1348.
- [4] H. Cheng, J.M. DePuydt, J.E. Potts and T.L. Smith, *Appl. Phys. Letters* 52 (1988) 147.
- [5] K. Akimoto, T. Miyajima and Y. Mori, *Japan. J. Appl. Phys.* 28 (1989) L531.
- [6] W. Stutius, *J. Crystal Growth* 59 (1982) 1.
- [7] K. Ohkawa, T. Mitsuyu and O. Yamazaki, *J. Crystal Growth* 86 (1988) 329.
- [8] M. Imami and W.L. Brost, *J. Chem. Phys.* 61 (1974) 1115.
- [9] D.C. Cartwright, S. Trajmar, A. Chutjian and W. Williams, *Phys. Rev. A* 16 (1977) 1041.
- [10] H. Cheng, J.M. DePuydt, J.E. Potts and M.A. Haase, *J. Crystal Growth* 95 (1989) 512.
- [11] J. Nishizawa, K. Itoh, Y. Okuno and F. Sakurai, *J. Appl. Phys.* 57 (1985) 2210.
- [12] M. Kitagawa, *Doctoral Thesis Kyoto Univ.* (1982).
- [13] Y. Shirakawa and H. Kukimoto, *J. Appl. Phys.* 51 (1980) 2014.
- [14] R.N. Bhargava, *J. Crystal Growth* 59 (1982) 15.
- [15] P.J. Dean, W. Stutius, G.F. Neumark, B.J. Fitzpatrick and R.N. Bhargava, *Phys. Rev. B* 27 (1983) 2419.

$(\text{ZnSe})_m-(\text{ZnTe})_n$ short-period strained layer superlattices prepared by atomic layer epitaxy

Yasushi Takemura, Hideki Nakanishi, Makoto Konagai, Kiyoshi Takahashi

Department of Electrical and Electronic Engineering, Tokyo Institute of Technology, 2-12-1 Ookayama, Meguro-ku, Tokyo 152, Japan

Yoshio Nakamura * and Nobuo Otsuka

School of Materials Engineering, Purdue University, West Lafayette, Indiana 47907, USA

$(\text{ZnSe})_m-(\text{ZnTe})_n$ short-period strained layer superlattices (SLSs) were grown by atomic layer epitaxy using the molecular beam epitaxy technique. Transmission electron microscopy, X-ray diffraction and Raman scattering measurements were carried out to evaluate the grown SLSs. It was proved that the atomic layer epitaxy enabled growth of fine short-period superlattice structures which have abrupt interfaces with at most one-monolayer steps.

1. Introduction

Wide-bandgap II–VI compound semiconductors, especially ZnS, ZnSe and ZnTe, are materials promising for visible light emitting devices. A combination of ZnSe and ZnTe in the form of strained layer superlattices (SLSs) provides potentially attractive features: a wide range of modulation in the band gap energy from 1.9 to 2.4 eV [1] and realization of amphoteric conduction doping [2]. The atomic layer epitaxy (ALE) has become attractive as a new technique to grow II–VI compound semiconductors [3,4] and strained layer superlattices (SLSs) with large strain [5–7]. We have already reported successful growth and characterization of ZnSe and ZnTe films [8], and preliminary results of ZnSe–ZnTe SLSs [9] by ALE. In this paper, growth and characterization of the short-period SLSs are presented in detail.

2. Experiments

The conventional molecular beam epitaxy (MBE) system with solid sources was used for the ALE growth. Three K-cells contained elemental Zn, Se and Te, and a shutter above each cell was manipulated with a stepping motor controlled by a personal computer. The shutters of Zn and chalcogens were alternately opened and closed for 7 s with an interval of 1 s. The ideal ALE growth, i.e., one-monolayer growth per cycle, was achieved in the substrate temperature range of 250–350 °C for ZnSe [8]. As for ZnTe, high intensity of the Te beam is required to obtain a growth rate of one monolayer per cycle but degrades its surface morphology with hillocks, which may consist of Te precipitates. In order to obtain high-quality ZnTe films, we employed low intensity of the Te beam [10]. Under this condition, the growth rate per cycle is less than one monolayer and depends on substrate temperature. With alternating supply of Zn and Te, ZnTe films with good surface morphology were grown at 250 °C. This temperature is also suitable for the ALE of ZnSe.

* Permanent address: Department of Metallurgy, Tokyo Institute of Technology, 2-12-1 Ookayama, Meguro-ku, Tokyo 152, Japan.

$(\text{ZnSe})_m-(\text{ZnTe})_n$ ($m, n = 1-4$) short-period SLSs were grown on (100) InP substrates. The substrates were chemically etched by a solution of H_2SO_4 , H_2O_2 and H_2O . Before the growth, thermal treatment was carried out at 450°C for 15 min without molecular beams. Then a few monolayers of ZnSe and ZnTe were alternately grown without buffer layers. The substrate temperature was 250°C , which is 70°C lower than that used for the conventional MBE. The growth rates were exactly one monolayer per cycle for ZnSe and 0.5 monolayer per cycle for ZnTe. Therefore, one monolayer of ZnTe was grown with two cycles of the supply sequence. The total film thickness was 1500–2500 Å.

3. Results and discussion

3.1. TEM study

Transmission electron microscopy (TEM) was performed to investigate the SLS structures. Fig. 1 shows the transmission electron diffraction pattern of the $(\text{ZnSe})_3-(\text{ZnTe})_3$ SLS for the [010] electron beam incidence. The satellite spots (from the 0th to the third) along the [100] direction are clearly observed, which indicates a fine superlattice structure. The diffraction pattern also includes that from the InP substrate, and the diffraction spots for InP coincide with those for the SLSs. This suggests that the lattice constant of the SLS along the growth direction is equal to that of InP. Since the lattice constant of InP is an average of those of ZnSe and ZnTe, it can be said that the numbers of monolayers in each ZnSe and ZnTe layer were the same. The lattice-match with the substrate is also seen in X-ray diffraction, as will be mentioned later.

Fig. 2 shows the dark field image of the $(\text{ZnSe})_2-(\text{ZnTe})_2$ SLS for the 200 diffraction beam. High-contrast stripes, which consist of a dark stripe for ZnSe and a bright stripe for ZnTe, are clearly observed. Abruptness and flatness of the interfaces are not as good as those for the $(\text{GaAs})_2-(\text{AlAs})_2$ superlattice grown by metalorganic chemical vapour epitaxy [11] or the $(\text{GaAs})_4-(\text{AlAs})_4$ superlattice grown by MBE [12].

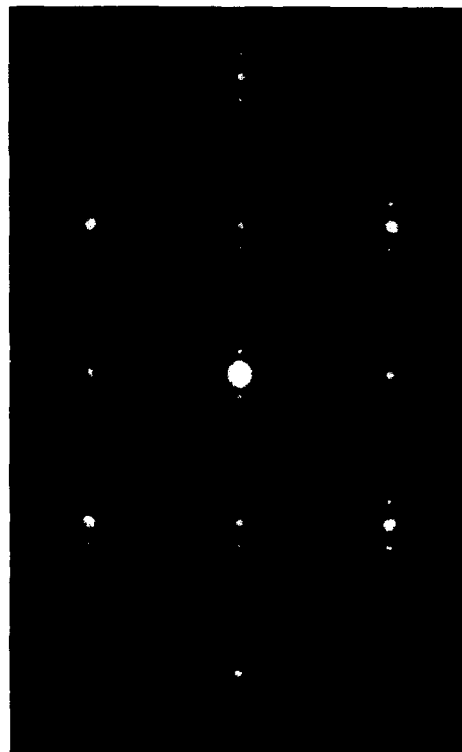


Fig. 1. Transmission electron diffraction pattern of the $(\text{ZnSe})_3-(\text{ZnTe})_3$ SLS for the [010] electron beam incidence.

But for the facts that the $(\text{ZnSe})_2-(\text{ZnTe})_2$ SLS involves 7% lattice mismatch and was heteroepitaxially grown on InP substrate, the TEM micrograph shows presence of a fine superlattice structure which has an abrupt interface with at most one-monolayer steps.

Fig. 3 shows a high-resolution TEM image of the $(\text{ZnSe})_3-(\text{ZnTe})_3$ SLS for the [011] electron beam incidence. Alternating layers of ZnSe and ZnTe were observed after a few periods. The numbers of monolayers in each ZnSe and ZnTe layer are estimated to be 3 on average. In the image, bright and dark stripes correspond to ZnSe and ZnTe layers, respectively. Interfaces of ZnTe on ZnSe appear to be smoother than those of ZnSe on ZnTe. This difference may be due to that ZnSe layer was grown by ALE but that ZnTe layer was not. The poor uniformity in thickness of the ZnTe layer was already discussed in terms of



Fig. 2. Dark field TEM image of the $(\text{ZnSe})_2-(\text{ZnTe})_2$ SLS for the 200 diffraction beam.

the photoluminescence spectrum of the $(\text{ZnSe})_1-(\text{ZnTe})_1$ monolayer superlattice [9,13]. Dislocations observed in fig. 3 and stacking faults observed in the dark field image may have been caused by residual oxide on InP.

3.2. X-ray diffraction measurements

Fig. 4 shows the conventional X-ray diffraction patterns of the $(\text{ZnSe})_n-(\text{ZnTe})_n$ ($n = 2, 3, 4$) SLSs. As observed by TEM, the lattice constants of the SLSs along the growth direction are equal to that of InP. In the X-ray diffraction, the lattice-match with substrate is confirmed by coincidence of the diffraction angle for the 0th satellite from the SLS with that of InP, as shown in fig. 4. The figure also shows the theoretical angles and intensities of the satellites. It was found that the actual numbers of ZnSe and ZnTe monolayers were equal to the designed numbers for all the samples. Poor uniformity in thickness of the ZnTe layer as mentioned in the TEM analysis causes a slight difference between experimental and theoretical angles in the diffraction pattern.

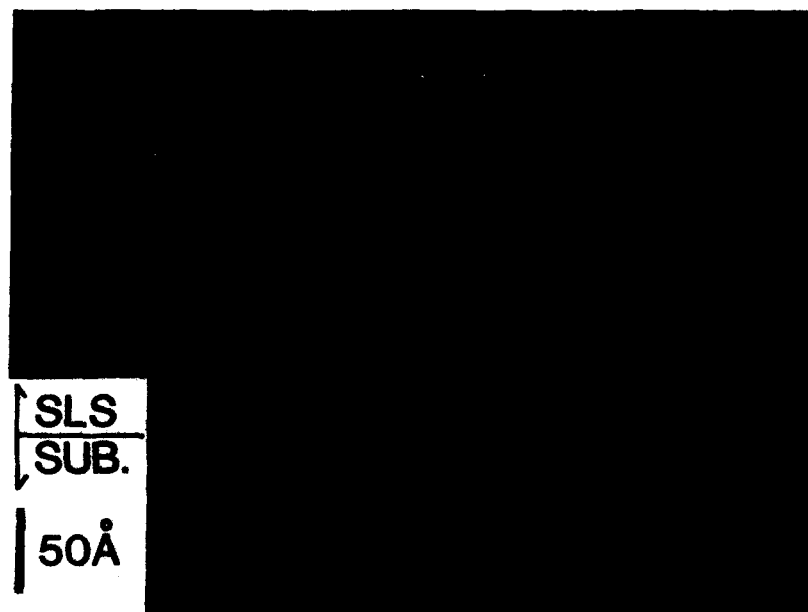


Fig. 3. High-resolution TEM image of the $(\text{ZnSe})_3-(\text{ZnTe})_3$ SLS for the [011] electron beam incidence.

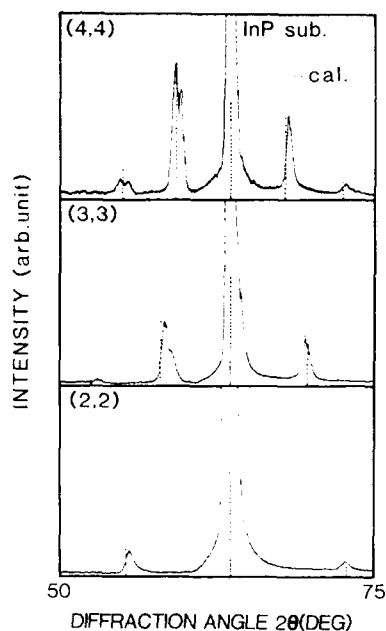


Fig. 4. X-ray diffraction patterns of the $(\text{ZnSe})_n-(\text{ZnTe})_n$ SLSs ($n = 2, 3, 4$).

3.3. Raman scattering measurements

Raman scattering measurements were performed at room temperature in the backscattering arrangement along the $[100]$ direction with the Ar-ion laser line (5145 Å). In the Raman spectra, the wave number of the LO phonon is shifted from the bulk value by strain. As shown in fig. 5, the spectra consist of two peaks of lorentzians: the lower-energy peak associated with the LO phonon of ZnTe and the higher-energy peak associated with the LO phonon of ZnSe. Arrows in the figure show wave numbers of the LO phonons for bulk ZnSe and ZnTe. The $(\text{ZnSe})_4-(\text{ZnTe})_4$ SLS is lattice-matched with the InP substrate and the ZnSe and ZnTe layers accommodate the same amount of strain, which is seen in the Raman spectrum, showing the same amount of shifts from the values for bulk ZnSe and ZnTe. The spectrum of the $(\text{ZnSe})_4-(\text{ZnTe})_2$ SLS shows that the amount of shift of the ZnSe-LO from its bulk value is smaller than that of the ZnTe-LO. The wave number of the LO phonon for ZnSe in the

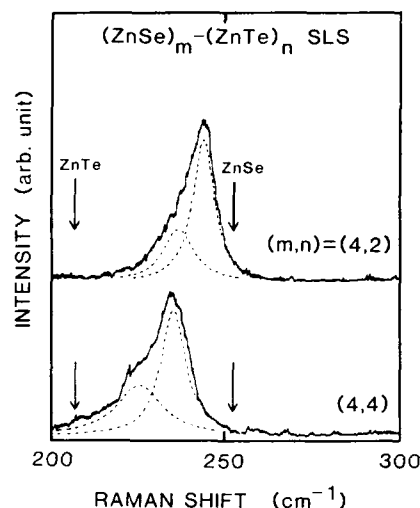


Fig. 5. Raman spectra of the $(\text{ZnSe})_4-(\text{ZnTe})_2$ and the $(\text{ZnSe})_4-(\text{ZnTe})_4$ SLSs.

SLS structures with various layer thickness were theoretically estimated, assuming the free standing configuration [14]. An effect of a short periodicity on the phonon frequency was not taken into account. The parameters used in the calculation are adopted from ref. [15]. As shown in fig. 6,

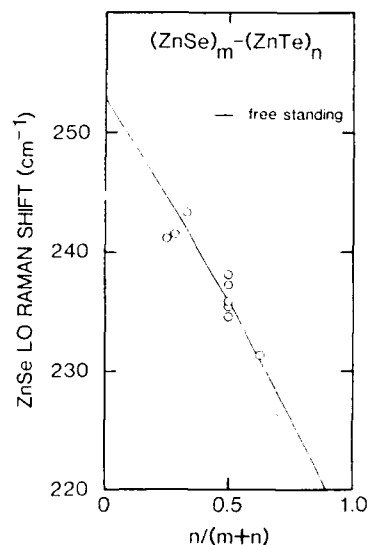


Fig. 6. Raman shift of ZnSe-LO phonon in $(\text{ZnSe})_m-(\text{ZnTe})_n$ SLSs.

experimental results well agree with the theoretical calculation. the assumptions that the SLs studied here were in the free standing configuration, and that lattice mismatch between two materials were completely relaxed by strain, are found valid.

4. Conclusions

$(\text{ZnSe})_m-(\text{ZnTe})_n$ short-period SLs were grown by ALE. From the TEM study, it was found that short-period SLs with the designed numbers of ZnSe and ZnTe monolayers were grown and that interfaces had abruptness with one-monolayer steps. In the X-ray diffraction, slight differences in angles and intensities of the satellite peaks between experiments and theory are seen. This may be due to poor uniformity in thickness of the ZnTe layer, which was confirmed by TEM. Raman scattering measurements showed that each layer was strained in the free standing configuration to relax the lattice mismatch between them.

Acknowledgments

This work was supported by a Grant-in-Aid for Scientific Research on Priority Areas, New Functionality Materials - Design, Preparation and

Control, The Ministry of Education, Science and Culture, No. 491940111653.

References

- [1] M. Kobayashi, N. Mino, H. Katagiri, R. Kimura, M. Konagai and K. Takahashi, *J. Appl. Phys.* 60 (1986) 773.
- [2] M. Kobayashi, S. Dosho, A. Imai, R. Kimura, M. Konagai and K. Takahashi, *Appl. Phys. Letters* 51 (1987) 1602.
- [3] T. Suntola and J. Anton, US Patent 4,058,430 (1977).
- [4] T. Yao and T. Takeda, *Appl. Phys. Letters* 48 (1986) 160.
- [5] T. Takeda, T. Kurosu, M. Lida and T. Yao, *Surface Sci.* 174 (1986) 548.
- [6] S. Dosho, Y. Takemura, M. Konagai and K. Takahashi, *J. Crystal Growth* 95 (1989) 580.
- [7] T. Karasawa, K. Ohkawa and T. Mitsuyu, *J. Crystal Growth* 101 (1990) 118.
- [8] S. Dosho, Y. Takemura, M. Konagai and K. Takahashi, *J. Appl. Phys.* 66 (1989) 2597.
- [9] Y. Takemura, S. Dosho, M. Konagai and K. Takahashi, *J. Crystal Growth* 101 (1990) 81.
- [10] M. Konagai, Y. Takemura, R. Kimura, N. Teraguchi, H. Nakanishi and K. Takahashi, *Acta Polytech. Scand.* 195 (1990) 81.
- [11] N. Watanabe and Y. Mori, *Surface Sci.* 174 (1986) 10.
- [12] P.M. Petroff, A.C. Gossard, W. Wiegmann and A. Savage, *J. Crystal Growth* 44 (1978) 5.
- [13] M. Konagai, Y. Takemura, R. Kimura, N. Teraguchi and K. Takahashi, *Mater. Res. Soc. Fall Meeting*, E5.1, Boston, MA, 1989.
- [14] B. Jusserand, P. Voisin, M. Voos, L.L. Chang, E.E. Mendez and L. Esaki, *Appl. Phys. Letters* 46 (1985) 678.
- [15] M. Kobayashi, M. Konagai, K. Takahashi and K. Urahe, *J. Appl. Phys.* 61 (1987) 1015.

Determination of refractive index and study of absorption in wide gap II–VI semiconductor superlattices

Aidong Shen, Jie Cui, Yunliang Chen, Hailong Wang

Shanghai Institute of Optics and Fine Mechanics, Academia Sinica, P.O. Box 800-216, Shanghai 201800, People's Rep. of China

and

Aizhen Li

Shanghai Institute of Metallurgy, Academia Sinica, 865 Chang Ning Road, Shanghai 20050, People's Rep. of China

The refractive indices of ZnSe–ZnTe and ZnSe–ZnS strained-layer superlattices (SLSs) were determined by double-beam reflectance measurements at 300 K. A discontinuity was found in the index spectra at about the energy equal to the transition energy $E_t(e-h)$ between $n = 1$ confined electron and hole levels. Large difference was found between the indices of the SLSs and those of the compositional bulk materials. Using the effective infinite-well model within effective mass approximation and taking into account the large strain effect, we also calculated the shifts of the exciton peaks with applied electric fields for ZnSe–ZnS multiple quantum wells (MQWs).

1. Introduction

Zinc-chalcogenides have generated a great deal of interest in the optoelectronics arena because of their direct wide band gaps, high electro-optic coefficients, wide range of transmission and continuously adjustable refractive indices of ternary alloys. Strained-layer superlattices (SLSs) composed of alternate layers of these lattice-mismatched materials have been thought to be particularly promising for producing blue light emitting diodes (LEDs), tunable color LEDs and short wavelength semiconductor lasers.

High quality ZnSe–ZnTe, ZnSe–ZnS and ZnTe–ZnS SLSs have been grown by MBE [1,2], MOCVD [3], MOMB [4], etc. Structural and optical properties such as X-ray diffraction [2–4], photoluminescence [1,3–5], Raman spectra [6,7] and bistability [8] have been studied by various groups.

In this paper, we report our measurements of the refractive indices of ZnSe–ZnTe and ZnSe–ZnS SLSs using double-beam reflectance [9]. A

calculation of the shifts of the exciton peaks with applied electric field for ZnSe–ZnS is presented in section 3.

2. Refractive indices of ZnSe–ZnTe and ZnSe–ZnS SLSs

For optoelectronic device designing, the refractive index is a very important parameter. Suzuki and Okamoto [9] have measured the refractive index of GaAs–AlAs superlattices. Kahen and Leburton [10] reported a study on the optical properties such as the dielectric constant and the GaAs–AlAs superlattice index. But, to the authors' knowledge, there are no reports on the measurements of the refractive indices of ZnSe–ZnTe and ZnSe–ZnS SLSs. We report here, for the first time, the determination of the indices of ZnSe–ZnTe and ZnSe–ZnS SLSs using double-beam reflectance measurement, which compare the reflectance of the sample with that of a mirror of

known reflectance (a aluminium-glass interface). The reflective spectra were measured using an infrared reflective spectrometer.

The SLs were grown by MBE techniques on (100) GaAs substrates at 320°C with ZnSe as buffer layers. The samples were unintentionally doped. The crystal qualities were examined by in situ reflection high energy electron diffraction (RHEED). X-ray diffraction measurements, combined with the growth rates of monolayers, determined by RHEED oscillation periods, have been used to determine the thicknesses of individual layers. The transition energy $E_1(e-h)$ between $n = 1$ confined electron and hole levels was determined by photoluminescence measurements.

The superlattice layer can be regarded as a Fabry-Pérot etalon sandwiched between the air ($n_1 = 1$) and the layer of the buffer combining with the substrate (n_2 , the effective index of the buffer and the substrate). In the reflectance-wavelength chart, the interference ripple can be seen in the region where the photon energy is below the band gap and thus the optical absorption in the epilayer is negligible. Using the following relations:

$$R = \left(\frac{n_2 - n^2}{n_2 + n^2} \right)^2, \quad m = \text{odd for } d = m \frac{\lambda}{4n}, \quad (1)$$

$$R^+ = \left(\frac{n_2 - 1}{n_2 + 1} \right)^2, \quad m = \text{even for } D = m \frac{\lambda}{2n}, \quad (2)$$

we can obtain the $n \sim \lambda$ curve, where n is the refractive index of the SLs, and R^- and R^+ are the reflectance minima and maxima.

From eq. (2) we can obtain relation between n_2 and λ . From $n_2 \sim \lambda$ curve, combined with eq. (1), we can determine the index of SLs, n for different wavelength λ .

Fig. 1 shows the refractive indices of ZnTe-ZnSe and ZnSe-ZnS SLs as a function of wavelength. We can see that a jump occurs at about the photon energy equal to $E_1(e-h)$. This discontinu-

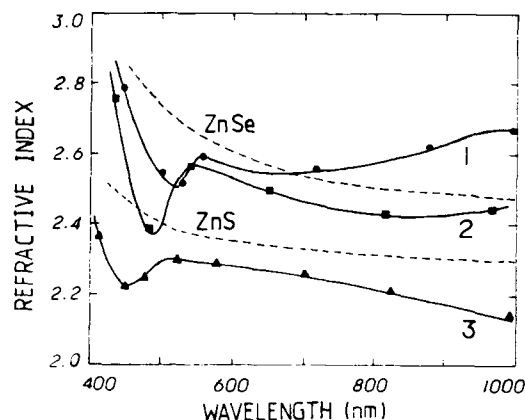


Fig. 1. The refractive index dispersion curves for ZnSe-ZnTe and ZnSe-ZnS SLs: (1) ZnSe-ZnTe (62 Å, 46 Å); (2) ZnSe-ZnTe (59 Å, 39 Å); (3) ZnSe-ZnS (29 Å, 26 Å). The dashed lines show the indices of bulk ZnSe and ZnS.

ity cannot be found in the index curves of bulk ZnS and ZnSe materials.

Kahen and Leburton reported that the difference between the refractive indices of a GaAs-AlGaAs superlattice and those of its corresponding AlGaAs alloy can be as large as 20%. Our results show that the difference between the indices of the SLs and those of their compositional materials are even much larger. This may result from the elastic strain caused by the large lattice mismatch, which shifts the quantized levels for a few hundred meV.

3. Electroabsorption in ZnSe-ZnS MQWs

The confinement of carriers in quantum well structures causes phenomena remarkably different from those of bulk materials. When an external electric field is applied perpendicular to the quantum well layers, the exciton absorption peaks will shift significantly to lower energies. This behavior was first observed by Miller et al. [11] in GaAs-GaAlAs MQWs, and was called the quantum-confined Stark effect (QCSE). A detailed explanation of this phenomenon was given in ref. [12]. Based on QCSE, various kinds of devices such as modulators and switches have been fabricated. The electroabsorption in InGaAs-InP, InGaAs-GaAs,

InGaAs-InAlAs and GaSb-AlGaSb MQWs was also demonstrated.

In ZnSe-ZnS MQWs, the strain-induced effect due to large lattice mismatch plays a very important role. The strain distorts the lattice cube into a tetragonal shape. The lattices constant a^{\parallel} parallel to the plane of the interface can be expressed by [13,14]:

$$a^{\parallel} = \frac{a_{\text{ZnS}} G_{\text{ZnS}} h_{\text{ZnS}} + a_{\text{ZnSe}} G_{\text{ZnSe}} h_{\text{ZnSe}}}{G_{\text{ZnS}} h_{\text{ZnS}} + G_{\text{ZnSe}} h_{\text{ZnSe}}}, \quad (3)$$

$$G_i = 2(C_{11}^i + 2C_{12}^i)(1 + C_{12}^i/C_{11}^i), \quad (4)$$

where a is the unstrained lattice constant, h the individual layer thickness and C_{ij} the elastic constant. The strain tensor element ϵ_x in the ZnSe layer is

$$\epsilon_{xx} = (a^{\parallel} - a_{\text{ZnSe}})/a_{\text{ZnSe}}. \quad (5)$$

The shifts of both the heavy-hole and the light-hole energy level are given by [15]:

$$\Delta E_{\text{HH}} = 2aS\epsilon_{xx} - bS'\epsilon_{xx}, \quad (6)$$

$$\Delta E_{\text{LH}} = 2aS\epsilon_{xx} + bS'\epsilon_{xx} - 2b^2(S')^2\epsilon_{xx}^2/\Delta, \quad (7)$$

$$S = \frac{S_{11} + 2S_{12}}{S_{11} + S_{12}}, \quad S' = \frac{S_{11} - S_{12}}{S_{11} + S_{12}}, \quad (8)$$

where $\Delta = 0.43$ eV is the spin-orbit coupling, $S_{11} = 21.1$ (T Pa) $^{-1}$ and $S_{12} = -7.8$ (T Pa) $^{-1}$ are the elastic compliance constants, $a = -5.4$ and $b = -1.2$ [16] are the deformation potentials. Using the parameters given in table 1, we obtained $\Delta E_{\text{HH}} = 57$ meV and $\Delta E_{\text{LH}} = 200$ meV.

Using the effective infinite-well model [12] within effective mass approximation, we calculate the energy shifts with field for electron, heavy- and light-hole states, as shown in fig. 2a. The strain-induced shifts have been added to heavy- and light-hole energy. The shifts of the exciton

Table 1
Parameters used in this study

	h (Å)	a (Å)	C_{11} (10^{11} dyn/cm 2)	C_{12} (10^{11} dyn/cm 2)
ZnSe	20	5.6676	8.1	4.9
ZnS	50	5.4041	10.0	6.5

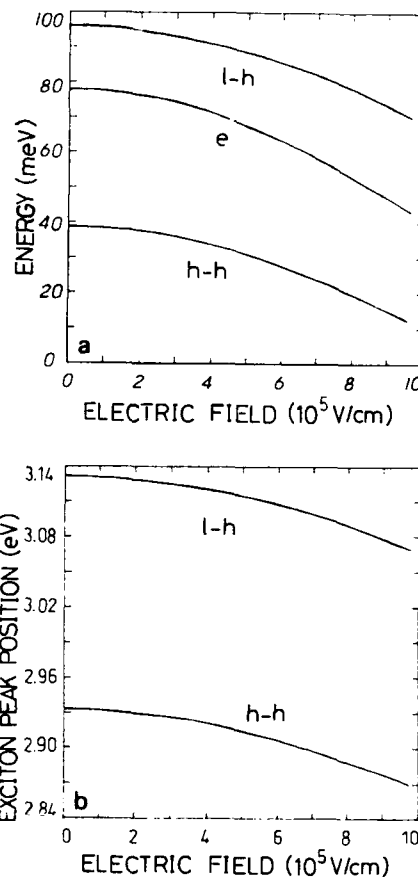


Fig. 2. (a) Energies of the first electron, heavy-hole and light-hole states with applied perpendicular electric field; (b) position of the exciton peaks with applied perpendicular field. All the results are obtained for the ZnSe-ZnS MQWs with $L_w(\text{ZnSe}) = 20$ Å and $L_b(\text{ZnS}) = 50$ Å.

peaks with field are presented in fig. 2b. In the calculation, effective masses of $0.16m_0$, $0.78m_0$ and $0.15m_0$ are used for electron, heavy- and light-hole, respectively.

because of the relatively narrow well width of ZnSe-ZnS MQWs compare to that of GaAs-GaAlAs MQWs, the ground state energy in ZnSe well will be higher and a larger field must be applied to the ZnSe-ZnS MQWs to produce the same shift as in GaAs-GaAlAs MQWs.

Experiment for electroabsorption measurement in ZnSe-ZnS MQWs is in progress. A p-i-n

diode structure with the ZnSe-ZnS MQWs grown on a p-type GaAs substrate and covered by a thin Cl-doped n-type ZnSe layer is proposed.

4. Summary

We have, for the first time, determined the refractive indices of ZnSe-ZnTe and ZnSe-ZnS SLSs by double-beam reflectance measurements. A discontinuity was found in the index spectra at about the photon energy equal to that of the electron-hole transition $E_g(e-h)$. The difference between the index of the SLSs and those of the compositional bulk materials is rather large.

Using the effective infinite-well model within effective mass approximation and taking into account the large strain effect, we calculated the shifts of exciton peaks with applied electric fields for ZnSe-ZnS MQWs. For a (20 Å–50 Å) sample, an electric field of about 5×10^5 V/cm must be applied to produce a exciton peak shift of nearly 20 meV.

Acknowledgements

The authors would like to thank Dr. L. Xu and Ms. Y.H. Shen for their help in the growth of the samples.

Reference

- [1] M. Kobayashi, R. Kimura, M. Konagai and K. Takahashi, *J. Crystal Growth* 81 (1987) 495.
- [2] T. Karasawa, K. Ohkawa and T. Mitsuyu, *J. Crystal Growth* 95 (1989) 547.
- [3] T. Yokogawa, M. Ogura and T. Kajiwara, *Appl. Phys. Letters* 49 (1986) 1702.
- [4] A. Taïke, N. Teraguchi, M. Konagai and K. Takahashi, *Japan. J. Appl. Phys.* 26 (1987) L989.
- [5] M. Kobayash, N. Mino, H. Katagiri, R. Kimura, M. Konagai and K. Takahash, *J. Appl. Phys.* 60 (1986) 773.
- [6] S. Nakashima, Y. Nakakura, H. Fujiyasu and K. Mochizuki, *Appl. Phys. Letters* 46 (1986) 236.
- [7] S. Nakashima, A. Wada, H. Fujiyasu, M. Aoki and H. Yang, *J. Appl. Phys.* 62 (1987) 2009.
- [8] H. Wang, L. Xu, A. Shen, Y. Chen, J. Cui, P. Qiu, Q. Li, D. Zhuang, C. Zhang, S. Yang and W. Wang, *J. Appl. Phys.*, to be published.
- [9] Y. Suzuki and H. Okamoto, *J. Electron. Mater.* 12 (1983) 397.
- [10] K.B. Kahen and J.P. Leburton, *Phys. Rev. B* 33 (1986) 5465.
- [11] D.A.B. Miller, D.S. Chemla, T.C. Damen, A.C. Gossard, W. Wiegmann, T.H. Wood and C.A. Burrus, *Phys. Rev. Letters* 53 (1984) 2173.
- [12] D.A.B. Miller, D.S. Chemla, T.C. Damen, A.C. Gossard, W. Wiegmann, T.H. Wood and C.A. Burrus, *Phys. Rev. B* 32 (1985) 1043.
- [13] J.W. Matthews and A.E. Blakeslee, *J. Vacuum Sci. Technol.* 14 (1977) 989.
- [14] G.C. Osbourn, *J. Appl. Phys.* 53 (1982) 1586.
- [15] P. Voisin, *Surface Sci.* 168 (1986) 546.
- [16] A. Blacha, H. Presting and M. Cardona, *Phys. Status Solidi (b)* 126 (1984) 11.

The study of phonons and lattice strains in ZnSe–ZnTe and ZnS–ZnSe strained-layer superlattices by Raman and far-infrared reflectivity spectra

Jie Cui, Hailong Wang, Fuxi Gan

Shanghai Institute of Optics and Fine Mechanics, Academia Sinica, P.O. Box 800-216, Shanghai 201800, People's Rep. of China

and

Aizhen Li

Shanghai Institute of Metallurgy, Academia Sinica, 865 Chang Ning Road, Shanghai 200050, People's Rep. of China

We have observed, for the first time, the confined LO_m phonon modes in the ZnSe layer of the ZnSe–ZnTe strained-layer superlattice (SLS) and the folded longitudinal acoustic (LA) phonon modes in the ZnS–ZnSe SLS by off-resonance Raman scattering at room temperature. The relation between LO mode shifts and the superlattice structure parameters has been determined for the ZnSe–ZnTe SLS. We conclude that the critical thickness for the ZnSe–ZnTe SLS is about 40 Å. We have calculated the red shifts of LO phonon frequencies due to confinement and the shifts induced by the elastic strains, which are much larger than the red shifts due to confinement. The blue shifts induced by tensile strain in the ZnSe layer and the red shifts induced by compressive strain in the ZnTe layer made the confined LO modes in two individual layers overlap. Therefore, the folded LO mode had been observed in the ZnSe–ZnTe SLS. We have also studied the transverse optical (TO) phonon modes in the two SLS systems by means of far-infrared reflectivity spectra. ZnSe layers are under different stress in the two SLS systems.

1. Introduction

The vibrational properties of semiconductor superlattices have been given considerable attention recently [1]. For modes with the wave vectors perpendicular to the layers (the z direction), folded and confined phonons have been identified. The folded modes propagate through the entire superlattice. These modes fall in the frequency region for which a substantial overlap exists in the phonon density of states of the bulk materials that form the superlattice. One of these regions comprises the acoustical frequencies. On the other hand, the confined modes are localized in one of the layers of the superlattice, which have frequencies in the optical spectral range. For the modes that propagate with the wave vector parallel to the layer surfaces (the x , y directions), the so-called interface modes arise.

In addition to the effects mentioned above, for a strained-layer superlattice (SLS), one has to consider the effects of elastic strains induced by lattice mismatch on the phonon frequencies. This is particularly important for the II–VI wide gap compounds ZnSe, ZnTe and ZnS because of the large lattice mismatch between the individual layers. The elastic strain caused by lattice mismatch influences the growth habits of the epitaxial layers and plays a major role in determining the final values of the parameters such as forbidden gaps, band offsets, subband level shifts and carrier mobilities. There are two kinds of growth described as pseudomorphic (or commensurate) and free-standing. In the pseudomorphic growth, the in-plane lattice constants of the individual strained layers are equal. All of the lattice mismatch is accommodated by layer strains without the generation of misfit dislocations if the individual layers

are below the critical thicknesses for dislocation generation. High crystalline quality will not generally be obtainable if the layer thicknesses exceed the critical thickness values. The free-standing structure would be expected to minimize the elastic strain energy by distributing the layer strains among the two types of SLS layers according to the thicknesses and the elastic properties to balance the misfit dislocation energies, since the resulting in-plane lattice constant of the free-standing SLS does not correspond to either layer.

Various experimental and theoretical studies have been carried out on the phonon modes of III-V compounds semiconductor superlattices and II-VI strained layer superlattices. Olego et al. have reported the confined LO modes in the ZnSe layer of the ZnSe-Zn_xSe_{1-x} SLS with resonant Raman scattering at low temperatures [2]. Menendez et al. [3] obtained the confined LO_m modes in the ZnTe and CdTe layers of the CdTe-ZnTe SLS with the near resonance Raman scattering at 10 K. We report, for the first time, the confined LO_m modes of the ZnSe-ZnTe SLS; the measurements were performed at room temperatures and under off-resonance conditions. There are some reports on folded LA phonons in ZnSe-ZnTe and ZnSe-Zn_{1-x}Mn_xSe SLS [4,5]. We report here folded LA phonons in the ZnS-ZnSe SLS, for the first time.

There are a lot of studies on strain in the SLS, for a brief review, see ref. [6]. The major questions are the critical thickness [7], the effects of strains on the electronic properties [8] and band offsets [9], and the relationship between strain and the SLS structure parameters [10]. Raman scattering

and far-infrared reflectivity spectra [11] provide powerful techniques for the study of crystalline quality and especially strain fields of SLSs. By measuring phonon frequencies and their shifts, we can determine the strength of the strains in superlattice layers. In this paper, we report the strain effect on the phonon modes and the critical thickness of individual layers in a ZnSe-ZnTe SLS, and we also show the far-infrared reflectivity spectrum of TO modes in the ZnS-ZnSe SLS, which are forbidden in Raman spectra in a backscattering geometry.

2. Experiments

In the experiments, we use two ZnS-ZnSe and five ZnSe-ZnTe samples, which were grown at 320°C by MBE. X-ray diffraction measurements combined with the growth rates of monolayers determined by RHEED oscillation periods, has been used to determine the thicknesses of individual layers. The main parameters of these samples are listed in table 1.

The Raman spectra were excited in a backscattering geometry with the 488 nm line of an Ar⁺ ion laser, the laser power on the sample was 70–100 mW, for details, see ref. [12].

The far-infrared reflection measurements were performed at near-normal incidence at 300 K using a Fourier spectrometer, the resolution is 2 cm⁻¹.

3. Results and discussion

3.1. Confined LO_m modes in ZnSe-ZnTe SLS

Fig. 1 shows the Raman spectrum from the ZnSe-ZnTe sample ST-3. Six confined LO_m phonon modes in the ZnSe layers have been observed. We have calculated the confined phonon frequencies by considering the red shifts due to confinement and the shifts induced by elastic strain. Table 2 lists the calculated and measured frequencies of the confined LO_m modes in the ZnSe layer. We use the methods described in ref. [2] to calculate the red shifts of confined modes in the absence of strain using the dispersion curves of

Table 1
Parameters of samples used in present experiments

Sample	d_{ZnS} (Å)	d_{ZnSe} (Å)	d_{ZnTe} (Å)	N	Buffer	Substrate
SS-1	26	29		150	ZnS	GaAs
SS-2	12	12		100	ZnSe	GaAs
ST-3		27	29	100		InP
ST-4		10	11	200		InP
ST-5		41	39	25		InP
ST-6		59	63	25		InP
ST-7		98	102	21		InP

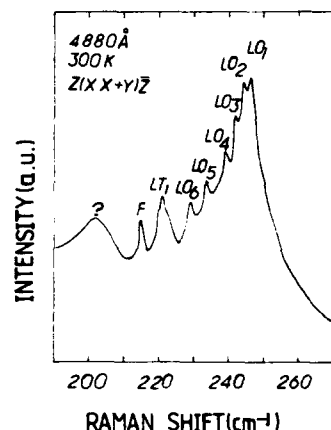


Fig. 1. Confined LO_m phonon modes in ZnSe layer of the ZnSe-ZnTe SLS sample ST-3. LT_1 is confined LO mode in ZnTe layer, the F peak is attributed to folded LO mode and the ? band to interface vibration or delocalized optical phonon. $x = (110)$, $y = (110)$ and $z = (001)$.

phonons of ZnSe and ZnTe given in refs. [13,14]. The shifts induced by strain [15] were calculated using the parameters in ref. [16]. The lattice constants of ZnSe and ZnTe are 5.6687 and 6.104 Å, respectively. The lattice is as large as 7.3%, which is the source of tensile strain in the ZnSe layers and compressive strain in the ZnTe layers in the (100) plane. The tensile strain induces the red shifts, 6.5 cm^{-1} , of the confined LO_m frequencies in the ZnSe layer, and it is much larger than the red shift due to confinement, 0.5 cm^{-1} (for $m = 1$ mode). The compressive strain in the ZnTe layer induces a blue shift as large as 15 cm^{-1} , which is greater than the red shift due to confinement, 0.3

Table 2
Measured and calculated frequencies of confined LO_m modes in ZnSe layer

m	ω_{meas} (cm^{-1})	ω_{cal} (cm^{-1})
1	246	246
2	244	244.5
3	242.5	242.5
4	239	239.2
5	233.5	234.3
6	228.5	229
7		222

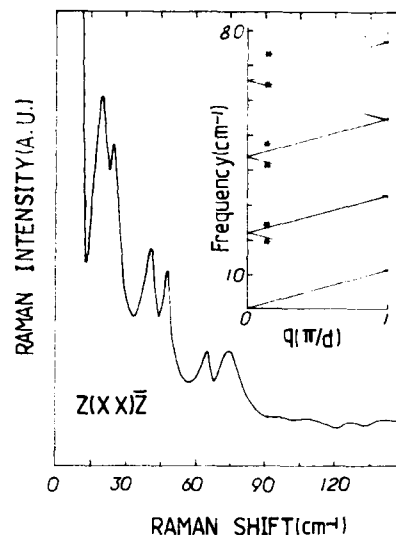


Fig. 2. Low-frequency region Raman spectrum for the ZnS-ZnSe SLS sample SS-1, which shows three folded LA doublets. The inset is the calculated dispersion curve using the sound velocities and bulk densities listed in ref. [16], without considering the strain effect; (*) experimental q values.

cm^{-1} (for $m = 1$ mode). Thus the two groups of phonon dispersion curves under the strain field would overlap in the region about $210\text{--}220 \text{ cm}^{-1}$. Therefore, an overlap exists between the ZnTe-like LO mode and the confined LO_m modes in ZnSe layers with $m \geq 7$. The mode labeled by F must be identified as due to scattering by the folded LO mode, and our calculations show that the frequency of mode F is equal to the $m = 8$ confined LO_8 mode in the ZnSe slab and the $m = 4$ confined LO_4 mode in the ZnTe slab. The frequencies of two modes which have the same symmetry of A_1 are in the overlapping range and the modes can propagate throughout the entire superlattice. The mode labeled by the question mark would be an interface mode or a delocalized mode.

3.2. Folded LA modes in ZnS-ZnSe SLS

Fig. 2 shows the Raman spectrum of the folded LA modes for the ZnS-ZnSe SLS sample SS-1. In the region $10\text{--}90 \text{ cm}^{-1}$, three doublets were seen at room temperature near 22, 44 and 67 cm^{-1} , the separation between the components of the doublet

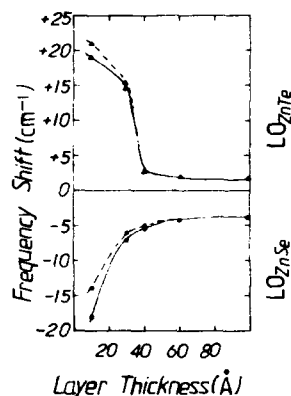


Fig. 3. The relationship between the shifts of LO phonon modes frequencies and the individual layer thicknesses: (—) measured values including the strain induced shifts and the red shifts due to confinement; (---) strain induced shifts.

is about 5 cm^{-1} . The inset of the figure is a calculated dispersion curve for the LA phonons using the Rytov model with strain-free parameters, for ZnSe, $\rho = 5.264 \text{ g cm}^{-3}$ and $v = 4.07 \times 10^5 \text{ cm/s}$ and for ZnS, $\rho = 4.083 \text{ g cm}^{-3}$ and $v = 5.047 \times 10^5 \text{ cm/s}$ [16]. The disagreement with the experiment may come from the neglect of the strain effects on the sound velocity or the phonon dispersion curve. As we know, in the [001] direction, the ZnSe layer is under tensile strain, while the ZnS layer is under compressive strain. Therefore, the dispersion curve of ZnSe should shift down while that of ZnS should shift up, and the sound velocity should decrease in the ZnSe layer and increase in the ZnS layer. This effect broadens the peaks and the separation of the components of the doublet is larger than the calculated value.

3.3. Critical thickness of ZnSe-ZnTe SLS

Fig. 3 shows the relationship between shifts of LO phonon frequencies and the thickness of ZnSe-ZnTe SLS layers. All the samples have the equal thicknesses for two individual layers, see table 1. The solid lines show the measured shifts including the red shifts due to confinement and the shifts induced by the elastic strain; the dashed lines are the shifts induced by the elastic strain. As we see, when the individual layer thickness ex-

ceeds 40 Å , the shifts are almost constant and comparatively small, but when the thickness is smaller than 40 Å , the shifts change sharply. For the sample with layer thickness of 10 Å , the shifts give better agreement for the calculated value [10], assuming that the two individual layers are commensurate. Therefore, the sample is in a commensurate configuration, and the large elastic strain is accommodated in the layers instead of forming misfit defects. But this is not true for the samples whose individual layers exceed 40 Å . For these samples, there are no large elastic strains in the layers, because of small shifts of the phonon frequencies. These samples should be in free-standing configurations (or incommensurate growth). We estimate that the critical thickness for a ZnSe-ZnTe SLS with 7% lattice mismatch is 40 Å , the commensurate-incommensurate transition occurs between 10 and 40 Å for individual layer thickness. In the transition region, the layer must be graded so as to relax some strain to make the elastic strain energy balance the misfit dislocation energies. For the sample ST-3, we assume that the ZnTe layer is coherent with the InP substrate on one side and is commensurate with the ZnSe layer on the other side; the resulting frequency shifts are 14 and 6 cm^{-1} , and give better agreement with the measured values of 15 and 6.5 cm^{-1} .

3.4. Far-infrared reflectivity spectrum

TO phonon modes have been obtained by far-infrared reflectivity spectra. The same behavior as

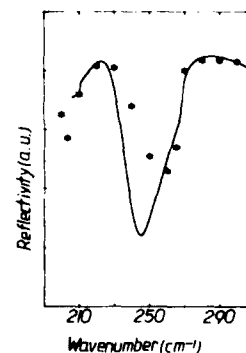


Fig. 4. Measured (*) and fitted (—) far-infrared reflectivity spectrum of the ZnS-ZnSe SLS sample SS-2 at 300 K.

Table 3

Phonon parameters giving best fit to the measured reflectivity curve for a ZnS-ZnSe SLS; buffer is ZnSe and substrate is GaAs

Layer	ϵ_{∞}	ω_{TO} (cm^{-1})	S	γ	d (\AA)
ZnS	5.1	270.1	4.05	8.9	12
ZnSe	5.8	214.6	6.4	25.5	12
Buffer	6.0	210.5	1.8	27.0	2000
Substrate	11.5	268.2	5.9	0.45	

LO phonon modes had been found. In the ZnSe-ZnTe SLS, the ZnSe-like LO and TO modes have red shifts because the ZnSe layer is under tensile strain in the (001) plane, while in the ZnS-ZnSe SLS, the ZnSe-like LO and TO modes have blue shifts for the ZnSe layer is under compressive strain. The shifts for TO modes are smaller than those of LO modes. Fig. 4 shows the spectrum for the ZnS-ZnSe SLS sample SS-2. Fitting the experimental data with long-wavelength dielectric response theory and the reflection theory of multiple absorbing layers, we have determined the phonon parameters such as the transverse optical phonon frequency ω_{TO} , mode damping constant γ , mode oscillation strength S and high frequency dielectric constant ϵ_{∞} , as listed in table 3.

4. Conclusions

We have obtained the confined LO_m in the ZnSe-ZnTe SLS, and overlap exists between the confined LO_m modes in the ZnSe layers and that in the ZnTe layers because of the large shifts of frequencies induced by the very large elastic strain. The folded LO phonon mode has therefore been observed and the folded LA phonon modes in ZnS-ZnSe SLS also have been obtained, for the first time. We have determined the critical thickness of the ZnSe-ZnTe SLS to be approximately 40 \AA . The TO phonon modes have been studied, also by far-infrared reflectivity spectrum, and these show the same behavior as the LO phonon modes.

Acknowledgements

The authors would like to thank Dr. A.D. Shen, Mr. Y.L. Chen, Dr. L. Xu and Ms. Y.H. Shen for their assistances in the preparation of the samples. Part of the Raman measurements were performed in the National Laboratory for Semiconductor Superlattices and Microstructures, P.O. Box 912, Beijing, People's Rep. of China.

References

- [1] M.V. Klein, IEEE J. Quantum Electron. QE-22 (1986) 1760.
- [2] D.J. Olego, K. Shahzad, D.A. Cammack and H. Cornelissen, Phys. Rev. B38 (1988) 5554.
- [3] J. Menendez, A. Pinczuk and J.P. Valladares, Appl. Phys. Letters 50 (1987) 1101.
- [4] Y.H. Wu, H. Yang, A. Ishida and H. Fujiyasu, Appl. Phys. Letters 54 (1989) 239.
- [5] E.K. Suh, D.U. Bareholomew, A.K. Ramdas, S. Rodriguez, S. Venugopalan, L.A. Kolodziejewski and R.L. Gunshor, Phys. Rev. B36 (1987) 4316.
- [6] G.S. Osbourn, IEEE J. Quantum Electron. QE-22 (1986) 1677.
- [7] R.H. Miles, T.C. McGill, S. Sivananthan, X. Chu and J. P. Faurie, J. Vacuum Sci. Technol. B5 (1987) 1263.
- [8] G.S. Osbourn, J. Vacuum Sci. Technol. B1 (1983) 379.
- [9] K. Shahzad, D.J. Olego and C.G. Van de Walle, Phys. Rev. B38 (1988) 1417.
- [10] S. Nakashima, Y. Nakakura, H. Fujiyasu and K. Mochizuki, Appl. Phys. Letters 48 (1986) 236.
- [11] J. Cui, F.X. Gan, H.L. Wang and Y.L. Chen, to be published.
- [12] Z.P. Wang, D.S. Jiang and K. Ploog, Solid State Commun. 65 (1988) 661.
- [13] N. Vagelatos, D. Wehe and J.S. King, J. Chem. Phys. 60 (1974) 3613.
- [14] B. Hennion, F. Moussa, G. Pepy and K. Kunc, Phys. Letters 36A (1971) 376.
- [15] F. Cerdeira, C.J. Buchenaure, F.H. Pollak and M. Cardona, Phys. Rev. B5 (1972) 580.
- [16] Landolt-Börnstein Tables, Vol. II-17b, Eds. O. Madelung, H. Schulz and H. Weiss (Springer, Berlin, 1982).

Growth and properties of new wide-gap quantum well structures: $\text{Zn}_{1-x}\text{Mn}_x\text{Se}/\text{Zn}_{1-y}\text{Cd}_y\text{Se}$

N. Samarth, H. Luo, J. Buschert, J.K. Furdyna

Department of Physics, University of Notre Dame, Notre Dame, Indiana 46556, USA

W.J. Walecki, A.V. Nurmikko

Department of Physics and Division of Engineering, Brown University, Providence, Rhode Island 02912, USA

R.G. Alonso, Eun-Soon Oh, A.K. Ramdas

Department of Physics, Purdue University, West Lafayette, Indiana 47907, USA

and

N. Otsuka

Department of Materials Engineering, Purdue University, West Lafayette, Indiana 47907, USA

We report the MBE growth and characterization of a new system of wide-gap II–VI heterostructures: $\text{Zn}_{1-x}\text{Mn}_x\text{Se}/\text{Zn}_{1-y}\text{Cd}_y\text{Se}$. We have grown single and multiple quantum well structures as well as superlattices with low lattice mismatch ($\leq 0.3\%$) and with good interface quality for $x \leq 0.30$, $y \leq 0.25$. All these structures show robust confinement effects and efficient excitonic luminescence in the blue-green spectral region. Magneto-optical measurements yield a valence band offset of 30 ± 5 meV.

Wide-gap heterostructures involving ZnSe-based alloys are of current interest because of potential optoelectronic applications in the blue-green region of the spectrum [1]. The combinations investigated in recent years include $\text{ZnSe}/\text{Zn}_{1-x}\text{Mn}_x\text{Se}$ [2] and $\text{ZnSe}/\text{Zn}_{1-x}\text{Cd}_x\text{Se}$ [3]. $\text{ZnSe}/\text{Zn}_{1-x}\text{Mn}_x\text{Se}$ structures have exhibited optically pumped lasing at low lattice temperatures [4], while room temperature lasing action has been recently demonstrated in $\text{ZnSe}/\text{Zn}_{1-x}\text{Cd}_x\text{Se}$. [5] These heterostructures are strained-layer systems, with a typical lattice-mismatch of 1%–2% using alloy compositions of interest. While not a limitation for thin structures containing a few pseudomorphic strained quantum wells, the lattice-mismatch could have detrimental effects in thicker structures where the criti-

cal thickness is exceeded. In anticipation of future applications, it is therefore important to investigate II–VI heterostructures with lower strain configurations. We discuss here the growth and properties of $\text{Zn}_{1-x}\text{Mn}_x\text{Se}/\text{Zn}_{1-y}\text{Cd}_y\text{Se}$ heterostructures, in which the lattice mismatch can be reduced by appropriately adjusting the alloy compositions [6,7].

The epitaxial growth and properties of the alloys $\text{Zn}_{1-x}\text{Mn}_x\text{Se}$ and $\text{Zn}_{1-x}\text{Cd}_x\text{Se}$ have been reported earlier in the literature [2,3,8]. Fig. 1 shows the schematic variation of the room temperature energy gap in both these alloys as a function of lattice parameter, indicating the opportunity for fabricating lattice-matched $\text{Zn}_{1-x}\text{Mn}_x\text{Se}/\text{Zn}_{1-y}\text{Cd}_y\text{Se}$ heterostructures. Notice also that, in comparison to both $\text{ZnSe}/\text{Zn}_{1-x}\text{Mn}_x\text{Se}$ and

$\text{ZnSe}/\text{Zn}_{1-y}\text{Cd}_y\text{Se}$, the lattice-matched heterostructures should have better confinement due to the larger difference between the energy gaps of barriers and wells. Our primary interest lies in the composition range $0.10 \leq y \leq 0.20$ for the $\text{Zn}_{1-y}\text{Cd}_y\text{Se}$ wells and $0.20 \leq x \leq 0.30$ for the $\text{Zn}_{1-x}\text{Mn}_x\text{Se}$ barriers. Both $\text{Zn}_{1-x}\text{Mn}_x\text{Se}$ and $\text{Zn}_{1-y}\text{Cd}_y\text{Se}$ epilayers show a rapid deterioration in quality for Mn and Cd concentrations much above these upper limits [3,8]. The composition range is also dictated by the desire to have optical transitions in the blue-green region of the spectrum while at the same time having sufficient confinement of the carriers.

Crystal growth was carried out in a Riber 32 R & D system, with elemental sources of Zn, Mn and Se, and a compound CdSe source. Substrates employed were commercially polished (100) GaAs, and were prepared in the standard manner before use. The sample surface was monitored by reflection high energy electron diffraction (RHEED) at 10 keV, and showed a (2×1) reconstruction under typical growth conditions. The composition of the alloy samples was determined by assuming a linear variation of the lattice constant (Vegard's law). Optimal growth temperatures for $\text{Zn}_{1-x}\text{Mn}_x\text{Se}$ are typically in the range $300\text{--}320^\circ\text{C}$, while those for $\text{Zn}_{1-y}\text{Cd}_y\text{Se}$ lie in the range $230\text{--}300^\circ\text{C}$, depending on the composition. Wherever thick buffer layers of $\text{Zn}_{1-x}\text{Mn}_x\text{Se}$ were required,

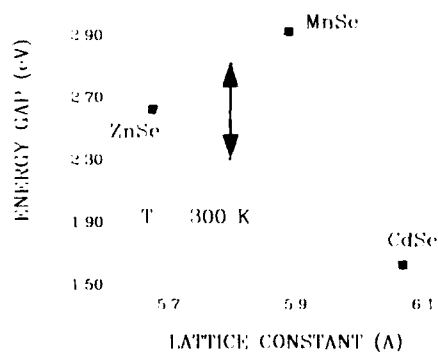


Fig. 1. Schematic depiction of energy gap (at 300 K) versus lattice parameter in the alloys $\text{Zn}_{1-x}\text{Mn}_x\text{Se}$ and $\text{Zn}_{1-y}\text{Cd}_y\text{Se}$. For experimental data showing detailed bowing effects, see refs. [2,3].

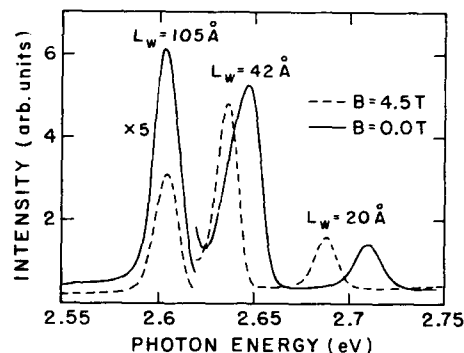


Fig. 2. Photoluminescence spectra of three isolated $\text{Zn}_{1-x}\text{Mn}_x\text{Se}/\text{Zn}_{1-y}\text{Cd}_y\text{Se}$ ($x = 0.15$, $y = 0.16$) quantum wells at $T = 2$ K. The dashed curve shows the PL in a magnetic field of 4.5 T.

we used a substrate temperature of 300°C . However, $\text{Zn}_{1-x}\text{Mn}_x\text{Se}/\text{Zn}_{1-y}\text{Cd}_y\text{Se}$ quantum wells and superlattices were grown at a substrate temperature of 250°C , hence optimizing the quality of the quantum well material. Studies of single quantum wells in which the temperature was cycled between the two optimal temperatures for the well and barrier materials showed no particular improvement in optical properties.

For characterization purposes, we fabricated $\text{Zn}_{1-x}\text{Mn}_x\text{Se}/\text{Zn}_{1-y}\text{Cd}_y\text{Se}$ quantum wells of varying thicknesses. The heterostructures were grown on top of buffer layers consisting of $0.5\text{ }\mu\text{m}$ ZnSe followed by $0.5\text{ }\mu\text{m}$ $\text{Zn}_{1-x}\text{Mn}_x\text{Se}$. The low temperature PL spectrum of one such structure is shown in fig. 2. The sample contains three quantum wells of $\text{Zn}_{1-y}\text{Cd}_y\text{Se}$ ($y = 0.15$) with well widths of 105, 42 and 20 Å, respectively, isolated by 500 Å $\text{Zn}_{1-x}\text{Mn}_x\text{Se}$ ($x = 0.16$) barriers. At low temperatures, the energy gap difference between the barriers and wells is 238 meV. The lattice mismatch is about 0.3%. Transmission electron microscopy (TEM) shows that the misfit dislocation density is quite low ($\leq 10^6\text{ cm}^{-2}$) compared to that in typical strained II-VI heterostructures. The photoluminescence (PL) spectrum in fig. 2 shows efficient excitonic recombination associated with the $n = 1$ to hh transition from each of the quantum wells, with strong confinement-related blue-shifts. A comparison between reflectivity and PL spectra indicates a relatively small Stokes shift

(≤ 7 meV), despite the presence of the alloy in the quantum well. The structure shows a very high luminescence efficiency up to 80 K.

The diluted magnetic semiconductor (DMS) nature of the barrier material can be exploited for determining band offsets [9]. DMS alloys such as $\text{Zn}_{1-x}\text{Mn}_x\text{Se}$ show a large Zeeman splitting of the band-edges at low temperatures due to the sp-d exchange interaction between band electrons and magnetic ions. In a quantum well structure with DMS barriers, the confined states experience some of this exchange interaction due to the penetration of the wavefunction into the barriers. The resulting magneto-optical shifts in PL spectra can then be fitted to theoretical calculations, yielding direct information about band alignments. The calculations employ a variational method that properly accounts for excitonic effects in the case of small valence band offsets [10].

In fig. 2, the dashed curve represents the PL spectrum for the $\text{Zn}_{1-x}\text{Mn}_x\text{Se}/\text{Zn}_{1-x}\text{Cd}_x\text{Se}$ quantum well structure in a magnetic field of 4.5 T in the Faraday configuration (B perpendicular to the layer plane). The emission from the two narrower wells shows a sizeable red-shift, due to the large penetration of the wavefunction into the DMS barrier. In fig. 3, we show the experimental Zeeman shift of the PL from the 42 Å well along with the theoretically calculated shift for several values of the valence band offset. A comparison with the experimental data yields a valence band

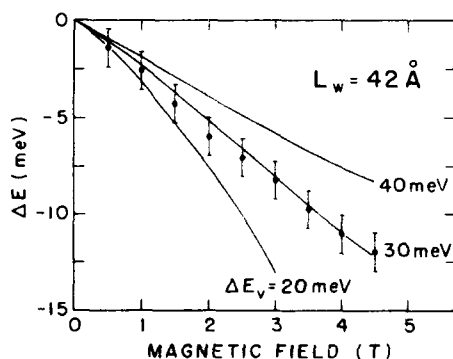


Fig. 3. Magneto-optical shift of the PL emission from the 42 Å quantum well in fig. 2. The solid lines show the theoretical shift for different values of the valence band offset.

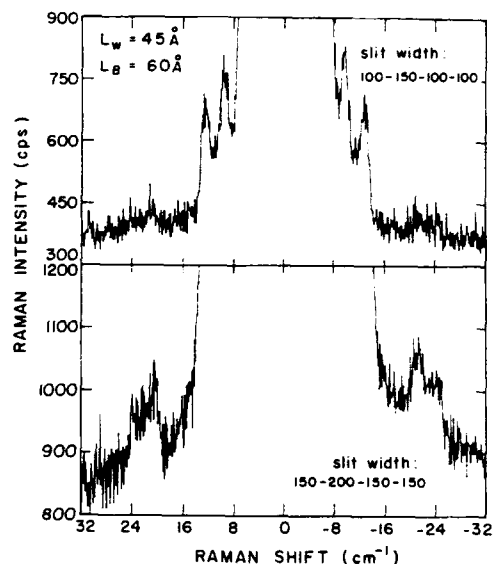


Fig. 4. Observation of folded acoustic phonons in a 50 period $\text{Zn}_{0.70}\text{Mn}_{0.30}\text{Se}/\text{Zn}_{0.85}\text{Cd}_{0.15}\text{Se}$ superlattice with $\text{Zn}_{1-x}\text{Mn}_x\text{Se}$ and $\text{Zn}_{1-x}\text{Cd}_x\text{Se}$ layer thicknesses of 60 and 45 Å, respectively. The upper panel shows the first order doublet and the lower panel shows a weak second order doublet.

offset of 30 ± 5 meV, implying a conduction band offset of 208 ± 6 meV.

In addition to quantum well structures, we have also investigated $\text{Zn}_{1-x}\text{Mn}_x\text{Se}/\text{Zn}_{1-x}\text{Cd}_x\text{Se}$ superlattices. PL spectra from these superlattices also show strong excitonic features and clear quantum confinement effects [6]. Further studies of $\text{Zn}_{1-x}\text{Mn}_x\text{Se}/\text{Zn}_{1-x}\text{Cd}_x\text{Se}$ superlattices using magneto-luminescence and Raman spectroscopy are currently underway. Preliminary analysis of magneto-optical data yields valence band offsets consistent with those obtained from the single quantum well measurements described earlier. Room temperature Raman measurements show the presence of folded acoustic phonons (fig. 4), attesting to the formation of superlattices with uniform layer thicknesses and well defined interfaces. The positions of the first and second order doublets are in good agreement with the predictions of a standard model [11] that accounts for zone-folding effects. Detailed Raman and magneto-optical studies of these superlattices will be described elsewhere.

To summarize, we have demonstrated the growth of low-strain $\text{Zn}_{1-x}\text{Mn}_x\text{Se}/\text{Zn}_{1-x}\text{Cd}_x\text{Se}$ quantum wells and superlattices with promising structural and optical properties. The close lattice match substantially reduces the density of misfit dislocations, and quantum wells and superlattices show efficient excitonic luminescence and strong confinement. Some crucial challenges still remain for future work. Paramount among these is the growth of *high quality* $\text{Zn}_{1-x}\text{Mn}_x\text{Se}$ buffer layers which are necessary to take full advantage of lattice-matching the $\text{Zn}_{1-x}\text{Mn}_x\text{Se}/\text{Zn}_{1-x}\text{Cd}_x\text{Se}$ structures. We believe that a solution may be offered by the recent growth of defect-free $\text{Ga}_{1-x}\text{In}_x\text{As}$ single-crystals [12] which can be used as high quality substrates lattice-matched to $\text{Zn}_{1-x}\text{Mn}_x\text{Se}$. This possibility is currently being investigated.

We thank U. Debska for the purification of the source materials. This work was supported by DARPA under the University Research Initiative Program (N00014-90-J-1582) and by the National Science Foundation (at Notre Dame and Purdue DMR-8913706; at Brown ECS-8916026).

References

- [1] R.L. Gunshor, L.A. Kolodziejski, A.V. Nurmikko and N. Otsuka, *Ann. Rev. Mater. Sci.* 18 (1988) 325.
- [2] L.A. Kolodziejski, R.L. Gunshor, T.C. Bonsett, R. Venkatasubramiam, S. Datta, R.B. Bylisma, W.M. Becker and N. Otsuka, *Appl. Phys. Letters* 47 (1985) 169.
- [3] N. Samarth, H. Luo, J.K. Furdyna, S.B. Qadri, Y.R. Lee, R.G. Alonso, A.K. Ramdas and N. Otsuka, *Appl. Phys. Letters* 56 (1990) 1163.
- [4] R.B. Bylisma, W.M. Becker, T.C. Bonsett, L.A. Kolodziejski, R.L. Gunshor, M. Yamanishi and S. Datta, *Appl. Phys. Letters* 47 (1985) 1039.
- [5] H. Jeon, J. Ding, A.V. Nurmikko, H. Luo, N. Samarth, J.K. Furdyna, W. Bonner and R.E. Nahory, *Appl. Phys. Letters*, submitted.
- [6] N. Samarth, H. Luo, J.K. Furdyna, S.B. Qadri, Y.R. Lee, R.G. Alonso, E.K. Suh, A.K. Ramdas and N. Otsuka, *Surface Sci.* 228 (1990) 226.
- [7] W. Walecki, A.V. Nurmikko, N. Samarth, H. Luo and J.K. Furdyna, *Appl. Phys. Letters* 57 (1990) 466.
- [8] S.B. Qadri, N. Samarth and J.K. Furdyna, *J. Appl. Phys.* 66 (1989) 3622.
- [9] Q. Fu, D. Lee, A.V. Nurmikko, R.L. Gunshor and L.A. Kolodziejski, *Phys. Rev. B* 39 (1989) 3173.
- [10] J.W. Wu and A.V. Nurmikko, *Phys. Rev. B* 38 (1988) 1504.
- [11] E.-K. Suh, D.U. Bartholomew, A.K. Ramdas, S. Rodriguez, S. Venugopalan, L.A. Kolodziejski and R.L. Gunshor, *Phys. Rev. B* 36 (1987) 4316.
- [12] W.A. Bonner, B.J. Skromme, E. Berry, H.L. Gilchrist and R.E. Nahory, in: *Proc. 16th Intern. Symp. on GaAs and Related Compounds*, Atlanta, GA, 1988, *Inst. Phys. Conf. Ser.* 96, Ed. J.S. Harris (Inst. Phys., London-Bristol, 1989) p. 337.

Characterization of CdSe/ZnTe heterojunctions

M.C. Phillips, E.T. Yu, Y. Rajakarunanayake, J.O. McCaldin, D.A. Collins and T.C. McGill

T.J. Watson, Sr., Laboratory of Applied Physics, California Institute of Technology, Pasadena, California 91125, USA

We have measured the valence band offset in a cubic CdSe/ZnTe (100) heterojunction by X-ray photoelectron spectroscopy (XPS). Our preliminary result, based on analysis of one heterojunction, is 0.65 ± 0.08 eV. The electrical characteristics of a doped n-CdSe/p-ZnTe heterojunction appear to be dominated by traps. We have attempted to verify the band offset through capacitance–voltage measurements, but have been unable to extract a consistent value for the flat band voltage from scans taken at different temperatures and frequencies.

1. Introduction

Inability to dope ZnTe n-type has frustrated attempts to base an efficient green light emitting diode on the 2.25 eV, direct band gap of ZnTe. One solution would be to find an n-dopable material with a conduction band alignment that allows electron injection into p-ZnTe. CdSe can be doped heavily n-type and, though its equilibrium structure is wurtzite, in thin layers it will grow readily in cubic form on ZnTe with a lattice mismatch of only 0.44% [1]. Unfortunately, since the room temperature band gap of cubic CdSe is 1.67 eV [1] and since the valence band of CdSe lies below that of ZnTe, the conduction band offset in a CdSe/ZnTe heterojunction is many times kT at room temperature.

Though the conduction band offset is unfavorable for injection from n-CdSe into p-ZnTe, it may still be possible to inject from a lattice-matched, n-type $(\text{CdSe})_{1-x}(\text{ZnTe})_x$ alloy into p-ZnTe. To evaluate this possibility we must have information about the dopability and miscibility of these alloys, and about the band offset of at least the binary materials. This paper gives a preliminary value for the CdSe/ZnTe offset as measured by XPS, and describes the electrical characteristics of a CdSe(Al)/p-ZnTe heterojunction.

2. Experiment and discussion

We grew the CdSe and ZnTe layers in a Perkin-Elmer 430P MBE loaded with 99.9999% elemental sources; the substrate temperature was 270°C for growth of both materials. For the XPS sample we started with a GaSb epilayer on a GaSb substrate, transferred through UHV to the II–VI chamber, then alternately grew ZnTe or CdSe epilayers and characterized them in the XPS chamber. Transfer between growth and analysis chambers was also through UHV, eliminating complications associated with exposing surfaces to atmosphere.

The thickest CdSe layer was about 400 Å. During the growth of this layer the RHEED pattern changed very little from that of the initial 2×1 reconstructed ZnTe surface. The upper XPS spectrum in fig. 1 is from this CdSe layer and is followed by a spectrum from a thick ZnTe layer. The third spectrum is from approximately 25 Å of ZnTe on CdSe. Applying the method of Kraut et al. [2] to these spectra, we find a valence band offset of 0.65 ± 0.08 eV, shown in fig. 2 amidst a wide range of theoretical predictions [3–10]. The strain in the layers was not measured; since, however, the lattice constants of ZnTe and cubic CdSe differ by only 0.44%, and since those of ZnTe and

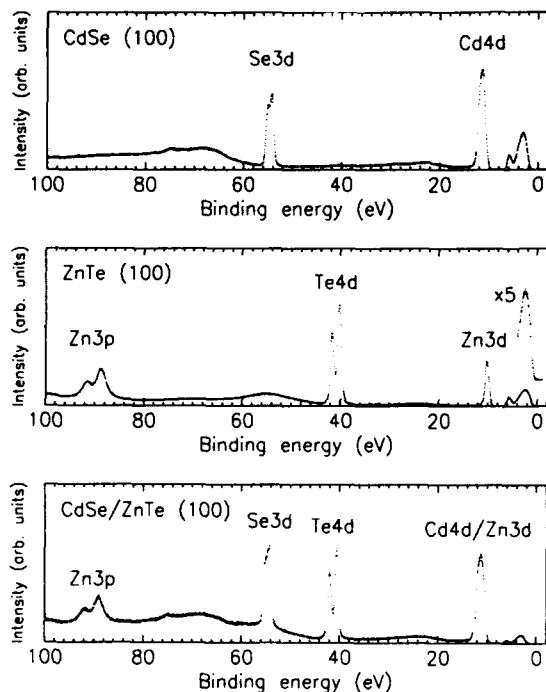


Fig. 1. XPS spectra for bulk CdSe (100), bulk ZnTe (100), and a CdSe/ZnTe (100) heterojunction.

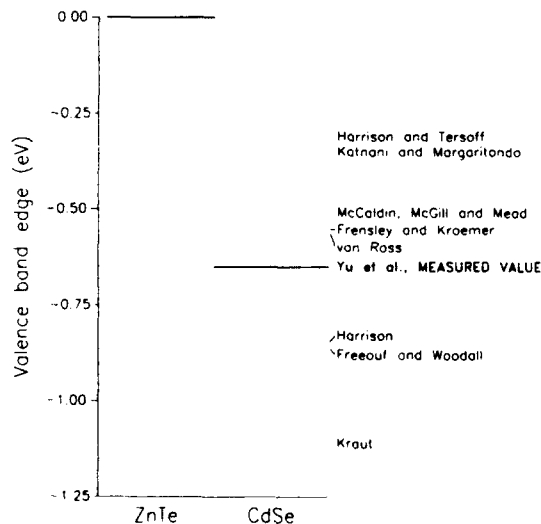


Fig. 2. Predicted values for the relative position of the ZnTe and CdSe valence band edges [3-10]. The figure also includes our experimentally measured value, indicated in bold.

GaSb differ by only 0.15%, strain effects can be neglected within the error bounds. The value quoted above is based on analysis of only one heterojunction; we will publish a detailed discussion when more samples have been studied.

The GaSb/ZnTe valence band offset is too large to allow a back contact suitable for electrical measurements to be made through a GaSb substrate. Since single-crystal, oriented ZnTe substrates are not commercially available, the sample for electrical characterization was grown on a randomly oriented, polycrystalline ZnTe substrate with an average grain size of a few millimeters and a room temperature hole concentration of about 10^{17} cm^{-3} . The structure consists of a nominally undoped, 400 Å ZnTe layer, 600 Å of CdSe heavily doped with Al, and an in situ Zn cap applied at room temperature. Due to a problem with the Se shutter, there was a 34 min growth interrupt between the ZnTe and the CdSe while the Se source heated from idling to growth temperature. During this time the substrate was lowered out of the Se

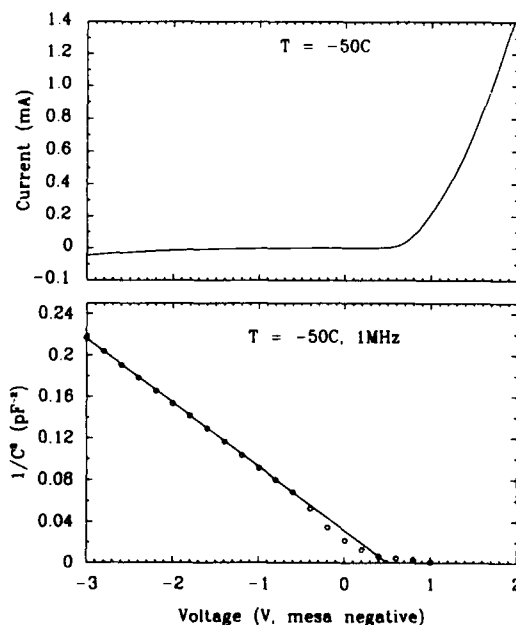


Fig. 3. Measured I - V and C - V for an 80 μm diameter mesa containing an n-CdSe/p-ZnTe heterojunction.

flux and held at the growth temperature, but impurities may have collected at this interface.

We evaporated a large area Au back contact after removing the sample from UHV, and then etched through the heterojunction to leave circular mesas with Zn caps. Since the grain boundaries were evident after etching, we were able to study only mesas lying within single grains. At room temperature these devices turn on exponentially with an ideality factor of 2.3 until an ohmic series resistance dominates the current. Fig. 3 shows current-voltage and capacitance-voltage measurements taken at -50°C ; the lower temperature reduces the reverse current and thus extends the voltage range over which the C - V data are useful. The infinite-capacitance intercept in the lower plot should be the flat band voltage, but a flat band voltage of 0.5 V gives a band offset of about 1 V. C - V scans taken at different temperatures and frequencies are not consistent with a simple model of depletion layer capacitance and suggest that the electrical characteristics of this device are dominated by charging of and recombination at traps. Some of these traps may be from impurities gettering at the interface during the long growth interrupt.

3. Conclusions

We were unable to extract information about the band offset from electrical measurements on our first doped heterojunction. The growth interrupt which may have introduced traps at the interface was necessary only because of a mechanical

malfunction. Eliminating this growth interrupt and starting with better substrate material should improve the results.

The heterojunction for XPS was grown on a high quality substrate and no problems were evident in the RHEED pattern during growth. Though the value of 0.65 eV should be considered tentative until checked with more samples, the procedure used has produced consistent results for several other heterojunctions.

Acknowledgment

This work was funded by the Office of Naval Research under contract N00014-90-J-1742.

References

- [1] N. Samarth, H. Luo, J.K. Furdyna, S.B. Qadri, Y.R. Lee, A.K. Ramdas and N. Otsuka, *Appl. Phys. Letters* 54 (1989) 2680.
- [2] E.A. Kraut, R.W. Grant, J.R. Waldrop and S.P. Kowalczyk, *Phys. Rev. Letters* 44 (1980) 1620.
- [3] W.A. Harrison and J. Tersoff, *J. Vacuum Sci. Technol.* B4 (1986) 1068.
- [4] A.D. Katnani and D. Margaritondo, *Phys. Rev.* B28 (1983) 1944.
- [5] J.O. McCaldin, T.C. McGill and C.A. Mead, *Phys. Rev. Letters* 36 (1976) 56.
- [6] W.R. Frensley and H. Kroemer, *Phys. Rev.* B16 (1977) 2642.
- [7] O von Ross, *Solid-State Electron.* 23 (1980) 1069.
- [8] W.A. Harrison, *J. Vacuum Sci. Technol.* 14 (1977) 1016.
- [9] J.L. Freeouf and J.M. Woodall, *Appl. Phys. Letters* 39 (1981) 727.
- [10] E.A. Kraut, *J. Vacuum Sci. Technol.* B2 (1984) 486.

Fabrication of $\text{ZnS}/(\text{ZnSe})_n/\text{ZnS}$ single quantum well structures and photoluminescence properties

T. Yao

*Department of Electrical Engineering, Hiroshima University, Higashi-Hiroshima 724, Japan
and
Electrotechnical Laboratory, Tsukuba 305, Japan*

M. Fujimoto *, S.K. Chang ** and H. Tanino

Electrotechnical Laboratory, Tsukuba 305, Japan

ZnS/ZnSe single quantum well structures are fabricated for the first time by a combination of molecular beam epitaxy and atomic layer epitaxy. The quantum wells thicker than 3 monolayers (ML) emit a sharp excitonic emission with half width of 15–30 meV, while a broad emission (half width of around 100 meV) with low-energy tail is observed from quantum wells thinner than 2 ML. From the analysis of the dependence of emission energy on well width, it is concluded that the conduction band offset at the ZnSe/ZnS interface is very small (almost zero). It is suggested that the luminescence broadening in thin quantum wells is caused by fluctuations not only associated with the quantum confinement effect along the growth direction, but also with the lateral quantum confinement effect in “quantum slabs” formed on islands and valleys at the interface.

1. Introduction

The interface roughness of heterostructures has been characterized by utilizing free excitonic emission from a superlattice or quantum well structure as a probe, in which the half width of the emission is closely correlated with the interface roughness [1]. The interface roughness implies fluctuations in the position of the barrier along the growth direction and the presence of islands and valleys at the interface. For interfaces formed under optimal growth conditions, the fluctuation of the barrier along the growth direction is expected to be a monolayer distance. The spectral width of an excitonic transition is given by the width of the probability distribution of lateral dimensions of

islands and valleys. It is intuitive to see that the transitions become sharp if the lateral dimensions of valleys and islands are either much larger or smaller than the exciton size, and that they become very broad when the lateral fluctuations are comparable to the excitonic size.

It is obvious that a single quantum well (SQW) structure is preferable to characterize the interface roughness compared to multi-quantum well (MQW) or superlattice structures, since a fluctuation in layer thickness present in MQW and superlattice structures give additional broadening in energy spectrum. In fact, the characterization of the interface roughness in III–V heterostructures has been mostly conducted with SQW structures [2].

Recently, there has been increasing interest in II–VI wide band gap superlattices such as CdTe-ZnTe [3], ZnTe-ZnSe [4,5], ZnSe-ZnMnSe [6], and ZnSe-ZnS [7,8] for use in optoelectronic devices in the short wavelength region. In particular, ZnSe-ZnS superlattices have been grown on (100)

* On leave from Tokai University, Hiratsuka 259-12, Japan.
Present address: Canon Inc., Shimomaru-ku, Ota-ku, Tokyo 146, Japan.

** On leave from Department of Physics, College of Science, Yonsei University, Seoul 120-749, South Korea.

GaAs substrates by hot wall epitaxy [9], molecular beam epitaxy (MBE) [10], metalorganic chemical vapor deposition [7,8], and metalorganic molecular beam epitaxy [11] methods because of potential applications such as optical waveguides [12] and blue lasers [13]. Although the interface quality has a crucial effect on the performance of these devices, the interface quality has not been extensively characterized because of the broad emission spectrum from II-VI superlattice structures.

This paper presents the first fabrication of ZnS/ZnSe SQWs by a combination of MBE and atomic layer epitaxy (ALE), in which ZnS barrier layers are grown by MBE, while the ALE technique [14] is adopted to grow thin ZnSe well layers. Photoluminescence (PL) spectra of the ZnS/ZnSe SQWs are measured for various well thicknesses. The interface roughness and its influence on PL spectra will be discussed.

2. Fabrication of $\text{ZnS}/(\text{ZnSe})_n/\text{ZnS}$ single quantum well structures

Fig. 1 shows a schematic picture of a ZnS/ZnSe SQW structure. A $0.15\text{ }\mu\text{m}$ thick GaAs buffer layer was grown on a (100)GaAs substrate by MBE in a separate growth chamber. The sample was transferred to the II-VI growth chamber via magnetic feedthrough and a ZnS barrier layer

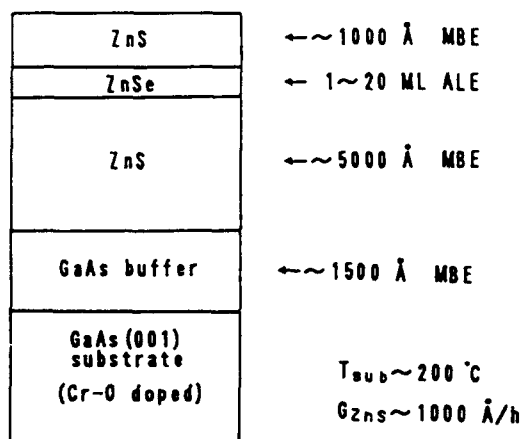


Fig. 1. Schematic of fabricated single quantum well structures.

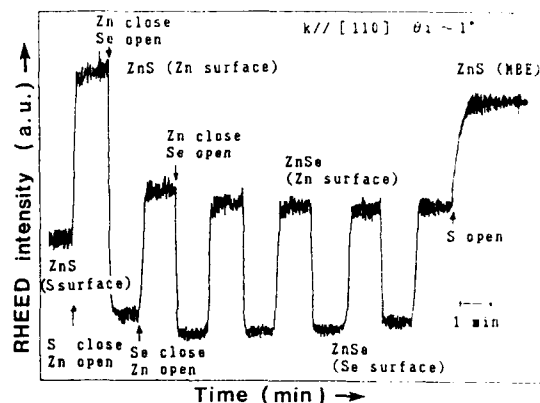


Fig. 2. The intensity variation of the RHEED specular beam intensity during the growth of ZnSe well.

whose thickness ranged from 0.1 to $0.5\text{ }\mu\text{m}$ was subsequently grown by MBE. The typical growth rate for ZnS was $0.1\text{ }\mu\text{m}/\text{h}$. Although the lattice mismatch between GaAs and ZnS is 4.5% , the ZnS layer was thick enough to be fully relaxed. The ZnSe well layer was grown by ALE, in which the ALE cycle was as follows: the open periods of the Zn and Se shutters were 60 s and the interval period in between each open period of the shutter was 5 s . The ALE growth conditions were examined by RHEED investigations [15]. The thickness of the ZnSe well ranged from 1 to 20 ML . Finally, a ZnS barrier layer whose thickness ranged from 0.03 to $0.1\text{ }\mu\text{m}$ was grown by MBE. The substrate temperature during growth of II-VI compounds was varied between 130 and $210\text{ }^\circ\text{C}$.

Fig. 2 shows an example of the variation of the RHEED specular beam intensity during the ALE growth of a ZnSe well of 5 monolayers (ML) . RHEED observation conditions were: acceleration voltage 11 keV ; azimuth $\parallel[110]$ direction; incidence angle 1° . After the succeeding formation of S- and Zn-covered surfaces, ALE growth of ZnSe was initiated by opening the Se shutter. The S-covered surface of ZnS showed a (2×1) reconstruction RHEED pattern, while the Zn-covered surface showed a (1×1) RHEED pattern. It is interesting to note that the RHEED intensity for the Zn-covered surface was stronger than that for the S-covered surface. This relationship is the same as for ZnSe and ZnTe [15]. After the growth

of 5 ML of ZnSe which was terminated by opening the Zn shutter, the MBE growth of ZnS was restarted by opening the S shutter with the Zn shutter being kept open. The observed persistent RHEED intensity oscillations during growth are indicative of atomic layer-by-layer growth of ZnSe.

3. Photoluminescence properties

PL spectra were measured at 4.2 K using the 3250 Å line from a He-Cd laser as an excitation source. As shown in fig. 3, PL spectra from ZnS/ZnSe SQWs show dominant excitonic emission presumably due to radiative annihilation of the free exciton. It should be noted that the free excitonic emission even from a 1 ML thick ZnSe SQW was observed with sufficient emission intensity, which is indicative of high internal quantum efficiency of ZnS/ZnSe SQWs. The emission en-

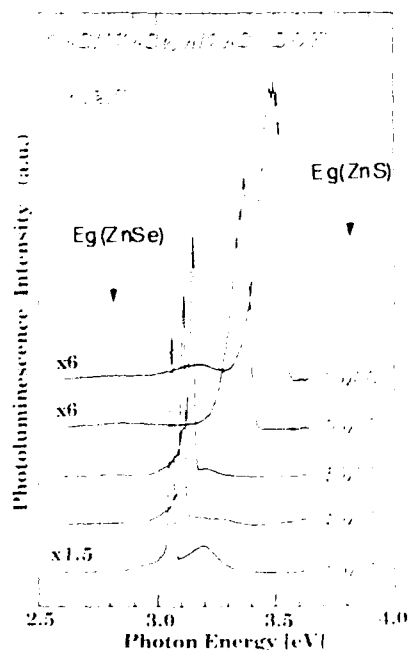


Fig. 3. Photoluminescence spectra from single quantum well structures.

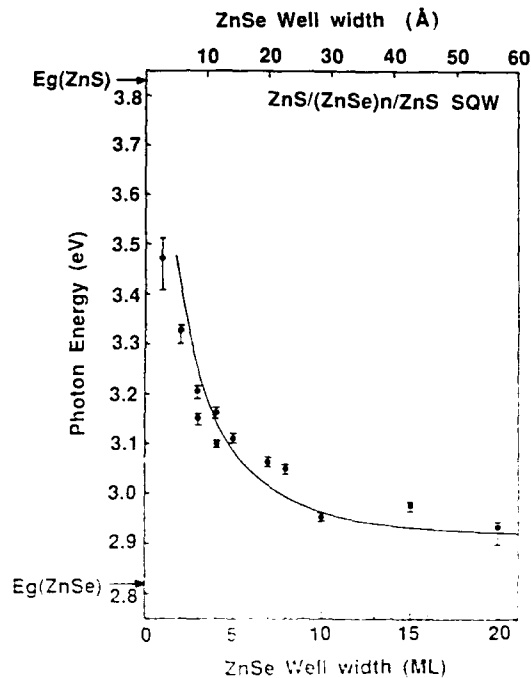


Fig. 4. The dependence of emission energy on the well thickness.

ergy of a ZnS/ZnSe SQW with 1 ML thick ZnSe well reaches around 3.5 eV, which is the shortest wavelength ever obtained from II-VI heterostructures. The linewidth of the emission peak from quantum wells thicker than 3 ML varied from 15 to 30 meV, which is narrower than the reported half-width for ZnSe-ZnS superlattices [7-11]. Such sharp emission is in contrast to the broad emission from ZnSe-ZnTe superlattices, which fall in the category of type II superlattices [4,5]. However, as the well width is reduced below 2 ML, the emission line shows a prominent band tail on its low energy side and the half width increases abruptly: 86 meV for 2 ML and 115 meV for 1 ML.

Fig. 4 plots the emission peak energy against the ZnSe well width. The half width value is shown by a vertical bar. As the well width de-

creases from 20 to 1 ML, the emission increases from 2.92 to 3.47 eV. Since the SQW emission exhibits a sharp peak with the peak energy being situated in between the band gap energies of ZnSe (2.82 eV) and ZnS (3.83 eV), the ZnS/ZnSe superlattice falls in the category of type I.

The solid curve shows the dependence of the calculated emission energy on the well thickness based on a simple square well potential model. In the calculation, the effect of strain – that is, biaxial compressive strain – is accounted for. Although there have been reported values ranging from 270 to 940 meV for the valence band offset of ZnSe/ZnS heterostructures [15], it is generally considered that the conduction band offset is very small compared to the valence band. We tentatively assumed for simplicity in the calculation that $\Delta E_c = 0$ and $\Delta E_v = \Delta E_g = 1$ eV. This assumption is consistent with the observation that only one emission line was observed, even at high temperature (up to 110 K). The calculation agrees fairly well with the experimental results except for well widths of 1–3 ML. Although Harrison's linear combination of atomic orbital theory predicts that the band structure of the ZnS–ZnSe interface represents type I ($\Delta E_c = 0.2$ eV and $\Delta E_v = 0.8$ eV) [17], it is likely that the conduction band offset is much smaller than 0.2 eV. In fact, recent study of PL of ZnSe/ZnS superlattices suggests that the conduction band offset for a well width of 40 Å is expected to be zero due to the strain [7]. There is considerable discrepancy in the emission energy for very thin wells (1–3 ML) between the calculation and experiment. In such thin quantum wells, the effective mass approximation is not a good approximation and a more rigorous treatment would be needed. Moreover, even in the calculation of the emission energy based on the simple square-well potential model, the variation of binding energy with the well thickness should be considered. The binding energy of 3D exciton is 21 meV, while that of a two-dimensional limit is 84 meV. The enhancement of the exciton binding energy becomes important thin quantum wells. These factors are not considered in the present calculation, and should be responsible for the deviation of the calculation from the experimental results.

4. Discussion

The broadening mechanisms of the PL line width are: (i) interface roughness, (ii) the interaction of excitons with phonons, and (iii) band filling due to high carrier concentration. The broadening due to the interaction of excitons with phonons becomes dominant at high temperature [18], but is less important at low temperature compared to other mechanisms in the case of weak electron–phonon coupling. The broadening due to the band filling becomes important in a thick well, when the excitation intensity is relatively high. Therefore, the luminescence broadening due to the interface roughness would be responsible for the luminescence broadening observed in the present experiments. It is observed that the linewidth scattered around 20 meV for quantum wells above 3 ML, while it increases abruptly as the well width decreases below 3 ML. Such abrupt broadening cannot be explained only by considering the fluctuation in the energy level of excitons caused by quantum confinement along the growth direction, but also considering an additional “lateral” quantum confinement effect of excitons.

When 1 ML thick ZnSe is deposited on a ZnS surface which has a surface roughness of one monolayer, there would be formation of ZnSe islands whose thickness is 1 ML, as schematically shown in fig. 5a. If the lateral dimensions of these islands is small compared to the de Broglie wavelength of electrons, additional “lateral” quantum confinement effects should be considered. In terms of RHEED characterization, the surface of the ZnS buffer layer is not atomically smooth compared to the GaAs surface. Therefore, it is natural to consider that there are many small islands and valleys whose lateral dimensions are much smaller than the de Broglie wavelength. After the deposition of ZnSe by ALE, a ZnS barrier layer is subsequently deposited. If the surface roughness of ZnS is assumed to be 1 ML, as shown in fig. 5a, the ZnSe islands formed by the surface roughness (terraces and valleys) of ZnS are three-dimensionally covered by ZnS, which results in a three-dimensional quantum confinement of electrons and holes. Thus the situation is similar to the quantum

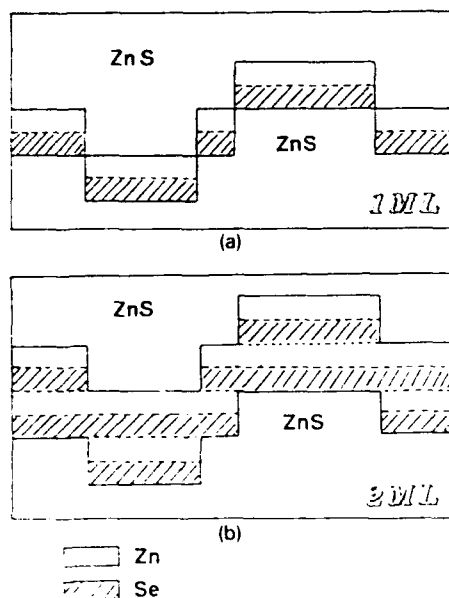


Fig. 5. Schematic depicting ZnSe growth on an atomically rough ZnS surface: (a) 1 ML thick ZnSe; (b) 2 ML thick ZnSe.

box, but with strong anisotropy. Such confinement would realize "quantum slabs", in which the confinement in the growth direction is of the order of an atomic layer, while the lateral confinement is of the order of excitonic size. It is expected that such anisotropic "quantum slabs" would yield interesting optical phenomena. Since the lateral dimensions of such "quantum slabs" are distributed almost randomly, the energy spread of the quantum level would become significant. Consequently, the luminescence broadening occurs.

Fig. 5b schematically shows the situation after the growth of 2 ML of ZnSe well. It is obvious that the lateral confinement is weakened because of the lateral extension of the interface layer. Thus, the energy spread due to the lateral confinement is decreased, which results in a decrease in luminescence broadening compared to the 1 ML quantum well. Further deposited ZnSe smears out the lateral quantum confinement abruptly. As a consequence, the luminescence broadening in thick quantum wells is mainly determined by the fluctuations due to the quantum confinement effect along the growth direction.

It should be pointed out that the thick well (15–20 ML) showed rather broad linewidth (30 meV) with weak luminescence. It is most likely that there occurs the generation of misfit dislocations in these films, which produces nonradiative centers and broadens the luminescence.

5. Conclusions

ZnS/(ZnSe)_n/ZnS ($n = 1-20$) single quantum well structures were fabricated by a combination of MBE and ALE. The SQW structure shows dominant excitonic emission which shows quantum confinement effect. The analysis of the dependence of the emission energy on the well width indicates that the conduction band offset is very small, or practically zero. The luminescence from wells thicker than 3 ML shows a sharp peak whose line width is typically 15–30 meV, while thinner quantum wells show much broader luminescence, which cannot be explained only by fluctuations in the electronic energy level associated with quantum confinement effect along the growth direction. It is suggested that "quantum slab" structures are formed on the ZnS surface at the beginning of epitaxy, which causes additional lateral quantum confinement. The lateral fluctuation of the "quantum slab" size causes additional luminescence broadening.

References

- [1] J. Singh, K.K. Bajaj and S. Chaudhari, *Appl. Phys. Letters* 44 (1984) 805.
- [2] D.F. Welch, G.W. Wicks and L.F. Eastman, *Appl. Phys. Letters* 46 (1985) 991.
- [3] G. Monfroy, S. Sivananthan, X. Chu, J.P. Faurie, R.D. Knox and J.L. Staudenmann, *Appl. Phys. Letters* 49 (1986) 152.
- [4] H. Fujiyasu, A. Ishida, H. Kuwabara, S. Shinohara and H. Murase, *Surface Sci.* 142 (1984) 579.
- [5] M. Kobayashi, N. Mino, H. Katagiri, R. Kimura, M. Konagai and K. Takahashi, *Appl. Phys. Letters* 48 (1986) 296.
- [6] L.A. Kolodziejski, R.L. Gunshor, N. Otsuka, S. Datta, V.M. Becker and A.V. Nurmikko, *IEEE J. Quantum Electron.* QE-22 (1986) 1666.

- [7] Y. Kawakami, T. Taguchi and A. Hiraki, *J. Crystal Growth* 93 (1988) 714.
- [8] T. Yokogawa, M. Ogura and T. Kajiwara, *Appl. Phys. Letters* 49 (1986) 702.
- [9] H. Fujiyasu, H. Takahashi, H. Shimizu, A. Sasaki and H. Kuwabara, in: *Proc. 17th Intern. Conf. on Physics of Semiconductors*, San Francisco, CA, 1984, Eds. J.D. Chadi and W.A. Harrison (Springer, Berlin, 1985) p. 539.
- [10] K. Mohamed, D.J. Olego, P. Newbury, D.A. Cammack, R. Dalby and H. Cornelissen, *Appl. Phys. Letters* 50 (1987) 1820.
- [11] M. Konagai, M. Kobayashi, R. Kimura and K. Takahashi, *J. Crystal Growth* 86 (1988) 290.
- [12] T. Yokogawa, M. Ogura and T. Kajiwara, *Appl. Phys. Letters* 52 (1988) 20.
- [13] D.A. Cammack, R.J. Dalby, H.J. Cornelissen and J. Khurgin, *J. Appl. Phys.* 62 (1987) 3071.
- [14] T. Yao and T. Takeda, *Appl. Phys. Letters* 48 (1986) 160.
- [15] T. Yao, Z.Q. Zhu, K. Uesugi, S. Kamiyama and M. Fujimoto, *J. Vacuum Sci. Technol.* A8 (1990) 997.
- [16] J.O. McCaldin, in: *Optical Properties of Low-Dimensional II-VI Wide Band Gap Compounds*, Eds. T.C. McGill, W. Streiber and C. Sotomayor-Torres (Plenum, New York, 1989).
- [17] W.A. Harrison, *J. Vacuum Sci. Technol.* 14 (1977) 1016.
- [18] J.L. Lee, E.S. Koteles and M.O. Vassell, *Phys. Rev.* B33 (1986) 5512.

Blue (ZnSe) and green (ZnSe_{0.9}Te_{0.1}) light emitting diodes

J. Ren, K.A. Bowers, B. Sneed, F.E. Reed, J.W. Cook, Jr. and J.F. Schetzina

Department of Physics, North Carolina State University, Raleigh, North Carolina 27695-8202, USA

We report the successful fabrication of ZnSe p–n junction light emitting diodes in which Li and Cl are used as p-type and n-type dopants, respectively. These p-on-n structures emit blue light at room temperature. Double heterostructures in which the active region is either a ZnSe_{0.9}Te_{0.1} layer or a ZnSe–ZnSe_{0.9}Te_{0.1} multilayer have also been fabricated by molecular beam epitaxy. These structures emit green electroluminescence over a wide temperature range.

1. Introduction

Fabrication of ZnSe blue light emitting diodes (LEDs) and lasers requires the formation of p–n junctions or heterostructures through controlled substitutional doping [1–9]. Devices of this type are currently sought for a number of applications including their use in full-color electroluminescent displays, as read–write laser sources for high-density information storage on magnetic and optical media, and as sources for undersea optical communications. In addition, ZnSe is closely lattice-matched to GaAs ($\Delta a/a \sim 0.25\%$). Thus, in principle, ZnSe devices can be integrated with Al–GaAs–GaAs devices to form sources, amplifiers, modulators, and detectors in a multicolor optoelectronics technology that could be used for both optical communications and optical signal processing (optical computing).

In this paper, we report the successful fabrication of ZnSe p–n junction LEDs in which Li and Cl are used as p-type and n-type dopants, respectively. These LEDs emit blue light at room temperature.

Double heterostructures (DH) in which the active region is either a ZnSe_{0.9}Te_{0.1} layer or a ZnSe–ZnSe_{0.9}Te_{0.1} multilayer have also been successfully prepared. These LED structures emit green electroluminescence over a wide temperature range.

2. Experimental details

The LED structures were grown by molecular beam epitaxy (MBE) in a special system designed and constructed at North Carolina State University (NCSU) specifically for growing II–VI compound semiconductors [10]. High purity (6N) Zn, Se, and Te from Osaka Asahi Metals Company were used as primary MBE source materials. ZnCl₂(5N5) was used as a solid Cl doping source for growth of the n-type layers. Pure Li metal (3N5) was used to dope the p-type layers.

The ZnSe diode structures (fig. 1a) were grown on n-type ($\sim 4 \times 10^{18} \text{ cm}^{-3}$) (100) GaAs:Si substrates. First, a 1.7 μm thick n-type ($n_0 \sim 2 \times 10^{18} \text{ cm}^{-3}$) ZnSe:Cl base layer was grown, followed by deposition of a 0.8 μm thick p-type ZnSe:Li layer. The ZnSe_{0.9}Te_{0.1} LED structures consisted of a DH in which the active region was either a ZnSe_{0.9}Te_{0.1} layer or a ZnSe–ZnSe_{0.9}Te_{0.1} multilayer sandwiched between doped ZnSe layers (fig. 1b). For each of the above structures, ohmic contact to the back surface of the GaAs:Si substrate was obtained by thermal evaporation of a Au_{0.88}Ge_{0.12} eutectic layer. Diode structures were then completed by depositing 0.8 μm Au dots onto the top ZnSe:Li layer using a metal mask.

Diode I – V characteristics at 300 K were measured using a Tektronix 370 curve tracer. Electroluminescence spectra were obtained for selected

a	
Au	
p-Type ZnSe:Li	0.8 μm
n-Type ZnSe:Cl	1.7 μm
n-Type GaAs:Si Substrate	
Au-Ge	

Blue Light Emitting Diode

b	
Au	
p-Type ZnSe:Li	0.8 μm
ZnSeTe Active Region	0.1 μm
n-Type ZnSe:Cl	1.7 μm
n-Type GaAs:Si Substrate	
Au-Ge	

Green Light Emitting Diode

Fig. 1. Schematic diagram of (a) ZnSe LED and (b) $\text{ZnSe}_{0.9}\text{Te}_{0.1}$ LED.

diodes at temperatures ranging from 4.2 to 300 K. In these experiments, gold wires were attached to the top and bottom electrodes and the diodes were placed in a liquid-He optical cryostat. The diodes were forward-biased using 6–8 V voltage pulses (1000 Hz, 10% duty cycle) from a Hewlett-Packard model 214-A pulse generator. The emitted electroluminescence was then detected and analyzed using a computer-controlled SPEX double monochromator equipped with a GaAs photomultiplier tube.

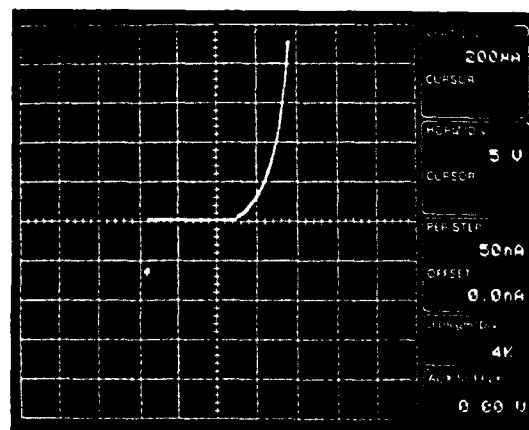
3. Results and discussion

3.1. ZnSe blue LEDs

The ZnSe diodes exhibit good rectification properties as shown in fig. 2. The forward-bias turn-on voltage is 2.5–3 V for our best diodes; reverse bias breakdown generally exceeds 10 V. It should be noted that the ZnSe diode structure described here is essentially the *reverse* of the

ZnSe diode structure recently reported by Haase and co-workers [3,11] of 3M Company. The 3M ZnSe LED structure consists of a p-type ZnSe:Li film deposited onto a p⁺-GaAs substrate. This is followed by deposition of an n-type ZnSe:Cl layer. Although this structure is reported by Haase et al. to emit blue light (463 nm) at room temperature, they also report a forward bias turn-on voltage in excess of 15 V. This large turn-on voltage, which cannot be tolerated in a laser structure, is attributed to a high resistivity layer caused by misfit dislocations at the GaAs–ZnSe interface. Part of this voltage, no doubt, is also due to the large *valence band* offset voltage (~ 1.3 eV) at the interface between these two materials, which blocks the transport of holes to the junction. By reversing this structure, as we have done using a p-on-n configuration, problems associated with the ZnSe–GaAs interface have been eliminated. In this case, under forward bias conditions, electrons flow toward the junction from the n-type layers. There is no blockage to transport at the GaAs–ZnSe interface, since the *conduction band* offset is essentially zero [12]. In addition, it appears that our samples are not plagued by a high resistivity layer at this interface, which contributes to the very high (> 15 V) turn-on voltage reported by the 3M group for their p-on-n diode structures.

There is a problem, however, in obtaining a good ohmic contact to p-type ZnSe, which the

Fig. 2. I - V characteristics of ZnSe LED at 300 K.

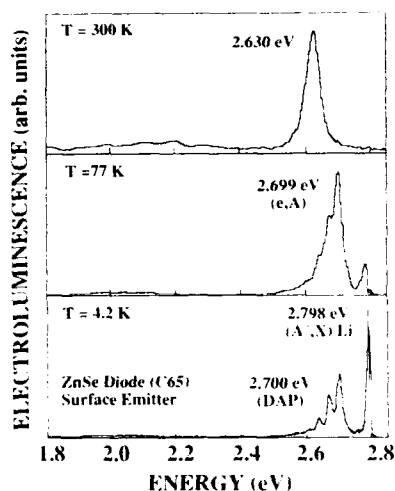


Fig. 3. Electroluminescence spectra obtained for ZnSe LED at 300, 77, and 4.2 K.

structure shown in fig. 2 requires. We have chosen to use gold for this contact, which produces a Schottky barrier of ~ 1 V on ZnSe, as determined from X-ray photoemission spectroscopy (XPS) studies [13]. As a consequence, the forward-bias turn-on voltage for our structure is larger than expected for an "ideal" ZnSe p-n junction, since the gold Schottky barrier is reverse-biased. It is also for this reason that the forward-bias I - V characteristics are "soft", after the 2.5–3 V turn-on. We have completed detailed measurements of the forward-bias characteristics of these initial diode structures using a Hewlett-Packard model 4142B circuit analyzer. We obtain a diode ideality factor $n = 1.3$ for forward-bias currents up to 10^{-6} A. For currents greater than 10^{-4} A, $n > 2$ because of appreciable series resistance ($R \sim 500$ – 1000 Ω) associated with the reverse-biased gold-ZnSe:Li contact.

Electroluminescence (EL) spectra for a typical ZnSe LED is shown in fig. 3. The 300 K electroluminescence spectrum consists of a single near-edge peak centered in the blue at 2.630 eV (471 nm) having a full-width at half maximum FWHM = 54 meV. At 77 K, peak emission occurs at 2.699 eV (459 nm). At 4.2 K, the main electroluminescence emission peak is at ~ 2.786 eV (445 nm) and is of excitonic origin. The EL emission ap-

pears at the edges of the 30 mil opaque circular gold dot. At 300 K, the emission appears very bright to the eye. However, LED absolute efficiency measurements have not yet been completed.

3.2. ZnSe_{0.9}Te_{0.1} LEDs

The substitution of 10% Te for Se in ZnSe to form the alloy ZnSe_{0.9}Te_{0.1} reduces the band gap by approximately 300 meV ($E_g \sim 2.4$ eV). In addition, the index of refraction of ZnSe is less than that of the alloy. Thus ZnSe can serve as a cladding layer in optical confinement structures containing ZnSe_{0.9}Te_{0.1}. As a consequence, we have employed a ZnSe_{0.9}Te_{0.1} alloy in the active region of the DH LEDs shown in fig. 1. Two types of active regions were investigated: (1) a 1000 Å layer of ZnSe_{0.9}Te_{0.1}, and (2) a superlattice consisting of ten (100 Å) layers of ZnSe_{0.9}Te_{0.1} alternating with nine (100 Å) layers of ZnSe. Both types of DH LED structures exhibited I - V curves similar to that shown in fig. 2. In addition, the ZnSe_{0.9}Te_{0.1} LEDs emitted green light over a wide temperature range. This is illustrated by the EL spectra shown in fig. 4. At the top is shown the emission spectra at 300 K, which peaks in the green at ~ 2.38 eV. Spectra obtained at 200 and 100 K are also shown

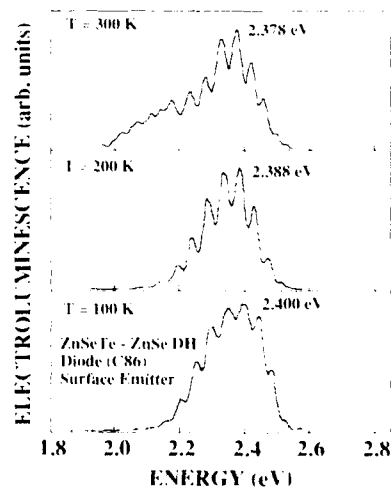


Fig. 4. Electroluminescence spectra obtained for ZnSe_{0.9}Te_{0.1} LED at 300, 200, and 100 K.

for comparison. Two features of the EL spectra are apparent: (1) The EL peak is relatively broad (FWHM > 200 meV) at all temperatures – much broader than the EL observed for the ZnSe LEDs, for example. This luminescence broadening is a known property of ZnSeTe alloys, which has been attributed to efficient decay of localized excitons self-trapped at Te sites that is triggered by alloy potential fluctuations [14,15]. It should be noted that, with this peak broadening, the integrated luminescence intensity at a given temperature is up to 100 times greater for the ZnSe_{0.9}Te_{0.1} LEDs compared to the ZnSe LEDs. (2) The EL peaks show regular periodic oscillations in intensity. This feature is due to interference effects which result from the fact that the EL comes from a thin (1000–2000 Å) confinement structure and thus has a relatively high degree of spatial coherence.

4. Summary and conclusions

Successful fabrication of ZnSe p–n junction light emitting diodes in which Li and Cl are used as p-type and n-type dopants, respectively, has been achieved. These p-on-n structures emit blue light at room temperature. Double heterostructures in which the active region is either a ZnSe_{0.9}Te_{0.1} layer or a ZnSe–ZnSe_{0.9}Te_{0.1} multilayer have also been successfully fabricated by molecular beam epitaxy. These LED structures emit bright green electroluminescence over a wide temperature range.

The question of Li diffusion throughout the LED structures is a potential problem that must be addressed. At NCSU, we intend to initiate a systematic set of annealing experiments together with SIMS measurements, to study this question.

Acknowledgements

This work was supported by the Defense Advanced Research Projects Agency (DARPA) through a University Research Initiative (URI) grant administered by the Office of Naval Research. Joe Matthews and M. Bennett provided assistance with some of the experiments.

References

- [1] T. Yasuda, I. Matsuishi and H. Kukimoto, *Appl. Phys. Letters* 52 (1988) 57.
- [2] K. Akimoto, T. Miyajima and Y. Mori, *Japan. J. Appl. Phys.* 38 (1989) L531.
- [3] M.A. Haase, H. Cheng, J.M. Depuydt and J.E. Potts, *J. Appl. Phys.* 67 (1990) 448.
- [4] R. Park, J. Mar and N. Salansky, *J. Appl. Phys.* 58 (1985) 1047.
- [5] T. Mitsuyu, K. Ohkawa and O. Yamazaki, *Appl. Phys. Letters* 49 (1986) 1348.
- [6] H. Cheng, J. Depuydt, J. Potts and T. Smith, *Appl. Phys. Letters* 52 (1987) 147.
- [7] J. DePuydt, T. Smith, J. Potts, H. Cheng and S. Mohapatra, *J. Crystal Growth* 86 (1988) 318.
- [8] K. Akimoto, T. Miyajima and Y. Mori, *Phys. Rev. B* 39 (1989) 3138.
- [9] J. DePuydt, M. Haase, H. Cheng and J. Potts, *Appl. Phys. Letters* 55 (1989) 1103.
- [10] J. Ren, K.A. Bowers, S. Hwang, J.W. Cook, Jr. and J.F. Schetzina, *J. Crystal Growth* 111 (1991) 772.
- [11] J.M. DePuydt, H. Cheng, M.A. Haase and J.E. Potts, *Mater. Res. Soc. Symp. Proc.* 161 (1990) 97.
- [12] L. Kassel, H.A. Abad, J.W. Garland, P.M. Raccach, J.E. Potts, M.A. Haase and H. Cheng, *Appl. Phys. Letters* 56 (1990) 42.
- [13] S.P. Kowalczyk, E.A. Kraut, M.R. Waldrop and R.W. Grant, *J. Vacuum Sci. Technol.* 21 (1982) 482.
- [14] D. Lee, A. Mysyrowies, A.V. Nurmikko and B.J. Fitzpatrick, *Phys. Rev. Letters* 14 (1987) 1475.
- [15] Q. Fu, D. Lee, A.V. Nurmikko, L.A. Kolodziejski and R.L. Gunshor, *Phys. Rev. B* 39 (1989) 3173.

Limited thickness epitaxy of semiconductors and Si MBE down to room temperature

D.J. Eaglesham, H.-J. Gossmann, M. Cerullo, L.N. Pfeiffer and K.W. West

AT&T Bell Laboratories, 600 Mountain Avenue, Murray Hill, New Jersey 07974, USA

Si MBE on smooth Si(100) surfaces is shown to occur at temperatures down to room temperature. We demonstrate that Si deposition at constant temperature becomes amorphous after growth of a limiting epitaxial thickness h_{epi} . At room temperature, h_{epi} is $\approx 10\text{--}30$ Å and increases rapidly at higher temperatures with a rate-dependent activation energy in the range 0.4–1.5 eV. Experiments suggest that neither impurity segregation nor defect build-up cause the ultimate nucleation of the amorphous phase, and the effect may be linked to surface roughening during growth at low temperatures. The possibility that some step arrangements may be sufficient to trigger nucleation of the amorphous phase is discussed. We show that dopants are active even at very low growth temperatures, so that limited-thickness epitaxy provides a solution to the “doping problem” of thermally-activated surface segregation of dopants in Si MBE. Our observations of Si/Si(111), Ge/Si(100), and GaAs/GaAs(100) suggest that limited-thickness epitaxy may occur in MBE deposition of almost any semiconductor.

According to the textbooks, there should be a minimum temperature T_{epi} for growth of a given material to occur epitaxially [1]. This critical temperature is attributed to the point at which, for a given growth rate, surface diffusion of incoming atoms ceases to be thermally activated. Below T_{epi} vacuum deposition should produce an amorphous overlayer, as opposed to a crystalline epitaxial film above T_{epi} . Here we present data to show that the notion of a T_{epi} is probably not appropriate in MBE growth of any semiconductor, even at a fixed growth rate. We demonstrate for the first time the existence of a limiting thickness h_{epi} for an epitaxial film, beyond which the amorphous phase nucleates. The epitaxial thickness h_{epi} follows an exponential temperature dependence, which has previously been mistaken for an abrupt cut-off in epitaxy.

We begin by studying Si MBE on the Si(100) surface, perhaps one of the most-studied epitaxial systems. The minimum epitaxial temperature T_{epi} is particularly important in Si MBE, since thermally-activated diffusion leads to very marked segregation of electrical dopants to the Si surface. This limits both the maximum dopant concentrations achievable and the sharpness of dopant pro-

files [2–5]; this is known as the “doping problem”. A large variety of techniques have previously been used to determine the epitaxial temperature in Si MBE; surprisingly, however, no clear consensus has emerged for T_{epi} , with measured values varying from 300°C to room temperature [6–8]. We shall show that these discrepancies are attributable to the existence of an amorphous-crystalline transition in a film growing at fixed temperature. This allows us to control Si epitaxy (of limited thicknesses) down to room temperature.

The epitaxy of Si at low temperatures was studied using cross-section and plan-view transmission electron microscopy (TEM) to study Si layers deposited under a variety of typical MBE conditions. Several different MBE chambers were used with pressures typically 10^{-10} to 10^{-9} Torr during growth. Deposition rates between 10 and 0.05 Å s^{-1} were studied using electron guns and Knudsen cells as the Si source; dopants were deposited using either K-cells or heavily doped Si E-guns. The surface was prepared by growth of a buffer at 550–700°C on nominally (100) oriented Si substrates from which a protective oxide had been sputtered or thermally desorbed. In order to clarify the interface between the high-temperature

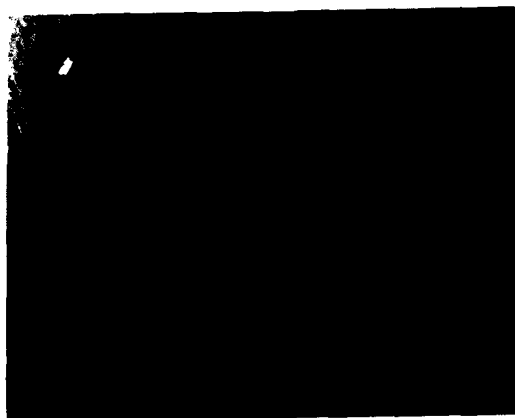


Fig. 1. Si film MBE-grown at $\approx 190^\circ\text{C}$ on Si(100) following growth of a 3 monolayer thick Ge marker layer at 580°C , showing a transition from crystalline epitaxy to amorphous deposition beyond the epitaxial thickness h_{epi} . Bright field image of $\{011\}$ cross-section, at the (400) Bragg position. Control samples show that this phenomenon is independent of the Ge marker layer.

buffer and the low-temperature epilayer an additional marker layer of 1–3 monolayers of Ge was frequently deposited (at high temperature) on this buffer. Since direct measurement of substrate temperature is difficult below $\approx 500^\circ\text{C}$, thermocouple measurements of the substrate holder temperature were calibrated by extrapolation from pyrometer measurements above 500°C ; while relative temperatures in a given chamber can easily be

measured to within $\pm 5^\circ\text{C}$, absolute values reported here are probably accurate only to within $\approx \pm 25^\circ\text{C}$. Substrate temperatures were held stable to within $\pm 5^\circ\text{C}$ throughout the low-temperature growth stage.

Fig. 1 shows a typical Si layer deposited at $\approx 190^\circ\text{C}$ on a Ge marker layer. Although the temperature was held constant during the low-temperature growth, we clearly see epitaxy over an initial thickness of $\approx 330 \text{ \AA}$, followed by nucleation of amorphous material. In fact, at all temperatures between 300 and 50°C , we observe epitaxy up to some finite thickness, which we call the epitaxial thickness h_{epi} ; beyond h_{epi} , the deposited film remains amorphous. The breakdown in crystallinity at h_{epi} is thus a property of Si MBE at constant temperature. This observation implies that, at least for Si homoepitaxy on Si(100), the concept of a minimum temperature for epitaxial growth is wholly misleading.

The epitaxial thickness observed prior to nucleation of the amorphous phase was observed to be strongly temperature-dependent, suggesting a thermally activated process. A sequence of layers was grown under otherwise identical conditions (900°C anneal to desorb a Shiraki oxide, 580°C Si buffer grown at 0.7 \AA s^{-1} with an 8 \AA thick 580°C Ge marker grown at 0.1 \AA s^{-1} , both from E-gun sources, followed by deposition of 1500 \AA of Si at 0.7 \AA s^{-1} at low temperature) to determine the temperature dependence of h_{epi} . Fig. 2

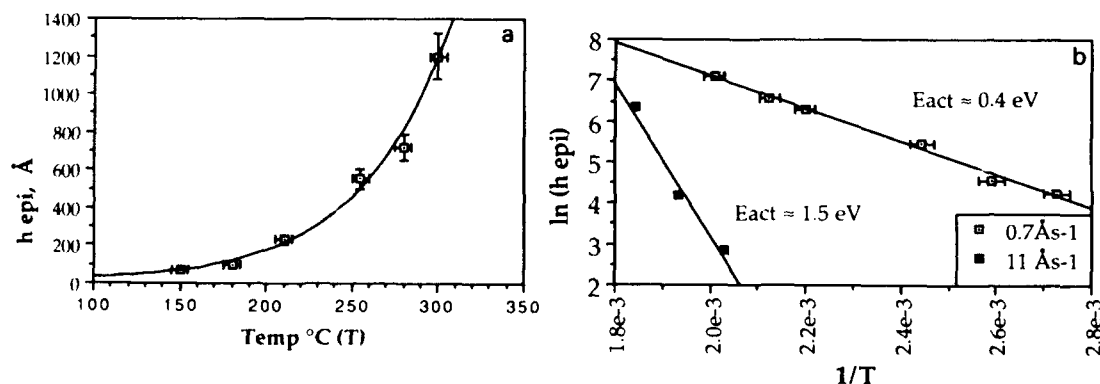


Fig. 2. Temperature dependence of the limiting epitaxial thickness h_{epi} (a), and plotted in Arrhenius form at growth rates of both 0.7 and 11 \AA s^{-1} (b). The very steep increase near 200°C in (a) explains why previous reports of an epitaxial temperature were usually close to this value. The activation energy suggested by the Arrhenius plot is 0.4 eV at 0.7 \AA s^{-1} and 1.5 eV at 11 \AA s^{-1} .

shows the result along with an Arrhenius plot of $\ln(h_{\text{epi}})$ against $1/T$. h_{epi} does indeed appear to increase in a thermally activated exponential, with a activation energy E_{act} of 0.4 ± 0.05 eV. Surprisingly, increasing the deposition rate of the low-temperature layer to 11 \AA s^{-1} produces a large increase in the apparent activation energy for h_{epi} , as shown in fig. 2b.

For amorphous growth to take place after growth of h_{epi} , the surface must be evolving either structurally or chemically. While surface segregation of impurities may be linked to amorphous deposition (particularly H_2 [9]), we have carried out a number of experiments which suggest that the phenomenon is independent of impurities [10]. We conclude that during growth at very low temperatures the (100) surface evolves structurally, rather than chemically: surface roughening is the most obvious explanation, although it is also possible that the step structure (rather than density) changes, and a change in the local surface reconstruction could also be responsible. RHEED oscillation studies of Si growth [11,12] show that at temperatures and growth rates similar to those reported here the (100) surface roughness will indeed evolve over thicknesses of the order 50–500 Å. Annealing to 500°C following growth of a thickness just less than h_{epi} allows us to deposit a further epilayer, up to $2 \times h_{\text{epi}}$ (so that we can grow 1000 Å at 200°C using 4 intermediate flashes to 500°C): thus the evolution of the surface during low temperature growth must be reversible.

Two previous studies have speculated on the possibility of a limiting h_{epi} . In order to explain the inconsistency between observations of RHEED oscillations on Si(100) at room temperature [12,11] and measurements made on thick films, Aarts and Larsen [11] postulated a breakdown with increasing thickness at constant temperature, but did not provide a model for the phenomenon. More recently, Jorke et al. [7] proposed a model to explain their observed T_{epi} based on the continuous build-up of disorder in the growing film. As they noted, a limiting h_{epi} at constant temperature is implicit in their model: thus it is tempting to believe that the actual observation of an h_{epi} provides some confirmation of this model. However, other predictions of their model do not appear to tally with

our experimental observations, and in particular constant temperature films (fig. 2) do not show the linear increase in the amorphous fraction given by the Jorke model. Examination of the defect microstructure suggests, on the contrary, that the amorphous phase appears fairly abruptly after extended growth of material with a low defect density. In contrast to the earlier model, we would therefore identify a limiting thickness as an intrinsic feature of Si MBE at low temperatures, as opposed to a consequence of the continuous build-up of crystal defects. The most probable conclusion is that the surface roughness built up during the early stages of growth plays some central role in nucleating the amorphous phase. The growth of a finite h_{epi} may thus be viewed as a manifestation of the nucleation barrier to forming the amorphous phase on a perfectly flat crystalline substrate.

This picture of limited-thickness epitaxy is not restricted to Si(100), and suggests that the effect may be general in low-temperature growth. We have now carried out similar experiments to those described above for MBE of Si/Si(111), Ge/Si(100) [13] and GaAs on GaAs(100) [14], at lower temperatures than those normally reported for epitaxy. Fig. 3 shows layers of Si/Si(111) (with Ge marker) and GaAs/GaAs(100) (with AlAs marker) grown at 350 and 240°C , respectively. All of the systems studied to date show limited-thickness epitaxy in the low-temperature regime, although with some significant differences. Ge/Si(100) shows a crystalline-amorphous transition even at temperatures where earlier RHEED experiments showed Ge/Ge epitaxy occurring to apparently arbitrary thickness, suggesting that h_{epi} is strain-dependent (possibly through the strain-dependence of the free energy of the crystalline phase). For Si/Si(111) the temperature-dependence of h_{epi} is exceptionally steep, so that limited-thickness epitaxy is only observable over a very narrow temperature range. As can be seen in fig. 3, the roughness of the amorphous-crystalline interface produced during limited-thickness epitaxy on (111) is considerably greater ($\approx \frac{1}{2}h_{\text{epi}}$) than that in Si/Si(100) ($\approx \frac{1}{4}h_{\text{epi}}$) or GaAs/GaAs(100) ($\approx \frac{1}{4}h_{\text{epi}}$). In GaAs, we also observe a very strong dependence on the Ga/As flux ratio,

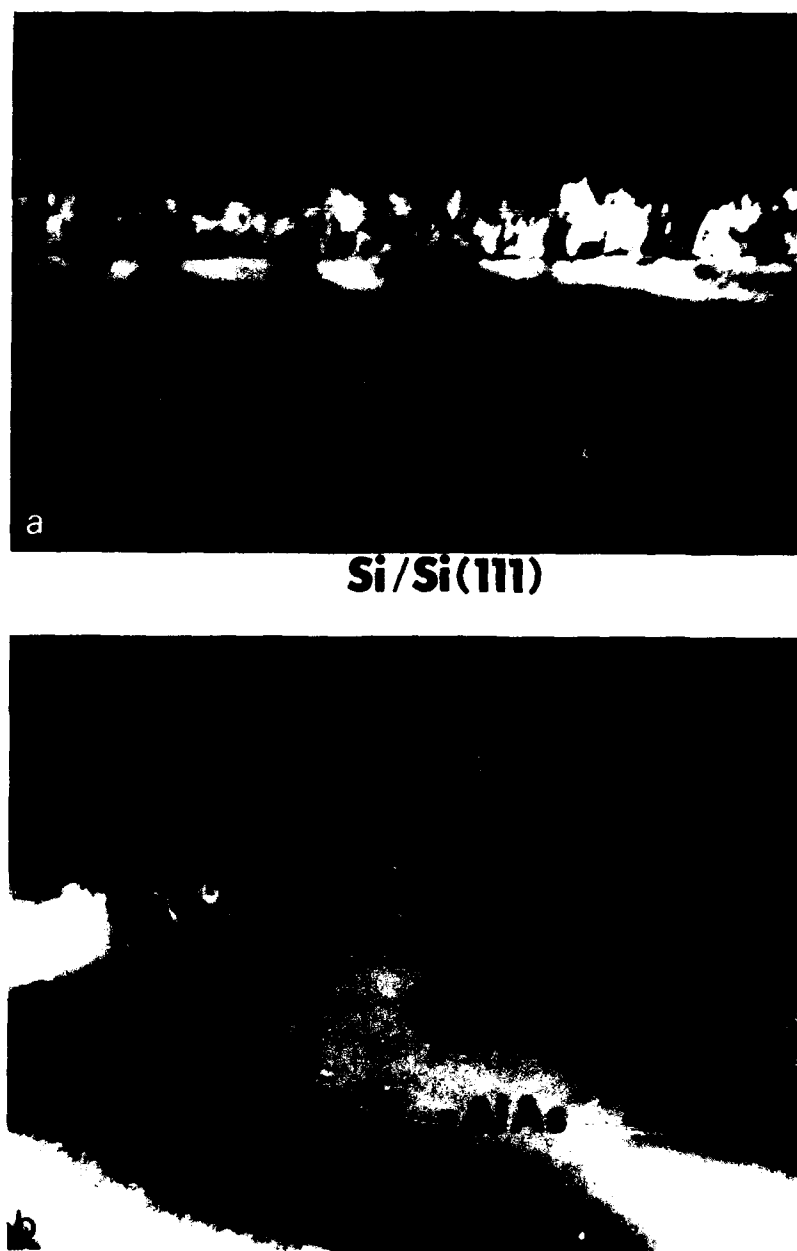


Fig. 3. The epitaxial thickness effect (a) in Si/Si(111) (MBE grown at 350°C on a Ge marker layer) and (b) in GaAs/GaAs(100) (240°C, AlAs marker).

with excess Ga producing a much larger h_{epi} , and an abrupt drop in the epitaxial thickness at $\approx 210^\circ\text{C}$ [14]. These results suggest that limited-

thickness epitaxy may be universal in semiconductor MBE. In addition, we also note that previous studies of plasma-enhanced CVD of Si(100) at

temperatures near 200°C show features consistent with limited-thickness behaviour [15].

Finally, we address the technological significance of our observations of Si MBE. Jorke et al. [17] recently described experiments on doping (100) Si at temperatures below 300°C and found activation levels of only $\approx 20\%$ for Sb incorporation at the 10^{18} cm^{-3} level: thus low temperature Si epitaxy appears to be of purely academic interest. However, we have carried out a series of experiments on doping low temperature films with both Sb and B, generally using temperatures as high as 250°C to attain sufficiently large epilayer thicknesses [18,19]. For both dopants, δ -doped layers (with a low-temperature epitaxial Si cap deposited on a monolayer of dopants established at high temperature) show no precipitation and less than 10 Å segregation in TEM, implying incorporation to the 10^{21} cm^{-3} level. Furthermore, both the δ -doped layers (for both Sb and B) and continuous films grown with lower doping levels ($\approx 10^{18}$ to 10^{20} cm^{-3}) show 100% electrical activation, within experimental error. (This implies an upper limit of $\approx 10^{16} \text{ m}^{-3}$ defect states, showing that the material has a low density of point defects as well as extended defects.) Thus, in obtaining a more complete understanding of low-temperature growth we have provided a solution to what is known as the "doping problem" in Si MBE.

In conclusion, we have demonstrated experimentally that there is an epitaxial thickness h_{epi} in low-temperature semiconductor MBE, as opposed to an epitaxial temperature. The breakdown of epitaxy is not due to segregation, but appears to arise from roughening of the surface during growth below some critical temperature. h_{epi} follows an Arrhenius curve, with an activation energy of 0.4 eV. Annealing to 500°C allows us to repeat the growth sequence to 2 (or n) $\times h_{\text{epi}}$. Low temperature growth solves the doping problem in Si MBE, giving activation levels of $\approx 100\%$ at dopant con-

centrations in the 10^{21} cm^{-3} regime, and 10 Å abruptness.

We would like to thank Stuart Wolff, Randy Headrick and Len Feldman for a number of useful discussions.

References

- [1] J.A. Venables, in: *Epitaxial Growth*, Part B, Ed. J.W. Matthews (Academic Press, New York, 1975) p. 389.
- [2] J.C. Bean, *Appl. Phys. Letters* 33 (1978) 654.
- [3] S.S. Iyer, R.A.A. Kubiak and E.C.H. Parker, in: *Silicon Molecular Beam Epitaxy*, Vol. I, Eds. E. Kasper and J.C. Bean (CRC Press, Boca Raton, FL, 1988) p. 221.
- [4] S.A. Barnett and J.E. Greene, *Surface Sci.* 151 (1985) 67.
- [5] H. Jorke, *Surface Sci.* 193 (1988) 569.
- [6] H.-J. Gossmann and L.C. Feldman, *Appl. Phys.* A38 (1985) 171.
- [7] H. Jorke, H.-J. Herzog and H. Kibbel, *Phys. Rev.* B40 (1989) 2005.
- [8] F. Jona, *Appl. Phys. Letters* 9 (1966) 235.
- [9] S.H. Wolff, S. Wagner, J.C. Bean, R. Hull and J.M. Gibson, *Appl. Phys. Letters* 55 (1989) 2017; see also N. Shibita, K. Fukuda, H. Ohtoshi, J. Hanna, S. Oda and I. Shimitsu, *Mater. Res. Soc. Symp. Proc.* 95 (1987) 225, for a link between H_2 and amorphous deposition in CVD.
- [10] For details, see D.J. Eaglesham, H.-J. Gossmann and M. Cerullo, *Phys. Rev. Letters*, in press.
- [11] J. Aarts and P.K. Larsen, in: *RHEED and Reflection Electron Imaging of Surfaces*, Eds. P.K. Larsen and P.J. Dobson (Plenum, New York, 1988) p. 449.
- [12] T. Sakamoto, N.J. Kawai, T. Nakagawa, K. Ohto and T. Kojima, *Appl. Phys. Letters* 47 (1985) 617.
- [13] D.J. Eaglesham and M. Cerullo, to be published.
- [14] D.J. Eaglesham, L.N. Pfeiffer, K. West and D. Dykaar, to be published.
- [15] J. Vanhellemont, K. Baert, J. Symons, J. Nijs and R. Mertens, in: *Electron Microscopy 1988*, *Inst. Phys. Conf. Ser.* 93, Eds. P.J. Goodhew and H.G. Dickinson (Inst. Phys., London-Bristol, 1988) Vol. 2, p. 95.
- [16] H. Jorke, H. Kibbel, F. Schäffler, A. Casel, H.-J. Herzog and E. Kasper, *Appl. Phys. Letters* 54 (1989) 819.
- [17] H.-J. Gossmann, E.F. Schubert, D.J. Eaglesham and M. Cerullo, to be published.
- [18] R.L. Headrick, B.E. Weir, A.F.J. Levi, D.J. Eaglesham and L.C. Feldman, to be published.

Buried, ordered structures: boron in Si(111) and Si(100)

R.L. Headrick, B.E. Weir, A.F.J. Levi, D.J. Eaglesham and L.C. Feldman

AT&T Bell Laboratories, Murray Hill, New Jersey 07974, USA

Two-dimensional, metastable, ordered structures have been prepared by deposition atop unique surface reconstructions. This discovery that surface superlattice structures can be buried in crystalline semiconductors suggests possibilities for ordered doping and ordered alloy structures with new electronic properties. In this paper we summarize our recent results in forming ordered structures of boron on Si(100) and Si(111) and the preservation of these structures under subsequent Si deposition.

The first realization of preserving a surface reconstruction under a deposited layer was in the a-Si/Si(111) system where the complex 7×7 structure remained at the interface formed by clean Si(111)- 7×7 and subsequent deposition of amorphous silicon (a-Si) [1]. The realization that ordered surface structures can be preserved at a buried interface suggests possibilities for new metastable materials and interesting two dimensional phenomena. In this paper we describe our recent observations of buried structures in systems consisting of ordered boron adsorbates on $\langle 111 \rangle$ -oriented Si surfaces [2–4]. This atomic configuration behaves electrically as a dopant sheet of atoms with high electrical activity. Similar results have recently been reported by Akimoto et al. [5] and Tatsumi et al. [6]. In addition, we report new results of buried ordered boron layers in $\langle 100 \rangle$ -oriented silicon.

Samples were prepared in a molecular beam epitaxy chamber equipped with an electron gun evaporator to deposit silicon, a quartz-crystal thickness monitor, and a Knudsen cell to deposit boron from HBO_2 . Oriented $\langle 111 \rangle$ and $\langle 100 \rangle$ Si substrates were prepared by chemical growth of a thin protective oxide layer, and then transferred into the vacuum chamber. Once in the vacuum chamber, the oxide was desorbed from the sample and boron was deposited onto the surface up to a coverage of between zero and one monolayer. After cooling to room temperature, low energy

electron diffraction (LEED) and Auger electron spectroscopy measurements were performed. Finally, the surface was capped with silicon at various temperatures. All other measurements, including grazing incidence X-ray diffraction, ion scattering/channeling, transmission electron microscopy, and low temperature ($T = 4.2$ K) Hall effect measurements were done after removing the capped samples from the vacuum system.

Glancing angle X-ray diffraction, scanning tunneling microscopy and first-principles theoretical calculations have established the structure of the Si(111)-B- $\sqrt{3} \times \sqrt{3}$ surface as boron in a subsurface site, arranged in a $\sqrt{3} \times \sqrt{3}$ configuration [3,7]. Fig. 1 shows this site and compared it to the more common $\sqrt{3} \times \sqrt{3}$ configuration (T_4 site) for Ga and other adsorbates. The stability of boron in the subsurface site relative to the T_4 adatom site is related to relief of subsurface strain by the mechanism of substituting a smaller boron atom for silicon [3].

The fact that this ordered structure is maintained upon room temperature deposition of a-Si is shown in fig. 2, which compares the glancing angle X-ray diffraction of both the Ga and B structures. Retention of the strong third order diffraction intensity in the boron case clearly indicates that the boron retains its $\sqrt{3} \times \sqrt{3}$ structure while Ga becomes disordered. Detailed Auger measurements show that the Ga surface segregates during Si deposition at room temperature, while

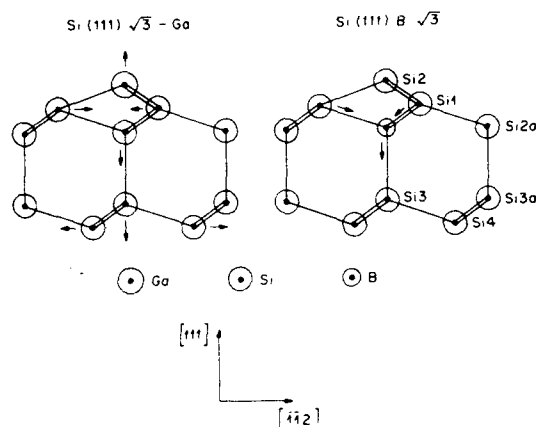


Fig. 1. Model of the Si(111)-Ga- $\sqrt{3}$ structure and proposed structure for Si(111)-B- $\sqrt{3}$ (right). Arrows indicate the direction of displacements from the ideal tetrahedrally bonded configuration.

boron remains in a buried, ordered in configuration. Such segregation behavior is consistent with the buried site for boron and an atop site for Ga.

A desired configuration would correspond to epitaxial Si atop the ordered boron configuration.

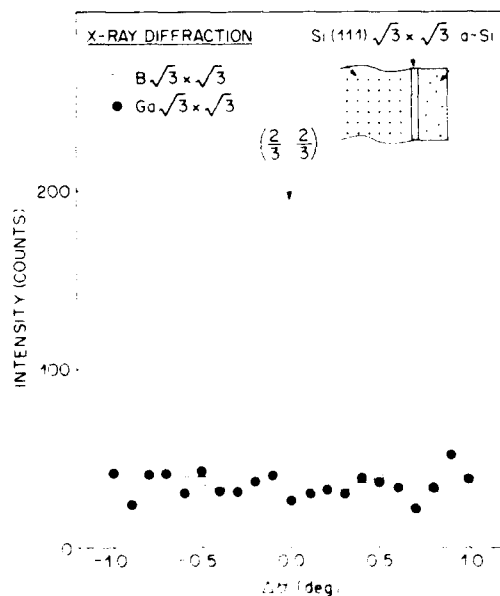


Fig. 2. Rocking scan through the $(\frac{2}{3}, \frac{2}{3})$ surface X-ray diffraction rod for buried boron and gallium surface structures on Si(111).

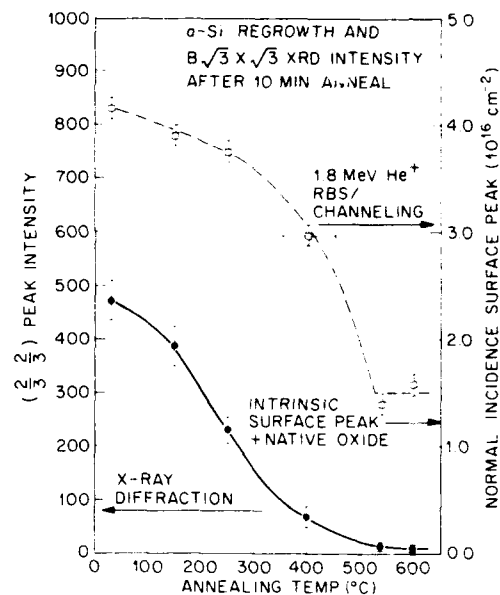


Fig. 3. Dependence of the $(\frac{2}{3}, \frac{2}{3})$ surface X-ray diffraction integrated intensity as a function of annealing temperature for the boron $\sqrt{3} \times \sqrt{3}$ surface structure originally covered with a-Si ($\sim 100 \text{ \AA}$) (filled in circles). Also shown is the temperature dependence of normal incidence channeling for the Si overlayer indicating complete epitaxial regrowth at $\sim 500^\circ\text{C}$.

Two possible methods of achieving this structure are: (1) epitaxial regrowth of the amorphous layer or (2) high temperature deposition of Si for epitaxial growth. Neither method works ideally in the Si(111)-B- $\sqrt{3} \times \sqrt{3}$ case. Fig. 3 shows the decrease of the $\sqrt{3} \times \sqrt{3}$ intensity with regrowth temperature. Epitaxy in the Si overgrown layer is indicated by channeling measurements which indicate crystallization with increasing temperature. The X-ray intensity corresponding to the $\sqrt{3}$ structure deteriorates with regrowth, indicating a disordering of the boron structure as epitaxial regrowth occurs. High temperature ($\sim 550^\circ\text{C}$) deposition of Si also results in boron disordering and surface segregation, indicating that the metastable structure associated with the ordered, δ -layer is not stable at Si epitaxy temperatures. A separate series of measurements indicated that the lowest temperature for Si(111) epitaxy is $\sim 400^\circ\text{C}$, however even at this low temperature some boron disordering occurs.

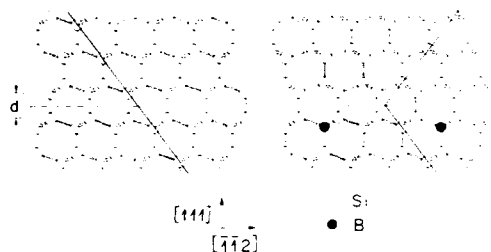


Fig. 4. Ball and stick models for the film orientation and interface structure for 0 (left) and 0.33 ML (right) boron coverages. The $\sqrt{3} \times \sqrt{3}$ reconstruction of the interface is introduced because boron occupies substitutional sites, occupying every third site in a single monolayer at the interface.

An interesting phenomenon is observed for Si epitaxial growth on the $B\sqrt{3}$ structure at low temperatures. Evidently the initial layers of Si epitaxial growth are strongly influenced by the Si-B interaction, giving rise to a 180° rotated configuration of the grown layer of Si (fig. 4). The existence of this layer is most strikingly demon-

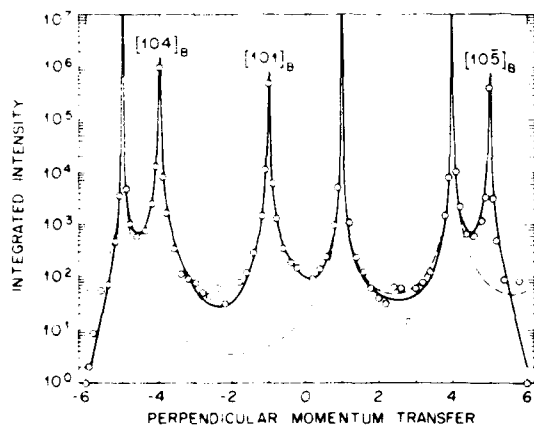


Fig. 5. (10) rodscan for a 350 Å rotated Si film on Si(111). A four-circle diffractometer and $\text{Cu K}\alpha$ radiation was used for the measurement. The diffraction profiles are indexed relative to a hexagonal unit cell appropriate for the Si(111) surface with in-plane lattice parameters $a = b = 3.84$ Å and out-of-plane lattice parameter $c = 9.41$ Å. The hexagonal indices are derived from cubic indices by $[10]_{\text{hex}} = \frac{1}{2}([422]_{\text{cub}} + [111]_{\text{cub}})$. Rotated reflections are indexed by replacing l by $-l$. Structure factors at $-l$ were obtained by the symmetry relation $|10\bar{l}| = |01l|$. The dashed line is the calculated intensity from a "bulk-like" structure, the full line is for a 350 Å rotated film atop a bulk crystal.

strated in fig. 5 which shows glancing X-ray diffraction intensity from a 350 Å Si layer grown at $\sim 400^\circ\text{C}$ on $\text{Si}(111)-B\sqrt{3}$ at and then further annealed.

The X-ray crystal truncation rod method using integer h and k but continuous l , originally developed for determination of surface structures, is used to identify this thin film structure. A total of 66 data points in the form of structure factors $F_{hk}(l)$ were obtained by numerical integration of rocking curves and corrected for the Lorentz factor ($\sin 2\theta$) and active area ($\sin 2\theta$). We compared (10/) crystal truncation rod data for a 350 Å silicon film grown at 400°C and annealed at 1000°C for 2 h to structure factors calculated in the kinematic approximation (fig. 5). The film is rotated 180° with respect to the substrate about the normal (111) axis, forming a single twin at the interface. The dashed line is the square of $F_{\text{Si}}(l)$, the structure factor $F_{10}(l)$ for the semi-infinite silicon substrate with double-layer termination. There are three prominent peaks that do not correspond to the substrate. The new peaks are accounted for by adding the 350 Å thick rotated film into the calculated structure factor. The solid line shows the results of a calculation with a 233 monolayer, rotated layer. The optimum interface separation was $d = 2.35 \pm 0.09$ Å, i.e. the same as the bulk layer spacing. This shows that the simple twin stacking sequence is the correct interface structure. Transmission electron microscopy confirms this assignment showing that the layer is at least 90% crystallographically pure [8].

We have recently reported a new boron-induced (2×1) surface reconstruction at $1/2$ monolayer boron coverage on $\langle 100 \rangle$ oriented silicon [9]. To our knowledge this reconstruction has not been reported previously, presumably because of the difficulty in distinguishing the $\text{Si}(100)-(2 \times 1)$ clean surface from the (2×1) boron structure. In sharp contrast to the results on $\langle 111 \rangle$ -oriented silicon discussed above, we find that this reconstruction can be preserved within high-quality, crystalline silicon by low-temperature epitaxial overgrowth at $\approx 300^\circ\text{C}$. For boron coverages at and below the completion of the (2×1) surface phase and silicon overlayer growth temperatures of 300°C and above, 100% of the boron is electrically active.

Fig. 6 shows grazing incidence X-ray diffraction azimuthal scans through the $(\frac{1}{2}0)$ surface reflections for two ordered interfaces. The open squares are for a 100 Å cap grown at room temperature, and the filled circles are for a 100 Å cap grown at 300°C. The boron coverage is 1/2 monolayer in both cases. Comparison of the data demonstrates that the reconstruction capped at 30°C gives a factor of two smaller integrated intensity in the diffraction signal than the reconstruction capped at room temperature. Boron segregation studies using Auger electron spectroscopy for films grown at 300°C reveal a broadening of the ideal monolayer distribution by ≈ 5 Å. This is consistent with the observation that $\approx 50\%$ of the boron remains in the ordered layer.

Cross-sectional transmission electron microscopy and ion channeling studies show that the 100

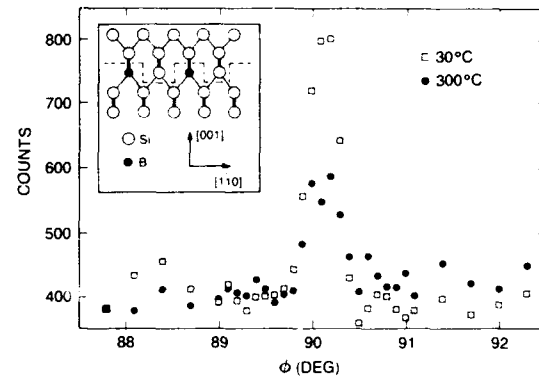


Fig. 6. Comparison of grazing incidence X-ray diffraction azimuthal scans through the $(\frac{1}{2}0)$ diffraction spot for Si(100)-(2 × 1) boron buried structures capped by growth at room temperature, and at $\approx 300^\circ\text{C}$. The boron coverage was 1/2 monolayer in both cases and the silicon growth rate was 0.1 Å/s. The inset shows a proposed model of the (2 × 1) structure.

Table 1
4.2 K Hall effect results for Si(111)/a-Si interface reconstructions

Reconstruction		a-Si thickness (Å)	T_{anneal} (°C)	Boron coverage (10^{14} cm^{-2})		Carrier density (10^{14} cm^{-2})	Mobility ($\text{cm}^2\text{ V}^{-1}\text{ s}^{-1}$)
Initial	Final			SIMS	NRA		
$\sqrt{3}$	$\sqrt{3}$	100	90	3.4	3.5	2.2	36.6
$\sqrt{3}$	$\sqrt{3}$	60	90	2.6	2.7	1.7	30.5
$\sqrt{3}$	$\sqrt{3}$	50	90	3.1	3.4	1.8	25.9
$\sqrt{3}$	3D	100	700	3.4	3.5	3.2	47.9
$\sqrt{3}$	Oxide	0	90	3.1	3.4	0	-
$\sqrt{3}$	3D	60	500	2.6	2.7	2.4	31.9
7×7	7×7	50	90	0.1	-	0	-

Table 2

Film thickness (Å)	T_{growth} (°C)	T_{anneal} (°C)	Anneal time (min)	Boron coverage (ML)	Carrier density (ML)	Mobility ($\text{cm}^2\text{ V}^{-1}\text{ s}^{-1}$)
100	300	90	20	0.44	0.45	21
100	30	90	20	0.50	0.24	1
100	30	90	20	0.50	0.18	3
100	30	90 ^{a1}	≈ 3000	0.47	0.12	19
100	30	400	1	0.11	0.07	14
100	30	400	1	0.31	0.18	21
100	30	400	1	0.51	0.32	16
100	30	400	1	0.83	0.33	18
100	30	400	60	0.50	0.35	17

^{a1} Boiled in distilled water.

Å thick films grown at 300°C are high quality crystalline silicon indistinguishable from bulk silicon, while room temperature growth results in an amorphous layer. Channeling measurements (in $\langle 100 \rangle$ normal incidence and $\langle 111 \rangle$ off-normal incidence) using the $^{11}\text{B}(p, \alpha)^8\text{Be}$ nuclear reaction to detect boron, show a reduced yield compared to random incidence after silicon overgrowth at 300°C, indicating that boron occupies a substitutional site buried within crystalline material.

We now discuss the electrical activity of boron doped silicon structures prepared via the (2×1) and $(\sqrt{3} \times \sqrt{3})$ reconstruction. Tables 1 and 2 gives carrier densities and mobilities from low temperature ($T = 4.2$ K) Hall effect measurements for silicon overlayers grown at 30 and 300°C, and annealed at various temperatures. There was no carrier freeze-out and no significant magnetoresistance for any of the samples measured. Units of monolayers are used for clarity, where one monolayer is defined as $6.8 \times 10^{14} \text{ cm}^{-2}$ for Si(100) and $7.8 \times 10^{14} \text{ cm}^{-2}$ for Si(111). The optimum conditions for producing electrically active ordered doping layers in epitaxial silicon (100) are a boron coverage of 1/2 monolayer and a silicon growth temperature of 300°C. Under these conditions 100% electrical activity and a mobility of $21 \text{ cm}^2 \text{ V}^{-1} \text{ s}^{-1}$ are obtained. This mobility is comparable to that obtained for very high boron concentrations in bulk silicon [10].

Conclusions: We have shown that two-dimensional ordered layers of boron can be preserved at

the Si(111) and Si(100) surfaces. In the Si(100) case epitaxial Si can be grown atop the ordered structure. All systems show a high p-type electrical activity, between 50% and 100% electrically active.

References

- [1] J.M. Gibson, H.-J. Gossmann, J.C. Bean, R.T. Tung and L.C. Feldman, *Phys. Rev. Letters* 56 (1986) 355; H.-J. Gossmann, L.C. Feldman and W.M. Gibson, *Phys. Rev. Letters* 53 (1984) 294; *Surface Sci.* 155 (1985) 413; H.-J. Gossmann and L.C. Feldman, *Phys. Rev. B* 32 (1985) 6.
- [2] R.L. Headrick, L.C. Feldman and I.K. Robinson, *Appl. Phys. Letters* 55 (1989) 442.
- [3] R.L. Headrick, I.K. Robinson, E. Vlieg and L.C. Feldman, *Phys. Rev. Letters* 63 (1989) 1253.
- [4] R.L. Headrick, A.F.J. Levi, H. Luftman, J. Kovalchick and L.C. Feldman, *Phys. Rev. B*, to be published.
- [5] K. Akimoto, J. Mizuki, I. Hirose, T. Tatsumi, H. Hirayama, N. Aizaki and J. Matsui, in: *Extended Abstracts 19th Conf. on Solid State Devices and Materials* (Business Center for Academic Societies, Tokyo, 1987) p. 463.
- [6] T. Tatsumi, I. Hirose, T. Nino, H. Hirayama and J. Mizuki, *Appl. Phys. Letters*, 57 (1990) 73.
- [7] P. Bedrossian, R.D. Meade, K. Mortensen, D.M. Chen and J.A. Golovchenko, *Phys. Rev. Letters* 63 (1989) 1257; I.-W. Lyo, E. Kaxiras and Ph. Avouris, *Phys. Rev. Letters* 63 (1989) 1261.
- [8] R.L. Headrick, B.E. Weir, D.J. Eaglesham and L.C. Feldman, *Phys. Rev. Letters* 65 (1990) 1128.
- [9] R.L. Headrick, B.E. Weir, A.F.J. Levi, D.J. Eaglesham and L.C. Feldman, *Appl. Phys. Letters*, to be published.
- [10] G. Masetti, M. Severi and S. Solmi, *IEEE Trans. Electron Devices* ED-30 (1983) 764.

Redistribution of delta-doped Sb in Si

S.J. Fukatsu, S. Kubo, Y. Shiraki and R. Ito

Research Center for Advanced Science and Technology, The University of Tokyo, 4-6-1 Komaba, Meguro-ku, Tokyo 153, Japan

Redistribution of delta-doped Sb in Si with various areal concentrations upon post-growth annealing was investigated by means of secondary ion mass spectrometry (SIMS). The diffusion profiles are dependent on the initial doping density and non-Gaussian profiles were obtained except for the lowest-doped sample. The doped layers are stable up to 550 °C, regardless of the doping density. For treatment at temperatures higher than 700 °C, the upper limit of the doping density was found to be set at 0.01 monolayer (ML). It was also found that there is no crystalline quality difference affecting the diffusion of Sb between the recrystallized and the MBE-grown layers.

1. Introduction

There has been a growing demand for defining sharp interfaces between the regions of different doping levels to an atomic scale. Delta-doping provides the way to confine dopants to within a single atomic plane. In such systems, even small spreading of atoms out of the initial location affects the desired properties. A thermal stability study is of primary significance, since the delta-doped structures often encounter high temperature environments during their growth and processing. Aside from the study of the effect of growth temperatures on the redistribution of the delta-doped layers in Si [1], we conducted a systematic investigation of profile changes during the course of post-growth annealing.

In this paper, we report on the diffusion measurements on the delta-doped Sb in Si with varying areal concentrations. We demonstrate the evolution of unusual diffusion profiles which are characteristic to the delta-doped impurities. The structural stability of delta-doped layers is discussed, where we set the upper limit on the doping level for practical use.

2. Experimental

The samples used in this study were grown on Si(100) substrates in Si molecular beam epitaxy

Table 1
Sample characteristics

Sample	Doping density ^{a)} (ML)	Peak Sb concentration ^{b)} (cm ⁻³)	Overlayer thickness (nm)	Growth mode of buffer layer
a	0.0023	1.8×10^{17}	80	MBE
b	0.03	2.5×10^{18}	80	MBE
c	0.06	4.5×10^{18}	80	MBE
d	0.11	1.3×10^{19}	120	MBE
e	0.14	1.5×10^{19}	120	SPE
f	1.0	1.2×10^{20}	80	MBE

^{a)} 1 ML = 6.78×10^{14} cm⁻².

^{b)} As determined from SIMS.

(MBE) systems [2]. Sample characteristics are listed in table 1. The required amount of Sb was deposited at around 100 °C. The capping layers were grown at 550 °C by solid phase epitaxy (SPE). The details of the sample preparation were presented elsewhere [2]. The samples were furnace-annealed at temperatures T_a of 550 °C up to 950 °C for 60 min, in a flowing 94-6 N₂:H₂ ambient.

3. Results

Fig. 1 shows the atomic distributions of Sb in sample c with a moderate Sb concentration. The full width at half maximum (FWHM) of the as-grown profile is comparable to the resolution limit

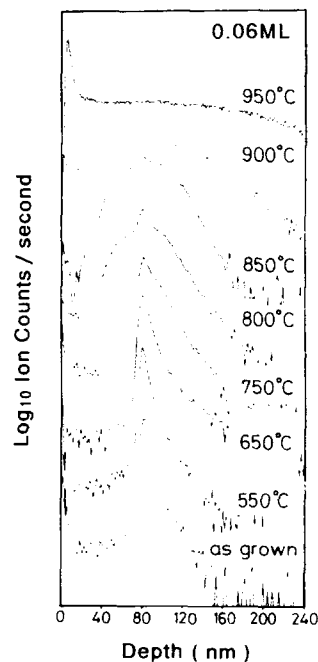


Fig. 1. SIMS profiles of Sb after isochronal annealing in sample c (0.06 ML). Anneal temperature is shown at the foot of the individual profile. Kink develops at around 710°C. Segregation at the SiO₂/Si interface is seen in the uppermost profile.

of the profiling. Above 650°C, significant spreading was observed and a pronounced kink was developed. The profile is a superposition of two components, one pinned at the original spike while the other (shoulders) extended into the neighboring regions. Concomitantly, preferential movement of Sb atoms toward the surface sets in, leading to their pile-up at the SiO₂/Si interface. The situation is more pronounced in the profile at $T_a = 950^\circ\text{C}$. Profile changes in samples b, d and e are qualitatively the same, although the kink developing temperatures are slightly different. On the other hand, the spike persists even at 950°C with a 20 nm wide peak in sample f with 1 ML Sb (fig. 2). The lowest-doped sample a, in contrast, shows only small spreading at the spike, followed by surface segregation at temperatures of up to 950°C, as shown in fig. 3.

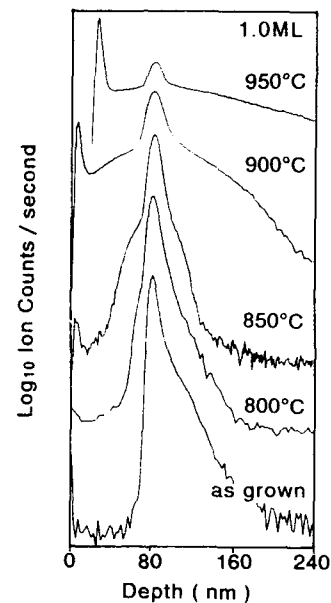


Fig. 2. Diffusion profiles of Sb in sample f (1.0 ML). The kink appears at $750 < T_a < 800^\circ\text{C}$. The remnant of the doping spike, 20 nm in width, is still observed at 950°C. Shoulder shapes are obliterated by and superposed on the segregation profile at the surface side of the spike.

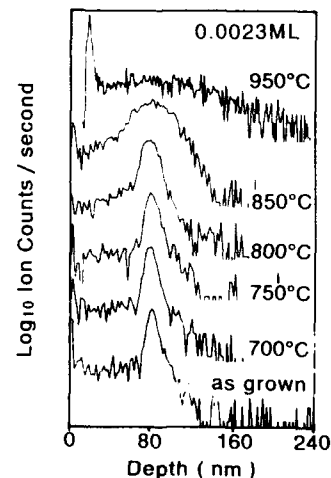


Fig. 3. Diffusion profiles of Sb in sample a (0.0023 ML). Kink development is not observed.

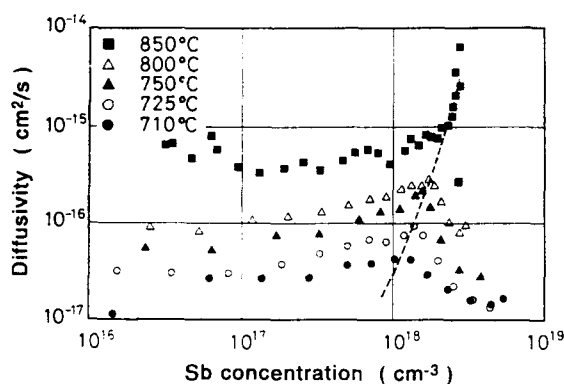


Fig. 4. Calculated diffusivity of Sb as a function of Sb concentration at various temperatures. Note that the bulk diffusivity at any specific temperature is much smaller than the calculation. The kink concentration (indicated by the broken curve) is an order of magnitude smaller than the solid solubility limit.

We evaluated the net diffusivity D of Sb atoms according to the Boltzmann–Matano analysis [3]:

$$D(C) = - \frac{XC(X, t)}{2t \partial C(X, t) / \partial t}.$$

where X denotes the distance from the spike, t the time and C the concentration. Figure 4 shows the diffusivity calculated from the profile at the surface side of the spike in sample d against the Sb concentration, $n(\text{Sb})$. The calculation gives values larger than the bulk diffusivity [4] and concentration dependence appears over $n(\text{Sb}) \approx 5 \times 10^{17} \text{ cm}^{-3}$. The kink concentration (indicated by the broken curve) is weakly temperature dependent and is by an order of magnitude lower than the solid solubility limit of Sb in Si [5]. The uprise approximately follows a curve with a fractional exponent as $n(\text{Sb})^{1/3}$, for $710 < T_a < 850^\circ\text{C}$, in contrast to the result on Be and Zn in GaAs with integral concentration exponents [4].

The activation energy was evaluated from the temperature dependence of the profile width, and two activation energies of 0.4–0.6 and 0.8 eV were obtained for Sb atoms pinned at the spike and for those extended, respectively. It should be pointed out that they are much smaller than that in the bulk, 4 eV [5].

4. Discussion

The diffusion mechanism seems complicated and the diffusivity is not described by a simple representation. The smaller activation energy for the less mobile Sb's suggests that interstitial-related and vacancy mechanisms operate for Sb's at the spike and at the shoulders, respectively. In addition, the fractional exponent indicates that the atomic spacing of Sb plays a role for the kink to develop. The kink may arise from the dopant aggregate or the two-stream diffusion [4]. The former can be applied to sample f [6], but a Hall measurement excludes the possibility of aggregation in samples with lower concentrations [2]. Detailed electrical measurements on the activity of Sb atoms are now under way. The aggregate is again unlikely since the kink concentration is much lower than the solid solubility limit. The two-stream diffusion model requires that two almost independent diffusion mechanisms with different diffusivities operate, and the slower of them must be the majority. This, alternatively, means that the matrix should have many defects. A prominent example is seen in an ion-implanted B in Si [4]. But the requisite condition is not fully satisfied in the samples studied, since they are not so much defective. Although we considered other possibilities, such as the substitutional-interstitial mechanism or pair diffusion, none of them satisfactorily explains the observation. In order to give a full account for the diffusion behavior, a new mechanism related to the strain modulation, due to atomic size difference between Sb and Si, should be taken into account. Further study is now in progress.

Next, we discuss the structural stability of the doped layers. Diffusion profiles at $T_a = 550^\circ\text{C}$ in all samples exhibited negligible spreading within the measurement resolution. It is thus concluded that the structural integrity is maintained up to the SPE growth temperature (550°C) regardless of the initial doping density. On the other hand, we note small spreading in the lowest-doped sample for $700 < T_a < 850^\circ\text{C}$, compared to the complex and significant broadening of the profiles in samples with higher doping densities. This, in turn, sets the upper limit on the doping level at as

high as 0.01 ML for device applications requiring high-temperature treatment.

Finally, the effect on the diffusion of the crystalline quality difference was examined. Slijkerman et al. attributed the diffusion enhancement to the abundance of defects in SPE layers with respect to MBE layers [7]. In order to see this more closely, we also examined sample e with an SPE buffer layer. The result is that there was no significant difference affecting the diffusion behavior between SPE and MBE layers. Thus the enhancement at the surface side must be driven in otherwise, possibly by surface oxide layers or field drift due to ionized donors [8].

5. Conclusion

Delta-doped Sb in Si exhibits characteristic diffusion profiles depending on the initial doping density and the annealing temperature. The diffusion mechanism involves two dominant processes with small activation energies and concentration-dependent diffusivity. The doped structure is stable up to 550°C. The asymmetrical diffusion enhancement of Sb is not due to crystalline quality difference between SPE-grown and MBE-grown layers.

Acknowledgements

We are greatly indebted to K. Nakagawa of the Central Research Laboratory, Hitachi Ltd., for the samples. We also acknowledge the support from M. Kishi, H. Yaguchi, K. Fujita and S. Ohtake, The University of Tokyo.

References

- [1] K. Nakagawa, M. Miyao and Y. Shiraki, *Thin Solid Films* 183 (1989) 315, and references therein.
- [2] A.A. Van Gorkum, K. Nakagawa and Y. Shiraki, *J. Appl. Phys.* 65 (1989) 2485.
- [3] M. Ghezzi, *J. Electrochem. Soc.* 119 (1972) 977.
- [4] S.M. Hu, in: *Atomic Diffusion in Semiconductors*, Ed. D. Shaw (Plenum, New York, 1973) ch. 5.
- [5] S.M. Sze, *Physics of Semiconductor Devices* (Wiley, New York, 1981).
- [6] K. Nakagawa, M. Miyao and Y. Shiraki, unpublished.
- [7] W.F. Slijkerman, P.M. Zagwijn, J.F. van der Veen, A.A. van Gorkum and G.F.A. van de Walle, *Appl. Phys. Letters* 55 (1989) 963.
- [8] E.F. Schubert, J.M. Kuo, R.F. Kopf, H.S. Luttman, L.C. Hopkins and N.J. Sauer, *J. Appl. Phys.* 67 (1990) 1969.

Dopant incorporation in epitaxial germanium grown on Ge(100) substrates by MBE

V.P. Kesan, S.S. Iyer and J.M. Cotte

IBM Research Division, T.J. Watson Research Center, Yorktown Heights, New York 10598, USA

We have conducted the first studies of dopant incorporation (gallium, boron, and antimony) in MBE germanium grown on Ge(100) substrates. Excellent germanium films have been grown on Ge substrates with little demarcation of the substrate–epi interface. A first order kinetic incorporation model has been used to describe the behavior of gallium in germanium. Gallium doping of germanium takes place through an adlayer at the growth front and between growth temperatures of 450 and 550 °C successful p-doping of germanium by gallium can be accomplished. Boron is an excellent p-dopant in germanium with good activation at high concentrations and sharp transition profiles. The incorporation of antimony in germanium at growth temperatures ≥ 450 °C is poor and needs further investigation.

1. Introduction

There is renewed interest in germanium-based devices for FET and bipolar applications. High carrier mobilities at room temperature and 77 K, superior projected high frequency performance, and the possibility of a wide bandgap silicon emitter are some of the advantages of a germanium-based technology.

There have been several studies describing growth of Ge on GaAs or vice versa by MBE [1–3]. Attempts to grow gallium-doped germanium layers on GaAs have been quite unsuccessful, with poor dopant activation [3]. In this paper we report the first studies of both p-type (gallium- and boron-doped) and n-type (antimony-doped) doping in MBE germanium grown on Ge(100) substrates.

2. Substrate preparation and growth conditions

Ge(100) substrates were cleaned using a modified RCA clean suitable for germanium. The first step consisted of a degrease in a 1 : 1 : 4 solution of HCl : H₂O₂ : H₂O at room temperature for 3 min followed by a rinse in de-ionized water. The Ge

wafers were then etched in H₂O₂ for 3 min while stirring continuously, and then rinsed in de-ionized water. This was followed by a quick dip in 1 : 10 HF : H₂O for 10 s which leaves the wafer surface hydrophobic and then loaded into the MBE system. The wafers were heated at 650 °C for 1–2 min in the MBE growth system just prior to growth. It is important to keep this step short, since long term heating of Ge wafers at high temperatures before growth results in a rough, undulating substrate (see fig. 1). Fig. 1 shows a cross-sectional TEM of a boron-doped Ge film grown at 450 °C on such a Ge substrate and subsequent growth on this rough Ge substrate is seen to cover the rough substrate–epi interface. Also, germanium films grown at high (> 650 °C) temperatures exhibit poor morphology. Fig. 2 shows a cross-sectional TEM of a boron-doped Ge film grown at 450 °C on a Ge substrate cleaned using the procedure described above. The substrate–epi interface is significantly better than in fig. 1. The excellent quality of the epitaxial boron-doped Ge layer is also evident in fig. 2. Germanium films grown at temperatures between 350–550 °C on Ge substrates consistently resulted in excellent epitaxial layers.

In order to study the incorporation of p and n



Fig. 1. Cross-sectional TEM micrograph of a boron-doped Ge film grown on a Ge substrate at 450°C. Prior to growth, the Ge substrate was taken to elevated temperatures ($> 650^{\circ}\text{C}$), which results in a rough, undulating, substrate-epi interface.

dopants in MBE grown germanium, effusion cell sources were used for antimony and gallium, and boron doping was achieved with a custom e-beam source. The Ge layers were analyzed using SIMS, spreading resistance analysis (SRA), and planar and cross-sectional TEM. The spreading resistance profiles were primarily used to determine dopant activation only, since the transition between doped

and undoped layers in spreading resistance profiles are often inaccurate particularly when the layer thicknesses are less than $0.5\text{ }\mu\text{m}$. Absolute values of carrier concentration in the SRA profiles are within $\pm 20\%$. A kinetic model for dopant incorporation was used to analyze the observed doping behavior in germanium, and this is described in the next section.

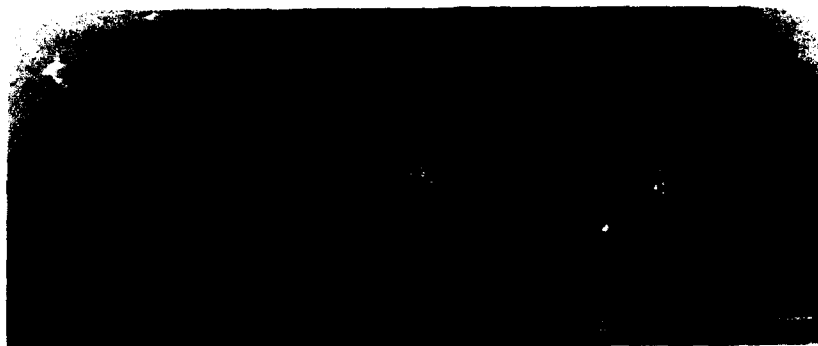


Fig. 2. Cross-sectional TEM micrograph of a boron-doped Ge film grown on a Ge substrate at 450°C. Prior to growth the Ge substrate was cleaned using a modified RCA clean suitable for germanium and the improved substrate-epi interface (compared to fig. 1) is evident.

3 Model for dopant incorporation

The kinetics of spontaneous dopant incorporation during epitaxial germanium growth by MBE can be described by a simple adsorption-incorporation-desorption model [4]. In the most general form this is

$$dN_{DS}/dt = F_D - \sum_p K_{Dp}(N_{DS})^p - K_I N_{DS}, \quad (1)$$

where N_{DS} is the surface concentration of the adsorbed dopant species at the growth front, F_D is the dopant flux, K_D is the desorption coefficient, p is the order of desorption, and K_I is the incorporation coefficient. The incorporation and desorption processes are activated processes with characteristic energies associated with them. Eq. (1) can be solved once a value for p is chosen.

The case $p = 1$ is the most relevant and has been used to describe dopant incorporation in silicon [4]. Eq. (1) then reduces to

$$dN_{DS}/dt = F_D - K_D N_{DS} - K_I N_{DS}. \quad (2)$$

Analyzing eq. (2) in the steady state, i.e., with $dN_{DS}/dt = 0$, we get

$$N_{DS} = F_D / (K_D + K_I). \quad (3)$$

Once steady state has been reached, the number of incident atoms per second is equal to the sum of those that desorb and incorporate per second. Hence, the rate of incorporation is given by

$$dN_{inc}/dt = K_I F_D / (K_D + K_I). \quad (4)$$

The rate of the number of atoms that incorporate to those that are incident, on a per unit time basis in steady state, is the sticking coefficient, s . Thus

$$s = \frac{dN_{inc}/dt}{F_D} = \frac{K_I}{K_I + K_D}. \quad (5)$$

The resultant steady state bulk doping concentration N_{DB} in the epitaxial Ge film is given by

$$N_{DB} = \frac{dN_{inc}/dt}{F_{Ge}} N_0, \quad (6)$$

where N_0 is the number of germanium atoms per cm^3 . Simplifying eq. (6), we get

$$N_{DB} = s(F_D/F_{Ge}) N_0. \quad (7)$$

Let us now consider a clean host surface and apply a step flux, F_D ; i.e., at $t < 0$, $F_D = 0$ and at $t \geq 0$, $F_D = F_D$. We then have

$$dN_{DS}/dt = F_D - (K_I + K_D) N_{DS}, \quad (8a)$$

$$N_{DS}(t) = \frac{F_D}{K_I + K_D} (1 - e^{-(K_I + K_D)t}). \quad (8b)$$

The time constant of importance here, τ , is given by

$$\tau = (K_I + K_D)^{-1}, \quad (9)$$

and is the characteristic dopant incorporation time. When the Ge-dopant system is subjected to a sudden change of flux, the system approaches its new steady state in an exponential manner in time. The initial rate of approach is given by $1/\tau$.

Since the incorporation rate follows the surface concentration behavior, the bulk doping concentration as a function of time is

$$N_{DB}(t) = s \frac{F_D}{F_{Ge}} N_0 \{1 - \exp[-(K_I + K_D)t]\}. \quad (10)$$

If the growth rate is constant the temporal variation is easily transformed to a spatial variation by

$$x = vt, \quad (11)$$

where x is the coordinate of film thickness and v the velocity of growth. This velocity is given by

$$v = F_{Ge}/N_0. \quad (12)$$

Hence,

$$N_{DB}(x) = s \frac{F_D}{F_{Ge}} N_0 \left\{1 - \exp\left[-\left(\frac{K_I + K_D}{v}\right)x\right]\right\}. \quad (13)$$

In the above transient analysis we have assumed that K_I and K_D are constants, which means that the temperature is constant and there are no saturation effects. The quantity $[(K_I + K_D)/v]^{-1} = \lambda$ is the spatial counterpart of τ . It represents the thickness of film over which variations in doping density occur in response to sudden changes in doping flux. Further, both τ and λ become smaller as the temperature of growth is increased.

The dopant and germanium fluxes are determined from growth rates and effusion cell calibration. The characteristic dopant incorporation time, τ , can be determined from the slope of the trailing/leading edge of the dopant profile in the epitaxial Ge layer and from eqs. (7) and (13). Using eqs. (3) and (9), we can determine the surface concentration of the adsorbed dopant species, N_{DB} . The incorporation coefficient, K_I , can then be determined from eqs. (3), (7), and (9). Since τ is known, we can now compute the desorption coefficient, K_D , and the sticking coefficient, s . This model is now applied to study gallium incorporation in germanium.

4. Gallium doping of germanium

The gallium K-cell was calibrated by growing amorphous Si films at 250°C and a wide range of gallium flux from 10^{10} – 10^{13} atoms/cm²·s have been examined in these experiments. Gallium does

not readily incorporate in germanium and instead doping takes place through the formation of an adlayer at the growth front. Fig. 3a shows the SIMS profile of a 4000 Å Ga doped Ge layer grown on a 1000 Å undoped Ge buffer with a 1000 Å undoped Ge cap at 550°C. The transition between the doped and undoped layers on the leading and trailing edges of the Ga doped film is gradual clearly indicating incorporation from an adlayer at the growing surface. Fig. 3b, which shows a spreading resistance profile of the same layers seen in fig. 3a, indicates about 22% gallium activation in the doped germanium layer. Also seen is some gallium segregation at the Ge substrate–epi interface and fig. 3b shows this gallium at the interface to be active. In addition to thick Ga doped Ge films, 1000 Å Ga doped Ge films separated by 1000 Å undoped layers were grown at different growth temperatures between 350°C and 550°C at different Ga fluxes. Fig. 4a shows the SIMS profile of such a film with a total thickness of 1.1 μm and grown at 550°C. A

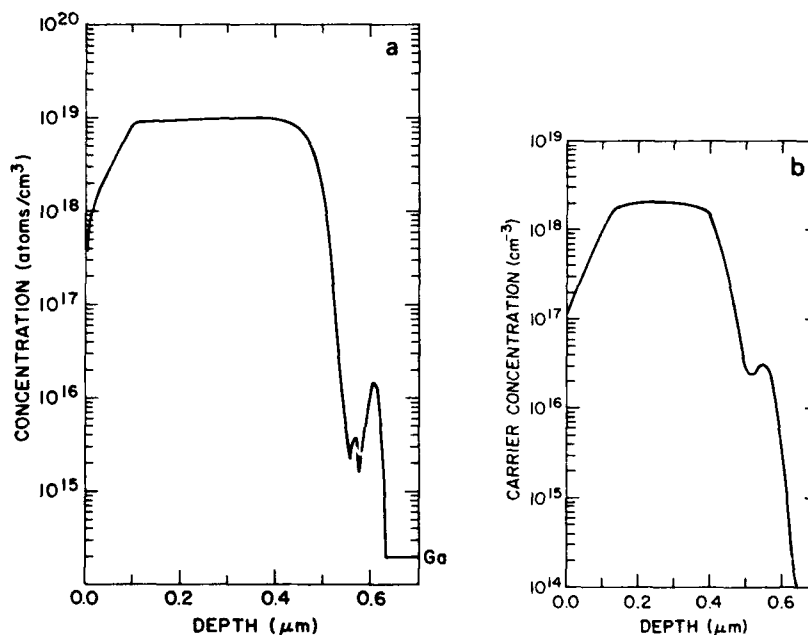


Fig. 3. (a) SIMS profile of a 4000 Å Ga-doped Ge layer grown on a 1000 Å undoped Ge buffer with a 1000 Å undoped Ge cap at 550°C. The transition between the doped and undoped layers on the leading and trailing edges of the Ge-doped film is gradual, indicating incorporation from an adlayer at the growing surface. (b) Spreading resistance (SRA) profile of the same sample as in (a).

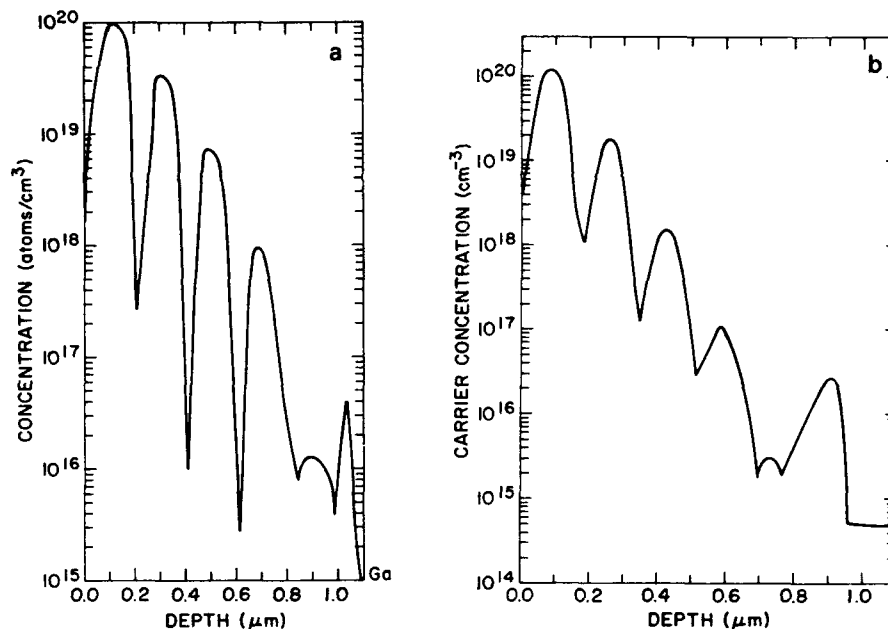


Fig. 4. (a) SIMS profile of 1000 Å Ga-doped Ge films separated by 1000 Å undoped layers grown at 550°C at different Ga fluxes. The total film thickness is 1.1 μm. (b) Spreading resistance profile of the same film as seen in (a).

spreading resistance profile of the same film is seen in fig. 4b. Ga doped Ge layers similar to the ones shown in figs. 3 and 4 were grown at different temperatures and their SIMS and SRA profiles were analyzed using the model described in the previous section.

The characteristic dopant incorporation time, τ , for a growth temperature of 450°C was 150–250 s and at 550°C, τ was 50–100 s. Fig. 5 shows the incorporation coefficient, K_1 , for two different growth temperatures as a function of surface gallium concentration, N_{DB} . The incorporation coefficient is constant with increasing surface coverage indicating that an increase in surface gallium concentration translates directly into higher incorporation in the bulk layer (see eqs. (5) and (7)). In addition, fig. 5 shows that no saturation effects (as indicated by a decreasing K_1) are observed for surface coverages up to 0.5–1.0 ml. The incorporation coefficient also increases by almost an order of magnitude between growth at 450 and 550°C, and hence the resulting gallium concentration in films grown at 550°C is almost an order of mag-

nitude larger than in films grown at 450°C. The activation energy for incorporation obtained from a plot of K_1 versus $1/T$ was found to be ap-

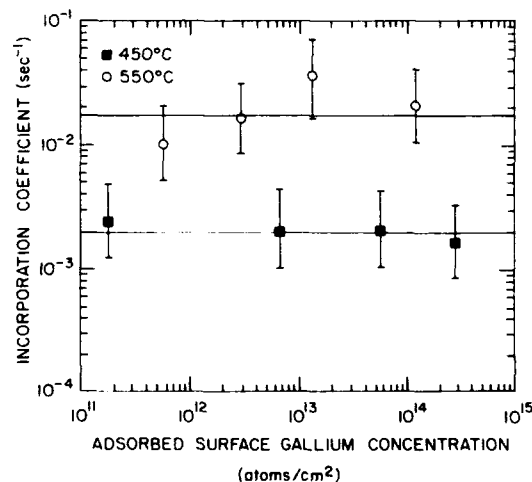


Fig. 5. Incorporation coefficient, K_1 , for two different growth temperatures as a function of surface gallium concentration, N_{DB} .

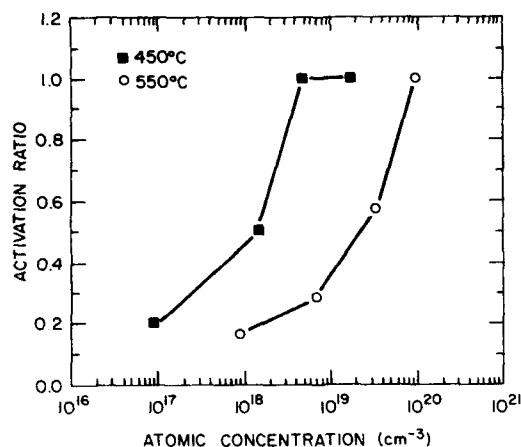


Fig. 6. Activation ratio obtained from SIMS and SRA data for two different growth temperatures as a function of the SIMS atomic doping concentration.

proximately 1.3 eV. This value is very similar to the activation energy for incorporation of gallium in silicon [5]. This suggests that gallium incorporation in germanium, like in silicon, involves the clustering of gallium atoms on the surface, with subsequent incorporation proceeding by gallium

atoms breaking away from the periphery of these clusters and surface diffusing to an available nearby kink site. If this mechanism were true, then the activation energy for incorporation obtained in our experiments should match data on the surface diffusion activation energy for gallium on germanium. The desorption coefficient, K_D , was less than 5×10^{-3} and the sticking coefficient, s , for gallium on germanium was between 0.25 and 1.0 for the entire range of growth conditions examined.

Fig. 6 shows a plot of the activation ratio obtained from SIMS and SRA data for two different growth temperatures as a function of the SIMS atomic doping concentration. The dopant activation of gallium increases with increasing atomic concentration and reaches unity at doping levels greater than 10^{19} cm^{-3} . The unity activation at high doping maybe due to band-tailing effects. The poor activation at higher growth temperatures, for a particular value of atomic concentration (see fig. 6), may be attributed to the fact that there is increased clustering of gallium atoms at the surface at higher temperatures. Here, it is important to note that no gallium precipitates

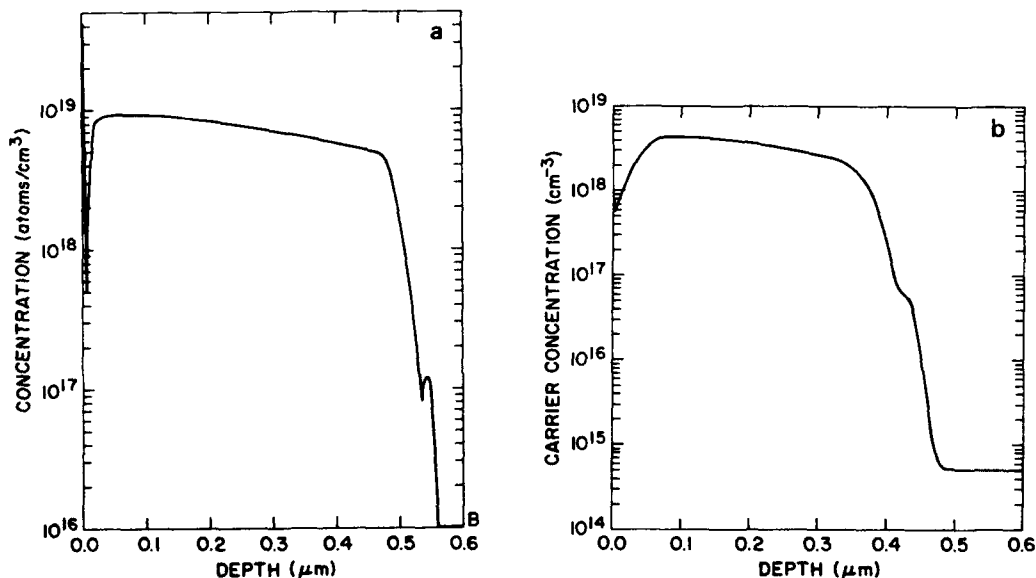


Fig. 7. (a) SIMS profile of a 4000 Å boron-doped Ge film grown on a 500 Å undoped buffer at 450°C. (b) The corresponding spreading resistance profile of the same sample.

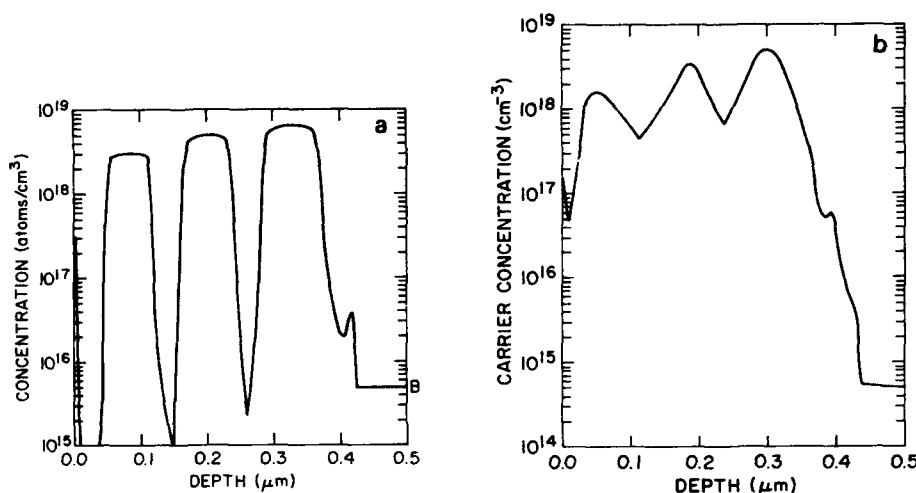


Fig. 8. (a) SIMS profile of 500 Å boron-doped germanium pulses separated by 500 Å undoped Ge layers grown at 450 °C. (b) SRA profile of the same sample.

were seen in cross-sectional TEM even at the highest doping levels obtained of 10^{20} cm^{-3} . While growth at high temperatures around 550 °C may result in increased dopant incorporation, the fraction that is active is actually reduced compared to growth at 450 °C. Thus the window for optimal growth of gallium doped Ge films is quite small, between 450 and 550 °C. Through the use of pre-buildup and flash-off techniques [4], it may be possible to obtain gallium doped germanium with sharp transition profiles.

5. Boron doping of germanium

Boron doping of germanium was accomplished using an e-beam source for boron. Fig. 7a shows the SIMS profile of a 4000 Å boron-doped Ge film grown on a 500 Å undoped buffer at 450 °C and fig. 7b shows the corresponding spreading resistance profile. Fig. 8a shows the SIMS profile of a sample with 500 Å boron-doped germanium pulses separated by 500 Å undoped Ge layers and fig. 8b shows the SRA profile of the same sample. The limited dynamic doping range seen in this film is due to our custom e-beam source. The interfacial boron spike [6] can be seen in both samples shown in figs. 7 and 8. By comparing the

SRA and SIMS profiles in figs. 7 and 8, it can be seen that 85–100% of the boron in germanium is active. Fig. 2, which shows a TEM cross-section of a boron-doped Ge film, also points to the excellent quality of these layers. Hence, boron is clearly the preferred p-dopant in germanium and uniform doping profiles at high concentrations with sharp transitions can be achieved.

6. Antimony doping of germanium

The antimony K-cell was calibrated using amorphous Si films grown at 250 °C and a wide range of antimony flux from 10^{11} to 5×10^{13} atoms/cm²·s were examined. Fig. 9 shows the SIMS profile of a 0.9 μm Ge film intended to produce 1000 Å thick antimony-doped Ge pulses separated by 1000 Å undoped Ge layers and grown at 450 °C. The leading edge transition of the first antimony-doped layer is sharp, but over a wide range of surface coverage, the bulk antimony doping concentration is relatively constant and does not turn off even when the surface atomic concentration of antimony is not replenished during growth of the undoped Ge layers. The same film as shown in fig. 9, when grown at 550 °C, results in lower bulk antimony concentration. SRA profiles

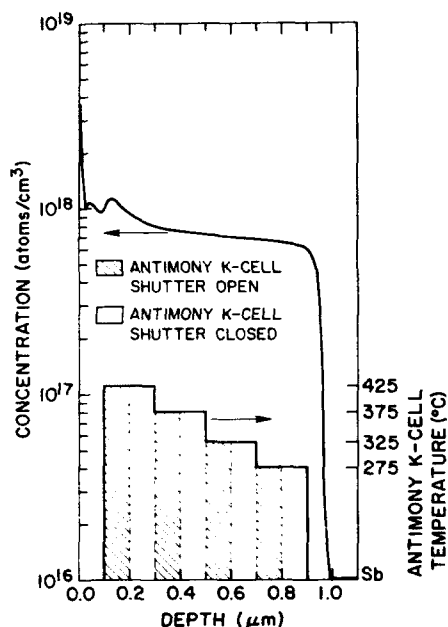


Fig. 9. SIMS profile of a 0.9 μm Ge film intended to produce 1000 Å thick antimony-doped Ge pulses separated by 1000 Å undoped Ge layers and grown at 450°C. The antimony K-cell temperature during growth and the K-cell shutter status is shown in the inset.

on these samples showed 20–30% activation of the antimony in the germanium layers. Fig. 10 shows a TEM cross-section of the same sample described in fig. 9. A number of “hair-pin” defects of stacking faults can be seen at the top of the film. It may be possible to achieve spontaneous antimony incorporation by reducing the growth temperature to around 300°C, but the defect density in Ge

fims grown at such low temperatures is correspondingly higher. Clearly, antimony doping of germanium does not proceed along similar lines as in silicon and will be studied in greater detail in the future.

7. Conclusion

In summary, we have studied dopant incorporation (gallium, boron, and antimony) in MBE germanium grown on Ge(100) substrates. Excellent germanium films have been grown on Ge substrates with little demarcation of the substrate–epi interface. Gallium doping of germanium takes place through an adlayer at the growth front, and between growth temperatures of 450°C and 550°C, successful p-doping of germanium by gallium can be accomplished. Boron is an excellent p-dopant in germanium with good activation at high concentrations and sharp transition profiles. The incorporation of antimony in germanium at growth temperatures $\geq 450^\circ\text{C}$ is poor. Further reduction in the growth temperature to around 300°C may increase antimony incorporation, with a penalty of increasing defect density in these films.

Acknowledgements

We would like to acknowledge the excellent technical assistance of Bruce Ek and F.K. LeGoues for the invaluable TEM work.



Fig. 10. TEM cross-section of the same sample described in fig. 9. A number of “hair-pin” defects of stacking faults can be seen at the top of the film.

References

- [1] R.W. Grant, J.R. Waldrop, S.O. Kowalczyk and E.A. Kraut, *J. Vacuum Sci. Technol.* B3 (1985) 1295.
- [2] N. Chand, J. Klem and H. Morkoç, *Appl. Phys. Letters* 48 (1986) 484.
- [3] S. Strite, M.S. Unlu, K. Adomi, G.-B. Bao and H. Morkoç, *IEEE Electron Device Letters* EDL-11 (1990) 233.
- [4] S.S. Iyer, in: *Epitaxial Silicon Technology*, Ed. B.J. Baliga (Academic Press, Orlando FL, 1986).
- [5] S.S. Iyer, PhD Dissertation, Univ. of California, Los Angeles (1981).
- [6] S.S. Iyer, S.L. Delage and G.J. Scilla, *Appl. Phys. Letters* 52 (1988) 486.

B doping effect on gas source Si-MBE growth: a comparison of B_2H_6 gas doping and HBO_2 Knudsen cell doping

Hiroyuki Hirayama *, Masayuki Hiroi, Kazuhisa Koyama and Toru Tatsumi

Microelectronics Research Laboratories, NEC Corporation, Miyazaki 4-1-1, Miyamae-ku, Kawasaki 213, Japan

In Si_2H_6 gas source Si-MBE, B doping is achieved using HBO_2 Knudsen cell or B_2H_6 gas dopant. B doping effect on gas source Si-MBE growth was studied for these two different doping sources. At high B doping using HBO_2 cell, RHEED intensity oscillation was found to extinguish. This is thought to be due to the scattering for Si_2H_6 surface migration by B adsorbates from HBO_2 cell on a growing surface. In fact, RHEED oscillation extinguished for B adsorption of 0.15 monolayer on Si(100) surfaces, whereas the oscillation continued on Si(111) $\sqrt{3} \times \sqrt{3}$ -B in which B occupies a subsurface site under the top layer. On the other hand, RHEED oscillation did not extinguish in B_2H_6 gas doping. This is because B_2H_6 is incorporated into the epitaxial layer via the same process as Si_2H_6 .

1. Introduction

For a high speed bipolar transistor fabrication, precise controls for the film thickness and doping profile of the collector, base and emitter layers are essential. From these view points, Si molecular beam epitaxy (Si-MBE) is a promising technique. Si-MBE has such advantages of low epitaxial growth temperature, good film thickness control in monolayer scale, and an abruptness in doping profile [1–3]. However, in addition to these advantages, a selective epitaxial growth for self-aligned processing is strongly desired in recent large scale integrated (LSI) circuit technology. But, unfortunately, a selective epitaxial growth is very difficult in conventional electron-gun evaporator type Si-MBE. To make this selective epitaxial growth possible, the authors had studied gas source Si-MBE [4–6].

In gas source Si-MBE, selective epitaxial growth has been found to be possible. But, for self-aligned processing, a selective doping technique is also required. Therefore, we devised an original gas mixing system [7] and studied B doping method

using B_2H_6 as a gas dopant source. The similar molecular structure of B_2H_6 as Si_2H_6 perhaps will have the same incorporation mechanism to Si_2H_6 , which enables the selective doping. In this study, the effect of B doping on gas source Si-MBE growth was studied using B_2H_6 gas. This effect was compared with that of the conventional HBO_2 cell doping.

2. Experimental apparatus

The experimental apparatus is schematically shown in fig. 1. The MBE chamber consists of a HBO_2 Knudsen cell for solid source B doping, a gas cell for gas source Si-MBE growth and gas doping, an electron cyclotron resonance (ECR) cell for low temperature surface cleaning [8] and surface H-termination [9], a reflection high energy electron diffraction (RHEED) gun and a fluorescent screen. RHEED intensity oscillations were observed with an aperture and a photomultiplier system [10]. Four-inch Si(100) and Si(111) wafers were used as substrates. B doping was achieved using HBO_2 or B_2H_6 gas. The effect of the B doping on gas source Si-MBE growth was monitored by RHEED intensity oscillation. The oscilla-

* Present address: Fritz-Haber-Institut der Max-Planck-Gesellschaft, Faradayweg 4–6, W-1000 Berlin 33, Germany.

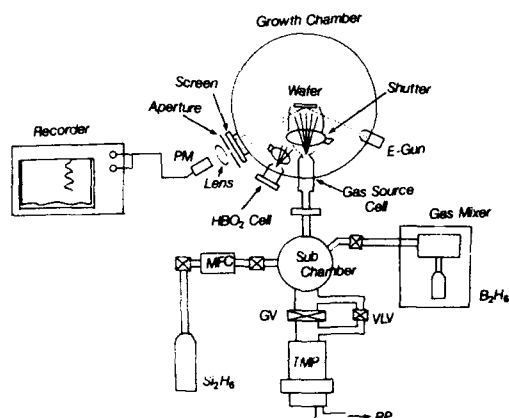


Fig. 1. Gas source Si-MBE apparatus.

tion was measured concerning a specular spot. Gas source Si-MBE growth was performed using 100% Si_2H_6 . B gas doping was achieved using 5% B_2H_6 diluted by H_2 . These gas flow rates were controlled by a gas mixing system [7]. These gas were first introduced to the subchamber, and then supplied to the growth chamber through the gas cell. The subchamber worked as a buffer chamber. The growth chamber pressure was less than 2×10^{-5} Torr, though it depended on the source gas flow rate to the growth chamber.

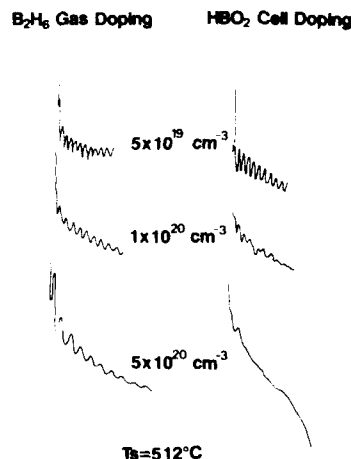
3. HBO_2 cell doping effect

RHEED intensity oscillations on Si(100) surfaces were observed during gas source Si-MBE growth with HBO_2 [11]. Experimental results are shown in fig. 2. In this study, B doping was achieved with a constant B_2H_6 flow rate or HBO_2 beam intensity. The doping concentration was increased by decreasing the Si_2H_6 flow rate. The substrate temperature was kept at 512°C . As shown in the right-hand side of fig. 2, oscillations were observed without HBO_2 doping. But, at high B doping above 10^{20} cm^{-3} , the oscillation extinguished. There are two possible reasons for this extinction of RHEED oscillation. One reason is that the surface dangling bonds are terminated by B dopant atoms. Gas source Si-MBE growth is governed by the dissociative adsorption of Si_2H_6

at Si dangling bond sites [12–14]. With the increasing doping concentration, the B coverage on the surface increases. Therefore, at high dopings, all surface dangling bonds may be terminated by B. In this case, gas source Si-MBE growth stops and the RHEED oscillation extinguishes. The other possible reason is the retardation of the Si_2H_6 surface migration by B atoms. In some previous studies on Si_2H_6 adsorption, a precursor state of Si_2H_6 has been reported [12]. As a first step for the dissociative adsorption, Si_2H_6 adsorbs molecularly in the precursor state. After the surface migration, Si_2H_6 dissociates at a dangling bond site and contributes to the epitaxial growth [14]. B adsorbates hinder the surface migration and the following two-dimensional growth. At high B doping concentrations, the scattering becomes dominant, which may cause the extinction of RHEED oscillation.

In 10^{20} cm^{-3} doping dilutions, the inter-distance between B dopants is in the order of a few nms, and B's are not expected to terminate all dangling bonds. Therefore, the extinction of the RHEED oscillation at high B doping is thought to be due to the retardation of surface migration by B adsorbates. This was also confirmed by the following two experiments.

RHEED oscillation for non-doped gas source Si-MBE growth was measured on Si(100) surfaces

Fig. 2. RHEED oscillation during HBO_2 Knudsen cell and B_2H_6 gas doping.

which have a B coverage between 0 and 0.2 monolayer. No RHEED oscillation was observed at the coverage above 0.15 monolayer. This result suggests that the extinction of RHEED oscillation was caused by the retardation of surface migration.

RHEED oscillation for non-doped gas source Si-MBE growth was also measured on Si(111) surfaces with a $1/3$ monolayer B. The $1/3$ monolayer B formed $\sqrt{3} \times \sqrt{3}$ -B surface superstructure at 800°C , while a 1×1 surface structure was observed at room temperature [15]. The RHEED oscillation was observed on B-Si(111) $\sqrt{3} \times \sqrt{3}$, whereas the oscillation was not observed on Si(111) 1×1 -B. On the B-Si(111) $\sqrt{3} \times \sqrt{3}$ surface, B occupies a subsurface site under the top layer [16]. The subsurface site B atom does not scatter the surface migration. On the other hand, B adsorbed on the top surface gives a B-Si(111) 1×1 structure. The special B site for the B-Si(111) $\sqrt{3} \times \sqrt{3}$ structure is the reason for RHEED oscillation in spite of its large B coverage ($1/3$ monolayer). This experimental result also supports that the extinction of RHEED oscillation is due to the retardation of surface migration by B adatoms.

4. B_2H_6 gas doping effect

Using B_2H_6 , B doping is also possible in gas source Si-MBE. An example of B_2H_6 gas doping is shown in fig. 3. In this experiment, the substrate temperature was kept at 561°C . The B_2H_6 flow

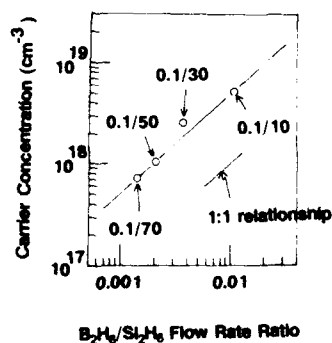


Fig. 3. B doping concentration in B_2H_6 gas doping.

rate was fixed at 0.1 SCCM, whereas the Si_2H_6 flow rate was varied in the range between 0 and 70 SCCM. As shown in the figure, the B concentration was found to be proportional to the $\text{B}_2\text{H}_6/\text{Si}_2\text{H}_6$ ratio. However, here we must pay attention to the Si_2H_6 flow rate dependence of the growth rate [7,10]. For Si_2H_6 flow rate below 30 SCCM, the growth rate increased linearly with the flow rate. But, for the Si_2H_6 rates above 30 SCCM, the growth rate did not depend on the flow rate. This is because that gas source Si-MBE has two competing rate-limiting steps [10]. One is the Si_2H_6 incidence. The other is the H thermal desorption from the growing surfaces. For large flow rates, the Si_2H_6 incident rate exceeds the H desorption rate. In this case, the H desorption becomes a rate-limiting step and thus the growth rate does not depend on the Si_2H_6 flow rate. For low flow rates, the Si_2H_6 incident rate is the rate-limiting process, where the growth rate is proportional to the Si_2H_6 flow rate. However, the B doping concentration is proportional to the $\text{B}_2\text{H}_6/\text{Si}_2\text{H}_6$ ratio, independent of the two different rate-limiting processes. This experimental result suggests that B_2H_6 is incorporated into the epitaxial film by the same adsorption process as that for Si_2H_6 . Specifically, B_2H_6 adsorbs in a precursor state, and after migration, the B_2H_6 dissociates at surface dangling bonds and is incorporated into the epitaxial film.

RHEED oscillation for B_2H_6 gas doping was also measured on Si(100) surfaces. Results are shown in fig. 2. As shown in the figure, for B doping concentrations above 10^{20} cm^{-3} , the oscillation for the HBO_2 cell doping extinguished, whereas the oscillation for the B_2H_6 doping still persisted. The extinction for the HBO_2 cell doping is caused by the retardation of the surface migration by B adsorbates. In HBO_2 cell doping, B atoms adsorb directly on Si(100) surface and act as scattering centers in surface migration. On the contrary, B_2H_6 is thought to have the same adsorption process as Si_2H_6 . Namely, B_2H_6 migrates in a precursor state, and then is incorporated by the subsequent dissociation at dangling bond sites. In the latter case, all B atoms are incorporated in the epitaxial layer and there are no B atoms on the growing surface. This is thought to be the reason

why the oscillation persists only for the B_2H_6 gas doping.

5. Summary

The B doping effect on gas source Si-MBE growth was studied using HBO_2 and B_2H_6 gas. In the HBO_2 cell doping, RHEED oscillation stopped for high B doping above 10^{20} cm^{-3} . This is due to the retardation of the Si_2H_6 precursor's surface migration by B adsorbates in the case of HBO_2 doping. This assumption was confirmed by the extinction of the RHEED oscillation on B-precovered Si(100) surfaces and the continuous oscillation on the Si(111) $\sqrt{3} \times \sqrt{3}$ -B surface.

In B_2H_6 gas doping, RHEED oscillation was found to persist even for high doping concentrations. This result suggests that B_2H_6 is incorporated in the epitaxial layer through the same process as that of Si_2H_6 . Namely, B_2H_6 is incorporated by dissociation at the dangling bond site after the surface migration in the precursor state.

Acknowledgements

The authors would like to thank Dr. M. Ogawa, M. Nakamae and N. Aizaki for their continuous encouragement.

References

- [1] Y. Ohta, *Thin Solid Films* 106 (1983) 3.
- [2] J.C. Bean, *J. Crystal Growth* 81 (1987) 411.
- [3] T. Tatsumi, H. Hirayama and N. Aizaki, *Appl. Phys. Letters* 52 (1988) 895.
- [4] H. Hirayama, T. Tatsumi, A. Ogura and N. Aizaki, *Appl. Phys. Letters* 51 (1987) 2213.
- [5] H. Hirayama, T. Tatsumi and N. Aizaki, *Appl. Phys. Letters* 52 (1988) 1484.
- [6] H. Hirayama, T. Tatsumi and N. Aizaki, *J. Crystal Growth* 95 (1989) 476.
- [7] H. Hirayama, M. Hiroi and K. Koyama, unpublished.
- [8] H. Hirayama and T. Tatsumi, *J. Appl. Phys.* 66 (1989) 629.
- [9] H. Hirayama and T. Tatsumi, *Appl. Phys. Letters* 54 (1989) 156.
- [10] M. Hiroi, K. Koyama, T. Tatsumi and H. Hirayama, unpublished.
- [11] H. Hirayama, M. Hiroi, K. Koyama and T. Tatsumi, *Appl. Phys. Letters*, in press.
- [12] F. Bozso and Ph. Avouris, *Phys. Rev.* B38 (1988) 3943.
- [13] Y. Suda, D. Lubben, T. Motooka and J.E. Green, *J. Vacuum Sci. Technol.* A8 (1990) 61.
- [14] H. Hirayama, K. Koyama, M. Hiroi and T. Tatsumi, in: *Proc. Mater. Res. Soc. 1990 Spring Meeting*, to be published.
- [15] H. Hirayama, T. Tatsumi and N. Aizaki, *Surface Sci.* 193 (1988) L47.
- [16] E. Kaxiras, K.C. Pandey, F.J. Himpsel and R.M. Tromp, *Phys. Rev.* B41 (1990) 1262.

Limitations of selective epitaxial growth conditions in gas-source MBE using Si_2H_6

Ken-ichi Aketagawa

ANELVA Corp., 5-8-1, Yotsuya, Fuchu-shi, Tokyo 183, Japan

Toru Tatsumi

Microelectronics Laboratories, NEC Corp., 4-1-1, Miyazaki, Miyamae-ku, Kawasaki 213, Japan

and

Junro Sakai

ANELVA Corp., 5-8-1, Yotsuya, Fuchu-shi, Tokyo 183, Japan

The limiting conditions of selective epitaxial growth (SEG) on SiO_2 patterned $\text{Si}(001)$ substrate were studied for Si gas-source molecular beam epitaxy (MBE) by use of 100% Si_2H_6 . In the initial stage of growth, epitaxial Si was selectively grown on a Si surface in the temperature range of 500 to 850°C. On the other hand, polycrystalline Si nucleation on a SiO_2 surface was intimately related to the impinging density of the Si_2H_6 molecules on SiO_2 , so that SEG was limited by the supply gas volume. Under optimum SEG conditions such as substrate temperature of 700°C and Si_2H_6 flow rate of 60 SCCM, a SEG layer could be deposited at a rate as high as 645 Å/min.

1. Introduction

Silicon gas-source molecular beam epitaxy (MBE) using Si_2H_6 has many advantages such as low temperature process, no spitting defect, high growth rate, and selective epitaxial growth (SEG) on SiO_2 patterned Si. Especially, SEG is one of the most important technologies for fabricating future ultra-large scale integration circuits (ULSIs).

Several papers have been reported on SEG by chemical vapor deposition (CVD), low or ultra-low pressure CVD (LP-, ULP-CVD) using SiH_4 , $\text{SiH}_4/\text{H}_2/\text{HCl}$, $\text{SiCl}_4/\text{HCl}/\text{H}_2$, $\text{SiH}_2\text{Cl}_2/\text{HCl}/\text{H}_2$, SiH_4/H_2 , and $\text{SiHCl}_3/\text{HCl}/\text{H}_2$ systems. Yew and Reif [1] reported that the SEG temperature using HCl should be higher than 900°C. However, they found also low temperature SEG by using ULPCVD of SiH_4 . Hirayama et al. [2,3]

succeeded in SEG in a gas-source MBE system with SiH_4 and Si_2H_6 . Gas-source MBE is one of the most promising methods for low temperature SEG. However, Hirayama et al. [3] reported that SEG conditions were restricted to the low molecular beam intensity and consequently the growth rate was very low.

In this study, we tried to find the critical conditions of Si-SEG on a SiO_2 patterned $\text{Si}(001)$ substrate in a gas-source MBE system by use of pure Si_2H_6 .

2. Experimental

Fig. 1 shows a schematic diagram of the gas-source MBE system (ANELVA GBE-620), which consists of a loadlock chamber and a growth chamber with liquid nitrogen shrouds. The growth

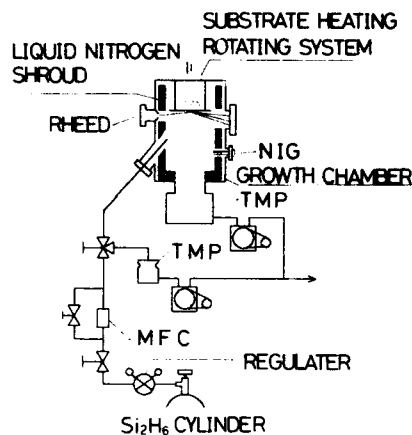


Fig. 1. Schematic diagram of gas source Si-MBE.

chamber is evacuated to the background pressure of 1.5×10^{-9} Torr by a 1000 L/s turbo molecular pump (Seiko Seiki STP-H1000C) and liquid nitrogen shrouds. The source gas, Si_2H_6 , is introduced from a cell port through a mass flow controller (MFC). According to the change of flow rate from 1 to 60 SCCM, the steady state pressure in the growth chamber varied from 2×10^{-6} to 5×10^{-5} Torr at the liquid nitrogen temperature of the shrouds. The substrate temperature was measured by a thermocouple located in the space between an IR radiation heater and the substrate. The substrate temperature was calibrated by RHEED observation of the Si(001) surface. According to a previous report [4], the temperature at which the superstructure patterns appear on the (001) surface was defined as 815°C . The substrate was a 4-inch (001) Si wafer patterned with CVD- SiO_2 and rinsed by an etching solution ($\text{H}_2\text{O}:\text{H}_2\text{O}_2:\text{NH}_4\text{OH} = 20:6:1$) before loading. After thermal cleaning in the growth chamber at 850°C for 10 min, films were grown at several temperatures. The presence of SEG was observed by RHEED pattern. In order to extend the lifetime of the RHEED gun filament, RHEED pattern observation was carried out periodically. The growth rate was calculated from a step height measured at the edge of the epitaxial layer after taking off the SiO_2 pattern by HF solution. The surface morphology of the SEG pattern was observed by scanning

electron microscope (SEM), and the cross sectional structure of the film was observed by transmission electron microscope (TEM).

3. Results and discussions

The SEM images of the perfect SEG film and the imperfect SEG film are shown in figs. 2a and 2b, respectively. The films were deposited at 700°C with Si_2H_6 flow rate of 15 SCCM for 4 min (fig. 2a) and 22 min (fig. 2b) growth. The thicknesses of the epitaxial layer were 640 \AA (fig. 2a) and 3000 \AA (fig. 2b). When the RHEED pattern showed 2×1 with halo, the SEM image did not show the existence of poly-Si on SiO_2 as in fig. 2a. When the RHEED pattern changed to

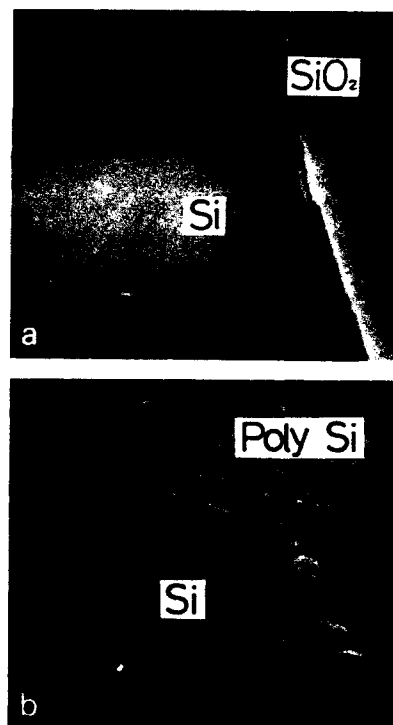


Fig. 2. Scanning electron microscopy (SEM) images of substrate surface taken from the films deposited at 700°C with Si_2H_6 flow rate of 15 SCCM for (a) 4 min and (b) 22 min growth. The thicknesses of the epitaxial Si layer were (a) 640 \AA and (b) 3000 \AA .

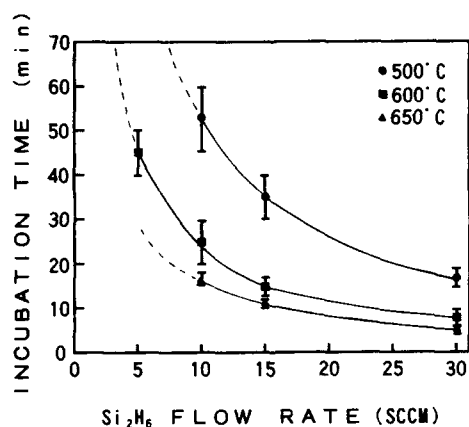


Fig. 3. Flow rate dependence of incubation time. When Si_2H_6 gas was supplied over the incubation time, poly-Si was nucleated on the SiO_2 .

2×1 overlapped with rings, poly-Si was deposited on SiO_2 as shown in fig. 2b.

RHEED observation showed that poly-Si nucleation started after an incubation time of initial growth. As shown in fig. 3, the incubation time was inversely proportional to Si_2H_6 flow rate at fixed substrate temperature. Therefore, the product of the incubation time by the gas flow rate, which means the total volume of gas supplied during the incubation time, should be constant at fixed temperature. Furthermore, the critical volume of supply gas above which poly-Si nucleation appears is predicted at various temperatures.

Fig. 4 shows the critical volume of supply gas as a function of the substrate temperature. Below

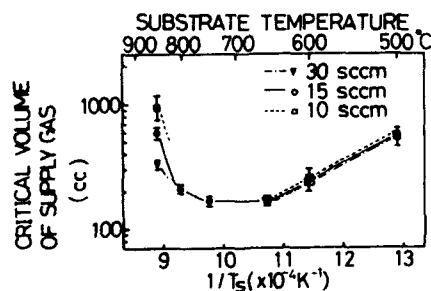


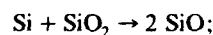
Fig. 4. Critical volume of supply gas for poly-Si nucleation on SiO_2 versus substrate temperature. The critical volume of the supply gas was introduced as the product of incubation time and gas flow rate.

700°C , the critical volume of supply gas decreases with increasing substrate temperature, independent of gas flow rate, whereas above 700°C the critical volume increases with substrate temperature. Moreover, at 850°C the critical volume decreases with increasing gas flow rate.

The critical volume of supply gas suggests that there is a critical adatom coverage on the SiO_2 surface to start poly-Si nucleation, since the number of adatoms decomposed from impinged Si_2H_6 molecules is proportional to the volume of supply gas under molecular flow region. While Si_2H_6 molecules are decomposed and contribute to the epitaxial growth on the Si surface, most of the molecules impinging on the SiO_2 surface are reflected and some portion is probably decomposed and stay as adatoms. As far as the density of these adatoms does not exceed the critical coverage, SEG continues on the Si surface.

In the low temperature region below 700°C , the surface decomposition rate of Si_2H_6 was increased with temperature; thus the critical volume of supply gas was decreased with increasing temperature.

In the high temperature region above 700°C , the SiO_2 surface was etched by decomposed Si_2H_6 . Tabe [5] reported that at high temperature, Si and SiO_2 react as



then the volatile SiO is evaporated at the growth temperature. Since the amount of adsorbed molecules necessary for Si island nucleation is decreased, the critical volume of supply gas is increased with temperature. By increasing the gas flow rate at a constant temperature, the poly-Si nucleation rate becomes higher than the SiO evaporation rate. Therefore, the critical volume of supply gas decreased with increasing gas flow rate.

The critical volume of supply gas well indicated the limitation of perfect SEG conditions. When Si_2H_6 was supplied under the critical volume obtained in fig. 4, perfect SEG Si could be obtained in various flow rates and substrate temperatures. Fig. 5 shows the substrate temperature dependence of the perfect SEG-Si growth rate. As seen from fig. 5, the deposition rate depends strongly

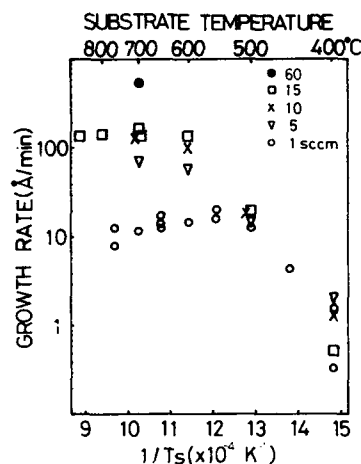


Fig. 5. Substrate temperature dependence of the SEG-Si growth rate. The upper limitation of growth rate under 700°C was determined by the reaction on the surface and the activation energy was introduced at 30 kcal/mol.

on the substrate temperature in the low temperature region and its transition temperature to a temperature-independent region increases with the increase in gas flow rate. So the temperature-independent region is regarded as a gas flow rate limited process. Under the temperature controlled condition, the activation energy of the reaction is estimated at 30 kcal/mol. From fig. 5, in order to obtain a thick SEG layer as far as possible without

poly-Si nucleation, the gas flow rate should be controlled to keep the flow rate limited condition for each substrate temperature.

The maximum growth rate of 645 Å/min was obtained at 700°C and gas flow rate of 60 SCCM. Fig. 6 shows the cross sectional TEM image of the SEG film with a thickness of 1290 Å deposited under these conditions. As seen in this photograph, the contact of the epitaxial Si layer with the side wall of SiO_2 was satisfactory.

4. Conclusion

In the selective epitaxial growth of Si by Si_2H_6 gas source MBE, poly-Si nucleation on a SiO_2 surface appears after a certain incubation time. It was found that poly-Si nucleation on SiO_2 starts after exceeding the critical volume of the supply gas. As far as the total Si_2H_6 gas supply was kept less than the critical volume, perfect SEG-Si could be obtained independent of both flow rate and substrate temperature. The maximum growth rate of SEG obtained in this study was 645 Å/min at 700°C , which was a conspicuously lower temperature than that of the CVD results. The maximum film thickness grown under the optimum SEG conditions is expected to extend over 3000 Å .

Acknowledgements

The authors would like to thank Dr. Z. Oda for helpful suggestions, and Dr. M. Ogawa, Dr. M. Nakamae and Dr. S. Murakami for their continuous encouragement.

References

- [1] T.-R. Yew and R. Reif, *J. Appl. Phys.* 65 (1989) 2500.
- [2] H. Hirayama, T. Tatsumi, A. Ogura and N. Aizaki, *Appl. Phys. Letters* 51 (1988), 2213.
- [3] H. Hirayama, T. Tatsumi and N. Aizaki, *Appl. Phys. Letters* 52 (1988) 2242.
- [4] Y. Mikata, T. Inoue, T. Usami, T. Ohta and H. Hirano, in: *Extended Abstracts 1st Intern. Symp. on Si-MBE*, Toronto, 1985 (Electrochemical Society, Pennington, NJ, 1985) p. 166.
- [5] M. Tabe, *Japan. J. Appl. Phys.* 21 (1982) 534.

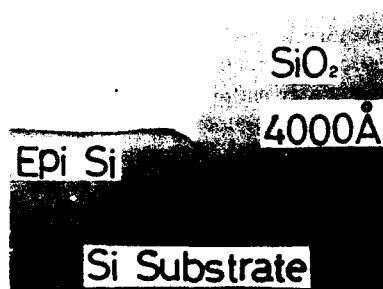


Fig. 6. Cross sectional TEM image showing an epitaxial layer grown selectively on the exposed Si window without poly-Si grown on SiO_2 . The film was deposited at a growth rate of 645 Å/min with a thickness of 1290 Å at 700°C and a gas flow rate of 60 SCCM.

Simulation with animation: microscopic growth kinetics of Si(001) homoepitaxy

M.R. Wilby

The Blackett Laboratory and Interdisciplinary Research Center for Semiconductor Materials, Imperial College, London SW7 2BZ, UK

M.W. Ricketts

IBM UK Scientific Centre, Winchester, Hampshire SO23 9DR, UK

S. Clarke and D.D. Vvedensky

The Blackett Laboratory and Interdisciplinary Research Center for Semiconductor Materials, Imperial College, London SW7 2BZ, UK

We present a description of the use of animation applied to simulation studies of molecular beam epitaxy. The animations generated are transferred to domestic video, which allows them to be used as demonstration and teaching tools. The major advantage gained from animation is the introduction of a temporal dimension when analysing the simulation. This allows the easy examination of fluctuations, where the enormity of the data produced usually forces the monitoring of only averaged quantities.

1. Introduction

Molecular-beam epitaxy (MBE) offers unprecedented control in the growth of low-dimensional semiconductor structures with novel electronic and optical properties. Underlying the utility of many such low-dimensional structures is the facility to grow atomically-abrupt interfaces. Under suitably-chosen operating conditions, growth proceeds in a layer-by-layer fashion [1,2], that is, a given layer is almost complete before growth of the next layer is initiated. When the lateral dimensions of the structures are large on an atomic scale (≈ 1000 Å), the details of the growth process are not a limiting factor. However, with lateral dimensions of heterostructures approaching as low as 10 atomic spacings, atomic-scale imperfections in the growth can undermine the integrity of the interface of two materials. Furthermore, in the growth of quantum wires and other sub-monolayer structures by MBE and variants such as migration-enhanced epitaxy, the growth front is comprised of

step edges, whose reduced dimensionality compared with the planar growth front of quantum wells means that fluctuations become increasingly important. In these situations, the growth process itself determines the extent to which the fabricated structure behaves as a structurally ideal heterostructure.

The inability to probe small length- and time-scale kinetic phenomena has led to the development of computer simulations of MBE growth to enable a better understanding of the formation of microscopic structures. Two principal techniques that have been utilized are Monte Carlo simulations [6–9] and molecular dynamics [10,11]. Molecular dynamics is restricted by the enormous computational overhead required to solve the equations of motion for every atom in the system at each time step, which is less than an atomic vibrational frequency ($\approx 10^{-13}$ s) [10]. Monte Carlo simulations, on the other hand, because of the simplicity of the representation of the substrate and of the kinetics, have the advantage of

allowing realistic substrate temperatures and growth rates (typically 1 monolayer/s). This can be maintained for extended periods of time (up to 1500 monolayers) on large lattices (up to 500×500). However, Monte Carlo simulations do present a problem in the sheer enormity of the data produced.

The problem we face is not unique to Monte Carlo simulations of MBE. The last three decades have witnessed an unprecedented increase in the power and availability of computers. This has fostered an explosion of activity in many areas of physics, with an accompanying expansion in the volumes of data being generated by computational physicists. Fortunately, developments in computer graphics have complemented this expansion, in particular leading to the introduction of "data visualization" techniques for presenting large quantities of data in ways that can be assimilated more readily. The fact that so much information is generated, makes data analysis a major problem. One way to address this difficulty is to take snapshots of the simulation. But while a single snapshot can characterize the system at a particular time, it may still remain difficult to ascertain the extent of activity within the system or to follow the trajectory of the system through phase space from one snapshot to the next. A more appropriate visualization of data streams from simulations is video animation, and in this paper we describe the application of animation techniques to the simulations of growth by MBE.

2. The model

We have implemented a model for GaAs and Si homoepitaxy based upon the solid-on-solid (SOS) model for crystal growth developed by Weeks and Gilmer [12]. We treat the substrate as a simple cubic lattice in which vacancies and overhangs are forbidden, and kinetic activity restricted to surface atoms. We allow two surface processes: deposition and migration. Evaporation of surface atoms is usually neglected, as at typical growth temperatures negligible desorption flux is observed [13]. Growth is initiated by the random deposition of atoms onto the substrate. The surface migration

kinetics are then modelled by prescribing an isotropic inter-site hopping probability with an Arrhenius form: $k(E, T) = k_0 \exp(-E/k_B T)$ in which k_0 is a surface vibrational term, k_B is Boltzmann's constant, T is the substrate temperature, and E is the barrier to migration.

A surface atom has a configurational diffusion barrier E comprising a substrate term and a term representing the number of nearest-neighbor bonds formed parallel to the substrate: $E = E_s + n_{\perp} + n_{\parallel} E_{\parallel}$, where E_s is the substrate term, E_{\perp} is the nearest-neighbor barrier in the direction perpendicular to of the dangling bond of the surface atom, n_{\perp} represents the number of bonds in that direction with E_{\parallel} and n_{\parallel} being the same quantities in the parallel direction. For Si(001) we set $E_{\parallel} = E_{\perp}/10$ and, as the direction of the dangling bond rotates through 90° on successive layers, the direction of the barrier anisotropy changes accordingly. The justification for the anisotropy comes from step-energy calculations performed by Chadi [15] and Aspnes and Ihm [16], where it was found that steps that form parallel to the direction of the dangling bond are energetically less stable than the perpendicular steps. The parameters used in all the animations are: $E_s = 1.3$ eV, $E_{\perp} + E_{\parallel} = 0.5$ eV and $k_0 = 10^{13} \text{ s}^{-1}$.

3. Animation

Animation introduces a temporal dimension into the visualization of data, and can exploit an observer's ability to correlate visual data in time as well as in space. For this reason, animation is obviously suited to addressing the representation of simulation data. Video has the particular advantage of accessibility, and in this format an animation can be presented or studied using only conventional domestic equipment. To generate the animation, we used general-purpose graphic research software developed at the IBM UK Scientific Centre [17] to generate raster images of solid models representing the surfaces. One such image was generated for each unique frame of the video tape, there being many hundreds of such frames in the final animations. A typical image took about 10 min to generate, though for this particular

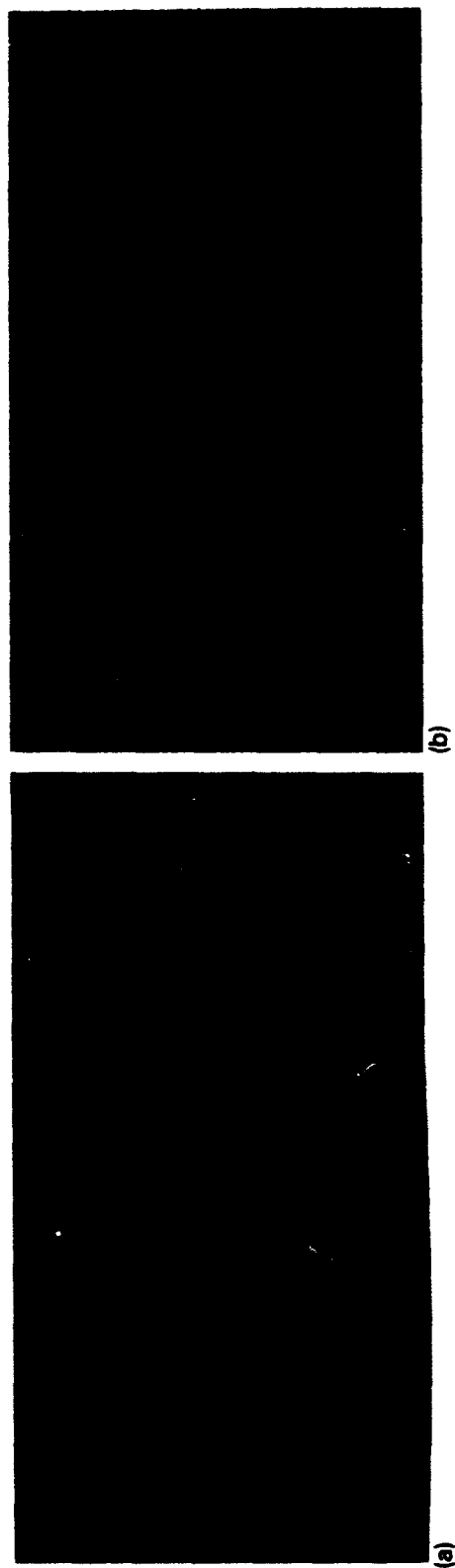


Fig. 1. Snapshots taken from a video showing the morphology of a substrate with four monatomic steps after the deposition of (a) 1.5 and (b) 2.5 layers of material at a substrate temperature of 750 K and a flux of 1 monolayer/s. The substrate is of dimension 120×120 , and two colors represent the two domains.

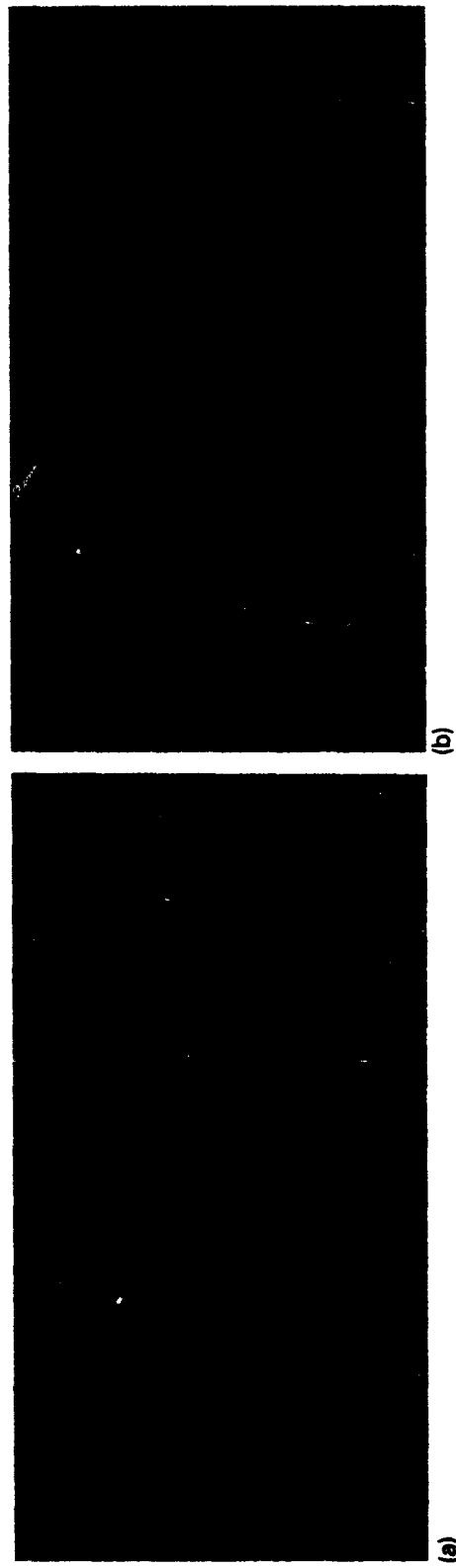


Fig. 2. Same as in fig. 1, except for a substrate with two biatomic steps.

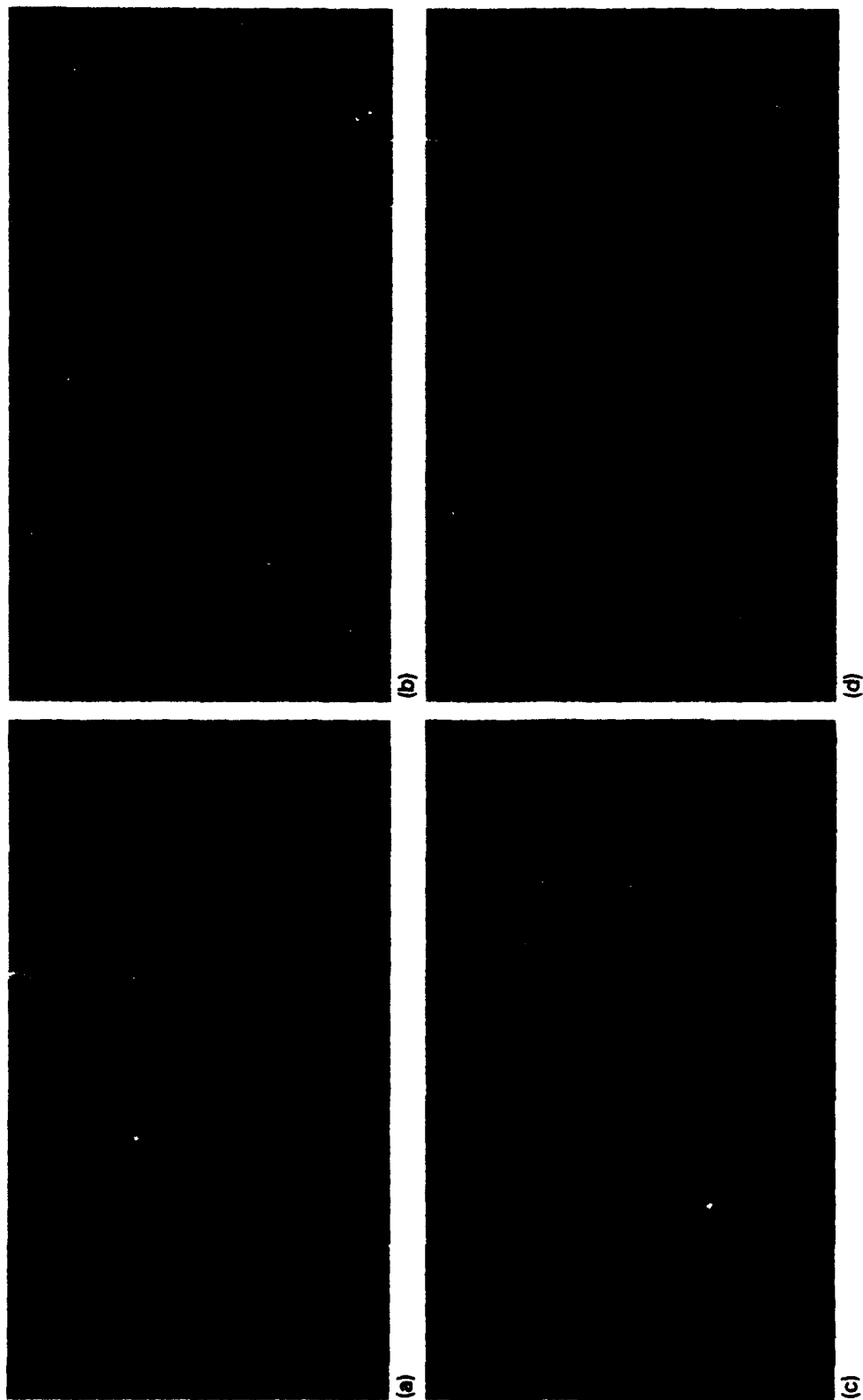


Fig. 3. Snapshots taken from a video showing the morphology of a substrate with 10 monatomic steps after the deposition of (a) 0, (b) 0.1, (c) 0.6, and (d) 1.0 monolayers after the surface has been heated at 850 K for 5 s. The substrate is of dimension 120×120 , the flux is 1 monolayer/s, and two colors again represent the same domains as in figs. 1 and 2.

application, specially-designed software could have taken advantage of features in the graphics, such as polygonal shading to substantially reduce the required computational resources. More details of the animation process for MBE may be found in ref. [18].

4. Animations of Si(001) homoepitaxy

There are a number of ways in which the animation of a physical process such as MBE are beneficial. All of these stem from the level of detail concerning the kinetic activity contained in the animation. While an average description of the process can be easily obtained with quantities such as the density of surface steps or a diffraction pattern, the statistical fluctuations are much more difficult to address theoretically. Animation provides a very natural medium for observation of high temperature fluctuations, since for any process involving a dynamic or evolutionary aspect, an animation is more likely to convey the activity of the process than any static rendering, be it line graphs or sophisticated graphics. The animations have demonstrated growth mode transitions on vicinal surfaces and have drawn attention to the details of step profile fluctuations which were not apparent in prior analyses of the simulations [18]; stills from the video demonstrate the irregularity of the step structure, but can not convey how it is likely to alter with time.

The animations have proved particularly useful in adding to our understanding of Si(001) homoepitaxy. In this case we used a 120×120 substrate. The increased degree of realism in comparison with the 40×40 lattices used earlier eliminates finite-size effects, but drastically increases the graphical processing requirements. An important feature of homo- and heteroepitaxy on Si(001) is the strong dependence of the growth characteristics upon the temperature and duration of substrate annealing prior to growth. For Si(001) homoepitaxy on a surface subjected to extended high-temperature ($\approx 1000^\circ\text{C}$) annealing, sustained oscillations in reflection high-energy electron-diffraction (RHEED) specular intensity are ob-

served, exhibiting either a monolayer or bilayer period, depending upon the azimuthal orientation of the electron beam [19]. However, for homoepitaxy on a surface prepared without such an annealing, there is a decaying envelope to the RHEED oscillations, which exhibit a monolayer period independent of the azimuth [20].

Even in the case of nucleation dominated growth on Si(001), where the behaviour was well understood from analysis of averaged quantities, a demonstration of the actual growth sequence is dramatic and shows clearly the degree to which a domain must complete before the next layer is formed. This is something that is not clear without including the temporal dimension that animation facilitates. Figs. 1 and 2 show the morphology of the surface after 1.5 and 2.5 monolayer deposition, on single- and double-domain surfaces, respectively. They show quite clearly the change in the direction of cluster elongation, but fail to convey the cooperative and remarkably rapid coalescence of the clusters, and the way their structure prevents the formation of the next layer until this has been achieved.

Monoatomic steps on a vicinal Si(001) alternate in stability. This means that one type of step, the unstable one, is more susceptible to fluctuations than the other, with the relatively stable steps thus showing smooth profiles and the relatively unstable steps showing a comparatively rough profile. This has been confirmed by scanning tunnelling microscopy [21,22]. During growth the less stable step advances (fig. 3), so that the predominant amount of the surface is terminated with an unstable step, but during surface recovery it recedes, so that there is approximately an equal amount of each type of surface. Experimentally, this is observed by monitoring the half-order beams, whose intensity is a measure of the relative coverages of 1×2 and 2×1 domains [23–25]. From the animation it is apparent that this relaxation back to equal coverage is caused by the unstable step attempting to maximise its degree of fluctuation. The fluctuations are bounded by the stable steps and hence its optimum average position is half-way between them. Such an effect would be difficult if not impossible to identify without such a continuous way of observing temporal behavior.

5. Conclusions

The ability to view the temporal evolution of individual atomic configurations has significantly added to our understanding of the solid-on-solid model and to the microscopic growth kinetics of MBE. Particularly fruitful have been the applications to GaAs(001) and Si(001), which have reproduced experimentally observed growth modes and highlighted the dynamic nature of terraced surfaces at higher temperatures. The development of visualization techniques such as those described here hold promise of an exciting future in the presentation and analysis of scientific data, including possible applications for emerging computer technologies which take advantage of the inherent concurrency of animating a simulation.

Acknowledgement

S.C. thanks the UK Science and Engineering Research Council for support.

References

- [1] J.H. Neave, B.A. Joyce, P.J. Dobson and N. Norton, *Appl. Phys.* A31 (1983) 1.
- [2] J.M. Van Hove, C.S. Lent, P.R. Pukite and P.I. Cohen, *J. Vacuum Sci. Technol.* B1 (1983) 741.
- [3] M.J. Kelly and R.J. Nicholas, *Rept. Prog. Phys.* 48 (1985) 1699.
- [4] P.M. Petroff, A.C. Gossard, R.A. Logan and W. Wiegmann, *Appl. Phys. Letters* 41 (1982) 635.
- [5] J.M. Gaines, P.M. Petroff, H. Kroemer, R.J. Simes, R.S. Geels and J.H. English, *J. Vacuum Sci. Technol.* B6 (1988) 1378.
- [6] S. Clarke and D.D. Vvedensky, *Phys. Rev. Letters* 58 (1987) 2235.
- [7] A. Madhukar and S.V. Ghaisas, *Appl. Phys. Letters* 47 (1985) 247.
- [8] A. Kobayashi and S. Das Sarma, *Phys. Rev. B* 37 (1988) 1039.
- [9] S.A. Barnett and A. Rockett, *Surface Sci.* 198 (1988) 133.
- [10] A. Schneider, I.K. Schuller and A. Rahman, *Phys. Rev. B* 36 (1987) 1340.
- [11] E.T. Gawalinski and J.D. Gunton, *Phys. Rev. B* 36 (1987) 4774.
- [12] J.D. Weeks and G.H. Gilmer, *Advan. Chem. Phys.* 40 (1979) 157.
- [13] J.R. Arthur, *J. Appl. Phys.* 39 (1968) 4032.
- [14] S. Clarke and D.D. Vvedensky, *Phys. Rev. B* 36 (1987) 9312.
- [15] D.J. Chadi, *Phys. Rev. Letters* 59 (1987) 15.
- [16] D.E. Aspnes and J. Ihm, *Phys. Rev. Letters* 57 (1986) 3054.
- [17] J.M. Burrige, B.M. Collins, B.N. Galton, A.R. Halbert, T.R. Heywood, W.H. Latham, R.W. Phippen, P. Quarendon, P. Reilly, M.W. Ricketts, J. Simmons, S.J.P. Todd, A.G.N. Walter and J.R. Woodward, *IBM Systems J.* 28 (1989) 548.
- [18] M.W. Ricketts, D.D. Vvedensky and S. Clarke, *Phys. World* 2(12) (1989) 39.
- [19] T. Sakamoto, N.J. Kawai, T. Nakagawa, K. Ohta and T. Kojima, *Appl. Phys. Letters* 47 (1985) 617.
- [20] J. Aarts, W.M. Gerits and P.K. Larsen, *Appl. Phys. Letters* 48 (1986) 931.
- [21] A.J. Hoeven, J.M. Lenssinck, D. Dijkkamp, E.J. van Loenen and J. Dieleman, *Phys. Rev. Letters* 63 (1989) 1830.
- [22] Y.-W. Mo, B.S. Swartzentruber, R. Kariotis, M.B. Webb and M.G. Lagally, *Phys. Rev. Letters* 63 (1989) 2393.
- [23] K. Sakamoto, T. Sakamoto, K. Miki and S. Nagao, *J. Electrochem. Soc.* 136 (1989) 2705.
- [24] K. Sakamoto, K. Miki, and T. Sakamoto, *Thin Solid Films* 183 (1989) 229.
- [25] A.J. Hoeven, E.J. van Loenen, D. Dijkkamp, J.M. Lenssinck and J. Dieleman, *Thin Solid Films* 183 (1989) 263.

Molecular dynamics and quasidynamics simulations of low-energy ion/surface interactions leading to decreased epitaxial temperatures and increased dopant incorporation probabilities during Si MBE

M. Kitabatake, P. Fons and J.E. Greene

Department of Materials Science, Coordinated Science Laboratory, and Materials Research Laboratory, University of Illinois, 1101 West Springfield, Urbana, Illinois 61801, USA

Molecular dynamics and quasidynamics simulation utilizing the Tersoff many-body potential, have been used to investigate ion/surface interaction kinetics and mechanisms, including defect formation and annihilation, associated with the use of low-energy ion irradiation during Si film growth by MBE to decrease epitaxial temperatures and increase dopant incorporation probabilities. The irradiation events were initiated at an array of points in the primitive unit cell of 2×1 terminated Si(001) lattice.

1. Introduction

Several groups have demonstrated reduced epitaxial temperatures during Si MBE experiments in which a fraction of the incident condensing beam is ionized and accelerated to energies ≤ 200 eV [1–3]. In addition, low-energy accelerated-ion doping during Si MBE has been shown to overcome problems associated with low dopant incorporation probabilities and profile broadening due to surface segregation [4,5]. Low-energy ion-doped MBE Si films exhibit excellent opto-electronic properties, with no evidence of residual ion damage, as determined by temperature-dependent Hall [6], deep-level transient spectroscopy [6], and photoluminescence [7] measurements.

In this paper, we present results obtained using molecular dynamics (MD) and quasidynamics (QD) simulations to investigate ion/surface interactions which control the kinetics and mechanisms of ion-induced low-temperature Si epitaxy and defect formation/annihilation during MBE with ion doping. Irradiation events were initiated with 10 and 50 eV Si atoms incident normal to the surface at an array of points in the Si(001) 2×1 primitive unit cell. Each event was followed to determine kinetic energy redistribution in the lattice as a function of time, projectile and lattice

atom trajectories, and the nature, number, and depth of residual defects. Minimum energy diffusion paths and defect formation and migration activation energies as a function of near-surface lattice position, including relaxation around defects, were also calculated. Events resulting in low-temperature epitaxy (due to both projectiles and lattice atoms coming to rest at epitaxial sites) were analyzed in detail.

2. Simulation procedure

The simulations were carried out using a combination of MD and modified QD techniques, discussed in detail in refs. [8,9], employing the many-body Tersoff potential [10]. In QD simulations, the positions and velocities of each atom are computed in a fully dynamic mode until both the total system force and potential energy values reach minima, at which point the velocity of each atom is set to zero and the system allowed to evolve further. The procedure is repeated until stable atom positions, with approximately zero net force, are obtained.

The computational cell for the 10 eV (50 eV) bombardment events included 360 (1920) atoms, 10 (20) Si(001) layers with dimensions 6×6 ($8 \times$

12) atoms. All violent collisional effects were found to subside within the first 6 (14) layers. Increasing the size of the cell by a factor of three had no significant effects on the results. Layers 7 and 8 (17 and 18) were momentum damped to minimize kinetic energy reflection and layers 9 and 10 (19 and 20) were fixed. The surface layer was allowed, following the procedure described in ref. [8], to relax, yielding a (2×1) dimerized surface. Periodic boundary conditions were applied to the four (110) boundary planes. The starting temperature for the simulations was 0 K, however lattice atoms involved in collision cascades attained kinetic energies ≥ 0.5 eV, corresponding to temperatures well above those used during typical MBE Si growth experiments (900–1050 °C). Simulations carried out with initial crystal temperatures up to 1000 K showed that the primary results – including the maximum penetration depth of the projectile, the average stopping depth, and the average position of residual bulk defects – are essentially the same as those obtained in $T = 0$ K simulations. Trajectories obtained from simulations initiated at $T = 0$ K correspond to an average over a very large number of simulations initiated at a high temperature and the same impact geometry [8].

3. Results and discussion

Fig. 1 shows the 36 points in the primitive surface unit cell of the 2×1 reconstructed Si(001) lattice used to initiate 10 and 50 eV collision sequences. The points were chosen to explore both high and low symmetry regions [8]. Each collisional event was followed for ≥ 800 ps, with time steps adaptively increased from 0.2 to 4 fs as the calculation proceeded, until the maximum kinetic energy per atom was < 0.5 eV.

3.1. Ten electron-volt irradiation

The 10 eV Si projectiles came to rest in positions ranging from an epitaxial bridge site above the surface dimers to the fourth layer, with an average stopping position of 0.5 Å below the surface (between the first and second layers). Split (S) and hexagonal (H) interstitials were obtained in the second to sixth layers with the largest concentrations being in the third and fourth layers. No residual vacancies were observed.

The only collision sequence resulting in projectile reflection was initiated at impact point 10 (see fig. 1) in the center of four dimers. In every case in which energetic projectiles were incident

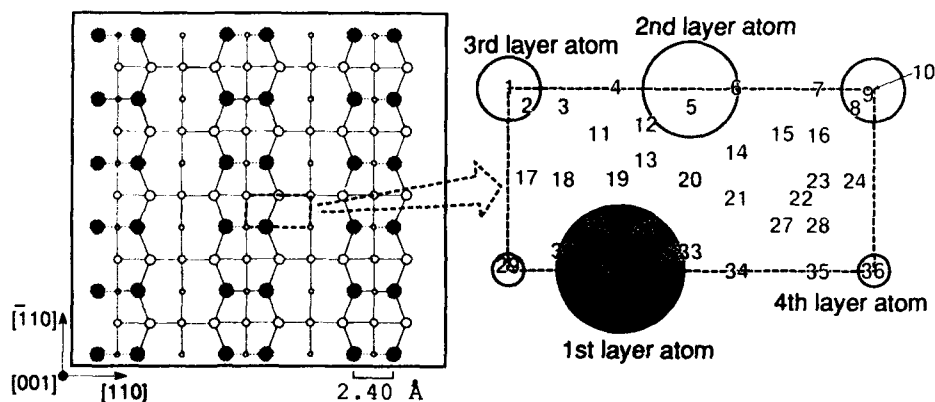


Fig. 1. A Si(001) 2×1 reconstructed surface, calculated using a modified quasidynamics technique, showing the 36 points in the primitive surface unit cells used to initiate 10 and 50 eV Si collision sequences.

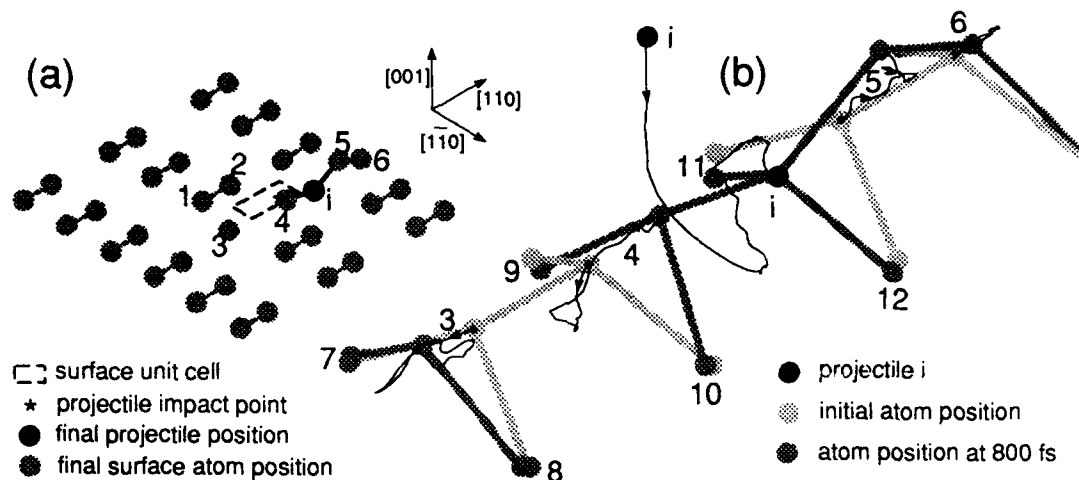


Fig. 2. (a) Calculated stable surface-atom and projectile positions exhibiting exchange epitaxy following 10 eV Si bombardment at surface unit cell point 27 (see fig. 1). (b) Projection view showing trajectories of projectile i and surface-atoms 3 through 6 following bombardment.

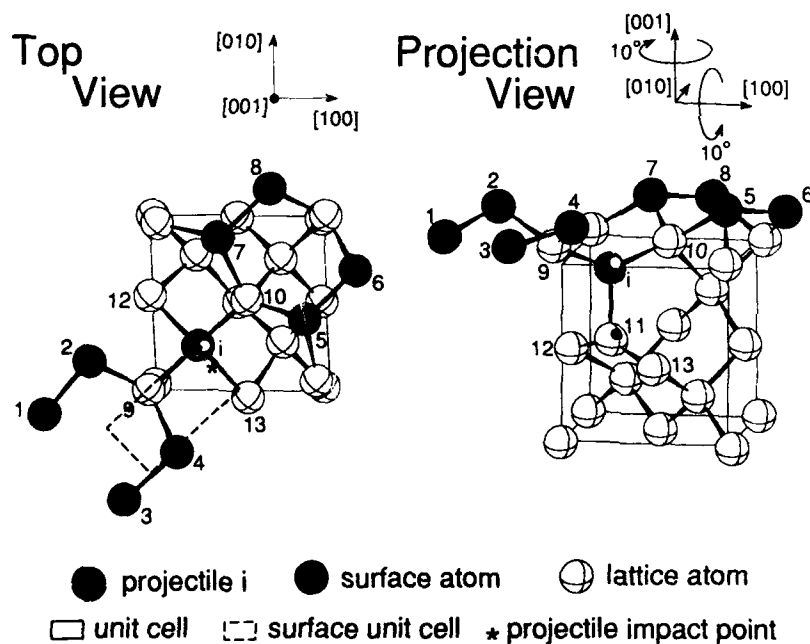


Fig. 3. Top and projection views of a Si lattice with a (001)2x1 reconstructed surface after bombardment by a 10 eV Si atom at surface unit cell point 24 (see fig. 1) indicated by ★.

near dimers, surface reactions (dimer opening, epitaxial growth, and surface defect creation) were observed. Fifteen of the 36 collision sequences opened surface dimers. Ten events resulted in epitaxy, eight of which occurred without residual bulk defects and five involved the opening of additional dimers. In the epitaxial events, the projectile came to rest either at an epitaxial bridge site position or, through an exchange process, at a lattice site with the displaced surface atom at an epitaxial position. An example of the latter, corresponding to bombardment at impact point 27, is illustrated in fig. 2a. The projectile *i* broke dimer 3–4, then, after interacting with second and third layer atoms, exchanged positions with atom 5 which came to rest in an epitaxial position between *i* and atom 6. The trajectories of atoms 3–6 and *i* are shown in fig. 2b.

Dimer atom interstitials were created following head-on or nearly head-on collisions with a dimer atom (impact points 30–33). Weak projectile/surface interactions due to ion incidence between the dimers resulted in residual bulk projectile interstitials. Ten S interstitials (impact points 6, 7, 12, 16, 24, 28, 30, 32, 35, and 36) and four H interstitials (points 22, 23, 31, and 33) were observed. Fig. 3 shows top and projection views illustrating an S interstitial created following bombardment at impact point 24. S is composed of projectile *i* and atom 11, oriented along the [001] direction, and centered on the original position of atom 11 in the third layer. Incident atom *i* interacted strongly only with atom 11 causing it to be displaced downward. Impact at points 28, 35, and 36 near the projected position of fourth-layer atom 13 also produced, through the same mechanism, S interstitials.

3.2. Fifty electron-volt irradiation

Raising the projectile energy from 10 to 50 eV resulted in an increase in: the average stopping depth from 0.5 to 1.6 Å (between layers $\ell=2$ and 3), the total number of epitaxial events from 10 to 13, the total number of residual bulk defects from 16 to 63 (note that the ratio of epitaxial events to residual bulk defects decreased), the number of projectiles ending in substitutional sites from 7 to

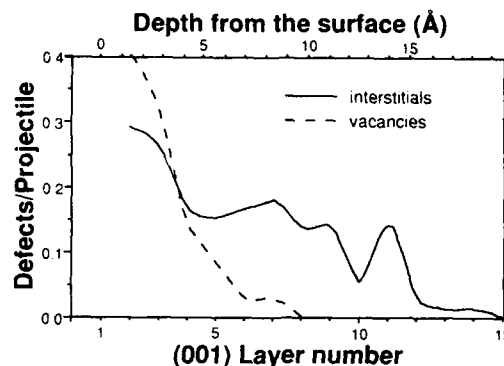


Fig. 4. The average number of lattice interstitials and vacancies produced per projectile for 50 eV Si atoms incident at the 36 points in the Si(001)2×1 primitive surface unit cell shown in fig. 1.

24, and the ratio of purely lattice-atom interstitials to projectile interstitials from 5/11 to 58/5. 50 eV irradiation also created residual vacancies (V), bonding defects, and defects which we have named pentagonal interstitials (P). Fig. 4 shows the depth distribution of interstitials ($\ell=2-14$) and vacancies ($\ell=2-7$). One sputtering event was observed in which a dimer atom was ejected following impact at surface unit cell point 34.

Thirty-five of the simulation runs resulted in the formation of more than one residual interstitial. In total, there were 40 S interstitials, 12 H interstitials, 4 tetrahedral (T) interstitials, 4 bond-centered (B) interstitials, and 3 pentagonal (P) interstitials. Fig. 5 shows a P interstitial in which atoms 1–4 occupy the area initially filled by atoms a, b, and c. The calculated formation energy E_f of a bulk P interstitial is 3.7 eV, while E_f for T, S, H,

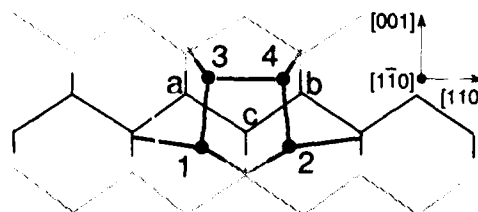


Fig. 5. A pentagonal interstitial in bulk Si. Atoms 1–4 occupy the area initially filled by atoms a, b, and c.

and B interstitials are 3.5, 4.7, 4.9, and 5.5 eV, respectively. P interstitials are more stable since all but one of the atoms in the defect have four-fold bonds whose lengths are within 6% of the initial 2.35 Å bond length. E_f for interstitials decreases as the surface is approached due to increased lattice relaxation, causing dilation, in the [001] direction. For example, E_f values for T and S interstitials located in $\ell = 3$ and H interstitials between layers 2 and 3 were 2.9, 2.7, and 2.6 eV, respectively. The probability of obtaining residual interstitials was large in lattice regions directly beneath the center of rectangles formed by four dimers. This gave rise to the maxima at $\ell = 7$ and 11 in the interstitial depth distribution shown in fig. 4.

A total of 36 V were observed and the average depth was 2.9 Å ($\ell \approx 3$). The maximum V concentration was in the second layer. Eleven bonding-defects were obtained in layers 3 to 11.

3.3. Defect annihilation

Diffusion and annihilation of ion-induced defects were investigated using QD by allowing one to several atoms, depending upon the defect, to migrate in steps of < 0.1 Å. During each diffusional step, all lattice atoms were fully relaxed and the diffusing species were relaxed in the plane orthogonal to the diffusion direction. The calculated trajectories coincided with minimum energy paths. Interstitial migration activation energies E_m were always ≤ 1.4 eV, except for P interstitials for which $E_m \leq 1.8$ eV, and decreased with decreasing ℓ . Due to the low E_f value for T interstitials and the strong effect of surface relaxation, the primary diffusion path for annealing of interstitials was along THT toward the surface. The annihilation activation energy for bonding defects was ≤ 1.2 eV. Vacancies, however, were found to be very stable with $E_m = 2.3$ eV, more than 1.5 times larger than E_m for all interstitials except P.

4. Conclusions

The simulations provide detailed insights into mechanisms associated with low-energy ion-bombardment-induced epitaxy and defect produc-

tion/annihilation. Several collision sequences resulted in the opening of additional dimers thus providing 1×1 sites for migrating adatoms during crystal growth. This suggests, in agreement with experimental results [11], that low-energy self-ion irradiation during vapor-phase film deposition may be useful for decreasing the epitaxial temperature even when the ion flux is only a small fraction of the total condensing atom flux. Trapping probabilities for both 10 and 50 eV projectiles were essentially unity. While residual bulk defects were also formed in many of the collision events, the interstitials and bonding defects were easily annealed out over times corresponding to monolayer deposition (of the order of one to several s) at typical growth temperatures. Full annealing of vacancies, however, requires interactions with deeper interstitials (see fig. 4) moving toward the surface and incident Si atoms.

Acknowledgements

The authors gratefully acknowledge the financial assistance of the Joint Services Electronics Program, the Semiconductor Research Corporation, the National Center for Supercomputing Applications, and the Space Vacuum Epitaxy Center funded by NASA.

References

- [1] T. Narasawa, S. Shimizu and S. Komiya, *J. Vacuum Sci. Technol.* 16 (1979) 377.
- [2] P.C. Zalm and L.J. Beckers, *Appl. Phys. Letters* 41 (1982) 167.
- [3] T. Ohmi, T. Ichikawa, T. Shibata, K. Matsudo and H. Iwabuchi, *Appl. Phys. Letters* 53 (1988) 45.
- [4] M.A. Hasan, J. Knall, S.A. Barnett, J.-E. Sundgren, L.C. Markert, A. Rockett and J.E. Greene, *J. Appl. Phys.* 65 (1989) 172.
- [5] W.-X. Ni, J. Knall, M.A. Hasan, G.V. Hansson, J.-E. Sundgren, S.A. Barnett, L.C. Markert and J.E. Greene, *Phys. Rev. B* 40 (1989) 10449.
- [6] J.-P. Noël, N. Hirashita, L.C. Markert, Y.-W. Kim, J.E. Greene, J. Knall, W.-X. Ni, M.A. Hasan and J.-E. Sundgren, *J. Appl. Phys.* 65 (1989) 1189.
- [7] J.-P. Noël, J.E. Greene, N.L. Rowell, S. Kechang and D.C. Houghton, *Appl. Phys. Letters* 55 (1989) 1525.

- [8] M. Kitabatake, P. Fons and J.E. Greene, *J. Vacuum Sci. Technol.* A8 (1990) 3726.
- [9] M. Kitabatake, P. Fons and J.E. Greene, *J. Vacuum Sci. Technol.*, in press.
- [10] J. Tersoff, *Phys. Rev.* B38 (1988) 9902.
- [11] See, for example, the following review article and references therein:
J.E. Greene, S.A. Barnett, J.-E. Sundgren and A. Rockett, in: *Ion-Beam Assisted Film Growth*, Ed. T. Itoh (Elsevier, Amsterdam, 1978) ch. 5.

Scanning tunneling microscopy studies of the growth process of Ge on Si(001)

Y.-W. Mo and M.G. Lagally

Department of Materials Science and Engineering, College of Engineering, University of Wisconsin, Madison, Wisconsin 53706, USA

The growth process of Ge on Si(001) has been investigated using a scanning tunneling microscope (STM) and a comprehensive picture of the major kinetic processes is obtained. Surface diffusion of Ge on Si(001) is found to be anisotropic. The two types of monatomic steps are shown to have different lateral sticking coefficients for Ge adatoms. The transition from 2D to 3D growth is found to occur via a kinetic pathway – a novel type of intermediate 3D cluster.

1. Introduction

The growth of Ge on Si(001) has attracted much attention recently because of the potential application of this heterojunction structure in opto-electronic devices [1–4]. Although this system has been studied with a variety of techniques [5–9] many aspects of its growth are still not well understood.

Film growth is a nonequilibrium process in which kinetics plays an essential role [10]. Deposition of adatoms onto a surface drives the system into supersaturation, from which the system tries to relax back to equilibrium by forming a condensed phase, e.g., 2D islands for an adlayer that wets the substrate. Adatoms move randomly on the surface and, when meeting each other, form islands. All islands larger than the critical nucleus will grow by further addition of adatoms until the supersaturation is eliminated. Another means of removing the supersaturation is by the adsorption of adatoms on those substrate steps that are good sinks. The surface diffusion coefficient determines the relative rates of these processes. From an atomistic point of view, kinetic processes in growth can be categorized into pure migration of adatoms on a flat terrace and the interactions of adatoms with surface steps. Of particular interest are the

possible anisotropies in these aspects for a surface with low symmetry, e.g., two-fold symmetry for Si(001). The lateral sticking coefficient of adatoms at steps is one of the most important issues for growth kinetics. The conventional wisdom that all steps are good sinks for adatoms has been shown to be invalid for Si/Si(001) [11], and we will show that this is also the case for Ge/Si(001).

Because of the lattice mismatch between Si and Ge, 2D growth eventually becomes unfavorable because of the buildup of strain energy in the 2D film, and 3D clusters form to relax the strain. The transition process from 2D to 3D structures in such a Stranski–Krastanov process is an interesting problem. Phase succession has been known to occur in many phase transition processes [12], i.e., one or more intermediate phases with lower nucleation barriers form and dissolve prior to the final equilibrium phase. We will show that there is such a kinetic pathway for the 2D to 3D transition of Ge/Si(001).

Scanning tunneling microscopy (STM), because of its atomic resolution and ability to scan large areas (e.g., 1.5 μm), provides an ideal tool for studying growth processes at the atomistic level. In this paper, we report an STM study of the growth process of Ge/Si(001), addressing the anisotropies in surface migration of Ge adatoms and

in the lateral sticking coefficient of adatoms at steps, and the transition process from 2D to 3D structures.

2. Experimental

The experiments are carried out in a UHV system equipped with a home-made STM, LEED optics, and a Ge deposition source. The base pressure of the system is 6×10^{-11} Torr. The substrates used for this study are nominally flat Si(001) wafers, with an actual miscut angle of 0.04° . Thermal cleaning of the substrates is carried out by DC heating to 1550 K [13]. The sample temperature is measured with an IR pyrometer. The Ge deposition source is a DC-heated wafer and the deposition rate is determined by measuring the surface coverage of Ge after a submonolayer is deposited onto the substrate at 470 K, a temperature at which only a negligible amount of adatoms is lost to surface steps [14].

The sample is quenched to room temperature immediately after deposition and then transferred in situ to the STM. All scans are carried out at room temperature at which no change in the surface structure can be observed even after several hours of scanning.

3. Submonolayer growth: anisotropies in surface migration and sticking to steps

The anisotropies in surface migration of adatoms and their interactions with surface steps can be studied by the analysis of denuded zones in the spatial distribution of the islands formed by deposition. A denuded zone is a striped area on the surface along a step where the island density is lower than that far away from the step, which is formed because adatoms arriving from the vapor and landing near the step can diffuse and stick to it before colliding with each other to form islands on the terrace. The length of a denuded zone depends on the following factors: how fast adatoms migrate on the surface; to what degree the step acts as sink for adatoms; whether a large energy barrier exists at the step for adatoms to

cross. By choosing specific step configurations, one can study each of these factors separately.

If a terrace is bounded by two different types of steps, the relative length of the two denuded zones near the steps is determined only by the relative value of the lateral sticking coefficients and energy barriers for crossing the two, because the adatom migration on the terrace is the same toward both steps. A high asymmetry in the denuded zone lengths will indicate very different properties of the two types of steps.

Furthermore, if a step separates two different terraces so that the diffusion of adatoms toward the step on the two terraces is along two different characteristic surface directions, then the two denuded zone lengths around this step will be different if diffusion is anisotropic. The ratio of the two lengths will provide quantitative information on the diffusion anisotropy. A condition for this analysis, however, is that this step is not only a good sink but also a symmetric sink for adatoms, i.e., adatoms from either the up- or the down-terrace will stick equally well upon reaching this step. This condition can be tested independently by choosing a configuration in which diffusion is symmetric from above and below.

The Si(001) surface forms a (2×1) reconstruction, with top-layer atoms dimerizing to reduce the number of dangling bonds. This establishes two characteristic directions on the surface: either along or perpendicular to the dimer rows. A natural question is whether the surface diffusion of adatoms is different in these two different directions [15,16]. Due to the tetrahedral structure of silicon, each monatomic step separates two degenerate reconstruction domains (2×1 and 1×2 domains) with dimer rows perpendicular to each other. Also there are two different types of monatomic steps [17]: one is perpendicular to the up-terrace dimer rows and is called an S_B step, and the other is parallel to the up-terrace dimer rows and is called an S_A step. An alternative description is that S_B is formed at the end of the dimer rows and S_A at the side of the dimer rows. Because the energy of forming kinks in an S_A step is higher than that in an S_B step [18], S_A steps are typically smooth while S_B steps are rough [19]. At issue here is the relative magnitude of the lateral

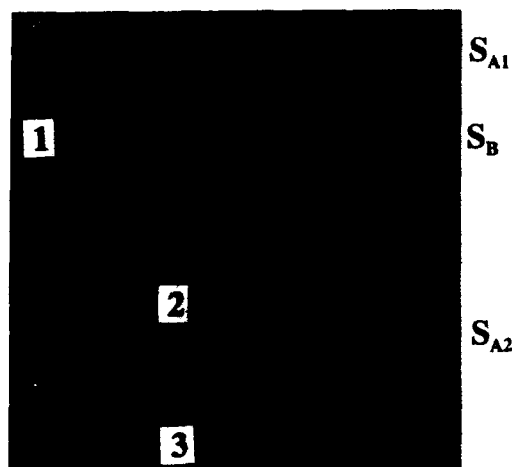


Fig. 1. STM image of the spatial distribution of Ge 2D islands relative to substrate steps, after ~ 0.2 ML Ge is deposited on Si(001) at 550 K substrate temperature. The scan range is 5000×5000 Å.

sticking coefficients for Ge adatoms at these two different types of steps.

To study these anisotropies, a submonolayer dose of Ge is deposited on the Si(001) substrate at temperatures at which growth is primarily by island formation rather than by step flow. Spatial distributions of 2D Ge islands are observed with STM. Fig. 1 is a large-scale STM scan showing 2D Ge island distributions relative to different types of monatomic steps. In the figure, the third terrace from the upper left (terrace 3) is bounded by S_B to the upper left and S_A at the lower right (S_{A2}). It can be seen that the island density close to the S_B step is almost zero while it gradually increases towards S_{A2} . This suggests that the denuded zone due to the S_B step is actually larger than the width of this terrace. One can imagine that if S_{A2} were moved farther away, one would see the island density increase until it reaches the uniform value seen on terrace 1, far enough from the S_B step. Terrace 1 is essentially the same as terrace 3 except the width is much larger. The S_B bounding step is far out at the upper left and not shown in the figure. It can be seen that on this terrace, in the area close to S_{A1} the island density is as high as that far from it. Therefore we conclude that S_B steps (the ends of dimer rows) are good sinks for

Ge adatoms and there is no large energy barrier for adatoms to cross downward over an S_B step, and that S_A steps (the sides of dimer rows) are poor sinks for adatoms. An interesting point is that initially adsorbed Ge adatoms decorate S_B steps of the Si(001) substrate, and further adsorption of Ge adatoms is actually by S_B steps made of Ge atoms.

The anisotropy in lateral sticking coefficients of adatoms at S_A and S_B steps is also reflected in the very anisotropic growth shape of 2D Ge islands, as shown in fig. 1. The islands are long in the dimer row direction, indicating that adatoms stick to the end of dimer rows much better. Here again the steps themselves are made of Ge atoms. Annealing of the growth structure results in a much less anisotropic equilibrium shape [11], which is determined by the ratio of the free energies of the steps, rather than the kinetic sticking coefficients.

Now we concentrate on the two denuded zones around the S_B step in fig. 1. It can be seen that they are not symmetric. The denuded zone on terrace 2 is much shorter than the one on terrace 3. Since the dimer rows in terrace 3 are perpendicular to the step while the dimer rows in terrace 2 are parallel to the step, this denuded zone asymmetry is clear evidence for diffusion anisotropy: surface diffusion of Ge adatoms on Si(001) is faster along substrate dimer rows than perpendicular to them. By preparing a sample in a configuration in which steps are at 45° to the dimer rows ($\langle 100 \rangle$ steps), such that the diffusion toward steps on each terrace is identical, we observe that denuded zones above or below each step have the same length, indicating that S_B steps are symmetric sinks for Ge adatoms from either up or down terraces. Steps with $\langle 100 \rangle$ orientations are made of alternating S_A and S_B step segments. However, as we have shown in fig. 1, S_A steps are very poor sinks, and hence we can assume that only the S_B segments actually adsorb adatoms, and therefore the adsorption behavior of the $\langle 100 \rangle$ steps reflects the properties of S_B steps.

Comparison of computer simulation results of the dependence of the denuded-zone length on the diffusion coefficient with quantitative measurements of the denuded zone asymmetry yields a diffusion coefficient that is at least 1000 times

faster along the dimer rows than perpendicular to them [20]. Note that the fast diffusion direction is perpendicular to the long axis of the growth shape of 2D islands. As mentioned earlier, the anisotropy of the growth shape is caused by the sticking coefficient anisotropy, and is not a consequence of diffusional anisotropy.

The above results on the microscopic aspects of surface kinetics are all essentially the same as for Si/Si(001). A detailed description of the denuded-zone analysis can be found in ref. [20].

4. Multilayer growth: kinetic pathway in 2D to 3D transition

After growth of about 3 monolayers (ML) at typical temperatures (e.g., 775 K), STM scans show that the growth mode is still two-dimensional, although with a rough growth front that typically involves 3 layers in a 600×600 Å area, as shown in fig. 2. This roughness is reduced after annealing at higher temperatures (e.g., 10 min at 875 K), confirming that 2D growth for doses less than 3 ML is an equilibrium structure rather than a result of kinetic limitations [1–9].

Growth beyond 3 ML results in 3D island formation. However, in addition to the “macro-



Fig. 2. STM image of rough 2D layers after 3 ML of Ge is deposited at ~ 775 K. Scan range is 600×600 Å. Displayed in the normal grey scale mode.

scopic” 3D islands that have been observed previously [5–9], we find a large concentration of generally much smaller clusters with well defined shapes, facet structure, and orientations distinctly differing from those of the “macroscopic” ones. Fig. 3 shows two STM images of these clusters. The smaller clusters have predominantly a prism shape (with canted ends). To distinguish them from the “macroscopic” clusters, we shall refer to



Fig. 3. STM images of two types of Ge 3D clusters on Si(001). (a) A “macroscopic” cluster surrounded by many “hut” clusters. The scan range is 8000×8000 Å. The “macroscopic” cluster is ~ 250 Å high. The image is shown in a curvature mode, to remove the large height difference. (b) Perspective view of some “huts” and a corner of a “macroscopic” cluster. Typical heights of the “huts” are between 20 and 50 Å. The scan range is 1500×1500 Å.

them as "hut" clusters. By detailed STM measurements, we determine that all four facets of the "hut" are {105} planes [21].

There are three interesting features of these "hut" clusters. One is the perfection of the facet planes. We never observe a partially completed layer on a facet. This observation, as well as a second one, namely that the number density of "huts" increases rapidly while their size grows only slowly with the Ge dose, is in accord with well known concepts about the stability of low-energy surfaces, for which a nucleation process is required for each new layer but once this occurs, the layer completes very rapidly. The third feature of the "hut" clusters is their generally elongated base shape and their orientations. Because all four facets are the same, they must have the same surface free energy and sticking coefficient for arriving atoms. The prism axes are at 45° to the dimer row directions, and therefore the Si substrate does not provide any preference in terms of surface stress or anisotropic diffusion. One possible explanation for the elongated shapes is that $\langle 100 \rangle$ steps (running 45° to the dimer row directions), formed in the 2D Ge layers during growth, act as nucleation sites. There are two orthogonal sets of these steps, corresponding to the principal axes of the clusters we observe. We have made limited STM measurements on samples miscut toward $\langle 100 \rangle$ by 2.5° that appear to support this idea of the role of $\langle 100 \rangle$ steps. "Hut" clusters predominantly form with their principal axis aligned parallel to these steps. Because the step density in these samples is greater, the number density of "huts" is much larger and their size reduced [20a]. However, additional measurements will be required to confirm this explanation.

In addition, several observations indicate that the "hut" clusters are a metastable and intermediate phase between the 2D layers and "macroscopic" 3D clusters. The "hut" clusters form preferentially at low growth temperatures, $T < 800$ K. Growth at 850 K results in only "macroscopic" clusters. Upon annealing at 850 K for 10 min almost all "hut" clusters formed at low growth temperatures vanish and more "macroscopic" clusters form. Furthermore the concentrations of the "hut" and "macroscopic" clusters, formed at

$T < 800$ K, are drastically different, being, for example, 7×10^{10} and $3.8 \times 10^7 \text{ cm}^{-2}$, respectively for the conditions shown in fig. 3. Hence, it appears that the formation barrier is much lower for the "hut" clusters than for the "macroscopic" clusters.

Therefore we propose the following scenario. The "macroscopic" clusters are the final equilibrium state. The "hut" clusters form more easily and hence preferentially nucleate first. "Hut" nucleation slows as their concentration gets large and the available $\langle 100 \rangle$ step sites for nucleation decrease. We suggest that the consequent increase in the supersaturation of Ge adatoms causes the nucleation of the "macroscopic" clusters. The "huts" therefore provide an easy way for 3D structures to appear at the surface initially, and consequently delay the onset of the formation of the "macroscopic" clusters. This idea of a competition between "hut" and "macroscopic" clusters is supported by the measurement of the concentration of "macroscopic" clusters after deposition to the same dose of Ge as that in fig. 3, but at 850 K substrate temperature. In this case, "hut" clusters are not observed, but the concentration of "macroscopic" clusters is $6.3 \times 10^7 \text{ cm}^{-2}$, larger than that in fig. 3, contrary to the typical relation between island number density and the growth temperature in a diffusion-limited growth process. We believe that this is because the "huts" are not stable at this growth temperature and therefore the supersaturation of Ge adatoms is kept higher, forcing nucleation of more of the "macroscopic" clusters.

5. Conclusions

We have used STM to investigate the initial growth of Ge on Si(001). By analyzing the spatial distribution of 2D Ge islands after submonolayer deposition, we measured the anisotropies both in surface diffusion and in the lateral sticking coefficients of Ge adatoms at different types of steps. We find that surface diffusion of Ge on Si(001) is very anisotropic, with the fast direction being along the substrate dimer rows. The two types of monatomic steps are found to have very different lateral

sticking coefficients for Ge adatoms: S_B steps are good sinks, while S_A steps are poor sinks.

A metastable "hut" cluster phase is found to provide a kinetic pathway for the transition between the 2D Ge layers and "macroscopic" 3D clusters. The "hut" clusters have {105} facet planes, and they preferentially nucleate at $\langle 100 \rangle$ steps. The nucleation barrier for the "huts" is lower than that of the "macroscopic" clusters, and therefore they provide an easier way for accommodating Ge adatoms from the gas phase than the direct formation of the "macroscopic" clusters.

Acknowledgments

This research was supported by ONR, Chemistry Program. We would like to thank D.E. Savage, B.S. Swartzentruber, M.B. Webb, R. Kariotis, J. Kleiner, and M. Schacht for discussions and assistance. We thank Dr. P. Wagner, Wacker Chemitronic, Germany, for supplying us with high quality wafers for this study.

References

- [1] J.A. Moriarty and S. Krishnamurthy, *J. Appl. Phys.* 54 (1983) 1892.
- [2] R. People, J.C. Bean, D.V. Lang, A.M. Sergent, H.L. Störmer, K.W. Wecht, R.T. Lynch and K. Baldwin, *Appl. Phys. Letters* 45 (1984) 1231.
- [3] T.P. Pearsall, H. Temkin, J.C. Bean and S. Luryi, *IEEE Electron Device Letters* EDL-7 (1986) 330.
- [4] T.P. Pearsall, J. Bevk, L.C. Feldman, J.M. Bonar, J.P. Mannaerts and A. Ourmazd, *Phys. Rev. Letters* 58 (1987) 729.
- [5] B.-Y. Tsaur, M.W. Geis, J.C.C. Fan and R.P. Gale, *Appl. Phys. Letters* 38 (1981) 779.
- [6] M. Asai, H. Ueba and C. Tatsuyama, *J. Appl. Phys.* 58 (1985) 2577.
- [7] K. Sakamoto, T. Sakamoto, S. Nagao, G. Hashiguchi, K. Kuniyoshi and Y. Bando, *Japan. J. Appl. Phys.* 26 (1987) 666.
- [8] Y. Koide, S. Zaima, N. Ohshima and Y. Yasuda, *Japan. J. Appl. Phys.* 28 (1989) 690.
- [9] P.M.J. Marée, K. Nakagawa, F.M. Mulders and J.F. van der Veen, *Surface Sci.* 191 (1987) 305.
- [10] J.D. Mathews, Ed., *Epitaxial Growth* (Academic Press, New York, 1975);
B. Lewis and J.C. Anderson, *Nucleation and Growth of Thin Films* (Academic Press, New York, 1978).
- [11] Y.W. Mo, B.S. Swartzentruber, R. Kariotis, M.B. Webb and M.G. Lagally, *Phys. Rev. Letters* 63 (1989) 2393.
- [12] P. Verhoven, *Fundamentals of Physical Metallurgy* (Wiley, New York, 1975).
- [13] B.S. Swartzentruber, Y.W. Mo, M.B. Webb and M.G. Lagally, *J. Vacuum Sci. Technol.* A7 (1989) 2901.
- [14] M.G. Lagally, Y.W. Mo, R. Kariotis, B.S. Swartzentruber and M.B. Webb, in: *Kinetics of Ordering and Growth at Surfaces*, Ed. M.G. Lagally (Plenum, New York, 1990).
- [15] A. Rockett, *Proc. SPIE* 944 (1988) 63.
- [16] S. Stoyanov, *J. Crystal Growth* 94 (1989) 751.
- [17] D.J. Chadi, *Phys. Rev. Letters* (1987) 1691.
- [18] B.S. Swartzentruber, Y.W. Mo, R. Kariotis, M.G. Lagally and M.B. Webb, *Phys. Rev. Letters* 65 (1990) 1913.
- [19] E. Bauer and W. Telieps, in: *Reflection High-Energy Electron Diffraction and Reflection Electron Imaging of Surfaces*, Eds. P.K. Larsen and P.J. Dobson (Plenum, New York, 1988).
- [20] (a) Y.-W. Mo, PhD Dissertation, University of Wisconsin-Madison (1991), unpublished;
(b) Y.-W. Mo and M.G. Lagally, *Surface Sci.*, in press;
(c) J. Kleiner, Y.-W. Mo and M.G. Lagally, *Surface Sci.*, submitted.
- [21] Y.W. Mo, D.E. Savage, B.S. Swartzentruber and M.G. Lagally, *Phys. Rev. Letters* 65 (1990) 1020.

Group IV element (Si, Ge and α -Sn) superlattices – low temperature MBE

K. Eberl, W. Wegscheider and G. Abstreiter

Walter Schottky Institut, Technische Universität München, W-8046 Garching, Germany

Si/Ge and Sn/Ge heterostructures and short-period superlattices are grown by a modified molecular beam epitaxy (MBE) technique on Si and Ge substrates. Low energy electron diffraction and Auger electron spectroscopy are used in order to optimize the growth conditions with respect to interface roughness, segregation and intermixing. Transmission electron micrographs reveal that the interface quality of short period superlattices is improved by substrate temperature modulation during deposition. For Si/Ge superlattices we use a temperature range between 250 and 400 °C. However, due to the extreme tendency of Sn to segregate on the film surface, it is necessary to further decrease the substrate temperature during overgrowth of the Sn layers. The optimized growth conditions for high-quality Sn/Ge superlattices were found to be in the temperature range between 45 and 300 °C. It is demonstrated that low temperatures, low growth rates, and temperature variations during deposition of the individual layers in MBE open the possibility to synthesize structures far beyond thermodynamic equilibrium conditions.

1. Introduction

Heterostructures and superlattices (SLs) based on the group IV elements Si, Ge and α -Sn are of fundamental interest due to the prospect of novel physical phenomena and of device applications. The basic properties can be tailored in a wide range by the structural parameters like layer thickness, composition and lateral strain distribution [1]. The band gap of Si/Ge strained alloy layers or SLs, for example, covers the energy range from 1.1 to about 0.55 eV [2–4]. $\text{Sn}_x\text{Ge}_{1-x}$ alloys are expected to have a band gap tunable from 0.75 eV to zero. Especially in the compositional range of $0.2 < x < 0.6$, a direct band gap semiconductor is predicted [5]. The Brillouin zone reduction in Si/Ge [6,7] and Sn/Ge [8,9] short period SLs leads to additional changes of the band structure. Pioneering work on Si/SiGe heteroepitaxy has been performed by Kasper et al. [10]. The lattice mismatch of about 4% between Si and Ge, however, turned out to cause problems in growth, especially for SiGe alloys with increased Ge concentrations. The limited thickness for lattice matched growth, the transition from two-dimensional to three-dimensional growth mode and Ge

segregation are the main difficulties. Bean and coworkers made an essential step forward by lowering the growth temperature [11]. In order to achieve high quality short period SLs, further modifications of the MBE conditions were necessary [12–14].

The difference in the lattice constants of α -Sn and Ge is about 13%. Besides the critical thickness for pseudomorphic growth of SnGe alloys on Ge, there are two further difficulties which must be considered. The solid solubility of the two materials in each other is less than 1% and there is a strong tendency of Sn to segregate on the alloy surface even at substrate temperatures as low as 150 °C [15]. The latter aspects inhibit the fabrication of Sn-rich alloy layers ($x > 0.2$) lattice matched to Ge or GaAs substrates [15–17]. This means that realization of both Si/Ge and Sn/Ge SLs requires non-equilibrium epitaxial growth conditions and in some cases also a large temperature variation during deposition of the individual layers.

We use a specially designed MBE system equipped with in situ analysis – low energy electron diffraction (LEED) and Auger electron spectroscopy (AES) – to optimize the growth condi-

tions. In this contribution we first present LEED and AES investigations on the formation of the Si/Ge and Ge/Si interface. Based on these results a variation of the substrate temperature was used to synthesize high quality Si/Ge SLs on (001) Si and Ge substrates. In the last part we briefly discuss the growth of short period Sn/Ge SLs on (001) Ge.

2. Si/Ge heterostructures

The MBE system is equipped with a rear view LEED system combined with a Vidicon camera and AES to obtain information about the morphology and the chemical composition of the surface. As a Si source, we use a specially designed sublimation cell. Ge and Sn are evaporated from conventional Knudsen type effusion cells. We use extremely low growth rates of about 1–5 Å/min or less. The pressure during growth is within the 10^{-11} mbar region. The substrate is heated by radiation. A very important feature is the capability to cool the substrate holder alternatively with water or liquid nitrogen. This allows precise temperature control and rapid variation down to very low temperatures. For more details about the MBE system, see refs. [14,18]. Typical growth temperatures (T_g) for Si/Ge and Sn/Ge SLs are in the range of 250 to 400 °C and 40 to 300 °C, respectively.

In order to determine the optimum growth temperature for the individual interfaces, we performed detailed LEED and AES measurements. First we studied the surface flatness and the interface sharpness of one monolayer (ML) Si on (001) Ge and 1 ML Ge on (001) Si as a function of T_g . Fig. 1 shows the mean terrace width measured by spot profile analysis in a Vidicon based LEED system following the concept of Henzler [19]. The mean terrace width is beyond the detection limit of about 200 Å of our system for 1 ML Si on Ge grown at $T_g = 350$ °C and decreases to about 70 Å at $T_g = 250$ °C. For 1 ML Ge on Si there is a maximum in surface flatness in the temperature range of 310 to 360 °C. However, the mean terrace width is considerably smaller in this case. Additionally, the measured mean terrace widths of

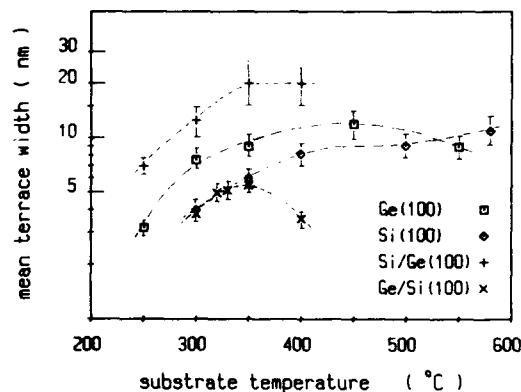


Fig. 1. Mean terrace width on the surface of Si (001) and Ge (001) homoepitaxial layers and for 1 ML Si on Ge (001) and 1 ML Ge on Si (001) as a function of the growth temperature.

Si and Ge homoepitaxial layers grown at these low temperatures are shown in fig. 1. Optimum surface quality is achieved at 450 °C and about 700 °C for Ge and Si homoepitaxy, respectively. These higher temperatures are used for growth of appropriate homoepitaxial buffer layers on Si or Ge substrates before we deposit the superlattice structures on top of it. Fig. 2 shows the condensate/substrate ratio of the AES intensities of the Si(92 eV) and Ge(47 eV) lines as a function of T_g for 1 ML Ge on (001) Si (fig. 2a) and 1 ML Si on (001) Ge (fig. 2b). The escape length of the Auger electrons is 5.5 Å for Si(92 eV) and 7.5 Å for Ge(47 eV). The dashed and the pointed arrows mark the expected Auger ratio of ideal atomically sharp heterostruc-

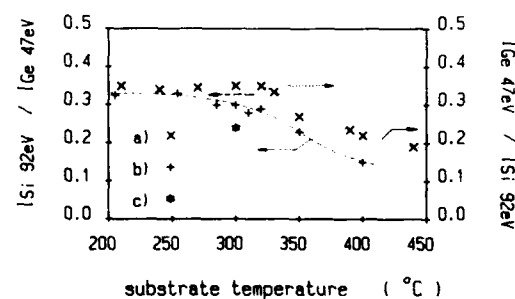


Fig. 2. Normalized condensate/substrate ratio of the AES intensities of the Si(92 eV) and Ge(47 eV) lines as a function of growth temperature: (a) for 1 ML Ge on Si (001), (b) 1 ML Si on Ge (001) and (c) 2 ML $\text{Si}_{0.5}\text{Ge}_{0.5}$ alloy on Ge.

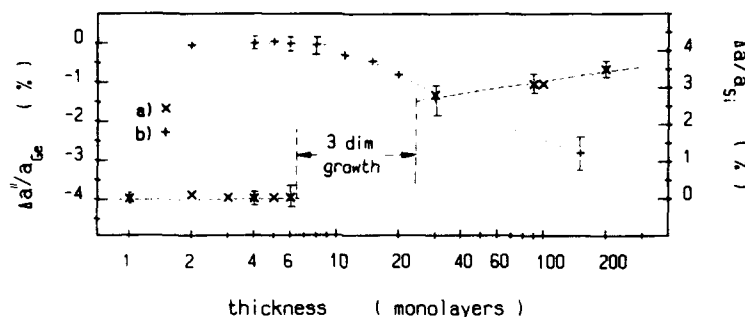


Fig. 3. Relative change of the lateral lattice constant as a function of thickness for (a) Ge on Si (001) (right scale) and (b) Si on Ge (001) substrate (left scale). The growth temperature was $T_g = 310^\circ\text{C}$ for both heteroepitaxial layers.

tures. For 1 ML Ge on Si we observe a deviation from the ideal ratio at $T_g > 330^\circ\text{C}$. At higher temperatures, intermixing and three-dimensional growth occurs. The AES results for 1 ML Si on Ge substrate in fig. 2 indicate a deviation from the ideal curve (dashed arrow) already at $T_g = 280^\circ\text{C}$. This is basically due to Ge segregation on the Si layer [20,21]. At higher temperatures, intermixing must also be taken into account [14]. As a comparison, we also included the measured AES ratio for 2 ML $\text{Si}_{0.5}\text{Ge}_{0.5}$ alloy grown at $T_g = 300^\circ\text{C}$ on Ge (fig. 2c). It indicates the sensitivity of this method. The measured value corresponds to the signal obtained from nominally 1 ML Si on Ge grown at $T_g = 350^\circ\text{C}$.

The information in figs. 1 and 2 as well as similar AES and LEED measurements within pseudomorphic Si/Ge SLs on Si and Ge substrates demonstrate that T_g should be kept at about 280 and 320°C during the formation of the Si/Ge and the Ge/Si interface, respectively, in order to achieve maximum interface abruptness and still relatively large lateral uniformity. LEED spot profile analysis is also used as a sensitive instrument to follow the lateral lattice constant of the structures and thus the relaxation process with increasing thickness by evaluating the spot separation [18]. Fig. 3 shows the relative change of the lateral lattice constant as a function of the thickness for Ge on (001) Si (fig. 3a) and for Si on (001) Ge (fig. 3b) grown at $T_g = 310^\circ\text{C}$. Parallel to these measurements, we again determined the mean terrace width for both heterostructures as plotted in fig. 4. The Ge overlayer adapts to the

lattice constant of the Si substrate up to 6 ML [22]. However, the mean terrace width is only about 50 Å for the first three ML Ge and then decreases with increasing thickness. Three-dimensional (3D) growth occurs beyond 6 ML (Stranski–Krastanov growth mode). The surface quality improves again after 30 ML Ge. A nearly smooth surface is regained after the deposition of about 100 ML. The Ge film then provides a lateral lattice constant which is about 3.1% larger than that of the Si substrate, that means, the Ge film is partly relaxed. The width of the region of 3D growth (additional LEED spots owing to facets) and the level of $\Delta a/a_{\text{Si}}$ depend strongly on the growth temperature. At higher temperatures there is a much stronger tendency to island formation

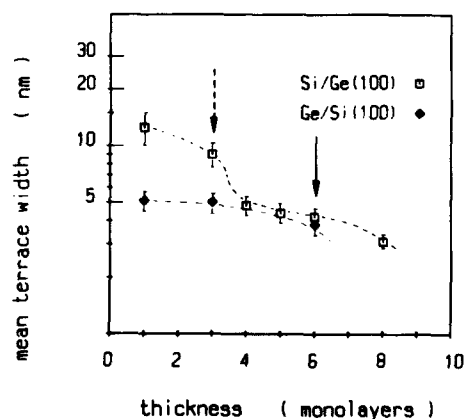


Fig. 4. Mean terrace width on the surface of Si on Ge (001) and Ge on Si (001) as a function of the thickness of the corresponding layer. The growth temperature was $T_g = 310^\circ\text{C}$.

[23,24]. The behaviour of $\text{Si}_x\text{Ge}_{1-x}$ alloys on Si is similar, but the beginning of island formation is shifted towards larger thicknesses depending on the Ge content [25].

The change of the lateral lattice constant as well as the flatness of the surface for Si on (001) Ge is also demonstrated in figs. 3b and 4, respectively. Up to about 8 ML, the Si overlayer is laterally extended by 4.2% to match the Ge substrate. For higher coverages, the Si film begins to relax towards its intrinsic lattice constant by formation of misfit defects. In contrast to Ge, on Si there is no pronounced 3D growth mode at $T_g = 310^\circ\text{C}$. The mean terrace width at the surface is close to the detection limit of the LEED system up to 3 ML Si, in contrast to the case of inverse strain (compressive) for Ge on Si. After 3 ML Si on Ge there is a significant decrease of the mean terrace width. Between 6 and 8 ML Si the film starts to relax as determined from detailed analysis of the energy dependence of the LEED spot profiles. Consequently, in both cases – Si on Ge and Ge on Si – the LEED results show that the surface of a 6 ML film exhibits already many random steps of different atomic height, but the interface is still pseudomorphic. Therefore 6 ML is the critical thickness for lattice matched growth of Si on Ge and Ge on Si substrate (arrow in fig. 4). The limit of two-dimensional growth is, however, reached already at 3 ML Si (indicated by the dashed arrow in fig. 4).

The basic conclusion from figs. 3 and 4 is that the limitation in thickness of the individual Si (Ge) layer of pseudomorphic Si_mGe_n SLs composed of m ML Si and n ML Ge on [001] oriented Ge (Si) substrates is 6 ML. However, it is also demonstrated, that the best SLs can be realized on Ge substrates if the thickness of the Si layers is less than 4 ML. For asymmetrically strained Si/Ge SLs, a overall superlattice critical thickness must be taken into account, which limits the achievable thickness [27]. It depends on the ratio m/n and the growth temperature.

3. Si/Ge superlattices

The LEED and AES measurements discussed in the last section demonstrate that T_g should be

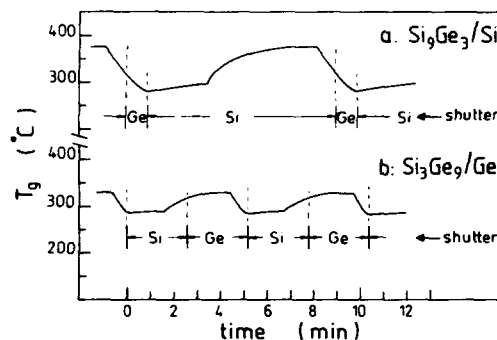


Fig. 5. Optimized substrate temperature during growth of (a) a Si_9Ge_3 SL on Si (001) and (b) a Si_3Ge_9 SL on Ge (001) substrate. The growth rates are 5 Å/min for Ge and 1.5 Å/min for Si. The dashed vertical lines mark the times when the shutter of the Si or Ge source is opened.

below 325°C during the formation of the interfaces of Si/Ge SLs. On the other hand, especially for Si homoepitaxy higher growth temperatures are recommended to obtain good surface flatness. Therefore, best crystalline quality for short period Si/Ge SLs can only be achieved by variation of T_g during deposition of the individual layers following the SL periodicity. Fig. 5 shows such an optimized substrate temperature profile during growth of a pseudomorphic Si_9Ge_3 SL on (001) Si (fig. 5a) and a Si_3Ge_9 SL lattice matched to a (001) Ge substrate (fig. 5b). The growth rates are 5 Å/min for Ge and 1.5 Å/min for Si. The dashed vertical lines mark the times when the shutter of the Si source or the Ge source is opened. In both cases of figs. 5a and 5b the minimum temperature ($T_g = 280^\circ\text{C}$) is adjusted at the time when the Ge shutter is closed and the Si shutter opens, i.e. during the formation of the Si/Ge interface. This lowering of the temperature is necessary to avoid Ge segregation (see fig. 2). After deposition of about 3 to 4 ML Si on Ge, T_g is increased slowly to about 380°C , which is reached at 8 ML Si (fig. 5b). This is necessary in order to achieve reasonable surface flatness for Si. According to fig. 1, even higher temperatures would be required for optimum conditions. However, a variation of T_g by more than 100°C would demand growth interruptions and would also cause intermixing. The substrate temperature is adjusted to $T_g = 320^\circ\text{C}$

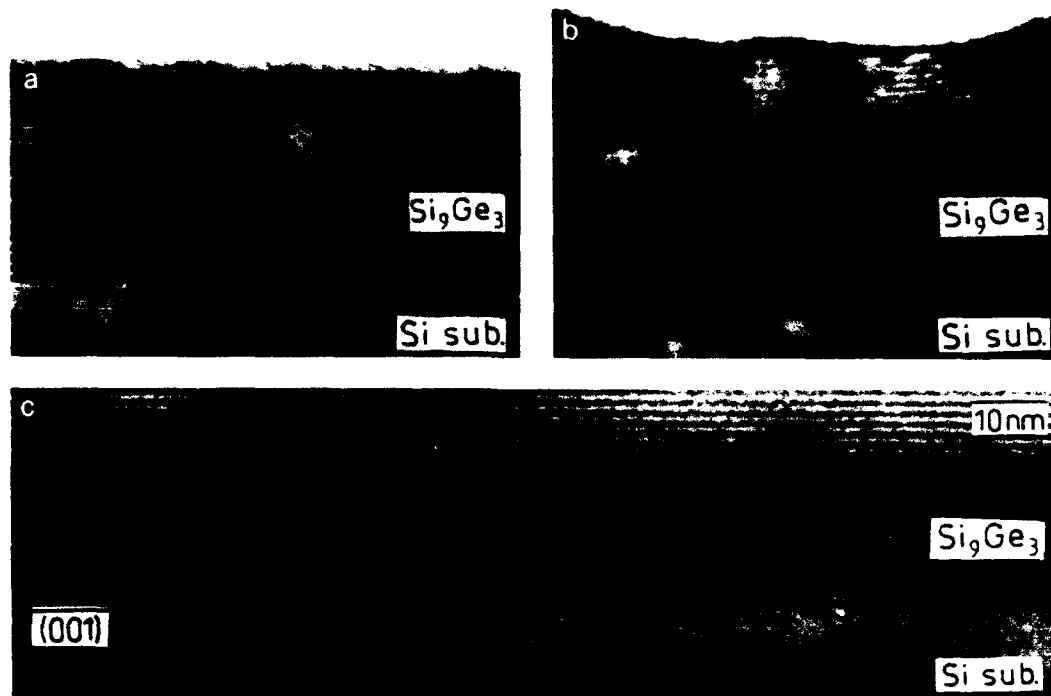


Fig. 6. TEM cross-sectional bright field images of Si_9Ge_3 SLs on Si (001) substrates. The samples have been grown at different temperature profiles: (a) $225 < T_g < 310^\circ\text{C}$, (b) $T_g = 400^\circ\text{C}$ constant and (c) $280 < T_g < 380^\circ\text{C}$.

when the Si shutter closes and the next Ge layer starts. This is based again on the results shown in fig. 2.

Fig. 6 shows TEM micrographs of three Si_9Ge_3 SLs on (001) Si substrates grown at different temperature profiles. The sample obtained with a temperature variation as described in fig. 5a is shown in fig. 6c. It provides an excellent lateral uniformity and a clear contrast between the individual layers. The SL contains 20 periods and has a total thickness of 335 \AA , which is far below the critical thickness of about $(800 \pm 200 \text{ \AA})$ for this SL composition [27]. This means that the Ge layers are laterally compressed by 4%, whereas the Si layers are unstrained. In cross-sectional TEM specimens of this sample, there was no indication of misfit dislocations over the whole examined area. The sample in fig. 6a has been grown by varying the temperature between $T_g = 225^\circ\text{C}$ and 310°C . Sample 6b was prepared with a constant substrate temperature of $T_g = 400^\circ\text{C}$. The TEM

image in fig. 6a shows sharp and flat interfaces in the first few periods of the Si_9Ge_3 SL. However, with increasing thickness the interfaces between the individual layers become more and more wavy and finally the periodic structure is almost lost. This is a consequence of the extremely low substrate temperatures which have been used in this case. Fig. 6b shows the result of a Si_9Ge_3 SL which was grown at too high temperature. The contrast between the individual layers is very weak compared to the two other samples. This indicates considerable intermixing between the individual layers. In addition, also misfit defects appear in this TEM image. The surface roughness is due to the increased tendency to three-dimensional growth with higher temperatures. AES measurements which have been performed on this sample show that during the overgrowth of the first 3 ML Ge film about 1.5 ML Ge segregate on top of the growing Si layer, which are then slowly incorporated. This continues throughout the deposition of

the whole SL and results in an increased Ge content with increasing SL thickness.

Detailed LEED, AES, Raman spectroscopy and TEM studies on Si/Ge SLs which are lattice matched to Si clearly indicate that much better interface sharpness can be achieved by variation of the substrate temperature during growth.

On (001) Ge substrates the mean terrace width which can be achieved for Si overlayers up to 3 ML thickness is considerably larger, as pointed out in figs. 1 and 4. As a consequence, the interface uniformity of short period Si_mGe_n SLs on Ge is usually superior to those on Si substrates, especially for $m < 4$. Raman spectra [28] and TEM micrographs [26] demonstrate the excellent structural properties of the Si/Ge SLs which have been grown on Ge substrates at a constant temperature of $T_g = 310^\circ\text{C}$. Additional improvement in the interface sharpness can be achieved by using the optimized temperature profile for a Si_3Ge_9 SL on Ge shown in fig. 5b. At the Si/Ge and the Ge/Si interface, T_g is again 280 and 320°C , respectively. The maximum temperature of about 340°C is achieved within the 9 ML Ge film. For Ge homoepitaxy there is no substantial improvement of the surface flatness with higher temperature, which would demand for a further increase of this temperature, as can be seen in fig. 1.

4. Sn/Ge superlattices

In this last section we discuss first results of MBE growth of short period Sn/Ge SLs. The growth temperature of a $\text{Sn}_2\text{Ge}_{20}$ SL on (001) Ge as a function of time is shown in fig. 7. The growth rates are $5 \text{ \AA}/\text{min}$ for both materials. The dashed vertical lines mark the times when the shutter of the Ge or Sn source is opened. Within the time intervals marked by crosses, the growth process is interrupted to adjust the appropriate temperature before the deposition is continued. The temperatures during the formation of the interfaces are again chosen by following the results of LEED and AES measurements on Sn/Ge heterostructures. Due to the lattice mismatch between Sn and Ge of about 13%, the critical thickness for Sn on (001) Ge is only 2 ML. The extreme

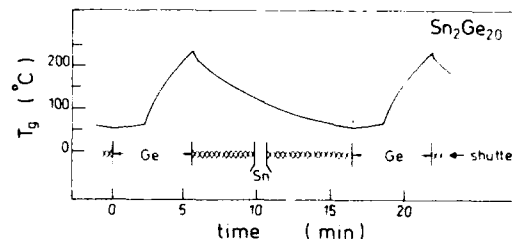


Fig. 7. Growth temperature of a $\text{Sn}_2\text{Ge}_{20}$ SL on Ge (001) substrate as a function of time. The growth rates are $5 \text{ \AA}/\text{min}$ for Ge and Sn. The dashed vertical lines mark the times when the shutter of the Ge or Sn source is opened. Within the time intervals marked by crosses the growth process is interrupted to change the temperature.

tendency of Sn to segregate on the Ge film during overgrowth demands a minimum temperature of less than 50°C at the Ge/Sn interface. The Sn segregation on the surface increases drastically with the growth temperature of the Ge layer as measured by AES [29]. For good epitaxial growth of Ge, it is on the other hand necessary to go to $T_g = 250^\circ\text{C}$. As a compromise we varied T_g by about 200°C during deposition, as shown in fig. 7. This considerable temperature variation is achieved within a reasonable time by effective cooling of the substrate holder with liquid nitrogen. Fig. 8 shows a TEM cross-sectional image of a 20 period $\text{Sn}_2\text{Ge}_{20}$ SL on (001) Ge substrate. The temperature profile shown in fig. 7 has been recorded during growth of this sample. The dark and bright lines correspond to the Sn and Ge layers, respectively. The SL is lattice matched to



Fig. 8. TEM cross-sectional bright field image of a 20 period $\text{Sn}_2\text{Ge}_{20}$ SL on Ge (001) substrate. The sample was grown with the temperature profile shown in fig. 7.

the Ge substrate. This means that the Sn layers are laterally compressed by 12.8%. Despite the large variation of T_g during growth, there exists still considerable intermixing at the Sn/Ge interface. The results, however, demonstrate that far away from thermodynamic equilibrium conditions, it is possible to achieve new kinds of SLs which consist of extremely dissimilar materials like α -Sn and Ge.

5. Conclusions

We have demonstrated that short period Si/Ge and Sn/Ge SLs can be realized on Si and Ge substrates by low temperature MBE. Detailed LEED and AES measurements were performed to determine the optimum growth parameters for the different heterostructures. Based on these results and additional ex situ characterization techniques like TEM and Raman spectroscopy, it is possible to optimize the temperature modulations during growth in order to achieve nearly atomically sharp interfaces and high quality short period superlattices.

Acknowledgements

We are grateful to H. Cerva and H. Oppolzer from the Siemens Research Laboratories for the fruitful collaboration and help in the TEM analysis. The work benefitted from the financial support of the Siemens AG and the Deutsche Forschungsgemeinschaft.

References

- [1] G. Abstreiter, K. Eberl, E. Friess, U. Menczgar and W. Wegscheider, in: *Proc. NATO Workshop on Low-Dimensional Systems*, Marmaris, 1990.
- [2] D.V. Lang, R. People, J.C. Bean and M.A. Sergeant, *Appl. Phys. Letters* 47 (1985) 1333.
- [3] R. People, *IEEE J. Quantum Electron.* QE-22 (1986) 1696.
- [4] G. Abstreiter, H. Brugger, T. Wolf, R. Zachai and Ch. Zeller, in: *Two-Dimensional Systems: Physics and New Devices*, Springer Series in Solid State Sciences 67, Eds. G. Bauer, F. Kuchar and H. Heinrich (Springer, Berlin, 1986) p. 130.
- [5] S. Oguz, W. Paul, T.F. Deutsch, B.Y. Tsaur, D.V. Murphy, *Appl. Phys. Letters* 43 (1983) 848.
- [6] U. Gnatzmann and K. Clausecker, *Appl. Phys.* 3 (1974) 9.
- [7] M.A. Gell, *Phys. Rev. B* 38 (1988) 7535, and references therein.
- [8] W. Wegscheider, K. Eberl, U. Menczgar, J. Olajos, G. Abstreiter and P. Vogl, in: *Proc. 20th Intern. Conf. on Physics of Semiconductors*, Thessaloniki, 1990 (World Scientific, Singapore, in press).
- [9] P. Vogl, to be published.
- [10] E. Kasper, H.J. Herzog and H. Kibbel, *Appl. Phys.* 8 (1974) 199.
- [11] J.C. Bean, L.C. Feldman, A.T. Fiory, S. Nakahara and J.K. Robinson, *J. Vacuum Sci. Technol.* A2 (1984) 436.
- [12] J. Bevk, A. Ourmazd, L.C. Feldman, T.P. Pearsall, J.M. Bonar, B.A. Davidson and J.P. Mannaerts, *Appl. Phys. Letters* 50 (1987) 760.
- [13] E. Kasper, H. Kibbel, H. Jorke, H. Brugger, E. Friess and G. Abstreiter, *Phys. Rev. B* 38 (1988) 3599.
- [14] K. Eberl, W. Wegscheider, E. Friess and G. Abstreiter, in: *Heterostructures on Silicon: One Step Forward with Silicon*, Eds. Y.I. Nissim and E. Rosencher (Kluwer, Dordrecht, 1989) p. 153.
- [15] P.R. Pukite, A. Harwit and S.S. Iyer, *Appl. Phys. Letters* 54 (1989) 2142.
- [16] S.I. Shah, J.E. Greene, L.L. Abels, Q. Yao and P.M. Raccach, *J. Crystal Growth* 83 (1987) 3.
- [17] H. Höchst, M.A. Engelhardt and I. Hernández-Calderón, *Phys. Rev. B* 40 (1989) 9703.
- [18] K. Eberl, G. Krötz, T. Wolf, F. Schäffler and G. Abstreiter, *Semicond. Sci. Technol.* 2 (1987) 561.
- [19] M. Henzler, in: *Electron Spectroscopy for Surface Analysis*, Topics in Current Physics, Vol. 4, Ed. H. Ibach (Springer, Berlin, 1977).
- [20] S.S. Iyer, J.C. Tsang, M.W. Copel, P.R. Pukite and R.M. Tromp, *Appl. Phys. Letters* 54 (1989) 329.
- [21] P.C. Zalm, G.F.A. Van de Walle, D.J. Gravensteijn, A.A. Van Gorkum, *Appl. Phys. Letters* 55 (1989) 2520.
- [22] This was already measured using RBS, by J. Bevk, J.P. Mannaerts, L.C. Feldman, B.A. Davidson and A. Ourmazd, *Appl. Phys. Letters* 49 (1986) 286.
- [23] Y. Kataoka, H. Ueby and C. Tatsuyama, *J. Appl. Phys.* 63 (1988) 749.
- [24] D.J. Eaglesham, D.M. Maher, E.P. Kvam, J.C. Bean and C.J. Humphreys, *Phys. Rev. Letters* 62 (1990) 187.
- [25] K. Eberl, E. Friess, W. Wegscheider, U. Menczgar and G. Abstreiter, *Thin Solid Films* 183 (1989) 95.
- [26] W. Wegscheider, K. Eberl, H. Cerva and H. Oppolzer, *Appl. Phys. Letters* 55 (1989) 448.
- [27] G. Abstreiter, K. Eberl, E. Friess, W. Wegscheider and R. Zachai, *J. Crystal Growth* 95 (1989) 431.
- [28] G. Abstreiter, *Thin Solid Films* 183 (1989) 1.
- [29] W. Wegscheider, K. Eberl, U. Menczgar and G. Abstreiter, *Appl. Phys. Letters* 57 (1990) 875.

Silicon heteroepitaxy: interface structure and physical properties

H. von Känel, E. Müller, H.-U. Nissen, W. Bacsa, M. Ospelt, K.A. Mäder, R. Stalder

Laboratorium für Festkörperphysik, ETH – Hönggerberg, CH-8093 Zürich, Switzerland

and

A. Baldereschi

IRRMA, PH-Ecublens, CH-1015 Lausanne, Switzerland

The interfaces in strained-layer Si_mGe_n superlattice (SLs) characterized by X-ray diffraction, Raman scattering and scanning tunneling microscopy are shown to deviate from the idealized form assumed in most calculations on electronic and optical properties. Electron microscopic investigations reveal that along the interfaces there exist thin regions of ordered alloys. In Si-rich SLs, the structure of these regions is dominated by growth-induced rhombohedral RS2 order, whereas with increasing Ge-content the fraction of RS1 domains becomes larger. The RS1 structure is found to be reversible, while the RS2 structure is not. Theoretical models, taking into account either growth kinetics or ground state properties, cannot explain all of the observed features.

1. Introduction

The structure of the interfaces in semiconductor superlattices (SLs) may have a profound effect on their optical and electrical properties. In theoretical calculations interfaces are often considered to be ideal, i.e. perfectly flat and abrupt and free of any defects. Experimentalists, however, are often plagued by considerable deviations from ideality. This is true in particular for strained-layer systems like Si/Ge which for years were difficult to control [1]. One of the main challenges in this field are ultra-short period SLs composed of alternate layers of pure Si and Ge with thicknesses approaching monolayer dimensions. Following the first attempts of Bevk and coworkers [2] to fabricate such SLs on Si(100) and increasing number of research teams has joined the effort [3].

Meanwhile short-period Si_mGe_n SLs grown pseudomorphically on Si(100) and Ge(100) have indicated [4,5] the new optical transitions expected theoretically [6,7]. Thickness limitations [1] imposed by the lattice mismatch of 4.2% have led to the concept of strain symmetrization [8]. In this

approach, thick Si_mGe_n SLs are grown on a $\text{Si}_{1-x}\text{Ge}_x$ alloy buffer layer with a lattice constant intermediate between those of Si and Ge. Although photoluminescence results obtained on this kind of structure have also been interpreted in terms of band structure effects [9], the elucidation of the electronic structure has remained unsatisfactory until now, due to the high defect density ($> 10^9 \text{ cm}^{-2}$) at the surface of relaxed buffer layers [10]. We present here a detailed study of the interface structure of Si_mGe_n SLs, lattice-matched to either Si(100) or to various $\text{Si}_{1-x}\text{Ge}_x$ buffer layers including pure Ge ($x = 1$). The investigation has been triggered by the surprising discovery of atomic ordering along the interfaces [11] which appears to be analogous to the ordering in strained and unstrained $\text{Si}_{1-x}\text{Ge}_x$ alloys [12–14].

2. Experimental

Details of the MBE growth procedure have been given elsewhere [15,16]. All heterostructures have been grown on the two domain (2×1)- and

(1 × 2)-reconstructed Si(100) surface. The substrate temperatures T_G ranged from 673 to 750 K for the growth of all SLs. For the $\text{Si}_{1-x}\text{Ge}_x$ buffer layers, T_G was chosen as high as possible, but sufficiently low (typically < 820 K) to avoid surface roughening [15]. Buffers of Ge with good crystalline quality (etch pit density $\leq 10^6 \text{ cm}^{-2}$) were obtained by growing the first $\sim 0.1 \mu\text{m}$ at 690 K and then slowly ramping the temperature up to 800 K and by annealing at 970 K. Defects were revealed by diffusing Sb ($\sim 10^{19} \text{ cm}^{-3}$) to a depth of $\sim 0.2 \mu\text{m}$ and a subsequent HF etch. The growth rates for the SLs were varied between 0.05 and 0.1 nm/s, depending on the substrate and T_G . For SLs lattice-matched to Si a sufficiently high Ge growth rate ($\sim 0.1 \text{ nm/s}$) was found to be crucial in order to avoid the formation of islands. All SLs and buffer layers were examined by Rutherford backscattering (RBS) and X-ray diffraction (XRD) in order to determine the composition and the amount of strain relaxation as well as the degree of crystalline perfection. For the RBS and channeling experiments, 2 MeV He^+ ions were used. Most XRD measurements were carried out on a conventional computer-controlled powder diffractometer equipped with a bent quartz crystal monochromator allowing nearly complete suppression of the $\text{Cu K}\alpha_2$ line. A few SLs grown on Si(100) were characterized by high resolution XRD using both symmetric and asymmetric Bragg reflections. X-ray topography in combination with these measurements showed that these structures are pseudomorphic and free of defects [17]. The Raman measurements were carried out in backscattering configuration with a conventional setup described in ref. [18]. Some SL surfaces were investigated with a special type of scanning tunneling microscope (STM) [19], in which the STM is located in a separate chamber attached to the analysis chamber of the MBE system.

For the electron microscopic investigations, two different specimen preparation techniques were applied. The samples were thinned by ion milling using argon gas, and, in order to ensure that the observed diffraction effects were not due to ion beam damage, the experiments were repeated using specimens cleaved along (110) planes. The specimens were subsequently studied using a 300 kV

transmission electron microscope (Philips CM 30), equipped with a $\pm 30^\circ$ tilting goniometer.

3. Results

The quantitative characterization of interfaces becomes increasingly difficult when the relative volume of the interface regions increases, i.e. when the SL period becomes smaller. Therefore results on high-resolution XRD are scarce; this is perhaps due in part to the difficulty to observe the high-angle SL satellites for periods below typically 3 nm [20]. Raman scattering from longitudinal (LO) optic phonons has become an important tool for interface characterization. The spectra are dominated by a three-mode structure attributed to mainly Ge-Ge, Ge-Si and Si-Si vibrations, with energies increasing in the same order. The exact positions of the Raman peaks depend, however, on strain, alloying and confinement effects [9,16, 21–23], all of which have to be separated if quantitative statements are to be made. Interface abruptness is often judged qualitatively by comparing the height of the Si-Ge peak with that of the other two peaks. Since, with decreasing layer thickness, the relative peak intensities become dominated by resonance effects, this method is not free from ambiguities.

As an example, fig. 1 presents the Raman spectra of a 31 period Si_3Ge_9 SL grown on a relaxed 2 μm thick Ge buffer layer at $T_G = 673 \text{ K}$. The laser wavelengths 514 and 458 nm have been chosen for the upper and the lower curve, respectively. Obviously, the intensity ratio between the Si-Ge and the Si-Si peak is rather different in the two cases. It should be emphasized that this particular SL is one of the few with periods below 2 nm in which the high-angle (-1) SL satellite has been observed by XRD besides the (400) reflection. From the separation of the 0th-order SL reflection from the Si(400) reflection the Si layers are found to be coherently strained. The question to what extent the Si layers are actually alloyed with Ge is difficult to answer on the basis of the Raman experiments, since strain, alloying and confinements effects all shift the Si-Si peak position to lower energies [9,16,21–23]. A comparison of the various

peak heights would, on the other hand, require detailed modeling [24]. The position of the Ge-Ge peak yields more quantitative information in this case. It lies at 296.8 cm^{-1} . For the buffer layer, the corresponding peak is found to be at 299.4 cm^{-1} , somewhat below the position for bulk Ge due to the expansive strain caused by the different thermal expansion of the Si substrate. The difference of 2.6 cm^{-1} must be attributed to confinement or alloying or to both. Neglecting confinement effects puts the upper limit of the average Si content in the Ge layers to $\sim 7\%$. Hence the interfaces cannot be considered abrupt on an atomic scale, although the inclusion of confinement effects would lower the upper limit of 7% somewhat. This follows also from a consideration of the growth mode. Growth by two-dimensional nucleation of islands having monolayer height can be inferred from the observation of RHEED intensity oscillations on SLs grown lattice-matched to Si [25]. The damping of the oscillations indicates, however, an increasing roughness of the surface as the growth continues. An estimate of the degree of roughness which is to be expected for the present growth conditions can also be obtained from scanning tunneling microscopy.

Fig. 2a shows the surface of the same Si_3Ge_5 SL as that presented in fig. 1, terminated by Si.

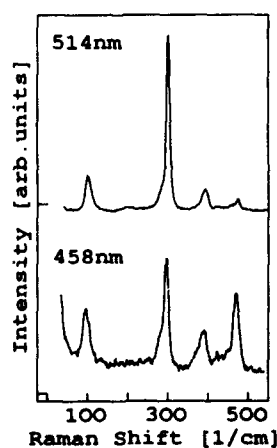


Fig. 1. (a) Raman spectrum of a 31 period Si_3Ge_5 SL (No. 557) grown lattice-matched to a $2 \mu\text{m}$ thick Ge-buffer layer at 673 K. Laser wavelength is 514 nm; (b) Raman spectrum of the same SL as in (a) excited at 458 nm.

The structure of the islands of monolayer height is exactly the same as for a homoepitaxial layer of Si grown under identical conditions. The surface of homoepitaxial Ge grown in the same way as the Ge layers in the SL (rate 0.1 nm/s , $T_G = 673 \text{ K}$) has an entirely different appearance (fig. 2b): the same irregular step structure occurs as for Ge grown at higher temperatures in the step flow regime. Considering the observations of RHEED intensity oscillations at temperatures above 673 K and for lower growth rates [25], we have to assume that in the present case all Ge atoms in two-dimensional islands have diffused towards the step edges during cool-down. Our STM results therefore do not allow us to describe the microscopic surface structure of the Ge layers during the growth of a SL. The Si/Ge interface, on the other hand, is probably microscopically rough due to the presence of a large number of monolayer steps such as those shown in fig. 2a.

For SLs lattice-matched to Ge, "sharp" interfaces have been obtained at much smaller growth rates and lower substrate temperatures [9,22,26]. Our own experiments indicated that at T_G around 720 K substantial interdiffusion or "intermixing" during growth cannot be prevented, even for deposition rates around 0.1 nm/s . At the same time, however, the morphology, i.e. planar growth, could be controlled. The situation is different for structures lattice-matched to Si for which there is compelling evidence that Ge tends to form clusters, and this poses the major growth technological problem. "Sharp" interfaces can, however, be obtained if the Ge deposition rates are chosen sufficiently high. As an example, the Raman spectrum of a 25 period SL grown at $T_G = 730 \text{ K}$ is shown in fig. 3. The thickness of the Ge layers is close to the critical value of 6 ML for pseudomorphic growth [2]. Since (quasi-) confinement effects in Ge layers of this thickness are small [16,23], the Ge-Ge mode is affected primarily by strain and alloying. The observed position of the resolution-limited peak at 315 cm^{-1} is consistent with pure Ge layers strained to the Si lattice constant [16,23], the shoulder on the low energy side of the Ge-Ge peak and the size of the Si-Ge peak reflect the presence of thin alloyed regions at the interfaces. From high resolution XRD the size of these re-

gions is estimated to be of the order of 1 ML [17]. Reducing the Ge deposition rate to 0.05 nm/s, two-dimensional growth could no longer be maintained at the same substrate temperature.

The results on SLs, lattice-matched to Si or Ge, indicate that excellent crystalline quality and reasonably sharp interfaces can be obtained if the thicknesses are below the critical values estab-

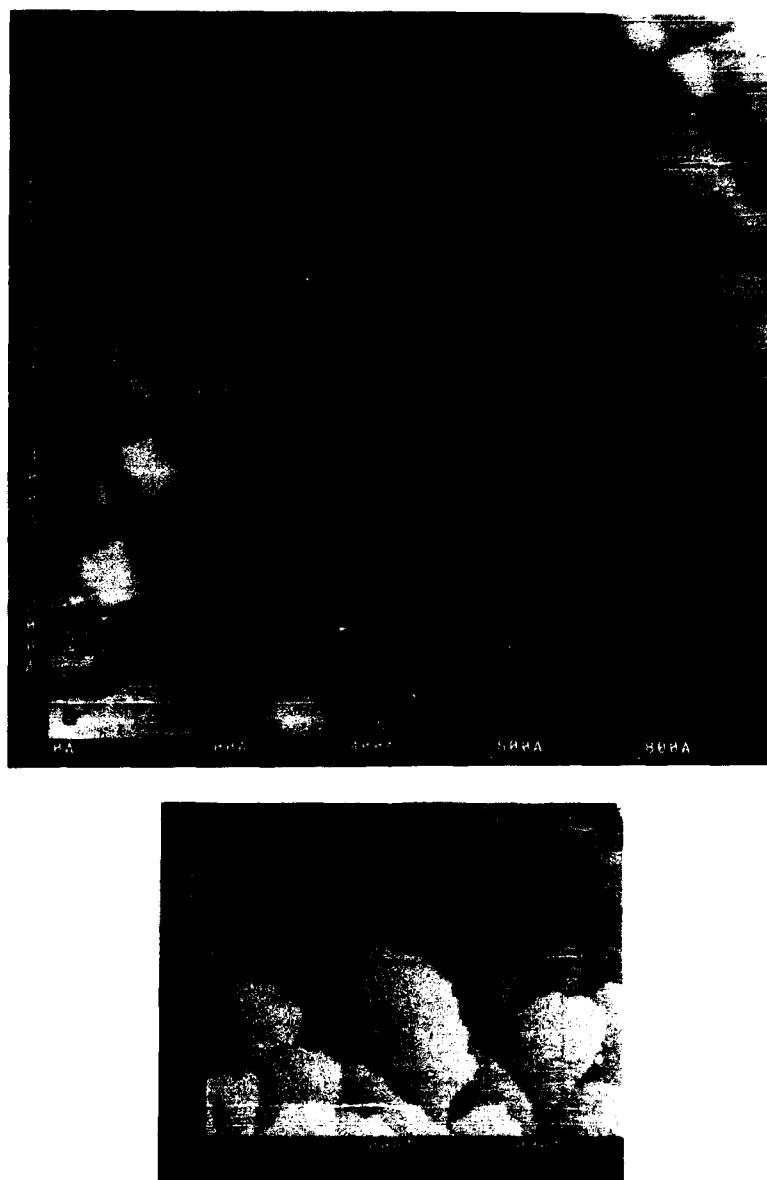


Fig. 2. (a) Scanning tunneling microscope (STM) image of the Si_3Ge_4 SL No. 557 terminated by Si; (b) STM image of Ge grown homoepitaxially on a 2 μm Ge buffer layer at the same temperature and growth rates as SL No. 557 (673 K, 0.1 nm/s).

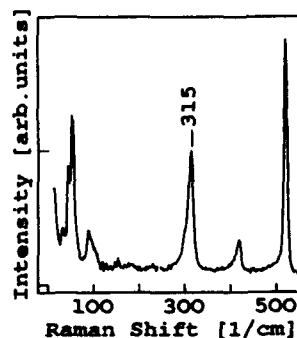


Fig. 3. Raman spectrum of SL No. 232 grown lattice-matched to Si at 730 K. Excitation wavelength 514 nm.

lished by People and Bean for growth at 550°C [27]. Unfortunately, this is not the case for strain-symmetrized SLs grown on alloy buffer layers. In this case all results known from XRD and RBS channeling reveal poor crystallinity compared with the case of elemental substrates [16,20]. This is due exclusively to the essentially unsolved problem of preparing a relaxed alloy buffer layer with good morphology and low defect density [10,16]. The sharpness of interfaces in symmetrically strained SLs does not suffer to the same extent as long as growth temperatures are kept low enough, typically at 673 K or below [8,9,16,26,28].

All results presented so far indicate that, irrespective of the substrate and the growth procedure, the interfaces in elemental Si/Ge SLs cannot be considered sharp on a monolayer scale. This is corroborated by transmission electron microscopy (TEM), which also proves that the interdiffusion zones along the interfaces are not simply random alloys but ordered structures [11]. As an example, fig. 4a shows a selected area electron diffraction pattern (SAD) obtained on the same Si_3Ge_9 SL as discussed previously. The corresponding pattern for a Si-rich strain-symmetrized SL, i.e. $(\text{Si}_6\text{Ge}_4)_{110}$, is displayed in fig. 4b. Apart from the SL satellites, additional spots at $\{\frac{1}{2}h \frac{1}{2}k \frac{1}{2}l\}$ are present for h, k, l all odd, as well as streaks through these spots along the growth direction. For all SLs lattice-matched to Ge, the half-order spots are surrounded by SL satellites. SLs grown on Si substrates do not show this feature and those on $\text{Si}_{1-x}\text{Ge}_x$ only very weakly. The half-order

spots or just streaking have been observed in all investigated SLs (at least 18) as well as in alloy buffer layers of the same average composition grown and investigated for comparison. In SLs for which Raman and high resolution XRD indicate sharp interfaces within the limits discussed above, it has often been difficult to observe the additional diffraction effects since in those cases the streaking may be extremely weak. From the symmetry of the observed SAD patterns doubling of the period along $\langle 111 \rangle$ directions can be concluded; this has been explained in terms of an alternate bilayer stacking of Si and Ge atoms, respectively. There are two possible stacking sequences. The first sequence, SiSiGeGeSiSiGeGe , is characterized by the occupation of the widely spaced $\{111\}$ planes with the same type of atom [12]. Henceforth this rhombohedral stacking structure will be called structure RS1, in accordance with ref. [29]. In the other type of stacking structure, RS2, the closely spaced $\{111\}$ planes are occupied by atoms of the same kind. In the original observations of order in $\text{Si}_{1-x}\text{Ge}_x$ alloys [12,13] structure RS2 was dismissed because it is microscopically strained and therefore is less stable according to theoretical predictions [29,30]. LeGoues et al. have shown, however, that the RS2 phase is present in unstrained alloys [14]. In order to determine the nature of the observed order in the present case the relative intensities of different diffraction spots have been compared. The diffraction patterns can only be structurally interpreted by comparing the experimental data to diffraction intensities derived

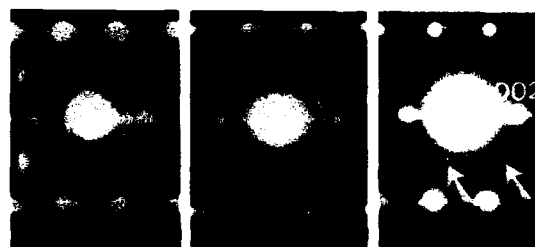


Fig. 4. (a) SAD of SL No. 557 (Si_3Ge_9); (b) SAD of SL No. 273 consisting of 110 periods of Si_4Ge_8 lattice-matched to an alloy buffer layer of the same mean composition; (c) SAD of SL No. 257 consisting of 80 periods of Si_2Ge_7 lattice-matched to a Ge buffer layer.

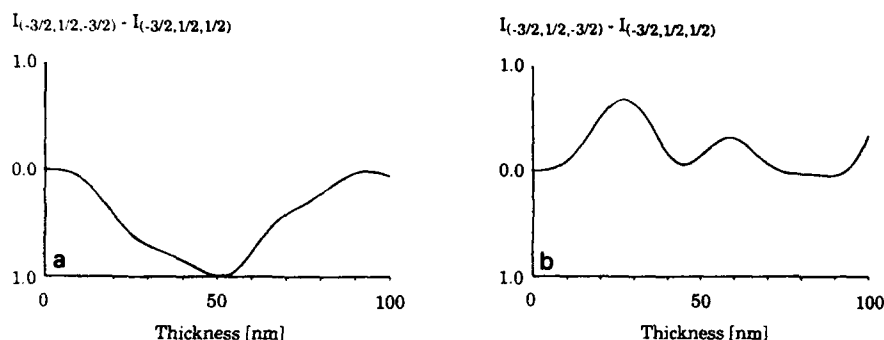


Fig. 5. (a) Calculated intensity difference between the $(\frac{3}{2}\frac{1}{2}\frac{3}{2})$ and the $(\frac{3}{2}\frac{1}{2}\frac{1}{2})$ reflections as a function of specimen thickness for RS1 order; (b) same as in (a) but for RS2 order.

from computer simulations. As a consequence of the dynamical scattering of the electron beam, a kinematical calculation is not satisfactory. Therefore the intensities were determined by a Bloch-wave calculation [31]. Fig. 5 presents the respective calculations of the intensity difference between the $(\frac{3}{2}\frac{1}{2}\frac{3}{2})$ and the $(\frac{3}{2}\frac{1}{2}\frac{1}{2})$ reflections, $I(\frac{3}{2}\frac{1}{2}\frac{3}{2}) - I(\frac{3}{2}\frac{1}{2}\frac{1}{2})$, as a function of the specimen thickness, for both models (in arbitrary units). The intensity of the $(\frac{3}{2}\frac{1}{2}\frac{3}{2})$ reflection is always equal to or smaller than $I(\frac{3}{2}\frac{1}{2}\frac{1}{2})$ for structure RS1 (fig. 5a), while for structure RS2, $I(\frac{3}{2}\frac{1}{2}\frac{3}{2})$ is always equal to or greater than $I(\frac{3}{2}\frac{1}{2}\frac{1}{2})$ (fig. 5b). The intensity of the $(\frac{3}{2}\frac{1}{2}\frac{3}{2})$ reflection had to be used for this calculation instead of that of the $(\frac{3}{2}\frac{1}{2}\frac{1}{2})$ reflection, because otherwise spots which belong to two differently oriented domains would be compared. A comparison of the observed and the calculated diffraction

patterns shows that the RS2 structure dominates in the cases of Si-rich SLs and alloys (fig. 4b). In the case of mere streaking such as observed in SLs lattice-matched to Si, e.g. in the one discussed in fig. 3, an unambiguous assignment of the interface structure is not possible. In symmetrically strained SLs, however, that assignment is possible since in this case the additional spots are sharp (fig. 4b).

With increasing Ge-content the contribution of RS1 domains by volume becomes more important (fig. 4c). This follows also from the structural changes induced by annealing. In all specimens, i.e. SLs as well as alloys, SAD patterns indicate that the RS2 domains vanish upon annealing to $T_A > 820$ –850 K. The RS1 domains in Ge-rich samples, however, can be assumed to persist above this temperature range. Fig. 6a shows, as an example, the SAD pattern of an 80 period Si_2Ge_7

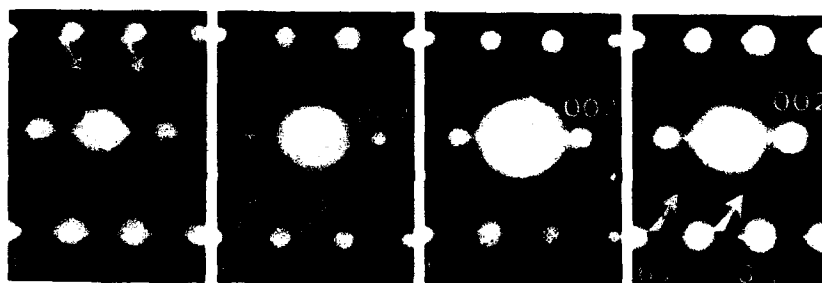


Fig. 6. (a) SAD pattern of SL No. 257 (Si_2Ge_7 , grown lattice-matched to Ge at 720 K and annealed to 870 K for 30 min); (b) SAD pattern of the partly relaxed $\text{Si}_{0.65}\text{Ge}_{0.35}$ as grown alloy No. 500; (c) SAD pattern of alloy No. 500 after annealing to 970 K for 30 min; (d) SAD pattern of alloy No. 500 after annealing to 970 K for 4 h.

(nominal composition) SL, lattice matched to Ge after annealing to 870 K for $\frac{1}{2}$ h. Whereas the SL satellites have vanished, the half order spots due to the RS1 structure are still present. It should be emphasized that the relatively high growth temperature of this SL, i.e. 720 K, leads to appreciable interdiffusion. The as-grown SL is thus composed of $\text{Si}_{1-x}\text{Ge}_x$ instead of pure Si layers. Accordingly, the ordering effects appear very clearly in the SAD patterns.

All ordered domains vanish eventually when the samples are heated to above 1070 K and cooled down rapidly. Upon slow cooling, however, the RS1 structure reappears, and this proves that the corresponding phase transition is reversible. In fig 6b–6d, the SAD patterns obtained on a Si-rich $\text{Si}_{1-x}\text{Ge}_x$ alloy are presented for the as-grown case (fig. 6b), after annealing to 970 K for 30 min only (fig. 6c) and after prolonged (4 h) annealing at 970 K (fig. 6d). The as-grown sample, as indicated by the SAD pattern, has pronounced RS2 ordering (fig. 6b), and this ordering completely disappears after annealing to 970 K (fig. 6c). When the same sample is annealed at 970 K for a long time, however, RS1 order is found to reappear (fig. 6d).

4. Discussion

As has been discussed in the preceding section, the interfaces in strained-layer Si_mGe_n SLs can be assumed to consist of domains of RS1 and RS2 order instead of being atomically sharp. Since similar observations have been made on SLs grown at even lower temperatures [32,33], it may be concluded that the observed features are of general significance and have to be related to the growth process. Results obtained by other groups on Ge segregation at surprisingly low temperatures point in the same direction [34–36]. The first model for the process of ordering induced by surface growth kinetics has been put forth by LeGoues et al. [37]. These authors have explained the RS2 type order in their relaxed alloy layers by site-dependent surface stresses associated with the (2×1) surface reconstruction [38]. From this it follows that there is a tendency for Si and Ge atoms to occupy alternate sites in the third and

fourth monolayers in such a way that equal atoms lie above one another. Monte Carlo simulations performed for alloys lattice-matched to Ge substrates [39] indicate that for this case the site-dependent occupation in the third monolayer is almost completely absent. Accordingly, the preference for RS2 type order is much less pronounced; and this explains our observations for Ge-rich samples. One serious drawback of the model proposed by LeGoues et al. is that the assumption of growth by the motion of bilayer steps [37] is hard to reconcile with observations of RHEED intensity oscillations implying monolayer growth [25]. Moreover, the model cannot explain the observed reversibility of the transition to the RS1 structure. Recently, Mäder et al. [40] have shown that order, confined to a few monolayers, can occur at interfaces despite bulk instability of the resulting phase. The model takes into account both strain and chemical effects, which generally compete with each other in lattice-mismatched systems. In superlattices, the mutual elastic interaction between interfaces can even further enhance the stability of confined order. As in other ground state models [29,30], the RS1 structure is found to be more stable, although in the presence of an interface even RS2-type order becomes more favorable compared with the corresponding bulk phase. Even though growth-related aspects are neglected in this model, it does, at least, provide a valid description of elastic interface interaction once the interfaces have been formed. The model can therefore explain the absence of streaking in the SAD patterns of the short-period SLs, since interface interaction causes the order to be a truly three-dimensional phenomenon.

5. Conclusions

On the basis of the available experimental data, it is concluded that interfaces in strained-layer Si_mGe_n SLs are characterized by ordered alloyed regions instead of being sharp on a monolayer scale. Whereas for SLs and alloys with cell parameters close to that of Si, growth-induced RS2 order is dominant, the fraction of RS1 domains becomes larger with increasing Ge content. At present,

theoretical models taking into account either growth kinetics or ground state properties can at best explain part of the experimental observations. In order to account for the occurrence of both ordered structures, one of which (RS1) is found to be reversible, a model combining growth-related aspects and ground state properties has to be developed.

Acknowledgments

The authors are indebted to Mr. H.-J. Gübeli for his excellent technical expertise. Financial support by the Swiss Science Foundation and the Board of the Swiss Federal Institutes of Technology is gratefully acknowledged.

References

- [1] J.C. Bean, *Mater. Res. Soc. Symp. Proc.* 91 (1987) 269.
- [2] J. Bevk, J.P. Mannaerts, L.C. Feldman, B.A. Davidson and A. Ourmazd, *Appl. Phys. Letters* 49 (1986) 286.
- [3] See, e.g., E. Kasper and E.H.C. Parker, Eds., *Silicon Molecular Beam Epitaxy, Proc. 3rd Intern. Symp. on Si-MBE, Strasbourg, 1989*, Eds. E. Kasper and E.H.C. Parker (North-Holland, Amsterdam, 1989 [Thin Solid Films 183 (1989)]).
- [4] T.P. Pearsall, J. Bevk, L.C. Feldman, J.M. Bonar, J.P. Mannaerts and A. Ourmazd, *Phys. Rev. Letters* 58 (1987) 729.
- [5] T.P. Pearsall, J.M. Vandenberg, R. Hull and J.M. Bonar, *Phys. Rev. Letters* 63 (1989) 2104.
- [6] S. Froyen, D.M. Wood and A. Zunger, *Phys. Rev. B* 37 (1988) 6893.
- [7] M.S. Hybertsen and M. Schlüter, *Phys. Rev. B* 36 (1987) 9683.
- [8] E. Kasper, H. Kibbel, H. Jorke, H. Brugger, E. Friess and G. Abstreiter, *Phys. Rev. B* 38 (1988) 3599.
- [9] G. Abstreiter, K. Eberl, E. Friess, W. Wegschneider and R. Zachai, *J. Crystal Growth* 95 (1989) 431.
- [10] B. Holländer, S. Mantl, W. Jäger, F. Schäffler and E. Kasper, in ref. [3], p. 157.
- [11] E. Müller, H.-U. Nissen, M. Ospelt and H. von Känel, *Phys. Rev. Letters* 63 (1989) 1819.
- [12] A. Ourmazd and J.C. Bean, *Phys. Rev. Letters* 55 (1985) 765.
- [13] D.J. Lockwood, K. Rajan, E.W. Fenton, J.-M. Baribeau and M.W. Denhoff, *Solid State Commun.* 61 (1987) 465.
- [14] F.K. LeGoues, V.P. Kesan and S.S. Iyer, *Phys. Rev. Letters* 64 (1990) 40.
- [15] M. Ospelt, K.A. Mäder, W. Bacsá, J. Henz and H. von Känel, in: *Heterostructures on Silicon: One Step Further with Silicon*, NATO ASI Series E, Vol. 160, Eds. Y.I. Nissim and E. Rosencher (Kluwer, Dordrecht, 1989) p. 129.
- [16] M. Ospelt, W. Bacsá, J. Henz, K.A. Mäder and H. von Känel, *Superlattices and Microstructures* 5 (1989) 71.
- [17] L. Tapfer, to be published.
- [18] W. Bacsá, H. von Känel, K.A. Mäder, M. Ospelt and P. Wachter, *Superlattices and Microstructures* 4 (1988) 717.
- [19] R. Stalder and H.J. Gübeli, to be published.
- [20] J.-M. Baribeau, D.J. Lockwood, M.W.C. Dharma-Wardana, N.L. Rowell and J.P. McCaffrey, in ref. [3], p. 17.
- [21] J. Menéndez, A. Pinczuk, J. Bevk and J.P. Mannaerts, *J. Vacuum Sci. Technol. B* 6 (1988) 1306.
- [22] K. Eberl, W. Wegschneider, E. Friess and G. Abstreiter, in: *Heterostructures on Silicon: One Step Further with Silicon*, NATO ASI Series E, Vol. 160, Eds. Y.I. Nissim and E. Rosencher (Kluwer, Dordrecht, 1989) p. 153.
- [23] J.C. Tsang, S.S. Iyer, P. Pukite and M. Copel, *Phys. Rev. B* 39 (1989) 13545.
- [24] M.W.C. Dharma-Wardana, G.C. Aers, D.J. Lockwood and J.-M. Baribeau, *Phys. Rev. B* 41 (1990) 5319.
- [25] K. Miki, K. Sakamoto, T. Sakamoto, H. Okumura, N. Takahashi and S. Yoshida, *J. Crystal Growth* 95 (1989) 444.
- [26] K. Eberl, E. Friess, W. Wegschneider, U. Menczgar and G. Abstreiter, in ref. [3], p. 95.
- [27] R. People and J.C. Bean, *Appl. Phys. Letters* 47 (1985) 322; Erratum, *Appl. Phys. Letters* 49 (1986) 229.
- [28] S.J. Chang, C.F. Huang, M.A. Kallel, K.L. Wang, R.C. Bowman and P.M. Adams, *J. Crystal Growth* 95 (1989) 451.
- [29] S. Ciraci and I.P. Batra, *Phys. Rev. B* 38 (1988) 1835.
- [30] J.L. Martins and A. Zunger, *Phys. Rev. Letters* 56 (1986) 1400.
- [31] P.A. Stadelmann, *Ultramicroscopy* 21 (1987) 131.
- [32] D.E. Jesson, S.J. Pennycook and J.-M. Baribeau, in: *Mater. Res. Soc. Symp. Proc., Symp. E. Spring Meeting*, San Francisco, CA, April 1990.
- [33] K. Eberl, private communication.
- [34] S.S. Iyer, J.C. Tsang, M.W. Copel, P.R. Pukite and R.M. Tromp, *Appl. Phys. Letters* 54 (1989) 219.
- [35] P.C. Zalm, G.F.A. van de Walle, D.J. Gravesteijn and A.A. van Gorkum, *Appl. Phys. Letters* 55 (1989) 2520.
- [36] E.T. Croke, T.C. McGill, R.J. Hauenstein and R.H. Miles, *Appl. Phys. Letters* 56 (1990) 367.
- [37] F.K. LeGoues, V.P. Kesan, S.S. Iyer, J. Tersoff and R. Tromp, *Phys. Rev. Letters* 64 (1990) 2038.
- [38] P.C. Kelires and J. Tersoff, *Phys. Rev. Letters* 63 (1989) 1164.
- [39] E. Müller, H.-U. Nissen, K.A. Mäder, M. Ospelt and H. von Känel, *Phys. Rev. Letters*, submitted.
- [40] K.A. Mäder, H. von Känel and A. Baldereschi, *Superlattices and Microstructures*, to be published.

MBE Si_mGe_n strained monolayer superlattices

M.A. Kallel, V. Arbet-Engels, K.L. Wang and R.P.G. Karunasiri

Device Research Laboratory, Electrical Engineering Department, University of California, Los Angeles, California 90024, USA

Si_mGe_n strained monolayer superlattices (SMSs) have been fabricated by molecular beam epitaxy (MBE) and characterized using photoluminescence (PL) for optical properties and using Raman scattering and X-ray diffraction to verify their structural integrity. Luminescence features below the Si energy bandgap have been observed and attributed to either dislocations in the buffer layer or to energy band transitions in the SMS. The effect of rapid thermal annealing (RTA) on the superlattice structure and on these transitions is reported and a model is proposed to explain the obtained results.

1. Introduction

Advances in SiGe-MBE have allowed the growth of high quality Si_mGe_n SMSs. Due to the 4.2% lattice mismatch between Si and Ge, layers of either material can be pseudomorphically grown only up to a critical thickness. The lattice mismatch, on the other hand, causes pseudomorphically grown layers to be strained, which can be positively exploited for engineering the optical properties of SMSs. Also, the strain of the constituent layers of a superlattice may be symmetrized through the use of a buffer layer of the appropriate Ge concentration [1]. In this manner, SMSs do not have the limitation of a critical thickness.

The concept of achieving a direct bandgap material by virtue of combining two indirect bandgap materials to form a superlattice was first recognized by Gnutzmann and Clausecker [2]. The observation of new optical transitions in a Si_4Ge_4 SMS by means of electroreflectance spectroscopy [3] triggered a lot of interest and intensified the efforts towards understanding the nature of the bandgap of SMSs. The properties of Si_mGe_n SMSs have been examined theoretically [4] and, with the proper choice of the superlattice periodicity and the strain conditions, were found to be promising candidates for direct bandgap materials.

PL has become a very important tool in studying the optical properties of Si_mGe_n SMSs. After

Eberl and coworkers [5] observed luminescence in Si_3Ge_9 superlattices with different thicknesses, a lot of effort has been directed towards the study of the luminescence dependence on the periodicity and the strain conditions of the superlattice [6,7].

In this paper, we study the luminescence of strain symmetrized Si_mGe_n superlattices. We attribute the observed PL to either dislocations in the buffer layer or to energy band transitions in the SMS. We also study the effect of RTA on the superlattice structure and on these transitions.

2. Experimental

The Si_mGe_n SMSs have been grown by SiGe-MBE at 380 °C. The details of the growth can be found elsewhere [8]. Two superlattices, $\text{Si}_{32}\text{Ge}_8$ and $\text{Si}_{16}\text{Ge}_4$, each grown on a $\text{Si}_{0.8}\text{Ge}_{0.2}$ buffer layer, have been investigated. The buffer layer is designed to be fully relaxed (2 μm thick) so that strain symmetrization in the superlattice can be achieved. The strain distribution is identical for both samples and is calculated to be $\epsilon_{\text{Si}} = 0.8\%$ and $\epsilon_{\text{Ge}} = -3.2\%$. The total superlattice thickness is 3000 Å for both SMSs.

PL data were taken at 4.2 K. Samples were cooled in a helium storage cryostat. All the lines of an argon ion laser were used for excitation and the beam was focused on the sample to a power

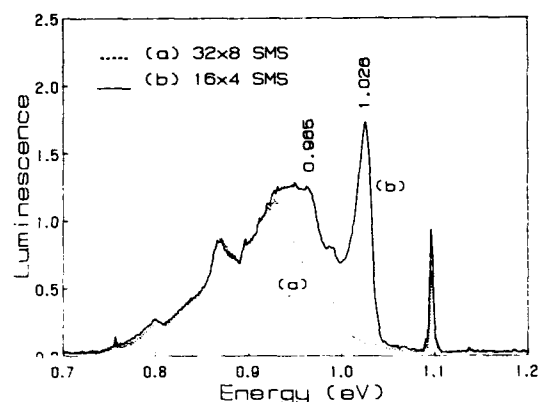


Fig. 1. PL spectra of (a) $\text{Si}_{32}\text{Ge}_8$ SMS, showing the Si exciton and a broad low energy feature, and (b) $\text{Si}_{16}\text{Ge}_4$ SMS, showing, in addition, a peak at 1.026 eV and a shoulder at 0.965 eV.

density of 8 W/cm^2 . Emitted light was collected and then dispersed with a 0.5 m spectrometer and detected by a liquid nitrogen cooled Ge detector. Signals were then measured using a standard lock-in technique.

3. Results and discussion

The PL spectrum for the 32×8 SMS is shown as curve (a) of fig. 1. We observe the Si substrate bound exciton at 1.096 eV and a broad low energy feature around 0.9 eV. Curve (b) shows the spectrum for the 16×4 SMS. In addition to the features observed for the 32×8 SMS, a strong sharp (33 meV FWHM) peak at 1.026 eV and a shoulder at 0.965 eV emerge. These seem to originate from the SMS and not from the buffer layer since both samples have the same buffer layer. The buffer layer, with a 20% Ge concentration, should have a bandgap of 1.06 eV [9], if we assume that it is totally relaxed. This transition, however, is not observed in the PL spectrum of either sample.

To verify that the peak and the shoulder originate from the superlattice and not from the buffer layer, chemical etching was employed to gradually remove the 16×4 SMS and the PL spectra were obtained after each etching step. The results are shown in fig. 2. The original spectrum is repeated as curve (a) for convenience. When

half the SMS is removed, curve (b) is obtained. Notice that the 1.026 eV peak intensity drops by about 50% and that the 0.965 eV shoulder becomes softer. When the SMS is totally removed, the peak and the shoulder both disappear, as shown in curve (c), and the spectrum becomes very similar to the 32×8 SMS spectrum of fig. 1.

The low energy feature observed in the spectra of both samples is due to dislocations in the buffer layer [10,11]. Although undesirable, these dislocations are unavoidable since the buffer layer thickness exceeds the critical thickness, creating misfit dislocations at the buffer layer/substrate interface that partially propagate through the buffer layer. These dislocations may be responsible for quenching the bandgap luminescence of the buffer layer [10].

RTA was then employed to monitor the peak and the shoulder of the 16×4 SMS as a function of annealing temperature. Different pieces cut from the same wafer were annealed at temperatures ranging from 600 to 950°C for a period of 60 s each. Fig. 3 shows the evolution of the peak as a function of annealing temperature. We can see that low temperature RTA (up to 750°C) enhances the peak intensity and slightly moves the peak to higher energy. RTA at higher temperatures reduces the peak intensity and considerably moves the peak to higher energy. The peak eventually disappears upon a 900°C RTA. (Although not shown here, the shoulder follows the same

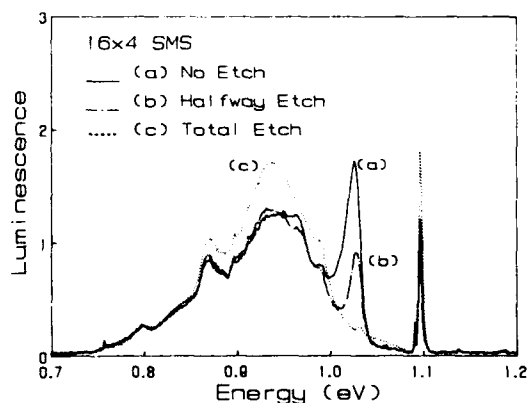


Fig. 2. PL spectra of $\text{Si}_{16}\text{Ge}_4$ SMS with (a) no etching, (b) half the SMS being removed and (c) the whole SMS being removed.

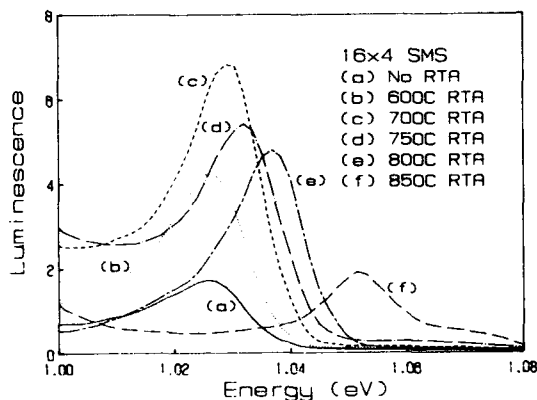


Fig. 3. Evolution of the peak of $\text{Si}_{16}\text{Ge}_4$ SMS as a function of annealing temperature for (a) no RTA, (b) 600°C RTA, (c) 700°C RTA, (d) 750°C RTA, (e) 800°C RTA and (f) 850°C RTA.

behavior.) The enhancement of the observed transitions after a low temperature RTA could be attributed to carrier lifetime improvement or to localization of electronic states (due to interface mixing) [12]. Further study, however, needs to be done to understand the underlying mechanism.

To study the structural variations of the 16×4 SMS as a function of annealing temperature, Raman scattering and X-ray diffraction have been used. Fig. 4 shows the effect of RTA on the folded transverse acoustic modes of the Raman spectrum. Curve (a) of the as-grown sample shows the first and second order modes at 90 and 178 cm^{-1} , respectively. After a 700°C RTA, the spectrum does not change, as shown in curve (b). After a 800°C RTA, however, the second order peak disappears and the first order peak decreases in intensity. The effect of RTA on the X-ray spectrum is shown in fig. 5. Five satellites are present in the spectrum of the as-grown sample, indicative of sharp interfaces. There is no noticeable change upon a 700°C RTA and only a slight decrease in the magnitude of the satellites after a 800°C RTA. A 900°C RTA, however, causes a lot of interdiffusion, and only two satellites can be observed. All of these indicate that there is only minimal interdiffusion for low temperature RTA.

High temperature RTA (800°C and higher), however, causes considerable interdiffusion and a loss of interface sharpness.

To explain the effect of RTA on the optical transitions observed for the 16×4 SMS, we propose the model of fig. 6. In the as-grown sample, interface mixing is minimal and the Si/Ge interfaces are sharp, as shown in fig. 6a. Due to high temperature RTA-induced interdiffusion, what used to be a Si/Ge superlattice becomes a Si/SiGe/Ge/SiGe superlattice, as shown in fig. 6b, where the thickness of the SiGe layers increases with temperature. The energy band diagram has been constructed, based on this model, for different SiGe layer thicknesses. These layers have been assumed to have a 50% Ge concentration, for simplicity, and the energy band offsets have been obtained from the calculations of Van de Walle and Martin [13]. Using the Kronig-Penney model to calculate the energy band transitions, it was found that the closest transition to the observed 1.026 eV peak occurs between the LH ($n=1$) and the X2 ($n=1$) bands and that this transition, and the other energy transitions as well, shift to higher energy as the SiGe layer thickness increases, or, equivalently, as the annealing tem-

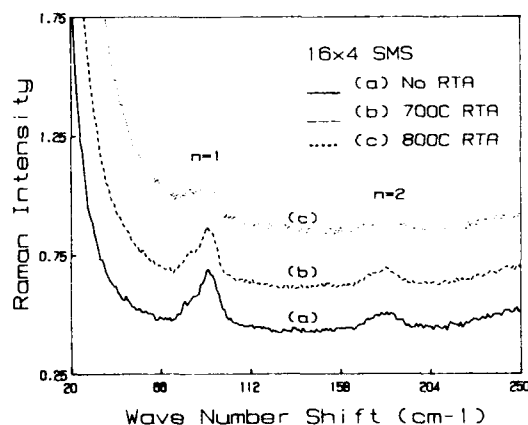


Fig. 4. Folded acoustic phonon Raman spectrum of $\text{Si}_{16}\text{Ge}_4$ SMS (a) before RTA, (b) after a 700°C RTA and (c) after a 800°C RTA.

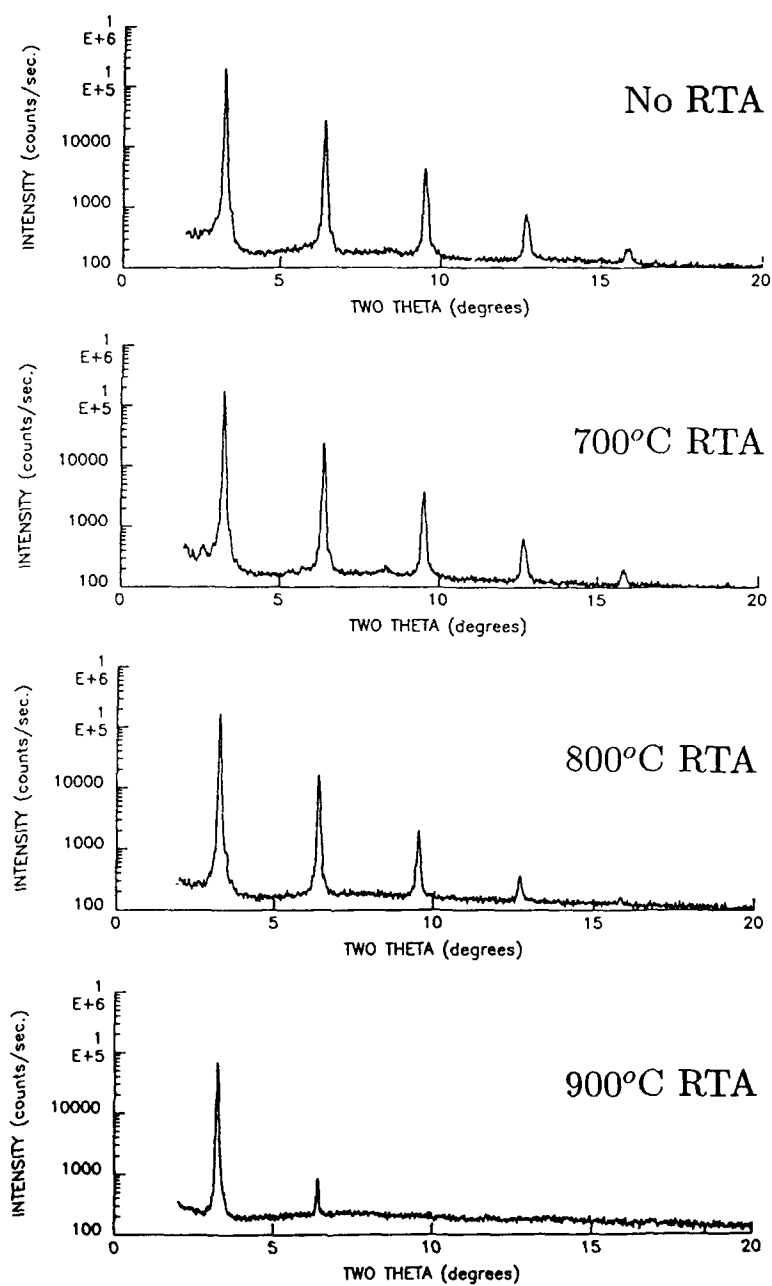


Fig. 5. Evolution of the X-ray diffraction spectrum of $\text{Si}_{16}\text{Ge}_4$ SMS as a function of annealing temperature. Shown are the spectra for no RTA, 700°C RTA, 800°C RTA and 900°C RTA.

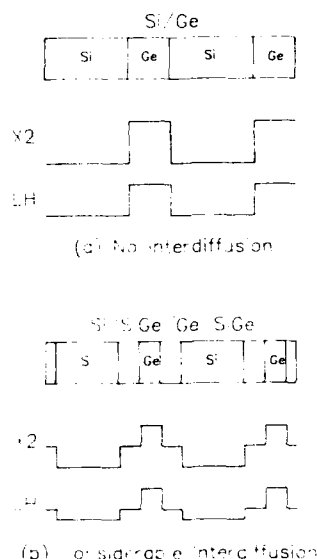


Fig. 6. Effect of RTA-induced interdiffusion on the structural and compositional properties and on the band diagram of the superlattice, (a) showing no interdiffusion and idealized energy band and (b) showing considerable interdiffusion and approximate energy band.

perature increases, as was obtained from the PL measurements.

4. Conclusion

PL spectra have been obtained for $\text{Si}_{12}\text{Ge}_8$ and $\text{Si}_{16}\text{Ge}_4$ SMSs grown on a strain symmetrizing $\text{Si}_{0.8}\text{Ge}_{0.2}$ buffer layer. Broad low energy features have been attributed to dislocations in the buffer layer of both samples. The spectrum of the 16×4 SMS also shows a peak at 1.026 eV and a shoulder at 0.965 eV, both of which have been attributed to energy band transitions in the superlattice. Low temperature annealing has been shown (1) not to affect the interface sharpness of the superlattice,

(2) to enhance the luminescence of the observed transitions and (3) to move them slightly to higher energy. Higher temperature annealing, on the other hand, causes (1) considerable interdiffusion and a loss of interface sharpness, (2) a decrease in the luminescence of the transitions and (3) a considerable shift of these transitions to higher energy.

Acknowledgements

The authors would like to thank D. Nayak for the RTA and P.M. Adams for the X-ray data. This work is in part supported by the Semiconductor Research Corporation and the Office of Naval Research.

References

- [1] E. Kasper, H. Kibbel, H. Jorke, H. Brugger, E. Friess and G. Abstreiter, *Phys. Rev. B* **38** (1988) 3599.
- [2] U. Gnutzmann and K. Clausecker, *Appl. Phys.* **3** (1974) 9.
- [3] T.P. Pearsall, J. Bevk, L.C. Feldman, J.M. Bonar, J.P. Mannaerts and A. Ourmazd, *Phys. Rev. Letters* **58** (1987) 729.
- [4] S. Satpathy, R.M. Martin and C.G. Van de Walle, *Phys. Rev. B* **38** (1988) 13237.
- [5] K. Eberl, G. Krötz, R. Zachar and G. Abstreiter, *J. Physique* **48** (1987) C5-333.
- [6] E.A. Montie, G.F.A. van de Walle, D.J. Gravesteijn, A.A. van Gorkum and C.W.T. Bulle-Lieuwma, *Appl. Phys. Letters* **56** (1990) 340.
- [7] R. Zachar, K. Eberl and G. Abstreiter, *Phys. Rev. Letters* **64** (1990) 1055.
- [8] V. Arbet, S.J. Chang and K.L. Wang, *Thin Solid Films* **183** (1989) 57.
- [9] J. Weber and M.I. Alonso, *Phys. Rev. B* **40** (1989) 5683.
- [10] R. Sauer, J. Weber, J. Stolz, E.R. Weber, K.-H. Küsters and H. Alexander, *Appl. Phys. A* **36** (1985) 1.
- [11] D.J. Robbins, R.A.A. Kubiak and E.H.C. Parker, *J. Vacuum Sci. Technol.* **B3** (1985) 588.
- [12] A. Sasaki, M. Kasu, T. Yamamoto and S. Noda, *Japan. J. Appl. Phys.* **28** (1989) L1249.
- [13] C.G. Van de Walle and R.M. Martin, *Phys. Rev. B* **34** (1986) 5621.

Structure dependence of photoluminescence in Ge_n/Si_m strained-layer superlattices

Kazushi Miki, Hajime Okumura, Kunihiro Sakamoto, Hirofumi Matsuhata, Tsunenori Sakamoto and Sadafumi Yoshida

Electrotechnical Laboratory, 1-1-4 Umezono, Tsukuba, Ibaraki 305, Japan

Ge_n/Si_m strained-layer superlattices (SLSs) grown on Si(001) substrate by molecular beam epitaxy using phase-locked epitaxy method were investigated by X-ray diffraction, transmission electron micrograph (TEM), and photoluminescence. In the TEM image, neither threading dislocations nor Ge clusters were observed over the whole superlattice area. In the substrate, however, misfit dislocations due to lattice mismatch between superlattice and substrate were observed. The photoluminescence spectra of Ge_n/Si_m ($n = 4, 5, 6$) SLSs exhibited an intense emission peak, while $\text{Ge}_n/\text{Si}_{4n}$ ($n = 2, 4, 6$) SLSs showed no intense emission. This result indicates that the optical properties of the Ge_n/Si_m SLS strongly depend not only on the superlattice periodicity but also on the thickness ratio of Ge to Si.

1. Introduction

Silicon is not suitable for optical devices since its optical transition probability is small due to the indirect band gap. However, recent development in molecular beam epitaxy (MBE) techniques makes it possible to fabricate an artificial crystal structure, giving us a chance to overcome this problem. Gnutzmann and Clausecker proposed to introduce a periodic one-dimensional potential into materials with indirect optical band gaps (e.g., Si or Ge) and theoretically predicted that the folding of conduction band minima into the Γ point enhances the optical transition probability [1]. Pearsall et al. observed new intense transition peaks at 0.76 and 1.25 eV in an electroluminescence measurement on a strained-layer superlattice (SLS) of $(\text{Ge}_4/\text{Si}_4)_5$ grown on Si(001) [2]. This experiment stimulated several theoretical works to explain the result, but their conclusions were controversial [3–10]. Recently some promising experimental results have been reported. Zachai et al. have observed an intense emission peak at around 0.84 eV in the photoluminescence spectrum of Ge_4/Si_6 SLS on GeSi alloy (001) substrate [11], which suggests a direct transition. Strong evidence has been reported by us that $\text{Ge}_4/\text{Si}_{12}$ SLS on

Si(001) exhibits intense emission around 0.8 eV and its absorption coefficient follows the curve typical of a direct optical transition [12].

In the present study, two series of SLSs, $\text{Ge}_n/\text{Si}_{3n}$ and $\text{Ge}_n/\text{Si}_{4n}$, were grown on Si(001) substrate by MBE to examine the superlattice structure dependence of the photoluminescence spectra. These superlattice structures were investigated by X-ray diffraction and transmission electron micrograph (TEM). The $\text{Ge}_n/\text{Si}_{3n}$ SLSs exhibit an intense emission, while $\text{Ge}_n/\text{Si}_{4n}$ SLSs show no intense emission. The results indicate that the luminescent property of the $\text{Ge}_n/\text{Si}_{3n}$ SLS strongly depends not only on the superlattice periodicity, but also on the thickness ratio of Ge to Si.

2. Experimental

The substrates used were well oriented Si(001) ($< 0.1^\circ$) and prepared to form a 2×1 single-domain structure [13]. Ge_n/Si_m SLSs were grown by MBE method at a growth temperature of 400°C . During the growth of Ge and Si layers, reflection high-energy electron diffraction (RHEED) intensity oscillations were observed to control layer thickness precisely [15]. The growth periods of Si

(~ 0.2 ML/s) and Ge (~ 0.05 ML/s) were constant during the growth. The total number of atomic layers of the SLSs was about 1100 monatomic layers (ML), which corresponds to a thickness of ~ 150 nm. To protect the SLS layers from oxidation, a 100 ML Si capping layer was grown on them. The photoluminescence measurements were carried out at 4.2 K in liquid He using a 488 nm line of an Ar^+ laser as an excitation light, and the emission signals were detected by a Ge detector cooled with liquid nitrogen. Details of the sample preparation and optical measurement conditions have been described elsewhere [12–15]. Part of the high resolution electron microscopic experiment was carried out by 400 kV electron microscopy at the Kyushu University.

3. Results and discussion

Fig. 1 shows typical RHEED intensity oscillations observed during the growth of $\text{Ge}_4/\text{Si}_{12}$ SLS. In the phase-locked epitaxy (PLE) technique, oscillations in the RHEED intensity are used to control the growth period of Si and Ge. The oscillation damped during the Ge growth and

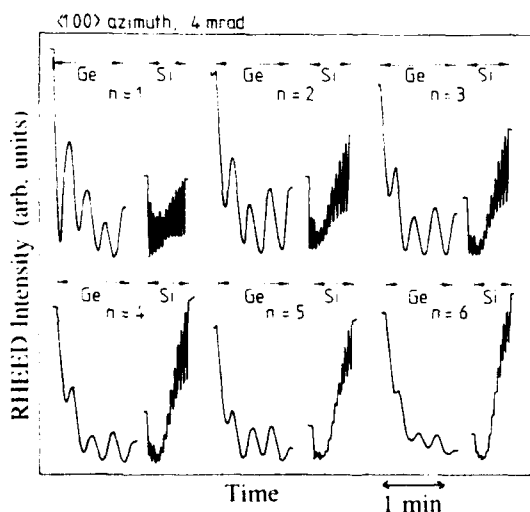


Fig. 1. Typical RHEED intensity oscillations observed during the growth of a $\text{Ge}_4/\text{Si}_{12}$ SLS. The glancing angle of the electron beam was 4 mrad in the azimuth of $\langle 100 \rangle$.

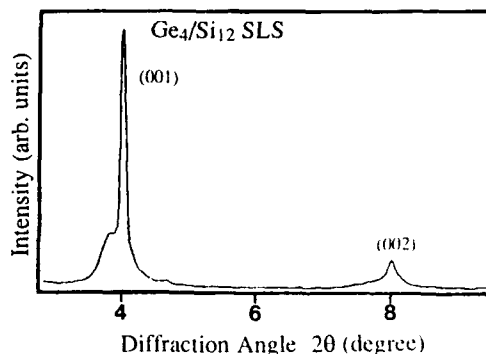


Fig. 2. The X-ray diffraction spectrum of the $\text{Ge}_4/\text{Si}_{12}$ SLS grown on a $\text{Si}(001)$ substrate.

recovered during the Si growth, and it was observed sequentially. This fact suggests that the surface was roughened during the growth of Ge and was smoothed out by the Si overgrowth. With the help of this oscillation recovery effect, the PLE method is applied for $\text{Ge}_4/\text{Si}_{12}$ SLS up to a total thickness of about 130 ML (~ 17 nm). After the RHEED intensity oscillation had damped, a time-control method was adapted. The growth interval time was precisely calibrated from the RHEED intensity oscillation.

The SLSs were examined by using X-ray diffraction with $\text{CuK}\alpha$ radiation. Fig. 2 shows a diffraction pattern of the $\text{Ge}_4/\text{Si}_{12}$ SLS. The diffraction peaks were observed at $2\theta = 4.02^\circ$ and 8.08° . These peaks are attributed to (001) and (002) diffraction peaks of its superlattice structure respectively, which indicates that the $\text{Ge}_4/\text{Si}_{12}$ SLS structure was fabricated as designed. The superlattice structures of the other SLS samples were also confirmed in the same way.

Fig. 3 shows the cross sectional view of the $\text{Ge}_4/\text{Si}_{12}$ SLS grown on $\text{Si}(001)$. Neither threading dislocations nor Ge clusters were observed over the whole superlattice area, although the total thickness of the SLS (~ 150 nm) is larger than the critical thickness (~ 100 nm) of the alloy $\text{Ge}_{0.25}\text{Si}_{0.75}$, which nominally has the same composition as $\text{Ge}_4/\text{Si}_{12}$ SLS. Black and white vertical fringes (~ 10 nm) were observed in the superlattice region, which is attributed to the strain introduced by lattice mismatch between super-



Fig. 3. A transmission electron microscopy (TEM) image of the $\text{Ge}_4\text{Si}_{12}$ SLS grown on a Si(001) substrate.

lattice and substrate. Also, misfit dislocations were observed in the Si substrate.

Fig. 4 shows the photoluminescence spectra measured for $\text{Ge}_4/\text{Si}_{12}$, $\text{Ge}_5/\text{Si}_{15}$ and $\text{Ge}_6/\text{Si}_{18}$ SLSs at 4.2 K. The spectrum of $\text{Ge}_6/\text{Si}_{18}$ SLS showed two types of peaks; one type, labeled as D_1 and D_2 , are particularly sharp peaks with a peak width of ~ 2 meV, and the other type, labeled as E1, is an intense peak with a peak width of 20–30 meV. These peaks are observed in the spectrum of $\text{Ge}_n/\text{Si}_{3n}$ SLSs. As the parameter n increased, the energy of peak E1 shifted lower. Meanwhile, the peak positions of D_1 and D_2 were unchanged. Further, the larger the parameter n , the more remarkable the peaks were. These results indicate that peak E1 and peaks D_1 , D_2 are due to different origins.

The energy of emission peaks at 807 meV (D_1) and 873 meV (D_2) observed in our experiment coincide with the peaks due to relaxed dislocation in Si [16], and peaks like D_1 and D_2 are observable in the spectrum of a $\text{Ge}_6/\text{Si}_{18}$ SLS whose Ge layers thickness is almost equal to the critical thickness [17,18]. Therefore, peaks D_1 and D_2 are due to dislocations caused by lattice mismatch between the Si substrate and the SLS. In fact, in the TEM image of $\text{Ge}_4/\text{Si}_{12}$ SLS, we observed misfit dislocations in the Si(001) substrate. From these results, it is concluded that the origin of

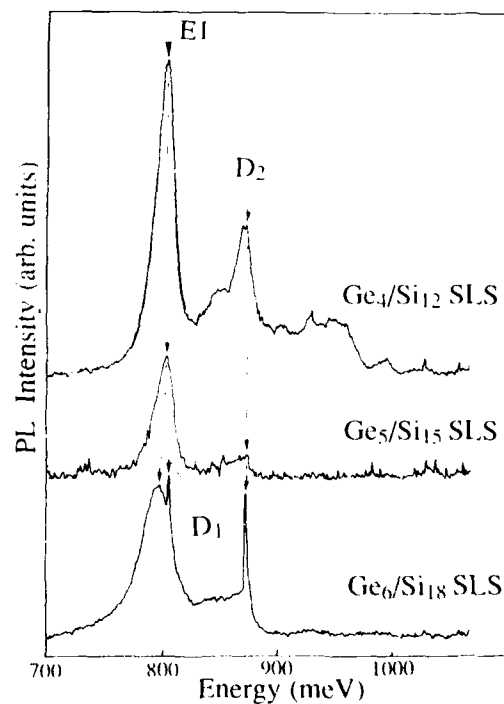


Fig. 4. Typical photoluminescence spectra measured for the $\text{Ge}_4/\text{Si}_{12}$ and the $\text{Ge}_6/\text{Si}_{18}$ SLS at 4.2 K. Peak E1 is attributed to a direct optical transition and peaks D_1 and D_2 are attributed to misfit dislocation in the Si(001) substrate.

peaks D_1 and D_2 is a misfit dislocation in the Si(001) substrate.

On the other hand, the intense emission of peak E1 is considered to be different from defect related emission. The absorption coefficient of $\text{Ge}_4/\text{Si}_{12}$ SLSs followed a $(h\nu - E_g)^{1/2}/h\nu$ law, where $h\nu$ is the energy of incident light and E_g is the band gap energy. The band gap energy estimated from the absorption coefficient curve was found to be just below the energy position of peak E1 [12]. These results provide evidence that the emission peak E1 is due to a direct optical transition.

In comparison to the $\text{Ge}_n/\text{Si}_{3n}$ SLSs, the $\text{Ge}_n/\text{Si}_{4n}$ SLSs exhibited only a weak broad emission band in the spectral region between 700 and 900 meV. This fact shows that the optical properties of the Ge_n/Si_m strongly depend not only on the superlattice periodicity but also on the thickness ratio of Ge to Si. In general, the number of Ge atomic layers in superlattice unit cell strongly influences the band structure. In addition, we would like to point out a possibility that the band structure of Ge_n/Si_m SLS strongly depends on strain in the superlattice, which is affected by the thickness ratio of Ge to Si. Pseudomorphic growth of Ge_n/Si_m superlattice on Si(001) makes the strain in the Ge layers compressive in plane, and consequently makes the Ge-Ge bond length shorter. And, as the thickness of Ge layers in the superlattice increases, the Ge-Ge bonds should tend to expand to the bulk bond length. Actually, the misfit dislocation in Si(001) substrate observed in our TEM image is thought to be one proof of such a tendency for Ge-Ge bonds. That is to say, the in-plane expansion of SLS layer induced the misfit dislocation. The change of bond length in the SLS layer should influence the band structure. To clarify the bond length dependence of the band structure of Ge_n/Si_m SLS, further theoretical and experimental studies are needed.

Our results indicate a great possibility that $\text{Ge}_n/\text{Si}_{3n}$ SLS grown on Si(001) has a direct band gap. Most of the theoretical studies treat only Ge_n/Si_n SLSs ($n = 2-6$) [3-9]; calculations corresponding to our sample have not yet been reported. Compared with the Ge_n/Si_n treated in the theoretical studies, the periodicity of our SLS sam-

ples is larger and the extent of zone-folding is higher. In the case of such large periodicity, the effect of such a long-range potential must be considered. In addition, theoretical studies have not considered the following points. First, the thickness ratio of Ge to Si strongly influences the length and angle of Ge-Ge bonds in the SLS layer. Second, there should be a distribution of bond lengths and angles perpendicular to the layer in the Ge layer. The bond length and angle depend also on the crystal growth condition. Therefore, the flatness of the interface between Ge and Si layers of actual Ge_n/Si_m SLS and interdiffusion around the interface during growth should be considered.

In conclusion, in the TEM image of $\text{Ge}_4/\text{Si}_{12}$, neither threading dislocations nor Ge clusters were observed over the whole superlattice area. However, in the Si(001) substrate, misfit dislocations were observed. The photoluminescence spectra of $\text{Ge}_n/\text{Si}_{3n}$ ($n = 4, 5, 6$) SLSs exhibited an intense emission peak while $\text{Ge}_n/\text{Si}_{4n}$ ($n = 2, 4, 6$) SLSs showed no intense emission. Our results suggest a possibility that the $\text{Ge}_n/\text{Si}_{3n}$ SLSs have a direct band gap and that the optical properties of the Ge_n/Si_m strongly depends on the thickness ratio of Ge to Si. The structural conditions for fabricating such properties should be investigated in further studies to clarify the possibility of direct band gap transition caused by zone-folding.

Acknowledgments

The authors wish to thank Dr. Y. Tomikiyo and Mr. T. Manabe for an opportunity to use the 400 kV electron microscope at the Kyushu University. They gratefully acknowledge the technical assistance by Mr. N. Takahashi, Mr. T. Goto, Mr. M. Furuyama and Mr. S. Unoki. They also wish to thank Dr. T. Tsurushima and Dr. K. Tanaka for their continuing encouragement.

References

- [1] U. Gnatzmann and K. Clausecker, *Appl. Phys.* 3 (1974) 9.
- [2] T.P. Pearsall, J. Bevk, J.C. Bean, J.M. Bonar, J.P. Mannearts and A. Ourmazd, *Phys. Rev. Letters* 58 (1987) 729.

- [3] R. People and S.A. Jackson, Phys. Rev. B36 (1987) 1310.
- [4] M.S. Hybertsen and M. Schüler, Phys. Rev. B36 (1987) 9683.
- [5] L. Brey and C. Tejedor, Phys. Rev. Letters 59 (1987) 1022.
- [6] I. Morrison and M. Jaros, Phys. Rev. B37 (1988) 916.
- [7] S. Froyen, D.M. Wood, and A. Zunger, Phys. Rev. B36 (1987) 4574.
- [8] K.B. Wong, M. Jaros, I. Morrison and J.P. Hagon, Phys. Rev. Letters 60 (1988) 2221.
- [9] M.A. Gell, Phys. Rev. B38 (1988) 7535.
- [10] S. Satpathy, R.M. Martin and C.G. van de Walle, Phys. Rev. B38 (1988) 13237.
- [11] R. Zachai, E. Friess and G. Abstreiter, in: Proc. 19th Intern. Conf. on Physics of Semiconductors, Warsaw, 1988, Ed. R. Zawadzki (Inst. Phys., Warsaw, 1988).
- [12] H. Okumura, K. Miki, S. Misawa, K. Sakamoto, T. Sakamoto and S. Yoshida, Japan. J. Appl. Phys. 28 (1989) L1893.
- [13] T. Sakamoto and G. Hashiguchi, Japan. J. Appl. Phys. 25 (1986) L78.
- [14] K. Sakamoto, T. Sakamoto, S. Nagao, G. Hashiguchi, K. Kuniyoshi and Y. Bando, Japan. J. Appl. Phys. 26 (1987) 666.
- [15] K. Miki, K. Sakamoto, T. Sakamoto, H. Okumura, N. Takahashi and S. Yoshida, J. Crystal Growth 95 (1989) 444.
- [16] R. Sauer, J. Weber, J. Stolz, E.R. Weber, K.-H. Küsters and H. Alexander, Appl. Phys. A36 (1985) 1.
- [17] J. Bevk, J.P. Mannaerts, L.C. Feldman, B.A. Davidson and A. Ourmazd, Appl. Phys. Letters 49 (1986) 286.
- [18] K. Miki, K. Sakamoto and T. Sakamoto, in: Chemistry and Defects in Semiconductor Heterostructures, Eds. M. Kawabe, E.R. Weber and R.S. Williams (Materials Research Society, Pittsburgh, PA, 1989).

Elemental boron and antimony doping of MBE Si and SiGe structures grown at temperatures below 600°C

A.R. Powell, R.A.A. Kubiak, S.M. Newstead, C. Parry, N.L. Matthey, D.W. Smith, J.C. Brighten, C.J. Emeleus, T. Naylor, E. Basaran, T.E. Whall, M.G. Dowsett, R.D. Barlow, E.H.C. Parker

Physics Department, University of Warwick, Coventry CV4 7AL, UK

and

D.K. Bowen

Engineering Department, University of Warwick, Coventry CV4 7AL, UK

This paper considers the low temperature doping of (100) Si and SiGe structures with elemental B and Sb sources particularly with regard to obtaining very narrow delta doping spikes. B is found to be an excellent dopant at SiGe growth temperatures incorporating in an active state at concentrations up to 10%. B delta layers of 1 nm or less have also been grown. Sb is also shown to be capable of providing delta doped layers less than 2 nm wide. The B delta layers have been incorporated into modulation doped structures yielding an order of magnitude increase in mobility at 77 K.

1. Introduction

The growth of high quality pseudomorphic Si/SiGe structures by MBE requires substrate temperatures (T_s) of < 600°C. Growth at such low T_s presents problems in achieving controllable co-evaporation doping, particularly as selective doping of Si and SiGe layers < 5 nm in width is often required. For example, the most commonly used n-type dopant in Si MBE, Sb, suffers severe surface accumulation effects at these temperatures with poor incorporation efficiencies and loss of control over dopant transitions. Despite the success of techniques such as potential enhanced doping [1] at $T_s > 750^\circ\text{C}$, at SiGe growth temperatures recourse has to be made to growth interruptions and heavy Sb coverages, both of which can disrupt epitaxial growth. Similarly, B is a well behaved dopant in Si MBE, but little work has been performed to elucidate its behaviour at low T_s and in SiGe.

We report the use of B and Sb doping in Si and SiGe structures. B is shown to excel as a dopant at SiGe growth temperatures, exceeding expectations in terms of achievable doping levels and activation efficiency. Preliminary results on B-doping of SiGe, and on the growth of 2DHG structures are given. We also report on growth procedures enabling high quality and very narrow B and Sb delta-doping to be obtained.

2. Experimental

The Si and Si/SiGe structures were grown in VG V80 and V90S MBE systems. Sb doping was performed from a conventional in house constructed effusion cell, and B from a high temperature directly current heated graphite crucible [2]. The small thermal mass of the latter source enables rapid thermal changes to the cell temperature, permitting abrupt dopant transitions.

The epilayers were characterized structurally by SIMS, cross-sectional TEM and X-ray diffraction, and electrically using electrochemical CV (ECV), Hall, spreading resistance and 4 point probe measurements, as appropriate.

3. Boron doping

3.1. Bulk boron doping

To ascertain the incorporation kinetics in (100) Si, 50 nm B "spikes" were introduced at 200 nm intervals with T_s varying from 900 to 450 °C. B incorporation was found to be well behaved for doping levels up to $\sim 3 \times 10^{19} \text{ cm}^{-3}$ over the entire temperature range exhibiting sharp doping transitions and complete electrical activation. At higher doping levels, the SIMS profile in fig. 1 shows significant deviation from the ideal structure for $T_s > 700^\circ\text{C}$, caused by B segregating and precipitating on the surface [3] and providing a secondary source for B-incorporation in the "undoped" spacer regions. The similarity with the work of Jackman et al. [4] indicates that oxygen incorporation due to their use of B_2O_3 compound source was not responsible for the segregation. At T_s below 700 °C, the segregation process becomes kinetically limited, resulting in the incorporation of B onto substitutional sites.

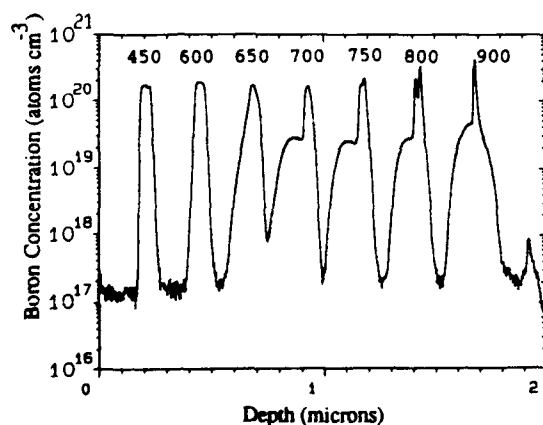


Fig. 1. The SIMS dopant concentration versus depth profile for a structure with B doped layers grown at successively lower substrate temperatures (°C).

Electrical measurements indicate complete electrical activation at all temperatures for doping levels below $\sim 3 \times 10^{19} \text{ cm}^{-3}$. The profile distortions noted above at higher doping levels and temperatures exceeding 700 °C are reflected in an electrical activation ceiling in the low 10^{19} cm^{-3} range. Nevertheless, at $T_s < 600^\circ\text{C}$, there is no surface accumulation smearing and the B is fully activated. This suggests that B-doping lends itself well to the conditions needed for SiGe growth; our preliminary work into B-doping of strained $\text{Si}_{0.8}\text{Ge}_{0.2}$ ($T_s = 550^\circ\text{C}$) at doping levels up to $2 \times 10^{19} \text{ cm}^{-3}$ confirms complete activation and material with Si bulk-like mobilities.

It appears, therefore, that B-doping holds excellent prospects in applications where low growth temperatures are essential, and two examples are described in the following sub-sections.

3.2. Two-dimensional hole gas (2DHG)

Separation of carriers from the dopant site by confinement in a quantum well holds prospects for high mobility devices. Structures have been grown containing four 1 nm thick $4 \times 10^{19} \text{ cm}^{-3}$ B-doped Si regions separated by 8 nm from 8 nm thick $\text{Si}_{0.5}\text{Ge}_{0.5}$ wells. Hall measurements at 100 K yield a sheet carrier density of $2.5 \times 10^{12} \text{ cm}^{-2}$ in each of the wells. The hole mobility of $250 \text{ cm}^2 \text{ V}^{-1} \text{ s}^{-1}$ at 77 K is an order of magnitude higher than for bulk Si, and the low temperature dependence confirms two-dimensional hole confinement.

3.3. Boron delta doping

Planar doping has applications in short channel FET structures [5]. Delta layer structures have been grown at 450 °C by deposition of B onto a Si buffer layer followed by a Si capping layer. Hall measurements on a typical structure yielded a sheet carrier density of $3.5 \pm 0.6 \times 10^{14} \text{ cm}^{-2}$. Comparison with the chemical B content of $3.8 \pm 0.4 \times 10^{14} \text{ cm}^{-2}$ measured using SIMS indicates complete activation, even at this extremely high doping level.

The distribution of the quasi-planar dopant was investigated using double crystal X-ray dif-

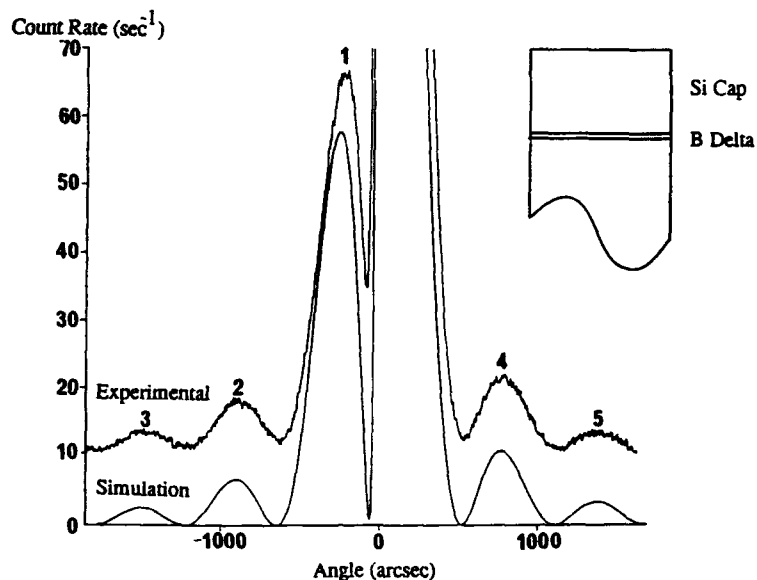


Fig. 2. Experimental X-ray diffraction rocking curve of a $3 \times 10^{14} \text{ cm}^{-2}$ B delta layer along with a simulation (smooth line) assuming a 0.7 nm wide square profile for the B dopant (the main substrate peak has a maximum value of 110,000 counts per second).

fraction with a four bounce beam conditioner [6]. The [113] asymmetric reflection rocking curve taken at glancing incidence is shown in fig. 2. The numbered fringes are due to the diffracted beams from the cap and delta layers interfering with those from the underlying Si. The sharpness of the interference fringes obtained indicates that the capping layer is of good crystalline quality (as the diffraction peaks are broadened by the presence of dislocations) implying that the underlying delta grew pseudomorphically with tetragonal contraction along the [100] direction. Also shown is a dynamical theory simulation [7,8] to which no detector noise offset has been added.

From such modelling using various B-distribution profiles for the delta layer, the factors influencing the rocking curve can be investigated. The spacing of the interference fringes numbered in fig. 2 allows determination of the depth of the delta layer which is found to be $52 \pm 1 \text{ nm}$ (in agreement with the growth schedule and the SIMS profile). The relative heights of the interference peaks, and in particular the ratio of the heights of peaks 3 and 5 which are particularly sensitive as shown in fig. 3, enable the delta layer thickness to

be found. For the experimental curve this ratio is 0.80 ± 0.05 giving the delta layer width as $< 1 \text{ nm}$ and implying an average B concentration in the delta layer of 10%. By considering the positions of the fringes with respect to the main Si substrate peak the total contraction in the [001] direction has been accurately determined to be $31 \pm 2 \text{ pm}$. This gives a volume contraction per atom at 10 at% B in Si of $(1.7 \pm 0.2) \times 10^{-23} \text{ cm}^{-3}$, which is

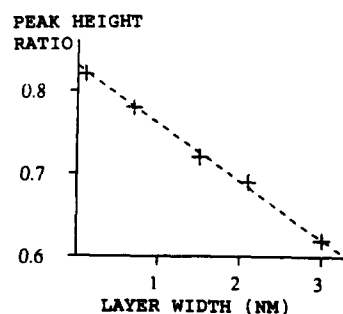


Fig. 3. The ratio of heights of peaks 3 and 5 obtained from simulating the rocking curve for various widths of square profile whilst keeping the total dopant concentration constant.

consistent with the values obtained at lower doping densities by ourselves and others [9].

4. Antimony doping

In order to prepare Sb delta layers, Si was grown at 650°C and then with the matrix flux shuttered off $2 \times 10^{14} \text{ cm}^{-2}$ of Sb deposited on this, T_s was then reduced to <250°C where surface segregation effects disappear [10,11] and a Si cap is grown. The sample was then annealed at 800°C to ensure activation of the Sb. SIMS analysis (fig. 4) shows two Sb delta layers where the capping layer was deposited at (a) $T_s < 250^\circ\text{C}$ but in (b) T_s was not allowed to fall below 250°C. Surface segregation can be seen to have produced appreciable broadening of the Sb delta layer, with the segregated layer acting as a secondary source of doping and producing an Sb shoulder on the growth side of the delta layer. X-ray diffraction

[12] measurements similar to those described for the B delta have shown the structures to have good crystalline quality, demonstrating that pseudomorphic growth took place with tetragonal expansion along the [100] direction and that the widths of the Sb delta layers grown with $T_s < 250^\circ\text{C}$ are <1.5 nm. TEM has confirmed these results and revealed a low density of precipitates ($< 10^7 \text{ cm}^{-2}$).

5. Conclusion

At low temperatures B is an excellent dopant allowing very sharp profile control and high doping densities. Sb doping, despite some problems with surface segregation, nevertheless enables the growth of n-type delta layers of good structural quality.

Acknowledgments

This research was supported by SERC under the Low Dimensional Structures and Devices program. One of us benefited from the support of VG Semicon through the SERC CASE scheme.

References

- [1] R.A.A. Kubiak, W.Y. Leong and E.H.C. Parker, *J. Electrochem. Soc.* 132 (1985) 2739.
- [2] R.A.A. Kubiak, W.Y. Leong and E.H.C. Parker, *J. Vacuum Sci. Technol.* B3 (1985) 592.
- [3] C.P. Parry, S.N. Newstead, R.D. Barlow, P. Augustus, R.A.A. Kubiak, M.G. Dowsett, T.E. Whall and E.H.C. Parker, *Appl. Phys. Letters*, in press.
- [4] T.E. Jackman, D.C. Houghton, J.A. Jackman, M.W. Denhoff, Song Kechang, J. McCaffrey and A. Rockett, *J. Appl. Phys.* 66 (1989) 1984.
- [5] E.F. Schubert, A. Fischer and K. Ploog, *IEEE Trans. Electron Devices* ED-33 (1986) 625.
- [6] L. Hart, G. Fisher and D.K. Bowen, *Advan. X-ray Anal.* 33 (1990) 55.
- [7] Bede Scientific Instruments Ltd., Bowburn, Durham DH65PF, UK.
- [8] D.K. Bowen, N. Loxley, B.K. Tanner, L. Cooke and M.A. Capano, *Proc. Mater. Res. Soc. Symp. Proc.*, in press.
- [9] A. Fukuhara and Y. Takano, *Acta Cryst.* A33 (1977) 137.

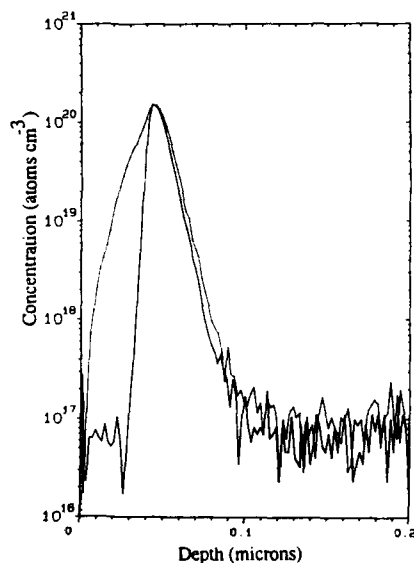


Fig. 4. This SIMS profile shows two Sb delta layer structures with capping and delta layers grown at, (a) $T_s < 250^\circ\text{C}$ (b) $T_s > 250^\circ\text{C}$. A shoulder can be seen on (b) due to surface accumulation problems during growth.

- [10] N.L. Matthey, M. Hopkinson, R.F. Houghton, M.G. Dowsett, T.E. Whall, E.H.C. Parker, G.R. Booker and J. Whitehurst, *Thin Solid Films* 15 (1990) 184.
- [11] H.P. Zeindl, T. Wegehaupt, I. Eisele, H. Oppolzer, H. Reisinger, G. Tempel and F. Koch, *Appl. Phys. Letters* 50 (1987) 1164.
- [12] A.R. Powell, R.A.A. Kubiak, T.E. Whall and D.K. Bowen, *J. Phys. D*, in press.

High hole mobility in strained Ge channel of modulation-doped p-Si_{0.5}Ge_{0.5}/Ge/Si_{1-x}Ge_x heterostructure

Masanobu Miyao, Eiichi Murakami, Hiroyuki Etoh, Kiyokazu Nakagawa and Akio Nishida

Central Research Laboratory, Hitachi, Ltd., P.O. Box 2, Kokubunji, Tokyo 185, Japan

Characterization and application of a new heterostructure (p-Si_{0.5}Ge_{0.5}/Ge/Si_{1-x}Ge_x) fabricated by MBE are comprehensively studied. The strain field in the Ge channel is precisely controlled by changing the X values in the Si_{1-x}Ge_x buffer layer. This enables sufficient confinement of a 2D hole gas at the p-Si_{0.5}Ge_{0.5}/Ge interface. In addition, alloy scattering in the channel region is avoided by the utilization of a pure Ge layer. As a result, a p-channel MODFET with ultra high field effect mobility (10000 cm²/V·s, 77 K) is achieved.

1. Introduction

Si-Ge hetero-epitaxy is the key technology for introducing the new concept of band engineering into Si-LSI work [1]. Modulation-doped heterostructures, i.e. n-Si_{1-x}Ge_x/Si and/or p-Si/Si_{1-x}Ge_x, have been formed by molecular beam epitaxy (MBE). This enabled the formation of two-dimensional (2D) gas systems with electrons and/or holes [2]. Recently, People [3] and Wagner and Janoko [4] suggested that very high hole mobility without alloy scattering can be obtained using the pure Ge channel of a p-Si_{1-x}Ge_x/Ge structure. However, band discontinuity (ΔE) at the hetero-interface was not large enough to confine a high concentration of holes. Thus, high mobility was not achieved.

To solve this problem, we have proposed [5,6] a new heterostructure consisting of p-Si_{0.5}Ge_{0.5}/Ge/Si_{1-x}Ge_x, where the strain field in the p-Si_{0.5}Ge_{0.5} and Ge channel layers are controlled by the Si mole fraction ($1 - X$) of the Si_{1-x}Ge_x buffer layer. This can enlarge the ΔE value and enable sufficient confinement of the 2D hole gas. This paper describes the formation and characterization of this new heterostructure.

2. Experimental

The sample structure is schematically shown in fig. 1. Prior to the MBE growth, the Sb-doped Ge substrate ((100) orientation) was cleaned by chemical etching and thermal heating (650°C, 20 min) in a UHV chamber. Then, thick Si_{1-x}Ge_x buffer layers (200–1000 nm, $0.20 \leq 1 - X \leq 0.40$) were grown incommensurately at high temperature (520°C). Next, a thin Ge channel layer (20 nm) and a Si_{0.5}Ge_{0.5} spacer layer (15 nm) were grown commensurately at low temperature (400°C). A p-type doping was performed by adsorption of Ga atoms at a substrate temperature below 100°C.

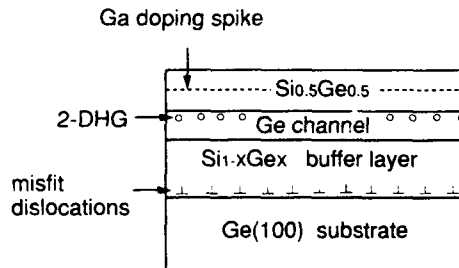


Fig. 1. Cross-sectional view of a new heterostructure consisting of p-Si_{0.5}Ge_{0.5}/Ge/Si_{1-x}Ge_x.

Finally, an amorphous Si_{0.5}Ge_{0.5} film (15 nm thick) was deposited and crystallized by annealing (450 °C, 1 h) in the UHV.

Strains in the p-Si_{0.5}Ge_{0.5}/Ge/Si_{1-X}Ge_X layers were characterized by Raman spectroscopy. In addition, the electrical properties of the 2D hole gas were evaluated by Hall effect measurements and by modulation-doped field effect transistor (MOD-FET) characteristics at 77 K.

3. Strain control of the Ge channel layer by a Si_{1-X}Ge_X buffer layer

In the Raman spectrum, four peaks from different lattice vibrations (i.e., Si-Si, Si-Ge, and Ge-Ge modes in the Si_{0.5}Ge_{0.5} layers, and Ge-Ge mode in the Ge channel layer) were observed. The frequency difference ($\Delta\omega$) between the strained Ge-Ge peaks from the Ge channel layers and the strain-free Ge-Ge peak from the bulk Ge are summarized in fig. 2, as a function of the Si mole fraction ($1-X$) in the buffer layers. Using the relationship of $\Delta\omega = -4.132\epsilon$ [8], the compressive strain (ϵ) was determined to be $\epsilon(\%) = -4.0(1-X)$. This agreed well with a theoretical relation, which was obtained assuming Vegard's law for the lattice constant of Si_{1-X}Ge_X. In this way, accurate control of the strain in the Ge channel layers becomes possible by changing the X value in the buffer layer.

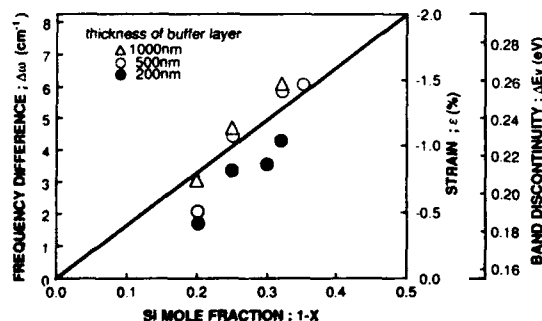


Fig. 2. Wave number differences of Raman shift, strain, and valence band discontinuity as a function of the Si mole fraction ($1-X$) of buffer layers.

Using People's equation [3], the relation between ΔE values and X values was found to be $\Delta E = 0.5(0.84 - 0.53X)$. The results shown in fig. 2 indicate the ΔE reaches 0.22 eV at the strained (1.0%) hetero-interface of p-Si_{0.5}Ge_{0.5}/Ge, which was commensurately grown on a Si_{1-X}Ge_X ($1-X = 0.25$) buffer layer. This value is considered to be large enough to confine the 2D hole gas to the interface.

4. Electrical properties and crystallinity of the strained Ge channel layer

The electrical properties of the heterostructures were evaluated by Hall measurements at 77 K, as shown in figs. 3a and 3b. The results indicated that the hole concentration and hole mobility (μ) increased with the strain in the low strain region (0.5%–1.0%). However, in the high strain region (1.0%–1.5%), they decreased with the strain. Maximum hole mobilities were obtained at $\epsilon = 1.0\%$. These values increased with buffer layer thickness (d), i.e., $\mu = 2400, 4500$, and $7600 \text{ cm}^2/\text{V}\cdot\text{s}$ for $d = 200, 500$ and 1000 nm , respectively.

The relations between hole mobilities and hole concentrations were determined from data shown in figs. 3a and 3b. These relations indicated that mobilities increased proportionally with the hole concentration, which is a typical feature of 2D hole gas [9]. In addition, angular (θ) dependence on magneto-resistance measured at 77 K showed the $\sin^2\theta$ dependence. This means that the magneto-resistance is only influenced for a field component normal to the hetero-interface. Thus, the existence of the 2D hole gas was confirmed.

To understand the phenomena in the high strain region, the crystal quality was examined as a function of X and d in the buffer layer. Observations using a transmission electron microscope showed that roughness at the p-Si_{0.5}Ge_{0.5}/Ge interface as well as threading defects significantly increased when the $(1-X)$ value exceeded 0.25, i.e., $\epsilon \geq 1.0\%$. These defects were found to decrease with an increase in the buffer layer thickness. These results provide ample explanations of why the maximum mobilities are obtained at $\epsilon = 1.0\%$ and why they increase with buffer layer thickness.

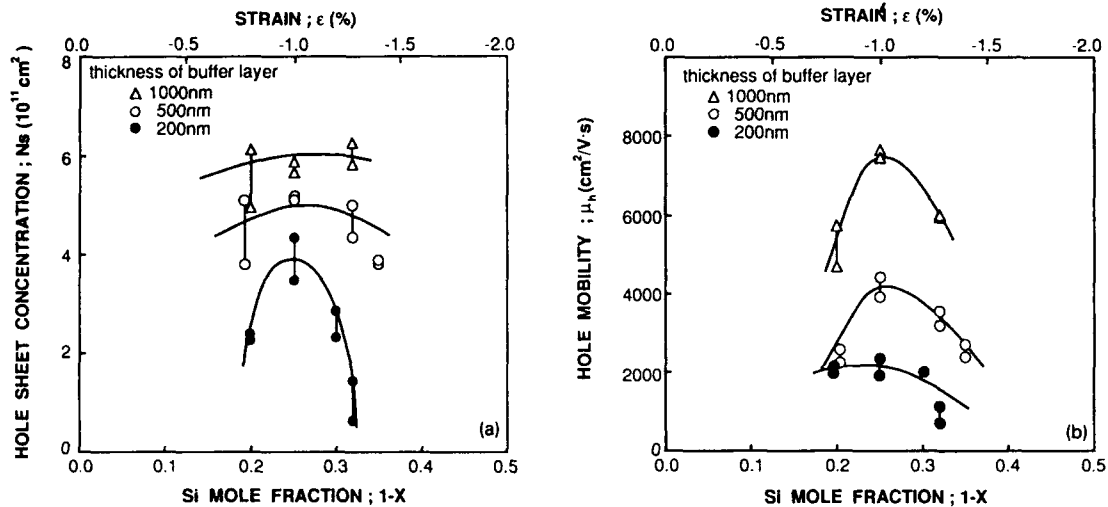


Fig. 3. (a) Two-dimensional hole concentration at the $p\text{-Si}_{0.5}\text{Ge}_{0.5}/\text{Ge}$ interface summarized as a function of $(1-X)$ and/or strain. (b) Two-dimensional hole mobilities at the $p\text{-Si}_{0.5}\text{Ge}_{0.5}/\text{Ge}$ interface summarized as a function of $(1-X)$ and/or strain.

5. Fabrication of a strain controlled modulation-doped FET

A p-channel MODFET was fabricated under the condition of $\epsilon = 1.0\%$ ($1-X = 0.25$). The gate oxide was made of CVD SiO_2 (50 nm), and the source and drain electrodes were made by AuGa alloying (330°C). Gate lengths (L_g) of the MODFETs were 4, 8, and $50 \mu\text{m}$, the gate width (W_g)

was $50 \mu\text{m}$, and spacing between the gate and source was $1.5 \mu\text{m}$.

Typical current-gain characteristics and transfer characteristics of the FET ($L_g/W_g = 50 \mu\text{m}/50 \mu\text{m}$) measured at 77 K are shown in figs. 4a and 4b, respectively. Gate capacitance and source resistance of the FET were $6 \times 10^{-8} \text{ F/cm}^2$ and 350Ω . The calculated values of maximum intrinsic transconductance were almost proportional to

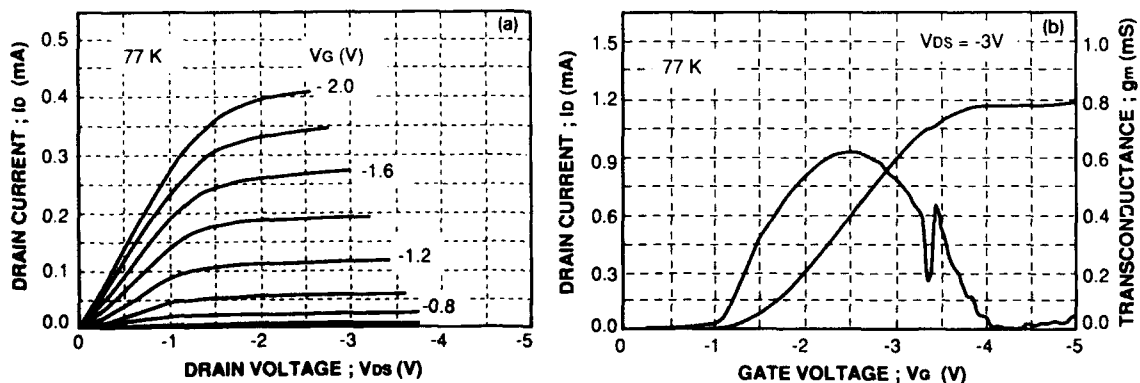


Fig. 4. (a) Current-voltage characteristics of the MODFET ($L_g/W_g = 50 \mu\text{m}/50 \mu\text{m}$) at 77 K. (b) Transfer characteristics of the MODFET ($L_g/W_g = 50 \mu\text{m}/50 \mu\text{m}$) at 77 K.

$1/L_g$ and reached 130 mS/mm at $L_g = 4 \mu\text{m}$, which is a very large value when the small gate capacitance of the present FET is considered. As a result, an extremely high field effect mobility ($10000 \text{ cm}^2/\text{V} \cdot \text{s}$, 77 K) was obtained in the strain-controlled MODFET ($L_g = 4\text{--}50 \mu\text{m}$). These values were ten times higher than those of a previously reported SiGe heterostructure ($600 \text{ cm}^2/\text{V} \cdot \text{s}$, 77 K) [7].

6. Conclusion

A new strain-controlled Ge-channel heterostructure (p-Si_{0.5}Ge_{0.5}/Ge/Si_{1-x}Ge_x/Ge) was fabricated by MBE. The strain field in the Ge channel layer was accurately controlled by changing the x -values in the Si_{1-x}Ge_x buffer layer. This enlarged the ΔE values and enabled the confinement of the hole gas to the p-Si_{0.5}Ge_{0.5}/Ge interface. As a result, ultra high mobility of the 2D hole gas ($10000 \text{ cm}^2/\text{V} \cdot \text{s}$) was obtained at 77 K.

Acknowledgements

The authors wish to thank Professor S. Furukawa of the Tokyo Institute of Technology, Pro-

fessor C. Tatsuyama of the Toyama University, and Professor Y. Shiraki of the Tokyo University for stimulating discussions and encouragement through the course of this study.

References

- [1] B.W. Dodson, L.J. Schowalter, J.E. Cunningham and F.H. Pollak, Eds., Layered Structure - Heteroepitaxy, Superlattice, Strain and Metastability, Mater. Res. Soc. Symp. Proc., Vol. 160 (Mater. Res. Soc., Pittsburgh, PA, 1989).
- [2] E. Kasper et al., Eds., Silicon Molecular Beam Epitaxy (CRC Press, Boca Raton, FL, 1988).
- [3] R. People, Phys. Rev. B34 (1986) 2508.
- [4] G.R. Wagner and M.A. Janoko, Appl. Phys. Letters 54 (1989) 66.
- [5] E. Murakami, H. Etoh, K. Nakagawa and M. Miyao, Japan. J. Appl. Phys. 29, Part 2 (1990) 29.
- [6] M. Miyao, E. Murakami, H. Etoh and K. Nakagawa, in ref. [1], p. 777.
- [7] T.P. Pearsall and J.C. Bean, IEEE Trans. Electron Device Letters EDL-7 (1986) 308.
- [8] F. Cerdeira, A. Pinczuk, J.C. Bean, B. Batlogg and B.A. Wilson, Appl. Phys. Letters 45 (1984) 1138.
- [9] K. Hirakawa and H. Sakaki, Phys. Rev. B33 (1986) 8291.

Transport properties of p-Si/SiGe single-modulation-doped heterostructures grown by MBE

D.J. Gravesteijn, T. Mishima *, C.W. Fredriksz, G.F.A. van de Walle and R.A. van den Heuvel

Philips Research Laboratories, P.O. Box 80.000, 5600 JA Eindhoven, Netherlands

Electrical properties have been examined for single Si/Si_{1-x}Ge_x p-channel modulation-doped heterostructures grown by MBE. Heterostructures with the doped layer on top have a higher hole mobility than structures with the doped layer on the substrate side. This difference is caused by B segregation during growth. The effects of B concentration and Ge content on the electrical properties are studied. Hole mobilities as high as 6000 cm²/V·s at 2 K have been obtained, which are the highest values reported so far.

1. Introduction

p-Si/SiGe modulation-doped heterostructures have been studied extensively recently [1–3]. The bandgap offset in these structures is mainly present in the valence band, in contrast to the III–V systems. In the potential well at the SiGe/Se interface a two-dimensional hole gas (2DHG) is formed. For practical applications, a high transconductance is essential, i.e. both a high sheet-carrier density and a high mobility are required. A high sheet-carrier concentration can be obtained by forming 2DHGs at both the surface side (a “normal” 2DHG) and the substrate side (an “inverted” 2DHG) of the SiGe layer. However, the quality of both interfaces is not necessarily the same, because of MBE-growth-related effects such as dopant or Ge segregation [4,5], leading to differences in mobilities between a normal and an inverted 2DHG.

The purpose of this paper is to study normal and inverted p-Si/SiGe single-modulation-doped heterostructures. It will be shown that very high conductances can be achieved by adjusting dopant concentration, Ge content and spacer layer thickness.

2. Experimental

The heterostructures were grown in a Vacuum Generators Silicon MBE system. The oxide was removed by a 5 min flash-off at 880 °C. The layers were deposited at a substrate temperature of 550 °C, except for the i-Si buffer layer which was grown at 690 °C. The layers were deposited by means of electron beam evaporation from i-Ge, i-Si and heavily B-doped Si slugs.

The Ge content and the crystalline quality were assessed by means of Rutherford backscattering spectroscopy (RBS). Secondary ion mass spectrometry (SIMS) was used to determine B and Ge profiles. Electrical characterization was performed using conventional Hall–Van der Pauw measurements between 4 and 300 K.

3. Results and discussion

Typical normal and inverted modulation-doped heterostructures that were studied are shown in fig. 1. The spacer layer thickness between the p-Si and the Si_{1-x}Ge_x layer, W_{sp} , was chosen to be 3 or 10 nm. Fig. 2 shows the temperature-dependence of the mobility, μ , and sheet-hole concentration, p_s , for a normal and an inverted modulation-doped heterostructure with $x = 0.2$, a B concentration of $2 \times 10^{18} \text{ cm}^{-3}$ and a spacer thickness of 3 nm. The

* Exchange researcher from Hitachi Central Research Laboratories, Tokyo, Japan.

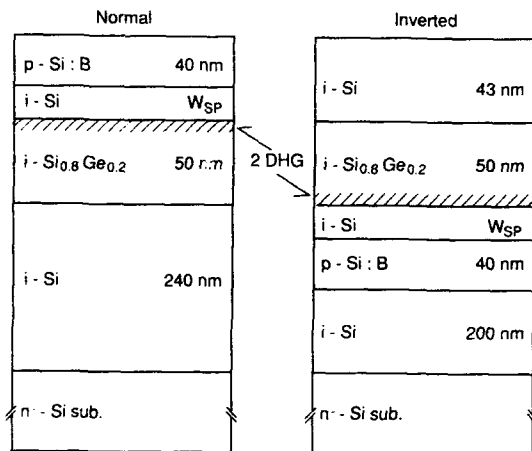


Fig. 1. Normal and inverted p-Si/SiGe modulation-doped heterostructures considered in this study.

behaviour of p_s is almost identical. A strong temperature-dependence is found for temperatures above 70 K, which is caused by the temperature-dependence of the conduction in the p-Si; below this temperature the conduction in the p-Si freezes out and the 2DHG becomes observable. The temperature-dependence of μ is quite different, however. At low temperatures the mobility increases

Table 1

Electrical characteristics of the p-Si/SiGe modulation-doped heterostructures

x	Normal/ inverted	W_{sp} (nm)	[B] (cm^{-3})	μ at 6 K ($\text{cm}^2/\text{V}\cdot\text{s}$)	p_s at 6 K (cm^{-2})
0.2	N	3	2.0×10^{18}	2300	0.99×10^{12}
0.2	I	3	2.0×10^{18}	800	0.94×10^{12}
0.2	I	10	2.0×10^{18}	3800	0.49×10^{12}
0.2	N	10	5.5×10^{18}	3900	0.65×10^{12}
0.2	I	10	5.5×10^{18}	820	1.10×10^{12}
0.4	N	3	5.5×10^{18}	1500	2.80×10^{12}

to much higher values for the normal 2DHG than for the inverted 2DHG ($2300 \text{ cm}^2/\text{V}\cdot\text{s}$ versus $800 \text{ cm}^2/\text{V}\cdot\text{s}$, see also table 1). This difference in mobility may be attributed to segregation of a small fraction of the B into the SiGe channel, as will be shown below. As a result, increased ionized impurity scattering will occur, leading to a low mobility. In the normal structure, with the high hole mobility, the B-doped layer is grown after the SiGe layer, hence no B segregation into the conduction channel is possible. This explains the higher mobility in this case.

Attempts were made to demonstrate B segregation in the inverted structure by means of SIMS analysis. However, no indication of B segregation was found, probably because of limited depth resolution. In order to prove that surface segregation influences the electrical properties, an inverted modulation-doped heterostructure was prepared, where the p-Si layer was grown at 690°C instead of the normal 550°C . The B segregation is stronger at this higher growth temperature [5]. After growth of this layer, the temperature was lowered to 550°C and growth was resumed. Now SIMS showed a distinct B spike at the SiGe/Si interface (fig. 3), which is due to segregation during the growth of the p-Si layer at 690°C . Some segregation will still occur during subsequent growth at 550°C . Due to the presence of more ionized impurities and also more B segregated into the conduction channel, the mobility is expected to decrease significantly. Experimentally a low-temperature mobility of only $330 \text{ cm}^2/\text{V}\cdot\text{s}$ is found at 6 K and p_s has almost doubled to $1.8 \times 10^{12} \text{ cm}^{-2}$. Both observations are in accor-

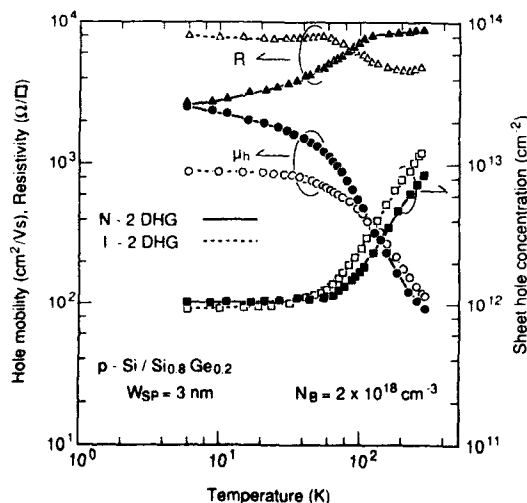


Fig. 2. Temperature-dependent electrical properties for a normal and inverted p-Si/Si_{0.8}Ge_{0.2} modulation-doped heterostructure with a spacer layer of 3 nm thickness.

dance with the segregation model. Even during continuous growth at 550°C some segregation will occur, reducing the mobility of the inverted with respect to the normal structures.

A larger W_{sp} is expected to give rise to an increase in mobility due to reduced remote ionized impurity scattering, and to a smaller p_s . The mobilities and sheet-hole concentration for structures with a spacer layer thickness of 10 nm are shown in table 1. A hole mobility as high as 3800 cm²/V·s is observed at 6 K, and increases to 6000 cm²/V·s at 2 K. The sheet carrier density is 4.9×10^{11} cm⁻². The high mobilities found in these structures compare very favourably with literature data on UHV-CVD-grown double-modulation-doped heterostructures [3]. It shows that very high quality modulation-doped heterostructures can be grown with MBE.

In order to obtain a higher p_s , the B concentration was increased to 5.5×10^{18} cm⁻³ for a normal and an inverted structure with a 10 nm spacer. The mobility and p_s values are shown in table 1. For the normal structure a sheet carrier concentration of 6.5×10^{11} cm⁻² was determined which is slightly higher than that of the low B doping heterojunctions. The mobility, however, is still very high, viz. 3900 cm²/V·s. The observed high mobility is in accordance with the expectations for a normal structure: B segregation does not play a role. In the inverted structure, the B segregation in

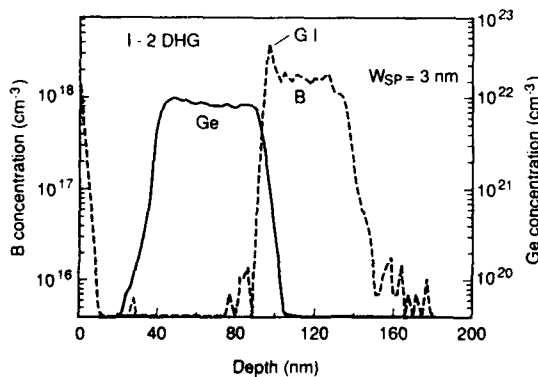


Fig. 3. B and Ge SIMS profiles for a heterostructure with a p-doped layer, grown at 690°C. G.I. Indicates the position where the growth was interrupted and the temperature was lowered to 550°C.

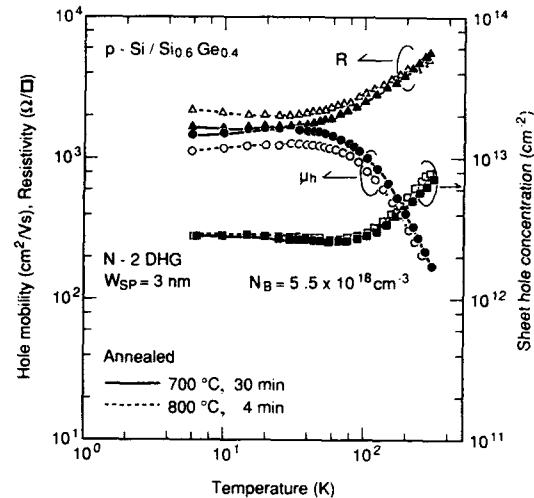


Fig. 4. Temperature-dependence of hole mobility and sheet-hole concentration for a normal p-Si/Si_{0.6}Ge_{0.4} modulation-doped heterostructure with a spacer layer thickness $W_{sp} = 3$ nm and a boron concentration of 5.5×10^{18} cm⁻³. Also shown are the results for a 30 min anneal at 700°C, and a 4 min anneal at 800°C. The results for the 700°C anneal and the 600°C standard anneal are identical, therefore only the 700°C result is given.

the SiGe channel is enhanced due to the higher dopant concentration. Consequently, p_s increases to 1.1×10^{12} cm⁻², but on the other hand an inferior mobility of 820 cm²/V·s was found.

A higher sheet-hole concentration is also expected if the valence band offset is increased. This can be achieved by increasing the Ge content of the strained layer. To study the effect of a higher Ge content, a normal structure was grown, with $W_{sp} = 3$ nm, a B concentration of 5.5×10^{18} cm⁻³ and a Ge fraction of 0.4. The thickness of the Si_{0.6}Ge_{0.4} layer was chosen to be 20 nm, in order to prevent strain relaxation. The temperature-dependent electrical properties are shown in fig. 4. At 6 K, p_s is found to be 2.8×10^{12} cm⁻² (cf. table 1), which is 2.8 times higher than that for the samples with a Si_{0.8}Ge_{0.2} strained layer, while μ was still 1500 cm²/V·s at 6 K. The conductance is 6.5×10^{-4} Ω⁻¹, which is about 30% higher than the highest value (5×10^{-4} Ω⁻¹) reported so far for double-modulation-doped structures [3].

The thermal stability of the modulation-doped structures was also examined by measuring the changes in electrical characteristics. Anneals for either 3 min at 700°C or for 4 min at 800°C were used and the results were compared to the 30 min 600°C anneal that was used to activate the contact implants. Assuming B diffusion to be the main cause of thermal degradation, a diffusion depth of 0.5 nm for the 700°C anneal and 1 nm for the 800°C anneal is expected, based on bulk B-diffusion data. Fig. 4 shows the temperature dependence of p_s and hole mobility of the annealed samples of the highly doped, 40% Ge structure. The 600 and 700°C data are indistinguishable, thus only the 700°C curve is given. After the 800°C anneal, the mobility is distinctly reduced. A similar reduction in mobility was found for all 3 nm samples, with both normal and inverted 2DHGs. This effect is in accordance with the B diffusion mechanism. For the inverted structure with $W_{sp} = 10$ nm, one would expect a smaller decrease in mobility, because diffusion only reduces the effective W_{sp} slightly from 10 to ≈ 9 nm. However, in this case a mobility reduction of $\approx 25\%$ is found like in the structures with $W_{sp} = 3$ nm. This observation seems to suggest that some strain relaxation occurs, reducing the bandgap offset. High resolution XRD does not show any indications of strain relaxation in this sample, however. This subject is being studied in more detail.

4. Conclusions

It was shown that MBE-grown normal p-Si/SiGe modulation-doped heterostructures have a higher mobility than the inverted structures. The origin of this difference is believed to be due to the segregation of B during growth which leads to increased ionized impurity scattering in inverted structures. The quality of the heterostructures ap-

pears to be very good: hole mobilities of 6000 $\text{cm}^2/\text{V} \cdot \text{s}$ have been obtained at 2 K for a normal structure. A thicker spacer layer leads to a higher mobility and a lower sheet-hole concentration. Increasing the B concentration gives rise to moderate increases in p_s . In this case the segregation becomes more severe in inverted structures. By increasing the Ge content, the valence band offset increases, giving rise to very high sheet-hole concentrations. A sheet carrier concentration of $2.5 \times 10^{12} \text{ cm}^{-2}$ was found at 6 K. Further, a conductance as high as $6.5 \times 10^{-4} \Omega^{-1}$ was measured for this single 2DHG structure, exceeding by 30% the values reported for double-modulation-doped structures. The structures appear to be at least stable with respect to thermal anneals for 30 min at 700°C.

Acknowledgments

The work described in this paper has been carried out as part of the researcher exchange programme of Hitachi, Ltd. and Philips. One of the authors (T.M.) gratefully acknowledges the hospitality of Philips Research Labs. The authors are indebted to L.J. van IJzendoorn for his expert RBS analysis, and to P.C. Zalm and C.J. Vriezema for their excellent SIMS analyses.

References

- [1] R. People, IEEE J. Quantum Electron. QE-22 (1986) 1696.
- [2] R. People, J.C. Bean, D.V. Lang, A.M. Sergent, H.L. Störmer, K.W. Wecht, T.R. Lynch and K. Baldwin, Appl. Phys. Letters 45 (1984) 1231.
- [3] P.J. Wang, B.S. Meyerson, F.F. Fang, J. Nocera and B. Parker, Appl. Phys. Letters 55 (1989) 2333.
- [4] P.C. Zalm, G.F.A. van de Walle, D.J. Gravesteijn and A.A. van Gorkum, Appl. Phys. Letters 55 (1989) 2420.
- [5] T. Tatsumi, H. Hirayama and N. Aizaki, Japan. J. Appl. Phys. 27 (1988) L954.

Dislocation-related photoluminescence in $\text{Si}_{1-x}\text{Ge}_x/\text{Si}(100)$ grown by molecular beam epitaxy

Koichi Terashima

Microelectronics Research Laboratories, NEC Corporation, 4-1-1, Miyazaki, Miyamae-ku, Kawasaki 216, Japan

Michio Tajima

Institute of Space and Astronautical Science, 3-1-1, Yoshinodai, Sagami-hara 229, Japan

Akira Sakai

Fundamental Research Laboratories, NEC Corporation, 34, Miyukigaoka, Tsukuba 305, Japan

and

Toru Tatsumi

Microelectronics Research Laboratories, NEC Corporation, 4-1-1, Miyazaki, Miyamae-ku, Kawasaki 216, Japan

Photoluminescence (PL) in $\text{Si}_{1-x}\text{Ge}_x$ alloys grown on Si(100) by molecular beam epitaxy (MBE) has been studied over the composition range $0 \leq x \leq 0.5$. For $x \geq 0.15$, strong deep-level luminescence has been observed. Sharp lines which are similar to the dislocation-related D-lines in Si appear in the spectra for $x = 0.15$ and 0.26. Transmission electron microscopy (TEM) for these samples reveals that there are a lot of dislocations at the $\text{Si}_{1-x}\text{Ge}_x/\text{Si}$ interface and in the Si substrate. The dislocations in the Si substrate are considered to be the origin of the sharp luminescence lines. These PL lines for $x = 0.15$ cannot be observed in the case of thin layers. In that case, the density of the dislocations near the interface is much lower. For $x = 0.38$ and 0.50, broad bands appear in the spectra. The TEM observations in these cases reveal that there are many dislocations in the $\text{Si}_{1-x}\text{Ge}_x$ layers and that the dislocation density in the Si substrate is very low. The broad bands are considered to originate from the dislocations in the $\text{Si}_{1-x}\text{Ge}_x$ layer.

1. Introduction

$\text{Si}_{1-x}\text{Ge}_x$ layers on Si substrates have attracted much attention in recent years. In the applications of $\text{Si}_{1-x}\text{Ge}_x/\text{Si}$ heterostructures to device fabrications, remarkable results such as heterojunction bipolar transistors (HBTs) have been reported [1,2]. Generation of misfit dislocations at the $\text{Si}_{1-x}\text{Ge}_x/\text{Si}$ interface is receiving physical interest [3]. Moreover, the enhanced mobility and the appearance of a direct band gap have been reported for strained Si–Ge superlattices [4,5].

Photoluminescence (PL) is one of the powerful

methods for investigating the electronic properties of semiconductors and for the characterization of impurities and defects. Rowell et al. [6] reported the PL spectra of $\text{Si}_{1-x}\text{Ge}_x/\text{Si}$ grown by molecular beam epitaxy (MBE). They observed deep-level luminescence. However, the origin of the observed PL lines was not analyzed in detail. Recently, several authors [5,7–9] reported PL spectra of strained Si–Ge superlattices. Although new PL lines reported by these authors are believed to be the evidence of a newly appearing direct band gap, these lines are rather broad and their positions are different from one report to another.

In this paper, we report the PL spectra of $\text{Si}_{1-x}\text{Ge}_x/\text{Si}(100)$ grown by MBE over the composition range $0 \leq x \leq 0.5$. In order to investigate the relationship between the deep-level luminescence and dislocations, the sample is observed by transmission electron microscopy (TEM).

2. Experimental

Undoped $\text{Si}_{1-x}\text{Ge}_x$ layers are grown on Si substrates by MBE at a substrate temperature of 650°C . The substrates are 100 mm diameter (100) Czochralski-grown (CZ-grown) Si wafers with a resistivity of $10\text{--}50\ \Omega\text{ cm}$ doped with P. The alloy composition is determined by Rutherford backscattering (RBS) using 2.275 MeV He ions and a backscattering angle of 160° .

The thickness of the $\text{Si}_{1-x}\text{Ge}_x$ layers studied in this work is $1000\text{--}5000\ \text{\AA}$. For larger x , the thickness is considered to be thicker than the critical thickness where misfit dislocations are introduced.

PL spectra are measured at 4.2 K in the wavelength region of $1000\text{--}1800\text{ nm}$. The samples are immersed in liquid helium in a glass cryostat. They are excited by the 647 nm line of a Kr ion laser or the 488 nm line of an Ar ion laser. This enables us to investigate the dependence of the PL spectra on the penetration depth of the excitation light, since the penetration depth of the 488 nm line of an Ar laser is about $1\ \mu\text{m}$ while that of the 647 nm line of a Kr laser is $10\ \mu\text{m}$ for Si. The excitation power density is about $6\text{ mW}/\text{mm}^2$ for a Kr ion laser and $8\text{ mW}/\text{mm}^2$ for an Ar ion laser. The emission from the sample is analyzed by a 32 cm grating monochromator with a 600 groove/mm grating blazed at $1\ \mu\text{m}$ and detected by a cooled Ge detector. The spectral response of the measurement system is calibrated using blackbody radiation.

All the samples are investigated by cross-sectional and plan-view transmission electron microscopy (TEM) observations. Specimens for cross-sectional TEM observations are prepared with Ar ion milling after bonding the samples together face-to-face and mechanically polishing from both sides. Plan-view TEM specimens are prepared by mechanically polishing and chem-

ically etching from the substrate side. Thinned specimens are examined using Akashi EM002B at 200 kV.

3. Results and discussion

The PL spectra of $\text{Si}_{1-x}\text{Ge}_x/\text{Si}(100)$ over the composition range $0 \leq x \leq 0.5$ are shown in Figs. 1 and 2 under the excitations with a Kr and an Ar laser, respectively. The thickness of the $\text{Si}_{1-x}\text{Ge}_x$ layer is $3000\text{--}5000\ \text{\AA}$. Sharp lines near 1100 nm can be observed for all the cases. These lines are associated with the near-band-gap emission of the Si substrate. In the spectra for $x = 0$, these lines appear near 1100 nm in addition to the emission from the Si substrate. From the energy positions of these new lines, these lines are considered to be the near-band-gap emission of the $\text{Si}_{1-x}\text{Ge}_x$ layer [10]. This idea is supported by the fact that their relative intensities are stronger under the 488 nm

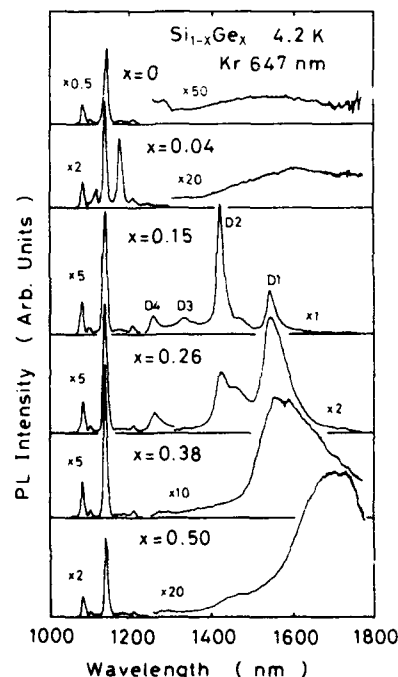


Fig. 1. Photoluminescence spectra of $\text{Si}_{1-x}\text{Ge}_x/\text{Si}(100)$ at 4.2 K under the 647 nm excitation. Spectral band pass is 10 nm.

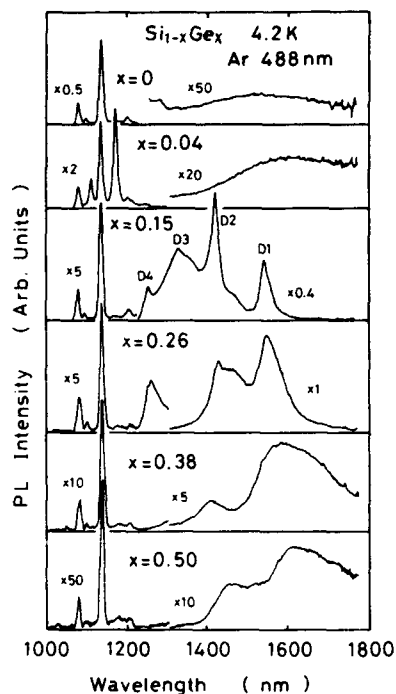


Fig. 2. Photoluminescence spectra of $\text{Si}_{1-x}\text{Ge}_x/\text{Si}(100)$ at 4.2 K under the 488 nm excitation. Spectral band pass is 10 nm.

excitation than under the 647 nm excitation: these new lines are from the part nearer to the surface.

For $x \geq 0.15$, strong deep-level luminescence can be observed. Four sharp lines labelled D1–D4 appear in the spectra for $x = 0.15$. These lines appear at the same wavelength positions as the dislocation-related D-lines in Si. A plan-view TEM image shows that there are a lot of dislocations in this sample. They are mainly misfit dislocations at the $\text{Si}_{1-x}\text{Ge}_x/\text{Si}$ interface. However, the cross-sectional TEM image of $x = 0.15$ shown in fig. 3 reveals that there are many dislocations in the Si substrate. These dislocations in the Si substrate are considered to be the origin of the lines D1–D4. In the case of the Ar laser excitation, the lines D1–D4 are accompanied by the broad background. This indicates that the broad background comes from near the surface. The broad background may be related to the dislocations at the $\text{Si}_{1-x}\text{Ge}_x/\text{Si}$ interface or in the $\text{Si}_{1-x}\text{Ge}_x$ layer.

The PL spectra of $\text{Si}_{0.85}\text{Ge}_{0.15}/\text{Si}(100)$ for the different thickness of the epitaxial layer are shown in fig. 4. In addition to the near-band-gap emission of the Si substrate, sharp lines near 1200 nm can be observed in some cases. These lines are



Fig. 3. Cross-sectional TEM image of $\text{Si}_{0.85}\text{Ge}_{0.15}/\text{Si}(100)$. Marker represents 0.5 μm .

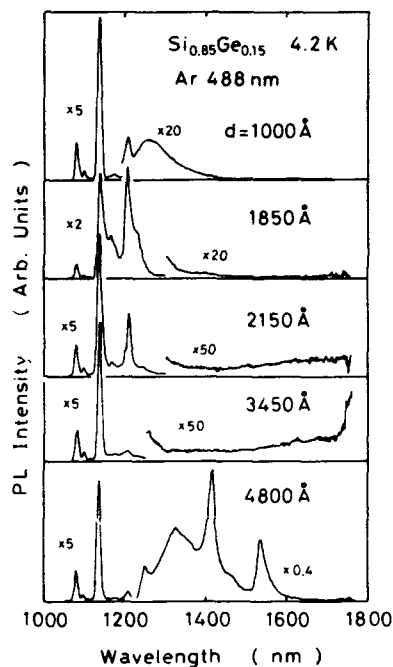


Fig. 4. Photoluminescence spectra of $\text{Si}_{0.85}\text{Ge}_{0.15}/\text{Si}(100)$ for the for different thicknesses of the epitaxial layer.

considered to be the near-band-gap emission of the $\text{Si}_{1-x}\text{Ge}_x$ layer [10]. When the layer is thin, the sharp deep-level PL lines cannot be observed.

Weak background can be seen in that case. This background becomes stronger as the epitaxial layer becomes thicker. When the sharp deep-level PL lines do not appear in the spectra, dislocations in the Si substrate cannot be observed in the cross-sectional TEM image. However, misfit dislocations can be seen in the plan-view TEM image. The background observed in the spectra is considered to originate from the misfit dislocations at the $\text{Si}_{1-x}\text{Ge}_x/\text{Si}$ interface. The dislocations in the Si substrate, which are considered to be the origin of the sharp PL lines, may be introduced when the epitaxial layer becomes thicker than a certain thickness. This thickness is different from the critical thickness where misfit dislocations are introduced.

The D-lines can be observed also in the PL spectra for $x = 0.26$ in figs. 1 and 2. However, the features of the spectra are different from the case of $x = 0.15$. The lines become broader and the line D3 disappears. A shoulder can be seen in the longer wavelength side of the line D2. In the TEM observation, dislocations near the $\text{Si}_{1-x}\text{Ge}_x/\text{Si}$ interface for $x = 0.26$ are similarly observed as in the case for $x = 0.15$, but the interface is rough. This may explain the difference of the PL spectra.

The broad bands which are different from the D-lines appear in the spectra for $x = 0.38$ and



Fig. 5. Cross-sectional TEM image of $\text{Si}_{0.62}\text{Ge}_{0.38}/\text{Si}(100)$. Marker represents $0.3 \mu\text{m}$.

0.50. The cross-sectional TEM image of $x = 0.38$ is shown in fig. 5. There are a lot of dislocations in the $\text{Si}_{1-x}\text{Ge}_x$ layer. On the other hand, the dislocation density in the Si substrate is very low in contrast to the case of $x = 0.15$. The broad bands in the PL spectra for $x = 0.38$ and 0.50 are considered to originate from the dislocations in the $\text{Si}_{1-x}\text{Ge}_x$ layer.

It should be noticed that the deep-level luminescence observed in this work is very strong. The PL spectra of strained Si-Ge superlattices reported recently are believed to be evidence of a newly appearing direct band gap [5,7-9]. However, some of these spectra are very similar to those obtained in the present work. We would like to point out that the appearance of the strong luminescence line is not necessarily evidence of the direct band gap and that the dislocations might be the origin of the luminescence of strained Si-Ge superlattices.

4. Conclusions

Photoluminescence in $\text{Si}_{1-x}\text{Ge}_x/\text{Si}(100)$ grown by MBE has been studied over the composition range $0 \leq x \leq 0.5$. Strong deep-level luminescence has been observed. TEM observations show that there are many dislocations near the $\text{Si}_{1-x}\text{Ge}_x/\text{Si}$ interface. For $x = 0.15$ and 0.26, the dislocations in the Si substrate are considered to be the origin of the sharp PL lines. For $x = 0.38$ and 0.50, the broad bands may originate from the dislocations in the $\text{Si}_{1-x}\text{Ge}_x$ layer. The variety of the PL spec-

tra is explained primarily by the difference in the generated position of the dislocations near the $\text{Si}_{1-x}\text{Ge}_x/\text{Si}$ interface.

Acknowledgments

We are grateful to M. Ogawa, M. Nakamae, and N. Aizaki for helpful discussions and great encouragement. We are also grateful to A. Ogura and A. Tanikawa for helpful discussions. We would like to thank T. Niino for the sample preparation.

References

- [1] T. Tatsumi, H. Hirayama and N. Aizaki, *Appl. Phys. Letters* 52 (1988) 895.
- [2] G.L. Patton, J.H. Comfort, B.S. Meyerson, E.F. Crabbe, G.J. Scilla, E. de Fresart, J.M.C. Stork, J.Y.-C. Sun, D.L. Harnage and J.N. Burghartz, *IEEE Electron Device Letters* ED-11 (1990) 171.
- [3] R. Hull and J.C. Bean, *Appl. Phys. Letters* 54 (1989) 925.
- [4] G. Abstreiter, H. Brugger, T. Wolf, H. Jorke and H.J. Herzog, *Phys. Rev. Letters* 54 (1985) 2441.
- [5] G. Abstreiter, K. Eberl, E. Friess, W. Wegscheider and R. Zachai, *J. Crystal Growth* 95 (1989) 431.
- [6] N.L. Rowell, J.M. Baribeau and D.C. Houghton, *J. Electrochem. Soc.* 135 (1988) 2843.
- [7] H. Okumura, K. Miki, S. Misawa, K. Sakamoto, T. Sakamoto and S. Yoshida, *Japan. J. Appl. Phys.* 28 (1989) L1893.
- [8] E.A. Montie, G.F.A. van de Walle, D.J. Gravesteijn, A.A. van Gorkum and C.W.T. Bulle-Lieuwma, *Appl. Phys. Letters* 56 (1990) 340.
- [9] R. Zachai, K. Eberl, G. Abstreiter, E. Kasper and H. Kibbel, *Phys. Rev. Letters* 64 (1990) 1055.
- [10] K. Terashima, M. Tajima and T. Tatsumi, *Appl. Phys. Letters* 57 (1990) 1925.

The determination of strain in Si–Ge superlattices by electron diffraction in a scanning transmission electron microscope

W.T. Pike *, L.M. Brown

Cavendish Laboratory, University of Cambridge, Madingley Road, Cambridge CB3 0HE, UK

R.A.A. Kubiak, S.M. Newstead, A.R. Powell, E.H.C. Parker and T.E. Whall

Department of Physics, University of Warwick, Coventry CV4 7AL, UK

The nanometre scale of the novel strained layer electronic devices now being grown requires characterisation techniques of a corresponding resolution. This work employs the subnanometre probe of a dedicated scanning transmission electron microscope to investigate individual layers in a cross-sectioned SiGe superlattice. Using recently developed instrumentation, microdiffraction patterns have been obtained at very high resolution and the strains in each layer quantified by analysing the position of the deficit higher order Laue zone lines in the zero order beam. The experimental patterns are fitted to computer simulations incorporating possible dynamical effects. The results from a 10 nm SiGe layer are shown to be in good agreement with bulk X-ray diffraction analysis, with an accuracy limited only by the fundamental constraints of diffraction from a laterally finite sample. Hence surface relaxation, a major complication with previous applications of electron microscopy to strain measurement, can be ignored for the specimen geometry that the small probe allows. It is anticipated that the technique can in future be applied to multilayer structures which are not amenable to bulk characterisation.

1. Introduction

High quality crystal growing techniques such as molecular beam epitaxy (MBE) are capable of incorporating metastable strains into multilayer structures [1]. The quantification of such strains is essential to an understanding of the novel electronic properties that such structures possess. X-ray diffraction, Rutherford backscattering, Raman scattering and ion channeling are all used routinely to measure the strains in bulk samples. However these techniques cannot probe the structure of the individual layers, a limitation which prevents the complete strain analysis of the more complicated structures, such as compositionally graded growth, now being grown.

The major technique for such microstructural

characterisation is conventional transmission electron microscopy (CTEM) of cross sectioned specimens. However the thin, electron transparent foils needed for CTEM examination allow elastic relaxation at their surfaces. Hence direct measurement of strain through atomic resolution micrographs and selected area diffraction do not give results representative of the the bulk [2,3]. The surface relaxation can be modelled using Fourier analysis [4] and finite element analysis, and has then been incorporated into the simulation of image contrast from parallel sided foils [5] and cleaved wedge specimens [6]. Such determinations of strain are necessarily indirect: the strain in the bulk sample can only be deduced from the surface relaxation effects that it produces in the thin specimen.

This present work uses a scanning transmission electron microscope (STEM) to measure directly the strains from specimens thicker than normally used in CTEM. A convergent beam of electrons,

* Now at Jet Propulsion Laboratory, California Institute of Technology, 4800 Oak Grove Drive, Pasadena, California 91109, USA.

less than 1 nm in diameter, is focussed on to the specimen and the diffraction pattern acquired at high resolution. This technique differs only in scale from convergent beam electron diffraction (CBED) in CTEM: the high brightness field emission gun (FEG) of STEM allows the formation of a probe limited mainly by the aberration of the probe forming lens, whilst in CTEM the probe size is determined by the size of the thermal emission source [7]. A CTEM probe is thus at least an order of magnitude larger than a STEM probe. Plan view specimens which should not show surface relaxation have been analysed using CBED [8] but the determination of strain in such samples is very difficult. CBED has also been used to determine strains in cross-sectioned Si-Ge layers using the displacement of deficit higher order Laue zone (HOLZ) lines in the transmitted direct beam [9], but surface relaxation affected the results. The small probe used in microdiffraction enables the investigation of thin layers which should not show surface relaxation.

This paper will describe the acquisition of high

quality microdiffraction patterns from individual strained SiGe layers, the analysis of the deficit HOLZ lines in the direct beam incorporating dynamical effects and a comparison with bulk X-ray diffraction measurements.

2. Sample preparation and experimental technique

The samples examined were grown in a Vacuum Generators V90S MBE machine. The [100] silicon substrates were initially cleaned at 850°C under a Si flux to remove the native oxide before the growth of a 19 nm Si buffer layer. The structure consisted of a twenty period superlattice each 54 nm period of nominal composition 9 nm 85 at% Si-15 at% Ge and 45 nm Si grown at a substrate temperature of $560 \pm 5^\circ\text{C}$. The specimens were prepared in cross-section for the electron microscope through cleaving and ion beam thinning, producing {110} surface normals.

The specimens were examined in a VG HB501 dedicated STEM with a nominal accelerating volt-

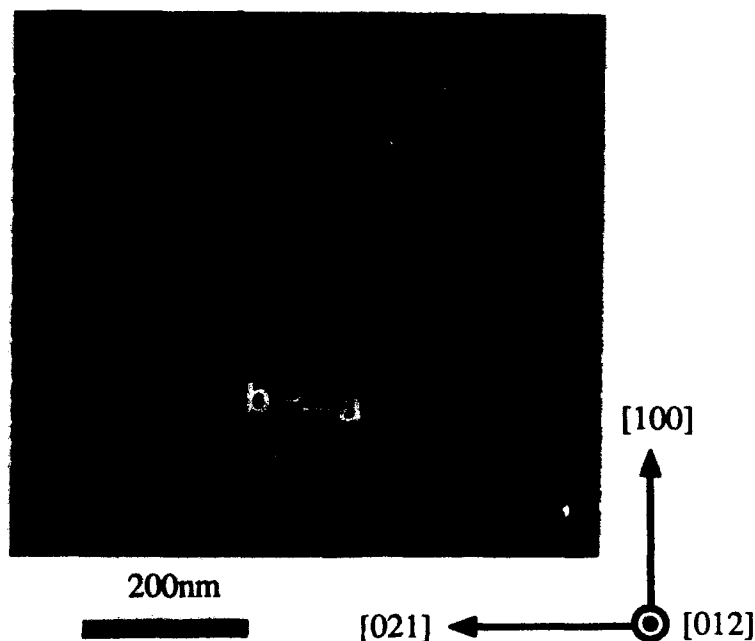


Fig. 1. ADF image of superlattice structure. The position of the probe when acquiring the patterns shown in the later figures is denoted by (a) centre of third Si layer and (b) centre of fourth SiGe layer.

age of 100 keV. Imaging of the structures was achieved with a scanned probe using the transmitted annular dark field (ADF) signal, which gives better contrast and noise statistics for thicker specimens than the conventional bright-field or dark-field signals. Fig. 1 shows an ADF image of the structure. Microdiffraction patterns were obtained by positioning the stationary probe at the desired place on the specimen and recording the transmitted signal. The acquisition of good quality microdiffraction patterns is problematic. Normal electron microscope photographic plates cannot be introduced into the vacuum as they would destroy the UHV necessary for STEM. Phosphor screens which can be viewed from outside the column give low resolution and very poor counting statistics. By replacing the spectrometer at the top of the column with a high efficiency phosphor screen fibre optically coupled to a low light level camera the performance can be considerably enhanced [10] at the cost of the loss of the electron energy loss spectroscopy (EELS) facility. Previous work on SiGe layers [11] used photographic film

separated from the vacuum by a thin Kapton window [12] to obtain good quality patterns, though of too low a camera length to resolve the deficit HOLZ lines.

This present work uses a newly developed technique using instrumentation initially designed for parallel EELS (PEELS): three quadrupoles are placed after the spectrometer to magnify the dispersion of the electrons which are imaged using a scintillator coupled to a low light level CCD camera. Through suitable adjustment of the quadrupoles to produce a point rather than the line focus necessary for PEELS, and closing down the slits at the exit to the spectrometer, microdiffraction patterns can be imaged at very high resolution (0.05 mrad), excellent detective quantum efficiency and large dynamic range [13]. In addition, as the electrons have passed through a spectrometer, the resulting pattern is energy filtered and hence the inelastic contribution to the microdiffraction pattern can be removed, improving the visibility of the HOLZ lines. A schematic diagram of the instrumentation is shown in fig. 2.

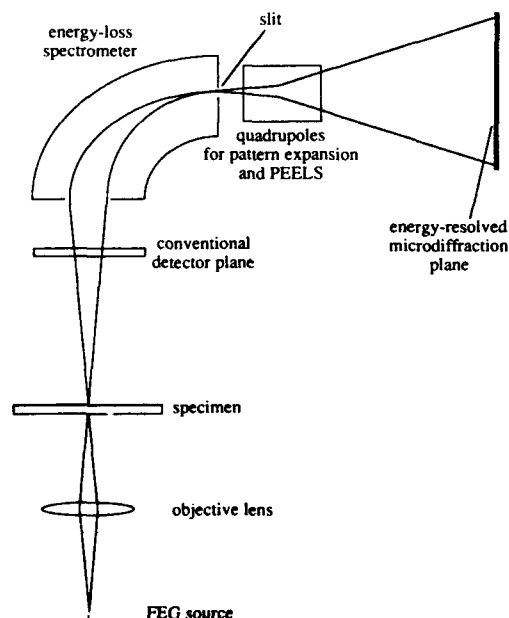


Fig. 2. Schematic diagram of the high resolution microdiffraction system.

3. Results and calculations

Microdiffraction patterns were taken from the Si buffer layer and from each layer in the first six periods of the superlattice structure in fig. 1. The buffer near the superlattice and the first two periods showed HOLZ line splitting indicating surface relaxation [14], but patterns from layers later in the growth sequence exhibited no such effects. Figs. 3 and 4 show two microdiffraction patterns from the [012] zone axis taken from the positions marked in fig. 1, namely the third Si and fourth SiGe layer. The patterns are elliptically distorted as isotropic dispersion for the three quadrupoles of the PEELS system is not attainable. Only the direct beam is shown, crossed by the deficit HOLZ lines corresponding to high angle reflections in the higher order Laue zones. The position of these lines is highly sensitive to all three lattice parameters and below each experimental pattern is a computer-simulated kinematical fit. The applicability of kinematical theory is justified by the very long extinction lengths associated with the high

angle HOLZ reflections. In general there are four unknowns in such a simulation, the three lattice parameters (assuming no shear) and the wavelength of the electrons in the material, λ . However the deficit line pattern can only be used to solve for two unknowns. The Si layer pattern can be used to determine λ assuming a lattice parameter of 0.5431 nm for pure silicon. This value of a , corresponding to an energy E of 96.1 ± 0.1 keV

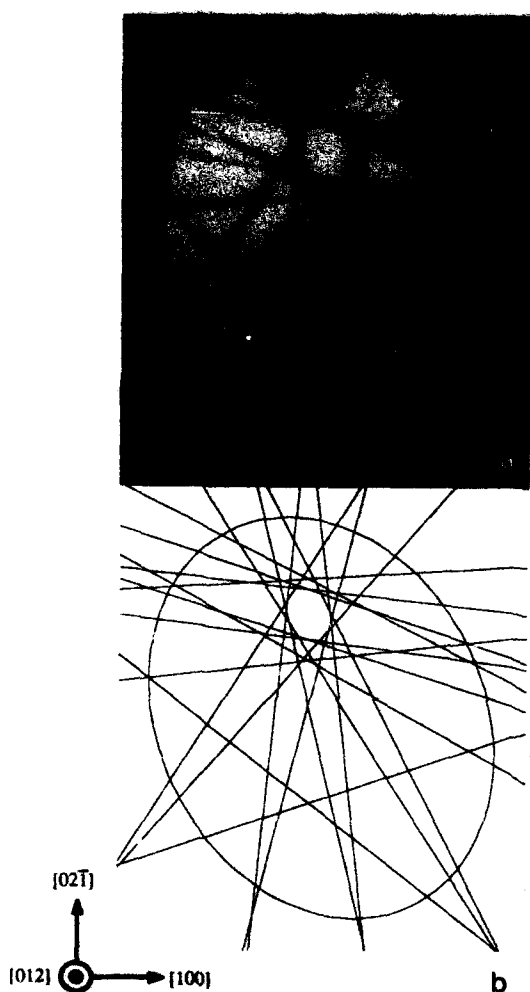


Fig. 3. (a) Microdiffraction pattern from the 45 nm Si layer on [012] with (b) a kinematical simulation with $E = 96.1$ keV, $a_{100} = a_{010} = a_{001} = 0.541$ nm. The objective aperture is about 15 mrad in diameter.

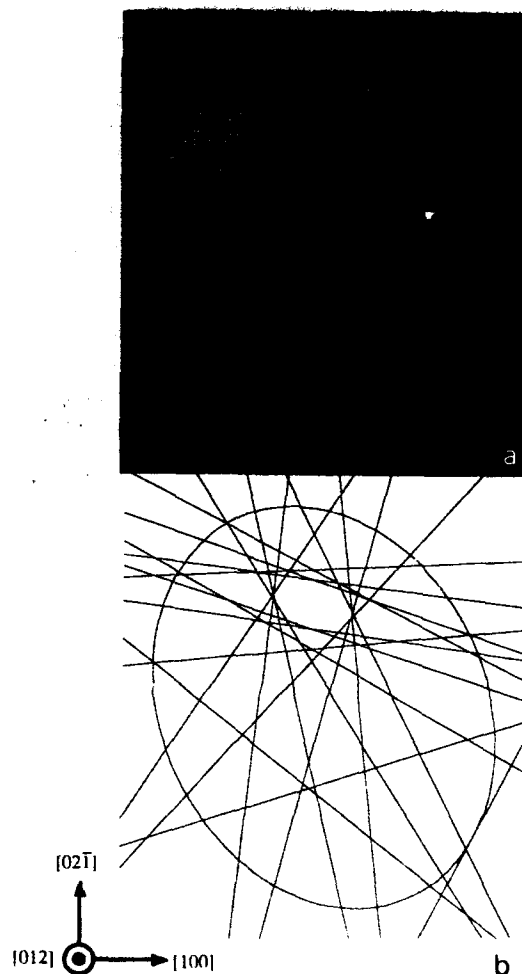


Fig. 4. (a) Microdiffraction pattern from the 9 nm SiGe layer on [012] with (b) a kinematical simulation with $E = 96.0$ keV, $a_{100} = 5.485$, $a_{010} = a_{001} = 0.5431$ nm.

for the electrons in the specimen, not only indicates a discrepancy between the nominal and actual accelerating voltage, but also takes into account the mean crystal potential and the shift of the dominant branch of the dispersion surface from the Ewald sphere due to dynamical interactions with reflections in the zero order Laue zone (ZOLZ) [15]. These last two effects depend on the chemical composition of the specimen and so λ will in general be different between the substrate

and alloy layers. The mean crystal potential, which affects both the diffracted and undiffracted beams equally, has virtually no effect on the position of the HOLZ lines, but dynamical interactions in the ZOLZ can produce a considerable shift of the HOLZ lines from their kinematical positions. The size of the shift, which is greatest on high symmetry zone axes and for the lower order HOLZ, can be quantified by calculating the ZOLZ dispersion surface as a function of composition [16], but has been neglected in previous CBED work [9]. For the [012] zone axis, the dynamical shift from Si to 85 at% Si corresponds to a drop in E of 100 eV for the first order Laue zone for the dominant first Bloch wave, which although equal to the error in ascertaining the accelerating voltage, has been taken into account.

The pattern from the alloy layer is simulated for $E = 96.0$ keV and assuming perfect epitaxy, i.e., $a_{010} = a_{001} = 0.5431$ nm. A best fit to the centre of the HOLZ lines is obtained for $a_{100} = 0.5485 \pm 0.0005$ nm. The accuracy of the fit is limited by the broadening of the HOLZ lines corresponding to reflections in the growth direction. This broadening is a consequence of the finite lateral extent of the strained layers [14] and can be considered as the fundamental constraint of determining a periodicity from a finite sample. By tilting onto a two beam condition and measuring the thickness fringes [17], the thickness of the specimen in the beam direction was calculated to be 320 ± 20 nm. As the layers themselves are only 10 nm wide in the growth direction, surface relaxation should not greatly affect the strain measurements. From the values determined from the simulation, the alloy layers have a tetragonal distortion, ϵ_1 , defined as the relative difference between the lattice parameter parallel and perpendicular to growth of $0.99 \pm 0.09\%$. Assuming perfect epitaxy and no surface relaxation, the tetragonal distortion as derived from elasticity theory should be

$$\epsilon_1 = \frac{s_{11} - s_{12}}{s_{11} + s_{12}} f, \quad (1)$$

where f is the bulk lattice parameter misfit between the silicon and alloy layers and s_{ij} is the compliance of the alloy. From eq. (1), f is $0.56 \pm$

0.05% for an interpolated value of s_{ij} for a 85 at% Si-15 at% Ge alloy. This value of f corresponds to a Ge proportion of 13.6 ± 1.4 at% for a bulk Ge lattice parameter of 0.5658 nm. A repeated self-consistent calculation, taking into account the discrepancy between the nominal and the deduced value of the composition, gives a negligible difference in the final result. X-ray diffraction has also been performed on the bulk wafer. From the strain measurements, $f = 0.62 \pm 0.04$. The better accuracy of the X-ray result is a result of sampling the complete structure of twenty strained layers, rather than the single layer analysed in microdiffraction.

4. Conclusions

Electron microdiffraction using a dedicated STEM with high resolution recording has been able to determine the structure of an individual layer in a Si-Ge superlattice. The strain can be measured to an accuracy determined by the growth thickness of the layers, in this case just under the accuracy of X-ray diffraction from the entire superlattice. A low symmetry zone axis has been used to minimise the dynamical shifts of the HOLZ lines. Agreement between the two techniques is good, confirming that with suitable geometry, elastic relaxation at the surfaces of the thick specimen does not have to be considered. Hence this is the first lattice parameter determination from an individual layer in cross-section which gives the values of strain measured in the bulk material. The technique should thus be able to be applied to multilayer structures where bulk strain parameter determinations are not possible.

References

- [1] A.T. Fiory, J.C. Bean, L.C. Feldman and I.K. Robinson, *J. Appl. Phys.* 56 (1984) 980.
- [2] J.M. Brown, N. Holonyak Jr., R.W. Kaliski, M.J. Ludowski, W.T. Dietze and C.R. Lewis, *Appl. Phys. Letters* 44 (1984) 1158.
- [3] M. Kobayashi, M. Konagai, K. Takahashi and K. Urabe, *J. Appl. Phys.* 61 (1987) 1015.

- [4] M.M.J. Treacy, J.M. Gibson and A. Howie, *Phil. Mag. A* 51 (1985) 389.
- [5] D.D. Perovic, G.C. Weatherly and D.C. Houghton, *Phil. Mag. A*, submitted.
- [6] U. Bangert and P. Charsley, *Phil. Mag. A* 59 (1989) 629.
- [7] L.M. Brown, J.M. Rodenburg and W.T. Pike, in: *Electron Microscopy 1988* (Proc. 9th European Congr.), York, 1988, Inst. Phys. Conf. Ser. 93, Eds. P.J. Goodhew and H.G. Dickinson (Inst. Phys., London-Bristol, 1988) Vol. 2, p. 3.
- [8] D. Cherns and A.R. Preston, *J. Electron Microsc. Tech.* 13 (1989) 111.
- [9] D.M. Maher, H.L. Fraser, C.J. Humphreys, R.V. Knoell and J.C. Bean, *Appl. Phys. Letters* 50 (1987) 574.
- [10] J.M. Cowley, *Scanning Electron Microsc.* 1 (1980) 61.
- [11] W.T. Pike, *Mater. Res. Soc. Symp. Proc.* 160 (1990) 111.
- [12] J.M. Rodenburg and D. McMullan, *J. Phys.* E18 (1985) 949.
- [13] D. McMullan, J.M. Rodenburg and W.T. Pike, in: *Proc. 12th Intern. Congr. on Electron Microscopy*, Seattle, WA, 1990, in press.
- [14] W.T. Pike, PhD Thesis, Cambridge (1990).
- [15] P.B. Hirsch, A. Howie, R.B. Nicholson, D.W. Pashley and M.J. Whelan, *Electron Microscopy of Thin Crystals* (Krieger, Melbourne, FL, 1977) p. 208.
- [16] Y.P. Lin, D.M. Bird and R. Vincent, *Ultramicroscopy* 27 (1989) 233.
- [17] P.M. Kelly, A. Jostons, R.G. Blake and J.G. Napier, *Phys. Status Solidi (a)* 31 (1975) 771.

Strain modification by ion-assisted molecular beam epitaxy in the $\text{Si}_x\text{Ge}_{1-x}$ alloy system: a kinetic analysis

C.J. Tsai, P. Rozenak *, H.A. Atwater and T. Vreeland

Thomas J. Watson Laboratory of Applied Physics, California Institute of Technology, Pasadena, California 91125, USA

Significant changes in strain are produced in $\text{Si}_x\text{Ge}_{1-x}$ epitaxial films grown on Si and Ge (001) substrates as a result of low energy ion beam assisted molecular beam epitaxy (IAMBE). Films grown in the temperature range of 200 to 450°C with concurrent Ar^+ or Xe^+ ion bombardment are coherently and uniformly strained in the growth direction by up to 1.5% in Ge films and 0.5% in Si films and contain no dislocations. Analysis of the strain modification kinetics suggests that defect complexes produced by the injection of ion beam induced native point defects and trapped gas are responsible for the strain changes. The dependence of film strain on ion/atom flux ratio can be explained by a steady state analysis in which beam-generated defects are annihilated at the growth surface. The dependence of strain modification on ion energy and ion species indicates the relative importance of surface defects and bulk defects in the free volume expansion of the films. Evolution of strain upon post-growth isochronal annealing suggests the complex nature of as-grown defects and rearrangement of defects during annealing. The relative roles of native defects and trapped gas in strain modification and thermal stability are discussed.

1. Introduction

The requirement of increased control over the microstructure and properties of thin epitaxial films has generated interest in alternatives to conventional thermal epitaxial growth. One approach is to utilize concurrent low energy ion bombardment during epitaxy to promote useful changes in film growth kinetics. Low energy ion bombardment has been employed as a method for surface cleaning during growth in plasma-enhanced chemical vapor deposition of Si [1]. Other applications include enhancement of dopant incorporation via concurrent ion bombardment during growth in Si [2], and increasing critical thickness for layer-by-layer growth of strained InAs on Si [3]. Direct low energy ion beam deposition has also produced epitaxial films of SiC and GaAs [4], and notably has yielded thick epitaxial Si films at temperatures as low as 100°C [5]. Of particular interest for high quality epitaxial films is the identification

of two regimes: one, in which surface processes, such as surface diffusion and adatom incorporation at growth sites, can be enhanced at low temperatures while avoiding bulk damage, and another in which controlled damage can be employed in useful ways.

2. Experiment

Films were grown in a custom-designed molecular beam epitaxy system with two electron beam sources and a Kaufmann-type ion source capable of producing Ar^+ or Xe^+ ion beams at energies of 50–1200 eV. The base pressure of the system was 1×10^{-10} Torr, and during the operation of ion gun the system was backfilled with Ar or Xe gas to a typical pressure of 8×10^{-5} Torr. Strain-modified films 100 nm thick were grown at constant rate in the range 0.1–0.7 nm/s on (001) Ge substrates and 0.08–0.2 nm/s on (001) Si substrates, following growth of a 50 nm buffer layer of pure Ge or Si by conventional molecular beam epitaxy. Ion/atom flux ratios were typically in the range 1:10–1:100. Temperature was measured

* Permanent address: Department of Materials Engineering, Ben-Gurion University of the Negev, Beer-Sheva 84105, Israel.

using a calibrated optical pyrometer. Growth temperatures were in the range of 200–450 °C. Films were analyzed in-situ using reflection high energy electron diffraction (RHEED), and following growth by X-ray rocking curve (XRC) measurement with a four crystal monochromator [6] using $\text{Cu-K}\alpha$ radiation, Rutherford backscattering (RBS), and transmission electron microscopy (TEM). Post-growth annealing was performed in vacuum with a pressure of 5×10^{-6} Torr.

3. Results and discussion

The strain state for a 100 nm thick Ge film on (001) Ge grown by IAMBE is illustrated by the diffraction intensity in fig. 1a, taken around the (004) and (224) Bragg diffraction using $\text{Cu-K}\alpha$ radiation. The film was grown at $T = 300^\circ\text{C}$, at a growth rate of 0.3 nm/s with a Ar^+ energy of $E_i = 200$ eV and ion/atom flux ratio of $J_i/J_a = 0.03$. In both cases, sharp Bragg peaks without

defect broadening were observed. Comparison of experimental X-ray data to a dynamical X-ray diffraction model, allowed strain to be extracted [7]. The results indicate the presence of a coherent film, i.e. $\epsilon_{\parallel} = 0\%$, with perpendicular strain resulting in a tetragonal distortion such that $\epsilon_{\perp} = 0.82\%$. The post-growth RHEED pattern taken at 20 keV along a [110] azimuth provides a qualitative indication of a smooth surface morphology with (2×1) surface reconstruction. Cross-sectional transmission electron microscopy indicated the 100 nm film to be free of misfit dislocations, threading dislocations and stacking faults, indicating that strain modification did not occur as a result of introduction of linear or planar defects. Fig. 1b shows XRC and RHEED results for a $\text{Si}_{0.2}\text{Ge}_{0.8}$ layer grown on Ge (100) by IAMBE at a growth rate of 0.25 nm/s with an Ar^+ energy of $E_i = 200$ eV and ion/atom flux ratio of $J_i/J_a = 0.03$. In the rocking curve scan around (004) diffraction plane, the Bragg peak from the 250 nm film occurs at $\Delta\theta = +0.11^\circ$ with respect to the substrate Bragg

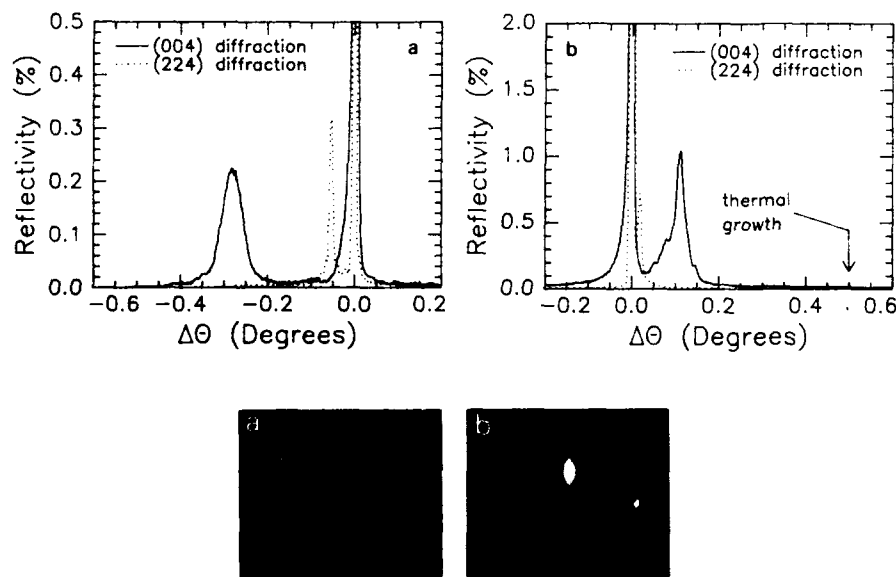


Fig. 1. (a) X-ray rocking curve around (004) Bragg peak for 100 nm Ge film grown on (001) Ge by IAMBE at $T = 300^\circ\text{C}$ for an ion/atom flux ratio $J_i/J_a = 0.03$, and incident Ar^+ ion beam energy $E_i = 200$ eV. Also shown is a rocking curve around the (224) Bragg peak. 20 keV RHEED pattern at incidence angle of 2° is shown below. (b) X-ray rocking curve around (004) and (224) Bragg peaks for 250 nm $\text{Si}_{0.2}\text{Ge}_{0.8}/(001)$ Ge grown by IAMBE at $T = 300^\circ\text{C}$; ion/atom flux ratio $J_i/J_a = 0.03$; incident Ar^+ ion beam energy $E_i = 200$ eV. 20 keV RHEED pattern at incidence angle of 2° is shown below.

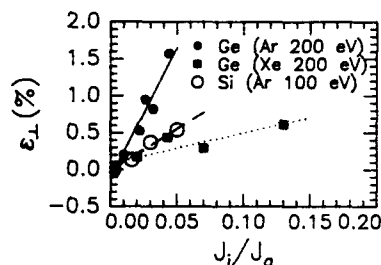


Fig. 2. Variation of perpendicular strain ϵ_{\perp} with ion/atom flux ratio J_i/J_a at the surface for 100 nm thick Ge films grown on Ge (001) by IAMBE at $T = 300^\circ\text{C}$ with (●) Ar^+ ion energy $E_i = 200$ eV, and with (■) Xe ion energy $E_i = 200$ eV, and for 100 nm thick Si films grown on Si(001) by IAMBE at $T = 350^\circ\text{C}$ with (○) Ar^+ ion energy $E_i = 100$ eV. Uncertainty in measurement is indicated by the size of the symbol.

peak. It should be noted that a coherent film with this alloy composition grown by conventional MBE exhibits a Bragg peak at $\Delta\theta = +0.5^\circ$, with an associated strain of $\epsilon_{\perp} = -1.3\%$. The magnitude and sign of strain modification are nearly equal for the pure Ge film and $\text{Si}_{0.2}\text{Ge}_{0.8}$ alloy, strongly suggesting that the normally tensile strain in the $\text{Si}_{0.2}\text{Ge}_{0.8}$ alloy was compensated by point defects introduced by IAMBE growth. RHEED pattern also indicates a smooth surface morphology.

The variation of perpendicular strain, ϵ_{\perp} , with ion/atom flux ratio J_i/J_a , for 100 nm thick Ge films grown on Ge (001) with Ar^+ 200 eV and Xe^+ 200 eV at $T = 300^\circ\text{C}$ and for 100 nm thick Si films grown on Si (001) with Ar^+ 100 eV at $T = 350^\circ\text{C}$ by IAMBE is shown in fig. 2. The expansion of the lattice constant in the growth direction in Xe^+ bombarded films is less than that for Ar^+ bombarded films with the same ion-atom flux ratio. This is consistent with the assumption that Xe^+ ions produce less bulk defects than Ar^+ ions with the same energy and the projectile range of Xe^+ is shallower than that of Ar^+ [8]. An approximately linear relationship exists between perpendicular strain ϵ_{\perp} and ion/atom flux ratio. This result can be pictured by considering the defect kinetics to be governed by a set of coupled

first order rate equations assuming defect interactions and higher order terms can be ignored:

$$\frac{dn_v}{dt} = G - k_v n_v - k_0 n_i n_v, \quad (1)$$

$$\frac{dn_i}{dt} = G - k_i n_i - k_0 n_i n_v, \quad (2)$$

$$\frac{dn_m}{dt} = G' - k_m n_m, \quad (3)$$

where G and G' are native defect generation rate and incident ion trapping rate, respectively, which are proportional to the ion/atom ratio; n_v , n_i , and n_m represent the concentration of vacancies, interstitials and trapped gas, respectively. The parameters k_v , k_i , and k_m are rate constants for the annihilation of vacancies, interstitials, and trapped gas to fixed sinks, and k_0 is the rate constant for vacancy and interstitial recombination. For steady state, two cases can be discussed in this simple picture. First, when bimolecular recombination is the dominant annihilation process simplified expressions for vacancy, interstitial and trapped ion concentrations can be obtained:

$$n_v \approx \sqrt{Gk_i/k_v k_0}, \quad n_i \approx \sqrt{Gk_v/k_i k_0},$$

$$n_m = G'/k_m.$$

Second, when fixed sink annihilation is the dominant process:

$$n_v \approx G/k_v, \quad n_i \approx G/k_i, \quad n_m = G'/k_m.$$

The second case is consistent with the observation of linear dependence of strain on ion/atom flux ratio, indicating that defects recombine at a fixed sink (most probably the growth surface). However, this kinetic analysis cannot further specify the relative roles of native defects and trapped gas in strain modification.

The variation of perpendicular strain, ϵ_{\perp} , with incident ion energy, E_i , for Ge films grown on Ge substrates by IAMBE at $T = 300^\circ\text{C}$ with $J_i/J_a = 0.02$, and for Si films grown on Si substrate by IAMBE at $T = 350^\circ\text{C}$ with $J_i/J_a = 0.016$ are shown in fig. 3. A monotonic increase in strain with increasing incident ion energy in the energy range $E_i = 70$ –300 eV is observed. In both cases, no detectable strain modification is observed for ion energy below 70 eV. Although the determination of threshold energy for strain modification is affected by the instrument sensitivity and the

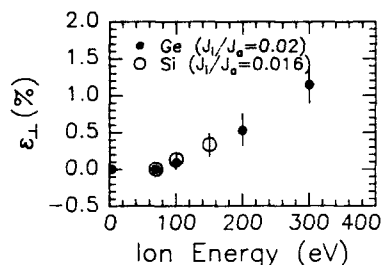


Fig. 3. Variation of perpendicular strain, ϵ_{\perp} , with incident ion energy E_i , (●) for 100 nm thick Ge films grown on Ge substrates by IAMBE at $T = 300^\circ\text{C}$ with fixed ion/atom flux ratio $J_i/J_a = 0.02$, and (○) for 100 nm thick Si films grown on Si substrate by IAMBE at $T = 350^\circ\text{C}$ with fixed ion/atom flux ratio $J_i/J_a = 0.016$. Error bars indicate the uncertainty introduced by possible variations in the ion/atom flux ratio J_i/J_a .

threshold is expected to be temperature dependent, the close agreement between the theoretical estimate of the transitional energy regime for onset of bulk displacements in Ge by Brice et al. [8], and this experiment is noteworthy.

Previous work on Ge epitaxial films grown on (001) GaAs substrate done by Haynes et al. [9] using mass-selected 40 eV Ge beams showed a small expansion of lattice parameter in the growth direction. This small free volume expansion was presumably caused by the native defects of Ge, since no inert gas was involved in their work. To elucidate the relative roles of native point defects and trapped gas in strain modification, Xe concentration in Ge films grown at $T = 300^\circ\text{C}$ and Ar concentration in Si films grown at $T = 350^\circ\text{C}$ were measured using RBS. The results indicate that the amount of trapped gas is approximately proportional to the strain. If we assume that strain is generated only by trapped gas and Vegard's law can be applied for the lattice parameter in this case with $\epsilon_i = 0\%$ and $a_{\text{Ar}} = 1.88 \text{ \AA}$, close agreement can be obtained between experimental value and calculated value for Ar in Si films. This suggests that Ar atoms in Si play an important role.

Fig. 4 shows the strain behavior as a function of annealing temperature of an Ar^+ bombarded Ge film grown at $T = 300^\circ\text{C}$ with $J_i/J_a = 0.02$, a Xe^+ bombarded Ge film grown at $T = 300^\circ\text{C}$

with $J_i/J_a = 0.04$, and an Ar^+ bombarded Si film grown at $T = 350^\circ\text{C}$ with $J_i/J_a = 0.04$. The annealing time for Ge films is 1 h and for Si film is 30 min. RBS results suggest that the Ar concentration in annealed Si samples was practically constant in the annealing temperature range. If the annealing behavior is explained by the segregation of Ar atoms to form bubbles or the aggregation of native point defects to form extended defects, a monotonic decrease in strain with respect to annealing temperature should be expected. This seems to suggest at least two processes of defect annihilation or aggregation occurred during annealing. From this observation it was deduced that migration of either Ar atoms or native point defects alone is not able to explain the annealing behavior. The local strain field around a trapped gas atom is expected to be large, which may cause the inert gas atom to form a complex in order to relax the local strain. On the other hand, a native defect (e.g. vacancy) may increase the trapping probability for inert gas atoms. The nonmonotonic behavior leads us to speculate that the strain modification is related to Ar-defect complex formation.

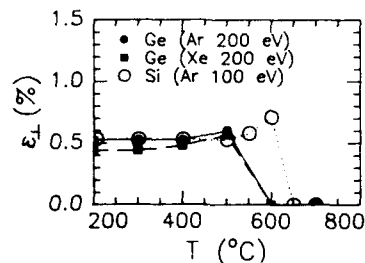


Fig. 4. Variation of perpendicular strain, ϵ_{\perp} , with annealing temperature for (●) 100 nm thick Ge film grown on Ge substrate at growth temperature $T = 300^\circ\text{C}$, Ar^+ ion energy $E_i = 200 \text{ eV}$, and ion/atom flux ratio $J_i/J_a = 0.02$, for (■) 100 nm thick Ge film grown on Ge substrate at growth temperature $T = 300^\circ\text{C}$, Xe^+ ion energy $E_i = 200 \text{ eV}$, and ion/atom flux ratio $J_i/J_a = 0.04$, and for (○) 100 nm thick Si film grown on Si substrate at growth temperature $T = 350^\circ\text{C}$, Ar^+ ion energy $E_i = 100 \text{ eV}$ and ion/atom flux ratio $J_i/J_a = 0.04$. The annealing time for Ge films is 1 h and for Si film is 30 min. Uncertainty in measurement is indicated by the size of the symbol. The lines are a guide to the eye.

4. Conclusion

In summary, we have observed large changes in $\text{Si}_x\text{Ge}_{1-x}$ layer strain, by up to 1.5% in Ge and 0.5% in Si during concurrent molecular beam epitaxial growth and low energy ion bombardment (IAMBE). The films are coherent and dislocation-free. The dependence of layer strain on ion energy, ion/atom flux ratio and temperature are consistent with a model in which misfit strain is accommodated by free volume changes associated with injection of a uniform dispersion of defects consisting of native point defects and/or trapped inert gases. An increase in strain of the films during annealing was observed. Migration of trapped gas atoms or native point defects alone cannot explain the annealing behavior.

In this work we demonstrate that low energy ion bombardment during epitaxy can lead to large changes in strain in *coherent* epitaxial films as a result of defect injection. The observed ion bombardment-generated strain changes have two important implications for epitaxy:

- The measured strain changes are an extremely sensitive indication of bulk defect generation in epitaxial layers. Hence any growth process that employs ion bombardment to enhance surface kinetics but seeks to avoid bulk defect generation must avoid growth conditions leading to the observed strain changes. This requirement can be used to define an upper limit to the ion energy that can be employed for a given ion-substrate combination.

- Strain "engineering" by controlled ion beam defect injection may have interesting implications for lattice-mismatched heteroepitaxy. Since low

energy ion bombardment produces strain changes without producing extended defects, such as dislocation and stacking faults, high quality epilayers can be grown on top of such layers. In the present work, we describe only changes in perpendicular strain. If equivalent changes in in-plane strain can be produced, it may be possible to accommodate film-substrate lattice mismatch in a novel manner.

Acknowledgments

This work was supported by the National Science Foundation P.Y.I.A. program (DMR-8958070) and the Materials Research Group program (DMR-8811795).

References

- [1] W.R. Burger and R. Reif, J. Appl. Phys. 62 (1987) 4255.
- [2] J.E. Greene, CRC Critical Rev. Solid State Mater. Sci. 2 (1983) 47.
- [3] C.-H. Choi, L. Hultman and S.A. Barnett, J. Vacuum Sci. Technol., to be published.
- [4] R.A. Zuhr, S.J. Pennycook, T.S. Noggle, N. Herbots, T.E. Haynes and B.R. Appleton, Nucl. Instr. Methods B37/38 (1989) 16.
- [5] P.C. Zalm and L.J. Beckers, Appl. Phys. Letters 41 (1982) 167.
- [6] W.J. Bartels, J. Vacuum Sci. Technol. B1 (1983) 338.
- [7] C.R. Wie, T.A. Tombrello and T. Vreeland, J. Appl. Phys. 59 (1986) 3743.
- [8] D.K. Brice, J.Y. Tsao and S.T. Pieraux, Nucl. Instr. Methods 44 (1989) 68.
- [9] T.E. Haynes, R.A. Zuhr, S.J. Pennycook, B.C. Larson and B.R. Appleton, J. Vacuum Sci. Technol. A7 (1989) 1372.

Si/SiGe heterostructures grown on SOI substrates by MBE for integrated optoelectronics

V.P. Kesan, P.G. May, F.K. LeGoues and S.S. Iyer

IBM Research Division, T.J. Watson Research Center, Yorktown Heights, New York 10598, USA

We have investigated the structural, electrical, and optical quality of epitaxial Si and SiGe films grown by MBE on SIMOX (separation by implanted oxygen) silicon substrates. Epitaxial films grown on these SOI substrates have been characterized using planar and cross-sectional TEM, SIMS, and Seeco chemical etching to delineate defects. We have fabricated the first Si/SiGe integrated waveguide-photodetector for long wavelength applications. Low reverse leakage current densities were seen in these device structures. The detector exhibited a responsivity of 0.43 A/W at 1.1 μm with an impulse response time of 200 ps.

1. Introduction

The use of silicon-germanium heterostructures permits the realization of Si-based optoelectronic detectors in the 1.3 μm wavelength regime, without the use of III-V technology. P-i-N photodetectors and avalanche photodiodes (APDs) using Si/SiGe strained layers have been fabricated by Temkin and co-workers [1,2]. Silicon-on-insulator (SOI) structures are useful for Si-based integrated optoelectronics since the buried oxide layer forms a low index confinement region that permits effective waveguiding in the silicon overlayer. The use of SOI thus permits the integration of active optoelectronic devices with passive waveguide elements. In order to realize these integrated device structures epitaxial growth of Si/SiGe strained layer heterostructures on SOI substrates is required.

We have investigated the structural, electrical, and optical quality of epitaxial silicon films grown by MBE on SIMOX (separation by implanted oxygen) silicon substrates. We have fabricated the first Si/SiGe superlattice p-i-n integrated rib waveguide and detector structures on SOI substrates with excellent electrical and optical characteristics. MBE and CVD epitaxial films grown on SIMOX substrates were characterized using planar and cross-sectional TEM, SIMS, and Seeco

chemical etching to delineate defects. The P-i-N Si/SiGe integrated waveguide-detector exhibited low reverse leakage currents (10–30 pA/ μm^2 at 15 V reverse bias) and 50% internal quantum efficiency at 1.1 μm with an impulse response time of 200 ps.

2. Bulk silicon films grown on SOI

The SIMOX substrate used in these experiments employed a three stage implant/anneal cycle resulting in an integrated dose of 1.8×10^{18} ions/ cm^2 at 200 keV with a total anneal cycle of 6 h at 1300°C. This results in a 4000 Å SiO₂ layer buried 2000 Å beneath the top silicon surface of the substrate. Fig. 1a shows a bare SIMOX wafer examined with an optical microscope using Nomarski image contrast to possess a distinct medium “orange peel” look. The defect density in the virgin SIMOX wafers was determined using the Seeco etch [3] (2:1 HF:K₂Cr₂O₇ (0.15M)). The Seeco etch was chosen since it has been shown to delineate most defects and provide an upperbound on the defect density in Si wafers [4]. Fig. 1b shows a SIMOX wafer that has been Seeco etched 3000 Å to reveal defects in the buried oxide layer. Characteristic raised defects, probably oxygen clusters, can be seen in fig. 1b, and one



Fig. 1. (a) A bare SIMOX wafer examined with an optical microscope using Nomarski image contrast. A distinct medium "orange peel" look can be seen. (b) A SIMOX wafer that has been Secco etched 3000 Å to reveal defects in the buried oxide layer. Characteristic raised defects, probably oxygen clusters, can be seen in this region. (c) One such defect is clearly shown here. The magnification in (b) and (c) is ten times lower than in (a).



Fig. 2. A high resolution TEM cross-section of the Si/SiO₂ top interface. Atomic fringes can be clearly seen in the silicon overlayer.



Fig. 3. (a) A $1\text{ }\mu\text{m}$ MBE Si film grown on SIMOX on the bottom half, with the top half showing the same film Secco etched $5000\text{ }\text{\AA}$ to reveal defects; (b) shows the etched Si film in detail and the film has taken a rough appearance with some distinctly shaped defects, one of which is shown in (c). The magnification in (a) and (b) is ten times lower than in (c).

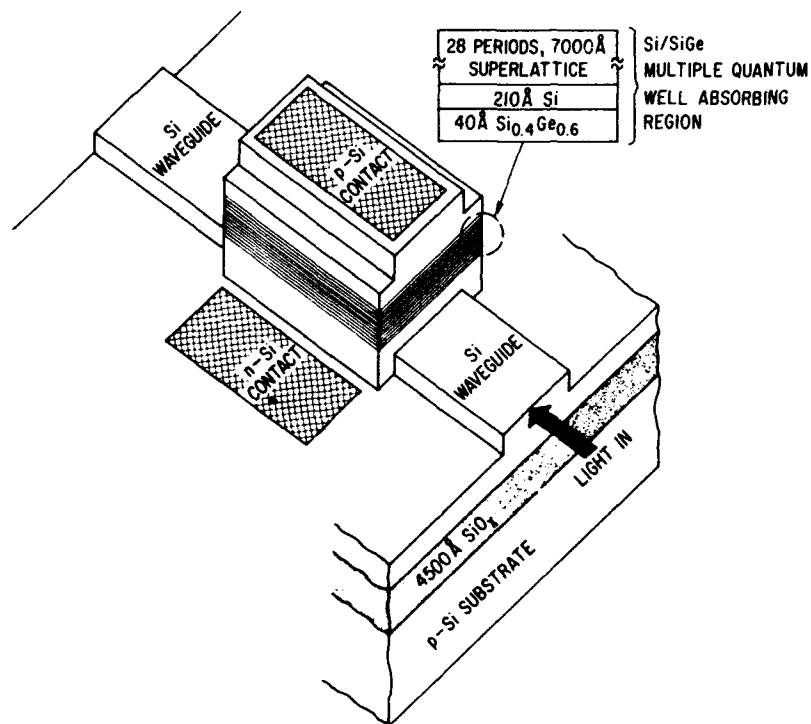


Fig. 4. Schematic view of the integrated waveguide-detector structure showing both device geometry and epitaxial layer structure.

such defect is clearly shown in fig. 1c. The delineation of defects by Seeco etching in an oxide matrix needs further study. A defect density of $(2-5) \times 10^3/\text{cm}^2$ was seen in the silicon overlayer after etching. Fig. 2 shows a high resolution TEM cross-section of the Si/SiO₂ top interface. The Si overlayer can be seen to be defect free (below TEM resolution) and atomic fringes in the film point to its good structural quality.

Thick ($\approx 1 \mu\text{m}$) nominally undoped epitaxial Si films were grown on these SIMOX substrates by MBE and high temperature (1050°C) conventional CVD. Fig. 3a shows a MBE Si film grown on SIMOX on the bottom half, with the top half showing the same film Seeco etched. Fig. 3b shows the etched Si film in detail and the film appears to have taken a rough appearance with some distinctly shaped defects, one of which is shown in fig. 3c. Defect densities in both the MBE grown and CVD grown Si were found to be around $10^3/\text{cm}^2$, suggesting that these defects originate

from the SIMOX substrate. More details regarding the structural quality and defect distribution in SIMOX wafers and in epitaxial Si films grown on them will be presented elsewhere [5].

3. Integrated waveguide and P-i-N detector

Si/SiGe P-i-N integrated waveguide-detector structures were grown on SIMOX substrates by MBE (see fig. 4). The undoped Si waveguide layer was grown at 650°C , after which the substrate temperature was dropped to 375°C for the growth of the Si/SiGe multilayer structure. The substrate temperature was raised back to 450°C for the growth of the p^+ contact layer. The device geometry consisted of a nominally undoped, Si/Si_{1-x}Ge_x multiple quantum well absorbing region, with Si p^- and n^- doped cladding layers on either side, grown on a Si waveguide structure (see fig. 4). The

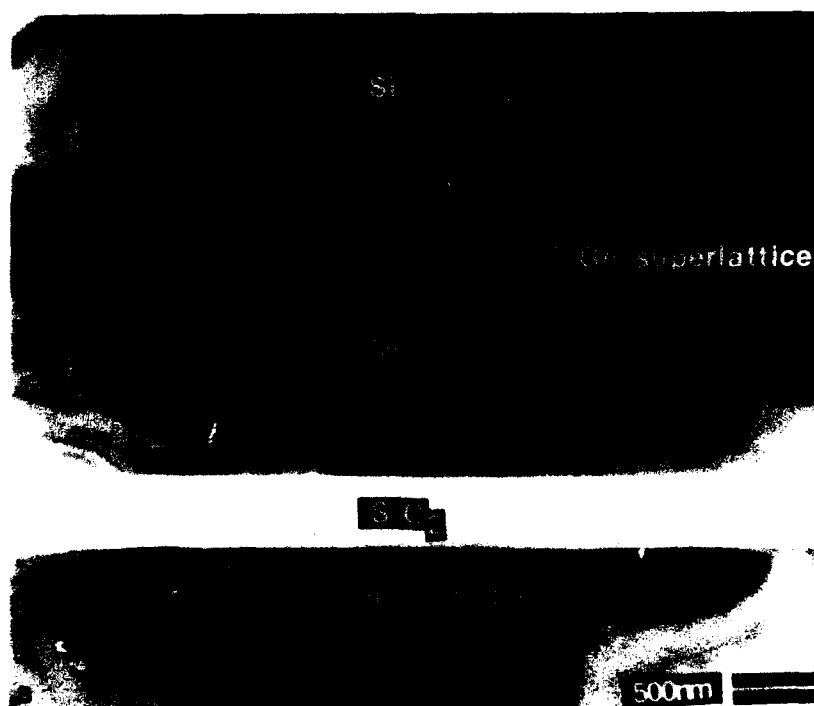


Fig. 5. (a) TEM cross-section of the entire P-i-N Si/SiGe structure grown on SIMOX.

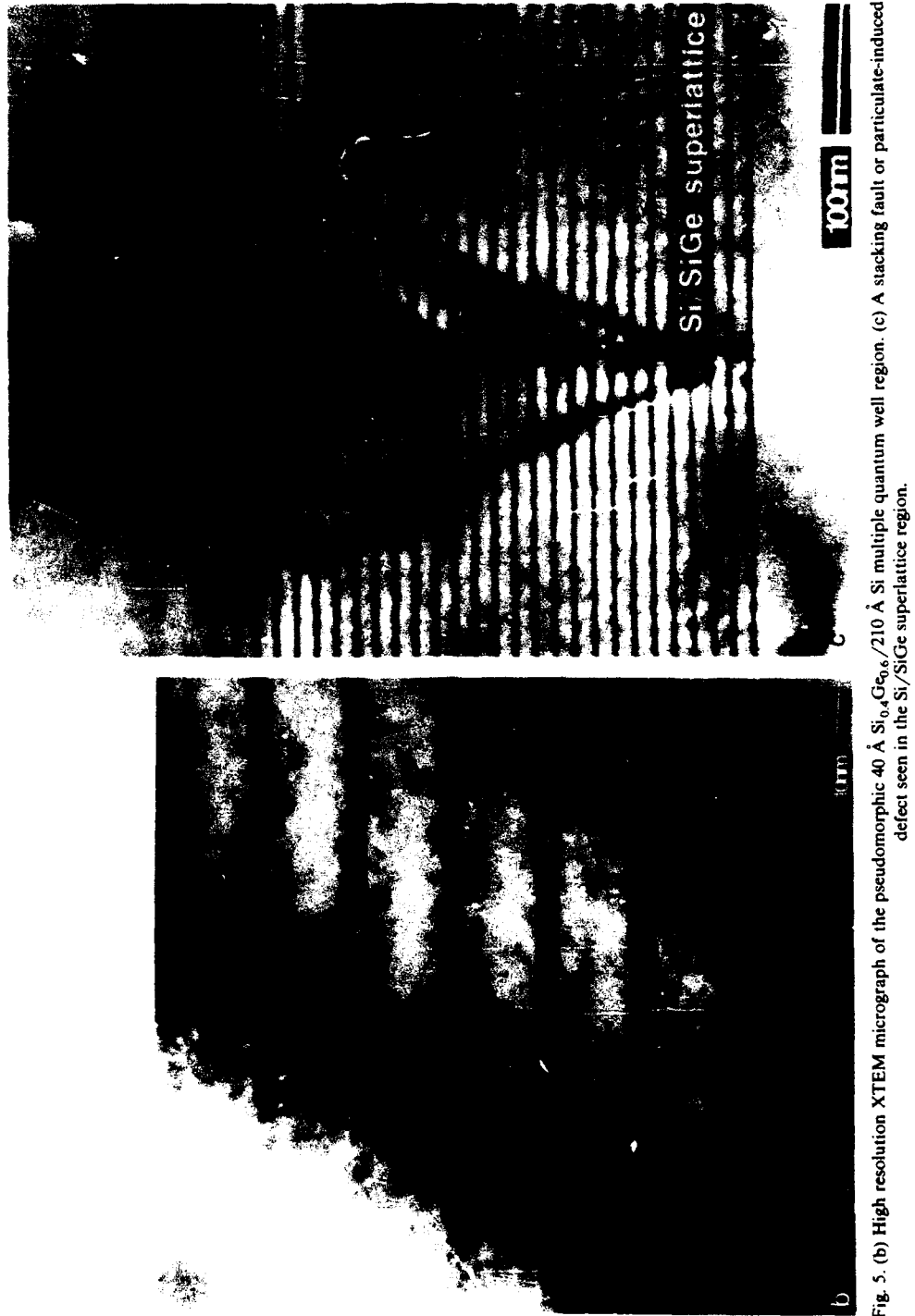


Fig. 5. (b) High resolution XTEM micrograph of the pseudomorphic 40 \AA $\text{Si}_{0.4}\text{Ge}_{0.6}/210 \text{ \AA}$ Si multiple quantum well region. (c) A stacking fault or particulate-induced defect seen in the Si/SiGe superlattice region.

absorbing region consisted of a 40 Å $\text{Si}_{0.4}\text{Ge}_{0.6}$ /210 Å Si, 28 period, superlattice (corresponding to an average Ge composition of 10% in this region).

Cross-sectional TEM showed the structural and interface quality of the complete device structure to be excellent (see fig. 5a), and fig. 5b shows the pseudomorphic SiGe/Si superlattice region in greater detail. Defects, which are either stacking faults or induced by particulates, originating in the SiGe/Si superlattice region are seen in fig. 5a. One such defect is shown in fig. 5c. The effective Ge concentration in the Si/SiGe layers and the doping concentration in the contact layers were determined by RBS and SIMS respectively. The waveguide-detector structure (see fig. 1) was fabricated using conventional silicon fabrication techniques - RIE etched mesas, PECVD oxide passivation, and Ti/Al contacts. For comparison, P-i-N detectors were fabricated on both Si and SIMOX substrates. I - V characteristics measured on large area devices grown on SOI, and ranging from $100\text{ }\mu\text{m} \times 100\text{ }\mu\text{m}$ to $260\text{ }\mu\text{m} \times 260\text{ }\mu\text{m}$, showed low reverse-leakage current densities. At 5 and 15 V reverse bias, the leakage current density was 1-3 and 10-30 $\text{pA}/\mu\text{m}^2$, respectively, with a reverse breakdown voltage of 35-40 V (see fig. 6).

Optical measurements were made by coupling light both directly into the Si/SiGe absorbing region and into the silicon waveguide, remote from

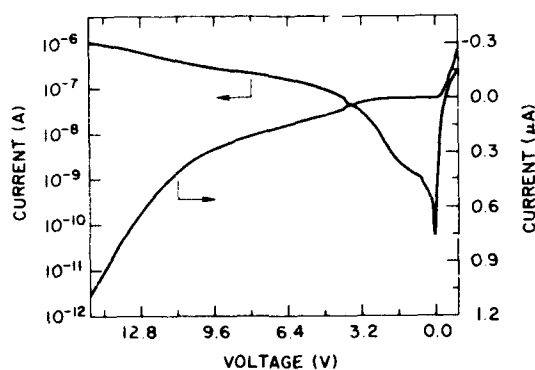


Fig. 6. Logarithmic (left vertical axis) and linear (right vertical axis) DC I - V characteristics of the Si/SiGe p-i-n detector fabricated on SOI with an on-chip device area of $260\text{ }\mu\text{m} \times 260\text{ }\mu\text{m}$. The reverse leakage current density at 15 V reverse bias is $16\text{ pA}/\mu\text{m}^2$.

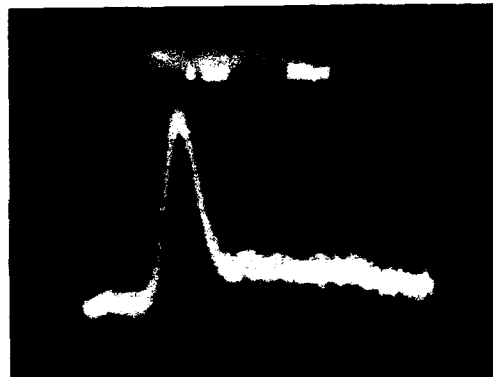


Fig. 7. Device impulse response when illuminated by 100 ps pulses from a $1.3\text{ }\mu\text{m}$ Nd:YAG laser at 20 V reverse bias. The full width half maximum of the impulse response is 200 ps.

the detector active area. In separate experiments, optical waveguides $30\text{ }\mu\text{m} \times 1\text{ }\mu\text{m} \times 1\text{ mm}$ were fabricated in $1\text{ }\mu\text{m}$ epitaxial Si films grown on SOI. These waveguides exhibited low attenuation losses of 1-2 dB/cm at $1.3\text{ }\mu\text{m}$. The P-i-N detectors with an active device area of $930\text{ }\mu\text{m} \times 30\text{ }\mu\text{m}$ exhibited an internal quantum efficiency of 50% at $1.1\text{ }\mu\text{m}$ (external quantum efficiency of 12%) at 10 V reverse bias. The impulse response time (full width at half maximum) of the detector when illuminated by 70 ps pulses at $1.06\text{ }\mu\text{m}$ and 100 ps pulses at $1.3\text{ }\mu\text{m}$, both obtained from a Nd:YAG laser, was 200 ps (see fig. 7). The speed of the detector appears to be limited by the RC time constant of the device. The detector exhibited a peak spectral response at $1.06\text{ }\mu\text{m}$ at room temperature, in good agreement with calculated transition energies between confined light hole valence band states to four-fold electron conduction band states in the Si/SiGe multiple quantum well structure. The peak response of the detector is hence tunable by varying the physical parameters of the multiple quantum well structure. The DC electrical and optical characteristics, i.e., reverse leakage current, quantum efficiency, and speed, are the best reported so far for Si/SiGe p-i-n detectors. More details regarding the optical performance of these detectors will be reported elsewhere [6].

4. Conclusion

We have investigated the structural, electrical, and optical quality of epitaxial Si and SiGe films grown by MBE on SIMOX (separation by implanted oxygen) silicon substrates. We have fabricated the first Si/SiGe integrated waveguide-photodetector for long wavelength applications. Low reverse leakage current densities were seen in these device structures. The detector exhibited a responsivity of 0.43 A/W at 1.1 μm with an impulse response time of 200 ps. Our results show promise for an integrated preamplifier/detector for an all Si-based long wavelength receiver.

Acknowledgements

We would like to thank B. Ek for excellent technical support, T. Sedgwick for providing in-

sights in defect etching, and J.-M. Halbout for many useful discussions. We would also like to acknowledge the continuing support and encouragement of T.P. Smith for this work.

References

- [1] H. Temkin, T.P. Pearsall, J.C. Bean, R.A. Logan and S. Luryi, Appl. Phys. Letters 48 (1986) 963.
- [2] H. Temkin, A. Antreasyan, N.A. Olson, T.P. Pearsall and J.C. Bean, Appl. Phys. Letters 49 (1986) 809.
- [3] F. Seeco d'Aragona, J. Electrochem. Soc. 119 (1972) 948.
- [4] D.G. Schimmel, J. Electrochem. Soc. 123 (1976) 734.
- [5] V.P. Kesan, G. Kroesen and S.S. Iyer, unpublished.
- [6] V.P. Kesan, P.G. May and S.S. Iyer, unpublished.

The growth and electronic properties of α -Sn thin films grown on InSb(100) and $(\bar{1}\bar{1}\bar{1})$ substrates by molecular beam epitaxy (MBE)

W.T. Yuen *, W.K. Liu **, R.A. Stradling *** and B.A. Joyce *

Imperial College of Science, Technology and Medicine, Prince Consort Road, London SW7 2BZ, UK

The growth and electronic properties of α -Sn films grown on InSb(100) and $(\bar{1}\bar{1}\bar{1})$ are investigated by RHEED, Shubnikov–De Haas (SDH) and magneto-optical studies. Two new structures, $p(2 \times 2)$ and $c(4 \times 4)$ apart from the commonly observed two-domain (2×1) , are observed on the (100) surfaces when the overlayer thicknesses approach 500 Å and 1000 Å respectively. The α -Sn/InSb($\bar{1}\bar{1}\bar{1}$) surface exhibits a (3×3) reconstruction up to an overlayer thickness of 1000 Å and a (3×1) is developed on further growth. It is found that not only the surface structures of the α -Sn film vary with substrate orientations and the thicknesses of the overlayer, the charge concentration of the two dimensional electron gas (2DEG) at the interface also exhibits similar behaviour. The properties of the 2DEG are investigated by Shubnikov–De Haas (SDH) experiments and possible mechanisms responsible for the occurrence of the 2DEG are discussed. Magneto-optical data indicate the presence of carriers due to the α -Sn layer with m^* ranging from $0.028m_0$ to $0.034m_0$.

1. Introduction

The observation of a two-dimensional electron gas (2DEG) at the interface of a lattice-matched nonpolar–polar system, namely the α -Sn/InSb heterostructure [1], has already been reported. Results from samples with various film thicknesses seem to suggest that the electronic properties, in particular the 2DEG, may be related to the surface structures of the substrate and the overlayer. In this paper we will present a brief report of the growth and electronic properties of α -Sn films grown on InSb(100) and $(\bar{1}\bar{1}\bar{1})$ surfaces as studied by reflection high energy electron diffraction (RHEED) [2], Shubnikov–De Haas (SDH) and magneto-optical measurements. The properties of the 2DEG will then be discussed in the light of the various experimental results. A detailed analysis of the SDH and magneto-optical data for the α -Sn films will be reported elsewhere [3].

The growth of α -Sn and α -Sn_{1-x}Ge_x thin films has recently been the subject of considerable interest following the pioneering work of Farrow et al.

[4]. Several groups have independently reported the growth of high quality n-type α -Sn thin films on CdTe [5–9] and InSb [10] substrates. The confinement of carriers in the thin film (quantum size effect) has recently been reported [8], but apparently a 2DEG was not observed.

2. Experimental

The samples investigated were 0.02–0.35 μm thick α -Sn overlayers grown on InSb(100) and $(\bar{1}\bar{1}\bar{1})$ surfaces (Cd doped to 10^{14} cm^{-3} for the p-type and Te doped to 10^{14} cm^{-3} for the n-type; both supplied by MCP, UK), using a three-chamber MBE machine. Details of the growth and sample preparation have been reported in earlier papers [1,2] and will not be repeated here.

3. Results and discussion

3.1. Surface structures of α -Sn(100) and $(\bar{1}\bar{1}\bar{1})$ films

Surface structures of the α -Sn films grown on InSb substrates have been studied by RHEED using a multi-azimuthal approach. Diffraction

* Interdisciplinary Research Centre for Semiconductor Materials.

** Blackett Laboratory.

streaks in several Laue zones of the RHEED patterns obtained from three different azimuths are examined as a function of film thicknesses. This "multi-azimuthal, multi-Laue zone" diffrac-

tion analysis is essential for the study of complex surface structures in which several surface domains coexist at the same time. For instance, half order streaks along $\langle 110 \rangle$ azimuths together with an integral streak along $[100]$ can both be found in the zeroth Laue zone of two-domain (2×1) as well as two-domain $c(4 \times 2)$ structures. The difference between these two structures can only be distinguished from the diffraction streaks in higher order Laue zones [2].

The growth of α -Sn on InSb(100)- (4×2) starts with the quenching of the substrate superstructure for the first 20 Å, leaving a bulk structure together with strong background in the RHEED patterns. Using a growth rate of about 0.5 $\mu\text{m/h}$, the surface structures of the α -Sn films undergo a thickness dependent change: two-domain (2×1) , $p(2 \times 2)$ and $c(4 \times 4)$ structures are observed at film thicknesses of 20, 500 and 1000 Å respectively. When the film thickness exceeds 1000 Å, the surface structure becomes very complicated: 1D disorder accompanied by atomic steps is observed. The presence of these structures on the α -Sn(100) surface has been compared with that of Si(100), and a dimer model [2] has been proposed to account for the occurrence of these structures on the α -Sn(100) surface.

The growth of α -Sn/InSb($\bar{1}\bar{1}\bar{1}$)- (3×3) is simpler than that of the (100) surface: a (1×1) bulk structure is observed for the first 20 Å of growth and then a (3×3) structure takes over until the thickness exceeds 1000 Å. Further growth reduces the intensity of the $1/3$ order streak along $[1\bar{1}2]$ and a (3×1) structure begins to develop as the film thickness reaches about 1200 Å. The observation of the (3×3) structure agrees with that re-

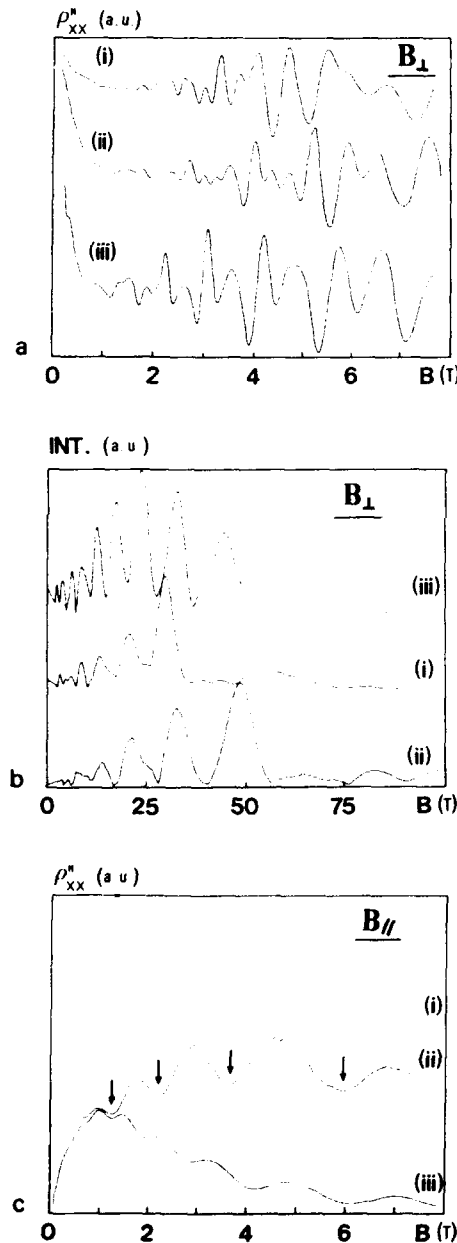


Fig. 1. (a) Experimental recordings of the second derivative of the magnetoresistance of an α -Sn/InSb structure at 4.2 K with the magnetic field applied perpendicular to the plane of the sample for the (i) 200 Å and (ii) 3000 Å thick film grown on InSb(100), and (iii) 1200 Å thick film grown on InSb($\bar{1}\bar{1}\bar{1}$) surfaces (b) The corresponding FFT power spectrum for these three samples and (c) diamagnetic resonances due to depopulation of carrier into lower subbands when magnetic field is applied parallel to the plane of the sample. Depopulation fields of individual subbands are indicated by the arrows.

ported by Kasukabe et al. [11] but differs from the (1×1) structure observed by Hochst et al. [12].

Note that the surface structures of the α -Sn films depend on the overlayer thickness and substrate orientations. It is found that the 2DEG exhibits similar behaviour: the carrier concentration of the 2DEG seems to be affected by the orientation as well as the thickness of the sample (see section 3.2 below).

3.2. Shubnikov-De Haas results

Hall measurements indicated that the first few structures grown in the reactor were p-type but that later samples were n-type even for films only 200 Å thick. The presence of a high-density 2DEG is evident from the complicated magnetoresistance structures as depicted in fig. 1a. Note the remarkable difference between the peak structures observed from the thick (3000 Å) and the thin (200 Å) films. Due to the complicated oscillatory structures in the magnetoresistance, fast Fourier transform (FFT) of the magnetoresistance data is required to determine the $(1/B)$ periodicity and to identify individual subbands. The FFT power spectrum shown in fig. 1b indicates distinctly the existence of as many as nine subbands in the α -Sn/InSb($\bar{1}\bar{1}\bar{1}$) sample. When the magnetic field is applied parallel to the sample surface, the bottom of the electric and magnetic hybrid subbands will be shifted upwards through the Fermi level. As a result, charge carriers will be redistributed to the lower subbands. The reduction in inter-subband scattering gives rise to "diamagnetic resonances". Fig. 1c shows parallel field measurements which consistently demonstrate the presence of a large number of subbands in the thin film.

The results of "tilting" experiments in which the magnetic field is rotated to a variable angle θ with respect to the normal of the growth plane can be very informative. For a true 2DEG the fundamental fields of the Shubnikov-De Haas series should increase as $1/\cos \theta$, i.e. the separation of the Landau levels should decrease with increasing θ . On the other hand, spin-splitting should be independent of θ for isotropic conduction bands with the result that it should become progressively more significant as θ increases. Rotation measure-

INT. (a.u.)

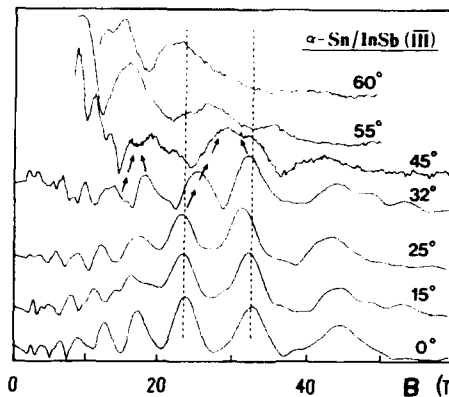


Fig. 2. The FFT power spectra for the α -Sn/InSb($\bar{1}\bar{1}\bar{1}$) sample with the magnetic field applied at angle θ to the normal of the surface plane. Note that the fundamental field for the subbands has been scaled to the $B \cos \theta$ term, i.e. for a perfect 2DEG the peaks should follow the dashed line. At about $\theta = 45^\circ$ some peaks appear to merge together: this could be attributed to the change of Landau level spacing relative to that of the spin-splitting as θ increases.

ments were performed with α -Sn/InSb(100) and ($\bar{1}\bar{1}\bar{1}$) samples and the results for the ($\bar{1}\bar{1}\bar{1}$) surface are shown in fig. 2. With this sample, spin-splitting apparently became dominant at an angle of approximately 45° . Up to 32° , the Fourier peaks from the first two subbands showed little influence of spin whereas the spin-splitting terms for subbands with $i > 3$ became much weaker on rotation. Note that almost all of the subbands follows the $1/\cos \theta$ rule. On the other hand, experiments taken with small intervals in θ with spike-doped InSb grown at low temperature (240°C) showed some deviation from the $1/\cos \theta$ relationship at small angles [3]. While diffusion of Si dopant in these sample is expected to be low [13], it may still be significant on the scale of the cyclotron radius. Moreover, Fourier analysis data on δ -doped InSb samples indicated that the spin-splitting terms did not become dominant until $\theta > 50^\circ$. The significant differences between the α -Sn structures and the δ -InSb layers suggest that the 2DEG in the former case involves the α -Sn layer itself and that little intermixing of the Sn and InSb has occurred away from the interface, i.e. an abrupt heterojunction is formed.

Substrates subjected to the cleaning procedure without subsequent epitaxial growth do not exhibit any SDH oscillations, demonstrating that the 2DEG is not created by substrate cleaning artefacts. The 2DEG charge density seems to be affected by the thickness of the α -Sn film in a complex manner: for film thickness below 3000 Å it increases with overlayer thickness but it shows an opposite trend when the overlayer thickness exceeds 3000 Å. Similarly, on reducing the thickness of a 3000 Å α -Sn film by etching in HCl for 2 min, the total charge density falls by about 10%. One possibility is that the shape of the potential well may change because the dielectric constant of the α -Sn films varies with film thickness [14]. Dielectric effects can also alter the potential of the well via the image force. We detect no SDH structures from films grown on n-type InSb substrates even using field modulation techniques. However, the effect may have been masked by the high conductance of the n-InSb substrate.

One important question remaining to be answered is the origin of the 2DEG. Quantum size effects cannot be fully responsible for the 2DEG: for a square well, the difference of the consecutive subband energies as well as their occupancy dif-

ference should increase with decreasing film thickness. Fig. 1b indicated that the reverse trend is true for α -Sn/InSb films and that the ratio of the subband occupancies E_n/E_{n+1} are relatively constant (~ 1.5) for both thin and thick films [3].

Hall measurements indicated that the apparent bulk carrier concentration of α -Sn films grown on low doped p-InSb(100) is of the order of 10^{17} cm^{-3} . At 4.3 K the Fermi levels for the α -Sn and p-InSb are about 20 and 1 meV above the valence bands of the two materials, respectively. Using the valence band offset of $400 \pm 75 \text{ meV}$ determined by core-level photoemission studies [15], the vacuum Fermi level of α -Sn would be about $420 \pm 75 \text{ meV}$ above that of InSb. In view of the narrow bandgap and high carrier concentration of the α -Sn layer, most of the band bending will occur in the wider bandgap InSb (250 meV) and the space charge region could extend several thousand ångströms into the bulk. However, a large concentration of interface states, which should vary with surface orientation, will alter the interfacial potential substantially.

3.3. Magneto-optical results

In order to understand the nature of the 2DEG as well as the properties of the carriers present in the bulk of the α -Sn films, high resolution magneto-optical experiments have been performed in the Faraday configuration. Fig. 3 shows the photoconductivity response from 3000 and 200 Å thick overlayers at a laser wavelength of $96 \mu\text{m}$. The two structures labelled S_1 and S_2 are the bound hole (s-p) transitions of the p-InSb while the structures A and B are the cyclotron resonances of carriers in the bulk α -Sn film. An effective mass of $0.033m_0$ with

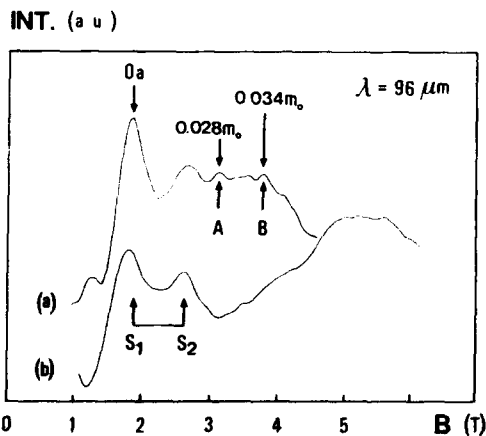


Fig. 3. The magneto-optical spectrum for (a) 3000 Å and (b) 200 Å thick α -Sn films grown on p-InSb(100) surface. Laser wavelength = $96 \mu\text{m}$. The two peaks S_1 and S_2 are due to the bound hole (s-p) transitions of the p-InSb while the structures A and B are the cyclotron resonances of carriers in the bulk α -Sn film.

broad resonance structure has also been observed in α -Sn/CdTe samples [16].

4. Conclusion

Surfaces of α -Sn(100) films exhibit two-domain (2×1), $p(2 \times 2)$ and $c(4 \times 4)$ structures depending on the film thickness while $(\bar{1}\bar{1}\bar{1})$ films show (3×3) and (3×1) reconstructions.

The properties of the 2DEG at the interface of α -Sn/InSb have been investigated by Shubnikov-De Haas measurements and data from various thicknesses of α -Sn overlayers grown on InSb(100) and $(\bar{1}\bar{1}\bar{1})$ indicate that cross-doping may not be the only factor responsible for the occurrence of the 2DEG. Although the α -Sn overlayers do affect the properties of the 2DEG, it is believed that interface states due either to the formation of a dipole layer when a nonpolar material is grown on a polar substrate [17,18], or to the localized states induced by the epilayer [19], may be important factors responsible for the occurrence of the 2DEG. In order to reveal the interfacial energy band diagram of this nonpolar/polar system, further information concerning the electronic and structural properties of α -Sn layers in the interfacial region is needed.

Due to the overlapping of transition energies of bound holes and cyclotron resonance structures, magneto-optical data could not unambiguously indicate the presence of carriers due to the InSb substrate. On the other hand, carriers due to α -Sn films with effective masses ranging from $0.028m_0$ to $0.034m_0$ are observed from thick film samples.

Acknowledgements

We would like to thank the Science and Engineering Research Council and the Imperial Col-

lege Surface Science and Technology Group for financial assistance. One of us (W.K.L.) would like to thank the CVCP for the award of an ORS studentship

References

- [1] W.T. Yuen, W.K. Liu, S.N. Holmes and R.A. Stradling, *Semiconductor Sci. Technol.* 4 (1989) 819.
- [2] W.T. Yuen, W.K. Liu, R.A. Stradling and B.A. Joyce, *Semiconductor Sci. Technol.* 5 (1990) 373.
- [3] W.T. Yuen, W.K. Liu, E. Skuras, R.A. Stradling and B.A. Joyce, paper in preparation.
- [4] R.F.C. Farrow, D.S. Robertson, G.M. Williams, A.G. Cullis, G.R. Jones, I.M. Young and P.N.J. Dennis, *J. Crystal Growth* 54 (1981) 507.
- [5] L.W. Tu, G.K. Wong and J.B. Ketterson, *Appl. Phys. Letters* 54 (1989) 1010.
- [6] L.W. Tu, G.K. Wong and J.B. Ketterson, *Appl. Phys. Letters* 55 (1989) 1327.
- [7] L.W. Tu, G.K. Wong, S.N. Song, Z. Zhao and J.B. Ketterson, *Appl. Phys. Letters* 55 (1989) 2643.
- [8] S.N. Song, X.J. Yi, J.Q. Zheng, Z. Zhao, L.W. Tu, G.K. Wong and J.B. Ketterson, *Appl. Phys. Letters* 65 (1990) 227.
- [9] C.A. Hoffman, J.R. Meyer, R.J. Waagner, F.J. Bartoli, M.A. Engelhardt and H. Hochst, *Phys. Rev.* B40 (1989) 11693.
- [10] M.T. Asom, A.R. Kortan, L.C. Kimerling and R.F.C. Farrow, *Appl. Phys. Letters* 55 (1989) 1439.
- [11] Y. Kasukabe, M. Iwai and T. Osaka, *Japan. J. Appl. Phys.* 27 (1988) L1201.
- [12] H. Hochst and I. Hernandez-Calderon, *J. Vacuum Sci. Technol.* A3 (1985) 911.
- [13] R.L. Williams, E. Skuras, R.A. Stradling, R. Dropad, S.N. Holmes and S.D. Parker, *Semiconductor Sci. Technol.* 5 (1990) S338.
- [14] J.G. Broerman, *Phys. Rev. Letters* 45 (1980) 747.
- [15] P. John, T. Miller and T.C. Chiang, *Phys. Rev.* B39 (1989) 3223.
- [16] T. Wojtowicz, M. Dobrowolska, G. Yang, H. Luo, J.K. Furdyna, L.W. Tu and G.K. Wong, *Semiconductor Sci. Technol.* 5 (1990) S248.
- [17] W.A. Harrison, E.A. Kraut, J.R. Waldrop and R.W. Grant, *Phys. Rev.* B18 (1978) 4402.
- [18] H. Kroemer, *J. Crystal Growth* 81 (1987) 193.
- [19] W.E. Spicer, I. Lindau, P. Skeath, C.Y. Su and P. Chye, *Phys. Rev. Letters* 44 (1980) 420.

Control of misoriented grains and pinholes in CoSi_2 grown on Si(001)

L.J. Schowalter, J.R. Jimenez

Physics Department and Center for Integrated Electronics, Rensselaer Polytechnic Institute, Troy, New York 12180, USA

L.M. Hsiung *, K. Rajan

Materials Engineering Department and Center for Integrated Electronics, Rensselaer Polytechnic Institute, Troy, New York 12180, USA

Shin Hashimoto **

Physics Department and Institute for Particle–Solid Interactions State University of New York, Albany, New York 12222, USA

R.D. Thompson and S.S. Iyer

IBM Thomas J. Watson Research Center, Yorktown Heights, New York 10598, USA

Two types of growth conditions have been obtained that consistently overcome the formation of epitaxially misoriented grains in $\text{CoSi}_2/\text{Si}(001)$. One is by codeposition of Co and Si at Co-rich ratios at a substrate temperature of $\sim 500^\circ\text{C}$. This method yields films of low resistivity ($16\ \mu\Omega\ \text{cm}$) and low ion channeling minimum yield ($\chi_{\text{min}} \approx 2\%$), but the misfit dislocation densities are of the order of $10^5\ \text{cm}^{-1}$. The second way uses a template method of growth after an epitaxial Si buffer layer. Films grown this way have somewhat higher resistivities than those grown by the first method, but have lower misfit dislocation densities. The strain relief mechanism in these films also appears to be different from that of codeposited films. Pinhole densities in films grown by both methods are below our detection limit of $10^3\ \text{cm}^{-2}$.

1. Introduction

Epitaxial CoSi_2 on silicon is a material system of interest because of possible applications such as buried epitaxial metal layers and use in novel devices such as the metal–base transistor. Most work has focused on $\text{CoSi}_2/\text{Si}(111)$, because very high quality films [1–3], and even multilayers [1,4], with essentially perfect interfaces can be routinely obtained. Current silicon field-effect transistor technology uses the (001) surface; however, so that the growth of CoSi_2 on Si(001) would have greater technological impact. Furthermore, in applications

like the metal–base transistor, the transport of hot electrons across the CoSi_2/Si interface must conserve crystal momentum parallel to the interface. A recent calculation [5] of the CoSi_2 band structure has shown that appropriate momentum states do not exist in CoSi_2 for injection of electrons along the (111) direction near the Si conduction band minima, but do exist for injection along the (001) direction.

Unfortunately, in contrast to the growth of CoSi_2 on Si(111), the epitaxial growth of CoSi_2 on Si(001) by molecular beam epitaxy (MBE) [6] is rather challenging. The growth conditions used to obtain high-quality epitaxial CoSi_2 on Si(111) substrates will result in films with varying amounts of misoriented grains when applied to Si(001) substrates. The relative difficulty in growing good quality CoSi_2 on Si(001) by MBE, as compared to

* Present address: Department of Materials Science, University of Virginia, Charlottesville, Virginia 22903, USA.

** Present address: Central Research Laboratories, Matsushita Electric Ind. Co., Ltd., Moriguchi, Osaka 570, Japan.

growing on the $\text{Si}(111)$ surface, may be due to a higher interface free energy for $\text{CoSi}_2(001)/\text{Si}(001)$ as compared to $\text{CoSi}_2(111)/\text{Si}(111)$ [7]. Yalisove et al. [8] have employed a template technique of growth and have observed two dominant epitaxial orientations, $\text{CoSi}_2(001)$ on $\text{Si}(001)$ and $\text{CoSi}_2(110)$ on $\text{Si}(001)$. They reported obtaining films with greater than 95% of either orientation by varying growth conditions. It was reported that room-temperature deposition of an appropriate template of Co and Si was necessary because direct codeposition at temperatures greater than 200°C resulted in polycrystalline or islanded films. Since epitaxial Si overgrowth requires CoSi_2 films of a single epitaxial orientation, it is desirable to obtain a reliable method for growing (001) CoSi_2 on (001) Si without misoriented grains. In this paper, we show that pure (001) CoSi_2 (i.e., free of misoriented grains to within detection limits) with good resistivity ($16\ \mu\Omega\text{ cm}$) and good crystal quality ($\chi_{\text{min}} = 2\%$), may be obtained by direct codeposition of Co and Si at high temperature ($\sim 500^\circ\text{C}$) and at Co-rich stoichiometries. Some template recipes, when used on epitaxially-grown Si buffer layers, also result in pure (001) CoSi_2 , but the resistivity of single-orientation films obtained in this manner is somewhat higher ($20\text{--}24\ \mu\Omega\text{ cm}$). The pinhole densities for both of these growth techniques are below our detection limit of 10^3 cm^{-2} .

2. Growth

Epitaxial layers of CoSi_2 were grown on 5-inch Si wafers in a MBE system with base pressure of 3×10^{-11} mbar. Pressures during growth were in the mid 10^{-10} mbar range. n-Type wafers were used, with resistivities between 3 and $16\ \Omega\text{ cm}$, and with surfaces oriented within 0.2° of the (001) axis. They were loaded into the MBE system within 15 min of an RCA chemical cleaning, were thermally cleaned at high temperature ($\sim 850^\circ\text{C}$), and then ramped down to the growth temperature. Cobalt was deposited at a rate of $0.2\ \text{\AA/s}$, and the stoichiometry of the codeposited film was controlled by independently setting the silicon deposition rate. Deposition rates were monitored by

electron-impact emission spectroscopy (EIES) and feedback-controlled to within 2%. Three main growth methods were investigated: deposition of Co at various temperatures ($400\text{--}600^\circ\text{C}$), codeposition of Co and Si at various temperatures and stoichiometries, and use of what has been called the template method [2,3], where an ultrathin silicide layer is formed by room temperature codeposition followed by an anneal, before subsequent codeposition of metal and Si to form a thicker film.

3. Experimental results and discussion

As shown previously [9], films grown by deposition of Co alone (cobalt-deposited films) were found to contain misoriented grains, pinholes, and misfit dislocations. Detailed transmission electron microscopy (TEM) analysis on films grown at ~ 460 and $\sim 500^\circ\text{C}$ showed misoriented grains with epitaxial relationship $\text{CoSi}_2(22\bar{1})//\text{Si}(001)$. Cross-sectional TEM revealed that these cobalt-deposited films to have roughened interfaces, with faceting along (111) planes, and $(22\bar{1})$ grains aligned with (111) facets. The $(22\bar{1})$ misoriented grain may then be understood as arising from twinning on (111) facets, which is consistent with the fact that type-B CoSi_2 is observed to grow preferentially on $\text{Si}(111)$. Fig. 1 is a cross-sectional TEM micrograph of a film grown by deposition of cobalt at $\sim 500^\circ\text{C}$, showing the misoriented grains lying on (111) facets. Faceting may be due to the large amount of mass transport (necessary for the formation of the disilicide phase) which facilitates the formation of energetically preferred interfaces. In addition, the misoriented grains in these films are always associated with pinholes [9].

Since the formation of misoriented grains in cobalt-deposited films is associated with the faceting of the interface, one may try to prevent them from forming by reducing the amount of diffusion necessary across the CoSi_2/Si interface. However, films grown by codeposition of Co and Si in stoichiometric (1:2) ratio at $\sim 500^\circ\text{C}$, in which no diffusion is necessary, were still found to contain $(22\bar{1})$ misoriented grains. Films grown by stoichiometric codeposition at lower temperatures

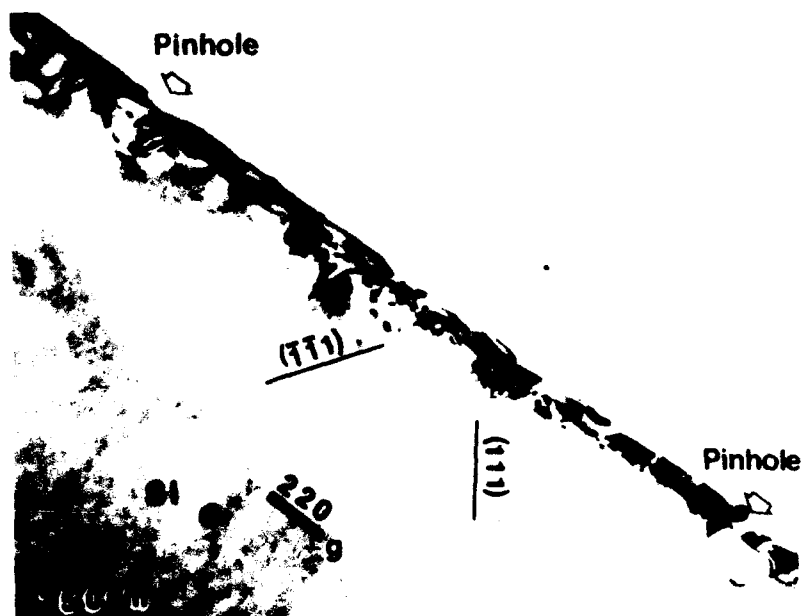


Fig. 1. Cross-sectional TEM micrograph of a 360 Å thick CoSi_2 film grown by deposition of Co at $\sim 500^\circ\text{C}$, showing $(22\bar{1})$ misoriented grains aligned with (111) facets.

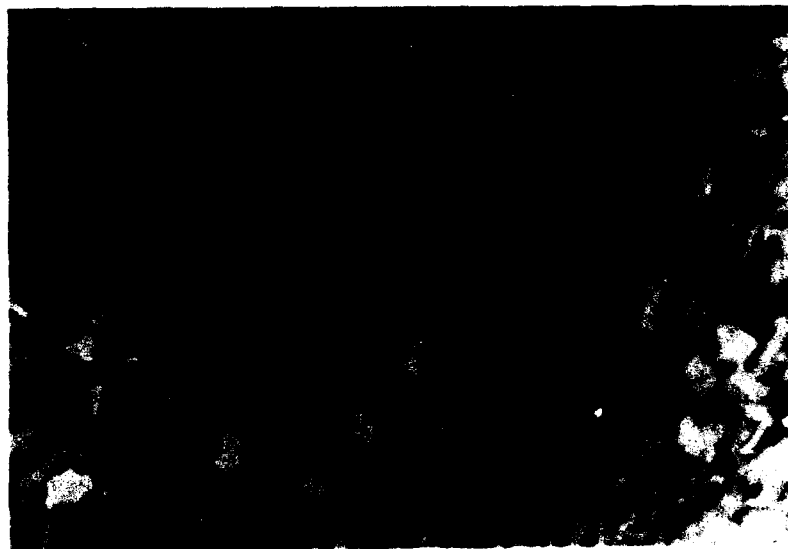


Fig. 2. Planar view, bright field TEM image of a 360 Å thick CoSi_2 film codeposited at $\sim 500^\circ\text{C}$ in 1:2 ratio, showing $(22\bar{1})$ misoriented grains (bright areas) and dislocations ($Z \approx [001]$, $g \approx \langle 220 \rangle$).

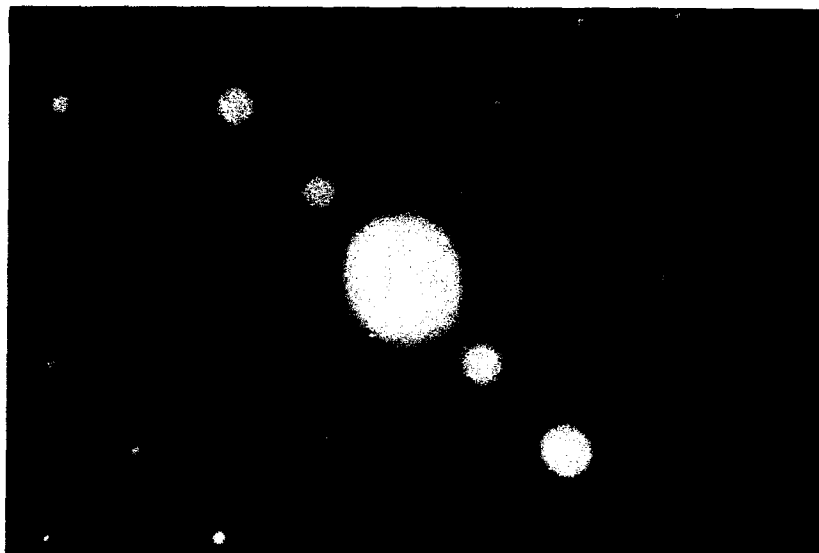


Fig. 3. TEM diffraction pattern for the same film shown in fig. 2, tilted $\sim 12^\circ$ away from the $[001]$ axis, towards the $[0\bar{1}0]$ direction, in order to reveal spots due to $(22\bar{1})$ grains.

were found to be inferior with poor ion channeling minimum yields. Fig. 2 is a TEM micrograph of a 360 \AA thick film grown by codeposition at $\sim 500^\circ\text{C}$ at the correct stoichiometric ratio, showing misfit dislocations and $(22\bar{1})$ misoriented grains. Unlike the cobalt deposited films, these grains are not associated with pinholes. Since TEM diffraction spots from $(22\bar{1})$ grains coincide with diffraction spots from the (001) -oriented film when taken along the $[001]$, one has to tilt slightly from the $[001]$ zone axis to reveal extra spots due to $(22\bar{1})$ misoriented grains. Fig. 3 shows such a TEM diffraction pattern for the film in fig. 2, with extra spots due to misoriented grains. The only misfit dislocations observed in these films were edge dislocations with a Burgers vector of the type $\frac{1}{2}\langle 110 \rangle$ (as determined from conventional diffraction contrast experiments). For films grown by codeposition of Co and Si in stoichiometric ratio, we expect the mechanism for the formation of misoriented grains to be different from that in cobalt-deposited films, since no diffusion or mass transport through the CoSi_2/Si interface is necessary in the former. Improving the surface quality by growing epitaxial Si buffer layers prior to CoSi_2

growth still does not result in single-orientation films, although it did improve CoSi_2 grown by the template technique, as will be shown later. Although the mechanism for the nucleation of misoriented grains on stoichiometrically-codeposited films is not understood, we observed that it is possible to suppress it by forming the CoSi_2/Si interface below the original substrate surface. This requires Co-rich codeposition ratios, so that sufficient diffusion occurs across the CoSi_2/Si interface to suppress the nucleation of misoriented grains. However, the Co content should not be rich enough to facilitate faceting, which would again result in misoriented grains.

A set of CoSi_2 films were grown in which the Co-to-Si codeposition ratio was varied between 1:2 and 1:0. Films grown at Co to Si codeposition ratios of 1:1.8 and 1:1.6 were found to be pure (001) -oriented CoSi_2 films, free of misoriented grains to within the limits of the TEM technique. Fig. 4 is a plane-view TEM micrograph of a 360 \AA film grown by codeposition of Co and Si in 1:1.8 ratio at $\sim 500^\circ\text{C}$. Fig. 5 is a cross-sectional TEM micrograph of the same film, showing a flat interface. No extra diffraction spots due to



Fig. 4. Bright field TEM image of a 360 Å thick CoSi_2 film codeposited in 1:1.8 ratio at $\sim 500^\circ\text{C}$. Only dislocations are visible ($Z \approx [011]$, $g \approx \langle 220 \rangle$).

misoriented grains were observed even when the sample was tilted. Ion channeling minimum yields (χ_{\min}) for these films were reproducibly $\sim 2\%$.

Fig. 6 shows Rutherford backscattering (RBS) channeling and random spectra for a film with a codeposition ratio of 1:1.8. Incident ions were 2



Fig. 5. Cross-sectional TEM micrograph of the same film shown in fig. 4, showing a flat interface.

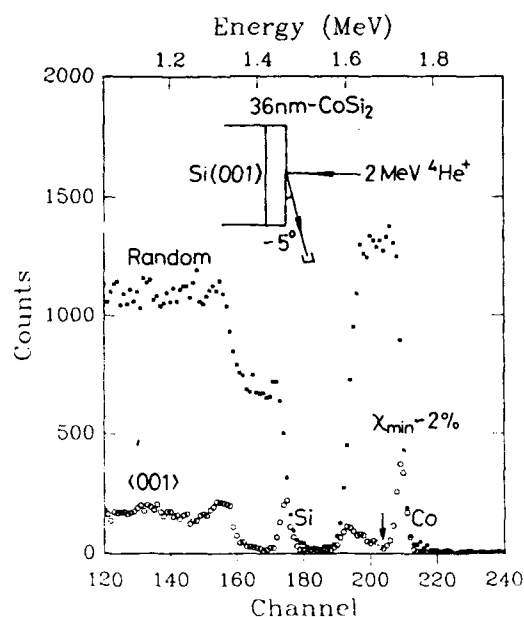


Fig. 6. RBS channeling and random spectra of a 360 Å thick CoSi₂ film codeposited in 1:1.8 ratio at ~500°C, with χ_{\min} ~2%, using 2 MeV ⁴He⁺ ions and a grazing exit angle geometry.

MeV ⁴He⁺, and a grazing exit angle detector geometry (~5° from surface) was used. The resistivity of films grown in this manner was the lowest (16 μΩ cm) among all the (001) CoSi₂ films, including those grown by other methods. The accuracy of codeposition ratios is set by the calibration of deposition rates, which were accurate to

better than 10%. Table 1 summarizes the results of varying the Co to Si codeposition ratio. Faceting is found to occur at a 1:1 codeposition ratio. Misoriented grains are found to occur at 1:1 and 1:2 codeposition ratio. Films of single (001) orientation occur at ratios of 1:1.6 and 1:1.8. The resistivities and channeling minimum yields do not vary significantly over the range of ratios 1:1.4 to 1:1.8. Thus, the growth of high-quality, single-orientation (001) CoSi₂ on Si is possible by the direct codeposition of Co and Si at high temperatures and at Co-rich codeposition ratios.

The template technique of silicide growth [2,3] has been used to grow high quality CoSi₂ and NiSi₂ on Si(111). The template technique was also investigated in this study. Several template recipes were used. One of these involved depositing an initial 2 Å of Co, then codepositing 2 Å of Co and 7.2 Å of Si, all at room temperature, followed by an anneal at ~330°C to form a 14 Å thick layer of CoSi₂. (For reference, called template I.) Yalisove et al. have used these template recipes to grow CoSi₂ layers on Si(001) [8]. A second recipe involved codeposition of 4 Å of Co and 14.4 Å of Si at room temperature, followed by an anneal at ~330°C. (For reference, called template II.) Growth on these templates was done at temperatures ranging from 330 to 500°C. We find that films grown from these templates by codeposition at ~330 and ~375°C contain (110) misoriented grains, i.e., with epitaxial relationship CoSi₂(110) // Si(001), in agreement with Yalisove et al. [8]. In addition, we find that films codeposited on

Table 1

Epitaxial orientations, resistivities, ion channeling minimum yields (χ_{\min}), and other characteristics for a series of CoSi₂ films grown at ~500°C with different Co-to-Si codeposition ratios; the χ_{\min} 's were measured at minimum yield just behind the surface peak of the Co spectrum (however, the finite energy resolution of the detector prevented complete resolution of the surface and interface peaks on the 120 Å thick film, which would partially account for its higher χ_{\min} value)

Co:Si	Orientations	χ_{\min} (%)	ρ (μΩ cm)	Microstructure	Film thickness (Å)
1:1	(001), (221)	8	22	Faceting, pinholes	360
1:1.0	(001), (221)	4	17	Faceting, pinholes	360
1:1.4	NA ^{a)}	2	17	NA	360
1:1.6	(001)	2	16	Flat interface, no pinholes	360
1:1.8	(001)	2	17	Flat interface, no pinholes	360
1:2.0	(001), (221)	<13	21	Flat interface, no pinholes	120

^{a)} NA = not available.

these templates at higher temperature ($\sim 500^\circ\text{C}$) have (221) misoriented grains, which is not reported in Yalisove et al.'s work. Cross-sectional TEM shows the interface of template-grown films to be flat, in contrast to the rough and faceted interfaces observed on films grown by deposition of Co only at a substrate temperature of $\sim 500^\circ\text{C}$.

Yalisove et al. [8] have suggested, among other possibilities, that the misoriented grains are nucleated at defects and impurities on the starting Si surface. If this is so, then improving the quality of the starting Si surface may significantly reduce (110) -oriented grains. We have grown silicide films using the described template recipes, after an initial 500 Å thick epitaxial Si buffer layer was deposited on the Si substrate to assure a pristine Si surface. Films grown using template II were found to contain misoriented grains even with the use of a Si buffer layer. However, pure (001) -oriented films, free of misoriented grains to within the detection limits of the TEM technique, have been obtained by using template I and an initial Si buffer layer. Several areas in the film were examined in the effort to look for misoriented grains. Fig. 7 is a TEM micrograph of this film. The

observed misfit dislocations have their Burgers vector in the $\langle 011 \rangle$ directions and are of lower density than those of directly codeposited films. Again, no extra diffraction spots due to misoriented grains was observed. An ion channeling χ_{\min} typical of ideal single crystals was observed, with a very small interface peak in the channeling spectrum. However, the resistivity of single-orientation films grown in this way ranged from 20 to 24 $\mu\Omega\text{ cm}$, even for films annealed at $\sim 500^\circ\text{C}$, the same temperature at which directly codeposited layers of low resistivity were grown.

Pinhole densities on films grown by both methods were studied by both TEM and scanning electron microscopy (SEM). No pinholes were observed by TEM, but since TEM examines a relatively small area, TEM observations set an upper bound on pinhole density of $\sim 10^6\text{ cm}^{-2}$. SEM can be used to examine much larger areas but may miss small pinholes. The SEM resolution can be improved by using a CF_4 plasma etch [10,11]. The CF_4 plasma selectively etches Si over CoSi_2 so that, even if pinholes below the detection limit of SEM are present in the as-grown Si_2 film, they would be detectable after the CF_4 plasma etch



Fig. 7 Planar view, bright field TEM image of a 120 Å thick CoSi_2 film codeposited on template I at $\sim 330^\circ\text{C}$, with a 500 Å thick Si buffer layer. Dislocations and clusters of point defects are visible ($Z \approx [001]$, $g \approx \langle 220 \rangle$).

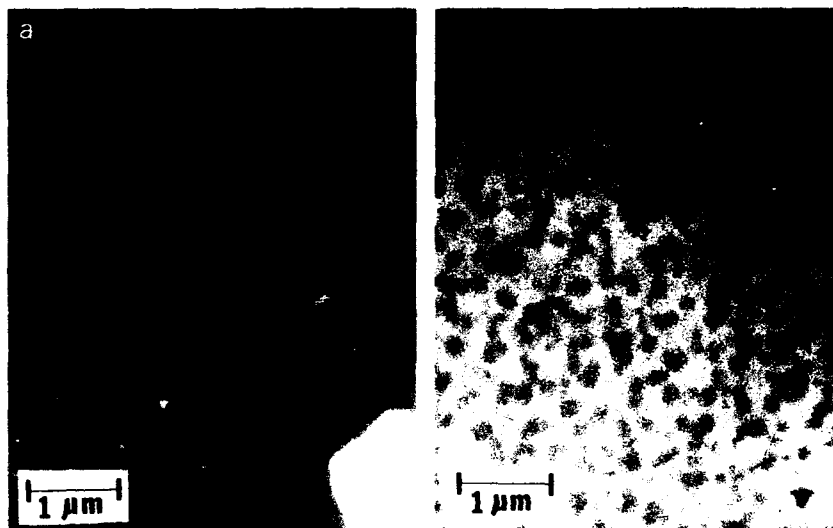


Fig. 8. SEM micrographs of a 260 Å thick CoSi_2 film grown by codeposition of Co alone at $\sim 500^\circ\text{C}$: (a) before CF_4 plasma etching and (b) after CF_4 plasma etching.

[10,11]. Using this technique, no pinholes were observable on films grown by codeposition at 1:1.8 ratio, although they were observable on films grown by deposition of Co only, as shown in fig. 8. From prior work [10], we know this technique will reveal pinholes that are 10 nm in size or larger. We have never observed pinholes smaller than this diameter. The plasma etch technique allows us to set the upper bound on pinhole density to 10^3 cm^{-2} .

4. Conclusion

In summary, CoSi_2 films of single (001) orientation have been grown both by direct codeposition of Co and Si at Co-rich stoichiometries, and by using the template method of growth on epitaxially-grown Si buffer layers. Although the mechanism for the nucleation of misoriented grains in stoichiometrically codeposited films is not understood, it appears this mechanism is suppressed by allowing a small amount of mass transport across the CoSi_2/Si interface. However, if too much mass transport is required by making the deposited film too Co-rich, the formation of facets along the CoSi_2 interface is facilitated which again results in (221)-misoriented grains. In this

case, however, the formation mechanism is clearly different from the stoichiometrically-deposited films, since the misoriented grains are always associated with pinholes. Single-orientation films grown by direct codeposition of Co and Si have somewhat lower resistivities than single-orientation template-grown films. The method of direct codeposition has the additional advantage over the template method of being easier to use and requiring less time. Pinhole densities are below the detection limit of 10^3 cm^{-2} on films grown by both methods.

Acknowledgements

We would like to acknowledge B.A. Ek for his technical assistance, and K.V. Ramanathan for initial discussions. K. Rajan wishes to acknowledge partial support through a grant from the AMAX Research Foundation.

References

- [1] B.D. Hunt, N. Lewis, E.L. Hall, L.G. Turner, L.J. Schowalter, M. Okamoto and S. Hashimoto, Mater. Res. Soc. Symp. Proc. 56 (1986) 151.

- [2] R.T. Tung and F. Schrey, *Appl. Phys. Letters* 54 (1989) 852.
- [3] R.T. Tung and F. Schrey, *Appl. Phys. Letters* 55 (1989) 256.
- [4] H. von Känel, J. Henz, M. Ospelt and P. Wachter, *Phys. Scripta* T19 (1987) 158.
- [5] L.F. Mattheiss and D.R. Hammann, *Phys. Rev. B* 37 (1988) 10623.
- [6] For work on CoSi_2 on $\text{Si}(001)$ by methods other than MBE, see, for example:
A.E. White, K.T. Short, R.C. Dynes, J.P. Garno and J.M. Gibson, *Appl. Phys. Letters* 50 (1987) 95;
C.W.T. Bulle-Lieuwma, A.H. van Ommen and J. Hornstra, *Mater. Res. Soc. Symp. Proc.* 102 (1988) 377.
- [7] K. Ishibashi and S. Furukawa, *Japan. J. Appl. Phys.* 24 (1985) 912.
- [8] S.M. Yalisove, R.T. Tung and D. Loretto, *J. Vacuum Sci. Technol. A* 6 (1989) 1472.
- [9] L.M. Hsiung, J.R. Jimenez, L.J. Schowalter, K.V. Ramanathan, S.S. Iyer and K. Rajan, presented at the The Metals, Minerals, and Materials Society (TMS) Fall Meeting, Indianapolis, IN, Sept. 1989.
- [10] B.D. Hunt and L.J. Schowalter, private communication.
- [11] T.L. Lin, R.W. Fathauer, P.J. Grunthaner and C. d'Anter-oches, *Appl. Phys. Letters* 52 (1988) 804.

Characterization and application of fine-patterned Si/CoSi₂/Si double heterostructures fabricated by self-aligned, two-step MBE

Masanobu Miyao, Kiyokazu Nakagawa, Nobuo Nakamura and Takashi Ohshima

Central Research Laboratory, Hitachi, Ltd., P.O. Box 2, Kokubunji, Tokyo 185, Japan

The formation and characterization of fine-patterned Si/CoSi₂/Si double heterostructures are comprehensively studied. Using self-aligned and selective MBE growth, a new sub-micron patterning method of CoSi₂ films is developed. In addition, a high-quality double heterostructure is formed by two-step MBE of the Si overlayer on CoSi₂/Si, i.e., low-temperature growth followed by high-temperature growth. The interfaces between CoSi₂ and Si are atomically abrupt and smooth. Finally, permeable base transistors with high performance ($g_m = 50$ mS/mm, $f_T = 4$ GHz) are fabricated using these new techniques.

1. Introduction

Double heteroepitaxy of Si/silicide/Si is a key technique for overcoming Si-LSI fabrication limitations [1]. This is because crystalline silicide wire embedded in a Si lattice enables the development of sophisticated devices for ultra-high-frequency operation [2,3], i.e., permeable base transistors (PBTs) and metal base transistors. In addition, it makes possible a three-dimensional connection between devices, which is useful for ultra-high-density LSIs. However, to realize such applications, the following two techniques should be developed: the fine patterning of silicide in the submicron range and the formation of high-quality double heterostructures (Si/silicide/Si). This paper describes the authors' recent molecular beam epitaxy (MBE) developments in relation to these techniques [4,5].

2. Experimental

MBE growth of CoSi₂ and Si was performed in a UHV chamber (2×10^{-11} Torr). Prior to growth, Si (111) substrates were cleaned by low-temperature thermal etching (800°C, 5 min). Then CoSi₂ films were grown on the Si substrates (300–600°C) using codeposition of Co and Si during which the Co-to-Si beam ratio was kept constant (Co/Si =

0.50) to an accuracy of $\pm 2\%$. Finally, a Si overlayer was grown on the CoSi₂ in the same UHV chamber. The growth rate of both CoSi₂ and Si was about 0.1 nm/s.

The crystallinity of CoSi₂ and Si films was examined using reflection high energy electron diffraction (RHEED) and a cross-sectional transmission electron microscope (XTEM). Surface morphology was investigated using a Nomarski microscope and a scanning electron microscope (SEM). In addition, the electrical property of the Si/CoSi₂/Si heterostructure was evaluated by measuring the Schottky diode and the PBT characteristics.

3. Fine patterning of CoSi₂ films by self-aligned MBE

The main idea behind the fine patterning of CoSi₂ films is a selective MBE growth on patterned Si substrates, as illustrated in fig. 1a. In this process, damage-free grooves of the submicron scale (0.5 to 1.5 μ m lines and spaces with 1.0 μ m depth) were formed on Si (111) substrates by photolithography and plasma etching using SF₆ + C₂Br₂F₄ gas. Then, single-crystalline CoSi₂ was grown by MBE.

Measurement of electrical conductance between CoSi₂ films on the top and the bottom

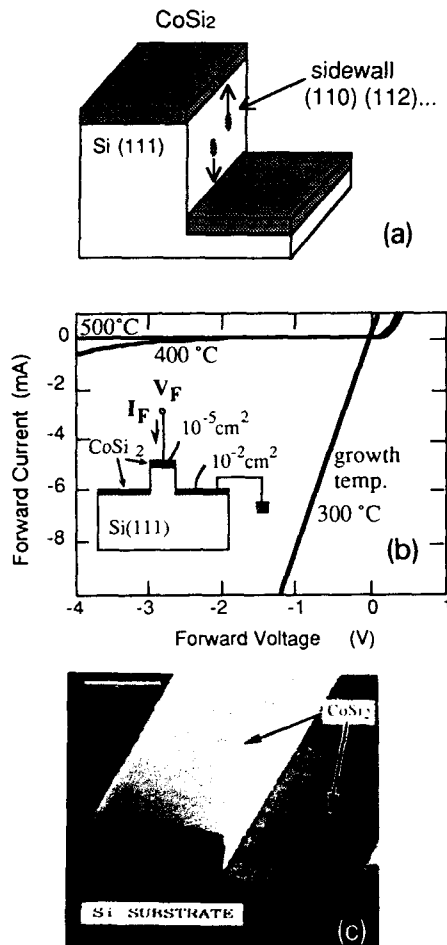


Fig. 1. (a) Schematic illustration of the self-aligned and selective MBE growth of CoSi₂ films on an etched-groove Si substrate. (b) Current-voltage characteristics between CoSi₂ films on the top and the bottom surfaces of the grooves as a function of growth temperature. (c) SEM micrograph after CoSi₂ MBE growth (450°C) on the etched grooves in the (111) Si substrate. Marker represents 1 μm.

surfaces of the grooves is shown in fig. 1b. Results indicated that the films were electrically connected after the low-temperature MBE growth ($\leq 300^\circ\text{C}$). However, after high-temperature growth ($\geq 400^\circ\text{C}$), the films were electrically isolated. This suggested that the CoSi₂ films deposited on the side walls ({112} and {110} orientation) of the grooves flowed away during high temperature

growth. In contrast, Nomarski microscope observation indicated that pin-hole-free CoSi₂ films i.e., pin-hole density $\leq 10^0 \text{ cm}^{-2}$, were obtained on the flat (111) Si surfaces. These phenomena are attributed to the fact that the interface energy is greater on Si {112} and {110} surfaces than on a Si (111) surface [6].

An SEM image taken after the growth of CoSi₂ film (450°C) on the etched grooves is shown in fig. 1c. The photograph clearly shows the features of the selective growth of CoSi₂. Thus, submicron patterning of CoSi₂ films was established with self-alignment to the etched grooves by choosing a proper growth temperature (400–500°C).

4. Formation of a Si/CoSi₂/Si double heterostructure by two-step MBE

To obtain high-quality Si overlayers on the CoSi₂/Si substrates, two-step Si-MBE growth was developed. Here, very thin Si (2 nm) layers were grown at low temperatures (300–400°C) to stabilize the CoSi₂ surface atoms. Then, on top, thick Si (50–200 nm) layers were grown at high temperatures (500–600°C). Nomarski microscope and RHEED observations shown in figs. 2a and 2b, respectively, indicate that the Si/CoSi₂/Si structure has good surface morphology and crystallinity. In addition X-ray photoelectron spectroscopy (XPS) measurements suggested that no segregation of CoSi₂ had occurred during Si MBE growth. This is in contrast to Si overgrowth on NiSi₂/Si substrates [7], where segregation does occur.

The atomic structure of the hetero-interfaces was observed by using XTEM and is shown in fig. 2c. The lattice image of the double heterostructure indicates that the upper and lower interfaces between CoSi₂ and Si are atomically abrupt and smooth. Thus, a high-quality Si/CoSi₂/Si double heterostructure was realized using the two-step MBE.

5. Fabrication and characterization of permeable base transistors

PBTs were fabricated utilizing these newly developed MBE processes, where n-type Si ($n = 10^{16}$

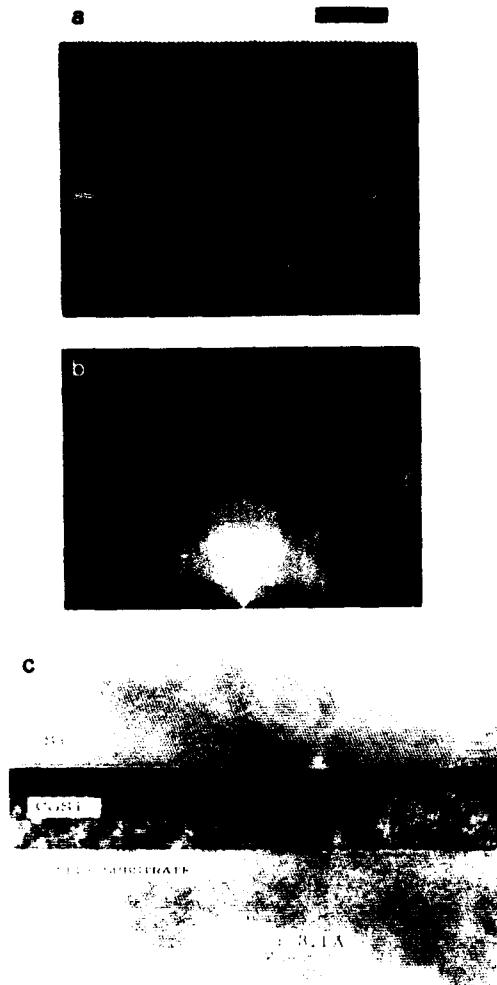


Fig. 2. (a) Surface morphology of the Si/CoSi₂/Si double heterostructure observed by the Nomarski microscope. Markers represent 10 μm . (b) RHEED pattern obtained after Si/CoSi₂/Si double heteroepitaxy. (c) Cross-sectional lattice image of the Si/CoSi₂/Si double heterostructure observed by TEM.

cm^{-3})/n⁺-type Si ($n = 10^{20} \text{ cm}^{-3}$) were used as the substrates. First, an n⁺-Si source region was formed by P⁺ ion implantation (50 keV, $1 \times 10^{15} \text{ cm}^{-2}$) and subsequent annealing (900°C, 5 min). Then, grooves (1.0 μm deep with a 0.5 to 1.5 μm width and spacing) were formed on the Si substrates by dry etching. Next, CoSi₂ electrodes (10

nm) were formed on the top and bottom Si surfaces of the grooves. Finally, Si overlayers were grown by two-step MBE. A cross-sectional view and plan view of the PBT (before Al electrode fabrication) are shown in figs. 3a and 3c, respectively.

The Schottky diode characteristics between the source and gate showed a reasonable ideality factor (*n*-value) of 1.05 under a forward bias condition. The current-voltage (*I*-*V*) characteristics exhibited triode like features as shown in fig. 3b.

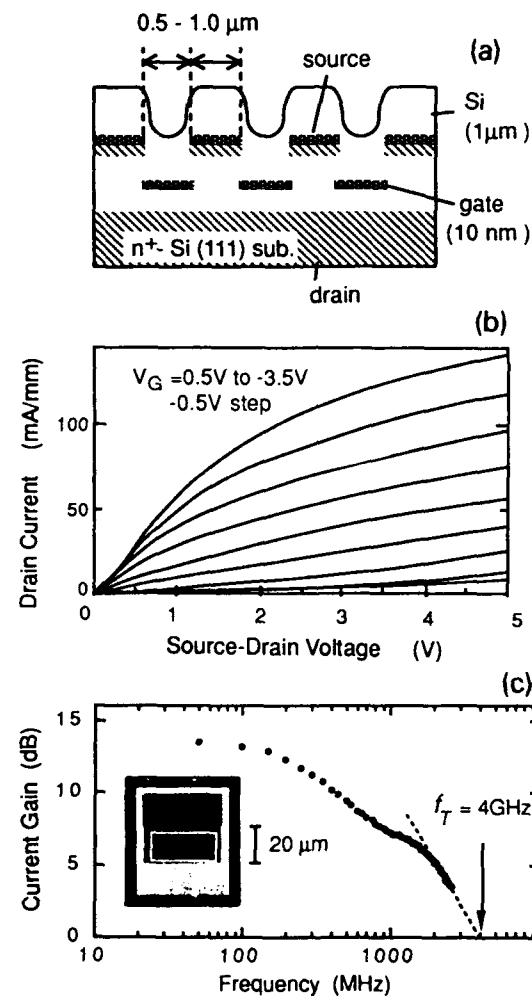


Fig. 3. (a) Cross-sectional view of PBT. (b) Typical current-voltage characteristics of PBT. (c) Typical high-frequency characteristics of PBT. The plan view of PBT is also shown.

The highest transconductance (g_m) was 50 mS/mm, which is about 10 times higher than that of previously reported Si PBTs [8,9] using a buried electrode. High-frequency characteristics shown in fig. 3c indicated that the highest unity gain frequency (f_T) was 4.0 GHz. The g_m value and the I - V characteristics agree well with the results of computer simulation. In addition, the f_T value is satisfactory, considering the existence of parasitic capacitance from the large pad region ($40 \times 20 \mu\text{m}^2$). Still, significant improvement in f_T (70–100 GHz) is possible by reducing the area of the pad region ($5 \times 5 \mu\text{m}^2$) and by using a deep submicron patterned gate ($\leq 0.1 \mu\text{m}$).

6. Conclusion

The authors have achieved a selective CoSi₂-MBE growth in a self-aligned fashion and a two-step Si-MBE. These processes make possible the formation of submicron-patterned Si/CoSi₂/Si double heterostructure without removal from the ultra-high vacuum chamber. This eliminates the introduction of any defects or contaminants during device fabrication processes. Results of high-performance PBTs ($g_m = 50\text{mS/mm}$, $f_T = 4\text{GHz}$) indicate that the newly developed MBE techniques are powerful tools for developing future, deep-submicron devices.

Acknowledgements

The authors gratefully acknowledge Professor S. Furukawa (Tokyo Institute of Technology) and Professor Y. Shiraki (University of Tokyo) for valuable suggestions and discussions. This work was performed under the management of the R&D Association for Future Electron Devices as part of the R&D of Basic Technology for Future Industry supported by the New Energy and Industrial Technology Development Organization.

References

- [1] B.W. Dodson, L.J. Schowalter, J.E. Cunningham and F.H. Pollak, Eds., *Layered Structure – Heteroepitaxy, Superlattice, Strain and Metastability*, Mater. Res. Soc. Symp. Proc., Vol. 160 (Mater. Res. Soc., Pittsburgh, PA, 1989).
- [2] R.A. Bojak and G.D. Alley, IEEE Trans. Electron Devices ED-30 (1983) 877.
- [3] R.D. Rathman, N.P. Economou, D.J. Silversmith, R.W. Mountain and S.M. Cabral, in: IEDM Tech. Digest, San Francisco, CA, 1982, p. 650.
- [4] T. Ohshima, N. Nakamura, K. Nakagawa and M. Miyao, Thin Solid Films 184 (1990) 275.
- [5] M. Miyao, T. Ohshima, N. Nakamura and K. Nakagawa, in ref. [1], p. 275.
- [6] D.J. Chadi, Phys. Rev. B29 (1984) 785.
- [7] T. Ohshima, K. Nakagawa, N. Nakamura and Y. Shiraki, J. Crystal Growth 95 (1989) 490.
- [8] K. Ishibashi and S. Furukawa, IEEE Trans. Electron Devices ED-33 (1986) 322.
- [9] G. Glastre, E. Rosencher, F. Arnaud d'Avitaya, C. Puisseant, M. Pons, G. Vincent and J.C. Pfister, Appl. Phys. Letters 52 (1988) 898.

$\sqrt{3} \times \sqrt{3}$ -B structure on a 5×5 Ge_xSi_{1-x}/Si(111) surface and its electrical conduction

T. Tatsumi

Microelectronics Research Laboratories, NEC Corporation, 4-4-1, Miyazaki, Miyamae-ku, Kawasaki 213, Japan

I. Hirose

Fundamental Research Laboratories, NEC Corporation, 34, Miyukigaoka, Tsukuba, Ibaragi 305, Japan

T. Niino, H. Hirayama

Microelectronics Research Laboratories, NEC Corporation, 4-4-1, Miyazaki, Miyamae-ku, Kawasaki 213, Japan

and

J. Mizuki

Fundamental Research Laboratories, NEC Corporation, 34, Miyukigaoka, Tsukuba, Ibaragi 305, Japan

The electric activation efficiencies for an a-Si/B- $\sqrt{3} \times \sqrt{3}$ /Si(111) system were measured by Hall measurement. The result strongly suggests that almost all boron atoms are activated at the a-Si/Si(111) interface because of $\sqrt{3} \times \sqrt{3}$ structure formation. A $\sqrt{3} \times \sqrt{3}$ -B structure was also found to be formed on a 5×5 Ge_xSi_{1-x}/Si(111) surface on which Ga or Sn atoms did not form any superstructures. A Si epitaxial overlayer can be grown on the $\sqrt{3} \times \sqrt{3}$ -B/50 Å Ge_{0.4}Si_{0.6}/Si(111) structure at a growth temperature of 300°C, preserving a large fraction of the $\sqrt{3} \times \sqrt{3}$ -B structure due to strain compensation.

1. Introduction

When group III metal atoms such as Al, Ga, or In are deposited onto a clean Si(111) 7×7 surface, various superstructures appear [1-3]. It has been known that they show quite similar behavior on a Si(111) surface. However, few studies have been reported for B/Si(111) systems because the low vapor pressure of B makes it difficult to deposit B with good controllability. We have previously reported that HBO₂ has a high vapor pressure and is applicable for controlled B doping in Si-MBE [4]. Using this B source, we have found that it also forms a $\sqrt{3} \times \sqrt{3}$ structure on a Si(111) surface [5]. Recent studies have revealed that this B- $\sqrt{3}$

$\times \sqrt{3}$ structure was different from the $\sqrt{3} \times \sqrt{3}$ structures formed by other group III elements. Akimoto et al. have reported that B- $\sqrt{3} \times \sqrt{3}$ structures can be preserved on Si(111) after subsequent Si deposition [6]. Headrick et al. have reported that B occupies the S₃ subsurface site rather than the T₄ adatom site [7]. The possibility of preserving a two-dimensional structure at a buried interface raises possibilities for new materials which have, for example, high mobility at very low temperatures, where ion scattering is dominant.

In this paper, we report the electric activation efficiencies for a-Si/B- $\sqrt{3} \times \sqrt{3}$ /Si(111) and Si epitaxial growth on a B- $\sqrt{3} \times \sqrt{3}$ /Ge_xSi_{1-x} structure.

2. Experimental

Boron-containing interface structures were formed on 100 mm diameter n-type (111) and (100) Czochralski silicon wafers with 10–20 Ω cm resistivity. Wafers were precleaned using a chemical solution ($\text{NH}_4\text{OH}:\text{H}_2\text{O}_2:\text{H}_2\text{O} = 1:6:20$) to form a thin protective oxide layer. The wafers were then loaded into MBE equipment (ANELVA MBE-430) in which the base pressure was 1.2×10^{-10} Torr. A thin amorphous silicon layer (10 Å) was then formed on the oxide layer. The wafer was preheated at 780°C to evaporate the oxide layer. This cleaning technique has previously been reported elsewhere [8]. Boron was deposited in the form of HBO_2 , an accurately controllable doping source for Si-MBE [4], using a Knudsen cell. The boron deposition rate was 2.9×10^{12} atoms cm^{-2} s^{-1} , which value was determined from the doping concentration of Si-MBE growth layers by Hall measurement and secondary ion mass spectrometry (SIMS). An a-Si layer was then deposited on this boron-deposited surface at room temperature. The a-Si layer thickness was 100 Å. Al electrodes were evaporated onto the a-Si layer after the sample was taken out from the MBE chamber. The sheet carrier concentration was determined by Hall measurement using the Van der Pauw technique.

3. Results and discussion

Fig. 1 shows, for a-Si/B/c-Si structures, the sheet carrier concentration dependence on the substrate temperature at which HBO_2 was deposited. Also indicated here are the AES peak height for oxygen and the RHEED pattern, both of which were observed just after HBO_2 deposition. Oxygen was detected when the substrate temperature was below 700°C, as previously reported [4]. The surface structure did not change and the RHEED patterns of Si(111) and Si(100) remained 7×7 and 2×1 , respectively. When HBO_2 was deposited at temperature above 700°C, oxygen was not detected, and the RHEED pattern of Si(111) changed from 7×7 to $\sqrt{3} \times \sqrt{3}$. On the other hand, on Si(100) the RHEED pattern remained 2×1 even at temperatures above 700°C.

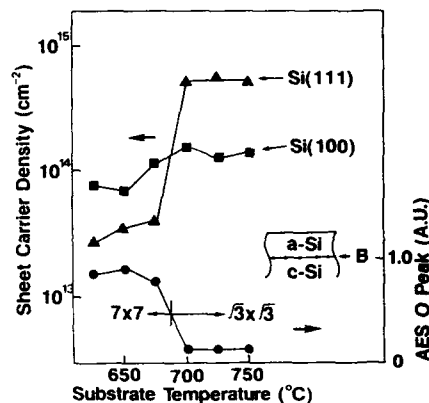


Fig. 1. Sheet carrier concentration dependence on the substrate temperature at which HBO_2 was deposited, for Si(111) (Δ) and Si(100) (\blacksquare). Also indicated here are the AES peak height for oxygen and the RHEED pattern, both of which were observed just after HBO_2 deposition.

While the sheet carrier density for (100) stayed essentially the same when temperatures were increased to over 700°C, that for (111) increased drastically, from the level equivalent to the density for (100) to the level approximately six times larger. Fig. 2 shows the sheet carrier concentration dependence on annealing temperature. The annealing time at each temperature was 10 min. While the carrier concentration for Si(111) did not change with temperature, that for Si(100) began to increase at 200°C and reached the level of Si(111) at approximately 400°C. Robinson and co-workers have reported that an a-Si overlayer on a clean Si overlayer on a clean Si surface started to

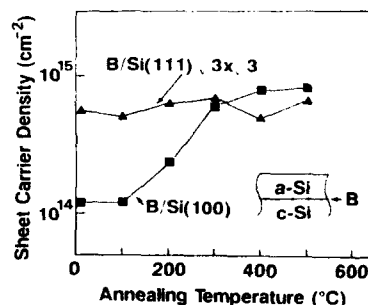


Fig. 2. Sheet carrier concentration dependence of a-Si/B/c-Si on annealing temperature in N_2 atmosphere. Annealing time at each temperature was 10 min.

recrystallize at about 200°C [7]. For (100), then, B may be considered to have been activated because of such an a-Si overlayer-recrystallization occurring in the annealing process. The difference in activation efficiency between (100) and (111) strongly suggests that B is activated at the a-Si/Si(111) interface because of the $\sqrt{3} \times \sqrt{3}$ structure formation.

On Si(111) at substrate temperatures above 700°C, oxygen atoms are desorbed and B forms a $\sqrt{3} \times \sqrt{3}$ structure. The sheet carrier density is sufficient because B atoms replace B_5 -site Si atoms and are activated. In the case of Si(100), B atoms are considered to exist at the adatom sites. B atom sites on the surface are not unique compared with the B_5 site on Si(111) where B atoms occupy the exact lattice sites. Thus, B atoms are not activated on Si(100) with a-Si overlayer fabrication.

The hole mobility was 5–30 $\text{cm}^2/\text{V} \cdot \text{s}$ at room temperature and there was little difference between Si(111) and Si(100). At 77 K, sheet carrier density decreased by about two orders. This was probably because the holes move from the interface into the a-Si overlayer and were trapped at a deep level in the a-Si. Thus, to obtain the electrical conduction at the two-dimensional $\sqrt{3} \times \sqrt{3}$ interface, it is necessary to contain holes within the $\sqrt{3} \times \sqrt{3}$ plane. Then, we tried the substantial preservation of the $\sqrt{3} \times \sqrt{3}$ -B structure beneath an epitaxial Si cap. This was achieved by the deposition of B on a $\text{Ge}_x\text{Si}_{1-x}$ substrate. The $\sqrt{3} \times \sqrt{3}$ -B structure was also formed on a 5×5 $\text{Ge}_x\text{Si}_{1-x}$ surface. In the $\text{Si}/\sqrt{3} \times \sqrt{3}$ -B/ $\text{Ge}_x\text{Si}_{1-x}$ structure, the hetero-interface coincides with the $\sqrt{3} \times \sqrt{3}$ two-dimensional plane. Thus, holes can be contained within the $\sqrt{3} \times \sqrt{3}$ plane by the band bending formed at the hetero-interface.

Fig. 3 shows the dependence of the critical B coverage θ_B on the Ge concentration x in the substrate layer. At this coverage the 7×7 pattern disappears and only the $\sqrt{3} \times \sqrt{3}$ pattern is visible. θ_B is 0.1 monolayer (ML) (1 ML = $7.8 \times 10^{14} \text{ cm}^{-2}$) when B atoms are deposited on the 7×7 Si(111) clean surface.

θ_B increases linearly with increasing Ge concentration x in the substrate layer until $x = 0.6$, and saturates at 0.3 ML. As Ge atoms are about 4% larger than Si atoms, compressive strain is

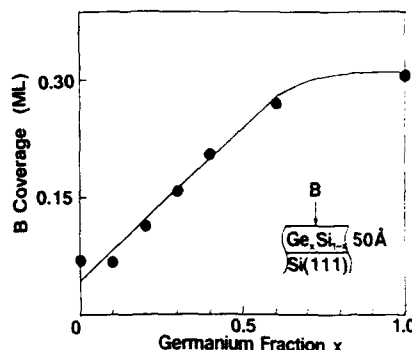


Fig. 3. Dependence on the substrate Ge concentration x of the critical B coverage, at which the 7×7 pattern disappears and only the $\sqrt{3} \times \sqrt{3}$ pattern is visible. (1 ML = $7.8 \times 10^{14} \text{ cm}^{-2}$).

produced in the $\text{Ge}_x\text{Si}_{1-x}$ alloy surface. The increased θ_B on the $\text{Ge}_x\text{Si}_{1-x}$ surface suggests that the compressive strain produced by the presence of Ge compensates for the tensile strain produced by $\sqrt{3} \times \sqrt{3}$ -B formation. Stress compensation in epitaxial Si films by simultaneous doping of a counterbalancing atom has been reported by several authors [9,10]. In the case of B and Ge, it has been reported that lattice defects in heavily B doped layers were reduced because the stress in the heavily doped layer was compensated by the presence of Ge [11]. The same mechanism may also be operating in the $\sqrt{3} \times \sqrt{3}$ -B case.

If the interface strain produced by B obstructs the burial of the $\sqrt{3} \times \sqrt{3}$ structure at the interface between epitaxial layer and substrate, the $\sqrt{3} \times \sqrt{3}$ structure on the $\text{Ge}_x\text{Si}_{1-x}$ layer, with less strain than that on Si(111), should be better preserved at the interface. Fig. 4 shows diffraction profiles from samples of 100 Å epitaxial $\text{Si}/\sqrt{3} \times \sqrt{3}$ -B/50 Å $\text{Ge}_{0.4}\text{Si}_{0.6}$ /Si(111) and 100 Å epitaxial $\text{Si}/\sqrt{3} \times \sqrt{3}$ -B/Si(111) structures. Diffraction peaks were observed at the $(-2/3, 4/3)$ fractional reciprocal lattice points. The amount of B coverage in each case was 0.3 ML, and an epitaxial overlayer was grown at 300°C. The RHEED pattern of each sample was 7×7 , somewhat streaky and diffuse. The intensity of the diffraction peak of $\sqrt{3} \times \sqrt{3}$ -B on Si(111) after epitaxial overlayer growth at 300°C. We considered that the $\sqrt{3} \times \sqrt{3}$ structure between the Si epitaxial overlayer and Si(111) is destroyed be-

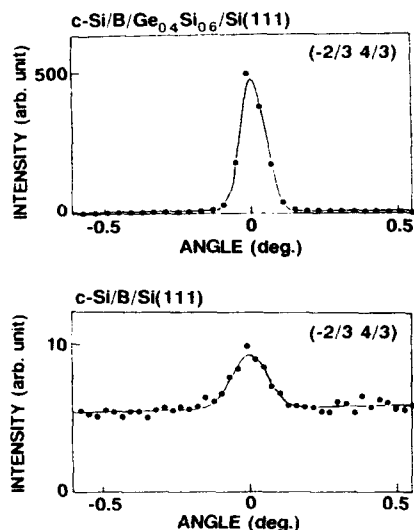


Fig. 4. Diffraction profiles from samples of 100 Å epitaxial Si/ $\sqrt{3} \times \sqrt{3}$ -B/50 Å Ge_{0.4}Si_{0.6}/Si(111) and 100 Å epitaxial Si/ $\sqrt{3} \times \sqrt{3}$ -B/Si(111) structures. Diffraction peaks were observed at the $(-2/3, 4/3)$ fractional reciprocal lattice points. The amount of B coverage in each case was 0.3 ML, and an epitaxial overlayer was grown at 300 °C.

cause of the large strain produced by B which replaces Si.

4. Conclusion

The electric activation efficiencies for a-Si/B- $\sqrt{3} \times \sqrt{3}$ /Si(111) and a-Si/B/Si(100) systems were measured, before and after annealing, by Hall measurement. The difference in the activation efficiencies between Si(100) and Si(111) strongly suggests that boron atoms are activated at the a-Si/Si(111) interface because of $\sqrt{3} \times \sqrt{3}$ structure formation. We found that the B- $\sqrt{3} \times \sqrt{3}$ structure was also formed on a 5×5 Ge_xSi_{1-x}

surface. A Si epitaxial overlayer can be grown on the $\sqrt{3} \times \sqrt{3}$ -B/50 Å Ge_{0.4}Si_{0.6}/Si(111) structure at a growth temperature of 300 °C, preserving a large fraction of the $\sqrt{3} \times \sqrt{3}$ -B structure due to strain compensation.

Acknowledgments

The authors wish to thank Dr. H. Ogawa and N. Aizaki for their suggestions and encouragement. The continual and helpful suggestions about the MBE system by J. Sakai of ANELVA Corp. are also gratefully acknowledged.

References

- [1] J.J. Lander and J. Morrison, *Surface Sci.* 2 (1964) 553.
- [2] D. Bolmont, P. Chen, C.A. Sebenne and F. Proix, *Surface Sci.* 137 (1984) 280.
- [3] H. Hirayama, S. Baba and A. Kinbara, *Japan. J. Appl. Phys.* 25 (1986) L452.
- [4] T. Tatsumi, H. Hirayama and N. Aizaki, *Appl. Phys. Letters* 50 (1987) 1234.
- [5] H. Hirayama, T. Tatsumi and N. Aizaki, *Surface Sci.* 193 (1988) L47.
- [6] K. Akimoto, J. Mizuki, I. Hirasawa, T. Tatsumi, H. Hirayama, N. Aizaki and J. Matsui, in: *Extended Abstracts of 19th Conf. on Solid State Devices and Materials* (Business Center for Academic Societies, Tokyo, 1987) p. 463.
- [7] R.L. Headrick, L.C. Feldman and I.K. Robinson, *Appl. Phys. Letters* 55 (1989) 442.
- [8] T. Tatsumi, I. Hirose, T. Niino, H. Hirayama and J. Mizuki, unpublished.
- [9] J. Nisizawa, T. Terasaki, K. Yagi and N. Miyamoto, *J. Electrochem. Soc.* 122 (1975) 664.
- [10] H.J. Herzog, L. Csepregi and H. Seidel, *J. Electrochem. Soc.* 131 (1984) 2969.
- [11] H. Hirayama, T. Tatsumi and N. Aizaki, *Appl. Phys. Letters* 52 (1988) 1335.

Growth and properties of high T_c films in $Y_1Ba_2Cu_3O_{7-x}$ perovskite by molecular beam epitaxy

J. Kwo

AT&T Bell Laboratories, Murray Hill, New Jersey 07974, USA

Thin film synthesis of the high temperature superconductors in $Y_1Ba_2Cu_3O_{7-x}$ perovskite has been successfully carried out by the advanced molecular beam epitaxy technique. The development of an efficient activated oxygen source led to in-situ growth of high quality films of $Y_1Ba_2Cu_3O_{7-x}$ and $Dy_1Ba_2Cu_3O_{7-x}$ without high temperature annealing. Excellent superconducting properties have been achieved: the T_c , ΔT_c , normal state resistivity ρ , and critical current density J_c equal to the best records reported to date for $Y_1Ba_2Cu_3O_{7-x}$ films. This paper reviews in-situ MBE growth, structural and superconducting characteristics of the films. The results of tunneling in planar junctions of $Y_1Ba_2Cu_3O_{7-x}$ /native barrier/Pb are also presented in the context of quasiparticle tunneling and Josephson behavior.

1. Introduction

Recent discovery of high temperature superconductivity in the layered perovskite oxides has generated much interest in synthesizing high T_c superconducting films for both fundamental and device research. Many experimental studies suggest that the occurrence of superconductivity is directly connected with its layered, intergrowth structure. The molecular beam epitaxy (MBE) technique is best known for its capabilities of low temperature and layer-by-layer growth, as has been demonstrated successfully for semiconductor materials. It is therefore anticipated that the MBE method is ideally suited for the thin film synthesis of high T_c oxide superconductors. Furthermore, it provides opportunities of fabricating artificial oxide heterostructures or metastable phases tailored on atomic scale. Studies of these synthetic, layered oxides may shed light on the theoretical mechanism responsible for high T_c superconductivity, which, in turn, offer promise of producing even higher T_c materials.

The paper reviews our recent successful application of the molecular beam epitaxy method to produce high T_c $Y_1Ba_2Cu_3O_{7-x}$, and $Dy_1Ba_2Cu_3O_{7-x}$ thin films on a number of substrates includ-

ing MgO, SrTiO₃, and LaAlO₃. The growth techniques are described, along with the design and operation of an activated oxygen source. Based on in-situ observations by RHEED, a model is proposed for the growth mode of the perovskites. Typical superconducting properties are the following: $T_c(R=0) = 92$ K, $\Delta T_c(\text{inductive}) = 0.4$ K, $\rho(100\text{ K}) = 55\ \mu\Omega\text{ cm}$, and $J_c(77\text{ K}) = 4.5 \times 10^6\text{ A/cm}^2$. Furthermore, tunneling studies on thin film junctions consisting of $Y_1Ba_2Cu_3O_{7-x}$ /native barrier/Pb indicated that the in-situ film surface exhibits quasiparticle tunneling characteristics similar to etched bulk single crystal. Josephson behavior was observed for the first time in this type of planar junctions.

2. MBE growth aided with an activated oxygen source

Two basic requirements are demanded for the MBE growth of high T_c perovskites; namely, precise compositional control, and an efficient activated oxygen source for oxidation [1–3]. In ordinary MBE growth process, the first requirement is met with relative ease. However, for our present research it remains as a challenging task

due to a large chemical unit cell containing multiple cation species. Discussions on this subject will be given later in the section.

The necessity of activated oxygen species follows from the oxidation characteristics intrinsic of the $Y_1Ba_2Cu_3O_{7-x}$ compound. The thermodynamic phase diagram of oxygen partial pressure versus temperature determined for $Y_1Ba_2Cu_3O_{7-x}$ indicates that for a given oxidation state there exists at a given temperature a minimal oxygen partial pressure below which that phase becomes unstable [1,2]. For instance, at a growth temperature of 650°C , the minimal oxygen pressure of forming $Y_1Ba_2Cu_3O_6$ is 6.0×10^{-3} Torr. However, the molecular flow regime generic to MBE requires that the mean free path be greater than typical source to substrate distance ($\sim 20\text{--}40$ cm), and such condition implies an operating pressure less than 1×10^{-4} Torr. The abundance of activated oxygen species enables oxidations of the cation elements at an oxygen partial pressure of several orders lower, while still sustaining the long free path necessary for MBE.

The in-situ growth of oxides in our work was achieved by reacting metal flux with neutral oxygen radicals (primarily atomic oxygen and excited molecular oxygen) at the substrates held at an elevated temperature [3–6]. The design of our activated oxygen source is based on the concept of a down-stream plasma excited by microwave discharges contained in a fast flow reactor. Due to a distance 20 inch long between the discharge and the substrates, it is essential to achieve a high flow rate exceeding 10 SCCM to minimize wall recombinations. The initial design using a simple straight tubing with a small hole near the end experienced a loss of activated species by as much as 60% in the flow path due to a low flow rate [3,4]. The latest design shown in fig. 1 has succeeded to retain the activated oxygens by as high as 87% of those initially produced near the discharge [5,6]. Furthermore, the usage of a quartz ring containing multiple holes allows uniform depositions over a 1.0 inch diameter area. The pressure near the discharge is $\sim 2 \times 10^{-1}$ Torr, and the oxygen pressure near the substrates is low 10^{-3} Torr. The overall chamber pressure during growth is maintained at low 10^{-5} Torr. The activated oxygen

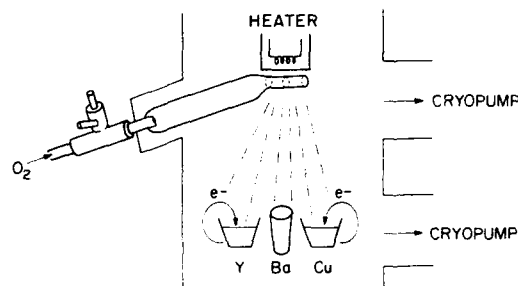


Fig. 1. The design of an activated oxygen source using a fast flow tube reactor, and the internal system configuration.

flux near the substrates is estimated to be about 2×10^{16} species/s \cdot cm 2 .

Metal cations are evaporated from individual thermal sources using a combination of effusion cells and e-beam evaporators. The coevaporation method is used, and no shuttered growth is employed thus far. The alkaline earths like Ba are evaporated from effusion cells at $\sim 600^\circ\text{C}$. The flux detection and control of e-beam evaporation are made by Inficon Sentinel monitors based on electron impact emission spectroscopy. While this method proved to be very successful for pure metal depositions [7], the interference of the metal cation signal (especially for Y) with a large oxygen signal from the background pressure makes the rate control of Y quite difficult. The deposition of Cu is less affected because its light emission occurs at a different wavelength. An alternative solution is to use effusion cells to evaporate the rare earths as well as Cu. Recently, $Dy_1Ba_2Cu_3O_{7-x}$ thin films were produced by evaporating Dy from an effusion cell held at $\sim 1150^\circ\text{C}$ [8]. The Dy flux was kept constant within 1% by regulating the cell temperature, and varied very little with the O_2 pressure. The precise compositional control is necessary for producing a highly ordered superconducting structure free of impurity phases.

A number of provisions were also made in the construction of the sample manipulator to be compatible with a highly oxidizing environment. Refractory materials like molybdenum and tantalum were avoided because they are subject to oxidation easily, and their oxides are highly volatile at 650°C . The substrate block material is now replaced by nickel due to its less volatile oxide

than Mo, and a better thermal conductor than other oxidation resistant materials like stainless steel [9]. The heater is made of 0.020 inch rhenium wire wound into a flower pattern. The substrate temperature is measured by an infrared pyrometer. Consistent readings between the pyrometer and the thermal-couple methods have been obtained once the Ni block surface became oxidized after multiple depositions.

Good thermal contact between the substrates and the sample block is crucial for growing the perovskites due to poor thermal conductivity of the substrate materials. Presently Ag pastes are used to provide the thermal contact. The substrate temperature at which the best films were produced occurred in a range of 650–700°C. Following the deposition, the films were cooled to 200°C in an oxygen pressure 4 times higher than during growth, while keeping the plasma running continuously.

3. Structural properties

Reflection high energy electron diffraction (RHEED) was used during growth to optimize the deposition conditions [3]. Sharp streaky pattern accompanied with Kikuchi arcs were generally seen. Typical diffraction patterns along azimuthal [100] and [110] axes are shown in figs. 2a and 2b. This observation, in general, implies that the growth takes place in a layer by layer mode,

producing a highly ordered, atomically smooth film surface. Furthermore, the alignments of the in-plane axes of $Y_1Ba_2Cu_3O_{7-x}$ films with those of the underlying substrates of MgO(100) and SrTiO₃(100) are evidence for epitaxial growth.

The overall crystal structure was examined by X-ray diffraction [3]. Under present deposition conditions, growth on epitaxial substrates of (100) orientation including MgO, SrTiO₃, and LaAlO₃ produces *c*-axis oriented $Y_1Ba_2Cu_3O_{7-x}$ films. There is little evidence for *a*-axis oriented grains. Typical rocking curve of the (005) Bragg reflection is less than 0.3°.

The detailed growth mechanism of the oxides still remains an interesting subject of study. Recently, strong oscillations of the specular RHEED intensity during growth of several perovskites including $Y_1Ba_2Cu_3O_{7-x}$, were observed by Terashima et al using the reactive evaporation method [10]. Furthermore, one period of oscillation corresponds to the height of one minimal unit cell which satisfies charge neutrality. The result is shown in fig. 3. In contrast to the layer-by-layer growth mode commonly known for metals or semiconductors, the growth of the perovskites is described by the unit-by-unit fashion. Presumably, it is related to the strong character of the ionic bond of oxides. This observation has an important implication that the oxide growth occurs by the formation of a 2D nuclei which is the minimum unit satisfying electrical neutrality. Moreover, it also suggests that within each growth unit the

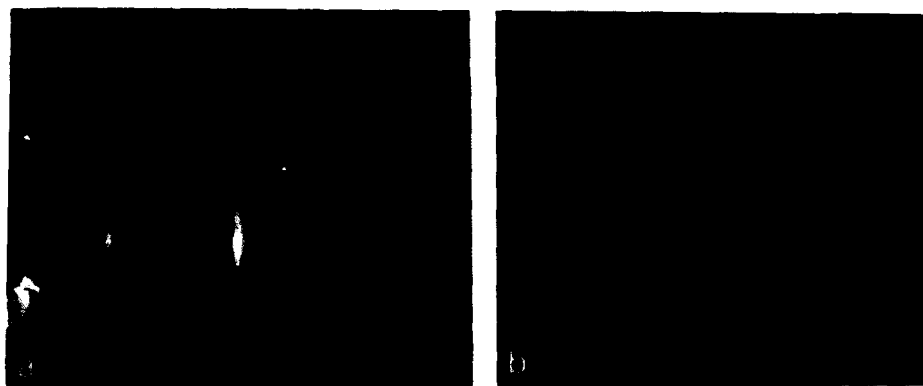


Fig. 2. RHEED patterns along azimuthal (a) [100] and (b) [110] axes of a $Y_1Ba_2Cu_3O_{7-x}$ film 1000 Å thick grown on MgO(100).

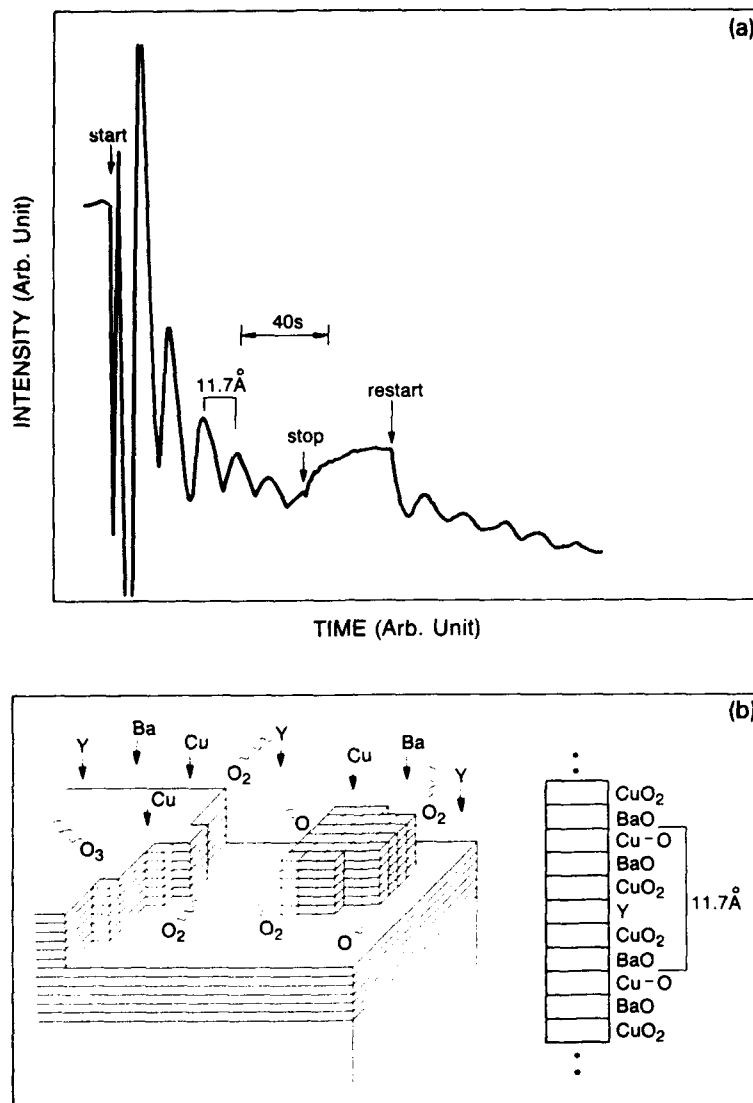


Fig. 3. (a) RHEED specular intensity as a function of the deposition time and (b) a proposed model for the $Y_1Ba_2Cu_3O_{7-x}$ film growth, after Terashima et al. [10].

stacking sequence starts and ends with specific cation-oxide layers.

4. Superconducting properties

MBE grown $Y_1Ba_2Cu_3O_{7-x}$ and $Dy_1Ba_2Cu_3O_{7-x}$ films showed excellent superconducting

properties including T_c ($R=0$), J_c , and normal state resistivity ρ . Depositions on a variety of substrates including $MgO(100)$, $SrTiO_3(100)$, and $LaAlO_3(100)$ have produced comparably good results, although the best superconducting transport properties were usually found for $SrTiO_3(100)$ of closest lattice match ($\sim 1.0\%$) with $Y_1Ba_2Cu_3O_{7-x}$ [8]. In comparison, the very large lattice mismatch

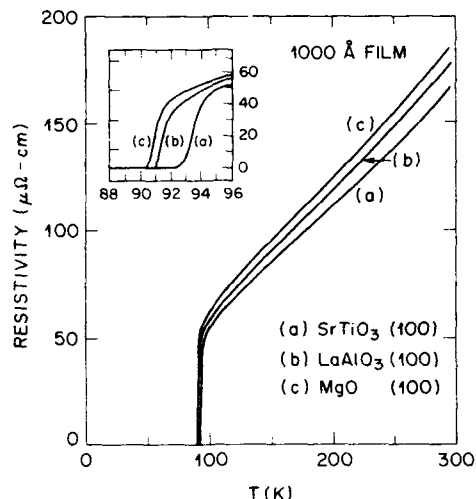


Fig. 4. Resistivity versus temperature for $Dy_1Ba_2Cu_3O_{7-x}$ films 1000 Å thick grown on (a) $SrTiO_3(100)$, (b) $LaAlO_3(100)$, and (c) $MgO(100)$. The superconducting transitions in details are plotted in the inset.

(~ 9%) between $Y_1Ba_2Cu_3O_{7-x}$ and MgO conduces to a lower T_c onset by ~ 2 K, and a higher $\rho(100\text{ K})$ by ~ 10%.

The temperature dependence of the normal state resistivity for typical $Dy_1Ba_2Cu_3O_{7-x}$ films 1000 Å thick is shown in fig. 4 for three different substrates. The ρ versus T curves show a linear temperature dependence above T_c , a common feature for current conduction along the Cu-Ox planes in the cuprates. The ratios of $\rho(300\text{ K})/\rho(100\text{ K})$ in all three cases are 3.0, and the ρ versus T curves extrapolate to zero resistivity at $T=0$. The detailed superconducting transition is plotted in the inset for each substrate. Notable difference in the shape of the transition was observed. Specifically, the $T_c(R=0)$ is 92.3, 91, and 90.5 K for films grown on $SrTiO_3$, $LaAlO_3$, and MgO , respectively. The 10%-90% transition widths are ~ 1.2 K for $SrTiO_3$ and $LaAlO_3$, and is only 0.5 K for MgO . The value of normal state resistivity $\rho(100\text{ K})$ has been commonly used in the high T_c field as a figure of merit to assess the materials quality. Note that $\rho(100\text{ K})$ of the film grown on $SrTiO_3$ is as low as $55\text{ }\mu\Omega\text{ cm}$, which equals to the best value reported for bulk single crystals at present.

Screening measurements on $Dy_1Ba_2Cu_3O_{7-x}$ films showed a sharp superconducting transitions at 90 K, and a width less than 0.4 K [11]. The penetration depth derived from the screening measurement followed a temperature dependence of a mean field BCS behavior with a T_c of 90 K. It was also concluded that such behavior is true only for good film qualities in the absence of cracks or inhomogeneities [11]. The critical current densities, J_c , at 77 K in zero field were measured by the transport method. The typical values are 4.5×10^6 and $2.0 \times 10^6\text{ A/cm}^2$ for $SrTiO_3(100)$ and $MgO(100)$, respectively. Our J_c results equal to the highest record reported by other groups using different growth techniques including reactive evaporation, pulsed laser deposition, and inverted cylindrical magnetron sputtering [12-14].

Thinner films generally show slightly poorer superconducting transport properties due to the lattice clamping effect and an increasing tendency of forming a tetragonal structure near the interface. For instance, reducing the film thickness to 500 Å has led to an increase in the resistivity by about 10%. The $T_c(R=0)$ decreases to 90.6 and 88.5 K, for films grown on $SrTiO_3$ and MgO , respectively. Continuing reduction of the film thickness to below 100 Å gives rise to substantially broadened transitions, especially for films grown on MgO . For a 90 Å $Y_1Ba_2Cu_3O_{7-x}$ film on MgO , the zero resistivity is not reached until 70 K [6].

5. Tunneling studies of planar junctions

The high T_c perovskites exhibit dramatic variations in conductivities with minor variations in the cation compositions and oxygen stoichiometry. This unusual property has offered new exciting possibilities of fabricating novel electronic devices in configurations of S/I/S or S/N/S oxide heterostructures. In comparison, such freedom in materials choices for devices was not available for traditional Josephson technology using low T_c Nb based superconductors. However, the progress toward fabricating all high T_c tunneling devices has been hampered due to the following difficulties. First, the coherence lengths of the high T_c super-

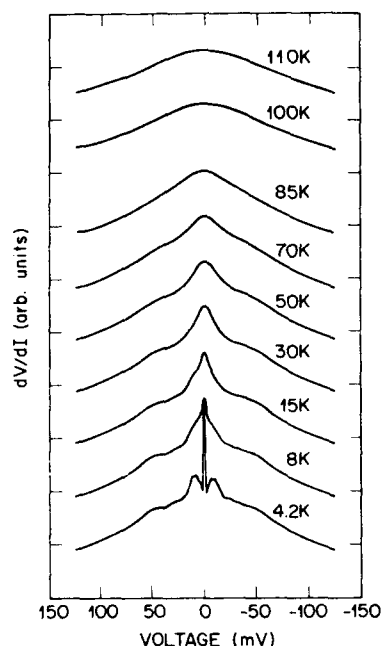


Fig. 5. Quasiparticle tunneling data of dynamic resistance versus bias for a $Y_1Ba_2Cu_3O_{7-x}$ film/native barrier/Pb junction at different temperatures.

conductors are very short and highly anisotropic. Secondly, the surface does not exhibit superconductivity consistent with the bulk of materials.

In order to better characterize the S/I inter-

faces and to obtain meaningful tunneling results, in the first phase of study we focused the efforts on a simpler junction configuration consisting of a $Y_1Ba_2Cu_3O_{7-x}$ thin film, native barrier, and a low T_c superconductor, Pb [15]. Low leakage tunnel barriers were formed by native insulating oxides of the in-situ grown $Y_1Ba_2Cu_3O_{7-x}$ film surface exposed to room air or annealed at 450°C for 10 min in O_2 . At the moment, the exact nature of the barrier is not clear, and still awaits further surface chemical analysis. However, empirically, the junction resistance appears to correlate with the film resistivity, and varies from a few Ω to a few hundred Ω . Typical junction area in the planar geometry is $0.3\text{ mm} \times 0.5\text{ mm}$.

The low leakage junctions formed with the native barriers warrant that the current conduction across the junction is caused primarily by the tunneling process. Reproducible current-voltage characteristics were observed, and are discussed in the following. As for the quasiparticle tunneling characteristics, below the T_c ($R \approx 0$) of $Y_1Ba_2Cu_3O_{7-x}$, a gap-like structure $\sim 20\text{ mV}$ developed in the tunneling conductance, with additional asymmetric modulations up to 50 mV . There is another feature of at $\pm 4\text{ mV}$ appearing below 28 K . The data of dynamic resistance versus bias are shown in fig. 5, and are in good agreement with the etched bulk single crystal data [16].

In contrast to the BCS tunneling density of

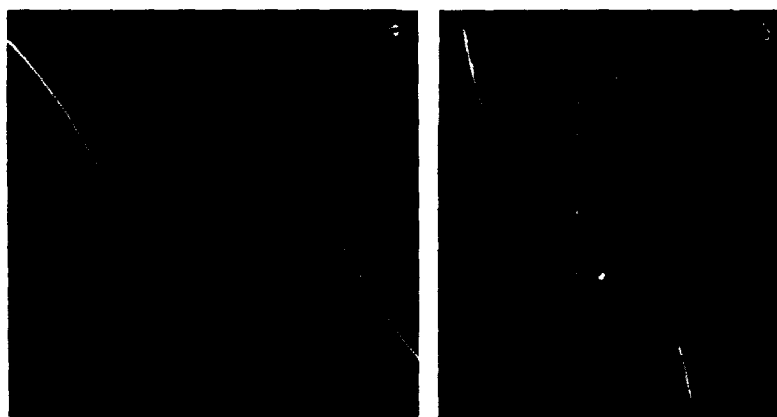


Fig. 6. Current-voltage characteristics at low bias at 1.5 K for a junction of a resistance of $80\ \Omega$. The x axis scale is 0.5 mV per large division for (a) and (b). The y axis is (a) $10\ \mu\text{A}$ and (b) $2\ \mu\text{A}$.

states of conventional superconductors, tunneling results of the high T_c cuprate of $Y_1Ba_2Cu_3O_{7-x}$ showed reproducibly three unusual features: (1) a weak, underdeveloped gap structure; (2) presence of finite states inside the gap persistent to low temperature; (3) an asymmetric, linear normal state conductance versus bias. Although many of these features could be attributed to materials-related imperfections near the surface, the reproducibility and consistency of these recent data suggest that the unusual properties could be intrinsic to the high T_c cuprates.

Junctions of lower resistance show at temperature below T_c of Pb the development of supercurrent at zero bias and associated hysteretic sub-gap structure with an $I_c R$ varying from 500 to 800 μV [15]. The present $I_c R$ product is about 10%–20% of the maximum theoretical value. Typical $I-V$ characteristics at low bias at $T = 1.5$ K are shown in fig. 6 for a junction of a resistance of 80 Ω and a critical current I_c of 5 μA . The $I-V$ shows a nearly complete Stewart McCumber hysteresis with numerous Fiske steps due to geometric resonances. The supercurrent modulates with magnetic field and microwave radiations in a manner expected for DC and AC Josephson effects. Although the present experimental evidence is highly suggestive of Josephson tunneling, the possibility due to a high $I_c R$ shorts is not ruled out completely.

6. Conclusions

Molecular beam epitaxy aided with an activated oxygen source has successfully produced $Y_1Ba_2Cu_3O_{7-x}$ epitaxial films of excellent structural and superconducting properties. The present results in single layer films provide a basis for future fabrications of sophisticated multilayer structures. Such approach has now opened up an exciting field of "molecular engineering of oxides", which will be vital for both basic research and device work. Our tunneling study observed for the first time the Josephson current between a high temperature superconductor and a conventional superconductor in a planar junction. This result

establishes an important criterion for theoretical postulations of high temperature superconductivity. Furthermore, it is also a major advance toward developing a Josephson technology based on all high T_c superconductors.

Acknowledgements

The author would like to thank valuable collaborations with M. Hong, T.A. Fulton, D.J. Trevor, R.M. Fleming, A.F. Hebard, P.L. Gammel, A.E. White, A.R. Kortan, R.C. Farrow, and K.T. Short, and excellent technical assistance from J.P. Mannaerts.

References

- [1] P.P. Freitas and T.S. Plaskett, Phys. Rev. B36 (1987) 5723.
- [2] R. Bormann and J. Nölting, Appl. Phys. Letters 54 (1989) 2148.
- [3] J. Kwo, M. Hong, D.J. Trevor, R.M. Fleming, A.E. White, R.C. Farrow, A.R. Kortan and K.T. Short, Appl. Phys. Letters 53 (1988) 2683.
- [4] J. Kwo, M. Hong, D.J. Trevor, R.M. Fleming, A.E. White, R.C. Farrow, A.R. Kortan and K.T. Short, in: Science and Technology of Thin Film Superconductors, Eds. R.D. McConnell and S.A. Wolf (Plenum, New York, 1989) p. 101.
- [5] J. Kwo, M. Hong, D.J. Trevor, R.M. Fleming, A.E. White, J.P. Mannaerts, R.C. Farrow, A.R. Kortan and K.T. Short, Physica C162–164 (1989) 623.
- [6] J. Kwo, M. Hong, T.A. Fulton, P.L. Gammel and J.P. Mannaerts, in: Processing of Films for High T_c Superconducting Electronics, SPIE Proc., Vol. 1187 (1989) p. 57.
- [7] J. Kwo, in: Thin Film Growth Techniques for Low-Dimensional Structures, Eds. R.C. Farrow, S.S.P. Parkin, P.J. Dobson, J.H. Neave and A. Arrott (Plenum, New York, 1986) p. 337.
- [8] J. Kwo, in: Proc. Conf. 2nd ISTEC Workshop on Superconductivity, Kagoshima, May 1990.
- [9] The Ni substrate block was suggested by John Talvachio at Westinghouse R&D Center, Pittsburgh, PA.
- [10] T. Terashima, Y. Bando, K. Iijima, K. Yamamoto, K. Hirata, K. Hayashi, K. Kamigaki and H. Terauchi, Phys. Rev. Letters 65 (1990) 2684.
- [11] A.T. Fiory, A.F. Hebard, P.M. Mankiewich and R.E. Howard, Appl. Phys. Letters 52 (1988) 2165.
- [12] T. Terashima, K. Iijima, K. Yamamoto, Y. Bando and H. Mazaki, Japan. J. Appl. Phys. 27 (1988) L91.
- [13] T. Venkatesan, X.D. Wu, B. Dutta, A. Inam, M.S. Hegde,

- D.M. Hwang, C.C. Chang, L. Nazar and B. Wilkens, Appl. Phys. Letters 54 (1989) 581.
- [14] X.X. Xi, G. Linker, O. Meyer, E. Nold, B. Obst, F. Ratzel, R. Smithey, B. Strehlau, F. Waschenfeld and J. Geerk, Z. Physik 74 (1989) 13.
- [15] J. Kwo, T.A. Fulton, M. Hong and P.L. Gammel, Appl. Phys. Letters 56 (1990) 788.
- [16] M. Gurvitch, J.M. Valles, Jr., A.M. Cucolo, R.C. Dynes, J.P. Garno, L.F. Schneemeyer and J.V. Waszczak, Phys. Rev. Letters 63 (1989) 1008.

Growth of superconducting $\text{Bi}_2\text{Sr}_2\text{Ca}_{n-1}\text{Cu}_n\text{O}_x$ thin films by atomically layered epitaxy

J.N. Eckstein, I. Bozovic

Varian Research Center, Palo Alto, California 94303, USA

D.G. Schlom and J.S. Harris, Jr.

Department of Electrical Engineering, Stanford University, Stanford, California 94305, USA

We have developed a technique for atomically layering crystallized films of $\text{Bi}_2\text{Sr}_2\text{Ca}_{n-1}\text{Cu}_n\text{O}_x$, in-situ, on SrTiO_3 substrates. These compounds have a layered structure along the c -axis of the unit cell. To grow c -axis oriented films, atomic monolayers of the constituent atoms were sequentially deposited on hot substrates by shuttering the fluxes from thermal effusion cells in such a way as to build up the crystal structure of the film. Various stable and metastable phases were grown in this way, along with atomically precise superlattice structures. Oxidation of the films was accomplished during growth using a beam of ozone. The films were superconducting as grown, with complete resistive transitions as high as 86 K. Moreover, reflection high energy electron diffraction (RHEED) patterns observed during growth, as well as post growth analysis by X-ray diffraction (XRD) and high resolution scanning electron microscopy indicate the films to be single crystal and heteroepitaxial.

High temperature superconductors comprise, by now, a large set of complex layered compounds. In many cases the superconducting properties of the material depends intimately on details of the crystallographic layering, such as in the low and high T_c phases of the Bi and Tl families of compounds. It is of interest, therefore, for practical reasons to develop techniques of synthesis that allow specific layerings to be accomplished. Besides approaches derived from molecular beam epitaxy [1-3], techniques relying on both sputtering [4] and laser ablation [5] have been developed incorporating kinetic control during growth. Here we describe progress in atomically layering epitaxial films of metastable phases and superlattice structures in the Bi family of compounds. The resulting thin films are single crystal in nature and have superconducting transitions as high as 86 K.

The films described here were fabricated using a technique developed for growing synthetically structured epitaxial superconducting films [1]. The

growth system consists of an ultra-high vacuum chamber that has a base pressure of 1.0×10^{-8} Torr and contains thermal effusion cells equipped with beam shutters for the controlled, sequential evaporation of individual elements. Prior to growth, the beam flux from each metal source was measured individually using an ionization gauge, and the measured beam flux was used to correct for long term drift in the sources. Overall beam flux calibration was accomplished by means of Rutherford back scattering analysis of test films.

To atomically layer the growing crystal film, the beams from the metal sources were sequentially turned on and off by means of a set of computer controlled shutters. The shuttering times were chosen to deposit individual monolayers of each element, one at a time, thereby synthetically structuring the film. For example, during the growth of the 2223 phase films the sequence used for each unit cell grown was -Bi-Bi-Sr-Cu-Ca-Cu-Ca-Cu-Sr- where each elemental symbol represents an integrated flux burst of one mono-

layer or about 6.9×10^{14} atoms cm^{-2} . Typically, the whole sequence was repeated 15 to 50 times to grow films 300 to 1000 Å thick.

To oxidize the growing crystal structure a beam of ozone-enriched oxygen from a discharge generator/silica gel cold-trap separator system was used [6]. We estimate the ozone fraction of the beam flux to have been greater than 30% based on measurements with a remote quadrupole mass spectrometer.

The growths discussed here were carried out on {100} SrTiO_3 substrates at temperatures ranging between 650 and 750 °C. The substrates were thermally cleaned in-situ to about 750 °C in the presence of an ozone flux, and exhibited streaky reflection high energy electron diffraction (RHEED) patterns characteristic of a single crystal surface. Typical growth rates used were 500–1000 Å/h. During growth, the crystal surface was monitored by RHEED. When good calibration was achieved, at specific layer stoichiometries a diffraction pattern characteristic of a single-crystal surface was observed. An example of such a pattern observed during the growth of a 2223 phase film is shown in fig. 1; the electron beam was incident along the SrTiO_3 $\langle 110 \rangle$ direction. This RHEED pattern is similar to that observed during the growth of $\text{Bi}_2(\text{SrCa})_3\text{Cu}_2\text{O}_x$ [4]. The most intense lines are due to a surface periodicity of about 2.7 Å. The fainter lines halfway in between them indicate the *a*- or *b*-axis lattice constant of about 5.4 Å. Thus the film [100] and [010] directions are parallel to the substrate $\langle 110 \rangle$ direction. Surrounding the more intense streaks are satellite streaks that are characteristic of an in-plane structure of about 25 to 30 Å, presumably due to the incommensurate *b*-axis structure modulation. As many as six satellite streaks around each main streak have been observed. The linewidth of the satellite pattern, comparable to the RHEED linewidths of the single crystal SrTiO_3 substrate itself, indicates an in-plane crystallographic coherence length of at least 200 Å. Post growth analysis with high resolution scanning electron microscopy with resolution down to about a hundred ångströms has shown the films to consist of a featureless field region, in which are embedded isolated, small defects with densities between 10^3

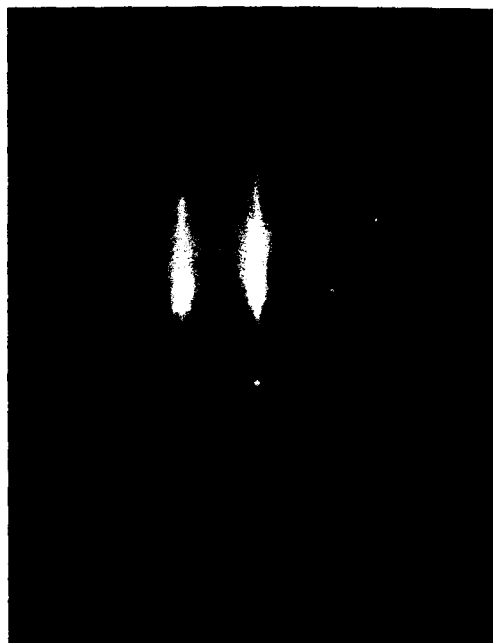


Fig. 1. RHEED pattern observed along a substrate $\langle 110 \rangle$ direction during growth of $\text{Bi}_2\text{Sr}_2\text{Ca}_2\text{Cu}_3\text{O}_x$ thin film on SrTiO_3 substrate. The streak spacings indicate that the film [100] and [010] directions are parallel to the substrate $\langle 110 \rangle$ directions.

and 10^8 cm^{-2} . Thus, we suggest the field region to be a single crystal, heteroepitaxial film.

During growth the RHEED patterns evolved in a complex manner reflecting the nature of the instantaneous surface chemistry occurring. In particular, after growth of the bismuth layers in each unit cell atomically smooth surfaces were observed, as indicated by the RHEED pattern shown here. We have also observed a similar behavior during the growth of 2201, 2212, and 2234 phases.

The highest resistive transition in a 2223 film, directly from the chamber, was 86 K, full zero. Fig. 2 shows a typical resistive transition from a sample from the same growth that exhibits a T_c ($R = 0$) of 84 K. This film was cooled from 725 °C in an oxygen/ozone flow approximately 20 times that used during growth. The transition seen here is broad, starting above 100 K. Just above the superconducting transition, the film had a resistivity of about $100 \mu\Omega \text{ cm}$.

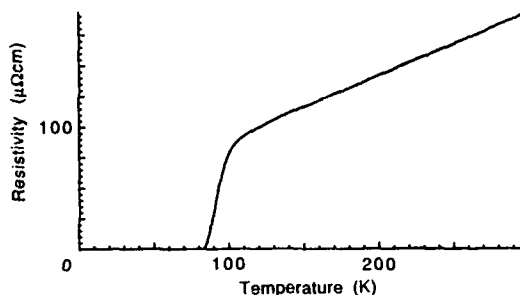


Fig. 2. Resistivity versus temperature for an in-situ grown $\text{Bi}_2\text{Sr}_2\text{Ca}_2\text{Cu}_3\text{O}_x$ film showing a critical temperature of 84 K.

The crystallographic properties of the films were also characterized by X-ray diffraction (XRD) measurements. The 2223 film can be indexed to a c -axis lattice constant of 37.2 Å, in good agreement with the range of measured values. Other scans sensitive to the in-plane structure show the film to be completely epitaxially aligned to the substrate. There is no evidence of 2223 phase growth with any other orientation. When the c -axis is aligned normal, the widths of the individual film peaks can be used as a measure of the regularity of the atomic layering throughout the film thickness. The linewidths of the 002 and 00 $\bar{1}0$ peaks indicate coherent Bragg scattering of the incident X-rays from the entire film thickness, which demonstrates the ability of atomically layered epitaxy to artificially synthesize the crystallographic structure of the film.

Other layerings of bismuth containing superconducting compounds are known to exist. Specifically, compounds with m CuO_2 layers, having chemical composition $\text{Bi}_2\text{Sr}_2\text{Ca}_{m-1}\text{Cu}_m\text{O}_x$, form a sequence that differ little in internal energy. Single phase films are thus hard to obtain using equilibrium synthesis techniques. With atomically layered growth, however, single phase samples can easily be grown by utilizing the inherent kinetic control of the sequenced growth process. Fig. 3 shows XRD pattern aligned close to the substrate {001} for five different films. Here compounds containing between one and five CuO_2 layers were grown as evidenced by the single phase XRD patterns observed.

Besides stabilizing the growth of metastable phases in the BiSrCaCuO system, atomic layer epitaxy is also capable of growing completely synthetic structures. As an example of this, superlattices consisting of different phases from the BiSrCaCuO system have been grown. In these experiments, the composition of each superconducting molecular layer is alternated. This is also easily achieved using the computer-controlled shuttering capability of the growth system. Growth conditions were similar to those described above when single phase films were grown. In such a regular structure consisting of alternating unit cells that are similar in their atomic arrangement, half of the XRD peaks that otherwise would be seen from the extended unit cell are approximately

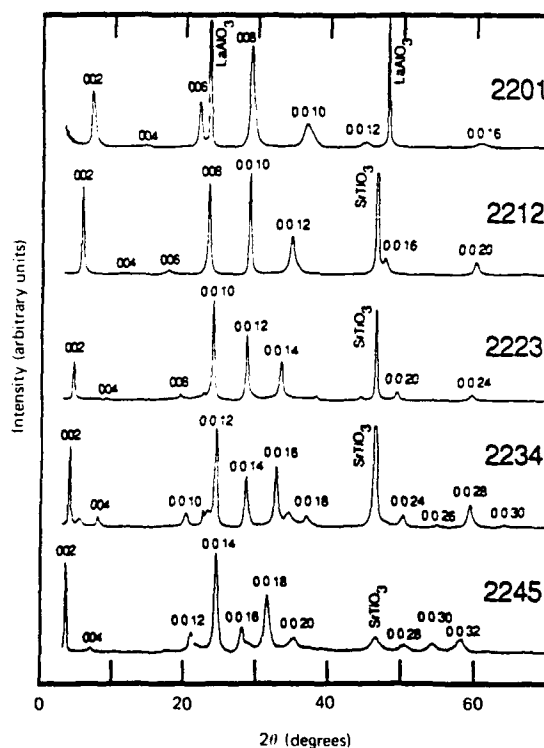


Fig. 3. X-ray diffraction patterns obtained from five different growths in which compounds containing from one to five CuO_2 layers per unit cell were grown.

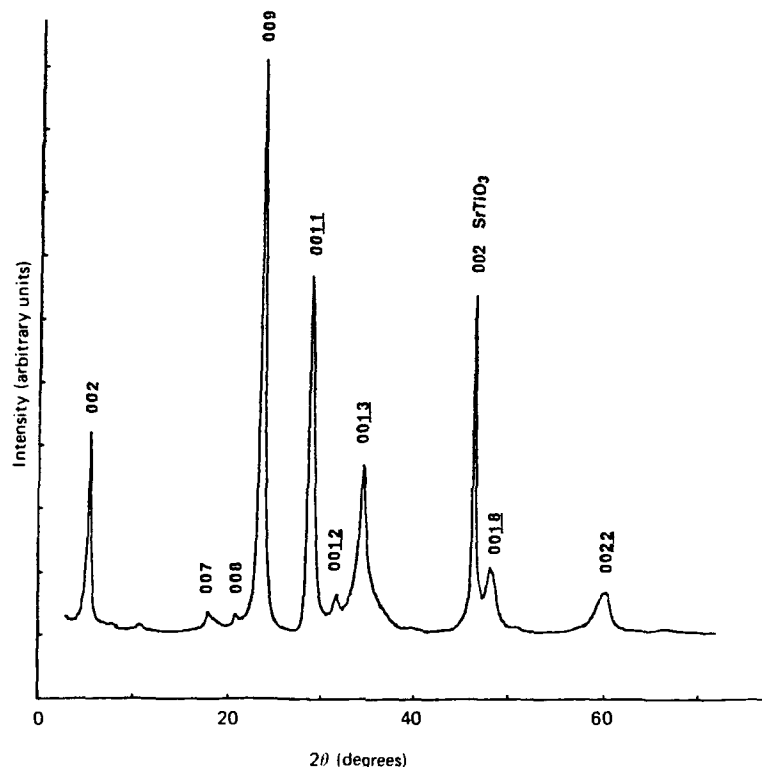


Fig. 4. X-ray diffraction pattern of superlattice consisting of alternating unit cells of the 2212 and 2223 compounds.

suppressed by symmetry. Fig. 4 shows an XRD pattern of a superlattice consisting of alternating 2212 and 2223 unit cells. In the region of the $00\bar{1}0$ reflections, the even peaks are suppressed and the odd peaks appear much higher, while at lower and higher angles the opposite is true.

To demonstrate that the c -axis lattice constant is in fact due to the regular ordering of an artificial structure and not due to a random mixture of the two unit cells, a careful low angle scan was performed to look for the 001 peak. In a disordered system such as described by Hendricks and Teller [7], no low angle peak would be seen. Fig. 5 shows such a low angle scan of a superlattice consisting of alternating layers of 2201 and

2223 unit cells. Here, the approximate symmetry is not as strong as it is in the previous superlattice discussed, due to the larger difference between the structure factors of the constituent unit cells, especially at low angles. Therefore the suppression of the odd order peak at low angles is not as strong. A strong 001 peak was found and demonstrates conclusively that the modulated structure grew as a regular, atomically layered superlattice. This can be viewed as a new compound with the extended c -axis unit cell.

In summary, single crystal films of Bi-Sr-Ca-Cu-O superconductors can be heteroepitaxially grown, in situ, by atomically layering, using ozone as a source of reactive oxygen. Such films have

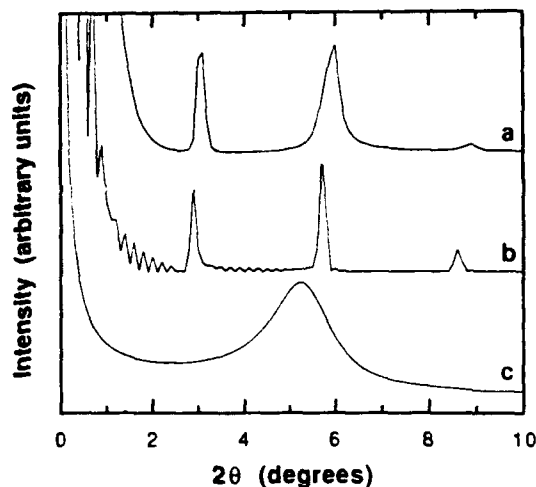


Fig. 5. (a) Low angle X-ray diffraction pattern obtained from a superlattice film consisting of alternating unit cells of the 2201 and 2223 compounds; (b) theoretical calculations for a 15 period 2201/2223 ordered superlattice and (c) the predictions of Hendricks and Teller's theory for a film consisting of a randomly layered mixture of 50% 2201 and 50% 2223 unit cells.

superconducting transitions as high as 86 K. By atomically layering the growth, metastable phases can be stabilized, and artificial structures, such as

layer by layer superlattices of different compounds, can be synthesized.

This project has been supported by ONR and DARPA through contract N00014-88-C-0760.

References

- [1] J.N. Eckstein, D.G. Schlom, E.S. Hellman, K.E. von Dessonneck, Z.J. Chen, C. Webb, F. Turner, J.S. Harris, Jr., M.R. Beasley and T.H. Geballe, *J. Vacuum Sci. Technol.* B7 (1989) 319.
- [2] D.G. Schlom, J.N. Eckstein, E.S. Hellman, S.K. Streiffer, J.S. Harris, Jr., M.R. Beasley, J.C. Bravman, T.H. Geballe, C. Webb, K.E. von Dessonneck and F. Turner, *Appl. Phys. Letters* 53 (1988) 1660.
- [3] Y. Nakayama, H. Ochimizu, A. Maeda, A. Kawazu, K. Uchinokura and S. Tanaka, *Japan. J. Appl. Phys.* 28 (1989) L1217.
- [4] J. Fujita, T. Yoshitake, H. Igarashi and T. Satoh, *Appl. Phys. Letters* 56 (1990) 259.
- [5] T. Kawai, M. Kanai, H. Tabata and S. Kawai, in: *Science and Technology of Thin Film Superconductors*, Eds. R.D. McConnell and S.A. Wolf (Plenum, New York, 1989) p. 21.
- [6] D.D. Berkley, B.R. Johnson, N. Anand, K.M. Beauchamp, L.E. Conroy, A.M. Goldman, J. Maps, K. Mauersberger, M.L. Mecartney, J. Morton, M. Tuominen and Y-J. Zhang, *Appl. Phys. Letters* 53 (1988) 1973.
- [7] S. Hendricks and E. Teller, *J. Chem. Phys.* 10 (1942) 147.

MBE growth of ferromagnetic metastable epitaxial MnAl thin films on AlAs/GaAs heterostructures

J.P. Harbison, T. Sands, R. Ramesh, L.T. Florez, B.J. Wilkens and V.G. Keramidas

Belcore, Red Bank, New Jersey 07701-7040, USA

Epitaxial ferromagnetic films of τ -MnAl in thickness from 3 to 60 nm have been successfully grown on AlAs/GaAs heterostructures using the molecular beam epitaxy (MBE) growth technique. This magnetic phase is a non-equilibrium metastable structure, stabilized in part by its close epitaxial registry with the underlying III–V semiconductor. The growth window is very narrow due to the metastability of the τ -phase. Growth has been achieved through the use of predeposited MnAl template layers of 1–3 bilayers, which effectively separate the nucleation and growth steps. Template formation and subsequent metal growth are monitored by reflection high energy electron diffraction (RHEED). RHEED has also been used to monitor preliminary attempts at III–V semiconductor overgrowth on the magnetic MnAl films. The data indicate that the overgrowth proceeds in a three-dimensional island growth mode of single crystal III–V semiconductor.

Recent advances in the field of heteroepitaxy have provided us with the ability to integrate dissimilar materials with markedly differing properties together within monolithic monocrystalline heterostructures. One particularly exciting possibility which couples two technologically very important classes of materials is that of magnetic materials grown epitaxially on underlying semiconductor structures. For magnetic materials which have a relatively isotropic magnetization energy, the shape anisotropy imposed by the large aspect ratio of a thin film dictates that the magnetic moment lie in the plane of the film. This is found to be the case in much of the work done over the last decade on elemental ferromagnetic metals on III–V compounds (e.g., Fe on GaAs) [1]. However, for magnetic storage applications, the highest storage density can be achieved with the magnetization direction perpendicular to the film. Furthermore, magneto-optic storage or switching applications require the material's magnetic moment to be along the direction of light propagation. Since in many such applications the optical beam comes in perpendicular to the surface of the material, perpendicular magnetization is again preferred. And finally, to fully exploit the

intimate heteroepitaxial coupling between the magnetic film and underlying semiconductor device structures, a perpendicular moment pointing either into or out of the semiconductor is the desirable configuration. An important goal, therefore, in the growth of magnetic films on semiconductors is to establish a strong enough magnetic anisotropy so as to bring the magnetization out of the shape-anisotropy-dictated in-plane direction and into the perpendicular configuration.

We have recently reported work involving the growth of MnAl/AlAs/GaAs heterostructures [2]. The work is an outgrowth of our earlier work on NiAl/AlAs/GaAs and CoAl/AlAs/GaAs heterostructures [3]. Whereas the cubic NiAl and CoAl materials are nonmagnetic, the tetragonal τ -MnAl material is ferromagnetic possessing a strong *magnetocrystalline anisotropy* favoring the magnetic moment lying along the *c*-axis. A summary of its structure and key magnetic properties is shown in fig. 1 in comparison with two elemental magnetic elements, Fe and Co, which have also been grown epitaxially on GaAs [1]. Though its saturation magnetization is less than that of Fe and Co, it is preferable to them in two respects. Its Curie temperature is closer to room

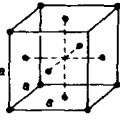
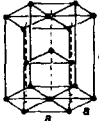
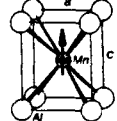
Magnetic Metal	Fe	Co	MnAl
Saturation Magnetization, M_s (Gauss)	21,580	17,900	6200
Curie Temperature, T_c ($^{\circ}\text{C}$)	770	1131	380
Anisotropy Field, H_A (Oersted)	557	5,750	40,000
Easy Magnetization Direction	(100)	c-axis	c-axis
Structure	 fcc	 hcp	 tetragonal

Fig. 1. A comparison of the structure and magnetic properties of three ferromagnetic materials which have been grown epitaxially on GaAs using MBE.

temperature, making it more appropriate, for example, for thermal write/erase applications. More importantly, it has a distinctly higher magneto-crystalline anisotropy as indicated by its high anisotropy field.

The crystal structure of τ -MnAl, also shown in fig. 1, is a tetragonally distorted version of the CsCl structure of NiAl and CoAl which we have previously grown within III-V semiconductor/metal heterostructures [3]. Since its chemistry is expected to be similar to those materials, it should be relatively stable in contact with III-V compounds in general, and AlAs in particular. This makes it a better candidate for elevated temperature metal growth and semiconductor overgrowth. In addition, its pronounced tetragonality ($c_0/a_0 = 1.278$) and favorable lattice constant ($a_0 = 0.277$ nm is within 2% of $a/2$ of GaAs and AlAs) give it a strong tendency to orient with its c -axis, and hence its strong magnetic direction, perpendicular to the (100) semiconductor substrate, the desired orientation discussed above. Equally important, this close epitaxial relationship may assist in stabilizing this tetragonal ferromagnetic τ -phase which is only metastable in the bulk [2]. This metastability issue, as it relates to the thin film growth of the material, will be discussed further below.

Though τ -MnAl is only metastable, it has been prepared previously both in the bulk by quenching [4] and in thin film form by sputtering onto glass substrates [5], neither of which result in monocrystalline growth or even in a predominance of c -axis orientation along any given direction. It is to achieve this highly desirable directionality that we have chosen epitaxial growth by molecular beam epitaxy (MBE). The entire deposition takes place in a single growth chamber of a Riber MBE 1000 growth system. The Mn source is a standard resistively-heated effusion cell with a pyrolytic graphite crucible, chosen to minimize reactions with the Mn (all other effusion cell sources used employed pyrolytic boron nitride crucibles). The cell was heated to 900–950 $^{\circ}\text{C}$ to provide a MnAl deposition rate of ~ 0.1 $\mu\text{m/h}$, and though there seem to be no catastrophic reaction problems between the Mn and the graphite crucible, the CO quadrupole mass analyzer peak rises significantly when the Mn cell is up to temperature, with the background chamber pressure rising from the low 10^{-10} Torr range to the low 10^{-8} Torr range. This is not expected to have effects on the metal deposition, but as a precaution, the Mn cell is idled at a much lower 400 $^{\circ}\text{C}$ during all semiconductor deposition, where it seems to have no appreciable effect. The monocrystalline semiconductor sub-

strates consist of a bulk (100) GaAs wafer on which a buffer layer of 0.5 μm or more of GaAs plus a thin (typically 10 nm) AlAs epitaxial layer are first deposited under normal arsenic-stabilized growth conditions at 580°C. The presence of an adjacent semiconductor layer sharing the same group III element, Al, with the MnAl minimizes any driving force for interfacial reactions. The growth of the GaAs/AlAs epitaxial layers is followed by a pause on the order of 1–2 h during which time the arsenic cell is turned off and allowed to cool and the substrate temperature is dropped to the desired value for metal growth.

The issues surrounding the growth of a phase which is only metastable are rather complex. Our findings for the case of MnAl may well serve as a guide for the growth of other metastable materials. The choice of substrate temperature is critical. Below the low temperature limit, we find amorphous metal growth, as the kinetics are too sluggish, preventing even the fraction of a nanometer atom movements required to form the lower energy crystalline phases. As one would expect, too high a temperature allows equilibrium phases to form, as the barriers separating them from the desired metastable phase become kinetically surmountable. For the case of τ -MnAl, these low and high temperature limits are remarkably close together, lying at about 180 and 260°C respectively. In most cases, the temperature values reported have been derived from thermocouple readings, linearly adjusted to two fixed points: the observed melting point of the indium solder holding the wafer to the heated Mo block, and the initial desorption temperature of the surface oxide from the starting GaAs wafer observed by RHEED. These two fixed points are 156 and 580°C respectively.

This rather narrow growth window, $\sim 80^\circ\text{C}$, is found to narrow even further with subsequent growth. We attribute this to the fact that once properly nucleated, as discussed below, the τ -phase continues to grow until a growth defect is formed which serves as a nucleation point for one of the competing equilibrium phases. Once a competing phase is nucleated, it will continue to grow until it eventually takes over completely from the less stable τ -phase. The rate at which such defects

occur is greater in the lower end of the growth temperature window, and hence only thin layers of the τ -phase can be grown at these temperatures before equilibrium phases take over. Hence, in order to grow thicker metastable films, the substrate temperature must be higher, further narrowing the growth window. Specifically, while films only a few nm thick can be grown at the lower 180°C limit, films with thicknesses of 60 nm can only be achieved near the upper limit of 260°C. Films thicker than 60 nm would require even higher substrate temperatures to avoid the above mentioned defects throughout, but this would mean exceeding the upper temperature limit where equilibrium phases can form. Of course the exact numbers depend on variables such as exact film composition and starting template perfection, neither of which we have yet systematically explored. The qualitative trend of the effective growth window narrowing with increasing film thickness, however, is expected to remain the same under any set of initial conditions.

A second issue related to the question of optimum substrate temperature is the issue of initial nucleation of the metastable phase. The lowered interface energy resulting from a c -axis aligned τ -phase on the AlAs is expected to favor the initial nucleation of τ -MnAl, as discussed above. However, here kinetics are also expected to play an important role, and it is not obvious from the outset that the optimum growth temperature will be the same as the optimum nucleation temperature. If one simply begins growth abruptly by co-depositing Mn and Al directly on AlAs, the two stages of nucleation and growth are interrelated, and a compromise substrate temperature must be sought. One way around this is the use of a starting template. In our previous work on heterostructures of NiAl and CoAl we have found that the predeposition of a thin template layer is essential in nucleating a single crystallographic variant [2,6]. Following a similar approach, a few atomic layers of Mn and Al are first deposited at a low temperature. This predeposit is then heated slowly while watching the reflection high energy electron diffraction (RHEED) pattern to ascertain the precise point at which a good c -axis τ -phase template is formed. Once the template forms, the

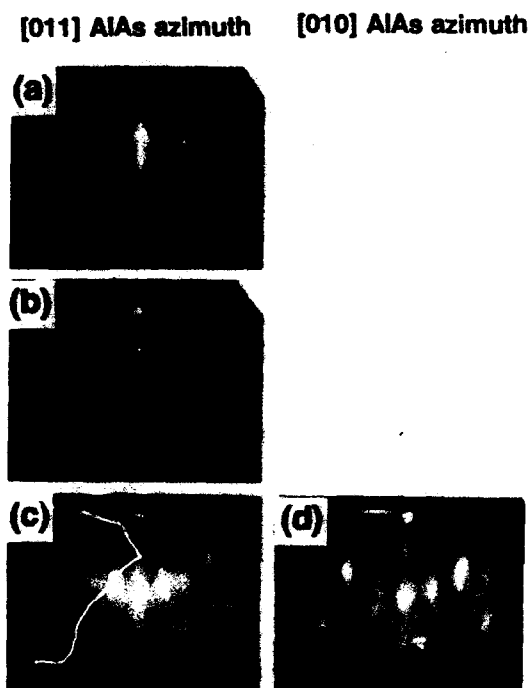


Fig. 2. RHEED sequence illustrating the formation of an equilibrium phase template instead of the desired τ -MnAl from a 5 bilayer template predeposition which is too thick. (a) $c(4 \times 4)$ AlAs surface; (b) 5 bilayers MnAl predeposited, $T_{\text{sub}} = 170^\circ\text{C}$, layer amorphous; (c), (d) heated to 250°C to crystallize mixture of τ plus equilibrium phases (equilibrium phases take over during subsequent growth).

substrate temperature can be changed to a different optimum growth temperature, at which point continuous co-deposition of Mn and Al can commence. Thus the template method is used here to decouple the nucleation from the growth and make possible the growth of the metastable phase.

In order to explore further the problem of initial nucleation, we have grown a series of templates which can be grouped into two categories, "thick" and "thin". The former consists of anything thicker than a few bilayers where one bilayer is defined here as the number of Al and Mn atoms in one complete tetragonal unit cell (see fig. 1). A RHEED sequence using such a thick template, consisting of 5 bilayers, is shown in fig. 2. The initial AlAs starting surface (fig. 2a) is completely covered with an amorphous layer once the prede-

position takes place (fig. 2b). The kinetics of converting such a "thick" amorphous layer to a crystalline τ -phase template are too sluggish for the τ -phase to preferentially nucleate alone. By the time the atoms are mobile enough at 250°C to crystallize the film, the equilibrium phases have already preferentially nucleated (fig. 2c). Once they nucleate, they dominate and subsequent τ -phase growth becomes impossible.

The case of "thin" predeposits favors the amorphous-to-crystalline conversion taking place at a lower temperature thus favoring the formation of the τ -phase. Such a sequence as documented by RHEED is shown in fig. 3. In this case, an amorphous predeposit of 2 bilayers is used. It is amorphous even after only a single bilayer is deposited as shown in fig. 3b. The lack of any strong AlAs pattern at this point is strong evidence for complete surface coverage at this low substrate temperature (0°C), even for a single unit cell of deposition. Once the 2 bilayers have been deposited, the substrate temperature is gradually increased, and by 200°C the properly oriented τ -phase template pattern appears, as seen in figs. 3c and 3d along two azimuths. Subsequent MnAl deposition on this template, shown on the bottom three panels of this figure, shows that under these growth conditions, pure τ -phase is present for a thickness as high as 6.5 nm (fig. 3e). By the time 16 nm are grown, equilibrium phases appear and soon begin to take over (figs. 3f and 3g). In exploring a series of template sequences we have found that all sequences involving 1, 2 or 3 bilayers can result in proper τ -phase templates.

In another series of experiments we have explored forming the initial amorphous predeposit as a layered sequence of alternating Mn and Al monolayers. The motivating idea was that the alternating layer structure of the c -axis τ -MnAl could already be in place in the amorphous starting deposit. There is some evidence that such a sequence indeed leads to the τ -phase formation at a slightly lower temperature. What is perhaps a more important factor, however, in determining the τ -phase onset temperature, which varies between 100 and 250°C , is the exact stoichiometry of the MnAl film. The *absolute* control of film stoichiometry is very difficult. The "ideal" con-

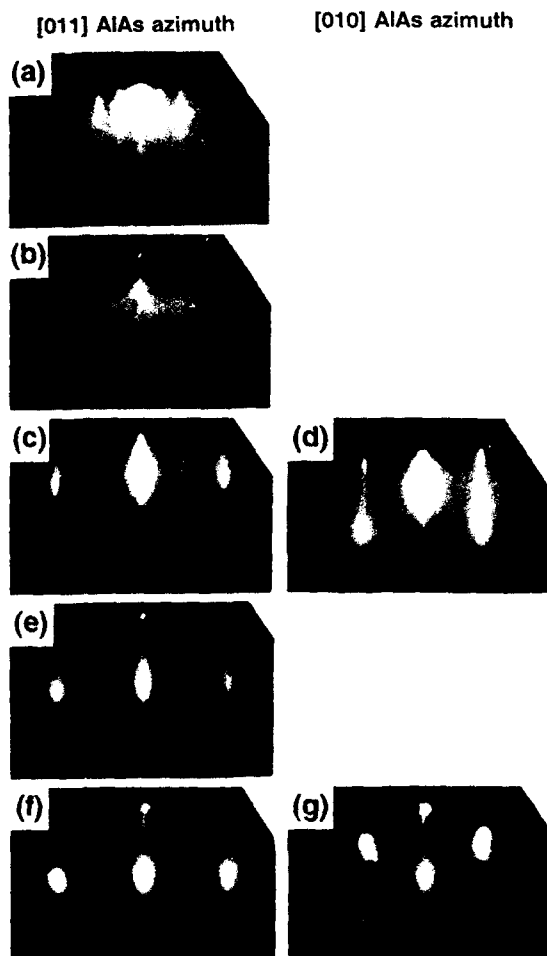


Fig. 3. RHEED sequence of a good τ -MnAl template on AlAs using a 2 bilayer predeposited template. Growth on the template begins τ -phase and eventually becomes an equilibrium phase mixture. (a) $c(4 \times 4)$ AlAs surface; (b) 1 bilayer MnAl predeposited at $T_{\text{sub}} = 0^\circ\text{C}$, the layer is amorphous; (c), (d) 2 bilayers MnAl predeposited at 0°C and annealed to $\sim 200^\circ\text{C}$, τ phase has formed; (e) 6.5 nm τ -MnAl grown at 200°C ; (f), (g) 16 nm τ -MnAl grown at 200°C , equilibrium phases present.

centration in bulk τ -MnAl is 54 at% Mn. Since we are using a non-rotating substrate, unavoidable composition gradients occur across the wafer. By spatially probing with RHEED we have determined that the relatively more Al-rich regions convert to τ -phase earlier than the more Mn-rich

regions. The precise understanding of these effects must await a more thorough experimental examination. Nevertheless, the layers formed in the manner described above are indeed the ferromagnetic τ -MnAl phase with the proper perpendicular c -axis orientation, as we have shown previously with both X-ray and magneto-transport measurements [2,7].

As a final demonstration of the flexibility achieved by growing the magnetic phase epitaxially on the underlying AlAs/GaAs substrate, we have attempted to perform single crystal semiconductor overgrowth over the τ -MnAl to form an embedded ferromagnetic metal layer. The MnAl/AlAs film couple is expected to be reasonably stable, even at the elevated temperatures needed for overgrowth. Fig. 4 shows the RHEED sequence as overgrowth proceeds on a starting 7 nm τ -MnAl surface (fig. 4a). In the overgrowth sequence we have previously optimized for III-V overgrowth on NiAl [2,6], the metal surface is intermittently pulsed with single monolayers of Al, at a rate of about 1 monolayer/min, while the As cell temperature is raised. This approach prevents formation of multivariant NiAs and becomes the starting AlAs template. The technique also works here in the MnAl case. An AlAs-like RHEED pattern is already forming upon heating and exposure to As (fig. 4b), indicating that the stability requirement seems to be satisfied. The complication arises in the growth mode of the subsequently overgrown GaAs/AlAs material. A spotty RHEED pattern, indicative of 3D island growth, can be seen from the very beginning (fig. 4c). This persists well beyond 100 nm of growth. These observations are similar to the wetting problems associated with GaAs overgrowth on ErAs [3]. In that case 3D island growth is attributed to the relatively low surface energy of the exposed ErAs layer. Based on that similarity, we presume that the island-like overgrowth observed here is due to the fact that the surface energy of τ -MnAl is lower than that of NiAl and CoAl which do not exhibit severe islanding overgrowth problems. These findings are of course only preliminary. A more complete experimental study of the overgrowth is needed to understand and discover ways around this problem.

[011] AlAs azimuth

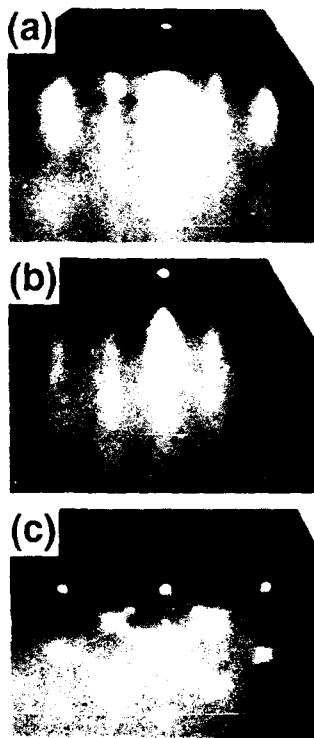


Fig 4. RHEED sequence of III-V semiconductor overgrowth on an epitaxial τ -MnAl/AlAs/GaAs heterostructure. Overgrowth is monocrystalline, but proceeds in a pronounced 3D island growth mode. (a) 7 nm τ -MnAl, $T_{\text{sub}} = 250^\circ\text{C}$; (b) annealed to 450°C . As flux coming up, AlAs surface forming; (c) 60 nm GaAs overgrowth, $T_{\text{sub}} = 450^\circ\text{C}$, epitaxial but in 3D island growth mode.

In summary, epitaxial ferromagnetic films of metastable τ -MnAl have been successfully grown by MBE on AlAs/GaAs heterostructures. Metastability and the problems resulting from the associated narrow growth window have been addressed by utilizing a template approach, thus separating the nucleation and subsequent growth parts of the problem. Initial attempts at semiconductor overgrowth result in a 3D island type growth mode. Nevertheless, preliminary indications are that the two materials are stable in contact with one another even at the elevated temperatures required to grow ferromagnetic layers epitaxially in III-V heterostructures.

References

- [1] G.A. Prinz and J.J. Krebs, Appl. Phys. Letters 39 (1981) 397; J.J. Krebs, Appl. Phys. A49 (1989) 513.
- [2] T. Sands, J.P. Harbison, M.L. Leadbeater, S.J. Allen, Jr., G.W. Hull, R. Ramesh and V.G. Keramidas, Appl. Phys. Letters 57 (1990) 2609.
- [3] For a recent review, see: T. Sands, C.J. Palmstrom, J.P. Harbison, V.G. Keramidas, N. Tabatabaie, T.L. Cheeks, R. Ramesh and Y. Silberberg, Mater. Sci. Reports 5 (1990) 99.
- [4] H. Kono, J. Phys. Soc. Japan 13 (1958) 1444.
- [5] A. Morisako, M. Matsumoto and M. Naoe, J. Appl. Phys. 61 (1987) 4281.
- [6] J.P. Harbison, T. Sands, N. Tabatabaie, W.K. Chan, L.T. Florez and V.G. Keramidas, Appl. Phys. Letters 53 (1988) 1717.
- [7] M.L. Leadbeater, S.J. Allen, Jr., F. DeRosa, J.P. Harbison, T. Sands, R. Ramesh, L.T. Florez and V.G. Keramidas, in: Proc. 35th Conf. on Magnetism and Magnetic Materials, San Diego, CA, 1990 (J. Appl. Phys., to be published).

MBE growth and properties of $\text{Fe}_3(\text{Al},\text{Si})$ on $\text{GaAs}(100)$

M. Hong, H.S. Chen, J. Kwo, A.R. Kortan, J.P. Mannaerts, B.E. Weir and L.C. Feldman

AT & T Bell Laboratories, Murray Hill, New Jersey 07974, USA

We report a successful epitaxial growth of an intermetallic compound $\text{Fe}_3(\text{Al},\text{Si})$ on $\text{GaAs}(100)$. $\text{Fe}_3(\text{Al},\text{Si})$ has a BiF_3 (DO_3) structure with a lattice constant which can be adjusted to achieve a perfect lattice match with $\text{GaAs}(100)$ face by tuning the relative concentration of Al to Si. The crystal growth was carried out in an MBE system consisting of dual growth chambers, one for III–V compound semiconductors and the other for growing metals or group IV like Si. Sharp, elongated streaks were observed in the reflection high energy electron diffraction (RHEED) pattern after the deposition of one monolayer (ML) of $\text{Fe}_3(\text{Al},\text{Si})$, indicating the attainment of an atomically smooth surface. The streaky RHEED pattern sharpened further until a 34 Å (12 MLs) thickness was reached, and retained similar quality in thicker films. The crystal structure of the films was also characterized by high-resolution X-ray diffraction and Rutherford backscattering/channeling analysis. A rocking curve as narrow as 0.03° full width half maximum along (400) Bragg reflection was obtained for an $\text{Fe}_{2.9}(\text{Al}_{0.4}\text{Si}_{0.7})$ film 1000 Å thick.

1. Introduction

Epitaxial metal–semiconductor heterostructures continue to receive much attention due to interest in the studies of fundamental physics such as Schottky barrier formation, as well as potential applications for electronic and optoelectronic devices. Notable examples for applications are monolithic vertical integration in microelectronics, hot-electron high-speed devices, and metallic quantum well devices. Recent efforts have also been extended to the area of epitaxial magnetic films and their integration with semiconductors.

Many metallic elements and intermetallic compounds have been shown to grow epitaxially on GaAs. Examples for the former are Al [1], Ag [2], and Fe [3]. All these elements have large lattice mismatches with GaAs. Moreover, their interfaces with GaAs are thermodynamically unstable. Growth or post anneal at modest temperatures has led to interdiffusion and formation of some compound phases.

As for the growth of intermetallic compounds on GaAs or its related III–V compound semiconductors, two notable groups have been found to form stable interfaces in good lattice matches with the compound semiconductors: The first group

has a cubic CsCl (B2) crystal structure, which includes NiAl, CoAl, FeAl, CoGa, NiGa, etc. [4]. Their lattice parameters are usually 1–3% larger than one half the lattice constant of GaAs. Rare earth (RE) monopnictides belong to the second group with a NaCl (B1) structure. The members include ErAs, LuAs, YbAs, Er(P,As), and (Sc,Er)As [5]. Their lattice constants are closely matched to that of GaAs.

Interesting results on crystal growth and electrical transport using the first group of materials on GaAs/AlAs have been reported. The quality of the materials may be further improved if lattice parameters of the metallic compounds can be made closer to that of GaAs or AlAs. One approach of fine tuning the lattice constant is to insert a third element rather than exhausting the possibilities in binary systems.

Our study along this direction has led to identify an Fe–Al–Si system in the crystal structure of BiF_3 (DO_3) [6]. This material system fulfills the necessary structural and thermodynamical requirements: (1) a material has a lattice constant close to that of GaAs, (2) compositions of Al and Si can be adjusted to achieve a perfect lattice match with GaAs, and (3) a material is thermodynamically stable with GaAs at a typical growth

temperature range, i.e. $\sim 500^\circ\text{C}$, and has a high melting point about 1500°C . In this paper, we report the epitaxial growth of $\text{Fe}_3(\text{Al},\text{Si})$ on $\text{GaAs}(100)$ by molecular beam epitaxy (MBE), along with its structural properties. The electrical and magnetic properties will be published elsewhere.

2. Experimental

The crystal growth was carried out in a multi-chamber MBE system in which one chamber with solid sources is used to grow III-V (GaAs , AlGaAs , InGaAs) materials and another chamber equipped with two electron guns and four effusion cells is used to grow metals and group IV materials like Si . In the second chamber for metal growth, no As chunk has ever been evaporated. This would, therefore, remove the possibility of As -contamination in the metal films, which is usually a primary concern if the metal films are prepared in the same growth chamber of As -based III-V materials.

The growth sequence began with a standard GaAs buffer layer $0.5\ \mu\text{m}$ thick on $\text{GaAs}(100)$ wafers. The growth temperatures were at 580 – 600°C . The samples were cooled in the III-V chamber to 250 – 300°C within 15 min and then transferred to the second growth chamber through several connecting chambers over a period of 5–10 min. The vacuum of these connecting chambers was kept at 1×10^{-10} Torr. Once the samples were in the second chamber, they were heated up to $\sim 550^\circ\text{C}$ to remove excess As to obtain a Ga -stabilized or an As -stabilized surface. The substrate temperatures were then lowered to 300 – 450°C for the growth of $\text{Fe}_3(\text{Al},\text{Si})$.

Fe and Si were evaporated from electron beam sources, and Al from an effusion cell. The evaporation rates of Fe and Si were controlled by Inficon Sentinel rate monitors based on electron impact emission spectroscopy (EIES). For Fe and Si , the feedback-loop controls formed with the rate monitors maintain constant deposition rates with fluctuations less than 2%. The evaporation rate of Al was controlled simply by the cell temperature, and is known to be quite accurate. The

growth rates of these three elements were further calibrated by a quartz crystal monitor located at the substrate position before the deposition. The quartz monitor was retracted during the growth in order to avoid interference with the film deposition. The deposition rate for Fe_3Al or $\text{Fe}_3(\text{Al},\text{Si})$ was $0.5\ \text{\AA}/\text{s}$. The compositions and thickness of the $\text{Fe}_3(\text{Al},\text{Si})$ films are also measured by Rutherford backscattering spectrometry (RBS). The results were then fed back to the rate calibration. In-situ reflection high energy electron diffraction (RHEED) was used to study both the III-V and the $\text{Fe}_3(\text{Al},\text{Si})$ growth.

High resolution X-ray diffraction was used for structural characterizations of the $\text{Fe}_3(\text{Al},\text{Si})$ films. These measurements were made on a 12 kW rotating anode source equipped with a triple-crystal four-circle diffractometer. A pair of flat $\text{Ge}(111)$ crystals used as monochromator and analyzer has provided a longitudinal resolution of $10^{-4}\ \text{\AA}^{-1}$ at $\text{Cu K}\alpha$ radiation. The triple-crystal four-axes geometry allows for scans to be made in any direction in reciprocal space, and in particular, is capable of separating ϕ from 2θ , thereby revealing the true mosaic of the samples. RBS/channeling analysis was performed using a 1.8 MeV $^4\text{He}^+$ beam with detection at both normal and grazing exit angle.

3. Results and discussion

$\text{Fe}_3(\text{Al},\text{Si})$ has a $\text{DO}_3(\text{BiFe}_3)$ structure, in which Al and Si share the same lattice site and are 100% fully miscible with each other on that site. Therefore, the lattice constants vary continuously from $5.64\ \text{\AA}$ (Fe_3Si) to $5.74\ \text{\AA}$ (Fe_3Al). Among them, $\text{Fe}_3(\text{Al}_{0.13}\text{Si}_{0.87})$ has a 0% lattice mismatch with $\text{GaAs}(100)$. Interestingly, the Fe-Al-Si with a composition close to $\text{Fe}_{2.95}(\text{Al}_{0.36}\text{Si}_{0.69})$, called *Sendust*, has unusually high magnetic permeabilities [7].

Let us first examine the results of Fe_3Al . Fe and Al were co-evaporated onto the GaAs . A sequence of RHEED patterns taken during the MBE growth of Fe_3Al on the As -stabilized $\text{GaAs}(100)$ surface along $[011]$ and $[001]$ directions are shown in fig. 1. For one monolayer (ML)

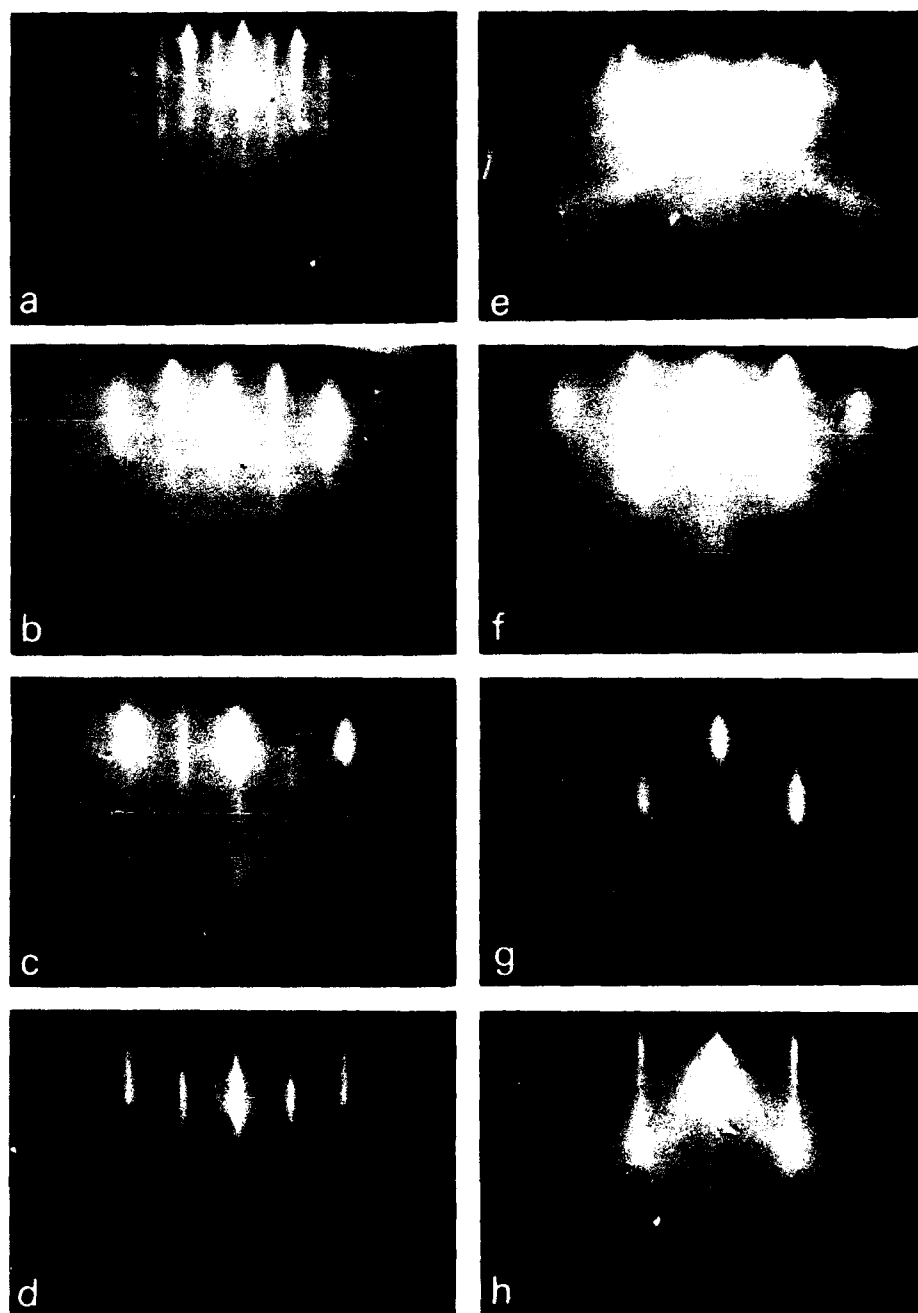


Fig. 1. A sequence of RHEED patterns recorded during the MBE growth of Fe_3Al on $\text{GaAs}(100)$. (a)–(d) Patterns recorded along $[011]$ direction and (e)–(h) recorded along $[001]$. (a), (e) As-stabilized surface of AsAs; (b), (f) RHEED patterns after growth of 1 ML of Fe_3Al ; (c), (g) RHEED patterns after growth of 3 ML of Fe_3Al ; (d), (h) RHEED patterns after growth of 12 ML (34 Å) of Fe_3Al .

growth of Fe_3Al , we have observed elongated sharp streaky RHEED pattern as shown in figs. 1b and 1e. This indicates an atomically smooth Fe_3Al surface after the growth of only 1 ML. The RHEED patterns continue to sharpen further when the Fe_3Al films grow thicker. For an Fe_3Al film 12 ML thick, the presence of Kikuchi arcs is an indication of a well-ordered single crystal film surface.

The epitaxial orientational relationship between Fe_3Al and GaAs was determined by RHEED and later confirmed by X-ray diffraction: The [011] direction of Fe_3Al is parallel with [011] of GaAs, and the film orientation (100) of Fe_3Al is aligned with the substrate orientation (100) of GaAs. The same orientational relationship also occurred in Fe_3Al or $\text{Fe}_3(\text{Al,Si})$ on GaAs, AlAs, or InGaAs. Judging from the close lattice constants between Fe_3Al and GaAs and the thermodynamical stability of Fe_3Al with GaAs, such orientational relationship is indeed consistent with our expectation. Note that the $\text{Fe}_3(\text{Al,Si})$ phase extends over a finite range of compositions according to the phase diagram. Consequently, even for film compositions which deviate from the ideal 3:1 of $\text{Fe}:(\text{Al,Si})$, the DO_3 structure could still form, but with a slightly different lattice constant. In that case, site exchanges take place, e.g. some Al or Si would occupy the lattice sites of Fe and vice versa.

The present epitaxial growth is seemingly different from a previous study of NiAl on AlAs by Harbison et al. [4]. In their study, the co-deposition of Ni and Al was preceded by the deposition of one or two MLs of Ni. Different orientational relationships were obtained unless the Ni was first deposited. Their explanation was that an initial reaction occurs between the Ni and the underlying AlAs to form an epitaxial Ni₃AlAs template layer. In the case of $\text{Fe}_3(\text{Al,Si})$ (including Fe_3Al and Fe_3Si), no such intermediate template layer is needed. Note that the lattice constant of $\text{Fe}_3(\text{Al,Si})$ is close to that of GaAs, while the lattice constant of NiAl is roughly half of that of GaAs.

High-resolution X-ray diffraction measurements on the Fe_3Al films gave a rocking curve full width half maximum (FWHM) of 1.2° for a film 150 Å thick and 0.7° for another film 300 Å thick. These rocking curve values are quite large com-

pared with 0.004° for the GaAs buffer layer. Longitudinal scans along the colinear direction with GaAs(400) peak indicated a significant tetragonal distortion of the films from their cubic lattice due to a 1.5% lattice mismatch between Fe_3Al and GaAs. A planar lattice contraction on the films by this 1.5% lattice mismatch causes the unit cell to expand by 0.14 Å for the 300 Å film and by 0.19 Å for the 150 Å film along the perpendicular direction to the interface.

The width extracted from the same longitudinal scans revealed that the size of the coherent grains is 140 Å for the film 300 Å thick and that reduces to 105 Å for the film 150 Å thick. In both cases, the coherent grains are less than the film thickness. This may be due to a strain-relaxed film and/or some rough but crystalline Fe_3Al at the top. The possibility of forming rough or defective materials at the top could be caused by the high reactivity of Fe and Al with the room air. Large values of rocking curves are also consistent with a picture of partially strain-relieved film.

We have also grown $\text{Fe}_3(\text{Al,Si})$ and Fe_3Si films on GaAs. Their RHEED patterns show the same comparably good quality as those in fig. 1. The rocking curve (FWHM) of a nominal $\text{Fe}_{2.9}(\text{Al}_{0.4}\text{Si}_{0.7})$ 1000 Å thick was measured to be as low as 0.03° . More work is underway to study the $\text{Fe}_3(\text{Al,Si})$ on GaAs in terms of their interfacial structures, the crystal quality as a function of film thickness, etc.

RBS spectra of the Fe_3Al film 150 Å thick were fit using a theoretical simulation [8], and the analysis indicates a stoichiometric Fe_3Al film grown to an average thickness of 150 Å. Grazing exit angle spectra revealed roughness in the film, estimated to be on the order of 60 Å. Channeling analysis was performed at normal exit angle, and the χ_{min} for the Fe was found to be 40%. For this 150 Å film, taking the entire Fe intensity ratio (including the surface peak), we estimate the ideal χ_{min} to be 11%. The observed increase in χ_{min} could be explained by a rough but crystalline Fe_3Al layer or by defective crystal material. This again is consistent with the observation in the high-resolution X-ray diffraction measurements. Studies on the methods of protecting Fe and Al from reacting with the room atmosphere and preserving the

crystallinity of $\text{Fe}_3(\text{Al},\text{Si})$ films are now in progress.

4. Conclusion

In this work, high quality single crystal films of $\text{Fe}_3(\text{Al},\text{Si})$, a BiF_3 structure, have been epitaxially grown on $\text{GaAs}(100)$. We have also shown by in-situ RHEED that an atomically smooth growth of 1 ML $\text{Fe}_3(\text{Al},\text{Si})$ or Fe_3Al has been achieved. The growth has been carried out in a multi-chamber MBE system, in which the metals were grown in an As-free ultra-high vacuum environment. Future studies include a fine tuning in the compositions of Fe, Al, and Si to achieve a perfect lattice match between $\text{Fe}_3(\text{Al},\text{Si})$ and GaAs , and an overgrowth of GaAs on $\text{Fe}_3(\text{Al},\text{Si})$ for fabricating

semiconductor/metal/semiconductor heterostructures.

References

- [1] A.Y. Cho and P.D. Dernier, *J. Appl. Phys.* 49 (1978) 3328.
- [2] J. Massies and N.T. Linh, *J. Crystal Growth* 56 (1982) 25.
- [3] G.A. Prinz and J.J. Krebs, *Appl. Phys. Letters* 39 (1981) 397.
- [4] J.P. Harbison, T. Sands, N. Tabatabaie, W.K. Chan, L.T. Florez and V.G. Keramidas, *Appl. Phys. Letters* 53 (1988) 1717.
- [5] C.J. Palmstrom, N. Tabatabaie and S.J. Allen, Jr., *Appl. Phys. Letters* 53 (1988) 2608.
- [6] A. Taylor and R.M. Jones, *J. Phys. Chem. Solids* 6 (1958) 16.
- [7] R.M. Bozorth, *Ferromagnetism* (Van Nostrand, New York, 1964) p. 95.
- [8] L.R. Doolittle, *Nucl. Instr. Methods B9* (1985) 344.

Overgrowth and strain in MBE-grown GaAs/ErAs/GaAs structures

J.D. Ralston, J. Wagner, F. Fuchs, P. Hiesinger

Fraunhofer-Institut für Angewandte Festkörperphysik, Tullastrasse 72, W-7800 Freiburg, Germany

and

J. Schmälzlin

Fakultät für Physik, Universität Freiburg, Hermann-Herder-Strasse 3, W-7800 Freiburg, Germany

The molecular-beam epitaxial overgrowth of GaAs on single ErAs layers of varying thickness is studied, as well as the growth of, and strain accommodation in, ErAs/GaAs multilayer films on GaAs substrates. Resonant Raman scattering and Rutherford backscattering are used to characterize the crystal quality of overgrown GaAs layers, while Fourier-transform infrared absorption spectra of the crystal-field-split Er^{3+} intra 4f-shell transitions, at $1.54\ \mu\text{m}$, are exploited as a novel probe of strain accommodation in the ErAs layers. Overgrowth of GaAs of good crystal quality on ErAs, as well as growth of ErAs/GaAs multilayer structures, are both demonstrated, but only for ErAs layers less than about 5 monolayers in thickness. Such thin ErAs layers are found to be tetragonally distorted due to elastic strain accommodation. Single buried ErAs films are found to be electrically continuous down to a thickness of 5 monolayers.

1. Introduction

The unique properties of metallic quantum wells [1], including low sheet resistance, ease of contactability, and large subband spacing relative to kT , offer the potential for novel quantum effect devices. A particularly promising example is found in the recent demonstration of resonant tunneling through metallic NiAl quantum wells buried in GaAs/AlAs heterostructures [1]. The successful epitaxial growth of a number of semimetallic rare-earth/Group V compounds on III–V semiconductors has made available another new class of compounds for the fabrication of epitaxial metal/semiconductor heterostructures. Using molecular-beam epitaxy (MBE) and gas-source MBE (GSMBE), various research groups have to date demonstrated the deposition on GaAs of YbAs [2], ErAs [3–5], LuAs [4], ScAs [6], ErP [7], and the lattice-matched ternaries $\text{Sc}_{0.32}\text{Er}_{0.68}\text{As}$ [6] and $\text{ErP}_{0.6}\text{As}_{0.4}$ [7]. Erbium phosphide, ErSb, and the

lattice-matched ternary $\text{ErP}_{0.5}\text{Sb}_{0.5}$ have also been successfully deposited by GSMBE on InP [8]. The above rare-earth (RE) compounds all share a NaCl crystal structure, demonstrate good single-crystal epitaxial growth on their respective III–V hosts, and display metallic conductivities. However, a potentially serious limitation in applications requiring buried metallic layers is poor subsequent overgrowth of III–V semiconductors on top of the metallic RE compounds [3–5]. This behaviour appears to be due to the poorly understood interface chemistry involved in the transition between a NaCl structure primarily ionic in bonding and a primarily covalently-bonded zincblende structure. No improvement has been observed in the case of overgrowth on the lattice-matched ternary RE compounds.

In the present work the MBE overgrowth of GaAs on single ErAs layers of varying thickness is studied, as well as the growth of, and strain accommodation in, ErAs/GaAs multilayer films

on GaAs substrates. ErAs has a 1.6% lattice mismatch with respect to GaAs. Resonant Raman scattering and Rutherford backscattering are used to characterize the crystal quality of overgrown GaAs layers, while Fourier-transform infra-red (FTIR) absorption is utilized as a novel probe of strain accommodation in the ErAs layers.

2. Experimental procedures

2.1. Sample preparation

Samples were grown in a Riber 2300 MBE machine on undoped, semi-insulating (100) GaAs substrates using indium-free substrate mounts. Growth rates and beam flux ratios are similar to those reported in ref. [5]. Growth rates were determined both from the measurement of (weak) RHEED intensity oscillations and from SEM thickness measurements on 500–800 nm thick single ErAs films. Two sets of samples are studied in the present paper. In all cases, undoped GaAs buffer layers 200–300 nm in thickness were first deposited at a substrate temperature of 580–600 °C. For the first set of seven samples, a superlattice buffer (100 periods of 12 nm $\text{Al}_{0.3}\text{Ga}_{0.7}\text{As}$ / 8 nm GaAs) was then grown at 680 °C, followed by an additional 100 nm of GaAs grown at 580 °C. Growth was then interrupted for 120 s to adjust the substrate temperature to 450 °C for the deposition of a single ErAs layer. Layer thicknesses were 1, 2, 5, 7, 20, 40, and 60 monolayers (ML). Undoped GaAs cap layers 50 nm in thickness were then grown with no change in substrate temperature and without any additional growth stop. For the second set of 6 samples, no superlattice buffer was grown. Upon completion of the GaAs buffer, growth was interrupted for 60 s and the substrate temperature decreased to 540–550 °C. An ErAs/GaAs multilayer structure was then deposited, consisting of 6 nm GaAs layers alternating with ErAs layers from 1 to 6 monolayers in thickness. The total ErAs thickness was kept constant by varying the number of periods from 600 to 100, respectively. Undoped GaAs capping layers 40 nm in thickness were then de-

posited, again with no change in substrate temperature and without any additional growth stop.

2.2. Sample characterization

Resonant Raman scattering by longitudinal optical (LO) phonons has been shown to be a sensitive probe for the crystalline perfection of GaAs [9]. This technique is used in the present investigations to study the crystalline quality of GaAs overgrown both on single ErAs layers and on ErAs/GaAs multilayer structures. Spectra were excited with a Kr^+ laser at a photon energy of 3.00 eV, in resonance with the E_1 bandgap of GaAs [9]. The probing depth for this excitation energy is roughly 8 nm, which is much less than the 40 or 50 nm thickness of the GaAs cap layers. Hence, only the cap layer is probed, both for samples containing single ErAs layers and for those containing ErAs/GaAs multilayer structures.

RBS axial channeling measurements have previously been used to directly assess crystal quality and strain accommodation in MBE-grown ErAs/GaAs heterostructures [5,10]. RBS measurements in the present work utilized a 7 MV Van de Graaff accelerator and a detector with an energy resolution of 18 keV at a scattering angle of 165°.

It has recently been demonstrated that the crystal-field splittings observed in FTIR absorption spectra of ErAs/GaAs multilayer structures allow one to distinguish between samples in which the lattice mismatch is elastically accommodated, via tetragonal distortion of the ErAs layers, or inelastically relieved [10]. This technique has also been utilized in the present work to characterize strain accommodation in the ErAs/GaAs multilayer samples. FTIR absorption measurements were made using a Bomem DA-3 spectrometer. Spectra were typically recorded using a resolution of 1 cm^{-1} .

Electrical characterization of buried single ErAs layers was carried out using Hall measurements. Cross-shaped Hall patterns were fabricated using optical lithography and wet chemical etching. Electrical contacts to the ErAs layer were formed by alloying Sn through the GaAs capping layer.

3. Results and discussion

3.1. Single ErAs layers

Fig. 1 shows room-temperature Raman spectra from 50 nm thick GaAs cap layers grown on top of single ErAs layers with thickness between 1 and 20 monolayers. The spectra were recorded in backscattering geometry from the (100) surface with the polarization of both the incident and scattered light parallel to the same (100) direction [$x(zz)\bar{x}$]. For this configuration, Fröhlich-induced intrinsic 2LO phonon scattering is allowed, and dipole-forbidden but defect-induced 1LO phonon scattering can also be observed [9]. Deformation potential 1LO phonon scattering is, on the other hand, suppressed. For GaAs grown on top of 1 and 2 monolayers of ErAs, the Raman spectra are very similar to those of pure GaAs, with the strength of the 2LO phonon line exceeding that of the defect-induced 1LO peak. For GaAs layers overgrown on 5 ML and thicker ErAs layers, the 2LO/1LO intensity ratio decreases rapidly, indicating a substantial increase in the defect con-

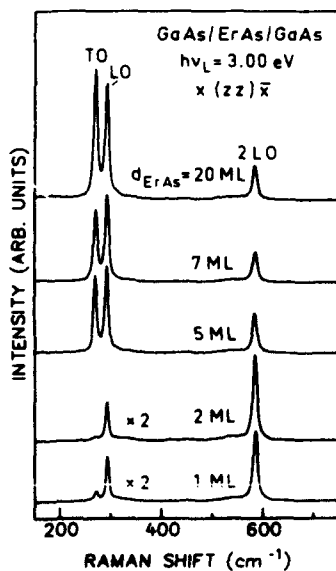


Fig. 1. Room-temperature Raman spectra from 50 nm thick GaAs layers overgrown on single ErAs films ranging in thickness from 1 to 20 monolayers.

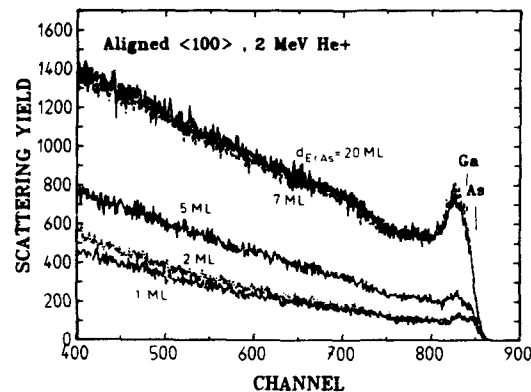


Fig. 2. Aligned [100] Rutherford backscattering spectra from the same five samples as in fig. 1. The plotted channels include only backscattering from Ga and As. The spectra corresponding to ErAs layer thicknesses of 7 and 20 monolayers overlap almost completely.

centration in the overgrown GaAs layers. Along with degradation of the 2LO/1LO intensity ratio, scattering by transverse optical (TO) phonons, which is forbidden in backscattering from a perfect (100) surface, increases to an intensity comparable to that of the defect-induced 1LO line. This behaviour is indicative of considerable roughening of the sample surface.

Fig. 2 shows aligned [100] RBS spectra from the same five samples as in fig. 1. The plotted channels correspond only to backscattering from Ga and As. The much weaker backscattering from Er in the single ErAs layers is centered roughly at channel 950, and is not included in fig. 2. The low backscattering yields from the first two samples indicate good GaAs crystal quality. Some degradation is already observed in the GaAs cap layer overgrown on 5 ML ErAs, while the backscattering yields from the samples containing 7 and 20 ML ErAs indicate polycrystalline or amorphous GaAs overgrowth. Random RBS spectra (not shown) were also recorded. The following GaAs minimum channeling yields (χ_{\min}) were calculated by taking the ratio of the integrated yields in the aligned and random spectra between channels 780 and 800: 1 ML, 6.2%; 2 ML, 7.3%; 5 ML, 12.1%; 7 ML, 34.7%; 20 ML, 31.4%. The RBS results are in good agreement with the Raman scattering results shown in fig. 1, at least for

the extreme cases of very good GaAs overgrowth (on top of 1 and 2 ML ErAs) and very poor GaAs overgrowth (on top of 7 ML or thicker ErAs). The Raman spectra, however, do not so clearly demonstrate the "intermediate" behaviour observed in the RBS spectra for GaAs overgrown on 5 ML ErAs. This difference may simply reflect the different samples areas (~ 1 mm spot diameter for RBS versus $50\text{ }\mu\text{m}$ spot diameter for Raman) and sample depths (several hundred nm for RBS versus roughly 8 nm for Raman) probed by the two techniques. The Raman spectra will thus be more sensitive to any spatial inhomogeneity in defect density or surface roughness.

Degraded overgrowth of GaAs on top of ErAs films has previously been reported [3–5] and attributed to poor GaAs wetting of the ErAs surface, giving rise to rough, island-like GaAs growth. Recent high-resolution transmission electron microscopy investigations [11] have revealed localized growth of (111) GaAs on (100) ErAs, leading to extensive twinning of the overgrown GaAs. Tentative explanations for this behaviour were oxidation of, or impurity adsorption on, the relatively reactive ErAs surface, as well as poor GaAs wetting of the underlying ErAs. Palmström and coworkers [12] have very recently reported that, for substrate temperatures between 350 and 400 °C during growth, one- and two-monolayer-thick ErAs films grown on GaAs are sufficiently pinholed to allowing seeding-enhanced GaAs overgrowth. In contrast, 3-monolayer-thick ErAs layers were observed to be continuous, and subsequent GaAs overgrowth degraded. The present results, indicating degraded GaAs overgrowth on ErAs layers thicker than roughly 5 ML, may reflect the persistence of a pinholed morphology for ErAs layer thicknesses up to 4 or 5 ML, simply due to the higher substrate temperatures (450 °C) used during growth.

Electrical characterization offers further support for the above interpretation of the overgrowth results. The single buried ErAs films were found to be electrically continuous down to a thickness of 5 monolayers (~ 1.4 nm). The four thickest ErAs films (7, 20, 40, and 60 ML) demonstrated metallic resistivities ranging between 114 and 200 $\mu\Omega$ cm. These values are somewhat larger

than those previously measured for single ErAs films 150 nm in thickness [5], which were consistently on the order of 60–70 $\mu\Omega$ cm for a relatively large range of MBE growth temperatures. The 5 ML ErAs film showed an increase in resistivity to 680 $\mu\Omega$ cm, while the samples containing 1 and 2 ML thick ErAs layers were measured to be highly resistive. Electrically continuous MBE-grown ErAs layers as thin as 3 ML, buried in GaAs, have recently been reported [11], but again using growth temperatures of 350–400 °C. Further investigations are required to better understand the role of layer and interface morphology, as well as quantum size effects, in determining the electrical behaviour of such extremely thin metallic films.

3.2. ErAs/GaAs multilayer samples

Raman spectra (not shown) from GaAs cap layers grown on top of the ErAs/GaAs multilayer structures demonstrate behaviour very similar to those in fig. 1. Degradation of the 2LO/1LO intensity ratio, as well as an increase in the intensity of forbidden TO scattering, are both observed as the thickness of the individual ErAs layers exceeds 2 ML. Both of the above effects, however, indicate an abrupt deterioration at an ErAs thickness of 6 ML. RBS spectra, presented in figs. 3 and 4, support this observation. Fig. 3 shows random and aligned backscattering, for both [100] and [110] channeling directions, from a 120-period multilayer structure containing 5 ML ErAs layers. Fig. 4 shows similar spectra from a 100-period structure containing 6 ML ErAs layers. Due to the large total epitaxial layer thicknesses, backscattering due to Er is not separately resolved from the background due to Ga and As. Also, the depth resolution in the above measurements (~ 20 nm) is insufficient to resolve individual layers in the ErAs/GaAs multilayer structures. Comparing the aligned [100] spectra in figs. 3 and 4, it is apparent that an abrupt increase in dechanneling occurs at the leading edge of the GaAs backscattering profile (\sim channel 850) as the ErAs layer thickness increases from 5 to 6 monolayers. This behaviour indicates an abrupt degradation in the crystallinity of the GaAs cap layer. In addition, an abrupt

increase in dechanneling also occurs at the leading edge of the Er backscattering profile (\sim channel 950), indicating accumulated degradation due to poor overgrowth within the multilayer structure itself. The peak observed between channels 800 and 850 in the [110] spectra in figs. 3 and 4 is due to enhanced overlap between backscattering from Er (at the bottom of the multilayer structure) and Ga and As (at the surface of the cap layer) arising from the larger effective multilayer thickness at [110] incidence. The following values for χ_{\min} were calculated for the first 15 channels in the [100] Er backscattering profiles, corresponding to a depth of about 80 nm or roughly the upper most 13 periods of the multilayer structures: 600 periods/1 ML ErAs, 4%; 300 periods/2 ML ErAs, 13%; 200 periods/3 ML ErAs, 6%; 150 periods/4 ML ErAs, 8%; 120 periods/5 ML ErAs, 8.3%; 100

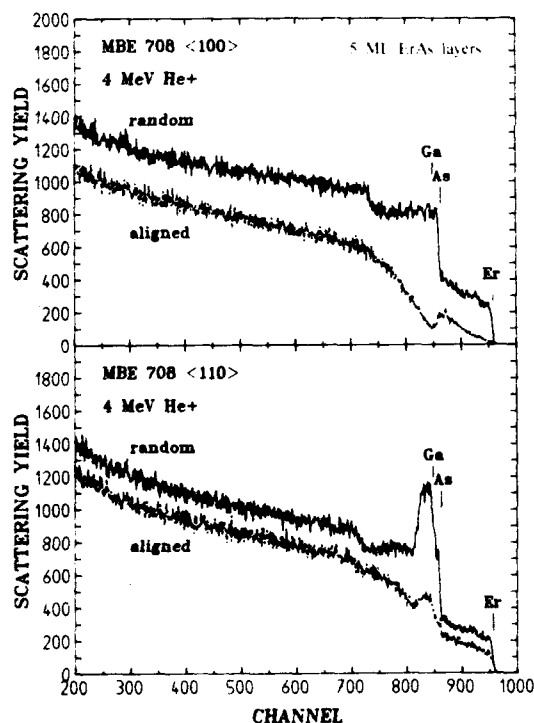


Fig. 3. Random and aligned Rutherford backscattering [100] and [110] axial channeling spectra of a 120 period ErAs/GaAs multilayer structure (5 monolayers ErAs/6 nm GaAs), capped with 40 nm GaAs.

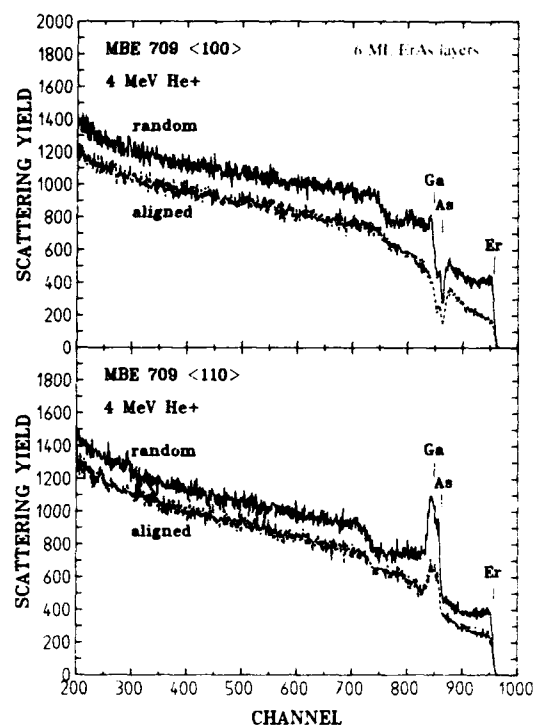


Fig. 4. Random and aligned Rutherford backscattering [100] and [110] axial channeling spectra of a 100 period ErAs/GaAs multilayer structure (6 monolayers ErAs/6 nm GaAs), capped with 40 nm GaAs.

periods/6 ML ErAs, 42%. These values clearly demonstrate relatively good multilayer crystal quality for ErAs layers up to 5 ML in thickness, and the abrupt degradation for 6 ML ErAs.

Strain relaxation in the above multilayer samples has been investigated via FTIR absorption. Fig. 5 presents FTIR absorption from all six samples, recorded at 300 K, along with that of a single strain-relieved 830 nm ErAs film grown on GaAs by MBE. Sharp intra 4f-shell transitions, centered at $1.54 \mu\text{m}$ (6500 cm^{-1}), are clearly resolved in all cases, corresponding to absorption between the crystal-field-split $^4I_{15/2}$ ground state and $^4I_{13/2}$ first excited state of Er^{3+} ($4f^{11}$) ions in ErAs [5]. The absorption spectra of all six multilayer samples show pronounced changes in the energies, linewidths, and relative intensities of the crystal-field-split lines, with respect to those of the

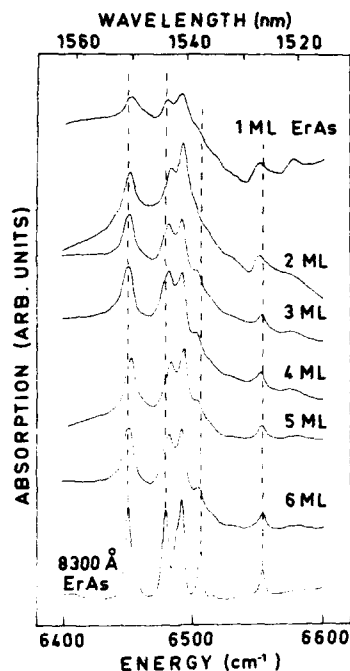


Fig. 5. Room-temperature FTIR absorption spectra of ErAs/GaAs multilayer structures containing 1–6 monolayer-thick ErAs layers alternating with 6 nm GaAs layers. Also plotted is the corresponding absorption spectra of a single 830 nm thick ErAs film grown on GaAs.

strain-relieved sample. In particular, the line originally observed at 6478 cm^{-1} shifts to higher energy, while the 6554 cm^{-1} line shifts to lower energy, and the 6506 cm^{-1} line decreases in intensity and eventually vanishes. Such behaviour has previously been observed in similar ErAs/GaAs multilayer structures in which the ErAs layers were coherently strained [10]. In contrast, FTIR absorption spectra from multilayer samples containing thicker, strain-relieved ErAs layers are essentially identical to those of single, thick, strain-relieved ErAs films [10]. Variations in the energies and relative intensities of the crystal-field-split spectral lines among the various multilayer samples in fig. 5 may indicate an inhomogeneous strain distribution resulting from the degraded overgrowth.

The detailed layer and interface morphology of the above multilayer samples has not yet been investigated. The fact that substantially higher growth temperatures ($540\text{--}550^\circ\text{C}$) were found to be required than in the case of overgrowth on single ErAs layers may further hint at the role played by pinhole-induced seeding of GaAs overgrowth on ErAs.

4. Conclusions

The Raman scattering and RBS results presented above indicate that, at least for the MBE growth parameters used here, GaAs can be successfully overgrown only on ErAs layers less than about 5 ML in thickness, beyond which the crystal quality of the overgrown GaAs rapidly degrades. Correspondingly, it is found that ErAs/GaAs multilayer samples containing several hundred periods and demonstrating good crystal quality can also be grown, but only when the thickness of the individual ErAs layers is 5 ML or less. FTIR absorption results indicate that such thin ErAs layers remain tetragonally distorted due to elastic accommodation of the lattice-mismatch-induced strain. Although single buried ErAs films are found to be electrically continuous down to a thickness of 5 ML, the severely degraded subsequent overgrowth presents a serious obstacle for such applications as tunneling devices, where high quality epitaxial semiconductor layers are required both above and below metallic quantum wells. However, much work remains to be done in exploring a wider range of growth parameters and substrate orientations, as well as various other lattice-matched or lattice-mismatched rare-earth/Group V compounds on III–V semiconductors.

Acknowledgements

The technical assistance of G. Bihlmann, H. Hoffmann, and B. Matthes is gratefully acknowledged. The authors also wish to thank Professor P. Koidl, Professor R. Brenn, and Dr. H. Ennen for their continuing support and encouragement.

References

- [1] J.P. Harbison, T. Sands, R. Ramesh, N. Tabatabaie, H.L. Gilchrist, L.T. Florez and V.G. Keramidas, *J. Vacuum Sci. Technol.* B8 (1990) 242, and references therein.
- [2] H.J. Richter, R.S. Smith, N. Herres, M. Seelmann-Eggebert and P. Wennekers, *Appl. Phys. Letters* 53 (1988) 99.
- [3] C.J. Palmström, N. Tabatabaie and S.J. Allen, Jr., *Appl. Phys. Letters* 53 (1988) 2608.
- [4] C.J. Palmström, K.C. Garrison, S. Mounier, T. Sands, C.L. Schwarz, N. Tabatabaie, S.J. Allen, Jr., H.L. Gilchrist and P.F. Miceli, *J. Vacuum Sci. Technol.* B7 (1989) 747.
- [5] J.D. Ralston, H. Ennen, P. Wennekers, P. Hiesinger, N. Herres, J. Schneider, H.D. Müller, W. Rothmund, F. Fuchs, J. Schmäzlin and K. Thonke, *J. Electron. Mater.* 19 (1990) 555.
- [6] C.J. Palmström, S. Mounier, T.G. Finstad and P.F. Miceli, *Appl. Phys. Letters* 56 (1990) 382.
- [7] A. Le Corre, J. Caulet and A. Guivarc'h, *Appl. Phys. Letters* 55 (1989) 2298.
- [8] A. Guivarc'h, J. Caulet and A. Le Corre, *Electron. Letters* 25 (1989) 1050.
- [9] J. Wagner, *Appl. Phys. Letters* 52 (1988) 1158, and references therein.
- [10] J.D. Ralston, F. Fuchs, J. Schneider and J. Schmäzlin, *J. Appl. Phys.* 68 (1990) 2176.
- [11] J.G. Zhu, Clive B. Carter, C.J. Palmström and S. Mounier, *Appl. Phys. Letters* 56 (1990) 1323.
- [12] C.J. Palmström, T.L. Cheeks, R.E. Nahory, B.J. Wilkens, J.A. Martinez, P.F. Miceli and V.G. Keramidas, Paper N1, 1990 Electronics Materials Conf., University of California, Santa Barbara, CA, June 1990, paper N1.

RHEED studies of epitaxial growth of CoGa on GaAs by MBE – determination of epitaxial phases and orientations

T.C. Kuo, T.W. Kang * and K.L. Wang

Device Research Laboratory, Department of Electrical Engineering, University of California at Los Angeles, Los Angeles, California 90024-1600, USA

Epitaxial growth of single crystal CoGa is investigated in-situ using reflection high energy electron diffraction (RHEED). The formation of different phases of CoGa (different stoichiometric compounds and epitaxial orientations) due to various initial growth conditions has been probed with X-ray diffraction and correlated with the RHEED patterns. The growth of (100)CoGa or (110)CoGa is found strongly dependent on the termination of the GaAs surface, with either Co or Ga, before the epitaxial deposition of CoGa. When the flux ratio is deviated from the proper stoichiometric range, additional Co–Ga–As compounds are found in the X-ray diffraction measurement. It is concluded that the CoGa phases and orientations can be determined by pre-deposition of Co or Ga with a control of stoichiometry in the proper range. The high quality epitaxial CoGa has potential applications in thermodynamically stable contacts, and more importantly for fabrication of GaAs/metal/GaAs quantum well structures.

1. Introduction

Thermodynamically stable metal contacts on GaAs are very important for both Ohmic and Schottky contacts. Since only W and Mo in the element metal form do not react with GaAs, intermetallic compounds have attracted great deal of interest in the past few years [1]. These intermetallic compounds, such as CoGa [2], RhGa [3], NiAl [4], and NiGa [5], have a CsCl structure and the lattice constants are close to half of the lattice constant of GaAs. Thus, epitaxial deposition of these intermetallic compounds on GaAs is plausible.

CoGa has certain advantages which make it a good candidate for metal contact on GaAs. First, there exist only two stable phases of Co/Ga compounds, which are CoGa and CoGa₃ [6], and this makes it easier to control the growth of single phase CoGa on GaAs. Second, the stoichiometry of Co_{1-x}Ga_x can be varied from 31% to 62% [7], and this flexibility of stoichiometric variation makes the flux ratio control less critical. Further-

more, the lattice mismatch of different stoichiometric CoGa's with GaAs (half of the lattice constant), varies from 1.8% to 0.5% as Ga content is adjusted from 31% to 61% [8]. In bulk Co_{1-x}Ga_x, electric and magnetic properties are known to depend on the stoichiometry [9–11]. However, the properties of epitaxial Co_{1-x}Ga_x on GaAs are still relatively unknown. Recent studies by Baugh et al. [12] have shown that the Ga rich condition may be thermodynamically more stable than the Co rich condition. Palmstrøm et al. [2] have demonstrated the growth of CoGa on GaAs and observed the surface reconstruction using reflection high energy electron diffraction (RHEED).

In this paper, we demonstrate the control of growth of single phase CoGa on GaAs and the epitaxial orientation in molecular beam epitaxy (MBE), by controlling the initial growth condition with in-situ RHEED diffraction.

2. Experimental

The substrate used in this study was undoped semi-insulating (100)GaAs. The wafer was first degreased, etched in H₂SO₄:H₂O₂:H₂O = 8:1:1

* Permanent address: Department of Physics, Dongguk University, 3-26 Chungku, Seoul 100-715, South Korea.

at 20°C for 4 min, and then indium-mounted on a molybdenum holder. The epitaxial growth was carried out in a two stage MBE chamber with a base pressure at about 5×10^{-10} Torr. Ga and As were from temperature controlled Knudsen cells. Co was evaporated from a electron beam evaporator, and the flux was monitored by an Inficon IC6000 crystal monitor. A RHEED system was used for in-situ analysis of the surface.

The sample was first heated up to 600°C with the As₄ shutter open. When the oxide layer was removed at about 600°C, an As(2 × 4) RHEED pattern was observed, and then, an undoped 1000 Å GaAs buffer layer was grown to smooth the surface. After growth of a buffer layer, the substrate was cooled down with the As₄ shutter remained open until the substrate temperature dropped down to below 400°C. The RHEED pattern changed to c(4 × 4) when the temperature was below 450°C. This condition indicated that the surface was now covered by excess As [13]. In order to avoid the residual As incorporation in the CoGa growth, the growth was allowed to resume after the As partial pressure was pumped down to about 1×10^{-9} Torr, and this process took about 2–3 h. In growth of CoGa, the Co flux used was about 0.3 Å/s, and the Ga flux was equivalent to a GaAs growth rate of 0.4 μm/h. The growth rate of CoGa under this condition was about 2000 Å/h (calibrated by Rutherford backscattering, RBS). CoGa film of 500–700 Å thickness was grown at different Co:Ga flux ratios and at different temperatures. In experiments, CoGa films have been grown on both Ga and Co terminated GaAs surfaces keeping other growth conditions the same as above. The growth pressure for GaAs buffer layers was about 5×10^{-7} Torr, and about 1×10^{-8} Torr for CoGa. X-ray diffraction was used for identifying the different phases of CoGa films formed, and finally the correlation of the CoGa phases with the initial conditions as determined by RHEED was established.

3. Results

Under a proper stoichiometry (Ga ratio between 40% and 60%), a single phase CoGa can be

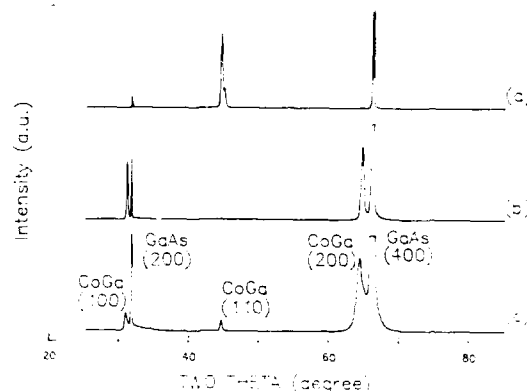


Fig. 1. X-ray diffraction patterns of different samples under different growth conditions: (a) with Ga pre-deposit; (b) with Co pre-deposit; (c) without any pre-deposit. All the films are of the same thickness.

obtained even at room temperature. However, at this low growth temperature, the RHEED pattern obtained is broad and spotty after a few minutes of growth, indicating poor crystalline quality and surface morphology. On the other hand, Baugh et al. [12] suggest that CoGa is not stable when annealed at 500°C both in the Co-rich or Ga-rich condition. To achieve high crystalline quality and to keep CoGa stable at the same time, we, therefore, use an intermediate growth temperature at about 300°C. In one case, a small amount of Ga is deposited, and the RHEED pattern is observed to change from As c(4 × 4) into Ga(4 × 6) or other Ga rich reconstructions. At the initial stage of this growth, a broad RHEED pattern is seen. However, as the growth proceeds, the RHEED pattern becomes streaky within one minute or so. For films grown under this condition, the X-ray diffraction shows a peak corresponding to (110)CoGa as shown in fig. 1a. For comparison, standard GaAs c(4 × 4) RHEED patterns are given in figs. 2a and 2b for looking along the (010) and (011) azimuth angles respectively, while fig. 3 gives the projections of GaAs and CoGa. The RHEED pattern of single phase CoGa(110) is shown in fig. 4, and we can see clear Kikuchi bands indicating a good crystalline quality. For convenience of comparison with the GaAs substrate as well as for being consistent, all the directions marked on

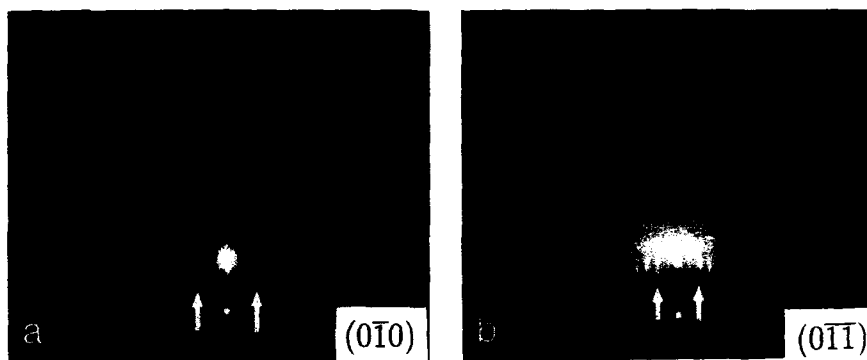


Fig. 2. As $c(4 \times 4)$ RHEED patterns after growing a 1000 Å GaAs buffer layer: (a) $(0\bar{1}0)$ and (b) $(0\bar{1}\bar{1})$; the two arrows indicate the fundamental lines from bulk diffraction.

CoGa RHEED patterns are referred to GaAs substrate. We see that the distance between the two fundamental lines from the bulk CoGa lattice in the $(0\bar{1}\bar{1})$ direction showing in fig. 4d is the same

as GaAs in $(0\bar{1}\bar{1})$ direction in fig. 2b. Furthermore, the distance in $(0\bar{1}\bar{1})$ (fig. 4b) is $\sqrt{2}$ times that in the $(0\bar{1}\bar{1})$ direction (fig. 4d). The relations of the lattice constant and orientation in (100) GaAs,

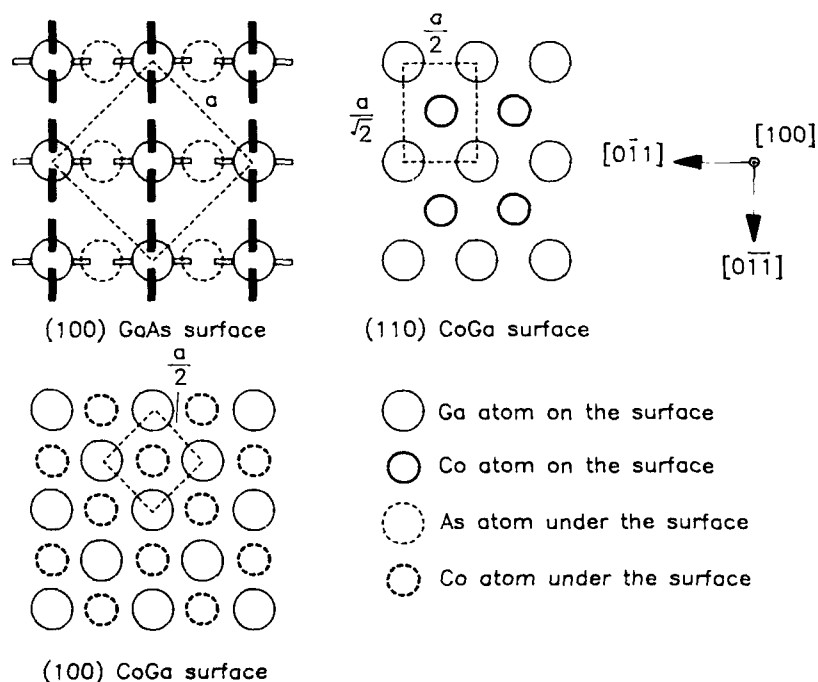


Fig. 3. Projective view of the surfaces of (100) GaAs, (100) CoGa, and (110) CoGa. They show the relations of the lattice constant and orientation. The dark lines in the top left figure indicate the upward bonds of Ga atoms.

(100)CoGa and (110)CoGa can be seen in fig. 3. Since the (110) surface of CoGa has a rectangular symmetry with sides $(1, \sqrt{2})$, the symmetry directions will appear at 0° and $\tan^{-1}(1/\sqrt{2}) \sim 35^\circ$. In the later case, if we rotate the sample 35° from $(0\bar{1}\bar{1})$ toward $(0\bar{1}0)$ or $(00\bar{1})$, we obtain another symmetric pattern, in which the distance between two fundamental lines is $\sqrt{3}$ times that of $(0\bar{1}\bar{1})$ as expected. Therefore, we can conclude that the growth direction when the surface is initially terminated with Ga is $(110)[001]$ CoGa on $(100)[011]$ GaAs. As the flux ratio of Co to Ga (still within 40% to 60%) is changed, there is no change of the epitaxial orientation.

For the second case, the growth temperature is kept constant at about 300°C , and some small amount of Co (\sim one monolayer) is deposited

until the RHEED pattern of As $c(4 \times 4)$ changes prior to the growth. In this case, an entirely different result from the Ga pre-deposited condition is obtained. Under this condition, the resulting films show a dominant (100)CoGa epitaxial growth. The corresponding X-ray diffraction is shown in fig. 1b. The RHEED pattern shown in fig. 5 reveals streaky lines with clear Kikuchi bands, indicating a good crystalline quality. From figs. 3 and 5, we can see that the distance between the two fundamental line of CoGa in the $(00\bar{1})$ direction (fig. 5a) is $1/\sqrt{2}$ times that in the $(0\bar{1}\bar{1})$ direction (fig. 5b), which is the same as the GaAs in the $(0\bar{1}0)$ direction, when compared with GaAs $c(4 \times 4)$ pattern. From the pattern in fig. 5, we conclude that the epitaxial direction in this case is $(100)[011]$ CoGa on $(100)[011]$ GaAs. Similar to the Ga pre-de-

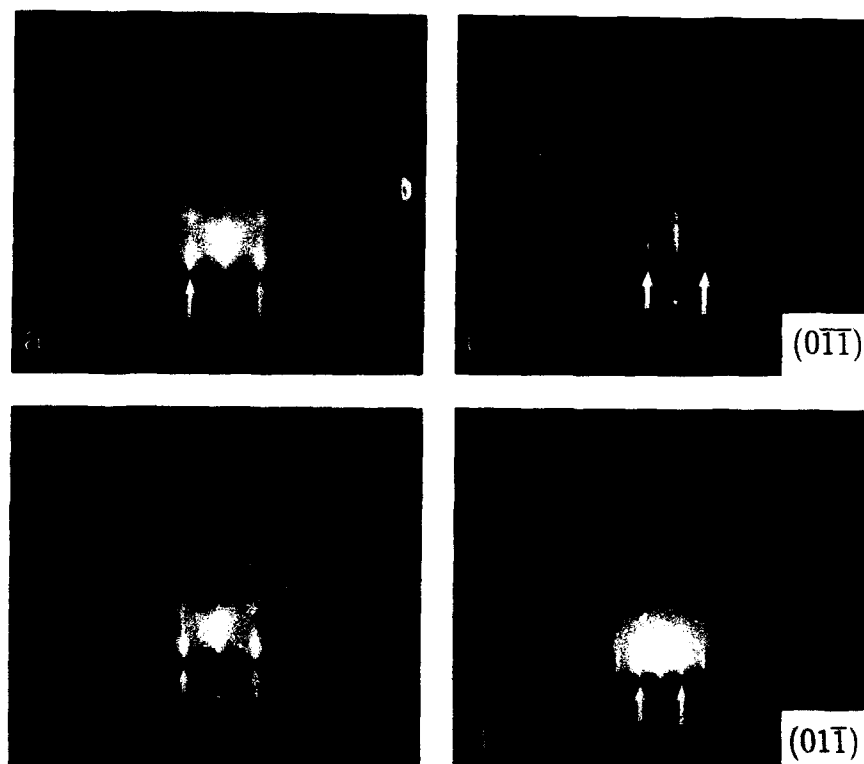


Fig. 4. RHEED patterns from the (110)CoGa sample after 500 Å growth: (a) about 35° from $(0\bar{1}\bar{1})$ toward $(0\bar{1}0)$, (b) $(0\bar{1}\bar{1})$, (c) about 35° from $(0\bar{1}\bar{1})$ toward $(00\bar{1})$, and (d) $(0\bar{1}\bar{1})$.

posited situation, the results will not be affected by the flux ratio as long as the Ga fraction is within 40% to 60%.

If CoGa is deposited directly onto the GaAs $c(4 \times 4)$ surface without the pre-conditioning, a mixture of (100)CoGa and (110)CoGa pattern is seen as given in fig. 6. It is clear that the pattern in fig. 6 is rather spotty and broad compared with the RHEED patterns in figs. 4 and 5, and, in addition, the Kikuchi bands disappear. The X-ray diffraction shown in fig. 1c indicates a mixed phase. Although, the (100)CoGa is the dominant one, there is (110)CoGa present.

The determination of epitaxial orientations and phases appear independent of the surface morphology. In order to verify that the anchoring of epitaxial orientation is independent of the surface morphology, several deposited films with and without a GaAs buffer layer are compared.

Without a buffer layer, the surface of a GaAs substrate after thermal cleaning is always rough as revealed in RHEED in contrast with the smooth buffer layer surface. For CoGa films deposited at different initial conditions without a buffer layer, the orientation and phase of CoGa are the same as the cases of a smooth GaAs buffer layer surface.

The composition deviation away from the proper stoichiometric range ($\text{Ga} \leq 40\%$ or $\geq 60\%$) results a mixture of CoGa and other Co-Ga-As compounds. Under Co-rich conditions, if the growth temperature is kept at room temperature, the X-ray diffraction data show that both CoGa and pure Co exist. If the flux ratio is fixed and the growth temperature is increased to 300°C , the X-ray diffraction data show that CoGa, CoGa_3 and CoAs co-exist while pure Co disappears. From previous work [14], pure Co deposited on GaAs substrate is known to react with GaAs at about

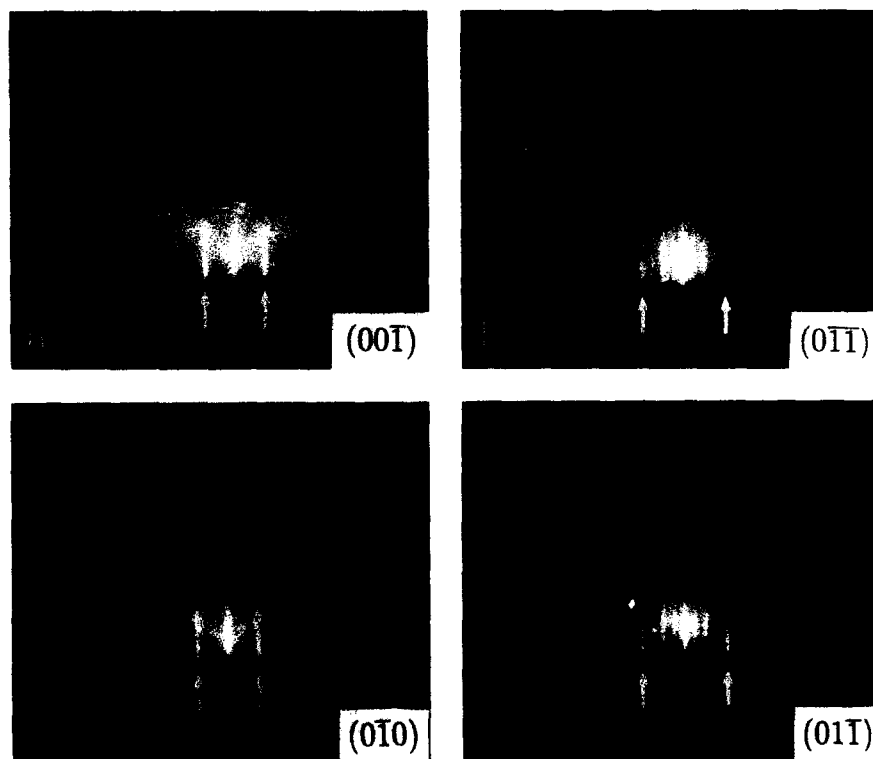


Fig. 5. RHEED pattern from the (100)CoGa sample after 500 Å growth: (a) $(00\bar{1})$, (b) $(0\bar{1}\bar{1})$, (c) $(0\bar{1}0)$, and (d) $(0\bar{1}\bar{1})$.

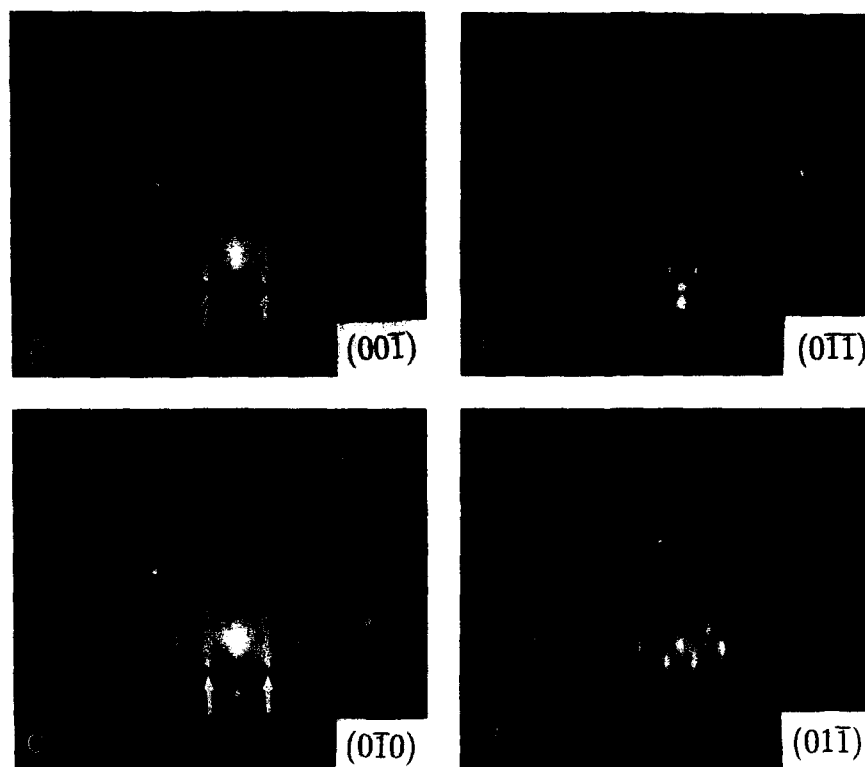


Fig. 6. RHEED patterns from the mixture of (100)CoGa and (110)CoGa after 500 Å growth: (a) (001), (b) (011), (c) (010), and (d) (011). We can not define the fundamental lines in (b) and (d) due to spotty patterns.

350°C; therefore it may be concluded that the formation of CoGa₃ is due to the reaction between the excess Co and the substrate. In the Ga rich condition, the X-ray data of the room temperature and 350°C grown samples show both CoGa and CoGa₃ peaks. For both the Co rich and Ga rich depositions (outside the previously stated desired range), the CoGa grown at 300°C shows broad RHEED patterns. As the growth temperature is increased to above 400°C, the RHEED pattern becomes streaky, and it becomes very similar to the CoGa(100) pattern. However, a strong peak of CoGa₃ in addition to CoGa is detected by the X-ray diffraction. Thus, for high quality single phase CoGa, surface pre-conditioning needs to be carefully done.

4. Summary

In summary, a single phase epitaxial CoGa is obtained by the co-deposition of Co and Ga at 300°C. Two epitaxial orientations, (100)CoGa and (110)CoGa, can be obtained by controlling the pre-deposit condition. A similar result was observed by Harbison et al. [15] in this case of NiAl grown on AlAs. Streaky patterns are observed for both (100)CoGa and (110)CoGa. The epitaxial direction is then independent of the flux ratio and the surface morphology after it is set by the initial growth condition. The composition deviation away from the proper stoichiometric range results in other Co-Ga-As compounds. In the latter case, although the patterns look streaky at high growth

temperature, X-ray diffraction detects the presence of CoGa_3 or other Co-As compounds. These results may be used for controlling growth of a thermodynamically stable metal contact on GaAs, and more importantly for fabrication of GaAs/metal/GaAs quantum well structures.

Acknowledgements

The authors would like to thank Dr. G. Bai for help in the RBS measurement. This work is sponsored by SDIO-IST monitored by ONR.

References

- [1] T. Sands, V.G. Keramidas, K.M. Yu, J. Washburn and K. Krishnan, *J. Appl. Phys.* 62 (1987) 2070.
- [2] C.J. Palmstrøm, B.-O. Fimland, T. Sands, K.C. Garrison and R.A. Bartynski, *J. Appl. Phys.* 65 (1989) 4753.
- [3] A. Guivarc'h, M. Secoué and B. Guenais, *Appl. Phys. Letters* 52 (1988) 948.
- [4] T. Sands, *Appl. Phys. Letters* 52 (1988) 197.
- [5] A. Guivarc'h, R. Guerin and M. Secoué, *Electron. Letters* 23 (1987) 1004.
- [6] R. Beyers, K.B. Kim and R. Sinclair, *J. Appl. Phys.* 61 (1987) 2195.
- [7] W.G. Moffatt, *The Handbook of Binary Phase Diagrams* (Genium, Schenectady, NY, 1984).
- [8] K. Schubert, H.L. Lukas, H.-C. Meissner and S. Bhan, *Z. Metallk.* 50 (1959) 534.
- [9] J.V. Yakhmi, *J. Phys. F (Metal Phys.)* 13 (1983) 659.
- [10] Y. Ochiai and J.O. Brittain, *Phys. Letters* 73 (1979) 347.
- [11] D. Berner, G. Geibel, V. Gerold and E. Wachtel, *J. Phys. Chem. Solids* 36 (1975) 221.
- [12] D.A. Baugh, Y.K. Kim and R.S. Williams, paper presented at 119th TMS Annual Meeting, Anaheim, CA, February 1990.
- [13] R.Z. Barchrach, R.S. Bauer, P. Chiaradia and G.V. Hanson, *J. Vacuum Sci. Technol.* 18 (1981) 797.
- [14] M. Genut and M. Eizenberg, *Appl. Phys. Letters* 50 (1987) 1358.
- [15] J.P. Harbison, T. Sands, N. Tabatabaie, W.K. Chan, L.T. Florez and V.G. Keramidas, *Appl. Phys. Letters* 53 (1988) 1717.

Molecular beam epitaxial growth of Cr/Fe, Ag/Fe, Ag/Cr and Ag/Co superlattices on MgO (001) substrates

P. Etienne

Laboratoire Central de Recherches, Thomson-CSF, F-91404 Orsay Cedex, France

J. Massies

Laboratoire de Physique du Solide et Energie Solaire, CNRS, Sophia Antipolis, F-06560 Valbonne, France

S. Lequien, R. Cabanel

Laboratoire Central de Recherches, Thomson-CSF, F-91404 Orsay Cedex, France

and

F. Petroff

Laboratoire de Physique des Solides, Université de Paris XI, Bâtiment 510, F-91405 Orsay Cedex, France

Cr/Fe and Ag/Cr, Fe, Co superlattices (SLs) have been grown by molecular beam epitaxy on MgO (001) substrates. The results are compared with those previously obtained on GaAs (001), on the basis of reflection high-energy electron diffraction, sputter-depth Auger profile and X-ray diffraction experiments. It is shown that MgO substrates, which are easier to prepare than GaAs prior to epitaxial growth, allow the growth of high quality metallic SLs.

1. Introduction

During the last few years, molecular beam epitaxy (MBE) has facilitated the growth of high quality magnetic multilayer structures. Among them, sandwiches or superlattices (SLs) of Ag/Fe and Cr/Fe have exhibited new and exciting properties, including perpendicular magnetization for Ag/Fe sandwiches and SLs [1–3] and antiferromagnetic coupling and giant magnetoresistance effects for Cr/Fe SLs [4]. Up to now, the MBE growth of SLs in these material systems has been mainly performed on GaAs (001) substrates. The successful use of such substrates necessitates the growth of a buffer layer in order to obtain a smooth and well ordered surface suitable for the subsequent growth of the metallic SLs. This requirement obviously complicates the growth pro-

cess. Moreover, when a GaAs buffer layer is grown, residual arsenic molecules resulting from the GaAs growth may affect the overall SL properties by reacting with Fe layers. We report here on the use of MgO (001) as an alternative substrate for the growth of high quality Ag/Fe and Cr/Fe SLs. The results show that the overall properties of SLs grown on MgO and GaAs substrates are similar. Moreover, it is shown that MgO (001) substrates can also be used to grow high quality Ag/Cr and Ag/Co SLs.

2. Experimental detail

The growth experiments have been performed in an MBE system designed in our laboratory and equipped with high-temperature effusion cells

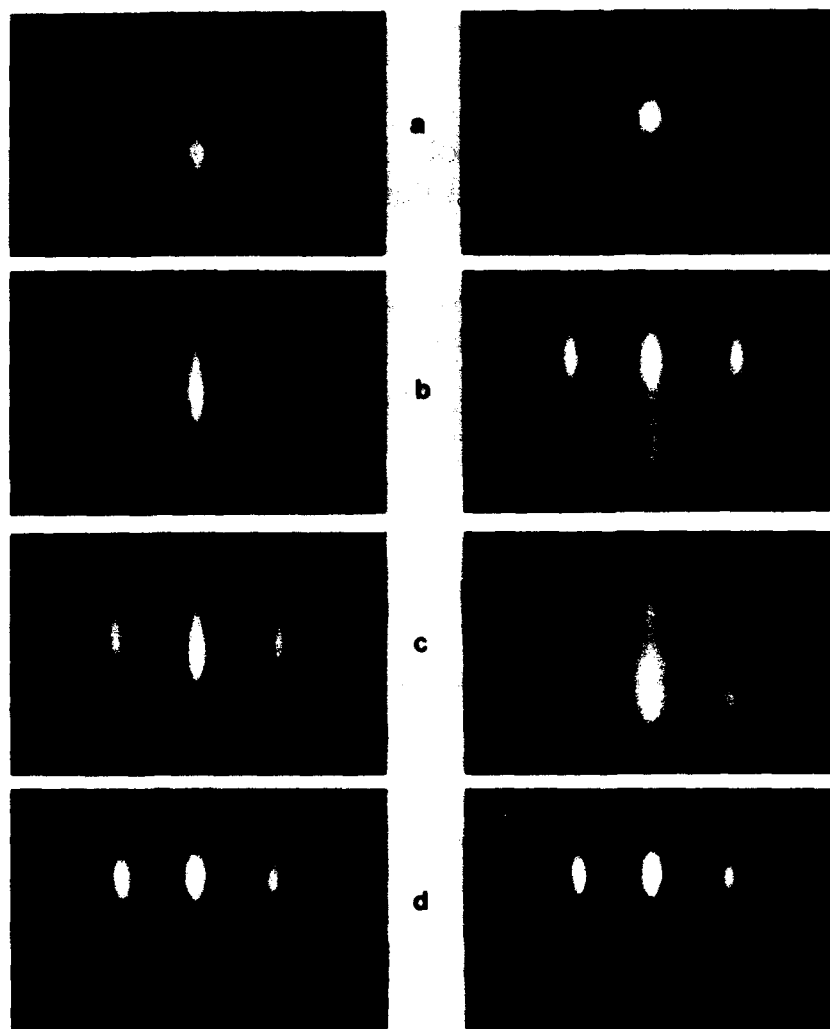


Fig. 1. Characteristic RHEED patterns of (a) MgO substrate after heating at 450°C for 15 min (left, $\langle 100 \rangle$ azimuth; right, $\langle 110 \rangle$ azimuth); (b) 20th period of a (Ag 60 Å/Fe 7 Å)₂₀ SL (left, Ag, right, Fe); (c) 30th period of a (Ag 30 Å/Cr 5 Å)₃₄ SL (left Ag, right Cr); (d) 2nd period of a (Cr 12 Å/Fe 5 Å)₃₀ SL (left Cr, right Fe).

heated by electron bombardment. Additional details can be found elsewhere [5]. Prior to epitaxial growth, the GaAs substrates were simply deoxidized by dipping into a HCl/methanol solution [6]. By heating in the 450–550°C temperature range under a suitable As₄ partial pressure, it is then possible to induce a standard 2×4 reconstruction surface. However, at this stage the surface is still rough and the growth of a GaAs buffer

layer is required in order to obtain high-quality epitaxial metallic multilayers [7–9]. Before the subsequent growth of metallic SLs, the residual arsenic pressure, resulting from the GaAs growth should be decreased down to the 10^{-10} Torr range. The growth process on MgO substrates is simpler. MgO substrates (from Sumitomo) are simply heated in the MBE chamber around 450°C for 15 min, without preliminary chemical etching. A 1×1

reflection high-energy electron diffraction (RHEED) pattern exhibiting strong Kikuchi features, and characteristic of a smooth surface, is then obtained (fig. 1a). However, it should be noted that RHEED observations on the bare substrate are more difficult than for GaAs due to strong charging effects, which are difficult to eliminate.

On both GaAs and MgO substrates, metallic SLs are grown using a relatively low growth rate of 500 Å/h for all the elements, and a low growth temperature (30–60°C). Growth was continuously monitored using RHEED. Since the growth chamber is connected under vacuum with a scanning Auger system, surface analysis could be performed at the different stages of the growth, and ion-beam sputter depth profiles of the grown structures could also be easily performed. Finally, the structural properties of SLs are controlled by standard X-ray diffraction techniques.

3. Results and discussion

3.1. Ag/Fe, Ag/Cr and Cr/Fe superlattices

One of the main differences between the growth on MgO (NaCl structure, $a = 4.20$ Å) and GaAs (zinc-blende, $a = 5.65$ Å) substrates is the occurrence of different epitaxial relationships for the metals involved in the superlattices. In particular, while the (112) orientation is found when Cr is grown on GaAs (001) [7], it is the (001) orientation which occurs on MgO (001). On the other hand, the growth of Ag on MgO gives rise only to the (001) orientation, eliminating the problem encountered in the case of GaAs substrates, for which both Ag (011) and (001) orientations can be present at the same time [8,9]. However, a better Ag (001) single-crystal film is obtained when a thin nucleation layer (10–20 Å) of Fe (001) or Cr (001) is first deposited on MgO (001). As previously reported [8,10,11], such a nucleation layer is a strict prerequisite for the growth of high quality Ag/Fe SLs on GaAs (001). However, in that case Cr, which is oriented (112), does not allow the growth of a good single-crystal Ag layer. Another difference between the two substrates is that, while a clearly defined (6×6) reconstruction is observed

when Ag is grown (via a Fe nucleation layer) on GaAs, a 1×1 unit cell is always obtained for the growth on MgO (via a Fe or Cr nucleation layer).

The epitaxial relationships observed when using MgO substrates are summarized as follows:

$$\text{Fe}_{\text{bcc}}, \text{Cr}_{\text{bcc}} \{001\} \langle 110 \rangle \parallel \text{Ag}_{\text{fcc}},$$

$$\text{MgO}_{\text{NaCl}} \{001\} \langle 100 \rangle$$

with $a_{\text{Fe}} = 2.86$ Å, $a_{\text{Cr}} = 2.88$ Å, $a_{\text{Ag}}/\sqrt{2} = 2.89$ Å and $a_{\text{MgO}}/\sqrt{2} = 2.97$ Å.

In the case of GaAs substrates, epitaxial relationships have been previously reported [5,7–9].

Apart from these differences, the overall structural characteristics of Ag/Fe, Ag/Cr and Cr/Fe superlattices are almost identical. Since results obtained using GaAs substrates have been previously reported [5,7–9], we focus here on structural features associated with the growth on MgO substrates.

Typical examples of RHEED patterns recorded during the growth of Ag/Fe, Ag/Cr and Cr/Fe SLs are given in fig. 1. As in the case of GaAs substrates, the RHEED patterns observed for the Ag/Fe (fig. 1b) and Ag/Cr (fig. 1c) couples are indicative of a rather smooth growth front. The transition between the characteristic patterns corresponding to Ag and Fe or Cr layers is rapid, within one or two monolayers, indicating the formation of sharp interfaces. Also, in analogy with the behaviour observed on GaAs substrate, Fe or Cr layers are always slightly rougher than the Ag ones. Therefore the interfaces are not strictly symmetrical; for each period, Ag (lower surface energy) smoothens the Fe or Cr layer surface. Presumably because of this smoothing effect, there is no noticeable degradation of the RHEED patterns even after the deposition of several thousand ångström thick SLs. On the contrary, even if the first grown Cr/Fe SL periods exhibit RHEED patterns characteristic of sharp interfaces and good single-crystal growth (fig. 1d), a slight but continuous degradation occurs as the growth proceeds further. Such degradation is observed for both GaAs and MgO substrates. This similarity is found despite the fact that there is compressive strain for Fe and Cr epitaxially deposited on GaAs (001)

($\Delta a/a = +1.4\%$ and $+2.0\%$ respectively), while severe tensile strain results from the growth on MgO (001) ($\Delta a/a = -3.5\%$ and -3% respectively). With the aim of decreasing the epitaxial strain energy, we have used thick Ag buffer layers ($\Delta a/a = -0.7\%$ and -0.1% for Fe/Ag and Cr/Ag respectively) or even quasi-lattice matched $\text{In}_{0.28}\text{Ga}_{0.72}\text{As}$ buffer layers [9]. No significant improvement was found. It can therefore be concluded that substrate-induced strain is not the driving force behind the observed disordering when increasing the thickness of Cr/Fe superlattices.

In order to confirm that there is no significant intermixing between individual layers of the SLs or between MgO substrates and SLs, ion beam (Ar⁺, 1 keV) sputter-depth Auger profiles have been performed. Auger electron signal intensities were deduced from dN/dE peak-to-peak heights measured using kinetic energy windows centered on the most intense line of Ag (336–361 eV), O (495–520 eV), Cr (520–538 eV), Fe (688–708 eV), and Mg (1171–1191 eV). The results corresponding to 4 periods SLs of Ag(60 Å)/Fe(30 Å), Ag(60 Å)/Cr(30 Å) and Cr(45 Å)/Fe(45 Å) are presented in figs. 2a, 2b and 2c, respectively. Although Auger measurements are more difficult for SLs grown on MgO substrates than for those grown on GaAs substrates due to charging effects, the measured profiles are similar. The contributions of each individual layer are clearly resolved even in the case of Cr/Fe superlattice (fig. 2c). Moreover, intermixing between the MgO substrate and the SL layers, if present, is limited to the first deposited SL layer, and is probably less than 15 Å in thickness, which is the estimated depth resolution in the present experiments.

Finally, X-ray diffraction was performed in order to determine the overall structural properties, and in particular the periodic ordering of the superlattices. Diffraction measurements were performed in the $\theta/2\theta$ geometry using Cu K α radiation monochromatized after the sample by a pyrolytic graphite (002) reflection) which also eliminates the Fe fluorescence. Spectra corresponding to (Ag 60 Å/Fe 7 Å) \times 15, (Ag 30 Å/Cr 30 Å) \times 34 and (Cr 12 Å/Fe 20 Å) \times 30 superlattices grown on MgO are presented in figs. 3a,

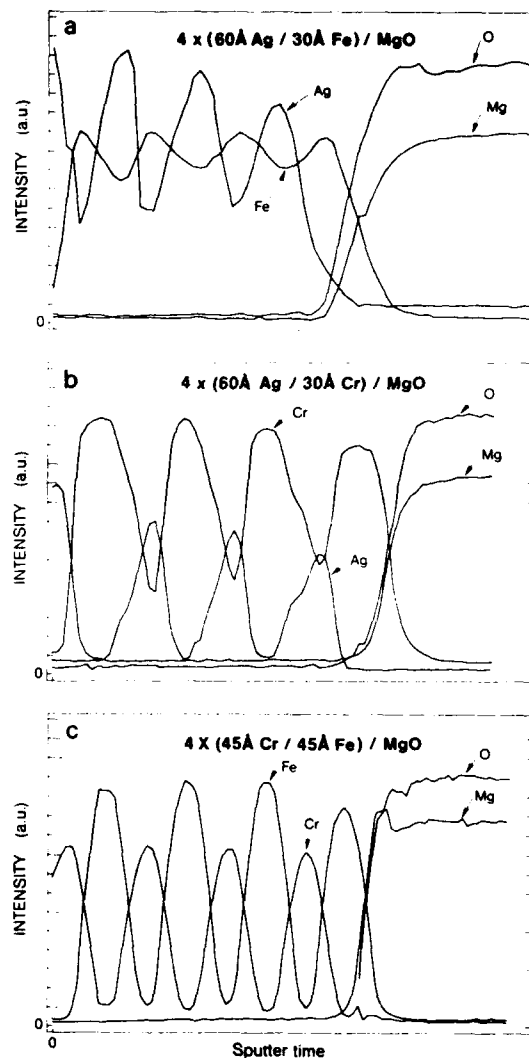


Fig. 2. Ion beam sputter depth Auger profiles of four period SLs grown on MgO (001): (a) Ag(60 Å)/Fe(30 Å); (b) Ag(60 Å)/Cr(30 Å); (c) Cr(45 Å)/Fe(45 Å).

3b and 3c, respectively. The spectra are similar to those obtained for SLs grown on GaAs [9]. In particular several satellites are identified for both Ag/Fe and Ag/Cr SLs between Ag and Fe (or Cr) Bragg peaks. These satellites indicate that well-ordered SL structures with sharp interfaces are achieved for Ag/Fe and Ag/Cr. Simulations

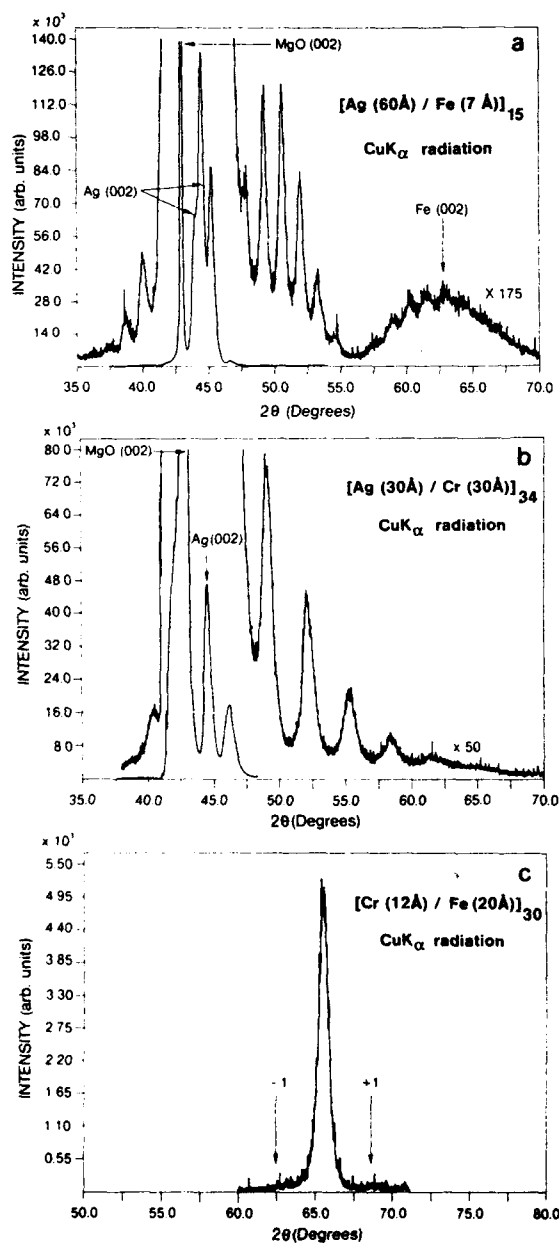


Fig. 3. X-ray $\theta/2\theta$ diffraction patterns around the first Bragg peaks for different SLs grown on MgO (001). Note that we observe in spectrum (a) two Ag (002) peaks, due to buffer and SL layers, respectively.

are in progress to estimate the influence of the two interfaces (Ag/Fe and Fe/Ag or Ag/Cr and Cr/Ag) on the satellite intensities, and to determine if they give rise to the asymmetry in the number of satellites observed around the (002) Bragg peaks. On the other hand, we only detected two weak satellites on each side of the (002) Cr/Fe SL reflection, despite the fact that there is no substrate peak obscuring their observation. One of the origins of these weak intensities is the absorption of X rays by Fe. We plan to carry out further experiments near the K-absorption edge of Cr in order to enhance the peak satellite intensity as in Fe/Mn SLs [12] and to better understand the nature of the interfaces for this system.

Concerning the magnetic properties of SLs grown on MgO (001), it should be noted that up to now no perpendicular magnetization has been found in Ag/Fe SLs grown on MgO (001), although such behavior has been observed in identical structures grown on GaAs (001) [3]. This difference may be related to the fact that for Ag layers grown on MgO no surface reconstruction occurs, while when grown on GaAs a clear (6×6) reconstruction is observed. Also, no RHEED oscillations are observed during the growth of Ag on MgO in contrast with the behavior found on GaAs [8]. It seems therefore that Ag layers are of lower quality when grown on MgO, although X-ray diffraction results on Ag/Fe SLs grown on MgO and GaAs substrates are comparable. The difficulty of obtaining perpendicular magnetization in the case of MgO substrates indicates that it is probably very sensitive to the atomic-scale perfection of the interface between Ag and Fe layers.

3.2. Ag/Co superlattices

Co-based multilayer structures have recently attracted considerable attention [13–18] because of their magnetic properties, such as perpendicular magnetic anisotropy, potentially of interest for high-density magnetic recording. Moreover, epitaxial strain in such systems may impose the formation of Co metastable phases, giving rise to new magnetic properties. Depending on the substrate structure and/or superlattice structural param-

ters (individual layer thickness, nature of the alternating metals), the Co layers crystallize in the usual hcp or in fcc [17,21–23] and bcc [2,19–21] metastable phases.

Among the different metals which can be alternated with Co to give single-crystal SLs, Ag has been studied less than other noble metals such as Au [14,15], Pt [13], Pd [13] or Cu [16]. However, very recent results indicate that the Ag/Co couple is a good candidate to obtain enhanced magneto-resistance effects [23,24].

When Co is directly deposited on MgO (001) substrates at room-temperature, it crystallizes in the (001) hcp orientation. However, if Ag is intercalated between MgO and the Co layer, it is the fcc phase which occurs with the following epitaxial relationship:

$$\text{Co}_{\text{fcc}}\{001\}\langle 100\rangle \parallel \text{Ag}_{\text{fcc}}\{001\}\langle 100\rangle.$$

After a nucleation layer of 20 Å, of Cr on MgO, a thin Ag layer (~60 Å) is in fact sufficient to impose the fcc phase of Co. The RHEED pattern of this phase is observed up to 400 Å, the thickest Co layer deposited in the present work. However, nuclear magnetic resonance (NMR) experiments [25], although confirming the presence

of the metastable fcc phase, indicate also a contribution of the hcp phase.

Different superlattice structures have been grown at room-temperature with individual layers ranging from 30 to 60 Å for Ag and 5 to 60 Å for Co. Although the RHEED pattern associated with the fcc Co phase is always observed for a 30 period SL of Ag(30 Å)/Co(5 Å), change in the RHEED pattern occurs with increasing Co layer thickness. It is tentatively associated to the phase transition from fcc to hcp. For a superlattice consisting of alternating layers of 60 Å Ag and 10 Å, 20 Å or 60 Å Co, the transition appears after ~15, 3 and 1 periods of growth, respectively. This result is in contrast to the fact that for a single layer of Co on Ag (001) the fcc phase is still present after several hundred angstroms deposition. It is clearly more difficult to preserve the fcc phase when alternating growth of Ag and Co is performed. This is probably due to the fact that the structural quality of the Ag layers grown on top of the Co layers degrades as a function of individual and integrated thicknesses of the Co layers, as deduced from the RHEED pattern evolution. Indeed the RHEED pattern of the fcc Co phase disappears when the Ag layer assumes

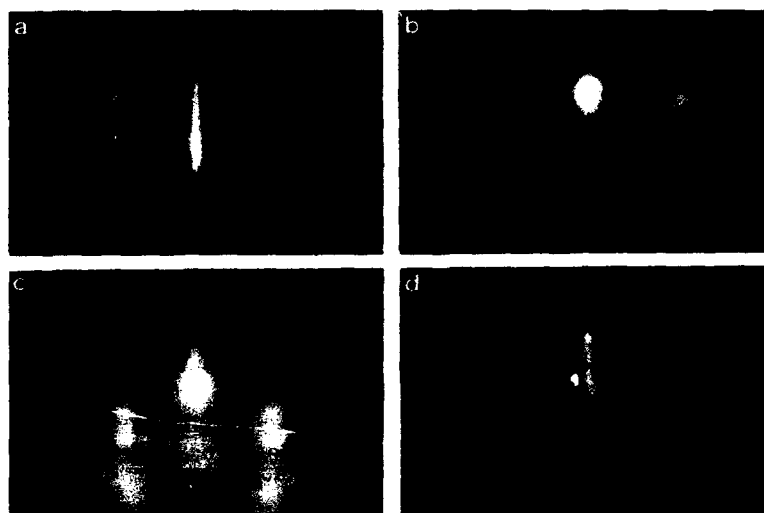


Fig. 4. Characteristic RHEED patterns of a (Ag 60 Å/Co 20 Å)₁₈ SL: (a) first Ag layer ((001) single orientation); (b) first Co layer (fcc phase); (c) last Ag layer (non-single orientation); (d) last Co layer (hcp phase).

several orientations. Another remarkable point is that when Co is grown on Ag (001), it assumes its bulk lattice parameter (3.54 Å) from the very first monolayers deposited. In other words, there is no pseudomorphic growth in this system.

Typical RHEED patterns taken during the growth of a (Ag 60 Å/Co 20 Å) \times 18 are presented in figs. 4a–4d. Figs. 4a and 4b correspond respectively to Ag and Co layers in the first SL period while figs. 4c and 4d correspond to Ag and Co layers in the last SL period, i.e. at a stage where the Ag layer is no longer of a single orientation and the Co layer is mainly in the hcp phase. From the point of view of transport properties, Ag/Co SLs epitaxially grown on MgO (001) appear to be promising structures. The magnetoresistance ratio attains 20% at 4.2 K with magnetoresistance peaks at ± 200 Oe [26].

4. Conclusion

It is shown that a MgO (001) substrate can be used instead of GaAs (001) for the MBE growth of high quality Cr/Fe, Ag/Fe, Ag/Cr, and Ag/Co epitaxial superlattices.

The structural properties of these superlattices grown on both substrates are similar. The main difference resides in the epitaxial relationships between the metals and the substrates. In particular, Cr and Ag take the (001) orientation on MgO (001) while on GaAs (001) the observed orientations are (112) for Cr and (110) and/or (001) for Ag. Another difference is that for Ag layers grown on MgO no surface reconstruction occurs, while when grown on GaAs a clear (6 \times 6) reconstruction is observed. This difference may be related to the fact that no perpendicular magnetization has been found, at least up to now, for Ag/Fe SLs grown on MgO, contrary to the case of identical SLs on GaAs (001).

On the other hand, in the present early state of our investigations, it seems easier to grow Ag/Co superlattices on MgO than on GaAs. It is found that thin layers of Co epitaxially grown on Ag (001) are mainly in the fcc metastable phase, the transition towards the hcp phase being rapidly

observed in SL structures when increasing the Co thickness. These superlattices have already exhibited promising transport properties such as enhanced magnetoresistance effect.

References

- [1] B. Heinrich, K.B. Urquhart, A.S. Arrott, J.F. Cochran, K. Myrtle and S.T. Purcell, *Phys. Rev. Letters* 59 (1987) 1756.
- [2] N.C. Koon, B.T. Jonker, F.A. Volkening, J.J. Krebs and G.A. Prinz, *Phys. Rev. Letters* 59 (1987) 2463.
- [3] R. Cabanel, P. Etienne, S. Lequien, G. Creuzet, A. Barthélémy and A. Fert, *J. Appl. Phys.* 67 (1990) 5409.
- [4] M.N. Baibich, J.M. Broto, A. Fert, F. Nguyen Van Dau, F. Petroff, P. Etienne, G. Creuzet, A. Friederich and J. Chazelas, *Phys. Rev. Letters* 61 (1988) 2472.
- [5] P. Etienne, J. Chazelas, G. Creuzet, A. Friederich, J. Massies, F. Nguyen Van Dau and A. Fert, *J. Crystal Growth* 95 (1989) 410.
- [6] A. Saletes, J. Massies and J.P. Contour, *Japan. J. Appl. Phys.* 25 (1986) L48.
- [7] P. Etienne, G. Creuzet, A. Friederich, F. Nguyen Van Dau, A. Fert and J. Massies, *Appl. Phys. Letters* 53 (1988) 162.
- [8] P. Etienne, J. Massies, F. Nguyen Van Dau, A. Barthélémy and A. Fert, *Appl. Phys. Letters* 55 (1989) 2239.
- [9] P. Etienne, S. Lequien, F. Nguyen Van Dau, R. Cabanel, G. Creuzet, A. Friederich, J. Massies, A. Fert, A. Barthélémy and F. Petroff, *J. Appl. Phys.* 67 (1990) 5400.
- [10] B.T. Jonker, J.J. Krebs and G.A. Prinz, *Phys. Rev.* B39 (1989) 1399.
- [11] R.F.C. Farrow, V.S. Speriosu, S.S.P. Parkin, C. Chien, J.C. Brauman, R.F. Marks, P.D. Kirschner, G.A. Prinz and B.T. Jonker, *Mater. Res. Soc. Symp. Proc.* 130 (1989) 281.
- [12] N. Nakayama, I. Moritani, T. Shinjo, Y. Fujii and S. Sasaki, *J. Phys.* F18 (1988) 429.
- [13] N. Nato, *J. Appl. Phys.* 64 (1988) 6424.
- [14] E. Velu, C. Dupas, D. Renard, J.P. Renard and J. Seiden, *Phys. Rev.* B37 (1988) 688.
- [15] C.H. Lee, Hui He, F.J. Lamelas, W. Vavra, C. Uher and R. Clarke, *Phys. Rev. Letters* 62 (1989) 653.
- [16] A. Cebollada, J.L. Martinez, J.M. Callego, J.J. de Miguel, R. Miranda, S. Ferrer, F. Batallan, G. Fillion and J.P. Rebouillat, *Phys. Rev.* B39 (1989) 9726.
- [17] F.J. Lamelas, C.H. Lee, Hui He, W. Vavra and R. Clarke, *Phys. Rev.* B40 (1989) 5837.
- [18] R. Krishnan, V. Cagan, M. Porte and M. Tessier, *J. Magnetism Magnetic Mater.* 83 (1990) 65.
- [19] G.A. Prinz, *Phys. Rev. Letters* 54 (1985) 1051.
- [20] M. Komuro, Y. Kozondo, S. Narishige, M. Hanazono and Y. Sugita, *Japan. J. Appl. Phys.* 27 (1988) L2105.
- [21] Hong Li and B.P. Tonner, *Phys. Rev.* B40 (1989) 10241.

- [22] C.M. Schneider, P. Bressler, P. Schuster, J. Kirschner, J.J. de Miguel and R. Miranda, *Phys. Rev. Letters* 64 (1990) 1059.
- [23] J.A.C. Bland, A.D. Johnson, C. Norris and H.J. Lauter, *J. Appl. Phys* 67 (1990) 5397.
- [24] D.H. Mosca, A. Barthélémy, F. Petroff, A. Fert, P.A. Schroeder, W.P. Pratt, Jr., R. Laloe and R. Cabanel, *E-MRS Spring Meeting, Strassbourg, 1990 (J. Magnetism Magnetic Mater., to be published).*
- [25] K. Le Dang and P. Veillet, private communication.
- [26] F. Petroff, A. Barthélémy and A. Fert, unpublished.

p-Type diluted magnetic III–V semiconductors

H. Munekata, H. Ohno *, R.R. Ruf, R.J. Gambino and L.L. Chang

IBM Research Division, T.J. Watson Research Center, P.O. Box 218, Yorktown Heights, New York 10598, USA

Diluted magnetic III–V semiconductors $\text{In}_{1-x}\text{Mn}_x\text{As}$ with p-type conduction have been successfully grown by molecular beam epitaxy under the specific growth conditions of substrate temperatures above 275°C with Mn compositions $0.001 \leq x \leq 0.03$. No MnAs second phase was detected in these films in which the Mn ions serve the dual purpose of providing conduction holes and local spins. Hole concentrations fall in the range of 5×10^{17} to 10^{20} cm^{-3} depending on the Mn composition, and they can be varied with donor impurities such as Sn. Magnetotransport at low temperatures exhibits striking hysteretic characteristics, suggesting the occurrence of ferromagnetic order induced by the presence of holes.

1. Introduction

Diluted magnetic III–V semiconductors are novel semiconductor materials in which high concentrations of magnetic ions are incorporated in the host III–V semiconductors. As recently exemplified by the epitaxy of $\text{In}_{1-x}\text{Mn}_x\text{As}$ ($x \leq 0.2$) films, formation of such systems was made possible by molecular beam epitaxy under low growth temperatures in the $200\text{--}300^\circ\text{C}$ range [1–3]. In diluted magnetic semiconductors, various cooperative effects can occur in both magnetic and electronic properties through the spin-exchange interaction between free carriers and magnetic ions [4]. These effects and their applications can now be pursued in technologically important III–V semiconductors and related heterostructures.

Previously, two types of $\text{In}_{1-x}\text{Mn}_x\text{As}$ epitaxial films were found under two different growth conditions. At low substrate temperatures ($\sim 200^\circ\text{C}$), homogeneous alloys with paramagnetic characteristics were grown at least up to $x = 0.18$. These films exhibited n-type conduction. Under the second growth condition of relatively high growth temperatures ($\sim 300^\circ\text{C}$) with large x values, the

films were ferromagnetic, arising apparently from the presence of MnAs clusters.

In this paper, we report the growth of homogeneous p-type $\text{In}_{1-x}\text{Mn}_x\text{As}$ films and their physical properties associated with carrier-induced magnetism. We have found in the growth-parameter space a specific regime, defined by the substrate temperatures $T_s \geq 275^\circ\text{C}$ and the Mn compositions $0 \leq x \leq 0.03$, where Mn ions serve the dual purpose of providing both local spins and conduction holes. Within this regime, the formation of MnAs-like clusters is suppressed, and a variety of p-type samples with different hole concentrations can be produced. The highest hole concentration so far obtained is $p \sim 10^{20} \text{ cm}^{-3}$ at $x = 0.004$. The number of holes at a fixed Mn composition has also been found to be controllable by doping with conventional donor impurities, such as Sn. In this case, the hole concentration decreases with an increasing incorporation of Sn, leading eventually to the conversion to n-type conduction. The p-type samples thus prepared exhibit very striking hysteretic characteristics in magnetotransport at low temperatures, together with the appearance of remanent magnetization [5]. In contrast, no anomalous behavior is observed for the n-type samples. These observations strongly suggest that the magnetic order is induced by carriers as a result of the rather strong

* Permanent address: Department of Electrical Engineering, Hokkaido University, Sapporo 060, Japan.

ferromagnetic spin-exchange interaction between the holes and Mn ions.

2. Epitaxy of p-type $\text{In}_{1-x}\text{Mn}_x\text{As}/\text{InAs}/\text{GaAs}$ (100)

A large number of thick epitaxial films (1–2.5 μm) were grown by molecular beam epitaxy on $\text{InAs}(20\text{ nm})/\text{GaAs}(300\text{ nm})/\text{GaAs}(100)$ surfaces under various combinations of growth parameters. $T_s = 200\text{--}380^\circ\text{C}$, $[\text{As}_4]/[\text{In} + \text{Mn}] = 1\text{--}10$, and $x = 0.001\text{--}0.05$, for substrate temperatures, flux ratios, and Mn compositions, respectively. The growth rate was $\sim 1.2\text{ }\mu\text{m/h}$ for all the films. The x values of the samples were evaluated by electron micro-probe analysis using a 10 keV beam. The flux ratio does not appear to have a significant influence on the physical properties of the films except that very high As_4 fluxes tend to induce three-dimensionally nucleated islands. The substrate temperature, however, is a rather critical growth parameter which is responsible for the resulting properties. The conduction is usually dominated by extrinsic donor states of unknown origin and thus n-type for films grown at $T_s = 200\text{--}265^\circ\text{C}$, whereas p-type conduction takes place for samples grown at $T_s \geq 275^\circ\text{C}$. The hole concentrations, as evaluated by low-field (4 kOe) Hall effect measurements, are in the range of $10^{19}\text{--}10^{20}\text{ cm}^{-3}$, greater than the values obtained in the conventional Mn-doped III-V compounds [6–8]. They are also strongly dependent on the Mn composition x , as shown in fig. 1 for samples grown at $T_s = 300^\circ\text{C}$. In the region of low Mn compositions ($0.001 \leq x \leq 0.004$), hole concentration increases monotonically with increasing x , reaching the highest concentration of $p \sim 10^{20}\text{ cm}^{-3}$ at $x = 0.004$. The hole concentration is reasonably close to the number of Mn atoms, indicating that Mn in these films are acceptors (Mn^{2+} plus one hole) with an activation efficiency being nearly 100%. Beyond $x = 0.004$, however, the numbers of holes decrease drastically with increasing Mn composition. The reduction is more than two orders of magnitude from $x = 0.004$ to 0.026, at which point the hole concentration is as low as $p \sim 5 \times 10^{17}\text{ cm}^{-3}$.

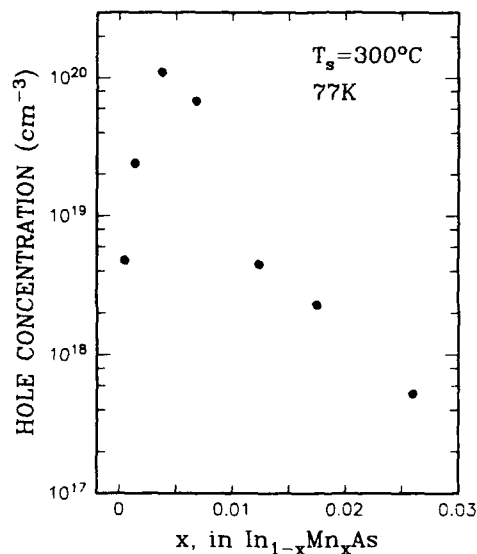


Fig. 1. Hole concentrations at 77 K of $\text{In}_{1-x}\text{Mn}_x\text{As}$ films grown at a substrate temperature of 300°C with different Mn compositions.

The influence of the Mn composition on film homogeneity in terms of the existence of ferromagnetic MnAs phase was examined by magnetization measurements. Hysteresis loop studies were performed at -150°C (123 K) using a vibrating sample magnetometer, with which a total MnAs concentration of $\sim 10^{18}\text{ cm}^{-3}$ could be selectively detected out of diamagnetic backgrounds of a glass sample holder and an undoped semi-insulating GaAs(100) substrate. Great care was taken to subtract these backgrounds for quantitative analyses of small sample signals ($10^{-6}\text{--}10^{-4}\text{ emu}$). Magnetization data thus obtained are shown in fig. 2 for samples with two different Mn compositions, $x = 0.026$ and 0.046. Both samples were grown at the same substrate temperature of $T_s = 300^\circ\text{C}$. As can be seen, the magnetization of the $x = 0.026$ sample, consisting only of a paramagnetic component as expected for a homogeneous alloy, does not show any evidence of the hysteretic component within the detection limit. In contrast, both components are clearly visible in the case of $x = 0.046$. The hysteresis disappears at $\sim 320\text{ K}$, which is consistent with the Curie temperature of ferromagnetic MnAs [9]. The MnAs

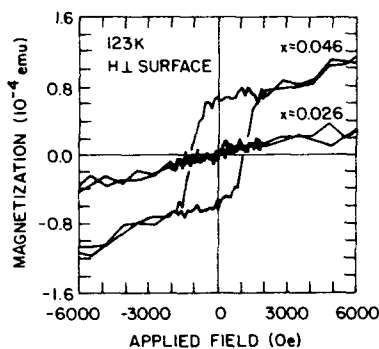


Fig. 2. Magnetization data at -150°C (123 K) of $\text{In}_{1-x}\text{Mn}_x\text{As}$ films with two different Mn compositions. Films were grown at a substrate temperature of 300°C . Magnetic field was applied perpendicular to the film surface.

composition, estimated from a known value of 800 emu/cm^3 of a bulk MnAs , is $x_{\text{MnAs}} = 0.0065$ which corresponds to 13% of the total Mn composition of the $x = 0.046$ sample. Further investigations have confirmed that all samples with $x \leq 0.026$ do not exhibit any hysteretic characteristics reminiscent of MnAs at 123 K. It is probably surprising that no hysteretic trace is observed even for an $x = 0.012$ sample grown at $T_s = 380^{\circ}\text{C}$. These results head to the conclusion that the formation of MnAs clusters is critically dependent on the x value with a critical Mn composition being around $x \sim 0.03$ at T_s above 275°C .

This observation suggests that p-type samples with $x \leq 0.026$ are virtually homogeneous, so that the reduction in hole concentrations (fig. 1) cannot be attributed to a decrease in the number of Mn acceptors due to the MnAs clustering. One possible mechanism responsible for the reduced hole concentration may be the self-compensation effect as frequently encountered in doping II-VI compounds, in which point defects or complexes are formed during the growth to electrically compensate for the charges of the impurities [10].

We now discuss the influence of intentional doping on conduction properties of p-type $\text{In}_{1-x}\text{Mn}_x\text{As}$ films. It has been found that the number of holes at a fixed Mn composition is controllable by doping with conventional donor impurities, such as Sn. The hole concentration decreases with an increasing incorporation of Sn,

and a conversion to n-type conduction occurs under extremely high-doping condition. Typical results are shown in fig. 3 for $x = 0.012$ samples grown at $T_s = 300^{\circ}\text{C}$, in which carrier concentration is plotted as a function of effusion cell temperature of Sn. The equilibrium vapor pressures range from 7.5×10^{-7} Torr (750°C) to 1×10^{-4} Torr (990°C), which are common values used for intentional doping in molecular beam epitaxy [11]. The hole concentration in the undoped sample is $4.5 \times 10^{18}\text{ cm}^{-3}$, as indicated in the figure with the left-most data point. The reduction in hole concentration is noticeable for samples grown with Sn-cell temperatures above 750°C , and conversion to n-type conduction takes place over $\sim 850^{\circ}\text{C}$. Above this cell temperature, electron concentrations continue to increase up to at least $\sim 1000^{\circ}\text{C}$. Composition analyses of the heavily doped films have confirmed that the Mn composition retains the same value as that of the undoped sample. It is interesting to note that the electron concentration decreases with increasing Mn composition at a fixed Sn cell temperature. For example, at the cell temperature of 950°C , electron concentrations are $n = 1.2 \times 10^{20}$, 9.6×10^{19} , and $1.4 \times 10^{18}\text{ cm}^{-3}$ for $x = 0$, 0.0038, and 0.012, respectively. This trend indicates that Sn atoms pre-

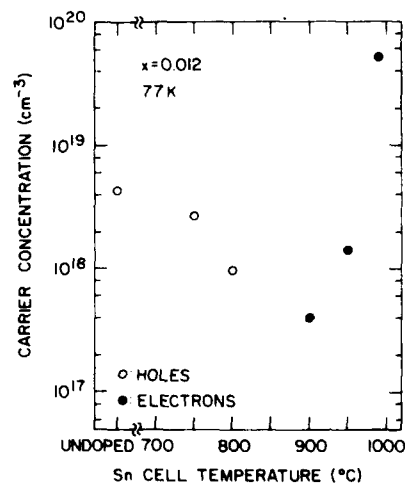


Fig. 3. Carrier concentrations at 77 K of Sn-doped films ($x = 0.012$) as a function of cell temperature of the Sn source. Open and solid circles represent hole and electron concentrations, respectively.

dominantly substitute for the sites of group III element.

3. Transport properties

The p-type samples thus prepared exhibit very striking hysteretic characteristics in magnetotransport at low temperatures [5]. In fig. 4, we show one of these results, transverse magnetoresistance ρ_{xx} and Hall resistance ρ_{xy} at 4.2 K for an undoped $x = 0.012$ sample patterned into a Hall-bar geometry. Numbers and arrows in the figure represent the sequence and sweeping direction of an applied field H . For the ρ_{xx} component, a very large negative magnetoresistance is accompanied by the hysteretic behavior, but a zero-field resistance remains at a constant value regardless of the history of the applied field. For the ρ_{xy} component, the ρ_{xy} - H curve forms a hysteresis loop with a small coercive force of ~ 200 Oe, so that the zero-field value depends on the polarity of H . Deviation from the ideal inversion-symmetry in the measured ρ_{xy} curve is due to a finite contribution of the ρ_{xx} component. These results indicate that ferromagnetic order takes place in the film,

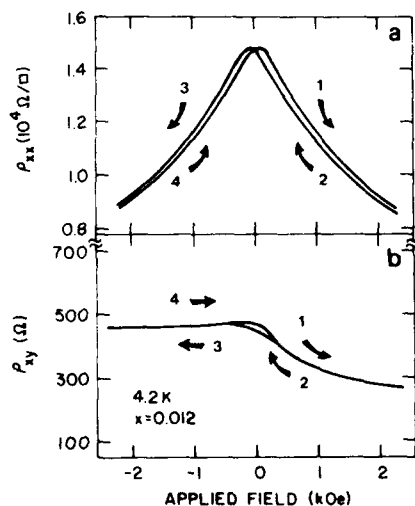


Fig. 4. Transverse magnetoresistance ρ_{xx} (a) and Hall resistance ρ_{xy} (b) at 4.2 K of a p-type sample with $x = 0.012$. The sample was patterned into a Hall bar by conventional photolithography and wet-etching processes.

and that the transport behavior is strongly influenced by the remanent magnetization. An anomalous increase in low-field (50 Oe) magnetization, detected with a SQUID magnetometer at temperatures below ~ 8 K, is consistent with these observations. In addition, it is important to mention that these characteristics are totally absent in n-type $\text{In}_{1-x}\text{Mn}_x\text{As}:\text{Sn}$ samples.

It is very likely that the observed effects arise from ferromagnetic order induced by the presence of conduction holes. In other words, a ferromagnetic spin-exchange interaction exists between the holes and Mn ions. The interaction of holes with MnAs clusters can not possibly be responsible for these results, since the coercive force (~ 2000 Oe) and the Curie temperature (~ 320 K) of this ferromagnetic material do not agree at all with present observations. Superparamagnetism due to ultrafine MnAs clusters, if any, might cause a weak remanent magnetization [12], but the interaction of carriers with such clusters, usually considered to be fairly small, is not known at the present stage. One of the intriguing and possible mechanisms is the Ruderman-Kittel-Kasuya-Yoshida (RKKY) interaction in which high numbers of free carriers can indirectly cause a long range ferromagnetic or antiferromagnetic order among magnetic ions. In diluted magnetic semiconductors, such carrier-induced magnetization was examined experimentally in the p-type PbSnMnTe (Mn $\sim 3\%$) system [13], where high hole concentrations of the order of 10^{20} cm^{-3} were found necessary for the carrier-induced ferromagnetic order. In contrast, in the present system, both hole and Mn concentrations are relatively low; for example, $p = 4.5 \times 10^{18} \text{ cm}^{-3}$ at 77 K and $x = 0.012$ for the sample in fig. 4. This fact implies that spin-exchange interaction is strong for the p-type $\text{In}_{1-x}\text{Mn}_x\text{As}$, in which Mn ions are the sources for both local spins and conduction holes.

Acknowledgements

We gratefully acknowledge A. Boulding for performing the electron micro-probe analyses, H. Lilienthal and T.R. McGuire for their collaboration in the low-temperature low-field magnetiza-

tion measurements, and S. von Molnár for fruitful discussions. This work is partially sponsored by the Army Research Office.

References

- [1] H. Munekata, H. Ohno, S. von Molnár, A. Segmüller, L.L. Chang and L. Esaki, *Phys. Rev. Letters* 63 (1989) 1849.
- [2] H. Munekata, H. Ohno, S. von Molnár, A. Harwit, A. Segmüller and L.L. Chang, *J. Vacuum Sci. Technol.* B8 (1990) 176.
- [3] S. von Molnár, H. Munekata, H. Ohno and L.L. Chang, European MRS Meeting, Strassbourg, 1990 [*J. Magnetism Magnetic Mater.*, to be published].
- [4] See, e.g., J.K. Furdyna and J. Kossut, Eds., *Semiconductors and Semimetals*, Vol. 25, *Diluted Magnetic Semiconductors* (Academic Press, Boston, MA, 1986).
- [5] H. Ohno, H. Munekata, S. von Molnár and L.L. Chang, unpublished; also H. Ohno, H. Munekata, S. von Molnár and L.L. Chang, presented at 35th Conf. on Magnetism of Magnetic Materials, San Diego, CA, 1990 [*J. Appl. Phys.*, to be published].
- [6] M. Illegems, R. Dingle and L.W. Rupp, Jr., *J. Appl. Phys.* 46 (1975) 3059; D. DeSimone, C.E.C. Wood and C.A. Evans, Jr., *J. Appl. Phys.* 53 (1982) 4938.
- [7] H. Asahi, Y. Kawamura, M. Ikeda and H. Okamoto, *Japan. J. Appl. Phys.* 20 (1981) L187.
- [8] D.G. Andrianov, V.V. Karataev, G.V. Lazareva, Yu.B. Muraviev and A.S. Savrl'ev, *Soviet Phys.-Semicond.* 11 (1977) 738, and references therein.
- [9] C.P. Beam and D.S. Rodbell, *Phys. Rev.* 126 (1962) 104.
- [10] See, e.g., Y.S. Park and B.K. Shin, in: *Electroluminescence*, Ed. J.I. Pankove (Springer, Berlin, 1977) pp. 133-170.
- [11] See, e.g., A.Y. Cho, in: *Molecular Beam Epitaxy and Heterostructures*, Eds. L.L. Chang and K. Ploog (Nijhoff, Dordrecht, 1985) pp. 191-226.
- [12] See e.g., A.H. Morrish, *The Physical Principles of Magnetism* (Wiley, New York, 1965, republished by Krieger, Melbourne, FL, 1980) pp. 360-363.
- [13] T. Story, R.R. Galazka, R.B. Frankel, and P.A. Wolff, *Phys. Rev. Letters* 56 (1986) 777.

Growth and novel properties of magnetic heterostructures by molecular beam epitaxy

J.M. Hong, D.D. Awschalom, F. Agulló-Rueda * and L.L. Chang

IBM Research Division, T.J. Watson Research Center, P.O. Box 218, Yorktown Heights, New York 10598, USA

Diluted magnetic semiconductor $\text{Cd}_{1-x}\text{Mn}_x\text{Te}$ – $\text{Cd}_{1-y}\text{Mn}_y\text{Te}$ heterostructures of various layer thickness, where $0 \leq x, y \leq 0.4$, were grown by molecular beam epitaxy for optical and magnetic studies of reduced-dimensional systems. X-ray diffraction patterns, low-temperature photoluminescence spectra (PL), and AC magnetic susceptibility measurements were used to verify the integrity of these structures. The carrier quantization in the quantum wells were revealed by the magnetic response in a magneto-optic microsusceptometer as well as by the results of PL measurement. These SLs were used to study the dimensional cross-over of the spin-glass phase. In addition, a magnetic-field-induced transition from type I to type II superlattice was observed.

1. Introduction

The advent of epitaxial crystal growth techniques such as the molecular beam epitaxy (MBE), with the ability to grow multilayer structures of monolayer resolution and selected chemical compositions, has made possible the experimental realization of heterostructures of semiconducting, magnetic, and insulating materials for studies of systems of reduced dimensions [1–5]. Among these materials, the diluted magnetic semiconductors (DMSs), a class of compound semiconductors containing a random distribution of magnetic moments, exhibit interesting magnetic effects as well as semiconducting properties [6]. For example, the systematical change of magnetic dilution results in different magnetic phases, namely, paramagnetic, spin-glass, or antiferromagnetic states, depending on the concentration of the magnetic ions and the temperature. Furthermore, DMSs exhibit novel magneto-optic and magneto-transport effects, such as the huge Faraday rotation, enhanced Zeeman splitting, and large negative magnetoresistance, due to the exchange interactions of the localized magnetic moments with the charge carriers.

While there have been extensive studies on the bulk properties of DMSs, the manifestations, in particular, the magnetic manifestations, of reduced dimensionality in DMS heterostructures have just started to be explored. The capability of MBE to select a particular magnetic phase by fine-tuning the magnetic dilution and to tailor the magnetic layer thickness allowed magnetic studies of dimensional crossover [7]. And the ability to generate carriers and confine them in magnetic wells allows the probing of carriers–magnetic-moments exchange interaction in a local scale [8,9].

In the first part of the following section the growth of DMS CdMnTe and CdMnTe – CdMnTe SLs will be discussed in detail. The materials were characterized by the X-ray diffractometer and low temperature photoluminescence (PL) measurements, supplemented by the photoluminescence excitation (PLE) measurements. In the second part the results from the magnetic and magneto-optical studies will be presented.

2. MBE growth and characterization

The host crystals of DMS can be $\text{A}^{\text{II}}\text{B}^{\text{VI}}$ compounds (binary and ternary compounds of group II and group VI elements), $\text{A}^{\text{IV}}\text{B}^{\text{VI}}$, Cd_3As_2 and Zn_3As_2 , chalcopyrites [6], and, recently, $\text{A}^{\text{III}}\text{B}^{\text{V}}$ [10]. The magnetic species can be transition metals

* Present and permanent address: Departamento de Física Aplicada C-IV, Instituto de Ciencia de Materiales de Madrid (CSIC), Universidad Autónoma, Cantoblanco, E-28049, Madrid, Spain.

or rare earth elements. The most-studied DMSs are the family of compounds with the form of $A^{II}_{1-x}M^{II}_x B^{VI}$, where A^{II} can be Cd, Hg, Zn, ..., M^{II} can be Mn, Fe, Eu, Gd, ..., and B^{VI} can be O, S, Se, or Te. The host binary $A^{II}B^{VI}$ compounds crystallize mainly in either zincblende (e.g., CdTe) or wurzite (e.g., MnTe) structures at atmospheric pressure.

Several crystal growth techniques have been employed to grow epitaxially thin-film $A^{II}B^{VI}$ compounds [3,11–14]. The first reported successful preparation of the DMS $A^{II}M^{II}B^{VI}$ thin films was HgCdMnTe by the close-spaced isothermal vapor transport growth technique [11]. The epitaxial growth was achieved by deposition of evaporating HgTe on the CdMnTe substrate and mutual interdiffusion. But, since then, vast amounts of the thin films have been CdMnTe and CdMnTe–CdMnTe heterostructures prepared by the MBE technique on GaAs (100) substrates [3,12,13]. The GaAs (100) substrates have advantages of providing large areas of good-quality and flat surface, well-established substrate cleaning methods, and controllable surface reconstructions. Recently, CdTe substrates having relatively large areas of minimal twins became available and were used to grow CdMnTe [15,16].

In our laboratory $Cd_{1-x}Mn_xTe$ layers were epitaxially grown on CdTe buffer layers deposited on semi-insulating GaAs substrates of either nominal (100) or 2° off towards $[0\bar{1}1]$ (see ref. [17]) in a MBE system with a base pressure of $< 2 \times 10^{-10}$ Torr. Substrates were prepared using the standard procedures of degreasing and etching, indium-bonded onto molybdenum blocks, and outgassed in the loading chamber before being transferred to the growth chamber. After the thermal surface-oxide desorption the reflection high energy electron diffraction (RHEED) pattern showed a streaking $3 \times$ reconstruction along the $[0\bar{1}1]$ azimuth, indicating an As-stabilized surface condition. The substrate temperature was then decreased to the typical growth temperature of 300°C . Compound CdTe was used as the source material in growing CdTe layers because it provided the right flux ratio of Cd and Te_2 beams as suggested by Farrow et al. [18]. For growing $Cd_{1-x}Mn_xTe$ additional effusion cells containing

elemental Mn and Te were used to maintain the stoichiometry. Typical growth rate of CdTe was $0.5 \mu\text{m/h}$. Depending on the growth conditions employed either CdTe/ $Cd_{1-x}Mn_xTe$ (111)B or (100) could be obtained. The former orientation was chosen resulting in the following orientation relationships in the film plane: $[011] \parallel \text{GaAs}[0\bar{1}1]$ and $[\bar{2}11] \parallel \text{GaAs}[0\bar{1}\bar{1}]$ [19–22]. The lattice mismatch in the former direction was 14.6% but was only -0.7% in the latter. The RHEED patterns initially exhibited elongated spots, but became streaking after the deposition of only a few atomic layers, despite the presence of the initial lattice mismatch. As the buffer layer thickness was increased, $2 \times$ reconstruction appeared in the RHEED pattern in both $\langle 011 \rangle$ and $\langle \bar{2}11 \rangle$ azimuths and remained throughout the growth, indicating the existence of layer by layer epitaxial growth.

For evaluation of the periodic structures, X-ray analysis was performed, employing a computer-controlled diffractometer with a well collimated $\text{Cu K}\alpha_1$ (wavelength $\lambda = 1.540562 \text{ \AA}$) as the source radiation [23]. The magnetic susceptibility measurement was performed utilizing a thin-film integrated miniature dc SQUID susceptometer circuit [24]. For the magneto-optic measurement an improved, ultra-low-noise DC-SQUID-based microsusceptometer was employed [25]. The transparent quartz substrate used allowed the light to be directly incident on the sample.

2.1. CdTe films

The X-ray diffraction studies (θ – 2θ scan) on CdTe (111) films of various thickness revealed that the perpendicular lattice constant of the thin films quickly approached that of a thick CdTe (111) film [26]. For example, a film of 64 \AA thick (17 monolayers) already had an almost identical lattice constant. The PL spectrum at 4.8 K of undoped CdTe (111) layers [3] typically exhibited several strong and well-defined exciton peaks, comparable to those observed in bulk CdTe [27,28]. Those peaks consisted of three dominant bound exciton peaks as well as a weaker peak of free excitons at higher energy. In addition, much weaker features present at lower energies corre-

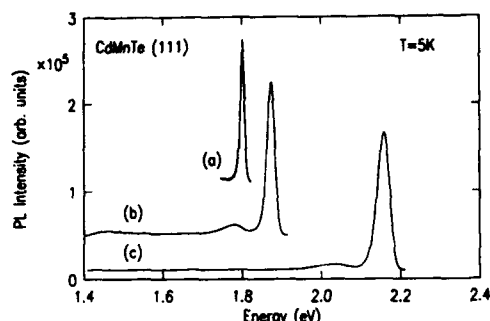


Fig. 1. The PL spectra at 5 K of three CdMnTe films. The MnTe percentage, PL peak position and FWHM of the dominant peaks are (a) 13%, 1.802 eV, 12.0 meV; (b) 17.5%, 1.874 eV, 23.3 meV; (c) 35.5%, 2.161 eV, 34.3 meV. An Ar^+ laser was used as the pumping source.

sponded to the first longitudinal optical (LO) phonon replica of the exciton peaks.

2.2. CdMnTe films

The ability to grow good-quality CdTe films on GaAs substrates permitted the epitaxial growth of bulk films of $\text{Cd}_{1-x}\text{Mn}_x\text{Te}$ and superlattices of $\text{Cd}_{1-x}\text{Mn}_x\text{Te}-\text{Cd}_{1-y}\text{Mn}_y\text{Te}$ on a more similar CdTe than GaAs substrate. Typically, an 1500 Å thick CdTe buffer layer was used. The $2 \times$ reconstruction patterns were maintained throughout the growth. The concentration of Mn was determined by electron microprobe measurements, the peak position of the low temperature PL spectra, and high temperature magnetic susceptibility data. The concentration determined from these methods was self-consistent within experimental errors. Typical PL spectra at 5 K of $\text{Cd}_{1-x}\text{Mn}_x\text{Te}$ layers are shown in fig. 1. In contrast to what was observed in CdTe films only one strong but broader peak is observed. For curve 1a the observed peak is centered at an energy of 1.802 eV and has a full width at half maximum (FWHM) of 12.0 meV, a value comparable to those observed in bulk $\text{Cd}_{1-x}\text{Mn}_x\text{Te}$ with a similar Mn concentration [29,30]. The observed peak corresponds to recombinations of excitons localized near magnetic fluctuations of the magnetic Mn^{2+} ions [29]. The value of x was determined to be 0.13 in this film. As the MnTe concentration is increased the

FWHM of the dominant peaks also increases as evidenced from curves 1b and 1c. The peak positions and FWHM are 1.874 eV and 23.3 meV for curve 1b and 2.161 eV and 34.3 meV for curve 1c, respectively. In addition, broader peaks at lower energies appear, which have been attributed to the formation of bound magnetic polarons around the acceptor site [29]. Introduction of superlattice buffer of CdTe–CdMnTe at the interface between the CdTe and CdMnTe films seemed to slightly increase the luminescence efficiency but did not affect the FWHM. The increase of FWHM as a function of MnTe percentage in CdMnTe is shown in fig. 2, which shows an almost constant slope of increase. It is noticed that these CdMnTe films have luminescence efficiencies almost as high as those of the CdTe films and no other appreciable impurity- or defect-related peaks at lower energies were observed. The magnetic behavior of the films was also confirmed by the magnetic susceptibility measurement to be the same as that of bulk crystals.

2.3. CdMnTe heterostructures

The results described above show that high-quality CdTe and $\text{Cd}_{1-x}\text{Mn}_x\text{Te}$ can be grown by MBE, which is the necessary step towards achieving high-quality $\text{Cd}_{1-x}\text{Mn}_x\text{Te}-\text{Cd}_{1-y}\text{Mn}_y\text{Te}$ heterostructures. In order to explore the paramagnetic–spin-glass region of the phase diagram, the magnetic concentrations, x and y , were varied

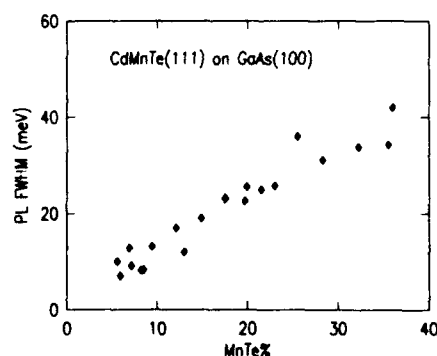


Fig. 2. The FWHM of the dominant peak of CdMnTe at 5 K as a function of the MnTe concentration.

from 0% to 40%. The thickness of each layer ranged from 20 to 200 Å.

The X-ray diffraction pattern in the vicinity of the CdTe (111) reflection of a 25 period $\text{Cd}_{0.89}\text{Mn}_{0.11}\text{Te}-\text{Cd}_{0.65}\text{Mn}_{0.35}\text{Te}$ superlattices is shown in fig. 3. The nominal thicknesses of both the wells and the barriers are 108 Å. The thickness of CdTe buffer in this sample was increased to 2 µm. As in the case of GaAs-AlAs SLs [23,31,32] and CdTe- $\text{Cd}_{0.8}\text{Mn}_{0.2}\text{Te}$ SLs [3] several diffraction peaks associated with the SL are observed. The strong zero-order reflection from the SL occurs at $\theta = 11.911^\circ$ and almost coincides with the slightly stronger (111) reflection from the CdTe buffer layer at $\theta = 11.848^\circ$. The weaker superlattice reflections on the high-angle side are designated as +1, +2, and +3 satellites and those on the low-angle side as -1, -2, and -3 satellites. The periodicity of SL determined from the angular positions of the peaks was 220 Å [32], very close to the nominal value designed from the growth rate measurements. The perpendicular lattice constant of this CdMnTe SL is smaller than that of the CdTe buffer layer and the lattice mismatch of the two determined from the peak positions is -0.5%, in contrast to the case of CdTe- $\text{Cd}_{0.8}\text{Mn}_{0.2}\text{Te}$ SL [3].

The PL spectra at 5 K of two CdMnTe SLs are shown in fig. 4. In fig. 4a the $\text{Cd}_{0.88}\text{Mn}_{0.12}\text{Te}-$

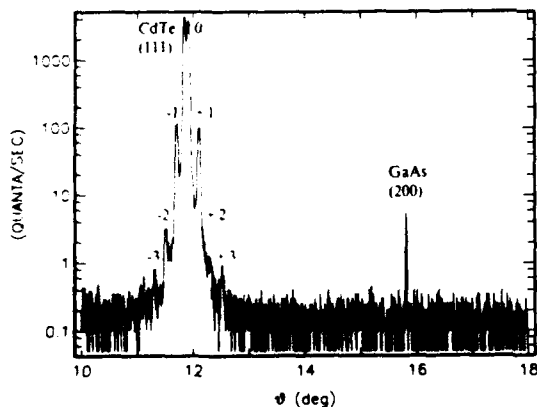


Fig. 3. The X-ray diffraction pattern ($\theta-2\theta$ scan) of a 25 period $\text{Cd}_{0.89}\text{Mn}_{0.11}\text{Te}(108 \text{ Å})-\text{Cd}_{0.65}\text{Mn}_{0.35}\text{Te}(86 \text{ Å})$ diluted magnetic semiconductor superlattice in the vicinity of the CdTe(111) reflection. The X-ray energy and intensity used were 50 kV and 60 mA, respectively.

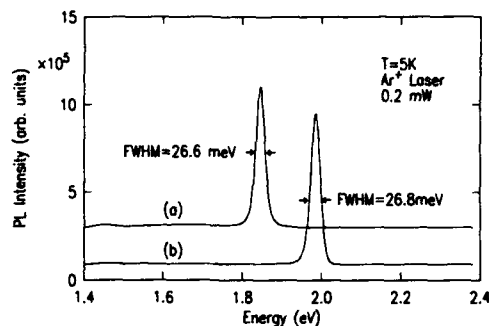


Fig. 4. (a) The PL spectrum of a 60 period $\text{Cd}_{0.88}\text{Mn}_{0.12}\text{Te}(41 \text{ Å})-\text{Cd}_{0.65}\text{Mn}_{0.35}\text{Te}(86 \text{ Å})$ SL; (b) same sample configuration, but the MnTe concentration in the well was increased to 22%.

$\text{Cd}_{0.65}\text{Mn}_{0.35}\text{Te}$ SL has a well and barrier thickness of 41 and 86 Å, respectively. The spectrum shows a strong and dominant peak at 1.846 eV with a FWHM of 26.6 meV. When the Mn concentration in the well is increased to 22%, the PL spectrum, shown in fig. 4b, is still dominated by a strong peak at a higher energy of 1.987 with a FWHM of 26.8 meV. The blue shift of the peaks relative to those of the $\text{Cd}_{0.88}\text{Mn}_{0.12}\text{Te}-\text{Cd}_{0.78}\text{Mn}_{0.22}\text{Te}$ indicates the quantum confinement of charge carriers in those wells. Although the excitation source employed has an energy larger than the bandgap of either wells or $\text{Cd}_{0.65}\text{Mn}_{0.35}\text{Te}$ barriers at this temperature, no other peaks with appreciable intensities were observed, similar to those observed in $\text{Ga}_{1-x}\text{Al}_x\text{As}-\text{GaAs}$ SLs.

3. Novel properties of CdMnTe heterostructures

The DMS CdMnTe heterostructures exhibited interesting and novel magnetic behavior and three examples are described in the following. The first concerns the intrinsic magnetic behavior of the DMS SLs, while the remaining two exploit the strong spin-spin exchange interaction between the charge carriers and local magnetic moments of Mn^{2+} ions.

3.1. Dimensional cross-over studies

Enormous theoretical effort has been expended on the role of dimensionality for spin-glasses and

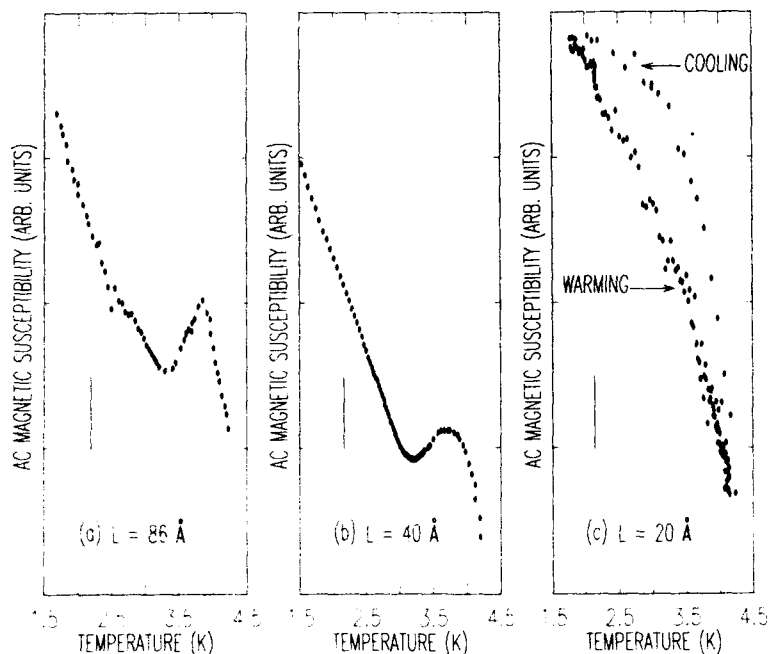


Fig. 5. Magnetic susceptibility of $\text{Cd}_{0.8}\text{Mn}_{0.2}\text{Te}$ - CdTe superlattices with 86 Å CdTe layers and (a) magnetic layer thickness $L = 86$ Å, 25 periods, (b) magnetic layer thickness $L = 40$ Å, 50 periods, and (c) magnetic layer thickness $L = 20$ Å, 100 periods. The vertical scale markers correspond to 2×10^{-6} emu/g.

the question of the lower critical dimension (the dimension below which systems cannot support long-range spin-glass order) [33]. Our results, in the following, on spin-glass behavior in the DMS CdMnTe - CdTe SLs, as the magnetic layer thickness is systematically reduced towards the two-dimensional (2D) limit, suggest that the 3D system can support long-range spin-glass order at finite temperatures, but that the 2D system cannot. These data are consistent with theoretical expectations that the lowest critical dimension for spin-glasses is greater than or equal to two [33].

Examples of the magnetic measurements may be seen in fig. 5, showing the AC magnetic susceptibility of $\text{Cd}_{0.8}\text{Mn}_{0.2}\text{Te}$ - CdTe superlattices with systematically thinner magnetic layers. The thickness of the nonmagnetic CdTe was kept constant at 86 Å, whereas that of the magnetic $\text{Cd}_{0.8}\text{Mn}_{0.2}\text{Te}$ was varied from 86 to 18 Å. The data for the geometry of fig. 5a yields results which are similar to those obtained from bulk

$\text{Cd}_{0.8}\text{Mn}_{0.2}\text{Te}$ crystals of the same Mn dilution, showing a cusp at the spin-glass transition temperature of $T_g = 3.8$ K and a $1/T$ divergences in the lower temperatures [34].

As the width of the magnetic layer is reduced by a factor of two, but still above the magnetic percolation threshold for this geometry [7], the magnetic response is considerably different, as shown in fig. 5b. This thinner 40 Å layer shows a rounding and broadening of the transition at T_g , consistent with there being no true spin-glass order in two-dimensional systems. The rounded maximum signals the development of significant short-range order, but its broadness implies that the establishment of long-range order has been blocked. This therefore suggests that the absence of a spin-glass transition in fig. 5b reflects the inability of the 2D system to support spin-glass order.

Data taken for a still thinner sample are shown in fig. 5c. Here even the broadened maximum of

fig. 5b has disappeared; the susceptibility increases monotonically with decreasing temperature, demonstrating the limited capacity of these thin layers to sustain even short-range order in the temperature range studied. Again, this system is close to but still above its percolation threshold and so one cannot expect a transition to occur except at extremely low temperatures. Furthermore, a hysteresis behavior is observed only in these thinnest samples, suggesting that its occurrence is associated with this system's reduced capacity to sustain even short-range order in equilibrium near the bulk T_g .

3.2. Magnetic manifestation of carrier confinement

The carrier confinement in CdMnTe quantum wells can be revealed not only by traditional methods of studies such as optical absorption, PL, and PLE measurements, but also by the study of the optically induced magnetism in these systems. The magnetism is induced by the spin-polarized carriers, created by circularly-polarized laser light, through the local spin-spin exchange interaction with the magnetic moments. The regions of magnetization, therefore, match the spatial extent of the carrier wavefunctions, which can be easily varied by changing the width of the quantum well or by exciting the carriers into higher quantum levels.

Shown in fig. 6 are the magnetic data of three quantum wells with systematically-reduced well widths [8]. The optical excitation is in the form of picosecond pulses from a tunable dye laser synchronously pumped by a frequency-doubled, mode-locked Nd-YAG laser and the data is time-averaged. There is an increase in the magnetic response when the pumping energy coincides with the excitonic energy of the levels. In the sample with 84 Å well width (fig. 6a), the effect of the quantum levels is clearly seen, with definite peaks at about 1.75 and 1.88 eV and a weaker feature at 1.98 eV, approximately the energies calculated from a simple Kronig-Penney model for excitons associated with $n = 1, 2$, and 3 subbands. For samples with narrower well widths the number of peaks is reduced and the peak energies shift to relatively higher energies as expected.

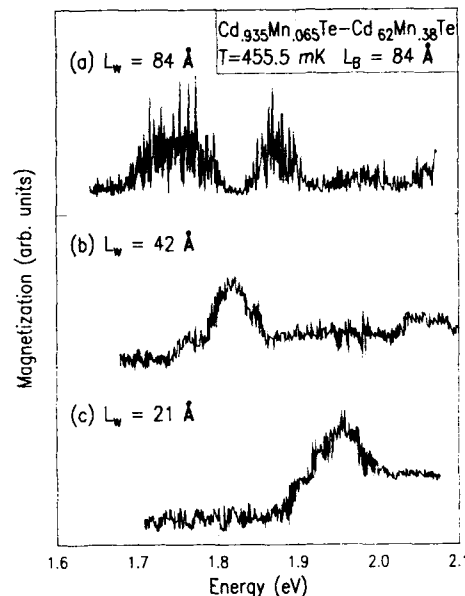


Fig. 6. Magnetic response as a function of pumping energy of 3 Cd_{0.935}Mn_{0.065}Te-Cd_{0.62}Mn_{0.38}Te superlattices with fixed barrier thickness of 86 Å and varying well thickness.

3.3. Magnetic-field-induced type I to type II transition

The exchange interaction between the magnetic ions and carriers in DMS leads to a large spin splitting in these materials with the applied magnetic fields, B [35]. This effect and the possible small value of the valence band offset ΔE_v lead to the observation of a type I to type II SL transition as induced by the magnetic fields in ZnSe-ZnFeSe [36] and CdTe-CdMnTe SLs [37]. In the former a very small ΔE_v and a large strain made the system a Type II SL at $B = 0$. In the latter, for example, a 25 period CdTe(86 Å)-Cd_{0.93}Mn_{0.07}Te(86 Å) SL, the experimental results from PL, PLE, and reflectivity measurements and theoretical calculation indicated that the SL was of type I at $B = 0$. As B was gradually increased a well-marked bump in the field-dependence of the σ^+ -component of the fundamental E_1 -HH₁ excitonic transition and a break in the variation of the associated luminescence efficiency revealed that the SL became a type II at approximately $B = 2$ T.

Based on these experimental results a theoretical calculation, taking into account the change in excitonic binding energy with B , obtained a value of $\Delta E_v/\Delta E_g = 15\text{--}20\%$ at $B = 0$, where ΔE_g is the bandgap difference between CdTe and $\text{Cd}_{0.93}\text{Mn}_{0.07}\text{Te}$.

4. Summary

The $\text{Cd}_{1-x}\text{Mn}_x\text{Te}$ – $\text{Cd}_{1-y}\text{Mn}_y\text{Te}$ DMS SLs grown by MBE were shown to exhibit excellent structural and optical qualities for various magnetic concentrations and magnetic layer thicknesses. Tuning these two magnetic layer parameters allowed the study of magnetic behavior in systems of reduced dimensions. Among the examples mentioned are the dimensional crossover studies of the spin-glass transition, magnetic manifestation of carrier confinement, and type I to type II SL transition as induced by the magnetic field.

Acknowledgements

We would like to thank A. Segmüller for performing X-ray diffraction measurements and G. Bastard, J.A. Brum, G. Grinstein, and E.E. Mendez for helpful discussions. This work was supported in part by the US Army Research Office.

References

- [1] See, for example, L.L. Chang and K. Ploog, Eds., *Molecular Beam Epitaxy and Heterostructures* (Nijhoff, Dordrecht, 1985).
- [2] J. Kwo, E.M. Gyorgy, D.B. McWhan, M. Hong, F.J. diSalvo and C. Vettier, *Phys. Rev. Letters* 55 (1985) 1402.
- [3] J.M. Hong, D.D. Awschalom, L.L. Chang and A. Segmüller, *J. Appl. Phys.* 63 (1988) 3285.
- [4] D.D. Awschalom, J.M. Hong and L.L. Chang, *Surface Sci.* 228 (1990) 220.
- [5] A. Garvin, J.R. Childress, C.L. Chien, B. Martinez and M.B. Salamon, *Phys. Rev. Letters* 64 (1990) 2438.
- [6] For recent reviews, see:
N.B. Brandt and V.V. Moshchalkov, *Advan. Phys.* 33 (1984) 193;
J.K. Furdyna and J. Kossut, Eds., *Semiconductors and Semimetals*, Vol. 25 (Academic Press, New York, 1988).
- [7] D.D. Awschalom, J.M. Hong, L.L. Chang and G. Grinstein, *Phys. Rev. Letters* 59 (1987) 1733.
- [8] D.D. Awschalom, J. Warnock, J.M. Hong, L.L. Chang, M.B. Ketchen and W.J. Gallagher, *Phys. Rev. Letters* 62 (1989) 199.
- [9] M.R. Freeman, D.D. Awschalom, J.M. Hong and L.L. Chang, *Phys. Rev. Letters* 64 (1990) 2430.
- [10] H. Munekata, H. Ohno, S. von Molnar, A. Segmüller, L.L. Chang and L. Esaki, *Phys. Rev. Letters* 63 (1989) 1849.
- [11] U. Debska, M. Dietl, G. Grabecki, E. Janik, E. Kierzek-Pecold and M. Klimkiewicz, *Phys. Status Solidi (a)* 64 (1981) 707.
- [12] L.A. Kolodziejski, R.L. Gunshor, S. Datta, T.C. Bonsett, M. Yamanishi, R. Frohne, T. Sakamoto, R.B. Bylisma, W.M. Becker and N. Otsuka, *J. Vacuum Sci. Technol. B3* (1985) 714.
- [13] R.N. Bicknell, N.C. Giles-Taylor, D.K. Blanks, R.W. Yanka, E.L. Buckland and J.F. Schetzina, *J. Vacuum Sci. Technol. B3* (1985) 709.
- [14] T.J. Gregory, J.E. Nicholls, J.J. Davies, J.O. Williams and N. Naunh, *Semicond. Sci. Technol.* 3 (1988) 1193.
- [15] D.L. Dreifus, R.M. Kolbas, R.L. Harper, J.R. Tassinio, S. Hwang and J.F. Schetzina, *Appl. Phys. Letters* 53 (1988) 1279.
- [16] S.M. Durbin, J. Han, Sungki O, M. Kobayashi, D.R. Menke, R.L. Gunshor, Q. Fu, N. Pelekanos, A.V. Nurmikko, D. Li, J. Gonsalves and N. Otsuka, *Appl. Phys. Letters* 55 (1989) 2087.
- [17] In general, the films grown on substrates (100) 2° off have better PL characteristics. Recently, it was suggested that by growing on substrates with even larger misorientation, CdTe (111) with improved quality could be obtained. See: J. Cibert, Y. Gobil, K. Saminadayar, S. Tatarenko, A. Chami, G. Feuillet, Le Si Dang and E. Ligeon, *Appl. Phys. Letters* 54 (1989) 828.
- [18] R.F.C. Farrow, G.R. Jones, G.M. Williams and I.M. Young, *Appl. Phys. Letters* 39 (1981) 954.
- [19] P.P. Chow, D.K. Greenlow and D. Johnson, *J. Vacuum Sci. Technol. A1* (1983) 562.
- [20] H.A. Mar, K.T. Chee and N. Salansky, *Appl. Phys. Letters* 44 (1983) 237.
- [21] C. Hsu, S. Sivananthan, X. Chu and J.P. Faurie, *Appl. Phys. Letters* 48 (1986) 908.
- [22] J. Yoshino, H. Munekata and L.L. Chang, *J. Vacuum Sci. Technol. B5* (1987) 683.
- [23] A. Segmüller, P. Krishna and L.L. Esaki, *J. Appl. Cryst.* 10 (1977) 1.
- [24] J. Rozen and D.D. Awschalom, *Appl. Phys. Letters* 49 (1986) 1649.
- [25] D.D. Awschalom, J.R. Rozen, M.B. Ketchen, W.J. Gallagher, A.W. Kleisasser, R.L. Sandstrom and B. Bumble, *Appl. Phys. Letters* 53 (1988) 2108.
- [26] J.M. Hong, A. Segmüller and L.L. Chang, unpublished.
- [27] R. Triboulet, Y. Marfaing, A. Cornet and P. Siffert, *J. Appl. Phys.* 45 (1974) 2759.

- [28] S. Suga, W. Dreybrodt, F. Willman, P. Hiesinger and K. Cho, *Solid State Commun.* 15 (1974) 871.
- [29] A. Golnik, J. Ginter and J.A. Gaj, *J. Phys.* C16 (1983) 6073.
- [30] J. Warnock, R.N. Kershaw, D. Ridgle, K. Dwight, A. Wold and R.R. Galazka, *Solid State Commun.* 54 (1985) 215.
- [31] L.L. Chang, L. Esaki, A. Segmüller and R. Tsu, in: *Proc. 12th Intern. Conf. on Physics of Semiconductors, Stuttgart, July 1974*, p. 668.
- [32] V.S. Speriosu and T. Vreeland, Jr., *J. Appl. Phys.* 56 (1984) 1591.
- [33] K. Binder and A.P. Young, *Rev. Mod. Phys.* 58, 801 (1986).
- [34] R.R. Galazka, S. Nagata and P.H. Keesom, *Phys. Rev.* B22 (1980) 3344.
- [35] J.A. Gaj, R. Planel and G. Fishmann, *Solid State Commun.* 29 (1979) 435.
- [36] X. Liu, A. Petrou, J. Warnock, B.T. Jonker, G.A. Prinz and J.J. Krebs, *Phys. Rev. Letters* 63 (1989) 2280.
- [37] E. Deleporte, J.M. Berroir, G. Bastard, C. Delalande, J.M. Hong and L.L. Chang, *Phys. Rev.* B23 (1990) 5891.

Evaluation of a new plasma source for molecular beam epitaxial growth of InN and GaN films

W.E. Hoke, P.J. Lemonias and D.G. Weir

Raytheon Research Division, Lexington, Massachusetts 02173, USA

An RF plasma source has been integrated into a molecular beam epitaxial system for growth of nitride films. Using an optical detector on the source, the presence of nitrogen atoms in the N_2 plasma region is deduced as a function of operating conditions. The plasma source has been used to grow hexagonal wurtzite films of InN and GaN. The film–substrate interface is more abrupt for GaN than InN films. For site competition the active nitrogen species from the plasma is found to incorporate more readily than As_2 .

1. Introduction

Of the various III–V compound systems, the nitride system is one of the least developed. However, column III-nitrides have attractive material properties. For example, most of the compounds are direct semiconductors and have large bandgaps. Consequently the potential for various optical applications is present. Also InN has been reported by one group [1] to have a relatively high electron mobility for its bandgap of 1.9 eV. However, InN is a difficult material to prepare due to its low thermal stability. The material decomposes at 500°C in a N_2 ambient [2] and at 300°C in air [3]. Consequently low growth temperatures are required with a reactive nitrogen species present. Film growth with NH_3 or amine compounds is made difficult by the relatively high thermal stability of these compounds at low temperatures. Also the presence of a reactive nitrogen species complicates material growth in reactor systems operated near atmospheric pressure due to gas phase reactions.

InN films have been deposited using N_2 plasmas directly [4–7] as well as RF sputtering [1,8–10]. In this work we examine the nitriding capabilities of a new radical source for growth of InN and GaN films. The source utilizes an RF plasma and is compatible with molecular beam epitaxy (MBE) technology.

2. Experimental

The nitride films were grown in a diffusion pumped VG-80H MBE machine which was continuously cooled with LN_2 . Standard high purity solid sources were used for gallium, indium, and arsenic. High purity N_2 , Ar, and/or H_2 were flowed through the plasma source mounted on the growth chamber. For a nitrogen flow of 10 SCCM the system pumping speed produced a chamber pressure of 2×10^{-4} Torr. The corresponding mean free path at room temperature for N_2 is 25 cm.

A major challenge in the growth of nitride films is the generation of a sufficient flux of reactive nitrogen species. In this work an Oxford Applied Research radical source (Model MPD21S) shown in fig. 1 was used as a remote nitrogen plasma source. The source operates at 13.56 MHz with a maximum power of 500 W. The bakable radical source is conflat flange mounted in an MBE furnace port with the conventional distance of 15 cm between the end of the radical source and the substrate. To minimize contamination of III–V films the discharge is electrodeless and the plasma is contained in a PBN (pyrolytic boron nitride) discharge tube capped with a PBN exit plate. Since the plasma is at the end of the radical source, recombination of excited species is reduced. An important feature of the design is that a

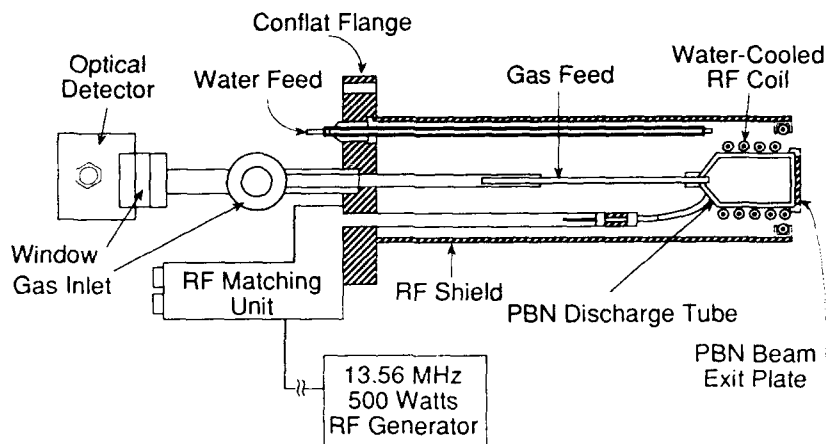


Fig. 1. Schematic of MBE compatible radical source.

silicon photodiode sites down the center of the plasma to detect radiation coming from the plasma region. Due to the higher plasma pressures the radical source produces considerably fewer ions than an ECR source. It is also less expensive.

Nitride films were deposited on GaP(111), GaAs(100), and GaAs(111) substrates. Prior to growth the substrates were heated in an arsenic flux to remove the surface oxides. For substrate temperatures above 450°C, an Ircon Model V pyrometer was used to measure temperature. Below 450°C the substrate temperatures are estimates based on the correlation at higher temperatures between the substrate thermocouple temperatures and pyrometer readings.

3. Plasma operating characteristics

The radical source has been used to create plasmas in N_2 , Ar, H_2 , and various mixtures of these gases. The plasmas are contained in the discharge tube and do not extend into the growth chamber. Two beam exit plates were used with conductances of 3.4 and 10 L/s. With on-flange tuning nitrogen plasmas could be matched with less than 1 W reflected power. No perturbation of nearby thermocouple readings or temperature control circuitry has been observed with input powers up to 500 W.

Various studies on nitrogen plasmas have shown that nitrogen atoms are predominantly produced in the ground 4S state [11]. These atoms can then recombine to form an excited N_2 molecule with internal energy nearly 10 eV above the ground electronic state. An important relaxation pathway involves the allowed $B^3\Pi_g \rightarrow A^3\Sigma_u^+$ transitions which produce the yellow Lewis-Rayleigh afterglow with the strongest emission line at 5820 Å. Neglecting temperature effects, the intensity of this afterglow has been shown to be proportional to the pressure, P , and the square of the ground state atomic nitrogen concentration, $[N(^4S)]$ (see refs. [11,12]):

$$I \propto [N(^4S)]^2 P. \quad (1)$$

Consistent with this relationship is the observation that $B^3\Pi_g \rightarrow A^3\Sigma_u^+$ transitions (5000–7000 Å) were necessary for plasma deposition of silicon nitride [13].

The capability of the radical source for producing ground state nitrogen atoms was qualitatively examined using the optical detector. Filters were placed in front of the detector so that the 5000–7000 Å emission band was measured as a function of nitrogen flow and input power. In fig. 2 are plotted the detected emission signal as a function of flow rate at 350 W input power for the two orifices. For the 3.4 L/s orifice, the emission initially increases rapidly with flow and then be-

gins to level off at roughly 12 SCCM. The corresponding curve for the 10 L/s orifice is skewed to higher flows since the increased conductance reduces the pressure and consequently the recombination rate in the plasma. Evidence of reduced recombination can actually be observed. With the 10 L/s orifice, a purplish-blue fluorescence from an excited species is observed in the growth chamber which is only very weakly seen with the 3.4 L/s orifice.

The power dependence of the emission is also given in fig. 2 for the lower conductance orifice and a N_2 flow of 10 SCCM. Below approximately 80 W the plasma is not stable resulting in low emission. Above 80 W the intensity initially rises rapidly and then begins to level off. From eq. (1) and the data in fig. 2, the estimated atomic nitrogen concentration at 250 W is approximately 80% of that at 500 W. A similar power dependence curve is obtained for the 10 L/s orifice.

The presence of ions in the radical beam was also examined. A $3\frac{1}{2}$ inch diameter tantalum disc was mounted on the substrate manipulator and

used as a Faraday cup. With the 3.4 L/s orifice, 10 SCCM flow of N_2 , and 400 W power, a small negative current of 10 μA was measured. However, under the same conditions with the 10 L/s orifice a positive current of 200 μA was observed which increased with increasing input power. A likely explanation is that the lower plasma pressure with the 10 L/s orifice reduces the recombination of N_2^+ ions. The presence of N_2^+ ions is often observed in nitrogen discharge [11]. Consistent with this explanation is that the ion current is reduced with increasing flow rate and thus plasma pressure. These results indicate that orifice size has an important effect on recombination of atoms and ions. However, the ion densities measured here (less than 0.1%) are still considerably less than that obtained with an ECR source.

4. Nitride film growth

Due to the above mentioned thermal instability of InN, growth of InN is a critical test of the

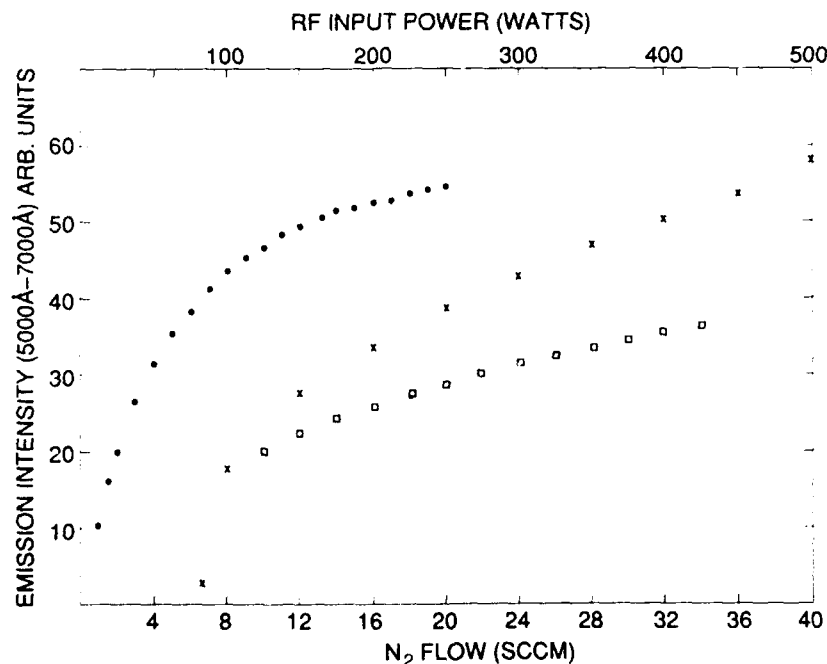


Fig. 2. Detected emission signal (5000–7000 Å wavelength band) at 350 W power as a function of flow for the 3.4 L/s orifice (●) and the 10 L/s orifice (□). Detected emission signal as a function of input power (×) for the 3.4 L/s orifice at 10 SCCM N_2 flow.

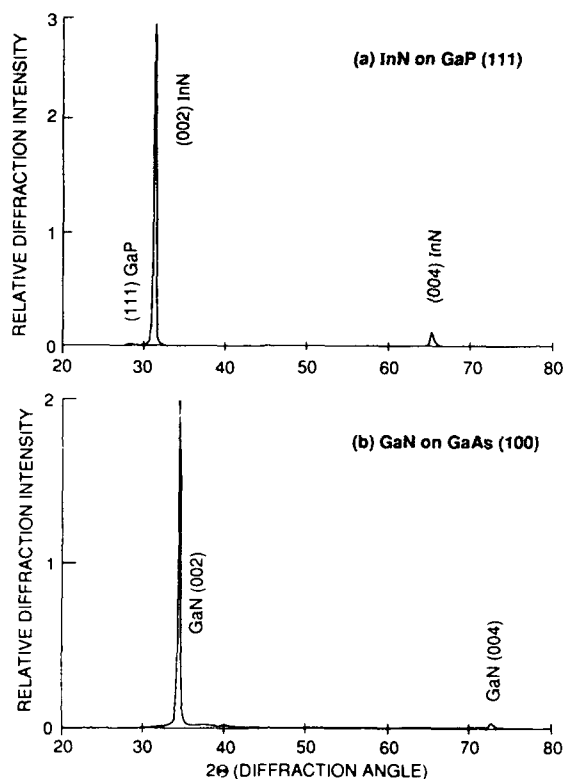


Fig. 3. X-ray diffraction spectra of a (1) 5000 Å InN film on GaP(111) and (b) 5000 Å GaN film on GaAs(100) substrate. For clarity the substrate diffraction peaks have been attenuated.

radical source's capability for production of sufficient fluxes of reactive nitrogen atoms and molecules. Initial InN runs were made with the lower conductance orifice at 300–400°C and 10–30 SCCM flow of N_2 . The X-ray spectra of the films indicated powder-like InN films with (101), (110), (102), and (103) reflections observed. By changing the orifice to 10 L/s film quality significantly improved. Fig. 3a is an X-ray spectrum using Cu $K\alpha$ radiation of a 5000 Å InN film grown on (111) GaP. The film was deposited at 350°C with a N_2 flow of 30 SCCM and a growth rate of 0.25 $\mu\text{m}/\text{h}$. The InN film has the hexagonal wurtzite crystal structure with the c -axis perpendicular to the film surface. Only the InN (002) and (004) planes are observed. The reason for the improvement in film quality is probably due to the reduced recombination in the plasma source with

the higher conductance orifice. Hexagonal InN films were also grown on GaAs (111) and (100) substrates. Due to the significant lattice mismatch between substrate and film the narrowest X-ray linewidth for these initial InN films was 0.7°. Improvements in crystal quality should be possible for thicker films grown on sapphire substrates with an AlN buffer layer [14].

The effect of substrate temperature on InN growth was examined using the 10 L/s orifice. Typical growth conditions were a nitrogen flow of 30 SCCM, plasma power of 350 W, and indium flux resulting in a growth rate of 0.25 $\mu\text{m}/\text{h}$. (The reactive nitrogen flux from the plasma at 5 SCCM is sufficient for InN growth. The effect of the lower flows on InN film properties has not been studied yet.) Under these growth conditions InN films were deposited from approximately 80 to 450°C. The smoothest surface morphology was obtained at 350°C with the red-tinted films being quite reflective to the eye. The surface morphology became increasingly rougher in going from 400–450°C. Fig. 4a is an Auger depth profile of a 5000 Å InN film grown on a GaP substrate at 350°C for 2 h. The nitrogen content is not profiled due to interference with the strong indium Auger signal. Some interdiffusion at the substrate–film interface is indicated in fig. 4a.

The growth of GaN films was examined. Due to the stronger gallium–nitrogen bond and related higher thermal stability of GaN compared to InN, the nitrogen flow requirements were less for GaN growth than InN growth. Also, GaN films could be more readily obtained with the 3 L/s orifice. An X-ray diffraction spectrum is given in fig. 3b of a GaN film grown with the 10 L/s orifice at 600°C and only 1 SCCM of nitrogen diluted in argon. The (002) and (004) diffraction peaks indicate that the film has the hexagonal wurtzite crystal structure with the c -axis normal to the film surface. An Auger depth profile is given in fig. 4b of the 5000 Å thick film which was grown for 2½ h at 600°C on a GaAs substrate. The substrate–film interface is quite abrupt and much sharper than that obtained with InN despite the considerably higher growth temperature. The higher strength of Ga–N bonds compared to In–N bonds may be a primary reason for this result.

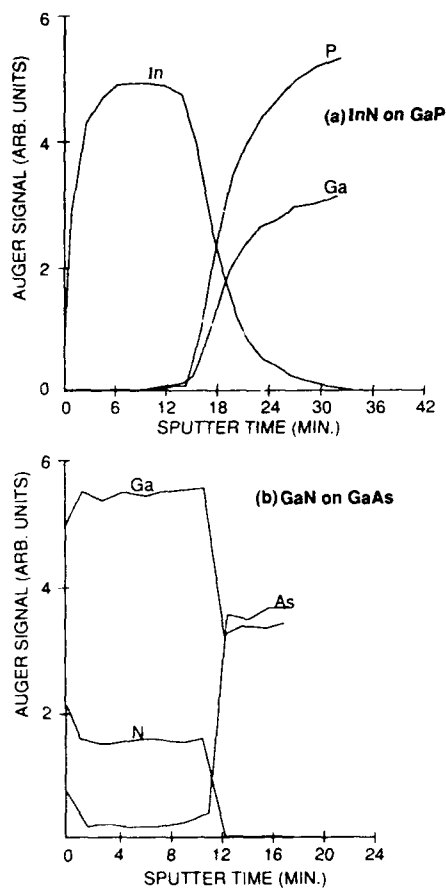


Fig. 4. Auger depth profile of a (a) 5000 Å InN film on a GaP(111) substrate and (b) 5000 Å GaN film on a GaAs(100) substrate.

A final growth experiment investigated the relative reactivity of the active nitrogen derived from the plasma source and As_2 , which is more reactive than As_4 . A film was grown at 600°C with gallium and As_2 fluxes directed at the substrate and with 1 SCCM N_2 flow through the plasma. The As_2 flux was sufficient for GaAs growth. From

X-ray diffraction measurements the resulting film was determined to be GaN indicating the highly reactive nature of active nitrogen species.

In conclusion a new plasma source has been integrated into an MBE machine for growth of hexagonal InN and GaN films. Using an optical detector the presence of nitrogen atoms has been examined as a function of operating conditions. The plasma orifice size has an important effect on recombination of atoms and ions which affects nitride film growth. Film-substrate interdiffusion is observed to be significantly less for GaN as compared to InN. The active nitrogen is found to be considerably more reactive than As_2 .

References

- [1] T.L. Tansley and C.P. Foley, *Electron. Letters* 20 (1984) 1066.
- [2] J.B. MacChesney, P.M. Bridenbaugh and P.B. O'Connor, *Mater. Res. Bull.* 5 (1970) 783.
- [3] M.D. Lyutaya and V.F. Bukhanevich, *Russ. J. Inorg. Chem.* 7 (1962) 1290.
- [4] K. Osamura, S. Naka and Y. Murakami, *J. Appl. Phys.* 46 (1975) 3432.
- [5] J.W. Trainor and K. Rose, *J. Electron. Mater.* 3 (1974) 821.
- [6] A. Wakahara and A. Yoshida, *Appl. Phys. Letters* 54 (1989) 709.
- [7] Y. Sato and S. Sato, *Japan. J. Appl. Phys.* 28 (1989) L1641.
- [8] H.J. Hovel and J.J. Cuomo, *Appl. Phys. Letters* 20 (1972) 71.
- [9] B.T. Sullivan, R.R. Parsons, K.L. Westra and M.J. Brett, *J. Appl. Phys.* 64 (1988) 4144.
- [10] K. Kubota, Y. Kobayashi and K. Fujimoto, *J. Appl. Phys.* 66 (1989) 2984.
- [11] A.N. Wright and C.A. Winkler, *Active Nitrogen* (Academic Press, New York, 1968) pp. 13-82.
- [12] J. Berkowitz, W.A. Chupka and G.B. Kistiakowsky, *J. Chem. Phys.* 25 (1956) 457.
- [13] L. Bardos, J. Musil and P. Taras, *J. Phys. D (Appl. Phys.)* 15 (1982) L79.
- [14] S. Yoshida, S. Misawa and S. Gonda, *J. Vacuum Sci. Technol.* B1 (1983) 250.

Heteroepitaxial growth by Van der Waals interaction in one-, two- and three-dimensional materials

Atsushi Koma, Keiji Ueno and Koichiro Saiki

Department of Chemistry, University of Tokyo, Bunkyo-ku, Tokyo 113, Japan

The lattice matching condition usually encountered in heteroepitaxial growth has been found to be relaxed greatly when the interface between constituent materials has Van der Waals nature and forms no direct chemical bonds. Layered transition metal dichalcogenides are the typical materials having that nature, and a variety of heterostructures can be grown by using them. This kind of approach has been proved to be applied also to heteroepitaxial growth between such quasi-one-dimensional materials as tellurium and selenium, that onto dangling-bond terminated three-dimensional material substrates, and that of organic materials forming Van der Waals type crystals.

1. Introduction

Molecular beam epitaxy has opened a new way to grow ultrathin heterostructures with atomic order thickness. But so far good heterostructures can be grown only between very limited combinations of constituent materials because of the severe lattice matching condition to be satisfied. This comes from the fact that there are usually dangling bonds on the surface of a substrate material and that those dangling bonds can not be connected to the atoms of grown materials without good lattice matching between the substrate and the grown materials (see fig. 1a). The lattice matching condition, however, has been found to be greatly relaxed, when the heteroepitaxial growth proceeds with Van der Waals interaction. A typical example is the growth of a layered material onto a cleaved face of the other layered material having no dangling bonds (see fig. 1b). We have called that type of epitaxy Van der Waals epitaxy [1–4]. It has been proved that an ultrathin film with its own lattice constant can be grown by the Van der Waals epitaxy even under the existence of lattice mismatch as large as 50%. It has also been shown that a very abrupt interface with small amounts of defects can be fabricated by Van der Waals epitaxy because of the nonexistence of the dangling bonds [5]. As will be shown in the follow-

ing, the idea of Van der Waals epitaxy can be applied to rather a wide choice of materials, indicating its usefulness to realize various kinds of heterostructures.

2. Materials to which Van der Waals epitaxy is applicable

Table 1 shows a variety of materials to which we have proved Van der Waals epitaxy is applicable. The materials extend from quasi-one-dimensional ones to three-dimensional ones.

2.1. Quasi-one dimensional materials

Selenium and tellurium are column VI element semiconductors and have peculiar crystal structures consisting of atoms in spiral chains. The atoms in a chain are bound to each other with strong covalent forces, whereas the chains are held together only via weak Van der Waals forces. Thus they are considered as quasi-one-dimensional ones in the sense that the atoms are strongly bound to each other only in one direction. The crystal can be cleaved easily along the chains without producing dangling bonds on their surfaces, onto which Van der Waals epitaxy is

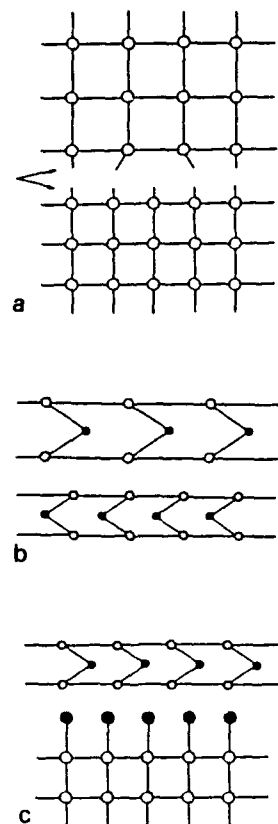


Fig. 1. Interfaces connected by (a) active bonds, (b) Van der Waals gap, and (c) quasi Van der Waals gap.

possible. Although the lattice mismatch along the *c*-axis (the chain axis) is as large as 20%, ultrathin selenium film of good quality has been proved to grow on a cleaved face of tellurium [6]. Recently we have also succeeded in growing heterostructures of Te/Se/Te.

2.2. Quasi-two-dimensional materials (layered materials)

Transition metal dichalcogenides (TX_2 , T = transition metal X = chalcogen) are the most suitable materials for the Van der Waals epitaxy. They have layered crystal structures, which are

formed of unit layers consisting of transition metal atoms sandwiched by chalcogen atoms. Atoms in a unit layer are bound to each other by strong covalent bonds, whereas the layers are held together only via weak Van der Waals forces. Thus they are easily cleaved parallel to the layers, and no dangling bonds appear on their cleaved surface. Therefore it is expected that growth of a layered material onto such surfaces proceeds via Van der Waals forces, resulting in the relaxation of the lattice matching condition. There are such insulators as HfS_2 , such semiconductors as MoS_2 and MoSe_2 , and such superconducting metals as NbS_2 and NbSe_2 among TX_2 's. So, the fabrication of various kinds of heterostructures using those as constituent materials has become a distinct possibility. Van der Waals epitaxy is possible between any combination of those materials.

Recently, Van der Waals epitaxial growth of MoSe_2 has been successfully made on a cleaved face of SnS_2 [7], which is also a layered material but different from TX_2 's. Moreover, it has been proved that MoSe_2 and NbSe_2 can be grown on a cleaved face of muscovite, a kind of mica [8,9]. Although muscovite is a layered material, it has a much more complicated crystal structure than TX_2 and its lattice constant is larger than that of TX_2 by 50%. It is expected from those facts that Van der Waals epitaxy is possible between any layered materials regardless of their crystal structures and of their lattice constants.

Table 1
Materials grown with Van der Waals epitaxy: TX_2 denoted a transition metal dichalcogenide

Material group	Materials grown with VdWE	Ref.
Quasi-1D	Se/Te Te/Se/Ta	[5]
Quasi-2D	TX_2/TX_2 TX_2/SnS_2 TX_2/mica	[1-4] [7] [8,9]
Quasi-2d on 3D	$\text{TX}_2/\text{S-GaAs}(111)$ $\text{TX}_2/\text{CaF}_2(111)$	[12] [12]
Organic	Phthalocyanine/ TX_2	

2.3. Van der Waals epitaxy onto dangling-bond-terminated surfaces

So far, Van der Waals epitaxy has been limited to the heteroepitaxial growth between quasi-one- or quasi-two-dimensional materials. If it can be applied to widely used three-dimensional materials, its application field will be greatly extended. As is mentioned above, there appear dangling bonds on a clean surface of an ordinary material, which prevents good heteroepitaxial growth of a layered material on it. But growth with Van der Waals forces becomes possible if regular termination of the surface dangling bonds is accomplished as is shown in fig. 1c and if it is kept stable even at high temperatures required for good epitaxial growth. Sulfide treated GaAs (111) surface seems to be the most suitable candidate for that purpose, since it was found that the surface dangling bonds are regularly terminated with sulfur atoms up to 520 °C [10]. Epitaxial growth of semiconducting MoSe₂ and superconducting NbSe₂ on (NH₄)₂S_x-treated GaAs (111) surfaces have been tried successfully [11].

Another promising three-dimensional substrate material is CaF₂. It has been found that the (111) surface of CaF₂ (cleaved face) is covered with F atoms resulting in its very inactive nature [12]. This inactive nature brings about difficulty in good heteroepitaxial growth of such a typical three-dimensional material as GaAs on it [13], but it is favorable to Van der Waals epitaxy of a layered material on it. We have succeeded in growing an ultrathin film of MoSe₂ on a cleaved face of CaF₂ [14]. CaF₂ is a well-known insulating material lattice-matched to silicon, and good heteroepitaxial films can be grown on Si [13]. Thus the present method makes it possible to grow heteroepitaxial layers of various transition metal dichalcogenides on a Si(111) substrate by putting an intermediate CaF₂ layer between them.

2.4. Organic materials

Van der Waals epitaxy seems to have potential application to heteroepitaxial growth of organic material thin films, because many organic material crystallize with Van der Waals force. Very recently

we have succeeded to grow Pb-, Cu- and VO-phthalocyanine films on cleaved faces of MoS₂. Cu- and VO-phthalocyanine molecules have been found to form square lattices on cleaved faces of MoS₂, whereas Pb-phthalocyanine forms rectangular lattices. The axes of those lattices align to that of hexagonal lattice of MoS₂, which result in forming three equivalent domains. This is our first application of Van der Waals epitaxy to organic materials, and this type of approach will be extended to the growth of thin films of vast organic materials.

3. Characterization of ultrathin heterostructures grown with Van der Waals epitaxy

In situ observations of reflection high energy electron diffraction (RHEED) have been done during the growth of all materials mentioned above. The most striking finding from the RHEED observation is that the heteroepitaxially grown film has its own lattice constant even at the interface with a substrate material having large lattice mismatch. This is much different from the case of strained superlattice, in which the lattice constant is forced to be the same as that of a substrate [15]. Nevertheless, the crystal axes of the grown film and the substrate align well to each other. Such features have also been confirmed by recent transmission electron microscope observation of a MoSe₂/SnS₂ heterostructure [7]. Thus the substrate and the film grown on it with Van der Waals epitaxy are usually incommensurate, but they are rotationally-commensurate. This is the most characteristic feature of Van der Waals epitaxy, which causes the relaxation of the lattice matching condition.

The abruptness of the interfaces of heterostructures grown with Van der Waals epitaxy has been measured by non-destructive in-depth profiling by low-energy electron energy loss spectroscopy [5]. The interfaces between MoSe₂/MoS₂ [5], MoSe₂/CaF₂ [14] and NbSe₂/S-GaAs [11] have been found to have abruptness as sharp as 0.1 nm.

The top surfaces of heterostructures grown with Van der Waals epitaxy are almost free from contamination, even under atmospheric pressure, be-

cause of the nonexistence of dangling bonds on them. This feature is especially preferable to the observation of their surfaces by a scanning tunneling microscope (STM). Recently, we have succeeded to get clear STM images of ultrathin MoSe_2 films on a SnS_2 [7] or a MoS_2 substrate. In addition to well-resolved atom images, a moiré-type modulation structure named wagon wheel structure was observed. This structure has been considered to arise from abrupt change in the lattice constant at the interface, which is characteristic of Van der Waals epitaxy. It has been concluded from the observed modulation structure that the lattice constant of the grown film agrees with its own one within the error of 0.1% and that the crystal axis of the grown film aligns with that of the substrate within 0.1° . In the next step, the STM observation is expected to disclose the details of Van der Waals epitaxial growth in atomic resolutions.

4. Summary

In conclusion, we have proved that good quality ultrathin heterostructures can be fabricated by Van der Waals epitaxy by using various kinds of materials ranging from quasi-one-dimensional to three-dimensional ones as constituents. The present technique has opened a new way to prepare many kinds of heterostructures consisting of superconductor, metal, semiconductor or insulator films with any thickness from subnanometer by using a variety of transition metal dichalcogenides and other materials having no dangling bonds on their surfaces. This method has been found to be useful also in preparing organic thin films. It is expected that Van der Waals epitaxy is especially useful to create new man-made materials formed of stacked ultrathin films of many kinds of materials.

Acknowledgments

The authors would like to thank Drs. B.A. Parkinson and F.S. Ohuchi for the STM experiments and stimulating discussions. The present work is supported by a Grant-in-Aid for Special Distinguished Research (No. 02102002) from the Ministry of Education, Science and Culture of Japan.

References

- [1] A. Koma, K. Sunouchi and T. Miyajima, *Microelectron. Eng.* 2 (1984) 129.
- [2] A. Koma, K. Sunouchi and T. Miyajima, *J. Vacuum Sci. Technol.* B3 (1985) 724.
- [3] A. Koma, K. Sunouchi and T. Miyajima, in: *Proc. 17th Intern. Conf. on Physics of Semiconductors*, San Francisco, 1984, Eds. J.D. Chadi and J.D. Harrison (Springer, Berlin, 1985) p. 1465.
- [4] A. Koma, in: *Proc. 1st Intern. Conf. on Electronic Materials*, Tokyo, 1988 (Materials Research Society, Pittsburgh, PA, 1989) p. 105.
- [5] A. Koma and K. Yoshimura, *Surface Sci.* 174 (1986) 556.
- [6] N. Aoto, K. Sunouchi and A. Koma, in: *Extended Abstracts 15th Conf. on Solid State Devices and Materials*, Tokyo, 1983, p.309.
- [7] F.S. Ohuchi, B.A. Parkinson, K. Ueno and A. Koma, *Appl. Phys.* 68 (1990) 2168.
- [8] K. Saiki, K. Ueno, T. Shimada and A. Koma, *J. Crystal Growth* 95 (1989) 603.
- [9] K. Ueno, K. Saiki, T. Shimada and A. Koma, *J. Vacuum Sci. Technol.* A8 (1990) 68.
- [10] H. Oigawa, J.-F. Fan, Y. Nannichi, K. Ando, K. Saiki and A. Koma, *Japan. J. Appl. Phys.* 28 (1989) L340.
- [11] K. Ueno, T. Shimada and K. Saiki and A. Koma, *Appl. Phys. Letters* 56 (1990) 327.
- [12] K. Saiki, Y. Sato and A. Koma, *Japan. J. Appl. Phys.* 28 (1989) L134.
- [13] H.C. Lee, H. Ishiwara, S. Kanemaru and S. Furukawa, *Japan. J. Appl. Phys.* 26 (1987) L1734.
- [14] A. Koma, K. Saiki, and Y. Sato, *Appl. Surface Sci.* 41/42 (1989) 451.
- [15] G.C. Osbourn, *J. Appl. Phys.* 53 (1982) 1586.

Growth of MoSe₂ thin films with Van der Waals epitaxy

F.S. Ohuchi, T. Shimada *, B.A. Parkinson

Central Research and Development Department, Experimental Station, E.I. du Pont de Nemours and Company, Wilmington, Delaware 19880, USA

K. Ueno and A. Koma

Chemistry Department, University of Tokyo, Hongo, Bunkyo-ku, Tokyo 113, Japan

The concept of Van der Waals epitaxy that has been recently introduced removes severe lattice matching requirement by using materials which only have strong bonding in two dimensions. We demonstrate that an epilayer of MoSe₂ deposited on various substrates can produce films of high crystalline quality despite of large mismatch. RHEED oscillation, observed in-situ for growing MoSe₂ epilayers, shows a layer-by-layer growth with evidence for bilayer type growth, from which the 2H₆ polytype is determined. STM provides real space images of the morphology of the epilayer, and shows novel structures resulting from the large lattice mismatch where the epilayer atoms are commensurated.

1. Introduction

Heteroepitaxy with a large lattice mismatch offers the possibility of combining materials with a wide variety of properties. Today, much effort has been paid to molecular beam epitaxy (MBE) with strained or graded layers to accommodate the lattice mismatching, yet the concept of Van der Waals epitaxy (VDWE), recently introduced by us [1,2], removes this constraint by using materials which have strong bonding only in two dimensions (2D). The materials which crystallize in 2D structures include many transition metal dichalcogenides, monochalcogenides, and tin sulfides and selenides. VDWE is the growth of such 2D materials, one upon the other, where the layers are bound together by the relatively weak Van der Waals forces. Many metal chalcogenide materials have 2D structures characterized by chalcogen-

metal (metal)-chalcogen layers held together by Van der Waals forces, thus a pronounced structural anisotropy resulting from strong chemical bonds in 2D results in these materials having unique properties. Changing either the metal or chalcogen can alter the electronic structure from superconducting to insulating. Therefore the flexibility for fabrication of multilayer structures containing different materials selected for their specific physical and chemical properties, rather than their lattice match, makes this an exciting new area for investigation.

We present VDWE growth of MoSe₂ thin films on SnS₂(0001), MoS₂(0001) and GaAs(111) surfaces. While the identity of the substrate strongly influences the growth process in conventional epitaxy, the substrates that have been selected in the present investigation differ from each other both electronically and structurally, yet a high quality epitaxial thin film can be grown by VDWE. In this paper we focus on the growing process of VDWE and resultant unique properties of the heterointerfaces.

* Also at Chemistry Department, University of Tokyo, Hongo, Bunkyo-ku, Tokyo 113, Japan.

2. Experimental

The MBE system used in the present investigation is described in detail elsewhere [3]. Briefly, the system consists of growth and analysis chambers separated by a gate valve. In the growth chamber, a conventional Knudsen cell and an electrostatically focused evaporation source provide Se and Mo molecular beams, respectively, which are directed toward the heated substrate. Reflection high energy electron diffraction (RHEED) was used to monitor the growth process. The variation of RHEED patterns can be recorded with a video camera and the video signals are further processed to extract RHEED oscillations during the growth. Further details are found elsewhere [4]. In the analysis chamber, a double pass cylindrical mirror analyzer was used to analyze the composition and the electronic structure of the epitaxial films. After growth of the desired thickness of MoSe₂, the specimens were removed from the MBE system and further characterized by various methods including X-ray photoelectron spectroscopy (XPS), transmission electron microscopy (TEM), low energy electron diffraction (LEED), and scanning tunneling microscopy (STM). Unlike conventional materials, the present materials are inert to ambient conditions (O₂, H₂O), which makes ex-situ analysis valuable.

3. Results and discussion

3.1. Growth characteristics

The RHEED patterns from a substrate have information about the substrate cleanliness and crystallinity. Elongated streaks from [11 $\bar{2}$ 0] and [10 $\bar{1}$ 0] azimuthal angles of these substrates reveal no surface reconstructions. Prior to initiation of MoSe₂ growth, the substrate surface was exposed to a Se flux at a temperature of more than 250°C. No changes in the streak intervals were identified, indicating that the Se species do not adsorb or react with the surfaces. When the Mo flux was initiated, the substrate patterns immediately faded out for a short period of time, then reappeared as

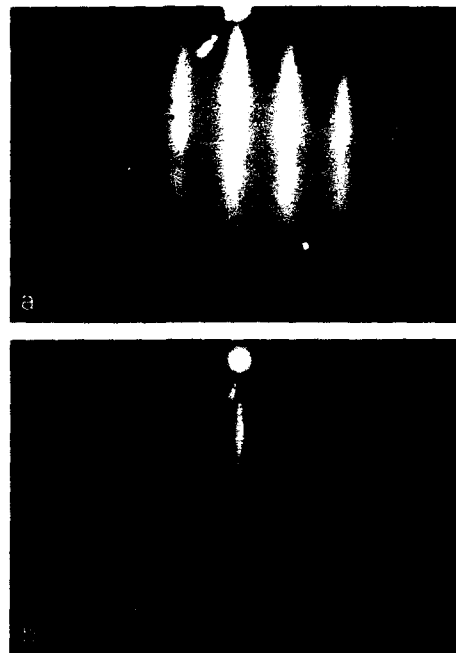


Fig. 1. RHEED patterns observed from (1) [11 $\bar{2}$ 0] and (b) [10 $\bar{1}$ 0] azimuthal angles for MoSe₂ thin film epitaxially grown on a SnS₂ substrate with a coverage less than 1 monolayer.

the deposition proceeded along with streaks associated with MoSe₂. In all three cases, the streaks from the substrate and the growing thin film are azimuthally aligned, suggesting the overlayer is epitaxially grown with their hexagonal edge aligned to those from the substrate. Shown in fig. 1 are RHEED patterns obtained from MoSe₂ deposition on a SnS₂ substrate, in which the lattice mismatch is about 10%. Co-existence of both substrate and deposit RHEED streaks is an indication of formation of a fractional monolayer coverage. The lattice constant for the deposit calculated from the streak interval was 3.29 ± 0.05 Å, close to the published value of 3.288 Å for 2 H_{1/2}-MoSe₂, suggesting that even for less than one monolayer, the MoSe₂ films are grown with their own lattice constants maintained despite the lattice mismatch. Further growth of the MoSe₂ layer resulted in substrate patterns completely fading out, leaving only the epilayer streaks indicating the formation of a crystalline MoSe₂ thin film. The high crystalline quality of

the epilayer is evidenced by sharp elongated RHEED streaks. Nearly identical LEED patterns to those observed from single crystalline MoSe₂ specimens have also been observed. Azimuthal alignment for the epilayer to the substrate was further confirmed by selected area electron diffraction (SAD) in the transmission electron microscope. The observed SAD pattern consists of a mixture of two rotationally aligned hexagonal patterns, corresponding to those from the substrate and the epilayer. Detailed discussion can be found elsewhere [3].

Much interest has recently been focused on the observed oscillations in the intensity of RHEED patterns during epitaxial growth. In MoSe₂ thin film growth, an oscillation in RHEED intensities has been observed. While the observed oscillatory behavior is an indication of 2D layer-by-layer growth of MoSe₂ thin films, further analysis allows us to determine the polytype (variation in layer stacking sequences) of MoSe₂ thin film crystals. Shown in fig. 2 is the RHEED intensity versus time plot during the growth of MoSe₂ on (111)GaAs at 620°C, where intensities of the specular and the non-specular (say (1,0,11.5)) diffracted beams have been chosen for display. While the oscillation period from the specular beam corresponds precisely to the time required to deposit

one monolayer of MoSe₂ on the substrate, the observed period from the (1,0,11.5) beam is exactly twice that from the specular beam, indicating a bilayer growth mode. This bilayer-mode oscillation is related to the stacking structure of the growing films. Bulk MoSe₂ single crystals exhibit several polytypes. The 2H_b polytype has the adjacent layers rotated by 180° [5]. In this polytype the *c*-axis of the unit cell contains two layers, accounting for the bilayer-mode oscillations. Kinematic theory also predicts that the diffraction maxima will occur in the bilayer-mode for 2H_b-MoSe₂. This model predicts a prominent bilayer-mode oscillation occurring at either (1,0,3.5) or (1,0,11.5). The (1,0,11.5) diffracted beam was used in the present experiment.

3.2. Epilayer structures

An epilayer of one 2D material deposited with VDWE onto another can produce films of high crystalline quality despite large lattice mismatches most likely because there is no covalent bonding between these layers. However, the Van der Waals forces which hold the layers together in the pure crystal still operate on the epilayer. The most stable site for a chalcogenide atom of the epilayer is one of the trigonal sites between the chalcogenide atoms of the substrate and above one of the trigonal sites containing a metal atom. Subsequent deposition will produce a strongly 2D bonded epilayer with the two HCP lattices going in and out of phase. A 2D model of the interface with the substrate and epilayer represented as different sized circles is shown in fig. 3. The results is that the lattice of the epilayer can be slightly distorted by the substrate lattice. This distortion can be measured by scanning tunneling microscopy (STM) due to the superior *z* resolution of the STM which is, in principle, less than the width of an atom. Shown in fig. 4 is STM image of several monolayers of MoSe₂ grown on a MoS₂ substrate (lattice mismatch of 4%). Triangular regions can be clearly seen and appear to be commensurate even when a molecular step is present. The size of the substructures, *D*, can be predicted using the moiré equation and the *a*-axis lattice constants of the two material (*d*₁ and *d*₂): $D = d_1 d_2 / |d_1 - d_2|$.

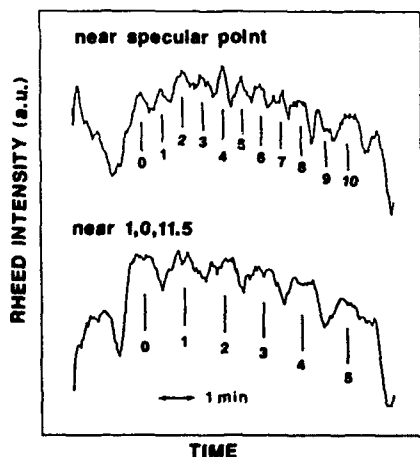


Fig. 2. RHEED intensity variation with time during the growth of MoSe₂ thin film on GaAs(111).

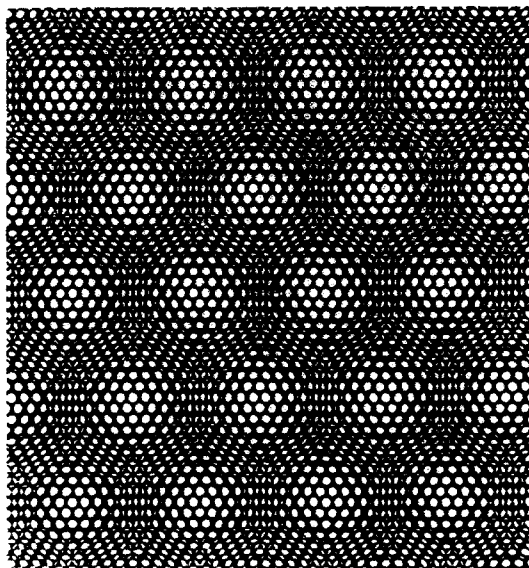


Fig. 3. A top view of the interface of two unrotated hexagonal closest packed lattices with a 10% lattice mismatch.

which gives a value of 80 Å whereas the actual size varies between 70 and 80 Å. The size of the structures with the extent of the lattice mismatch was also examined for MoSe_2 grown on SnS_2 , where the lattice mismatch is 10%. The resulting structure shows similar morphology, but with a

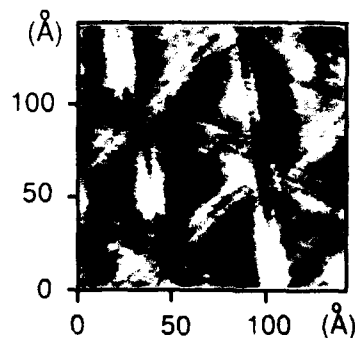
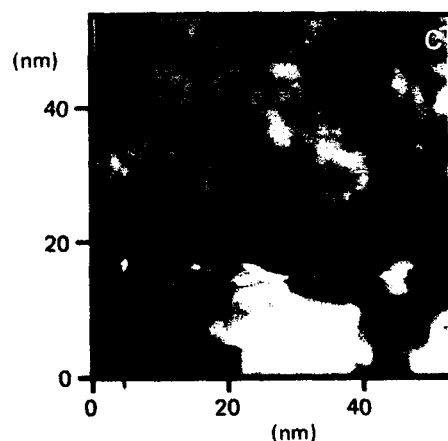
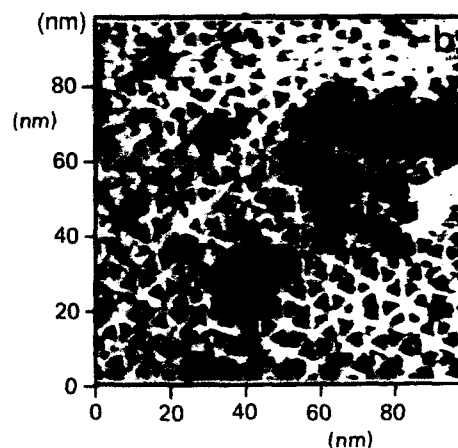
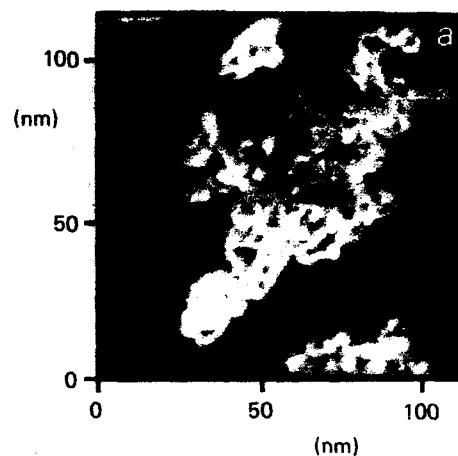


Fig. 4. A constant height atomic resolution STM image of several monolayers of MoSe_2 grown on a MoSe_2 substrate.

Fig. 5. A series of STM images for (a) 0.3, (b) 1.0 and (c) 2.0 monolayer coverages of MoSe_2 on a MoS_2 substrate.



different spacing (30–40 Å), close to that predicted by the moiré equation (33 Å).

STM images of various epilayer coverages of MoSe₂ grown on MoS₂ provide a further insight into the growth mechanism of VDWE. A series of STM images taken for 0.3, 1.0 and 2.0 monolayer coverages of MoSe₂ on MoS₂ are shown in figs. 5a, 5b and 5c, respectively. Here the coverage was estimated from the time required to form a complete monolayer. For a fractional monolayer, growth structure can be seen in the MoSe₂ islands, but no long range order can be seen. Fig. 5b shows an epilayer coverage of about one monolayer where the moiré substructure patterns become evident, however, islands on the layer as well as holes indicate incomplete growth of the first layer before nucleation of the second layer. For multilayer growth (fig. 5c), the moiré patterns from the second layer are rotationally aligned with respect to those from the first complete layer. Evidently the distortion of the first layer, induced by the lattice mismatch, influences the subsequent growth of additional layers. Information about the extent of these structures to a large number of epilayers has not yet been obtained but identical structures have been observed on up to 10 layers of MoSe₂ on MoS₂.

The apparent height of the structures measured with the STM was surprisingly large (2–4 Å) since it was expected that the geometric relaxation of the epitaxial atoms into the trigonal sites would produce a modulation of less than 0.5 Å. Enhanced *z* modulation of atomic features on 2D materials has been attributed to imaging a single wave function rather than mapping surface topography [6]. The nodal structure of the periodic wave functions can lead to large corrugations with the periodicity of the unit cell, which in our case has been determined by moiré pattern distance. The structures we observed may be considered analogous to charge density waves (CDWs), in that the CDW is a structural distortion producing a new electronic state by lowering the electronic degeneracy of the system while the structures we observe are a result of forcing a periodic structural distortion which breaks the degeneracy of the normally planar structures, leading to new electronic states.

CDWs have also shown enhanced *z* modulation in STM images.

4. Conclusions

A variation of molecular beam epitaxy, called Van der Waals epitaxy, is described where a material with primarily 2D bonding is epitaxially grown. Lattice matching difficulties, which limit the choice of materials in MBE of 3D systems, are circumvented since the interlayer bonding is from weak van der Waals interactions. We have demonstrated epitaxial growth of MoSe₂ on various substrates with lattice mismatches exceeding 10%. RHEED oscillations, observed in-situ for growing MoSe₂ epilayers, show a layer-by-layer growth with evidence for bilayer type growth, suggesting the 2H₁ polytype for the epilayer. STM provided real space images of the morphology of the epitaxial layer and showed novel structures resulting from the large lattice mismatch where the epilayer atoms are commensurated. The flexibility for fabrication of multilayer structures containing different materials selected for their specific properties, rather than their lattice matching requirements, has been discussed.

Acknowledgement

Sue Riggs is acknowledged for her technical assistance in the STM studies.

References

- [1] A. Koma, K. Sunouchi and T. Miyajima, J. Vacuum. Sci. Technol. B3 (1985) 724.
- [2] A. Koma and J. Yoshimura, Surface Sci. 174 (1986) 556.
- [3] F.S. Ohuchi, B.A. Parkinson, K. Ueno and A. Koma, J. Appl. Phys. 68 (1990) 2168.
- [4] T. Shimada, H. Yamamoto, K. Saiki and A. Koma, Japan. J. Appl. Phys. 29 (1990) L2096.
- [5] F. Levy, Ed., Crystallography and Crystal Chemistry of Materials with Layered Structures (Reidel, Dordrecht, 1976).
- [6] J. Tersoff, Phys. Rev. Letters 57 (1986) 440.

Reconstruction structure at $\text{Ga}_2\text{Se}_3/\text{GaAs}$ epitaxial interface

D. Li, Y. Nakamura, N. Otsuka

School of Materials Engineering, Purdue University, West Lafayette, Indiana 47907, USA

J. Qiu, M. Kobayashi and R.L. Gunshor

School of Electrical Engineering, Purdue University, West Lafayette, Indiana 47907, USA

A highly developed reconstruction structure was found at the $\text{Ga}_2\text{Se}_3/\text{GaAs}$ epitaxial interface by transmission electron microscope observations. The atomic structure of the reconstruction was derived by the analysis of electron diffraction patterns and high resolution transmission electron microscope images. The structure, which is described as an ordered arrangement of structural vacancies on the Ga sublattice, suggests that the reconstruction results from the valence mismatch at the $\text{Ga}_2\text{Se}_3/\text{GaAs}$ interface.

1. Introduction

The development of advanced thin film growth techniques such as molecular beam epitaxy (MBE) and metalorganic chemical vapor deposition (MOCVD) has led to the growth of heterostructures of a variety of combinations of semiconductor materials. Among such heterostructures, those represented by II–VI/III–V and III–V/IV semiconductor heterostructures possess great significance for both device technology and fundamental materials science. These heterostructures consist of semiconductor materials having similar lattice structures but belonging to chemically different families. Due to the difference of valences of constituent atoms, electron-excess or electron-deficient chemical bonds may form at the interfaces of these heterostructures. The formation of the electron-excess or electron-deficient chemical bonds is a result of one form of mismatch between two materials at the interface which may be called “valence mismatch” in order to be distinguished from conventional “lattice constant mismatch”. The valence mismatch is a direct conflict of the

lattice structure with the basic mechanism of chemical bonds in the semiconductors, and, hence, the study on structures and properties of valence mismatched interfaces provides us with an opportunity to explore the fundamental character of chemical bonds in these materials.

During the course of the study on the ZnSe/GaAs interface, we have succeeded in the growth of $\text{Ga}_2\text{Se}_3/\text{GaAs}$ heterostructures by MBE. Ga_2Se_3 crystallizes in the zincblende structure similarly to III–V and II–VI semiconductors [1] and, hence, the $\text{Ga}_2\text{Se}_3/\text{GaAs}$ interface is also a representative of the valence mismatched interfaces. We have found a highly developed reconstruction structure at this interface by the transmission electron microscope (TEM) observation. This finding adds a new member to the group of interface reconstructions, the existence of which has been found for the first time in the last few years [2–6]. The atomic structure derived by the analysis of electron diffraction patterns and high resolution transmission electron microscope (HRTEM) images indicates that this reconstruction results from the valence mismatch at the

$\text{Ga}_2\text{Se}_3/\text{GaAs}$ interface. In this paper, we present results of the TEM observation and structure analysis of the reconstruction structure.

2. Experimental procedure

The $\text{Ga}_2\text{Se}_3/\text{GaAs}$ heterostructures were grown by using a 430 modular MBE system which has three separate growth chambers connected by an ultra-high vacuum transfer tube. A GaAs epilayer was first grown on a (100) GaAs substrate in one chamber and then transferred to another chamber for the growth of a Ga_2Se_3 epilayer. Prior to the growth of the Ga_2Se_3 epilayer, the GaAs surface was heated without being exposed to fluxes, which gave rise to an As deficient surface exhibiting a (4×3) surface reconstruction [7]. The Ga_2Se_3 epilayer with a thickness of 450 Å was grown at 400 °C with a growth rate of 5 Å/min. For the TEM observation, (010), (001), (011) and (0 $\bar{1}1$) cross-sectional samples and (100) plan-view samples were prepared by ion thinning. A JEM 2000 EX electron microscope with a top-entry goniometer was used at an operating voltage of 200 kV. The spherical aberration coefficient of the objective lens pole piece is 0.7 mm.

3. Results and discussion

TEM observations of cross-sectional and plan-view samples have shown the formation of a single crystal Ga_2Se_3 film having a zincblende structure. Ga_2Se_3 is known to crystallize in a stable zincblende structure in which one third of Ga sites are left as structural vacancies [1]. The presence of the structural vacancies is explained as a result of the valence mismatch of Ga and Se atoms in the perfect form of the zincblende structure. The lattice parameter of the Ga_2Se_3 epilayer is 5.43 Å which is close to that of stoichiometric Ga_2Se_3 . Both electron diffraction patterns and HRTEM images have shown a parallel epitaxial relation of the (100) Ga_2Se_3 crystal with the (100) GaAs crystal. Existence of misfit dislocations at the interface was observed in (011) and (0 $\bar{1}1$) HRTEM images. The lattice mismatch between GaAs and

Ga_2Se_3 is 4%, with which one can expect a critical thickness of a few tens of ångströms. Electron diffraction patterns of the Ga_2Se_3 epilayer exhibit diffuse scattering, indicating a short-range ordered arrangement of structural vacancies in the epilayer.

The existence of the reconstruction structure at the interface was found by [010] and [001] cross-sectional electron diffraction patterns. Fig. 1 is a [010] cross-sectional diffraction pattern taken from an area including the $\text{Ga}_2\text{Se}_3/\text{GaAs}$ interface. Due to a long exposure, Bragg spots of Ga_2Se_3 and GaAs became broader and overlapped each other in the pattern. Many bright lines radiating from the direct spot were caused by deflection of electrons in the path of the electron microscope column. Reflection rods resulting from the reconstruction structure are clearly seen in the pattern. One group of reflection rods connect Bragg spots of GaAs, while the other group appear between the Bragg spots, corresponding to superstructure reflections. Locations of superstructure reflection rods are defined as $(0, l)$, where l is an odd

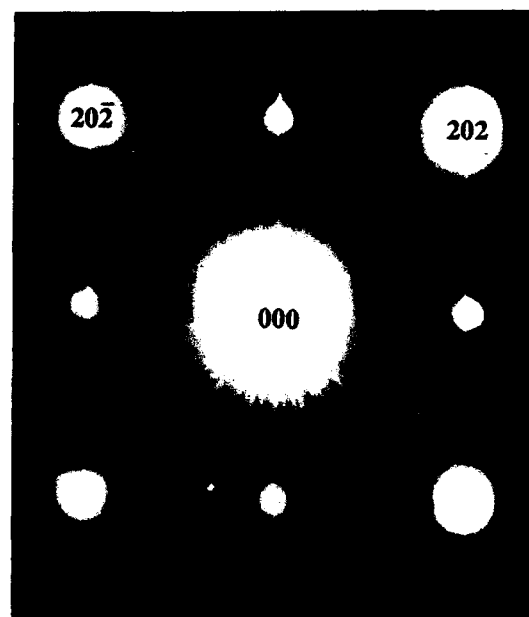


Fig. 1. [010] cross-sectional electron diffraction pattern of the $\text{Ga}_2\text{Se}_3/\text{GaAs}$ heterostructure.

integer. These reflection rods exhibit intensity modulation suggesting a pseudo-two-dimensional nature of the reconstruction. The period of the modulation is a^* , and the positions of intensity maxima and minima of reflection rods of the first group are shifted from those of the second group by $\frac{1}{2}a^*$, where a^* is the length of the reciprocal lattice vector of the cubic GaAs lattice. Similar reflection rods were observed in $[001]$ diffraction patterns. In $[011]$ and $[0\bar{1}1]$ diffraction patterns, only reflection rods connecting Bragg spots of GaAs were observed. Superstructure reflection rods observed in $[010]$ and $[001]$ patterns appear as very weak spots in $[100]$ plan-view patterns at the positions of forbidden reflections of the zincblende structure. These cross-sectional and plan-view patterns indicate that the reconstruction structure is described as a $c(2 \times 2)$ lattice if the structure is projected to a plane parallel to the interface.

Direct images of the reconstruction structure were obtained in $[010]$ and $[001]$ cross-sectional HRTEM images. Fig. 2 is a $[010]$ cross-sectional HRTEM image of the $\text{Ga}_2\text{Se}_3/\text{GaAs}$ interface. One can see a periodic arrangement of bright spots corresponding to the reconstruction structure along the interface with a spacing of 5.65 Å which is twice greater than that of (002) lattice planes of GaAs. Such a periodic arrangement of bright spots were seen in many parts of the interface, suggesting the existence of a highly developed reconstruction structure at the interface. The

close examination of the HRTEM images has shown that more than one row of the ordered arrangement of bright spots appears in some parts of the interface. The spacing of these rows in the $[100]$ direction is 4.9 Å, and the positions of bright spots of the second row is shifted from those of the first row by a half of the period of the ordered arrangement of bright spots.

As explained earlier, one third of the Ga sites in the Ga_2Se_3 crystal are left as structural vacancies. One may, therefore, suggest that the reconstruction structure at the interface is an ordered arrangement of these structural vacancies. Observations of electron diffraction patterns and HRTEM images support such a structure model. The ordered arrangement of bright and dark spots along the interface is clearly seen in the HRTEM images with relatively high contrasts even at very thin areas of the sample, which cannot be explained based on a model of an ordered arrangement of As and Se atoms or that of displacements of interface atoms. Diffraction patterns with excitation of only $h00$ type reflections exhibit a distinct reflection rod with intensity maxima at the positions of 1, 0, 0 and $\bar{1}$, 0, 0. This observation cannot be explained by a model of displacements of atoms along the interface. We have derived a model of an ordered arrangement of structural vacancies which can explain all main features of observed diffraction patterns and HRTEM images. Figs. 3a and 3b schematically show this model. In the model, only a half of the sites of the first Ga

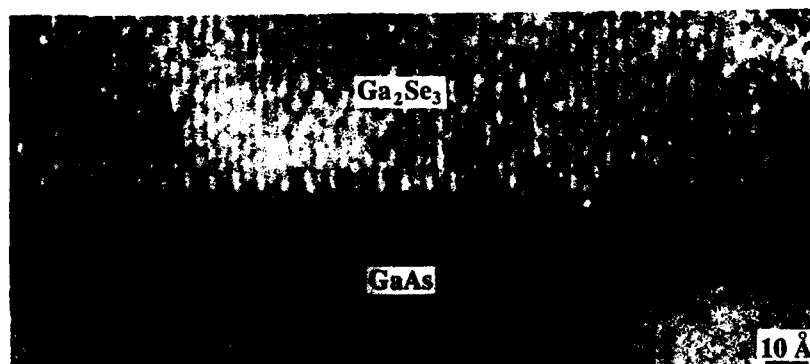


Fig. 2. $[010]$ high resolution transmission electron microscope image of the reconstruction structure at the Ga_2Se_3 interface.

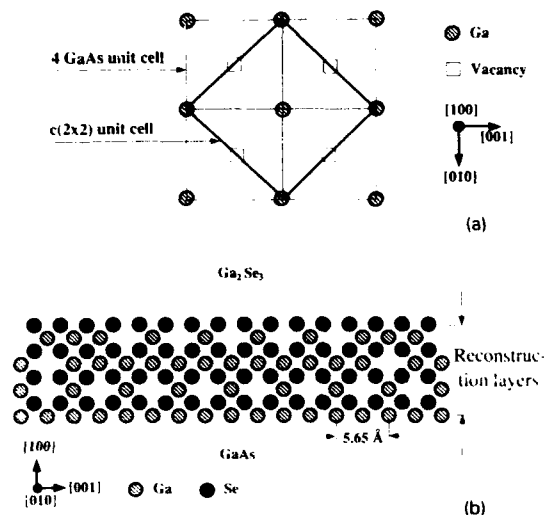


Fig. 3. Model of the atomic structure of the reconstruction. (a) Vacancy arrangement in the first Ga layer; (b) [010] projection of the reconstruction structure.

layer of the Ga_2Se_3 epilayer are occupied by atoms, leaving the remaining sites as structural vacancies. These vacancies form a $c(2 \times 2)$ superlattice in this layer as shown in fig. 3a. The second Ga layer in the epilayer, on the other hand, is almost fully occupied by atoms. In the third Ga layer, structural vacancies locally form the $c(2 \times 2)$ ordered structure which is shifted by half a period from that of the first Ga layer. In Ga layers beyond the third one, structural vacancies form a nearly random arrangement. Fig. 3b shows a sequence of these Ga layers viewed in the [010] direction. Intensity distributions of reflection rods calculated based on this model are in an excellent agreement with the observed ones. Details of the analysis of the reconstruction structure will be reported in a separate paper [8].

The ordered arrangement of structural vacancies in the model of the reconstruction structure is different from that found in bulk crystals of Ga_2Se_3 [9]. In the reconstruction structure, the fraction of structural vacancies varies from one Ga layer to the next Ga layer as shown in fig. 3b. The size of the variation rapidly decreases in the

growth direction, leading to the average fraction of vacancy in Ga_2Se_3 . In the ordered structure of bulk Ga_2Se_3 , on the other hand, all (100) Ga layers have the same fraction of structural vacancies, i.e., $\frac{1}{3}$. Despite this difference of ordered arrangements, the number of the nearest neighbor Ga atoms of one Se atom in the reconstruction is very close to that of the ordered structure of bulk Ga_2Se_3 . In the ordered structure of bulk Ga_2Se_3 , two thirds of the Se atoms have three nearest neighbor Ga atoms, and the remaining one third of Se atoms have two nearest neighbor Ga atoms. The average number of the nearest neighbor Ga atoms is, therefore, $\frac{8}{3}$. In the reconstruction structure, each Se atom has three nearest neighbor Ga atoms as seen in fig. 3b. With the similarity of the number of the nearest neighbor atoms, one can suggest that the reconstruction structure forms as a transient structure from the GaAs crystal to the Ga_2Se_3 crystal, maintaining the valence matching of constituent atoms of the interface region; if a Ga_2Se_3 crystal having the structure of the bulk crystal directly forms on the GaAs surface, atoms at the interface cannot maintain the valence matching because of the nearly complete occupation of the top Ga layer of the GaAs crystal [8].

Acknowledgements

This research was supported by Air Force Office of Scientific Research grant No. 89-0438 and Defense Advanced Research Project Agency/Office of Naval Research - University Research Initiative Program N0014-86-K0760.

References

- [1] H. Hahn and W. Klingler, *Z. Anorg. Chem.* 259 (1949) 135.
- [2] J.M. Gibson, H.J. Gossmann, J.C. Bean, R.T. Tung and L.D. Feldman, *Phys. Rev. Letters* 56 (1986) 355.
- [3] K. Akimoto, J. Mizuki, T. Tatsumi, N. Aizaki and J. Matsui, *Surface Sci.* 183 (1987) L297.
- [4] J. Mizuki, K. Akimoto, I. Hirose, K. Hirose, T. Mizutani and J. Matsui, *J. Vacuum Sci. Technol.* B6 (1988) 31.
- [5] K. Akimoto, I. Hirose, J. Mizuki, S. Fujieda, Y. Matsumoto and J. Matsui, *Japan. J. Appl. Phys.* 27 (1988) L1401.

- [6] D. Lorette, J.M. Gibson and S.M. Yalisove, Phys. Rev. Letters 63 (1989) 198.
- [7] J. Qiu, Q.D. Qian, R.L. Gunshor, M. Kobayashi, D.R. Menke, D. Li and N. Otsuka, Appl. Phys. Letters 56 (1990) 1272.
- [8] D. Li, Y. Nakamura, N. Otsuka, J. Qiu, M. Kobayashi and R.L. Gunshor, to be published.
- [9] D. Lubbers and V. Leute, J. Solid State Chem. 43 (1982) 339.

MBE as a production technology for AlGaAs lasers

Haruo Tanaka and Masato Mushiage

Rohm Co., Ltd., 21, Saiin Mizosaki-cho, Ukyo-ku, Kyoto, Japan

We are the first to succeed in the mass production of AlGaAs visible-wavelength semiconductor laser on a commercial basis using MBE. Single-transverse-mode self-aligned AlGaAs double heterostructure (DH) lasers were fabricated by a two-step molecular beam epitaxial technique. A GaAs layer was thermally etched selectively in the MBE system just prior to regrowth. There was no problem associated with the regrowth of an AlGaAs layer after the thin GaAs passivation layer was removed. This self-aligned structure by MBE affords high control of transverse and longitudinal modes, which results in high quality laser for various applications such as compact disc, video disc, laser beam printer and optical memory disc.

1. Introduction

MBE offers planar, uniform and high quality over large wafer areas, as compared with conventional LPE. The first current injection AlGaAs DH laser was prepared by Cho and Casey [1] in 1974. In 1979, Tsang [2] first obtained AlGaAs DH lasers by MBE with threshold currents at least as low as those prepared by LPE. In the 1980s, Tsang demonstrated MQW and GRIN-SCH lasers [3,4] by MBE. For the industrial production of lasers using MBE, however, mainly two problems needed to be overcome: (1) poor reproducibility and (2) no stripe structure fit for MBE. In this paper, we report the mass-production of transverse-mode-controlled self-aligned AlGaAs DH lasers using a two-step molecular beam epitaxy technique [5], and the characteristics of these lasers.

2. Device fabrication

Modified conventional MBE Riber 32P systems was used, operating day and night with computer-controlled. The requirements for mass-production MBE are: (1) one-touch substrate mounting; (2) large volume cells (2400 h); (3) precise substrate temperature control ($\pm 5^\circ\text{C}$); (4) shutter reliability.

Fig. 1 shows the room temperature photoluminescence intensity of DH samples as a function of time. After the MBE system is reloaded, the system is baked (72 h, 200°C) and sources are purified. About two days of growth are enough to obtain high quality DH wafers. Usually, if the PL intensity is higher than the dashed line level, high quality AlGaAs DH lasers can be fabricated reproducibly.

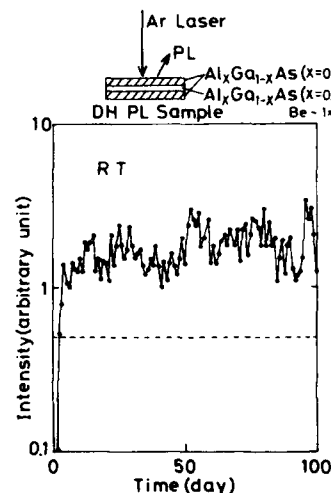


Fig. 1. Room temperature photoluminescence intensity of DH sample as a function of time. If the intensity is higher than the dashed line level, high quality AlGaAs DH lasers can be fabricated reproducibly.

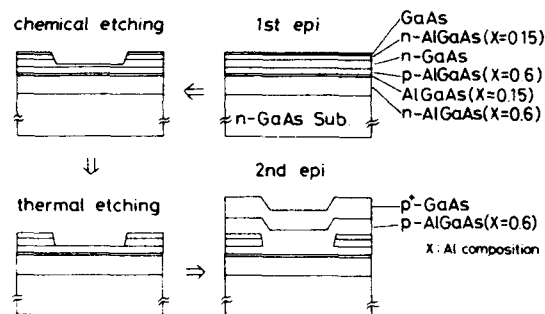


Fig. 2. Schematic illustrations of the process and structure of the self-aligned laser fabricated by MBE.

producibly. The devices were grown on a (100) oriented Si-doped GaAs substrate (2 inch wafer). Growth rates were $1.2 \mu\text{m/h}$ for GaAs and $3.0 \mu\text{m/h}$ for AlGaAs ($x = 0.6$). An active layer was grown at 690°C . Schematic illustrations of the process and structure of the self-aligned laser are shown in fig. 2. In the first growth of the two step technique, six layers were grown: (1) n-AlGaAs ($x = 0.6$, Si: $5 \times 10^{17} \text{ cm}^{-3}$), $1.3 \mu\text{m}$; (2) undoped AlGaAs ($x = 0.15$) active layer, $0.07 \mu\text{m}$; (3) p-AlGaAs ($x = 0.6$, Be: $5 \times 10^{17} \text{ cm}^{-3}$), $0.35 \mu\text{m}$; (4) n-GaAs (Si: $5 \times 10^{18} \text{ cm}^{-3}$), $0.24 \mu\text{m}$; (5) n-AlGaAs ($x = 0.15$, Si: $5 \times 10^{18} \text{ cm}^{-3}$), $0.07 \mu\text{m}$; (6) undoped-GaAs, $0.04 \mu\text{m}$. After the first growth step, the wafer was taken out from the MBE system, and stripes were opened along the $\langle 110 \rangle$ direction with a conventional photo-lithographic technique. The width of the stripes used in this work was $4 \mu\text{m}$. The channels were etched into the wafer using a $\text{H}_2\text{SO}_4 : \text{H}_2\text{O}_2 : \text{H}_2\text{O}$ mixture. A thin GaAs layer about 1000 \AA was left on the p-AlGaAs layer for passivation as shown in fig. 2. The wafer was then inserted into the MBE system for the second MBE growth step. Prior to regrowth, the thin GaAs passivation layer on the p-AlGaAs cladding layer and the n-AlGaAs current confinement layer was thermally desorbed under As_4 pressure. The thermal desorption rate of GaAs at 740°C under As_4 pressure was about $2 \mu\text{m/h}$ while that of AlGaAs ($x \geq 0.15$) under the same conditions was negligible. The wafer was heated for 15 min at 740°C under As_4 pressure. After the thin GaAs layers was selectively desorbed, two layers were grown: (1) p-AlGaAs ($x = 0.6$, Be:

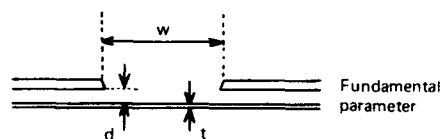
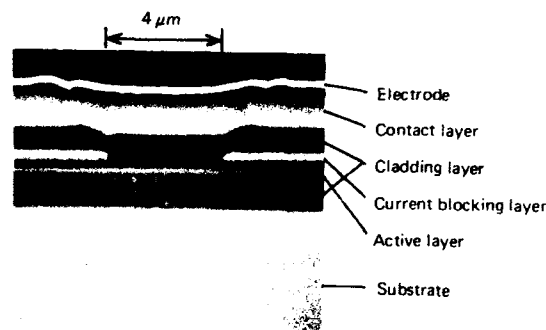


Fig. 3. A cross-sectional SEM photograph of the self-aligned laser by MBE and fundamental parameters of the lasers.

$5 \times 10^{18} \text{ cm}^{-3}$), $1.3 \mu\text{m}$; (2) p⁺-GaAs (Be: $2 \times 10^{19} \text{ cm}^{-3}$), $1.5 \mu\text{m}$. Fig. 3 shows a cross-sectional SEM photograph of the self-aligned laser by MBE. In this two-step molecular beam epitaxy method, the thickness of each layer was controlled within the accuracy of MBE. Metal contacts of Ti-Au

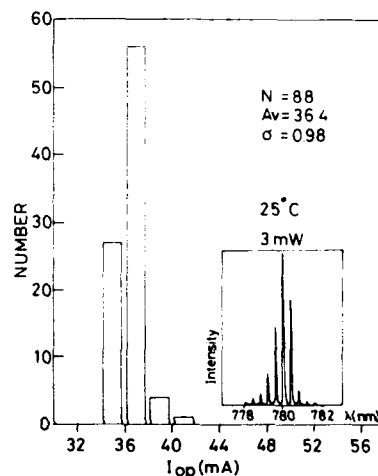


Fig. 4. Histogram of operation currents at an optical output of 3 mW and lasing spectrum.

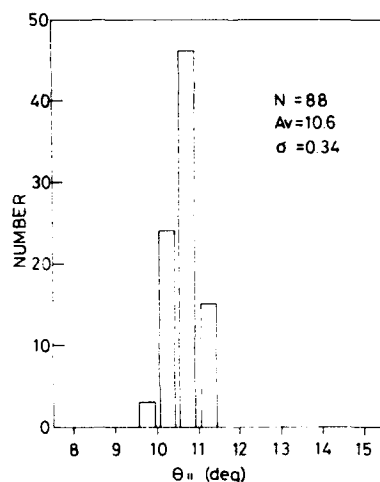


Fig. 5. Histogram of beam divergences parallel to junction plane.

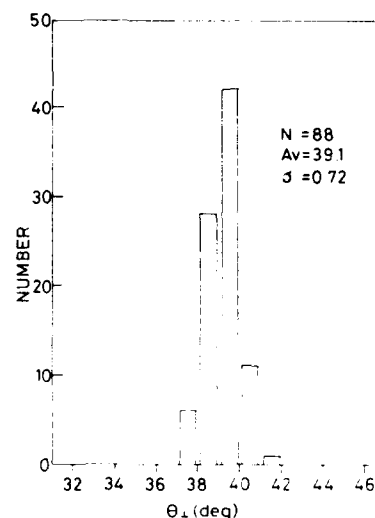


Fig. 6. Histogram of beam divergences perpendicular to junction plane.

and alloyed Au-Ge were then formed on the wafer. There was no additional current confinement such as oxide stripes on the surfaces. Devices with a 250 μm long cavity were fabricated as usual by cleaving, sawing and coating.

3. Device characteristics

Fig. 4 shows a histogram of operation currents at 3 mW and lasing spectrum. Low operation current has been realized by optimizing the carrier concentration of the first p-AlGaAs cladding layer to minimize the lateral current spreading and carrier out-diffusion from the stripe. The laser operates in a multi longitudinal mode at 3 mW. This means that mode changes are performed smoothly by the return light and that low noise is maintained, even if the optical path is shorter than the coherence length.

Fig. 5 and fig. 6 show histograms of beam divergences parallel and perpendicular to the junction plane. Due to excellent control of the film thickness by MBE, the variability of these optical

characteristics are one-third that of the conventional LPE lasers.

Fig. 7 shows the results of 1000 h continuous operation at the temperature of 80°C and the optical output of 5 mW. Since the carrier concentration has been optimized and the operation current has thus been lowered, the operation current at 80°C comes between 60 to 80 mA and degradation rate is very low.

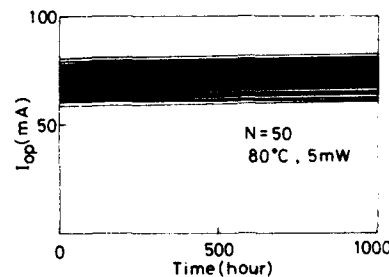


Fig. 7. Life-testing results of 1000 h continuous operation at a temperature of 80°C and optical output of 5 mW.

4. Summary

We are the first to succeed in the mass-production of AlGaAs visible-wavelength semiconductor laser using MBE. The self-aligned structure by MBE affords high controllability of transverse and longitudinal modes, which provides the laser with various applications such as compact disc, video disc, laser beam printer and optical memory disc.

References

- [1] A.Y. Cho and H.C. Casey, Jr., *Appl. Phys. Letters* 25 (1974) 288.
- [2] W.T. Tsang, *Appl. Phys. Letters* 34 (1979) 473.
- [3] W.T. Tsang, *Appl. Phys. Letters* 39 (1981) 786.
- [4] W.T. Tsang, *Appl. Phys. Letters* 40 (1982) 217.
- [5] H. Tanaka, M. Mushiage, Y. Ishida and H. Fukada, *Japan. J. Appl. Phys.* 24 (1985) L89.

Substrate temperature dependence of SQW alloy and superlattice lasers grown by MBE using As_2

C.T. Foxon

Philips Research Laboratories, Redhill, Surrey RH1 5HA, UK

P. Blood

Department of Physics, University of Wales, P.O. Box 913, Cardiff CF1 3TH, Wales, UK

E.D. Fletcher, D. Hilton, P.J. Hulyer

Philips Research Laboratories, Redhill, Surrey RH1 5HA, UK

and

M. Vening *

Department of Physics, University of Surrey, Guildford GU2 5XH, UK

Until recently most semiconductor device structures grown by MBE have used As_4 . In such structures during the growth of (Al,Ga)As alloys a characteristic roughness is observed under some growth conditions. The threshold current of lasers grown using As_4 is also strongly influenced by the choice of substrate temperature. It is possible therefore that these two factors are related. We have compared the morphology of thick films of $\text{Al}_{0.5}\text{Ga}_{0.5}\text{As}$ grown using As_2 and As_4 over the temperature range 610 to 710 °C. For films grown with As_4 the characteristic roughness in such structures is observed but over the whole temperature range films grown with As_2 have a specular appearance. We have grown, using As_2 , a series of graded refractive index separate confinement heterostructure single quantum well (57 Å) lasers with and without pre-layers at temperatures from 610 to 710 °C. In this series of samples the Al and Ga fluxes were kept constant, the nominal Al fractions for the outer confinement and barrier regions were 50% and 25%, respectively. A similar set of stepped separate confinement structures with prelayers was grown for comparison. In a fourth series of structures the separate confinement and part of the outer cladding regions were replaced by short period superlattices. Contrary to previous reports for structures grown using As_4 , no strong dependence of threshold current on growth temperature was observed. Results for four sets of lasers will be discussed in detail. An additional benefit of using As_2 is the reduced loss of Ga at high temperatures due to a reduction of free metallic group III element present on the surface during growth.

1. Introduction

In the growth of III–V compounds by MBE the group V element is often supplied by sublimation from the solid in the form of a tetramer molecule. It is, however, possible to dissociate this molecule

into two dimers using a two-zone cracker furnace. The basic growth mechanisms for the two processes are different [1,2] and it has been shown in a number of studies that films grown with the dimer are superior to those grown with the tetramer. The concentration of deep levels in GaAs grown with As_2 is lower than in films grown with As_4 [3] and the optical properties are also im-

* Industrial Trainee.

proved [4]. For (Al,Ga)As–GaAs double heterostructures a lower interface recombination velocity is also observed using As_2 compared to As_4 [5]. In addition, in the growth of (Al,Ga)As films with As_4 a characteristic surface roughness is commonly observed in the so-called forbidden temperature regime (600–680°C) [6], but in films grown with As_2 this problem is not observed [7].

For double heterostructure (DH) lasers grown with As_4 the choice of substrate temperature strongly influences the threshold current [8], and it is now clear that the lowest threshold current is only obtained for films grown under conditions where no surface roughness is observed for the growth of (Al,Ga)As [9]. Prior to this observation a number of techniques have been used to improve the threshold current of DH and quantum well (QW) lasers including the use of off-orientation substrates [10], which are known to smooth the surface of (Al,Ga)As grown in the so-called forbidden temperature range [11]. It has also been shown that the use of pre-layers reduces the threshold current of graded refractive index (GRIN) separate confinement heterostructure (SCH) single quantum well (SQW) lasers [12]. Finally it has been shown recently that extremely low threshold current GRIN-SCH-SQW lasers can be obtained by replacing the alloy regions by short period (SP) superlattices (SLs) [13]. In all the above studies the use of high temperatures (about 700°C) results in a temperature dependent loss of Ga from the surface, small variations in substrate temperature across the slice during growth therefore leads to unacceptable variations in operating wavelength.

We have therefore studied the effect of replacing As_4 with As_2 for a variety of laser structures including conventional GRIN-SCH-SQW structures grown with alloys, similar structures incorporating a SP-SL prelayer, abrupt SCH-SQW lasers with SP-SL pre-layer and similar SCH-SQW lasers with the alloy region of the waveguide replaced by a SP-SL. In each case we have studied the effect of varying the substrate temperature over the range 610 to 690 or 710°C where there is a transition from rough to smooth growth for (Al,Ga)As alloys, i.e., inside and outside the so-called forbidden temperature regime.

2. Experimental technique

The samples were grown in a 2 inch Varian GEN-II MBE system using an indium bonded substrate holder. With this system using roughened blocks, the substrate temperatures measured using a radiation pyrometer (operating at 2 μm using an emissivity setting of 0.62 of Si doped substrates) agree with the thermocouple estimate to within 20°C. In this system using an As flux with a beam equivalent pressure of 1×10^{-5} Torr, with no other fluxes impinging on the sample, there is a transition from the As-stable (100) (2×4) reconstructed surface pattern to a Ga-stable (3×1) pattern in less than 2 s on closing the As shutter at 640°C.

The samples were grown using a GaAs growth rate of 1 monolayer (ML) per second, the growth rates were established using the familiar RHEED oscillation technique [14]. Growth rates for Al were adjusted in a similar manner to give the required alloy fraction. In the SCH-SQW structures a 5 min interrupt was used to reset the Al cell temperature but for all other structures growth was continuous. Doping densities were kept low enough to avoid disordering the SP-SLs, i.e. $< 10^{18} \text{ cm}^{-3}$, and this was confirmed both by TEM and X-ray analysis on selected samples. No adjustment was made to the Ga flux to allow for Ga re-evaporation at high temperatures in order to avoid this complication. As_2 was produced using the commercially available Varian cracker cell operating under the nominally suggested conditions. Apart from the expected reduction in system pressure and more rapid coating of the windows we have no independent indication of the cracking efficiency of this cell.

Prior to the growth of all laser structures the minority carrier lifetime at 300 K was established in intentionally doped (Be at $2 \times 10^{16} \text{ cm}^{-3}$) MQW structures. Experience has shown that this lifetime correlates well with the threshold current of lasers grown by MBE. We have previously shown that this is a good measure of the radiative efficiency in the (Al,Ga)As or AlAs regions close to the heterointerface with the GaAs well [15]. A minimum lifetime of 30 ns was achieved prior to the growth of the structures described above. Struc-

tures grown with As_2 had significantly longer lifetimes (approximately $3 \times$) than the equivalent samples grown with As_4 immediately before or afterwards.

The wafers were processed into oxide isolated $50 \mu\text{m}$ stripe lasers with a cavity length of $500 \mu\text{m}$ and the threshold current and wavelength measured as a function of temperature using pulsed techniques. The fabrication and testing procedures have been described in detail elsewhere [16]. For some wafers broad area devices were also fabricated to give a better guide to the true threshold current density and to make a more meaningful comparison with other low-threshold current devices.

3. Experimental results

$1 \mu\text{m}$ thick layers of $\text{Al}_{0.5}\text{Ga}_{0.5}\text{As}$ were grown using both As_2 and As_4 over the temperature range 610 to 710°C . In agreement with earlier observations we observed the characteristic surface roughness [6] when using As_4 as a group V source but this was entirely eliminated when using As_2 in

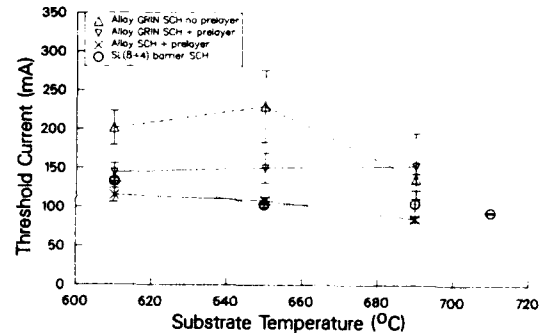


Fig. 2. Variation in threshold current with substrate temperature for four sets of oxide isolated $50 \mu\text{m}$ stripe lasers. The error bars correspond to two standard deviations.

agreement with our earlier unpublished observations and those reported in the literature [7]. Lower oval defect densities were also observed in films grown with the dimer compared with those grown using the tetramer.

Fig. 1 shows the structures that we have grown for this study. Fig. 2 shows the effect of substrate temperature on the threshold current of the four sets of structures. The first series consist of

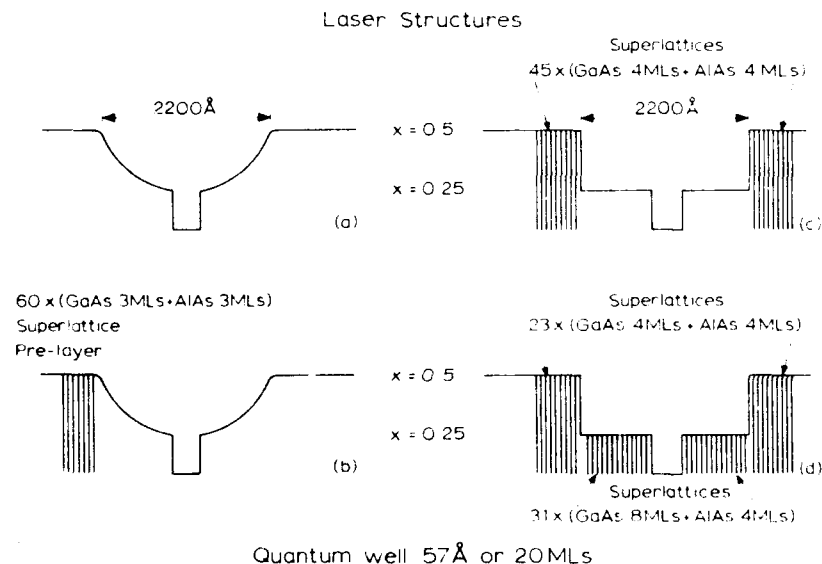


Fig. 1. Schematic composition profiles for the four sets of lasers grown in this study.

GRIN-SCH-SQWs (57 Å, 20 MLs), the second series have a 60 period GaAs(3 ML)/AlAs(3 ML) SL placed immediately before the GRIN region, the third series are abrupt SCH-SQW (57 Å, 20 MLs) lasers with 45 period GaAs(4 ML)/AlAs(4 ML) SL immediately before and after (to make the optical confinement symmetrical with respect to the SQW) the SC region. In the fourth series the 25% (Al,Ga)As alloy parts of the SCH region were replaced by a 31 period GaAs(8 ML)/AlAs(4 ML) SP-SL structure which gives an approximately equivalent band gap material.

In all cases there is evidence for only a weak effect of varying the substrate temperature, contrary to the results reported for samples grown with As₄. We also see little variation in laser wavelength with substrate temperature and the measured values agree with those predicted for the nominal structure within experimental error. From this it is evident that the use of As₂ under these conditions has resulted in little loss of Ga over the whole temperature range used for growth. As we have recently shown [17] and will report elsewhere at this conference in more detail, this is consistent with the observation that the rate of loss of Ga (In) from the surface is higher from free metallic Ga (In) than from the group III element already incorporated into the lattice. Using the dimer reduces the amount of free metallic group III present on the surface during growth and this in turn reduces the loss at high temperature.

We have observed no significant variation with growth temperature of other laser properties such as the external differential efficiency, junction threshold voltage and resistance of the devices. In most cases no significant trend was observed except for a small increase in external differential efficiency from 40% to 60% with increasing substrate temperature for the fourth set of devices with SLs in the separate confinement region.

Broad area devices have been fabricated on a number of the wafers and the lowest threshold current densities achieved for the alloy and SL barrier lasers were 236 and 232 A cm⁻², respectively. This compares favourably with other data present in the literature for lasers of similar cavity length operating at the same wavelength (~ 820 nm) [12,13].

4. Conclusions

We have shown that the use of As₂ enables "state-of-the-art" lasers to be grown over a wide range of substrate temperatures (610–710°C) compared with the situation using As₄ where it is essential to go to the highest temperature (710°C) to obtain low threshold current devices. This improvement correlates with the fact that the morphology of (Al,Ga)As layers grown with As₂ is good over the whole temperature range, whereas those grown with As₄ in the so-called forbidden substrate temperature region exhibit a characteristic surface roughness. An additional benefit in the use of As₂ is the reduced loss of Ga at high temperatures due to a lower amount of free metallic Ga present on the surface during growth. The use of As₂, therefore, enables acceptable growth to take place in the temperature range where small variations in substrate temperature across the slice become unimportant, leading to better control of thickness, alloy composition and hence lasing wavelength.

References

- [1] C.T. Foxon and B.A. Joyce, *Surface Sci.* 64 (1977) 293.
- [2] C.T. Foxon and B.A. Joyce, *Surface Sci.* 50 (1975) 434.
- [3] J.H. Neave, P. Blood and B.A. Joyce, *Appl. Phys. Letters* 36 (1980) 311.
- [4] H. Kunzel and K. Ploog, *Appl. Phys. Letters* 37 (1980) 416.
- [5] G. Duggan, P. Dawson, C.T. Foxon and G.W. 't Hooft, *J. Physique* 43 (1982) C5-129.
- [6] H. Morkoç, T.J. Drummond, W. Kopp and R. Fischer, *J. Electrochem. Soc.* 129 (1982) 824.
- [7] L.P. Erickson, T.J. Mattford, P.W. Palmberg, R. Fischer and H. Morkoç, *Electron. Letters* 19 (1983) 631.
- [8] W.T. Tsang, F.K. Reinhart and J.A. Ditzenberger, *Appl. Phys. Letters* 36 (1980) 118.
- [9] H. Meier, private communication.
- [10] H.Z. Chen, A. Ghaffari, H. Morkoç and A. Yariv, *Appl. Phys. Letters* 51 (1987) 2094.
- [11] R.K. Tsui, J.A. Curless, G.D. Kramer, M.S. Peffley and G.W. Wicks, *J. Appl. Phys.* 59 (1986) 1508.
- [12] T. Fuji, S. Yamakoshi, K. Nambu, O. Wada and S. Hiyamizu, *J. Vacuum Sci. Technol.* B2 (1984) 259.
- [13] P.S. Kop'ev, *Surface Sci.* 228 (1990) 514.
- [14] J.J. Harris, B.A. Joyce and P.J. Dobson, *Surface Sci.* 103 (1981) L90.

- [15] P. Dawson, G. Duggan, H.I. Ralph and K. Woodbridge, *Superlattices and Microstructures* 1 (1985) 173.
- [16] P. Blood, E.D. Fletcher and K. Woodbridge, *Appl. Phys. Letters* 47 (1985) 193.
- [17] E.M. Gibson, C.T. Foxon, J. Zhang and B.A. Joyce, *Appl. Phys. Letters* 57 (1990) 1203.

Vertical cavity top-surface emitting lasers with thin Ag mirrors and hybrid reflectors

M. Hong, L.W. Tu

AT&T Bell Laboratories, Murray Hill, New Jersey 07974, USA

J. Gamelin

Department of Electrical Engineering, University of California, Berkeley, California 94720, USA

Y.H. Wang, R.J. Fischer, E.F. Schubert, K. Tai, G. Hasnain, J.P. Mannaerts, B.E. Weir, J.D. Wynn, R.F. Kopf, G.J. Zyzik and A.Y. Cho

AT&T Bell Laboratories, Murray Hill, New Jersey 07974, USA

Three types of vertical cavity surface emitting lasers based on GaAs/AlGaAs have been grown by molecular beam epitaxy (MBE). The laser structures with top emission have been evolved from a simple double heterostructure (DH) with n-type distributed Bragg reflectors (DBR) as the bottom mirror and a semitransparent Ag as the top mirror, to a DH structure with a hybrid reflector consisting of a thin metal and a few pairs of p-DBR as the top mirror, and to a 3-QW structure again with a hybrid reflector as the top mirror. MBE growth of these three device structures is discussed, particularly on the in-situ growth of metals on GaAs. Devices have been fabricated and measured. A theoretical model has been used to gain an understanding of the parameters in each design. The MBE growth techniques have been improved to modify the heterostructural interface in the DBR to reduce the series resistance. The laser performance has been improved from a high threshold current in the first structure to a much lower threshold current in the second structure and finally to a cw room temperature operation with low threshold currents in the third structure.

1. Introduction

Vertical cavity surface emitting lasers (SELs) have recently attracted a lot of interest due to their unique features and potential applications [1–4]. For example, fabrication of integrated optical structures such as high density laser arrays or chip-to-chip communication elements with high speed and high data rate transmission could be realized. Also, SEL arrays could serve as drivers in optical logic systems.

To date, SELs have shown room temperature continuous wave (cw) performance using GaAs or InGaAs quantum wells (QWs) or GaAs/AlGaAs double heterostructures (DHs) [1–4]. Although most of the reported SELs emit light from the substrate side, light emission in a SEL can be

taken from the epitaxial side (top emission). Top emission simplifies processing since substrate removal is not necessary [4,5].

In this work, three types of top emitting SELs are reported as shown in fig. 1. The design concept has been evolved from a simple DH structure with a thin metal mirror, to a DH structure with a hybrid mirror (thin metal plus a few pairs of semiconductor distributed Bragg reflectors, DBRs), and finally to a QW structure with a hybrid mirror. We have gained a better understanding of the parameters in each design as the structure becomes more sophisticated. At the same time, we have improved our growth techniques including a more precise control in the growth rates and the ability to reduce the series resistance in the p-DBR by modifying the AlAs/GaAs inter-

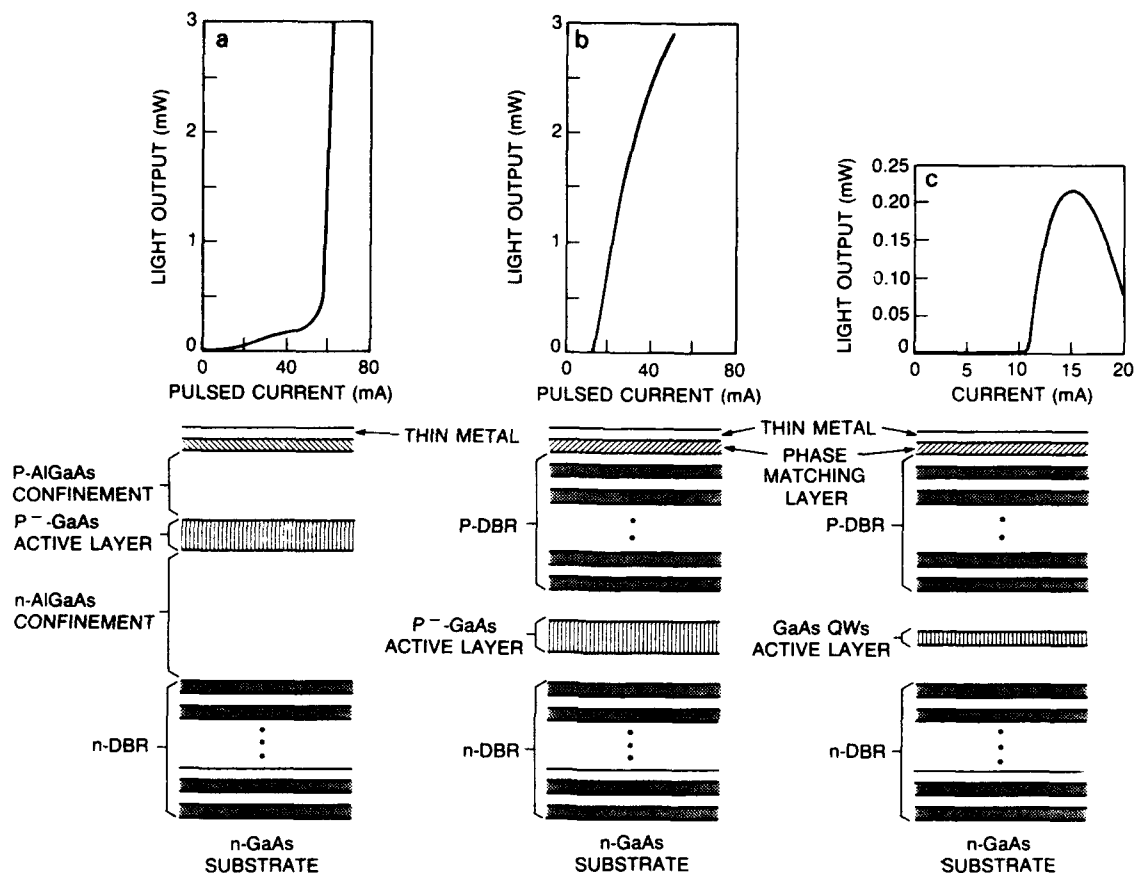


Fig. 1. Schematic representation of the vertical cavity surface emitting laser diodes and their light output power versus current ($L-I$) curves: (a) a DH structure with n-DBR as the bottom mirror and a semitransparent Ag as the top mirror; (b) a DH structure using a hybrid reflector consisting of a thin metal and a few pairs of p-DBR as the top mirror; (c) a 3-QW structure with a hybrid reflector as the top mirror.

face. Using this understanding, the laser performance has been improved: low threshold currents under cw operation.

2. Experimental

The first structure, labeled (a) in fig. 1, has a lightly p-doped bulk GaAs ($5 \times 10^{17} \text{ cm}^{-3}$) active layer $0.6 \mu\text{m}$ thick. The confinement layers are $0.5 \mu\text{m}$ p- $\text{Al}_{0.3}\text{Ga}_{0.7}\text{As}$ ($5 \times 10^{18} \text{ cm}^{-3}$) on the top and $2-3 \mu\text{m}$ n- $\text{Al}_{0.25}\text{Ga}_{0.75}\text{As}$ ($7 \times 10^{17} \text{ cm}^{-3}$) at the bottom. A thin heavily p-doped $\text{Al}_{0.1}\text{Ga}_{0.9}\text{As}$ ($\geq 5 \times 10^{19} \text{ cm}^{-3}$) was put on the very top to facilitate

the ohmic contact. The bottom mirror consists of 22.5 pairs of a quarter-wave n-type doped $\text{AlAs}(730 \text{ \AA})/\text{Al}_{0.1}\text{Ga}_{0.9}\text{As}(620 \text{ \AA})$ multilayer DBR. Thin Ag layers with various thickness from 300 to 2000 \AA used as the top mirror were deposited at 120°C in a separate e-beam evaporator. The n-DBR mirror, doped to a level of $1 \times 10^{18} \text{ cm}^{-3}$ with Si, was grown at a substrate temperature of $580-600^\circ\text{C}$. All the quarter-wave DBR mirrors mentioned in this work have been grown in this temperature range. A few attempts to grow the DBR mirrors at a higher temperature $\geq 620^\circ\text{C}$ proved to be unsatisfactory.

The second structure, also a DH and labeled

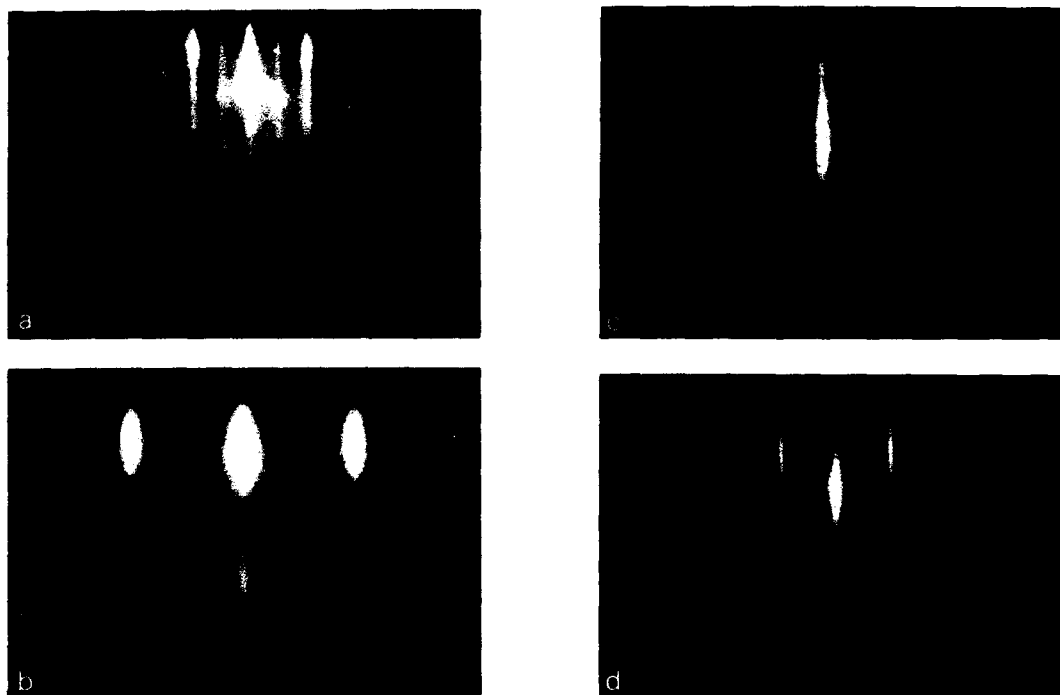


Fig. 2. Sequence of RHEED patterns recorded during the MBE growth of a Au/Ag/Fe/GaAs structure. All patterns were recorded along [110]. Pattern (a) shows a GaAs As stabilized surface. Pattern (b) was recorded after the growth of 35 Å Fe at 180°C. Pattern (c) was recorded after the growth of 100 Å Ag at 180°C on Fe. Pattern (d) was recorded after the growth of 200 Å Au at 180°C on Ag.

(b) in fig. 1, has a smaller cavity length, of 0.89 μm , corresponding to 3.5λ (optical wavelength) between two mirrors. The bottom mirror is an n-DBR identical to that used in the first structure. The top mirror is a thin metal/semiconductor p-DBR hybrid reflector. The p-DBR mirror consists of 7.5 pairs of quarter-wave $\text{AlAs}/\text{Al}_{0.1}\text{Ga}_{0.9}\text{As}$ with a linearly graded interface, and was doped to a level of $3 \times 10^{18} \text{ cm}^{-3}$ with Be. The thin metal in this second structure is an in-situ epitaxially grown composite, and consists of Au/Ag/Fe (200/100/35 Å).

The in-situ epitaxial metal growth on GaAs are discussed in the following. Unlike the growth of $\text{Al}(001)$ single crystal on $\text{GaAs}(001)$ in which a 45° azimuthal rotation occurs to minimize a large lattice mismatch between Al and GaAs, the growth

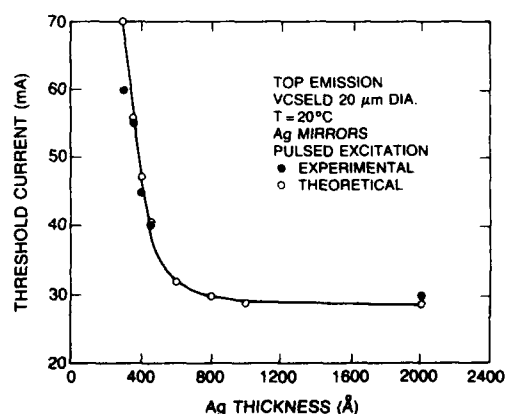


Fig. 3. Lasing threshold currents versus thickness of Ag mirror: experimental and theoretical data. The Ag contact is 20 μm in diameter.

of Ag single crystal on GaAs(001) was found to be much more difficult. Streaky reflection high energy diffraction (RHEED) patterns of the Ag were observed only after the deposition of films at least 500 Å thick. Somewhat surprisingly, there is no azimuthal rotation for Ag(001) on GaAs(001). For growing thin flat Ag single crystal (with thickness of less than 200 Å) on GaAs, a buffer layer may be needed to screen the GaAs surface anisotropy. A thin layer of Fe 35 Å thick [6] provides a successful subsequent growth of thin Ag and Au as indicated by the RHEED pattern and shown in fig. 2. Note that the Au on top of the Ag is for the protection of the devices beneath during wet chemical processing.

The third structure, labeled (c) in fig. 1, is similar to the second structure with the following differences: (1) the active layer consists of 3 GaAs QWs, (2) the number of periods in the p-mirrors is increased to 11.5 with a higher p-doping of $5 \times 10^{18} \text{ cm}^{-3}$ for the first 4.5 pairs and of $1 \times 10^{19} \text{ cm}^{-3}$ for the rest of the mirror, (3) the number of periods in the n-mirror is increased to 30.5, (4) the thin metal layer in the hybrid is ex-situ deposited Ag as in the first structure, and (5) two-step interfaces are used in the DBRs to reduce the series resistance in the p-DBR.

3. Results and discussion

3.1. GaAs bulk active region and thin metal as top mirror

Lasers using the structure of fig. 1a were fabricated and electrically pumped using a fine probe through the thin Ag. Here, the thin Ag acts both as the mirror and the electrode. The electroluminescence (EL) spectra of the SEL 20 µm in diameter with Ag 450 Å thick show four Fabry-Pérot (FP) modes in the wavelength range of 0.82 to 0.9 µm. The positions of these FP modes and the separation (~200 Å) between them are in good agreement with a theoretical calculation of this structure. A detailed description of the lasing measurement and characteristics was given in a separate publication [5].

Lasing threshold currents under pulsed operation versus the thickness of Ag mirrors are shown in fig. 3. The lasing threshold current is 30 mA for a Ag 2000 Å thick, and remains roughly at this value down to 800 Å. As Ag thickness is further reduced, the threshold rapidly increases. The trend of threshold current versus Ag thickness is shown in fig. 3 and is in good agreement with a theoretical model based on the reflectivity/loss characteristics of Ag as a function of thickness. This theoretical curve is plotted in fig. 3 for comparison. The discrepancy between the experimental and the theoretical threshold values is small and is within experimental error such as exact size of the Ag dots, or flatness and thickness of the Ag films. The optical constant (n, k) of Ag used in the theoretical calculation is (0.163, 5.95) [7]. The theoretical model used in this work will be described in a later paper [8].

The threshold current of this structure with Ag 450 Å is as high as 40 mA. This high threshold is due to the low reflectivity of the thin Ag. The threshold could be reduced by using thicker Ag; however, the thick Ag is opaque, and the structure can not emit light from the top surface.

3.2. GaAs bulk active region and hybrid mirror with thin metal and semiconductor DBR

A new design based on the work of hybrid reflector [2] and thin semitransparent metal [5] was then proposed [8,9] to provide high reflectivity and low resistance for a top-emission structure. The reflectivity of this hybrid structure consisting of a thin metallic composite Au/Ag/Fe (200/100/35 Å) and 7 pairs of AlAs/Al_{0.1}Ga_{0.9}As p-doped DBR is 97%. For comparison, the reflectivity of 300 Å Ag and 7 pairs of the DBR is ~80% and 91%, respectively. The second SEL structure discussed here and shown in fig. 1b was constructed with the top mirror based on this hybrid design. The doping concentration was as low as $3 \times 10^{18} \text{ cm}^{-3}$ through the entire p-DBR. Device fabrication was carried out using annular contacts and H⁺ ion implantation for isolation [9]. The threshold is 12 mA pulsed for a 10 µm size.

The reason why this structure could not lase cw is because of heating caused by the high voltage drop across the p-DBR. This high voltage drop occurred despite the effort in reducing the resistance by linearly grading the interface between the AlAs and $\text{Al}_{0.1}\text{Ga}_{0.9}\text{As}$. The increase in p-doping to the level of high 10^{18} cm^{-3} certainly would drastically reduce the resistance, but at the same time it would only slightly increase the threshold current as is discussed in one of our publications on the effect of Be doping on the performance of SELs [10].

3.3. GaAs MQW active region and hybrid mirror with thin metal and semiconductor DBR

From the results of the above two SEL structures, we have learned that:

- (1) Thin semitransparent metals when properly prepared may give low resistance but would not have high enough reflectivity needed to obtain low threshold currents. A hybrid reflector of thin metal and a few pairs (in the range between 6 and 12 pairs) of DBR would certainly provide high reflectivity and low series resistance.
- (2) Be doping in the high 10^{18} cm^{-3} range in the p-DBR lowers the series resistance, but does not substantially increase the threshold current.

Based on the above considerations, we then designed a new structure as shown in fig. 1c. This SEL lases cw at room temperature with top emission [9]. Voltage at the threshold current of 11 mA is 3.2 V and 100 Ω differential series resistance is obtained in devices 10 μm in diameter.

4. Conclusion

From the device characteristics of the MBE grown SELs and with the aid of the theoretical model, we have obtained a better understanding on the parameters in each design. A semitransparent thin metal alone as the mirror does not

offer high enough reflectivity to obtain low threshold currents. The hybrid structure consisting of a thin metal and a few pairs of semiconductor DBR provides high reflectivity and low series resistance. The in-situ grown metal films are better than the ex-situ ones in terms of flatness and electrical properties. However, a systematic comparison study on the performance of devices using these two different forms of metals is needed to assess the role of in-situ metal films in these devices.

The modifications in the heterojunction between AlAs/AlGaAs in the p-DBR whether by a linearly graded interface or a two-step one has reduced the series resistance. However, a Be doping in the high 10^{18} cm^{-3} in the p-DBR (after a few quarter-wave pairs away from the active region) is needed to ensure a room temperature cw operation in the present SEL structures.

References

- [1] F. Koyama, S. Kinoshita and K. Iga, Appl. Phys. Letters 55 (1989) 221.
- [2] K. Tai, R.J. Fischer, C.W. Seabury, N.A. Olsson, T.-C.D. Huo, Y. Ota and A.Y. Cho, Appl. Phys. Letters 55 (1989) 2473.
- [3] Y.H. Lee, J.L. Jewell, A. Scherer, S.L. McCall, J.P. Harbison and L.T. Florez, Electron. Letters 25 (1989) 1377.
- [4] Y.H. Lee, B. Tell, K. Brown-Goebeler, J.L. Jewell and J.V. Hove, Electron. Letters 26 (1990) 710.
- [5] L.W. Tu, E.F. Schubert, R.F. Kopf, G.J. Zydzik, M. Hong, S.N.G. Chu and J.P. Mannaerts, Appl. Phys. Letters 57 (1990) 2045.
- [6] P. Eitenne, J. Massies, F. Nguyen-Van-Dau, A. Barthelemy and A. Fert, Appl. Phys. Letters 55 (1989) 2239.
- [7] D.W. Lynch and W.R. Hunter, in: Handbook of Optical Constants of Solids, Ed. E.D. Palik (Academic Press, New York, 1985) p. 356.
- [8] M. Hong, J. Gamelin and R.J. Fischer, to be published.
- [9] G. Hasnain, K. Tai, J.D. Wynn, Y.H. Wang, R.J. Fischer, M. Hong, B.E. Weir, G.J. Zydzik, J.P. Mannaerts, J. Gamelin and A.Y. Cho, Electron. Letters, to be published.
- [10] Y.H. Wang, R.J. Fischer, J. Gamelin, M. Hong, J.P. Mannaerts and A.Y. Cho, to be published.

Reduced current thresholds in GaAs/AlGaAs vertical cavity surface emitting lasers using 4° off-oriented (001) GaAs substrates

Y.H. Wang *, K. Tai, Y.F. Hsieh, S.N.G. Chu, J.D. Wynn, M. Hong, R.J. Fischer and A.Y. Cho

AT&T Bell Laboratories, Murray Hill, New Jersey 07974, USA

GaAs/AlGaAs vertical cavity surface emitting lasers (VCSELs) with two semiconductor distributed Bragg reflectors (DBRs) were grown by molecular beam epitaxy. The threshold current was found to be 20-50% less on an average for the bulk VCSELs with an active layer of 0.47 μm thick grown on the 4° off-orientation (001) substrates than those on the on-orientation ones. The lower threshold current was attributed to the smoother interfaces of the $\text{Al}_{0.1}\text{Ga}_{0.9}\text{As}/\text{AlAs}$ DBRs in the off-orientation growth observed by transmission electron microscopy.

1. Introduction

The development of vertical cavity surface emitting lasers (VCSELs) [1-7] has made them attractive for many applications, ranging from monolithic optoelectronic integration, chip-to-chip optical interconnection, high power arrays, and to low cost discrete devices. Distributed Bragg reflectors (DBRs) [2-7] consisting of periodic quarter wavelength stacks of low and high refractive index compound semiconductors are very promising for the implementation of the novel VCSEL structure. The advantages of incorporating DBRs in VCSELs are epitaxial growth compatibility and uniform vertical current injection through the doped semiconductor reflectors. To achieve high reflectivities of $\sim 99\%$ for low threshold current $\text{In}_x\text{Ga}_{1-x}\text{As}/\text{GaAs}$ or $\text{GaAs}/\text{AlGaAs}$ VCSELs, ~ 20 pairs or more of quarter wavelength $\text{Al}_x\text{Ga}_{1-x}\text{As}/\text{Al}_y\text{Ga}_{1-y}\text{As}$ ($x \sim 0$ and $y \sim 1$) are required.

Surface morphologies on the growth of $\text{Al}_x\text{Ga}_{1-x}\text{As}$ ($x < 0.3$) on GaAs have been studied previously [8-11]. However, the growth of high quality thick $\text{Al}_x\text{Ga}_{1-x}\text{As}/\text{Al}_y\text{Ga}_{1-y}\text{As}$ DBR structure with AlAs mole fraction near unity was difficult [8,9]. As shown in fig. 1a, the transmission electron microscopy (TEM) cross-sectional

image of the $\text{Al}_{0.1}\text{Ga}_{0.9}\text{As}/\text{AlAs}$ DBR structure grown by molecular beam epitaxy (MBE) on a (001) Si-doped GaAs substrate indicates quasi-periodic zigzag roughness appearing in the uppermost $\text{Al}_{0.1}\text{Ga}_{0.9}\text{As}/\text{AlAs}$ interfaces as the number of layers becomes large even though the starting substrate and the lower hetero-interfaces near the substrate are flat. Another growth instability of the quarter wavelength stack can also be observed as shown in fig. 1b which is the n-mirror ($\text{Al}_{0.1}\text{Ga}_{0.9}\text{As}/\text{AlAs}$) of a VCSEL. The initial periods from substrate have smooth hetero-interfaces. The $\text{Al}_{0.1}\text{Ga}_{0.9}\text{As}$ layer can smooth out the roughness of the AlAs layer as can be seen in the $\text{AlAs}/\text{Al}_{0.1}\text{Ga}_{0.9}\text{As}$ interface. The roughness of AlAs surface is still observed and becomes more serious as the number of period increases. The rough hetero-interface introduces diffraction and scattering loss, deforms the wavefront of the reflected optical wave, and thus reduces the effective reflectivity of the DBR structures. The quality of the active layers grown subsequently on the top of the DBR structures may also be degraded. It is thus important to avoid this spatial instability in the MBE growth of VCSELs employing the DBR structures.

In this paper, we show that the roughness in thick AlGaAs DBR structures may be eliminated when employing the misoriented substrates. Threshold currents of the GaAs/AlGaAs VCSELs

* Present address: Department of Electrical Engineering, National Cheng-Kung University, Tainan, Taiwan, ROC.

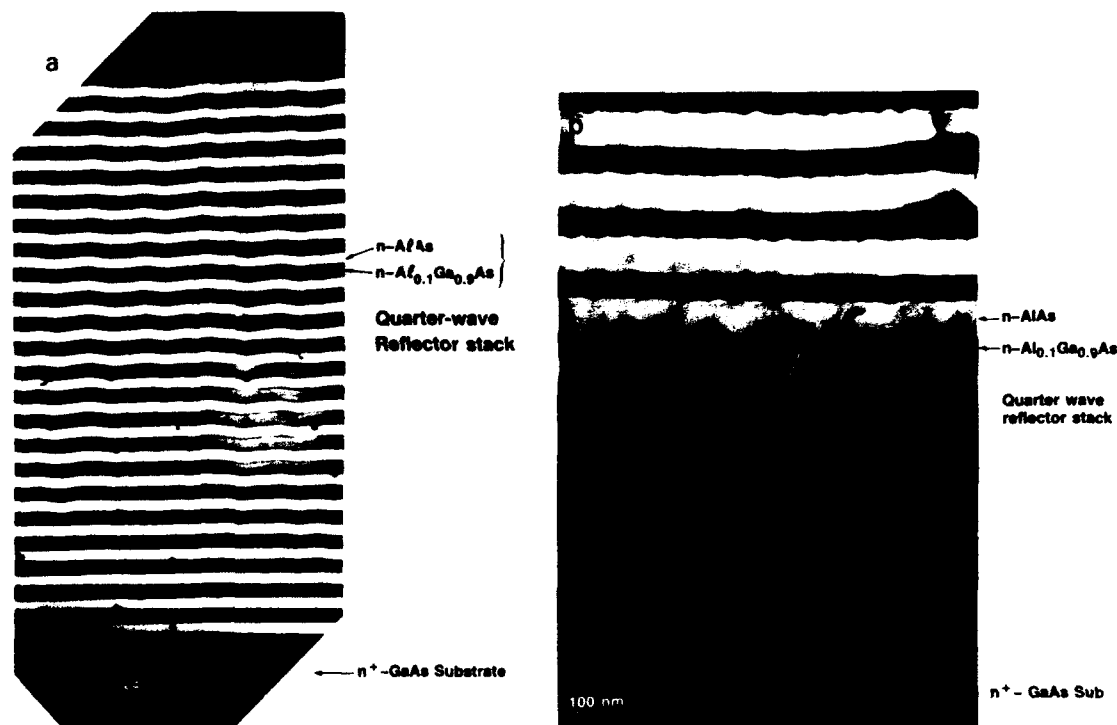


Fig. 1. TEM cross-sectional image of (a) a 22.5-pair n-type $\text{Al}_{0.1}\text{Ga}_{0.9}\text{As}/\text{AlAs}$ DBR structure with a nominal Si doping concentration of $5 \times 10^{17} \text{ cm}^{-3}$ and (b) an n-mirror of a VCSEL.

were observed to be lower for those grown on substrates with 4° off-(001) orientation toward (111)A face than those on substrates with the (001) orientation. Consistency was found in the TEM cross-section study where the smoother DBR interfaces were observed for the off-orientation samples. We note that improved performance on edge emitting lasers grown on the off-orientation substrates was previously reported [10].

2. Experimental

We will first describe the layer structure of the GaAs/AlGaAs VCSELs grown by molecular beam epitaxy, followed by the discussion of the effects of the substrate orientation on the interfacial flatness on the DBR structures and on the lasing threshold of VCSELs. The VCSELs studied here contain, starting from the GaAs substrate, a

17.5-pair n-type ($\text{Si}, 5 \times 10^{17} \text{ cm}^{-3}$) quarter-wavelength $\text{AlAs}/\text{Al}_{0.1}\text{Ga}_{0.9}\text{As}$ (720/618 Å) DBR, an n-type ($\text{Si}, 5 \times 10^{17} \text{ cm}^{-3}$) 0.13 μm thick $\text{Al}_{0.3}\text{Ga}_{0.7}\text{As}$ confinement layer, a three-period $\text{GaAs}/\text{Al}_{0.3}\text{Ga}_{0.7}\text{As}$ (10/10 Å) superlattice, a p-type ($\text{Be}, 5 \times 10^{16} \text{ cm}^{-3}$) 0.47 μm thick GaAs active layer, a p-type ($\text{Be}, 5 \times 10^{18} \text{ cm}^{-3}$) 0.13 μm thick $\text{Al}_{0.3}\text{Ga}_{0.7}\text{As}$ confinement layer, and a 5-pair p-type ($\text{Be}, 10^{19} \text{ cm}^{-3}$) quarter-wavelength $\text{Al}_{0.7}\text{Ga}_{0.3}\text{As}/\text{Al}_{0.1}\text{Ga}_{0.9}\text{As}$ (700/618 Å) DBR. The three-period $\text{GaAs}/\text{Al}_{0.3}\text{Ga}_{0.7}\text{As}$ (10/10 Å) superlattice grown between the n- $\text{Al}_{0.3}\text{Ga}_{0.7}\text{As}$ confinement and GaAs active layers enhances the quality of the active layer [12]. The DBR structures were designed to have peak reflectivity at 0.87 μm wavelength. To eliminate the parameter variation on the growth, the on-orientation and 4° -off (001) GaAs substrates were mounted side-by-side on the rotating Mo-block. The nominal substrate temperature during the growth of the

n-type 17.5-pair $\text{Al}_{0.1}\text{Ga}_{0.9}\text{As}/\text{AlAs}$ DBR, measured by an infrared (IR) pyrometer, was either 580 or 630°C. The substrate temperature for the subsequent growth of the n- $\text{Al}_{0.3}\text{Ga}_{0.7}\text{As}$ confinement layer, GaAs active layer, p-type $\text{Al}_{0.3}\text{Ga}_{0.7}\text{As}$ layer and p-type DBR were 680, 570, 585 and 550°C, respectively. The device processing of the VCSELs for the epitaxially grown DBR vertical cavity structures involves mesa formation by wet chemical etching, ohmic contact formation by E-beam evaporation of metals, and etching holes in the substrate for light transmission. The details were stated previously [6,7].

3. Results and discussion

Fig. 2 shows a section of TEM cross-sectional profiles of the on-orientation and 4°-off GaAs/

AlGaAs VCSEL wafers grown at the same run with a substrate temperature of 630°C during the n-type $\text{Al}_{0.1}\text{Ga}_{0.9}\text{As}/\text{AlAs}$ DBR growth. Rough interfaces are evident in the top several n-type DBR layers of the on-orientation substrate, while much smoother interfaces throughout the whole VCSEL structure were seen for the off-orientation substrate. As previously mentioned, the roughness originated from the inherent spatial instability in the AlAs growth regardless of the flat starting substrate. The use of the mis-oriented substrate seemed to avoid the growth instability [11,13]. It is well known that substrate misorientation towards (111)B leads to a rough surface morphology for both AlGaAs and GaAs, while misorientation towards (111)A leads to a smooth surface morphology [9–11]. The implication is that the extra dangling bonds associated with the surface ledges for (111)B misoriented substrate increase the

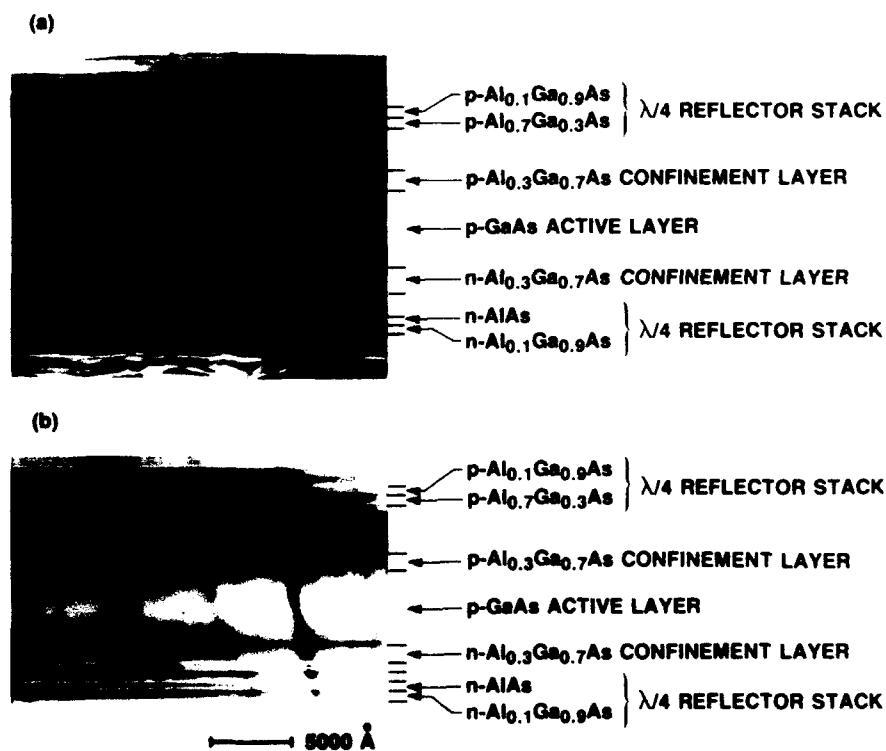


Fig. 2. A section of TEM cross-sectional images, which shows only the top three n-DBR pairs and n-confinement layers, of the GaAs/AlGaAs VCSELs grown on (a) the (001) on-orientation and (b) the 4° off (001) GaAs substrates.

chemical reactivity of the surface, which, in turn, initiates the three-dimensional growth mode that the surface impurities which produce similar extra dangling bonds on a (100) substrate may have the same effect on the growth morphology. The rough surface morphology eventually is revealed in the roughness of the interfaces in a heterostructure. The amount of the surface impurity accumulated during the growth thus determines the degree of the roughness in the interfaces [4]. For (111)A misorientation surfaces, the number of dangling bonds is less than (100) on-orientation surfaces due to the presence of Ga-like surface ledges. The reduced chemical reactivity renders a higher surface mobility for the adatoms, which may produce the smooth surface morphology.

The upper 5-pair p-type $\text{Al}_{0.1}\text{Ga}_{0.9}\text{As}/\text{Al}_{0.7}\text{Ga}_{0.3}\text{As}$ DBR structure was grown at a lower substrate temperature of 550°C and a higher As_4/III ratio to achieve a Be doping concentration of 10^{19} cm^{-3} [15]. Not shown in fig. 2, flat interfaces in the p-type DBR structure were seen for the two samples. The growth of thick Al GaAs/GaAs/AlGaAs double-heterostructure active region ($\sim 0.8 \mu\text{m}$) and the incorporation of superlattice region prior to the growth of the active GaAs layer [12] planarized the active surface on which the p-type DBR layers was deposited subsequently. The surface morphology of the VCSEL structures, examined under a Nomarski optical microscope, is essentially flat, independent of the substrate orientation.

The spatial instability shown in fig. 1 and 2a was found to be reduced by employing a lower substrate temperature of 580°C in the growth of the n-type DBR structure instead of 630°C. Substantial improvement on the interface flatness was observed by TEM. However the off-orientation growth exhibited smoother interfaces than the on-orientation one, although the contrast of zigzag roughness was not as drastic as shown in fig. 2.

A single longitudinal mode lasing characteristic with a side mode suppression ratio of 40 dB and a resolution-limited linewidth of 2 Å was observed for VCSELs independent of the substrate orientation. Due to the thickness variation of the sample, the emission wavelength varied from 850 to 880 nm across the wafer. The typical light output

versus current characteristics of the off-orientation axis grown VCSELs at room temperature were measured under pulsed condition with a pulse width of 200 ns and a duty cycle of 2%. The peak output power is greater than 6 mW with a slope efficiency of 0.2 mW/mA. The operating voltage at the threshold is 3.5 V. Similar lasing characteristics were seen for the on-orientation grown VCSEL with higher threshold currents on an average.

The threshold current (I_{th}) of VCSEL depends on the mirror reflectivity and emission wavelength. Due to the short cavity length, the wavelength of the Fabry-Pérot resonant mode (lasing wavelength) varies with the nonuniform spacer and DBR layer thicknesses. The threshold current of the off-orientation VCSELs varied from 12 to 40 mA. Correlations between the threshold current and emission wavelength were found, where devices with low threshold currents of 12 to 20 mA have the emission wavelength in a spectral region of 860–875 nm. For the on-orientation VCSELs, larger variation in I_{th} of 20 to 60 mA was seen, even with a substrate growth temperature of 580°C for smoother n-DBR growth. Both the larger I_{th} variation and the higher I_{th} value indicate lower effective mirror reflectivities in the VCSELs grown on the on-orientation substrates than on the off-orientation ones, in agreement with the TEM study discussed earlier.

Other lasing characteristics such as the circular two-dimensional Gaussian-like far-field and near-field spatial distributions, and linear polarization were similar to previously reported [6,7].

4. Conclusion

The instability in the MBE growth of thick AlGaAs DBR structures was observed by transmission electron microscopy. The instability results in rough hetero-interfaces and can be reduced by employing a lower substrate temperature. More importantly we observed that the instability can be suppressed by using mis-oriented substrates for a wide range of growth temperature. A 20–50% reduction in the threshold current was achieved for the GaAs/AlGaAs VCSEL with the

active layer of $0.47\text{ }\mu\text{m}$ thick grown on the 4° -off (001) toward (111)-A substrate than on the on-orientation (001) ones.

Acknowledgements

The authors would like to acknowledge N. Chand, J.F. Chen, D. Sivco and R. Hull for useful discussion.

References

- [1] F. Koyama, S. Kinoshita and K. Iga, *Appl. Phys. Letters* 55 (1989) 221.
- [2] J.L. Jewell, A. Scherer, S.L. McCall, Y.H. Lee, S.J. Walker, J.P. Harbison and L.T. Florez, *Electron. Letters* 25 (1989) 1123.
- [3] A. Ibaraki, K. Kawashima, K. Furusawa, T. Ishikawa, Y. Yamaguchi and T. Niina, *Japan. J. Appl. Phys.* 28 (1989) L667.
- [4] D. Botez, L.M. Zinkiewicz, T.J. Roth, L.J. Mawst and G. Peterson, *IEEE Photonics Technol. Letters* 1 (1989) 205.
- [5] R.S. Geels, S.W. Corzine, J.W. Scott, D.B. Young and L.A. Coldren, *IEEE Photonics Technol. Letters* 2 (1990) 234.
- [6] K. Tai, R.J. Fischer, C.W. Seabury, N.A. Olsson, T.-C.D. Huo, Y. Ota and A.Y. Cho, *Appl. Phys. Letters* 55 (1989) 2473.
- [7] K. Tai, R.J. Fischer, K.W. Wang, S.N.G. Chu and A.Y. Cho, *Electron. Letters* 25 (1989) 1644.
- [8] J. Faist, J.D. Ganiere, P. Buffat, S. Sampson and F.K. Reinhart, *J. Appl. Phys.* 66 (1989) 1023.
- [9] N. Chand and S.N.G. Chu, unpublished.
- [10] H.Z. Chen, A. Ghaffari, H. Morkoç and A. Yariv, *Appl. Phys. Letters* 51 (1987) 2094.
- [11] R.K. Tsui, J.A. Curless, G.D. Kramer, M.S. Peffley and D.L. Rode, *J. Appl. Phys.* 59 (1986) 1508.
- [12] R.J. Fischer, J. Klem, T.J. Drummond, W. Kopp, H. Morkoç, E. Anderson and H. Pion, *Appl. Phys. Letters* 44 (1984) 1.
- [13] D.L. Rode, W.R. Wagner and N.E. Schumaker, *Appl. Phys. Letters* 30 (1977) 75.
- [14] P.M. Petroff, R.C. Miller, A.C. Gossard and W. Wiegmann, *Appl. Phys. Letters* 44 (1984) 217.
- [15] Y.C. Pao, J. Franklin and J.S. Harris, Jr., *J. Crystal Growth* 95 (1989) 301.

GaInAs/InP MQW and DBR growth for surface emitting lasers by CBE

T.K. Uchida, T. Uchida, K. Mise *, N. Yokouchi, F. Koyama and K. Iga

Tokyo Institute of Technology, 4259 Nagatsuta, Midori-ku, Yokohama 227, Japan

Growth rates of 1 to 6 $\mu\text{m}/\text{h}$ were obtained for $\text{Ga}_{0.47}\text{In}_{0.53}\text{As}$ using all gas-source chemical beam epitaxy. Using these high growth rates, quantum wells and distributed Bragg reflectors were grown to study thickness controllability and material quality. Growth rate linearity of GaInAs was observed from growth times of 2 s to 1 h. The photoluminescence linewidth of 29 meV was obtained for 38 Å wells at room temperature. We also investigated doping with Si and Be at high growth rates; as high as $2 \times 10^{20} \text{ cm}^{-3}$ of Be doping in GaInAs was obtained. Finally, using high Si-doped GaInAs and InP, a multi-layered Bragg reflector was grown yielding 85% reflectivity at a wavelength of 1.6 μm .

1. Introduction

Since the first continuous wave operation of surface emitting (SE) laser was achieved [1], vertical cavity (wave propagates perpendicular to the interfaces) SE lasers are drawing increasing interest in optoelectronics. To obtain high performance SE lasers, the use of distributed Bragg reflectors (DBRs) and quantum wells (QWs) has been investigated [2–4]. However, these technologies have yet to be applied to long-wavelength (1.3–1.6 μm) SE lasers. For developing such sophisticated devices, the $\text{Ga}_{1-x}\text{In}_x\text{As}/\text{InP}$ system is one very attractive choice. To grow high-reflective DBRs and high-quality QWs in the 1.3–1.6 μm range, fast growth rates with precise thickness control are highly desirable because a typical SE laser needs a total epitaxial layer of more than 5 μm . Also, a set of DBRs with 95% reflectivity itself grows to be more than 5 μm [5]. To grow long wavelength SE lasers, especially with semiconductor DBRs, growth rate is then a crucial parameter.

Chemical beam epitaxy (CBE), which uses metalorganics and hydride gases under ultra-high vacuum conditions can be advantageously used to grow GaInAs(P)/InP at high growth rates [6,7].

However, to grow GaInAs/InP SE laser structures at such high growth rates by CBE, we still need to know some fundamental growth conditions. We have then grown and characterized QWs and DBRs for future applications to SE lasers. It is also very useful to have optical characteristics of quantum wells at room temperature, especially for device oriented crystal growth as a reference.

2. Experimental

A Riber-made two-chamber CBE system and our originally designed cracking cell made of boron nitride and tantalum were used for the experiment. For group III sources, 7% trimethylindium (TMI) and 20% triethylgallium (TEG) in hydrogen carrier gas were used. Pure arsine (AsH_3) and phosphine (PH_3) were used for the group V sources. Cracking temperature was kept at 900°C and valves were used instead of mechanical shutters. The substrate temperature was fixed at 540°C and constantly monitored by a pyrometer which was calibrated against the melting point of InSb. For doping, solid Si and Be were used in conventional effusion cells.

* On leave from Anritsu Co., Atsugi-shi, Kanagawa 243, Japan.

3. Results and discussion

We used TMI flow rates to change InP and GaInAs growth rates; the results are shown in fig. 1. Also plotted in the figure are TEG flow rates to maintain the lattice-matching condition. All samples were grown for 30 min. Growth rates of InP linearly increased with TMI flow rates from about 0.5 to 2.3 $\mu\text{m/h}$. However, GaInAs growth rates did not increase linearly. The incorporation of indium for a given arsenic is higher than that of gallium; therefore a larger amount of TEG is needed to maintain lattice-match resulting in a non-linear growth rate increase. The highest growth rate obtained with a mirror-like surface was 6 $\mu\text{m/h}$ for GaInAs.

Using growth rates of 7 \AA/s (2.52 $\mu\text{m/h}$) and 14 \AA/s (5.04 $\mu\text{m/h}$), quantum wells were grown by changing growth time from 2 to 10 s. In fig. 2, well thickness obtained from a transmission electron microscope (TEM) and X-ray diffraction spectrum are plotted for growth time. The slopes of these lines are in agreement with growth rates obtained from bulk growth. Also, the intersections of these lines are near the origin. This is different from results obtained by metalorganic chemical vapor deposition (MOVPE) [8]. Room temperature photoluminescence spectra of QWs grown at 7 \AA/s are shown in fig. 3. The narrowest linewidth obtained was 29 meV at room temperature and at 77 K, a linewidth of 8 meV was obtained for QW samples grown at GaInAs growth rates of 7 and 14 \AA/s [9]. In fig. 4, a typical X-ray diffraction

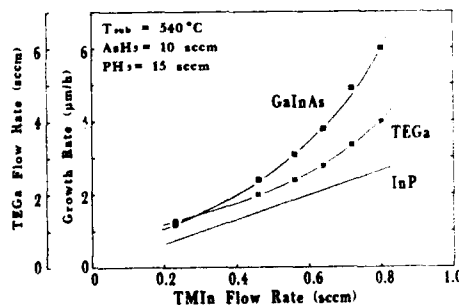


Fig. 1. GaInAs and InP growth rates are shown for TMI flow rates. For lattice-matching and non-linear increase of GaInAs, TEG flow rates are also shown.

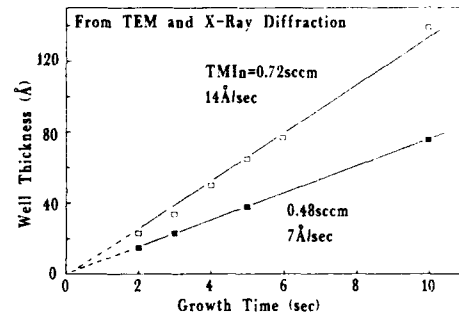


Fig. 2. Quantum well thickness for growth time is plotted for GaInAs growth rates of 7 and 14 \AA/s . The thinnest well was about 14 \AA at 7 \AA/s .

spectrum where up to 8 satellite peaks can be observed is shown. These results indicate that CBE is capable of growing materials at relatively high growth rates without losing controllability or crystal qualities.

Silicon and beryllium were doped in GaInAs and InP using growth rates of 14 \AA/s for GaInAs and 6 \AA/s for InP. Hole and electron concentrations are plotted for the reciprocal of each effusion cell temperature in fig. 5. In GaInAs, we successfully doped up to $2 \times 10^{20} \text{ cm}^{-3}$ with Be [10] and $1.5 \times 10^{19} \text{ cm}^{-3}$ with Si.

The absorption edge of GaInAs is 1.67 μm , but this can be shifted to shorter wavelengths by doping GaInAs to highly n-type [11,12]. As a pre-

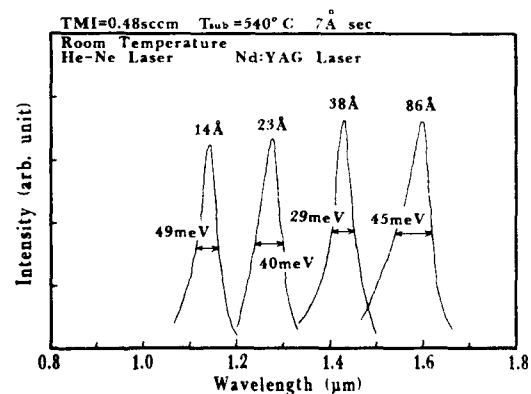


Fig. 3. Photoluminescence spectra of quantum wells grown at 7 \AA/s are shown. Well thickness and linewidth are also indicated in the figure.

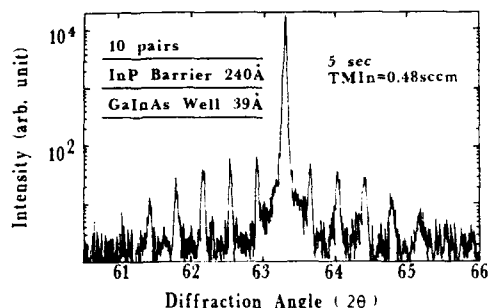


Fig. 4. Double-crystal X-ray diffraction spectrum is shown to indicate periodicity of GaInAs well and InP barrier. Up to 8th order of satellite peak can be observed.

liminary experiment, we designed and grew an 18-pair Si-doped ($1 \times 10^{19} \text{ cm}^{-3}$) GaInAs/InP DBR for a wavelength of $1.6 \mu\text{m}$ at growth rates of 14 Å/s for GaInAs and 6 Å/s for InP. Reflectivity of this DBR was measured and is shown in fig. 6. The highest reflectivity obtained was 85% at $1.6 \mu\text{m}$. For a typical DBR growth, we must have less than 2% of fluctuations in thickness to have a maximum reflectivity at a desired wavelength. This result shows that we have good thickness controllability and periodicity using CBE at high growth rates. The use of GaInAs/InP for DBRs, however,

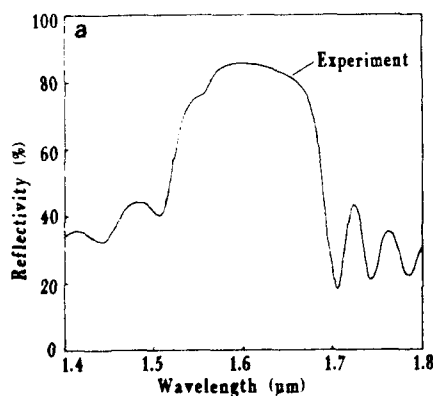


Fig. 6. (a) Reflectivity of an 18-pair GaInAs/InP DBR; GaInAs was doped to $1 \times 10^{19} \text{ cm}^{-3}$ with Si. (b) Scanning electron microscope picture.

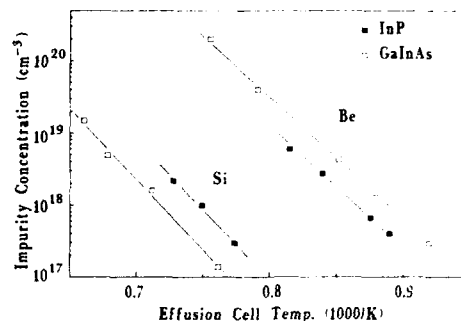


Fig. 5. Hole and electron concentrations are shown for reciprocal of each effusion cell temperature. In GaInAs, $2 \times 10^{20} \text{ cm}^{-3}$ of Be doping was achieved.

is still in consideration because of the impurity absorption due to high doping. Further investigation is necessary.

4. Conclusions

We have grown QWs and DBRs at relatively high growth rates by CBE. Even at high growth rates, high quality QWs were obtained and wavelength could easily be selected. For DBR growth, it would be unrealistic to use slower growth rates for real time device growths. Doping levels were also well-controlled and we have shown high dop-



ing was possible at high growth rates. Such results indicate that CBE has good growth controllability and feasibility to grow QWs and DBRs for application to SE lasers.

Acknowledgements

The authors would like to acknowledge Professor Y. Suematsu, President of Tokyo Institute of Technology, for his encouragement of this work. They also thank Mr. T. Miyamoto for his technical assistance. This work was supported by the Scientific Research Grant-in-Aid 61065002 from the Japanese Ministry of Education, Science and Culture.

References

- [1] F. Koyama, S. Kinoshita and K. Iga, *Trans. Inst. Electron. Information Commun. Engrs.* E-71 (1988) 1089.
- [2] T. Sakaguchi, F. Koyama and K. Iga, *Electron. Letters* 24 (1988) 928.
- [3] Y.H. Lee, J.L. Jewell, A. Scherer, S.L. McCall, J.P. Harbison and L.T. Florez, *Electron. Letters* 25 (1989) 1377.
- [4] R.S. Geels, S.W. Corzine, J.W. Scott, D.B. Young and L.A. Coldren, *IEEE Photonic Technol. Letters* 2 (1990) 234.
- [5] T.K. Uchida, F. Koyama and K. Iga, *Trans. Inst. Electron. Information Commun. Engrs.* E-72 (1989) 1084.
- [6] K. Tai, S.L. McCall, S.N.G. Chu and W.T. Tsang, *Appl. Phys. Letters* 51 (1987) 826.
- [7] W.T. Tsang, *J. Crystal Growth* 95 (1989) 121.
- [8] K.W. Carey, R. Hull, J.E. Fouquet, F.G. Kellert and G.R. Trott, *Appl. Phys. Letters* 51 (1987) 910.
- [9] T.K. Uchida, T. Uchida, N. Yokouchi, K. Mise, F. Koyama and K. Iga, in: *Extended Abstracts, 8th Intern. Conf. on Solid State Devices and Materials, Sendai, Aug. 1990*, in press.
- [10] T.K. Uchida, T. Uchida, K. Mise, F. Koyama and K. Iga, *J. Crystal Growth* 105 (1990) 366.
- [11] E. Burstein, *Phys. Rev.* 93 (1954) 632.
- [12] D.G. Deppe, N.D. Gerrard, C.J. Pinzone, R.D. Dupuis and E.F. Schubert, *Appl. Phys. Letters* 56 (1990) 315.

MBE grown, visible, surface emitting harmonic generation lasers

R.L. Williams, F. Chatenoud

Solid State Optoelectronics Consortium, Molecular Beam Epitaxy, National Research Council, Ottawa, Ontario, Canada K1A 0R6

and

R. Normandin

Optoelectronic Devices, National Research Council, Ottawa, Ontario, Canada K1A 0R6

Using an MBE grown GaAs/AlGaAs multilayer structure in a waveguide geometry, we show that an enhancement for surface emitting harmonic generation in excess of 10 million can be achieved. Based upon this effect, we propose a design giving monolithic surface emitting laser sources tuneable from red to blue in the visible spectrum.

1. Introduction

Previous work by Normandin and Stegeman [1], has reported the non-linear mixing of oppositely propagating guided waves. The resultant field in such an instance is coupled to radiation modes and propagates in a direction perpendicular to the waveguide surface in the case of equal frequency fundamentals. The overlap of the two oppositely propagating fields may be viewed as giving rise to a non-linear polarisation source:

$$P_z^{nl} = \epsilon_0 d_{ij} E_+(y) E_-(y) \times [\exp(2i\omega t) + \exp(-2ikx)], \quad (1)$$

where d_{ij} is the second harmonic coefficient, and the oppositely propagating fields are given by

$$E_{\pm} = E_{\pm}(y) \exp[i(\omega t \pm kx)]. \quad (2)$$

In bulk media, such a process is non-radiative due to the simultaneous requirements of energy and momentum conservation in all directions. This is not the case for the waveguide geometry depicted in fig. 1.

The formal approach to evaluate the radiated field is based on a surface Green function approach first developed by Sipe [2]. From eq. (1) we see that the non-linear polarisation will depend strongly on the exact shape of the mode amplitude distribution and polarisation. We consider the

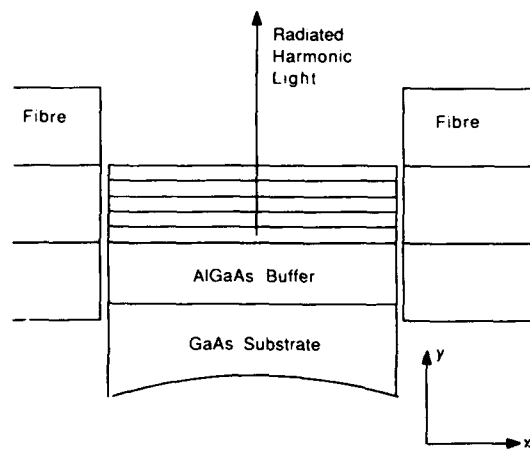


Fig. 1. Experimental geometry used for non-linear harmonic cross-section measurements.

polarisation distribution as a series of thin dipole sheets parallel to the waveguide surface:

$$P(y') = P_z^{nl}(y)\delta(y - y'), \quad (3)$$

and then integrate the contributions from each sheet following the actual amplitude and phase distribution of the non-linear polarisation.

If the depth variation of the refractive index is small for the radiated field, then its form will be given by

$$E_{\pm}^{\infty}(y) = E_{\pm}(y) \exp(\mp i k' y), \quad (4)$$

where + and - indicate the presence of both surface and substrate directed harmonics. The wavevector, $k' = nk$, is at the harmonic frequency, with n the index of refraction, again at the harmonic frequency. Substitution of eq. (4) into Maxwell's equations, with the non-linear driving term

$$P(y) = \int_{-\infty}^{\infty} P_z^{nl}(y')\delta(y - y') dy', \quad (5)$$

gives the field intensity radiated from the surface as proportional to SS^* , where,

$$S = \int_{-\infty}^0 \frac{P_z^{nl}(y')}{n(y')} \exp\{-ik_0 n(y')y'\} dy'. \quad (6)$$

Experimentally, a more useful quantity is the harmonic cross-section, A_{nl} , defined as the harmonic radiated intensity, normalised to an area of $1 \text{ mm} \times 1 \text{ cm}$, for fundamentals of unit intensity:

$$I^{2\omega} = A_{nl} I_1 I_2. \quad (7)$$

2. Results and discussion

As an example, and neglecting materials losses, the cross-section for a thin GaAs layer is shown in fig. 2. This calculation is for $1.06 \mu\text{m}$ for the fundamental, and was performed several years ago by Vella et al. [3].

Strong interference effects are evident, which can be explained when it is realised that, to a first approximation, dipole sheets which are separated by half a wavelength will produce contributions

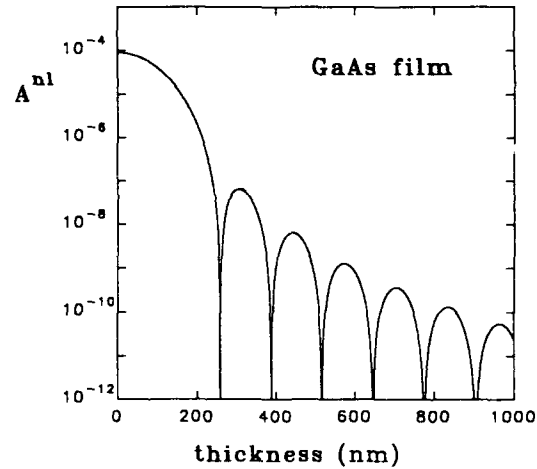


Fig. 2. Harmonic cross-section for a free standing GaAs layer, with fundamentals at $1.06 \mu\text{m}$.

that cancel exactly in the far field. The situation is more complex in reality, since the non-linear polarisation varies in magnitude throughout the waveguide. For a fixed input intensity, the guided fundamental field decreases with increasing guide thickness, resulting in a sharp reduction in radiated harmonic.

In order to get usable devices, the second harmonic interaction cross-section, A_{nl} , must be improved and its decrease with thickness controlled, even in the presence of substantial materials losses at the harmonic frequency. We have achieved this by tailoring the refractive index variation with depth, $n(y')$ in eq. (6), so that all non-linear field contributions are in phase in the far field. This is achieved by introducing alternating layers of GaAs and AlGaAs into the waveguide structure.

Assuming similar non-linear coefficients for GaAs and AlGaAs, calculations were performed, using fully complex refractive indices and hence including absorption losses, for alternating AlGaAs layers of various compositions in a waveguide geometry, with an AlGaAs buffer layer. The results of this calculation, for alternating layers of $\text{Al}_{0.9}\text{Ga}_{0.1}\text{As}$ and $\text{Al}_{0.7}\text{Ga}_{0.3}\text{As}$ on an $\text{Al}_{0.9}\text{Ga}_{0.1}\text{As}$ buffer, at a wavelength of $1.06 \mu\text{m}$ for the fundamental, are shown in fig. 3, together with a similar

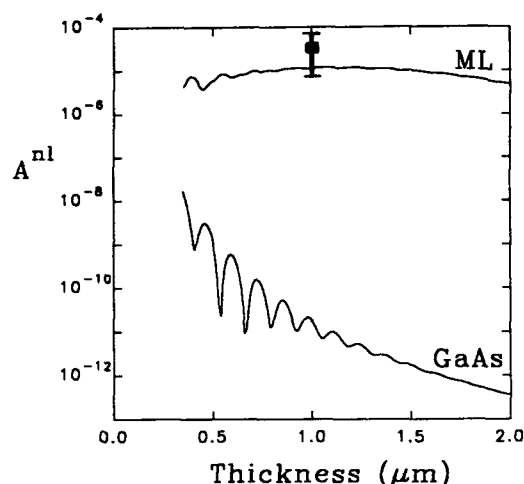


Fig. 3. Harmonic cross-section for an $\text{Al}_{0.9}\text{Ga}_{0.1}\text{As}/\text{Al}_{0.7}\text{Ga}_{0.3}\text{As}$ multilayer waveguide, and a uniform GaAs waveguide, both with an $\text{Al}_{0.9}\text{Ga}_{0.1}\text{As}$ buffer. The point shown is the experimentally determined cross-section for this sample design. The fundamental is at $1.06\text{ }\mu\text{m}$.

calculation for a uniform GaAs waveguide on the same buffer. Note the uniform cross-section with thickness, as well as the enhancements in excess of 10 million in some regions of the diagram.

Considering that the layer spacings in the waveguide are at half wavelengths of the harmonic light (i.e. of the order of $600\text{ }\text{\AA}$), and that the total waveguide thickness is approximately $1\text{ }\mu\text{m}$, there cannot be many layers active in the film. To indicate the non-critical nature of the "tuning" in these structures, fig. 4 shows the variation with period of the harmonic cross-section for a thickness of $1\text{ }\mu\text{m}$. The overall log curve is similar to that from an antenna array in aperture microwave designs, to which it is related. It is clear from this

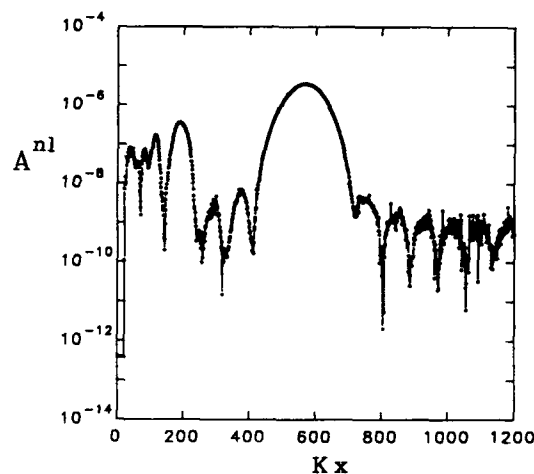


Fig. 4. Harmonic cross-section versus multilayer period, with a total thickness of $1\text{ }\mu\text{m}$, for an $\text{Al}_{0.9}\text{Ga}_{0.1}\text{As}/\text{Al}_{0.7}\text{Ga}_{0.3}\text{As}$ multilayer waveguide with an $\text{Al}_{0.9}\text{Ga}_{0.1}\text{As}$ buffer. The fundamental is at $1.06\text{ }\mu\text{m}$.

diagram, that because the number of layers is small, the main resonance peak is extremely broad. Thus the overall design is not sensitive to variations in material composition or layer design.

Initial experiments using the geometry depicted in fig. 1 have been performed to gauge the validity of the theory described above. The average power coupled into the waveguide was less than $70\text{ }\mu\text{W}$, with a repetition rate of 7.7 kHz and pulse widths of 200 ns . The $1.06\text{ }\mu\text{m}$ light source was an unpolarised CVI Nd-YAG laser. Because of the orientation of the (100) substrates, a mixture of TE and TM polarisation must propagate in the waveguide in order to have any harmonic signal generated. Substrates with a (111) orientation are being used to overcome this limitation. The mode

Table 1
Predicted and measured harmonic cross-section enhancements over uniform GaAs for three different multilayer waveguide structures; the fundamental is at $1.06\text{ }\mu\text{m}$

Layer 1	Layer 2	Waveguide thickness (μm)	Predicted enhancement	Measured enhancement
$\text{Al}_{0.4}\text{Ga}_{0.6}\text{As}$	GaAs	0.6	$750\times$	$800\times$
$\text{Al}_{0.8}\text{Ga}_{0.2}\text{As}$	GaAs	0.6	$3000\times$	$2400\times$
$\text{Al}_{0.9}\text{Ga}_{0.1}\text{As}$	$\text{Al}_{0.7}\text{Ga}_{0.3}\text{As}$	1.0	$1000000\times$	$5000000\times$

beating expected in the harmonic signal was clearly visible when imaging the harmonic, green, surface emission. The mode beating gave rise to a surface array of sources spaced a few hundred micrometers apart. As the coherent array radiated, several sharp side lobes could readily be seen with the eye. The results of harmonic cross-section measurements on three different multilayer waveguide structures are given in table 1. These structures were grown by MBE in a Vacuum Generators V80H deposition chamber at growth rates of approximately $1 \mu\text{m h}^{-1}$ and at substrate temperatures of approximately 700°C .

In a laser cavity, the circulating power is several orders of magnitude greater than that used in our test experiments. In a ridge geometry, further confinement exists in the plane of the guide and power densities are increased by another order of

magnitude. If we view the electromagnetic field propagating in a laser cavity, consisting of a waveguide for light confinement, as two contra-propagating fields of identical wavelength, then applications of the second harmonic enhancement discussed above are obvious.

As an example, a possible geometry for an electrically pumped, visible, surface emitting, harmonic generation laser, on a (111) orientation substrate, is shown in fig. 5. The device consists of two separate regions, an active region and a radiating region, with the layer structure for both regions being identical prior to any post growth processing. The active region, to the right in fig. 5, is a standard p-i-n SCH semiconductor diode laser structure, except that the quantum well is embedded in a multilayer waveguide. The material above the multilayer waveguide is the p-type cladding region common to typical diode lasers.

The radiating region, to the left in fig. 5, has the material above the multilayer waveguide removed, to allow harmonic radiation from the surface. This process can easily be facilitated with the inclusion of an etch stop layer. The laser mirrors are the front and back cleaved edges of the chip. Indeed, by providing 100% mirrors for the fundamental wavelength, the overall lasing threshold can be substantially lower than that of a conventional laser. By using conservative estimates of the ridge width and length, and of the intra-cavity lasing power of a typical InGaAs laser for example, a radiated field of better than 0.1 mW CW is obtained for green operation. The full visible spectrum can be reached by using InP (red), InGaAs (yellow, green) or GaAs (blue).

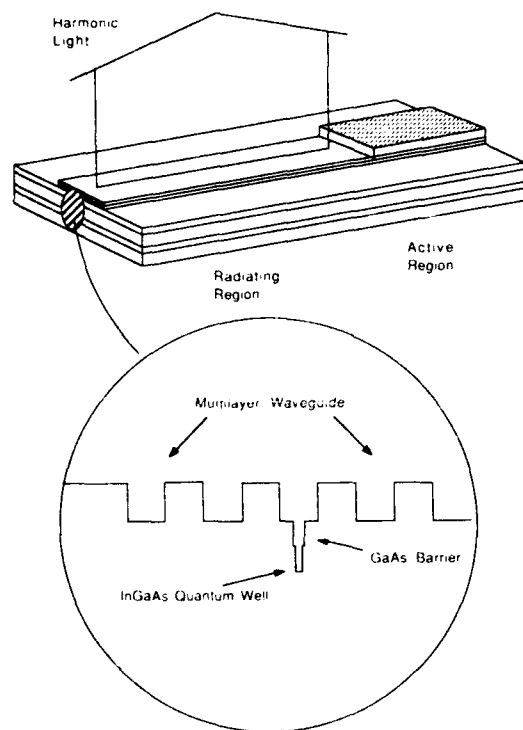


Fig. 5. Geometry for an electrically pumped, visible, surface emitting harmonic generation laser using an InGaAs QW embedded in a multilayer AlGaAs waveguide. Lasing and radiating regions differ only by the controlled etch off of the p-type cladding regions for the radiator.

3. Conclusions

By using an AlGaAs multilayer structure in a waveguide geometry, we have shown the feasibility of enhancing the harmonic surface emission by factors in excess of 10 million. Harmonic cross-section measurements on MBE grown multilayer structures in this geometry show good agreement with theoretical predictions. A possible geometry for electrically pumped, surface emitting, visible, harmonic generation lasers is discussed.

References

- [1] R. Normandin and G.I. Stegeman, Opt. Letters 4 (1979) 58.
- [2] J.E. Sipe, Surface Sci. 84 (1979) 75.
- [3] P.J. Vella, R. Normandin and G.I. Stegeman, Appl. Phys. Letters 38 (1981) 759.

A simple way to reduce series resistance in p-doped semiconductor distributed Bragg reflectors

M. Hong, J.P. Mannaerts

AT&T Bell Laboratories, Murray Hill, New Jersey 07974, USA

J.M. Hong

IBM Thomas J. Watson Research Center, Yorktown Heights, New York 10598, USA

R.J. Fischer, K. Tai, J. Kwo, J.M. Vandenberg, Y.H. Wang

AT&T Bell Laboratories, Murray Hill, New Jersey 07974, USA

and

J. Gamelin

Department of Electrical Engineering, University of California, Berkeley, California 94720, USA

A novel method has been used to smooth out the energy band discontinuity at the heterojunction of AlAs and GaAs in quarter-wave distributed Bragg reflectors (DBRs) by linearly grading the Al and Ga compositions. This has been achieved by simply varying the cell temperatures of Al and Ga. No shutter operation was used during the MBE growth of these DBR mirrors. Low series resistance at a moderate doping ($3 \times 10^{18} \text{ cm}^{-3}$) and high optical reflectivity have been obtained in the p-type DBRs using our approach. These p-DBRs were characterized by high-resolution X-ray diffraction, optical reflectivity, and electrical measurements.

1. Introduction

Distributed Bragg reflectors (DBRs) consisting of periodic quarter-wave stacks of low and high refractive index compound semiconductors find applications in many optoelectronic devices such as vertical cavity surface emitting lasers [1–3]. For the GaAs/AlAs system, very high reflectivity has been achieved by choosing the largest possible refractive index difference between the two constituents, with compositions of the chosen constituents being determined by the need of the experiments. However, the potential barriers at the heterointerfaces (between the two constituents, for example, GaAs and AlAs) due to the energy bandgap difference impede the carrier flow and

give large series resistances, particularly in the p-type doped case. In the case of vertical cavity surface emitting lasers, the series resistance in the DBR mirrors causes thermal heating and thus deteriorates the laser performance.

As has been known, the series resistance can be reduced when the barrier height at the heterojunctions is lowered. Experimentally, lowering of the barrier height has been achieved by modifying the band discontinuity by inserting an AlGaAs region with either one intermediate composition [4] or a range of smoothly graded Al compositions [4,5]. The latter approach of using graded Al compositions has been implemented by growing 10–20 Å short periods of multilayers with a variable duty cycle such that the average Al content is smoothly

graded. Recently, another approach using two or three AlGaAs layers of intermediate compositions was applied to the growth of p-DBRs to lower the series resistance [6,7].

Shutter operation during the MBE growth has been employed in all the methods mentioned above. Particularly for the approach using short-period multilayers, over 20 shutter operations have been used for the growth of each period in the DBR mirror. As a consequence, several hundred shutter operations are needed for one single growth of a vertical cavity surface emitting laser. Any fault in shuttering, even if only once during the entire growth, will ruin the device performance.

In this paper, we present a simple approach to smooth out the band discontinuity at the heterojunction of GaAs/AlAs by linearly grading at Al and Ga compositions *without any shutter operation* during the MBE growth. This has been achieved by varying the effusion cell temperatures of Al and Ga simultaneously, and repeating the sequence of the temperature profiles. We have achieved excellent results in the p-DBRs using our present approach, i.e. low series resistance at a moderate doping level and high optical reflectivity. The growth rate of AlAs, GaAs, and graded AlGaAs regions has been kept almost the same; thus a constant doping profile has been maintained throughout the entire DBR. We have reduced the specific series resistance in the p-DBR of 8 pairs of GaAs/AlAs to $5 \times 10^{-4} \Omega \text{ cm}^2$ for a doping concentration of $3 \times 10^{18} \text{ cm}^{-3}$, and to $7 \times 10^{-5} \Omega \text{ cm}^2$ for a doping concentration of $8 \times 10^{18} \text{ cm}^{-3}$.

2. Experimental

The growth rates of GaAs, AlAs, and AlGaAs as functions of cell temperatures of Al and Ga have been calibrated initially using RHEED oscillations and from the flux gauge readings. A more accurate determination of the growth rates has been carried out by high-resolution X-ray diffraction [8] and optical reflectivity measurements on DBRs of at least 5 periods. The growth rate information was fed into a computer program which tailors the change of Al and Ga cell temperatures

as a function of time to produce a desired graded interface. The temperature controllers used here are the Eurotherm 822, and the power suppliers are the Hewlett-Packard (HP) System Power Supply with a capacity of 0–60 V, 0–50 A, and 1000 W.

Typical temperature profiles from the thermocouple readings of Al and Ga effusion cells are plotted in fig. 1. During the growth of an AlAs layer as indicated by (a) in the figure, the Ga cell temperature was lowered to 780°C to give pure AlAs growth. In the case of AlGaAs growth, the Ga cell temperature was raised slightly higher to produce an AlGaAs layer with a designed composition. For the growth of GaAs (as indicated by (c) in the figure) or the Ga-rich AlGaAs, the Al cell temperature was lowered to produce a desirable composition. Regions (b) and (d) are the composition graded area in which the Al cell temperature was varied from 980 to 1150°C and that of Ga from 930 to 780°C . The temperature profiles for Al and Ga were chosen to keep the total growth rate of the AlGaAs constant and the same as those of the AlAs and GaAs.

Note that growth rate versus temperature is not linear. A linearly graded Al (or Ga) content throughout the region has been approximated.

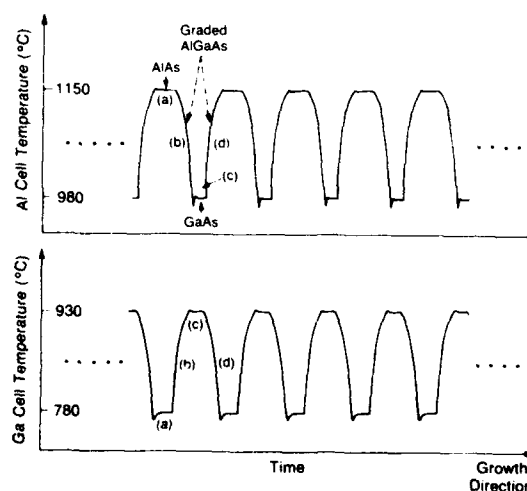


Fig. 1. Temperature profiles of Al and Ga cells as function of time for a growth of a DBR mirror with linearly graded interfaces.

therefore, by an adjustment in temperature ramp rate versus time (i.e. distance).

The series resistance measurements were performed on samples grown with the following sequence. A buffer layer of n-GaAs followed by one of p-GaAs both $0.5\ \mu\text{m}$ thick was grown on the n-GaAs substrate before the growth of p-DBRs. The DBR layers have nominal Be doping concentrations of 3×10^{18} and $8 \times 10^{18}\ \text{cm}^{-3}$, respectively. The very top layer ($100\ \text{\AA}$) of the DBRs has been doped heavily to $3 \times 10^{19}\ \text{cm}^{-3}$ for the contact. Alloyed AuBe or Ag metals were used as electrodes.

A direct I - V measurement was performed on mesas $30\ \mu\text{m}$ in diameter. The mesas were formed by wet chemical etching down to the n-type GaAs layer. The series resistance was determined from the forward diode current versus voltage (I - V) characteristics between 2 and 2.5 V. Another electrical measurement was a standard transmission line measurement [9] performed before and after etching away all the DBR layers between the metal contact pads.

High-resolution X-ray diffraction (HRXRD) has been implemented to evaluate the structural quality of the AlAs/GaAs DBRs. The X-ray studies were carried out with a previously described HRXRD geometry [10]. X-ray scans were taken along the $[h00]$ direction in the vicinity of the (400) and (200) reflection with the diffractometer run in the θ - 2θ mode.

3. Results and discussion

Using our method described above, the growth rates for AlAs, GaAs, and graded AlGaAs were kept constant. This has been achieved by using one Al and one Ga cell. In the case of one or two intermediate layers in the DBRs, two Al and two Ga cells may have to be employed to achieve a similar result [6,7].

With the cell temperature varying up and down in the graded region, we notice that there is an overshooting during the temperature rising and an undershooting during the lowering of temperature.

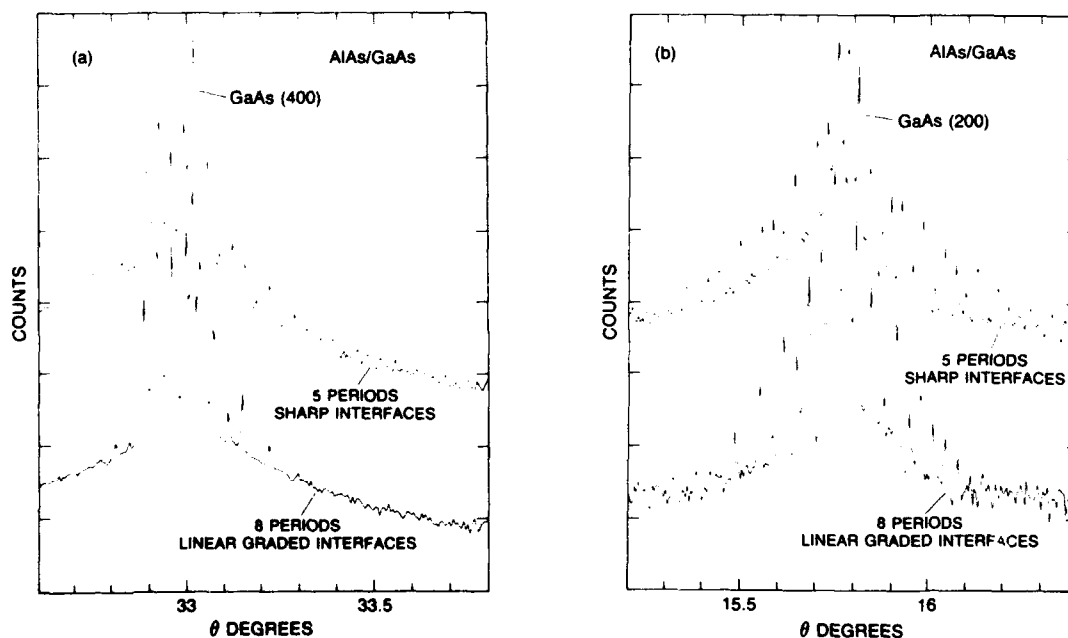


Fig. 2. X-ray scans of 5-period ($1571\ \text{\AA}$) and 8-period ($1398\ \text{\AA}$) AlAs/GaAs DBRs in the vicinity of (a) (400) and (b) (200) reflections.

This is clearly shown in fig. 1 for both Al and Ga cells. The overshooting or undershooting in temperature is inevitable because the variation is over the growth of such thin layer as 100–300 Å. It is very difficult for any temperature controller to regulate the cell temperature in such a short period of time with a temperature change of $\sim 150^\circ$. The length of time to grow the graded region is between 0.5 to 2.0 min, depending on the thickness of the region. However, the performance of the DBR as a mirror would not be affected because this temperature overshooting or undershooting has periodically repeated itself as shown in fig. 1. As long as the temperature variation repeats itself, the periodic multilayered DBR is obtained as indicated by the high-resolution X-ray diffraction patterns (fig. 2). As a consequence, the reflectivity as a function of wavelength and the position of peak reflectivity for the DBR mirrors prepared by our method fulfill what we have originally designed for.

Fig. 2 shows the X-ray scans of a 5-period (sharp interfaces) and a 8-period (linearly graded interfaces) AlAs/GaAs DBR grown on GaAs (100). The strong and sharp satellite peaks are generated by the well-defined periodicity of the DBRs, irrespective of the presence of interfacial grading. The periodicity of the DBRs is consistent with the repetition of the temperature variation as shown in fig. 1. The period of the DBR as calculated from the position of the satellite peaks is 1571 Å for the 5-period and 1398 Å for the 8-period DBR. The calculated periodicity from X-ray diffraction measurement is consistent with the growth rates deduced from the RHEED oscillations and with the optical reflectivity measurement.

The (400) satellite intensities are predominantly affected by the strain modulation, while the (200) satellite intensities are more sensitive to the chemical modulation. Although the composition and corresponding strain in the interfaces of the 8-period AlAs/GaAs DBR are linearly graded, the presence of strong, sharp satellite peaks still demonstrates a well-defined periodic structure. The scans of the 5-period AlAs/GaAs DBR show the presence of slightly more, higher-order weak satellite peaks further away from the main peak than is

the case for the 8-period DBR. This is to be expected since interfacial composition grading in the 8-period DBR causes the intensities of the satellite peaks to decrease with increasing order number.

Optical reflectivity of the DBRs with sharp interfaces and those with linearly graded interface, in theoretical calculations, shows a small difference in the peak reflectivity, while the one with sharp interfaces has a larger bandwidth. An extra pair or two added to the DBR with linearly graded interfaces, however, increases the peak reflectivity over the one with sharp interfaces. Our experimental measurements on various types of DBRs are in good agreement with the theoretical calculations. However, we should caution that there is an uncertainty in the measurement of peak reflectivity. The measurement on the bandwidth, on the other hand, is more accurate.

Recently, several new designs of the p-type semiconductor quarter-wave DBR have been made to lower the series resistance by reducing the sharpness of the interfaces in the mirrors: For example, in the case of GaAs/Al_{0.7}Ga_{0.3}As, modifications have been made by inserting an intermediate layer 200 Å thick of Al_{0.35}Ga_{0.65}As or superlattices of GaAs(10 Å)/Al_{0.7}Ga_{0.3}As(10 Å) at the GaAs/Al_{0.7}Ga_{0.3}As heterointerfaces. The specific DBR series resistance was found to be reduced by two orders of magnitude to about $6 \times 10^{-5} \Omega \text{ cm}^2$ for a doping concentration of $\sim 10^{19} \text{ cm}^{-3}$ [4]. These modifications have not much altered the optical reflectivity, though at these doping levels, free carrier absorption loss becomes significant.

For a lower doping level of $\sim 10^{18} \text{ cm}^{-3}$, the DBR using only one intermediate layer may not have low enough resistance. Therefore, for the DBR consisting of AlAs/GaAs, which has a higher potential barrier than the one with Al_{0.7}Ga_{0.3}As/GaAs, the low resistance in the DBR can be achieved by the approaches using graded interface or two intermediate layers. Using our method discussed above, we have reduced the specific series resistance in the quarter-wave DBR of 8 pairs of GaAs/AlAs to $5 \times 10^{-4} \Omega \text{ cm}^2$ for a doping concentration of $3 \times 10^{18} \text{ cm}^{-3}$. With a doping level at $8 \times 10^{18} \text{ cm}^{-3}$, the specific series

resistance in the 8-pair DBR (AlAs/GaAs) was measured to be $7 \times 10^{-5} \Omega \text{ cm}^2$. Note that the optical reflectivity of the DBRs with a graded interface should be higher than those with one or two intermediate layers.

4. Conclusion

We have shown a simple method to reduce the series resistance in p-DBR mirrors while maintaining their high reflectivity. The energy band discontinuity at the heterojunction of AlAs and GaAs has been modified (minimized) by inserting an intermediate layer with linearly graded Al and Ga compositions. Experimentally, this has been achieved by varying temperatures of one Al and one Ga cells. No shutter operation was used during the MBE growth. From the presence of strong, sharp satellite peaks in the high-resolution X-ray diffraction patterns, a well-defined periodicity of the DBRs, irrespective of the interfacial grading, has been achieved. The optical reflectivity measurements on these DBRs are consistent with the theoretical calculations, which is expected based on the results of X-ray diffraction. Constant growth rates of GaAs, AlAs, and AlGaAs have been achieved throughout the course of mirror

growth, thus maintaining a constant doping level. Low specific series resistance has been achieved in the p-DBR of 8 pairs of GaAs/AlAs to be $5 \times 10^{-4} \Omega \text{ cm}^2$ for a doping level of $3 \times 10^{18} \text{ cm}^{-3}$.

References

- [1] F. Koyama, S. Kinoshita and K. Iga, *Appl. Phys. Letters* 55 (1989) 221.
- [2] R.J. Fischer, K. Tai, M. Hong, J.M. Vandenbreg, J.Y. Ying, J.P. Mannaerts and A.Y. Cho, *J. Vacuum Sci. Technol. B8* (1990) 336.
- [3] Y.H. Lee, J.L. Jewell, A. Scherer, S.L. McCall, J.P. Harbison and L.T. Florez, *Electron. Letters* 25 (1989) 1377.
- [4] K. Tai, L. Yang, Y.H. Wang, J.D. Wynn and A.Y. Cho, *Appl. Phys. Letters* 56 (1990) 2496.
- [5] R.S. Geels, S.W. Corzine, J.W. Scott, D.B. Young and L.A. Coldren, *IEEE Photonic Technol. Letters* 2 (1990) 234.
- [6] Y.H. Lee, B. Tell, K. Brown-Goebeler, J.L. Jewell and J.V. Hove, *Electron. Letters* 26 (1990) 710.
- [7] R.J. Fischer, Y.H. Wang, J. Gamelin, M. Hong and A.Y. Cho, unpublished results.
- [8] J.M. Vandenberg, M. Hong, J.P. Mannaerts, K. Tai, S.N.G. Chu and A.Y. Cho, *J. Mater. Res.*, submitted.
- [9] R.K. Willardson and A.C. Beer, Eds., *Semiconductors and Semimetals*, Vol. 7, Part A (Academic Press, New York, 1971) p. 180.
- [10] J.M. Vandenberg, R.A. Hamm, M.B. Panish and H. Temkin, *J. Appl. Phys.* 62 (1987) 1278.

MBE growth of InP/InGaAs MQW modulators

E.G. Scott and M.A.Z. Rejman-Greene

British Telecom Research Laboratories, Martlesham Heath, Ipswich IP5 7RE, UK

Matched Stark effect MQW optical modulators in the InP/InGaAs materials system have been grown using double sided epitaxy (DSE) on both sides of a single InP wafer by gas source MBE. Coupled multi-quantum well stacks have been used to reduce the operating voltage of the devices (1.2 dB at -6 V unbiased), and group III cells incorporating conical crucibles have greatly improved the area uniformity (exciton absorption peak ± 3 nm over 2 inches) making feasible the fabrication of modulators operating at the same wavelength over an entire wafer.

Parallel optical processing is becoming increasingly important in overcoming electrical wiring bottle-necks in high capacity data transfer. Achieving spatially parallel interconnects using Stark effect modulator arrays [1,2] places stringent demands on the growth of device material. The requirement for large area arrays, low voltage operation, sharp absorption edges, and novel optical architectures has necessitated the growth of MQW's in the InP/InGaAs materials system with excellent lateral and vertical uniformity and morphology, growth on both sides of the wafer, and the development of coupled multi-quantum well devices.

The growth was carried out by gas source MBE using a VG V80-H chamber with conventional solid sources for the group III elements and dopants, and 100% arsine and phosphine gas for the group V sources. The gas flows were controlled by mass flow controllers and pre-cracked using a low pressure tantalum catalytic cracking cell operated at 1000 – 1050°C . The growth rates for InP and InGaAs were ~ 1 and $2 \mu\text{m h}^{-1}$, respectively, at a growth temperature of 525°C . Abrupt InP/InGaAs heterojunctions were achieved using a group III source ramping technique to eliminate flux transients due to shutter operation and a growth interrupt of the order of 15 s to allow pumpdown of group V gases between layers [3,4].

Improvements in thickness and compositional area uniformity in InP/InGaAs MQWs have been achieved by attention to geometric factors involving the sources and the substrate. The use of group III sources with conical crucibles having walls 7.5° to the normal and an orifice diameter of 29 mm, a source to substrate distance of 145 mm, and an angle of 24° between the sources and the normal through the centre of the wafer yields thickness and compositional uniformities of $\pm 1.5\%$ and ± 50 parts per million respectively. Fig. 1 shows a Fourier transform infra red (FTIR) absorption spectrum line scan from the middle to the edge of a 2 inch wafer in 5 mm steps. The wavelength of the absorption edge varies by ± 3 nm over a 2 inch wafer making feasible the fabrication of modulators operating at the same wavelength over the entire wafer.

The use of conical crucibles in the group III cells lead to flux transients due to shutter operations which were too large and long lived to permit the ramping technique to be used effectively. In this case it was found that the In and Ga fluxes responded in unison to the opening of the shutter so that the problem was the less serious one of change of growth rate rather than of mismatch.

Double sided polished [100] InP ($S \sim 1 \times 10^{19} \text{ cm}^{-3}$) wafers were used. The wafer preparation consisted of etching with H_2SO_4 , HNO_3 and 10%

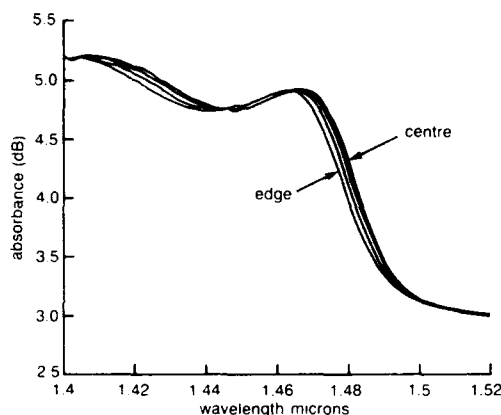


Fig. 1. FTIR absorption line scan of an InP/InGaAs MQW stack measured at 5 mm intervals from centre to edge of a 2 inch wafer grown using group III sources incorporating conical crucibles.

HCl before mounting in an indium-free sample holder. The sample holder consisted of a molybdenum ring containing a whole 2 inch InP wafer with a sapphire backing slice mounted slightly out of contact with the InP.

An important feature of indium-free mounting is the preservation of the integrity of the back of the wafer during growth. For the DSE growth, after the first epitaxial layers (side A) were grown the wafer was removed from the MBE reactor, turned over and with no further cleaning or preparation replaced in the reactor. Epitaxial layers were then grown under the same conditions on the second side (side B).

DSE allows matched or different devices to be grown on the back and front of the wafer. For the MQW optical modulator this provides a powerful way of gaining extra modulation depth at the same operating voltage or extra functionality on the chip. By working in the InP/InGaAs materials system where the substrate is transparent at the operating wavelength it has been possible to adopt a parallel optical bus architecture where wafers are "stacked" together and the light beam is transmitted through the stack perpendicular to the [100] faces of the wafers [5].

The DSE layer structure is shown in fig. 2. The p-n junction was formed subsequent to the epilayer growth by Zn diffusion through a 60 nm

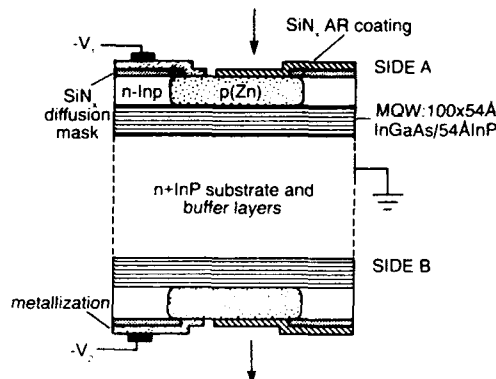


Fig. 2. Fabrication details and layer structure of the double sided MQW modulator device.

window. 2×2 arrays of optically coupled devices $125 \mu\text{m}$ apart with separate electrical addressing have been fabricated. For this structure containing 100 quantum wells on each side of the wafer a total modulation depth of 3.8 dB was achieved for a -10 V excursion from a -10 V bias voltage.

Fig. 3 shows the (FTIR) absorption spectra from the MQW layers on both sides of the wafer compared with the individual contributions from adjacent points on each side (within $\sim 0.5 \text{ mm}$ of each other), measured by cleaving the wafer and etching off the epilayers from the side opposite to the side being measured. The wavelength, step height and gradient of the absorption edge are

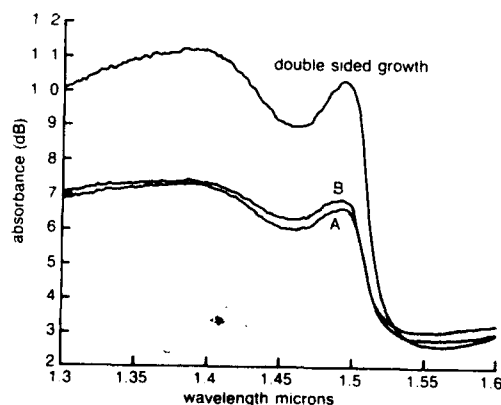


Fig. 3. FTIR absorption spectra from the entire double sided structure and from the A and B sides separately.

identical within experimental error for the layers on the A and B sides of the wafer.

Double crystal X-ray diffraction patterns also indicate that the crystalline quality, period and mismatch in the MQWs are very similar between the A and B sides of the wafer as can be seen in fig. 4. The area uniformity is dominated by the system geometry and it is found that the A and B sides closely resemble each other over the entire wafer, exhibiting circular symmetry due to substrate rotation. Furthermore, modelling of X-ray diffraction results has shown that the InP/InGaAs interfaces are extremely narrow, of the order 2–3 monolayers [4].

The complexity of double sided processing is illustrated in fig. 5 which shows the difference in transmission with voltage for the A and B side devices. The B side device has a larger modulation depth for a given voltage than the A side. This is probably due to a Zn diffusion "push-on" effect shifting the position of the A side pn junction into the MQW stack during the subsequent Zn diffusion of the B side.

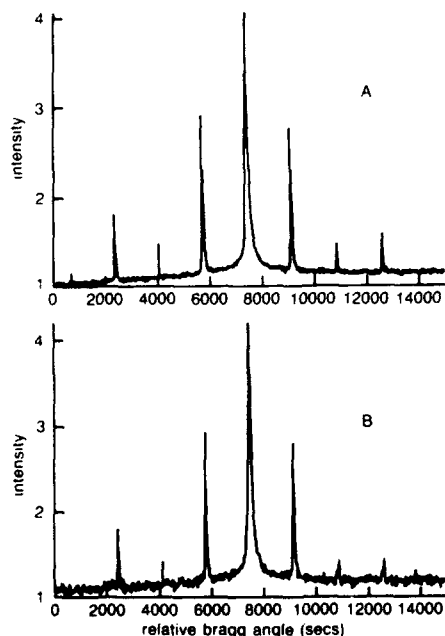


Fig. 4. Double crystal X-ray diffraction patterns from the A and B sides of the double sided structure.

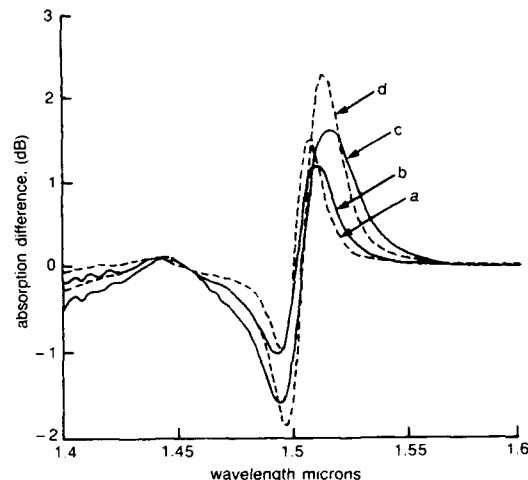


Fig. 5. Absorption difference spectra for the double sided modulator. Bias voltages relative to -10 V offset: (a), (b) at -5 V; (c), (d) at -10 V; (—) A side; (---) B side.

Optical modulator devices comprising a conventional 200 period InP/InGaAs MQW stack as the i region of a pin structure typically operate at a voltage of ~ -30 V to give a modulation depth of 3 dB. The magnitude of the applied voltage can be a limitation of this device in a practical circuit. This may be overcome by operating a smaller voltage swing from a fixed bias voltage, e.g. the conventional 200 period structure gives ~ 1.75 dB modulation depth for a -6 V applied on a -15 V bias. Where bias voltages are not desirable coupled multi-quantum wells can be used. In a coupled well system the quantum well wavefunctions are made more sensitive to the applied field by inserting a thin (20 Å) barrier in the middle of the quantum well. A modulation depth of 1.2 dB for an unbiased -6 V applied voltage has been achieved. The coupled multi-quantum well structures consisted of 200 periods of (60 Å InP/30 Å InGaAs/20 Å InP/30 Å InGaAs) in the MQW region of the device. The morphological defect count was $\sim 400 \text{ cm}^{-2}$ and after fabrication 99% of devices had leakage currents less than 10 nA at -10 V. These results allowed working arrays of 10×10 devices (pitch $125 \mu\text{m}$) to be made. Speed measurements carried out on a 4×4 array showed a data rate of $100 \text{ Mbits}^{-1} \times 16$ channels in a

parallel interconnect system. In this case the data rate was limited by the speed of the CMOS drive circuitry; the bandwidth of a Stark effect MQW optical modulator in the GaAs/AlGaAs system has been measured to be at least 5.5 GHz [6].

The authors would like to acknowledge Dr. M.A.G. Halliwell for the X-ray diffraction analysis and Dr. G.J. Davies for useful discussions.

References

- [1] M.A.Z. Rejman-Greene, E.G. Scott and E. McGoldrick, *Electron. Letters* 24 (1988) 1583.
- [2] R. Sahai, R.B. Bailey, C. Lastufka, S.C. Hong, W.Q. Li, J. Singh and P.K. Bhattacharya, in: *Proc. SPIE Conf. 1151: Optical Information Processing Systems and Architectures*, San Diego, CA, 1989.
- [3] E.G. Scott, S.T. Davey, M.A.G. Halliwell and G.J. Davies, *J. Vacuum Sci. Technol.* B6 (1988) 603.
- [4] E.G. Scott, M.H. Lyons, M.A.Z. Rejman-Greene and G.J. Davies, *J. Crystal Growth* 106 (1990) 249.
- [5] N. Barnes, P. Healey, P. McKee, A.W. O'Neill, M.A.Z. Rejman-Greene, E.G. Scott, R.P. Webb and D. Wood, *Electron. Letters*, to be published.
- [6] G.D. Boyd, J.E. Bowers, C.E. Socolich, D.A.B. Miller, D.S. Chemla, L.M.F. Chirovsky, A.C. Gossard and J.H. English, *Electron. Letters* 25 (1989) 558.

Quantum-confined Stark effect in InGaAs/InP multiple quantum wells grown by solid source molecular beam epitaxy

P.A. Claxton, M. Hopkinson

Department of Electronic and Electrical Engineering, University of Sheffield, Mappin Street, Sheffield S1 3JD, UK

J. Kovac

Microelectronics Department, Slovak Technical University, 812 19 Bratislava, Czechoslovakia

G. Hill, M.A. Pate and J.P.R. David

Department of Electronic and Electrical Engineering, University of Sheffield, Mappin Street, Sheffield S1 3JD, UK

We report the first observation of the quantum-confined Stark effect (QCSE) in $\text{In}_{0.53}\text{Ga}_{0.47}\text{As}/\text{InP}$ multiple quantum wells (MQWs) grown by solid source molecular beam epitaxy (SSMBE). MQW PIN diodes have been fabricated with reverse bias leakage currents of ≈ 10 nA at -35 V, for $400\text{ }\mu\text{m}$ diameter mesas. Room temperature photocurrent measurements on diodes with nominal $55\text{ }\text{\AA}$ wells show well resolved excitonic absorption at around $1.55\text{ }\mu\text{m}$ and exhibit shifts of up to 39 meV at -35 V.

1. Introduction

The quantum confined Stark effect (QCSE) [1], in semiconductor quantum well structures, is of considerable technological interest as it can form the basis of high speed modulators and switches for use in optical fibre communication systems. The application of an electric field perpendicular to the plane of the quantum wells results in a shift of the exciton absorption to longer wavelength. Light, of appropriate wavelength, incident in the plane of the quantum wells can then be modulated by this change in absorption. There has been extensive development of QCSE in the GaAs/AlGaAs system where high contrast optical modulators have been fabricated [2,3]. However, for longer wavelength applications, other material systems are required which can operate in the 1.3 to $1.55\text{ }\mu\text{m}$ range for low loss in optical fibres.

For long wavelength operation work has been concentrated on two quantum well systems, InGaAs with InP barriers and InGaAs with AlInAs

barriers. Both systems are lattice matched to InP substrates. Until recently, metalorganic vapour phase epitaxy (MOVPE) has been preferred for the growth InGaAs/InP multi-quantum wells (MQWs) [4], and molecular beam epitaxy with solid sources (SSMBE) for the InGaAs/AlInAs MQWs [5]. This situation has arisen because of the difficulty of handling phosphorus in MBE systems and the problem of growing high quality aluminium containing materials by MOVPE. More recently, gas source molecular beam epitaxy (GSMBE) [6] and chemical beam epitaxy (CBE) [7] have emerged as hybrid techniques which have demonstrated the ability to achieve high quality interfaces in the InGaAs/InP material system.

In this paper we show that, despite the difficulty of controlling elemental phosphorus, the growth of high quality low leakage $\text{In}_{0.53}\text{Ga}_{0.47}\text{As}/\text{InP}$ MQW PIN diodes is possible by SSMBE. The simplicity and inherent safety of this technique may lead to continued interest in the use of elemental sources.

2. Experimental

Growth of the InGaAs/InP MQW PINs was performed in a specially modified VG V80H MBE system, incorporating dimer arsenic and phosphorus sources, a turbomolecular pumped phosphorus handling system, and liquid nitrogen cooled shutters to improve the shuttering of the group V sources. Full details of this system appear elsewhere [8].

The (100) InP substrates were indium soldered to a 3 inch silicon wafer, which was held in an indium free molybdenum ring holder. The InGaAs and InP layers were grown at a temperature of $\approx 500^\circ\text{C}$, with a growth rate of $1\ \mu\text{m/h}$ for the InP and $1.9\ \mu\text{m/h}$ for the lattice matched InGaAs. Growth took place under As or P dimers generated by K-cells incorporating 900°C graphite baffle furnaces. The use of cracker cells is essential for rapid switching of the As and P fluxes using liquid nitrogen cooled shutters, and for the safe handling of phosphorus.

Two device structures were produced for this work. The first, shown in fig. 1a, was grown on a semi-insulating substrate, and the second, shown in fig. 1b, on an n^+ substrate. Be doping was used for the $p^+ \approx 10^{18}\ \text{cm}^{-3}$ and $p \approx 10^{17}\ \text{cm}^{-3}$ and Si for the $n^+ \approx 10^{18}\ \text{cm}^{-3}$ and $n \approx 10^{17}\ \text{cm}^{-3}$ layers. As there is evidence of Be diffusion from the p-type region into the MQW, undoped InP spacers were used between the MQW and the p-type contact layers. Structures with no spacers, or

spacers of the less than $1000\ \text{\AA}$, gave inferior diode characteristics with leakage currents increased by up to four orders of magnitude. The MQW and spacer layers were all nominally undoped. Circular $400\ \mu\text{m}$ diameter mesa diodes were fabricated using standard lithography and wet chemical etching. The n-type ohmic contacts were InGe/Au and the p-type Au/Zn/Au.

3. Results and discussion

Transmission electron microscopy measurements show highly uniform multilayers, and confirm the nominal well and barrier thicknesses. The "i" region thickness for diode (a) was $1.5\ \mu\text{m}$ and for diode (b) was $1.11\ \mu\text{m}$. Capacitance-voltage measurements show the background doping level in the undoped "i" regions to be $n \approx 5 \times 10^{15}\ \text{cm}^{-3}$.

Current-voltage characteristics of the diodes were measured at room temperature. Structure (a) has a reverse bias breakdown of $\approx 70\ \text{V}$ (electric field $E = 4.5 \times 10^5\ \text{V cm}^{-1}$) and leakage current of $10\ \text{nA}$ at $35\ \text{V}$; structure (b), with thinner barriers and thinner total "i" region, has a reverse bias breakdown voltage of $\approx 55\ \text{V}$ ($E = 4.9 \times 10^5\ \text{V cm}^{-1}$) and leakage current of $10\ \text{nA}$ at $28\ \text{V}$. The shape of the I - V curves is similar for both diodes, and is shown for structure (b) in fig. 2. From the shape of the curve it is possible to identify three regions; up to $20\ \text{V}$ the conduction

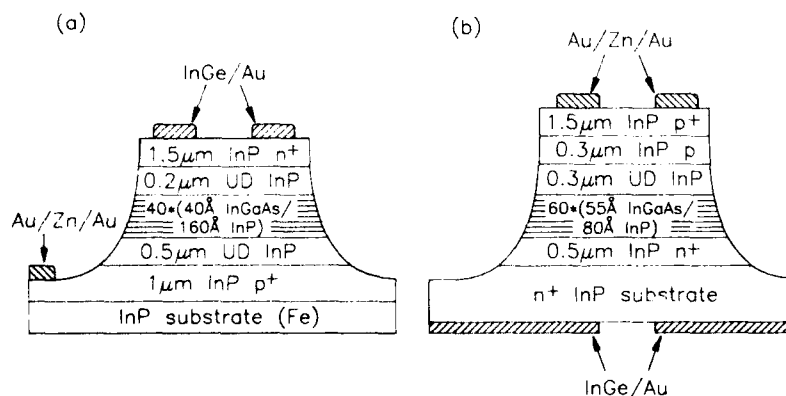


Fig. 1. $400\ \mu\text{m}$ diameter $\text{In}_{0.53}\text{Ga}_{0.47}\text{As}/\text{InP}$ MQW PIN diodes: (a) on semi-insulating substrate; (b) on n^+ substrate.

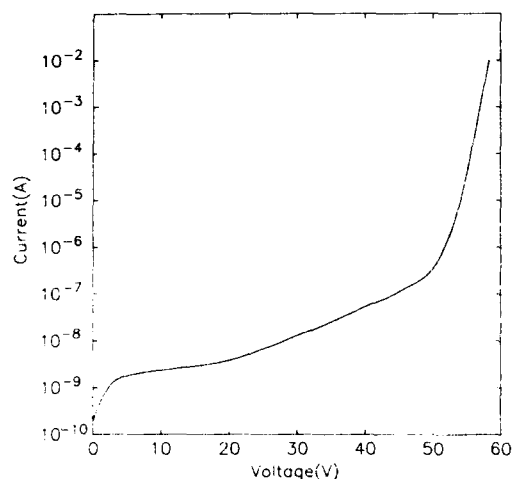


Fig. 2. Current-voltage characteristic for diode (b), the "i" region is $1.11 \mu\text{m}$ thick and the mesa diameter is $400 \mu\text{m}$.

is dominated by generation/recombination and diffusion currents; from 20 to 55 V evidence of tunneling is observed; and above 55 V avalanche breakdown occurs.

Photocurrent measurements were performed at room temperature by illuminating the diodes using a monochromated white light source. The diodes were reverse biased and lock-in techniques were used to measure the photocurrent as a function of wavelength; this was repeated for a range of bias voltages. In the presence of an electric field the exciton absorption shifts to longer wavelength and broadens. In the case of device (a) the absorption edge shifts from $1.4990 \mu\text{m}$ at -5 V to $1.5255 \mu\text{m}$ at -35 V , an energy shift of 14.4 meV at an electric field of $2.25 \times 10^5 \text{ V cm}^{-1}$. For device (b) there is a larger shift from $1.550 \mu\text{m}$ at -5 V to $1.629 \mu\text{m}$ at -35 V , a shift of 38.8 meV at a field of $3.15 \times 10^5 \text{ V cm}^{-1}$. The photocurrent spectra and the QCSE shift with bias for device (b) are shown in figs. 3 and 4. The shifts observed in this work are in good agreement with those calculated by Temkin et al. [9] for $1.0 \mu\text{m}$ thick superlattice structures, and for device (b) is, as far as we are aware, the largest shift reported in $\text{In}_{0.53}\text{Ga}_{0.47}\text{As}/\text{InP}$ for 55 \AA QWs grown by any technique.

The photocurrent increases with increasing reverse bias until it saturates at a voltage of ≈ -10

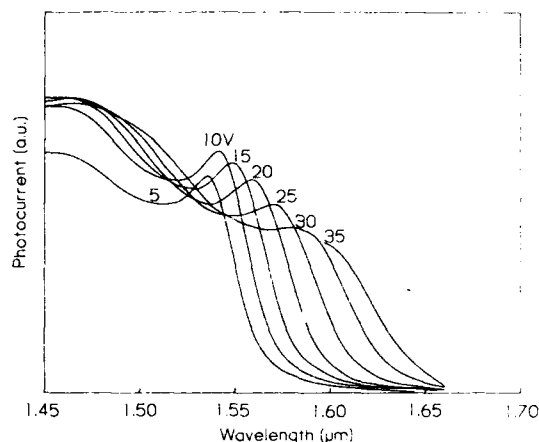


Fig. 3. Photocurrent response spectra of diode (b), with 55 \AA thick wells of $\text{In}_{0.53}\text{Ga}_{0.47}\text{As}$.

V. This indicates that at low fields not all the photoexcited carriers are extracted. Shorthose et al. [10] attribute this increase to enhanced tunneling as the field is increased. At zero bias the photocurrent is small and the exciton peaks are considerably broadened by the space charge present. For clarity we do not include the zero bias spectrum, but note no observable shift in the exciton absorption between zero and -5 V bias.

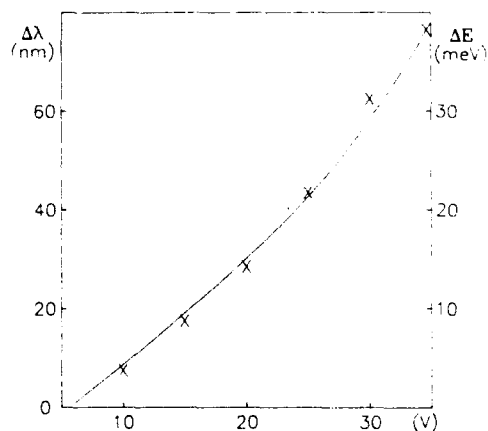


Fig. 4. Quantum confined Stark shift for diode (b). Experimentally determined points are shown, the continuous line is drawn to guide the eye.

4. Conclusion

High quality, low leakage, $\text{In}_{0.53}\text{Ga}_{0.47}\text{As}/\text{InP}$ multiquantum well PIN diodes have been grown by solid source molecular beam epitaxy. Room temperature photocurrent measurements have shown exciton absorption edge shifts of 38 meV for structures with 55 Å quantum wells, which we believe is the highest value reported.

References

- [1] D.A.B. Miller, D.S. Chemla, T.C. Damen, A.C. Gossard, W. Wiegmann, T.H. Wood and C.A. Burrus, *Phys. Rev. Letters* 53 (1984) 2173.
- [2] T.H. Wood, E.C. Carr, C.A. Burrus, J.E. Henry, A.C. Gossard and J. English, *Electron. Letters* 23 (1987) 916.
- [3] M. Whitehead, G. Parry, J.S. Roberts, P. Mistry, P. Li Kam Wa and J.P.R. David, *Electron. Letters* 23 (1987) 1048.
- [4] D.R.P. Guy, L.L. Taylor, D.D. Besgrove, N. Apsley and S.J. Bass, *Electron. Letters* 24 (1988) 1253.
- [5] K. Wakita, Y. Kawamura, Y. Yoshikuni and H. Asahi, *Electron. Letters* 22 (1986) 907.
- [6] M.B. Panish, *J. Crystal Growth* 81 (1987) 249.
- [7] W.T. Tsang, *J. Crystal Growth* 81 (1987) 261.
- [8] P.A. Claxton, J.S. Roberts, J.P.R. David, C.M. Sotomayor-Torres, M.S. Skolnick, P.R. Tapster and K.J. Nash, *J. Crystal Growth* 81 (1987) 288.
- [9] H. Temkin, D. Gershoni and M.B. Panish, *Appl. Phys. Letters* 50 (1987) 1776.
- [10] M.G. Shorthose, A.C. Maciel, J.F. Ryan, M.D. Scott, A.J. Moseley, J.I. Davies and J.R. Riffat, *Appl. Phys. Letters* 51 (1987) 493.

Critical issues in the MBE growth of $\text{Ga}_{0.47}\text{In}_{0.53}\text{As}$ for waveguide/PIN/JFET integration

H. Künzel, R. Kaiser, W. Passenberg, D. Trommer and G. Unterbörsch

Heinrich-Hertz-Institut für Nachrichtentechnik Berlin GmbH, Einsteinufer 37, W-1000 Berlin 10, Germany

The critical issues for the optimization of the MBE grown layer sequence for the integration of an optical waveguide, a PIN photodiode and a junction field effect transistor (JFET) to form a monolithic integrated receiver chip are discussed. For the JFET layer sequence low residual carrier density of the thick buffer layer has been successfully achieved. The growth of a p^+/p^{++} gate contact layer with minimized acceptor diffusion behaviour is described. For the hybridly grown MOVPE(LPE) GaInAsP/MBE GaInAs PIN/waveguide structure optimum crystallinity is achieved; however, donor accumulation at the interface is detected. MBE grown AlGaInAs as an alternative for the waveguide layer has been investigated. Due to its high resistivity at growth temperatures below 500 °C device isolation can be achieved.

1. Introduction

For long wavelength optical communication InP-based optoelectronics is the basic prerequisite. Monolithic integration of optoelectronic devices (OEIC) offers the potential of improvement in performance and functionality as well as reduction of size and costs compared to hybrid circuits. An integrated receiver module comprising a waveguide, detector and transistors on the same substrate forms a basic building block for a variety of complex OEICs.

In this contribution, we report on the critical issues in the MBE growth of $\text{Ga}_{0.47}\text{In}_{0.53}\text{As}$ (referred to as GaInAs) for the integration of a rib waveguide (WG), a PIN photodiode and a junction field effect transistor (JFET). On the basis of the integration scheme presented MBE growth conditions are adjusted for an integrable JFET and a PIN/WG module.

2. WG/PIN/JFET integration concept

In fig. 1 the underlying scheme for WG/PIN/JFET integration is schematically depicted. The layer structure is grown on a semi-insulating

InP:Fe substrate for integration purposes. The sequence consists of an undoped 1 μm thick GaInAsP layer with a composition corresponding to a band gap of 1.18 eV followed by an undoped 1 μm thick GaInAs layer. The sequence proceeds with a 0.2 μm n-GaInAs:Si and a 0.3 μm p^+ -GaInAs:Be layer. Doping concentrations are $n \approx 1 \times 10^{17} \text{cm}^{-3}$ and p^+ as high as possible, respectively. The GaInAsP layer serves as the WG layer and, together with the undoped GaInAs layer which simultaneously forms the i-region of the PIN diode, forms the buffer layer of the JFET. Due to the PIN diode being placed on top of the WG layer light detection is based on leaky coupling [1]. Theoretical calculations as well as ex-

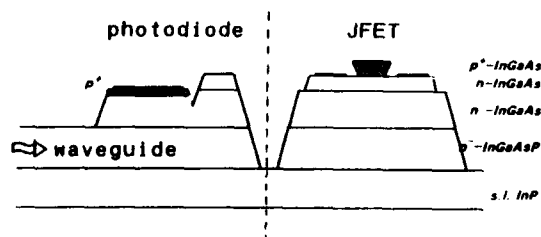


Fig. 1. Basic concept for WG/PIN/JFET integration on InP:Fe.

perimental data suggest a minimum thickness of approximately $1\text{ }\mu\text{m}$ for the i-layer in order to obtain optimum internal quantum efficiency [2]. The n-GaInAs layer acts as the JFET channel layer and is also used to form the PIN diode n-contact. A channel thickness of $0.2\text{ }\mu\text{m}$ in combination with a doping level of $1 \times 10^{17}\text{ cm}^{-3}$ are chosen such that depletion mode transistors with high transconductance are obtainable. The p^+ -GaInAs layer serves as the JFET gate layer and is utilized to facilitate fabrication of a low resistivity ohmic gate contact.

On the basis of the integration scheme presented in fig. 1 it is clearly seen that the optimization of the layer sequence can be separated into two parts, as indicated by the broken line. Accordingly, the critical items in the MBE growth can be divided into two groups related to the fabrication of the JFET and the PIN/WG. With respect to the MBE growth of the JFET layer sequence, the residual carrier concentration of the thick buffer layer and the extremely highly doped gate layer represent the critical issues. For the PIN/WG component MBE grown GaInAs for the PIN layer sequence is grown onto a MOVPE (LPE) GaInAsP WG layer. For this hybrid epitaxial growth process the interface quality of this layer sequence plays the important role.

3. Integrable JFET

The JFET buffer layer formed by GaInAsP/GaInAs, as described above, has a total thickness of $2\text{ }\mu\text{m}$. To facilitate abrupt pinch-off of the JFET device the residual carrier concentrations in these layers must be minimized. Since high resistivity and even semi-insulating GaInAsP material can be used for the WG, only the GaInAs residual carrier concentration needs to be reduced to a minimum. Using an adequate substrate material, a proper cleaning procedure, high quality source materials and a proper bakeout of the In source a residual carrier concentration below $2.5 \times 10^{15}\text{ cm}^{-3}$ is reached routinely. Best values achieved are $N_D - N_A = 7.4 \times 10^{14}$ and $4.1 \times 10^{14}\text{ cm}^{-3}$ and electron mobilities $\mu = 12580$ and $53000\text{ cm}^2/\text{V}\cdot\text{s}$ at 300 and 77 K, respectively.

To further reduce the free carrier concentration, reduction of the growth temperature is a possibility for the MBE growth of GaAs [3,4]. In fig. 2 the results for the growth temperature dependence of the 300 K electrical characteristics of MBE GaInAs are depicted. In contrast to GaAs, no reduction of the electron concentration at low growth temperatures down to 300°C is observed. On the contrary, an increase of the residual electron concentration by an order of magnitude at growth temperatures below 400°C is noticed. This effect is connected with a slight reduction of the mobility. Above 400°C , up to the onset of In desorption at 600°C , no influence of the growth temperature on the electrical characteristics is found since the scatter of the data between 6×10^{14} and $2.5 \times 10^{15}\text{ cm}^{-3}$ corresponds to the variation from layer to layer even at a fixed growth temperature. On the other hand, at 77 K a dramatic reduction of the free electron concentration is obtained for samples grown below 500°C . Below 400°C high resistivity material is attained. Hence, the reduction of the growth temperature to below 500°C results in an increase of the amount of the free carrier freeze-out. Further details of the influence of growth temperature on impurity incorporation in MBE GaInAs will be published elsewhere [5].

Using a standard growth temperature of 500°C , n/n⁺-GaInAs active/buffer junctions are pre-

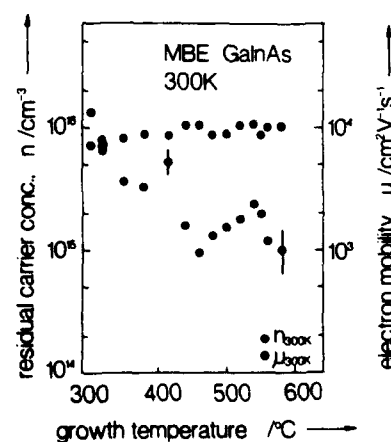


Fig. 2. Growth temperature dependence of 300 K electrical characteristics of undoped MBE GaInAs.

pared. Single n-GaInAs JFET channel layers are characterized by a mobility of 9000 and 10250 $\text{cm}^2/\text{V}\cdot\text{s}$ for a free electron concentration of 15×10^{16} and $9.5 \times 10^{16} \text{ cm}^{-3}$ at 300 and 77 K, respectively. $C-V$ measurements of the impurity distribution indicate perfectly flat profiles. At the n/n^- junction an abrupt change of the impurity concentration by nearly two orders of magnitude is measured. From the decay of the impurity concentration at the n/n^- interface the smearing of the impurity profile is found to be less than 0.05 μm including Debye length effects. A residual impurity concentration below $2 \times 10^{15} \text{ cm}^{-3}$ is also confirmed by the $C-V$ technique.

The achievement of non-alloyed very low resistance ohmic contacts to the gate layer requires very high hole concentrations near the surface. Be doping during MBE growth is suitable to reach high acceptor concentrations. Nevertheless, at doping levels in excess of $5 \times 10^{19} \text{ cm}^{-3}$ surface roughening and a deviation of the free hole concentration from the concentration of incorporated Be atoms is found to occur [6].

These detrimental effects can be directly correlated with acceptor diffusion during growth [7]. A marked increase of the diffusion coefficient at acceptor concentrations in excess of $5 \times 10^{19} \text{ cm}^{-3}$ is inferred from SIMS profile measurements [8]. Since a doping concentration of at least $5 \times 10^{19} \text{ cm}^{-3}$ is necessary to achieve very low contact resistivity, this doping level is applied near the surface, whereas a reduced Be concentration of $5 \times 10^{18} \text{ cm}^{-3}$, resulting in a reduction of the Be diffusion coefficient by two orders of magnitude, is utilized to form the p^+/n gate/channel junction. The resulting Be profile in the gate layer grown at 500°C as measured by SIMS is depicted in fig. 3a. A comparison of the intended profile given by the broken line and the measured Be distribution clearly demonstrates, however, drastic diffusion effects manifesting themselves in a reduction of the surface concentration, a Gaussian type diffusion profile at the p^+/p^+ junction, and a diffusion tail extending far into the layer. Since this tail with an acceptor concentration of 10^{18} cm^{-3} overcompensates the adjacent n-doped channel layer this gate doping configuration is not suitable for the JFET device structure.

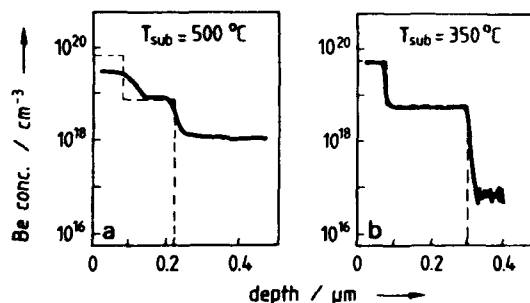


Fig. 3. SIMS Be concentration profile of a JFET p^+/p^+ -GaInAs gate contact layer. The broken line gives the Be distribution projected from the beam flux density. The growth temperature is (a) 500°C and (b) 350°C .

The growth temperature has a great influence on the diffusion of Be during growth. Reducing this growth parameter from 500 to 350°C results in a reduction of the acceptor diffusion by more than an order of magnitude [8] without affecting the free hole concentration [7] and the achievable contact resistance [8]. The resulting dopant distribution for a gate layer grown at a reduced temperature of 350°C is shown in fig. 3b. A sharp rectangular profile, which is in excellent agreement with the profile predicted by the flux density profile (broken line) and the low Be concentration outside the p-doped region demonstrate the successful realization of an optimized gate configuration.

$1 \mu\text{m}$ gate-length JFET devices have been fabricated on the basis of the optimized MBE growth described above. The gate/source diode is characterized by an ideality factor of 1.12 and a leakage current of 100 nA at -2 V reverse voltage. The output behaviour exhibits a pinch-off voltage of -4.5 V and a transconductance of 140 mS/mm . The electron mobility in the channel as deduced from the linear regime of the channel conductance is extracted to be $4500 \text{ cm}^2/\text{V}\cdot\text{s}$, representing a reduction by a factor of two compared to bulk material with the same doping level. Excellent high-frequency properties of the devices are indicated by very high cut-off frequencies for this type of FET of $f_T = 28 \text{ GHz}$ and $f_{\text{max}} = 38 \text{ GHz}$. Further details of the device properties are given in ref. [9].

4. Integrated PIN / WG component

Since solid source MBE used in this work cannot be used for the growth of the InGaAsP WG layer, either LPE or MOVPE material has been utilized. Consequently, application of a hybrid growth technique is necessary if the well established MBE grown GaInAs JFET/PIN structure has to be incorporated. By using an appropriate cleaning technique to reduce surface contamination before introduction of the GaInAsP/InP wafers into the MBE growth chamber, smooth surface MBE GaInAs can be grown. As judged from $C-V$ profiling measurements to assess the GaInAsP/GaInAs interface, cleaning with diluted HF was found to be most appropriate. X-ray diffraction measurements demonstrate a high crystalline quality of the MBE layer, showing a FWHM value of the rocking curve of below 20 arc sec, which is a typical figure of our MBE layers on InP substrates. This finding is true for both LPE and MOVPE grown GaInAsP layers.

Accumulation of impurities is expected to occur at the LPE(MOVPE)/MBE interface. To separate accumulation effects from heterostructure effects during $C-V$ profiling, MBE n -GaInAs was grown onto LPE n -GaInAs for comparison. The corresponding net dopant profile is represented in fig. 4. The measured profile clearly shows a mid-

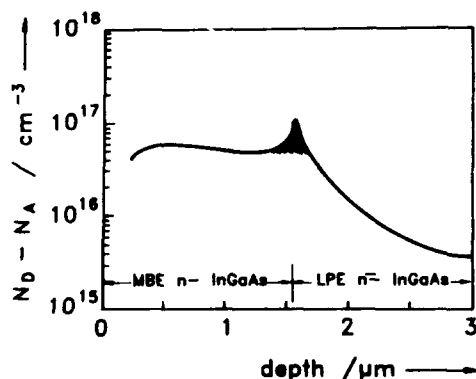


Fig. 4. $C-V$ donor concentration profile of a MBE n -GaInAs/LPE n -GaInAs sequence. The shaded area marks donor accumulation at the growth interrupted interface.

10^{16} cm^{-3} doping concentration of the MBE layer and the decrease of the concentration to below $5 \times 10^{15} \text{ cm}^{-3}$ in the undoped LPE layer. At the interface a donor-type accumulation is clearly detected which corresponds roughly to an areal density of $1 \times 10^{12} \text{ cm}^{-2}$. This density appears to be extremely high compared to interface state densities reached in MBE grown GaInAs/AlGaInAs heterostructures.

The high accumulation density and the relatively large thickness of the WG layer which unfavourably adds to the i -GaInAs layer (both forming the buffer of the JFET) leads to problems with respect to a sharp pinch-off behaviour of the transistor. An alternative approach to circumvent these problems is the use of high resistivity WG material. As an additional advantage, only the GaInAs layer needs to be mesa-etched to electrically isolate the different devices. Either iron doped semi-insulating MOVPE GaInAsP or high resistivity MBE AlGaInAs may be applicable.

AlGaInAs ($E_g = 1.18 \text{ eV}$) as the WG material offers the advantage of requiring only the MBE technique which leads to a low interface state density of as low as $1 \times 10^{10} \text{ cm}^{-2}$, as calculated from $C-V$ measurements. In addition, the AlGaInAs material is of high perfection, which manifests itself in optimum surface morphology and X-ray diffraction peak half-widths of again 20 arc sec. The electrical behaviour can be varied within wide limits. For growth temperatures in excess of 550°C conductive material with $n = (1-2) \times 10^{15} \text{ cm}^{-3}$ and mobilities in the range of $1500-2000 \text{ cm}^2/\text{V}\cdot\text{s}$ are obtained. Reducing the growth temperature to 500°C results in an increase of the resistivity to beyond $10^3 \Omega \text{ cm}$. A further reduction of the growth temperature is expected to yield semi-insulating material whilst retaining good crystalline and WG properties which make this material suitable for the WG/PIN integration as well as for the JFET buffer.

So far, integrated PIN/WG components based on hybrid growth on undoped LPE GaInAsP and semi-insulating MOVPE GaInAsP:Fe have been fabricated. Devices with an area of $A = 2.3 \times 10^{-5} \text{ cm}^2$ are characterized by a dark current of 2 nA ($V_r = -10 \text{ V}$), a breakdown voltage of 25 V ($I_r = 10 \mu\text{A}$) and an ideality factor of 1.25. The external

quantum efficiency is 16% ($\lambda = 1.55 \mu m/V = 0 V$) and the internal quantum efficiency is estimated to be $90\% \pm 10\%$. The 3 dB cut-off frequency is determined to be in excess of 2.0 GHz, which represents the upper limit of our measurement system used.

5. Conclusions

JFET devices on thick GaInAsP/GaInAs buffer layers and an integrated PIN/WG component forming substructures for the integration of a receiver module have been successfully fabricated. JFET devices with superior characteristics are demonstrated on the basis of optimized buffer and gate contact layer growth. Integration of a WG and PIN photodiode using LPE or MOVPE grown GaInAsP layers in conjunction with hybrid MBE GaInAs growth is achieved with promising device performance. Quaternary AlGaInAs MBE grown material has been demonstrated to be an alternative to form the WG layer to circumvent problems related to donor interface accumulation occurring in the hybrid epitaxial approach currently used to combine GaInAsP WGs with MBE grown PIN/JFET structures.

Acknowledgements

The authors wish to thank N. Grote for critically reviewing the manuscript. The work was funded by the "German Ministry for Research and Technology (BMFT)" under contract number TK 04477.

References

- [1] C. Bornholdt, W. Döldissen, F. Fiedler, R. Kaiser and W. Kowalsky, *Electron. Letters* 23 (1987) 2.
- [2] M.C. Amann, *Electron. Letters* 23 (1987) 17.
- [3] G.M. Metzger, A.R. Calawa and J.G. Mavroides, *J. Vacuum Sci. Technol.* B1 (1983) 166.
- [4] T. Murotani, T. Shimano and S. Mitsui, *J. Crystal Growth* 45 (1978) 302.
- [5] H. Künzel, R. Gibis, P. Harde and W. Passenberg, to be published.
- [6] R.A. Hamm, M.B. Panish, R.N. Nottenburg, Y.K. Chen and D.A. Humphrey, *Appl. Phys. Letters* 54 (1989) 2586.
- [7] W. Passenberg, H. Künzel, R. Bochnia, R. Gibis and P. Harde, in: *Proc. 19th ESSDERC*, Eds. A. Heuberger, H. Ryssel and P. Lange (Springer, Berlin, 1989) p. 55.
- [8] W. Passenberg, P. Harde, H. Künzel and D. Trommer, in: *Proc. 2nd Intern. Conf. on Indium Phosphide and Related Materials*, Denver, CO, 1990, IEEE Catalog No. 90CH 2859-7, p. 195.
- [9] D. Trommer, A. Umbach, W. Passenberg, G. Mekonnen and G. Unterbörsch, *Electron. Letters* 26 (1990) 734.

Investigation of a double barrier resonant tunnelling structure which incorporates an optical window layer in the top contact

M. Henini, C.R.H. White *

Department of Physics, University of Nottingham, Nottingham NG9 2RD, UK

P.E. Simmonds **

Royal Signals and Radar Establishment, St. Andrews Road, Great Malvern, Worcestershire WR14 3PS, UK

L. Eaves

Department of Physics, University of Nottingham, Nottingham NG9 2RD, UK

M.S. Skolnick

Royal Signals and Radar Establishment, St. Andrews Road, Great Malvern, Worcestershire WR14 3PS, UK

D.K. Maude, O.H. Hughes

Department of Physics, University of Nottingham, Nottingham NG7 2RD, UK

and

J.C. Portal ***

SNCI-CNRS, F-38042 Grenoble, France

The electrical and optical properties of a double barrier resonant tunnelling device based on n-GaAs/(AlGa)As and incorporating a heavily doped (AlGa)As window layer are described. The window layer is located between the quantum well and the top surface and has a band gap which exceeds the energy of the quantum well photoluminescence. The incorporation of this layer does not impair the electrical properties of the device.

* Also at RSRE, St. Andrews Road, Great Malvern, Worcestershire WR14 3PS, UK.

** Also at department of Physics, University of Nottingham, Nottingham NG7 2RD, UK.

Permanent address: Department of Physics, University of Wollongong, P.O. Box 1144, Wollongong, NSW 2500, Australia.

*** Also at LPS-INSa, F-31077 Toulouse, France.

Magnetic field measurements [1–3] and photoluminescence spectroscopy (PL) [4,5] are powerful techniques for investigating charge build-up and electron energy relaxation processes in double barrier resonant tunnelling structures (DBRTSs). Most studies reported to date have used structures in which the doped semiconductor contact layers

on either side of the barriers are of the same material as the quantum well, for example doped GaAs contact layers in GaAs/(AlGa)As DBRTS. This layer is usually fairly thick, typically $> 0.5 \mu\text{m}$, to prevent degradation of the barrier and quantum well (QW) regions when Au/Ge alloyed contacts are made to the top surface. This type of structure has a disadvantage for PL measurements, since the quantum confinement energy of the electrons and holes gives rise to a PL emission energy from the QW which exceeds the band gap energy of the contact layer. The excitation light and the PL therefore suffer strong attenuation as they traverse the contact layer.

In this paper we investigate a DBRTS which has been specially designed for spectroscopic investigation, in which a thick heavily doped (AlGa)As layer is incorporated in the top contact layer. The (AlGa)As layer, which we term a "window" layer, greatly reduces the attenuation since, by choosing the correct Al concentration, it is possible to produce a band gap greater than the recombination energy of the QW.

The structure was grown by molecular beam epitaxy and is shown schematically in fig. 1. Note the undoped spacer layers of GaAs immediately adjacent to the tunnel barrier [3]. The layers were processed into $100 \mu\text{m}$ diameter mesas with annular top contacts to allow optical access. The (AlGa)As window layer has a band gap energy of 1.9 eV , which is considerably larger than the QW recombination energy of 1.562 eV . No difficulties with electron capture at DX are encountered since

25nm	GaAs	$2 \times 10^{18} \text{ cm}^{-3}$	Top Cap
1 μm	$\text{Al}_{0.33}\text{Ga}_{0.67}\text{As}$	$2 \times 10^{18} \text{ cm}^{-3}$	Window Layer
51nm	GaAs	$2 \times 10^{18} \text{ cm}^{-3}$	
35nm	GaAs	$1 \times 10^{18} \text{ cm}^{-3}$	
7.6nm	GaAs	Undoped	Spacer Layer
8.5nm	$\text{Al}_{0.4}\text{Ga}_{0.6}\text{As}$	Undoped	Barrier
7.6nm	GaAs	Undoped	Well
8.5nm	$\text{Al}_{0.4}\text{Ga}_{0.6}\text{As}$	Undoped	Barrier
7.6nm	GaAs	Undoped	Spacer Layer
51nm	GaAs	$1 \times 10^{18} \text{ cm}^{-3}$	
51nm	GaAs	$1 \times 10^{17} \text{ cm}^{-3}$	
2 μm	GaAs	$2 \times 10^{18} \text{ cm}^{-3}$	
n+ GaAs Substrate			

a

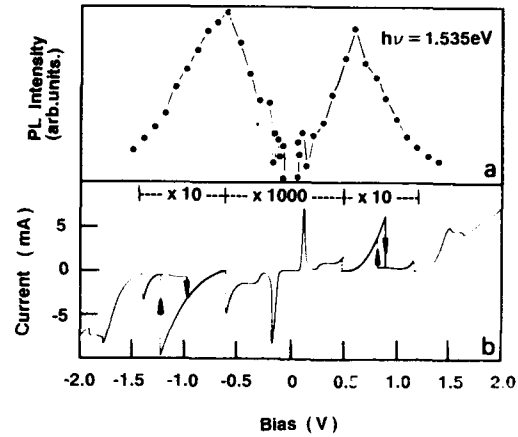


Fig. 2. (a) The dark $I(V)$ characteristic of the device, measured at 4.2 K . (b) The variation of PL integrated intensity with bias for an excitation energy of 1.535 eV .

any electron that might be captured at the DX level is ionised when the sample is illuminated due to the persistent photoconductivity effect.

Fig. 2a shows the dark $I(V)$ characteristic of the device. Forward bias ($V > 0$) corresponds to electrons tunnelling from the substrate to the top contact. There are three clear peaks in the current in each bias direction. These occur at 0.10 V (-0.11 V), 0.9 V (-1.0 V) and 1.5 V (-1.8 V) for forward (reverse) bias, and correspond to electrons tunnelling from the two-dimensional electron gas (2DEG), which forms in the emitter accumulation layer, into the first (ϵ_1^w), second (ϵ_2^w) and third (ϵ_3^w) quasi-bound states of the QW. The

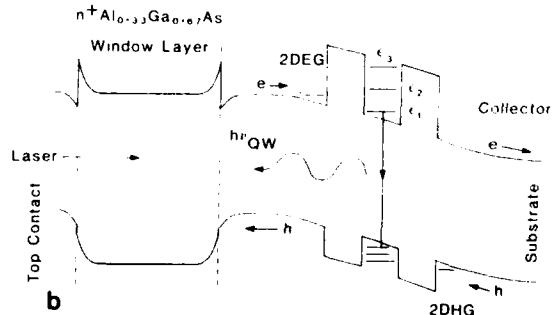


Fig. 1. (a) The layer structure of the device. (b) A schematic diagram of the conduction and valence band edge profiles for a DBRTS.

existence of three bound QW states for a well width of 7.5 nm is consistent with effective mass theory. Note the high degree of symmetry in the $I(V)$ characteristic with respect to bias direction. This shows that the inclusion of the window layer does not adversely affect the electrical properties of the device. This is further emphasized by the excellent peak to valley ratios at the first and second resonances which, at 4.2 K, are 40:1 and 20:1 respectively for both bias directions.

The first (low voltage) resonance is sharply peaked. This is characteristic of the situation when only a very small electronic space charge builds up in the QW during resonant tunnelling. In contrast, the second resonance, which corresponds to a much larger current flow, is spread over a wide range of voltage (in forward bias, from a threshold at around 0.4 V to a peak at 0.9 V). This is accompanied by pronounced intrinsic bistability in $I(V)$. Over this voltage range, electrons resonantly tunnel from the 2DEG in the emitter into the ϵ_2^w state of the QW. The electrons can then undergo inter-subband scattering into the ϵ_1^w state by the emission of a longitudinal optic (LO) phonon [2]. The charge stored in the QW over the voltage range of the second resonance resides almost entirely in this lower energy state. This is confirmed by the photoluminescence experiments described below.

Let us consider the main features of figs. 3a and 3b. The dependence on magnetic field of the various features in figs. 3a and 3b are shown by the fan diagram plotted in fig. 4. We will concentrate on the forward bias case, since similar remarks apply for reverse bias. In the presence of a perpendicular magnetic field ($B \parallel J$), the 2DEG systems in the emitter accumulation layer and the QWs become quantised into Landau levels whose energies are given by:

$$\epsilon^a(B) = \epsilon^a(0) + n\hbar\omega_c, \quad \epsilon_q^w(B) = \epsilon_q^w(0) + n'\hbar\omega_c,$$

where $\omega_c = eB/m^*$ is the cyclotron frequency, n and n' are integers and $q = 1, 2$ or 3. Feature RP₁ (fig. 4) corresponds to resonant tunnelling of electrons from the accumulation layer into the lowest state ϵ_1^w of the QW with conservation of Landau level index ($\Delta p = n' - n = 0$). At slightly higher

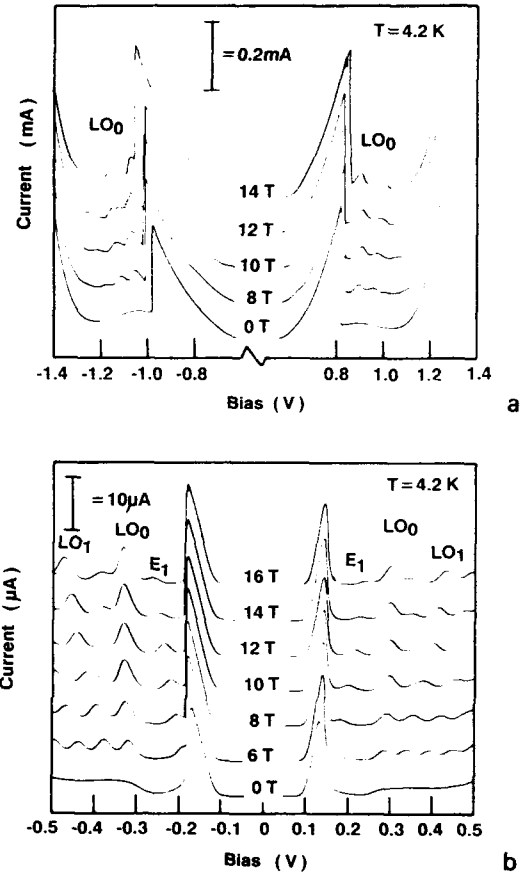


Fig. 3. (a) $I(V)$ curves for the first electron resonance measured with various magnetic fields, the field been applied parallel to the current ($B \parallel J$). (b) $I(V)$ curves for the second electron resonance measured with various magnetic fields ($B \parallel J$).

voltage, a weak feature, E_1 , corresponds to tunnelling accompanied by elastic scattering with $\Delta p = 1$. The other features at higher voltages correspond to tunnelling of electrons with the emission of an LO phonon. This can occur either with ($\Delta p = 1, 2, 3, \dots$) or without ($\Delta p = 0$) change of Landau level index. Fig. 4 shows a number of LO phonon-related peaks at voltages beyond the first and second resonant peaks in the $I(V)$. By using the cyclotron energy, $\hbar\omega_c$ to calibrate the voltage axis [6] we can determine the energy of the LO phonon emitted. By extrapolating to zero mag-

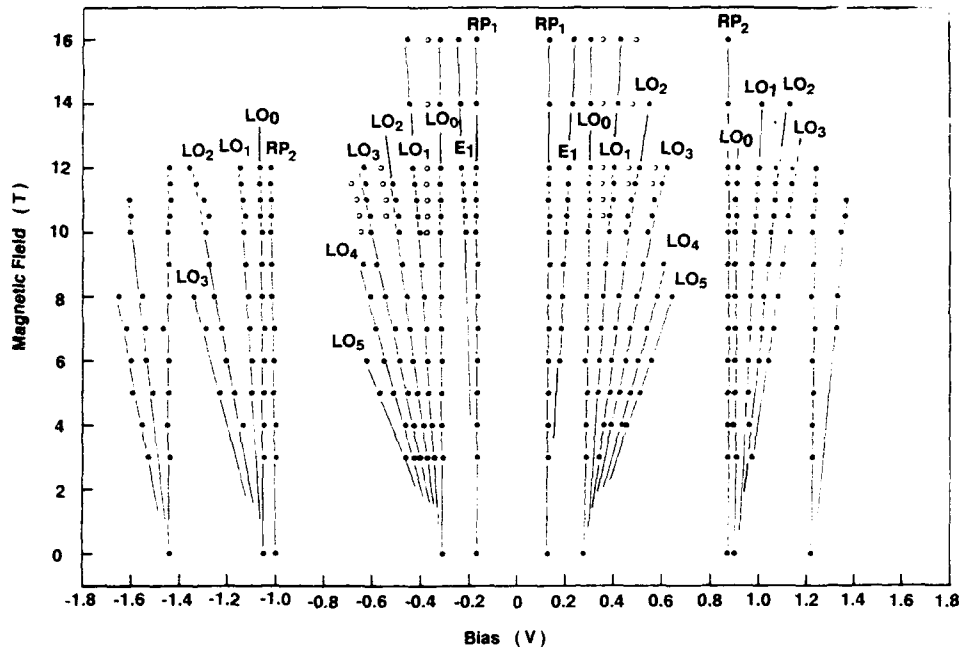


Fig. 4. The fan chart of the elastic and inelastic assisted resonant tunnelling features observed in figs. 3a and 3b.

netic field, the fan-shaped series of lines through the closed circles just beyond RP_1 gives an LO phonon energy of 33 meV. This is close to the energy of the GaAs LO phonon mode (36 meV). The two weaker peaks (positions indicated by open circles in fig. 4) extrapolate back to give an LO phonon energy of 48 meV, which we attribute to the AlAs-like LO phonon mode in the barrier [7]. For these LO phonon-assisted transitions beyond the first resonance, we estimate the relative strengths of the GaAs and AlAs LO phonon emission processes to be in the ratio 8:1.

The fan of points which occurs beyond the second resonant peak at 0.9 V is also related to the resonant tunnelling of an electron with the emission of an LO phonon. However, the space charge build-up and intrinsic bistability which occurs on the second resonance makes it difficult to determine the LO phonon energy accurately.

The charge confined in the QW under resonant tunnelling conditions can be determined from a line-shape analysis of the QW PL emission spectra [5]. Fig. 5 shows a set of PL spectra obtained over

a wide range of voltage covering the three resonances. For all the spectra, the energy of the peak intensity of the QW PL spectra corresponds to the recombination of electrons in the ϵ_1^W state of the conduction band QW with holes in the lowest state of the valence band QW. This is the case even at bias voltages above 0.4 V where the electrons are tunnelling into the second (ϵ_2^W) or third (ϵ_3^W) states of the QW and provides clear evidence for a sequential tunnelling process in which the electrons undergo inter-subband scattering into the lowest bound state of the QW [2,5]. This process involves the emission of an LO phonon and occurs on a time scale typically ≈ 1 ps. Note also that as the bias is increased there is an overall shift in the peak intensity position to lower energies. This is due to the quantum confined Stark effect [8].

Direct evidence for the large electron space charge build up in the QW at the second resonance is provided by the increase of the PL line-width between 0.7 and 0.8 V (see fig. 5). When the device comes off resonance (0.9 V) the electronic

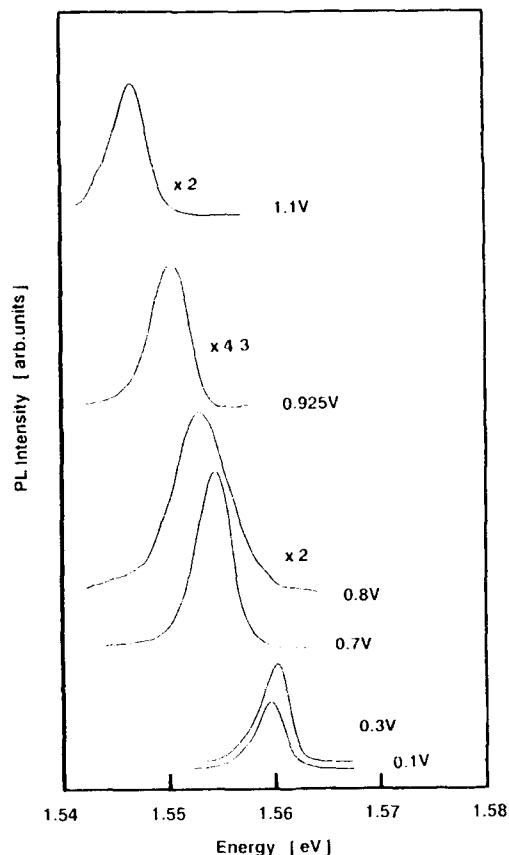


Fig. 5. PL spectra measured at a series of forward bias voltages corresponding to the three electron resonances, in forward bias.

space charge is ejected from the QW and the line-width narrows again. This can be seen by comparing the line-width for the spectra taken at 0.8 and 0.925 V (see fig. 5). From the line-shape analysis we estimate a sheet charge density of $n_w = 2 \times 10^{11} \text{ cm}^{-2}$ in the ϵ_1^w at the peak of the second resonance in $I(V)$.

The very low attenuation of the excitation light and the PL emission in the window layer also allows us to study the device in a convenient way for both bias directions. This provides information about the mechanism for the hole generation and capture processes. In a conventional structure, the PL intensity from the QW is highly asymmetric with respect to bias direction. A typical ratio is

5:1 in favour of the bias direction in which the holes are created in the top contact layers and then tunnel into the QW [4,5] where they recombine radiatively with the electrons. In contrast, for the device with the window layer, there is a high degree of symmetry in the integrated PL intensity (I_{PL}) with respect to bias direction, as shown in fig. 2b. The PL excitation energy used for this study was 1.535 eV, which is 27 meV below that required for direct excitation in the QW and 12 meV above the GaAs band gap energy. Thus holes cannot be generated directly in the QW. The observed PL arises from holes which tunnel into the well from the contact regions. The integrated PL intensity shows a weak peak at low bias corresponding to the small build-up of electronic space charge in the QW at the first resonance. This peak occurs at the same voltage as the first resonant peak in $I(V)$. Beyond the first resonance there is always a small residual electronic charge in the QW. The steady increase in the integrated PL intensity up to 0.6 V is due to increasing electronic space charge build-up as the peak of the second resonance is approached. However, the PL intensity starts to fall before the second resonant peak is reached due to the decrease in the capture efficiency of the photo-created holes in the valence band QW [5].

As stated earlier, the illumination energy of 1.535 eV is insufficient for direct excitation in the QW. Hence the only mechanism by which holes can enter the QW is via tunnelling. Because I_{PL} is symmetrical it can be concluded that the hole density (n_h) in the QW is also symmetrical with respect to bias direction. However, the total number of holes created above and below the barriers is very different, since there is only 80 nm of GaAs on the top side of the barriers. Thus only 10% of the incident light will be absorbed in the relatively thin GaAs layer above the QW (absorption coefficient $\alpha \approx 1 \times 10^4 \text{ cm}^{-1}$). The rest of the light will be absorbed below the barrier system. If the diffusion of holes towards the barrier is the dominant hole collection process, and the diffusion length is relatively long ($> 200 \text{ nm}$) then in reverse bias (holes drift from the substrate to the top contact) I_{PL} would be expected to be much stronger than for forward bias. This conclusion is

reached since the hole production rate is much greater in the thick GaAs region below the QW than in the relatively thin (80 nm) GaAs layer above the QW. Thus in order to explain the nearly symmetrical $I_{PL}(V)$ results in fig. 2b, it is concluded that the hole diffusion length must be less than 100 nm in this sample, and that drift towards the barriers of the holes created close to the barrier or in the high field collector region is very likely the dominant hole collection process.

Conclusion. In conclusion we have fabricated and studied a double barrier resonant tunnelling device which incorporates a heavily doped (AlGa)As window layer. This layer prevents reabsorption of PL emission from the QW. The PL intensity is symmetric with respect to applied bias, in contrast to previous results obtained for conventional structures. The incorporation of the window layer does not impair the electrical properties of the device.

This work is supported by SERC (UK), CNRS (France) and the European Community. P.E.S. acknowledges SERC for the provision of a visiting

fellowship. We are grateful to Drs. G. Hill and M.A. Pate for processing this layer.

References

- [1] V.J. Goldman, D.C. Tsui and J.E. Cunningham, *Phys. Rev.* B35 (1987) 9387.
- [2] L. Eaves, G.A. Tombs, F.W. Sheard, C.A. Payling, M.L. Leadbeater, E.S. Alves, T.J. Foster, P.E. Simmonds, M. Henini, O.H. Hughes, J.C. Portal, G. Hill and M.A. Pate, *Appl. Phys. Letters* 52 (1988) 212.
- [3] M.L. Leadbeater, E.S. Alves, F.W. Sheard, L. Eaves, M. Henini, O.H. Hughes and G.A. Toombs, *J. Phys. Condens. Matter* 1 (1989) 10605.
- [4] J.F. Young, B.M. Wood, G.C. Aers, R.L.S. Devine, H.C. Liu, D. Landheer, M. Buchanan, A.J. SpringThorpe and P. Mandeville, *Phys. Rev. Letters* 60 (1988) 2085.
- [5] M.S. Skolnick, D.G. Hayes, P.E. Simmonds, A.W. Higgs, G.W. Smith, H.J. Hutchinson, C.R. Whitehouse, L. Eaves, M. Henini, O.H. Hughes, M.L. Leadbeater and D.P. Halliday, *Phys. Rev.* B41 (1990) 10754.
- [6] M.L. Leadbeater, L. Eaves, M. Henini, O.H. Hughes, G. Hill and M.A. Pate, *Solid State Electron.* 32 (1989) 1467.
- [7] O.K. Kim and W.G. Spitzer, *J. Appl. Phys.* 50 (1979) 4362.
- [8] D.A.B. Miller, D.S. Chemla, T.C. Damen, A.C. Gossard, W. Wiegmann, T.H. Wood and C.A. Burrus, *Phys. Rev.* 32 (1985) 1043.

Transport in $\text{Al}_x\text{Ga}_{1-x}\text{As}/\text{In}_y\text{Ga}_{1-y}\text{As}$ resonant tunneling diodes with asymmetric layers

Hyungmo Yoo *, Stephen M. Goodnick and John R. Arthur

Center for Advanced Materials Research, Department of Electrical and Computer Engineering, Oregon State University, Corvallis, Oregon 97331, USA

$\text{Al}_x\text{Ga}_{1-x}\text{As}/\text{In}_y\text{Ga}_{1-y}\text{As}$ resonant tunneling diodes (RTDs) grown by molecular beam epitaxy with symmetric and asymmetric spacer layers have been fabricated and studied by electric and magnetic field measurements. Pseudomorphic (pm) $\text{Al}_{0.35}\text{Ga}_{0.65}\text{As}/\text{In}_{0.1}\text{Ga}_{0.9}\text{As}$ RTDs with asymmetric spacer layers exhibit novel tunneling phenomena depending upon the bias direction. Tunneling is through the ground state energy of the $\text{In}_{0.1}\text{Ga}_{0.9}\text{As}$ well when the thick spacer layer is in the leading edge of the device while it is through the first excited state of the $\text{In}_{0.1}\text{Ga}_{0.9}\text{As}$ well when the thick spacer layer is in the trailing edge of the diode. Shubnikov–De Haas oscillations obtained from the pm-RTDs of asymmetric spacer layers also show different features depending upon the bias direction. Improved device performance is observed when a thick spacer layer is on the substrate side rather than the top contact side, which is evidence of silicon dopant atom outdiffusion during molecular beam epitaxial growth.

1. Introduction

Considerable progress has been made in the fabrication of compound semiconductor devices over the past decades through advances in epitaxial growth technology. These techniques make possible the growth of structures composed of different semiconductor materials with layer thickness precisely controlled to within a few angstroms. As the device dimensions are reduced, quantum mechanical phenomena which do not have classical analogies, become increasingly important. One such device which depends explicitly on quantum interference is the resonant tunneling diode (RTD) whose transport properties were first investigated by Tsu and Esaki [1].

The RTDs fabricated by numerous groups usually contain undoped GaAs layers (referred to as spacer layers) adjacent to tunnel barriers to reduce ionized impurity scattering [2,3]. In this paper we report on transport of pm- $\text{Al}_{0.35}\text{Ga}_{0.65}\text{As}/\text{In}_y\text{Ga}_{1-y}\text{As}$ RTDs with symmetric and asymmet-

ric spacer layers through current–voltage and magneto-transport measurements.

The RTDs studied here were grown by MBE on silicon doped ($n = 2 \times 10^{18} \text{ cm}^{-3}$) $\langle 100 \rangle$ GaAs substrates. The $\text{Al}_{0.35}\text{Ga}_{0.65}\text{As}/\text{In}_y\text{Ga}_{1-y}\text{As}$ RTDs consist of the following layers, in order of growth from the n^+ -GaAs substrate: $1 \mu\text{m}$ of $n = 1 \times 10^{18} \text{ cm}^{-3}$ GaAs buffer layer, undoped GaAs spacer layer whose thickness is ranging from 35 to 500 Å, 85 Å of undoped $\text{Al}_{0.35}\text{Ga}_{0.65}\text{As}$ barrier, 50 Å of undoped $\text{In}_y\text{Ga}_{1-y}\text{As}$ well ($y = 0$ and 0.1), 85 Å of undoped $\text{Al}_{0.35}\text{Ga}_{0.65}\text{As}$ barrier, undoped GaAs spacer layer of thickness from 35 to 500 Å and 4000 Å of silicon $1 \times 10^{18} \text{ cm}^{-3}$ doped top (emitter) contact layer. After the epitaxial growth of the RTD structure, devices of lateral dimensions ranging from 50×50 to $200 \times 200 \mu\text{m}^2$ were fabricated and wire bonded in an integrated circuit (IC) package for measurements.

2. Influence of InGaAs layer on RTD performance

Figs. 1a and 1b, respectively, are I – V curves of the lattice matched $\text{Al}_{0.35}\text{Ga}_{0.65}\text{As}/\text{GaAs}$ and the pm- $\text{Al}_{0.35}\text{Ga}_{0.65}\text{As}/\text{In}_{0.1}\text{Ga}_{0.9}\text{As}$ RTDs with a 50

* Present address: Department of Materials Science and Engineering, University of Washington, Seattle, Washington 98195, USA.

Å thick spacer layer measured at 77 and 1.8 K. The two RTDs have the same structural parameters except for the well. The lattice matched device shows somewhat better device performance (PVCR, valley width, and peak current) at lower temperature while the pseudomorphic device does not. This difference may be due to the fact that the latter experiences alloy scattering due to the presence of the InGaAs layer in the well. InGaAs grown pseudomorphically on GaAs substrate is strained due to lattice mismatch (7% for InAs on GaAs). This strain may result in additional intrinsic crystal imperfections, even below the critical thickness [4]. The InGaAs layer may also suffer from increased interface roughness scattering due to In atom segregation during MBE growth [5]. Most of the scattering processes associated with the presence of the InGaAs layer, such as alloy

and interface roughness scatterings, are not strongly temperature dependent so the performance of pm-RTDs at lower temperature shows less improvement than RTDs from the lattice matched system.

3. The pm-RTDs with asymmetric spacer layers

Pseudomorphic RTDs with asymmetric spacer layer thicknesses were grown with $\text{Al}_{0.35}\text{Ga}_{0.65}\text{As}$ barriers and $\text{In}_{0.1}\text{Ga}_{0.9}\text{As}$ wells. For one pm-RTD, a 50 Å spacer was grown on the top (emitter) side and a 500 Å spacer was placed on the substrate (collector) side for one sample, while the other sample had the spacer layer order reversed. RTDs with asymmetric spacer layer configurations are denoted as 50/500 RTDs (50 Å on top and 500 Å on substrate) and 500/50 RTDs after the spacer layer order from top to substrate. RTDs with asymmetric spacer layer configurations show very asymmetric I - V characteristics depending upon the bias direction.

Typically I - V characteristics of the 50/500 and 500/50 RTDs measured at 77 K are shown in fig. 2. The inset figure is the current-bias profile of the 50/500 RTD at thermal equilibrium. The calculated ground state energy in the InGaAs well lies slightly below the Fermi level due to the effect of charge storage in the well, which raises the ground state energy. The I - V curves of the RTD show several interesting features. Large differences in the peak voltage (V_p) and the peak current density (J_p) are found to depend upon the bias polarity. The measured values of $V_p = 0.45$ at 77 K in forward bias (V_{CE} positive) appear to be due to tunneling through the first excited state, while the peak voltage of 0.12 V for negative V_{CE} corresponds to tunneling through the ground state of the InGaAs well, based on the calculated position on these levels at zero bias. For positive V_{CE} , electrons from the emitter side must tunnel through the emitter and the collector barriers as well as the thick collector spacer barrier. Part of the thick collector spacer layer acts as a pseudo-barrier to ground state tunneling because the energy level in the well lies below the spacer barrier. The thick collector spacer barrier reduces the tun-

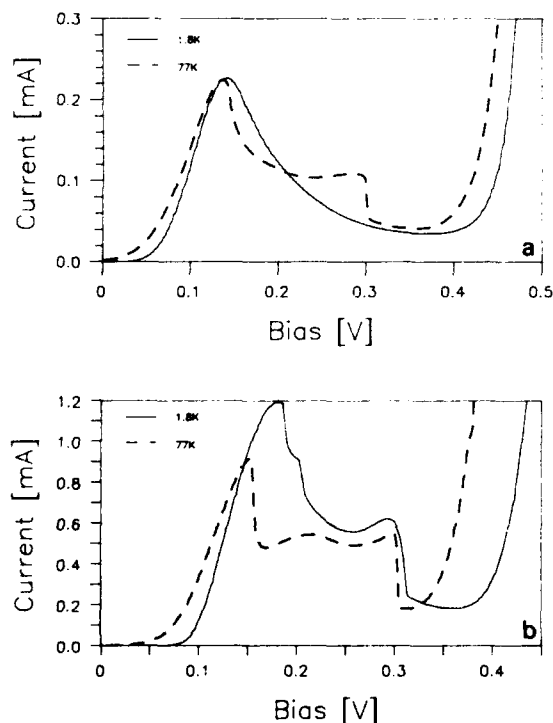


Fig. 1. I - V characteristics of (a) the pm- $\text{Al}_{0.35}\text{Ga}_{0.65}\text{As}/\text{In}_{0.1}\text{Ga}_{0.9}\text{As}$ RTD and (b) the lattice-matched $\text{Al}_{0.35}\text{Ga}_{0.65}\text{As}/\text{GaAs}$ RTD with 50 Å thick spacer layers measured at 77 and 1.8 K.

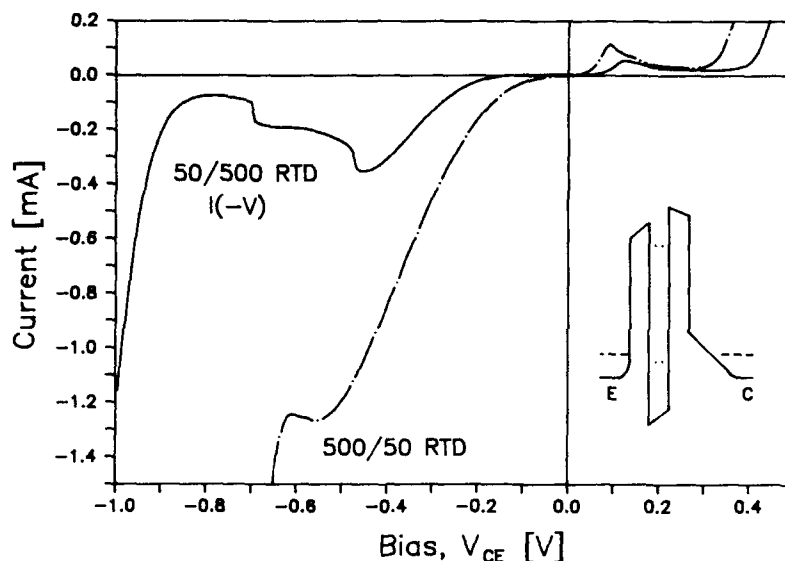


Fig. 2. I - V characteristics of the 50/500 and 500/50 RTDs measured at 77 K. Inset figure shows the current-bias profile of the pm-500/50 RTD at thermal equilibrium.

neling probability, which makes ground state tunneling undetectable in forward bias. However, tunneling through the ground state energy in reverse bias is possible via a two step transport processes. Electrons from the collector side are first accumulated in front of the collector barrier, which modifies the CB profile and the energy level in the accumulation layer is aligned with the ground state in the well at resonance. The accumulated electrons in the collector spacer layer tunnel through the rest of the double barrier as a second step. Thus V_p and J_p are smaller in reverse bias rather than in forward bias.

The general trends of the 500/50 RTD are similar to the previous 50/500 RTD except that the bias polarity is reversed. The interpretations given for the 50/500 RTD are valid for this device too. However, the PVCr and valley width of the 500/50 RTD are inferior to the previous 50/500 RTD while the current densities are higher. The PVCr's of the 500/50 RTD are 4.2 and 1.02:1 in forward and reverse bias, respectively. It is worth mentioning that the PVCr's of the 50/500 RTD are 3.0 and 4.7:1 for the same bias configurations.

The reduction in the PVCr of the 500/50

sample, particularly in reverse direction is possibly due to silicon outdiffusion in which silicon atoms in GaAs segregate during molecular beam epitaxy due to Fermi level pinning at the semiconductor surface [6]. The 50/500 RTD which has a thicker collector spacer layer (i.e. a thicker diffusion barrier for silicon from the substrate side) than the 500/50 RTD reduces ionized impurity scattering in the well. The higher current through the 50/500 RTD appears to be associated with leakage current through the double barrier structure which could be due to the detrimental effect of impurity outdiffusion.

To ascertain whether tunneling is through the ground state or first excited state, a set of five identical samples with symmetric spacer layers were studied. The samples have the same structural parameters as the pm-AlGaAs/InGaAs RTDs with asymmetric spacer layer, except for the spacer layer configuration. The samples contain 35, 50, 100, 250, and 500 Å thick symmetric spacer layers and show V_p 's of 0.15, 0.145, 0.232, and 0.336 V respectively at 77 K, as shown in fig. 3. The straight line in the figure is a least-squares fit of the V_p 's as a function of the spacer layer thickness.

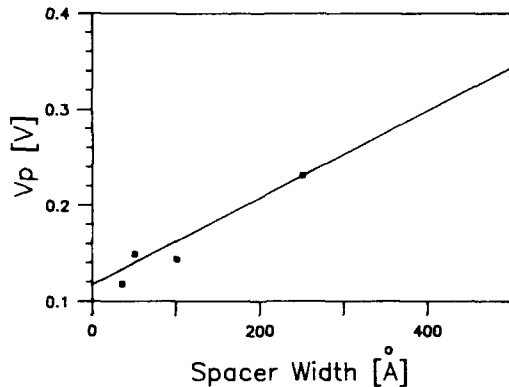


Fig. 3. Peak voltage position of the $\text{pm-Al}_{0.35}\text{Ga}_{0.65}\text{As}/\text{In}_{0.1}\text{Ga}_{0.9}\text{As}$ RTD with symmetric spacer layers measured at 77 K. The straight line is a result of a least squares fit.

According to the data shown in fig. 3, the spacer layer has to be approximately 1000 Å thick on both sides for a V_p of 0.45 V to indicate ground state tunneling; in fact the layers were 50 and 500 Å. Thus the V_p of 0.45 V is believed to be evidence of tunneling through the first excited level tunneling.

4. Magnetic field study

Fig. 4 shows the magneto-quantum oscillation period of the 500/50 and the 50/500 RTDs as a function of applied bias. The former is forward biased and the latter is reverse biased, so electrons first encounter the thicker of the two spacer layers for both cases. When both RTDs are oppositely biased, the conductance of the RTDs either decreases quadratically without any oscillations or shows very weak oscillations up to a magnetic field strength of 8 T. The squares and the triangles are the oscillation periods as a function of bias for the 50/500 and the 500/50 RTDs, respectively. The solid lines are a least-squares fit of the magneto-quantum periods. The origin of oscillations is either the bulk, the accumulation layer or quasi-bound state in the well and they show different features depending upon their origin [7,8]. In the present work, bulk oscillations may be eliminated as the source of the observed oscillation since the

RTDs fabricated with thin spacer layers (below 50 Å) did not show any oscillation up to a magnetic field strength of 8 T. Oscillations associated with Landau levels in the accumulation layer passing through the Fermi energy E_F of the contact layer occur when $E_F = E_a$. The oscillations due to the electrons tunneling into the Landau levels in the well and scattering into another Landau level, possibly with longitudinal optical (LO) phonon emission, occur when $E_a = E_q + \hbar\omega$ [9]. The oscillation period in $\Delta(1/B)$ of the former case is given by $\hbar e/m^*(E_F - E_{a0})$, while that for the latter is $\hbar e/[m^*(E_{a0} - E_{q0}) - \hbar\omega_L]$ [10]. The slope of the least-squares fit of the 500/50 and the 50/500 RTDs are 34.5 and 20.75 T/V, respectively. The slope is either $m^*\alpha/\hbar$ or $m^*\beta/\hbar$, depending on its origin. The higher slope corresponds to a higher α or β which signifies a larger portion of the applied voltage drop occurs across the 500 Å spacer layer of the 500/50 RTD compared to that of the 50/500 RTD. Thus a 500 Å spacer layer placed in the collector side becomes effectively narrower than that in the emitter side, which agrees well with a directional Si atom diffusion toward the surface due to surface Fermi level pinning during MBE growth.

Assuming the origin of the oscillations is the accumulation layer, its periodicity is directly related to the carrier density by $n_{2D} = 2eB/\hbar$, where $1/B_f = \Delta(1/B)$ and n_{2D} is a two-dimensional carrier density [11] which is shown in the right

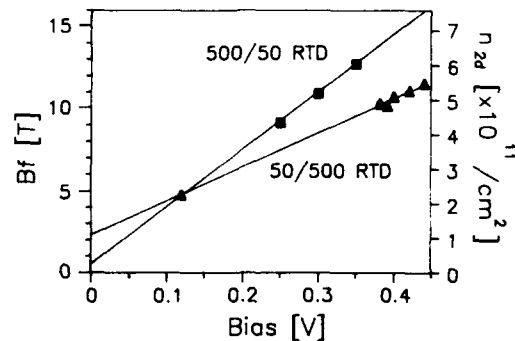


Fig. 4. SdH oscillation period of the 50/500 and 500/50 RTDs as a function of the applied bias. The right ordinate shows a two-dimensional carrier concentration with the corresponding B_f .

ordinate of fig. 4. The 500/50 RTD shows a higher n_{2D} which is consistent with a higher current through the 500/50 RTD.

5. Summary

An electrical and magnetic field study of the pseudomorphic and lattice-matched $\text{AlGaAs}/\text{InGaAs}$ RTDs grown by molecular beam epitaxy has been presented. The general performance (PVC, valley width and peak current) of the pm-RTDs studied is inferior to the lattice matched diodes due to alloy scattering from the InGaAs layer as well as interface roughness scattering due to possible indium segregation. pm-RTDs with asymmetric spacer layers exhibited very strong evidence that the spacer layer plays different roles depending upon their position. pm- $\text{AlGaAs}/\text{InGaAs}$ RTDs with asymmetric spacer layers show novel tunneling phenomena depending upon the bias direction. The asymmetric pm-RTD with a thick spacer layer on the substrate side yields better performance than when the thick spacer layer is on the top side. This result may be due to growth artifacts as follows. Silicon impurities tends to outdiffuse during MBE growth due to surface Fermi level pinning. Thus, the RTD with a thicker spacer layer on the substrate side shows better performance. Analysis of the Shubnikov-De Haas oscillation period of the two diodes provides evidence of silicon outdiffusion which agrees well with the analysis obtained from I - V characteristics.

Acknowledgements

The authors would like to express their thanks to L. Ungier, J. Lary, and Dr. J. Wager for useful discussions related to the work, and to S.B. Kim for the deposition of the plasma enhanced chemical vapor deposition oxide. They acknowledge partial support from Office of Naval Research contract No. N00014-89-J-1894.

References

- [1] R. Tsu and L. Esaki, *Appl. Phys. Letters* 22 (1973) 562.
- [2] H.M. Yoo, S.M. Goodnick and J.R. Arthur, *Appl. Phys. Letters* 56 (1990) 86.
- [3] P. Cheng and J.S. Harris, Jr., *Appl. Phys. Letters* 55 (1989) 572.
- [4] J.W. Matthews and A.E. Blakeslee, *J. Crystal Growth* 27 (1974) 118.
- [5] J.T. Ebner and J.R. Arthur, *J. Vacuum Sci. Technol.* A5 (1987) 2007.
- [6] E.F. Schubert, *J. Vacuum Sci. Technol.* A8 (1990) 2980.
- [7] H.M. Yoo, S.M. Goodnick, J.R. Arthur and M.A. Leed, *J. Vacuum Sci. Technol.* B8 (1990) 370.
- [8] L. Eaves, G.A. Toombs, F.W. Sheard, C.A. Payling, M.L. Leadbeater, E.S. Alves, J.C. Portal, G. Hill and M.A. Pate, *Appl. Phys. Letters* 52 (1988) 212.
- [9] V.J. Goldman, P.C. Tsui and J.E. Cunningham, *Phys. Rev.* B36 (1987) 7635.
- [10] H.M. Yoo, S.M. Goodnick and J.R. Arthur, in: *Proc. SPIE, Quantum Well and Superlattice Physics III*, to be published.
- [11] C.A. Payling, C.R.H. White, L. Eaves, M.L. Leadbeater, J.C. Portal, P.D. Hodson, D.J. Robbins, R.N. Wallis, J.I. Davis and A.C. Marshall, *Superlattices and Microstructures* 6 (1989) 193.

MBE growth and post-growth annealing of GaAs-based resonant tunneling structures, viewed in relation to interface roughness

H. Riechert, D. Bernklau, J.-P. Reithmaier * and R.D. Schnell

Siemens Research Laboratories, P.O. Box 830952, W-8000 München 83, Germany

Device-oriented double barrier quantum well structures of very high quality were grown by MBE on GaAs substrates. We present electrical characteristics of structures with GaAs and pseudomorphic InGaAs wells in correlation with the growth parameters we used. Post-growth annealing experiments show that the peak-to-valley current ratios of even our best structures can still be improved and that electrical measurements on such structures can very sensitively detect interface degradation occurring at temperatures above 800°C. We discuss our electrical data in relation to interface quality, concluding that they yield information about interface roughness on a scale smaller than that probed by photoluminescence.

1. Introduction

Double barrier quantum well (DBQW) structures for resonant tunneling are one of the simplest forms of a quantum electronic device. Therefore the optimisation of their performance presents an important task to both epitaxial technology and structural design.

Key parameters are the peak current density j_p at the resonance voltage U_p at which the negative differential resistance sets in as well as the peak-to-valley current ratio $PVR = j_p/j_v$ with j_v being the current minimum ("valley") at a voltage just beyond the resonance. Whereas j_p depends exponentially on the barrier thickness, the factors influencing PVR are theoretically not so clear. Recent work [1] has shown that inelastic scattering processes limit the practically obtainable PVR and that for a given structure the interface roughness is the most important growth-related parameter. Thus electrical characteristics of DBQWs may be an important way of judging interface quality, complementary to photoluminescence.

We have recently reported DBQW structures

on GaAs substrates with much improved PVRs [2], amongst them a special structure containing an InGaAs "prewell" adjacent to one barrier on which we obtained the highest room temperature PVR (5.9) ever reported for GaAs-based structures.

In this paper results on two types of structures will be presented and discussed in relation to the roughness of the heterojunction interfaces: (i) conventional GaAs/GaAlAs structures (type A); (ii) structures with InGaAs of varied In content as the central potential well (type B).

2. Experimental

After structural optimizations [2,3] we concentrated on DBQW structures as depicted in fig. 1. All results reported here pertain to the same GaAlAs barrier/well dimensions of 30 Å/40 Å with an Al content of 0.6 in the barriers and to the same two-step Si-doping profile which symmetrically embeds the DBQW.

The DBQW structures were grown in a VG Semicon V 80H MBE system, using elemental sources. The substrates used were 2 inch, n^+ -doped (Si or Te), $(100) \pm 0.5^\circ$ or 2° off-oriented. The substrate temperature was measured by a short

* Work performed under a Siemens PhD grant. Present address: IBM Research Laboratory, Säumerstrasse 4, CH-8803 Rüschlikon, Switzerland.

0.2 μm	GaAs	$n = 1 \times 10^{18} \text{ cm}^{-3}$
0.1 μm	GaAs	$n = 1 \times 10^{17} \text{ cm}^{-3}$
150 Å	GaAs	undoped
30 Å	Ga _{0.4} Al _{0.6} As	undoped
40 Å	(In)GaAs	undoped
30 Å	Ga _{0.4} Al _{0.6} As	undoped
150 Å	GaAs	undoped
0.1 μm	GaAs	$n = 1 \times 10^{17} \text{ cm}^{-3}$
0.6 μm	GaAs	$n = 1 \times 10^{18} \text{ cm}^{-3}$
n ⁺ GaAs - Substrate		

Fig. 1. Schematic cross section through our double barrier quantum well structures.

wavelength pyrometer, as required by the In-free mounting technique we employed. The GaAs oxide desorption temperature, taken as 580°C, was routinely used as a calibration point. In the central part of the structure the GaAs growth rate was about 0.6 Å/s. No growth interruptions at the interfaces were employed.

The processing into diodes and details on electrical measurements are given in refs. [2,3].

Post-growth annealing experiments were performed to assess the process stability of our structures and to examine if improvements like those observed in the photoluminescence yield of pseudomorphic InGaAs/GaAlAs QWs [4] could be found. To this purpose, quarters of 2 inch wafers were capless annealed under AsH₃ employing a 5 min temperature ramp and holding the samples at the specified temperature for a further 25 min. These annealing conditions were found to give damage free surfaces suitable for shallow channel (< 500 Å) MESFET application [5], ensuring that the DBQW structure is not influenced by surface degradation. The wafers were subsequently processed into diodes, such that each piece was annealed at only one temperature.

3. Results and discussion

Room temperature electrical data for our GaAs/GaAlAs structure are given in table 1. The

Table 1

Data of GaAs/Ga_{0.4}Al_{0.6}As DBQW structures

T_g (°C)	$j_p(+)$ (kA/cm ²)	$U_p(+)$ (mV)	PVR(-)	PVR(+)	PVR _{max}
605	5.8	1430	3.4	3.6	3.9
605	6.0	1410	3.6	3.8	4.1
525	6.4	1400	4.1	4.4	4.6
520	7.0	1410	3.9	4.5	4.8
505	5.0	1280	4.0	4.6	4.8

T_g : growth temperature.

U_p : bias voltage at which peak current is observed.

(+) and (-) refer to electron injection from the top and from the substrate, respectively.

All electrical data taken at room temperature.

average PVR values given ((+) and (-) designating electron injection from the top and from the substrate, respectively) are the mean values of 10–12 examined test diodes taken across a 35 mm diameter area in the center of the 2 inch wafer. There is a tendency towards higher peak currents and higher resonance voltages towards the edge of the wafer, due to decreasing layer thickness. The PVR values, however, are very uniform over the 35 mm diameter area. Results from DBQWs grown on differently oriented substrates were within this variation of data.

The PVRs obtained represent a significant improvement over the highest room temperature values previously reported in this material system [6] and are achieved with slightly higher peak current densities (7 kA/cm²). Note that the high quality of the structures grown at 605°C is still exceeded by those grown around 520°C, a growth temperature uncommonly low for heterostructures in this material.

The DBQWs of type B which we have grown are identical to the GaAs/GaAlAs structure except for the In contents of 8%, 11% and 15% in the well layers. The In contents were closely monitored by optical absorption and photoluminescence studies on InGaAs/GaAs MQW layers [8] grown with the same flux settings, usually on the same day.

The growth temperature for the active part of the structure was below 530°C. The electrical data obtained at room temperature for these structures are presented in table 2. Contrary to previ-

Table 2

Data on $\text{In}_y\text{Ga}_{1-y}\text{As}/\text{Ga}_{0.4}\text{Al}_{0.6}\text{As}$ DBQW structures; for explanations see table 1

y	$j_p(-)$ (kA/cm^2)	$U_p(-)$ (mV)	PVR(-)	PVR(+)	PVR _{max}
0.08	3.3	750	3.95	3.85	4.1
0.11	1.0	400	2.83	2.56	3.4
0.15	0.6	310	2.35	2.06	2.6

ous results in the literature ($\text{PVR} < 2$; see, e.g., ref. [7]), the PVR values of our structures can be almost comparable to those of our GaAs/GaAlAs structures. The desired reduction in the resonance voltage U_p is clearly achieved. We find a more pronounced variation of PVR on the wafer than on type A structures. Having checked by photoluminescence that the In content is constant to within .1% we attribute this to a dependence of PVR on the substrate temperature, which is more critical than for GaAs. Note the asymmetry in the I - V curves, which is generally smaller but always opposite to that found for structures of type A. This will be explained below.

Post-growth annealing experiments were performed with quarters of 4 wafers, 2 with structures of type A and 2 of type B with 8% In in the well.

For each type one wafer of the highest and one of somewhat lower quality underwent the anneals. Again, the higher PVRs were obtained on material grown at the slightly lower substrate temperatures (505–508°C rather than 515–520°C). The complete results are given in table 3, from which we extract the following information.

First, annealing improves the PVRs (again measured at room temperature) of all samples, even in those which from their as-grown data, are among our very best. Maximum PVRs are obtained after annealing at 800–820°C.

Secondly, there is a clear trend that rising annealing temperatures cause a moderate increase in the peak current density j_p and the resonance voltage U_p , particularly in the structures with In-GaAs wells. We attribute this to a narrowing of the potential well by a slight diffusion of Al from the barriers. As the energy of the quantized well state goes up, the transmission function broadens, which would explain the increase in j_p .

Thirdly, while the thermal stability of all structures is quite good, we find drastic changes in the electrical data of sample A1 after the 820°C anneal, as shown in fig. 2. The resonance voltage rises by about 40%, and the peak current drops sharply. This must be due to a more severe Al

Table 3

Room temperature data of annealed samples

Sample	Temperature (°C)	$j_p(+)$ (kA/cm^2)	$U_p(+)$ (mV)	PVR(+)	PVR(-)	PVR _{max}
A1	525	4.8	1580	4.41	4.27	4.6
	750	4.9	1520	4.29	4.14	4.5
	800	5.6	1600	4.74	4.54	4.9
	820	1.5	2200	4.35	4.07	5.1
A2	505	4.5	1200	4.61	3.98	4.8
	820	5.5	1260	4.86	3.99	5.1
	840	5.6	1320	4.67	4.21	4.9
B1	520	1.5	690	2.73	2.93	3.1
	750	1.6	720	2.74	2.92	3.4
	800	2.5	920	2.56	2.81	3.2
B2	508	1.5	560	3.72	3.65	3.9
	820	1.2	700	4.02	3.46	4.3
	840	2.8	840	3.72	3.79	4.1

A1 and A2 with GaAs wells; B1 and B2 with $\text{In}_{0.08}\text{Ga}_{0.92}\text{As}$ wells.
The lowest temperatures are the growth temperatures.

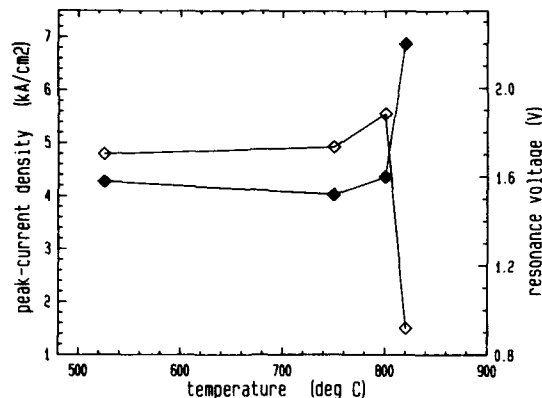


Fig. 2. Peak current density (open symbols) and resonance voltage (full symbols) of sample A1 after different anneals. The lowest temperature is the growth temperature.

diffusion causing the potential barrier to widen significantly, which in turn leads to the decrease on j_p . Thus, the electrical data give a very clear indication of a thermal degradation.

Last, we recall the correlation between interface quality and PVR, which we discussed in a forthcoming publication (ref. [3] and references therein) and extend it by the data presented here. Citing recent theoretical and experimental results we concluded that the PVR is a valid measure for interface roughness. We interpret the fact that our best PVRs are obtained by growth at temperatures far below those which give best optical quantum well performance by considering the different probe scales of optical and tunneling experiments: Tunneling involves hot electrons which probe lengths of the order of their de Broglie wavelength (≥ 30 Å) whereas photoluminescence averages over the typical exciton diameter of ≤ 300 Å.

Thus from our results on PVRs of structures grown at different temperatures (table 1) we have to conclude that heterointerfaces grown at $> 600^\circ\text{C}$ must contain roughness on a 50 Å scale in contradiction to generally accepted ideas of monolayer-flat islands of ≥ 300 Å size, at least for the upper GaAs/GaAlAs interface.

Recently, however, strong evidence has been brought up against this simple explanation of

optical data [10]. Adopting the view taken in ref. [10] that one always has to consider a roughness spectrum, we can simply reconcile our electrical data with common results of optical experiments by assuming that at low growth temperatures we optimize the interface roughness periodicity on the de Broglie wavelength scale, whereas at higher growth temperatures we minimize the roughness periodicities around the exciton diameter, which then leads to narrowest QW photoluminescence linewidths.

Furthermore, based on a comparison of the electrical characteristics of structures with and without In in the potential well we explained the origin of the asymmetry in the I - V curves: $R = \text{PVR}(+)/\text{PVR}(-) > 1$ if the upper barrier/well interface is of higher quality, as it is the case for GaAs wells. For InGaAs wells $\text{PVR}(+)/\text{PVR}(-) < 1$, which we attribute to the fact that pseudomorphic InGaAs shows a stronger tendency for 3D growth than GaAs [9].

On the basis of this model we can differentiate between the quality of the top and bottom interfaces by measuring under positive or negative bias. Thus, we can determine which interface is more affected by the anneals: In both of the better samples, the highest PVRs are attained in conjunction with a significant increase in R , in both samples the top interface is improved, in sample B2 the bottom interface is slightly worse than without anneal. Both samples, however, show an improvement of the bottom interface with the anneal at 840°C .

Also, it is interesting to note that the top interface of the GaAs well can be improved, i.e. that on the small scale probed by tunneling electrons there was still some roughness present after growth.

4. Conclusions

We have reported the growth of high performance double barrier quantum well structures which we believe set a new standard for the room temperature performance of GaAs-based structures. Particularly large improvements were attained for structures containing pseudomorphic

InGaAs wells. Both pseudomorphic and conventional DBQW structures are stable under 20 min anneals of up to 840°C, thermal degradation of the interfaces is sensitively detected by electrical measurements. We argue that the use of low growth temperatures minimizes electron scattering by interface roughness on a ≈ 50 Å scale. Thus, electrical data yield information which is complementary to that found from photoluminescence.

Acknowledgements

The authors gratefully acknowledge the collaboration of R. Höger on optical investigations and the encouragement by H. Schlötterer, G. Packeiser and H. Kniepkamp.

References

- [1] F. Chevoir and B. Vinter, *Appl. Phys. Letters* 55 (1989) 1859.
- [2] H. Riechert, D. Bernklau, J.-P. Reithmaier and R.D. Schnell, *Electron. Letters* 26 (1990) 340.
- [3] H. Riechert, D. Bernklau, J.-P. Reithmaier and R.D. Schnell, in: *Resonant Tunneling: Physics and Applications*, Ed. E.E. Mendez (Plenum, New York, 1990).
- [4] A. Forchel, H. Leier and J.-P. Reithmaier, unpublished.
- [5] S. Gisdakis and R.D. Schnell, unpublished.
- [6] C.I. Huang, M.J. Paulus, C.A. Bozada, S.C. Dudley, U.R. Evans, C.E. Stutz, R.L. Jones and M.E. Cheney, *Appl. Phys. Letters* 51 (1987) 121.
- [7] C.H. Young and H.D. Shih, *Electron. Letters* 24 (1988) 553.
- [8] J.P. Reithmaier, R. Höger and H. Riechert, *Appl. Phys. Letters* 56 (1990) 536.
- [9] J.-P. Reithmaier, H. Riechert, H. Schlötterer and G. Weimann, *J. Crystal Growth* 111 (1991) 407.
- [10] C.A. Warwick, W.Y. Yan, A. Ourmazd and T.D. Harris, *Appl. Phys. Letters* 56 (1990) 2666.

MBE growth of GaAs/AlAs double-barrier structures on GaAs channeled substrates

S. Shimomura, N. Okamoto *, M. Takeuchi, E. Tamaoka **, Y. Yuba, S. Namba, S. Hiyamizu

Research Center for Extreme Materials and Faculty of Engineering Science, Osaka University, 1-1 Machikaneyama, Toyonaka, Osaka 560, Japan

M. Shigeta, T. Yamamoto and K. Kobayashi

ATR Optical and Radio Communications Research Laboratories, Sanpeidani Inuidani, Seika-cho, Soraku-gun, Kyoto 619-02, Japan

Overgrowth of GaAs and GaAs/AlAs heterostructures on GaAs channeled substrates by MBE was studied. Grooves along $[01\bar{1}]$ were made on a (100) GaAs substrate by selective etching. There are two kinds of crystal planes on the substrate: a (100) plane (flat region) and a (111)A plane (slope region). We first demonstrated the resonant tunneling of electrons preferentially through a small (111)A slope region (12 μm wide) of GaAs/AlAs double-barrier structures grown on the channeled substrates.

1. Introduction

MBE overgrowth of GaAs/AlGaAs heterostructures on channeled substrates, which has laterally several kinds of facets on its surface, has three advantages for fabricating low-dimensional electron structures: (1) The effective band gap in a quantum well structure can be laterally modulated because of different growth rates for different facets owing to the different incident angles of the molecular beam fluxes and the different dissociation rates of molecular species. (2) The lateral dimension of the structures can be precisely controlled because of the fine controllability of both etching processes and MBE growth. (3) Defect-free low-dimensional structures can be realized, because the final stage of fabrication, which often

includes formation of an active region of the structure, is made by MBE.

Recently, many investigations of MBE growth of III–V compound semiconductor materials on channeled substrates have been reported: they are observation by scanning electron microscope (SEM) [1–3], investigation of growth modes [2,3], growth simulation of MBE overgrowth [3], observation by transmission electron microscope (TEM) [4–6] and by cathodoluminescence (CL) [5–7], Si doping characteristics of GaAs [8], Raman and photoluminescence measurements of AlGaAs [9], laser diodes [2,7,9–11], and fabrication of quantum well wires [12].

When this technique (overgrowth on channeled substrates) is applied to fabrication of the low-dimensional structures, it is very important to understand electrical and electronic properties of an overgrown layer both in the flat region (typically (100) plane) and in the slope region (often (111)A or (311)A facet planes). There have been, however, few reports on characterization of epitaxial layers, especially on the slope region because of technical difficulties. This paper reports the first fabrication

* Present address: Fujitsu Laboratories, 10-1 Morinosato-Wakamiya, Atsugi 243-01, Japan.

** Present address: Research Center R&D Headquarters, Sanyo Electric Co. Ltd., 1-18-13 Hashiridani, Hirakata 573, Japan.

of GaAs/AlAs resonant tunneling diodes (RTDs) on GaAs channeled substrates and preliminary, but successful, observation of negative-differential resistance due to a resonant tunneling current preferentially through the (111)A side slope region of double-barrier structures.

2. Experiments

Grooves along [011] were made by selective etching on (100) GaAs substrates with the use of an AZ-1350J resist mask and an etchant of $\text{H}_3\text{PO}_4:\text{H}_2\text{O}_2 = 1:10$. The etching depth was about 10 μm . The upper and lower (100) planes are connected by the (111)A facet slope. After removing the resist, the surface of the substrate was degreased and was slightly etched by $\text{H}_3\text{PO}_4:\text{H}_2\text{O}_2:\text{H}_2\text{O} = 3:1:50$.

First, we studied surface morphology and electrical properties (n-type or p-type conductivity) of Si-doped GaAs (doping concentration of $1 \times 10^{18} \text{ cm}^{-3}$) on the channeled substrates as a function

of substrate temperature (T_s) and V/III pressure ratio, because the RTDs require good surface morphology and n-type conductivity on the (111)A slope region as well as on the (100) region.

Fig. 1 shows SEM photographs of the 1.0 μm thick Si-doped GaAs layer grown at $T_s = 550^\circ\text{C}$ and V/III pressure ratios of 15 to 60 using a Varian GEN-II Modular MBE system. The substrate was rotated at 60 rpm in order to eliminate a shadowing effect of some molecular beams by a structure of the channeled substrate. At V/III = 15, we obtained the good morphology on the (100) surface, but on the (111)A slope region a lot of Ga droplets could be seen due to insufficient As_4 supply. The surface also became rough at V/III = 60 because of the excess As_4 flux. At V/III = 30, however, quite good surface morphology was obtained on both (100) and (111)A regions.

Conductivity of the GaAs films was n-type on the (111)A slope at V/III = 30 and 60; on the other hand, it was p-type at V/III = 15. Therefore, V/III = 30 was chosen for growth of RTDs on channeled substrates. Details of the surface

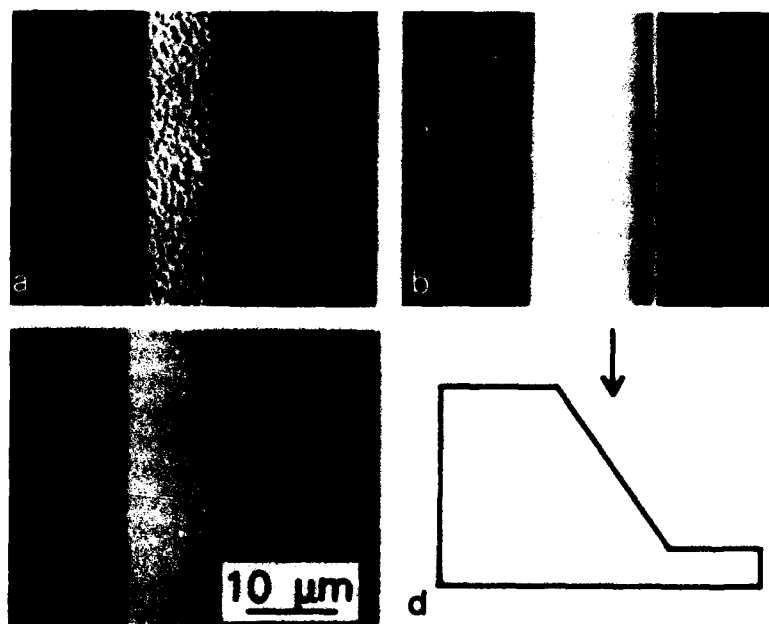


Fig. 1. SEM photographs of surface morphology of GaAs grown on the GaAs channeled substrates at 550°C , and V/III = 15 (a), 30 (b), 60 (c). The central part corresponds to GaAs on the (111)A slope region.

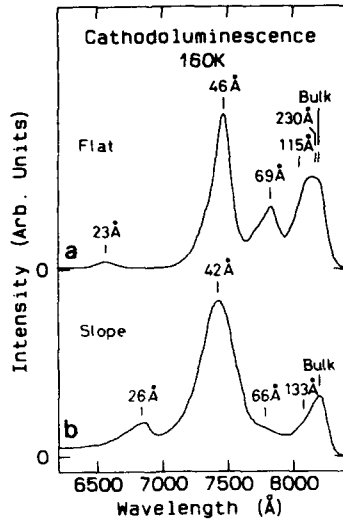


Fig. 2. Cathodoluminescence (CL) spectra at 160 K from the (100) flat region (a) and from the (111)A slope region (b).

morphology and the p-n conversion of Si-doped GaAs on channeled substrates will be reported elsewhere.

CL measurements at 160 K were made for GaAs/AlAs quantum well structures grown on the channeled substrates at $T_s = 630^\circ\text{C}$ and $V/III = 30$ to compare the well widths and quality of GaAs/AlAs quantum wells on the (111)A slope region with those on the (100) surface. The growth rates of GaAs and AlAs were 1 and $0.43 \mu\text{m/h}$, respectively. On the (100) flat region, GaAs quantum well widths (L_w) are 23, 46, 69, 115 and 230 Å and AlAs barrier layers are 500 Å thick. The CL spectrum from the (100) flat region is shown in fig. 2a. The peak around 8200 Å comprises luminescences from the 115 and 230 Å wells and bulk GaAs. The other three peaks are identified to be the luminescences from 69, 46 and 23 Å quantum wells as indicated in the figure. These three peaks are 75 meV ($L_w = 69$ Å), 148 meV (46 Å), and 378 meV (23 Å) higher in energy than that of the bulk GaAs. These observed shift energies agree well with the calculated value based on the electron masses of $0.0665m_0$ (GaAs) and $0.15m_0$ (AlAs), the heavy hole masses (in the [100] direction) of $0.34m_0$ and $0.75m_0$, and the conduction

band offset energy (ΔE_c) of 1053 meV, and the valence band offset energy (ΔE_v) of 569 meV.

The spectrum from the (111)A slope region has three apparent peaks (fig. 2b). The two higher energy peaks come from 26 Å and 42 Å quantum wells. These values of well widths on the (111)A region are 57% and 61% of the corresponding well width for (100) region. The heavy hole masses in the [111] direction are $0.9m_0$ (GaAs) and $1.06m_0$ (AlAs). The angle between the (111)A slope and the (100) flat plane is 54.7° , then the molecular beam flux intensity on the (111)A slope facet during growth becomes 57.7% of that on the (100) flat plane, if the unit sticking coefficient of Ga or Al is assumed. Expected wavelengths of CL emitted from other two quantum wells with $L_w = 66$ Å (57.7% of 115 Å) and 133 Å (57.7% of 230 Å) are indicated by bars in fig. 2b. Slight shoulders at these wavelengths can be seen in the spectrum. Hence the calculated quantum well widths seem to be quite reasonable.

The FWHM (full width at half maximum) of the luminescence from the 46 Å quantum well on the (100) flat region was 40 meV and there could be seen the considerable tailing on the higher energy side of all peaks. This is possibility due to the high temperature (160 K) and quite heavy excitation by the incident electron beam (1×10^{-8} A per 1–2 μm diameter, 15 kV). The FWHM of the luminescence from the 42 Å quantum well on the (111)A region is quite large (76 meV). This broadness is partly owing to the fact that the slope gradually changes from (111)A to (211)A ($54^\circ \rightarrow 35^\circ$) at the foot of the slope region in this experiment. Then, quantum well width may be considered to increase at the lower part of the slope region. The higher energy side tailing of the peaks can be considered similar to the case of the (100) flat region.

Epitaxial growth for RTDs on the channeled substrate was carried out at $T_s = 550^\circ\text{C}$. The other growth conditions were the same as the quantum well structures for CL measurements. An undoped AlAs(34 Å)/GaAs(70 Å)/AlAs(34 Å) double-barrier structure sandwiched between two undoped GaAs spacer-layers (117 Å) was grown on an n-GaAs layer ($n = 5 \times 10^{17} \text{ cm}^{-3}$), as shown in fig. 3. The top n⁺-GaAs ($n = 1 \times 10^{19} \text{ cm}^{-3}$) was

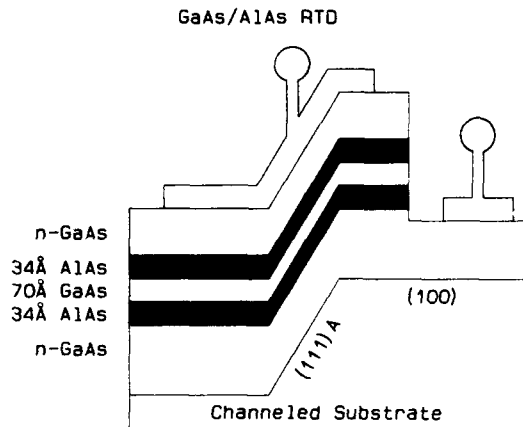


Fig. 3. Schematic cross-sectional structure of the resonant tunneling diode on the channeled substrate.

grown to make non-alloy ohmic contacts. These layer thicknesses are values for the (100) region. The RTD was fabricated by a photolithographic technique and wet etching. The schematic structure of the RTD is also shown in fig. 3.

Fig. 4 shows the current-voltage characteristics of the RTD structure with a $40 \times 40 \mu\text{m}^2$ area, which includes the (111)A slope region ($12 \mu\text{m}$ wide). The current peak at 0.38 V results from the resonant tunneling current in the (100) flat region,

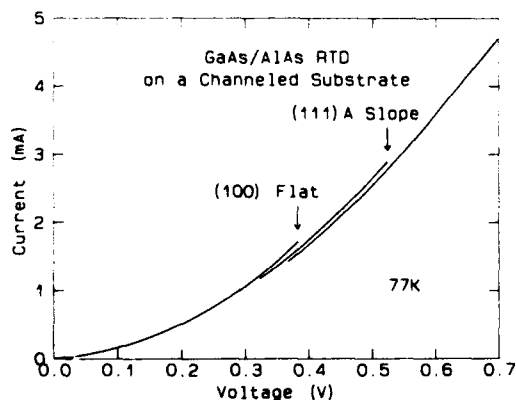


Fig. 4. Current-voltage characteristics of a resonant tunneling diode fabricated on the channeled substrates, which includes both the (100) flat region and the (111)A slope region. The peak current at 0.38 V is due to the resonant tunneling of electrons preferentially through the (111)A slope region.

while another peak at 0.52 V is considered to be due to the resonant current through the (111)A slope region. The calculated values are 0.131 V for the (100) region and 0.288 V for the (111)A region. The differences between measured peak voltages and calculated values results mainly from a high contact resistance of the device. Peak-to-valley (P/V) current ratios were 1.48 for the (100) flat region and 2.0 for the (111)A slope region. These rather small P/V ratios are probably due to the quality of the double-barrier structure on the (111)A facet and the parallel conduction through the (100) flat and the (111)A slope regions.

3. Summary

The current-voltage characteristics of a GaAs/AlAs resonant tunneling diode (RTD) fabricated on a GaAs channeled substrate, which has the (100) flat plane and (111)A slope plane on its surface, were measured at 77 K. The resonant tunneling currents preferentially through the (111)A slope region were observed for the first time. Furthermore, cathodoluminescence (CL) spectra from quantum wells indicate that reasonable quantum wells were grown on the (111)A slope facet of a channeled substrate. These results imply that a resonant tunneling barrier structure fabricated on channeled substrates with a microscopic slope region will provide us potential means to realize the lateral confinement of electrons emission.

Acknowledgments

The authors wish to express their thanks to Y. Okamoto (Kubota Corp.) for his stimulating discussion and assistance with characterization of samples. Appreciation should also be expressed to S. Yamakawa, M. Hisada, A. Inoue and C. Wu for their assistance and discussion. This work was supported in part by a Grant-in-Aid for Scientific Research on Priority Area, "Electron Wave Interference Effects in Mesoscopic Structures" from the Ministry of Education, Science and Culture.

References

- [1] W.T. Tsang and A.Y. Cho, *Appl. Phys. Letters* 30 (1977) 293.
- [2] J.S. Smith, P.L. Derry, S. Margalit and A. Yariv, *Appl. Phys. Letters* 47 (1985) 712.
- [3] M. Ohtsuka and S. Miyazawa, *J. Appl. Phys.* 64 (1988) 3522.
- [4] E. Kapon, M.C. Tamargo and D.M. Hwang, *Appl. Phys. Letters* 50 (1987) 347.
- [5] M.E. Hoenk, C.W. Nieh, H.Z. Chen and K.J. Vahala, *Appl. Phys. Letters* 55 (1989) 53.
- [6] E.M. Clausen, Jr., E. Kapon, M.C. Tamargo and D.M. Hwang, *Appl. Phys. Letters* 56 (1990) 776.
- [7] H.P. Meier, E. Van Gieson, W. Walter, C. Harder, M. Krahl and D. Bimberg, *Appl. Phys. Letters* 54 (1989) 433.
- [8] D.L. Miller, *Appl. Phys. Letters* 47 (1985) 1309.
- [9] T. Yuasa, M. Mannoh, T. Yamada, S. Naritsuka, K. Shinozaki and M. Ishii, *J. Appl. Phys.* 62 (1987) 764.
- [10] Y. Wu, M. Werner, K. Chen and S. Wang, *Appl. Phys. Letters* 44 (1984) 834.
- [11] E. Kapon, J.P. Harbison, C.P. Yun and L.T. Florez, *Appl. Phys. Letters* 54 (1989) 304.
- [12] K. Kojima, K. Mitsunaga and K. Kyuma, *Appl. Phys. Letters* 56 (1990) 154.

Highly strained pseudomorphic $\text{In}_x\text{Ga}_{1-x}\text{As}/\text{AlAs}$ based resonant tunneling diodes grown on patterned and non-patterned GaAs(100) substrates

R.M. Kapre, A. Madhukar and S. Guha

Photonic Materials and Devices Laboratory, University of Southern California, Los Angeles, California 90089-0241, USA

Resonant tunneling diodes (RTDs) with strained well and spacer regions made of $\text{In}_x\text{Ga}_{1-x}\text{As}$ alloys or $(\text{InAs})_M/(\text{GaAs})_N$ short period multiple quantum well (SPMQW) have been fabricated on GaAs(100) substrates. With increasing x , the presence of strain results in generation of misfit dislocations and/or change to three-dimensional island mode of growth, both detrimental to the performance of the RTDs. Consequently, a systematic study of the electrical and structural properties of RTDs with $0.10 \leq x \leq 0.33$ was carried out with emphasis on control of the growth kinetics. This has led to RTDs with $(\text{InAs})_1/(\text{GaAs})_2$ wells having room temperature peak to valley ratios (PVR) of 4.7 with peak current densities (J_p) of 125 kA/cm^2 . This is the first time that devices grown on GaAs substrate without any thick strain relieving intermediate layers have shown simultaneously high PVRs and J_p .

1. Introduction

Resonant tunneling diodes (RTDs) have been fabricated in various material systems including GaAs/AlGaAs, $\text{In}_{0.53}\text{Ga}_{0.47}\text{As}/\text{AlAs}$, and InAs/AlSb grown on GaAs, InP, and InAs substrates, respectively. Considering the usual figures of merit of peak current density (J_p) and peak-to-valley ratio (PVR), strained RTDs with $\text{In}_{0.53}\text{Ga}_{0.47}\text{As}/\text{InAs}$ wells and AlAs barriers grown on InP substrate have shown the best results: a room temperature PVR of 30 with $J_p = 6 \text{ kA/cm}^2$ [1] and a PVR of 3–4 with $J_p = 400\text{--}500 \text{ kA/cm}^2$ [2]. Lattice matched GaAs/AlGaAs RTDs on GaAs(100) substrates have shown room temperature PVRs of 4–5 with $J_p = 10\text{--}20 \text{ kA/cm}^2$ [3] and PVR of 2–2.5 with $J_p = 100\text{--}200 \text{ kA/cm}^2$ [4]. Strained $\text{InGaAs}/\text{AlAs}$ RTDs on GaAs(100) have shown comparable behaviour with PVR of 4.7 and $J_p = 10\text{--}12 \text{ kA/cm}^2$ [5]. InAs/AlSb devices based on thick $n^+\text{-InAs}$ epilayers on top of GaAs (i.e. very low strain in the RTD) have yielded room temperature $J_p = 200\text{--}400 \text{ kA/cm}^2$ with PVR of 3–4 [6]. For GaAs based optoelectronic device integration, it is important to achieve good performance for RTDs grown directly on GaAs sub-

strates, since thick intervening strain relieving layers of other materials such as InAs can compromise the desired objective as InAs is optically absorbing in the long wavelength regime of interest.

The key to improving the PVR of RTDs while maintaining high J_p is to use barrier and well materials with high conduction band (CB) discontinuity (ΔE_c). In the GaAs/ $\text{Al}_x\text{Ga}_{1-x}\text{As}$ system while the $\Gamma\text{--}\Gamma \Delta E_c$ can reach 1.0 eV for $x = 1.0$, it is the $\Gamma\text{--}X \Delta E_c$ of only 0.194 eV which is operative thus reducing the effectiveness of the barrier in cutting down non-resonant valley current. Use of the lower bandgap $\text{In}_x\text{Ga}_{1-x}\text{As}$ for the well region offers increasingly larger $\Gamma\text{--}X \Delta E_c$ with increasing x . However, being lattice mismatched to GaAs and AlAs, it poses two severe difficulties for high quality growth. First, for $x \sim 0.5$, the critical thickness for misfit (3.5%) induced defect formation, if a 2D layer-by-layer mode of growth could be maintained, is ≤ 10 monolayers for the individual layer itself. For $x \geq 0.30$ there is in general a tendency for the growth mode to change over to the 3D island formation after a few monolayers of growth depending upon the growth conditions employed. Second, the large differences in

the surface mobilities of In, Ga, and Al as well as the congruent temperatures of InAs, GaAs and AlAs, impose severe limitations on optimizing growth conditions for simultaneous high quality growth of AlAs barriers and $\text{In}_x\text{Ga}_{1-x}\text{As}$ well layers. It has been demonstrated that growth of $\text{In}_x\text{Ga}_{1-x}\text{As}$ on pre-patterned GaAs mesas results in reduction of misfit dislocation density [7]. Consequently this technique was explored in this work on the growth of strained $\text{In}_x\text{Ga}_{1-x}\text{As}$ / AlAs RTDs. For RTDs with high In ($\geq 25\%$), the strain appeared to be large enough for the onset of 3D island growth after the deposition of ~ 10 monolayers (ML) under most growth conditions employed earlier [5,9]. Substrate patterning on $20\ \mu\text{m} \times 20\ \mu\text{m}$ scale did not improve the situation. Consequently, to maintain layer-by-layer growth, new growth conditions providing better control of growth kinetics were explored and employed in the present work. In addition, we have examined the use of $(\text{InAs})_M/(\text{GaAs})_N$ short period superlattice (SPSL) as the strained layers. This was motivated by previous work on such strain layer modulated structures [8] where good quality interfaces were realized.

2. Resonant tunneling structures

The resonant tunneling structures discussed here are of the triple-well double-barrier type consisting of undoped top and bottom $\text{In}_x\text{Ga}_{1-x}\text{As}$ spacers, undoped AlAs barriers, and undoped $\text{In}_y\text{Ga}_{1-y}\text{As}$ well. The presence of an undoped spacer well was shown in our previous work [9] to

be effective in reducing non-resonant valley current as compared to the usual undoped GaAs spacers. The undoped tunneling structures were grown on top of $0.7\ \mu\text{m}$ $n^+\text{-GaAs}$ epitaxial layers on $n^+\text{-GaAs}(100)$ substrates and capped with $0.6\ \mu\text{m}$ $n^+\text{-GaAs}$. RTDs with $\text{In}_{0.1}\text{Ga}_{0.9}\text{As}$ well and spacer layers have resulted in room temperature $J_p \sim 11\ \text{kA}/\text{cm}^2$ and PVR 3.2 [9], while those with $\text{In}_{0.25}\text{Ga}_{0.75}\text{As}$ well and spacer gave $J_p = 10\text{--}20\ \text{kA}/\text{cm}^2$ and PVR = 4.5 [5]. Further improvement requires $x > 0.25$. By optimizing MBE growth kinetics based upon reflection high energy electron diffraction (RHEED) pattern and intensity, we have successfully grown a series of samples with In content in the well regions from 30% to 33%. RTD device structures are summarized in table 1. RTDs No. 19 and No. 21 have a doping density $N_D = 1 \times 10^{18}\ \text{cm}^{-3}$, while the others have $N_D = 2 \times 10^{18}\ \text{cm}^{-3}$ in the contact layers. RTDs No. 19 and No. 29 have conventional homogeneous random alloy InGaAs layers while the remaining contain SPMQW layers. Growth conditions used for these RTDs are summarized in table 2. A substrate temperature increase/decrease was typically accomplished in 60/120 s by interrupting growth and rapidly adjusting the power input to the substrate heater. Rapid changes in As_4 pressure were made possible by using two As_4 cells. Monolayer delivery times, τ_{ML} , were determined by RHEED intensity oscillations on InAs and GaAs substrates immediately prior to the growth of the actual structures. During the RTD growth, the RHEED pattern was used to infer growth front morphology with streaky/spotty pattern indicating 2D/3D growth. The As_4 pres-

Table 1

Structural parameters of the RTDs reported; RTDs No. 19 and No. 29 have conventional homogeneous random alloy $\text{In}_x\text{Ga}_{1-x}\text{As}$ layers while the others have $(\text{InAs})_M/(\text{GaAs})_N$ short period multiple quantum well layers; the thicknesses are specified in units of monolayers (1 ML = 2.83 Å)

RTD No.	Spacer material	Well material	d_{sp} (ML)	b (ML)	w (ML)
19	$\text{In}_{0.3}\text{Ga}_{0.7}\text{As}$	$\text{In}_{0.3}\text{Ga}_{0.7}\text{As}$	20	9	23
29	$\text{In}_{0.3}\text{Ga}_{0.7}\text{As}$	$\text{In}_{0.3}\text{Ga}_{0.7}\text{As}$	15	8	18
21	$(\text{InAs})_1/(\text{GaAs})_2$	$(\text{InAs})_1/(\text{GaAs})_2$	15	10	24
23	$(\text{InAs})_1/(\text{GaAs})_4$	$(\text{InAs})_1/(\text{GaAs})_2$	15	8	18
28	$(\text{InAs})_1/(\text{GaAs})_4$	$(\text{InAs})_1/(\text{GaAs})_2$	15	6	18
31	$(\text{InAs})_1/(\text{GaAs})_4$	$(\text{InAs})_1/(\text{GaAs})_2$	15	4	18

Table 2

Growth conditions used for the RTDs reported; the substrate temperature read by a calibrated pyrometer, As_4 pressure read by a beam flux monitor, and the monolayer delivery time, τ_{ML} , are tabulated

RTD No.	Spacer and well layer			Barrier layer		
	T_{sub} ($^{\circ}\text{C}$)	P_{As} (10^{-6} Torr)	τ_{ML} (s)	T_{sub} ($^{\circ}\text{C}$)	P_{As} (10^{-6} Torr)	τ_{ML} (s)
19	555	6.5	2.8	555	6.5	3.5
29	425	2.3	2.7	525	3.7	4.2
21	475	2.8	4	600	7.0	3.5
23	475	4.8	4	600	4.8	2
28	425	1.6	4	525	3.7	4.2
31	425	1.6	4	525	3.7	4.2

tures for samples No. 19, No. 21, and No. 23 were chosen to maintain sufficiently As-stabilized growth conditions, since barely As-stabilized conditions were earlier found to be detrimental to RTD performance [9]. The As_4 pressures for samples No. 28, No. 29, and No. 31 were chosen such that the As incorporation rate was about 1.5 times that of the group III elements. For this, the As incorporation rate was determined by performing As controlled RHEED oscillation experiments [10]. The SPMQW essentially equivalent to 20% and 33% alloys were grown by deposition of 1 ML of InAs followed by 4 ML or 2 ML of GaAs with a 5 to 10 s growth interruption before deposition of the next period. In order to study the effect of growth on finite substrates, a portion of the GaAs(100) substrates for RTD's No. 19, No. 21, and No. 23 was patterned into $20\text{ }\mu\text{m} \times 20\text{ }\mu\text{m}$ wide and $1\text{ }\mu\text{m}$ deep mesas. The grown structures were processed into $12\text{ }\mu\text{m} \times 12\text{ }\mu\text{m}$ mesas with AuGe/Ni top and In back alloyed ohmic contacts.

3. Results and discussion

Fig. 1a shows the 77 K I - V characteristics from the patterned region of RTD No. 19 containing $\text{In}_{0.3}\text{Ga}_{0.7}\text{As}$ alloy in the spacer and well layers. A weak negative differential resistance (NDR) effect is seen for both polarities. The +polarity indicates top of the mesa biased positive with respect to the bottom. The non-patterned region of this sample did not show a NDR. Figs. 1b and

1c show the cross-sectional TEM micrographs from the patterned and non-patterned regions. Both regions show that a 3D island mode of growth had set in and a high density of dislocations of $\sim 5 \times 10^9\text{ cm}^{-2}$, as measured by TEM,

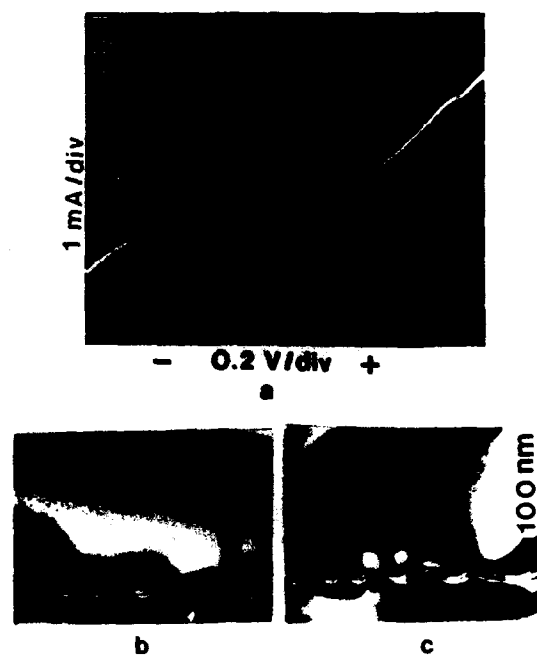


Fig. 1. (a) 77 K typical I - V characteristics of $12\text{ }\mu\text{m} \times 12\text{ }\mu\text{m}$ size RTDs made from the patterned region of RTD No. 19 containing conventional $\text{In}_{0.3}\text{Ga}_{0.7}\text{As}$ alloys. The symbol + refers to top of mesa biased positive with respect to the bottom. Cross-sectional TEM micrographs of RTD No. 19 from (b) patterned region, (c) non-patterned region.

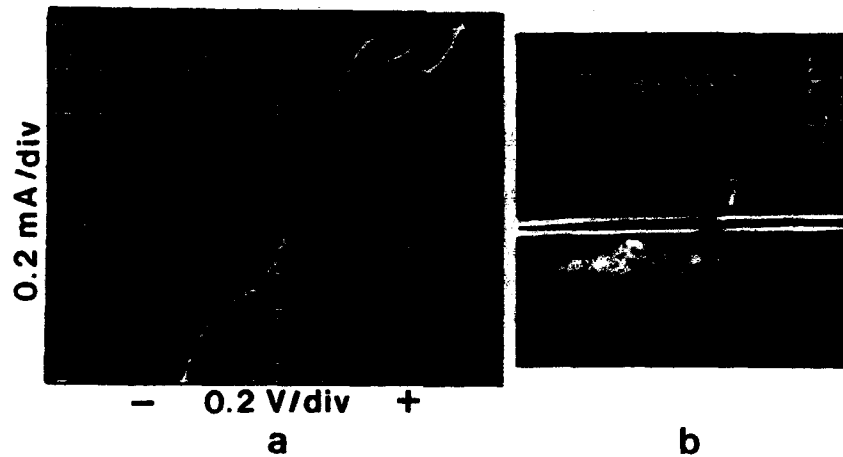
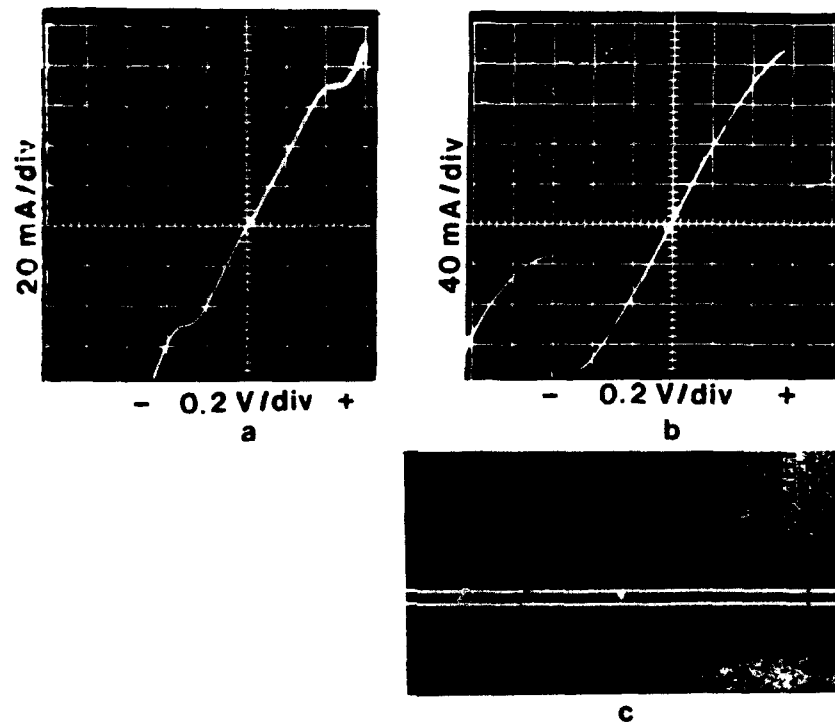


Fig 2. (a) 300 K typical I - V characteristics of $12\ \mu\text{m} \times 12\ \mu\text{m}$ size RTDs made from the non-patterned region of RTD No. 21 containing $(\text{InAs})_1/(\text{GaAs})_2$ SPMQW. The symbol + refers to top of mesa biased positive with respect to the bottom. (b) A cross-sectional TEM micrograph of RTD No. 21 from the non-patterned region.



Figs 3. 300 K typical I - V characteristics of $12\ \mu\text{m} \times 12\ \mu\text{m}$ size RTDs made from the non-patterned region of (a) RTD No. 23 with wells grown at 475°C , (b) RTD No. 28 with wells grown at 425°C . Both the RTDs contain $(\text{InAs})_1/(\text{GaAs})_2$ SPMQW spacer and $(\text{InAs})_1/(\text{GaAs})_2$ SPMQW well regions. (c) A cross-sectional TEM micrograph of RTD No. 28 (non-patterned).

have propagated through the cap layer. Due to the 3D mode of growth, the advantages that accrue from patterning in the layer-by-layer growth regime of strained $\text{In}_x\text{Ga}_{1-x}\text{As}$ are lost [11]. Consequently, only a marginal effect of patterning on resonant tunneling is observed. The I - V characteristics at 300 K from the non-patterned region of RTD No. 21 (<33% In SPMQW) are shown in fig. 2a. Note (table 2) that the growth temperature has been lowered to 475 from 555°C for RTD No. 19. Here the NDR effect is stronger than for RTD No. 19, though much inferior to state-of-the-art RTDs. Results from the patterned region were similar to that from the non-patterned. The improvement over RTD No. 19 correlates well with the superior morphology observed in TEM (fig. 2b). A 3D mode of growth had set in and a dislocation density of $\sim 1 \times 10^9 \text{ cm}^{-2}$ measured by TEM is observed. A large asymmetry is seen in the I - V characteristics with the improved NDR measured for tunneling from the substrate into the cap layer. This is indicative of the expected roughening of the interface with thicker growth of strained layers. To relieve the influence of increasing strain, but without compromising the relevant ΔE_c between the well and barrier layers, we examined structures with lower In composition in the spacer layer only. Fig. 3a shows the I - V characteristics from the non-patterned region of RTD No. 23 (<20% In SPMQW spacers, <33% In SPMQW well layer), the results from the patterned region being again similar. A much higher current density at resonance is observed, consistent with the higher contact layer doping of $2 \times 10^{18} \text{ cm}^{-3}$ used in this sample. However, the NDR effect is small, indicative of poor interfacial quality as is the case for RTDs No. 19 and No. 21. RHEED studies of <33% In SPMQW indicated that a 2D layer-by-layer growth mode could be maintained to a much higher thickness at a growth temperature of 425°C as compared to 475°C. Hence RTD No. 28 was grown at 425°C with the As_4 beam equivalent pressure (BEP) reduced to 1.6×10^{-6} Torr. The AlAs barriers were grown at a temperature of 525°C to avoid deterioration of the strained films and also to reduce the growth interruption time required for temperature changes. The I - V characteristics from RTD No.

28 at 300 K are shown in fig. 3b. The figure shows a J_p of 125 (104) kA/cm^2 with a PVR of 4.7 (4.7) for positive (negative) bias. At 77 K, a J_p of 128 (111) kA/cm^2 with PVR of 7.6 (6.7) is seen. To our knowledge, this is the first time a high room temperature PVR has been obtained simultaneously with $J_p > 100 \text{ kA/cm}^2$ in RTDs grown directly on GaAs substrate without any intermediate, thick strain relieving layers. The high degree of symmetry in the I - V characteristics is indicative of good interfacial quality. The high structural quality of the RTD is also corroborated by the cross-sectional TEM micrograph shown in fig. 3c. A search over a wide area did not reveal any misfit dislocations. The excellent results obtained for RTD No. 28 compared to RTD No. 23, which is a structure identical to it (except for a small difference in barrier thickness), indicate that the growth conditions play a major role in 3D island formation. The RHEED pattern remained streaky all the way through the growth of RTD No. 28 as opposed to RTDs No. 19, No. 21, and No. 23 where it turned spotty during the growth. RTD No. 31 was grown under conditions identical to RTD No. 28 and resulted in a 77 K J_p of 319 (250) kA/cm^2 with PVR of 2.3 (2.12) for positive (negative) bias. Due to high power dissipation in RTD No. 31, when tested at room temperature, the devices were destroyed. RTD No. 29 with conventional alloy $\text{In}_{0.3}\text{Ga}_{0.7}\text{As}$ layers showed a J_p of 32 (32) kA/cm^2 with PVR of 4.7 (5.2) for positive (negative) bias at room temperature. The growth conditions were identical to RTD No. 28.

Acknowledgements

This work was supported by the Air Force Office of Scientific Research, the Joint Services Electronics Program at the University of Southern California, and the Office of Naval Research.

References

- [1] T.P.E. Broekart, W. Lee and C.G. Fonstad, *Appl. Phys. Letters* 53 (1988) 1545.
- [2] T.P.E. Broekart and C.G. Fonstad, in: *IEEE Intern. Electron Devices Meeting Tech. Digest*, 1989, p. 559.

- [3] P. Cheng and J. Harris, Appl. Phys. Letters 56 (1990) 1676.
- [4] S.K. Diamond, E. Ozbay, M.J.W. Rodwell, D.M. Bloom, Y.C. Pao, E. Wolak and J. Harris, IEEE Electron Device Letters EDL-10 (1989) 104.
- [5] R. Kapre, A. Madhukar and S. Guha, IEEE Electron Device Letters EDL-11 (1990) 270.
- [6] J.R. Soderstrom, T.C. McGill, E.R. Brown, C.D. Parker and L.J. Mahoney, presented at Electronic Materials Conf., Santa Barbara, CA, June 1990.
- [7] S. Guha, A. Madhukar, K. Kaviani and R. Kapre, J. Vacuum Sci. Technol. B8 (1990) 149.
- [8] M.Y. Yen, A. Madhukar, B.F. Lewis, R. Fernandez, L. Eng and F.J. Grunthaner, Surface Sci. 174 (1986) 606.
- [9] R. Kapre, A. Madhukar, K. Kaviani, S. Guha and K.C. Rajkumar, Appl. Phys. Letters 56 (1990) 922.
- [10] B.F. Lewis, R. Fernandez, A. Madhukar and F.J. Grunthaner, J. Vacuum Sci. Technol. B4 (1986) 560.
- [11] S. Guha, A. Madhukar, Li Chen, K.C. Rajkumar and R. Kapre, in: Proc. Society of Photo-Optical Instrumentation Engineers, Bellingham, WA, Vol. 125, in press.

Comprehensive analysis of epitaxial $\text{Al}/\text{Al}_x\text{Ga}_{1-x}\text{As}$ Schottky barriers made by MBE: barrier heights and band edge discontinuities

M. Missous, E.H. Rhoderick, K.E. Singer and W.S. Truscott

*Department of Electrical Engineering and Electronics and Centre for Electronics Materials,
University of Manchester Institute of Science and Technology, P.O. Box 88, Manchester M60 1QD, UK*

Extremely high quality epitaxial aluminium on $\text{Al}_x\text{Ga}_{1-x}\text{As}$ Schottky diodes have been prepared by MBE. The excellent electrical properties of the MBE grown AlGaAs layers, with residual deep-level concentrations of less than 10^{14} cm^{-3} , combined with the in-situ deposition of single crystal epitaxial aluminium resulted in Schottky diodes with accurately exponential current–voltage characteristics over up to 6 decades of current and with ideality factors, for all but one of the diodes, less than 1.04 for x from 0 (GaAs) to 1 (AlAs). The dependence of the Schottky barrier heights on the aluminium mole fraction was determined using I/V and C/V measurements. A comparison of the data from n- and p-type diodes shows the pinning level responsible for the barrier height to be the same in both cases; the sum of the barrier heights giving a bandgap dependence on composition consistent with other data. The compositional trends of the barrier heights are shown to be in close agreement with accepted GaAs/AlGaAs conduction and valence band offsets, supporting the idea of a relationship between Schottky barriers and heterojunction band offsets.

1. Introduction

The use of MBE to produce Schottky contacts by in-situ deposition of metal on freshly-grown surfaces has allowed diodes with much improved electrical characteristics to be produced [1]. In the case of $\text{Al}_x\text{Ga}_{1-x}\text{As}$, the in-situ growth of epitaxial aluminium overlayers can be expected to lead to even more dramatically improved contacts as the high reactivity of $\text{Al}_x\text{Ga}_{1-x}\text{As}$ surfaces has made it extremely difficult to fabricate conventional ex-situ Schottky diodes [2,3].

From a more fundamental point of view, it has recently been suggested by Tersoff [4] that the band lineups at semiconductor heterojunctions are simply related to the difference in the Schottky barrier heights formed by the same metal to the individual semiconductors forming the heterojunction pair. In essence this means that the physical mechanism responsible for the pinning of the Fermi level in Schottky barrier formation also determines the band lineups in heterostructures. The position of the Fermi level in a metal–semiconductor contact (as determined by the barrier height) would then provide a reference level which,

by a comparison of the barrier heights of a given metal to GaAs and AlGaAs, provides a direct measure of the band offset between the two semiconductors. For the case of diodes to p-type material this will be the valence band offset, and for n-type, the conduction band offset.

Unlike some other experimental procedures, this technique is applicable in both the direct and indirect gap regions of the alloy system. It should be noted, however, that the calculation of the offset is the result of the subtraction of two relatively similar numbers and thus for any meaningful results, it is necessary that utmost care is taken in measurement of barrier heights and, more importantly, that the diodes used are of the highest quality. The MBE growth of epitaxial aluminium on AlGaAs is shown to produce near-ideal Schottky diodes, allowing a precise test of Tersoff's assertion to be made.

Langer et al. [5] have recently assessed the validity of Tersoff's ideas by drawing on earlier Schottky barrier data [2,6]. The conclusions reached by Langer et al. [5], i.e. that the MIGS model was not applicable, was based on the data available at that time and apart from the work of

Eizenberg et al. [6], all the diodes assessed were produced by conventional means with the corresponding problems associated with the highly reactive AlGaAs surface.

In this study we report on the electrical properties of extremely high quality epitaxial Al on AlGaAs diodes with the aluminium concentration, x , varied from 0 (GaAs) to 1 (AlAs). A detailed analysis of the characteristics of the characteristics of the near ideal characteristics has allowed a critical test of Tersoff's assertion as well as an assessment of current theories of Schottky barrier formation [7,8].

2. Experimental

All the layers used in this study were grown by molecular beam epitaxy in a VG V90H system using solid sources. The growth sequence of all the samples studied consisted of a 0.5 μm GaAs buffer layer doped p-type to $2 \times 10^{18} \text{ cm}^{-3}$ grown at 580°C followed by a 10 period GaAs-AlAs superlattice (approximately 0.1 μm thick) and a 0.1 μm graded Al_xGa_{1-x}As and finally 0.5 to 1 μm of Al_xGa_{1-x}As active layer doped with Be to $(1-4) \times 10^{16} \text{ cm}^{-3}$. The growth temperature was raised during the graded alloy layer from 580 to 690°C without changing the As₄ flux impinging on the surface resulting in a very strong (3×1) reconstructed surface.

After growth termination, the As, Ga, Be and Al cells were lowered to their idling temperatures and the Al_xGa_{1-x}As films which still exhibited a (3×1) surface reconstruction, were kept at high temperatures (500–580°C) until the As overpressure in the growth chamber dropped to below 10^{-8} Torr, at which point the substrate was then lowered to room temperature. When the system pressure was below 4×10^{-10} Torr and the substrate temperature reached 50°C, aluminium was evaporated on the (3×1) Al_xGa_{1-x}As surface at a rate of 0.01 Å/s for 5 min, then this was increased to 2000 Å/h for 1 h.

The aluminium concentration was measured using a double crystal X-ray diffractometer. These data closely correlated with beam flux measurements and (for $x < 0.3$) with photoluminescence.

The relative errors in aluminium content ($\Delta x/x$) are estimated to be less than $\pm 5\%$. Schottky barrier heights were determined by conventional I - V and C - V measurements on photolithographically-defined 0.5 mm diameter diodes.

3. Results

The procedure adopted for aluminium epitaxy was essentially identical to that described earlier for GaAs [1] and n-type AlGaAs [9]. The grown AlGaAs surfaces exhibited a (3×1) reconstruction which on commencement of aluminium deposition transformed gradually to a (1×1) structure. Initially aluminium nucleated in islands with a mixture of (100) and (110) orientations. After growth of approximately 30 nm this gradually gave way to a predominantly (100) orientation. The RHEED patterns from the aluminium remained characteristic of a smooth single crystal surface throughout the growth of the film.

The forward I - V characteristics of some typical epitaxial Al on p-type Al_xGa_{1-x}As are shown in fig. 1. The characteristics follow an exponential law for over 4 decades for Al on GaAs to more than 6 decades for the Al/Al_{0.58}Ga_{0.42}As Schottky diodes with very little component of recombina-

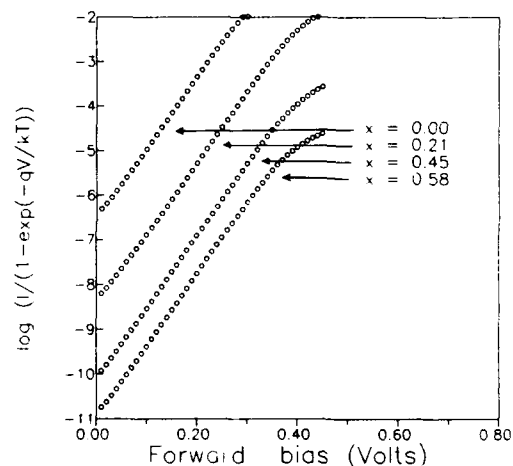


Fig. 1. Typical logarithmic plots of $I/[1 - \exp(-qV/kT)]$ versus forward voltage for aluminium on p-type AlGaAs of various compositions.

Table 1
Experimental values for the Schottky barrier heights, and ideality factors for the epitaxial Al on p-AlGaAs diodes

x	Φ_b (I/V)	n	Φ_b (C/V)
0	0.60	1.03	0.64
0.21	0.77	1.04	0.74
0.32	0.82	1.06	0.83
0.45	0.88	1.03	0.89
0.58	0.93	1.03	0.93
0.92	1.10	1.03	1.12

nation current present. The Schottky barriers exhibited very low values for the ideality factor (< 1.04 , apart from the devices made on the $x = 0.32$ material). A correction was made to the barrier for the effect of image force lowering, which for our samples amounted to a value of 0.025 to 0.035 eV depending on the doping of the layers. The C^{-2} versus V plots of the Al/AlGaAs Schottky diodes were almost ideal as indicated by the linearity of the plots. From the slopes of the lines the free hole concentrations were determined, and the barrier heights computed from the extrapolated intercepts of the lines with the voltage axis. All the data on the p-type diodes are summarized in table 1.

4. Discussion

The GaAs/AlAs ternary system provides an excellent series of materials for testing the validity of various theories of Schottky barrier formation. These models predict a barrier height on the assumption of a particular model of Fermi level pinning at the interface. The more prominent amongst the theories are the anti-site model of Allen and Down [7] in which pinning is assumed at interface states due to cations on arsenic vacancies, the anion vacancy defect model of Daw and Smith [8], and the modified metal-induced gap states (MIGS) model due to Tersoff [10]. It is usual to couch the predictions of these models in terms of the variation with composition of the barrier height to p-type material. We have recently shown from measurements on n-type diodes [9]

that in terms of the variation of barrier height with aluminium content an excellent quantitative fit can be obtained to both the anion vacancy model [8] and the anti-site model [7]. There is also a close quantitative fit to the absolute values predicted by the anion vacancy model, but owing to the uncertainties in the theory, this result should be treated with caution. This conclusion was obtained by calculating the barrier height to p-type material of a given composition by subtracting the measured barrier height from the band gap; an approach which relies on the pinning level responsible for the barrier formation being the same in both n- and p-type material, and also on a precise knowledge of the variation of E_g with x .

This work extends these measurements to barriers formed on p-type material. The data are summarised in table 1. Taken with our earlier data on n-type material [9] it is possible to compare the sum of the barrier heights to n- and p-type material with the known bandgap variation of AlGaAs. In the direct gap region a linear fit of the barrier height to x yields the derivatives given in table 2.

Langer et al. [5] have recently reviewed the AlGaAs bandgap data in the light of revised determinations of the precise aluminium content. The earlier accepted values of 12.5 meV/% now appears too low and more recent measurements give values in the range of 13.4 to 14.6 meV/%. The variation in the sum of the barrier heights measured in this work is thus in close agreement with all the other measurements.

Fig. 2 plots the $C-V$ measured barrier heights to both p-type AlGaAs (this work) and our earlier results on n-type [9] as a function of x . The barrier heights are plotted relative to a common reference level shown by the horizontal line. All energies are referenced to the barrier height to p-type GaAs. The solid lines are the best fits to the overall data

Table 2
Derivatives of linear fit of barrier height to x in direct gap region

Data from	$d\Phi_n/dx$ (meV/%)	$d\Phi_p/dx$ (meV/%)	$d(\Phi_n + \Phi_p)/dx$ (meV/%)
$I-V$	8.2 ± 0.3	4.8 ± 0.4	13.0 ± 0.7
$C-V$	8.6 ± 0.2	5.0 ± 0.3	13.6 ± 0.5

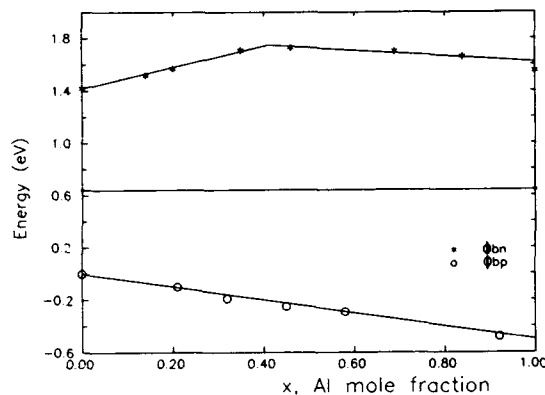


Fig. 2. C-V barrier heights to p-AlGaAs (this work) and n-AlGaAs (ref. [9]) referenced to the barrier height to p-type GaAs. The solid lines are average values of ΔE_c and ΔE_v from ref. [5].

on band edge discontinuity data derived from a variety of measurements and reviewed in ref. [5]. For the purposes of comparison the energies are referenced to the GaAs valence band edge. It can be seen that there is an excellent agreement between the Schottky barrier data and the other measurements. In the direct gap region the ratio of the conduction band to valence band offsets (calculated by equating $\Delta E_c/\Delta E_g$ to $d\Phi_n/dx/(d\Phi_n/dx + d\Phi_p/dx)$) is 63:37. This figure is identical to that calculated by Langer et al. [5] from earlier offset data in the light of more accurate values of x . Note, however, that the present results do not rely on any measured variation of AlGaAs band gap; if the Tersoff assertion is correct, the offsets are measured to each band independently.

The close agreement between band offsets determined by our Schottky barrier measurements and those by other techniques suggests an interesting result. Given the uncertainties in the quantitative predictions of the MIGS [10] and defect theories [7,8] of barrier formation, the barrier height variation with x measured here does not allow any firm conclusions to be drawn about the relative validity of these models. However, the extremely close correlation between our barrier height data and other band offset measurements strongly points to a common mechanism being

responsible for band lineups and Fermi level pinning in Schottky barriers. All indications are that the concentration of defects at the GaAs/AlGaAs heterointerface is far too small to account for the degree of pinning. This points to the conclusion that Tersoff's primary assertion, that for both heterojunctions and Schottky barriers the mechanism for aligning the bands is due not to defects but to electric dipoles resulting from dielectric screening at the interface, is correct.

5. Conclusions

Extremely high quality single crystal aluminium on p-type AlGaAs Schottky barriers have been made by MBE for the full range of alloy composition. The near-ideal characteristics of these diodes have allowed a more precise determination of barrier heights than has been possible with earlier experiments. Taken with similar results on n-type AlGaAs, the data points to a common pinning level being responsible for the barrier heights in materials of both types. The bandgap variation with x calculated from the two sets of data is in close agreement with other measurements. The variation of barrier height with x agrees qualitatively with both the defect [7,8] and the MIGS [10] models. The compositional trends of the barrier heights were found to be practically the same as that of the GaAs/AlGaAs conduction band offsets thus pointing to a strong correlation between Schottky barriers and heterojunction band offsets as proposed by Tersoff [10].

Acknowledgements

We would like to acknowledge much useful discussion with Professor J.M. Langer. This work has been supported by a grant from the Science and Engineering Research Council.

References

- [1] M. Missous, E.H. Roderick and K.E. Singer, *J. Appl. Phys.* 59 (1986) 3189.

- [2] Y.A. Gol'dberg, T.Y. Rafiev, B.V. Tsarenkov and Y.P. Yakovlev, *Soviet Phys.-Semicond.* 6 (1972) 398.
- [3] J.S. Best, *Appl. Phys. Letters* 34 (1979) 522.
- [4] J. Tersoff, *J. Vacuum Sci. Technol.* B3 (1985) 1157.
- [5] J.M. Langer, C. Delerue, M. Lannoo and H. Heinrich, *Phys. Rev.* B38 (1988) 7723.
- [6] M. Eizenberg, M. Heiblum, M.I. Nathan, N. Braslau and P.M. Mooney, *J. Appl. Phys.* 61 (1987) 1516.
- [7] R.E. Allen and J.D. Dow, *Phys. Rev.* B25 (1982) 1423.
- [8] M.S. Daw and D.L. Smith, *Appl. Phys. Letters* 36 (1980) 690.
- [9] M. Missous, W.S. Truscott and K.E. Singer, *J. Appl. Phys.* 68 (1990) 2239.
- [10] J. Tersoff, *Phys. Rev.* B32 (1985) 6968.

Author index

- Abernathy, C.R., S.J. Pearton, D.A. Bohling and G.T. Muhr. The roles of aluminum and hydrogen in impurity contamination of AlGaAs grown by MOMBE 111 (1991) 574
- Abstreiter, G., see Eberl 111 (1991) 882
- Aers, G.C., see Wasilewski 111 (1991) 70
- Agulló-Rueda, F., see Hong 111 (1991) 1016
- Aketagawa, K., T. Tatsumi and J. Sakai. Limitations of selective epitaxial growth conditions in gas-source MBE using Si_2H_6 111 (1991) 860
- Akita, K., see Hiratani 111 (1991) 570
- Allovon, M., M. Quillec, M. Blez and C. Kazmierski. MBE growth of graded index AlGaInAs MQW lasers on InP 111 (1991) 484
- Alonso, R.G., see Samarth 111 (1991) 816
- Ando, H., see Sandhu 111 (1991) 559
- Andrew, N.L., see Woodbridge 111 (1991) 339
- Arbet-Engels, V., see Kallel 111 (1991) 897
- Arthur, J.R., see Yoo 111 (1991) 1095
- Asahi, H., see Hasegawa 111 (1991) 371
- Asahi, H., see Takeyasu 111 (1991) 502
- Asahi, H., see Kaneko 111 (1991) 638
- Asami, K., see Takeyasu 111 (1991) 502
- Asom, M.T., G. Livescu, M. Geva, V. Swaminathan, L.C. Luther, R.E. Leibenguth, V.D. Mattern, E.F. Schubert, J.M. Kuo and R. Kopf. Comparison of delta doped GaAs grown by MBE and GSMBE using different arsenic species 111 (1991) 246
- Asom, M.T., V. Swaminathan, G. Livescu, M. Geva, L.C. Luther, R.E. Leibenguth, V.D. Mattern and T. Hayes. Hydrogen passivation of delta doped GaAs 111 (1991) 260
- Atwater, H.A., see Tsai 111 (1991) 931
- Awschalom, D.D., see Hong 111 (1991) 1016
- Azzam, W.J., see Bahl 111 (1991) 479
- Bachem, K.H., see Köhler 111 (1991) 295
- Bacsa, W., see Von Känel 111 (1991) 889
- Bahl, S.R., W.J. Azzam and J.A. del Alamo. Orientation dependence of mismatched $\text{In}_{0.1}\text{Al}_{0.9}\text{As}/\text{In}_{0.45}\text{Ga}_{0.55}\text{As}$ HFETs 111 (1991) 479
- Baldereschi, A., see Von Känel 111 (1991) 889
- Baldwin, K.W., see Pfeiffer 111 (1991) 333
- Ballingall, J.M., see Ho 111 (1991) 233
- Barlow, R.D., see Powell 111 (1991) 907
- Barski, A., see Garcia 111 (1991) 578
- Barthe, F., see Moisson 111 (1991) 141
- Bartoli, F.J., see Youngdale 111 (1991) 693
- Basaran, E., see Powell 111 (1991) 907
- Baur, B., see Heinecke 111 (1991) 599
- Beall, R.B., see Harris 111 (1991) 239
- Beck, W.A., see Svensson 111 (1991) 450
- Becker, E.E., see Chand 111 (1991) 20
- Benz II, R.G., B.K. Wagner, D. Rajavel and C.J. Summers. Chemical beam epitaxy of CdTe, HgTe, and HgCdTe 111 (1991) 725
- Bernklau, D., see Riechert 111 (1991) 1100
- Beserman, R., see Turco-Sandroff 111 (1991) 762
- Bhattacharya, P.K., see Chen 111 (1991) 228
- Bhattacharya, P.K., see Kim 111 (1991) 633
- Blez, M., see Allovon 111 (1991) 484
- Block, T.R. and B.G. Streetman. Correlation between the dampening of RHEED oscillations and the photoluminescence of quantum wells in the presence of AsO 111 (1991) 98
- Blood, P., see Foxon 111 (1991) 1047
- Blunier, S., see Tiwari 111 (1991) 730
- Boggess, T.F., see Hasenberg 111 (1991) 388
- Bohling, D.S., see Abernathy 111 (1991) 574
- Bove, P., see Garcia 111 (1991) 578
- Bowen, D.K., see Powell 111 (1991) 907
- Bowers, K.A., see Ren 111 (1991) 772
- Bowers, K.A., see Pen 111 (1991) 829
- Bozovic, I., see Fekstein 111 (1991) 973
- Brandt, O., L. Tapfer, K. Ploog, M. Hohenstein and F. Philipp. Growth processes and relaxation mechanisms in the molecular beam epitaxy of InAs/GaAs heterostructures 111 (1991) 383
- Brasil, M.J.S.P., see Turco-Sandroff 111 (1991) 762
- Brennan, T.M., see Tsao 111 (1991) 125
- Brighten, J.C., see Powell 111 (1991) 907
- Briones, F., see González 111 (1991) 120
- Briones, F. and A. Ruiz. Atomic layer molecular beam epitaxy (ALMBE): growth kinetics and applications 111 (1991) 194
- Brown, A.S., see Metzger 111 (1991) 4-5
- Brown, L.M., see Pike 111 (1991) 925
- Brown-Goebeler, K., see Chang 111 (1991) 475
- Buchan, N.L., see De Lyon 111 (1991) 564
- Buschert, J., see Samarth 111 (1991) 816
- Cabanel, R., see Etienne 111 (1991) 1003
- Cardone, F., see De Lyon 111 (1991) 564
- Carlin, J.F., see Rudra 111 (1991) 589
- Castagné, J., see Harris 111 (1991) 239

- Cerullo, M., see Eaglesham 111 (1991) 833
 Chalmers, S.A., see Petroff 111 (1991) 360
 Chalmers, S.A., H. Kroemer and A.C. Gosard, The growth of (Al,Ga)Sb tilted superlattices and their heteroepitaxy with InAs to form corrugated-barrier quantum wells 111 (1991) 647
 Chamberlain, J.M., see Stanley 111 (1991) 14
 Chand, N., T.D. Harris, S.N.G. Chu, E.E. Becker, A.M. Sargent, M. Schnoes and D.V. Lang, Variation of background impurities in $\text{Al}_x\text{Ga}_{1-x}\text{As}$ ($0.3 \leq x \leq 0.4$) with growth temperature: implications for device leakage current and surface/heterointerface roughness 111 (1991) 20
 Chang, A.M., see Chin 111 (1991) 466
 Chang, L.L., see Munekata 111 (1991) 1011
 Chang, L.L., see Hong 111 (1991) 1016
 Chang, S.K., see Yao 111 (1991) 823
 Chang, T.Y., see Chin 111 (1991) 466
 Chang, T.Y., N.J. Sauer, J.E. Zucker, K.L. Jones, B. Tell, K. Brown-Goebeler, M. Wegener and D.S. Chemla, High quality GaInAs/AlGaInAs/AlInAs heterostructures on Si ion implanted semi-insulating InP substrates for novel high performance optical modulators 111 (1991) 475
 Chang, W.S.C., see Niki 111 (1991) 419
 Chapman, J.N., see Kean 111 (1991) 189
 Chatenoud, F., see Williams 111 (1991) 1066
 Chemla, D.S., see Chang 111 (1991) 475
 Chen, H.S., see Hong 111 (1991) 984
 Chen, J.F. and A.Y. Cho, Tellurium doping study of GaSb grown by molecular beam epitaxy using SnTe 111 (1991) 619
 Chen, J.F., L. Yang, M.C. Wu, S.N.G. Chu and A.Y. Cho, Studies of the tunneling currents in the InAs/AlSb/GaSb single-barrier interband tunneling diodes grown on GaAs substrates 111 (1991) 659
 Chen, Li, K.C. Rajkumar, A. Madhukar, Wei Chen, S. Guha and K. Kaviani, Realization of sharp excitonic features in highly strained GaAs/ $\text{In}_x\text{Ga}_{1-x}\text{As}$ multiple quantum wells grown on GaAs(100) substrates 111 (1991) 424
 Chen, M., see Wu 111 (1991) 252
 Chen, Wei, see Chen 111 (1991) 424
 Chen, Y.C., P.K. Bhattacharya and J. Singh, Strained layer epitaxy of InGaAs by MBE and migration enhanced epitaxy - comparison of growth modes and surface quality 111 (1991) 228
 Chen, Y.C., see Kim 111 (1991) 633
 Chen, Yunliang, see Shen 111 (1991) 807
 Cheng, Xingyu, see Li 111 (1991) 736
 Chi, A., see Fashe 111 (1991) 677
 Chikyow, T., see Koguchi 111 (1991) 688
 Chin, A., T.Y. Chang, A. Ourmazd, E.M. Monberg, A.M. Chang and C. Kurdak, Effects of substrate orientation, pseudomorphic growth and superlattice on alloy scattering in modulation doped GaInAs 111 (1991) 466
 Chiu, T.H., J.E. Cunningham, J.A. Ditzenberger, W.Y. Jan and S.N.G. Chu, Characterization of the GaAs:C and AlGaAs:C doping superlattice grown by chemical beam epitaxy 111 (1991) 274
 Cho, A.Y., Advances in molecular beam epitaxy (MBE) 111 (1991) 1
 Cho, A.Y., see Chen 111 (1991) 619
 Cho, A.Y., see Chen 111 (1991) 659
 Cho, A.Y., see Hong 111 (1991) 1052
 Cho, A.Y., see Wang 111 (1991) 1057
 Choi, H.K., see Eglash 111 (1991) 669
 Chow, D.H., see Collins 111 (1991) 664
 Chow, D.H., R.H. Miles, C.W. Nieh and T.C. McGill, Growth of InAs/ $\text{Ga}_{1-x}\text{In}_x\text{Sb}$ infrared superlattices 111 (1991) 683
 Chow, P.C., see Fashe 111 (1991) 677
 Chu, S.N.G., see Chand 111 (1991) 20
 Chu, S.N.G., see Chiu 111 (1991) 274
 Chu, S.N.G., see Chen 111 (1991) 659
 Chu, S.N.G., see Wang 111 (1991) 1057
 Chu, T.Y., A. Dodabalapur, A. Srinivasan, D.P. Neikirk and B.G. Streetman, Properties and applications of $\text{Al}_x\text{Ga}_{1-x}\text{As}$ ($0 \leq x \leq 1$) grown at low temperatures 111 (1991) 26
 Cingolani, R., see Crook 111 (1991) 184
 Clarke, S., see Wilby 111 (1991) 864
 Claxton, P.A., M. Hopkinson, J. Kovac, G. Hill, M.A. Pate and J.P.R. David, Quantum-confined Stark effect in InGaAs/InP multiple quantum wells grown by solid source molecular beam epitaxy 111 (1991) 1080
 Clegg, J.B., see Harris 111 (1991) 239
 Collins, D.A., D.Z.-Y. Ting, E.T. Yu, D.H. Chow, J.R. Söderström, Y. Rajakarnanayake and T.C. McGill, Interband tunneling in InAs/GaSb/AlSb heterostructures 111 (1991) 664
 Collins, D.A., see Phillips 111 (1991) 820
 Colombo, P., see Hoke 111 (1991) 269
 Cook, Jr., J.W., see Lansari 111 (1991) 720
 Cook, Jr., J.W., see Ren 111 (1991) 772
 Cook, Jr., J.W., see Ren 111 (1991) 829
 Cooke, D.C., see Svensson 111 (1991) 450
 Cooke, D.C., see Uppal 111 (1991) 623
 Cotte, J.M., see Kesan 111 (1991) 847
 Covington, B.C., see Fashe 111 (1991) 677
 Cray, S.B., see Sherwin 111 (1991) 594
 Crook, G.E., I. Tapfer, L. Däweritz, R. Cingolani and K. Ploog, Control of initial surface configuration for GaAs-on-Si MBE using a Si buffer layer? 111 (1991) 184
 Cui, Jie, see Shen 111 (1991) 807

- Cui, Jie, Hailong Wang, Fuxi Gan and Aizhen Li, The study of phonons and lattice strains in ZnSe-ZnTe and ZnS-ZnSe strained-layer superlattices by Raman and far-infrared reflectivity spectra 111 (1991) 811
- Cunningham, J.E., see Chiu 111 (1991) 274
- Cunningham, J.E., T.Y. Kuo, A. Ourmazd, K. Goossen, W. Jan, F. Storz, F. Ren and C.G. Fonstad, Gas source molecular beam epitaxy growth of heterojunction bipolar transistors containing 1 monolayer δ -Be 111 (1991) 515
- Datye, A., see Klem 111 (1991) 628
- David, J.P.R., see Claxton 111 (1991) 1080
- Davies, A.G., J.E.F. Frost, D.A. Ritchie, D.C. Peacock, R. Newbury, E.H. Linfield, M. Pepper and G.A.C. Jone, The growth and physics of high mobility two-dimensional hole gases 111 (1991) 318
- Däweritz, L., J. Griesche, R. Hey and J. Herzog, Dynamics and roughness spectrum of the GaAs(001) surface during the MBE process 111 (1991) 65
- Däweritz, L., see Crook 111 (1991) 184
- Dawson, M.D., see Hasenberg, 111 (1991) 388
- De Lyon, T.J., N.I. Buchan, P.D. Kirchner, J.M. Woodall, D.T. McInturff, G.J. Scilla and F. Cardone, Use of CCl_4 and CHCl_3 in gas source molecular beam epitaxy for carbon doping of GaAs and $\text{Ga}_{1-x}\text{In}_x\text{P}$ 111 (1991) 564
- Del Alamo, J.A., see Bahl 111 (1991) 479
- Deppert, K., see Paulsson 111 (1991) 115
- Desai, Y.M., see Webb 111 (1991) 309
- Ditzenberger, J.A., see Chiu 111 (1991) 274
- Dodabalapur, A., see Chu 111 (1991) 26
- Dodson, B.W., Stress accommodation in large-mismatch systems 111 (1991) 376
- Dowsett, M.G., see Powell 111 (1991) 907
- Droopad, R., see Puechner 111 (1991) 43
- Drummond, T.J., see Sherwin 111 (1991) 605
- Duh, K.H.G., see Ho 111 (1991) 233
- Durbin, S.M., see Han 111 (1991) 767
- Eaglesham, D.J., H.-J. Gossmann, M. Cerullo, L.N. Pfeiffer and K.W. West, Limited thickness epitaxy of semiconductors and Si MBE down to room temperature 111 (1991) 833
- Eaglesham, D.J., see Head, 111 (1991) 838
- Eaves, L., see Henini 111 (1991) 1089
- Eberl, K., W. Wegscheider and G. Abstreiter, Group IV element (Si, Ge and α -Sn) superlattices - low temperature MBE 111 (1991) 882
- Eckstein, J.N., see Webb 111 (1991) 309
- Eckstein, J.N., I. Bozovic, D.G. Schlom and J.S. Harris, Jr., Growth of superconducting $\text{Bi}_2\text{Sr}_2\text{Ca}_{n-1}\text{Cu}_n\text{O}_x$ thin films by atomically layered epitaxy 111 (1991) 973
- Eglash, S.J., see Turner 111 (1991) 105
- Eglash, S.J., H.K. Choi and G.W. Turner, MBE growth of $\text{GaInAsSb}/\text{AlGaAsSb}$ double heterostructures for infrared diode lasers 111 (1991) 669
- Elta, M.E., see Sherwin 111 (1991) 594
- Elta, M.E., see Sherwin 111 (1991) 605
- Emeleus, C.J., see Powell 111 (1991) 907
- Emeny, M.T., L.K. Howard, K.P. Homewood, J.D. Lambkin and C.R. Whitehouse, A photoluminescence study of indium desorption from strained $\text{Ga}_{1-x}\text{In}_x\text{As}/\text{GaAs}$ 111 (1991) 413
- Etienne, P., J. Massies, S. Lequien, R. Cabanel and F. Petroff, Molecular beam epitaxial growth of Cr/Fe, Ag/Fe, Ag/Cr and Ag/Co superlattices on MgO (001) substrates 111 (1991) 1003
- Etoh, H., see Miyao 111 (1991) 912
- Farrell, H.H., see Tamargo 111 (1991) 741
- Farrow, L.A., see Turco-Sandhoff 111 (1991) 762
- Fashe, R., J.T. Zborowski, T.D. Golding, H.D. Shih, P.C. Chow, K. Matsuichi, B.C. Covington, A. Chi, J. Zheng and H.F. Schaake, MBE growth and characterization of $\text{In}_x\text{Ga}_{1-x}\text{Sb}/\text{InAs}$ strained layer superlattices 111 (1991) 677
- Faurie, J.P., R. Sporken, S. Sivananthan and M.D. Lange, New development on the control of homoepitaxial and heteroepitaxial growth of CdTe and HgCdTe by MBE 111 (1991) 698
- Feldman, L.C., see Headrick 111 (1991) 838
- Feldman, L.C., see Hong 111 (1991) 984
- Feuerbacher, B.F., see Ploog 111 (1991) 344
- Fewster, P.F., see Woodbridge 111 (1991) 339
- Fischer, A., see Ploog 111 (1991) 344
- Fischer, R.J., see Hong 111 (1991) 1052
- Fischer, R.J., see Wang 111 (1991) 1057
- Fischer, R.J., see Hong 111 (1991) 1071
- Fletcher, E.D., see Foxon 111 (1991) 1047
- Floeder, W., see Tiwari 111 (1991) 730
- Florez, L.T., see Harbison 111 (1991) 978
- Fons, P., see Kitabatake 111 (1991) 870
- Fonstad, C.G., see Vlcek 111 (1991) 56
- Fonstad, C.G., see Cunningham 111 (1991) 515
- Foxon, C.T., see Zhang 111 (1991) 93
- Foxon, C.T., E.M. Gibson, J. Zhang, B.A. Joyce and D.E. Lacklison, A comparison of MBE and MOMBE/CBE growth mechanisms using modulated beam mass spectrometry and RHEED 111 (1991) 539
- Foxon, C.T., P. Blood, E.D. Fletcher, D. Hilton, P.J. Hulyer and M. Vening, Substrate temperature dependence of SQW alloy and superlattice lasers grown by MBE using As_2 111 (1991) 1047

- Fredriksz, C.W., see Gravesteijn 111 (1991) 916
 Frost, J.E.F., see Ritchie 111 (1991) 300
 Frost, J.E.F., D.A. Ritchie and G.A.C. Jones,
 The growth of shallow high mobility
 two-dimensional electron gas structures 111 (1991) 305
 Frost, J.E.F., see Davies 111 (1991) 318
 Fuchs, F., see Ralston 111 (1991) 989
 Fujii, T., see Sandhu 111 (1991) 559
 Fujimoto, I., see Shigeta 111 (1991) 284
 Fujimoto, M., see Yao 111 (1991) 823
 Fujisaki, Y., see Ohishi 111 (1991) 792
 Fujita, Sg., see Wu 111 (1991) 757
 Fujita, Sz., see Wu 111 (1991) 757
 Fukada, T., see Matsumura 111 (1991) 787
 Fukamachi, T., see Yamada 111 (1991) 584
 Fukatsu, S.J., S. Kubo, Y. Shiraki and R. Ito,
 Redistribution of delta-doped Sb in Si 111 (1991) 843
 Fukushima, Y., see Matsumura 111 (1991) 787
 Furdyna, J.K., see Samarth 111 (1991) 816
 Fuwa, K., see Shigetomi 111 (1991) 110
- Gaborit, F., see Lambert 111 (1991) 495
 Gailhanou, M., see Houdré 111 (1991) 456
 Gambino, R.J., see Munekata 111 (1991) 1011
 Gamelin, J., see Hong 111 (1991) 1052
 Gamelin, J., see Hong 111 (1991) 1071
 Gan, Fuxi, see Cui 111 (1991) 811
 Ganière, J.-D., see Houdré 111 (1991) 456
 Ganser, P., see Köhler 111 (1991) 295
 Garcia, J.C., P. Maurel, P. Bove, J.P. Hirtz
 and A. Barski, Chemical beam epitaxy
 growth of GaAs/Ga_{0.5}In_{0.5}P heterostruc-
 tures: growth kinetics, electrical and opti-
 cal properties 111 (1991) 578
 Gentile, P., see Ulmer 111 (1991) 711
 Gérard, J.M., see Moisson 111 (1991) 141
 Gérard, J.M., J.Y. Marzin and B. Jusserand,
 Modulated molecular beam epitaxy: a
 successful route toward high quality highly
 strained heterostructure 111 (1991) 205
 Gerber, D.S., see Puechner 111 (1991) 43
 Gershoni, D., see Nagle 111 (1991) 264
 Geva, M., see Asom 111 (1991) 246
 Geva, M., see Asom 111 (1991) 260
 Gibis, R., see Künzel 111 (1991) 461
 Gibson, E.M., see Zhang 111 (1991) 93
 Gibson, E.M., see Foxon 111 (1991) 539
 Gill, D.M., see Uppal 111 (1991) 623
 Giugni, S., T.L. Tansley and G.J. Griffiths,
 Graded compositional heterostructures in
 the GaAs/Al_xGa_{1-x}As system 111 (1991) 50
 Golding, T.D., see Fashe 111 (1991) 677
 Goldstein, L., see Lambert 111 (1991) 495
 Gomyo, A., see Suzuki 111 (1991) 353
 Gonda, S., see Takeyasu 111 (1991) 502
 Gonda, S., see Kaneko 111 (1991) 638
 González, L., see González 111 (1991) 120
- González, Y., L. González and F. Briones,
 In-situ monitoring of antiphase domain
 evolution during atomic layer MBE (AL-
 MBE) and MBE growth of GaAs/Si(001)
 by reflectance difference 111 (1991) 120
 Goodnick, S.M., see Yoo 111 (1991) 1095
 Goossen, K., see Cunningham 111 (1991) 515
 Gossard, A.C., see Petroff 111 (1991) 360
 Gossard, A.C., see Chalmers 111 (1991) 647
 Gossmann, H.-J., see Eaglesham 111 (1991) 833
 Gotoh, H., see Nagao 111 (1991) 511
 Gotoh, H., see Nagao 111 (1991) 521
 Gravesteijn, D.J., T. Mishima, C.W. Fre-
 driksz, G.F.A. van de Walle and R.A. van
 den Heuvel, Transport properties of p-Si/
 SiGe single-modulation-doped hetero-
 structures grown by MBE 111 (1991) 916
 Greene, J.E., see Kitabatake 111 (1991) 870
 Griesche, J., see Däweritz 111 (1991) 65
 Griffiths, G.J., see Giugni 111 (1991) 50
 Grimes, R.T., see Stanley 111 (1991) 14
 Grote, N., see Künzel 111 (1991) 461
 Gueissaz, F., see Houdré 111 (1991) 456
 Gueissaz, F., R. Houdré and M. Ilegems,
 High electron density and mobility in
 single and double planar doped InGaAs/
 InAlAs heterojunctions on InP 111 (1991) 470
 Guha, S., see Chen 111 (1991) 424
 Guha, S., K.C. Rajkumar and A. Madhukar,
 The nature and control of morphology
 and the formation of defects in InGaAs
 epilayers and InAs/GaAs superlattices
 grown via MBE on GaAs(100) 111 (1991) 434
 Guha, S., see Kapre 111 (1991) 1110
 Gunshor, R.L., see Qiu 111 (1991) 747
 Gunshor, R.L., see Han 111 (1991) 767
 Gunshor, R.L., see Li 111 (1991) 1038
- Haddad, G.I., see Sherwin 111 (1991) 594
 Haddad, G.I., see Sherwin 111 (1991) 605
 Hafich, M.J., H.Y. Lee, P. Silvestre and G.Y.
 Robinson, GSMBE growth of GaAs at
 low AsH₃ cracking temperatures 111 (1991) 507
 Hafich, M.J., see Lee 111 (1991) 525
 Hagerott, M., see Han 111 (1991) 767
 Hagino, M., see Nomura 111 (1991) 61
 Hall, E.L., see Ho 111 (1991) 233
 Hamilton, A., see Ritchie 111 (1991) 300
 Hammons, B.E., see Tsao 111 (1991) 125
 Han, J., S.M. Durbin, R.L. Gunshor, M.
 Kobayashi, D.R. Menke, N. Pelekanos,
 M. Hagerott, A.V. Nurmikko, Y. Naka-
 mura and N. Otsuka, Quantum wells with
 zincblende MnTe barriers 111 (1991) 767
 Harada, K., see Hashimoto 111 (1991) 393
 Harbison, J.P., T. Sands, R. Ramesh, L.T.
 Florez, B.J. Wilkens and V.G. Keramidas,

- MBE growth of ferromagnetic metastable epitaxial MnAl thin films on AlAs/GaAs heterostructures 111 (1991) 978
- Harmand, J.C., see Inoue 111 (1991) 313
- Harris, J.J., J.B. Clegg, R.B. Beall, J. Castagné, K. Woodbridge and C. Roberts, Delta-doping of GaAs and Al_{0.33}Ga_{0.67}As with Sn, Si and Be: a comparative study 111 (1991) 239
- Harris, Jr., J.S., see Lee 111 (1991) 131
- Harris, Jr., J.S., see Pao 111 (1991) 489
- Harris, Jr., J.S., see Eckstein 111 (1991) 973
- Harris, K.A., see Yanka 111 (1991) 715
- Harris, T.D., see Chand 111 (1991) 20
- Hasegawa, S., M. Sato, K. Maehashi, H. Asahi and H. Nakashima, Formation of quantum well wire-like structures by MBE growth of AlGaAs/GaAs superlattices on GaAs (110) surfaces 111 (1991) 371
- Hasenberg, T.C., D.S. McCallum, X.R. Huang, A.L. Smirl, M.D. Dawson and T.F. Boggess, Optical studies of InAs/GaAs on GaAs short-period strained-layer superlattices grown by MBE and MEE 111 (1991) 388
- Hashimoto, S., see Schowalter 111 (1991) 948
- Hashimoto, Y., K. Hirakawa, K. Harada and T. Ikoma, Strain induced change in band offsets at pseudomorphically grown InAs/GaAs heterointerfaces characterized by X-ray photoelectron spectroscopy 111 (1991) 393
- Hasnain, G., see Hong 111 (1991) 1052
- Hata, M., A. Watanabe and T. Isu, Surface diffusion length observed by in situ scanning microprobe reflection high-energy electron diffraction 111 (1991) 83
- Hata, M., see Isu 111 (1991) 210
- Hata, M., see Watanabe 111 (1991) 554
- Hayes, T., see Asom 111 (1991) 260
- He, Li, see Li 111 (1991) 736
- Headrick, R.L., B.E. Weir, A.F.J. Levi, D.J. Eaglesham and L.C. Feldman, Buried, ordered structures: boron in Si(111) and Si(100) 111 (1991) 838
- Heinecke, H., B. Baur, R. Höger, A. Miklis and R. Treichler, Growth of GaInAs and GaInAsP lattice matched by InP by metalorganic MBE 111 (1991) 599
- Hendriks, H.T., see Hoke 111 (1991) 269
- Henige, J.A., see Metzger 111 (1991) 445
- Henini, M., C.R.H. White, P.E. Simmonds, L. Eaves, M.S. Skolnick, D.K. Maude, O.H. Hughes and J.C. Portal, Investigation of a double barrier resonant tunneling structure which incorporates an optical window layer in the top contact 111 (1991) 1089
- Heremans, J.P., see Partin 111 (1991) 614
- Heremans, J.P., see Youngdale 111 (1991) 693
- Herzog, J., see Däweritz, 111 (1991) 65
- Hey, R., see Däweritz, 111 (1991) 65
- Hiesinger, P., see Ralston 111 (1991) 989
- Hill, G., see Claxton 111 (1991) 1080
- Hilton, D., see Foxon 111 (1991) 1047
- Hirakawa, K., see Hashimoto 111 (1991) 393
- Hiratani, Y., Y. Ohki, Y. Sugimoto and K. Akita, In-situ selective-area epitaxy of GaAs using a GaAs oxide layer as a mask 111 (1991) 570
- Hirayama, H., M. Hiroi, K. Koyama and T. Tatsumi, B doping effect on gas source Si-MBE growth: a comparison of B₂H₆ gas doping and HBO₂ Knudsen cell doping 111 (1991) 856
- Hirayama, H., see Tatsumi 111 (1991) 961
- Hiroi, M., see Hirayama 111 (1991) 856
- Hirosawa, I., see Tatsumi 111 (1991) 961
- Hirose, H., see Iizuka 111 (1991) 429
- Hirtz, J.P., see Garcia 111 (1991) 578
- Hiyomizu, S., see Shimomura 111 (1991) 1105
- Ho, P., S.C. Wang, T. Yu, J.M. Ballingall, P.A. Martin, K.H.G. Duh, S.M.J. Liu, G.A. Hutchins and E.L. Hall, Improved device performance by migration-enhanced epitaxy 111 (1991) 233
- Hoffman, C.A., see Youngdale 111 (1991) 693
- Höger, R., see Heinecke 111 (1991) 599
- Hohenstein, M., see Brandt 111 (1991) 383
- Hoke, W.E., P.J. Lemonias, P.S. Lyman, H.T. Hendriks, D. Weir and P. Colombo, Carbon doping of MBE GaAs and Ga_{0.7}Al_{0.3}As films using a graphite filament 111 (1991) 269
- Hoke, W.E., P.J. Lemonias and D.G. Weir, Evaluation of a new plasma source for molecular beam epitaxial growth of InN and GaN films 111 (1991) 1024
- Holland, M.C., see Stanley 111 (1991) 14
- Holland, M.C., see Kean 111 (1991) 189
- Homewood, K.P., see Emeny 111 (1991) 413
- Hong, J.M., D.D. Awschalom, F. Agulló-Rueda and L.L. Chang, Growth and novel properties of magnetic heterostructures by molecular beam epitaxy 111 (1991) 1016
- Hong, J.M., see Hong 111 (1991) 1071
- Hong, M., H.S. Chen, J. Kwo, A.R. Kortan, J.P. Mannaerts, B.E. Weir and L.C. Feldman, MBE growth and properties of Fe₃(Al,Si) on GaAs(100) 111 (1991) 984
- Hong, M., L.W. Tu, J. Gamelin, Y.H. Wang, R.J. Fischer, E.F. Schubert, K. Tai, G. Hasnain, J.P. Mannaerts, B.E. Weir, J.D. Wynn, R.F. Kopf, G.J. Zydzik and A.Y. Cho, Vertical cavity top-surface emitting lasers with thin Ag mirrors and hybrid reflectors 111 (1991) 1052
- Hong, M., see Wang 111 (1991) 1057

- Hong, M., J.P. Mannaerts, J.M. Hong, R.J. Fischer, K. Tai, J. Kwo, J.M. Vandenberg, Y.H. Wang and J. Gamelin, A simple way to reduce series resistance in p-doped semiconductor distributed Bragg reflectors 111 (1991) 1071
- Hopkinson, M., see Claxton 111 (1991) 1080
- Horikoshi, Y., M. Kawashima and N. Kobayashi, Optical investigation of GaAs growth process in molecular beam epitaxy and migration-enhanced epitaxy 111 (1991) 200
- Horikoshi, Y., see Ramesh 111 (1991) 752
- Houdré, R., F. Gueissaz, M. Gailhanou, J.-D. Ganière, A. Rudra and M. Illegems, Characterization of InGaAs and InAlAs layers on InP by four-crystal high resolution X-ray diffraction and wedge transmission electron microscopy 111 (1991) 456
- Houdré, R., see Gueissaz 111 (1991) 470
- Houzay, F., see Moisson 111 (1991) 141
- Howard, L.K., see Emeny 111 (1991) 413
- Hsieh, Y.F., see Wang 111 (1991) 1057
- Hsiung, L.M., see Schowalter 111 (1991) 948
- Huang, X.R., see Hasenberg 111 (1991) 388
- Huang, Yi, see Zhou 111 (1991) 288
- Hughes, O.H., see Henini 111 (1991) 1089
- Hugill, K.J., see Myers-Beaghton 111 (1991) 328
- Hulyer, P.J., see Foxon 111 (1991) 1047
- Hutchins, G.A., see Ho 111 (1991) 233
- Hwang, S., see Lansari 111 (1991) 720
- Hwang, S., see Ren 111 (1991) 772
- Iga, K., see Uchida 111 (1991) 1062
- Iizuka, K., T. Yoshida, T. Suzuki and H. Hirose, Observation of dark line defects in InGaAs/GaAs strained layer superlattices by photoluminescence topography 111 (1991) 429
- Ikei, T., see Takano 111 (1991) 216
- Ikoma, T., see Hashimoto 111 (1991) 393
- Illegems, M., see Houdré 111 (1991) 456
- Illegems, M., see Gueissaz 111 (1991) 470
- Illegems, M., see Rudra 111 (1991) 589
- Ino, S., see Shigetomi 111 (1991) 110
- Inoue, K., J.C. Harmand and T. Matsuno, High-quality $\text{In}_{0.1}\text{Ga}_{0.9}\text{As}/\text{InAlAs}$ modulation-doped heterostructures grown lattice-mismatched on GaAs substrates 111 (1991) 313
- Inoue, M., see Yano 111 (1991) 397
- Inoue, M., see Yano 111 (1991) 609
- Inoue, M., see Yoh 111 (1991) 643
- Inoue, N., MBE monolayer growth control by in-situ electron microscopy 111 (1991) 75
- Inoue, Y., see Nagao 111 (1991) 511
- Inoue, Y., see Nagao 111 (1991) 521
- Ishikawa, H., see Sandhu 111 (1991) 559
- Isu, T., see Hata 111 (1991) 83
- Isu, T., M. Hata and A. Watanabe, Real-time μ -RHEED observations of GaAs surfaces during growth with alternating source supply 111 (1991) 210
- Isu, T., see Watanabe 111 (1991) 554
- Itani, Y., see Kaneko 111 (1991) 638
- Ito, R., see Fukatsu 111 (1991) 843
- Ivanov, S.V., P.S. Kop'ev and N.N. Ledentsov, Thermodynamic analysis of segregation effects in MBE of $\text{A}^{\text{III}}\text{-B}^{\text{V}}$ compounds 111 (1991) 151
- Iwai, Y., see Yano 111 (1991) 397
- Iwai, Y., see Yano 111 (1991) 609
- Iwawaki, T., see Yano 111 (1991) 397
- Iyer, S.S., see Kesan 111 (1991) 847
- Iyer, S.S., see Kesan 111 (1991) 936
- Iyer, S.S., see Schowalter 111 (1991) 948
- Jan, W.Y., see Chiu 111 (1991) 274
- Jan, W.Y., see Cunningham 111 (1991) 515
- Jeppesen, S., see Paulsson 111 (1991) 115
- Jimenez, J.R., see Schowalter 111 (1991) 948
- Jin, Weimin, see Zhou 111 (1991) 288
- Jo, J., see Santos 111 (1991) 366
- Johnson, D.A., see Puechner 111 (1991) 43
- Jones, G.A.C., see Ritchie 111 (1991) 300
- Jones, G.A.C., see Frost 111 (1991) 305
- Jones, G.A.C., see Davies 111 (1991) 318
- Jones, K.L., see Chang 111 (1991) 475
- Jönsson, J., see Paulsson 111 (1991) 115
- Joyce, B.A., see Zhang 111 (1991) 93
- Joyce, B.A., see Foxon 111 (1991) 539
- Joyce, B.A., see Yuen 111 (1991) 943
- Jusserand, B., see Moisson 111 (1991) 141
- Jusserand, B., see Gérard 111 (1991) 205
- Kadoya, Y., A. Sato, H. Kano and H. Sakaki, Electrical properties and dopant incorporation mechanisms of Si doped GaAs and (AlGa)As grown on (111)A GaAs surfaces by MBE 111 (1991) 280
- Kaiser, R., see Künzel 111 (1991) 1084
- Kallel, M.A., V. Arbet-Engels, K.L. Wang and R.P.G. Karunasiri, MBE Si_mGe_n strained monolayer superlattices 111 (1991) 897
- Kanaya, Y., see Takano 111 (1991) 216
- Kaneko, T., see Takeyasu 111 (1991) 502
- Kaneko, T., H. Asahi, Y. Itani, Y. Okuno and S. Gonda, MOMBE growth of GaSb and InAsSb using triethylstibine and triethylarsine 111 (1991) 638
- Känel, H. von, E. Müller, H.-U. Nissen, W. Bacsá, M. Ospelt, K.A. Mäder, R. Stalder and A. Baldereschi, Silicon heteroepitaxy: interface structure and physical properties 111 (1991) 889
- Kang, T.W., see Kuo 111 (1991) 996
- Kano, H., see Kadoya 111 (1991) 280

- Kapre, R.M., A. Madhukar and S. Guha, Highly strained pseudomorphic $\text{In}_x\text{Ga}_{1-x}\text{As}/\text{AlAs}$ based resonant tunneling diodes grown on patterned and non-patterned $\text{GaAs}(100)$ substrates 111 (1991) 1110
- Karasawa, T., see Ohkawa 111 (1991) 797
- Kargodorian, T.V., see Metzger 111 (1991) 445
- Karunasiri, R.P.G., see Kallel 111 (1991) 897
- Katahama, H., see Shigeta 111 (1991) 284
- Katoh, M., see Nagao 111 (1991) 521
- Kaviani, K., see Chen 111 (1991) 424
- Kawakami, Y., see Wu 111 (1991) 757
- Kawanishi, E., see Nagao 111 (1991) 511
- Kawashima, M., see Horikoshi 111 (1991) 200
- Kazmierski, C., see Allovon 111 (1991) 484
- Kean, A.H., see Stanley 111 (1991) 14
- Kean, A.H., C.R. Stanley, M.C. Holland, J.L. Martin and J.N. Chapman, Gallium desorption from $(\text{Al},\text{Ga})\text{As}$ grown by molecular beam epitaxy at high temperatures 111 (1991) 189
- Keramidas, V.G., see Harbison 111 (1991) 978
- Kesan, V.P., S.S. Iyer and J.M. Cotte, Dopant incorporation in epitaxial germanium grown on $\text{Ge}(100)$ substrates by MBE 111 (1991) 847
- Kesan, V.P., P.G. May, F.K. LeGoues and S.S. Iyer, Si/SiGe heterostructures grown on SOI substrates by MBE for integrated optoelectronics 111 (1991) 936
- Kim, J.H., D. Yang, Y.-C. Chen and P. Bhat-tacharya, Growth and properties of $\text{InAs}_x\text{Sb}_{1-x}$, $\text{Al}_x\text{Ga}_{1-x}\text{Sb}$, and $\text{InAs}_x\text{Sb}_{1-x}/\text{Al}_x\text{Ga}_{1-x}\text{Sb}$ heterostructures 111 (1991) 633
- Kirchner, P.D., see De Lyon 111 (1991) 564
- Kitabatake, M., P. Fons and J.E. Greene, Molecular dynamics and quasidynamics simulations of low-energy ion/surface interactions leading to decreased epitaxial temperatures and increased dopant incorporation probabilities during Si MBE 111 (1991) 870
- Klem, J.F., S.R. Kurtz and A. Dartye, Growth and properties of $\text{GaAsSb}/\text{InGaAs}$ superlattices in InP 111 (1991) 628
- Kobayashi, K., see Shigeta 111 (1991) 284
- Kobayashi, K., see Shimomura 111 (1991) 1105
- Kobayashi, M., see Qiu 111 (1991) 747
- Kobayashi, M., see Han 111 (1991) 767
- Kobayashi, M., see Li 111 (1991) 1038
- Kobayashi, N., see Horikoshi 111 (1991) 200
- Kobayashi, N., see Ramesh 111 (1991) 752
- Koguchi, N., S. Takahashi and T. Chikyow, New MBE growth method for InSb quantum well boxes 111 (1991) 688
- Köhler, K., P. Ganser, M. Maier and K.H. Bachem, Modulation doped inverted and normal $\text{GaAs}/\text{Al}_x\text{Ga}_{1-x}\text{As}$ heterostructures: influence of Si -segregation on the two-dimensional electron gas 111 (1991) 295
- Koma, A., K. Ueno and K. Saiki, Heteroepitaxial growth by Van der Waals interaction in one-, two- and three-dimensional materials 111 (1991) 1029
- Koma, A., see Ohuchi 111 (1991) 1033
- Konagai, M., see Yamada 111 (1991) 584
- Konagai, M., see Takemura 111 (1991) 802
- Kondo, K., see Saito 111 (1991) 544
- Kop'ev, P.S., see Ivanov 111 (1991) 151
- Kopf, R.F., see Asom 111 (1991) 246
- Kopf, R.F., see Hong 111 (1991) 1052
- Kortan, A.R., see Hong 111 (1991) 984
- Kovac, J., see Claxton 111 (1991) 1080
- Koyama, F., see Uchida 111 (1991) 1062
- Koyama, K., see Hirayama 111 (1991) 856
- Kroemer, H., see Miller 111 (1991) 323
- Kroemer, H., see Petroff 111 (1991) 360
- Kroemer, H., see Chalmers 111 (1991) 647
- Kubiak, R.A.A., see Powell 111 (1991) 907
- Kubiak, R.A.A., see Pike 111 (1991) 925
- Kubo, M. and T. Narusawa, A novel in-situ molecular beam epitaxy monitoring system using low energy ion scattering 111 (1991) 136
- Kubo, S., see Fukatsu 111 (1991) 843
- Kudo, K., J.S. Lee, K. Tanaka, Y. Makita and A. Yamada, Fabrication and characterization of MBE grown InAs/GaAs strained-layer superlattices on variously oriented substrates 111 (1991) 402
- Künzel, H., R. Gibis, W. Schlaak, L.M. Su and N. Grote, MBE overgrowth of implanted regions in $\text{InP}:\text{Fe}$ substrates 111 (1991) 461
- Künzel, H., R. Kaiser, W. Passenberg, D. Trommer and G. Unterbörsch, Critical issues in the MBE growth of $\text{Ga}_{0.47}\text{In}_{0.53}\text{As}$ for waveguide/PIN/JFET integration 111 (1991) 1084
- Kuo, J.M., see Asom 111 (1991) 246
- Kuo, T.C., T.W. Kang and K.L. Wang, RHEED studies of epitaxial growth of CoGa on GaAs by MBE - determination of epitaxial phases and orientations 111 (1991) 996
- Kuo, T.Y., see Cunningham 111 (1991) 515
- Kurdak, C., see Chin 111 (1991) 466
- Kurtz, S.R., see Klem 111 (1991) 628
- Kwo, J., Growth and properties of high T_c films in $\text{Y}_1\text{Ba}_2\text{Cu}_3\text{O}_{7-x}$ perovskite by molecular beam epitaxy 111 (1991) 965
- Kwo, J., see Hong 111 (1991) 984
- Kwo, J., see Hong 111 (1991) 1071
- Lacklison, D.E., see Foxon 111 (1991) 539
- Legally, M.G., see Mo 111 (1991) 876
- Lambert, M., L. Goldstein, A. Perales, F. Gaborit, C. Starck and J.-L. Lievin, High quality InP and $\text{In}_{1-x}\text{Ga}_x\text{As}_y\text{P}_{1-y}$ grown by gas source MBE 111 (1991) 495

- Lambkin, J.D., see Emeny 111 (1991) 413
 Lang, D.V., see Chand 111 (1991) 20
 Lange, M.D., see Faurie 111 (1991) 698
 Lansari, Y., Z. Yang, S. Hwang, F.E. Reed, A.T. Sowers, J.W. Cook, Jr. and J.F. Schetzina, Very low temperature growth and doping of Hg-based epilayers and superlattices 111 (1991) 720
 Lanzillotto, A.-M., see Santos 111 (1991) 366
 Ledentsov, N.N., see Ivanov 111 (1991) 151
 Lee, H.Y., see Hafich 111 (1991) 507
 Lee, H.Y., M.J. Hafich, G.Y. Robinson, K. Mahalingam and N. Otsuka, Improved InGaP/GaAs heterointerfaces during gas-source MBE growth 111 (1991) 525
 Lee, J.S., see Kudo 111 (1991) 402
 Lee, W.S., G.W. Yoffe, D.G. Schlom and J.S. Harris, Jr., Accurate measurement of MBE substrate temperature 111 (1991) 131
 LeGoues, F.K., see Kesan 111 (1991) 936
 Leibenguth, R.E., see Asom 111 (1991) 246
 Leibenguth, R.E., see Asom 111 (1991) 260
 Lemonias, P.J., see Hoke 111 (1991) 269
 Lemonias, P.J., see Hoke 111 (1991) 1024
 Lequien, S., see Etienne 111 (1991) 1003
 Levi, A.F.J., see Headrick 111 (1991) 838
 Li, Aizhen, see Shen 111 (1991) 807
 Li, Aizhen, see Cui 111 (1991) 811
 Li, D., see Qiu 111 (1991) 747
 Li, D., Y. Nakamura, N. Otsuka, J. Qiu, M. Kobayashi and R.L. Gunshor, Reconstruction structure at $\text{Ge}_2\text{Se}_3/\text{GaAs}$ epitaxial interface 111 (1991) 1038
 Li, Jie, Li He, Wei Shan, Xingyu Cheng and Shixin Yuan, Atomic layer epitaxy of $(\text{CdTe})_m(\text{ZnTe})_n\text{-ZnTe}$ multiquantum wells on (001)GaAs substrate 111 (1991) 736
 B.W. Liang and C.W. Tu, The roles of group-V species in metalorganic molecular-beam epitaxy and chemical-beam epitaxy of III-V compounds 111 (1991) 550
 Lievin, J.-L., see Lambert 111 (1991) 495
 Linfield, E.H., see Ritchie 111 (1991) 300
 Linfield, E.H., see Davies 111 (1991) 318
 Liu, S.M.J., see Ho 111 (1991) 233
 Liu, W.K., see Yuen 111 (1991) 943
 Livescu, G., see Asom 111 (1991) 246
 Livescu, G., see Asom 111 (1991) 260
 Longenbach, K.F., L.F. Luo, S. Xin and W.I. Wang, Resonant tunneling in polytype InAs/AlSb/GaSb heterostructures 111 (1991) 651
 Lopez, M., see Takano 111 (1991) 216
 Low, T.S., see Miller 111 (1991) 30
 Lu, Y.T., see Petroff 111 (1991) 360
 Lui, M., see Metzger 111 (1991) 445
 Luo, H., see Samarth 111 (1991) 816
 Luo, L.F., see Longenbach 111 (1991) 651
 Luther, L.C., see Asom 111 (1991) 246
 Luther, L.C., see Asom 111 (1991) 260
 Lyman, P.S., see Hoke 111 (1991) 269
 MacKinnon, A., see Myers-Beaghton 111 (1991) 328
 Mäder, K.A., see Von Känel 111 (1991) 889
 Madhukar, A., see Chen 111 (1991) 424
 Madhukar, A., see Guha 111 (1991) 434
 Madhukar, A., see Kapre 111 (1991) 1110
 Maeda, T., see Saito 111 (1991) 544
 Machashi, K., see Hasegawa 111 (1991) 371
 Magnea, N., see Ulmer 111 (1991) 711
 Mahalingam, K., see Melloch 111 (1991) 39
 Mahalingam, K., see Lee 111 (1991) 525
 Maier, M., see Köhler 111 (1991) 295
 Makita, Y., see Kudo 111 (1991) 402
 Maksym, P.A., see McCoy 111 (1991) 178
 Malik, R.J., see Nagle 111 (1991) 264
 Mannaerts, J.P., see Hong 111 (1991) 984
 Mannaerts, J.P., see Hong 111 (1991) 1052
 Mannaerts, J.P., see Hong 111 (1991) 1071
 Mao, Jianmin, see Zhou 111 (1991) 288
 Maracas, G.N., see Puechner 111 (1991) 43
 Mariette, H., see Ulmer 111 (1991) 711
 Martel, D.C., see Svensson 111 (1991) 450
 Martin, J.L., see Kean 111 (1991) 189
 Martin, P.A., see Ho 111 (1991) 233
 Martin, R.J., see Tamargo 111 (1991) 741
 Martin, R.J., see Turco-Sandhoff 111 (1991) 762
 Marzin, J.Y., see Gérard 111 (1991) 205
 Massies, J., see Moisson 111 (1991) 141
 Massies, J., see Etienne 111 (1991) 1003
 Matsuhata, H., see Miki 111 (1991) 902
 Matsuichi, K., see Fashe 111 (1991) 677
 Matsumura, N., T. Fukada, K. Senga, Y. Fukushima and J. Saraie, Photo-assisted MBE growth of ZnSe on GaAs substrates 111 (1991) 787
 Matsuno, T., see Inoue 111 (1991) 313
 Matterna, V.D., see Asom 111 (1991) 246
 Matterna, V.D., see Asom 111 (1991) 260
 Matthey, N.L., see Powell 111 (1991) 907
 Matuhata, H., see Yao 111 (1991) 221
 Maude, D.K., see Henini 111 (1991) 1089
 Maurel, P., see Garcia 111 (1991) 578
 May, P.G., see Kesan 111 (1991) 936
 McCaldin, J.O., see Rajakarunanyake 111 (1991) 782
 McCaldin, J.O., see Phillips 111 (1991) 820
 McCallum, D.S., see Hasenberg 111 (1991) 388
 McCoy, J.M. and P.A. Maksym, Monte Carlo simulation of MBE growth of the 2×4 reconstructed GaAs(001) surface 111 (1991) 178
 McCray, L.G., see Metzger 111 (1991) 445
 McGill, T.C., see Collins 111 (1991) 664
 McGill, T.C., see Chow 111 (1991) 683
 McGill, T.C., see Rajakarunavake 111 (1991) 782
 McGill, T.C., see Phillips 111 (1991) 820

- McInturff, D.T., see De Lyon 111 (1991) 564
- Melloch, M.R., K. Mahalingam, N. Otsuka, J.M. Woodall and A.C. Warren, GaAs buffer layers grown at low substrate temperatures using As₂ and the formation of arsenic precipitates 111 (1991) 39
- Menke, D.R., see Qiu 111 (1991) 747
- Menke, D.R., see Han 111 (1991) 767
- Metiu, H., see Petroff 111 (1991) 360
- Metzger, R.A., A.S. Brown, W.E. Stanchina, M. Lui, R.G. Wilson, T.V. Kargodorian, L.G. McCray and J.A. Henige, Growth and characterization of low temperature AlInAs 111 (1991) 445
- Meyer, J.R., see Youngdale 111 (1991) 693
- Migita, M., A. Taike and H. Yamamoto, n-Type and p-type conductivity control of ZnSe grown by metalorganic molecular beam epitaxy using methyl iodide and ammonia 111 (1991) 776
- Mii, Y.J., see Wu 111 (1991) 252
- Miki, K., H. Okumura, K. Sakamoto, H. Matsuhata, T. Sakamoto and S. Yoshida, Structure dependence of photoluminescence in Ge_n/Si_m strained-layer superlattices 111 (1991) 902
- Miklis, A., see Heinecke 111 (1991) 599
- Miles, R.H., see Chow 111 (1991) 683
- Miller, J.N. and T.S. Low, Low-temperature growth of GaAs and AlGaAs by MBE and effects of post-growth thermal annealing 111 (1991) 30
- Miller, M.S., C.E. Pryor, H. Weman, L.A. Samoska, H. Kroemer and P.M. Petroff, Serpentine superlattice: concept and first results 111 (1991) 323
- Miller, M.S., see Petroff 111 (1991) 360
- Miner, C.J., see Wasilewski 111 (1991) 70
- Mise, K., see Uchida 111 (1991) 1062
- Mishima, T., see Gravesteijn 111 (1991) 916
- Missous, M., E.H. Rhoderick, K.E. Singer and W.S. Truscott, Comprehensive analysis of epitaxial Al/Al_xGa_{1-x}As Schottky barriers made by MBE: barrier heights and band edge discontinuities 111 (1991) 1116
- Mitsuyu, T., see Ohkawa 111 (1991) 797
- Miyake, R., see Yamada 111 (1991) 584
- Miyao, M., see Nomura 111 (1991) 61
- Miyao, M., E. Murakami, H. Etoh, K. Nakagawa and A. Nishida, High hole mobility in strained Ge channel of modulation-doped p-Si_{0.5}Ge_{0.5}/Ge/Si_{1-x}Ge_x heterostructure 111 (1991) 912
- Miyao, M., K. Nakagawa, N. Nakamura and T. Ohshima, Characterization and application of fine-patterned Si/CoSi₂/Si double heterostructures fabricated by self-aligned, two-step MBE 111 (1991) 957
- Mizuki, J., see Tatsumi 111 (1991) 961
- Mizutani, T., see Tsuda 111 (1991) 88
- Mo, Y.-M. and M.G. Lagally, Scanning tunneling microscopy studies of the growth process of Ge on Si(001) 111 (1991) 876
- Mohnkern, L.M., see Yanka 111 (1991) 715
- Moisson, J.M., F. Houzay, F. Barthe, J.M. Gérard, B. Jusserand, J. Massies and F.S. Turco-Sandroff, Surface segregation in III-V alloys 111 (1991) 141
- Monberg, E.M., see Chin 111 (1991) 466
- Moore, K.J., see Woodbridge 111 (1991) 339
- Moriuchi, T., see Yoh 111 (1991) 643
- Muhr, G.T., see Abernathy 111 (1991) 574
- Müller, E., see Von Känel 111 (1991) 889
- Munekata, H., H. Ohno, R.R. Ruf, R.J. Gambino and L.L. Chang, p-Type diluted magnetic III-V semiconductors 111 (1991) 1011
- Munns, G.O., see Sherwin 111 (1991) 594
- Munns, G.O., see Sherwin 111 (1991) 605
- Murakami, E., see Miyao 111 (1991) 912
- Murray, J.J., see Wu 111 (1991) 252
- Mushiage, M., see Tanaka 111 (1991) 1043
- Myers, T.H., see Yanka 111 (1991) 715
- Myers-Beaghton, A.K. and D.D. Vvedensky, Nonlinear diffusion equation for epitaxial growth and recovery on vicinal surfaces 111 (1991) 162
- Myers-Beaghton, A.K., J.P.G. Taylor, D.D. Vvedensky, K.J. Hugill and A. MacKinnon, Growth kinetics and electronic characteristics of quantum wires 111 (1991) 328
- Nagao, S., Y. Inoue, E. Kawanishi and H. Gotoh, Residual impurities originating from AsH₃ in GS-MBE grown GaAs 111 (1991) 511
- Nagao, S., M. Takashima, Y. Inoue, M. Katoh and H. Gotoh, Abruptness of GaAs/AlInP hetero-interfaces grown by GS-MBE 111 (1991) 521
- Nagle, J., R.J. Malik and D. Gershoni, A comparison of atomic carbon versus beryllium acceptor doping in GaAs grown by molecular beam epitaxy 111 (1991) 264
- Nahory, R.E., see Tamargo 111 (1991) 741
- Nahory, R.E., see Turco-Sandroff 111 (1991) 762
- Nakagawa, K., see Miyao 111 (1991) 912
- Nakagawa, K., see Miyao 111 (1991) 957
- Nakahara, H., see Yao 111 (1991) 221
- Nakamura, N., see Miyao 111 (1991) 957
- Nakamura, Y., see Han 111 (1991) 767
- Nakamura, Y., see Takemura 111 (1991) 802
- Nakamura, Y., see Li 111 (1991) 1038
- Nakanishi, H., see Takemura 111 (1991) 802
- Nakashima, H., see Hasegawa 111 (1991) 371
- Namba, S., see Shimomura 111 (1991) 1105
- Narusawa, T., see Kubo 111 (1991) 136
- Naylor, T., see Powell 111 (1991) 907

- Neikirk, D.P., see Chu 111 (1991) 26
- Newbury, R., see Davies 111 (1991) 318
- Newstead, S.M., see Powell 111 (1991) 907
- Newstead, S.M., see Pike 111 (1991) 925
- Nieh, C.W., see Chow 111 (1991) 683
- Niino, T., see Tatsumi 111 (1991) 961
- Niki, S., W.S.C. Chang, H.H. Wieder and T.E. Van Eck, Molecular beam epitaxial growth and properties of highly strained $\text{In}_x\text{Ga}_{1-x}\text{As}/\text{GaAs}$ multiple quantum wells 111 (1991) 419
- Nishida, A., see Miyao 111 (1991) 912
- Nishinaga, T., see Tanaka 111 (1991) 168
- Nishinaga, T., see Suzuki 111 (1991) 173
- Nishine, S., see Shigeta 111 (1991) 284
- Nissen, H.-U., see Von Känel 111 (1991) 889
- Noda, T., M. Tanaka and H. Sakaki, Characterization of lateral correlation length of interface roughness in MBE grown GaAs/AlAs quantum wells by mobility measurement 111 (1991) 348
- Nomura, T., H. Ogasawara, M. Miyao and M. Hagino, Composition control of GaAsP grown by molecular beam epitaxy 111 (1991) 61
- Normandin, R., see Williams 111 (1991) 1066
- Nozaki, S., see Yamada 111 (1991) 584
- Nurmikko, A.V., see Han 111 (1991) 767
- Nurmikko, A.V., see Samarth 111 (1991) 816
- Ogasawara, H., see Nomura 111 (1991) 61
- Oh, E.-S., see Samarth 111 (1991) 816
- Ohishi, M., H. Saito, H. Torihara, Y. Fujisaki and K. Ohmori, Ultraviolet irradiation effect on the MBE growth of ZnSe/GaAs observed by RHEED 111 (1991) 792
- Ohkawa, K., T. Karasawa and T. Mitsuyu, Doping of nitrogen acceptors into ZnSe using radical beam during MBE growth 111 (1991) 797
- Ohki, Y., see Hiratani 111 (1991) 570
- Ohmori, K., see Ohishi 111 (1991) 792
- Ohno, H., see Munekata 111 (1991) 1011
- Ohshima, T., see Miyao 111 (1991) 957
- Ohuchi, F.S., T. Shimada, B.A. Parkinson, K. Ueno and A. Koma, Growth of MoSe_2 thin films with Van der Waals epitaxy 111 (1991) 1033
- Okada, Y., see Yao 111 (1991) 221
- Okamoto, N., see Shimomura 111 (1991) 1105
- Okano, Y., see Shigeta 111 (1991) 284
- Okumura, H., see Miki 111 (1991) 902
- Okuno, Y., see Kaneko 111 (1991) 638
- Ono, K., see Saito 111 (1991) 544
- Ospelt, M., see Von Känel 111 (1991) 889
- Otsuka, N., see Melloch 111 (1991) 39
- Otsuka, N., see Lee 111 (1991) 525
- Otsuka, N., see Qiu 111 (1991) 747
- Otsuka, N., see Han 111 (1991) 767
- Otsuka, N., see Takemura 111 (1991) 802
- Otsuka, N., see Samarth 111 (1991) 816
- Otsuka, N., see Li 111 (1991) 1038
- Ourmazd, A., see Chin 111 (1991) 466
- Ourmazd, A., see Cunningham 111 (1991) 515
- Pak, K., see Takano 111 (1991) 216
- Pao, Y.C. and J.S. Harris, Jr., Molecular beam epitaxial growth and structural design of $\text{In}_{0.52}\text{Al}_{0.48}\text{As}/\text{In}_{0.53}\text{Ga}_{0.47}\text{As}/\text{InP}$ HEMTs 111 (1991) 489
- Parker, E.H.C., see Powell 111 (1991) 907
- Parker, E.H.C., see Pike 111 (1991) 925
- Parkinson, B.A., see Ohuchi 111 (1991) 1033
- Parry, C., see Powell 111 (1991) 907
- Partin, D.L., J. Heremans and C.M. Thrush, Indium antimonide doped with lead telluride grown by molecular beam epitaxy 111 (1991) 614
- Partin, D.L., see Youngdale 111 (1991) 693
- Passenberg, W., see Künzel 111 (1991) 1084
- Pate, M.A., see Claxton 111 (1991) 1080
- Paulsson, G., K. Deppert, S. Jeppesen, J. Jönsson, L. Samuelson and P. Schmidt, Reflectance-difference probing of surface kinetics of (001) GaAs during vacuum chemical epitaxy 111 (1991) 115
- Peacock, D.C., see Ritchie 111 (1991) 300
- Peacock, D.C., see Davies 111 (1991) 318
- Pearson, S.J., see Abernathy 111 (1991) 574
- Pelekanos, N., see Han 111 (1991) 767
- Pepper, M., see Davies 111 (1991) 318
- Perales, A., see Lambert 111 (1991) 495
- Petroff, F., see Etienne 111 (1991) 1003
- Petroff, P.M., see Miller 111 (1991) 323
- Petroff, P.M., M.S. Miller, Y.T. Lu, S.A. Chalmers, H. Metiu, H. Kroemer and A.C. Gossard, MBE growth of tilted superlattices: advances and novel structures 111 (1991) 360
- Pfeiffer, L.N., H.L. Störmer, K. West and K.W. Baldwin, Quantum wire structures by MBE overgrowth on a cleaved edge 111 (1991) 333
- Pfeiffer, L.N., see Eaglesham 111 (1991) 833
- Phillipp, F., see Brandt 111 (1991) 383
- Phillips, M.C., E.T. Yu, Y. Rajakarunanyake, J.O. McCaldin, D.A. Collins and T.C. McGill, Characterization of CdSe/ZnTe heterojunctions 111 (1991) 820
- Pike, W.T., L.M. Brown, R.A.A. Kubiak, S.M. Newstead, A.R. Powell, E.H.C. Parker and T.E. Whall, The determination of strain in Si-Ge superlattices by electron diffraction in a scanning transmission electron microscope 111 (1991) 925
- Ploog, K., see Crook 111 (1991) 184
- Ploog, K., A. Fischer, L. Tapfer and B.F. Feuerbacher, Narrow luminescence linewidth in GaAs single quantum wells by insertion of thin AlAs smoothing layers 111 (1991) 344

- Ploog, K., see Brandt 111 (1991) 383
 Portal, J.C., see Henini 111 (1991) 1089
 Powell, A.R., R.A.A. Kubiak, S.M. Newstead, C. Parry, N.L. Matthey, D.W. Smith, J.C. Brighten, C.J. Emeleus, T. Naylor, E. Basaran, T.E. Whall, M.G. Dowsett, R.D. Barlow, E.H.C. Parker and D.K. Bowen, Elemental boron and antimony doping of MBE Si and SiGe structures grown at temperatures below 600 °C 111 (1991) 907
 Powell, A.R., see Pike 111 (1991) 925
 Proctor, M.J., see Rudra 111 (1991) 589
 Proctor, M.J., see Tiwari 111 (1991) 730
 Pryor, C.E., see Miller 111 (1991) 323
 Puechner, R.A., D.A. Johnson, K.T. Shiralagi, D.S. Gerber, R. Droopad and G.N. Maracas, Electrical and optical characterization of gas source and solid source MBE low temperature buffers 111 (1991) 43
 Qian, Q.-D., see Qiu 111 (1991) 747
 Qiu, J., D.R. Menke, M. Kobayashi, R.L. Gunshor, Q.-D. Qian, D. Li and N. Otsuka, ZnSe/GaAs heterovalent interfaces: interface microstructure versus electrical properties 111 (1991) 747
 Qiu, J., see Li 111 (1991) 1038
 Quillec, M., see Allovon 111 (1991) 484
 Rajakarunanyake, Y., see Collins 111 (1991) 664
 Rajakarunanyake, Y., J.O. McCaldin and T.C. McGill, Electric field assisted doping of semiconductors during epitaxial growth 111 (1991) 782
 Rajakarunanyake, Y., see Phillips 111 (1991) 820
 Rajan, K., see Schowalter 111 (1991) 948
 Rajavel, D., see Benz 111 (1991) 725
 Rajkumar, K.C., see Chen 111 (1991) 424
 Rajkumar, K.C., see Guha 111 (1991) 434
 Ralston, J.D., J. Wagner, F. Fuchs, P. Hiesinger and J. Schmäzlin, Overgrowth and strain in MBE-grown GaAs/ErAs/GaAs structures 111 (1991) 989
 Ramdas, A.K., see Samarth 111 (1991) 816
 Ramesh, R., see Harbison 111 (1991) 978
 Ramesh, S., N. Kobayashi and Y. Horikoshi, High-quality ZnSe/GaAs superlattices: MEE growth, and structural and optical characterization 111 (1991) 752
 Reed, F.E., see Lansari 111 (1991) 720
 Reed, F.E., see Ren 111 (1991) 829
 Reithmaier, J.-P., H. Riechert, H. Schlötterer and G. Weimann, Indium desorption during MBE growth of strained InGaAs layers 111 (1991) 407
 Reithmaier, J.-P., see Riechert 111 (1991) 1100
 Rejman-Greene, M.A.Z., see Scott 111 (1991) 1076
 Ren, F., see Cunningham 111 (1991) 515
 Ren, J., K.A. Bowers, S. Hwang, J.W. Cook, Jr. and J.F. Schetzina, Substitutional doping of ZnSe films 111 (1991) 772
 Ren, J., K.A. Bowers, B. Sneed, F.E. Reed, J.W. Cook, Jr. and J.F. Schetzina, Blue (ZnSe) and green (ZnSe_{0.9}Te_{0.1}) light emitting diodes 111 (1991) 829
 Rhoderick, E.H., see Missous 111 (1991) 1116
 Ricketts, M.W., see Wilby 111 (1991) 864
 Riechert, H., see Reithmaier 111 (1991) 407
 Riechert, H., D. Bernklau, J.-P. Reithmaier and R.D. Schnell, MBE growth and post-growth annealing of GaAs-based resonant tunneling structures, viewed in relation to interface roughness 111 (1991) 1100
 Ritchie, D.A., J.E.F. Frost, D.C. Peacock, E.H. Linfield, A. Hamilton and G.A.C. Jones, The growth and characterisation of back-gated high mobility two-dimensional electron gas structures 111 (1991) 300
 Ritchie, D.A., see Frost 111 (1991) 305
 Ritchie, D.A., see Davies 111 (1991) 318
 Roberts, C., see Harris 111 (1991) 239
 Robinson, G.Y., see Hafich 111 (1991) 507
 Robinson, G.Y., see Lee 111 (1991) 525
 Rozenak, P., see Tsai 111 (1991) 931
 Rudra, A., see Houdré 111 (1991) 456
 Rudra, A., J.F. Carlin, M. Proctor and M. Illegems, Luminescence and transport properties of high quality InP grown by CBE between 450 and 550 °C 111 (1991) 589
 Ruf, R.R., see Munekata 111 (1991) 1011
 Ruiz, A., see Briones 111 (1991) 194
 Saiki, K., see Koma 111 (1991) 1029
 Saito, H., see Ohishi 111 (1991) 792
 Saito, J., T. Maeda, K. Ono and K. Kondo, Background pressure dependence of GaAs and AlGaAs growth rates in gas-source molecular beam epitaxy 111 (1991) 544
 Sakai, A., see Terashima 111 (1991) 920
 Sakai, J., see Aketagawa 111 (1991) 860
 Sakaki, H., see Kadoya 111 (1991) 280
 Sakaki, H., see Noda 111 (1991) 348
 Sakamoto, K., see Miki 111 (1991) 902
 Sakamoto, T., see Miki 111 (1991) 902
 Samarth, N., H. Luo, J. Buschert, J.K. Furdyna, W.J. Walecki, A.V. Nurmikko, R.G. Alonso, E.-S. Oh, A.K. Ramdas and N. Otsuka, Growth and properties of new wide-gap quantum well structures: Zn_{1-x}Mn_xSe/Zn_{1-x}Cd_xSe 111 (1991) 816
 Samoska, L.A., see Miller 111 (1991) 323
 Samuelson, L., see Paulsson 111 (1991) 115
 Sandhu, A., T. Fujii, H. Ando, T. Takahashi, H. Ishikawa and N. Yokoyama, P⁺/N GaAs-AlGaAs heterostructures grown by

- gas source MBE using gaseous p- and n-type dopant sources 111 (1991) 559
- Sands, T., see Harbison 111 (1991) 978
- Santos, M., J. Jo, M. Shayegan and A.-M. Lanzillotto, Fabrication of quasi-three-dimensional electron systems and superlattices in wide parabolic wells 111 (1991) 366
- Saraie, J., see Matsumura 111 (1991) 787
- Sato, A., see Kadoya 111 (1991) 280
- Sato, M., see Hasegawa 111 (1991) 371
- Sauer, N.J., see Chang 111 (1991) 475
- Schaae, H.F., see Fashe 111 (1991) 677
- Schetzina, J.F., see Lansari 111 (1991) 720
- Schetzina, J.F., see Ren 111 (1991) 772
- Schetzina, J.F., see Ren 111 (1991) 829
- Schlaak, W., see Künzel 111 (1991) 461
- Schlom, D.G., see Lee 111 (1991) 131
- Schlom, D.G., see Eckstein 111 (1991) 973
- Schlötterer, H., see Reithmaier 111 (1991) 407
- Schmälzlin, J., see Ralston 111 (1991) 989
- Schmidt, P., see Paulsson 111 (1991) 115
- Schnell, R.D., see Riechert 111 (1991) 1100
- Schnoes, M., see Chand 111 (1991) 20
- Schowalter, L.J., J.R. Jimenez, L.M. Hsiung, K. Rajan, S. Hashimoto, R.D. Thompson and S.S. Iyer, Control of misoriented grains and pinholes in CoSi_2 grown on $\text{Si}(001)$ 111 (1991) 948
- Schubert, E.F., see Asom 111 (1991) 246
- Schubert, E.F., see Hong 111 (1991) 1052
- Scilla, G.J., see De Lyon 111 (1991) 564
- Scott, E.G. and M.A.Z. Rejman-Greene, MBE growth of InP/InGaAs MQW modulators 111 (1991) 1076
- Senga, K., see Matsumura 111 (1991) 787
- Sergent, A.M., see Chand 111 (1991) 20
- Seto, H., see Shigeta 111 (1991) 284
- Shan, Wei, see Li 111 (1991) 736
- Shank, S.M. and G.W. Wicks, Electrooptic effects of piezo-electrically strained AlGaAs/GaAs(111) quantum wells 111 (1991) 440
- Shayegan, M., see Santos 111 (1991) 366
- Shen, Aidong, Jie Cui, Yunliang Chen, Hailong Wang and Aizhen Li, Determination of refractive index and study of absorption in wide gap II-VI semiconductor superlattices 111 (1991) 807
- Sherwin, M.E., G.O. Munns, M.E. Elta, E.G. Woelk, S.B. Cray, F.L. Terry and G.I. Haddad, The optimization of In_{0.5}Ga_{0.5}As and InP growth conditions by CBE 111 (1991) 594
- Sherwin, M.E., G.O. Munns, E.G. Woelk, T.J. Drummond, M.E. Elta, F.L. Terry and G.I. Haddad, The design of an ECR plasma system and its application to InP grown by CBE 111 (1991) 605
- Shibli, S.M., see Tamargo 111 (1991) 741
- Shigeta, M., Y. Okano, H. Seto, H. Katahama, S. Nishine, K. Kobayashi and I. Fujimoto, Si doping and MBE growth of GaAs on tilted (111)A substrates 111 (1991) 284
- Shigeta, M., see Shimomura 111 (1991) 1105
- Shigetomi, J., K. Fuwa, S. Shimizu, H. Yamakawa and S. Ino, Initial growth stage of InAs/GaAs studied by RHEED-TRAXS method 111 (1991) 110
- Shih, H.D., see Fashe 111 (1991) 677
- Shimada, T., see Ohuchi 111 (1991) 1033
- Shimizu, S., see Shigetomi 111 (1991) 110
- Shimomura, S., N. Okamoto, M. Takeuchi, E. Tamaoka, Y. Yuba, S. Namba, S. Hiyamizu, M. Shigeta, T. Yamamoto and K. Kobayashi, MBE growth of GaAs/AlAs double-barrier structures on GaAs channelled substrates 111 (1991) 1105
- Shirakashi, J., see Yamada 111 (1991) 584
- Shiraki, Y., see Fukatsu 111 (1991) 843
- Shiralagi, K.T., see Prochner 111 (1991) 43
- Silvestre, P., see Hafich 111 (1991) 507
- Simmonds, P.E., see Henini 111 (1991) 1089
- Singer, K.E., see Missous 111 (1991) 1116
- Singh, J., see Chen 111 (1991) 228
- Sivananthan, S., see Faurie 111 (1991) 698
- Skolnick, M.S., see Henini 111 (1991) 1089
- Skromme, B.J., see Tamargo 111 (1991) 741
- Smirl, A.L., see Hasenberg 111 (1991) 388
- Smith, D.W., see Powell 111 (1991) 907
- Sneed, B., see Ren 111 (1991) 829
- Söderström, J.R., see Collins 111 (1991) 664
- Sowers, A.T., see Lansari 111 (1991) 720
- Sporken, R., see Faurie 111 (1991) 698
- SpringThorpe, A.J., see Wasilewski 111 (1991) 70
- Srinivasan, A., see Chu 111 (1991) 26
- Stalder, R., see Von Känel 111 (1991) 889
- Stanaway, M.B., see Stanley 111 (1991) 14
- Stanchina, W.E., see Metzger 111 (1991) 445
- Stanley, C.R., M.C. Holland, A.H. Kean, J.M. Chamberlain, R.T. Grimes and M.B. Stanaway, $4 \times 10^{15} \text{ cm}^2 \text{ V}^{-1} \text{ s}^{-1}$ peak electron mobilities in GaAs grown by solid source MBE with As₂ 111 (1991) 14
- Stanley, C.R., see Kean 111 (1991) 189
- Starck, C., see Lambert 111 (1991) 495
- Störmer, H.L., see Pfeiffer 111 (1991) 333
- Storz, F., see Cunningham 111 (1991) 515
- Stradling, R.A., see Yuen 111 (1991) 943
- Streetman, B.G., see Chu 111 (1991) 26
- Streetman, B.G., see Block 111 (1991) 98
- Su, L.M., see Künzel 111 (1991) 461
- Sugimoto, Y., see Hiratani 111 (1991) 570
- Summers, C.J., see Benz 111 (1991) 725
- Suzuki, T., see Tanaka 111 (1991) 168

- Suzuki, T. and T. Nishinaga, Surface diffusion and atom incorporation kinetics in MBE of InGaAs and AlGaAs 111 (1991) 173
- Suzuki, T. and A. Gomyo, Re-examination of the formation mechanism of CuPt-type natural superlattices in alloy semiconductors 111 (1991) 353
- Suzuki, T., see Iizuka 111 (1991) 429
- Svensson, S.P., W.A. Beck, D.C. Martel, P.N. Uppal and D.C. Cooke, Influence of non-uniform charge distribution in In_{0.53}Ga_{0.47}As on the interpretation of dopant incorporation 111 (1991) 450
- Svensson, S.P., see Uppal 111 (1991) 623
- Swaminathan, V., see Asom 111 (1991) 246
- Swaminathan, V., see Asom 111 (1991) 260
- Tai, K., see Hong 111 (1991) 1052
- Tai, K., see Wang 111 (1991) 1057
- Tai, K., see Hong 111 (1991) 1071
- Taike, A., see Migita 111 (1991) 776
- Tajima, M., see Terashima 111 (1991) 920
- Takahashi, K., see Yamada 111 (1991) 584
- Takahashi, K., see Takemura 111 (1991) 802
- Takahashi, S., see Koguchi 111 (1991) 688
- Takahashi, T., see Sandhu 111 (1991) 559
- Takano, Y., M. Lopez, T. Torihata, T. Ikei, Y. Kanaya, K. Pak and H. Yonezu, Realization of mirror surface in (111)- and (110)-oriented GaAs by migration-enhanced epitaxy 111 (1991) 216
- Takashima, M., see Nagao 111 (1991) 521
- Takemura, Y., H. Nakanishi, M. Konagai, K. Takahashi, Y. Nakamura and N. Otsuka, (ZnSe)_m-(ZnTe)_n short-period strained layer superlattices prepared by atomic layer epitaxy 111 (1991) 802
- Takeuchi, M., see Shimomura 111 (1991) 1105
- Takeyasu, N., H. Asahi, S.J. Yu, K. Asami, T. Kaneko and S. Gonda, Gas source MEE (migration enhanced epitaxy) growth of InP 111 (1991) 502
- Tamaoka, E., see Shimomura 111 (1991) 1105
- Tamargo, M.C., R.E. Nahory, B.J. Skromme, S.M. Shibli, A.L. Weaver, R.J. Martin and H.H. Farrell, Surface stoichiometry effects on ZnSe/GaAs heteroepitaxy 111 (1991) 741
- Tanaka, H. and M. Mushiage, MBE as a production technology for AlGaAs lasers 111 (1991) 1043
- Tanaka, K., see Kudo 111 (1991) 402
- Tanaka, M., T. Suzuki and T. Nishinaga, Surface diffusion of Al and Ga atoms on GaAs (001) and (111)B vicinal surfaces in molecular beam epitaxy 111 (1991) 168
- Tanaka, M., see Noda 111 (1991) 348
- Tanino, H., see Yao 111 (1991) 823
- Tansley, T.L., see Giugni 111 (1991) 50
- Tapfer, L., see Crook 111 (1991) 184
- Tapfer, L., see Ploog 111 (1991) 344
- Tapfer, L., see Brandt 111 (1991) 383
- Tatsumi, T., see Hirayama 111 (1991) 856
- Tatsumi, T., see Aketagawa 111 (1991) 860
- Tatsumi, T., see Terashima 111 (1991) 920
- Tatsumi, T., I. Hirose, T. Niino, H. Hirayama and J. Mizuki, $\sqrt{3} \times \sqrt{3}$ -B structure on a 5×5 Ge_xSi_{1-x}/Si(111) surface and its electrical conduction 111 (1991) 961
- Taylor, J.P.G., see Myers-Beaghton 111 (1991) 328
- Tell, B., see Chang 111 (1991) 475
- Terashima, K., M. Tajima, A. Sakai and T. Tatsumi, Dislocation-related photoluminescence in Si_{1-x}Ge_x/Si(100) grown by molecular beam epitaxy 111 (1991) 920
- Terry, F.L., see Sherwin 111 (1991) 594
- Terry, F.L., see Sherwin 111 (1991) 605
- Thompson, R.D., see Schowalter 111 (1991) 948
- Thrush, C.M., see Partin 111 (1991) 614
- Thrush, C.M., see Youngdale 111 (1991) 693
- Ting, D.Z.-Y., see Collins 111 (1991) 664
- Tiwari, A.N., W. Floeder, S. Blunier, H. Zogg and M.J. Proctor, Heteroepitaxy of CdTe(100) on Si(100) using BaF₂-CaF₂(100) buffer layers 111 (1991) 730
- Torihara, H., see Ohishi 111 (1991) 792
- Torihata, T., see Takano 111 (1991) 216
- Treichler, R., see Heinecke 111 (1991) 599
- Trommer, D., see Künzel 111 (1991) 1084
- Truscott, W.S., see Missous 111 (1991) 1116
- Tsai, C.J., P. Rozenak, H.A. Atwater and T. Vreeland, Strain modification by ion-assisted molecular beam epitaxy in the Si₃Ge_{1-x} alloy system: a kinetic analysis 111 (1991) 931
- Tsang, W.T., A review of CBE, MOMBE and GSMBE 111 (1991) 529
- Tsao, J.Y., T.M. Brennan and B.E. Hammons, Oscillatory As₄ surface reaction rates during molecular beam epitaxy of AlAs, GaAs and InAs 111 (1991) 125
- Tsuda, H. and T. Mizutani, A reflection high-energy electron diffraction study of growth processes at step edges during molecular beam epitaxy of GaAs and AlAs 111 (1991) 88
- Tu, C.W., see Liang 111 (1991) 550
- Tu, L.W., see Hong 111 (1991) 1052
- Turco-Sandhoff, F.S., see Moisson 111 (1991) 141
- Turco-Sandhoff, F.S., R.E. Nahory, M.J.S.P. Brasil, R.J. Martin, R. Beserman, L.A. Farrow, J.M. Worlock and A.L. Weaver, Molecular beam epitaxy of Zn(Se,Te) alloys and superlattices 111 (1991) 762
- Turner, G.W. and S.J. Eglash, Application of frequency-domain analysis to RHFED oscillation data: time dependence of Al-GaAs growth rates 111 (1991) 105
- Turner, G.W., see Eglash 111 (1991) 669

- Uchida, T., see Uchida 111 (1991) 1062
- Uchida, T.K., T. Uchida, K. Mise, N. Yokouchi, F. Koyama and K. Iga, GaInAs/InP MQW and DBR growth for surface emitting lasers by CBE 111 (1991) 1062
- Ueno, K., see Koma 111 (1991) 1029
- Ueno, K., see Ohuchi 111 (1991) 1033
- Ulmer, L., N. Magnea, H. Mariette and P. Gentile, Application of the RHEED oscillation technique to the growth of II-VI compounds: CdTe, HgTe and their related alloys 111 (1991) 711
- Unterbörsh, G., see Künzel 111 (1991) 1084
- Uppal, P.N., see Svensson 111 (1991) 450
- Uppal, P.N., D.M. Gill, S.P. Svensson and D.C. Cooke, Transport properties of heterostructures based on GaSb, InAs and InSb on GaAs substrates 111 (1991) 623
- Van de Walle, G.F.A., see Gravesteijn 111 (1991) 916
- Van den Heuvel, R.A., see Gravesteijn 111 (1991) 916
- Van Eck, T.E., see Niki 111 (1991) 419
- Vandenberg, J.M., see Hong 111 (1991) 1071
- Vening, M., see Foxon 111 (1991) 1047
- Vlcek, J.C. and C.G. Fonstad, Precise computer control of the MBE process - application to graded InGaAlAs/InP alloys 111 (1991) 56
- Von Känel, H., E. Müller, H.-U. Nissen, W. Bacsa, M. Ospelt, K.A. Mäder, R. Stalder and A. Baldereschi, Silicon heteroepitaxy: interface structure and physical properties 111 (1991) 889
- Vreeland, T., see Tsai 111 (1991) 931
- Vvedensky, D.D., see Myers-Beaghton 111 (1991) 162
- Vvedensky, D.D., see Myers-Beaghton 111 (1991) 328
- Vvedensky, D.D., see Wilby 111 (1991) 864
- Wagner, B.K., see Benz 111 (1991) 725
- Wagner, J., see Ralston 111 (1991) 989
- Walecki, W.J., see Samarth 111 (1991) 816
- Wang, Hailong, see Cui 111 (1991) 811
- Wang, Hailong, see Shen 111 (1991) 807
- Wang, K.L., see Wu 111 (1991) 252
- Wang, K.L., see Kallel 111 (1991) 897
- Wang, K.L., see Kuo 111 (1991) 996
- Wang, S.C., see Ho 111 (1991) 233
- Wang, W.I., see Longenbach 111 (1991) 651
- Wang, Y.H., see Hong 111 (1991) 1052
- Wang, Y.H., K. Tai, Y.F. Hsieh, S.N.G. Chu, J.D. Wynn, M. Hong, R.J. Fischer and A.Y. Cho, Reduced current thresholds in GaAs/AlGaAs vertical cavity surface emitting lasers using 4° off-oriented (001) GaAs substrates 111 (1991) 1057
- Wang, Y.H., see Hong 111 (1991) 1071
- Warren, A.C., see Melloch 111 (1991) 39
- Wasilewski, Z.R., G.C. Aers, A. Spring-Thorpe and C.J. Miner, Growth uniformity studies in molecular beam epitaxy 111 (1991) 70
- Watanabe, A., see Hata 111 (1991) 83
- Watanabe, A., see Isu 111 (1991) 210
- Watanabe, A., M. Hata and T. Isu, Metalorganic molecular beam epitaxy of GaAs using hydrogen radical beam 111 (1991) 554
- Weaver, A.L., see Tamargo 111 (1991) 741
- Weaver, A.L., see Turco-Sandroff 111 (1991) 762
- Webb, C., J.N. Eckstein and Y.M. Desai, Anisotropy in electronic transport of modulation doped structures having strained InGaAs wells 111 (1991) 309
- Weimann, G., see Reithmaier 111 (1991) 407
- Weir, B.E., see Headrick 111 (1991) 838
- Weir, B.E., see Hong 111 (1991) 984
- Weir, B.E., see Hong 111 (1991) 1052
- Weir, D.G., see Hoke 111 (1991) 269
- Weir, D.G., see Hoke 111 (1991) 1024
- Wegener, M., see Chang 111 (1991) 475
- Wegscheider, W., see Eberl 111 (1991) 882
- Weman, H., see Miller 111 (1991) 323
- West, K.W., see Pfeiffer 111 (1991) 333
- West, K.W., see Eaglesham 111 (1991) 833
- Whall, T.E., see Powell 111 (1991) 997
- Whall, T.E., see Pike 111 (1991) 925
- White, C.R.H., see Henini 111 (1991) 1089
- Whitehouse, C.R., see Emeny 111 (1991) 413
- Wicks, G.W., see Shank 111 (1991) 440
- Wieder, H.H., see Niki 111 (1991) 419
- Wilby, M.R., M.W. Ricketts, S. Clarke and D.D. Vvedensky, Simulation with animation: microscopic growth kinetics of Si(001) homoepitaxy 111 (1991) 864
- Wilkens, B.J., see Harbison 111 (1991) 978
- Williams, R.L., F. Chatenoud and R. Normandin, MBE grown, visible, surface emitting harmonic generation lasers 111 (1991) 1066
- Wilson, R.G., see Metzger 111 (1991) 445
- Woelk, E.G., see Sherwin 111 (1991) 594
- Woelk, E.G., see Sherwin 111 (1991) 605
- Woodall, J.M., see Melloch 111 (1991) 39
- Woodall, J.M., see De Lyon 111 (1991) 564
- Woodbridge, K., see Harris 111 (1991) 239
- Woodbridge, K., K.J. Moore, N.L. Andrew and P.F. Fewster, Indium incorporation in GaInAs/GaAs quantum wells grown on GaAs 111 (1991) 339
- Worlock, J.M., see Turco-Sandroff 111 (1991) 762
- Wu, B.J., Y.J. Mii, M. Chen, K.L. Wang and J.J. Murray, Reduced silicon donor incorporation in MBE grown GaAs layers using cracker-generated dimer arsenic 111 (1991) 252
- Wu, M.C., see Chen 111 (1991) 659
- Wu, Y., Y. Kawakami, Sz. Fujita and Sg. Fujita, Growth and characterization of ZnSe on (NH₄)₂S_x-treated GaAs substrates: effect of GaAs surface microstructure on the growth rate of ZnSe 111 (1991) 757

- Wynn, J.D., see Hong 111 (1991) 1052
Wynn, J.D., see Wang 111 (1991) 1057
- Xin, S., see Longenbach 111 (1991) 651
- Yamada, A., see Kudo 111 (1991) 402
Yamada, T., S. Nozaki, R. Miyake, T. Fukamachi, J. Shirakashi, M. Konagai and K. Takahashi, MOMBE growth and characterization of heavily carbon-doped In GaAs 111 (1991) 584
- Yamakawa, H., see Shigetomi 111 (1991) 110
Yamamoto, H., see Migita 111 (1991) 776
Yamamoto, T., see Shimomura 111 (1991) 1105
Yang, D., see Kim 111 (1991) 633
Yang, L., see Chen 111 (1991) 659
Yang, Z., see Lansari 111 (1991) 720
- Yanka, R.W., K.A. Harris, L.M. Mohnkern and T.H. Myers, A novel technique for the MBE growth of twin-free HgCdTe 111 (1991) 715
- Yano, M., K. Yoh, T. Iwawaki, Y. Iwai and M. Inoue, Structural stability of ultrathin InAs/GaAs quantum wells grown by migration enhanced epitaxy 111 (1991) 397
- Yano, M., H. Yokose, Y. Iwai and M. Inoue, Surface reaction of III-V compound semiconductors irradiated by As and Sb molecular beams 111 (1991) 609
- Yano, M., see Yoh 111 (1991) 643
- Yao, T., H. Nakahara, H. Matuhata and Y. Okada, Fabrication of AlAs/Al/AlAs heterostructures by molecular beam epitaxy and migration enhanced epitaxy 111 (1991) 221
- Yao, T., M. Fujimoto, S.K. Chang and H. Tanino, Fabrication of ZnS/(ZnSe)_n/ZnS single quantum well structures and photoluminescence properties 111 (1991) 823
- Yoffe, G.W., see Lee 111 (1991) 131
- Yoh, K., see Yano 111 (1991) 397
- Yoh, K., T. Moriuchi, M. Yano and M. Inoue, Electrical characteristics dependence on aluminum mole fraction in (Al_{0.5}Ga_{0.5})Sb/InAs/(Al_xGa_{1-x})Sb heterostructure 111 (1991) 643
- Yokose, H., see Yano 111 (1991) 609
Yokouchi, N., see Uchida 111 (1991) 1062
Yokoyama, N., see Sandhu 111 (1991) 559
Yonezu, H., see Takano 111 (1991) 216
- Yoo, H., S.M. Goodnick and J.R. Arthur, Transport in Al_xGa_{1-x}As/In_yGa_{1-y}As resonant tunneling diodes with asymmetric layers 111 (1991) 1095
- Yoshida, S., see Miki 111 (1991) 902
Yoshida, T., see Iizuka 111 (1991) 429
- Youngdale, E.R., J.R. Meyer, C.A. Hoffman, F.J. Bartoli, D.L. Partin, C.M. Thrush and J.P. Heremans, Strong nonlinear optical enhancement in MBE-grown Bi_{1-x}Sb_x 111 (1991) 693
- Yu, E.T., see Collins 111 (1991) 664
Yu, E.T., see Phillips 111 (1991) 820
Yu, S.J., see Takeyasu 111 (1991) 502
Yu, T., see Ho 111 (1991) 233
- Yuan, Shixin, see Li 111 (1991) 736
- Yuba, Y., see Shimomura 111 (1991) 1105
- Yuen, W.T., W.K. Liu, R.A. Stradling and B.A. Joyce, The growth and electronic properties of α-Sn thin films grown on InSb(100) and (111) substrates by molecular beam epitaxy (MBE) 111 (1991) 943
- Zborowski, J.T., see Fashe 111 (1991) 677
- Zhang, J., E.M. Gibson, C.T. Foxon and B.A. Joyce, Modulated molecular beam study of group III desorption during growth by MBE 111 (1991) 93
- Zhang, J., see Foxon 111 (1991) 539
Zheng, J., see Fashe 111 (1991) 677
- Zhou, Junming, Weimin Jin, Jianmin Mao and Yi Huang, Effect of neutron irradiation on transport in heterostructures 111 (1991) 288
- Zogg, H., see Tiwari 111 (1991) 730
- Zucker, J.E., see Chang 111 (1991) 475
- Zydzik, G.J., see Hong 111 (1991) 1052

Subject index

- Adsorption 93, 110, 125, 162, 407, 413, 456, 502, 787, 792, 847, 856
- Alloys 978
- Aluminum
- antimonide 360, 651, 659, 664
 - arsenide 88, 125, 168, 221, 305, 978, 1071, 1105, 1110
 - gallium antimonide 631, 643, 647
 - gallium arsenide 20, 26, 30, 50, 75, 98, 105, 173, 189, 239, 269, 274, 280, 295, 318, 323, 328, 360, 366, 371, 440, 544, 559, 574, 1043, 1047, 1052, 1057, 1066, 1089, 1095, 1116
 - gallium arsenide antimonide 669
 - gallium indium arsenide 475, 484
 - indium arsenide 445, 456, 461, 470, 475, 479, 489
 - indium phosphide 521
 - organic 274, 574
- Antimony
- organic 638
- Apparatus
- for thin film growth
 - by chemical beam epitaxy
 - of II-VI compounds 725
 - by gas source molecular beam epitaxy
 - of silicon 860
 - for miscellaneous purposes
 - ECR plasma injector for chemical beam epitaxial growth 605
- Arsenic
- organic 638
- Bismuth
- antimonide 693
 - strontium calcium cuprate 973
- Boron 838
- Cadmium
- manganese telluride 1016
 - mercury telluride 698, 711, 715, 720, 725
 - organic 725
 - selenide 820
 - telluride 698, 725, 730, 736, 1016
- Characterization methods
- by absorption spectroscopy 388, 419, 424, 720, 807, 1076
 - by Auger electron spectroscopy 669, 677, 882, 1003, 1024
 - by cathodoluminescence 698, 1105
 - by deep level transient spectroscopy 43
 - by electrical methods 14, 20, 26, 30, 43, 50, 228, 233, 246, 252, 260, 264, 269, 280, 288, 295, 300, 305, 309, 313, 318, 333, 348, 366, 440, 445, 450, 461, 466, 470, 479, 484, 489, 495, 507, 511, 515, 559, 578, 584, 589, 594, 605, 614, 619, 623, 633, 643, 647, 651, 659, 664, 669, 683, 698, 720, 741, 747, 762, 767, 772, 776, 820, 829, 838, 847, 856, 902, 912, 916, 936, 957, 961, 965, 973, 978, 989, 1011, 1071, 1076, 1080, 1084, 1089, 1095, 1100, 1105, 1110, 1116
 - by electroluminescence 829
 - by electron diffraction 1038
 - by electron microscopy 20, 39, 50, 75, 83, 189, 210, 221, 233, 305, 353, 371, 383, 402, 407, 419, 434, 456, 489, 495, 521, 584, 628, 647, 683, 688, 698, 720, 747, 752, 767, 802, 833, 847, 860, 882, 889, 897, 920, 925, 936, 948, 957, 973, 1038, 1043, 1057, 1105
 - by electron probe microanalysis 371
 - by electro-optical methods 440
 - by emission 1024
 - by Fourier transform infrared 677, 989, 1076
 - by infrared spectroscopy 811
 - by ion scattering 136
 - by low energy electron diffraction 882
 - by magnetic properties 318, 366, 816, 943, 978, 1011, 1016
 - by mass spectrometry 93, 507, 539, 570
 - by medium energy electron diffraction 787
 - by neutron irradiation 288
 - by optical microscopy 131, 570, 762, 767, 807, 936, 957
 - by photoluminescence 20, 30, 43, 98, 184, 205, 233, 246, 260, 264, 284, 323, 344, 360, 388, 397, 402, 407, 413, 424, 429, 445, 495, 502, 507, 511, 578, 589, 599, 605, 628, 698, 730, 736, 741, 752, 767, 772, 776, 787, 797, 816, 823, 829, 897, 920, 1016, 1043, 1062, 1089
 - by Raman spectroscopy 205, 383, 609, 802, 811, 816, 889, 897, 912, 989
 - by reflectance 70, 209, 693, 931, 1062, 1071
 - by reflectance difference 115, 120, 194
 - by reflection high energy electron diffraction 65, 83, 88, 98, 105, 110, 125, 162, 168, 173, 184, 189, 194, 210, 221, 228, 284, 339, 388, 397, 424, 434, 461, 489, 502, 521, 539, 609, 688, 711, 730, 736, 741, 752, 757, 792, 823, 856, 897, 902, 965, 973, 978, 984, 996, 1003, 1033
 - by refractive index 807
 - by Rutherford back scattering 948, 989
 - by scanning tunneling microscopy 876, 889, 1033
 - by secondary ion mass spectrometry 50, 239, 246, 252, 260, 295, 366, 445, 484, 495, 511, 544, 559, 564, 599, 843, 847, 907, 916, 1084
 - by thermochemical properties 609
 - by transmission spectroscopy 131, 683, 711, 715
 - by X-ray methods 56, 110, 184, 269, 274, 344, 383, 402, 445, 456, 461, 470, 515, 525, 578, 584, 599, 623, 628, 669, 677,

- 683, 698, 736, 752, 762, 772, 802, 838, 897, 902, 907, 931, 961, 973, 984, 996, 1003, 1016, 1024, 1062, 1071, 1076
- by X-ray photoelectron spectroscopy 393, 521, 747, 820, 957
Cobalt
- disilicide 948, 957
- gallium 996
Computer simulation 870
- Devices 1, 20, 26, 59, 136, 228, 233, 305, 419, 440, 461, 470, 475, 479, 484, 489, 515, 559, 633, 664, 669, 776, 847, 912, 916, 957, 965, 1043, 1047, 1052, 1057, 1062, 1066, 1071, 1076, 1080, 1084, 1089, 1095, 1100, 1105, 1110, 1116
Diffusional control 83, 151, 239, 348, 515, 782, 843, 870, 876, 1076
Dislocations 233, 309, 376, 383, 434, 683, 698, 715, 897, 902, 920, 948
Distribution coefficient 141
Dopants 1, 30, 239, 246, 252, 260, 264, 269, 274, 280, 284, 288, 295, 300, 305, 309, 313, 318, 450, 515, 559, 564, 584, 614, 623, 651, 669, 720, 730, 772, 776, 782, 797, 829, 833, 843, 847, 856, 870, 907, 916, 1076, 1095
- Erbium
- arsenide 989
Etching
- chemical 936
- Gallium
- aluminum arsenide 269
- antimonide 360, 550, 619, 623, 638, 651, 659, 664
- arsenide 14, 30, 39, 43, 50, 65, 70, 75, 83, 88, 93, 98, 115, 120, 125, 131, 136, 168, 178, 184, 189, 200, 210, 216, 233, 239, 246, 252, 260, 264, 269, 274, 280, 284, 288, 295, 300, 305, 318, 333, 339, 344, 348, 371, 393, 424, 507, 511, 515, 521, 539, 544, 550, 554, 559, 564, 570, 574, 578, 584, 683, 741, 747, 833, 978, 989, 1052, 1057, 1066, 1071, 1089, 1100, 1105
- arsenide antimonide 628
- arsenide phosphide 61
- indium antimonide 683
- indium arsenide 339, 413, 461, 466, 475, 599, 1062, 1084
- indium arsenide antimonide 413, 669
- indium arsenide phosphide 599
- indium phosphide 353, 564, 578
- nitride 1024
- organic 115, 274, 539, 544, 550, 554, 570, 574, 578, 599, 638
- phosphide 564
- selenide 1038
Germanium 833, 847, 876, 882
Grain boundary 715
- Heterojunction 20, 50, 194, 205, 221, 233, 280, 288, 295, 300, 305, 309, 313, 318, 323, 376, 383, 388, 393, 397, 419, 470, 479, 489, 515, 521, 525, 559, 578, 599, 609, 623, 628, 643, 647, 651, 659, 664, 669, 698, 747, 767, 820, 823, 829, 912, 916, 920, 936, 973, 978, 989, 996, 1016, 1033, 1076, 1089, 1095, 1116
- Impurity 274, 284, 450, 511, 559, 574, 776, 847
Inclusions 39
Indium
- aluminum arsenide 313, 456, 470
- antimonide 614, 623, 633, 688
- arsenide 93, 110, 125, 205, 383, 388, 393, 397, 402, 434, 550, 623, 633, 651, 659, 664, 677, 683
- arsenide antimonide 633, 638
- arsenide phosphide 61
- gallium aluminum arsenide 56, 313
- gallium antimonide 677, 683
- gallium arsenide 173, 228, 233, 309, 313, 339, 407, 413, 419, 429, 434, 450, 456, 461, 466, 470, 475, 479, 489, 584, 594, 599, 628, 1062, 1076, 1080, 1095, 1110
- gallium arsenide phosphide 495, 599
- gallium phosphide 525
- manganese arsenide 1011
- nitride 1024
- organic 578, 599, 638
- phosphide 495, 502, 564, 589, 594, 599, 605, 1076, 1080
Interface 98, 141, 189, 221, 274, 328, 348, 383, 397, 407, 461, 521, 525, 559, 599, 609, 643, 647, 677, 698, 741, 747, 757, 767, 823, 889, 902, 920, 936, 961, 989, 1029, 1057, 1076, 1095, 1100, 1116
Iron
- aluminum silicide 984
- Kinetics
- of anneal 65
- of antiphase domain annihilation 120
- of atom incorporation 173
- of defect creation 870
- of dopant incorporation 239
- of growth 1, 43, 61, 65, 75, 83, 93, 105, 115, 136, 162, 178, 189, 194, 210, 216, 233, 252, 280, 328, 339, 353, 360, 371, 407, 434, 539, 544, 550, 554, 578, 594, 599, 638, 647, 711, 730, 757, 762, 833, 847, 856, 860, 876, 907, 948, 973, 978, 989, 1003, 1057, 1062
- of interface control 20, 30, 141, 189, 194, 344, 376, 388, 515, 578, 599, 864, 973, 1003
- of nucleation 110, 194, 402, 948, 1003
- Lasers 1043, 1047, 1052, 1057, 1062, 1066
Lattice mismatch 56, 120, 221, 313, 376, 445, 479, 489, 584, 594, 599, 628, 688, 984, 1029, 1033
Light emitting diode 829
- Manganese
- aluminum 978
- telluride 767
Mercury
- cadmium telluride 698, 711, 715, 720, 725
- telluride 720, 725
Metals 1003
Molybdenum
- diselenide 1033
Monte Carlo method 178, 328, 864

- Morphological stability 189, 376
 Morphology of growth 1, 65, 216, 233, 434, 489, 589, 605, 647, 720, 833, 864, 876, 882, 936, 948, 1003
- Nonlinear optics 693
 Nucleation 162, 168, 194, 210, 383, 402, 864, 876, 948, 1003
- Perfection of crystals 1, 56, 98, 136, 228, 288, 383, 407, 429, 434, 450, 698, 715, 720, 736, 762, 772, 870, 931, 948, 989, 1076
 Phenomenological theory 61, 376
 Polymorphism/polytypism 651
- Quantum wells/size effects 1, 20, 50, 98, 189, 264, 309, 323, 328, 333, 339, 344, 348, 366, 371, 388, 397, 402, 407, 413, 419, 424, 440, 475, 484, 578, 643, 647, 651, 664, 688, 720, 736, 767, 807, 816, 823, 829, 936, 989, 1016, 1047, 1066, 1076, 1080, 1089, 1095, 1100, 1110
- Segregation 141, 151, 239, 295
 Silicon 833, 838, 843, 856, 860, 864, 870, 882, 889, 907, 916, 936, 957
 - germanium 889, 897, 902, 907, 912, 916, 920, 925, 931, 936, 961
 Statistical mechanics, molecular theory 864
 Stefan problem or moving boundary problem 162
 Step 65, 88, 125, 168, 173, 184, 328, 353, 847, 864
 Strain 1, 205, 221, 339, 376, 383, 388, 393, 397, 402, 407, 413, 419, 424, 429, 434, 440, 445, 466, 623, 677, 715, 736, 807, 811, 882, 897, 902, 912, 916, 925, 931, 936, 1095
- Superconductivity 965, 973
 - characterization 965, 973
 - crystal chemistry 965, 973
 - high T_c 965, 973
 - thin films 965, 973
- Superlattices 1, 194, 205, 274, 323, 333, 353, 360, 366, 371, 376, 383, 388, 402, 429, 466, 628, 647, 677, 683, 720, 736, 752, 762, 802, 807, 811, 816, 829, 838, 882, 889, 897, 902, 912, 925, 936, 957, 989, 1003, 1016, 1033, 1047, 1076
- Surface energy, determination of 847
 Surface processes 61, 353, 847, 864, 870
 Surface structure 20, 65, 75, 88, 115, 136, 184, 194, 221, 353, 429, 489, 570, 594, 609, 792, 876, 943, 961, 1033
- Tellurium
 - organic 725
 Thermodynamics 151, 173
 Thin film growth
 - by atomic layer epitaxy
 - - of II-VI compounds 736
 - by atomic layer molecular beam epitaxy
 - - of gallium arsenide 120
 - - theory of 194
 - by chemical beam epitaxy
 - - of aluminum gallium arsenide 274
 - - of gallium arsenide 274, 578
 - - of gallium indium phosphide 578
 - - of indium gallium arsenide 594, 1062
 - - of indium phosphide 589, 594, 605
 - - of III-V compounds 550
 - - of II-VI compounds 550, 725
 - - review of 529
 - by gas source molecular beam epitaxy
 - - of aluminum gallium arsenide 544
 - - of gallium arsenide 246, 507, 511, 515, 521, 544, 559, 564, 570
 - - of gallium indium phosphide 564
 - - of indium gallium arsenide phosphide 495
 - - of indium gallium phosphide 525
 - - of indium phosphide 495, 502
 - - of low temperature buffers 43
 - - of silicon 860
 - - review 529
 - by migration enhanced epitaxy
 - - of aluminum arsenide 221
 - - of gallium arsenide 200, 210, 216
 - - of indium arsenide 397
 - - of indium gallium arsenide 228
 - - of indium phosphide 502
 - - of zinc selenide 752
 - - improved device performance by 233
 - by metalorganic molecular beam epitaxy
 - - of aluminum gallium arsenide 574, 1043
 - - of gallium antimonide 638
 - - of gallium arsenide 539, 554, 570, 574, 584
 - - of indium arsenide antimonide 638
 - - of indium gallium arsenide 584, 599
 - - of indium gallium arsenide phosphide 599
 - - of III-V compounds 550, 599
 - - review of 529
 - by modulated molecular beam epitaxy
 - - theory of 205
 - by molecular beam epitaxy
 - - of aluminum antimonide 651, 659, 664
 - - of aluminum arsenide 88, 125, 168, 221, 1071, 1105, 1110
 - - of aluminum gallium antimonide 647
 - - of aluminum gallium arsenide 20, 26, 30, 50, 75, 98, 105, 189, 239, 269, 280, 295, 318, 366, 371, 440, 544, 559, 1043, 1047, 1052, 1057, 1066, 1089, 1095, 1116
 - - of aluminum gallium arsenide antimonide 669
 - - of aluminum gallium indium arsenide 484
 - - of aluminum indium arsenide 445, 456, 461, 470, 479, 489
 - - of aluminum indium phosphide 521
 - - of bismuth antimonide 693
 - - of boron 838
 - - of cadmium manganese telluride 1016
 - - of cadmium selenide 820
 - - of cadmium telluride 698, 730, 1016
 - - of cobalt disilicide 948, 957
 - - of cobalt gallium 996
 - - of erbium arsenide 989
 - - of gallium aluminum arsenide 269
 - - of gallium antimonide 559, 619, 623, 651, 659, 664
 - - of gallium arsenide 14, 30, 39, 43, 50, 65, 70, 75, 83, 88,

- 93, 120, 125, 131, 136, 168, 184, 189, 200, 210, 216, 233, 239, 246, 252, 260, 264, 269, 274, 280, 284, 288, 295, 300, 305, 318, 333, 339, 344, 371, 393, 424, 507, 511, 515, 521, 539, 544, 550, 559, 741, 747, 833, 989, 1052, 1057, 1066, 1071, 1089, 1100, 1105
- - of gallium arsenide antimonide 628
- - of gallium arsenide phosphide 61
- - of gallium indium arsenide antimonide 413, 669
- - of gallium nitride 1024
- - of gallium selenide 1038
- - of germanium 833, 847, 876, 882
- - of indium antimonide 614, 623, 688
- - of indium arsenide 93, 110, 125, 205, 383, 388, 393, 397, 402, 434, 550, 623, 651, 659, 664, 677, 683
- - of indium gallium aluminum arsenide 56
- - of indium gallium antimonide 677, 683
- - of indium gallium arsenide 228, 233, 309, 339, 407, 413, 419, 429, 434, 450, 456, 461, 466, 470, 475, 479, 489, 628, 1076, 1080, 1084, 1095, 1110
- - of indium gallium arsenide phosphide 495
- - of indium gallium phosphide 525
- - of indium manganese arsenide 1011
- - of indium nitride 1024
- - of indium phosphide 495, 502, 1076, 1080
- - of iron aluminum silicide 984
- - of manganese aluminum 978
- - of manganese telluride 767
- - of mercury cadmium telluride 698, 711, 715, 720
- - of mercury telluride 720
- - of metals 1003
- - of molybdenum diselenide 1033
- - of silicon 833, 838, 843, 856, 870, 882
- - of silicon germanium 889, 897, 902, 907, 912, 916, 920, 925, 931, 936, 961
- - of III-V compounds 1, 125, 141, 151, 173, 194, 313, 360, 475, 550, 564, 609, 623, 633, 643
- - of tin 882, 943
- - of II-VI compounds 811, 816
- - of Van der Waals crystals 1029, 1033
- - of yttrium barium cuprate 965
- - of zinc selenide 741, 757, 772, 776, 787, 792, 797, 802, 823, 829
- - of zinc selenide telluride 762, 829
- - of zinc sulphide 823
- - of zinc telluride 782, 802
- - growth uniformity study of 70
- - review of 529
- - simulation with animation of 864
- - theory of 1, 61, 162, 178, 323, 328, 539
- by solid source molecular beam epitaxy
- - of gallium arsenide 14
- - of low temperature buffers 43
- by vacuum chemical epitaxy
- - of gallium arsenide 115
- by vapor phase epitaxy
- - through metalorganic chemical vapor deposition
- - - of gallium indium phosphide 353
- Three-five (III-V) compounds 1, 125, 141, 151, 173, 194, 313, 360, 475, 550, 564, 599, 609, 623, 633, 643, 1011
- Tin 882, 943
- Twinning 698, 715, 736
- Two-six (II-VI) compounds 550, 711, 725, 736, 807, 811, 816
- Uniformity of growth 70, 269, 599
- Van der Waals crystals 1029, 1033
- Yttrium
- barium cuprate 965
- Zinc
- cadmium selenide 816
- manganese selenide 816
- selenide 741, 747, 752, 757, 772, 776, 787, 792, 797, 802, 807, 811, 823, 829
- selenide telluride 741, 762, 829
- sulphide 807, 811, 823
- telluride 736, 782, 802, 807, 811